IGARSS'96

1996 International Geoscience and Remote Sensing Symposium

IEEE

University of Nebraska Lincoln

NASA

NOAA

OFFICE OF NAVAL RESEARCH 50th Anniversary 1946-1996

U.R.S.I.

Remote Sensing for a Sustainable Future

Volume I

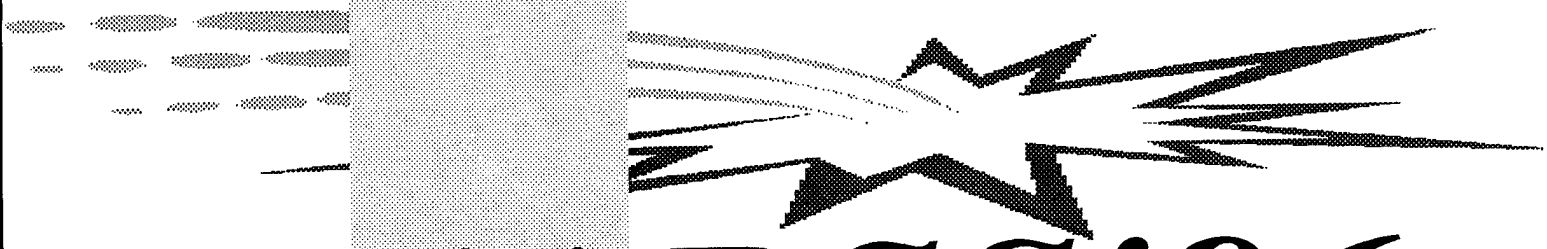
Burnham Yates Conference Center
Lincoln, Nebraska USA
27-31 May 1996

IEEE Catalog Number 96CH35875
Library of Congress Number: 95-80706

DISCLAIMER NOTICE



THIS DOCUMENT IS BEST QUALITY AVAILABLE. THE COPY FURNISHED TO DTIC CONTAINED A SIGNIFICANT NUMBER OF PAGES WHICH DO NOT REPRODUCE LEGIBLY.



IGARSS'96

1996 International Geoscience and Remote Sensing Symposium

Remote Sensing for a Sustainable Future

Volume I

DTIC QUALITY INSPECTED 2

19970520 021

IEEE Catalog Number 96CH35875
Library of Congress Number: 95-80706

Editor: Tammy I. Stein
Editorial Assistant: Jennetta Brunk
Production: IEEE Publications

Copyright and Reprint Permission: Abstracting is permitted with credit to the source. Libraries are permitted to photocopy beyond the limit of U.S. copyright law for private use of patrons those articles in this volume that carry a code at the bottom of the first page, provided the per-copy fee indicated in the code is paid through Copyright Clearance Center, 222 Rosewood Drive, Danvers, MA 01923. For other copying, reprint or reproduction permission, write to the IEEE Copyrights Manager, IEEE Service Center, 445 Hoes Lane, P.O. Box 1331, Piscataway NJ 08855-1331. All rights reserved. Copyright @1996 by the Institute of Electrical and Electronics Engineers, Inc.

IEEE Catalog Number 96CH35875
ISBN 0-7803-3068-4 (softbound edition)
ISBN 0-7803-3069-2 (casebound edition)
ISBN 0-7803-3070-6 (microfiche edition)
Library of Congress Number 95-80706

Additional copies of the IGARSS'96 Digest are available from the following source:

Institute of Electrical and Electronics Engineers, Inc.
Single Copy Sales
445 Hoes Lane
PO Box 1331
Picataway NJ 08855-1331

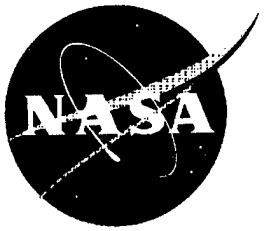
IGARSS'96 SPONSORS



IEEE Geoscience and Remote Sensing Society



University of Nebraska, Lincoln



National Aeronautics and Space Administration (NASA)



National Oceanic & Atmospheric Administration (NOAA)



Office of Naval Research (ONR)

IGARSS'96 TECHNICAL SPONSOR



U.S. National Committee
Union Radioscientifique Internationale

IGARSS'96 COOPERATIVE SPONSORS

Canon/Modern Methods Inc.

Center for Advanced Land Management Information Technologies, UNL

Center for Communication and Information Science, UNL

Center for Electro-Optics, UNL

Center for Laser Analytical Studies of Trace Gas Dynamics, UNL

Centurion International, Inc.

College of Engineering and Technology, UNL

Department of Electrical Engineering, UNL

ERDAS, Inc.

High Plains Climate Center, UNL

Li-Cor, Inc.

U.S. Geological Survey EROS Data Center

IGARSS'96 ORGANIZING COMMITTEE

Ram Narayanan
General Chairman

Robert McIntosh
Technical Program Co-Chairman

Calvin Swift
Technical Program Co-Chairman

Barbara Emil
Finance Chairman

James Merchant
Publications Chairman

Steve Reichenbach
CD ROM Chairman

Jim Lacy
WWW Chairman

Tammy Stein
Director of Conferences and Information Services, GRSS

LOCAL HOST COMMITTEE

Dennis Alexander
Mark Anderson
Ezekiel Bahar
Blaine Blad
John Boye
Mark Cockson
Natale Ianno
Robert Maher
Robert Palmer
Donald Rundquist
Karen St. Germain
Khalid Sayood
Tracy Soukup
Elizabeth Walter-Shea
Jon Welles

Dennis Alexander, University of Nebraska-Lincoln
Werner Alpers, University of Hamburg
Mark Anderson, University of Nebraska-Lincoln
Ghassem Asrar, NASA Headquarters
Kultegin Aydin, Penn State University
Ezekiel Bahar, University of Nebraska-Lincoln
Ronald Birk, Sverdup Technology Inc.
Andrew Blanchard, University of Missouri-Columbia
Dan Cress, Sandia National Laboratories
John Curlander, Vexcel Corporation
John Curtis, US Army WES
Don Deering, NASA Goddar Space Flight Center
Craig Dobson, University of Michigan
Fernando Echavarria, University of Nebraska-Lincoln
Edwin Engman, NASA Goddard Space Flight Center
Stephen Frasier, University of Massachusetts
Prasad Gogineni, University of Kansas
Richard Gomez, US Army TEC
Bill Grant, NASA Langley
Martti Hallikainen, Helsinki University of Technology
Jim Irons, NASA Goddard Space Flight Center
Akira Ishimaru, University of Washington
Thomas Jackson, USDA Hydrology Lab
James Kalshoven, NASA Goddard Space Flight Center
Timothy Kane, Pennsylvania State University
Roger Kassebaum, Millard North High School-Omaha
Wolfgang Keydel, Institut fur Hochfrequenztechnik
Nahid Khazenie, NASA Goddard Space Flight Center
Roger Lang, George Washington University
Ellsworth LeDrew, University of Waterloo
Fuk Li, Jet Propulsion Laboratory
Charles Luther, Office of Naval Research
Harlan McKim, US Army CRREL
David McLaughlin, Northeastern University
James Mead, University of Massachusetts
Nasir Memon, Northern Illinois University
James Merchant, University of Nebraska-Lincoln
David Meyer, EROS Data Center
Wooil Moon, University of Manitoba
Richard Moore, University of Kansas
Ram Narayanan, University of Lincoln-Nebraska
Eni Njoku, Jet Propulsion Laboratory
Robert Palmer, University of Nebraska-Lincoln
William Plant, University of Washington
Jeff Plaut, Jet Propulsion Laboratory
Paul Racette, NASA Goddard Space Flight Center
John Reagan, University of Arizona
Steven Reichenbach, University of Nebraska-Lincoln
Jack Rinker, US Army TEC
Christopher Ruf, Pennsylvania State University
Donald Rundquist, University of Nebraska-Lincoln
Khalid Sayood, University of Nebraska-Lincoln
Thomas Schmugge, USDA/ARS Hydrology Laboratory
Khalid Siddiqui, SUNY College at Fredonia
Alois Sieber, Joint Research Centre-Ispra
Karen St. Germain, University of Nebraska-Lincoln
Mikio Takagi, University of Tokyo
Jim Tilton, NASA Goddard Space Flight Center
Dennis Trizna, Naval Research Labs
Leung Tsang, University of Washington
Fawwaz Ulaby, University of Michigan
Bruce Wallace, Army Research Laboratory
Elizabeth Walter-Shea, University of Nebraska-Lincoln
JoBea Way, Jet Propulsion Laboratory
Edward Westwater, NOAA/ERL/WPL
Simon Yueh, Jet Propulsion Laboratory



IGARSS'96

1996 International Geoscience and Remote Sensing Symposium

Table of Contents

INTERACTIVE AREA 1 -- Atmosphere

1. Dual-Frequency Three-Dimensional Images of Clouds 1
Firda, J.M., S.M. Sekelsky and R.E. McIntosh

2. Preliminary Backscatter Lidar Measurements of Atmospheric Boundary Layer and Cirrus Clouds in Buenos Aires 34.6 S / 58.5 W 4
Lavorato, M.B., G.J. Fochesatto , E.J. Quel and P.H. Flamant

3. Improvement of a Standard Doppler Dealiasin Technique for Weather Radars Operating in Heavy Clutter Environment 7
Giuli, D., L. Facheris, F. Frattura and L. Baldini

4. Time-Frequency Analysis of Backscattered Lidar Signal to Study Atmosphere Dynamics 10
Molinaro, F., H. Bencherif, M. Bessafi and J. Leveau

5. Estimating RCS of the Sea Surface Perturbed by Rain for Rainfall Rate Retrieval 13
Capolino, F., D. Giuli , L. Facheris and F. Sottili

6. Assessment of Multiple Scattering Effects on Aerosol Retrievals from AVHRR NA
Ignatov, A., L. Stowe and R. Singh

7. Dielectric Constants for Melting Hydrometeors as Derived from a Numerical Method 16
Meneghini, R., and L. Liao

8. Analysis and Modeling of Atmospheric Transport of Water Vapor and Other Trace Constituents NA
Johnson, D.R.

9. Second Order Microwave Radiative Transfer Equation Solution with SSM/I Data NA
Souffez, S.H., and J.R. Givri

10. Adaptive Optical Aerosol Model of the Earth's Atmosphere NA
Smokty, O., and N. Kobjakova

11. Monitoring of Clouds Moisture for Problems of Increase Precipitation Artificially NA
Ruzhentsev, N.V., Yu.A. Kuzmenko and V.P. Bakhanov

12. Optical Remote Sounding of Aerosol Formations on the Base of Numerical Simulation of the Scattering Radiation 19
Belyaev, B.I., L.V. Katkovsky, V.P. Kabashnikov and V.P. Nekrasov

13. Investigation of the Anisotropy of the Atmospheric Turbulence Spectrum in the Low Frequency Range 22
Lukin, V.

14. Benguela Upwelling System: Satellite and Shipborne Data Analysis NA
Kazmin, A.S.

INTERACTIVE AREA 1 -- SAR Processing and Applications

15. A Simulation-Based Validation of Some Improvements in Automatic Stereo-Radargrammetry 25
Nocera, L., S. Dupont and M. Berthod

16. Detection and Localization of Lost Objects by SAR Technique 28
Dionisio, C.

NA -- Not available at time of printing.

INTERACTIVE AREA 1 *continued* -- SAR Processing and Applications

17. REX -- An Automated Road Extraction Algorithm for SAR Imagery NA
Bergen, Z.D., D. Kaiser and R.E. Carande

18. Automated Matching Experiments With Different Kinds of SAR Imagery 31
Gelautz, M., G. Jakob, G. Paar, S. Hensley and F. Leberl

19. Detecting Man-Made Features in SAR Imagery 34
Carlotto, M.J.

20. Texture Analysis by Universal Multifractal Features in a Polarimetric SAR Image 37
Martinez, P., D. Schertzer and K. Pham

21. Reading CEOS-SAR Tapes: A New General Reader and a Proposed New Standard 40
Pierce, L.

22. RADARSAT Processing at ASF 43
Leung, K., M. Chen, J. Shimada and A. Chu

23. Radar Speckle: Noise or Information? 48
Xia, Z.G., and Y. Sheng

24. SAR and One-Bit Coding: New Ideas 51
Franceschetti, G., M. Tesauro and S. Wall

25. Preserving Exponentials in Synthetic Aperture Radar Data 54
Pepin, M.P., and J.J. Sacchini

26. Improved Multiple Look Technique 57
Yeo, T.S., W.L. Lay, Y.H. Lu, W.E. Ng, I. Lim and C.B. Zhang

27. Partially Correlated K-Distribution for Multi-Look Polarimetric SAR Imagery 60
Yu, Y., A. Torre and S. Huan

28. Speckle Reduction and Enhancement of SAR Images in the Wavelet Domain 63
Sveinsson, J.R., and J.A. Benediktsson

29. Adaptive Filtering Algorithms for SAR Speckle Reduction 67
Lu, Y.H., S.Y. Tan, T.S. Yeo, W.E. Ng, I. Lim and C.B. Zhang,

INTERACTIVE AREA 2 -- Marine/Ocean

1. Multispectral and Multisatellite Data for Investigation of Black Sea Upper Layer Processes NA
Stanichny, S.V., and D.M. Solov'ev

2. A Software Package for the Quality Assessment of the Low Bit Rate Mediterranean Scatterometer and Altimeter Products:ERS-1.WSC.DWP and ERS-1.ALT.MPR NA
Bartoloni, A., C. Celani, C. D'Amelio, G. Milillo and R. Viggian

3. Estimation of Adjacent Effects Over the Coastal Zone by Polarization Measurements NA
Kusaka, T., S. Sado and Y. Kawata

4. An Eolian and Marine Phenomena Characterization in Dune Sectors by Image Processing 70
Delignon, Y., L. Moreau and P. Clabau

5. Retrieval of Arctic Surface Conditions and Cloud Properties from AVHRR Data: A Time Series for the Beaufort Sea 73
Meier, W., J. Maslanik, J. Key and C. Fowler

6. Sensitivity Study of the Aerosol Size Parameter Derived from AVHRR's Channels 1 and 2 Over Oceans NA
Ignatov, A.

7. Evaluation of Remote Sensing Algorithms for the Retrieval of Optically-Active Components in Turbid Natural Waters 76
Kutser, T., A. Blanco and H. Arst

8. Comparison of Sea Traffics in Tokyo and Osaka Bays With JERS-1/OPS Data 79
Takasaki, K., T. Sugimura and S. Tanaka

9. NASA Scatterometer Near-Real-Time, Value Added Products for Meso/Synoptic-Scale Marine Forecasting 82
Spencer, M.W.

10. Wavelet Analysis of AVHRR Images for Feature Tracking 85
Liu, A.K., W.Y. Tseng and S.Y.S. Chang

11. Flourescence as a Potential Indicator of Coral Health 88
Holden, H., D. Peddle and E. LeDrew

12. Satellite Synthetic Aperture Radar, CODAR, and In Situ Measurements of Oceanic Features in Monterey Bay NA
Fernandez, D.M.

13. Variability of Rossby Wave Propagation in the North Atlantic from TOPEX/POSEIDON Altimetry 91
Cipollini, P., D. Cromwell and G.D. Quartly

14. Chlorophyll Retrieval from CZCS: Influence of Atmospheric Aerosols 94
Moldenhauer, O., M.L. Steyn-Ross and D.A. Steyn-Ross

15. A Global Sea Level Variability Study From Almost a Decade of Altimetry 97
Naeije, M.C., and R. Scharroo

16. Variability and Frontogenesis in the Large-Scale Oceanic Frontal Zones Derived from the Global Satellite Measurements NA
Kazmin, A.S.

17. Vertical Distribution of PAR and Diffuse Attenuation Coefficient Modeling and In Situ Measurements 100
Volynsky, V.A., A.I. Sud'bin and J. Marra

18. Determination of Optical Properties of Ocean Upper Layers by Reflectance Spectra Measurements NA
Parishikov, S.V., M.E. Lee and O.V. Martynov

19. Oil Spills Detection in the Sea Using ALMAZ-1 SAR NA
Ivanov, A.Yu., V.V. Zaitsev, O.V. Ivlev and V.Yu. Raizer

20. Detection of Convective Instability in Atmospheric Boundary Layer Over the Ocean by Airborne Ku- Band Real Aperture Radar 103
Mityagina, M.I., Y.A. Kravtsov, V.G. Pungin, K.D. Sabinin and V.V. Yakovlev

21. Analyzing the Discharge Regime of a Large Tropical River Through Remote Sensing, Ground-Based Climatic Data, and Modeling 106
Schloss, A.L., C.L. Vorosmarty, C.J. Willmott and B.J. Choudhury

INTERACTIVE AREA 3 -- Sea Ice

1. Using Temporal Information in an Automated Classification of Summer, Marginal Ice Zone Imagery 109
Haverkamp, D., and C. Tsatsoulis

2. Texture Representation of SAR Sea Ice Imagery Using Multi-Displacement Co-Occurrence Matrices 112
Soh, L.K., and C. Tsatsoulis

3. Phase Correction for Coherent Noise Reduction in Short-Range Radar Measurements 115
Beaven, S.G., S.P. Gogineni and P. Kanagaratnam

4. In-Situ Measurement of the Complex Dielectric Constant of Sea Ice From 1 to 10 GHz 118
Nassar, E., R. Lee, K. Jezek and J. Young

5. Nearshore Ice Surface Roughness Surveys on Lake Superior 121
Pilant, D.

6. Error Characteristics of the SIRF Resolution Enhancement Algorithm 124
Early, D.S., and D.G. Long

7. The Quantification of Sea Ice Melt Features from Low Level Aerial Photographs 127
Derksen, C.P., J.M. Piwowar and E.F. LeDrew

8. Electromagnetic Waves Scattering From Sea Ice with Inhomogeneous Dielectric Permittivity Profile NA
Timchenko, A.I., and A.O. Perov

9. Investigation of the Fast Troposphere Parameters Variations by Using Method of the Radioacoustic Sounding NA
Rapoport, V.O., N.I. Belova, V.V. Chugurin, Y.G. Fedoseev, Y.A. Sazonov and V.A. Zinichev

10. Applications of the Remote Sensing for Experimental Study of the Boundary Layer's Dynamics in the Coastal Zone of the Black Sea NA
Kontar, E.A., A.I. Ginzburg and M.M. Domanov

11. Modelling Inter-Annual Snow Variability in Eastern Canada NA
Lewis, J.E., and L. Lee

12. Mapping Snow Properties for Spatially Distributed Snow Hydrological Modeling in Mountainous Areas Using Passive Microwave Remote Sensing Data 130
Wilson, L.L., L. Tsang and J.N. Hwang

13. Snow Classification from SSM/I Data over Varied Terrain Using an Artificial Neural Network Classifier 133
Sun, C., C.M.U. Neale, J.J. McDonnell and H.D. Cheng

14. Snow Mapping with SIR-C Mulpolarization SAR in Tienshan Mountain 136
Li, Z., and J. Shi

15. Recent Progress in Development of the Moderate Resolution Imaging Spectroradiometer Snow Cover Algorithm and Project 139
Riggs, G., D.K. Hall and V.V. Salomonson

16. Relation Between Radiative and Microphysical Properties of Snow: New Efficient Approach NA
Zege, E.P., and A.A. Kokhanovsky

17. Variations in Radar Backscatter Across the Great Ice Sheets 142
Noltimier, K.F., and K.C. Jezek

18. Geophysical Data Management System 145
Baggeroer, P.A., K.C. Jezek and D.G. Hart

19. Ice Sheet Margin Detection Using ERS-1 Synthetic Aperture Radar 148
Sohn, H.G., and K.C. Jezek

INTERACTIVE AREA 3 -- Soil

20. Microwave Effective Permittivity Model of Frozen Soil and Applications to Passive Remote Sensing NA
Tikhonov, V.V.

21. Flood Monitoring in Norway Using ERS-1 SAR Images 151
Weydahl, D.J.

22. Relating Microwave Satellite Radiometer Observations to Land Surface Parameters: A Physical Approach 154
Karam, M.A., and A. Stogryn

23. Analysis of ERS-1 SAR Data to Study Soil Moisture Content in Rocky Soils 157
Sano, E.E., A.R. Huete, D. Troufleau, M.S. Moran and A. Vidal

24. Determining Water Stress in Potato Fields Using Infrared Thermometry NA
Peterson, J.R., J.M. Giarrusso and M.C. MacDonald

25. An Automated Overland Flow Model Based Upon Remote Sensing and GIS 160
Leu, C.H.

26. Analysis for Soil Moisture and Land Cover Studies ERS-1 and JERS-1 SAR Data 163
Rao, Y.S., P.V.N. Rao, L. Venkataratnam and K.S. Rao

27. Spatio-Temporal Dynamics of Soil Moisture in Tallgrass Prairie Using ERS-1 SAR Image Time Series: First Year Results 166
Henebry, G.M., and A.K. Knapp

28. Mapping Methane Emission from Arctic Tundra Using Satellite Data, a Digital Elevation Model, and Discriminant Functions Based on Field Data 169
Shippert, M.M.

INTERACTIVE AREA 4 -- Crustal Movements/Vegetation

1. Neogene-Quaternary Kinematics of the Northern Mediterranean Microplates NA
Yutsis, V.V., and V.N. Vadkovsky

2. Water Content Influence on Scattering Properties of Vegetation Cover 172
Roenko, A.N., Yu.F. Vasilyev, B.D. Zamaraev and V.L. Kostina

3. Experimental Study of Fire Risk by Means of Passive Microwave and Infrared Remote Sensing Methods 175
Liberman, B., A. Grankov, A. Milshin, S. Golovachev and V. Vishniakov

4. Investigation and Cataloguezation of Backscattering Characteristics of Different Earth Covers in Millimeter Wave Band 178
Vasilyev, Yu.F., B.D. Zamaraev, V.L. Kostina and A.N. Roenko

5. Classification Using Multi-Source Data Using and Predictive Ability Measure 180
Chong, C.C., and J.C. Jia

6. Center Pivot Irrigation System Analysis Using Airborne Remotely Sensed Imagery: A Commercial Remote Sensing Case Study 183
MacDonald, M.C.

7. The Sensitivity of a Land Surface Parameterization Scheme to the Choice of Remotely-Sensed Landcover Data Sets 186
Oleson, K.W., K.L. Driese, J.A. Maslanik, W.J. Emery and W.A. Reiners

8. Using the Wavelet Method for a Multispectral Remote Sensing Study of Plant Community Spatial Processes in Broad Range of Spatial Scales 189
Mikheev, P.V., S.S. Kheeroug, G.Y. Yakin and J. S. Todhunter

9. A Multi-Parameter Land Data Set for Regional Modeling 192
Thames, P., J. Maslanik, K. Oleson and W. Emery

10. Coincident Diurnal and Spatial Variations in Dielectric Constant Properties as Measured Along a Vertical Gradient in Stems of Norway Spruce NA
McDonald, K., R. Zimmermann and E.D. Schulze

11. Spatio-Temporal Land Cover Dynamics in the Pantanal Assessed Using Lacunarity Analysis on an ERS-1 SAR Image Time Series 195
Henebry, G.M., and H.J.H. Kux

12. Accuracy Analysis and Validation of Global 1 Km Land Cover Data Sets 198
Scepan, J., J.E. Estes and W.J. Starmer

13. Potential of SIR-C Data to Study Vegetation Over Gujarat Test Site, India 201
Rao, K.S., Y.S. Rao, L. Venkataratnam and P.V.N. Rao

14. Intercomparison of Several BRDF Models for the Compositing of Spaceborne POLDER Data over Land Surfaces 204
Hautecoeur, O. and M. Leroy

15. Monitoring Arid and Semi-Arid Regions with ERS-1 Wind Scatterometer Data NA
Frison, P.L. and E. Mougin

16. Estimation of Seasonal Dynamics of Pasture and Crop Productivity in Kazakhstan Using NOAA/AVHRR Data 209
Gitelson, A., F. Kogan, E. Zakarin and L. Lebed

17. The Reflectance of Pleurozium Schreberi as a Function of Water Status and Its Implications on Understory Reflectance Variations for BOREAS Sites 212
Fernandes, R., H.P. White, D.R. Peddle, J.R. Miller and L.E. Band

18. Mapping Species Rich Boreal Wetlands Using Compact Airborne Spectrographic Imager (CASI) NA
Jelinski, D.E., J.R. Miller, R. Steinauer, S. Narumalani and J. Freemantle

19. Seasonal NDVI Trajectories to Response to Disturbance: Toward a Spectral-Temporal Mixing Model for Tallgrass Prairie 215
Goodin, D.G., and G.M. Henebry

20. Analysis of the Canadian Boreal Forest Using Enhanced Resolution ERS-1 Scatterometer Imagery 218
Wilson, C.J., III, and D.G. Long

21. Comparison of Interferomertic SAR and Radar Profiling in Forest Mapping NA
Axelsson, S.R.J.

22. Land Cover Change Dynamics of a Himalayan Watershed Utilizing Indian Remote Sensing Satellite (IRS) Data 221
Krishna, A.P.

23. Classification of Cover Types in the Lower Delta of the Parana River Using a Multitemporal Approach NA
Karszenbaum, H., P. Kandus, L.A. Frulla and D.A. Gagliardini

24. Remote Sensing of Crop Responses to Ozone and Carbon Dioxide Treatments 224
Leblanc, E., C.S.T. Daughtry and C.L. Mulchi

25. Radar Profiling for Forest Inventory NA
Axelsson, S.R.J., M. Eriksson and S. Hallidin

26. Examination of Multi-Temporal ERS-1 Radar over the Rainwater Basin 227
Keithley, C., and M. Roberts

27. Application of Remote Sensing Measurements for Research an dService of Agriculture in Bulgaria NA
Kazandjiev, V.

28. A Comparison of NDVI and Spectral Mixture Analysis for Estimating Biophysical Properties in Boreal Forest Terrain 230
Peddle, D.R., F.G. Hall and E.F. LeDrew

29. Global Landcover Classification Training and Validation Issues and Requirements 233
Muchoney, D., J. Borak and A. Strahler

30. An Automatic Road Extraction Method Using a Map-Guided Approach Combined with Neural Networks for Cartographic Database Validation Purposes 236
Fiset, R., F. Cavayas, M.C. Mouchot, B. Solaiman and R. Desjardins

31. Plant Condition Remote Monitoring Technique 239
Fotedar, L.K., and K. Krishen

INTERACTIVE AREA 4 -- Geophysical Modelling

32. Feature Selection Using Decision Trees -- An Application for the MODIS Land Cover Algorithm 243
Borak, J.S., and A.H. Strahler

33. Regional Land Cover Characterization Using Multiple Sources of Intermediate-Scale Data 246
Vogelmann, J.E., S. Howard and T. Sohl

34. Multisensor Studies Using Landsat TM, SPOT and ERS-1 in Monitoring of Vegetation Damage in Nikel (Russia) and Varanger (Norway) NA
Lauknes, I. and H. Tommervik

35. Calibration and Classification of SIR-C SAR Data in Moderate Slope Areas 248
Holecz, F., T.R. Michel and M. Keller

36. A New Quick-Look Optical SAR Processor with Digital Input/Output 251
Litovechenko, K., P. Lemaire and C. Barbier

37. The Modeling of Forested Areas for Real and Synthetic Aperture Imaging Radar Simulation 254
Stuopis, P.A., J.M. Henson, R.E. Davis and K. Hall

38. Use of Geometrical SAR Simulation for Visibility Prediction: Application to Mission Planning and Urban Study 257
Gouinaud, C., and I. Pons

39. Modelling of Microwave Backscatter Using a Tree-Growth Model for Boreal Forests Within the NOPEX Test Site 260
Woodhouse, I.H., and D.H. Hoekman

INTERACTIVE AREA 4 *continued* -- Geophysical Modelling

40. Modeling Wetland Vegetation Using Polarimetric SAR 263
Slatton, K.C., M.M Crawford, J.C. Gibeaut and R.O. Gutierrez

41. Rain Pattern Detection by Means of Packet Wavelets 266
Marazzi, A., P. Gamba and R. Ranzi

INTERACTIVE AREA 5 -- Missions and Programs

1. The Development of the Seawinds Scatterometer Electronics Subsystem (SES) 269
Boller, B.D., R.D. Crowley, M.C. Smith and R.S. Roeder

2. Phase B and Breadboard Results for the TOPEX POSEIDON FOLLOW-ON Mission 273
Rey, L., N. Suinot, P. Oudart and G. Carayon

3. Science Data Collection with Polarimetric SAR 276
Dall, J., K. Woelders and S.N. Madsen

4. Spaceborne Rain Radar Mission and Instrument Analysis 279
Vincent, N., J. Chenebault, N. Suinot and P.L. Mancini

5. SIR-C/X-SAR Campaign on Ruegan Island, Germany - First Results 282
Prietzsch, C., and A. Bachem

6. The Indian Remote Sensing (IRS) Mission NA
Yang, J.

INTERACTIVE AREA 5 -- Electromagnetic Problems

7. Phase Fluctuations for Waves of Different Spatial Frequencies and Their Use in Determination of Inhomogeneous Dielectric Permittivity Profile NA
Timchenko, A.I.

8. Volume Scattering Function of Light for a Mixture of Polydisperse Small Particles with Various Optical Properties 285
Haltrin, V.I., A.D.Weidemann and W.E. McBride III

9. Simulation of RAR Reflectivity Maps of the Sea Surface for Remote Sensing Applications 290
Corsini, G., G. Manara and A. Monorchio

10. A Simplified Hybrid Model for Radiation Under Discontinuous Canopies 293
Li, X., W. Ni, C. Woodcock and A. Strahler

11. Estimation of Some Characteristics of Ocean Waters Using Optical Data (Case I) 296
Volynsky, V.A., J. Marra and C. Knudson

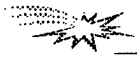
12. The Synthesis of Optimal Structure of Radar Using Polarization Adaptation 299
Loutin, E.A., A.I. Kozlov and A.I. Logvin

13. A Method and Algorithm of Computing Apparent Optical Properties of Coastal Sea Waters 305
Haltrin, V.I., and A.D. Weidemann

14. Scene Understanding from SAR Images 310
Datcu, M.

15. Microwave Specific Attenuation by Lossy Raindrops of Spheroidal Shapes: An Exact Formulation NA
Li, L.W., T.S. Yeo, P.S. Kooi and M.S. Leong

16. Theoretical Research on New Concepts for the Remote Sensing of Hydrometeors 315
Martin-Neira, M., J. Bara, A. Capms, F. Torres, I. Corbella and O. Gasparini



INTERACTIVE AREA 6 -- Educational Initiatives

1. Helping Students and Teachers Make Sense of Remote Sensing Via the Internet NA
Croft, S.K., and R.J. Myers

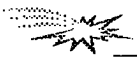
2 "Winds of Change" A Multi-Media Tool to Aid Teachers in Teaching Global Climate 321
Yanow, G., A. Sohus and B. Payne

3 From Surfer to Scientist: Designing a Canadian Remote Sensing Service for the Internet Audience 324
Langham, C.W., A.M. Botman and T.T. Alfoldi

4 Earth System Science Education Using Remote Imagery and Environmental Data Access NA
Fortner, R.W.

5 Using Weather Satellite Images in the Classroom of the Future NA
Keck, C.L.

6 The Use of Technology Driven Investigations in Geoscience and Remote Sensing Education: Findings from an Evaluation of the JASON Project NA
Coan, S.M., and C.J. Moon



INTERACTIVE AREA 7 -- SAR Interferometry

1. Linear Structures in SAR Coherence Data 330
Hellwich, O., and C. Streck

2. Detection and Velocity Estimation of Moving Objects in a Sequence of Single-Look SAR Images 333
Kirscht, M.

3. A Discrete Minimization Approach to Phase Unwrapping NA
Bartoloni, A., C. D'Amelio, A., Mariani, G. Milillo and M. Mochi

4. Comparison of Multigrid and Wavelet Techniques for InSAR Phase Unwrapping NA
Datcu, M.

5. Comparative Analysis of Phase Unwrapping Methods Using Self-Affine (Fractal) Models 336
Valero, J.L., and I. Cumming

6. A Workstation for Spaceborne Interferometric SAR Data 339
van der Kooij, M.W.A., B. Armour, J. Ehrismann, H. Schwichow and S. Sato

7. A Comparison of Phase to Height Conversion Methods for SAR Interferometry 342
Small, D., P. Pasquali and S. Fuglistaler

INTERACTIVE AREA 7 *continued* -- SAR Interferometry

8. Along-Track SAR Interferometry for Motion Compensation NA
Pasquali, P., B. Fritsch and D. Nuesch

9. SAR Interferometry: A Multigrid Markovian Approach for Phase Unwrapping with a Discontinuity Model 345
Labrousse, D., S. Dupont and M. Berthod

10. Echoes Covariance Modelling for SAR Along-Track Interferometry 347
Lombardo, P.

11. On the Survey of Volcanic Sites: The SIR-C/X-SAR Interferometry 350
Coltelli, M., G. Fornaro, G. Franceschetti, R. Lanari, M. Migliaccio, J.R. Moreira, K.P. Papathanassiou, G. Puglisi, D. Riccio and M. Schwabisch

12. DEM Generation by Repeat-Pass SAR Interferometry NA
Herland, E.A.

INTERACTIVE AREA 8 -- Techniques and Instrumentation

1. Atmospheric Induced Errors on Interferometric DEM Generation 353
Kenyi, L.W., and H. Raggam

2. Wavelet Projection Pursuit for Feature Extraction and Cloud Detection in AVIRIS 356
Bachmann, C.M., E.E. Clothiaux and D.Q. Luong

3. Atmospherical Correction of Satellite and Aircraft Spectral Image Without Calibration NA
Zege, E.P., I.L. Katsev and A.S. Prikhach

4. Absolute in Flight Calibration of Airborne Multichannel MM-Wave Imaging Radiometer 360
Cherny, I.V., A.A. Pankin and S.Y. Pantzov

5. Analysis of Map Speckle Suppression Algorithm 363
Zaitsev, V.V., and V.V. Zaitsev

6. Space "MSU-E" and "MSU-SK" Scanner Images Using for Evaluation of Antropogenic Pollution of Snow Cover NA
Mironov, V.L., S.A. Komarov, A.V. Yevtyushkin, I.N. Dubina, V.N. Yushakov and T.V. Baikalova

7. Laboratory and In-Flight Spectrometer Calibration Technique in Visible and Near Infrared Spectral Ranges 366
Belyaev, B.I., L.V. Katkovsky and V.P. Nekrasov

8. An Attempt to Differentiate Specific Absorption Characteristics by Solving Inverse Problem NA
Volynsky, V.A.

9. Secondary Processing Algorithm for Two-Frequency Aircraft Radiomapping System NA
Ruzhentsev, N.V., Yu.A. Kuzmenko and V.P. Churilov

10. Duct Detection over the Sea by TRANSIT Measurements 369
Gaikovich, K.P., A.N. Bogaturov, A.S. Gurvich, S.S. Kashkarov, S.N. Krivonozhkin, B.M. Shevtcov, V.K. Ivanov and V.D. Freylikher

11. The Abilities of Radioacoustical Sounding Method for Atmosphere Processes Diagnostic NA
Rapoport, V.O. and V.V. Tamoikin

12. An Investigation of the Textural Characteristic for Geological Purposes 372
Pasaribu, D.P.

13. Estimating Microwave Observation Depth in Bare Soil Through Multi-Frequency Scatterometry NA
Troch, P.A., F. Vandersteene and Z. Su

14. Validation of ERS-1/SAR Data to Map the Rio Amazonas Floodplain According to the Cartographic Accuracy Standards 374
Kux, H.J.H., and V. Barbosa da Silva

15. Detail-Preserving Segmentation of Polarimetric SAR Imagery 377
Andreadis, A., G. Benelli and A. Garzelli

16. Detection and Analysis of Ship Waves in ERS-1 SAR Imagery 380
Peng, C.Y., A.K. Liu and S.Y.S. Cheng

17. ROME: The Rosetta Microwave Experiment for the Investigation of the Cometary Nucleus 383
Fedele, G., G. Picardi and R. Seu

18. On the Use of Whitening Filter and Optimal Intensity Summation to Produce Multi-Look SAR Images 387
Bruniquel, J., A. Lopes, J.G. Planes, F. Cazaban and M. Deschaux-Beaume

19. Channel Design of the ADEOS-II/GLI (Global Imager) 390
Nakajima, T.Y., T. Nakajima and M. Nakajima

20. Atmospheric Effects on CO2 Differential Absorption Lidar Performance 393
Petrin, R.R., D.H. Nelson, J.R. Quagliano, M.J. Schmitt, C.R. Quick, R.K. Sander, J.J. Tiee and M. Whitehead

21. Improved Feature Classification by Means of a Polarimetric IR Imaging Sensor 396
Sadjadi, F., and C. Chun

22. A Comparison of Scintillation Crosswind Methods 399
Poggio, L., M. Furger and W.K. Graber

23. A Multi-Frequency, Dual-Polarization, Microwave Link for Rainfall Estimation 402
Rincon, R.F., S.W. Bidwell, A.R. Jameson and O.W. Thiele

24. Radiometric Normalization of Landsat/TM Images in Multitemporal Classification Procedures NA
Frulla, L., J. Milovich and H. Karszenbaum

25. Cost-Effective Parallel Processing for Remote Sensing Applications 405
Kim, H.J., and H.S. Kim

26. Design of a Geographic Information System Using OPS5 408
Menon, A.K., P. Jayaprakash and P.V. Usha

27. Multiresolution De-Speckle Based on Laplacian Pyramids 411
Alparone, L., B. Aiazzi, S. Baronti and C. Susini

28. Classification and Feature Extraction with Enhanced Statistics 414
Benediktsson, J.A., K. Arnason, A. Hjartarson and D. Landgrebe

29. Modeling and Simulation of Real Aperture Radar Images NA
Menegasssi Menchik, M.T., and D. Fernandez

30. A Rain Profiling Algorithm for the TRMM Precipitation Radar NA
Iguchi, T., T. Kozu, R. Meneghini and K. Okamoto

31. Application of Radar Target Decomposition Technique for Flood Detection: Results from SIR-C Data NA
Hess, L.L., Y. Wang and J.M. Melack

32. Solar Irradiance Determination by Using ATSR-2 Data 417
Xue, Y., D.T. LLewellyn-Jones and S.P. Lawrence

33. Automatic Interaction Detector (Aid) Application on Image Classification NA
Ho, L.L. and J.A. Quintanilha

34. Comparison of Linear Least Squares Unmixing Methods and Gaussian Maximum Likelihood Classification 420
Fernandes, R., J. Miller and L.E. Band

35. Development and Test of a Raster Scanning Laser Altimeter for High Resolution Airborne Measurements of Topography 423
Rabine, D.L., J.L. Bufton and C.R. Vaugh

36. Optical Correction of Scene Fractions for Estimating Regional Scale Ocean Coral Abundance in Fiji 427
Peddle, D.R., E.P. LeDrew and H.M. Holden

37. Development of SAR Interferometry at I.I.T. Bombay, India 430
Sukhatme, J.S., V. Walavalkar, Y.S. Rao, G. Venkataraman, M.V. Khire and K.S. Rao

38. Improved Procedures for the Retrieval of Stratospheric Trace Gases from Spectra of a Ground-Based Millimeter Wave Radiometer 433
Kuntz, M.

39. A New 278 GHz Ground-Based Radiometer for Vertical Profile Sounding of C10 and 03 in the Upper Atmosphere 436
Hochschild, G., and R. Krupa

40. Polarimetric SAR Image Classification Based on Target Decomposition Theorem and Complex Wishart Distribution 439
Du, L.J., and J.S. Lee

41. Hydrometeors Investigation by Means of 3 Millimeter Coherent Radar 442
Kosov, A.S., V.D. Gromov, S.N. Maleev, S.S. Kiselev, D.P. Skulachev and I.A. Strukov

42. Vegetation Obscuration Effects on Mid-Infrared Laser Reflectance of Soil 445
Guenther, B.D., and R.M. Narayanan

43. Applying Principal Components Analysis to Image Time Series: Effects on Scene Segmentation and Spatial Structure 448
Henebry, G.M., and D.R. Rieck

44. D.A.T.E. -- Dip Algorithm Testing and Evaluating Workbench 451
Kerzner, M.G.

45. High Resolution VHF SAR Processing Using Synthetic Range Profiling 454
Lord, R.T., and M.R. Inggs

46. A Region-based Approach to the Estimation of Local Statistics in Adaptive Speckle Filters 457
Fjortoft, R., F. Lebon, F. Sery, A. Lopes, P. Marthon and E. Cubero-Castan

47. A Precision Processor for Radarsat NA
Hughes, W., I. Arnon, K.A. Gault, D. MacGregor, L. Mikulin, L. Lightstone and J. Princz

48. Reversible Inter-Frame Compression of Multispectral Images Based on a Previous-Closest-Neighbor Prediction 460
Aiazzi, B., P.S. Alba, L. Alparone, S. Baronti and P. Guarnieri

49. Color Correction of HSI Transformed Images Using Color Space Transformation NA
Hosomura, T., and K. Katou

50. Lossless Compression of Multispectoral Images Using Permutations 463
Arnavut, Z., and S. Narumalani

51. Algoritms to Compute the Top-of-the-Atmosphere ALBEDO for Clear-Sky Conditions from Multi-Angle Data NA
Borel, C.C., and S. A.W. Gerstl

52. Parametric Representation of Atmospheric Disturbances NA
Mukherjee, D.P., P. Pal and J. Das

53. Radar Altimeter Return Noise Signals Identification 466
Maotang, L., J. Jingshan, W. Jingli and Y. Zhiqiang

54. Range and Angle Error Correction Measure for the Low Elevation Angle in Remote Sensing Data Analysis 469
Choi, J.

55. Potential and Use of Radar Images for Characterization and Detection of Urban Areas 474
Gouinaud, C., F. Tupin and H. Maitre

56. Phase Preservation in SAR Processing: The Interferometric Offset Test 477
Rosich Tell, B., and H. Laur

57. The Automation of Radar Operation and Calibration of NASA/JPL Airborne Multi-Frequency Polarimetric and Interferometric Synthetic Aperture Radar System NA
Lou, Y., and Y. Kim

58. Robust Restoration of Microwave Brightness Contrasts from the DMSP SSM/I Data 481
Petrenko, B.Z.

59. Advanced Airplane Version of the HUT 93 GHz Imaging Radiometer 484
Kemppinen, M., T. Auer, I. Mononen and M. Hallikainen

60. Ingara Dual Pass Cross Track Interferometry NA
Stacy, N.J.S., and G.G. Nash

61. A Low Range-Sidelobe Pulse Compression Technique for Spaceborne Rain Radar 487
Sato, K., H. Hanado and H. Kumagai

62. Pulse Compression With - 65 dB Sidelobe Level for a Spaceborne Meteorological Radar 490
Vincent, N., J. Richard, N. Suinot, M. Yarwood and C. Mavrocordatos

63. A SAR Antenna Calibration Method 493
Stevens, D., P. Bird and G. Keyte

64. Inflight Vertical Antenna Patterns for SIR-C from Amazon Rain-Forest Observation 496
Fang, Y., and R.K. Moore

65. A Contribution to Imaging Radiometer Sampling and Integration Period Determination 499
Kemppinen, M.

66. Radarclinometry for ERS-1 Data Mapping 503
Paquerault, S., H. Maitre and J.M. Nicolas

67. Millimeter-Wave Backscatter Measurements in Support of Surface Navigation Applications 506
Snuttjer, B.R.J., and R.M. Narayanan

68. A Novel Design of Return Signal Simulator for Radar Altimeters 509
Wu, J., and L. Lin

69. Polarimetric Calibration of Bistatic Radars Using Active Calibrators NA
Hevizi, L.G., and D.J. McLauglin

70. Calibration of Airborne Multiparameter Precipitation Radar with an Active Radar Calibrator 512
Hanado, H., H. Kumagai, T. Iguchi, T. Kozu, K. Nakamura and H. Horie

71. On the Accurate Calibration of the Sea Winds Radar Antenna: A Cylindrical Near-Field Measurement Approach 515
Hussein, Z.A., and Y. Rahmat-Samii

72. Detection of Pollutants in Liquids by Laser Induced Breakdown Spectroscopy Technique 520
Arca, G., A. Ciucci, V. Palleschi, S. Rastelli and E. Tognoni

73. Review of Vicarious Calibration of the Visible and Near-Infrared Channels of the Advanced Very High Resolution Radiometer NA
Rao, C.R.N., and J. Chen

74. Contextual Dynamic Neural Networks Learning in Multispectral Images Classifications 523
Solaiman, B., M.C. Mouchot and A. Hillion

TPAM -- Land Cover Mapping: Models and Applications

1. The Use of AVHRR Data for Creation of a New Global Land Cover Product for IGBP/DIS NA
Belward, A., and T.R. Loveland

2. From Leaf to Scene: A Scaling Problems in Remote Sensing of Vegetation 526
Goel, N.S., and W. Qin

3. Global Land Cover Classes Compatible with Radiative Transer Theory NA
Nemani, R., S. Running and R. Myneni

4. ART Neural Networks for Remote Sensing: Vegetation Classification from Landsat TM and Terrain Data 529
Carpenter, G.A., M.N. Gjaja, S. Gopal and C.E. Woodcock

5. New Approaches to Classification in Remote Sensing Using Hybrid Decision Trees to Map Land Cover 532
Brodley, C.E., M.A. Friedl and A.H. Strahler

6. Proportional Estimation of Land Cover Characteristics From Satellite Data 535
DeFries, R., M. Hansen and J. Townshend

7. Fuzzy ARTMAP Classification of Global Land Cover From AVHRR Data Set 538
Gopal, S., C.E. Woodcock and A.H. Strahler

8. Exploring the Interannual Variability of Vegetation Activity Using Multitemporal AVHRR NDVI Imagery 541
Mora, F., and J.W. Merchant

9. Correction of Land-Cover Area Estimates from Low Spatial Resolution Remotely Sensed Data 544
Moody, A.

10. Landsat Pathfinder Data Sets for Landscape Change Analysis 547
Dwyer, J.L., K.L. Sayler and G.J. Zlystra

TPAA -- Radar Remote Sensing and Precipitation

1. Factors Affecting NEXRAD-Based Point Rainfall Rate Estimation in the Seattle Area 551
Seliga, T.A., and C. Chen

2. Analysis of Dual-Wavelength Dual-Polarization Returns from Frozen Hydrometeors 554
Meneghini, R., T. Iguchi and L. Liao

3. Polarimetric Method for Ice Water Content Determination 557
Ryzhkov, A.V., and D.S. Zrnic

4. Simulation of Dual-Polarization Bistatic Scattering from Rain and Hail 560
Aydin, K., and S.H. Park

5. Computational Study of Millimeter Wave Scattering form Bullet Rosette Type Ice Crystals 563
Aydin, K., and T.M. Walsh

6. Multiparameter Radar Snowfall Estimation Using Neural Network Techniques 566
Xiao, R., and V. Chandrasekar

TPAA *continued* -- Radar Remote Sensing and Precipitation

7. Probing Electric Fields Near Sprites and Jets Using Multiparameter Radar and Chaff 569
Seliga, T.A., J.D. Sahr and R. H. Holzworth

8. Weather Radars with Pulse Compression Using Complementary Codes: Simulation and Evaluation 574
Mudukutore, A., V. Chandrasekar and R.J. Keeler

TPCP -- Remote Sensing: Boreal Ecosystems

1. Mapping of Boreal Forest Biomass Using SAR 577
Ranson, K.J., G. Sun, B. Montgomery and R.H. Lang

2. Carbon Dynamics in Northern Forests Using SIR-C/X-SAR Imagery 580
Bergen, K.M., M.C. Dobson and L.E. Pierce

3. Winter and Spring Thaw as Observed with Imaging Radar at BOREAS NA
Way, J.B., R. Zimmermann, K. McDonald and E. Rignot

4. Land Applications of ERS-1 Wind Scatterometer in Boreal Forest Zone 583
Pullianinen, J., N. Walker, T. Manninen, M. Hallikainen and J. Grandell

5. Monitoring Boreal Ecosystems in Siberia with the ERS-1 Windscatterometer NA
Schmullius, C., V. Wismann and K. Boehnke

6. Changes in Water Flux, Xylem Sap Composition, and Dielectric Constant Along a Vertical Gradient in Stems of Norway Spruce NA
Zimmermann, R., K. McDonald and E.D. Schulze

7. Spatial and Temporal Variability of Surface Cover at BOREAS Using Reflectances from a Helicopter Platform 586
Loechel, S.E., C.L. Walthall, E. Brown de Coulston, J.M. Chen and B.L. Markham

8. Use of Compact Airborne Spectrographic Imager (CASI) Data and Separability Measures for Classifying Complex Wetland Vegetation NA
Shepherd, P.R., D.E. Jelinski and J.R. Miller

9. Modeling Solar Radiation Transmission in Boreal Conifer Forests 591
Ni, W., X. Li, C.E. Woodcock, R.J. Roujean, R. Davis and A. Strahler

10. The Impacts of Environmental Conditions on Microwave Radiometry of Vegetation: A Physical Approach 594
Karam, M.A.

TPED -- Remote Sensing Applications of Sea Surface Modelling

1. Optimization of a Composite Surface Model for the Radar Backscattering Cross Section of the Ocean Surface as Measured by Wind Scatterometers 597
Romeiser, R.

2. A Physically-Based Two-Scale Electomagnetic Model for Backscatter From Ocean-Like Surfaces 600
Elfouhaily, T., and B. Chapron

3. An Application of the Two-Scale Model from the Point of View of the Small Slope Approximation to Radar Observations from the Ocean 603
Skirta, E.A., and A.N. Keane

4. A Comparison of Wind Wave Spectra Used in Ocean Remote Sensing Modeling 606
Elfouhaily, T., and B. Chapron

5. Evolution of Surface Waves of Finite Amlitude in Field of Inhomogeneous Current 609
Bakhanov, V.V., O.N. Kemarskaya, V.P. Pozdnyakova, J.A. Okomel'kova and I.A. Shereshevsky

6. Study of the Second Order Approximation of the Velocity Bunching in SAR Imaging Process Using the Bispectrum 612
Le Caillec, J.M., R. Garello and B. Chapron

7. Bistatic Sea Clutter: Simulations and Measurements 615
Khenchaf, A., F. Daout, Y. Hurtaud and J. Saillard

8. Verification of Microwave Scattering Mechanisms Using Optical Polarimetric Imagery 618
Barter, J.D., and P.H.Y. Lee

9. Fetch and Wind Speed Dependence of SAR Azimuth Cutoff and Higher Order Statistics in a Mistral Wind Case 621
Kerbaol, V., B. Chapron, T. Elfouhaily and R. Garello

10. Combined Radar and Cross-Polarizational Radiometer System for Detection and Identification of Some Anomalous Formations Originated on Sea Surface Due to Changes of Long and Short Waves Characteristics 625
Arakelian, A.K., and A.K. Hambaryan

TPES -- Youth Enhancing Space: KidSat

1. KidSat: Youth Enhancing Space 628
Choi, M.Y, G. Nagatani, J.B. Way and E.J. Stork

2. The Education Element of the KidSat/Youth Enhancing Space Project 631
McGuire, J., B. Fisher, R. Kassebaum, D. Barstow, K. Rackley, P. Bixler, M.A. Jones and J. Hunt

3. The Space Element of the Youth Enhancing Space Project NA
Lane, J., A. Leach, S. Davis, A. Ramirez and J. Baker

4. Mission Operations in the Classroom NA
Rackley, K., P. Bixler and H. Haugen

5. Youth Enhancing Space: Data System Element NA
Kirchner, C., M. Minino, R. Kassebaum, J. Lawson and P. Andres

6. Exploration Results from Charleston NA
Cowen, R., K. Rackley and the Fifth Grade Students of Buist Academy

7. Exploration Results from San Diego NA
Austin, A., S. Akpa, R. Anderson, P. Bixler and R. Ebel

8. Exploration Results from Pasadena NA
Brammer, C., M.A. Jones and the Fifth Grade Students of Washington Accelerated

TPF -- Remote Sensing for the Arctic Climate System

1. Future Opportunities and Issues in Radar Remote Sensing of Earth's High Latitudes 634
Carsey, F., and C. Wales

2. Satellite Remote Sensing of Atmosphere and Ice over the Arctic Ocean: A Perspective NA
Rothrock, D.A.

3. Expected Errors in Satellite-derived Estimates of the High Latitude Surface Radiation Budget 636
Key, J.R., R.S. Stone and A.J. Schweiger

4. Multitemporal Analysis of Fast Sea Ice Albedo Using AVHRR Data 639
De Abreu, R.A., and E.F. LeDrew

5. Assessing Variability and Trends in Arctic Sea Ice Distribution Using the Satellite Data 642
Belchansky, G.I., I.N. Mordvintsev and D.C. Douglas

6. Image Time Series Analysis of Arctic Sea Ice 645
Piwowar, J.M., G.R.I. Wessel, and E.F. LeDrew

7. An Analysis of Odden Event Intra- and Inter-Annual Variability 648
Fischer, K.W., C.A. Russel, R.A. Shuchman and E.G. Josberger

8. Remote Sensing Data Availability from the Earth Observation System (EOS) via the Distributed Active Archive Center (DAAC) at NSIDC 651
Weaver, R.L., and V.J. Troisi

9. CIDAS Climatological Ice Data Archiving System NA
Chagnon, R.

10. The Radarsat Geophysical Processor System NA
Rothrock, D., H. Stern, and R. Kwok

TPP -- SAR Interferometry: Processing Algorithms and Systems

1. Algorithms for Calculation of Digital Surface Models from the Unwrapped Intereferometric Phase 656
Goblirsch, W., and P. Pasquali

2. Elevation Correction and Building Extraction from Interferometric SAR Imagery 659
Burkhart, G.R., Z. Bergen, R. Carande, W. Hensley, D. Bickel and J.R. Fellerhoff

3. Unbiased Estimation of the Coherence from Multi-Look SAR Data 662
Touzi, R., A. Lopes, J. Bruniquel and P. Vachon

4. Automated Rapid Mapping with Interferometric Synthetic Aperture Radar Data 665
Ngai, F.M., and R.E. Carande

5. Ultra-Wideband and Low-Frequency SAR Interferometry 668
Ulander, L.M.H., and P.O. Frolind

6. Medium Resolution Efficient Phase Preserving Focusing for Interferometery 671
Gatelli, F., A. Monti Guarnieri, C. Prati and F. Rocca

7. EMISAR Single Pass Topographic SAR Interferometer Modes 674
Madsen, S.N., N. Skou, K. Woelders and J. Granholm

8. Parametric Estimation of Time Varying Baselines in Airborne Interferometric SAR 677
Mohr, J.J., and S.N. Madsen

9. On the Baseline Decorrelation 680
Franceschetti, G., A. Iodice, M. Migliaccio and D. Riccio

TPT -- Daytime Operation of Lidar Systems

1. Micro Pulse Lidar Daytime Performance: Simulations and Observations 683
Reagan, J.A., A.E. Galbraith and J.D. Spinhirne

2. Daytime Raman Lidar Measurements of Atmospheric Water Vapor NA
Whiteman, D., S.H. Melfi, G. Schwemmer, R. Ferrare and K. Evans

3. Lidar Studies of the Atmosphere NA
Carswell, A.I.

4. Daytime Temperature Measurements with a Sodium-Vapor Dispersive Faraday Filter in Lidar Receiver NA
Chen, H., M.A. White, D.A. Krueger and C.Y. Che

5. Rayleigh Lidar Observations During Arctic Summer Conditions 686
Thayer, J.P., N.B. Nielsen, R.B. Kerr and J. Noto

6. Daytime Tropospheric Water Vapor Profile Measurements by Raman Lidar 691
Bisson, S.E., and J.E.M. Goldsmith

7. A Differential Absorption Lidar System for Day and Night Measurements of Tropospheric Ozone NA
Langford, A.O., amd M.H. Proffitt

8. Spatial Properties of the Atmospheric Boundary Layer as Observed by Lidar NA
Cooper, D.I., and W. Eichinger

9. High Spectral Resolution, Low-Coherence Technique for Daytime Doppler Wind Measurements with Lidar 694
Fischer, K.W.

10. Field Calibration and Sensitivity Analysis of Coherent Infrared Differential Absorption Lidars 697
Richter, P.I., I. Peczeli, S. Borocz, L. Gazdag, J. Leonelli and T. Dolash

TPV -- Image Segmentation

1. Task-Specific Segmentation of Remote Sensing Images 700
Xuan, J., and T. Adah

2. Hybrid Image Segmentation for Earth Remote Sensing Data Analysis 703
Tilton, J.C.

3. Unsupervised Statistical Segmentation of Multispectral SAR Image Using Generalized Mixture Estimation 706
Marzouki, A., Y. Delignon and W. Pieczynski

4. Segmentation of SAR Images by Means of Gabor Filters Working at Different Spatial Resolution 709
Baraldi, A., and F. Parmiggiani

5. Markov Random Field Based Image Segmentation with Adaptive Neighborhoods to the Detection of Fine Structures in SAR Data 714
Smits, P.C., S. Dellepiane and S.B. Serpico

TPV *continued* -- Image Segmentation

6. Unsupervised Multiresolution Segmentation of Textured Image and Its Interpretation Using Fully Polarimetric SAR Data — NA
Liu, G., S. Huang and A. Torre

7. SAR Image Segementation by Mathematical Morphology and Texture Analysis — 717
Ogor, B., V. Haese-Coat and J. Ronsin

TPZ -- Microwave Remote Sensing of Vegetation

1. Analysis of Polarimetric Radar Backscatter of Moss-Bedded Conifers in Boreal Forest — NA
Saatchi, S.S., and M. Moghaddam

2. Scattering from Cultural Grass Canopies: A Phase Coherent Model — 720
Stiles, J.M., and K. Sarabandi

3. Scattering from Cultural Grass Canopies: Measured and Modeled Data — 723
Stiles, J.M., K. Sarabandi and F.T. Ulaby

4. Forest Backscatter Modeling: Simulation Versus Discrete Random Media Approach — 726
Lang, R.H., and R. Landry

5. Wave Scattering and Scene Image of Trees Generated by Lindenmayer Systems — 728
Zhang, G., and L. Tsang

6. Extraction of Biomass from SAR Data: A Realistic Approach — NA
Amar, F., M.S. Dawson, A.K. Fung and M.T. Manry

7. Estimation of Moisture Content of Forest Canopy and Floor From SAR Data, Part I: Volume Scattering Case — 730
Moghaddam, M., and S. Saatchi

8. Estimation of Moisture Content of Forest Canopy from SAR Data — NA
Moghaddam, M., and S. Saatchi

9. Investigating Correlations Between Radar Data and Characteristics of Mangrove Forests — 733
Proisy, C., E. Mougin and F. Fromard

10. Monitoring Vegetation Features with Multi-Temporal SAR Data — 736
Amodeo, G., P. de Matthaeis, P. Ferrazzoli, S. Paloscia, P. Pampaloni, G. Schiavon, S. Sigismondi and D. Solimini

TEAM -- Microwave Sensor Calibration

1. RADARSAT Calibration Studies NA
Lukowski, T.I., R.K. Hawkins, C. Cloutier, L.D. Teany, J. Iisaka and T. Sakurai-Amano

2. Near-Field Effect of Extended Targets on Absolute Calibration of Microwave Sensors 739
Wu, J., and J. Jiang

3. Calibration of an Airborne W-Band Polarimeter Using Drizzle and a Trihedral Corner Reflector 743
Galloway, J., A. Pazmany and R. McIntosh

4. Calibration of Bistatic Polarimetric Scatterometers 746
Daout, F., A. Khenchaf and J. Saillard

5. Accurate Antenna Reflector Loss Measurements for Radiometer Calibration Budget 749
Skou, N.

TEF -- Volume Scattering I

1. Electromagnetic Scattering Based on Pair Distribution Functions Retrieved from Planar Snow Sections 754
Zurk, L.M., L. Tsang, J. Shi and R.E. Davis

2. Modeling of Electromagnetic Wave Scattering from Time-Varying Snowcover 757
Ding, K.H., Y.E. Yang, S.E. Shih, J.A. Kong and R.E. Davis

3. Pulsed Beam Scattering from a Layer of Discrete Random Medium: With Applications to Spaceborne Weather Radars 760
Kilic, O., and R.H. Lang

4. TM Wave Scattering by Multiple Two-Dimensional Scatterers Buried Under One-Dimensional Multi-Layered Media 763
Cui, T.J., and W. Wiesbeck

5. TE Wave Scattering by Multiple Two-Dimensional Scatterers Buried Under One-Dimensional Multi-Layered Media 766
Cui, T.J., and W. Wiesbeck

TEH -- Subsurface Sensing and Material Properties I

1. High Resolution Imaging Techniques in Step-Frequency Subsurface Radars NA
Martinez-Madrid, J.J., J.R. Casar Corredera and G. de Miguel-Vela

2. Numerical Simulation of Scattering from Objects Embedded in a Medium with Randomly Rough Boundary 772
Tjuatja, S., Z.J. Li, A.K. Fung and C. Terre

3. A High-Resolution Imaging of Small Objects for Subsurface Radar Data Processing 775
Sato, T., T. Wakayama, K. Takemura and I. Kimura

4. Ground-Penetrating Radar Antenna Modeling 778
Haung, Z., K. Demarest and R. Plumb

5. 3-D SAR Imaging of Targets Obscured by Dielectric Media NA
Fortuny, J., and A.J. Sieber

TEM -- Land Cover: Innovation Classification Methods I

1. A Hierarchial Fuzzy Clustering Algorithm Using Pyramid Linking Data and Land-Cover Classification Experiments 781
Naka, M., T. Miyazaki and Y. Iwata

2. Fractal Concept to the Classification of Crop and Forest Type in IRS Data 784
Jeyarani, K., and K. Jayaram Hebbar

3. A Comparison of Three Neural Network Classifiers for Remote Sensing Classification 787
Gopal, S., and M. Fischer

4. A Decision Tree Classifier Design for High-Dimensional Data with Limited Training Samples 790
Tadjudin, S., and D.A. Landgrebe

5. Classification Accuracy Improvement and Delineation of Mixed Pixels Using Hierarchical Image Classification 793
Ediriwickrema, D.J., and S. Khorram

TEP -- SAR Interferometry

1. High Resolution 3-D SAR via Multi-Baseline Interferometry 796
Homer, J., D. Longstaff and G. Callaghan

2. Interferometric Analysis of Multifrequency and Multipolarisation SAR Data 799
Papathanassiou, K.P., and J.R. Moreira

3. Fusing L, C, and X Band Interferometric Phase Images by Means of Kalman Filtering Techniques NA
Loffeld, O., R. Kraemer, A. Hein, L. Dutra, G. Fornaro, R. Lanari, M. Migliaccio, J.R. Moreira, K.P. Papathanassiou, D. Riccio and M. Schwabisch

4. Quality Assessment of InSAR-Derived DEMs Generated with ERS Tandem Data 802
Schwabisch, M., M. Matschke,W. Knopfle and A. Roth

5. Atmospheric Heterogeneity: Effects on Multi-Pass Space Borne SAR Interferometry NA
Rossi, M., H. Vadon and A. Arnaud

TES -- Ocean Winds and Waves I

1. Surface Winds in a Midlatitutde Storm Seen by Satellites and Numerical Models 805
Katsaros, K.B., S. Dickinson, A. Bentamy, Y. Quilfen, S.S. Atakturk and R.A. Brown

2. The Comparison Between Active and Passive Microwave Data for Geophysical Ocean Surface Parameters Retrieval NA
Givri, J.R., S.S. Souffez and K. Bourbigot

3. Microwave Backscatter from the Sea Surface at Grazing Incidence 808
Buckley, J.R., and R.S. Johnson

4. Doppler-Radar-Radiometer Method of Near Sea Surface Wind Speed, Long Waves Roughness Degree, Water and Air Temperatatures Determination 811
Arakelian, A.K., and A.K. Hambaryan

5. An Offset between Scatterometer Directional Anisotropy and Wind Direction across the Equatorial Pacific Ocean 814
Rufenach, C.L.

TET -- Educational Initiatives

1. The Role of Remote Sensing in Training Activity of Tuscany Region 817
Cuomo, S., D. Giuli and G. Federici

2. Development of a Remote Sensing Core Curriculum Submitted for the Sessions on Educational Initiatives in Geoscience and Remote Sensing 820
Estes, J.E., and T. Foresman

3. NASA/JPL's Imaging Radar Outreach Program 823
Freeman, A., E. O'Leary, B. Chapman and J. Trimble

4. What Kind of Images Do I Need? What Is the Delay to Obtain Them? NA
Houzelle, S., P. Bellemain, J. Amalric and P. Herry

5. Geoscience Field Trainings in Russian Universities NA
Yutsis, V.V., and V.T. Trofimov

WAAM -- Land Cover: Tropical Forests and Vegetation

1. Discrimination of Africa's Vegetation Using Reconstructed ERS-1 Imagery 827
Hardin, P.J., D.G. Long and Q.P. Remund

2. The JERS-1 Amazon Multi-Season Mapping Study (JAMMS) 830
Freeman, A., B. Chapman and M. Alves

3. Forest Classification by Means of Pattern Recognition Method Applied to Scatterometer Data 833
Dechambre, M., and M. Bourdeau

4. Use of Polarisation Synthesis for Deforestation Studies Based on SIR-C/XSAR Data Analysis 836
Soyris, J.C., T. Le Toan, N. Floury, L. Thomasson, C.C.Hsu and J.A. Kong

5. Can the ERS-1 Scatterometer Be Used to Forecast the Inundation Extent in the Pantanal Wetland? 839
Wismann, V.R., and K. Boehnke

6. Forest Mapping and Monitoring in French Guiana: From Deforestation Mapping to a GIS for a Future National Park NA
Vedel, S., and D. Girou

7. Use of ERS-1 SAR Data for Forest Monitoring in South Sumatra 842
Le Toan, T., F. Ribbes, T. Hahn, N. Floury and U.R. Wasrin

8. Tropical Forest Monitoring Using Data from the ERS-1 Wind Scatterometer 845
Woodhouse, I.H., and D.H. Hoekman

9. Mapping and Monitoring the Mangrove: First Regional Map of Mangrove Using Remote Sensing and Geographic Information Systems NA
Girou, D., S. Vedel and O. Laroussinie

10. A Comparison of Reconstructed Ku-Band Scatterometry, C-Band Scatteromentry, and SSM/I Imagery for Tropical Vegetation Classification 848
Hardin, P.J., D.G. Long, Q.P. Remund and D.R. Dawn

WAAA -- Sensors and Remote Methods for Detecting Environmental Contaminants

1. Advances in Fiber Optic Based Laser-Induced Flourescence Sensors for In Situ Measurement of Petroleum Hydrocarbons in Soils — NA
Lieberman, S.H., and D.S. Knowles

2. Determination of Contaminants in the Enviroment Using Instrumentation Based on Laser-Induced Breakdown Spectroscopy — NA
Cremers, D.A., and M.J. Ferris

3. Trace Detection of Environmental Contaminants by Laser Photogragmentation / Fragment Detection Spectrometry — 851
Sausa, R.C.

4. Detection of Environmental Contaminants by Time Resolved Laser Induced Breakdown Spectroscopy Technique — 854
Arca, G., A. Ciucci, V. Palleschi, S. Rastelli and E. Tognoni

5. Influences on Detectability of Heavy Metals in Soils by Laser-Induced Breakdown Spectroscopy — 857
Alexander, D.R., D.E. Poulain, M.S. Khlif and E.R. Cespedes

6. Development and Testing of Electrochemical Sensors for Rapid Detection of Explosive Contaminants in Soils — NA
Cespedes, E.R.

7. Commercialization of the Laser Spark Continuous Metal Emissions Montor — NA
French, N.B.

8. Measurements of the Radar Backscattering Over Different Oceanic Surface Films During the SIR-C/X-SAR Campaigns — 860
Gade, M., W. Alpers , M. Bao and H. Huehnerfuss

9. Airborne CASI Imaging Spectrometer Used in Monitoring of Vegetation Damage in the Pasvik Area — NA
Tommervik, H., I. Lauknes and B. Johansen

10. Preliminary Evaluation of a Millimeter-Wave System for Air Pollution Monitoring — 863
Nadimi, S.A., and J.W. Bredow

WACP -- Microwave Synthetic Aperture Interferometric Radiometry

1. Two-Dimensional Aperture Synthesis Radiometers in a Low Earth Orbit Mission and Instrument Analysis — 866
Kraft, U.R.

2. Integration of MIRAS Breadboard and Future Activities — 869
Martin-Neira, M. , J.M Goutoule, A. Knight, J. Claude, J. Bara, A. Camps, F. Torres, I. Corbella, A. Lannes, E. Anterrieu, V. Laursen and N. Skou

3. Design and Implementation of the MIRAS Digital Correlator — 872
Batz, O., U. Kraft,W. Lindemer and H. Reichel

4. Characteristics of the Baseline Off-Nadir Angle of Supersynthesis Radiometer — 875
Komiyama, K., and Y. Kato

5. Icestar: Next Major Advance in Sea Ice Remote Sensing — NA
Cavalieri, D.J., L.L. Thompson, D.M. Le Vine and J.A. Weinman

6. Calibration of Synthetic Aperture Radiometers in Space: Antenna Effects 878
Le Vine, D.M., and D.E. Weissman

7. RADSAR Synthetic Aperture Radiometer Test Results NA
Edelsohn, C.R.

8. Development of a 37GHz Synthetic Apeture Microwave Radiometer NA
Goodberlet, M.A., C.S. Ruf and C.T. Swift

9. Application of Sparse Phased Arrays to Millimeter-Wave Radiometry 881
Loveberg, J., S. Clark, D. Wilkner and B. Wallace

10. Radiometer System with Cross-Polarization and Correlation of the Channels of Observation 885
Arakelian, K.A., and A.K. Arakelian

WAED -- Remote Sensing of Littoral Submesoscale Processes I

1. Spatial Variations of Microwave Backscatter Magnitude and Angular Distribution: Response of the Short Waves to Wind and Surface Changes 888
Weissman, D.E., W.J. Plant, W.C. Keller and V. Hesany

2. Seagulls and SAR: Atmospheric Convection Effects in SAR Images over the Ocean 891
Vesecky, J.F., F.L. Ludwig, J.M. Daida, N. Chinchilla and G. Kimbreau

3. Evidence of a Land Breeze in an ERS-1 SAR Image of the New Jersey Coastline 893
Sikora, T.D., D.R. Thompson, G.S. Young and N.S. Winstead

4. Atmospheric Signatuares in SAR Imagery 896
Beal, R.C., D.R. Thompson, G.S. Young, H.N. Shire and T.D. Sikora

5. SAR Response to Spatially and Temporally Varying Wind Fields 899
Lyzenga, D.R.

6. Synthetic Aperture Radar Imagery of the Coastal Ocean Near Cape Hatteras, NC NA
Marmorino, G.O., D.R. Lyzenga, J.A.C. Kaiser and C.L. Trump

7. An End-To-End Simulation of Radar Signatures from the HI-RES 1 Rip Feature 902
Chubb, S.R., A.L. Cooper, R.W. Jansen and C.Y Shen

8. Low Grazing Angle Dual Polarized Doppler Radar Measurements of Oceanic Fronts 905
Allan, N., D.B. Trizna and D.J. McLaughlin

9. Effects of Wave Breaking on SAR Signatures Observed Near the Edge of the Gulf Stream 908
Lyzenga, D.R.

10. Issues Surrounding Surfactant Effects Upon Radar Imagery of Convergent Ocean Surface Flows with Application to the Hi-Res I Rip Feature 911
Cooper, A.L., S.R. Chubb and J.A.C. Kaiser

WAES -- Educational Initiatives I

1. Satellite Remote Sensing of the Environment: New Opportunities for the Educator NA
Winokur, R.S.

2. An Overview of Remote Sensing Education Projects Sponsored by the NASA Space Grant Program 914
Wersinger, J.M., and E. Ward

3. Mission to Planet Earth On-Line Earth Systems Science Course 917
Blurton, C., and S. McGee

4. Remote Sensing Data for Educational Purposes: The Policy of the European Space Agency and Its Achievements with the Meteosat Data NA
Le Ber, J.

5. Earth Observation Satellite Date and its Application to Environmental Education 920
Goto, A.

6. Applications of Satellite Imagery, Visualizations and Remote Sensing in Environmental/Science: An Earth Systems Science Approach 922
Moore, J.D.

7. Do We Really Understand What We See? Cognitive Issues in Remote-Sensing From the Perspective of a Scientist and an Educator 925
Barstow, D., and E. Frost

8. National Weather Service Portable Multimedia Presentations to Teachers and Students NA
Gird, R., and J. Von Ahn

9. Interdisciplinary Earth System Science and Earth Observations From the International Space Station: Partners in Education 929
Willis, K.J., D.L. Amsbury, C.D. McLaughlin and T. Miewald

10. Applied Environmental Problem-Solving Using Remote Sensing Technology: A Summer Practicum for Undergraduate Faculty NA
Panah, A.A.

WAF -- Sea Ice Remote Sensing (Models, Techniques and Applications) I

1. Global Sea Ice Monitoring from Microwave Satellites 932
Johannessen, O.M., M.W. Miles and E. Bjorgo

2. Sea Ice Identification Using Dual-Polarized Ku-Band Scatterometer Data 935
Yueh, S.H., R. Kowk, S.H. Lou and W.Y. Tsai

3. Temporal Mixture Analysis of SMMR Sea Ice Concentrations 938
Piwowar, J.M., D.R. Peddle and E.F. LeDrew

4. Polarimetric Backscattering at 23 cm Wavelength from Antarctic Lead Ice and Estimation of Ice Thickness 941
Winebrenner, D.P.

5. Characterization of Ice in the Chukchi Sea at the Start of the Growing Season Using Satellite SAR 944
Onstott, R.G.

6. Bistatic Microwave Investigations of Sea Ice-Like Media 947
May, G.C., J.W. Bredow, J. Juying, S.A. Nadimi and A.K. Fung

7. Validation of a Sea Ice Model Using Forward Simulation of ERS-1 SAR Data: A Case Study in the Beaufort Sea 950
Heinrichs, J., J. Maslanik and K. Steffen

8. The Influence of Cloud Cover on the Microwave Scattering Coefficient (σ°) of First-Year and Multiyear Sea Ice 953
Barber, D.G., and A. Thomas

9. Comparison of Aircraft and DMSP SSM/I Passive Microwave Measurements over the Bering Sea in April 1995 956
Cavalieri, D.J., D.K. Hall and J.R. Wang

10. Multi-Channel Algorithm Approach to Determining Melt for Arctic Sea Ice Using Passive Microwave Data 959
Anderson, M.R.

WAP -- SAR Interferometry and Geoscience Applications

1. Differential SAR Interferometry for Detection of Small Terrain Movements NA
Cavallo, A., D. Tarchi and A.J. Sieber

2. Satellite Radar Measurements of Land Subsidence 963
van Halsema, D., and M.W.A. van der Kooij

3. Flood Monitoring Using ERS-1 SAR Interferometry Coherence Maps 966
Geudtner, D., R. Winter and P.W. Vachon

4. Determination of Vegetation Height from SAR Interferometry: A Theoretical Study 969
Sarabandi, K.

5. Application of Interferometry to Studies of Glacier Dynamics 972
Mohr, J.J., and S.N. Madsen

6. Relating Forest Paramters to Interferometric Data 975
Floury, N., T. Le Toan and J.C. Souyris

7. Estimating Vegetation and Surface Topographic Parameters from Multibaseline Radar Interferometry 978
Treuhaft, R., M. Moghaddam, J. van Zyl and K. Sarabandi

8. On the Detection of Spatially Varying Current Fields at the Ocean Surface by Along-Track Interferometric Synthetic Aperture Radar 981
Romeiser, R., and D.R. Thompson

9. Study of Integration Time Effects on Coherent Radar Imagery of the Sea Surface 984
Moller, D., S. Frasier and R.E. McIntosh

10. Recent Earth Crust Movement of the Black Sea and Adjacent Areas: Application of Remote Sensing Data NA
Yutsis, V.V., V.G. Talitsky and A.F. Vasilevsky

WAT -- Lidar/Spectrometry

1. Daytime Performance Simulation of PN-Code Modulated Micro-Joule Lidar 987
Schoening, V.L., J.A. Reagan and P.A. Delaney

2. Application of Wideband Signals to Airborne Laser Bathymetry 990
Pillai, S.R., and A. Antoniou

3. Low Light-Level IR Detectors for Use in Lidar Systems 993
Mayer, T.S., and T.J. Kane

4. Scanning for a Satellite Radar Wind Sounder (RAWS) 996
Moore, R.K., B. Beh and S. Song

5. Feasibility Study of a Compact Low Cost Correlation LIDAR Using a Pseudo Noise Modulated Diode Laser and an APD in the Current Mode 999
Bundschuh, B.O., D. Schneider and M. Grindel

6. Remote Sensing Spectrometry of a Temperate Deciduous Forest -- A Modeling Approach 1002
Demarez, V., J.P. Gastellu-Etchegorry, F. Zagolski, E. Mougin, G. Marty, E. Dufrene and V. Le Dantec

7. A Revised Measurement Methodology for Spectral Optical Properties of Conifer Needles 1005
Middleton, E.E., S.S. Chan, M.A. Mesarch and E.A. Walter-Shea

8. Airborne Imaging Spectrometry in National Forest Inventory 1010
Makisara, K., and E. Tomppo

9. An Approach for Obtaining Best Estimates of Spectral Optical Depths and Calibration Intercepts from Solar Radiometer Data Corrupted by Temporal Variations 1014
Erxleben, W.H., and J.A. Reagan

10. Estimation of Abundances in Two-Component Mineral Mixtures Using Mid-Infrared Laser Reflectance Ratios 1017
Narayanan, R.M., K.K. Warner and R.F. Diffendal, Jr.

WAV -- Data Compression in Remote Sensing

1. Near Lossless Transform Coding of Multispectral Images 1020
Tescher, A.G., J.T. Reagan and J. A. Saghri

2. Progressive Model-Based VQ for Image Data Archival and Distribution 1023
Manohar, M., and J.C. Tilton

3. Effect of Compression on Physical Parameters Derived from Polar Ice Radiances 1026
St. Germain, K.M., and K. Sayood

4. Lossless Seismic Data Compression Using Adaptive Linear Prediction 1029
Mandyam, G., N. Magotra and W. McCoy

5. Performance of An Enhanced DCT Compression System for Space Applications 1032
Yeh, P.S., W.H. Miller and S. Hou

6. End-to-End System Consideration of the Galileo Image Compression System 1035
Cheung, K., K. Tong and M. Belongie

7. A Bounded Distortion Compression Scheme for Hyper-Spectral Image Data 1039
Memon, N.D.

8. Lossless Image Compression Based on a Generalized Recursive Interpolative DPCM 1042
Aiazzi, B., P.S. Alba, L. Alparone and S. Baronti

9. Image Sequence Compression Using Adaptive Wavelet Packet 1045
Sarita, S., and P. Nagabhushan

10. Using ATM Networks for Processing Global Earth Data 1048
Kess, B.L., P.R. Romig III, S.E. Reichenbach and A. Samal

WAZ -- Soil Moisture I

1. Applications of Passive Microwave Observations of Surface Soil Moisture 1051
Schmugge, T.

2. Spatial and Temporal Trends in Land Surface Moisture and Temperature Observable Using Data from the Nimbus-7 Microwave Radiometer 1054
Njoku, E.G., and B.W. Rague

3. Application of Microwave Remotely Sensed Surface Soil Moisture for Estimation of Sub-Surface Soil Hydraulic Properties 1058
Engman, E.T., N.M. Mattikalli, L.R. Ahuja and T.J. Jackson

4. Investigation of the Accuracy of Soil Moisture Inversion Using Microwave Data and Its Impact on Watershed Hydrological Modeling 1061
O'Neill, P.E., A.Y. Hsu, T.J. Jackson, E.F. Wood and M. Zion

5. Surface Soil Moisture Estimation with Radarsat: Early Results NA
Brisco, B., R.J. Brown and T.J. Pultz

6. SIR-C/X-SAR as a Bridge to Soil Moisture Estimation Using Current and Future Operational Satellite Radars 1064
Jackson, T.J., T.L. Li, E.F. Wood, A. Hsu, P.E. O'Neill and E.T. Engman

7. Backscattering over Bare Soils: Measurements and Simulations Using SIRC/XSAR and ERASME 1994 Data over Orgeval 1067
Zribi, M., Taconet, O., S. Le Hegarat-Mascle, D. Vidal-Madjar, C. Emblanch, C. Loumagne and M. Normand

8. Polarimetric Backscattering Measurements of Herbaceous Vegetation: A Sensitivity Study for Soil Moisture Retrieval 1070
Chiu, T.C., K. Sarabandi and F.T. Ulaby

9. Comparison of Spatial Statistics of SAR-Derived and In-SITU Soil Moisture Estimates 1073
Hirsave, P.P., R.M. Narayanan, B.T. Tracy , B.L. Gwilliam R.L. Bolus, T. Pangburn and H.A. McKim

10. Soil Moisture and Temperature Determination by Recursive Assimilation of Multifrequency Observations Using Simplified Models of Soil Heat and Moisture Flow and Emission 1076
Galantowicz, J.F., and D. Entekhabi

WPAM -- Land Cover: Radar for Forest Mapping

1. Radar Backscatter Components from Ponderosa Pine Forests 1077
Wang, Y., and F.W. Davis

2. The Applications of Space Born SAR on Forestry NA
Zeng, Q., J. Jiao, Z. Li and X. Che

3. The Suitability of Multifrequency, Multipolarimetric and Multitemporal Radar Data for Forest Monitoring 1080
Haas, A., and B. Forster

4. Sensitivity of Modeled C-Band from Loblolly Pine Forest Backscatter to Soil Surface Roughness and Moisture 1083
Wang, Y., J.L. Day and F.W. Davis

5. Multifrequency and Polarimetric Analysis of Forests with SIR-C/X-SAR Data 1086
Seifert, F.M., H. Kietzmann and M. Zink

6. Optimization of a Scanning Radar Altimeter for Forest Inventory: A Simulation Method 1089
Hyyppa, J., and M. Hallikainen

7. Temporal Stability of Northern Forest Biophysical Retrievals Using SIR-C/X-SAR 1092
Dobson, M.C., L.E. Pierce, K.M. Bergen and F.T. Ulaby

8. Regional Stability of an ERS/JERS-1 Classifier 1093
Kellndorfer, J.M., M.C. Dobson and F.T. Ulaby

9. Radar Modeling of Forest Spatial Structure 1096
Sun, G., and K.J. Ranson

10. Comparative Analysis of Forests Types Classification Methods Using SIR-C Multifrequency, Multipolarization and Repeated Orbits Interferometry Data NA
Zaitsev, V.V., and A.I. Zakharov

WPAA -- Weather Information Systems

1. Knowledge Based System for Weather Information Processing and Forecasting 1099
Siddiqui, K.J.

2. A Database Program to Archive and Analyze Current Weather Data 1102
Parkin, S.H. and J.P. Refling

3. Neural Network-Based Cloud Detection/Classification Using Textural and Spectral Features 1105
Azimi-Sadjadi, M.R., M.A. Shaikh, B. Tian , K.E. Eis and D. Reinke

4. An FFT-Based Algorithm for Computation of Gabor Transform with its Application to Cloud Detection/ Classification 1108
Tian, B., M.R. Azimi-Sadjadi, M.A. Shaikh and K.E. Eis

5. A Prototype Sea Ice Mapping System Using a Geographical Information System and Expert Knowledge 1111
Williams, R.N., and J. Hartnett

6. Campaign of Validation of Aerosol Optical Depth from Satellites in the Canary Islands Zone NA
Exposito, F.J., J.P. Diaz, M. Arbelo, J.C. Guerra and F. Herrera

7. A Split-Window Equation with Variable Coefficients to Obtain SST in Midlatitudes NA
Arbelo, M., V. Caselles, F.J. Exposito and F. Herrera

8. Pluviometry and Vegetation Monitoring in the Canary Island Zone Using the NOAA Advanced Very High Resolution Radiometer NA
Hernandez, P.A., M. Arbelo, F.J. Exposito and F. Herrera

9. Combined Use of Radar and Satellite Information for Precipitation Estimation in Hungary 1114
Csiszar, I., and J. Kerenyi

10. DSP Architecture for Dual Waveband Meteorological Data Processing NA
Malinovski, V.

WPCP -- Polarimetric Radiometry

1. The AEOLIS Program: Prospects for Future Low-Cost, Space-Borne Vector Wind Sensors 1117
Van Woert, M.L.

2. Polarimetric Scanning Radiometer for Airborne Microwave Imaging Studies 1120
Piepmeier, J.R., and A.J. Gasiewski

3. Ocean Surface Wind Direction Retrievals Using Microwave Polarimetric Radiometer Data 1123
Gaiserl, P.W., P. Chang and L. Li

4. Polarimetric Observation of Ocean Internal Waves by Microwave Radiometers During the Coastal Ocean Probing Experiment 1126
Irisov, V.G., and Yu.G. Trokhimovski

5. Broadband Phenomena in Oceanic Passive Wind Direction Signatures: The Sensitivity to Wave Asymmetry, Foam, and Atmospheric Profile 1129
Kunkee, D.B., and A.J. Gasiewski

6. A Numerical Study of Ocean Thermal Emission NA
Johnson, J.T., R.T. Shin, J.A. Kong, L. Tsang and K. Pak

7. A Comparison of Sea Emission Between Experimental Data and Model Predictions NA
Chen, K.S., S.J. Lai, A.K. Fung and S.Y. Yueh

8. Modelling of Wind Direction Signals in Polarimetric Sea Surface Brightness Temperatures 1132
Yueh, S.H., W.J. Wilson and F.K. Li

9. The Atmosphere Influence on Sea-Surface Polarized Microwave Emission 1135
Pospelov, M.N.

10. Oceanic Wind Vector Determination Using a Dual-Frequency Microwave Airborne Radiometer - Theory and Experiment 1138
Jacobson, M.D., W.J. Emery and E.R. Westwater

WPED -- SAR Applications for Oceanography

1. A PC-Based Remote Sensing System for Detection and Classification of Oceanic Fronts 1141
Askari, F., E. Malaret, D. Lyzenga, M. Collins, T. Donato, A. Skoelv, T. Jenserud and C. Brownsword

2. A Lightweight Spectrasat Concept for Global Ocean Wave Monitoring 1143
Beal, R.C., D.Y. Kusneirkeiwicz, J.L. MacArthur, F.M. Monaldo and S.F. Oden

WPED *continued* -- SAR Applications for Oceanography

3. Using the CCRS Along Track InSAR to Measure and Interpret Ocean Surface Currents 1146
Campbell, J.W.M., A.L. Gray, J.H. Clark, J. Gower and K.E. Mattar

4. Comparison of Wave Parameters Measured from the SIR-C On-Board Processor with WAM Predictions in the Southern Ocean 1149
Monaldo, F.M.

5. Estimation of Thermocline Depths From SAR Imagery and a Two Layer Density Model 1152
Porter, D.L., and D.R. Thompson

6. Validation of SAR Ocean Wave Measurements: ERS-1 and CV-580 Cross Spectra and CV-580 Along-Track InSAR 1155
Vachon, P.W., C. Bjerkelund, J. Buckley, J. Campbell, F.W. Dobson, A.L. Gray, H. Johnsen and R. Lalbeharry

7. Coast Watch - 95: ERS - 1/2 SAR Applications of Mesoscale Upper Ocean and Atmospheric Boundary Layer Process off the Coast of Norway 1158
Johannessen, O.M., J.A. Johannessen, A.D. Jenkins, K. Davidson, D.R. Lyzenga, R Shuchman, P. Samuel, H.A. Espedal, J. Knulst, E. Dano and M. Reistad

8. Evaluation of RADARSAT Synthetic Aperture Radar Data for Ocean Wave Measurements and Ship Detection NA
Olsen, R.B., P. Bugden, P. Hoyt, M.Henschel and M.R. Lewis

9. The Imaging of Submarine Sandwaves with Multi-Band SAR NA
Vogelzang, J.

10. Ocean Surface Slope Measurement Using Polarimetric SAR 1162
Lee, J.S. and D.L. Schuler

WPES -- Educational Initiatives II

1. Studying the Earth's Environment From Space - A Curriculum Workshop 1165
Alfultis, M.A.

2. NASA-NOAA Summer School for Earth Science - Processes of Global Change and Global Change Workshop for Teachers NA
Syvertson, M., S. Ride, D. McCleese and W. Mohling

3. Mission: Arkansas - Curriculum Enhancement and Dissemination of K-12 Science Mathematics Using Space Based Data and Geographic Information Systems NA
Hehr, L.H.

4. Constructing Earth System Science Learning Through Multidisciplinary Studies of Global Change 1166
Fortner, R.W., and V.J. Mayer

5. A CD-ROM Study Package on Current Forest Issues for Use in Secondary School Science Classes 1169
Hassol, S., and C.J. Tucker

6. Using Distributed Multimedia Systems to Enable Earth Systems Education in the Earth System Science Community NA
Keeler, M.,and F. Mahootian

7. Our Role in the Earth System: One K-12 School District's Science Education Initiative 1172
Lindgren, P.D.

8. Earth System Science Education: A Continuing Collaboration 1175
Johnson, D.R., M. Ruzek and M. Kalb

9. OMSI-NSF Young Scholars Research Participation Program, Oregon Museum of Science and Industry 1178
Gottfried, J.

10. Alaska SAR Facility Education Outreach 1181
Sandberg, D., and F. Carsey

WPF -- Research Progress Under the ONR Sea Ice Electromagnetics ARI

1. Observations of Sea Ice Physical Properties During the Sea Ice Electromagnetics Initiative 1184
Gow, A.J., and D.K. Perovich

2. Physical and Electrical Characteristics of Snow on Sea Ice: Implications for Forward Scattering Model Development 1187
Barber, D.G., S.D. Drobot and J. Iacozza

3. Sea Ice Polarimetric Backscatter Signatures at C Band 1190
Nghiem, S.V., R. Kwok, S.H. Yueh, J.A. Kong, A.J. Gow, D.K. Perovich, S. Martin and R. Drucker

4. Polarimetric Properties of Simulated Sea Ice with Special Focus on Property Retrieval and Important Scattering Processes 1193
Onstott, R.G.

5. Ultra-Wideband Radar Measurements of over Bare and Snow-Covered Saline Ice 1196
Gogineni, S.P., P. Kanagaratnam and K. Jezek

6. Microwave and Thermal Infrared Emission from Young Sea Ice and Pancake Ice 1199
Grenfell, T.C.

7. Modeling of Ice Thickness Effect and Its Application to Data Interpretation 1202
Fung, A.K, and R.G. Onstott

8. Electromagnetic Inversion of the Physical Properties of Sea Ice NA
Golden, K.M.

9. Inversion of Wideband Microwave Reflectivity to Estimate the Thickness of Arctic Lead-like Sea Ice 1205
Winebrenner, D.P., and J. Sylvester

10. Thickness Retrieval Using Time Series Electromagnetic Measurements of Laboratory Grown Saline Ice 1208
Shih, S.E., K.H. Ding, S.V. Nghiem, C.C. Hsu, J.A. Kong and A.K. Jordan

WPP -- SAR Processor Systems and Algorithms

1. ASF SAR Processing System Performance Overview NA
Jin, M., K. Leung, M. Chen and A. Chu

2. Vexcel Corporations' SAR Processing Ground Station: An Overview 1211
Compton, M., and R.E. Carande

3. Azimuth and Range Scaling for SAR and ScanSAR Processing 1214
Moreira, A., R. Scheiber and J. Mittermayer

WPP *continued* -- SAR Processor Systems and Algorithms

4. High Precision Processing of SIR-C ScanSAR Data 1217
Mittermayer, J., A. Moreira, G. Davidson, R. Bamler and Y.L. Desnos

5. A Comparison of the Range-Doppler and Chirp Scaling Algorithms with Reference to RADARSAT 1221
Hughes, W., K.A. Gault and J. Princz

6. Comparison of Medium Resolution Algorithms for Spacecraft On-Board SAR Image Generation 1224
Vidal, A., and J. Rosello

7. Registration SAR Images Using the Chrip Scaling Algorithm 1227
Fernandes, D., G. Waller and J. R. Moreira

8. Autofocus of Wide Azimuth Angle SAR Images by Contrast Optimisation 1230
Berizzi, F., G. Corsini, M. Diani and M. Veltroni

9. High Frequency Phase Errors in SAR Imagery and Implications for Autofocus 1233
Marechal, N.

10. Phase Errors Compensation in SAR Imaging 1241
Isernia, T., V. Pascazio, R. Pierri and G. Schirinzi

WPT -- Clouds, Aerosols and Boundary Layer

1. Cirrus Cloud Detection by Micro Pulse Lidar: Algorithm Development and Testing 1244
Galbraith, A.E., J.A. Reagan and J.D. Spinhirne

2. Cloud Masking with Satellite Infrared Images over Polar Oceans 1247
Schlueter, N., and T. Markus

3. Cloud Corrections for Satellite Images NA
Peltoniemi, J.I.

4. The Estimation of Aerosol Models by the Reflectance Analysis of the Airborne POLDER Data 1250
Yamazaki, A., K. Ueda, Y. Kawata and T. Kusaka

5. Particle Size Distributions and Extinction Determined by a Unique Bistatic Lidar Technique 1253
Stevens, T.D., and C.R. Philbrick

6. Remote Sensing of the Marine Atmospheric Boundary Layer and Oean Surface Winds: Observations from the LITE Correlative Flights 1257
Palm, S.P., G. Schwemmer, D. Vandemark, D. Hines and S.H. Melfi

7. Remote Measurement of Coastal Marine Atmospheric Boundary Layer (MABL) Features 1260
Jordan, M.S., C.H. Wash and K.L. Davidson

8. Estimation of the Ocean/Atmosphere Boundary Layer Height of Water Vapor from Space 1263
Ruf, C.S., and S.E. Beus

9. Rain Measurement with SIR-C/X-SAR 1266
Moore, R.K., A. Mogili, Y. Fang, B. Beh and A. Ahamad

10. Investigations of Atmospheric Boundary Layer by Using 5-Millimeter Radiometer NA
Kadygrov, E.N., and A.V. Troitsky

WPV -- Calibration and Correction Algorithms for Radiometric and Reflectance Measures

1. Artifact Correction and Absolute Radiometric Calibration Techniques Employed in the Landsat 7 Image Assessment System 1270
Boncyk, W.C., B.L. Markham, J.L. Barker and D.L. Helder

2. Landsat-7 Enhanced Thematic Mapper Plus In-Flight Radiometric Calibration 1273
Markham, B.L., J.L. Barkerm,W.C. Boncyk, E. Kaita and D.L. Helder

3. Short Term Calibration of Landsat TM: Recent Findings and Suggested Techniques 1276
Helder, D., W. Boncyk, J.L. Barker and B.L. Markham

4. Comparison of Scene-Dependent Radiometric Validation Methodologies for EOS-AM1 MODIS Level-1 Products NA
Barker, J.L., and S.G. Ungar

5. In-Flight Radiometric Calibration Plans for the Earth Observing System -- Multi-Angle Imaging Spectroradiometer 1279
Bruegge, C., R.Woodhouse, and D. Diner

6. Cross-Calibration of Two Small Footprint Sensors 1283
Gustafson-Bold, C.L., and K.J. Thome

7. Evaluation of The Aerosol Scattering Phase Function from PGAMS Observation of Sky Path Radiance 1286
Schiller, S., and J. Luvall

8. RADARSAT CALIBRATION: The Operational System and Initial Results 1290
Srivastava, S.K., T.I. Lukowski, R.K. Hawkins, C. Cloutier, L.D. Teany, N.W. Shepherd, R.B. Gray, A.P. Luscombe and R. Banik

9. Calibration Methods and Results for the Advanced Solid-State Array Spectroradiometer (ASAS) NA
Dabney, P.W., M.R. Tierney, J.R. Irons,W.M. Kovalick, M.C. Bur and C.A. Russell

10. Calibration of the AVHRR Thermal Infrared Channels: Determining the Temperature of the Internal Calibration Target 1293
Steyn-Ross, D.A., M.L. Steyn-Ross and S. Clift

WPZ -- Soil Moisture II

1. The Influence of Soil Moisture on Temporal CVV- and LHH- Signatures from Vegetated Fields - Summary of the DLR E-SAR Cleopatra Campaign NA
Schmullius, C., and J. Nithack

2. A Modified IEM Model for Scattering from Soil Surfaces with Application to Soil Moisture Sensing 1297
Fung, A.K., M.S. Dawson, K.S. Chen, A.Y. Hsu, E.T. Engman, P.O. O'Neill and J. Wang

3. Soil Moisture Retreival Using the Danish L- & C-Band Polarimetric SAR 1300
Ji, J., P. van der Keur, A. Thomsen and H. Skriver

4. Remote Sensing of Soil Moisture Using EMAC ESAR Data 1303
Su, Z., P.A. Troch and F.P. De Troch

5. Use of Polariztion Synthesis From Polarimetric SAR Data for Roughness Estimation over Bare Fields 1306
Mattia, F., J.C. Souyris, T. Le Toan, G. De Carolis, N. Floury, F. Posa and G. Pasquariello

6. Microwave Remote Sensing of Land Surfaces Soil Moisture at Global Hydrology and Climate Center 1309
Wu, S.T.S.

WPZ *continued* -- Soil Moisture II

7. Soil Hydraulic Characterization Derived from Landsat TM-5 Data 1312
Bresci, E., and I. Becchi

8. An Optical Reflectance Technique for Soil Moisture Measurement - Part I: Theory, Description and Application 1315
Belisle, W.R., A. Sharma and T.L. Coleman

9. Accuracy of Soil Moisture Determination by Means of Passive Microwave Remote Sensing Method: Modeling and Experiments 1320
Liberman, B., and A. Milshin

10. Microwave Dielectric Behavior of Wet Soils in Region of Transition Moisture 1323
Belyaeva, T.A., and Yu.M. Sosnovsky

WEAM -- Infrared and Optical Remote Sensing of the Ocean Surface

1. Ocean Skin Temperature Modulation by Swell Waves NA
G.A. Wick, Hesany and A.T. Jessup

2. Monitoring of the Sea Surface Thermal Patterns in a Marginal Sea Affected by an Ocean NA
Nakamura, S.

3. Sensitivity Analysis of a Coupled Optical Remote Sensing and Three Dimensional Hydrodynamic Model NA
Bostater, C., and T. McNally

4. Ocean Ripple Statistics Measured with a Scanning-Laser Glint Sensor 1328
Shaw, J.A., and J.H. Churnside

5. The Remote Technique of Sea Surface Waves by Optical Sensors 1331
Titov, V.I., and E.M. Zuykova

WEF -- Volume Scattering II

1. Radio Wave Propagation Along Mixed Paths Through Four-Layered Model of Rain Forest: A Closed Form Solution NA
Li, L.W., T.S. Yeo, P.S. Kooi and M.S. Leong

2. A Coherent Scattering Model for Forest Canopies Based on Monte Carlo Simulation of Fractal Generated Trees 1334
Lin, Y.C., and K. Sarabandi

3. A Numerically Derived Electromagnetic Scattering Model for Grass Grain Heads 1337
Siqueira, P., and K. Sarabandi

4. Electromagnetic Scattering by Multiple Three-Dimensional Scatteres Buried Under One-Dimensional Multi-Layered Media 1340
Cui, T.J., and W. Wiesbeck

5. Electromagnetic Wave Transmission in Randomly Distributed Inhomogeneous Spherical Particles NA
Osharin, A.M.

WEH -- Subsurface Sensing and Material Properties II

1. Wave Reflection From a Target Immersed into Disordered Medium NA
Kanzieper, E., and V. Freilikher

2. The Modified Rayleigh-Gans Approach and Scattering Waves 1343
Yildirim, O.

3. An Inverse Algorithm for Integral Equation Formaultion of Dielectric Loaded Cavities 1346
Sabet, K.F., K. Sarabandi, J.G. Yook and L.P.B. Katehi

4. Method for Retrieval of Media Structural Parameters from Frequency Dependence of Transmission Coefficient NA
Boyarskii, D.A.

5. Application of SIR-C L/C/X-Band Radar Data for Mineral Exploration Experiment in Hwanggangni Mining District, Korea NA
Jiang, W.W., C.S. So, Y. Yamaguchi, W.M. Moon and S.K. Choi

WEM -- Remote Sensing Missions and Programs

1. Early Images from the RADARSAT Synthetic Aperture Radar 1352
Luscombe, A.P., R. Gray, N. Shepherd, S. Srivastava, D. Meier and W. Jeffries

2. The Development of the ENVISAT-1 Advanced Synthetic Aperture Radar 1355
Mancini, P., J.L. Suchall, Y.L. Desnos, R. Torres, J. Guijarro and G. Graf

3. Processing and Validation of the ERS-1 Radar Altimeter Data at the Italian PAF NA
Celani, C., A. Bartoloni, G. Milillo and F. Nirchio

4. An Alaska SAR Overview in the RADARSAT Era 1358
Cuddy, D., and K. Leung

5. Cassini Radar Investigation of Titan NA
Wall, S., C. Elachi and L. Roth

WEP -- Active and Passive Remote Sensing of Precipitation

1. Validation and Ground Truth for TRMM Precipitation Radar Using the MU Radar 1361
Sato, T., T. Teraoka and I. Kimura

2. Preliminary Results of Ground-Based Rain Measurements with a Dual-Frequency Multiparameter Radar-Radiometer 1364
Horie, H., R. Meneghini and T. Iguchi

3. Active and Passive Microwave for Rainfall Monitoring 1367
Nativi, S., L. Baldini, D. Giuli and P. Mazetti

4. Study of Potential of a Profile-Based Algorithm for Precipitation Retreival from MIMR NA
Panegrossi, G., S. Dietrich, F.S. Marzano and A. Mugnai

5. Investigation of Multifrequency Multipolarisation Radar Signatures of Rain Cells, Derived From SIR-C/X-SAR Data 1370
Melsheimer, C., W. Alpers and M. Bao

WESF -- Land Cover: Innovative Classification Methods II

1. Mathematical Morphology, Urban Change, Image-Oriented Geographic Information Systems 1373
Maupin, P., and B. Solaiman

2. Fuzzy Classification Techniques for Urban Area Recognition 1376
Console, E., and M.C. Mouchot

3. Robust Mixed Pixel Classification Using the Hypothesis Testing Hough Transform 1379
Bosdogianni, P., M. Petrou and J. Kittler

4. Improving Automated Land Cover Mapping by Identifying and Eliminating Mislabeled Observations from Training Data 1382
Brodley, C.E., and M.A. Friedl

5. An Automatic Technique for Detecting Land-Cover Transitions NA
Serpico, S.B., L. Bruzzone, F. Roli and M.A. Gomarasca

WES -- Ocean Waves and Winds II

1. A Not Pointwise Approach to the Wind Field Retrieval from Scatterometer Data NA
Bartoloni, A., C. D'Amelio and G. Milillo

2. X-Band Coherent Measurements of Ocean Backscatter from an Airship NA
Hesany, V., W.J. Plant, W.C. Keller and K. Hayes

3. Observations of the Ocean Surface Using an Aircraft Radar Altimeter, Scatteromenter and ROWS 1385
Vandemark, D., D. Hines, B. Chapron, J. Carswell and W. Donnelly

4. Dependence of Altimeter Returns on Wind Stress and Wave Age 1389
Elfouhaily, T., B. Chapron, V. Kerbaol, J. Gourrion, J. Tournadre, K. Katsaros and D. Vandemark

5. Correcting SeaWinds Scatterometer Measurements for Atmospheric Attenuation 1392
Moore, R.K., N. Kambhammettu and S. Song

WET -- Remote Sensing of Surface Waters

1. Spectrometry of Turbidity in Surface Water 1395
Han, L.

2. Validation of an Optical Remote Sensing Model Using Reflectance Signatures Collected From an Airborne Sensor NA
Bostater, C., W. Ma, T. McNally, M. Keller and M. Gimond

3. Quantitative Remote Estimation of Algal Density, Pigment Concentrations and Non-organic Suspended Matter in Aquatic Environments, Principles and Techniques NA
Gitelson, A.A., Y.Z. Yacobi and S. Plotnizky

4. SeaWiFS and MERIS: A Comparison of Their Performance for the Estimation of Optically Active Components in Ocean Water 1398
Cipollini, P., and G. Corsini

5. A Numerical Study of the Composite Surface Model for Ocean Scattering 1401
Johnson, J.T., R.T. Shin, J.A. Kong, L. Tsang and K. Pak

6. Algorithm Requirements for Operational Use of Airborne Remote Sensing in Inland Water Management NA
Dekker, A.G., H.J. Hoogenboom and M. Rijkeboer

THAAM -- Retrieval of Ecosystem Parameters from BRDF Data and Models

1. Kilometer-Scale Global Albedo from MODIS 1405
Wanner, W., A.H. Strahler, B. Zhang and P. Lewis

2. The Influence of Directional Sampling on Bidirectional Reflectance and Albedo Retrieval Using Kernel-Driven Models 1408
Wanner, W., P. Lewis and J.L. Rougean

3. Semiempirical Modelling of Bidirectional Utilizing the MODIS BRDF/Albedo Algorithm Models 1411
White, H.P., J.R. Miller, R. Soffer and W. Wanner

4. Analytic Forms of Bidirectional Reflectance Functions for Earth Radiation Budget Studies 1414
Manalo-Smith, N., and G.L. Smith

5. The Use of Bidirectional Reflectance to Estimate Broadband Hemispherical Albedo Over Tasmania 1417
Russell, M., and M. Nunez

6. A Technique for Combining Geometrical and Spectral BRDF Information for Retrieval of Plant Canopy Characteristics Uing AVHRR Optical Data NA
Braswell, B.H., J.L. Privette and D.S. Schimel

7. Estimating Hemispherical Reflectance and Selected Biophysical Parameters for Boreal Forest Canopies Using Spectral Bidirectional Reflectance Data Acquired by ASAS NA
Russell, C.A., J.R. Irons and P.W. Dabney

8. An Integrated Approach to Estimating LAI Using Multitemporal and Multidirectional Remote Sensing Measurements 1420
Qi, J., and M.S. Moran

9. Comparison of Vegetation Index Compositing Scenarios: BRDF Versus Maximum VI Approaches 1423
van Leeuwen, W.J.D., A.R. Huete, S. Jia and C.L. Walthall

10. Retrieval of Canopy Structural Parameters from Multi-Angle Observations Using an Artificial Neural Network 1426
Abuelgasim, A.A., S. Gopal and A.H. Strahler

THAAA -- Microwave/Millimeter-Wave Atmospheric Absorption and Scattering Models

1. Observations and Modelling of Radiometric Signatures of Storms in the Frequency Range of 90-220 GHz 1429
Wang, J.R., C. Kummerow, P. Racette, W. Olson and J. Zhan

2. Atmoshperic Water-Vapor Microwave Absorption - A Review of Models and Measurements NA
Rosenkranz, P.W.

3. Model Based Retrievals of Water Vapor Profiles from Microwave Radiances NA
Wilheit, T.T., C.B. Blankenship and S.L. Moore

4. Observed and Theoretical Millimeter Wave Emission in the Tropics 1432
Snider, J.B., and D.A. Hazen

5. Atmospheric Microwave Absorption Parameter Estimation Near 22 GHz 1435
Cruz Pol, S.L., C.S. Ruf and SJ. Keihm

6. Atmospheric Water Vapor and the Total GPS Signal Delay NA
Gutman, S.I., D.E. Wolfe and R.B. Chadwick

THAAA *continued* -- Microwave/Millimeter-Wave Atmospheric Absorption and Scattering Models

7. Recent Advances in Satellite Sounding at the U.K. Meteorological Office 1438
Barwell, B.R.

8. Wind Speed and Total Integrated Water Vapor Measurements Over the Ocean Using the Special Sensor Microwave/Imager (SSM/I) NA
Manning, W.

9. Influence of Scattering in the Absorbing Line Structure in Two-Phase Media 1441
German, M.L., V.P. Nekrasov and E.F. Nogotov

10. Atmospheric Effects Due to Different Particle Shapes on Propagation 1444
Yildirim, O.

THACP -- Microwave Remote Sensing of Ocean Surface Winds I

1. JPL Wind Radiometer Measurements NA
Wilson, W.J., and S.H. Yueh

2. Surface and Airborne Radiometric Observations During the Coastal Ocean Probing Experiment: An Overview 1450
Westwater, E.R., V.G. Irisov, L.S. Fedor and Yu.G. Trokhimovski

3. Surface Wind Measurements by Radiometer- Polarimeters in Frame of Russia Airspace Programs 1454
Kravtsov, Yu.A., A.V. Kuzmin, M.N. Pospelov and A.I. Smirnov

4. Observation of the Ocean Brightness Temperature Anisotrophy During the Coastal Ocean Probing Experiment 1457
Irisov, V.G., and Yu.G. Trokhimovski

5. High Altitude Aircraft Mapping of Near Surface Ocean Winds 1460
Hood, R.E., and R.W. Spencer

6. Performance Analysis for the Sea Winds Scatterometer 1463
Long, D.G., and M.W. Spencer

7. Remote Sensing of the Near Surface-Ocean Wind Vector Under Low-Wind Conditions Using Scatterometry 1466
Carswell, J., W. Donnelly and R. McIntosh

8. Ku-Band Ocean Backscatter Functions for Surface Wind Retrieval 1469
Nghiem, S.V., F.K. Li and G. Neumann

9. Scatterometer Measurements of Ocean Surface Stress Magnitude and Direction from Aircraft During SWADE and from ERS-1 1472
Weissman, D.E.

10. Statistics of Radar Backscatter from Wind Waves 1475
Long, D.G., R. Reed and D.V. Arnold

THAED -- Remote Sensing of Littoral Submesoscale Processes II

1. An Analysis of Drainage Flow Exit Jets Over the Chesapeake Bay as Seen in an ERS-1 SAR Image NA
Winstead, N.S., G.S. Young, D.R. Thompson and H.N. Shirer

2. Study of Katabatic Wind Fields by Using ERS-1 Synthetic Aperture Radar Imagery of the Ocean Surface 1478
Alpers, W., U. Pahl, G. Gross and D. Etling

3. A Coupled Wind — Internal Wave System 1481
Smirnov, A.V.

4. A Large-Scale Evaluation of Features for Automatic Detection of Oil Spills in ERS SAR Images 1484
Schistad Solberg, A.H., and R. Solberg

5. Ocean Features Evaluation from RADARSAT SAR Imagery NA
Staples, G.C.

6. Meteorological Explanation of a Sea Surface Roughness Streak Imaged by ERS-1 SAR Near Block Island, New York NA
Winstead, N.S., H.N. Shirer, T.D. Sikora and R.C. Beal

7. Internal Waves in the Strait of Messina Observed by the ERS1/2 Synthetic Aperture Radar 1487
Brandt, P., A. Rubino and W. Alpers

8. Studies of Rainfall Footprints on the Sea Conducted by Spaceborne SAR "Almaz" and Shipborne Microwave Radiometers 1490
Bulatov, M.G., M.D. Raev and E.I. Skvortsov

9. The Microwave Radar Signal Doppler Spectrum and the Problem of Ocean Surface Slicks Detection 1493
Kanevsky, M.B., and V.Y. Karaev

10. The Remote Sensing of the Ocean Surface in the Frontal Zone 1495
Lavrenov, I.

THAES -- Educational Initiatives III

1. The Weather Visualizer: A Java Tool for Interactive Learning 1498
Hall, S.E., M.K. Ramamurthy, R.B. Wilhelmson, J. Plutchak, D. Wojtowicz and M. Sridhar

2. Lessons Learned From Using GIS/RS as an Integrative Tool for Interdisciplinary Learing and Teaching in a Senior-Level Capstone Course on Global Change at Westminster College of Salt Lake City 1501
Ford, R.E., and J. Hipple

3. Classroom Applications of Marine and Environmental Remote Sensing Data 1504
Alfultis, M.A., and M.R. Hicks

4. A Model for Environmental Earth Science Module Design 1506
Meyers, R.J., J.A. Botti and K.D. Gonzalez

5. Remote Sensing and Inner City Youth: A Pilot Collaboration of the Aspen Global Change Institute's Ground Truth Studies and the 4-H After School Programs 1509
Katzenberger, J.

6. The Arctic Observatory: An Educational Tool for Intercomparison Studies and Time-Series Analysis Using Five Arctic Parameters on CD-Rom NA
Keeler, M., and F. Mahootian

7. Texas Space Grant Consortium: Educational Opportunites in Earth Science and Remote Sensing 1512
Neuenschwander, A.

THAF -- Sea Ice Remote Sensing (Models, Techniques and Applications) II

1. The SIMMS'93 SAR Polarimetry Experiment: Combined Surface and Airborne Radar Measurements for Winter Sea Ice 1515
Livingstone, C.E., D.G. Barber, F. Spring and W. Liu

2. Ice Roughness Classification and ERS SAR Imagery of Arctic Sea Ice: Evaluation of Feature-Extraction Algorithms by Genetic Programming 1520
Daida, J.M., R.G. Onstott, T.F. Bersano-Begey, S.J. Ross and J.F. Vesecky

3. A Microwave Technique for Mapping Ice Temperature in the Arctic Seasonal Ice Zone 1523
St. Germain, K.M., and D.J. Cavalieri

4. A Neural Network Sea Ice Edge Classifier for the NASA Scatterometer 1526
Alhumaidi, S.M., W.L. Jones, J.D. Park, S. Ferguson and M.H. Thursby

5. Fusion of Satellite SAR and SSM/I Data for Thin Sea Ice Concentration NA
Beaven, S.G.

6. Comparison of Open Water and Thin Ice Areas Derived from Satellite Passive Microwave Data with Aircraft Measurements and Satellite Infrared Data in the Bering Sea 1529
Markus, T., and D.J. Cavalieri

7. Lake Superior Ice Concentration Using SSM/I NA
Pilant, D.

8. Measuring Sea Ice Floe Size During Summer with ERS SAR Imagery NA
Holt, B., and S. Martin

9. Separating Ice-Water Composites and Computing Floe Size Distributions 1532
Soh, L.K., D. Haverkamp and C. Tsatsoulis

THAH -- Emerging Technologies and Techniques

1. Laser Diode Based New Generation Lidars 1535
Reagan, J.A., H. Liu and J.F. McCalmont

2. Antartic Miniature Lidar 1538
Rall, J.A.R., and J.B. Abshire

3. Fulfilling the Promise of Imaging Spectrometry: Underappreciated Aspects of Sensor Performance Which Affect Data Utility NA
Chrien, T.G., M.L. Eastwood, R.O. Green, C.M. Sarture and G.H. Bearman

4. Use of FT-IR and UV Spectrometers for Monitoring Multiple Pollutants in the Lower Troposphere 1541
Gibbs, D.P., and B. Krenek

5. Multimeter Wave Imaging Technology 1544
Huguenin, G.R.

6. Synthetic Aperture Radiometers for Microwave Remote Sensing from Space 1547
Le Vine, D.M., and C.T. Swift

7. Capabilities and Recent Results From the ER-2 Doppler Radar (EDOP) 1550
Bidwell, S.W., G.M. Heymsfield and I.J. Caylor

8. Millimeter-wave Radars for Remotely Sensing Clouds and Precipitation 1553
Mead, J.B., A.L. Pazmany, S.M. Sekelsky, R. Bambha and R.E. McIntosh

9. Airborne SAR Interferometry: Potential and Future Applications NA
Moreira, J.

10. Satellite SAR Interferometry: Present Status and Future Technologies NA
Guarnieri, A. M., C. Prati and F. Rocca

THAP -- SAR Speckle and Classification

1. Polarimetric Image Classification Using Optimal Decomposition of Radar Polarization Signatures 1556
Dong, Y., B. Forster and C. Ticehurst

2. A Comprehensive Evaluation of Filters for Radar Speckle Suppression 1559
Sheng, Y., and Z.G. Xia

3. SIR-C Polarimetric Image Segmentation by Neural Network 1562
Sergi, R., G. Satalino, B. Solaiman and G. Pasquariello

4. Determining the Number of Classes for Segmentation in SAR Sea Ice Imagery 1565
Soh, L.K., and C. Tsatsoulis

5. A Multi-Temporal Classifier for SIR-C/X-SAR Imagery 1568
Bergen, K.M., L.E. Pierce, M.c. Dobson and F.T. Ulaby

6. Study on Target Detection Using Multi-Look Polarimetric SAR Data NA
Xiong, H., G. Liu and S. Huang

7. Optimal Multi-look Polarimetric Speckle Reduction and Its Effects on Terrain Classification 1571
Liu, G., S. Huang, A. Torre and F. Rubertone

8. Polarimetric Signature Preservation in SAR Speckle Filtering 1574
Lee, J.S., G. De Grandi, M.R. Grunes and E. Nezry

9. Reduction of Multiplicative Noise in SAR Imaging by Wiener Filtering 1577
Pascazio, V., and G. Schirinzi

10. Statistical Characterization of the Phase Process in Interferometric SAR Images 1580
Di Bisceglie, M., and C. Galdi

THAV -- Image Processing: Restoration Problems

1. Aerosol Properties From Blurring Effect in Remotely Sensed Images 1584
Leone, A., B. Bulgarelli, M. Garello and G. Perona

2. Deriving the Anisotropic Atmospheric Point Spread Function of ASAS Off-Nadir Images and Removal of the Adjacency Effect by Inverse Filtering 1587
Hu, B., X. Li and A.H. Strahler

3. Quantitative Evaluation of Edge Preserving Noise-Smoothing Filter 1590
Pasaribu, D.P.

THAV *continued* -- Image Processing: Restoration Problems

4. A Constructive Deconvolution Procedure of Bandpass Signals by Homomorphic Analysis 1592
Marenco, A.L., and V.K. Madisetti

5. Cubic Covolution for One-Pass Restoration and Resampling 1597
Reichenbach, S.F., and K. Haake

THAV -- Image Processing: Registration and Resampling

6. Quantitative Aspects of the Radiometric Normalization of Multi-Temporal Satellite Scenes in the Creation of Large Area Image Mosaics NA
Guindon, B.

7. Landsat Thematic Mapper Band-to-Band Registration 1600
Barker, J.L., and J.C. Seiferth

8. Digital Resampling for Image Processing and Fusion of SSM/I Data 1603
Pellegrini, P.F., E. Piazza and A. Nervi

9. Spatial Resolution Enhancement of SSM/I Data: Vegetation Studies of the Amazon Basin 1606
Long, D.G., D.R. Daum and P.J. Hardin

10. Automated Image Registration for Change Detection from Landsat Thematic Mapper Imagery 1609
Dai, X., S. Khorram and H. Cheshire

THAZ -- The World's Airborne SAR Facilities I: Conventional Frequencies & Respective Applications

1. NASA/JPL Airborne Three-Frequency Polarimetric/Interferometric SAR System 1612
Kim, Y., Y. Lou, J. van Zyl, L. Maldonado, T. Miller, T. Sato and W. Skotnicki

2. Hughes Integrated Synthetic Aperture Radar 1615
Bayma, R.W.

3. Ingara: An Integrated Airborne Imaging Radar System 1618
Stacey, N.J.S., M.P. Burgess, M.R. Muller and R. Smith

4. The Canadian Airborne R&D SAR Facility: The CCRS C/X SAR 1621
Livingstone, C.E., A.L. Gray, P.W. Vachon, M. Lalonde, R.K. Hawkins, T.I. Lukowski, K. Mattar and J.W. Campbell

5. The DLR Airborne SAR Project E-SAR 1624
Horn, R.

6. EMISAR: C- and L-Band Polarimetric and Interferometric SAR 1629
Lintz Christensen, E., J. Dall, N. Skou, K. Woelders, J. Granhohm and S.N. Madsen

7. First Results and Status of the PHARUS Phased Array Airborne SAR 1633
Greidanus, H., P. Hoogeboom, P. Koomen, P. Snoeij and H. Pouwels

8. Development of NASDA Airborne Synthetic Aperture Radar (NASAR-1) 1636
Shimada, M., H. Oaku and M. Yamanashi

9. The NEC Interferometric SAR System "NEC-SAR" 1639
Nagata, H., H. Shinohara, M. Murata, M. Miyawaki, H. Nagata, H. Shinme, M. Sugawara, H. Totuka, Y. Ohura and H. Nohmi

THPAM -- BRDF Model Development, Validation and Inversion II

1. Angular Signatures, and a Space-Borne Measurement Concept 1642
Gerstl, S.A.W.

2. Estimation of Leaf Size from Hotspot Observation 1645
Qin, W., N.S. Goel and B. Wang

3. Multiple Scattering Approximations and Coherent Backscattering Theory for Soil Bidirectional Reflectance 1648
Liang, S.

4. A Four-Level Bidirectional Reflectance Model Based on Canopy Architecture and its Inverstion 1651
Chen, J.M., and S.G. Leblanc

5. Validation of a BRDF Model for Boreal Forest 1654
North, P.R., S.E. Plummer and D.W. Deering and M. Leroy

6. Assessing Canopy Biomass and Vigor by Model-Inversion of Bidirectional Reflectances: Problems and Prospects 1657
Brakke, T.W., J. Otterman, J.R. Irons and F.G. Hall

7. Retrieval of Forest Biophysical Parameters from Remote Sensing Images with the DART Model 1660
Pinel, V., J.P. Gastellu-Etchegorry and V. Demarez

8. Extracting Sub-Pixel Vegetation Endmember Bidirectional Reflectance for Canopy Model Inversion Using NOAA AVHRR Satellite 1663
Asner, G.P., J.L. Privette, C.A. Wessman and C.A. Bateson

9. Estimation of Bidirectional Reflectance Distribution Function from Land Surfaces Using Airborne POLDER Data 1666
Takemata, K., T. Yonekura, M. Asae and Y. Kawata

10. Validation of Kernel-Driven Semiempirical BRDF Models for Application to MODIS MISR Data 1669
Hu, B., W. Wanner, X., Li and A.H. Strahler

THPAA -- Passive Remote Sensing of the Environment

1. A Scanning 60 GHz Radiometer to Measure Air-Sea Temperature Difference: Recent Results During Cope 1672
Trokhimovski, Yu.G., E.R. Westwater, V.G. Irisov and V.Ye. Leuskiy

2. Measurements of Integrated Water Vapor and Cloud Liquid from Microwave Radiometers at the DOE ARM Cloud and Radiation Testbed in the U.S. Southern Great Plains 1675
Liljegren, J.C., and B.M. Lesht

3. Performance Evaluation of a Spinning Flat Reflector for Millimeter-Wave Radiometry 1678
Jacobson, M.D., and W.M. Nunnelee

4. Observations of Water Vapor and Cloud Liquid from an Airborne Dual-Frequency Radiometer During VORTEX'95 1681
Fedor, L.S., E.R. Westwater and M.J. Falls

5. Applications of Kalman Filtering to Derive Water Vapor Profiles from Raman Lidar and Microwave Radiometers 1685
Han, Y., E.R. Westwater and R.A. Ferrare

6. Application of Neural Nets to Rain Rate Retrieval from Simulated Multichannel Passive Microwave Imagery 1688
Gasiewski, A.J., G.A. Showman and G.M. Skofronick

7. Prediction of Water Vapor Scale Height from Integrated Water Vapor Measurements 1692
Boback, J.P., and C.S. Ruf

8. Feasibility of a New Ground-Based Microwave Measurement Method for the Atmospheric Water Vapor 1695
Hashimoto, S., N. Yamashita and T. Mikami

9. Determination of Humidity Profiles from Measurements of Up Going Radiation at Wavelengths 0.3 and 1.35 cm 1698
Markina, N.N., and A.P. Naumov

10. Recovering of Atmospheric Water Vapor and Liquid Water Contents by Multifrequency Radiometer: Experiments and Modeling 1701
Perfiliev, Y.P.

THPCP -- Microwave Remote Sensing of Ocean Surface Winds II

1. A Simple Model for Deriving Ocean Surface Wind Direction from the DMSP Special Sensor Microwave Imager (SSM/I) 1704
Boucher, D.J., B.H. Thomas, D.N. Ricci and A.M. Kishi

2. Ocean Surface Wind Speed and Direction Retrievals from the SSM/I 1707
Li, L., and P. Chang

3. Assessing the Ocean Surface Vector Wind Signal in SSM/I Data Using Neural Networks 1710
Bates, J.J., and K.C. McColl

4. The Effects of Tropospheric Water Vapor and Cloud Liquid Water on Ocean Surface Wind Vector Retrievals Using Polarimetric Radiometers NA
Gaiserl, P.W., and P. Chang

5. Surface Winds from the SSM/I Using Neural Networks 1712
Krasnopolsky, V.M., L.C. Breaker and W.H. Gemmill

6. Development of a Statistical Method for Eliminating Improbable Wind Aliases in Scatterometer Wind Retrieval 1715
Oliphant, T.E., and D.G. Long

7. Advanced Techniques for Improving Wind Direction Ambiguity Removal in Scatterometry 1718
Huddleston, J.N., R.D. West, S.H. Yueh and W.Y. Tsai

8. Geophysical Modeling Error in Wind Scatterometry 1721
Johnson, P.E., D.G. Long and T.E. Oliphant

9. Cramer-Rao Bound for Wind Estimation from Scatterometer Measurements 1724
Oliphant, T.E., and D.G. Long

10. Atmospheric Effects on the Wind Retrieval Performance of Satellite Radiometers 1727
West, R.D., and S.H. Yueh

THPED -- Remote Sensing of the Space/Time Characteristics of Water Surfaces

1. Laboratory Studies on Frequency-Wavenumber Spectrum of Short Wind Waves — NA
Hara, T., E.J. Bock and M. Donelan

2. Nonlinearities and Reverse Travelling Energy Observed in Wavenumber-Frequency Spectra of X-Band Ocean Backscatter — 1730
Frasier, S., and R. McIntosh

3. In Situ Measurements of Small Scale Wind-Waves and Their Moduation by Ocean Currents and Atmospheric Forcing — NA
Bock, E.J., T. Hara and J.B. Edson

4. Observed Space-Time Structure of Radar Backscatter from the Ocean Surface — 1733
Hesany, V., W.J. Plant, W.C. Keller and K. Hayes

5. Surface Wave Dispersion Observed With Airborne Spotlight Imaging Systems — NA
Dugan, J.

6. Optical, Radar and In Situ Measurements of Internal Wave Dispersion — 1736
Gotwols, B.L., E. Aarholt, R.D. Chapman and R.E. Sterner II

7. The Coastal Ocean Probing Experiment: Further Studies of Air-Sea Interactions with Remote and In-Situ Sensors — 1739
Kropfli, R.A. and S.F. Clifford

8. The Estimation of Ocean Current From ω-k Analysis of Radar Data — 1742
Lamont-Smith, T.

9. High Resolution Polarimetric Radar Scattering Measurements of Low Grazing Angle Sea Clutter — 1745
Twarog, E.M., D.J. McLaughlin and N. Allan

10. Simultaneous CODAR and OSCR Measurements of Ocean Surface Currents in Monterey Bay — 1749
Fernandez, D.M., and J.D. Paduan

THPES -- Land Cover: Multitemporal Analysis and Change Detection

1. A Comparative Analysis of ERS-1/SAR and Landsat/TM Multitemporarl Scenes for Land Use Studies in Sao Paulo State, Brazil — NA
Damiao, D.P., and H.J.H. Kux

2. A Multitemporal Land-Cover Change Analysis Tool Using Change Vector and Principal Components Analysis — 1753
Parra, G.A., M.C. Mouchot and C. Roux

3. Assessing Inter-Annual Variability for the Central Grassland Region of the US Using the 1990 Seasonal Land Cover Classification — NA
Stretch, L., B. Reed and D. Ojima

4. Land-Cover Dynamics in Eastern Amazonia, 10 Years of Change as Viewed by Landsat TM — NA
Roberts, D.A., G. Batista, J. Pereira and B. Nelson

5. Monitoring Land Cover of the Desert Fringes of the Eastern Nile Delta, Egypt — 1756
El-Khattib, H.M., N.M. El-Mowilhi and F. Hawela

6. Temporally Invariant Classifiers and the Classification of Floristics — NA
Fitzgerald, R.W.

THPES *continued* -- Land Cover: Multitemporal Analysis and Change Detection

7. Retrieval of Forest Parameters from Multitemporal Spaceborne SAR Data 1759
Kurvonen, L., J. Pulliainen, M. Hallikainen and P. Mikkela

8. Monitoring of the Change of Vegetative Conditions Using Multitemporal SAR Data 1763
Suga, Y., S. Takeuchi and H. Tsu

9. C- and L-Band Multi-Temporal Polarimetric Signatures of Crops 1766
Skriver, H., F. Nielsen and A. Thomsen

10. Characterization of Oklahoma Reservoir Wetlands for Preliminary Change Detection Mapping Using IRS-1B Satellite Imagery 1769
Mahlke, J.

THPF -- Microwave Remote Sensing of the Antarctic

1. RADARSAT Antarctica Mapping System: System Overview 1772
Norikane, L., B. Wilson and K. Jezek

2. RADARSAT: The Antarctic Mapping Project 1775
Jezek, K.C., J. Curlander, L. Norikane, F. Carsey, J.P. Crawford, C. Wales and J. Muller

3. The McMurdo Ground Station (MGS): Ready for SAR Acquisition 1777
Wales, C.

4. Calibration of Data from the Antarctic Mapping Mission 1780
Williams, J.

5. A Robust Threshold Retracking Algorithm for Extracting Ice-Sheet Surface Elevations from Satellite Radar Altimeters 1783
Davis, C.H.

6. Individual Weather Correction for Antarctic Sea-Ice Concentration from SSM/I 1788
Thomas, C.H., and G.C. Heygster

7. The Effect of the Grounded Tabular Icebergs in Front of Berkner Island on the Weddell Sea Ice Drift as Seen from Satellite Passive Microwave Sensors 1791
Markus, T.

8. Mueller Matrix Associated with Diffuse Scattering from Two-Dimensional Random Rough Surfaces -- Full Wave Analysis 1794
Lee, B.S., and E. Bahar

THPH -- Optical Remote Sensing Instrumentation and Techniques

1. Development and Present Configuration of the NASA GSFC/WFF Helicopter-Based Remote Sensing System 1797
Walthall, C.L., D.L. Williams, B.L. Markham, J.E. Kalshoven and R.F. Nelson

2. System Requirments for Active Optical Search and Rescue 1800
Field, C.T., and P.S. Millar

3. Shortwave Infrared Spectral Reflectance of Plant Litter and Soils 1803
Nagler, P.L., C.S.T. Daughtry and S.N. Goward

4. Using Laser Echo Recovery and a Scannable Field-of-View Telescope to Determine Vegetation Structure and Sub-Canopy Topography Over Wide Swaths 1806
Blari, J.B., D.J. Harding and D.B. Coyle

5. An Active Optical Remote Sensing System for Vegetation Index Determination 1809
Kalshoven, J.E., and D.P. Rosten

6. Effects of Excitation Wavelength on the Chlorophyll Flourescence Ratio F685/F730 nm 1812
Corp, L.A., J.E. McMurtrey, E.W. Chappelle, M.S. Kim and C.S.T. Daughtry

7. An Improved Aircraft Underflight Instrument for the Derivation of Band Gains in Satellite Sensors 1816
Abel, P., and B. Subramanya

8. Radiometric Corrections of Visible/Infrared Satellite Data Over Terrestrial Environments: Angular, Atmospheric and Topographic Effects 1823
Moreno, J.F.

9. Comparison of Lidar Water Vapor Measurements Using Raman Scatter at 266 nm and 532 nm 1826
Harris, R., F. Balsiger and C.R. Philbrick

10. Computer Modeling of Adaptive Optics and Sites for Telescopes Design 1830
Lukin, V.P.

THPP -- SAR Applications and Signal Processing

1. Mapping Geologic Structure on Barrier Islands Using Polarimetric SAR NA
Slatton, K.C., M.M. Crawford, J.C. Gibeaut and R.O. Gutierrez

2. Integration of SIR-C/X-SAR and Landsat TM Data for Geologic Mapping and Resource Exploration 1833
Wever, T., and M. Frei

3. Retrieval of Man-Made Structures in Siberia with INSAR Techniques Using ERS SAR Data 1836
Streck, C., and O. Hellwich

4. Angular Dependence of SAR Backscatter Around Mt. Taranaki, New Zealand 1839
Pairman, D., and S. Belliss and S. McNeill

5. Edge Detection in Speckled SAR Images Using the Continuous Wavelet Transform 1842
Chabert, M., J.Y. Tourneret and G. Mesnager

6. Heterogeneity in SAR Images NA
Mueller, H.J

7. Intersystem Normalization of Multifrequency Radar Imagery for Discrimination of Unvegetated Lava Surfaces NA
Kaupp, V.H., J.F. Hug, W.P. Waite, H.C. MacDonald and C.M. Ting

8. Removing RF Interferences from P-Band Ariplane SAR Data 1845
Cazzaniga, G., and A. Monti Guarnieri

THPV -- Methods of Data Analysis

1. Hybrid Consensus Theoretic Classification 1848
Benediktsson, J.A., J.R. Sveinsson and P.H. Swain

2. A Framework for Multi-Date Multi-Sensor Image Interpretation 1851
Murni, A., A.K. Jain and J. Rais

3. Optimal Projection Selection for Projection Pursuit in High Dimensional Feature Reduction NA
Velipasaoglu, E.O., and O.K. Ersoy

4. Automated Training Sample Labeling Using Laboratory Spectra 1855
Hsieh, P., and D.A. Landgrebe

5. Modified Divisive Clustering Useful for Quantitative Analysis of Remotely Sensed Data 1858
Prakash, H.N.S., S.R. Kumar, P. Nagabhushan and K.C. Gowda

6. Surface Information Retrieval From Optical/Microwave Data: Potentials and Limits of Synergistic Approaches 1861
Moreno, J.F., and S.S. Saatchi

7. Sensor Data Simulations Using Monte-Carlo and Neural Network Methods 1864
Kiang, R.K.

8. Model-Based Technique for Super Resolution and Enhanced Target Characterization Using a Step-Frequency Radar: A Simulation Study 1867
Chakrabarti, S., P. Kanagaratnam and P. Gogineni

9. Contextual Simulation of Landscape Based on Remotely Sensed Data 1870
Jung, M.,THPF: Microwave Remote Sensing of the Antarctic and M.M. Crawford

10. Intelligent Fusion and Analysis of AIRSAR Data for SEIDAM 1873
Bhogal, A.S., D.G. Goodenough, D. Charlebois, H. Barclay, S. Matwin and O. Niemann

THPZ -- The World's Airborne SAR Facilities II: Extraordinary Frequencies and Special Applications

1. Multi-Channel SAR with Phased Array: The Experimental Airborne System AER-II NA
Ender, J.H.C.

2. The German DO-SAR Sytem Abstract NA
Fritsch, B.

3. The Experimental Airborne VHF SAR Sensor CARABAS: A Status Report 1877
Gustavsson, A., L.M.H. Ulander, L.E. Anderson, P.O. Frolind, H. Hellsten, T. Jonsson, B. Larsson and G. Stenstrom

4. A H igh Resolution, Four-Band SAR Testbed with Real-Time Image Formation 1881
Walker, B., G. Sander, M. Thompson, B. Burns, R. Fellerhoff and D. Dubbert

5. The Lincoln Laboratory Millimeter-Wave Synthetic Aperture Radar NA
Murphy, T.J., and J.C. Henry

6. ONERA Airborne SAR Facilities NA
Boutry, J.M.

7. The Army Research Laboratory Ultra Wideband BoomSAR
Ressler, M.A. 1886

8. Status of the SASAR System 1889
Inggs, M.

9. Overview of the P-3 UWB SAR System NA
Sheen, D.R., and T.B. Lewis

10. YSAR: A Compact, Low-Cost Synthetic Aperture Radar 1892
Thompson, D.G., D.V. Arnold, D.G. Long, G.F. Miner and T. Karlinsey

FAAM -- Land Cover Characterization Using BRDF Models and Data

1. Nadir and Bidirectional Surface Measurements of Arctic Tundra: Site Differentiation and Vegetation Phenology Early in the Growing Season 1897
Vierling, L.A., D.W. Deering and T.F. Eck

2. Analysis of Airborne POLDER Data on Boreal Forest Covers 1901
Bicheron, P., M. Leroy and O. Hautecoeur

3. Variability of BRDF with Land Cover Type for the West Central HAPEX-Sahel Super Site 1904
Brown de Colstoun, E.C., C.L. Walthall, A.T. Cialella, E.R. Vermotel, R.N. Halthore and J.R. Irons

4. Use of BRDF Models to Normalize Angular Reflectances to NADIR for Temporal Compositing Schemes NA
Jia, S., A.R. Huete and W.J.D. van Leeuwen

5. Detection and Correction of the Bidirectional Effects in AVHRR Measurements Over Northern Regions NA
Li, Z., J. Cihlar, X. Zheng and L. Moreau

6. Conifer Shoot Bidirectional Scattering: Methodology and Preliminary Results 1908
Walter-Shea, E.A., M.A. Mesarch and L. Chen

7. Assymmetry in the Diurnal Variation of Surface Albedo 1911
Mayor, S., W.L. Smith, Jr., L. Nguyen, T.A. Alberta, P. Minnis, C.H. Whitlock and G.L. Schuster

FAAA -- Active Remote Sensing of the Lower Atmosphere

1. Retrieval of Boundary-Layer Turbulence Using Spaced-Antenna Wind Profilers 1914
Holloway, C.L., R.J. Doviak, S.A. Cohn and R.J. Lataitis

2. A Buoy-Mounted Wind Profiler for Remote Measurement of Ocean Winds 1917
Mead, J.B., P.M. Langlois and R.E. McIntosh

3. Frequency Domain Interferometry in the Planetary Boundary Layer: First Results 1920
Corner, B.R., R.D. Palmer and R.M. Narayanan

4. A Digital Beamforming Radar Profiler for Imaging Turbulence in the Atmospheric Boundary Layer 1923
Mead, J.B., G. Hopcraft, B. Pollard, R.E. McIntosh

5. Preliminary Results From the Arecibo 430 MHz Spatial Interferometry System 1926
Howell, P.B., R.D. Palmer, R.M. Narayanan, M.F. Larsen and J.Y.N. Cho

6. Measurements of Vertical Velocities and Divergence in the Atmosphere Using the MU Radar in Japan 1929
Ren, Y., R.D. Palmer, S. Fukao, M. Yamamoto and T. Nakamura

FAAA *continued* -- Active Remote Sensing of the Lower Atmosphere

7. Structure of the Atmosphere in an Urban Planetary Boundary Layer from Lidar and Radiosonde Observations — NA
Eichinger, W., and D. Cooper

8. Volume Imaging Lidar Observations of the Convective Boundary Layer — NA
Eloranta, E., and A. Piironen

9. Low-level Jet Detection in Snow with a Noncoherent Weather Radar — NA
Melnikov, V.M., and A.V. Ryzhkov

FACP -- Subsubsurface Electromagnetic Sensing at Deeper Depths

1. Radar Sounding of Glaciers in Greenland — 1932
Allen, C., B.P. Wolhletz and S. Gogineni

2. Sensing of Gradient Electromagnetic Fields from Subsurface Conducting Targets — 1935
Cress, D.H., and L.C. Bartel

3. Modeling the Electromagnetic Detection of Buried Cylindrical Conductors — 1938
Moses, R.W., R.E. Kelly and J.M. Mack

4. Marine Sediment Mapping with Airborne Electromagnetics — NA
Mozley, E.C., and J. Reynaud

5. Electromagnetic Modeling of Subsurface 3D Structures — 1941
Newman, G.A., and D.L. Alumbaugh

6. Demonstration of the Lasi High-Resolution Electromagnetic Sounding System at the Nevada Test Site — NA
Sternberg, B.K., and M.M. Poulton

7. Statistical Law of Surface Impedance Distribution — 1945
Bashkuev, Yu.B., V.B. Haptanov and L.H. Angarkhaeva

8. The Prediction Map of Geoelectric Sections of Australia, New Zealand and New Guinea — 1947
Bashkuev, Yu.B., V.R. Advokatov and L.H. Angarkhaeva

9. The Influence of Ground Stratification Upon a Field of Magnetic Loop — 1950
Dmitriev, W.V.

FAED -- Remote Sensing of Littoral Submesoscale Processes III

1. Frontal Signatures in Radar Imagery — NA
Vogelzang, J., K.G. Ruddick and J.B. Moens

2. Detection and Location of Internal Waves in Ocean SAR Images by Means of Wavelet Decomposition Analysis — 1953
Rodenas, J.A., and R. Carello

3. Imaging the Multiscale Structure of Atmospheric Turbulence Using Satellite-Based Synthetic Aperture Radar (SAR) — NA
Mourad, P.D.

4. Spectral Analysis of Non-Stationary Ocean SAR Images Using the Wigner-Ville Transform — 1956
Grassin, S., R. Garello and M. Prevosto

5. Results of Airborne Backscatter Measurements During the Surface Wave Dynamics Experiment 1959
Nghiem, S.V., F.K. Li G. Neumann and S.H. Lou

6. Quantitative Analysis of Radar Signatures of Underwater Bottom Topography According to a Bragg-Based Composite Surface Model 1962
Romeiser, R.

7. Near Nadir Microwave Specular Returns From the Sea Surface -- Measurements of Winds From Breeze to Hurricane 1965
Wu, J.

8. Spectral Variations of Sea Surface Emission at MM-Wave Frequencies Under Influence of Synoptical Oceanic Eddies 1968
Cherny, I.V., and V.P. Nakonechny

9. Examination of Sea Surface by Airborne Microwave Radar and Radiometers in Joint US/Russia Internal Waves Remote Sensing Experiment NA
Kuzmin, A.V., M.I. Mityagina and V.V. Yakovlev

10. Surface Wave Observation in the Gulf Stream Area Using ALMAZ-1 SAR 1971
Grodsky, S.A., V.N. Kudryavtsev, A.Y. Ivanov, V.A. Zaitsev and D.M. Solov'ev

FAES -- Land Cover: Agricultural

1. Land Cover Mapping in the Eastern Slopes of the Andes Using ERS-1 and Landsat Data NA
Echavarria, F.R., and C. Keithley

2. A Multisensoral Approach for Landuse Classifications and Grassland Monitoring Based on the Possibility Theory 1974
Stolz, R., and W. Mauser

3. Spectral Angle Mapper Classification and Vegetation Indices Analysis for Winter Cover Monitoring Using JERS-1 OPS Data 1977
Kim, C., and S. Cho

4. Comparison of Classification Techniques for Agricultural Crops Using Temporal Multiparameter Airborne DLR E-SAR Images NA
Schmullius, C., S. Erasmi and P. Hurlemann

5. SIR-C Polarimetric Backscatter Features of Agricultural Land Cover Types Early and Late During the Growing Season 1980
Davidson, M.W.J., R. Steingießer, W. Kuhbauch, F. Vescoui and F. Tano

6. Use of ERS-1 SAR Data for Field Rice Mapping and Rice Crop Parameters Retrieval 1983
Ribbes, F., and T. Le Toan

7. Textural Processing of Multi-Polarization SAR for Agricultural Crop Classification 1986
Treitz, P.M., O.R. Filho, P.J. Howarth and E.D. Soulis

8. Early Diagnostic of Disease Erisiphe Graminis with Using Remote Sensing Measurements NA
Kazandjiev, V.

9. Study on Auto-Extraction of Winter Wheat Planting Area from TM Image Based on Pattern Recognition Technology 1989
Yang, X., N. Wang and P. Qin

10. Spring Wheat Yield Prediction for Western Canada Using Weekly NOAA AVHRR Composites 1992
Hochheim, K.P., D.G. Barber and P.R. Bullock

FAF -- Microwave Remote Sensing of Snow

1. Snow and Ice Observations During the European Multi-Sensor Airborne Campaign in 1995 — 1995
Noll, J., M. Wooding and E. Attema

2. Overview of EMAC-95 Snow and Ice Airborne Campaign in Finland — 1998
Hallikainen, M., P. Ahola, K. Rautiainen, J. Pihlflyckt, T. Tirri, M. Makynen, J. Lahtinen, H. Servomaa, P. Makkonen, J. Grandell, M. Kemppinen, M. Nikulainen, H. Taskinen, S. Tauriainen and M. Roschier

3. First Results From EMAC '95 Snow Experiment in Norway — NA
Guneriussen, T., R. Solberg, K. Sand, J. Noll and D. Weydal

4. Estimation of Snow Water Equivalence Using SIR-C/X-SAR — 2002
Shi, J., and J. Dozier

5. Estimation of Snow Water Equivalent Using Passive Microwave Radiation Data — 2005
Tait, A.

6. Microwave Remote Sensing of Snow: Modeling and Measurements — NA
Hallikainen, M., J. Grandell, T. Pyhalahti and V. Jaaskelainen

7. Scattering and Emission from Dry Snow in the Range 35-120 GHz — 2008
Tjuatja, S., A.K. Fung and J.C. Comiso

8. Multi-Frequency FMCW Radar Profile of Snow Cover — NA
Koh, G., and N.E. Yankielun

9. Observations of Snow Crystal Shape in Cold Snowpacks Using Scanning Electron Microscopy — 2011
Foster, J.L., D.K. Hall, A.T.C. Chang, A. Rango, W. Wergin and E. Erbie

10. Dramatic Decrease in Radar Cross Section over Greenland Observed by the ERS-1 Scatterometer Between 1991 and 1995 — 2014
Wismann, V.R., and K. Boehnke

FAH -- UWB and Ground Penetration Radar

1. An Ultrawideband Imaging Radar for Sea Surface Studies — 2017
Sletten, M.A., and D.B. Trizna

2. Development of a Low Cost SFCW Ground Penetrating Radar — 2020
Langman, A., S.P. Dimaio B.E. Burns and M.R. Inggs

3. A Range Algorithm for Ground Penetrating Radar — 2023
Caffey, T.W.H.

4. Results of a Remote Sensing Experiment Using a Low Frequency Ultra-Wideband SAR to Investigate the Phenomenology of Landmines — 2027
Sturgess, K., L. Happ, J. Kurtz and M. Collins

5. Processing the Ground Penetrating Radar Data Using Its Correlation Property — NA
Jen, L., J. Li and M.X. Wang

6. Signal Processing Aspects of Polarimetric Random Noise Radar Data for Shallow Subsurface Imaging — 2030
Xu, Y., P.D. Hoffmeyer, R.M. Narayanan and J.O. Curtis

7. An Interferomic Techniques for Synthetic Aperture Ground-Penetrating Radar 2033
Leuschen, C., N. Goodman, C. Allen and R. Plumb

8. Subsurface Imaging Using Ground-Penetrating Radar Measurements 2036
Goodman, N., C. Leuschen, R. Plumb and C. Allen

9. Multi-Layer Detection Tracking for Monostatic Ground Penetrating Radar 2038
Rampa, V., and U. Spagnolini

10. Analysis of Response of the Electromagnetic Induction for Detecting of Buried Objects 2041
Zhu, K.



FAP -- SAR Interferometry Processing Algorithms

1. Region Growing Algorithm for InSAR Phase Unwrapping 2044
Xu, W., and I. Cumming

2. A Comparison of Phase Unwrapping Techniques NA
Collins, J.D., G. Sessenrath and N. Marechal

3. A Theoretical Analysis on the Robust Phase Unwrapping Algorithms for SAR Interferometry 2047
Fornaro, G., G. Franceschetti, R. Lanari and E. Sansosti

4. SAR Interferometry: A Multigrid Markdown Approach to Phase Unwrapping with a Discontinuity Model NA
Labrousse, D., and M. Berthod

5. A Multiresolution Approach to Improve Phase Unwrapping 2050
Davidson, G.W., and R. Bamler

6. Maximum Entropy Solution for Interferometric SAR Phase Unwrapping 2054
Datcu, M.

7. Consistent 2-D Phase Unwrapping Guided by a Quality Map 2057
Flynn, T.J.

8. Absolute Phase Determination in SAR Interferometry 2060
Chiaradia, M.T., L. Guerriero, G. Pasquariello, A. Refice and N. Veneziani

9. Determination of Absolute Interferometric Phase Using the Beam-Amplitude Ratio Technique 2063
Bickel, D.L., and W.H. Hensley



FAV -- Method of Data Analysis

1. Multisource Data Integration Using Neural Networks: Optimal Selection of Net Variables for Lithologic Classification 2068
Yang, G., M.J. Collins and P. Gong

2. Multisensor Data Analysis Based on Neural Networks NA
Blonda, P., G. Pasquariello, V. la Forgia, A. Bennardo, G. Stalino, R. Sergi and R. Loizzo

3. A Completely Fuzzy Classification Chain for Multispectral Remote Sensing Images 2071
Gamba, P., A. Marazzi, A. Mecocci and P. Savazzi

4. A Raster-Based Fuzzy Expert System for Forestry Evolution 2074
Saint-Joan, D., and J. Desachy

FAV *continued* -- Method of Data Analysis

5. Evolving Feature-Extraction Algorithms: Adapting Genetic Programming for Image Analysis in Geoscience and Remote Sensing — 2077
Daida, J.M., T.F. Bersano-Begey, S.J. Ross and J.F. Vesecky

6. Radar Imaging of Three-Dimensional Targets in the Laboratory — 2080
Bertrand, J., and P. Bertrand

7. Use of Confocal Techniques in the Generation of Three Dimensional Images Using Conventional SAR — NA
Byrd, M., A.J. Blanchard and B. Krenek

8. Reconstrucion of Complex Dielectric Profiles via Quadratic Models — 2083
Pierri, R., T. Isernia, V. Pascazio and A. Tamlourrino

9. Topographic Measurements Using Polarimetric SAR Data — 2086
Schuler, D.L., J.S. Lee and G. De Grandi

10. A New Method for Extracting Topographic Information From a Single Multispectral Image — 2089
Carlotto, M.J.

FAZ -- Surface Temperatures: Observations and Applications

1. Thermal Emission from Rough Terrain: Anisotropy and Its Possible Consequences on Satellite Image Interpretation — 2092
Jamsa, S.

2. Validation of Land-Surface Temperature Retrieval from Space — 2095
Wan, Z., W. Snyder and Yulin Zhang

3. Model Simulations of the Effect of the Atmosphere on the Remote Sensing of Earth Surface Parameters with the Advanced Very High Resolution Radiometer — NA
Rao, C.R.N., and N. Zhang

4. Land Surface Temperature Retrieval From AVHRR: Influene of Surface Emissivity and Atmospheric Water Vapor — 2098
Steyn-Ross, M.L., and D.A. Steyn-Ross

5. TIR Observations in FIFE From Field, Aircraft and Satellite Platforms — 2101
Schmugge, T.J., and G.M. Schmidt

6. A Simple Method for Estimating Surface Energy Fluxes and Air Temperatures From Satellite Observations — 2104
Anderson, M.C., J.M. Norman, G.R. Diak and W.P. Kustas

7. Unmixing of Satellite Thermal Images: Simulation and Application to TM/Landsat Data — 2107
Zhukov, B., D. Oertel, F. Lehmann and P. Strobl

8. SSM/I-Based Surface Temperature Retrieval Method for Boreal Forest Zone — 2110
Pullianinen, J., J. Grandell and M. Hallikainen

9. Analyzing Thermal Properties of Forests Using Multitemporal Space Borne Thermal Data — NA
Lohi, A., and Y. Awaya

10. Visualisation of Urban Surface Temperatures Derived from Satellite Images — 2113
Nichol, J.

FPAM -- Rough Surface Scattering Effects on Remote Sensing of Terrain

1. A Further Study of the IEM Surface Scattering Model 2116
Fung, A.K., and C.Y. Hsieh

2. On the Use of the Quasi Specular Model for Surface Parameter Estimation 2119
Marchand, R., and G.S. Brown

3. Electromagnetic Scattering from Slightly Rough Surfaces with Inhomogeneous Dielectric Profile 2122
Sarabandi, K., and T. Chiu

4. Electromagnetic Wave Scattering From Real-Life Rough Surface Profiles and Profiles Based on Averaged Spectrum 2125
Pak, K., L. Tsang, R. Weeks, J.C. Shi and H. Rott

5. Analytical, Experimental, and Numerical Studies of Angular Memory Signatures of Waves Scattered from One-Dimensional Rough Surfaces 2128
Kuga, Y., C.T.C. Le and A. Ishimaru

6. The SIR-C/X-SAR Experiment: The Sensitivity of Microwave Backscattering to Surface Roughness of Bare Soils 2131
Coppo, P., G. Macelloni, P. Pampaloni, S. Paloscia and S. Sigismondi

7. Using SIR-C SAR and Cloude's Decomposition for the Determination of Soil Moisture in Vegetated Areas 2134
Chadwick, D.J., and J.R. Wang

8. Interferometric Technique of Determining the Average Height Profile of Rough Surfaces 2137
Ishimaru, A., C.T.C. Le, Y. Kuga, J.H. Yea, K. Pak and T.K. Chan

9. Detection of a Target in a Inhomogeneous Medium Using Angular Correlation Function 2140
Chan, T.K., Y. Kuga and A. Ishimaru

10. Numerical Study of Detection of a Buried Object Under a Single Random Rough Surface with Angular Correlation Function 2143
Tsang, L., G. Zhang and K. Pak

FPAA: Earth Radiation Budget

1. Remote Sensing of Land Surface Temperature: The Directional Viewing Effect 2146
Smith, J.A., N. Chauhan and J. Ballard

2. A Simulation of Topographic Solar Radiative Forcing over a Mountainous Region Using Geostationary Satellite Data 2149
Loechel, S., R.O. Dubayah, J. Barnett, C. Gautier and M. Landsfeld

3. Modeling Area-Averaged Fluxes over Partially Vegetated Land Surfaces Using Aircraft and In-Situ Thermal Data 2152
Friedl, M.A.

4. A One-Dimensional Hydrology/Radiobrightness Model for Freezing/Thawing Bare Soils 2155
Liou, Y.A., and A.W. England

5. On the New Long-Wave Radiation Determination from Satellite Data 2158
Xue, Y., S.P. Lawrence and D.T. Llewellyn-Jones

FPAA *continued* -- Satellite Measurements

6. Landsat 7 System Design Overview 2160
Andary, J., P. Spidaliere, S. Jurczyk and T. Arvidson

7. Landsat 7 and Beyond 2161
Irons, J.R., D.L. Williams and B.L. Markham

8. Reducing the Effects of Space-Varying Wavelength-Dependent Scattering in Multispectral Imagery 2164
Carlotto, M.J.

9. RADARSAT for Landuse Monitoring: Early Results NA
Brown, R.J., T.J. Pultz, B.G. Brisco, Y. Crevier and L. Tighe

FPCP -- Surface Scattering

1. An Exact Technique for Calculating Low Grazing Angle Backscatter from Rough Surfaces NA
Kasilingam, D.

2. Fractal Analysis of Bidimensional Profiles and Application to Electromagnetic Scattering of Soils 2167
Rouvier, S., P. Borderies, I. Chenerie, J.C. Souyris, T. Le Toan and N. Floury

3. Like and Cross Polarized Cross Sections for Two Dimensional Random Rough Surfaces: Bistatic Single and Double Scatter 2170
El-Shenawee, M., and E. Bahar

4. A Knowledge-Based Inversion of Physical BRDF Model and Three Examples 2173
Li, X., and A. Strahler

5. Scattering Cross Sections of Composite Rough Surfaces New Unified Full Wave Solutions 2177
Bahar, E., and Y. Zhang

6. Scatter Cross Sections for Two-Dimensional Random Rough Surfaces-Full Wave Analysis 2180
Bahar, E., and B.S. Lee

7. The Measured Polarized Bidirectional Reflectance Distribution Function of a Spectralon Calibration Target 2183
Betty, C.L., A.K. Fung and J. Irons

8. Energy Conservation in Soil Surface Scattering in the Optical Region 2186
Li, Z., A.K. Fung, S. Tjuatja, C. Betty and J. Irons

9. Optical Versus Radar Roughness in Agricultural Tillage 2189
Colpitts, B.G.

10. The Soil Surface Reflectivity in the Partial Coherent Microwaves at the Frequencies 300 and 900 MHz 2192
Bobrov, P.P., and I.M. Schetkin

FPED -- Laboratory Studies of Ocean Surface Scattering

1. Laboratory Investigations of the Hydrodynamics and Radar Backscattering Properties of Breaking Waves 2195
Meadows, G., E.B. Dano, D.R. Lyzenga, H. VanSumeren, R. Onstott and D.E. Lund

2. Doppler Characteristics and Angular Dependence of Radar Backscatter From Laboratory Breaking Waves 2198
Dano, E.B., D.R. Lyzenga and G. Meadows

3. Dependence of Polarimetric Doppler Spectra on Breaking-Wave Energy 2201
Lee, P.H.Y., J.D. Barter, K.L. Beach, B.M. Lake, H. Rungaldier, J.C. Shelton, H.R. Thompson, Jr., and R. Yee

4. Laboratory Study of the Fine Structure of Breaking Waves for Scatterometry Applications 2204
Rozenberg, A., W.K. Melville and M. Ritter

5. Small Grazing Angle Radar Scattering from a Breaking Water Wave: Demonstration of Brewster Angle Damping 2207
West, J.C., J.M. Sturm and M.A. Sletten

6. Dominant Wave Effects in Wavetank Measurement of Microwave Doppler Spectra 2210
Plant, W.J., V. Hesany, W.C. Keller and M.A. Donelan

7. Comparison of Experimental and Theoretical Ocean Wavenumber Spectra for Gravity-Capillary and Capillary Waves NA
Keller, M.R., and B.L. Gotwols

8. Depolarization in Microwave Scatterometry 2213
Lee, P.H.Y., J.D. Barter, K.L. Beach, B.M. Lake, H. Rungaldier, J.C. Shelton, H.R. Thompson, Jr., and R. Yee

9. Influences of Wind Bursting on Radar Return 2216
Savtchenko, A., S. Tang and J. Wu

10. Measuring Small-Scale Water Surface Waves: Nonlinear Interpolation and Integration Techniques for Slope-Image Data 2219
Daida, J.M., R.R. Bertram, D.R. Lyzenga, C. Wolf, D.T. Walker, S.A. Stanhope, G.A. Meadows, J.F. Vesecky and D.E. Lund

FPES -- Spatial Decision Support Systems: Cost/Benefit Analysis

1. Remote Sensing: Economic Viability Environmental Monitoring 2222
Macauley, M.K., and T.J. Brennan

2. Ecosystem Management: A Decision Support GIS Approach 2225
Ji, W.

3. Dawn of a New Era: The Image Information Age 2228
Jordan, III, L.E.

4. Non Point Source Pollution 2231
Subra, W., and J. Waters

5. A Genetic Approach to Ecosystem Modeling: Do the Benefits Warrant the Costs? NA
Morain, S., and A. Budge

6. Cost-Effective Environmental Consulting Using Geographic Information Systems and Remote Sensing 2234
Gibas-Tracy, D.R.

FPES *continued* -- Spatial Decision Support Systems: Cost/Benefit Analysis

7. Land Surface Remote Sensing and Geographical Information Systems for Water Quality Modeling 2237
Mattikalli, N.M., and E.T. Engman

8. Satellite Remote Sensing and Geographic Information System for Monitoring Morphodynamics of the Active Yellow River Delta, China 2240
Yang, X., M.C.J. Damen, R. van Zuidam, A. van Gelder, J.H. van den Berg and G. Chen

9. Remote Sensing and Core Data Needed to Support Planning and Policy Decision Making 2242
Foresman, T.W., J.E. Estes, J.J. Garegnani and D.L. Porter

FPF -- Snow, Glaciers and Permafrost

1. Analysis of Snow Cover in Alaska Using Aircraft Microwave Data (April 1995) 2246
Hall, D.K., J.L. Foster, A.T.C. Chang, D.J. Cavalier, J.R. Wang and C.S. Benson

2. Estimation of Snow Surface Albedo Using Landsat Thematic Mapper 2249
Shi, J., T.H. Painter and J. Dozier

3. Estimating Alpine Snow Cover with Unsupervised Spectral Unmixing 2252
Rosenthal, W.

4. Airborne and Spaceborne SAR Interferometry: Application to the Athabasca Glacier and Area 2255
Vachon, P.W., D. Geudtner, L. Gray, K. Mattar, M. Brugman, I. Cumming, and J.L. Valero

5. Effects of System Errors on Combined MM/IR Neural Network Inversion of Surface Snow Properties 2258
Jackson, S.R., and R.M. Narayanan

6. Machine-Based Snow Line Determination and the Identification of Ice Sheet Features in Visible and SAR Imagery 2261
Lin, I.I., and W.G. Rees

7. Thawing of Soils in Siberia Observed by the ERS-1 Scatterometer Between 1992 and 1995 2264
Boehnke, K., and V.R. Wismann

8. Passive Microwave Freeze/Thaw Classification for Wet Tundra Regions 2267
Kim, E.J., and A.W. England

9. Freeze / Thaw Classification for Prairie Soils Using SSM/I Radiobrightnesses 2270
Judge, J., J.F. Galantowicz, A.W. England and P. Dahl

FPH -- Advanced Sensors

1. Integrating Global Positioning Systems with Satellite Remote Sensing: Avoiding Major Pitfalls 2273
Leavitt, B.C., and S.L. Payton

2. Remote Sensing with Hyperspectral Imagery Using DASI -- An Imaging Interferometer 2276
Hammer, P.D., D.L. Peterson, W.H. Smith, S.E. Dunagan, L.F. Johnson, A.W. Strawa, J. Zott and G. Langford

3. Multi-Mission Radar Altimeter: Concept and Performance 2279
Jensen, J.R., and R.K. Raney

4. Backscatter Characteristics of Buried Targets Measured Using an Ultrawideband Polarimetric Random Noise Radar 2282
Hoffmeyer, P.D., Y. Xu, R.M. Narayanan and J.O. Curtis

5. Airborne 14-Channel Microwave Radiometer HUTRAD 2285
Hallikainen, M., M. Kemppinen, K. Rautiainen and J. Pihlflyckt

6. Experimental Investigation of Diffraction Gratings for Millimeter/Submillimeter-Wave Instruments 2288
Nadimi, S.A., J.W. Bredow and G.C. May

7. Ground Segment for ERS-2 GOME Sensor at the German D-PAF 2291
Balzer, W.

8. Dual Polarized L-Band Microstrip Patch Array for the AIRSAR/TOPSAR System 2294
Rostan, F., W. Wiesbeck and J.J. van Zyl

9. Self-adapting Sensor for Atmospheric Electricity Measuring 2297
Yanovsky, F.J.

10. Spectrometry From Airborne Platforms: Examples and Analysis of the Italian Research Council (CNR) MIVIS Campaigns Over Different Test Sites NA
Bianchi, R., R.M. Cavalli and S. Pignatti

FPP -- Land Cover: Inventory and Monitoring

1. Integration of Multispectral Land Ecological Data for Characterizing Montane Meadow Communities in the Greater Yellowstone Ecosystem 2300
Jakubauskas, M.E., D. Debinski and K. Kindscher

2. Case-Based Reasoning and Software Agents for Intelligent Forest Information Management 2303
Charlebois, D., D.G. Goodenough, A.S. Bhogal and S. Matwin

3. The Suitability of Future High-Resolution Satellite Imagery for Forest Inventory 2307
Solberg, R., A.H. Schistad Solberg, H. Koren and K. Aas

4. Applications of Multi-Frequency, Multi-Polarization and Multi-Incident Angle SAR Systems in Urban Land Use and Land Cover Mapping 2310
Xia, Z.G.

5. Variations in Land Cover Areas Estimated from Remotely Sensed Data 2315
Yang, W., and J.W. Merchant

6. Recent Experiences in Mapping Land Cover From AVHRR Data: People's Republic of China Test Sites 2318
Qiu, Z., L. Yang and T.R. Loveland

7. Validating Global Landcover Classification Pattern Using Spatial Resoluton -- Independent Landscape Metrics 2321
Frohn, R.C., and J.E. Estes

8. Using Geoinformation System and Space Imagery to Monitor Environmetal Changes in the Aral Sea Ecological Disaster Area 2324
Glushko, E.V., A.V. Ptichnokov and V.S. Tikunov

9. Limitations for Multispectral Classification of Temperate Forests -- Scaling Problems of Groundtruth and Satellite Data 2326
Kellenberger, T.W., and K.I. Itten

FPV -- SAR Geocoding and Orthorectification

1. Practical SAR Orthorectification 2329
Pierce, L., J. Kellndorfer, F. Ulaby and L. Norikane

2. Optimization of the Tie-Pointing Procedure for the Terrain Correction of SAR Data 2332
Roth, A., W. Knoepfle and M. Matschke

3. Applicability of Automatic Tie-Pointing for Geocoding and Mosaicking of Overlapping SAR Images NA
Raggam, H., A. Bauer and W. Hummelbrunner

4. Geocoding and Classification of ERS/JERS-1 Composites 2335
Kellndorfer, J.M., M.C. Dobson and F.T. Ulaby

5. Experiences In Multi-Sensoral SAR Geocoding 2338
Roth, A., D. Kosmann, M. Matschke, B. Mueshen and H. John

6. Design, Performance and Technology Aspects in Relation to a Next Generation High Resolution Spaceborne SAR Instrument 2341
Bottger, H., C.Heer and J.J. Wilson

7. Development of a High-Resolution Ground-Based Synthetic Aperture Radar 2344
Morrison, K., and J.C. Bennett

8. Integrated Design of Synthetic Aperture Radars for Unmanned Aircraft 2347
Vesecky, J.F., and J.M. Cornwall

9. ER-2 IFSAR Digital Terrain Matrix Collection System 2349
Malliot, H.A.

FPZ -- Vegetation Properties

1. Novel Algorithms for Remote Sensing of Chlorophyll Content in Higher Plant Leaves 2355
Gitelson, A.A., M.N. Merzlyak and Y. Grits

2. Chlorophyll Flourescence Measurements of Several Plant Species Compared with MNDVI-Images in Air Pollution Affected Sites in Varanger, Northern Norway NA
Tommervik, H.

3. An Approach for Mapping Light-Use Efficiency on Regional Scales Using Satellite Observations 2358
Norman, J.M., M.C. Anderson and G.R. Diak

4. Detecting Spatial and Temporal Patterns of Aboveground Production in a Tallgrass Prairie Using Remotely Sensed Data 2361
Su, H., J.M. Briggs, A.K. Knapp, J.M. Blair and J.R. Krummell

5. Assimilation of Shortwave Remote Sensing Observations Within an Agrometeorological Model -- Crop Production Estimation 2366
Moulin, S., A. Fischer and G. Dedieu

6. Mapping Field Crop Evapotranspiration Using Airborne Multispectral Imagery 2369
Ahmed, R.H., and C.M.U. Neale

7. Effects of Shadows on Vegetation Indices 2372
Huemmrich, K.F.

8. Multisensor Estimation of Vegetation Characteristics 2375
Zhang, J., R.M. Narayanan, B.T. Tracy, B.L. Gwilliam, R.L. Bolus, T. Pangburn and H.L. McKim

9. Subpixel Spatio Temporal Pattern Analysis of Remote Sensing Observations for Predicting Grassland Ecological and Biophysical Parameters 2377
Csillag, F., A. Davidson , S. Mitchell, B. Wylie, D. Wedin, H. Peat and M. Kertesz

10. Retrieval of Crop Biomass in 1989 by Using ANN MODEL of 1988 2380
Jin, Y.Q.



IGARSS'96

1996 International Geoscience and Remote Sensing Symposium

Technical Papers

Dual-Frequency Three-Dimensional Images of Clouds

John M. Firda, Stephen M. Sekelsky, and Robert E. McIntosh
Microwave Remote Sensing Laboratory
Dept. of Electrical & Computer Engineering
University of Massachusetts
Amherst, MA 01003
T: 413.545.0779 / F: 413.545.4652 / firda@alex.ecs.umass.edu

Abstract— **This paper presents a method of forming three-dimensional representations of clouds and precipitation by combining series of two dimensional scans. In April of 1995 the Cloud Profiling Radar System (CPRS) collected dual-frequency Doppler radar data of several cloud scenarios. Images of reflectivity and linear depolarization ratio are presented from different viewpoints of a precipitating cloud with a well defined melting layer.**

I. Introduction

Observations of cloud structure and geometry provides insight into the development and progression of storms. Geometric variables such as cloud base height and cloud top height are useful for estimating the total amount of liquid-water and ice in the clouds. Such studies are limited with only vertically orientated measurements, however, because the measurement consists of the antenna volume at only one location over time. A more complete picture of the clouds can be created by performing scans to observe the adjacent pixels.

The Cloud Profiling Radar System attained such measurements during the Ground Based Remote Sensing Intensive Observation Period (GBRS-IOP). Successive RHI scans were stacked in time to create a three-dimensional representation of a precipitating cloud. The images provide a unique perspective to examine cloud structure and may be valuable for comparison with satellite imagery or obtaining two-dimensional measurements of cloud base height.

II. Radar System

The Cloud Profiling Radar System (CPRS) is a fully polarimetric Doppler radar consisting of two subsections at 33 and 95 GHz [1]. Parameters for the radar system are shown in Table 1. Both radar subsections transmit and receive vertical and horizontal polarized pulses through a single 1-meter lens antenna [2]. The single antenna design ensure both frequencies are sampling the same cloud volume. The transmit polarization can be selected on a pulse to pulse basis and each sub-system has receiver channels to record the amplitude and phase of co-pole and cross-pole backscattered signals simultaneously. The data acquisition system consists of an HP VXI card cage containing identical, independent configurations for the two frequencies. Each is composed of six digitizers to record the log-magnitude, I and Q for each receiver channel, and a DSP card to perform averaging and compute either pulse-pairs or FFTs. The entire radar system is mounted on an azimuth over elevation positioner to perform RHI, PPI, VAD, and Raster scans.

TABLE I
CPRS System Parameters

	Ka-band Radar	W-band Radar
Frequency	33.12 GHz	94.92 GHz
Peak Power	100 kW	1.5 kW
Average Power	120 W	15 W
PRF	200 Hz - 3 kHz (20 kHz bursts)	1 Hz - 80 kHz
Pulsewidth	200 - 2000 ns	50 - 2000 ns
Noise Figure	11 dB	13 dB
3 dB Bandwidth	2, 5 MHz	2, 5 MHz
3 dB Beamwidth	0.5 deg	0.18 deg

CPRS is capable of measuring reflectivity (Z_e), linear depolarization ratio (LDR), mean fall velocity, velocity spectral width, as well as the full Doppler spectrum. Polarimetric measurements such as differential reflectivity (Z_{DR}), correlation magnitude ($|\rho_{hv}(0)|$), and specific differential phase (K_{DP}) are also attainable.

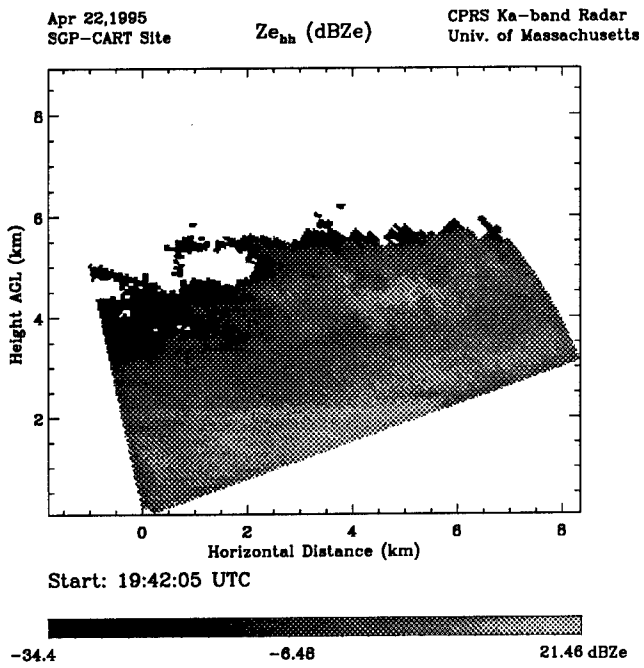
III. Experiment

In April and May of 1995, CPRS participated in the Atmospheric and Radaition Measurement (ARM) program's GBRS-IOP at the Department of Energy's Cloud and Radiation Testbed (CART) site in Billings, OK. The role of CPRS was to collect Doppler radar data of clouds and precipitation in support of site instruments. During this part of the year a variety of conditions are encountered across the southern great plains. Typically, squall-line systems develop to the south-west of the CART site and move either east or north-east producing heavy rain and sometimes hail. Large formations of cirrus and stratus clouds are encountered as well.

CPRS performed successive RHI scans at different ranges in elevation while pointing cross-wind in azimuth. The scan speed was selected to be low enough not to

This work was support by the Department of Energy under grant No. DE-FG02-90ER61060

0-7803-3068-4/96$5.00©1996 IEEE



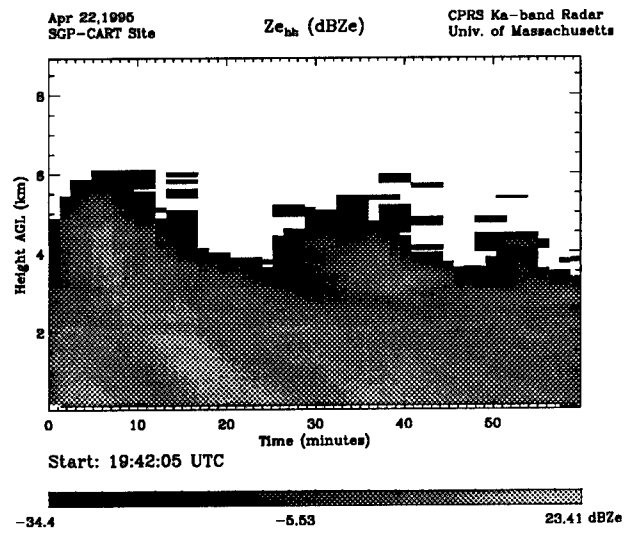
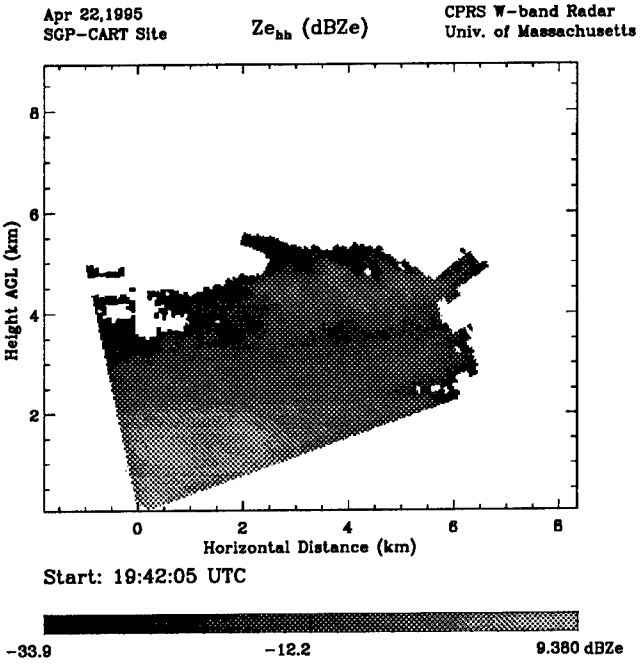


Fig. 1. 33 GHz images of reflectivity. The top image is the first RHI scan ofthe series. The bottom image is a time-height plot taken at 90 degrees elevation.



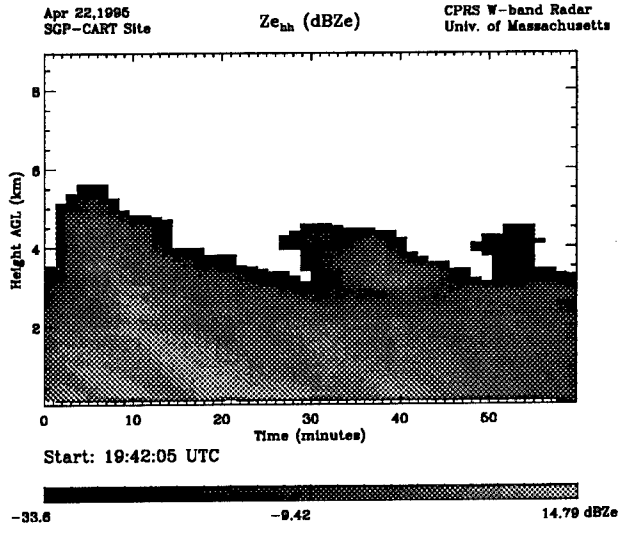


Fig. 2. 95 GHz images of reflectivity. The top image is the first RHI scan of the series. The bottom image is a time-height plot taken at 90 degrees elevation.

loose sensitivity but fast enough to minimize changes in the cloud from scan to scan. For example, a scan from 30 to 100 degrees in elevation would take between 40 to 60 seconds. Performing these scans creates snap-shots to observe structural changes in the clouds and movement of hydrometeors.

IV. Measurements

On April 22, a series of 50 RHI scans were performed over 60 minutes during a precipitation event. The radar scanned from 20 to 110 degrees in elevation while pointing cross-wind in azimuth. After stacking the scans in time, a three-dimensional representaion was created.

Fig. 1 shows the first RHI scan in the series and a time-hieght plot at 90 degrees elevation for 33 GHz reflectivity, and the corresponding 95 GHz images are shown in Fig. 2. A melting layer located at 2 km with a thickness of 400 m can be identified by the bright band. Measurements of depolarization indicate LDR of -11 db and fall velocity changing from 1.5 m/s to 5.0 ms at 2 km. The effects of attenuation are evident as the 95 GHz sensistivity decreases while the path length through the rain and

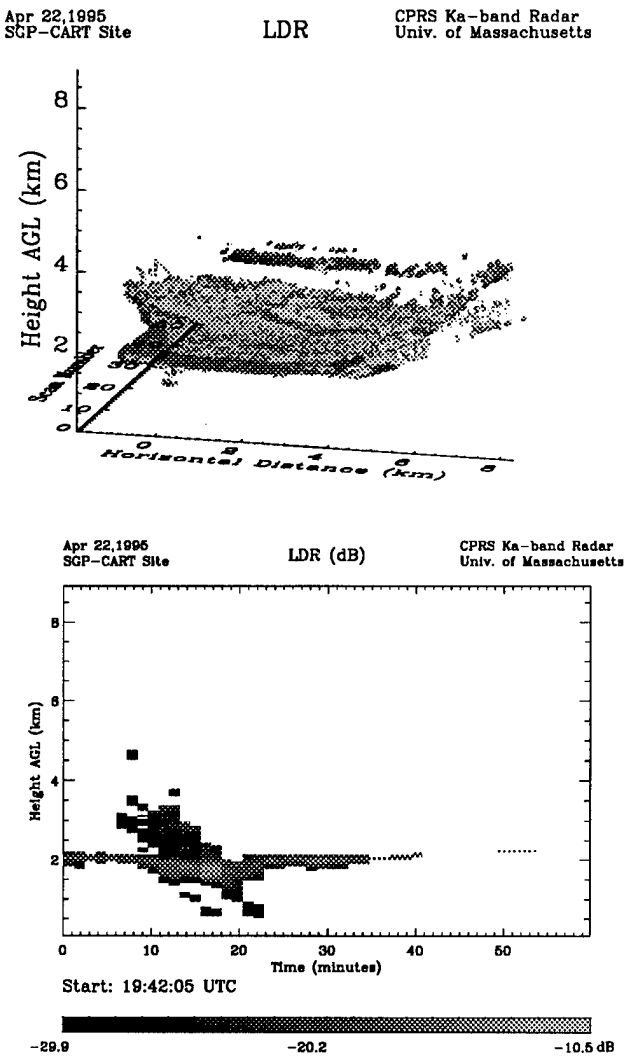


Fig. 3. 33 GHz images of Linear Depolarization Ratio. The top image is a three-dimension represenatation. The bottom image is a time-height plot taken at 90 degrees elevation.

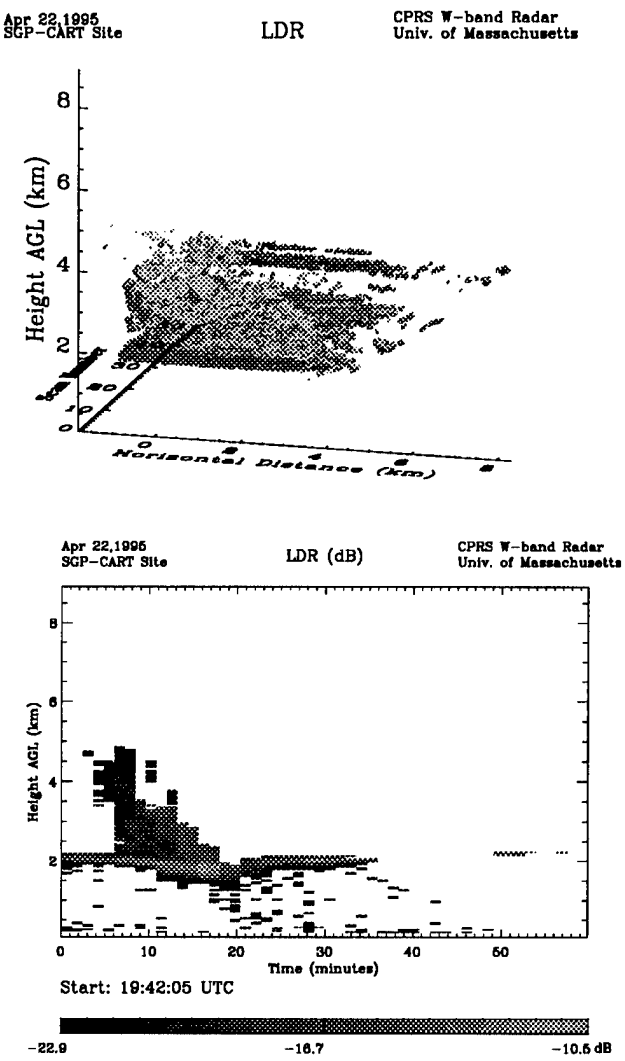


Fig. 4. 95 GHz images of Linear Depolarization Ratio. The top image is a three dimensional representation. The bottom image is a time-height plot taken at 90 degrees elevation.

melting layer increases.

Fig. 3 shows a three-dimensional image and a time-hieght plot at 90 degrees elevation for 33 GHz depolarization, and Fig. 4 shows the 95 GHz images. Snow and ice in the cloud above the melting layer fall and combine with mixed phase particles causing the melting layer to double in thickness to 800 m. The particles then fall and the melting layer returns to 400 m thick. Towards the end of the scan series, the melting layer weakens and falls apart.

V. Conclusion

The method presented has been applied to cases with and without precipitation, and the results show promise of a straight-forward method to interpolate cloud structure from simple scanning routines. Another scanning method used in conjuction this is to scan upwind of an approaching storm to study the development of anvil clouds. By combining the two methods, the life cycle of an anvil and storm can be characterized in detail.

References

[1] Sekelsky, S.M. and McIntosh, R.E. Cloud observations with a polarimetric 33 GHz and 95 GHz radar. *Meteorology and Atmospheric Physics*, 58:123–140, 1996.

[2] Mooradd., D.C. Design, development and construction of a dual-frequency, dual-polarized millimeter wave cloud profiling radar antenna. Master's thesis, University of Massachusetts at Amherst, 1993.

Preliminary Backscatter Lidar Measurements of Atmospheric Boundary Layer and Cirrus Clouds in Buenos Aires (34.6 S / 58.5 W).

M.B. Lavorato, G.J. Fochesatto, E.J. Quel.
CEILAP (CITEFA - CONICET)
Zufriategui 4380, 1603 Villa Martelli, Buenos Aires, Argentina.
email lavorato@udceilap.edu.ar; phone: 54 -1- 761 0131; fax: 54 -1- 760 3210
P. H. Flamant.
Lab. de Météorologie Dynamique du CNRS,École.Polytech., 91128. Palaiseau, France.

Abstract - **We present preliminary backscatter lidar measurements of atmospheric boundary layer and height, geometric and optical thickness of cirrus. In addition, aerosols and clouds were detected at Buenos Aires. The lidar system is based on a pulsed Nd-YAG laser at 532 nm and a Newtonian telescope. A photomultiplier tube is used in the detection system. Differents methods of backscattering lidar signal processing for these atmospheric parameters are discussed.**

I. INTRODUCTION

Atmospheric monitoring by a LIDAR system allows remote acquisition of atmospheric backscattering signal to retrieve aerosol concentration, thickness and cloud height, presence and characterization of cirrus and boundary layer [1].

LIDAR system presents the advantage of operating in real time with good spatial resolution, lower cost and permanent monitoring, in contrast to satellite measurements that have small spatial resolution and low precision but cover greater areas. Therefore the LIDAR system is more useful for calibration and validation measurement data.

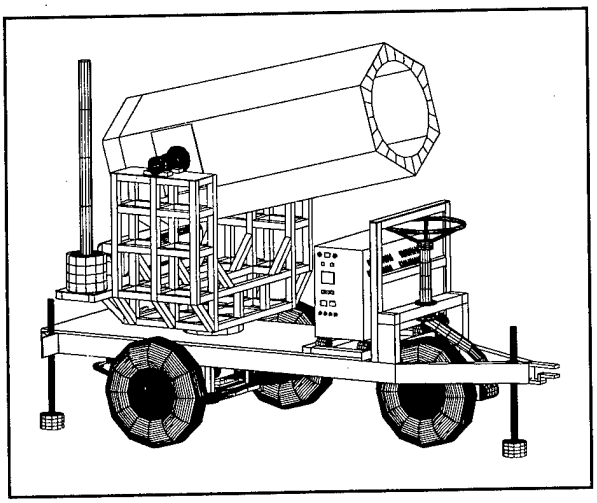


Fig. 1. LIDAR SYSTEM (schematic)

0-7803-3068-4/96$5.00©1996 IEEE

II. LIDAR SYSTEM.

We present a Lidar Station for atmospheric boundary layer (ABL) monitoring, measurements of height, geometric and optical thickness of clouds, aerosols and cirrus. This was accomplished at times during the past year at our LIDAR station developed in CEILAP (CITEFA-CONICET) - Villa Martelli - Prov. of Buenos Aires - Rep. Argentina (34.6S / 58.5W).

The Lidar emitter is a pulsed, doubled frequency (532 nm), 310 mJ of energy per pulse, 10 Hz and 0.3 mrad divergence Nd-YAG laser. The telescope is field of view adjustable between 0.1 to 10 mrad. The backscattering radiation detection is achieved by a telescope with a Newtonian parabolic mirror f/2 type of 50 cm in diameter, coupled to a photomultiplier detector and data acquisition system.

The output laser emission is vertically oriented and the detection system is aligned with the output emission. The telescope was designed to be guided to elevate between -10° and 90° and between 0° and 300° in azimuth as shown in figure 1. Thus, we can take different types of atmospheric measurements.

III. ATMOSPHERIC BOUNDARY LAYER (ABL).

The ABL is the section of the troposphere where the most important parameter of the atmosphere are directly influenced by the presence of the Earth surface. The dynamic nature of this influence is due to hot and humid air flows and the sun and surface winds [2].

This is due to two factors: a hot air concentration under a heavy cold and stable layer, with cyclic daytime evolution.

Figure 2 show a typical backscattering signal for the ABL measurement. We noted a sharp variation in the backscattering signal around 700 meters.

The signal processing of ABL monitoring is based on the follow up of the discontinuity or slope breakdown derived from the converted signal logarithms. The procesed data signal contain the information about the molecular atmospheric density variations [3].

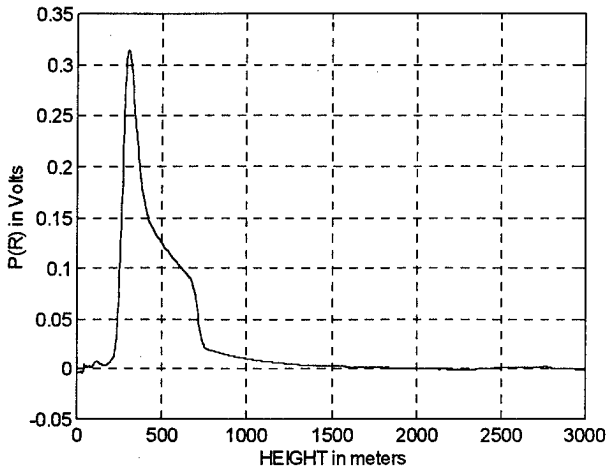


Fig. 2. ABL (August 30,1995 - 10:55AM - Av.=20)

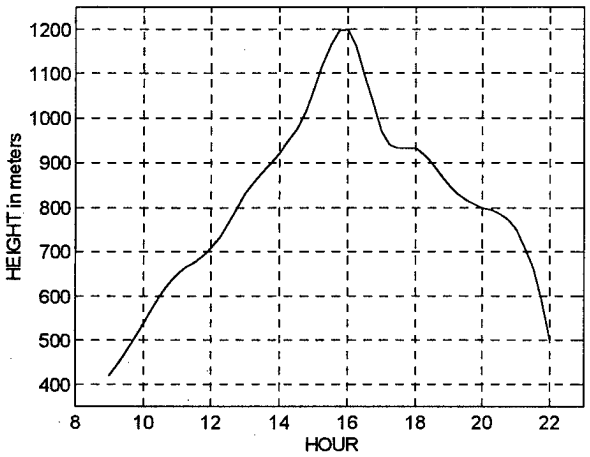


Fig. 3. ABL daily evolution (15 minutes per sample)

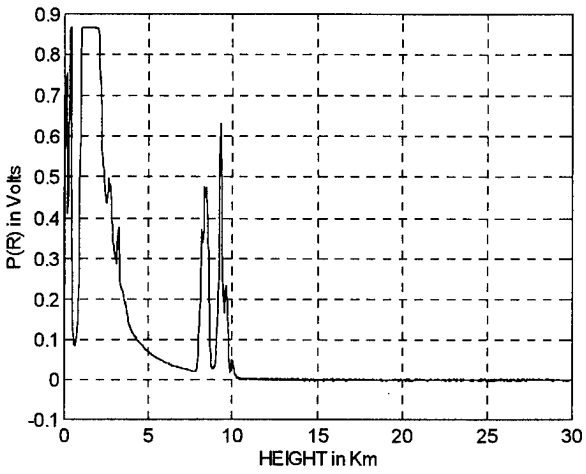


Fig. 4. Cirrus: 28 aug. 95 - 8:07:05 PM - Av.=50

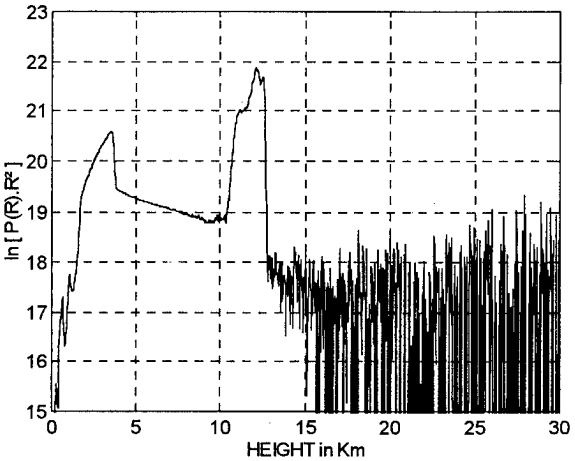


Fig. 5. Cirrus:23 aug. 95 - 6:30 to 8:30 PM - Av.=18000

Figure 3 shows the ABL daily evolution monitoring. We noted the ABL limits (maximum and minimum) throughout a full day of monitoring.

We can see in a clear day (oct. 13,1995), the maximum (1200-1300 m) and the minimum (300-400 m) limits which depend of the climate conditions and the seasons of the year.

III. CIRRUS AND CLOUDS.

Clouds and cirrus are found in the troposphere, the later occur in the high troposphere and they have a significant effect on the radiative budget. They permanently make up a large part of atmosphere and they have a significant impact on the radiation budget of the earth. Hence, it is necessary to study their optical and physical properties which are used in climate model [4].

We present monitoring of the optical and geometrical properties of cirrus by Lidar. The processing of the signal backscatter gives access to properties such as the total volume backscattering coefficient, and the geometric and optical thickness and height of cirrus and clouds.

Figure 4 shows an example of a multilayer cirrus between 8 to 10 Km and tropospheric aerosols located at 3 to 4 Km for 50 shots averaged. Based on the slope method we obtained in the figure 5 the optical thickness (0.55) and geometrical thickness (~ 2.75 Km). The attenuation coefficient is approximately ($\alpha = 2.0\ 10^{-4}\ m^{-1}$).

Real time and long term evolution of cirrus and clouds during daytime and nightime is one of the main capabilities of our Lidar system. Therefore, seasonal and instantaneous evolution can be monitored.

IV. SIGNAL PROCESSING METHODS.

The signal processing method is based on the backscattering Lidar equation:

$$P(R) = \frac{c}{2}\eta\, EA \frac{1}{R^2}\beta(R)\,[T(R)]^2$$

where $T(R) = \exp\left(\int_0^R \alpha(\xi)d\xi\right)$ and

A is the telescope area, η the detector efficiency, $T(R)$ the optical transmission, E energy per pulse, α the total attenuation, absorption and extinction coefficient, and β is total backscattering coefficient.

ABL signal processing is based on a sharp variation of backscattering signal due to the discontinuity of the potential temperature profile in the troposphere.

There are several methods to determine ABL heigth [3].
The *Derivative method* is based on the derivative of the logarithmically corrected [P(R).R^2] backscattering signal. Then for ABL monitoring we determine the minimum of this corrected signal.
The *Break Slope method* is a graphic determination of the ABL position. Based on a simple model of the ABL which works from a sharp atmospheric density variation at the point of measurements.
The *Standard deviation method* is based on the monitoring of a fixed point around the limit of the ABL. The strong temporary variations in backscattering intensity is due to the movement of the aerosols trapped in thermal columns reach a maximum height. Thus, the covariance is affected if the measures are made at regular time intervals. The covariance graphics will present a maximum at the top of the ABL.

Cirrus and cloud measuring methods are based on an inversion of the lidar equation. The optical and geometrical properties of cirrus can be determined by adequately processing signals. The solution is known as the "inverse problem" because there are two unknown parameters, the backscattering coefficient (β) and the extinction coefficient (α).

In order to solve the lidar equation a relationship between β and α is usually assumed $\beta = \kappa\,\alpha^g$ where k is the backscatter-to-extinction ratio and g=1 usually. Two solution forms are available that use either the variables P(R).R^2 or S(R)=ln[P(R).R^2], called linear and logarithmic solution respectively, where P(R) is the received power converted to a mV and R is the range in Km.

The most important methods of data analysis of cirrus and clouds are [4]:
The *slope method:* used to obtain optical thickness assuming simple molecular scatter (k=1 is considered). In this method optical signal backscattering beyond cirrus clouds is required.
The *Linear method* this method required a calibrated lidar system and k must be a constant throughout the cloud.
The *LMD1 method* is an integration process of the backscattering profile adapted to cirrus and based on the Klett integration method.
The *LMD3 method* is based on the determination of the coefficient α where is g unitary for a given altitude.

IV. CONCLUSIONS.

To improve the signal to noise ratio in the ABL and Cirrus monitoring we used the signal averaging technique. Thus, electrical noise and sky background radiation were eliminated.

DC and low frequency noise generated by the atmosphere (variable during the day) were eliminated by means of the aquisitions of a second signal having the same number of averaging and the same condition of the measured signal, but no laser radiation.

Precision in the results of the lidar equation coefficients is obtained by increasing the number of measurements in the same time interval.

For monitoring ABL evolution is necessary to carry out measurements during the whole day.

Thus the variance method permits us to determine precisely the ABL break point and its spatial fluctuations.

The backscattering-extinction ratio k and the atmospheric attenuation coefficient α are the most important parameters to be calculated.

The slope method is simple and most adequate to determinate the coefficients of Lidar equation for a thin and homogeneous atmospheric layer. It also permits calculation of the optical and geometric cirrus thickness. We monitored in the nighttime and daytime cirrus from 7.5 to 13.5 Km.

The authors wishes to thank Salem Elouragini, Rene Valentin, Jacques Pelon and Mauricio Pagura for fruitful discussions and practical aids. This work was supported by CONICET and CIC.

V. REFERENCES.

1- "Laser monitoring of Atmosphere". E.D.Hinkley. Springer Verlag. 1976.
2- Roland B. Stull. An introduction to boundary layer meterology. Atmospheric Science Library. Kluwer Academic Publishers
3- Etude de la Couche Limite Atmospherique par télédétection lidar active. R. Claudon et P. Pailloux. Laboratoire de Météorologie Dynamique. France.1989
4- Etude des proprietés óptiques et géometriques des cirrus par télédétection optique active (lidar) et passive (radiométrie). These de Doctorat de l'Universite Paris 6. Salem Elouragini. 1991.

Improvement of a standard Doppler dealiasing technique for weather radars operating in heavy clutter environment

D. Giuli, L. Facheris, F. Frattura, L. Baldini
Dipartimento di Ingegneria Elettronica, Universita di Firenze
Via di Santa Marta, 3, 50139, Firenze, Italy
Tel: +39 55 4796370-274 Fax: +39 55 494569 e-mail: giuli@ingfi1.ing.unifi.it

Abstract -- Techniques devised to correct aliased Doppler velocity PPI maps obtained from meteorological radars seem to have not accounted for the possible presence of extended areas of ground clutter and/or practical absence of signal due to beam screening. This is a severe limit for radars operating in hilly terrain. Dealiasing methods are necessarily based on hypotheses of continuity of the radial velocity field, which are quite harder to exploit when such field is corrupted by ground clutter, or even void of data over relatively vaste areas. In this paper we discuss this topic, first showing some drawbacks that a classical dealiasing technique undergoes when utilized in such a context. Data utilized are those gathered by a dual polarization Doppler weather radar sited in Tuscany, in a quite orographically complex environment. After that, we describe a modified algorithm that overcomes the limitations of the original technique, and show that the proposed modifications are useful to make the algorithm work correctly even under severe clutter/beam screening conditions.

INTRODUCTION

The Local Environment Dealiasing (LED) technique is the most cited and probably most efficient method for deliasing mean Doppler velocity PPI maps obtained by weather radars [1]. LED works exploiting the hypothesis of local continuity of radial velocity data in both range and azimuth, by sequentially processing range cells of each single radar ray while accounting for data previously processed in azimuthally contiguous cells. In the literature, on the other hand, there is not much evidence of the problems arising when unreliability of average Doppler velocity data makes more complex the task of exploiting the hypothesis of local continuity. Unreliability of data is caused primarily by partial or total beam screening and related clutter effects, which become major problems for those radars that operate in hilly or mountaineous terrain.

We address here the problem of an efficient dealiasing procedure that may be applied also to Doppler velocity maps where a great percentage of data cannot be utilized due to screening/clutter impairments. We first discuss typical problems encountered by applying the LED technique to data collected by the dual polarization radar POLAR 55C: such radar, sited in a very hilly environment near Montagnana (Florence), is able to collect data over major basins of Tuscany. Still at an elevation angle of 2°, which allows monitoring such basins, screening/clutter effects are relevant in other areas covered by the radar. We then show improvements obtained by introducing some modifications and range adaptive parameters to the basic LED technique, devised in order to obtain a general uniformity of the LED behaviour. In fact, the need of discarding unreliable data over relatively large clutter zones in the radar coverage area implies that range cells which may be farther than usual get involved in the comparisons. Thus, the general principle of the modified dealiasing procedure is to allow lower continuity constraints for data referring to farther cells: this has repercussions on every part of the original LED algorithm, influencing also the criterion by means of which the first radar ray to be processed should be selected in order to avoid propagation of errors.

The starting point of the modified dealiasing procedure is the classification of radar data in 'reliable' and 'unreliable', made by resorting to a polarimetric clutter classification technique [2] that utilizes mean absolute and differential reflectivity maps, besides dry clutter maps and Doppler velocity maps.

THE LED TECHNIQUE

We briefly recall here the basic steps of the LED technique, so that the modifications introduced in the procedure we propose can be more easily understood in the next paragraph.

The LED technique is based on an initial radial continuity check and on subsequent error checks:

i) *Radial continuity check*

Initially, the velocity of the current range gate is compared with that of a 'valid' (already checked) preceding range cell, but not farther than 4 cells. If the difference between the two velocities is lower than a given threshold, then the velocity examined is kept unchanged. Instead, if the difference exceeds the threshold, the current velocity is dealiased, if this is possible, by adding or subtracting one or more Nyquist intervals, and the new value is taken as valid.

Should this initial check fail, an average of nine surrounding cells - four of which belonging to the current ray and closer to the radar and five in the adjacent ray - is computed. The current velocity is compared with this average using a different threshold: if it cannot be dealiased, the current velocity is considered not valid and the algorithm proceeds with the error checks. In case that none of the velocities that should be utilized for the average is valid, the algorithm begins a local search for a valid velocity

0-7803-3068-4/96$5.00©1996 IEEE

considering, first, the current ray up to 5 km backward and, if no valid datum is found, the adjacent ray up to 2.5 km forward. If this check fails too, the velocity is assumed as not valid.

ii) *Error checks*

Besides that, the routine makes a few checks with the purpose to avoid the propagation of possible errors occurred during the radial continuity check. Three kinds of checks have been implemented in order to detect these errors.

The first check is activated when five consecutive not valid velocities are detected. The first datum is considered, and the initial radial continuity check is executed again, comparing this datum with the preceding one, this time with a larger threshold. If the check fails, the comparison is made utilizing an average of 15 velocities of the preceding ray.

The second check - the azimuthal check - determines whether the difference between the velocities of 17 azimuthally adjacent gates along the current ray and the preceding ray is lower or higher than a fixed threshold. If all pairs considered do not fall within the threshold, the velocities in the current ray are corrected using a least squares technique.

The third check - the radial check - verifies if there are large differences, in the current ray, between the velocities of two consecutive gates. If there are, the velocity data are not used for the azimuthal check when proceeding with the following ray.

RANGE ADAPTIVE MODIFICATION OF THE LED TECHNIQUE

In case the radar operates in hilly terrain and at low elevation angles, it is possible to have relevant effects of screening and related ground clutter. In areas where these effects prevail, velocity data are unreliable or even missing due to excessive power loss. As evidenced in the next section, the presence of a great percentage of such areas brings about serious problems if the LED technique is directly applied, without modifications.

The main modification with respect to the LED technique is the a priori removal of radar data classified as 'unreliable'. For this, a polarimetric method, that allows the classification of radar data in 'reliable' and 'unreliable', has been used before applying the modified dealiasing procedure. Such method combines in a more complex classification test some simple elementary tests performed on clear air reflectivity maps taken at the given elevation angle, absolute and differential reflectivity maps, besides mean Doppler velocity maps [2].

The presence of clutter areas gives rise also to a not negligible problem, i.e. the absence of data, due to excessive power loss. This is another aspect the dealiasing technique we propose accounts for in several points that follow.

a) The local search performed when the initial radial continuity check fails is extended by adopting a iterative procedure that stops as soon as a valid datum is found. Given the current gate, at the generic n-th step the algorithm checks whether the cell located n gates backwards along the current ray has a valid datum. If this does not happen, the check is made in the preceding ray: first utilizing the cell adjacent to the one just 'removed', and then the cell located n gates ahead with respect to the current one.

b) The first error check (replacement of 5 consecutive not valid velocities) has been modified: the number of gates of the preceding ray to be taken into account for computing the average when such check fails has been increased from 15 to 21. Furthermore, the gates are taken symmetrically with respect to the current cell.

c) Since the radial error check cannot be always performed on a continuous set of valid data, it is not possible to obtain a general uniformity of results utilizing the 'standard' LED technique. For this reason, such error check has been removed, thus simplifying the algorithm and reducing the processing time.

d) The choice of the ray where the whole algorithm is started is relevant since velocities belonging to such ray are never checked through the azimuthal error check. Therefore, dealiasing errors possibly occurred during the initial radial continuity check applied to this ray may propagate to rays processed later. For this reason, a few not-optimal starting areas have been identified on Doppler velocity maps. Such areas are located near extended clutter zones. On the other hand, given the starting ray, no appreciable differences could be evidenced by processing velocity maps clockwise or counterclockwise.

Another aspect that cannot be neglected is the fact that the distance between azimuthally adjacent gates is variable: in fact, the farther the cells are from the radar, the greater is the azimuthal distance. This fact has induced the introduction of further modifications that follow:

e) The procedure performed adopts a different choice of the range gates used for the computation of the average taken as comparison reference when the initial radial continuity check fails. The number of cells taken along the current ray has been increased from 4 to 6, considering also that some data may be missing because of the clutter. The 5 cells in the adjacent ray, which are symmetrical with respect to the current cell, are introduced in the average only if the distance between this cell and the radar does not exceed 50 km. This modification is justified by the fact that getting farther from the radar the distance between two azimuthally adjacent cells is more than 900 m, while 750 m is the distance from the sixth preceding gate along the current ray (we refer to POLAR 55C parameters, i.e. an azimuth beamwidth and a pulse duration of approximately 1° and 1 ms, respectively).

f) The thresholds used for comparing velocity data pertaining to adjacent rays have been set adaptively in order to account for the distance: 8 m/s within the first 300 range cells, 12m/s for the following 300 cell, 19.2 m/s for the last 380 range cells.

g) The azimuthal error check has been performed on a more limited area: in this way, pairs of gates differing in distance too much from eachother are not taken into account for such check. Besides that, the processing time of the algorithm is heavily reduced.

RESULTS

The proposed modified dealiasing technique has been applied to Doppler velocity maps obtained during an intense precipitation event occurred on October 30, 1992, extended over a great part of Tuscany. A preliminary polarimetric classification of radar data has been applied to each map, since a slight variation of elevation angle influences position and size of areas with data classified as unreliable. Unreliable data have been then totally removed from any further processing, typically leaving a number of reliable data ranging from 33% to 47% of the total covered area at elevation angles ranging from 1.5° to 2.5°. Removed data are represented in white in Fig. 1: we show them together with those of Fig. 2 as a quite general example of the results that have been obtained by means of the modified algorithm. The presence of a narrow strip extended from north-west to south-east with a clear discontinuity in the velocity field is evident in Fig. 1. In fact, radial velocities in this area exhibit jumps from values close to the maximum unambiguous velocity V_n (16 m/s) to values close to $-V_n$. Fig. 2 shows the velocity map obtained after the application of the modified algorithm. The mean Doppler velocity field exhibits now a uniform variation all over the radar coverage area, with no residual discontinuities. This is particularly evident in the aforementioned north-west south-east strip, where the initial discontinuity has been removed. It must also be pointed out that the presence of a high percentage of unreliable data, which implies missing velocity data for the dealiasing technique, does not affect the algorithms effectiveness. At this regard, notice in particular the center map, where a vaste clutter area has been removed without causing any error propagation problem in other zones.

ACKNOWLEDGMENTS

This work has been supported by the Italian Ministry for University and Scientific Research and by the National Council for Research.

REFERENCES

[1] Michael D. Eilts, Steven D. Smith: "Efficient Dealiasing of Doppler velocities using local environment constraints", Journal of Atmosperic and Oceanic Technology, Vol. 7, February 1990, 118-128

[2] M. Gherardelli, A. Freni, T.A. Seliga, K. Aydin: "Rainfall versus clutter discrimination by means of dual-linear polarization radar measurements", Journal of Atmosperic and Oceanic Technology, Vol. 8, December 1991, 777-789

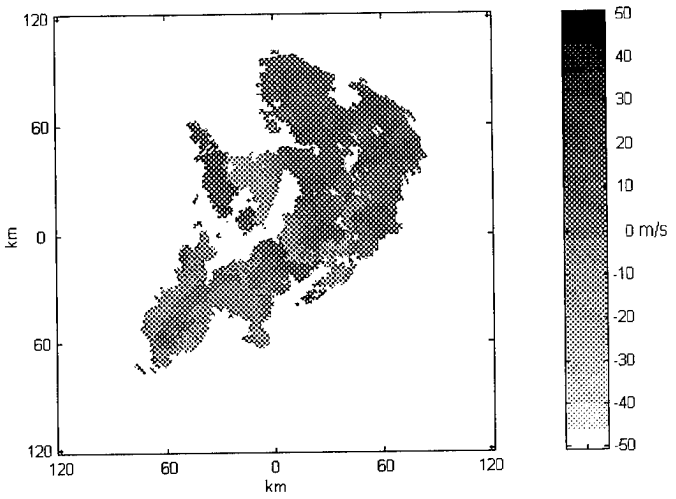


Figure 1 Sample mean Doppler velocity map with an evident aliasing phenomenon in a area surrounded by extended clutter and missing data (the former removed from the originally measured map through the polarimetric classification procedure). The same palette is used as in Fig. 2 for easier comparison. Antenna Elevation: 2.15°.

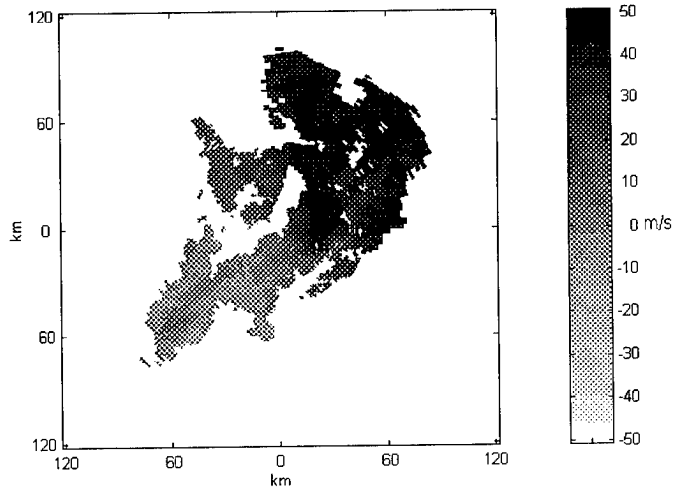


Figure 2 The same map as in Fig. 1 after application of the modified LED technique.

Time-Frequency Analysis of Backscattered Lidar Signal to Study Atmosphere Dynamics

Franck Molinaro, Hassan Bencherif, Miloud Bessafi, Jean Leveau
Laboratoire de Physique de l'Atmosphère, Université de la Réunion
15 Av. René Cassin, BP 7151, 97715 Saint Denis cedex 9, France
Tel : (262)93-82-53 Fax : (262)93-81-66 Mail : molinaro@univ-reunion.fr

Abstract -- The Lidar is a laser beam which sent vertically monochromatic pulses in the atmosphere. The analysis of the backscattered light provides information about the vertical structure, composition and density of the atmosphere versus height. The temperature profile is deduced from the recorded density profile. Temperature perturbations are associated with gravity waves phenomenon. It is now widely recognized that atmospheric gravity waves play a major role in determining the large scale circulation and structure of the middle atmosphere. The aim of the study is to identify characteristics of these particular waves (vertical wavelength, height...) above Reunion island. Different perturbation signals are analysed with an usual parametric time-frequency tool and a comparison is made for two representative periods.

1. INTRODUCTION

Tropical gravity waves are an important contributor of the general stratospheric circulation [1]. To study this phenomenon, Reunion island has a very interesting geographical position (20°S, 55°E).

A perform remote sensing system is efficient to survey middle atmospheric dynamics : the LIDAR (Light Detection and Ranging). It operates as an "optical radar". A typical lidar system employs a laser source to transmit light pulses into the atmosphere. An optical telescope mounted adjacent to the laser is used to intercept backscattered echoes from scatterers in the path of the transmitted pulses. Thus, temperature profile is deduced from recorded density profile assuming that the density is in hydrostatic equilibrium and obeys to the perfect gas law [2]. The profile is limited upwards by the signal to noise ratio at 70-80 km an downward by the aerosols contribution which are superposed to Rayleigh signal. Study of perturbation signals will give gravity waves characteristics.

In a previous work [3] the Smoothed Pseudo Wigner-Ville Distribution (SPWVD) was applied on this kind of signal. At high heights (45-60 km) we have obtained gravity waves characteristics for different nights. In this study we focus on the evolution of wavelengths versus heigth. Magnitude of gravity waves increases with height. An inconvenient of the SPWVD is its difficulty to show on the same representation multicomponent signal with low and high magnitude. For this paper, we prefer parametric time-frequency representations which are less sensitive on the magnitude and more accurate with low number of samples. We represent wavelength evolution with parametric modeling based on Autoregressive model. The aim of the paper is to study gravity waves performances during two periods, austral summer and winter, and also for different atmospheric layers.

2. INSTRUMENTAL LIDAR SYSTEM

The use of lidars for atmospheric studies has known a large development in the last two decades. The possibility it offers to probe at a distance and without perturbing the medium several physical parameters as density, temperature, wind, turbulence as well as the concentration of specific atmospheric constituants has opened a whole domain of application for studying the environment. The lidar is a good tool to survey atmosphere due to its possibility to give a continuity of measurements, to its easy handling and to its low cost of operation. Shorter wavelength range gives lidar systems the oppotunity for sensing atmospheric constituents and properties to which radar was insensitive.

Our lidar configuration is classical : it is a monostatic system in which the laser beam is projected through the receiving telescope. Backscattered photons collected by the telescope are focused onto a photomultiplier which yields an electronic signal proportional to the received light flux. Then, the signal is sampled, digitized and stored in a microcomputer.

The diagram on Fig.1 shows that lidar system can be divided into three subsystems described in the following lines : emission source, reception device and detection and storage unit. Lidar characteristics of emission and reception are given Table 1.

3. TEMPERATURE PERTURBATION SIGNAL

The backscattered photons by atmospheric constituants from layer at a given altitude are proportional to the atmospheric density. These backscattered photons which result in an elastic interaction between emitted laser pulses and the atmosphere are collected by the telescopes and computed after reaching the photomultiplier tubes. Thus, a temporal analysis of the number of backscattered photons reveals the vertical structure of the atmosphere layers crossed by the laser beam. According to the Rayleigh theory, when the atmosphere is typically molecular, the backscattered photons number is right away proportional to the atmospheric density.

Assuming that the atmosphere obeys the perfect gaz law, is in hydrostatic equilibrium, and the molecular air mass is constant, the temperature profile is then computed from the density profile [4]. A mean profile is obtained with a lowpass filter from the initial temperature profile. By subtraction set of these two profiles we obtain the temperature perturbation profile (see fig.2). Study of perturbation signals will give gravity waves characteristics.

Table 1 - Lidar characteristics

EMISSION		RECEPTION	
Laser	Nd-YAG	Area	0,67 m^2
Wavelength	532 nm	Resolution	150 m
Pulse energy	300 mJ	Det. mode	Phot. Count.
Emission rate	10 Hz	Field of view	3.10^{-4} rad
Beam div.	0,5 10^{-4} rad	Operation	Mai 1994

0-7803-3068-4/96$5.00©1996 IEEE

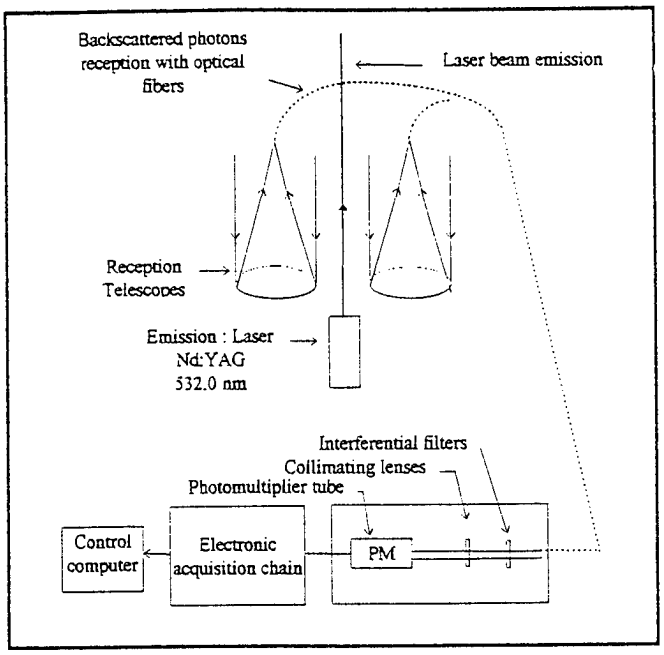


Figure 1 - Instrumental Lidar system

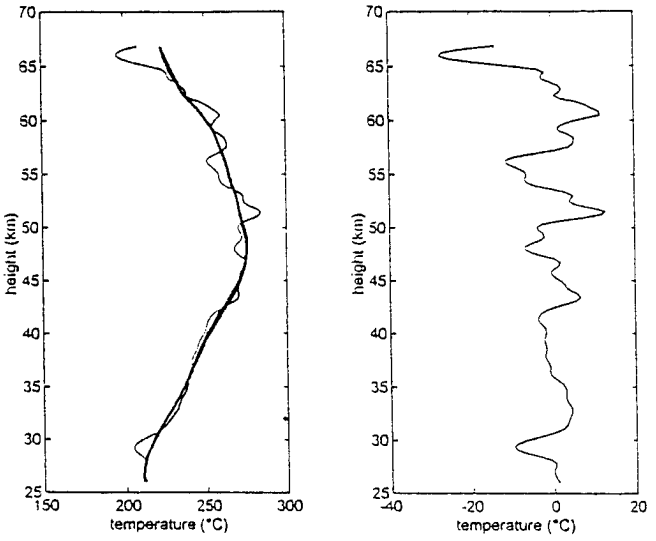


Figure 2 - Left side : initial temperature and temperature mean profile (in Heavy). Right side : Perturbations obtained by substraction of these profiles

4. GRAVITY WAVE

It is now widely recognized that atmospheric gravity waves play a major role in determining the large scale circulation and structure of the middle atmosphere. Gravity waves are generated in the lower atmosphere. Various processes have been proposed to explain the excitation of gravity waves : interaction of surface winds with topography, wind shear associated with jet-streams, geostrophic adjustement, cumulonimbus convection and various meteorological disturbances [1].

5. PARAMETRIC TIME-FREQUENCY REPRESENTATION

5.1 Autoregressive model

For an order p autoregressive (AR) signal modeling, the signal $x(n)$ at time n is modeled as a linear combination of the previous p samples :

$$x(n) = -\sum_{k=1}^{p} a_k x(n-k) + e(n) \qquad (1)$$

$e(n)$ is the model error [5].

5.2 Time-Frequency representation

An advantage of this model is its high frequency resolution for signal with small number of samples. On the opposite, FFT methods depends directly on the signal size. In our case, temperature perturbation signal have around 120-150 samples, it is not enough to obtain accurate time-frequency diagrams with a spectrogram (classical time-frequency representation issue from FFT technics).

To obtain a time-frequency representation, we have computed an AR spectrum on a sliding window. The "instantaneous" spectrum is given by :

$$S_x(f,t) = \sigma_e^2 / \left[1 + \sum_{k=1}^{p} a_k \exp(-j2\pi f k) \right]^2 \qquad (2)$$

t is the center of the sliding window, σ_e^2 is the error power.

6 TIME-FREQUENCY ANALYSIS

Four representative nights are selected for this time-frequency study : two in winter (22 and 23 june) and two in summer (1 and 10 november). The associated perturbation signal is represented in Fig.3. Height resolution is 300 m. We compute an AR model of order 10 on a sliding window of 30 samples (9 km). Four time-frequency representations are shown in Fig.4, they show wavelength evolution versus heigth.

In june (Fig.4.a,b), the waves are localized in 6-8 km wavelength range in stratosphere and low mesosphere. They are relatively stable because it is austral winter and in this season there are less meteorological disturbance. The jet-stream subtropical gets closer to Reunion in august, convection has a low level... These waves seem to be inertio-gravity waves generated by the topography (Reunion Island has a maximum heigth of about 3 km). Different waves appear in austral summer (Fig.4.c,d). Wavelength range is between 1,5 and 8 km and their energy are more important than in june (see fig.3). In the two diagrams appeared two wave components. Wavelengths are more disturbed, but we can notice that they decrease in low mesosphere where components of 2-3 km wavelength appear. In this season convection level is very high, it can explain the disturbance of wavelength and the increasing of energy.

7. CONCLUSION

In this study, different temperature perturbation signals coming from a lidar remote sensing system are analysed in term of wavelength versus height. A classical parametric time-frequency method is used to analyse four representative days.

Comparison between time-frequency diagrams indicates that waves are more stable and more localized in term of wavelength in austral winter. In this season, one component is predominant which wavelength belong to the 6-8 km

bandwith. We suppose that this kind of wave have topography origin. On the opposite, in austral summer, wavelengths are more disturbed and have higher amplitude. We explain this phenomenon by the high convection level in this season.

REFERENCES

[1] L.Pfister and al, "Gravity Waves Generated by a Tropical Cyclone During the STEP Tropical Field Program : A Case Study", J. of Geophys. Res., vol 98, p8611-8638, may 20, 1993.

[2] R. M. MEASURES, Laser Remote Sensing : Fundamentals and Applications. New York, NY : Wiley, 1984.

[3] F. MOLINARO, H.BENCHERIF, M. BESSAFI, Analyse temps-fréquence du signal rétrodiffusé d'un Lidar pour l'étude des ondes de gravité dans l'atmosphère, p1331-1334, GRETSI 1995.

[4] A. HAUCHECORNE, M.L. CHANIN, Density and temperature profiles obtained by lidar between 35 and 70 km, Geophys. Res. Lett., p565-568, 1980.

[5] M. KAY, Modern Spectral Estimation, Theory and application, Prenctice Hall, 1987.

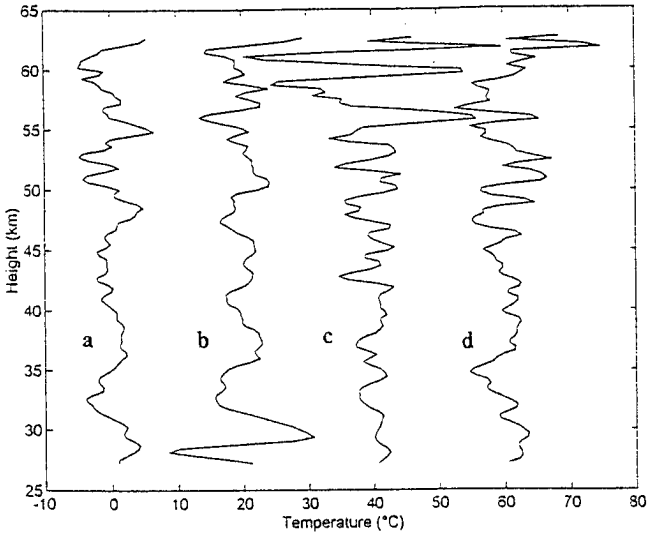


Figure 3 - Temperature perturbation signals
a:22/06/94, b:23/06/94, c:01/11/94, d:10/11/94

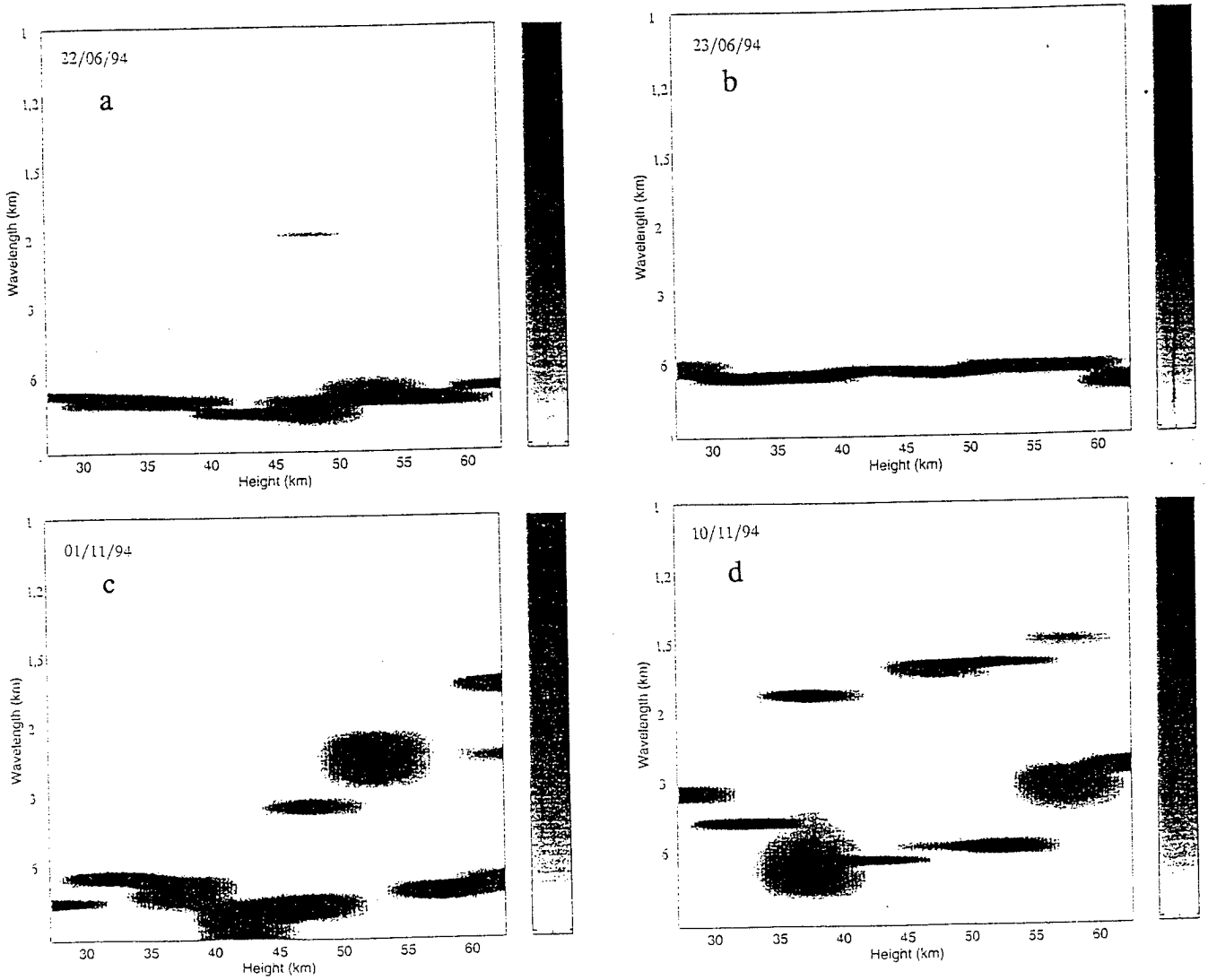


Figure 4 - Time-frequency analysis of temperature perturbations. Wavelengths versus heights are given for the four days.

Estimating RCS of the sea surface perturbed by rain for rainfall rate retrieval

F.Capolino, D. Giuli, L.Facheris, F. Sottili
Dip. Ingegneria Elettronica, University of Florence, via di S.Marta 3, 50139 Florence, Italy
Tel: +39-55-4796370 Fax: +39- 55-494569 e-mail: giuli@ingfi1.ing.unifi.it

Abstract -- The problem of improving estimates of rainfall intensity over the sea surface through spaceborne rain radars is addressed. The backscattered signal is composed of volumetric contribution due to rainfall and of the sea surface contribution. When trying to estimate the NRCS of the sea surface, one of the major difficulties is that different scale of roughness of the sea surface should be accounted for in the same e.m. model: the larger due to wind and the smaller due to the raindrop splashes. While in the first case several models are available in the literature, in the second case only a few experimental results or theoretical studies are at disposal. In this paper, a model which accounts for the additional roughness due to the effects of the raindrop splashes is analysed. Furthermore, an enhanced algorithm is proposed here for retrieving rainfall rate profiles, which utilises the relationship between sea NRCS and rainfall rate.

INTRODUCTION

Retrieval of rainfall intensity over sea surface by means of spaceborne rain radars is getting increasing importance for monitoring environmental parameters on a global scale. Let us consider a downward-looking spaceborne rain radar operating at attenuating frequency. One drawback of attenuation retrieval techniques is the heavy additional attenuation due to the possible presence of the melting layer, that is not easy at all to predict and model.

One of the most utilised class of algorithms considers the case of a single wavelength radar. It has been shown that surface the referenced technique (kZS) performs generally better than other single frequency methods [1], but it is based on the knowledge of σ_S (Normalized Radar Cross Section, NRCS, of the sea surface), which is commonly predictable only very approximately. It becomes essential to determine the NRCS of the sea and how it is influenced by the surface corrugation induced by rain. In order to obtain an e.m. formulation to predict the NRCS that takes into account of both the roughness contribution induced by the effects of wind and raindrop splashes, the Full Wave Model (FWM) for rough surface is considered [2]. It will be shown that at C-band the additional effects of the rain are negligible respect to those of wind, thus the NRCS at C-band could be utilised to retrieve the corrugation parameters due to wind. It will be shown that the Ku-band is sensitive to the induced corrugation of the rain and its behaviour when varing the rainfall rate R is predicted and utilised in rain rate retrieval. Due to the strong sea return, the modified σ_S alone permits rainfall rate retrieval directly by means of differential echo measurements pertinent to the first two range cells above the sea surface. At nadir, for example, the first range cell is substantially affected only by the sea echo (that is much powerful than the volumetric one present in the same range cell), while the second range cell is affected only by the volumetric echo due to rainfall. The two power measurements relative to the two different cells show opposite behaviours with respect to the variation of the rainfall rate, thus allowing the estimation of rainfall rate at sea level directly by comparison.

E.M. MODELING OF SEA SURFACE

Let us consider a sea surface corrugated by wind and by the effects of raindrop splashes. It has been shown that the crown and stalks phases, following raindrop splashes, are important features to be considered for analysing backscattering near grazing incidence angle, while ring waves are important for backscattering at incidence angles near nadir [3]. In our case, only ring waves have been considered, and been modeled as a random process with characteristics similar to those of the waves generated by wind. Since our purpose was an accurate and complete polarimetric description of the sea radar return when corrugated by two statistically independent phenomena (wind and rain), we considered the e.m. model described in [2],[4]. We assumed that roughness is due to the superposition of the two random processes due to rain and wind. The roughness due to wind and to rain will be referred to as large scale and small scale phenomenon, respectively.

As a preliminary example, for the sea surface roughened by wind we resorted to the Pierson-Moscowitz spectrum as in [2], with a zero mean Gaussian surface height distribution. The distribution of the local surface slope has also been assumed as zero mean Gaussian, like that used for the height of the surface roughened by rain, assumed as a random process with a wavenumber spectrum as that yielded from experimental results given in [5].

The height standard deviation h_R(rms) for roughness due to rain is of the order of a few millimeters, and its correlation length of the order of a few centimeters. Under these hypotheses, and considering the values for the wind roughness given in [2], it can be easily verified that the average radius of curvature of the rain roughness is much larger than that of the wind roughness. The NRCS has been calculated by means of a statistical average over the slopes and over the heights. Indicating with L_R and L_W the correlation lengths of the roughness due to rain and to the

0-7803-3068-4/96$5.00©1996 IEEE

wind, respectively, we have $L_W >> L_R$. Assuming also the two random processes as statistically independent, we can write the total NRCS σ_S as the sum of two NRCS:

$$\sigma_S^{pq} = \sigma_W^{pq} + \sigma_R^{pq} \quad (1)$$

where

$$\sigma_W^{pq} = Q_W(\vec{n}^f, \vec{n}^i) \int_{\vec{n}} A^{pq}(\vec{n}^f, \vec{n}^i, \vec{n}) \cdot |\chi^R(\vec{v} \cdot \vec{n})|^2 p(\vec{n}) d\vec{n} \quad (2)$$

and

$$\sigma_R^{pq} = \int_{\vec{n}} A^{pq}(\vec{n}^f, \vec{n}^i, \vec{n}) \quad (\vec{n} \cdot \vec{a}_y) \cdot Q_R(\vec{n}^f, \vec{n}^i, \vec{n}) p(\vec{n}) d\vec{n} \quad . (3)$$

The term σ_R^{pq} is the NRCS contribution of the wind roughness perturbed by rainfall, σ_R^{pq} is the NRCS contribution due to rainfall, *pq* is the arbitrary polarisation of incident and radiated waves (H,V); the symbols we adopted are those defined in [4], in particular the term $A^{pq}(\vec{n}^f, \vec{n}^i, \vec{n})$ includes the Fresnel reflection coefficients. The terms $|\chi^R(\vec{v} \cdot \vec{n})|$ and $Q_{W,R}$ account for the statistics of the phase of the e.m. wave determined by the height distribution of the rough surface and their expression are in [4]. The integration in the variable $d\vec{n}$ means that the result is averaged along the slopes of the large scale surface due to the wind. Notice It is important to note that the terms $Q_R(\vec{n}^f, \vec{n}^i, \vec{n})$ in the σ_R^{pq} component are weighted by the slope of the large scale surface. This corresponds to compute the NRCS component corresponding to the ring waves by means of a statistical average over the slopes of the surface roughened by the wind.

SEA NRCS BEHAVIOUR AT C- AND Ku-BAND

Some preliminary numerical results of the NRCS computations are discussed in the following for the frequencies of 5.6 and 13.75 GHz. Wind speed is supposed to be 4.3 m/s as in [2]. Surface roughness due to rainfall is described in terms of standard deviation h_R(rms). Indeed, h_R is related to the rainfall rate R, by the approximated law

$$h_R(\text{mm}) = 0.1631\sqrt{R(\text{mmh}^{-1})} \quad (4)$$

calculated through the graph in [3] obtained for an artificial rain falling from 1m height and using energetic consideration in order to find the relationship for raindrops falling at terminal velocity. Nevertheless, an accurate description of such relationship is not available in the literature, and for this reason, we have simply chosen h_R as the parameter describing sea roughness and rainfall intensity; one can obtain the NRCS as a function of h_R using the formula (4).

In Fig. 1 the VV component of the NRCS at 5.6 GHz is plotted versus incidence angle in the absence of rainfall, and in the case that additional perturbation due to rainfall is present, for different values h_R(rms) of the surface roughness. At this frequency, the NRCS of the sea is strongly dependent on sea wind conditions, while it is slightly dependent on rainfall intensity as shown by the Figure.

In Fig. 2 the VV component is plotted at a frequency of 13.75 GHz. When increasing rainfall intensity (increasing h_R(rms)), a decrease of the NRCS is correspondingly obtained for incidence angles close to nadir; this phenomenon can be observed for all incidence angles ranging from 0° to 10°. On the other hand, at incidence angles ranging from around 10° to 35° an opposite trend is present, i.e. for increasing intensity an increase of the sea surface NRCS shows up, as also observed in the laboratory experiment described in [3]. At this higher frequency, the NRCS is rather sensitive to rainfall intensity.

We point out that using the results for small incidence angles at C-band, it is possible to extract the component of the surface roughness only due to the wind. On the other hand, when the wind condition are known, at Ku band we can predict the roughness due to the corrugation induced by rain.

TWO-CELL ALGORITHM

The variation at nadir incidence of the NRCS of the sea surface can be utilised to compute the rainfall rate at sea level by comparing the first two contiguous range-cells above the sea surface. From that comparison the rain rate and the value of the NRCS of the sea surface can be obtained. Due to the powerful sea return, sea backscatter prevails in the first cell, while in the second cell only rainfall backscatter is present. If P_1 and P_2 are the powers of echoes referred to the first and second range cell, respectively, a simple relation is [6]:

$$\sigma_s(R) = \frac{P_1 C}{P_2 C_s} \alpha \cdot K(R)^{\beta} \cdot e^{0.46 \Delta r K(R)} \quad (5)$$

where R is the rainfall rate, $_s(R)$ is the NRCS of the sea surface depending on the rainfall rate and K(R) is the attenuation factor for propagation in rainfall. Knowing the dependence of the NRCS as a function of the rainfall rate, it is possible to compute R by means of the ratio between the two power measurements P_1 and P_2 . The key point of this inversion is that K(R) and σ_s(R) have an opposite trend with respect to rainfall rate variations. In Fig. 3, a numerical simulation that rapresent the estimation of the σ_s(R) as a function of a simulated rainfall rate R is reported. The numerical simulation is performed by finding the zeros of Eq. (5) considering: α as a random process and random errors in the relationships K(R) and σ_s(R) as in [1] with the mean value of the random process σ_s(R) obtained by means of Eq. (1). In Fig 3, the continuos and dashed lines represent the

mean value and the standard deviation of the solution of expression (5), respectively. The corresponding rainfall rate is found through Eq. (4). When the rainfall rate R is available at sea level, it can be used as the starting value in the *k*ZS algorithm, aiming at extracting the rainfall rate height profile.

CONCLUSIONS

Several models are available in the literature that characterise the sea surface interaction with e.m. waves, when such surface is roughened by wind. In this paper, a model that takes into account the additional surface roughness due to rainfall is considered, in order to achieve a full polarimetric description of the radar return. Results can be utilised for rainfall rate retrieval or to overcome some of the inherent ambiguities associated with the retrieval algorithms. These first results can already be utilised for a more detailed characterisation of the sea surface return. The same model and results could also be exploited to evaluate algorithms for scatterometer wind speed computation, in order to cancel the bias introduced by the rain roughness contribution. An algorithm for rain rate retrieval is proposed; it is shown how theoretical relationships between the sea NRCS $_s(R)$ and the rainfall rate R can be exploited. Such information can be directly used to retrieve the rainfall rate at sea level by direct comparison between the power echoes pertinent to the two first range cells above the sea surface. This technique is independent of possible ambiguities, like that induced by the melting layer of precipitation, or by the attenuation factor along the path from the second cell to the radar.

Acknowledgments --- This work has been supported by the Italian Space Agency and by the Italian Ministry for University and Scientific Research.

REFERENCES

[1] M. Marzoug, and P. Amayenc, "A Class of Single- and Dual- Frequency Algorithms for Rain Rate Profiling from a Spaceboorne Radar. Part I: Principle and Tests from Numerical Simulations", *Journal Atm. Oceanic Techn.*, V. 11, pp. 1480-1506, Dec. 1994.

[2] E. Bahar, and M.A. Fitzwater, Scattering Cross Sections for Composite Rough Surfaces Using the Unified Full Wave Approach", IEEE Trans. Antennas Propagat., AP-32, N.7,1984

[3] F.L. Bliven, H. Branger, P. Sobieski, J-P. Giovanangeli, "An Analysis of Scatterometers Returns from a Water Surface Agitated by Artificial Rain: Evidence that Ring-Waves are the Main Features", *Int. J. of Remote Sens.*, 14, N.12, 1993.

[4] E. Bahar, "Review of the Full Wave Solutions for Rough Surface Scattering and Depolarization: Comparison with Geometric and Physical Optics, Perturbation, and Two-scale Hybrid Solutions", *Journ. . .Geophys. Res.*, V.92, N. C5, pp. 5209-5224, May 1987.

[5] L. F. Bliven, P. W. Sobieski, T. Elfouhaily, "Ring Wave Frequency Spectra: Measurements and Model", *IGARSS'95,* Florence, Italy, July 10-14 1995.

[6] F. Capolino, G. Biffi Gentili, L. Facheris, M. Gherardelli, D. Giuli," Improving Rainfall Measurement Accuracy in Spaceborne Rain Radar over Sea", *IGARSS'95*, Florence, Italy, July 10-14 1995.

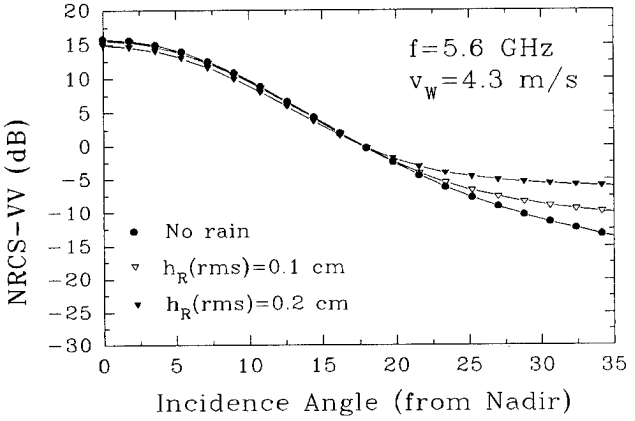


Fig. 1

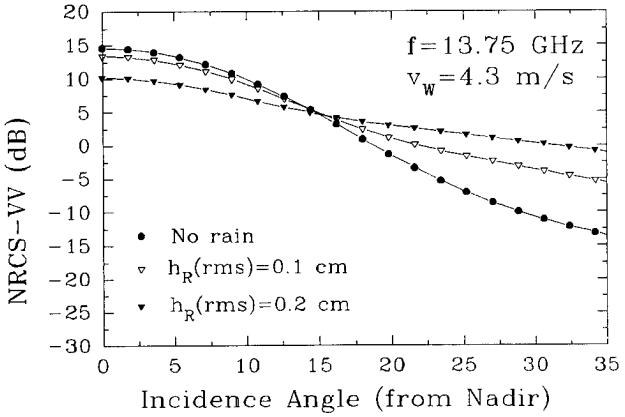


Fig 2

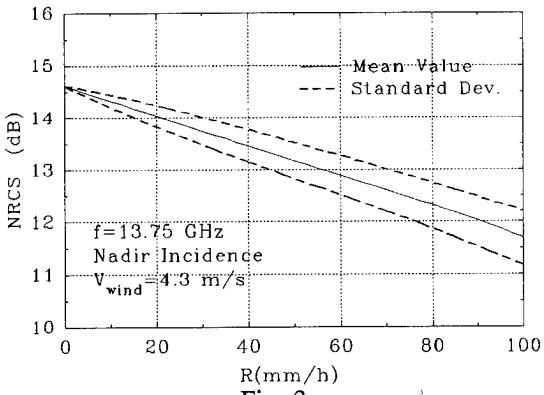


Fig. 3

Dielectric Constants for Melting Hydrometeors as derived from a Numerical Method

Robert Meneghini, Code 975, NASA Goddard Space Flight Center, Greenbelt, MD 20771
Ph: 301-286-9128, FAX: 301-286-1761, email: bob@meneg.gsfc.nasa.gov
Liang Liao, Caelum Research Co., Silver Spring, MD, 20901
Ph: 301-286-5855, FAX: 301-286-1761, email: lliao@meneg,gsfc.nasa.gov

INTRODUCTION AND BACKGROUND

A critical element in the modelling of melting hydrometeors is the characterization of the complex dielectric constant. One of the most commonly used mixing formulas is that given by Maxwell Garnett (1904). Unlike the Debye and the Bruggeman formulations, the Maxwell Garnett equation is asymmetric with respect to the roles of the background matrix and the inclusions. In particular, an ice matrix with water inclusions yields a dielectric constant that differs significantly from a water matrix with ice inclusions with the same fractional volume contents. Despite the expectation that the Maxwell Garnett (MG) formulation of an ice matrix with water inclusions be applicable to a partially melted hydrometeor with small fractional water content, a reversal of the ice and water components seems to better reproduce certain properties of the scattering characteristics of single particles (Bohren and Battan, 1980, 1982) as well as characteristics of the radar bright band. On the other hand, experimental measurements with acrylic-water mixtures indicate that for small fractional volume contents of water, the MG formula with water as the inclusion must be used to obtain reasonable agreement with the measured data [Chylek et al., 1988].

To resolve these apparent discrepancies, accurate representations are needed for the distributions of air, ice, and water within the melting graupel particle or snow aggregate. What is needed, in addition, is a numerical method flexible enough to provide the scattering properties of mixed-phase particles with complex structure. In this paper we focus on the latter requirement using spherical particles in which the melt water within the ice particle is taken to be uniformly distributed. Generalizations of the results to ice-water-air mixtures and to non-uniform distributions of melt water within the particle are mentioned briefly.

CG-FFT METHOD

Unlike conventional methods where the electric field integral equation is solved by a direct inversion of the full matrix, the conjugate gradient (CG) approach solves the integral equation by means of iterative algorithms. As the terms in the series solution can be expressed as convolutions, the fast Fourier transform (FFT) can be used to reduce the demands on computation time and memory allocation. Several applications of the CG-FFT approach to electromagnetic scattering problems can be found in the literature [e.g., Liao and Sassen, 1994]. In general, the method has great flexibility with respect to the shape and material of the particle. Comparisons between the CG-FFT and Mie theory for pure ice for a size parameter of 0.11 shows the percentage error in the CG-FFT estimates of σ_e and σ_b to be less than 2% for both the 16x16x16 and the 32x32x32 cell approximations. For pure water particle at the same size parameter, the errors in σ_e and σ_b are less than 6% if a 32x32x32 cell approximation is used.

RESULTS FOR UNIFORM ICE-WATER MIXTURES

To compare the various mixing formulas, the backscattering and extinction coefficients of spheres are computed using Mie theory where the dielectric constant of the scatterer is determined from either the Debye, Bruggeman or Maxwell-Garnett mixing formulas. The accuracy of the mixing formulas are evaluated relative to the results of numerical computations using the conjugate gradient- fast Fourier transform method (CG-FFT). To perform the numerical computations, the sphere is divided into a NxNxN grid of equal-volume cells. To represent the distribution of water within the particle, the probability that melt water is present at a particular cell is prescribed. For the case of uniformly distributed water in an ice matrix, where the fraction of water by volume is f, a random number generator is used to provide sets of numbers that are uniformly distributed in the interval between zero and 1. For the jth grid point of the particle ($j = 1,..,N^3$), the cell containing ice is replaced by water if the random number is less than f. A realization of a particle with a uniform distribution of melt water is shown in Fig. 1 for a fractional melt water, by volume, of 0.46. In this figure the cells in gray represent ice, the cells in black water where the temperatures of the ice and water are assumed to be 0 C. Having constructed the mixed phase particles in this manner, the scattering computations are made as a function of f using the CG-FFT method.

Figs. 2 and 3 show, respectively, the extinction, σ_e, and backscattering, σ_b, coefficients for a sphere of 1.3 mm

0-7803-3068-4/96$5.00©1996 IEEE

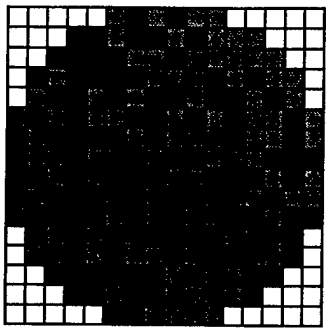


Fig. 1: 2-D view of a realization of an ice-water sphere with a water fraction (in black) of 0.46.

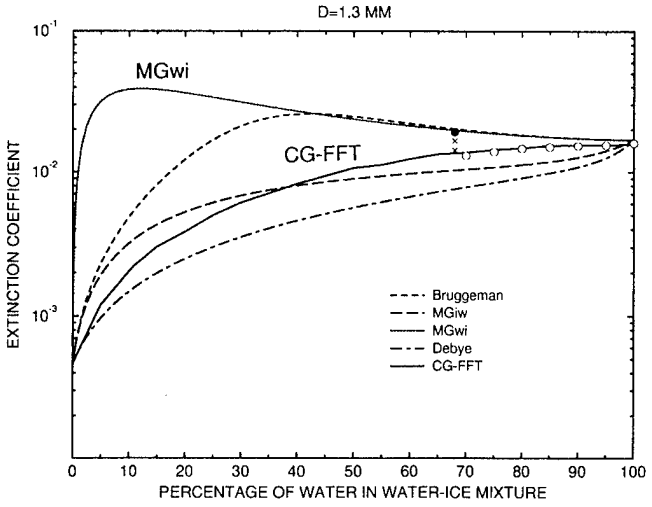


Fig. 2: Extinction coefficients versus the fraction of water by volume, f, in an ice-water sphere.

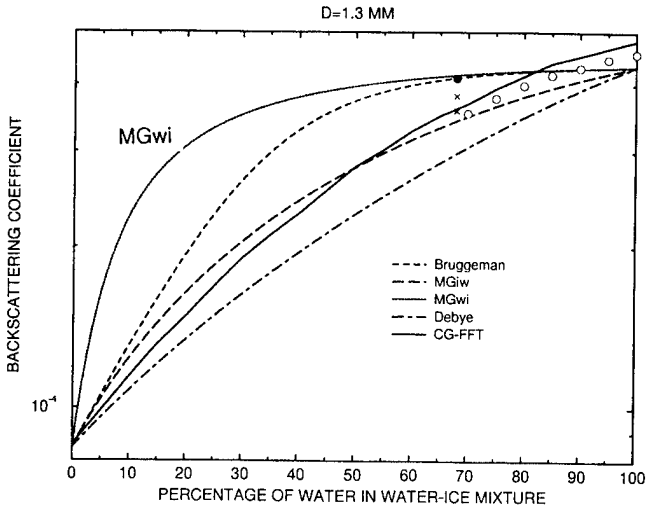


Fig. 3: Same as Fig. 2 but for the backscattering coefficients.

diameter at a wavelength of 3.9 cm ($\pi D/\lambda = 0.105$) as a function of the volume fraction of water, f, in the ice-water mixture. Shown in each figure are the results of 4 mixing formulas (using Mie theory) as well as the results derived from the CG-FFT method. The results of the CG-FFT method are represented by the solid line and can be seen to be closest to the Debye and MG_{IW} (ice matrix/ water inclusions) results for f less than about 0.7. For $f > 0.5$, however, the CG-FFT results begin to move away from the MG_{IW} values toward the MG_{WI} (water matrix/ ice inclusions) and Bruggeman values. Comparisons of the various formulations for the backscattering coefficient, σ_b, are shown in Fig. 3 and follow the same general behavior as that for σ_e. Two additional features of Figs. 2 and 3 should be noted. The values of the scattering coefficients computed by the CG-FFT and shown as the solid lines were done for $N = 16$; as the fractional water content increases, however, the accuracy of the method degrades. For this reason, the CG-FFT was recomputed for $f \geq 0.7$ using $N = 32$ and are represented in these figures by the open circles. A second point is that if the available melt water is distributed in increasingly higher concentrations near the boundary of the particle, the CG-FFT scattering coefficients increase toward the MG_{WI} results. The three points (*, X and ●) at $f = 0.64$ show an example of this progression. Although this provides an insight into how the radial distribution of water can affect the scattering properties, the remainder of the paper will focus on the case of uniform mixing.

As the CG-FFT computations described above take several orders of magnitude longer to compute than the Mie calculations, they are of limited value in bright-band modelling unless the computation time can be drastically reduced. Moreover, for larger particles, the CG-FFT can fail to converge. To circumvent these limitations, the foregoing results can be used to deduce the dielectric constant, ϵ_{CG}, which, when substituted into Mie theory, reproduces the CG-FFT results shown in Figs. 2 and 3. This procedure can be described in the following way: for a fixed value of the fractional melt water, f, the extinction and scattering cross sections can be computed by means of Mie theory for any value of ϵ selected in the complex plane. This process is continued until an ϵ ($= \epsilon_{CG}$) is found that yields the backscattering and extinction coefficients closest to those estimated from the CG-FFT results. The results of these calculations are given in Figs. 4a and 4b where the heavy solid lines represent the real and imaginary parts of ϵ_{CG}. Also shown on the figures are the real and imaginary parts of the dielectric constants, ($\epsilon_{MG\,WI}$, $\epsilon_{MG\,IW}$) as predicted by the MG_{WI} and MG_{IW} formulas, respectively. Inspection of the results shows that for small values of f ϵ_{CG} is well approximated by the MG_{IW} results but that as f increases beyond about 0.7, the ϵ_{CG} values tend toward the MG_{WI} estimate.

A pertinent question is whether ϵ_{CG} can be accurately expressed as a linear combination of the $\epsilon_{MG\ WI}$ and $\epsilon_{MG\ IW}$ functions. The behavior of ϵ_{CG} illustrated in Figs. 4 suggests that functions approximating the unit step function are appropriate choices. One such parameterization can be written:

$$\mathrm{Re}[\epsilon_{CG}] = 0.5\ \{(1-\mathrm{erf}(x))\ \mathrm{Re}(\epsilon_{MG\ WI}) + (1+\mathrm{erf}(x))\ \mathrm{Re}(\epsilon_{MG\ IW})\} \quad (1)$$

$$\mathrm{Im}[\epsilon_{CG}] = 0.5\ \{(1-\mathrm{erf}(x))\ \mathrm{Im}(\epsilon_{MG\ WI}) + (1+\mathrm{erf}(x))\ \mathrm{Im}(\epsilon_{MG\ IW})\} \quad (2)$$

where

$$\mathrm{erf}(x) = (2/\sqrt{\pi}) \int_0^x \exp(-y^2)\, dy \quad (3)$$

$$x = [(1-f)/f - t]/\sqrt{2}\, q \quad (4)$$

and where Re and Im denote the real and imaginary parts. Displayed in Fig. 4a as a function of f are the values of the right hand side of Eq. (1) for t = 0.2 and q = {0.25, 0.1}. The corresponding pair of curves are shown in Fig. 4b for the imaginary parts. As in Fig. 4a, t is set equal to 0.2 and plots of Eq. (2) are shown for q = {0.25, 0.1}. Examination of the results indicate that Eqs. (1) and (2) with t = 0.2 and q = 0.1 yield fairly good approximations to the real and imaginary parts of ϵ_{CG}; stated differently, a weighted sum of the Maxwell Garnett mixing formulas, with the roles of matrix and inclusion interchanged, provides an accurate representation of the dielectric constant as derived from the numerical results.

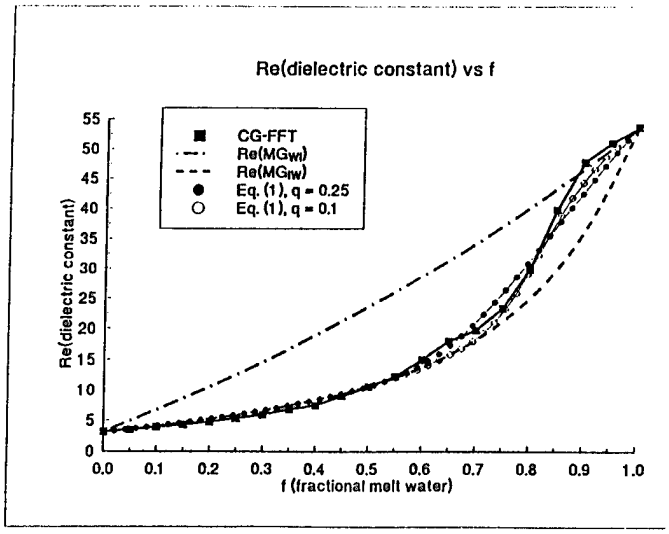


Fig. 4a: Real parts of the dielectric constant as derived from the CG-FFT, Maxwell-Garnett formula, and Eq. (1).

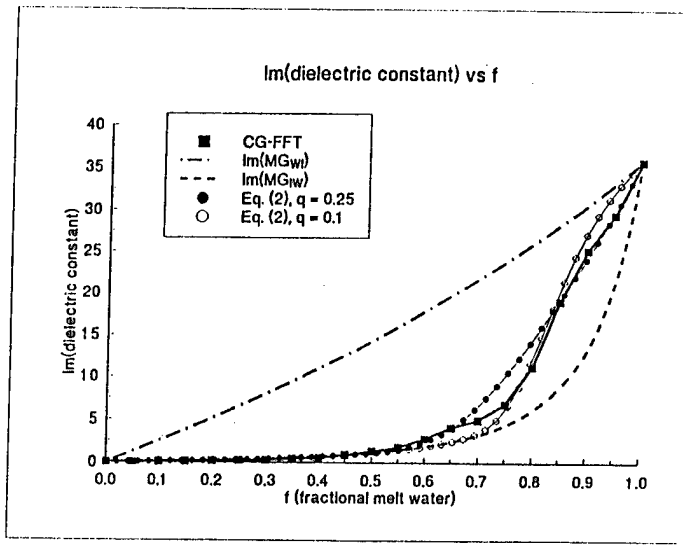


Fig. 4b: Imaginary parts of the dielectric constant as derived from the CG-FFT, Maxwell-Garnett formula, and Eq.(1).

SUMMARY

Using a conjugate gradient numerical method, calculations of the scattering coefficients for mixed phase hydrometeors were made. For the uniform ice-water mixtures considered, an effective dielectric constant was derived and compared with the predictions from the Maxwell Garnett formula. The flexibility of the numerical method with respect to the spatial distribution of the component materials offers the potential to model the scattering characteristics of complex, mixed-phase hydrometeors.

REFERENCES

Bohren C.F., and L.J. Battan, 1982: Radar backscattering of microwaves by spongy ice spheres. J. Atmos. Sci., 39, 2623-2629.

Chylek, P., V. Srivastava, R.G. Pinnick, and R.T. Wang, 1988: Scattering of electromagnetic waves by composite spherical particles: experiment and effective medium approximations. Appl. Optics, 27, 2396-2404.

Liao, L., and K. Sassen, 1994: Investigation of relationships between Ka-band radar reflectivity and ice and liquid water contents. Atmos. Res., 34, 231-248.

Maxwell Garnett, J.C., 1904: Colors in metal glasses and in metallic films. Phil. Trans. Roy. Soc. London, A203, 385-420.

Optical Remote Sounding of Aerosol Formations on the Base of Numerical Simulation of the Scattering Radiation

B.I.Belyaev, L.V.Katkovsky, V.P.Kabashnikov, V.P.Nekrasov
Remote Photometry Laboratory, Scientific Research Institute of Applied Physics Problems,
Kurchatova St., 7, Minsk, Republic Belarus, 220064;
Phone: (017) 2780409; Fax: (017) 2780417

The multispectral technique for passive remote sensing of aerosol formations (chimney smoke tails of energy plants, vehicle engine exhaust gas tails and others) is described. It is based on the measurements and analysis of the spectral-angular distribution of the solar radiation scattered by the aerosol formation using the spectrometer as, for example, "GEMMA 2-video" [1] (of our own development) and TV camera linked to it in order to visualize the observed area of the object. The field of view of the spectrometer is depicted on the video frame as a slit. The measurements are assumed to be made from the board of a helicopter, airplane or the ground surface .

To solve the inverse problem we have to get the analytical expression for radiation escaped from the tail, which involves some unknown parameters, such as optical thickness and so on. The analytical approximation were obtained by fitting the numeric Monte-Carlo calculation curves. The values of unknown parameters, including optical thickness and phase function parameter of aerosol particles are then calculated by using least square non-linear regression method.

NUMERICAL MODELING OF THE SCATTERING OF SOLAR RADIATION BY AXIALLY SYMMETRICAL TAILS

To solve the direct problem we have to get the elementary volume optical parameters: particle concentration, N, particle size distribution function, $f(r)$, extinction coefficient, phase function and optical thickness. This information is received by the Mie theory calculations. Monte-Carlo calculations of radiative transfer inside the axially symmetrical vehicle engine exhaust gas and aerosol tail are then made. These numerical simulations give the directed reflectance coefficients of the tail. At that the real processes in the contrail such as condensation of the water vapor and chloride hydrogen and water deposition on the soot particles were taken into account. In many cases the industrial aerosols consist of insoluble particles of soot for which the imaginary part of refractive index close to 1. The water covering the particles lead to changing of the particles' optical properties and transformation of the initial size distribution function. These aerosols are described by the two-layer particle model [2,3]. There are some restrictions when the complete scattering matrix is being calculated for the cases of the small core, small envelope thickness', large diffraction parameters with absorbing core. The restrictions arise when logarithmic derivative of Riccati-Bessel function with complex argument is calculated. In our algorithm [4] of the two-layer particle scattering matrix calculation the expansion of the logarithmic derivative of Riccati-Bessel function into the chain fraction is used. Due to some algebraic operations, avoiding of using the complex arithmetic, and some optimizations the program effectiveness was improved considerably. The double precision is not needed. There are no restrictions on the diffraction parameter and the optical properties. The calculation speed has increased at least the order of magnitude comparing to [2,3]. Results of calculations by the program were compared with the results of [5] for complex refractive index $m = 1{,}32 - i\,1000$ and the diffraction parameters $x = 2\pi r/\lambda = 0.2 - 610.61$. Complete coincidence of the all meaning figures was achieved. For the two-layer particles the comparison was carried out with the results of [2,3].

At the beginning the smoke tail has approximately an axially symmetrical form. It may be modeled by several cylinders with the different radii. The transversal sizes of the smoke contrails are usually much less then the longitudinal ones. It is possible to use the indefinite cylinder approximation for the scattering coefficients' calculations of cylinder when transversal radiation fluxes are much more longitudinal ones. This approximation reduces the computational time because of photon drawings in Monte-Carlo algorithm carried out only in the plane perpendicular to the cylinder axes.

We have considered the sun light scattered by condensed particles and products of burning in a contrail behind a rocket. The boundary conditions for the contrail equations are the gas dynamic parameters at the end of the rocket exhaust. In particular, at the height 10 km the boundary conditions for this model are: jet radius 5 m, temperature 1000°K, gas speed relatively ambient air 200m/s, mole parts of water vapor and chlorine hydrogen are 0.03 and 0.02 respectively. Monodispersive soot particle's concentration with size 0.1μm is considered to be equal $5 \cdot 10^6$ cm^{-3}. The condensation is an equilibrium process, because of the slowness of the contrail parameter changes. Condensation of water vapor and chloride hydrogen is calculated using the approach [6]. It is assumed that the all condensate deposits

0-7803-3068-4/96$5.00©1996 IEEE

on the soot particles. The obtained for this process particle size is considered to as average size. Scattering coefficient Al_2O_3 at the beginning of the contrail is $0.5 \cdot 10^{-1}$ cm^{-1}. Elementary volume phase function was determined as average weighted of phase functions for Al_2O_3 particles and for soot particles. Particle size distribution function has a form $f(r) = Nr\exp(-\alpha r^2)$. The contrail parameters at the altitude 10 km for the time moments from the beginning of condensation t = 1, 7, 20, 100 s were, respectively, the following: contrail radii (m) - 9, 14, 22, 55; soot particle concentrations (1/cm3) - 1.3E+6, 5.0E+5, 2.0E+5, 3.5E+4; average soot particle radii (μm) - 0.1, 0.188, 0.565, 0.555.

The directed scattering coefficient $k(\vec{\Omega}^*)$ is obtained by dividing the scattered flux into the direction $\vec{\Omega}^*$ on the incident radiation capacity and is measured in units of $ster^{-1}$. There are the directed scattering coefficients calculated for the aforementioned data for wavelength λ=0.5 μm and different angles of view in the Tab. 1 and 2. The sun rays are perpendicular to the cylinder axis. The signs ↑, ⊥, ↓ mean, correspondingly, that observation is carried out in the plane of the sun beam arrival in opposite direction (back reflection), perpendicular the plane and in the direction arrival (transmittance). θ is the view angle in each of this planes relatively to the cylinder axis.

The tables show that the contrail optical thickness and the directed scattering coefficient of cylinder increase with the beginning condensation. Only in the direction backward to ray arrival direction the scattering coefficient decreases with the increasing of optical thickness. It is caused by phase function changing because of the condensation.

Table 1

	τ = 1,9 t = 1 s			τ = 4,2 t = 7 s		
θ°	↑	⊥	↓	↑	⊥	↓
30°	3.1E-2	3.6E-2	4.5E-2	3.4E-2	4.1E-2	4.9E-2
60°	4.2E-2	6.2E-2	1.4E-1	5.3E-2	6.6E-2	1.4E-1
90°	5.2E-1	5.8E-2	5.7E-0	1.8E-1	7.4E-2	574E-1

Table 2

	τ = 21 t = 20 s			τ = 8.14 t = 100 s		
θ°	↑	⊥	↓	↑	⊥	↓
30°	8.3E-2	4.9E-2	1.5E-2	5.9E-2	4.5E-2	3.1E-2
60°	1.6E-2	6.8E-2	3.1E-1	1.0E-1	8.5E-2	8.3E-2
90°	2.1E-1	1.0E-1	5.6E-1	1.3E-1	9.3E-2	2.1E-2

THE METHOD OF DETERMINING THE AEROSOL PARAMETERS

Let $B_\lambda(\vec{\Omega}^*)$ be the spectral brightness of the radiation, scattered by the fixed area of the tail along the observation direction $\vec{\Omega}^*$. Then for the brightness measured from the distance L along this direction it may be written down [7]:

$$I_\lambda(L,\vec{\Omega}^*) = B_\lambda(\vec{\Omega}^*)\exp\left[-\tau_\lambda^*(0,L)\right] + \int_0^L \varepsilon_\lambda(l) S_\lambda(l,\vec{\Omega}^*)\exp\left[-\tau_\lambda^*(l,L)\right] dl \quad (1)$$

Here $\varepsilon_\lambda = \sigma_\lambda + \alpha_\lambda$ - spectral extinction coefficient in the atmosphere, τ_λ^* the spectral optical thickness in the atmosphere and $S_\lambda(l,\vec{\Omega}^*)$-the source function of the atmosphere at the point l in the direction $\vec{\Omega}^*$.

When there is clear sky or unbroken clouds the source function may be considered the constant along the sounding path [7], i.e. instead of (1) it may be written

$$I_\lambda(L,\vec{\Omega}^*) = B_\lambda(\vec{\Omega}^*)\exp\left[-\tau_\lambda^*(0,L)\right] + S_\lambda(\vec{\Omega}^*)\left\{1 - \exp\left[-\tau_\lambda^*(0,L)\right]\right\} \quad (2)$$

From this equation it directly follows, that with good accuracy the source function for assign direction is determined by measurement of the atmospheric brightness at the infinity (observation beside the object, close to it). Practically it is sufficient that $\tau_\lambda^* > 3 \div 4$ in order to

$$I_\lambda(\infty,\vec{\Omega}^*) \cong (0{,}95 \div 1) \cdot S_\lambda(\vec{\Omega}^*). \quad (3)$$

There are the known techniques of determination the atmospheric extinction coefficient by measuring the brightness of two contrasting surfaces from two different distances [8]. To obtain the atmospheric extinction coefficient ε_λ along the path it is sufficient to measure the smoke tail, B_λ and nearby background brightness spectra B_λ^* at two different distances along the same direction: $B_{\lambda 1}, B_{\lambda 1}^*$, $B_{\lambda 2}, B_{\lambda 2}^*$. Than coefficient ε_λ is calculated by the formula:

$$\varepsilon_\lambda = \frac{1}{\Delta L} \cdot ln\left(B_{\lambda 1}^* - B_{\lambda 1}\right) / \left(B_{\lambda 2}^* - B_{\lambda 2}\right), \quad L_1 > L_2 \quad (4)$$

where ΔL is the distance between two points of measuring (L_1, L_2). Thus, if only $S_\lambda(\vec{\Omega}^*)$ and ε_λ have found, the haze influence is excluded from (2), and the values $B_\lambda(\vec{\Omega}^*)$

of the spectral brightness of the tail are restored. Father, we can consider that (we omit argument λ hereinafter)

$$B(\vec{\Omega}^*)/B_1(\vec{\Omega}^*) = k(\vec{\Omega}^*)/k_1(\vec{\Omega}^*) = F(\vec{\Omega}^*, a_1, a_2, \ldots) \quad (5)$$

where $B_1(\vec{\Omega}^*)$, $k_1(\vec{\Omega}^*)$ - are the brightness and directed scattering coefficient of the tail, respectively, calculated in singl-scattering approximation, $a_1, a_2, \ldots$ - are some parameters. The analytical form of $F(\vec{\Omega}^*, a_1, a_2, \ldots)$ have been investigated on the base of calculations the ratio $k_{MC}(\vec{\Omega}^*)/k_1(\vec{\Omega}^*)$, i.e. the ratio of the scattering coefficient, which takes into account the all multiple-scattering, $k_{MC}(\vec{\Omega}^*)$, to that one in the single-scattering approximation, $k_1(\vec{\Omega}^*)$. The coefficient $k_{MC}(\vec{\Omega}^*)$ was calculated using Monte-Carlo simulation procedure for the homogeneous infinite cylindrical tail with various radius optical thickness', τ_R , and with various scattering phase functions. This approach is most convenient if $k_{MC}(\vec{\Omega}^*)$ is the function of one variable, therefore the some fixed detecting plane, containing cylinder axes, was chosen. For example, in the case when this plane is normal to the solar rays incident plane the ratio $k_{MC}(\vec{\Omega}^*)/k_1(\vec{\Omega}^*)$ is well approximated by the following function:

$$F(\theta^*) = k_{MC}(\theta^*)/k_1(\theta^*) = 1 + \left\{1 - exp(-\tau^*) - 0{,}5\tau^* exp(-\tau^*)\left[1 + a_3 cos^2(\theta^* - \theta_s)\right]\right\} \times \times \left[a_1 - a_2 Ch(\theta^* - \theta_s)\right] \quad (6)$$

Where θ^*, θ_s - observing and solar incidence direction angles with cylinder axes, τ^* is the effective optical thickness of the cylinder. The function $F(\theta^*)$ contains four unknown parameters: τ^*, a_1, a_2, a_3 and adding some ones, which $B_1(\vec{\Omega}^*)$ depends on, we thus get from (5) the parameter dependent function for every λ and θ^*, which serves to finding the unknown parameters:

$$B(\theta^*) = B_1(\theta^*, \tau_R, g) F(\theta^*, a_1, a_2, a_3), \quad (7)$$

g - phase function asymmetry factor. In (7) $B(\theta^*)$ -is the experimentally measured value, F -is received by numerical modeling, $B_1(\theta^*, \tau_R, g)$ - is analytically calculated. It is also supposed, that the solar flux on the tail level, which B_1 depends on, is measured at the experiment using neutral attenuating filter.

By now the calculations and retrievals of the parameters τ_R and g have been made for not large optical thickness', $\tau_R \lesssim 2$ using the direct problem Monte-Carlo results. The accuracy of retrieval was about 15-30%. At this the initial data were also given with not high accuracy (Monte-Carlo calculations errors was about 10%).

The following conclusion may be made:

- the proposed technique of passive aerosol remote sensing may be used for determining the basic aerosol parameters with the satisfactory practical accuracy after some additional work will be done.

REFERENCES

[1] B.I. Belyaev, Veller V.V., Kiselevskii L.I, "Interactive micro-processor-based videospectropolarimetric system "Gemma 2-video," Thesis's of papers of Inter-department scientific-technical conference "Statistical Methods and Data Processing systems for the Remote Sensing of the Environment," Minsk, pp. 74-75, 1989. (in Russian).

[2] C.F. Borhen, D.R. Huffman, "Absorption and scattering of light by small particles," John Wiley & Sons, Inc., 1983.

[3] J.M. Krekov, R.F. Rahimov, "Optics-location model of continental aerosol," Eds. Novosibirsk: Nauka, 1982, 199 p.

[4] V.P. Nekrasov, K.I. Fefilov, "New calculation algorithm for two-layer particle scattering matrix and sea aerosol optical characteristic investigation," Thesis of reports at the conference Problems of complex automatization of hydrophysical investigation. - Sevastopol, 1989, p. 90-91 (in Russian).

[5] A.R. Jones, "Calculation of the ratios of complex Riccati-Bessel functions for Mie scattering," J. Phys., vol. D16, pp. 49-52, 1983.

[6] J.W. Meyer, "Kinetic model for aerosol formation in rocket contrails," AIAA J., vol. 17, No 2, pp. 135-144, 1979.

[7] B.I. Belyaev, L.V. Katkovsky, V.P. Nekrasov, A.L. Birjukov, "Multispectral Technique for Passive Remote Sensing of Aerosol Atmospheric Pollution Using Ground Based or Aircraft Measurements," in Proceedings of the International Aerosol Symposium, Moscow, 21-25 March, 1994, vol. 1, Moscow, Aerosol Technology Ltd., pp. AT1-21--AT1-38.

[8] M.V. Kabanov, D.M. Kabanov, S.M. Sakerin, "Aerospace borne methods of optical atmospheric depth and light extinction coefficients determination," Atmospheric Optics, vol. 1, No 1, pp. 107-114, 1988.

Investigation of the Anisotropy of the Atmospheric Turbulence Spectrum in the Low Frequency Range

Vladimir P. Lukin

Institute of Atmospheric Optics,Siberian Branch of the RAS,
av.Academicheski, 1, Tomsk, 634055, Russia
tel.:(382-2)25-9606, fax: (382-2)25-9086, e-mail:ZUEV@IAO.TOMSK.SU

Abstract - This paper deals with the analysis of optical measurements data on the atmospheric turbulence characteristics. Some conclusions are drawn on the variability of the most large scale component of the turbulent inhomogeneities, spectrum for the atmosphere as a whole and for the boundary atmospheric layer as well. We will analyze several years experimental studies.

INTRODUCTION IN MODEL OF ATMOSPHERIC TURBULENCE

The fact must be taken into account that for large scale inhomogeneities close in size to the outer scale of turbulence the assumption on local isotropy is not strictly correct for the real atmosphere [1-3]. Nevertheless, in the practical calculations of fluctuations of the optical fields various models are used to describe spectrum in the region of large scales [4, 5]. These models have already had two parameters, one of which was the so called outer scale of turbulence.

It is well known that the atmospheric turbulence as any motion with dissipation, can exist as the stationary phenomenon only in the presence of energy sources. Energy enters into the turbulent from the larger scales of motions. All these motions breaking down due to the instability serve as a basis for the entire spectrum of the turbulent inhomogeneities. The region of the large scale inhomogeneities is most closely related with all local meteorological parameters, first of all, with the fields of the wind velocity and temperature and their gradients. Naturally, the properties of the corresponding statistical characteristics of optical waves are also dependent on the direction [8-10].

Let us consider the pecularities of the random displacements of the image formed in the surface layer of the atmosphere on the horizontal atmospheric path. Therefore, if the atmospheric turbulence spectrum is anisotropic, the anisotropy of jitter in the low-frequency range could be expected.

Experiments were performed under conditions of the model thermal turbulence and in the real atmosphere on the uniformly near ground paths. The sharp, especially at low altitudes, difference of the variances of the random displacement of the beam in the vertical and transverse directions was observed that indicated on the turbulence anisotropy. With increase of the altitude the inhomogenuities became more isotropic while the variances became comparable [2,9].

Measurements were performed at the scientific station of the Institute of Atmospheric Optics of the RAS. From the measurements of the position of the maximum in the spectra we can estimate the outer scale of the turbulence Lo as well as its components. The ratio of the variances characterizing the anisotropy of the turbulence spectrum in the low-frequency range varied from the value of the order of 1 to 2.1. And as early as in these first measurements (1978) it was found that the value outer scale by itself and its components vary as functions of the value and sign of the parameter of the thermodynamic stability of the atmosphere. The outer scales of the turbulence were calculated from the optical measurements and it was found [3-5, 9] that they lay in the range from 80 cm to 2.5m.

EXPERIMENTAL SETUPS

First, we will give the specifications of the used measuring facilities. For some reason, if the model parameter Lo was adjusted based on simultaneous measurements of fluctuations of some optical parameter and the turbulence intensity they certainly must be followed by the measurements of the mean meteorological parameters, such as mean gradients of temperature and the wind velocity, transverse component of the mean wind velocity at the altitude of the optical radiation propagation, and the variance of the wind velocity fluctuations. In the experiments two classes of measuring devices were employed: measurers of the temperature and wind velocity at fixed altitudes (measured quantities were used for calculating the structure temperature parameter and the instability parameter B), and an optical meter of fluctuations of angle of arrival along two perpendicular directions.

INVESTIGATION OF THE ANISOTROPY OF THE SPECTRUM OF ATMOSPHERIC TURBULENCE

Together with the dependence of the outer scale of turbulence on variations of meteorological parameters of the atmosphere, there exists anisotropy of the atmospheric properties, in other words, inhomogeneities with dimensions exceeding several meters possess the properties that depend on direction. As a consequence, the properties (correlation characteristics) of some parameters of optical waves appear to be direction-dependent. For example, random displacements of an image, which is formed by the optical radiation passed through the surface atmospheric layer along a hori-

0-7803-3068-4/96$5.00©1996 IEEE

zontal path, exhibit such properties.

Investigations of the fluctuations of image displacements occurring due to the atmospheric turbulence were conducted along a horizontal path 100m in length located at the altitude of 2.5m over the ground surface covered with approximately 20cm long plant canapies. A collimated laser beam (0.63μm wavelength and 1.3cm diameter) was used as a radiation source. Random displacements were measured with a tracking system [2, 9] at the focus of an objective (220-270cm focal length). The displacements of the image in two perpendicular directions were recorded simultaneously. Meteorological measurement support of this optical experiment involved measurements of the mean temperatures and wind velocities at heights 5m and 1.25m and at the height of the beam propagation the pulsations of these parameters have also been measured. In addition, at this height the pulsations and mean values of the vertical and horizontal components of the transverse wind velocity were measured. The primary sensors of the meteorological measurement system were mounted on a mast installed in the vicinity of the optical receiver.

For estimating the anisotropy of the turbulence spectrum in the low-frequency region the comparison of the corresponding variances can be used. The so-called coefficient of anisotropy K, being obtained immediately in the experiment, varied in the interval from 0.62 to 2.57 with the mean value Km = 1.57 that indirectly indicated that the temperature induced optical inhomogeneities, which produce the phase fluctuations, were anisotropic in the large-scale. In addition, the relationship is quite obvious between the K value and the instability parameter B.

Let us compare the measured variances (and their ratios) with those calculated using the model of the turbulence spectrum allowing for the finiteness of the turbulence outer scale. In the numerical calculations we use the model of the turbulence spectrum that makes it possible to introduce two scales for the outer scale of turbulence.

In the general case for estimating the observed anisotropy of the image jitter K one should use appropriate formula. It follows from this formula that the measured K values can be explained with the help of the spectrum as a model with two different projections of the outer scale of turbulence into the vertical and horizontal directions. In addition vertical component of outer scale is always smaller than horizontal component.

INVESTIGATION OF THE ATMOSPHERIC TURBULENCE DYNAMICS ON THE BASIS OF ASTROCLIMATIC OBSERVATIONS

Let us finally analyze the data on the astroclimatic characteristics obtained in the region of the Elbrus mountain. These measurements were conducted at the Special Astrophysical Observatory. In our analysis of the experimental data we assume that the atmosphere is stratified and its inhomogeneities have the shape of elongated ellipsoids of revolution. This implies that: (1) In the case of vertical propagation (precisely along the zenith direction) the image jitter must be practically isotropic. (2) If the underlying surface is isotropic then the anisotropy of the jitter of an optical source image must be maximum for the case of horizontal propagation and will be determined by the atmospheric instability.

In the experiment we have used the measurer of fluctuations of the angles of arrival of the optical waves based on the telescope as a photoelectric adapter. This adapter was manufactured based on the soviet dissector LI-609 [1]. The parameters of the telescope and the measurer ensure the determination of angular position of the center of gravity of the focal spot with the accuracy of about 0.08" and the measurements of its deviation in the frequency range from 0.01 to 100Hz. The signals proportional to the deviations of the center of gravity along two perpendicular directions were processed on a computer. We calculated the corresponding variances, spectral densities of the processes, as well as the distribution probability densities in the case of 256 levels of digitizing.

The meteorological instrumentation allowed obtaining the data for calculating the structure parameter of temperature, mean wind velocity at the altitude of 2.5m above the underlying surface, the mean gradients of temperature and wind velocity. In the first stage, the measurements were conducted under the controlled conditions of a homogeneous horizontal path. To this end a point light source, i.e., the electric bulb supplied by a source of stabilized voltage, was placed at the distance of 1685m from the telescope. As a result we have obtained the values of the variance of an image jitter and theirs orthogonal components

However, under the near-surface conditions one can expect a strong anisotropy of the turbulence that leads to the anisotropy of the jittering process. We shall use the value K the ratio of variances, to characterize the measure of anisotropy of the image jitter process. The data of synchronous meteorological and optical measurements carried out along a near surface path, each being averaged over 16 measurements, are presented.

It is obvious from the data that at small wind velocities the increase of the temperature instability (the positive growth of the temperature gradient) reduces the turbulence intensity, but causes an enhancement of the anisotropy of the temperature field (growth of K). The earlier indications of the anisotropy of a source image jitter in the surface atmospheric layer can be found in Ref.9.

At the next stage jittering of images of stars caused by the atmospheric turbulence were observed. During the whole observation period more than 2000 realizations (with their

durations ranging from 10 to 500s) of the star image jitters were obtained. About 40 different stars were used in the measurements. The position of an observed star is described by two angles, i.e., the azimuthal A and zenith Q angles. In the process of the jitter recording we have determined the zenith and azimuth angles of a star while its stellar magnitude was available from a catalog. The sensitivity of the photoelectric measurer provided reliable measurements of the star image jitters with the brightness as low as +4.

It is well known [6, 7] that under conditions of uniform underlying surface the length of atmospheric column is solely the function of the zenith angle and is independent of the azimuth. In the so-called approximation of "flat Earth" the assumption is made that with the change of elevation angle the variance of an image jitter scales as 1/cosQ. In this context we can replace the measured value of the variance of a stellar image jitter along the direction Q_1 by that in the other direction Q_2 by multiplying the former value by $\cos Q_2/\cos Q_1$. It should be noted that the approximation (1/cosQ) is valid with stars in two cases, i.e., under conditions of uniform underlying surface (steppe, sea) and for isolated mountain peaks [1,2]. This approximation must be valid for all azimuthal angles. Alternatively, if the mountain peak, at which the telescope is located, is not single but is surrounded by other peaks being even higher than the peak of the telescope location, then the characteristics of jitter of the image formed by the telescope will be dependent both on the elevation and azimuthal angles. As in the case of horizontal paths, the measurements of variance of the jitter performed for the stars observed at large zenith angles (Q is of order 70^o-75^o) are indicative of a strong anisotropy (K=1.6-2.4). At the same time, for the stars, observed at small zenith angles (Q=20^o -30^o) , jitter is practically isotropic (K = 0.9-1.15). These data confirm my earlier assumptions.

It is difficult to obtain reliable data on the outer scale of turbulence from these measurements [11-13] because the real altitude distribution of the turbulence intensity is unknown. At the same time, indirect information about the outer scale can be obtained by examining the dependence of the variance of a jitter of a star on the diameter of a receiving aperture.

In our measurements aperture dependence of star jitter was examined with the help of a sufficiently bright star. The diameter of the receiving aperture has been varied with the help of an aperture diaphragm. successively. diameters of the diaphragms were 2R = 152, 215, 313, 492, and 600mm. All observations were performed sufficiently fast so that the stellar zenith angle could be considered constant and no significant variations of the meteorological conditions occurred. However, the experimental data do not follow the theory [6, 7]. This failure can be justified, for example, as follows: the aperture diameter 2R is comparable to the outer scale of the turbulence. From our experiments it was revealed that: (1) In the ground atmospheric layer the outer scale of turbulence is comparable to the height above the underlying surface. (2) The value of this outer scale appears to be dependent on the atmospheric stability. (3) In the ground atmospheric layer the most large-scale inhomogeneities of the atmospheric turbulence are anisotropic. One of the consequences of this situation is the difference of vertical and horizontal dimensions of the outer scale. (4) From the standpoint of vertical distribution of the atmospheric inhomogeneities one can conclude that the atmosphere is a stratified medium.

REFERENCES

1. S.M. Gubkin, O.N. Emaleev, and V.P. Lukin, "Experimental investigations of astroclimatical characteristics of Elbrus region", Astron. Zh., vol.60, pp.790-795, 1983.
2. V.P. Lukin and V.V. Pokasov, "Optical wave phase fluctuations". Appl. Opt.. vol.20, pp.121-135, 1981.
3. V.P. Lukin, "Optical measurements of outer scale of atmospheric turbulence", Atmos. Oceanic Opt., Vol.5, No.4, pp.229-242, 1992.
4. B.V.Fortes, V.P.Lukin, "Modeling of the image observed through the turbulent atmosphere", Proc.SPIE, vol.1668, P.477-488, 1992..
5. Vladimir P.Lukin, "Investigation of some peculiarities in the structure of large scale atmospheric turbulence", Proc. SPIE, vol.2200, pp.384-395, 1994.
6. M.S. Belenkii, V.P. Lukin, V.L. Mironov, and V.V. Pokasov, Coherence of Laser Radiation in the Atmosphere, Nauka, Novosibirsk, 1985.
7. A.S. Gurvich, A.I. Kon, V.L. Mironov, and S.S. Khmelevtsov, Laser Measurement in the Turbulent Atmosphere, Nauka, Moscow, 1976.
8. G.M.B. Bouricius, S.F. Clifford, "Experimental study of atmospherically induced phase fluctuations in an optical signal", J.Opt.Soc.Am., vol.60, p.1484, 1970.
9. V.P. Lukin, V.V. Pokasov, and S.S. Khmelevtsov, "Investigation of time characteristics of phase fluctuations of optical waves propagating in the atmospheric layer near the earth", Izv.Vyssh.Uchebn.Zaved. Radiofizika, vol.15, pp.1861-1866, 1972.
10. R.S. Lawrence, "Tracking systems requirements for atmospheric steering compensation", Applied Optics, vol.14, p.2750. 1975.
11. J.-M.Mariotti and G.P.Di Benedetto, Pathlenght stability of synthetic aperture telescopes. The case of the 25cm CERGA interferometer, I.A.U.Coloq.79, Garching, Apr.9-12 1984.
12. M.Mark Colavita, Michael Shao, and David H.Staelin, Applied Optics, 1987, V.26, No.19, pp.4106-4112.
13. D.F.Bucher. A Thousand and One Nights of Seeing on Mt.Wilson, Proc. SPIE, 1994, V.2200, pp.260-271.

A Simulation-Based Validation of Some Improvements in Automatic Stereo-Radargrammetry

Lucien Nocera
INRIA*
nocera@sophia.inria.fr

Stephane Dupont
ISTAR†
sdupont@gandalf.inria.fr

Marc Berthod
INRIA*
berthod@gandalf.inria.fr

Abstract

In this paper, the main problems of automatic stereo-radargrammetry are analyzed. An algorithm for reconstruction is presented including an alternative formulation for the restitution function. We present a few experimental results and emphasize on some of the difficulties encountered during the matching process. We show that these difficulties are due to the correlation function. Some solutions are proposed and discussed.

INTRODUCTION

Many papers present stereo-radargrammetry but only a few of them propose an automatic implementation [7, 4]. Most of the results in this domain are based on a manual approach [5], which is in contrast with the fast evolution of the automatic techniques for the optical sensors [8]. This is mainly due to the intrinsic characteristics of the Synthetic Aperture Radar imaging (SAR).

In this paper, we discuss the problems of automatic stereo-radargrammetry and we propose some improvements. Quantified results are presented on synthetic images.

The first part of the paper describes the stereoscopic algorithm used for the reconstruction. It is a cross-correlation algorithm implemented with a pyramidal strategy. A generic formulation of the reconstruction function is proposed, which integrates viewing parameters. We show that this method has a low sensitivity to the matching errors in azimuth. Thus, one could apply less strict epipolar constraints.

The second part of the paper presents reconstruction results from which we formulate the intrinsic problem of radargrammetry. This can be divided into three parts: (1) the speckle noise, (2) the influence of the surface effects correction factor (3) the foreshortening effect. The two first problems are radiometric problems, the last one is geometric. We discuss methods that quantify and solve these effects.

ALGORITHM DEFINITION

Stereoscopic algorithms proceed in three separate stages: (1) sensor calibration, (2) matching and (3) reconstruction. Because we aim to use calibrated (synthetic) images, we will examine points (2) and (3) only.

The goal of matching is to pair image primitives. For SAR images, correlation-based methods are usually run in order to obtain a dense disparity map. Cross-correlation [3] reduces the errors induced by the low level signal-to-noise ratio. Selecting the match as the maximum of the correlation peak imposes a uniqueness constraint. Regions which violate the uniqueness constraint are foreshortening areas. We show below that these areas may be treated in a special manner, so that uniqueness constraint can be applied.

The advantages of a hierarchic strategy are (1) to increase the robustness because of the signal to noise ratio enhancement (divided by a factor $\sqrt{N}$, if N is the number of averaged samples) and (2) to decrease the computational time.

The coarse disparity map obtained after the matching process, requires a processing stage before the reconstruction. This is essential to eliminate false matches and to interpolate the missing information. It can be done by means of a filtering, a smoothing and an interpolation of the disparity map. Those treatments and a pyramidal strategy impose a continuity constraint. This constraint may be violated on SAR imagery because of the existence of so-called layovers. Only a local and complex treatment can cope with such a problem.

Geometric constraints used in automatic stereo-radargrammetry are poorly known. Thus the epipolar constraint can only be imposed on delimited image regions for which deformations due to the satellite path orientation are small enough. For zero Doppler frequency and quasi-parallel tracks, images can be registrated along azimuth and the matching process may be performed as a 1-D search.

Finally, the reconstruction stage, computes 3-D information from paired pixels. Usually, a simplified scheme is used for this purpose [10], giving the altitude of the reconstructed point

*INRIA : 2004 Route des Lucioles - 06902 SOPHIA ANTIPOLIS Cedex - FRANCE
†ISTAR : Espace Beethoven Bâtiment 2 - Route des Lucioles - 06902 SOPHIA ANTIPOLIS Cedex - FRANCE

0-7803-3068-4/96$5.00©1996 IEEE

above the reference ellipsoid. A least square formulation deduced from the Doppler cones and distance equations is preferable. Using index 1 and 2 to reference the stereo pair images, the cost function F can be written as,

$$F = \sum_{i=1,2} \left\{ \left(\frac{f_{Di} - \widehat{f}_{Di}(\mathbf{M})}{\sigma_{f_{Di}}} \right)^2 + \left(\frac{r_i - \widehat{r}_i(\mathbf{M})}{\sigma_{r_i}} \right)^2 \right\} + P$$

with $\widehat{f}_{Di}$ and $\widehat{r}_i$, $i = 1, 2$, the estimated Doppler frequencies and the distances estimated in terms of $\mathbf{M}$, (the searched 3-D point). The reference distance r_1 (respectively r_2) is known for calibrated images. The Doppler frequency f_{D1} (respectively f_{D2}) is a constant defined by the SAR image processing. Figure 1 shows that two solutions exist for SAR reconstruction. In this figure, all the positions are defined in a geocentric reference frame $(G, \mathbf{i}, \mathbf{j}, \mathbf{k})$ and satellite positions corresponding to a match are noted as $\mathbf{S_1}$ and $\mathbf{S_2}$.

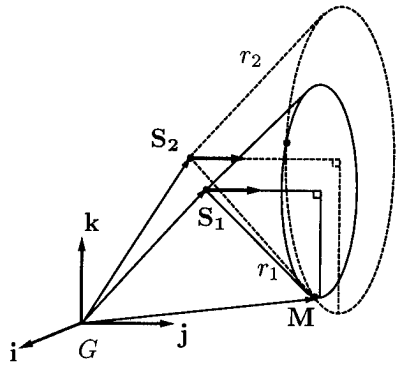


Figure 1: Doppler cones and reconstruction

To select the proper (realistic) solution among the two possible ones, one can add a penalty term P. This term can be chosen equal to the altitude of $\mathbf{M}$ above the ellipsoid. P can only be used to initialize the process. The first solution is then propagated to the rest of the reconstruction.

An alternative formulation of the cost function F consist in searching the $\mathbf{M}$ that projected in the stereo pair minimizes the distance to the matched pixels. However, it is more time consuming because it needs the inverse projection of $\mathbf{M}$.

To ensure a fast convergence, minimization of F can be performed using a conjugate gradient algorithm. Moreover, for easy implementation, derivatives of F can be calculated analytically.

The reconstruction tests show a low sensitivity to azimuth matching errors because the solution is adjusted along the mean azimuthal direction. This property avoids exact image registration along the azimuthal axis.

RESULTS AND DISCUSSION

Synthetic images used to test the algorithm have been generated by SAMI (Simulateur Appliqué à la Modélisation Interferométrique), an Insar Simulator [1]. The chosen example is on a hilly test-site, Aix-Marseille (FRANCE). The Digital Elevation Model (DEM) used for the simulation is part of a DEM kit freely available through the CEOS WGCV Terrain Mapping sub group. It has been provided by IGN and obtained by stereoplotting from aerial photographs at a scale of 1:30000 and has a 10 m grid size. Its accuracy has been evaluated to be around 1 m. The ERS-1 slant range image is 5 looks (1 in slant range x 5 in azimuth) and has a dimension of 1500 x 1200. It has been processed from a SLC product. The backscatter coefficient used for each pixel of the DEM has been generated from a normalized orthoimage of the scene. During the processing we take the surface effects [9, 2] into account.

Using a polynomial modelisation for the orbits and the appropriate cartographic projection allow us to compare the reconstructed DEM with the reference DEM.

Figure 2 shows a couple of synthetic SAR images with viewing geometry of 20 and 23 degrees (the baseline between the two orbits is 40 Km), and the reconstructed DEM. Noisy versions of these images have been generated using a multiplicative noise model following a gamma law.

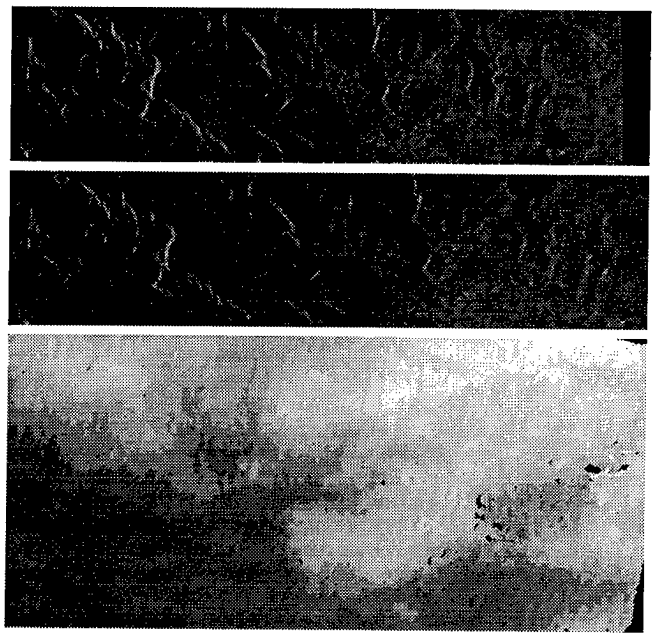


Figure 2: Stereo pair and reconstructed DEM

Table 1 shows the cartographic errors obtained with both noiseless and noisy images. In the case of noiseless images, statistical results validate the algorithm because the rms (root

mean square) is of the order of the resolution (i.e. $\simeq 10\,m$). Errors for the y axis are small because of the perfect registration of the orbits. This axis is also mainly parallel to the azimuth axis. We note that extremal errors are due to shadow areas.

	noise	mean (m)	min (m)	max (m)	rms (m)
x	noiseless	12.17	-19.08	36.92	3.42
	noisy	10.91	-55.52	61.66	10.62
y	noiseless	2.12	-3.73	7.35	0.88
	noisy	1.90	-10.53	11.69	1.97
h	noiseless	-0.56	-103.83	134.53	14.45
	noisy	-5.98	-208.73	285.47	45.59

Table 1: Errors along the DEM axes

Speckle

Statistical results on noisy images shows that the rms is, on average, three times higher than for noiseless images. Image filtering can be a solution but it is costly and not very effective. Moreover image filtering remove information and deteriorates the matching process. An alternate solution would be to use a correlation function which takes into account the speckle noise statistics, instead of assuming the noise to be Gaussian (as in a classical correlation function $(I_1 - I_2)^2$). We are presently studying this kind of alternative correlation function.

Surface correction

Synthetic aperture assumes the ground to be flat. This assumption introduces uncertainty in the radiometry estimation and the matching process becomes problematic. A study of the characteristics of the ground (slope and roughness) can lead to a qualitative estimation of the validity of the classical correlation function. In the following cases, the classical correlation function should not be applied: (1) for smooth surfaces when the incidence angle (angle between the surface normal and the incident beam direction) falls to zero, or (2) for rough surfaces with varying slopes. The first case can be considered rather rare. The second case happens more often. Shape from shading algorithms (known as radarclinometry) are advisable to obtain the 3-D information in such areas.

Foreshortening

Because of the difference of viewing angles, the reconstruction of foreshortening areas can produce errors. These kind of errors can be visualized on an orthoimage with the reconstruction error superimposed. For the studied examples, we can see that these errors are not spatially correlated to the foreshortening. This can be explained by using a model based on a simplified viewing geometry [6]. Such models show that these effects arise only in regions which include long steep slopes along the range axis.

CONCLUSION

In this paper, the problem of radargrammetry is analyzed. An automatic algorithm is presented. An alternate approach for the reconstruction is proposed, deduced from the SAR geometry. The results show that speckle noise is the main source of errors for the reconstruction. The roughness of the ground is the second source of errors. Foreshortening influence can be considered less important. More precisely, the Gaussian noise correlation function is not adapted to the SAR imaging. Thus, we propose to apply a correlation function which includes a speckle noise model and to apply locally a shape from shading algorithm.

References

[1] S. Dupont, F. Perlant, and M. Berthod. Sami: An insar simulator to improve sar calibration. In *Proceedings of IGARSS'95 Symposium*, Firenze, Italy, July 1994.

[2] S. Dupont, F. Perlant, and M. Berthod. A generalized method to radiometrically correct sar images. In *Proceedings of Satellite Remote Sensing II*, Paris, France, September 1995.

[3] P. Fua. A parallel stereo algorithm that produces dense depth maps and preserves image features. *Machine Vision and Applications*, 6(1), 1993. Also available as INRIA research report 1369.

[4] F. Leberl, K. Maurice, J.K. Thomas, and M.Millot. Automated radar image matching experiment. *ISPRS Journal of Photogrammetry and Remote Sensing*, 49(3):19–33, 1994.

[5] F. Leberl, W. Mayr, and G. Domik. Sir-b stereo-radargrammetry of australia. *IJRS*, 9(5), july 1988.

[6] L. Nocera. *Reconstruction du Relief en imagerie Radar à Ouverture de Synthèse : Stéréoscopie et Ombrages*. PhD thesis, Universite Paris 7, Paris, France, 1996.

[7] H. Ramapriyan, J. Strong, Y. Hung, and C. Murray Jr. Automated matching of pairs of sir-b images for elevation mapping. *IEEE Transaction on Geoscience and Remote Sensing*, GE-24(4), july 1986.

[8] L. Renouard. *Restitution automatique du relief à partir de couples stéréoscopiques d'images du satellite SPOT*. PhD thesis, Ecole Polytechnique, 1991.

[9] P. Rosen. Application of interferometrically derived terrain slopes: Normalization of backscatter and the interferometric correlation coefficient. In *Second ERS-1 Symposium*, volume SP-361, Hamburg, Germany, October 1994. ESA.

[10] J. Thomas, V. Kaupp, W. Waite, and H. MacDonald. Considerations for optimum radar stereos. In *Proceedings of IGARSS'87 Symposium*, pages 1531–1536, may 1987.

DETECTION AND LOCALIZATION OF LOST OBJECTS BY SAR TECHNIQUE

C. Dionisio
Consorzio Spazio Ambiente
via Saccomuro 24, Roma
00131, Italy
Tel: +39 6 41512138
fax: +39 6 4191391

ABSTRACT
The increased sensibility of Public Opinion and Governments for Environment and its health status together with the research of new applications for Remote Sensing small satellites technologies lead to identify future space missions.
It was recognized that during the Worldwide navigation, vessels and ships loss a significant number of containers and pallets due to different reasons, but mainly for bad weather conditions. Those can transport dangerous or valuable goods. Therefore it comes out the need of a system capable to detect and localize the position of the lost objects so permitting their recovery. More in general Search and Rescue systems like COSPAS-SARSAT present same problems related to interference and poor localization accuracy.
A simple architecture based on: a micro satellite weighting less than 100 Kg, embarching a small SAR (Synthetic Aperture Radar) sensor; a transponder installed in the container and one or more ground stations, can comply the mission at inexpensive cost. Whether the container drops in the water a floating housing is unhooked and the internal transponder is switched-on. Initially it works in a low power consumption status and then, when activated by the small satellite beacon, starts the full operations . The azimuth localization is performed by a synthetic aperture or Doppler analysis processing. In the range direction short pulse is used. The radar transmitted frequency is shifted inside the transponder, maintaining the coherence. This avoid any problem of time ambiguities in the radar because the receiver chain operates at a different frequency from the transmitter. The micro satellite should be equipped with GPS system for determining its position along the orbit. The received signals are preprocessed on board and then transmitted to the Satellite Control Station. A requirement of four/five days can be met by a single satellite while up to four's are needed for one day revisit time.
This paper deals with the description of such innovative system, its dimensioning and possible implementation solutions for the micro satellite radar and the electronics contained into the transponder.
The system can be used for other applications which require tracking or accurate phase measurements. For instance a transponder and differential Interferometry permit to detect mm's movements of man made objects like monuments or dikes; the direction of a oil slick could be tracked by a buoy (displaced by an aircraft).
Key words: new sensors, SAR, S&R, small satellites .

1. INTRODUCTION

The capability to detect and localize objects on the Ocean surface can be easily achieved by space based systems.
A study case is derived from an analysis /1/ conducted about the naval traffic and its problematic. It showed that during navigation a significant number of containers is lost both in the World oceans and in the European seas. The containers can transport dangerous or valuable goods which need to be recovered. Therefore a system able to detect and locate the lost containers could be useful and a routine timely service for Navigation Companies could be provided at a low cost.
The existing systems are generally based on the combination of a localization equipment like GPS plus a telecommunication equipment to send the information to the remote station or on Doppler measurement (COSPAS-SARSAT) of a beacon transmitted by the lost object.
In the following section a new design is presented based on radar techniques.
The system project is called "SCAMSAT & Balize Morte" and the architecture has been elaborated by Alenia Spazio for and together with the following Organizations: Consorzio Spazio & Ambiente (Roma), CRITT (France), Consorzio IESI (La Spezia).

2. REQUIREMENT

The requirement of a system to detect and locate lost objects on the ocean are identified in the table 1.
The main constraint in the realization of this system is surely the cost. Infact the possibility to sale the service to the users , generally Assurance and Navigation Companies, depends on the low cost of the proposed solution. Especially the equipment to be installed on the containers must be simple, reliable, accomodable and costs a fraction of the container , that is less than 100 $.

3. SYSTEM DESCRIPTION

A preliminary design has been carried out to understand the architecture and the feasibility of the system.

0-7803-3068-4/96$5.00©1996 IEEE

The system is composed of three elements (see figure 1.):

- One or more micro satellites in polar orbit; increasing the number of satellites is reduced the delay between the lost and the detection.
- A few ground stations able to link automatically with the micro satellites and the users in case of a container drops into the water.
- The electronics to link the micro satellite and installed in a suitable box attached to the containers. It signals the position of the container and provides its code number.

In case the container drops into the ocean during the navigation, the box with the electronic is unhooked and floats on the water surface . A humidity sensor activates partially the transponder in stand-by mode to save power consumption. When the satellite passes over the box than the reception of a beacon signal fully activate the electronic which receives and retransmits the radar signal.
Many different options are under studying for the radar architecture in order to get the localization requirement and to simplify the overall system, only one solution is presented here as example.
The earth coverage requirement of five days is satisfied by flying the satellite in a 500 Km altitude polar orbit with a swath in the order of 550 Km . The access region of the radar shall vary within the incident angle of 20° and 58°.

Space Segment

The space segment is realized by a micro satellite with a weight lower than 100 Kg , it is composed of:
- standard platform
- payload including:
    - radar
    - communication receiver for code identification
    - star sensor
    - GPS receiver

The presence of the star sensor is dictated from the need to know very accurately the pointing position of the radar antenna. The GPS receiver is used for navigation and to know precisely the satellite position along the orbit.
The in-flight radar is a monostatic, coherent instrument in X band which derives the distance measurement by transmitting a short or a chirp pulse and the azimuth measurement by the synthesis of the antenna pattern or by the frequency Doppler computation. The presence of the transponder in the box permits the transmission of a low power level pulse, in the order of 30 watts. The range resolution is achieved by a 2 microsecond long CW pulse. The azimuth resolution can be obtained by synthesizing the range pulse phases. An integration time of only 20 ms is needed for the 250 m resolution. In order to reduce the radar complexity non ambiguous PRF is selected that is about 200 Hz. This PRF value is too low to sample the azimuth synthetic antenna . Fortunately the azimuth ambiguities shall fall down the receiver noise because of the low transmitted power. Furthermore despite the subsampling, generally a submultiple of needed PRF, the real from the gost targets can be discriminated by S/W processing. A second technique, now used as baseline, consists of alternating the burst of short range pulses with 10 ms long pulses for frequency Doppler computing. The complete coherence of the system permits the achievement of very good accuracy with simple FFT processing.
The radar transmits and receives the signals by an two beams electronically steered antenna or two antennas in both the cases 100 MHz bandwidth is requested because the frequency translation operated in the transponder. The telecommunication channel still uses the X band and is received by the same radar antenna. The antenna shall have a gain better than 25 dB. The telecommunication channel is devoted to the container code reception and to associate the position and the kind of transported goods. In the present design the FSK modulation has been selected.

Ground segment

The ground segment shall include one Mission Control Ground Station and a certain number of simple secondary receiving station which should use commercial H/W. The satellite is programmed to trar smit data to ground in VHF or S band in correspondence to the receiving secondary station

Container electronic

The principle block diagram of the electronic in the box is given in figure 2. The transponder translates the received signal in X band of 96 MHz. The beating frequency is extracted by a second signal in S band which is divided by 10. Later the up-converted signal is amplified and transmitted back by a second antenna.
This approach avoids the drawbacks of a monostatic configuration that is a costly circulator or the loss of signal level coming from the implementation of a hybrid device.
The complete antenna is composed of three patches as in figure 3. Each X band patch is matched to its operative frequency (different Tx and Rx) so increasing the isolation between transmitting and receiving chains. A third S band patch is accommodated for the reception of the local oscillator signal. The patch antenna was selected because of low cost, wide coverage angle, reasonable gain.

4. OTHER APPLICATIONS

Other applications could be envisaged like differential phase measurement to measure displacement of object like monuments and dikes . This technic has been already investigated by using ERS-1/2 SAR but here is proposed to realize a real service with high revisit time and fast delivery of data.
A second example could be the tracking by floating buoys of oil slicks or currents at very low cost.

Moreover a solid state memory buffer can be added to the satellite permitting the exchange of messages between ship and vessels and remote stations.

5. CONCLUSIONS

The preliminary definition of a system architecture capable to detect and locate lost objects on the ocean water has been performed. The following activity shall consist of reviewing the design, dimensioning of electronics and definition of budget and interfaces. In parallel shall continue the market exploration and the cost evaluation for the system implementation and service.

7. REFERENCES

/1/ Avant Project de Balize Morte, CRITT

/2/ Consideration on detection and localization of lost objects into the sea water, Alenia Spazio internal memo

/3/ Total Information Processor for 121.5/243 MHz SARSAT Signals

PARAMETER	VALUE	REMARKS
localization accuracy	> 1 Km min > 250 m goal	
time of delay	> 3 days min. > 1 day goal	
coverage	Europe seas min. global goal	Mediterran Bacin Baltic and North sea, Atlantic coasts
identification capability	the container should be able to transmit its code number	
minimun cost and complexity impacts on Container	reduced dimension and power consumption	

TABLE 1.

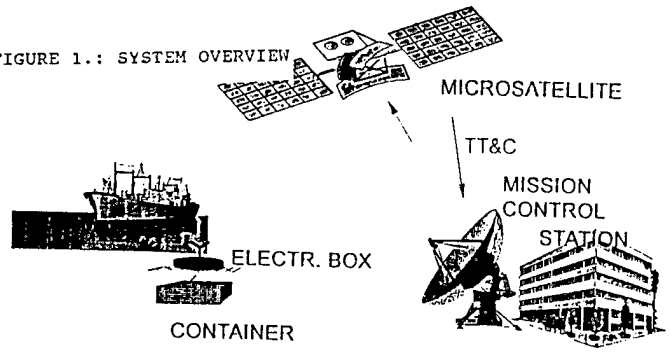


FIGURE 1.: SYSTEM OVERVIEW

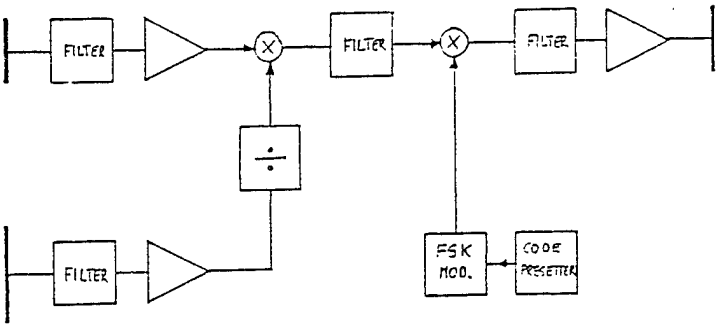


FIGURE 2. : TRANSPONDER BLOCK DIAGRAM

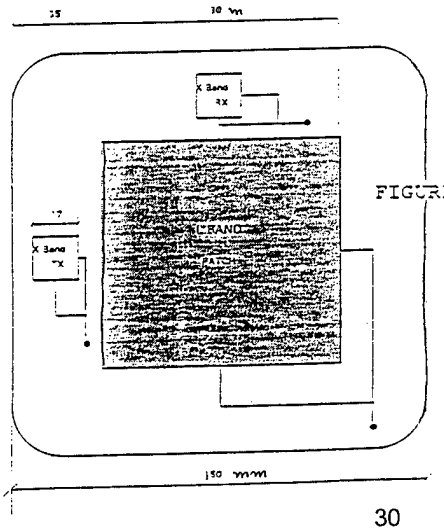


FIGURE 3. PATCH ANTENNA LAYOUT

Automated Matching Experiments with Different Kinds of SAR Imagery

M. Gelautz [1], G. Jakob [2], G. Paar [2], S. Hensley [3], F. Leberl [1]

[1] Institute for Computer Graphics, Technical University Graz
Münzgrabenstraße 11, A-8010 Graz, Austria
Tel.: ++43/316/873-5031, Fax: ++43/316/873-5050, Email: gelautz@icg.tu-graz.ac.at
[2] JOANNEUM RESEARCH, Institute for Digital Image Processing
Wastiangasse 6, A-8010 Graz, Austria
Tel.: ++43/316/876-716, Fax: ++43/316/876-720, Email: paar@pdib40.joanneum.ac.at
[3] Jet Propulsion Laboratory, California Institute of Technology
4800 Oak Grove Drive, Pasadena, CA 91109

ABSTRACT

We carry out tests with two readily available automated matching algorithms in their application to (a) Magellan SAR stereo images, and (b) ERS-1 and X-SAR real-simulated images. The match points are examined visually, and an accuracy analysis on Magellan data is performed by comparison with manual measurements.

1. INTRODUCTION

Existing literature on SAR image matching can basically be divided into two groups: (a) matching of stereo image pairs for the computation of a Digital Elevation Model (DEM), and (b) matching of real with simulated imagery for the purpose of geocoding and the refinement of sensor parameters. Early automated stereo matching experiments on SIR-B data are reported in [10]. Reference [8] carried out investigations on Magellan and aircraft stereo images, and compared the results to those obtained from optical data. Magellan data are also included in the test data set we employ in this study, however the matching algorithms applied are different. Seasat data are the subject of real-simulated image matching investigations carried out in [2], [7], and [6]. In the last work, the authors show that the choice of the backscatter model used in the simulation has a significant influence on the accuracy of the matching results. The issue of accuracy analysis is particularly addressed in [3], a study on real-simulated ERS-1 data.

Two available matching algorithms are applied to Magellan stereo data, as well as to real-simulated ERS-1 and X-SAR data. The match points found are superimposed on the images for visual inspection, and an accuracy analysis on Magellan images shows that an rms error of less than 2 pixels can be achieved.

2. TEST DATA

The data set used for stereo analysis consists of SAR images of planet Venus from NASA's Magellan Mission. The pixel size is 75 m x 75 m, resampled from an original ground resolution of the radar of approximately 130 m x 120 m. It should be noted that the Magellan images we investigate are already geocoded to a low-resolution (over 26 km/pixel) DEM available from the earlier Pioneer Mission. Therefore, stereo analysis means the detection of remaining distortions between the two images, which can then be used to compute higher frequency topographic information not includud in the coarser Pioneer DEM.

The test site for our investigations on real-simulated ERS-1 and X-SAR imagery is the Oetztal, a rugged terrain in the Austrian Alps, partially covered with snow and glaciers. The simulation program used to generate the synthetic images is part of the RSG software package [5]. It assumes a cosine reflectance model, and no ground truth data is incorporated into the simulation. The 12.5 m x 12.5 m pixel size of the ERS-1 and X-SAR images was obtained by resampling from the original radar resolution of 25 m x 25 m. No previous speckle filtering was applied to the images.

3. MATCHING ALGORITHMS

We carry out tests with two different matching algorithms, a hierarchical correlation-based algorithm (ALG1) specially suited to SAR imagery corrupted by speckle noise, and a so-called Hierarchical Feature Vector Matcher (ALG2), which uses local image statistics to describe correspondence.

The mathematical background of ALG1 is described in [1], and its application to DEM generation from Magellan stereo data is reported in [4]. Therefore, the basic concepts of the algorithm are only briefly outlined. Matching is performed in a hierarchical manner, with successively smaller window sizes. At each level, a two-dimensional normalized cross-correlation is carried out, and the shape of the correlation surface along with a local scene noise estimate is then used to compute a confidence measure. This confidence measure is a two-dimensional covariance matrix for the match which can be used for weighting information differently in the two directions and propagating matching error forward in stereo solutions. The confidence matrix serves to filter out bad matches, and to suppress speckle noise. In our tests, the algorithm was run with the suggested default values, no attempt was made to optimize the parameters, which can greatly effect matcher performance.

ALG2 has originally been developed for stereo matching to compute dense disparity maps from optical stereo images of natural terrain. A detailed description of the algorithm can be found in [9]. Its principles can be described as follows: First, for each pixel of both images a

0-7803-3068-4/96$5.00©1996 IEEE

feature vector is derived from local properties, e.g. convolutions, in the surrounding of each pixel. For each pixel in the reference image, its feature vector is compared to the feature vectors in the expected search area in the other image. Using Euclidian distance, the minimum distance vector defines the corresponding pixel. Median filtering is applied to smooth the resulting disparity images, and undefined disparities are interpolated. These steps are carried out for several resolution levels, using the low resolution results as prediction. In principle, on each pixel of the two matched images a disparity vector is gained. As confidence measure, a so-called backprojection error is computed, which is the inconsistency after left-right and right-left matching. Since the algorithm was originally designed for optical imagery, parameter tuning had to be carried out in order to adapt it to SAR imagery.

4. ANALYSIS AND RESULTS

Match points can be visually inspected in Figs.1 and 2. In the reference (left) image, a regular set of grid points was chosen, and the algorithm searches for the corresponding match points in the right image. Missing grid points mean that based on the internally computed confidence value the corresponding match was classified as bad, and therefore discarded. Fig.3 shows the gray-level encoded range disparity image corresponding to Fig.1.

A lack of texture was found to be the main reason for inaccurate or missing match points. Steep slopes in the terrain, which lead to extreme foreshortening or even layover situations, pose special problems in stereo matching, due to the different geometric appearance associated with the different viewing angles. On the other hand, foreshortening and layover areas can provide particularly useful features for real-simulated matching, since they provide highly textured regions with good contrast.

A quantitative analysis of the matching accuracy was carried out for the Magellan data by comparing the automatically determined match points with manual matches acquired by an experienced human stereo operator. The manual measurements we use as reference exhibit an uncertainty of +/- 0.6 pixels. This was determined by repeat measurements, as described in [8]. Table 1 shows the differences between manual and automated match points in range (r) and azimuth (a) direction, expressed as mean value and standard deviation σ. The percentage of matches which exhibit an error Δ in the disparity measurement of less than two pixels is also given.

Table 1 Analysis of Magellan stereo match points

Algorithm	number of matches	$\bar{r}$ pixel	σ_r pixel	$\bar{a}$ pixel	σ_a pixel	$\Delta < 2$ %
ALG1	272	0.4	2.2	0.4	0.6	57
ALG2	302	0.2	1.2	0.1	1.3	76

When examining the real-simulated match points visually, no clearly discernible mismatches were found. Since for this data set no manually acquired reference matches of sufficient accuracy were available, a first comparison between the two matching algorithms was carried out by analyzing the differences between the matches produced by ALG1 and ALG2. Mean value and standard deviation σ of the differences in range and azimuth direction are listed in Table 2. When applying ALG2 to X-SAR data, 71 % of the match points were classified as bad, as opposed to 26 % rejected by ALG1. In a practical application, such a high percentage of outliers may cause problems, since valid match points are too sparse. The determination of the absolute accuracy of the two algorithms with respect to suitable refence values remains the subject of further investigations.

Table 2 Analysis of ERS-1 and X-SAR real-simulated match points

Data	$\bar{r}$ pixel	σ_r pixel	$\bar{a}$ pixel	σ_a pixel
ERS-1	0.3	3.0	1.5	2.0
X-SAR	0.7	2.2	2.2	3.5

5. SUMMARY AND OUTLOOK

Tests on Magellan stereo pairs have shown that up to 76 % of the automatically acquired match points differed from the corresponding manual reference matches by less than two pixels. The immediate next step will be to employ the real-simulated match points for a refinement of the corresponding sensor flight path. Then, match points between stereo image pairs will be used together with the improved sensor parameters to compute a DEM of the Oetztal test site. Our investigations aim at studying the potential accuracy and limitations of a completely automated approach of DEM generation from SAR stereo images in a practical application.

6. ACKNOWLEDGMENTS

The authors wish to thank Walter Kellerer-Pirklbauer for his help in preparing the manuscript. The X-SAR and ERS-1 data were made available by Dr. Helmut Rott of the University of Innsbruck. We gratefully acknowledge his cooperation. The manual stereo measurements were obtained from Vexcel Corporation, Boulder. This study was supported by the Austrian Science Foundation (Grants 7003.3 and 7001.4) and JOANNEUM RESEARCH.

7. REFERENCES

[1] R. Frankot, S. Hensley, and S. Shafer: Noise resistant estimation techniques for SAR image registration and stereo matching, Proceedings of IGARSS'94, Pasadena, CA, pp. 1151 - 1153, 1994.

[2] B. Guindon and H. Maruyama: Automated matching of real and simulated SAR imagery as a tool for ground control point acquisition, Canadian Journal of Remote Sensing, vol. 12, nr. 2, pp. 149 - 158, 1986.

[3] B. Guindon: Performance evaluation of real-simulated image matching techniques in the acquisition of ground control for ERS-1 image geocoding, ISPRS Journal of Photogrammetry and Remote Sensing, vol. 50, nr. 1, pp. 2 - 11, 1995

[4] S. Hensley and S. Shafer: Automatic DEM generation using Magellan stereo data, Proceedings of IGARSS'94, Pasadena, CA, pp. 1470 - 1472, 1994.

[5] JOANNEUM RESEARCH: RSG - Remote Sensing Software Package Graz, Software User Manual, Release Nr. 3.0, Institute for Digital Image Processing, 1993.

[6] H. Kimura and T. Iijima: Automated matching of real and simulated SAR imagery for geometric correction, Proceedings of IGARSS'90, Washington, D.C., pp. 309 - 312, 1990.

[7] R. Kwok, J. Curlander, and S. Pang: An automated system for mosaicking spaceborne SAR imagery, International Journal of Remote Sensing, vol. 11, nr. 2, pp. 209 - 233, 1990.
[8] F. Leberl, K. Maurice, J. Thomas, and W. Kober: Automated radar image matching experiment, ISPRS Journal of Photogrammetry and Remote Sensing, vol. 49, nr. 3, pp. 19 - 33, 1994.
[9] G. Paar and W. Poelzleitner: Robust disparity estimation in terrain modelling for spacecraft navigation, Proceedings 11th ICPR, 1992.
[10] H. Ramapriyan, J. Strong, J. Hung, and C. Murray: Automated matching of pairs of SIR-B images for elevation mapping, IEEE Trans. Geosc. Remote Sensing, GE-24, nr. 4, 1986.

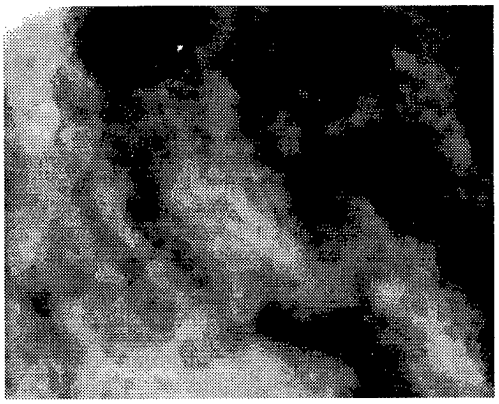


Figure 3: Range disparity map corresponding to Fig.1, produced by ALG2.

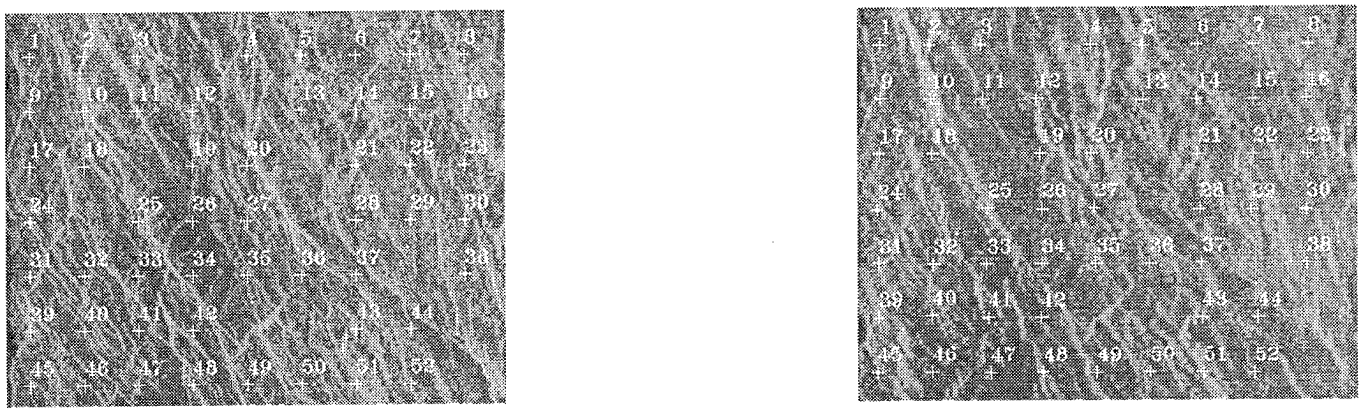


Figure 1: Subscene of a Magellan stereo pair with superimposed match points produced automatically by ALG1. The scene was illuminated from the left, with a look angle of 40 deg (left) and 21 deg (right). The area shown is located on Venus at about 8 deg S, 74 deg E. Image size is 460 x 360 pixels.

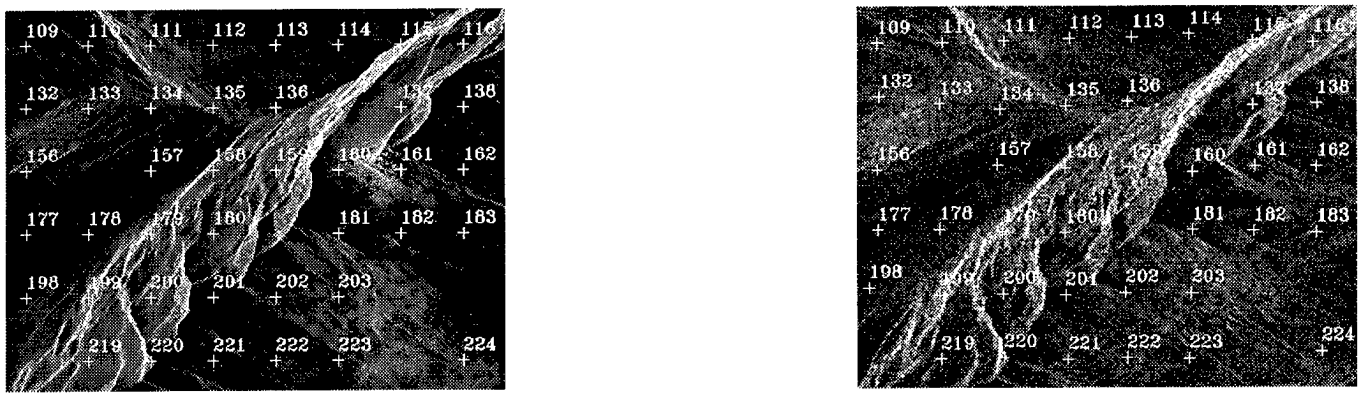


Figure 2: Simulated (left) and corresponding real (right) ERS-1 detail of the Oetztal, Austria, with automated match points from ALG2 overlaid. The scene was acquired from ascending orbit with a nominal sensor look angle of 23 deg. Image size is 512 x 387 pixels.

DETECTING MAN-MADE FEATURES IN SAR IMAGERY

Mark J. Carlotto (mjcarlotto@ma.psrw.com)
PSR Corp., 1400 Key Blvd., Suite 700, Arlington VA 22209

Abstract -- A method for detecting man-made features in synthetic aperture radar (SAR) imagery is described. The method is based on matching the local histogram against a family of Weibull densities. The Weibull density is defined by two parameters, the median and the skewness (Weibull parameter). Regions containing man-made objects have Weibull parameter values that are smaller than those containing natural features. In experiments performed with aircraft SAR imagery, man-made features are effectively discriminated from natural features using this method.

INTRODUCTION

Object detection techniques generally rely on edges or specific textures to indicate the presence of man-made objects in optical imagery. Instead of attempting to detect man-made objects directly, fractal techniques [1,2] model and remove the natural background. Certain sensors provides other opportunities to detect man-made features. For example, in multispectral imagery surface materials associated with man-made features can often be identified by their spectral signature. SAR texture modeling and discrimination approaches based on a variety of methods have been developed and evaluated [3].

In SAR clutter statistics provide an indication of type of surface material present [4]. Areas containing natural features (e.g., sparse vegetation, forested areas, and water) can often be modeled by the Rayleigh density. On the other hand in areas containing man-made features the clutter density has heavy tails and is better modeled by the log-normal density. Our method exploits the probability density of the clutter in SAR to detect man-made features. In particular we model the clutter by a family of densities and pick the density that best describes the clutter on a local basis.

METHOD

The image $X = \{x(i,j)\}$ is divided into non-overlapping regions. Let $p_{i,j}(x)$ denote the local histogram computed over the $r \times r$ pixel region $R(i,j)$ centered at pixel (i,j). We use the local histogram normalized to unit area as an estimate of the density in $R(i,j)$. Within each region, a family of Weibull densities for a range of parameter values are generated. The Weibull density [5] is given by

$$p_\alpha(x) = \frac{\alpha}{x_m}\left(\frac{x}{x_m}\right)^{\alpha-1} \exp\left[-\left(\frac{x}{x_m}\right)^{\alpha}\right] \qquad (1)$$

where α is the Weibull parameter which relates to the skewness of the distribution and x_m is the median value. The power of the Weibull is that it becomes different densities by changing the Weibull parameter. For $\alpha = 2$ it becomes the Rayleigh density, for $\alpha = 1$ it becomes the exponential density. Between the two the Weibull can approximate a log-normal density. Thus a single parameterized model can be used to model the clutter in regions containing natural features as well as in regions containing man-made features.

Figure 1 plots a family of Weibull densities for x_m=128 and $1 \le \alpha \le 4$. We use the median value of the local histogram computed over $R(i,j)$ as an estimate of x_m. In effect we are adjusting the model locally based on the brightness values within the window. This should also compensate for variations in brightness caused by changes in slope in the direction of the illumination.

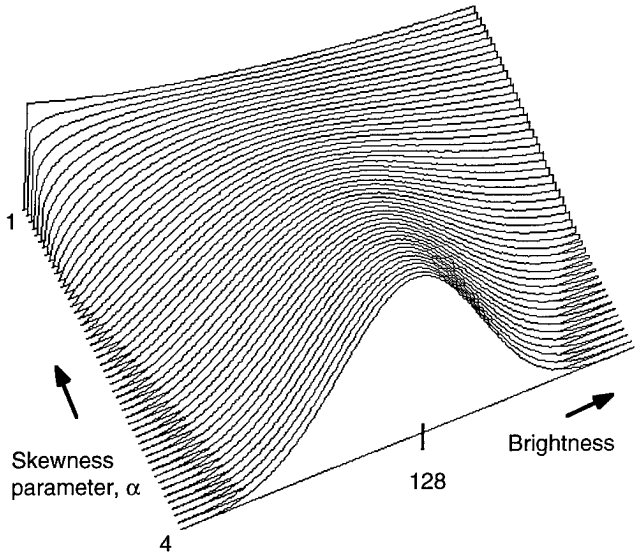


Figure 1 Family of Weibull densities

The model densities $p_\alpha(x)$ are then compared to the normalized local histogram. Let $P_\alpha(x)$ and $P_{i,j}(x)$ denote the cumulative distributions of the model densities and normalized local histogram. We use the maximum difference between cumulative distributions to find the model density that is most similar to the local histogram [5]. The maximum differences are

$$D(i,j,\alpha) = \max_x \left| P_{i,j}(x) - P_\alpha(x) \right| \qquad (2)$$

0-7803-3068-4/96$5.00©1996 IEEE

The Weibull parameter with the smallest maximum difference

$$\alpha = \arg\min_{\alpha'} D(i,j,\alpha') \tag{3}$$

is output in the form of a parameter image $\alpha(i,j)$. The parameter image indicates which of the model densities best matches the image in each region. We also output the smallest maximum difference

$$D = \min_{\alpha'} D(i,j,\alpha') \tag{4}$$

as a "model fit" image $D(i,j)$. The model fit image identifies those regions that are not described well by any of the model densities.

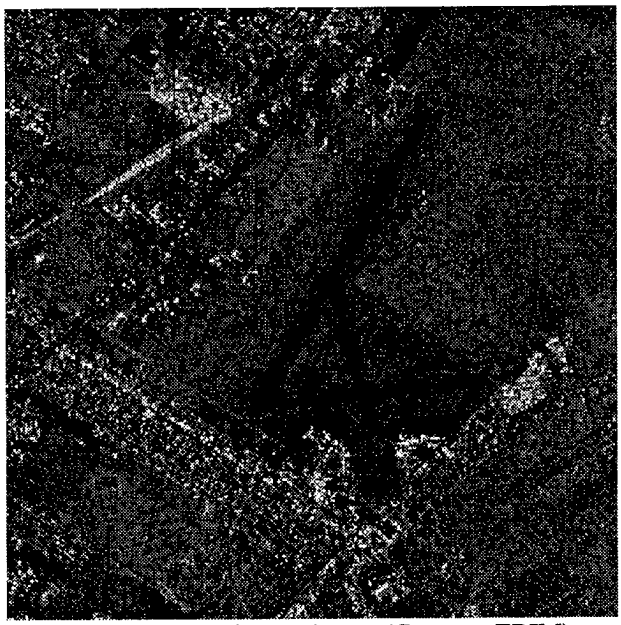


Figure 2 Aircraft SAR image (Courtesy ERIM)

EXPERIMENTAL RESULTS

Figure 2 is a 512 x 512 pixel aircraft SAR image over Willow Run Airport in Michigan. Figure 3 shows the computed parameter image for an 8 x 8 pixel window. The range of parameter values used was $1 \le \alpha \le 4$ in 32 discrete steps. Built up areas have low Weibull parameter values. These are the darker areas in Figure 3. A histogram over a built up area in this image is shown in Figure 4a. In built up areas, the histograms have very heavy tails and are thus better modeled by log-normal or even exponential densities. Natural features (e.g., sparse vegetation, forested areas, and water) on the other hand are better modeled by Rayleigh densities. In regions containing natural features the Weibull parameter values are higher. These are the brighter areas in Figure 3. Histograms over wooded and grassy areas in this image are shown in Figure 4b and c.

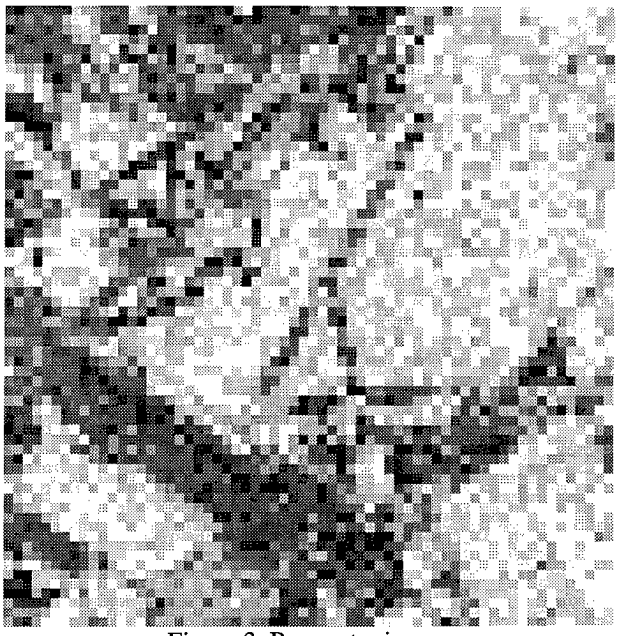
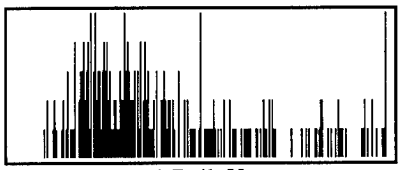
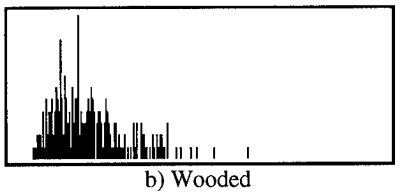


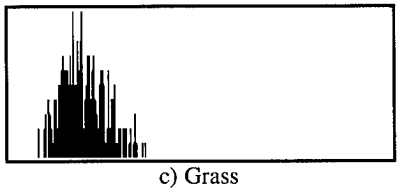
Figure 3 Parameter image



a) Built Up



b) Wooded



c) Grass

Figure 4 Selected histograms from image

Figure 5 depicts the model-fit errors, i.e., areas in the image that did not match any of the model densities. In many of these areas the densities have more than one mode thus indicating a mixture of two or more materials. This effect is particularly evident near features that are about the size of the processing window (e.g., the roads and the runways).

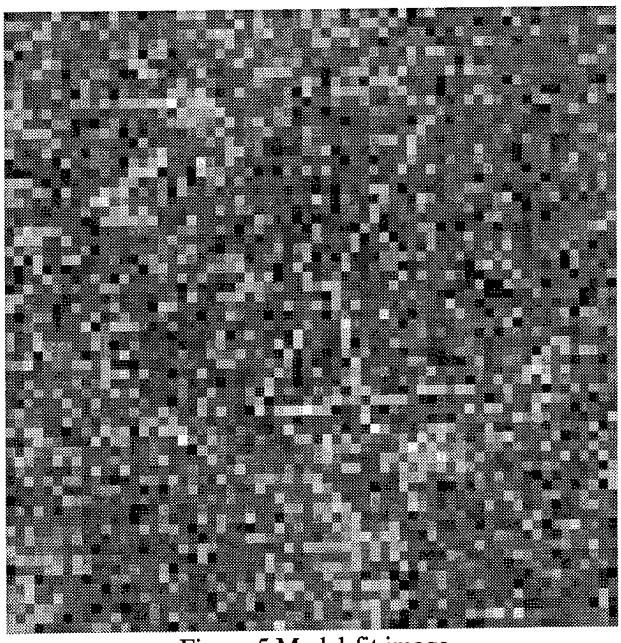


Figure 5 Model-fit image

Man-made and natural features are separated by thresholding the parameter image (Figure 3). The threshold value used ($\alpha = 2.7$) was between the two modes in the parameter image histogram (Figure 6). Values less than the threshold are classified as man-made. Regions containing man-made and natural features are shown in Figures 7 and 8.

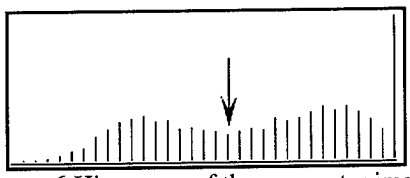


Figure 6 Histogram of the parameter image

CONCLUSION

A method for detecting man-made features in SAR imagery has been described and demonstrated. Additional testing is underway to determine the stability of the threshold for discriminating between man-made and natural features for a given SAR sensor. We are also determining the extent to which the method is insensitive to the topographic modulation of brightness mentioned in the paper. Future applications include the detection of man-made changes in imagery and use together with other texture measurements for land use classification.

References

[1] M.C. Stein, "Fractal image models and object detection," *SPIE*, Vol. 845, pp 293-300, 1987.

[2] T. Peli, "Multiscale fractal theory and object characterization," *J. Optical Society of America*, Vol. 7, No. 6, pp 1101-1112, June 1990.

[3] V. Kluth, H. Henning, M. Sharp and D. Winsand, "Detecting man-made objects in low resolution SAR using fractal texture discriminators," *IGARSS*, May 1992.

[4] M.I. Skolnik, *Introduction to Radar Systems*, McGraw-Hill, 1980.

[5] M.H. DeGroot, *Probability and Statistics*, Addison-Wesley, 1975.

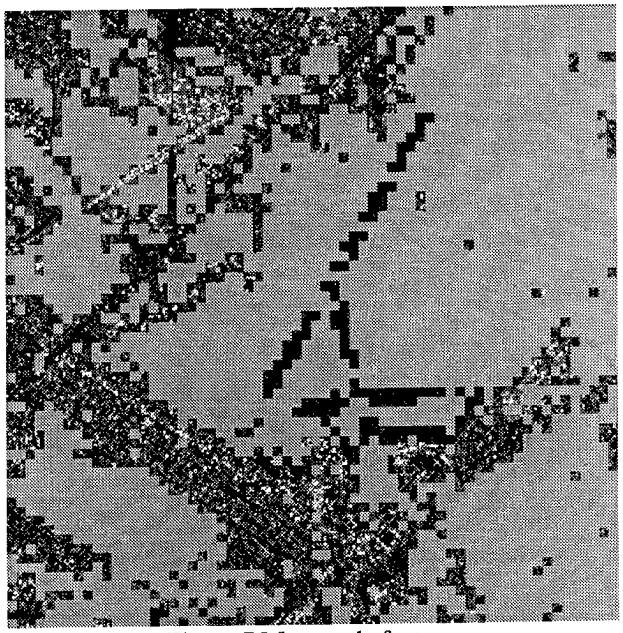


Figure 7 Man-made features

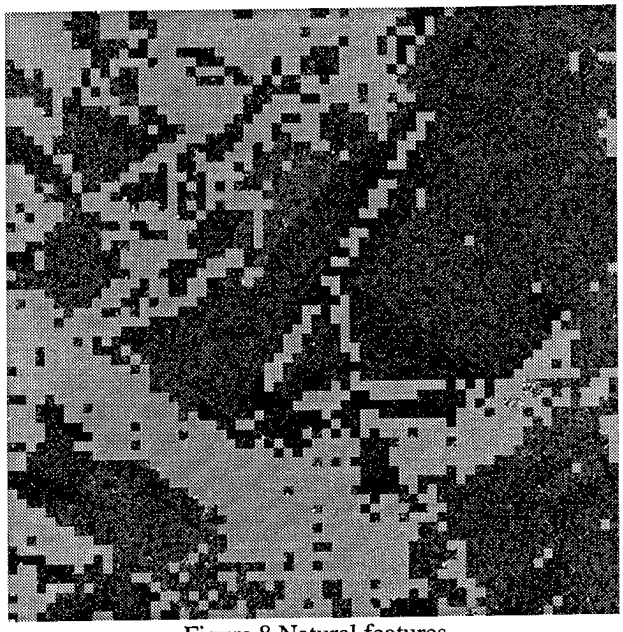


Figure 8 Natural features

Texture Analysis by Universal Multifractal Features In a Polarimetric SAR Image

P. Martinez[1)], D. Schertzer[2)], K. Pham[1)]

[1)] THOMSON-CSF/AIRSYS/RDT, 7 rue des Mathurins, 92223 Bagneux Cedex, France.
Tel (33 1) 40 84 33 56, e-mail: martinez@dedale.thomson-csf.fr

[2)] Laboratoire de Météorologie Dynamique, CNRS, Université Pierre et Marie Curie, Tour 15-25, Boite 99, 4 place Jussieu, Paris 75005, France. Tel (33 1) 44 27 49 63, e-mail: schertzer@lmd.jussieu.fr

Abstract

Multifractal features have been widely used in geophysics to characterize natural phenomenons but seldom in image processing. Therefore, in this study, we show that these features can also be efficient in texture classification. We assume that a natural image texture is the result of a specific two-dimensional multifractal cascade process and so, according to the *universal multifractal theory*, few parameters are enough to entirely describe this process and therefore the texture. As the multifractal parameters are quite linearly separable, a very simple and fast algorithm is run for the supervised segmentation. In practice, we have computed these features on a SIR-C L-band polarimetric SAR image, and used them to segment this image into five classes (sea, shore, forest, urban areas and cultivated fields).

1. Introduction

The introduction of the fractal geometry few years ago [1] brought up a new approach in texture analysis and classification : a surface can be described by its roughness which is quantatively evaluated with its fractal dimension. First, this feature has been widely used, with quite good performance [2]-[3], but some authors have pointed out that the single fractal dimension may not be a successful tool for fully discriminating textures; some studies[4][5] on different textures showed that despite obvious visual differences, the fractal dimensions remained quite identical. So, we attempted to find out a more accurate description of the texture.

In previous studies in geophysics, many physical phenomenons such earthquakes, rain falls, clouds, etc... [6] have been modeled by multiplicative cascade processes. The main characteristic of these cascades is their multifractal behavior and so, according to the *universal multifractal theory*, is completely described with only two parameters which are easily computed from the raw data. Moreover, in remote sensing, the computation of these multifractal parameters of some physical phenomenons like clouds or sea ice, pointed out a certain stability of their value whatever the remotely sensed data sources[7] are.

In this paper, a study on multifractal interest in classification is performed on the SIR-C L-band polarimetric SAR image of the Landes area in France. First, we introduce the multifractal parameters and then we propose our simple segmentation algorithm with the obtained results using the multifractal features, added to the intensity mean and variance computed on each pair of polarizations.

2. Multifractal Parameters

2.1 Scale Invariance

Before estimating any fractal or multifractal features, we must ensure that the principal property of a fractal process is respected: *the scale invariance*. Computing the *power spectral density* is a convenient and fast way to check this invariance for second order moment. In case of fractal data, the spectrum in *log* versus *log* scale presents a linear part corresponding to a scaling behavior of the fractal set. Precisely, this linearity corresponds to the power law :

$$\langle P(f) \rangle \propto 1/f^{\beta} \qquad (1)$$

where f is the frequency in the Fourier space and β the spectral exponent. For isotropic data, the linear part covers the totality of the scale range, whereas for anisotropic one the spectrum is distorded. Unfortunately, real textures are seldom isotropic and, even when they are, image shooting conditions like sensor orientation, make them anisotropic. Some methods[8] allow to compute the multifractal parameters even in anisotropic cases, but it takes too much time to keep the segmentation efficient. So in order to avoid this waste of time, the valid frequency range and so the valid scale range was chosen experimentally where the anisotropic distortion is estimated to be not so significant compared with the real image texture characteristic influence. Observations on natural textures of size 256 x 256 pixels taken from the SIR-C polarimetric SAR image, give a valid scale range from 2 pixels to 32 pixels. This choice has also been motivated keeping in mind the time computation: taking too many scales does not improve parameter estimation enough with regard to the computation time. Fig.1 shows the power spectra of different textures, the hashed zones indicate the non-considered scales. At the high scale, the spectrum curvatures translate the anisotropic behavior of the studied textures.

Note that in case of monofractal processes, the unique fractal dimension D is a function of β. For a n-dimensional

0-7803-3068-4/96$5.00©1996 IEEE

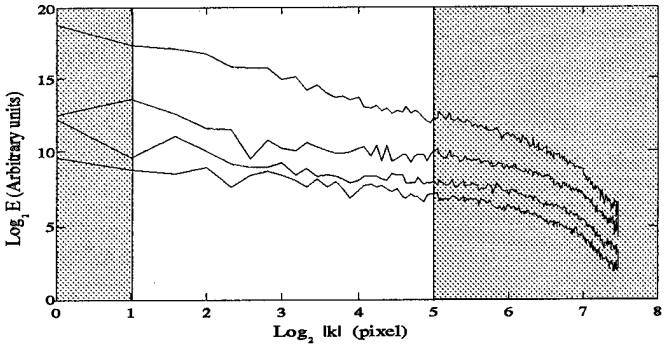


Fig. 1. Spectral density of different textures. From top to bottom : shore, cultivated fields, sea and forest. The spectra have been vertically offset so as not to overlap

Fractional Brownian Motion the fractal dimension is given[4] by the relation :

$$D = n + (3 - \beta)/2$$

This relation is obviously no longer applied to multifractal processes.

2.2 Multifractal processes

First, assuming that a texture is the result of a multifractal cascade process, we call $\varphi_{i,\Lambda}$ the i^{th} elementary energy flux of the cascade at the finest scale which represents the pixel level for the image texture. Let $\lambda = L/l$ be the scale ratio where L is the outer scale and l the scale of interest and, reducing the resolution consists in multiplying l by 2. Identically to $\varphi_{i,\Lambda}$, we define $\varphi_{i,\lambda}$ at the scale ratio λ; $\varphi_{i,\lambda}$ is the mean of all the $\varphi_{j,\Lambda}$ inside a square of size l.

One particular property of a multifractal field is that the energy flux $\varphi_{i,\lambda}$ follows the scale law (2) where γ_i is its order of singularity [8]. Higher is γ_i and higher is the singularity i.

$$\varphi_{i,\lambda} \approx \lambda^{\gamma_i} \; i \in [1..\lambda^2] \tag{2}$$

Further more, in multifractal processes, the fractal dimension of the subset of all the $\varphi_{i,\lambda}$ higher than a threshold $\tau(\gamma)$, with $\tau(\gamma) = \lambda^{\gamma}$, is a decreasing function of γ, whereas in monofractal processes like Brownian motions, this fractal dimension is constant. This behavior is described by eq.3 which shows the link between the singularity order and the fractal dimension. For convenience, the codimension $c(\gamma) = D - d(\gamma)$ where D is the embedding space dimension and $d(\gamma)$ the fractal dimension of the subset of the $\varphi_{i,\lambda}$ higher than $\tau(\gamma)$, was introduced[9]. We can say that $c(\gamma)$ describe the *sparseness* of the field intensities.

$$Pr(\varphi_{i,\lambda} \geq \lambda^{\gamma}) \approx \lambda^{-c(\gamma)} \tag{3}$$

If we now consider the q^{th} order statistical moment $\langle \varphi_{\lambda}^{q} \rangle$, we can define the multiple-scaling exponent $K(q)$:

$$\langle \varphi_{i,\lambda}^{q} \rangle \approx \lambda^{K(q)} \; with \; \lambda > 1 \tag{4}$$

which is related to the codimension function $c(\gamma)$ via a Legendre transform [9]. This exponent function $K(q)$ fully characterizes the multifractal process[9], and is easily and practically computed via a generalization of the partition function methods to stochastic processes called "Trace Moments" [8]. But even if $K(q)$ entirely describes multifractal processes, practically, it is not very easy to distinguish two multifractal processes by using it because of the infinity of points to compare. The same problem occurs with $c(\gamma)$.

2.3 Multifractal Universality

Since neither $c(\gamma)$ nor $K(q)$ were suitable for process comparisons, we had to look towards universal multifractals. There, it was shown [10] that a nonlinear multiplicative conservative flux possesses a stable and attractive generator which can be described by relations (5) and (6).

$$K(q) = \begin{cases} \left(\frac{C_1}{\alpha-1}\right)(q^{\alpha} - q) & , \alpha \neq 1 \\ C_1 q \log q & , \alpha = 1 \end{cases} \tag{5}$$

$$c(\gamma) = \begin{cases} C_1 \left(\frac{\gamma(\alpha-1)}{C_1 \alpha} + \frac{1}{\alpha}\right)^{\frac{\alpha}{\alpha-1}} & , \alpha \neq 1 \\ C_1 \exp(\frac{\gamma}{C_1} - 1) & , \alpha = 1 \end{cases} \tag{6}$$

These relations show that $K(q)$ and $c(\gamma)$ can be defined by only two parameters: C_1 and α. The first one, C_1, is the mean singularity of the multifractal process and is a fixed point of $c(\gamma)$, so we have :

$$\gamma_1 = C_1 = c(\gamma_1) = c(C_1) \tag{7}$$

This parameter is bounded by 0 and d, the embedding space dimension (in our case $d = 2$) and, in our study, C_1 is computed by the relation (8), according to the relations described in [9].

$$C_1 = \left(\frac{dK(q)}{dq}\right)_{q=1} \tag{8}$$

Then, the second one, α, is the Levy index and characterizes the field multifractality degree. It belongs to [0,2] and its extremal values correspond to β model (monofractal process) when α=0, and to the *log-normal* model when α=2. To compute this parameter, the *Double Trace Moment*[11] is chosen.

Thus, α and C_1 completely describe two conservative multifractal processes, and so we now use them to compare image textures.

3. Application on SAR Image

The multifractal feature description done, we can now point out their relevance in an L-band polarimetric SAR image acquired from the SIR-C satellite, see Fig.2. The scene covers the south of the Arcachon oyster bed in Landes country (France) and, is of size 9920 x 1190 pixels. Its resolution is 6.66 meters in distance and 5.22 meters in azimuth.

First, the multifractal parameters and the intensity mean and variance are computed, for each pair of polarizations HH,HV,VV, on windows of size 64 x 64 pixels



Fig. 2. Original SIR-C polarimetric SAR image in L-band, representing Les Landes area (France)



Fig. 3. Segmentation result. From the darkest grey level to the lightest: deep water (ocean, lake), forest, cultivated fields, wet land(shore, Arcachon oyster bed), artificial zones (urban areas, pieces of roads)

overlapping with a step of 14 pixels horizontally and 7 pixels vertically, giving 704 x 157 pixels feature images. In a previous study[12], the multifractal features were compared to the classical features to show their relevance, but here they are combined in order to improve the texture classification. Indeed, multifractal are not able to distinguish a dark texture from a light one if they result from the same cascade process.

For the learning stage, we have selected one window of size 20 x 20 pixels per texture, in the feature images, and computed the mean of these features inside this window. This yields fifteen attributes, noted $f_k^{(n)}$ with $(k \in [1..15])$, for the n^{th} texture. Then, the classification is performed as follow ($\langle . \rangle$ is the spatial averaging) :

- for the k features $k \in (\beta, C_1, \alpha, \bar{x}, \sigma^2)$
  - for each element (i,j) of the k^{th} feature image
    - $f_k(i,j) = \langle f_k(i',j') \rangle$, with $i-1 \leq i' \leq i+1$ and $j-1 \leq j' \leq j+1$
    - for the n textures
      - $f^{(n)}(i,j) += \min(f_k(i,j)/f_k^{(n)}, f_k^{(n)}/f_k(i,j))$
    - end for n
  - end for each element
- end for k

then, an element (i,j) belongs to the texture which corresponds to the maximum of all the $f^{(n)}(i,j)$.

Fig.3 presents the classification into five classes of the image presented Fig.2.

4. Conclusion

In this work, we studied terrain classification on the polarimetric SAR image of Les Landes (France), using universal multifractal theory. Therefore, we have described image textures with both their universal multifractal parameters and their intensity mean and variance. The mix of these features gives a good result because of the complementarity of their discrimination aptitude. We can also note that the features are relevant enough to avoid using a complicated segmentation algorithm and so to gain time.

The good results obtained in this study are promising; further works on other SAR images will validate the method. Furthermore, it should be interesting to qualify the multifractal model relevance in terrain characterization.

5. Acknowledgments

We would like to thank gratefully Mrs Le Toan from the CESR at Toulouse (France) who made available the radar data being used for these tests. This work was supported by the CNES (France). Special thanks to Mr S. Lovejoy from Mc Gill university (Canada).

References

[1] Mandelbrot, B.: The fractal geometry of nature. San Francisco: Freeman, 1983.

[2] Pentland, A. P.: Fractal-based description of natural scenes. IEEE Trans. on Pattern Analysis And Machine Intelligence **6** (1984), 661–674.

[3] Peleg, S.; Naor, J.; Hartley, R.; Avnir, D.: Multiple resolution texture analysis and classification. IEEE Trans. on Pattern Analysis and Machine Intelligence **6** (1984), 518–523.

[4] Mandelbrot, B. B.; Ness, J. V.: Fractional brownian motions, fractional noises and applications. SIAM Rev **10** (1968), 422–450.

[5] Voss, R.: Random fractals : characterization and mesurement. – In: Scaling Phenomena in Disordered Systems. New york: Plenum, 1986.

[6] Tessier, Y.; Lovejoy, S.; Schertzer, D.: Universal multrifractal: theory and observations for rain and clouds. J. Appl. Meteor **32** (1993), 223–250.

[7] Lovejoy, S.; Schertzer, D.: Multifractals and resolution dependence of remotely sensed data. 16^{th} Canadian Symposium on Remote Sensing, june 1993. 775–780.

[8] Schertzer, D.; Lovejoy, S.: Physical modeling and analysis of rain and clouds by anisotropic scaling multiplicative processes. J. Geophys. Res **92** (1987), 9693–9714.

[9] Parisi, G.; Frisch, U.: A multifractal model of intermittency. – In: Turbulence and predictability in geophysical fluid dynamics and climate dynamics. North-Holland: M. G. et al, 1985, 84–88.

[10] Schertzer, D.; Lovejoy, S.: Nonliear variability in geophysics: Multifractal simulations and analysis. – In: Fractals: Their physical origins and properties. Pietronero, L. (ed.). New York: Plenum Press, 1989, 49–75.

[11] Lavallée, D.; Lovejoy, S.; Schertzer, D.; Ladoy, P.: Nonlinear variability and landscape topography: analysis and simulation. – In: Fractals in Geography. Cola, L. D.; Lam, N. (eds.). Prentice Hall, 1993, 158–192.

[12] Martinez, P.; Schertzer, D.; Schmitt, F.; Pham, K.: Polarization influence on multifractal processing for terrain classification in a SAR image. EUSAR'96, Königswinter (Germany), 1996.

Reading CEOS-SAR Tapes: A New General Reader and a Proposed New Standard

Leland Pierce

The University of Michigan, Radiation Lab
Ann Arbor, MI 48109-2122 USA
FAX: +1-313-747-2106 email: lep@eecs.umich.edu

ABSTRACT

All recent scientific SAR data is formatted in compliance, more or less, with the CEOS standard developed recently. If this standard were followed meticulously by each organization producing SAR data a single tape-reader could read all of the data. However, there are small but significant differences in how each sensor's data is formatted and this has led to the need for a different reader for each sensor, and even for each format from the same sensor. This makes using the data difficult for most users, as the first step is to read it in to some kind of image processing system, such as ERDAS, PCI, GRASS, KHOROS, etc.

The solution to this problem has been for data providers and commercial vendors to write tape readers for their customers. Unfortunately, these readers do not read all the ancillary data and do not allow easy porting to use with other image processing systems. A new general reader has been developed that solves all these problems. It uses simple text "format" files to define the data that is to be read in: variable name and type, location in file, and format. It also allows the user to write interface code to read the data (ancillary and image) into the user's image processing system.

Despite this solution, a better format would make things even easier both for the data provider and for the user. A new format is proposed which addresses the following issues: (1) a single file per image, with a single record-length per file; (2) Ancillary data in ASCII: KEYWORD = value ; comment; (3) Self-documenting via comments and strict syntax; (4) Self-reading, so that a program can read input file and generate code that can read in all data in input file; (5) Addition of new parameters is simple, and users can generate readers for the new format with the program in #4.

This code is written and works now.

1. INTRODUCTION

This paper presents a solution to the problem of constantly writing new software to read in, and otherwise process, a SAR image every time a new format must be supported. The basic problem is that the CEOS standard for SAR data is not being meticulously followed, hence there is a new format to deal with whenever receiving data from a different sensor or different processing facility. Section 2 details the problems with the present standard, and section 3 presents a computer program that solves these problems in a way that requires no programming from the user. Section 4 gives a detailed example of a format-file that is used for that solution. Section 5 then goes on to propose a new standard that would be better for both data provider and data user. A detailed example of this new standard is given in section 6, followed by the conclusions in section 7.

0-7803-3068-4/96$5.00©1996 IEEE

2. PRESENT TROUBLES

To any SAR data user who uses data from different sensors or different processing facilities the problems with the present standard for this data is obvious: the formats are nearly identical, but not exactly. When they aren't exactly identical in areas that matter to the user, the solution involves writing a custom computer program for each format type. In our lab this has quickly become a prohibitive time sink with 2 or 3 new formats every year. The solution presented here is a code-generator: a program that writes the source code for another program.

But back to the problems: how serious are they? It all depends on the kind of processing required: which parameters you need. Some example problems include: (1) one needs the resolution of a pixel, not spacing, to estimate the number of looks applied, and it's not there; (2) one needs a calibration constant to give you an absolutely-calibrated image, for comparison with other images, and that constant is zero or missing. The kinds of problems encountered so far are summarized below:

1. missing data (zero or not supplied at all)
2. wrong data (the value is wrong or inconsistent)
3. data with different meanings (eg.: one facility uses sensor resolution, while another uses image resolution)
4. data in different places and/or different formats (eg.: date formats)

5. data is not in the same form as in another format. Requires writing a program to calculate required parameter(s).

6. poorly-defined parameters (eg.: polynomial coefficients for doppler centroid do not give a clue as to the polynomial equation they go with.)

3. SOLUTION

The proposed solution to most of these problems involves the user writing a simple ASCII "format-file" for each file-type, describing what to read, where to read it, and the format. This can take care of problem #4 above. The format file also allows one to assign default values and to do arbitrary processing of the values to produce new ones. This will solve problems #3 and #5, and can solve #1, #2, and #6 under most circumstances. To solve problem #6 and sometimes #1, one must resort to asking the data provider for more information. This is usually very difficult since the question usually involves something rather detailed or esoteric. Often, things that are missing or wrong are predictable for a particular format (from a particular sensor and processing facility) and so default values can be used instead. The data with different meanings is also a constant for a particular file-type and so can usually be transformed so that it has a standard meaning as desired by the user. However, there still may be unresolvable problems that the "format-file" approach cannnot solve, eg.: no calibration constant. But since this "format-file" scheme solves most problems it saves lots of time and is still worth using in most cases.

Each format file that a user writes specifies how to read in ancillary and image data as provided by a particular processing facility in one among several formats that are specific to the sensor involved. For example, four format files would be written in order to read data from: (1) ERS-1 as provided by Gatineau (Canada) in MLD format, (2) ERS-1 as provided by DLR (Germany) in PRI format, (3) SIR-C as provided by JPL (USA) in SLC format, (4) X-SAR as provided by DLR (Germany) in SSC format. Each is different, each has its own quirks, but these quirks are predictable for each and can be encoded in the format files that the user must write.

These format files are detailed enough so that a computer program is genertaed from them. The new program is capable of reading the data as specified in the format file. There are two main reasons for this method:

1. The generated code can easily be customized to work with different image processing packages. This is through the use of a few standardized calls to subroutines/functions that are package-specific. When compiling the program one merely links using the library appropriate for the image processing package of choice,

2. The resultant data sets, from disparate sensors and processors, can all have the exact same set of ancillary data. This is due to the translation and calculation abilities built in to the format file specification. For instance: All the dates can be MM-DD-YYYY, all the distances can be meters, all the calibration constants can be multiplicative as applied, etc.

Both of these are major advantages when one must write code to perform further processing. For example, our lab uses four different orthorectification programs for four different SAR formats. This is a nightmare of wasted effort in writing and maintaining them. One orthorectifier is all that should be needed with this new tape reader and re-formatter.

4. EXCERPT FROM EXAMPLE FORMAT-FILE

```
% format file for: Gatineau ERS-1/MLD
file_type: DEFAULT="format",LOCAL
format_name: DEFAULT="ers_ccrs_mld",LOCAL
int_format: DEFAULT="2s-complement",LOCAL
int_byte_order: DEFAULT=[4,3,2,1],LOCAL
%
voldesc: RECORD-ID=5:5,"BIU8",192;6:6,
   "BIU8",192;7:7,"BIU8",18;8:8,"BIU8",18
%
tapeID:  READ="voldesc",45:60,"A32"
sensor:  READ="voldesc",61:76,"A16"
%CCODE=if(strncmp(sensor,"ERS",3) !=0 ) {
%CCODE=    printf("Error: Expecting ERS
           sensor, got: %s\n",sensor);
%CCODE=    return(error); }
%
totpix:  READ="imop_fdesc",249:256,"I8"
totlin:  READ="imop_fdesc",237:244,"I8"
%
% Now the image data:
imgbfr:  DATA="image",193:$,BIU16
```

5. PROPOSED NEW FORMAT

Despite this solution, a better standard would be welcome. What are the requirements of this standard? The most basic requirement is that it be used by the data providers. I formulated the following list with that in mind, as well as ease of use by the data users:

1. One file per image (can be multi-channel).

2. All records in file same length.

3. All ancillary data in ASCII at start of file:
   KEYWORD = value ; comment

4. Self-Documenting:
   - parameters clearly defined with comments
   - parameter types unambiguous via syntax rules

5. Self-Reading: Developed code that can read in any file and output the source code for a program that will read in the file. As in the general reader for present CEOS-SAR data, the same customization to a user's own image processing system is available.

6. Must have a set of parameters (and definitions) that all data providers agree to that would be mandatory for all data sets. Optional parameters for different types of sensors can be defined as well.

7. Addition of new parameters by the data providers is as simple as adding the parameter name, value and comment. Users can then read the "new format" after creating a reader for it by running the program in #5.

Each of these is easy to accomplish by the data providers, and will allow for increased ease-of-use by the end-users. Becasue SAR is still in rapid development there are constantly new requirements in the ancillary data that no standardizing committee could hope to keep up with. That is why the present standard (CEOS-2) has a special record that is to be used for anything extra that the data provider thinks is important. The new standard proposed here makes the entire header area like this so that there is nothing special about new ancillary data: making it special just makes it more work to write a program to read it in. So all ancillary data is in the top of the file, in the same format, as given in point #3 above. Adding new keywords is easy for the data provider, since the ordering of the keywords and thier positions is completely arbitrary. Old programs that don't read these new keywords still work, since they effectively ignore any data that they weren't told to read. All common scalar, vector, and matrix data types are supported and have a unique syntax so that their data-types are unambiguous. Various required keywords specify important details concerning the image data such as data-type and byte-ordering. All capabilities in the old format are preserved in this new format, such as geocoding line-by-line, since vectors of arbitrary length are a supported ancillary data type. The ASCII header can be displayed at the terminal very simply, since all that is needed is a translation from the end-of-keyword character used in the data file to the end-of-line character used by the computer. The image itself no longer has any header or trailer in each line so that it is very simple to read it in with standard programs if one wishes to do so. Also, a record of image data on the tape is one line in the image, allowing the user to easily extract a subset while reading the tape, if necessary.

Lastly, because it is strongly typed, the data file can be used as a template by a code-generator to produce a new tape-reading program that will read in all of the ancillary data, thus alleviating the end-user of the task of writing a new tape reader for each new format. On the processing facility side, there is another program which can read a data file, but generate code to *write* a data file of that kind. With all this in hand, the user will never again need a hard-copy of the tape format describing fields byte-by-byte.

6. EXCERPT FROM EXAMPLE NEW FORMAT

Note that many of the comments have been deleted in an effort to save space for this article.

```
%START-OF-HEADER
RECORD_LENGTH= 512
FILE_FORMAT="CEOS-3 SAR"
NHEADER_RECORDS= 30
% Example fmt for CEOS-3 SAR Image Data.
%
DATA_START_RECNO= 31
NUMBER_OF_IMAGE_LINES=512 % No. of lines
% (y-dir) in the image for a single band.
% (NOT #records)
NUMBER_OF_IMAGE_PIXELS=512 %No. of pixels
% (x-dir) in the image for a single band.
%
DATA_TYPE="signed integer"
DATA_NUMBERS_PER_PIXEL=1
DATA_BYTES_PER_NUMBER=1
DATA_INTEGER_FORMAT="2s-complement"
DATA_BAND_INTERLEAVING="pixel"
%
TAPEID="EOC1003"
PROCESSOR_VERSION="V1.0.3"
SENSOR_NAME="SRL-1, SIR-C"
DATA_FORMAT_CODE="MLD"
DATA_FORMAT_NAME="Multi-Look Detected"
ACQUISITION_DATE="01-13-1960" %dd-mm-yyyy
ACQUSITION_TIME="13:45:23.023"
                          % hh:mm:ss.xxx
RESOLUTION_AZIMUTH=30.  % Resolution in
%              azimuth direction, meters.
RESOLUTION_SLANT_RANGE=30.  % Resolution
%       in slant range direction, meters.
```

7. CONCLUSIONS

Two new programs have been written that can help both SAR data users and providers to save time and do their work better. The first program can read several format-files, describing different formats of CEOS-SAR data files, and create a program that will distinguish between the different formats and will read them in so that both the ancillary data and the image data are in a uniform format for use by other processing programs. The second program is really a set of programs that allows a user and data provider to read and write a new format that is flexible and powerful enough to satisfy all data formatting needs for SAR data in the forseeable future. This set of programs alleviates the need for users or providers to ever write a format-reader or format-writer ever again. These programs are available to any non-commercial user. Just email the author for more information.

RADARSAT Processing System at ASF

K. Leung, M. Chen, J. Shimada, A. Chu
Jet Propulsion Laboratory
California Institute of Technology
4800 Oak Grove Drive, M/S 300-243, Pasadena, CA 91109 USA
Phone: (818) 393-9045 / Fax: (818) 393-0202 / E-mail: kon.leung@jpl.nasa.gov

ABSTRACT

RADARSAT is a Canadian polar orbiting remote sensing satellite launched in November 1995. Its only instrument is a synthetic aperture radar (SAR) that is capable of operating in a number of imaging modes, including the first operational ScanSAR in space. As one of the data reception, processing, and archive facilities for RADARSAT data, the Alaska SAR Facility (ASF) has responded to its science users by establishing a RADARSAT processing system to handle the data processing of all RADARSAT modes. This paper outlines the ASF RADARSAT data processing requirements as driven by the science users and describes the RADARSAT processing system design and implementation approach to meet the challenge of providing ASF with an integrated operational SAR image production facility. Design and implementation attributes that facilitate system growth in handling future SAR missions such as Envisat and HIROS are also addressed.†

INTRODUCTION

The Alaska SAR Facility (ASF), situated at the University of Alaska at Fairbanks, has been acquiring, processing, and archiving synthetic aperture radar (SAR) data from a fleet of international polar orbiting satellites since 1991, including the European ERS-1/2 and the Japanese JERS-1 [1,2]. ASF has also been selected to provide similar services for SAR data from the Canadian RADARSAT, which was launched in November 1995. The Jet Propulsion Laboratory was tasked in 1993 to upgrade ASF to be capable of handling all four operating satellites. In addition to upgrading the current facility to handle, process, and archive a fourfold increase in data volume, new processing capabilities are also needed to deal with the novel ScanSAR-mode and special beam mode data that are unique to RADARSAT. In order to keep the operations costs in check in the face of increased system complexity, operability and maintainability become important system design issues as well. This paper provides an overview of the RADARSAT data processing requirements levied on ASF and a perspective on the resulting increase in system complexity. Major system design and implementation issues are then discussed, followed by descriptions of the SAR Processing System architecture and subsystem designs. The paper concludes with a brief summary of the development experience and a report on the current status of this activity.

RADARSAT PROCESSING REQUIREMENTS OVERVIEW

RADARSAT is the first in a series of Canadian remote-sensing satellites. Its single payload is a C-band SAR with characteristics given in Table I. In addition to operating in the customary continuous (strip) mode, RADARSAT is the first operational spaceborne SAR system to operate in a ScanSAR mode that allows up to 500-km coverage over a single orbit pass [3]. To fully exploit the capabilities afforded by RADARSAT, a list of data processing requirements has been developed under the guidance of a team of science users [4]. This section discusses the throughput requirements for RADARSAT, ERS-1/2, and JERS-1, as well as the general requirements applicable to all ASF systems.

RADARSAT Standard Beam Mode Processing Requirements

RADARSAT can operate in any one of seven standard radar beam modes, each covering 150 km in swath and having incidence angles ranging from 20° to 50°. ASF is required to process a total of 58 minutes of standard beam mode data from any combination of ERS-1/2, JERS-1, and RADARSAT data within a 16-hour day.

RADARSAT ScanSAR Beam Mode Processing Requirements

In the ScanSAR modes, wide-swath coverage of 300 km and 500 km is achieved by sweeping the antenna beam electronically in the range dimension to generate multiple overlapping subswaths, each extending about 150 km in range. The resulting echo data for each subswath appears in the form of discrete "bursts" of echo returns rather than a continuous sequence. Two 4-beam modes provide a maximum swath width of about 500 km, with incidence angles ranging from 20° to 50°. One 3-beam mode and one 2-beam mode yield the 300-km swaths. ASF is required to process 42 minutes of RADARSAT ScanSAR data, all modes combined, in an 11-hour day.

†The research described in this paper was carried out by the Jet Propulsion Laboratory, California Institute of Technology, under a contract with the National Aeronautics and Space Administration.

0-7803-3068-4/96$5.00©1996 IEEE

Table I
RADARSAT SAR CHARACTERISTICS

Incidence angle (degrees)	20 - 50
Radar frequency (GHz)	5.3
Polarization	HH
Pulse repetition frequency (Hz)	1200 - 1400
Chirp slope (KHz/μs)	-721.4 -416.2 -279.3
Transmit bandwidth (MHz)	30.299 17.48 11.731
Transmit pulse width (μs)	42.0
Sampling frequency (MHz)	32.32 18.46 12.92

RADARSAT Special Beam Mode Processing Requirements

RADARSAT is also equipped to operate 15 special beam modes that include three wide-swath beams, five fine-resolution beams, six high-incidence beams, and one low-incidence beam. ASF is required to process at least 5 minutes of special beam mode data in a 5-hour day.

General Requirements

All subsystems within the ASF SAR Processing System (SPS) are required to follow project-wide guidelines regarding subsystem interfaces, systems standards, coding standards, user interfaces, and error reporting [5]. The emphasis is on applying, to the greatest extent possible, commercial off-the-shelf hardware, software, standards, and technology. Communication between the SPS subsystems follows a client-server model, with the raw data conditioner and image generation processors acting as production servers to a control processor client. With the exception of the existing hardware-based Alaska SAR Processor, where additional new custom hardware is unavoidable, all other subsystems in the SPS are being implemented with commercial high-performance workstations and mini-supercomputers that run operating systems based on System V Release 4 (SVR4) UNIX.

ASF SPS OVERVIEW

ASF Overview

ASF is a full-service data processing and archiving organization. It can assume end-to-end SAR data processing and handling functions that include receiving and cataloging data ordering information from users, communicating data acquisition requests to respective flight agencies, collecting satellite downlink data, processing SAR data into various forms of data products, and archiving and distributing the respective products back to the individual users. Figs. 1 and 2 depict the current and upgraded configurations of ASF, respectively.

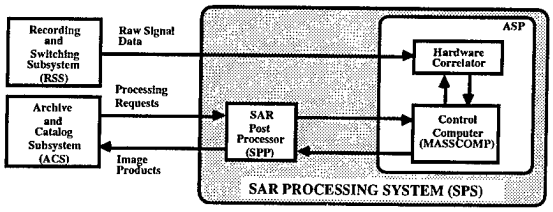


Fig. 1. Current ASF Configuration

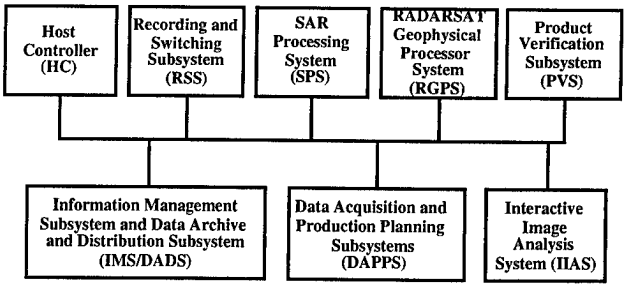


Fig. 2. New ASF Configuration

Current SPS Configuration

The ASF SAR Processing System (SPS) is responsible for reducing the SAR raw data downlinked from the satellites into various forms of image products. The current SPS, also shown in Fig. 1, consists of the Alaska SAR Processor (ASP) subsystem and the SAR Post Processor (SPP) subsystem. To date, 130,000 ERS-1 and JERS-1 image frames have been produced by the SPS.

The ASP is a SAR data processor developed by JPL in the late 1980s. It was commissioned in August of 1990 to support ERS-1 data processing and underwent a modification in 1991 to accommodate JERS-1. This subsystem consists of a hardware correlator and a control computer hosted on a MASSCOMP workstation. The hardware-based ASP is a custom-built pipeline SAR correlator that executes a fast Fourier correlation technique in both range and azimuth processing [6]. The ASP is capable of processing strip-mode SAR data at very high throughput rates, producing a 100-km by 100-km ERS scene in 6 minutes. For input, the ASP receives playback SAR signal data from an Ampex DCRSi high density digital recorder (HDDR).

The SAR Post Processor (SPP) subsystem provides data quality assurance and interface functions between the SPS and the Archive and Catalog Subsystem. This subsystem is hosted on a DEC MicroVAX-II running the VMS operating system.

SPS Configuration in the RADARSAT Era

New System Description: To accommodate RADARSAT and to allow for easy expansion to include future satellites, the SPS is being reconfigured and upgraded using an integrated system approach. As depicted in Fig. 3, the new SPS configuration consists of five subsystems:

- an upgraded version of the current ASP that handles RADARSAT and ERS-2 data in addition to ERS-1 and JERS-1 data;
- new ScanSAR Processors (SSPs) for handling ScanSAR-mode data from RADARSAT;
- new Precision Processors (PPs) for handling RADARSAT special beam modes, as well as processing of all strip-mode data into high-precision image data products;
- a new Raw Data Scanner (RDS) for reading and deformatting raw signal data from the various satellites for ingestion by the SSP and PP, and for determining raw data availability;
- a new Control Processor (CP) for coordinating all SPS processing controls and interfaces.

Fig. 3 shows the external interfaces of the SPS with the Recording and Switching Subsystem (RSS), which houses the HDDRs used for nominal raw signal data input; the Production Planning Subsystem (PPS), which is a subsystem of the Data Acquisition and Planning Subsystem; and the Information Management / Data Archive and Distribution Subsystems (IMS/DADS).

System Design Approach: The design of the new SPS has been driven not only by numerical throughput requirements, but also by the ASF project directives and overall goals of expandability and ease of use. To those ends, the following elements have been incorporated into the SPS:

- Resource management is centralized at the CP. In particular, the CP houses a large disk array for temporary storage of decoded raw data files and completed image products. The other SPS subsystems have only enough local storage to meet their processing requirements for one job request. Placing most of the disk space at the CP reduces the need to have large amounts of storage distributed at each subsystem and reduces the software development costs associated with having to manage distributed data stores.
- Centralized control of SPS operations through the CP means that the SPS operator can monitor operations from a single location and user interface development for the SPS is almost completely confined to the CP. This also greatly simplifies the addition of new SAR processors.
- As described earlier, the SAR data processors (ASP, PP, and SSP) and data conditioner (RDS) all behave as product servers to the client CP. The CP uses an identical communications protocol and common software library with each of these servers to send and receive job information and send control messages for subsystem initialization and shutdown. Development of the library has been greatly aided by the fact that the operating systems on all these platforms are based on SVR4 UNIX and are POSIX-compliant.

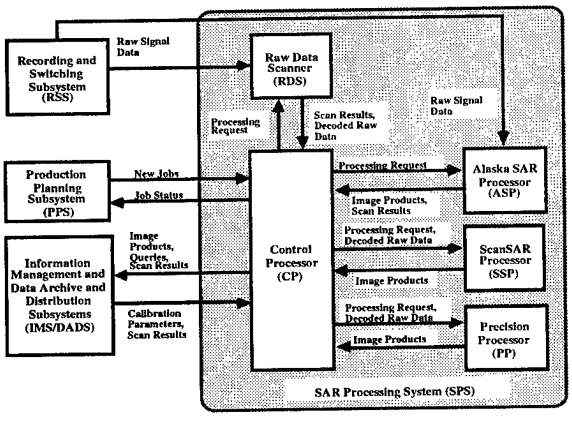


Fig. 3. New SPS Configuration

THE ASF SPS SUBSYSTEMS

The Alaska SAR Processor (ASP)

In the new SPS configuration, the ASP becomes just one of several SAR data processors within the SPS. The main function of the ASP is to continue to provide a high-throughput strip-mode data processing capability for the SPS by augmenting its system to accommodate RADARSAT and ERS-2. The new ASP subsystem will continue to be based on the existing hardware correlator which will be fed by three data deformatters for ERS, JERS, and RADARSAT strip mode data. A number of modifications are also being implemented to enhance system performance and maintainability and to allow it to conform to the new project-mandated client-server interface protocol. The new ASP configuration is expected to yield a 50% increase in processing throughput, allowing the ASP to generate a 100-km by 100-km scene within 4 minutes. As with the current data processing options available for ERS-1/2 and JERS-1, the ASP can produce any of the four user selected image products for RADARSAT: standard low-resolution, standard full-resolution, complex, and computer-compatible signal data (CCSD). Brief specifications for these four products are shown in Table II.

The new ASP subsystem (Fig. 4) uses a DEC Alpha workstation with 128 MB RAM in place of the MASSCOMP as the control computer. The Alpha generates processing and control parameters for the hardware correlator and buffers image data to the CP storage disks. For ingestion of RADARSAT data from the RSS, a new deformatter has been

Table II
RADARSAT Standard-Mode Product Specifications

PRODUCT	Number of Looks	Pixel Spacing (Resolution) (m)	Pixel Format	Swath (km)
Low-resolution	256	100 (240)	Byte Amplitude	100 x 100
Full-resolution	4	12.5 (30)	Byte Amplitude	100 x 100
Complex	1	natural (10)	16I/16Q	40 x 50
CCSD	N/A	N/A	8I/8Q	N/A

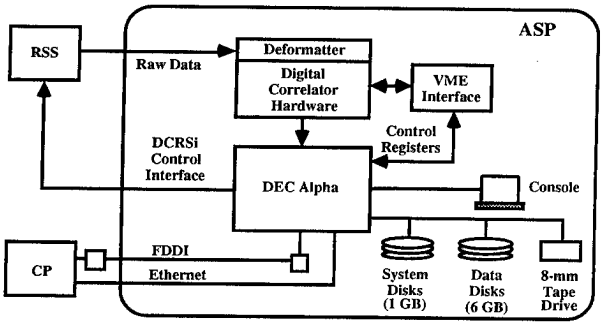


Fig. 4. New ASP System Configuration

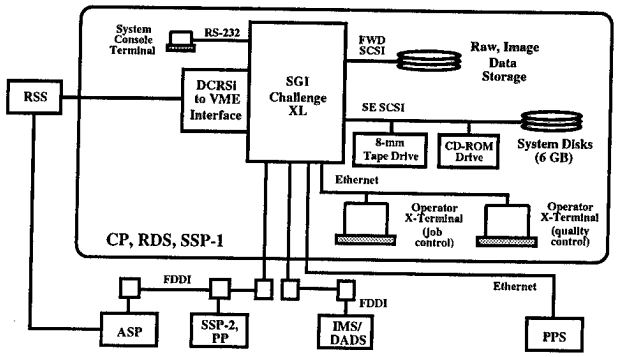


Fig. 5. CP, RDS, SSP-1 System Configuration

added to the front end of the ASP hardware correlator. A new VMEbus interface has also been introduced to serve as a control signal interface between the Alpha and the hardware correlator.

ScanSAR Processor (SSP)

The function of the SSP is to provide the SPS with the capability of processing RADARSAT ScanSAR-mode data. The implementation of the SSP has been divided into two phases. Under Phase 1, a prototype processor has been built for the evaluation of ScanSAR processing algorithms. The final version of the prototype shall meet all image performance requirements. Its throughput rate is projected to be approximately one three-hundredth real-time or one 500-km by 500-km ScanSAR image frame in about 6 hours. This prototype is also expected to participate in the initial RADARSAT downlink validation at ASF. Phase 2 involves the implementation of high-throughput processors that are capable of processing 42 minutes of ScanSAR data in an 11-hour day (or approximately one fifteenth real-time). Various types of ScanSAR image products produced by the SSP include a number of standard products and special products for internal system calibration support. Table III lists the characteristics of these ScanSAR data products.

The Phase 1 prototype processor is cohosted with the CP and RDS subsystems on an SGI Challenge XL computer with four MIPS R4400 CPUs and 256 MB RAM (Fig. 5). Processing control is initiated by the CP in accordance with a client-server model. The ScanSAR processing algorithm capitalizes on the burst nature of the data by processing one burst at a time [7-12]. Each burst is first range-compressed using an FFT correlation approach. The resulting data burst is then corner-turned followed by azimuth processing, which utilizes an efficient deramp-FFT algorithm. The resulting burst is then geometrically rectified and radiometrically compensated. At this point, data from adjacent bursts are merged and averaged into a final multi-look image before a projection process is applied to form the final ScanSAR image product.

For Phase 2, three IBM SP-2 mini-supercomputers, two equipped with 8 processing nodes and one with 4 nodes, are being used [13]. Each SP-2 is expected to operate independently as a server to the CP, processing upward of 17 minutes of ScanSAR data in an 11-hour day. The SP-2 is a distributed-memory machine well suited for the burst-mode nature of the ScanSAR data and its processing algorithm, with each processing node handling integral data bursts efficiently without the need for frequent I/O. The Phase 2 processors will inherit the core processing code from the prototype unit with massive parallelization employed to achieve high throughput. The SSP-2 platform configuration is depicted in Fig. 6.

Table III
RADARSAT ScanSAR Product Specification

PRODUCT	Number of Looks	Pixel Spacing (Resolution) (m)	Pixel Format	Swath (km)
Standard - Geocoded	8 - 28	50 / 100 / 400 (75 / 150 / 600)	Byte Amplitude	500/300
Standard - Terrain-Corrected	8 - 28	50 / 100 / 400 (75 /150 / 600)	Byte Amplitude	500/300
Special - Single-look	1	100 (150)	Byte Amplitude	150
Special - Multi-look	8 - 28	100 (150)	Byte Amplitude	500/300

Precision Processor (PP)

The main function of the PP is to provide a processing capability to handle the RADARSAT special beam mode

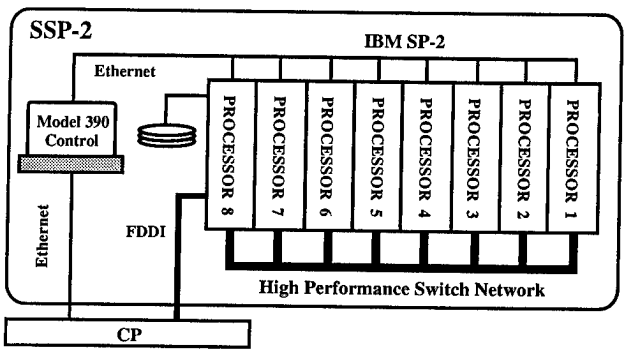


Fig. 6. SSP-2 System Configuration

data. It is also designed to be flexible so that modern SAR processing algorithm technology can be implemented efficiently with relative ease. Current throughput is expected to be on the order of processing 5 minutes of nominal 100-km swath strip-mode data per 5-hour day.

The PPs are being cohosted on the same IBM SP-2s used for processing ScanSAR data (Fig. 6). It is expected that each 8-node SP-2 will be capable of processing 2.5 minutes of data in 5 hours.

Raw Data Scanner (RDS)

The main function of the RDS is to deformat and decode raw signal and ancillary (ephemeris and engineering) data that are embedded in the high-rate data stream from each satellite. The decoded SAR signal data and ancillary data are then fed to either the SSP or the PP for image generation. (Recall that the ASP has its own raw data decoding and scanning capability.) A second function of the RDS is to provide an efficient scanning capability to determine how much of the downlinked data can actually be processed into image products. The RDS is expected to scan 200 minutes of data and supply the SSP and PP with 47 minutes of deformatted and decoded data during each 16-hour day.

The RDS software is hosted on the same SGI Challenge platform as the SSP-1 software (Fig. 5). An Ampex VME interface has been included to provide access to the Ampex DCRSi HDDRs at the RSS. The RDS software has been implemented as a single multithreaded application capable of taking its input from either DCRSi tape or from disk.

Control Processor (CP)

The main function of the CP is to provide overall control of all the other SPS subsystems through a single operator interface. This interface allows the SPS operator to initialize and shut down the various subsystems without having to physically log onto each subsystem's host platform. The CP has been designed to automate the SAR processing to the greatest extent possible. Incoming jobs from the PPS are automatically routed to the appropriate subsystem or subsystems and completed image products are delivered to the IMS/DADS subsystems, with minimal intervention required from the operator. The CP also hosts the image data quality control functions for the SPS, providing the ability to check completed products at a centralized location prior to delivery.

The main part of the CP software shares the SGI Challenge XL with the RDS (Fig. 5). A DigiData Z9000 RAID-3 subsystem with 128 GB of storage serves as temporary local storage for the deformatted data files used by the SSP and PP and for the completed image products prior to their delivery to the IMS/DADS. To better enable fast transfer of large volumes of data within the SPS and to the DADS, the SGI utilizes two separate FDDI connections. The main application is a multithreaded program that manages the various processing jobs within the SPS and allows the operator to monitor and control the processing through an X/Motif GUI. Multiple threads of execution allow parallel processing of X events and input and output messages to and from the subsystems that interface with the CP. The other CP applications are used for the quality control functions and for interfacing with the PPS and IMS/DADS subsystems. These applications also utilize X/Motif GUIs and/or threads as appropriate.

SUMMARY AND STATUS

This paper has provided a comprehensive overview of the new SAR Processing System at ASF, with special emphasis on its processing capabilities and accommodation of the various operating modes of RADARSAT. The various SPS subsystems have been undergoing testing using test data modified from SIR-C as well as test data sets supplied by the Canadian Space Agency. The new ASF SPS is approaching a major delivery to ASF in the summer of 1996. By then all SPS subsystems and capabilities described in this paper will be operational except for the Precision Processor, which is to be delivered in November 1996.

ACKNOWLEDGMENTS

The authors wish to thank the Alaska SAR Facility Project for supporting the work described in this paper.

REFERENCES

[1] D. Cuddy, M. Chen, T. Bicknell, "Alaska SAR Processor Implementation for ERS-1," IGARSS '92, Houston, May 26-29, 1992.

[2] D. Cuddy, M. Chen, T. Bicknell, "Alaska SAR Processor Implementation for JERS-1," IGARSS '93, Tokyo, April 1993.

[3] R. Keith Raney *et al,* "RADARSAT," *Proceedings of the IEEE,* Vol. 79, No. 6, June 1991.

[4] F. Carsey, *Science Requirements RADARSAT/ERS-2 Modifications for the Alaska SAR Facility,* Version 1.0, JPL Internal Document D-10443, May 6, 1993, revised August 31, 1994.

[5] D. Cuddy, T. Bicknell, M. Tankenson, "ASF Design Considerations for RADARSAT/ERS-2," IGARSS '94, Pasadena, August 8-12, 1994.

[6] M. Y. Jin and C. Wu, "A SAR Correlation Algorithm which Accommodates Large Range Migration," *Geoscience and Remote Sensing,* Vol. GE-22 No. 6, November 1984.

[7] M. Jin, "Range Compression Using Deramp-FFT Approach," JPL Internal Memorandum, April 14, 1992.

[8] M. Jin, "RADARSAT ScanSAR Azimuth Compression," JPL Internal Memorandum, June 15, 1992.

[9] M. Chen, "RADARSAT Image Resampling Operations," JPL Internal Memorandum, March 9, 1993.

[10] M. Jin, "RADARSAT Pointing Estimation Algorithm," JPL Internal Memorandum, June 26, 1992.

[11] M. Jin, "Radiometric Compensation for RADARSAT ScanSAR," JPL Internal Memorandum, November 6, 1992.

[12] K. Leung, M. Jin, "Processing of ScanSAR Mode Data For RADARSAT," IGARSS '93 Technical Program, Volume III, pp. 1185-1188, Tokyo, April 14, 1993.

[13] K. Leung *et al,* "Parallel Computing Implementation for ScanSAR Mode Data," unpublished.

Radar Speckle: Noise or Information?

Zong-Guo Xia and Yongwei Sheng
Department of Geography, University of Massachusetts at Boston
100 Morrissey Boulevard, Boston, MA 02125-3393
Phone: (617) 287 - 5285, FAX: (617) 265 - 7173, E-mail: zgx@earth.geog.umb.edu

Abstract -- In this paper, we examine radar speckle from a non-traditional perspective. Instead of viewing radar speckle as noise, we attempt to assess the information content of radar speckle. A speckle identification algorithm is developed to separate speckle from pixels of "normal" returns. The relationships between land cover types and the density and roughness of speckle are examined.

INTRODUCTION

The presence of speckle in an image reduces the detectability of ground targets, obscures the spatial patterns of surface features, and decreases the accuracy of automated image classification. In digital image processing and visual image interpretation, radar speckle has been conventionally considered as disturbing noise. Arsenault and April[1] analyzed the information content of images degraded by speckle noise and found that speckle seriously decreased the information content. Many studies[2,3] have been carried out to design filters for suppressing the so-called "speckle noise".

However, from the physical point of view, speckle is the result of interactions between scatterers inside a pixel at the subpixel level. Therefore, the speckle pattern should reflect the conditions of ground surface. From this perspective, speckle should also contain some meaningful messages about ground targets. So far, however, very little is known about the kind and amount of information that can be extracted from analyzing speckle pattern. Hoekman[4] tried to extract subpixel spatial information over forested areas from SLAR data by analyzing the power density spectrum of speckle. This paper presents some preliminary results of our attempt in examining the relationship between landcover types and radar image speckle patterns.

ORIGIN OF RADAR SPECKLE

With the development of laser technology, a lot of research[5,6,7,8] has been done on laser speckle since the early 1960's. Goodman[5] elaborated eloquently the theory of laser speckle from the view of physics. Radar speckle has similar properties as laser speckle. Goodman's laser speckle theory has been applied to describe radar speckle[9,10]. Radar speckle arises from coherent scattering of a number of random scatterers within each pixel. The waves emitted by active sensors travel in phase and interact minimally on their way to the target area. After interacting with surface objects, these waves are no longer in phase. Once out of phase, radar echoes interfere either constructively or destructively to produce light and dark pixels known as speckle. It is known that radar speckle is multiplicative,

$$R_{i,j}=R0_{i,j}*SP_{i,j} \quad (1)$$

where i,j are the row and column number; $R_{i,j}$ is the recorded value of radar return; $R0_{i,j}$ is the real value without coherent interference; $SP_{i,j}$ is the speckle factor.

In general, speckle patterns depend both on the coherence of the incident signal and the detailed properties of the random surface. Dainty[6] pointed out that the most obvious application of speckle analysis was to the measurement of surface roughness. For a given radar system, the incident signal can be considered constant in each image. The speckle pattern is produced by coherent interference of random scatterers on a rough surface. Thus, it should reflect the properties of ground targets. For example, the SIR-C/X-SAR system has three bands at a ground sampling resolution of 30m. Natural surface is so complicated that one pixel is generally a mixture of different landcovers at subpixel level. Even for a pixel of macroscopically uniform landcover, it includes numerous individual objects such as trees, grass, soil particles, etc. The objects are oriented in different ways and have different physical properties. The constructive and destructive interference of returns from these objects generates the salt and pepper appearance of radar images.

IDENTIFICATION OF SPECKLE

In order to analyze speckle pattern, speckled pixels must be distinguished from those normal pixels. Radar speckle has a unique property that a speckled pixel is very different from its neighbors. It has much higher or lower brightness value than its neighboring pixels. Speckle is commonly shown as isolated pixel. On the other hand, features usually distribute in a linear or block pattern with several pixels together.

The median filter uses the median value and eliminates the higher and lower values in the moving window, which likely correspond to the bright and dark speckles. Thus, the median filter can be considered as a speckle-suppressing filter[11]. The visual inspection of radar images seems to indicate that bright speckle and dark speckle display quite different patterns. As a result, they are considered separately.

Based on the above considerations, an algorithm was developed for identifying radar speckle. First, signal-dependent multiplicative speckle can be converted to

0-7803-3068-4/96$5.00©1996 IEEE

additive signal-independent terms by using logarithmic transformation, that is,

$$V_{i,j}=Ln(R_{i,j})=Ln(R0_{i,j})+Ln(SP_{i,j}). \quad (2)$$

Four directional subwindows in a 3x3 moving window (see Fig. 1) are then taken for the purpose of distinguishing speckle from features. The median value $Med(Win_k)$ is used as the estimation of normal radar return in the kth subwindow.

The algorithm is as follows:

$MMin=0.0$
$for\ (k=1, 4)$
$\{\ MMin=Min(MMin, abs(V_{i,j}-med(Win_k)))$
$index=k\ \}$
$if\ \ V_{i,j}-med(Win_{index})>0.0$
$\{\ Bright_Speckle_{i,j}=1\ \}$
$else\ \{\ if\ V_{i,j}-med(Win_{index})<0.0$
$\{Dark_\ Speckle_{i,j}=1\ \}$
$else\ \{\ Bright_Speckle_{i,j}=0$
$Dark_\ Speckle_{i,j}=0\ \}\}$

By using this algorithm, both bright speckle and dark speckle are converted to 0-1 images.

SPECKLE PATTERN ANALYSIS

It becomes possible to analyze the relationship between the speckle patterns and landcover types after speckle identification. In this preliminary study, speckle density and speckle roughness are characterized for some selected uniform areas of different landcover types.

1. Speckle Density:

For each area, speckle density is defined as the ratio of the number of speckled pixels to the total number of pixels in the area. For bright speckle, dark speckle and total speckle density, we have

$$Bright_Density=\frac{\sum Bright_Speckle \in parcel}{\sum pixel \in parcel}, \quad (3)$$

$$Dark_Density=\frac{\sum Dark_Speckle \in parcel}{\sum pixel \in parcel}, \quad (4)$$

$$Speckle_Density=Bright_Density+Dark_Density. \quad (5)$$

2. Speckle Roughness:

The standard deviation of speckle value is used to derive the speckle roughness in each area:

$$Roughness=\sqrt{\frac{\sum_{i=1}^{n}(R_i-\overline{R})^2}{n-1}} \quad (6)$$

where n is the number of speckles in the area; R_i is the speckled radar value; $\overline{R}$ is the mean of speckled pixel values.

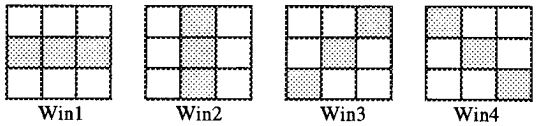


Fig1. Four Subwindows in a 3x3 Neighborhood

A CASE STUDY

The L-band radar image of Flevoland, the Netherlands, acquired by the SIR-C/X-SAR system on April 14, 1994, was used for our study. A subimage (600x700) was clipped, where six categories of landuse are identified: built-up area (City of Harderwijk and Zeewolde town), canal, arable land, meadow, meadow with poplar, and forest.

In order to analyze the speckle patterns of different landuse categories, areas of homogeneous landuse were delineated on the computer screen with the support of the local landuse map. The digitized parcels are shown in Fig.2, while the corresponding landuse types are listed in Tab. 1.

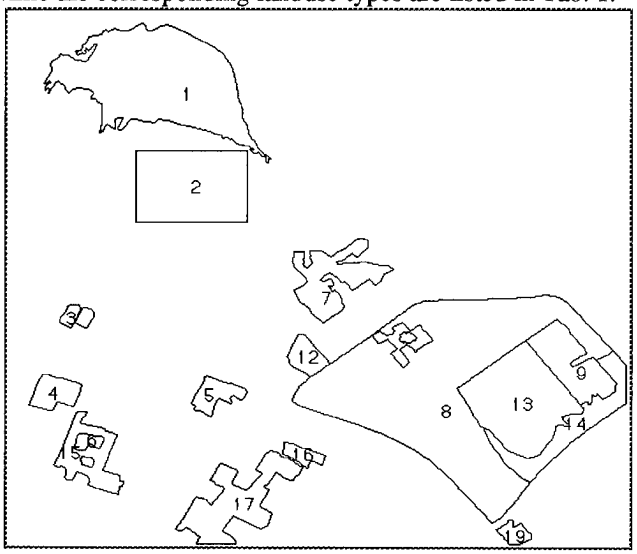


Fig. 2 Landuse Map of Selected Areas

The above speckle identification algorithm was carried out on this image. The identified bright speckle map is shown in Fig.3. The speckle density and roughness for areas of different landuse are shown in Tab. 2 and Tab. 3.

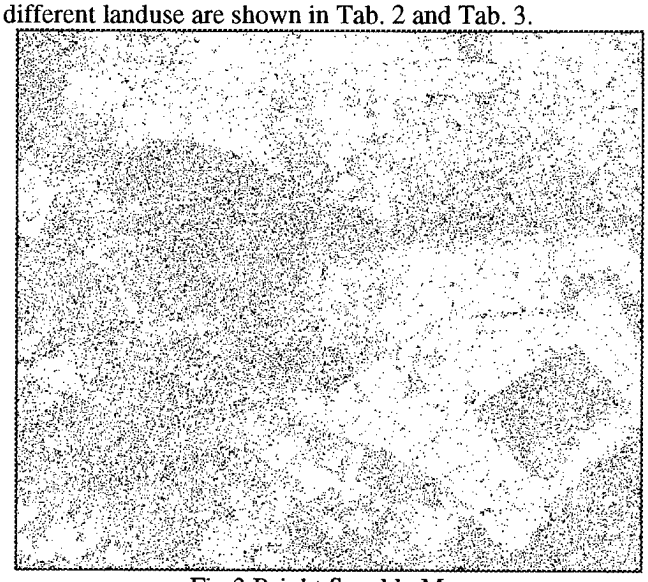


Fig 3 Bright Speckle Map

Tab.1 Landuse Type of Digitized Parcels

Landuse Code	Landuse Type	Parcel No.
1	built-up area	1, 7
2	water	2
3	arable area	4, 5, 6, 9, 12
4	meadow	3, 15
5	meadow with poplar	17
6	forest	14, 16

Tab. 2 Speckle Density of Selected Parcels

Landuse Code	Parcel No.	Speckle Density	Bright Density	Dark Density	$\frac{Bright_Density}{Dark_Density}$
1	1	0.168	0.026	0.142	0.183
1	7	0.203	0.057	0.146	0.390
2	2	0.291	0.119	0.172	0.692
3	4	0.292	0.112	0.180	0.622
3	5	0.286	0.103	0.183	0.563
3	6	0.285	0.111	0.174	0.638
3	9	0.278	0.102	0.176	0.580
3	12	0.273	0.102	0.170	0.600
4	3	0.217	0.099	0.118	0.839
4	15	0.270	0.101	0.169	0.598
5	17	0.193	0.039	0.154	0.253
6	14	0.151	0.012	0.139	0.086
6	16	0.135	0.005	0.130	0.038

Tab. 3 Speckle Roughness of Selected Parcels

Landuse Code	Parcel No.	Bright Speckle		Dark Speckle	
		Mean	Roughness	Mean	Roughness
1	1	212.925	43.310	154.828	53.502
1	7	215.943	26.865	116.419	55.069
2	2	61.421	26.865	7.706	10.571
3	4	165.422	32.439	83.601	33.860
3	5	173.583	35.528	92.026	31.253
3	6	139.811	35.462	44.265	29.228
3	9	167.454	33.912	88.491	32.197
3	12	197.625	35.897	112.181	34.868
4	3	60.671	52.799	12.310	15.188
4	15	72.630	39.897	13.882	26.368
5	17	219.000	36.530	115.667	42.441
6	14	220.068	26.578	184.131	37.798
6	16	217.000	25.910	202.663	39.203

The speckle density of forested areas is quite different from the others, while it is not easy to separate built-up area from meadow with poplar, meadow from water and arable area. However, all these overlapping categories can be distinguished by their properties in speckle mean and roughness.

CONCLUSION

Radar speckle patterns are related to the interactions between radar signal and land surface. The close relationship between speckle patterns and landcover types shows that there is some information content in radar speckle. If we only treat speckle as noise, some useful information may be lost. Further research is needed to develop techniques for speckle identification and speckle characterization.

REFERENCES

[1] H.H. Asenault and G.April, "Information content of images degraded by speckle noise," SPIE, International Conference on Speckle, Vol. 556, pp. 191-195, 1985.

[2] J.S. Lee and I. Jurkevich, "Speckle filtering of synthetic aperture radar images: a review," Remote Sensing Review, Vol. 8, pp. 313-340, 1994.

[3] Y. Sheng and Z.G. Xia, "A comprehensive evaluation of filters for radar speckle suppression," Proceedings of IGARSS'96 Symposium, 1996.

[4] D.H. Hoekman, "Extraction of small-scale spatial information from SLAR raw data of forests through an analysis of speckle," Proceedings of IGARSS'88 Symposium, pp. 1257-1261, 1988.

[5] J.W. Goodman, "Statistical properties of laser speckle patterns," in Laser Speckle and Related Phenomena. J.C. Dainty, Eds. Berlin: Springer-Verlag, 1975, pp.9-75.

[6] J.C. Dainty, "Introduction," in Laser Speckle and Related Phenomena. J.C. Dainty, Eds. Berlin: Springer-Verlag, 1975, pp.1-7.

[7] M. Francon, Laser Speckle and Applications in Optics, Translated by H.H. Arsenault, New York: Academic Press, 1979.

[8] J.W. Goodman, Statistical Optics, New York: John Wiley & Sons, 1985.

[9] J.S. Lee, "Digital image enhancement and noise filtering by use of local statistics," IEEE Trans. on Pattern Analysis and Machine Intelligence, Vol. 2, No. 2, pp. 165-168, 1980.

[10] F.W. Leberl, Radargrammetric Image Processing, Norwood, Massachusetts: Artech House, 1990.

[11] P.V.N. Rao, M.S.R.R. Vidyadhar, T.Ch. M. Rao and L. Venkataratnam, "An adaptive filter for speckle suppression in synthetic aperture radar images," Int. J. Remote Sensing, Vol. 16, No. 5, pp. 877-889, 1995.

SAR and one-bit coding: new ideas

Giorgio Franceschetti[1,2], *IEEE Fellow*, Manlio Tesauro[1], Steve Wall[3]

[1]Università di Napoli Federico II, *Dipartimento di Ingegneria Elettronica*, Via Claudio 21, 80125 Napoli, Italy.
☎ +(39)-81-7681111 fax+(39)-81-5934438 email: francesc@irece1.irece. na.cnr.it
[2]UCLA, Department of Electrical Engineering,405 Hilgard Ave, Los Angeles, CA, USA
[3] Jet Propulsion Laboratory (JPL), 4800 Oak Grove Drive, Pasadena, CA, 91109 USA.
☎ +(1)-818-3547424 fax +(1)-818-3549476 email: steve.wall@radar-email.jpl.nasa.gov

Abstract --One-bit coded processing of SAR data is revisited. Quantitative results on real data are discussed.

INTRODUCTION

Active microwave systems are powerful tools to observe the Earth. Among them the Synthetic Aperture Radar (SAR), an high-resolution active microwave system, has demonstrated its ability to detect important natural features [1].

Spaceborne SAR systems have on-board hardware consisting of a transmitting unit with analog-to-digital (A/D) converter, usually coded at 4-8 bits, followed by a realtime downlink with a high data rate to the Earth station where processing is performed. The data rate is proportional to the pulse repetition frequency (PRF), to the sampling rate for each received pulse, and to the number of quantization bits for each sample [1]. There are some possibilities to reduce the data rate, but these will deteriorate the system performance. A reduction of PRF will increase azimuth ambiguities unless a longer azimuth antenna is used but the azimuth resolution would be degraded. A reduction of the system bandwidth will decrease the range resolution.

Within such a framework, the ability to benefit of raw data bit rate reduction is matter of great relevance. One-bit coding is a very attractive technique in SAR applications [2], because it drastically alleviates transmission problems from space to ground station. But there is another important reason why this technique is worth of extensive exploration and experimentation: provided that all the processing is performed at one-bit, convolution can be implemented by using only phase-shifters and adders, i. e., with a robust and inexpensive hardware. In addition, convolution can be performed in time-domain, [3] and real time operations are attainable with today's technology, using a lightweight processor of limited power consumption. This is a first step in the direction of on-board processing.

It is evident that one-bit coding generates images of degraded quality compared to those obtained by using the conventional 4-8 bits. However, degradation may be acceptable in view of other benefits or requierements. Accordingly, a trade-off between image quality and complexity of data compression algorithm is an important point in SAR system design. Also, it may be surmised that one-bit operation can be optimized in order to limit its inherent deficiencies. The starting point of such effort is the developement of a very accurate model for one-bit operations, explicitly accounting for both raw signal and reference function hard-limiting.

We present suggestions to improve one-bit processing. We make reference to two-dimensional processing, which is inherently superior to the conventional range-doppler approach and is crucial in the proposed one-bit procedure. Possible improvements are all based on the elimination of unwanted signal components in the one-bit coded reference (*reference sterilization*).

SIGNUM CODED SAR THEORY

Consider a transmitted chirped pulse,

$$f_T(t') = b\exp\left[i\left(\omega t' + \frac{\alpha}{2}t'^2\right)\right]\mathrm{rect}\left[\frac{t'}{\tau}\right] \tag{1}$$

which is backscattered by the illuminated scene and generates the received segnal $f(t)$, t being the retarded time. This is decomposed in the sum of the desired signal, i.e., the one scattered by the target (the considered pixel in SAR applications), and all other returns, i.e., the superposition of all the signals backscattered by all other targets,

$$f(t) = a\exp\left[i\left(\omega t + \frac{\alpha}{2}t^2\right)\right]\mathrm{rect}\left[\frac{t}{\tau}\right] + u_I(t) + i\,u_Q(t) = \\ = f_I(t) + if_Q(t) \tag{2}$$

Real and imaginary part of the signal $f(t)$, eq.(2), are passed through a hard-limiter, thus generating the hard-limited signal (HLS):

$$h(t) = \mathrm{sgn}\left[f_I(t)\right] + i\,\mathrm{sgn}\left[f_Q(t)\right] = \frac{1}{\pi i}\mathrm{rect}\left[\frac{t}{\tau}\right]\sum_{n=0}^{\infty} h_n(t),$$

$$h_n(t) = \varepsilon_n i^n\left\{A_n^I(t)\cos\left[n\left(\omega t + \frac{\alpha}{2}t^2\right)\right] + \right. \\ \left. + iA_n^Q(t)\cos\left[n\left(\omega t + \frac{\alpha}{2}t^2 - \frac{\pi}{2}\right)\right]\right\} \tag{3}$$

wherein ε_0=1 and ε_n=1 for $n\neq 0$.By using results of Ref.[4] we have:

$$A_n^{I,Q}(t) = \int_{-\infty}^{+\infty}\frac{d\xi}{\xi}J_n(a\xi)\exp\left[j\xi u_{I,Q}(t)\right] =$$

0-7803-3068-4/96$5.00©1996 IEEE

$$= \begin{cases} \frac{2}{n}\cos\left[n\sin^{-1}\left(\frac{u_{I,Q}(t)}{a}\right)\right]\mathrm{rect}\left[\frac{u_{I,Q}(t)}{2a}\right], & \text{for } n \text{ odd} \\ \frac{2i}{n}\sin\left[n\sin^{-1}\left(\frac{u_{I,Q}(t)}{a}\right)\right]\mathrm{rect}\left[\frac{u_{I,Q}(t)}{2a}\right], & \text{for } n \text{ even} \end{cases} \quad (4)$$

where $J_n(\cdot)$ is the n-th order Bessel function. For n=0, we get:

$$A_0^{I,Q}(t) = \begin{cases} i\pi\,\mathrm{sgn}\left[u_{I,Q}(t)\right] & ,\left|u_{I,Q}(t)\right| > a \\ 2i\sin^{-1}\left[\frac{u_{I,Q}(t)}{a}\right] & ,\left|u_{I,Q}(t)\right| \le a \end{cases} \quad (5)$$

Superposition of all the series terms (3) reconstruct the HLS. The term n=0 is a smoothed version of the final hard-limited signal; the successive terms, $h_1(t)$, $h_2(t)$, ..., appear in the form of narrow spikes, if $\left|u_{I,Q}(t)\right| >> a$ for most of the time, and their superposition reconstructs the switch sharp of the HLS arround a zero.

The same hard-limiting operation is performed also on the reference function

$$w(t) = \exp\left[i\left(\omega t - \frac{\alpha}{2}t^2\right)\right]\mathrm{rect}\left[\frac{t}{\tau}\right] = w_I(t) + iw_Q(t). \quad (6)$$

The hard-limited one, $g(t)$ exhibits the same formal expression of eq.(3) with eq.(4) substituted by

$$B_n^{I,Q}(t) = \int_{-\infty}^{+\infty}\frac{d\xi}{\xi}J_n(\xi) = \begin{cases} \frac{2}{n}, & \text{for } n \text{ odd} \\ 0, & \text{for } n \text{ even} \end{cases}. \quad (7)$$

and $B_0^{I,Q} = 0$.

Convolution between the raw and reference HLSs is in order by using the pertinet series expansions. Only terms with equal indexes are focused and dominante the other ones. The n=1 term provides the wanted signal; elimination of the others is desirable.

Consider the additiional reference function:

$$w_3(t) = \exp\left(i\frac{\pi}{3}\right)w(t) \quad (8)$$

whose hard-limited expression is readily obtained from eq.(3):

$$g_3(t) = \frac{1}{\pi i}\mathrm{rect}\left[\frac{t}{\tau}\right]\sum_{\substack{n=1 \\ n\ odd}}^{\infty} i^n\left\{B_n^I\cos\left[n\left(\omega t + \frac{\alpha}{2}t^2 + \frac{\pi}{3}\right)\right]\right. \quad (9)$$
$$\left. + iB_n^Q\cos\left[n\left(\omega t + \frac{\alpha}{2}t^2 - \frac{\pi}{2} + \frac{\pi}{3}\right)\right]\right\}$$

The new reference function $g(t)+g_3(t)$ is free of its third order component while the fundamental one is multiplied by a constant factor. Accordinly, the n=3 term desappears in the convolution. We refer to this procedure as *reference function sterilization*. It is noted that one-bit processing can be implemented by convolving the raw HLS with the two reference HLSs along two parallel channels.

RESULTS

In this Section we present experimental results which implement reference HLS sterilization. ERS-1 data are used relative to Mt. Etna (Sicily, Italy) site. Original raw data coded at 5 bits have been recoded for our purpuse.

Four experiments have been performed: raw HLS and refercence HLS without (case I) and with sterilization (case II); raw HLS and conventional reference signal (case III); conventional raw and reference signals (case IV). The correspondent images are presented in Fig.1.

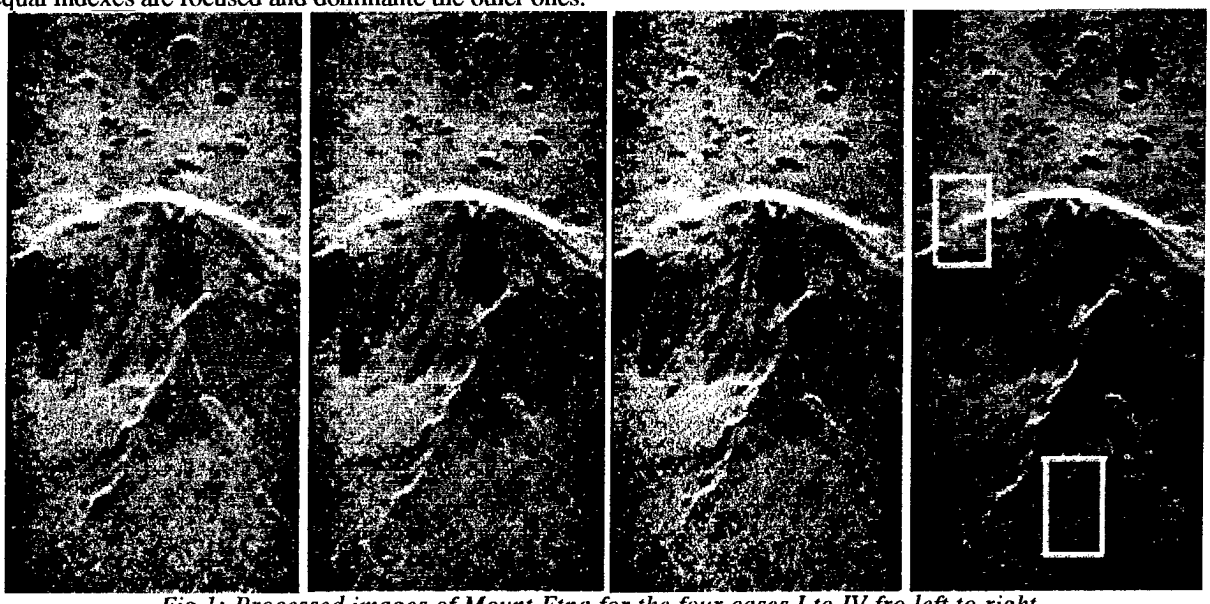


Fig.1: Processed images of Mount Etna for the four cases I to IV fro left to right. Boxes in the last picture are examined in Fig.2 and 3.

Visual inspection of the immages allows only a qualitative assessment of their similarity; qualitative estimates are desirable.

Normalized moments of two different areas of 200x400 pixels are reported in Fig.2. The two chosen areas are indicated in Fig.1 and are relative to an uniform and a non uniform site. In the first site (A) the statistics is clearly Rayleigh, and coincident for all the cases; on the contrary, some differences arise with reference to the other site (B). However, these differernces are not substantial.

In addition to this first order statistical test, we also performed a second order one, computing the autocorelation of several patches for each image: the corresponding curves are practically coincident, showing that the geometrical resolution is not impaired.

An interesting test is the "similiarity" between the images. Letting $s, \tilde{s}$ the reference and test images, respectivevely, an estimate of their similiarity is [5]:

$$\rho = \frac{\mathrm{E}\{\|s-\tilde{s}\|\}}{\sqrt{\mathrm{E}\{\|s\|\}\,\mathrm{E}\{\|\tilde{s}\|\}}}. \qquad (10)$$

This, however, requires an appropriate amplitude normalization of $\tilde{s}$ because it is normalized to its mean square deviation. If the latter is multiplied by the factor

$$k = \frac{\mathrm{Re}\left[\mathrm{E}\left(s\tilde{s}^{*}\right)\right]}{\mathrm{E}\left(\|\tilde{s}\|\right)} \qquad (11)$$

the *similarity index*, eq.(10), is minimized. The normalized histogram of $\mathrm{Re}[s-\tilde{s}]$ is depicted in Fig.3 for test cases I; II; III compared to the conventional image (case IV). The corresponding values of ρ are equal to 0.52, 0.42, 0.34.

CONCLUSIONS

In this paper we presented a comparison between processing of one-bit coded raw signal with three different reference functions. We can conclude that geometrical resolution is not impared and that the first order statistics are marginally different. Similarity between I (and Q) channels processed data shows that the sterilization of the filter function is beneficial. This result may be relevant for interferometric application, a point that is worth of further study (phase preserving procedure).

Further effort is needed along two research lines. First of all, the raw HLS generates images that are normalized to their square mean deviation, a space varying quantity. Then, raw data sampling generates replicas of $h_n(t)$, $n>1$, within the $h_1(t)$ bandwidth. Both problems are under study and solutions are being experimented.

REFERENCES

[1] J. C. Curlander, R. N. McDonough, *Synthetic Aperture Radar: Systems and Signal Processing*, New York,: John Wiley, 1991.

[2] G. Franceschetti, V. Pascazio, G. Schirinzi, "Processing of signum coded SAR signal: theory and experiments", *Proc. IEE F, Commun., Radar & Signal Process.*, 1991, **138**, (3) pp. 192-198.

[3] G. Alberti, G. Franceschetti, V. Pascazio, G. Schirinzi, "Time-domine convolution of one-bit coded radar signals", *Proc. IEE F, Commun., Radar & Signal Process.*, 1991, **138**, (5) pp. 438-444.

[4] I. Gradshteyn, I. M. Rizhik, *Tables of integrals, series and products*, Academic Press,1980, p. 743, n.6.693.1

[5] B. S. Steinberg, "A theory on the effect of hard limiting and other distortions upon the quality of the microwave images", *IEEE Trans. Acoustics, Speech, and Sig. Proc.*, **ASSP-35**(10), 1987, pp. 1462-1472.

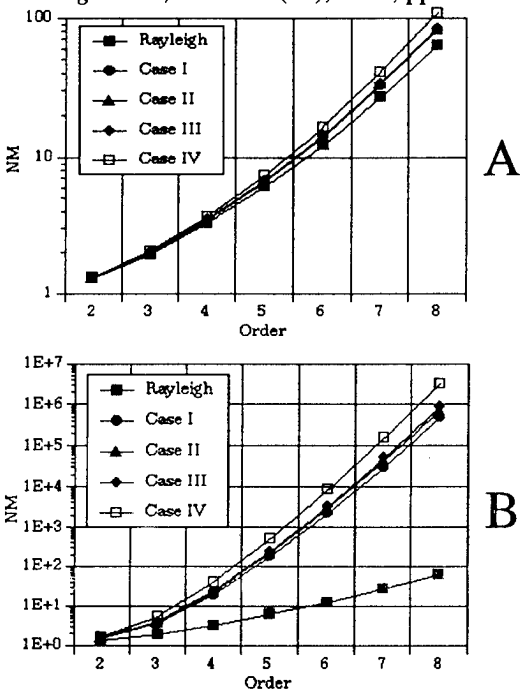


Fig.2: Normalized moments for two sites of the images.

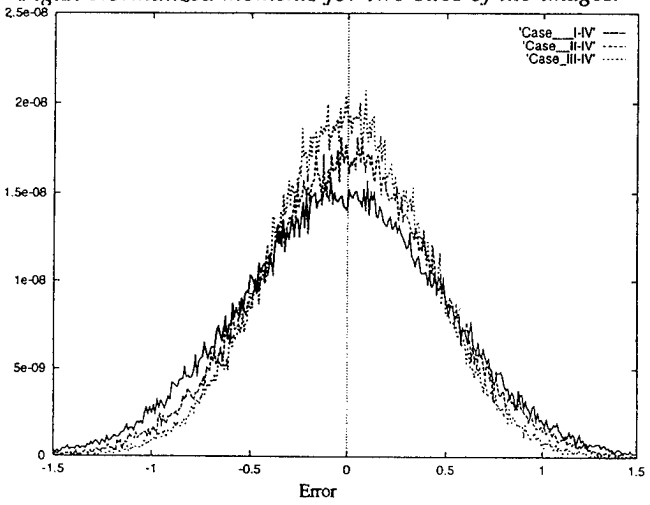


Fig.3: Histogram of $\mathrm{Re}[s-\tilde{s}]$ *for site A.*

Preserving Exponentials in Synthetic Aperture Radar Data

Matthew P. Pepin and Joseph J. Sacchini

Department of Electrical and Computer Engineering
Air Force Institute of Technology; AFIT/ENG
Wright-Patterson AFB, Ohio 45433-7765 USA

ABSTRACT

This paper examines the conditions necessary to preserve damped exponentials in synthetic aperture radar (SAR) phase histories. A small number of 2-D damped exponentials can model SAR data when the radar return is due to a few point scatterers. Error in parametric estimation of the exponential parameters results from the method of data collection, spotlight SAR or radar chamber measurement. This error is quantified and compared to the estimation bound (Cramér-Rao). Methods to reduce this error and preserve true point scatterer locations are successfully applied. Also, a fast method of focusing SAR data to the point scatterer locations is developed.

1. INTRODUCTION

A spatial ($\mathbf{k} = [\ k_x \quad k_y\ ]^T$) and temporal frequency (ω) domain analysis of Synthetic Aperture Radar (SAR) data collection shows that SAR data may be used directly in exponential estimation algorithms with the addition of an interpolation step. In this interpolation step, the $\mathbf{k}-\omega$ domain data or phase history is transformed from the sampling grid on which it was attained (polar for chamber data, or polar-linear for airborne data) to a rectangular grid. This interpolation step may be skipped provided the $\mathbf{k}-\omega$ domain data are collected on a grid that is very nearly rectangular. The error induced by this approximation is examined later. Exponential estimation techniques model SAR data directly; thus any modification of the data will degrade the estimates. The use of filter windows, zero-padding, or inappropriate means of fitting the $\mathbf{k}-\omega$ domain data to a rectangular grid significantly degrades the performance of estimation techniques.

SAR data collection is modeled here in a two-dimensional perspective as shown in Figure 1. In airborne SAR data is collected by spotlighting a ground target location. For a linear flight path, the collection geometry involves a line (the flight path) and a non-colinear point (the target). The collection occurs entirely in the plane represented by the point and the line. The target signature collected is in a view orthogonal to this plane. The spectrum of received

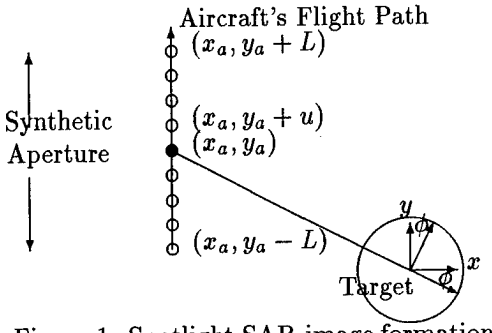


Figure 1: Spotlight SAR image formation geometry

radar signal is [6]

$$S(k_u, \omega) \propto e^{j\sqrt{4k^2 - k_u^2}x_a + jk_u y_a} F(\sqrt{4k^2 - k_u^2}, k_u), \quad (1)$$

where (x_a, y_a) is the center of the synthetic aperture, $k \equiv \frac{\omega}{c}$ where c is the wave propagation speed, $k_u \equiv k_y$, and F is the 2-D Fourier transform of the target reflectivity function $f(x, y)$. Equation 1 reduces the problem of calculating $f(x, y)$ to interpolating the data samples collected in the (k, k_u) domain to the (k_x, k_y) domain.

2. FITTING THE EXPONENTIAL MODEL

When the target $f(x, y)$ consists of point scatterers the phase history $F(k_x, k_y)$ consists of exponentials with damping to account for wave divergence. The difficulty in applying this model lies in the sampling. When samples are taken uniformly in u the samples are not uniform in k_x, and when the flight path is circular (chamber data), the samples are on a polar grid in the (k_x, k_y) plane. The sampling grid for the airborne and chamber cases are plotted in Figures 2. Interpolation must be performed between the data sampling grid and the rectangular grid needed to estimate damped exponential parameters. Focusing methods assume that a point scatter at each pixel and imposing a point spread function on the data which degrades parametric estimation methods. Inappropriate means of interpolating a SAR image such as the zero-padding in X-PATCH data also destroy the performance of exponential estimation techniques [4]. This leaves three solutions: 1) collect data on an almost rectangular grid, 2) interpolate the data, 3) estimate from nonuniform data.

0-7803-3068-4/96$5.00©1996 IEEE

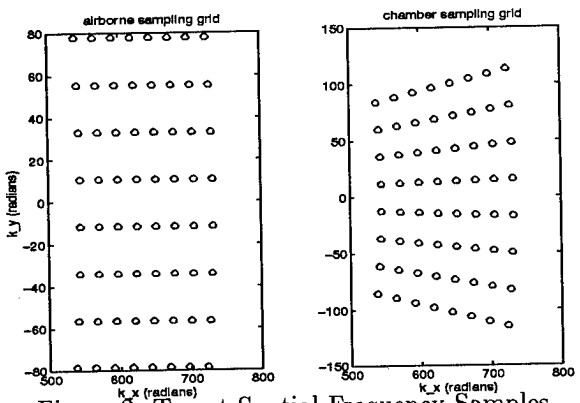


Figure 2: Target Spatial Frequency Samples

2.1. Rectangular Assumption

The rectangular assumption has been used in exponential estimation of SAR data [1]. The error incurred by using the polar or polar-rectangular grid data directly is determined by examining the deviation of these grids from the rectangular grid. For chamber data in the broadside case ($\phi = 0$) the data are collected at angles to the target $\theta \in [-\theta_b, \theta_b]$, and at frequencies $k \in [k_{\min}, k_{\max}]$.

To achieve better than Fourier resolution each sample, $F(k_n, \theta_m)$ $n = 1, \ldots, N; m = 1, \ldots, M$, must lie in a separate cell in the rectangular grid. If the first sample in a row is lower than the last sample of the previous row then resolution of a scatterer to less than a pixel (Fourier bin) is not possible. This occurs first in top row of samples when $k_{\min} < \frac{N-2}{N-1} k_{\max}$ (pixel boundary condition).

Frequency estimation accuracy (scatterer location) is bounded by the maximum k_x or k_y deviation of samples within a column or row of the rectangular grid. This error consists of two orthogonal components, e_{k_x} and e_{k_y}. The error in the k_x direction is greatest at the outer ring is

$$e_{k_x} = k_{\max} \cos 0° - k_{\max} \cos \theta_b = k_{\max}(1 - \cos \theta_b). \quad (2)$$

The error in the y direction is the deviation of the radial lines from parallel beam center and is

$$e_{k_y} = k_{\max} \sin \theta_b - k_{\min} \sin \theta_b = (k_{\max} - k_{\min}) \sin \theta_b. \quad (3)$$

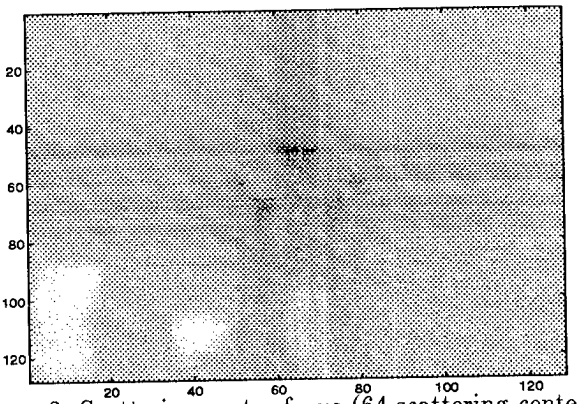
The maximum error is then the maximum of these errors. Airborne SAR is regularly sampled in the k_y direction and thus contains only the e_{k_x}error term.

2.2. Scattering Center Focus

A simple form of interpolation, phase-shifting the data to a rectangular grid is described below. More complex methods of interpolation include 1-D and 2-D Lagrange interpolation polynomials [2], and inverse distance [5].

F can be written as 2-D damped exponential data from p point scatterers and noise W

$$F[n,m] = \sum_{i=1}^{p} s_i \lambda_i^n \gamma_i^m + W[n,m] \quad \begin{matrix} 0 \le n \le N-1 \\ 0 \le m \le M-1. \end{matrix} \quad (4)$$


Figure 3: Scattering center focus (64 scattering centers)

where the λ_i and γ_i are the complex spatial frequencies and the s_i are the complex amplitudes of the scatterers and $W[n,m]$ is circular white Gaussian noise. Arranging F in an $N \times M$ matrix

$$F = GSH^T + W, \quad (5)$$

$$G = [\ \mathbf{g}_1 \quad \mathbf{g}_2 \quad \cdots \quad \mathbf{g}_p\ ] \quad \mathbf{g}_i = \Psi_N(\lambda_i), \quad (6)$$

$$S = \mathrm{diag}([\ s_1 \quad s_2 \quad \cdots \quad s_p\ ]) \quad (7)$$

$$H = [\ \mathbf{h}_1 \quad \mathbf{h}_2 \quad \cdots \quad \mathbf{h}_p\ ] \quad \mathbf{h}_i = \Psi_M(\gamma_i), \quad (8)$$

$$\Psi_K(z) = [\ 1 \quad z \quad z^2 \quad \cdots \quad z^M\ ]^T. \quad (9)$$

This model assumes that the data are sampled on a rectangular grid. A reformulation of Equation 5 shows how the rectangular grid is involved in the model and how it may be replaced with a different grid to reflect the data collection. Consider, a 2-D damped exponential with a single mode in each dimension. The matrix form may then be expressed as $F = s_i \lambda_i^{\mathbf{X}} \odot \gamma_i^{\mathbf{Y}}$

$$\mathbf{X} = \begin{bmatrix} 1 & 1 & \cdots & 1 \\ 2 & 2 & \cdots & 2 \\ \vdots & \vdots & & \vdots \\ N & N & \cdots & N \end{bmatrix}, \mathbf{Y} = \begin{bmatrix} 1 & 2 & \cdots & M \\ 1 & 2 & \cdots & M \\ \vdots & \vdots & & \vdots \\ 1 & 2 & \cdots & M \end{bmatrix}$$

where the scalar λ_i taken to a matrix power results in a matrix of the same size with elements $\lambda_i^{x_{nm}}$ where x_{nm} is the nm^{th} element of $\mathbf{X}$ and $\odot$ represents the element-wise product of two matrices. $\mathbf{X}$ and $\mathbf{Y}$ represent the coordinates of the sampling grid on which the data is taken. To express a damped exponential which is sampled with a non-rectangular grid, simply replace the matrices $\mathbf{X}$ and $\mathbf{Y}$ with the rectangular coordinates of that grid. In multimode case $F = \sum_{i=1}^{p} s_i \lambda_i^{\mathbf{X}} \odot \gamma_i^{\mathbf{Y}}$. Each element of F is

$$F_{nm} = \sum_{i=1}^{p} s_i \lambda_i^{x_{nm}} \gamma_i^{y_{nm}} = \sum_{i=1}^{p} (s_i \lambda_i^n \gamma_i^m)\, \lambda_i^{x_{nm}-n} \gamma_i^{y_{nm}-m}.$$

The damped exponential model is thus distorted at each pixel by the weighting factors $\{\lambda_i^{x_{nm}-n} \gamma_i^{y_{nm}-m}\}_{i=1\ldots p}$.

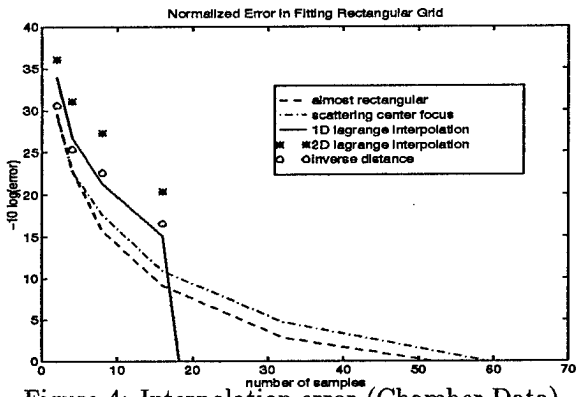


Figure 4: Interpolation error (Chamber Data)

For conversion to the polar grid these weights are $\lambda_i^{k_n \cos\theta_m - k_n} \gamma_i^{k_n \sin\theta_m - \theta_m}$. Assume that the λ_i and γ_i are undamped exponentials; then $\lambda_i^{x_{nm}-n} \gamma_i^{y_{nm}-m}$ simply applies a phase shift to each term F_{nm} and the average is

$$\angle_{nm} = \frac{1}{p} \sum_{i=1}^{p} \angle\lambda_i^{k_n \cos\theta_m - k_n} + \angle\gamma_i^{k_n \sin\theta_m - \theta_m}. \qquad (10)$$

Equation 10 is easily implemented by estimating the λ_i and γ_i, by picking the brightest pixels in the image and calculating their spatial frequency. Since only the pixel locations are required, the DFT of $F(k_n, \theta_m)$ provides good results. This method also provided a fast means of improving SAR image quality when 2-D interpolation methods are too intensive. Figure 3 shows the focusing method on chamber data of a C-29 aircraft.

2.3. 1-D and 2-D Interpolation

For the 1-D Lagrange interpolation polynomial, the k_x dimension for chamber data was interpolated. An order-N interpolation polynomial was formed for each frequency then evaluated at the rectangular grid points. The most computationally intensive techniques were 2-D. The inverse distance method used the 2-D gradient to interpolate, and a Lagrange polynomial interpolated the stacked columns of the 2-D data. An image of two point sources was sampled on an 'almost rectangular' polar grid, then interpolated by each technique. Figure 4 shows the energy loss of the methods as measured with $\bar{e} = \frac{\|F - \hat{F}\|_F}{\|F\|_F}$ using the F, Frobenius norm.

3. RESULTS

Mean Square Error's (MSE's) for two exponentials in white Gaussian noise in a 8×8 snapshot were calculated using Monte Carlo simulations each with 50 independent experiments. Several 2-D methods [3] which attain the Cramér-Rao bound (CRB) were tested for accuracy without interpolation, and with focusing. Figures 5 and 6 show the CRB and resultant MSE's for estimated frequency. The solid lines are the 2-D CRB and multi-trial 1-D bound.

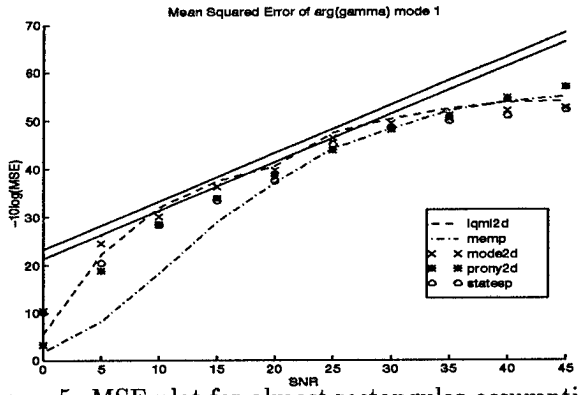


Figure 5: MSE plot for almost rectangular assumption

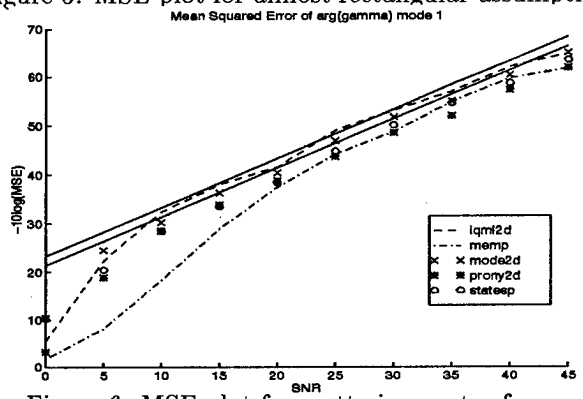


Figure 6: MSE plot for scattering center focus

Degradation away from the CRB is observed even for this small 8×8 snapshot. The 'almost rectangular' assumption fails quickly. When the sample grid is greater than 32×32, the pixel boundary condition is violated. Each of the interpolation methods improves the performance of the algorithms. Figure 6 shows that scattering center focus enhances estimation performance.

4. REFERENCES

[1] Y. Hua, E. Baqui, Y. Zhu, and D. Heilbronn, "Imaging of Point Scatters from Step-Frequency ISAR Data," IEEE Trans AES, 29:1, pp. 195-204, Jan. 1993.

[2] P. Lancaster and K. Salkauskas, *Curve and Surface Fitting,* London: Academic Press, 1986.

[3] M. P. Pepin and M. P. Clark, "On the Performance of Several 2-D Harmonic Retrieval Techniques," in *Proc. IEEE Asilomar,* Oct. 1994.

[4] M. P. Pepin and M. P. Clark, "On the Applicability of 2D Damped Exponential Models to Synthetic Aperture Radar," in *Proc. IEEE ICASSP*, May 1995.

[5] D. T. Sandwell, "Biharmonic spline interpolation of GEOS-3 and SEASAT altimeter data," *Geophysical Research Ltrs*, 2, pp. 139, 1987.

[6] M. Soumekh, *Fourier Array Imaging,* Englewood Cliffs, NJ: Prentice Hall, 1994.

Improved Multiple Look Technique

T.S. Yeo, W.L. Lay, Y.H. Lu, W.E. Ng, I. Lim and C.B. Zhang
Radar Signal and Processing Lab
Department of Electrical Engineering
National University of Singapore
10 Kent Ridge Crescent Singapore 119260
Tel: (65)7722119, Fax: (65)7791103
Email:eleyeots@leonis.nus.sg

I. ABSTRACT

Synthetic aperture radar (SAR) images are contaminated by speckle noise. To suppress speckle, N lower resolution images (looks) are generated and averaged. This improves the signal-to-speckle noise ratio (SSNR) by a factor of $\sqrt{N}$, assuming that the corresponding pixels in these looks have equal mean intensities. In practice this assumption is not always valid and as such SSNR is degraded. A new adaptive technique that replaces the conventionally averaged resultant pixel with one of the N available pixels is found to produce better SSNR under these circumstances.

II. INTRODUCTION

SAR images are inherently granular in appearance due to speckle noise. One technique of speckle suppression involves the use of post-image formation filters and is known as **Image Domain Filtering** (IDF) [1]. The other technique, known as **Discrete Mixed Integration** (DMI), divides the azimuth reference function in either the time or frequency domain into N discrete contiguous segments. The segments are then used to generate N lower resolution images which are incoherently averaged to achieve a speckle-suppressed image. Ideally, this latter technique is able to achieve an improvement factor of $\sqrt{N}$ in SSNR, provided that the mean intensity in each look is equal. In practice, the mean intensities of the different looks differ due to the non-uniformity of the antenna azimuthal gain pattern and the aspect dependence of terrain backscattering. As such, SSNR improvement is often lower than the theoretical value.

As an illustration, we tabulate the mean and variance of pixel intensities for the various looks of a homogeneous patch in an ESAR image of Oberpfaffenhofen, Germany. As can be seen, the means of the different looks are not equal.

Table 1 Mean and Variance of Pixel Intensity of an uniform area in the various single looks

	1st Look	2nd Look	3rd Look	4th Look
Mean	79	89	72	65
Variance	1693	2210	1620	1142

In this paper, we propose a new speckle suppression method, known as **Adaptive Sampling Technique** (AST), that is able to achieve better SSNR over that of conventional DMI.

0-7803-3068-4/96$5.00©1996 IEEE

III. EVALUATION OF DMI TECHNIQUE

The SSNR used to quantify the improvement in speckle noise reduction, is defined as

$$\text{SSNR} = E(x)\Big/\sqrt{E\left(x^2\right)-E^2(x)} = E(x)\Big/\sqrt{Var(x)} \qquad (1)$$

where x is the intensity (square of amplitude) of a pixel. $E(x)$ and $Var(x)$ represents the expectation and the variance of x respectively. When the pixel consists of many scattering centres distributed over a rough surface, the observed intensity from a pixel in each look follows an exponential distribution [2] and is given by

$$f(x_i) = {}^{1}\!/_{P_i}\exp(-{}^{x_i}\!/_{P_i}) \qquad (2)$$

where x_i and P_i are the intensity value and mean intensity in the i^{th} look respectively. In the DMI technique, the resultant intensity pixel x of the multiple look image is given by

$$x = \sum_{i=1}^{N} x_i \qquad (3)$$

From (2) and (3) the SSNR can be easily evaluated to be

$$\text{SSNR} = \sum_{i=1}^{N} P_i \Big/ \sqrt{\sum_{i=1}^{N} P_i^{\,2}} \qquad (4)$$

Fig. 1 shows a plot of achievable SSNR of a 4-look image *i.e.* $N = 4$ (using DMI) against varying mean in one look when the other 3 looks have equal unit mean *i.e.* $P_1 = P_2 = P_3 = 1$. We see that when the mean intensity in each look is the same *i.e.* $P_4 = 1$, the SSNR obtained is $\sqrt{N}$. However, when the mean intensity of any one look deviates, SSNR is reduced.

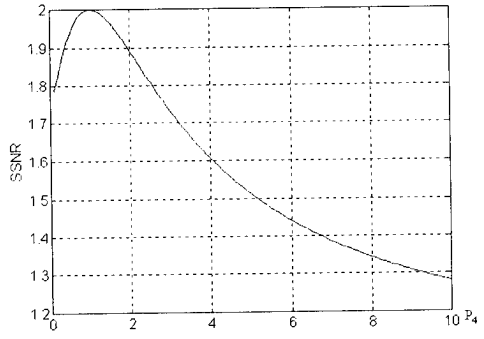


Fig. 1: Plot of SSNR for conventional DMI technique when $N = 4$ and mean intensities $P_1 = P_2 = P_3 = 1$.

IV. THE SAMPLING TECHNIQUE

The AST is derived from the DMI technique. Unlike DMI however, it adaptively samples one of the N available single-look pixel intensities as its resultant pixel value (instead of averaging the N looks). In this section, we shall first show (without derivation) the different probability density functions (pdf) of the resultant pixel intensity, due to different sampling of the N pixel intensities in their sorted order. Subsequently, we make comparisons by showing plots of the achievable SSNRs based on the different sampling criteria. For coherency in discussion, the case for $N = 4$ is presented.

A. Sample maximum intensity

Let x_1 be the resultant pixel intensity employing Replacement by the maximum intensity pixel intensity value

$$f(x_1) = \sum_{i=1}^{N} \frac{1}{P_i} \exp\left(-\frac{x_1}{P_i}\right) \prod_{\substack{j=1 \\ j\neq i}}^{N} \left[1 - \exp\left(-\frac{x_1}{P_j}\right)\right] \tag{5}$$

When $N = 4$, the pdf is given by

$$\begin{aligned} f(x_1) = & \sum_{1}^{4} \frac{1}{P_i} \exp\left(-\frac{x_1}{P_i}\right) - \sum_{i=1}^{4}\sum_{j>i}^{4} \left(\frac{1}{P_i} + \frac{1}{P_j}\right) \exp\left(-x_1\left(\frac{1}{P_i} + \frac{1}{P_j}\right)\right) \\ & + \sum_{i=1}^{4}\sum_{j>i}^{4}\sum_{k>j}^{4} \left(\frac{1}{P_i} + \frac{1}{P_j} + \frac{1}{P_k}\right) \exp\left(-x_1\left(\frac{1}{P_i} + \frac{1}{P_j} + \frac{1}{P_k}\right)\right) \\ & - \sum_{i=1}^{4} \frac{1}{P_i} \exp\left(-x_1\left(\sum_{j=1}^{4} \frac{1}{P_j}\right)\right) \end{aligned} \tag{6}$$

B. Sample second maximum intensity

Let x_2 be the resultant pixel intensity due to sampling the second maximum intensity pixel:

$$f(x_2) = \sum_{i=1}^{N} \frac{1}{P_i} \exp\left(-\frac{x_2}{P_i}\right) \sum_{\substack{j=1 \\ j\neq i}}^{N} \exp\left(-\frac{x_2}{P_j}\right) \prod_{\substack{k=1 \\ k\neq j \\ k\neq i}}^{N} \left[1 - \exp\left(-\frac{x_2}{P_k}\right)\right] \tag{7}$$

When $N = 4$, the pdf is given by

$$\begin{aligned} f(x_2) = & \sum_{i=1}^{4}\sum_{j>i}^{4} \left(\frac{1}{P_i} + \frac{1}{P_j}\right) \exp\left(-x_2\left(\frac{1}{P_i} + \frac{1}{P_j}\right)\right) \\ & - 2\sum_{i=1}^{4}\sum_{j>i}^{4}\sum_{k>j}^{4} \left(\frac{1}{P_i} + \frac{1}{P_j} + \frac{1}{P_k}\right) \exp\left(-x_2\left(\frac{1}{P_i} + \frac{1}{P_j} + \frac{1}{P_k}\right)\right) \\ & + 3\sum_{i=1}^{4} \frac{1}{P_i} \exp\left(-x_2\left(\sum_{j=1}^{4} \frac{1}{P_j}\right)\right) \end{aligned} \tag{8}$$

C. Sample third maximum intensity

Let x_3 be the resultant pixel intensity due to sampling the third maximum intensity pixel:

$$f(x_3) = \sum_{i=1}^{N} \frac{1}{P_i} \exp\left(-\frac{x_3}{P_i}\right) \sum_{\substack{j=1 \\ j\neq i}}^{N} \exp\left(-\frac{x_3}{P_j}\right) \sum_{\substack{k=1 \\ k\neq j \\ k\neq i}}^{N} \exp\left(-\frac{x_3}{P_k}\right) \prod_{\substack{l=1 \\ l\neq k \\ l\neq j \\ l\neq i}}^{N} \left[1 - \exp\left(-\frac{x_3}{P_l}\right)\right] \tag{9}$$

When $N = 4$, the pdf becomes

$$\begin{aligned} f(x_3) = & \sum_{i=1}^{4}\sum_{j>i}^{4}\sum_{k>j}^{4} \left(\frac{1}{P_i} + \frac{1}{P_j} + \frac{1}{P_k}\right) \exp\left(-x_3\left(\frac{1}{P_i} + \frac{1}{P_j} + \frac{1}{P_k}\right)\right) \\ & - 3\sum_{i=1}^{4} \frac{1}{P_i} \exp\left(-x_3\left(\sum_{j=1}^{4} \frac{1}{P_j}\right)\right) \end{aligned} \tag{10}$$

D. Sample minimum intensity

Let x_4 be the resultant pixel intensity when the minimum intensity pixel is used:

$$f(x_4) = \sum_{i=1}^{N} \frac{1}{P_i} \exp\left(-\frac{x_4}{P_i}\right) \prod_{\substack{j=1 \\ j\neq i}}^{N} \left[\exp\left(-\frac{x_4}{P_j}\right)\right] \tag{11}$$

When $N = 4$, the pdf becomes:

$$f(x_4) = \sum_{i=1}^{4} \frac{1}{P_i} \exp\left(-x_4\left(\sum_{j=1}^{4} \frac{1}{P_j}\right)\right) \tag{12}$$

E. Comparison of achievable SSNRs

To derive the SSNRs for the various sampling criteria for N=4, $E(x)$ and $Var(x)$ are first evaluated using the respective pdfs as shown in (6), (8), (10) and (12). Subsequently, they are substituted into (13) where i = 1,2,3,4 indicates the different sampling criterion.

$$\mathrm{SSNR}_i = E(x_i) \Big/ \sqrt{Var(x_i)} \tag{13}$$

Fig. 2 shows a plot of the achievable SSNRs for the various methods as a function of varying mean P_4 , with P_1 = P_2 = P_3 = 1. SSNR_j denotes the SSNR obtained by DMI.

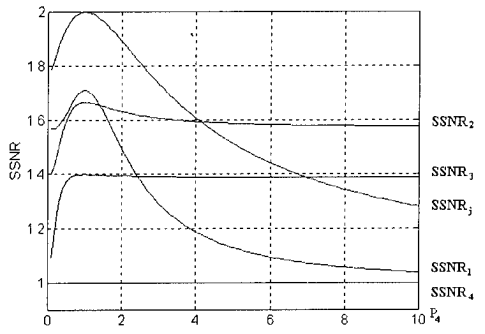


Fig. 2: SSNR for various methods for the case N = 4 with $P_1 = P_2 = P_3 = 1$.

From Fig. 2 it is evident that as the mean pixel intensity in any look begins to deviate from the rest, the sampling technique is able to produce a better SSNR compared to DMI. In this particular case, when $P_4 > 4$ one should employ the sample second maximum intensity method instead of the DMI. Although the ideal improvement factor of $\sqrt{N}$ is not

obtained, incorporation of the sampling technique into DMI nevertheless maximizes the achievable SSNR

Fig. 3 shows another plot of achievable SSNR as a function of P_4, however with a different set of mean intensities P_1 = P_2 =1 P_3 = 5. It is observed that when P_4 <1 the sample second maximum intensity method gives a higher SSNR. On the other hand when P_4 > 1, conventional DMI produces better results.

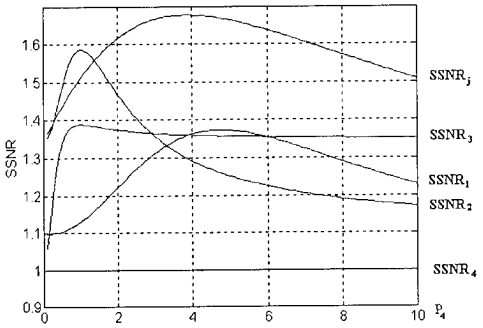


Fig. 3: SSNR for various methods for the case N = 4 with P_1 = P_2 =1 P_3 = 5.

These isolated cases highlight the need for an adaptive approach for the determination of the appropriate sampling criterion to be used, based on the mean pixel intensity variation. From both Fig. 2 and 3 we also note that unit SSNR is always achieved for the case when the minimum intensity is sampled. This is equivalent to not employing multiple look processing at all and hence should not be used.

V. ADAPTIVE IMPLEMENTATION

The implementation of the sampling technique requires the knowledge of the mean intensity of pixels in each look. However, since only the pixel intensity of the looks is available, we estimate the mean intensity using local statistics. Choice of the appropriate window is determined by image resolution. In practice, image pixels in the azimuthal direction are much smaller than the resolution cell length. Averaging pixels within the resolution cell to estimate the mean is therefore expected to be fairly accurate since the pixels can be assumed to be quasi-uniform. An illustration of this adaptive implementation is shown in Fig. 4.

VI. EVALUATION WITH ESAR IMAGES

Fig. 5 and 6 show the same section of an ESAR image of Oberpfaffenhofen (Campaign OP93AF), processed using the conventional DMI technique and the proposed AST. A 1×10 window in the azimuth direction was used to estimate the pixel mean, corresponding to resolution cell size of 1.5m×0.8m. It is noted from the image that the latter approach reduces the speckle noise more significantly, resulting in the visibility of terrain features that were otherwise smoothed out by the former method which employs averaging.

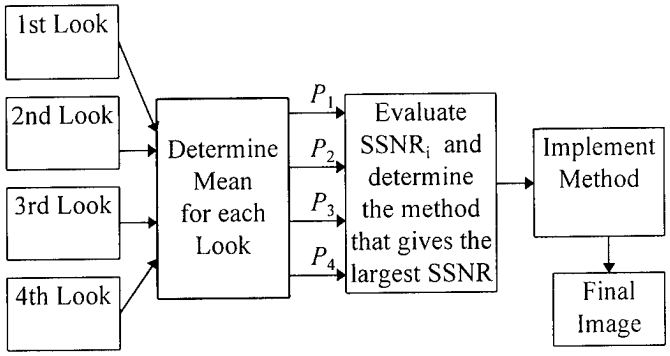


Fig. 4: Implementation of Adaptive Algorithm based on estimated mean intensity in the various looks.



Fig. 5: ESAR image processed by conventional DMI technique.



Fig. 6: ESAR image processed by Sampling Technique.

VII. REFERENCES

[1] Fuk-Kwok Li, "Comparison of Several Techniques to obtain Multiple-Look SAR Imagery," *IEEE Trans. on Geoscience and Remote Sensing*, vol. Ge-21, No 3, Jul 1983

[2] J.W.Goodman, "Some Fundamental Properties of Speckle," *J.Opt, Soc, Amer.*, vol 66 no.11, pp. 1257-1260, Nov 1976

Partially Correlated K-distribution for Multi-look Polarimetric SAR Imagery

Yongjian Yu, Andrea Torre*, and Shunji Huan

Dept. of Electronic Engineering,
Univ. of Electronic Science and Technology
of China, Chengdu, Sichuan 610054, PRC.
Tel: +86-28-3201140. Fax: +86-28-3334131

*** Alenia Spazio S.p.A.**
Via Saccomuro 24,
Roma 00131, ITALY.
Tel: +39-6-41512046.Fax: +39-6-41512171.

Abstract -- A partially correlated polarimetric K-distribution model is presented to characterize statistical properties of multi-look polarimetric SAR data from urban areas. The model was derived using a more general matrix form of the product model that uses separate Gamma distributed texture variables for different polarization channels and assumes that these texture variables be partially correlated. Experimental assessment of the model was conducted using NASA/JPL polarimetric SAR data from an urban area, showing improvement in better characterizing urban polarimetric backscattering.

1. INTRODUCTION

To construct algorithms for higher level object statistical polarimetric classification and characterization as well as optimal SAR image speckle reduction applications using high resolution polarimetric SAR data associated with a scene or field that contains not only various kinds of natural objects such as terrain, crops, forests and etc. but also complex urban objects, it is essential to have an unified and precise polarimetric statistical model applicable to all kinds of interested objects within the scene. Furthermore, to assure the algorithms' robustness and effectiveness in diverse environments, the model should be physically based and compact in form.

It has been shown that polarimetric K-distribution(PKD) [1] is promising for statistically describing high resolution polarimetric backscatter of ocean, vegetation, crops, and forest which could have heterogeneous texture structures. More significantly, PKD was set up on the basis of certain mathematical and physical assumptions about radar echo; and also had a closed mathematical form. Naturally, it is desirable that PKD could be used as an unified and precise polarimetric statistical model for the aforementioned purpose.

However, some experiments indicated that PKD is not precise enough to characterize complex urban polarimetric scatter.

In this research, we are concerned with generalizzing PKD to overcome its shortcoming in urban scatter description.

2. PARTIALLY CORRELATED POLARIMETRIC K-DISTRIBUTION

Multi-look PKD can be formulated by using the so called product model which permits a varying texture structure to modulate the homogeneous complex Wishart speckle pattern. A common random variable is used to characterize the texture sensed with HH, HV, VH, and VV polarization; or equivalently, the SAR measurements of the texture with the four polarization are presumed to be the outcomes of four random variables that obey the same statistics and are completely correlated. In this paper, it is assumed that the SAR observations of texture structure in urban areas with high resolution POL-SAR HH, HV, VH, and VV polarization are outcomes of four partially correlated random variables.

For simplicity and without losing generalization, we just consider a dual-polarization, for instance, a single-channel (say channel 1) transmission, dual-channel (say channel 1 and 2) reception , SAR system. Let *Sij* denote the channel *i* transmitted and channel *j* received signal, where *i, j* =1,2. Thus, the measured 1-look polarimetric scattering vector y at each pixel consists of two complex elements: $y_1 = S_{11}$, and $y_2 = S_{12}$.

We assume that y is a product of a bivariate, zero mean, complex Gaussian vector X,referred to as texture-free scattering vector, and a two by two diagonal texture matrix G, i.e.

$$y = G \cdot X = \begin{pmatrix} \sqrt{g_1} & 0 \\ 0 & \sqrt{g_2} \end{pmatrix} \cdot \begin{pmatrix} x_1 \\ x_2 \end{pmatrix} \qquad (1)$$

Let $y(k)$be the k-th look scattering vector. From (1), and under the assumption that g_1 and g_2 are independent of k for pixels included in the multi-look processing, the measured n-look polarimetric covariance matrix at each pixel is given by

$$Y = (1/n)\sum_{k=1}^{n} y(k)[y(k)]^{+} = GZG^{+} \qquad (2)$$

here , $Z = (1/n)\sum_{k=1}^{n} X(k)[X(k)]^{+}$, a Wishart distributed n-look texture-free covariance matrix.

For given values of g_i (i=1,2), the conditional pdf of the random matrix Y is also a Wishart, i.e.,

$$f(Y/g_1, g_2) = \frac{n^{2n}|Y|^{n-2}}{R(n)(g_1 g_2 |\Sigma|)^n} \exp[-nTr\ (G^{-1}\Sigma^{-1}G^{-1}Y)] \quad (3)$$

where $R(n) = n\Gamma(n)\Gamma(n+1)$, and Σ is the texture-free polarimetric characteristic covariance matrix,

$$\Sigma = \begin{pmatrix} \sigma_1 & \Psi\rho_0 \\ \Psi\rho_0^{*} & \sigma_2 \end{pmatrix} \qquad (4)$$

where $\sigma_i = \left\langle |x_i|^2 \right\rangle$, ($i$=1,2), is the backscattering coefficient of the ith polarization channel, ρ_0 is the polarimetric correlation coefficient, $\rho_0 = \left\langle x_1 x_2^{*} \right\rangle / \Psi$, and $\Psi = \sqrt{\sigma_1 \sigma_2}$. It worthies

0-7803-3068-4/96$5.00©1996 IEEE

noting that Σ is related to the textured characteristic covariance matrix $C[Y]$ of Y by

$$C[Y]=\begin{pmatrix}\sigma_1 & TCF\Psi\rho_0\\ TCF\Psi\rho_0^* & \sigma_2\end{pmatrix} \quad (5)$$

where $TCF=\left\langle\sqrt{g_1g_2}\right\rangle$, is the texture correlation function .

If we model the texture scaling multipliers g_1 and g_2 as partially correlated Gamma distributed variables each of which having unity mean, their joint pdf is given by [2] :

$$p(g_1,g_2)=\frac{\upsilon^{\upsilon+1}(g_1g_2/\rho)^{(\upsilon-1)/2}}{\Gamma(\upsilon)(1-\rho)}\exp\left(-\upsilon\frac{g_1+g_2}{1-\rho}\right)I_{\upsilon-1}\left(2\upsilon\frac{\sqrt{\rho g_1g_2}}{1-\rho}\right) \quad (6)$$

where $I_n(x)$ is the modified Bessel function of the first kind of order n; υ is the texture shape parameter; ρ is a positive correlation coefficient; and $\Gamma(x)$ is the gamma function.

Using (6), we can obtain the texture correlation function:

$$\left\langle\sqrt{g_1g_2}\right\rangle=\begin{cases}1, i=j\\ \dfrac{(1-\rho)^{\upsilon}}{\upsilon\Gamma(\upsilon)}\displaystyle\sum_{k=0}^{\infty}\frac{[\Gamma(\upsilon+k+0.5)]^2}{\Gamma(k+1)\Gamma(\upsilon+k)}, i\neq j\end{cases}$$

For $\rho=0$, $\left\langle\sqrt{g_1g_2}\right\rangle=[\Gamma(\upsilon+0.5)/\Gamma(\upsilon)]^2/\upsilon$, approaches zero as υ becomes large; for $\rho=1$, TCF=1.

From (3) and (6), we found the partially correlated K-distribution for the n-look polarimetric covariance matrix Y,

$$f(Y)=\frac{2n^{2n}|Y|^{n-2}\upsilon^{2n}}{R(n)|\Sigma|^n\Gamma(\upsilon)(1-\rho)^{2n-\upsilon}}\sum_{k=0}^{\infty}\frac{\rho^k}{k!\Gamma(k+\upsilon)}\cdot$$

$$\left\langle\left(\frac{|\Sigma(\theta)|}{|\Sigma|}\right)^{k+\upsilon-n}\frac{K_{2(n-k-\upsilon)}(U'_\theta)}{(U'_\theta/2)^{2(n-k-\upsilon)}}\right\rangle_\theta \quad (7)$$

here $U'_\theta=2\sqrt{n\upsilon Tr\left\{[\Sigma(\theta)]^{-1}Y\right\}}$, $\Sigma(\theta)=R\Sigma R$,

$$R=\begin{pmatrix}1/\sqrt{(1+\theta)} & 0\\ 0 & 1/\sqrt{(1+1/\theta)}\end{pmatrix},\langle(\cdots)\rangle_\theta=\int_0^\infty(1/\theta)(\cdots)d\theta\cdot$$

When ρ is close to zero, (7) takes, approximately, the form of Taylor series about ρ around ρ =0. In this case, the PDF of Ycould be evaluated by using only the first few terms in the summation of (7), However, it is impractical to use (7) when ρ is close to 1. In this case, we would better have the PDF of Yexpressed as Taylor series about ρ around ρ=1.

The first order partially correlated multi-look K-distribution suitable for computation under the condition of high texture correlation, i.e., $\rho\le 1$, can be expressed as

$$f(Y)\approx f_0(Y)+f_1(Y) \quad (8)$$

where $f_0(Y)$ is the usual multi-look polarimetric K-distribution as (10) in [1], and $f_1(Y)$ is a small term given by

$$f_1(Y)=\frac{n^{2n}\upsilon^{\upsilon}(1-\rho)|Y|^{n-2}}{R(n)|\Sigma|^n\Gamma(\upsilon+1)}\{2n\upsilon F_{\upsilon-2n}+$$

$$(V')^2HF_{\upsilon-2n-1}+(V')^3QF_{\upsilon-2n-2}+(V')^4WF_{\upsilon-2n-3}\}, \quad (8)$$

here $F_n=(V')^nK_n(U'), H=2n(n+1)-2\upsilon-\upsilon(\tilde{A}+\tilde{A}'+\tilde{B}),$

$$Q=(\upsilon-2-2n)(\tilde{A}+\tilde{A}')+(\upsilon-2n-1.5)\tilde{B},$$

$$W=(\tilde{A}+\tilde{B}/2)^2+(\tilde{A}'+\tilde{B}/2)^2, U'=2\sqrt{n\upsilon Tr(\Sigma^{-1}Y)},$$

$$V'=U'/(2\upsilon),\tilde{A}=n\sigma_1Y_{22}/|\Sigma|,\tilde{A}'=n\sigma_2Y_{11}/|\Sigma|, \quad \text{and}$$

$$\tilde{B}=2n\,\mathrm{Re}(\Psi\rho_0^*Y_{12})/|\Sigma|.$$

3. MARGINAL PDFS

Equation (7) has six dimensions, difficult to be validated. Its marginal PDFs are more suitable for later validation.

3.1. The multi-look amplitude ratio distribution

The normalized amplitude ratio is defined as $w=r\cdot v$, where $r=\sqrt{g_1/g_2}$, $v=|x_1|/(\sqrt{\tau}|x_2|)$, and $\tau=\sigma_1/\sigma_2$.

Neglecting derivation, we have that

$$f(w)=\frac{2\Gamma(2n)\Gamma(2\upsilon)(1-|\rho_0|^2)^n(1-\rho)^{\upsilon}}{[\Gamma(n)]^2[\Gamma(\upsilon)]^2}w^{2n-1}I(w)$$

with $I(\sqrt{w})=\int_0^\infty du(w+u)(1+u)u^{n+\upsilon-1}/$

$$\left\{\left[(w+u)^2-4|\rho_0|^2wu\right]^{n+1/2}\left[(1+u)^2-4u\rho\right]^{\upsilon+1/2}\right\}.$$

3.2. Multi-look Phase difference and normalized amplitude distributions

The multi-look phase difference Ψ_{12} is defined as the argument of the off-diagonal element Y_{12} of Y in (2). Because g_1 and g_2 are real variables, the phase difference is independent of them. So, the PDF of Ψ_{12} can be found by replacing $\Psi$and ρ in (15) in [1] with Ψ_{12} and ρ_0, respectively.

The normalized multi-look amplitude distribution is identical with its counterpart(11) in [1].

4. TEST OF PARTIALLY CORRELATED DISTRIBUTION

In this section, we conduct an initial test of (7) to see whether it could be used to better characterize urban scatter compared to PKD using Sanfrancisco L-band polarimetric SAR data. The test site is an urban area containing 51x101 nominal 4-look pixels.

To compute the marginal pdfs, we need an estimate of ρ_0 from the test data set. While $\arg(\rho_0)$ can be directly computed, $|\rho_0|$ can not because its estimate is coupled with *TCF*.

From plots of *TCF* as function of ρ for different values of υ, we found that if υ is larger than 1, then *TCF* will be larger than 0.9 for any value of ρ no less than 0.5. As well known, υ is an indicator of the roughness of the texture structure; the larger the υ,the more homogeneous the imaging scene is. Lee in [2] has obtained a υ = 12.8 for forest texture using 4-look data. From this order of magnitude of υ ,it could be expected that for υ less than 1, the image scene would have become extremely rough.

In this test, we assume that υ is larger than 1 and that ρ is not close to zero for the test urban area, making it possible to neglect *TCF* in the estimation of $|\rho_0|$. Under this assumption,

1) Equivalent number of looks(ENL) and an initial estimate of υ are obtained by using the same method used in [1].

2) An accurate υ is found by testing various values in a wide neighborhood of the initial υ estimate for best match between derived PDFs and histograms for HH, HV, and VV amplitudes.

3) ρ is found by testing various values in the interval of (0,1) for best match between derived PDFs and histograms for normalized $|HH|/|VV|$, $|HH|/|HV|$, and $|HV|/|VV|$.

To echo above assumption about the data set, we use a nominal 16-look data . The test site then consists of 26x51 nominal 16-look pixels. Fig.1 shows the histogram of HH-HV phase difference and corresponding theoretical PDF when ENL =8. An acceptable fit can be noted. Fig.2 shows the histogram of HH normalized amplitude and the corresponding theoretical PDF when ENL=8 and υ=3.3. Again, a good fit exists. An acceptable fit is also found between histograms and PDF for normalized $|HH|/|HV|$ amplitude ratio when ρ =0.9, as shown in Fig.3. In Fig.3 the amplitude ratio pdf derived from the PKD in [2] is also plotted for comparison. It is shown in Fig.3 that our model fits experimental curve better. Since the obtained ρ and υ are in the valid range of our assumption, the test is effective.

5. CONCLUSION

A generalization of polarmetric K-distribution is proposed for high resolution urban scatter statistics description. A test is conducted using a real nominal 16- look urban data set, showing that the model outperforms PKD.

ACKNOWLEDGMENTS

This work was supported by the Alenia Spazio S.p.A., Italy, and was performed there as a Cooperative Research between the University of Electronic Science and Technology of China and the company. The authors wish to thank Mr. F. Rubertone and Mr. G. Perrotta for fostering this work and for many helpful discussions throughout the course of the work.

REFERENCES

[1] Lee, J.S., Schuler, D.L., et al., "K-distribution for multi-look processed polarimetric SAR imagery," IGARSS'94(1994), pp.2179-2181.

[2] Armstrong, B.C., and Griffiths, H.D.," Modeling spatially correlated K-distributed clutter," Electronics Letters, Vol.27, No.1, Feb.,1994,pp.53-58.

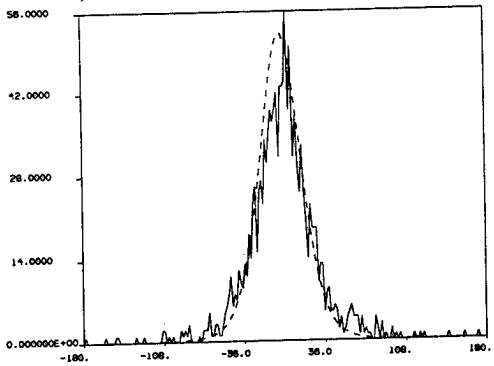


Fig.1 . Comparison of HH-HV phase difference PDF(dashed plot) with corresponding histogram test (solid). (ENL=8).

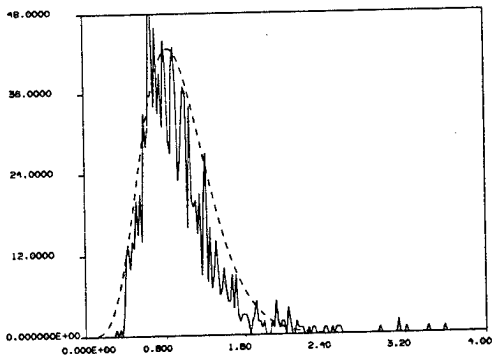


Fig.2. Comparison of normalized |HH| amplitude PDF(dashed plot) with corresponding histogram test(solid). (ENL=8, υ =3.3).

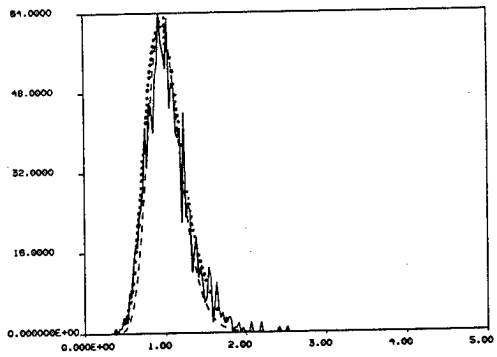


Fig.3. Comparison of normalized $|HH|/|HV|$ amplitude ratio PDF(dotted plot) with corresponding histogram test(solid). The dashed plot is computed using PKD derived amplitude ratio PDF (ENL=8,υ =3.3, ρ =0.9).

Speckle Reduction and Enhancement of SAR Images in the Wavelet Domain

Johannes R. Sveinsson and Jon Atli Benediktsson

Engineering Research Institute, University of Iceland,
Hjardarhagi 2-6, Reykjavik, IS-107, Iceland
E-mail: sveinsso@verk.hi.is.

ABSTRACT

Three methods are investigated for speckle reduction and enhancement of synthetic aperture radar (SAR) images in the orthogonal wavelet domain. The first method is a non-linear method based on soft thresholding the wavelet coefficients for logarithmically transformed SAR image data [1]. The second method uses enhanced adaptive Lee filter [2] of the wavelet coefficients of SAR images. Finally, the third method introduces non-linear speckle reduction based on adaptive sigmoid thresholding of the wavelet coefficients for logarithmically transformed SAR images. The wavelet methods show great promise for speckle removal and hence provide better detection performance for SAR based recognition.

1. INTRODUCTION

The role of SAR, in gathering information from the Earth's surface, is very important since SAR has the ability to operate under all weather conditions. However, processing of SAR images has one major problem, i.e., they contain speckle or coherent noise. The speckle noise can typically be modeled as multiplicative i.i.d. Gaussian noise [3]. Logarithmic transformation of an SAR image converts the multiplicative noise model to an additive noise model. When information details in the SAR image are important, speckle causes degradation of the image. Hence, speckle reduction is a necessary procedure before automatic and efficient class discrimination can be performed.

The discrete wavelet transformation (DWT) is a relatively new technique for multi-resolution decomposition of images and has been used for both noise reduction and compression of SAR images [1].

This paper studies speckle reduction and image enhancement for digitized SAR images. Shi and Fung [4] have compared several speckle filters, e.g., the Lee, Kuan, Enhanced Lee, Frost, Enhanced Frost, and Gamma MAP filters. They showed that all these filters had some trade-off between speckle reduction and preservation of useful information in the image.

This paper uses the adaptive statistic filter of Lee together with thresholding in the wavelet domain for speckle reduction and image enhancement. A logarithmic transformation is used to get an estimate of the signals from multiplicative noise models. The speckle reduction and image enhancement are then obtained by thresholding the wavelet coefficients of the estimated signals. A novel thresholding method which operates in the wavelet domain is proposed. This method uses a sigmoid function similar to the activation function used in neural networks. Also, soft thresholding will be studied and the results will be compared.

2. DENOISING OF SAR IMAGES

This section describes three non-linear methods for speckle reduction of SAR images. For a digitized SAR image, we define $z(j,k)$ as the gray level (or the observed image intensity) of the (j,k)-th pixel of the image. For clarity, we will omit the pixel in the indices in the rest of this paper. Hence, the pixel level of a SAR image can be written as

$$z = xe$$

where x is the desired texture information and e is the multiplicative noise. Arsenault and April [5] showed that for a logarithmically transformed SAR image, the speckle is approximately Gaussian additive noise, i.e.,

$$\tilde{z} = \tilde{x} + \tilde{e}$$

where $\tilde{z} = \ln(|z|)$. In what follows $\tilde{y}$ will represent a logarithmically transformed gray level (or intensity), y.

All speckle reduction methods are applied within the wavelet multiresolution representation, i.e., if z represents the original image and $\mathcal{W}$ is the multi-level DWT, then a multiresolution representation is given by the equation

$$y = \mathcal{W}z \qquad (\text{or } \tilde{y} = \mathcal{W}\tilde{z}).$$

This work was sported in part by the Research Fund of the University of Iceland.

0-7803-3068-4/96$5.00©1996 IEEE

The noise level (variance), σ, in the multiresolution representation is not known in advance and has to be estimated from the data. In this paper an estimate of σ is taken to be the standard derivation of the high/high subband-image of the first level of the DWT [6]. Also, no filtering or thresholding is done on the low/low subband-image at the final level of the DWT.

Below we present a general formula for processing these subband-images to accomplish speckle reduction and enhancement of SAR images. Let f be a non-linear function designed to reduce speckle for selected subband-images. Then, an enhanced subband-image $\hat{y}$ may be given by

$$\hat{y} = f(y).$$

The speckle reduced image is then obtained from the inverse DWT of the enhanced subband-image $\hat{y}$.

2.1. Soft Thresholding

In [7] Donoho proposed a non-linear method for reconstruction of an unknown signal from noisy measurements. The method is based on shrinkage or thresholding in the orthogonal wavelet domain. If the signal of interest, $\tilde{x}$, has been corrupted by measurement noise (or any other noise), then the signal $\tilde{y}$ is obtained as

$$\tilde{y} = \tilde{x} + \sigma\tilde{e}$$

where $\tilde{e}$ is unit-variance, zero-mean Gaussian white noise and σ is the noise level. The recovery of the unknown signal, $\tilde{x}$, such that the mean square error between the estimate $\hat{\tilde{x}}$ of $\tilde{x}$ and $\tilde{x}$ itself, $\frac{1}{N}\mathrm{E}\left[\|\hat{\tilde{x}} - \tilde{x}\|\right]$, is optimized, can simply be done by thresholding in the wavelet domain. This method was extended to SAR images in [1] and can be described in three steps:

1. Logarithmically transform the SAR image to obtain, $\tilde{z}$. Then apply the orthogonal DWT to get the wavelet coefficients corresponding to the noise data, $\tilde{y}$.

2. Choose a threshold $t = \gamma\sigma$ (where γ is a constant to be chosen) and apply the soft thresholding

$$f(\tilde{y}) = \begin{cases} \tilde{y} - t & \text{for } \tilde{y} > t \\ 0 & \text{for } |\tilde{y}| \le t \\ \tilde{y} + t & \text{for } \tilde{y} < -t \end{cases}$$

   to obtain the enhanced wavelets coefficients, $\hat{\tilde{y}}$.

3. Apply the inverse orthogonal DWT and the exponential transformation to get the denoised signal, $\hat{x}$.

2.2. Adaptive Sigmoid Thresholding

In [8] a continuous function was introduced for image enhancement. The function is based on the sigmoid function, similar to the activation function commonly used in neural networks. For an input image, $\tilde{y}$, with maximum absolute amplitude, $\tilde{y}_{\max}$, the image range $[-\tilde{y}_{\max}, \tilde{y}_{\max}]$ is mapped onto the interval $[-1, 1]$ with the function $f(\tilde{y})$ given by

$$f(\tilde{y}) = a\,\tilde{y}_{\max}\left[\mathrm{sigmoid}\left(c\left(\frac{\tilde{y}}{\tilde{y}_{\max}} - b\right)\right) - \mathrm{sigmoid}\left(-c\left(\frac{\tilde{y}}{\tilde{y}_{\max}} - b\right)\right)\right]$$

where

$$a = \frac{1}{\mathrm{sigmoid}\,(c\,(1-b)) - \mathrm{sigmoid}\,(-c\,(1-b))}$$

and $\mathrm{sigmoid}(\tilde{y})$ is defined by

$$\mathrm{sigmoid}(\tilde{y}) = \frac{1}{1 + \exp\,(-\tilde{y})}.$$

Because of the normalization, the transformation parameters, a, b, and c can be set independently of the dynamic range of the input image.

Here we propose an adaptive denoising method based on this function. It is described below:

1. Logarithmically transform the SAR image to obtain, $\tilde{z}$. Then apply the orthogonal DWT to get the wavelet coefficients corresponding to the noise data $\tilde{y}$.

2. Choose the parameters $c = \gamma_1\sigma$ and $b = \gamma_2\sigma/\tilde{y}_{\max}$ (γ_1 and γ_2 are constants to be chosen) where $\tilde{y}_{\max}$ is the maximum absolute amplitude value of subband-images for the DWT multiresolution representation. Apply the non-linear function $f(\tilde{y})$ from above.

3. Apply the inverse orthogonal DWT and the exponential transformation to get the denoised signal, $\hat{x}$.

2.3. Lee Filtering

For the (enhanced) Lee filter, the multiplicative model of the SAR image is at first approximated by a linear model. Then the minimum mean square error criterion is applied to this linear model. Following [2], the speckle reduction filter can be formulated as

$$\hat{x} = \begin{cases} \bar{z} & \text{for } C_z \le C_e \\ zw + \bar{z}(1-w) & \text{for } C_e < C_z < C_{\max} \\ z & \text{for } C_z \ge C_{\max} \end{cases}$$

where

$$w = \exp\left[-k(C_z - C_e)/(C_{\max} - C_z)\right]$$

is the weighting function and $\bar{z}$ is the mean of z. The variation coefficients of the image and the noise (speckle) are given by

$$C_z = \frac{\sigma_z}{\bar{z}}, \quad C_e = \frac{\sigma}{\bar{e}}$$

respectively, and $C_{\max} = \sqrt{3}$ for single look SAR image.

We propose applying the (enhanced) Lee filter on the subband-images in the wavelet domain. The method can be described as follows:

1. Apply the orthogonal DWT to get the wavelet coefficients corresponding to the noise data, y.

2. Choose the variation parameters $C_e = \gamma_1\sigma$, $C_{\max} = \gamma_2\sigma$ (where γ_1 and γ_2 are constants to be chosen). Calculate the variation coefficients, $C_y = \sigma_y$'s, for each subband-image for the DWT multiresolution representation. For these parameters apply the (enhanced) Lee filter to each subband-image to obtain enhanced wavelets coefficients, $\hat{y}$.

3. Apply the inverse orthogonal DWT to get the denoised image, $\hat{x}$.

3. EXPERIMENTAL RESULTS

In the experiments we applied the three denoising methods described in the previous section to a single look SAR image which is a 256 × 256, 256-gray-scale image. There are several parameters that need to be chosen for the denoising methods. It is needed to choose the type of wavelet to be used, the length of the wavelet filters, and the number of wavelet decomposition levels. In all our experiments we used a Daubechies orthogonal wavelet [6] along with 4-tap wavelet filters (i.e., D_4). A 4-level wavelet-decomposition was used for all the denoising methods. The thresholding coefficients for the denoising methods were chosen as: (i) $t = 1.2\sigma$ for the soft-thresholding method; (ii) $\gamma_1 = \gamma_2 = 10$ for the sigmoid thresholding method; and (ii) $C_e = 1.6\sigma$, $C_{\max} = 2.0\sigma$, and C_y was calculated using a 3 × 3 window for Lee filtering in the wavelet domain. The speckle phenomena is clearly visible in the original image (Figure 1) and greatly removed in the denoised images in Figures 2-4.

4. CONCLUSIONS

This paper developed methods for speckle reduction and enhancement of SAR images in the wavelet domain. The methods can significantly reduce the speckle while preserving the resolution of the original SAR image. Cleaner images should improve classification and recognition.

5. REFERENCES

[1] H. Guo, J.E. Odegard, M. Lang, R.A. Gopinath, I. Selesnick and C.S. Burrus, "Wavelet based speckle reduction with application to SAR based ATD/R," in *Proc. IEEE Int. Conf. Image Processing*, vol. 1, pp. 75-79, Austin, TX, Nov. 1994.

[2] A. Lopes, R. Touzi, and E. Nezary, "Adaptive speckle filters and scene heterogeneity," *IEEE Trans. Geosci. Remote Sensing*, vol. GE-28, pp. 992-1000, Nov. 1990.

[3] J.S. Lee, "Digital image enhancement and noise filtering by use of local statistics," *IEEE Trans. Pattern Anal. Machine Intell.*, vol. PAMI-2, pp. 165-168, Mar. 1980.

[4] Z. Shi and K.B. Fung, "A comparison of digital speckle filters," in *Proc. IEEE IGARSS'94*, vol. IV, pp. 2129-2133, Aug. 1994.

[5] H.H. Arsenault and G. April, "Properties of speckle intergrated with a finite aperture and logarithmically transformed," *J. Opt. Sco. Am.*, vol. 66, pp. 1160-1163, Nov. 1976.

[6] I. Daubechies, *Ten Lecture on Wavelets*, SIAM, USA, 1992.

[7] D.L. Donoho, "De-noising by soft-thresholding," *IEEE Trans. Inform. Theory.*, vol. IT-41, pp. 613-627, May 1995.

[8] A.F. Lain, S. Schuler, J. Fan, and W. Huda "Mammographic feature enhancement by multiscale analysis," *IEEE Trans. Medical Imaging*, vol. 13, pp. 725-735, Dec. 1994.



Figure 1: Original SAR image.

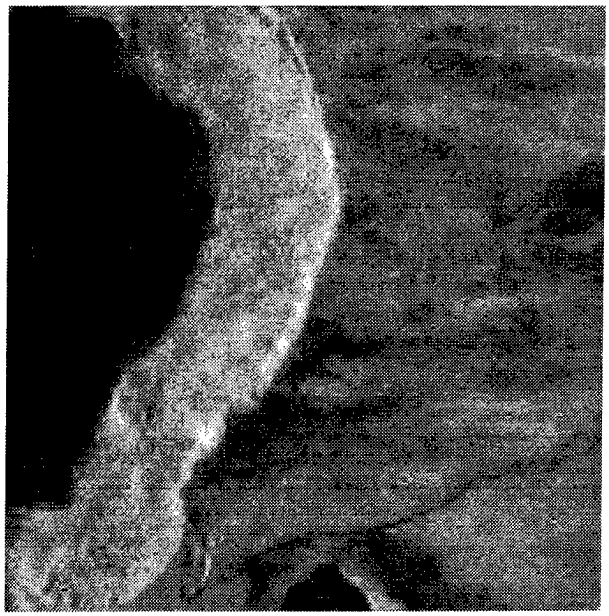


Figure 3: Denoised SAR image with sigmoid thresholding $\gamma_1 = \gamma_2 = 10$ for D_4 4-level filter.

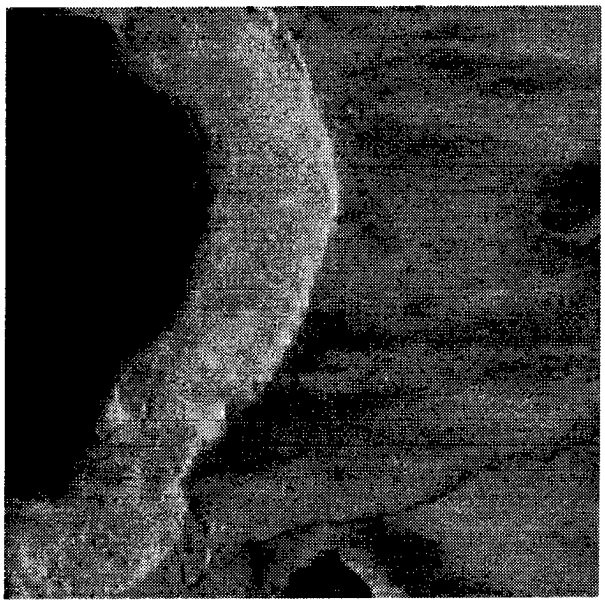


Figure 2: Denoised SAR image with soft-thresholding $t = 1.8\sigma$ for D_4 4-level filter.

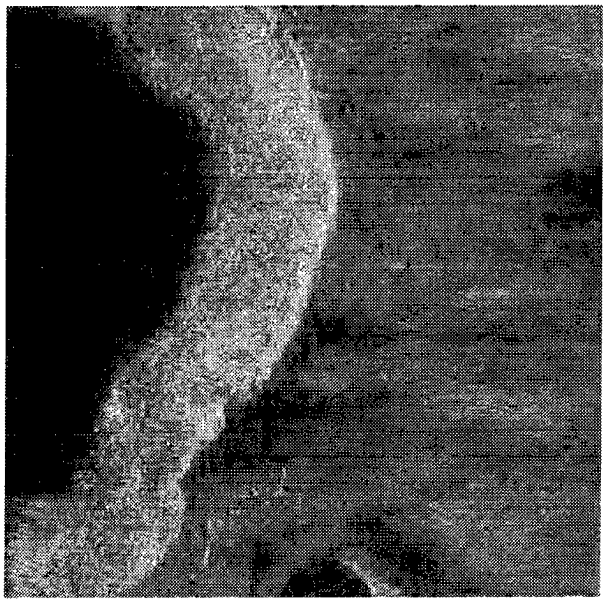


Figure 4: Denoised SAR image with Lee filtering in the wavelet domain with $C_e = 1.6\sigma$ and $C_{\max} = 2.0\sigma$ for D_4 4-level filter.

Adaptive Filtering Algorithms for SAR Speckle Reduction

Y.H. Lu, S.Y. Tan, T.S. Yeo, W.E. Ng, I. Lim and C.B. Zhang
Radar and Signal Processing Laboratory
Department of Electrical Engineering
National University of Singapore
10 Kent Ridge Crescent , Singapore 119260
Tel. : (65)7726471, Fax. (65)7791103
Email: eleluyh@leonis.nus.sg

I. ABSTRACT

Speckle noise in synthetic aperture radar (SAR) images reduces target feature detection. Two of the better known post-processing speckle suppression filters are the Lee (1986) and Kuan filter (1987). In this paper, we present modifications that have been made to the Lee and Kuan filters, such that there is an improvement in speckle suppression in regions of large back-scattering variations. Improvement over the original algorithms are illustrated using SEASAT images of Flevoland (Netherlands). Quantitative measures of performance for various types simulated terrain will also be presented.

II. INTRODUCTION

Many adaptive speckle reduction techniques developed in recent years make use of homomorphic transformation [1] and gamma maximum *a priori* probability (MAP) [2]. Examples include the Frost [3], Lee [4] and Kuan [5] filters. Adaptive linear filters, based on image properties, assume a multiplicative speckle model and make use of local statistics. It has been accepted that while some of these filters display superior performance in smoothing speckle in homogeneous areas, others give better performance at preserving features *e.g.* edges. In this study, the Lee and Kuan algorithms are modified in an attempt to bridge these two areas of concern.

III. SAR SPECKLED IMAGE MODEL

It is well established that speckle manifests itself in the form of multiplicative noise, characterized by a Rayleigh probability density function of image magnitude [6].

Let $z_{i,j}$ be the amplitude of an observed image pixel and $x_{i,j}$ be the noise-free image pixel to be recovered. With the multiplicative noise model,

$$z_{i,j} = x_{i,j}\, v_{i,j} \tag{1}$$

in which $v_{i,j}$ represents the multiplicative noise with unit mean and standard deviation σ_v (σ_v is independent of $x_{i,j}$.). To simplify notation, subscripts i, j will be omitted henceforth.

IV. THE LEE FILTER

Lee adopted the additive noise filter to multiplicative noise by transforming (1) into the sum of signal and an additive noise (independent of signal) via linear approximation. From the multiplicative noise model, the *a priori* mean $\bar{x}$ and variance var(x) of x can be estimated *in terms of* $\bar{z}$ and var(z), which are in turn approximated by the local mean and variance of the speckle-corrupted image. Using first-order Taylor expansion about $(\bar{x}, \bar{v})$, Lee estimated x by minimizing the mean square error (MMSE) of (3):

$$\tilde{x} = \bar{x} + k(z - \bar{x}) \tag{2}$$

$$\xi = \mathrm{E}(\mathrm{x} - \tilde{\mathrm{x}})^2 \tag{3}$$

The factor k for the Lee algorithm is:

$$k = \frac{\mathrm{var}(x)}{\mathrm{var}(x) + \sigma_v^2 \bar{x}^2} \tag{4}$$

This algorithm is effective in flat regions as var(x) ≈ 0, thus $\tilde{x} \approx \bar{x}$ (neighborhood average). In regions of high contrast, var(x) is large compared with $\sigma_v^2 \bar{x}^2$, as such $\tilde{x} \approx z$ (retains pixel value). Consequently, speckle near high contrast edges and objects is not suppressed.

A. *Second Order Taylor Expansion*

In our work, we extended the Taylor expansion to second-order. The new factor obtained after MMSE becomes:

$$k' = \frac{\mathrm{var}(x)}{\mathrm{var}(x)(1+\sigma_v^2) + \bar{x}^2\sigma_v^2}$$

$$= k\left(\frac{1}{1+k\sigma_v^2}\right) \approx k(1 - k\sigma_v^2) \tag{5}$$

Although better performance can be achieved using the 2nd order Lee filter, we find that the new factor k' is still unable to achieve the desired suppression near edges.

B. *Modified Lee algorithm*

Empirically, we derive a new factor based on the idea of adaptively modulating the factor k when $(z - \bar{x})$ is large:

$$k_e = \frac{\mathrm{var}(x)}{\mathrm{var}(x) + \bar{x}^2\sigma_v^2}\left(1 - \frac{|z - \bar{x}|}{(z - \bar{x})|_{\max}}\right) = k \cdot w_e \tag{6}$$

$$\tilde{x} = \bar{x} + k w_e (z - \bar{x}) \tag{7}$$

When $(z - \bar{x})$ is large, w_e becomes small to allow $\tilde{x}$ to take on the value of $\bar{x}$. On the other hand, when variation is small *i.e.* $(z - \bar{x}) \approx 0$, (7) reduces to the original (2). Experimental results show that this modified algorithm is better able to suppress speckle in regions of large back-scattering variations.

0-7803-3068-4/96$5.00©1996 IEEE

V. THE KUAN FILTER

The Kuan filter was also developed from the additive noise filter. Correlation properties of speckle were used and a local MMSE (LMMSE) filter using local statistics was proposed. For easy numerical computation, LMMSE and MAP speckle filters were also presented for cases when pixel-to-pixel correlation can be neglected. This occurs when the sampling interval of the speckled intensity image is of the order of the correlation length of speckle (image resolution). The image samples can then be assumed to be independent.

A. Analysis of the Kuan filter

Kuan assumed an image model which has nonstationary mean and variance (NMNV). As in (1), a multiplicative speckle intensity model was used. Assuming no correlation, the LLMMSE filter reduces to a set of scalar equations and the simplified Kuan filter becomes:

$$\tilde{x}_{\text{LLMMSE}} = \bar{x} + \frac{\text{var}(x)}{\text{var}(x) + \bar{x}^2 + \text{var}(x)}(z - \bar{x}) \qquad (8)$$

where $\bar{x}$ is the local mean estimate of x, and var(x) is the local variance estimate of x.

B. Modified Kuan filter

Recalling the k' factor in our second-order extension of the Lee filter and assuming that $\sigma_v^2 \rangle\rangle \bar{v}^2$, we are able to derive a modified factor that resembles the original Kuan filter.

$$k' = \frac{\text{var}(x)}{\text{var}(x) + \bar{x}^2\sigma_v^2 + \text{var}(x)\sigma_v^2}$$

$$= \frac{\text{var}(x)}{\text{var}(x) + \sigma_v^2\left(\frac{\text{var}(z) + \bar{z}^2}{\bar{v}^2 + \sigma_v^2}\right)}$$

$$\approx \frac{\text{var}(x)}{\text{var}(x) + \bar{x}^2 + \text{var}(z)} = k_{\text{modified, kuan}} \qquad (9)$$

This new factor incorporates a var(z) in place of a var(x) in the original Kuan filter. As var(z) ≥ var(x), the ability of the modified Kuan filter in suppressing speckle in regions of large variation will be greater, with $k_{\text{modified,kuan}} \leq k_{\text{kuan}}$.

VI. EVALUATION OF THE FILTERS

As discussed previously, higher speckle smoothing may be achieved at the expense of feature fidelity. Filters should obtain minimum variance estimation and ensure good spatial and radiometric resolution. In this section, we attempt to quantify and compare the performance of the various filters along with the non-adaptive box (local average) filter.

A. SEASAT SAR data

We first carry out a visual evaluation of the filters using a SEASAT image of Flevoland, characterized by patches of varying back-scattering terrain. From Fig. 1, we see that the original image is badly corrupted by speckle. Fig. 2 and 3 show the results after original and modified Lee filtering respectively. We see that the modified algorithm is better able to suppress speckle without losing significant feature characteristics. Kuan filtering as depicted in Fig. 4 loses out in spatial resolution when compared with the Lee algorithms. However, after modification, it is able to reach a better compromise in terms of speckle suppression and spatial resolution. See Fig. (5).

B. Simulated smooth varying terrain

An important feature of the improved filters is the ability to perform in areas of high back-scattering variations. A smooth varying terrain is simulated to evaluate this property, the results of which are tabulated in Table 1. Results show that both modified filters are able to give lower mean error as compared to the original algorithms.

Table 1: Resultant mean error for the various filters.

Image	$E(\lvert x - \tilde{x}\rvert)$
Box filter	8.7552
Lee filter	9.8969
Lee (modified) filter	9.5282
Kuan filter	8.7558
Kuan (modified) filter	8.7550

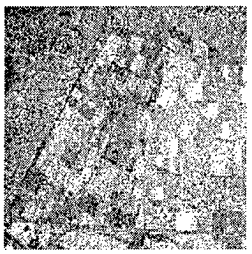


Fig. 1: Original Image

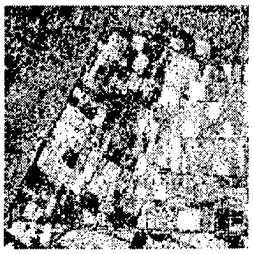


Fig. 2: Lee Filter



Fig. 3: Modified Lee



Fig. 4: Kuan Filter



Fig. 5: Modified Kuan

C. *Simulated homogeneous terrain*

The four filters are applied to the image of a simulated homogeneous terrain and compared using ENL (effective number of looks, ENL = $\bar{x}^2 / \sigma_x^2$). Fig. 6 shows the histograms of the image after application of the various filters. Table 2 gives the comparative ENL.

We see that the Lee filter gives the lowest ENL as compared to the Kuan and modified filters. Performance of the modified Kuan filter approaches the box filter, which has been shown to give the best performance in speckle suppression for homogenous terrain.

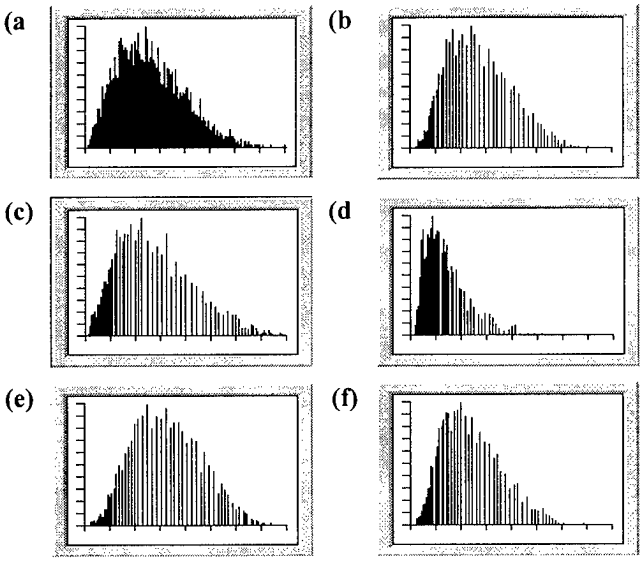


Fig. 6 : Histogram of a) Original 1-look, b) Box filter, c) Lee filter, d) Modified Lee, e) Kuan filter, f) Modified Kuan

Table 2 : Equivalent number of looks (ENL) by the filters on a 1-look simulated image. Filtering is performed using a 5 by 5 window.

Image	ENL
Original simulated 1-look	3.572
Box filter	61.718
Lee filter	37.058
Lee (modified) filter	46.530
Kuan filter	56.801
Kuan (modified) filter	59.351

D. *Simulated flat patterned feature terrain*

Evaluation is next carried out using the patterned feature (checkered box) terrain as developed in [7]. The filters are applied again and the contrast at the sharp edges are tabulated in Table 2.

Table 3 : Averaged contrast at sharp edges for the various filters.

Simulated 1-look Image	Averaged contrast at sharp edges (Gray Levels of 256)
Box filter	22.92
Lee filter	25.34
Lee (modified) filter	24.61
Kuan filter	23.78
Kuan (modified) filter	23.89

Results show that the modified Lee gives a lower contrast at edges as compared to the original algorithm. As for the modified Kuan algorithm, contrast is improved.

VII. CONCLUSION

A 2nd order extension of the adaptive Lee filter has been derived and we have used it to make modfications to the Kuan filter. Modifications have also been made to the Lee using empirical reasoning. Results show that these modified adaptive algorithms display excellent speckle suppression ability. Evaluation has been carried out using both simulated images as well as an actual SEASAT SAR image. We have shown that the modified filters are able to give better suppression in homogenous terrain. As for regions of large terrain back-scattering variations, better compromises between speckle suppression ability and feature fidelity have been achieved. The modified algorithms are also conceptually simple and computationally efficient.

VIII. REFERENCES

[1] H.H. Arsenault and M. Levesque, "Combined homomorphic and local-statistics processing for restoration of images degraded by signal-dependent noise," *Appl. Opt.*, vol. 23, no. 6, March 1984.

[2] E. Nerzy et. al. , "Detection of structural and textural features for SAR images filtering," *Proc of IGARSS '91*, pp. 2169-2172, June 1991.

[3] V.S. Frost, J.A. Stiles, K.S. Shanmugan, and J.C. Holtzman, "A model for radar images and its application to adaptive digital filtering for multiplicative noise," *IEEE Trans. Patt. Analy. and Mach. Intell.*, PAMI-4, pp. 157-166, Mar 1982.

[4] J.S. Lee, , "Speckle suppression and analysis for synthetic aperture radar images," *Opt. Eng.*, vol. 20, pp. 636-643, May 1986.

[5] D.T. Kuan and Alexander A. Sawchuk, "Adaptive restoration of images with speckle," *IEEE Trans. Acoustics, Speech and Sig. Proc.*, vol. ASSP-35, pp. 373-383, March 1987.

[6] J.W. Goodman, "Some fundamental properties of speckle," *J. Opt. Soc. Amer.*, vol. 66, pp. 1145-1149, Nov. 1976.

[7] Y.H. Lu, P.S. Kooi, T.S. Yeo, W.E. Ng, C.B. Zhang, "A new speckle SAR data source for examination of radiometric isolation of SAR imagery," *Sym. Int. Retrieval of Bio- and Geo. parameters for SAR data for land appl.*, p. 91.

An eolian and marine phenomena characterization in dune sectors by image processing.

Yves Delignon*, Loïc Moreau*, Philippe Clabaut**

*Ecole Nouvelle d'Ingénieurs en Communication, rue Marconi, 59650 Villeneuve d'Ascq-France
** 14 rue Paul Doumer, 59110 La Madeleine-France

Abstract -- The North of the French coastline is partly subject to coastal erosion that is due to the sandy coast retreat. Many dune sectors are moving because of the wind dynamics due to the small quantity of vegetation on their surface. In order to analyze and control these phenomena that endanger the littoral and its tourist activities, several scientific programs have been initialized whose a part uses the aerial remote sensing images.
In this paper, we deal with the coastal environment analysis by image processing. The algorithm recognizes, localizes and quantifies the different components of the littoral such as the sand, the dune with lime grass and the bush vegetation. By working with an image set representing the North of France and dating from the sixties to our days, the algorithm provides the evolution thematic map of the site.
From an algorithmic viewpoint, the thematic map is obtained by an unsupervised method of classification which is independent of the ambient luminosity, of the sensor adjustment, of its altitude and of its orientation. This method belongs to the family of SEM algorithms and uses the Bayesian strategy minimizing the error of classification.
Our algorithms have been applied to a set of images representing the region of Wissant (Pas de Calais - France). As result, we analyze from the thematic map the speed of the coast line retreat, the movement of the dunes on the urban zones and the impact of the plantation program on the coastal environment.

I. Coastal erosion

On a world scale, coasts have a tendency to erosion: a report realized for the International Geographical [1] shows that more than 70% of sandy coasts have been eroded during the last decades, against 20 to 30% of stable and less of 10% prograding; comparable results are obtained for French coast. The Nord-Pas de Calais coast presents this general characteristic as well. The coast is eroding at a speed of 1m/year on approximately 3/4 of its length, reaching locally 7m/year at the center of the Wissant Bay. Cliffs of Boulonnais area retreat at a speed of 0.2 to 0.5 m/year [2]. These phenomena consequences are a loss of ground of high ecological, recreational and scientific interest. Damages are also caused to sea-walls or to some urban zones (Platier d'Oye, Wissant..).
Since several decades, the phenomenon has leaded to realize many coastal defenses. They fill 51 km of coast, with 21 km of harbors piers. 2/3 of the regional coast (66 km of dunes, 24 km of cliffs and 7 km of estuaries) remain natural [3].
Recent studies have been initiated in order to understand sedimentary mechanisms between dunes, beaches and the nearshore area in areas of significant extension [4]. Indeed, the phenomenon of erosion indicates a sedimentary imbalance between dunes, beaches and the small marine area. Relevant factors, multiples and interactive, are linked to the global context (sea - level variations) of the sea, weakness of current sedimentary contributions). Local parameters are natural (tidal current, wind, swell, dune vegetation), or human (houses, tourist activities).

II. Characterization of the phenomena by image processing

We propose an image segmentation algorithm for the study of the coastal area evolution. The aim of segmentation is to split the image in thematic regions [5] (lime-grass dune, black dune of brushwood, non-vegetalized dune...). Applied to a set of aerial photography images, segmentation provides a dynamic mapping of these topics.

II.1. Models for the images

When considering statistical segmentation of images authors generally suppose the existence of two random fields : the field of "classes" $\xi = \{ \xi_S : s \in S \}$ and the field of measurements $X = \{ X_S : s \in S \}$. These two fields are supposed homogeneous and compound of independent random variables. Each ξ_S takes its value in a finite set $\Omega = \{\omega_1, \omega_2, \omega_3\}$ of classes where ω_1 = 'sand', ω_2 = 'dune with lime grass' and ω_3 = 'bush vegetation'. So the problem of segmentation is the problem of the estimation of an ignored realization of ξ from an observed realization of X [6].
The hierarchical model adopts this proceeding, it consists of two random fields. One governs the grouping of the pixels, called region process and the other consists of 3 random fields which represent the noise degraded appearance of the nature of the classes. These three random fields modelize class inherent statistical properties and system inherent noise. We have chosen Kelly and Derin's image model for two reasons.

0-7803-3068-4/96$5.00©1996 IEEE

Firstly, this model clearly points out the idea that the "observed noise" is not only a worthless disturbance, but carries information on the nature of the ground. Secondly, the hierarchical character fits well to Bayesian decision theory and this model allows quite easily the generation of a great number of synthesized images.

Region process : The region process is responsible for the distribution of pixels within the different classes. An image consists of a few different region types.
Since the region process is assumed homogeneous and independent, its distribution is entirely defined by the probabilities $\Pi_1 = P_\xi(\omega_1)$, $\Pi_2 = P_\xi(\omega_2)$ and $\Pi_3 = P_\xi(\omega_3)$.

Noise process : This field cannot be observed, so the noise process modelizes the marginal statistics of each type of observed nature. In case of optical data, the distributions of X conditional to $\xi = \omega_i$ are normal $N(\mu_i,\sigma_i^2)$. The parameters μ_i,σ_i^2 are different from a class to another and also on the acquisition moment. Indeed the (μ_i,σ_i^2) parameters are function of the ambient luminosity and the vegetation growth at the acquisition.
Thus, the distribution of (ξ,X) is defined by P_ξ, the distribution of ξ, and the family P_X^ξ of distribution of X conditional to $\xi = \omega$.

II.2. SEM ALGORITHM

We explain in this paragraph the classical SEM algorithm. Its aim is to estimate all parameters defining the components of the distribution mixture.

Initialization : $P^{t=0}$ and parameters defining $f^{t=0}$ are chosen at random.

Step S : For each x_i we draw a realization $e^t(x_i)$ from the set E with regards to the conditional distribution knowing $X_i = x_i$. We obtain a new partition $(Q_1,...,Q_K)^t$ of the image in K classes with the help of the couple $(P_k,f^k)^t$.

Step M : Parameters defining f_k^{t+1} are estimated in the selection Q_k^t by the classic moment method. We estimate P_k^{t+1} by : $P_k^{t+1} = \dfrac{\text{card}(Q_k)}{\text{card}(S)}$

Step E :We compute the distribution $P_k^{t+1}(\omega_i)$ and return to step S.

II.3. BAYESIAN STRATEGY

The density of the distribution of X conditional to $\xi = \omega$ and the distribution of the classes X define the distribution of (ξ,X) and therefore the conditional distribution of ξ knowing that $X = x$, which we denote P^x. The Bayesian rule r_g for a 0-1 cost function is then defined by :

$$r_g(x) : \hat{\xi} \Leftrightarrow P^x\left[\hat{\xi}\right] = \sup_\varepsilon P^x[\varepsilon]$$

it can be also expressed as follow :

$$r_g(x) : \hat{\xi} \Leftrightarrow P_{\hat{\xi}}.f_X^{\hat{\xi}} = \sup_\varepsilon P_\varepsilon.f_X^\varepsilon$$

The functions are called "discriminating".

III. RESULTS

Applied on three aerial photographs of French National Geographical Institute (IGN) of Wissant West surroundings in 1963, 1977 and 1989 (scale : 1/20 000), this site has been chosen for two reasons: the importance of the erosion and the knowledge acquired on its evolution in the framework of several in-situ studies [7,8].
After a preliminary processing (the scale and the orientation of the three plugs of views are adjusted), these images are segmented according to the described algorithm. The knowledge acquired by the in-situ data are therefore materialized and quantified by the superposition of the three segmented images.
Fig. 1, 2 represent respectively the resulting images from year 1977 and 1989. The main points are the following:
- the recession of the line of coast to the South due to the marine erosion: whereas the front of dune was located ahead of military blockhouses, it was in 1989 behind them.
- under the eolian action, the dunes move towards South and East in 1963 and 1977. The mobile sands of the dune d'aval invade the wooded zone that separates it from the urban zone, and the marsh of Tardinghen (Fig. 3). This phenomenon is the consequence of the absence of dune vegetation. In 1989, the dune is vegetalized, thanks to the Pas de Calais region council (espace naturel Régional) and the Conservatoire du Littoral.
On others sites of the regional coast, the segmented images point out the progressive colonization of the dune by vegetation and local degradation of the vegetation due to the important pedestrian traffic.
Future developments will be proposed dealing with the coastal erosion for better urban zone management, and with the dynamic mapping of littoral.

BIBLIOGRAPHY

[1] E.C.F Bird, "Coastlines changes, a global review", Wiley, Chichester, 1985.

[2] P.M. Clique, "Catalogue sédimentologiques sur le littoral de Wissant (site des caps, Boulonnais)", Annales de la Société Géologique du Nord, tCV, p. 169-178.

[3] F. Victor, "Le coût de dix années de protection contre la mer en Nord-Pas de Calais", Erosion côtière symposium, Obs. de l'Env. du Litt et Marin, Boulogne sur mer, 1994 .

[4] A. Bryche and al, "The French and Belgian coast from Dunkirk to De Panne : a case study of trans border cooperation ... ", Am Soc of Civil Eng , pp. 245-257, 1993 .

[5] L. Moreau, Y. Delignon, P. Clabaut, "Coastline evolution highlighting using image segmentation", in LARUS, December 1995, France

[6] A. Marzouki, Y. Delignon, W. Pieczynski, "Segmentation of SAR images", OCEANS'94 symposium, Brest, 13-16 September 94.

[7] P. Clabaut, H. Chamley, "Observations sedimentologiques sur le littoral de Wissant (Site des caps boulonnais)", Annales de la societe de geologie du Nord, t.CV, pp. 169-178, 1986

[8] C. Augris, P. Clabaut, O. Vicaire, "Le domaine marin du Nord Pas de Calais (co-édition IFREMER et Région Nord Pas de Calais).

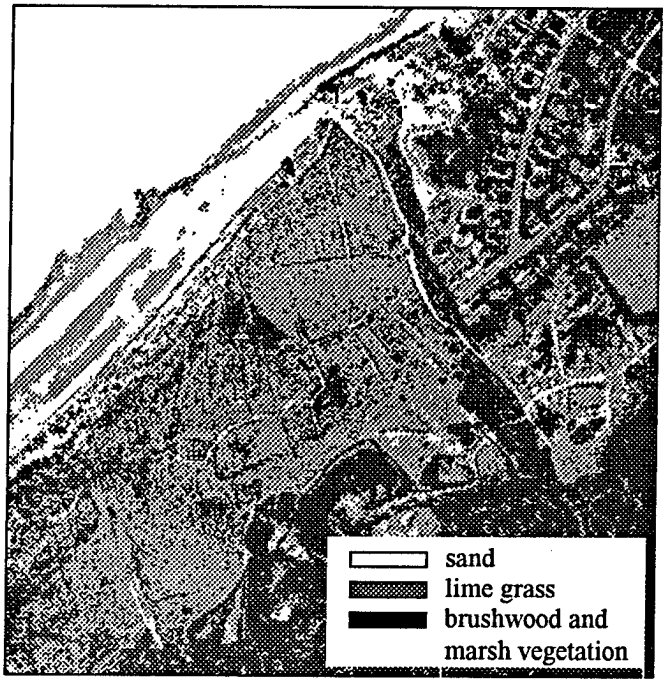


Figure 2: Segmented image (1989)



Figure 1: Segmented image (1977)

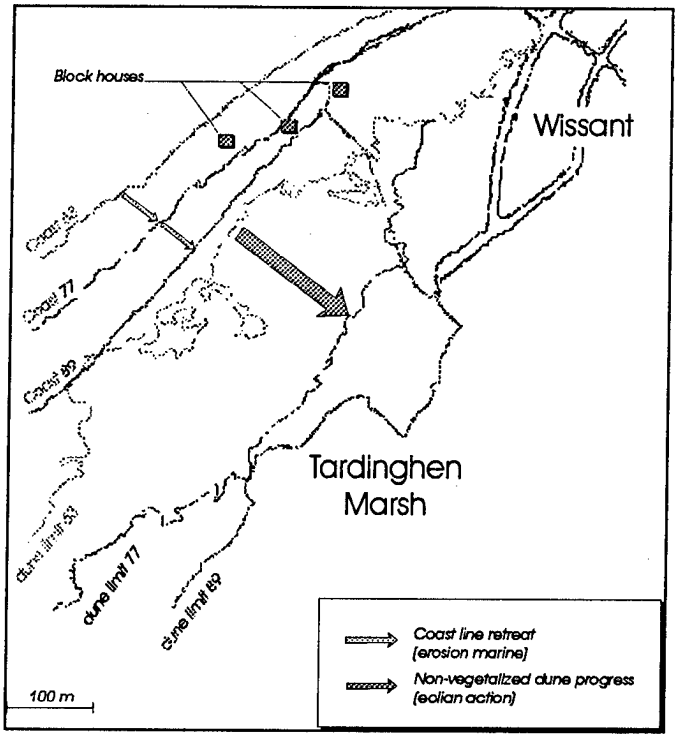


Figure 3: Resulting dynamic map (63, 77, 89)

Retrieval of Arctic Surface Conditions and Cloud Properties from AVHRR Data: A Time Series for the Beaufort Sea

Walter Meier*, James Maslanik*, Jeffrey Key†, and Charles Fowler*

*University of Colorado, Campus Box 431, Boulder, CO, 80309
Ph: (303) 492-1241; FAX: (303) 492-2825; email: walt@colorado.edu
†Boston University, Dept. of Geography, 675 Commonwealth Ave., Boston, MA 02215
Ph: (617) 353-2841; FAX: (617) 353-8399; email: jkey@bu.edu

Abstract -- Generation of an integrated set of remotely-sensed products for sea-ice monitoring and modeling is tested using AVHHR data of the Arctic Beaufort Sea region for June 1992 through July 1993. The resulting product set includes a suite of parameters applicable to energy balance calculations and monitoring of detailed sea ice processes. Using calibrated and navigated AVHRR 1.1 km imagery, cloud fraction, ice surface temperature, surface albedo, downwelling radiative fluxes, ice motion vectors, and cloud properties such as optical depth, phase and droplet effective radius are estimated. Here, we describe the processing strategy and use these products to summarize conditions during the study period.

INTRODUCTION

The polar regions play an important role in the global climate due in part to the effects of sea ice cover on surface albedo and heat transfer. A combination of observations, modeling, and remote sensing is needed to gain a better understanding of sea ice variability and the ice-climate system. In particular, model parameterizations and validation can benefit from uniform, gridded data products that are coincident in time and cover large areas for relatively long time periods. Ideally, these data products should describe the distribution of the ice cover and the energy balance components that affect growth and melt of the ice pack [1]. Advanced Very High Resolution Radiometer (AVHRR) data is capable of providing many of these parameters over a time span sufficient to study interannual variability.

The objective of this work is to demonstrate the combination of fully-automated algorithms and simple parameterizations to produce a suite of products suitable for monitoring and modeling the Arctic ice-climate system. These products include cloud fraction, ice surface temperature and albedo, downwelling radiative fluxes, ice motion vectors, and cloud properties such as optical depth, phase and droplet effective radius for the Beaufort Sea region in the Arctic Ocean.

STUDY AREA AND AVHRR PRE-PROCESSING

This study uses NOAA-11 AVHRR 1.1 High Resolution Picture Transmission (HRPT) data acquired by the Canadian Atmospheric Environment Service (AES) at their Edmonton, Alberta receiving station. The region studied, from 69° N to 80° N latitude and 120° W to 150° W longitude, is defined by the Arctic Ocean coverage available within the Edmonton station mask. This 1.5 million square kilometer area includes the Beaufort Sea and portions of the Canadian Arctic Basin.

For this study, AVHRR images were collected from June 12, 1992 to August 4, 1993 with a two-month data gap from August 14, 1992 to October 11, 1992 and other smaller gaps. Overall, imagery for 293 days over a 412 day period were purchased from AES. Since the NOAA satellites are in sun-synchronous orbits, each day's data was obtained at approximately the same time, between 12:47 pm and 3:30 pm local time. Five channels are retrieved from the processing. Two visible channels, hereafter referred to as Channel 1 and Channel 2, are centered at approximately 0.6 and 0.9 microns. Thermal channels are at 3.8 microns (Channel 3), 11.0 microns (Channel 4), and 12.0 microns (Channel 5). The AVHRR images have a nominal field of view of 1.1 km at nadir.

The initial processing of the data included calibration using NOAA-11 specific coefficients, and precise geolocation using an orbital ephemeris and ground control points. Channels 1 and 2 were calibrated using coefficients developed as part of the NOAA/NASA AVHRR Pathfinder Calibration Working Group. Non-linear calibrations obtained from NOAA were applied to Channels 3, 4, and 5.

The calibrated data were georeferenced to earth coordinates using an orbital ephemeris model with orbit and clock time corrections [2, 3] to yield sub-pixel registration accuracy. Satellite azimuth, satellite elevation, solar zenith and solar azimuth were calculated from the date and time of each pixel in the image and the ephemeris model. The result is a suite of once-per-day 16-bit, 1024 by 1024 pixel images, with 1.2 kilometer resolution per pixel, for each of the five AVHRR channels and the four angle files.

PRODUCT GENERATION

The basic processing sequence to generate the product suite from the calibrated and navigated AVHRR radiances involves: cloud detection and estimation of cloud properties; calculation of clear-sky surface temperature and broadband albedo; estimations of short and longwave fluxes; and ice motion calculations.

0-7803-3068-4/96$5.00©1996 IEEE

The cloud detection routine used here employs AVHRR channels 3, 4 and 5 to distinguish between clear and cloudy sky [4]. Separate procedures are used for daylight and polar night conditions. The daytime scheme defines channel 3 reflectances used as thresholds to detect clouds. The nighttime mask uses the difference between channel 4 and channel 5 brightness temperatures as cloud-detection thresholds.

Optical depth, effective radius, cloud phase and cloud top temperature and pressure are retrieved using the Cloud and Surface Parameter Retrieval (CASPR) software toolkit for AVHRR analysis [4]. CASPR combines a variety of parameterizations, model-derived lookup tables, and radiative transfer code to determine the cloud properties, as well as radiative fluxes.

The surface temperature algorithm is a function of channel 4 and 5 brightness temperatures and scan angle [5].

Top-of-the-atmosphere (TOA) measurements by AVHRR are converted to surface albedo through several steps. Calibrated channel 1 and channel 2 TOA values are corrected for sun-satellite-surface geometry dependence [6]. Then, narrow-band surface albedo is retrieved by correcting the TOA albedo for atmospheric attenuation [7]. Finally, the narrow-band values are converted to broadband albedo for clear and cloudy sky conditions individually.

To determine ice velocities, two-dimensional cross correlations are used to match feature locations between pairs of co-registered images typically separated by one to three days [8]. Vectors are filtered based on the local cross-correlation coefficient and correlation of individual vectors with neighboring vectors. The ice velocity is calculated by dividing the ice displacement in a pair of images by the time between the images.

RESULTS

The results of surface temperature, cloud fraction, and albedo are discussed here in terms of means summed over the entire model domain. Monthly average surface temperatures range from 233 K for January up to 273 K during the summer. These are within the expected ranges of values for this region and compare well with existing climatologies [9] and data sets [10] (Table 1) and other analyses of AVHRR-derived ice temperatures (e.g. [12]).

Monthly mean cloud fraction varies from 45% in April to near 80% in late summer and fall (Table 1). The AVHRR-derived cloud fractions lie between the observation-based climatology [9] and the International Satellite Cloud Climatology Project (ISCCP) fractions (an average of cloud fractions for 1984-1991). Relative to observations, both satellite-derived data sets tend to underestimate cloud amount in spring and summer, but the difference is much less pronounced in the AVHRR products generated here. As with the temperature data cited above, comparisons of remotely-sensed data from a single year with climatological data can only provide a general idea of the agreement among the data sets.

Albedo is also reasonably consistent with previous results (Table 1) with lower values in spring reflecting some inclusion of coastal ocean in the study area. The monthly average albedo is a high of 0.75 in April and then drops sharply to 0.45 by the summer.

The relatively high resolution of the AVHRR data provides considerable information on cloud distribution, morphology and cloud type. Though not included here, these cloud properties, as well as radiative fluxes, are consistent with the ranges of values expected in the Arctic.

	Surface Temperature (K)			Cloud Cover (%)			Albedo			Sensible Heat Flux (W/m2)		
	avhrr	E&C [9]	B&P [10]	avhrr	E&C [9]	isccp	avhrr	E&C [9]	Scha. [11]	avhrr	E&C [9]	L&R [12]
Jan	233	240	238	73	81	50	-	0.83	-	30	-2	10
Feb	242	240	235	77	78	60	-	0.83	-	24	-3	27
Mar	243	242	233	56	81	50	0.70	0.82	-	22	-3	21
Apr	254	250	247	45	71	41	0.75	0.81	-	30	-4	12
May	269	263	264	67	78	30	0.70	0.80	0.78	18	-2	-
Jun	273	272	271	59	83	30	0.51	0.80	0.71	1	3	15
Jul	272	273	273	50	85	39	0.43	0.45	0.56	-2	-5	15
Aug	272	272	269	74	81	43	0.44	0.46	0.53	7	-2	-
Sep	-	265	262	-	85	45	-	0.75	-	-	-3	20
Oct	249	254	248	74	89	50	-	0.78	-	30	1	23
Nov	241	246	244	77	78	48	-	0.80	-	31	1	33
Dec	236	243	241	72	78	55	-	0.82	-	27	-1	23

Table 1: AVHRR-derived parameters and comparison with model and observed values. (Comparison values estimated from figures in [9, 10, 11, 12]).

As noted earlier, ice transport is a key element controlling the evolution of the sea ice cover. Thus, it is useful to have ice motion information available in conjunction with the energy-budget related products described above. For the Beaufort series considered here, AVHRR provides useful long-term ice motion calculation, particularly as a complement to other ice motion detection schemes (buoys, SAR, etc.), and can provide detailed ice motion information where cloud cover permits [13].

EXAMPLES OF COMBINING MULTIPLE PARAMETERS

To demonstrate the utility of combining these various data types, we investigated the relationship between the AVHRR-derived albedo and skin temperature, and estimated sensible heat fluxes using AVHRR temperatures and passive microwave-derived (SSM/I) ice fractional coverage. For areas with at least 50% ice cover based on the SSM/I data, mean albedo in spring is 0.77 until skin temperatures reach about 265 K, at which point albedo decreases linearly at 0.046/degree. Climate models typically prescribe an albedo decrease beginning at 273 K, so the decrease observed here prior to melt warrants additional investigation.

Sensible heat fluxes were calculated using a simplified version of the strategy of [12], with the AVHRR temperature adjusted slightly to represent air temperatures, a fixed wind speed of 5 m/s, and fluxes estimated separately for open water (at 271.2 K) and ice fractional coverage as defined by the SSM/I data. The relatively large mean fluxes (Table 1; positive fluxes represent heat loss to the atmosphere) likely reflect the inclusion of thin ice in the open-water fraction estimated by SSM/I as well as the marginal ice zone character of some of the study area.

CONCLUSION

A year long AVHRR data set of the Beaufort Sea region has been processed, including calibration and georeferencing. The data set was then used in conjunction with several algorithms to calculate surface and cloud physical parameters, which show good agreement with previous model and observational values. This time series of a suite of polar variables should prove useful for a variety of studies, as demonstrated by the brief examples here. Work is underway to produce a multi-year time series of polar AVHRR products as part of the NASA Pathfinder effort.

ACKNOWLEDGMENTS

Thanks are due to AES and NSIDC for data. This work is funded by NASA's Mission to Planet Earth (MTPE) and the EOS POLES project.

REFERENCES

[1] Barry, R.G., M.C. Serreze, J.A. Maslanik, and R.H. Preller, The Arctic sea ice-climate system: Observations and modeling, Reviews of Geophysics, vol. 31, 4, pp. 397-422, 1993.

[2] Rosborough, G.W., Baldwin, D.G., and W.J. Emery, Precise AVHRR navigation, Transactions on Geoscience and Remote Sensing, vol. 32, pp. 644-657, 1995.

[3] Baldwin, D., and W.J. Emery, Spacecraft attitude variations of NOAA-11 inferred from AVHRR imagery, Int. J. Remote Sensing, vol. 16, 531-548, 1995.

[4] Key, J., The Cloud and Surface Parameter Retrieval (CASPR) System for Polar AVHRR: User's Guide, Version 1.0A, Cooperative Institute for Research in Environmental Sciences, University of Colorado, 71 pp., 1995.

[5] Key, J. and M. Haefliger, Arctic ice surface temperature retrieval from AVHRR thermal channels, Journal of Geophysical Research, vol. 97(D5), pp. 5885-5893, 1992.

[6] Taylor , V.R. and L.L. Stowe, Atlas of reflectance patterns for uniform earth and cloud surfaces (NIMBUS-7 ERB-61 days), NOAA Technical Report NESDIS 10, U.S. Department of Commerce, 66 pp., 1984.

[7] Koepke, P., Removal of atmospheric effects from AVHRR albedos, Journal of Applied Meteorology, vol. 28, pp. 1341-1348, 1989.

[8] Fowler, C.W., Ice Motion Derived from Satellite Remote Sensing with Application to Ice Studies in the Beaufort Sea, Doctoral Thesis, University of Colorado, June 1995.

[9] Ebert. E., and J. Curry, An intermediate one-dimensional thermodynamic sea ice model for investigating ice-atmosphere interactions, Journal of Geophysical Research, vol. 98 (C6), pp. 10085-10109, 1993.

[10] Banks, H.C., and E.N. Partanen, Meteorological observations, in Scientific Studies at Fletcher's Island, T-3, 1952-1955, vol. II, edited by V. Bushnell, pp. 1-49, 1959.

[11] Scharfen, G., R.G. Barry, D.A. Robinson, G. Kukla, and M.C. Serreze, Large-scale patterns of snow melt on Arctic sea ice mapped from meteorological satellite imagery, Annals of Glaciology, vol. 9, pp. 1-6, 1987.

[12] Lindsay, R.W., and D.A. Rothrock, Arctic sea ice surface temperature from AVHRR, Journal of Climate, vol. 7 (1), pp. 174-183, 1995.

[13] Fowler, C.A., J.A. Maslanik, W.J. Emery, Observed and simulated ice motion for an annual cycle in the Beaufort Sea, IGARSS '94, Pasadena, CA, pp. 1303-1305.

Evaluation of Remote Sensing Algorithms for the Retrieval of Optically-active Components in Turbid Natural Waters

Tiit Kutser[1], Alberto Blanco[2] and Helgi Arst[1]
1) Estonian Marine Institute, Lai 32, Tallinn, EE-0001, Estonia
Telephone: +372 2 451 968; Facsimile: +372 6 313 004; Email: tiit@phys.sea.ee
2) Department of Geophysics, University of Helsinki, Fabianinkatu 24a, Helsinki, Finland
Telephone: +358 0 191 22028; Facsimile: +358 0 191 23385; Email: alberto.blanco@helsinki.fi

Abstract -- A simple mathematical model is elaborated for estimation of chlorophyll, yellow substance and suspended matter concentrations in turbid coastal and inland waters from diffuse reflectance spectra of the water body measured using remote or underwater spectrometers. Measurements were carried out on the Baltic Sea, Estonian and Finnish lakes. Correlation between measured and estimated by means of model calculations concentrations of optically active components were calculated.

INTRODUCTION

Blue to green ratios or the same kind of spectral characteristics have been widely used in remote detection of concentrations of optically active constituents in the water bodies. Chlorophyll retrieval algorithms for Case I waters were elaborated by number of authors ([1], [2], [3] and many others). Situation becomes much more complicated if to try to estimate concentrations of optically active substances, like chlorophyll pigments (CHL), yellow substance or dissolved organic carbon (DOC) and suspended matter (SM), in turbid coastal and inland waters using water reflectance measurements. Some success has been achieved in estimation of concentrations of optically active substances in turbid coastal and inland waters, but remote sensing algorithms used by different authors seem to have local and seasonal character [4],[5],[6]. It means algorithms that were useful in estimation of chlorophyll concentration (for example) in one particular water body (or region of water body) cannot be used for the same purposes in the other waterbody (or other region of the same waterbody). Occur that remote sensing algorithms are depending on stage of biological activity and dominating algae assemblage in the water body besides many other reasons. Huge amount of measurements is needed to clear up seasonal changes in water color even in one water body.

We have started to elaborate a simple mathematical model that enables to calculate diffuse reflectance spectra beneath and just above the water surface to avoid shortcomings of above mentioned method

METHOD DESCRIPTION

The main principle of our method is comparison of full modelled water color spectrum with full measured spectrum. We suppose that if the shape and multitude of modelled spectrum is close to measured one then concentrations of optically active substances used in calculation of the most closest spectrum correspond to real ones in the water under investigation. Note that for this kind of comparison normalised spectral curves may also be used.

To build up our model we assumed that there are three optically active constituents in the water that influence on water reflectance spectrum in visible part of wave band. They are chlorophyll like pigments, dissolved organic carbon and suspended matter. Under these conditions the total spectral absorption coefficient of the water, a_λ, is described by the following formula:

$$a_\lambda = a_{w,\lambda} + a_{CHL,\lambda}C_{CHL} + a_{DOC,\lambda}C_{DOC} + a_{SM,\lambda}C_{SM}, \quad (1)$$

where $a_{w,\lambda}$ is the spectral absorption coefficient of pure water; $a_{CHL,\lambda}$, $a_{DOC,\lambda}$, $a_{SM,\lambda}$ are spectral specific absorption coefficients of chlorophyll, dissolved organic carbon and suspended matter respectively and C_{CHL}, C_{DOC}, and C_{SM} their respective concentrations in the water. The values of specific absorption coefficients of pure water, chlorophyll and suspended matter were obtained from Plass, Humphreys and Kattawar [7]. The values of $a_{DOC,\lambda}$ were calculated by the formula from Topliss, Miller and Irvin [8]:

$$a_{DOC,\lambda} = 0.565\exp[-\gamma(\lambda - 380)], \quad (2)$$

where γ =0.013±0.005 and λ is given in nm. By our investigation γ=0.017 is the best value for describing specific absorption coefficient of DOC in the Baltic coastal waters, Estonian and Finnish lakes.

The total backscasttering coefficient, b^*_λ is given by

$$b^*_\lambda = 0.5b_{w,\lambda} + \beta b_{SM,\lambda}C_{SM}, \quad (3)$$

where $b_{w,\lambda}$ is the spectral scattering coefficient of the pure water and $b_{SM,\lambda}$ is the specific scattering coefficient of suspended matter, β is the ratio of the hydrosol backscattering coefficient to its scattering coefficient. The values of $b_{SM,\lambda}$ and β were estimated from physical models of scattering properties of sea water by Kopelevich [9]. It is assumed that 50% of scattered light scatters backwards in pure water.

On the basis of the values of a_λ and b^*_λ we can calculate the diffuse reflectance of the water ($r_{D,\lambda}$) just below the water surface (z= - 0) using formula by Kirk [10]. To use Kirk's formula in remote sensing we used assumption that $r_D(z=+0) \approx 0.5r_D(z=-0)$ [11]. Then we get :

$$r_{D,\lambda}(z=+0) \approx 0.5[(0.975 - 0.629\mu_0)\frac{b^*_\lambda}{a_\lambda}], \quad (4)$$

0-7803-3068-4/96$5.00©1996 IEEE

where μ_0 is the cosine of direct solar beam in the water (after refraction). Note, that time, date and place of the measurement are taken into account through solar zenith angle.

Different combinations of optically active substances may give similar shape of reflectance spectra. Therefore we use averaged concentrations from three, five or ten best fitting spectra besides the closest to measured spectrum in correlation analysis.

Concentrations of DOC we put in the model (and get as results) are in mg/l, C_{CHL} are in mg/m^3 and C_{SM} are in relative units if to use specific absorption and scattering coefficients from above mentioned literature. We have investigated relationship between concentrations of SM and relative units of SM given by Plass et al. [2]. After investigation of water samples appeared that 1 mg/l of suspended matter is 7-12 relative units in the case of the Baltic Sea, Estonian and Finnish lakes. We used approximation 10 relative units = 1mg/l to give estimations of SM in physical units.

RESULTS AND DISCUSSION

Field experiments, where concentrations of all three optically active components of water, that we used in our model, were measured simultaneously with optical measurements, have been carried out in 1993 to 1995. During the first year small Estonian lakes, Pärnu Bay and Gulf of Riga were studied. Telespectrometer "Pegasus" was used for remote measurements. In 1994 some Finnish lakes were under investigation, besides above mentioned regions and in 1995 measurements were carried out also in different regions of the Baltic Sea. LI-COR 1800UV underwater spectrophotometer was used in 1994 and 1995 expeditions simultaneously with remote measurements.

It must be noted that both remote and underwater spectral measurements data can be used in evaluation of our model, whereas the only difference between using our model in solving optical inverse problem in the water and above the water is coefficient 0.5 in formula (4). 49 stations (15 during two expeditions on the Baltic sea and 34 during four expeditions on Estonian lakes) were investigated in 1993 and underwater spectral measurement data was collected in six lakes (12 stations) in 1994. Five Finnish and seven Estonian lakes were investigated twice during summer 1995 and expeditions on R/V Aranda and Marina were carried out in different regions of the Baltic Sea. Concentrations of CHL varied from 0.51 to 38.3 mg/m^3; DOC from 1.15 to 91 mg/l and SM from 1.5 to 26 mg/l.

Water reflectance spectra just beneath the water surface were calculated from LI-COR 1800UV measurements dividing upwelling diffuse radiance spectrum with downwelling radiance spectrum. Different scattering models were used in our model. The best results were obtained when β=0.17 (β=0.02 in clear Case I waters). Better results were achieved in estimation of DOC and CHL in lake waters. The correlation between measured chlorophyll concentration and estimated by our model is 0.94 and correlation between measured and estimated yellow substance concentration is 0.91. Comparison of normalised to wavelength 520 nm spectral curves were used to obtained these results. Correlations are worse if to compare not normalised spectra (0.55 and 0.76 correspondingly). Correlation between measured and calculated suspended matter was weak. Correlation coefficient R=0.62 and not normalised spectra were used to obtain this result. Due to "grey" absorption spectrum suspended matter influences more on absolute values of reflectance spectra than the shape of spectra and therefore using of normalised spectra is not reasonable.

Problems appeared in interpretation of remote measurement data. Correlation coefficients between measured and calculated concentrations of optically active substances were below 0.7 if we put together sea and lake measurements. Correlation coefficients were 0.7 between measured and calculated CHL and 0.75 between measured and calculated DOC for marine expeditions separately. For some expeditions correlation coefficients were as high as 0.95 for CHL and 0.92 for DOC, but even separation of marine and lake results did not give us good correlation between measured and calculated concentrations of suspended matter. Exceptional case was expedition on Estonian lakes in May 1993 (8 lakes) when correlation between measured and calculated SM was 0.86 and correlation between measured and calculated DOC was 0.3.

Grid steps of concentrations in model calculations were not constant. To minimise calculation time we used smaller grid steps for smaller concentrations and raised it step by step to higher concentrations. Selection of grid steps was made visually looking on effect of different concentrations of each substance on the shape of reflectance spectra. Occurred that decreasing of grid step made possible to obtain better correlations between measured and calculated concentrations of CHL, DOC and SM, but optimising of the grid steps is essential for reasonable calculation time. Decreasing grid steps a little bit may cause increasing of calculation time from seconds to hours and still not give us better correlation coefficients between measure and estimated concentrations of optically active substances. At present it takes 20-30 seconds on PC with 90 Mhz Pentium processor to compare a measured spectrum with calculated spectra and obtain estimations of concentrations of chlorophyll, yellow substance and suspended matter in the water under investigation. The model could be also used in interpretation of remotely measured images whereas computational time per pixel is small.

In most of cases concentrations of CHL, DOC and SM obtained from the best fitting spectrum gave better correlations with measured concentrations of optically active substances than concentrations obtained by averaging of concentrations from three, five or ten most closest spectra.

It must be noted that the shape of reflectance spectra is very sensitive to small concentration changes especially when concentrations of other ingredients are low, but the

same effect may occur in case of higher turbidity, too . For example small increase of yellow substance concentration may overshadow influence of relatively high concentrations of chlorophyll in blue region of visible spectrum. The opposite effect may occur with high concentrations of suspended matter. There exists certain saturation level where increase of concentration of suspended matter do not influence shape and multitude of diffuse reflectance spectra.

To test efficiency of our model we compared our results with chlorophyll, yellow substance and suspended matter concentration estimations obtained by means of color index method. We used turbid water algorithms proposed by Tassan [3] for interpretation of SeaWiFS data:

$$X_c=[R(\lambda_2)/R(\lambda_5)][R(\lambda_1)/R(\lambda_3)]^{-0.5} \quad (5)$$

$$X_y=[R(\lambda_1)/R(\lambda_3)]R(\lambda_2)^{0.25} \quad (6)$$

$$X_s=[R(\lambda_5)+R(\lambda_6)][R(\lambda_3)/R(\lambda_5)]^{-1.2} \quad (7)$$

$$\log(CHL)=0.36-4.38\log(X_c) \quad (8)$$

$$\log(A_y(440)=-4.36-6.08\log(X_y) \quad (9)$$

$$\log(SM)=1.82+1.23\log(X_s) \quad (10)$$

Here yellow substance concentration is expressed through absorption coefficient in wavelength 440 nm, and reflectances $R(\lambda_i)$ are measured in SeaWiFS sensors wavelengths i=412,443,490,510,555,670 nm. Correlation coefficient between measured concentrations of optically active substances and calculated by formulae (5-10) is below 0.4 that is lower than correlations between measured CHL, DOC and SM values and our estimations made using the above described model.

CONCLUSIONS

The efficiency of this method depends essentially on the validity of the mathematical model describing the reflectance spectra. The principle difficulty is with the detailed description of absorption and scattering properties of optically active material in the water (i.e. different types of phytoplankton pigments, organic and inorganic substances), especially the determination of backscattering coefficients. Our estimations show that scattering (and backscattering) coefficients presented in handbooks and monographs (mainly for the open ocean waters) are unsuitable for turbid coastal and inland waters.

Data about vertical distribution of optically active substances in euphotic zone is needed to test the model. Water samples for CHL, DOC and SM measurements, taken from surface layer only, cannot be used in case of lakes where concentrations of optically active substances may vary significantly, due to stratification.

More information is necessary on the type, size distribution and backscattering properties of living and non-living suspended matter. Bigger particles may give us higher SM concentrations, but they do not influence proportionally to their concentration on optical properties of the water under investigation. There are also problems with the determination of chlorophyll specific absorption coefficients: due to package effect those coefficients may differ more than twice for the same phytoplankton species growing under different illumination conditions. Data about scattering and absorption properties of dominating algae species should improve applicability of the model for certain water body or region under investigation.

In spite of the difficulties related with elaboration of the model our results confirm the understanding that the correlation of optical remote sensing data with concentrations of optically active substances in the water is not a random phenomenon even in turbid waters and it is possible to get qualitatively authentic results of spatio-temporal changes of those characteristics using optical remote sensing and model simulations.

REFERENCES

[1] D.K. Clark, "Phytoplankton pigment algorithms for the NIMBUS-7 CZCS," Oceanography from space, pp. 227-237, 1981.

[2] T. Kutser, H. Arst, T.Miller, L. Käärmann, and A. Milius, "Telespectrometrical estimation of water transparency, chlorophyll-a and total phosphorus concentration of Lake Peipsi," International Journal of Remote Sensing, vol. 16, pp.3069-3085, 1994.

[3] S. Tassan, "Local algorithms using SEAWIFS data for the retrieval of phytoplankton pigments, suspended sediment, and yellow substance in coastal waters," Applied Optics, vol. 33, pp.2369-2378, 1994.

[4] H. Arst, and T. Kutser, "Data processing and interpretation of sea radiance factor measurements," Polar Research, vol. 13, pp 3-12, 1994.

[5] R.P. Bukata, J.H. Jerome, K.Y. Kondratyev, and D.V. Pozdnjakov, "Satellite monitoring of optically-active components of inland waters: an essential input to regional climate change impact studies," Journal of Great Lakes Research, vol. 17, pp.470-478.

[6] O. Buttner , and Voros, " Investigation of Hungarian lakes by means of Landsat data," Advanced Space Research, vol. 1, pp. 177-179.

[7] G.N. Plass, T.J. Humphreys, and G.W. Kattawar, "Color of the ocean," Applied Optics, vol. 17, pp. 1432-1446, 1978.

[8] G.N. Topliss, J.R. Miller, and B. Irwin, "Ocean optical measurements - 1. statistical analysis of data from the Western North Atlantic," Continental Shelf Res., vol. 9, pp. 113-131, 1989.

[9] O.V. Kopelevich, "Few-parameter model of the optical properties of the sea water " in Optics of the ocean, A.S Monin, ed., pp. 208-235, Nauka, Moscow, 1983 (in Russian).

10] J.T.O. Kirk, "The assessment and prediction of optical water quality," Australian Water and Waste water Association 13th Federal convention, pp. 504-507, 1989.

[11] H.R. Gordon, O.B. Brown, and M.M. Jacobs, "Computed relationships between the inherent and apparent optical properties of a flat homogenous ocean," applied Optics, vol. 14, pp. 417-427, 1975.

Comparison of Sea Traffics in Tokyo and Osaka Bays with JERS-1 /OPS Data

K.Takasaki, T.Sugimura and S.Tanaka
REMOTE SENSING TECHNOLOGY CENTER OF JAPAN
Roppongi-First Bldg., 8F, Roppongi, Minato-ku, Tokyo 106 JAPAN
email: takasaki@restec.or.jp

ABSTRACT

The authors developed an algorithm of sea traffic monitoring using JERS-1/OPS that observes a stereo pair image in one orbit. The stereo pair consisting of forward and nadir viewing has an observation time gap about 20 seconds. Measuring the displacement of moving objects on the pair image, we can obtain the speed vectors. Traffic information in any sea area can be obtained under the same condition through this procedure.

This study focuses on a comparison of sea traffic patterns in Tokyo Bay and Osaka Bay. This work also discusses the performance of OPS data and its applicability for general speed vector measurements.

INTRODUCTION

Sea traffic in Tokyo Bay was restricted in the period of the construction of the Trans-Tokyo Bay Highway. Sea traffic condition during the restriction period, on September 9, 1992, was observed by OPS data. Contrary to this, the condition in restriction-free period also was analyzed using the OPS data on February 19, 1994. Two results show an influence of construction against the sea traffic in Tokyo Bay. Number of anchored ships in Osaka Bay was found to be relatively small. This is due to the difference of Tokyo and Osaka Bays in the routes connecting the bay area and the open sea. It depends upon also the difference of location of petrochemical facilities in two bay areas.

Ships are navigated freely in Osaka Bay because of no navigation control. Contraries to this, all large ships are controlled in Tokyo Bay by the Tokyo-Wan Traffic Advisory Service Center to avoid the traffic accident in the narrow channel.

TEST SITE AND DATA

JERS-1/OPS characteristics are as follows.

Swath width	75 km
Ground resolution	18.3m x 24.2m
Stereo angle	15.3°

VNIR spectral bands :

Band1 0.52-0.60 μ m (Nadir View)
Band2 0.63-0.69 μ m (Nadir View)
Band3 0.76-0.86 μ m (Nadir View)
Band4 0.76-0.86 μ m (Forward View)

Data used in this study were stereo image products, in which a stereo pair image was projected to the UTM and recorded.

Test site of Tokyo and Osaka Bay are shown in Fig.1, and followings JERS-1/OPS data are used in this study.

(1) Tokyo Bay observed on Sep. 9.1992
(2) Tokyo Bay observed on Feb. 9.1994
(3) Osaka Bay observed on July.22.1993

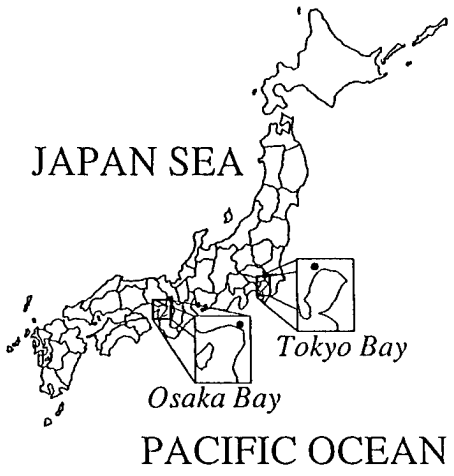


Fig.1 Test site

GENERATION OF VECTOR MAP

Registration process is required for accurate measurement of the moving objects. About 10 GCPs are selected from the coastal area. Because, the image observed by forward viewing is distorted by earth surface undulation. The orientation accuracy was fitted into one pixel and geometric correction was done by referring the nadir image.

After the correction, a stereo pair image became possible to composite each other on the display. The color composite image show the displacements of moving object. So, the moving speed was calculated by the displacement divided by time gap. They were shown by the expanded arrow in green color, and yellow circle for anchored ship.

A flow of this process is as follows, and generated speed

0-7803-3068-4/96$5.00©1996 IEEE

vector maps of Tokyo and Osaka Bay are shown in Fig.2, Fig.3 and Fig.4. The number of ships are shown in Table 1.

(1) Selection of GCP and orientation.
(2) Geometric correction of forward view image.
(3) Color composition of stereo pair image.
(4) Measurement of the displacement of moving objects.
(5) Overlay of the speed vectors on the color composite image.

Table 1 Detected ships in the image of Tokyo Bay and Osaka Bay.

Image Name	*Anchored*	*Navigating*	*Total*
Tokyo Bay in 1992	140	282	422
Tokyo Bay in 1994	189	338	527
Osaka Bay in 1993	32	454	486



Fig. 3 Vector map of Tokyo Bay in 1994



Fig. 2 Vector map of Tokyo Bay in 1992



Fig. 4 Vector map of Osaka Bay in 1993

COMPARISON OF SEA TRAFFICS IN TOKYO BAY

Sea traffics in Tokyo Bay which was restricted by Trans-Tokyo Bay Highway construction in 1992 and 1994 were compared. In the image of 1992, all navigating ships were avoiding the constructing area. Therefore, sea traffics were crowded at the sea front of Kawasaki and Yokohama city. In the image of 1994, sea traffics became possible to navigate in the constructing area. Magnified images around the constructing area were shown in Fig.5 and Fig.6. The influence of construction to the sea traffics are estimated from comparison of these vector maps.



Fig.5 Vector map around the constructing area in 1992

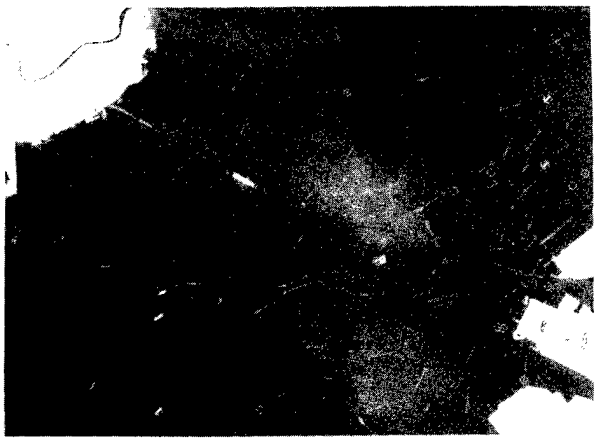


Fig.6 Vector map around the constructing area in 1994

COMPARISON OF SEA TRAFFICS IN TOKYO AND OSAKA BAY

There are some differences of sea traffic in Tokyo and Osaka Bay.

(1) The number of large or anchored ships.

(2) The navigation control.

Some reasons of the above differences were discussed as follows.

In Tokyo Bay, one narrow channel is connecting the bay and sea. In Osaka Bay, two channels are connecting them. However, each channels of Osaka Bay are narrower than the one of Tokyo. In narrow channel, large ships disturb the other ship navigation. Because, slow speed and large body are effect to other small ship navigation. Therefore, in Osaka Bay, petrochemical facilities are located on the out of the bay.

In Tokyo Bay, all ships are navigated regularly, but in Osaka Bay, they are navigated freely. Because, in the Tokyo Bay, navigation of all ships are controlled by Tokyo-Wan Traffic Advisory Center. However, in Osaka Bay, ships navigation are not controlled.

CONCLUSION

This study finds the following facts concerning with the performance of JERS-1/OPS data.

1. Minimum size of moving objects that can be recognized as ship by the 18 m resolution needs to be larger than about 50 meters. Moving object of less than one pixel can be detected in the pair image, but it is difficult to be discriminated from the other object or noise.
2. Observation time gap of about 20 seconds is suitable for the detection of moving objects as ships on the sea. Accuracy of the measured speed depends upon the image registration accuracy. When obtaining the accuracy of one pixel registration, the accuracy of speed vector becomes within about 1.5 knots.
3. Sea traffic of main Japanese bays as Tokyo and Osaka Bays expand over the sea area about several tens of kilometers. Field of view of 75 km in the JERS-1/OPS is the minimum size for this kind of observation.

REFERENCES

[1] K.Takasaki,T.Sugimura,S.Tanaka: Speed Vector Measurement of Moving Objects Using JERS-1/OPS Data, IGARSS'93, vol. II, pp.476-478

[2] K.Takasaki, T.Sugimura,S.Tanaka:A Measurement of moving objects using JERS-1/OPS data, Journal of The Remote Sensing Society of Japan, vol.14,pp.11-17, 1994

[3] -----: RADAR VESSEL-DATA PROCESSING SYSTEM, Marine Safety Agency, 1992

NASA Scatterometer Near-Real-Time, Value Added Products for Meso/Synoptic-Scale Marine Forecasting

Michael W. Spencer

California Institute of Technology, Jet Propulsion Laboratory
MS 300-319, 4800 Oak Grove Drive, Pasadena, CA 91109-8099
Tel: (818) 354-1175, email: mws@shiokaze.jpl.nasa.gov

Abstract -- The potential for near-real-time NASA Scatterometer (NSCAT) data to contribute to operational marine forecasting is described. A description of the NSCAT Value Added Product (VAP) activity -- an effort to provide near-real-time wind images to the public and operational forecasters -- is presented.

INTRODUCTION

Spaceborne scatterometers are radar instruments specifically designed to measure ocean surface wind speed and direction. This technique was initially demonstrated with the 1978 flight of the Ku-Band Seasat Scatterometer (SASS) [1], and has most recently been demonstrated with the successful operation of the C-band ERS-1 scatterometer [2]. In August of 1996, the Ku-Band NASA Scatterometer (NSCAT) will be launched aboard the Japanese Space Agency Advanced Earth Observation Satellite (ADEOS) [3]. NSCAT will operate for three years and make accurate measurements of ocean surface wind speed and direction in two 600 km swaths on either side of the spacecraft, thus providing a significant expansion and improvement of the current scatterometer data base.

The application of scatterometer data to oceanographic and climatological research is well documented [4]. Ocean wind stress is a primary factor in driving ocean circulation and thus the global energy balance. In addition to its applicability to the study of wind forced ocean circulation and global climate change, scatterometer wind data, made available to users on a sufficiently timely basis, is also of great value in mesoscale and synoptic-scale marine forecasting. It is these "operational" applications of the NSCAT data which are the focus of this paper.

OPERATIONAL APPLICATIONS

Several potential operational applications of scatterometer data have been noted elsewhere [5]. Below we include a list of several areas where scatterometer measurements are likely to have the highest impact.

A. Marine Hazard Warning: Perhaps the most noteworthy operational application of scatterometer data is determining the location, structure, and strength of storms at sea. Severe marine storms -- which include tropical cyclones (hurricanes, typhoons) and mid-latitude cyclones -- are among the most destructive of all natural phenomena. In the United States alone, hurricanes have been responsible for at least 17,000 deaths since 1900, and hundreds of millions of dollars in damage annually. If worldwide statistics are considered, the numbers are substantially higher. Although typically not as violent as tropical cyclones, severe mid-latitude storms nevertheless exact a heavy toll in casualties and material damage [5]. Cloud imagery from satellites has significantly enhanced the forecasters ability to detect and track storms. Scatterometer data will augment these familiar images by providing a direct measurement of the surface wind to compare to the cloud patterns. Scatterometer data can thus assist in the identification of the storm center locations, storm related fronts, and the location of the most damaging winds within the storm structure. Scatterometer derived winds can also be used as inputs to models that forecast wave height and flooding.

B. Ocean Ship Routing: Scatterometer observations of winds can be of particular significance to ocean going cargo ships. In today's world of international commerce, billions of dollars worth of food, fuel, raw materials, and manufactured goods are transported by sea yearly. Besides the benefits derived from the ability of NSCAT to locate and identify storms which may cause harm to vessels or crew, satellite wind data can also allow sea captains to chart their courses more efficiently. With a knowledge of the winds, the ship master can choose a route to avoid heavy seas or high headwinds which can slow the ship's progress and consume an excessive amount of fuel. Previous to the flight of spaceborne scatterometers, ship captains had to rely completely on sporadic and potentially unreliable reports from other ships, and widely spaced measurements from buoys. A satellite based instrument allows a much more regular and extensive assessment of the winds. This is particularly advantageous in remote regions of the world where there are few, if any, other wind measurements.

C. Drilling and Mining Operations: Oil and gas production has been undertaken at many offshore sites around the world -- the Gulf of Mexico, the North Sea, and the Persian Gulf being prominent examples. Thorough knowledge of the historic wind and wave conditions at a specific location are important to the appropriate design of drilling platforms. Accurate knowledge of the current sea state as well as warnings of impending storms are critical to safe and efficient drilling operations. In the event of an oil spill, the surface wind is

0-7803-3068-4/96$5.00©1996 IEEE

a key factor in determining how the oil will spread. Wind data from NSCAT can thus be used by clean-up and containment crews to minimize the environmental impact of such a disaster.

NSCAT SYSTEM

The NASA Scatterometer (NSCAT) is scheduled for launch aboard the Japanese Advanced Earth Observing Satellite (ADEOS) in August 1996. The NSCAT instrument is a Ku-band radar which measures global ocean surface wind speeds and directions at up to 25 km resolution. The wind measurement is accomplished by first measuring the normalized backscatter cross section (σ_0) of the ocean at three different azimuth angles and two different polarizations using eight fan-beam antennas. Wind vectors are then retrieved during ground data processing using an empirical geophysical model function which relates σ_0 to wind speed and direction.

The NSCAT system offers several enhancements over previous scatterometers. With respect to SASS, which measured backscatter cross section at two azimuth angles on either side of the spacecraft, NSCAT makes additional measurements at a third azimuth angle. This has been demonstrated, both in analyses and with the ERS-1 experience, to greatly enhance the ability of ground processing to remove wind direction ambiguities which are inherent to the wind retrieval process [3]. Because NSCAT has two 600 km swaths on either side of the spacecraft, the overall ocean coverage will be enhanced relative to the ERS-1 and ERS-2 systems. NSCAT will cover approximately 77% of the worlds oceans in 24 hours, and 95% in 48 hours. This will be a particular advantage to operational users, for whom measurement coverage and revisit time is extremely important in order to follow fast-developing meteorological phenomena.

The main NSCAT science data stream will be sent from Japan, and processed to winds by the Science Data Processing System within two weeks. The science data stream will be calibrated and Earth located to a very high accuracy. The NSCAT science data will be distributed to researchers via the Physical Ocean Distributed Active Archive Center (PODAAC).

NEAR REAL-TIME PROCESSING

Although the main science data stream has the high accuracy necessary for research purposes, it is not available on a sufficiently timely basis for use by operational users. To allow near real-time access by operational users, NOAA, in coordination with NASA and JPL, has invested in a satellite data downlink and wind processing infrastructure that will allow access to scatterometer wind measurements within 2-4 hours after data take.

As the first element of the near real-time processing system, the scatterometer data will be downlinked directly from ADEOS to NASA ground receiving stations at Wallops Island, Virginia, and at the Alaska SAR facility in Fairbanks, Alaska. Each downlink pass over these stations will playback the most recently acquired NSCAT data.

From the ground receiving stations, the data will be transmitted to NOAA in Suitland, Maryland for wind processing. For this step, JPL has developed a special version of the NSCAT wind processor which is able to generate wind estimates from the raw data in near real-time -- ten minutes of processing for each orbit's worth of NSCAT data. Although the radiometric and Earth location accuracy is not to the high research standards of the main science product, the near real-time product generated by NOAA is judged to be of sufficient accuracy for operational users where the timeliness of the data is all important. The NOAA scatterometer data will be provided to the National Meteorological Center (NMC) for the development of improved numerical forecasts, the National Hurricane Center for the study of severe tropical storms, and other domestic and international operational weather organizations.

VALUE ADDED PRODUCTS

As an additional effort to foster the utilization of scatterometer data by the public and the operational meteorological community, the NSCAT project at JPL has initiated the Value Added Product (VAP) activity. The VAP activity, working very closely with the larger NOAA near real-time effort, will also receive and process the NSCAT data in near real-time. A "value added" step will then be performed to create images to be made available to the public via the Internet. The goal of the valued added images is to display the wind data in a visually informative way, and provide a convenient means of access by commercial and educational users.

One important element of the value added processing is the coregistration of NSCAT wind data with geosynchronous cloud imagery. Such a visual correlation will add additional information to traditional cloud images. For instance, hurricanes begin their lives as rather ill-defined masses of clouds in the Eastern tropical Atlantic. The addition of scatterometer wind data to these images will clearly identify features where strong cyclonic circulation has begun to form.

Another value added step to be performed is the interpolation of NSCAT data between swaths. Successive NSCAT orbits do not touch each other at the equator or mid-latitudes, and thus produce gaps in coverage for short time periods. Furthermore, a 400 km "nadir gap" exists in the center of the swath about the ADEOS orbit track. To allow users to view a continuous near real-time wind field, it is necessary to invoke a two dimensional spatial interpolation scheme. The interpolation technique must match the "true" data within the swath with a minimum of smoothing, while providing a reasonably accurate estimate of the "missing" data. To accomplish this, an interpolation scheme based on the objective analysis approach will be employed [6]. Taking advantage of

current display technology, animations of the wind field data will also be created for transfer over the Internet. In addition to being simply a novelty, animation is capable of visually emphasizing features not readily apparent in still images.

CONCLUSIONS

Scatterometer data has the potential to revolutionize areas of operational marine forecasting. To explore and support the development of scatterometer data for operational users, NASA and NOAA are sponsoring efforts to provide near real-time wind products to the public and the meteorological community.

ACKNOWLEDGMENTS

The author would like to acknowledge the efforts of R. Dunbar, of JPL, and P. Chang, of NOAA, in the development of the near real-time wind processor. This research was performed at the Jet Propulsion Laboratory, California Institute of Technology, under contract with the National Aeronautics and Space Administration.

REFERENCES

[1] W.L. Grantham, E.M. Bracalente, C.L. Britt, Jr., F.J. Wentz, W.L. Jones, Jr., and L.C. Schroeder., "Performance Evaluations of an Operational Spaceborne Scatterometer," IEEE Trans. Geosci. and Remote Sensing, vol. GE-20, July, 1982.

[2] E.P.W. Attema, "The Active Microwave Instrument On-Board the ERS-1 Satellite," Proceedings of the IEEE, Vol. 79, No. 6, June 1991.

[3] F. Naderi, M.H. Freilich, and D.G. Long, "Spaceborne Radar Measurement of Wind Velocity Over the Ocean -- An Overview of the NSCAT Scatterometer System," Proceedings of the IEEE, Vol. 79, No. 6, June 1991.

[4] M.H. Freilich, "Science Opportunities Using the NASA Scatterometer on N-ROSS," JPL Publication 84-57, February 1, 1985.

[5] P.G. Black, R.C. Gentry, V.J. Cardone, J.D. Hawkins, "Seasat Microwave Wind and Rain Observations in Severe Tropical and Midlatitude Marine Storms," Advances in Geophysics, Volume 27, Academic Press, Inc., 1985.

[6] G.J. Tripoli and T.N. Krisnamurti, "Low-Level Flows over the GATE Area during Summer 1972," Monthly Weather Review, Volume 103, March 1975.

Wavelet Analysis of AVHRR Images for Feature Tracking

Antony K. Liu
NASA Goddard Space Flight Center, Code 971
Greenbelt, Maryland 20771
TEL: (301) 286-8534, FAX: (301) 286-0240
E-mail: liu@neptune.gsfc.nasa.gov

William Y. Tseng
NOAA/NESDIS, Washington, D.C. 20233

Steve Y.-S. Chang
Caelum Research Corporation, Silver Spring, Maryland

ABSTRACT

The Advanced Very High Resolution Radiometer (AVHRR) images collected from NOAA polar orbiting operational satellites were used in this study. The Laplacian of the Gaussian (Mexican hat) wavelet transform can be used as an edge detector to separate the high/low sea surface temperature (SST) areas from ambient water. The histogram of each satellite image will first be examined for ocean feature enhancement by gray scale. The enhanced image will then be wavelet transformed with various scales to separate various texture or features. The Mexican hat wavelet will be used as a band-pass-filter, and its first derivative as a threshold for feature detection. Heuristic edge linking methods will be used to further enhance the images. Finally, a binary image can be produced in order to reduce the data volume. By overlaying sequential binary images from different imaging time, the evolution of mesoscale features such as fronts, oil spills, and eddies can be monitored by wavelet analysis using satellite data from subsequent passes.

INTRODUCTION

A new method for time-varying signal analysis, called the Wavelet Transform, has been developed for image processing at NASA/GSFC during the past three years, and gives spectral decompositions via the scale concept. Basically, wavelet transforms are analogous to Fourier transforms, but are localized both in frequency and time, i.e., they enable the study of processes by localizing their properties in both time and frequency [1].

The two-dimensional wavelet transform is a highly efficient band-pass-filter, which can be used to separate various scale processes and shows their relative phase/location information [2]. Two-dimensional Gaussian wavelet (often referred to as Mexican hat) transform of SAR imagery for small scale features can be used with threshold as an edge detector. In the marginal ice zone study by Liu et al. [3], the ice edge in each SAR image has been delineated by using two-dimensional wavelet transform.

The combined use of AVHRR, SeaWiFS/OCTS, and ERS-2/RADARSAT SAR can provide frequent high resolution coverage of the coastal area for the evolution study of processes caused by sea surface temperature, high pigment or surface roughness from a sequence of satellite images of the coastal zone. Simultaneous satellite images, in-situ measurements from moorings and ship operations, and wind records from buoys and meteorological stations can be used to detect and monitor the ocean environment. By using repeat satellite coverage, the mesoscale features, such as internal waves, ship wakes, fronts, ice-edge meanders, oil spills, surface slicks, upwelling, and eddies associated with coastal processes can be tracked through multitemporal satellite data analysis lead to an important data product: satellite derived maps for tracking mesoscale features in the coastal zone.

In this paper, wavelet analysis of sequential SST images from Bering Sea and the Persian Gulf (the Gulf of Oman) will be demonstrated for feature tracking and the corresponding oceanic processes will be interpreted.

TWO-DIMENSIONAL GAUSSIAN WAVELET

The wavelet transform, Ws(a,b), of a function, s(r), where r = (x,y), is expressed in terms of the complex valued wavelet function, w(r), as follows :

$$W_s(a,b) = \iint s(r)\, w^*_{a,b}(r)\, dr = 1/a^2 \cdot \iint s(r)\, w^*\,[(r-b)/a]\, dr \qquad (1)$$

in which the wavelet function is dilated by a factor a, and shifted by b. The function w(r) is the basic wavelet which must satisfy the admissibility condition, but is otherwise subject to choice within certain limits. The superscript * indicates complex conjugate. For data analysis, the mother wavelets frequently used are: a Gaussian modulated sine and cosine wave packet (the Morlet wavelet); the second derivative of a Gaussian (the Mexican hat). In this study, the analyzing wavelet is defined as the second derivative of a Gaussian as follows:

$$W(x,y) = 1/a \cdot [2-(x^2+y^2)/a^2] \cdot \exp[-(x^2+y^2)/2/a^2] \qquad (2)$$

0-7803-3068-4/96$5.00©1996 IEEE

Since convolution is commutative with respect to differentiation, the resulting wavelet transform is the Laplacian of a Gaussian smoothed function.

WAVELET ANALYSIS FOR FEATURE TRACKING

AVHRR data will first be examined with coastal land and clouds masked. The histogram of each subscene will also be examined for data screening. The promising subscenes will then be wavelet transformed with various scales to separate various texture or features. The Laplacian of the Gaussian (Mexican hat) wavelet will be used as a band-pass-filter, and its first derivative as a threshold for feature detection. Heuristic edge linking methods will be used to enhance the images. Finally, a binary image can be produced in order to reduce the data volume. By overlaying binary images from subsequent passes, the evolution of mesoscale features such as ice edge, fronts, surface film, ship wakes, and eddies can be monitored by wavelet analysis.

Fronts

The Mexican hat wavelet transform can be used as an edge detector to separate dark areas from bright areas in the image. An AVHRR image of 512 * 512 pixels (with pixel spacing of 0.01°) of sea surface temperatures collected over the Bering Sea on April 27, 1995 during the FOCI field program is shown in Fig. 1. First the cloud/land and ocean features are separated by using different gray scales for different temperature ranges. Then, the cloud and Aleutian Islands (dark areas) are delineated by the white lines and the ocean surface high temperature features (brighter areas) are extracted by dark lines using wavelet transforms with a small scale (a = 4 units of pixel spacing) as an edge detector with a threshold about 1.5 and 0.5 standard deviation, respectively. The method of edge linking based on the neighboring point was applied and the short segments were removed. By combined use of gray scale and wavelet transform, we can detect (with gray scale), track (with wavelet transform), and enhance (with edge linking) the satellite images.

Oil Slicks

Satellite remote sensing has become a useful tool to study marine pollution [4, 5]. For tracking of temperature front, we can use sequential AVHRR images. Figure 2a shows an AVHRR image with 512 * 512 pixels (pixel spacing of 1 km) of the Gulf of Oman collected on March 31, 1994 at 12:47 UT. Note that the land has higher temperature during the daytime, and an oil spill with mild temperature located behind the sharp turn in the Strait of Hormuz. Similar procedure is applied as in the previous case to separate the land and ocean features by using different gray scales for different temperature ranges. The wavelet transform with a small scale (a = 4) and the threshold of one standard deviation are used to separate the land (white contours) and high ocean temperature front (black contours). The same procedure is applied to the AVHRR image of the same area collected on April 1, 1994 at 1:21 UT in Fig.2b. Note that the land now has lower temperature at night, and the oil spill has disappeared in the image. The oil spill may not have a significant different temperature signature from the surrounding water at night or it may be sinking below the water surface. By overlaying two wavelet transformed images, a schematic diagram can be drawn to show the approximated flow pattern by following the motion of frontal features. Note that three small eddies persist near the frontal boundary. This type of analysis can help for the numerical modeling of flow circulation in the Strait.

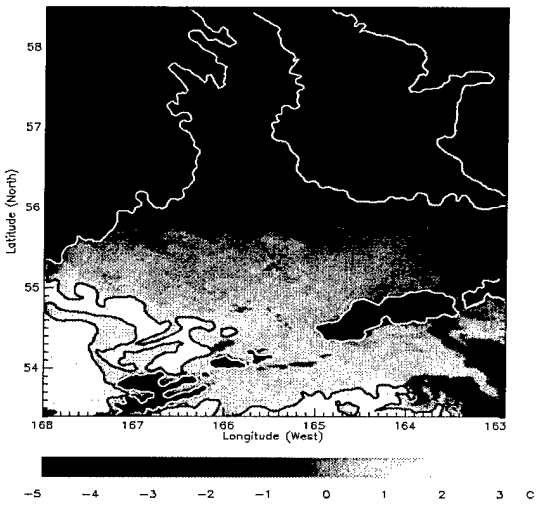


Fig. 1. An AVHRR-channel 4 image of Bering Sea from April 27, 1995 with clouds and islands delineated by white lines and high sea surface temperature areas by dark lines processed by the wavelet transform.

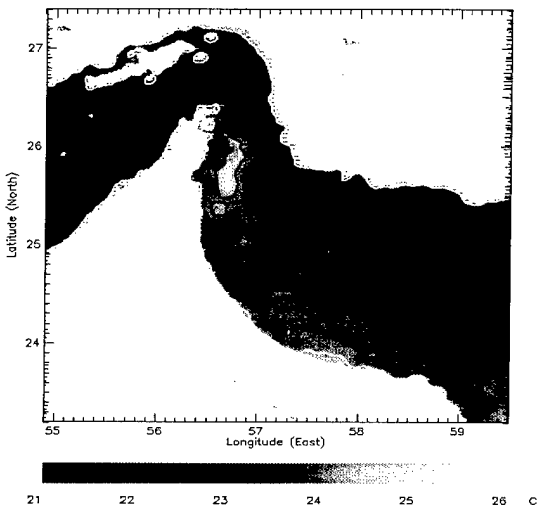


Fig.2a. An AVHRR-channel 4 image of the Gulf of Oman from March 31, 1994 processed by the similar procedure as in the previous case of Bering Sea.

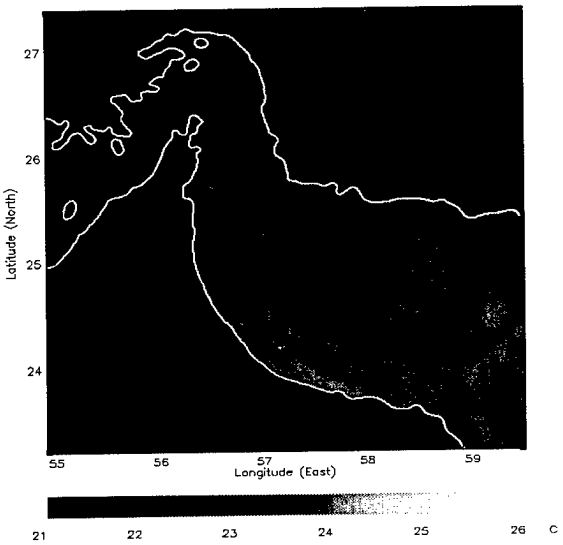


Fig.2b. An AVHRR-channel 4 image from April 1, 1994 at the same position as in Fig.2a. The land now has lower temperature at night.

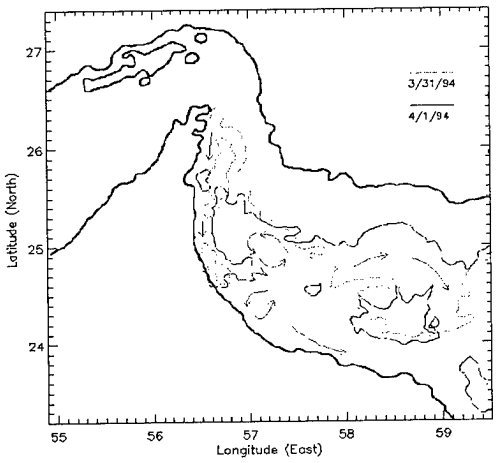


Fig.3. A schematic diagram derived by overlaying the feature lines in Fig.2a and Fig.2b.

COASTAL MONITORING AND DISCUSSION

The NOAA CoastWatch program provides near real-time mapped satellite and in-situ data and information for U.S. coastal waters for hazard warning, ice and ocean monitoring, and environmental management [6]. A development project is underway to add SAR data and products to the CoastWatch product suite. One of the major areas of interest will be the coast of Alaska. We plan to evaluate the use of the wavelet transform techniques for the automated analysis of SAR, AVHRR, and SeaWiFS images to detect ocean features for CoastWatch applications. The developed algorithms will be transferred to the NOAA CoastWatch program and will be applied/tested in other U.S. coastal areas.

In this paper, the wavelet transform has been applied to satellite AVHRR imagery and we have demonstrated the feasibility of this technique for feature extraction. The evolution of mesoscale features such as fronts, oil slicks, and eddies can be easily tracked by the wavelet analysis using satellite data. The wavelet transforms of satellite images can be used as a near real-time "quick look" of satellite data screening (feature detection), data reduction (binary image), and image enhancement (edge linking). Wavelet analysis can provide a more cost-effective monitoring program that would keep track of changes in important elements of the coastal ecosystem. Reliable imaging of such mesoscale features by certain sensors (e.g., SAR, ocean color and IR) and definition of the conditions under which imaging is possible will provide the understanding of processes caused by sea surface temperature, high pigment or surface roughness.

ACKNOWLEDGMENTS

The authors would like to thank NOAA/NESDIS for providing AVHRR images.

REFERENCE

[1] Combes, J.M., Grossmann, A., and Ph. Tchamitchian, "Wavelet: time frequency methods and phase space," Proceedings of the International Conference, Dec. 1987, Marseille, France, Springer-Verlag, 331pp, 1989.

[2] Liu, A. K., and C. Y. Peng, "Ocean-ice interaction in the marginal ice zone," Proceedings of Second ERS-1 Symposium, 1993.

[3] Liu, A. K., C. Y. Peng, and T. J. Weingartner, "Ocean-ice interaction in the marginal ice zone using SAR, J. Geophys. Res., to appear, November, 1994.

[4] Park, P. K., J. A. Elrod, and D. R. Kester, "Application of satellite remote sensing to marine pollution studies," Chemistry and Ecology, 5, 57-73, 1991.

[5] Tseng Y. W., and L. S. Chiu, "AVHRR observations of Persian Gulf oil spills," Proceedings of IGARSS'94, 1994.

[6] Pichel, W., J. Sapper, C. Duda, E. Maturi, K. Jarva, and J. Stroup, "CoastWatch operational mapped AVHRR imagery," Proceedings of IGARSS'94, 1994.

Fluorescence as a Potential Indicator of Coral Health

Heather Holden, Derek Peddle and Ellsworth LeDrew
University of Waterloo, Department of Geography
Waterloo, Ontario, Canada N2L 3G1
(519) 885-1211 ext 6070 (phone)
(519) 888-6768 (fax)
hmholden@cousteau.uwaterloo.ca

Abstract -- Distinct coral chlorophyll fluorescence peaks have been measured in the field using an Analytical Spectral Device (ASD) radiometer. Bleached coral reveals a distinctly different reflectance spectra than healthy coral due to the presence of photosynthetic pigments. This spectral difference provides the distinction necessary to identify bleached coral from a remote sensing platform with a sensor of spectral sensitivity similar to that of the ASD. Field results are presented, and potential remote sensing applications are discussed in the context of in situ profile radiometer measures for the optical correction of hyperspectral airborne imagery.

INTRODUCTION

Coral reefs are considered sensitive indicators of climate variability, and thus it is important to monitor their state of health. A healthy coral possesses symbiotic zooxanthellae which is the photosynthetic pigment that gives the coral its color. When corals are subjected to any stress (thermal pollution, extreme water temperature change resulting from El Niño-Southern Oscillation (ENSO) events, decreased salinity, etc.), they expel their zooxanthellae thus loosing their color and becoming bleached. Traditionally, surveying of coral reefs has been done via ship and SCUBA divers; both methods are expensive and often subjective. Furthermore, these methods are inaccurate when dealing with large, or inaccessible regions, so remote sensing is being evaluated as a potential alternative for precisely monitoring coral health on a regional scale.

In preparation for future airborne hyperspectral remote sensing endeavors in identifying coral health, we have investigated the hypothesis that bleached corals are spectrally dissimilar to healthy corals on the basis of chlorophyll fluorescence. The exact location of spectral peaks of chlorophyll fluorescence differs between species [1], but distinct natural fluorescence peaks can be found at approximately 700 nm. We hypothesize that this difference in amount of zooxanthellae can be identified with sensitive hyperspectral devices and used as the basis for monitoring coral bleaching events over time which would be of use in climate change studies.

STUDY AREA

Beqa Lagoon, in the Fiji Islands of the South Pacific (15°-23° S - 177° E-178° W), is 390 km^2, and almost entirely surrounded by its own barrier reef of volcanic origin. The particular location of Beqa Lagoon is suitable for this type of exploratory work, as it is relatively unaffected by external oceanic influences which ensures roughly consistent water optical properties. The water is extremely clear, particularly in the winter season, with near-surface chlorophyll values estimated to be less than 0.2 mg m^{-3} [2]. The clarity and homogeneity of the water is maintained by its constrained nature, lack of major incoming tributaries, and low surface chlorophyll. In addition, the lagoon is easily accessible by boat, and extensive local knowledge of the surrounding coral reefs allowed for expeditious sampling techniques.

The *in situ* water temperature profile indicates a well-mixed upper 60 m, with no thermocline apparent (Fig. 1A). This is significant since chlorophyll fluorescence has a maximum at the base of the thermocline which is indicative of a population of phytoplankton supported by nutrients from below [3]. It can therefore be assumed that there is no phytoplankton bloom to complicate substrate identification. Photosynthetically available radiation (PAR) is attenuated with no significant deviations from the characteristic logarithmic profile that is to be expected from pure water [2], (Fig.1B).

DATA COLLECTION

Nadir hyperspectral target radiance was collected with a hand-held Analytical Spectral Device (ASD) field spectrometer from a variety of individual targets such as bleached coral and assorted species of healthy coral. These high spectral resolution field measurements were taken at high tide in a flat bottom boat, so that the instrument could be as close to the substrate as possible and water optical attenuation could be minimized. In addition, great care was taken to ensure a cloudless sky at the time of radiance measurement. Simultaneous photographs were taken of the substrate with a Nikonos V underwater camera, so that the various individual targets could be catalogued with their respective spectral profiles and compared.

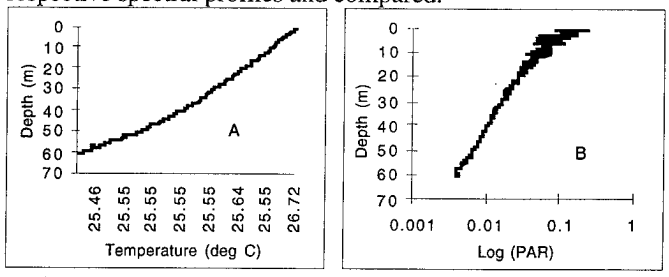


Fig. 1A is the temperature profile revealing a lack of a thermocline; Fig.1B is the log of PAR profile revealing a lack of a phytoplankton bloom.

0-7803-3068-4/96$5.00©1996 IEEE

Water optical properties were measured with a Profiling Reflectance Radiometer (PRR-600) in the SeaWiFS bands: 412, 443, 488, 510, 560, 665, 683nm. This dropsonde was allowed to drop from the side of the boat collecting reflected radiance and incoming irradiance at incremental depths throughout the water column. A hand-held Global Positioning System (GPS) was used to record geographic location, while a sonar verified the water depth measurements taken by the PRR-600.

ANALYSIS

Several processing steps are involved in converting ASD spectra from raw radiance values to calibrated reflectance. These include reference panel calibration; solar zenith angle determination; spectral and angular interpolation; and reflectance computation [4]. The approach outlined by [4] is quite flexible in that panel calibration data for any solar zenith angle can be derived based on a procedure for spectral and angular interpolation of panel measurements obtained over a range of view angles [4].

Over one hundred in-water hyperspectral reflectance profiles collected with the ASD hyperspectral radiometer of substrates ranging from dead coral debris to healthy coral were plotted and compared. A healthy coral profile is compared to that of bleached coral in Fig.2. A spectral peak in reflectance at approximately 760 nm is apparent in all profiles of healthy corals due to the presence of chlorophyll in the photosynthetic zooxanthellae. In contrast, the profiles of bleached coral and dead coral debris reveal a distinct lack of any such spectral peak indicating a lack of photosynthetic zooxanthellae. These findings are consistent with accepted theories on coral bleaching which state that a coral will turn white when it expels its photosynthetic zooxanthellae.

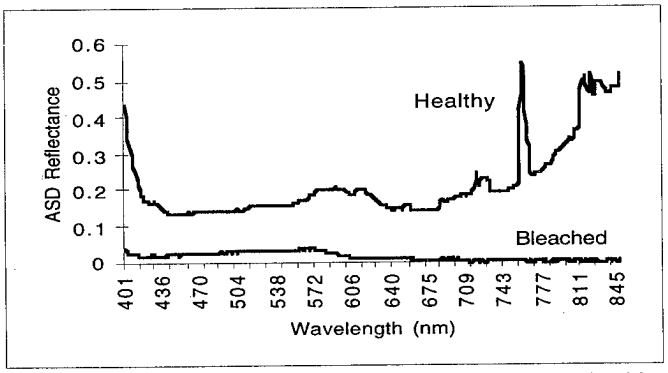


Fig. 2: The fluorescence reflectance peak in the healthy coral's spectra is at 760 nm, but is noticeably absent in the bleached coral's spectra.

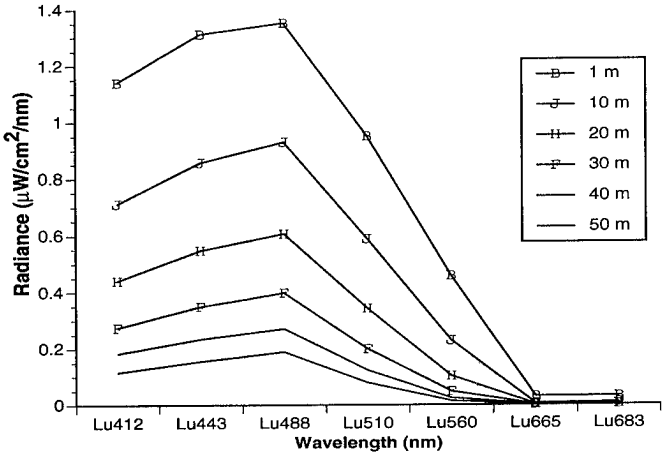


Fig.3: At all depths, the 488nm wavelength has the highest radiance and thus the least attenuation.

The radiance profiles collected by the PRR-600 characterize the optical extinction of light with increased depth. The wavelength which is least attenuated by water is 488nm (Fig.3) but there is little distinction between bottom types in this wavelength (Fig.4). Unfortunately, there is considerable attenuation of light in the wavelengths capable of sensing the fluorescence peak, so it may only be possible to use this technique in shallow waters of 10-15 meters.

For future remote sensing applications of coral reef mapping, an attenuation coefficient will be required to remove the effects of the water column from the coral signal. The slope of the log of radiance versus depth provides an estimate of the amount of energy attenuated with increased depth, as in Fig.5.

DISCUSSION

These field data reveal an exciting possibility for accurate identification of areas of coral bleaching using an airborne hyperspectral remote sensing platform. The spatial and spectral resolution of satellite sensors are inappropriate for such sensitive mapping. For example, the SPOT HRV sensor operates in wavelengths unsuitable for detecting fluorescence, and its spectral resolution (20x20m) further complicates the detection of individual features.

Alternatively, the Compact Airborne Spectrographic Imager (*casi*) system is compatible with ASD wavelengths, and could thus be a feasible option for remotely identifying coral bleaching. The spectro-radiometer data were not corrected for the water volume attenuation of energy with increased depth, as the data were collected very near the surface. However, if the *casi* system is to be used for identification of coral bleaching at greater water depths, an attenuation coefficient would have to be applied to correct for the logarithmic reduction of light energy through the water column near the 700nm wavelengths.

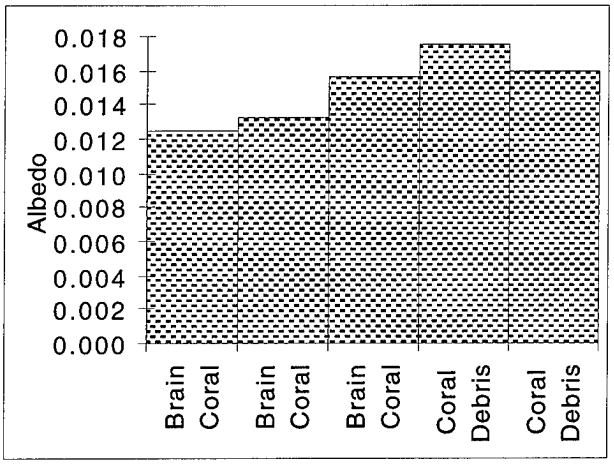


Fig.4: There is little distinction between the albedos of healthy and dead coral at 488nm (from PRR-600 measurements).

The PRR-600 wavelength which corresponds most closely to the fluorescence peaks collected by the ASD is 683nm, so the slope of this profile could be used in reflectance algorithm (1) by [6] to correct remotely sensed imagery for the effects of water attenuation. The reflectance values are taken from the remotely sensed image, the attenuation coefficient from the slope of *in situ* irradiance profiles (Fig.5), and the depth from bathymetric soundings. The resulting albedo of the bottom surface can then be considered unaffected by the water column.

$$R_\lambda = R_{\infty\lambda}+(A_\lambda-R_{\infty\lambda})\exp(-2K_\lambda Z) \quad (1)$$

where
R_λ = Reflectance below water
$R_{\infty\lambda}$ = Reflectance of deep water
A_λ = Albedo of bottom
K_λ = Attenuation Coefficient
Z = Depth

The approximate 400 to 900 nm spectral sensitivity of *casi* airborne data coupled with algorithm (1) would be appropriate for mapping of bottom albedo on a regional scale. The catalogued spectral signatures measured by the ASD could then be used to classify a bottom albedo map to determine areas of bleached corals. The spectral and spatial resolution attainable with this airborne sensor is superior to that possible using a satellite sensor, so a more sensitive analysis could be performed on a regular basis.

The implications for coastal zone management are enormous. With an established data base of coral spectral signatures, regular over-flights with the *casi* system would enable repetitive processing of coral bleaching maps to be analyzed over time to monitor environmental change. Since coral reefs appear to be sensitive to large-scale climatic processes such as the well-known ocean-atmosphere phenomenon of the El Niño-Southern Oscillation, impacts could be effectively monitored over time. Similarly, corals are sensitive to industrial pollution, river runoff and deforestation sedimentation, which could all be regulated more closely through repetitive mapping of coral reef ecosystems.

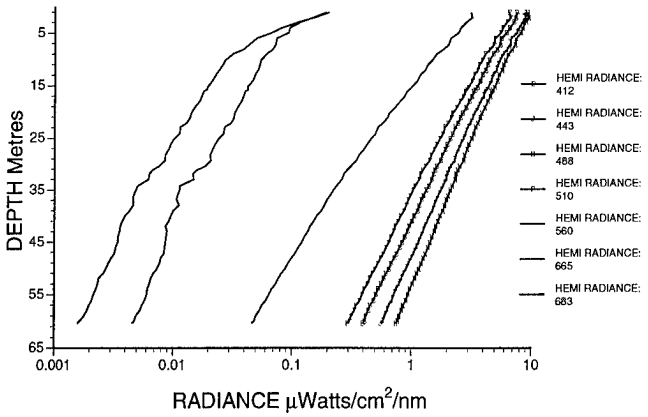


Fig.5: The slope of the log of radiance vs depth estimates the optical attenuation of energy through the water column in these wavelengths.

ACKNOWLEDGMENTS

We would like to thank Biospherical Instruments for the use of their PRR-600 spectral radiometer. This research was supported by a Natural Sciences and Engineering Research Council grant to E. LeDrew.

REFERENCES

[1] J.Hardy, F.Hoge, J.Yungel and R.Dodge, "Remote Detection of Coral Bleaching using Pulsed-laser Fluorescence Spectroscopy," Marine Ecology Progress Series, vol. 88, pp. 247-255, 1992.

[2] N. Jerlov, Optical Oceanography, Elsevier Publishing Company, 1976.

[3] M.Hamilton, C.Davis, W.Rhea, S.Pilorz and K.Carder, "Estimating Chlorophyll Content and Bathymetry of Lake Tahoe Using AVIRIS Data", Remote Sensing of Environment, vol.44, 1993.

[4] D.Peddle, H.White, R.Soffer, J.Miller and E.LeDrew,"Reflectance Processing of Field Spectrometer Data in Boreas", Proceedings of the 17th Canadian Symposium on Remote Sensing, 1995.

[5] D.Lyzenga, "Shallow Water Bathymetry Using combined LIDAR and Passive MSS Data", International Journal of Remote Sensing, vol.6, 1995.

[6] N.O'Neill and J.Miller, "On Calibration of Passive Optical Bathymetry Through Depth Soundings Analysis and Treatment of Errors Resulting From the Spatial Variation of Environmental Parameters",International Journal of Remote Sensing, vol.10, 1989.

Variability of Rossby Wave Propagation in the North Atlantic from TOPEX/POSEIDON Altimetry

P. Cipollini[1], D. Cromwell[1] and G. D. Quartly[2]
[1] James Rennell Division for Ocean Circulation, Southampton Oceanography Centre
[2] Remote Sensing Applications Development Unit, Southampton Oceanography Centre
European Way, Southampton SO14 3ZH, UK
Tel.+44-1703-596405 Fax +44-1703-596400
E-mail: cipo@soc.soton.ac.uk, ddc@soc.soton.ac.uk, gdq@soc.soton.ac.uk

Abstract — This paper deals with the study of westward-travelling, long-wavelength Rossby waves in the North Atlantic from TOPEX/POSEIDON altimeter data. Nearly three years of altimeter data have been used, starting from November 1992, in order to investigate the variability of this phenomenon. Corrections which are applied to the data set are briefly described: they account for radar propagation effects and geophysical phenomena such as ocean tides. After applying these corrections, we analyse time series of sea surface height anomalies to find the signature of Rossby waves. This analysis is carried out in a hybrid spatial-temporal frequency domain. It allows us to determine the wavelength, period and phase speed of the various signals which are present in this region. The results show evidence of Rossby waves which are particularly noticeable in the latitude range 33°-35° N. Detailed results are given in the paper for latitude 34° N. In particular, as the waves generated in the eastern basin traverse the Mid-Atlantic Ridge a change in the wavelength and speed of the propagating energy is observed.

INTRODUCTION AND BACKGROUND

The northeast Atlantic has traditionally been a region of interest for physical oceanographers and many observations have been gathered in order to elucidate the regional ocean circulation. Satellite observations are particularly useful to observe medium and large-scale features of the circulation. In particular, altimeter measurements of sea surface height (SSH) allow one to monitor propagation of long-wavelength Rossby waves.

Rossby or planetary waves arise from the conservation of potential vorticity when a water parcel is displaced northward or southward from a position of equilibrium. They appear as large-scale undulations which tend to propagate zonally in a westward direction across the ocean basins. Tokmakian and Challenor [1] and Le Traon and De Mey [2] have reported Geosat altimetric evidence for periodic SSH signals in the northeast Atlantic with typical wavelengths of 300-1200 km and periods of 120-700 days. Some of these signals correspond to Rossby waves. Moreover, analysis of Along-Track Scanning Radiometer (an instrument on ERS-1) average sea surface temperature data has shown thermal features propagating westward at about 2 km/day [3]. The present study utilises nearly three years of data from the state-of-the-art TOPEX/POSEIDON (T/P) radar altimeter.

A satellite altimeter measures its height above the sea surface by means of radar reflection. The shape of the sea surface is determined primarily by the Earth's gravitational field and, to a much smaller degree, by the dynamics of ocean circulation. In order to convert the altimeter height into a quantity of use to oceanographers, accurate satellite tracking is required together with various atmospheric and geophysical range corrections [4]. The SSH signal due to ocean circulation is obtained by taking the difference of the satellite's range to the sea surface and the computed height of the satellite's orbit above a reference ellipsoid, and then removing an estimate of the geoid. Atmospheric corrections compensate for the effect of radar propagation delays due to the presence of the ionosphere, and air and water vapour in the atmospheric column. Geophysical corrections account for tides (solid earth, ocean and polar), inverse barometer effect and electromagnetic bias (arising from the radar backscatter cross-section being larger at wave troughs than at crests).

DATA PROCESSING

The T/P data used in this study were extracted from the geophysical data records (GDRs) provided on CD-ROMs by AVISO. The data extracted from the GDRs consist of geo-located, approximately one-second average SSH estimates. An area of the Atlantic Ocean was selected between longitudes 5°–75° W and latitudes 10°–60° N (see Figure 1). Cycles 6 to 106, covering the period 11 November 1992 to 10 August 1995, were used in the analysis. The first five cycles were excluded from the analysis as altimeter mispointing problems have been reported for those cycles.

Values of SSH are corrected at each along-track location for the atmospheric and geophysical effects discussed above, and values of geoid height for that position are subtracted,

This work has been partially supported by the Commission of European Communities through a Research Training Fellowship to Paolo Cipollini (HCM contract no. ERBCHBGCT930440).

0-7803-3068-4/96$5.00©1996 IEEE

using a global geoid model. A summary of the corrections is presented in table 1.

The altimeter sampling position of SSH varies along-track. The corrected, geoid-removed SSH values are therefore collocated onto a reference grid. Apart from along-track variations in sampling position, there are also cross-track variations as the satellite does not exactly repeat its ground track; the across-track variations are usually kept within 1 km of the nominal path. This may introduce errors in the SSH if the cross-track geoid gradients are significant. In order to minimise this, a gradient reduction correction was used [Matt Jones, pers. comm.] whereby the difference between a model mean sea surface at the reference point and at the interpolated along-track point is added to the interpolated along-track SSH value. For both the along-track resampling and the cross-track gradient correction, we chose cycle 18 as the reference grid, as it is very close to the nominal ground track.

Table 1 Atmospheric and Geophysical effects corrections applied to T/P data [4]

correction	TOPEX	POSEIDON
Ionospheric	Dual frequency altimeter	DORIS model
Dry tropospheric	ECMWF model pressure field	
Wet tropospheric	TOPEX microwave radiometer	
E.m. bias	Gaspar et al. 4-parameter model [5]	
Inverse barometer	ECMWF model pressure field	
Solid earth tide	Cartwright and Edden model	
Ocean tide	Texas model CSR 3.0	
Polar tide	Wahr model	
Geoid height	OSU 91A model	

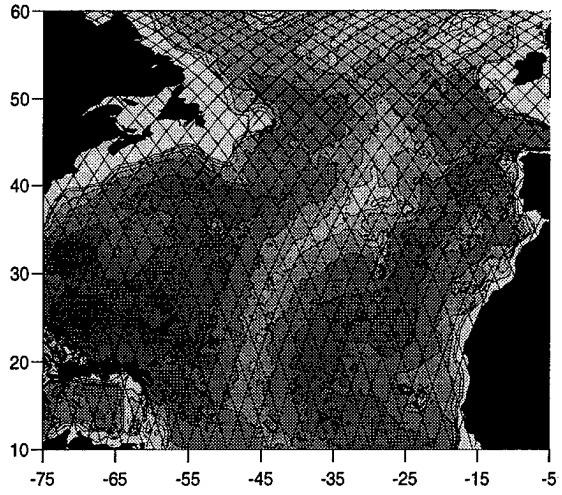


Fig.1 North Atlantic bathymetry at 1000 m intervals with 10-day repeat TOPEX/POSEIDON tracks superimposed.

The SSH time-mean over cycles 6 to 106 was calculated for each reference point from the gradient-reduced, collocated SSH data, and subtracted from individual SSH cycles to obtain the SSH anomaly for each cycle. Finally, the SSH anomalies were gridded onto a regular 1° by 1° grid. This was accomplished by means of Gaussian interpolation using a full-width half-maximum of 150 km and a search radius of 200 km.

It is possible to produce a movie of SSH anomalies which clearly shows interesting dynamic phenomena. Apart from the obvious high-energy area associated with the Gulf Stream, another interesting area extends zonally just south of the Azores and could be related to the Azores Current. We can study zonal waves by choosing a latitude value and considering the longitude-time plot or corresponding power spectrum obtained by Fast Fourier Transform (FFT).

RESULTS

We have analysed longitude-time and FFT plots east and west of the Mid-Atlantic Ridge (MAR). The largest signal related to Rossby waves is at 34°N; the signal quickly attenuates moving south or north of 34°N. The results for 34° N are shown in Figure 2 for the basin to the east of the MAR (east of 38°W) and in Figure 3 for that on the west of the MAR (west of 38°W). Although the overall energy in the eastern basin is lower, two peaks in the FFT (Figure 2b) are easily distinguishable and are explicable in terms of Rossby waves: these appear as diagonal stripes in the longitude-time plot (Figure 2a). The lower frequency peak corresponds to a time period of ~500 days and a spatial wavelength of ~1250 km. These values are consistent with the signal reported in [1]. The higher frequency peak approximately appears as a 2nd harmonic of the previous one, with a time period of ~250 days and a wavelength of ~600 km, as discussed in [2].

In the western half of the North Atlantic, although the Gulf Stream dominates the ocean dymanics, we observe waves continuing west across the MAR, with apparently increased phase speed from ~2.3 km/day to more than 4 km/day. This can be easily detected from the change of slope in the longitude-time plot in Figure 3a. The energy spectrum in this basin is richer and several higher frequency signals appear. However, the lower frequency peak is still evident while the high frequency peak is shifted towards longer time periods. It is believed that generation of topographic Rossby waves at, or near, the MAR could play a role in the change of energy characteristics [1]. Indeed, a distinct change of slope and the splitting of some wave tracks can be observed in the area between 50°W and 45°W.

Note that the observed main periodic signals can not be due to tidal aliasing since the T/P orbit produces tidal aliases of much shorter periods than those observed here [6].

REFERENCES

[1] R. T. Tokmakian and P. G. Challenor, "Observations in the Canary Basin and the Azores Frontal Region Using Geosat Data," J. Geophys. Res., vol. 98 (C3), pp. 4761-4773, 1993.

[2] P.-Y. Le Traon and P. De Mey, "The eddy field associated with the Azores Front east of the Mid-Atlantic Ridge as observed by the Geosat altimeter," J. Geophys. Res., vol. 99 (C5), pp. 9907-9923, 1994.

[3] D. Cromwell, J. P. Bishop, and M. S. Jones, "An atlas of ATSR averaged sea surface temperature maps of the NE Atlantic for 1992-94," J. Rennell Div. for Oc. Circ., Internal Doc. No. 24, 77 pp. (unpubl. manuscr.), 1995.

[4] L.-L. Fu, E. J. Christensen, C. A. Yamarone, M. Lefebvre, Y. Menard, M. Dorrer and P. Escudier, "TOPEX/POSEIDON mission overview," J. Geophys. Res., vol. 99 (C12), pp. 24369-24381, 1994.

[5] P. Gaspar, F. Ogor, P.-Y. Le Traon and O.-Z. Zanife, "Estimating the sea state bias of the TOPEX and POSEIDON altimeters from crossover differences," J. Geophys. Res., vol. 99 (C12), pp. 24981-24994, 1994.

[6] B. V. Sanchez and N. K. Pavlis "Estimation of main tidal constituents from TOPEX altimetry using a Proudman function expansion," J. Geophys. Res., vol. 100 (C12), pp. 25229-25248, 1995.

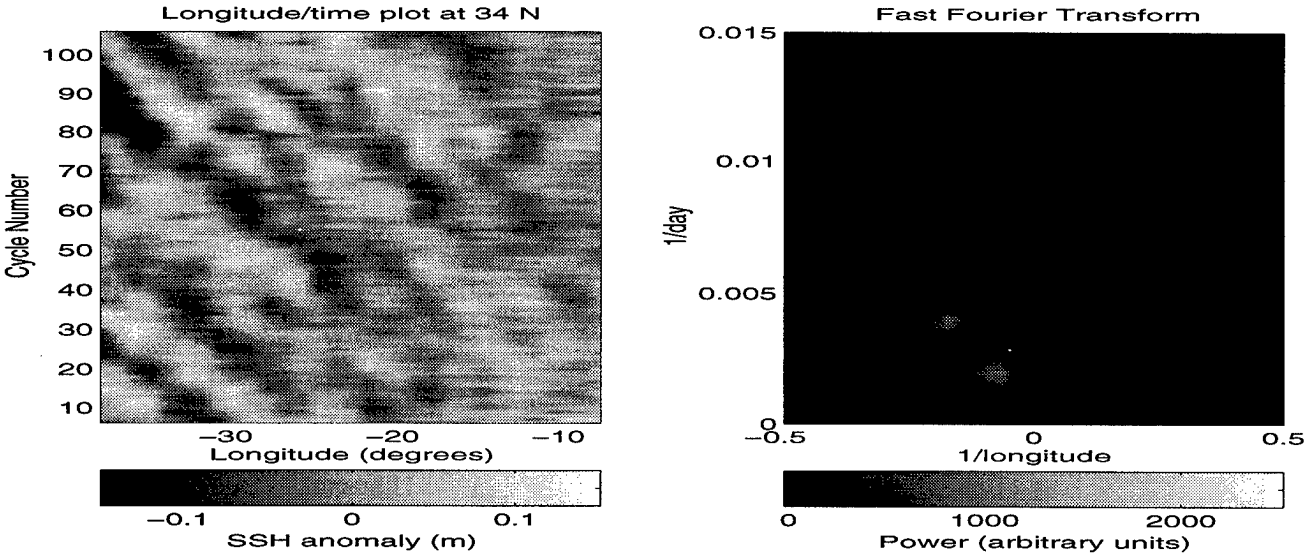


Fig. 2 a) Longitude-time plot and b) related FFT of the altimeter SSH anomalies at 34°N - eastern basin (38°W to 8°W)

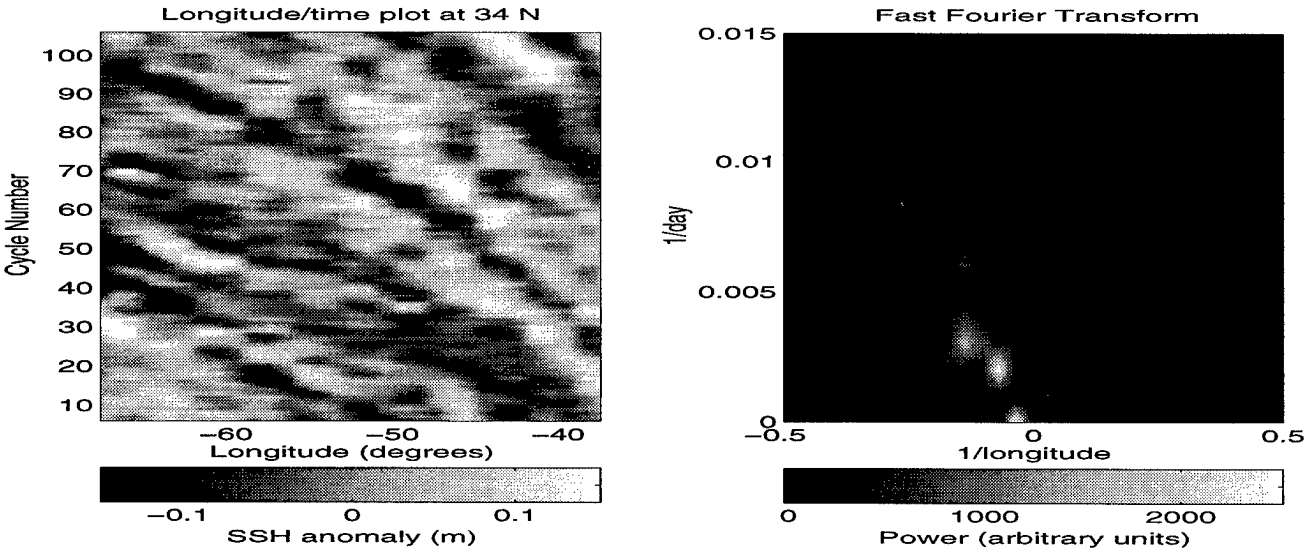


Fig. 3 a) Longitude-time plot and b) related FFT of the altimeter SSH anomalies at 34°N - western basin (68°W to 38°W)

Chlorophyll Retrieval from CZCS: Influence of Atmospheric Aerosols

Oliver Moldenhauer*, Moira L. Steyn–Ross†, and D. A. Steyn–Ross†

***Schuetzenweg 42/2/113, 26129 Oldenburg, Germany 0441/7775234**
***O.Moldenhauer@aida.comlink.de / http://www.hrz.uni-oldenburg.de/~oliver**
†Physics Dept, Univ. of Waikato, P.B. 3105, Hamilton, New Zealand / asr@waikato.ac.nz

Abstract -- Accurate chlorophyll concentration retrieval from satellite data is hampered by the aerosol scattering effects of the intervening atmosphere. We present an algorithm which employs a multivariate-optimisation to correct for atmospheric scattering. The method returns a value for chlorophyll concentration as well as a first estimate for aerosol content at pixel resolution. We demonstrate the method using *in situ* data co-located with CZCS data. Results indicate the method yields chlorophyll amounts to within expected uncertainties.

INTRODUCTION

The Coastal Zone Color Scanner (CZCS), launched on board the NIMBUS-7 satellite in 1978, was designed as a prototype to investigate the feasibility of obtaining global distributions of oceanic phytoplankton. Over its eight-year life-time, it returned radiances in the visible (channels 1-4: 443, 520, 550, 670 nm), near infrared (ch.5: 750 nm), and thermal infrared (ch.6: 0.5-12.5 μm). Channels 1 to 4 in the visible are the most useful for detecting ocean pigment.

Many algorithms have been developed to retrieve chlorophyll concentration [1]. Most model the radiance received at the satellite as the sum of the water-leaving radiance plus the optical-path contribution due to scattering and reflected skylight from the sea surface. As the optical-path radiance contributes up to 90 percent of the satellite signal, it is crucial that path radiances be accurately determined on a pixel-by-pixel level to enable reliable pigment retrieval.

The standard CZCS atmospheric correction algorithm [1] assumes that the instrument is able to view "clear water" ocean, that is, a region of ocean in which the chlorophyll concentration is less than 0.25 mg/m^3. The channel-4 (670 nm) water-leaving radiance is approximately zero; the normalised water-leaving radiances in channels 2 and 3 are (approximately) known, thus the ratios of aerosol-scattered radiance for the channel pairs 4, 2, and 4, 3 can be computed, and the corresponding 4, 1 ratio found by extrapolation. Thus the path radiance in all channels may be determined.

However, problems arise when the image contains no clear water. Also the required ratios may vary over the image due to changes in aerosol type.

We present a new chlorophyll concentration retrieval algorithm which uses the Fischer MOMO computer code [2]. MOMO is a full radiative transfer bio-optical model characterised by scattering and absorption of the various water- and air-suspended constituents. We employ a novel technique to correct for the atmosphere: Using satellite observed radiances and the equation of transfer for the ocean-atmosphere system, we perform a multivariate-optimisation which returns that chlorophyll concentration which is most consistent with a given atmospheric aerosol content.

THEORY: EQUATION OF TRANSFER

To obtain the radiance sensed by the satellite, we model the atmosphere-ocean system via the equation of transfer:

$$\begin{aligned}\mu \frac{d}{d\zeta} L(\hat{\xi},\zeta) \;=\; & -L(\hat{\xi},\zeta) \\ & + \;\omega(\zeta) \int L(\hat{\xi}',\zeta)\, \tilde{\beta}(\zeta,\hat{\xi}' \to \hat{\xi})\, d\Omega(\hat{\xi}') \\ & + \;\omega(\zeta)\, \pi F_0\, \tilde{\beta}(\zeta,\hat{\xi}_0 \to \hat{\xi})\, \exp(-\zeta/\mu_0)\end{aligned} \tag{1}$$

where $L(\hat{\xi},\zeta)$ is the spectral radiance (radiative power per unit area, per unit solid angle, per unit wavelength). The second term on the right-hand side of (1) describes scattering and absorption of radiation by ocean or atmospheric components; the third term indicates the attenuation of the direct solar flux. The integral is over the unit sphere where $d\Omega(\hat{\xi}')$ is the infinitesimal solid angle centered on the

0-7803-3068-4/96$5.00©1996 IEEE

direction $\hat{\xi}'$. The symbols $\hat{\xi}$ and $\hat{\xi}_0$ represent unit vectors in the direction of the light ray and the solar radiance respectively; μ and μ_0 are the zenith and solar zenith cosines; F_0 is the solar radiance.

$\zeta = \int c(z)dz$ is the optical depth (zero at the top of the atmosphere), where the extinction coefficient c (with unit m^{-1}) is defined as the sum $c = a + b$ of the absorption coefficient a and the scattering coefficient b. $\omega = b/a$ is the single scattering albedo, and β is the volume scattering function.

We model the absorption coefficient of pure sea water and gelbstoff (colored, dissolved organic matter) following Mobley [3].

To obtain the coefficients of the pigment-dependent absorption coefficient we adopted the model of Morel [4].

For the scattering coefficient of pure sea water, we used the model of Morel [5] .

The scattering and backscattering coefficients dependent on chlorophyll used in our model are that of Mobley [3]. However, we modify the volume scattering coefficient to render it more pigment-dependent.

DATA SETS

CZCS satellite data and coincident ground truth were obtained from the NASA Goddard Space Flight Center. We found that the pre-navigated satellite images contained residual positioning errors of ~7 km, so we fine-tuned the navigation by optimizing the correlation between image coastline features and coastlines extracted from the public-domain CIA World Database II.

The most important molecular absorber for the CZCS channels is ozone. Ozone concentrations were obtained from coincident TOMS (total ozone mapping spectrometer) data.

METHOD

The equation of transfer (1) was solved using the computer program MOMO, version 2.1a [2]. MOMO solves for radiative transfer in the atmosphere-ocean system using a matrix-operator adding technique. The diffuse radiation is calculated via the matrix operator method, while the direct unscattered solar flux is computed using the Beer-Lambert law.

Using a Mie scattering program developed by Heinemann [6], we calculated the extinction ceofficients for three types of aerosols (maritime, urban, continental) defined by the World Climate Project [7]. The ratio of continental to urban aerosols was fixed at 9:1, as defined by the ratio of their extinction coefficients at 550 nm; we refer to the variable fraction of maritime aerosol to this mixture as the aerosol-ratio.

For the optimization merit function we used a χ^2-like expression to compare the measured and predicted at-satellite radiances, taking the standard deviation of the set of measured radiances in a given channel as an estimate of the error in a single measurement.

RESULTS

Rather than adopting the standard radiance calibration method for CZCS (the standard method is optimized to match Gordon's algorithm [1]), we recalibrated the sensor to fit our algorithm. This was done by assuming an aerosol-ratio of 0.5, fixing the pigment concentration to the sea-truth value, then minimizing the deviation between predicted and measured radiances by varying the aerosol concentration for the first 141 points in our data set. The average of the ratios between the measured and the predicted radiances is taken as the correction factor to be applied to the calibration provided by GSFC. The resulting calibration correction factors are:

Channel 1: 1.081
Channel 2: 1.026
Channel 3: 1.011
Channel 4: 0.792

We applied these radiance corrections to the second half of our data set (n = 139). We then calculated the pigment concentrations (Fig. 1), aerosol concentrations, and aerosol ratios (Fig. 2) which minimized the deviation between predicted and measured radiances for the second data set.

The Fig. 1 log-log plot of retrieved versus surface-measured pigment concentrations has a correlation coefficient of r = 0.43, an encouraging result in the context of the large atmospheric uncertainties and wide dynamic range of the measurements (almost three orders of magnitude).

Our values for retrieved aerosol concentrations (not shown here) seem reasonable, with optical depths at 550 nm ranging between 0.10 and 0.18.

The Fig. 2 scatter plot shows that the aerosol ratio is varying over the our data set, indicating qualitatively that the

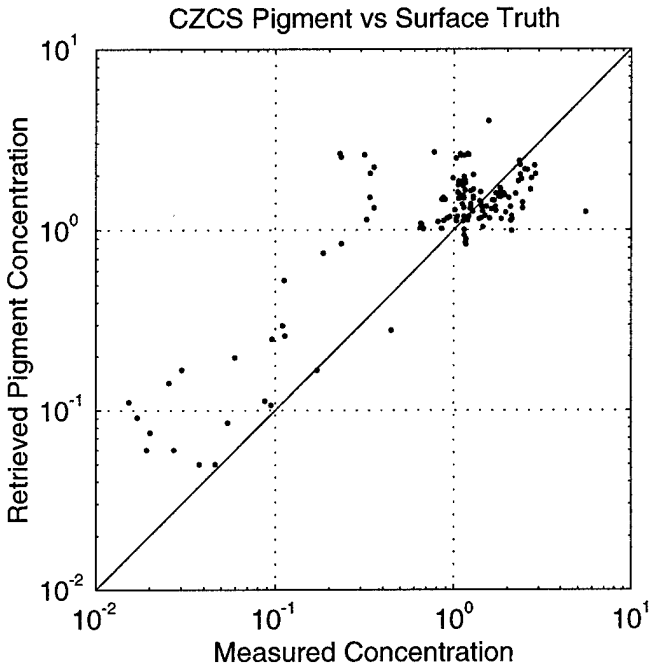


Fig. 1 Log-log plot of CZCS retrieval for ocean pigment concentration (mg/m^3) versus *in situ* concentration measurements.

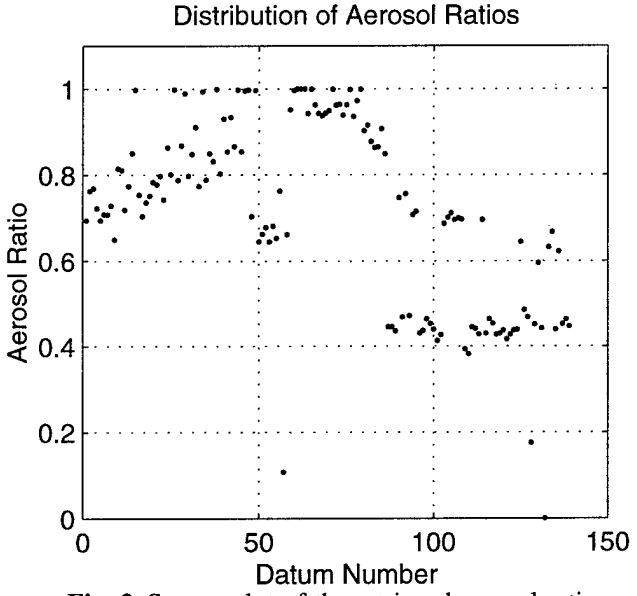


Fig. 2 Scatter plot of the retrieved aerosol ratios from our data set.

algorithm seems to be able to distinguish between the different types of aerosol.

Considering the limitations of our rather simplistic aerosol model, and the inherent problems associated with the retrieval of chlorophyll by remote sensing, we feel that these results are quite encouraging, and could form the basis of further research relevant to future ocean sensors such as SEAWiFS.

ACKNOWLEDGMENTS

We wish to acknowledge Frank Fell, Jürgen Fischer, and Ralf Bennartz from the FU Berlin for providing the radiative transfer code MOMO. Also, thanks are due to NASA Goddard Space Flight Center (GSFC) and the DAAC for providing the CZCS data, the sea truth, and the information describing how to decode these data.

REFERENCES

[1] Gordon, H.R., Clark, D.K., Brown, J.W., Brown, O.B., Evans, R.H., and Broenkow, W.W., Phytoplankton pigment concentrations in the middle atlantic bight: Comparison of ship determinations and CZCS estimates, *Appl. Opt.*, 22 (1), pp. 20-36, 1983.

[2] Fischer, J., Fernerkundung von Schwebstoffen im Ozean, PhD thesis, Universitat Hamburg, 1983.

[3] Mobley, C.D., Light and water: Radiative Transfer in Natural Waters, Academic Press, 1994.

[4] Morel, A., Light and marine photosynthesis: a spectral model with geochemical and climatological implications, *Prog. Oceanogr.*, 26, p. 263, 1991.

[5] Morel, A., Optical properties of pure water and pure sea water, In Jerlov, N. G. and E.S. Nielsen, eds, Optical Aspects of Oceanography, Academic Press, 1974.

[6] Heinemann, T. Fernerkundung von Aerosolen, Master's Thesis, FU Berlin, 1994.

[7] WCP Report 55: Experts meeting on aerosols and their climatic effects, 1983.

A Global Sea Level Variability Study from almost a Decade of Altimetry

Marc C. Naeije and Remko Scharroo
Delft University of Technology – Institute for Earth-Oriented Space Research (DEOS)
Kluyverweg 1, 2629 HS Delft, The Netherlands
Tel: +31 15 2783831, Fax: +31 15 2783444, Email: Marc.Naeije@lr.tudelft.nl

Abstract— Altimeter data of the GEOSAT, ERS-1 and TOPEX/POSEIDON (T/P) missions have been used to study large-scale seasonal and long-periodic changes in the sea level. The radial orbit error is reduced by crossover minimization. We computed large-scale global dynamic topographies with a time resolution of 7 days and a space resolution of about 5°. EOF and DFT analyses show a dominant annual cycle for most regions. Time-longitude sections reveal ENSO warm and cold events accompanied by Kelvin and Rossby waves. A secular change of 4.9 mm/yr is evident both from the ERS-1 and T/P data.

1. INTRODUCTION

In recent years satellite altimetry has been used for studying ocean dynamics on a variety of time and space scales, the biggest advantage over *in situ* measurements being the global coverage. Most of the altimeter missions, however, cover only a few years, which makes it hard to evaluate long-periodic sea level changes like interannual and decadal variability. In turn, this hampers the utility of altimetry in describing and understanding the climate system. We made an effort to patch the data available from the GEOSAT, ERS-1, and T/P missions, spanning almost a decade of altimetry. Here we briefly summarize the results of analyzing a dynamic topography time series computed from these data.

This work was supported by the Space Research Organisation Netherlands SRON and the Netherlands Remote Sensing Board BCRS

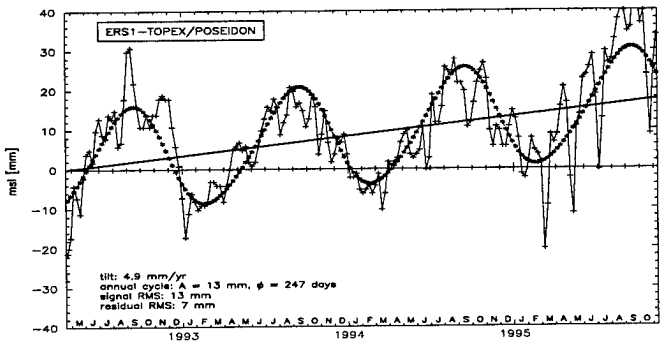


Figure 1. Mean sea level history.

2. DATA AND METHOD

We selected 1-Hz altimeter data from the GEOSAT archive (NOAA T2GDR) from November 1986 to November 1988, ERS-1 (ESA OPR2) from April 1992 to January 1995, and T/P (Aviso M-GDR) from November 1992 to November 1995. Besides the standard corrections, JGM-3 orbits and the Grenoble FES-95.2 tide model has been used. A weekly representation of the global dynamic topography was obtained by interpolating/filtering the sea level data corrected for orbit error and calibrated altimeter bias, and referenced to a hybrid JGM-3 and OSU91A geoid model, to a 1°-resolution grid. The data were grouped into batches of 17 days (GEOSAT, ERS-1) and 10 days (T/P), and processed separately to preserve the large-scale seasonal signal. The radial orbit error is then reduced by crossover minimization, accounting for a bias and a 1 cycle/rev signal. Subsequently, 36-degree spherical harmonic expansions have been computed to extract only the large-scale features of the ocean circulation. The solutions were merged together from one mission to the other by removing a shift in the latitude-longitude plane resulting from incompatibilities of the coordinate frames. For this we compared 1-degree spherical harmonics of the long-term averages. It appeared that the C_{10} and C_{11} terms of GEOSAT differ by 5 cm from T/P, whereas ERS-1 only differs less than 1 cm. After merging, finally only T/P data are used during the T/P mission. In addition, a 2.5 mm/yr TOPEX instrument drift is applied.

3. DISCUSSION ON RESULTS

From the complete time series a long-term (6-years) mean topography and variability grid was computed. The variability (not shown here) exhibits, apart from the enhanced levels in the western boundary currents, high levels in the equatorial Pacific and Indian Ocean due to the El Niño/Southern Oscillation (ENSO) phenomenon and

0-7803-3068-4/96$5.00©1996 IEEE

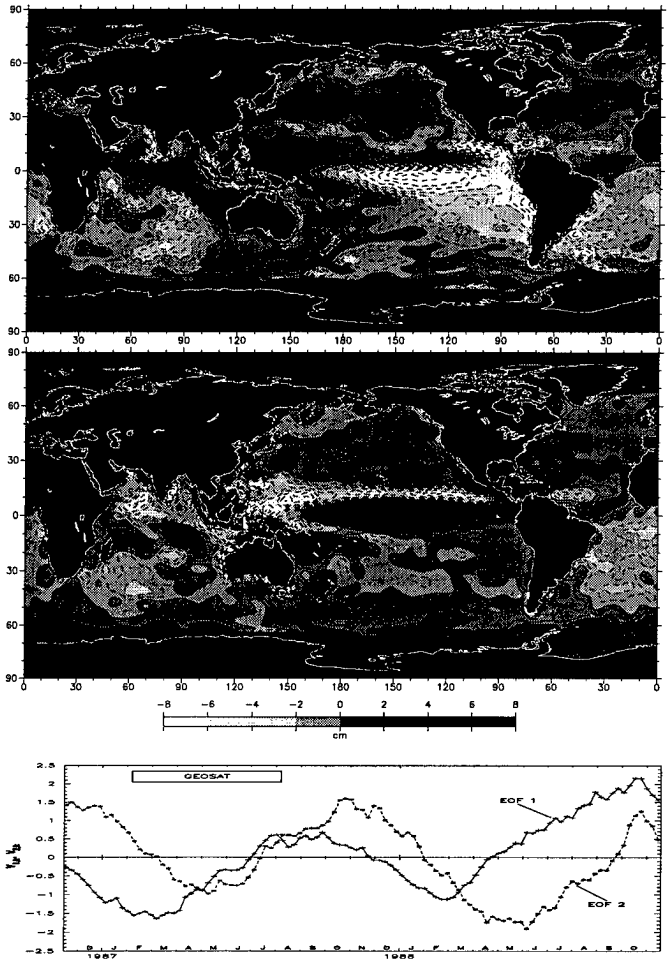


Figure 2. First two EOFs in the GEOSAT data.

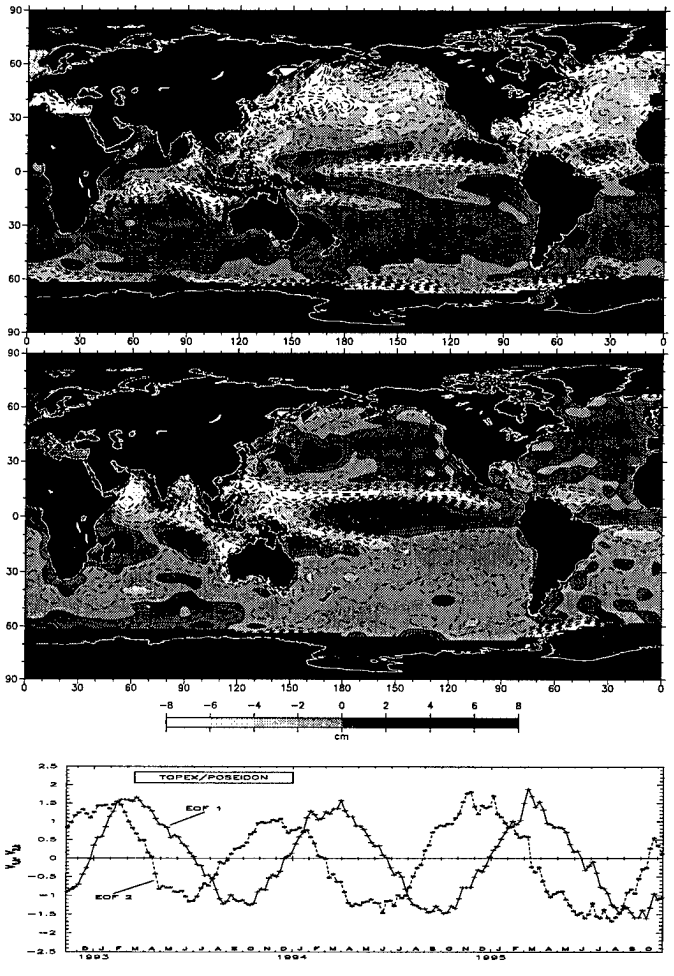


Figure 3. First two EOFs in the T/P data.

monsoon systems. This is also apparent from DFT analyses on the variations in the time series. The *annual* cycle is identified as being most dominant in all regions with an intensification in the northern hemisphere, whereas the *semiannual* cycle pops up in equatorial regions like the Northwest Indian Ocean, and a *biannual* signal accounts for the ENSO.

A global mean sea level was computed for each of the dynamic topographies by averaging the total height representation of the spherical harmonics weighted by the cosine of the latitude. The history of this mean sea level is given in Fig. 1. A simultaneous estimate of the annual and semiannual cycle and a tilt, reveals an average sea level change rate of 4.9 mm/yr over the 1992-95 period. We independently analyzed the ERS-1 data, which reveals a 4.7 mm/yr rise. So we are very confident about this rather high value. The GEOSAT result (not shown here) shows a decline but suffers from instrument drift and an increasing ionospheric correction error.

We applied singular value decomposition (SVD) on the GEOSAT and T/P data matrices to recover the first two EOFs. The results are given in Fig. 2 and Fig. 3. The upper two panels give the geographical distribution of the first two EOFs, whereas the bottom panel gives the **V** matrix, or time function. The first two EOFs explain about 40% of the data in both cases. The annual cycle is very dominant, both in EOF1 and EOF2. In EOF1 we notice the 180° out of phase signature in the sea level in the two hemispheres due to the thermal expansion related to the Earth's motion about the sun. There is strong evidence of ENSO and monsoon in EOF2. The GEOSAT and T/P results are quite similar, the ENSO being stronger in the GEOSAT results. To investigate this in detail we followed the variations in the dynamic topography series in time in the equatorial region. Fig. 4 gives a time-longitude plot for the equatorial cross-section. Focusing on the eastern equatorial Pacific between 120°E and 80°W we observe the evolution of ENSO warm and cold events (high and low anomalies, respectively). The pattern is very regular and seems to have a biannual cycle. We easily notice up- and downwelling Kelvin waves, propagating eastward with an average speed of 2.8 m/s, which is consis-

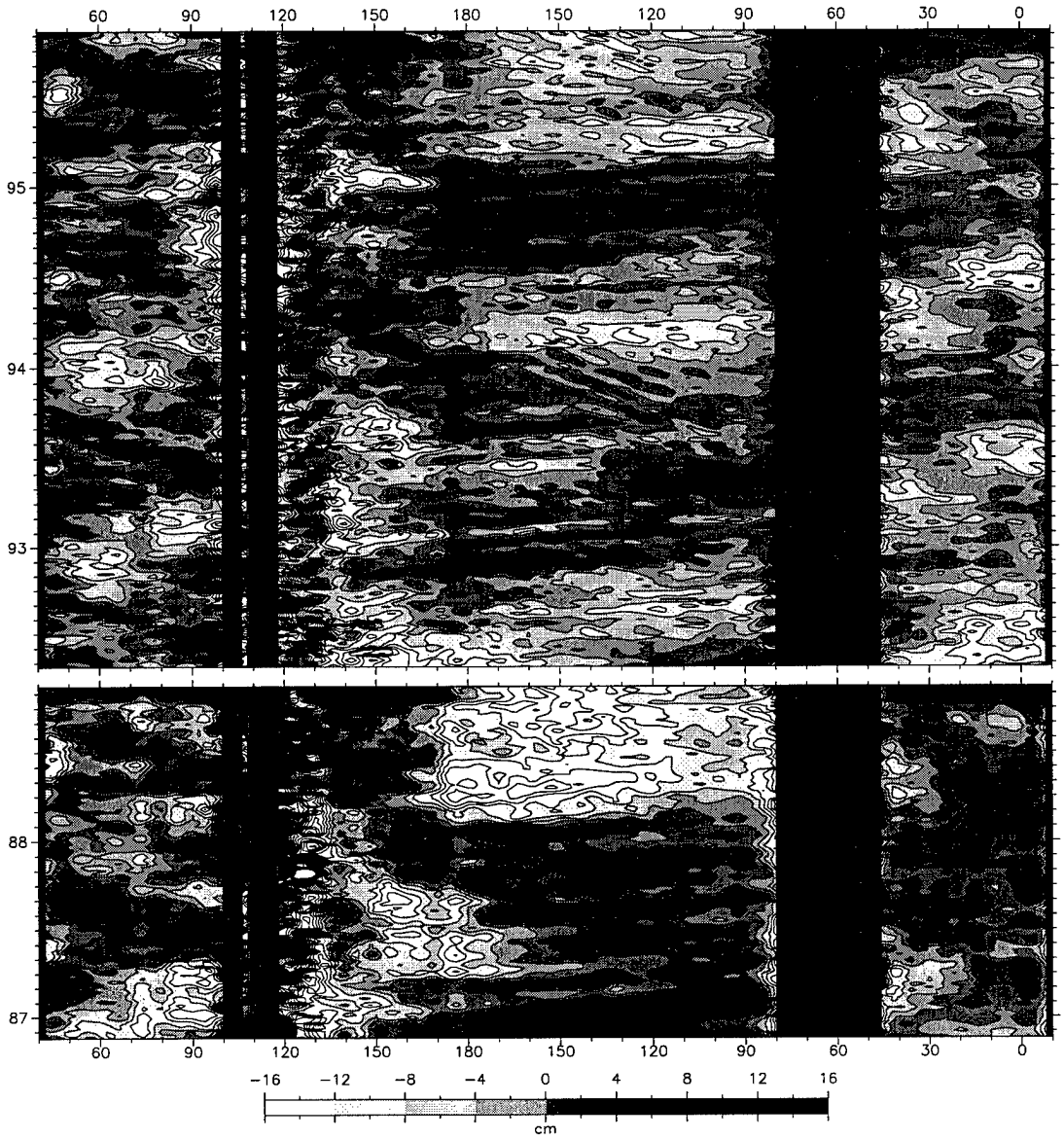


Figure 4. Time-longitude section of sea level anomalies along the equator.

tent with the first baroclinic mode. Also westward propagation by Rossby waves can be identified of which the phase speed is about 60 cm/s, consistent with the first-mode Rossby waves. The waves are clearly reflected by natural boundaries. There seems to be a barrier at about 175°E. We found that this must be due to the presence of the Gilbert Islands. The equatorial Atlantic also reveals an annual cycle with high levels bouncing up the east and west coast.

Though this paper can only describe a fraction of the total analyses conducted, we think it demonstrates that a long record of altimeter data is capable of recovering long-periodic changes in the sea level. We quiver to study more years worth of data.

4. REFERENCES

Fu, L.-L., and R. E. Cheney (1995), Application of satellite altimetry to ocean circulation studies: 1987–1994, *Rev. Geophys., Suppl.*, pp. 213–223, July 1995.

Naeije, M.C. (1995), Evaluating 2 years' worth of T/P sea level data, *T/P Research News, JPL 410–42, Issue 4*, 17–21, August 1995.

Various authors (1990), Geosat special issues, *J. Geophys. Res.*, *95*(C3&C10), 2833–3179 & 17,865–18,052.

Various authors (1994), 1st TOPEX/POSEIDON Special Issue, *J. Geophys. Res.*, *99*(C12), 24,369–25,062.

Vertical distribution of PAR and diffuse attenuation coefficient: modeling and in situ measurements

Vladimir A.Volynsky, Anatoly I. Sud'bin
P.P.Shirshov Institute of Oceanology, 23 Krasikova, 117218, Moscow, Russia
tel:(7-095)-335-8506; e-mail: vvladm@mx.iki.rssi.ru

John Marra
Lamont-Doherty Earth Observatory of Columbia University, Palisades, NY 10964, USA
tel:(914)-365-8891; fax: (914)-365-8150; e-mail: marra@ldeo.columbia.edu

INTRODUCTION

Vertical distributions of the photosynthetically available radiation, PAR, is of great importance for understanding of biological matter behavior, estimation of primary productivity, in evaluation of the heath budget and in some other problems. Numerical modeling of PAR penetration was carried on using diffuse attenuation coefficient, Kd(440), in the upper 10 meters layer as an input parameter. These calculations were done for different types of the Kd(Z) profiles [1]. Numerical results were compared with experimental data of PAR measurements. It was shown that correlation between PAR and Kd(440) in the upper 10 meters layer are very close as for model and for experimental data.

MODELING OF PAR PENETRATION.

Penetration of PAR in ocean water in the wavelength band of 400-700 nm is determined as

$$PAR(Z) = \int_{400}^{700} Eo(\lambda)\exp[-\int_{0}^{Z} Kd(\lambda,z)dz]d\lambda, \quad (1)$$

where $Eo(\lambda)$ is a surface downwelling spectral irradiance, and $Kd(\lambda,z)$ is the spectral diffuse attenuation coefficient.
In (1) $Eo(\lambda)$ was taken as an averaged of about 100 $Eo(\lambda)$ spectra normalized by Eo(490) (Tab. 1). The diffuse attenuation coefficient spectrum was calculated using Kd(440) and an improved combination of [3] with two eigenvectors and [2] algorithms. The value of Kd(440) in the upper 10 m layer was varied from 0.023 to 0.4 m^{-1}.
The decrease of PAR with the depth can be described by depths where it is equal to 10%, 1% and 0.1% of the surface value. We evaluated these depths, Z(10%), Z(1%) and Z(0.1%), for non-stratified and stratified waters through numerical modeling. Correlation between Kd(440nm;0-10m) and Z(x%) was found in the form $Z(x\%) = A\ Kd(440;0\text{-}10m)^{-B}$ for two different stratification types of Kd profiles: 1-non-stratified waters; and 2-for stratified waters, which described by Kd(0-Zef)=1.01 Kd(0-10) - 0.0046, where Zef = 4/Kd(0-10) (Tab. 2).

Table 1
Normalized sea-surface downwellig irradiance

λ,nm	Eon	λ,nm	Eon	λ,nm	Eon
390	.48	500	1.0	610	.82
400	.54	510	1.0	620	.78
410	.62	520	.995	630	.75
420	.69	530	.99	640	.72
430	.74	540	.99	650	.71
440	.79	550	.98	660	.70
450	.84	560	.97	670	.69
460	.88	570	.94	680	.68
470	.92	580	.91	690	.67
480	.96	590	.88	700	.67
490	1.0	600	.87		

Table 2
Correlation coefficients

Non-stratified waters			Stratified waters		
	A	B		A	B
Z(10%)	4.25	0.67	Z(10%)	3.5	0.78
Z(1%)	8.07	0.76	Z(1%)	7.06	0.87
Z(0.1%)	12.8	0.76	Z(0.1%)	13.0	0.87

0-7803-3068-4/96$5.00©1996 IEEE

The relationship between Kd(440nm;0-10m) and Z(PAR10%,1% and 0.1%) is illustrated by Fig. 1.

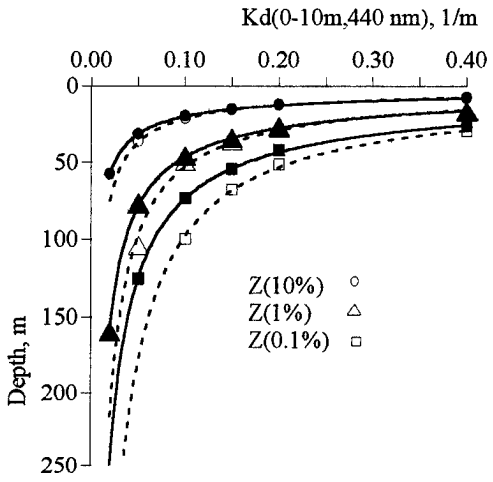


Fig. 1. Correlation between Kd(0-10m, 440nm) and Z(x%) for non-stratified (solid lines) and startified waters (dashed lines)

In the frame of this modeling research it was found a relationship between Kd(440;0-10m) and the Secchi disk depth (for 109 points with correlation coefficient is 0.91, $r^2 = 0.83$, and the standard error is equal to 0.51) in different regions of the World Ocean where these two optical characteristics were measured simultaneously. This relationship is

$$Kd(440;0\text{-}10m) = 4.94\ (Zsd)^{-1.35}, \qquad (2)$$

where Zsd is the Secchi disk depth (m). (Fig. 2).

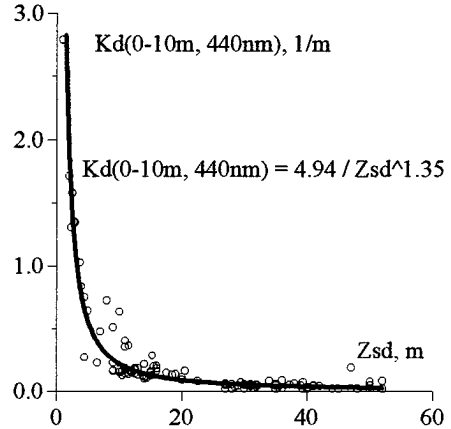


Fig. 2. Correlation between Kd(0-10m,440nm) and Secchi disk depth, Zsd

The modeling results were compared with measurements data of P16 WOCE expeditions. Bio-optical stations of P16 expedition going along 152° W longitude from south to north. Optical data were collected using a Profiling Spectroradiometer, MER-2040

For measured profiles of PAR(Z) there were determined the depths of 10%, 1% and 0.1% attenuation of the surface PAR(0), which were compared with the same modeling values. The Kd(440,0-10m) values determined from measured downwelling irradiance were correlated with values Z(10%, 1%, 0.1%) calculated from measured PAR(Z). Analogous results were obtained in this case too (Fig. 3).

The comparison shows a satisfied coincidence of Z(10%) with average relative error of 12%. For Z(1%) and Z(0.1%) the relative errors are twice more.

Fig. 4 illustrates meridianal distribution of Z(x%). The satisfied coincidence of Z(PAR10%) calculated from measurements and the same values obtained from modeling for non-stratified waters suggests that the upper layer up to the depth Z(PAR10%) is weakly stratified. The depth of the euphotic zone (corresponding to the depth of 1% of surface PAR) varied from 149-120 m in the two northern-most stations and 90-100 m in the 10 southern-most stations to 80-90 m in the middle part of this section.

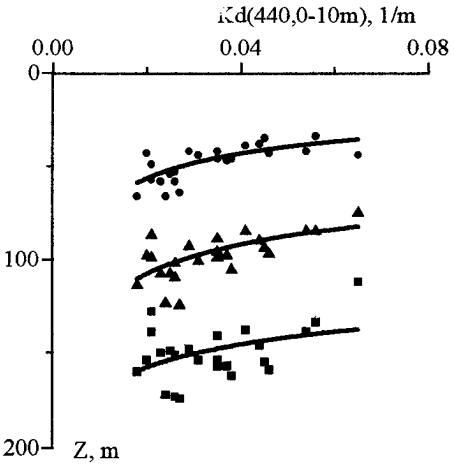


Fig. 3. Measured values of Kd(440,0-10m) and Z(PAR10%, 1%, 0.1%)

On the basis of improved models and using data of: a) Kd(495) distribution in the upper layer of the World Ocean [4]; b) seasonal distribution of Zsd, there were created PAR vertical distribution macroscale maps. This approach allows to use remote sensor data such as Kd(490) to estimate PAR penetration with relative error of about 30%.

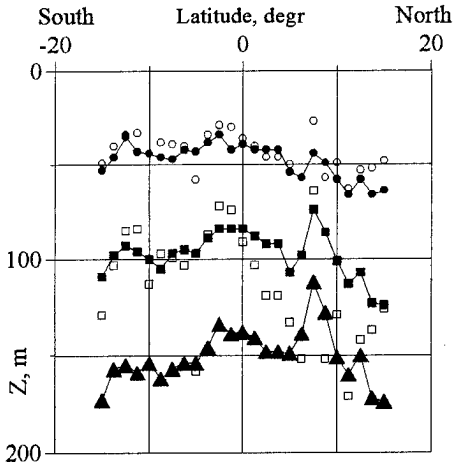


Fig.4. Meridional Distribution (152 deg W) of Z(PAR10%,1%,0.1%)

Z(10%) ○
Z(1%) □ Filled - measurements
Blank - modeling
Z(0.1%) △

References

[1] V.A. Volynsky and A.I.Sud'bin, "Vertical attenuation coefficient investigation in upper and deep layers," Proc. SPIE, 2048, 1993, pp. 73-79.

[2] R.W. Austin and T.J.Petzold, "Spectral dependence of the diffuse attenuation coefficient of light in ocean waters: A re-examination using new data," Proc. SPIE, Ocean Optics X, 1302, 1990, pp. 79-93.

[3] V.A. Volynsky and A.I.Sud'bin, "Statistical analysis of spectra of vertical attenuation coefficient," Oceanology, 32, 1992, pp. 821-829.

[4] J.-Y. Simonot and H.A. Trout, "A Climatological Field of Mean Optical Properties of the World Ocean," J. of Geophys. Res., 91(5), 1986, pp. 6642-6646.

Detection of Convective Instability in Atmospheric Boundary Layer Over the Ocean by Airborne Ku-band Real Aperture Radar.

M.I.Mityagina, Yu.A.Kravtsov, V.G.Pungin, K.D.Sabinin, V.V.Yakovlev.
Space Research Institute, Russian Academy of Sciences
Profsoyuznaya, 84/32, 117810, Moscow, Russia
Telephone:095-333-5279; Fax:7-095-333-1056
E-mail:kravtsov@asp.iki.rssi.ru;vyakovlev@asp.iki.rssi.ru;vpungin@iki3.iki.rssi.ru

ABSTRACT

The paper examines structural features of radar images obtained under unstable stratification of ocean-atmosphere boundary layer. Manifestations of the dry and moist convective cells are of special interest. Near surface convective processes in radar images are investigated at different sounding direction relative to mean surface wind. Images recorded by airborne side looking real aperture radar at wave length 2.25 cm are considered. Radar images under discussion were recorded during joint Russia/US experiment JUSREX conducted in July 1992 in an area off the U.S. coast, roughly 80 km south east of Long Island, New York [1].

MANIFESTATIONS OF THE BOUNDARY LAYER CONVECTIVE PROCESSES IN RADAR IMAGES

Results of Ku-band. radar measurments from TU-134 aircraft laboratory are presented. The radar swath is 12.5 km on each side of ground track. Alternate pulses of horizontal and vertical polarizations are transmitted to produce simultaneous HH and VV images. Spatial resolution is of about 25x25 meters.

High sensitivity of VV radar images to instability of boundary atmosphere layer is their most impressive feature in the obtained data. Under stable stratification, when air temperature is higher than that of water, VV and HH radar images of sea surface are qualitatively similar to each other.

The radar image (July 18, 1992) given in fig.1 illustrates this fact. Surface manifestations of internal waves are distinctively seen both at HH and VV polarizations, although VV contrasts are less pronounced.

Fig. 2 presents HH and VV sea surface radar images obtained on July 24, 1992 under unstable stratification of boundary layer. Near-surface wind variations induced by intensive convection in the boundary layer produce high contrast cellular pattern in the VV image . The typical size of this cells is of about 1.5-2 km. There is an increase of mean backscattered signal from the bottom to the top of the image, caused by speeding up of mean surface wind . Internal waves in ocean are clearly observed in the HH image (left) and are not visible in the VV image(right).

Similar phenomena are observed in radar images obtained over a number of years of experiments in the North-West Pacific, near the Kamchatka peninsula. An extension of analysis of numerous images recorded under stable, unstable and neutral atmospheric boundary layer conditions shows that cellular-type structures in VV radar images are distinctively visible every time when the sea surface is warmer than the near surface air and are never detected under other conditions. It means that an analysis of Ku-band radar images at vertical polarization makes it possible to determine the type of the boundary layer stratification and radar images clutter patterns at vertical polarization are to be regarded as an indicator of boundary layer conditions. When a cellular type structure appears in vertical-polarization radar images, the sea surface is estimated to be warmer than air. Occurrence of this type of clutter is strongly correlated with presence of an unstable atmospheric boundary layer. This is important because the modern models for ocean-atmosphere interaction include the stability parameter.

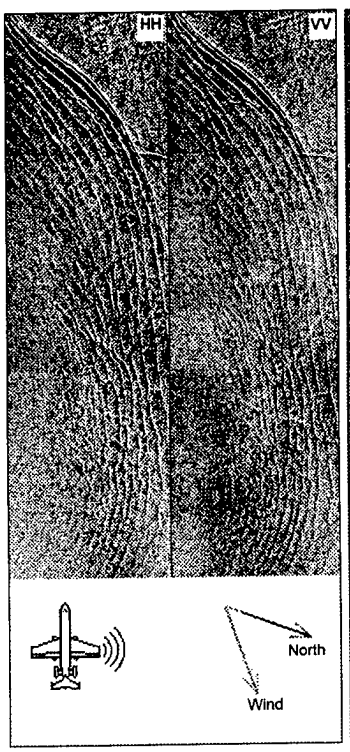


Fig.1 Radar image of the sea surface obtained under stable conditions

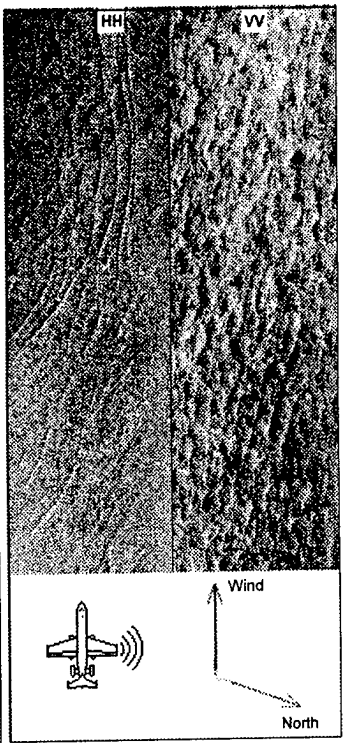


Fig.2 Radar image of the sea surface obtained under unstable conditions

0-7803-3068-4/96$5.00©1996 IEEE

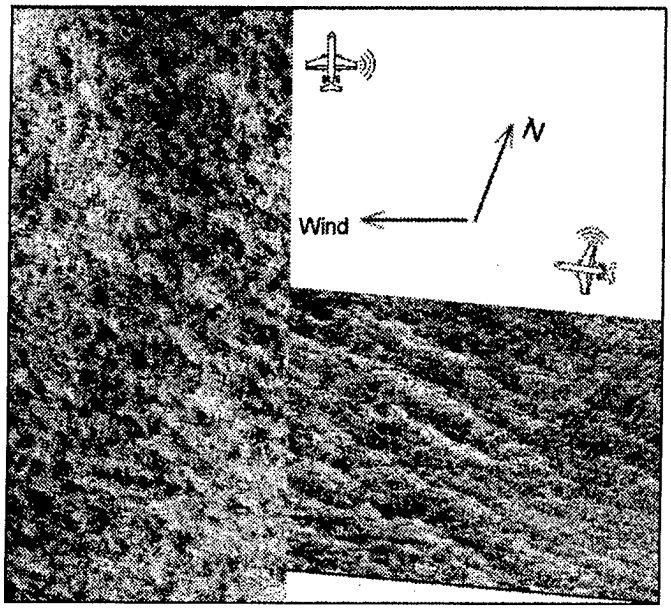


Fig.3 Superposition of radar images obtained under unstable condition in upwind (left) and crosswind (right) sounding directions.

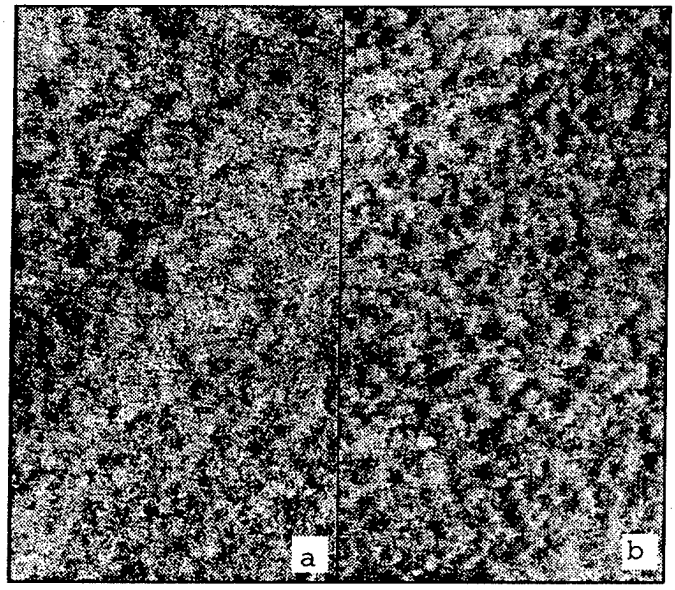


Fig.4 Fragments of radar images of sea surface under unstable atmospheres; a) in daytime, b) at night.

IMPACT OF VIEW DIRECTION

Two superposed fragments of images obtained by cross- and upwind sounding directions are shown in the figure 3. Time interval between two records is half an hour. The main orientation of cellular structures is noted in both of them, but in crosswind sounding direction it is more pronounced. The orientation of the coherent structure is shifted to the right from mean surface wind direction by 30 degree. It is natural to suppose that this structure has connection with geostrophic wind. It might be that cloud system , located at some altitude, changes energy balance on sea surface. The presence of pronounced orientations in radar images pattern may be explained by different growth increment of resonant scattering ripples in different directions as well as by viscosity variations. When convective cells are carried by wind, the most pronounced imprint is produced by the elements stretching along the wind direction. This imprint results in surface temperature variations and hence in viscosity variations. The same viscosity variations are clearer marked in radar images formed by cross wind ripple components, because the energy income to components of ripples propagating in wind direction is greater and they are less influenced by variations of the viscosity. Hence the same viscosity variations are clearly seen in crosswind radar measurements than in down- or upwind images.

ESTIMATION OF SPATIAL SCALES

Fig. 4a and b show radar images recorded 24.07.092 in daytime ant at night. The day before an atmosphere front had passed over the test area. Air temperature and moisture were rapidly decreased , and this resulted in convection development. Fig. 5 gives boundary layer stability parameter z/L calculated using technique given in [2] and corresponding contact measurements taken by the research vessel "Academic Joffe". Here z is the height at which the measurements were performed (20 m), L - the Monin-Obukhov length. Atmosphere vertical temperature profiles recorded by radio sonde close to the time of radar measurements are shown in figs.6a,b.

Both images have cellular structures of about 1 km in size. In both cases the vertical temperature gradient passes through dry adiabatic point at approximately 350 m. At this altitude the buoyancy frequency for dry air turns into zero (see figs. 7a,b). Above the level of 350m the buoyancy frequency has real values and under it imaginary values.This implies, that atmosphere temperature stratification above

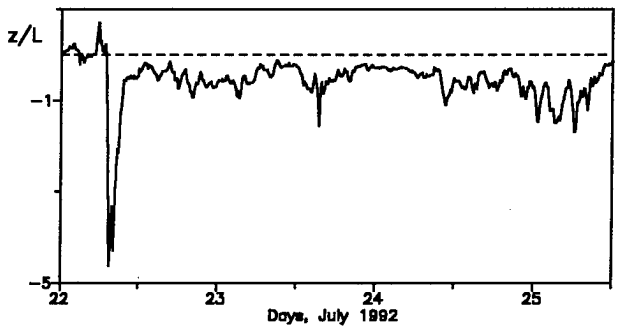


Fig.5. Boundary layer stability parameter

this level does not permit the development of the dry convection confining it in lower layers only.

Therefore 1 km cellular elements in the given radar images can be considered as surface manifestations of dry convective cells in the near surface layer (below 350 m). While the radar image recorded at night has cells of about the same sizes, the day time image contains different cells (1 km as well as up to 2.5 km in size) mostly located in the area of more intensive radar signal. The corresponding temperature profile has an inversion point approximately at 800 m , that is by 200 m higher than the condensation level calculated according to the simplified formula:

$$h = -\frac{\ln f_0}{\lambda\gamma_a - \frac{1}{H}},$$

where f_0 is initial air moisture at the surface, λ is approximation parameter of saturated vapor pressure temperature dependence, γ_a is dry adiabatic gradient, H is height scale.

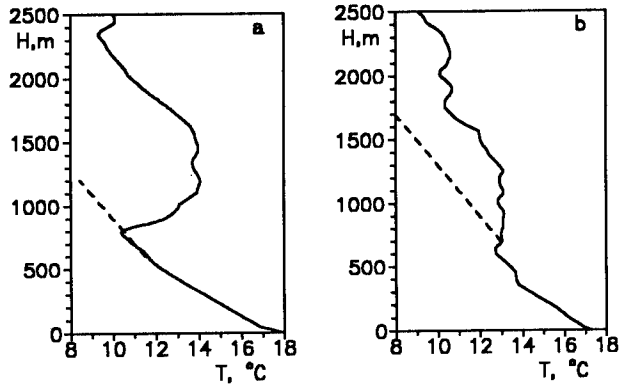


Fig.6 Vertical profiles of air temperature:
a) in day time, b) at night.

Dashed lines in figs. 6a,b indicate moist adiabatic curves corresponding to the experimental conditions and starting from the heights of condensation. It is clearly seen that in day time between the condensation height and the inversion base the air temperature decreased quicker than it occures during moist adiabatic lifting of an element of air with saturated water vapor. This is an implication of possible moist convective development in the specified layer. So, 2.5 km cellular elements are considered to be surface manifestations of moist convective cells between the sea surface and the inversion point accompanied by convective clouds.

In both cases of dry convection (in day time and at night) as well as in the case of moist convection seen in the day time image only, horizontal scales of convective cells are approximately 3 times greater than estimated vertical sizes of this structures. It is close to the theoretical ratio of 2.8 for the Rayleigh-Benard convection and agrees with experimental values between 2 and 4 obtained during observations of atmosphere convection [3,4].

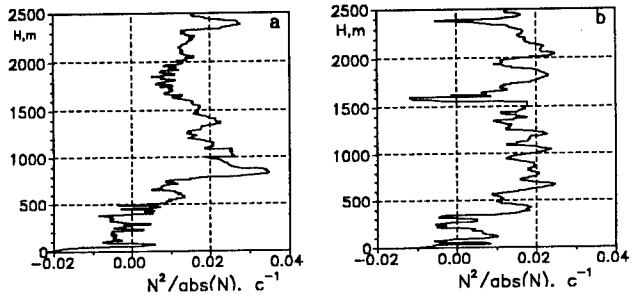


Fig.7.The parameter of the dry adiabatic stability of atmosphere $\tilde{N} = \frac{N^2}{|N|}$, N- the buoyancy frequency;
a) in day time, b) at night

CONCLUSIONS

Analysis of Ku-band radar images at vertical polarisation of sounding signal permits to determine the type of atmosphere boundary layer stratification. This is of large importance, because modern remote sensing techniques designed to retrieve parameters of ocean state and energy exchange in the ocean-atmosphere system should take into account the boundary layer stability.

Centimeter band radar is a promising tool to study dry and moist convection. The extensive use of this radar will increase the amount of information registred by remote sensing systems.

REFERENCES

[1] R.F.Gasparovic and V.S.Etkin, "An overview of the joint US/Russia Internal Wave Remote Sensing Experiment",. in Proceedings of IGARSS'94, Pasadena, California U.S. pp. 741-743, August 1994 .

[2] S. Smith., "Coefficients for sea surface wind stress, heat flux, and wind profiles as a function of wind speed and temperature", Journal of Geophysical. Research, vol. 93, C12, pp. 15467- 15 472, 1988.

[3] W.Alpers and B.Brümmer., "Imaging of atmospheric boundary layer rolls by the synthetic aperture radar abord the European ERS-1 satellite", in Proceedings of IGARSS'93, Tokyo, pp. 540-542, 1993.

[4] R.Kelly, "Horizontal Rolls and boundary layer interrelationships observed over lake Michigan", Journal. Atmospheric Sciences., 41, p p. 1816- 1826, 1984.

Analyzing the Discharge Regime of a Large Tropical River through Remote Sensing, Ground-based Climatic Data, and Modeling

Annette L. Schloss, Charles J. Vörösmarty
Institute for the Study of Earth, Oceans and Space,
University of New Hampshire, Durham, NH, 03824, USA
603-862-1792, annette.schloss@unh.edu

Cort J. Willmott
Center for Climatic Research, Dept. of Geography,
University of Delaware, Newark, DE

Bhaskar J. Choudhury
Hydrological Sciences Branch, NASA/GSFC, Greenbelt, MD

Abstract -- This study demonstrates the potential for applying passive microwave satellite sensor data to infer the discharge dynamics of large river systems, using the mainstem Amazon as a test case. The methodology combines a). interpolated ground-based meteorological station data, b). horizontally and vertically-polarized temperature differences (HVPTD) from the 37 GHz Scanning Multichannel Microwave Radiometer (SMMR) aboard the Nimbus-7 satellite and c). a calibrated Water Balance/Water Transport Model (WBM/WTM). Monthly HVPTD values at 0.25 degree latitude x longitude resolution were re-sampled spatially and temporally to produce an enhanced HVPTD time series at 0.5 degree grid-cell resolution for the period May 1979 through February 1985. Enhanced HVPTD values were regressed against monthly discharge derived from the WBM/WTM for each of 40 grid-cells along the mainstem over a calibration period from May 1979 to February 1983 to provide a spatially-contiguous estimate of time-varying discharge. HVPTD-estimated flows generated for a validation period from March 1983 to February 1985 were found to be in good agreement with both observed and modeled discharges over a 1400 km section of the mainstem Amazon. Both the WBM/WTM and HVPTD-derived flow rates reflect the significant impact of the 1982-83 ENSO event on water balances within the basin.

INTRODUCTION

The water cycle is an important component of the Earth System. River discharge can provide validation for both empirical water balance models and climate change scenarios. River heights and flows are also of importance to landscape processes including the generation and transport of sediment, nutrients and carbon, and through floodplain inundation, the consequent generation of trace gases.

Hydrological features are distinguishable with microwave sensors. The Scanning Multichannel Microwave Radiometer (SMMR) aboard the Nimbus-7 satellite collected horizontally and vertically-polarized brightness temperatures at 37 GHz between 1978 and 1987, at a spatial resolution of about 25 km. The difference (^{O}K) between the horizontally and vertically-polarized temperatures (HVPTD) are related to the dipolar moment of water and the sensor should yield an HVPTD value of 60 ^{O}K for pixels composed entirely of open water, 4 ^{O}K for closed canopy, and intermediate values for vegetated floodplains [1]. Temporal variations in the HVPTD have been related to floodplain inundation in tropical regions dominated by periodically-inundated floodplains [2]. HVPTD values have been shown to be positively correlated with variations in water level for many large South American rivers and wetland systems [3].

The purpose of this study is to demonstrate the potential for applying 37 GHz passive microwave data to generate remotely-sensed, contiguous discharge hydrographs along the mainstem Amazon River, and to test the limits of the approach. It prepares a framework for monitoring other large rivers and for exploring the use of contemporary and future passive microwave data sets in conjunction with hydrological models.

METHODS

Study Area

The setting for this analysis is the Amazon River drainage basin (Fig.1a). We consider the mainstem Amazon River to begin in the Brazilian State of Amazonas (ca. 71.5 degrees West; 4.0 deg. South), progress downstream through the large floodplain-dominated channel system, and end at a point close to the city of Óbidos (ca. 56.0^{O} W; 2.0^{O} S), the farthest downstream location not influenced by coastal tides.

Climatic Time Series

Representative climatic time series of monthly air temperature (T) and precipitation (P) were estimated from station data [4] that were spatially interpolated by methodology developed by Willmott and Robeson [5]. Their algorithm makes use of a climatological (long-term average)

0-7803-3068-4/96$5.00©1996 IEEE

monthly $\bar{P}$ or $\bar{T}$ field to assist in interpolating any particular monthly P or T field of interest. Termed *climatologically-aided interpolation* or *CAI,* the procedure improves upon the simple interpolation from station observations by exploiting the spatial colinearity between P and $\bar{P}$ (or between T and $\bar{T}$), and the knowledge that $\bar{P}$ and $\bar{T}$ are available at meaningfully higher spatial resolutions than are observations of P and T. Using *CAI*, monthly fields of P and T were interpolated to a 0.5^{o} grid for the period April 1979 to March 1985 (for a full description of *CAI* as used in this study, see [6]).

Simulated Discharges

The Water Balance/Water Transport Model (WBM/WTM) was used to generate a six-year monthly time series of discharge for each 0.5 degree cell representing the entire Amazon drainage basin. The WBM relies on a series of biophysical data sets which specify land surface properties and time-varying fields of precipitation and temperature to predict monthly water balances, specifically soil moisture, evapotranspiration, and runoff on independent grid cells [7].

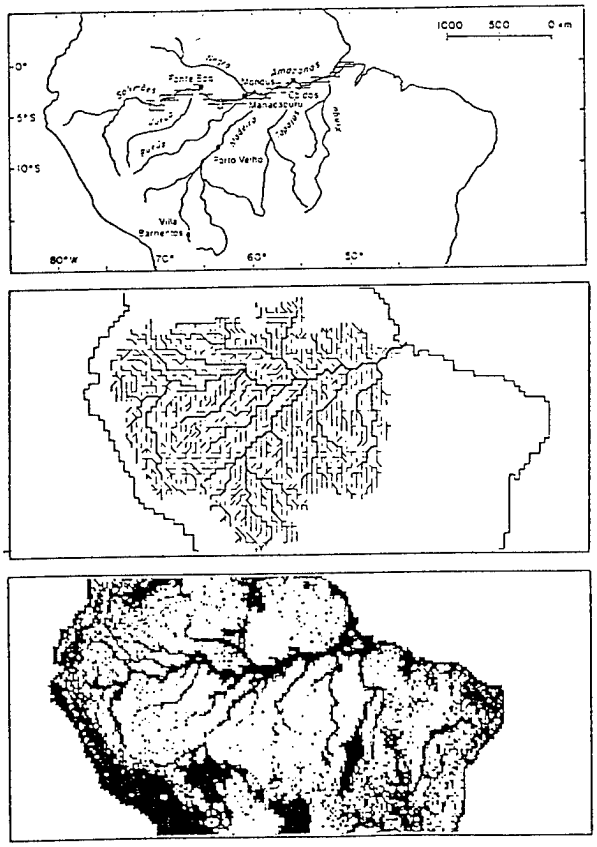


Fig.1.a) The mainstem Amazon River. b) The overall simulated network topology used to route distributed runoff downstream. c) An image of mean HVPDT for April. River corridors are clearly apparent in contrast to dense forest.

The WTM routes runoff using a simulated network topology (Fig.1b) and a system of coupled differential equations. The WTM is a quasi-linear cascade model, with linear flow within channels and temporary storage of water along floodplains during high flow periods. The WBM/WTM was calibrated to match published discharge hydrographs [8].

Since there are few published high resolution time series, the modeled flows represent a sensible interpolation of the available discharge fields which are distributed hundreds of kilometers apart and subject to numerous sharp gradients brought about by tributary inflows. Use of these simulated flows allows us to characterize the discharge regime along much of the mainstem river that would not otherwise be possible.

Passive Microwave Radiometer Data

Monthly values of the SMMR 37 GHz horizontally and vertically-polarized temperature differences (^{o}K) were obtained from NASA's Pilot Land Data System Archive [9, Fig.1c]. Three corrections were made to the original PLDS data set (Fig.2). To account for the sensor geolocation error of the beam center, on the order of 12 km, the original data were first re-sampled to 0.5 x 0.5 degree resolution using a simple spatial integration procedure that gave proportional weighting to each 0.25 degree signal based on its areal extent within the larger 0.5 degree cell. Next, each monthly HVPTD value at 0.5 degree resolution was averaged with the corresponding value from each of its five adjacent upstream cells, to minimize the effect of local variations in river morphology. Lastly, since the original monthly HVPTD time series was based upon a single observation taken during the named month (the second lowest of the daytime values), a temporal error was embedded within the data set. To compensate for this, a weighted moving average was applied (Fig.2).

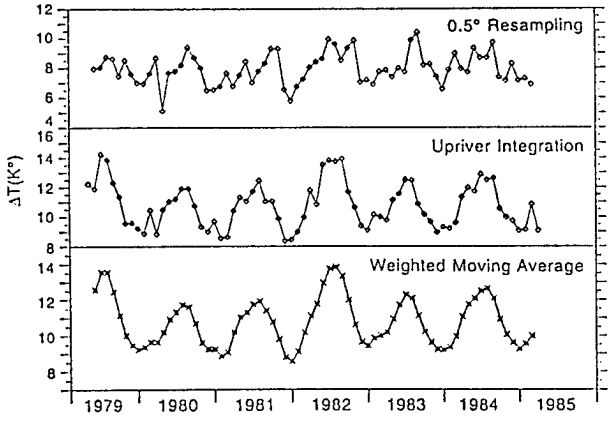


Fig.2 Example of enhancements of the 37 GHz HVPDT time series. top). weighted re-sampling at 0.5^{o}, middle). partial integration using data from five additional upstream cells, bottom). application of a weighted moving average as: $HVPTD_t = 0.25\ HVPTD_{t-1} + 0.50\ HVPTD_t + 0.25\ HVPTD_{t+1}$, where t is month.

For each mainstem grid-cell, a linear regression of monthly enhanced HVPTD values and WTM-derived flows was generated for the calibration period, May 1979 through February 1983. The regressions were used to generate HVPTD-derived flows for the validation period, March 1983 through February 1985. The analysis is discussed in [6].

RESULTS

Flows derived from both the climate-based WTM and the remotely-sensed HVPTD provide a useful synoptic view of how Amazon River discharge varies over space and time (Fig.3). Both models show the progressive downriver increase in discharge and the influence of tributary inflows. The magnitudes depicted by each model are quite similar. The WTM clearly shows inter-annual variations in discharge, the most dramatic of which are associated with the 1982-83 ENSO event. The HVPTD also captures the ENSO discharge dynamics. The most upstream sites show less seasonal variability with HVPTD than with WTM-derived fields, suggesting that the influence of greater amounts of vegetated area and thus less water-filled area limit the general utility of the 37 GHz HVPTD model in this region.

SUMMARY AND CONCLUSIONS

This study demonstrated the concurrent use of ground-based meteorological station data, passive microwave radiometer data, and calibrated water balance and transport models to infer flow regime in a large, floodplain-dominated river. Although there are limits to the use of such satellite-derived discharge models, this research has clearly demonstrated their potential to remotely monitor the status of river systems in real time. Through collaborative research with the University of California (Santa Barbara) we are currently developing methods to couple the onset and cessation of floodplain inundation as derived from 37 GHz time series data from both the SMMR and its successor, the SSM/I, to our hydrology model in the Amazon, Paraná, and Orinoco Rivers.

We have demonstrated the possibility of monitoring the dynamics of a large tropical river with a relatively coarse passive microwave sensor. Both the SSMR and SSM/I time series provide an excellent synoptic tool for providing time series in large floodplain-dominated rivers. An operational capacity for smaller river systems will require higher resolution sensors and techniques that exploit synergistic optical, passive and active microwave sensors.

ACKNOWLEDGMENTS

National Aeronautics and Space Administration (grants NAGW1884, 1888, 2669) and the Environmental Protection Agency (ca. CR816278) partially funded this research.

REFERENCES

[1] B.J.Choudhury, "Monitoring global land surface using Nimbus-7 37 GHz data theory and examples," Int.J.Rem. Sens.,vol.10,pp.1579-1605,1989.

[2] S.J.Sippel, S.K.Hamilton, J.M.Melack, and B.J. Choudhury, "Determination of inundation area in the Amazon River floodplain using the SMMR 37 GHz polarization difference," Rem.Sens.Env., vol.48,pp.70-76,1994.

[3] L.Giddings and B.J.Choudhury, "Observation of hydrological features with Nimbus-7 37 GHz data, applied to S America," Int.J.Rem.Sens.,vol.10,pp.1673-1686,1989.

[4] D.R.Legates, and C.J.Willmott, "Global air temperature and precipitation data archive," Dept. of Geography, U. Delaware, Newark, DE.,1988.

[5] Willmott,C. J. and S.M.Robeson, Climatologically-aided interpolation (CAI) of terrestrial air temperature, Internat.J. Clim., vol.15,pp.221-229,1995.

[6] C.J.Vörösmarty et al., "Analyzing the discharge regime of a large tropical river through remote sensing, ground-based climatic data, and modeling," in press.

[7] C.J.Vörösmarty et al., "Continental scale models of water balance and fluvial transport: An application to South America," Glo.Biogeochem.Cyc., vol.3,pp.241-265,1989.

[8] J.E.Richey, L.A.K.Mertes, T.Dunne, R.L.Victoria, B.R. Forsberg, A.Tancredi, and E.Oliveira, "Sources and routing of the Amazon River flood wave," Glo.Biogeochem.Cyc., vol.3,pp.191-204,1989.

[9] B.J.Choudhury and B.Meeson, "Microwave Vegetation Index: Data Set Documentation, Product Description, and User's Guide," [NASA Pilot Land Data System User Publication, May 1992].

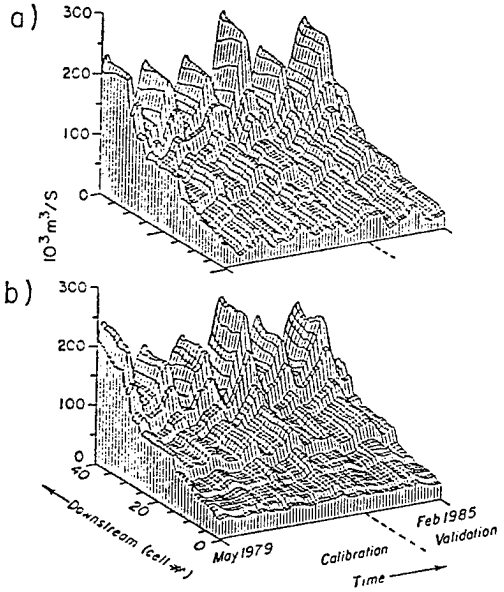


Fig.3. Time series for river discharge along the mainstem Amazon, generated by a). the calibrated WaBM/WTM and b). the 37 GHz HVPTD statistical model.

Using Temporal Information in an Automated Classification of Summer, Marginal Ice Zone Imagery*

Donna Haverkamp and Costas Tsatsoulis
Department of Electrical Engineering and Computer Science
The University of Kansas, Lawrence, KS

Center for Excellence in Computer-Aided Systems Engineering
2291 Irving Hill Road, Lawrence, KS 66045
Tel: (913)864-7767 Fax: (913)864-7789
E-mail: haverkam@cecase.ukans.edu

Abstract -- Synthetic aperture radar (SAR) imagery is difficult to classify under summer melt conditions, even with the human eye. Backscatter instability causes the intensities of the firstyear ice, multiyear ice, and open water classes to intermix, thus making an intensity-based classification invalid.

The method presented in this paper supplements backscatter information from SAR data with wind and temporally-analyzed temperature records and regional statistics in order to achieve an automated ice/no-ice classification of summer imagery in the marginal ice zone (MIZ). Referring to a database of prior area statistics (ice percentages, ice types, temperatures), an expert system forms conclusions to guide a current classification of the same area. Using parameters set by the expert system, an algorithmic floe extraction procedure divides the image into two classes (one assumed to contain floes and the other assumed not to contain floes) and then subdivides those two classes into ice and water. Classification results are then compared to the expected values derived from temporal adjustments of prior ice percentages. Unacceptable differences are called to the attention of the user for further inspection and possible manual correction.

The study area for testing is the Beaufort Sea, with data taken from the ERS-1 SAR. Results show that temporally-accumulated data can be used to provide a basis for an automated classification of MIZ imagery under summer melt conditions.

INTRODUCTION

Satellite remote sensing provides data for the continuous monitoring of sea ice distributions and concentrations over the polar oceans. The amount and thickness of ice in the polar regions is a key indicator of global climate, particularly in the summer season [1].

Although summer ice concentrations are no less important to obtain than winter ice concentrations, the analysis of summer ice imagery remains as yet unautomated. The backscatter contrast between first-year and multi-year ice is stable only from October through May; the summer season is characterized by nearly indistinguishable backscatters for all ice types [2]. Surface melt affects the backscatter of the ice adversely, and different ice thicknesses cannot be distinguished based upon backscatter alone.

A source of information which heretofore has not been utilized for summer sea ice imagery is *time*. Combining cumulative previous knowledge of an area's ice/water concentrations and melt state with temperature and wind data, a current interpretation of that same area can be guided, resulting in the automated measurement of ice distributions in MIZ areas during the summer season.

BACKGROUND

The summer ice season consists of several stages [3], beginning with the *early melt* stage in which the snow pack begins to undergo transformation due to melt/freeze cycling which ends when moisture is continuously present in the snow cover. This phenomenon also marks the beginning of the *melt onset* stage, which is characterized by dampness at the snow - ice interface and an average surface temperature near the melting point. This stage ends when most of the snow cover has become completely saturated, signalling the beginning of the *advanced melt* stage. From this point, the ice continues to decay until the freeze-up season begins.

While the signatures of the different ice types/thicknesses are stable under winter conditions (with multi-year ice typically having a higher backscatter than first-year ice), once the melt season begins, the signatures quickly begin to move closer together. After converging, they remain indistinguishable until midsummer [3,4]. At this point, because of the cumulative effect of melt on the perceived roughness, a backscatter reversal between first-year and multi-year ice occurs. Melt and drain cycles subsequently cause multiple backscatter reversals until the end of the summer, when the backscatters of multi-year and first-year ice again stabilize [4,5].

In [6], a number of notable conclusions are made concerning the backscatter changes in the summer ice cover: 1) when the snow begins to melt in early summer, the contrast between multiyear and first-year signatures vanishes, 2) when no snow remains in the first-year ice, the winter contrast between first-year and multiyear ice is reversed, which causes the first-year ice returns to exceed the multiyear ice returns by a few decibels - the shift can occur in less than a week, 3) the melting of superimposed ice can cause the reversed contrast to disappear in less than a week, and

*This work is supported in part by NASA Graduate Students Researcher Fellowship NGT-5064.

0-7803-3068-4/96$5.00©1996 IEEE

Table 1: Compositions of floe and non-floe classes corresponding to melt stage.

	Early Melt		Melt Onset		Advanced Melt		Freeze-Up	
Wind	< 4m/s	> 4m/s	< 4m/s	> 4m/s	< 4m/s	> 4m/s	< 4m/s	> 4m/s
Floe Class	ice	water	ice+ matrix	water+ matrix	ice+ matrix	water	ice	water
Non-floe Class	matrix+ water	ice+ matrix	matrix+ water	ice+ matrix	water	ice+ matrix	matrix+ water	ice+ matrix

4) because of the rapid fluctuations in the backscatter of first-year and multiyear ice, it is very difficult to classify C- and X-band radar images using intensity-based algorithms.

These investigations indicate that, due to backscatter fluctuations and general instability of sea ice signatures during the melt season, any attempt at an automated classification of corresponding imagery cannot depend upon intensity alone. It was therefore decided that additional information was needed in order to classify summer ice.

Pre-existing work at the University of Kansas performs segmentation of summer ice imagery into floe and non-floe classes in order to calculate floe statistics in the MIZ [7]. Rather than discard this body of work, which is based upon local dynamic thresholding and feature extraction techniques as described in [8], it was decided that it should be used as a central part of the summer ice classification procedure.

The major problem with the segmentation procedure was that it had no knowledge concerning the imagery which it segmented. A human operator had to look at the image and "tell" the segmentation procedure in what gray-level range it might expect to find floes. After dividing the image into floe and non-floe classes, it then subdivided those two classes based on the assumption that the floes class is composed of ice floes and "undesignated" areas while the non-floe class is composed of background matrix (usually consisting of ice bits) and open water. These assumptions work only in the ideal case (when they happen to be true).

However, the state of melt of an area, along with temperature and wind information, can supply guidelines for estimating the average backscatter of ice floes with respect to other classes present in the image, and for estimating the composition of the floe and non-floe areas found in the segmentation process (see Table 1).

METHODOLOGY

The approach used here is to utilize expert systems to interpret information such as time-of-year, latitude, wind, and previous knowledge of area conditions (including temperature and previous ice distribution statistics) to assist an algorithmic classification of SAR imagery into ice/no-ice categories during summer melt conditions in the MIZ.

Expert systems can provide interpretation of wind and melt stage information (and thus expectations of the relative backscatter of the floe class *and* of the compositions of the floe and non-floe classes), and guidelines for expected ice percentages based upon previous percentages in the same area. Combining this with local, dynamic thresholding and a feature extraction technique, we are provided with an expert system-guided segmentation and classification of SAR summer, MIZ imagery. The technique separates an image into ice floes, background matrix (assumed, for ice percentages, to consist of ice), and water.

IMPLEMENTATION

The system utilizes expert information along with a segmentation procedure to differentiate between ice and water and to define individual ice floes in synthetic aperture radar imagery of the MIZ during the melt season. It is necessary to coordinate several components, including two expert systems and a database, in order to realize the complete classification system. The study area has been limited to the Beaufort Sea, in the interest of both time and space.

Database

Information from analyses of different areas of the Beaufort Sea are kept in a database, indexed to nearest latitude and longitude degree blocks. Temperature records are also included, along with current melt state, ice percentages, and floe size distributions. This database is updated with such information as it becomes available from incoming data and from expert system analyses.

Algorithmic Parameters Expert System

This expert system determines the settings of key parameters used by the algorithmic segmentation and classification procedure. The parameters are determined by melt conditions (requiring analysis of cumulative temperature information) and wind - these are the factors which indicate whether the floes in the image will be bright or dark or "in-between" relative to other ice forms in the image. This information is used by the segmentation and feature extraction technique to determine the floe and non-floe classes. These factors also indicate what classes will be similar in backscatter and will combine to form the floe and non-floe classes subsequently found in the image segmentation. This information is used by the classification to further segment the floe and non-floe areas into ice and water classes.

This expert system generates the updated melt stage information and updates the database accordingly.

Segmentation and Feature Extraction

A dynamic thresholding and feature extraction procedure for segmenting SAR imagery into unlabeled classes already

exists [8], and it has been adapted to segment summer MIZ SAR imagery into two classes, assumed to be simply floe and non-floe [7].

The summer adaptation of the dynamic thresholding and feature extraction technique will be utilized to divide the image into floe and non-floe regions. Floe class will be selected as dark or bright according to parameters set by the algorithmic parameters expert system.

Classification: Ice/No-Ice

Variables set by the algorithmic parameters expert system indicate the expected compositions of the floe and non-floe classes found (see Table 1). Within these classes, shape characteristics are used to distinguish floes, and texture measures are applied to the raw imagery to distinguish water areas. The remaining features are assumed to consist of background matrix (ice).

Floe Analysis

After the classification is complete, floe analyses are performed to calculate floe statistics of the area based upon floe size distributions. This information is entered into the database.

Post-Classification Expert System

In this stage, there are three error checks performed on the data.

1) Based upon prior ice percentages of the same area and cumulative temperature data, a projected set of ice percentages are calculated. These numbers must agree reasonably with the new percentages.

2) Ice floe size distributions should reflect a decrease in floe size over the summer (as the ice melts).

3) Ice type distributions should also agree with historical information taken from the area (over past years), at least in a general sense (i.e., "at x time of year, there is usually more ice than water present in the area" should hold true for current statistics).

If any of the above do not hold, attention is called to the user to verify (or negate) the current classification. The database is then updated with the new regional statistics.

RESULTS

The system was run on a small collection of test images from the Beaufort Sea. A SAR strip was acquired for three consecutive passes, each spaced three days apart.

In all cases, the sea ice was in a state of advanced melt. Tthe imagery did, however, exhibit varying wind speeds. Based upon these and a fabricated temperature record for corresponding areas, the system was run on the test images. The floe and non-floe classes and their subclasses were all assigned properly according to visual evaluation. Results were within expected error bounds, with the exception of the results from one test image which exhibited very poor contrast. In that case, notification of error was made to the user, and a manual correction of the statistics was allowed.

CONCLUSIONS

Automated classification of summer, MIZ SAR imagery is a desired, if difficult, task. Supplementing intensity data with wind and temperature data, a classification can be made which is at least semi-automated. By analyzing classification results with respect to prior area statistics, the classification can be evaluated for correctness, and the need for user intervention can be assessed (and minimized).

REFERENCES

[1] Bentley, C. R., "Some Aspects of the Cryosphere and its Role in Climatic Change", in *Geophysical Monograph 29: Climate Processes and Climate Sensitivity*, J. E. Hansen and T. Takahashi, editors. American Geophysical Union, 1984, pp. 207-220.

[2] Thomas, R. H., "Ice Sheet Margins and Ice Shelves", in *Geophysical Monograph 29: Climate Processes and Climate Sensitivity*, J. E. Hansen and T. Takahashi, editors. American Geophysical Union, 1984, pp. 265-274.

[3] Livingstone, C. E., K. P. Singh, and A. L. Gray, "Seasonal and Regional Variations of Active/Passive Microwave Signatures of Sea Ice", *IEEE Transactions on Geoscience and Remote Sensing*, vol. GE-25, no. 2, March 1987, pp. 159-172.

[4] Onstott, R. G., "SAR and Scatterometer Signatures of Sea Ice", in *Geophysical Monograph 68: Microwave Remote Sensing of Sea Ice*, F. D. Carsey, editor. American Geophysical Union, 1992, pp. 73-104.

[5] Onstott, R. G., T. C. Grenfell, C. Matzler, C. A. Luthre, and E. A. Svendsen, "Evolution of Microwave Sea Ice Signatures During Early Summer and Midsummer in the Marginal Ice Zone", *Journal of Geophysical Research*, vol. 92, no. C7, June 1987, pp. 6825-6835.

[6] Gogineni, S. P., R. K. Moore, T. C. Grenfell, D. G. Barber, S. Digby, and M. Drinkwater, "The Effects of Freeze-Up and Melt Processes on Microwave Signatures", in *Geophysical Monograph 68: Microwave Remote Sensing of Sea Ice*, F. D. Carsey, editor. American Geophysical Union, 1992, pp. 329-341.

[7] Soh, L. K., D. Haverkamp, and C. Tsatsoulis, "Separating Ice-Water Composites and Computing Floe Size Distributions", *IGARSS 1996*.

[8] Haverkamp, D., L. K. Soh, and C. Tsatsoulis, "A Comprehensive, Automated Approach to Determining Sea Ice Thickness from SAR Data", *IEEE Transactions on Geoscience and Remote Sensing*, vol. 33, no. 1, Jan. 1995, pp. 46-57.

Texture Representation of SAR Sea Ice Imagery Using Multi-Displacement Co-Occurrence Matrices

Leen-Kiat Soh and Costas Tsatsoulis
Department of Electrical Engineering and Computer Science
University of Kansas, Lawrence, Kansas
address: Center for Excellence in Computer-Aided Systems Engineering
2291 Irving Hill Road, Lawrence, KS 66045
tel: (913)864-7767 fax: (913)864-7787 e-mail: lksoh@cecase.ukans.edu

Abstract -- In this paper, we desribe multi-displacement co-occurrence matrices for representing sea ice textures of SAR imagery. Our design of co-occcurrence matrices captures local relationships among neighboring pixels and global links among distant pixels, an advantage over other existing versions of co-occurrence matrices. As a result, it can adequately represent micro textures, such as grainy details, and macro textures, such as patchy blocks. We have conducted experiments to compare our multi-displacement co-occurrence matrices with other existing versions using Bayesian linear discrimination. We have found that our design is the most texturally representative in terms of classification accuracies in both training and test datasets. In addition, we have applied this design to sea ice texture analysis which includes detection and localization, and subsequent image-texture mapping.

INTRODUCTION

Statistical texture analysis has been important in SAR sea ice imagery research since, with it, sea ice regions can be better represented and thus classified, compared to analysis based on only intrinsic gray levels. For example, [1] classified one SAR image (over the Beaufort Sea) to new/first-year ice and multiyear ice with an overall accuracy of more than 65% using derived textural descriptors on X-band (HV polarization). Standard statistics and higher order texture statistics generated from co-occurrence matrices were used to classify SAR sea ice data with an overall accuracy of 89.5% [2]. Statistical textures have also been used in classifying other sea ice imagery such as Landsat Thematic Mapper (TM) Antarctic scenes [3]. In this paper, we concentrate on the statistical textural contexts of SAR sea ice regions for identifying structural composition of ice-water patterns, instead of surfacial textures that have been used for determining ice types.

We have chosen the gray level co-occurrence method as our texture analysis basis for three reasons. First, perceptual psychology studies [4] have shown this method to match a level of human perception. Second, studies [5,6] have shown this method to outperform the others in texture discrimination. Third, co-occurrence matrices have been used successfully in many applications [7-10] and also in SAR imagery classification [11,12].

In this paper, we present a study of different designs of co-occurrence matrices on SAR sea ice imagery. We investigate the effects of the quantization and displacement, factors on implementing co-occurrence matrices for SAR sea ice imagery. We also present a classification experiment using Bayesian linear discrimination that compares different implementations of co-occurrence matrices. Finally, we apply the best implementation on SAR sea ice imagery to generate textural maps.

This work is supported in part by NASA Grant NAGW-3043

BACKGROUND ON CO-OCCURRENCE MATRICES

The original definition of gray-level co-occurence matrices is shown in [7]. Briefly, the texture-context information is specified by the matrix of relative frequencies P_{ij} with two neighboring pixels separated by distance d occur on the image, one with gray level i and the other with gray level j. Such matrices of gray level co-occurrence frequencies are a function of the angular relationship and distance between the neighboring pixels. To implement co-occurrence matrices, one needs to identify the number of quantization levels, the orientation and displacement factors, given which one can determine the most representative co-occurrence matrix for certain application. An algorithm for selecting the matrix with the highest χ^2 value was proposed such that one can determine the displacement and orientation parameters of the optimal matrix for classification [13].

EXPERIMENTS

Our experiments were designed to assess the best quantization and displacement values for representing SAR sea ice textures. Before conducting the experiments, we identified seven sea ice texture types: 1) *Web-like*, where the image consists of mostly multiyear ice with high ridge content, 2) *High-deformation*, where crushing of ice floes creates extreme deformations, usually found at marginal ice zones (MIZs), 3) *Fractal-like*, where the image consists mostly of new ice and melt ponds, especially at the end of summer melt season, 4) *Pebble-like*, where tiny round floes are embedded in younger ice formations, at the start of summer melt season, 5) *Smooth*, where floes are minimally deformed, with low ridge content, 6) *High-contrast*, where large dark multiyear ice floes and large refrozen young and thin pancake ice coexist, resulting from mobile floes that create water lodgings and yet are stationary enough for pancake or young ice to form, and 7) *Packed*, where the image consists of packed multi year ice occasionally broken up by leads. Beside their geophysical implications, these texture types were identified also because of their frequent

0-7803-3068-4/96$5.00©1996 IEEE

occurrences during a study of a database of about 2000 SAR sea ice images. We conducted three experiments as follows:

Experiment 1: Number of Quantization Levels

This experiment used uniform quantization. We extracted sample sites, each 64 x 64, from 18 images with different textural regions. We devised a test using four textural features (energy, contrast, entropy, and homogeneity) and six different quantization schemes: 8, 16, 32, 64, 128, and 256 levels. The displacement was 1 and orientations were 0°, 45°, 90°, and 135°. Taking the average of the orientations yields for each sample site a two-dimensional vector. The degrees of similarity or disimilarity among samples, as derived from the vectors, were more stable across higher number of quantization levels, indicating that we should not use small number of quantization levels.

Experiment 2: Displacement Parameter

The displacement, *d*, is important in the computation of co-occurrence matrices. Applying a large displacement value to a fine texture would yield a co-occurrence matrix that does not capture the textural information, and vice versa. For our experiment, we used $d = 1, ..., 32$. As a result, we generated a curve for each textural feature, for each quantization scheme. We concluded that across quantization schemes, each textural curve preserves nicely, indicating that it is sufficient to use one quantization scheme with a range of displacement values since the dynamics of the curves are similar.

Experiment 3: Implementations and A Comparative Study of Co-Occurrence Matrices

Experiments 1 and 2 provided us some ideas on designing a general co-occurrence matrix to represent SAR sea ice textures. Combining the conclusions of the experiments, we conjectured that a co-occurence matrix with a 64-level quantization and a range of displacement values should sufficiently and efficiently represent textures in sea ice. For SAR sea ice imagery, there are no systematic patterns based on orientation: ice floes position themselves in all possible orientations. We thus used 0°, 45°, 90°, and 135°. In this experiment, we had three implementations of co-occurrence matrices. The first implementation was called the mean displacement and mean orientation (MDMO) matrix. Textural measures are averaged over orientation and displacement values. This design assumes that every matrix of specific displacement and orientation values is partially representative for each region; and that the third order measurement, the average of the textural curve values, is constructive. The second implementation was called the χ^2-optimal displacement and mean orientation (ODMO) matrix. χ^2 values of all 4 matrices of different orientations are calculated and averaged for each displacement value, and the matrix accumulating the most χ^2 value is the optimal matrix. This design assumes that only the matrix whose χ^2 value is the highest with specific displacement is truly and sufficiently representative for the sample. The third one is called the χ^2-optimal displacement and χ^2-optimal orientation (ODOO) matrix. This design assumes that the matrix whose χ^2 value is the highest with specific displacement and orientation is truly and sufficiently representative for the sample. To study these three implementations comparatively, we used a Bayes classifier. A Bayes classifier estimates covariance matrices from the different classes of training dataset and generates classifying rules. In testing, each rule will be used to compare an unknown instance to a certain class. The rule that yields the largest probability of membership gives the class of the unknown instance.

First, we used 240 sample sites, and seven texture groups. After training, we obtained seven classifying rules. We then re-applied all the samples as unknown instances to the rules, and the resubstitution or training set classification accuracies of the MDMO, ODMO, and ODOO implementations were 90.79%, 62.28%, and 51.75%, respectively. This exercise tells us that MDMO has the best capability in creating the necessary inter-class decision boundaries among the seven texture groups Second, to test the generality of our MDMO Bayes classifier, we divided the data set into two, trained the classifier on one and applied the trained classifier to the other. The training and test set classification accuracies were 99.19% and 94.17%, respectively. We have concluded from these experiments: 1) The MDMO implementation is the most representative of SAR sea ice textures, 2) The range of displacement values as a whole is more representative than a displacement value alone. This indicates that MDMO, using a third order measurement (i.e., the average of the curve), is able to capture local and global details of a texture, and 3) Matrices with the highest χ^2 value did not provide useful information. We named the MDMO implementation Multi-Displacement Co-Occurrence Matrix.

RESULTS

We have applied Multi-Displacement Co-Occurrence Matrix to generate texture maps of SAR sea ice imagery, thereby detecting and locating regions with high/low ridge content, high/low deformation, high/low melt, etc. For example, Fig.1 shows an original image and Fig.2 shows a texture classification of the image: 53.62% Web-like, 31.26% Fractal-like, 10.79% Pebble-like, 7.79% Smooth, and 3.56% High-contrast. The texture classification and mapping results have been encouraging, and our planned future work includes gathering more diversified test sets and improving the classification power of our co-occurrence matrix.

CONCLUSIONS

We have implemented a texture representation technique for SAR sea ice imagery and shown that it has more classification power than co-occurrence matrix that uses only a single displacement value. We have also shown that a straight 64-level quantization scheme is able to discriminate different textures adequately. In addition, we have also applied this design to SAR sea ice imagery which includes

localization of surface deformation, high ridge content, and melt pond regions, which is useful in sea ice geophysical analysis.

REFERENCES

[1] Q. A. Holmes, D. R. Nuesch, and R. A. Shuchman, "Textural Analysis and Real-Time Classification of Sea-Ice Types Using Digital SAR Data," IEEE Transactions on Geoscience and Remote Sensing, vol. 22, no.2, pp. 113-120, 1984.

[2] J. A. Nystuen and F. W. Garcia, Jr., "Sea Ice Classification Using SAR Backscatter Statistics," IEEE Transactions on Geoscience and Remote Sensing, vol. 30, no. 3, pp. 502-509, 1992.

[3] J. Chou, R. C. Weger, J. M. Ligtenberg, K.-S. Kuo, R. M. Welch, and P. Breeden, "Segmentation of Polar Scenes Using Multi-Spectral Texture Measures and Morphological Filtering," International Journal of Remote Sensing, vol. 15, no. 5, pp. 1019-1036, 1994.

[4] B. Julesz, E. N. Gilbert, L. A. Shepp, and H. L. Frisch, "Inability of Humans to Discriminate Between Visual Textures that Agree in Second-Order Statistics—Revisited," Perception, vol. 2, pp. 391-405, 1973.

[5] J. S. Weszka, C. R. Dyer, and A. Rosenfeld, "A Comparative Study of Texture Measures for Terrain Classification," IEEE Transactions on Systems, Man, and Cybernetics, vol. 6, pp. 269-285, 1976.

[6] R. W. Conners and C. A. Harlow, "A Theoretical Comparison of Texture Algorithms," IEEE Transactions on Pattern Analysis and Machine Intelligence, vol. 2, no. 3, pp. 204-222, 1980.

[7] R. M. Haralick, K. Shanmugan, and I. H. Dinstein, "Textural Features for Image Classification," IEEE Transactions on Systems, Man, and Cybernetics, vol. 3, pp. 610-621, 1973.

[8] R. P. Kruger, W. B. Thompson, and A. F. Turner, "Computer Diagnosis of Pheumoconiosis," IEEE Transactions on Systems, Man, and Cybernetics, vol. 4, no. 1, pp. 40-49, 1974.

[9] Y. P. Chien, and K. -S. Fu, "Recognition of X-Ray Picutre Patterns," IEEE Transactions on Systems, Man, and Cybernetics, vol. 4, no. 2, pp. 145-156, 1974.

[10] S. P. S. Kushwaha, S. Kuntx, and G. Oesten, "Applications of Image Texture in Forest Classification," International Journal of Remote Sensing, vol. 15, no. 11, pp. 2273-2284, 1994.

[11] K. Shanmugan, V. Narayanan, V. S. Frost, J. A. Stiles, and J. C. Holtzman, "Textural Features for Radar Image Analysis," IEEE Transactions on Geoscience and Remote Sensing, vol. 19, no. 3, pp. 153-156, 1981.

[12] D. G. Barber and E. F. LeDrew, "SAR Sea Ice Discrimination Using Texture Statistics: A Multivariate Approach," Photogrammetric Engineering and Remote Sensing, vol. 57, no. 4, pp.385-395, 1991.

[13] S. W. Zucker and D. Terzopoulos, "Finding Structure in Co-Occurrence Matrices for Texture Analysis," Computer Graphics and Image Processing, vol. 12, pp. 286-308, 1980.

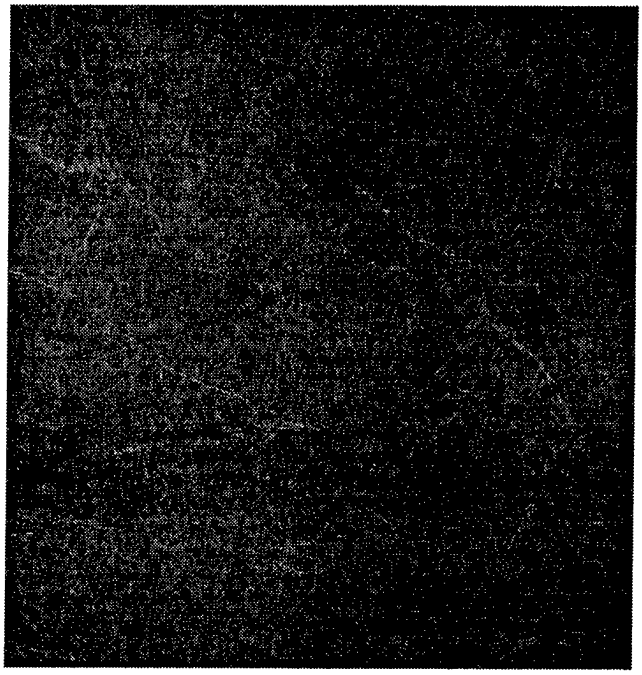


Fig.1 The orignal SAR image, Mar 27, 1992, at 73.46°N, 156.19°E. Copyright ESA.



Fig.2 The texture map of Fig.1. More than half (bright regions) of the image has been classified as Web-like.

Phase Correction for Coherent Noise Reduction in Short-Range Radar Measurements

S.G. Beaven[1], S.P. Gogineni[2], and P. Kanagaratnam[2]

[1] Naval Command, Control and Ocean Surveillance Center
Research, Development, Test & Evaluation Division
52111 Mammal Road, San Diego, CA 92152-7670
Phone: (619) 553-4186 * FAX: (619) 553-5366
Email: sbeaven@nosc.mil

[2] Radar Systems and Remote Sensing Laboratory
University of Kansas Department of Electrical and Computer Engineering
2291 Irving Hill Road
Lawrence, Kansas 66045-2969
Phone: (913) 864-7734 * FAX: (913) 864-7789
Email: gogineni@rsl.ukans.edu

Abstract -- Short-range scatterometer systems are used to obtain radar backscatter signatures for understanding the interaction between electromagnetic energy and geophysical media in a number of remote sensing applications. Unlike long-range and intermediate-range radar systems, the sensitivity of short-range radars is not limited by thermal noise, but rather by reflections and leakage signals from the antenna and RF section[1]. These leakage signals and their sidelobes are the primary sources of unwanted signals (coherent noise) in short-range FM radar systems. We have employed coherent noise reduction techniques to reduce the effects of these unwanted signal sources. Reduction of these coherent noise sources is critical to obtaining accurate backscatter measurements from geophysical targets. Recent advances include the use of phase correction to overcome limitations due to drift of local oscillators and effects of temperature changes on the system. Here we present results from the standard and phase-corrected coherent noise reduction techniques. These techniques increased the dynamic range of field and laboratory measurements of radar backscatter from sea ice and allows us to use data from past experiments that had previously been discarded due to low signal-to-noise ratio.

INTRODUCTION

Typically, measurements in which no target is present, or sky measurements, are used to determine coherent noise sources in FM scatterometer data. These measurements often are not feasible when performing measurements in the field because of limitations in the experiment set-up. Furthermore, time taken to perform sky measurements reduces experiment time that is better spent observing backscatter changes that may occur on short time scales due to rapid geophysical changes. In addition, the movement of the radar system to obtain these measurements often results in flexing of the cables used to couple the radar system with the antenna. This reduces the effectiveness of noise reduction with sky measurements.

We have developed coherent noise reduction techniques that use only the measurements from the distributed geophysical targets, and do not require sky measurements. These techniques rely on the property that signals from distributed targets vary spatially and temporally, whereas returned signals from systematic sources do not vary spatially, and only vary slowly with time. We have also added a phase correction method to account for variations in the phase of the systematic noise sources. This extends the noise reduction method to apply to systems whose phase stability is not optimum, and situations in which measurements are obtained over long periods of time. The coherent noise reduction technique, with phase correction reduced systematic noise sources by as much as 50 dB in experiments performed in the field. These methods have allowed us to process data obtained from past experiments of radar backscatter from sea ice that had been previously discarded due to low signal-to-noise ratio.

COHERENT NOISE REDUCTION (CNR)

Since 1992 we have used a coherent noise reduction (CNR) technique to process scatterometer data. This technique is described in detail in previous work [2]. Essentially, the algorithm capitalizes on the fact that unwanted systematic reflections within the system are phase coherent, whereas reflections from the target of interest are not coherent from sample to sample. The method uses only

0-7803-3068-4/96$5.00©1996 IEEE

samples obtained from the measurements from the geophysical target of interest (e.g. sea ice) and do not require special calibration. The only limitation is that the system must be coherent over the period of time in which measurements are used to compute the coherent noise sources. The performance of the CNR technique is limited by the amplitude and phase fluctuations which occur in any system due to temperature effects or movement of cables. Typical phase and amplitude shifts have been shown to be capable of significantly degrading the performance of the standard CNR [3]. The coherent noise reduction algorithm previously used has been successful for most data sets analyzed, but is subject to these limitations.

PHASE-CORRECTED CNR (PC-CNR)

Significant improvement in the CNR method can be obtained by introducing a phase correction to the process. The phase drift from the systematic noise sources is estimated for each sample to be used. Each measurement is corrected by this phase to force the systematic noise sources to be fully coherent. This requires a dominant systematic noise source, such as the primary antenna reflection, which is ubiquitous in FM scatterometer measurements.

The technique to correct for phase variations between measurements consists of five steps. First, one of the radar return signals is designated the reference signal (v_0) and subsequent return signals (v_i) are phase corrected to this. Second, a prominent coherent reflection (usually the primary antenna reflection) is located in the IF spectrum of v_0 and designated as the reference spike. Third, both the reference signal and each v_1 are filtered around the reference spike. Fourth, the phase difference between the filtered signals is determined. Fifth, the return signal v_1 is advanced in phase according to the phase difference measured to correct for phase errors.

The phase-corrected coherent noise reduction (PC-CNR) process was applied to data obtained with a C-band FM radar systems and a recently developed wideband, plane-wave step-frequency radar [4]. Results of PC-CNR for both radar systems are presented below.

PC-CNR RESULTS

The phase-corrected coherent noise reduction process (PC-CNR) was applied to data obtained with FM radar systems during a field experiment in 1991 and to data obtained during experiments at the US Army Cold Regions Research and Engineering Laboratory (CRREL) experiments between 1988 and 1995. We've also applied an extension of the technique to data from the wideband plane wave system used during CRREL'95.

The result for the phase-corrected, coherent noise reduction, applied to FM radar data is shown in Fig. 1a as the solid curve, with the original spectrum (no CNR) as the dashed curve. Here each of the coherent noise signals is reduced by approximately 25 dB, and the IF spectrum is clearly improved. The true test of the improvement, though, is illustrated by a direct comparison of the PC-CNR process with the standard CNR process for these data in Fig. 1b. Here we observe that the standard CNR suppresses the noise spikes by less than 5 dB. This is caused by the fact that the data were obtained over a long period of time (nearly 24 hours), and any of a number of sources of phase drift have resulted in a degradation of the CNR process. However, the PC-CNR result has reduced the coherent portions of the spectrum by an additional 10 to 15 dB. The improvement of PC-CNR over standard CNR may be better illustrated on a linear scale as depicted in Fig. 2. Here it is clear that the return from the target (sea ice) at a range of approximately 23 m is the dominant return after phase-correction. The standard CNR does not significantly reduce the unwanted noise spikes for these data.

We also applied the PC-CNR process for wideband data to measurements obtained during CRREL'95 and the results are shown in Fig. 3. These results demonstrate that the PC-CNR improves the measurement over the standard CNR. The PC-CNR improves the SNR in the vicinity of the surface return by 20 to 25 dB.

CONCLUSIONS

We have developed coherent noise reduction (CNR) and phase-corrected coherent noise reduction (PC-CNR) techniques to improve radar backscatter measurements with short-range FM and step-frequency radar systems. Short-range radar systems are not limited by thermal noise, but by the leakage and reflection signals from the antenna and RF sections. The coherent noise reduction techniques developed here reduce the effects of these leakage and reflection signals. These schemes hinge on the fact that the returns from distributed targets are non-coherent from sample to sample and that the returns from systematic sources are coherent from sample to sample. Phase-correction algorithms for improving the CNR process in the presence of phase variations caused by oscillator drift, cable flexing or temperature fluctuations were also developed. These algorithms result in measurements whose sensitivity approaches the thermal noise floor, rather than being limited by systematic leakage and reflection signals.

ACKNOWLEDGMENTS

This work was sponsored in part by Office of Naval Research (ONR) grant #N00014-89-J-1456 and an ONR Doctoral Fellowship.

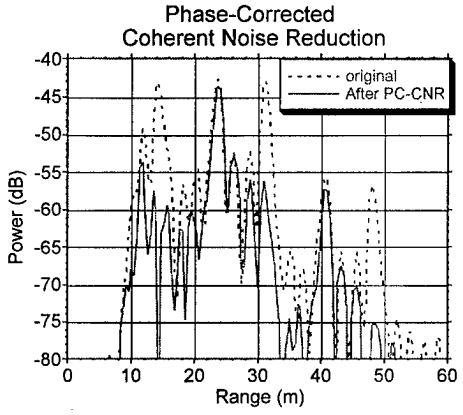
REFERENCES

[1] W.K. Saunders, CW and FM Radar, in *Radar Handbook*, edited by M. Skolnik (New York:McGraw-Hill), 14.1-14.45, 1990.

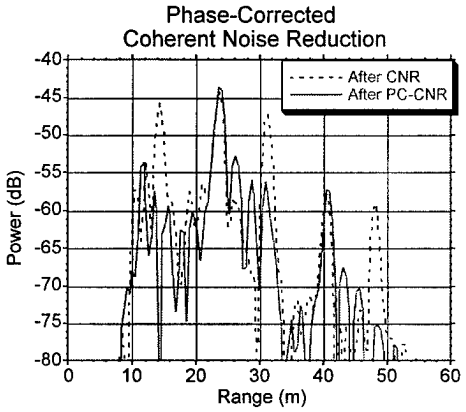
[2] S. Beaven, and S.P. Gogineni, "Shipborne Radar Backscatter Measurements from Arctic Sea Ice During the Fall Freeze-Up," *Remote Sensing Reviews,* vol. 9, nos. 1-2, pp. 3-25, 1994.

[3] S.G. Beaven, "Sea Ice Radar Backscatter Modeling, Measurements, and the Fusion of Active and Passive Microwave Data," Ph.D. Dissertation, University of Kansas, 1995.

[4] Gogineni, S.P., K. Jezek, L. Peters, J. Young, S. Beaven, and E. Nassar, Application of plane waves for accurate measurement of microwave scattering from geophysical surfaces, *IEEE Transactions on Geoscience and Remote Sensing*, May, 1995.



a)



b)

Fig. 1. Result of coherent noise reduction with phase correction. (a) The corrected IF spectrum is plotted along with the original to demonstrate the suppression of unwanted coherent noise spikes. (b) Result of CNR with phase correction, compared to CNR without phase correction.

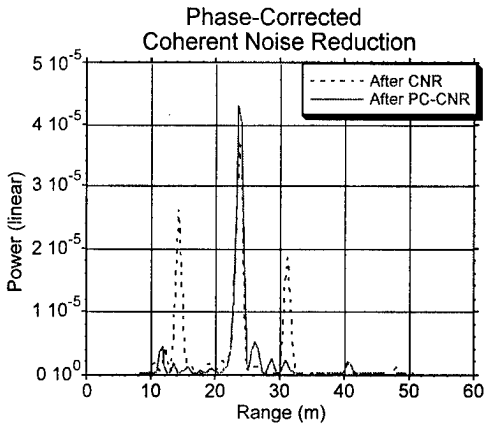


Fig. 2. Result from Fig. 1a, plotted on a linear scale to illustrate the suppression of coherent noise in the IF spectrum.

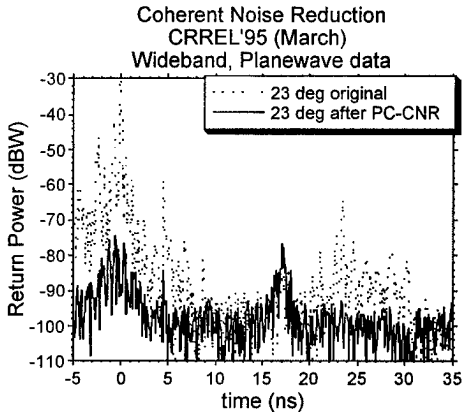


Fig. 3. PC-CNR for wideband, step-frequency radar measurements, compared to the original spectrum The antenna reflection is reduced by 50 dB, whereas standard CNR (not shown) resulted in 25-dB suppression.

In-Situ Measurement of the Complex Dielectric Constant of Sea Ice From 1 to 10 GHz

Elias Nassar[1], Robert Lee[1], Ken Jezek[2] and Jonathan Young[1]
[1] ElectroScience Lab., The Ohio State University, 1320 Kinnear Road,
Columbus, OH 43212, Phone: 614-292-7981.
[2] Byrd Polar Research Center, The Ohio State University, 1090 Carmack Road,
Columbus, OH 43210, Phone: 614-292-6531.

Abstract – We have developed a new electromagnetic, hand-held, ultra wide-band probe for the In-Situ measurement of the complex dielectric constant of sea ice in the frequency range of 1 to 10 GHz. The probe uses two antennas mounted on a cylinder. One of the antennas transmits a wide-band pulse that propagates through the ice and is received by the second antenna. From the received signal we can extract the complex dielectric constant. In order to calibrate the results we developed a numerical model for the probe using the FDTD technique. With this model we can reproduce the measurements and introduce calibration factors in order to extract the dielectric constant. A brief description of the probe and its FDTD model will be given. Results for sea ice grown at the CRREL facility will be presented.

INTRODUCTION

In recent years the scattering behavior of sea ice has been widely investigated, and efforts are made to develop forward and inverse scattering models that will give insight into the composition of sea ice from remotely recorded radar signatures. Therefore there is a need to determine the dielectric constant behavior of sea ice versus such parameters as depth, temperature, salinity and frequency. Most of the previous attempts to measure the dielectric constant of sea ice were done in laboratory settings where a slab of ice was cut and transported to the measuring device. These types of measurements usually introduce uncertainties in the results since, unlike freshwater ice, sea ice has embedded in it brine inclusions and air gaps [1, 2]; these inclusions will be significantly perturbed by the extraction and transportation process due to melting and draining of the sea ice sample. The first section deals with the design of the electromagnetic probe and its FDTD model, then in the following section we show some dielectric constant results obtained for sea ice grown at the CRREL facility.

0-7803-3068-4/96$5.00©1996 IEEE

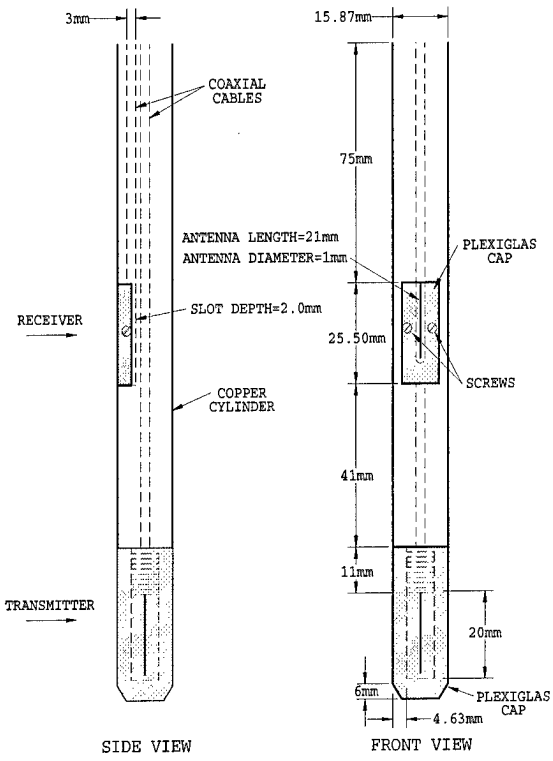


Figure 1: Geometry of the Electromagnetic Probe

PROBE DESIGN AND FDTD MODEL

A schematic diagram for the ice probe is shown in Fig. 1.

Two semi-rigid coaxial cables are inserted into a copper cylinder having the dimensions shown; One of the cables extends to the end of the cylinder and the other to a distance of 5 cm from the end.

The middle antenna is located in a semi-circular slot of radius 2 mm, see Fig. 2.

Both antennas are covered with plexiglass caps of the same diameter as the copper cylinder.

The separation between the two antennas is chosen to give a significant path length in the material while still insuring a good spatial resolution when measuring dielectric constant profiles.

In order to perform a measurement, the probe is connected to a network analyzer which is controlled by a personal computer. The network analyzer sweeps through frequencies from 1 to 10 GHz.

A hole of the same diameter as the probe is drilled and the probe inserted in the material.

To minimize any measurement errors, care should be taken to eliminate any air gaps between the probe and the material walls. Also any reflections from the edges of the sample should be gated out so they don't interfere with the direct signal between the transmitter and receiver.

In order to calibrate and interpret the measurements done with the probe, we developed a numerical model using the FDTD technique.This technique first proposed by Yee [3] has recently been used to model antennas. In this model we use the PML medium formulation introduced by Berenger [4].

The building blocks of the model are as follows:

1. Space and time steps

   The coaxial cable radius is .15 cm and the cell sizes in the x,y and z directions, Δx, Δy and Δz respectively, were chosen to be .15 cm. This space step is one twentieth of a wavelength at 10 GHz. The time step Δt is computed according to the Courant stability condition for the three-dimensional FDTD algorithm and is given by:

   $\Delta t \leq 2.89ps$; we choose $\Delta t = 2.59ps$; The code was executed for 1500 time steps giving a total running time of 3.89 ns.

2. Source and receiver

   The coaxial cables are simulated using four cells in the x-y plane backed by a perfect electric conductor as shown in Fig. 2.

   The center conductor of the coax was modeled using contour integration method, by setting the electric field in the z-direction, E_z, to zero at the intersection of the four cells and using special updating expressions for transversal magnetic fields in the x and y-directions.

   Both coaxes are terminated with a PML absorbing boundary condition to absorb the waves propagating in the negative z-direction.

   In order to launch the source pulse, which is a differentiated Gaussian, we initialize the four transversal electric fields in the coax to simulate a TEM wave (Fig. 2). the received signal is sampled inside the coax connected to the middle antenna.

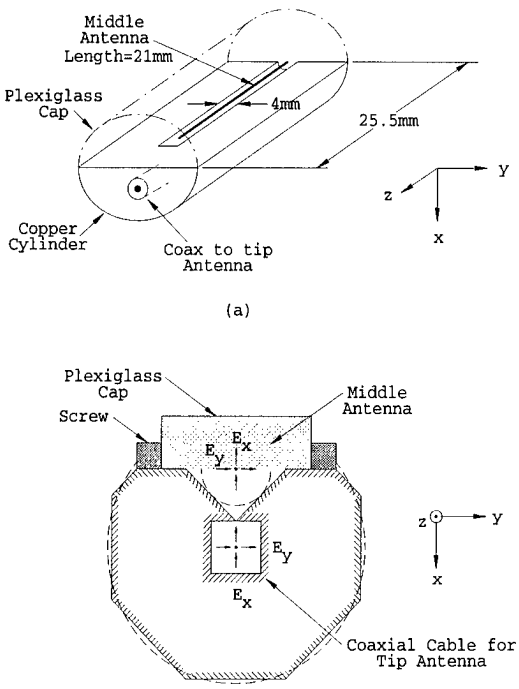


Figure 2: Detailed Geometry Near Middle Antenna,(a) 3-D plot of middle antenna,(b) 2-D cut showing the FDTD models of Cylinder, Cap, Screws, Slot and Coaxial Cable

3. Antennas

   The two antennas are also modeled with the same thin wire approximations used for the center conductor of the coaxial cables.

   The plexiglass caps around the antennas were modeled by setting the real part of the dielectric for the corresponding cells to 2.7, that of plexiglass; the conductivity for this material is $4*10^{-4}$. Stair-step approximation is used for the circular cap surface.

4. Copper Cylinder

   In order to model the circular conducting cylinder we made use of the half-cell contour integral formulation as shown in Fig. 2. Each of the screws holding the middle cap to the cylinder is modeled by one FDTD cell.

5. Absorbing Boundary Condition

   The space around the probe is terminated by the Perfectly Matched Layer (PML ABC) introduced by Berenger [4]. This type of ABC gives very low levels of reflection at the boundary by using a lossy

material that is matched to the material in the computation space in the three Cartesian coordinate directions. We use a PML layer made up of 13 FDTD cells having a dielectric constant $\epsilon_{PML} = \epsilon_m$ and a conductivity

$$\sigma_{PML} = \sigma_{max} \left(\frac{i * \Delta x}{d} \right)^2 + \sigma_m \qquad (1)$$

where

$\sigma_{max} = 8.0, d = 13 * \Delta x = 0.0195$ m, and i goes from 1 to 13.

ϵ_m and σ_m are the real part of the dielectric constant and conductivity of the material surrounding the probe in the cells adjacent to the PML absorbing layer.

NUMERICAL RESULTS

The computed and measured transmission coefficient($S21$, between the probe antennas when the surrounding medium is free space are shown in Fig. 3. The two curves are within 2 dB for the frequency range from 1 to 11 GHz, hence the FDTD model is a good numerical representation of the actual probe.

After running the code for several values of real part and conductivity values we get a set of factors that we use to calibrate the sea ice measurements. A plot of the calibrated real and imaginary parts for a sample of sea ice at a depth of 6 cm and temperature of -4.82 degrees is shown in Fig. 4 .

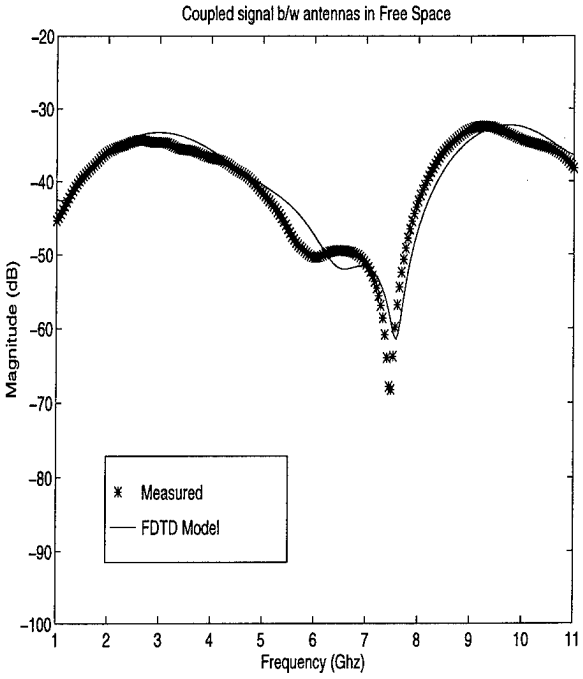


Figure 3: S21 in free space, Measured and FDTD results

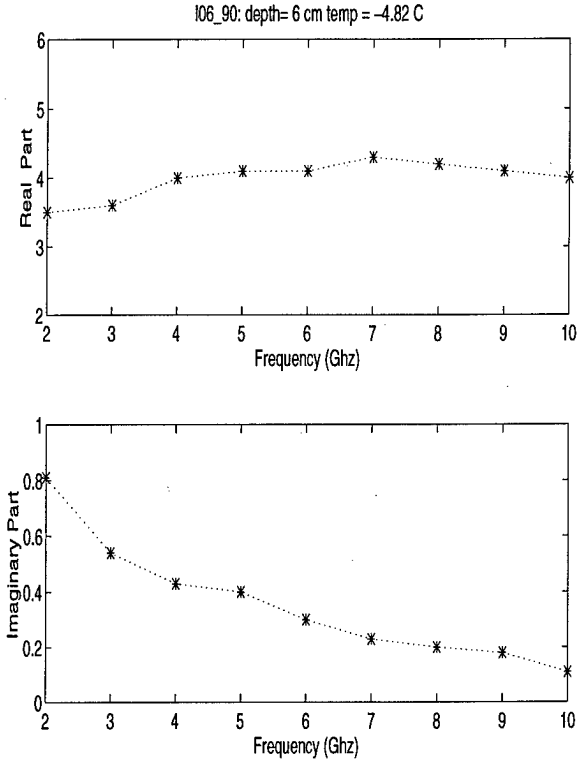


Figure 4: Complex Dielectric Constant of Artificially Grown Sea Ice

REFERENCES

[1] F.D.Carsey, "Microwave Remote Sensing of Sea Ice," Geophysical Monograph 68, American Geophysical Union, 1992.

[2] M.R.Vant, R.O.Ramseir, V.Makios, "The Complex Dielectric Constant of Sea Ice at Frequencies in the range 0.1 to 40 GHz," Journal of Applied Physics, vol. 49(3), March 1978.

[3] K.S.Yee, "Numerical Solution of Initial Boundary value Problems involving Maxwell's Equations in Isotropic Media," IEEE Trans. Antennas and Propag. Vol AP 14, pp 302-307, May 1966.

[4] J.P.Berenger,"A Perfectly Matched Layer for the Absorption of Electromagnetic Waves,"Journal of Computational Physics, Vol 114,No 2, pp 185-200, October 1994.

Nearshore Ice Surface Roughness Surveys on Lake Superior

Drew Pilant
Laboratory of Atmospheric Remote Sensing
Department of Geological Engineering and Sciences
Michigan Technological University
Houghton, MI 49931
T: 906.487.3199 F: 906.487.3371 EMail: anpilant@mtu.edu

ABSTRACT

Nearshore ice surface roughness and snow thickness were surveyed with an autolevel on Lake Superior for application to multisensor satellite remote sensing of Great Lakes ice cover. Topographic transects across four commonly occurring ice facies were measured with 0.2 cm vertical and 5.0 cm horizontal resolutions. The four ice facies rank in roughness as follows *(RMS roughness (cm) / correlation length (cm) in parentheses)*: single large pressure ridge (30/125), series of small pressure ridges (16/110), ball ice zone (8/70) and young ice cakes (5/145). Thin snow cover was widespread on the nearshore facies, with potential for generating diurnally-varying melt related changes in electromagnetic signatures during spring warming.

INTRODUCTION

Ice cover is a major component of the Great Lakes annual hydrometeorological cycle, governing winter and spring mass and energy fluxes at the lakes surfaces, weather, shipping season duration and shoreline processes. Current ice monitoring programs employ combinations of shore, ship, aircraft and multisensor satellite observations to produce ice cover information products. Radar sensors are used increasingly to provide day/night, weather independent, high spatial resolution (10-100 m), volume and surface sensitive information about ice cover.

Ice backscatter from freshwater ice is very dependent upon surface roughness both for SAR and radar altimetry, thereby necessitating *in situ* surface roughness studies. In general, the physical-electromagnetic properties of Great Lakes ice have received less attention than polar sea ice. Previous studies of Great Lakes ice properties include [1-4], and specific microwave studies include [5-6].

This paper is primarily descriptive in nature, part of an ongoing process to develop on-ice ground truth for multisensor remote sensing of Great Lakes ice cover. Ice roughness profiles and statistics presented here may be useful to readers interested in Great Lakes and, comparatively, sea ice roughness characteristics.

FIELD OBSERVATIONS

Four study transects were surveyed with an autolevel in late February 1996 at two sites on Michigan's Keweenaw Peninsula (Fig. 1) with the objective of measuring ice surface roughness and snow thickness. Ice heights are collected by sighting through the autolevel to the stadia positioned at regular intervals along the transect (Fig. 2). Supraice snow thickness was measured concurrently.

Autoleveling is advantageous in that it is relatively inexpensive, requires no sophisticated electronic equipment and permits surveying of long (10-100 m scale) transects. The disadvantage here is the relatively coarse horizontal resolution (limited by the width of the stadia base, ~4.0 cm).

This is a 'macro-roughness' study, in contrast with sub-cm resolution micro-roughness surveys which require more specialized equipment [7,8]. A 5.0 cm horizontal sampling interval makes these ice roughness data perhaps more pertinent to backscatter at longer radar wavelengths (e.g., L and P bands). The data apply also to mapping multi-km scale surface roughness zones that influence passive microwave emissivity.

Four common and morphologically distinct ice facies were surveyed: 1) a portion of a single large pressure ridge, 2) a rafted accretionary sequence of several small pressure ridges, 3) a ball ice zone and 4) young ice cakes (Table 1; Fig.3). They appear by visual inspection to be representative of major ice types in the region. The four ice facies fall into two thermal signature categories evident in Fig. 1: facies 1-3 occur in colder, thicker, older, deformed shore fast ice; facies 4 represents warmer, thinner young ice that probably formed in a Great Lakes -wide freezing event around February 2, 1996. Transects 1-3 were oriented perpendicular to shore; transect 4 was oriented to cross two ice cakes.

This study was funded in part by NASA Fellowship for Global Change Research #1956-GC92-0312 and Michigan Space Grant Consortium Seed Grant #79827.

0-7803-3068-4/96$5.00©1996 IEEE

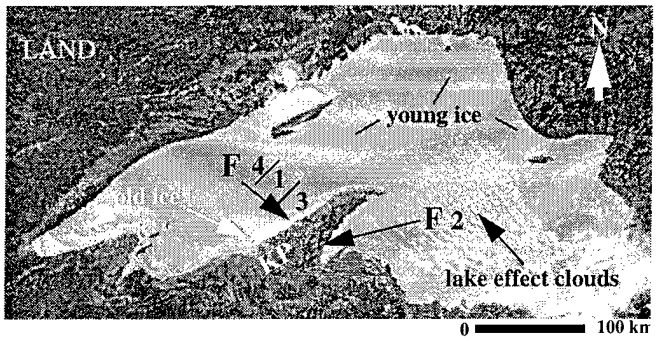


Fig. 1. Locations of ice topographic transects (Facies (F) 1-4) on Michigan's Keweenaw Peninsula (KP) on Lake Superior. Thermal infrared image (band 4 AVHRR) 8:11 UTC Feb. 4, 1996. Old, deformed ice (F 1-3) appears in brighter grey-white tones (-24 to -18 C°) and young ice (F 4) in medium grey tones (-17 to -2 C°). The lake is extensively ice covered with young ice; open water is confined primarily to the area beneath *(and source of)* the lake effect snow clouds in the eastern basin.

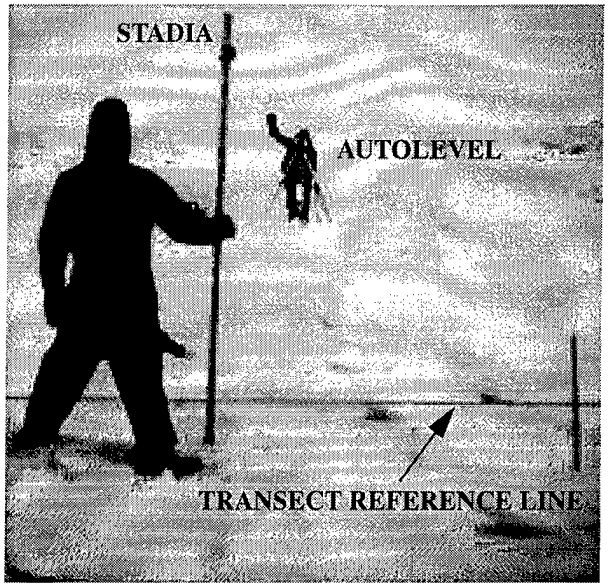


Fig. 2. Autoleveling survey in the small pressure ridge facies.

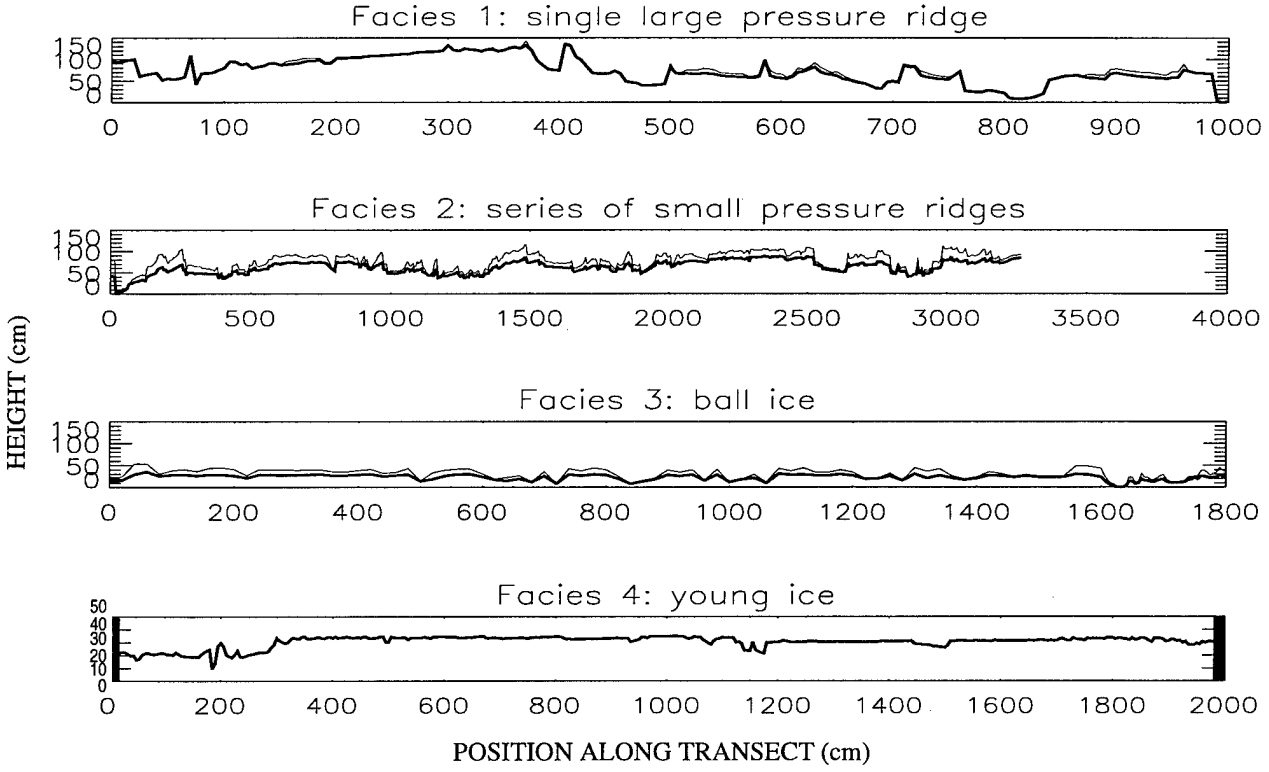


Fig.3. Topographic profiles of the four ice facies. Thick line=ice height above local base level; thin line=snow thickness above ice. Profiles 1-3 extend lakeward from 0 position.

Table 1: Field measured ice roughness and snow thickness parameters

facies	RMS roughness (cm)	correlation length (cm)[a]	mean height (cm)	ice slab thickness (cm)	min-max snow thickness (cm)	mean/std. dev. snow thickness (cm)	transect length (m)	horizontal sampling interval (cm)
1. large pressure ridge: rafted clear thick congelation ice	30.2	125	72	30-40	0-14	3.2 / 3.8	10	5.0
2. small pressure ridges: accretionary sequence of rafted clear thin congelation ice	15.7	110	63	4-6	1-38	13.9 / 6.8	32	5.0
3. ball ice: ice balls and slush ice conglomerate	7.8	20	21	10-40 *(ball diameter)*	0-24	7.9 / 5.3	18	20.0[b]
4. young ice: 2 clear ice cakes and interstitial brash ice	4.8	145	30	20-30	negligible snow	n.a.	20	5.0

a. Correlation length: distance at which normalized autocorrelation function=1/e.
b. 20 cm for first 16 m of transect; 5 cm for final 2 m.

RESULTS

The ice surface roughness and snow depth data collected in this study will be applied to interpretation of multisensor satellite imagery of Great Lakes ice cover. Two major morphogenetic regimes were sampled; old, moderately deformed shore fast ice, and clear, young congelation ice. These two regimes are readily discriminable in AVHRR thermal and infrared imagery, and should be discriminable in satellite radar imagery. Snow cover was nearly ubiquitous on the shore fast facies, with potential for generating areally extensive, diurnally-varying, melt-induced electromagnetic signature changes upon spring warming.

ACKNOWLEDGMENTS

The author thanks a host of undergraduate and graduate student colleagues for their enthusiastic field assistance: Matt Wachholz, Ashok Agarwal, Kindra Wicklund, Dan Brugeman, Dan Wrona, Heather Shocker, Jon French, Seth Lemke, Bill Schulz and Michelle Mars. Commentary provided by Dave Schneider. AVHRR satellite image is courtesy of NOAA Satellite Active Archive.

REFERENCES

[1] W.M. Marsh, B.D. Marsh and J.D. Dozier, "Formation, structure, and geomorphic influence of Lake Superior icefoots", Am. J. Sci., vol. 273, pp. 48-64, 1975
[2] E.W. Marshall, "The geology of the Great Lakes ice cover", unpublished. Ph.D. dissertation, Geology, Univ. of Michigan, 614 p., 1977.
[3] S.J. Bolsenga, "Nearshore Great Lakes ice cover", Cold Regions Sci. and Tech., vol. 15, pp. 99-105, 1988.
[4] R.A. Assel, F.H. Quinn, G.A. Leshkevich and S.J. Bolsenga, "Great Lakes Ice Atlas", NOAA Great Lakes Environmental Research Laboratory, 1983.
[5] M.L. Bryan and R.W. Larson, "The study of freshwater ice using multiplexed imaging radar", J. Glaciology, vol. 14, num. 72, pp. 445-458, 1975.
[6] B.B. Hagman, "On the use of microwave radiation for Great lakes ice surveillance", NOAA Tech. Mem. ERL-GLERL-13, 1976.
[7] F. Johnson, B. Brisco and R.J. Brown, "Evaluation of limits to the performance of the surface roughness meter", Canadian J. Remote Sensing, vol. 19, num. 2, pp. 140-145, 1993.
[8] M. Simila, M. Lepparanta, H.B. Granberg and J.E. Lewis, "The relation between SAR imagery and regional sea ice ridging characteristics from BEPERS-88". Int. J. Remote Sensing, vol. 13, num. 13, pp. 2415-2432, 1992.

Error Characteristics of the SIR Resolution Enhancement Algorithm

David S. Early and David G. Long
Brigham Young University
459 CB, Provo, UT 84602
801-378-4884, FAX: 801-378-6586, e-mail: earlyd@newt.ee.byu.edu

Abstract: To improve the utility of the scatterometer for land and ice studies, the Scatterometer Image Reconstruction (SIR) resolution enhancement algorithm has been developed to exploit the frequent overlapping coverage provided by the scatterometer. In this paper, we examine the effects of feature motion on SIR imagery and show the similarity of SIR motion imagery to low pass filtered truth images. Also, resolution improvement is qualified by examining radiometric accuracy as a function of spatial frequency. The SIR algorithm applied to ERS-1 scatterometer data provides a 33% gain in radiometric accuracy when compared to simple image reconstruction of raw scatterometer data.

INTRODUCTION

Spaceborne scatterometers are currently used to monitor and study near surface ocean winds on a global scale. The temporal and spatial resolution of the scatterometer make it a useful instrument for studying these atmospheric processes. Recently, the scatterometer has also been used to study non-ocean surface conditions (e.g. [1] [2] [3]). However, while the temporal coverage of the scatterometer is good for rapid repeat coverage of the Earth's surface, the nominal spatial resolution of 50 km is inadequate for detailed classification of non-ocean surface conditions.

In order to improve the resolution of the scatterometer data, a resolution enhancement technique has been developed to exploit the frequent, overlapping coverage of the spaceborne scatterometer [4]. The Scatterometer Image Reconstruction (SIR) algorithm is particularly useful for polar ice studies because of the high temporal and spatial coverage provided by scatterometers, and in fact the algorithm has been applied successfully to Seasat scatterometer data over Greenland glacial ice in [3]. It can also be used with ERS-1 data.

ERS-1 AND SIR

The ERS-1 scatterometer measurements are delivered on a 25 km grid of cells or resolution elements for each orbit. Each cell has cos^2 response as illustrated in Fig. 1 which is a result of averaging several discrete pulses into a single reading. The general effect of this averaging is a low pass filter on the collected data. The high frequency loss is accentuated by the fact that the ERS-1 roll off function extends to a radius of nearly 50km, larger than the nominal 25 km grid spacing.

SIR attempts to recover as much of the frequency information as possible from the scatterometer data stream. By using several days worth of data, multiple overlapping cells are algebraically recombined in a weighted iterative process. Resolution enhancement is achieved by backprojecting the data onto a higher resolution grid. The achievable enhancement is determined in part by the overlap characteristics of the cells and the cell shape. Seasat data, for instance, can be enhanced to greater resolution than ERS-1 data because the cell shape is oblong, resulting in a higher spatial sampling in one direction. Recombination of several days of data with various cell orientations results in a greater resolution enhancement than is possible with the larger, circular ERS-1 cell shapes. However, SIR does provide resolution enhancement to increase the use and applicability of ERS-1 data over land and ice.

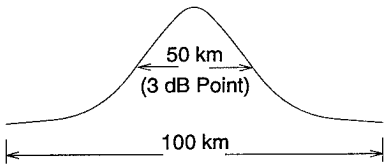


Figure 1: Geometry of the ERS-1 Footprint. Each measurement cell has a latitude and longitude that specify the center of the cell. The σ^o is assumed to have a cosine-squared roll off characteristic, with the 3 dB point at 50km. (Personal Communication, E. Attema)

This paper addresses the issue of radiometric and frequency error in the SIR algorithm for ERS-1 data. Because SIR was originally developed for use over the Amazon where microwave signatures are relatively stable over periods of days, there is a need to characterize the behavior of the algorithm over the more dynamic polar ice regions. For brevity, we consider only the simple characterization of the SIR algorithm as a low pass filter for surfaces in motion and radiometric accuracy of SIR compared to nominal ERS-1 resolution.

METHODOLOGY

Simulated data is used to characterize the SIR imagery. High resolution test scenes are processed using cell location, azimuth and incidence angle information extracted from actual ERS-1 scatterometer data. The cell response shown in Fig. 1 is used in calculating the simulated σ^o values. For the purposes of this simulation, we assume that this response is exact and that there is no location error in the latitude and longitude extracted from the actual ERS-1 data.

We model σ^o as a linear function of incidence angle:

$$\sigma^o_{dB} = \mathcal{A} + \mathcal{B}(\theta - 40°) \quad (1)$$

0-7803-3068-4/96$5.00©1996 IEEE

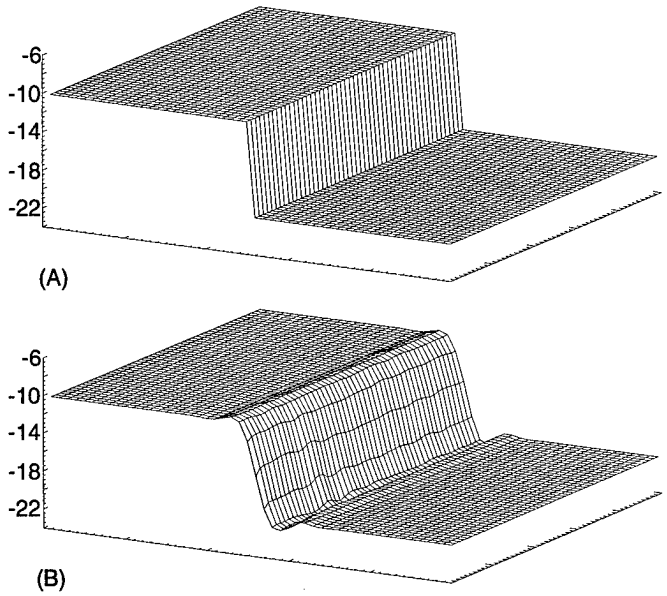


Figure 2: Example test image and SIR output. Plot (A) is the original single step image. Plot (B) is the output of SIR.

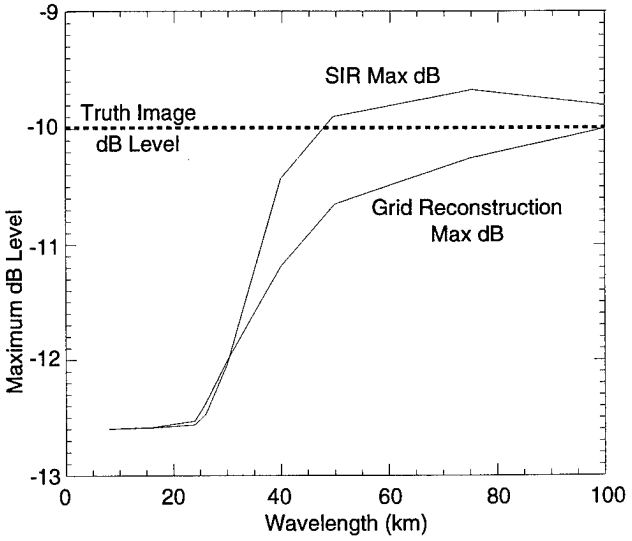


Figure 3: Convergence of the maximum dB levels for the SIR algorithm and a simple single pass reconstruction. Note SIR becomes more accurate relative to the true dB level faster than the simple grid reconstruction even with the overshoot.

where θ has been normalized to 40°, the median incidence angle in the data. Each test scene consists of two colocated images: an $\mathcal{A}$ image and a $\mathcal{B}$ image. In this study, the test scenes are at 1 km/pixel resolution. For any given cell measurement, we assume that the incidence angle is identical for each pixel in the footprint. For each pixel, the σ^o value for that pixel is calculated based on the $\mathcal{A}$ and $\mathcal{B}$ values from the test images and the incidence angle associated with the cell using (1). The cos^2 weighting function is applied and the weighted average of the pixels within a footprint represent a linear estimate of σ^o for the test 'surface'.

The simulated data stream is then processed with SIR. Surface plots of sample input and output image are shown in Fig. 2. The test scenes used in this study are two-level scenes as illustrated in Fig. 2(A). Step sizes vary from 2 dB to 20 dB, but the results for various step sizes have negligible differences.

A total of 5 days of location, azimuth and incidence data are extracted from the ERS-1 data set. Motion scenes are created using five $\mathcal{A}$ and $\mathcal{B}$ image sets, one for each day. The scenes are considered stationary over each day period. Motions of 2 km/day, 5 km/day, 10 km/day, 15 km/day and 30 km/day are considered, although a sustained speed of 30 km/day in sea ice is unlikely.

Comparison images

Comparison of SIR imagery to low pass filtered versions of the original high resolution imagery is used to assess the SIR algorithm performance. Each test scene in this study is low pass filtered to create a 'truth' image for comparison with the SIR output. The low pass filter used to create comparison 'truth' images is ideal with a spatial cutoff frequency equivalent to the resolution of the SIR imagery. For motion over multiple days, each day's image is low pass filtered and the truth image is created by averaging the individually filtered daily images.

RESULTS

Because the ERS-1 footprint extends beyond the nominal 25km grid spacing (approximately a 100 km diameter circle), significant reduction of the spatial frequency content of the original image is expected at wavelengths less than 100km. The SIR algorithm enhances the frequency content and results in a reconstructed image that is accurate at higher spatial frequencies than the nominal data provides. This is illustrated in Fig. 3. The SIR image converges to within 0.5dB of the true dB level at wavelengths of around 40km, although there is a slight overshoot. The idealized data does not reach this level of accuracy for wavelengths less than about 60km.

We note that the shape and size of the ERS-1 footprint severely limits the resolution enhancement achievable by the SIR algorithm. In a previous study using Seasat, SIR achieved a much greater resolution enhancement because of the shape and distribution of the scatterometer measurement cells [5]. It is expected that SIR will perform similarly well using NSCAT data.

Motion

Fig. 4 shows profile comparisons of SIR imagery with the low pass 'truth' images. Note that as the magnitude of the motion increases, the overshoot and undershoot of the truth images are reduced by the averaging of the individually filtered day images, but that the transition region between the high and low dB levels is the same for both SIR and the low pass truth

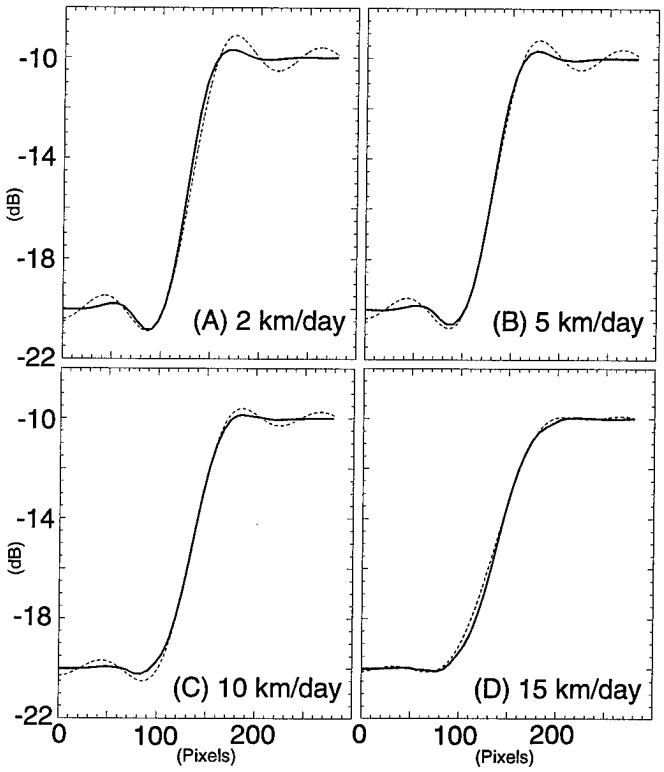


Figure 4: Cross sections of several motion examples. The solid lines are SIR image profiles, the dotted lines are low pass filtered truth image profiles.

images. Also note that the SIR images have less over- and undershoot and ripple than the low pass truth images.

Figs. 5(A) and 5(B) show a comparison of 15 km/day motion and 30 km/day motion. The ripples in the 30 km/day transition region are because the scatterometer passes over the regions at various ascending and descending angles which result in unique distributions of overlapping cells in any given scene. Because SIR uses multiple overlapping cells to reconstruct the images, areas in a scene that have limited or reduced cell coverage may not be as accurately reconstructed. In Fig. 5(A), where the underlying motion is more reasonable, the textural anomalies in the transition region are less significant.

SUMMARY

The ability of the SIR reconstruction algorithm to create accurate images at higher spatial frequencies is illustrated. SIR provides more accurate dB estimates at lower wavelengths resulting in an approximately 33% resolution gain for errors less than 0.5 dB when compared to simple grid reconstructions even with the severe limitations of the ERS-1 cell response. The SIR algorithm also produces images of stationary scenes and scenes in motion that are similar to low pass filtered versions of the original scenes allowing the algorithm to be characterized as a low pass filter. Because of the non-linearities of the SIR algorithm, the overshoot and undershoot characteristic of low

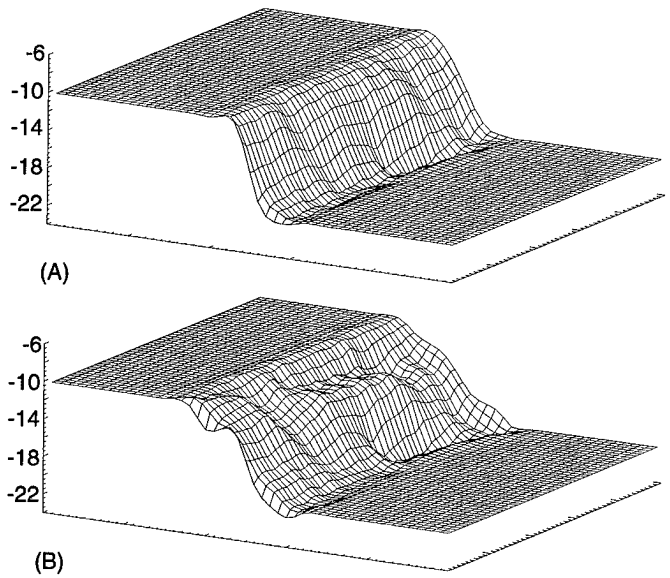


Figure 5: Comparison of two motion images. Plot (A) is 15 km per day motion, plot (B) is 30 km per day. Note the textural similarities in the transition regions and the very flat response in the extremities.

pass filtering are reduced in SIR imagery. This suggests that SIR is more effective than simple construction of imagery from raw ERS-1 scatterometer data.

REFERENCES

[1] A. R. Hosseinmostafa, V. I. Lytle, K. C. Jezek, S. P. Gogineni, S. F. Ackley, and R. K. Moore, "Comparison of radar backscatter from antarctic and arctic sea ice," *Journal of Electromagnetic Waves and Applications*, vol. 9, no. 3, pp. 421--438, 1995.

[2] P. Lecomte, A. Cavanie, and F. Gohin, "Recognition of sea ice zones using ERS-1 scatterometer data," in *Proceedings of IGARSS 93*, pp. 855--857, IEEE, 1993.

[3] D. Long and M. Drinkwater, "Greenland Ice Sheet Surface Properties Observed by the Seasat-A Scatterometer at Enhanced Resolution," *Journal of Glaciology*, vol. 40, pp. 213--230, 1994.

[4] D. Long, P. Hardin, and P. Whiting, "Resolution Enhancement of Spaceborne Scatterometer Data," *IEEE Transactions on Geoscience and Remote Sensing*, vol. 31, pp. 700--715, 1993.

[5] D. Daum, D. Long, and W. Davis, "Reconstructing Enhanced Resolution Images From Spaceborne Microwave Sensors," in *Proceedings of IGARSS 94*, pp. 2231--2233, IEEE, 1994.

The Quantification Of Sea Ice Melt Features From Low Level Aerial Photographs

C.P.Derksen, J.M.Piwowar, and E.F.LeDrew
Waterloo Laboratory for Earth Observations
Department of Geography
University of Waterloo
Waterloo, Ontario, Canada
N2L 3G1
Phone: (519) 888-4567 ext 6070
Fax: (519) 888-6768
email: chris@glenn.uwaterloo.ca

Abstract -- The transition from a dry snow cover over Arctic sea ice to a prevalence of melt pond features can occur quickly -- on the order of two weeks or less. As the energy absorption and scattering properties of a ponded sea ice surface differ radically from those of a snow covered surface, calculating the rate at which the snow cover to melt pond ratio changes is of great significance. With their high spatial resolution, low level aerial photographs are an excellent data source for monitoring the evolution of sea ice melt features. In this study we use a time series of low level sea ice photographs to quantify the changing evolution of melt pond coverage as the spring melt progresses. The data were collected as a component of the Seasonal Sea Ice Monitoring and Modeling Site (SIMMS) field experiment of 1995 conducted near Resolute, Northwest Territories in the Canadian Arctic Archipelago.

INTRODUCTION

The variable nature of Arctic sea ice is one of its defining properties. Not only does the areal extent change vastly from season to season and subtly from year to year, but the physical characteristics of the sea ice surface itself vary greatly as well. One of these variable parameters is the presence of water on and within the sea ice and overlying snow pack, and the resultant changes in surface albedo. While snow covered sea ice has an albedo ranging from 0.6 to 0.9, the albedo for standing water over sea ice can drop below 0.2 [1],[2]. During the spring melt season the scattered presence of melt ponds thereby causes great spatial variation in ice pack albedo.

While the processes of ice and snow ablation are very complicated and not well understood, Arctic sea ice undergoes a positive feedback cycle every spring season which illustrates the relationship between albedo and ice decay [3]. During winter and early spring, the snow covered sea ice surface reflects nearly all incident radiation. This, in combination with cold surface temperatures, maintains relatively static ice conditions.

The spring is marked by an increase in ambient temperature, incident solar radiation, cloud cover, and precipitation. As surface temperatures warm, snow pack temperatures also warm and as the spring transition begins the snow pack becomes markedly wetter. This increase in snow pack water content begins to lower the surface albedo and energy absorption increases. This furthers the warming process and melt pond features begin to form on the ice surface with the actual spatial distribution of melt ponds dependent on the heterogeneity of surface characteristics such as snow cover and ice roughness. The areas of standing water greatly increase energy absorption, acting as solar radiation sinks, which accelerates the expansion of pond area and increases further energy absorption [4]. While the onset of melt can be slow to occur, the initial presence of water in the snow pack triggers the rapid development of melt pond features.

With a fine spatial resolution and user defined temporal resolution, a time series of aerial photographs is ideal for investigating the spatial and temporal patterns of melt feature growth. This study quantifies the rate at which melt features evolve spatially utilizing low level aerial photographs acquired from a tethered balloon flown during the Seasonal Sea Ice Monitoring and Modeling Site (SIMMS) field experiment of 1995. The raw images were enhanced using a noise reduction filter and segmented into image classes of melt and non-melt features. From these images the changing ratio of melt pond coverage to residual snow cover can be calculated. Results from an intensive study region are compared to a second area in order to investigate the consistency of results across spatially disparate images. A final objective was to compare areas of melt pond coverage in late spring with pre-melt period images and note which early spring surface characteristics effect the spatial pattern of melt pond development later in the melt season.

DATA

Low level aerial photographs of a first-year sea ice study area were collected from a tethered balloon as a component of the SIMMS'95 field season conducted near Resolute NT (Fig. 1). SIMMS is a multidisciplinary field experiment which operated from April 4 (Day 94) to June 19 (Day 160), 1995 with balloon flights occurring daily from June 7 (Day 158) to June 19 (Day 160). This analysis uses a time series of images collected at a balloon flying height of 300 meters with photographic infrared film. Cameras were attached to a gimbal mount and suspended below a helium filled Raven Industries TRF-900 balloon. Complete technical details are given in [5]. After the field season the images were scanned into digital form for analysis at a resolution of 1536 pixels by 1024 lines.

0-7803-3068-4/96$5.00©1996 IEEE

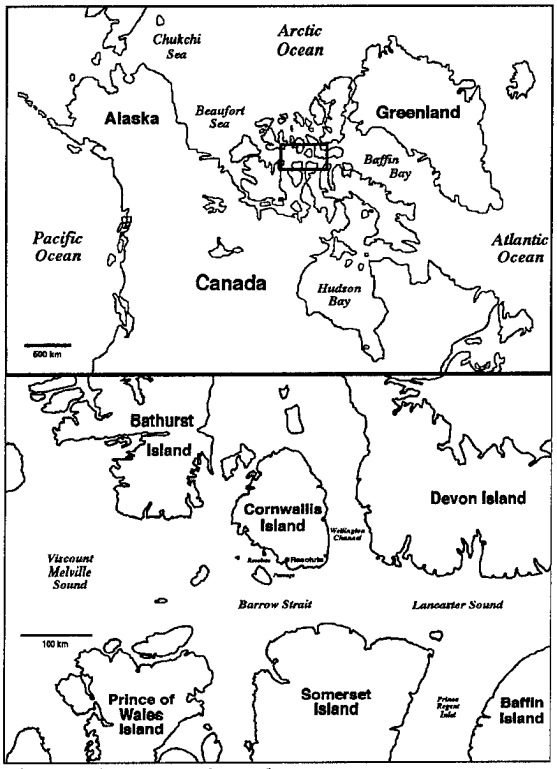


Fig. 1. The SIMMS study area.

Although the balloon was flown over the same study area each day, wind induced drift created changes in the photographic coverage of each image. In order to isolate a common area the time series of data was co-registered using the PCI Image Analysis System (V5.3). Certain days in the time series (Table 1) were omitted because of poor image quality caused by foggy conditions which are very prevalent during this season.

ANALYSIS PROCEDURE

Preliminary image analysis showed that standing water with a depth greater than 10 centimeters is relatively easy to isolate as an image class because of its low spectral reflectance. Also of interest, however, are transitional melt areas which can consist of very shallow standing water, extremely high snowpack wetness, and water beneath an apparent snow surface. These areas return speckled gray tones that can be very similar to the areas of residual snow cover and therefore are lost in an image thresholding procedure. To include these transitional areas in the melt feature class, and improve overall thresholding accuracy, a noise reduction filter was used on the raw images to adjust gray tone values. Noise was reduced using a median filter with which the center pixel in a 3x3 neighbourhood was replaced by the median pixel value in that neighbourhood.

Other methods of image adjustment such as simple range and variance texture operators were explored, and each technique improved the overall accuracy of thresholding. The noise reduction filter was chosen, however, because it created an especially strong contrast between melt features and snow cover, while the integrity of fine discontinuous zones of water and snow were maintained The analysis procedure therefore consisted of noise reduction filtering, thresholding the time series of imagery into melt and non-melt feature classes (Fig. 2), and calculating the changing spatial ratio of these classes. Finally, while the first days of the time series show no standing water, these early spring images were also thresholded and analyzed in order to examine any correlation between bare ice and snow covered areas in early spring, and the relative location of melt features in late spring.

Table 1. Image acquisition days and times

Day	Time	Day	Time
158	1745	163	1300
159	1200	167	1230
159	1700	169	1200
160	1200	169	1700
160	1700		

RESULTS

The primary goal of this work was to establish the rate at which the ratio of snow cover to melt feature areal extent changes on first-year Arctic sea ice during the spring melt period. Calculations using low level aerial photographs show a strong linear growth rate from the onset of melt to approximately a 50:50 snow cover:melt feature ratio (Fig. 3). The first day of imagery used in the analysis (Day 159) had no standing water or apparent melt features in the study area. During Day 160 melt feature growth started slowly and progressed to 8% coverage in one day. By Day 163, 25% of the image area was in the melt feature class and this growth trend continued until Day 169 when just over 53% of the study area was classified as melt feature. At this point the growth trend appears to level off with no significant change in melt pond area occurring within the span of Day 169.

As a means of exploring the spatial consistency of results, the study area images from Day 163, 167, and 169 were compared to supplementary images of first-year sea ice collected over different sea ice areas on the same days. While the results indicate a close relationship in values (Table 2), additional supplementary first-year sea ice images would be necessary to more rigorously examine the reproducibility of these results.

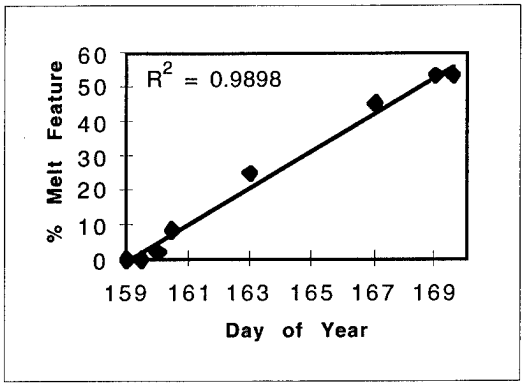


Fig. 3. Percent area in the melt feature class.

Table 2. Comparison of intensive site and supplementary image results (Ratios are snow cover:melt feature)

Day	Intensive Ratio	Supplementary Ratio	Difference
163	25:75	28.8:71.2	3.8%
167	54.6:45.4	53.7:46.3	0.9%
169	46.4:53.6	48.1:51.9	1.7%

A second objective of the study was to link the areas of standing water in late spring images with those same areas in early spring before the appearance of melt ponds. The results of this comparison show that the areas of ice with little or no snow cover during the winter evolve to contain water and become melt features during the spring. Fig. 4 shows the bare ice areas of Day 159 overlaid on the image from Day 167. The early season bare ice areas (black) are in the same locations as late season melt ponds (gray) which are surrounded by late season residual snow cover (white). While the areas do not match exactly, the relationship is clear enough that future areas of standing water can be extrapolated from early season images.

DISCUSSION

The time series of imagery used in this study has shown a strong linear trend in the proportion of sea ice surface area covered by melt features as the spring melt progresses. In a relatively short period of ten days a 100% snow covered sea ice surface with a consistently high albedo was transformed to over 50% standing water and, therefore, a spatially erratic surface albedo. This rapid change clearly has ramifications in regards to energy absorption and reflection at the ice/snow/water surface and for the acquisition of sea ice information by remote sensing during the melt season.

Further study of the temporal rate of melt pond coverage is important as thermodynamic sea ice modeling efforts have shown sensitivity to parameters associated with melt feature area and depth [6], [7]. Additionally, local scale spatial fluctuations in melt pond coverage and corresponding albedo, as discussed in this work, influence the derivation of regional scale albedo values used in sea ice models.

After this initial stage of research several outstanding issues remain. Of a technical nature, which type of imagery is most effective: panchromatic or photographic infrared?



Figure 4. Overlay of Day 159 bare ice (black) on Day 160 melt feature (gray) and snow cover (white) image.

What influence do lighting conditions have on image quality and accuracy? For example, are photos collected under diffuse lighting conditions more effective than those collected under an unobscured solar disk?

It would also be of interest to note what other surface variables change in accordance with the growth of melt features. For example, parameters such as ice temperature, snow pack temperature and net all-wave radiation show a similar linear trend to our rate of melt feature growth during this study period.

The variable nature of Arctic sea ice is clearly represented through the rapid evolution and growth of melt features. The drastic changes in surface parameters such as albedo that are caused by the growth and spatial discontinuity of melt features makes the examination of that growth rate an important procedure.

ACKNOWLEDGMENTS

This work was supported by funding through the Natural Science and Engineering Research Council (Operating Grant - E. LeDrew) and the Northern Studies Scientific Training Program (Grants - C. Derksen, J. Piwowar). Special thanks are given to the Polar Continental Shelf Project for logistical support and appreciation is extended to the SIMMS'95 field crew.

REFERENCES

[1] R. De Abreu, D. Barber, K. Misurak, and E. Le Drew, "Spectral albedo of snow covered first-year and multi-year sea ice during spring melt," *Ann. of Glaciol.*, vol 21, pp. 337-342, 1995.

[2] T. Grenfell and K. Perovich, "Spectral albedo of sea ice and incident solar irradiance in the Southern Beaufort Sea," *J. Geophys. Res.* vol 89 (C3) 3573-3580, 1984.

[3] E. LeDrew, D. Barber, T. Agnew, and D. Dunlop, "Canadian Sea Ice Atlas from Remotely Sensed Imagery," Ottawa: Canada Communications Group, 1992.

[4] W. Tucker, D. Perovich, and A. Gow, "Physical properties of sea ice relevant to remote sensing," in *Microwave Remote Sensing of Sea Ice*, F. Carsey ed., Washington D.C.: American Geophysical Union, Geophysical Monograph 68, 1992, pp. 9-28.

[5] J. Piwowar, "Balloon Data" in *SIMMS'95 Data Report*, K. Misurak, C. Derksen, E. LeDrew, and D. Barber, Eds. Waterloo: Earth Observations Laboratory Technical Report, 1995.

[6] E. Ebert and J. Curry, "An intermediate one-dimensional thermodynamic sea ice model for investigating ice-atmosphere interactions," *J. Geophys. Res.* vol 98 (C6) 10 085-10 109, 1993.

[7] K. Shine and A. Henderson-Sellers, "The sensitivity of a thermodynamic sea ice model to changes in surface albedo parameterization," *J. Geophys. Res.* vol 90 (D1) 2243-2250, 1985.

Mapping Snow Properties for Spatially Distributed Snow Hydrological Modeling in Mountainous Areas Using Passive Microwave Remote Sensing Data

Larry L. Wilson, Leung Tsang, and Jenq-Neng Hwang
Department of Electrical Engineering, Box 352500
University of Washington, Seattle, WA 98195
tel: (206) 685-0760; fax: (206) 543-3842
sterling@u.washington.edu

Abstract -- A method to incorporate passive microwave remote sensing measurements in a spatially distributed snow hydrology model is investigated. The difference in scale is tackled using an electromagnetic scattering model and parameter estimation techniques. An important aspect is accounting for the lack of homogeneity within the area of the sensor footprint.

INTRODUCTION

Snowpack properties exhibit high spatial variability in mountainous regions. This is particularly true of snow water equivalent (SWE), which is an important variable in hydrology and water resources engineering. However, point measurements of snow properties, such as the SNOTEL (SNOwpack TELemetry) measurements of SWE, are sparsely distributed and not representative of the parameter spatial variability. This makes it difficult to incorporate these measurements into basin-scale spatially distributed snow models.

Passive microwave remote sensing holds potential for overcoming this deficiency through spatial measurements of snowpack properties. Through microwave dependencies on snow properties such as grain size, temperature, depth, and density, passive microwave remote sensing measurements may be able to provide the required spatial distribution of snowpack parameters. However, with the exception of [1] little has been done in fully exploiting this information in combination with a snow hydrology model. One of the difficulties in implementing this is the solution of the many-to-one inverse problem from brightness temperatures to snow parameters. Another problem is the differences in spatial resolution between a hydrology model (1 km) and the footprint resolution of the microwave measurements (25 km).

To tackle these problems we combine a spatially distributed snow model with remote sensing measurements and parameter estimation techniques to estimate the time evolution of snow parameters in a mountain environment.

BASIN AND DATA CHARACTERISTICS

The basin chosen for the investigation of the technique is the upper portion of the Rio Grande River in the mountains of Colorado. The basin is defined by the streamgauge at Del Norte, Colorado and has an area of 3419 km^2 with an elevation range of 2432–4215 m. This basin has been used in previous snow-remote sensing studies [1]. The basin topographical characteristics are determined from 30 arc-second digital elevation model (DEM) output. The basin topography from the DEM is shown in Fig. 1.

Defense Mapping Satellite Program (DMSP) Special Sensor Microwave Imager (SSM/I) brightness temperatures for 1992–1993 are obtained from the Distributed Active Archive Center (DAAC) at the Marshall Space Flight Center. The SSM/I measures microwave emission for four frequencies with dual-polarization. We selected the 19 and 37 GHz frequencies, using both polarizations. Each day that contains nighttime measurements over the basin is determined. Daily SWE values for selected points in the basin were obtained from the SNOTEL measurement network. These are used to assist in refining the estimation procedure.

METHODOLOGY

The method we investigate uses snowpack parameter outputs from a spatially distributed snow hydrology model as input to a microwave scattering model. Estimated brightness temperatures at 1 km resolution are aggregated and compared with the remotely sensed 25 km measurements. The difference is disaggregated and used to adjust the 1 km brightness temperatures which are then inverted to give updated snowpack parameter values that are returned to the snow hydrology model.

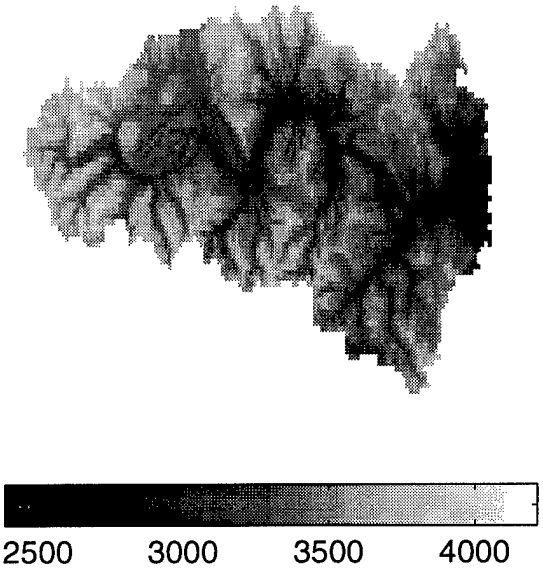


Figure 1 Topography of the upper Rio Grande River basin.

0-7803-3068-4/96$5.00©1996 IEEE

The snow model contains three components: accumulation, surface energy balance, and metamorphism. The accumulation is based on point precipitation with air temperature records to determine the snow/no-snow boundary for the time step. It is calibrated using annual streamflow volume from the basin and checked with the SNOTEL SWE values. The snow surface energy balance is based on the point model of [2], which is generalized to a spatial model, incorporating the topography of the basin through the DEM. It is driven using elevation adjusted point meteorological measurements. The snow metamorphism algorithm, which describes the evolution of snowpack properties such as snow grain size and density is taken from the SNTHERM model of [3], but simplified to operate for a one-layer snowpack. The snowpack parameter estimates obtained from the model are grain size, depth, density, and snow temperature.

The electromagnetic scattering model used to simulate the microwave interaction with the snowpack is the dense medium radiative transfer (DMRT) model [4,5]. Unlike traditional radiative transfer models, this model takes into account the collective effects of snow grain scattering. This is important in dense materials such as snow. The model incorporates a particle size distribution using a modified gamma distribution, accounting for the different particle sizes in the pack. A neural network representation of the DMRT is employed similar to that of [6] and [7].

At the end of each day for which there is basin coverage from the sensor, the neural network forward approximation to the DMRT is used to estimate the four microwave brightness temperatures from the four snowpack parameters at pixel resolution (1 km). The pixel brightness temperatures are then averaged to the footprint scale (25 km) for each measurement. The difference between the pixel integrated brightness temperatures and SSM/I measured brightness temperatures is distributed back to the pixels and a least mean square error scheme is used to update the snow parameters for each pixel using a neural network inversion of the DMRT. The snow hydrology model then continues forward with the updated parameters until the next SSM/I observation.

RESULTS

The critical point in the previously described procedure is in going from the 1 km scale to the 25 km scale and then back to the 1 km scale. The remote sensing measurements cover approximately a 25 km area and thus represent a spatial average of snow properties that may be quite heterogeneous. Depending on the location of the pixel with respect to the center of the footprint, the pixel-to-footprint measurement relationship can vary from day-to-day.

To examine the possible fluctuations in remote sensing measurements due to footprint position, we compared SNOTEL sites with brightness temperatures assigned to a pixel based on the degree of footprint coverage. Fig. 2a shows brightness temperatures for a coverage area with radius of 12.5 km, the actual footprint size. Fig. 2b shows the brightness temperatures using a coverage area radius of 5.0 km from the footprint center. As the pixel of interest becomes nearer to the center of the footprint, it should be more closely related to the footprint measurement. From the figures we see that the amount of fluctuation is reduced as the distance from pixel to footprint center is reduced, showing more clearly the expected trend of decreasing brightness temperatures with increasing snow depth.

The previously described updating methodology is applied to this site using a coverage radius of 5.0 km. In the time interval from day 88–104, four remote sensing measurements met this criterion. The snow hydrology model is run independently using only the meteorological forcings to drive it. It is then run again incorporating the updating information derived from the remote sensing measurements.

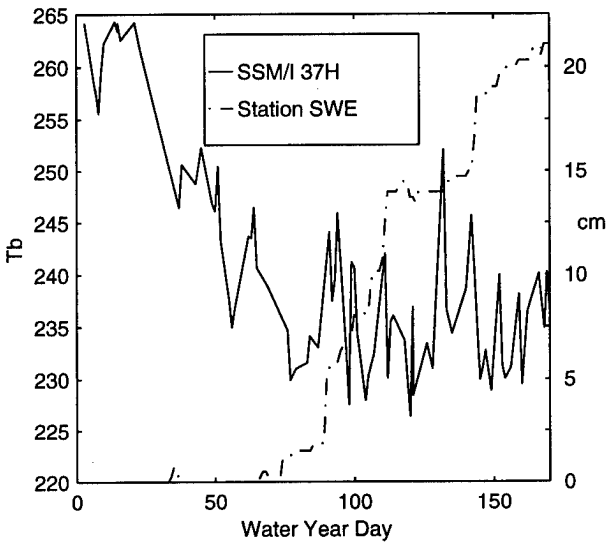


Figure 2a Brightness temperature and station SWE as a function of time for coverage radius of 12.5 km.

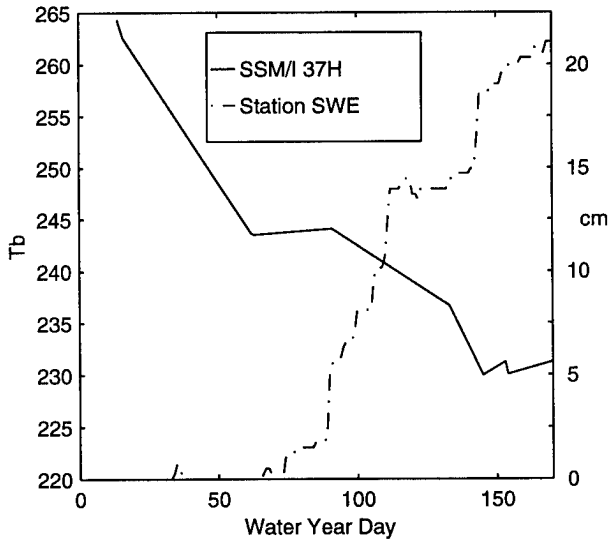


Figure 2b Brightness temperature and station SWE as a function of time for coverage radius of 5.0 km.

Fig. 4 shows the SWE values at this pixel for measured, modeled, and modeled with updating cases. The two model cases follow each other until Day 90, the first updated day. The output from the end of Day 90 is adjusted using the brightness temperature measurements taken that night. The updated values are used as the initial values for the start of the Day 91 simulation. In between updatings, both modeling schemes parallel each other, relying solely on the meteorological data to determine the SWE. The updating technique provides more information to the model and is able to improve upon the SWE estimate that would be obtained from the hydrology model without remote sensing input. This method was applied to all pixels within the basin and a spatial image of SWE at the end of the updating run (Day 104) is shown in Fig. 5.

CONCLUSION

The presented methodology for updating a spatially distributed snow model using remote sensing appears promising. The methodology is able to handle the scale differences between the two levels of snow parameter estimation. The most critical step in the methodology is determining the appropriate updating plan for the pixel, which is under continuing investigation

ACKNOWLEDGMENTS

This work was supported by NASA Grant NAGW 4251. The assistance of the Marshall Space Flight Center in providing the SSM/I passive microwave measurements and the Natural Resources Conservation Service for providing the SNOTEL data are also gratefully acknowledged.

REFERENCES

[1] A. Rango, J. Martinec, A.T.C. Chang, J.L. Foster, and V.F. van Katwijk, "Average areal water equivalent of snow in a mountain basin using microwave and visible satellite data", IEEE Trans. Geosci. Remote Sens., 27(6), 740–745, 1989.

[2] D. Marks, "Climate, energy exchange, and snowmelt in Emerald Lake watershed, Sierra Nevada", Ph.D. dissertation, University of California, Santa Barbara, 1988.

[3] R. Jordan, "A one-dimensional temperature model for a snow cover, technical documentation for SNTHERM.89", Spec. Rep. 91-16, CRREL, Hanover, NH, 1991.

[4] L. Tsang, "Passive microwave remote sensing of dense nontenuous media", J. Electromag. Waves Applic., 1(2), 159–173, 1987.

[5] L. Tsang, "Dense media radiative transfer theory for dense discrete random media with particles of multiple sizes and permittivities", in Progress in Electromagnetics Research 6, 181–230, New York: Elsevier, 1992.

[6] L. Tsang, Z. Chen, S. Oh, R.J. Marks II, and A.T.C. Chang, "Inversion of snow parameters from passive microwave remote sensing measurements by a neural network trained with a multiple scattering model", IEEE Trans. Geosci. Remote Sens., 30(5), 1015–1024, 1992.

[7] D.T. Davis, Z. Chen, L. Tsang, J.N. Hwang, and A.T.C. Chang, "Retrieval of snow parameters by iterative inversion of a neural network", IEEE Trans. Geosci. Remote Sens., 31(4), 842–852, 1993.

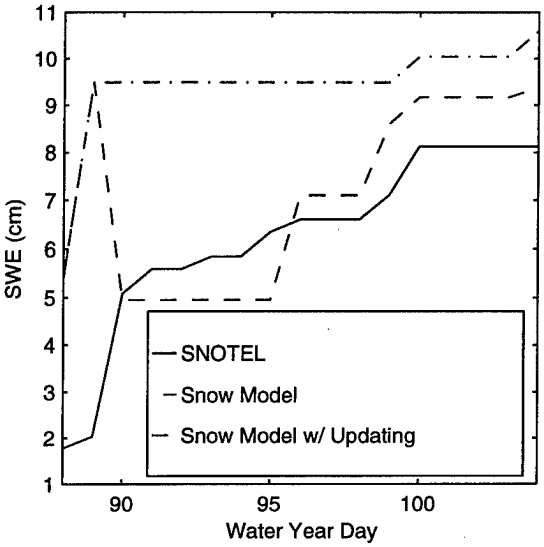


Figure 4 Comparison between the different estimation techniques with measured SWE at a SNOTEL site.

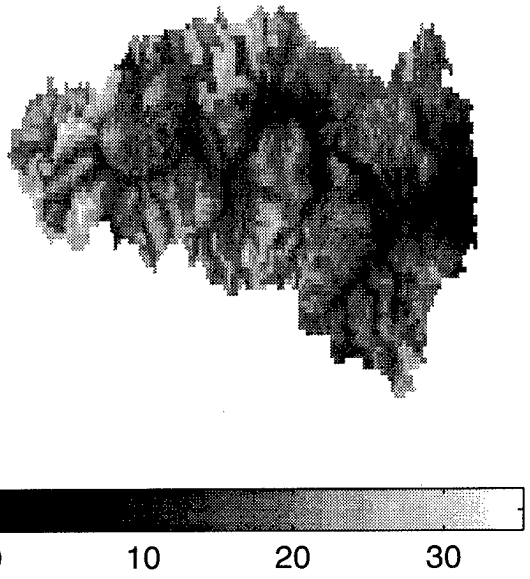


Figure 5 Spatial distribution of SWE (in cm) on Day 104 for the upper Rio Grande River basin from the snow hydrology model with remote sensing updates.

Snow Classification from SSM/I Data over Varied Terrain Using an Artificial Neural Network Classifier

Changyi Sun
Forest Resources, Utah State University, Logan, UT 84322-5215, USA
Tel: (801)797-1041 Fax: (801)797-4040 Email: csun@indigo.ecob.usu.edu

Christopher M.U. Neale
Biological and Irrigation Engineering, Utah State University, Logan, UT 84322-4105, USA
Tel: (801)797-3689 Fax: (801)797-1248 Email: neale@indigo.ecob.usu.edu

Jeffrey J. McDonnell
College of Environmental Science and Forestry, SUNY, Syracuse, NY 13210-2779, USA
Tel: (315)470-6565 Fax: (315)470-6956 Email: jemcdonn@mailbox.syr.edu

Heng-Da Cheng
Computer Science, Utah State University, Logan, UT 84322-4205, USA
Tel: (801)797-2054 Fax: (801)797-3265 Email: cheng@hengda.cs.usu.edu

Abstract -- The brightness temperatures (Tb's) observed by the Special Sensor Microwave/Imager (SSM/I) radiometer are sensitive to the changes in land surface snow conditions. Previously developed SSM/I snow classification algorithms have limitations and do not work properly for terrain where forests overlay snow cover. In this study, we applied unsupervised cluster analysis to define 6 snow classes in Tb observations, assessing both sparse- and medium-vegetated region classes. Typical SSM/I Tb signature, in terms of cluster means, of each snow class was determined by calculating the mean Tb's of the corresponding cluster. A single-hidden-layer backpropagation (backprop) artificial neural network (ANN) classifier was designed to learn the 6 Tb patterns. Classification performance, in terms of error rate (%), was as small as 2.4%. This study confirms the potential of using cluster means in ANN supervised learning, and suggests a nonlinear retrieval method towards making the inferences of snow classes from SSM/I data over varied terrain operational. Improvement is expected by identifying more SSM/I Tb signatures of different land surface types to train the ANN classifier.

INTRODUCTION

The Special Sensor Microwave/Imager (SSM/I) radiometer [1], flown on the Defense Meteorological Satellite Program (DMSP) satellites, is a useful tool for monitoring snow covered land surface, because its brightness temperature (Tb) observations are sensitive to the changes in snow physical and dielectric properties. The SSM/I is a seven-channel, four-frequency, linearly polarized, passive microwave radiometric system. It measures both vertically (V) and horizontally (H) linearly polarized Tb's, at 19.35, 37.0, and 85.5 GHz and only vertical polarization at 22.235 GHz.

To date, SSM/I snow classification algorithms (e.g., [2], [3]) have been developed using regression approaches with Tb observations over sparse-vegetated terrain. Vegetation will mask the microwave emission from the snow below, resulting a higher Tb observations [4]. Thus, algorithms developed for sparse-vegetated region have limitations and do not work properly for terrain where forests overlay snow cover.

Consequently, there exists a need of a robust snow classification algorithm by which different snow conditions over varied terrain can be determined simultaneously. Study in [5] has shown that artificial neural networks (ANNs) have the potential to learn Tb patterns. According to [6], unsupervised cluster analysis may provide typical Tb signatures for the various snow types by the average of all the data in each class. Following [7], an ANN trained from cluster means has shown a reliable generalization capability in pattern classification.

A possible research framework would be to determine the typical SSM/I Tb signatures of desired snow classes from an unsupervised cluster analysis, and use them as a prelude to train an ANN classifier. The purpose of this study is to explore the above concept towards making the inference of snow classes from SSM/I data over varied terrain operational.

METHODS

A study area bounded by latitude of 40°N to 45°N and longitude of 100°W and 115°W, which contained both plains and mountainous region in the western United States, was selected. SSM/I Tb's from the DMSP-F8 satellite and ground-based snow data from the SCS SNOTEL [8] and NOAA weather stations in Oct. 1, 1989 to May. 30, 1990, were obtained. Due to the increase in noise level of both SSM/I 85.5 GHz channels on DMSP-F8 satellite, only 5 Tb's of the lower frequency channels, denoted as T19V, T19H, T22V, T37V, and T37H, were used in this study. SSM/I data at each footprint were integrated with ground-based snow measurements, using a neighborhood merging method [5]. Only data of snow-covered footprints were considered as the valid data elements in the database.

0-7803-3068-4/96$5.00©1996 IEEE

The average linkage clustering method [9] was used to explore the possible clusters with respect to the 5 SSM/I Tb variables. A hypothetical true snow condition was then assigned to each cluster according to its typical Tb's signature (cluster means) in relation to the emission behavior of various snow conditions. Only data of the 6 mostly representative clusters (i.e., dry snow with sparse (DsSv) or medium (DsMv) vegetation, wet snow with sparse (WsSv) or medium (WsMv) vegetation, and refrozen snow with sparse (RsSv) or medium (RsMv) vegetation) were selected for ANN supervised training.

A single-hidden-layer ANN was created. It consisted of one input layer of 5 nodes representing the inputs of SSM/I Tb's, one output layer of 6 nodes representing the 6 snow conditions, and a hidden layer of nodes set up at 5, 10, 20, and 30, respectively. The error backpropagation (backprop) algorithm [10] was applied to train the ANN. The root-mean-squared (RMS) error, computed after each training epoch, was used as the stopping criterion. Training epoch repeated until a specified RMS error was reached. RMS tolerance was set between 0.1 and 0.3 by trial and error.

After training, a test data set, sampled from each snow cluster, was applied to evaluate the classification performance of the resulting ANNs. Classification result, in terms of error rate (%), was calculated for each ANN. The ANN with the minimum error rate was eligible for the SSM/I ANN snow classifier. A two-way contingency table was used to summarize the classification performance of the qualified ANN on test data.

RESULTS AND DISCUSSION

Fig. 1 displays the cluster means of the 6 snow classes. Evidently, for each dry, wet, and refrozen snow class, SSM/I Tb's of medium-vegetated were higher than those of sparse-vegetated. Depolarization effects by the overlaying vegetation were also distinct between sparse- and medium-vegetated snow conditions. A higher Tb at T37H rather than at T19H found in WsSv snow condition could be the evidence of a rapid increase in Tb at 37.0 GHz horizontal polarization with an increase in liquid water content in snowpack [11]. For refrozen snow, because the melting and refreezing resulted in larger snow crystals, more scattering and consequently much lower Tb's were observed at 37.0 GHz than at 19.35 GHz. As noted above, these interpretations provide the theoretical basis for using the 6 SSM/I Tb signatures as the appropriate inputs in ANN supervised training.

Results of the ANN training performance (Table 1) show that the smallest error rate (2.4%) was reached by the 5-10-6 ANN at RMS tolerance of 0.2. There was no evidence to indicate that a smaller RMS tolerance may ensure a better ANN performance. The increases in error rates as RMS tolerances decreased could be a sign of overtraining [12]. Regarding the number of nodes in the hidden layer, there is no evidence to show that the more nodes in the hidden layer the better ANN performance. The best ANN was only resulted from a number of training runs by trial and error.

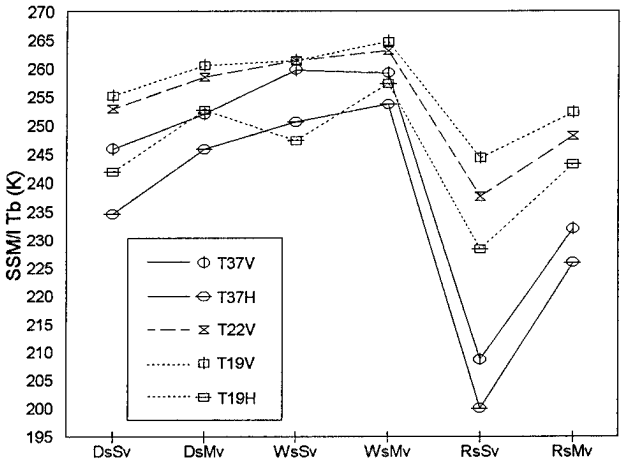


Fig. 1 Cluster means of SSM/I Tb for 6 snow conditions.

Table 2 summarizes the classification accuracy of the best ANN applied to the test data in relation to the snow classes defined by cluster analysis. Error rates were 3.8% (2/52) for DsSv, 2.9% (3/102) for DsMv, 3.2% (3/93) for WsSv, 0.0% (0/73) for WsMs, 0.0% (0/19) for RsSv, and 2.7% (2/75) for RsMv. The most misclassified Tb patterns were found in medium-vegetated wet snow cluster, i.e., 6 of the 79 SSM/I Tb patterns in WsMv cluster were classified as either DsMv or WsSv conditions by the ANN. Such misclassification could be due to the depolarization effect caused by the vegetation which made the SSM/I Tb patterns of different overlaid snow cover similar. Overall, the results indicate that the ANN may be useful in classifying snow conditions from SSM/I Tb observations over varied terrain.

CONCLUSIONS

To date, no single existing SSM/I classification algorithm has been able to identify land surface snow conditions over varied terrain. This study confirms the potential of cluster means in ANN supervised learning, and suggests a nonlinear retrieval method that overcomes the drawbacks and limitations of the existing classification methods for SSM/I land surface snow classification.

Since the ANN was trained with only 6 snow classes, application of the SSM/I ANN classifier may require pre- and/or post-treatment procedures to distinguish snow-free or other snow conditions. Improvement is expected by identifying more SSM/I Tb signatures of different land surface types to train the ANN classifier.

ACKNOWLEDGMENT

This study was supported by the NASA WetNet Project (Contract NAG8-897).

TABLE I
TRAINING PERFORMANCES OF THE ANNS AT DIFFERENT RMS TOLERANCE

ANN Topology	RMS Tolerance	Training Epochs	Error Rate (%)	ANN Topology	RMS Tolerance	Training Epochs	Error Rate (%)
5-5-6	0.215	1743	10.9	5-20-6	0.230	1708	8.7
	0.200	2908	3.9		0.215	2597	5.6
	0.185	7772	4.6		0.200	2603	6.0
5-10-6	0.300	1159	3.4	5-30-6	0.240	1998	10.1
	0.200	5243	2.4		0.230	2552	7.2
	0.190	4329	4.1		0.220	2098	16.9

TABLE 2
CLASSIFICATION PERFORMANCE OF THE ANN CLASSIFIER ON TEST DATA SET

Snow Class by ANN	Snow Class by Cluster Analysis						Total
	DsSv	DsMv	WsSv	WsMv	RsSv	RsMv	
DsSv	50	1	1	0	0	0	52
DsMv	0	99	0	3	0	0	102
WsSv	0	0	90	3	0	0	93
WsMv	0	0	0	73	0	0	73
RsSv	0	0	0	0	19	0	19
RsMv	1	0	0	0	1	73	75
Total	51	100	91	79	20	73	414

REFERENCES

[1] J. P. Hollinger, DMSP Special Sensor Microwave/Imager calibration/validation, Final Report, Vol. I. Naval Research Laboratory, Washington, D.C., USA, 1989.

[2] C. M. U. Neale, M. J. McFarland, and K. Chang, "Land-surface-type classification using microwave brightness temperatures from the Special Sensor Microwave/Imager," IEEE Trans. Geosci. Remote Sens., vol. 28, no. 5, pp. 829-838, 1990.

[3] M. J. McFarland and C. M. U. Neale, "Land parameter algorithms validation and calibration," in DMSP Special Sensor Microwave/Imager calibration/validation, Final Report, Vol. II, J. P. Hollinger, Ed. Naval Research Laboratory, Washington, D.C., USA, 1991, pp. 1-108.

[4] D. K. Hall, M. Sturm, C. S. Benson, A. T. C. Chang, J. L. Foster, H. Garbeil, and E. Chacho, "Passive microwave remote and in-situ measurements of Arctic and Subarctic snow cover in Alaska," Remote Sens. Environ., vol. 38, pp. 161-172, 1991.

[5] C. Sun, H. D. Cheng, C. M. U. Neale, and J. J. McDonnell, "SSM/I land surface snow classification using a neural network," in Proc IASTED International Conference on Signal and Image Processing-SIP-95, pp. 155-158, 1995.

[6] S. R. Rotman, A. D. Fisher, and D. H. Staelin, "Analysis of multiple-angle microwave observations of snow and ice using cluster-analysis techniques," J. Glaciology, vol. 27, no. 95, pp. 89-97, 1981.

[7] C. Sun and H. Cheng, "The use of class means in error backpropagation training for species identification of iris data," in Proc. 2nd Annual Joint Conference on Information Sciences, pp. 556-559, 1995.

[8] West National Technical Center, Snow survey and water supply products reference, Soil Conservation Service, Portland, OR, USA, 1988.

[9] SAS Institute Inc., SAS/STAT Users Guide, Release 6.03 Edition, SAS Institute Inc., Cary, NC, USA, 1988.

[10] J. M. Zurada, Introduction to artificial neural systems. West Publishing Co., St. Paul, MN, USA, 1992.

[11] Ulaby, F. T., R. K. Moore, and A. K. Fung, Microwave Remote Sensing: Active and Passive, Volume II: Radar Remote Sensing and Surface Scattering and Emission theory, Artech House, Dedham, MA, USA, 1982.

[12] Masters, T., Practical neural network recipes in C++, Academic Press Inc., San Diego, CA, USA, 1993.

Snow Mapping with SIR-C Mulpolarization SAR in Tienshan Mountain

Zhen Li and Jiancheng Shi*
Institute of Glaciology and Geocryology,
Academia Sinica, Lanzhou, 730000, China
Tel (86/931) 8841462, Fax (86/931) 8885241 ggcheng@bepc2.ihep.ac.cn
*Center for Remote Sensing and Environmental Optics (CSL/CRSEO)
University of California, Santa Barbara, CA 93106, USA

Abstract -- The areas covered by snow and glacial ice are important parameters in climatological and hydrological investigations, particularly in alpine regions. The most common use of remote sensing in snow studies is to monitoring snow-covered area to measure the change as an index in a snowmelt runoff model. Active microwave sensors can discriminate snow and glacier from other surfaces in all weather conditions. The radar polarization signature of an object permits a more accurate description of the object of interest than single-polarization measurements. Our study aid to examine the usage of multi-frequency mulpolarization SAR data to map snow- and glacier-cover in Tienshan Mountain. The results showed that C-band VV/HH images can discriminate between wet-snow and snow-free areas with the accuracy of 83-87% and some difficult in discriminating glacier ice from snow and rock, L-band HH/VV images can separate snow-cover areas from other targets with the accuracy of 89-93%, but there are problem to discriminate between rock and snow, and the cross-polarization SAR images can be used to solve this problem. So the multi-frequency mulpolarization SAR data are fairly good use to snow-cover map in alpine areas.

I. INTRODUCTION

For climatological and hydrological investigations, the areas covered by snow and glacial ice are important parameters, particularly in alpine regions. Snow and ice also play important interactive roles in the regional climates through its effect of increasing surface albedo. Understanding of processes in the seasonal snow cover is also important for studies detail of climate dynamics and climate. It has been suggested that this information might make snow-cover extent a useful index for detecting and monitoring such change.

The most common use of remote sensing in snow studies is to monitoring snow-covered area to measure the change as an index in a snowmelt runoff model and prediction of local or regional climatic change. High resolution sensors provide a means for monitoring the variations of seasonal snowpack parameters in alpine basins. Visible and near-infrared sensors have been used extensively to measure these quantities[1], but are hampered by cloud cover, which can be pervasive in some regions. In particular, snow cover must be measured on a timely basis to be useful for operational hydrology, and the opportunities for obtaining suitable data from these sensors can be infrequent. Microwave remote sensing is a methodology that is less influenced by cloud conditions, depending on frequency. Active microwave sensors have shown sensitivity to snowpack parameters, such as snow density, depth, free liquid water content, ice particle size and size variation[2], are capable of discriminating between snow and bare ground, and have a spatial resolution compatible with the topographic variation in alpine regions[3]. The radar polarization signature of an object provides a more accurate description of the object of interest than single-polarization measurements.

The major problem we are facing in using SAR to map snow covered areas in alpine region is the effects of topography and selection of different bands and polarization state. In this paper, we will discuss (1) the techniques to derive coefficients of mulpolarization SAR data from the measured stokes matrix, (2) the topographic effects and the method of correction, (3) classification of snow- and glacier-covered areas using multi- frequency mulpolarization data, (4) measurement accuracy of the SAR compared with the TM image.

II. DATA AND CAICULATION OF BACKSCATTERING COEFFICIENT

We map snow and glacier ice with data at the eastern of Tienshan Mountain (43^0 3.5'N, 87^0 10.7'E) of China in this study. Altitudes in the site rang from 3300 to 5445 m. The peak of the mountain are covered by glaciers and there are a lot of irrigation files depend on snowmelt runoff under this mountain. Our study aid to examine the usage of multi-frequency mulpolarization SAR data to map snow- and glacier-cover at this area. The multi-frequency(C, L Bands) mulpolarization(HH, VV, HV and VH) SAR data, from Space borne Imaging Radar-C and X- Synthetic Aperture Radar (SIR-C/X-SAR) on Apr.16, 1994, as part of NASA's Mission to Planet Earth, was analyzed. The flight altitude is 225km, image range is az48.2km × rg8.9km and incidence angle at image center is $21^0$54'. The data were processed at JPL and made available in a single-look

0-7803-3068-4/96$5.00©1996 IEEE

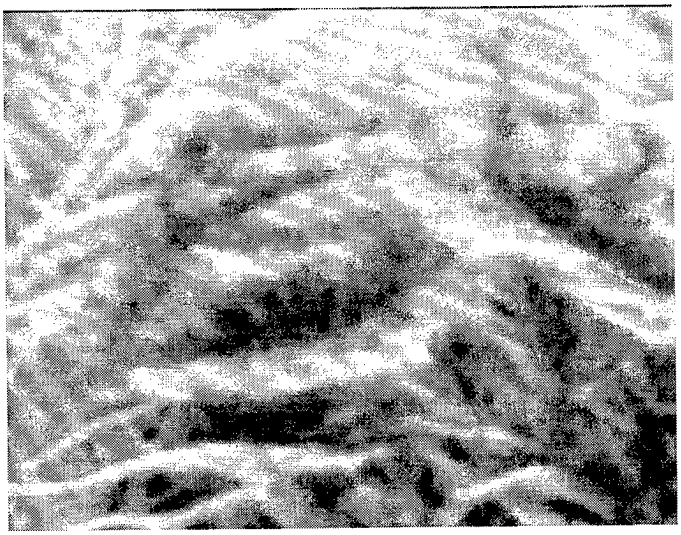


Fig.1 C-band HH polarization SAR image of the study site

complex-data format with 6.2 m azimuth resolution and 21.4 m slang-rangeresolution. Figure 1 shows a C-band image of the study site with HH polarization in a slant-range presentation.

Both theory and field measurements of microwave signals from snowpacks and glacier show that these have different characters of the backscattering coefficient from other targets. We rely mainly on the backscattering coefficient in order to distinguish snow and glacier covered area from other targets, such as bare ground or vegetation areas. SIR-C/X-SAR provided multi-frequency mulpolarization SAR data in form of nine independent real elements of the Stokes' matrix, which describes how the scattering mechanisms in each pixel transform the illuminating electromagnetic wave back to the receiving antenna[4]. The polarization feature derived from the Stokes' matrix, is the radar cross section as a function of the antenna polarization state and is useful in interpreting the scattering mechanisms within a resolution cell. The backscattering coefficient of different polarization states were calculated from the Stokes' matrix according to the theory of radar polarimetry[5].

III. TOPOGRAPHIC EFFECTS AND CORRECTION

The radar cross section depends on polarization, frequency, viewing geometry, illuminated area, and the dielectric properties and geometric structure of the targets. The study [6] indicates that the topographic effects on radiometric properties measured from spaceborne SAR can be explained by variation in imaged pixel area and in local incidence angle. For this regions, we mainly consider two factors caused topographic effects on radar images: (1) variations in imaged ground range pixel area (2) local incidence angle, are more serious at near range than at far range. When good topographic data are available, the effect can be corrected.

Using topographic (DEM) information of the study area , we radiometrically calibrated the SAR images (in slant-range presentation) and geocoded SAR images (in ground-range presentation). Because the backscattering signals depend on the local incidence angle, the absolute power of the signal is unlikely to be reliable for discrimination unless the local incidence angle is included in the classification procedure, or unless time series of images are available. In order to reduce the angular dependence of backscattering coefficients, we used the normalized backscattering coefficient.

Normalization Backscattering Coefficient

Generally, we consider the backscattering coefficient as a product of

$$\sigma^0(\theta_i) = \sigma_n^0 \times f(\theta_i) \qquad (1)$$

θ_n^0 is the normalized backscattering coefficient related to the target backscattering properties, and $f(\theta_i)$ represents the angular dependence of backscattering coefficients of the given target, depending on the dominant scattering mechanism. Therefore, the angular dependence of backscattering coefficients can be reduced if we normalize the measured backscattering coefficients by the function $f(\theta_i)$. We need to find θ_i for each pixel from the map of the local incidence angles.

The local incidence angle θ_i can be calculated from[7] :

$$\mathrm{Cos}(\theta_i) = \mathrm{Cos}(S) \times \mathrm{Cos}(\theta_0) + \mathrm{Sin}(S) \times \mathrm{Sin}(\theta_0) \times \mathrm{Cos}(T\text{-}A) \qquad (2)$$

S and A are the slope and aspect of pixel, can be known from DEM. T is flight direction, and θ_0 is radar incidence angles.

According the study [6], we select $f(\theta_i) = Cos_{\theta_i}^{2.2}$ to normalize the VV polarization SAR imagines, and $f(\theta_i) = Cos_{\theta_i}^{1.9}$ to HV polarization SAR imagines. $f(\theta_i) = Cos_{\theta_i}^{1.5}$ to HH polarization SAR imagines, $f(\theta_i) = Cos_{\theta_i}^{2.2}$ to VH polarization SAR imagines. Target discrimination can be significantly improved by using the normalized standard deviation of the backscattering coefficients.

Correction to Ground Range Presentation

Correction from slant range presentation to ground range presentation in alpine is accounted for by:

$$\Delta g = \frac{\Delta s \times \cos(S)}{\sin(\theta - S)} \qquad (3)$$

Table 1. Results (%) of classification of multi-frequency mulpolarization.

C-band				L-band			
HH	VV	HV	VH	**HH**	**VV**	**HV**	**VH**
87	83	81	79	**89**	**93**	**80**	**76**

slant range Δs to the imaged area. Here Δg is the ground range, S is the local slope, and θ is local incident angle.

IV. CLASSIFICATION

To reduce the effect of image speckle and to improve the classification performance, the multi- frequency mulpolarization SAR image all were smoothed with a 5 * 5 filter.

We defined two surface types to be classified from the radar images: snow (include glacier ice), and other surfaces, mainly rock, and alpine vegetation. Both TM and C, L-band mulpolarization SAR images were classified with a supervised Bayes classification.

Table 1 shows the all classification results compared with TM data. The results showed that C-band VV/HH images can discriminate between snow and snow-free areas with the accuracy of 83-87%, L-band VV/HH images can separate snow-cover areas from other targets with the accuracy of 89-93%, but there are problem to discriminate between rock and snow. We find that the cross-polarization SAR image can be used to solve this problem during the classification.

Comparing with TM data, the result of the classification shows very good agreement for almost all snow and glacier regions except very small amount of rock being classified as glacier and glacier being classified as rock. So we firstly discriminated glacier ice from other objects using HV/VH polarization images.

V. CONCLUSIONS

This paper reports the results on mapping snow and glaciers in Tienshan Mountain with SIR-C Mulpolarization SAR and the topographic information. C-band VV and HH polarization have similar capabilities for snow and glacier mapping at the same viewing geometry. They provide good capability to map wet snow and ice-free surfaces, but they poorly separate glacier ice from snow and rock. L-band VV and HH polarization SAR can distinguish snow or glacier from other surfaces but cannot discriminate between snow and glacier ice. The results of classification of cross-polarization HV/VH SAR images of C, L-bands can solve the problem in distinguishing glacier ice from snow and rock. So, the multi-frequency mulpolarization SAR data are fairly good use to snow-cover map in alpine areas.

Overall, TM is better than SAR for mapping glacier ice in alpine regions, because the backscattering measurements from SAR have much greater fluctuations than TM reflectance. These fluctuations are caused by greater sensitivity to the surface characteristics of the glacier ice, larger effect of topography and viewing geometry, and random signal fading (image speckle) caused by the coherent property of SAR sensors. Therefore, TM images may be used to monitor glacier boundaries when timely measurement is not needed. However, SAR can be used in all weather conditions Timely measurements of snow extent are required by hydrological investigations. This results can be used to map seasonally snow-covered area and monitor the change of the snow-line on glaciers. when ERS-1 (with C-band SAR) and JERS-1 (with L-band SAR) are running in the sky.

REFERENCES

[1] A. Rango, "An international perspective on large-scale snow studies,"Hydrol. Sci. Bull.,vol.50, no. 4, pp. 225-238, 1985.

[2] J. Shi, "Modeling and observation of polarimetric SAR response to dry snow," Proceeding IGARSS'93, III, pp. 1042-1045, 1993.

[3] J. J. van Zyl, P. Dubois, and J. Shi, "The effect of topography on SAR calibration," IEEE Trans. Geosci. Remote Sens., vol. 31, no. 5, pp. 1036-1043, 1993.

[4] Jakob J. van Zyl, Howard A. Zebker, and Charles Elachi, "Imaging radar polarization signatures: Theory and observation," Radio Science, vol. 22, no. 4, pp. 529-543, 1987.

[5] F. T. Ulaby, C. Elachi, Radar polarimetry for geoscience application, Norwood, MA. : Artch House, Inc., 1990.

[6] J. Shi, J. Dozier, "Snow mapping in alpine regions with synthetic aperture Radar," IEEE Trans. Geosci. Remote Sens., vol. 32, no. 1, pp. 152-158, 1994.

[7] J. Dozier, Frew J, "Rapid calculation of terrain parameters for radiation from elevation data," IEEE Transl. Geosci. Remote Sens., vol. 28, no.5, pp. 963-969, 1990.

Recent Progress in Development of the Moderate Resolution Imaging Spectroradiometer Snow Cover Algorithm and Product

George Riggs
Research and Data Systems Corp., 7833 Walker Drive, Suite 550, Greenbelt, MD 20770, tel 301-286-6811, e-mail griggs@ltpmail.gsfc.nasa.gov

Dorothy K. Hall
Code 974, NASA/GSFC, Greenbelt, MD 20771, tel 301-286-6892, fax 301-286-1758, email dhall@glacier.gsfc.nasa.gov

Vincent V. Salomonson
Code 900, NASA/GSFC, Greenbelt, MD 20771, tel 301-286-8601, fax 301-286-1738, email vinces@farside.gsfc.nasa.gov

Abstract -- In preparation for the launch of the Moderate Resolution Imaging Spectroradiometer (MODIS) on the first NASA Earth Observing System platform in 1998, an algorithm to generate a global snow cover map is being developed. Status of the snow mapping algorithm and description of the data product is described in this paper.

INTRODUCTION

Monitoring the spatial and temporal extent of seasonal snow cover at synoptic, regional and local scales is important to the research, modelling and operational monitoring communities concerned with snow cover [1]. A snow algorithm and data product are being developed for the future Moderate Resolution Imaging Spectroradiometer (MODIS) instrument to be flown aboard the Earth Observing System (EOS), a part of NASA's Mission to Planet Earth (MTPE). Landsat Thematic Mapper (TM) and MODIS Airborne Simulator Data (MAS) are used as surrogates for MODIS data during development of the algorithm.

BACKGROUND

The objective for the MODIS snow algorithm, SNOMAP, is to generate a consistent, well described, global snow cover data product. The spatial resolution planned for the snow cover data product is 500 m with daily and ten day composites of the product generated and archived.

MODIS is an imaging radiometer consisting of a cross track scan mirror, collection optics and set of linear detector arrays with spectral interference filters in four focal planes. MODIS has 36 discrete bands between 0.4 and 15 μm selected for diagnostic significance in Earth science. The different spectral bands have spatial resolutions of 250 m, 500 m or 1 km at nadir. Complete description of the MODIS instrument can be found at the MODIS homepage http://ltpwww.gsfc.nasa.gov/MODIS/MODIS.html. Orbital characteristics of the EOS platform will allow MODIS to have near daily repeat coverage over much of the globe and in the mid to upper latitudes swath overlap will provide multiple daily views of some regions. Those multiple views open the option of the algorithm to select and analyze the "best" observation(s) of a location for the day.

Processing and generation of MODIS data products will be done at several levels. The levels are defined by temporal and spatial manipulations done on the data to arrive at a product. Information about the data processing system and these data levels can be found at the Earth Observation System and Data Information System (EOSDIS) home page http://spsosun.gsfc.nasa.gov/ESDIShome.html. The lowest level is a short segment of an orbital swath, while the next levels involve spatial and temporal manipulations, including gridding of data, to generate products covering larger spatial areas. Within the MODIS land group of investigators there is a gridding and tiling scheme to assemble MODIS swaths into geographically referenced and gridded tiles for common use among products.

The SNOMAP algorithm is composed of three algorithms for product generation at the swath level, daily composite, and ten day composite. Products from the swath flow to daily compositing, which flow to the ten day composite. Ten day compositing follows the compositing scheme laid out by the Science Working Group [EOS] AM Platform (SWAMP). The ten day compositing periods are defined as: first ten days of the month, days 11 - 21, then day 21 to end of month.

Other MODIS data products such as the cloud mask and static land/water mask are being integrated into SNOMAP to mask large water bodies and assist with discriminating snow from cloud. For information on other MODIS data products and the Earth Science Data Information System (ESDIS) in general begin at http://spsosun.gsfc.nasa.gov/ESDIShome.html.

The snow cover products are generated in HDF format composed of global attributes (metadata), product specific attributes (metadata and quality information) and the snow cover 'map' as a scientific data array.

0-7803-3068-4/96$5.00©1996 IEEE

TECHNIQUE

The SNOMAP algorithm at the swath level employs criteria tests and decision rules with universal threshold values, to identify snow by its reflectance features in the visible and near infrared wavelengths (NIR). Techniques are briefly described here; greater discussion is presented in [2]. A principle key to identification of snow is the Normalized Difference Snow Index (NDSI). The NDSI is defined as (visible reflectance - NIR reflectance) / (visible reflectance + NIR reflectance) or for TM (band 2 - band 5) / (band 2 + band 5). Snow and cloud discrimination is also achieved with the NDSI, though confusion with cirrus (ice clouds) is a problem. Water may also have a high NDSI and thus be confused with snow but, that confusion is largely eliminated by use of far red threshold test which discriminates water from snow because water absorbs whereas snow reflects through the red. If observation results lie in the snow decision region of the decision rule, the pixel is identified as snow covered.

TM data is converted to radiance then reflectance using methods described by [3] using pre-flight gains and offsets, or by using recorded gains and offsets [4] when available, prior to applying the snow decision tests. We have found that use of observed reflectances increases the accuracy of snow cover identification. MODIS data input will be at-sensor reflectances. Work is in progress to incorporate atmospheric correction.

In addition to the criteria tests and decision rules for snow, the full-up version of SNOMAP will contain internal checks for data integrity that will affect algorithm flow in cases of missing or out-of-range data. During execution of the algorithm, several pieces of metadata are accumulated to provide summary information with the snow cover map and serve as indicators of quality assessment (QA). Metadata such as counts of out-of-range data and total snow area are generated and written as attributes in the HDF output file. A general QA flag based on metadata and QA criteria rules is also written as an attribute.

SNOMAP at the second level composites the results of the swath outputs from overlapping orbits into a daily snow cover product. An intermediate algorithm assembles all the swaths into tiles of a grid, SNOMAP then employs a series of criterion tests to select the 'best' observation(s) of multiple observations. If there are multiple 'best' observations, the mode of the SNOMAP swath level result is used as the result for the day.

SNOMAP at the third level composites the level 2 results for a ten day period. The technique used is to sum the number of snow observations for that period to generate a snow cover summation product. That product contains the number of days that a cell was snow covered, along with summary metadata of snow cover.

RESULTS & DISCUSSION

Runs have been undertaken on over 25 TM scenes to generate snow cover maps. Snow cover extent identified by SNOMAP has agreed to within a few percent of snow cover identified with intensive classification methods (e.g. supervised classification and spectral mixture modelling [2]) on several TM scenes. Identified snow extent has also agreed with ground observations and with regional snow maps generated by the National Operational Hydrologic Remote Sensing Center (NOHRSC). SNOMAP continues to be validated against other techniques and data sources of snow cover.

The most commonly encountered error in SNOMAP is confusion of cirrus clouds with snow. No consistent trend has been observed in confusing snow with cirrus clouds. In some situations cirrus clouds over non-snow covered land may be identified as snow, while in other seemingly similar situations it will not; cirrus clouds over snow are also inconsistently confused. Means of sorting out this confusion are being explored. Much of the confusion may be alleviated with the integration of the MODIS cloud mask, developed by another MODIS investigator team, which has the capability of identifying cirrus clouds.

Solar zenith angle (SZA) has been observed to have an effect on identification of snow. A study is in progress to determine if there is a crucial SZA above which snow identification becomes erroneous. This appears to be an issue related to high SZA. If a crucial SZA is determined, then a bound on acceptable SZAs will be incorporated into SNOMAP.

A simulated weekly snow composite has been generated with SNOMAP from a pseudo time series of TM data to demonstrate the information content of the composited product. SNOMAP higher level products have been generated with simulated MODIS data. Simulated MODIS data are used to test the flow of SNOMAP through all levels of product generation. The higher level products exhibit consistent snow cover extent results among levels. Lack of validation data for composites precludes significant comment to be made for the composited snow covers.

SUMMARY

Results obtained with SNOMAP and review of products and techniques by the community [1,2] indicate that the snow identification technique and products being developed will be of general utility to sections of the community. Research is continuing to improve snow identification techniques, including conditional bounding of factors such as SZA, defining metadata and quality indicators for the SNOMAP products. Concurrent with research is the programming task of preparing the program code to be run in the production environment of EOSDIS. Expectations are that MODIS will be launched aboard the EOS AM platform in mid 1998, and that data product generation will begin shortly after MODIS is declared operational.

REFERENCES

[1] D.K. Hall, (Editor) "First Moderate Resolution Imaging Spectroradiometer (MODIS) Snow and Ice Workshop", NASA Conference Publication 3318, Sept 13-14, 1995, Greenbelt, MD

[2] D.K. Hall, G.A. Riggs, and V.V. Salomonson. "Development of Methods for Mapping Global Snow Cover Using Moderate Resolution Imaging Spectroradiometer Data", Remote Sens. Environ. 54:127-140 (1995).

[3] B.L. Markham and J.L. Barker, "Thematic Mapper Bandpass Solar Exoatmospheric Irradiances", Int. J. Remote Sens., 8:517-523 (1987).

[4] P.S. Chavez, "Radiometric Calibration of Landsat Thematic Mapper Multispectral Images", Photgram. Eng. Remote Sens., 55:1285-1294 (1989).

Variations in Radar Backscatter Across the Great Ice Sheets

Katy F. Noltimier and Kenneth C. Jezek
Byrd Polar Research Center and The Department of Geological Science
The Ohio State University, 1090 Carmack Rd., Columbus, OH 43210
Tel: (614) 292-6531, Fax: (614) 292-4697 e-mail: kfn@iceberg.mps.ohio-state.edu

ABSTRACT

Radar backscatter over the great ice sheets is modulated by the near surface properties of polar firn. These properties (grain size, density, stratigraphy, wetness) change in time and from region to region. Information was compiled on the spatial variation in backscatter across selected parts of Antarctica and Greenland from ERS-1 SAR data. The SAR-derived σ° compared favorably with both in situ and the ERS-1 scatterometer data obtained from literature. These results will be used to refine processing schemes for the Radarsat Antarctic Mapping Project.

A difference plot of the azimuthal anisotropy of SAR-derived σ° was created to determine the magnitude of azimuthal anisotropy on a pixel by pixel basis. Azimuthal variability for a region of the Antarctic Peninsula was found to vary from 0 to 14dB.

INTRODUCTION

Radar backscatter over the great ice sheets is related to the near surface properties of polar firn. These properties (grain size, density, stratigraphy, wetness) change in time and from region to region.

Histograms of SAR-derived σ° (Fig. 1, 2) across selected parts of Antarctica and Greenland (Fig. 3, 4) were created to determine the backscatter distribution for ESA ERS-1 SAR PRI (European Space Agency European Remote Sensing Synthetic Aperture Radar Precision Image) images. A difference plot (Fig. 5) was created from overlapping ascending and descending orbits of SAR-derived σ° over the Antarctica Peninsula area.

PROCEDURE

Histograms:

Geographic locations (Fig 3, 4) were obtained from the GDMS home page [1]. Histograms (Fig. 1, 2) of the SAR-derived σ° were created from the 12.5m resolution PRI data and binned at 0.5dB intervals [3]. All images are representative of the winter season.

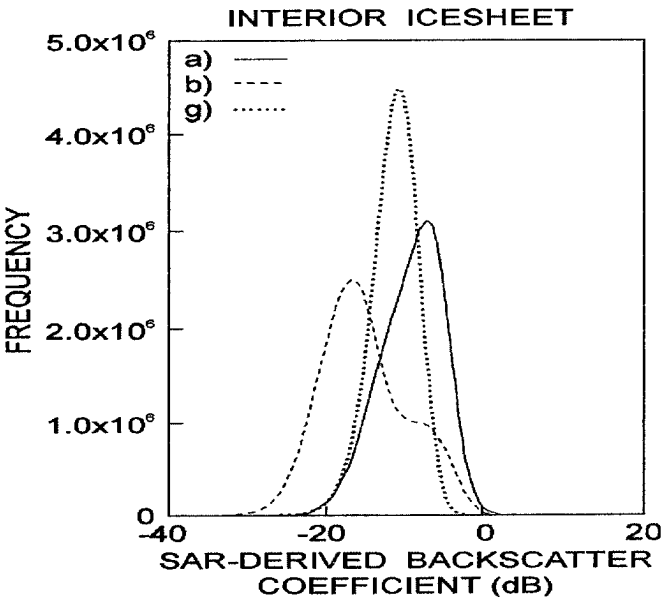


Fig. 1. Histogram of σ° for the interior ice sheet of Antarctica (a), (b) and Greenland (g). Letters correspond to geographic locations on Fig. 3, 4.

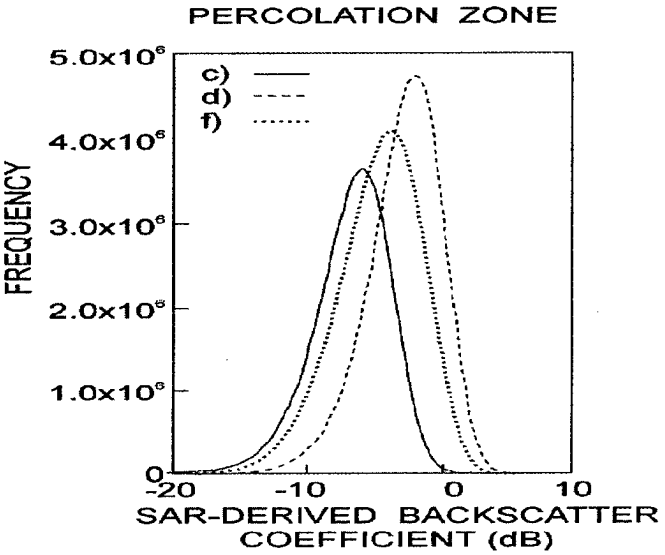


Fig. 2. Histogram of σ° for the percolation zone of Antarctica (c), (d) and Greenland (f). Letters correspond to geographic locations on Fig. 3, 4.

[1] Sponsored by NASA Office of Polar Programs

0-7803-3068-4/96$5.00©1996 IEEE

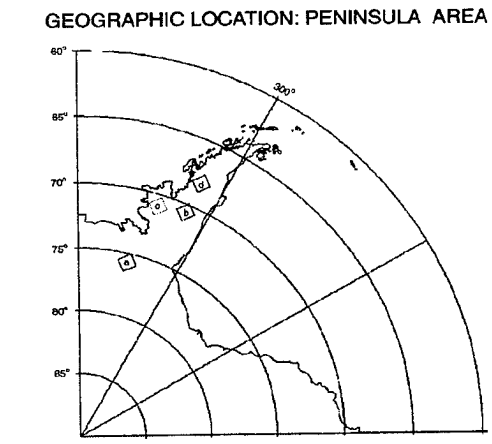


Fig 3. Geographic location of images where (a) (b) correspond to interior ice sheet on Fig. 1 and (c) (d) to percolation zone on Fig. 2.

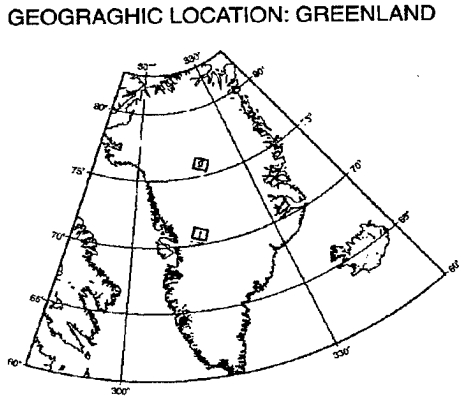


Fig. 4. Geographic location of images where (g) corresponds to interior ice sheet on Fig.1 and (f) to percolation zone on Fig. 2.

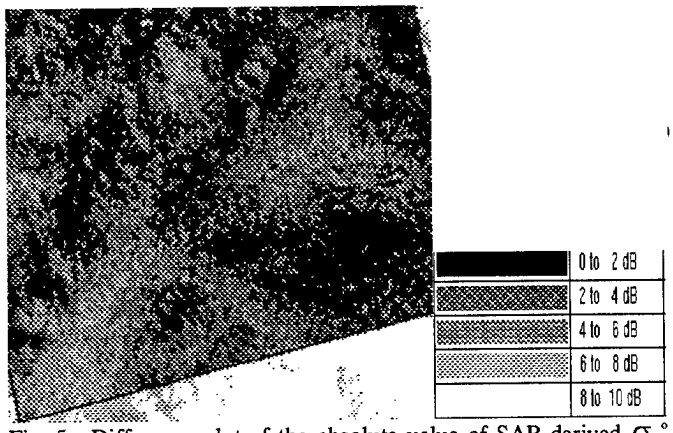


Fig. 5. Difference plot of the absolute value of SAR-derived σ° from overlapping ascending and descending orbits depicting azimuthal anisotropy variations (Antarctica).

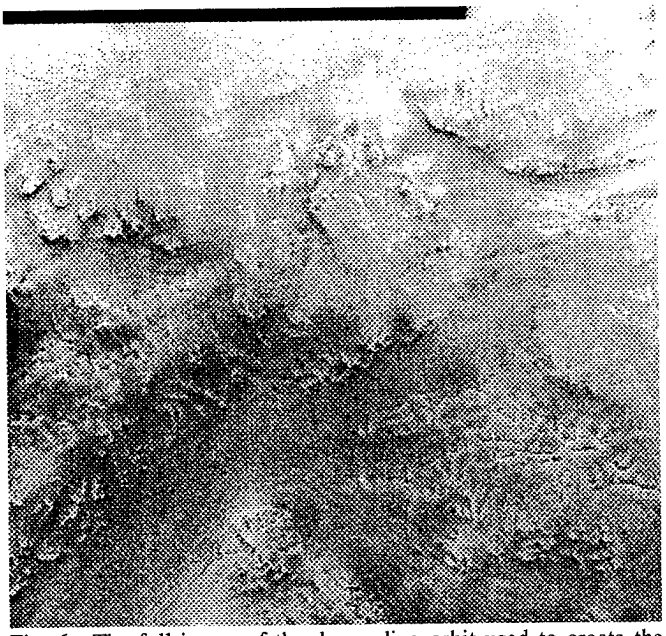


Fig. 6. The full image of the descending orbit used to create the difference plot.

Azimuthal Anisotropy:

A difference plot of the σ° from overlapping ascending and descending orbits over the Antarctic Peninsula is created from 12.5m resolution PRI data and binned at 2dB intervals (Fig. 5). The azimuthal separation between the ascending and descending orbit is 93.75°. The images are geocoded and rectified (Fig. 6). To reduce inherent speckle a 9x9-pixel mean-filter is applied to the resultant image. The difference plot is created by level slicing using a 2dB intervals to determine the magnitude of azimuthal anisotropy on a pixel by pixel basis.

DISCUSSION

Histograms:

Interior Ice Sheet: SAR-derived σ° for Antarctica have an approximate mean of -7dB and -16dB, where SAR-derived σ° for the Greenland interior ice sheet correspond to an approximate mean of -10dB. These low values of σ° occur over the interior ice sheet where volume scattering from individual snow grains dominates.

Rack [4] reports a range of σ° calculated from the ERS-1 scatterometer data over Antarctica (incidence angle 30°) of -5dB to -13dB during the austral winter. In 1992, Jezek and others [2] performed surface-based microwave radar measurements at 5.3 GHz with VV polarization on the western flank of the Greenland Ice Sheet. At incidence angle of 25° the glacier surface has a σ° of -12dB. The variation between VV and HH polarization at low incidence angles is negligible [6].

Percolation Zone: Mean σ° for Antarctica are about -3dB and -6dB. Mean σ° for Greenland are about -4dB. These higher values of σ° are caused by extensive near surface ice lenses formed during summer melt events.

Rack [4] report ERS-1 scatterometer measurements of σ° that range from -4dB to -7dB during the Antarctic austral winter. Jezek and others [2] report a total surface σ° from the western flank of the Greenland Ice Sheet of -2dB.

Table I. Summary of SAR-derived σ°(dB) and data obtained from literature. AP=Antarctic Peninsula, GL=Greenland.

	INTERIOR		PERCOLATION	
REFERENCE	AP	GL	AP	GL
SAR-derived	-16 and -7	-10	-6 and -3	-4
Scatterometer [4]	-13 to -5	-	-7 to -4	-
Surface-based [2]	-	-12	-	-2

The SAR-derived σ° compare favorable with both the in situ and the ERS-1 Scattterometer data obtained from literature.

Azimuthal Anisotropy:

A difference plot of SAR-derived σ° from overlapping ascending and descending orbits was created to determine the magnitude of azimuthal anisotropy on a pixel by pixel basis. Fig. 6 is one of the images used to create the difference plot. It shows a glacier surrounded by rugged mountains exposed through the ice sheet. Surface features of high relief are illuminated on the side facing the sensor while the side away from the sensor will be in shadow. The areas most illuminated by one direction and least illuminated by the other direction will have a range of relatively high azimuthal anisotropy. Low relief areas will be illuminated uniformly from both directions, giving a low azimuthal anisotropy, unless there is a change in the physical characteristics of the surface.

High azimuthal anisotropy in Fig. 5 correspond with two main features in Fig. 6. The mountains show up as isolated areas of high azimuthal anisotropy (> 8 dB) surrounded by relatively low azimuthal anisotropy (2-4dB). Examples of these areas are clearly evident in the upper right and middle far left of Fig. 5. Sections of the glacier also show high azimuthal anisotropy as evident in the lower left and lower middle of Fig. 5. Rott and Rack [5] report high azimuthal anisotropy (5.75dB) in areas of strong winds recorded by ERS-1 scatterometer measurements. Hence, drainage wind channeled by the glacial valley may explain our results.

CONCLUSION

The SAR-derived backscatter distributions, discussed earlier, compare favorably with both the in situ and the ERS-1 scatterometer data obtained from literature. Azimuthal anisotropy calculated from ascending and descending SAR-derived σ° ranges from 0 to 14dB.

REFERENCES

[1] Baggeroer, P. A. "Geophysical Data Management System" in press.

[2] Jezek, K., P Gogineni, and M. Shanableh, 1994. "Radar Measurements of Melt Zones on the Greenland Ice Sheet". Geophysical Research Letters, **21**, 33-36.

[3] Laur, H., 1992. ERS-1 SAR Calibration: Derivation of backscattering coefficient in ERS-1.SAR.PRI products. ESA ESRIN, 16 pp.

[4] Rack, W., 1995. "Streuverhalten und morphologie der antarktischen schneedecke aus scatterometer-messungen von ERS-1". Diploma Thesis, Science Faculty, University of Innsbruck.

[5] Rott, H. and W. Rack, 1995. "Characterization of Antarctic Firn by Means of ERS-1 Scatterometer Measurements". IGARRS' 1995 Digest, Cat. #95CH35770, 3, 2041-2043.

[6] Rott, H., K. Sturm, and H. Miller, 1993. "Active and passive microwave signatures of Antarctic firn by means of field measurements and satellite data". Annals of Glaciology, **17**, 337-343.

Geophysical Data Management System

P. A. Baggeroer, K. C. Jezek, D. G. Hart

The Ohio State University
Byrd Polar Research Center
1090 Carmack Road
Columbus, OH 43210

Tel: (614) 292-1107, Fax: (614) 292-4697, e-mail: pab@polestar.mps.ohio-state.edu

ABSTRACT

The geoscience community relies heavily on the use of a variety of data sets in its research efforts. Data sets range from remotely sensed satellite imagery covering large geographical areas to locally sampled data of regional interest. Researchers acquire much of this data in varying quantities ranging from tens to tens of thousands of data sets. Smaller collections of data sets can usually be handled manually and are rarely shared amongst research groups. Larger collections of data sets are usually handled by large scale database systems such as the EOS Data and Information System under development by NASA [1]. However, this still leaves a large number of researchers with data set collections somewhere between these two extremes. Often times, researchers pursuing the same ultimate objective or working in collaboration with colleagues will share data sets on a limited basis. In order to archive these "medium sized" data set collections in an organized and easily accessible manner and to facilitate distribution of data sets on a limited basis, we have developed a system to provide researchers with a simple to use archive and browse system.

SYSTEM DESCRIPTION

The GDMS system consists of four basic components: load utilities, archive, browse functions and the GUI (Fig. 1). These utilities are extendible to additional remote nodes which may be accessed via WWW (World Wide Web) based hyperlinks (Fig. 2).

The current, beta version of GDMS is implemented in PERL (Practical Extraction & Report Language), CGI (Common Gateway Interface) and HTML (Hypertext Markup Language). A useful feature of the local GDMS system at BPRC is the ability to automatically ingest ERS-1 and JERS-1 SAR data sets directly from the distribution media. A browse image is also produced by the ingest procedure (50-100 Kbytes). The loader functions are implemented in C and can be controlled from the GDMS WWW interface. Access to these functions and the ability to modify a local data archive is restricted to authorized local individuals.

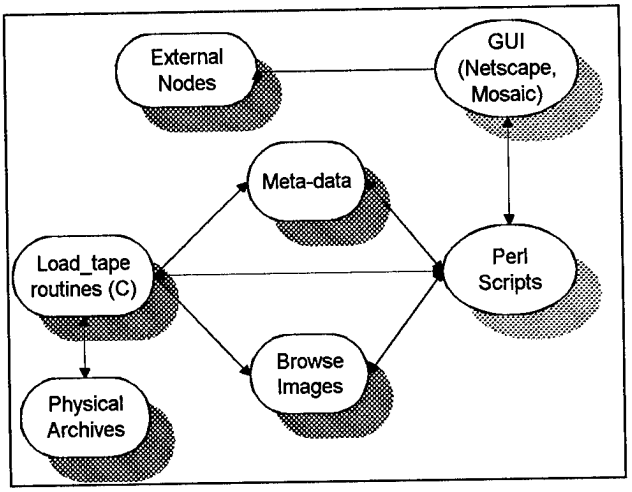


Figure 1. Level 1 system diagram for GDMS.

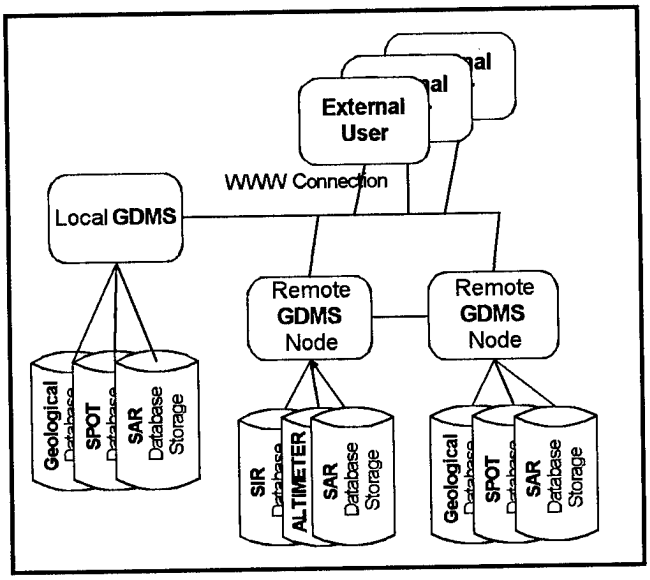


Figure 2. Level 0 System diagram

0-7803-3068-4/96$5.00©1996 IEEE

USER INTERFACE

GDMS provides the user with a GUI based interface (Fig. 3) for searching and viewing data sets, in both remote and local archives. The system is WWW based. This makes the system accessible from most of the widely varying computer platforms used by scientists and researchers.

A user may conduct searches on data archives by specifying search parameters or by using an interactive coverage map. Hyperlinks to data set images and coverage maps (Fig. 4) showing geographical locations of data sets make GDMS a powerful search and browse tool. The browse images (Fig. 5) are reduced considerably in resolution to facilitate rapid downloading and viewing over the internet.

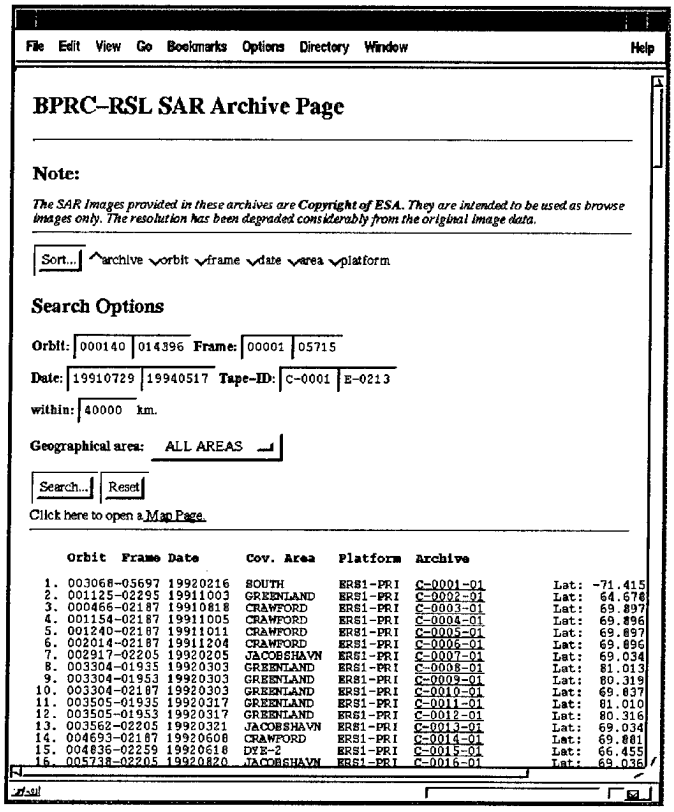


Figure 3. GDMS client search interface accessed using Netscape WWW browser. BPRC local SAR image archive.

Users may access the system as clients simply by using a WWW browser such as Netscape or NCSA Mosaic. A user may also maintain a GDMS server to archive local data sets on-line and make selected data sets available on-line to client users. Hyperlinks to published archive locations provided from the GDMS homepage.

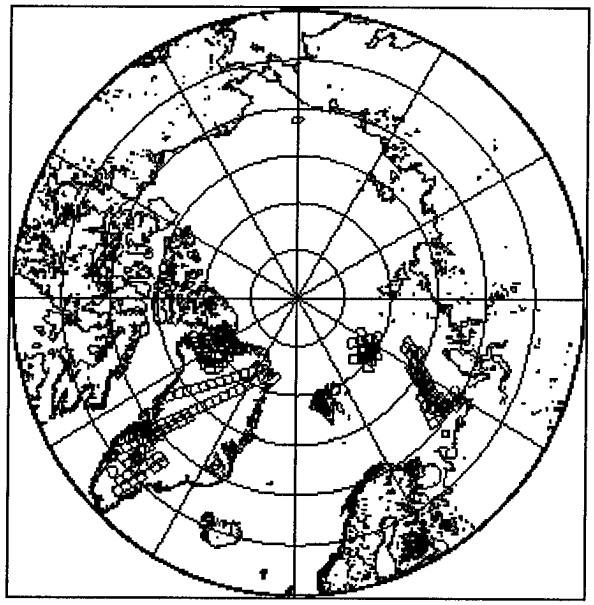


Figure 4. GDMS coverage map showing locations of SAR images. Map is a clickable image map. North polar projection.

APPLICATIONS

GDMS is implemented as a beta version at the Byrd Polar Research Center. The archive contains almost 500 synthetic aperture images primarily of polar regions. The archive has proven to be a valuable tool for assisting researchers at BPRC in identifying and locating data relevant to their particular research project. Some examples of how GDMS has been used are listed below.

- Selection of SAR imagery over the Antarctic Peninsula for use in studies to determine the feasibility of use of SAR in regional geomorphology.
- GDMS has been used to visually inspect SAR images of Antarctica in for selection of tie points to be used for terrain correction of the SAR mosaic to be produced by the Radarsat Antarctic Mapping Project. GDMS will also be used to monitor the progress of data acquisition during the 18 day Antarctic mapping mission. Access to the local archive has been provided to co-investigators as necessary.
- **The Byrd Center's GDMS archive can be accessed at** *http://polestar.mps.ohio-state.edu/gdms/GDMS.html*

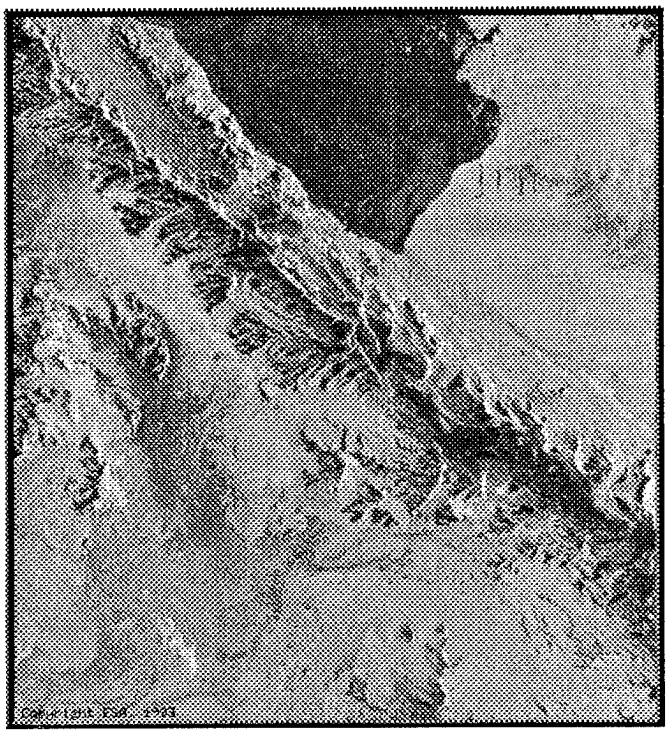


Figure 5. Synthetic aperture radar image of Alexander Island and George VI Sound in Antarctica. The image is used in an attempt to identify structural features of the glacier and underlying surface features.

FUTURE DEVELOPMENT

The Geophysical Data Management System will continue to be developed as a research tool for PI's and individual researchers. Some features to be added to the system for subsequent versions are listed below.

- Ability to conduct cross archive searches, thus allowing a researcher to search several archives for the desired data sets.
- Ability to ingest and archive a wide variety of data types not limited to SAR.
- Allow local archives to be easily configurable by users to accommodate the needs of a particular archive.

REFERENCES

[1] EOS Data and Information System (EOSDIS), 1995 MTPE / EOS Reference Handbook.

Ice Sheet Margin Detection Using ERS-1 Synthetic Aperture Radar

Hong-Gyoo Sohn and Kenneth C. Jezek
The Ohio State University, Byrd Polar Research Center, 1090 Carmack Road, Columbus, OH 43210
Tel: 614) 292-1107, Fax: 614) 292-4697, e-mail: sohn@iceberg.mps.ohio-state.edu

ABSTRACT

A portion of the Greenland ice sheet margin near the Jakobshavn area is mapped using an automatic, hierarchical approach applied to ERS-1 Synthetic Aperture Radar (SAR). Image tone and texture variability between the bare ice facies near the ice sheet margin and recently deglaciated rocks are used to map the ice sheet margin. This process involves integration of an anisotropic diffusion algorithm, local dynamic thresholding method, and edge following scheme.

INTRODUCTION

Ice sheet margin advances and recessions are highly correlated with climatic change over the western part of Greenland [6]. This suggests that consistent and long-term observations of the ice sheet margin change may provide a useful indicator of changing climate.

SAR imagery has shown potential to monitor ice sheet margin changes[2]. ERS-1 SAR imagery supplies high-resolution image information of ice sheet margin regardless of weather conditions, day and night.

An automatic ice sheet margin detection algorithm is implemented to monitor and detect the margin fluctuations using ERS-1 SAR imagery. A portion of the Greenland ice sheet margin near the Jakobshavn area is mapped using an automatic, hierarchical approach applied to ERS-1 SAR imagery.

APPROACH

Image texture and tone variation of SAR imagery between bare ice facies at the margin of the ice sheet and recently deglaciated rock are used to map the ice margin. Fig.1 shows the schematic diagram for the approach.

The ice sheet margin is detected by application of several different algorithms. First of all, original SAR imagery is geocoded and terrain corrected using the available digital elevation model produced in Denmark at Kort- og Matrikelstyrelsen (KMS). Fig. 2 represents the geocoded and terrain corrected ERS-1 SAR imagery of August 20, 1992 with resolution of 100m.

An anisotropic diffusion algorithm proposed by [4] is used to minimize noise while not perturbing the position and magnitude of significant edge features.

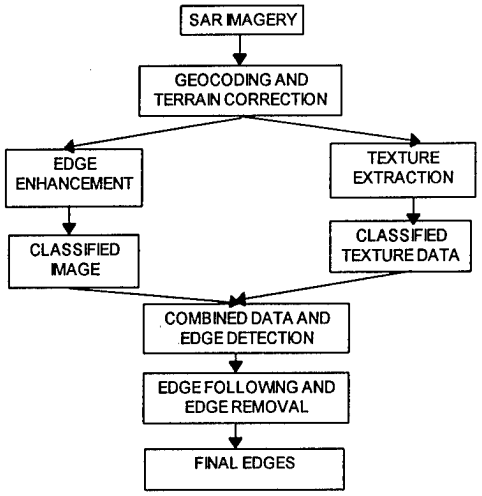


Fig. 1. Schematic diagram for margin detection algorithm.

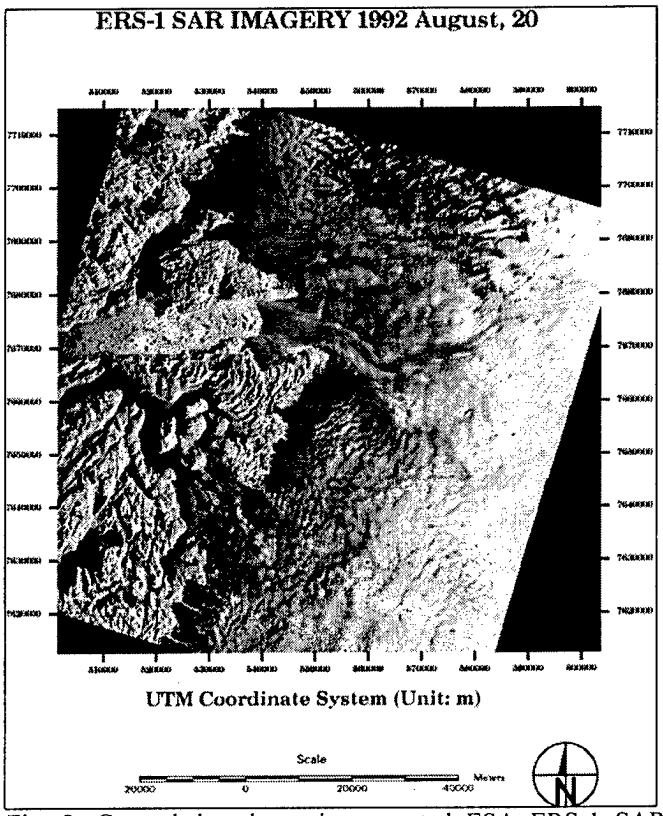


Fig. 2. Geocoded and terrain corrected ESA ERS-1 SAR imagery.

0-7803-3068-4/96$5.00©1996 IEEE

Fig. 3 shows the resultant image after applying the anisotropic diffusion. As shown in Fig. 3, noise is reduced without smoothing or displacing the significant edge features.

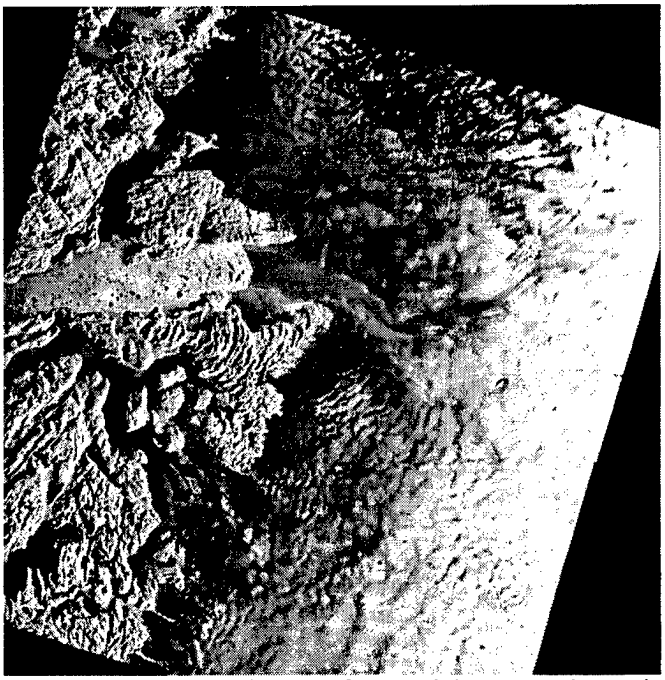


Fig.3. The resultant image after applying an anisotropic diffusion algorithm on Fig.2 using the inverse form for directional diffusion coefficient (K=5, iterations = 50).

Texture data is created by using second order statistics in a small-area image patch. After creating texture data, the local dynamic thresholding algorithm [3] is applied to both the resultant statistical data of texture and the edge enhanced image of Fig. 3. This procedure segments the images into three different gray level classes.

Fig. 4 is the classified image after applying local dynamic thresholding algorithm to Fig. 3. Fig. 5 represents the classified image after applying the local dynamic thresholding algorithm to gray level converted texture data.

A final image was created by combining the results of Fig. 4 and Fig. 5. This was done by selecting the same class, for example the rock, in both Fig. 4 and Fig. 5 and then filtering out the other two classes. Edge detection is performed on the final image using Roberts edge detection method [5].

Unwanted small edges are identified within both the ice sheet and rock area. A recursive line following scheme is implemented by using chain code [1] to detect the small edges. The binary line image is scanned line by line for points from which to start a chain. Every continuous line is chain coded and the length of each line is stored. Global constraint is set to identify the ice sheet boundary and reomve the unwanted small edges by calculating the length of edges.

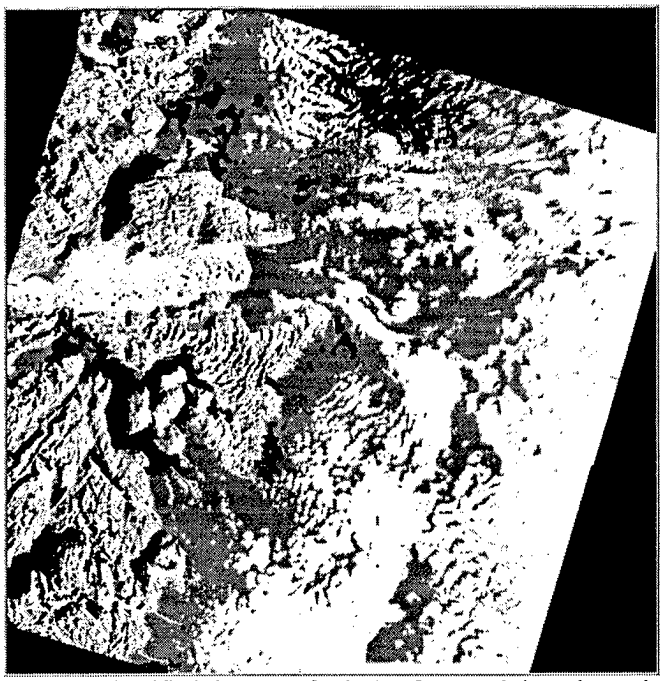


Fig. 4. Classified image of Fig.3 after applying dynamic thresholding

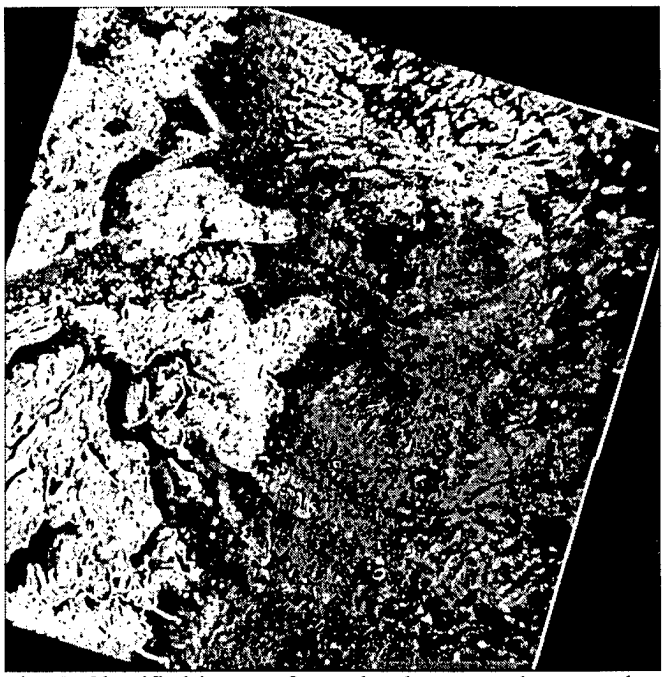


Fig. 5. Classified image of gray level converted texture data after applying the dynamic thresholding method.

RESULTS

Fig. 6 is the final result of ice sheet boundary after removing unwanted boundaries. The constraint on the length of an edge for this result is 3000 pixels (size of image is 1024x1024). Fig. 7 shows the image of the detected ice sheet boundary draped on Fig. 1. The detected ice sheet boundary matches with the visually-inspected ice sheet margin to within several pixels (300m).

CONCLUSION

We presented steps for automatic ice sheet margin extraction by integrating several different algorithms. A consistent, long-term application of the algorithm will aid in monitoring whether the ice sheets are retreating or advancing and how the patterns are and in modeling the local/global climate models.

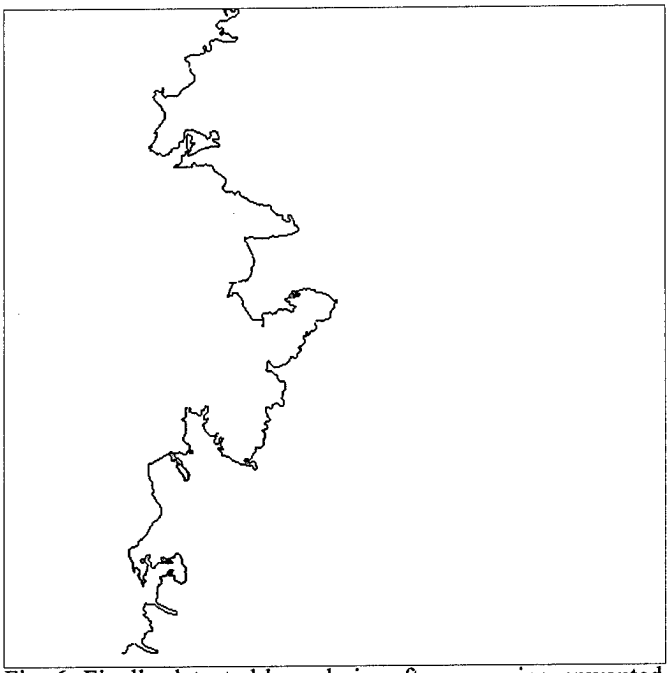


Fig. 6. Finally detected boundaries after removing unwanted edges.

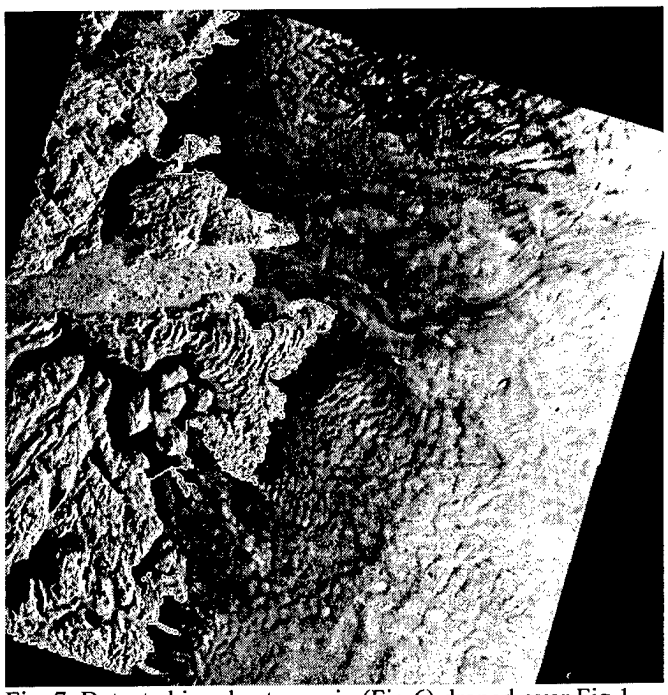


Fig. 7. Detected ice sheet margin (Fig.6) draped over Fig.1.

REFERENCES

[1] Ballard, D.H. and Brown, C.M., 1982, Computer Vision, Prentice-Hall, Inc., New Jersey

[2] Fahnestock, M.A., Bindschadler, R.A., 1993, Description of a program for SAR investigation of the Greenland ice sheet and an example of margin change detection using SAR, Annals of Glaciology, pp. 332-336.

[3] Haverkamp, D, Soh, L.K., and Tsatsoulis, C., 1995, A Comprehensive, Automated Approach to Determining Sea Ice Thickness from SAR Data, IEEE Transactions On Geoscicence and Remote Sensing, Vol. 33, No. 1, pp. 46-57.

[4] Perona, P and Makik, J, 1990, Scale-Space and Edge Detection Using Anisotropic Diffusion, IEEE Transactions on PAMI, Vol 12, No. 7, pp 629-639.

[5] Pratt, W.K., 1978, Digital Image Processing, John Wiley & Sons, Inc.

[6] Weidick, A., Boggild, C.E., and Knudsen, N.T., 1992, Glacier inventory and atlas of West Greenland, Grønlands Geologiske Undersøgelse, Rapport 158.

Flood Monitoring in Norway Using ERS–1 SAR Images

Dan Johan Weydahl
Norwegian Defence Research Establishment, PO Box 25, N–2007 Kjeller, Norway
Phone:+47 63 80 70 00 Fax:+47 63 80 72 12 E–mail:dan–johan.weydahl@ffi.no

ABSTRACT

The all–weather capability of SAR makes it interesting for flood monitoring. A major flood occurred in south Norway in June 1995. Several ERS–1 SAR images was acquired over the region during the flooding. Change detection techniques was applied using additional ERS–1 SAR images taken before the flooding. The location and extend of the flooded regions was then registered in areas that had moderate wind conditions. In the future, RADARSAT may prove to be an alternative for flood monitoring since it can operate at higher incidence angles and therefore be more independent of the wind conditions.

INTRODUCTION

ERS–1 SAR images have previously been used to study the flood in St. Louis in summer 1993 [1], the flood in western Europe in December 1993 and January 1994 [2], and flooded areas near the Tanaro river in Italy in November 1994 [3]. Each ERS–1 SAR image covers an area of 100 x 100 km, with a resolution of 25 m. This will give good possibilities for covering large flooded areas while still capturing fine details like bridges and small rivers.

In late May and early June 1995, the south–eastern parts of Norway was struck by one of the largest spring flooding in Norway in this century. The flooding caused large damages in agricultural areas as well as towns located along the rivers. The two main rivers involved in the flooding are called Gudbrandsdalslågen and Glomma. These rivers run through agricultural and forested landscape in the Gudbrandsdalen and Østerdalen valleys respectively on their 300 km long way from the high mountains to the North Sea. During the flooding period that lasted more than 2 weeks, the river level rose by several meters. The flooding culminated the first week of June.

THE DATA SET

Three ERS–1 SAR full resolution images (FRI) was acquired at about 12:20 local time over the flooded areas the 4 and 7 June 1995. These images are processed and delivered by Tromsø Satellite Station in Norway. The image acquired the 4 June covered the flooding in Østerdalen from Flisa to Kongsvinger (see fig. 1.1). The two SAR images from the 7 June covered flooded areas in Østerdalen and Mjøsa, from Koppang in the north to Sarpsborg in the south.

Strong wind conditions on the 7 June made it impossible to distinguish between water bodies and land surface in these ERS–1 SAR images. On the contrary, the 4 June SAR image gave good contrast between vegetation and areas covered by water. In the data arch3ve at Norwegian Defence Research Establishment (FFI), an ERS–1 SAR image from 25 August 1994 covers the same areas as the flooding in the 4 June image. A Landsat Thematic Mapper (TM) image from 1 July 1994 is also available at FFI.

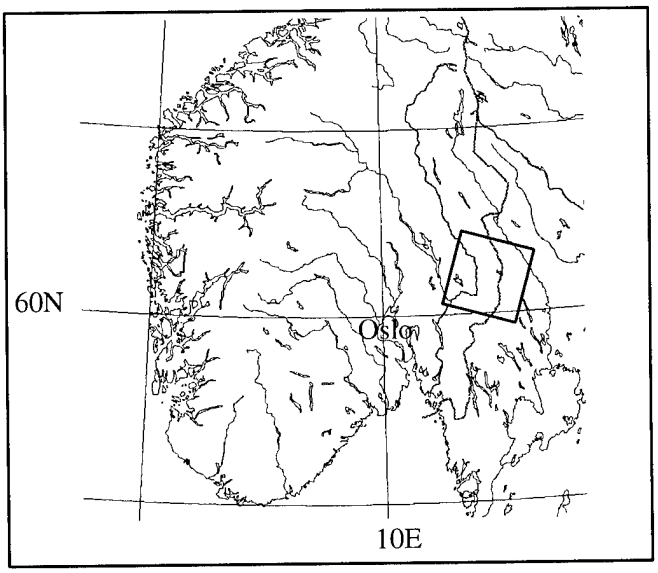


Figure 1.1 A map over south Norway indicating the ERS–1 SAR image acquired over the flooded areas along the Glomma river in Østerdalen the 4 June 1995.

0-7803-3068-4/96$5.00©1996 IEEE

METHODOLOGY

Good flood monitoring can be achieved using a change detection technique between SAR images taken under the flooding, and SAR images taken before the flooding.

ERS–1 SAR is operating with a wavelength of 5.6 cm and an incidence angle of only 23 degrees. These parameters indicate that the SAR signal will be very sensitive to the water surface roughness. A prerequisite for good flood monitoring using ERS–1 SAR is therefore moderate wind conditions. In our case, only the 4 June ERS–1 SAR image could therefore be used for flood monitoring.

Both the 25 August 1994 SAR image and the 4 June 1995 SAR image cover the flooded area Flisa–Kongsvinger in Østerdalen. These images are taken from ascending and descending satellite pass respectively.

First, the images has to be registered to each other. This is done by selecting 9 ground control points taken from bridges and other structures that are visible along the Glomma river in both SAR images. The 24 August image is then resampled and transformed into the geometry of the 4 June image with an accuracy of about 30 m along the river. No topographical corrections are made during the registration process because the geometrical SAR effects are assumed to be negligible along the flat, flooded areas next to the river.

RESULTS

The changes that are caused by the flooding can be visualized on a computer by simply showing the two registered SAR images as a color composite where the 4 June image is loaded into the red and green channel, while the 25 August image is loaded into the blue channel. The flooded areas will then get a blue color. This is because the flooded areas will give little SAR backscatter the 4 June, but a lot of backscatter from the vegetation cover the 25 August. Fig. 1.2 shows a SAR image composite from the flooded areas round Flisa in Østerdalen.

It may be difficult to geographically locate the flooded areas by looking at a SAR image. The flooded areas can therefore first be extracted manually or automatic using the two SAR images, and then the extracted areas can be plotted onto a Landsat TM image, or a map.

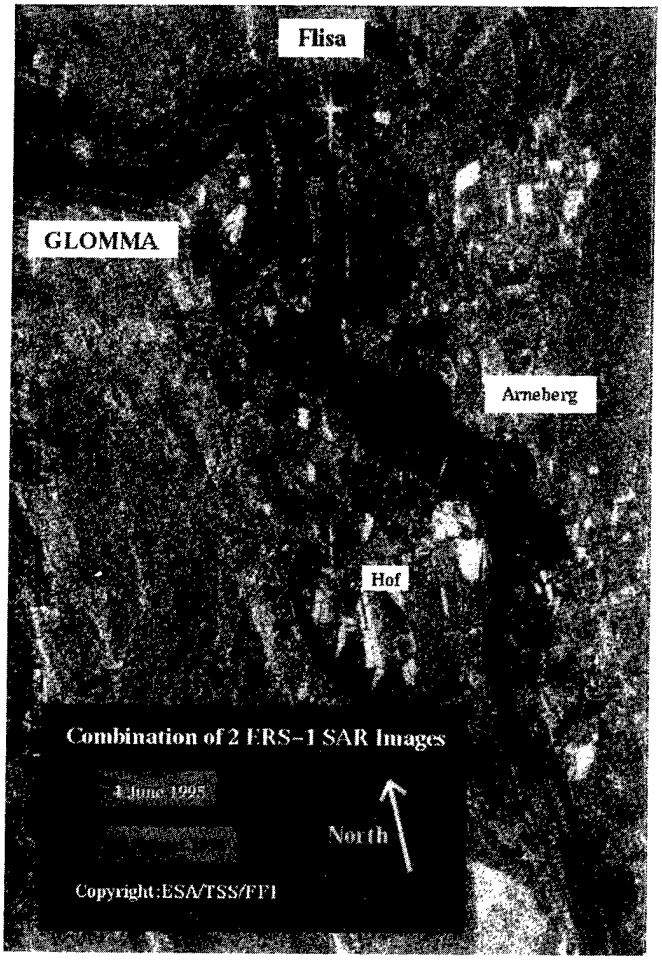


Figure 1.2 A composite of the 25 August 1994 and 4 June 1995 image. The flooding is shown as dark areas along the Glomma river.

In this way it is easier to recognize the geographical location of the flooded areas. In fig. 1.3, the flooded areas are plotted onto a Landsat TM satellite image. The flooded areas were here manually extracted from the ERS–1 SAR images using an interactive image processing system.

The registered flooded areas can also be put into a geographical information system (GIS) for further investigation and analysis.

Analysis along a 50 km long part of the Glomma river from Flisa to Kongsvinger (see fig. 1.3) indicated that about 23.8 km2 was flooded the 4 June 1995.

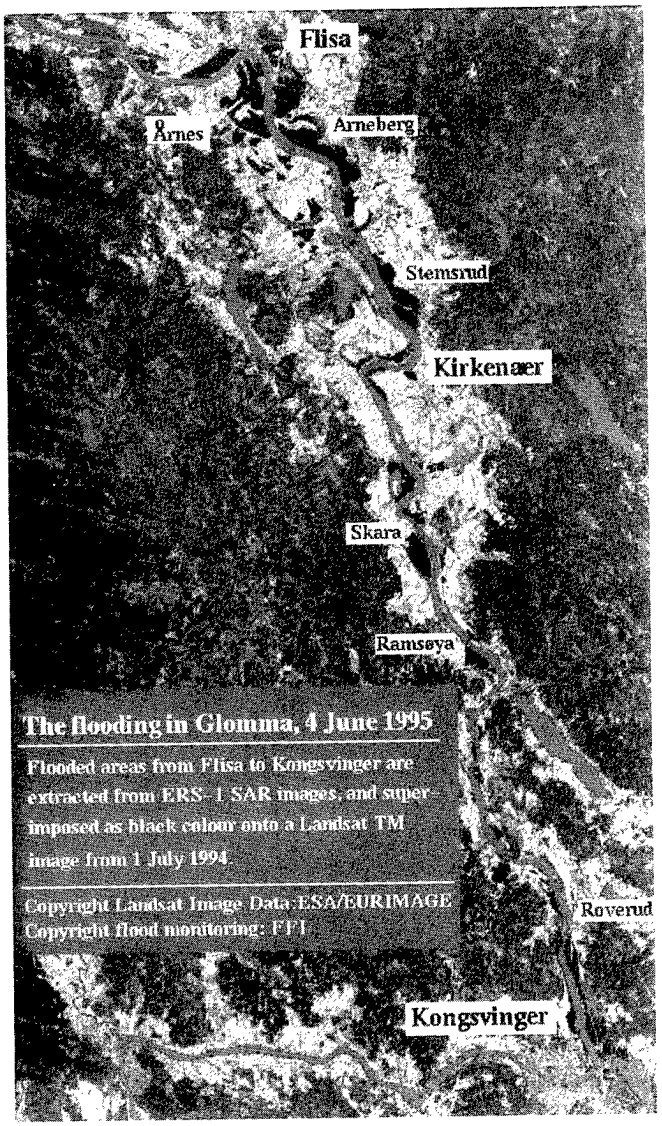


Figure 1.3 Flooded areas from Flisa to Kongsvinger were extracted from ERS–1 SAR images and superimposed as black areas onto the Landsat TM image from 1 July 1994.

CONCLUSIONS

It is an advantage to use satellite SAR in flood monitoring because these sensors can image the Earth surface regardless of day light and cloud conditions.

Flooded areas can be extracted from a SAR image by detecting changes along the rivers with respect to another SAR image that is taken under normal conditions. It is then an advantage if the two SAR acquisitions are close to each other in time, otherwise the flood analysis may be disturbed by large seasonal variations and plant growth.

The ERS–1 SAR operating frequency and incidence angle require moderate wind conditions for discriminating water bodies and surrounding land areas. This clearly puts limitations on the use of ERS–1 SAR for flood monitoring.

It would be an ad vantage to use L–band rather than C–band SAR. This is because the water surface normally gives a lower backscatter in L–band images than in C–band images, regardless of the wind conditions.

An ERS–1 revisit frequency of 1 week at latitudes of south Norway does not match operational requirements. The time–critical phase lasts normally only a few days, and the flood release team would therefore need daily updates. It would therefore be more interesting to use RADARSAT that will have a nearly daily coverage at latitudes above 60 degrees North. RADARSAT will also have the possibility of operating at higher incidence angles than 23 degrees, giving the possibility for good SAR change detection even when the wind is roughening the water surface.

ACKNOWLEDGMENT

We are grateful to Tromsø Satellite Station in Norway that processed and delivered the SAR data.

REFERENCES

[1] "Landsat and ERS–1 data fusion", EOSAT Notes, vol.8, no.3/4, 1993.

[2] "Floods visit western Europe", EOSAT Notes, vol.9, no.1, 1994.

[3] G. Calabresi, "Flood monitoring – workshop report", Earth Observation Quarterly, no.49, September 1995.

Relating Microwave Satellite Radiometer Observations to Land Surface Parameters : A Physical Approach

M. A. Karam* and A. Stogryn
GenCorp Aerojet
1100 W. Hollyvale Street, Azusa, CA 91702, USA
Phone : (818) 812-1154, Fax : (818) 969-5772, e-mail : karamm@post.aes.com

.ABSTRACT

A physically based algorithm relating microwave satellite radiometer brightness temperatures to land surface parameters is developed, through integrating physical algorithms previously developed at Aerojet for the scattering, absorption, and emission characteristics of land surface and atmosphere components. Numerical simulations based on the algorithm showed how the radiometer observations are influenced by the atmosphere. They also revealed some factors limiting the radiometer ability in monitoring the variation in soil moisture along the canopy depth..

INTRODUCTION

For over thirty years Aerojet has played a leading role in microwave satellite radiometry through designing radiometers, and through developing mathematical algorithms describing the absorption, scattering, and emission characteristics of several surface and atmosphere components such as vegetation, sea ice, precipitation, sea surface, water vapor, oxygen , etc. Those algorithms have two common features, not available in other similar published algorithms :(i) they are physically based algorithms, and (ii) they are applicable over a wide frequency bands ranging from microwave to millimeter wave frequencies. In the area of satellite microwave radiometry, as in other areas of remote sensing, physical rather than empirical algorithms have the merits of evaluating the performance of operating sensors, and of generating simulated observations for sensor configurations (polarization, frequency, and incidence angles) not covered by current sensors. The applicability of the algorithms over a wide frequency bands enable us to compare the performance of radiometers operating at different frequencies and to determine the optimum frequency bands required for the retrieval of certain land-surface parameters. In this study, the description of some of the algorithms that have been already developed at Aerojet are outlined and then integrated to develop a physically based algorithm relating the satellite borne radiometer observations to both land surface parameters and the atmospheric parameters. Numerical simulations are performed using the algorithm to investigate (i) the effect of atmosphere on radiometer observations, and (ii) the potential of the current operating radiometers in monitoring soil moisture.

ALGORITHM DEVELOPMENT

The mathematical algorithms developed at Aerojet can be placed into three groups: (i) algorithms for land surface components, (ii) algorithms for lower atmosphere, and (iii) algorithms for upper atmosphere. Only the first two groups of algorithms are considered here, because in relating radiometer observations to land surface parameters lower millimeter wave frequencies should be used, e.g. below 85 GHz. In this frequency range the effect of the upper atmosphere on the radiometer observations is negligible. In the first group of algorithms, electromagnetic field theory is applied to relate the absorption, scattering, and emission characteristics of land surface components to the geometric properties (such as surface roughness, biomass, type of vegetation cover, etc.) and physical properties (such as soil moisture, land surface temperature, vegetation water contents, etc.) of such components. Geometric properties determine the propagation direction, and the polarizations of the radiations received by the radiometers. Physical properties determine the dielectric properties of the medium under consideration, and hence the level of the radiometer brightness temperatures. In this study, the scattering, absorption, emission characteristics of land surface components are integrated through solving the radiative transfer equations, or applying strong fluctuation theory to formulate the land surface emissivity and brightens temperature. In the second group of algorithms, only the absorption and emission properties of the precipitation and atmospheric gases, e.g., oxygen and water vapor are considered. This is because, at microwave frequencies as well as millimeter wave frequencies, and in the absence of hydrometeors,

0-7803-3068-4/96$5.00©1996 IEEE

the scattering characteristics of the intervening atmosphere are negligible. The absorption and emission characteristics, are derived from the frequency intensity and width of the oxygen and water vapor absorption lines. Then by solving the radiative transfer equation in the atmosphere, and using the surface temperature and reflectivity as a boundary conditions the radiometer brightness temperature can be formulated in terms of both land surface and atmospheric parameters.

NUMERICAL SIMULATIONS

The results of the numerical simulations are presented in Figs. 1 - 4. Figure 1 gives the emitted sky brightness temperature at the land surface at two different observation angles : 20°, and 65°. In Fig. 2, atmospheric transmissivity calculated at the satellite as a function of frequency at the same observation angles considered in Fig. 1.

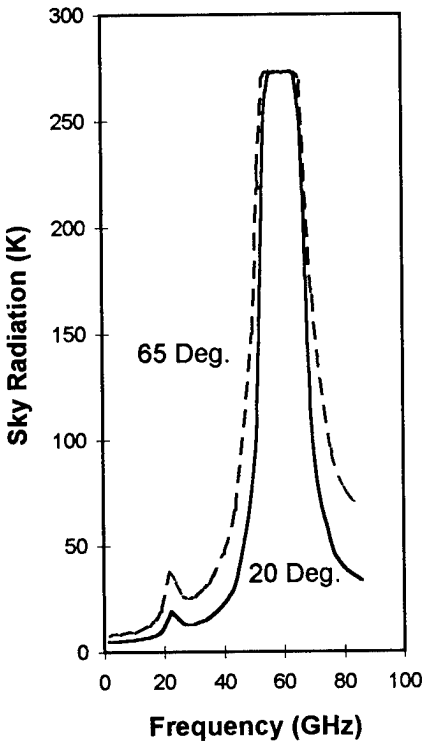


Fig. 1 The sky radiation at land surface as a function of frequency.

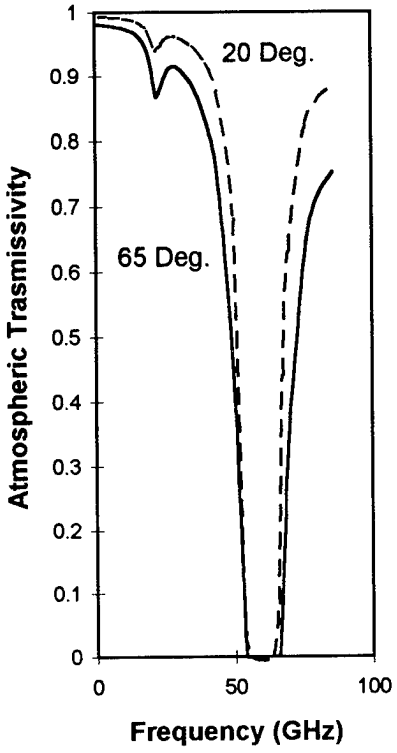


Fig. 2 The atmospheric transmissivity as a function of frequency.

Both figures are calculated under clear sky conditions, e.g. there is no clouds and precipitation in the sky. USA standard atmosphere is used to provide the atmospheric conditions required as input for the algorithm, e.g. water vapor profile and temperature profile.

Figure 3 depicts the variation in satellite brightness temperature as a function of soil depth along which the soil moisture is varying. The soil is taken to have an exponential moisture profile to a certain depth and is assumed to be uniform beyond that depth. The volumetric soil moisture at the soil surface is equated to 25 % and its value beyond the variation depth is equated to 70%. Figure 3 is calculated at 37 GHz for 65° observation angles and a plane soil interface. both vertical and horizontal polarizations are considered in Fig. 3. Figure 4 gives the horizontally polarized brightness temperature at the same observation angle used in Fig. 3 at three different frequencies : 19, 22, and 37 GHz.

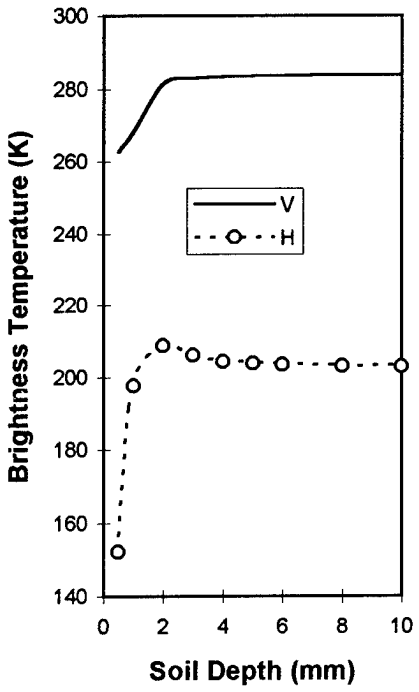


Fig. 3 The radiometer brightness temperature as a function of soil depth for a plane soil surface.

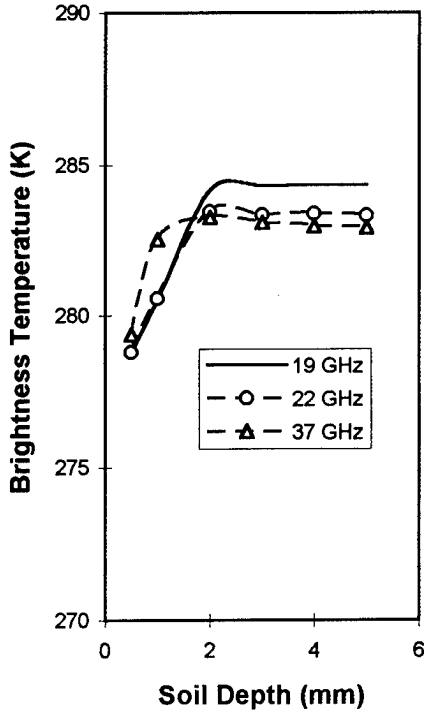


Fig. 4 The radiometer brightness temperature as a function of soil depth for a rough soil surface.

The soil surface in Fig. 4 is taken to be rough with a variance equal to 1 cm.

DISCUSSIONS

From Figs. 1 and 2 we see that both the sky radiation at land surface and atmospheric trasmissivity follow the variations in atmospheric absorption with frequency. Higher absorption values for the atmosphere (at 22.235 GHz, where the first absorption line for water vapor occurs, and around 60 GHz, where the first set of oxygen absorption lines occur) are associated with higher sky radiation values and lower trasmissivity values. From Figs. 3 and 4 we see that (i) at 37 GHz, the radiometer can sense a variation in soil moisture occurring along a depth not exceeding 2 mm, (ii) the horizontally polarized temperatures are more sensitive to the variation in soil moisture profile than the vertically polarized temperature, and (iii) the soil surface roughness decrease the radiometer sensitivity to the variation in soil moisture along the soil depth.

REFERENCES

[1] A. Stogryn, "The emissivity of sea foam at microwave frequencies, " J. Geophysical Res. vol. 2, pp. 1658-1666, 1972

[2] A. Stogryn , "Equations for calculating the dielectric constant of saline water," IEEE Trans. Microwave Theory and Techniques, vol. MTT-19, pp. 733-736, 1971.

[3]A. Stogryn, "Mesospheric temperature sounding with microwave radiometers, " IEEE Trans. Geoscience and Remote Sensing, vol. 27, pp. 332-338, 1989.

[4] M. A. Karam, D. M. LeVine, Y. M. M. Antar, and A. Stogryn, " Improvement of the Rayleigh approximation from a small scatterer," IEEE Trans. Antennas and Propagation, vol. 43, pp. 681-688, 1995.

[5]M. A. Karam, "A physical model for microwave radiometry of vegetation. I. Brightness temperature formulation," Unpublished.

Analysis of ERS-1 SAR Data to Study Soil Moisture Content in Rocky Soils

E.E. Sano[(1)], A.R. Huete[(1)], D. Troufleau[(2)], M.S. Moran[(3)], A. Vidal[(2)]

(1) University of Arizona, 429 Shantz Bldg # 38, Tucson, AZ, 85721, USA Email: sano@ccit.arizona.edu
(2) LCT CEMAGREF-ENGREF, 500 rue J.F. Breton, 34093 Montpellier, Cedex 5, France
(3) USDA-SWRC, 2000 E. Allen Road, Tucson, AZ, 85719, USA

Abstract --The objective of this research was to analyze the potential of ERS-1 SAR data to study the surface soil moisture content of rocky soils in semi-arid regions. The study took place at the Walnut Gulch Experimental Watershed, Tombstone, AZ. Field soil moisture contents and dry bulk densities in the top 5 cm were obtained from 51 different sampling sites in the watershed during a satellite overpass on July 25, 1994. One set of 22 points was characterized by a sandy soil, 3-15% slope, and vegetation dominated by shrubs. Another set of 29 sampling sites was characterized by a clayey soil, 0-3% slope, and covered by grasses and forbes. Soil roughness was measured at eight of these sites. The SAR image was georeferenced in the Universal Transverse Mercator (UTM) coordinate system and calibrated using a digital elevation model (DEM). In general, the correlation between volumetric soil moisture content and the radar backscatter signal was poor, but improved ($r^2 = 0.78$ and 0.41 for the first and second sets, respectively) when limited to sites with volumetric moisture contents higher than 10%. The low correlation was due to the dominant influence of soil roughness which was directly related to the proportion and size of rock fragments. Although roughness seems to explain much of the variance from the radar backscatter signal, it was not clear how best to parameterize the roughness properties. Continued research includes modeling and separating moisture and roughness influences.

INTRODUCTION

A number of authors ([1], [2], [3]) have addressed the use of remote sensing to estimate soil moisture content. Experiments with truck-mounted, aircraft, and spaceborne microwave sensors have shown good prediction potential for soil moisture within the top 5 centimeters of soil. Soil moisture can be estimated from microwave data because of the large contrast between the dielectric properties of liquid water (80) and dry soil (3-5). Thus, as the soil moisture increases, even slightly, the dielectric constant can increase to a value of 20 or greater [3]. Other strengths of microwave sensors are their capabilities of day/night operation, cloud penetration, and large-scale mapping within a short time and reasonable cost [4].

However, one major difficulty in mapping soil moisture using microwave sensors is the influence from both vegetation canopy and soil roughness ([5], [6]). Most authors have shown that there is a linear relationship between the radar backscatter coefficient ($\sigma°$) and soil moisture content, but this relationship does not remain valid for sites with dense vegetation cover and/or rough soil surface. For instance, agricultural fields with furrows oriented perpendicular to the radar incident energy or sites with a high percent of rock fragments can result in a low correlation between $\sigma°$ and soil moisture. The objective of this research was to analyze the potential of ERS-1 SAR data to study surface soil moisture content from rocky soils and sparse vegetation cover in semi-arid regions. The study took place at the Walnut Gulch Experimental Watershed (WG) in Tombstone, southeastern Arizona.

EXPERIMENTAL DESIGN

This study was based on the ERS-1 SAR image obtained on July 25, 1994 at approximately 11:00 AM (local time). This sensor operates at 5.3 GHz (C- band), VV polarization, 23° incidence angle and 12.5 meters of nominal spatial resolution. The date was chosen to coincide with the summer "monsoon" season in July and August. The goal was to obtain a high soil moisture content during the overpass so that this parameter could be evaluated appropriately. An average of 10.3 millimeters precipitation, with a standard deviation of 3.1 millimeters occurred during the two days before the satellite overpass, calculated from 89 rain gages located across the watershed.

The image was calibrated (i.e., corrected to account for the real backscatter area of each pixel) and georeferenced in the Universal Transverse Mercator (UTM) coordinate system using a digital elevation model (DEM) [7]. Radar backscatter coefficients were extracted from this calibrated and georeferenced image using the following equation:

$$\sigma° \text{ (dB)} = 10 \log\langle DN^2\rangle - K \quad (1)$$

where DN^2 = average value of 200 squared digital numbers at the site,
K = calibration constant given by European Space Agency (ESA).

Gravimetric soil moisture samples within the top 5 cm (three replicates) were collected in the same day of the satellite overpass over two different surface conditions. One set of 29

0-7803-3068-4/96$5.00©1996 IEEE

sites was located at the eastern part of the watershed over a clayey Forrest-Bonita complex soil unit [8], 0-3% slope and vegetation dominated by grasses and forbes. Another set of 22 sites was located at the western part of the watershed, over a sandy Mabray-Chiricahua outcrop complex soil unit, 3-15% slope and vegetation dominated by shrubs. Dry bulk density data were also obtained for each sampling point, allowing the calculation of volumetric soil moisture. Finally, eight field soil roughness measurements (three replicates) were made after analyzing the scatterplot of σ° and soil moisture. The field roughness measurements were collected using a device developed by the USDA/ARS, which measures 100 heights of soil surface per meter [9]. These heights were digitized in a GIS software package (Arc/Info) to calculate the standard deviation (in centimeters) that corresponded to the soil roughness of the site (Table 1).

RESULTS

The scatterplot of σ° and soil moisture (Figs. 1 and 2) showed very low correlation over both soil units ($r^2 = 0.08$ and 0.02 for Mabray-Chiricahua and Forrest-Bonita soil units, respectively). Some improvement was found ($r^2 = 0.78$ and 0.41 for Mabray-Chiricahua and Forrest-Bonita soil units, respectively) when the analyzed data was limited to only sites having volumetric moisture contents higher than 10%. However, the correlation was still lower than those reported by others (e.g., correlation coefficients higher than 0.85, [10]).

This low correlation was most likely due to the dominant influence of soil roughness at the Walnut Gulch Experimental Watershed (over 20% of rock fragments and less than 1 kg/m^2 of biomass), which is particularly important in C-band data [11]. For instance, the Forrest-Bonita soil unit exhibited two sets of sites (Set 1 and Set 2, Fig. 2) that behaved opposite to that expected. Set 1 presented low moisture contents (less than 6%) but relatively high σ° (more than -8.5 dB). Set 2 presented high moisture contents (more than 13%), but low σ° (less than -9.6 dB). The soil roughness data collected over these two sets (Table 1) indicated a rougher surface with Set 1(more than 1.6 cm of soil roughness) and thus higher σ° values while the relatively smooth surface of Set 2 (less than 1.1 cm of soil roughness) explained its low σ° values. Although we can expect only attenuation effects in the σ° for WG's sparsely vegetated watershed, the differences in the total green biomass for each site probably contributed for the low correlation between σ° and soil moisture as well.

Therefore, at the Walnut Gulch conditions, soil roughness presented a strong (if not dominant) effect on the backscatter coefficient. In order to retrieve soil moisture from radar data in regions similar to the Walnut Gulch Watershed, the influence of both soil moisture and roughness need to be modeled and separated. One approach to reduce the influence of the roughness is the simple ratio (SR) technique. Assuming that two multitemporal images acquired at the same geometrical and spectral configurations present approximately the same roughness effect (valid for WG conditions), the SR image can produce a better correlation between soil moisture and σ°. This approach will be tested in the future, using a dry season ERS-1 SAR image (DOY 116, 1992). Another difficulty in retrieving soil moisture content from radar data in semi-arid regions is, as highlighted by [12], the typically small range of soil moisture values, less than 20% volumetric soil moisture, even during the "monsoon" season. Future research includes more soil roughness measurements, analysis of relationship between σ° and rainfall data, and modeling and separating moisture and roughness influences.

ACKNOWLEDGMENTS

This work was supported by the NASA-EOS Interdisciplinary Research Program (NASA IDP-88-086). Special thanks are due to J. Epiphanio, L. Accioly, F. Rahman, C. Unkrich, G. de Lira and K. Batchily for their help in the field soil moisture sampling.

REFERENCES

[1] F.T. Ulaby, and P.P. Batlivala, "Optimum radar parameters for mapping soil moisture", IEEE Trans. Geosci. Electronics, vol. 14, n. 2, pp. 81-93, 1976.

[2] E.T. Engman, and N. Chauhan, "Status of microwave soil moisture measurements with remote sensing", Remote Sens. Environ., v. 51, pp. 189-198, 1995.

[3] T.J. Schmugge, "Remote sensing of soil moisture: recent advances", IEEE Trans. Geosci. Remote Sens., vol. 21, n. 3, pp. 336-344, 1983.

Table 1
Field soil roughness measurements (cm) for eight sites in Mabray-Chiricahua soil unit.

Set #	Site	Roughness (cm)
1	1	2.21
	2	1.69
	3	1.86
	4	1.74
2	1	0.66
	2	1.02
	3	0.75
	4	1.02

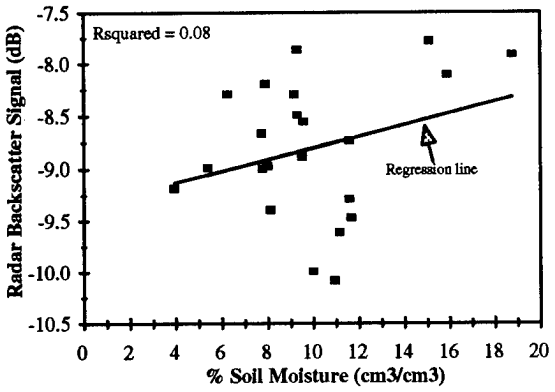


Fig.1 - Scatterplot of soil moisture and radar backscatter coefficients for Mabray-Chiricahua soil unit.

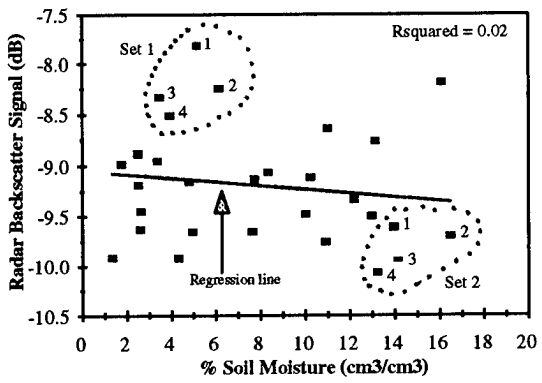


Fig.1 - Scatterplot of soil moisture and radar backscatter coefficients for Mabray-Chiricahua soil unit. Sets 1 and 2 correspond to the soil roughness measurement sites.

[4] C. Schmullius, and R. Furrer, "Frequency dependence of radar backscattering under different moisture conditions of vegetation-covered soil", Int. J. Remote Sens., vol. 13, n. 12, pp. 2233-2245, 1992.

[5] E.P.W. Attema, and F.T. Ulaby, "Vegetation modeled as a water cloud", Radio Sci., vol. 13, n. 2, pp. 357-364, 1978.

[6] L. Prevot, I. Champion, and G. Guyot, "Estimating surface soil moisture and leaf area index of a wheat canopy using a dual-frequency (C and X bands) scatterometer", Remote Sens. Environ., vol. 46, pp. 331-339, 1993.

[7] A. Beaudoin, M. Deshayes, L. Piet, N. Stussi, and T. Le Toan, "Retrieval and analysis of temperate forest backscatter signatures from multitemporal ERS-1 data over hilly terrain", 1st Symp. ERS-1 Pilot Project, Toledo, Spain, 23-25 June 1994, pp. 283-289.

[8] USDA, Soil Survey, Walnut Gulch Experimental Watershed, unpublished.

[9] J.R. Simanton, R.M. Dixon, and I. McGowan, "A Microroughness meter for evaluating rainwater infiltration", Proceedings of Hydrology and Water Resources in AZ and the Southwest, v. 8, pp. 171-174, 1978.

[10] R. Bernard, P.H. Martin, J.L. Thony, M. Vauclin, and D. Vidal-Madjar, "C-band radar for determining surface soil moisture", Remote Sens. Environ., v. 12, pp. 189-200, 1982.

[11] A. Beaudoin, T. Le Toan, and Q.J.H. Gwyn, "SAR observations and modelling of the C-band backscatter variability due to multiscale geometry and soil moisture", IEEE Trans. Geosci. Remote Sens., vol. 28, n. 5, pp. 886-894, 1990.

[12] D. Troufleau, A. Vidal, A. Beaudoin, M.S. Moran, M.A. Weltz, D.C. Goodrich, J. Washburn, and A.F. Rahman, "Using optical-microwave synergy for estimating surface energy fluxes over semi-arid rangeland", Proceedings of VI Int. Symp. on Physical Measurements and Signatures on Remote Sensing, 17-21 Jan., Vald'Isere, France, 1994.

An Automated Overland Flow Model Based Upon Remote Sensing and GIS

Cheng-Hua Leu
Associate Professor, Dept. of Civil Engineering
National Chung Hsing University, Taichung, Taiwan, ROC.
TEL:886-4-2853472 FAX:886-4-2862857 e-mail:402chleu@vax9k.nchu.edu.tw

ABSTRACT: This research uses remote sensing and raster-based GIS technology to establish an automated overland flow model in watershed hydrologic simulations. the basic framework is to construct watershed grid-based geographical feature data base. Based upon these raster watershed characteristics, the required hydrologic parameters for computer simulation can then be extracted automatically. Also, through watershed digital terrain model and simulated grid flow algorithms, a hydrologically ordered cell-to-cell flow sequence can thus be dictated. Finally, by combining the digital watershed flow algorithms with the kinematic-wave hydrologic modeling and using finite-difference method to solve the system equations, the output runoff hydrographs can thus be produced.

INTRODUCTION

Recently, hydrologic models which simulate watershed runoff process have made tremendous improvement on both estimation accuracy and computer running speed. However, for most hydrologic models, to perform rainfall-runoff simulation, the values of related hydrologic parameters have to be determined in advance and then used as input for simulation. Thus, the entire modeling processes sometimes needs to be broken-in-steps. Nowadays, owing to the rapid progress of personal computer technologies and the integrated concept of remote sensing and geographical information systems, an automated hydrologic model which links up 1)basic thematic mapping, 2)parameter estimation and 3)runoff simulation processes in a continuous manner is thus quite possible.

This study uses remote sensing and grid-based GIS technology to construct the main database core for related watershed analyses. The first step is to generate the required watershed digitized thematic maps such as topographic, soil type and land use maps. Through vector-raster transformation, a grid based geographic feature database can be obtained. Also, watershed landuse characteristics can be found through image processing on SPOT satellite data. Based on these watershed grid-based data, through expert systems(ES) and associate database management system, the values of required hydrologic parameter for simulation can then be extracted automatically. As for the hydrologic simulations, through watershed digital terrain modeling, a hydrologically ordered cell-to-cell flow sequence can be dictated quite easily. Finally, by combining 1)digital watershed grid flow algorithms,2)parameter estimation and 3)the kinematic-wave hydrologic theory and using finite-difference method to solve the system equations, the output runoff hydrographs can thus be produced. Figure 1 presents the scheme of the analysis procedures for this study.

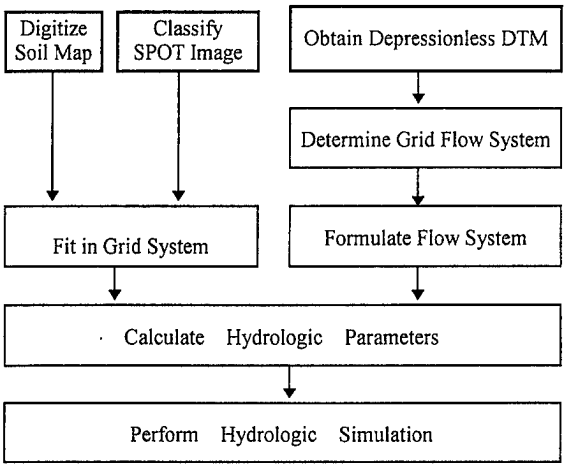


Figure 1 A schemaitc of the automated hydrologic modeling

Test area: Der-Chi Reservoir watershed The overall objective of test study was to evaluate the simulation accuracy of the rainfall-runoff modeling based on the proposed geographic database. The Der-Chi Reservoir watershed, at the center part of Taiwan Island, was selected for this study simply because it is a typical important forest watershed in Taiwan. The watershed area ia about 523 square kilometers. Figure 2 is a 3-dimensional plot of watershed, which is constructed from a 40mx40m digital terrain model (DTM). Also, in this research, multispectral image collected by French satellite SPOT was used in watershed landuse classification. A world wide image process software ERDAS was used for image analysis.

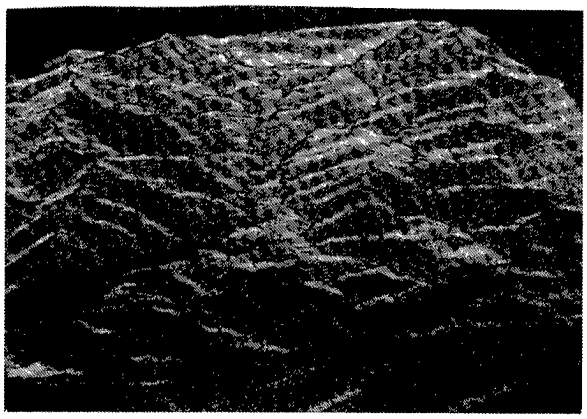


Figure 2 3-D topographic map of Der-Chi Reservoir watershed

Hydrologic Simulation Model

The basic hydrologic theory used in watershed rainfall-runoff simulation of this study is the kinematic-wave model In estimation rainfall loss amount, SCS curve number method [1] was introduced. Thus, the basic governing equations for this study are

0-7803-3068-4/96$5.00©1996 IEEE

$$\frac{\partial y}{\partial t} + \frac{\partial q}{\partial x} = r \quad \text{.....(1)}$$

$q = \alpha y^m$ .....(2)

y : depth

t : time

q : flow rate per unit width

x : flow direction

α,m : constant

The above equations can be solved through finite-difference iterations.

WATERSHED GEOGRAPHIC DATABASE

Due to rapid advancing on the technologies in geographical information systems, the complicated spatial analyses on ground features turns to be more convenient. First, all kinds of map data such as topographic map, soil type map, etc., can be stored as different layers in computer through GIS digitizing techniques. Therefore, these thematic maps can be constructed as watershed geographic database and applied to hydrologic studies. In this study, in order to meet the requirements of hydrologic simulation, watershed geographic database should contain the following layers. They are watershed digital terrain model, soil type and land use. All the hydrologic parameters can thus be obtained from this database. Through GIS analysis, the resulted Der-Chi Reservoir watershed database is summarized as below.

Topographic feature The DTM of the watershed, provided by Research Center of Space and Remote Sensing Technology, National Central University, was used to obtain watershed topographic features such as slope, aspect, etc., which are important to determine direction of grid overland flow. The 3-D plot of the watershed DTM has been shown in Figure 2.

Soil type Soil type is an important factor in determining rainfall loss and Manning's roughness n.[2] In this research, watershed soil map was first digitized in vector mode. Through vector-raster transformation, a grid base soil type map was generated and used in hydrologic parameter estimation,[3]

Land use As mentioned previously, SPOT satellite 3-band multispectral image data were used to determine watershed land use characteristics.In this study the general statistics of landuse characteristics within the watershed are shown in Table 1.

Table 1 Land use Statistics of Der-Chi Reservoir watershed

Land use	Area (km^2)	Percentage
Conifer	154.28	29.50
Hardwood	338.64	64.75
Orchard	12.40	2.37
Grass	8.00	1.53
Farm	9.68	1.85

By combining the above data layers, a complete GIS database of Der-Chi Reservoir watershed is thus established. This database was then used to obtain the required parameters for hydrologic simulation. The detailed procedures to determine the parameter values are discussed in next section.

HYDROLOGIC PARAMETERS

To perform the hydrologic modeling, a group of parameters need to be determined. First, the runoff processes are simulated based upon grid-flow system. In this study, the entire watershed was divided into about 340000 grids, the rainfall runoff relationship is then simulated from the upper stream grid to watershed outlet according to the grid flow network. The basic parameters regarding to the simulation processes are discussed as below.

Grid flow system The basic framework of this study is to establish a hydrologically ordered grid-to-grid flow sequence which is subsequently used to dictate the order of flow computations. First of all, a depressionless watershed DTM was processed to remove pits and depressions which would lead to computer divergence in simulation iterations. Flow directions of each grid are then assigned on the basis of steepest descent away from the current grid. Figure 3 is the diagram of flow direction codes for each grid. To determine the watershed draining to a specifed outlet grid, a watershed growing procedure is thus used. First the algorithm examines all grids neighboring the selected outlet grid. Those grids flowing into the outlet grid become the primary watershed drainage area. As no neighbors of existing watershed grids can be found the flow into the watershed, the drainage area is considered to have been fully defined. Using the watershed growing procedure, the flow direction for each grid are also dictated. These flow directions are then used in overland and channel flow routing.

↖ 1	↑ 2	↗ 3
← 4	5 ×	6 →
↙ 7	8 ↓	9 ↘

Figure 3 Diagram of flow direction codes for cell X

Slope and aspect Based upon watershed DTM data, since the GIS software owns the function in 3-D analysis. The grid-by-grid slope and aspect values can be easily calculated.

Rainfall loss Basically, interception and infiltration are the major parts of the rainfall loss in rainfall-runoff simulation. Usually, the loss amount is determined mainly by soil types, land use and antecedent condition, which can be estimated through SCS curve-number method [1]. Since the soil type and landuse within the watershed have been stored on grid base, the grid-by-grid CN values can be obtained easily. These CN values can then be used in estimation of effective rainfall amount through SCS method.

Surface roughness Watershed surface roughness is an important factor in kinematic-wave modeling, which is determined mainly by land use. Crawford and Linsley[4] have designated a series of roughness values for different ground

covers. Since a detailed land use map has built in watershed GIS database, the surface roughness values for each grid can be calculated by weighting procedures.

PARAMETER ESTIMATION

In the previous section, the parameters such as grid flow system and grid slope can be obtained directly from the GIS database. On the other hand, the parameters of rainfall loss (in terms of curve number) and surface roughness have to be obtained through experience rules. In this study, an expert system which collects all the experimental and experienced rules is used to determine curve number and surface roughness in the grid mode within the watershed. From the interactive computer module, these two parameters can be obtained through database management and built-in expert system. Figure 4 and 5 are the examples showing the values for selected grid of these two paramaters from computer screen output.

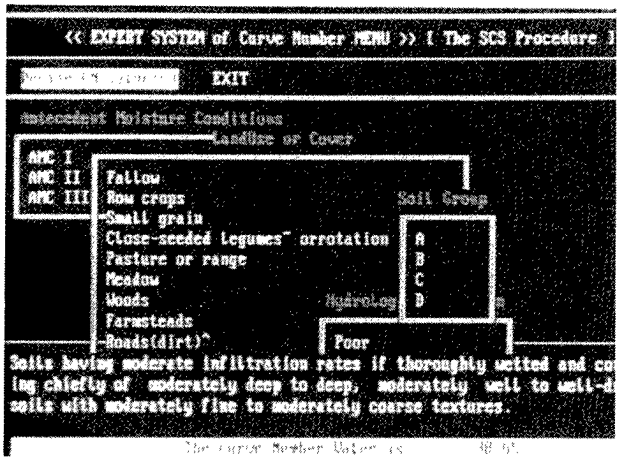


Figure 4 Estimation on curve number using expert system

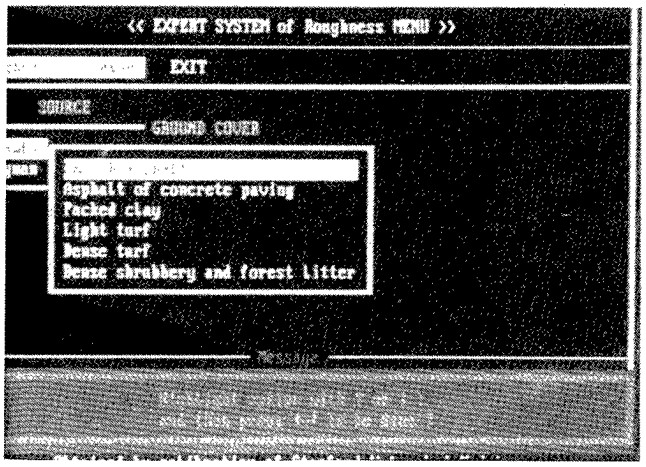


Figure 5 Estimation on surface roughness using expert system

RESULTS OF SIMULATION

Since all the grid-based values of the required parameters have been obtained, the hydrologic simulation can thus be performed. Through finite-difference iterations, with the input rainfall and antecedent data, the runoff hydrographs can be generated. Figure 5 is the general output of modeling results. By comparing the simulation results with the measured runoff rates, it is shown that the proposed model, with the parameters values estimated from GIS data base and expert system, works quite sucessfully in estimating overland flow for Der-Chi Reservoir watershed.

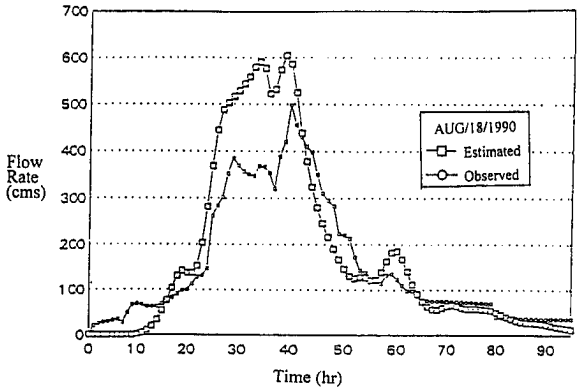


Figure 6 Hydrologic simulation result

CONCLUSIONS

This research uses GIS and expert system technologies in determining the hydrologic paramaters of the watershed and links all the modeling procedures through computer interfacing. In estmating the parameter values, the GIS grid-based method have been tested sucessfully. Moreover, by fitting those parameter values wirh kinematic-wave based hydrologic modeling, the simulation results have also been shown with good accuracy in estimating runoff rates.

REFERENCES

[1]U.S. Soil Conservation Service. 1964. Watershed Planning in Hydrology. National Engineering Handbook, Part I.

[2]Bras, R.L. 1990. Hydrology: an Introduction to Hydrologic Science. Addison-Wesley Publishing Company. ISDN 0-201-05922-3

[3]Environmental System Research Institution Inc., 1989. Arc/INFO User's Guide.

[4]Crawford, N.H. and R.K.Jr. Linsley. 1966. Digital Simulation in Hydrology. Stanford Watershed Model IV., Dept. of Civil Engineering Technical Report N0.39. University of Stanford, USA.

ERS-1 and JERS-1 SAR Data Analysis for Soil Moisture and Land Cover Studies

Y.S. Rao, P.V.N. Rao*, L. Venkataratnam* and K.S. Rao

Centre of Studies in Resources Engineering
Indian Institute of Technology, Powai, Bombay-400 076, India
Fax: +91-22-5783480, Email: ksrao@powai.cc.iitb.ernet.in

*** National Remote Sensing Agency, Agriculture and Soil Group**
Balanagar, Hyderabad-500 037, India

Abstract:- ERS-1 and JERS-1 SAR data acquired with one day difference were compared to each other to study the effect of frequency and incidence angle on soil moisture and various land cover features. Optical data from IRS-1 satellite were also used for comparison with microwave data. Temporal ERS-1 SAR data acquired in three months (3 scenes) were also included in the analysis.

The response of ERS-1 SAR data for soil moisture is better than that of JERS-1 SAR data. Effect of roughness and vegetation on soil moisture was observed in both the SAR data sets. The temporal changes in soil moisture using three ERS-1 SAR scenes were clearly seen. Classification accuracy of various land cover features are very poor in microwave data as compared to optical data.

INTRODUCTION

There has been growing interest in remote sensing community to use microwave SAR data of JERS-1, ERS-1,2 and Radarsat satellites due to its availability irrespective of cloud cover and sun illumination. Recent studies [1]-[5] using SAR data have been shown that ERS-1, JERS-1 SAR and SIR-C systems are useful for observing soil moisture and dynamics of agriculture crops as well as providing land cover mapping and area estimation.

The objective of this research is to study the ability of ERS-1 and JERS-1 SAR data for soil moisture and land cover classification. For this, we have used the available data of JERS-1, ERS-1 SAR and optical data of Indian Remote Sensing (IRS-1) satellite. In the subsequent sections, study area, ground truth, data sources and results and discussions are given.

0-7803-3068-4/96$5.00©1996 IEEE

STUDY AREA AND DATA SOURCES

The study area for the analysis of three sensor data is located around Rajahmundry town with Latitude 17°.1' and Longitude 81°.47', Andhra Pradesh, India. The area contains wide variety of cover types such as reserved forest, plantation, croplands (paddy, sugarcane, pulses), barren land, urban area, hilly terrain and water bodies. Some part of the study area is inundated with water in rainy season and later used for plantation of commercial crops such as tobacco, chilly and cotton in the winter.

The details on data acquisition from different sensors are given in Table I.

GROUND TRUTH DATA

In January, many fields were harvested paddy fields. Some harvested fields were used for growing second crops such as pulses (green and black gram) and sunhamp. The crops were grown and fully covered the soil surface. Some harvested area were again planted with paddy and it was grown about 30 cm height. Many sugarcane fields were closed to harvesting stage and some fields were harvested. Low-lying water logged areas in rainy season were used for growing commercial crops such as tobacco, chilly, tomato etc. in winter season. The height of the tobacco was 1.2 m with big leaves and flowers. Water content in a single leaf was 42 grams. Each plant had for about 13 leaves. Therefore, the tobacco plant with leaves and stalk (diameter 2 cm) may have highest water content as compared to other crops. The area also covers mango, cashew plantation and reserved scrub and highly grown thick forest. The soil moisture in many crops vary from 5% to 18% of weight in January 1993.

Table I. Different sensors and their data on different dates used for the analysis.

Sensor	Band	Resolution	Acqs. Date
JERS-1 SAR	L-band	18 m	Jan. 22, 1993
ERS-1 SAR	C- band	30 m	Jan. 21, 1993
(SAR)			Dec. 17, 1992
			Feb. 25, 1993
IRS-1	2,3,4 bands	36.25 m	Jan. 2, 1993

DATA PROCESSING

ERS-1 and JERS-1 SAR data were resampled to IRS-1 optical data (36.25 m) and co-registered all the images. Different color combinations using ERS-1, JERS-1 SAR and IRS-1 data were made for better identifications of various features. Principal component and IHS analysis were also done. Ground truth soil moisture locations were identified in January SAR images and average digital numbers (DN) of 3x3 window were taken.

RESULTS AND DISCUSSIONS

Fig. 1 shows 42 km by 36 km area of JERS-1, ERS-1 SAR images on different dates. From comparison of JERS-1 and ERS-1 SAR images in January, it is observed that various features can easily be identified in JERS-1 SAR imagery as compared to that of ERS-1. Paddy fields are seen as dark tone (extreme lower right area) in ERS-1 imagery, whereas it is bright in the JERS-1. This can be attributed to the larger incidence angle (35°) of JERS-1 as compared to that of ERS-1 (23°). Just above paddy area, pulse crop is seen dark tone in JERS-1. The same area is bright in ERS-1. The centre of the image is mango-cashew plantation which can be seen clearly in JERS-1.

Temporal ERS-1 SAR scenes show variations in brightness. Out of three ERS-1 scenes, Dec. 17 scene is very bright due to cyclone and rainfall in this month. Maximum tonal variations is observed mainly in agricultural areas as compared to highly grown plantation and forest areas. In February, overall imagery is dark due to dry soil conditions in this month.

Soil Moisture Analysis

Ground truth soil moisture values in January 22 of bare smooth, medium rough, rough, and crop fields were plotted against backscattering coefficient (σ°) in Figs. 2 and 3 for ERS-1 and JERS-1 SAR respectively. DN values were converted to backscattering values using available calibration equations [6],[7]. It can be seen from Figs. 2 and 3 that points related to tobacco and rough fields were deviated from fitted line obtained with smooth bare, medium rough and sparce vegetation fields. Even though the soil moisture in tobacco fields were low, its σ° values were high due to high vegetation water content in tobacco. High correlation is observed between ERS-1 σ° and soil moisture. However, the sensitivity is low as compared to JERS-1 SAR. Large scattering in JERS-1 Plot may be attributed to the restrictions on the use of JERS-1 calibration equation.

All the images were classified individually and combinely using supervised maximum-likelihood classifier and the classification accuracy is given in Table II. The classification accuracy using single SAR data is about 30%, whereas optical data gives 67%. Combinations of optical and microwave data gives a small increment (10%) in classification accuracy.

CONCLUSIONS

JERS-1 and ERS-1 SAR data were analysed for soil moisture and land cover classification. Large differences in the tone of image were observed between ERS-1 and JERS-1 for paddy and pulses. Correlation between σ° and soil moisture is higher for ERS-1 as compared to JERS-1. The relations are to be verified using more ground truth data points. Temporal variations in ERS-1 SAR data using three scenes show that the sensor is suitable for soil moisture monitoring. As the classification accuracy is very poor using SAR data and supervised maximum-likelihood classifier, new techniques based on texture and neural networks can be applied.

ACKNOWLEDGMENTS

The authors are thankful to Prof.V.S. Chandrasekaran, Head, CSRE for his constant encouragement and support for this work. We are grateful to DST for the financial support under the grant ES/23/131/91.

REFERENCES

[1] M.C. Dobson, K. Sarabandi and F.T.Ulaby, "Preliminary analysis of ERS-1 SAR for forest ecosystem studies," IEEE Trans Geosci. and Remote sensing, Vol 30, No 4, pp. 203-211, 1992.

[2] S. Mohan et al., "Estimation of soil moisture using ERS-1 SAR data, Proc. second ERS-1 symposium, Hamburg, Germany, Oct. 11-14, pp. 241, 1993.
[3] K. Musiake et al., "Extraction of soil moisture information using JERS-1 SAR image," JERS-1 information exchange meeting presentation materials, August 15, 16, 1993, Kogakuin University, Tokyo, Japan, pp. 311-326.
[4] T. Nishidai, "Early results of Fuyo-1, Japanese Earth Resources Satellite (JERS-1)." Int. J. Remote Sensing, Vol 14, No 9, pp 1823-1833, 1993.
[5] P.C. Dubios, J. van Zyk abd T. Engman, "Measuring soil moisture with imaging radars," IEEE Trans. Geosci. and Remote Sensing, Vol. 23, No.4, pp. 915-926, 1995.
[6] User's guide to NASDA's SAR products, EOC, NASDA, Japan, March 10, 1993.
[7] D.R. Paudyal and J.Aschacher, "ERS-1 SAR data calibration at the Indian National Remote Sensing Agency," Asian-Pacific Remote Sensing Journal, Vol. 6, No.2, PP. 117-119, 1994.

Table II. Classification accuracy of different features using various combinations of sensor systems.

Sensors / Classes	JERS	ERS	ERS+ JERS	Temp. ERS	T.ERS +JERS	IRS B432	B4 E&J	B432 E&J	Total pixels
Settlement	59.8	88.6	92.8	93.8	99.0	55.7	97.9	100.0	92
Tobacco	51.4	71.4	71.4	97.1	97.1	100.0	100.0	100.0	35
Pulses	49.4	57.1	63.3	59.2	65.3	83.7	75.5	87.8	49
Paddy	0.0	5.0	79.3	91.4	67.9	99.3	72.9	100.0	140
Fallow	0.0	2.8	44.4	38.9	68.1	100.0	100.0	100.0	72
R.forest	0.0	3.8	3.9	0.0	18.2	63.6	68.8	84.4	77
Mango	52.1	2.0	47.9	20.8	45.8	41.7	43.7	37.5	48
Tapioka	47.7	0.0	25.0	9.1	2.0	27.3	43.2	20.5	44
Water	27.2	14.9	43.9	85.1	86.0	17.5	97.4	57.9	114
Sugarcane	15.6	62.2	55.6	66.7	77.8	48.9	88.9	77.8	45
Sand	64.2	0.0	0.0	1.2	4.9	100.0	7.4	100.0	81
Overall	33.4	30.0	48.0	51.2	57.5	67.1	72.3	78.7	

Temp. - Temporal; B-bands; E-ERS-1; J-JERS-1

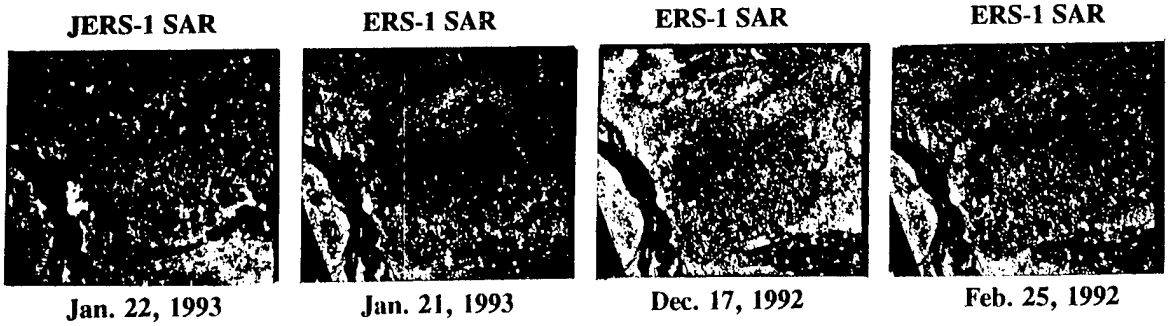


Fig. 1. JERS-1 and ERS-1 SAR images of an area 42 km by 36 km acquired on different dates.

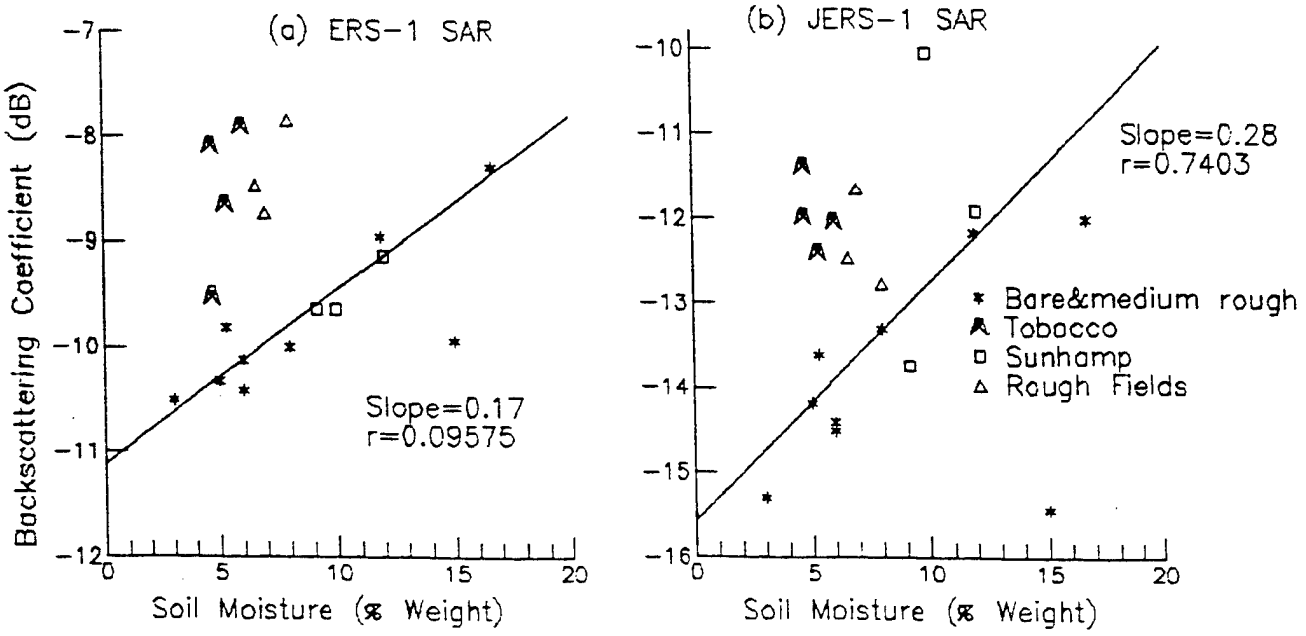


Fig. 2. Backscattering coefficient (σ°) versus soil moisture for (a) ERS-1 SAR and (b) JERS-1 SAR data in January.

Spatio-temporal dynamics of soil moisture in tallgrass prairie using ERS-1 SAR image time series: first year results

Geoffrey M. Henebry
Kansas State University
Division of Biology/Ackert Hall
Manhattan, KS 66506-4901 USA
T: 913.532.7997 F: 913.532.6653
gmh@unix.konza.ksu.edu

Alan K. Knapp
Kansas State University
Division of Biology/Ackert Hall
Manhattan, KS 66506-4901 USA
T: 913.532.7094 F: 913.532.6653
aknapp@lter-konza.konza.ksu.edu

Abstract -- Radar remote sensing of soil moisture has been demonstrated in croplands and rangelands. We are interested in synoptic estimates of soil moisture to aid long term ecological investigation of tallgrass prairie and have initiated a three year study to develop this technology. Our study area, Konza Prairie Research Natural Area (KPRNA), exhibits a variety of factors to complicate soil moisture estimation via synthetic aperture radar (SAR) including significant terrain variation, heterogeneous soil types and depths, and watershed-level experimental treatments including prescribed burning, grazing by large ungulates, and water supplementation. Several indicators of the moisture status of soil-water-vegetation continuum were gathered during the 1995 growing season including soil moisture via neutron probe and TDR, xylem pressure potential values, and aboveground biomass (wet and dry weights). Due to orbital track overlap, eleven ERS-1 SAR images of KPRNA were acquired from mid-April to early October. Spring through mid-summer were unusually cool and wet, thereby delaying phenological development and attenuating the water stress typical of the later growing season. Backscattering values show some consistent agreement with ground data. Watersheds burned in April showed markedly higher backscattering at the end of the growing season due to a lack of litter layer from previous seasons' growth. Grazed units that were also burned showed the highest backscattering caused by no litter layer and more exposed soil.

INTRODUCTION

In a recent review of microwave remote sensing of soil moisture, [1] lists key questions for future research including how the vegetation canopy affects backscattering as a function of plant and canopy geometry, water content, and growth stage. Previous scatterometer work at Konza Prairie has shown significant correlations between moisture in canopy and soil and backscattering from C-band illumination with HH-polarization, even at moderate (30^0) to high (45^0) incidence angles [2-4]. These relationships result from an increasing contribution of volume and surface-volume components to scattering [5] and from an attenuation of terrain slope modulation [2,4]. Further research on effect of accumulated litter layer on microwave backscattering and on the relationship between terrestrial slope variation and microwave backscatter was urged by [4]. We report here initial results of a project at Konza Prairie Research Natural Area to develop SAR-based soil moisture estimation techniques for ecological applications in a heterogeneous natural landscape.

METHODS

We obtained eleven ERS-1 SAR scenes during the 1995 growing season: (4/14, 5/3, 5/19, 6/7, 6/23, 7/12, 7/28, 8/16, 9/1, 9/20, 10/6). The data were processed by CCRS into Multi-Look Detected (MLD) format. The nominal spatial resolution is 25m with a pixel spacing of 12.5m. The ERS-1 SAR instrument operates at C-band (5.3GHz; 5.6cm wavelength) with VV polarization and 23^o incidence angle. A 10x10 pixel region within each of two well studied watersheds, 001D and 020B, was selected for sampling of the SAR digital counts. These areas were selected to avoid slopes with easterly aspects. Means and extremes were calculated: only means are reported but extremes exhibited the same seasonal dynamics.

During the 1995 growing season, soil moisture was monitored using neutron-probe (at 25cm and 50cm in

0-7803-3068-4/96$5.00©1996 IEEE

lowlands only) and TDR (at 15cm in upland and lowlands; 30cm in lowlands only). Canopy moisture status was monitored by xylem pressure potential (XPP) using a Scholander-type pressure chamber at both upland and lowland sites. Biomass data were also collected. It is not possible to present here either the TDR or the biomass data.

RESULTS

The seasonal course of canopy moisture (as XPP) and soil moisture (as percent of field capacity) is expressed in terms of growing degree days (GDD), an accurate bioclimatological time variable, for watersheds 001D (Fig.1) and 020B (Fig 2). The former is burned annually in spring (4/18 in 1995) while the latter watershed is on 20-year burn rotation (but was last burned 4/5/91 during a wildfire). Note the discrepancy between XPP and soil moisture at 25cm and 50cm during the early to middle growing season (1500-2300 GDD). The canopy was almost fully developed by GDD 2300. The XPP curves are not significantly different either by landscape position or burning treatment. This lack of effect was atypical and was caused by an unusually cool, wet spring and early summer, which delayed phenology and attenuated the water stress common in the later growing season. The average annual precipitation of 835 mm was reached by 8/16 and GDD 3000. Heavy precipitation near GDD 4000 reduced XPP and replenished soil moisture stores.

A few caveats on the backscattering data are in order. These ERS-1 data were not calibrated and no terrain corrections were performed. Slope and aspect effects on backscattering are twofold at KPRNA: the direct effects on sensor-target geometry and the indirect effects on vegetation status and stature. We are in the process of using interferometric techniques to construct a high resolution DEM from ERS Tandem data that should improve considerably on the current USGS 30m DEM. Untangling the effects of terrain and subpixel variability on soil moisture estimation is mentioned in [1] as an important area for future research.

The temporal sequence of mean digital numbers of C-band backscattering shows differences between watersheds and the associations with soil moisture (Figs. 3&4) and canopy moisture status (Figs. 5&6). There is more apparent dynamic range in backscattering during the growing season in the burned watershed. This accords with the observations of [2-4] but the relative difference might have been attenuated by the wetter than normal conditions.

Note the minimum values in each watershed occur at mid-season, just before GDD 2300, and that they appear better correlated with XPP than the soil moisture data. That the backscattering is not well correlated with relatively deep soil moisture is not surprising. The early to middle season association with XPP, however, is intriguing. To what extent is this related to the developing canopy? Why does this association appear to weaken later in the growing season (GDD > 2300)? Is this an artifact of a wet year? As we collect additional data during the next two growing seasons, we hope to be able to answer these questions.

Finally, and on a broader scale, the effects of management practices (grazing and burning) were clearly evident in the SAR image time series. Time since last burn is an important parameter since a litter layer accumulates in the absence of fire [6]. The litter layer changes the microclimate and directly affects backscattering [2-4]. Over a period of just a few years, significant changes in species composition can occur, including the invasion of woody species. Watersheds burned in April 1995 showed markedly higher backscattering at the end of the growing season (9/20 image) due to a lack of litter layer (data not shown). Grazed units that were also burned showed very high backscattering on the 9/20 image, due to a lack of litter layer combined ith the spatially heterogeneous mosaic of live canopy and exposed soil that characterizes grazed landscapes.

ACKNOWLEDGMENTS

This research was supported by National Science Foundation grants DEB-9527108 and BSR-9011662, and European Space Agency grant AO2.USA126.

REFERENCES

[1] E.T.Engman and N.Chauhan, "Status of microwave soil moisture measurements with remote sensing," Rem. Sens. Environ., vol. 51, pp.189-198, 1995.

[2] S. Gogineni, J. Ampe, and A. Budihardjo, "Radar measurements of soil moisture over Konza Prairie," Int.J.Rem. Sens. vol.12, pp.2425-2431, 1991.

[3] R.D. Martin, Jr. G. Asrar, and E.T. Kanemasu, "C-band scatterometer measurements of a tallgrass prairie," Rem. Sens. Environ., vol. 29, pp. 281-292, 1989.

[4] J.R.Wang, S.P. Gogineni, and J. Ampe, "Active and passive microwave measurements of soil moisture in FIFE," J.Geophy.Res., vol. 97(D), pp.18979-18985, 1992.

[5] A.K. Fung and H.J. Eom, "A comparison of active and passive sensing of soil moisture from vegetated terrains," IEEE Trans. Geosci. Rem. Sens., vol. GE-23, pp.768-775, 1985.

[6] A.K. Knapp and T.R. Seastedt, "Detritus accumulation limts productivity of tallgrass prairie," BioScience, vol. 36, pp.662-668, 1986.

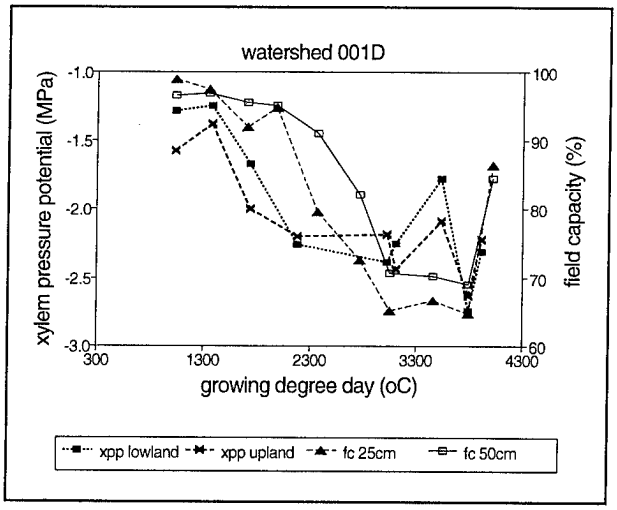


Figure 1

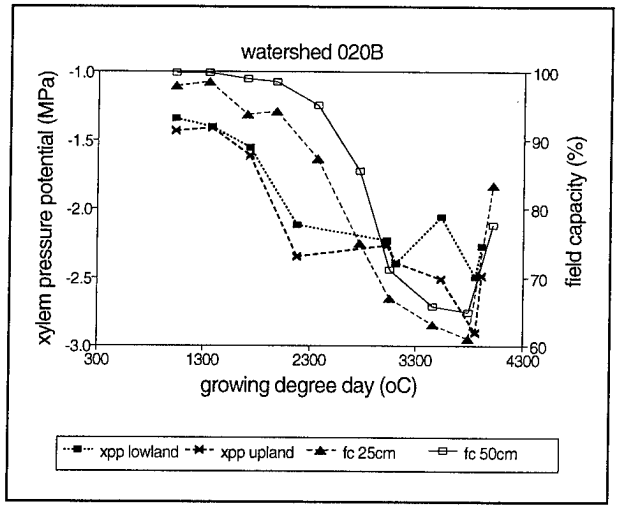


Figure 2

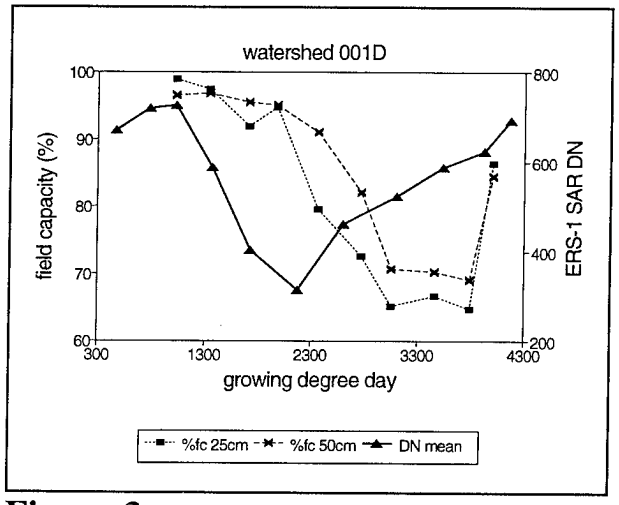


Figure 3

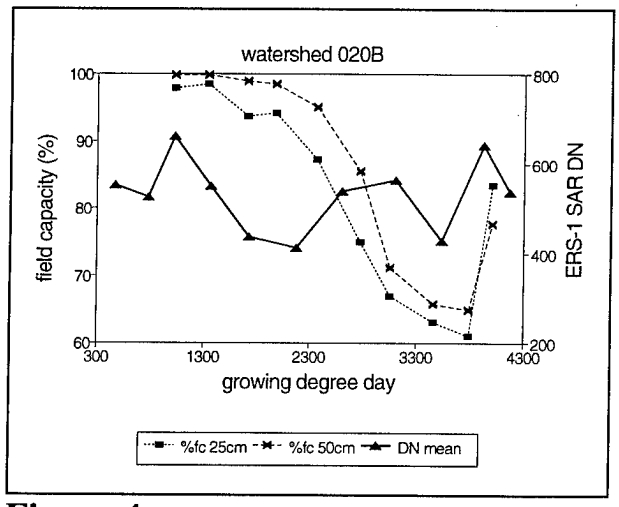


Figure 4

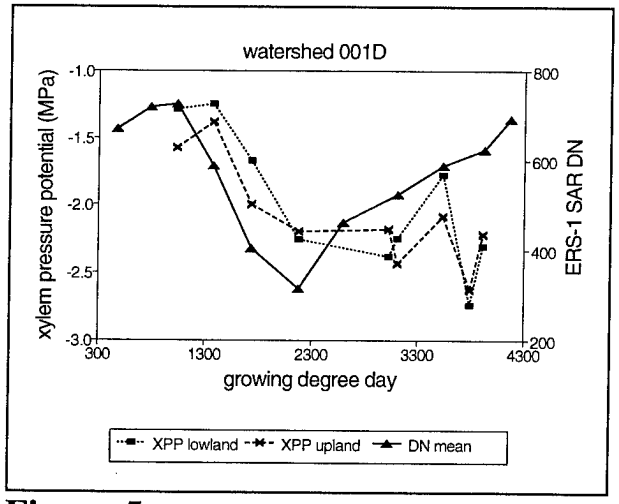


Figure 5

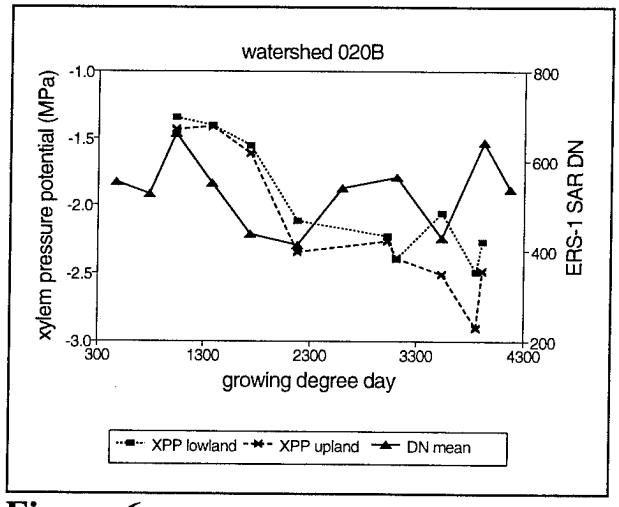


Figure 6

Mapping Methane Emission from Arctic Tundra Using Satellite Data, a Digital Elevation Model, and Discriminant Functions Based on Field Data

Margaret M. Shippert, Department of Geography and Cooperative Institute for Research in Environmental Sciences, University of Colorado, Boulder, Colorado 80309-0216, (303)492-5051, FAX: (303) 492-5070, shippert@crash.colorado.edu

ABSTRACT

Arctic tundra is a significant source of atmospheric methane. The size of this source and its variation across landscapes, however, is uncertain. Images representing environmental variables relevant to methane emission have been derived from satellite data and a digital elevation model. Multivariate functions relating these environmental variables to methane emission have been derived from field data. The images will be combined using these functions into a digital map of methane emission rates within the study area. The map will be used to spatially extrapolate seasonally integrated methane emission values for several vegetation types typical of the study area. The resulting map of seasonal methane emission will incorporate both spatial and temporal variation in more detail than previous emission estimates.

INTRODUCTION

Ice core data indicate that atmospheric methane concentration has more than doubled in the last 200 years, after varying by less than 30% during the previous 10,000 years [1, 2]. During the past decade, however, this rate of increase has declined [3]. Neither the cause of the increase nor the cause of its recent decline are well understood.

Long-wave radiation emitted by the earth is absorbed by greenhouse gases, such as methane, and re-emitted to the atmosphere rather than escaping to space. Concentrations of the various greenhouse gases largely determine the earth's surface temperature. Thus, continued increases in atmospheric methane and other greenhouse gases such as CO_2 are expected to result in global warming [4, 5]. More information about sources and sinks of atmospheric methane is needed, however, to understand the recent trends in atmospheric methane concentration and to predict future concentrations and consequent surface temperatures of the earth.

Methane is a greenhouse gas generated by microorganisms living in anaerobic environments. High latitude wetlands are significant sources of atmospheric methane because organisms that produce methane live in their waterlogged soils. Current global estimates of methane emission from arctic tundra range from 11 to 60 Tg/year, which is 2 to 18% of the total global emission [6, 7, 8]. The large range in these estimates is due to an incomplete understanding of the environmental factors controlling methane emission, the large variability in methane emission in space and time, and the lack of sufficient emission measurements to capture this variability [e.g., 9, 10, 11, 12, 13, 14, 15]. Further investigation of methane emission from arctic tundra is needed to more accurately estimate the size of the methane source from global tundra.

Past estimates of global tundra methane emission have been derived by multiplying the average methane emission measured at arctic tundra field locations by the area of the globe estimated to be covered by tundra [e.g., 16, 17, 18]. These studies use different strategies to account for spatial or temporal variation in methane emission rates within arctic tundra. To calculate a seasonal emission estimate, these global emission rates are then multiplied by the length of the thaw season. However, methane emission in arctic tundra varies significantly over a thaw season [16, 17, 18]. W. Reeburgh at the University of California at Irvine is currently addressing this question of temporal variation in tundra methane emission by collecting seasonally integrated methane emission data in several tundra types near Toolik Lake, in arctic Alaska. Reeburgh chose sampling sites typical of large areas of the Kuparuk River basin. These sites are located in areas with high, medium, and low emission rates. To extrapolate local methane emission data to landscape or regional scales, data quantifying the spatial and temporal variation in methane emission rates must be acquired and considered.

A MAP OF METHANE EMISSION FROM THE STUDY AREA

The overall objective of this project is to derive for an arctic tundra landscape a digital methane emission map that uses the most accurate data available regarding temporal and spatial variation in emission. This methane emission map will be derived using images representing relevant environmental variables. The images will be combined using discriminant functions derived from field measurements of these environmental variables and methane emission rates. The resulting map will represent emission at one point in time. It will subsequently be used to spatially extrapolate field measurements, collected by W. Reeburgh, of total methane emission from a whole growing season. This map of seasonal methane emission rates will be used to estimate

Support for this work is provided by NASA grant NGT-30266. Previous work was supported by NSF /OPP grant 9214959. SAR data was provided by NASA through the Alaska SAR Facility.

0-7803-3068-4/96$5.00©1996 IEEE

the total yearly value of methane emitted to the atmosphere from the study area.

STUDY AREA

The study area for this project is in the Kuparuk River watershed in the northern foothills of the Brooks Range in arctic Alaska. It includes Toolik Lake, which is the site of a research station operated by the Institute for Arctic Biology at the University of Alaska in Fairbanks. The vegetation includes tussock tundra, riparian shrublands, wet sedge meadows and upland heath communities. It is broadly representative of a much larger area of Alaskan arctic tundra.

IMAGES OF ENVIRONMENTAL VARIABLES

A SPOT (Systeme pour l'Observation de la Terre) image was used to calculate an image of the normalized difference vegetation index (NDVI) for the study area. A vegetation biomass image was derived from this NDVI image using an empirical relationship between field measurements of NDVI and aboveground vegetation biomass [19]. Field spectra were collected using a Personal Spectrometer II (Analytical Spectral Devices, Boulder, CO). Systematic differences between field and image NDVI were accounted for using an empirical relationship determined for broad vegetation categories [19]. The areas of different vegetation categories were identified in the image using a vegetation map of the study area [20].

A soil moisture image was derived from an ERS-1 (European Remote-Sensing Satellite 1) synthetic aperture radar (SAR) image for August 28, 1994, using an empirical relationship developed by Doug Kane and others at the University of Alaska between the SAR signal and soil moisture measured in the field:

$$V_{pixel} = 1.17*M + 115 \qquad R^2 = 0.50$$

where V_{pixel} is the value from a pixel in the SAR image, and M is the volumetric soil moisture [21]. Before this equation was applied to the ERS-1 image values, geometric and radiometric (incidence angle) corrections were applied.

To derive information about the spatial distribution of standing water in the study area, spectral mixture analysis was performed on the SPOT multispectral image. The dark endmember in this analysis is interpreted to correspond to standing water, topographic shade, and shadows within vegetation. A correction utilizing information from the biomass image was applied to minimize the contribution of shadows within vegetation. Additional corrections were applied to minimize the effects of topographic shade.

An image of cumulative net solar radiation late in the growing season will be derived from a digital elevation model of the study area. The relationship between cumulative net solar radiation over a growing season and soil temperature will be determined in the field during the summer of 1996. If significant, this relationship will be used to derive a soil temperature image from the net solar radiation image.

AN ALGORITHM FOR COMBINING ENVIRONMENTAL VARIABLES

Soil moisture, soil temperature, soil pH, aspect, slope, and aboveground vegetation biomass were measured at 62 points in the field for this study. Discriminant analysis using all data points resulted in functions that accurately predict methane emission rate classes for 88% of the sampling points (Table 1). When data are separated into two groups, with one group including sites that were inundated with water at the time of measurement, and one group including sites that were not, and separate discriminant functions derived for these two groups, emission categories for 92% of the sampling points are correctly predicted (Table 1). These functions require only soil moisture and soil temperature values. Biomass data have not yet been considered in this analysis. Emission rate classes used are low (less than 19 mg/m^2/day), medium (19 to 60 mg/m^2/day) and high (greater than 60 mg/m^2/day).

CONCLUSIONS

Equations that accurately predict methane emission rates from environmental conditions in the study area have been derived from field data. Images representing relevant environmental variables at the peak of the growing season have been generated. These images will be combined using the equations that predict emission rates to derive a digital map of methane emission rates in the study area. This map will be used to extrapolate field measurements of seasonal methane emission.

Table 1. Discriminant functions for the three emission rate classes. M=volumetric soil moisture (%), T=soil temperature (°C) at 14 cm depth.

All data	
low	-9.61 + 21.94*M + 1.53*T
med.	-19.93 + 30.00*M + 2.20*T
high	-19.74 + 31.37*M + 1.95*T
Inundated	
low	-21.43 + 45.57*M - 1.50*T
med.	-13.59 + 27.98*M + 0.38*T
high	-18.96 + 43.08*M - 0.93*T
Not inundated	
low	-14.41 + 33.76*M + 2.42*T
med.	-28.98 + 46.01*M + 3.33*T
high	-10.39 + 23.37*M + 1.52*T

ACKNOWLEDGMENTS

The author thanks W. Reeburgh, D. Walker, D. Kane and L. Hinzman for sharing unpublished results from their work in the study area, and R. Guritz for performing terrain and incidence angle corrections on the SAR data.

REFERENCES

[1] R.A. Rasmussen and M.A.K. Khalil, "Atmospheric methane in the recent and ancient atmospheres," Journal of Geophysical Research, vol. 89, pp. 11,599-11,605, December 1984.

[2] T. Blunier, J. Chappellaz, J. Schwander, B. Stauffer, and D. Raynaud, "Variations in atmospheric methane concentration during the Holocene epoch," Nature, vol. 374(2), pp. 46-49, March 1995.

[3] E. J. Dlugokencky, K.A. Masaire, P.M. Lang, P.P. Tans, L.P. Steele, and E.G. Nisbet, "A dramatic decrease in the growth rate of atmospheric methane in the northern hemisphere during 1992," Geophysical Research Letters, vol. 21(1), pp. 45-48, January 1994.

[4] I. Fung, J. John, J. Lerner, E. Matthews, M. Prather, L. Steele, and P. Fraser, "Three-dimensional model synthesis of the global methane cycle," Journal of Geophysical Research, vol. 96(D7), pp. 13,033-13,065, July 1991.

[5] K.P. Shine, R.G. Derwent, D.J. Wuebbles, and J-J. Morcrette, "Radiative forcing of climate," in Climate Change, The IPCC Scientific Assessment J.T. Houghton, G.J. Jenkins and J.J. Ephraums, Eds. Cambridge: Cambridge University Press, 1990, pp. 41-68.

[6] S.C. Tyler, "The global methane budget," in Microbial Production and Consumption of Greenhouse Gases J.E. Rogers and W.B. Whitman, Eds. Washington, D.C.: American Society for Microbiology, 1993, pp. 7-38.

[7] R.J. Cicerone and R.S. Oremland, "Biogeochemical aspects of atmospheric methane," Global Biogeochemical Cycles, vol. 2, pp. 299-327, December 1988. .

[8] I. Aselmann and P.J. Crutzen, "Global distribution of natural freshwater wetlands and rice paddies, their net primary productivity, seasonality and possible methane emissions," Journal of Atmospheric Chemistry, vol. 8, pp. 307-358, May 1989.

[9] P.M. Crill K.B. Bartlett, R.C. Harriss, E. Gorham, E.S. Verry, D.I. Sebacher, L. Madzer, and W. Sanner, "Methane flux from Minnesota peatlands," Global Biogeochemical Cycles, vol. 2, pp. 371-384, 1988.

[10] T.R. Moore and R. Knowles, "Methane emissions from fen, bog and swamp peatlands in Quebec," Biogeochemistry, vol. 11, pp. 45-61, September 1990.

[11] D.S. Bartlett, P.M. Crill, R.L. Sass, R.C. Harriss, and N.B. Dise, "Methane emissions from tundra environments in the Yukon-Kuskokwim Delta, Alaska," Journal of Geophysical Research, vol. 97(D15), pp. 16,645-16,660, October 1992.

[12] L.A. Morrissey and G.P. Livingston, "Methane emissions from Alaskan Arctic tundra: an assessment of local spatial variability," Journal of Geophysical Research, vol. 97, pp. 16,661-16,670, October 1992.

[13] J.L. Bubier, T.R. Moore, and N.T. Roulet, "Methane emissions from wetlands in the midboreal region of Northern Ontario, Canada," Ecology, vol. 74(8), pp. 2240-2254, December 1993.

[14] M.S. Torn and F. S. Chapin, III, "Environmental and biotic controls over methane flux from arctic tundra," Chemosphere, vol. 26(1-4), pp. 357-368, January 1993.

[15] N.B. Dise, "Methane emission from Minnesota peatlands: spatial and seasonal variability," Global Biogeochemical Cycles, vol. 7, pp. 123-142, March 1993.

[16] W.S. Reeburgh and S.C. Whalen, "High-latitude ecosystems as CH_4 sources," Ecological Bulletins, vol. 42, pp. 62-70, 1992.

[17] S.C. Whalen and W.S. Reeburgh, "Interannual variations in tundra methane emissions: a 4-year time series at fixed sites," Global Biogeochemical Cycles, vol. 6, pp. 139-159, June 1992.

[18] T.R. Christensen, "Methane emission from Arctic tundra," Biogeochemistry, vol. 21, pp. 117-139, 1993.

[19] M.M. Shippert, D.A. Walker, N.A. Auerbach, and B.E. Lewis, "Biomass and leaf-area index maps derived from SPOT images for Toolik Lake and Imnavait Creek areas, Alaska," Polar Record, vol.31(177), pp. 147-154, 1995.

[20] D. A. Walker, unpublished.

[21] D.L. Kane, L.D. Hinzman, J.Yu, and D.J. Goering, "The use of SAR satellite imagery to measure active layer moisture contents in arctic Alaska," unpublished.

"Water Content Influence on Scattering Properties of Vegetation Cover"

A.N.Roenko, Yu.F.Vasilyev, B.D.Zamaraev, V.L.Kostina.

Institute of Radiophysics and Electronics of National Academy of Sciences of Ukraine
Address: Proskura St.12, Kharkov 310085, UKRAINE.
Telephone: 0572-44-85-65.
Fax: 0572-44-11-05.
E-mail: yura@ire.kharkov.ua.

The problem of the influence of the parameters of underlying cover on its scattering properties is of a great interest of investigators. Most of all this is due to the possibility of receiveing a great economic benefit in the case of truly estimation and prediction of the state of vegetation covers, throught they are agricultural crops or other kinds of vegetation. The known theoretical models sometimes do not give a sutisfactory coincidence with experimental results. It may be explained by the variety of kinds of earth covers, by different approaches in development of theoretical models, by distinctions of methodics of receiveing an experimental data and for millimeter and submillimeter waves - by a small quantity of experimental data.

In proposed paper the analysis of influence of the parameters of underlying cover, such as vegetation water content and water content of the upper layer of soil, on scattering of millimeter waves is given.

Vegetation Canopy Model.

At present many different models of vegetation canopy are used. To our opinion, in some cases, one of the most convinient is the "cloud" model of vegetation canopy [1]. A great advantage of this model consists in its sufficient simplicity and physical base, and at the same time in quite enough accuracy of estimation and prediction the real values of backscattering coefficients of different vegetation covers. A detailed description of the model is given in [2]. According to this model

$$\sigma^{\circ}_{can}(\theta) = \sigma^{\circ}_{veg}(\theta) + \sigma^{\circ}_{soil}(\theta) =$$

$$= f(N)\cos\theta[1-\gamma^{2}(\theta)]+\gamma^{2}(\theta)C_{s}(\theta)m_{s}, \qquad (1)$$

where $\sigma^{\circ}_{veg}(\theta)$ - is the contribution of vegetation volume;
$\sigma^{\circ}_{soil}(\theta)$ - is the backscattering contribution of the soil surface in presence of vegetation cover;
θ - is angle of incidence relative to nadir;
$f(N) = \sigma_{v}/2k_{e}$ - is the function , depends from the density of the cover (the quantity of the particles N in a volume unit), and from the size, shape and orientation-distribution of the particles;
σ_{v} - canopy volume backscattering coefficient (m^{-1});
k_{e} - extinction coefficient (m^{-1});
$\gamma^{2}(\theta) = \exp(-2k_{e}h\,\mathrm{Sec}\theta)$ - is the two-way transmittance of the canopy (m^{2}/m^{2});
h - canopy height(m);
$C_{s}(\theta)$ - is a constant for a given wavelength and polarization configuration, and soil's surface roughness;
m_{s} - is a soil moisture content.

0-7803-3068-4/96$5.00©1996 IEEE

Description of Experiments.

Detailed description of measurement equipment and technique is given in [3]. But according to conducted measurements [3], [4] this time as a control parameters of vegetation cover water content of vegetation, the quantity of dry biomass, soil water content were chosen. A 35GHz ground-based scatterometer was used to measure σ°, at vertical polarization, angle of incidence of 40 degrees, one time a day – in the morning, five times a week. In order to determine water contents the samples of vegetation and soil were taken twice a week. It's explained by restricted sizes of investigated area, covered with vegetation. For determination the vegetation water content plants at five randomly located sites, each with a square of $1dm^2$, were cut at ground level and carefully placed in plastics bags to avoid losing any internal or surface water. These samples were analized gravimetrically for total plant moisture. Then the averaged value of water content was calculated. Similarly, the values of soil moisture were determined and averaged value was calculated.

Results of Experiments.

According to described model we may write that

$$\sigma^\circ_{can}(\theta) = \sigma^\circ_{veg}(\theta) + \sigma^\circ_{soil}(\theta),$$

although at angles of incidence $\theta \geq 40^\circ$,in the cases of rather thick covers, we may asssume that

$$\sigma^\circ_{veg} \gg \sigma^\circ_{soil},$$

and the influence of the soil is rather negligible. But in 1994 at the investigated area the grass cover was rather thin, and even visually it was determined the transparance of the cover and the influence of the soil on backscattering signal.

In practice sometimes, it's very difficult to define exactly some parameters of the cover, i.e. σ_v, k_e and C_s, so the formula (1) is not convinient enough. So, assume that σ°_{veg} and σ°_{soil} are given in the following forms

$$\sigma^\circ_{veg} = K(1-e^{-\beta\Delta}) \qquad (2),$$

$$\sigma^\circ_{soil} = Me^{-\beta\Delta} \qquad (3),$$

where $\Delta(g/dm^2)$ – is the water content of the canopy per unit area.

This assumption is based on the supposition that parameter $e^{-\beta\Delta}$ is proportional to γ^2; factor K – to the function f(N) and factor M – to $C_s m_s$; i.e. the main influence on backscattering of the cover is made by the water contents of vegetation and soil (during the investigations upon one site of the landscape the surface geometry is practically constant). The angular dependence we will miss, because we examine the received experimental dependence at fixed angle of incidence $\theta=40^\circ$, although this angular dependence in general may be taken into account.

Let examine the coefficients K and M in detailes. We may rename them as a weight factors and express in the form:

$$K = ke^{c\Delta}, \qquad (4)$$

$$M = me^{dW}, \qquad (5)$$

where c, d, k and m – constants,
W – soil moisture.

The reasons of such selection are as follows:
1) for our opinion function f(N) depends not only upon the factors noted in [2], but also on water content of the cover Δ, since at

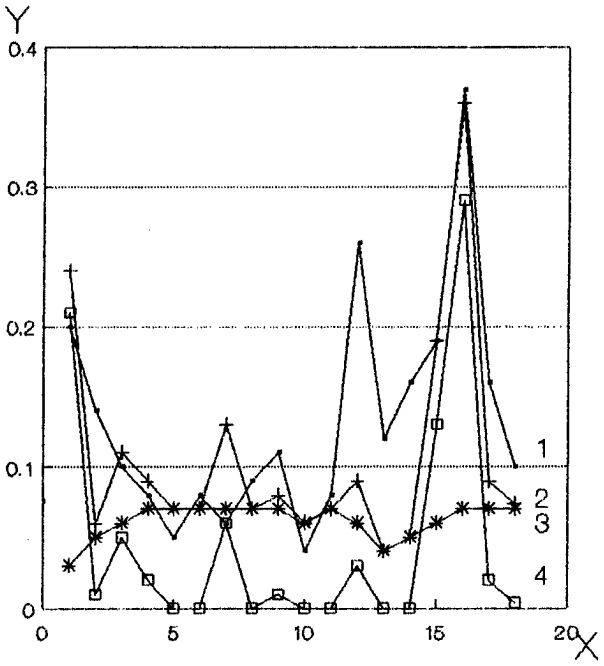


Fig.1

small values of ε k_e is proportional to Δ;
2) the technique of the measurements gives more reliability for big deviation of investigated parameter, but not for small ones, which are compared with the error of measurements, and the exponential function emphasizes the big changes of investigated parameters, but the small fluctuations, which are the result of receiver noise, small errors of experiments - to a lesser extent. So, we may write:

$$\sigma^{\circ}_{can} = \sigma^{\circ}_{veg} + \sigma^{\circ}_{soil} =$$

$$= ke^{c\Delta}(1-e^{-\beta\Delta}) + me^{dW}e^{-\beta\Delta}, \qquad (6)$$

Expression (6) includes two physical parameters and five coefficients - c,d,k,m and β.Their values were defined using the least-squares technique, as a criterion - the minimum of divergence of averaged values and maximum of correlation between measured and calculated values were taken. So, the defined values of coefficients are as follows:

$$c = 0,\ d = 0.5,\ k = 0.5,$$

$$m = 5/10^5,\ \beta = 1/3.$$

The correlation coefficient between calculated according formula (6) σ°_{can} and experimental σ°_{can} is 0.76. Fig.1 presents the received experimental σ°_{can}(1) and calculated σ°_{can}(2) dependences and also calculated σ°_{veg}(3) and σ°_{soil}(4). On X-axis the experiment days numbers are plotted, and on Y-axis - relative values of σ°.

So, conducted experimental measurements confirm the using of "cloud" model for some kinds of covers, for example for grass cover.

References.

[1] E.P.W.Attema and F.T.Ulaby "Vegetation Modeled as a Water Cloud", "Radio Science" 13/2/1978, p.357-364.

[2] F.T.Ulaby, C.T.Allen and G.Eger III "Relating the Microwave Backscattering Coefficient to Leaf Area Index", "Remote Sensing of Environment",14, p.113-133, 1984.

[3] F.V.Kivva, B.D.Zamaraev, Yu.F.Vasilyev, A.N.Roenko "Angular and Seasonal Dependences of the Backscattering Coefficients From Vegetation at 35 GHz", Turkish journal of Physics v.19, No.8, 1995.

[4] F.V.Kivva, A.N.Roenko B.D.Zamaraev, Yu.F.Vasilyev "Correlation Between Backscattering Coefficient and Vegetation Water Content" Turkish journal of Physics v.19, No.10, 1995.

EXPERIMENTAL STUDY OF FIRE RISK BY MEANS OF PASSIVE MICROWAVE AND INFRARED REMOTE SENSING METHODS

Dr. Boris Liberman, Dr. Alexander Grankov, Alexander Milshin, Sergey Golovachev
Institute of Radioengineering and Electronics, Russian Academy of Sciences,
Friazino, Russia Institute of Geoinformatics, Ltd., Friazino, Russia
141120 Friazino, Moscow reg., Vvedensky sq. 1, IRE RAS
Tel. (007-095) 526-91-50, Fax. (007-09656) 4-52-30. Email: bml246@ire216.msk.su

Dr. Valery Vishniakov
Designing bureau "SALUT" of State Scientific and Industrial Center, named after Hrunichev,
Novozavodskaya str., 18, 123290, Moscow, Russia
Tel. (007-097) 142-50-11

ABSTRACT

Some results of experimental testing of fire risk by means of passive microwave and infrared remote sensing methods in the forests of Moscow region are presented. Used equipment, procedure of measurements, some results of processing are described. The intercorrelation between natural fire risk and remotely obtained data is studied. It is shown, that passive microwave and infrared remote sensing methods can be used for the classification of forest state.

INTRODUCTION

Remote sensing (RS) methods (from the board of satellites, aircrafts, etc.) played now very important role in forest state monitoring, give possibility of its seasonal and year dynamics study. Now optical and infrared RS means are used for solving of different forest problems, for example, illnesses, fire detection, degradation after fire, etc.[1]

It was shown theoretically and by experiments, that radiophysical methods are very effective for "soil - canopy system" study [2, 3].

The screen influence of the forest cover on the RS determination of soil moisture in the forests, relationships between microwave radiation and number of forest parameters, statistics of forest radiation in different waveranges from the fire risk determination point of view were studied [4, 5].

The experiments on fire risk determination were conducted jointly by Institute of Geoinformatics, LTD, Institute of RadioEngineering and Electronics, RAS, Designing bureau "SALUT" of State Scientific and Industrial Center, named after Hrunichev together with forestry service of Moscow region.

The natural fire risk was used as a parameter for remote sensing determination. Natural fire risk is more or less stable parameter, which depends firs of all on trees and soil types, ground water level, relief and some other data, which in some meteorological conditions increased the probability of fire appearance and propagation.,

REGION OF EXPERIMENTS. METEO CONDITIONS. EQUIPMENT. PROCEDURE OF MEASUREMENTS.

Experiments were conducted in Shatura and Egorievsk regions of Moscow regions. The coniferous,

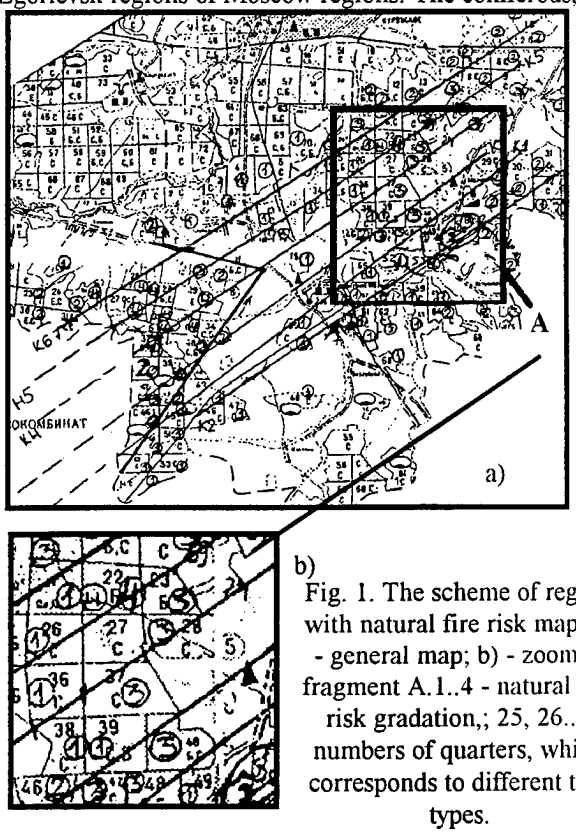


Fig. 1. The scheme of region with natural fire risk map. a) - general map; b) - zoomed fragment A.1..4 - natural fire risk gradation,; 25, 26.. - numbers of quarters, which corresponds to different tree types.

0-7803-3068-4/96$5.00©1996 IEEE

deciduous and mixture forests with general area about 500 sq. km were studied. The scheme of region with natural fire risk map, obtained from the forest service is given on Fig.1a. The zoomed fragment "A" of this region is presented on Fig.1b. The region was characterized by presence of different tree types, bushes, marshes, peatbogs, etc.

Air temperature at the testing region varies from + (23 - 24° C) in ground layer till +(10 - 12° C) on the 1500 m height. There were some cumulus clouds above test region. There were no raining for about 1 week before the measurements.

The base of used equipment were microwave radiometers, elaborated and manufactured in Institute of Geoinformatics, Ltd. Main characteristics of used equipment is given in Table 1. All passive microwave and infrared radiometers were trace type, portable and light and in principle are ready for installation on any platform. During described experiment airplane AN-2 was used. The antennas were nadir looking. For decimeter radiometers were used microstrip antenna. Centimeter radiometer use horn.

Table 1

Trace MCW radiometers	
Waverange, cm	2.25, 21, 27
Operating range, K	10 - 350
Sensitivity with integration time 1 S, K	0.1
Integration time, S	0.5
Output signal, (analog form)	- 5...+5
Supply voltage, V	27 (+7,-4)
Power supply, VA	<30
Weight, Kg	6
Spatial resolution, degrees	35
2-channel trace IR radiometer	
Waveranges, mkm	8 - 12
Sensitivity, K	0.1
Spatial resolution, degrees	3

All information was recorded on the IBM PC compatible computer.

Experiment procedure includes measurements along the flight lines on different altitudes (from 70 till 1500) and thematic mapping from 200 m height.

RESULTS AND DISCUSSION

The spatial distribution of microwave radiation in decimeter and centimeter waveranges was compared with variations of natural fire risk along the flight lines. The example of mentioned comparison for the trace 2 are presented as two - dimensioned diagram (Fig. 2). It's one of the best versions, when MCW clusters , which corresponds to different fire danger degrees are really separated.

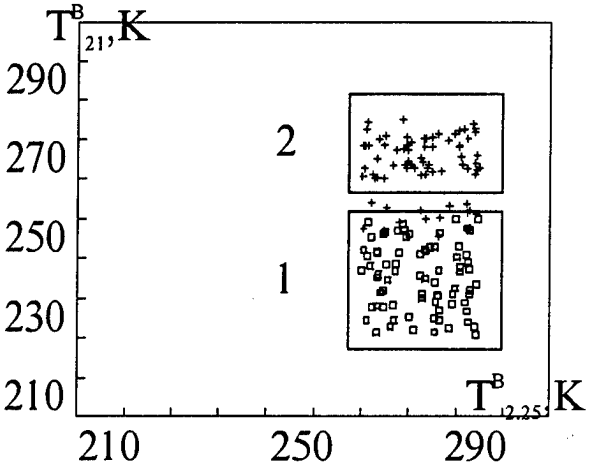


Fig. 2. The results of comparison between microwave radiation on centimeter (2.25 cm) and decimeter (21 cm) wavelengths, obtained along the trace 2 (Moscow region,, 23.09.1994). 1 - first class of fire danger; 2 - second class of fire danger.

The joint processing of IR radiation spatial distribution and microwave radiation on the 21 cm wavelength in marked regions (A, B, C, D, E, F) on tested region with really different fire risk degree was done.

The examples of thermodynamic (Fig. 3) and microwave (Fig. 4) maps were used. The regions A and B - are characterizes by high level of fire danger (3, 4); C, D and E - corresponds to minimum level of fire risk (1, 2); F - is free of forest cover.

The results of comparison between calculated value

$$r = 1 - T_{IR}/T^B_{21}$$

and thermodynamic temperature T_{IR}, obtained using IR radiometer are presented on Fig. 5.

As it's well seen from the figure, there is good correlation between chosen regions on fig.5 and fire risk gradations.

CONCLUSION

Obtained results shows the principle possibility of nonscanned passive microwave and IR remote sensing methods application for heat and water exchange processes monitoring, which is directly connected with fire danger. It was shown, that for mentioned above region good correlation

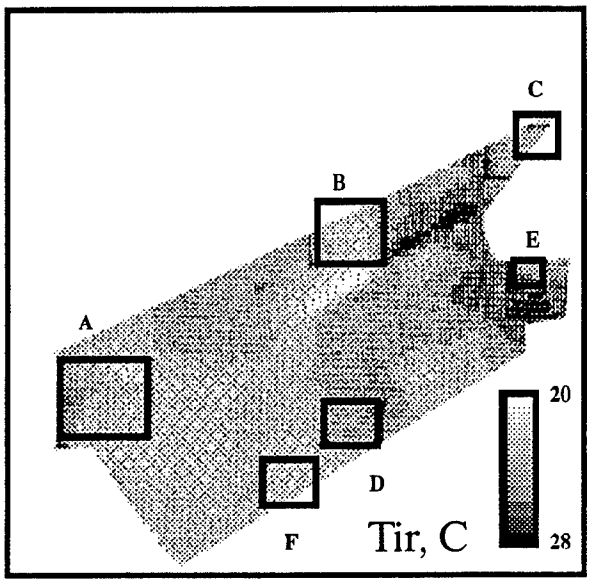


Fig. 3. The thermodynamic temperature map of the tested forest region. 24.09.1994.

between natural fire risk and MCW and IR radiation intensity variations took place. These conclusions coincides with the same, obtained during experiments in another regions of Europe (East and West Germany, Poland, Belorussia), but for the last decision about mentioned methods application and for elaboration of software for remote sensing fire risk determination it's necessary to continue theoretical study and experiments in different conditions and climatic zones.

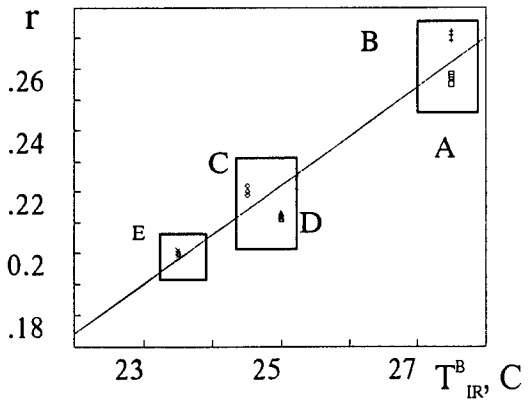


Fig. 5. The relationships between MCW and IR radiation intensity variations and natural fire risk degree. A, B - 3, 4 degree of fire risk; C, D, E - 1, 2.

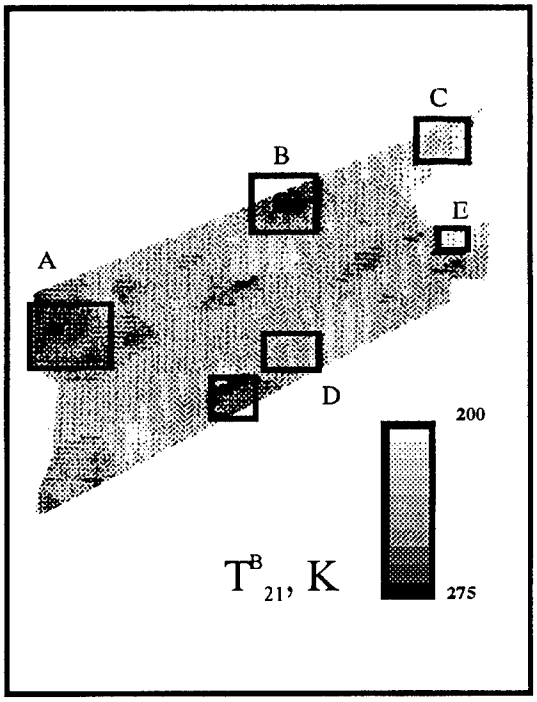


Fig. 4. The radiobrightness temperature map of the tested forest region. Waverange 21 cm. 24.09.1994.

REFERENCES

[1] V. V. Kozoderov, V. S. Kosolapov, "New applications of air-satellite measurements for the forest ecosystems study", Issledovaniya Zemli iz Cosmosa, 1994, v. 4, 68 - 80 (translation).

[2] A. M. Shutko, "Microwave radiometry of water surface and grounds, "Moscow, Publishing House Nauka, 1986, p.189, (English translation).

[3] A. A. Chuhlantsev, S. P. Golovachev, "Attenuation of Microwave radiation in canopy cover", Radiotechnika i Electronica, 1989, v 11, 2269 - 2278 (English translation).

[4] A. G. Grankov, B. M. Liberman, A. M. Shutko, " Spectral passive microwave remote sensing method of natural objects classification and some results of its applications," Metodi i sredstva obrabotky signalov, Moscow, 1987, 17 - 28.

[5] K. P. Kirdiashev, V. P. Savorsky, "On the statistic estimation of fire risk using thermal radiation measurements," Radiotechnika i Electronica, 1989, v 11, 2269 - 2278 (English translation).

"Investigation and Cataloguezation of Backscattering Characteristics of Different Earth Covers in Millimeter Wave Band"

Yu.F.Vasilyev, B.D.Zamaraev, V.L.Kostina, A.N.Roenko.

Institute of Radiophysics and Electronics of National Academy of Sciences of Ukraine
Address: Proskura St.12, Kharkov 310085, UKRAINE.
Telephone: 0572-44-85-65.
Fax: 0572-44-11-05.
E-mail: yura@ire.kharkov.ua.

Radar methods, using mm-waves, allow to solve by one hand different agricultural problems, such as controlling the state of agricultural crops, the state of gidrological, irrigation systems, determining of water and salt contents of the soil, and by other hand - such technical problems, as designing of the navigational systems of the flying vehicles, which use radar images of different landscapes and radar features of separate elements according to background landscape.

The problems at this scientific direction have a spesific features for each concrete task. So, if anybody wants to control the state of agricultural crops during the period of plant growth, it's necessary to know all possible data about links of signal parameters with changeable characteristics of surface and vegetation cover (water content, plant growth stage, etc); but for designing of navigational systems it's necessary to know the most conservative and invariant under seasonal and weather conditions characteristics of landscapes.

Nowadays, the large quantity of theoretical and experimental data on backscattering characteristics of different Earth surfaces, both natural and artificial, is accumulated. But the application of this data for purposes of developing the remote sensing and navigational systems is rather difficult, because the theoretical models use rather rough and unadequate methods of interaction of mm-waves with different objects, and the experimental investigations were made at various seasonal and weather conditions and according to different methodics. Most of all, making the procedure of determining the backscattering characteristics, it's necessary to measure with high accuracy the amplitude of the signals and to make equipment calibration on standart reflectors. For this purpose it's necessary to ensure the high spartial selection of backscattering signals. All these problems, at random distributed signals, are connected with some difficulties, particularly when the airborne radar systems are used.

These circumstances require the necessity of conducting the cycle of measurements of backscattering properties of different Earth surfaces in mm-wave band in order to create the catalogue of backscattering characteristics of different Earth covers, both natural and artificial, as a universal data base for all-weather navigational systems. It was determined, that the catalogue must include all typical objects of Earth surfaces and will be created in general according to experimental data. Theoretical results may be used only for summarising and approximation of experimental data, for example, to other wave length, angles of incidence and so on. For receiveing the experimental data the single methodic may be used, which allows to reproduce the conditions of experiments and to

0-7803-3068-4/96$5.00©1996 IEEE

Table No.1

No.	Surface	$\sigma^{\circ}(0^{\circ})$	$\sigma^{\circ}(0^{\circ})$ (dB)	$D_{\sigma^{\circ}}(0^{\circ})$ (dB)	$\sigma^{\circ}(40^{\circ})$ (dB)
1	Water surface (calm)	50	17	∓3	-17
2	Ice, covered with snow	1.0	0	∓5	-11
3	Concrete surface (clean run-way)	10	10	∓2	-17
4	Concrete surface, covered with snow	1.0	0	∓5	-11
5	Field (september - january)	0.6	2	∓5	-10
6	Field (february)	4.0	6	∓1	-11
7	Field (march)	1.5	2	∓4	-11
8	Field (april - may)	0.15	-8	∓2	-11
9	Field (june - august)	0.3	-5	∓3	-7

compare the results on the base of multiyear measured data, which embrace all seasonal, weather conditions by the sufficient statistical reliability.

According to this structure the catalogue must be the seasonal one. For each object it must include the experimental data for three seasons - winter, summer and transitional one. All typical objects, included in the catalogue, are devided into three classes - surface-distributed, linear-distributed and dotted, in the scale of resolution element. So, the catalogue consists of 9 tables (3 seasons • 3 types of objects). Each table, except the values of backscattering intensity from typical objects, includes the accuracy value of their determination for concrete season, angular and azimuth dependences and also some parameters of this objects. This tables make it possible for each type of landscape, with known kinds of objects, quikly determine and take a decision about possibility of using concrete navigational system.

For experimental investigations two radar systems were made. First ground-based scatterometer, second airborne side-scan radar. The calibration of ground-based scatterometer was made upon the metalic cylinder of "infinite" length, and the airborne equipment was calibrated on concrete surface, using methodics from [2].

For example, table No.1 presents some values of backscattering intensity for different Earth surfaces, received in mm-wave band on geographical latitude of Central Russia.

References.

[1] Yu.A.Melnik "Radar methods of Earth investigation",Sov.radio 1980, p.264.

[2] Yu.F.Vasilyev, B.D.Zamaraev V.G.Kolesnikov "Application of concrete surface as a standard one during the measurements with airborne radar", "Propagation and diffraction of radiowaves", Naukova dumka, Kiev, 1984.

Classification of multi-source data using predictive ability measure

C C Chong J C Jia
ed2624874@ntuvax.ntu.ac.sg ejjia@ntuvax.ntu.ac.sg
School of Electrical and Electronic Engineering
Nanyang Technological University, Nanyang Avenue, Singapore 2263

ABSTRACT

The predictive ability of an evidence source for an uncertain event is referred to the ability of the evidence source to predict the probability of the event concerned. A new algorithm which incorporates the predictive ability of the multi-source data into the classification process is presented. The algorithm was developed based on the concept of second-order probability. Experimental results obtained show that the new algorithm outperformed the conventional multivariated Gaussian maximum likelihood classifier when applied to untrained test data. It is also shown to be more consistent in performance.

1 INTRODUCTION

Classification of remotely sensed images is typically done by applying a decision rule to each pixel and classifying it based on spectral information. To further improve classification accuracies, researchers had proposed the use of ancillary data, such as the texture and topographic information. When using this multi-source data for classification, different evidence sources usually exhibit different merit in identifying different classes. That is, the predictive ability of each evidence source varies across the individual class. The differences in predictive abilities can affect the outcome of the inferencing process disproportionately and consequently increase classification error. This means that the evidence sources need to be weighted, for different classes, according to their predictive abilities.

One fundamental assumption when using most conventional approaches for classification is that the probability distribution obtained from each evidence source can be represented by "perfect" point values defined over the possible set of propositions. The main problem of this assumption is that it neglects the differences in the predictive abilities of the evidence sources in different decision situation, since such differences cannot be captured by the point probability distribution [4, page 242].

Existing methods to incorporate the qualities (or reliability) of the evidence sources, for classification of remotely sensed images, include the Bayesian approach proposed by Lee *et al.* and Benediktsson *et al.* [5, 1], where reliabilities of the evidence sources are incorporated into the classification process. Another method proposed by Lee *et al.* [5] is an evidential calculus approach based on the Dempster-Shafer theory. These approaches although successfully incorporated the reliability into the classification process. It, however, does not take into account the differences in reliability of the evidence source for different classes. Further more, the Bayesian approach described does not generate a resultant reliability.

2 THE PREDICTIVE ABILITY APPROACH

Let $\beta_{i,j}$ be a measure quantity of the predictive ability of source e_i for class w_j. It can take on any value between 0 and 1, ranging from 'no' predictive ability to 'perfect' predictive ability.

To obtain the measure quantity of the predictive ability, one possibility is to obtain the classification accuracy of an evidence source using the training samples. That is, from the training samples, if the classification accuracy of evidence source e_i is high for class w_j, then the predictive ability $\beta_{i,j}$ is high, and vice-versa. Using the training samples we can also derived the predictive ability using other statistical measures such as separability measure and error in class modelling. Although, the concepts consider in these approaches are similar to to some of those described in [5, 1] for the estimation of reliability. The reliability obtained from these statistical measures, however, represents the overall 'quality' of the entire source. It does not indicate how the quality is distributed across the individual classes. The sources could, and frequently do, exhibit drastically differing quality for different classes. In contrast, the approach considered here explicitly determine the quality (predictive ability) of the evidence source for estimating the probability of each class.

2.2 Second Order Probability

Suppose that there are m evidence sources, $E_m : e_1, .., e_i, .., e_m$, which bear information in terms of the probability distributions define over a sample space of $\Omega : w_1, .., w_j, .., w_n$. During classification process, these probability distributions, $P_{i,j}$, are combined to form a resultant probability distribution over Ω. However, due to the different predictive abilities of each evidence source for different classes, we are not likely to fully commit ourself to the first order probability value, $P_{i,j}$, obtained and excluding its immediate neighbours. Instead, we are more willing to say that "it is *more likely* that the probability of class w_j is $P_{i,j}$". So that at the same time we can also consider its immediate neighbours.

To take into account our "doubt" on the first order probability value, the second order probability approach is proposed. A second order probability, $P(P(w_j/e_i))$, that proposition w_j is true can be defined as "probability of the probability that proposition w_j is true". It allows us to express the predictive ability of the evidence source through the 'variance' of the second order probability distribution function. Consider the graphical display as shown in Fig.1, the x-axis represents the first order probability $P_{i,j}$ defined over class w_j. The actual first order probability value obtained from e_1, say, for class w_j is denoted as $\hat{P}_{1,j}$. Instead of confining ourself to the estimated first order probability $\hat{P}_{1,j}$, we now spread our belief around

0-7803-3068-4/96$5.00©1996 IEEE

$\hat{P}_{1,j}$ through the second order distribution function. Using the Bayesian approach, the second order probability distributions correspond to different sources can be combined as fallow:

$$P(P(w_j)) \propto P(P(w_j|e_1))\ P(P(w_j|e_2))\ ...\ P(P(w_j|e_m)) \quad (1)$$

2.3 Combination of normal distributions

For representational and simple analysis purposes, the Normal distribution function is employed as the second order probability function to represent our belief in the first order probability. The distribution's mean, μ represent the first order probability, $\hat{P}_{i,j}$, and the variance, σ^2, is related to the predictive ability as follow:

$$\sigma^2 = \frac{1-\beta_{i,j}}{\beta_{i,j}}$$

Let normal functions, $N(\hat{P}_{1,j}, \sigma^2_{1,j})$ and $N(\hat{P}_{2,j}, \sigma^2_{1,j})$, represents the information obtained from evidences e_1 and e_2, for class w_j. From Eqn.1, the combination of the two functions using the Bayesian approach [2, page 74] is the normal function $N(\hat{P}_{1\oplus 2,j}, \sigma^2_{1\oplus 2,j})$ where

$$\hat{P}_{1\oplus 2,j} = \sigma^2_{1\oplus 2,j}\left(\frac{\hat{P}_{1,j}}{\sigma^2_{1,j}} + \frac{\hat{P}_{2,j}}{\sigma^2_{2,j}}\right) \quad , \quad \frac{1}{\sigma^2_{1\oplus 2,j}} = \frac{1}{\sigma^2_{1,j}} + \frac{1}{\sigma^2_{2,j}}$$

The subscript, $1 \oplus 2$, represent the resultant from the combination of evidence e_1 and e_2. The combination can be illustrated graphically as shown in Fig.1. Notice that the resultant second order probability distribution, corresponds to the combined evidence $e_{1\oplus 2}$, has a sharper peak than either of the contributing distributions. This corresponds to a gain of information, hence increase in predictive ability, compared to its contributing sources, e_1 and e_2. In the case when $\beta_{2,j} > \beta_{1,j}$, that is e_2 has higher predictive ability than e_1 for class w_j as illustrated by the sharper peak of e_2. The 'mean' of the resultant distribution, $\hat{P}_{1\oplus 2,j}$, is closer to $\hat{P}_{2,j}$ than to $\hat{P}_{1,j}$. This indicates that e_2 has greater inference on the resultant probability, $\hat{P}_{1\oplus 2,j}$, than e_1. It follows that the combination of m evidences, $e_1, e_2, ..., e_m$, results in the following quantities:

$$\hat{P}_{1\oplus 2\oplus ...\oplus m,j} = \sigma^2_{1\oplus 2\oplus ...\oplus m,j} \sum_{i=1}^{m} \frac{\hat{P}_{i,j}}{\sigma^2_{i,j}} \quad (2)$$

$$\frac{1}{\sigma^2_{1\oplus 2\oplus ...\oplus m,j}} = \sum_{i=1}^{m} \frac{1}{\sigma^2_{i,j}} \quad (3)$$

$$\beta_{1\oplus 2\oplus ...\oplus m,j} = \frac{1}{\sigma^2_{1\oplus 2\oplus ...\oplus m,j} + 1} \quad (4)$$

where $\hat{P}_{1\oplus 2\oplus ...\oplus m,j}$, $\sigma^2_{1\oplus 2\oplus ...\oplus m,j}$ and $\beta_{1\oplus 2\oplus ...\oplus m,j}$ are the resultant probability of class w_j, variance and resultant predictive ability, respectively.

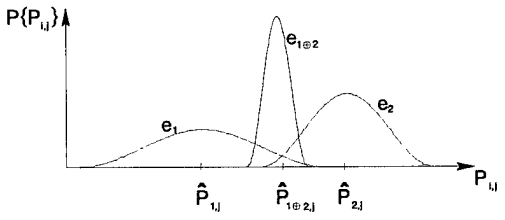


Figure 1: Second order probability distribution.

3 EXPERIMENT

3.1 Data

The classification performances were obtained based on the classification of a study area in the central of Singapore. This area consists of both natural land-cover and several different urban land-use. The data sources used include:

- SPOT HRV data (three channels)
- topographic data - elevation and slope (two channel)
- texture information (one channel)

The three spectral images of the study area are the SPOT HRV satellite images acquired on 4 March 1991. Each image pixel has a spatial resolution of $20m \times 20m$. The topographic data, elevation and slope, were derived from a 1:25,000-scale topographic map with contour interval 10 meters with supplementary contour 5 meter. The resultant elevation and slope data were co-registered with the spectral images. The texture information was extracted from the spectral image (band-1) using the Grey Level Co-Occurrence Matrices (GLCM).

The land-use categories to be classified were split into the following 7 categories:- 1-high density residential, 2-low density residential, 3-commercial, 4-water, 5-grass field, 6-forest and 7-industrial. Two sets of samples, 314 training samples and 500 test samples, were randomly selected from the image. The ground truth required for the evaluation of the classification results was derived from a 1:20,000-scale aerial photograph and a 1:50,000-scale topographical map, supplemented with manual interpretation of the color composite image of the SPOT scene.

3.2 Classifiers

MGML: As a comparison, the Multivariate Gaussian Maximum Likelihood (MGML) classifier was also employed in this experiment. The three ancillary sources were combined with the spectral sources to form a "six-bands" data source. Classification was performed based on the multivariate Gaussian model, which was estimated using the training data.

BUSP: The other classification method used in the experiment was the Bayesian Update of Second order Probability (BUSP), which is referred to the new classification approach proposed in section 2. Due to the difference in inferencing nature of the classification process between BUSP and MGML, the multivariate Gaussian models for the three spectral bands are not suitable for the BUSP when combined with other ancillary sources. Each spectral source was, therefore, treated separately, where data classes from each source were modelled by the gaussian distributions separately. Probability distributions from the other three ancillary sources were obtained directly from their respective normalized histogram of the training data.

To take into account the correlation between the three spectral bands, which is common among spectral information, we modelled the effect of the correlation into the classification process using a correlation factor, ρ. For example, if source e_i is correlated with any other source, its 'inference' will be reduced during the classification process. From Eqn. 2 and Eqn. 3, increasing/decreasing the variance σ^2 of the second order distribution will decrease/increase the inference of an

evidence source. We can, therefore, revised the inference of an evidence source using the correlation factor [3] as follow

$$\sigma_{(new)}^2{}_{i,j} = \sigma_{i,j}^2 \sum_{k=1}^{m} \rho_{i,k} \quad (5)$$

where the correlation $\rho_{i,k}$ between sources e_i and e_k can be derived directly from the correlation matrix.

In this experiment, the predictive ability was derived directly from the classification accuracy of the training samples of each data source for each individual class.

4 RESULTS AND DISCUSSION

Tables 1 and 2 show the classification performances of the two classifiers for the training and test samples, respectively. The classification performances are presented in terms of the overall kappa values and classification accuracy for each individual class.

For the BUSP classifier, three sets of classification performances were obtained. The first set, indicated as 'Perfect', was obtained without the inclusion of the correlation factor and predictive ability. Where we assumed perfect predictive ability with $\beta_{i,j} = 0.9999$ for all i and j. The second set, indicated as 'Correlation', was obtained with the inclusion of the correlation factor but predictive ability was not used. The last set was obtained with the correlation factor and predictive ability, indicated as 'Predictive A.' in the tables.

Without the inclusion of the correlation factor and predictive ability, the BUSP obtained lower classification performances (0.7341, 0.6913) for both training and test samples, as compared to the MGML classifier (0.9118, 0.8358). This is mainly due to the existence of correlation between sources, in particular between spectral band2 and band3, which resulted in over-inference from these correlated sources. When correlation factors were used, classification performances (0.8216, 0.7184) for both training and test samples, although improved, are still relatively lower than that of the MGML. When predictive abilities were used, classification performances of the training and test samples are further improved (0.8908, 0.9020). Although, the training performance is somewhat lower, its test performance outperformed the MGML significantly. Tables 1 and 2 also show that, when predictive abilities were used, classification performances for all the classes are improved.

Results also show that when predictive ability was used, classification performances obtained for both training and test samples are highly consistent. The high consistency in classification performances indicates that the BUSP classifier is robust. In contrast, performances of the MGML decreased significantly when applied to the test samples. This is likely due to the dissimilarity between the test data distribution and the data model assumed. The main different between the BUSP and MGML is that the nature of the inferencing process of the former approach is "additive" which has an "averaging" effect. This has contributed to its robustness and consistency of performance. The nature of the inferencing process of the MGML, on the other hand, is "multiplicative" which has a "reinforcement" effect. Hence, this approach tend to be more sensitive to the distribution model than that of the BUSP approach.

Table 1: Classification results of training data.

	classification accuracies for individual class							
	1	2	3	4	5	6	7	Kappa
MGML	0.85	0.98	0.85	1.00	0.86	0.83	0.94	0.9118
BUSP								
Perfect	0.69	0.81	0.81	0.97	0.93	0.89	0.61	0.7341
Correlation	0.86	0.86	0.70	0.95	0.84	0.87	0.87	0.8216
Predictive A.	0.87	0.94	0.82	1.00	0.92	0.90	0.94	0.8908

Table 2: Classification results of test data.

	classification accuracies for individual class							
	1	2	3	4	5	6	7	Kappa
MGML	0.94	0.92	0.80	0.99	0.76	0.70	0.88	0.8364
BUSP:								
Perfect	0.56	0.87	0.83	0.95	0.86	0.80	0.46	0.6913
Correlation	0.71	0.83	0.69	0.87	0.65	0.64	0.83	0.7184
Predictive A.	0.87	0.92	0.89	1.00	0.88	0.85	0.98	0.9020

5 CONCLUSION

Based on the concept of second order probability, a new approach, BUSP, for the classification of multi-source data is presented. This algorithm takes into account the predictive ability of the data source for each individual class. This form of quality measure of the data source is highly desirable as it expressed the quality of the sources for each individual class explicitly. The algorithm not only determines the resultant probability distribution for the sample space, it also generates the resultant predictive ability of the combined evidence. So that the combined evidence can be further updated in the light of new evidence.

Experimental results show that the BUSP classifier, with the inclusion of predictive ability measures, outperformed the MGML classifier when untrained test data is employed. This is mainly attributed to the fact that the BUSP was provided with more information in terms of the predictive ability of the evidence source for each class, and also its robustness and insensitivity to the anomaly of the data distribution.

In the area of pattern recognition, the proposed algorithm is suitable for classification of multi-source data, such as remotely sensed images employed in this paper, where the information sources are not equally reliable and exhibit different merit in identifying different classes.

REFERENCES

[1] J A Benediktsson, P H Swain, and O K Ersoy. "Neural Network approaches versus statistical methods in classification of multi-source remote sensing data." *IEEE Transactions on Geoscience and Remote Sensing,* (4):540-552, July 1990.

[2] George E P Box and George C Tiao. *Bayesian Inference in Statistical Analysis,* Addison-Wesley Publishing Company, 1973.

[3] C C Chong. "Classification using multi-source data with different reliability and predictive ability - An experiment," *unpublished Internal Report IV,* Dec. 1995.

[4] Peter Gardenfors and Nils-Eric Sahlin. *Decision, Probability and Utility - Selected readings.* Cambridge University Press, 1988.

[5] T Lee, J A Richards, and P H Swain. "Probabilistic and evidential approaches for multisource data analysis." *IEEE Transactions on Geoscience and Remote Sensing,* (3):283-293, May 1987.

Center Pivot Irrigation System Analysis Using Airborne Remotely Sensed Imagery: A Commercial Remote Sensing Case Study

Michael C. MacDonald
TRW Systems Integration Group
495 Java Drive, Sunnyvale, CA 94088-3510, MS 203
(408) 738-2888 x5517, (408) 743-6425 (FAX), e-mail: michael_macdonald@smtp.svl.trw.com

Abstract -- TRW's Ag Resource Mapping agricultural remote sensing program operated a commercial airborne remote sensing service in the state of Washington during the growing season of 1994. As part of the remote sensing program, TRW offered a prototype irrigation management service that was targeted at the early season verification/evaluation of the functionality of center pivot irrigation systems. Initial commercial market evaluation regarding this service indicated a substantial number of potential customers over a wide area. Initial concepts for the fulfillment of the service indicated good economics (based on number of fields covered per flight and cost per field imaged). During the study, it was demonstrated that the remote sensing of center pivot irrigation systems can be successfully addressed with high resolution film based remote sensing systems. However, our experience indicates that servicing a very large number of customers over a wide area can be economically problematic and that the difficulties are an interplay of complex market, system, weather, geographic, crop, and customer related factors.

INTRODUCTION

Center pivot irrigation systems are widely used in the automatic irrigation of high value agricultural crops. With use, these systems can develop malfunctions that can disrupt the proper the irrigation of the crop and effect its development and subsequently its cash value. To address this problem TRW has developed a commercial remote sensing system targeted at agricultural surveillance applications, one of which is irrigation system management.

The service was flown for the early part of the growing season in the State of Washington and was successful in detecting irrigation problems for many growers in the subscribing customer set. Acquired imagery was usually analyzed and delivered the next day (24 hour turnaround). Among the irrigation system defects and problems detected were missing nozzles, plugged nozzles, mismatched nozzles, stuck (non-rotating) sprinklers, system joint leaks, system "spoking" due to field slope characteristics or faulty pivot movement switches, system pressure problems associated with "end arm" activation, etc. The system evaluations provided in the service were the motivating factor for many growers to perform specific maintenance or corrective activities on their systems. It was seen that certain irrigation system problems (e.g. partially blocked nozzles) required image resolutions of significantly less than a meter while others could be detected with coarser resolutions.

Difficulties resulting from lack of specific knowledge of detailed customer irrigation practices, weather complications, variable soil characteristics, the broad area of required coverage, and limited flight opportunities caused some contract compliance, schedule and economic problems. These problems prompted the development of a more sophisticated contracting, scheduling, interpretation, quality assurance, and flight planning process. Prompt product delivery over such a large region as the Columbia River Basin also proved problematic. Some of the problems encountered in this venture are discussed in the following sections.

CENTER PIVOT IRRIGATION SYSTEM DESCRIPTION

Figure 1 shows a plan view diagram of a center pivot irrigation unit. There are several components. The central support pivot that anchors the fixed end of the irrigation arm is located at "A". This unit supports the inner end of the pivot arm and this is where the irrigation controls are located. The pivot arm extends from this point to the outer edge of the field. The arm portion rotates like the hand of a clock to provide irrigation coverage for the entire field. The arm carries the water supply pipes and hosts the sprinkler heads. At the tip of the end arm there is a "end gun" sprinkler which extends the coverage of the system.

The pivot arm is comprised of multiple segments which are supported by a series of spaced posts which are connected to sets of wheels. These wheels allow the pivot segments to move. The rotation speed of the pivot is set by the outer segment which moves at a continuous controlled rate. As the outer segment moves (leaving the inner segments lagging behind) an angular deflection is detected by sensors at each joint in the pivot (at each inner wheelset).

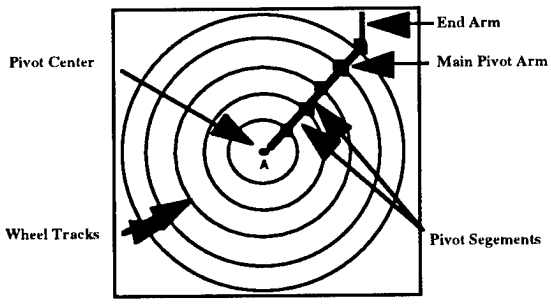


Figure 1 Center Pivot Irrigation Diagram

0-7803-3068-4/96$5.00©1996 IEEE

The detection of a deflection at a joint causes the system to rotate the wheels at that joint to correct the deflection. This is how the pivot moves around the field.

A series of sprinklers are mounted along the pivot arm. The sizing (and resultant output) of these sprinklers is calculated as a function of arm movement speed and water pressure. Some are static nozzles, some are rotating impact type sprinklers. Sprinklers are mounted both on the arm itself or hanging downward on lines from the arms.

SYSTEM DIAGNOSIS

These automated systems can develop a number of mechanical and pressure related problems. Many problems are the result of human installation errors (mis-sizing of sprinklers) while others are the result of system wear and tear (worn nozzles, plugged nozzles, etc.). Most of these problems are readily detectable in remotely sensed imagery. Example irrigation system problems are listed in Table 1.

Missing and worn sprinklers will have high water output rates. (Sprinkler nozzles get worn by the trace amounts of sediment found in irrigation water and their aperture widens with time, increasing output flow). Plugged or partially plugged nozzles result in relative dry rings. Non-rotating impact sprinklers exhibit a dry ring associated with an adjacent very thin, very dark wet ring. Pressure problems manifest themselves as large radial wedges that are drier and/or wetter that the remainder of the field. These are cause by pressure drops related to field slope effects (pumping uphill reduces water pressure) and pivot end arm actuation (the sprinklers on the end arm turn "on" and take up water reducing overall pressure at nozzles on the main arm).

For each of these problems there is an associated image feature in the soil (wet ring, dry ring, intermittent watering) that can be seen using good quality imagery of reasonable resolution. Given a good image, the interpreter can evaluate the system effectively. Given the ability to cover a large number of fields in one flight, the economics of irrigation remote sensing initially seem very straight forward and promising.

Sprinkler Problems	**Image Feature**
• Missing	Wet ring, overwater
• Worn	Wet ring, overwater
• Mis-sized	Wet or dry rings
• Partially plugged	Dry ring, underwater
• Fully plugged	Dry ring, underwater
• Non-rotating	Combo wet & dry ring
• Intermittent rotating	Variable wet/dry ring
• End gun mis-timing	Wet/dry areas
Pivot Problems	**Image Feature**
• Pressure problems	"X Pattern Spoking"
• Leaks	Large wet areas
• Stuck wheels	"Local Spoking"

Table 1 Mechanical Problems

This is how most companies enter the remote sensing market: i.e. with uncomplex views of the task to be completed. These preliminary views are what initial venture capital funding and market estimates are based upon. By experience it has been seen that the science and business of agricultural remote sensing gets very complex very quickly when you finally have get the job done on time and on budget.

UNCERTAIN GROWER IRRIGATION SCHEDULES

In the beginning of the season the growers' primary concern is getting his crop in the ground and properly irrigated. One must be aware that growers will not schedule irrigation at the convenience of an aerial survey firm. They irrigate when it is right for the crop. This includes weekends and holidays. Even at night sometimes. Often times when asked when they were going to irrigate the growers cannot not say with any specificity. Sometimes when they do specify a date and time, the irrigation system will not be turned on until a day later due to communication time lags with their irrigation managers. Some growers may irrigate multiple times in the early portion of the season giving you several imaging opportunities, while others will irrigate only once making it a "do or die" situation. In short, the timing for the survey of a particular customer field is in reality controlled by the customer and usually the irrigation schedule is often not very firm, is not well known, and is open to daily change from a wide variety of factors. Because of this, the simple coordination of overflight with an irrigation event can be very difficult.

DATA INTERPRETABILITY PROBLEMS

In order to see irrigation defects in the center pivot systems, you need to get a good look at the sprinkler watering patterns on the field. This is best done when the field is dry and the pivot is beginning to rotate and irrigate around the field. An aerial image of the field then shows the wedge-shaped wetness pattern on the field. The key location to interpret is the back edge of the wet area termed the "drying wedge". This area has been wetted and has had time to start drying. Its drying pattern depend on how much water was received in each local area. A missing sprinkler results in a very localized wet ring (because the water is gushing out uncontrolled). A plugged sprinkler results in a dry band at its location along the pivot. The resultant contrast of the light toned drying soil and the darker wet soil shows up the irrigation inconsistencies well. A perfectly regulated irrigation system in a perfect world will leave a well behaved gradual drying pattern at this trailing edge.

Problems occur, however, when this model it is applied to the real world. In many circumstances it is difficult to get a good "drying wedge" which is critical to spotting the subtle problems such as partially plugged or mis-sized nozzles. If

the grower is irrigating heavily, and the sun and wind are not drying the soil to any degree, there may
be no dry portion anywhere on the 360 degrees of the field. If the weather is poor and it rains, the field will also not be drying and in any case images acquired will not be interpretable (significant rain tends to "erase" any irrigation patterns). Soils with high water retention characteristics will also dry slowly (muck soils). Conversely, if the irrigation was too light, the field will dry too quickly and not provide an interpretable pattern (too indistinct). Table 2 shows some common drying related interpretation problems.

Each of these problems has a temporal period of effect. For example, the too wet field, might have dried sufficiently by the next day and provide good conditions for interpretation or may not have dried by as late as the next week. The difficulty is that the grower will want the information as soon as is possible so he will have sufficient time to correct any problems before irretrievable damage has been done to the emerging crop. Any mis-timing in imaging the field with respect to any of these dynamically changing conditions could result in an image that cannot be used. The only sure way to know if a field is ready for imaging is to go look at it. This drying prediction problem is a very significant restriction to scheduling cost effective aerial survey because it can requiring multiple revisits to properly image a field.

Additional interpretation problems occur with fields that show multiple problems that can tend to mask each other. An example of this would be in fields with highly variable soil moisture retention characteristics, that when combined with a partially plugged sprinkler set can make for difficulties in interpretation. The inherent soil moisture retention variation may tend to hide the effects of the low output sprinklers, and you may not detect this problem during interpretation.

IRRIGATION PUMP/WELL LIMITATIONS

The characteristics of irrigation water sources often control how and when fields are irrigated. In many water conservation areas, growers can only take so much water per hour from the canals and other water sources. In other situations growers are working off well water and can only draw from the number of wells available. Water wells are expensive to drill, so growers usually have a few as is possible. Sometimes pump equipment availability can also restrict the irrigation process. If the grower has one pump or well, but ten fields, each of which takes 18 hours to irrigate, he/she will only be able to irrigate about one per day for ten days straight. This means that any survey aircraft contracted to evaluate his irrigation systems will have to be over the property every day for the week to have a chance to service all his needs. The hard fact is that the grower usually cannot change pump, well, or water restrictions like these in any way. This problem is perhaps a single most significant controlling element in the irrigation survey problem because it is an inherent limit to what you can do in one flight for one customer.

Problems	Results in Imagery
• Overwatering	No drying
• Underwatering	Dries too fast
• Continuous watering	No drying
• No sun, no wind	No or slow drying
• High wind	Dries fast, water blows
• Muck soils	No drying

Table 2 Image Interpretation Problems

OTHER FACTORS EFFECTING IRRIGATION SURVEY OPERATIONS

Flight restrictions -- Commercial business aircraft can only fly when the conditions for safe flight permit. Windy days , turbulent air, etc. may preclude survey flights.

Breezy days -- Wind will cause the water from the sprinklers to be blown away from its usual pattern. Most growers will not irrigate when the wind is high (too much evaporation/loss) but in some cases they have no choice due to high evapotranspiration rates caused by a warm dry wind. In any case the irrigation pattern for field irrigated under high wind conditions is difficult to interpret.

CONSEQUENCES OF A BAD ANALYSIS

The grower is counting on the survey firm to provide a good evaluation of the irrigation systems in the beginning of the season. If the irrigation system check is done improperly and system problems are not identified early in the season, they will manifest themselves later in the season as crop damage. It is easy to spot irrigation related crop damage because it follows the familiar circular irrigation pattern. Because of this it is imperative to use proper image data sets in the interpretation process. There simply is no substitute.

RECOMMENDATIONS

The following recommendations are suggested to mitigate some of the difficulties in agricultural remote sensing:

- Ensure grower cooperation (commitment) in communicating field irrigation schedules. This is imperative.
- Monitor local weather and model (estimate) expected field dying characteristics to avoid imaging fields at improper times
- Plan realistic and strict schedules around pump/well usage or other restrictions
- Take into account a number of required re-flights in planning flight operations and resultant product cost estimations

The Sensitivity of a Land Surface Parameterization Scheme to the Choice of Remotely-Sensed Landcover Data Sets

K.W. Oleson,* K.L. Driese,† J.A. Maslanik,* W.J. Emery,* W.A. Reiners†
* University of Colorado, Campus Box 431, Boulder, CO. 80309
303-492-1241, Fax: 303-492-2825, oleson@frodo.colorado.edu
† University of Wyoming, P.O. Box 3165, Avent Nelson Building, Laramie, WY. 82071
307-766-2484, Fax: 307-766-2851, gap@botsun2.uwyo.edu

Abstract -- The characteristics of satellite-derived landcover data for climate models vary depending on sensor properties and processing options. To better understand the first order effects of differences in landcover data on a land surface parameterization scheme (VBATS), stand-alone model runs were performed for two adjacent 2.8° by 2.8° GCM gridcells in Wyoming using landcover from two satellite-derived maps (AVHRR, TM) and a global landcover data set commonly used in GCMs. Substantial differences in prescribed landcover were found between the three datasets. Despite these differences, the VBATS simulated surface fluxes were similar in the eastern gridcell for the two satellite data sets. In the western gridcell, the partitioning of net radiation into sensible and latent heat fluxes was affected by the relative proportions of wet cover types (i.e., inland water and irrigated crop) prescribed by the two satellite data sets. This emphasizes the importance of accurately estimating the proportion of wet cover types within a GCM gridcell in arid regions. Spatial aggregation of the satellite data sets reduced the number of cover types used to represent each GCM gridcell. In the western gridcell, a reduction in the number of cover types from 11 to 2 resulted in differences in annual averages of sensible and latent heat fluxes of about 10%. Other simulations involving these data sets suggest that these differences could be reduced if the wet cover types are accounted for. In this respect, fine spatial resolution information is required for some cover types whereas coarser resolution may be adequate for other types. Landcover classifications for land surface modeling need to be based more on model sensitivities than on traditional vegetation-type schemes.

INTRODUCTION

Landcover data sets used within most general circulation models (GCMs) are derived from a wide variety of map and atlas sources, e.g., [1] [2]. The accuracy of these data sets suffers from several limitations. Reference [3] quantified the extent of these inadequacies by noting the significant disparities in estimates of cover type area and spatial distribution between several ground-based data sets.

Remote sensing offers the most promising means for deriving improved global landcover maps [3]. Several issues arise, however, regarding choices in remote sensing instruments, classification methodology, and data processing to best meet the needs of GCMs [4].

The goal of our work was to quantify the effects of some of these choices by studying the effects of forcing a stand-alone vectorized version of the Biosphere-Atmosphere Transfer Scheme (VBATS) [5] with three landcover data sets, two of which are derived from satellite data, sampled at four spatial resolutions for two GCM gridcells in Wyoming.

Through comparisons of output from VBATS simulations conducted with these data sets, this work addresses the following questions in the context of these two gridcells:

1. *Do the satellite-derived data sets, when aggregated to GCM gridcell resolution, yield a different landcover type than the GCM-prescribed type, and if so, is this difference significant in terms of surface fluxes predicted by VBATS?*
2. *Is VBATS sensitive to the differences in landcover prescribed by the two satellite-derived data sets?*
3. *Is VBATS sensitive to a reduction in the number of cover types resulting from spatial aggregation of the data sets?*

APPROACH

The first of the three data sets used (denoted here as NC2) is a standard map/atlas-based data set ([2] as adapted by [6]) and is used in the National Center for Atmospheric Research (NCAR) Community Climate Model 2 (CCM2) GCM. The NC2 data set was derived by associating one of the 18 BATS types with each of the [2] types and aggregating by dominant cover type to 2.8° resolution.

The second (EDC) is based on 1km advanced very high resolution radiometer (AVHRR) data and was created by the EROS Data Center using temporal normalized difference vegetation index (NDVI) profiles and a variety of ancillary data [7]. The EROS Data Center has translated their 159 original classes into BATS types.

The third (GAP) was assembled in response to the need for a highly resolved and accurate landcover map of Wyoming for use with animal habitat models [8]. Degraded resolution (100m) Thematic Mapper (TM) data were used to create a digital false color composite image which served as a basis for manual photointerpretation of nearly 17,000 vector polygons into 41 landcover types which were then mapped into BATS types.

We aggregated the EDC and GAP data sets to coarser spatial resolutions of 0.2° and 0.4° by assigning the dominant BATS landcover type from the finer-resolution data to each coarser-resolution cell.

The areas chosen for analysis correspond to two standard CCM2 2.8° by 2.8° gridcells contained within the state of Wyoming. Both cells extend from 41.9° N to 44.7° N latitude. The western cell (denoted GWEST) extends from 108.3° W to 111.1° W longitude, while the eastern cell (GEAST) extends from 105.5° W to 108.3° W longitude.

0-7803-3068-4/96$5.00©1996 IEEE

In VBATS, the GCM gridcell is represented as a subcell mesh. Vertical fluxes are assumed to dominate over horizontal ones, so each of the subcells has its own independent connection to the atmosphere. The land surface parameterizations within VBATS are identical to those of BATS [6], but the vectorized nature of the VBATS code allows for efficient simulations of multiple gridcells.

We performed eight VBATS simulations for each of the GWEST and GEAST gridcells to address the three questions posed in the introduction. These simulations used landcover prescribed by the NC2, GAP, and EDC data sets at spatial resolutions of 2.8°, 0.4°, and 0.2°, and at the full spatial resolution of each satellite-derived data set (100m and 1km for GAP and EDC, respectively). The number of VBATS subcells for each simulation was determined by the number of cover types prescribed by each version of the data set. To yield GCM gridcell fluxes, subcell fluxes were weighted according to each landcover type's areal coverage within the 2.8° gridcell and then summed.

One year's worth of half-hourly atmospheric forcings were derived from the daily climate data of the Vegetation/Ecosystem Modeling and Analysis Project (VEMAP) database [9]. Simulations were run for 20 years and results were taken from the last year of each simulation.

RESULTS

First, we examined the sensitivity of VBATS to differences between NC2, EDC, and GAP dominant cover types. Both EDC and GAP, when aggregated to 2.8° resolution using a dominant cover type rule, prescribed the VBATS cover type semi-desert (SD) in the GWEST domain while NC2 prescribed evergreen needleaf (EN). In GEAST, NC2 and EDC prescribed short grass (SG) while GAP prescribed SD.

The consequences of choosing EN or SD in GWEST results in substantially different values for Q and QH (Table 1). The lower Q for SD is primarily due to its higher albedo (0.25 vs. 0.14 for EN). Within VBATS, the important differences between the SD and EN cover type parameterizations, besides albedo, are a high fractional vegetation cover for EN (0.7-0.8) compared to SD (0.0-0.1), a lack of prescribed seasonality in leaf area index (LAI) for EN, and a larger roughness length for EN (1.0m) compared to SD (0.1m). Due to the relatively dry climate forcings used here (average monthly precipitation < 30 mm), the significance of the interaction of moisture with vegetation (interception, transpiration) was greatly reduced. Hence, the predicted QE differed by only a small amount annually (1.4 W/m^2). The difference in Q between SD and EN was therefore primarily accounted for by QH.

In GEAST, the effects on surface fluxes of choosing between SG or SD for the gridcell landcover are smaller. The VBATS parameterizations of SG and SD are quite similar in most respects. Of the 14 biophysical parameters that represent VBATS cover types, only two (maximum fractional vegetation cover and maximum LAI) are notably different between these two cover types. SD is parameterized by a small maximum fractional vegetation cover (0.1 vs. 0.8 for SG) and high maximum LAI (6 vs. 2 for SG). The results indicate that for these atmospheric forcings, the combination of high LAI and low fractional vegetation cover produces nearly the same surface fluxes as low LAI and high fractional vegetation cover.

Second, we examined the sensitivity of VBATS to differences between full resolution EDC and GAP land cover. In GWEST, EDC prescribes the gridcell landcover as 27% SD, 20% EN, 17% mixed woodland (MW), 10% each of crop/mixed farming and SG, and less than 5% each of other cover types. In contrast, GAP landcover consists of 36% SD, 34% EN, and 9% evergreen shrub, with other cover types each occupying less than 4% of the gridcell. In GEAST, the EDC landcover components are 44% SG, 38% SD, and less than 5% each of other cover types. GAP prescribes 58% SD, 20% SG, 10% EN, and smaller proportions of other cover types.

Despite these substantial differences in landcover, the GWEST and GEAST simulated annual surface fluxes were similar (EDC.F and GAP.F in Table 1). This can be explained in part by the similar VBATS parameterizations of EN and MW, and SG and SD. If each of these similar pairs of cover types are grouped into a single cover type, then EDC and GAP agree on 75% of the gridcell landcover for GWEST and 80% for GEAST.

Monthly flux differences were of the same magnitude as the annual flux differences with the exception of QE in GWEST where differences in QE were up to 8 W/m^2 in the summer months. An analysis of the subcell fluxes revealed that this difference in QE was primarily related to the relative proportions of the wet cover types (inland water (IW) and irrigated crop (IC)) prescribed by each data set. Within VBATS, the IW and IC cover types are modeled as saturated

Table 1. Annual averages of net radiation (Q), sensible (QH), and latent (QE) heat fluxes in W/m^2 for GWEST and GEAST simulations. EN (evergreen needleaf), SD (semi-desert), and SG (short grass) refer to simulations where the gridcell consists of 100% of these cover types . The GAP.F and EDC.F simulations use landcover prescribed by the full spatial resolution of the GAP (100m) and EDC (1km) data sets. The GAP.2 and GAP.4 simulations use landcover prescribed from the GAP data set at 0.2° and 0.4° spatial resolution. # refers to the number of cover types modeled within the gridcell as prescribed by each data set.

	GWEST						GEAST			
	EN	SD	GAP.F	EDC.F	GAP.2	GAP.4	SG	SD	GAP.F	EDC.F
#	1	1	11	10	7	2	1	1	9	9
Q	129.9	99.9	111.9	111.3	114.7	115.2	100.3	94.4	100.6	100.0
QH	93.2	68.7	73.0	74.6	78.9	81.2	72.9	71.2	73.4	73.6
QE	38.2	36.8	41.7	39.2	39.1	37.5	30.3	29.4	32.3	30.8

soil and soil at field capacity, respectively. GAP and EDC classified 6% and 2% of the gridcell as inland water/irrigated crop. For the dry climatic forcings used here, even small proportions of these wet cover types substantially increased the availability of moisture in the gridcell. The larger proportion of wet cover types in GAP relative to the EDC data caused a higher QE during the summer months when energy was present to evaporate the increased available soil moisture. In GEAST, the wet cover types only occupy 3% and 1% of the GAP and EDC gridcell landcover, respectively, so differences in QE are smaller.

Lastly, we looked at VBATS sensitivity to a reduction in the number of landcover types modeled within a gridcell. For brevity, we focus on a comparison between VBATS simulations using the reduced resolution versions of the GAP data set (GAP.2, GAP.4) and the full resolution GAP data set (GAP.F) in GWEST only. Average annual Q was slightly higher for GAP at coarse spatial resolution than at finer spatial resolution (Table 1). QH increased and QE decreased as the number of cover types was reduced with aggregation. The changes in QH and QE were largest in the months of April-October. Part of the reduction in QE, and therefore, some of the increase in QH during these months can be attributed to the reduction or elimination of the wet cover types in the coarser resolution data sets. The reduction in QE was largest for GAP, which at full resolution had the largest wet cover type component (6%). In the winter months, snow and cold temperatures combined to reduce the effects of the wet cover types on surface fluxes at the various spatial resolutions.

CONCLUSIONS

Comparison of two satellite-derived landcover data sets with a standard map/atlas based data set commonly used in GCMs, revealed substantial differences in the areal proportions of landcover types within two 2.8° × 2.8° Wyoming GCM gridcells. Aggregation of the satellite-derived landcover data to the GCM gridcell resolution resulted in a different designation of landcover for both gridcells than is used in the standard map/atlas product. In the western gridcell, this resulted in substantial differences in surface fluxes simulated by a land surface parameterization scheme. In the eastern gridcell, the resulting differences in surface fluxes were smaller because of the similar biophysical parameterization of the two cover types prescribed by the data sets. These results support the assertion that accurate satellite-derived landcover data sets are needed to replace outdated and inaccurate prescriptions of landcover within current GCMs [3].

The sensitivity of VBATS to small proportions of wet cover types (e.g., inland water and irrigated crop) when landcover heterogeneity is explicitly modeled, emphasizes that the consequences of ignoring the potential contribution of certain cover types to the relative distribution of surface fluxes can often be disproportionate with respect to their areal coverage within the gridcell. Land surface parameterizations have advanced to the point where gridcell landcover can now be modeled using more than one landcover type. The choice of which landcover types to use should be evaluated with respect to the landcover composition within the gridcell and each cover type's response within the model to the range of atmospheric forcing it might experience.

In general, these results suggest that the value of high resolution landcover data sets depends on the presence of certain critical landcover types and on the biophysical differences among other types. Landcover classification schemes for climate modeling should ideally be flexible in terms of spatial resolution and information content to take account of model sensitivities to different surface conditions.

ACKNOWLEDGMENTS

The authors acknowledge the financial support of NASA's Earth Observing System (EOS) program as part of one of its InterDisciplinary Science (IDS) teams (Principle Investigator R. Dickinson). K. Oleson was supported in part by a grant from the National Science Foundation (NSF) (#BIR-9413218).

REFERENCES

[1] E. Mathews, "Global vegetation and land use: new high-resolution data bases for climate studies," J. Climate Appl. Meteor., vol. 22, pp. 474-487, March, 1983.

[2] J.S. Olson, J.A. Watts, and L.J. Allison, "Carbon in live vegetation of major world ecosystems," DOE/NBB Rep. No. TR004, Oak Ridge National Laboratory, Oak Ridge, TN.

[3] J.G. Townshend, C. Justice, W. Li, C. Gurney, and J. McManus, "Global land cover classification by remote sensing: present capabilities and future possibilities," Remote Sens. Environ., vol. 35, pp. 243-255, February, 1991.

[4] F.G. Hall, J.R. Townshend, and E.T. Engman, "Status of remote sensing algorithms for estimation of land surface state parameters," Remote Sens. Environ., vol. 51, pp. 138-156, January, 1995.

[5] A. Seth, F. Giorgi, and R.E. Dickinson, "Simulating fluxes from heterogeneous land surfaces: explicit subgrid method employing the biosphere-atmosphere transfer scheme (BATS)," J. Geophys. Res., vol. 99, pp. 18651-18668, September, 1994.

[6] R.E. Dickinson, A. Henderson-Sellers, and P.J. Kennedy, "Biosphere-atmosphere transfer scheme (BATS) version 1e as coupled to the NCAR community climate model," NCAR Technical Note, TN-387+STR, 1993.

[7] T.R. Loveland, J.W. Merchant, D.O. Ohlen, and J.F. Brown, "Development of a land-cover characteristics database for the conterminous U.S.," Photogramm. Eng. Remote Sens., vol. 57, pp. 1453-1463, November, 1991.

[8] K.L. Driese, W.A. Reiners, E.H. Merrill, and K. Gerow, "A digital land cover map of Wyoming: A tool for vegetation analysis," unpublished.

[9] T.G.F. Kittel, N.A. Rosenbloom, T.H. Painter, D.S. Schimel, and VEMAP Modeling Participants, "The VEMAP integrated database for modeling United States ecosystem/vegetation sensitivity to climate change," in press.

USING THE WAVELET METHOD FOR A MULTISPECTRAL REMOTE SENSING STUDY OF PLANT COMMUNITY SPATIAL PROCESSES IN BROAD RANGE OF SPATIAL SCALES

Petr V.Mikheev, Sergey S.Kheeroug, Gavriil Yu.Yakin, John S.Todhunter †
Botanical Gardens at Kazan State University
18, Lenin str., Kazan, 420008, Russia
843-238-0424, 843-238-0843 (fax), root@bg.ksu.ras.ru, mikheev@open.ksu.ras.ru
†Westinghouse Science and Technology Center
Pittsburgh, PA, USA
412-256-1606, 412-256-2205 (fax), jst@osmosis.pgh.wec.com

INTRODUCTION

Landscapes are the complex systems changing in time, which include components described in different spatial scales. Plant communities (PCs) are their components, in which different processes of dynamic interaction with the environment are taking place in their own spatial scales. Hence, many problems of our understanding of PCs in their landscape context such as scaling from PCs to the landcape, vegetation mosaics and landscape pattern and within-community spatial processes demand multiresolution approaches for their resolving. Therefore, use of wavelet approach (WA) seems to be prospective for these studies, because multiresolution methods enable the extraction of a spatial structure hierarchy of vegetation in the defined spatial limits.

A special property of PCs as an object of the study is a multilevel organization of their mosaic spatial structure. This makes it somewhat difficult to state the study odject within PCs. The use of WA might essentially simplify the situation.

In the present study the possibility is addressed of the use of wavelet-method to obtain the thematic map of PCs within the landscapes and making the map usable for comparative analysis with the maps of different factors, effects of which is studied.

The necessity of the use of multispectral images (MSIs) is due to the demand of large number of spectral zones to obtain information needed for segmentation of natural (including plant) object image. Output of this procedure is essentially enriched due to a synergetic effect, which might be discribed in terms of polyfeatures compozed by spectral features (particularly brightnes) of MSIs.

Conducted by authors analysis of many-dimensional gistogram of MSIs, received at research of plant communities (PCs) and other natural objects, has shown, in particular, that the compactness of spectral patterns of objects tends to grow with increasing of dimension of the space of spectral attributes (number of channels of a scanner). This fact may be interpreted as follows: in the feature space with an increase of its number of components of MSI the distances, determined, for example, as an Euclidean metric, between pixels, belonging to the same object or class of objects, will be reduced concerning distances between pixels, belonging to objects of different classes. Hence, with increasing of number of components of MSI (its dimension), the strengthening of synergetic effect can be expected. The specified effect consists of the fact that the semantic information of MSI is contained more than it is possible to receive at consecutive interpretation of a sum of its zone components.

Success of a solution of the task of semantic labelling of the segmented domains of MSI is largely dependent on the presentation form of the studied video-information for its constructive interpretation. The traditional approach of semantic labelling on the basis of learning patterns is often unacceptable for plant patterns due to their particular variety. Therefore, the method of the expert evaluation is more adequate which requires facilitation not only of the use of professional knowledge and experience, but aslo psychofisiological conditions of image perception by the specialist.

USING THE WAVELET APPROACH IN SEGMENTATION OF MULTISPECTRAL IMAGES

Not being segmentational, the WA can obviously be used in large segmentation algorythms with multiple sorting out for its optimization and calculation amount minimization according to the following scheme:

- zonal components of a given MSI are wavelet-transformed, providing a set of MSIs with a lowered spatial resolution;
- the wavelet transform pyramid level is chosen to assure successful segmentation, and segmentation of the chosen image is carried out;
- basing on the segmentation results performed at the above stage, the segmentation of the subsequent MSI situated lower in the pyramide is carried out with a higher resolution.

The most interesting from this point of view is the case of segmentation by the hierarchical clustering (HC). The HC method has been proposed quite a time ago and is successfully applied with relatively small set of selected elements (that is, much smaller than the number of pixels in the images practically used), while the number of features

0-7803-3068-4/96$5.00©1996 IEEE

analysed is high enough (several hundreds). Taxonomy is an example of a successful application of the method. The set dimension is limited because of the globality of HC transform, thus increasing in a geometric progression manner the number of calculations with the set dimesions.

Segmentation of MSIs by HC method looks promising because, on one hand, it allows to analyse the MSI of high dimension, and on the other hand, it allows to present the results as an hierarchical structure. It is interesting to compare the hierarchical clustering method to the wavelet one, and to combine them in a more powerfull MSI analysis method.

The HC method allows to analyse adequately the morphological structure of the studied objects, while WA allows to analyse their spatial organization. It should be noticed that WA does not limit the size of the data set used, because the transforms used are local, but limits significantly the dimension of the data analysed (for the first thing, the dimension of the output set is increased during the wavelet transform; secondly, increasing the dimension of the feature space its volume grows in a geometric progression mode while the data volume is not changed, rising therefore the number of useless calculations). As far as we know, the HC method has not been used priveously for image segmentation. Therefore we state here its brief description.

Multispectral image hierarchical clustering method:

Let $G(i^{(1)},...i^{(n)},...,i^{(N)})$ is N-dimensional historgam of the MSI $I(x,y)=\{Ij(x,y)\}$, $(x,y)\in W$, $0\le I_j(x,y)\le M$, $j=1,..,N$ in discrete feature space of N-dimension, where n - zone component number, $N=max(n)$, W - picture plane domain.

Let us define set connectivity. Let H - metric set. H - r-connected, if for arbirary pair (a, b) of elements of set H such sequence of elements $\{x1,...,xn\}$ of this set, $x_1=a$, $x_n=b$ exists, that distances $d(x_i,x_{i+1})$ are not more than r. Denote the r-connected set by H_r. Consider set G of nonempty cells of histogram $G(i^{(1)},..,i^{(N)})$. Denote its connectivity by R and define it:

$$R = min\ (r \mid G \text{ - } r\text{-connected}) \qquad (1)$$

Then $G=G_R$. It is possible to separate subsets G_{R-1} of set G_R, then repeating this procedure for G_{R-2} and so on, we obtain following hierarchy of feature space subsets:

$$G_R = \bigcup_{j_1} G_{R-1,}(j_1),$$

. . . . . .

$$G_r(j_1,..,j_{R-r}) = \bigcup_{j_{R-r+1}} G_{r-1,}(j_1,..,j_{R-r+1})$$

. . . . . .

$$G_1(j_1,..,j_{R-1}) = \bigcup_{j_R} G_0(j_1,..,j_R). \qquad (2)$$

The obtained hierarchy (1) correspond graph, nodes of which can be described by following system of numbers $(r,j_1,..,j_{R-r})$. A unique lable $M_{r,j1,..,jR-r}$ is assigned to every element of each branch of graph on level r. Then one obtains set of segmented images $\{S_r(x,y)\}$.

If the above procedure is difficult to execute due to a large number of calculations, it is possible to carry out this task by using the WA within the above scheme.Obviously in the feature space the historgam of MSI can differ from histogram of the wavelet-transformed image so that clusters of contiguous objects on the image would be percolated on histogram of the wavelet-transformed image and nonpercolated on histogram original one. Therefore the procedure of HC of MSI would be economizer if it would fulfill in two or three step: at first an upper level image of waveletpyramid is segmented, which consists of significantly less pixel than lower level images; then the domains created by projection of upper segments are processed separately. This procedure can be repeated antill bottom of wavelet pyramid is attained.

HIERARCHICAL REPRESENTATION OF THE MULTISPECTRAL IMAGE AND ITS INTERPRETATION

The methods of the clustering analysis and wavelet analysis are used at revealing of various aspects of a hierarchical structure of data. As it is can be seen from their comparison stated above, they mutually complement each other and, hence, can be used for revealing a generalized hierarchical MSI structure. We propose the following circuit of a combination of these methods:

- Hierarchical clustering of the MSI is carried out, as a result of which hierarchical set of the images is received, which present the structural information on the initial MSI with a various degree of detailed elaboration.
- The researcher involving his expert opportunities conducts choosing of levels of hierarchy, and the scale of research given to objects.
- The segmented images of chosen levels of hierarchy are subjected to wavelet transform for the analysis of features space organization of set of objects - PCs detected on the image.

At interpretation submitted with the method stated above of MSI the user has a opportunity to analyze a graph and hierarchical set of the resulting images by moving within the hierarchy either in the vertical (for choice of the level of interpretation of the image), or in the horizontal direction (for the visual analysis of a chosen segment of the image on any of hierarchical levels and supervision of changes, occurring in a structure of a of given segment at moving from one level to the other).

The object determined by level (cluster, received semantic label) can be subjected to the analysis and at lower levels of hierarchy, on which it is possible to reveal details of its structural and space organization. The specified procedure appears especially useful at analysis of such objects, as PCs.

It should be noticed, that in common case the results of clustering depend on choice of the metric of the feature space. The choice of Euclidian metric assumes, that the space of

attributes is isotropic. Therefore, for realization of a correct HC it is necessary to normalise the data so that the attributes of researched object in all zones would have the same average significances and variances. In case of several researched objects, possessing attributes of various nature, at normalization of the zone images there are the contradictions. The opportunities, created by the proposed method, permit to conduct research of objects at different hierarchical levels. By virtue of that linear brightness transformations influence only the level of hierarchy in cluster-hierarchical representation of the objects of MSI, on which they are displayed, therefore the mentioned normalizing problem is avoided.

RESULTS AND DISCUSSION

We used the airborn MSI of vicinities of Kazan, received by 5-channel scanner, two of which channels were in visible, two - in near IR and one - in the far IR.

To obtain a thematic map of PCs and test its interpretation the segmented image was compared with the topographical map of scale 1:10000. Testing and correction of segmentation results was carried out on the basis of the on-ground observation and expert knowledge.

The results of HC, executed with developed method, were submitted as an hierarchical database, containing till each of hierarchical levels information about quantity of clusters, the sizes of each cluster in pixels and quantity of lower levels, on which the given cluster continues to be divided on subclusters.

The interpretation of received hierarchy of objects has shown, that at the top levels of graph separation on classes of antropogenical and natural objects takes place, further - on a branch of natural objects: water, soil and plant objects; further along the plant branch - on PCs types: herbs, brushwoods, forests, etc.; then - on pure PCs and so on - up to separate plant populations. Thus, the initial levels of branching of the classification tree correspond to division of objects into large classes, and finally, at the sufficient space resolution, correspond to individual objects.

Between these extremal cases, the hierarchic levels are situated which have the elements classified by objects with increasing specificity studied in the downward hierarchical direction.

On the thematic map reflecting the data of one of the lowest segmentation levels of multizonal image studied, the terminal clasters were chosen which were shown by the on-ground observations to correspond to the following objects:

- mixed leaf forest (Tilia cerdata Mill., Acer platanoides L., Betula pubescens Ehrh.);
- Pinus sylvestris L. area;
- Populus tremula L. area, etc.

Obtained space patterns of specified PCs or populations were transformed into the form of the binary images, which then were subjected wavelet-transform. Received for each of researched objects the multiresolusion sets of the images were used for the comparative analysis of these components of a landscape with various factors, submitted at appropriate levels of resolution.

The interpretation of received results has shown, that the proposed method permits to divide reliably on the image the areas, distinguished not only for a plant type, but also on complex factors, influencing on conditions of flora. So the leaf forest file, two clusters are submitted, one of which corresponds to the mixed leaf forest on hillside, other - mixed leaf forest on low humid plain near the river coast. If the population Populus tremula takes the area on the bottom of ravines, Pinus sylvestris has appeared less similar and was precisely divided into two subpopulation, located on hillsides of ravines and low humid plain.

The wide opportunities of the proposed method are demonstrated by the example of revealing on the interpretive MSI clusters, containing objects, sizes of which are less sizes of a image pixel in the object space. In this case such objects as country cottages have appeared, the average area of which made in a whole 5-10 % of the pixel area. These objects were not located on anyone zone image, however the synergetic effect of the joint analysis of five components of MSI realized by the proposed method allowed to allocate the clusters appropriate to them already at the top levels of its hierarchical representation.

CONCLUSION

For the analysis of landscapes, the method of MSI representation as a uniform space-morphological hierarchy of the segmented images is proposed, convenient for their direct interpretation by a person and for the classification on the basis of expert knowledge. The basis of the proposed segmentation method the HC approache in a combination with wavelet-transform. In the proposed method the wavelet-transform is used for the solving of two problems:

- Preparation of data for convenient HC, enabling to execute MSI segmentation.
- To present MSI in a form, convenient for recognition by generalization of a spatial and morphological structure in a uniform hierarchy.

It is shown in the above examples, that the proposed method gives the expert an opportunity to successfully interprete MSI on the basis of brightness polyfeatures, using the expert knowledge.

This result may be useful for different geobotanical, syntaxonomical and ecological interpretations. Analysis of this type of representation has a large potential for yielding information about influence of different factors on the environment.

The proposed methods provide a promising approach to understanding the vegetation patterns by analyzing the remotely sensed MSIs.

A Multi-Parameter Land Data Set for Regional Modeling

Paul Thames, James Maslanik, Keith Oleson, William Emery
University of Colorado at Boulder, Campus Box 431, Boulder, Colorado 80309-0431
Corresponding Author: Paul Thames, tel. (303) 492-1241, FAX (303) 492-2825, Paul.Thames@Colorado.Edu

Abstract --Regional climate simulations can benefit from data sets that depict seasonal and inter-annual variability of surface conditions at relatively fine spatial resolution. Remotely-sensed data can provide such information. However, a variety of data processing and algorithmic issues become apparent when attempting to link satellite products with modeling. Here, we review the assembly of existing remotely-sensed products to support a regional climate modeling experiment, and summarize lessons learned regarding applicability of existing land products to modeling applications.

OBJECTIVES

The work presented here describes the data-assembly component of a regional modeling experiment designed to explore the application of moderate-resolution satellite data for simulations of land surface processes. This experiment represents a "prototype" of the regional modeling applications to be supported by the Earth Observing System Distributed Information System (EOSDIS) when the Earth Observing System (EOS) is fully operational. The goal of this data-assembly component of the prototype is to explore the practical problems of identifying and applying satellite-derived products as land-surface boundary conditions and parameterizations within climate simulations. Objectives are to: 1) locate and assemble data sets most applicable to land components of climate models; 2) from these data sets, derive specific products suited for regional modeling; and 3) recommend data processing strategies to facilitate modeling uses of EOS data.

INTRODUCTION

In the last decade, the importance of land surface effects in climate modeling has been increasingly recognized. Research into the influences of surface conditions on regional and global climate has resulted in a new understanding of land surface effects and progress toward simulating them. Remotely-sensed data sets can contribute to the development and applications of surface process models as sources of improved time- and space-varying parameterizations [1], as well as for the more typical applications as validation sets. However, practical problems arise in locating and assembling the large amounts of data needed to cover model domains. More fundamental concerns are involved in reconciling differences between the information requirements of models and the types of information obtainable from satellites.

To define data requirements and processing strategies for climate modeling during the EOS era, a prototype EOS-era data set is being assembled to support regional climate simulations for flood and drought years in the Upper Mississippi Drainage Basin. The modeling applications of these data are twofold: 1) to provide inter-annually varying surface conditions in place of the prescribed parameters and climatologies in the model; and 2) as validation data for comparison to model output. This database covers a model domain of 1440 km by 1440 km. Included are time series of AVHRR imagery, SSM/I brightness temperatures, derived parameters from NASA Pathfinder sets, and ancillary information such as drainage networks, digital elevation data, and ground observations of flood conditions.

SURFACE-MODEL DATA REQUIREMENTS

The remote sensing requirements considered here address the information needs of the Biosphere-Atmosphere Transfer Scheme (BATS) model [2], a land-atmosphere transfer scheme (LATS) typical of the type found in many climate models, including CCM2 and the regional climate model, RegCM2 [3,4]. BATS treats a variety of processes that control the transfer of heat, moisture, and momentum between the land surface and atmosphere, and thus includes information pertaining to a range of surface conditions. Our specific application of BATS involves modifying the BATS scheme to accept parameters from remotely sensed data in stand-alone mode (e.g., uncoupled from the atmosphere), for eventual application of this BATS version within the fully-coupled RegCM2 model. These time- and space-varying remotely-sensed surface conditions are then used in place of the existing climatology-based prescriptions in BATS

Of the parameters used in BATS to specify surface conditions, six parameters have been identified with the potential to be derived from the remotely sensed data sets and which will incorporate the desired variability into the model. These are the fraction of vegetation, bare soil, and water, green leaf area index (LAI), aerodynamic roughness, and broadband albedo.

0-7803-3068-4/96$5.00©1996 IEEE

SATELLITE REMOTE SENSING PRODUCTS

In keeping with the project objectives, the remotely-sensed products must provide these parameters in sufficient spatial and temporal detail and with sufficient accuracy (or potential accuracy using EOS instruments) such that the data sets help minimize uncertainties in the climate model. With this in mind, the satellite remotely-sensed data sets assembled to date into a common projection within a geographic information system are the Pathfinder AVHRR Land (PAL) data, NOAA/NASA Pathfinder SSM/I Land Products, Conterminous U. S. 14-day Normalized Difference Vegetation Index (NDVI) Composite, and Conterminous U. S. Land Cover data sets. Spectral and temporal coverage, spectral resolution, and availability were the criteria used to select these data sets. Additional observations of flooding and stream conditions were obtained from the recently released Global Energy and Water Cycle Experiment (GEWEX) Continental-Scale International Project (GCIP).

The PAL products consist of a processed set of data from AVHRR, distributed by the Goddard Space Flight Center (GSFC) Distributed Active Archive Center (DAAC). The PAL products, currently available from 1983 through August 1993, contain daily data sets, as well as a ten-day composite of NDVI data. at 8 km resolution derived from Global Area Coverage (GAC) imagery.

The Conterminous U.S. AVHRR Biweekly Composites are a product of the EROS Data Center (EDC), and are derived from AVHRR High Resolution Picture Transmission (HRPT) data and distributed at 1 km resolution [5]. NDVI and individual channel values have been produced for 1990-1993. A companion to the biweekly composites is the Conterminous U. S. Land Cover Characteristics product generated by EDC using the NDVI time series in conjunction with ancillary information to classify the surface into 159 cover types for 1990 [6]. Also included is the land cover mapped from those 159 types to the landcover classes used by BATS.

Assembly of these data sets involved collection of pertinent information from Internet sites and archive centers, including the EOS DAACs. In general, the availability of documentation, online links to other information, and availability of assistance in using the data represent substantial gains in improving the usefulness of data sets. A major shortcoming of the current Version 0. DAAC data retrieval system is the lack of a subsetting capability, which entailed ordering and processing large volumes of data beyond that needed for the model domain. This capability is planned for the DAACs. Other issues related to this data assembly effort include non-uniform media and formats from different data centers, and the fundamental difficulties of processing the data volumes needed to support climate simulations.

BATS PARAMETER DERIVATION

The following describes some of the basic steps being used to convert the above data sets into the specific parameters appropriate for ingest into the BATS model.

Vegetation Fractional Coverage This parameter has been derived from the 14-day NDVI composite data set, using a threshold algorithm described by Loveland, et al [6]. NDVI thresholds are used to determine whether vegetation is present in the sensor's nominal 1 km field of view. Since RegCM2 will be run using 60 km grid cells for our experiments, the data must be aggregated from the source resolution to the grid cell size of the climate model. The AVHRR derived fractional coverages thus provide the means to introduce spatial as well as temporal variability into the climate model, although the aggregation process must be done with modeling needs in mind [7].

Bare Soil and Water Fractional Coverages Originally, our intent was to use the EDC bi-weekly NDVI data to determine bare soil and water fractional coverages within the model domain. However, the compositing method to generate the original data set precludes this application. By compositing using the highest NDVI value (which works well for vegetation) this method gives indeterminate information on whether the non-vegetated pixels are bare soil, water, ice, snow, or clouds. To produce the fractional soil and water coverages therefore requires using the spectral information available from the PAL data sets, albeit with the tradeoff of 8 km versus 1 km resolution. The discrimination algorithm being implemented is a simple multispectral classifier using AVHRR channels 1, 2, and 4. An extension of this task is to quantify how much information is lost using the 8 km versus 1 km data, before and after aggregating to model resolution.

Leaf Area Index LAI is a measure of the biomass of the vegetative canopy. It can be determined from the fractional photosynthetically active radiation (FPAR), which is a linear function of the simple ratio [1] of the visible and near infrared channels of the AVHRR instrument, or from the NDVI which is also derived from those two channels. This data has been calculated from the 14-day NDVI composite coverage at 1 km resolution.

Other Parameters Vegetation types derived from the EDC conterminous U. S. products are supplied to BATS as boundary conditions. The original BATS classes in the EDC product include some apparent misclassifications. Selected EDC BATS class assignments were therefore modified based on further analysis. Additional products yet to be generated

for the Upper Mississippi model domain include albedo and aerodynamic roughness. Calculation of albedos required by BATS awaits selection of an appropriate method for conversion from spectral albedo to broadband or short-wave and near-infrared albedos. Plant canopy conditions provide some indication of aerodynamic resistance, used by BATS to estimate movement of heat, moisture, and momentum flux from a reference level to some other level in the overlying air. Roughness lengths will be estimated using the first-order closure model described by Sellers [4] that incorporates remotely-sensed vegetation parameters.

NOAA/NASA SSM/I Pathfinder land products contain data derived from the SSM/I instrument at 25 km resolution. As with the PAL data, coverage is global. One product of particular value to land surface modeling is the soil moisture content. This product, along with SSM/I derived precipitation rate, will be used for general comparison with model results rather than as forcing within the model, since uncertainties in the products remain quite large.

RESULTS AND CONCLUSIONS

In summary, multivariate data comparable to those planned for EOS have been assembled for use in regional climate modeling experiments. Decision rules are applied to these data to delineate fractional vegetation cover, bare soil, and flooded areas. These basic classes are combined with USGS AVHRR-derived landcover types to specify surface conditions for the regional model's vegetation-atmosphere transfer scheme. To better represent time-varying vegetation conditions within these classes, leaf area index values are derived from AVHRR for bi-weekly intervals. A combination of SSM/I and AVHRR data is planned to depict general soil moisture and saturated-soil conditions for comparison to the climate model output.

Spatial and temporal variability of surface conditions are represented with much greater detail in the remotely-sensed data than in existing climatologies. These differences are described in more detail in a companion paper by Oleson, et al [7]. Of particular note are differences that, while not necessarily substantial in terms of typical applications of satellite imagery for landcover mapping, are nevertheless significant for climate modeling. Future work will continue to identify such modeling-related issues pertaining to data sets.

ACKNOWLEDGMENTS

The authors would like to acknowledge the financial support of NASA's Earth Observing System (EOS) program as part of one of its InterDisciplinary Science teams (Principal Investigator R. Dickinson). The authors would also like to acknowledge the use of data from the following data centers: EROS Data Center, Goddard Space Flight Center DAAC, and Marshall Space Flight Center DAAC.

REFERENCES

[1] Sellers, P.J., C. J. Tucker, G. J. Collatz, S. O. Laos, C. O. Justice, D. A. Dazlich, D. A. Randall, A global 1° by 1° NDVI data set for climate studies. Part 2: The generation of global fields of terrestrial biophysical parameters from the NDVI, Int. J. Remote Sensing, Vol. 15, No. 17, 1994, pp. 3519-3545

[2] Dickinson, R.E., A. Henderson-Sellers, P. J. Kennedy, and M. F. Wilson, Biosphere-atmosphere transfer scheme (BATS) for the NCAR community climate model, NCAR Technical Note, NCAR/TN-275+STR, National Center for Atmospheric Research, Boulder, CO, 1986

[3] F. Giorgi, M. R. Marinucci, G. T. Bates, "Development of a second-generation regional climate model (RegCM2). Part I: Boundary-layer and radiative assimilation of lateral boundary conditions", Monthly Weather Review. Vol. 121, October 1993

[4] F. Giorgi, M. R. Marinucci, G. T. Bates, "Development of a second-generation regional climate model (RegCM2). Part II: Convective processes and transfer processes", Monthly Weather Review. Vol. 121, October 1993

[5] J. C. Eidenshink, "The 1990 conterminous U. S. AVHRR data set", Photogrammetric Engineering & Remote Sensing, Vol. 58, No. 6, June 1992, pp. 809-813

[6] T. R. Loveland, J. W. Merchant, D. O. Ohlen, J. F. Brown, "Development of a land-cover characteristics data base for the conterminous U. S.", Photogrammetric Engineering & Remote Sensing, Vol. 57, No. 11, November 1991, pp. 1453-1463

[7] K. W. Oleson, K. L. Driese, J. A. Maslanik, W. J. Emery, W. A. Reiners, "The sensitivity of a land surface parameterization scheme to the choice of remotely-sensed landcover data sets", IGARSS'96

Spatio-temporal land cover dynamics in the Pantanal assessed using lacunarity analysis on an ERS-1 SAR image time series

Geoffrey M. Henebry
Kansas State University
Division of Biology/Ackert Hall
Manhattan, KS 66506-4901 USA
T: 913.532.7997 F: 913.532.6653
gmh@unix.konza.ksu.edu

Hermann J. H. Kux
Instituto Nacional de Pesquisas Espaciais (INPE)
Caixa Postal 515
12227-010 São José dos Campos SP Brazil
T: 55.123.418977 F: 55.123.218743
hermann@klaus.ltid.inpe.br

Abstract -- The Pantanal of Brazil, the largest wetland on the planet, is a disturbance-maintained ecosystem: an unusual topography coupled with a seasonal cycle of flooding and drydown creates a collection of landscapes that are environmentally heterogenous in space and time. Dominant land cover types include freshwater and saline lakes, periodically inundated grasslands, and forested corridors and patches. These cover types are highly heterogeneous in spatial arrangement and in response to inundation. Spatio-temporal analysis of land cover dynamics from Synthetic Aperture Radar (SAR) image time series is relatively new research area but one that will expand given the increasing availability of SAR data. The Pantanal is well suited to microwave remote sensing because land cover types can exhibit great contrasts in backscattering. We have previously shown the efficacy of using lacunarity analysis with SAR imagery for quantifying land cover dynamics. In this presentation we extend that analysis to a total of seven ERS-1 SAR images from December 1992 to November 1993. This period includes both seasonal inundation followed by a significant climatic drought that transformed the spatial structure of backscattering across the landscape. Lacunarity analysis of the SAR image series captures the spatio-temporal rearranging and illustrates how complex land cover change can be quantified within a predictive framework.

INTRODUCTION

The efficacy of Synthetic Aperture Radar (SAR) image time series for environmental monitoring has been amply demonstrated in the past several years [1]. Most of this research has focused on the temporal shifts in backscattering that accompany alterations in land cover and changes in permittivity. Less attention has turned to the spatio-temporal analysis of image series, by which we mean the explicit quantification of temporal change in the spatial structure of an imaged scene. This definition is in contrast to the implicit spatio-temporal analysis found in a sequence of classified images. We seek robust spatio-temporal patterns, landscape trajectories, to use in higher-order change detection algorithms appropriate for environmental monitoring [2,3]. Here we illustrate how lacunarity analysis applied to a seven date SAR image series can uncover some typical spatio-temporal trajectories found within the very dynamic tropical landscape. This study extends our previous work in lacunarity analysis of SAR imagery [4-6].

LACUNARITY ANALYSIS

Lacunarity indices use multiscale windowing to measure the scale dependency of spatial heterogeneity and anisotropy in binary maps in terms of departures from translational and rotational invariance [4,7]. The indices are sensitive to the map density and local aggregation. Higher lacunarity indicates a more sparse, more clumped distribution within the map. Random maps show little persistent spatial structure under multiscale windowing and thus exhibit low lacunarity scores. Conversely, maps containing larger aggregates maintain high lacunarity scores until the extent of sampling window exceeds the extent of the aggregates. Thus for spatio-temporal analyses it is useful to track lacunarity using a constant window size. Anistropy can be estimated by the ratio of lacunarity indices obtained from rectangular windows with extreme but complementary shapes, e.g., $w(1j)$ and $w(j1)$ [6].

STUDY AREA

The Pantanal is the largest wetland habitat on the planet: an immense assemblage of alluvial fans formed during the Pleistocene, it covers 139,000 km^2 in Brazilian states of Mato Grosso and Mato Grosso do Sul [8,9]. The Pantanal is also one of the more radiometrically dynamic landscape in the

0-7803-3068-4/96$5.00©1996 IEEE

tropics due to extensive seasonal flooding by the Paraguay River and its tributaries. An ecotonal landscape that developed during the Holocene, the Pantanal is a complex mosaic of shallow lakes, periodically inundated grasslands, and islands and elevated corridors of forest, which together support an abundant and diverse fauna of birds, fish, reptiles, and mammals, including four million head of cattle [10].

The Pantanal is remarkable for its reduced declivity (2.5-5.0 cm/km). Local topographic features (2-4 m above the surrounding lands), resulting from either ancient Aeolian sandfields [8] or termite activity [11] are critical for determining habitat for both flora and fauna. Forested ribbons of higher ground known as *cordilheiras* are never flooded and serve as seasonal refuge for terrestrial animals. Where the water is deep, hydrophytes predominant; in areas with sufficient water flow, productive grasslands emerge [9] Highly permeable soils in the Pantanal lead to a substantial seasonal drydown (June to September) that favors xeric species on elevated soils.

The study area lies in the region of the Pantanal called Nhecolândia, located along the southern tier of the Taquari River alluvial fan. Nhecolândia is remarkable for the hundreds of freshwater and saline lakes that punctuate the landscape. We analyzed three typical landscapes: (1) a large quasi-perennial wetland with bordering woodlands, (2) a mosaic of lakes ringed by trees and interspersed among grasslands, and (3) a well formed channel with riparian forest.

METHODS

Our image time series spanned seven dates (Table 1). The SAR images were georeferenced, ground-range projected, real-valued, 3-look digital data processed by INPE. The nominal ground resolution of these data was 25 m with a pixel spacing of 12.5 m in both range and azimuth. For each landscape type the same scene (1024x1024 pixels = 655 km^2) was extracted at each date and registered to the corresponding December 1992 scene using linear offsets. The resulting misregistration was minimal (<2 pixels) and lacunarity is robust to misregistration errors when image extent is large relative to pixel resolution. To prepare the data for lacunarity analysis, the quartiles (Q1, Q2, Q3, Q4) of each subimage histogram were calculated and four binary images were thereby generated. Slicing the histogram into even quantiles controls the map density, thereby making lacunarity sensitive only to the scale dependency of aggregation. Lacunarity was estimated using square windows ranging from 1 to 64 pixels (0.0625 ha to 256 ha) with 1000 random samples at each window size. (For more detail on calculation of the lacunarity index, see [4-7].) Anisotropy was estimated using the zero-centered ratio of 4 ha windows of shape 1x64 and 64x1. Values close to 0 indicate an isotropic distribution. Values less (greater) than 0 indicate more (less) clumping west to east than north to south.

RESULTS

In earlier work [4,6] we had seen that most of the spatial heterogeneity was located in Q1 and Q4, corresponding to the lowest and highest backscattering values, while the middle 50 percent of the histogram was dominated by spatially random speckle noise. This was again the case for each landscape examined here. Together Q1 and Q4, although comprising 50 percent of the pixels, accounted for 72 to 91 percent of the total lacunarity. The partitioning of anisotropy, however, was a different matter. There was no significant difference between quartiles at a single date, although there was significant variation in anisotropy over the course of the image series.

If we plot the Q1+Q4 composite anisotropy ratio against the independently determined Q1+Q4 composite lacunarity index, where both were calculated at a maximal window dimension of 64 pixels, we obtain a spatio-temporal pattern that captures some essential elements of the land cover dynamics (Figures 1-3). In each landscape, there is a distinct periodicity of the spatial arrangement of backscattering. Note the counter-clockwise trajectory until Day of Year (DOY) 226 for the riparian scene (Fig. 1) and DOY 156 for the lake mosaic (Fig. 2). The divergence from periodicity thereafter likely arises from an extreme drought that struck the Pantanal during the later half of 1993. A similar, though not as clear, pattern of divergence can be seen in the wetland trajectory (Fig. 3).

How do we interpret these trajectories? Lacunarities near zero indicate a nearly random distribution of pixels. These low lacunarity values correspond to the period of peak flooding (DOY 121-156). Note the shift in the wetland (Fig. 3) and riparian (Fig. 1) landscapes to lower lacunarity from DOY 261 to 331, corresponding to the peak of dryness. In constrast, the punctuate landscape of the lake mosaic (Fig. 2) registers an increase in aggregation of highest and lowest backscatterers during the drought. The anisotropy time series reveals a similar grouping of the three landscapes. Both the wetland and riparian landscape exhibit an increase in anisotropy due to flooding and an attenuation of anisotropy during drying. Higher anisotropies, however, are observed in the lake mosaic during the drought (Fig. 2).

CONCLUSION

The spatio-temporal patterns revealed in this study are provocative; however, it is important to recall that these analyses were independent of backscattering magnitude, thus its explicit inclusion might enhance the trajectories. This study shows the utility in extracting latent yet robust spatio-temporal patterns for environmental monitoring, specifically, for the

definition of nominal behavior, the assessment of disturbance impacts, and, eventually, the predictive modeling of land cover dynamics. Although we do not think that this image series is exhaustively representative of the behavior of the region, the results are promising and we look forward to obtaining additional, longer image series from ERS-2.

ACKNOWLEDGMENTS

G.M.H. acknowledges support from NSF grant DEB-9527108, a Fulbright Research Fellowship at INPE during 1993-94, and NSF grant BSR-9011662, Long Term Ecological Research at Konza Prairie. H.J.H.K. acknowledges the support of an ERS-1 Pilot Project grant from the European Space Agency. The ERS-1 SAR data was processed by and acquired from INPE.

REFERENCES

[1] European Space Agency, New Views of the Earth: Scientific Achievements of ERS-1, Noordwijk, The Netherlands: ESTEC, 1995.

[2] G.M.Henebry, "Detecting change in grasslands using measures of spatial dependence with Landsat TM data," Remote Sens. Environ. vol. 46, pp.223-234, 1993.

[3] G.M.Henebry and H.Su, "Using landscape trajectories to assess the effects of radiometric rectification." Int. J. Remote Sens., vol. 14, pp. 2417-2423, 1993.

[4] G.M.Henebry and H.J.H.Kux, "Lacunarity as a texture measure for SAR imagery,". Int. J. Remote Sens., vol. 16, pp. 565-571, 1995.

[5] H.J.H.Kux and G.M.Henebry, "Multi-scale texture in SAR imagery: landscape dynamics of the Pantanal, Brazil," in Electronic Digest of IGARSS '94, Piscataway, NJ: IEEE, 1994, pp. 1359-1364.

[6] H.J.H.Kux and G.M.Henebry, "Evaluating anisotropy in SAR imagery using lacunarity functions," Int. Arch. Photogram. Rem. Sens., vol.30, no.7A, pp.141-145, 1994.

[7] R.E.Plotnick, R.H.Gardner, and R.V.O'Neill, "Lacunarity indices as measures of landscape texture," Landscape Ecology, vol. 8, pp. 201-211, 1993.

[8] G. Klammer, "Die paläowuste des Pantanal von Mato Grosso und die pleistozäne Klimageschichte der brasilianischen Randtropen," Zeitschift für Geomorphologie N.F., vol 26, pp. 393-416, 1982.

[9] C.T.Rizzini, A.F.Coimbra Filho, A.Houaiss, Ecossitemas Brasileiros/Brazilian Ecosystems, Rio de Janeiro: Index Editora, 1988.

[10] C.J.R. Alho, T.E. Lacher Jr., and H.C. Gonçalves, "Environmental degradation in the Pantanal ecosystem," BioScience, vol. 38, pp. 164-171, 1988.

[11] V.M.Ponce and C.N. da Cunha, "Vegetated earthmounds in tropical savannas of Central Brazil: a synthesis with special reference to the Pantanal do Mato Grosso," J. Biogeog., vol. 20, pp. 219-225, 1993.

TABLE 1: ERS-1 SAR data from track 210 & frame 3987

Acquisition Date	Orbit Number	Center Latitude	Center Longitude
1992 12 12	7369	S19° 12' 04"	E304° 02' 06"
1993 02 20	8371	S19° 12' 40"	E304° 01' 26"
1993 05 01	9373	S19° 15' 00"	E304° 01' 19"
1993 06 05	9874	S19° 11' 42"	E304° 02' 10"
1993 08 14	10876	S19° 11' 38"	E304° 01' 52"
1993 09 18	11377	S19° 12' 14"	E304° 01' 19"
1993 11 27	12379	S19°11' 56"	E304° 01' 55"

Figure 1 -- Riparian Forest

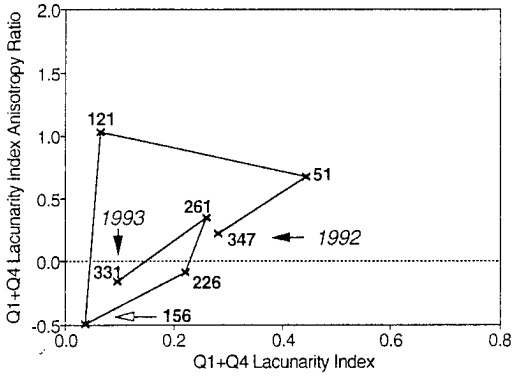


Figure 2 -- Lake Mosaic

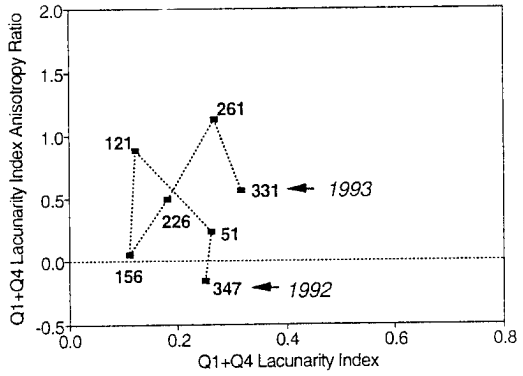
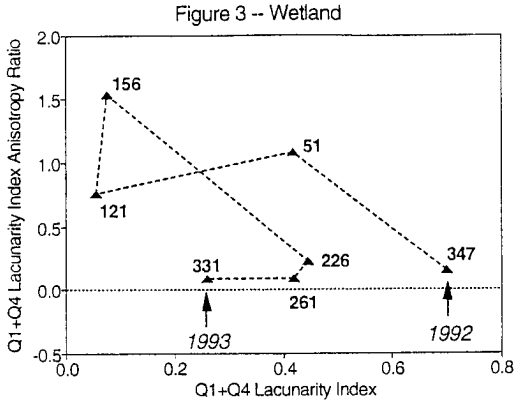


Figure 3 -- Wetland



Accuracy Analysis and Validation of Global 1 Km Land Cover Data Sets

Joseph Scepan, John E. Estes, and William J. Starmer
Remote Sensing Research Unit
Department of Geography
University of California
Santa Barbara, CA 93106-4060
805-893-3845
scepan@geog.ucsb.edu

ABSTRACT

In this study, an approach for analyzing and validating thematic and positional accuracy of high resolution global land cover data set is described. Portions of the International Geosphere/Biosphere Programme's (IGBP) 1 Kilometer Land Cover Data Set are used as a test bed to evaluate procedures for accuracy assessment and validation. The 1 Km Land Cover Data Set contains 17 land cover classes ranging from natural vegetation to developed land and non-vegetated classes.

This study focuses on developing statistical map accuracy procedures for data set validation through a continental scale cross validation exercise using the 1 KM land cover data set. The objective of this exercise is to assess the potential of the IGBP fast track validation procedures. These include implementation of an integrated overall map accuracy analysis as well as a detailed category specific thematic accuracy assessment for both a North American and African study site. Specific goals of this study are to: 1) determine whether different classification techniques employed for Africa and North America significantly affect the classification of the 1Km Land Cover data set; 2) determine whether systematic differences are introduced into the datasets by the separate processing flows; 3) examine and attempt to explain any non-systematic differences which may be identified, and; 4) derive a statistical estimate of these differences between the two datasets for each of the 17 Land Cover classes -- or as many of the classes as are adequately represented.

BACKGROUND

Global ecological and chemical cycle modeling is the most important scientific technique currently available to measure, monitor and predict critical physical and biological processes and environmental changes in the Earth's environmental system. Global ecological models are developed and implemented to provide information about a variety of ecological and biogeochemical regimes. Important among these are carbon cycles, hydrologic cycles, and terrestrial energy balance [1]. These processes are very complex and they must be addressed using numerical models. These global ecological models require spatially referenced terrestrial vegetation and land cover parameters as inputs. Requirements have been demonstrated for these data at spatial resolutions of 1 kilometer (and finer) and high temporal resolution. In the past these data have been spatially and temporally incomplete, inadequate and inaccurate [2]. Accurate scientifically valid continental or global scale land cover data sets do not currently exist for either the developed or the developing world [3]

To overcome these shortcomings, efforts are ongoing among international scientific organizations to provide timely, comprehensive, and accurate global scale land cover and vegetation datasets. The most important of these are derived from satellite imaging systems, including meteorological sensors such as AVHRR [4]. Since the early 1980's, a number of continental and global scale data sets have been produced using AVHRR data. The focus of our proposed research is the 1 Km Global Land Cover Data Set developed by The International Geosphere Biosphere Programme (IGBP) and the US Geological Survey EROS Data Center (USGS/EDC).

The IGBP 1 Km Global Land Cover Data Set is being assembled to meet data requirements for studies of climate, biogeochemical cycles, atmospheric chemistry, water, energy, vegetation, and ecosystems [5]. The data set is being compiled on an individual continental basis from AVHRR data collected daily through the efforts of a number of AVHRR receiving stations coordinated by USGS/EDC. An initial "fast-track" data set is being generated by researchers at EDC and the European Economic Commission's Joint Research Center (JRC) at Ispra, Italy.

The 1 Km Land Cover Data Set is being generated with 17 land cover classes ranging from natural vegetation to developed land and non-vegetated classes. These classes are:

1) Evergreen Needleleaf Forests
2) Evergreen Broadleaf Forests

0-7803-3068-4/96$5.00©1996 IEEE

3) Deciduous Needleleaf Forests
4) Deciduous Broadleaf Forests
5) Mixed Forests
6) Closed Shrublands
7) Open Shrublands
8) Woody Savannas
9) Savannas
10) Grasslands
11) Permanent Wetlands
12) Croplands
13) Urban and Built-up
14) Cropland/Natural Vegetation Mosaics
15) Snow and Ice
16) Barren
17) Water Bodies

A more thorough discussion of this classification scheme may be found in [6].

METHODOLOGY

For statistical analysis of this data set we are utilizing a directed random sampling procedure which follows the overall accuracy verification procedure developed through the IGBP for analysis of the complete 1Km Global Land Cover Data Set [7].

This strategy includes two elements: 1) a core sampling strategy to systematically assess the accuracy of each cover type included in the global land cover product and 2) the use of confidence sites where fine-resolution land cover information is available for a substantial region. The core sampling strategy will be based on visual interpretation of high resolution satellite image data coregistered with the AVHRR data. The sampling design takes into account the spatial variance of all cover classes. Decision rules and interpretation keys will also be developed to aid in visual interpretation of the high resolution data. Some important assumptions relate to the classification scheme and the classification method. It is assumed that the classification scheme is exhaustive (all pixels are assigned to a class); that it is exclusive (classes do not overlap); and that classes can be identified both on AVHRR data and higher resolution imagery. The classification methodology assumes that it is objective, consistent, reproducible and fully documented.

This procedure will be performed independently for both Africa and North America. Following initial data compilation, by-class area calculations will be performed for each data set and land cover difference maps will be produced. Area weighted estimates of overall map accuracy will then be calculated. Individual class accuracy statistics will be generated next and confusion matrixes produced for both EROS and JRC North America and Africa maps. These results will be statistically evaluated for variance between the two output products. We will stratify these samples by continent as well as processing technique in order to make inferences based on variances (if any) between continents. We will determine if statistically significant classification differences result from the different processing flows used in land cover data set compilation for each continent and, if so, we will address their sources and potential remedies.

This study will further identify those IGBP land cover classes, if any, which can not be mapped from processed AVHRR data and validated to acceptable accuracy standards using higher resolution Landsat/Spot data sets.

STATUS

Activities to date on this study have been focused on compilation of the 1 km Land Cover Data Sets covering North America and Africa. Currently, the classified 1 km coverage for the continent of North America has been completed by scientists at USGS/EDC. Initial by-class area calculations for the continent have also been generated (Tab.1). These by-class area figures were derived by simply summing the number of 1 km pixels present in each class within the data set. As outlined above, these are only the first steps in a more complex effort to validate the land cover classification procedures for the 1 km data set.

Tab.1.

Land Use Class	Class Area (km^2)	Percent Image
1	2844279	3.22
2	530527	0.60
4	1886191	2.14
5	1700355	1.93
6	575226	0.65
7	2461381	2.79
8	1455227	1.65
9	784579	0.89
10	1438454	1.63
11	36066	0.04
12	1330202	1.51
13	88933	0.10
14	2250978	2.55
15	2398183	2.72
16	1404335	1.59
17	65060904	73.69
18	1982163	2.25
0	58914	0.07
Image total	88286896	100.00

As outlined above, these are the first steps in a comprehensive study to validate the land cover classification procedures for the 1 Km Land Cover Data Set. Our preliminary examination of these data identified some issues which must be addressed before proceeding to a thorough statistical evaluation of the data set. As an example , Tab. 1 shows that a very small number of pixels in the data set (approximately .025 of the total area) remain unclassified. These are represented by Classes 0 and 18.

The next critical task to be performed is the selection and location of test sites for this study. We are currently examining the North America data set in preparation for identifying and locating appropriate study sites within North America and Africa. Adept identification of test subregions is a critical step in this study and optimal test site selection is dependent upon two related factors. Test sites must encompass the broadest range of 1Km Land Cover categories possible and be small enough to ensure availability of verification image data and to allow for the completion of processing and analysis. The subregions selected must be "adequately" covered by Landsat and/or SPOT imagery. Ideally, test sites will be covered by imagery that is currently compiled and archived by EOSAT or Spot Image or already in the hands of EDC and JRC researchers. These higher resolution images will form the basis upon which the validity of the AVHRR products are interpreted and assessed. In addition, available image data must be of adequate quality (cloud free or less than 10% cloud cover). Initial estimates indicate that optimally situated rectangular test subregions sized on the order of 1500 x 1500 Km should include most (12-15) of the 17 total 1Km Land Cover classes in Africa and North America. We initially see IGBP Classes 2,3,6,11, and 15 as potential problems. We will focus within the conterminous Unites States for selecting the North America test site.

EDC researchers are in the process of deriving the 1 km land use data set for the continent of Africa. Concurrently, researchers at JRC are producing classifications for Africa as well as North America.

CONCLUSIONS

This study is part of a broad scientific effort to develop and implement the Global 1Km Land Cover Data Set. The validation of this data set will establish quantitative statistical parameters of thematic accuracy of the data set. This will facilitate the use of the Land Cover Data Set and contribute accurate information on changes in global land cover types and can may also provide accurate baseline information for assessing changes in ecosystems and for input into continental or global scale hydrologic models.

ACKNOWLEDGMENTS

The authors wish to acknowledge the contributions which have been and are being made to this research by Mr. Thomas Loveland, and Drs. Alan Belward, Alan Strahler, and Clive Anderson. This work is being conducted as a part of National Aeronautics and Space Administration Research Grant NAGW-1743 and we also gratefully acknowledge the support of this agency.

REFERENCES

[1] Tucker, C.J., J.R.G. Townshend, and T.E. Goff. 1985. African land cover classification using satellite data. Science, 227, 369-375.

[2] Townshend, J.R.G., C.O. Justice, W. Li,, C. Gurney, and J. McManus. 1991. Global land cover classification by remote sensing: present capabilities and future possibilities. Remote Sensing of Environment, 35, 243-256.

[3] Estes, J.E. and W. Mooneyhan, 1994, Of maps and myths, Photogrammetric Engineering and Remote Sensing, Vol. 60, No. 5, pp. 517-524.

[4] Eidenshink, Jeffrey C. 1992. The 1990 Conterminous U.S. AVHRR Data Set. Photogrammetric Engineering and Remote Sensing, 58:6, pp.809-813.

[5] Belward, A. and T. Loveland. 1995. The IGBP-DIS 1Km Land Cover Project. International Geosphere Biosphere Programme. European Commission Joint Research Center, Ispra, Varese, Italy.

[6] Belward A. and Tom Loveland. 1995. The IGBP 1 Km Land Cover Project. Proceedings of the Remote Sensing Society Annual Conference, Southampton, England.

[7] Belward, A. (Ed.). 1995. The IGBP-DIS 1 Km Land Cover Data Set: A Validation Strategy Proposal. International Geosphere Biosphere Programme Draft Strategy Document. European Commission, Joint Research Centre. Ispra, Italy.

Potential of SIR-C Data to Study Vegetation Over Gujarat Test Site, India

K. S. Rao and Y.S. Rao

CSRE, Indian Institute of Technology, Bombay - 400 076, India
Email: ksrao@powai.cc.iitb.ernet.in Fax: + 91 22 5783480
and
L. Venkataratnam and P.V. Narasimha Rao
Agriculture & Soils Group, NRSA, Balanagar, Hyderabad 500 037, India

Abstract - Multifrequency Polarimetric SIR-C data acquired during April 1994 was processed to extract information on vegetation and salinity parameters. Signatures at different frequencies and polarizations were derived for several land categories. The polarization ratio of L (HV) to L (VV) is found to be a useful parameter for the discrimination of vegetation. Cross polarization is found to be very good for identification of field boundaries and road network.

INTRODUCTION

It can be seen from the literature that a good amount of research work was carried out by various researchers with an attempt to quantify Soil moisture, vegetation and Salinity [1]. Most of the above work was done with single frequency and single polarization SAR data. With the launch of SIR-C, it became possible to have simultaneous multifrequency multipolarization SAR data for efficient modelling of Geophysical parameter retrieval [2]-[4].

The aim of this paper is to see the potential of SIR-C/X-SAR data for the retrieval of vegetation and salinity through multifrequency multipolarization modelling. The subsequent sections deal with study area, ground truth collection, data processing and results & discussions.

STUDY AREA AND DATA SOURCES

Multifrequency polarimetric SIR-C/X-SAR data is unique and only data set so far available over Indian test sites. The first flight of SIR-C acquired data over Gujarat test site centered at 22° Lat. and 72° Long in mode 16X (L & C bands are fully polarimetric and X - band VV) on April 12, 14 and 15, 1994. Each pass covers about 500 km with a swath width of about 20 km, each pass at 50°, 36° and 24° incidence angle respectively.

0-7803-3068-4/96$5.00©1996 IEEE

GROUND TRUTH DATA

Synchronous with SIR-C flight, ground truth data were collected in terms of soil moisture, vegetation, surface roughness etc. The fields covered in this area are paddy, tomato, sugar cane, harvested wheat, bajra and many bare & ploughed fields. Also scattered prosopis juliflora plants are present at many places. Most of the fields are dry except irrigated areas. Soil moisture vary in the irrigated areas from 5 to 30 % by weight. All the saline soil fields are very smooth and agriculture fields were medium to very rough. The details on the ground truth data collected are given in [5].

DEPLOYMENT OF CORNER REFLECTORS

For SIR-C/X-SAR mission, we have fabricated three triangular trihedral corner reflectors suitable for L-, C- and X- bands. The details of these corner reflectors are as follows:

Size (L) (meters)	Gain values in dB		
	L - band	C - band	X - band
2.44	34.3	46.4	51.9
0.90	17.0	29.1	34.6
0.60	9.9	22.1	27.5

DATA PROCESSING

The pre-processing of SIR-C data was carried out using JPL software and EASI/PACE around IBM RISC 5000 computing system available at National Remote Sensing Agency, Hyderabad. We have taken several sub-scenes where the ground truth is collected. Optical data from Indian Remote Sensing Satellite (IRS-1B) were also acquired and registered with SIR-C data. The scenes of HH, VV and HV polarizations are generated at L- and C- bands. Colour

composites using different polarizations and frequencies were also generated.

Polarization ratio (L-HH/L-VV) of a sub-image was computed with a view to enhance the vegetation information content.

RESULTS AND DISCUSSION

It was noticed from the sub-image extending from Bhavnagar to Surendranagar that the cross polarization image gives more information on field boundaries and road networks compared to like polarizations. The sensitivity to the variations in soil moisture and vegetation is high for HH and VV compared to HV polarizations. Saline soils show low backscattering coefficient (σ°) for HV compared to like polarizations. Salt pans around Bhavnagar are clearly visible in all the three polarizations.

Fig. 1 shows the multifrequency multipolarization sub-images including colour composite and polarization ratio around Barwala town. The following points can be seen from the above figure :

- The (σ°) values are more or less in the same range for HH and VV where as they are very low for HV. The same phenomenon is observed for both L- and C- bands.
- The (σ°) values are higher for C- band compared to L-band.
- A colour composite generated with C(HV), L(HH) and L(HV) (RGB respectively) shows more classes compared to any one of the individual bands. Fields with different levels of soil moisture and vegetation types are clearly distinct in the colour composite.
- The polarization ratio of L (HV/VV) is computed for the sub-scene and made colour composite with L (VV) and L (HV). Certain vegetation classes which are not very clear in the previous colour composite are clearer in this one.

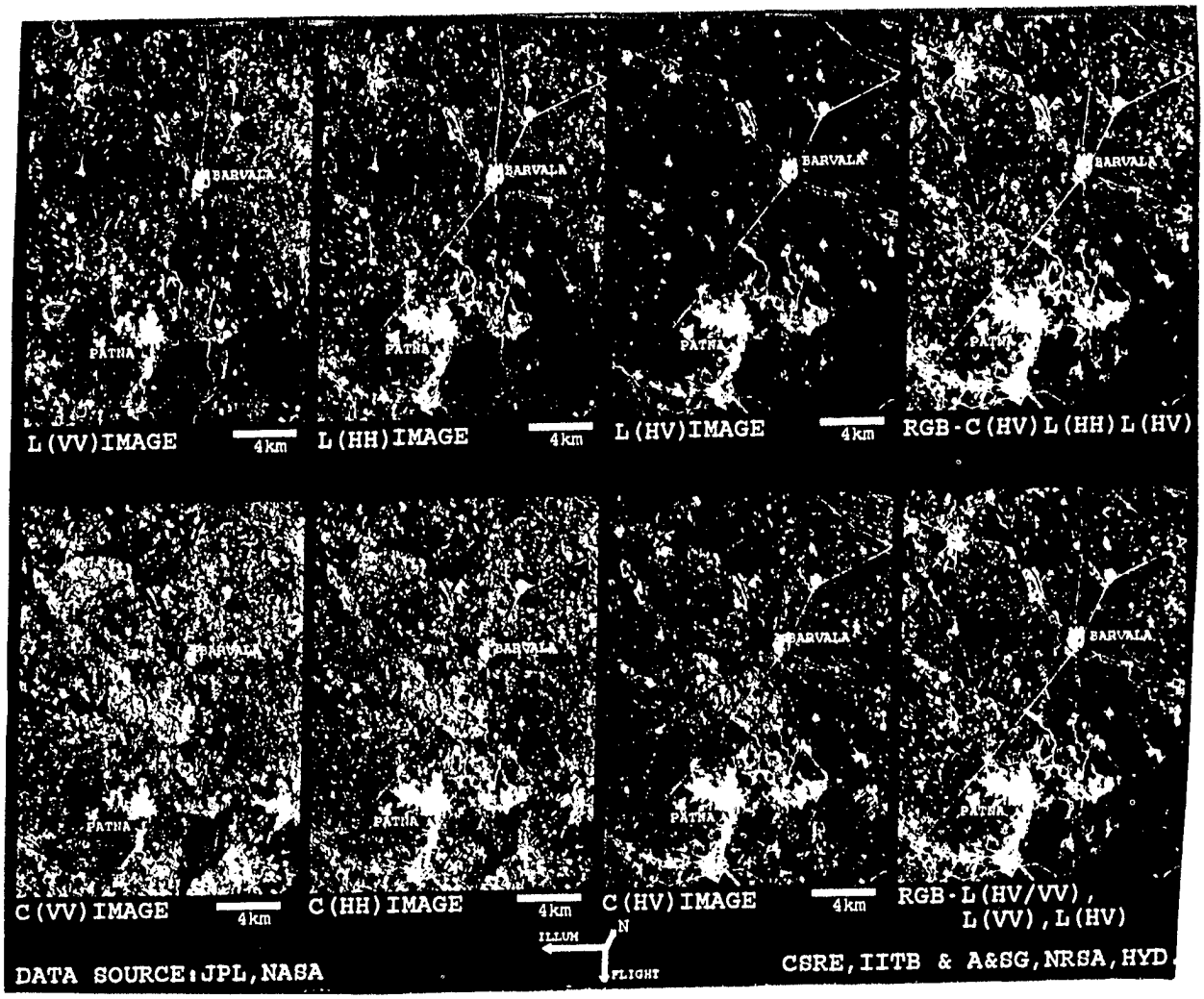


Fig.1. SIR-C images at different polarizations around Barvala town, Gujarat, India. Colour composite images are also seen using ratio of L(HV/VV) and direct combinations.

Fig. 2 shows the RGB colour composite of (a) L(HV), L(VV) and L(HH), (b) C(HV), C(VV) and C(HH), (c) L(VV), C(VV) and x(VV) and (d) IRS-1B colour composite for the area between Bhavnagar and Ahmedabad. It can be seen from the figure that

- in the submerged areas near to the coast, HH and VV dominates over HV for both L-and C- bands.
- with reference to the visible data, the vegetation along the river course are seen with high (σ°) values.
- The presence or the absence of water in the river could not be identified in SAR data where as that is very clearly seen in the visible data.
- In general, the contrast among different land covers is better in L- band as compared to C- band.

The sub-image extending from Bhavnagar to Navsari through gulf of Khambat is also analysed. Over the sea water, the (σ°) is higher for L- band compared to C- band, higher for HH and VV compared to HV. X- band shows the lowest values. From all the sub-images discussed above, the (σ°) values for different land covers are extracted (averaged for 3 x 3 pixels) and given below:

Feature	L-band (σ°)			C-band (σ°)		
	HH	VV	HV	HH	VV	HV
Urban	-4.8	-6.3	-6.0	-1.5	-0.5	-3.8
MP.	-5.8	-5.0	-18.9	-4.5	-4.2	-14.2
BF.	-13.6	-13.7	-26.4	-7.1	-6.2	-17.1
SP	-16.2	-15.7	-29.2	-13.3	-12.2	-22.3
Crop	-8.7	-10.2	-16.1	-5.8	-4.4	-12.5
Smooth	-17.9	-16.2	-32.5	-10.8	-10.2	-19.8

MP. - Mud plots, BF. - Bare Field, SP. - Salt pans

CONCLUSIONS

The preliminary analysis of SIR-C data indicates the potential for the identification of various vegetation types, different levels of soil moisture. HV is better for the identification of locations, where as HH and VV are better for analysis. Further work on Polarization Phase Difference, Polarization Index, Scattering Decomposition and Inversion is in progress.

ACKNOWLEDGMENTS

We are thankful to Prof. V.S. Chandrasekaran, Head, CSRE for his encouragement. Thanks are due to the scientists from JPL for generously giving the SIR-C data and software. Finally we thank DST for providing financial support to carryout the work.

REFERENCES

[1] M.C. Dobson and F.T. Ulaby, "Active microwave soil moisture research," IEEE Trans. Geosci. and Remote Sensing, GE -24, No.1, PP. 23 - 36, 1986

[2] E.R. Stofan et al., "Overview of Results of Spaceborne Imaging Radar - C, X-Band Synthetic Aperture Radar," IEEE Trans. Geosci. and Remote Sensing, GE-33, No.4, PP. 817 - 828, 1995.

[3] P.C. Dubois, J. van Zyl and T. Engman, "Measuring soil moisture with imaging radar," IEEE Trans. Geosci. and Remote Sensing, GE-33, No.4, PP. 915 - 926, 1995.

[4] K.J. Ranson, S. Saatchi and G. Sun, "Boreal forest ecosystem characterization with SIR-C/X-SAR," IEEE Trans. Geosci.and remote sensing, V0l. 33, No. 4, July 1995.

[5] K.S.Rao, J. Adinarayana and Y.S. Rao, "Ground truth data collection over Gujarat area synchronous with U.S. Space Shuttle SIR-C/X-SAR Mission," Final report submitted to DST, May 1995.

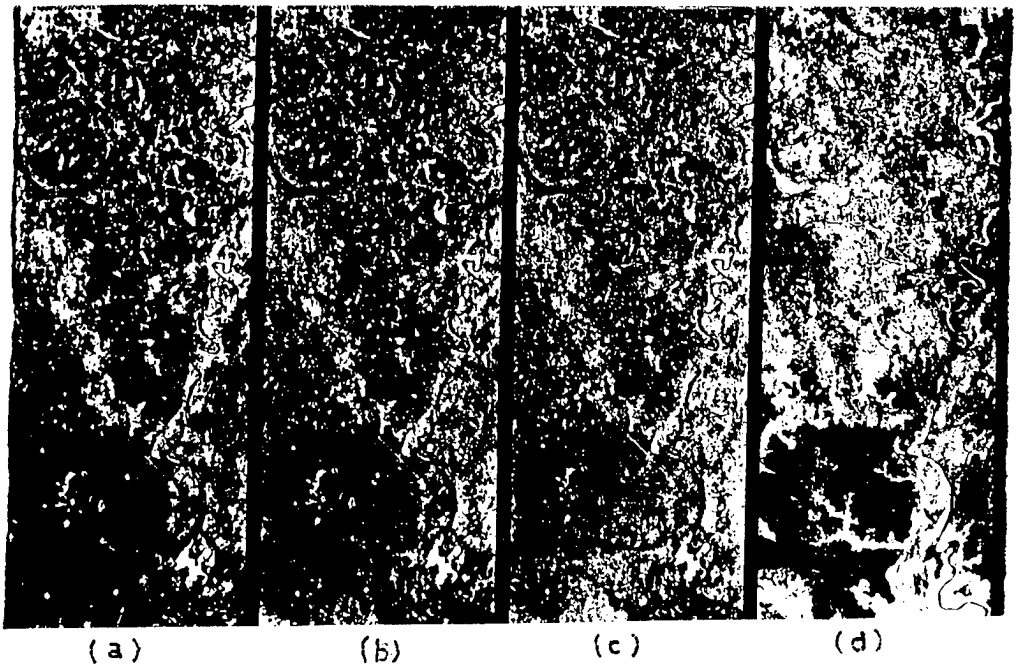


Fig.2. SIR-C/X-SAR colour composite images of an area between Bhavnagar and Ahmedabad. **(a)** L-HV(R), L-VV(G), L-HH(B); **(b)** C-HV(R), C-VV(G), C-HH(B), **(c)** L-VV(R), C-VV(G), X-VV(B) and **(d)** IRS-1B standard FCC.

Intercomparison of several BRDF models for the compositing of spaceborne POLDER data over land surfaces

Olivier Hautecoeur and Marc Leroy
Centre d'Etudes Spatiales de la Biosphère,
18 avenue Edouard Belin, 31055 Toulouse Cedex, France.

Abstract -- The surface reflectances derived from POLDER / ADEOS are operationally composited in time using an algorithm of adjustment of a BRDF model against POLDER directional reflectances. This paper compares several linear BRDF models as candidates for this algorithm. The various models are tested and compared against a variety of BRDF field data, and several criteria are examined.

INTRODUCTION

POLDER is a new instrument devoted to the global observation of the Bi-directional Reflectance Distribution Function (BRDF) and the Bi-directional Polarization Distribution Function (BPDF) of Earth's reflectances in the visible and near infrared [1]. It is scheduled to be launched in 1996 on the Japanese ADEOS platform. CNES (the French space agency) has started the development of 3 operational processing lines of science products, related to (1) land surfaces and atmosphere over land, (2) ocean color and aerosols over the ocean, and (3) Earth radiation budget, water vapor and clouds. The surface products of the 'land surfaces and atmosphere over land' processing line are, for each orbit segment, bi-directional reflectances corrected for atmospheric effects, and, every 10 days, global maps of surface directional signatures and hemispherical reflectances at 443, 670, 765, and 865 nm [2].

The choice of the compositing technique to apply to directional surface reflectances acquired each orbit, in order to generate a composite surface product at global scale and 10 day period, is one of the key questions to be solved. A data compositing method widely applied on AVHRR data is the MVC technique [3], whose principle is to select, over a given period of composition, the AVHRR data which maximizes the Normalized Differential Vegetation Index (NDVI). An alternative possibility, which can be used with AVHRR [4], and should be quite appropriate with POLDER directional reflectance measurements, is to adjust a parameterized BRDF model against a time series of BRDF measurements.

The choice of the BRDF model is a serious problem. The subject of this paper is to describe a detailed comparison of several available BRDF models to select one of them to be implemented in the 'land surface and atmosphere over land' processing line.

BRDF MODELS AND DATA SET

Many explicit analytical models of the surface BRDF exist in the literature. They are either linear or non linear, and either empirical, semi-empirical, or physically based. The model complexity increases with their degree of physical realism.

For the sake of simplicity and computer time limitations, only linear models were accounted for. We considered (see Table I): (1) the 4-parameter empirical model of Shibayama

Table I

θ_s , θ_v	*sun and view zenith angles*
ϕ	*relative azimuth angle* ($\phi < 180°$)
ξ	*phase angle* $\cos\xi = \cos\theta_s \cos\theta_v + \sin\theta_s \sin\theta_v \cos\phi$

Notations of model parameters have been made identical.

Shibayama and Wiegand [5], named 'Shibayama's model'

$$\rho(\theta_s,\theta_v,\phi) = k_0 + k_1 \sin\theta_v + k_2 \sin\theta_v \sin\frac{\phi}{2} + k_3 \frac{\sin\theta_v}{\cos\theta_s}$$

Walthall, Norman, Welles, Campbell and Blad [6], modified by Nilson and Kuusk [9], named 'Walthall's model'

$$\rho(\theta_s,\theta_v,\phi) = k_0 + k_1\theta_s\theta_v\cos\phi + k_2\theta_s^2\theta_v^2 + k_3\left(\theta_s^2+\theta_v^2\right)$$

Deering, Eck and Otterman [7], named 'Deering's model'

$$\rho(\theta_s,\theta_v,\phi) = k_0 + k_1\frac{(\pi-\phi)\cos\phi+\sin\phi}{4\left(\cot\theta_s+\cot\theta_v\right)} + k_2\frac{\sin\phi-\phi\cos\phi}{4\left(\cot\theta_s+\cot\theta_v\right)}$$

Roujean, Leroy and Deschamps [8], named 'Roujean's model'

$$\rho(\theta_s,\theta_v,\phi) = k_0 + k_1 f_1(\theta_s,\theta_v,\phi) + k_2 f_2(\theta_s,\theta_v,\phi)$$

$$f_1(\theta_s,\theta_v,\phi) = \frac{1}{2\pi}\left[(\pi-\phi)\cos\phi+\sin\phi\right]\tan\theta_s\tan\theta_v - \frac{1}{\pi}\left[\tan\theta_s+\tan\theta_v+\sqrt{\tan^2\theta_s\tan^2\theta_v-2\tan\theta_s\tan\theta_v\cos\phi}\right]$$

$$f_2(\theta_s,\theta_v,\phi) = \frac{2}{3\pi}\frac{(\pi-2\xi)\cos\xi+\sin\xi}{\cos\theta_s+\cos\theta_v} - \frac{1}{3}$$

Spherical harmonics, named 'Legendre's model'

$$\rho(\theta_s,\theta_v,\phi) = k_0 + k_1\left[\left(2\cos\theta_s-1\right)\left(2\cos\theta_v-1\right)\right] + k_2\sin\theta_s\sin\theta_v\cos\phi + k_3\left[\left(6\cos^2\theta_s-6\cos\theta_s+1\right)\left(6\cos^2\theta_v-6\cos\theta_v+1\right)\right] + k_4\left[\left(8\cos\theta_s-3\right)\left(8\cos\theta_v-3\right)\sin\theta_s\sin\theta_v\cos\phi\right] + k_5\sin^2\theta_s\sin^2\theta_v\cos 2\phi$$

0-7803-3068-4/96$5.00©1996 IEEE

Table II

Cover type	Reference	Number of data sets	Solar zenith angle range
Cobble	[10]	5	20° - 58°
Lava flow		6	21° - 73°
Playa		6	28° - 71°
Bare soil	[11]	10	16° - 69°
(3 roughness)		4	36° - 53°
		4	36° - 54°
Prairie grassland	[12]	4	22° - 62°
Soybean	[13]	5	20° - 49°
(3 dates)		6	21° - 38°
		12	31° - 61°
Spruce-Hemlock forest	[14]	6	35° - 76°
Corn	[15]	3	23° - 68°
Orchard grass		3	45° - 71°
Soybeans		3	48° - 63°
Grass lawn		3	42° - 70°
Plowed field	[16]	3	26° - 45°
Annual grassland		3	28° - 50°
Hard wheat		3	27° - 51°
Steppe grass		3	27° - 63°
Irrigated wheat		3	26° - 59°
Pine forest	[17]	3	23° - 59°
Deciduous forest		3	25° - 63°

and Wiegand [5], designed to fit the BRDF of wheat canopies, (2) a modified version of the empirical model of Walthall *et al.* [6] satisfying the reciprocity principle, as used by Nilson and Kuusk [9], (3) the semi-empirical model of Deering *et al.* [7], designed for arid and semi-arid soils, (4) the 3-parameter semi-empirical model of Roujean *et al.* [8], and (5) a linear decomposition of the BRDF on a basis of spherical harmonics. Spherical harmonics are functions of only 2 variables (say, θ_v and ϕ). The model was modified to become a reciprocal function of all 3 geometric angles.

These various models were tested over a variety of field data, available in free access data bases, acquired by various authors, on many different surface types: lava flow, cobble, sand, plowed soils, Kansas prairie, grass, cultures (soybean, wheat, orchard, corn), spruce and pine forests. Altogether a set of about 100 BRDF measurements were considered in the analysis, acquired over 18 different types of surfaces, with various sun zenith angles for each site (Table II). We acknowledge here that the models of Shibayama and Wiegand, and that of Deering *et al.* were used in this comparison because of their property of linearity but were tested on surface types differing much from the surface types for which they were designed

MODEL EVALUATION

The models were evaluated on the basis of several criteria:

(1) ability to fit BRDF measurements acquired at a given sun zenith angle. All BRDF data are considered in this test. The indicators of the comparison include:

- the rms error : $\sqrt{\frac{\sum_{i=1}^{n}(\rho_{imeas} - \rho_{i\,\mathrm{mod}})^2}{n}}$
- the signal to noise S/N ratio : $10\log_{10}\left(\frac{\sum_{i=1}^{n}(\rho_{imeas} - \overline{\rho_{meas}})^2}{\sum_{i=1}^{n}(\rho_{imeas} - \rho_{i\,\mathrm{mod}})^2}\right)$

Fig. 1 represents, for each BRDF data, in the visible and near infrared, S/N of each model as a function of S/N of the model of Roujean. The typical S/N is of the order of 0 to 20.

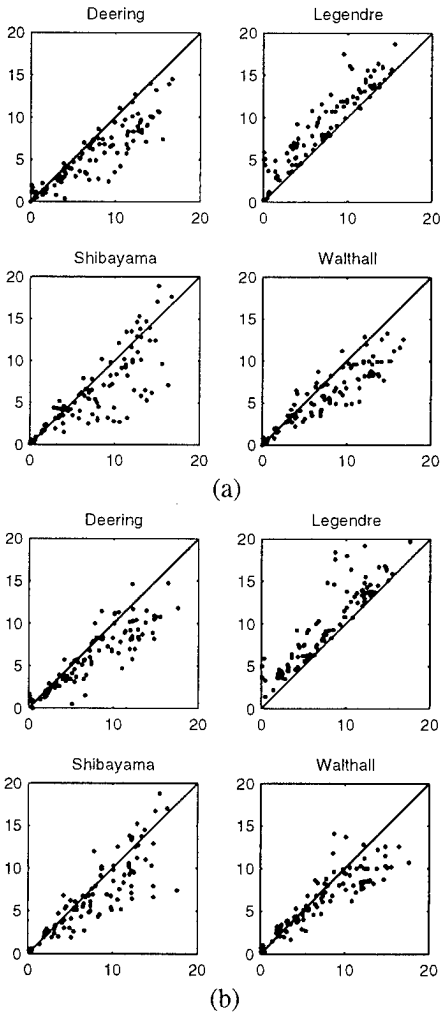


Figure 1: S/N ratio of each model compared to that of Roujean for each BRDF data set. (a) visible, (b) near infrared

Fig. 1 shows that the performance of the Legendre model is higher than that of Roujean, itself somewhat above that of the other models. Fig. 2 shows an example of BRDF restitution by each model, which illustrates the fact that some differences exist between the restituted BRDFs. Generally the most important errors are in the backscattering region in the vicinity of the hot spot, and sometimes also in the specular direction.

(2) ability to fit BRDF measurements acquired with a range of sun zenith angles. It is also important to test the ability of models to represent the BRDF for a significant range of variation of the sun zenith angle (typically variations of the order of 20°) representative of the variations of θ_s encountered in a one-month period of POLDER acquisitions. The considered data sets are listed in Table III, and the results are displayed in Fig. 3 in terms of S/N (in the same format as Fig. 1) and also in Table III in terms of rms error. Fig. 3 shows that S/N decreases relatively to the previous situation, and that the differences between models are less significant than before. However, the ordering of models remains approximately the same. Generally, the rms errors as shown by Table III are of the order of 0.005 to 0.02 in the visible and 0.02 to 0.04 in the near infrared. The performance of models is generally better on bare soils and cultures than on forests and grasslands.

(3) ability to simulate spectral directional hemispherical reflectances. For data sets which include the directional hemispherical reflectance data (*i.e.*, the bi-directional reflectance integrated over the half space of possible viewing directions), a comparison is made between the data and the models, at the exception of the model of Deering for which the functions can not be integrated analytically. Fig. 4 compares modeled and measured hemispherical reflectances in the visible and near infrared, and shows that all models restitute satisfactorily the hemispherical reflectances.

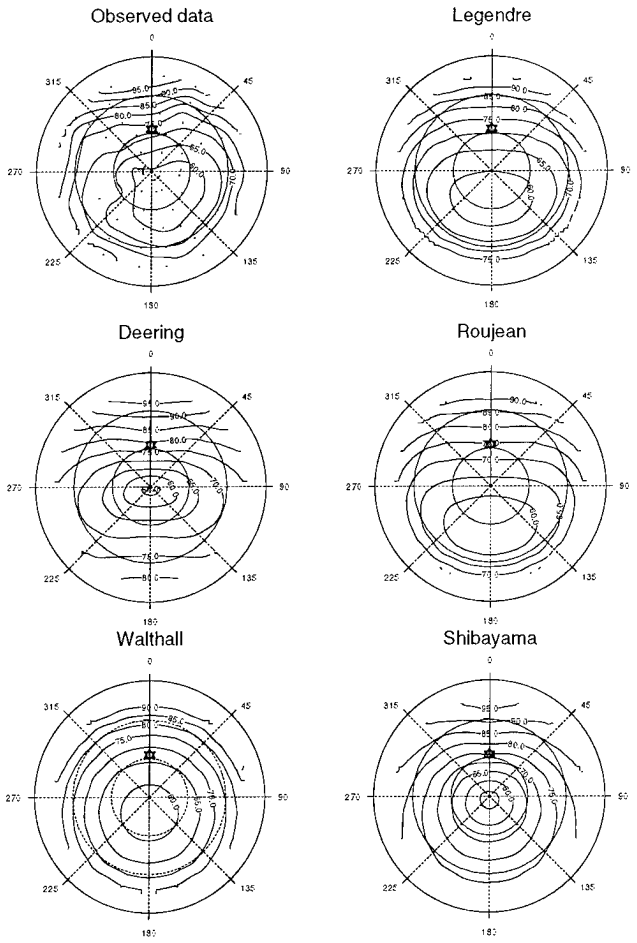


Figure 2: Observed and restituted BRDFs for the prairie grassland site in the near infrared.

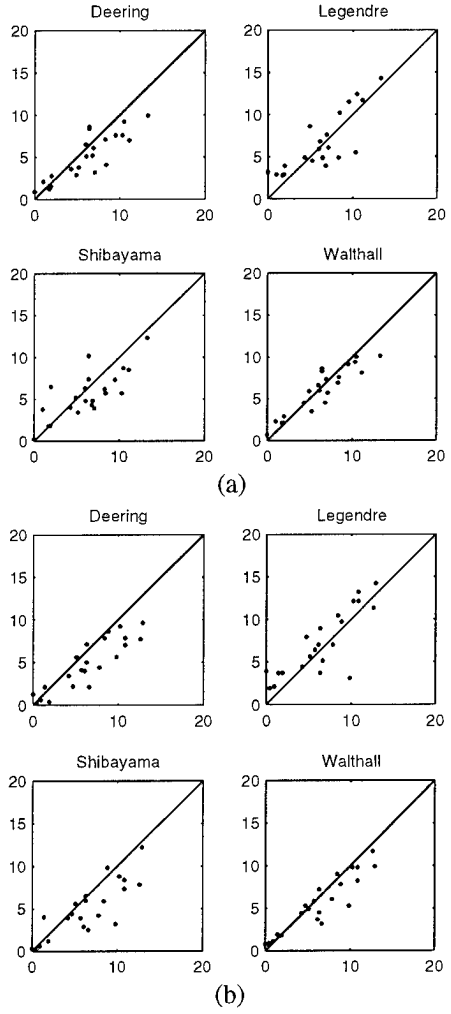


Figure 3: Same as Fig. 1 when BRDF data cover for each surface type a range of sun zenith angles.

Table III: rms error performance (% of reflectance).

	Sun zenith angle range (number of data sets)	Visible					Near Infrared				
		Deering	Legendre	Roujean	Shibayama	Walthall	Deering	Legendre	Roujean	Shibayam	Walthall
Spruce	35-45 (4)	1.8	1.5	2.0	1.5	1.9	11.6	10.5	13.1	9.5	11.3
Prairie grassland	22-33 (2)	2.3	1.5	2.0	1.9	2.4	9.0	4.4	5.5	7.5	6.0
Soybean 07/17/80	20-40 (4)	1.1	0.9	1.1	1.1	1.0	4.5	3.8	4.3	4.3	4.1
Soybean 07/24/80	21-38 (6)	0.7	0.6	0.7	0.7	0.6	4.0	3.4	3.8	3.8	3.7
Soybean 08/27/80	31-48 (10)	0.3	0.2	0.3	0.3	0.2	2.6	2.3	2.4	2.5	2.4
Bare soil 06/30/89	23-52 (8)	2.4	1.4	1.6	2.1	2.1	3.0	1.8	1.9	2.5	2.7
Bare soil 08/09/89	36-53 (4)	2.0	1.2	1.4	1.5	1.9	2.3	1.4	1.6	1.8	2.3
Bare soil 08/25/89	28-54 (7)	2.4	1.7	2.1	2.5	2.2	2.8	2.0	2.4	3.0	2.6
Annual grassland	28-50 (3)	1.8	1.4	1.7	2.3	1.6	2.9	2.4	2.6	3.4	2.5
Corn	23-46 (2)	1.3	0.9	1.1	1.2	1.1	2.4	1.7	1.5	2.2	1.8
Deciduous forest	25-45 (2)	1.1	0.8	0.6	1.0	0.9	5.2	4.6	5.7	3.4	5.2
Grass lawn	56-70 (2)	1.0	1.5	1.1	1.1	1.0	4.8	7.1	6.0	5.3	4.8
Orchard grass	45-58 (2)	0.8	0.7	0.8	0.7	0.9	3.2	4.1	2.7	3.5	3.2
Pine forest	41-59 (2)	1.1	1.5	0.7	1.5	1.2	2.8	3.3	2.4	3.1	3.1
Plowed field	26-45 (3)	2.7	1.4	1.9	2.9	2.1	3.2	2.1	2.6	3.4	2.7
Soybean	28-49 (2)	0.5	0.3	0.4	0.5	0.5	3.7	3.4	3.1	3.9	3.9
Steppe grass	27-35 (2)	2.6	2.0	2.1	2.6	2.1	2.5	2.0	2.2	2.5	2.2
Hard wheat	32-51 (2)	1.9	1.2	1.1	1.9	1.2	3.5	4.4	2.5	4.3	2.8
Irrigated wheat	26-42 (2)	1.0	0.7	0.7	1.0	0.8	3.1	4.8	4.0	2.5	3.1
Cobble	28-49 (3)	3.6	1.9	2.7	2.8	2.6	3.5	1.8	2.7	2.6	2.4
Lava	33-52 (3)	1.8	1.9	2.0	1.8	2.0	2.4	2.5	2.5	2.4	2.3
Playa	28-54 (4)	3.7	2.8	4.3	4.2	4.0	4.1	3.1	4.5	4.4	4.2

(4) robustness. Two criteria are established to measure the robustness of models. The first is to measure the standard deviation of the retrieved $k_0(\lambda)$ when θ_s varies (for a given surface) over the whole range of available sun angles. The coefficient $k_0(\lambda)$ corresponds to the 'Lambertian' basis of the BRDF for each model. Table IV reports the range of the above standard deviation of $k_0(\lambda)$ for the whole data set. This criterion favors the Legendre model; next come the Roujean and Walthall models.

Table IV: Range of standard deviation of k_0 (see text).

	Deering	Legendre	Roujean	Shibayama	Walthall
Visible	0.04	0.01	0.02	0.03	0.02
Near infrared	0.06	0.04	0.05	0.06	0.05

The second criterion is to examine the rms error when some data occupying part of the available directional space are discarded. This latter criterion is important since it measures the ability to extrapolate a model to sun or view angles which have not been used to retrieve the model parameters in the fitting procedure. Table V shows the rms performance of the Legendre and Roujean models on a few sites in 5 different situations : (1) all data, (2) forward scattering region only, (3) backscattering region only, (4) data with $\theta_v < 60°$ only (internal circlet), (5) data with $\theta_v > 50°$ only (external circlet). This table shows that in most situations the Legendre model is less robust than the Roujean model. This is not surprising since the Legendre model is completely empirical, while the semi-empirical nature of the model of Roujean permits to resist better to 'holes' in the BRDF data set.

Table V: rms error performance (% of reflectance).

	Soybean	Prairie	Bare soil	Spruce forest
Roujean model				
All data	0.35	1.47	1.42	1.24
Forward side	0.44	1.99	1.49	2.05
Backward side	0.55	1.92	1.51	1.56
Internal circlet	0.35	3.73	1.57	2.44
External circlet	0.51	1.95	1.56	1.27
Legendre spherical harmonics				
All data	0.30	1.06	1.29	0.98
Forward side	0.68	4.51	2.58	1.38
Backward side	0.49	2.50	9.58	3.81
Internal circlet	0.30	1.44	1.41	1.17
External circlet	0.49	7.81	11.94	1.00

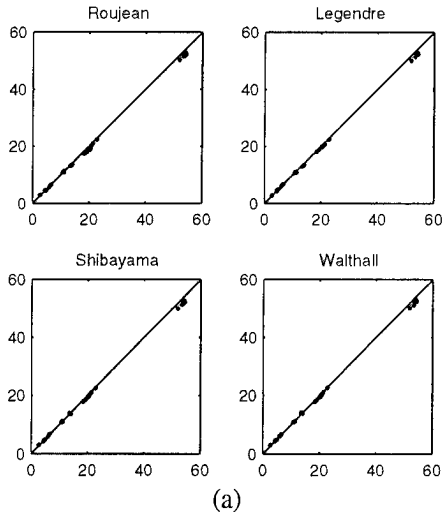


Figure 4: Modeled versus measured hemispherical reflectances (% of reflectance). (a) visible, (b) near infrared.

CONCLUSION

This study has compared several linear BRDF models as candidates for the compositing algorithm of POLDER surface reflectance data. The various models were tested against a variety of field BRDF data, and several criteria were examined. The paper shows that the purely empirical model based on spherical harmonics leads to the best adjustments of BRDF data, and that the semi-empirical model of Roujean *et al.* produces an adjustment less good than the Legendre model but somewhat better than the other models. On the other hand, the purely empirical nature of the Legendre model leads to more instability, when data are discarded from the data set, than the Roujean model. This is why we eventually chose the Roujean model for the POLDER algorithm. The overall shape of the BRDF is well reproduced by the model, except for the hot spot and specular directions. The model reproduces satisfactorily hemispherical reflectances, an important step for the estimation of surface albedo.

REFERENCES

[1] Deschamps P.-Y., Bréon F.-M., Leroy M., Podaire A., Bricaud A., Buriez J.-C. and Sèze G., 1994. The POLDER mission: Instrument characteristics and scientific objectives. *IEEE Transactions on Geoscience and Remote Sensing*, **32**, 598-615.

[2] Leroy M., Deuzé J.-L., Bréon F.-M., Hautecoeur O., Herman M., Buriez J.-C., Tanré D., Bouffiès S., Chazette P. and Roujean J.-L., 1996. Retrieval of atmospheric properties and surface bidirectional reflectances over land from POLDER / ADEOS. *Unpublished.*

[3] Tarpley J.P., Schneider S.R. and Money R.L., 1984. Global vegetation indices from NOAA-7 meteorological satellite. *Journal of Climate and Applied Meteorology*, **23**, 491-494.

[4] Leroy M. and Roujean J.-L., 1994. Sun and view angle corrections on reflectances derived from NOAA/AVHRR data. *IEEE Transactions on Geoscience and Remote Sensing*, **GE-32**, 684-696.

[5] Shibayama M. and Wiegang C.L., 1985. View azimuth and zenith, and solar angle effects on wheat canopy reflectances *Remote Sensing of Environment*, **18**, 91-103.

[6] Walthall C.L., Norman J.M., Welles J.M., Campbell G., and Blad B.L., 1985. Simple equation to approximate the bidirectional reflectance from vegetation canopies and bare soil surfaces. *Applied Optics*, **24**, 383-387.

[7] Deering D.W., Eck T.F., and Otterman J., 1990. Bidirectional reflectances of selected desert surfaces and their three-parameter soil characterization. *Agricultural and Forest Meteorology*, **52**, 71-93.

[8] Roujean J.-L., Leroy M., and Deschamps P.-Y., 1992. A bidirectional reflectance model of the Earth's surface for the correction of remote sensing data. *Journal of Geophysical Research*, **97**(D18), 20,455-20,468.

[9] Nilson T. and Kuusk A., 1989. A reflectance model for homogenous plant canopy and its inversion. *Remote Sensing of Environment*, **27**, 157-167.

[10] Arvidson R.E., Dale-Bannister M.A., Guiness E.A., Slavney S.H., and Stein T.C., 1991. Archive of Geologic Remote Sensing Field Experiment data. Release 1.0, CD-ROM Volume USA_NASA_PDS_GR_001, NASA Planetary Data System, Jet Propulsion Laboratory, California.

[11] Irons J.R., Campbell G. S., Norman J. M., Graham D.W., and Kovalick W.M., 1992. Prediction and measurement of soil bidirectional reflectance. *IEEE Transactions on Geoscience and Remote Sensing*, **30**(2), 249-260.

[12] Deering D.W., Middleton E M., Irons J.R., *et al.*, 1992. A comparison of prairie grassland bidirectional reflectances measured by different instruments at the FIFE site. *Journal of Geophysical Research*, **97**(D17), 18,870-18,903.

[13] Ranson K.J., Biehl L.L., and Bauer M.E., 1985. Variation on spectral response of soybeans with respect to illumination, view and canopy geometry. *International Journal of Remote Sensing*, **6**, 1827-1842.

[14] Deering D.W., Middleton E.M., and Eck T.F., 1994. Reflectance anisotropy for a spruce-hemlock forest canopy. *Remote Sensing of Environment*, **47**, 242-260.

[15] Kimes D.S., 1983. Dynamics of directional reflectance factor distributions for vegetation canopies. *Applied Optics*, **22**(9), 1364-1372.

[16] Kimes D.S., Newcomb W.W., Tucker C.J., Zonneveld I.S., Van Wijngaarden W., De Leeuw J., and Epema G.F., 1985. Directional reflectance factor distributions for cover types of northern africa. *Remote sensing of environment*, **18**, 1-19.

[17] Kimes D.S., Newcomb W.W., Nelson R.F., and Schuut J.B., 1986. Directional reflectance distributions of a hardwood and a pine forest canopy. *IEEE Transactions on Geoscience and Remote Sensing*, **GE-24**(2), 281-293.

Estimation of Seasonal Dynamics of Pasture and Crop Productivity in Kazakhstan Using NOAA/AVHRR Data

Anatoly Gitelson[α], Felix Kogan[β], Lev Spivak[χ], Edige Zakarin[χ], Lubov Lebed[ε]

[α]J. Blaustein Institute for Desert Research, Ben-Gurion University of the Negev, 84990 Israel; Phone: (972)-7-557 219; Fax: (972)-7-557 042; Email: gitelson@bgumail.bgu.ac.il; [β]National Environmental Satellite Data and Information Service, National Oceanic and Atmospheric Administration, USA; [χ]Institute for Space Research, Academy of Sciences, Kazakhstan. [ε]National Meteorological Administration, Kazakhstan

ABSTRACT

Recently, NOAA developed the AVHRR-based Vegetation Condition Index (VCI) for drought monitoring. This index was used for estimating pasture and crop productivity in Kazakhstan. The results of VCI-derived vegetation conditions were compared with vegetation density, biomass and reflectance measured in different climatic and ecological zones with elevation from 200 to 700 m and a large range of the NDVI variation (over space and season) from 0.05 to 0.47. An estimation error of AVHRR-derived vegetation density was less than 16 per cent. First time it was shown that the VCI-derived vegetation condition data can be effectively used for quantitative assessments of both vegetation state and productivity (density and biomass) over large areas.

INTRODUCTION

Drought is the typical phenomenon of the Kazakh climate which occurs every two to four years. In order to mitigate drought consequences thorough monitoring of drought start, expansion and duration is required. The goal of the work was to develop and test algorithms for using data obtained by the Advanced Very High Resolution Radiometer (AVHRR) flown on NOAA polar orbiting satellites for quantitative monitoring seasonal dynamics of pasture and crop conditions and production in Kazakhstan. In the paper we present comprehensive results of the validation of AVHRR-derived vegetation conditions with actually measured vegetation density.

DATA AND METHODS

Satellite data set contained Global Vegetation Index (16 km spatial resolution, 7 days temporal resolution) from NOAA-9, NOAA-11, and NOAA-14 (Ohring et al., 1989) in a period from 1985 to 1995. Ground data included historical set for the period from 1985 to 1995 on 10-day total precipitation (mm), average temperature, end of 10-day soil moisture, phenology and vegetation density (number of plants per square meter) from six weather stations located in different climatic zones of Kazakhstan. During the growing seasons of 1994 and 1995, the biomass of winter wheat and spring barley (three plots) and that of grass (four plots) were measured at two weather stations in Almaty region. Simultaneously upwelling radiance of vegetation and reference white plate were measured with hand-held radiometer in twenty different locations of each plot and average and median values were calculated. These measurements were made in the spectral bands corresponding to the red and near infra-red channels of the AVHRR sensor. The reflectance were determined as ratio of upwelling radiance of vegetation to that of reference plate. NDVI variation over space were studied also using airborne radiometer in the channels of NDVI.

The highest and the lowest NDVI values during 1985-1995 for each of the 52 weeks of the year and for each pixel was calculated. The weather component of the NDVI was enhanced by separating it from the ecosystem component [1-3]. The weather-related NDVI envelope was linearly scaled from zero (minimum NDVI) to 100 (maximum NDVI) for each grid cell and week. The resulting index was named the Vegetation Condition Index (VCI) defined by the following:

$$VCI = (NDVI - NDVI_{med}) / (NDVI_{max} - NDVI_{min})$$

where NDVI, $NDVI_{max}$ and $NDVI_{min}$ are the smoothed weekly NDVI [4], its multi-year maximum, and multi-year minimum, respectively, calculated for each pixel.

The average VCI data for the area of 48 km by 48 km (3 by 3 GVI pixels) were collected around six weather stations with the experimental plots. These stations are located in southern (Almaty region), central (Jeskazgan), and northern (Akmola) Kazakhstan. Analysis was done for two years with different weather conditions, 1991 dry and 1992 wet. Data on density of vegetation were measured several times (5 to 11) for the growing season in a period from 1985 to 1995. For comparison with VCI, the ground measurements of density were expressed in terms of multi-year variation. Each measurement, D_i, was expressed as a deviation from median, D_{med}, values and normalized to the range of multi-year fluctuation of the density, $(D_{max} - D_{min})$:

$$\delta D,(\%) = (D_i - D_{med})/(D_{max} - D_{min})$$

0-7803-3068-4/96$5.00©1996 IEEE

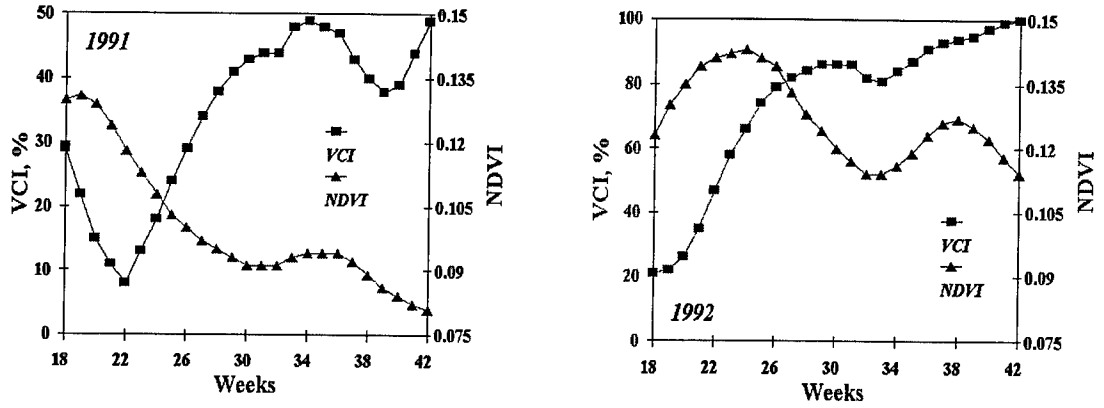


Fig 1. NDVI and VCI dynamics at station 36819 (Almaty region) in 1991 (dry) and 1992 (favorable conditions).

RESULTS AND DISCUSSION

NDVI and VCI dynamics on one of the test sites in Kazakhstan during two years with extremely different weather conditions are shown in Fig. 1. Although NDVI had very similar dynamics during these years, the VCI indicates that the dynamics of vegetation conditions were very different and VCI values in 1992 were two to three times larger than in 1991.

The attempt was made to find out whether AVHRR-derived VCI can be used as an quantitative indicator of vegetation productivity on a large area. The good match between VCI- and density-derived conditions shown in Figs. 2 and 3. Despite of the fact that six selected stations were located in very different climatic and ecological zones, with elevation changing from 300 to 700 m and a large range of NDVI variation (over space and season) from 0.05 to 0.47, all station points were located around the same correlation line (Fig. 4). Although there are some local differences, correlation was high $r^2 = 0.76$ with an estimating error of vegetation density of less than 16 percent. This error is less for low density, indicating that in cases of very unfavorable weather (such as drought) the accuracy of VCI-derived estimates is higher. One of the main causes for scattering of the VCI vs. Density relationship may be the difference between aerial estimates from satellite data and point measurements of ground density.

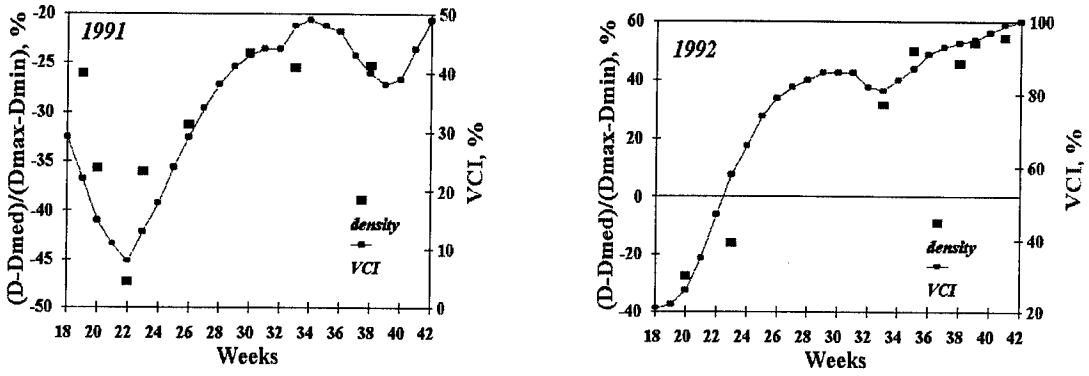


Fig. 2. Comparison of the VCI and multi-year density variation from median values in 1991 and 1992. Station 36819 (Almaty region)

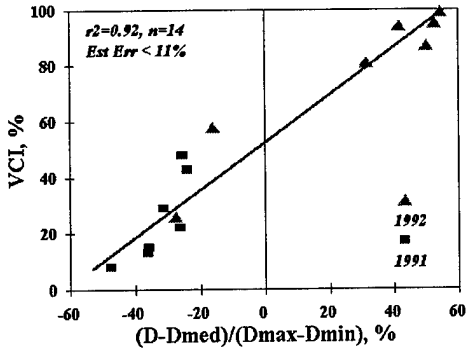


Fig. 3. Correlation between the VCI derived and actually measured density of vegetation. Station 36819 (Almaty region).

The findings are the first step in validating the VCI. First time it was shown that the VCI-derived vegetation condition data can be effectively used for quantitative assessments of density and biomass of vegetation over large areas.

REFERENCES

[1] Kogan, F.N., "Remote sensing of weather impacts on vegetation in non-homogeneous areas," Int. Journal of Remote Sensing, vol. 11, pp. 1405-1419, 1990.

[2] Kogan, F.N., "NOAA plays leadership role in developing satellite technology for drought watch," Earth Observation Magazine, September 1994, pp. 18-21, 1994.

[3] Kogan, F.N., "Drought of the late 1980s in the United States as derived from NOAA polar-orbiting satellite data," Bul. Of the Amer. Met. Soc., vol. 76, pp. 1-13, 1995.

[4] Ohring, G., K. Gallo, A. Gruber, W. Planet, L. Stowe, J.D. Tarpley, "Climate and Global Change: Characteristics of NOAA Satellite Data," Eos. Trans., Amer. Geophysical Union, vol. 70, pp. 889-901, 1989.

[5] Tucker, C.J., J.R.G. Townshend, T.E. Goff, "African Land Cover Classification Using Satellite Data," Science, vol. 227, No. 4685, January 25, pp. 369-375, 1985.

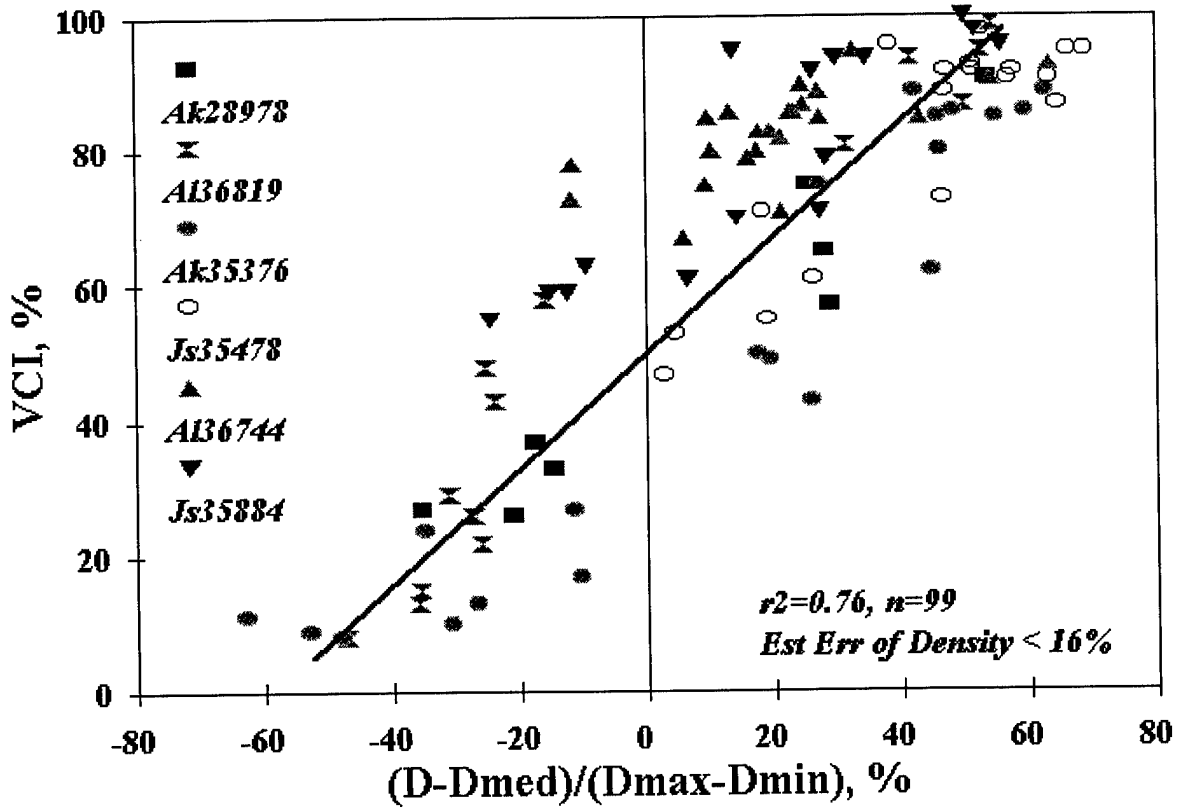


Fig. 4. Correlation between the VCI-derived and actually measured density of vegetation for six weather stations and for two years (1991 and 1992).

The Reflectance of Pleurozium Schreberi as a Function of Water Status and its Implications on Understory Reflectance Variations for BOREAS Sites

Richard Fernandes[1], H. Peter White[2], Derek R. Peddle[3], John R. Miller[2], Lawrence E. Band[1]
[1] Deptartment of Geography, University of Toronto, 100 St. George St., Toronto, Ontario, M5S 1A1, CANADA,
Tel: (416)978-5070, fernande@geog.utoronto.ca
[2] Deptartment of Physics & Astronomy, York University, 4700 Keele St., North York, Ontario, M3J 1P3, CANADA
[3]Department of Geography, University of Waterloo, Waterloo, Ontario, N2L 3G1, CANADA

ABSTRACT

A controlled laboratory experiment was conducted to test the null hypothesis that the nadir reflectance of Pleurozium scheberi (a feather moss) in the red (ρ_{RED}), near-infrared (ρ_{NIR}), and infrared (ρ_{IR}) bands is not a function of live layer moisture content. Reflectance spectra were acquired from replicate moss turves over five dry down stages ranging from 4.8 g water/g moss to 0 g/g. Replicate spectra showed a maximum 13.5% increase in ρ_{RED}; almost no significant change in ρ_{NIR}; and over 20% increase in ρ_{IR}. However, ρ_{RED} variations due to drying before desiccation were less than 2%. Inter-replicate differences in reflectance were often larger than dry down differences. NIR understory reflectance measured in a moss dominated BOREAS site showed a significant seasonal change in ρ_{NIR} which is not likely due to moisture variations.

INTRODUCTION

One of the aims of the BOReal Ecosystem Atmosphere Study (BOREAS) is to model spatial variations in carbon flux at various scales[1]. A large proportion of the northern boreal forest consists of Picea Mariana (black spruce) stands with a moss dominated understory[2]. The low canopy cover of back spruce stands suggests that factors influencing understory reflectance should be identified both to assist remote sensing efforts and to parameterize carbon flux models. Field measurements of Pleurozium scheberi dominated understories indicated some seasonal variations in nadir reflectance[3]. The relationship between moss moisture contents and changes in surface nadir reflectance (ρ) has not been investigated. This study represents an initial controlled experiment to determine if ρ variations observed in the field could be driven by, or even supplemented by, variations due to moisture content.

PURPOSE AND HYPOTHESES

The purpose of the experiment was to determine if the relationship between moss moisture content and ρ was significant enough to warrant further studies in situ. The experiment also addressed the lack of controlled characterizations of ρ of Pleurozium scheberi and feather mosses in general. Finally, the experiment provided information regarding the relative magnitude of between treatment versus between replicate variations of ρ. The experiment measured ρ over a large number of bands. However, for convenience, hypotheses referred to LANDSAT TM bands ρ_{RED} (630 nm to 690 nm), ρ_{NIR} (760 nm to 900 nm) and ρ_{IR} (1550 nm to 1750 nm).

The null hypothesis was that ρ_{RED}, ρ_{NIR}, ρ_{IR} of the surface of a live layer of Pleurozium scheberi is not related to live layer moisture content. The lack of controls and monitoring of other moss characteristics prohibited the definition of an alternate hypothesis that attributed changes in ρ to moisture alone. An additional null hypothesis that the between replicate differences in ρ are significantly different than the treatment differences was also tested. If ρ varied more between replicate rather than between treatments one would suggest that factors other than moisture may also cause variations ρ.

MATERIALS AND METHODOLOGY

The laboratory experiment used three turves (A,B, and C) of live moss. The turves were harvested near the end of a prolonged rain storm at a Scotch Pine stand at approximately 78° W longitude and 43°40' N latitude in Ontario, Canada. Each turve had a 20cm long x 20cm wide x 8cm deep live layer. The turves were acclimatized to the laboratory room for 24 hours. Loose litter was removed from the turves' surfaces. The live layer of each turve was removed and mounted on a pre-weighed mesh platform. A fourth turve (D) represented desiccated moss. This turve had been harvested at the BOREAS Northern Old Black Spruce (NOBS) field site and oven dried at a very low temperature until it was completely desiccated.

The York University BRDF facility was used to acquire radiance measurements. A 1000W halogen lamp with a collimated beam provided illumination at a 45 degree zenith angle. An ASD field spectrometer measured target nadir radiance in 1 nm bands from 350 nm to 1750 nm. A 2 degree field of view lens was used with the

0-7803-3068-4/96$5.00©1996 IEEE

spectrometer giving a 2.5 cm diameter target size. A Spectrolon panel was used as a white reference.

Turves A,B, and C dried down in four stages (including the initial wet stage) over a period of 30 hours. A table fan on its lowest setting was used to speed drying. Turve D was assumed representative of all turves at desiccation. The Spectrolon panel radiance was measured at the start of each dry-down stage. Each turve was weighed and nine non-overlapping radiance measurements were acquired. The ρ spectrum corresponding to a radiance measurement was estimated using the Spectrolon panel radiance measurement corresponding to the drydown stage. Mean spectra were computed for each set of nine ρ spectra.

OBSERVATIONS AND ANALYSIS

Fig. 1 shows the mean spectra for A at each dry down stage. Tables 1,2, and 3 give the mean and standard deviation of mean ρ_{RED}, ρ_{NIR}, and ρ_{IR} for A,B, and C. A "*" symbol is indicated beside measurements which provided evidence against the null hypothesis that there is no difference between reflectance at a given dry down stage compared to the initial wet stage at a 95% significance level. A "**" symbol is indicated besides stages where there was evidence against the null hypothesis that replicates A and B have the same mean reflectance at a 95% significance level. C started at a higher initial moisture content and was not used for testing the second null hypothesis.

A and B had almost identical initial moisture contents of 3.4 g/g and 3.27 g/g and dried to 1.25 g/g and 1.06 g/g respectively. C started at a moisture content of 4.8 g/g and dried down to 1.47 g/g. The moisture contents measured were lower than the range of 14.6 g/g to 1.27 g/g measured at the NOBS site during August 1994 and the field dry down rates were lower than those observed in the lab. However, moisture contents and dry down rates observed in the lab were similar to those reported at other black spruce sites [4].

Fig. 1 and Table 1 indicate a statistically significant increase in ρ_{RED} on the order of 1%. No significant further increase is seen with subsequent drying until desiccation occurs. At desiccation (stage 5) a 14.5% increase in ρ_{RED} in comparison to the stage 1 was noted. The increases in ρ_{RED} were likely due to a reduction in red absorption due to chlorophyll depletion bought about by moisture stress as demonstrated in [5]. Figure 2 shows moss dominated understory mean ρ at the BOREAS southern "Old Black Spruce" (OBS) site. The slight increase in ρ_{RED} over the growing season may be due to moisture differences rather than seasonal changes.

Fig. 1 and Table 2 indicate a significant change in ρ_{NIR} only between stage 1 and 2 and only for B and C. Both A and B show no evidence against the null hypothesis that ρ_{NIR} did not change with dry down between stages 1 to 4. C showed evidence against this null hypothesis at all stages. There was evidence against the null hypothesis that there are no replicate differences at all stages. The large inter-replicate differences in ρ_{NIR} suggested that moisture differences were not the primary cause of ρ_{NIR} variations duri.g drydown. Cellulose and lignin in plant matter give rise to scattering in NIR. The large inter-replicate ρ_{NIR} variations may be due to differences in moss shoot density and needle litter density in the turves. Fig. 2 shows a large increase in ρ_{NIR} over the growing season (which was not observed in a more northern site). This increase may be due to organic matter such as needles which have been trapped in the moss surface.

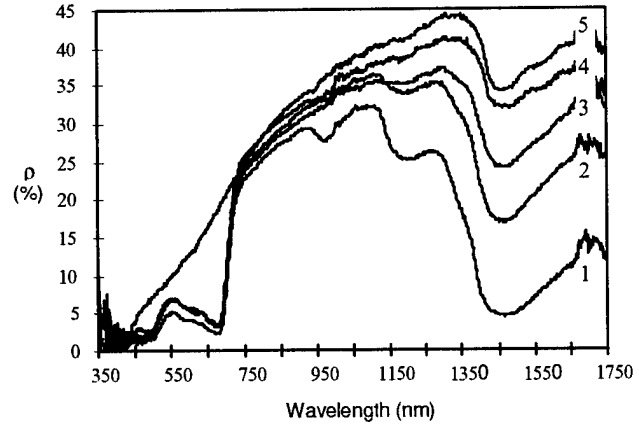


Fig. 1 Mean moss nadir reflectance at five dry down stages (Turve A)

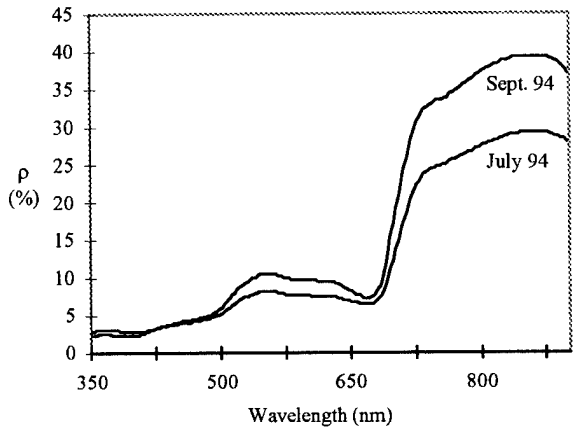


Fig. 2 Mean reflectance of moss dominated sunlit understory in the BOREAS Southern OBS site during middle and late growing season.

Fig. 1 and Table 3 indicate that there was evidence against the null hypothesis that moisture is unrelated to ρ_{IR} at all drydown stages for all replicates. A 30% absolute increase in ρ_{IR} was noted between stage 1 and 4. In addition, Fig. 1 indicates that the increase in ρ_{IR} is monotonic with decreasing moisture content. Only stage 2 showed evidence against the null hypothesis that there were no inter-replicate differences in ρ_{IR}.

Table 1 Mean & standard deviation of ρ_{RED} during drydown

	A		B		C	
Stage	ρ_{RED}	1σ	ρ_{RED}	1σ	ρ_{RED}	1σ
1	2.85	0.23	2.95	0.18	2.69	0.13
2**	3.49*	0.15	4.10*	0.23	4.01*	0.26
3**	3.31	0.26	4.42*	0.33	4.11*	0.39
4	3.68*	0.14	4.03*	0.28	4.09*	0.31
5	16.3*	0.91	16.3*	0.91	16.3*	0.91

Table 2 Mean & standard deviation of ρ_{NIR} during drydown

	A		B		C	
Stage	ρ_{NIR}	1σ	ρ_{NIR}	1σ	ρ_{NIR}	1σ
1**	22.3	2.1	26.3	0.53	29.8	1.1
2**	24.4	1.2	29.4*	1.7	35.1*	2.4
3**	20.8	1.4	28.1	1.6	35.8*	2.1
4**	21.8	1.0	25.9	1.4	33.3*	2.1
5	29.3*	1.5	29.3*	1.5	29.3	1.5

Table 3 Mean & standard deviation of ρ_{IR} during drydown

	A		B		C	
Stage	ρ_{IR}	1σ	ρ_{IR}	1σ	ρ_{IR}	1σ
1	11.4	1.0	11.3	0.57	9.2	0.83
2**	28.1*	1.6	24.7*	1.4	38.3*	1.6
3	30.8*	2.0	31.4*	2.7	43.4*	3.1
4	31.3*	1.3	34.4*	2.0	40.7*	2.4
5	39.6*	1.6	39.6*	1.6	39.6*	1.6

CONCLUSIONS

The turves tested spanned a plausible range of moisture contents and drydown rates. There was evidence against the null hypothesis that moss moisture content and nadir reflectance are not related in RED; no evidence in NIR; and strong evidence in IR. The absolute magnitude of the change in ρ_{RED} was near 1% until desiccation. where it jumped to over 10%. There was a monotonic increase in ρ_{IR} of up to 30% even before desiccation.

There was infrequent evidence against the null hypothesis that there are no inter-replicate differences in RED and IR; while there was strong evidence in NIR. It was suggested that the inter-replicate differences in NIR response are due to differences in structural organic matter, such as needles, trapped in the moss. The increase in NIR reflectance observed in the field may be due to an increase in needle litter and understory species later in the growing season.

The very small changes in ρ_{RED} during drying coupled with canopy absorption in RED suggest that both energy balance and remote sensing models need only consider moisture driven changes in ρ_{RED} when desiccation occurs. Coincident in situ measurement of moss moisture status and reflectance could be performed to determine the cause of seasonal changes in ρ_{IR}. Additional replicates would permit analysis of the proportion of ρ variation due to moisture alone. Significant changes in understory ρ_{IR} due to moisture may have an effect on understory PAR, surface heating, and top of canopy radiance The observed relationship between moss moisture status, if supported by further drydown measurements, could be incorporated in remote sensing models and may give information regarding spatial variations of surface moisture if atmospheric and canopy related effects can be modeled.

REFERENCES

[1] P. Sellers, et. al. "The Boreas Ecosystem-Atmosphere Study (BOREAS)"Proc. AGU Symposium, Baltimore M.D., May, 1995.

[2] G.B. Bonan and H.H. Shugart, "Environmental factors and ecological processes in boreal forests," Ann. Review of Ecology and Systematics, vol. 20, pp. 1-28m 1989.

[3] H. P. White, J. R. Miller, J. Chen, D.R. Peddle, "Seasonal Change in Mean Understory Reflectance for BOREAS Sites: Preliminary Results," Proc. 17th Can. Remote Sensing Symposium, vol. 1, pp. 182-187, 1995.

[4] O. Skre, W.C. Oechel and P.M. Miller, "Moss leaf water content and solar radiation at the moss surface in a mature black spruce forest in central Alaska," Can. J. For. Res., vol. 13, pp. 860-868, 1983.

[5] J.R. Busby, and D.W. Whitfield, "Water potential, water content and net assimilation of some boreal forest mosses." Can. J. Bot., vol. 56, pp. 1551-1558, 1977.

Seasonal NDVI Trajectories in Response to Disturbance: Toward a Spectral-Temporal Mixing Model for Tallgrass Prairie

Douglas G. Goodin
Department of Geography/Dickens Hall
Kansas State University
Manhattan, KS 66506
T: (913) 532-6727 F: (913) 532-7310
email: dgoodin@ksu.ksu.edu

Geoffrey M. Henebry
Division of Biology/Ackert Hall
Kansas State University
Manhattan, KS 66506
T: (913) 532-7997 F: (913) 532-6653
email: gmh@unix.konza.ksu.edu

Abstract -- Natural and anthropogenic disturbance in tallgrass prairie communities can induce changes in plant species composition, including shifts in abundance of C_3 vs. C_4 lifeforms. The asynchronous seasonalities in greenness that C_3 and C_4 species exhibit should enable monitoring of their relative abundance using sensor derived vegetation indices, such as NDVI. We used close-range measurements made over 22 experimental plots at the Konza Prairie Research Natural Area (KPRNA) to evaluate seasonal trajectories in canopy greenness as a function of C_3/C_4 ratio. NDVI data were collected from each plot at approximately ten day intervals throughout the 1995 growing season. Temporal trajectories were used to develop discriminant functions to model relative C_3/C_4 abundances. The discriminant model yielded values of Kendall's τ_b and Cohen's κ statistic of 0.794 and 0.781, indicating strong agreement between classes and an overall classification significantly better than random assignment. Results suggest the possibility of applying spectral-temporal mixture models derived from close-range sensing to larger scale monitoring of tallgrass prairie.

INTRODUCTION

Disturbance is a crucial element in maintenance of the tallgrass prairie ecosystem. Disturbance can be of natural or human origin. Fire and grazing, for example, are two common and important prairie disturbances that occur naturally but are also linked to human land use. Climatic perturbations (e.g., drought) are natural phenomena; whereas, supplementation of water and nutrients and the introduction of invasive exotic species are anthropogenic effects.

Both natural and anthropogenic disturbances in tallgrass prairie can induce changes in plant species composition, including the relative abundance of C_3 vs. C_4 lifeforms. These lifeforms are distinguished by the photosynthetic pathway by which carbon is fixed into carbohydrate. Typically, C_3 species are "cool season" plants, with lower light saturation levels and higher transpiration rates than C_4 "warm season" species [1]. These two vegetation types reach maximum phenological activity under different environmental conditions, hence they exhibit asynchronous seasonality in greenness. Accordingly, it should be possible to monitor their relative abundance using spectral-temporal sensing techniques. Here we explore the possibility of using seasonal trajectories of NDVI to develop a spectral mixing model for characterizing C_3/C_4 ratio.

STUDY SITE AND DATA COLLECTION

Close-range sensing data were collected from 22 experimental plots located at the Konza Prairie Research Natural Area (KPRNA) near Manhattan, KS. These experimental plots had been manipulated by a combination of burn frequency and nutrient addition over several years, resulting in a range of possible prairie canopy types varying both in lifeform and species composition. Eight separate sites within each plot were sampled, resulting in a total of 176 sampling locations. These data were collected at approximately ten day intervals during the 1995 growing season using a Cropscan MSR-87 eight band spectroradiometer. The radiometer was suspended over each measurement site on a hand-held mast at a height of approximately two meters above the level of the substrate. The MSR-87 has a field of view of 28°, yielding a circular measurement area with a diameter of one meter. Normalized difference was calculated as (NIR-RED)/(NIR+RED). We used MSR band 5 (635-685 nm) for red reflectance and MSR band 8 (757-870 nm) for near infrared reflectance.

Species composition within each measurement site was determined by sampling the site using a modified Daubenmire

0-7803-3068-4/96$5.00©1996 IEEE

procedure with a 20 x 50 cm quadrat. Individual species within the sampling frame were classified into four lifeform categories: C_3 graminoid, C_4 graminoid, C_3 forb, and woody vegetation.

THE SPECTRAL MIXING MODEL

Unlike many other mixture models applied to remote sensing data, our goal was not to estimate relative areas of cover type at a subpixel scale within a single scene. Instead, we seek to estimate the relative abundance of intermixed, spectrally similar components of a vegetative canopy. The separability of mixture components are revealed not in their spectral reflectivity at any one time, but in the temporal trajectory of their greenness. It was thus necessary to develop metrics to summarize the temporal behavior. Fig. 1 shows the mean NDVI for sites with nearly uniform coverage of C_3 and C_4 species, together with a trajectory from sites with roughly even proportions of both types plotted against growing degree day. There are clearly identifiable differences between these three trajectories during the growing season. It is also apparent that these differences can be summarized by the behavior of the curves at various growing degree days. Three indices seemed particularly sensitive to C_3/C_4 ratio: (1) the growing degree day at which the peak rate of greenup occurs (GDDUP); (2) GDD of peak greenness (GDDPEAK); and (3) mean rate of browndown (RATEDN). These indices were calculated by first smoothing the seasonal NDVI curve using a three-point moving average, then numerically differentiating the curve using a divided difference algorithm [2]. GDDUP and GDDPEAK were determined by noting the GDD at which maximum and zero derivative occurred, respectively. In addition, GDDPEAK required interpolating the position of zero between the last positive and first negative derivatives within the curve. RATEDN was determined by averaging derivatives for all growing degree days after the peak NDVI value.

Once the spectral-temporal metrics were calculated for each of the 176 measurement sites, they were submitted as dependent variables to discriminant analysis. Discriminant models have been used frequently in both remote sensing classification problems and in statistical analysis of mixtures [3,4]. Essentially, discriminant analysis forms groups by deriving probability density functions for class membership using a subset of the entire data set (i.e., training data), then assigning each measurement in the data set to its most probable class. The mathematics of discriminant models have been extensively described in the statistical literature [5].

Discriminant models require data grouped into categorical variables. We sorted the species composition data into two groups: C_3 graminoids and forbs vs. C_4 graminoids and woody vegetation. Classes were then developed based on the

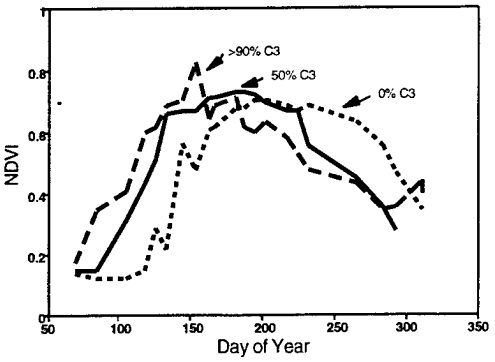


Figure 1. Temporal NDVI curves for sites with approximately 0, 50, and 100% C_3 species composition.

percentage of C_3 coverage at each measurement site. Initially, five classes were created: (1) plots with no C_3 grass or forb coverage; (2) plots with C_3 coverage ranging from 1-25%; (3) 26-50% C_3 coverage; (4) 51-75% C_3 coverage; and (5) 76-100% C_3 coverage. Preliminary analysis of this classification scheme revealed considerable confusion between classes. Based on the confusion matrix from this initial scheme (Table 1), the five classes were reduced to three by aggregating classes 1+2 and classes 3+4. Class 5 was retained and renamed class 3.

The results of the discriminant model are summarized in Table (2). Validation of the model is based on dividing the dataset into two roughly equal halves, each containing four of the eight measurement sites from each plot. One half was designated the training set and the other was used for model cross-validation. All categorical frequencies and measures of association presented in Table (2) result from classification of the validation dataset using the discriminant functions derived from the training dataset.

DISCUSSION

It is apparent from the information in Table 2 that the mixture model for three categories produced strong results.

Table 1. Confusion matrix for five classes

	Reference				
Observed	1	2	3	4	5
1	44	20	3	0	0
2	19	26	3	5	0
3	3	3	15	11	0
4	1	0	5	8	1
5	0	0	0	1	8

Table 2. Confusion Matrix and Agreement statistics for three classes.

	Reference		
Observed	1	2	3
1	55	4	0
2	5	19	0
3	0	0	5

τ_b=0.794
κ=0.782

Kendall's τ_b (a measure of association interpreted like a correlation coefficient) and Cohen's κ statistic indicate strong agreement between all classes and an overall classification significantly better than random assignment.

Within classes some patterns of confusion do emerge. By percentage, class 2 had the greatest confusion with 21% error. Class 1 had 7% error and class 3 had no misclassified cases. Every misclassified case was incorrectly placed into an adjacent category. In an ordered data set such as this one, this pattern means that the misclassified cases were "near-misses", as opposed to gross misclassifications.

Given the broad range of $\%C_3$ values comprising class 2, it seems reasonable that most of the error would be associated with this class. The most common error type, however, occurred when a case belonging to class 2 being misassigned to class 1. Examination of the cases plotted in the discriminant space (Figure 2) reveals class 2 to be less well defined than the others, as clearly evident in the dispersion of cases around the group centroid. Class 2 has two distinct clumps of outliers, one of which is well within the main cluster of class 1 values. Misclassified values in class 1 also comprise an outlying cluster contained within the main group of class 2 values. Subsequent examination of these cases reveal that all are borderline cases with $\%C_3$ values very close to 25, the threshold for group membership.

Our results show that low $\%C_3$ transitional values are the most difficult to classify. Transitional values at higher percentages of C_3 coverage appear to be more distinctive, since no values were misclassified. Apparently, as the $\%C_3$ values within and individual plot increase, the distinguishing spectral-temporal features become more prominent. Thus class 2, which spans a large range of $\%C_3$ values, shows considerable confusion at the low end of its range but no confusion at the higher end. Class 3 shows no confusion at all, although one class 3 datum did plot away from the main group in the discriminant space (Figure 2). Interpretation of the measures of agreement should be done with some caution due to the uneven class sizes and the small number of cases in class 3. These proportions, however, reflect the actual

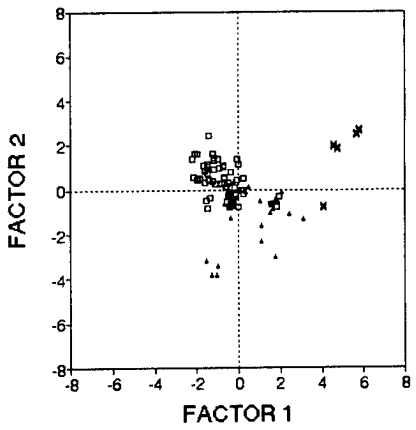


Figure 2. Plot of factors in discriminant space. Class 1 = □, class 2 = ▲, class 3 = ⁎.

$\%C_3$ values within the study site. However, oversampling any of the sites to balance these proportions would result in a model based on a training data set which did not reflect the actual site being studied.

CONCLUSIONS

Our results demonstrate both the effectiveness of seasonal trajectories of NDVI for detecting relative C_3/C_4 fractions in tallgrass prairie canopies and the use of discriminant based mixture models for categorization of observations based on these fractions. Relative C_3/C_4 ratio is diagnostic of a variety of surface disturbances of relevance to environmental impact and change processes, hence the techniques outlined here show promise for larger scale monitoring of tallgrass prairie using NDVI values derived from a variety of space-borne remote sensing instruments.

ACKNOWLEDGEMENTS

We thank Bill Rogers, Donna Rieck, and Kent Hilbert for help with species idetification and data reduction. This research was supported by EPA EMAP grant #R823605-01-0. KPRNA is owned by the Nature Conservancy and managed by the Division of Biology, Kansas State University.

REFERENCES

[1] P.G. Risser *et al.*, The True Prairie Ecosystem. Stroudsburg, PA: Hutchinson Ross, 1981.

[2] J.L. Buchanan and P.R. Turner, Numerical Methods and Analysis New York: McGraw-Hill, 1992.

[3] D.M. Titterington, A.F.M. Smith, and U.E. Makov, Statistical Analysis of Finite Mixture Distributions, Chichester: John Wiley, 1985.

[4] T.M. Lillesand and R.W. Kiefer, Remote Sensing and Image Interpretation, 3rd ed., New York: John Wiley, 1994.

[5] G.J. McLachlan, Discriminant Analysis and Statistical Pattern Recognition, New York: John Wiley, 1992.

Analysis of the Canadian Boreal Forest using Enhanced Resolution ERS-1 Scatterometer Imagery

Clarence J. Wilson III and David G. Long
Brigham Young University
459 CB, Provo, UT 84602
801-378-4884, FAX: 801-378-6586, e-mail: wilsonj@newt.ee.byu.edu

Abstract -- Scatterometer backscatter measurements (σ°) are primarily and traditionally used to estimate wind speed and direction over the ocean. This paper presents an investigation of the backscatter coefficient of boreal forest and neighboring vegetation regions. ERS-1 backscatter $\mathcal{A}$-values of the Canadian boreal forest are imaged using a resolution enhancement algorithm for this analysis. Regions of boreal forest, tundra, and grassland are individually analyzed over the extent of the ERS-1 scatterometer's data set (1992-1995). The annual variation of the mean σ° value for each region is presented. Distinct seasonal variations exist for these vegetation types. Boreal forests exhibit a stronger response (~2.5 dB) during warm summer months than during the snow and ice covered winter months. The results of this study indicate good potential for further analysis of boreal forest regions using ERS-1 scatterometer data.

INTRODUCTION AND BACKGROUND

Boreal forests are found in cool, temperate zones of the northern hemisphere, typically north of the 50^{th} parallel and south of the Arctic Circle. Because they cover such massive regions (~15 million km^2 worldwide), boreal forests are an important factor in understanding the global ecosystem. Boreal forest research has sought to determine how timber resources are being managed, the effects of increasing pollution from modern society (i.e., acid rain and global warming theories), the natural cycles of the forest, and how the forest adapts to change. Remote sensing techniques including aerial photography and SAR imagery have found use in studies requiring infrequent image collection (on the order of years) and studies of small (< 10 km^2) sections of forest. However, as Shubert et al. [1] have suggested, "The processes that control [boreal forest] patterns can change in importance as the space- and time-scales of the pattern of interest are changed." Thus, the understanding of boreal forest cycles over small sections or short time periods does not necessarily apply to the cycles of the forest on macroscopic levels or over long time periods. A means of monitoring the forests on such scales needs to be developed.

Scatterometer σ° Measurements and SIR Imagery

The European Remote Sensing satellite, ERS-1, carries a scatterometer radar which measures the radar backscattering coefficient (σ°) over the entire earth. The primary purpose of this measurement is to determine wind speeds and directions over the ocean; however, backscatter measurements over land surfaces are also useful. Kennett and Li [3, 4] demonstrated that the radar backscatter coefficient values over land are well modeled by the first-order linear function

$$10\,log_{10}\,\sigma^\circ(\theta) = \mathcal{A} + \mathcal{B}\,(\theta - 40^\circ)$$

where θ is the incidence angle of the observation. Such research has demonstrated a strong correlation between $\mathcal{A}$ and $\mathcal{B}$ and vegetation type and surface topology [2, 3, 4].

A major drawback of using spaceborne scatterometer σ° measurements to study vegetation and land surfaces is the coarse resolution of the scatterometer measurements (~50 km for ERS-1). However, spaceborne scatterometers offer the distinct advantages of frequent fly-overs at a wide variety of incidence angles over a period of many years. The ERS-1 scatterometer has provided repeated coverage of the entire world every 4-10 days for over four years. These characteristics make spaceborne scatterometer σ° measurements an attractive resource for studying vegetation on a regional or global scale.

A new resolution enhancement technique, called Scatterometer Image Reconstruction (SIR) [5], has the ability to increase ERS-1 resolution from >50 km/pixel to ~25 km/pixel or better. SIR imagery, along with the frequent coverage of spaceborne scatterometers like ERS-1, can aid in the study of large land regions with ecological significance. This paper investigates the use of enhanced resolution ERS-1 σ° measurement imagery as a technique for studying boreal forests over long time periods and large forest regions.

ANALYSIS OF BOREAL FOREST σ° PATTERNS

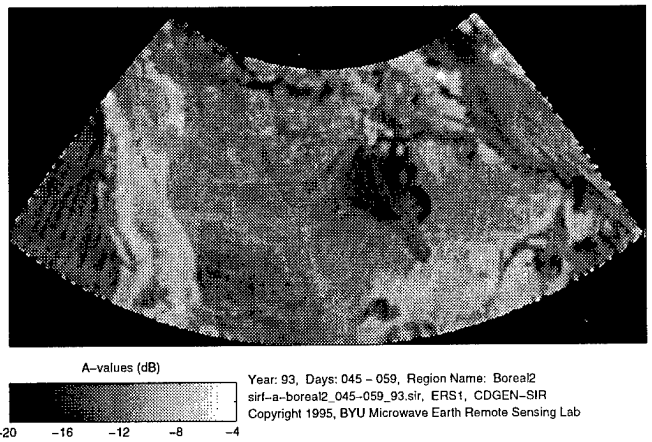
The potential of ERS-1 SIR imagery for studying boreal forest regions is investigated by first making imagery of the Canadian boreal forest region from original σ° measurements. Next, subregions of the different vegetation types in the study area are examined over a four year period to investigate interannual backscatter variations.

SIR Imagery

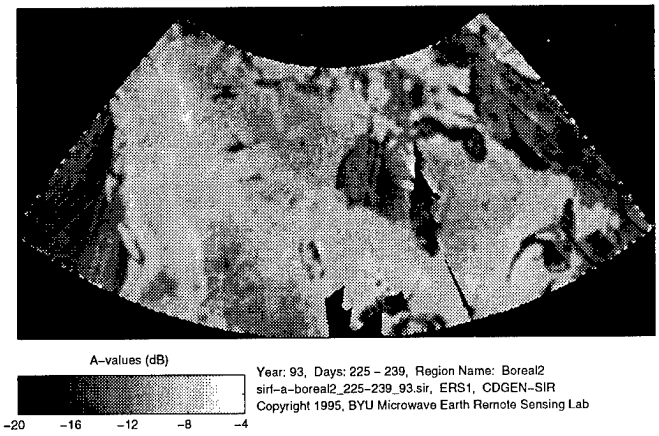
ERS-1 σ° data of the study region (50° N to 70° N, 140° W to 55° W) is grouped into 15-day periods from Jan. 1, 1992 through Oct. 31, 1995 (extent of the available data at press). Each 15-day data group is then processed using the SIR algorithm, producing an 8.9 km/pixel image of the backscatter's $\mathcal{A}$-value average for each 15-day period.

Fig. 1 shows two SIR images thus produced. Fig. 1(a) is the image for February 15-28, 1993. Snow and ice present during this winter period result in a nearly homogeneous backscatter

0-7803-3068-4/96$5.00©1996 IEEE



(a) Feb. 15-28, 1993



(b) Aug. 15-31, 1993

Figure 1: *SIR Images of Canada. The overall darkness in the upper image is the result of snow and ice coverage. The bright diagonal band in the lower image is the boreal forest.*

$\mathcal{A}$-value with little discrimination among vegetation types. However, several geographic features are still apparent.

Fig. 1(b) shows the region for August 15-31, 1993. Here, a distinctive band that stretches from the northwest to southeast corners of Canada and corresponds to the boreal forest is readily apparent. This image reveals higher contrast levels among the backscatter $\mathcal{A}$-values of the various vegetation types in the region.

One noticeable problem with Fig. 1(b) is the missing image data at the bottom center of the image. The missing data is due to SAR operation on ERS-1 over this area during this time period and is a problem for many of the images produced in this series.

Seasonal Variations

Six subregions of homogeneous vegetation are selected from the Canadian boreal forest and neighboring vegetation types. A map displaying the location of the six subregions is found in Fig. 2. Subregions 1 and 2 are needleleaf evergreen forest (boreal forest); subregions 3 and 4 are lichen woodland; subregion 5 is tundra; and, subregion 6 is grassland/farmland.

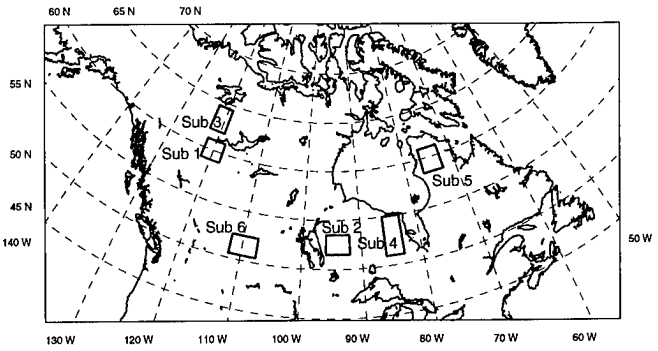


Figure 2: *A map of Canada indicating the six vegetation subregions.*

Fig. 3 is a graph of the mean $\mathcal{A}$-values estimated by the SIR algorithm for the needleleaf evergreen forest subregions (#1 and #2). In these plots, the dashed line represents the weighted average of the $\mathcal{A}$-values from all four years. Portions of the subregions missing data (as discussed above) are not included in calculating such statistics. The backscatter response is 2-3 dB stronger during the summer than the winter. Both plots display a distinctly increasing slope during early spring that climaxes around JD 120 (May 1). This is assumed to represent spring vegetation growth following the melt-off of winter snow and ice. A symmetric feature occurs in the late summer season as the autumn vegetation cycle and winter freezing begins. Note that this occurs earlier for the northern subregion (about JD 260, or mid-September) than the southern subregion (about JD 280, or mid-October).

Fig. 4 is a similar plot for lichen woodland subregions (#3 and #4). Here, again, the spring and autumn vegetation cycles are apparent yielding a 2.5-3 dB difference between winter and summer. The lichen woodland spring and autumn transitions are more rapid than those of the boreal forest. Note that for both vegetation types the northern subregions (#1 and #3) have more abrupt transitions than their southern counterparts.

In Fig. 5 the weighted mean $\mathcal{A}$-values for all six subregions are plotted for comparison. From this figure it is clear that the grassland subregion (#5) backscatter is significantly less than the boreal forests, lichen woodlands, and tundra year-round. The tundra region (#6) backscatter coefficient is less than the boreal forest and lichen woodlands during summer by about 1.5 dB, but during the winter season is approximately the same or slightly greater. It appears the boreal forest and lichen woodland regions all reach a peak in spring around JD 120. However, date of the autumn fall-off varies from region to region. Thus, the seasonal patterns of boreal forests and the surrounding vegetation regions are very pronounced.

CONCLUSION

Study of the boreal forest regions using enhanced resolution imagery produced by the SIR algorithm demonstrates that a dramatic seasonal transition exists for the boreal forest's backscatter coefficient. This annual variation is characterized by a much stronger response (2-3 dB) during the growing

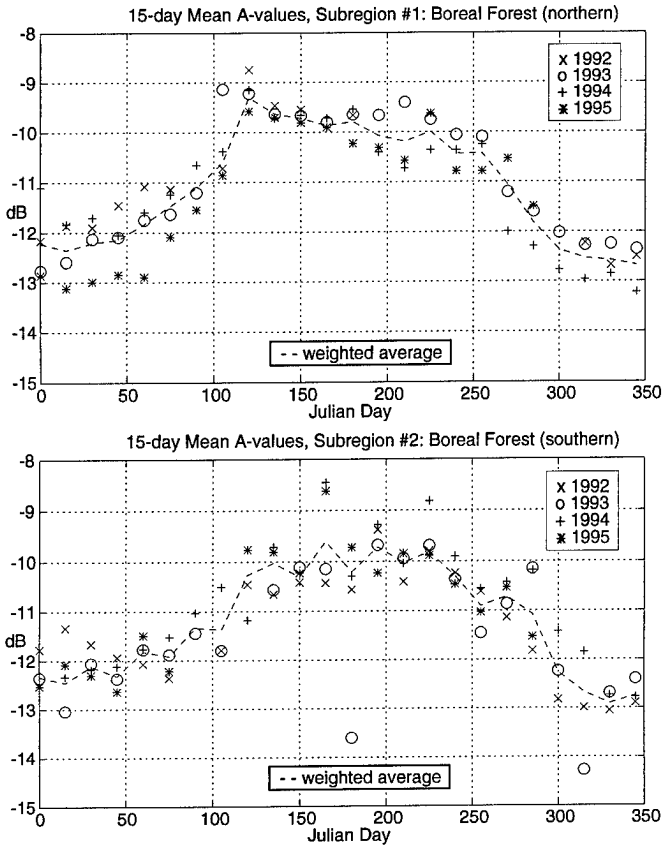


Figure 3: *Mean A-values for subregions 1 and 2 (boreal forest).*

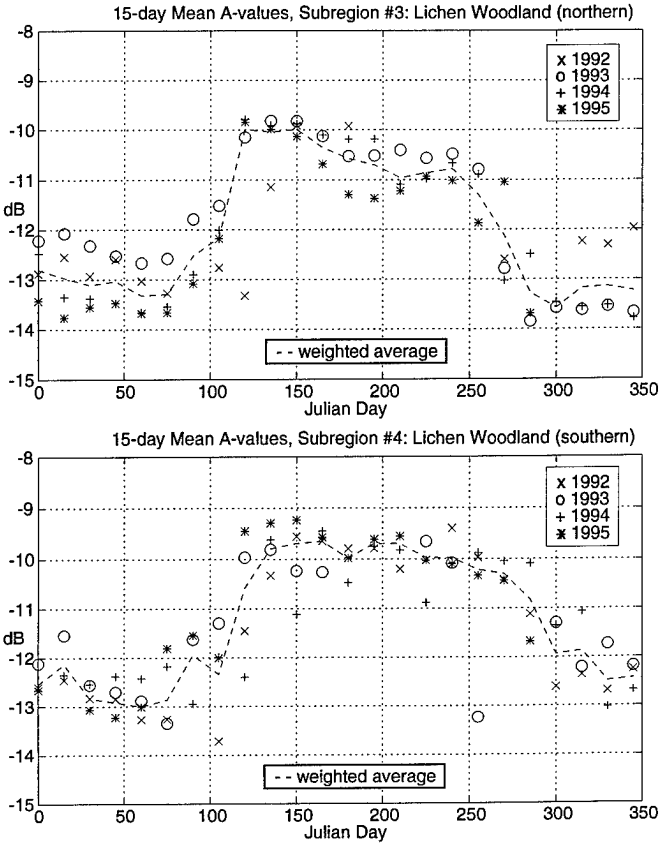


Figure 4: *Mean A-values for subregions 3 and 4 (lichen woodland).*

season throughout the summer than that of the snow and ice covered winter. An even more rapid transition is observed for neighboring lichen woodlands. Tundra has a similar response during winter but differs during summer by about 1.5 dB. Grasslands exhibit a much lower response year-round.

The use of spaceborne scatterometer measurements in combination with SIR image resolution enhancement is a valuable resource for the study of land regions such as boreal forests. With this technique, we have examined the boreal forest on a macroscopic level over several annual cycles. These successful results are substantial motivation for expanded research exploring the use of spaceborne scatterometer backscatter coefficient measurements for the study of boreal forest vegetation regions.

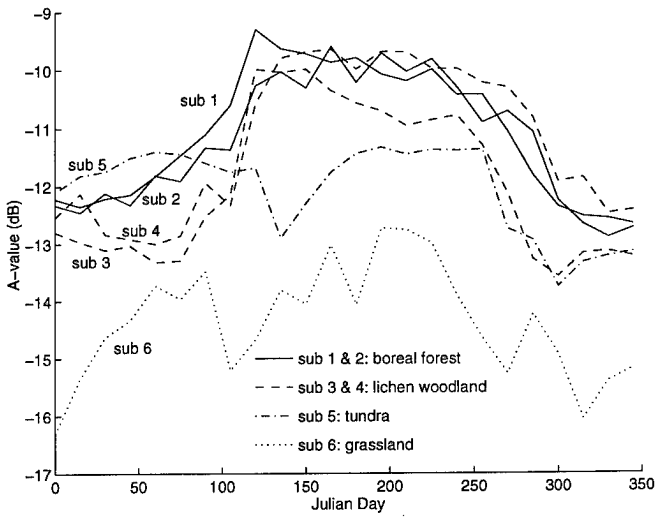


Figure 5: *Weighted Mean A-values over all six subregions*

REFERENCES

[1] H. Shugart, R. Leemans, and G. Bonan, eds., *A Systems Analysis of the Global Boreal Forest*. Cambridge, Great Britain: Cambridge University Press, 1992.

[2] E. Mougin, A. Lopes, P. Frison, and C. Proisy, "Preliminary Analysis of ERS-1 Wind Scatterometer Data over Land Surfaces," *International Journal of Remote Sensing*, vol. 16, no. 2, pp. 391--398, 1995.

[3] R. Kennett and F. Li, "Seasat over Land Scatterometer Data, Part I: Global Overview of the Ku-band Backscatterer Coefficients," *IEEE Trans. Geosc. Rem. Sens.*, vol. 27, pp. 592--605, 1989.

[4] R. Kennett and F. Li, "Seasat over Land Scatterometer Data, Part II: Selection of Extended Area Land-target Sites for the Calibration of Spaceborne Scatterometers," *IEEE Trans. Geosc. Rem. Sens.*, vol. 27, pp. 779--788, 1989.

[5] D. Long, P. Hardin, and P. Whiting, "Resolution Enhancement of Spaceborne Scatterometer Data," *IEEE Trans. Geosc. Rem. Sens.*, vol. 31, pp. 700--715, May 1993.

Land Cover Change Dynamics of a Himalayan Watershed Utilizing Indian Remote Sensing Satellite (IRS) Data

Akhouri Pramod Krishna
G.B. Pant Institute of Himalayan Environment and Development,
Sikkim Unit, P.O. Tadong, Gangtok 737102, Sikkim, INDIA
Telephone/facsimile: +91 3592 23335

Abstract - **This study of an anthropogenically vibrant Sikkim Himalayan watershed shows rapid land cover changes within it. The area is a typical environmentally fragile terrain undergoing tremendous pressure on its natural resources. Considering the watershed as basic resource unit, the impacts of development are noteworthy. Indian Remote Sensing Satellite (IRS 1A/1B) data have been used in this study alongwith other collateral information for deriving land cover change dynamics. The variations over a period of four years on the classified land covers were determined. At level I, the land covers are forest, agricultural land, waste-land, water bodies and built-up land. At level II, forest has six, agricultural land has three and waste land has two sub-classes.**

Interpretations have been done using optical bands of IRS/LISS II sensor with good spectral resolutions in visible to near infra-red range and spatial resolution of 36.25 meters. Multidate single band as well as normal false color composite (FCC) scenes have been used. Ground-truth studies were done with suitable ground control points (GCPs). Remote sensing technique has been found cost-effective and less time consuming. This has provided much needed information for developmental planning in such a mountain environment. Sustainable development and environmental conservation strategies are perceived to be worked out faster and precisely for such inaccessible and difficult terrain taking cue from the land cover change dynamics.

I. INTRODUCTION

In the context of mountain environment, land and water resources management are of paramount importance. In relatively younger mountain range like the Himalaya, this is much more complex because of its ecologically fragile nature. The inhabitants of such remote regions depend on the available natural resources locally. Their demand for food and livelihood are met primarily from the forests and scarce agricultural lands. The pressure on available resources increases day by day with growing population and family fragmentation leading to smaller land holdings. This is further compounded by non-scientific farming and forestry developmental activities.The broad environmental impact of these are manifested as rapid land cover change and are discernible on the earth resources satellite scenes. The remotely sensed data provide scope for quick monitoring of land cover dynamics [1]. The synoptic and repetitive coverage of the same region by satellites facilitate the study of dynamics of such changes even for remote and difficult hilly terrain. This study, carried out under institutional project on integrated watershed management in the Sikkim Himalaya, aims to demonstrate the potential of satellite remote sensing in environmental conservation and sustainable development planning at watershed level. The identification of ecological disturbances on the land surfaces and their dynamics are important for adopting suitable management and mitigating measures.

The watershed investigated encompasses an area of 3009 hectares and is situated in South district of Sikkim state. Its geographical co-ordinates are 27°12′3″N to 27°16′14″N and 88°19′2″E to 88°23′30″E and is known as Mamlay watershed (Fig. 1). There are three perennial and four seasonal major streams within it, and it lies in the catchment zone of Rangit river flowing along its western boundary. The drainage pattern is dendritic with drainage density value of 2.62 and stream frequency value of 3.06. Its elevation range is 300 meters to 2650 meters and is divided into three geomorphic divisions physiographically. These are lower hill slopes (<1000 meters), middle hill slopes (1000-2000 meters) and upper hill slopes (>2000 meters). The general slope range is 30° to 40°. An estimated 95 per cent population is

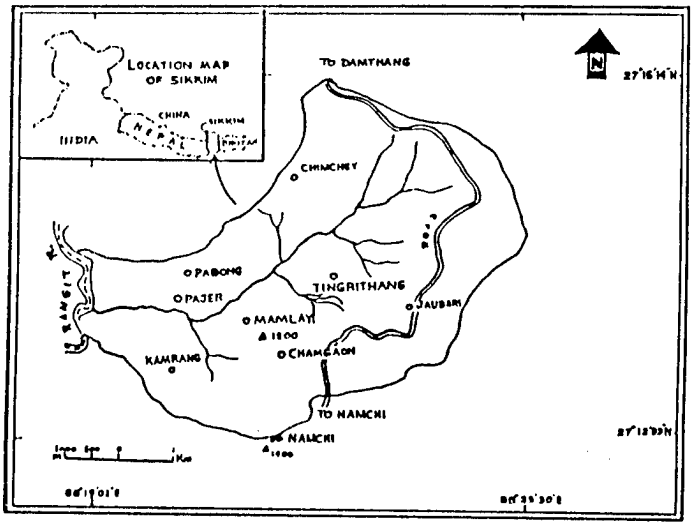


Fig.1 Location map of the study area.

0-7803-3068-4/96$5.00©1996 IEEE

concentrated in lower and middle hill slopes and rest 5 per cent in upper hill slopes. The topography becomes rugged from east to west. There is significant variation in land cover types depending on the micro-climate, lithology, soil types, slope aspects and altitude within this watershed. There is high rainfall in temperate region and shadowed rainfall in the valleys of sub-tropical region.

II. DATA AND METHODOLOGY DESCRIPTION

IRS 1A/1B LISS-II A2, geocoded single bands as well as normal FCCs of path/row - 19/48 on 1:50,000 scale were used. Table 1 shows the band ranges of this satellite. These bands cover important application areas like geology, forestry, hydrology and agriculture. The data used pertained to two specific dates of November 1988 and November 1992. Visual interpretation of these scenes was done using standard interpretation techniques [2] for deriving the land cover classes. All the terrestrial features have their own unique spectral signatures which help in their identification and delineation visually as well as by digital image processing of the scenes [3]. Eventhough the modern trend is to utilize computers, visual interpretation still has certain advantages for working on limited resource themes [4]. In this study also, interpretation on limited land cover classes was considered. This included detection of tone, color brightness and classification of tonal color groups. The spatial image analysis led to the establishment of relationships between these groups and the land covers.

All the interpretations were verified by ground truth studies with suitable ground control points. The field data collection in remote sensing analysis especially for first hand observations of land cover is important [5]. Such field studies were also necessary to minimize the shadow effects so characteristic of hilly terrain on the satellite scenes. Final details were observed on the FCCs. These scenes showed water bodies in blue or deep blue color according as the depths. Vegetation was observed in various shades of red depending on its health and density. Bare soils showed brighter tones as per quartz content variations. Built-up area showed bluish tone/color characteristic of the building materials and observations could be made for cluster settlements only.

TABLE 1
SPECTRAL BAND RANGES OF IRS 1A/1B

Band	Spectral range (microns)
1	0.45 - 0.52
2	0.52 - 0.59
3	0.62 - 0.68
4	0. 77 - 0.86

The statistics on each land cover was generated using precision digital planimeter and integrated with the collateral ground level information. This has provided quantified land cover status for these periods. Standard error estimation [6] for accuracy of classified land covers for the base year 1988 was done. Ground truth studies for 60 points in the watershed showed that 78 per cent points were correct and 22 per cent points were incorrect in the classification. Classification accuracy formula [7] was used for standard error as follows:

$$SE = \{(p \times q) / N\}^{1/2}$$

[SE - standard error in %, p - correct observations (%), q - incorrect observations (%) and N - sample size].

In this case, SE value obtained is 5.35 per cent. Therefore, 78 per cent correct observations can be taken to be a mean value with a standard error of ±5.35 per cent at 68 per cent significance level and ±10.7 per cent at 95 per cent significance level. The classification accuracy range, therefore, is 67.3 to 88.7 per cent at 95 per cent confidence interval.

The land cover area variations in each class over the period 1988 to 1992 was calculated by this formula:

$$\text{Variation}(\%) = [\{1992(\%) - 1988(\%)\}/1988(\%)]\times 100$$

This is indicative of the change dynamics showing the trend of land-use manipulations within all the land cover classes. The observations are presented in Table 2. The classes are given serial number according as their level I and II categories. The sub-classes at level II are assigned sub-serial numbers. The variations are calculated for both the levels and pesented in the table separately.

III. SUMMARY AND DISCUSSION

The use of multidate satellite data has indicated a trend of rapid land cover change within the watershed which is depicted in table 2. Forest category shows an overall negative variation of 10.9 per cent. Its level II sub-classes namely dense (canopy cover > 0.4), open (canopy cover 0.2-0.4) and sal (*Shorea robusta*) forest also show negative variation values of 21.52, 12.98 and 26.09 per cent respectively. Its other sub-classes are degraded forest (canopy cover 0.1-0.2), scrub land (canopy cover < 0.1) and forest blanks, which show positive variation values of 31.51, 33.52 and 21.21 per cent respectively. Agricultural land shows positive variation of 52.5 per cent. Its sub-classes rainfed land, irrigated land and fruit orchards also show positive variation of 58.2, 8.13 and 32.5 per cent respectively. The waste land category shows a positive variation of 10.64 per cent. Its sub-classes rock-outcrops and landslides show positive variation values of 7.09 and 100 per cent respectively. Water-bodies show a

TABLE 2
LAND COVER CHANGE DYNAMICS OF MAMLAY WATERSHED, SOUTH SIKKIM

S.No./ Level	Land cover class	Area (%) 1992	Area (%) 1988	Variation (%)
1/I	**Forest land**	**67.55**	**75.81**	**–10.90**
1.1/II	Dense forest	21.66	27.60	–21.52
1.2/II	Open forest	35.10	40.34	–12.98
1.3/II	Sal forest	0.34	0.46	–26.09
1.4/II	Degrad. forest	2.88	2.19	+31.51
1.5/II	Scrub land	6.97	5.22	+33.52
1.6/II	Forest blanks	0.40	0.33	+21.21
2/I	**Agricul. land**	**23.62**	**15.49**	**+52.5**
2.1/II	Rainfed land	21.83	13.80	+58.2
2.2/II	Irrigated land	1.33	1.23	+8.13
2.3/II	Fruit Orchards	0.53	0.40	+32.5
3/I	**Waste land**	**6.24**	**5.64**	**+10.64**
3.1/II	Rock-outcrops	6.04	5.64	+7.09
3.2/II	Land-slides	0.20	0.00	+100
4/I	**Water-bodies**	**0.60**	**0.67**	**–10.45**
5/I	**Built-up land**	**2.12**	**2.12**	**0**

negative variation of 10.45 per cent. Built-up land does not show significant variation. This is due to scattered settlement pattern and limitation of resolution. But some increase is expected in this category.

In Mamlay watershed, the forest has been meeting and satisfying the needs of majority of the population for fuel, timber and fodder [8]. Overall negative variation in forest land and positive variation in agricultural land very explicitly imply that this land is fast encroaching upon the forest land. Such situation will result into increased soil erosion and thereby the soil fertility and nutrient status will also be affected. The energy availability shall be directly influenced by depletion of forest cover. The positive variation in waste lands is due to improper upland farming practices leading to landslides in rainfed lands mainly. Negative variation in water-bodies is attributed to manipulations in small streams by the inhabitants. Land cover change dynamics thus derived provides a valuable source of information in evolving suitable watershed management options for sustainable development and environmental conservation. Ecosystem dynamics, effect of human activities on ecological processes, monitoring of resources and the techniques for watershed management are essential research areas [9]. Satellite data utilization shall make the task faster, easier and cost-effective with quick monitoring of such remote terrain.

ACKNOWLEDGMENTS

The author is thankful to Dr. L.M.S. Palni, Director, G.B. Pant Institute of Himalayan Environment and Development for all the institutional facilities provided.

REFERENCES

[1] K.G. Saxena, B.P. Kothyari and K.S. Rao, "Remote sensing for management of biological resources - a rational outlook for the Himalaya," in Mountain resource management and remote sensing, P.N. Gupta and A.K. Roy, Eds.Dehradun (India): Surya Pub., 1991, pp.185-194.

[2] F.F. Sabins (Jr.), Remote Sensing : Principles and Interpretations, New York: Freeman, 1986, pp. 100- 105.

[3] P.K. Akhouri, M.S. Bhagwat and A.D. Agnihotri, "Application of digital image processing for environmental studies of limestone deposits - a case study," Procd. 3rd NCB Int. sem. on cement and building materials, New Delhi, vol. VI, pp. 1-27, 1991.

[4] B.L. Deekshatulu, "Status of remote sensing in India," in Mountain resource management and remote sensing, P.N. Gupta and A.K. Roy, Eds.Dehradun (India): Surya Pub., 1991, pp.1-9.

[5] J.B. Campbell and J.O. Browder, "Field data collection for remote sensing analysis: SPOT data, Rondonia, Brrazil," *Int. J. Remote Sensing*, vol. 16, no. 2, pp.333 - 350, 1995.

[6] P.J. Curran, Principles of Remote Sensing, England: Longman, 1985, pp. 217-220.

[7] A. Hay, "Sampling design to test land use map accuracy," *Photogramm. Engg. and Remote Sensing*, vol. 45, pp. 529-533, 1979.

[8] R.C. Sundriyal and E. Sharma, "Anthropogenic pressure on tree structure and biomass in the temperate forest of Mamlay watershed in Sikkim," *Forest Ecology and Management*, 1996,in press.

[9] R.C. Sundriyal, S.C. Rai, A.P. Krishna and E. Sharma, "Watershed management for sustainable development in the Eastern Himalaya," in Prof. R.S. Ambasht festschrift volume, A.K. Srivastava, Ed. Varanasi (India),1996, in press.

Remote Sensing of Crop Responses to Ozone and Carbon Dioxide Treatments[1]

Éric Leblanc[2], C.S.T. Daughtry[3], C.L. Mulchi[2]
[2]University of Maryland, College Park, MD 20742 USA, (301) 405-1328
[3]USDA - ARS Remote Sensing and Modeling Lab., Beltsville, MD 20705-2350 USA, (301) 504-5015

Increases in tropospheric ozone (O_3) and carbon dioxide (CO_2) concentrations have been shown to alter crop responses such as gas exchange rates, leaf areas and specific leaf mass, plant biomass and yields. Leaf level alterations induced by exposure to pollutants are known to alter canopy reflectance characteristics. The objectives of this research are to evaluate the utility of non-imaging, ground-based, remote sensing measurements for detecting crop responses to alterations in atmospheric O_3 and CO_2 levels using crop plants grown in open-top chambers (OTCs). Winter wheat and soybeans were grown during the spring and summer months of 1995 in a 2X2 factorial arrangement of O_3 and CO_2 treatments. Canopy reflectance measurements were performed on several dates for both crops using a spectroradiometer (SE-590). Canopy reflectance, normalized reflectance, and the red edge response were determined and compared over gaseous treatments for use as a stress indicator for each crop. Spectral curves for both crops show minimal difference between treatments up to 700 nm but differ in soybeans for data beyond 700 nm. However, when reflectance data were normalized using the low O_3 + ambient CO_2 as control, high O_3 and/or CO_2 treatments were separated for both crop species with different patterns for each. Likewise, red edge effects were different between O_3 treatments.

INTRODUCTION

The increasing levels of tropospheric ozone (O_3) and carbon dioxide (CO_2) are inducing significant crop responses that result in decreased [2] and enhanced [1] plant productivity, respectively. Such physiological disturbances can induce biochemical and, if severe enough, physical alterations at the leaf level which modify its spectral characteristics. This is affecting the way the whole leaf, and consequently the whole plant, responds to incoming radiation [11].

Reflectance measurements can provide information for inferring plant status. The reflectance behavior of living vegetation can usually be described by low reflectance values in the visible range, caused mainly by chlorophyll absorption, and high reflectance values in the near-infrared due to internal leaf scattering. This change in reflectance occurs in just a few nanometers and is usually referred to as the red edge. This is characteristic of green vegetation only and permits discrimination of vegetation from the background [5]. It is also commonly used as a mean to study senescence [6] and detect plant stress [8].

Edward and Cure [3] showed that soybeans exposed to O_3 concentrations as low as 20 nmol mol^{-1} can be distinguished from soybeans exposed to ambient O_3 levels by film density of aerial photographs. Field bean (*Vicia faba* L.) leaves exposed to sulfur dioxide (SO_2) were also shown to have different spectral characteristics once exposed to concentrations of 200 nmol mol^{-1} during ten days [4]. Red edge measurements can provide additional information for the detection of early stress symptoms such as a change in chlorophyll status [7].

MATERIALS AND METHODS

Winter wheat (*Triticum aestivum* L., cvs. Gore and Susquehanna) seeds were sowed at the Beltsville Agricultural Research Center in Beltsville, MD in November 1994 in a Codorus silt loam. Open-top chambers (OTCs) were installed over 24 plots in March 1995. The experimental design consisted of a randomized complete block with two levels of O_3 and CO_2 in a 2X2 factorial. The low O_3 level was realized by using charcoal-filtered air, while the high O_3 treatment consisted of the addition of approx. 20 nmol mol^{-1} O_3 above ambient. Carbon dioxide treatments consisted of an ambient (355 µmol mol^{-1}), while the high treatment was ambient plus 150 µmol mol^{-1} CO_2. Plants were harvested in July. As soon after the harvest was completed, one-week old soybeans (*Glycine max* (L.) Merr., cvs. Essex and Forrest) grown in a greenhouse were transplanted into the OTCs in rows 0.6 m apart with plants spaced 0.1 m apart. The soybean harvest occurred in November.

Canopy reflectance was measured under clear skies between 1100 and 1300 EST using the SE-590 spectroradiometer which detects energy in the 400-1100 nm range. The instrument was installed on a hand-held boom, then positioned over the OTCs for a nadir view. Ten scans were acquired as the spectroradiometer was moved in a sweeping fashion over each canopy. The radiance of a Spectralon[4] (Labsphere Inc.) reference panel was measured every 10-15 min to calculate the reflectance factor. Canopy reflectance was measured on three dates for winter wheat and on 11 dates for soybeans. For each experimental unit, scans were averaged. Reflectance curves

[1]Scientific Article No. A7873, Contribution No. 9205, Maryland Agric. Exp. Sta., Univ. of MD, College Park, MD 20742 USA.
[4]Company and trade name are given for the benefit of the reader and do not imply any endorsement of the product or company.

0-7803-3068-4/96$5.00©1996 IEEE

were smoothed and predicted values were output using SAS/INSIGHT software [10]. Slopes and inflection points were determined and these values were analyzed as a mixed-effect model using the SAS/MIXED procedure [9]. Treatment means were compared using Duncan's Multiple Range Test.

RESULTS AND DISCUSSION

Table I shows the seasonal 7-h mean O_3 and CO_2 concentrations observed for the four treatments. Fig. 1 shows the canopy reflectance response of winter wheat immediately before heading. The mean canopy reflectance of winter wheat was not different between treatments; however, the normalized reflectance (right portion of the graph) indicated some differences. The normalized reflectance was calculated by ratioing the mean reflectance of every treatment to the mean reflectance of the low O_3 + ambient CO_2 treatment. High CO_2 treatments had higher ratios in the visible range compared to ambient CO_2 treatments, i.e. approx. 7.5 to 30 % more then the control.

For soybeans, mean canopy reflectance values in the visible and red edge area were similar (Fig. 2); however, for wavelengths greater than 750 nm, both high O_3 treatments had slightly lower reflectance values than the low O_3 treatments. High CO_2 treatments followed a different pattern compared with ambient CO_2 treatments; they showed higher normalized reflectance values in the chlorophyll absorption band, i.e. approx. 50% more for the low O_3 + high CO_2 treatment and nearly 10 % more for the high O_3 + high CO_2 treatment. This may be related to the seasonal leaf chlorophyll concentration which showed a decrease of 10% under high CO_2 treatments (data not shown).

Fig. 3 shows the red edge slope response of both species. Responses in the red portion of the visible range were again similar, but the slope of low O_3 treatments tended to be greater at the inflection point (peak) compared with high O_3 treatments. This difference was especially apparent in soybeans. Notice that winter wheat showed greater maximal slopes for all treatments.

Table I. Seasonal 7-h mean O_3 and CO_2 concentrations.

Treatment	$[O_3]$, (nmol mol^{-1})		$[CO_2]$ (μmol mol^{-1})
	Wheat	Soybeans	
Low O_3 + Amb. CO_2	26.4	28.5	355
Low O_3 + High CO_2	26.4	28.5	505
High O_3 + Amb. CO_2	57.1	67.0	355
High O_3 + High CO_2	57.1	67.0	505

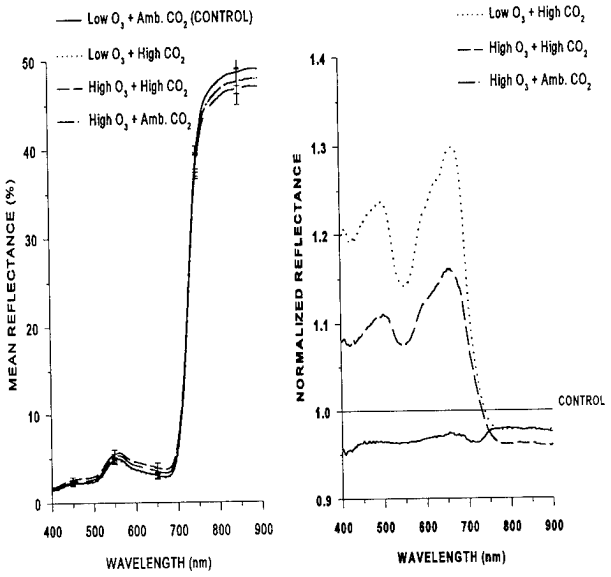


Figure 1. Mean (left) and normalized (right) winter wheat canopy reflectance measured on 27 April 1995.

Table II summarizes the red edge results calculated for both crops. In winter wheat, λ_{RE} shifted toward shorter wavelengths when comparing low vs. high O_3 treatments (under ambient CO_2). Even if not significant, trends indicate smaller S_{RE} and R_{RE} values under high O_3 conditions. For soybeans, the λ_{RE} also indicates a tendency to shift toward shorter wavelengths under

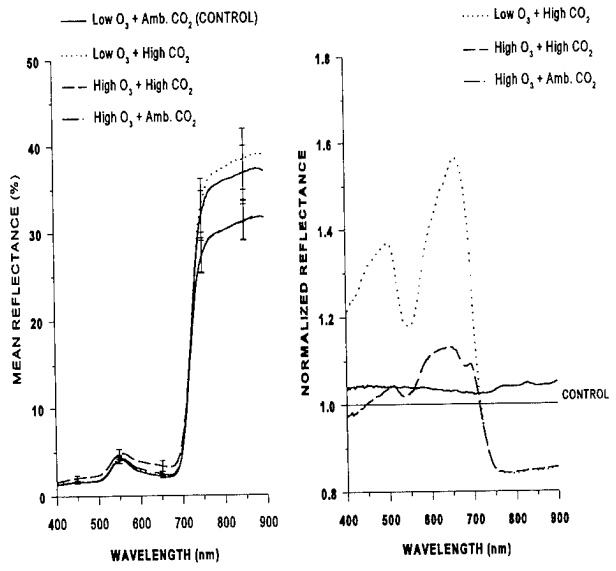


Figure 2. Mean (left) and normalized (right) soybean canopy reflectance measured on 22 August 1995.

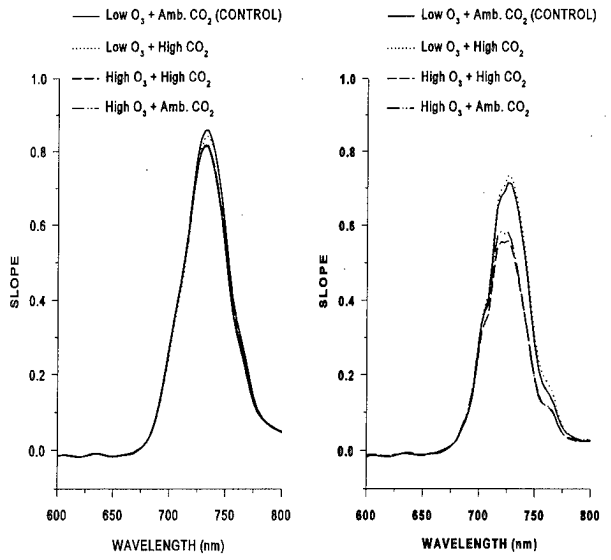


Figure 3. Winter wheat (left) and soybeans (right) slope (S_{RE}) response for the same dates as in Fig. 1 and 2.

Table II. Red edge wavelength (λ_{RE}), slope (S_{RE}), and reflectance (R_{RE}) of winter wheat and soybean canopies exposed to O_3 and CO_2 treatments[1,2]

Treatments	λ_{RE} (nm)	S_{RE}	R_{RE}(%)
Winter Wheat			
Low O_3 + Amb. CO_2	723 a	0.634 a	21.4 a
Low O_3 + High CO_2	721 ab	0.605 a	20.6 a
High O_3 + Amb. CO_2	717 b	0.566 a	18.8 a
High O_3 + High CO_2	719 ab	0.573 a	19.6 a
Standard error	0.5	0.032	1.0
Soybeans			
Low O_3 + Amb. CO_2	716 a	0.610 ab	19.4 a
Low O_3 + High CO_2	716 a	0.636 a	19.8 a
High O_3 + Amb. CO_2	712 a	0.509 b	16.6 a
High O_3 + High CO_2	713 a	0.528 ab	17.5 a
Standard error	1.9	0.049	1.7

[1]Variables are averaged over three dates for winter what and eleven dates for soybeans.
[2]For each species, means with same letter are not significantly different according to Duncan's Multiple Range Test (α=0.05).

high O_3 treatments (not significant). R_{RE} also showed the same behavior. The S_{RE} value for the healthiest treatment, i.e. low O_3 + high CO_2, is significantly higher (0.636) compared to most stressed treatment, i.e. the high O_3 + ambient CO_2 (0.509).

It is clear that the red edge constitutes a phenomenon that is worth measuring in order to investigate the responses of plants to factors such as O_3 and CO_2. Ozone hastened plant senescence and its impact was detected spectrally. Reflectance measurements and red edge determination provided valuable information partly because of their high sensitivity. However, it was not possible to recognize O_3 stress or CO_2 enrichment as such using this information.

REFERENCES

[1] Acock, B. 1990. Effects of carbon dioxide on photosynthesis, plant growth, and other processes. Impact of carbon dioxide, trace gases, and climate change on global agriculture. ASA special publication no. 53.

[2] Alscher, R.G., and Wellburn, A.R. 1994. Plant responses to the gaseous environment. Chapman and Hall. New York. 395 pp.

[3] Edwards, G.J., and Cure, W.W. 1989. The use of a spectroradiometer to study aerial photographs of ozone-treated soybeans. Int. J. Remote Sensing 10: 1913-1918.

[4] Gemmell, F.M., and Colls, J.J. 1992. The effects of sulphur dioxide on the spectral characteristics of leaves of *Vicia faba* L. Int. J. Remote sensing 13: 2547-2563.

[5] Horler, D.N.H., Dockray, M., and Barber, J. 1983. The red edge of plant leaf reflectance. Int. J. Remote Sensing 4: 273-288.

[6] Miller, J.R., Wu, Jiyou, Boyer, M.G., Belanger, M., and Hare, E.W. 1991. Seasonal patterns in leaf reflectance red-edge characteristics. Int. J. Remote Sensing 12: 1509-1523.

[7] Munden, R., Curran, P.J., and Catt, J.A. 1994. The relationship between red edge and chlorophyll concentration in the Broadbalk winter wheat experiment at Rothamsted. Int. J. Remote Sensing 15: 705-709.

[8] Rudorff, B.F.T., Mulchi, C.L., Daughtry, C.S.T., and Lee, E.H. 1995. Growth, radiation use efficiency, and canopy reflectance of wheat and corn grown under elevated ozone and carbon dioxide atmospheres. In press.

[9] SAS Institute, Inc. 1992. SAS Technical Report P-229. SAS/STAT Software: Changes and Enhancements. Release 6.07. pp. 287-366.

[10] SAS Institute, Inc. 1994. SAS/INSIGHT Software: Changes and Enhancements. Release 6.10. 204 p.

[11] Steven, M.D., and Malthus, T.J., Demetriades-Shah, T.H., Danson, F.M., and Clark, J.A. 1990. High-spectral resolution indices for crop stress. In: Applications of remote sensing in agriculture. Steven, M.D., Clark, J.A., eds. Butterworths, Boston. pp. 209-227.

Examination of multi-temporal ERS-1 radar over the Rainwater Basin

Chris Keithley
Miles Roberts, PhD
Department of Geography
CSU-Sacramento
Sacramento, CA 95819

Abstract – This study examined the use of multi-date radar to identify crops and other types of vegetation within the Rainwater Basin in south-central Nebraska. The Rainwater basin is comprised of a dense cluster of wetlands that have been greatly modified by agricultural production. Initial research indicates that the multi-date approach is effective in dinstinguishing between agricultural and wetland vegetation. Temporal curves constructed from 150 field observations show a pronounced seasonal variation in backscatter associated with crop phenology. Differences in backscatter among crop types was most pronounced in early and mid-summer images.

INTRODUCTION

The Rainwater Basin is a mosaic of wetlands and agriculture stretching across 17 counties in south central Nebraska. The region provides habitat for waterfowl and is a focus of spring waterfowl migration. During the past century, conversion of wetlands to agriculture has dramatically altered this landscape and its ecological function. Most wetlands in the Basin are shallow and small, with size dependent on recent meteorological conditions. For conservation and habitat restoration, new techniques are needed to reliably map such small yet important wetlands. This study examined the use multi-date ERS-1 Synthetic Aperture Radar (SAR) satellite imagery to identify land cover (crop type and wetlands) with radar data alone. Six images were acquired covering the Rainwater Basin during the 1995 growing season to examine the ability of SAR images to map land cover. These images were used to identify typical rural land cover types such as agricultural crops (corn, soybean, milo), wetlands, and grasslands.

The use of Synthetic Aperture Radar (SAR) to identify agricultural land cover and other vegetation characteristics has been investigated to some extent in the last two decades. Two well-documented advantages of imaging radar are cloud penetration and the capture of information about vegetation canopy structure. The ERS-1 satellite offers images that are comparable in spatial resolution to Landsat TM, but are imaged with an Active Microwave Imaging (AMI) sensor. The ERS-1 satellite uses a C-band SAR with VV polarization. The active SAR sensor emits a narrow bandwidth energy pulse and measures the reflected signal (called the backscatter or return), from the target. The strength of the SAR return is affected by target morphological factors such as surface slope and roughness, moisture content, and molecular structure [1]. Thus, SAR images capture distinctly different but complementary information compared to traditional V/IR images.

For agricultural applications, the radar backscatter has been found to be dependent on plant species and age, which generally determine plant morphology. For example, sugar beets were found to give a high return due to their high water content and large leaves [2]. In general, broad leaf crops produce a higher signal return than other crops for C band with VV polarization. VV polarized SAR reflectance is predominately caused by the physical structure of the plant canopy rather than understory characteristics [3].

As with the initial applications using Landsat V/IR images, initial ERS-1 SAR researchers have attempted to map various crop types. Bouman and Uenk [4], used simulated multidate ERS-1 radar to examine SAR backscatter changes over agricultural fields. They reported that a combination of early and late season SAR images provided the best discrimination between crops. Schmullis [5], reported that ERS-1 SAR returns from different fields of the same crop were more variable in the early season and converged with increasing canopy cover. Early season differences were attributed to differences in soil roughness. Thus, crop identification should be conducted using late summer data when the SAR reflectance is more affected by crop canopy than soil surface effects.

ANALYSIS AND RESULTS

Six ERS-1 images were acquired between May and September 1995 covering the eastern part of the Rainwater basin in Clay County, Nebraska. These images were rectified into the UTM coordinate system using nearest neighbor resampling to 30 m resolution and assembled into a single multiband image data set where each band is a single date of imagery. Four images were from the descending ERS-1 orbit (approximately 10:30 pm EST) and two images from the ascending orbit (approximately 10:30 am EST). Practically, the difference between the ascending and decending orbits means that while the look angle (23.5 degrees) is the same, the look direction is reversed. Inspection of the imagery

0-7803-3068-4/96$5.00©1996 IEEE

shows no discernable look direction effects for the relatively flat terrain of the study area.

One problem inherent in most SAR images is speckle, or noise, which is the result of echoes from the target surface [6]. This speckle is usually treated as a random effect and reduced by averaging adjacent pixels using spatial convolution filters. In this study, a 3 x 3 Sigma filter [7] was used to reduce image speckle while retaining edge information such as field boundaries.

Field observations were made in the study area to record crop type and condition for over 150 fields. The field boundaries were identified on the image data set and digitized to produce training polygons. This information provided the base for constructing temporal profiles of radar backscatter for crops and wetlands in the scene. Temporal signatures of radar backscatter were extracted for each of the 150 fields.

Histograms were used to examine the distribution of backscatter for the entire image and for individual fields. The raw data showed a high variance for the May 6, July 7 and September 23 images, although the distributions were remarkably normal. Graphs produced with the original DN values were influenced by extreme differences in standard deviation, which made comparison of profiles between agricultural fields difficult. To account for the difference in variance between dates the data was standardized to Z-scores and a scalar was added to return all Z-scores to a positive range. Inspection of covariance and correlation matrices indicated a strong positive relationship between brightness values on the July and August images.

Temporal curves were constructed to examine seasonal trends in backscatter. The mean value of backscatter was plotted using normalized Z-scores. The data reveals a strong temporal pattern of backscatter for vegetation throughout the growing season (**Fig. 1**). A separation between agricultural fields, wetlands, and grasslands was apparent for some dates.

The phenological cycle of vegetation becomes important in interpreting the graphs. The first image was acquired in early May during a very wet spring, and prior to most planting. Difference in backscatter from this date are attributed mainly to differences in soil and moisture content. The second image was acquired in mid June. Due to a wet spring the planting was delayed and while agricultural vegetation was emergent, the backscatter would still be influenced by the soil background. Winter wheat provides an exception to the general pattern in that the crop was mature in mid - June and close to harvest. The third image taken on July 7th consistently provides the greatest magnitude of backscatter as shown by the peak in the curve for all land cover types. This date also provides the greatest separation between crops. The temporal curves begin to converge during late July as the canopies thicken although there is still distinction between crops. The fifth image acquired in late August represents a full canopy for most crops and shows the least distinction in backscatter. The final image in September shows an increased variation in backscatter which could be attributed to the senescence of vegetation and the variation in harvesting schedules among crops.

In examining the temporal pattern of backscatter among crops a general pattern emerges as well, yet the temporal difference between crops is not as dramatic as the temporal difference between land cover classes. There is high variation between fields during the early image dates that is attributed to the soil background. Once vegetation in emergent, Corn shows the highest backscatter followed by Milo, Soybean, and Pasture. The stubble from winter wheat provides a consistently high backscatter. As the season progresses the separation between crops is most significant in early July. The variation in backscatter among crops is less in late July, and there is little distinction between crops by the late summer.

CONCLUSIONS AND FUTURE RESEARCH

This research indicates that multi-temporal radar can be used to track temporal changes in backscatter that are related to differences in crop phenology. Preliminary results suggest that the strongest distinction between crops occurs during the early to mid growing stages. Once crops reach a full canopy the ERS-1 C-band sensor appears to provide limited penetration of the vegetation canopy. This trend has been reported in other agricultural studies as well. The extreme variation in backscatter in early season images appears to be influenced by the soil background. Other factors include the differences in planting schedules that occurred due to wet spring weather. A clear distinction was present between major land cover types (crop, wetlands, grassland, etc.). This suggests that multi-date radar has potential for use with regional land cover mapping. Future work will explore the use of multi-date radar for classification of crops and wetlands in this region.

With the increase in the number of existing and proposed earth resource satellites that collect microwave radar data there is a need to develop new techniques to merge optical and microwave data for improved identification of crops and crop growth parameters. One area of research that needs to be addressed is the method in which the classification is performed. Traditional approaches to image classification use a pixel by pixel classifier and often assume a multi-variate normal distribution. This assumes that the spectral response of a given pixel is similar to its neighboring pixels and the classification will result in identifying homogeneous fields for a given crop. Because of the speckle inherent in the radar imagery this assumption may not hold. Future remote

sensing applications relying on multi-date or multi-sensor data sets will need to develop new ways in which these different sources of image information can be merged using data fusion techniques for information extraction.

ACKNOWLEDGMENTS

ERS-1 SAR images were provided by the European Space Agency (grant USA/124). Additional support was provided by the CALMIT lab at the University of Nebraska, and the Geography Dept. at CSU-Sacramento. Pat Starks, USDA provided Soils data. Additional assistance in field data collection and computer processing was provided by Fiona Renton, Brian Leavitt and Anthony Militar.

REFERENCES

[1] Lillesand, T.M. and R.W. Kiefer, Remote Sensing and Image Interpretation, John Wiley & Sons, 1987.
[2] Bouman, B.A.M. and D.H. Hoekman, Multi-temporal, multi-frequency radar measurements of agricultural crops during the Agriscatt-88 campaign in The Netherlands. Int. Journal of Remote Sensing. 14(8):1595-1614, 1993.
[3] Holmes, M.G., "Applications of Radar in Agriculture," Ch. 19 in Applications of Remote Sensing in Agriculture, M.D. Stevens and J.A. Clark, Eds. Butterworth Press, 1990.
[4] Bouman, B.A.M. and D. Uenk, "Crop classification possibilities with radar in ERS-1 and JERS-1 configuration," Remote Sensing of Environment. 40:1-13, 1992.
[5] Schmullius, C, Nithack, J. and M. Kern. 1994. Comparison of multitemporal ERS-1 and E-SAR image data for crop monitoring. Earth Obs. Quaterley. 43:9-12.
[6] Leberl, F.W. Radargrammetric Image Processing, Artech House, 1990.
[7] Lee, J.S., 1981. Speckle analysis and smoothing of synthetic aperture radar images. Computer Graphics and Image Processing. 17:24-32.

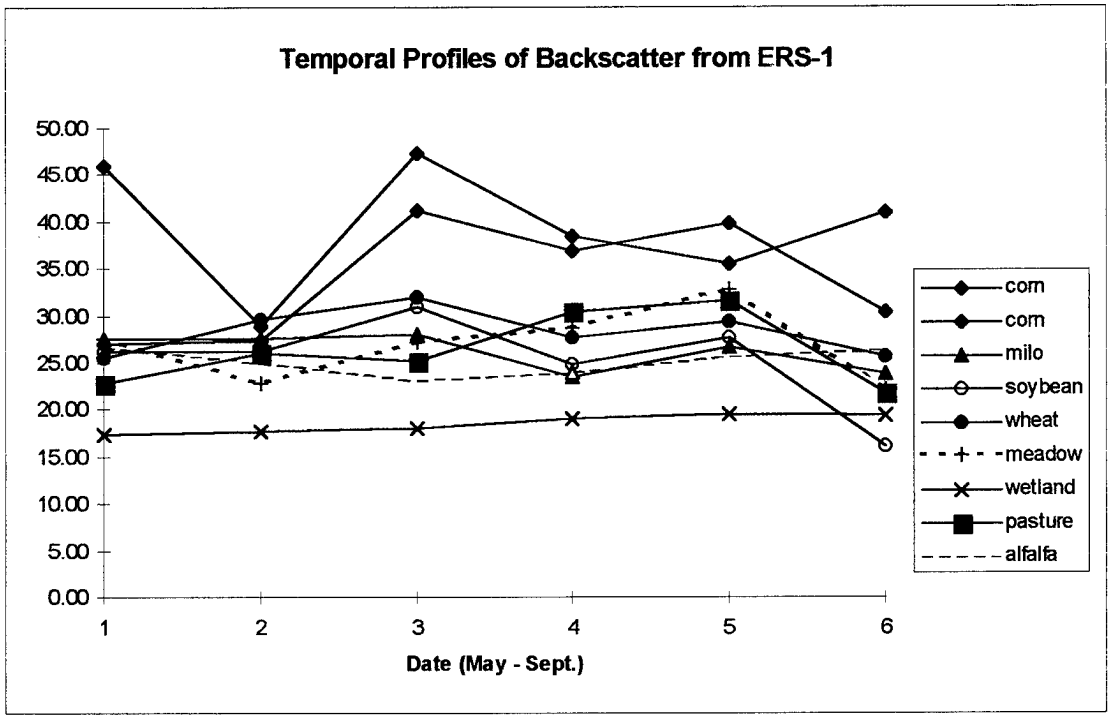


Figure 1. Multi-date ERS-1 SAR imagery was used to calculate the mean backscatter for land cover occuring within the Rainwater basin in Clay County, Nebraska

A Comparison of NDVI and Spectral Mixture Analysis for Estimating Biophysical Properties in Boreal Forest Terrain

Derek R. Peddle [1], Forrest G. Hall [2], and Ellsworth F. LeDrew [1]

[1] **Department of Geography, University of Waterloo**
Waterloo, Ontario N2L 3G1 Canada
(519) 885-1211 Fax: 888-6768
drp@wateol.uwaterloo.ca

[2] **NASA Goddard Space Flight Center**
Laboratory for Terrestrial Physics
Biospheric Sciences Branch, Code 923
Greenbelt, Maryland 20771 USA

Abstract -- Spectral mixture analysis is used to determine scene fractions of sunlit canopy, background, and shadow, which are compared to NDVI in terms of their relation to the biophysical parameters LAI, biomass and NPP. In all tests, the mixture fractions outperformed NDVI by large margins, with shadow fraction having an r^2=0.80 compared to 0.47 for NDVI. Solar zenith angle was an important factor in determining input component reflectance values for mixture analysis. The physical basis for these improvements is the sensitivity of mixture fractions to tree size and morphology.

INTRODUCTION

The North American Boreal Forest is one of the largest biomes on Earth and a major storehouse of organic carbon within the global carbon cycle. Studies of the terrestrial carbon budget in Boreal Forest environments require biophysical structural parameters such as biomass, leaf area index (LAI), and net primary productivity (NPP). A common approach to estimating these variables has used the Normalised Difference Vegetation Index (NDVI), however a number of investigators have reported problems in its use [1,2], such as the effects of background reflectance, shadows, and canopy geometry. To address these problems, we have been developing new applications of spectral mixture analysis (SMA, [3]) and canopy geometric-optical reflectance models [4] to capture individual scene fractions with respect to scene physics, canopy geometry and structure, and relate these fractions to the biophysical variables of interest. In this paper, we present a summary of some of the major findings from our SMA investigations to date [5,6,7], and compare these to results from NDVI.

STUDY SITE AND DATA

The study area is in the Superior National Forest (SNF), Minnesota, located near the southern limit of the Boreal Forest which may be particularly sensitive to climatic variability and change. A multispectral and biophysical characteristics data set was acquired during the summers of 1983 and 1984 over a gradient of forest densities. In this study we used biophysical data (biomass density, leaf area index, net primary productivity) collected from 31 stands of black spruce, the most common boreal forest dominant. Spectral reflectance measurements were acquired over each of the plots using a helicopter-mounted Modular Multi-band Radiometer (MMR) at several times during the growing seasons.

BIOPHYSICAL PARAMETER ESTIMATION

Spectral Mixture Analysis

Spectral mixture analysis is based on the fact that the IFOV represented by a pixel contains a number of individual surface components which together contribute to the overall pixel level reflectance received by a remote sensing instrument [3]. In the Boreal Forest, pixel level reflectance (R_p) can be expressed as linear combinations of the individual component (end-member) reflectances of sunlit canopy (R_c), sunlit background (R_b), and shadow (R_s), weighted by their areal fractions (C, B, and S, respectively), as:

$$R_p = C \cdot R_c + S \cdot R_s + B \cdot R_b \quad (1)$$

A system of equations is developed over all spectral bands from remotely sensed pixel level reflectance values together with input component reflectances, from which we solve for the unknown fractions using a constrained least squares approach [8]. These fractions are in turn related to the forest biophysical parameters of interest.

The input component end-member spectra (R_c,R_s,R_b) are critical to the SMA procedure. In this study, reflectance values for sunlit background (sphagnum moss) and shadow were obtained in the field. However, there were no available spectral measurements of sunlit canopy structures. Instead, we have tested cylinder, conical, and spheroid based geometric-optical (G-O) canopy reflectance models [4] for estimating values for R_c. Since it is known that R_c increases with SZA, we obtained estimates of R_c over a range of SZA corresponding to the solar position at the time of MMR acquisition.

NDVI

For each MMR acquisition, we also computed NDVI, defined as (NIR-RED)÷(NIR+RED). The analysis was performed over all SZA, and also for the three 7° SZA ranges centered at 30°, 45° and 60° for direct comparison with mixture analysis results, even though the computation of NDVI is the same

0-7803-3068-4/96$5.00©1996 IEEE

regardless of SZA. NDVI values and SMA fractions were compared in terms of their relationship to biomass, LAI, and NPP through a linear regression analysis over the full set of MMR sites.

RESULTS

Table 1 presents a summary of overall results obtained from mixture analysis and NDVI. In both cases, results are shown for the analysis of all black spruce stands over the full range of solar zenith angles. Since the SMA results were obtained at specific SZA, they were averaged to obtain the reported summary values. For all three biophysical parameters, overall results show that SMA provides significantly better correspondence with biophysical parameters compared to NDVI.

Table 2 provides more detailed results as it reports different SZA used in the three canopy geometric-optical reflectance models as part of the SMA. We see that SZA is important in the overall rankings obtained. In virtually all cases, the best results from SMA were obtained when sunlit canopy reflectance was estimated using canopy models run at SZA=45°. Similarly, the spheroid based geometric-optical mutual shadowing (GOMS) model provided better results compared to the cone and cylinder representation of canopy geometry. As with the overall results, NDVI was ranked in the last three positions in all but one case. It is clear from these results that (i) NDVI is not capturing the full information content available from these remotely sensed data sets in terms of biophysical variables, and (ii) the spectral mixture fractions provide significantly improved results which are consistent over a range of solar zenith angles and forest stand densities.

CONCLUSIONS

A thorough comparison of NDVI and spectral mixture analysis has been summarised, with the latter involving three canopy geometric-optical radiation models tested over a variety of solar zenith angles. In all tests performed, scene fractions from spectral mixture analysis were superior to NDVI in terms of their relationship to LAI, biomass and NPP. Overall r^2 values ranged from 0.74 to 0.80 for SMA, while NDVI results ranged from 0.40 to 0.47. The best overall results were r^2=0.83,0.86 and 0.82 for biomass, NPP and LAI, respectively. The basis for these improvements is the ability to separate scene components which are related to forest structure, as well as the physical basis of the canopy models and their characterisation of tree geometries. These important properties are impossible to capture from the simplistic two-band ratio NDVI technique. Current and future work is addressing the application of spectral mixture analysis and canopy radiation models to regional scales for biophysical parameter estimation in the BOREAS project, as well as in the Brazilian Amazon and other global data sets as part of EOS-MODIS.

ACKNOWLEDGEMENTS

Part of this work was completed while DRP was a Visiting Scientist at NASA/GSFC supported by USRA. This research has also been funded by NSERC. We are grateful to Drs. A. Strahler, X. Li and W. Wanner for collaboration through provision of geometric-optical modeling techniques, and to Dr. F. Huemmrich for assistance with the data set at Goddard.

REFERENCES

[1] Curran, P.J. and Williamson, H.D., 1987. GLAI estimation using measurements of red, near infrared, and middle infrared radiance. *Photogrammetric Engineering and Remote Sensing*, 53(2):181-186.

[2] Spanner, M.A., Pierce, L.L., Peterson, D.L., and Running, S.W., 1990. Remote sensing of temperate coniferous forest leaf area index: the influence of canopy closure, understorey vegetation and background reflectance. *International Journal of Remote Sensing*, 11(1):95-111.

[3] Adams, J.B., Smith, M.O. and Gillespie, A.R., 1993. Imaging spectroscopy: interpretation based on Spectral Mixture Analysis. *In* Topics in remote sensing IV: remote geochemical analysis, p. 145-166. Pieters and Englert (eds.). Cambridge.

[4] Li, X. and A.H. Strahler, 1992. Geometric-optical bidirectional reflectance modeling of the discrete crown vegetation canopy: effect of crown shape and mutual shadowing. *IEEE Transactions on Geoscience and Remote Sensing*, 30(2):276-292.

[5] Hall, F.G., Shimabukuro, Y.E. and Huemmrich, K.F., 1995. Remote sensing of forest biophysical structure in boreal stands of *picea mariana* using mixture decomposition and geometric reflectance models. *Ecological Applications*. 5(4):993-1013.

[6] Hall, F.G., D.R. Peddle, and E.F. LeDrew, 1996. Remote Sensing of Biophysical Variables in Boreal Forest Stands of *Picea Mariana*. *International Journal of Remote Sensing* (in press).

[7] Peddle, D.R., F.G. Hall, and E.F. LeDrew, 1996. Spectral mixture analysis and geometric-optical reflectance modeling of boreal forest biophysical structure. *Remote Sensing of Environment*, (in press).

[8] Shimabukuro, Y.S. and Smith, J.A. 1991. The least-squares mixing models to generate fraction images derived from remote sensing multispectral data. *IEEE TGARS*, GE-29(1):16-20.

OVERALL	BIOMASS		NPP		LAI	
	r^2	S.E.	r^2	S.E.	r^2	S.E.
SMA	0.74	2.14	0.80	0.06	0.79	0.55
NDVI	0.40	3.26	0.47	0.11	0.47	0.85

Table 1: Overall results summarised from linear regression coefficients (r^2) and standard error (S.E.) for NDVI and spectral mixture analysis (SMA) with biomass, net primary productivity (NPP), and leaf area index (LAI). Results shown for all MMR data (solar zenith angles ranging from 30° to 60°). SMA results from shadow fraction using a spheroid model of canopy geometry.

BIOMASS		NPP		LAI	
Ranking	r^2	Ranking	r^2	Ranking	r^2
1. SMA-GOMS 45°	0.83	1. SMA-GOMS 45°	0.86	1. SMA-GOMS 45°	0.82
2. SMA-CONE 45°	0.81	2. SMA-CONE 45°	0.85	2. SMA-CONE 45°	0.82
3. SMA-CYL 45°	0.76	3. SMA-CYL 45°	0.80	3. SMA-GOMS 60°	0.79
4. SMA-GOMS 30°	0.73	4. SMA-GOMS 60°	0.77	4. SMA-CYL 45°	0.78
5. SMA-CONE 30°	0.73	5. SMA-GOMS 30°	0.76	5. SMA-GOMS 30°	0.76
6. SMA-CYL 30°	0.66	6. SMA-CONE 30°	0.76	6. SMA-CONE 30°	0.76
7. SMA-GOMS 60°	0.65	7. SMA-CYL 30°	0.76	7. SMA-CYL 30°	0.76
8. SMA-CONE 60°	0.60	8. SMA-CONE 60°	0.66	8. NDVI 60°	0.60
9. SMA-CYL 60°	0.60	9. SMA-CYL 60°	0.66	9. SMA-CONE 60°	0.60
10. NDVI 45°	0.44	10. NDVI 60°	0.56	10. SMA-CYL 60°	0.60
11. NDVI 30°	0.39	11. NDVI 30°	0.53	11. NDVI 30°	0.54
12. NDVI 60°	0.37	12. NDVI 45°	0.46	12. NDVI 45°	0.44

Table 2: Results from linear regression analysis for predicting biophysical variables from NDVI and spectral mixture analyses at different solar zenith angles. Spheroid based geometric-optical mutual shadowing (GOMS), cone and cylinder (CYL) models of canopy geometry were tested in the SMA. Rankings shown by SZA and for all 12 test cases (ties resolved based on standard error values, not shown).

Global Landcover Classification Validation Issues and Requirements

Douglas M. Muchoney
Jordan Borak
Alan Strahler

Center for Remote Sensing, Boston University
675 Commonwealth Avenue
Boston, MA 02215 USA
Phone: 617-353-1049/Fax: 617-353-3200/email: muchoney@bu.edu

BACKGROUND

Global landcover mapping efforts using multitemporal AVHRR GAC and LAC data are current testbeds for developing continuous landcover characterization and monitoring approaches for use with planned EOS-era sensors, particularly MODIS (Moderate Resolution Imaging Spectroradiometer). While the remote sensing science community can address data handling and algorithm development issues, there are currently no adequate specifications or systems developed for training, validation and accuracy assessment requirements of global landcover. There are over 150 million land pixels for each global acquisition at 1-km resolution. A one-percent sample requires 1,500,000 observations for accuracy assessment. While sampling to support TM-based landcover mapping is well-developed, issues of training and validation at 1-km have not been resolved. Although there is utility in applying simple *a priori* landcover classification systems, there is a trade-off between simplicity of sampling and parameterization of landcover components so that reference data may be more useful to support different classification systems. It is obvious that traditional approaches to Earth-feature representation, field inventory and sampling for validation and accuracy assessment are inadequate for global mapping. New models of training and testing are required.

The overriding objectives of validation are to increase the integrity and utility of landcover products to the benefit of the global research and science communities. Validity implies determining that we are observing or measuring what we think we are measuring; in this sense validation is more closely related to calibration than to accuracy assessment. Whereas validation of a biophysical parameter might entail developing a quantitative estimate or sense of the physical meaning of the parameter under consideration [1], landcover validation provides an indication or estimate of confidence that a pixel or segment has been correctly labeled as to a thematic class. Therefore, validity is dependent on how we define landcover classes.

The critical issues related to landcover training and validation include: 1) development of an appropriate scene-remote sensing model, 2) sampling frame development, stratification and sampling, 3) plot sampling methods and parameters in relation to 1-km pixels, 4) remote sensing system sampling parameters (grid, orientation, sampling dimension), 5) data temporality and 6) the relationship of plot and classification system parameters. The purpose of this paper is to outline the relevant requirements and issues relating to training, validation and accuracy assessment. This paper focuses on the specific problems of developing training and validation (reference data) and techniques for algorithm and product validation.

ACCURACY ASSESSMENT AND VALIDATION

Accuracy assessment is the process of comparing products with some reference. It is designed to associate some indicator of "correctness" with a product. Although accuracy estimates are derived from some comparison , this does not necessarily imply that the reference is "truth". One of the principal problems confronting accuracy assessment of a global landcover product is determining what an appropriate reference dataset might be. The working assumption of global landcover validation is the need to place a bounded (per-pixel) estimate on the global accuracy of a classification. Current classification approaches are based on structure, function, geography and physiognomy, but generally not floristics [2],[3]. If the assumption is to place a bounded estimate on accuracy, then a formal sample design based on a random, random-stratified or systematic spatial sample is required [4]. Such sampling requires repetitive sampling at multiple sites distributed across the globe. Therefore, test sites for which high-resolution landcover data are available are proposed as an alternative. Because the test sites are a biased sample, accuracy statistics derived at test sites cannot be regarded as proper statements of global accuracy.

0-7803-3068-4/96$5.00©1996 IEEE

SOURCES AND NATURE OF ERROR

Sources of error introduced into the generation of landcover products include compositing, clouds, registration, gridding and binning, topographic data error, data dependencies and algorithms [5]. In addition, temporality can introduce error when validation data are not temporally coincident with remote sensing observation. This is especially a problem for detecting and describing change. Although data compositing is prescribed, it is necessary to define meaningful temporal generalizations of landcover based on successive observations. A further issue of temporality is assuring the temporal continuity of algorithms and processes.

Algorithm-induced errors are generated when the classification algorithm selects the wrong class. With respect to a particular class, errors of omission occur when pixels of a class are assigned wrong labels; errors of commission occur when other pixels are wrongly assigned the label of the class considered. Errors occur when the signal of a pixel is ambiguous, perhaps as a result of spectral mixing, or when the signal is produced by a cover type that is not accounted for in the training process. These errors, a normal part of the classification process, can be minimized, but not avoided entirely. While they cannot be identified on a pixel-by-pixel basis due to processing constraints, they can be characterized in a statistical sense.

TRAINING AND VALIDATION ISSUES

Test sites are promoted to take advantage of data that have already been generated and where research is continuing. This approach is not however fully developed. The test site data are not in any standard (classification) format, they are derived from a number of remote sensing and other sources and may be unvalidated. However, if the test sites are reasonably representative of their region (an unknown), test site statistics can at least indicate weaknesses and strengths in the datasets and allow users to anticipate how errors might impact their own research. The use of unvalidated, biased test site data for accuracy assessment is an extremely subjective and qualitative approach. It should not be considered in the same category as development of an objective, statistically valid sampling system. Site inventory should be classification-free; that is, landcover/vegetation/ ecosystem attributes should be parameterized so that the standard classification system can be modified and so that other classification systems can be used [6]. There must be a standard suite of variables recorded at each site pertaining to ecosystem structural and functional parameters that are either associated with a landcover or will aid in deriving the landcover type.

Reference data for training and validation are generally pre-existing maps, ancillary biogeophysical data, remote sensing data and test site field data. The quality and availability of adequate training/validation data derived from field sites and existing maps and tabular data is crucial to landcover and landcover change validation. This quality of reference map data is a function of their inherent locational and thematic accuracy. For individual test sites, the utility and quality of the ground truth are variable. Data utility is influenced by the classification system that is applied to the input parameters derived for a site and is also a function of the data source.

For map reference data, there are a number of global vegetation [7], potential natural vegetation [8], ecosystem [9] and landcover maps in existence and planned for the near future. It is not useful to intercompare classification systems without first analyzing their interrelationships and developing inter-classification translations (ie. cross-walking). Since all classification systems, whether by design or not, are appropriate to specific data, scales and levels of analysis, this proves problematic in many cases.

The quality of reference data is significantly affected by the underlying accuracy of the ground truth classification (which may not be known). Because factors relevant to validation vary considerably from test site to test site, validation requires assessment of each test site and most probably re-analyzing the site data to extract specific landcover and landcover change parameters. This strongly supports the development of a high-resolution reference dataset that is derived from other remote sensing sources, standardization of classification subunits or parameters, standardization of procedures for deriving classification subunits and parameters, and development of a global sampling scheme and associated database.

High spatial resolution imagery will be available from a number of sources including ASTER (which will be on the EOS-AM platform with MODIS), Landsat-7 ETM instrument (due for launch at about the time of the EOS-AM platform in a near-simultaneous orbit) and Lewis. Using these fine-scale data, spatial heterogeneity within the test sites can be further characterized. As a continuing data source, these instruments will also allow updating of landcover ground truth at test sites through the EOS era. Use of collateral remote sensing datasets provides additional benefits of redundancy and complementarity that are required by data integration and data fusion techniques.

STRATIFICATION AND SAMPLING FRAMES

Regionalization is the approach to stratification whose objective is to increase classification accuracy by subdividing the globe into regions that produce (presumably) higher accuracies by minimizing intra-strata variance and maximizing inter-strata variance. This contrasts with an ecoregional approach, although regionalization may ultimately be along ecological lines. Regionalization cannot be completely defined prelaunch because it must be a function of how MODIS data geographically organize themselves (what is the inherent global organization) rather than any based on a priori assumptions such as latitudinal range or continentality. An alternative is site stratification based on latitude, continentality, solar irradiation, precipitation, topography and other factors known to influence landcover patterns. Environmental gradient-based stratification and sampling are independent of the remote sensing data and classification systems. Thus, sampling is proportional to area while assuring sampling of all types. This stratification would provide the best independent means of determining and sampling the overall representativeness of the earth from a climate/vegetation perspective. The sampling frame also gives context for allocating global test sites based on their probable efficacy in minimizing uncertainty.

A sampling frame needs to be developed that has at least five components: 1) Stratification/regionalization: The stratification can be ecologically-relevant, geographically determined or based solely on inherent remote sensing data organization which will at least partly be a reflection of ecological and biophysical attributes, 2) systematic random: The sampling frame needs a systematic random component so that stratification and sampling are unbiased and so that an estimate of errors of omission can be characterized. Site access generally constrains the use of systematic random sampling but would be possible if this element was largely dependent on high-resolution remote sensing observation as afforded by ASTER, Lewis or TM, 3) Proportional sampling: A tier of sample points is allocated based on class proportions. This can either be based on MODIS data, or collateral environmental and physical data. Approaches such as gradsect sampling [10] are employed using primarily non-remote sensing data although proportional sampling should at least in part use remote sensing data, 4) Change detection optimized: As a postlaunch modification to the sampling scheme, points should be allocated based on perceived change. Prelaunch-defined sites will include areas that are likely to be dynamic based on history and management/use practices, and 5) Reduction of variance: Postlaunch, the initial sampling scheme should be augmented based on the assessment of where classification error and variance are high. Error probability contours can be generated and samples allocated accordingly.

CONCLUSION

The development of global landcover maps requires the parallel development of an efficient sampling frame, sampling mechanism and sampling technique. Test sites are not sufficient globally even if they were developed to be useful for comparison with MODIS landcover locally. A substantial effort is required to derive consistent units for these sites to become valid input to a global site database system and as a tier in a multistage sampling scheme. Given the geographic area and number of pixels, this will require the community to reexamine pixel models of classification and validation, as well as classification theory and remote sensing models for landscape characterization.

REFERENCES

[1] R.Kahn, R.D.Haskins, J.E.Knighton, A.Pursch and S. Granger-Gallegos, "Validating a Large Geophysical Dataset: Experiences with Satellite-Derived Cloud Parameters", Proc. 23rd Symp. on Interface, Computing Science and Statistics, pp.133-140, 1991.

[2] T.R.Loveland, J.W.Merchant, J.F.Brown, D.O.Ohlen, B.C.Reed, P.Olson and J. Hutchinson, "Seasonal Land-Cover of the United States", Annals Assoc. of Am. Geographers Vol.85(2), pp.339-355,1995.

[3] A.Belward and T.R.Loveland, "The IGBP 1km Land Cover Project", Proc. of the 21st Annual Conf. of the Remote Sensing Society, Southampton, UK, pp.1099-1106, 1995.

[4] W.G.Cochran, "Sampling Techniques". John Wiley and Sons, New York, 1977.

[5] A.H.Strahler, A.Moody and E.Lambin, "MODIS Landcover Product: Algorithm Theoretical Basis Document", 1995.

[6] D.M.Muchoney, "Relationships and Divergence of Vegetation and Mapping Classifications". Proc. of the 5th ASIS/CR Classification Research Workshop, pp.121-128, 1994.

[7] E.Matthews, " Global vegetation and land use: New high resolution data bases for climate studies", J. of Appl. Meteor., Vol.22, pp.474-487, 1983.

[8] A.F.W.Kuchler, "World map of natural vegetation", in Goode's World Atlas, 16 ed., Chicago, Rand McNally, pp.16-17, 1983.

[9] J.S.Olson and J.A.Watts, "Major World Ecosystem Complexes", Oak Ridge National Lab, Oak Ridge, TN, 1982

[10] B.G.Mackey, M.F.Hutchinson, J.P.MacMahon and P.M.Fleming, "Assessing Representativeness of Places for Conservation Reservation and Heritage Listing", Environmental Management Vol.12(4), pp.501-514, 1988.

An Automatic Road Extraction Method Using a Map-Guided Approach Combined with Neural Networks for Cartographic Database Validation Purposes.

R. Fiset* & **, F. Cavayas*, M. C. Mouchot, B. Solaiman** and R. Desjardins*****

***Université de Montréal, Département de Géographie**
C.P. 6128, Succ Centre-Ville, Montréal, Québec, Canada
****École Nationale Supérieure des Télécommunications de Bretagne**
Département Image et Traitement de l'Information
BP 832, 29285 Brest Cédex, France
*****Université du Québec à Montréal, Département de Géographie**
C.P. 8888, Succ A, Montréal, Québec, Canada
Tel: (514)343-8000*, (+33) 98 00 13 55** Fax: (514)343-8008*, (+33) 98 00 10 98**
Email: Robert.Fiset@enst-bretagne.fr

Abstract. In this paper a method is proposed to extract road intersections from a SPOT panchromatic image, using a map-guided approach combined with the application of a neural network. The results show an average increase of 36% of planimetric accuracy after applying the method instead of simply superimposing the roads on the geocoded image. Also, only 8 out 42 samples were previously correctly traced, compared to 27 after application of the algorithm.

I - INTRODUCTION

The information contained in most digital maps is usually obtained through areal photography using stereorestitution techniques. Some important geometrical distortions are present in this type of document. Consequently, some planimetric elements, such as roads, may present noticeable shifts from their real position on the ground. For example, when a rasterized road map is superimposed to the corresponding geocoded satellite image, it can be observed that many segments are shifted in a non-systematic fashion, some up to 3 pixels. In the framework of cartographic database validation and accurate automatic updating procedures, it is primordial to correctly extract road segments that are at par with reality. The road shapes already defined in the cartographic database may help us to perform this task. In fact, even if road segments shape and location on a map may sometimes differ from those on a satellite image, the information provided by the map could be used to locate the corresponding road segments on the image and thus correct the map information.

In previous works [1], [2], it has been shown that the use of a SPOT panchromatic image is very well adapted for this task due to their high spatial resolution wich yields a good precision at a scale of 1:50 000 corresponding to the scale of the cartographic database used in this procedure. Tests performed with a map-guided procedure in [2], [3] produced interesting results in urban and rural environments but were constrained by the determination of road pixels gray level value intervals. These intervals could be very different depending on the area examined.

This paper describes a new method to automatically extract road intersections from a SPOT panchromatic image using a procedure that combines the map-guided approach and neural networks. The first step of this procedure consists on a Multi Layer Perceptron (MLP) training over the examined image. The weight matrix thus obtained is used in the search procedure to evaluate the potential of the examined pixels instead of using gray level value intervals.

II - DATA AND PREPROCESSING

To develop this method, a test is performed on a geocoded SPOT panchromatic image of Charlesbourg near Québec City, acquired on August 19th, 1989 at 15:57 GMT. A 600 by 600 pixels subset has been extracted, geometrically corrected with approximatly 30 ground control points and resampled by cubic convolution at 10 meters resolution. For this particular test, a high degree of planimetric accuracy is not essential. Hence, a geometrically corrected image is used instead of an ortho-image.

The map roads are extracted from a digitized topographic document at a scale of 1:50 000 and rasterized at 10 meters resolution to create a binary map. These roads had no topology at all since the map itself was used mostly for illustration purposes. A topological relationship had to be created by finding every intersections. This preprocessing step is described in details in [3]. The resulting output is an indexed file containing every road segment and each segment pixel coordinates. A file containing each intersection coordinates and the corresponding connected segment numbers is also created.

III - TRAINING THE NEURAL NETWORK

The neural network used in this experiment is a backpropagation MLP inspired by the algorithm described in [4]. The training was performed with a learning

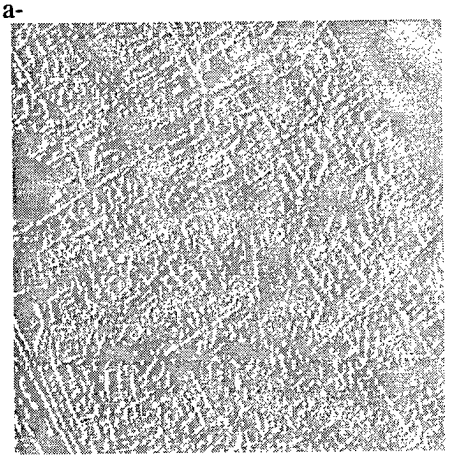
0-7803-3068-4/96$5.00©1996 IEEE

database containing over 90 patterns. A pattern is a 5 by 5 window representing either an example of road or a counter-example. The counter-examples are chosen to represent, as much as possible, every other class type present in the image. The architecture of the weight matrix is composed of an input layer of 25 neurons, 4 hidden layers of 75 neurons each and an output layer of one neuron representing the road class. The patterns are presented in a pseudo-random fashion; an order of presentation is randomly chosen and this sequence is repeated every iteration. The weights are ajusted immediately after each pattern is presented instead of waiting the end of the whole pattern set presentation. The training took over 13 hours on a Digital Alpha 200 station to reach an error lower than 0.01 for every pattern in the learning database.

A non-guided classification was performed with the obtained weight matrix to summerly evaluate the results (Fig. 1). Using a test database of 70 samples, it could be observed that only 55% of the road patterns are well classified, while 93% of the non-road patterns are well classified. The result was deemed acceptable for the present study.



a-



b-

Figure 1- Subset (256 X 256) of the SPOT image of Charlesbourg: a- Enhanced panchromatic band, b- Neural network binary road classification.

IV - SEARCHING THE INTERSECTIONS ON THE IMAGE

In previous works, one of the main problems encountered while searching road segments was that the search directions were either perpendicular to the local road axis [1] or restricted in six directions [2], [3], thus ignoring some positions that should have been examined. One way to correct this problem is to examine every pixels included in a square window. However, this brings another problem in the case of a straight road segment. For instance, a north-south straight road that would be shifted by two pixels to the right (east) and one pixel upward (north) would produce such a problem. In fact, the left-right shift would be very easy to detect since it is perpendicular to the road axis, but any position could be chosen for the upward-downward shift. To prevent these problems, it has been decided to examine intersections instead of segments alone. Since most intersections are composed of road segments connected at a certain angle, all directions should be taken into account while searching them on the image.

The cartographic database implicitly contains the shape of each road intersection. Therefore, this information is used to guide the search on the image. Each intersection coordinates in the database represents the center of a 7 by 7 search window on the image (Fig. 2a). Each of these 49 pixels is in turn the center of a window defined by the intersection shape (Fig. 2b). Each pixel defining the intersection represents the center of a 5 by 5 sub-window constituting the input layer of the previously trained weight matrix (Fig. 2c). The neural network outputs an activation value for every pixel defining the intersection shape. These values are used to compute a mean value of activation. For example, on Fig. 2, thirteen values would be used to compute each of the 49 mean values. The highest mean value of activation should represent the real position of the intersection on the image.

V - RESULTS AND DISCUSSION

A sample of 42 intersections was extracted from the image (Fig. 3). The choice of the samples was done to represent the widest possible range of conditions present on the image. At the same time, the samples were taken in order to cover as much ground as possible to be spatially representative. However, an intersection had to be visually discernible in order to be chosen, since it was the only "ground truth" used to judge the procedure's performance. Table I summarizes the sample root mean square (RMS) error, both before and after the procedure.

The results show a decrease of 36% of the RMS after applying the method. Also, only 8 out 42 samples were previously correctly traced, compared to 27 after the application of the algorithm. It should be noted that these results were obtained in spite of the fact that the weight

matrix used could only classify the image at a 55% rate of success. Nevertheless, almost 65% of the sampled intersections are precisely retraced and the global planimetric accuracy of the cartographic document is substantially increased.

VI - CONCLUSION

We are able to conclude that this method is very promising, especially considering that the weight matrix used in the procedure had only a 55% classification success rate. Superior results to all conventional image processing methods should be expected from a better trained weight matrix.

Further tests should also be performed on satellite images resampled at different resolutions to study the effect of the rasterization of the road vectors as well as on ortho-images in order to increase the planimetric accuracy of the images used, thus readily minimizing the shifts.

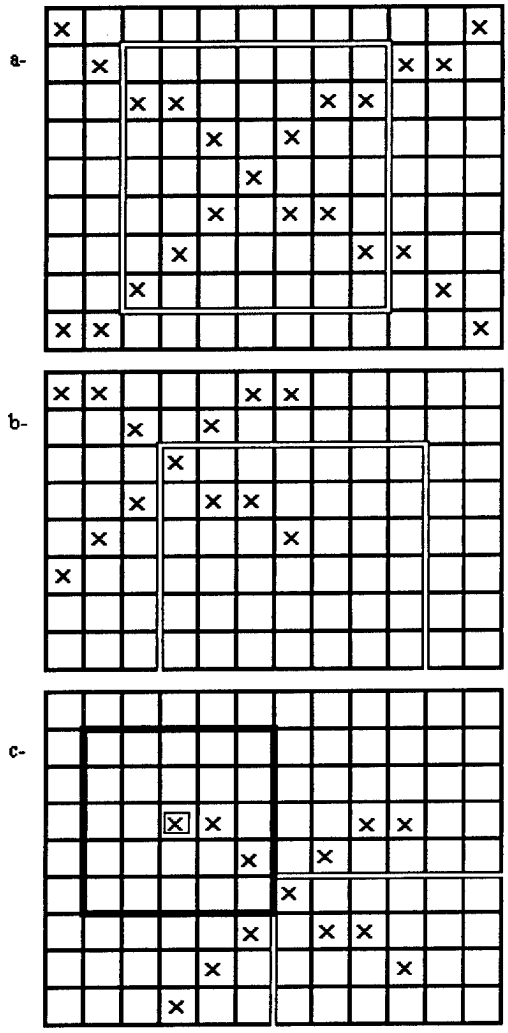


Figure 2- Description of the road intersection extraction method: a- Search area centered on the map road intersection, b- First subset searched according to the intersection shape, c- Image pixels fed to the neural network for each map road pixels in the intersection shape.

TABLE I- RMS Error Report

	X	Y	Total
RMS before procedure	0.121	0.130	0.178
RMS after procedure	0.067	0.092	0.114
RMS variation (%)	-44.6	-29.2	-35.95

REFERENCE

[1] P. MAILLARD and F. CAVAYAS, "Automatic map-guided extraction of roads from SPOT imagery for cartographic database updating", International Journal of Remote Sensing, vol. 10, no. 11, pp. 1775-1787, 1989.

[2] R. FISET and F. CAVAYAS, "Automatic comparison of a topographic map with remotely sensed images in a map updating perspective: the road network case", unpublished (submitted to Int. J. of R. S.).

[3] R. FISET, "Processus d'extraction automatique des routes des images du satellite SPOT à l'aide des donnees cartographiques à l'échelle 1:50 000, M.Sc. Thesis, Université de Montréal, Département de Géographie, 123 pages, 1993.

[4] M. CAUDILL and C. BUTLER, "Understanding neural networks: computer explorations (volume 1), The MIT Press, Cambridge, Massachusetts, 309 pages, 1992.

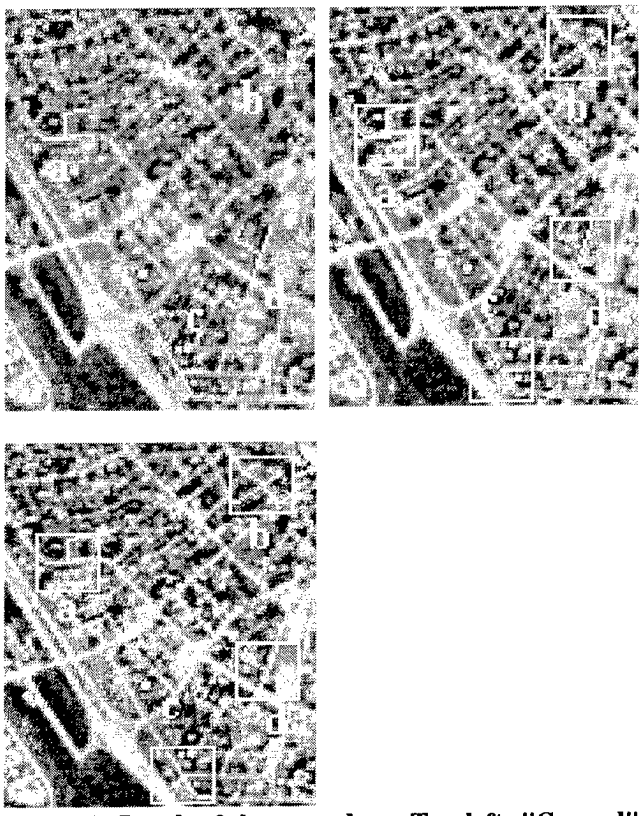


Figure 3- Result of the procedure: Top left- "Ground" truth, Top right- Original intersections superimposed on the geocoded image, Bottom left- Extracted intersections.

PLANT CONDITION REMOTE MONITORING TECHNIQUE

L.K. Fotedar
University of Texas Health Science Center
6431 Fannin Street
Houston, Tx 77030

K. Krishen, Ph.D.
Technology Transfer and Commercialization Office
NASA Johnson Space Center
Hourston, TX 77058

ABSTRACT

This paper summarizes the results of a radiation transfer study conducted on houseplants using controlled environmental conditions. These conditions included: (1) air and soil temperature; (2) incident and reflected radiation; and (3) soil moisture. The reflectance, transmittance, and emittance measurements were conducted in six spectral band: microwave, red, yellow, green, violet, and infrared, over a period of three years. Measurements were taken on both healthy and diseased plants. The data was collected on plants under various conditions which included: variation in plant biomass, diurnal variation, changes in plant pathological conditions (including changes in water content), different plant types, various disease types, and incident light wavelength or color. Analysis of this data was performed to yield an algorithm for plant disease from the remotely sensed data.

I. INTRODUCTION

One key applicaiton of the space technology developed by the national Aeronautics and Space Administration (NASA) has been in the area of global moitoring of earth resources [1]. In cooperation with the United States Department of Agriculture (USDA), NASA has established the potential for remote sensing through the Landsat program. This program is concerned with the estimation of crop yield from infrared and visible imagery. More recently, several organizations throughout the world are investigating the potential of microwave systems to complement the Landsat sensors for all weather predictions. Numerous publications on the subject of remote sensing of crops identify physical variables, such as: crop type, maturity/age, soil moisture, farming practices, crop health, and climatic factors, as significant contributors to the crop "signature" [2]. A mathematical model (based on both microwave and infrared data) which could separate these variables has, to our knowledge, not yet emerged.

The present study was undertaken to isolate and study the effect of plant condition/health on the reflectance/emittance in six spectral bands: microwave, red, yellow, green, violet, and thermal infrared. Disease in plants is brought about by infection with fungi, bacteria, viruses, nematodes, algae, and parasitic higher plants [3]. Deficiency of chemicals such as iron, nitrogen, calcium, and water may also cause disease.

In this project, plants with rust, smut, leaf spot, virus, and mineral deficiency diseases were studied [4]. Incident radiation on the plant undergoes three processes for each of the three parts of the electromagnetic spectrum: reflection, radiation emission, and transmission [5]. These three processes have a bearing on the plant's efficiency in the use of radiation and its adaptability for survival under stress conditions (disease) [6,7]. Different methods of plant disease detection have been incorporated. One method is by viewing leaf, stem, or root cross-sections under a microscope or more complex optical source [3,6]. Another method is just by visual observation of outward symptoms of the disease. Biochemical analysis of the plant biomass is also used [8,9]. All these methods, however, employ invasive and often destructive measures to detect diseases and are not economical or even accurate for large areas/volumes of vegetation. The key element of this investigation is that measurements were taken while the plant was living in its full biomass (in vivo), and undergoing normal energy processes.

Houseplants were chosen so that plants with slow and fast growth could be used in the present study. Any changes in the plant condition caused by disease or lack of moisture cause changes in the energy transfer processes (evapotranspiration, conduction, and convection) [10]. For this reason , the radiated or reflected energy in the visible, infrared, and microwave bands is different for diseased plants. Reflected and/or emitted energy provides an indication of the health of the plant. Measurements were taken on both healthy and diseased plants under laboratory type conditions. The data was collected under various conditions which included: plant biomass, diurnal variation, surrounding temperature, amount of light, pathological conditions (water content, frozen/unfrozen, algae, etc.) and incident lighting conditions. Establishing repeatability of the data was a key concern and was addressed throughout the study. For this reason, a controlled environment (room) was used to observe six types of houseplants. The added advantage of controlled environment was that the plant could be constantly observed under unperturbed conditions with full biomass and through a phase/history of diseases which interfered with its normal energy exchange processes. The plants were accessible day and night for these observations. The data shows that water deficiency in the plant, and the plant biomass have strong dependence in the microwave band. The diseased plants show

0-7803-3068-4/96$5.00©1996 IEEE

measurable difference compared to healthy plants in the reflected visible and emitted infrared bands. A mathematical formula was proposed on the basis of the observed dependencies for monitoring the plant condition. This algorithm is now ready for testing/evaluation under natural conditions.

II. INSTRUMENTS AND PROCEDURE

The development of the expression for the plant condition remote monitoring technique was based on the normalized integrated measurements of plant reflections/emissions at six wavelengths over a period of two years. The wavelengths used were 0.41, 0.45, 0.55, 0.65, and 11 microns, and 3cm. A PRT-5 radiometer and thermiscope were used at the 11 micron band.

The radiometer gives point measurements of the temperature on the leaves. The thermiscope showed temperature differences of the objects in imagery form and pictures were taken for record and analysis. The microwave system consisting of an antenna, transmitter, receiver, oscilloscope, amplifier, and a power meter, was used for the 3 cm band. In addition to these instruments, an accurate thermometer, a light exposure meter, and microscope were used to characterize the light environment and the plant status. A controlled environment (room) was made ready for some experiments by placing black cloth around the plant to absorb background radiation. The room temperatures were maintained to within 1 degree centigrade for the periods of observation. Several experiments were conducted in the patio under uncontrolled environmental conditions. Soil moisture data was also collected in addition to temperature and lighting data. Fig. 1, 2, 3 illustrate typical instrument block diagrams and set-up. The plants were rotated to cover all the foliage for the reflectance, transmittance and emissivity. An average was computed for each plant. Six types of plants (the Crassula, Philodendron, Ficus, Shefflera, Tradescantia, and Vriesea) were selected with four types of diseases (rust, fungus, virus, and deficiency). Data in the five spectral bands was taken daily with the following variables: (1) plant biomass; (2) diurnal variation (morning, afternoon, and night); (3) plant type; (4) disease type; (5) room temperature; and (6) incident radiation. The 3cm wavelength was found very sensitive to the water content of the plant (actual weight minus dry weight). Transmittance and reflectance measurements were taken for several plants in this band, and the plant was rotated to obtain an average value for the plant. Plots and tables for the average values and variances were computed along with a record of the plant biomass and stage of growth.

III. DATA COLLECTED

Several types of data were taken to account for the different variables involved in the experimentation of this technique. Fig. 4 shows the marked difference in the band readings between a diseased Schefflera plant and a healthy one. The healthy plant has a higher reflectance reading in the green, yellow, and red bands, a higher emission reading in the infrared, and a lower transmittance reading in the x-band (since the healthy plant has more foliage). In Fig. 5, different diseases were compared. The two diseases compared were nitrogen deficiency and rust fungus. The deficiency disease had a higher reading in the infrared band, and, again, a lower reading in the x-band. Additional data collected consisted of a photo image of the plant vs. the thermiscope image. In one case for the Philodendron, the disease was shown on the infrared scan two weeks before it showed up on the plant.

Fig. 6 shows the diurnal variation between a healthy Tradescantia plant and a diseased one. Both plants have the highest emittance readings in the afternoon, and the lowest in the morning. Fig. 7 shows the difference in microwave transmittance readings of Ficus and Palm plants. Specific weather conditions are tested in this experiment. The Palm plant (having frostbite) showed a considerably higher transmittance than the deficiency Ficus. In Fig. 8, plant biomass was tested.

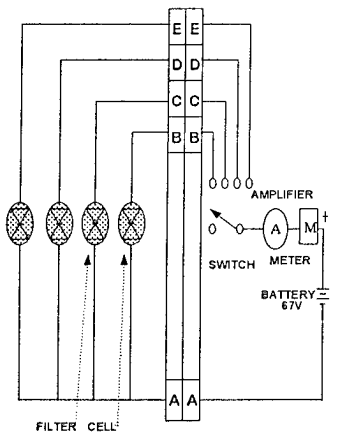


Fig.1 Visible spectrometer Circuit Diagram

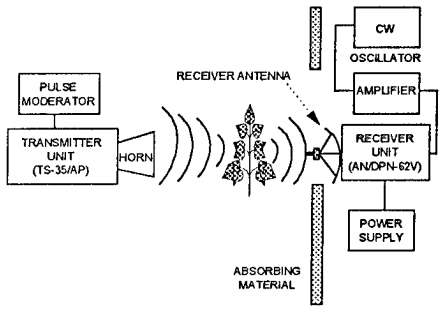


Fig. 2 Microwave Block Diagram

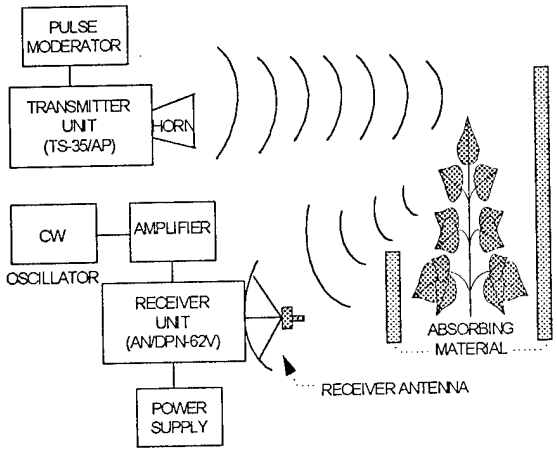


Fig. 3 Microwave Experimental Setup

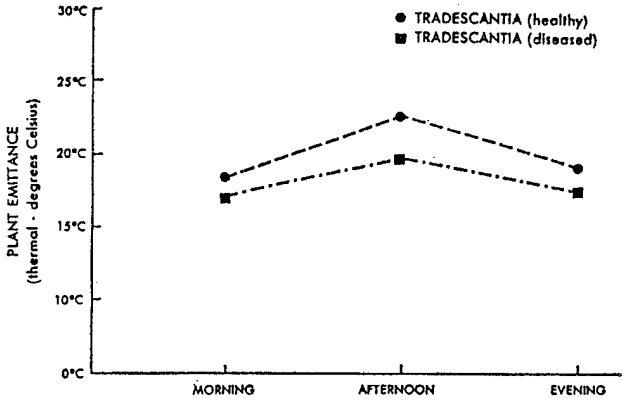


Fig. 6 Diurnal Variation (Average Values)

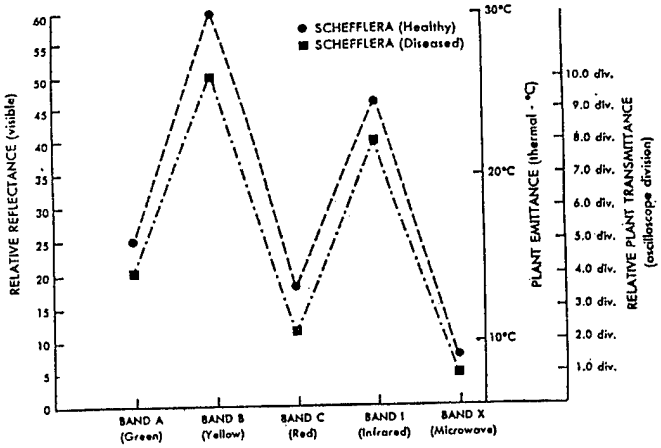


Fig. 4 Healthy Vs. Deseased Plant

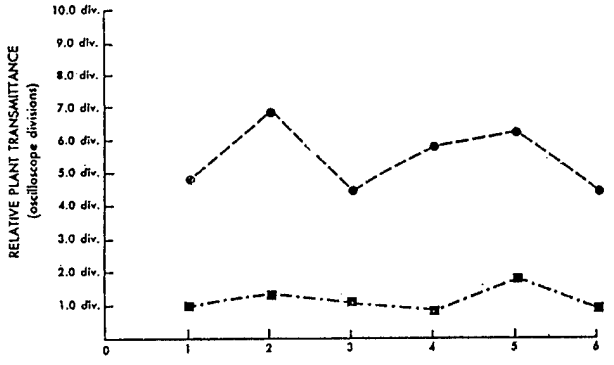


Fig. 7 Ficus (Nitrogen Deficiency) Vs Palm (Frostbite)

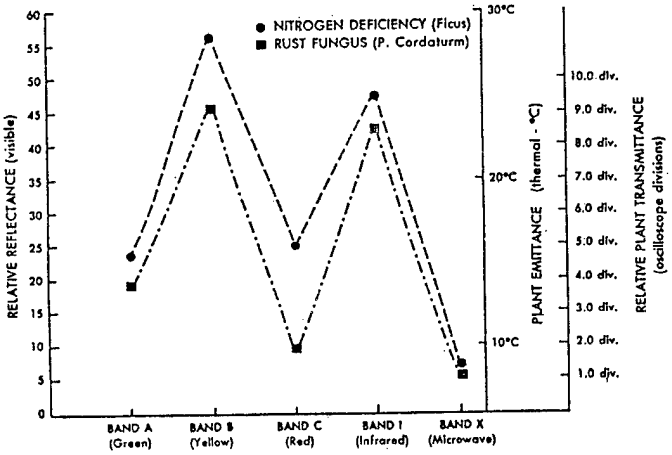


Fig. 5 Response With Disease Types

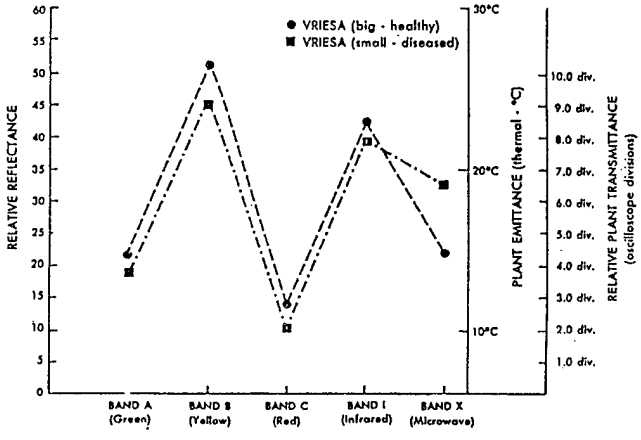


Fig. 8 Plant Biomass

Data taken in all five bands showed the larger Vriesea plant to have higher values than the smaller plant. The difference was especially noticeable in the X-band. Each of these samples of data showed proof of the basic hypothesis first presented.

IV. DETECTION TECHNIQUE

The repeatability of the measurements was ascertained to within 1%. The dependencies in the graphs indicate that the water deficiency in plants can be detected most accurately in the microwave band. The diseased plants show measurable differences compared to healthy plants in the reflected visible and emitted infrared bands. The parasitic and no-parasitic diseases of plants show differences in all the spectral bands investigated. Diurnal variation readings show that plant emittance is at its highest during the afternoon. Based on the graphs presented, a detection technique for the plant condition is proposed. The responses (relative emittance, reflectance, and transmittance) in the visible, infrared, and microwave bands are labeled as A_i's. These responses were measured for both healthy (A_i's) and diseased (B_i's) plants of the same type. Ratios B_i/A_i were computed for the known plant diseases. Based on these measurements, a quantity

$$K = \sum_i W_i(B_i/A_i)$$

where W_i are weighting factors forvarious bands that was computed to emphasize the use of a particular band for a specific disease. A matrix of W_i's and X_i's for various plant types, stages of growth, diseases, and environmental factors was developed under known conditions. The algorithm showed more than 96% correlation between the observed plant condition and the predicted disease/water deficiency.

V. CONCLUSIONS

In a particular application, data should be collected over known healthy vegetation (A_i's) using handheld, vehicle-mounted, aircraft, or spacecraft data. Data should also be collected under unknown conditions and labeled as B_i's. The value of K should be computed and compared with the memorized values in the computer. The memorized values are developed using known plant condition and laboratory observations. These values can be experimentally determined using controlled environments similar to what was done in this study. The comparison would then yield the unknown vegetation disease/condition.

The procedure was tested using the data presented in Section III. It was found to be accurate nine times out of ten for the diseases/conditions and plants for which the data was collected. The procedure could be applied to the commercially available Landsat data for large area applications [11]. In conclusion, this study successfully identifies a quantitative noninvasive remote monitoring technique to detect pathological or water deficiency related conditions in living plant based on significant and sensitive variation in their unique electromagnetic spectral signatures.

V. ACKNOWLEDGMENT

The authors wish to acknowledge the comments and suggestions given by Mr. Jerry Elliott, *High Eagle*, of NASA Johnson Space Center.

REFERENCES

[1] Sheffner, E. J., "The Landsat Program: Recent History and Prospects," Photogrammetric Engineering and Remote Sensing, 60: 735-744, 1994.

[2] Erickson, John D., "Satellite-Aided Global Crop Monitoring," Microwave Remote Sensing Symposium proceedings, sponsored by National Aeronautics and Space Administration, Johnson Space Center, December, 1977.

[3] Devling, Robert M., Plant Physiology, New York; Reinhold Publishing Corp., 1966.

[4] Corbett. m. Plant Virology, University of Florida, Florida, 1967.

[5] King, C., "Agricultural Terrain Scatterometer Observations with Emphasis On Soil Moisture Variation", University of Kansas, Tech. Rept. RSL 177-44, Kansas, 1973.

[6] Slayter, R.O., Plant Water Relationships, Academic Press, London, 1967.

[7] Ashby, Maurice, Introduction to Plant Ecology, St. Martin's Press, New York, 1969.

[8] Grodzinskii, D.N., Plant Biophysics, Jerusalem: Keterpress Enterprises, Inc., 1976.

[9] Bickford, E.D., and S. Dunn, Lighting for Plant Growth, Kent state University Press, Inc., 1972.

[10] Ulaby, F.T., R.Y. Li, and K.S. Shanmugam, "Crop Classification Using Airborne Radar and Landsat Data", university of Kansas, Kansas, Issued by NASA as SA-KI-04043 Report, Feb., 1981.

[11] Salomonson, V.V., J.R. Irons, and D.L. Williams, "The Future of Landsat: Implications for Commercial Development," Proceedings of the Conference on NASA Centers for Commercial Development of Space (NASA CCDS), M.S. El-Genk and R.P. Whitten (eds.), American Institute of Physics, New York, 353-359, 1995.

Feature Selection Using Decision Trees — An Application for the MODIS Land Cover Algorithm

Jordan S. Borak and Alan H. Strahler
Department of Geography and Center for Remote Sensing, Boston University,
725 Commonwealth Avenue, Boston, MA 02215, USA,
Phone +1-617-353-2088, Fax +1-617-353-3200, e-mail borak@crsa.bu.edu, alan@crsa.bu.edu

Abstract – One of the key issues involved in generating global-scale land cover maps from remote sensing data is the discarding of useless or redundant information. The decision tree offers a promising approach to extraction of meaningful features from large measurement spaces. This research examines the performance of several classifiers on subsets of features produced via decision trees.

INTRODUCTION

In the EOS era, large datasets will be available from such instruments as the Moderate Resolution Imaging Spectroradiometer (MODIS) that include information from spectral, spatial, temporal, and directional domains. However, the high dimensionality of these datasets means that literally hundreds of features (in the pattern recognition sense) will be available for input to algorithms such as land cover classification. Further, for the case of land cover classification, not all of these features will be useful in a given region. That is, a given data field may be useful in one vicinity, but redundant in another.

One way to extract relevant information from such high-dimension datasets is to employ feature selection using a binary decision tree classifier. The tree is a supervised classifier that partitions measurement space via binary rules and a heterogeneity- minimization function [1]. It is non-parametric, and is therefore effective in forming complicated decision surfaces. Additionally, it handles missing data relatively well. The decision tree algorithm can accept large numbers of input features, and the resulting tree structure provides for rapid and objective selection of the feature subsets that are most effective for separating classes based on the training data supplied. These subsets, in turn, may be used for large area classification beyond the training locations utilizing the decision tree or other classification algorithms, such as neural networks.

The present research investigates the utility of binary decision trees to aid in discrimination of land cover at the local scale of a test site in the southeastern Arizona desert, centered on Walnut Gulch. Here, a database developed from registered Landsat Thematic Mapper (TM) scenes provides information from the spatial, spectral, and temporal domains that simulates the information content of MODIS data. Feature selection is accomplished using decision trees, and a number of classification algorithms are compared for their accuracy in identifying a limited number of broad land cover types consistent with a global land cover product. Specifically, the intent is to examine the implications of feature selection on the generation of the 1-km global MODIS Land Cover Product (MLCP).

This work was funded by NASA under the MODIS project, NAS5-31369, Earth Observing System.

STUDY SITE

The study site investigated in this research is located in the southeastern corner of Arizona, and includes the Walnut Gulch watershed research area. The cover types in the study area are evergreen needleaf forest, evergreen broadleaf forest, deciduous broadleaf forest, mixed forest, woody savanna, grassland, closed shrubland, open shrubland, cropland, urban/built-up and barren. For presentation purposes, these are coded as 1 to 11 repectively in the tables below.

DATASET

The dataset employed in this research includes seven TM scenes collected in 1992 over the study site, a land cover map of the area based on the Gap Analysis Project vegetation layer for Arizona and a digital elevation model (DEM) subsetted from the 30 arc-second Digital Chart of the World. Thus, 57 data fields are assembled for each pixel in the study site. The satellite data have been atmospherically corrected to surface reflectance, and the classes in the vegetation layer have been remapped to the legend used in the International Geosphere-Biosphere Programme Data and Information System 1-km Land Cover Project [2], since these are the categories that the MLCP recognizes.

The TM data and vegetation map have been co-registered and spatially degraded to 1-km resolution in order to simulate the characteristics of the MODIS sensor. The DEM, already at approximately 1-km resolution, has been directly registered to the rest of the input dataset. Additonally, image texture and Soil Adjusted Vegetation Index layers have been derived from the reflectance data.

METHODS

Sampling of Training Data

Two sampling strategies are examined in this research. The first is a random stratified scheme which draws an equal proportion (0.20) of each cover type. The other is a random stratified sampling which draws an equal number of samples (300) from each cover class. Both strategies are implemented for both feature selection and classification.

Feature Selection

The high dimensionality of the input data set is reduced using the tree-based approach of Breiman et al. [1]. The algorithm recursively partitions input data based on a splitting rule that seeks to maximize the inter-subset variance at each split in the data, while maintaining an acceptable level of intra-subset

0-7803-3068-4/96$5.00©1996 IEEE

homogeneity. Operationally, a decision tree is grown using a training set that has the full dimensionality of the inputs, and only those features that contibute the most to the variance in the training data are retained for classification. Thus, a tree is grown that fits all of the training data, and then pruned back to reduce the fitting of noise in the inputs.

Classifiers

Three classification approaches are examined for performance on the reduced set of inputs. First, the predictive capability of the decision tree itself is explored. Although primarily used for feature selection in this analysis, the ability of the tree to label new data is of note because this indicates whether acceptable classification results may be produced without additional processing.

A second classification algorithm is a neural network known as Fuzzy ARTMAP [3]. Fuzzy ARTMAP (FA), which operates in a supervised mode, uses Adaptive Resonance Theory technology to relate input and output patterns, while avoiding some of the pitfalls (e.g. overtraining, failure to converge) that are associated with other neural network architectures such as back propagation. Additionally, input and output vectors are compared using fuzzy operators rather than traditional set-theory measures. For comparison, a classification has also been performed with FA using the full-dimensional training set.

The third approach is a maximum likelihood classifier (MLC). The intent is to use the performance of the MLC as a sort of measuring stick for evaluating the results generated by the more advanced techniques. In fact, MLC is expected to produce the lowest accuracies among the three approaches.

Results and Discussion

Proportional Sampling

For this sampling approach, the decision tree performs reasonably well in terms of overall accuracy (73.47%) because it characterizes the largest class, grassland, best (see Table 1). This is due in part to the sampling approach. Since grassland is the most common class in the training data, the tree tends to split on factors that reduce the intra-class variance for this category. The only other categories that have per-class accuracies that approach reasonable values are evergreen broadleaf and barren.

As illustrated in Table 2, the MLC performs poorly in terms of overall accuracy (56.30%) because it has problems with the grassland class (less than 50% correct). In the other classes, however, maximum likelihood seems to perform well. When the prior probabilities for the classes are adjusted to reflect the known proportions of the cover types in the study area, the performance of the MLC improves to 71.15% overall accuracy (see Table 3).

The Fuzzy ARTMAP classification, 78.40% overall accuracy, is the best in terms of overall accuracy (see Table 4). This is in part due to its high accuracy in the grassland class. In the smaller classes, FA produced results of varying strengths, but none were exceptionally weak. For comparison, Table 5 shows the results of running FA using the full-dimensional training set. The overall accuracy of this scenario (77.26%) is actually lower than that obtained using the reduced measurement space.

Equal Sampling

For the equal sampling approach, certain classes are too small for the analysis, and must be dropped. The remaining classes are evergreen broadleaf forest, mixed forest, grassland, open shrubland and crops.

The decision tree performs poorly in terms of overall accuracy (47.18%) because it characterizes grassland poorly (see Table 6). This means that when the tree does not have knowledge of which classes account for the most variance in the test data (as it did under proportional sampling), there may be problems with using the trained tree for predictive purposes.

As illustrated in Table 7, the MLC again performs poorly in terms of overall accuracy (54.43%) mostly due to an inability to label the grassland class accurately (less than 50% correct). In the other classes, again, maximum likelihood performs well.

The Fuzzy ARTMAP classification, 63.56% overall accuracy, is the best in terms of overall accuracy (see Table 8). Once again, this is in part due to its ability to discriminate the grassland class. On smaller classes, FA produced results of medium to high accuracy. For comparison, Table 9 shows the results of running FA using the full-dimensional training set. The overall accuracy of this scenario (64.06%) is only slightly higher than that obtained using the reduced measurement space.

Conclusions

For the proportional sampling strategy, with the exception of the MLC with equal prior probabilities, all of the classifiers produced nearly equivalent results. This indicates that the additional features do not add significantly to the information content for any of these algorithms. Conversely, for the equal sampling strategy, all of the classifers produced degraded results relative to the proportional approach, with the neural network being least sensitive to this phenomenon. As the latter strategy is a likely scenario for production of the MODIS Land Cover Product (at least in early versions), it is apparent that the neural network approach is the most stable across sampling strategies, and is the best candidate of the three examined here for production of this global land cover database.

References

[1] Breiman, L., J. H. Friedman, R. A. Olsen, and C. J. Stone, Classification and Regression Trees, Wadsworth, Inc., Belmont, California, 1984.

[2] Belward, A., and T. R. Loveland, "The IGBP-DIS 1-km land cover project," Proc. 21st Ann. Conf. Remote Sens. Soc., Southampton, UK, pp. 1099-1106, 1995.

[3] Carpenter, G. A., S. Grossberg, N. Markuzon, J. H. Reynolds, and D. B. Rosen, "Fuzzy ARTMAP: A neural network architecture for incremental supervised learning of analog multidimensional maps," IEEE Trans. Neural Networks, 3, pp. 698–713, 1992.

Table 1: Decision tree, proportional sampling

ref.→ ↓map	1	2	3	4	5	6	7	8	9	10	11	total
1	127	0	0	36	0	0	0	0	0	0	0	163
2	0	0	0	0	0	0	0	0	0	0	0	0
3	0	0	0	0	0	0	0	0	0	0	0	0
4	66	203	3	920	27	225	28	17	2	0	0	1491
5	0	0	0	0	0	0	0	0	0	0	0	0
6	1	86	14	123	171	7827	56	1317	504	76	7	10182
7	15	13	0	27	3	15	72	15	18	0	0	178
8	0	0	0	0	0	0	0	0	0	0	0	0
9	0	4	1	12	0	214	2	50	402	16	0	701
10	0	0	0	0	0	0	0	0	0	0	0	0
11	0	0	0	0	0	65	0	0	2	0	164	231
total	209	306	18	1118	201	8346	158	1399	928	92	171	12946

trace = 9512 (Overall Accuracy = 73.4744)

Table 2: MLC, proportional sampling, equal priors

ref.→ ↓map	1	2	3	4	5	6	7	8	9	10	11	total
1	136	0	0	82	2	1	2	0	0	0	0	223
2	2	218	6	314	7	541	12	21	2	0	0	1123
3	0	0	0	0	0	0	0	0	0	0	0	0
4	56	23	0	555	19	86	10	4	0	3	1	757
5	0	5	2	13	117	278	3	7	6	0	0	431
6	0	31	6	44	34	4021	7	135	116	40	0	4434
7	15	24	1	94	17	157	97	20	7	2	0	434
8	0	3	0	16	5	2774	21	1195	53	7	0	4074
9	0	2	3	0	0	405	6	15	743	3	1	1178
10	0	0	0	0	0	30	0	2	0	37	0	69
11	0	0	0	0	0	53	0	0	1	0	169	223
total	209	306	18	1118	201	8346	158	1399	928	92	171	12946

trace = 7288 (Overall Accuracy = 56.2954)

Table 3: MLC, proportional sampling, adjusted priors

ref.→ ↓map	1	2	3	4	5	6	7	8	9	10	11	total
1	121	0	0	46	0	1	1	0	0	0	0	169
2	1	185	5	216	5	219	11	9	1	0	0	652
3	0	0	0	0	0	0	0	0	0	0	0	0
4	74	30	0	685	23	68	19	7	0	3	1	910
5	0	2	0	9	79	66	2	0	3	0	0	161
6	0	69	11	105	89	6327	20	446	290	53	2	7412
7	13	19	0	53	5	36	79	11	4	0	0	220
8	0	0	0	4	0	1388	21	918	10	3	0	2344
9	0	1	2	0	0	187	5	7	620	3	1	826
10	0	0	0	0	0	7	0	1	0	30	0	38
11	0	0	0	0	0	47	0	0	0	0	167	214
total	209	306	18	1118	201	8346	158	1399	928	92	171	12946

trace = 9211 (Overall Accuracy = 71.1494)

Table 4: FA, proportional sampling

ref.→ ↓map	1	2	3	4	5	6	7	8	9	10	11	total
1	128	4	0	61	2	1	7	0	0	0	0	203
2	0	163	1	96	1	97	2	13	0	0	0	373
3	0	0	5	0	0	0	0	0	0	0	0	5
4	75	54	2	802	18	87	20	1	0	0	0	1059
5	1	0	0	4	115	120	0	0	0	0	0	240
6	0	80	10	146	60	7245	32	510	338	45	10	8476
7	5	5	0	8	3	17	81	7	0	0	0	126
8	0	0	0	1	2	585	15	855	31	8	0	1497
9	0	0	0	0	0	183	1	13	559	3	0	759
10	0	0	0	0	0	1	0	0	0	36	0	37
11	0	0	0	0	0	10	0	0	0	0	161	171
total	209	306	18	1118	201	8346	158	1399	928	92	171	12946

trace = 10150 (Overall Accuracy = 78.4026)

Table 5: FA, proportional sampling, full set of features

ref.→ 1 ↓map	2	3	4	5	6	7	8	9	10	11	total	
1	133	0	0	33	1	0	4	0	0	0	0	171
2	2	106	0	60	0	48	9	4	0	0	0	229
3	0	0	4	0	0	0	0	0	0	0	0	4
4	65	72	3	837	20	133	23	6	0	0	0	1159
5	0	0	0	0	81	60	0	0	0	0	0	141
6	0	120	11	162	94	7212	46	614	295	48	13	8615
7	9	5	0	22	1	14	64	0	1	0	0	116
8	0	3	0	1	4	651	10	766	22	7	0	1464
9	0	0	0	3	0	210	2	9	610	6	0	840
10	0	0	0	0	0	5	0	0	0	31	0	36
11	0	0	0	0	0	13	0	0	0	0	158	171
total	209	306	18	1118	201	8346	158	1399	928	92	171	12946

trace = 10002 (Overall Accuracy = 77.2594)

Table 6: Decision tree, equal sampling

ref.→ ↓map	2	4	6	8	9	total
2	255	343	732	23	0	1353
4	26	726	362	21	2	1137
6	17	18	2790	106	81	3012
8	3	18	3105	1129	38	4293
9	5	13	1357	120	807	2302
total	306	1118	8346	1399	928	12097

trace = 5707 (Overall Accuracy = 47.1770)

Table 7: MLC, equal sampling

ref.→ ↓ma	2	4	6	8	9	total
2	267	432	782	35	3	1519
4	19	643	123	5	1	791
6	12	27	3769	135	119	4062
8	4	15	3110	1191	91	4411
9	4	1	562	33	714	1314
total	306	1118	8346	1399	928	12097

trace = 6584 (Overall Accuracy = 54.4267)

Table 8: FA, equal sampling

ref.→ ↓map	2	4	6	8	9	total
2	304	218	638	22	2	1184
4	1	863	239	7	4	1114
6	0	21	4672	250	81	5024
8	1	7	1940	1064	55	3067
9	0	9	857	56	786	1708
total	306	1118	8346	1399	928	12097

trace = 7689 (Overall Accuracy = 63.5612)

Table 9: FA, equal sampling, full set of features

ref.→ ↓map	2	4	6	8	9	total
2	303	203	437	25	10	978
4	1	876	301	14	0	1192
6	2	32	4696	253	77	5060
8	0	6	1976	1054	21	3057
9	0	1	936	53	820	1810
total	306	1118	8346	1399	928	12097

trace = 7749 (Overall Accuracy = 64.0572)

Regional Land Cover Characterization Using Multiple Sources of Intermediate-Scale Data

J.E. Vogelmann, S.M. Howard, and T. Sohl
Hughes-STX Corporation
EROS Data Center
Sioux Falls, SD 57198
Telephone: 605-594-6062
Email: vogel@edcserver1.cr.usgs.gov

Abstract -- Many United States federal agencies need accurate, intermediate scaled, land cover information. While many techniques and approaches have been successfully used to classify land cover in relatively small regions, there are substantial problems in applying these techniques to large multi-scene regions. An evaluation was conducted of the multiple layer land characteristics data base approach for generating large area land cover information. Mosaicked leaves-on Landsat thematic mapper scenes were used in conjunction with leaves-off thematic mapper data, digital elevation (and derived slope, aspect and shaded relief) data, population census information, defense meteorological satellite program "city lights" data, land use and land cover data, digital line graph data, and national wetlands inventory data to derive land cover information. This approach was evaluated for Region III of the United States Environmental Protection Agency (middle Atlantic states).

Keywords: Landsat TM, land cover classification

INTRODUCTION

Many United States federal agencies, including the Environmental Protection Agency, United States Forest Service, National Biological Service, National Oceanic and Atmospheric Administration, and the U. S. Geological Survey, currently have needs for up-to-date intermediate-scale land cover data. Potential uses for such land cover data are many and varied, and include assessing ecosystem status and health, modelling nutrient and pesticide runoff, understanding spatial patterns of biodiversity, land use planning, and developing land management policy. Despite the need for current land cover data, much of the intermediate-scale spatial land cover data presently available for the entire United States is outdated and of questionable accuracy. The most recent intermediate-scale land cover data set generated for the conterminous United States (Land Use and Land Cover data; LUDA) was developed by the U. S. Geological Survey [1] in the 1970's via interpretation of high-altitude aerial photography. While this data set is still probably adequate for many applications, there is concern that many land cover changes have occurred since the data set was compiled. More recently, a land cover classification generated for the conterminous United States using 1 km advanced very high resolution radiometer data [2] [3] has been developed for use by the global change research community. However, this data set is spatially too coarse for assessing some of the issues of national concern.

The main objective of this project was to generate a generalized and consistent (i.e. seamless) land cover data layer for EPA Region III, which includes the states of Pennsylvania, Maryland, Delaware, Virginia, and West Virginia. In addition to enabling us to explore various methods for generating large area classifications, one of the ramifications of this project was that it afforded us the opportunity to evaluate the potential and practicality of generating an intermediate land cover data for the conterminous United States.

GENERAL PROCEDURES

Data sources

The primary source of data for this project was leaves-on (summer) Landsat TM data, acquired in 1991, 1992 and 1993. These data sets were referenced to Lambert Azimuthal coordinates. Additionally, leaves-off TM data sets were acquired and referenced. While most of the leaves-off data sets were acquired in spring, a few were from late autumn due to the difficulties in acquiring cloud-free TM data. A wider seasonal range of dates, covering a wider span of years, characterize the leaves-off data. In total, approximately 50 TM scenes were analyzed. In addition, other intermediate scale spatial data were acquired and utilized. These included 3-arc second Digital Terrain Elevation Dataset (DTED) and derivative DTED products (including slope, aspect and shaded relief), population density data, Defense Meteorological Satellite Program (DMSP) city lights data, LUDA, and National Wetlands Inventory (NWI) data. It is anticipated that Digital Line Graph (DLG) data and National Biological Service Gap Analysis Program (GAP) data will be incorporated at a future date.

Methods

The general procedure of this project was to (1) mosaic multiple summer TM scenes and classify them using an unsupervised classification algorithm, (2) interpret and label classes into twelve land cover categories using aerial photographs

0-7803-3068-4/96$5.00©1996 IEEE

as reference data, (3) resolve confused classes using the appropriate ancillary data source(s), and (4) incorporate land cover information from leaves-off TM data and NWI data to refine and augment the "basic" classification developed above.

The entire region was divided into two halves, which were analyzed separately. This was done in part to keep amounts of analyzed data reasonable, and in part because scenes from the west half of the region were acquired during late summer and early autumn, whereas scenes from the east half of the region were acquired during early summer. It was felt that the mosaicking of early summer and late summer scenes might create difficulties due to phenological differences. For mosaicking purposes, a base scene was selected, and other scenes were normalized to mimic spectral properties of the base scene following histogram equalization using pixels in regions of spatial overlap.

Following mosaicking, mosaicked scenes were clustered into 100 spectrally distinct classes using the Cluster algorithm developed by Los Alamos [4]. Clusters were assigned into Anderson level 1 and 2 land cover classes using National High Altitude Photography program (NHAP) aerial photographs as reference information. Almost invariably, individual spectral classes were confused between/among two or more "targeted" land cover classes. Separation of spectral classes into meaningful land cover units was accomplished using ancillary data. Briefly, for a given confused spectral class, digital values of the various ancillary data layers were compared to determine: (1) which data layers were the most effective for splitting the confused class into the appropriate land cover units, and (2) the appropriate thresholds for splitting the classes. Models were then developed using one to several data sets to split each confused class into the desired land cover categories. As an example, a spectral class might be confused between stressed deciduous forest and low density residential areas. In order to split this particular class into more meaningful land cover units, population density and city lights data were assessed to determine if they could be used to split the class into residential and forested categories, and if so, to define the appropriate thresholds to be used in the class splitting model.

Following the above class splitting steps, a "first order" classification product was constructed for each of the two halves of the study region. Leaves-off data were then clustered with the goal of discerning certain land cover features not easily discriminated using leaves-on TM data. Classes easily defined using leaves-off data included conifer vegetation and hay/pastures. Both are green in early spring and late autumn, and are readily discernable from each other and almost all other (non-green) land cover categories. This information was then incorporated into the classification product. Land cover classes that were spatially but not spectrally distinct (barren areas, clearcuts) were digitized off the screen and NWI data were incorporated into the land cover product. The east and west halves of the region were then mosaicked together. The resulting classification includes: water, low density developed, high density developed, hay/pasture/grass, row crops, conifer forest, mixed forest, deciduous forest, forested wetlands, emergent wetlands, barren (non-coal), and barren (coal mines).

RESULTS AND CONCLUSIONS

The approach above appears to have yielded a very good general land cover classification product for a very large region. While some refinement in the product will undoubtedly be necessary, and quantitative accuracy checks have yet to be conducted, the large area product appears to have many desirable characteristics (e.g. mostly seamless, reasonable in terms of accuracy based on visual inspection). GAP data will be incorporated as they become available, resulting in a much more detailed land cover product. It is envisioned that similar approaches could be used to enable efficient generation of land cover data for the rest of the United States.

ACKNOWLEDGMENTS

This work was performed by the Hughes STX Corporation under U.S. Geological Survey Contract 1434-92-C-40004.

REFERENCES

[1] United States Geological Survey, 1990, Land use and land cover digital data from 1:250,000- and 1:1000,000-scale maps, data users guide. Department of the Interior, U.S. Geological Survey, Reston, Virginia, USA.

[2] Brown, J.F., Loveland, T.R., Merchant, J.W., Reed, B.C. and Ohlen, D.O., 1993, Using multisource data in global land cover characterization: concepts, requirements, and methods. Photogrammetric Engineering and Remote Sensing 59, 977-987.

[3] Loveland, T.R., Merchant, J.W., Ohlen, D.O., and Brown, J.F., 1991, Development of a land-cover characteristics database for the conterminous U.S., Photogrammetric Engineering and Remote Sensing 57, 1453-1463.

[4] Kelly, P.M., and White, J.M., 1993, Preprocessing remotely sensed data for efficient analysis and classification, Applications of Artificial Intelligence 1993: Knowledge-Based Systems in Aerospace and Industry, Proceedings of SPIE, 1993, 24-30.

Calibration and classification of SIR-C SAR data in moderate slope areas

Francesco Holecz [1,2], Thierry R. Michel[2], and Markus Keller[3]

[1]Jet Propulsion Laboratory/California Institute of Technology
4800 Oak Grove Drive, M/S 300-243, Pasadena CA 91109, E-mail: franci@blacks.jpl.nasa.gov
[2]Remote Sensing Laboratories, University of Zürich, Switzerland
[3]Swiss Federal Institute for Forest, Snow and Landscape Research, Switzerland

ABSTRACT

The goal of this paper is to present the capabilities of SIR-C Synthetic Aperture Radar (SAR) magnitude data (dual frequency, dual polarization) for land cover classification purposes in areas with moderate slope variations. The work consists of two parts. In a first step SIR-C SAR data acquired during the SRL-2 mission over a hilly to mountainous area in Central Switzerland is geometrically and radiometrically calibrated, by taking into account high resolution Digital Elevation Model (DEM) data. In a second step the backscattering coefficient is classified using an unsupervised and a supervised method. The first one is a scale-space clustering algorithm, while the second one is a quadratic classifier. Since topographic variations correspond also to vegetation changes, additional a priori topographic information, such as elevation and slope data, must be included during the classification step. The different classification results are then compared with the digital ground truth. Results clearly shows that, in spite of strong relief-induced distortions, an accurate classification can be achieved, if the SAR data is correctly calibrated and a priori information is used.

Keywords: SAR calibration, backscattering coefficient, unsupervised and supervised classification

1. INTRODUCTION

An important requirement within most applications is the calibration of the SAR data, especially in areas with terrain variations, where active radar signals are distorted due to the projection of the scene topography into the slant range-Doppler plane. The primary effect of these variations is to change the physical size of the scattering area. A secondary but not negligible source of radiometric error is due to the topographic effects on the antenna gain pattern (AGP) , because the radar look angle is not known precisely as a result of the platform displacements and the local surface topography. For this reason each resolution cell must be radiometrically corrected, by taking into account platform displacements (position and attitude), position of the backscatter element (defined by DEM data), and system AGP.

The ability to acquire multifrequency polarimetric SAR data implies multidimensional data. Potentially, this improves the capability to obtain more information about backscatter signatures of various terrain types and land cover. However, the task of extracting the large amount of information present in these images is still a challenging problem. Furthermore, in the remote sensing case, a priori knowledge about the land cover is generally hard to come by, and therefore the use of supervised methods is prevented. On the other hand, unsupervised techniques, such as the cluster analysis, offers the opportunity to explore in an objective way the data. Roughly speaking, the goal of clustering is to partition a given data set into subgroups such that the data in each group is as compact.

The paper is organized as follows. In section 2 the data sets are presented, while in section 3 the SAR data ist calibrated according to the topography. In section 4 the calibrated SAR data are classified using an unsupervised and a supervised method. The conclusions are presented in section 5.

2. DATA SETS

The SAR data (DT110.00) used in this study were acquired during the second Shuttle Radar Laboratory (SRL-2) mission on October 7th 1994, over an hilly (450 msl) to mountainous (2800 msl) area of Central Switzerland, located at 47.00°N, 8.60°E. The SAR image (C- and L-band HH-, HV-polarization) collected with an incidence angle of 54.6° covers an area of around 1800 km^2.

Two DEMs were provided by the Swiss Federal Office of Topography. The first one is a high quality model (DHM25) derived from digitized map sheets, arranged in the Swiss national (Oblique Mercator) map projection at an original horizontal grid spacing of 25m, while the heights are quantized to integer decimeters. The second one, also in Oblique Mercator projection, has an original horizontal grid spacing of 250m and a height resolution of 1m (DHM250). In order to have the same spatial resolution as the DHM25, the DHM250 data were resampled to 25m grid size using a bilinear interpolator. Furthermore, for classification purposes, the 1979 Land Use Map (LUM) produced by the Swiss Federal Statistical Office has been used. The LUM has a 100m raster and contains 24 main classes. Since the SAR data were geocoded to a pixel spacing of 25m, corresponding to the DHM25 data, the LUM was resampled also to a grid spacing of 25m.

3. SAR CALIBRATION

From the radar equation for distributed targets it is known that the received power is modulated with the 2-way-antenna gain $G(\theta_\ell)^2$ and with the reciprocal value of $1/\sin\theta_i$, where θ_i is the local incidence angle. For each pixel these quantities are therefore dependent on the radar look angle θ_ℓ, the depression angle of the antenna, the sensor position and attitude, the position of the backscatter element, as well as on the processed pixel spacing in range and azimuth. Since SAR processing does not include topographic information, these two radiometric corrections are omitted during the processing step, and therefore they should be considered in a postprocessing step. A detailed discussion of the applied method is given in Holecz et al. (1994 and 1995). Figure 1 shows terrain geocoded and calibrated L-HH data with the corresponding local incidence angle map, AGP correction for L-band HH-polarization, and layover/shadow mask. It should be pointed out, that the achieved geometric accuracy amounts at less than half pixel, while the radiometric calibration distortions due to the topographic effects are up to 6.1 dB (local incidence angle), 1.2 dB (AGP L-HH, -HV), and 1.5 dB (AGP C-HH, -HV) in magnitude.

0-7803-3068-4/96$5.00©1996 IEEE

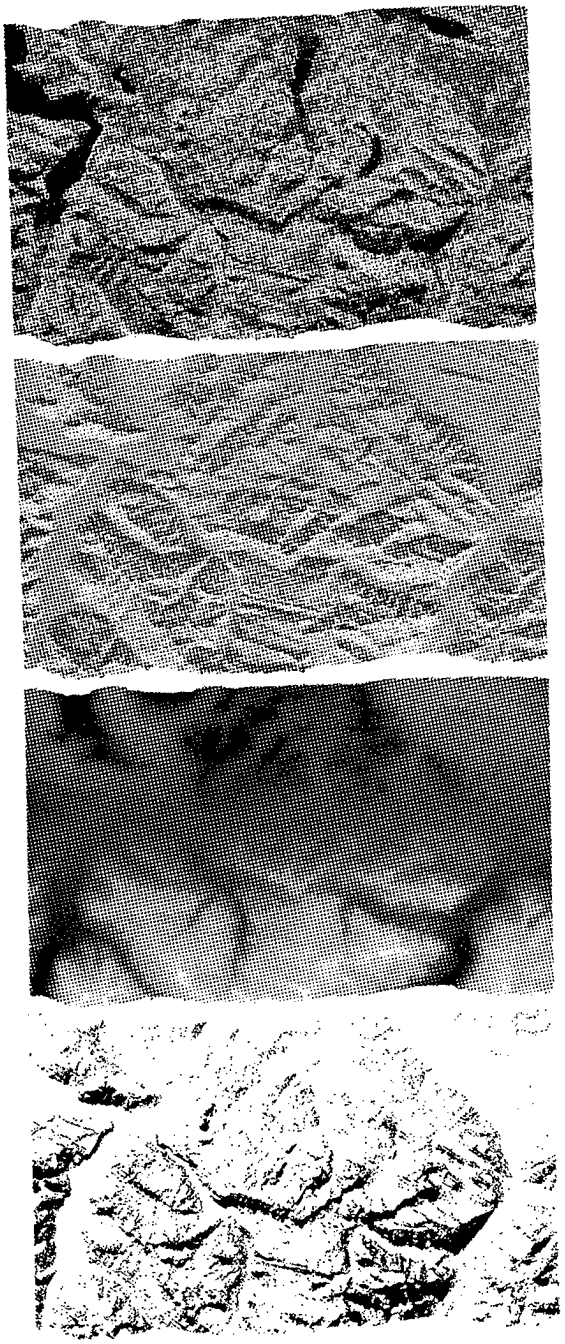


Figure 1: Terrain geocoded and calibrated L-HH data with the corresponding local incidence angle, AGP correction, and layover/shadow mask

An important issue by SAR calibration is the DEM accuracy. For this purpose, as already mentioned in Section 2, a high and low resolution DEM were used during the calibration step. The calibration differences in dB are shown in Figure 2. Dark values, which means no changes, are frequently located in flat areas (lakes and bottom of the valleys), while bright values, mainly situated in the mountainous areas, correspond to large variations, namely 3 to 4 dB in magnitude, with extreme changes up to 10 dB. However, even in the hilly area, variations in the order of 1 to 2 dB are observed. It has to be noted, that the DEM accuracy basically influences only the determination of the local incidence angle, while elevation errors of several meters do not affect the accuracy of the AGP correction (Holecz et al., 1995).

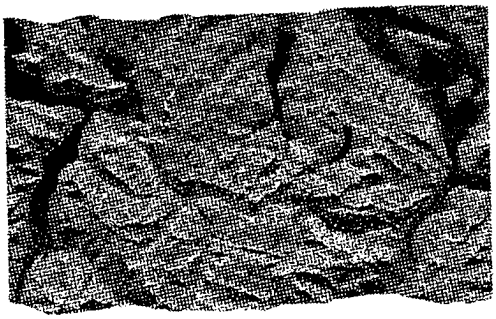


Figure 2: Calibration differences in dB using DHM25 and DHM250

What are the topographic effects on the SAR data? Figure 3 represents uncalibrated and calibrated L-HH, C-HH, L-HV and C-HV data for the whole image. Note, that layover and shadow areas were excluded by the histograms computation. From these plots it can be easily recognized, that SAR data not calibrated according to the topography (dashed lines) are spreaded out, strongly affecting the SAR statistic. A reduction of this dispersion, of course, do not mean a loss of information by the classification step: it is to understand as a much more homogeneous data, or statistically speaking robust.

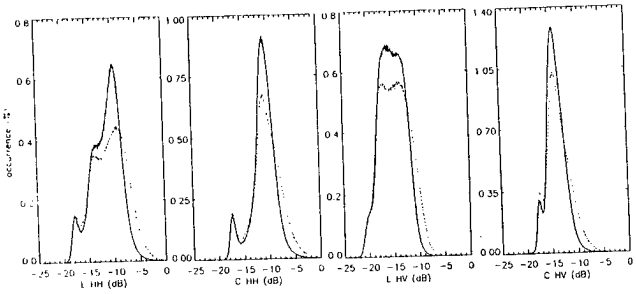


Figure 3: Uncalibrated (dashed) and calibrated (solid) L-HH, C-HH, L-HV and C-HV data for the whole image

4. LAND COVER CLASSIFICATION

In this section two different ways to extract qualitative information from SAR data are applied. The first one is a scale-based clustering algorithm (Wang and Posner, 1993). The probability distribution for the determination of a cluster center is chosen such that its entropy $(-\sum_x P(x)\log P(x))$ is maximized subject to a linear contraint $(-\sum_x e(x) = C$, where $e(x)$ is the Euclidean distance between the observation x and the cluster center y), namely:

$$P(x) = \frac{e^{-\beta(x-y)^2}}{\sum_x e^{-\beta(x-y)^2}}$$

with $\beta = 1/T$, where T has to be considered as temperature. It should be noted, that this approach does not assume any particular data distribution. The melting procedure starts with huge β, initializing every observation as a cluster. By increasing the temperature T the clusters merge, generating a tree of clusters. A criterion for determining the goodness of each cluster (defined as fractional free energy) is used. Moreover, a real cluster should remain stable over a long range of logarithmic scales. The second one is a supervised

Bayes classifier with equal a priori probability (Duda and Hart, 1973). In addition we assume that the probability density function of each class may be represented by a multivariate normal distribution or by a mixture of such normal components.

Figure 4 illustrates the classification results based on the unsupervised, supervised method including a priori topographic information, and LUM.

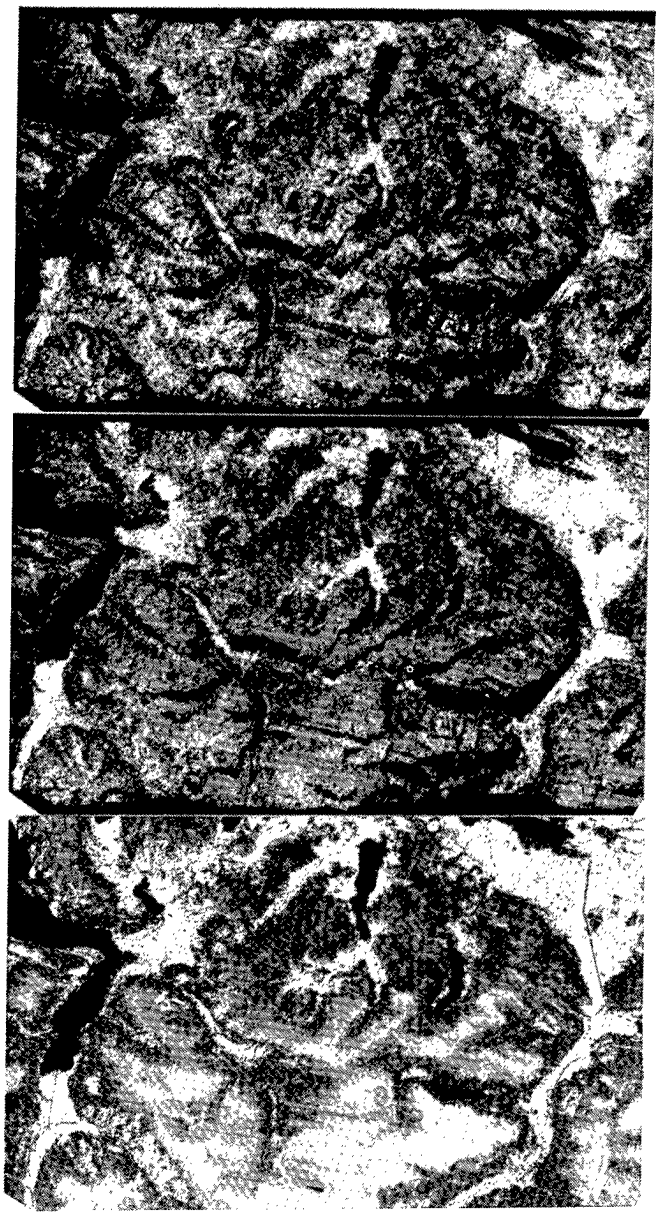


Figure 4: Unsupervised, supervised with topographic information, and LUM. From black to white: shadow/layover, water, forest, pasture, unvegetated, agricultural fields.

A visual comparison of the classified images with the LUM shows the classification accuracy and indicates, that the best result is obtained using a supervised classification including a priori topographic information. It is to be pointed out, that for the supervised method for each land cover type only 1 training sample was used. This is only possible when the data is fully calibrated. The a priori topographic information was included during the classification step by means of three simple conditions, i.e. 1) urban areas are not on sloped area, 2) agricultural fields are not located over a given altitude, 3) pasture is not in the flat areas. Omitting this topographic knowledge, significant classification errors occur for urban area vs rocks, agricultural fields vs pastures and pastures vs agricultural fields, due to the same radar return nature in both frequencies and polarizations. This is especially evident in the mountainous area where rocks are confused with urban area. In the surrounding surfaces unvegetated soil (in this case bare soil at about 2500 msl) is classified as agricultural fields. We should remember the acquisition date, namely October 7th. In this period of the year several agricultural fields are bare soil, and therefore from radar not discriminable from unvegetated soil at any frequency and polarization. The same situation occur between pasture and agricultural fields: some fields were not cultivated during the current year, or after the summer harvest grass is growing, or they still have some low crops such as raps or canola (Wegmüller, 1990). Basically, the classification result using the clustering algorithm, which contain the effective radar return information, are conform to the described situation.

5. CONCLUSIONS

From our results it is evident that an accurate SAR data calibration using a high resolution DEM is a fundamental requirement even for qualitative analysis. Furthermore, it was shown, that in spite of strong relief-induced distortions, an accurate classification over a large area (1800 km^2) having significant different terrain morphologies can be achieved, if a priori information (thematic and topographic information) is used. On the other hand, unsupervised methods, are useful to a) explore in a objective way the SAR data, b) determine which classes are, statistically speaking, robust, and c) indirectly interpret the scattering mechanisms of the radar.

ACKNOWLEDGMENTS

This study was supported by the Swiss Academy of Science and the Holderbank Foundation. A portion of the research described in this paper was performed at the Jet Propulsion Laboratory, California Institute of Technology, under a contract with the National Aeronautics and Space Administration. Thanks are due to the Swiss Federal Office of Topography for providing the DHM25, DHM250, and the Swiss Federal Statistical Office for the LUM.

REFERENCES

Duda R. and P. Hart, 'Pattern classification and scene analysis', John Wiley & Sons, New York, 1973.

Holecz F., E. Meier, J. Piesbergen, D. Nüesch, and J. Moreira, 'Rigorous derivation of the backscattering coefficient', IEEE GRS Newsletter, No. 92, 1994.

Holecz F., A. Freeman, and J. van Zyl, 'Topographic effects on the antenna gain pattern correction', Proceedings IGARSS'95 Symposium, Firenze, 1995.

Wang Y. and E. Posner, 'A new clustering algorithm applicable to multispectral and polarimetric SAR images', IEEE TGRS, Vol. 31, No. 3, 1993.

Wegmüller U., 'Remote sensing signature on agricultural fields with ground-based radiometry and scatterometry', Ph.D. Thesis, Bern, 1990.

A new quick-look optical SAR processor with digital input/output

Konstantin LITOVCHENKO, Philippe LEMAIRE, Christian BARBIER

Centre Spatial de Liège, Université de Liège
Parc Scientifique du Sart-Tilman, Avenue du Pré-Aily,
Angleur-Liège, B-4031 BELGIUM
Phone 32-41-676668
Fax 32-41-675613
E-mail CSLULG@VM1.ULG.AC.BE

Abstract -- A new optical SAR processor is developed and experimentally tested. The main procedure of two-dimensional spatial filtering as well as the phase perturbation correction are performed by means of classical Fourier optics in a tilted-plane configuration. The raw data are introduced by means of film inserted into laser beam. The image is detected by CCD camera, displayed and stored by PC. The possibility of data input by means of liquid crystal display is investigated theoretically. Different possible optical set-up configuration were analysed and tested from the point of view of geometrical and radiometric resolution. The processor is tested by simulated point targets raw data and by real raw data of ERS-1 and ALMAZ-1 satellites.

INTRODUCTION

There exist many applications where real time quick-look lower resolution SAR images are more desirable than off-line full resolution images. Such systems could be implemented as on-board processors of airborne or spaceborne SAR as well as compact ground-based (or shipborne) processors intended for direct utilisation by SAR imagery users. The optical integration of large array of data seems to be very competitive with respect to digital one as far as the processing speed is concerned. The development of modern optical SAR processor provides an alternative and attractive way to satisfy these demands.

The traditional optical processing were used for SAR data up to the time when considerable progress in computing technology were achieved. Such processors were bulky and incapable to operate in on-line regime. Now, using the novel technology of spatial light modulation, it is possible to combine the advantage of digital data storage and that of optical integration speed. This work is the first step in construction of such a processor. It comprises the development of the theoretical basis and laboratory tests of processor main features.

Up to now only one version of optical real-time SAR processor were proposed and described in publications - the processor based on "add-and-shift" CCD principle [1,2]. We propose here the more traditional version with two-dimensional simultaneous integration in range and azimuth and fully digital input and output of data by means of liquid crystal display (LCD) and CCD matrix respectively.

The main stages of the approach to the problem are as follows:

1. The analysis of all system features (i.e. the 2D integration procedure, the phase distortion suppression, the correct image scaling) by means of general SAR theory.
2. The experimental testing of a SAR processor with simulated point targets raw data and with real data of ERS-1 and ALMAZ-1 SARs using traditional data input by means of film.
3. The introducing of LCD as input data source.
4. The introducing of watching system for on-line processor parameters modulation.

The present paper covers the steps 1 and 2 and preliminary investigation concerning step 3, since the LCD was not available at a time of submission.

THEORY

Let us consider the SAR with chirp modulated transmitted pulse (this is a case for ERS-1 SAR). The expression for single point target raw data of such a SAR in most general case can be written in the following form:

$$h(x,y) = A_0 + A_1 \cos\left[2\pi\left(k_{10}x + k_{01}y + k_{20}x^2 + k_{02}y^2 + k_{11}xy + k_{21}x^2y\right)\right] \quad (1)$$

where x and y are the co-ordinates of data carrying medium (e.g. photographic film) corresponding to scene co-ordinates of azimuth and range respectively,

$$k_{10} = \frac{1}{p}\left(\frac{f_{of}}{V} + \frac{U}{V\lambda_0} - \frac{2f_0}{c}\tan\beta\right) \quad (2a)$$

$$k_{01} = \frac{1}{q}\left(\frac{2f_{of}}{c} + \frac{2U}{c\lambda_0} + \frac{2\alpha^2 R_0}{c^2}\tan^2\beta\right) \quad (2b)$$

$$k_{20} = -\frac{1}{p^2}\left(\frac{f_0}{cR_0} + \frac{3\alpha^2}{c^2}\tan^2\beta\right) \quad (2c)$$

$$k_{02} = -\frac{1}{q^2}\frac{2\alpha^2}{c^2} \quad (2d)$$

$$k_{11} = -\frac{1}{pq}\frac{4\alpha^2}{c^2}\tan\beta \quad (2e)$$

$$k_{21} = \frac{1}{p^2 q}\frac{2\alpha^2}{c^2 R_0} \quad (2f)$$

where λ_0 is the radar wavelength, f_0 is the radar carrier frequency, R_0 is the mean slant range, V is the platform velocity U is the velocity of scene motion caused by Earth rotation, α is the chirp rate, β is the angle between antenna beam position and normal to SAR velocity, f_{of} is the demodulated signal centre (offset) frequency (for ERS-1 f_{of}=0, for ALMAZ-1 f_{of}=750 Hz), p and q are the scaling factors between the scene and data carrier in azimuth and range respectively.

Expression (1) describes the transparency function of the

This work was supported by the fellowship awarded by the Services Fédéraux des Affaires Scientifiques, Techniques et Culturelles of Belgium

0-7803-3068-4/96$5.00©1996 IEEE

elliptical Fresnel lens with focal lengths determined by factors k_{20} and k_{02} in azimuth and range meridians respectively [3]:

$$F_a = \pm \frac{1}{2\lambda_l k_{20}}, \qquad F_r = \pm \frac{1}{2\lambda_l k_{02}} \tag{3}$$

where λ_l is the laser wavelength. As the azimuth focal length depends on target range, the azimuth focal plane of real data will be tilted against the range one by the angle:

$$\varphi = \operatorname{atan}\left(\frac{\lambda_0}{2\lambda_l}\frac{p^2}{q}\right) \tag{4}$$

The linear terms in (1) are responsible for the asymmetry of Fresnel pattern. The terms depending on both co-ordinates introduce phase distortion into diffracted wave and are known as range walk (term $k_{11}xy$) and range curvature (term $k_{21}x^2y$).

OPTICAL PROCESSOR DESCRIPTION

The optical system capable to focus the raw data of point target into a single point is shown in fig. 1. It consists of spherical and cylindrical telescopes bringing both azimuth and range focal planes of Fresnel lens into coincidence, and of the 2-lenses module correcting range walk and curvature. The lens L5 is appropriately tilted in range plane and rotated around system axis. The telescopic and tilted plane configuration allows to hold the uniform and adequate scaling over the final image. The screen with hole passes only converging diffracted wave and stops the diverging one and non-diffracted light.

This optical set-up is the most general configuration suitable in principle for any SAR system. The following expressions determine the angle χ between input beam and axis, the angle α of input and output data planes tilting, the angles of lens L5 tilt ψ_1 and rotation ψ_2 via SAR parameters:

$$\tan\chi = \lambda_l k_{10}, \qquad \tan\psi_1 = \lambda_l F^2 k_{21}/\pi \tag{5}$$

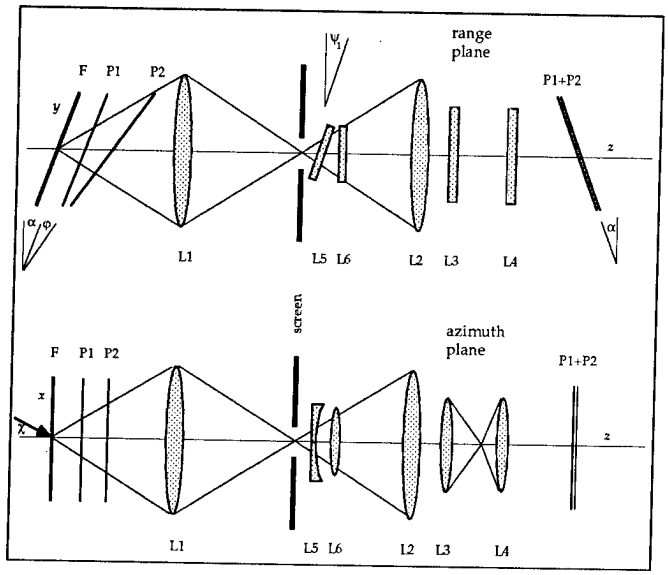


Fig. 1. The SAR tilted plane processor schematic diagram: L1-L2 - spherical telescope, L3-L4 - azimuth cylindrical telescope, L5-L6 - phase distortions correction module, F - plane of input data, P1 - plane of range focuses of input data, P2 - plane of azimuth focuses of input data, P1+P2 - the combined position of planes of range and azimuth focuses.

Table 1. Example of parameters set for ERS-1 case.

parameters of SAR system		
speed of light	300000	km/s
SAR carrier frequency	5.3	GHz
SAR wavelength	0.056604	m
mid-swath slant range	852.72	km
mid-swath incidence angle	23	deg
SAR velocity	6.656	km/s
pulse repetition frequency	1678.7	Hz
pulse duration	37.1	mcs
pulse bandwidth	14.3	MHz
sampling frequency	18.96	MHz
chirp factor (alpha)	620842	Hz
oversampling factor	2.651748	
sample interval in azimuth	3.964942	m
sample interval in range	7.911392	m
angle of antenna squint (beta)	1	deg
terrain velocity from Earth rotation	-200	m/s
parameters of raw data		
offset frequency	750	Hz
azimuth scale factor (p)	3.31E-06	
range scale factor (q)	1.66E-06	
k10	-312.381	mm^(-1)
k01	1.345819	mm^(-1)
k20	-1.86455	mm^(-2)
k02	-3.10696	mm^(-2)
k11	-0.05436	mm^(-2)
k21	0.000544	mm^(-3)
parameters of optical processor		
laser wavelength	0.6325	mcm
azimuth focal length	423.9712	mm
range focal length	254.433	mm
tilt angle of azimuth focal plane (fi)	16.47899	deg
focal length L1 and L2 - sphere	500	mm
focal length L3 - cylinder	200	mm
focal length L4 - cylinder	100.2307	mm
focal length L5 - cylinder	-90	mm
focal length L6 - cylinder	90	mm
angle of input film tilt (alpha)	5.361227	deg
distance between lenses L2 and L3	103.7444	mm
distance from lens L2 to image plane	754.433	mm
distance from frequency plane to lens L5	3.847722	mm
tilt angle of lens L5 (psi1)	1.569433	deg
rotation angle of lens L5 (psi2)	-0.98485	deg
angle between input beam and optical axis (hi)	-11.1766	deg

$$\tan\alpha = \frac{\sin\varphi}{(p/q)^2 - \cos\varphi}, \qquad \tan\psi_2 = \lambda_l F k_{11} \tag{6}$$

where F is the focal length of both spherical lenses. To provide the unity aspect ratio of an image the focal lengths of cylindrical lenses must satisfy the condition:

$$F_3/F_4 = p/q \tag{7}$$

The distance between L2 and L3 is adjusted in order to provide the coincidence of planes P1 and P2 in the image domain. The focal lengths of lenses L5 and L6 do not play important role but they must not disturb significantly the telescopic condition of the main system.

The total set of system parameters is calculated by the Excel worksheet (see example in table 1).

EXPERIMENTAL TESTS

The system was tested with simulated point target responses and with real raw data. The simulated data were calculated and printed by PostScript and LaserWriter. Then they were photo-reduced and realised as black-and-white film. With simulated data the problems of system resolution , adequate scaling and phase distortions suppression were investigated. These tests have confirmed all theoretical performances of the optical system.

As real data we used the raw data of ERS-1 and ALMAZ-1 satellites. The real data were transferred to the film in the similar manner. The results are illustrated by images obtained from the same raw data sets by means of standard digital and optical processing (fig. 2 and 3).

The system parameters were adopted in each case for the

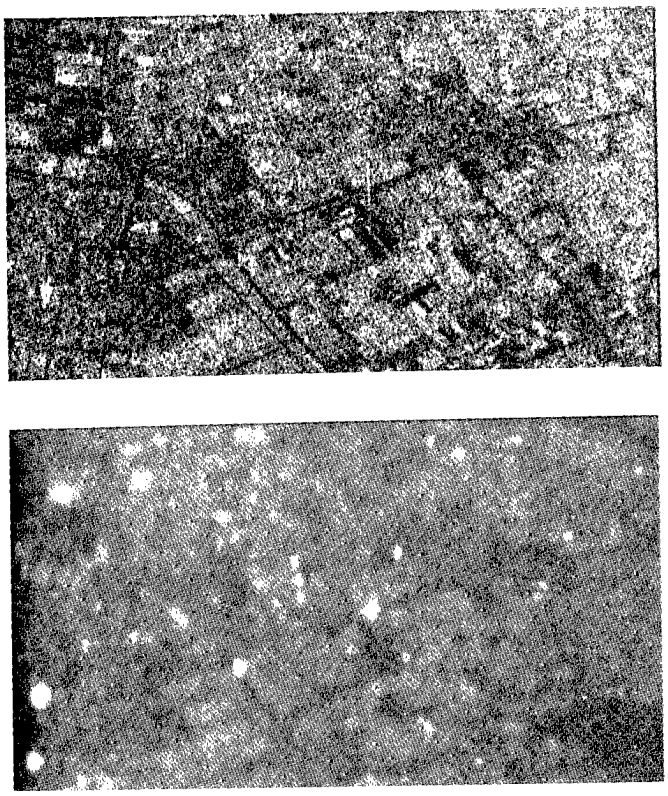


Fig. 2. The ERS-1 SAR image processed digitally (top) and optically (bottom).

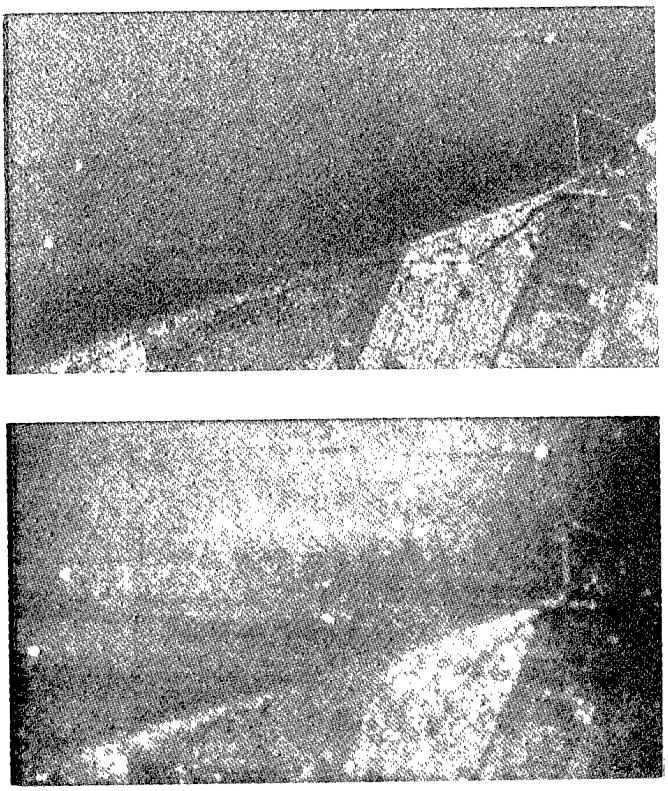


Fig. 3. The ALMAZ-1 SAR image processed digitally (top) and optically (bottom).

SAR parameters accounting, in particular for fact that for ALMAZ-1 only azimuth focusing is needed (as in ALMAZ-1 SAR no chirp pulse is implemented), while for ERS-1 the focusing in both dimensions is needed. The comparison with standard processing shows in both cases that the quality of optical processing has the evident lack of spatial resolution but the quality of image can be considered as sufficient for some quick-look applications.

FUTURE ACTIVITIES

The considered optical set-up is consisting of classical optical elements. Now modern electro-optical elements are available or will be available in near future. These are the LCD [4] or other spatial modulators of light with direct addressing of cells which transparency or reflectivity [5] as well as optical length is modulated by external electrical signal. The use of such elements opens two possibilities - the digital input of raw data by modulating the transparency of matrix used instead of input film and the synthesis of any arbitrary phase compensating function to perform the focusing. Such phase function can be realised as a light valve matrix (or matrices) and used instead of lens system with the same output result. All parameters of processing (both constant and variable) are introduced by applying the appropriate signal (from computer) to each cell thus modulating its phase or amplitude transfer factor.

The performance of such a system (and its size) depends however on a size of available electro-optical cells. The principal requirement for such a system is that a number of simultaneously lighting up pixels of input matrix must be enough to ensure the needed resolution. E. g. for ERS-1 this number is about 2000 if each pixel of raw data is used. The compactness of a system depends primarily on a size of light modulator. For example, the for above SAR images the pixel size of raw data was about 25 μm the total optical length of a system being about 2.5-3 m.

ACKNOWLEDGMENTS

The authors would like to thank Mr. J. Rosello (ESTEC) and Mr. P. Shirokov (NPO Mashinostroeniya, Russia) for the supply of, respectively, ERS-1 and ALMAZ-1 SAR data.

REFERENCES

[1] Psaltis D., Wagner K. Real time optical synthetic aperture radar (SAR) processor. *Opt. Eng.* **21** (5), pp. 822-828, 1982.

[2] Uhrich P. et al. Real time non coherent optical processor with CCD "add and shift" for synthetic aperture radar data. ONERA, T.P. n°1988-108, 1988.

[3] Goodman J. Introduction to Fourier Optics. McGraw-Hill, New-York, 1968.

[4] Burns D.C. et al. A 256x256 SRAM-XOR pixel ferroelectric liquid crystal over silicon spatial light modulator. *Optics Communications* , **119**, pp. 623-632, 1995.

[5] Feather G.A. Micromirrors and digital processing. *Photonics Spectra*, pp. 118-124, May 1995.

The Modeling of Forested Areas for Real and Synthetic Aperture Imaging Radar Simulation

Paul A. Stuopis; James M. Henson
Dept. of Electrical Engineering
University of Nevada
Reno, NV 89557
(702) 784-6929/Fax:(702) 784-6627/jmh@proton.ee.unr.edu

R.E. Davis
U.S. Army Corps of Engineers
Cold Regions Research and Engineering Laboratory
Kenneth Hall
U.S. Army Corps of Engineers
Waterway Experiment Station

Abstract -- The following paper provides a discussion of several procedures for generating elevation and terrain category database information for the modeling of deciduous, coniferous, and mixed forested areas. Specifically, techniques for the geometric modeling of individual pine and oak trees, based on measured or estimated location, height, and canopy diameter are presented. Techniques for randomly populating forested areas at user specified densities with individual trees are discussed. Considerable simulated imagery has been developed for both solid canopy forest and individual tree forest models. In the case of forests modeled as collections of individual trees, imagery has been developed for forests with varying tree densities. Simulated image presentations (grey level and pseudo-color) include sidelooking SAR range and ground range imagery and forward scan B-Scope and P-Scope range and ground range imagery. All modeling and simulation was accomplished using the Synthetic Aperture Reconnaissance, Tactical, And Camouflage (SARTAC) imaging radar simulation and analysis tool developed at the University of Nevada with the support of the U.S. Army Corps of Engineers Cold Regions Research and Engineering Laboratory (USACE/CRREL) and the U.S. Army Corps of Engineers Waterway Experiment Station (USACE/WES).

INTRODUCTION

The database modeling techniques described in the following sections were developed as part of the Synthetic Aperture Reconnaissance Tactical And Camouflage (SARTAC) Imaging Radar Simulation and Analysis Tool. At this time SARTAC resides on a Silicon Graphics Indigo workstation and consists of approximately 50,000 lines of 'C' code. The primary purpose of the program is the generation of simulated sidelooking and forward scan radar imagery. Required input data includes ground truth elevation, terrain type, and target information. User controlled inputs which directly affect simulated imagery include: altitude, depression angle, frequency, polarization, range resolution, cross-range resolution, antenna pattern, flight path, area of illumination and display options.

Also included in the program is a graphic terrain database editor which can be used for the creation of new databases as well as for the modification of existing ones. Tree/forest modeling is accomplished interactively through this editor.

0-7803-3068-4/96$5.00©1996 IEEE

TREE MODELING

In the case of both coniferous and deciduous tree models the required user specified inputs are average height, average (canopy) radius, height deviation, radius deviation, and canopy roughness factor. For any individual tree the tree height is computed as tree_height = average_height + (1.0 - 2.0(rand(0,1))(height_deviation). Similarly the tree_radius is computed as tree_radius = average_radius + (1.0 - 2.0(rand(0,1))(radius_deviation). After statistical placement of the tree centers based on a user specified density (trees/km^2), individual canopy elevation values within the specified tree radius are found based on the distance of a pixel from the tree center.

In the case of coniferous trees, the elevation of individual points (pixels) within the canopy are formed as

$$\text{elevation} = \text{ground_elev_tree_center} + \text{tree_height} - \Delta z,$$

where $\Delta z = 0.9 * \text{tree_height} * \text{distance_to_center} / \text{tree_radius}$. Finally the elevation is roughened using elevation = elevation + (0.5-rand(0,1)) * roughening_factor * tree_height. Figure 1 shows the relevant variables.

Assumptions underlying this model are:

1) Canopies in plan view are circular.

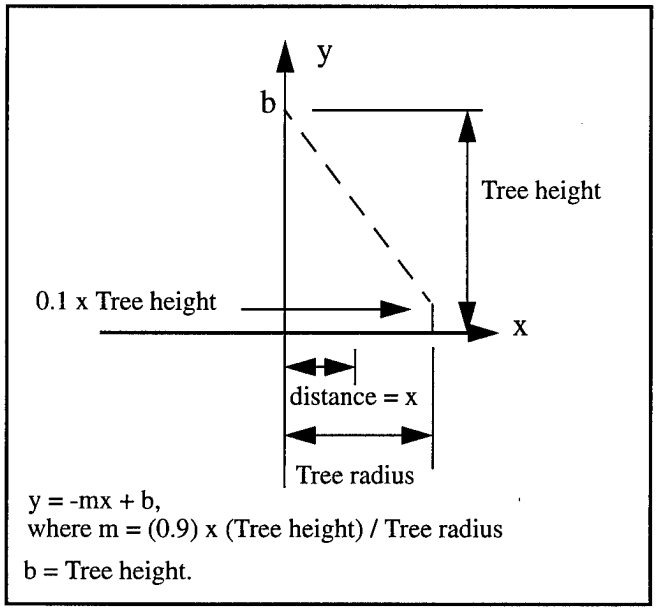


Figure 1. Evergreen Tree Canopy Modeling

2) Maximum canopy height occurs at tree center.
3) Canopy shape in side view is triangular.

In the case of deciduous tree canopies the elevation of a particular point on the top of the canopy is computed as

elevation = ground_elev_tree_center + tree height + Δz ,

where $\Delta z = \sqrt{\left[b^2 - \left(1 - \frac{x^2}{a^2}\right)\right]} - b = z - b,$

a = (Tree canopy diameter / 2), b = (Tree height / 2),

and $z = \sqrt{\left[b^2 - \left(1 - \frac{x^2}{a^2}\right)\right]}$

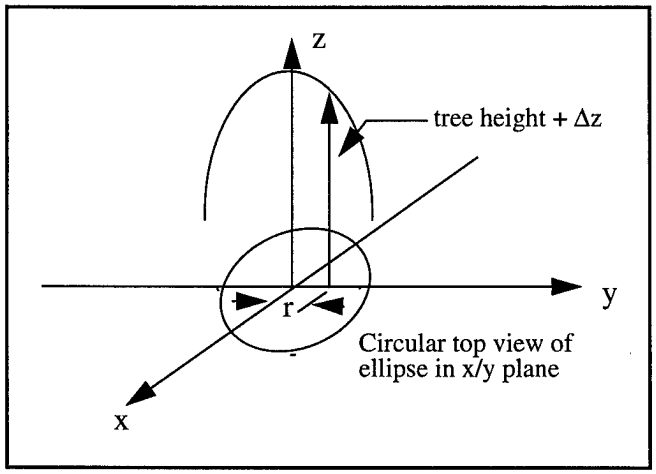


Figure 2. Deciduous Tree Canopy Modeling

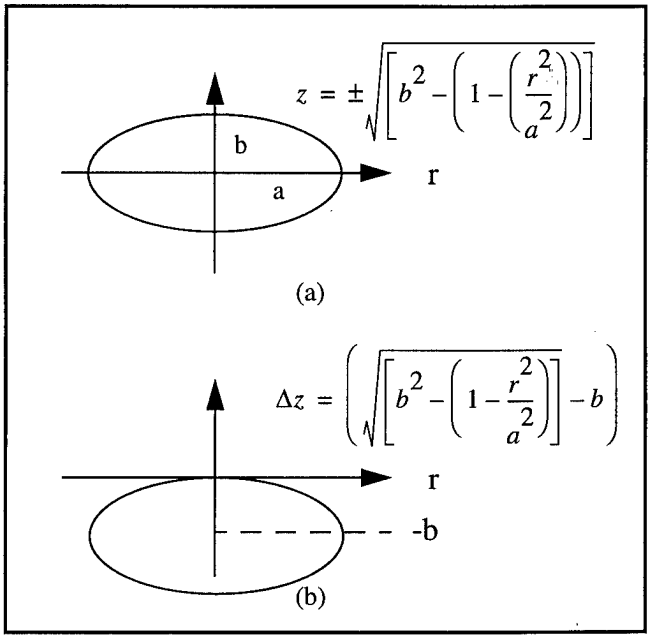


Figure 3. Deciduous Tree Canopy Computations

As shown in Figure 2 and 3, elevation values of the canopy depend on the (x,y) values of an ellipse with minor axis of 2a and major axis of 2b. Finally the elevation is roughened using elevation = elevation + (0.5-rand(0,1)) * roughening_factor * tree_height. In the case of deciduous tree models we have assumed:

1) Canopies are circular in plan view.
2) Maximum height occurs at tree center.
3) Canopies are elliptical in side view with ellipse_width = tree_radius and ellipse height = tree_height/2.

If the computed elevation is greater than the current elevation value, the current elevation value and tree category are replaced with the computed elevation and current tree category. Otherwise, the existing terrain is at an elevation greater than the canopy pixel.

TREE POPULATION AND PLACEMENT

Individual canopies for deciduous and coniferous trees are inserted in terrain elevation and terrain cover databases statistically based on the user specified value, trees/km^2. Areas for population can be selected by drawing closed areas directly into the database or by selecting an existing area. All terrain cover within the selected area is remapped to grass (or wasteland), prior to tree insertion. Individual trees (Deciduous, coniferous, or a mixture of the two types) are then generated as described above and inserted randomly in the area at the proper density.

Specifically, the user defined density is converted to trees

per database resolution cell. Notice that this value will typically be << 1.0,. If for example the distance between ground truth data points is 2 m and the user enters the value 10,000 trees/km^2, we find trees/cell = 0.04, or a tree center located in one out of 25 database cells, on average. At each pixel within the area to be populated, we compute a random value uniformly distributed between 0 and 1. If this value is less than the computed value, trees/cell, a tree center is located within the current cell (pixel). Note that the value, trees/cell is in effect a probability. If this probability is greater than the value uniformly sampled from the interval [0,1], a tree should be located within the current pixel area. The actual location of the tree center within the current cell is formed as x=row + z_1 and y = col + z_2, where (row,col) is the location of the current pixel and z_1 and z_2 are independent random values sampled uniformly between -0.5 and 0.5. This coordinate value (x,y), is then used for the center location of the tree canopy to be constructed as described previously.

SIMULATED RESULTS

Figure 4 shows a 250x300 m sidelooking ground range mapped image of a modeled forested area. The area is composed of the following tree types and densities. Quadrant 1: Mixed pine and deciduous at 10,000 trees/km^2 for each type. Quadrant 2: Pine trees at 10,000 trees/km^2. Quadrant 3: Deciduous trees at 10,000 trees/km^2. Quadrant 4: Mixed pine and deciduous at 2,000 trees/km^2 for each type. In all cases



Figure 4. Simulated Sidelooking Image

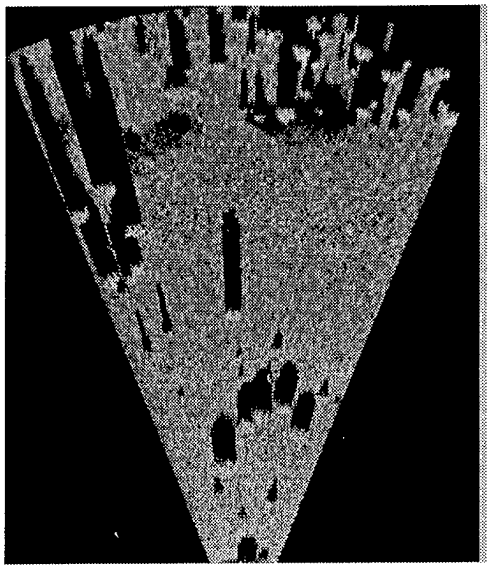


Figure 5. Simulated Forward Scan Image

average tree height for pine is 20 m, and 15 m for deciduous, and average canopy radius is 5 m. Radar parameters include: altitude = 10,000 m, depression angle to scene center = 30 degrees, frequency/polarization X H/H, 4-look noise averaging, 1m range and cross-range resolution. Figure 5 shows a forward scan ground range mapped image of a forrest section composed of a mixture of pine and oak trees whose location and size information was measured. Radar parameters were set as follows: altitude = 25 m, depression angle to near range edge = 40 degrees, frequency/polarization X H/H, range resolution = 1m, and far range crossrange resolution = 1 m.

REFERENCES

[1] Henson, J.M., and G. Velazquez, "SAR Simulation and Camouflage Assessment," Technical Report EL-2, Dept. of the Army, U.S. Corps of Engineers, Washington, D.C. 1992.

[2] Henson, J.M., SARTAC, An Imaging Radar, Terrain and Camouflage Simulation, Ph.D. Dissertation, University of Arkansas, 1991.

[3] Henson, J.M., "An Air to Ground Forward Scan B-Scope and PPI Imaging Radar Simulation for Diverse and Urban Terrain," IEEE International Geoscience and Remote Sensing Symposium, Tokyo, 1993.

[4] Ulaby, F.T., Moore, R.K., and Fung, A.K., Microwave Remote Sensing, Addison-Wesley Press, 1982.

[5] Ulaby, F.T., Handbook of Radar Scattering Statistics for Terrain, Artech House, 1988..

Use of geometrical SAR simulation for visibility prediction: Application to mission planning and urban study

Christophe Gouinaud† and Isabelle Pons††

†Département Images .Télecom Paris
46 Rue Barrault
75634 Paris CEDEX 13-FRANCE
Gouinaud@ima.enst.fr

††GEOSYS
3 Rue Hermes
Parc technologique de Toulouse Rammonville
31526 Rammonvile CEDEX-France
Ip@geosys.fr

ABSTRACT : The specification of future radar satellites and many remote-sensing applications need information about the geometrical distortions seen in a SAR image. The main geometrical distortions are those that are called "shadow" and "lay-over"; it is very difficult to quantify them with a lonely SAR image, but the use of many SAR images allows a numerical evaluation of these distortions. Unfortunately not only this procedure is very expensive, but also, before the launch of RADARSAT, only SIR C produced satellite multi-incidence radar images. On the contrary, digital elevation models are easy to access, for a large variety of countries and landscapes.

We show here the interest of geometrical SAR simulations in order to estimate the probability of geometrical distortions and extract practical information concerning visibility. We describe our approach of SAR simulation, based on an adaptation of ray-tracing to radar geometry, and expose two specific applications. The first one is used to specify the best incidence angle for the simulation with a representative DEM base (100 000 km^2, and the second one is used to predict the visibility of urban objects with specific satellites

This work is based on incidence angle specification for RADARSAT III, and emphasizes the radar potential for urban study.

1 Introduction

When we observe a SAR satellite image, we can see two major types of phenomena : speckle noise and, geometrical effect such as relief aspect or building backscatter. In a real image, those two phenomena are totally confused, so that cannot permit to make a quantification of one or other.

The use of simulation permits to quantify independently geometrical or backscattering effects. There are two major types of simulation : simulation of speckle effect with Goodman model and simulation of the surface variation of the radar echo du to the relief. We show in this paper our technique to realize geometrical simulation only, then we show two applications in the observation of incidence effect. First, we calculate the best radar incidence to maximize the visibility using a DEM base. Second, we show the inference of the incidence angle in the visibility of buildings.

0-7803-3068-4/96$5.00©1996 IEEE

2. Simulation scheme

we present here our algorithm to make SAR geometrical images.

2.1 Context and equations

The constraint of our simulator are :
- Simulate SAR satellite images.
- Simulate relief effect in small area of DEM.
- Give opportunity to quantify shadows and lay-over.

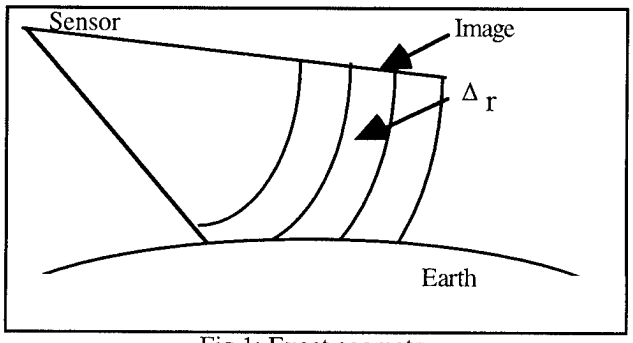


Fig 1: Exact geometry

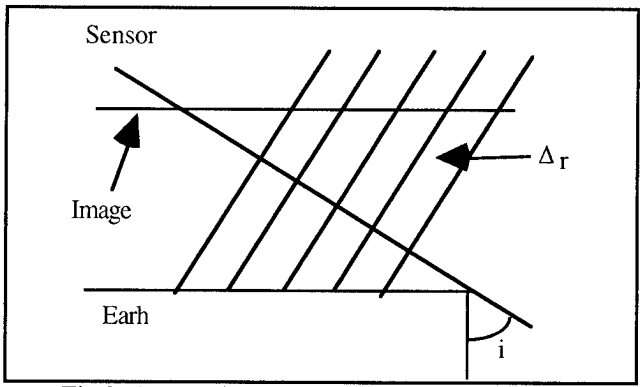


Fig 2: Approached geometry, i angle of incidence

So, we can make some approximations in modeling geometry of acquisition. The first point permits to use constant incidence angle because the high altitude allows small variations in viewing angle.

The second point assumes that wave fronts are plane. For ERS-1 (altitude 800km), this approximation gives a deviation of only few millimeters for 30 meters pixel. also, we assume that the trajectory of the satellite is a straight line.

Others aproximations consist to neglect earth curvature and to assume that cartographic projection of DEM [1] are exactly the ground surface. The calculus of the deviation inducted by ours approximations shows that it is (in use of ERS-1 parameters) neglected in a 10 kilometers range. So, we must only simulate small parts of ground or periodically update our simulation parameters.

These approximations have two principal advantages : first, a low computation coast, that gives possibilities of simulation in extensive DEM base; second, the sensor parameters are constant for one simulated image, so geometrical effects of SAR acquisition are constant.

2.2 Algorithm

Fig. 2 shows us the wave front separate of Δr (range resolution). Four steps are necessary for our simulation :

- we find shadow areas ,
- we compute DEM facet table for each pixel in SAR image,
- we use this table to characterize lay-over areas,
- we sum the facets contributions for each pixel,

The first step is realized using a simple geometrical condition : we follow the incidence plane for each DEM facet and mark as shadow the facet if one other intersection is find with the DEM.

The second step is computed using a distance-finding algorithm. For each pixel of simulated SAR image we find, all DEM facets that have a distance between $[n\Delta r ; (n+1)\Delta r]$ and satisfy the azimutal condition. Finally, a facet table is obtained for each pixel.

The third step consists in extracting lay-over areas from facet table. Lay-over pixels correspond to ones which have multiple facets contributions, so as count upper one in the table.

In the last step, we built the radiometric value of the pixel. For one pixel, we explore facet table, compute intersection between resolution cone and the facet (with a discrete algorithm) and sum each contribution. The contribution of facets is calculated according to the Lambertian model.



Fig 3: DEM of the Reunion and geometrical SAR image with ERS1 parameters

Finally, geometrical SAR image is obtained (Fig. 3). This image can be seen as a perfect de speckled image of a Lambertian uniform landscape.

3 Application

Typical application of simulation is to realize statistical analysis of phenomena that are too complex for direct estimations (in real images). Visibility prediction is the fundamental example. Two approachs can be used : one to specify the best sensor parameters to maximize visibility of a class of landscape or one to evaluate the visibility of a particular object with a defined sensor.

3.1 Specifying angle of incidence

Before the launch of Radarsat, there was no permanent multi-incidence SAR satellite sensor. Maximizing incidence game is very interesting for the research applications but increase the global coast of the sensor. According to this, we use simulations over a large base of DEM (100 000 km^2) to compute the means of shadow and lay-over ratio surfaces. Two types of products can be generated : an image of shadow or lay-over regions as a function of radar incidence and a graphic displaying shadow or lay-over as a function of the radar incidence.

Next, the summation of the two graphics (shadows and lay-over) permits to obtain a graph of the viewing probability for each angle of incidence (Fig. 4).

For the conclusion about this study, we have remarked that the best angle of incidence which maximizes the visibility, is between 30° and 55°. This conclusion coincides with the opinion of the majority of experts interviewed.

[1] Digital Elevation Model

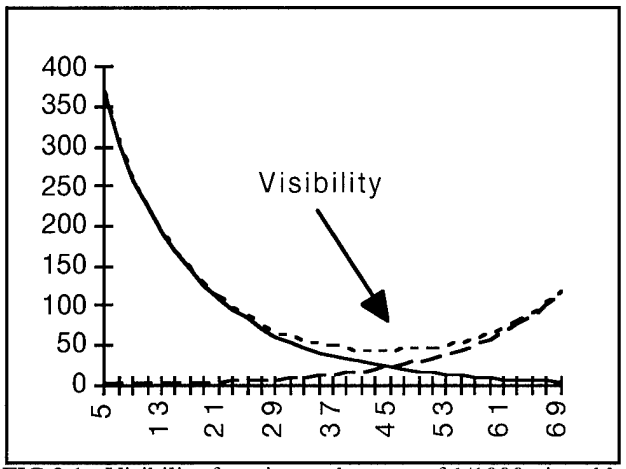


FIG 3.1 : Visibility function and means of 1/1000 viewable areas. continuous line foldover, - line shadows.

3.2 Visibility of a particular objects :

If we have the model of an object and if we want to acquire an image with an existent system, we need to make a choice between configurations. For example, with ERS-1, the choice between an ascending or a descending pass is needed. The same problem appears for the surveying of some particular objects in a town, or for the predicting of buildings masks.

The simulator permits to compute images and to choose the best way to acquire this area. Fig.5 shows an example of this kind of application.

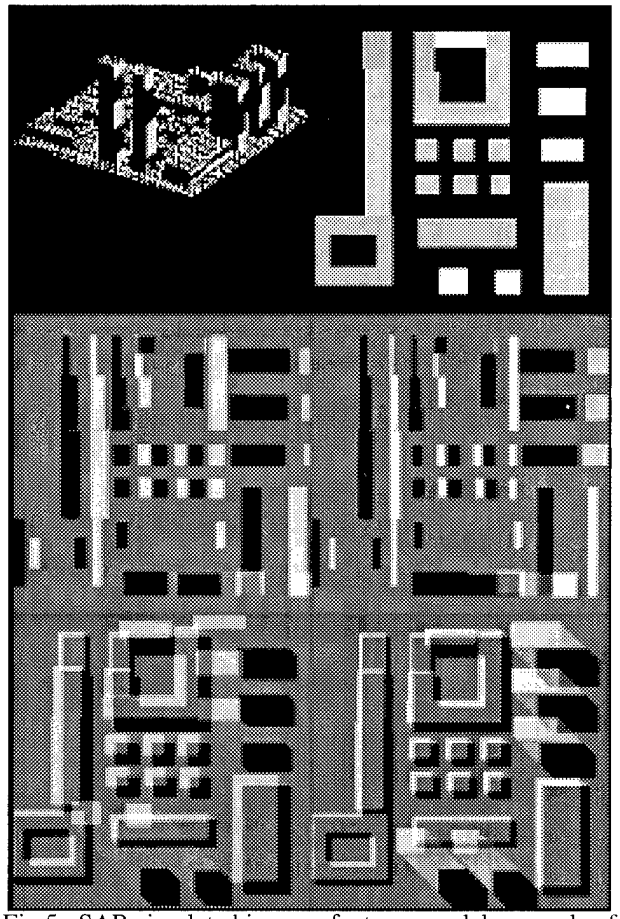
3.3 Other applications

One major other application of this geometrical simulation is assisted photo interpretation for geological survey. If we have a DEM of a volcano before an irruption and a acquired image after the irruption, we can compare real simulated image to detect changes.

Another application is an assisted learning of SAR geometry. Simulation allows to show many views of the same area, and so, to show an exhaustive demonstration.

4. Conclusions

We show here the interest to uncouple two major difficulties in the interpretation of SAR images : speckle and no usual aspects of relief effects. This method gives robust estimation to evaluate a set of parameters for a sensor system, in specification or acquisition phases.


Fig 5 : SAR simulated image of a town model, az angle of azimut, i angle of incidence.

3D perspective	DEM base
az : -90 i : 23	az : -90 in : 35
az : 45 i: 23	az : 45 in : 35

Bibliography :

[1] John C. Curlander and Robert N., Mc Donough.
Synthetic Aperture Radar
J. A. Kong series editor, 1991.

[2] Gouinaud Christophe.
Le monde selon sar.
Master's thesis, Paris VI, 1991.

[3J.W. Goodman.
Some fundamental properties of speckle.
J. Opt. Soc. Am., V66 N11 pp:1145--1150, 1976.

[4] Franz w. Leberl.
Radargrammetric image processing.
Artech House, 685 Canton Street Norwood, MA 02062, 1 edition, 1990.

[5] Gunter Schreier.
SAR Geocoding : Data and Systems.
WICHMANN, 1993.

Modelling Of Microwave Backscatter Using A Tree-Growth Model For Boreal Forests Within The NOPEX Test Site

Iain H. Woodhouse and Dirk H. Hoekman

Department of Water Resources
Wageningen Agricultural University, Nieuwe Kanaal 11
6709 PA Wageningen, The Netherlands
tel: +31-317-484288 fax: +31-3170-484885 email: woodhouse@rcl.wau.nl

ABSTRACT

The use of a tree growth model to provide statistical information about the scattering components of boreal-type forests is described. Such data is used as input to a radar backscatter model as an alternative to data obtained through intensive fieldwork and has been used to predict the total backscatter from three test stands at C-band frequency for three polarisation combinations (HH, VV and HV). The test sites consisted of two stands of Scots Pine and one of Norwegian Spruce. The modelled backscatter values are compared to measured C-band data from a polarimetric airborne Synthetic Aperture Radar (EMISAR). Differences between modelled and simulated backscatter values compare favourably with previous studies, with like- and cross-polarisation differences less than 2.5dB, with the modelled backscatter values generally less than those observed.

INTRODUCTION

There is increasing interest in the use of microwave instruments, such as Synthetic Aperture Radar (SAR), to monitor specific characteristics of forest ecosystems. The analysis of measured data however, requires the development and validation of theoretical models that can predict microwave scattering from vegetation and soils. To date the validation associated with such backscatter models has been limited, the effort needed to collect and analyse extensive ground truth being one of the principal reasons for the shortage of model/data comparisons. To circumvent this difficulty, this study utilises a tree growth model developed at the University of Wageningen which simulates the growth of typical trees within a forest stand, given information about its general characteristics [1]. This can allow for comparisons of modelled and observed backscatter values over large areas without a significant increase in ground truth measurements

The central focus of this study is the application of this model to a region of boreal-type forest within the test site of the Northern Hemisphere Climate Processes Land-Surface Experiment (NOPEX). Data from the tree growth model is used to drive the radiative transfer backscatter model and rough surface scattering model developed by Karam, *et al*, at the University of Texas [2]. This model was developed to simulate the microwave scattering of layered vegetation and is based on an iterative solution of the radiative transfer equation up to the second order to account for multiple scattering within the canopy and between the ground and the canopy. The canopy may be represented by up to three layers, with the branches and needles (or leaves) within each layer being grouped into different sizes each with their own orientation distribution. These scatterers are modelled as randomly positioned finite-length dielectric cylinders.

0-7803-3068-4/96$5.00©1996 IEEE

TEST SITE AND DATA COLLECTION

The measurement sites are located in the forest at Siggefora, 20 km north west of Uppsala, Sweden. The area is dominated by forests of predominately Norwegian Spruce (*Picea abies*) and Scots Pine (*Pinus sylvestris*). Topographic variation throughout the forest is small with a total change of elevation of less than 15-m over the 4-km^2 area of the Siggefora test site. Individual stands were chosen for ground truth measurements on the basis of species homogeneity and spatial uniformity.

Ground data collection of forest parameters involved destructive sampling of six representative trees of three different ages and species (*i.e.*, 3 each of Norwegian Spruce and Scots Pine). Measurements of age, shoots, number of branches, and details of physical dimensions (*i.e.*, diameter, length, angle of inclination) of each tree component were made in order to parameterise the tree growth model.

Tree Growth Model

The tree growth model uses species dependent branching statistics coupled with other local variables such as lighting conditions, maximum tree height, etc., to simulate the physical structure of trees of a given age, with branches represented by collections of cylinders. From such simulations, statistical distributions of branch characteristics may be determined and used as input to the backscatter model.

The model was used to simulate trees typical of those found in the Siggefora test site. An visual representation of

some simulated trees is shown in Fig. 1, illustrating different ages of a Scots Pine.

The model can produce a variety of statistical information about branch dimensions, ages, locations and angular distributions, which can be grouped together in terms of any parameter, such as cylinder dimensions or branch order. An example of the distributions obtained from a simulated 67 year old Scots Pine is shown in Fig. 2. The data from the tree growth model is therefore readily adapted for use as input to backscatter model.

Parameterisation of Forest Stands

Using a combination of field estimates of tree density, tree stand ages from forestry records, and the data from the tree growth model, individual stands can be characterised by number densities and angular distributions of cylindrical branch elements in different layers. A visual representation illustrating the three stands considered in this study is shown in Fig. 3. These modelled sites were two pine stands, (28 and 67 years old) and a 38 year old spruce stand.

The current study has concentrated on stands with dense forest cover to minimise the effect of surface characteristics.

The determination of the layering scheme is dependant upon the characteristics of each forest stand, but are generally one of three categories (each of which is clearly evident in the three cases shown in Fig. 1):

- 1 layer: (1) Small upright trunks, live branches, needles.
- 2 layer: (1) Small upright trunks, live branches, needles.
  (2) Upright trunks, dead branches.
- 3 layer: (1) Small upright trunks, live branches, needles.
  (2) Upright trunks, dead branches.
  (3) Large upright trunks.

Airborne SAR Data

Polarimetric, C-band SAR data of the Siggefora region were acquired on 23 June 1994 with the airborne SAR system of the Danish Centre for Remote Sensing (EMISAR) flown on a Gulfstream G-3 aircraft [3]. The flight of the EMISAR instrument covered a triangular flight line with an image centre incidence angle of 50° and a ground resolution of 2.0-m in both range and azimuth. The corresponding incidence angles (θ_i) over the Siggefora site ranged from 44 to 46°.

RESULTS AND DISCUSSION

The model results were computed at C-band over a range of incidence angles using the simulated stands as input to the scattering model. The model predictions for the total backscatter (given as $\gamma=\sigma^0/\cos\theta_i$) from the Siggefora forest stands are shown in Table 1 alongside the EMISAR measured values.

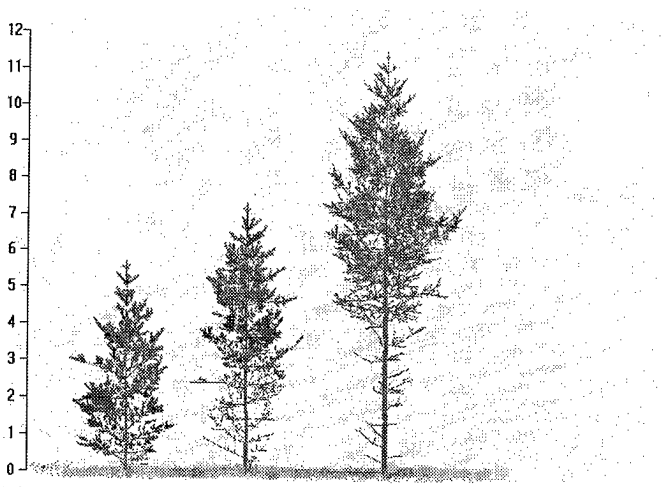


Fig. 1. Visual representation of 3 stages of growth of Scots Pine (15, 20 and 30 year old) using a tree growth model to simulate tree structure. The scale on the left is in metres.

For like-polarisation the experimental values are consistently higher than those predicted by the model by between 0.9 and 2.4 dB. This is comparable to earlier modelling studies which have encountered similar discrepancies between modelled and measured backscatter [2, 4].

The similarity of the HH and VV experimental values (differing by 0.1 to 0.3 dB) may indicate that the main scatterers are randomly orientated, which in turn may imply that the needles (or groups of needles) are the main contributors to the backscatter. The model results, on the other hand, consistently show higher values for HH, implying that the branches dominate in the modelled backscatter. This is most apparent in the spruce stand where there is a difference of 1.2 dB.

A likely explanation for the discrepancies observed is that

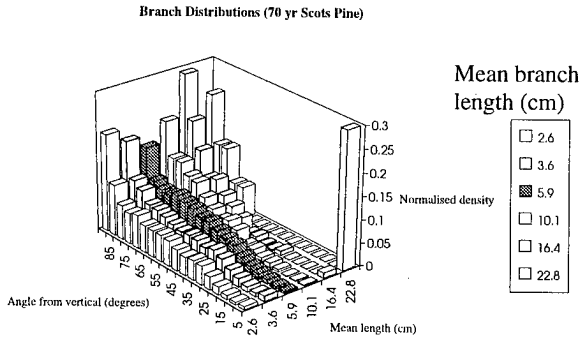


Fig. 2. An example of the discrete orientation statistics of various branch sizes for a simulated 67 year old Scots Pine using a tree growth model. Such data forms the basis of input parameters to the radar backscattering model.

in reality the needles are clustered around the smaller branches providing dense scattering centres, and are not evenly distributed throughout the canopy (forming an attenuating cloud) as in the model. Overcoming this problem will require a systematic method for representing needle-covered branches by equivalent dielectric cylinders.

CONCLUSION

In this paper we have introduced the use of a tree growth model to provide statistical information about the dimensions and angular distributions of scattering components of Scots Pine and Norwegian Spruce stands within the Siggefora forest. Such data has been used as input to a backscatter model as an alternative to using intensive field data and has been used to predict the total backscatter from three test stands at C-band frequency for three linear polarisation combinations (HH, VV and HV). The model predictions were compared with experimental data from the Danish EMISAR instrument and the differences and similarities were analysed. The simulation results show the model worked well for the Scots Pine stands but were significantly poorer for the Norwegian Spruce.

Future analysis will include the modelling of L-Band backscatter to compare with EMISAR data from the NOPEX 1995 campaign. Such comparisons should prove invaluable for developing a better understanding of the main factors affecting radar backscatter from boreal-type forests.

REFERENCES

[1] R. P. Leersnijder, *PINOGRAM: A Pine Growth Area Model.* Ph.D. Dissertation, Department of Forestry, Wageningen Agricultural University, 1992.

[2] M. A. Karam, A.K. Fung, R.H. Lang and N.S. Chauhan, "A microwave scattering model for layered vegetation". *IEEE Transactions on Geoscience and Remote Sensing*, Vol. 30, No. 4, pp. 767-784, 1992.

[3] E. L. Christensen, et al. "The Danish polarimetric SAR for remote sensing applications". *Proceedings, IGARSS '94*, International Geoscience and Remote Sensing Symposium, California, USA, 1994.

[4] N. S. Chauhan, R. H. Lang and K. J. Ranson. "Radar modeling of a boreal forest". *IEEE Trans. on Geosci. and Remote Sensing*, Vol. 29, No. 4, pp. 627-638, 1991.

Table 1: A comparison of simulated (γ_{MOD}) and experimental (γ_{SAR}) C-band backscatter values.

stand	*28 year old pine*			*67 year old pine stand*			*38 year old spruce*		
	HH	VV	HV	HH	VV	HV	HH	VV	HV
γ_{SAR}	-8.8	-8.4	-16.3	-8.5	-8.4	-16.7	-6.8	-6.9	-16.2
γ_{MOD}	-9.7	-10.1	-16.0	-10.5	-10.8	-17.6	-8.1	-9.3	-14.2
γ_{SAR}-γ_{MOD}	0.9	1.7	-0.3	2.0	2.4	0.9	1.3	2.4	-2.0

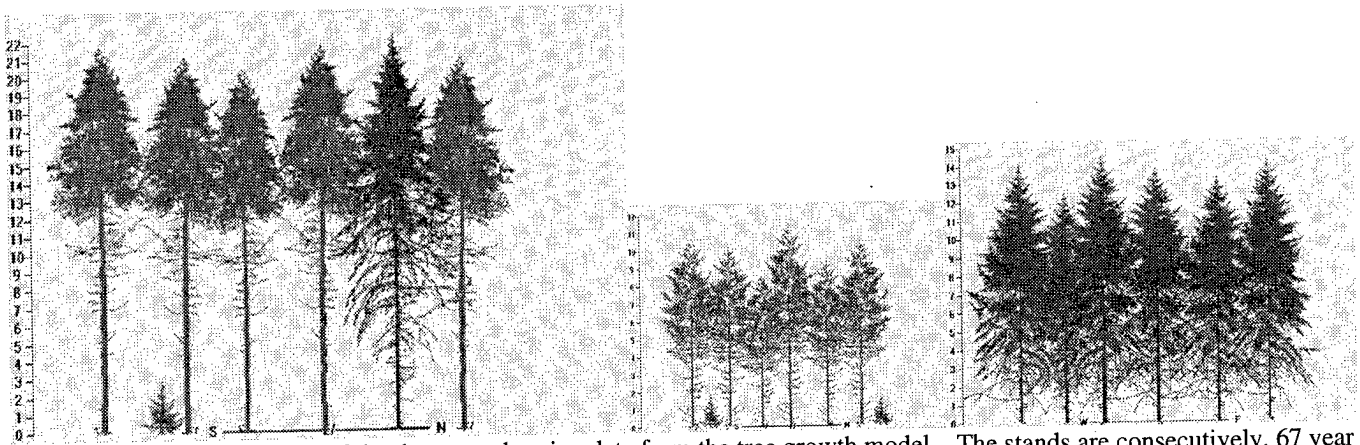


Fig. 3. Visual representation of the three stands using data from the tree growth model. The stands are consecutively, 67 year old pine (with a small proportion of spruce), 28 year old pine and 38 year old spruce. Height scales are in metres. (Undergrowth is represented here but was not incorporated into the modelling).

Modeling Wetland Vegetation Using Polarimetric SAR

K. Clint Slatton(*), Melba M. Crawford(*), James C. Gibeaut(**), Roberto Gutierrez(**)
(*): Center for Space Research, University of Texas at Austin
2901 N. IH-35, suite 300, Austin, TX 78722
(**): Bureau of Economic Geology, University of Texas at Austin
E-mail: slatton@csr.utexas.edu Ph: (512) 471-5506 Fax: (512) 471-3570

Abstract -- Airborne polarimetric Synthetic Aperture Radar (SAR) data are investigated for their potential in mapping herbaceous coastal wetlands. The subenvironments of coastal wetlands have very distinct vegetation cover and surface properties. Qualitative analysis of the SAR images reveals the relative importance of surface and vegetation scatter in these subenvironments. Furthermore, sampled SAR data distinctly separate the subenvironments, indicating that classification techniques could be used to discriminate among them. Although wetland environments are typically too vegetated to use empirical surface models to explain the SAR return, discrete scatterer models can be used to account for the scattering due to the vegetation. A discrete scatterer model fitted to a coastal wetland site on Bolivar Peninsula near Galveston, Texas provides insight into the dominant scattering mechanisms, and may aid in the accurate mapping of coastal wetlands.

INTRODUCTION

Modeling the scatter of microwave radiation by natural surfaces and vegetation is important for assessing the ability of radar remote sensing to accurately map terrain and land cover. Coastal wetlands comprise a critical ecosystem for specialized vegetation and wildlife habitats, as well as for the natural production of methane. The Synthetic Aperture Radar (SAR) backscatter coefficient (σ^0) is a complex function of local characteristics including topography, geological composition, soil moisture and salinity, and vegetation density and structure. Modeling the scatter from the vegetation is important for classifying land cover, monitoring change in dynamic environments, and discriminating among mechanisms of the backscattered return. The focus of this work is the analysis and modeling of the SAR return from coastal wetland vegetation. Both fully polarimetric SAR data in C, L, and P bands and fixed-baseline interferometric SAR (TOPSAR) data were acquired by the NASA/JPL AIRSAR system in April 1995. The data were acquired in support of a project to detect topographic change and relict geomorphic features on barrier islands for NASA's Topography and Surface Change Program. Imagery over a salt marsh is being used for a preliminary study of the effects of vegetation on the SAR return.

Interest in SAR response to wetland environments has increased in recent years. Ormsby and Blanchard [1] studied the effect of inundation on σ^0. Pope et al. [2] developed wavelength and polarization dependent indices of σ^0 which represent scattering mechanisms such as attenuation due to vegetation and depolarization due to vegetation multiple scattering. Such indices can be used as qualitative measures of the effect of vegetation cover on the total σ^0 return.

Understanding the scatter due to vegetation also helps relate the σ^0 return to surface properties such as soil moisture. Knowledge of the soil moisture distribution can then be used as an input for hydrological models. SAR's value in retrieving soil moisture estimates from barren and sparsely vegetated areas has been shown by Dubois et al., [3] and others. Typically, surface models that relate σ^0 to soil moisture are empirically derived for specific data sets. These models have difficulty separating the return due to soil moisture from the scatter due to surface roughness and vegetation multiple scatter. If the scattering due to vegetation could be well characterized, its effects might be accounted for, allowing for the estimation of soil moisture over vegetated areas.

Models that represent vegetation as a layer of discrete scattering elements have been developed to characterize the scatter due to vegetation. Most of this research has focused on forested areas, but some work has been done for herbaceous vegetation. Saatchi et al. [4] developed a model for grass canopies, and Durden et al. [5] modeled scatter from inundated rice fields. The model developed by Lang and Sidhu [6] was used to study the SAR return from a coastal wetland test site. Before such a model is fit to the data, the σ^0 values are often plotted versus incidence angle. These plots can be used to fit the model to the data, and to determine how well SAR is able to separate different environments. In this study, a variety of methods were used to study the SAR response to coastal wetlands, including visual interpretation, empirical surface modeling, and discrete scatterer modeling. Some preliminary observations from each method are discussed.

SITE DESCRIPTION

The test site is located on Bolivar Peninsula, Texas, shown in Fig. 1, and consists of an herbaceous salt marsh, vegetated upland flats, and an intermediate transition zone, shown in Fig. 2. The SAR scene contains a typical transition from a salt marsh to vegetated upland flats. This transition involves four subenvironments: a low salt marsh with barren tidal flats that is flooded often; a low salt marsh with nearly continuous vegetation cover that is less frequently flooded; a transition zone with occasional seawater

This work was supported by the National Aeronautics and Space Administration, under the Topography and Surface Change Program (Grant NAG5-2954).

0-7803-3068-4/96$5.00©1996 IEEE

flooding; and the vegetated upland flats. The entire peninsula is extremely low relief (<4 m), so even small changes in elevation can produce significant changes in the soil moisture and salinity. The peninsula is a sandy barrier spit formed during the last 4,000 years, primarily through spit accretion, and modified by washover and tidal inlet processes.

Because the uplands are higher in elevation and contain sandy soils, they are well drained and non-saline. The tidal-flat low marsh contains muddy (silt + clay) soils with high concentrations of organic material. It is flooded almost daily with seawater. The continuous-cover low marsh soils are similar to those found in the tidal-flat low marsh, but contain less organic material. The transition zone corresponds to the mean high water mark. Because of evaporation between seawater inundations, this area is extremely saline.

These variations in ground conditions give rise to variations in the vegetation cover. In the tidal-flat low marsh, tall grasses grow to heights of 2 m [7]. These grasses often occur in small groups intermixed with the barren tidal flats. The continuous-cover low marsh also contains tall grasses (< 1.5 m), but the plants are more consolidated creating a more uniform cover. Due to the high saline concentration in the transition zone, that area contains many barren salt flats, and supports mainly small succulent plants. The uplands have a drier, rougher surface, and support short (< 0.5 m) range grasses.

The variations in vegetation , soil type, soil moisture, and soil salinity all involve variations in electrical and geometric properties to which SAR is sensitive. It was therefore expected that SAR would be useful for mapping herbaceous wetlands.

ANALYSIS

Initial analysis of the SAR images consisted of visual interpretation. C-band showed subtle variations in vegetation, but was so strongly scattered by all vegetation that the subenvironments were not well delineated. The longer wavelength L- and P-band separated the four subenvironments very well.

Because of the extremely low relief, local slope changes were assumed to be unimportant in the σ^o return. Several σ^o indices were examined to qualitatively determine the relative importance of surface scatter and vegetation multiple scatter in the four subenvironments. The "canopy structure index" (csi) [2] was used as a measure of the vertical co-polarized return relative to the sum of the vertical and horizontal co-polarized returns. The csi reveals variations in the predominant orientation of vegetation structure. Because attenuation of σ^o_{vv} can be much greater than attenuation of σ^o_{hh} at P-band [8], the csi was also expected to reveal attenuation due to vegetation. As expected, the P-band csi image showed that most attenuation occurred in the dense vegetation of the continuous-cover low marsh. The tidal-flat low marsh produced less attenuation due to the lack of continuous vegetation cover. The transition zone showed the least attenuation.

A "volume scattering index" (vsi) was adapted from [2] and used as a measure of the depolarization relative to the sum of the co-polarized and cross-polarized returns. At L-band, the uplands exhibited the most volume scattering, while the continuous-cover low marsh exhibited the most volume scattering at P-band. It was therefore concluded that P-band was achieving some penetration of the upland vegetation. From the qualitative analysis of these indices, it appeared that there were scattering contributions from both the surface and vegetation in the uplands, the return from the transition zone was almost entirely due to surface scatter, the continuous-cover low marsh returns were mostly due to strong vegetation scatter, and the weaker returns from the tidal-flat low marsh were due to specular reflection off of the water surface.

In an effort to retrieve soil moisture estimates, empirical surface models were studied. Before any of these models could be applied, it was necessary to assess how the presence of the vegetation cover would affect the soil moisture estimates. The criterion developed in [3] was used to determine whether the vegetation cover over the test site was thick enough to reduce the accuracy of such models. That criterion consisted of the ratio $\sigma^o_{hv} / \sigma^o_{vv}$ at L-band. If this ratio is greater than -11 dB, the model is not recommended for estimating soil moisture. This criterion was exceeded over most of the Bolivar SAR image. Empirical surface models were therefore abandoned in favor of discrete scattering models.

In addition to the techniques mentioned above, σ^o data were sampled from the four subenvironments and plotted versus radar incidence angle. Fig. 3 shows one such plot for L-band. These plots clearly demonstrated polarimetric SAR's ability to separate the subenvironments and its potential for herbaceous wetland mapping. Strong σ^o_{hh}, due mostly to vegetation multiple scatter at L-band, occurs in the uplands. A marked decrease in σ^o_{hh} over the transition zone is due to that region's lack of vegetation and extremely smooth surface. The continuous-cover low marsh possesses strong σ^o_{hh} due to vegetation scatter. The decrease in σ^o_{hh} over the tidal-flat low marsh is due to specular reflection off of the water surface and is evidence of inundation. Using all available bands and polarizations should provide ample discriminators for the classification of these subenvironments.

The discrete scatterer model developed by Lang and Sidhu [6] was fitted to these data to gain insight into the scattering mechanisms in each subenvironment. The model represents the vegetation cover as a layer of discrete scattering elements over a flat half space. The lower half space was assumed to be saline water for the inundated tidal-flat low marsh [5], and soil for the other subenvironments. A soil dielectric mixing model adapted from [9] was used to compute the soil dielectric constant. The total σ^o is computed as the sum of the σ^o due to (i) direct scatter from the vegetation, (ii) scatter from a single-reflection ground/vegetation interaction, and (iii) scatter from a double-reflection ground/vegetation interaction. Preliminary attempts to fit the scattering model to the data have been

successful, but are difficult to interpret because there are insufficient ground data to properly constrain the model. Additional ground truth will be collected so that the model may be quantitatively applied to the data.

SUMMARY AND FUTURE WORK

It is clear that polarimetric multiband SAR has potential for mapping the major subenvironments associated with coastal herbaceous wetlands. A discrete scatterer model can be fitted to the data to gain insight into the scattering mechanisms that occur.

Additional ground data, such as soil and plant dielectric constants, will be collected to constrain the scattering model. Also, the effects of direct surface scattering will be included in the model to account for sparsely vegetated areas.

REFERENCES

[1] Ormsby, J. P., and B. J. Blanchard, "Detection of Lowland Flooding Using Active Microwave Systems," Photogrammetric Engr. and Remote Sensing, vol. 51, no. 3, pp. 317-328, 1985.

[2] Pope, K. O., J. M. Reybenayas, and J. F. Paris, "Radar Remote Sensing of Forest and Wetland Ecosystems in the Central American Tropics," Remote Sensing Environ., vol. 48, pp. 205-219, 1994.

[3] Dubois, P. C., J. J. van Zyl, and T. Engman, "Measuring Soil Moisture with Imaging Radars," IEEE Trans. Geosci. Remote Sensing, vol. 33, no. 4, pp. 915-926, 1995.

[4] Saatchi, S. S., D. M. Le Vine, R. H. Lang, "Microwave Backscattering and Emission Model for Grass Canopies," IEEE Trans. Geosci. Remote Sensing, vol. 32, no. 1, pp. 177-186, 1994.

[5] Durden, S. L., L. A. Morrissey, and G. P. Livingston, "Microwave Backscatter and Attenuation Dependence on Leaf Area Index for Flooded Rice Fields," IEEE Trans. Geosci. Remote Sensing, vol. 33, no. 3, pp. 807-810, 1995.

[6] Lang, R. H. and J. S. Sidhu, "Electromagnetic Backscattering From a Layer of Vegetation: A Discrete Approach," IEEE Trans. Geosci. Remote Sensing, vol. GE-21, no. 1, pp. 62-71, 1983.

[7] Webb, J. W., Typical Dune Vegetation of the Upper Texas Coast, non-published Texas A&M at Galveston document, pp. iii, 3.

[8] Le Vine, D. M., and M. A. Karam, "Dependence of Attenuation in a Vegetation Canopy on Frequency and Plant Water Content," in Proc. IGARSS'95, vol. I, pp. 607-609, 1995.

[9] Ulaby, F. T., A. K. Moore, A. K. Fung, Microwave Remote Sensing, Active and Passive, vol. 3, Artech House, pp. 2086-2103, 1986.

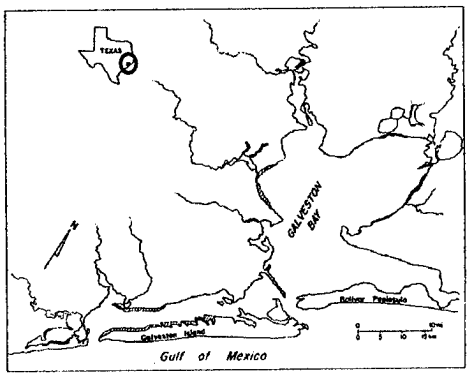


Fig. 1: Study area.

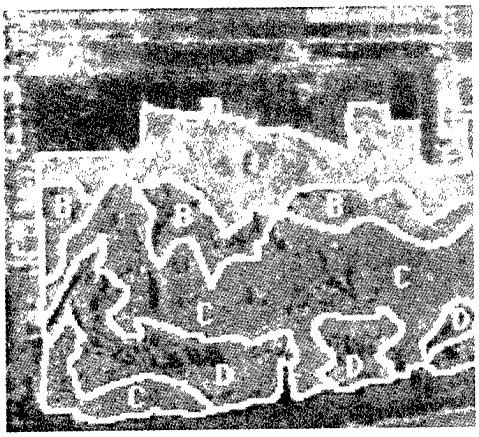


Fig. 2: L-band image of test site with subenvironments labeled as (A) vegetated upland flats, (B) transition zone, (C) continuous-cover low marsh, and (D) tidal-flat low marsh.

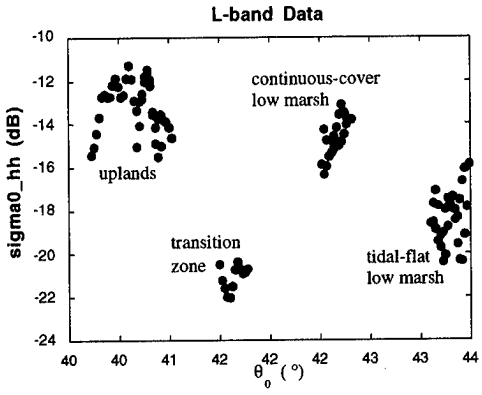


Fig. 3: L-band σ^0_{hh} values versus incidence angle for the four subenvironments.

Rain Pattern Detection by means of Packet Wavelets

Andrea Marazzi(*), Paolo Gamba(*) and Roberto Ranzi(†)
(*)Dipartimento di Elettronica, Università di Pavia, Via Ferrata, 1, I-27100 Pavia
Tel: +39-382-505923 Fax: +39-382-422583 E-mail:maraz@comel1.unipv.it
(†)Dipartimento di Ingegneria Civile, Università di Brescia, Via Branze, 38, I-25123, Brescia

Abstract – The recent advances in microwave telecommunications and the need for more precise weather forecasting systems are two of the many fields where is extremely important to be able to analyze quickly, precisely and, possibly, in a fully or partially automatic way, the data obtained by systems like metereological radars. In this work it is presented a wavelet packet based algorithm, combined with a C-means classifier, for rain patterns detection and tracking from this data. The use of this kind of classification chain is motivated by the high efficiency and low computational load of the wavelet transform algorithm and by the observation that a large class of natural textures can be modeled as quasi-periodic signal, whose dominant frequencies are located in the middle frequency channels, easily provided by this transform.

The chain was applied to a radar data sequence of a rain event on Northern Italy, interesting interpretation of the dynamics of storm structures at different meso-scales.

1. INTRODUCTION

Communication systems working in the microwave frequency domain above 10 GHz are now widely spread, and there is therefore an increasing need for very detailed investigations on the propagation characteristics of the atmosphere [1]. In particular, great interest is shown for the information on the spatial and temporal organization of precipitation patterns.

A very useful method to obtain these information is by means of weather-radars, that supply an estimation of the rain intensity for sufficiently wide geographic regions to consider large scale rain structures, but with a fine space resolution [2]-[3]. These data allow the study, within a coarse-to-fine strategy, of the spatial structure of precipitation. However, the raw records of radar reflectivities need a complex processing procedure to provide to the final user the information on the spatial/temporal characteristics of rain events. To achieve this goal, a system able to track the spatial evolution of rain patterns has to be determined, and this system must be able to tackle a number of problems. The tracking process is not, in fact, an easy task, even if performed by a human observer in real time: the temporal evolution of the rain events results from complex processes, organized at different space-time scales. Each scale, ranging from the synoptic external scale of frontal systems to the meso-gamma scale of convective cells, displays its own dynamic, which is sometimes coupled with the others, sometimes not. Thus the patterns to be tracked change continuously their shape while moving [5].

We propose a chain based on a wavelet representation of the rain data, on which a classification is performed in order to extract the textured rain patterns at different scales. A single image, representing the rain intensity in the environment around the radar, is preprocessed by a wavelet packet algorithm and divided in subimages, different representations of the same scene: the use of this transform is motivated by the observation that a large class of natural textures can be modeled as quasi-periodic signal, whose dominant frequencies are located in the middle frequency channels. The subband images are then processed by an envelope signal estimationto provide a method for features extraction: different textures have different "energy" in the detail subband related to the magnitude of oscillation of wavelet coefficients in each subband. The image can be finally seen as a multiband representation of the same scene and thus resolved as a multidimensional data clustering problem, and a C-means algorithm is applied to the image to achieve an efficient segmentation of the different rain patterns.

2. THE PACKET WAVELET TRANSFORM

The general structure and computational framework of the discrete wavelet transform (DWT) are similar to those found in subband coding system, but wavelet filters are required to be regular. In this study, we consider the discrete wavelet packet transform (DWPT), which corresponds to a general tree-structured filter bank.

Wavelet transforms are entirely specified in terms of a prototype filter h that satisfies the standard quadrature mirror filter condition:

$$H(z)H(z-1) + H(z)H(-z-1) = 1 \qquad (1)$$

where $H(z)$ denotes the z-transform of h. The filter h is also required to satisfy the lowpass constraint: $H(z)|_{z=1} = 1$. A complementary high pass filter is obtained by shift

0-7803-3068-4/96$5.00©1996 IEEE

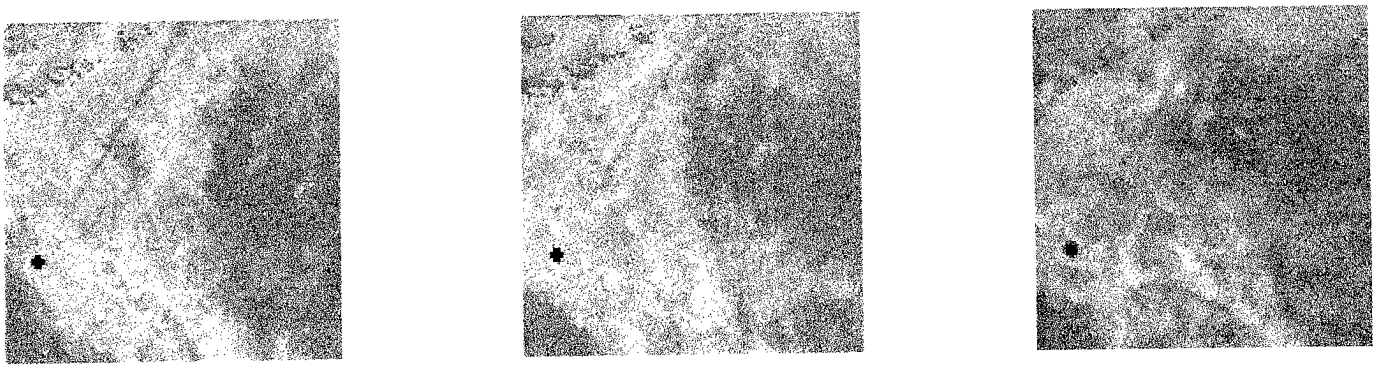


Figure 1: Three frames from the recorded radar data of a rain event in Northern Italy.



Figure 2: The two different meso-scale rain patterns detected from the images of fig. 1.

and modulation:

$$G(z) = zH(-z-1) \tag{2}$$

These prototypes are then used to generate, in an iterative fashion (initial condition $H_0(z) = 1$), a sequence of filters of increasing width (indexed by i):

$$\begin{aligned} H_{i+1}(z) &= H(z^{2i})H_i(z) \\ G_{i+1}(z) &= G(z^{2i})H_i(z) \quad (i = 0, \ldots, I-1) \end{aligned} \tag{3}$$

The pyramidal structure of the DWF decomposes a signal into a set of different frequency channels that have narrower bandwidths in the lower frequency region. The application of a simple DWF to a texture is completely useful for segmentation because a large class of natural textures can be modeled as quasi-periodic signal, whose dominant frequencies are located in the middle frequencies channels. Therefore, the concept of DWF must be generalized using a library of modulated waveform orthonormal basis called wavelet packets. The filtering is recursively applied to both the low frequency and high frequency components creating a binary tree. The 2-D wavelet can be seen by a tensor product of two 1-D wavelet basis function along the horizontal and vertical directions. the corresponding coefficients can be expressed as

$$h_{LL}(k,l) = h(k)h(l) \quad h_{LH}(k,l) = h(k)g(l)$$

$$h_{HL}(k,l) = g(k)h(l) \quad h_{HH}(k,l) = g(k)g(l) \tag{4}$$

where the first and second subscript denote the lowpass and highpass filtering in the x- and y- directions.

3. THE WAVELET CLASSIFICATION CHAIN

Exploiting the concept shown in the preceding section, a wavelet classification chain has been implemented, followed by a standard procedure able to measure, according to different methods, the velocities of the different rain patterns. The aim is to extract automatically how different rain patterns evolve during the recorded rain event. This wavelet-based method can be summarized in the following steps (for a more detailed description, refer to [7]):

1. First of all, a 2-D Battle-Lemarie packet wavelet transform is applied to each original radar image. By means of this operation, the components of the rain patterns at the different spatial and frequency scales are subdivided. This result allows to discard information related to high spatial frequencies, that individuate very short-term phenomena of little or no interest for our investigation. In particular, we discard all the data about very little rain cells, usually with life too short to be trackable within the frame

temporal frequency (an image each 15 min.) of our radar data.

2. Each of the chosen packet wavelet subimages is modified by an envelope estimation algorithm (EEA). It can be used a simple zero-crossing algorithm, where the maximum value between two adjacent zero-crossings is found and assigned to all points within the interval. The EEA is applied row-wise or column-wise depending to the wavelet-bank filter that originated each subimage.

3. The gray value of the subimages is normalized. This is done because the variance of the gray level can vary a lot from subimage to subimage. Remember that the result of the wavelet transform are coefficient and not gray level value, so they can have a range quite different from the usual 8-bit image coding.

4. The subimages can be considered as a multiband image of the same region and a clustering algorithm (the classical C-means or the more recent Fuzzy-C-means [6]) is applied to the wavelet coefficients obtained in the preceding steps.

The output of such a classification algorithm are, for each frame, the rain patterns associated to different values of the "energy" represented by the wavelet coefficients. The intensity of the rainfall field is derived from the reflectivity of a C-band Doppler Radar operating at the 5.5 cm wavelength. Reflectivity was converted into rainfall rate using the Marshall-Palmer formula, which was verified to be accurate in the event investigated. In fig. 1 three frames of a radar sequence are shown, that refer to the rain event that occurred on 4 October 1992 and that was examined in this study. It represents an episode of cyclogenesis in the lee of the Alps, whose occurrence is rather frequent in the Gulf of Genova. A deep and stationary low developed for more than five days, reaching a minimum of 989 hPa at 6.00 GMT of 4 October 1992. The convergence over the Italian Peninsula of southerly winds, carrying warm and moist air, with cold and dry air masses flowing over the Rodano Valley, in France, caused persistent precipitation over the Po Valley. Vertical soundings recorded over the meteorological stations of Milano Linate, Udine and S. Pietro Capofiume, close to Bologna, showed that warm advection occurred in the lower levels. The vertical wind profile recorded at S. Pietro Capofiume at 11.00 GMT of 4 October reveals the 0°C isotherms to be located at the 720 hPa level, at a height of about 2700 m a.s.l., where a bright band is detected by the radar. Several rainbands were observed in the structure of the cyclone, during its occluded stage of development. A large scale synoptic motion was detected from the geostationary METEOSAT satellite pictures and from the movement of the 0-isoallobaric contour line. A small scale motion of cell clusters was recognized to be consistent with the 700 hPa wind speed vector, which is directed toward N-NW, a different direction respect to the large-scale one. This de-coupled dynamic was recognized in the field after its wavelet decomposition into the small- and large-scale structures (see also [8]).

In fact, after classification, further operations are performed on the data to extract information on the behaviours of the rain patterns at the different meso-scales. In particular, since we are interested in their movement and life, a first operation is to detect their velocities by lag-correlation or by means of an advettive model with a single velocity or with more components. The velocities of the two patterns along the sequence of fig. 2 are obtained as de-coupled, as can be easily verified in the frames.

REFERENCES

[1] CCIR: "Radiometereological Data", Doc. 5/5049-E, Ref. 5/423.

[2] A. Pawlina, "Rain patterns motion over a region deduced from radar measurement," *Alta Frequenza*, Vol. LV (2), pp. 99-103, 1987.

[3] A. Pawlina, "Radar rain patterns: automatic extraction, collection and description for modeling purposes," *Alta Frequenza*, Vol. LVI (1-2), pp. 153-159, 1987.

[4] P.V. Hobbs, "Organization and structure of clouds and precipitation on the mesoscale and microscale in cyclonic storms," *Rev. of Geophysics and Space Physics*, Vol. 16 (4), pp. 741-755, 1978.

[5] P. Kumar and E. Foufoula-Georgiou, "Fourier domain shape analysis methods: a brief overview and an illustrative application to rainfall area evolution," *Water Resour. Res.*, Vol. 26 (9), pp. 2219-2227, 1990.

[6] I. Gitman and M.D. Levine, "A fuzzy relative of the ISODATA process and its use in detecting compact well-separated clusters", *Journ. Cybernetics*, 1973.

[7] A. Marazzi, A. Mecocci, P. Gamba, M. Barni, "Texture segmentation in remote sensing images by means of packet wavelets and fuzzy clustering," *European Symposium on Satellite Remote Sensing II*, Paris, 25-29 Sept. 1995.

[8] R. Ranzi, "The wavelet transform as a new technique for analysing spatial scales in rainfall fieldsg," *Proc. Int. Conference on "Atmospheric Physics and Dynamics in the Analysis and Prognosis of Precipitation Fields"*, Rome, 15-18 November pp. 211-214, 1994.

The Development of the SeaWinds Scatterometer Electronics Subsystem (SES)

B.D. BOLLER, R.D. CROWLEY, M. C. SMITH, R.S. ROEDER
E-Systems, Inc., ECI Division, P.O. Box 12448, Mail Stop 56, St. Petersburg, FL, USA 33733-2248
wdba@qmgate.eci-esys.com,rdca@qmgate.eci-esys.com,mcsb@qmgate.eci-esys.com,rsra@qmgate.eci-esys.com

Abstract - SeaWinds is a new spaceborne Ku-band scatterometer designed to accurately measure the amplitude backscatter return from the ocean and process the data to obtain global ocean surface wind vectors. The scatterometer is a pulsed 13.402 GHz dual polarization radar with a conical scan, pencil beam antenna. This paper provides a brief overview of the instrument and describes the major microwave and digital modules in the Scatterometer Electronics Subsystem (SES). The SES generates precise frequencies that drive the transmitter and synchronize the receiver. The received ocean backscatter signals are processed and measured to a precision of 0.15 dB in order to derive accurate wind vector data.

INTRODUCTION

SeaWinds is a next generation spaceborne Ku-band radar (scatterometer) designed to accurately measure wind vectors over the earth's global oceans. The instrument will provide long-term data measured through all weather conditions for studies of ocean circulation, air-sea interaction and weather forecasting. E-Systems under contract to NASA/JPL is developing the SeaWinds Scatterometer Electronics Subsystem (SES) which is the heart of a new radar approach. The radar along with other instruments will fly on the Japanese Advanced Earth Observing Satellite (ADEOS-II) illustrated in figure 1. The SeaWinds program is a continuing cooperative effort between the U.S. and Japan to monitor and evaluate global ocean changes.

SYSTEM CHARACTERISTICS

SeaWinds will orbit the earth at an altitude of 800 Km and scan a continuous swath width of 1800 Km. Over 90% of the global oceans will be measured every 2 days. The scatterometer precisely measures the pulse-by-pulse backscatter return from the oceans and telemeters the data to ground stations. The processed wind speed will be accurate to 2 m/sec over a range of 3 to 30 m/sec and wind direction will be accurate to 20° over 360°.

A comparison of SeaWinds vs. preceding satellite scatterometers is shown in figure 2. Various designs have been used, but all preceding systems have required large fan beam antennas. The SeaWinds scanning pencil-beam approach provides many advantages over the previous systems including; higher radar backscatter measurement accuracy, continuous wider swath ocean coverage without "nadir gaps", and fixed incidence angle measurement with reduced size.

0-7803-3068-4/96$5.00©1996 IEEE

SCATTEROMETER DESIGN

SeaWinds has three major subassemblies as shown in the system block diagram in figure 3, the SeaWinds Antenna Subsystem (SAS), the Electronics Subsystem (SES), and the Command and Data Subsystem (CDS). The conical scan pattern is illustrated in figure 4. The SAS is a 1 meter parabolic antenna that scans at 18 rpm providing multiple azimuth angle looks at the ocean. Dual offset feeds provide measurement with vertical polarization at a 46° elevation angle and horizontal polarization at a 40° elevation angle.

Figure 5 is a block diagram of the SES. The scatterometer controller/processor (SCP) provides multiple functions consisting of; communication with the CDS, processing of operating commands, timing and control of the SES, A/D conversion, power measurement of the backscatter signal, and collection of engineering telemetry that describes the operating state and health of the SES. A synthesizer/exciter with integral STALO generates precise frequencies for the RF drive to a Traveling Wave Tube Amplifier (TWTA), the local oscillator signals for the receiver and all other synchronization signals. The T/R module, besides being a T/R circulator, contains RF switches for redundant TWTA and receiver selection, antenna beam selection, receiver protection and in-flight loop-back scatterometer calibration. The receiver section downconverts the RF echo through two downconverters and provides baseband I and Q signals to the SCP. The SCP then provides a precise power measurement of the backscatter signal.

Figure 6 shows the packaging of the SES as it will be mounted on the ADEOS satellite. The electronics are fully redundant except for the T/R module. Louvers are mounted on the SES to provide proper thermal control throughout the orbit.

The characteristics of the scatterometer are given in figure 7. The system operates at 13.402 GHz with a nominal peak power of 110 watts. The pulse width, PRI and receive gate timing are commandable from the ground over a wide range of steps. Variations on selection of the pulse width, PRI and receive gate timing accommodate changes in slant range over the satellite orbit. Doppler corrections of ±600 kHz are made through commands to the transmitter tuning. These are required as a function of the antenna azimuth scan angle.

The receiver accepts a wide dynamic range of backscatter power level and provides quadrature I & Q signals to the SCP. The SCP processes the backscatter signal and receiver noise signals and provides a measurement of the received echo to a precision of 0.15 dB.

SES MODULE DESIGN

The Transmit Receive Switch (TRS) is a design based on previous proven flight hardware. Brazed aluminum waveguide construction is used to minimize weight and ferrite latching switch assemblies are used for both isolation, beam select and redundancy switching. The TRS contains preselect and harmonic filters. The TRS integrates the direct measurement of PtGr using the loopback technique. Loopback is achieved through a high attenuation coupler which incorporates two 50 dB precision cross-guide couplers connected with a short piece of waveguide. Thermistor monitoring of calibration path couplers, receive protect switches and beam select switch are provided to enhance calibration accuracy.

Three RF modules the Receiver, Synthesizer and Exciter provide dual-redundant electronics, with only one side being powered on at a time. All modules are post regulated, possess post EMI filtering and all microwave/RF assemblies are in sealed enclosures to minimize EMI leakage/radiation. Direct access ports are provided throughout the SES to provide diagnostics to the Support Equipment (SE) suite. The majority of microwave design realization techniques are microstrip on 0.025" thick alumina substrates with thin film resistors(TaN) resistors. The alumina is then reflowed soldered on gold plated kovar carriers. All microwave filters are integral to each assembly using a proprietary technique that enhances combline filter performance. Miniature blind mate connectors and multilayer boards are also used to reduce packaging density. These packaging techniques are indicative of typical spaceborne hardware built by E-Systems with a typical microwave assembly shown in figure 9.

The receiver provides low-noise amplification, bandpass filtering and double downconversion, and gain adjustment. The backscatter signal is downconverted to baseband, i.e. "video" band, centered about an intermediate frequency(IF) of 0 Hz. The resultant noise like signal spectrum is presented in two output channels, in-phase (I) and quadrature (Q) for processing. The receiver operates in two states wind observation mode and calibrate mode. In calibrate mode, receive gain is reduced to handle strong signals coupled in from the transmitter. All stages are >18 dB below the 1 dB compression point during wind observation mode.

The synthesizer module in figure 10, accepts a phased locked 775 MHz LO from the exciter that facilitates conversion to clock a Direct Digital Synthesizer for transmit IF signal spreading modulation, on-off keying, and Doppler compensation tuning. It also provides the transmitter and receiver local (2nd LO) synthesis.

The Exciter module provides the necessary 13.402 GHz output to the TWTAs, which are shown in figure 11, through one hybrid cross-strap network that monitors drive power. Other functions include phase coherent reference frequency synthesis, stable local oscillator (STALO) reference frequency generation, transmit intermediate-frequency (IF) signal upconversion/filtering and amplification and RF drive disabling during the receive portion of the transmit pulse repetition interval.

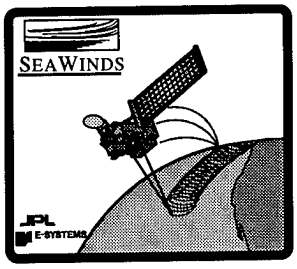
The I and Q outputs from the Receiver are processed by the Detector card, which is part of the SCP, shown in figure 12, . The Detector card provides analog anti-alias filtering and buffering before the signal is sampled. Samples are taken over a variable receive gate time. The samples in each channel are then processed by a narrow band (40 KHz) Echo filter and a wide band (500 KHz) Noise filter. The Echo filter is implemented as a two-stage decimated finite impulse response (FIR) filter. The first 8-tap filter stage has a bandwidth (BW) of 400 KHz, with the output decimated by four. The second 30-tap filter stage has a bandwidth of 40 KHz, with the output decimated by two. The Noise filter is implemented as a 5-tap filter. The I and Q outputs of each filter are squared and accumulated over the receive gate interval. The accumulated energy value is converted into a pseudo-floating point number to reduce telemetry bandwidth and sent to the Processor card in the SCP for insertion into the return science data stream sent to the CDS each PRF.

The Processor card in the SCP module performs the interfacing and timing functions for the SES. The SES does not transmit, receive, or process telemetry data unless it is commanded to so by the CDS. There is a serial bi-directional interface between the CDS and SES that is implemented on the Processor card. The Processor card receives the stable local oscillator (STALO), and uses divided versions of this signal to provide all the timing for the SES, including transmit and receive RADAR timing. Much of the telemetry generated by the SES is input to the Processor card, where analog and temperature signals are digitized, and combined with digital telemetry. The CDS can request a subset of the telemetry every PRI via the serial interface.

Prior to spacecraft launch, the SES will be put through extensive automatic test and precise calibration with the SE shown in figure 12 To meet the wind vector accuracies discussed earlier, the SE will measure the SES total worst case absolute PtGr error to <0.53 dB with total worst case repeatability to <0.085 dB.

SUMMARY

SeaWinds is a new instrument being developed to obtain continuous global wind vector measurements starting in 1999. An SES Engineering Model and the first set of SE have been delivered to JPL. The SES flight hardware and the second set of SE will be complete this year. The equipment is being designed to provide continuous mission operation for 3 years. SeaWinds will provide crucial ocean wind velocity measurements as part of the NASA/International Earth Observing System (EOS).



- Instrument on Japanese Advanced Earth Observing Satellite (ADEOS) II
- Provides Calibrated Wind Speed and Direction Over Ocean Areas
- Instrument Consists of Antenna, Command and Data, and Electronic Subsystem
- Electronic Subsystem is Similar to GEOSAT Follow-On Altimeter
- Contributes to NASA's Mission to Planet Earth Program

Figure 1. SeaWinds Scatterometer

	SASS	ERS-1/2	NSCAT	SEAWINDS
LAUNCH DATE	1978	1991,1994	1996	1999
FREQUENCY (GHZ)	14.6	5.3	13.995	13.402
ANTENNA/POLARIZATION	FAN BEAM/V-H	FAN BEAM/V ONLY	FAN BEAM/V-H	PENCIL BEAM/V-H
SPATIAL RESOLUTION	FIXED DOPPLER	RANGE GATE	VARIABLE DOPPLER	PENCIL BEAM
RESOLUTION (KM)	50/100	50	25/50	50
PEAK POWER (WATTS)	110	4800	129 (MAX)	129 (MAX)
SWATH KM	500 400 500	500	600 350 600	1800

Figure 2. Comparison of Past and Current Scatterometers

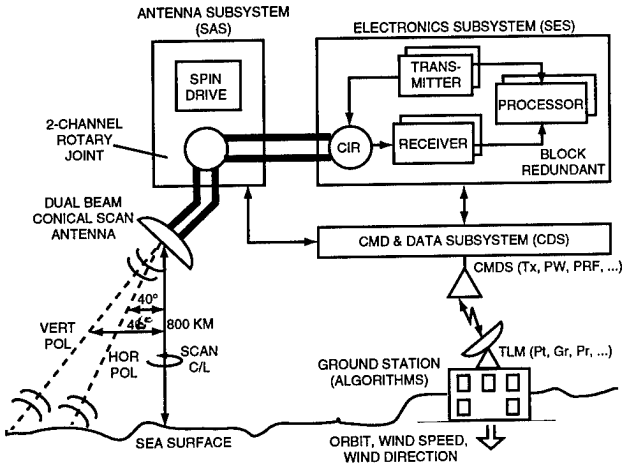


Figure 3. System Block Diagram

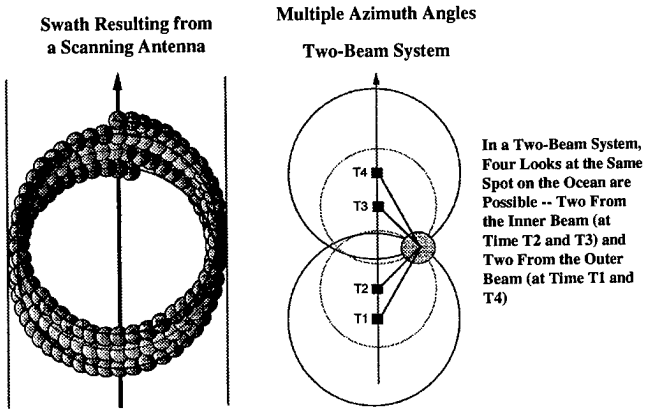


Figure 4. SeaWinds Scan Pattern

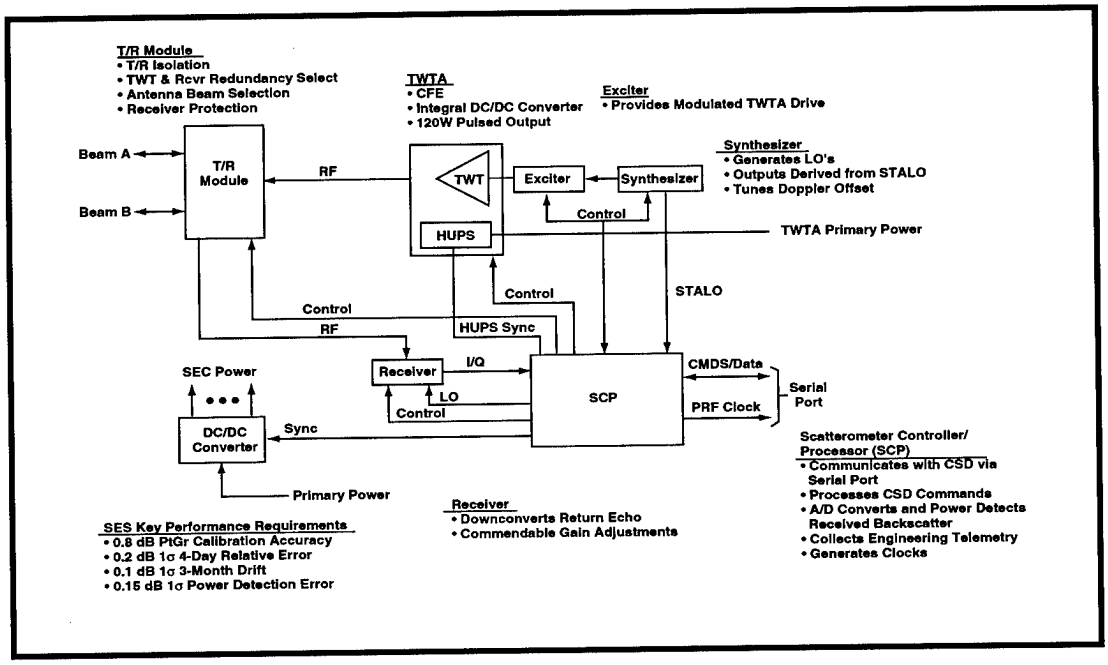


Figure 5. Scatterometer Electronics Subsystem (SES) Block Diagram

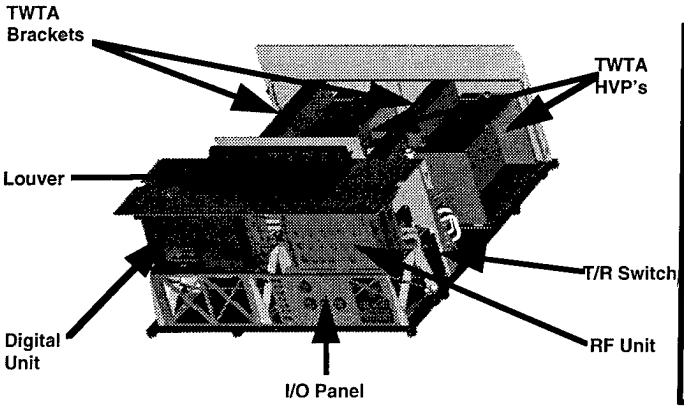


Figure 6. SES Configuration

Transmitter		
• Frequency	–	13.402 GHz ± 0.01 MHz
• Tuning range	–	± 600 kHz in 2 kHz steps
• Transmitter stability	–	10.0×10^{-8} short term
	–	10 ppm over life
• Output power	–	104 watts min (EOL)
• Pulse width (TLM CMD)	–	0.5 to 2.0 msec in 0.05 msec steps
• PRI range (TLM CMD)	–	4.7 to 6.0 msec in 0.1 msec steps
Receiver		
• Receive gate width (TLM CMD)	–	0.0 to 2.6 msec in 0.05 msec steps
• Receive gate delay (TLM CMD)	–	0.0 to 12.75 msec in 0.05 msec steps
• System noise figure	–	4.5 dB
• Power detection error	–	0.15 dB, 1s
• Gain adjustment (TLM CMD)	–	10 dB range, ± 0.1 dB accuracy
• Echo filter BW	–	80 kHz
• Noise filter BW	–	1 MHz

Figure 7. SES Electrical Characteristics

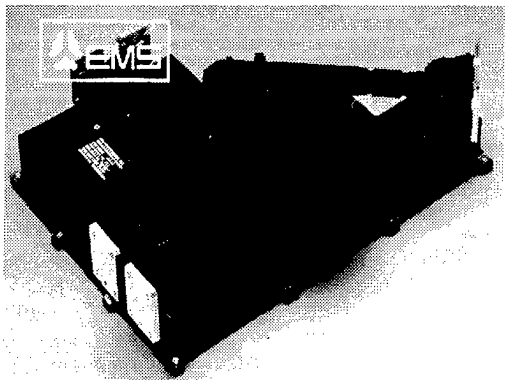


Figure 8. TRS Assembly

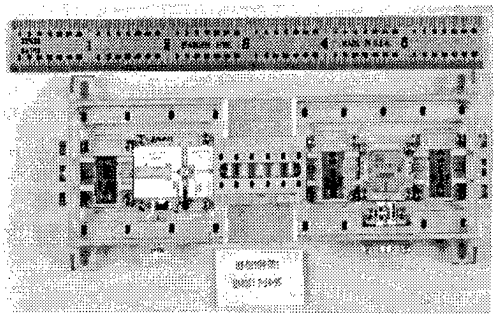


Figure 9. Ku-band Upconverter

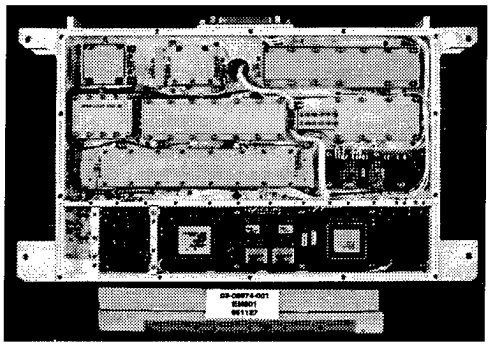


Figure 10. Synthesizer Module

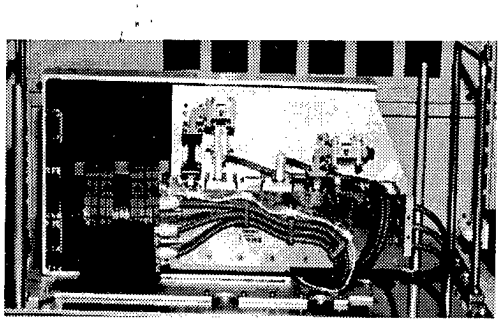


Figure 11. TWTA Assembly

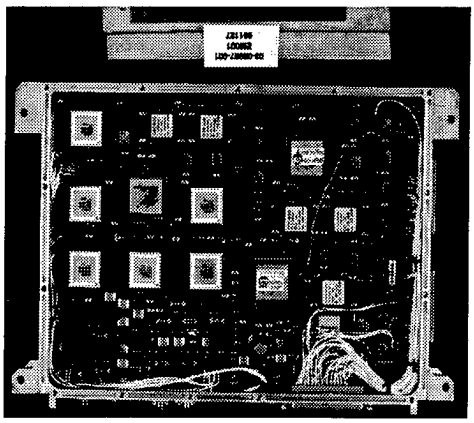


Figure 12. SCP Module

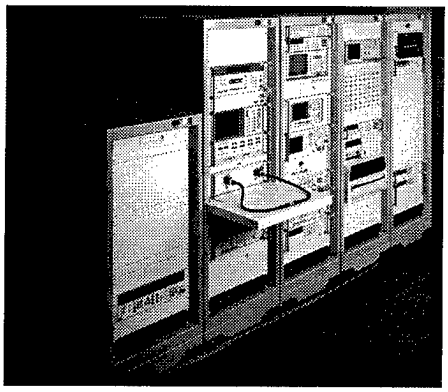


Figure 13. SES Support Equipment

Phase B and breadboard results for the TOPEX POSEIDON FOLLOW-ON mission

L. Rey, N. Suinot, P. Oudart
ALCATEL ESPACE, 26 Avenue J.F. Champollion, 31037 Toulouse Cedex, FRANCE
Telephone (33) 61 19 61 08, Fax (33) 61 19 61 63
G. Carayon
CNES, 18 Avenue Edouard Belin, 31055 Toulouse Cedex, FRANCE
Telephone (33) 61 28 25 68, Fax (33) 61 28 18 15

ABSTRACT

Pursuing the successful TOPEX POSEIDON altimetry mission, activities for the follow-on program are in progress. ALCATEL ESPACE completes the phase B of the next generation altimeter funded by the French Space Agency (CNES). The main evolution with respect to the former POSEIDON-1 rely upon the dual frequency (Ku & C bands) operation, and the doubled processed range depth within the same mass and power budgets. The altimeter design and development resulting from study and breadboarding activities are presented hereafter with regards to the function requirements and also the expected altimeter performances.

1. INTRODUCTION

ALCATEL ESPACE developped the first solid state altimeter (POSEIDON-1) for CNES which was integrated onto the TOPEX-POSEIDON satellite.
The success of the first experimental mission involves now the operational one named: TOPEX-POSEIDON FOLLOW ON (TPFO). The satellite will be composed of the new dual frequency altimeter and its antenna, a three band radiometer and its antenna, and a DORIS localization system, the whole payload borned on a small satellite (500 kg class).
Following the phase A study, lead by ALCATEL ESPACE [1], critical points was pointed out and during phase B study, breadboarding activities have been conducted in order to validate the new concept and design.

2. ALTIMETER MAIN CHARACTERISTICS

The spaceborne radar altimeter is used to measure three oceanographic parameters of scientific interest : the height of ocean surface with centimetric accuracy, the significant wave height (SWH) and the backscattering coefficient (σ_0) from which the wind speed at the sea surface can be derived.
The major part of the TPFO altimeter characteristics are similar to the POSEIDON-1 one as described in table 1. However, significant evolution have been taken into account to improve the parameter estimation accuracy:

- ionospheric effects are compensated by combining measurements at two different frequencies in Ku and C band,
- antenna mispointing estimation is computed on 128 points spectrum compared to 64 points on POSEIDON-1.

Moreover the mass (25 kg) and power consumption (55 W) allocated are still the same. The operational life time has been increased from 3 to 5 years.
The global performance is reached by a link budget requirement of SNR $\geq$ 10 dB with respect to a σ_0 (backscattering coefficient) of 8 dB in Ku band and a σ_0 of 12 B in C-band.

Mission		
Life-time	5 years	
Altitude	1347 km ± 15 km	
Inclination	63°	
General instrument requirements		
PRF	2100 Hz ± 10%	
Pulse duration	105.6 µs	
	Ku-band	C-band
Center frequency	13.575 GHz	5.3 GHz
Bandwidth	320 MHz	320/100 MHz
Peak power	> 5W	> 30 W
Spectrum analyzer	128 points	
Real time integration	50 ms	

Table 1: Mission and instrument characteristics

3. GENERAL INSTRUMENT ARCHITECTURE

The synoptic of the altimeter instrument, without its antenna, is described on figure 2. This architecture is composed of two main subsystems: the processing unit and the RF unit. The operation principle is based upon a wideband chirp generation of about 100 µs duration, the deramp compression, and the digital processor to compute the real time FFT operation and the Maximum Likelihood Estimation (MLE) algorithm [1]. The parameters estimation and the unprocessed waveforms are transmitted to ground on telemetry at low data rate.

0-7803-3068-4/96$5.00©1996 IEEE

The scheme of 6 Ku band pulses and 1 C band pulse, sequentially transmitted at the PRF rhythm, has been chosen in order to achieve the optimum performance in terms of ionosphere distortion estimation with minimum hardware duplication.

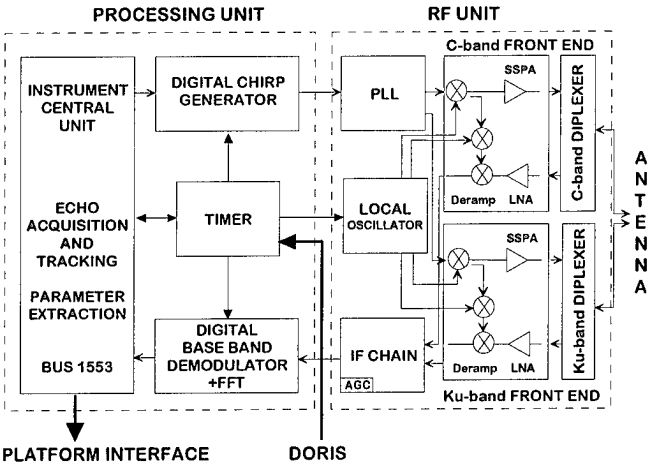


Figure 2: Instrument block diagram

This dual frequency altimeter design implies major modifications from the POSEIDON 1 architecture. The chirp generator has to generate two types of chirp band: 100 or 320 MHz for C-band transmission and 320 MHz for Ku-band. The new C-band front end with an SSPA RF peak power > 30 W has to be added without increasing the power and mass budgets. At the last, the receive chain including the digital baseband demodulator and the spectrum analyzer has to process the 128 points wide Brown echo.

Therefore, three main developments have been realized on the following proposed breadboards:

- digital chirp generation
- Solid State Amplifier (SSPA) in C-band
- digital baseband demodulation and Fast Fourier Transform ASICs design.

4. BREADBOARD RESULTS

Chirp generator

It is composed of a digital part which computes the chirp from memories in a reduced band: 10 MHz. The output signal is converted by a Digital to Analogue Converter (DAC) at a 80 MHz clock rate, to come into the analogue part composed of a phase locked loop enable to multiply the chirp phase by 32. A splitting circuit is used to eliminate the signal distortions and to deliver the appropriate output signal duration.

The current results are described on table 3.

Frequency	900	MHz
Bandwidth	320	MHz
Chirp duration	106	µs
Signal to noise ratio SNR	30	dB
Spurious	35	dBc

Table 3: Chirp generator performances

C-band SSPA

The requirement of such an amplifier was deduced from the signal to noise ratio to reach for the altimeter link budget. An output peak power >30 W is needed at the antenna access without disturbing the transmitted signal and performing low power consumption. The breadboard performances are shown on table 4.

Frequency	5,3	GHz
Peak power	40	W
Gain	20	dB
Amplitude ripple	0,2	dB in 350 MHz
Efficiency	41,1	%
Dimension	52 x 22	mm²

Table 4: C-band SSPA performances

Digital baseband demodulation (DAP) and Fast Fourier Transform ASICs design

The digital baseband demodulator consists of a 7,27 MHz clock digital data rate demodulation in I and Q channels, the filtering and undersampling operations, to obtain the near 1 MHz bandwidth signal. This first part of the process is designed in one ASIC and takes about a Pulse Repetition Interval (PRI) to compute. A second ASIC is needed for the 128 points FFT operation and takes a PRI to process. The performances completed are presented on table 5.

DAP: Filter characteristics		
Bandwidth	1,2	MHz
Rejection band at ± 635 kHz	40	dB
Amplitude ripple	< 0,1	dB peak to peak
DAP + FFT		
Spurious	-38	dBc
Noise level	-50	dBc
Overall computation time	1,3	ms

Table 5: Digital baseband demodulation and Fast Fourier Transform ASICs simulation performances

5. PERFORMANCES

Complementary to the breadboarding activities a performance altimeter simulator has been used. It alloows the breadboard measurements to be immediately analysed and the altimeter range accuracy to be estimated. The results can be given depending on the wave height (SWH), the satellite altitude motion, and the mispointing antenna. Simplified on-board MLE algorithm or full process can be compared. The performances including the main parameters of the phase B study are described on table 6.

Wave height	2 m	4 m	8 m
Altitude	1,5 cm	2,1 cm	3,3 cm
σ_0	< 0,05 dB	< 0,05 dB	< 0,1 dB
SWH	5 cm	8 cm	10 cm

Table 6: Estimation of altimetry parameter accuracy (including ionospheric corrections)

6. INSTRUMENT BUDGET

The link budget of the TPFO instrument presents a 2 dB margin for both Ku and C band signals. The power and mass budget estimated is in agreement with the small satellite mission as discussed on table 7.

SUBSYSTEMS	MASS	POWER
Processing	10 kg	30 W
RF	13 kg	30 W
Harness	2 kg	-
TOTAL	25 kg	60 W

Table 7: Altimeter budget

7. CONCLUSION

Thanks to the present results, we can say that the expected performances can be reached. The breadboard results have confirmed the necessary improvements from the POSEIDON-1 altimeter, in particular the choice of new microwave and new digital processing technologies. The small satellite requirements are achieved and the altimetry estimation performances are compatible with the TPFO objectives.

The overall payload phase B design is successfully completed for the incoming phase C/D.

REFERENCES

[1] C. Mavrocordatos, S. Gouenard, J. Richard, P. Raizonville "A compact Dual-Frequency Altimeter for TOPEX POSEIDON FOLLOW ON mission", Proc IGARSS 94 p 1516, Los Angeles, 1994.

Science Data Collection with Polarimetric SAR

J. Dall, K. Woelders and S. N. Madsen
Danish Center for Remote sensing, Department of Electromagnetic Systems
Technical University of Denmark, B348, DK-2800 Lyngby, Denmark
Phone: +45 4288 1444, Fax: +45 4593 1634, e-mail: jd@emi.dtu.dk

Abstract -- This paper discusses examples on the use of polarimetric SAR in a number of Earth science studies. The studies are presently being conducted by the Danish Center for Remote Sensing†. A few studies of the European Space Agency's EMAC programme are also discussed. The Earth science objectives are presented, and the potential of polarimetric SAR is discussed and illustrated with data collected by the Danish airborne EMISAR†† system during a number of experiments in 1994 and 1995. The presentation will include samples of data acquired for the different studies.

1. INTRODUCTION

SAR has been considered a promising technology for numerous applications for close to 20 years. The advent of new and/or better sensors, both airborne and space borne, has improved the feasibility of performing qualitative studies on the usefulness of SAR with respect to operational applications and scientific studies. The strategy applied for these studies is to focus on few applications but mapping test areas multiple times to better understand temporal and environmental variations.

The Danish Center for Remote Sensing (DCRS) uses data from multiple sensors, but the principal sensor is EMISAR [1], which has been developed by the Department of Electromagnetic Systems (EMI). It is a fully polarimetric C- and L-band SAR covering a slant range swath of 9.6 km in the 2x2 m resolution mode. It is flown on Gulfstream G-3 aircraft of the Royal Danish Airforce. These twin engine jet aircraft are well-suited for SAR campaigns as they are fast (420 kn), have a long range (6000 km), and typically operate at a high altitude (41000 ft).

The system has been designed to exhibit excellent stability, and no calibration targets need to be deployed in the sites to be mapped due to a unique internal calibration system [2]. A calibration test site supporting fully polarimetric calibration has been established in co-operation with the Research Centre Foulum (RCF), Denmark. Usually, this site is mapped on the first and the last day of a mission in order to check and possibly correct the radiometric and polarimetric calibration of the data from the entire mission. A performance evaluation based on the Foulum data is found in [1].

DCRS conducts research in both remote sensing technology and Earth science. Currently the latter includes seven study areas: Plant and Soil Mapping, Remote Sensing of Landscape Ecology, Determination of Aerodynamic Rougness, Microwave Sea Ice Signatures, Geologic Mapping in Greenland, Glacier Dynamics, and Sand Dune Dynamics. The Earth sciences are being pursued in collaboration with scientists outside DCRS.

Section 2 discusses the first five Earth science studies. The studies of Glacier Dynamics [3] and Sand Dune Dynamics are not discussed here, as they primarily rely on interferometry and not polarimetry. In Section 3 EMISAR's involvement in the EMAC campaigns is briefly addressed. Finally, the potential of using polarimetric SAR in the Earth sciences is discussed in Section 4.

2. DCRS EARTH SCIENCE STUDIES

Plant and Soil Mapping

The objective is to study the application of SAR to monitor agricultural crops, biomass, and soil physics. Mapping of extent, type, and state of agricultural crops are important for yield prediction and agricultural subsidiary policy enforcement. Soil moisture is an important but not very widely measured parameter in global climate models. It is a key factor in modeling evaporation, for calculating the capacity of land surfaces to absorb or release greenhouse gasses, and is expected to be a sensitive indicator of global change.

RCF is the DCRS science partner for this study, and the test site is the agricultural area surrounding RCF. Extensive *in-situ* measurements are conducted simultaneously with the acquisition of SAR data. The surface roughness is measured with a 2D scanning laser altimeter, and the soil moisture is measured using Time Domain Reflectometry (TDR). Spectral reflectance measurements in the visible and near infrared part of the spectrum are used to monitor biomass, leaf-area-index, foliage distribution, and orientation. These data are used in concert with the polarimetric EMISAR data for DCRS's studies of classification and decomposition algorithms as well as electromagnetic backscatter modeling. The polarimetric classification work is supported by crop maps comprising hundreds of fields in the Foulum area.

Remote Sensing of Landscape Ecology

Habitat fragmentation and deterioration are primary causes of biodiversity reduction and species loss. Therefore it is desirable to be able to continuously monitor landscape ecology over large areas in order to detect natural and man-made

† The Danish Center for Remote Sensing is established and funded by the Danish National Research Foundation.
†† Development of EMISAR was sponsored by the Thomas B. Thriges Foundation, the Danish Technical Research Counsil (STVF), the Royal Danish Air Force (RDAF), the Technical University of Denmark and the Joint Research Centre (JRC).

0-7803-3068-4/96$5.00©1996 IEEE

changes, and to identify habitat types, estimate habitat quality, and quantify landscape patterns in terms of for instance patch size, adjacency, and connectivity. Since the features to be mapped are hedgerows, ponds, single large trees etc., a high spatial resolution is required. DCRS and the National Environmental Research Institute (NERI) studies the applicability of airborne polarimetric SAR in this field.

A 12 by 12 km test area at Kalø near NERI's Department of Wildlife Ecology is used for the experiments. The ground reference data include vegetation maps and maps of the distribution of chosen species of birds and mammals.

Aerodynamic Roughness

The objective is to assess the potential of measuring the aerodynamic roughness of the Earth's surface with polarimetric SAR and to develop appropriate data processing techniques. The aerodynamic roughness influences the ability of wind to initiate sand and dust movement, and it is an important parameter when modeling vertical transport of heat and water vapour, since increasing roughness implies increasing turbulence and thereby more vertical transport.

The experiments are conducted in the vicinity of Foulum, were the vertical wind profiles and turbulence over different surfaces are measured using anemometers. The wind data are supplemented with soil moisture and biometric measurements as these parameters affect the SAR data, too.

Microwave Sea Ice Signatures

This study aims at establishing a basis for monitoring sea ice conditions using microwave remote sensing techniques. In addition to its impact on the navigation over polar waters, sea ice has a huge influence on the heat exchange between the oceans and the atmosphere. Classification of the principal types of sea ice requires detailed information about their microwave signatures. In particular the polarimetric SAR signatures are studied and related to the scattering mechanisms at the ice surface and within the ice.

Sea ice data are collected in the Greenland Sea and off the coast of East and South Greenland. The EMISAR data are supplemented by satellite SAR data (ERS and RADARSAT), satellite radiometer data (SSM/I), and satellite visible and infrared data (NOAA-AVHRR, LANDSAT) as well as airborne microwave radiometer data (TUDRAD) and airborne visible data (video). Data are collected from different seasons and include nearly simultaneous observations.

Geologic Mapping in Greenland

The application of SAR for geologic mapping in Greenland is investigated by DCRS in co-operation with the Danish Lithosphere Centre (DLC). In its research plan DLC has concentrated on two themes. One is continental break-up, hotspots and possible mantle plumes. The other is plate boundaries and crustal accretion in the Precambrian. A firm understanding of the distribution of different rock lithologies is important for both research areas.

The questions to be answered are: 1) Is it possible to discriminate different rock lithologies using high-resolution polarimetric SAR imagery? 2) Can individual lava flows and lava sequences be distinguished and traced over extensive areas? 3) How do faults and dike swarms manifest themselves in polarimetric SAR imagery?

The test site is 400 km SW of Scoresbysund in an area which is geologically well-known. Geologic maps have been generated through decades of field work. The terrain is characterised by an extreme topography as it also appears from the elevation contours of the geologic maps.

3. EMAC

The European Space Agency's European Multi-sensor Airborne Campaign (EMAC-94/95) is a programme providing support for the preparation of future satellite remote sensing programmes and their users [4]. The 1994 programme included coastal/ocean, agriculture, forestry and soils experiments with an optical multispectral scanner and two SAR systems. The NOrthern hemisphere climate Processes land-surface Experiment (NOPEX) was part of the EMAC programme. In 1995 the EMAC programme continued the NOPEX activities, but otherwise concentrated on snow and ice experiments in northern Europe where two SAR systems and two microwave radiometer systems collected data. Unlike previous snow and ice experiments the EMAC experiments emphasise the multi-temporal element.

In 1994 EMISAR collected polarimetric C-band data from the NOPEX test site at Uppsala, Sweden. In 1995 EMISAR collected both C- and L-band data from the following test sites: NOPEX, the Gulf of Bothnia (sea ice), Oulu, Finland (snow), and Okstindan, Norway (glacier and snow). DCRS's role in the EMAC programme is to collect, pre-process, and calibrate the fully polarimetric, dual frequency EMISAR data. DCRS is not directly involved with the interpretation of the data.

4. EARTH SCIENCE POTENTIAL

In the following the potential of polarimetric SAR for various Earth Science disciplines is discussed on the basis of the above-mentioned EMISAR data. Table I summarises some of the conclusions by classifying the ability to measure a number of geophysical parameters.

DCRS has applied several pixel-based supervised classification algorithms to the Plant and Soil data sets from Foulum, including the Maximum Polarimetric Contrast algorithm and a maximum likelihood classifier based on the Complex Wishard distribution. The results are promising, but in order to discriminate crops with similar structures such as different cereals, multi-temporal data sets are required [5]. In addition, due regard should be paid to the fact that the incidence angle varies over the swath.

These studies have also shown that SAR is not as independent of weather as often stated. Factors like precipitation and wind have been found to have dramatic effects in vegetated areas. This is especially true for vegetation which like

cereal has a vertical structure when no wind is present, and sufficient flexibility that the wind can change its orientation.

In combination with the *in-situ* measurements of soil moisture and surface roughness the Integral Equation Method (IEM) has been used to compute backscatter coefficients for a number of bare fields. These theoretical backscatter coefficients seem to be larger than those measured by EMISAR. Recent results indicate that one reason may be that the SAR signal is likely to be backscattered by a smoother subsurface layer [5]. The *in-situ* measured values of soil moisture and soil surface roughness agree very well with the estimates retrieved from the two co-polarised backscatter coefficients by using the empirical model developed by Dubois et al. [6]. It is desirable to complement the polarimetric SAR data by topographic data in order to correct the backscatter coefficient for the impact of the local incidence angle.

The application of polarimetric SAR data to map landscape ecology is very challenging. Unlike agricultural fields, the habitats to be classified are rarely homogeneous, e.g. meadows, mixed deciduous/coniferous forests. Also, the variety and the small extent of the features of interest complicate the use of SAR data. However, if the data is interpreted by an experienced human analyst many landscape classes and vegetation types can be discerned. For the forest studies the L-band data seem to be preferable as it takes much larger biomass densities at L-band to saturate the backscatter which is generally an increasing function of the biomass per unit area. Also, at L-band the relative cross-pol to like-pol ratio seems to be an indicator of tree height and biomass.

Encouraging results have been obtained with respect to the aerodynamic roughness. For five selected surfaces a linear relationship has been found between the cross-pol backscatter coefficient and the logarithm of the aerodynamic roughness [7]. The HH polarisation is also highly dependent on the vegetation density and hence the aerodynamic roughness, while the vertical polarisation is more sensitive to the soil moisture. These results are based on EMISAR data from the NOPEX site and they are confirmed by Foulum data associated with a wheat field. Previously, a high correlation between aerodynamic roughness and backscatter coefficient has been reported for three different types of arid surfaces [8].

A fully polarimetric C-band data set of sea ice was collected off the East Greenland coast in March 1995. Simultaneous ERS-1 data, microwave radiometer data, and video data were recorded, allowing many different ice types to be identified and exposed to polarimetric signature analysis. It is evident that the discrimination capability is greatly improved when fully polarimetric data are available [9].

Less encouraging are the results from geologic mapping in Greenland. Indeed, structural features like faults, dike swarms, and lava bedding are reflected quite well in the SAR imagery, but a geologic classification cannot be performed on the basis of polarimetric data [10]. Due to the glacial activity in this area lithological differences do not reflect in the surface morphology measured by the SAR. It is noted that in other areas of the world, where the lithology is related to a unique morphology, it can be possible to infer some information about lithology from SAR data.

TABLE I. Polarimetric SAR measuring capability

Parameter	High	Medium	None
Soil moisture	X		
Surface roughness	X		
Aerodyn. roughness		X	
Crop type	X		
Ice type	X		
Lithologic rock type			X
Geologic structure		X	
Landscape ecology		X	

CONCLUSIONS

Results from 1994 and 1995 have shown that SAR is a very useful sensor for land cover mapping particularly for biosphere studies, SAR is also very useful in relation to both sea and inland ice studies. It has been found that for most studies there will be a significant temporal/environmental variation and it is thus very important for most studies to acquire more than one data set. Our present understanding is, however, that SAR seems to be less generally applicable for geological studies, mainly being of use for mapping morphology and also topography.

REFERENCES

[1] E. Lintz Christensen, J. Dall, N. Skou, K. Woelders, J. Granholm, and S.N. Madsen, "EMISAR: C- and L-band Polarimetic and Interferometric SAR", these proceedings.

[2] J. Dall, Niels Skou, E. Lintz Christensen, "Pulse-based Internal Calibration of Polarimetric SAR", IGARSS'94, Pasadena, California, USA, August, 1984.

[3] J.J. Mohr, S. Nørvang Madsen, and N. Reeh, "Applications of Interferometry to the Studies of Glacier Dynamics", these proceedings.

[4] E. Attema and M. Wooding, "EMAC Experimenters Handbook, Programme for 1995", ESTEC.

[5] H. Skriver, J. Ji, J.Dall, K. Woelders, and A. Thomsen, "A Multi-Temporal and Multi-Frequency Study of Polarimetric Signatures of Soil and Crops", in press, EUSAR'96, Köningswinter, Germany, March, 1996.

[6] P. Dubois, J. van Zyl, and T. Engman, "Measuring Soil Moisture with Imaging Radar", IEEE Trans. Geoscience and Remote Sensing, vol. 33, pp. 915-926, 1995.

[7] A. van de Griend, "Progress report for the Forest Dynamo Project", EU report, 44 pp.

[8] R. Greeley and D.G. Blumberg, "Preliminary Analysis of Shuttle Radar laboratory (SRL-1) Data to Study Aeolian Features and Processes", IEEE Trans. Geoscience and Remote Sensing, vol. 33, pp. 927-933, 1995.

[9] B.B. Thomsen, L. Toudal Pedersen, and H. Skriver, "C-Band Polarimetric Signatures of Winter Sea Ice", these proceedings.

[10] J. Dall, S.N. Madsen, C.K. Brooks, and T. Nielsen, "Geologic Mapping in Greenland with Polarimetic SAR", IGARSS'95, Florence, Italy, August, 1995.

Spaceborne rain radar mission and instrument analysis

N. Vincent, J. Chenebault, N. Suinot

ALCATEL ESPACE, 26 av J.F Champollion, 31037 Toulouse Cedex, FRANCE
Phone : (33) 61 19 52 25, Fax : (33) 61 19 61 63, E-Mail : FRDK8N58@IBMMAIL.COM

P.L. Mancini

ESA-ESTEC, 2200 AG Noordwijk, THE NETHERLANDS
Phone : (31) 71 56 5 40 52, Fax : (31) 71 56 5 45 96

ABSTRACT

The main objective of this paper, based upon a Pre-phase A study founded by ESA, is to define a preliminary design of a spaceborne Rain Radar from a precise review of user requirements proposed for climate research and operational meteorology purpose.
A mission analysis defines the most suitable space segment, taking into account the instrument related aspects and mission constraints.
As a result of several trade-off, the dual frequency rain radar design is described presenting in particular the way pulse compression is implemented to achieve a pulse response with a side-lobe level lower than -60 dB.
Finally simulated performances shows this feasible spaceborne rain radar is in compliance with the user requirements.

1. INTRODUCTION

During the last few years, Earth Observation from space has demonstrated its growing scientific, social, economic and political importance by contributing to a better understanding and regular monitoring of the Earth and its environment. Considering the increasing community of users, the European Space Agency proposes to prepare an Earth Explorer Mission for research and demonstration purpose.
Among the nine possible candidates, the Precipitation Mission plan to observe precipitation especially in tropical regions.
For climate research, a typical requirement is a global mapping of the monthly rainfall with a grid resolution of 500 x 500 km^2 horizontally and 250 m vertically with an accuracy better than 10 %. The rain rate variability within a day is another important parameter for comparison with climate model.
This paper is based upon results of an ESA pre-phase A study, lead by ALCATEL ESPACE with three other European companies. Its objective is to determine precise user requirements and define adequate mission and instrument design.

0-7803-3068-4/96$5.00©1996 IEEE

2. MISSION DEFINITION

2.1 Instruments and platform

The payload of such a dedicated mission consists mainly in the association on a low orbiting platform of a rain radar, a visible/IR imager and a multichannel microwave radiometer.
The precipitation field, from 0 to 15 km altitude, is sampled in three dimensions by the radar with a footprint resolution of 3 km, compatible with the observation of deep convective cells.
The 400 km swath width avoids a too large degradation of the vertical resolution as well as a too severe contamination of the meteorological echo by the surface return.
According to the statistical distribution of the rainfall, the radar dynamical range should cover 0.5 to 60 mm/h in order to observe 95 % of the rainfall.
The role of the microwave radiometer is to extend the swath of the measuring system up to 1000 km by a conical scanning. Its poor sampling is compensated by the introduction in the inversion algorithm of the radar fine scale description of the precipitation field.

2.2 Mission selection

For a 500 * 500 km^2 grid mesh, meeting a sampling error on a monthly rainfall lower than 5 % requires a revisit time shorter than about 12 hours [1].
The mission analysis is based on this critical requirement as well as the global coverage of the geographical domain (± 60 degrees latitude with a particular interest in the ± 30 degrees tropical region) range and local hour sampling.
The orbit inclination is selected close to 56 degrees to get the required coverage together with a high drifting equator crossing time in order to sample the diurnal cycle.
Even if the considered swath is the radiometer's one, it is necessary to consider a two satellite mission with both satellites on a 500 km height orbit, with the same inclination and ascending nodes separated by 12 degrees [2].

Performances of this mission are summarized in Table 1.

PARAMETER	VALUE
Mean revisit time over [-60, +60 deg]	10.9 h
Mean revisit time over [-30, +30 deg]	13.5 h
% of [-60, +60 deg] domain with a mean revisit time lower than 12 hours	91 %
Coverage of the [-60, +60 deg] domain	99.4 %
Local hour coverage	< 34 days

Table 1 : Mission performances for 2 satellites

3. RAIN RADAR DESIGN

3.1 Concept selection

Three main concepts, based upon different rain rate retrieval algorithms, have been compared : Single Beam Single Frequency (SBSF), Single Beam Dual Frequency (SBDF) and Dual Beam Single Frequency (DBSF).

The DBSF concept (tilt angle of ± 15 deg related to nadir) has been discarded because of its algorithm instability and sensibility to non uniform beam filling.

Both other concepts meet the requirements but the SBDF concept is preferable as in the range 0.5 to 25 mm/h, its algorithm is insensitive to radar calibration, drop size distribution variability and it operates over land as well as over sea. The SBDF concept was therefore selected despite the increase of cost and design complexity.

3.2 Design

As represented in Figure 1, the baseline architecture is composed of five main parts : the digital electronic subsystem, the RF subsystem, the antenna, the mass storage unit and the instrument control unit (ICU).

A pulse compression is implemented and the selected pulse waveform is a broken line FM pulse, as described in Figure 2 [3].

Up and down conversions are performed from 5 MHz simultaneously to 13.7 and 24.15 GHz. High amplification is performed through travelling wave tubes that require less cost and technological risk than a distributed architecture, specially for K-band.

The antenna consists of a reflector illuminated by two adjacent single frequency feed arrays. Footprints are not simultaneously superimposed but antenna pointing ensures an overlapping higher than 90% along the orbit. The across-track beam steering is fulfilled by a feed array including a set of phase shifters whose commands are controlled by ICU.

Pulse compression consists mainly of a frequency domain multiplication of each echo with a replica computed by ICU from a calibration pulse. A breadboard developed for ESTEC [3] shows that this compensation procedure enables to meet point target response side-lobe level lower than -60 dB and to relax radar hardware distortions.

Digital processing unit, echoes are averaged in range and pulse to pulse in order to get for each beam position a single echo with a 250 m range resolution. Each coded echo is stored before being transmitted through the payload telemetry antenna. On ground, echoes can therefore be introduced in rain rate retrieval algorithms.

A calibration design is implemented to acquire the signal required to compute the replica, to compensate the manufacturing, thermal and ageing errors in the passive beam forming network and to guarantee the antenna sidelobe level.

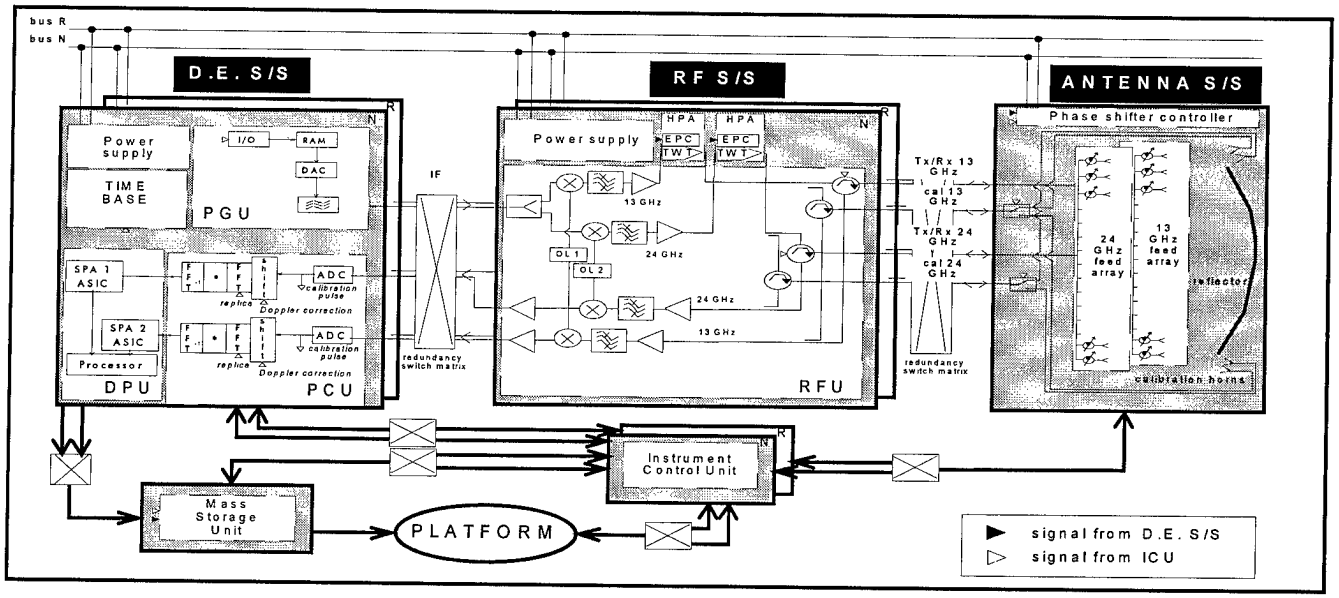


Figure 1 : Instrument block diagram

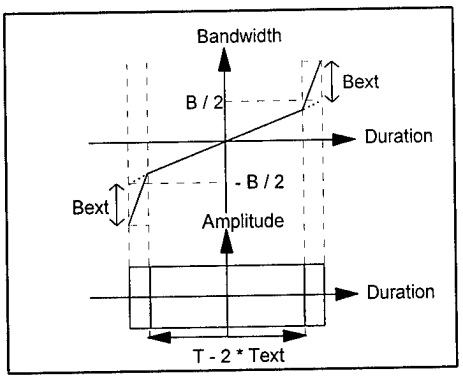


Figure 2 : Pulse waveform

Main system and instrument characteristics are summarized in Table 2.

PARAMETER	VALUE
Frequencies	13.70 and 24.15 GHz
Horizontal / range resolution	3 km / 250 m
Swath width	250 to 400 km
Observed altitude	15 km + 7 km (mirror echo)
Pulse bandwidth / duration	4.5 MHz / 60 µs
PRF	selectable < 3500 Hz
Reflector size	4.8 m height * 6 m width
Number of feeds	2 * 272

Table 2 : Main system/instrument characteristics

4. PERFORMANCES AND CONCLUSION

Simulations show that KZs algorithm, similar to Hitschfeld-Bordan method with surface echo processing, and Dual Frequency algorithm are complementary and provide satisfying rain rate retrievals.
Budgets and performances are described in Table 3.

PARAMETER	VALUE
Mass budget (margin of 20 %)	360 kg
Power consumption budget	340 W
Rain rate dynamic range	0.5 to 50 mm/h
Standard deviation and bias	< 10 %

Table 3 : Budgets and performances

In conclusion, this study has demonstrated the feasibility of a spaceborne rain radar which meets the performances needed for climate research. In addition, the proposed two satellite mission achieves the severe user requirements related with the revisit time, the coverage and the local hour sampling.

5. REFERENCES

[1] C.R. Laughlin, « On the effect of temporal sampling on the observation of mean rainfall », Precipitation measurements from Space, NASA publication, D5-D66, 1981.

[2] J. Testud, P. Amayenc, J. Chenebault, « Global Mapping of the Rainfall from a System of Spaceborne Rain Radars », Proc. IGARSS 95, Vol.2, pp.879 - 881.

[3] N. Vincent and al, « Pulse compression with -65 dB sidelobe level for a spaceborne meteorological radar », Proc. IGARSS 96, in press.

6. ACKNOWLEDGMENTS

This work has been supported by the European Space Agency under contract no. 10820/94/NL/NB. We would like to express our thanks to Mr. P. L. Mancini and D. Maccoll of ESTEC.

SIR-C/X-SAR Campaign on Ruegen Island, Germany - First Results

Corinna Prietzsch and Alexander Bachem
ZALF - Institute of Landscape Modeling, Eberswalder Strasse 84, D-15 374 Müncheberg
Tel: + 49 33432 82 239 Fax: +49 334[1]32 82 334, email: cprietzsch@zalf.de, abachem@zalf.de

Abstract -- The analysis of remotely sensed image data, that have been acquired during the SIR-C/X-SAR mission in October 1994 over Ruegen island, Germany, together with the application of a backscattering inversion technique for the retrieval of the soil water content is shown. The results are in agreement with the modeled soil water content and the RMS surface roughness (standard deviation of surface height), if compared to reference data from maps and field measurements. This way a spatial derivation of soil moisture information is possible.

INTRODUCTION

For a lot of ecological modeling approaches of landscapes or regions, spatial data are necessary. These are important not only for the retrieval of initial parameters, but as well as a verification database for geoecological modeling results. Most numeric ecological models have only been verified with point measurements so far. Remote sensing methods, however, offer the possibility of large area assessment of soil and plant physical parameters. Especially the use of weather and cloud independent synthetic aperture radar (SAR) data offers the possibility of spatial data retrieval.

Depending upon the water content, microwaves can penetrate into the ground and the backscattering of the incident wave is mainly influenced by the surface roughness and the soil dielectric behavior. The large difference between the dielectric constant of the soil (2-3) and of water (about 80 opens the possibility to calculate the dielectric constant from water content from the dielectric constant and this way from the backscattering coefficient.

The SIR-C systems recorded polarimetric radar image data in C- and L-band, which is 5.3 and 1.2 GHz, respectively. X-SAR records X-band VV data (9.6 GHz). Two 10-day campaigns were carried out in April and October 1994. During these periods synchronously to the shuttle overpass acquired field data have been collected and are an important reference data set for the modification, improvement and validation of algorithms.

INVESTIGATION AREA

This study was conducted on Ruegen island, which is located near the North East German coast of the Baltic Sea. The total size of the area is about 30 * 30 km. The region of interest consists mostly of agricultural fields and forests, bog areas and open water bodies and only a few small towns and cities. The substrates are glacial deposits and represent a large variety of texture classes ranging from clayey silt to sandy loam and sand. Main agricultural crops are rape seed, barley and corn. During the second SIR-C/X-SAR campaign 21 mm of precipitation were measured. October 7 did not receive any rain. The surface topography was mainly flat in the region of interest, so that no disturbances of the image geometry by topographic effects occurred.

FIELD MEASUREMENTS AND IMAGE DATA

Representative fields with the major occurring substrates were sampled with TDR probes (time domain reflectometry) that give a direct read-out of the volumetric soil moisture content in the upper 10 cm of the homogeneously wet soil profile. The empirical relationship between the soil dielectric constant, which modifies the runtime of the transmitted pulse from the TDR device into the soil and back, and the volumetric soil water content is described by [1]. The sampling locations were chosen following a 100 m x 100 m grid sampling strategy. Each field was covered with up to 120 measurement locations and at each location 3 repetitions were taken (field averages are shown in Tab. I). The probes were calibrated and their results are absolutely comparable.

The average soil water content across fields varies between 17 and 48 % Vol. with standard deviations per field of 2 to 11 % Vol. This large spatial variability is due to the very heterogeneous substrates. The averaging over whole agricultural fields was necessary to provide comparison data for the speckled image data that were averaged over whole fields as well.

Surface roughness was determined with a 3D-laser profiler over a 1x1m area and with a simpler approach that uses incremented measurements along a 2m transect at three location on each field. The spatial resolution of the laser in x and y directions was adjusted to 2, 12, 56 and 100 mm steps. Semivariograms were calculated for the soil water content and kriging interpolation (ordinary kriging) was applied to interpolate between point measurements. A GIS contains the land use, soil substrates, sample locations, and soil water content maps from the geostatistical analysis. Especially the

[1] This work was funded by the German Aerospace Agency (DARA), Bonn.

0-7803-3068-4/96$5.00©1996 IEEE

soil substrate maps are necessary to apply a local soil texture correction of the inversion model output [2].

In this study single look complex data in a slant range projection (SLC-product) in L-Band HH, VV, and VH polarization were used, because these geometrically uncorrected products contain the original unbiased backscattering amplitudes. The spatial resolution is 22.4 m in range direction and 6.6 m in azimuth direction. The image covers an area of 18.5 x 50 km at an incidence angle of 45.1° at the image center and contains amplitude data that are absolutely calibrated at an accuracy of +/- 2 dB.

Tab I: Reference data of representative substrates on Ruegen island during the SIR-C/X-SAR campaign on October 7, 1994.

Field	Mean m_v [% Vol]	Std.dev. m_v [% Vol]	Clay [%]	Sand [%]	s [cm]	l [cm]
KLN	18.81	11.15	6.0	70.9	1.83	8.4
KLS	17.63	3.04	6.3	70.7	1.69	6.4
VE	22.72	3.22	10.2	60.5	1.27	7.2
MO	48.32	7.14	21.5	44.7	0.60	6.2
VEI	28.41	1.94	9.6	60.7	0.60	6.2
RA	19.58	5.42	11.7	66.0	2.91	6.8

m_v: volumetric soil water content, s: RMS height, l: autocorrelation length.

REGRESSION ANALYSIS

Linear regression analysis (Tab. II) was applied to estimate the intensity of the relationship between measured soil water content and backscattering coefficients, that have been retrieved from the same areas in the image data. These are average values across whole fields, the location of the fields was determined with the GIS layer of investigation sites.

The regression results for the soil water content and the autocorrelation length at single polarizations are very low.

Tab. II: Regression analyses between the backscattering in L-Band at different polarizations and soil parameters.

r for the independent parameters

Polarization	m_v	s	l
HH	0.48	0.85	0.51
VV	0.19	0.72	0.41
VH	0.27	0.83	0.23
HV	0.32	0.85	0.28
all 4	0.67	0.46	0.99
VV, HH	0.98	0.90	0.57
VH, HV	0.39	0.85	0.34

m_v: volumetric soil water content, s: RMS height, l: autocorrelation length.

Only the use of both like polarizations raises r. If all polarizations are introduced into the analysis, the results are not improved, compared with the case of both like polarization for the soil water content and the RMS height. This may be due to the calibration problems in the cross polarized signatures.

The general trend for the regression between the soil water content and the backscattering in L-band can be described as follows: VV represents the highest backscatter followed by HH and the very low backscattering in HV (about 10 dB less) and the regression lines run parallel.

Regarding the soil water content, the best explanation is given, if the two like polarizations HH and VV are introduced into the analysis: R is 0.98 for the soil water content and 0.90 for the standard deviation of surface heights (RMS height). These results are an important prerequisite for the successful application of the theoretical backscattering model and the inversion model.

BACKSCATTER MODELING

Theoretical modeling with the empirical soil surface backscattering model MIMICS-UMICH [3] was then applied in order to learn about the influence of the radar parameters on the backscattering and the measured ground parameters. The empirical model was developed, because other modeling results for given surface conditions did not compare well enough with the imaging radar backscattering coefficient and the model should be applicable to a greater variety of soil surface conditions.

The validity criteria of these models are based on the radiometric surface roughness and were checked for the measured surface roughness conditions (Tab. III). This led to the result, that only the small perturbation model and the empirical model may be applied to the measured surface conditions.

Tab. III: Validity criteria for surface scattering models.

Model	Criteria
Geometrical Optics	$ks > 2$, $kl > 6$
Physical Optics	$kl > 6$, $m < 0.25$
Small Perturbation	$kl < 3$, $ks < 0.3$, $m < 0.3$
MIMICS-UMICH	$0.1 < ks < 0.6$, $2.6 < kl < 19.7$
	$0.009 < m_v < 0.31$

k: wave number, m: surface slope. Others as in Tab. I.

The backscattering results in VV polarization are always about 5 dB higher than in HH and 10 dB higher than in the VH polarization. The wetter the surface is, the higher the backscattering is. With increasing incidence angle, the backscattering decreases as the surface appears rougher than close to nadir incidence angles and the difference between VV and HH becomes about 2 dB larger. These general theoretical results support the possibility of estimating the soil water content and surface roughness from SAR data with an inversion algorithm. If wet mineral soils are compared (KLS and VEI, Tab. I), the difference in the water content is 10.78 % Vol. as opposed to a difference in the backscattering of 5.35 dB in VV, 7.95 dB in HH and 8.66 dB in VH as modeled by MIMICS-UMICH. It has to be taken into account that the roughness conditions are different and the calibration

accuracy for SIR-C which is +/- 2 dB reduces the difference even more.

INVERSION MODELING

The application of an inversion technique by SHI [4] allows the retrieval of soil water content and surface roughness parameters directly from L-band VV and HH polarized image data. Inversion techniques make use of the physical scattering properties of defined wavelength and polarization. For each pixel of the input SLC image data the appropriate rough surface model is selected: The ratio of the co-polarized signals determines the use of the model. Image speckle (multiplicative noise) is overcome due to the embedded multilooking procedure. Vegetated areas are excluded by a scattering based classification algorithm [5] that only selects pixels with single reflections. Two extreme classes of possible soil water contents are then tested and determine the range for the calculated dielectric constants. Some pixels that are out of range (densely vegetated, forested or built-up areas) are assigned missing values and appear black.

The resulting 3 channel image contains the dielectric constant of the soil, the standard deviation and the autocorrelation length of the surface roughness. It still appears very speckled, in a sense, that a large heterogeneity of the calculated dielectric constant an the RMS height can be observed.

An expression by Hallikainen [2] is used for the conversion of the dielectric constant into the volumetric soil water content depending on the sand, clay and water content at L-band. In a first step this conversion is carried out for the sampled fields only (Tab. IV) the next step is the calculation of soil water contents for the whole output image based on the digitized soil substrate map and the derived sand and clay content. As the soil water content and the surface roughness are estimated in the same equation, the underestimation of the one leads to an overestimation of the other, as reported by [6, 7]. This tendency has yet to be proven for the Ruegen Island data set. Most of the site water contents were underestima-

Tab. IV: Comparison of modeled (SHI 1991) and measured soil water contents and surface roughness.

Site	m_v	m_v (Shi)	s	s (Shi)
VE	0.227	0.209	1.27	2.11
KLN	0.188	0.123	1.83	1.91
KLS	0.176	0.076	1.69	1.57
VEI	0.284	0.161	0.60	1.48
MO	0.486	0.162	0.60	2.42
RA	0.196	0.195	2.91	2.52

m_v: volumetric soil water content, s: RMS height.

ted, only test site RA is almost fully recognized. A problem may be the large spatial heterogeneity of the soil conditions in each site, that can not be taken care of with averaging. The regression analysis between each pixel from the kriging map (measured soil water content) and the modelled dielectric constant will be presented.

RESULTS AND DISCUSSION

For a field average approach the following results can be summarized: The comparison of image data and soil data (regression analysis) for a few fields is satisfying. r reaches 0.98 for four polarisations. A multi-temporal approach even with only one frequency and polarization (C-band, VV) shows similar results [11]. The comparison of backscattering coefficients of modeling results (UMICH-MIMICS) and image data gives a first impression, but can not be used to invert image data on a spatial scale. The comparison of inversion technique results and ground truth leaves room for improved comparison techniques with GIS information. Inversion modeling can be used to calculate large area soil moisture and roughness maps from L-band polarimetric SAR data as stated by [10] as well.

REFERENCES

[1] M.A. Malicki and W.M. Skierucha (1989): A manually controlled TDR-soil moisture meter operating with 300 ps rise time needle pulse. Irrigation Sci., 10, 103-109.

[2] M. Hallikainen, F.T. Ulaby, M.C. Dobson, M.A. El-Rayes, and L.K.Wu (1984): Microwave dielectric behavior of wet soil. - Part I: Empirical models and experimental observations. IEEE Geosc. Rem. Sen., Vol. GE-23, No. 1, 25-34.

[3] Y. Oh, K. Sarabandi, and F.T. Ulaby (1992): An empirical model and an inversion technique for radar scattering from bare soil surfaces. IEEE Geosc. Rem. Sen., Vol. 30, No. 2, 370-381.

[4] J.C. Shi, E.T. Engman, and J.J. van Zyl (1991): SAR-derived soil moisture measurements for bare fields. Proc. IGARSS'91, Helsinki, Finland, Vol. 1, 393-396.

[5] J.J. van Zyl (1989): Unsupervised classification of scattering behavior using radar polarimetry data. IEEE Trans. Geosc. Rem. Sen., Vol. GE-27, No. 1, 36-45.

[6] P. Dubois, J.J. van Zyl, and E.T. Engman (1995): Measuring soil moisture with active microwaves: Effect of vegetation. Proc. IGARSS'95, IEEE, Florence, Italy, Vol. II, 495-497.

[7] P.E. O'Neill, A.Y. Hsu, and J.C. Shi (1995): Soil moisture estimation using time-series radar measurements of bare and vegetated fields in Washita'92, Proc. IGARSS '95, IEEE, Florence, Italy, Vol. II, 498-500.

[8] F. von Poncèt, M. Tapkenhinrichs, J.Hannemann, R. Schmidt, C. Prietzsch and H.-R. Bork (1995): Methodenentwicklung zur Nutzung von Satelliten-SAR-Daten für die Kartierung und Erfassung von Parametern und Phänomenen des Bodenwasserhaushalts. ZALF-Bericht, Nr. 17, Müncheberg.

Volume Scattering Function of Light for a Mixture of Polydisperse Small Particles with Various Optical Properties

Vladimir I. Haltrin
Naval Research Laboratory, Ocean Sciences Branch, Code 7331, Stennis Space Center, MS 39529-5004, USA
Phone: 601-688-4528, fax: 601-688-5379, e-mail: <haltrin@nrlssc.navy.mil>

Alan D. Weidemann
Naval Research Laboratory, Ocean Sciences Branch, Code 7331, Stennis Space Center, MS 39529-5004, USA
e-mail: <alanw@indyvih.nrlssc.navy.mil>

and

Walton E. McBride, III
Planning Systems Inc., 115 Christian Lane, Slidell, LA 70458, USA, <wmcbride@indyvih.nrlssc.navy.mil>

Abstract – Scattering of electromagnetic waves by a polydisperse system of small spherical hydrosol particles in the scalar approximation is considered. The equation for the scattering cross-section which generalizes the well-known Rayleigh-Gans-Rocar formula for a scattering medium containing particles characterized by continuous distributions in their dielectric permittivities at any given size is derived. For a natural situation, such as a coastal environment, the difference between volume scattering functions proposed in this paper and conventionally derived scattering functions can be as large as 50% for the particle size distributions with the maximum size of particles less than ten wavelengths of light.

INTRODUCTION

Conventional volume scattering function calculations use a particle size distribution and a fixed dielectric permittivity for each size class. This approach became widely accepted due to two main reasons: first, it is mathematically simpler compared to a more general approach, and, second, it is accurate enough for open ocean situations. In these simple cases we can divide all scattering particles into a few different particle types, each with an assigned dielectric permittivity. However, as emphasis has switched to coastal environments, the number of particle types in each size class has increased. We include this diversity of particle types in the calculation of the volume scattering function.

In order to incorporate this real-life complexity we utilize a two-dimensional distribution of particles with respect to particle size and dielectric permittivity. We consider multiple scattering but, because of the complexity of the problem, restrict ourselves to the case of small particles and use the scalar approximation to Maxwell's equations for electromagnetic theory. Using this approach we calculate the contribution to the volume scattering function due to small particles for various coastal-type hydrosols.

0-7803-3068-4/96$5.00©1996 IEEE

APPROACH

Consider the scattering of scalar electromagnetic waves in a medium represented by a polydisperse system of N particles. Let ε_0 denote the dielectric permittivity of the surrounding medium, while ε_n is the dielectric permittivity of a particle with index n. The dielectric permittivity of a mixture is a function of the random distribution of the particles' coordinates $\{\vec{r}_n\}$. For a particular configuration of a polydisperse mixture of hydrosol particles with different electric properties it can be represented in the following form [1, 2]

$$\tilde{\varepsilon}(\vec{r},\{\vec{r}_n\}) = \varepsilon_0 + \sum_{n=1}^{N} (\varepsilon_n - \varepsilon_0)\,\theta(a_n - |\vec{r} - \vec{r}_n|), \qquad (1)$$

where $\theta(x)$ is the Heavyside (or step) function defined as : $(\theta(\mu)=1, \mu>0; \theta(\mu)=0, \mu\le 0)$, and a_n is the size associated with the n^{th} particle determined from

$$a_n = (3V_n / 4\pi)^{1/3}, \qquad (2)$$

where V_n is the volume of the n^{th} particle. For a spherical particle, a_n coincides with its radius. In the above equation, $\vec{r}$ is the field vector, while $\vec{r}_n$ is the position vector of n^{th} particle. The field scattered by a system of N particles is a random function of both the coordinates and scattering properties of the particles in that system.

In order to calculate average values of physical quantities of interest, we use Foldy's probability distribution method [3] for the ensemble of possible configurations of the dielectric scatterers. Foldy represents "the probability of finding the scatterers in a configuration in which the first scatterer lies in the element of volume $d\vec{r}_1$ about the point $\vec{r}_1$ and has a scattering parameter lying between S_1 and $S_1 + dS_1$, the second scatterer lies in the element of volume $d\vec{r}_2$ about the point $\vec{r}_2$ and has a scattering parameter lying between S_2 and $S_2 + dS_2$, etc." as

$$F(\vec{r}_1,\vec{r}_2,...\vec{r}_N,S_1,S_2,...S_N)\,dr_1\,dr_2...dr_N\,dS_1\,dS_2...dS_N. \qquad (3)$$

In this article we consider only scattering properties such as the dielectric permittivity ε and the particle size x. Then: $dS_n = d\varepsilon_n dx_n$. To find the configurational average of a physical quantity f, we multiply its value for a particular configuration by (3) and integrate over all values of the $\vec{r}_n$ and S_n accessible to the scatterers:

$$\langle f \rangle = \iint F(\{S\},\{\vec{r}\})\, f\, d\{S\}\, d\{\vec{r}\}. \tag{4}$$

In the spirit of Foldy's article [3], we write

$$F(\{S\},\{\vec{r}\}) = n(S_1,\vec{r}_1)\, n(S_2,\vec{r}_2) \ldots n(S_N,\vec{r}_N), \tag{5}$$

which is equivalent to assuming that "the probability that a particular scatterer is located in some volume element and has a value of S located within some range dS is independent of the locations and scattering parameters of the other scatterers and is the same for all scatterers". We note that

$$n(S,\vec{r}) = n_{Foldy}(S,\vec{r})/N, \tag{6}$$

so that $n(S,\vec{r})\, d\vec{r}\, dS$ represents the *percentage* of scatterers in the element of volume $d\vec{r}$ about the point $\vec{r}$ with scattering parameters between S and $S+dS$.

In what follows, we restrict ourselves to spherical particles, neglect thermal and turbulent fluctuations of the medium and assume homogeneity. We can then write:

$$n(S,\vec{r}) = n(S) = V^{-1} f_x(\varepsilon)\, \varphi(x), \tag{7}$$

where V is the volume of the system, $f_x(\varepsilon)$ is the dielectric permittivity distribution function for a particle with size x, and $\varphi(x)$ is the size-distribution function. The distribution functions in (7) are normalized according to

$$\iint n(S,\vec{r})\, dS\, d\vec{r} = 1, \quad \int f_x(\varepsilon)\, d\varepsilon = 1, \quad \int_0^\infty \varphi(x)\, dx = 1. \tag{8}$$

Using (4) and (5) we can calculate the average dielectric permittivity of the medium from (1):

$$\left\langle \tilde{\varepsilon}(\vec{r},\{\vec{r}\}) \right\rangle = \varepsilon_0 + C_H\, \varepsilon_H, \tag{9}$$

In the above equation

$$C_H = N V_H / V \tag{10}$$

is the volume concentration of particles as a fraction of the total volume,

$$V_H = (4\pi/3)\int_0^\infty x^3 \varphi(x)\, dx \tag{11}$$

is the average particle volume, and

$$\varepsilon_H = \int_0^\infty \varepsilon_x\, \varphi(x)\, x^3 dx \Big/ \int_0^\infty \varphi(x)\, x^3 dx \tag{12}$$

is the standard deviation of the average dielectric permittivity ε_x due to the particles with respect to the dielectric permittivity ε_0 of the surrounding medium, such that

$$\varepsilon_x = \int (\varepsilon - \varepsilon_0) f_x(\varepsilon)\, d\varepsilon. \tag{13}$$

In this case the formula (1) for the dielectric permittivity of a mixture can be rewritten as

$$\tilde{\varepsilon} = \varepsilon_w - \varepsilon; \quad \varepsilon_w = \varepsilon_0 + C_H\, \varepsilon_H, \tag{14}$$

$$\varepsilon = C_H\, \varepsilon_H - \sum_{n=1}^{N} (\varepsilon_n - \varepsilon_0)\, \theta(a_n - |\vec{r} - \vec{r}_n|), \ \langle \varepsilon \rangle = 0. \tag{15}$$

The equation for a monochromatic scalar wave field in a scattering medium [4] will be

$$\left(\Delta + \tilde{\varepsilon}\, \omega^2/c^2\right)\tilde{\Psi} = f, \tag{16}$$

where $\Delta \equiv \nabla^2$ is the Laplace operator, ω is the circular frequency, c is the speed of light in vacuo, $\tilde{\Psi}$ is the wave field amplitude, and f is the source function. Let us introduce the following notation:

$$\kappa^2 = \varepsilon_w\, \omega^2/c^2; \quad \kappa_0^2 = \omega^2/c^2, \tag{17}$$

$$\tilde{\Psi} = \Psi + \varphi; \quad \langle \varphi \rangle = 0, \tag{18}$$

$$\hat{L} = \Delta + \kappa^2, \tag{19}$$

so that $\hat{L}$ is the Helmholtz operator.

We derive an equation for Ψ by averaging (16), and an equation for φ by subtracting the averaged equation from (16). Then we have the system of equations

$$\left.\begin{aligned} \hat{L}\, \Psi &= \kappa_0^2 \langle \varepsilon \varphi \rangle + f \\ \hat{L}\, \varphi &= \kappa_0^2\, \varepsilon\, \Psi + \kappa_0^2 [\varepsilon, \varphi] \end{aligned}\right\}, \tag{20}$$

where

$$[\varepsilon, \varphi] = \varepsilon \varphi - \langle \varepsilon \varphi \rangle. \tag{21}$$

The Helmholtz operator (19) has an inverse operator $\hat{G}$. Operator $\hat{G}$ is an integral operator with a Green function G (or a fundamental solution of the Helmholtz equation [5]) as kernel

$$(\hat{L})^{-1} = \hat{G}, \quad G(r) = -\exp(i\kappa r)/(4\pi r), \tag{22}$$

$$(\hat{G} f)(\vec{r}) = \int G(\vec{r} - \vec{r}')\, f(\vec{r}')\, d\vec{r}', \tag{23}$$

with

$$\hat{L}\hat{G} = \hat{G}\hat{L} = \hat{I}, \quad \hat{L} G(\vec{r}) = \delta(\vec{r}), \tag{24}$$

$$(\hat{I} f)(\vec{r}) \equiv \int \delta(\vec{r} - \vec{r}')\, f(\vec{r}')\, d\vec{r}' = f(\vec{r}). \tag{25}$$

Let us introduce a random operator $\hat{K}$, which acts on an arbitrary (random or deterministic) function F according to the rule

$$\hat{K} F = \hat{G}[\varepsilon, F] \equiv \hat{G}\left(\varepsilon F - \langle \varepsilon F \rangle\right). \tag{26}$$

When acting on a deterministic function F_0 it gives

$$\hat{K} F_0 = \hat{G}[\varepsilon, F_0] = \hat{G}\, \varepsilon\, F_0. \tag{27}$$

Let us also introduce the operator

$$\left(1 - \kappa_0^2 \hat{K}\right)^{-1} = \sum_{n=0}^{\infty} \kappa_0^{2n}\, \hat{K}^n, \tag{28}$$

and act with the operator $\hat{G}$ on the system of equations (20). Then, instead of (20) we get

$$\left(\hat{L} - \kappa_0^2 \langle \varepsilon \hat{Q} \rangle\right)\Psi = f, \quad \varphi = \hat{Q}\Psi, \tag{29}$$

where

$$\hat{Q} = \sum_{n=1}^{\infty} \hat{Q}_n \equiv \sum_{n=1}^{\infty} \kappa_0^{2n}\, \hat{K}^n. \tag{30}$$

Let us restrict ourselves presently to a first order approximation for which

$$\hat{L}^0 \Psi = \left(\hat{L} - \kappa_0^4 \langle \varepsilon \hat{G} \varepsilon \rangle\right)\varphi^0 = f, \quad \varphi^0 = \kappa_0^2\, \hat{G}\, \varepsilon\, \Psi^0 \tag{31}$$

Let us examine the structure of the operator

$$\hat{L}^0(1,2) = \hat{L}(1,2) - \kappa_0^4\, G(1,2)\, B_\varepsilon(1,2), \tag{32}$$

where the spatial correlation function

$$B_\varepsilon(1,2) = \langle \varepsilon(1)\, \varepsilon(2) \rangle = B_\varepsilon(\vec{r}_1, \vec{r}_2) = B_\varepsilon(\vec{r}_1 - \vec{r}_2), \tag{33}$$

and the square of field fluctuations is

$$\left\langle \varphi^0(1)\varphi^{*0}(1)\right\rangle = \kappa_0^4\, G(1,2)G^*(1,3)B_\varepsilon(2,3)\Psi^0(2)\Psi^{*0}(3)\ , \quad (34)$$

where asterisk denotes complex conjugates. In order to simplify the notation in what follows, we introduce numerical indices *1, 2,...* instead of $\vec{r}_1, \vec{r}_2, \ldots$, with implied integration over repeating indices.

When $N >> 1$, and with the use of (4) and (15), it is not difficult to derive the following expression for the correlation function $B_\varepsilon(R)$ (see APPENDIX):

$$B_\varepsilon(R) = \frac{N}{V}\int_{R/2}^{\infty} \frac{4\pi}{3} x^3\, \varepsilon_x^{(2)}\, \varphi(x)\left(\frac{R}{2x}-1\right)^2\left(\frac{R}{4x}+1\right)dx, \quad (35)$$

where $$\varepsilon_x^{(2)} = \int (\varepsilon-\varepsilon_0)^2\, f_x(\varepsilon)\, d\varepsilon. \quad (36)$$

represents the variance of the dielectric permittivity fluctuations.

The Fourier transform of this correlation function will be needed later and is given by:

$$\Phi_\varepsilon(k) = (2\pi)^{-3}\int B_\varepsilon(R)\exp(-i\,\vec{k}\,\vec{r})\, d^3R$$

$$= \left[1/(2\pi^2 k)\right]\int_0^{\infty} B_\varepsilon(R)\sin(kR)\, R\, dR. \quad (37)$$

Using (35) it is also not difficult to show that

$$\Phi_\varepsilon(k) = \frac{N}{V}\frac{1}{(2\pi)^3}\int_0^{\infty}\left[\frac{4\pi}{3}x^3\, f(kx)\right]^2 \varepsilon_x^{(2)}\, \varphi(x)\, dx, \quad (38)$$

where $$f(kx) = 3\left[\sin(kx) - kx\cos(kx)\right]/(kx)^3\,. \quad (39)$$

For a monodisperse hydrosol where $\varphi(x) = \delta(x-a)$, and $f_x(\varepsilon) = \delta(\varepsilon-\varepsilon_m)$, we find that

$$\Phi_\varepsilon^{mono}(k) = \frac{N}{V}\frac{(\varepsilon_m-\varepsilon_0)^2}{(2\pi)^3}\left[\frac{4\pi}{3}a^3 f(ka)\right]^2$$

$$= C_H\frac{(\varepsilon_m-\varepsilon_0)^2}{6\pi^2}a^3 f^2(ka). \quad (40)$$

SCATTERING CROSS-SECTION

Consider a plane-parallel wave $A_0\exp(i\kappa_0'\,\vec{n}\,\vec{r})$ falling on a certain part V_s of the volume V. (here $\vec{n}$ is a unit vector pointing in the direction of propagation; $\kappa_0' = \varepsilon_0\kappa_0$). The fluctuating field outside of the scattering volume V_s, caused by scattering due to the particles inside this volume, is given by (31):

$$\varphi^0 = \kappa_0^2\,\hat{G}\,\varepsilon\,\Psi^0; \quad (41)$$

where the average field Ψ^0 is represented by a plane-parallel wave [4] $$\Psi^0(\vec{r}) = A_0\exp(iq\,\vec{n}\,\vec{r}). \quad (42)$$

Here q is a wave vector. It corresponds to the Fourier transform of a bi-local Green function $G^0 = (\hat{L}^0)^{-1}$ and can be expressed by the equation

$$q^2 = \kappa^2 + \left(\kappa_0^4/q\right)\int_0^{\infty} B_\varepsilon(R)\exp(i\kappa R)\sin(qR)\, dR. \quad (43)$$

When the following condition is valid,

$$C_H\int\left(\varepsilon/\varepsilon_0 - 1\right)^2 f_x(\varepsilon)\, d\varepsilon \;<<\; 1, \quad (44)$$

the integral in (43) is small compared to κ^2 so that $q \cong \kappa$ Neglecting higher order terms we obtain

$$q = q' + i\,q'', \quad (45)$$

$$q' = \kappa\left[1 + (1/8)\left(\kappa_0/\kappa\right)^4\right]\int_0^{\infty} B_\varepsilon(z/2\kappa)\sin z\, dz, \quad (46)$$

$$q'' = (\kappa/2)\left(\kappa_0/\kappa\right)^4\int_0^{\infty} B_\varepsilon(z/2\kappa)\sin^2 z\, dz. \quad (47)$$

During the derivation of the scattering cross-section we will consider that the field point is situated in the Fraunhofer diffraction zone, *i. e.*

$$|\vec{r} - \vec{r}'| \cong \vec{r} - \vec{n}^s\,\vec{r}\,, \quad (\vec{n}^s \equiv \vec{r}/r).$$

Then

$$\left\langle \varphi^0\,\varphi^{*0}\right\rangle \cong \left[\kappa_0^4 A_0^2/\left(16\pi^2 r^2\right)\right]\times$$

$$\int_{V_s}\int_{V_s}\exp\{\, i[\kappa\,\vec{n}_s(\vec{r}'' - \vec{r}') - q'\,\vec{n}\,(\vec{r}'' - \vec{r}')] \quad (48)$$

$$-\, q''\,\vec{n}\,(\vec{r}' + \vec{r}'')\}\, B_\varepsilon(\vec{r}' - \vec{r}'')\, d^2\vec{r}'\, d^3\vec{r}''.$$

Introducing the new variable $\vec{R} = \vec{r}' - \vec{r}''$ and integrating over $\vec{r}''$, which under the assumption that $q''\,V_s^{1/3} << 1$ gives the scattering volume V_s, we get

$$\left\langle \varphi^0\,\varphi^{*0}\right\rangle \cong \frac{\kappa_0^4 A_0^2 V_s}{16\pi^2 r^2}\int_{V_s}\exp[-i(\kappa\,\vec{n}_s - q'\,\vec{n})\,\vec{R}]\, B_\varepsilon(\vec{R})\, d^3\vec{R}. \quad (49)$$

Regarding the linear size of the scattering volume as big in comparison with the correlation length a of the function B_ε (it corresponds to an average radius of an ensemble of scattering particles) $V_s << a^3$, we can expand the integration in (49) to infinity, and obtain

$$\left\langle \varphi^0\,\varphi^{*0}\right\rangle = \frac{\pi\kappa_0^4 A_0^2 V_s}{2\,r^2}\,\Phi_\varepsilon(\kappa\,\vec{n}_s - q'\,\vec{n}) \equiv \frac{\pi\kappa_0^4 A_0^2 V_s}{2\,r^2}\times$$

$$\Phi_\varepsilon\left(\sqrt{4\kappa^2\left[1-(q'-\kappa)/\kappa\right]\sin^2(\theta/2) + (q'-\kappa)^2}\right) \quad (50)$$

where $\theta = \cos^{-1}(\vec{n}\,\vec{n}')$ is the scattering angle. The energy scattered by the volume V_s in the direction of $\vec{n}_s$ in a solid angle $d\Omega$ will be

$$dE = \left[c\left\langle \varphi^0\,\varphi^{*0}\right\rangle/(8\pi)\right] r^2 d\Omega = S_0\,\sigma_s\, V_s\, d\Omega, \quad (51)$$

where $S_0 = c\,A_0^2/(8\pi c)$ is the energy flux density of the incident wave. From this equation we derive an effective scattering cross-section from a unit volume to a unit solid angle in the direction of $\vec{n}_s$

$$\sigma_s = \left(\pi\kappa_0^4/2\right)\Phi_\varepsilon\left(2\kappa\sqrt{[1+\Delta(\kappa)]\,\sin^2(\theta/2) + \Delta^2(\kappa)/4}\,\right), \quad (52)$$

where

$$\left.\begin{aligned} \Delta(\kappa) &= \frac{q'-\kappa}{\kappa} = \frac{\kappa^2}{2\varepsilon_w^2}\int_0^{\infty} B_\varepsilon(R)\sin R\, dR, \\ \text{or}\quad \Delta(\lambda) &= \frac{2\pi^2}{\varepsilon_w\lambda^2}\int_0^{\infty} B_\varepsilon(R)\sin R\, dR, \end{aligned}\right\} \quad (53)$$

$$B_\varepsilon(R)=\frac{4\pi N}{3V}\int_{R/2}^{\infty}\varepsilon_x^{(2)}\left(\frac{R}{2x}-1\right)^2\left(\frac{R}{4x}+1\right)x^3\varphi(x)\,dx, \quad (54)$$

$$\varepsilon_x^{(2)}=\int_0^{\infty}(\varepsilon-\varepsilon_0)^2 f_x(\varepsilon)\,d\varepsilon,\ \varepsilon_w=\varepsilon_0+C_H\,\varepsilon_H. \quad (55)$$

The transition from the scalar wave to the electromagnetic field is made by introducing the coefficient $\sin^2\chi$ [4, 6], which takes into account the vector nature of the electromagnetic field. Here $\chi=\cos^{-1}(\vec{n}^E\vec{n}^S)$, where $\vec{n}^E$ is the unit vector of polarization of the incident wave. Let β be the azimuthal angle between vector $\vec{n}^E$ and the projection of the scattering vector $\vec{n}^S$ on a plane orthogonal to the wave vector $q\vec{n}$. Then

$$\sin^2\chi=1-\cos^2\beta\ \sin^2\theta. \quad (56)$$

The scattering cross-section in this case will then become

$$\sigma_s(\theta,\beta)=\frac{\pi}{2}\kappa_0^4(1-\cos^2\beta\ \sin^2\theta)\times \Phi_\varepsilon\left(2\kappa\sqrt{[1+\Delta(\kappa)]\sin^2(\theta/2)+\Delta^2(\kappa)/4}\right). \quad (57)$$

If $q'\to\kappa$, then $\Delta\to 0$, and (57) will coincide with the well-known Rayleigh-Gans-Rocar equation [7, 8], averaged over the particle size distribution function (without considering depolarization effects inside particles which are irrelevant to the shape of phase function).

For unpolarized light (57) should be averaged over the azimuthal angle β, which gives

$$\sigma_s(\theta,\beta)=\frac{\pi}{2}\kappa_0^4(1-\cos^2\beta\ \sin^2\theta)\times \Phi_\varepsilon\left(2\kappa\sqrt{[1+\Delta(\kappa)]\sin^2(\theta/2)+\Delta^2(\kappa)/4}\right), \quad (58)$$

with Φ_ε given by (38).

PHASE FUNCTION

The phase function for scattering by a polydisperse inhomogeneous ensemble of dielectric particles is given by the following equation

$$p(\theta)=\left[2(1+\cos^2\theta)/A_p\right]\times \Phi_\varepsilon\left((2\pi/\lambda)\sqrt{\varepsilon_w\left\{[1+\Delta(\lambda)]\sin^2(\theta/2)+\Delta^2(\lambda)/4\right\}}\right), \quad (59)$$

where ε_w is given by (14), (15) and (10), and the constant of normalization can be computed according to

$$A_p=\int_0^{\pi}(1+\cos^2\theta)\ \Phi_\varepsilon\sin\theta\,d\theta. \quad (60)$$

The phase function (59) is normalized according to the condition

$$0.5\int_0^{\pi}p(\theta)\sin\theta\,d\theta=1. \quad (61)$$

Eqn. (59) together with (53)-(55), (12), (14) and (39) can be used to calculate the scattering phase function for a polydisperse system of particles of different types. The input parameters for calculation of $p(\theta)$ are: the size distribution function of particles $\varphi(x)$, the distribution function of values of dielectric permittivity for a given size $f_x(\varepsilon)$, and the volume concentration of particles C_H.

EXAMPLE

In order to demonstrate the difference in phase functions calculated by the polydisperse and monodisperse approaches we considered the following two simple cases:

Case 1.

The size distribution function is given by

$$\varphi(x)=\begin{cases}c_x\,x^{-2.5}, & a_x\le x\le b_x,\\ 0, & elsewhere,\end{cases} \quad (62)$$

here

$$c_x=1.5/\left(a_x^{-1.5}-b_x^{-1.5}\right). \quad (63)$$

The dielectric permittivity distribution function for a given size x is represented as a superposition of rectangular and Dirac delta-function:

$$f_x(\varepsilon)=\alpha_x\Pi(\varepsilon)+(1-\alpha_x)\delta(\varepsilon-\varepsilon_m), \quad (64)$$

here

$$\alpha_x=(x-a_x)/(b_x-a_x) \quad (65)$$

$$\Pi(\varepsilon)=\begin{cases}\pi_\varepsilon, & \varepsilon_0<\varepsilon<2\varepsilon_m-\varepsilon_0,\\ 0, & elsewhere,\end{cases} \quad (66)$$

$$\pi_\varepsilon=1/\left[2(\varepsilon_m-\varepsilon_0)\right]. \quad (67)$$

This case corresponds to a polydisperse hydrosol with the size-dependent dielectric permittivity distributed between values of ε_0 and $2\varepsilon_m-\varepsilon_0$.

Case 2.

The size distribution function is taken identical to the one used in *Case 1* and given by (62)-(63). The dielectric permittivity distribution function for a given size x is represented by Dirac delta function [5]:

$$f_x(\varepsilon)=\delta(\varepsilon-\varepsilon_m). \quad (68)$$

This case corresponds to a monodisperse hydrosol with the unique value for the dielectric permittivity equal to ε_m.

Due to spatial limitations we cannot display the pictures associated with both considered cases. We strongly emphasize that neglecting the dielectric permittivity distribution function will cause differences in the resulting phase function in the range of 50%, which can be regarded as very significant.

CONCLUSION

We have shown here that our formulation gives a more general expression for scattering of light by a polydisperse ensemble of dielectric particles than in the Rayleigh-Gans-Rocar approximation [7, 8]. For the special case of a particle size distribution represented by a single dielectric permittivity (a one-component hydrosol) our results reduce to the Rayleigh-Gans-Rocar approximation. For a natural situation such as a coastal environment, the difference between our volume scattering function and conventionally derived scattering functions can be as large as 50% for the particle size distributions $(x<10\lambda)$ considered here. In view of such

potential differences, a similar approach to deal with the larger particles in coastal waters should be considered.

ACKNOWLEDGMENT

The authors wish to thank continuing support at the Naval Research Laboratory through the Littoral Optical Environment (LOE 6640-06) and Optical Oceanography (OO 73-5051-05) programs. This article represents NRL contribution NRL/PP/7331–96–0002.

APPENDIX: DERIVATION OF THE CORRELATION FUNCTION

Using (15) we can write

$$\langle \varepsilon(\vec{r}_1)\,\varepsilon(\vec{r}_2)\rangle \equiv B_\varepsilon(\vec{r}_1,\vec{r}_2) = (C_H\varepsilon_H)^2 - C_F\varepsilon_H + \left\langle \sum_{n=1}^{N}(\varepsilon_n-\varepsilon_0)\big(\theta(a_n-|\vec{r}_1-\vec{r}_n|)+\theta(a_n-|\vec{r}_2-\vec{r}_n|)\big)\right\rangle + \quad (1a)$$

$$\left\langle \sum_{n=1}^{N}\sum_{m=1}^{N}(\varepsilon_n-\varepsilon_0)(\varepsilon_m-\varepsilon_0)\theta(a_n-|\vec{r}_1-\vec{r}_n|)\,\theta(a_m-|\vec{r}_2-\vec{r}_n|)\right\rangle,$$

The average in the second and third summations according to (1) and (14) is equal to $C_H\varepsilon_H$. In the double summation term we extract the $m=n$ term:

$$B_\varepsilon(\vec{r}_1,\vec{r}_2) = -(C_H\varepsilon_H)^2 + \left\langle \sum_{n=1}^{N}(\varepsilon_n-\varepsilon_0)^2\theta(a_n-|\vec{r}_1-\vec{r}_n|)\theta(a_n-|\vec{r}_2-\vec{r}_n|)\right\rangle + \left\langle \sum_{n=1}^{N}(\varepsilon_n-\varepsilon_0)\theta(a_n-|\vec{r}_1-\vec{r}_n|)\right\rangle \times \quad (2a)$$

$$\times\left\langle \sum_{m=1,m\neq n}^{N}(\varepsilon_m-\varepsilon_0)\theta(a_m-|\vec{r}_2-\vec{r}_m|)\right\rangle.$$

By neglecting the terms where $\sim 1/N$, (because $N>>1$) and explicitly introducing the averaging operation according to (4), (5) and (7), we have

$$B_\varepsilon(R) = (N/V)\int_V d^3\rho\int_0^\infty dx\,\varphi(x)\int d\varepsilon\, f_x(\varepsilon) \times(\varepsilon-\varepsilon_0)^2\theta(x-|\rho|)\theta(x-|\vec{R}+\vec{\rho}|). \quad (3a)$$

By integrating over the polar angle, we obtain

$$B_\varepsilon(R) = (2\pi N/V)\int_0^\infty \varepsilon_x^{(2)}\varphi(x)\,dx\int_0^x \rho^2 d\rho \times\int_{-1}^{1} d\eta\;\theta\left(x-\sqrt{\rho^2+R^2+2\rho R\eta}\right), \quad (4a)$$

where

$$\varepsilon_x^{(2)} = \int d\varepsilon\, f_x(\varepsilon)(\varepsilon-\varepsilon_0)^2. \quad (5a)$$

For convenience let us introduce the function

$$D(x,R,\rho) = (x^2-R^2-\rho^2)/(2R\rho), \quad (6a)$$

with which we can rewrite (4a) as

$$B_\varepsilon(R) = (2\pi N/V)\int_0^\infty \varepsilon_x^{(2)}\, I(x)\;\varphi(x)\;dx, \quad (7a)$$

where

$$I(x) = \int_0^x J(x,\rho)\rho^2 d\rho, \quad (8a)$$

and

$$J(x,\rho) = \int_{-1}^{1}\theta(D-\eta)\,d\eta = 2\,\theta(D-1)+(1+D)\,\theta(1-D^2). \quad (9a)$$

Integrating (9a) with (8a)and after analyzing the behavior of D in a $R\rho$-plane, we find

$$I(x) = (2/3)\theta(2x-R)\,x^3\left[R/(2x)-1\right]^2\left[R/(4x)+1\right]. \quad (10a)$$

After inserting (10a) in (7a), we obtain formula (35) for the correlation function

$$B_\varepsilon(R) = \frac{N}{V}\int_{R/2}^{\infty}\frac{4\pi}{3}x^3\varepsilon_x^{(2)}\varphi(x)\left(\frac{R}{2x}-1\right)^2\left(\frac{R}{4x}+1\right)dx. \quad (11a)$$

We also present here the value of the correlation function and its derivative at $R=0$

$$B_\varepsilon(0) = \frac{N}{V}\int_0^\infty\frac{4\pi}{3}x^3\varepsilon_x^{(2)}\varphi(x)\;dx = C_H\,\varepsilon_H^{(2)}, \quad (12a)$$

where

$$\varepsilon_H^{(2)} = \int_0^\infty \varepsilon_x^{(2)}x^3\varphi(x)dx\Big/\int_0^\infty x^3\varphi(x)dx, \quad (13a)$$

$$\left.\frac{\partial B_\varepsilon(R)}{\partial R}\right|_{R=0} = -\frac{N}{V}\int_0^\infty \pi x^2\varepsilon_x^{(2)}\varphi(x)\;dx = -\left[3C_H/(4a^3)\right]\int_0^\infty x^2\varepsilon_x^{(2)}\varphi(x)\;dx. \quad (14a)$$

REFERENCES

[1] V. I. Khalturin (*a.k.a.* Vladimir I. Haltrin), "On the Dielectric Permittivity of Sea Water" (in Russian), Marine Hydrophys Research [Morskie Gidrofizicheskie Issledovaniya], No. 3(78), pp. 121-144, 1977.

[2] V. I. Khalturin (*a.k.a.* Vladimir I. Haltrin), Computation of a Scattering Phase Function on a Hydrosol Particles in a Bi-Local Approximation (in Russian), Report # VINITI 249-84Dep., Marine Hydrophysical Institute, Sevastopol, 1984, p. 13.

[3] L. L. Foldy, "The Multiple Scattering of Waves. 1. General Theory of Isotropic Scattering by Randomly Distributed Scatterers", Phys. Rev., Vol. 67, No.3-4, pp.107-119, 1945.

[4] V. I. Tatarskii and M. E. Gertsenshteyn, "Propagation of Waves in a Medium with Strong Fluctuations of Refractive Index," JETP, Vol. 44, No. 2, pp. 676–685, 1963.

[5] V. S. Vladimirov, Equations of Mathematical Physics, Dekker, New York, 1971, p. 418.

[6] V. I. Tatarskii, The effects of Turbulent Atmosphere on Wave Propagation, NOAA Transl # TT-68-50464, Washington, D.C., 1971, p. 472.

[7] C. F. Bohren and D. R. Huffman, Absorption and Scattering of Light by Small Particles, John Wiley & Sons, New York, 1983, p. 530.

[8] K. S. Shifrin, Scattering of Light in a Turbid Medium, NASA Techn. Transl. F-477, Springfield, VA, 1968, p. 212.

Simulation of RAR Reflectivity Maps of the Sea Surface for Remote Sensing Applications

G. Corsini, G. Manara, A. Monorchio
Department of Information Engineering, University of Pisa
Via Diotisalvi 2, I-56126 Pisa, Italy -
Phone: +39-50-568511 Fax: +39-50-568522
E-mail: gcorsini@iet.unipi.it, manara@iet.unipi.it, mono@iet.unipi.it

Abstract - A numerical procedure for simulating the scattering from the sea surface is applied to the case of Real Aperture Radar (RAR) systems operating at low and intermediate incidence angles. The simulation scheme is based on a physical model of the sea surface derived from its two-dimensional directional spectrum. The scattered electromagnetic field is evaluated by resorting to a two-scale electromagnetic model. Physical parameters can be taken into account in simulations, as for instance the local wind velocity direction and intensity. Numerical results are presented and compared with experimental data available in the literature, in order to demonstrate the effectiveness of the simulation procedure proposed.

INTRODUCTION

Remote sensing observations of the sea performed by using active microwave systems are strongly influenced by a considerable number of physical phenomena at the air-water interface. Effective analytical models for describing the scattering from the sea surface cannot be defined for all weather conditions (sea state and wind velocity) and radar configurations. In this context, numerical analysis may represent a tool of remarkable importance for a deeper understanding of the different mechanisms contributing to the formation of the radar backscattered signal. In particular, a numerical simulator has been implemented, which allows to analyze the performance of Real Aperture Radars (RAR) operating in marine environments at low and intermediate incidence angles. Attention is focused on the determination of radar reflectivity maps.

The simulation procedure relies on a physical model of the interaction between electromagnetic waves and the sea surface. In particular, the sea surface is described in terms of a classical two-scale model. Given the two-dimensional surface height power spectrum, determined by the local wind velocity, a profile of the sea surface is generated. Moreover, the presence of long wavelength swells can be also considered. This allows to take into account a large variety of sea states and environmental conditions. The generated profile is modelled by means of planar facets that are large in terms of the incident electromagnetic wavelength, but sufficiently small to accurately interpolate the large scale sea components. A small scale roughness is considered on each facet, which is originated by the higher part of the sea spectrum. The scattering from each facet is evaluated by resorting either to Kirchhoff's method or to the small perturbation method, depending on the local incidence angle [1], [2]. Planar facets are interpreted as basic elements for describing the scattered field. This allows to simply account for the main effect to which radar cross-section modulation by ocean waves is usually attributed, i.e. tilting modulation. The differences between backscattered signal intensities observed at upwind and downwind directions have been taken into account by introducing, in the determination of the large scale profile, a modified version of the empirical bispectrum model recently proposed in the literature [3].

NUMERICAL SIMULATION SCHEME

The RAR system simulator is based on the physical model describing electromagnetic wave scattering from the sea surface. A classic two-scale electromagnetic model is adopted, neglecting, for the sake of simplicity, effects due to volumetric scattering. The numerical code requires as an input parameter the local wind field, through which the two-dimensional sea wave spectrum is defined. This spectrum is a function of the sea wave propagation vector $\overline{K}$ and can be expressed in polar coordinates as:

$$W(K,\Phi)\, K\, dK\, d\Phi = W(K)\, g(\Phi)\, K\, dK\, d\Phi, \qquad (1)$$

where $W(K)$ is the omnidirectional sea wave spectrum, Φ is the standard angular cylindrical coordinate and $g(\Phi)$ is a suitable directional function. A good compromise between accuracy and computational costs is obtained by using the directional function introduced in [3]:

$$g(\Phi) = \frac{1}{2\pi}\left\{1 + r\cos\left[2\left(\Phi - \Phi_w\right)\right]\right\}, \quad |\Phi - \Phi_w| \le \frac{\pi}{2}, \qquad (2)$$

where Φ_w indicates the wind direction with respect to a standard two-dimensional cylindrical coordinate system and r is a factor which depends on wind velocity.

0-7803-3068-4/96$5.00©1996 IEEE

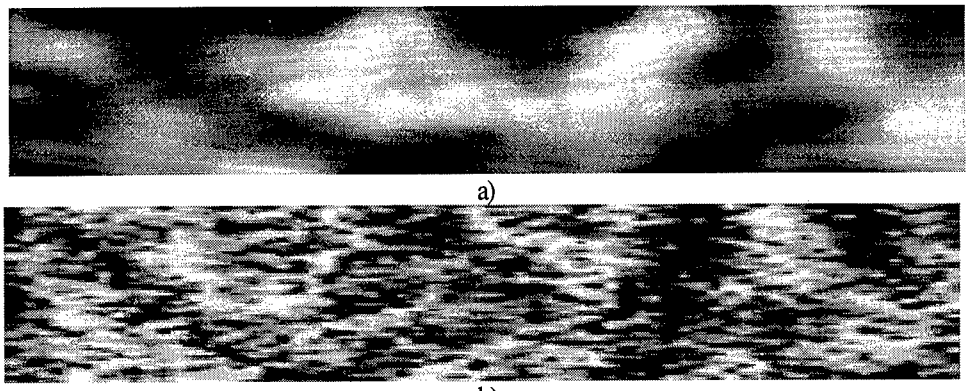


Fig. 1 *a) Sea surface height for a wind velocity of 14.5 m/s. The upwind direction forms an angle of 85° with respect to antenna bearing (range: right-oriented horizontal axis). b) Corresponding reflectivity map. Scene dimensions are 696 m (range) × 123 m (azimuth).*

In particular, the expression given by Pierson and Moskovitz [4] for $W(K)K$, represents a good fit to available experimental results.

Starting from the low frequency part of the two-dimensional power spectrum, a large scale profile of the sea surface is determined by summing up sinusoidal components with random amplitudes whose mean square value is related to $W(K)$. This profile is modelled by means of planar facets that are large in terms of the incident radar wavelength, but sufficiently small to closely interpolate the large scale sea components. Each facet is considered as a rough surface, with a small scale roughness determined by the higher part of the sea spectrum.

The scattering from each facet is calculated by resorting either to Kirchhoff's method [1] or to the small perturbation method [2], depending if the local incidence angle is smaller or greater than 15°, respectively. In the former case, it is assumed that the small-scale roughness does not affect significantly the backscattered signal, so that the facet surface can be considered smooth. Conversely, in the latter case, scattering is dominated by the facet surface roughness, with the small-scale RMS height which must be small, with respect to the incident wavelength, for the small perturbation method to represent a valid approximation. In particular, a random phase, uniformly distributed in the interval $[0,2\pi]$, is associated with field contributions from those facets treated with the small perturbation method. This ambiguity in the phase can be attributed to the unknown relative position of the Bragg's resonant ripple with respect to the facet. By summing up contributions from elementary facets the total backscattered field is obtained, which directly provides, through processing, the reflectivity map of the scene under investigation. In particular, the received base band signal is generated as the sum of the complex envelopes of the elementary echoes due to each facet belonging to the radar resolution cell.

As previously mentioned, the asymmetry between upwind and downwind scattering cross-section measurements of the ocean surface is introduced by a suitable bispectrum model [3]. This asymmetry is due to the difference in surface geometrical properties observed by the radar, caused by the presence of the wind. This latter, even under moderate blowing conditions, forces the crests of waves to be tilted towards the wind direction. Such effects are responsible for the nonlinearities often associated with ocean waves that are connected with higher-order statistics of the sea surface, eventually modifying the surface probability density function.

NUMERICAL RESULTS

Samples of numerical results are shown here to demonstrate the effectiveness of the numerical simulation procedure previously described. It is important to note that the first step of the simulation scheme consists in defining the proper sea wave spectrum, which is the main input parameter of the RAR simulator. An example of a large scale sea height generated for a wind speed of 14.5 m/s measured at an altitude of 19.5 m over the sea surface mean level, is shown in Fig. 1a. Wind velocity forms an angle of 85° with respect to antenna bearing (range), which corresponds to the horizontal axis in the figure. The corresponding reflectivity map obtained is shown in Fig. 1b. The figure is obtained with a carrier frequency of 1.28 GHz, for VV polarization and with an incident angle of 28°.

The behavior of Normalized Radar Cross Section (NRCS) as a function of the angle at which the electromagnetic wave impinges on the sea surface with respect

to grazing is analyzed next. In particular, numerical results obtained by the simulator (dots) are plotted in Fig. 2 and compared with experimental data presented in [5] (dashed line) and [6] (continuous line); the case shown is relevant to upwind observation and to the VV polarization case. The values of NRCS produced by the simulator have been obtained by averaging the value of the unit area backscattering coefficient over the illuminated scene and with a further average over 30 realizations of the reflectivity maps obtained. It is apparent that the simulator provides results that are contained in the range of variability of experimental data. Similar agreements have been obtained for HH polarization.

The possibility of predicting the discussed asymmetry for upwind and downwind observations through the introduction of the bispectrum model proposed in [3] is shown in Fig. 3. Again the agreement with experimental data is good. Statistical tests have also been performed in order to check the probability density function of the texture intensities of reconstructed reflectivity maps. In particular, it has been found that the K distribution fits very well the distribution of simulated data.

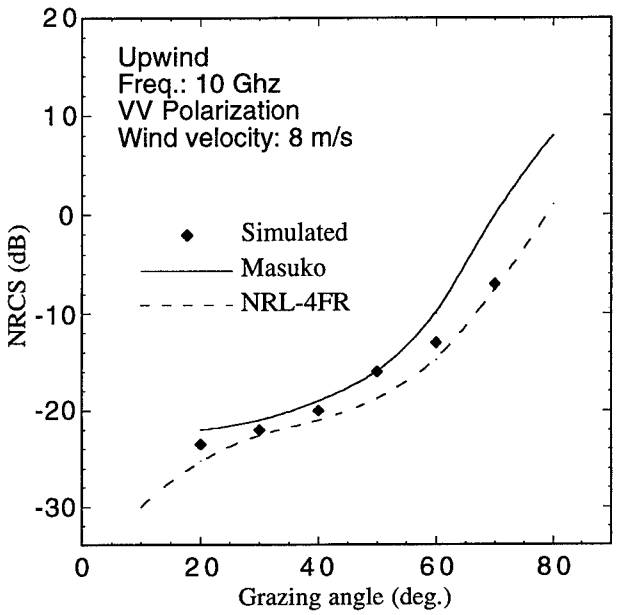


Fig. 2 *Normalized Radar Cross Section (NRCS) as a function of the grazing incidence angle.*

CONCLUSIONS

A simulation procedure has been described, which can be suitably used for generating realistic reflectivity maps of the sea. It is based on a physical model describing the interaction between electromagnetic waves and the sea surface. This latter is characterized through its two-dimensional power spectrum. Local wind field and

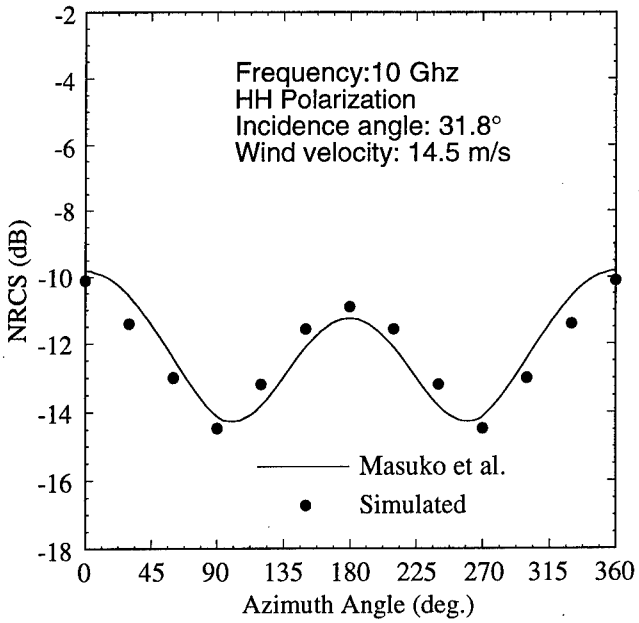


Fig. 3 *NRCS as a function of the angle between observation direction and upwind direction (azimuth angle).*

long wavelength swell are required at the input stage of the numerical algorithm, together with the characteristic parameters of the radar system. Comparisons with experimental results presented in the literature have demonstrated the effectiveness of simulations in different environmental conditions.

REFERENCES

[1] Ulaby F.T., Moore R.K., Fung A.K., *Microwave Remote Sensing*, Artech House Inc., Norwood, 1986.

[2] Ishimaru A., *Wave Propagation and Scattering in Random media*, Academic Press, New York, 1978.

[3] Chen K. S., Fung A. K., Amar F., "An empirical bispectrum model for sea surface scattering", *IEEE Trans. Geosc. Remote Sens.*, vol. 31, n.4, July 1993

[4] W.J. Jr. Pierson and L. Moskowitz, "A proposed spectral form for fully developed wind seas based on the similarity theory of S.A. Kitaigorodskii," *J. Geophys. Res.*, vol. 69, pp. 5181-5190, 1964.

[5] Masuko H., Okamoto K., Shimada M., Niwa S., "Measurements of Microwave Backscattering Signatures of the Ocean Surface Using X Band and Ka Band Airborne Scatterometers", *Journal of Geophysical Research*, Vol. 91(C11), 1986.

[6] Skolnik M. I., *Radar Handbook*, Second Edition, McGraw-Hill Publ. Co., New York, 1990, p. 13-10.

A Simplified Hybrid Model For Radiation Under Discontinuous Canopies

X. Li[1], W. Ni[1], C.E. Woodcock[1], and A. Strahler[1]
[1] Center for Remote Sensing and Department of Geography,
Boston University, 725 Commonwealth Ave., Boston MA, 02215, USA
Tel. +1-617-353-2088, Fax +1-617-353-3200, e-mail: wenge/lix/curtis/alan@crsa.bu.edu

Abstract – The hybrid geometric optical and radiative transfer (GORT) model [1] for the radiation climate under a discontinuous canopy is simplified for easier application by approximation of the multiple scattering. The approximation involves decoupling the multiple scattering into path scattering within the canopy layer and multiple bouncing between the canopy layer and the ground surface. A three-stream approximation is used for multiple bouncing. The path scattering (including reflectance and transmittance) is approximated as functions of mean depth of single scattering source distribution and leaf albedo by extending the analytical solutions of path scattering parameters for a homogeneous layer with limited optical thickness. The approximated path scattering agrees reasonably well with the numerical solutions of the GORT model.

By combining path scattering and multiple bouncing, the approximated downwelling radiation at the forest floor and upwelling radiation at top of the forest are close to the numerical solutions by the GORT model. The signature of the sunlit crown surface can also be approximated by the product of the canopy path reflectance parameter and the total gap probability in the discontinuous plant canopies. Through this, the signature of sunlit crown surface, a parameter required by the pure GO model can be derived. The calculated signature of sunlit crown surface agrees well with measurements made in a conifer forest in Howland, Maine.

INTRODUCTION

The hybrid geometrical-optical radiative-transfer (GORT) model was designed to simulate the radiation environment above, within, and below discontinuous forest canopies [1]. This model incorporates directly the three-dimensional effects of the canopy structure and leaf spectral properties on shortwave radiation. Our study [2] showed that GORT model has more advantages than either pure RT or pure GO approaches in modeling solar radiation transmission in discontinuous plant canopies. But in the GORT model, numerical integration is used for successive orders of scattering, which makes GORT too complicated to apply for canopy reflectance modeling. In this study, an approach based on the analytical solutions of path scattering of canopies is used to simplify the full hybrid GORT model.

PATH SCATTERING FOR DISCONTINUOUS PLANT CANOPIES

This study started with the investigation of the path scattering for a homogeneous layer with limited thickness. First a semi-infinite homogeneous layer was divided into a layer with limited thickness and a semiinfinite layer. Based on Hapke's solutions of the Kubelka-Munk equation for a semiinfinite homogeneous layer [3], the analytical formula of path scattering parameters can be obtained by decoupling the multiple scattering in the semiinfinite layer into multiple scattering within the limited optical thickness homogeneous layer and the multiple bouncing between the limited thickness layer and its lower bound which is also a semiinfinite layer. Detailed derivation is described in [4]. Fig.1 comparies the analytical solutions of path scattering with the numerical calculation from GORT model for homogeneous canopy layer. The parameter values used are: projected foliage density (isotropic); $\tau = 1.0m^{-1}$; thickness of the layer, h= 0.5 m, 1.5 m, 2.5 m, 3.5 m, 4.5 m, 5.5 m; leaf albedo, ω = 0.1, 0.3, 0.5, 0.7, 0.9, 0.95; solar zenith angle, $\theta_i = 0, 15^0, 30^0, 45^0, 60^0, 75^0, 85^0$.

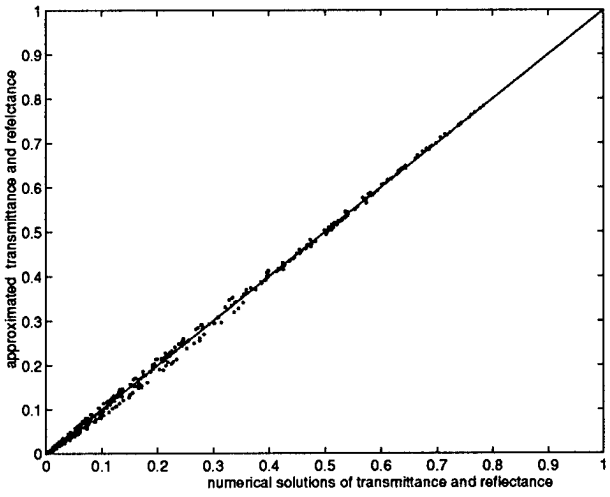


Figure 1: Comparison of analytical solutions of path scattering with the numerical solution for homogeneous layer with limited optical thickness

0-7803-3068-4/96$5.00©1996 IEEE

In a homogeneous layer, the single scattering source distribution has a maximum value at top of the layer and then decreases with the depth. But for a discontinuous plant canopy layer, the maximum value of the single scattering source is not at the top of the layer, but at a different depth depending on the solar zenith angle. The path scattering formula for a homogeneous layer can not directly apply to the discontinuous vegetation canopies.

But Hapke's hemisphere albedo [3] in a homogeneous semi-infinite layer was rewritten as a function of mean depth of single scattering source distribution (SSSD), and medium element albedo. In other words, no matter it is direct sun beam or isotropic diffuse skylight, the upwelling radiation from such a semi-infinite layer is a function of the mean depth of single scattering sources (and medium characteristics) of this layer. With the knowledge of the mean depth of single scattering source distribution for a discontinuous canopy layer, the path scattering can be approximated as functions of mean depth of single scattering source distribution and the medium characteristics by the same approach described above.

In our simplified model for discontinuous plant canopies, the collided and uncollided parts of beam and diffuse irradiance are still calculated through the GO approach. The collided radiation becomes the single scattering source (SSS) within canopies and the mean depth of its distribution can also be obtained through the GO approach. After that, the formula for the path scattering reflectance and transmittance in discontinuous plant canopy layer is approximated as functions of the mean depth of single scattering source distribution, leaf spherical albedo and depth of the canopy layer by an approach similar to the one used for the derivation of path scattering for the homogeneous layer. The approximated reflectance ρ and transmittance t are:

$$\rho(\Delta h) = \frac{R(\Delta h) - f_m R(h - \Delta h)}{1 - f_m^2} \quad (1)$$

$$t(\Delta h) = \frac{R(h - \Delta h) - f_m R(\Delta h)}{1 - f_m^2} \quad (2)$$

where

$$f_m = \frac{1-\gamma}{1+\gamma} e^{-2\gamma\tau h}$$

$$R(\Delta h) = \frac{1-\gamma}{1+2\gamma\tau\Delta h}$$

$$R(h-\Delta h) = \frac{1-\gamma}{1+2\gamma\tau(h-\Delta h)}$$

where h is the thickness of the canopy layer, Δh is the mean depth of single scattering distribution, $\gamma = \sqrt{1-\omega}$, where ω is the leaf albedo, and τ is the projected foliage volume density within a single crown.

For the NIR range, the approximated reflectance and transmittance in a conifer stand in Howland, Maine were compared with the numerical solutions by full GORT model, as shown in Fig.2. The tree parameters used in the calculation are: the horizontal crown radius is $R = 2.2m$, the ratio of the vertical radius to the horizontal radius is 1.6, the count density of the crowns is 0.1161 $1/m^2$. The crowns are randomly centered between 7.5 m to 12.3 m in height, effective leaf area index, $ELAI = 6.6$, the leaf albedo is 0.972, ground surface albedo is 0.0. The path scattering reflectance matches very well with the numerical solution by GORT, but the path scattering transmittance overestimates the numerical solution by GORT a little. In order to test the response of the approximated formula to the foliage volume density and the crown density, Fig.2 shows the comparison between the approximated formula and the GORT model by decreasing ELAI from 6.6 to 2.2, or by decreasing crown density from 0.116 $\frac{1}{m^2}$ to 0.0558 $\frac{1}{m^2}$. Fig.2 also shows that approximation accuracy is not so sensitive to the foliage volume density and the crown count density.

With the approximated path scattering formula for discontinuous plant canopies, combination of the path scattering with the canopy layer and the multiple bouncing between the canopy layer and the ground surface can be used to approximated the downwelling radiation at the bottom of the forest canopy and the upwelling radiation at top of the canopy. By using this approach, the first-order effects of crown geometry are retained while we take full advantage of analytical approximations derived from RT approach to handle multiple scattering.

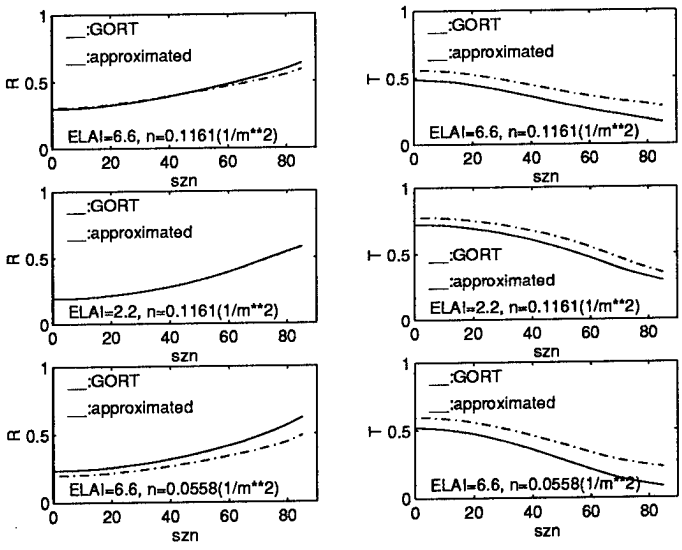


Figure 2: Comparison of approximated path scattering with the numerical solutions by GORT

APPROXIMATION FOR DIRECTIONAL REFLECTANCE

For the bidirectional reflectance (BRDF) calculation, the

pure GO approach requires the field measurements of the signature of sunlit crown surface. Applying the approach we described above, the signature of the sunlit crown surface can also be approximated. Since the signature of the sunlit crown surface is much larger than the signature of the shadowed crown surface, we can approximate the signature of sunlit crown surface by the product of the path reflectance and the total single scattering source proportion, which is $(1 - P_{gap})$. Table 1 shows the calculated and measured signature of sunlit crown surface in the conifer forest, Howland, Maine. Notice that "measured" signature is defined as the exiting radiance from the sunlit crown surface, and the "calculated" one contains the total upward radiance above the canopy, which includes the contribution from shaded crown surface. Further refinement and validation with field measurement is necessary.

Table 1: Calculated and measured signature of sunlit crown surface in Howland, Maine

szn(^{o})	measured	calculated
58.79	0.4506	0.4664
54.54	0.4169	0.4472
43.47	0.3498	0.4094
42.07	0.3425	0.3913

Meanwhile careful measurements over sunlit crown surface are being made now in China. Further validation and better approximation will be done in the future when these measurements are available.

DISCUSSION

Approximation of multiple scattering for discontinuous plant canopy agree reasonable well with the numerical solution of GORT model. The approximated path scattering parameters can also be used for the calculation of the signature of sunlit crown surface and shadowing crown surface for the bidirectionasal reflectance calculation.

ACKNOWLEDGMENT

This work is supported in part by U.S. Army Corps of Engineering under contract DACA89-93-k-00012, by NASA under contract NAS5-31369 and in part by China's NSF under grant 49331020.

References

[1] Li, Xiaowen, Strahler A. H. and Woodcock C.E., "A hybrid geometric optical-radiative transfer approach for modeling albedo and directional reflectance of discontinuous canopies", IEEE Transactions on Geoscience and Remote Sensing, 1995, vol.33, pp.466-480.

[2] W. Ni, X. Li, C.E. Woodcock, R.J. Roujean, R. Davis, and A. Strahler, "modeling solar radiation transmission in Boreal conifer forests", 1996 International Geoscience and Remote Sensing Symposium.

[3] Hapke, B., " Bidirectional reflectance spectroscopy", Journal of Geophysical Research, 1988, Vol.86, No.B4, pp3039-3054.

[4] W. Ni, X. Li, C.E. Woodcock, and A. Strahler, " Decoupling path-scattering of light in a homogeneous layer and multiple bouncing at its non-Lambertian bottom", 1996, to be submitted to Journal of Geophysical Research.

Estimation of some characteristics of ocean waters using optical data (Case I)

Vladimir A.Volynsky
P.P.Shirshov Institute of Oceanology, 23 Krasikova, 117218, Moscow, Russia
tel:(7-095)-335-8506; e-mail: vvladm@mx.iki.rssi.ru

John Marra, Carol Knudson
Lamont-Doherty Earth Observatory of Columbia University, Palisades, NY 10964, USA
tel:(914)-365-8891; fax: (914)-365-8150; e-mail: marra@ldeo.columbia.edu

INTRODUCTION

The connection between the optical characteristics of the sea water measured by remote and *in-situ* methods and concentration of specific elements may be formulated as an inverse problem. Here we present a new algorithm for estimation of water quality parameters such as chlorophyll pigment concentration (Cchl), absorption of "yellow substance" ("y.s") ($a_y(390)$), absorption of detritus ($a_d(400)$), and volume concentration of small and large particles, (Vsp and Vlp) from the spectral diffuse attenuation coefficient $Kd(\lambda)$ and other optical data. The inverse problem was solved by non-linear programming methods with adaptive strategy.

Optical data were collected at bio-optical stations of P16 WOCE expedition going along 152° W longitude from south to north using a Profiling Spectroradiometer, MER-2040 which measures spectral downwelling irradiance $Ed(z,\lambda)$ and upwelling radiance $Lu(z,\lambda)$ (for wavelengths 410, 441,488,520,565,665 nm) as well as beam attenuation c(z,660nm), and fluorescence Fl(z). Chlorophyll concentration values, measured in the surface layer and at fluorescence maximum as well as water type classification based on Kd(490) values allow to say that water belongs to Jerlov's water types (JWT) from IA to II which correspond to Case I, with phytoplankton predomination which is typical to open ocean [1,2].

Kd MODEL AND IT'S PARAMETERS

To obtain the water quality parameters from the vertical attenuation coefficient $Kd(\lambda)$, the two-flow approximation was used

$$Kd(\lambda) = a(\lambda) + b_b(\lambda), \quad (1)$$

where $a(\lambda)$ and $b_b(\lambda)$ are spectral coefficients of absorption and backscattering. For spectral reconstruction of Kd an improved method, which combined [3,4] algorithms was used.

Light field structure was taken into account, and Kd was divided into a diffuse, and a direct components,

$$Kd(\lambda) = [a(\lambda) + b_b(\lambda)]\ \{\mu(\lambda)\ D(\lambda,\theta) + [1 - D(\lambda,\theta)]/\mu_o\} \quad (2)$$

where θ is the solar zenith angle in water, and

$\mu_o = \sqrt{1 - \sin^2\theta / n^2}$, $n = 1.34$, $\mu(\lambda)$ is the average cosine for perfectly diffuse sky, which is should equal 1/1.16, $D(\lambda,\theta)$ = Ed_dif/(Ed_dif + Ed_dir) is determined the diffuse component, i.e. contribution of sky irradiance in the total flux of irradiance, and it depends on θ and wavelength [5]. The dependence of $D(\lambda,\theta)$ on wavelength and zenith angle, described in [6].

For the total volume attenuation coefficient the following model was used

$$a(\lambda) = a_w(\lambda) + Cchl\ a_{chl}^{sp}(\lambda) + a_y(\lambda) + a_d(\lambda), \quad (3)$$

where $a_w(\lambda)$ is the spectral absorption of clean water [7], $a_{chl}^{sp}(\lambda)$ is a specific absorption of phytoplankton pigments, $a_y(\lambda)$ is an absorption of "y.s.", and $a_d(\lambda)$ is absorption of detritus.

Spectral specific absorption of phytoplankton pigments was taken from [8].

For detritus absorption the model of [10] was used

$$a_d(\lambda) = a_d(400)\ \exp[-0.011\ (\lambda - 400)] \quad (4)$$

The model of "y.s." absorption [10] was used

$$a_y(\lambda) = a_y(400)\ \exp[-0.016\ (\lambda - 400)], \quad (5)$$

where the exponential coefficient was taken as an average value ranging from -0.014 to -0.019 nm^{-1}. In previous research [11] this absorption model was based on [9]

$$a_y(\lambda) = Aa_y(390)\ \exp[-\mu\ (\lambda - 500)], \quad (6)$$

where A=1, $\mu = 0.017\ nm^{-1}$ while $\lambda \le 490$ nm and A =0.154, $\mu = 0.011\ nm^{-1}$ when $\lambda \ge 500$ nm. That model supposed that "y.s." consists of two fractions, a variable fraction in spectral range $\lambda \le 490$ nm, and a conservative fraction for waveband $\lambda \ge 500$ nm. But one-parameter spectral dependence will vary together with significant variation of "y.s." content and would not express the conservative properties of the second fraction. On the other hand, the above mentioned detritus absorption (5) is much more like the second fraction of (6). The model (6) may be used as a rough one-parameter estimation of non-biological absorption.

0-7803-3068-4/96$5.00©1996 IEEE

Following [13,14] the scattering of suspended particles was divided into two components: scattering of large (mainly biological particles larger than 1 mm in size and having refraction index n=1.03) and small (mainly mineral particles less than 1 mm in size and with n = 1.15) particles. So the spectral scattering was described in [13] by the following equation

$$b(\lambda) = b_W(\lambda) + b_{sp}(\lambda)Vsp + b_{lp}(\lambda)Vlp, \quad (7)$$

where $b_W(\lambda)$ is backscattering of clean water, $b_{sp}(\lambda)=1.1513\ (400/\lambda)^{1.7}$ ($m^2\ g^{-1}$) and $b_{lp}(\lambda) = 0.3411(400/\lambda)^{0.3}$ ($m^2\ g^{-1}$) are the specific scattering coefficients for small and large particles, respectively, and Vsp and Vlp are volume concentration of small and large particles (in cm^3 of particles per m^3 of water). For back- and forward-scattering in [13] there were yielded the following expressions:

$$b_f(\lambda) = 0.5b_W(\lambda) + (1\text{-}Bs)b_{sp}(\lambda)\ Vsp + (1\text{-}B_l)b_{lp}(\lambda)Vlp \quad (8)$$

$$b_b(\lambda) = 0.5b_W(\lambda) + Bsb_{sp}(\lambda)Vsp + B_lb_{lp}(\lambda)Vlp\ , \quad (9)$$

where Bs = 0.039 and B_l = 0.00064 are the backscattering probability for small and large particles respectively.

From [12] we estimated volume concentration of large and small particles as

$$Vlp = 1.3910^{-2} + 1.68b(550nm) \quad (11)$$

and

$$Vsp = [b(550nm) - 0.312Vlp - 1.710^{-3}] / 1.34 \quad (12)$$

THE MODEL PARAMETERS BOUNDARIES

The inverse problem for the of determination of water quality parameters was formulated as following: to find model's parameters vector **X** which provide minimum of the function

$$\mathbf{F(X)} = \sum_{\lambda} [Kdexp(\lambda) - Kdm(\lambda,\mathbf{X})]^2 \rightarrow \min, \quad (13)$$

where Kdexp is experimentally measured and Kdm is model function of the diffuse attenuation. In addition to (13) there are two constraints put on the parameter vector **X** to provide a physically reasonable solution: one sets the upper and lower boundaries for vector **X,** and the other one constrains maximum deviation of model and experimental spectra. It was shown in [11] that while using the least square roots (LSR) method it is impossible to include above mentioned constraints, and in some cases the solution obtained was far from physically reasonable.

Two main problems of non-linear programming are: how to find an initial point of search and how to find physically reasonable boundaries of parameters vector, i.e. how to find the parameters constraints.

We estimated the boundaries of the model parameters by finding such parts of the optical characteristic spectrum where a single model parameter dominates. Then while neglecting the other model parameters, the upper boundary of this parameter may be obtained. And from the other part of spectrum we calculated the lower boundary. At the wavelength of 660 nm, phytoplankton absorption and forward scattering play the main role in contrast to absorption by "y.s." and detritus, together with backscattering of small particles. So forward scattering may be estimated as $b_f(660) = c(660) - Kd(660)$. Using (8,9), on the assumption that Vsp=0, the upper boundary of Vlp is

$$Vlp^{up} = [b_f(660) - 0.5\ b_w(660)] / (1\text{-}B_l)\ b_{lp}(660) \quad (14)$$

Then from (11, 12) with Vlp equals to Vlp^{up}, the lower boundary of Vsp^{lw} was derived.

Backscattering (9) was subtracting from Kds to obtain the absorbent part $Kda(\lambda) = Kds(\lambda) - b_b(\lambda)$. In the waveband 460-510 nm, Kda curves are convex [1]. We supposed that absorption of phytopigments dominates in this waveband, because both "y.s." and detritus absorption spectra have the concave shape. On the contrary in the waveband 550-570 nm where the Kda is concave, non-phytopigment absorption plays the main role. Thus the upper boundary of Cchl is determined by LSR fitting of $Kda(\lambda)$ by $a_{chl}^{sp}(\lambda)$ in the waveband 460-510 nm. In the same way, the upper boundary of a_y (390) from (8) can be determined by LSR fitting of $Kda(\lambda)$ by $a_y^{sp}(\lambda)$ in the waveband 550-570 nm. The lower boundaries of these parameters are obtained by the same way from $Kda(\lambda)$-$a_{clh}(\lambda)$ in the waveband 550-570 nm for a_y (390) and from $Kda(\lambda)$ - $a_y(\lambda)$ in the waveband 460-510 nm for Cchl.

The average of the upper and lower boundaries was used as the initial points for optimization.

RESULTS AND DISCUSSION

For upper layer model's parameter Cchl correlated with measured values of chlorophyll concentration, only two points are out of general correlation, where the model over estimates the concentration of Cchl by ~ 1.5 X (Fig.1).

As to lower layers , where fluorescence has maximum, and chlorophyll concentration is much higher correlation between measured and calculated chlorophyll concentration may be divided into two types of dependence: for north stations on the one hand , and equatorial and south stations on the other. We suggest two different types of phytoplankton population dominating north and south of the equator.

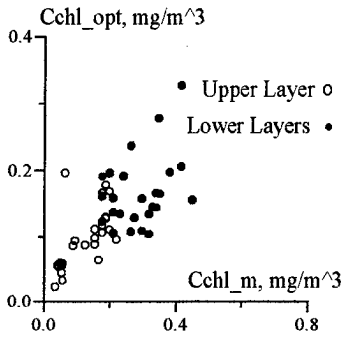


Fig. 1. Measured (_m) and calculated (_opt) chlorophyll concentration

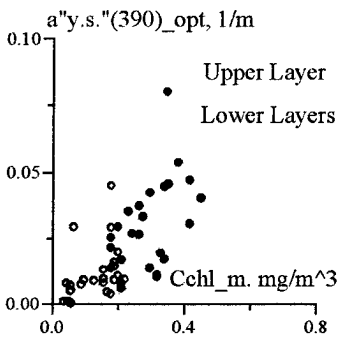


Fig. 2. "Yellow substance" and measured chlorophyll concentration.

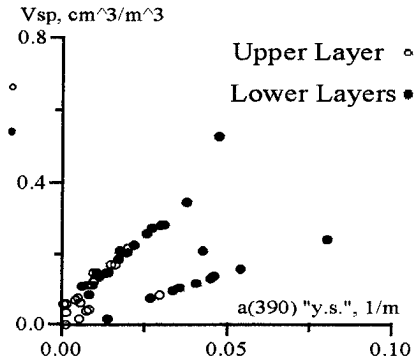


Fig. 3. Volume concentartion of small particles and "yellow substance"

The same results may be obtained from correlation between absorption of "y.s."-detritus in comparison with measured chlorophyll concentration (Fig.2). This correlation is more or less homogeneous for the upper layer and divided into two different dependence for lower layers. Existence of a high correlation between chlorophyll content and absorption of "y.s."-detritus is typical of Case 1 waters.

For relatively clean waters, the contribution of "y.s." and detritus could be hardly separated. But comparison of the model's parameter corresponding to volume concentration of small particles and absorption of "y.s."-detritus shows the high correlation between them. It may be interpreted that contribution of detritus absorption dominates in these waters. For small concentration of chlorophyll, detritus content is very small, and correlation is much lower. This effect is more obvious in the upper layer. For deeper layers the correlation is higher in comparison with the upper layer. Moreover for deeper layers it may be observed two type of dependence (Fig. 3).

This research showed how optical *in situ* measurements may be used for estimation of bio-optical properties of Case 1 waters primarily from the spectral diffuse attenuation coefficient. If beam attenuation were used in addition, the model permitted an estimation of back- and forward-scattering separately, which improved the solution accuracy.

The principle of the dominating parameter in specific spectral bands allows to find physically reasonable boundaries and initial points to solve the inverse problem by non-linear methods.

REFERENCES

[1] A.Morel, L.Prieur, "Analysis of variations in ocean color," Limnol. Oceanogr., 22, 1977, pp. 709-722.

[2] C.D.Mobly, "Light and Water," Acad. Press, 1994, 577p.

[3] V.A.Volynsky, A.I.Sud'bin, "Statistical analysis of spectra of vertical attenuation coefficient," Oceanology, 32, 1992, pp. 821-829.

[4] R.W.Austin, T.J.Petzold, "Spectral dependence of the diffuse attenuation coefficient of light in ocean waters: A re-examination using new data," Proc. SPIE, Ocean Optics X, 1302,1990, pp. 79-93.

[5] N.G.Jerlov, "Marine Optics," Elsevier, Amsterdam, 1976.

[6] V.N.Pelevin, "Solar radiation in ocean," Ocean optics, v.1, Chap. 10, Moscow, Nauka Pub., 1983.

[7] R.C.Smith, K.S.Backer, "Optical properties of clearest natural waters (200-800 nm)," Appl. Opt., 20, 1981, pp. 177-184.

[8] C.L.Gallegos, D.L.Correl, and J.W.Pierce, "Modeling spectral diffuse attenuation, absorption, and scattering coefficients in a turbid estuary," Limnol. Oceanogr., 35, 1990, pp. 1486-1502.

[9] O.V.Kopelevich, S.V.Ljutzarev, and V.V.Rodionov, "The spectral light absorption by the 'yellow substance' of ocean water," Oceanology, 29, 1989, pp. 409-414.

[10] C.S.Roesler, M.J. Perry and K.L.Carder, "Modelling in situ phytoplankton absorption from total absorption spectra in productive inland marine waters," Limol. Oceanogr., 34, 1989, pp. 1510-1523.

[11] V.A.Volynsky, "Adaptive optimization algorithms in inverse hydro-optics problems," Proc. SPIE, 2048, 1993, pp. 93-105.

[12] O.V.Kopelevich, "Small-parameter model of optical properties of sea water," Ocean optics, v.1, Chap. 8, Moscow, Nauka Pub., 1983.

[13] V.I.Haltrin, G. Kattawar, "Light fields with Raman scattering and fluorescence in sea water," Tech. Rept., Dept. of Pysics, Texas A&M Univ., College Station, 1991.

THE SYNTHESIS OF OPTIMAL STRUCTURE OF RADAR USING POLARIZATION ADAPTATION

Dr.,Prof. Loutin E.A., Dr.,Prof. Kozlov A.I., Dr.,Prof. Logvin A.I.

The Moscow State Technical University of Civil Aviation Kronstadtsky Blvd.,20 , 125838 ,Moscow ,Russia Tel: 007 095 4571207 ; Fax: 007 095 4571202

Abstract-This paper is devoted to a polarization signal processing of an active radar. The structure synthesis of the polarization adaptable radar receiver is made on the basis of the using nonlinear optimal Markov's filtration. It was derived equations of a measuring dispersion estimation of polarization parameters. The receiver construction features was detected taking into account a parameter correlation.

A radar, which use a polarization spacing of a signal , has the highest effectiveness if it adapts to the receiving signal polarization. Let's determine the structure of such radar and it's parameters.
Suppose that an elliptic polarized wave comes into areceiver input port

$$\bar{E}(t) = \bar{e}_1 \dot{E}_1(t) + \bar{e}_2 \dot{E}_2(t) \qquad (1)$$

where : $\vec{e}_1, \vec{e}_2$ - are a wave polarization basis; $\dot{E}_i(t)$ - are a component of an additive mixture of a signal $\dot{S}_i(t)$ and an interference $\dot{n}_i(t)$.
If wave unit vectors represent in a linear basis , signal components may be written as [1]:

$$\begin{cases} S_x(t) = \sqrt{\dfrac{P}{2}}\sqrt{1+\cos 2\varepsilon(t)\cos 2\beta(t)}\cos(\omega_0 t + \varphi_0) \\ S_y(t) = \sqrt{\dfrac{P}{2}}\sqrt{1-\cos 2\varepsilon(t)\cos 2\beta(t)}\cos(\omega_0 t + \varphi_0) \end{cases} \qquad (2)$$

where : P- is acoefficient' which is proportional to the radiated power; $\varepsilon(t)$ - is an ellipticity angle of a polarezation ellipse; $\beta(t)$ - is an orientation angle of a po ellipse; ω_0 - is a carrier frequency; φ_0 - is a phase shift.

Suppose, that all useful signal parameters are determind one, except the parameters, that characterize a wave polarization condion $\beta = \beta(t)$ and $\varepsilon = \varepsilon(t)$. AN adaptive radar structure is found with the help a nonlinear optimal Markov's filtration. A state vector is a two-component one in this instance

$$\Lambda(t) = \left\| \beta(t), \varepsilon(t) \right\|^T$$

where : T - means a transpasition sign
And the observation equation take a form:

$$\vec{E}(t) = S(\Lambda(t), t) + n(t)$$

where : $\vec{E}(t) = \left\| E_1(t), E_2(t) \right\|^T$ is a specified realization vector; $S(\Lambda(t),) = \left\| S_1(\Lambda(t), t), S_2(\Lambda(t), t) \right\|^T$ is a useful signal vector (here and below the vector sign don't use); n(t)= $\left\| n_1(t), n_2(t) \right\|^T$ is a noise interference vector , which has the following characteristics

$$\begin{aligned} &\langle n_i(t) \rangle = 0; \\ &\langle n_i(t) n_i(t+\tau) \rangle = N_{ij}\delta(1-\tau) \end{aligned} \qquad (4)$$

0-7803-3068-4/96$5.00©1996 IEEE

i = 1, 2 ; <.> - is a mathematical expectation sign; (.) - is a Dirak's delta function; N_{ij} - is a covariation matrix , which can be assumed as the diagonal one , when there are noncorrelation noises in receiver channels.

$$N_{ij} = \frac{1}{2}\begin{Vmatrix} N_i & 0 \\ 0 & N_j \end{Vmatrix} \qquad (5)$$

A radar structure optimization will be make in accordance with the nonlinear optimum Markov's filtration [2]. To simplify subsequent analyses let's assume , that there are an inherent receiver noise and Nx=Ny=0 . Suppose , that a component normal a posteriopi probability density has an average value and cumulant K_{ij} . A posteriori dispersion defines present filtering error. In this case the optimum filtering equation of a mathematical expectation ofcondion vector components can be received by a substitution (5) into the equation for priori probability density evaluation value.

$$\dot{\Lambda}^*(t) = \begin{Vmatrix} -\alpha_\beta & 0 \\ 0 & -\alpha_\beta \end{Vmatrix} \times \begin{Vmatrix} \Delta\beta \\ \Delta\varepsilon \end{Vmatrix} + \begin{Vmatrix} K_{\beta\beta} & K_{\beta\varepsilon} \\ K_{\varepsilon\beta} & K_{\varepsilon\varepsilon} \end{Vmatrix} \times \begin{Vmatrix} F_\beta^* \\ F_\varepsilon^* \end{Vmatrix} \qquad (7)$$

where : $\Delta\beta = \beta^* - \beta_0$; $\Delta\varepsilon = \varepsilon^* - \varepsilon_0$ is a polarization ellipse parameter definition; F - is a functional defined for signal nonenergy parameters ε and β in the form:

$$F(\beta,\varepsilon,t) = E^T(t) N_{i,j}^{-1} S(\Lambda^*(t),t);$$

$$F_\beta^* = \frac{\partial}{\partial\beta} F(\beta(t),\varepsilon(t),t)_{\beta=\beta^*}; \qquad (8)$$

$$F_\beta^* = \frac{\partial}{\partial\varepsilon} F(\beta(t),\varepsilon(t),t)_{\varepsilon=\varepsilon^*}.$$

A posteriori distribution cumulants can be determined as

$$\dot{K} = \begin{Vmatrix} \dot{K}_{\beta\beta} & \dot{K}_{\beta\varepsilon} \\ \dot{K}_{\varepsilon\beta} & \dot{K}_{\varepsilon\varepsilon} \end{Vmatrix} = \begin{Vmatrix} -\alpha_\beta & 0 \\ 0 & -\alpha_\varepsilon \end{Vmatrix} \times \begin{Vmatrix} K_{\beta\beta} & K_{\beta\varepsilon} \\ K_{\varepsilon\beta} & K_{\varepsilon\varepsilon} \end{Vmatrix} + \begin{Vmatrix} K_{\beta\beta} & K_{\beta\varepsilon} \\ K_{\varepsilon\beta} & K_{\varepsilon\varepsilon} \end{Vmatrix} \times \begin{Vmatrix} -\alpha_\beta & 0 \\ 0 & -\alpha_\beta \end{Vmatrix} +$$

$$+ \begin{Vmatrix} K_{\beta\beta} & K_{\beta\varepsilon} \\ K_{\varepsilon\beta} & K_{\varepsilon\varepsilon} \end{Vmatrix} \times \begin{Vmatrix} F_{\beta\beta}^* & F_{\beta\varepsilon}^* \\ F_{\varepsilon\beta}^* & F_{\varepsilon\varepsilon}^* \end{Vmatrix} + \begin{Vmatrix} K_{\beta\beta} & K_{\beta\varepsilon} \\ K_{\varepsilon\beta} & K_{\varepsilon\varepsilon} \end{Vmatrix} \times \begin{Vmatrix} \frac{1}{2}N_\beta & 0 \\ 0 & \frac{1}{2}N_\beta \end{Vmatrix} \qquad (9)$$

where : $N_{\beta\varepsilon}$ - is defined by the equation (4) , F_{ij}^* - is second mix function partial derivative matrix components F(Λ^*,t) defined by equation (8) .

Assume, that β (t) and ε (t) are priori independent to simplify the receiver realization. This assumption is correct for radiolocation signals. For instace independent changes of this parameters are possible when radiowaves are passing across nonhomogeneous mediums. In such case it is possible to assume in a stationary mode, that $K_{\varepsilon\beta} = K_{\beta\varepsilon} = 0$. Let's write down the equation (9) in expanded form to find out values of $K_{\beta\beta}$ and $K_{\varepsilon\varepsilon}$ taking this fact into consideration.

$$\begin{cases} \dot{K}_{\beta\beta} = \frac{1}{2} N_\beta - 2 N_\beta K_{\beta\beta} + K_{\beta\beta}^2 F_{\beta\beta}^* \\ \dot{K}_{\varepsilon\varepsilon} = \frac{1}{2} N_\varepsilon - 2\alpha_\varepsilon K_{\varepsilon\varepsilon} + K_{\varepsilon\varepsilon}^2 F_{\varepsilon\varepsilon}^* \end{cases} \quad (10)$$

Now let's determine the cumulants E_{ij} in a stationary mode using algebraic methods of a temporary averaging instead differential equations (10).

$$\begin{cases} \frac{1}{2} N_\beta - 2\alpha_\beta \overline{K}_{\beta\beta} + \overline{K}_{\beta\beta}^2 \overline{F}_{\beta\beta}^* \\ \frac{1}{2} N_\varepsilon - 2\alpha_\varepsilon \overline{K}_{\beta\beta} + \overline{K}_{\varepsilon\varepsilon}^2 \dot{F}_{\varepsilon\varepsilon}^* \end{cases} \quad (11)$$

Let's determine values of F and F for resolving the (11) equation system, which equal:

$$\overline{F}_{\beta\beta}^* = \overline{F}_{\varepsilon\varepsilon}^* = -\frac{P}{2N_0} = -q^2 \quad (12)$$

and heve been determined taking into account, that the members, which heve arguments β and ε, will be suppressed by filters or reductd considerably. Then it is possible to find the filtering process cumulants by using equation (10) taking into account the equation (12)

$$\begin{aligned} \overline{K}_{\beta\beta} &= \frac{2\alpha_\beta}{q^2}\left(\sqrt{1+\frac{q^2 N_\beta}{4\alpha_\beta^2}} - 1\right) \\ \overline{K}_{\varepsilon\varepsilon} &= \frac{2\alpha_\varepsilon}{q^2}\left(\sqrt{1+\frac{q^2 N_\varepsilon}{4\alpha_\varepsilon^2}} - 1\right) \end{aligned} \quad (13)$$

The last equation shows, that a signal-to-noise ratio increasing decrease a parameter evaluation dispersion and a wandering intensity increasing i.e. N_β and N_ε increase it. In this case in accordance with the expanded form of the optimal filtration equation for the polarization ellipse parameter mathematical expectation may be written in an operator form [3].

$$\begin{aligned} \Delta\beta &= \frac{\alpha_\beta}{\alpha_\beta + D} K_1 S_\beta A\left[E_{yb} - E_{xb}\right]\cos\omega_0 t \\ \Delta\varepsilon &= \frac{\alpha_\varepsilon}{\alpha_\varepsilon + D} K_2 S_\varepsilon C\left[E_{yb} - E_{xb}\right]\cos\omega_0 t \end{aligned} \quad (14)$$

where : S_β - is a controlling component characteristicslope in the evaluation circuit $\beta(t)$; S_ε - is a controlling component characteristic slope in the evaluation circuit $e(t)$; D=d/dt - is an differentiation operator.

An optimal receiver realizing diagram algorithm may be made with the help of the block diagram [Fid.1]. this diagram is in fact two servo systems reducing to zero an effective value difference and the e and в parameterevaluations. It is obvious that the A, B, C function calculation can be made both in an antenna device and on a reduced frequency after it's transforming. Such transforming may be made by a frequency fget generator converter (a multiplier) serves to derive low frequency spectrum components. This diagram transmission gain of the multiplier equals toone. If it is not so in the practice implementation and the transmission gain equal K_{ii} , it can be take into account by a

corresponding correction of the gain of the K_1 and K_2 amplifiers. In this case $K_1 = K_1 / K_{ii};\ K_2 = K_2 / K_{ii}$.

The assumed realization processing let to derive polarization ellipse parameter evaluations and automatic control system streams to minimize differences of β(t) - $\beta^*(t)$ and ε (t) - ε^*(t) , that in fact means a polarization basis. The forming coordinate transformer elements is shown by dotted line. This device may have a difference implementation.

A polarization ellipse indepence don't realized in some cases and then Keв = 0. The filtering algorithm (7) with allowance for (12) take form:

$$\Delta\beta = \frac{\alpha_\beta}{\alpha_\beta + D} S_\beta \left[E_{yb} - E_{xb}\right]\left[K_1 A + K_3 C\right]\cos\omega_0 t$$

$$\Delta\varepsilon = \frac{\alpha_\varepsilon}{\alpha_\varepsilon + D} S_\varepsilon \left[E_{yb} - E_{xb}\right]\left[K_2 C + K_4 A\right]\cos\omega_0 t \qquad (15)$$

A receiver development algorithm, adapting to a polarization in accordance with (15) let to synthesize the block diagram shown on Fig.2. The block diagram comparison (Fig.1 and Fig.2) shows, that if ε (t) and β (t) is correlated additional cross couplings are arriving between the e and в channels.

The equation to define the cumulants of the correlated channels can be written by using realizing algrithm as:

$$\begin{cases} \frac{1}{2} N_\beta - 2\alpha_\beta \overline{K}_{\beta\beta} + \overline{K}^2_{\beta\beta} + \overline{K}^2_{\beta\varepsilon} \overline{F}^*_{\varepsilon\varepsilon} = 0 \\ \frac{1}{2} N_\varepsilon - 2\alpha_\varepsilon \overline{K}_{\varepsilon\varepsilon} + \overline{K}^2_{\varepsilon\varepsilon} \overline{F}^*_{\varepsilon\varepsilon} + \overline{K}^2_{\varepsilon\beta} \overline{F}^*_{\beta\beta} = 0 \\ -\alpha_\varepsilon\left(\overline{K}_{\varepsilon\varepsilon} + \overline{K}_{\beta\varepsilon}\right) - \alpha_\beta\left(\overline{K}_{\beta\varepsilon} + \overline{K}_{\beta\beta}\right) + \overline{K}_{\beta\beta}\overline{K}_{\beta\varepsilon}\overline{K}^*_{\beta\beta} + \overline{K}_{\beta\varepsilon}\overline{K}_{\varepsilon\varepsilon}\overline{K}^*_{\varepsilon\varepsilon} = 0 \end{cases} \qquad (16)$$

The system (16) in an analyticalform can't be solved, that iswhy it's numerical methods solution is presented graphically on Fig.3. As follows from this graphics subject to the ε and β parameter equality the e and в parameter a posteriori dispersion are equal. As the ε parameter goes up, which means the $\varepsilon(t)$ priori dispersion decreasing, the $K_{\varepsilon\varepsilon}$ cumulant is decreased. The signal-to-noise ratio increasing decrease the $K_{\varepsilon\varepsilon}$ cumulant significantly, but with a high parameter meaning this decreasing is practically imperceptible. The same situation can be during a cumulant behavior analyses, when β and θ change.

So the structure of the optimal radar receiver adapting to polarization parameters is defined and there accurate characteristics is derived in this work, that let to define there maximum achievable values.

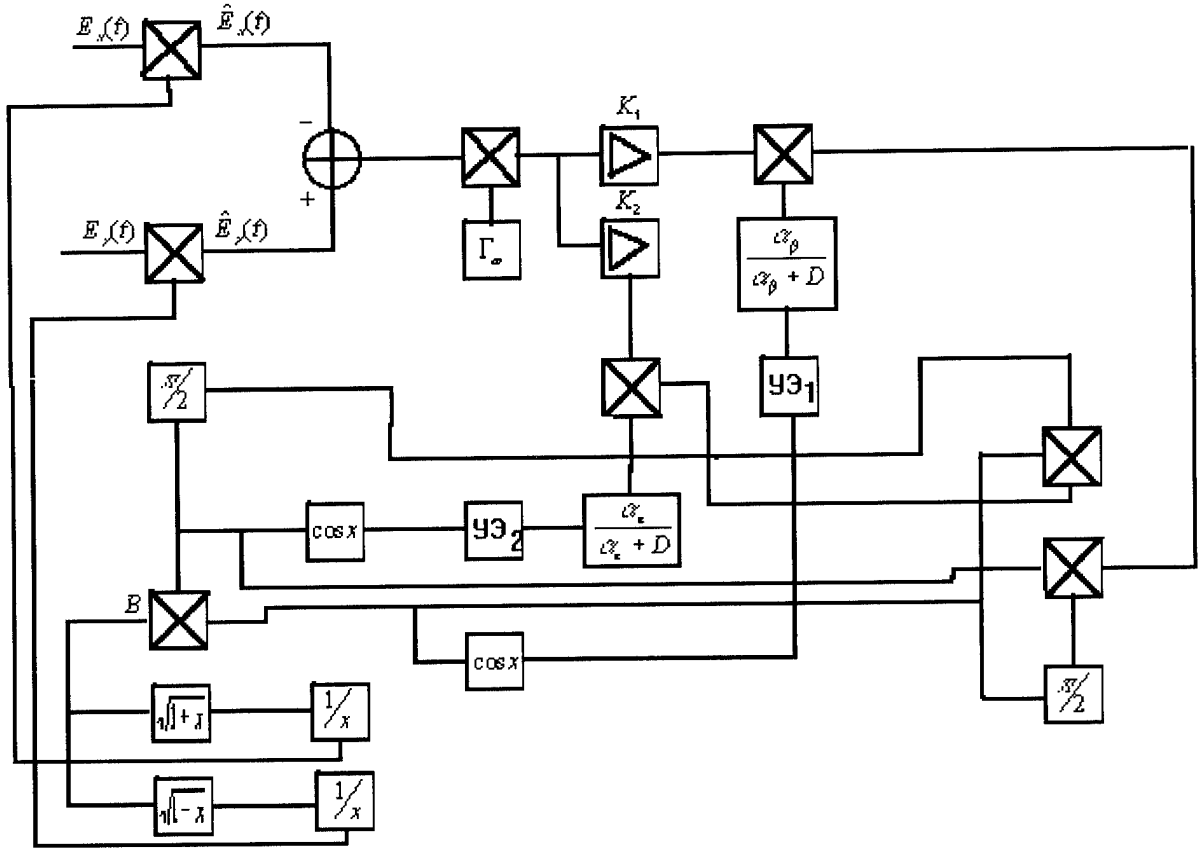


Fig 1. Block Diagram of optimal receiver as adopts to polarizational ellipse parameters

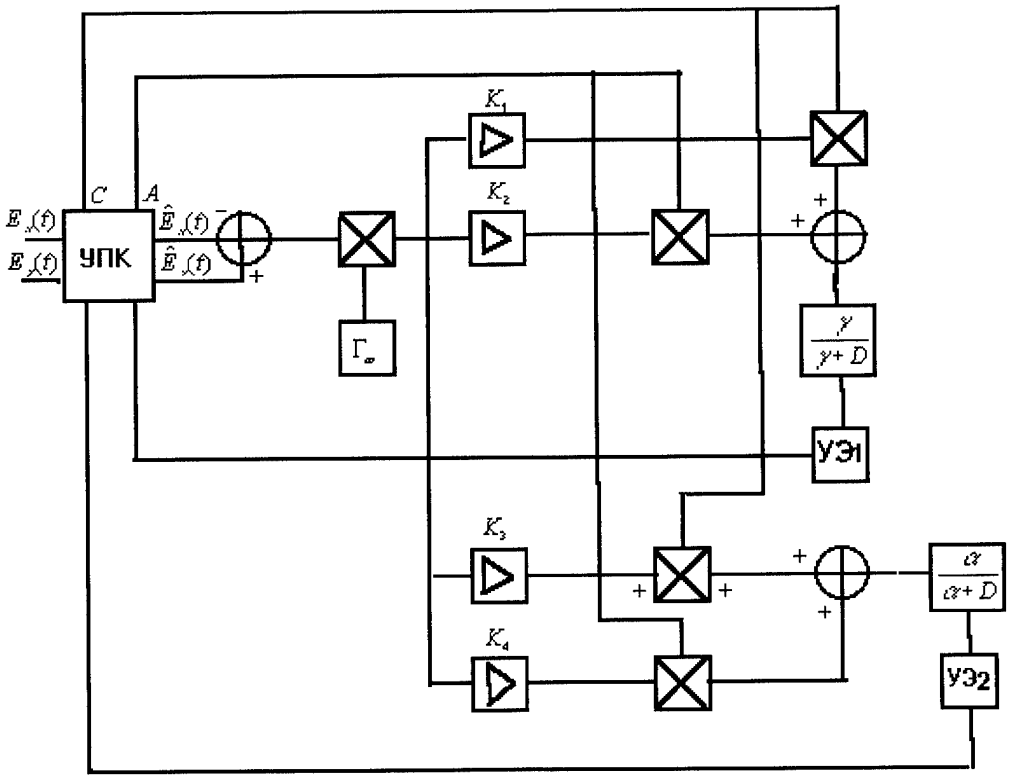


Fig 2. Block Diagram of optimal receiver separatingpolarizing ellipse geometric parameters in presence of statistic comunication between parameters

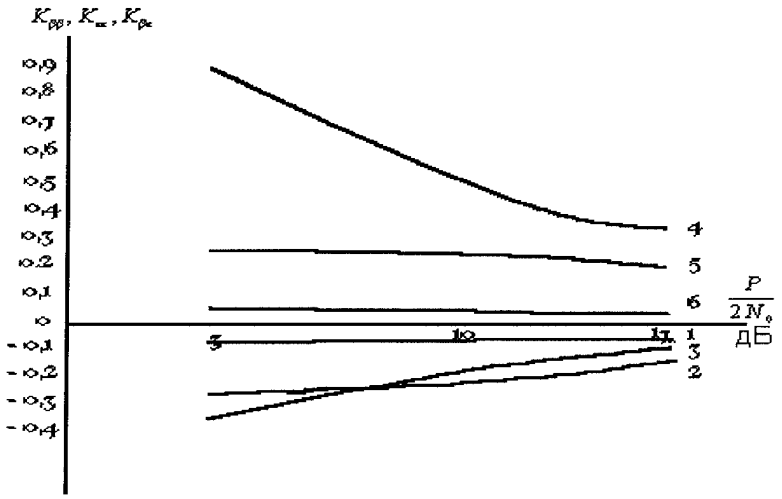


Fig 3. Dependent of a parameter apostoriori distribution cumulant from signal/noise ratio changing γ =10

REFERENCES

1. V.V.Bogorodski., B.D.Kanareikin., A.I.Kozlov " Polarization of earth's surface dissipated radio radiation".

2. M.C.Jarlikov " Application of Markov'snonlinear filtration theory in radiotechnique" M.: Sov. radio,1980, p. 360.

3. A.I.Logvin, E.A.Loutin " Polarized adaption effectivity for airborne radar receivers carrying out the ПАНХ tasks". From the book " Quality increasing of civil aviation radars receiver and operation processes ", M.:MIIGA, 1992

A Method and Algorithm of Computing Apparent Optical Properties of Coastal Sea Waters

Vladimir I. Haltrin
Naval Research Laboratory, Ocean Sciences Branch, Code 7331, Stennis Space Center, MS 39529-5004, USA
Phone: 601-688-4528, fax: 601-688-5379, e-mail: <haltrin@nrlssc.navy.mil>

and

Alan D. Weidemann
Naval Research Laboratory, Ocean Sciences Branch, Code 7331, Stennis Space Center, MS 39529-5004, USA
e-mail: <alanw@indyvih.nrlssc.navy.mil>

Abstract – A new approach is proposed for the calculation of irradiances, diffuse attenuation coefficients and diffuse reflectances in waters with arbitrary scattering and absorption coefficients, arbitrary conditions of illumination and a bottom with Lambertian albedo. The two-stream approach adopted here utilizes experimental dependencies of mean cosines from inherent optical properties in order to achieve appropriate accuracy. This approach can be successfully used for calculation of apparent optical properties in both open and coastal oceanic waters, lakes and rivers.

INTRODUCTION

For many practical applications of remote sensing such as the inference of the diffuse attenuation coefficient and component inversion it is sufficient to know only the integral characteristics of the light field such as upward and downward irradiances or reflectances. Present models used in remote sensing applications for radiative transfer employ simple two-flow or quasi-single scattering approximations which suffer from limited validity over the dynamic range of optical properties found in the ocean. However the limitation to open ocean water types restricts the general usage of these models. Remote sensing applications would be greatly enhanced if we add to it a simple model that can be used over all water types, turbid to open ocean. We present a semi-empirical model that incorporates laboratory and *in situ* measurements of optical properties [1, 2] to encompass the entire range of natural waters.

We start from an exact equation for irradiances derived from the scalar transfer equation. To make this equation solvable it is necessary, however, to approximate the resulting coefficients of the system of two-flow equations. Due to the inaccuracy inherent in the approximations, previous approaches [3] have resulted in insufficient accuracy over some portions of the natural range of optical parameters. We use two main steps to reduce the exact, but analytically unsolvable, system of equations to an approximate system which can be easily solved. The first step consists of replacing the initial arbitrary phase function with the transport phase function. This greatly simplifies the equations, but introduces excessive error. We reclaim the lost accuracy, in the next step, by introducing empirical relationships between the upward and downward cosines and total mean cosine derived from laboratory and *in situ* data [1].

In the case of coastal waters it will be more consistent to take into account variability of upward, downward and total mean cosines ($\overline{\mu}_u$, $\overline{\mu}_d$, $\overline{\mu}$) or their functional dependence on inherent optical properties. The experimental (modeled and measured *in-situ*) data of Timofeyeva [1, 2] show that with the change of $x = B\omega_0/(1-\omega_0+B\omega_0)$ between 0 and 1 (here ω_0 is the single-scattering albedo and B is the probability of backscattering) the total mean cosine $\overline{\mu}$ also varies between 0 and 1, the upward mean cosine $\overline{\mu}_u$ decreases from 1 to ~0.25 at $x \sim 0.08$ and then increases to 0.5 at $x = 1$, and the downward mean cosine $\overline{\mu}_d$ decreases from 1 to 0.5.

The main purpose of this work is to obtain equations which relate inherent optical to apparent optical properties for any input radiance distribution. These equations, which are convenient and precise, are valid in the complete range of variability of optical properties of natural water.

In transfer theory, requirements of both simplicity and precision are mutually exclusive. For a successful resolution of the problem, therefore, we have accepted a compromise by determining the degree of simplicity and precision.

In solving our problem we will use the *self-consistent method* proposed in [4]. For a better understanding of the idea of this method, we quote an example from classical mechanics [5], from which it was adopted. Suppose we have to obtain the equation of motion of a material body around some center of attraction. The law of attraction is unknown to us, or it is known only partially, but in addition we have some information on the shape of trajectories in the form of dependencies between integral parameters of these trajectories. This problem can be solved provided we use the available information to constrain the acceptable solutions. In this example the knowledge of additional information on *consequences* (trajectory parameters) has made it possible to compensate for the lack of information on *causes* (attraction forces).

In the theory of radiative transfer the main *causes* are the inherent optical properties such as the scattering law characteristics (volume scattering and single scattering albedo), and the main *consequences* are the apparent optical

0-7803-3068-4/96$5.00©1996 IEEE

properties, such as the angular distribution of radiance, as a functions of depth. In general, the volume scattering function is only approximately known, with unknown precision. It is impossible in general to calculate the volume scattering function of an actual medium because in many cases the shape of the scattering particles is irregular and often *exotic*, with the optical characteristics of these particles known only approximately. Experimental measurements of the volume scattering function in the small-angles regime becomes complicated due to difficulty in discriminating between unscattered and forward scattered light. The measurements of the volume scattering function in the range of angles close to the backward direction are in principal impossible because one cannot install a receiver before or behind an emitter without considerable distortion in the process of measurement. To overcome this, beam splitting of backscattered light has been utilized with some success. On the contrary because, as a rule, the angular distribution of the scattered light at depth is always less anisotropic than the volume scattering function, and the anisotropy of the direct light of the outer sources is known, the measurements of radiance distribution are less difficult, and the precision of these measurements is restricted only by the perfection of the measuring device.

Thus, in our attempts to solve the problem of light field calculation in a scattering and absorbing medium, we restrict ourselves to the simplest transport approximation of the volume scattering function. The information, which we lose through this simplification, is restored by accepting functional dependencies between integral parameters of the radiance angular distribution, which are derived from an approximation of experimental data.

FORMULATION OF THE PROBLEM

We shall start from the scalar equation describing the transport of optical radiation in a layer of a scattering and absorbing medium of thickness H

$$\left(\cos\theta\frac{\partial}{\partial z}+c\right)L_t(z,\theta,\varphi)=\frac{b}{4\pi}\int L_t(z,\theta',\varphi')\,p(\gamma)\,d\Omega', \quad (1)$$

where $L_t(z,\theta,\varphi)$ is the spectral density of the energetic radiance (or, simply, radiance) of light, θ and φ are the zenith and azimuth angles in the direction of light propagation, measured from the positive direction of the $0z$-axis, $c=a+b$ is the extinction (attenuation) coefficient, a is the absorption coefficient, b is the scattering coefficient, $d\Omega\equiv\sin\theta\,d\theta\,d\varphi$ is the element of solid angle, $p(\gamma)$ is the volume scattering function. Here γ is the light scattering angle, which is determined from the relation: $\cos\gamma=\mu\mu'+\sqrt{(1-\mu^2)(1-\mu'^2)}\cos(\varphi-\varphi')$, where $\mu=\cos\theta$, $\mu'=\cos\theta'$, and the phase function is normalized as follows: $\int p(\gamma)\,d\Omega'=4\pi$. The system of coordinates here is chosen so that the xy-plane coincides with the outer boundary of the medium on which the radiation is incident, while the $0z$-axis is oriented into the medium.

In an anisotropic light-scattering media the phase function $p(\gamma)$ has a distinct diffraction peak near $\gamma=0$. The light rays scattered in a small solid angle near the forward direction ($\gamma\cong 0$) form the halo part of the scattered light and are, for many applications, indistinguishable from the unscattered rays. This suggests that the halo part of the rays should not be regarded as scattered rays, *i.e.* the forward diffraction peak can be eliminated from the volume scattering function [4].

We separate the main part of the halo rays by representing the volume scattering function as a sum of isotropic and anisotropic components:

$$p(\gamma)=2B+(1-2B)\,p_h(\gamma),$$
$$p_h(\gamma)=[p(\gamma)-2B]/(1-2B),\quad \int p_h(\gamma)\,d\Omega'=4\pi, \quad (2)$$

where $B=0.5\int_{\pi/2}^{\pi}p(\gamma)\sin\gamma\,d\gamma$ is the probability of scattering into the backward hemisphere. When the elongation of the phase function is increased, the relation $\lim_{B\to 0}p_h(\gamma)=2\delta(1-\cos\gamma)\equiv 4\pi\,\delta(\varphi-\varphi')\delta(\mu-\mu')$ exists, where $\delta(x)$ is the Dirac delta-function. As $B\to 0$ the phase function $p(\gamma)$ equals the transport phase function

$$p_t(\gamma)=2B+2(1-2B)\delta(1-\cos\gamma),\quad \int p_t(\gamma)\,d\Omega'=4\pi. \quad (3)$$

Substituting $p(\gamma)\equiv p_t(\gamma)+(1-2B)[p_h(\gamma)-2\delta(1-\cos\gamma)]$ into (1), we get

$$\left(\mu\frac{\partial}{\partial\tau}+\alpha\right)L_t(\tau,\theta,\varphi)=\frac{x}{2\pi}\int L_t(\tau,\theta',\varphi')\,d\Omega'+$$
$$\frac{x(1-2B)}{4\pi B}\int[p_h(\gamma)-2\delta(1-\cos\gamma)]\,L_t(\tau,\theta',\varphi')\,d\Omega', \quad (4)$$

where $\alpha=1+x$, $x=b_b/(a+b_b)\equiv B\omega_0/(1-\omega_0+B\omega_0)$, $b_b=bB$ is the backscattering coefficient; $\omega_0=b/(a+b)$ is the single scattering albedo, and $\tau=z(a+b_b)$ is the *transport* optical depth.

Let $L_q(\mu,\varphi)$ be the radiance of external sources at $\tau=+0$ ($z=+0$) (below water surface) and $L(\tau,\mu,\varphi)$ be the radiance of the scattered component minus the halo rays at the optical depth τ. In this case the total radiance distribution $L_t(\tau,\mu,\varphi)\equiv L_t(z,\mu,\varphi)$ can be expressed as

$$L_t(\tau,\mu,\varphi)=L(\tau,\mu,\varphi)+L_q(\mu,\varphi)\theta(\mu)\exp(-\alpha\tau/\mu), \quad (5)$$

where $\theta(\mu)$ is the Heavyside (or step) function defined by: $\theta(\mu)=1,\mu>0;\theta(\mu)=0,\mu\le 0$. In this case α is the attenuation coefficient for the sum of forward and halo rays. In (5) we assume that either the layer of scattering medium is optically thick $\{\alpha(a+b_b)H\equiv(a+2b_b)H>>1\}$, or that its lower boundary reflects light according to Lambert's law. Substituting (5) into (4), we obtain an equation for the radiance of the scattered light (without halo)

$$\left(\mu\frac{\partial}{\partial\tau}+\alpha\right)L(\tau,\mu,\varphi)=\frac{x\,E_0(\tau)+g(\tau,\mu,\varphi)+\Delta(\tau,\mu,\varphi)}{2\pi}, \quad (6)$$

where $E_0(\tau)$ is the scalar irradiance by diffuse light,

$$E_0(\tau)=\int_0^{2\pi}d\varphi\int_{-1}^{1}L(\tau,\mu,\varphi)\,d\mu, \quad (7)$$

$g(\tau,\mu,\varphi)$ is the source function

$$g(\tau,\mu,\varphi)=\frac{x}{2B}\int_0^{2\pi}d\varphi\int_0^1 p(\gamma)L_q(\mu',\varphi')e^{-\frac{\alpha\tau}{\mu'}}d\mu' \qquad (8)$$
$$-\left[2\pi x(1-2B)/B\right]L_q(\mu,\varphi)e^{-\frac{\alpha\tau}{\mu}},$$

$$\Delta(\tau,\mu,\varphi)=\left[2xB/(1-2B)\right]\int_0^{2\pi}d\varphi'\times \qquad (9)$$
$$\int_{-1}^1\left[p_n(\gamma)-2\delta(1-\cos\gamma)\right]L(\tau,\mu',\varphi')d\mu'.$$

Equation (6) is totally equivalent to (1). Introduction of the function $\Delta(\tau,\mu,\varphi)$ in (6) corresponds to including the halo rays in the nonscattered light. The expression (9) completely vanishes in two limiting cases: (a) for isotropic scattering: $p(\gamma)=1$ at $B=0.5$, and (b) for extremely anisotropic scattering: $p(\gamma)=2\delta(1-\cos\gamma)$ at $B=0$.

ENHANCED TWO-FLOW APPROXIMATION

Equation (6) for arbitrary $p(\gamma)$ cannot be solved analytically. But if we neglect the term Δ compared to xE_0+g, we reduce the problem to the case of an exactly solvable transport approximation. However in doing so we decrease the accuracy of our results.

In order to overcome this shortcoming we propose to solve (6) in the terms of self-consistent approximation [4]. This consists of neglecting the value Δ in comparison with xE_0+g, and but then taking it into account later by evaluating the quantity xE_0+g through the two-flow approximation. This technique requires empirical dependencies between the integral parameters of radiance distribution, which have been derived from experimental data.

We introduce downward (E_d) and upward (E_u) irradiances by diffuse light (without halo)

$$E_d(\tau)=\int_0^{2\pi}d\varphi\int_0^1 L(\tau,\mu,\varphi)\,\mu\,d\mu, \qquad (10)$$

$$E_u(\tau)=-\int_0^{2\pi}d\varphi\int_{-1}^0 L(\tau,\mu,\varphi)\,\mu\,d\mu, \qquad (11)$$

and scalar irradiances by diffuse light (without halo)

$$E_{0d}(\tau)=\int_0^{2\pi}d\varphi\int_{-1}^0 L(\tau,\mu,\varphi)\,d\mu, \qquad (12)$$

$$E_{0u}(\tau)=\int_0^{2\pi}d\varphi\int_{-1}^0 L(\tau,\mu,\varphi)\,d\mu. \qquad (13)$$

Average downward and upward cosines of the diffuse light distribution (without halo) would be

$$\mu_d(\tau)=E_d(\tau)/E_{0d}(\tau),\quad \mu_u(\tau)=E_u(\tau)/E_{0u}(\tau). \qquad (14)$$

We introduce average cosine for the diffuse light distribution

$$\mu(\tau)=\int_0^{2\pi}d\varphi\int_{-1}^1 L(\tau,\mu,\varphi)\,\mu\,d\mu\Big/\int_0^{2\pi}d\varphi\int_{-1}^1 L(\tau,\mu,\varphi)\,d\mu, \qquad (13)$$

Applying the operators $\int_0^{2\pi}d\varphi\int_0^1 d\mu\ldots$, $\int_0^{2\pi}d\varphi\int_{-1}^0 d\mu\ldots$ on (6) with $\Delta=0$, using (10)-(14) and replacing the average cosines $\mu_i(\tau)$ $(i=1,2)$ (indices 1 and 2 are equivalent, respectively, to the indices d and u) by their values deep in the layer, we obtain from (6)

$$D_{ik}(\tau)E_k(\tau)=f_i(\tau),\qquad i,k=1,2, \qquad (16)$$

where

$$D_{ik}(\tau)=\begin{pmatrix}\dfrac{\partial}{\partial\tau}+\dfrac{1}{\mu_d} & -\dfrac{x}{\mu_u}\\ -\dfrac{x}{\mu_d} & -\dfrac{\partial}{\partial\tau}+\dfrac{1}{\mu_u}\end{pmatrix}, \qquad (17)$$

$$f_1(\tau)=(x/B)\int_0^{2\pi}d\varphi\int_0^1[2B-\psi(\mu)]L_q(\mu,\varphi)e^{-\frac{\alpha\tau}{\mu}}d\mu\ , \qquad (18)$$

$$f_2(\tau)=(x/B)\int_0^{2\pi}d\varphi\int_0^1\psi(\mu)L_q(\mu,\varphi)e^{-\frac{\alpha\tau}{\mu}}d\mu\ , \qquad (19)$$

$$\psi(\mu)=\frac{1}{2}\int_0^1 p_m(-\mu',\mu)d\mu',\quad p_m(\mu',\mu)\equiv\frac{1}{2\pi}\int_0^{2\pi}p(\gamma)d\varphi. \qquad (20)$$

Here and further in this paper repeated indices imply summation.

We shall look for solution of (16) in the form of a sum of the general and particular solutions

$$E_i(\tau)=A\,a_i\exp(\varepsilon_1\tau)+P\,p_i\exp(\varepsilon_2\tau) \qquad (21)$$
$$+\int_0^{\tau_B}G_{ik}(\tau-\tau')f_k(\tau')d\tau',\quad i,k=1,2,$$

where ε_1 and ε_2 are eigenvalues of equation (16), and G_{ik} is the Green's matrix of this equation, which satisfies the equation $D_{il}G_{lk}(\tau)=\delta_{ik}\delta(\tau)$.

Before writing down the solutions of (21) let us find eigenvalues ε_1 and ε_2. Inserting (21) into (16) we obtain

$$\varepsilon^2-\varepsilon(1/\mu_u-1/\mu_d)-(1-x^2)/(\mu_u\mu_d)=0, \qquad (22)$$

Before solving the quadratic equation (22), let us determine the functional dependencies of the average cosines μ_u, μ_d on optical parameters of the medium. In the majority of two-stream theories [3, 7] the quantities μ_u and μ_d are considered as independent of the optical properties of the medium and such an assumption leads to significant reduction of accuracy in those approaches.

In this work we shall adopt the following two suppositions of the self-consistent approach:

(a) We shall assume that neglecting Δ in (18)-(19) does not have any influence on the magnitude of the negative eigenvalue of the system of equations (16), *i.e.* we assume that it is equal to its exact value ε_e

$$-\varepsilon_1=\varepsilon_e\equiv(1-x)/\overline{\mu}\ . \qquad (23)$$

(b) We will suppose that values μ_u and μ_d are functions of the mean cosine $\overline{\mu}$ and adopt the functional dependencies $\mu_u(\overline{\mu})$ and $\mu_d(\overline{\mu})$ which results from experiment.

After accepting these assumptions we can express the parameter x on $\overline{\mu}$ by installing (23) into (22)

$$x=[\overline{\mu}+\mu_u(\overline{\mu})][\mu_d(\overline{\mu})-\overline{\mu}]/\left[\mu_u(\overline{\mu})\mu_d(\overline{\mu})+\overline{\mu}^2\right], \qquad (24)$$

By inserting into (24) experimental values of $\overline{\mu}$, μ_u and μ_d [1, 2], we obtain the corresponding values of x (see Table1). Table 1 makes it possible to obtain empirical dependencies which connect mean cosines, diffuse reflectance R_∞ and coefficient $k=R_\infty(x)/x$ to the medium parameter $x=b_b/(a+b_b)\equiv B\omega_0/(1-\omega_0+B\omega_0)$.

By imposing the condition of realization of asymptotic behavior of R_∞ at small x and $(1-x)$ given in [8]:

Table 1.

$\bar{\mu}$	$\bar{\mu}_d$	$\bar{\mu}_u$	R_∞	x	R_∞/x
0	0.5	0.5	1.0	1.0	1.0
0.1	0.5249	0.4831	0.671	0.9408	0.7132
0.2	0.5525	0.4545	0.443	0.7970	0.5550
0.3	0.5834	0.4202	0.283	0.6179	0.4580
0.4	0.6184	0.3745	0.171	0.4439	0.3852
0.5	0.6566	0.3311	0.095	0.2959	0.3211
0.6	0.7008	0.3003	0.048	0.1802	0.2664
0.7	0.7536	0.2857	0.0207	0.0967	0.2141
0.8	0.8217	0.3610	0.0082	0.0413	0.1985
0.9	0.9033	0.6849	0.0016	0.0101	0.1584
1.0	1.0	1.0	0.0	0.0	0.25
Experiment [1, 2]				Eqn. (24)	

$$R_\infty(x)=\begin{cases} x/4, & x\ll 1 \quad (\text{or } 1-\bar{\mu}\ll 1),\\ 1-4\sqrt{(1-x)/6}, & 1-x\ll 1 \quad (\text{or } \bar{\mu}\ll 1),\end{cases} \tag{25}$$

we can obtain from the data of Table 1 the following equations

$$\bar{\mu}=a_0+(1-a_0)\sqrt{1-x}+\sum_{n=1}^{6} a_n x^{\frac{n}{3}}, \tag{26}$$

$$\mu_d=\left[1-\bar{\mu}(1-\bar{\mu})^2\sum_{n=0}^{3} b_n\bar{\mu}^{2n}\right]\Big/(2-\bar{\mu}), \tag{27}$$

$$\mu_u=\left[1-\bar{\mu}(1-\bar{\mu})^2\exp\left(\sum_{n=0}^{4} c_n\bar{\mu}^{2n}\right)\right]\Big/(2-\bar{\mu}), \tag{28}$$

$$R_\infty\equiv\frac{1-\bar{\mu}/\mu_d}{1+\bar{\mu}/\mu_u}=\frac{(1-\bar{\mu})^2\left[1-\bar{\mu}(1-\bar{\mu})^2\sum_{n=0}^{3} b_n\bar{\mu}^{2n}\right]}{2-(1-\bar{\mu})^2\left[1+\bar{\mu}\exp\left(\sum_{n=0}^{4} c_n\bar{\mu}^{2n}\right)\right]}, \tag{29}$$

$$k=\frac{1}{4}+d_0\left(1-\sqrt{1-x}\right)+d_1\sqrt[3]{x}+\sqrt[3]{x^2}(1-x)\Big/\sum_{n=2}^{6} d_n x^{n-2}. \tag{30}$$

The values of coefficients a_n, b_n, c_n and d_n are given in Table 2. The correlation coefficients between the quantities of parameters given in Table 1 and those computed by (26)-(30) in all cases exceed 0.99, and mean quadratic deviations are less then 3%.

The functional dependencies of the experimental values of $\bar{\mu}, \mu_u, \mu_d, R_\infty$ and values computed with (26)-(30) are shown on Fig.1.

With inclusion of empirical equations (26)-(28), (22) and (23) will give us the following dependencies for the eigenvalues ε_1 and ε_2:

Table 2.

n	a_n	b_n	c_n	d_n	r_n
0	0.5918	0.0326	-0.0131	1.6330	0.7500
1	-0.7937	0.1661	8.4423	-0.8830	0.3750
2	4.8350	0.7785	-15.6605	0.4631	25.3315
3	-22.8150	0.0228	21.8820	2.3442	-83.6066
4	42.6859		-11.2257	-6.0841	24.7228
5	-35.8945			7.5933	130.6733
6	11.3905			-3.8215	-105.6769

$$-\varepsilon_1\equiv\alpha_\infty=(1-x)/\bar{\mu}\,, \tag{31}$$

$$\varepsilon_2\equiv\alpha_0=1/\mu_u-1/\mu_d+(1-x)/\bar{\mu}\,, \tag{32}$$

It is easy to show that the Green's matrix $G_{ik}(\tau)$ of (16) has the following form: (33)

$$G_{ik}(\tau)=\begin{pmatrix}1 & R_0\\ R_\infty & R_0R_\infty\end{pmatrix}\frac{\theta(\tau)e^{-\alpha_\infty\tau}}{1-R_0R_\infty}+\begin{pmatrix}R_0R_\infty & R_0\\ R_\infty & 1\end{pmatrix}\frac{\theta(-\tau)e^{\alpha_0\tau}}{1-R_0R_\infty},$$

and $$a_1=p_2=1,\qquad a_2=R_\infty,\qquad p_1=R_0\,, \tag{34}$$

where
$$R_\infty=\lim_{\tau\to\infty}E_u(\tau)/E_d(\tau)\equiv\left(1-\bar{\mu}/\mu_d\right)/\left(1+\bar{\mu}/\mu_u\right)$$
$$=\mu_u(1-\alpha_\infty\mu_d)/\left(x\,\mu_d\right)=x\,\mu_u/\left[\mu_d(1+\alpha_\infty\mu_u)\right], \tag{35}$$

is the diffuse reflectance of an infinitely thick layer at $\tau\gg 1$,

$$R_0=\lim_{\tau\to\infty}E_{0u}(\tau)/E_{0d}(\tau)\equiv\left(\mu_d-\bar{\mu}\right)/\left(\mu_u+\bar{\mu}\right)$$
$$=R_\infty\mu_d/\mu_u=\left(1-\alpha_\infty\mu_d\right)/x=x\,/\left(1+\alpha_\infty\mu_u\right), \tag{36}$$

Substituting (33) and (34) into (21) and imposing boundary conditions at $\tau=0$ and $\tau_H\equiv H(a+b_b)$:

$$E_d(0)=E_0\,,\quad E_u(\tau_H)=A_B[E_d(\tau_H)+E_d^f(\tau_H)] \tag{37}$$

where A_B is the albedo of the lower boundary and $E_d^f(\tau)$ is the total flux of the unscattered and halo rays

$$E_d^f(\tau)=\int_0^{2\pi}d\varphi\int_0^1 L_q(\mu,\varphi)\exp(-\alpha\tau/\mu)\,\mu\,d\mu\,, \tag{38}$$

we obtain the equations for the descending and ascending

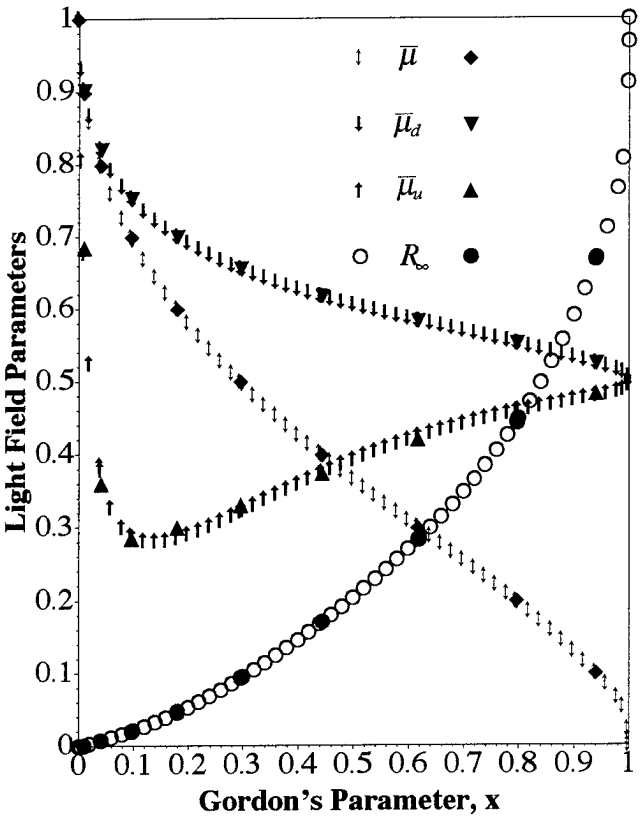


Fig.1 Dependencies of the integral light field parameters $\bar{\mu}$, $\bar{\mu}_d$, $\bar{\mu}_u$, and R_∞ on the parameter x. The filled symbols denote experimental values, while others correspond to computed ones.

fluxes of diffuse radiation (without halo)

$$E_d(\tau)=[E_0+M(\tau)]e^{-\alpha_\infty\tau}+R_0\,N(\tau)\left(e^{\alpha_0\tau}-e^{-\alpha_\infty\tau}\right), \quad (39)$$

$$E_u(\tau)=R_\infty[E_0+M(\tau)]e^{-\alpha_\infty\tau}+N(\tau)\left(e^{\alpha_0\tau}-R_0\,R_\infty\,e^{-\alpha_\infty\tau}\right) \quad (40)$$

where

$$M(\tau)=\left(1-R_0\,R_\infty\right)^{-1}\int_0^\tau\left\{\left[f_1(\tau')+R_0\,f_2(\tau')\right]e^{\alpha_\infty\tau'}-R_0\left[R_\infty\,f_1(\tau')+f_2(\tau')\right]e^{-\alpha_0\tau'}\right\}d\tau'. \quad (41)$$

$$N(\tau)=\left(A_B-R_\infty\right)\left(R_0\,\Delta_H\right)^{-1}\left[E_0+M(\tau_H)\right]e^{-\nu\tau_H}+\left(1-R_0\,R_\infty\right)^{-1}\int_\tau^{\tau_H}\left[R_\infty\,f_1(\tau')+f_2(\tau')\right]e^{-\alpha_0\tau'}d\tau'+ \quad (42)$$

$$A_B\left(R_0\,\Delta_H\right)^{-1}\int_0^{2\pi}d\varphi\int_0^1 L_q(\mu,\varphi)\exp\left[-\left(\alpha_0+\alpha/\mu\right)\tau_H\right]\mu\,d\mu,$$

$$\Delta_H=R_0^{-1}-A_B+(A_B-R_\infty)\,e^{-\nu\tau_H}, \quad (43)$$

$$\nu=\alpha_0+\alpha_\infty\equiv x\left(R_\infty^{-1}-R_0\right)/\mu_d.$$

For totally diffuse illumination of the medium we assume that the light flux from external sources passing through the upper boundary

$$E_q^0=E_d^f(0)\equiv\int_0^{2\pi}d\varphi\int_0^1 L_q(\mu,\varphi)\,\mu\,d\mu \quad (44)$$

is completely diffuse and we take it into account by the boundary condition $E_u^0(0)=E_q^0$, while we set $f_i(\tau)$ equal to zero. In addition, making the substitutions $E_0=E_q^0$, $M(\tau)=0$, $N(\tau)=(A_B-R_\infty)\,E_q^0\,(R_0\,\Delta_H)^{-1}e^{-\nu\tau_H}$ in (35), we obtain

$$E_d(\tau)=E_q^0\Delta_H^{-1}\left\{\left(R_0^{-1}-A_B\right)\exp(-\alpha_\infty\tau)+(A_B-R_\infty)\exp\left[-\alpha_0(\tau_H-\tau)-\alpha_\infty\tau_H\right]\right\}, \quad (45)$$

$$E_u(\tau)=E_q^0\Delta_H^{-1}\left\{R_\infty\left(R_0^{-1}-A_B\right)\exp(-\alpha_\infty\tau)+\left[(A_B-R_\infty)/R_0\right]\exp\left[-\alpha_0(\tau_H-\tau)-\alpha_\infty\tau_H\right]\right\}, \quad (46)$$

Now we calculate the transmittance of the layer $(0,\tau_H)$ for diffuse light $T(\tau)=E_d(\tau)/E_d(0)$ and the diffuse reflectance $R(\tau)=E_u(\tau)/E_d(\tau)$. Using (44)-(46), we obtain

$$T(\tau)=\frac{(R_0^{-1}-A_B)+(A_B-R_\infty)\,e^{-\nu(\tau_H-\tau)}}{(R_0^{-1}-A_B)+(A_B-R_\infty)\,e^{-\nu(\tau_H-\tau)}}\exp(-\alpha_\infty\tau), \quad (47)$$

$$R(\tau)=R_\infty\frac{(R_0^{-1}-A_B)+(A_B-R_\infty)(R_0\,R_\infty)^{-1}e^{-\nu(\tau_H-\tau)}}{(R_0^{-1}-A_B)+(A_B-R_\infty)\,e^{-\nu(\tau_H-\tau)}}. \quad (48)$$

The functional dependencies of $R_\infty, R_0, \alpha_\infty, \alpha_0$ upon the parameters of medium a and b_b are determined by (26)-(29), (31), (32), and (36).

In the limiting case of optically thick layer $(H>>[(\alpha_0+\alpha_\infty)(a+b_b)]^{-1}, R\to R_\infty)$ it is possible to express parameter $x=b_b/(a+b_b)$ in terms of the experimentally measurable quantity R_∞ Using the data of Table 1 and the asymptotic conditions given by (25), we get the following empirical equation

$$x=1-(1-R_\infty)^2\left\{r_1-r_0\,(1-R_\infty)+(1-R_\infty)^2\left[1+r_1-\sum_{n=2}^{6}r_n\,R_\infty^{\frac{n-3}{4}}\right]\right\}. \quad (49)$$

The coefficients r_n are given in Table 2. The correlation coefficient between the calculated via (49) values and experimental data exceeds 0.99.

CONCLUSION

Our method of calculation is found to produce results with accuracies in the range of 15% for all types of natural water optical situations (open ocean to coastal environments). Comparison with Monte-Carlo simulations shows that (49) can be used for processing remotely sensed data collected over coastal and open ocean areas with the same 15% precision.

ACKNOWLEDGMENT

The authors wish to thank continuing support at the Naval Research Laboratory through the Littoral Optical Environment (LOE 6640-06) and Optical Oceanography (OO 73-5051-05) programs. This article represents NRL contribution NRL/PP/7331–95–0087.

REFERENCES

[1] V. A. Timofeyeva, "Relation Between the Optical Coefficients in Turbid Media," Izvestiya USSR AS, Atmos. Ocean Physics, Vol. 8, pp. 654-656, 1972.

[2] V. A. Timofeyeva, "Determination of Light-Field Parameters in the Depth Regime from Irradiance Measurements," Izvestiya USSR Acad. Sci., Atmos. Ocean Physics, Vol. 15, pp. 774-776, 1979.

[3] W. E. Meador, and W. R. Weaver, "Two-Stream Approximations to Radiative Transfer in Planetary Atmospheres: A Unified Description of Existing Methods and a New Improvement," J. Atmos. Sciences, Vol. 37, pp. 630-643, 1980.

[4] V. I. Khalturin (a. k. a. Vladimir I. Haltrin), "The Self-Consistent Two-Stream Approximation in Radiative Transfer Theory for the Media with Anisotropic Scattering," Izvestiya USSR Acad. Sci., Atmos. Ocean Physics, Vol. 21, p.452-457, 1985.

[5] F. R. Gantmakher, Lectures on Analytical Mechanics, Chelsey Publ. Co., New York, 1970, p. 300.

[6] J. F. Potter, "The Delta-Function Approximation in Radiative Transfer Theory," J. Atmos. Sciences, Vol. 27, pp. 943-949, 1970.

[7] E. P. Zege, A. P. Ivanov, and I. L. Katsev, Image Transfer through a Scattering Media, Springer Verlag, Berlin, 1991, p. 349.

[8] L. F. Gate, "Comparison of the Photon Diffusion Model and Kubelka-Munk Equation with the Exact Solution of the Radiative Transfer Equation," Appl. Optics, Vol. 13, pp. 236-238, 1974.

Scene Understanding from SAR Images

An overview

Mihai Datcu

German Aerospace Research Establishment (DLR)
German Remote Sensing Data Center (DFD)
D–82234 Oberpfaffenhofen, Germany

Abstract

The major task of the Scene Understanding process is to find the scene which best explains the observed data.

In general the observed data, the same radar signals, can be generated by different scenes. To identify the scene we have to choose between competing hypotheses. The methods we analyze within the present paper arise from the fundamental approach of considering the probability theory as a set of normative rules for conducting inference. The scene inversion is a model based approach, and the models carry the thematic information. Model comparison is a delicate task, more complex models can always fit better the data, so the maximum likelihood choice would lead us to implausible over–parameterized models that generalize poorly. We propose as solution the Bayesian inference that penalizes the unnecessary complicated models and prefers the simpler and precise ones.

The paper presents comparatively the problem statement for scene understanding in the light of the Bayesian inference, Maximum Entropy principle and the methods of Simulated Annealing.

1. Models for SAR images

The success of data inversion depends critically on the accuracy of the assumed models. The complex SAR image is often described as a circular Gaussian process [15]. The model is only globally accurate: does not capture the local nature of the imaged scene. Models for image regions and speckle process have been introduced [4,5]. An image is assumed to be a puzzle of several different regions. Each region is assumed to be a Markov Random Field (MRF) having Gibbs distribution. The MRF assumption models the continuity in the image and the Gibbs model allows the parmetrization of the different image regions, the *cliques*. The SAR image is further hierarchically modeled: each pixel is a sample from a speckle process conditioned by the *clique* model. A variant of the hierarchical model was defined in [14]. The cross section is assumed to be Gamma distributed, resulting in an K–distributed intensity SAR image. An alternative of this model is the Weibull distribution [13].

The previously described models are all based on the same idea: the SAR image is described by a random walk process modulalated, by another statistical process describing the underlining cross–section. The SAR image formation process is reflected in the model by the statistic of the speckle and its autocorrelation.

Another class of SAR image models are based on extensive numerical simulations [6]. The models are more complete, taking into account the digital elevation model, the parameters of the imaging system, the orbit information and elements of scattering properties of the land cover. The statistic of the data is given by the physical and geometrical parameters of the modelled scene.

2. Parameter estimation

The theory of parameter estimation aims at the evaluation of a parameter generated by a noisy source of information. The observation space is transformed in the estimated data space by the estimation rule. Following are shortly presented and compared the basic estimators: the Minimum Mean Square Error (MMSE), the Maximum Likelihood (ML) and Maximum A posteriory (MAP). The notation used are, Θ represents the parameter to be estimated, D represents the observed data. The MMSE is defined as the conditional mean of the parameter (1). The estimator requires the knowledge of the Probability Distribution Function (PDF) $p(\Theta|D)$.

$$\tilde{\Theta}_{MSEE}(D) = \int_{-\infty}^{\infty} \Theta p(\Theta|D) d\Theta \tag{1}$$

If the parameter to be estimated is an unknown deterministic one, its estimate is the ML (2).

$$\frac{\partial}{\partial \Theta} \ln p(D|\Theta) = 0 \Big|_{\tilde{\Theta}_{MLE}} \tag{2}$$

If the PDF $p(D|\Theta)$ and $p(\Theta|D)$ are symmetric around its maximal value, the ML estimate is identical with the MMSE estimate. A

0-7803-3068-4/96$5.00©1996 IEEE

more complex estimate can be computed in the situation of known parameter model. The model is given in terms of PDF and it is equated in the Bayes relation as prior information $p(\Theta)$ (3).

$$p(\Theta|D) = \frac{p(D|\Theta)p(\Theta)}{p(D)} \tag{3}$$

The MAP estimate is found to be the solution of (4 and 5):

$$\frac{\partial}{\partial\Theta}\ln p(\Theta|D) = \frac{\partial}{\partial\Theta}\ln p(\Theta) + \frac{\partial}{\partial\Theta}\ln p(D|\Theta) \tag{4}$$

$$\frac{\partial}{\partial\Theta}\ln p(\Theta|D) = 0\Big|_{\tilde{\Theta}_{MAP}} \tag{5}$$

If the estimated parameter is modeled by a uniform PDF the MAP estimate is identical to the ML estimate. If the $p(\Theta|D)$ is symmetric the MAP estimate is identical with the MMSE estimate. The MAP estimate is qualitatively superior to the MMSE and ML estimates due to the consideration of the prior knowledge encapsulated in the model. The ML estimator is the best guess in the absence of any prior knowledge.
For the particular problem of SAR cross–section estimation from the measured speckled intensities in the frequentist approach the estimators are investigated in [2,13].

3. The Bayesian Inference

The Bayesian approach consists in interpreting probabilities based on a systems of axioms describing the incomplete information rather than randomness. The Bayesian and frequentist approaches are similar at certain extent, but the self consistent formulation of the modern Bayesian interpretation gives an alternative understanding of the information hidden in the measured data.
The estimation theory relies on the availability of some knowledge expressed as PDF's. The inference is the process, given a data set and a hypothesis space $\{H_i\}$, to assign probabilities to the hypothesis. Two levels of inference are introduced: the model fitting and the model comparison [12].

3.1 Level I: model fitting

The first level of inference assumes that the models to be inverted are true. The task is model fitting to the data. The results are often expressed as the most probable parameter values and a measure of the error.
The inference requires the knowledge of the prior model $p(\Theta|H_i)$,and the data prediction $p(D|\Theta, H_i)$.The inference pursues the Bayes rule and is applied separately for each of the models attached to $\{H_i\}$ (6).

$$p(\Theta|D, H_i) = \frac{p(D|\Theta, H_i)p(\Theta|H_i)}{p(D|H_i)} \tag{6}$$

The equation is similar to the MAP estimator (3 and 7):

$$Postreior = \frac{Likelihood\ x\ Prior}{Evidence} \tag{7}$$

The *evidence* term is generally neglected in the model fitting, result which was already obtained in the case of MAP estimation (4). The *evidence* term, is important in the second level of inference, and here is the novelty of the Bayesian approach in data inversion.

3.2 Level II: model comparison

The task of the second level of the Bayesian inference is to find the most plausible model given the data (8).

$$p(H_i|D) = p(D|H_i)p(H_i). \tag{8}$$

The inference relies on the evidence of H_i, carried by $p(D|H_i)$, and the subjective prior over the assumed hypothesis space, $p(H_i)$. $p(H_i)$ shows how plausible we thought the alternative models where before the data arrived. The hypothesis space can be structured using the Maximum Entropy principle (§4) to assign $p(H_i)$. The *reasons* for a certain model (hypothesis) will be expressed as constrains.
The second level of the Bayesian inference encapsulates the *Occam's razor* [12]: the unnecessarily complex models are not preferred to the simpler ones. The complicated overparametrized models, trying to generalize too much (H_2) are penalized under the Bayes rule. The simpler ones (H_1) are preferred, they are more *evident* (fig. 1), a better data prediction is accomplished in the validity interval C.

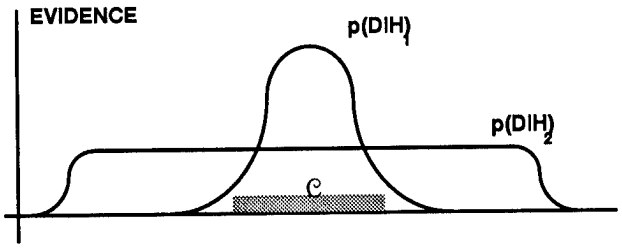


Figure 1

The model inference (8) is a ML estimate corrected by the *Occam's factor*: the ratio of the posterior accessible volume of H_i's parameters space to the prior accessible volume. The logarithm of the Occam's factor is interpreted as the information about the model at the data arrival.
The solution of ill–posed inverse problems is generally very sensible to the assumed model. This is the criticism of the inverse problem methods, they can introduce unrealistic behavior in the results. *The importance of the second level of the*

Bayesian inference consist in the possibility to select the best results which correspond to the the most plausible model given the data.

3.3 The Bayesian SAR cross–section estimation

The first level of the Bayesian inference can be used for this purpose. The SAR imaging system is described by the chain:

$$\Theta \rightarrow \quad \sigma \rightarrow \quad \varphi \rightarrow \quad y \tag{9}$$

where Θ represents the physical parameter of the scene, σ the cross–section, φ the scattered field, and y the SAR image. At its turn σ can be conditioned by scattering parameters or a texture. In [11] two inverse problems are studied: the inverse scattered field, the estimation of φ from y, and the inverse cross–section, the estimation of σ from $\mathbf{y}$. The previous methods consider the 2–dimensional end to end SAR system modeled as a convolution (10).

$$y = f * \varphi \tag{10}$$

The influence of the topography is not considered, the radiometric correction is assumed in the classical way.

3.4 The scene parameter inference

A complete 3–dimensional formalism can be derived from the generic view approach [7]. The image formation process is described by the operator f (11).

$$y_0 = f(x, \Theta); \quad y = y_0 + n \tag{11}$$

The noisy image y is described by the scene 3–dimensional geometry x, and its physical parameters, Θ. The goal of the inference is to find the posterior PDF (12):

$$p(\Theta|y) = \frac{p(y|\Theta)p(\Theta)}{p(y)} \tag{12}$$

The inference takes into account the image formation process and the noise (13,14).

$$p(y|\Theta, x) = p(y - f(x, \Theta)) \tag{13}$$

$$p(y|\Theta) = \int_x p(y|\Theta, x)\, dx \tag{14}$$

The result can always be equated as (15):

$$p(\Theta|y) = \frac{imaging * scattering}{geometry} \tag{15}$$

An intuitive comparison of (7) and (15) shows that the *likelihood* is physically interpreted as the descriptor of the imaging process, the *prior* is represented by a scattering model and the *evidence* is related to the geometrical description of the scene. Known the $p(\Theta|y)$ the MAP estimate of the parameter Θ can be evaluated according to (5).

4. The principle of Maximum Entropy

The principle of maximum entropy (ME) and the principle of minimum cross–entropy (MCE) are two methods of translating information into a probability assignment .

4.1 Maximum Entropy inference

The principle of Maximum Entropy (ME) and the principle of Minimum Cross–Entropy (MCE), which is a generalization of the prior, were first introduced as general methods of inference about unknown probability densities subject to a set of constraints. Later approaches showed that ME and MCE formalisms emerge as consequences of requiring that the methods of inductive inference be self–consistent, thus providing a more general framework by making no reference to information measures [9].

The ME principle states that of all distributions that satisfy certain constraints, one should choose the one with the largest entropy. The MCE principle is a generalisation that applies in cases when a prior distribution is known in addition to the constraints. The principle states that, of the distributions that satisfy the constraints, one should choose the one with the least cross–entropy.

4.2 Maximum Entropy approach in inverse problems

Inferring the data that satisfies the constraint set can be seen as solving an ill–posed inverse problem, with the entropy as regularizing functional. The ME formalisms provide coherent tools for incorporating new information (as constraints) into initial models and also an alternative tool for solving inverse problems. The set of constraints encode the effects of the imaging system with different image formation models, having various degrees of refinement [16,17]. The simplest approach is the end to end SAR system modeled as a convolution (16).

$$y = f * x \tag{16}$$

The input signal x is normalized to unit and interpreted as a PDF of entropy S (17).

$$S = -\sum xlog(x) \tag{17}$$

The condition of ME is now understood as the smoothness condition. The inversion of the observed data, y, is stated as an iterative method. The simulated data η, based on a guess of x, are compared with measured data y, in the sense of Mean Square Error (MSE). The ME solution is found as the maximum of the functional Q (18).

$$Q = S - \lambda\ MSE \tag{18}$$

ME fails to take noise into account, a factor that orthodox methods do deal with. So, they represent opposite reasoning formats: classical methods apply in cases where we have a sampling distribution (i.e. noise) of known properties but no prior information about other constrains; while ME is for cases where we have known the constrains but the noise is assumed null. To take into account the noise the full Bayesian approach has to be considered. An alternative solution is to measure the data misfit in terms of a statistic measure. The simplest choice is the chi–squared measure (16), where σ_n is noise variance:

$$\chi^2 = \frac{\sum \| y-\eta \|}{\sigma_n^2} \tag{19}$$

The solution is found as the maximum of the functional Q'(20).

$$Q' = S-\lambda\ \chi^2 \tag{20}$$

The unconstrained Bayes maximum can be reinterpreted also as a constrained ME maximum. A pure ME algorithm could be used to generate full Bayes solution by fixing Q at a nonzero value to allow for noise. Evaluation of the ME principle application to SAR cross–section estimation and SAR iamge enhancement are reported in [8,16].

5. The Simulated Annealing

A method to deal with the full noisy problem and the sets of constrains in a complete way is the stochastic relaxation [10]. In the above methods the prior knowledge was in the form of PDF of the data. There was no attempt to represent the correlations between the data and the different structural parameters to be estimated, i.e. the cross section in neighbouring pixels. A technique which meets these requirements is the simulated annealing (SA) method. The underlying cross–section model is a MRF, which is equivalent to characterizing the cross–section by a Gibbs distribution. For reconstruction the parameters of the scene are distorted randomly while the *system temperature* is gradually and slowly decreased such as the system evolves at each step through equilibrum states towards the maximisation of the global score, which in this case is the aposteriori distribution. A stochastic mechanism is set up for the acceptance of the transitions in order to avoid the local extremes of the score function. An energy function can be expressed in terms of the local potential. New constrains can be added.

A simple heuristic model on real scenes give generally poor results. A way to circumvent this difficulty is to perform an on–line dynamic adaptation of the prior model after a number of iterations. Another approach is to include in the neighbourhood system the sites of the elementary edges between the pixels and to perform a fine tuning of the model by assigning different weights for the possible neighbourhood configurations [10, 17, 18]. This corresponds to a combination of segmentation and restoration within the same process, since the pixel neighbourhood accounts for the local uniformity and the edge neighbourhood accounts for the local differences in the image.

6. Conclusions

The SAR data are strongly dependent on the geometry, elevation and structure of the imaged scene. For high complexity scenes or for scenes in mountainous areas the application of image analysis is a weak approach. Significant radiometric uncertainities remain unsolved and as a consequence the signature analysis, structural interpretation and classification are affected by errors. Alternatively, in this paper the scene understanding approach is proposed. Scene understanding is the attempt to extract knowledge about the physical characterization (scattering parameter), the structure and geometry of the three–dimensional scene from two–dimensional image. The problem statement is in the general frame of ill–posed inverse problems. The solutions are model based in the general frame of the Bayesian inference. The models encapsulate the prior knowledge and reflect the user–application thematic objectives.

Acknowledgments

The author is grateful to Dr. Cristian E. Toma and Dr. Richard Bamler for the stimulating discussions referring the Principle of Maximum Entropy and its applications in the field of SAR.

References

[1] Bamler R., Schättler B., *SAR Data Acquisition and Image Formation*, in: G. Schreier (Ed.), *SAR Geocoding: Data and Systems*, Wichmann, Karlsruhe, pp. 53–102, 1993.

[2] Blacknell D., *Comparison of parameter estimators for K–distribution*, IEE Proc. –Radar, Sonar Navig., Vol. 141, No.1, pp. 45–52, feb. 1994.

[3] Burch S.F., Gull S.F., Skilling J., *Image Restoration by a Powerful Maximum Entropy Method*, Comp. Vis. Graph. and Imag. Processing, Vol. 23, 113–128, 1983.

[4] Kelly D. A., Derin H., Hartt K. D., *Adaptive segmentation of speckled images using a hierarchical random field model*, in IEEE Trans. Acoust. Speech Sig. Process. ASSP–36(10), pp. 1628 – 1641, 1988.

[5] Derin H., Elliott H., *Modeling and Segmentation of Noisy and Textured Images Using Gibbs Random Fields*, in IEEE Tr. on Pattern Anal. Machine Intell., PAMI–9(1), pp. 39 – 55, 1987.

[6] Franceschetti G. et al., *SARAS: A Synthetic Aperture Radar (SAR) Raw Signal Simulator*, in IEEE Tr. on Geosci. and Remote Sensing, GE–30(1), pp. 110 – 123, 1992.

[7] Freeman T., *Exploiting the Generic View Assumption to Estimate Scene Parameters*, in Proc. ICIP'93, pp. 347 – 355, 1993.

[8] Frieden B.R., Bajkova, *Bayesian cross–entropy reconstruction of complex images*, Applied Optics, Vol.33, No.2, pp.219–226, 1994.

[9] Jaynes E.T., *On The Rationale of Maximum–Entropy Methods*, IEEE Proc., Vol. 70, No.9, p. 939–952, 1982.

[10] Geman S., Geman D., *Stochastic Relaxation, Gibbs Distribution and The Bayesian Restoration of images*, in IEEE Tr. Pattern Anal. Machine Intell., PAMI–6(6), pp. 721 – 741, 1984.

[11] Luttrell S.P., *The theory of Bayesian super–resolution of coherent images: a review*, Int. J. Remote sensing, Vol.2, pp. 303–314, 1991.

[12] MacKay D.J., *Bayesian interpolation*, Neural computation, Vol. 43, 1992.

[13] Oliver C.J., *Information from SAR images*, in J. Phys. D: Appl. Phys. 24(9), 1493 – 1514, 1991.

[14] Oliver C.J., *Optimum texture estimators for SAR clutter*, J. Phys.D: Appl. Phys.26, pp. 1824–1835, 1993.

[15] Raney, R.K., Wessels G. J., *Spatial Consideration in SAR Speckle Simulation*, IEEE Tr. on Geoscience and Remote Sensing, Vol. 26, No. 5, pp. 666–672, Sept. 1988.

[16] Toma Cr., Datcu M., *Maximum entropy and minimum crossentropy methods in image processing*, in SPIE Proc. Vol. 1827: Model–Based Vision, pp. 133–144, 1992.

[17] Toma Cr., Datcu M., *Genetic Algorithm for Maximum Entropy Image Restoration*, SPIE Proc. Vol. 2304: Neural and Stochastic Methods in Image and Signal Processing III, 1994.

[18] White R.G., *A simulated annealing algorithm for radar cross–section estimation and segmentation*, SPIE Vol. 2234, pp. 231–239, 1994.

Theoretical Research on New Concepts for the Remote Sensing of Hydrometeors

M. Martín-Neira[1],
J. Bará[2], A. Camps[2], F. Torres[2], I. Corbella[2],
O. Gasparini[3], M.V. Arbolino[3]

(1) European Space Agency, ESTEC, Postbus 299, 2200 AG Noordwijk, The Netherlands
(2) Polytechnic University of Catalonia, ETSE Telecommunications, 08071 Barcelona, Spain
(3) Dune S.r.I., via Tracia 4, 00183 Rome, Italy

ABSTRACT

There is an interest for climatology and meteorology to map hydrometeors, and in particular precipitation, both over the entire globe and across large defined regions. To achieve this goal at the proper spatial and temporal resolution which are required to satisfy the end users needs it has been proposed to use satellite based observations.

This paper presents the results of a theoretical study aiming to the research of new concepts for the remote sensing of hydrometeors with emphasis on precipitation. The concept proposed is a Focused Wide band millimeter wave INTERferometer (WINTER-F) comprising a constellation of two small satellites, flying close to each other. The two satellites, which are phase synchronized by the GNSS (Global Navigation Satellite System) signals, perform near field interferometry by passive (radiometer) and active (radar) means. The study comprises the realization of laboratory experiments to check the validity of the theoretical models.

INTRODUCTION: THE WINTER-F CONCEPT

The Winter-f (mm-Wave wide band INTERferometer - Focused) concept, which was first developed for a passive system, comprises the following main theoretical basis [1]:

- a radiometer can have range resolution much in the same way as a radar does [2],
- range resolution in the one direction is achieved by decorrelation;
- range resolution in another direction is obtained by doppler processing;

When these theoretical basis are applied to a spaceborne passive system for Earth remote sensing the following theoretical results are found:

- the signals from the ground and the continuous atmosphere can be filtered out by selecting a proper spatial frequency (satellite baseline) of observation;
- the signals originated by the hydrometeors (both through scattering and emission) can be observed by the properly chosen satellite baseline;
- the output of the passive system is proportional to the density of hydrometeor particles in the atmosphere.

Thus, the theoretical conclusion is that a radiometer system can be built able to measure directly the density of hydrometeor particles (i.e. rain rate) free of contamination from the background (ground and continuous atmosphere).

The same concept can be applied to an active system (radar) where time gating can be performed. In this case we have a third degree of freedom and the spatial resolution in the third dimension becomes possible.

WINTER-F IMPULSE RESPONSE

Let us compute the response to a point source consisting of an element of volume filled with short dipoles. The current through every short dipole is assumed to represent the processes of emissivity, absorption and scattering which occur in the interaction between matter and radiation.

Consider two receiving antennas at points P_1 and P_2. The signal from every small dipole arrives at point P_1 producing a voltage

$$V_1(t) = \int_{a.s.d.} dV_1(t) \qquad (1)$$

where dV_1 is the voltage produced by every single short dipole and *a.s.d* stands for *all short dipoles*. The signals of the short dipoles arrive at P_2 as well and a similar expression can be written for the voltage at the second antenna.

The antenna voltages constitute the input signals to the receivers and get thus filtered by their frequency response. The impulse response of the Winter-f system is given by the cross correlation of the two receiver outputs

0-7803-3068-4/96$5.00©1996 IEEE

which assuming coherence between the local oscillators becomes

$$\Gamma_{S_1S_2}(\tau) = B\left(\frac{\eta L}{2\lambda}\right)^2 \frac{\chi}{r_1 r_2} \langle |J|^2 \rangle \, \mathrm{sinc}\left[B(\tau - \Delta r/c)\right] e^{-jk\Delta r} \, dV \qquad (2)$$

where $\Gamma_{S_1S_2}(\tau)$ is the cross correlation evaluated at time τ, B the bandwidth, L the antenna effective length, η the intrincic impedance of vacuum, λ the wavelength, χ an obliquity factor, r_1 and r_2 the distances between the source point and the receivers, $\langle |J|^2 \rangle dV$ the intensity of the source, $\Delta r = r_1 - r_2$ the path difference, c the light speed and k the wavenumber.

RANGE DISCRIMINATION BY DECORRELATION

The impulse response (2) shows that the spatial distribution of the source intensity is weighted by the system filter response according to the sinc function. This fringe washing function accounts for the decorrelation of the signal due to the finite system bandwidth. Thus the system is only sensitive to that volume for which the decorrelation is not excessive, that is, to those points whose path delay is compensated by the system delay within the main lobe of the sinc function

$$\left|\tau - \frac{\Delta r}{c}\right| < \frac{1}{2B} \qquad (3)$$

The geometrical volume defined by this equation corresponds to the space between two hyperboloids with foci at the observation points P_1 and P_2 and has been depicted in Figure 1. By changing the system delay τ we can make the sinc function to peak on a different hyperboloidal volume. A range of values of τ correspond to a range of hyperboloidal shells. We realize in this way that we have built a radiometer system which has ranging capability based on near field observations from two points.

SYSTEM RESPONSE TO A DISTRIBUTED SOURCE

When the impulse response (2) is applied over a *uniform* distributed source such as the ground or the gaseous atmosphere it vanishes because $k\Delta r \gg 1$ over the volume of correlation:

$$\Gamma_{S_1S_2}(\tau) \to 0 \qquad (4)$$

In practice the interferometer would give an output equal to its radiometric sensitivity.

On the contrary, when the impulse response is applied to a *discrete* source such as a distribution of water particles a non zero value is found

$$\Gamma_{S_1S_2}(r_o) = B\left(\frac{\eta L}{2\lambda}\right)^2 \frac{\chi}{r_1 r_2} \langle |J_p|^2 \rangle \sum_{i=1}^{N} e^{-jk\Delta r_i} \qquad (5)$$

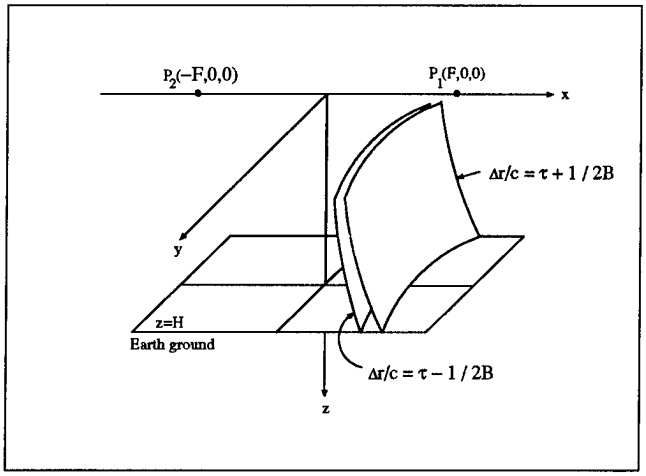


Figure 1: Range discrimination by decorrelation

where the subindex p denotes 'particle' and the summation extends only to the N particles contained inside the resolution volume, for which

$$r_o - \frac{r_c}{2} \le \Delta r_i \le r_o + \frac{r_c}{2} \qquad (6)$$

$r_c \equiv c/B$ being the correlation length. Assuming a random distribution of particles, the average (over the ensemble of particle distributions) of (5) yields

$$\langle \Gamma_{S_1S_2}(r_o) \rangle = 0 \qquad (7)$$

and its standard deviation

$$\sigma_\Gamma = B\left(\frac{\eta L}{2\lambda}\right)^2 \frac{|\chi|}{r_1 r_2} \sqrt{N} \langle |J_p|^2 \rangle \qquad (8)$$

This equation is the response of the Winter–f interferometer to hydrometeor particles and shows that the standard deviation of the cross correlation between the two receivers is proportional to the product of the square root of the number of particles in the resolution volume times the intensity of the particle. The standard deviation of the cross correlation can be measured by root mean square averaging of independent samples.

STUDY ON THE SATELLITE CONSTELLATION

The iso–delta range and iso–delta doppler family lines for a pair of satellites flying close to each other in different configurations have been computed. The optimum view geometry is that providing a perpendicular crossing between the iso–range and iso–doppler lines. One possible scenario was selected where the two satellites fly along the same orbit keeping a spacing of a few kilometers. The local oscillators of the radiometers of the two satellites

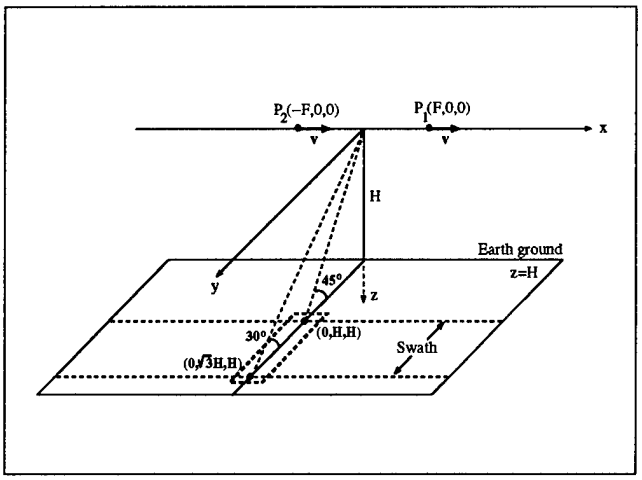


Figure 2: Selected orbital scenario and view geometry

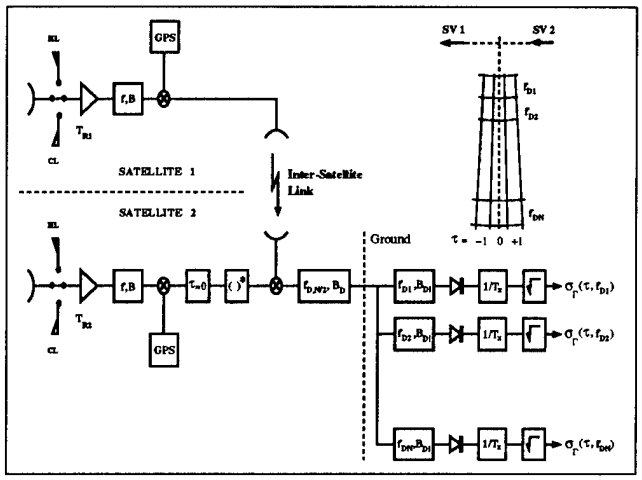


Figure 3: Winter–f block diagram

are derived from the GNSS signals and are thus coherent. The iso–delta range lines are across track while the iso–delta doppler lines are along track. This scenario has been depicted in Figure 2.

RANGE DISCRIMINATION BY DOPPLER

As seen from the system response in (5) the cross correlation of every particle has a different delta doppler shift, defined by

$$\Delta f_i(t) \equiv \frac{1}{\lambda}\frac{d\,\Delta r_i(t)}{dt} \qquad (9)$$

where the sub–index refers to particle i. The further a particle is from the satellites ground track the smaller the doppler is in its cross correlation function.

The cross correlation function is then passed through a bank of doppler sharpening filters to achieve spatial discrimination. The output of every filter corresponds to a different region limited by a pair of iso–delta doppler lines. The width of the doppler filters, and hence, the spatial resolution achievable by doppler, is limited by the transit time and the velocity of the particles.

WINTER–F BLOCK DIAGRAM

The conceptual block diagram of the Winter–f passive interferometer can be derived from the previous theoretical study and is shown in Figure 3. Typically a dual frequency sensor would most likely b mused. The satellites are provided with a radio link to be able to perform the cross correlation on board.

ACTIVE INTERFEROMETRY IN WINTER–F

The same concepts explained on the passive interferometer can be applied to the case when one satellite transmits a pulsed noise–like (or deterministic) signal and the two satellite receive the echo afterwards.

If S_M and S_B indicate the signals received by the transmitting satellite and the second satellite respectively we arrive at the result that the cross correlation $\langle S_M(t)S_B^*(t)\rangle$ is null while the autocorrelations $\langle S_M(t)S_M^*(t)\rangle$ and $\langle S_M(t)S_B^*(t)\rangle$ are proportional to the number of raindrops within the resolution volume.

The fourth order correlation $\langle S_M(t)S_M^*(t)S_B^*(t)S_B(t)\rangle$ is proportional to the product of the two second order autocorrelations, thus giving the number of raindrops within the resolution cell. The properties of the fourth order correlation as an estimator of rain density, both regarding the accuracy of the estimate and the spatial resolution are currently under investigation.

CONCLUSION

The study predicts, within the limitation of the models used, the possibility of a radiometer system with range capability which is sensitive to the hydrometeors but not to the background.

A laboratory experiment of the fundamental concepts is being undertaken to compare the theoretical predictions with the real world behaviour. The usefulness of this effort is worth in view of its potential for a satellite based Rain Detection System.

REFERENCES

1 M. Martín–Neira, "mm–Wave Wide Band Focused Interferometry", ESA/ESTEC Technical Note, XRI/134.95/MMN, 1995;

2 A.J. Skalafuris, "Microwave Geodesy by Interferometric Radiometry", Astrophysics and Space Science 137, pp 317–345, 1987;

"Helping students and teachers make sense of Remote Sensing via the Internet"

S.K. Croft and R.J. Myers
NASA Classroom of the Future
Wheeling Jesuit College,Wheeling, WV 26003
email: scroft@cotf.edu, bmyers@cotf.edu
PH: (304)243-2388, FAX (304)243-2497

INTRODUCTION

Remote sensing (RS) using aerial and satellite imagery can supply local, regional, and global views of the Earth and its different interrelated systems. It can provide a powerful means for students to visualize their place in the world and their effects on it, thus providing both a compelling introduction and continuing support to students' explorations of the state of the Earth and how to sustain it in the future [1]. The "translation" of professional-level RS data and results into useful educational materials for classroom use is a formidable task from the teacher's point of view, however. The data sets are immense in comparison to the memory capabilities of typical computers in schools; there are many different kinds of specialized data sets - each requiring a unique information base to understand; many data sets of high interest are too expensive; and the information content is complex and often intimidating. There are also challenging student-related issues: how to interest or involve the students in working with RS data, how to give students (and teachers) the tools needed even for elementary analysis, and how to find the time for RS-related studies in already crowded school curricula.

On the other hand, the potential opportunities are great. RS images are eye-catching. Working with RS images can be a primary learning tool for visual learners and a powerful adjunct for more traditional learners. With appropriate computers and software, students are able to use their own creativity in manipulating RS images and other cartographic data, making the visual information "their own" - increasing their involvement, understanding, and retention of the information.

THE "ETE" PROJECT

In our project [2], Exploring the Environment (ETE), we are exploring ways to take RS data efficiently and effectively into the classroom. We are developing Earth Science modules utilizing a problem-based learning pedagogy, which places students in the role of active investigators of complex, ill-structured problems that mirror real-world problems [3,4]. These modules are designed for delivery over the World Wide Web (Our Web site may be visited at http://www.cotf.edu/ETE).

One of the significant components of our modules is use of RS imagery to help define or investigate the central environmental problem. One objective for inclusion of the RS data is to allow the students to manipulate the images directly and to take their own measurements. Past experience indicates that having the students do their own processing and measurement more fully involves the student and gives them "ownership" of the problem [5]. The central problem of each module is open-ended because the emphasis in our primary problem-based learning modules is on problem solving and not on specific image processing skills.

However, to effectively deal with RS images, students (and teachers) need some image processing skills. Simply placing RS images in front of the students is not sufficient for effective use. The information content of remotely sensed images is not necessarily obvious to students or teachers. The images are often taken from overhead, an uncommon perspective for many, and in spectral bands that usually have no connection to the students' world and thus convey no meaning. A set of basic image processing skills can be applied to almost any set of images and problems, and hence can be applied in any number of our modules. So rather than include detailed step-by-step directions for processing the images associated with any single module, we are designing a short series of activities that teach basic image processing skills and concepts that the students will be able to use later on the images specific to each module. Giving the students a set of basic image processing skills to use in various situations also supports the objectives of our open-ended problem modules.

THE IMAGE PROCESSING SKILLS ACTIVITIES

To be consistent with the spirit of the problem based learning approach, we have written each activity as a simple problem scenario rather than as a linear, step-by-step instruction guide - although the step-by-step instructions are included since this is a training activity.

0-7803-3068-4/96$5.00©1996 IEEE

The objective is to give students a reason to learn a skill rather than to simply explain it. At this point we have completed three skills activities. The first introduces the concept of digital images, pixels, gray-scale and pseudo coloring, histograms, simple filtering and stretching. The activity is built around a first manned landing on Mars, where the students are given one of the original images of the terrain around the "face on Mars." They are not told directly about the "face," but are given the problem of finding a suitable (i.e., flat) landing site. However, if they do the simple processing activities correctly, the face "pops out" at them. Information about the "face" and the geology of the surrounding area are given in a separate "Teacher's Notes" section. The teacher's section is password protected so that guidelines and intended outcomes can be supplied to the teacher over the Internet while at the same time preventing easy student access to the same information - information which they should discover themselves by working through the activities. The second activity introduces setting image scales and making linear and areal measurements. The scenario is built around deciding what to do on a vacation in Honolulu, Hawaii. The third activity introduces spectral bands, true and false color composites, and how to recognize typical features such as bare rock, plants, open water, and man-made structures from their appearance in different bands and composites. The scenario is built around survival after being shipwrecked on a desert island.

We have also placed activities within existing problem-based-learning modules that show how to conduct animations and time comparisons, density slices and terrain classification, and simple image arithmetic. In time, the directions for these image processing skills will be written into separate training activities.

HARDWARE/SOFTWARE CONSIDERATIONS

We have written our activities for NIH Image, a powerful, freeware image processing program that can be run on a wide range of Macintosh computers. Copies of NIH Image and supporting documentation can be obtained via anonymous ftp from zippy.nimh.nih.gov [128.231.98.32]. This user-friendly program includes a great variety of tools for image processing, measurement, animation, arithmetic, mosaicing, and drawing. Two drawbacks to the program are: 1) GIS-type activities can be done, but not efficiently, and, more importantly, 2) NIH Image runs only on Macintosh computers, thus our image processing activities are as yet unavailable to PC or unix users (although a Macintosh emulator for the PC is under development). We are looking at other programs that will run on PCs, such as IDRISI, ARCVIEW, and MULTISPEC, but these programs are designed more for GIS applications and less for the general image processing skills available with NIH Image. In addition, these PC programs are not free (although educational discounts can be obtained). Eventually we are planning to rewrite as many of the activities as we can on a PC-compatible platform.

DISCUSSION

Obtaining suitable images for student use is an ongoing problem, simply because of the cost of many data types (such as Landsat and SPOT) and the sheer size of most RS images. For example, AVHRR and full-resolution SIR-C radar images are several megabytes in size, seven bands of a single TM Landsat scene are in excess of 400 megabytes, and AVIRIS data cubes and projected data sets from the fleet of MTPE satellites to be launched later this decade are an order of magnitude larger still. Although the memory capability of computers in schools is growing quickly, it will be several years before a typical school computer will be able to deal directly with image data sets hundreds of megabytes or gigabytes in size. And again, though the speeds of Internet connections available for schools is rapidly increasing, these large data sets would take hours or days to download for most existing school computers. Consequently at present, we take the large images and use our professional-scale hardware and software (ER Mapper) to cut or subsample the images down to sizes of a few hundred kilobytes or less for easy Internet delivery. This takes the students at least one step away from the raw data, but it does make available images of practical size for processing.

A final issue of importance in this context is the trade-off between the level of student expertise (and independence) in image processing and the time used in class to achieve that expertise. It takes time to learn to use a tool well. Once learned, however, the range of possible activities using the tool increases greatly, as well as the students' sense of ownership and achievement. Our main modules are designed to be flexible in time usage, ranging from a few class periods to an entire semester, depending on the level of involvement desired by the teacher. The skills activities are designed to take one to several class periods each, depending on the class. Thus completing the whole set of image processing activities could take several weeks - and that before the students

really engage the main modules. Consequently, several weeks of time must be invested to let the students properly learn basic image processing skills. But in the long run, once learned, these skills can be used to address a much wider range of problems and at a much higher level of involvement than previously possible.

REFERENCES

[1] S.A. Drury, A Guide to Remote Sensing: Interpreting Images of the Earth, Oxford, Oxford University Press, 1990.

[2] J. A. Botti and R. Myers, "Exploring the Environment: A Problem-Based Approach to Learning About Global Change," 1995 International Geoscience and Remote Sensing Symposium, Vol. I, pp. 391-393, July 1995.

[3] S.L. Finkle and L.L. Torp, "Introductory Documents," available from The Center for Problem-Based Learning, Illinois Math and Science Academy, 1500 West Sullivan Road, Aurora, IL 60506-1000, 1995.

[4] C.R. Ault, Jr., "Research on Problem Solving," in Handbook of Research on Science Teaching and Learning, D.L. Gobel, ed., New York: Macmillan, 1994, pp. 269-283.

[5] K. Tobin, D.J. Tippins, and A.J. Gallard, "Research on Instructional Strategies for Teaching Science," in Handbook of Research on Science Teaching and Learning, D.L. Gobel, ed., New York: Macmillan, 1994, pp. 45-93.

"Winds of Change" a Multi-Media Tool to Aid Teachers in Teaching Global Climate

Gilbert Yanow, Anita Sohus and Bruce Payne
NASA/Jet Propulsion Laboratory
4800 Oak Grove Drive, Pasadena, CA 91109, Mail Stop CS-530
(818) 354 6916, 354 6013
gilbert.yanow@jpl.nasa.gov

Abstract -- In an effort to help strengthen the nation's science, math and technology education and at the same time promote educational systemic change, all new space projects at the NASA/Jet Propulsion Laboratory (JPL) now incorporate in their mission plans detailed educational outreach efforts. These outreach programs are done in partnership with the educational leadership of national, state and local agencies, organizations and class room teachers. The Winds of Change is the first educational resource developed under these conditions that provides a new type of educational tool. Winds of Change has been sponsored by the NASA Scatterometer (NSCAT) mission as its first educational product and an example for other NASA or technical organizations who also wish to contribute to enhancing science education.

BACKGROUND

NASA, as one of the world's leading scientific and engineering organizations, takes its obligation to pass on new knowledge, technology and the excitement of discovery to the educational community very seriously [1]. The NASA Scatterometer (NSCAT) is an instrument being developed and managed at the Jet Propulsion Laboratory in Pasadena CA. This instrument will be carried on the ADEOS, a Japanese satellite. ADEOS will use multiple radar antennas to provide a global measurement every few days of the speed and direction of the winds of the world's oceans. This data will contribute to better understanding of the role of the oceans in short term weather and long term climate change. In 1994 NASA set aside funds not to develop public relations materials about NSCAT, but rather to develop a new type of educational resource that would give teachers and students new tools and incentives to study the various aspects of global climate.

THE "CORE" DEVELOPMENT TEAM

To ensure that the final product would be factually correct, to use mission information where appropriate, to educationally align and promote the paths given in documents such as the National Science Standards and the California Science Framework, and at the same time to produce a product that would be useful in the classroom to teachers and student, a broad -based development group called the "Core Team" was formed as an advisory and design Team. The membership of the Core Team combines NSCAT project engineers and scientists, a representative of the California State Department of Education, university educators, classroom teachers of different grade levels, and JPL CD-ROM designers and programmers. Two other components were added to this Team. An educational evaluator was included to design evaluation instruments that could be used during and after the development of the materials. and JPL also contracted with a curriculum consultant who had used a unique educational organization tool for science programs in Texas and Wyoming called "webbing"[2].

In addition to providing an educational resource for the topic of global climate, there was the desire to encourage the use of technology in the classroom. JPL has been a leader in the development of scientific data CD-ROM's and therefore the Core Team decided to use a CD-ROM as the media of this new educational tool. "Winds of Change" has been designed for middle school students, but should find use in grades 6-12. The CD-ROM is designed to run on both PC and Macintosh.

THE WINDS OF CHANGE EDUCATIONAL WEB

The Winds of Change Web, shown in Fig. 1, is not only the design tool for the CD-ROM, but is also the initial "point and click" graphic used to explore the subjects.

The concentric rings are themes used in education (e.g. The California State Science Framework). They represent very general natural concepts of scale and structure, measurement, energy, systems and interactions, patterns of change, evolution, stability and human interactions. Almost any topic could be studied by exploring it via these themes. The "spokes" of the web identify the topics to be examined. The user decides on one of the topics to investigate (weather, atmosphere, oceanography, livings things or climate) and simply "clicks" that subject. Next the choice of an intersection of ring and topic will show a research question to initiate a study. For example, if the topic of "atmosphere" is picked at the theme of evolution, the pop-up question is "How has Earth's atmosphere changed over time?"

0-7803-3068-4/96$5.00©1996 IEEE

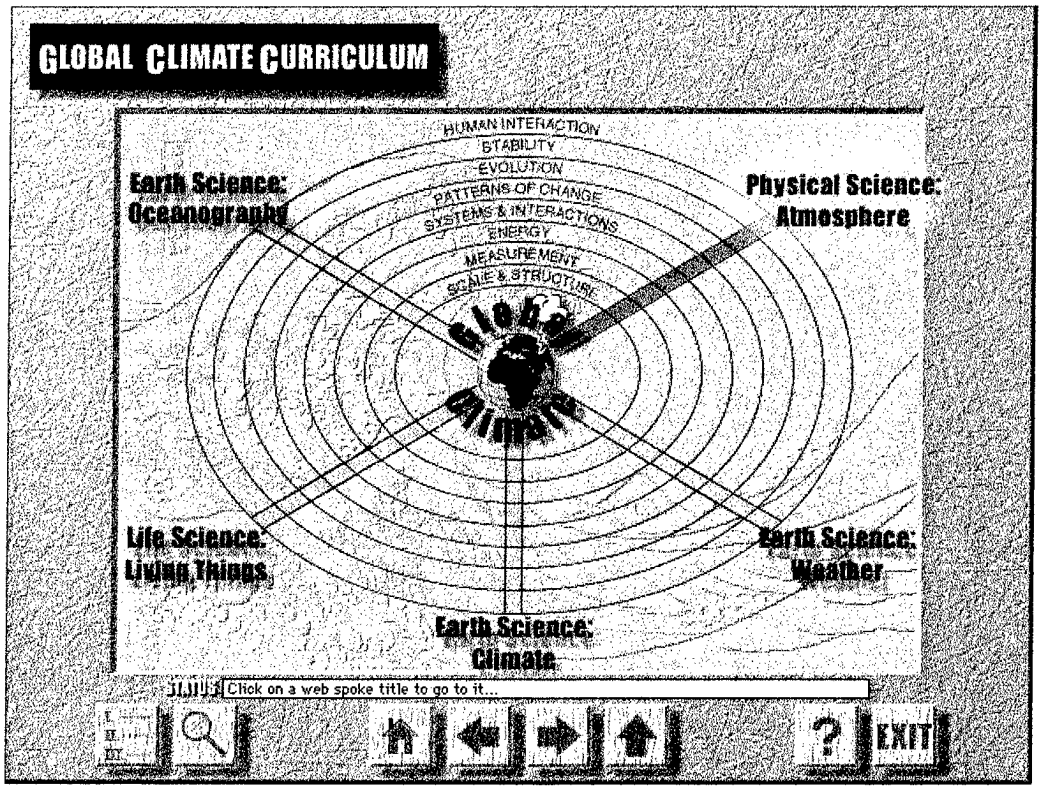


Fig 1- The introductory screen of the Winds of Change CD-ROM using the educational web organization.

The Core Team decided on the topics and all research questions.

If the user then clicks this question a whole library of reference materials are made available. For each one of these "bubble" questions there are several pages of background information (in Adobe PDF files), numerous classroom hands-on activities (also in PDF files), many still images and several movies. Professional curriculum writers prepared the background materials, classroom activities, captions and narration's.

USING WINDS OF CHANGE

Winds of Change can be used in any way that a teacher or student wishes-- it is a resource, not a curriculum. It is anticipated that teachers may use the CD-ROM for classroom presentations, to build up their own backgrounds or use the library of hands-on activities. The teacher may assign students to do independent study or to work in small groups investigating different subjects. We are compiling a data base of "tutorial profiles" of the various ways teachers and students use Winds of Change. This information will be made available on the NSCAT home page on the World Wide Web.

ASSESSING STUDENTS

The suggested and preferred method to obtain student assessment is by having the students prepare journals of their research. Currently, many teachers have students prepare electronic journals using tools such as Hyperstudio. With the click of the correct button, Winds of Change allows teachers and students to print any of the documentation, still images or any frame of a movie, as well as send any of this material to other forms of electronic media such as floppy disk or video tape.

FIELD TESTING

As the materials for each spoke were written, prepared and programmed on to the CD-ROM, test cuts were sent out to the Core Team for critical review of content and user interfacing Changes and modifications were incorporated after each review.

While Winds of Change was being developed, presentations were made at national teacher meetings and many local inservice groups. Teachers were solicited to volunteer, via written application, to be part of a field test once the CD-ROM was in near final form. Over 150

teachers sent in their requests to participate in the field test.

(The initial version of Winds of Change will implement three spokes-- weather, atmosphere and oceanography. The last two topics, climate and living things, will be added to a second version of Winds of Change after full field testing.)

Each of the field test teachers were sent a package containing evaluation instruments for the teacher response based on their reactions to using Winds of Change in their classrooms in a variety of ways (24 basic questions plus comments). There was also a shorter evaluation form to be filled in by the students themselves (13 questions and comments). The last component of evaluation was a tutorial profile questionnaire (20 questions and fill-in comments) that will be used to build a data base of how teachers use Winds of Change in their classrooms.

The results of all the returned evaluation forms were examined and the findings were used to make final modifications to the Winds of Change distribution CD-ROM's before wide spread distribution.

DISTRIBUTION OF WINDS OF CHANGE

To obtain an initial copy of Winds of Change, a teacher must fill out and mail to JPL a "no cost" order form. This will allow the development of a data base of teachers using the CD-ROM. Presentations illustrating the CD-ROM are being given at major national teacher meetings and in cooperation and coordination with NASA headquarter's teacher inservice training programs. At each of these presentations attending educators are give the order forms. They in turn are free to make copies for their colleagues. The CD-ROM is also given out at special educator conferences held at JPL.

Distribution copies of Winds of Change have the tutorial profile form attached with a request for teachers to fill them out and return to JPL after significant use.

NSCAT VALUE ADDED PRODUCTS

The NSCAT project will be showing current data on their home page for general use. To make this information is more valuable for the educational community, software tools are being identified and developed to allow teachers to use NSCAT data in coordination with Winds of Change.

JPL may be contacted on the World Wide Web at http://www.jpl.nasa.gov. The home page for the JPL Teaching Resource Center is http://learn.jpl.nasa.gov.

CONCLUSION

The Core Team has put in a great amount of work and resources in developing Winds of Change. The lessons learned with the making of this CD-ROM are now being applied to the production of CD-ROM's for other JPL projects.

JPL would be interested in forming partnerships with other scientific and research organizations to help them produce similar products for subject areas that relate to their fields of expertise.

REFERENCES

[1] NASA's Strategic Plan for Education. NASA EP 289, 1992.

[2[Payne B.C. and Steussy C., "8th Grade Science Model", Texas Education Agency, 1991.

From Surfer to Scientist: Designing a Canadian Remote Sensing Service for the Internet Audience

Christine W. Langham
Canada Centre for Remote Sensing, Natural Resources Canada
588 Booth Street, Ottawa, Ontario, CANADA K1A 0Y7
Tel: (613) 947-1315 Fax: (613) 947-1385
chris.langham@ccrs.nrcan.gc.ca

Anne Marie Botman
Geomatics International
Suite 610, 265 Carling Avenue, Ottawa, Ontario, CANADA K1S 2E1
Tel: (613) 947-1261 Fax: (613) 947-1385
anne.botman@ccrs.nrcan.gc.ca

Tom Alföldi
Canada Centre for Remote Sensing, Natural Resources Canada
588 Booth Street, Ottawa, Ontario, CANADA K1A 0Y7
Tel: (613) 947-1255 Fax: (613) 947-1385
tom.alfoldi@ccrs.nrcan.gc.ca

Abstract -- The World Wide Web site at the Canada Centre for Remote Sensing (CCRS) is much more than a passive, electronic brochure. With its long tradition and expertise in developing training materials for a variety of knowledge levels, CCRS is ideally placed to exploit the store front medium that the Internet provides for raising public awareness of remote sensing technology. The CCRS Web site is a multi-faceted didactic tool: providing information to the remote sensing specialist on the latest research; and to the surfer who wants to learn about applications that promote a sustainable future.

INTRODUCTION

The World Wide Web site at the Canada Centre for Remote Sensing (CCRS) began as an implementation project in December 1994 with a team of six people. The guiding principle behind the CCRS Web site is to provide service to the Canadian remote sensing community, namely knowledgeable geomatics professionals. A secondary, but still important goal is to foster an interest in, and an appreciation of remote sensing outside our traditional community, whether it is high school students, resource managers or the casual surfer. Our opening date was June 1, 1995. Ten months after the site opened, it is receiving over 3,000 "hits", or requests per day.

Planning the site has always encompassed a two-pronged objective: to inform and educate people about remote sensing. Initial content was culled from the Centre's extant materials, all of which had to be structured in a meaningful way to take advantage of the dynamic nature of the Web. We focused on information design as well as ease of navigation to construct "chapters" around specific themes:

- Tell them who we are: ("This is CCRS" and "The Remote Sensing Community")
- Tell them what we do: ("Images & Products" and "Satellites & Sensors")
- Kindle an interest in remote sensing: ("What is Remote Sensing?" and "In the Spotlight")

The navigational buttons and layout were designed to create a sense of corporate identity and contribute to the overall look and feel of the site. Following a strict policy on the usage of these buttons helps to create a sense of continuity and improves the user's ability to navigate through the Web site.

Informative Reference Materials

Last year was a very important year for Canada because RADARSAT, our first operational earth observation satellite, was launched. While awaiting the November 8, 1995 launch, we were able to build a RADARSAT chapter which catered to all interest levels - from the photos of the satellite under construction, with tongue in cheek captions - to detailed specifications, examples of our R&D with RADARSAT image simulations as well as the abstracts of published papers on RADARSAT. New research opportunities and programs related to RADARSAT are also highlighted in this chapter.

0-7803-3068-4/96$5.00©1996 IEEE

Remote sensing scientists are, of course, already hooked. How could we sustain their interest to make sure that the CCRS site is a well thumbed bookmark? We decided to offer our existing glossary of general remote sensing terms and, for the radar specialist, a technical radar glossary. We offer a searchable contacts list of Canadian companies involved in the remote sensing side of the geomatics industry, which has proven very popular. Our list of international conferences complete with hyper links to e-mail and Web site addresses of future conferences is a particularly handy tool. CCRS conducts a seminar series on various aspects of remote sensing research and the Web site contains not only the seminar schedule, but a full abstract of each presentation. Over 5,000 copies of the CCRS newsletter are printed and distributed three times a year. It appears almost simultaneously on our Web site. These on-line issues of printed newsletters continue to be dynamic and informative because we can update the research findings and amend the material by adding new links within the articles. On the lighter side, there are some amusing items such as our "unconventional" definitions of remote sensing where readers are invited to contribute their own definitions.

Information regarding remote sensing applications and our research and development is always in demand and the Web offers a way of delivering the most up-to-date results, complete with data examples, in a way that paper copy never can. We present overviews of most of the CCRS programs and short "Spotlights" on specific items of interest. Our scientists have reported a definite increase in feedback from interested colleagues as a direct result of publishing their work on our Web site. By constantly updating news on interesting applications and innovative R&D, we keep the specialist informed and show the newcomer our areas of expertise.

Educational and Training Materials

Remote sensing is blessed with eye-catching images that draw the attention of the casual surfer and leave one with a thirst to learn more. Once we were convinced that our site had sufficient depth of informative content, we had some time to catch our breath and concentrate on the potential of our site for delivering some educational material. We decided to target high school level students as well as the ever present, interested surfer. Remote sensing is not usually part of most Canadian high school curricula, unless students are fortunate enough to have a teacher with a background or particular interest in this field. As part of planning for this section, we knew that educators should be involved in the development of materials.

A high school geography teacher evaluated our Web site over the summer and provided feedback and suggestions for material that would be suitable for students. Armed with this information and input from colleagues who had produced educational materials for Canada's School Net, we designed our first educational tool.

Images of Canada, a remotely sensed tour of the country, was designed to appeal to students, really to anyone who wanted to learn more about interpreting remote sensing images and it could serve as a resource tool for geography teachers. Different images from across the country were selected to show various elements of remote sensing - at least one for each province and territory. The images covered a wide variety of satellite and airborne sensors including different image enhancements. Each image is fully described, points of interest within the image are highlighted, and the viewer is challenged by a skill testing question related to the image. Figure 1 shows an example of an ***Images in Canada*** page.

Feedback regarding ***Images of Canada*** has been extremely positive. Shortly after its Web debut, ***Images*** was selected as *"Canuck Site of the Day"*. It is also listed on the Canadian *Science Web's* Hall of Fame page and under the Canadian *School Net's* section on Science, where it is receiving rave reviews from teachers:

> *"I have to admit first that the Tour of Canada is the best satellite image page on the web. Congratulations on a job well done. It is extremely well organized as a learning tool. I am using the page(s) for a grade 13 assignment on satellite imaging and the web. Each student has only 25 minutes to complete the exercise..."*

Buoyed by the positive response to ***Images of Canada***, we decided to develop a more focused educational tool to cater to our visitors who want a more substantive introduction to remote sensing, image analysis and remote sensing applications. Working with an internationally known geomatics company that has a strong background in remote sensing training, a series of modules will be constructed that cover topics from the electromagnetic spectrum to radar applications. Included in these modules will be evaluation tools that will allow users to gauge their understanding of the materials.

FUTURE PROSPECTS

Plans are already underway to make the internationally recognized RESORS database (1971-1995) of over 90,000 bibliographic citations in remote sensing searchable from our Web site. Over the years, CCRS scientists have provided image interpretation and radar training workshops to resource managers all over the globe and in several languages - we still have much valuable training material that can be redesigned

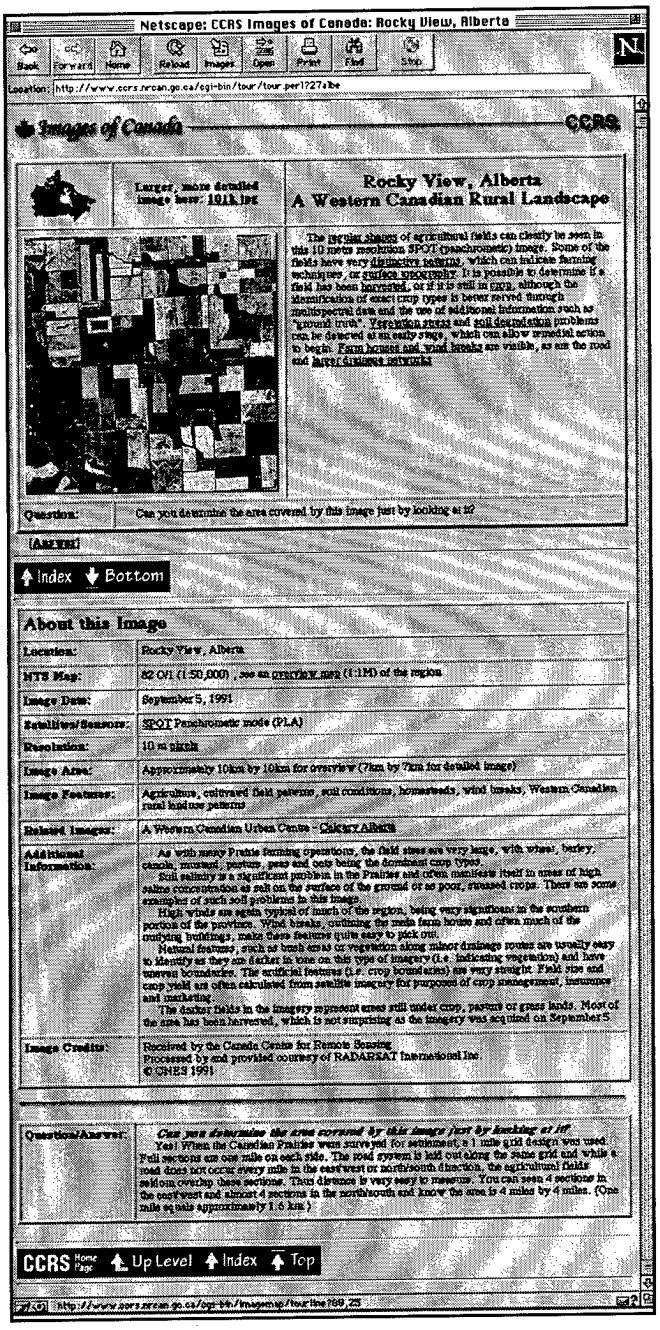


Figure 1. Example screen from ***Images of Canada.***

for distance learning. Another objective will be to offer some elementary training in image enhancement and data manipulation.

By using site-access statistics to gather intelligence about our visitors and which topics are most popular, we can clarify the requirements of our audience. This will result in improved design of multi-media learning materials to target diverse client needs. Further, by exploiting developing Web technologies (e.g. Java applets) we will be strategically placed to maximize the potential of our Web site to inform and educate.

ACKNOWLEDGMENTS

The authors acknowledge Anick Cantin, Mark Giovannetti and Rhonda Sabino of the Web implementation team for their dedication and hard work; and Jon Harris of the Carleton Board of Education for his valuable suggestions. Thanks to all our colleagues at the Canada Centre for Remote Sensing who contributed to the success of this project.

REFERENCES

The Canada Centre for Remote Sensing:
http://www.ccrs.nrcan.gc.ca
Images in Canada (in English):
http://www.ccrs.nrcan.gc.ca/ccrs/tour/toure.html
Images du Canada (in French):
http://www.ccrs.nrcan.gc.ca/ccrs/tour/tourf.html
Science Web:
http://scienceweb.dao.nrc.ca
School Net:
http://schoolnet2.carleton.ca

Earth Systems Science Education: Using Remote Imagery and Environmental Data Access

Rosanne W. Fortner, Professor. The Ohio State University, Earth Systems and Ohio Sea Grant Education Programs, 2021 Coffey Rd., Columbus, OH 43210. Voice phone 614/292-9826; fax 614/292-7432. Electronic mail: fortner.2@osu.edu

Abstract — The Ohio Sea Grant and Earth Systems Education programs at The Ohio State University have developed a CD-ROM, hard-copy materials and a teacher education program on "Environmental Data for Teaching About the Great Lakes." Support for the project has come from the Great Lakes Protection Fund, the George Gund Foundation of Cleveland, and the National Sea Grant College Program, for a three-year development and outreach program. Using the program materials, teachers can gain access to such environmental data as site-specific temperatures and precipitation for global sites reporting since 1890, the amount and types of toxic chemicals released by reporting sources anywhere in the United States, water quality data for streams, greenhouse gas concentration at global reporting sites, earthquake position and magnitude, wind patterns over water, and the status of remedial action planning in polluted areas. Some key areas for investigation are imaged with Landsat and aircraft photography. Creative teacher leaders are the first audience for the program. They are educated in how to use these new tools to effectively teach about the environment in relevant and exciting ways, and provided with support for conducting additional teacher education programs with them.

BACKGROUND

The Earth System Science concept was originally espoused by the National Aeronautics and Space Administration (NASA) as a means of imaging the complete scope of science, organized around and contributing to an understanding of the Earth. A large group of science educators found this approach appealing for organization of the science curriculum as well, and developed Earth Systems Education (ESE) programs for teacher enhancement to foster use of a systems approach in classrooms [1].

As science educators in the United States consider National Standards for Science Education [2] to guide the total science program in school contexts, and Benchmarks for Science Literacy [3] to identify levels of science understanding to be achieved by students after a given number of years in school, Earth Systems educators are finding justification for their approaches as well as new opportunities to influence the curriculum. Like the national curriculum restructure efforts recommend for all of science, ESE has always relied on interdisciplinary subject matter, collaborative learning, investigations, construction of knowledge from experiences, decisionmaking activities, and "real world" applications of science. Thus, instead of simply fitting into the plans of others for science education, Earth Systems Education should become part of the dialogue and help the public and the educational establishment see how the ideas of Earth systems science can be incorporated into new educational structures [4].

One of the basic understandings of ESE is that "The development of scientific thinking and technology increases our ability to understand and utilize Earth and space" [5]. Unfortunately, it is often the case that what emerges through the curriculum is not the *development* of scientific thinking and technology, but *facts we know* about science and technology. Students may never have the opportunity to collect original data or even use real data collected by scientists. Instead, they gather predictable numbers from a prescribed "experiment" or study a pre-interpreted graph in a textbook. It is easy to conclude, then, that following directions carefully results in "correct" data, and that data collected by real scientists is part of a complex TRUTH to be learned.

The tools of electronic networking and data recovery from archives are becoming more and more accessible to science classrooms in the United States and many other countries. Most teachers, however, are unaware of where to find such tools, how to use them, and how they might enhance the curriculum. A project at The Ohio State University helps teachers conquer these barriers. Users of the "Great Lakes Solution Seeker" CD-ROM and ancillary hard copy materials developed through the project are encouraged to develop an Earth System science question they feel would be important to answer. Examples might include a broad problem such as, Why is the catch of lake trout declining?, or a more student-relevant problem such as, Will it be safe to go swimming at the beach today?, assuming data are available on recent coliform counts or chemical spill dispersal or water temperature. Working cooperatively, they seek the data that will help them understand the complexity of the problem and what it would take to answer the question. A "Tool Kit" of resources on the general topic area gives a starting place for the investigations, and users are encouraged to pursue any productive avenues on-line or with the given data sets. Since few classrooms have all the technology desired for teaching, hard-copy and voice phone alternatives are provided. Some examples of the materials are described here.

Example 1. How much does a coastal region erode over time?

Many areas along the Great Lakes, as well as along other shorelines, are sites of dramatic erosion. Human developments exacerbate natural processes by changing runoff amounts and patterns, as well as removing protective vegetation [5]. Coastal

0-7803-3068-4/96$5.00©1996 IEEE

processes over the years can result in the loss of many cubic meters of waterfront property, including threatening or destroying human structures such as roads and houses. The data for studying such processes can be obtained from state agencies that have access to national databases of aerial photography. The data can be searched for old and new images of the same area, as in Fig. 1a-b. For easiest use, photos should be altered to be on about the same scale (using a copy machine or graphics software). Students in middle school and above can draw the early shoreline on tracing paper, then compare it with the more recent shoreline. Knowing the scale of the photos, they calculate the surface area of the land lost, and attempt to relate that to coastal processes, human impacts, storm events and such. In the case of these photos, the groins perpendicular to the shore have interrupted the longshore current and the protective beach has disappeared.

To find the volume of land lost requires that a topographic map be added to the available data types. Students examine the contour lines to find out how high the bluff is above the water, then multiply that height by the surface area lost. In this example, the area east of the groins lost land at the rate of 22,737 cu ft/yr year, while west of the groins the rate was 8421 cu ft/yr.



Figure 1a. Aerial photo of Painesville Township Park (OH) in 1954.



Figure 1b. Aerial photo of Painesville Township Park (OH) in 1973.

Newer technologies are now available for such studies. At this site the State of Ohio has installed a video monitor that records images every 15 minutes at the site. A computer registers the images and keeps a record of changes in wave action, slumping, and other factors. A Great Lakes Forecasting System computer model, available to the public at marinas and on the internet, enables students to get updates on wave heights and wind directions every six hours [6]. It is interesting for students to gather storm-related archival data from that system and match it with the video images taken at the same time.

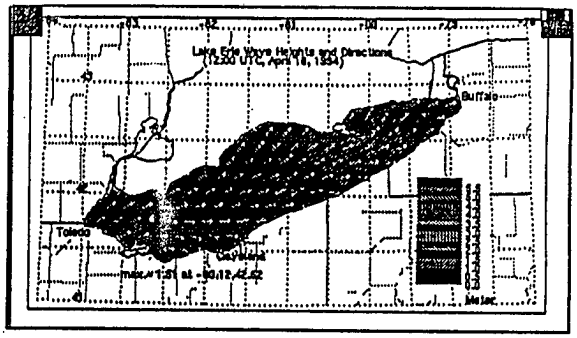


Figure 2. Wind directions on Lake Erie, as depicted by the Great Lakes Forecasting System.

Example 2. Are Great Lakes water levels related to regional precipitation? [7]

A second "Tool Kit" on the CD-ROM includes information for accessing large datasets: lake level measurements from the U.S. Army Corps of Engineers, and weather data from the National Climate Data Center of the National Oceanic and Atmospheric Administration (NOAA). Students can either access the data on the internet

http://sparky.nce.usace.army.mil
http://www.ncdc.noaa.gov

or call to request specific searches of the data for their lake and a nearby city. Comparison of the data requires that they analyze the graphing needs, amount and utility of data, and determine the most effective methods of arraying information to search for trends and relationships.

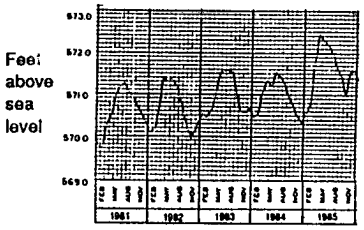


Figure 3. Water levels in Lake Erie from 1981-1985.

This example is from a 300-page book of instructional activities that utilize datasets to explore important questions about global change. The use of global change data helps students to understand media reports and also interpret what many see as frustrating disagreements among scientists. By critically examining data themselves, and by seeking a variety of data that can combine to help answer questions, students begin to appreciate how scientists approach data as tools. They will know that data from individual disciplines do not answer questions, and few datasets graph into neat, regular curves. It is a major goal of Earth Systems Education to create opportunities for students to examine the ways that scientists collect, analyze and interpret data about the ways in which the planet is changing [8].

Example 3. Toxic pollution issues in the Great Lakes

The CD-ROM for the project [9] includes a Hypercard stack about the 42 Areas of Concern (AOC, Fig. 4) that have been singled out in the region because water quality is impaired for some uses in those areas. Many of these sites are river mouths and harbors that for years received the wastes of cities and industries, and are now polluted to the point that fish, waterfowl, and perhaps even human consumers of fish have high levels of toxic chemicals in their bodies. Each AOC is represented on the CD by interactive information bases in which the problems are identified, characteristics of the area are shown on a satellite image, and Remedial Action Plans are presented. An audio challenge is given to the students at each site, to explore potential data sources or comparisons that can assist them in answering questions about the areas. The final CD will include a digital command that will access the internet address of the AOC or the Great Lakes Information Network on the internet.



Figure 4. The Great Lakes Areas of Concern

CONCLUSIONS

The use of environmental data and remote images enhances studies of the Earth system by enabling students to see how scientists function in their research. Such studies demonstrate to students that Earth system science does not have one scientific method, i.e. the experimental approach touted as the only correct way to do a science fair project, but instead employs descriptive and historical approaches and datasets. Using the materials from this project, teachers in the U.S. and Canada not only gain confidence in their ability to find and use environmental data, but also see the value of teaching in an Earth systems mode, integrating disciplines and exploring the answers to relevant questions.

REFERENCES

[1] V.J. Mayer and others, "The role of planet Earth in the new science curriculum," Journal of Geological Education, vol. 40(1), pp. 66-73, 1992.

[2] National Research Council, National Science Education Standards. Washington, DC: National Academy of Science, 1995.

[3] Benchmarks for Science Literacy. Washington, DC: AAAS Project 2061, 1994.

[4] R.W. Fortner, "A place for EE in the restructured science curriculum." In Confronting Environmental Challenges in a Changing World. J.H. Baldwin, Ed. Troy, OH: North American Association for Environmental Education, 1991. pp. 103-105.

[5] B.A. Kennedy and V.J. Mayer, Erosion Along the Great Lakes, EP-06. Columbus: Ohio Sea Grant, 1985.

[6] Great Lakes Forecasting System, K. Bedford, Director. Columbus, OH: The Ohio State University College of Engineering, 1994.

[7] "How is the precipitation of the Great Lakes Basin related to lake level change?" in Great Lakes Instructional Materials for the Changing Earth System (GLIMCES), R.W. Fortner, H. Miller and A. Sheaffer, Eds. Columbus: Ohio Sea Grant, 1996.

[8] R.W. Fortner and V.J. Mayer, "Making global change research data available to educators." in Earth Observations and Global Change Decision Making, 1990: A national partnership, I.W. Ginsberg and J.A. Angelo, Eds. Malabar, FL: Krieger Publ., 1991. pp. 313-318.

[9] Great Lakes Solution Seeker, CD-ROM for Great Lakes Environmental Data. Columbus: Ohio Sea Grant, 1996 draft.

Linear Structures in SAR Coherence Data

Olaf Hellwich[1], Claudia Streck[2]

[1]Chair for Photogrammetry and Remote Sensing
Technical University of Munich
Arcisstr. 21
D-80290 München, Germany
T: +49.89.2105.2677 F: +49.89.280.9573 EMail: olaf@photo.verm.tu-muenchen.de

[2]Kayser-Threde GmbH
Wolfratshauser Str. 48
D-81379 München, Germany

The extraction of thin linear structures like roads, rivers and railway lines from Synthetic Aperture Radar (SAR) scenes has been shown to be a difficult task owing to the speckle effects of coherent imaging (e.g. Hendri et al., 1988). Therefore, for line extraction it is reasonable to use all information SAR scenes offer, and not only the amplitude data. One source of additional information is the coherence data computed by interferometric processing of two SAR scenes.

The visibility of linear structures in SAR coherence data has been investigated. Scene pairs from the ERS-1 and the ERS-2 SAR sensors, the X-SAR experiment and a scene from a two-antenna airborne SAR system were evaluated. The time difference between the acquisitions of the spaceborne scenes forming interferometric scene pairs was one to 35 days. An optimal size of the correlation window used to derive coherence maps for linear structure extraction was determined by visual inspection. The correlation between the intensity and the coherence data was used to infer how much information the coherence adds to the information of the amplitude of both scenes.

DERIVATION OF SAR COHERENCE DATA

At the beginning of the interferometric processing of the spaceborne scenes three to four pairs of candidate conjugate points are identified and digitized interactively at the computer screen. The exact locations of these points are determined by a subpixel-accurate matching procedure seeking for the maximum complex correlation coefficient. From the successfully matched points mean translations of the second scene with respect to the first scene are computed.

With these translation values a coherence image is derived for a comparatively small region (e.g. 200x200 pixels) in the center of the region of interest. After the second scene is resampled to the geometry of the first scene using a bicubic-spline interpolation, the interferogram is derived in the original resolution of the scene. From this interferogram the interferogram of a "flat earth" is subtracted using the approach described by Hartl & Xia [1993]. Finally, the correlation, i.e. the coherence, is computed for a predefined window size. As the evaluated region is small, the coherence computation can be repeated very rapidly. Therefore, with a hill climbing procedure to maximize the average coherence the initial translation values can be refined by iteratively changing them and recomputing the coherence data.

After this coarse registration procedure precision registration is conducted. The complete region of interest is covered with a lattice which consists of a few grid points in each co-ordinate direction (e.g. 5x5 points). In each of those grid points, optimal translations are computed using the above hill climbing procedure for a small region (e.g. 80x80 pixels) starting with the translations from coarse registration. Then the final interferogram is derived. For the resampling, translations for each pixel are computed by bilinear interpolation between the grid points of the precision registration lattice. With a simple windowing operation coherence and smoothened phase are derived from the interferogram for varying window sizes.

TEST DATA

Five interferometric scene pairs from spaceborne SAR sensors were processed, and an interferometric data set from an airborne sensor was evaluated. Table 1 gives an overview of the data used.

data set	sensor	location	date of first scene	date of second scene	time diff. [days]	base -line [m]	Δf_{DC} [Hz]
1	ERS-1	Palatinate	91/11/24	91/11/30	6	220	40
2	ERS-1	Bavaria	92/06/01	92/07/06	35	230	30
3	ERS-1/2	Siberia	95/11/27	95/11/28	1	80	250
4	ERS-1/2	Siberia	96/01/01	96/01/02	1	110	240
5	X-SAR	Bavaria	94/10/08	94/10/09	1	140	230
6	TOP SAR	California	94/08/05			2.5	

Table 1. Test data. Δf_{DC}: difference of Doppler centroid frequencies; ERS-1/2: ERS-1 and ERS-2 SLC data sets from the tandem mission.

TEST RESULTS

The test mainly consisted of a visual inspection of various linear objects in the coherence and amplitude data. For each data set a principle component transformation was conducted for one frost-filtered amplitude data set and a coherence data set. In all cases amplitude and coherence were found to be uncorrelated to slightly correlated. This means that the coherence data set in general contains independent information about the imaged region. For particular objects, like roads etc., this is not true, as these are either darker or lighter than their surroundings in the amplitude as well as in the coherence data. So there will either be a positive or a

* This work was partially funded by the Deutsche Agentur für Raumfahrtangelegenheiten (DARA) GmbH under contract 50EE9423.

0-7803-3068-4/96$5.00©1996 IEEE

negative correlation. Nevertheless, the additional use of the coherence is valuable, as it increases the distance between the object data and the data of the surroundings. For the spaceborne data sets the correlation between the two amplitude images was computed. They were usually medium to highly correlated. Table 2 summarizes the results of the computations.

data set	correlation coefficient of amplitude and coherence	correlation coefficient of first and second amplitude	average coherence
1	0.24	0.84	0.54
2		0.29	
3	0.06	0.54	0.69
4	0.09	0.59	0.71
5	0.13	0.68	0.31
6	0.31		0.93

Table 2. Correlation between amplitude and coherence images, correlation between the two amplitude images and the average coherence in the region of interest.

The amplitude and coherence images of test data set 1, an ERS-1 scene pair of Ludwigshafen, Germany, are shown in Figs. 1 and 2. The coherence image shows interesting patterns of the agricultural areas. Some of the fields must have been cultivated between the two passes. Linear structures are not as clearly visible as in the amplitude image. This is mainly due to the reduced resolution of the coherence data which have to be computed inside of a window including several pixels. The coherence was computed for window sizes of 5x1, 11x3, 15x3 and 25x5 pixels. Though the 5x1 window offers the best chance to derive coherence data with a high resolution, it is not recommendable as the results are very noisy. The 25x5 window is also disadvantageous, as it smoothes over linear features and results in artifacts around highly coherent locations such as buildings. Therefore, the 11x3 and 15x3 window sizes are considered optimal for this application. For the further computations the 11x3 window was preferred, as it results in a slightly higher resolution than the 15x3 window.

The ERS-1 35-days-orbit scene pair of Oberpfaffenhofen, Bavaria, was largely incoherent. A reasonable interferometric processing was not possible.

Figs. 3 to 5 show the amplitude image of a Siberian test site and the corresponding coherence images derived from two scene pairs of the ERS-1/ERS-2 tandem mission (data sets 3 and 4). The scenes are highly coherent and the coherence data contains valuable information about rivers and pipelines crossing the scene. Figs. 6 and 7 show the coherence images of an enlarged section of the same area. The straight dark line in Fig. 6 is a road appearing to be comparatively incoherent. In the second data set (Fig. 7), the same road is more coherent than its surroundings. This phenomenon may be caused by height changes due to traffic between the acquisitions of the scenes of the first data set. A look into the phase data derived from data set 3 (Fig. 8) unveils that the road area is not completely decorrelated, as the phase data of the road is relatively constant. The phase difference between the road and its surroundings is surprisingly large (3 to 4 radians) indicating a change of height between the passes of ERS-1 and ERS-2.

The amplitude and coherence of the X-SAR data 5 is shown in Figs. 9 and 10. The average coherence is rather low which may be due to the fact that the X-SAR SSC data was not common-band filtered to eliminate the influence of the difference of the Doppler centroids of 230 Hz (Gatelli et al., 1994; Geudtner, 1995). In general, the residential and industrial areas have a considerably higher coherence than the agricultural and forested areas. The only linear object clearly visible in the coherence data is a runway at the right of the center of the image.

The airborne data set 6 shows a build-up area with city streets which are clearly visible in the amplitude and the coherence images (Figs. 11 and 12). The high resolution of the sensor as well as the high coherence of single path interferometry is very advantageous.

CONCLUSIONS

The tests have shown that coherence data contain information about linear objects, if these have a width slightly larger than the system resolution. Amplitude and coherence are largely uncorrelated. In coherence derived from ERS-1 and X-SAR scenes rivers and highways are visible. Railway lines usually could not be identified. For the extraction of linear structures we found a window size of 11x3 pixels for coherence computations to be optimal. Independent from the time difference between the acquisitions of the scenes, coherence of linear objects depends on the events occurring between the passes which makes the use of coherence data for object extraction rather difficult. Though data sets with varying time difference have been used, the assumption that man-made linear objects can be identified more easily in data sets with a larger time difference as they are changing to a lesser degree than the surrounding natural areas could not be verified. Furthermore, the visibility of linear objects depends on the surrounding objects and their coherence. A higher resolution, like that of an airborne sensor, would be very advantageous for the detectability of linear objects.

ACKNOWLEDGMENTS

We thank Stefan Prechler for implementing the essential interferometric processing routines, Cornelia Hecke for processing the test data sets, and the Deutsche Forschungsanstalt für Luft- und Raumfahrt, Oberpfaffenhofen, and Vexcel Corporation, Boulder, for providing most of the test data sets.

REFERENCES

Gatelli F., Monti Guarnieri A., Parizzi F., Pasquali P., Prati C., Rocca F. [1994], "The Wavenumber Shift in SAR Interferometry", IEEE Transactions on Geoscience and Remote Sensing, Vol. 32, No. 4, pp. 855-865.

Geudtner, D. [1995], *Die interferometrische Verarbeitung von SAR-Daten des ERS-1*, Deutsche Forschungsanstalt für Luft- und Raumfahrt, Forschungsbericht 95-28, 141 pages.

Hartl P., Xia Y. [1993], "Besonderheiten der Datenverarbeitung bei der SAR-Interferometrie", Zeitschrift für Photogrammetrie und Fernerkundung, No. 6, pp. 214-222.

Hendri A., Quegan S., Wood J. [1988], "The Visibility of Linear Features in SAR Images", Proc. IGARSS '88, Ref. ESA SP-284, (IEEE 88CH2497-6), pp. 1517-1520.



Fig. 1. Frost-filtered histogram-equalized amplitude of ERS-1 scene of 91/11/24.

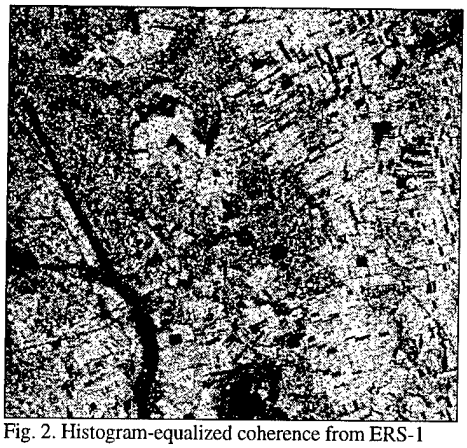


Fig. 2. Histogram-equalized coherence from ERS-1 scenes of 91/11/24 and 91/11/30.



Fig. 3. Frost-filtered histogram-equalized amplitude of ERS-1 scene of 95/11/28.

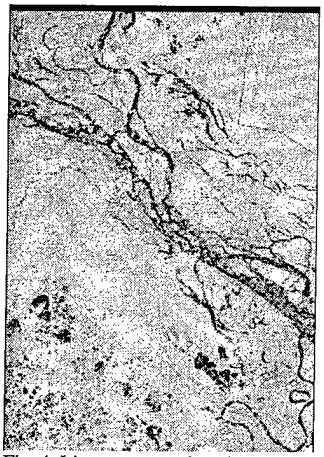


Fig. 4. Linear grey scale coherence from ERS-1/2 scenes of 95/11/27 and 95/11/28.

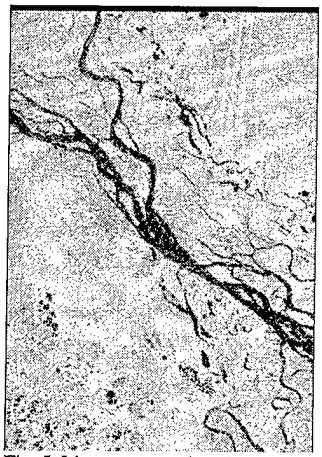


Fig. 5. Linear grey scale coherence from ERS-1/2 scenes of 96/01/01 and 96/01/02.

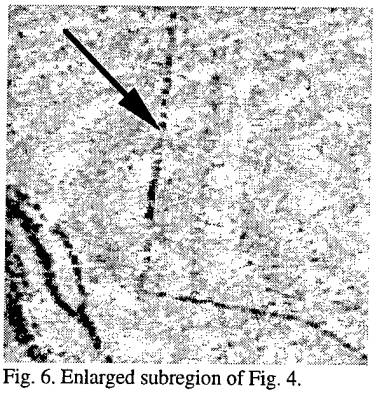


Fig. 6. Enlarged subregion of Fig. 4.

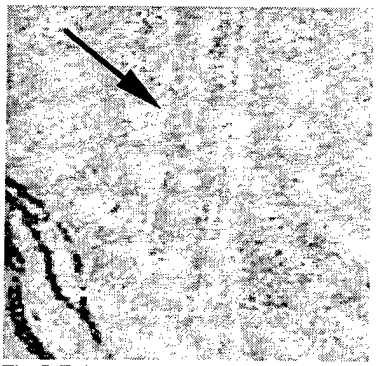


Fig. 7. Enlarged subregion of Fig. 5.

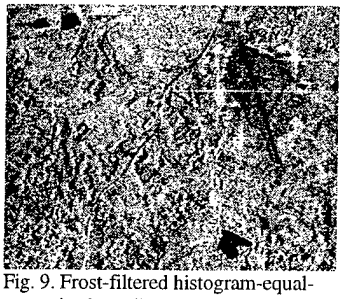


Fig. 9. Frost-filtered histogram-equalized amplitude of X-SAR scene of 94/10/08.

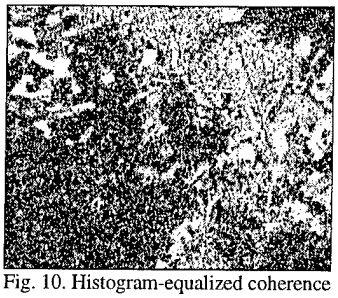


Fig. 10. Histogram-equalized coherence from X-SAR scenes of 94/10/08 and 94/10/09.

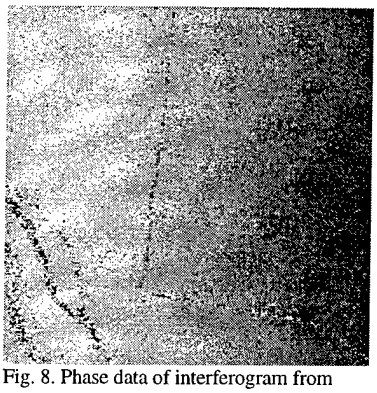


Fig. 8. Phase data of interferogram from ERS-1/2 scenes of 95/11/27 and 95/11/28.

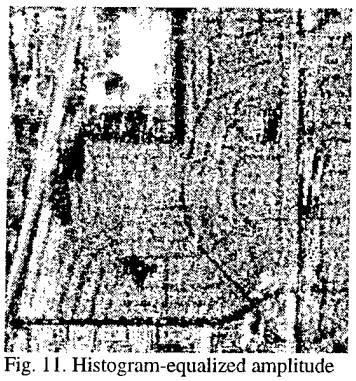


Fig. 11. Histogram-equalized amplitude of TOPSAR scene of 94/08/05.



Fig 12. Histogram-equalized coherence of TOPSAR scene of 94/08/05.

Detection and Velocity Estimation of Moving Objects in a Sequence of Single–Look SAR Images

Martin Kirscht
Institut für Theoretische Nachrichtentechnik und Informationsverarbeitung, Universität Hannover
Appelstr. 9A, D–30167 Hannover, Germany
Telephone: +49–511–762–5305 / Fax: +49–511–762–5333 / Email: kirscht@tnt.uni–hannover.de

Abstract — A method for detection of point–like moving objects and for estimation of their velocities with airborne synthetic aperture radar (SAR) is presented. This method is based on evaluation of the temporal correlation in a sequence of single–look SAR images which are processed using look filters with different center frequencies. In these images, candidates for moving objects are detected and a displacement vector estimation is performed for each candidate using a block matching algorithm as known from e. g. videotelephony. From the displacement vectors the velocities of the candidates in azimuth direction are calculated. The proposed algorithm has been applied to simulated and real raw data. The azimuth velocity component has been estimated with high accuracy, and a high detection probability with a low false alarm rate is reached.

INTRODUCTION

Synthetic aperture radar (SAR) is a powerful tool to produce high resolution microwave images of the ground. Since for SAR processing it is assumed, that the observed objects are static, moving objects cause errors in the SAR images. There are two significant kind of errors, depending on the direction of the motion. An object which moves in azimuth direction is defocused in azimuth direction whereas an object which moves in range direction is shifted in azimuth direction in the SAR image [1]. To compensate for these errors it is necessary to detect the moving objects and to estimate their velocities.

Most of the previously proposed algorithms for motion estimation of point–like moving objects are not able to detect objects which only have an azimuth velocity component. They usually work on range compressed SAR raw data, either transformed to the Doppler frequency domain (e. g. [2], [3]), or to a time–frequency domain [4]. A restriction is that the pulse repetition frequency (PRF) normally has to be much higher than the Doppler bandwidth of the clutter.

In this paper, a new method for detection of arbitrarily moving ground–based objects and for estimation of the azimuth velocity component is presented, which also works with a small PRF. This method is based on evaluation of the temporal correlation in a sequence of single–look SAR images. These images are processed from different overlapping frequency bands with constant look bandwidth out of the Doppler spectrum. The images show the ground at different look angles and therefore at different times. Thus, the objects appear at different positions in the several images and the velocities of the objects can be estimated.

The following paragraphs of the paper describe the generation of the sequence of single–look SAR images and the three main steps of the detection and velocity estimation algorithm. Afterwards main results concerning the detection probability and the estimation accuracy are given.

GENERATION OF THE SEQUENCE OF SAR IMAGES

The proposed method is based on estimation of the displacements of point–like moving objects in a sequence of single–look SAR images. The generation of this sequence is carried out as follows. First the Doppler spectrum of the range compressed SAR raw data is calculated by performing a fast Fourier transform (FFT) in azimuth direction. Then the Doppler spectrum is subdivided into several overlapping bands and a single–look image is processed from each band. The images show the ground at different (horizontal) look angles θ_i, which depend on the look center frequencies f_{li}, as given by

$$\theta_i = \arcsin\frac{f_{li}\,\lambda}{2\,v_{Ax}}, \qquad (1)$$

where v_{Ax} is the platform velocity, which moves in positive azimuth direction, denoted by x, and λ is the carrier wavelength. The different look angles also imply that the images show the ground at different times. The look bandwidth has to be chosen carefully. If it is too small, the azimuth resolution will decrease, on the contrary if it is too large, the quickly moving objects will be defocused and will lose the point–like property.

The images of the sequence are ground range corrected and then a range migration correction is performed by shifting the images in range direction according to the change of the distance between antenna and ground at different look angles. After this manipulation the stationary background in the images remains at the same position, whereas the positions of the moving objects change from image to image. Due to the single look processing the images contain a lot of speckle noise. This might be interpreted as a moving object in some cases. To avoid this, a three step algorithm is performed, which evaluates the images of the sequence consecutively, beginning at the image with the highest look center frequency. The first step is the detection of candidates for moving objects, which later are verified.

DETECTION OF CANDIDATES FOR MOVING OBJECTS

In each image of the generated sequence point–like objects are selected as candidates for moving objects. The search is

This work was supported by the German Federal Government. The SAR raw data have been delivered by DASA Dornier, Friedrichshafen, Germany.

0-7803-3068-4/96$5.00©1996 IEEE

performed by starting at the pixel with the highest intensity, which depends on the radar cross section. Then this pixel and the surrounding pixels are selected as one candidate if the following criteria are fulfilled:

- the brightest pixel of a candidate has a higher intensity than a threshold adapted to the mean global intensity of the image,
- the number of pixels belonging to one candidate is between a lower and an upper bound; the upper bound depends on the length of the objects in azimuth direction and is therefore be chosen according to the maximal detectable velocity;
- the mean intensity of the pixels of a candidate is noticeably higher than the mean intensity of the surrounding area,
- the candidate covers a closed area, and
- no pixel of one candidate adjoins a pixel of another candidate.

After the positive or negative finishing of this task, the previous steps are repeated for the remaining pixels with the same intensity and afterwards for those with less intensity until a threshold is reached.

VELOCITY ESTIMATION

After having detected candidates for moving objects, for each candidate a displacement vector is estimated using a block matching algorithm as known from e. g. videotelephony [5]. This algorithm estimates the displacement of parts of the image between two successive images s_1 and s_2 of the sequence, which are called frames in this chapter. To obtain the displacement vector, a window is positioned in the frame s_2, so that the candidate lies in the center of it. Then in frame s_1 another window is put at the same position. The aim is, to find the best match between the two windows by shifting the window in frame s_1 on every position within a neighborhood (full search method). For that, one of the following four matching criteria are used, the cross correlation coefficient (CCC), the normalized cross correlation function (NCCF), the mean square error (MSE), and the mean absolute difference (MAD). The NCCF criterion shows the best results. The results of the MSE criterion are nearly as good as the results of the NCCF, with the advantage of a faster implementation. The NCCF is defined by

$$C_{Ns_2s_1}(\Delta x, \Delta y) = \frac{\sum_{x,y}[s_2(x,y) \cdot s_1(x-\Delta x, y-\Delta y)]}{\sqrt{\sum_{x,y} s_2^2(x,y) \cdot \sum_{x,y} s_1^2(x-\Delta x, y-\Delta y)}}, \quad (2)$$

where (x, y) is one of the positions inside the window, and Δx and Δy are the position shifts between the two windows. Equation (2) has to be evaluated for each different position of the window in the first frame. The motion vector in pixel / frame for the selected candidate is then given by that shifts Δx and Δy which maximize the $C_{Ns_2s_1}$.

The azimuth velocity component is calculated from the displacement vector component $v_{Tx_{pix}} = \Delta x$ in azimuth direction and the range dependent time difference between two successive frames which is given by

$$\Delta t \approx \frac{\Delta\theta \; R_0}{v_{Ax}} \approx -\frac{\Delta f_l \; \lambda \; R_0}{2 v_{Ax}^2} \quad \text{for } \sin\theta \ll 1, \quad (3)$$

where $\Delta\theta$ is the difference between the look angles of adjacent frames, R_0 is the minimal distance between antenna and object candidate, and Δf_l is the difference between the look center frequencies.

Let δx be the pixel spacing in azimuth direction, then we can calculate the observed velocity in azimuth direction to

$$v_{Tx_{obs}} = \frac{v_{Tx_{pix}} \; \delta x}{\Delta t}. \quad (4)$$

This velocity is not the real one, because the objects do not appear at the right positions in the different images. Ouchi [6] showed that the azimuth velocity component has to be divided by a factor of 2 to get the real velocity. So the estimated velocity $v_{Tx_{est}}$ finally becomes

$$v_{Tx_{est}} \approx \frac{v_{Tx_{pix}} \; \delta x}{2 \; \Delta t} = -\frac{v_{Tx_{pix}} \; \delta x \; v_{Ax}^2}{\Delta f_l \; \lambda \; R_0}. \quad (5)$$

Here beside some other approximations, the assumption is made that $v_{Tx}/v_{Ax} \ll 1$.

Additionally, it deserves mentioning that the range velocity component cannot be well estimated that way, because the range migration correction causes a warping of the range position of those objects, whose range velocity component is not zero. However, this warping can be avoided if the Doppler shift due to motion in range direction is compensated prior to the generation of the sequence.

VERIFICATION OF MOVING OBJECTS

The candidates are verified to be moving objects if their displacement vectors remain quite constant during a fixed number of images. This means that the absolute value and the angle of motion may only change within a fixed range. If this is fulfilled, the counter for this candidate will be incremented and it will be finally detected as moving object, if the dedicated number of images is reached.

Finally, in order to improve the reliability of the estimated azimuth velocity component an averaging over all previously counted, estimated values is carried out.

RESULTS

The proposed method has been applied to simulated raw data and to real raw data. A PRF of 1.5 times the clutter bandwidth and a sequence with 16 images are used. The proposed algorithm estimates the azimuth velocity component with high accuracy, i. e. the average of the relative error is 8.0 % for positive v_{Tx}, and 18.9 % for negative v_{Tx} ranging from $\pm$ 10 km/h ($\pm$ 2.8 m/s) to $\pm$ 50 km/h ($\pm$ 13.9 m/s), respectively. The attained accuracy depends on the moving direction of the object due to the approximations in (5). For this results the

NCCF criterion and simulated raw data of moving objects superimposed by real clutter data with a signal–to–clutter ratio of 0 dB are used. The platform velocity is 300 km/h or 83 m/s. All moving objects with a minimum azimuth velocity component of 10 km/h are detected even if they move in direct neighborhood to a strong stationary scatterer. At smaller velocities the detection probability decreases slightly. The false alarm rate is about 2 %. The maximal detectable velocity can be adjusted; it depends on the maximal Δx in (2) and the maximal number of pixels for the detection of candidates.

The proposed method also works well if the objects have an additional range velocity component v_{Ty}. In an example two images out of a sequence with 16 images are shown. The azimuth direction x runs horizontal. The 5 moving objects in the scene have the velocity components v_{Tx}=30 km/h and v_{Ty} ranging from –20 to +20 km/h. Fig. 1 shows image No. 6 of the sequence, where 2 objects out of 5 are already detected, which is marked with a white square. In Fig. 2 image No. 11 of the sequence is shown, where all moving objects are detected.

First results by applying the method to real SAR raw data show that the detection probability slightly decreases, but that the algorithm still works well.

CONCLUSIONS

In this paper a new method for detection and estimation of the azimuth velocity component of moving objects has been presented, which works on a sequence of single–look SAR images. These images show the ground at different look angles and therefore at different times. So the object velocities can be estimated by evaluating the temporal correlation of successive images. The advantages of the method are, that it works with a small PRF and that also objects can be detected, whose range velocity component is zero. A high estimation accuracy is reached, even if the objects are superimposed by real clutter data. The method only works well for the azimuth velocity component, but it could be extended in order to estimate both components of the velocity if the Doppler shift due to motion in range direction is compensated prior to the generation of the sequence.

REFERENCES

[1] R. K. Raney, "Synthetic aperture imaging radar and moving targets," IEEE Trans. Aerospace and Electronic Systems, vol. AES–7, No. 3, pp. 499–505, May 1971.

[2] A. Freeman and A. Currie, "Synthetic aperture radar (SAR) images of moving targets," GEC Journal of Research, vol. 5, No. 2, 1987.

[3] E. D'Addio, M. Di Bisceglie, and S. Bottalico, "Detection of moving objects with airborne SAR," Signal Processing, vol. 36, No. 2, pp. 149–162, March 1994.

[4] S. Barbarossa and A. Farina, "A novel procedure for detecting and focusing moving objects with SAR based on the Wigner–Ville distribution," Proc. of IEEE Int. Radar Conf., Arlington, 1990.

[5] M. Bierling, "Displacement estimation by hierarchical blockmatching," 3rd SPIE Symposium on Visual Communications and Image Processing, Cambridge, USA, pp. 942–951, 1988.

[6] K. Ouchi, "On the multilook images of moving targets by synthetic aperture radars," IEEE Trans. Antennas and Propagation, vol. AP–33, No.8, pp. 823–827, 1985.

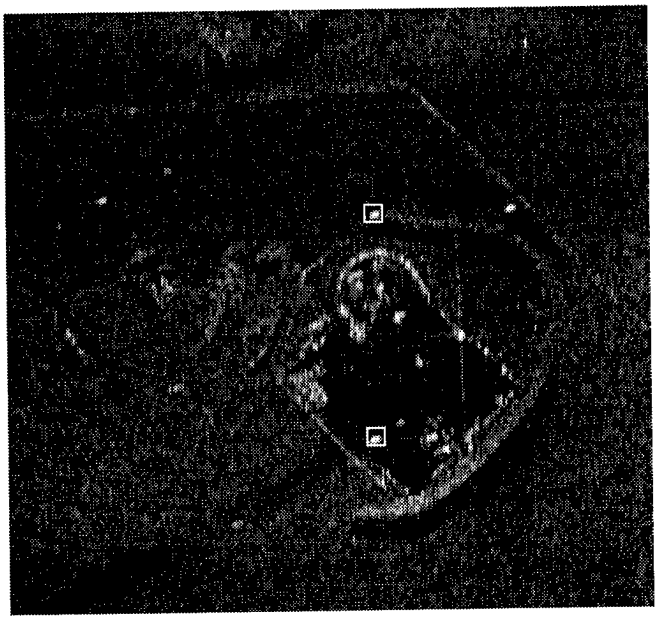


Fig. 1 Single–look image No. 6 from the generated sequence, look center frequency is 125 Hz; 2 out of 5 moving objects are detected (marked with a white square)

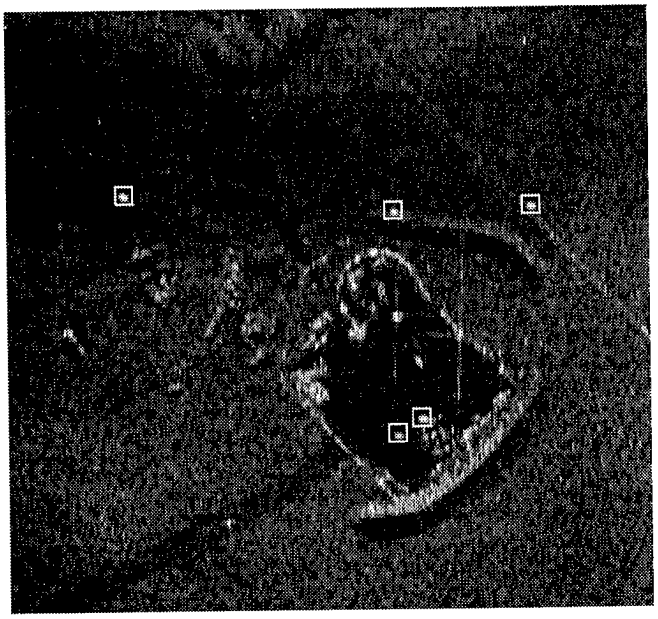


Fig. 2 Single–look image No. 11 from the generated sequence, look center frequency is –125 Hz; all moving objects are detected

Comparative Analysis of Phase Unwrapping Methods Using Self-Affine (Fractal) Models.

Juan-Luis Valero & Ian Cumming

Radar Remote Sensing Group, Dept. of Electrical Eng., Univ. of British Columbia
2356 Main Mall, Vancouver, BC, Canada, V6T 1Z4.
Tel: +1 604 822-4623, Fax: +1 604 822-5949, e-mail: ianc@ee.ubc.ca

ABSTRACT

The use of a self-affine surface to test three phase unwrapping algorithms, Cut-line, Least-Squares and a Region-Growing is discussed. The methods were chosen to be a representative set of modern phase unwrapping methods.

1. INTRODUCTION

Satellite radar interferometry is a promising technique for estimating the topography or small displacements of the Earth's surface. This is done by measuring the phase differences between two registered synthetic aperture radar (SAR) images, taken with a time lapse and/or a shift in the viewing angle of the sensor. Several aspects of the InSAR processing algorithms require improvement to form a fully operational technique, such as: calibration and phase unwrapping. The phase obtained by InSAR is multi-valued with an ambiguity of 2π: a wrapped phase. The process of estimating the un-ambiguous phase from wrapped phase is known as phase unwrapping. This is one of the most critical processes in InSAR.

We present an evaluation of several of the representative phase unwrapping methods [1] using realistic simulated test data. The chosen phase unwrapping methods are: A variation of the cut-line method reported by Joughin [2], a least-squares (LS) method presented by Ghiglia and Romero [3], and a region-growing method presented by Xu [4].

Simulated data are used because one can control the error sources and make a direct comparison with the expected results. In addition, the lack of accurate ancillary data does not allow a systematic comparison between actual satellite InSAR results and ground truth.

The authors wish to thank the Canada Centre for Remote Sensing, MacDonald Dettwiler, the Natural Sciences and Engineering Research Council, the BC Advanced Systems Institute and the BC Science Council for their financial support during the course of this work and Dr. Joughin and Dr. Xu for providing their phase unwrapping algorithm's code.

Section 2 describes the characteristics of the self-affine model used in our testing procedure, Section 3 presents the phase unwrapping algorithms tested, Section 4 summarizes our results and finally Section 5 presents our conclusions.

2. SELF-AFFINE TOPOGRAPHIC MODEL

The concept of fractal geometry was introduced in the 70's by Mandelbrot [5] for the description of natural landscapes. Since then, the fractal nature of a large number of natural landscapes has been experimentally confirmed by several authors [6]. The use of fractal concepts in remote sensing is not new but is still under development. It has been used for SAR scene segmentation, interpolation and analysis of digital elevation models (DEMs) and for the simulation of raw SAR data [7].

For clarity, we should recall that self-affinity is the scaling behavior of a topographic surface that relates the increase of the horizontal scale by a factor r to the increase of the vertical scale by a factor r^H, in order to keep the surface statistically identical. If an small portion of this kind of surface is sufficiently enlarged, the result is statistically indistinguishable from the whole surface. The exponent H is referred to as the Hausdorff measure or Hurst exponent [8], where $0 < H < 1$. And it is related to the surface's fractal dimension, D, as $D = 3 - H$.

The fractal dimension of a surface can be interpreted as its *roughness*: its value ranges between 2 (completely smooth) and 3. Usually, D ranges between 2.1 to 2.3 for natural landscapes.

A self-affine surface provides a model of Earth's topography which has realistic statistical properties over a limited range of scales, from few meters to thousand of meters.

The high frequency component of the topography is one of the origins of phase singularities or residues in real InSAR data. The use of high resolution DEMs to test phase unwrapping algorithms is limited because they are generated by stereomatching or by interpolating digital

0-7803-3068-4/96$5.00©1996 IEEE

contours maps. In both cases, the high frequency component of the topography does not appear in the DEMs. On the other hand, the spatial frequency components of a band-limited self-affine model are controllable during its generation, overcoming the limitation of the high resolution DEMs. Other sources of phase singularities as noise, phase aliasing or mis-registration can be easily added in the simulation.

We selected a Fractional Brownian Motion (fBM) function as a self-affine surface to perform tests on phase unwrapping algorithms. fBM has been used for the simulation of random surfaces found in nature such as mountainous terrain or clouds. It is an extension of the Brownian motion concept with a fractal dimension ranging from 2 to 3. The modeling of Earth's topography by a fBM does not mimic geomorphological processes, such as erosion, without additional processing. But is realistic enough for our purposes.

3. PHASE UNWRAPPING ALGORITHMS

The first algorithm considered is an improvement of Goldstein's cut-line algorithm [9]. This implementation was developed by Joughin [2] and uses a binary mask derived from the coherence values of the 2-D phase-map to identify the feasible areas to unwrap.

Cut-line algorithms are based on the identification of phase singularities or residues, and the connecting of these residues by a cut-line. In this way, the phase-map can be unwrapped without ambiguities. The main problem of any cut-line algorithm is the selection of the joining paths between residues. There are many possible paths, and only one is correct. The algorithm implemented by Joughin attempts to differentiate between the phase inconsistencies produced by noise from those produced by the topography of the area under observation.

The current version of the region-growing approach [4] uses the values of the coherence of the 2-D phase-map as the indicator of the quality of a point to be unwrapped. The unwrapped phase-map is divided into regions by the value of the coherence. Each of these regions is unwrapped beginning with a point with small phase variability in his surroundings. From this initial point, the phase unwrapping follows a path governed by the minimum phase variability. When a point is surrounded by a neighbourhood with high phase variability, it is either marked as an invalid point or is unwrapped in a later iteration. The individual regions are joined following the minimum phase variability of their common boundaries.

The third method is a path-independent approach based on a fast Poisson solver [3]. The current implementation uses a Picard iteration scheme with a variation described by Pritt and Shipman [10]. The solution of the Poisson equation is based on an FFT of a periodic extension of the 2-D phase-map, i.e. double reflection plus periodic boundary conditions.

4. TEST RESULTS

The three phase unwrapping algorithms were first tested in the following way: A) Generation of a fBM surface B) Scaling the fBM surface in order to generate a phase-map with enough dynamic range. In this way, the scaling generates several 2π ambiguities. C) Wrapping the fBM phase-map. D) Estimation of the coherence of the fBM phase-map for the use in the region-growing algorithm and after a binary conversion for the use in the cut-line and Picard iteration algorithms. E) Running the algorithms and comparing their output with the original self-affine phase-map.

Fig.1 shows the original and wrapped fBM phase-map (coherence, γ= 0.96). The three algorithms correctly unwrap this first example. The Picard iteration algorithm was tested with only half of the fBM phase-map because its convergence rate is very slow. Fig.2 shows the small difference between the original and unwrapped phase using the Picard iteration algorithm after 200 iterations.

A second test was carried out using a noisy version of the fractal phase-map. Enough Gaussian noise was added to the phase values to reduce the coherence to $\gamma = 0.71$. As in the previous case, the cut-line and region-growing methods unwrap this phase-map without errors.

As a third test, we added a jump near a 2π discontinuity to the noisy version of the fractal phase-map. The goal here is to check the behavior of the unwrapping algorithms when a phase jump is present. Note that in a real interferogram this situation could happen at layover areas or at areas with large topographic changes. However the coherence level in these areas is low in real interferograms, allowing the phase unwrapping algorithm to bypass them.

We created a quarter of a Gaussian surface in order to generate a phase discontinuity in the phase-map. This Gaussian surface was multiplied by a self-affine surface and added to the noisy version of the fractal phase-map.

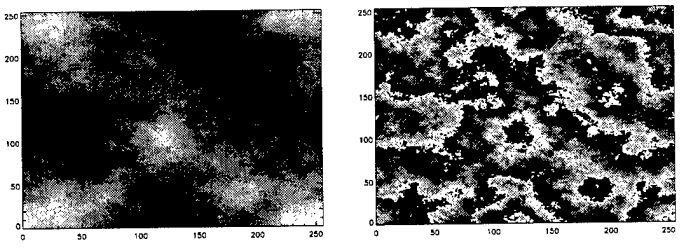


Figure 1: Original (unwrapped) and wrapped fractal phase-map used in the simulation: each cycle in the wrapped case represents a phase change of 2π.

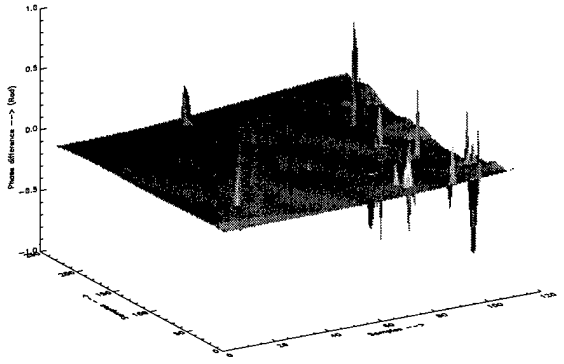


Figure 2: Phase difference between the original and unwrapped phase using the Picard iteration scheme after 200 iterations.

The cut-line algorithm failed this test.

Fig.3 shows the 2π ambiguity level of the noisy version of the fractal phase-map with an abrupt 2π jump and the output of the region-growing approach. The white spots on the right part of Fig.3 are non-valid regions excluded from the unwrapping process. In this case, a 2π error appears in region-growing unwrapping procedure (close to the location (100,100)).

5. CONCLUSIONS

The topographic modeling of Earth's topography by a self-affine surface Vs. real DEMs allows a direct comparison of phase unwrapping algorithms to the expected results, the control of error sources and the inclusion of higher spatial frequencies.

In our testing of 3 phase unwrapping algorithms we conclude: A) The three tested methods work properly with comparable accuracies when the phase-map has high coherence. B) If the coherence is low and the topography has cliffs edges, then 2π errors appear. This is expected given the characteristics of the Gaussian jump used. Each of the algorithms seems to localize phase unwrapping errors. C) In terms of speed, the cut-line approach is the fastest, while the Poisson solver is the slowest.

6. REFERENCES

[1] J. L. Valero and I. Cumming. A survey of phase unwrapping techniques with applications to InSAR. Technical report, Department of Electrical Engineering, UBC, June 1995.

[2] I. R. Joughin. *Estimation of ice-sheet topography and motion using interferometric synthetic aperture radar.* PhD thesis, Electrical Engineering, University of Washington, Seattle, March 13, 1995.

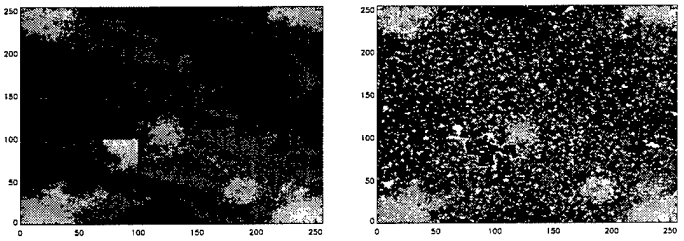


Figure 3: Left: Original Gaussian noisy phase plus an abrupt ambiguity (2π value) Right: region-growing method phase ambiguity, note the phase ambiguity error in the image.

[3] D. C. Ghiglia and L. A. Romero. Robust two-dimensional weighted and unweighted phase unwrapping that uses fast transforms and iterative methods. *J. Opt. Soc. Am. A*, 11(1):107–117, January 1994.

[4] W. Xu and I. Cumming. A region growing algorithm for InSAR phase unwrapping. In *IGARSS'96*, Lincoln, Nebraska, U.S.A., July 1996.

[5] B. B. Mandelbrot. *The Fractal Geometry of Nature.* W. H. Freeman, San Francisco, 1982.

[6] J. C. Russ. *Fractal surfaces.* Plenum Press, New York, 1994.

[7] G. G. Wilkinson, I. Kanellopoulos, and I. Megier, editors. *Fractal in Geoscience and Remote Sensing*, volume 1 of *Image Understanding Research.* European Commission, 1995.

[8] K. Falconer. *Fractal Geometry: Mathematical Fundations and Applications.* John Wiley, New York, 1990.

[9] R. M. Goldstein, H. A. Zebker, and C. L. Werner. Satellite radar interferometry: Two-dimensional phase unwrapping. *Radio Science*, 23(4):713–720, 1988.

[10] M. D. Pritt and J. S. Shipman. Least-squares two-dimensional phase unwrapping using FFT's. *IEEE Trans. Geo. Rem. Sensing*, 32(3):706–708, May 1994.

A Workstation for Spaceborne Interferometric SAR Data

M.W.A. van der Kooij, B. Armour, J. Ehrismann, H Schwichow and S. Sato

Atlantis Scientific Systems Group Inc.
1827 Woodward Drive, Ottawa, Canada K2C 0P9
tel: 613-727-1087; fax: 613-727-5853
E-mail: marco@atlsci.com

Abstract - The Atlantis Interferometric SAR (InSAR) Workstation is implemented in the ERGO*vista* image analysis software framework. It is specially designed for spaceborne repeat-pass interferometric SAR data and provides both research and operational users with a complete set of commands and tools to interact with interferometric SAR data, generate interferometric products and develop new functions. This paper describes the objectives, requirements and technical outline of the InSAR Workstation. Examples of interferometric products will be shown using JERS-1 data of the Hyogo Nanbu (Kobe, Japan) earthquake that occurred on January 17 1995.

INTRODUCTION

In the last decade SAR repeat-pass interferometry has been the subject of intensive research. Although it is still at a research stage, it has been recognized as a technique that yields highly quantitative information, for example height, large scale deformation and (subtle) change. It has the potential to routinely provide Digital Elevation Models (DEM's), maps of deformation and change, and to allow a full geocoding of SAR imagery. A growing number of applications have become feasible, and even more are being researched. Perhaps the most exciting new application of SAR interferometry is the 2-dimensional mapping of deformation with very high accuracy (mm- to cm-level). Applications include earthquake deformation detection and monitoring, monitoring of crustal movements, volcanic movement, land slides and land subsidence.

Based on its experience in building COTS (Commercial Off-The-Shelf) SAR processing and SAR image processing software, Atlantis is now developing a software product to be made available called the *InSAR Workstation*. The primary objectives for the design of the InSAR workstation are as follows.

1) To create an environment in which research users are able to manipulate InSAR data and generate products like interferograms, coherence maps, DEM's and deformation maps (sometimes referred to as "differential" InSAR). It should give them the ability to investigate different algorithms, add their own algorithms and validate the use of SAR interferometry for different applications.
2) To create an environment in which operational users are able to routinely generate geocoded InSAR products like DEM's, and deformation and change maps of high quality in a fast and user-friendly way.

Other objectives are:

1) To generate additional products like
   - coherence and scene coherence maps
   - terrain slope and incidence angle maps
2) the possibility to import data from any platform (RADARSAT, ERS-1/2, JERS-1, Almaz).
3) To import SAR SLC data from any SAR processor
4) To include easy-to-use toolkit facilities that enable the user to
   - process data of varying orbit accuracy
   - reduce/repair phase errors during and after the phase unwrapping process
5) To add tools for validation of the products e.g. comparing generated DEM's to an input DEM.
6) To include mosaic functions
7) To export and import existing DEM formats.

Details of the processing approach are given below. Examples of interferometric products are shown using JERS-1 interferometric SAR data of the Hyogo Nanbu (Kobe, Japan) earthquake

TECHNICAL OUTLINE

The InSAR workstation is developed in the ERGO*vista* image processing and function development framework. The ERGO*vista* SAR processor can be used to generate single-look complex SAR image data from raw SAR data. Seven distinct software elements can be distinguished:

Kernel Parameter Generator.
This element enables the user to validate the input master and slave datasets for InSAR use in terms of spatial overlap, spectral overlap and height sensitivity. It generates all parameters required by the other 6 kernel elements. Co-registration parameters are generated using the orbit state vectors at given epochs, dataset slant range and timing information and earth geometry parameters. In case of low

0-7803-3068-4/96$5.00©1996 IEEE

quality orbit data, user-friendly absolute and relative tiepointing facilities are available to improve master and slave state vectors. Fine co-registration parameters of the slave image are calculated relative to the previously determined (coarse) co-registration parameters. The slave state vector is updated such that it describes the updated parameters.

Interferogram Generator.
The master and slave images are filtered to minimize the effect of baseline decorrelation and azimuth spectral mismatch. The slave image is resampled using the co-registration parameters obtained in the kernel parameter generator. The phase variation due to a selected earth model or optionally from an input digital elevation model are removed. InSAR DEM's or DEM's from other origins can be used for this purpose. This "topography phase" removal is important for deformation analysis ("differential InSAR") but is also important to validate the accuracy of InSAR measurements (e.g. study of the effect of atmospheric heterogeneities) or to improve or update existing DEM data.

Interferogram Quality Analysis and Enhancement
Several interferogram enhancement techniques are available that attempt to smooth the phase noise and control the number of phase residues. An unwrapping control mask is generated for use in the phase unwrapping. A coherence map and optionally a signal-to-noise ratio map, a scene coherence map and a phase slope map are generated.

Interferogram Phase Unwrapping
Several phase unwrapping techniques are available that can operate in the context of the phase unwrapping-mask. A number of phase residue connection algorithms and several hierarchical strategies are available that can be configured such that the phase fidelity of the unwrapped phase map is optimized. Users have several user-friendly unwrapping control tools that allow them to interact directly with the unwrapping process and enable them to make repairs or adjustments to the unwrapping strategy

Slant-range DEM or Deformation map generator
This process translates an input image of absolute phase values to either height values or deformation values (depending on whether the user selected DEM or deformation map generation) using the parameters generated in the Kernel Parameter Generator.

Terrain Distortion Removal
This process also uses parameters generated by the Kernel Parameter Generator and resamples the slant-range DEM or deformation products on the basis of a supplied slant range DEM.

Resampling (Geocoding)
The geocoding is a parametrically controlled resampling process in two passes that generates geocoded InSAR products in standard map projections (UTM, UPS, LCC, etc.).

EXAMPLES OF INTERFEROMETRIC PRODUCTS

Figure 1, 2, 3 and 4 show results for the interferogram generated from JERS-1 data recorded on October 10, 1993 and on March 22, 1995 over Kobe, Japan. The size of the image is approximately 25 x 25 km. The areas covered by water (ocean) are masked out (grey). The perpendicular component of the interferometric baseline is approximately 540 m. Figure 1 shows the interferogram power. Figure 2 shows the filtered interferogram phase, where the "flat" earth and topographic fringes have been removed using an input DEM of the area. The remaining phase pattern is due to large scale deformation caused by the Hyogo-Nanbu earthquake on January 17, 1995. Figure 3 shows the unwrapped phase. The unwrapped phase has been calculated using a phase residue connection algorithm in combination with a path independent unwrapping algorithm that is available in the InSAR Workstation. The maximum absolute phase (white) is measured at Kobe harbor at the lower right, and is approximately +27 radians relative to the "stationary" background phase. Assuming a horizontal shift towards the southwest, this value corresponds to a deformation of 1.5 m. Figure 4 shows the phase coherence of the scene. Although the coherence is low (less than 0.4), the interferogram enhancement and unwrapping algorithm managed to generate good quality interferometric products.

CONCLUSIONS

The objectives, requirements, and technical outline of the Atlantis InSAR workstation have been described. It provides both research and operational users of spaceborne InSAR data with a complete set of commands and tools to interact with InSAR data and to generate interferometric products. Examples of data of the Hyogo Nanbu (Kobe) earthquake demonstrate the potential of repeat-pass interferometry and the capability of Atlantis to create an InSAR workstation.

ACKNOWLEDGEMENTS

The development of the InSAR Workstation is supported by the Canadian Space Agency under the RADARSAT User Development Program.

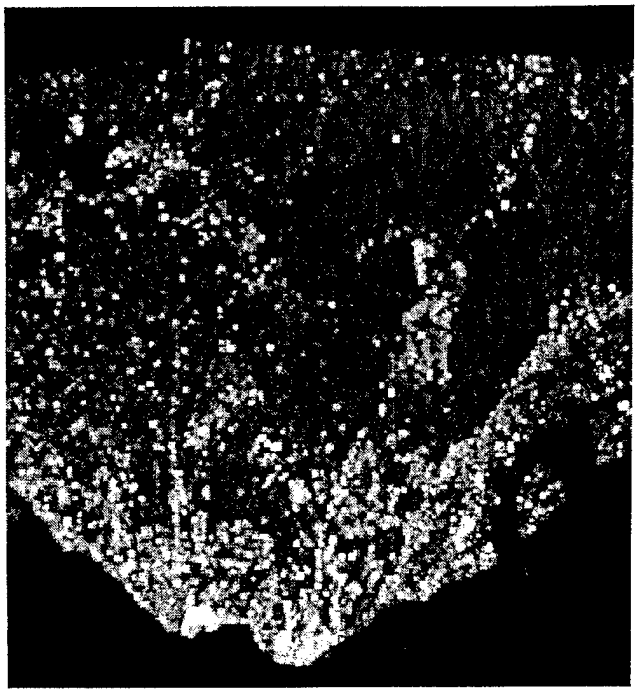


Fig. 1 Interferogram power of the JERS-1 scenes of October 10, 1993 and March 22 1995. © NASDA 1993, 1995 © NIED, Japan & Atlantis, Canada

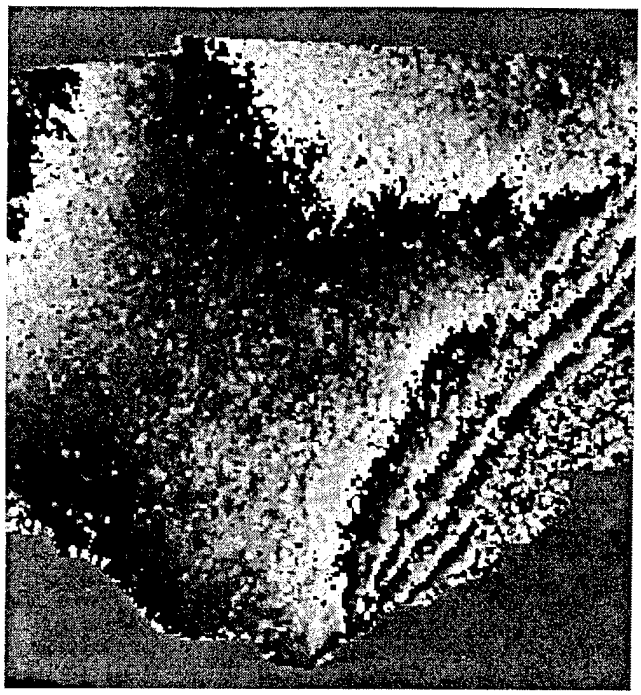


Fig. 2 Interferogram phase of the JERS-1 scenes of October 10, 1993 and March 22, 1995. "Flat earth" and topography phase have been removed. © NASDA 1993, 1995 © NIED, Japan & Atlantis, Canada

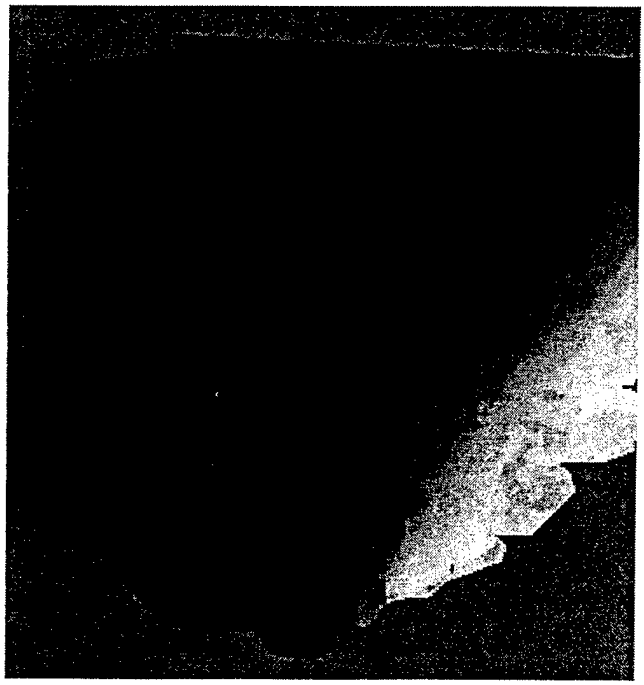


Fig. 3 Unwrapped JERS-1 interferogram. The deformation ranges from 0 (black) to 1.5 m (white). © NASDA 1993, 1995 © NIED, Japan & Atlantis, Canada

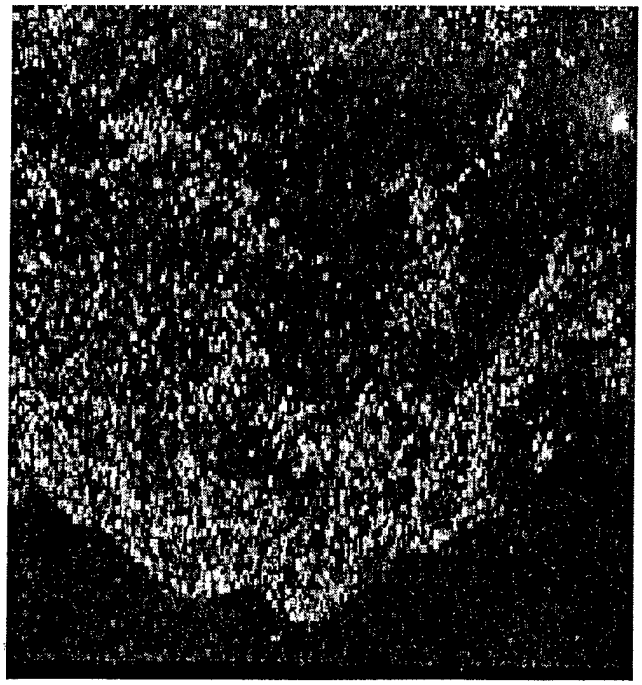


Fig. 4 Coherence image of the JERS-1 interferogram. The coherence ranges from 0 (black) to 0.5 (white). © NASDA 1993, 1995 © NIED, Japan & Atlantis, Canada

A Comparison of Phase to Height Conversion Methods for SAR Interferometry

David Small, Paolo Pasquali, and Stefan Füglistaler

Remote Sensing Laboratories (RSL); University of Zürich
Winterthurerstrasse 190; CH-8057 Zürich; Switzerland
E-mail: daves@rsl.geogr.unizh.ch; Tel: +41 +1 257-5164; FAX: +41 +1 362-5227

ABSTRACT

SAR Interferometry has been shown capable of producing accurate digital elevation models. InSAR height map generation always includes a transformation from the unwrapped phase to terrain height. Various methods for carrying out this step have been presented in the literature. This paper compares the different methods using both synthetic and real data for spaceborne and airborne geometries. The systematic errors introduced by each algorithm are analyzed. For each method, both the necessary number of parameters, as well as their required accuracies are evaluated with the goal of minimizing the required number of ground control points. The impact of the choice of geometry on the differential InSAR case is also investigated.

Keywords: SAR Interferometry, Geocoding, ERS-1, DEM

1. INTRODUCTION

SAR Interferometry makes use of the phase difference measured between two data acquisitions to generate height information. Assorted methods are described in the literature for conversion from interferometric phase difference to height values.

Our implementation of the interferometric processing consists of automatic orbital and fine registration, interferogram calculation, coherence calculation, and adaptive filtering. Phase unwrapping, height calculation, and geocoding steps follow [9]. This paper investigates methods for the transformation from phase difference to height. Error models are developed to investigate the question of whether or not systematic errors impede automation of the phase to height conversion step, with the goal a minimization of the number of ground control points.

1.1 Sources of Baseline Information

The InSAR baseline can be estimated in the following ways:

- *Fringe frequency* in flat area: the local fringe frequency within a flat area provides an estimate of the normal baseline component.
- *Orbit to orbit approach*: the baseline is calculated for each point in the reference orbit on the basis of a closest approach criterion or zero tangential component (Figure 1).
- *Tiepoints* + unwrapped phase: An iterative non-linear least squares fit can be used to adjust the baseline model and phase constant [11].
- *Image registration relationship*: The range image offset (known to subpixel accuracy) enables triangulation of the slant ranges to a point on a reference ellipsoid within the scene [6].
- *Image simulation*: Using precise orbits together with a reference ellipsoid, baselines are calculated for all points on a coarse grid distributed over the scene [8]. Range and azimuth trends are captured.

1.2 Baselines: 3D and 2D

In the repeat-pass case, given non-parallel tracks, one must choose between modelling the baseline either two or three-dimensionally.

Figure 1 shows a top-down cross-section of the InSAR geometry. One sees that for non-parallel tracks, the 3D baseline departs from the 2D approximation, with variation mainly in azimuth but also in range. Solving for the 3D baseline requires solution of the range-Doppler equations for each point, which vary with range. In the 2D baseline model, one sets as criterion either closest approach or zero tangential component.

For an ERS tandem pair over Bern, Switzerland in October 1995, we formed a differential interferogram from synthetic interferograms [10] calculated with 3D and 2D geometries. Systematic phase trends were observed to be mainly in azimuth. Within the scene tested, approximately 30° of total phase variation was observed. There were both range and azimuth phase trends, with the larger effect in azimuth.

Within the ERS tandem mission, the baseline typically has a vertical component much smaller than the horizontal. Figure 2 shows the variation in the baseline components over a day in October 1995. Using ERS precise orbit (PRC) data, the instantaneous angle between the orbital planes of the two satellites was measured over a day. Figure 3 shows the measured angle plotted against the satellite nadir latitude. Larger divergences have been observed in non-tandem interferometric pairs.

Although the 3D baseline model is most general, a two dimensional model is computationally simpler, and does not introduce unacceptable phase trends given a small baseline divergence. Solution of the Range-Doppler equations is required to correct errors from larger divergences. Correction of errors from larger divergences requires squint processing.

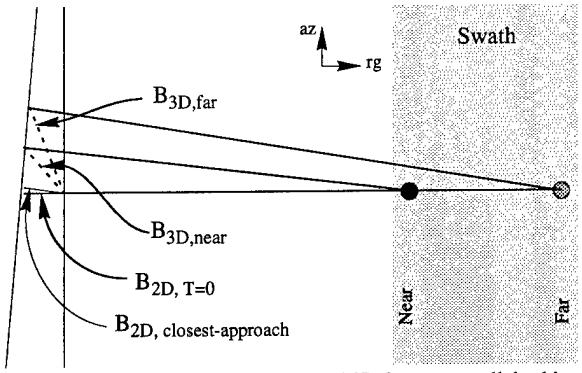


Figure 1: Baseline Geometries: 2D and 3D for non-parallel orbits

2. METHODS

We first describe the different methods studied, specifically, how they transform unwrapped phase values into height measurements. All require at least a single control point (h_0, θ_0, and/or ϕ_0) to "calibrate" their geometry: however their sensitivity to parameter errors differs significantly. We divide the methods into two categories: those that operate on the flattened phase, and those based on the "raw" interferogram phase.

Unwrapped Flattened Phase: In this class of methods, the interferogram is first flattened (e.g. using orbit data), and the flattened phase is unwrapped. This unwrapped flattened phase is then *directly* transformed into height.

Unwrapped Raw Interferogram Phase: This class of methods also first flattens the interferogram (to ease unwrapping) but

0-7803-3068-4/96$5.00©1996 IEEE

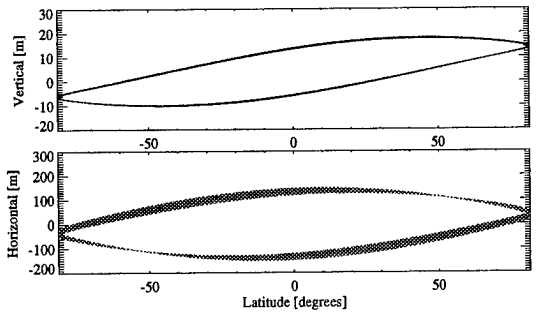


Figure 2: ERS tandem baseline components: variation over October 22-23, 1995

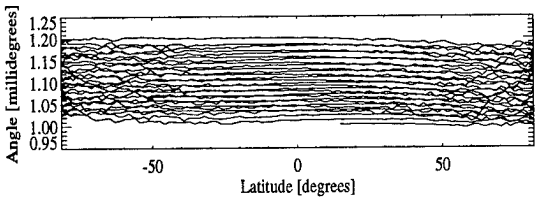


Figure 3: ERS tandem baseline angle: Variation over October 22-23, 1995 -- minimal deviation from parallel orbits

then *reintroduces* the absolute phase that was subtracted during flattening to produce a "raw" interferogram with unwrapped phase.

In the repeat-pass case, the difference in distance between the two acquisitions δ_r is related to the unwrapped "raw" interferogram phase ϕ_u as $\delta_r = \lambda/4\pi \cdot (\phi_u - \phi_c)$, where ϕ_c is a single phase constant shift for the unwrapped interferogram.

Far Field Approximation: It should be noted that assuming $B_{||}$ to be representative of the slant range difference is invalid for airborne geometries, and is also inaccurate for satellite geometries with large swaths. Figure 4 shows the approximation geometrically.

2.1 Normal Baseline

We consider one method that operates based on the unwrapped flattened phase. One of the earliest phase to height transformation methods published was [7]:

$$\Delta h = \frac{\lambda \cdot r_1 \cdot \sin\theta}{4\pi \cdot B_n} \cdot \Delta\phi, \qquad (1)$$

where r_1 is the slant range in the first image, B_n the normal component to the baseline, λ the radar wavelength, and θ the incidence angle. The above relationship is used to integrate across the image, transforming from phase to height values. The model's accuracy suffers from using only a single normal baseline value for all heights at the same slant range.

2.2 Integrated Incidence Angle

Another phase to height transformation integrates the incidence angle over the image, and bases the height estimates on these values [2]. Taking the derivative of $B_{||}=B_x\sin\theta_i - B_z\cos\theta_i$ (N.B. far field approximation), the incidence angle change $\Delta\theta$ is

$$\Delta\theta = \theta_{i+1} - \theta_i = \frac{\lambda}{4\pi\,(B_x\cos\theta_i + B_z\sin\theta_i)} \cdot \Delta\phi\ , \qquad (2)$$

where $B_n = B_x\cos\theta_i + B_z\sin\theta_i$. Comparing this far-field approximation with a differentiation of the non-simplified range difference shows that (2) results in an error of approximately $\lambda/4\pi \bullet B_{||,i} / (r_1 \bullet B_{n,i})$ at each step.

The local incidence angle is used to calculate the local height value h_i [3]: $h_i = H - r_1(i)\cos\theta_i$, where H is the satellite reference height.

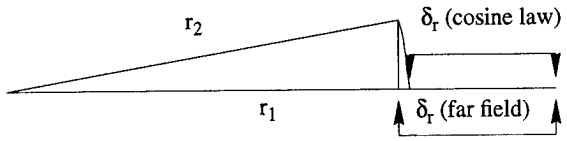


Figure 4: Far-field approximation

2.3 Baseline Rotation

The baseline rotation method operates by first estimating the internal angle between the baseline and a point in the scene, and then rotating the baseline through that angle to form a look-vector.

Far Field Approximation: To enable simplified models, the slant range "look" vectors for the two acquisitions may be assumed to be parallel (in the far field). The internal angle ψ in the Doppler plane between the baseline vector and the local look vector is then approximated [3] by: $\cos(\psi) = \delta_r/|\underline{B}|$ where the length of the baseline vector $\underline{B}$ is $|\underline{B}|$.

Cosine Law: For each point in the image, given knowledge of the difference in slant range distance between the two acquisitions δ_r, the slant range distance during the second acquisition $|\underline{r}_2|$ is then $|\underline{r}_2| = |\underline{r}_1| + \delta_r$. The cosine law [4] then allows calculation of the internal angle ψ:

$$\cos(\psi) = \frac{|\underline{B}|^2 + |\underline{r}_1|^2 - |\underline{r}_2|^2}{2 \cdot |\underline{B}| \cdot |\underline{r}_1|}. \qquad (3)$$

The baseline vector can now be rotated down to form the local look vector, and the height above the reference ellipsoid calculated [9].

2.4 Empirical Lookup Table

A newer method operates empirically, building up a set of coefficients that govern the phase to height conversion for a coarse grid covering the scene [8]. For a set of ellipsoid heights, forward geocoding methodology is used to calculate phase difference values for points in the grid. All points then have known heights and phase differences: matrix inversion provides a set of coefficients (modelled across the scene) that govern the transformation from absolute phase to height.

3. SIMULATIONS

The ERS geometry was simulated using a 3D curved Earth model. Various baselines were tested. The simplest model was a parallel baseline, with flat terrain, and B_x=100m, and B_z=10m. Baseline configurations matching typical ERS tandem mission values (with small horizontal and vertical baseline divergences) were also investigated. Systematic height errors inherent in the phase to height transformation methods were revealed.

The **normal baseline** method uses the same baseline and incidence angle reference values for all heights at a given slant range (reference is typically zero height). Although the method had no error for terrain constant at that reference level, any terrain departing significantly (i.e. 1000m) from that height results in serious errors (hundreds of metres), as the height-dependent change in the normal baseline component is not reflected in the model. The method is also dependent on an accurate initial height estimate h_0.

The **integrated incidence angle** method is similar, in that it uses the same knowledge of the normal baseline. It requires a single incidence angle θ_0 as initial condition. The results are

better than those obtained with the normal baseline method, as its method for calculation of the local normal baseline incorporates knowledge of the local incidence angle (see Equation (2)). The method also depends on the far-field approximation, causing small systematic height errors, even on flat terrain.

For cases with no orbital divergence, the assumption that the look vectors $\underset{\sim}{r}_1$ and $\underset{\sim}{r}_2$ are parallel causes systematic height errors on the order of 10's of meters for the cases studied. The assumption allows simplified estimation of the baseline based on tiepoints distributed in range (and azimuth if there is divergence). However, one should be aware that systematic errors are introduced. The simplification was originally applied [3] over a 16km swath: accurate results for larger areas require more careful treatment. In the case of azimuth divergence, both the normal baseline and integrated incidence angle methods must make a height assumption while transferring between azimuth lines. This can also introduce systematic errors.

The **baseline rotation** methods differ from the preceding two, in that they do not integrate across the scene. They operate on the unwrapped "raw" interferogram phase, and treat each pixel independently of the others. An estimate of the phase constant ϕ_c is required as the initial condition. The far-field approximation, if taken, results again in systematic height errors (tens of metres). Use of cosine law more accurately reproduces the true baseline geometry. In cases with larger orbital divergences, the systematic error increases due to the 2D baseline geometry used (Figure 5). These errors can be mitigated through tiepoint-based baseline tweaking [11].

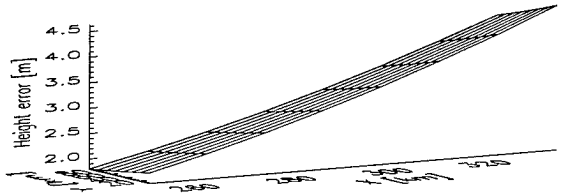


Figure 5: Horizontal orbital divergence cosine law baseline rotation simulation -- systematic 2D baseline errors, 8 millidegrees

The **empirical lookup table** method requires a single phase constant and captures the true 3D baseline through image simulation. Given highly precise knowledge of the baseline, and at the cost of increased complexity, orbit pairs with significant divergence can be accurately treated without requiring multiple tiepoints to tweak the baseline model.

4. GEOLOCATION

The location of each pixel may be determined by solving equations describing the slant range sphere, Doppler Frequency, and height above an oblate ellipsoid [10]. The generated set of irregularly spaced solutions are then regridded, with "holes" filled through interpolation from neighbours. Differences between such a forward geocoding algorithm and the conventional reference-DEM based terrain-geocoding [5] appear (not surprisingly) where the interferometrically measured height departs from the reference. Figure 6 shows the differences between forward and reverse geocoded interferometric heights for an area near Bonn, Germany. Height differences appear at gravel pits not considered in the reference DEM: differing height references result in planimetric shifts. Noisy height estimates within forested areas are also located differently. A kidney-shaped mask marks a forested area that was not penetrated by the phase-unwrapping algorithm.

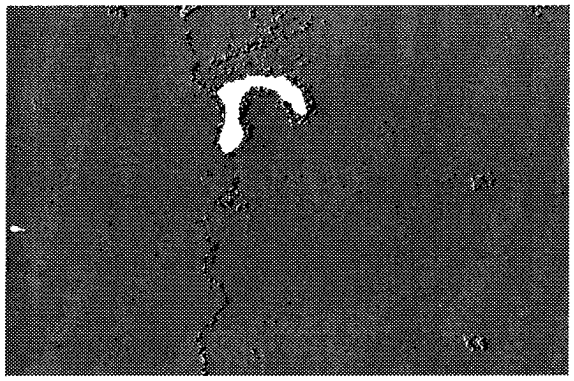


Figure 6: Height differences between forward and reverse geocoded datasets, saturation at ±5m - Bonn, Germany

5. CONCLUSIONS

The assumption of parallel look vectors in the far field allows simplified baseline estimation, but introduces systematic errors over large extents. Accurate results for larger swaths requires more careful treatment. The angle between the orbital planes of the two ERS satellites was found to be less than two millidegrees. No significant latitude-dependency was found. For such 1-day repeat tandem data, the difference between 2D and 3D baseline geometries, if not corrected with tiepoints, causes height errors on the order of less than a metre. Forward geocoding of interferometric height estimates results in planimetric accuracy comparable with that obtainable through conventional terrain-geocoding. Differences appear where the reference DEM is not up to date (e.g. gravel pits), and where the interferometric height is noisy (e.g. forested areas).

6. ACKNOWLEDGMENTS

Many thanks to ESA-ESRIN for providing the ERS data and precise orbits. Thanks are also due to Swiss Federal Office of Topography for providing the DHM25 reference elevation model, and to the D-PAF for the Bonn reference elevation model.

7. REFERENCES

[1] Gabriel A.K., Goldstein R.M, *Crossed Orbit Interferometry: Theory and Experimental Results from SIR-B*, Intl. J. Remote Sensing, 9(5), 1988, pp. 857-872.

[2] Hagberg J., Ulander L.M.H., *On the Optimization of Interferometric SAR for Topographic Mapping*, IEEE Trans. on Geoscience & Remote Sensing, 31(1), Jan. 1993.

[3] Li F.K. and Goldstein R.M., *Studies of Multibaseline Spaceborne Interferometric Synthetic Aperture Radars*, IEEE Trans. on Geoscience and Remote Sensing, 28(1), Jan. 1990, pp. 88-97.

[4] Massonnet D. and Rabaute T., *Radar Interferometry: Limits and Potential*, IEEE Trans. on Geoscience & Remote Sensing, 31(2), March 1993, pp. 455-464.

[5] Meier E., Frei U., and Nüesch D., *Precise Terrain Corrected Geocoded Images*, chapter in SAR Geocoding: Data and Systems, ed. G. Schreier, Herbert Wichmann Verlag GmbH, 1993.

[6] Pasquali P., *Generazione di Mappe Altimetriche con Interferometria SAR*, Ph.D. Thesis, Dipartimento di Elettronica e Informazione, Politecnico di Milano, Milan, Italy, 1995.

[7] Prati C., Rocca F., Guarnieri A.M., and Damonti E., *Seismic Migration For SAR Focusing: Interferometrical Applications*, IEEE Trans. Geoscience & Remote Sensing, 28(4), July 1990, pp. 627-640.

[8] Schwäbisch, M., *Die SAR-Interferometrie zur Erzeugung digitaler Geländemodelle*, DLR Forschungsbericht 95-25, August 1995.

[9] Small D., Werner C., and Nüesch D., *Geocoding and Validation of ERS-1 InSAR-derived Digital Elevation Models*, EARSeL Advances in Remote Sensing, 4(2), Oct. 1995, pp. 26-39, pp. I-II.

[10] Small D., Holecz F., Nüesch D., *Combination of Ascending / Descending ERS-1 InSAR Data for Calibration and Validation*, Proc. of IGARSS'95, July 10-14, 1995, pp. 553-555.

[11] Small D., Werner C., and Nüesch D., *Baseline Modelling for ERS-1 SAR Interferometry*, Proc. of IGARSS'93, Tokyo, Japan, August 18-21, 1993, pp. 1204-1206.

SAR Interferometry: a Multigrid Markovian Approach for Phase Unwrapping with a Discontinuity Model

David Labrousse
INRIA*
dlabrous@gandalf.inria.fr

Stéphane Dupont
ISTAR†
dupont@istar.fr

Marc Berthod
INRIA‡
berthod@gandalf.inria.fr

Abstract

In this paper, we present a solution for the phase unwrapping problem using a markovian modelization. The computational cost of this approach being particularly heavy in phase unwrapping, we propose to utilize a multigrid technique. An adaptative model is proposed in order to allow discontinuities in the unwrapped phase image. Results are presented on a real interferogram.

INTRODUCTION

Observation of interferometric images provided by Synthetic Aperture Radar (SAR) satellites enables the reconstruction of Digital Elevation Models (DEM) of a region. The elevation of a ground point is computed from the phase difference of two signals backscattered from the same point and emitted from two different positions of the satellite [2, 3]. Since the phase difference may only be measured modulo 2π, the problem consists of estimating the unwrapped phase for each point, that is the number of complete cycles of the phase. Thus, phase unwrapping is a labelling problem and can, therefore, be solved with a markovian modelization. An algorithm based on the Metropolis simulated annealing process with an energy function allowing phase discontinuities has been proposed in [1]. It reveals good robustness to noise but is penalized by a very high computational cost due to the residual gray level difference between the unwrapped phase image and the data (which does not allow the data potential to be a quadratic measure of the gray level difference but is instead 2π periodic). Hence, a multigrid algorithm is proposed in this paper which cuts down computation time significantly.

*INRIA: 2004 Route des Lucioles - 06902 SOPHIA ANTIPOLIS Cedex - FRANCE

†ISTAR: Espace Beethoven Bât. 2 - Route des Lucioles - 06902 SOPHIA ANTIPOLIS Cedex - FRANCE

‡INRIA: 2004 Route des Lucioles - 06902 SOPHIA ANTIPOLIS Cedex - FRANCE

0-7803-3068-4/96$5.00©1996 IEEE

PROPOSED METHOD

In a multigrid scheme, scales are usually built with different resolutions generating a sequence of coarser and coarser grids and a corresponding sequence of energy functions. The coarsening of a grid is done by dividing it into blocks and then identifying each block with one of its elements. In phase unwrapping, this method is not satisfactory because it increases the undersampling phenomena, called *aliasing*, which already exists in most real interferograms (i.e. the image of phase differences). In order to avoid this problem we propose the following method: First pseudo partial derivatives $\frac{\partial\hat{\varphi}(x,y)}{\partial x}$ and $\frac{\partial\hat{\varphi}(x,y)}{\partial y}$ are computed from the interferogram $\varphi(x,y)$ as follows:

$$\frac{\partial\hat{\varphi}(x,y)}{\partial x} = \varphi(x,y) - \varphi(x-1,y) + 2\hat{k}_x\pi \qquad (1)$$

$$\frac{\partial\hat{\varphi}(x,y)}{\partial y} = \varphi(x,y) - \varphi(x,y-1) + 2\hat{k}_y\pi \qquad (2)$$

where

$$\hat{k}_x = \arg\min_{k\in Z} |\varphi(x,y) - \varphi(x-1,y) + 2k\pi| \qquad (3)$$

$$\hat{k}_y = \arg\min_{k\in Z} |\varphi(x,y) - \varphi(x,y-1) + 2k\pi| \qquad (4)$$

Hence, the pseudo partial derivatives are an aproximation of the partial derivatives of the unwrapped phase image and are bounded below by $-\pi$ and above by π. The coarsening of a grid is then done by integrating the pseudo partial derivative with respect to x (resp. to y) along the upper (resp. left) edge of each block starting from the upper-left point. For each point of the new grid, three values are stored: the value of the upper-left point ($\varphi(x_0,y_0)$), and the results of the two integrations ($\varphi(x_0,y_0)+\sum_x \frac{\partial\hat{\varphi}(x,y_0)}{\partial x}$ and $\varphi(x_0,y_0)+\sum_y \frac{\partial\hat{\varphi}(x_0,y)}{\partial y}$). The potential functions P_x and P_y, defined on cliques of order two, are computed in the following way:

$$P_x(s_1,s_2) = P(\varphi(x_0,y_0) + \sum_{x\in\{x_0+1,x_1\}} \frac{\partial\hat{\varphi}(x,y_0)}{\partial x}, \varphi(x_1,y_0)) \qquad (5)$$

$$P_y(s_1, s_3) = P(\varphi(x_0, y_0) + \sum_{y \in \{y_0+1, y_1\}} \frac{\partial \hat{\varphi}(x_0, y)}{\partial y}, \varphi(x_0, y_1)) \quad (6)$$

where s_1 and s_2 (resp. s_1 and s_3) are two neighboring sites of the new grid in the x (resp. y) direction, x_0, x_1, y_0 and y_1 are the coordinates in the current grid coordinate system as shown in the figure 1 and P is the common potential function based on a discontinuity model and presented in [1]. The relaxation is then processed for each grid of the sequence. Beginning with the coarsest grid, our algorithm performs the Metropolis simulated annealing process at each level, transfering the result of one level to the next one and so on untill we get to the finest grid.

RESULTS

The advantage of our multigrid technique is that we obtain immediatly, i.e. at the coarsest grids, a rather good estimation of the global dynamic of the unwrapped phase image and therefore the entire relaxation process is much faster. We present a result on an (256 × 256) ERS-1 interferogram of the Interlaken site in Switzerland (figure 2). The whole sequence of grids, after relaxation, is shown in figure 3. For the coarsest grids, the relaxation is deterministic, the number of sites being small. The intermediate grids are the most important because too many errors would necessitate heavy computation during the relaxation of the last ones in order to correct them. At each level of resolution the results are given after integration of each resolution square of the pseudo partial derivative in the y direction so that their interpretation is easier. This explains why vertical lines appear in the coarsest grids: they are due to the errors of the pseudo partial derivatives.

CONCLUSION

We have presented a new algorithm for phase unwrapping based on a markovian modelization with a multigrid technic. The results are quite satisfactory from many points of view: robustness, sensitivity to noise and preservation of discontinuities. Furthermore, our multigrid approach allows rather fast computation.

ACKNOWLEDGMENTS

The authors would like to thank the CNES scientists for providing an ERS-1 image which enabled them to base their research on real SAR imagery.

References

[1] D. Labrousse, S. Dupont, Marc Berthod, "SAR interferometry: A markovian approach to phase unwrapping with a discontinuity model", *Proc. IGARSS'95*, Firenze, Italy, July 1995.

[2] D. Massonnet, T. Rabaute, "Radar Interferometry: Limits and Potential", *IEEE Trans. on Geoscience and Remote Sensing*, Vol. 31, No. 2, pp. 455-464, March 1993.

[3] H. Zebker, R. Goldstein, "Topographic Mapping from Interferometric Synthetic Aperture Radar Observations", *J. of Geophysical Research*, Vol. 91, pp. 4993-4999, April 1986.

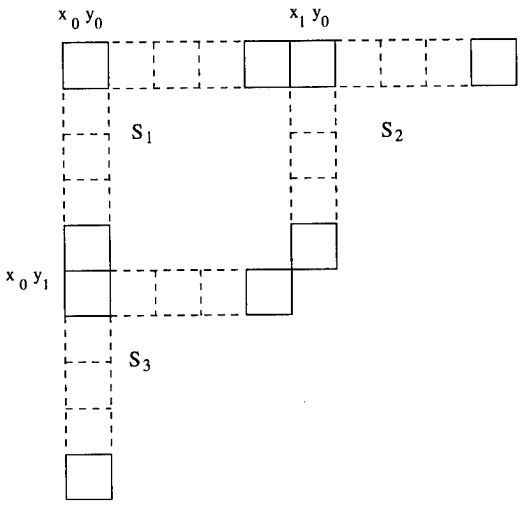


Figure 1: Coarsening scheme

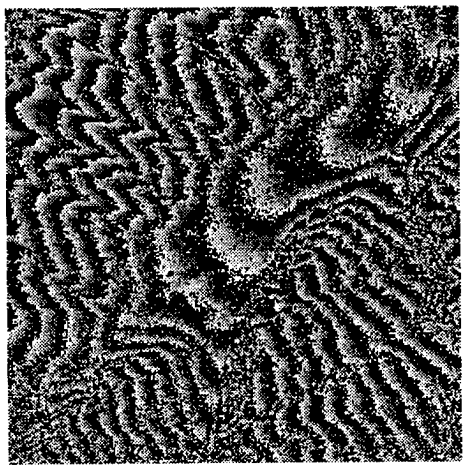


Figure 2: Interferogram (Interlaken site, Switzerland)

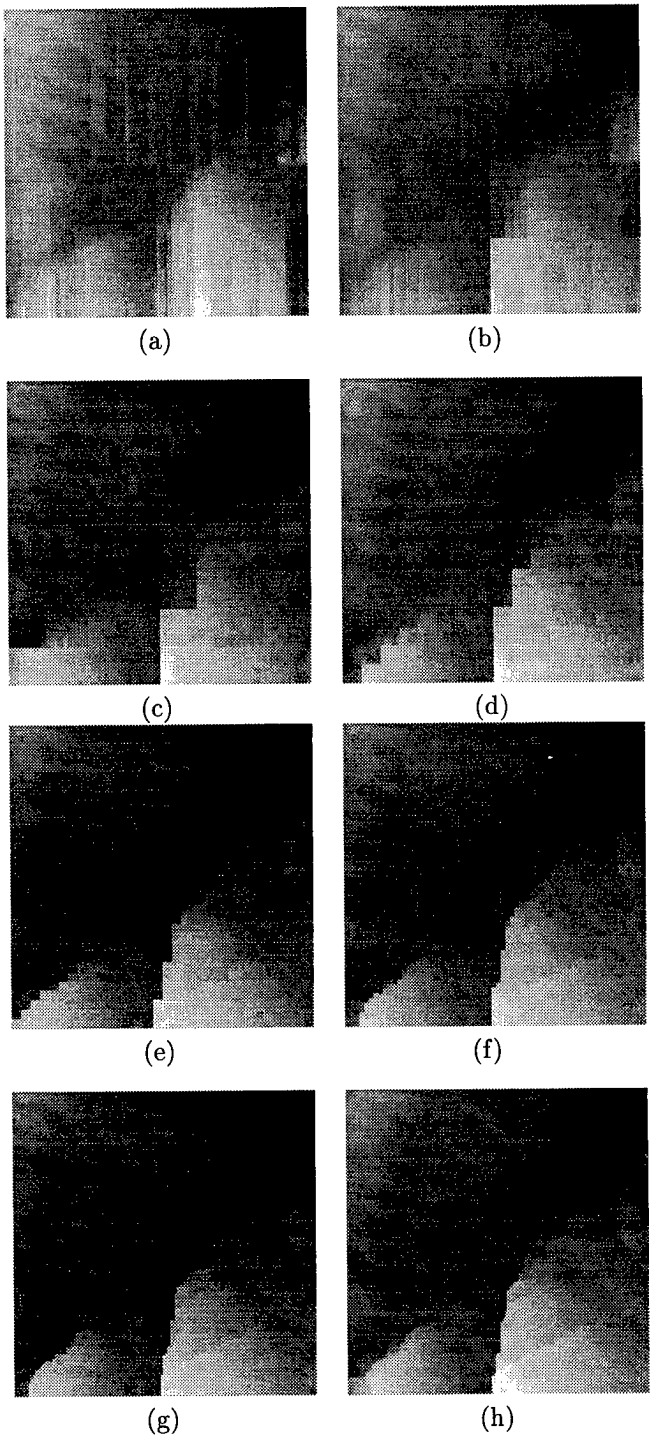


Figure 3: Grid sequence : (a) resolution 1 (4 sites). (b) resolution 2 (16 sites). (c) resolution 3 (64 sites). (d) resolution 4 (256 sites). (e) resolution 5 (1024 sites). (f) resolution 6 (4096 sites). (g) resolution 7 (16384 sites). (h) resolution 8 (65536 sites).

Echoes Covariance Modelling for SAR Along-Track Interferometry

Pierfrancesco Lombardo

Dpt. ECE, Syracuse University, 121 Link Hall, Syracuse, NY 13244-1240
Ph. +315-443-3260, Fax +315-443-2583, e-mail: plombard@mailbox.syr.edu

INTRODUCTION

Recently there is an increasing interest for Synthetic Aperture Radar (SAR) equipped with an along-track linear array of receiving antennas [1]. These systems, called multichannel SAR (M-SAR), allow doppler and angular informations to be decoupled by means of the along-track interferometric processing. Both the derivation of optimum estimation algorithms for physical parameters of the observed surface, in remote sensing applications, and of clutter cancellation schemes, in moving target detection, require the definition of a model for the covariance of the space-time clutter echoes to take full advantage of this potentiality. Moreover a proper representation space for the resulting space-time model is required to adequately interpret the results.

Both models and representations are available separately for single channel SAR, where the long observation time and the consequent non-linear phase history of the echoes are the main issues, and for multichannel systems [2], which assume, on the contrary, a short integration time and focus on the angular characteristics. Our aim is to build a closed form model for the M-SAR echoes, which takes into account both non-linear phase modulation and angular position at the same time and to define a proper representation space for it. Even though simple to handle, the model should encode all the main characteristics of the scattering from the observed scene.

M-SAR ECHOES MODEL

With reference to the slant plane geometry in Fig. 1, assume that the radar transmitting antenna moves, with constant velocity v, along a straight trajectory at a fixed distance Ro from the q axis (crossing the r axis at time $t=0$) and has a fixed pointing, orthogonal to the flight path. The sequence of echoes relative to the N pulses, transmitted with pulse repetition time PRT, is received by a uniform linear array of K antennas, parallel to the radar trajectory. The K receiving antennas have separate receiving channels and phase centers at distance $s_k=(k-(K-1)/2)\Delta$, $k=0,..,K-1$ from the transmitter.

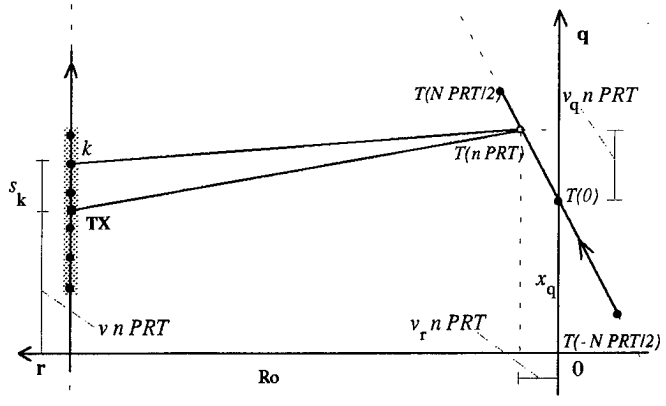


Fig. 1 - The multichannel SAR observation geometry

A pointlike scatterer T is assumed to be for $t=0$ on the q axis at the position x_q and to move with velocity components v_q and v_r along the two axes q and r, named along-track and cross-track. It is further assumed that: (i) the range cell migration is negligible or has been corrected for; (ii) the two way antenna pattern, for the channel k, has the gaussian shape $g_k[y]=1/(\sqrt{\pi}\,X_q)\exp[-(y-s_k/2)^2/X_q^2]$, being y the along-track position of the scatterer relative to the phase center of the transmitter; (iii) quadratic terms in the receiving antennas displacements can be neglected and the Fresnel approximation is valid for the distance of the scatterer from the transmitter (narrow antenna pattern). Thus the echo received by the k-th receiving antenna at time $t_n = (n-(N-1)/2)\,PRT$, $n=0,\ldots,N-1$ can be modeled as

$$s_k(n)=A_o\,z_k(t_n;x_q,v_q,v_r)=A_o/(\sqrt{\pi}X_q)\;e^{j\Phi}\;e^{j2\pi f_d t_n}$$
$$\exp\left\{-\left(1/X_q^2+j2\pi/(\lambda R_o)\right)\left[(v-v_q)t_n+s_k/2-x_q\right]^2\right\} \quad (1)$$

where Ao and Φ are constant amplitude and phase terms and $f_d = 2v_r/\lambda$, the doppler frequency due to the cross-track velocity for the wavelength λ. Eq. (1) takes indeed into account the central doppler frequency and direction of arrival (DOA) of the scatterer, which are the usual model for space-time processing techniques based on a short integration time. Moreover, the quadratic term encodes the time varying doppler and DOA, observed in the long SAR integration time.

The clutter echo $c_k(t)$, received at time t and receiving element k, is obtained by integrating the echoes from the infinitesimal clutter patches of dimension dx_q, modelled as eq. (1) with instantaneous reflectivity $A_o=\mu(x_q,t)\,dx_q$. The correlation of the clutter echoes received at times $t_{n_1}=t, t_{n_2}=t+\tau$ and receivers in s_{k_1}, $s_{k_2}=s_{k_1}+2\eta$ is

$$R(t_{n_1},t_{n_2},k_1,k_2)=<c_{k_1}^*(t_{n_1})\cdot c_{k_2}(t_{n_2})>=\int\int dx_q\,dx_q' \quad (2)$$
$$<\mu^*(x_q,t_{n_1})\mu(x_q',t_{n_2})>z_{k_1}^*(t_{n_1};x_q,v_q,v_r)z_{k_2}(t_{n_2};x_q',v_q,v_r)$$

the symbol <.> standing for the statistical expectation.

Homogeneous clutter

The model for homogeneous clutter is obtained in the hypothesis of factorization of the spatial and temporal correla-

0-7803-3068-4/96$5.00©1996 IEEE

tions, $\rho_x(x)$ and $\rho_t(\tau)$, of the clutter reflectivity:

$$< \mu^*(x_q,t)\,\mu(x'_q,t+\tau) >= \sigma_o^2\ \rho_t(\tau)\ \rho_x(x_q - x'_q) \qquad (3)$$

Using a gaussian spatial correlation, with variance σ_c^2, $\rho_x(x) = (\sqrt{2\pi}\ \sigma_c)^{-1} \exp[-x^2/(2\sigma_c^2)]$, the double integration in eq. (2) becomes a gaussian function of the space-time displacement, $z = (v - v_q)\,\tau+\eta$, of the two way phase center and is thus stationary in both space and time:

$$R(t_{n_1},t_{n_2},k_1,k_2) = \sigma_o^2 \rho_t(\tau) R_{HOM}(z;\sigma_c) = \sigma_o^2 \Sigma / X_q\, e^{j2\pi f_d \tau}$$
$$\rho_t(\tau)\ \ 1/\sqrt{2\pi(\Sigma^2+\sigma_c^2)}\ \ \exp\left\{-z^2/\left[2\,(\Sigma^2+\sigma_c^2)\right]\right\} \quad (4)$$

where $\Sigma^2 = 1/[1/X_q^2 + (2\pi\ X_q/(\lambda\ R_o))^2]$ is the square of the maximum SAR resolution. By taking the bidimensional Fourier transform of eq. (4) with respect to time: $t \rightarrow f$, and space: $\eta \rightarrow \sin(\theta)/\lambda \approx \theta/\lambda$, we obtain the power spectral density (PSD) as a function of frequency f and angle θ:

$$P(f,\theta) = \sigma_o^2 \Sigma / X_q \exp\left[-2\pi^2/\lambda^2\,(\Sigma^2+\sigma_c^2)\theta^2\right]$$
$$\Gamma_t[f - f_d - (v-v_q)/\lambda\ \ \theta] \qquad (5)$$

where $\Gamma_t[f]$, is the Fourier transform of $\rho_t(\tau)$. In the absence of temporal decorrelation ($\rho_t(\tau)=1$), $P(f, \theta)$ reduces to a sheet for $f=f_d+(v - v_q)\,\theta/\lambda$, whose gaussian shaped amplitude is controlled by the variance $\Sigma^2+\sigma_c^2$. This reduces to the square of the SAR resolution for uncorrelated reflectivity and grows with the spatial correlation σ_c^2 otherwise. This can be expecially important for the new generation of VHF SAR systems, to which the reflectivity of a natural scene can appear more correlated than to microwave sensors. It applies also in a number of remote sensing applications over smooth surfaces, as sea or ice covered regions and in some planet exploration missions, where the correlation of the surface scattering is not negligible and also a coherent contribution can be present in the echo. As expected, the mean cross-track velocity of the observed surface produces a constant frequency shift, whereas a mean along-track velocity changes the slope of the clutter ridge. The presence of temporal decorrelation, spreads the PSD around the straight line above, according to the function $\Gamma_t[f]$, while X_q controls its amplitude, affecting the angle over which the transmitted power is spread.

Nonhomogeneous clutter

The effect of the clutter non-homogeneity is discussed in the following, maintaining the factorization for spatial and temporal properties, and assuming the spatial independence:

$$< \mu^*(x_q,t_{n_1})\cdot\mu(x'_q,t_{n_2}) > = \sigma_o^2(x_q)\ \rho_t(\tau;x_q)\ \delta(x_q - x'_q) \quad (6)$$

In this condition a step reflectivity transition is addressed. This is a simple non-homogeneity model, which applies to a number of physical cases of interest, as the transitions from grass to wood, ground to sea, grass to airfield and grass to buildings. These clutter edges are points of major changes in environmental surface monitoring and likely to be used as hiding locations in an hostile environment. Thus we assume

$$\sigma_o^2(x_q)\ \rho_t(\tau;x_q) = \begin{cases} \sigma_{oa}^2\ \rho_t^a(\tau), & x_q < x_o \\ \sigma_{ob}^2\ \rho_t^b(\tau), & x_q > x_o \end{cases} \qquad (7)$$

where generically different reflectivities and temporal fluctuations are assumed on the two sides of the edge in x_o. For the sake of simplicity, different cross-track velocity components of the mean surface are assumed in the two regions, v_r and v_r^b, but the same along-track component. Under these conditions, and with $f_d^b = 2(v_r^b - v_r)/\lambda$ eq. (2) yields

$$R(t_{n_1},t_{n_2},k_1,k_2) = R_{HOM}(z;0)\ 1/2\cdot\left\{\sigma_{oa}^2\rho_t^a(\tau) + \right.$$
$$+\sigma_{ob}^2\ \rho_t^b(\tau)e^{j2\pi f_d^b\tau} + [\sigma_{oa}^2\rho_t^a(\tau) - \sigma_{ob}^2\ \rho_t^b(\tau)e^{j2\pi f_d^b\tau}]$$
$$\left. erf\left[\sqrt{2}/X_q\,(\beta - x_o - j\pi X_q^2\, z/\lambda R_o)\right]\right\} \qquad (8)$$

where $\beta = (v-v_q)(t_{n_1}+t_{n_2})/2 + (s_{k_1}+s_{k_2})/4$ encodes the non-stationarity of the average behaviour, due to the clutter edge. The contributions from the two clutter regions are combined in amplitude and phase according to its value in the error function *erf*. Now the covariance is not any more real, as it was in the homogeneous case thanks to the broadside antenna pointing, since the clutter edge destroys the average symmetry of the scattering process with respect to the antenna phase center. A space-time varying PSD must thus be defined to represent eq.(8), as a function of β. This general model can be used to represent the transition between ground and sea, where a mean doppler is considered only for the sea echoes. On the contrary, when the surfaces in the two sides of the edge have the same mean velocity components and temporal decorrelation, eq. (8) simplifies to

$$R(t_{n_1},t_{n_2},k_1,k_2) = R_{HOM}(z;0)\ \rho_t(\tau)(\sigma_{ao}^2+\sigma_{ab}^2)/2 \quad (9)$$
$$\left\{1 + \frac{\sigma_{ao}^2 - \sigma_{ab}^2}{\sigma_{ao}^2+\sigma_{ab}^2}\, erf\left[\sqrt{2}/X_q\,(\beta - x_o - j\,z\,\pi X_q^2/(\lambda R_o))\right]\right\}$$

still maintaining the nonstationary behaviour. Eqs. (8)-(9) are easily generalized to the case of double transitions, (e.g. road in grass, road in wood, ... or also man made objects).

Thus, with the assumption of a gaussian antenna pattern, a simple closed form model has been derived, which takes into account a number of physical phenomena. Despite the ideal assumptions at the basis of its evaluation, it allows to correctly represent the influence of the scene reflectivity properties on the covariance of the clutter echoes. This includes the effect of spatial and temporal correlations, non-homogeneity of the scene and mean surface motion.

REPRESENTATION

The angle-frequency plane (θ, f) in Fig. 2 is the preferred representation space for the clutter covariance in multichannel systems [2]. A short observation time is assumed, so that doppler frequency and DOA of the single scatterer are constant and the array of receivers is used to exploit the scatterers angle. The PSD in eq. (5) is directly mapped into this plane, which seems thus appropriate for homogeneous clutter.

Though, when the observation time is long, both DOA and doppler frequency of the clutter echo from the single surface scatterer depend on time (eq. (1)). This can't be represented in the (θ, f) plane, where the contribution from each patch of an homogeneous clutter moves in time along a line with constant slope (see arrows in Fig. 2). Since the scatterers that quit the antenna beam, are replaced by the new entered, in the average, the same PSD is observed. This doesn't apply for a nonhomogeneous clutter, which results in a nonstationary covariance and thus in a time-varying PSD. Specifically for the step transition in eq. (8), the clutter edge moves during the observation time over the gray area in Fig. 2. Moreover, since the time-varying characteristic of the echo's DOA and doppler spread its power over a line in the (θ, f) plane, the gain of the SAR coherent integration over the noise can't be related directly to doppler or angular filtering in this plane. This applies also for the detection of targets, with a motion different from the clutter patches.

The time-frequency plane (t,f) in Fig. 3 is the preferred representation space for single channel SAR, where a long observation time is considered. It allows the correct representation of the time varying characteristic of the doppler frequency but doesn't contain angular information. Thus the doppler frequency f of the generic scatterer, shown in this plane, relates to a combination of cross-track velocity and angular position: this ambiguity cannot be resolved. This is shown in Fig. 3, where solid and dashed lines represent the echo from the same homogeneous clutter patch, received by different channels. The clutter edge is localized in time in the (t,f) plane and the SAR coherent integration gain is now clear.

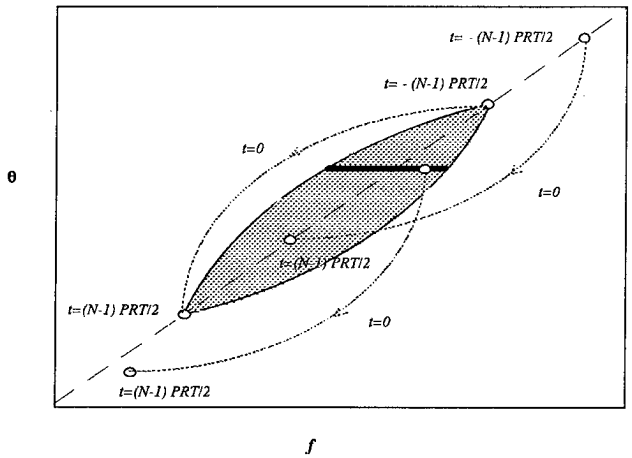


Fig. 2 - Frequency- angle plane

From the analysis above results that, to interpret properly the MSAR echoes, a higher dimensional space is required, which allows both doppler frequency and DOA to be represented as functions of time. The space-time-frequency space (θ, t, f), in Fig.4, is thus introduced. Its integration over the temporal axis, collapses it back into the (θ, f) plane, while the integration over the angular axis collapses it into the (t,f) plane. In this space the motion of the scatterer echoes in the doppler-angle limits of the antenna beam are correctly represented for both homogeneous and nonhomogeneous scene: (_ . _), as well it is a target echo: (_ . . _). The motion of the clutter edge is now fully represented, as shown in Fig. 4.

ACKNOWLEDGMENTS

The author acknowledges the support of Dr H Wang at Syracuse University and discussions with Dr A Farina of Alenia.

REFERENCES

[1] S.Barbarossa, A.Farina, "Space-Time-Frequency Processing of Synthetic Aperture Radar Signals", IEEE Trans. on AES, Vol. 30, No. 2, April 1994, pp. 341-358.

[2] R. Klemm, "Adaptive clutter suppression for airborne Phased Array Radars", IEE Proc F, Vol 130, Feb '83, pp 125-31

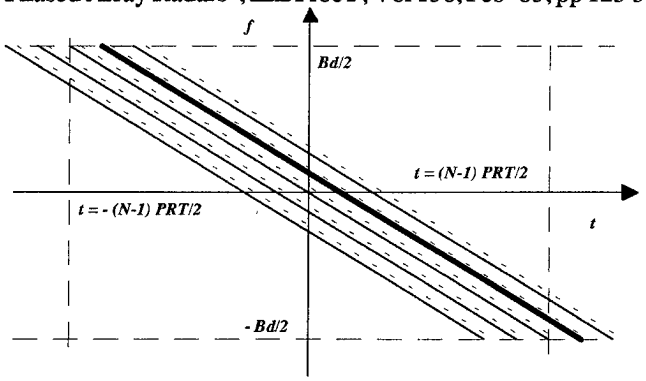


Fig. 3 - Time frequency plane

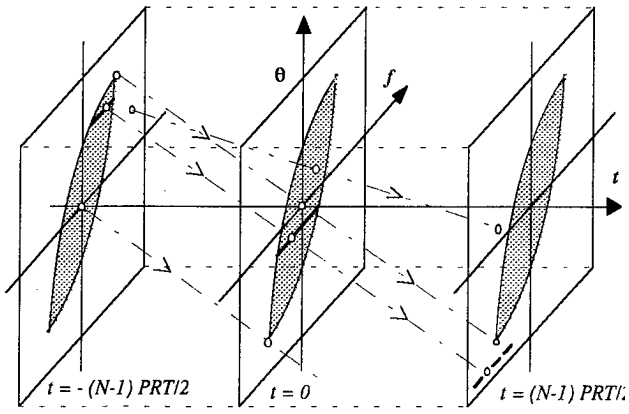


Fig. 4 - Space-time-frequency space

On the Survey of Volcanic Sites: the SIR-C/X-SAR Interferometry

The Florian Group:
Mauro Coltelli[1], Gianfranco Fornaro[2], Giorgio Franceschetti[2,3], *Fellow, IEEE*, Riccardo Lanari[3], *Member, IEEE*, Maurizio Migliaccio[4], *Member, IEEE*, João R.Moreira[5], *Member, IEEE*, Konstantinos P.Papathanassiou[5], Giuseppe Puglisi[1], Daniele Riccio[2], *Member, IEEE*, Marcus Schwäbisch[5]

[1]Consiglio Nazionale delle Ricerche, *Istituto Internazionale di Vulcanologia*, Piazza Roma 2, 95123 Catania, Italy.
tel +39-95-502795, fax +39-95-435801, email: geo@iiv.ct.cnr.it
[2]Università di Napoli, *Dipartimento di Ingegneria Elettronica*, Via Claudio 21, 80125 Napoli, Italy.
tel +39-81-7683114, fax +39-81-5934448, email: francesc@ irece1.irece.na.cnr.it
[3]Consiglio Nazionale delle Ricerche, *I.R.E.C.E.*, Via Diocleziano 328, 80124 Napoli, Italy.
tel +39-81-5707999, fax +39-81-5705734, email: lanari@irece1.irece.na.cnr.it
[4]Istituto Universitario Navale, *Istituto Teoria e Tecnica delle Onde Elettromagnetiche*, Via Acton 38, 80133 Napoli, Italy.
tel +39-81-5513976, fax +39-81-5521485, email: migliaccio@nava1.uninav.it
[5]DLR, *Deutsche Forschungsanstalt fur Lüft und Raumfahrt*, D-82234 Oberpfaffenhofen, Germany.
tel +49-8153-2822367, fax +49-8153-281135, email: hf39@vm.op.dlr.de

Abstract -- It is here presented an international cooperative work in the field of volcanoes monitoring by means of SAR interferometry. The case study of the SIR-C/X-SAR mission over Mt.Etna, Sicily, Italy is detailed.

INTRODUCTION

The problem of surveying field settings which are not practical or safe to be directly inspected is one the most prominent application of remote sensing [1].

Within this framework, the importance of volcanic sites is remarkable [1-4]. Syntethic Aperture Radar (SAR) is a challenging tool in order to accomplish such a task. In fact, SAR images contain information on physical characteristics of the surface [1]. As a consequence, a great deal of interest has been shown in the inverse problem, i.e. the extraction of qualitative and quantitative features from SAR images [2-4]. However, the extraction of geological features is by no means an easy task due to the fact that physical surface parameters are nonlinearly related (in an unknown manner) to the scattered field, thus making the inverse problem nontrivial [1]. Further, the presence of multiplicative noise over SAR image makes the problem even more cumbersome [1].

A new perspective to the problem is provided by the across-track SAR interferometry (IFSAR) and the recent availability of multifrequency multipolarization multipass sensors [3-4]. In this paper, we consider the SIR-C/X-SAR multifrequency multipass interferometry mission over the Mt. Etna, Sicily and we accomplish a supervised interpretation approach over the coherence maps and a fractal-based approach over the IFSAR Digital Elevation Models (DEM). The first permits to recognize different volcanic terrains and between vegetated and unvegetated areas while the second is able to validate the IFSAR DEMs and to detect geological structures. This latter analysis, accomplished over the photogrammetric DEM, is able to emphasize artifacts such as caused by digitizing and resampling; obviously, IFSAR DEMs are not affected by these problems. As a consequence we can state that IFSAR products are of valuable aid in geological interpretation.

PRODUCTS GENERATION

In this Section we briefly summarize the IFSAR products generation.

As input data complex SAR images processed by NASA/JPL (L and C bands) and DLR/DPAF (X band) have been used. These images are relevant to the two Shuttle passes over Mt.Etna of October 9 and 10, 1994.

The fundamental steps in order to generate the IFSAR products relevant to a single frequency data set can be summarized as follows:

-Slant range and azimuth filtering of the complex images: The complex SAR image pair have been filtered in azimuth and range in order to improve the coherence and the interferometric phase purity. Azimuth filtering allows to avoid the decorrelation effect caused by data pair different squint angles. Range filtering reduces the baseline decorrelation effect [5].

-Registration: The SAR image registration procedure has been performed by applying the maximum spectrum method [6]. The accuracy achieved is of the order of 1/8 of pixel.

-Complex inteferogram formation and flat earth phase removal: The complex interferogram has been computed by multiplying the first registered SAR image by the complex conjugate of the second one. This operation was followed by the flat-earth phase pattern removal which drastically simplifies the phase unwrapping step. The flat-earth phase pattern has been computed by means of L-band data [6] and properly rescaled (by a factor proportional to the wavelength) for the other bands.

-Evaluation of the interferometric phase patterns and of the coherence maps: In order to reduce the noise effect, the complex interferogram has been filtered by means of a filter

0-7803-3068-4/96$5.00©1996 IEEE

of 5 (range) x 13 (azimuth) pixels for the L and C bands and 3 x 7 pixels for the X-band. Then, the interferometric phase has been evaluated by applying the arc tangent function. The coherence maps have been computed by means of an 4 x 5 average window at all frequecies.

-Phase unwrapping: The phase unwrapping step has been accomplished by making use of the robust two-dimensional algorithm presented in [7]. In this case the basic phase unwrapping procedure has been modified to include the multifrequency information [6].

-DEM generation: The DEM generation has been performed by making use of a two step procedure [8]. First, the slant-range height map is computed by the unwrapped phase and then the geocoding step is accomplished. The WGS84 has been used [9].

PRODUCTS INTERPRETATION

In this Section, the interpretation of the IFSAR products is examined. In particular, first we consider a supervised approach which make use of the availability of multifrequency coherence maps and a detailed knowledge of the site. Then we apply a fractal-based model over the IFSAR DEMs. The rationales and the logical steps of these two interpretation analysis are hereitherto given. With regards to the interpretation procedure performed on the multifrequency coherence maps, we underline that other similar analysis have been able to detect among different surfaces [10] and therefore it is here employed.

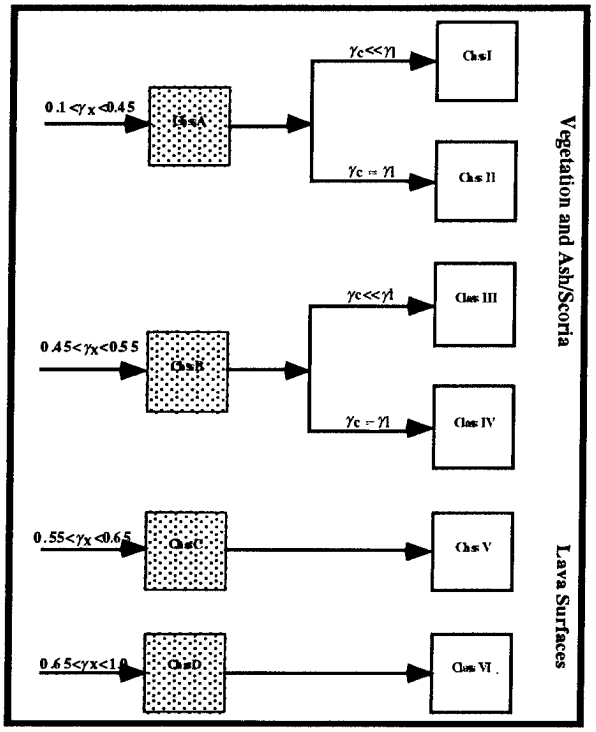


Fig.1 Relevant to the coherence maps classification scheme

The two logical steps in which this interpretation procedure can be seen are: the selection of the training areas and the choice of the decision rule.As a matter of fact, in the first step some training areas have been selected on the X-band coherence map and then a multifrequency decision rules have been found suitable. The block scheme is depicted in Fig.1. Results are shown in Fig.2. Class I pertains to high and dense vegetated areas (dark green), Class II to 1990 ash and scoria (violet), Class III to low and sparse vegetation (pale green), Class IV to old ash and scoria (grey), Class V to old lava flows (yellow) and Class VI to fresh lava flows (orange). It is evident that discrimination between vegetated and unvegetated areas is possible as well as the classification of some relevant volcanic materials. For a complete analysis of these results the interested reader can refer to [9].

Let us now examine the fractal-based approach performed over the IFSAR DEMs. The rationale of this approach is very simple: natural surfaces are well modelled by means of fractal geometry. In particular, the fractal Brownian model (fBm) has been demonstrating very powerful in describing natural landscapes. The interested reader can find a large amount of literature on this topic, e.g. [11]. For reader completeness we only recall that an fBm is described by two fractal parameter: the D and the K [12]. The D is the fractal dimension and is related to the roughness, K is related to the standard deviation σ of the increments [11]. The σ can be interpreted as a generalized slope. These fractal parameters can be estimated by means of the fractal plot procedure [12].

Accordingly, a large set of numerical examples have been performed [9] while here only a single fractal map is shown for saving space. We briefly outline the main results achieved. First of all, it seems to be confirmed that the D-maps are less informative than the σ-maps. By making use of the D-maps a first order quality analysis of the IFSAR DEMs compared to the available photogrammertric one was possible. This first analyis, demonstrated that the photogrammetric DEM (often dogmatically assumed as a reference!) is by no means error-free and this is mainly due to artifacts caused by digitizing and resampling [9].

Conversely, IFSAR DEMs do not suffer of such problems, but of course they are sensible to lack of coherence and its minimization is therefore of great relevance.

More interesting on the geological point of view seems the σ-map analysis [9]. In fact, it permits to detect several morphological and structural features of the Mt.Etna that represent the imprint of the main eruptive process occurred during its geological history [9]. A comparative analysis among the different IFSAR and photogrammetric DEMs demonstrated that the informative content of the IFSAR DEMs is valuable and in particular C and X bands provide excellent description of the geological structures while the L-band is definitely poorer; the photogrammetric DEM although showing some artifacts it was able to reveal the

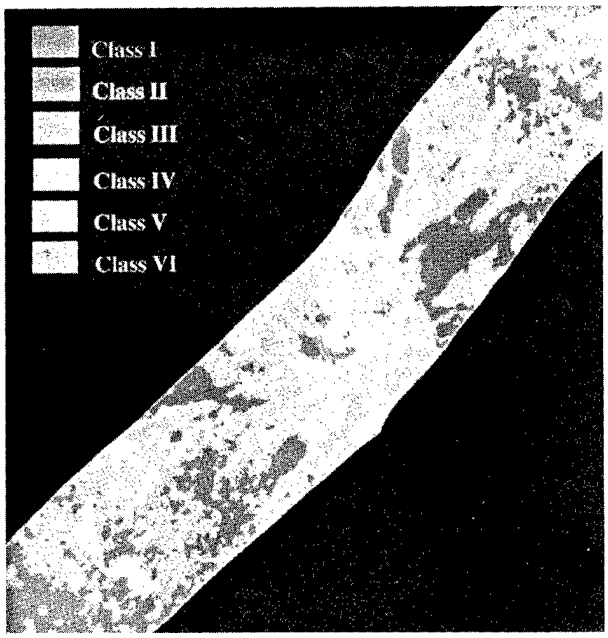


Fig.2 Classification by means of coherence maps

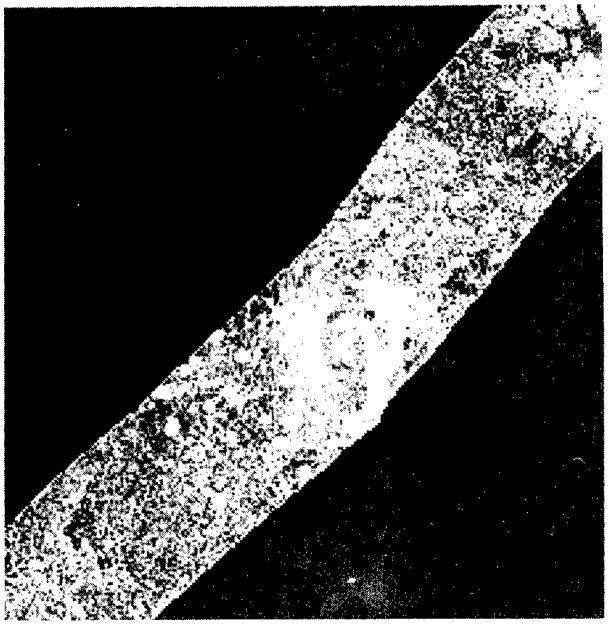


Fig.3 σ-map relevant to the X-band IFSAR DEM

geological features.

In Fig.3 the σ-map relevant to the X-band IFSAR DEM is shown. We here only note the lateral and sommital cones, the Cratere del Piano plateau and the Valle del Bove which can be easily identified. The interested reader can find a detailed analysis in [9].

CONCLUSIONS

In this paper, the capability of the multipass multifrequency across-track interferometry to generate useful geological thematic maps has been investigated. The SIR-C/X-SAR mission over Mt.Etna, Sicily has been considered. Results showed the effective capability of IFSAR products to be of valuable aid in geological interpretation.

ACKNOWLEDGMENTS

We are grateful to NASA/JPL and DPAF for processing the SIR-C/ XSAR images, the NASA/JPL for providing the orbital information, and the Italian Gruppo Nazionale per la Vulcanologia for providing the photogrammetric DEM of Mt.Etna. A special acknowledgment is finally due to Dr. W.Keydel and his staff for all the valuable support at DLR, Opferphaffenofen. The research described in this paper was conducted at the DLR under DARA contract FKZ 50 EE 9532.

REFERENCES

[1] C.Elachi, *Spaceborne Radar Remote Sensing: Applications and Techniques*, New York: IEEE Press, 1987.

[2] B.A.Campbell and D.B.Campbell, "Analysis of Volcanic Surface Morphology on Venus From Comparison of Arecibo, Magellan, and Terrestrial Airborne Radar Data", *J.Geophys. Res., 97*, 16293-16314, 1992.

[3] H.A.Zebker, P.A.Rosen, R.M.Goldstein, A.Gabriel, C.L.Werner, "On the Derivation of Coseismic Displacement Fields Using Differential Radar Interferometry: the Landers Earthquake, *J.Geophys. Res., 99*, 19617-16634, 1994.

[4] P.J.Mouginis-Mark, "Preliminary Observation of Volcanoes with the SIR-C Radar", *IEEE Trans. Geosci. Remote Sensing, GE-33*, 934-941, 1995.

[5] F.Gatelli, A.Monti-Guarnieri, F.Parizzi, P.Pasquali, C.Prati, and F.Rocca, "The Wavenumber Shift in SAR Interferometry", *IEEE Trans. Geosci. Remote Sensing, GE-32*, 855-865, 1994.

[6] M.Coltelli, L.Dutra, G.Fornaro, G.Franceschetti, R. Lanari,M.Migliaccio, J.R.Moreira, K.P.Papathanassiou, G.Puglisi, D.Riccio, M.Schwäbisch, *SIR-C/X-SAR Interferometry over Mt.Etna: DEM Generation, Accuracy Assessment and Data Interpretation, Forschungsbericht, DLR book*, 1996.

[7] G.Fornaro, G.Franceschetti, R.Lanari, "Interferometric SAR Phase Unwrapping Using Green's Formulation", in print on *IEEE Trans. Geosci. Remote Sensing*.

[8] M.Schwäbisch, "Die SAR-Interferometrie zur Erzeugung Digitaler Gelaendemodelle" (in German), *DLR-Forschungsbericht*, 1995.

[9] M.Coltelli, G.Fornaro, G.Franceschetti, R.Lanari, M.Migliaccio, J.R.Moreira, K.P.Papathanassiou, G.Puglisi, D.Riccio, M.Schwäbisch, "SIR-C/X-SAR Multifrequency Multipass Interferometry: a New Tool for Geological Interpretation", *submitted*.

[10] U.Wegmüller and C.L.Werner, "SAR Interferometric Signatures of Forest", *IEEE Trans. Geosci. Remote Sensing, GE-33*, 1153-1161, 1995.

[11] B.B.Mandelbrot, *The Fractal Geometry of Nature*, W.H. Freeman & Co., San Francisco, 1983.

[12] M.Migliaccio and D.Riccio, "Fractal Brownian Model for SAR Image Analysis: Edge Detection and Classification Issues", in *Proceeding of IGARSS'93*, 1605-1607, Tokyo, Japan, 1993.

Atmospheric Induced Errors in Interferometric DEM Generation

Lado W. KENYI and Hannes RAGGAM

Institute for Digital Image Processing, JOANNEUM RESEARCH
Wastiangasse 6, A-8010 Graz, AUSTRIA
Tel.: +43 316 876 735; Fax: +43 316 876 720
E-Mail: lado@pdib40.joanneum.ac.at

Abstract -- Atmospheric error impacts on interferometric DEM generation were assessed. It was found that atmospheric effects are manifested in the INSAR data as deviations from the local topography of the terrain. Local height errors of 50 m corresponding to a phase shift of about 247° in an INSAR image pair with a baseline of 160 m was found, while the RMS error of the INSAR generated DEM was about 11 m. Error analysis indicated that atmospheric induced errors in INSAR DEMs are significantly reduced in larger baselines data.

INTRODUCTION

Synthetic aperture radar interferometry (INSAR) allows the production of detailed and accurate three dimensional relief maps of the Earth's surface directly from two SAR complex image data that can be acquired either simultaneously by two SAR recievers in a single pass or by one SAR reciever in multiple passes at different times [4,6]. The assumption for the two pass INSAR systems is that the atmosphere does not disturb the propagation of the SAR signal in both overflights. However, the atmosphere is a refractive medium and the SAR signal does not propagate in a straight line throught it [3]. The implication is that path delay is introduced by the atmosphere into the measured radar signal.

In this paper, the effects of atmospheric distortion on INSAR digital elevation model (DEM) generation using ERS-1 single look complex (SLC) data were assessed. First, SLC data of suitable baseline were selected. The selection was based on approximate weather conditions at the time of the data acquisition, such that the orbits selected represent SLC data of dry and wet (turbulent) atmospheric conditions. The data were then interferometrically processed and a DEM was generated. For matters of comparison, a reference DEM was digitised from contour lines of a topographic map of the test area. From the SAR viewing geometry parameters, a theoretical error analysis of phase shifts against baselines was performed. The theoretically computed and practically estimated errors from the interferometric data were elaborately discussed and quantified.

DEM GENERATION PROCEDURE

A procedure to convert an absolute phase image pixel-by-pixel to the corresponding ground points $\vec{p}$ can be deduced from Fig. 1. First, the slant range difference δ_i is calculated for each pixel from phase Φ :

$$\delta_i = -\frac{\lambda}{4\pi} \cdot (\Phi_i + \Phi_c) \qquad \text{Equ. (1)}$$

Here, Φ_c is a constant phase offset, which has to be determined in advance by using ground control points.

Based on slant range R_1 and δ the slant range distance R_2 and the baselength B are calculated in a next step:

$$R_2 = R_1 + \delta \; ; \qquad B = |\vec{s}_2 - \vec{s}_1| \qquad \text{Equ. (2)}$$

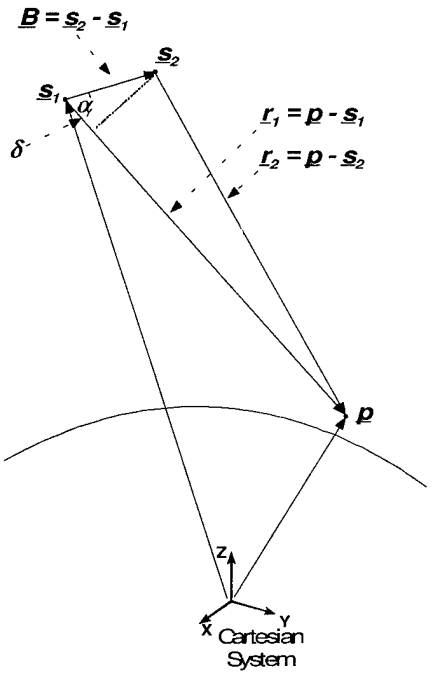


Fig. 1: Geometric INSAR imaging disposition.

These entities are used to determine the angle α between baseline vector $\vec{B}$ and pointing vector $\vec{r}_1$ in sensor position $\vec{s}_1$ by the equation:

$$\cos\alpha = \frac{R_2^2 + B^2 - R_1^2}{2 \cdot B \cdot R_1} \qquad \text{Equ. (3)}$$

Using $\vec{s}_1$, $\vec{B}$, α, R_1 and 3D vector relations, the pointing vector $\vec{r}_1$ and ground point $\vec{p}$ are calculated.

DEM ERROR ANALYSIS

The impact of phase deviations on the location accuracy of the ground coordinates derived from INSAR

0-7803-3068-4/96$5.00©1996 IEEE

data can be analysed by considering Fig. 2. According to equation (1) a certain phase shift $\Delta\phi$ results in a range error ΔR as:

$$\Delta\delta = \Delta R = \frac{\lambda}{4\pi}\Delta\phi \qquad \text{Equ. (4)}$$

In Fig. 2 the point displacement Q resulting from the range displacement ΔR can be approximated as:

$$\Delta\alpha \approx B\cos^2\theta/H \qquad \text{Equ. (5)}$$

$$Q \approx \frac{H}{B\cos^2\theta}\Delta R \qquad \text{Equ. (6)}$$

The location errors ΔP and ΔH in planimetry and height are then:

$$\Delta P = Q\cos\theta\ ; \quad \Delta H = Q\sin\theta \qquad \text{Equ. (7)}$$

Now, under the assumption of various baselines and phase shifts the location errors in height were computed using ERS-1 mid swath parmeters. Table 1 shows the calculated height errors. It is obvious that the error in height decreases with increasing baseline, i.e. atmospheric induced height errors might become insignificant in INSAR pairs of very large baselines.

DEM GENERATION

An ERS-1 phase B SLC image pair of the area of Weilerswist, west of the city of Bonn in Germany, acquired on the 14 and 29 March 1992 was interferometrically processed. The pair was selected on the fact that other authors reported phase anomalies in the same image pair [5]. Using the procedure described above, a digital elevation model was generated. 14 ground control points (GCPs) were selected simultaneously from a topographic map and the INSAR amplitude image in order to determine the phase constant. Then, the coordinates of the GCPs were calculated from the INSAR geometry geometry and subsequently compared to the values measured in the topographic map. The statistical parameters of the coordinates and phase residuals are summarised in Table 2.

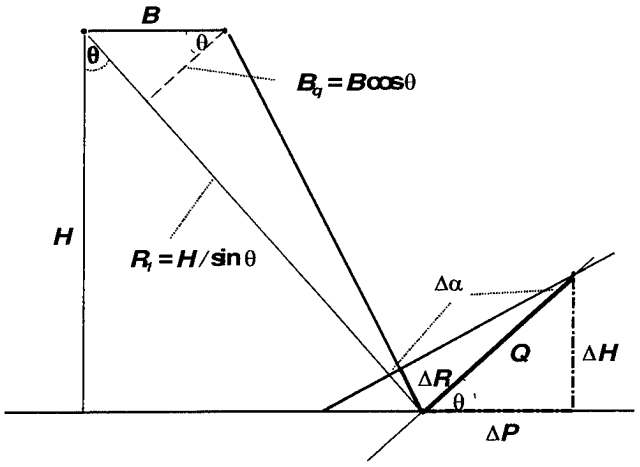


Fig. 2: Displacement due to range/phase error.

Table 1: Height errors versus baselines due to phase shifts.

Baseline [m]	Phase Shifts 45° ΔH	90° ΔH	135° ΔH	180° ΔH	225° ΔH	270° ΔH	315° ΔH	360° ΔH
50	26	51	77	102	128	154	179	205
100	13	26	38	51	64	77	90	102
150	9	17	26	34	43	51	60	68
200	6	13	19	26	32	38	45	51
250	5	10	15	20	26	31	36	41
300	4	9	13	17	21	26	30	34
350	4	7	11	15	18	22	26	29
400	3	6	10	13	16	19	22	26

Table 2: Statistics of GCP phase and coordinate residuals.

Residuals (14 GCPs)	*Phase* rad.	deg.	*GCP Coordinates* E	N	H
RMS	0.98	56°	28.2	25.4	8.9
Minimum	-1.72	-99°	-50.7	-58.4	-11.6
Maximum	1.96	112°	47.9	40.7	13.7

Fig. 3 shows the generated DEM in a colour coded presentation with the local topographic anomalies area indicated by a box. For comparison a DEM was created from digitised contour lines of a topographic map in a 1:50.000 scale. Fig. 4 shows this map-derived reference DEM in a colour coding similar to that of the INSAR generated DEM. In order to assess the errors introduced by the atmospheric effect, the difference of the two DEMs was computed. For the entire area the standard deviation of the elevation differences was about 11 m. This is slightly worse than the RMS height error of about 9 m for the GCPs (see Table 2). Moreover, the interferometric DEM is shifted on average by 2 meters in comparision to the map derived DEM. The maximum errors were around 50 m, whereas that of the GCPs was about 14 m. The 50 m error turned out as local deviations due to the atmospheric turbulences, (areas in box Fig. 3).

ATMOSPHERIC EFFECT

For verification purposes, meteorological data of the weather conditions around the time of the ERS-1 image acquisition, 10:26 UTC, were obtained from the *Deutscher Wetterdienst*. Table 3 shows the weather information taken at 10:00 UTC at the station of Euskirchen located within the test site.

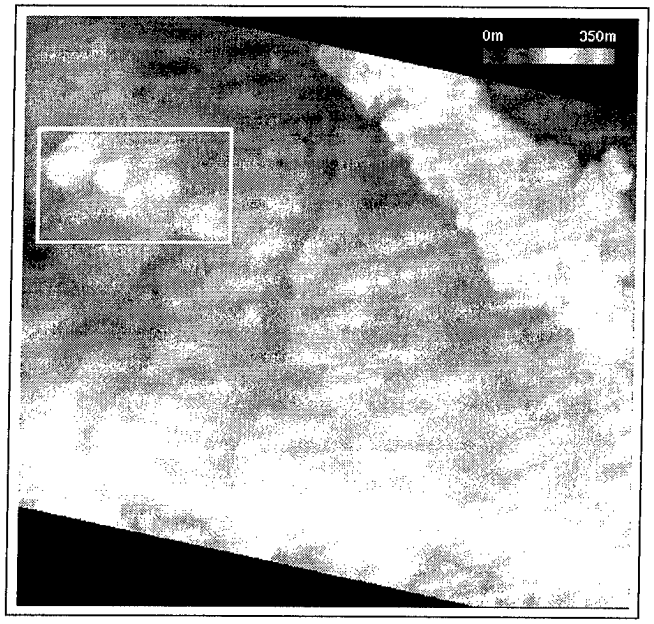


Fig. 3: INSAR derived DEM (colour coded).

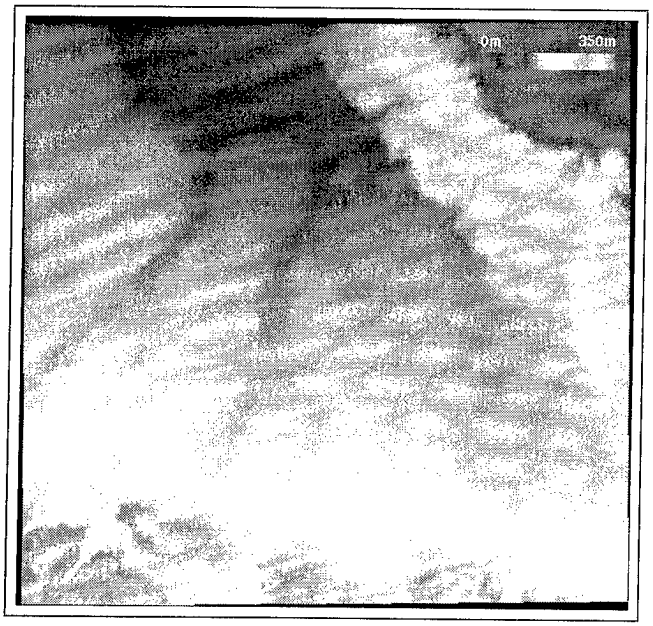


Fig. 4: Map Derived DEM (colour coded).

The weather data were modeled using the Hopfield tropospheric path delay estimation model [1,2]. The estimated total path delay was 114°. On the other hand, the average unwrapped phase differences estimated from the anomalies regions were 247°. Despite the poor correlation between these values, the deviations observed could be regarded as atmospheric effects due to their shape and when taking the Hopfield model error (± 60°), the time gap between image acquisition and meteorological measurements (26 minutes) and the meteorological measurement errors into consideration.

Table 3: Meteorological data at 10:00 UTC.

Date	**14.03.1992**	**29.03.1992**
Temperature in °C	4.4	4.7
Pressure in hPa	1010	1005
Relative humidity in %	52	73
Cloud Coverage	7/8	5/8
Remarks	Snowfall	No precipitation

CONCLUSIONS

Atmospheric induced errors in INSAR DEM generation have been analysed. It was found that atmospheric effects are manifested as local deviations in the INSAR topographic information. A maximum height error of 50 m corresponding to an average absolute phase value of 247° was estimated. This value is close to the theoretical error of 44 m calculated for an equvivalent phase shift. Whereas, the RMS for the GCPs was about 9 m the standard deviation of the difference DEM was 11 m. From the theoretical error analysis it can be concluded that atmospheric induced errors are significantly reduced in interferometric image pairs of very large baselines.

ACKNOWLEDGEMENTS

This work was part of a study on the "Feasibility of Atmospheric Effect in Interferometric Data and its Interpretation" supported by ESA under contract No. 9949/92/NL/PB. The effort of Dipl. Ing. E. Kubista of the Joanneum Research, Institute of Applied Systems Technology, for the provision of the weather data and the Hopfield tropospheric modeling is highly acknowledged.

REFERENCES

[1] H. S. Hopfield, "Two-quartic tropospheric reflectivity profile for correcting satellite data," Journal of Geophysical Research, Vol. 74, No. 18, August 1969.

[2] L. W. Kenyi, H. Raggam and E. Kubista, "Feasibility of atmospheric effect in interferometric data and its interpretation," ESA ESTEC-XEP Draft Report, Prepared by the Institutes of Digital Image Processing and Applied Systems Technology, Joanneum Research, December 1995.

[3] H. Tarayre and D. Massonnet, "Effects of refractive atmosphere on interferometric processing," Proceedings of IGARSS'94, pp. 717-719, 1994.

[4] C. Prati, F. Rocca and A. Monti-Guarnieri, "SAR interferometry experiments with ERS-1," Proceedings of 1st ERS-1 Symposium, Cannes, France, pp. 211-218, November 1992.

[5] U. Wegmueller, C. Werner, D. Small and D. Nueesch, "Analysis of land surface signatures using SAR interferometry," ESA ESTEC-XEP Report, prepared by Remote Sensing Laboratories, University of Zuerich, 28 June 1994.

[6] H. Zebker, C. Werner, P. Rosen and S. Hensley, "Accuracy of topographic maps derived from ERS-1 interferometric radar," IEEE Trans. Geoscience and Remote Sensing, Vol. 32, No. 4, pp. 823-836, 1994.

Wavelet Projection Pursuit for Feature Extraction and Cloud Detection in AVIRIS and AVHRR Imagery

Charles M. Bachmann *, Eugene E. Clothiaux †, Dong Q. Luong ‡

* Airborne Radar Branch
Radar Division,Code 5365
Naval Research Laboratory,
Washington, D. C. 20375
e-mail: bachmann@radar.nrl.navy.mil
tel.: (202) 767-3240; fax: (202) 404-7572

† Department of Meteorology
Pennsylvania State University
University Park, Pennsylvania 16802
e-mail: cloth@essc.psu.edu

‡ Lockheed Martin
2711 Jefferson Davis Highway
Arlington, VA 22202.

Abstract— **We examine a class of constrained Projection Pursuit (PP) algorithms for extracting textural features from multi-spectral remote sensing imagery. Based on the assumption that spatial frequency information is useful for separating classes of interest in the data, topological constraints are defined for the PP filter vectors. The constraint on each filter is imposed by a set of tunable meta-parameters which define each filter as an adaptive Gabor wavelet. We call this approach Wavelet Projection Pursuit (WPP). The application of the approach to cloud detection is described. The long-term goal is to develop algorithms for texture-based cloud masking applicable to future data from the Multi-Angle Imaging Spectrometer (MISR).**

I. Introduction

Projection Pursuit has a long history as a means of exploratory data analysis [10] and [12]. In our approach, the Projection Index which is minimized during the search procedure is based on the difference of higher moments of the projected data distribution; feature extraction, therefore, is unsupervised and can proceed without a priori knowledge of data labels. The unconstrained version of our PP algorithm was developed in [4] (BCM) and [15] (BCM-PP) and has been used in a number of applications including remote sensing [1], [2], [3], [13]. The model which we describe here constrains the BCM algorithm by requiring that search elements be inter-related topologically. In image processing applications such as cloud detection, this means that the search vector elements have the shape of an adaptable Gabor wavelet when plotted on a two-grid corresponding to the size of input data patches. The use of an unsupervised Projection Index for exploratory data analysis distinguishes this approach from other adaptive wavelet algorithms which are based on regression [16]. In our approach, regression occurs at a later stage of processing when textural features extracted by WPP or PP from each spectral channel are adaptively pooled and mapped to a classification. In [1] and [2], we applied BCM-PP to texture feature extraction from Gray-Level Difference Vector (GLDV) histograms and Sum-and-Difference Histograms (SADH), contrasting this approach to cloud detection with those based on fixed statistics of the histograms as described in [8], [9], and [20].

At minima of the search procedure for WPP and PP, multi-modal structure present in the data is revealed in data projections. In this paper, feature extraction is demonstrated on two different remote sensing databases: (1) AVIRIS imagery and (2) AVHRR LAC imagery obtained from northern latitudes. A goal of our work is to develop methods for cloud detection based on texture feature extraction which could be applied eventually to data from the Multi-Angle Imaging Spectrometer (MISR). End-to-end cloud detection using features extracted by BCM-PP and WPP from 12x12 pixel input boxes is demonstrated for AVIRIS scenes using bands which are close spectrally to those which will be available from MISR, albeit at higher spatial resolution than from MISR. The feature extraction stage is also demonstrated for AVHRR LAC channel 1 data from northern latitudes; AVHRR LAC has similar spatial resolution to that of one of the MISR modes, although is spectrally broad compared to MISR channels, with AVHRR channel 1 overlapping the MISR red channel at 670nm.

II. Feature Extraction by BCM Projection Pursuit

In the BCM model the Cost Function is closely related to Projection Indices based on standardized absolute cumulants [12] of the projected data distribution; however, since methods based on polynomial moments can be overly sensitive to outliers, the use of a saturating nonlinearity, with derivatives which go to zero at extreme values, is used to mitigate this effect [14]. Also, projections are jointly optimized as in neural network models, rather than serially.

In the BCM Projection Pursuit model, the ith projection in layer n of a multi-layer BCM network is: [1]

$$\tilde{c}_i^{(n)} = \sigma\Big(\sum_j L_{ij}^{(n)} c_j^{(n)}\Big) \quad (1)$$

$$with: \ \sigma(x) = a \tanh(a\lambda x), \quad (2)$$

$$c_j^{(n)} = \vec{w}_j^{(n-1)} \cdot \vec{\tilde{c}}^{(n-1)} + b_j^{(n)}, \quad (3)$$

[1] In the present study, BCM-PP and WPP networks had only a single layer of projections.

C. Bachmann is supported by grants from ARPA (program element 62712E, sponsor: Dr. Barbara Yoon) and ONR (program element 61153N, sponsor: Dr. Thomas McKenna). Computing resources were supplied by the DOD High Performance Computing Modernization Program which provided access to the Army Research Laboratory's SGI Power Challenge Array (ARLPCA) and the Maui High Performance Computer Center (MHPCC).

E. Clothiaux is supported by Jet Propulsion Laboratory contract 959034

D. Luong contributed to this work under contract to NRL.

0-7803-3068-4/96$5.00©1996 IEEE

$$and\ L_{ij}^{(n)} = \begin{pmatrix} 1-\mu, for\ i=j \\ -\mu, for\ i \neq j \end{pmatrix}$$

where $L_{ij}^{(n)}$ is a fixed constraint matrix, $\vec{w}_j^{(n-1)}$ is the jth modifiable projection vector, which weights inputs from layer $(n-1)$, and $b_j^{(n)}$ is the bias. Projection vectors and biases are modified by minimizing the cost of the projected data distribution over the cost function, $\xi^{(n)}$ (4) ; this leads to a semi-local Projection Index, $E[\xi^{(n)}]$, with no reference to training labels (unsupervised learning): [2]

$$Minimize: \quad E[\xi^{(n)}] = -(\sum_i \frac{E[(\tilde{c}_i^{(n)})^3]}{3} - \gamma \frac{E^2[(\tilde{c}_i^{(n)})^2]}{4}) \qquad (4)$$

$$By\ Gradient\ Descent: \quad \Delta\vec{w}_k^{(n-1)} = -\eta \frac{\partial E(\xi^{(n)})}{\partial \vec{w}_k^{(n-1)}} = \eta E[\sum_i \phi(\tilde{c}_i^{(n)}, \tilde{\theta}_i^{(n)})\,(\tilde{c}_i^{(n)})'\, L_{ik}^{(n)}\, \vec{\tilde{c}}^{(n-1)}] \qquad (5)$$

$$with: \quad \phi(\tilde{c}_i^{(n)}, \tilde{\theta}_i^{(n)}) = \phi_i^{(n)} = \tilde{c}_i^{(n)}(\tilde{c}_i^{(n)} - \gamma\tilde{\theta}_i^{(n)}), \quad \theta_i^{(n)} = E[(c_i^{(n)})^2], \quad (\tilde{c}_i^{(n)})' = \lambda(a - \tilde{c}_i^{(n)})(a + \tilde{c}_i^{(n)})$$

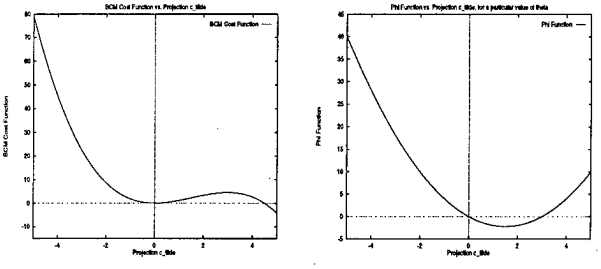


Fig. 1. (Left) The BCM Cost Function vs. $\tilde{c}_i^{(n)}$; the Cost Function favors at least bi-modal projections of the data; the two wells move during training, and the time scale is set by τ in Equation 7 ; the Projection Index is obtained by minimizing the cost of the data projections over this function, and then averaging over all projections. (Right) the ϕ-function vs. $\tilde{c}_i^{(n)}$; in a single-projection model, ϕ determines whether the projection response to a pattern is reinforced or weakened based on whether the pattern is above or below the dynamical threshold (the rightmost crossing point), $\gamma\theta_i^{(n)} = \gamma E[(c_i^{(n)})^2]$.

$\gamma\theta_i^{(n)}$ is the dynamic modification threshold above which the response to a particular input pattern is reinforced and below which it is weakened in a single projection model; this can be seen by writing:

$$\frac{d\tilde{c}^{(n)}}{dt} = \nabla_{\vec{w}}\tilde{c}^{(n)} \cdot \frac{d\vec{w}}{dt} \approx \eta\,(\,(\tilde{c}^{(n)})'\,\vec{\tilde{c}}^{(n-1)}\,)^2\phi \qquad (6)$$

Thus, the sign of ϕ, depicted graphically in Fig. 1, determines the sign of the change in the response to a particular pattern. Typically the expectation value in (4) is only approximated as a leaky integrator:

$$\theta_i^{(n)} = \frac{1}{\tau}\int_{t_0}^{t} e^{-\frac{t-s}{\tau}}(\tilde{c}_i^{(n)})^2(s)\,ds \qquad (7)$$

This minimization procedure biases projection vectors toward directions where the input pattern distribution is statistically skew or multi-modal when projected onto them. For a small and decreasing step-size, Equation 5 is well approximated by stochastic gradient descent [15].

III. Wavelet Projection Pursuit

A number of researchers have described adaptive wavelet methods; the majority of these are based on supervised adaptive learning (see for example [16]). In contrast, the particular method which we develop here is an unsupervised learning algorithm for exploratory feature extraction based on BCM: wavelet projection pursuit (WPP). In WPP, a set of meta-parameters imposes a modifiable wavelet constraint on the topology of the projection vector. The primary motivation for imposing such a constraint is that spatial frequency and localization are natural for representing texture. We emphasize that for detection applications, reconstruction of the texture is not the goal. Rather, we would like to find a limited set of texture projection vectors which capture important structure, by revealing clusters in the data.

A. BCM with Wavelet Meta-Parameters

We impose a wavelet constraint on the topology (Gabor wavelet constraint) of the Projection Pursuit filter vector in the following manner. For vector $\vec{w}_i$, we define:

$$w_{ij} = s_i e^{-\frac{(\vec{r}_j - \vec{\mu}_i)A_i(\vec{r}_j - \vec{\mu}_i)}{2}} cos(\vec{k}_i \cdot \vec{r}_j + p_i) \qquad (8)$$

where $\vec{k}_i$ is the wave-vector of the wavelet filter, p_i is the associated phase, $\vec{r}_j$ is the location of the jth input pixel with coordinates (x_j, y_j) in a 2D input grid, A_i is the scale matrix for the exponentially decaying envelope (in this case, initialized as a diagonal 2x2 matrix but permitted to develop off-diagonal elements during training), $\vec{\mu}_i$ is the location of the center of the envelope, and s_i is the amplitude. The set $\{\ \vec{k}_i,\ p_i,\ A_i,\ \vec{\mu}_i,\ s_i\ \}$ is composed of ten tunable meta-parameters for each filter vector. As in the unconstrained BCM model, the objective function for WPP is given by (4). The meta-parameters are modified by gradient descent in the Projection Index of of (4), according to:

$$\Delta s_i = -\eta_s \frac{\partial E(\sum_j \xi_n)}{\partial w_{ij}} \frac{\partial w_{ij}}{\partial s_i} = \eta_s E[\sum_\alpha \phi_\alpha^{(n)}\,(\tilde{c}_\alpha^{(n)})'\, L_{\alpha i}^{(n)}\, \vec{\tilde{c}}^{(n-1)} \cdot \frac{\vec{w}_i}{s_i}]\ . \qquad (9)$$

And defining,

[2] $E[]$ represents the expectation value.

$$T_{ij} = s_i e^{-\frac{(\vec{r}_j - \vec{\mu}_i) A_i (\vec{r}_j - \vec{\mu}_i)}{2}} sin(\vec{k}_i \cdot \vec{r}_j + p_i) \ , \qquad (10)$$

we also have:

$$\begin{aligned} \Delta \vec{k}_i &= -\eta_k \frac{\partial E(\sum_j \xi_n)}{\partial w_{ij}} \frac{\partial w_{ij}}{\partial \vec{k}_i} \\ &= -\eta_s E \left[\sum_\alpha \sum_j \phi_\alpha^{(n)} \, (\tilde{c}_\alpha^{(n)})' \, L_{\alpha i}^{(n)} \, \tilde{c}_j^{(n-1)} T_{ij} \vec{r}_j \ \right] \end{aligned} \qquad (11)$$

$$\begin{aligned} \Delta p_i &= -\eta_p \frac{\partial E(\sum_j \xi_n)}{\partial w_{ij}} \frac{\partial w_{ij}}{\partial \vec{k}_i} \\ &= -\eta_s E \left[\sum_\alpha \sum_j \phi_\alpha^{(n)} \, (\tilde{c}_\alpha^{(n)})' \, L_{\alpha i}^{(n)} \, \tilde{c}_j^{(n-1)} T_{ij} \ \right] . \end{aligned} \qquad (12)$$

For the Gaussian envelope, A_i, we also have:

$$\Delta A_i = \eta_A \sum_\alpha \sum_j \phi_\alpha^{(n)} \, (\tilde{c}_i^{(n)})' L_{\alpha i} w_{ij} \tilde{c}_j^{(n-1)} (\vec{d}_{ij} \otimes \vec{d}_{ij}) \ , \quad (13)$$

where:

$$\vec{d}_{ij} = \vec{u}_i - \vec{r}_j \qquad (14)$$

$$(\vec{d}_{ij} \otimes \vec{d}_{ij})_{lk} = (\vec{d}_{ij})_l (\vec{d}_{ij})_k \ . \qquad (15)$$

Finally, for $\vec{u}_i$, we have:

$$\begin{pmatrix} \Delta u_{i,0} \\ \Delta u_{i,1} \end{pmatrix} = -\eta_u E \left[\sum_\alpha \sum_j \phi_\alpha^{(n)} \, (\tilde{c}_\alpha^{(n)})' L_{\alpha i} w_{ij} \tilde{c}_j^{(n-1)} \begin{pmatrix} d_{ij0} A_{00} + \frac{A_{01} + A_{10}}{2} d_{ij1} \\ d_{ij1} A_{11} + \frac{A_{01} + A_{10}}{2} d_{ij0} \end{pmatrix} \right] . \qquad (16)$$

IV. Results

To evaluate the WPP algorithm and other methods of texture feature extraction for cloud detection, we have used two databases. The long-term goal is to develop algorithms for texture-based cloud masking applicable to future data from the Multi-Angle Imaging Spectrometer (MISR) [6]. Accordingly, one of our two data sets consists of 17 Airborne Visible and Infra-Red Imaging Spectrometer (AVIRIS) [19] scenes from which we have chosen a very limited subset of spectral channels (4 out of 224 channels), which correspond closely to those which will be available from MISR (443, 555, 670, and 865 nm) [7], albeit at significantly higher spatial resolution; each image is 614x512 pixels for each of the four spectral channels.

Our second database consists of a large corpus of Advanced Very High Resolution Radiometer 1.1 Km Local Area Coverage (AVHRR LAC) data. For the purposes of this paper, we have confined our attention mainly to feature extraction from one AVHRR scene (2048x3500 pixels per channel per scene) covering parts of northern Canada on August 1, 1993. A fragment of this scene is shown in Fig. 2. The AVHRR scene in the second database was chosen because northern latitudes are among the more challenging regions for feature extraction and cloud detection, particularly for texture-based methods because of ice and snow.



Fig. 2. Fragment (503x487pixels) of the channel 1 AVHRR scene (2480x3500 pixels per scene per channel) used for evaluating WPP feature extraction. The whole scene is an image of parts of Northern Canada and is partly over water.

In previous work [1] [2], we have reported our efforts to extract textural features from Gray-Level Difference Vector (GLDV) histograms and Sum-and-Difference Histograms (SADH) using the unconstrained BCM-PP algorithm. Features obtained by BCM-PP from these preprocessing steps were shown to be useful for detecting cloud pixels in the AVIRIS data set. Ensemble networks were used to pool these features from the four spectral channels for various window sizes, using these preprocessing steps as input; features from other representations, which encoded exact geometrical information (simply normalized pixel intensities), were also extracted using BCM. These features became the input to a higher level network trained using the backward propagation (BP) [18] algorithm with a cross-entropy cost function (BPCE) [17]. In some cases, BPCE ensembles of ensembles were also used to smooth the results for more robust performance across all training and testing images.

In this study, we show that the WPP algorithm, which we have formulated above is also useful for extracting textural features. In Figure 3, we show a subset of two projection vectors drawn from a WPP network trained on channel 1 of the AVHRR scene described above. In the figure, we compare the projected 2D histograms for samples of cloud-free input windows (24x24 pixels) with samples containing both classes, cloudy and clear. Analysis of the clusters shows that two clusters correspond to cloudy data windows and two to clear data windows.

For the AVIRIS database, we show an example of a cloud detection result (Fig. 4) obtained from an ensemble network experiment. Features from WPP networks, BCM-PP features from GLDV histograms and simply normalized data representations, as well as standard statisitical moments from GLDV as in [20], were pooled and adaptively weighted to obtain the detection model. In (Fig. 4), 94.0 % of the cloud pixels were correctly detected, with a false-alarm rate of 4.8 %.

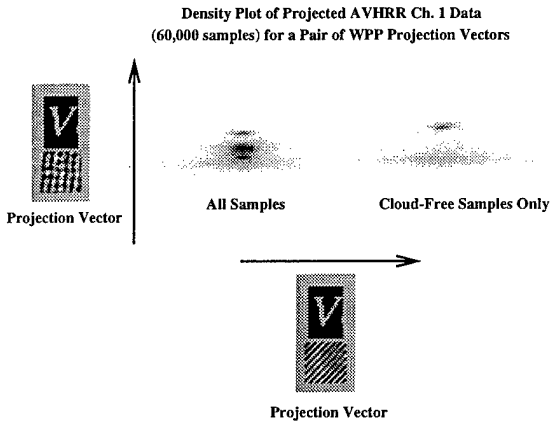


Fig. 3. Examples of Wavelet Projection Pursuit vectors are shown with 2D histograms of the AVHRR data projected through these vectors. Vectors were trained in a network which received inputs from 24x24 data windows of the AVHRR scene from Northern Canada (channel 1). The histogram at left shows the density of all 60,000 projected samples (a small subset of the total AVHRR scene) with multi-modal clusters revealed; the histogram at right shows that when only cloud-free data samples are retained in the histogram, two of the clusters disappear. From this, it is obvious that two of the clusters correspond to cloudy data, while the remaining clusters are associated with cloud-free data samples.

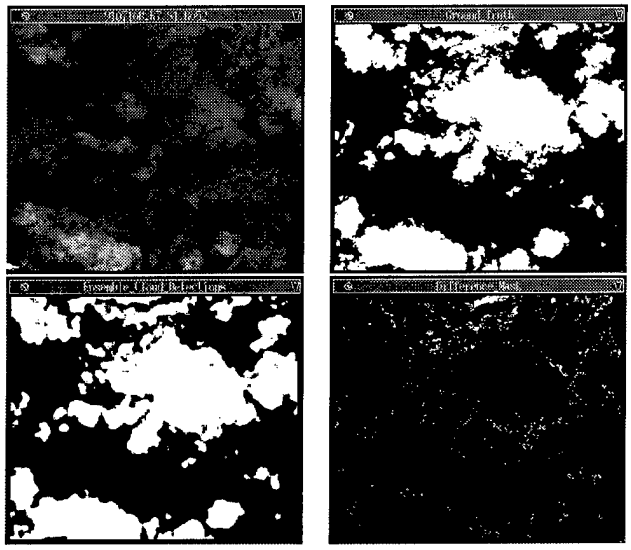


Fig. 4. An example of cloud detection from novel test data in the AVIRIS database. (Upper left) Near infra-red channel (865nm) for one of the AVIRIS scenes in the test set; spectral channel is one of 4 chosen to correspond spectrally to future MISR channels; colormap is black (low) to white (high). (Upper right) Human interpretation of cloud pixel location, white = cloud, black= no cloud. (Lower left) Cloud detection result from an example ensemble network using extracted WPP features, BCM GLDV features, BCM features from simply normalized pixel intensities, and standard standard statistical moments from GLDV as in (Welch et. al., 1992); features in the ensemble model were extracted from all four spectral channels; white = cloud, black = no cloud. (Lower right) difference mask: black = no error, gray = false-alarm, white = false negative; many of the errors are on cloud, no-cloud boundaries. Cloud detection rate for this novel test image was 94.0 % with a false alarm rate of 4.8 % .

REFERENCES

[1] C. M. Bachmann, E. E. Clothiaux, J. W. Moore, D. Q. Luong," Dynamically Reconfigurable Projection Pursuit Ensembles for Cloud Detection in AVIRIS Imagery," in Proceedings of the International Geoscience And Remote Sensing Symposium (IGARSS '95), Firenze, Italy, July 10-14, 1995, Vol. I, pp. 256-259.

[2] C. M. Bachmann, E. E. Clothiaux, J. W. Moore, D. Q. Luong, "Self-Pruning Projection Pursuit Models for Improved Cloud Detection in AVIRIS Imagery," in Neural Networks for Signal Processing V: Proceedings of the 1995 IEEE Workshop, Cambridge, MA, Sept., 1995, pp. 361 - 370.

[3] C. M. Bachmann, S. Musman, D. Luong, and A. Schultz, "Unsupervised BCM Projection Pursuit Algorithms for Classification of Simulated Radar Presentations," *Neural Networks*, Vol. 7, No. 4, pp. 709-728, 1994.

[4] E. L. Bienenstock, L. N. Cooper, P. W. Munro, "Theory for the Development of Neuron Selectivity: Orientation Specificity and Binocular Interaction in Visual Cortex," *J. Neuroscience*, Vol. 2, No. 1, pp. 32-48, 1982.

[5] D. W. Chen, S.K. Sengupta, and R.M. Welch, "Cloud Field Classification Based upon High Spatial Resolution Textural Features: 2. Simplified Vector Approaches," *J. Geophys. Res.*, 94, No. D12, 14749-14765, 1989.

[6] "A Multiangle Imaging SpectroRadiometer for Terrestrial Remote Sensing from the Earth Observing System," D. J. Diner, C. J. Bruegge, J. V. Martonchik, G. W. Bothwell, E. d. Danielson, E. L. Floyd, V. G. Ford, L. E. Hovland, K. L. Jones, M. L. White, International Journal of Imaging Systems and Technology, Vol. 3, 92-107, 1991.

[7] "MISR Level 2 Algorithm Theoretical Basis: Top-of-Atmosphere/ Cloud Product," D. J. Diner, C. C. Borel, E. Clothiaux, J. E. Conel, R. Davies, L. Di Girolamo, J. Muller, T. Varnai, D. Wenkert, JPL D-11399, Rev. A, Dec. 19, 1994.

[8] E. Ebert, "A Pattern Recognition Technique for Distinguishing Surface and Cloud Types in the Polar Regions," *J. Climate Appl. Meteor.*, 26, 1412-1427, 1987.

[9] E. Ebert, "Analysis of Polar Clouds from Satellite Imagery Using Pattern Recognition and a Statistical Cloud Analysis Scheme," *J. Appl. Meteorology*, Vol. 28, pp. 382 - 399, 1989.

[10] J. H. Friedman, J. W. Tukey, "A Projection Pursuit Algorithm for Exploratory Data Analysis," *IEEE Trans. Computers*, Vol. c-23, No. 9, pp. 881 - 890, 1974.

[11] , J. H. Friedman, "Exploratory Projection Pursuit," Journal of the American Statistical Association, March, 1987, Vol. 82, No. 397, Theory and Methods, pp. 249-266.

[12] P. J. Huber, "Projection Pursuit," *Annals of Statistics*, Vol. 13, No.2, 435-475, 1985.

[13] N. Intrator, "Feature Extraction Using an Unsupervised Neural Network," in Proceedings of the 1990 Connectionist Models Summer School, (eds.) D. S. Touretzky, G. L. Ellman, T. J. Sejnowski, Morgan Kaufmann, San Mateo, CA.

[14] N. Intrator, "Feature Extraction Using an Exploratory Projection Pursuit Neural Network," Ph.D. Dissertation, Brown University, May, 1991.

[15] N. Intrator, L. N. Cooper, "Objective Function Formulation of the BCM Theory of Visual Cortical Plasticity: Statistical Connections, Stability Conditions," *Neural Networks*, Vol. 5, pp. 3-17, 1992.

[16] S. G. Mallat, Z. Zhang, "Matching Pursuits with Time-Frequency Dictionaries," IEEE Trans. on Signal Processing, Vol. 41, No. 12, Dec. 1993.

[17] M. D. Richard, R. P. Lippman, "Neural Network Classifiers Estimate Bayesian a posteriori Probabilities," *Neural Computation*, 3, 461-483, 1991.

[18] D. E. Rumelhart, G. E. Hinton, R. J. Williams, "Learning Internal Representations by Error Propagation," in *Parallel Distributed Processing, Explorations in the Microstructure of Cognition*, Vol. 1, Rumelhart, D. E., McClelland, J. L. (eds.), MIT Press, Cambridge, MA, pp. 318-362, 1986.

[19] G. Vane, R. O. Green, T. G. Chrien, H. T. Enmark, E. G. Hansen,W. M. Porter, *The Airborne Visible/Infrared Imaging Spectrometer (AVIRIS)*, Remote Sens. Environ., 44: 127-143 (1993).

[20] R. M. Welch, S. K. Sengupta, A. K. Goroch, P. Rabindra, N. Rangaraj, M. S. Navar, "Polar Cloud and Surface Classification Using AVHRR Imagery: An Intercomparison of Methods," *J. Appl. Meteorology*, Vol. 31, pp. 405-420, May, 1992.

Absolute in Flight Calibration of Airborne Multichannel MM-Wave Imaging Radiometer

I.V.Cherny, A.A.Pankin, S.Yu.Pantzov

Center for Program Studies, Russian Space Agency,
Profsoyusnaya, 84/32, Moscow, 117810, Russia,
Fax: 7-(095)-420-2275, Email: solom@febes.msk.su

Abstract - In microwave radiometry, hot and cold black body targets of known brightness temperature are used to calibrate microwave radiometer. This paper discusses the procedure of absolute in flight calibration of airborne multichannel mm-wave radiometer, based on measuring of two scenes known (calculated) brightness temperature - radiohorizon and cold sky, during aircraft bank over a water surface.

INSTRUMENTS AND METHODS

Airborne scanning multichannel radiometer provides the two-polarization measuring of radiation at frequencies of 22.2, 31, 34, 37, 42, 48, 75 and 96 GHz [1]. Multifrequency feed horn antenna is used to conduct concurrently in space and time spectral and polarization measurements. Imaging configuration is based on circular conical scanning with viewing angle of 75° from nadir (Fig.1). To remain the invariant of viewing angle and polarization in scanning sector, the radiometer and horn antenna are continually rotated about the vertical axis.

Parameters of airborne mm-wave imaging technique are:
- angle of antenna beam incidence.....75°
- scanning sector (conical scanning in front and back hemisphere).....130°
- scanning period..... 30 s
- half-power beamwidth (75 GHz).....2°
- antenna footprint (75 GHz).....0.12H x 0.45H (H - flight height)
- swath width.....6.4H

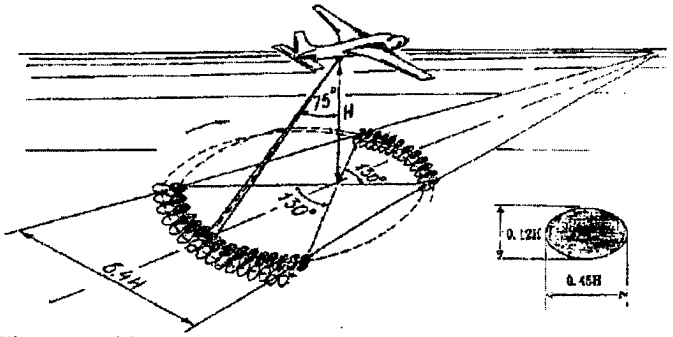


Figure 1. Airborne mm-wave imaging technique configuration.

CALIBRATION PROCEDURE

When aircraft bank is more than 25°, antenna beam looks through hot radiohorizon and cold sky (Fig.2)

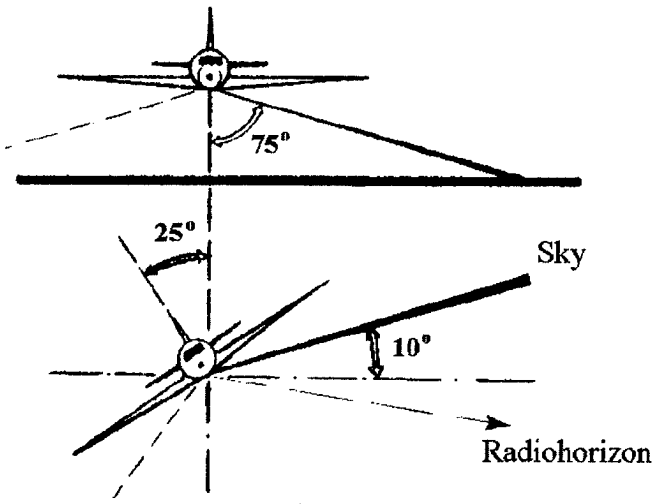


Figure 2.

The experimental distributions of brightness temperature T_b for frequencies of 22 GHz (horizontal polarization) and 75 GHz (vertical polarization) in scanning sector during aircraft bank of 25° are shown in Fig.3. The maximum of T_b corresponds to viewing radiohorizon, but minimum of T_b - cold sky.

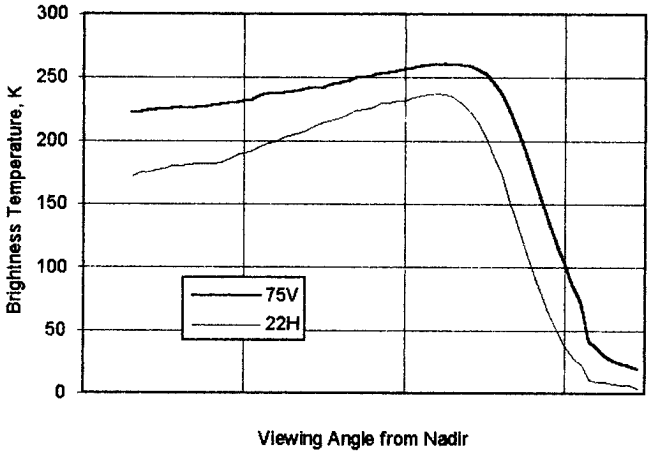


Figure 3. Experimental brightness temperature distribution in scanning sector according to Fig. 2. Flight height is 10 km over a ocean surface. Clear atmosphere, sea surface temperature 14°C, absolute humidity 9.5g/m³

0-7803-3068-4/96$5.00©1996 IEEE

CALCULATION OF BRIGHTNESS TEMPERATURE IN VIEWING NEAR RADIOHORIZON

The brightness temperature of calibration scenes is calculated, based on the following: U.S. standard atmosphere model; spherical form of the Earth; refraction in the atmosphere; "polarization coupling" effect; antenna pattern smoothing; scanning configuration parameters; aircraft navigation data.

The calculation of brightness temperature depends on the type of antenna beam trajectory [2] (See Fig. 4).

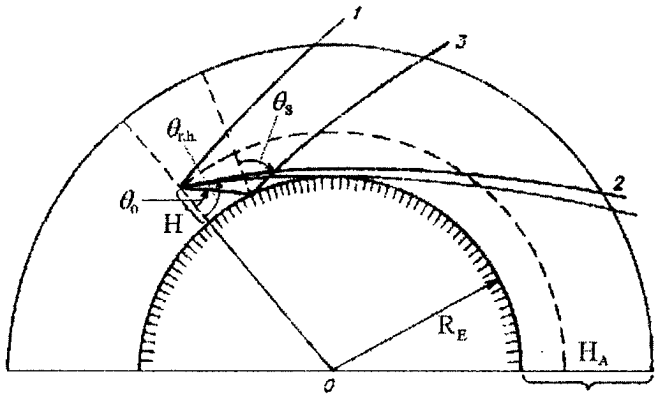


Figure 4. Three types of antenna beam trajectories for spherical-parallel atmosphere at normal refraction. θ_0 -viewing angle, $\theta_{r.h.}$ - angle of radiohorizon direction, θ_s - incident angle, R_E - Earth radius, H_A - height of atmosphere, H - viewing height.

When $90° \le \theta_0$ (type 1, Fig. 4), T_b is described as

$$T_{b\downarrow}(\theta_0, H) = \int_H^{H_A} \frac{\alpha(z)T(z)e^{-\tau(z,H_A)}dz}{\eta'(\theta_0,z)} + T_r e^{-\tau(H,H_A)} \qquad (1)$$

When $\theta_{r.h.} \le \theta_0 < 90°$, (type 2, Fig. 4) T_b is described as

$$T_{b\uparrow\downarrow}(\theta_0, H) = \int_{z_m}^{H} \frac{\alpha(z)T(z)e^{-\tau(z,H)}dz}{\eta'(\theta_0,z)} + \int_{z_m}^{H_A} \frac{\alpha(z)T(z)e^{-\tau(z,H_A)}dz}{\eta'(\theta_0,z)} \cdot e^{-\tau(z_m,H)} \qquad (2)$$

When $\theta_0 < \theta_{r.h.}$, (type 3, Fig. 4) T_b is described as

$$T_{bp\uparrow}(\theta_0, H) = \kappa_p(\theta_s)T_s e^{-\tau(0,H)} + \int_0^{H} \frac{\alpha(z)T(z)e^{-\tau(z,H)}dz}{\eta'(\theta_0,z)} + \left(1-\kappa_p(\theta_s)\right)\int_0^{H_A} \frac{\alpha(z)T(z)e^{-\tau(z,H_A)}dz}{\eta'(\theta_0,z)} \cdot e^{-\tau(0,H)} \qquad (3)$$

Where

$$\theta_{r.h.} = \arcsin\left(\frac{R_E \cdot m'(0)}{(R_E + H)\cdot m'(H)}\right)$$

m' - index of refraction of air, according to [3];

$\alpha(z)$ - atmosphere absorbtion coefficient, according to [4];

$T(z)$ - atmosphere temperature profile;

T_s - sea surface temperature;

$T_r = 2.73$ K - cosmic background temperature;

κ_p - sea surface emissivity, according to [5];

$p = v, h$ - polarization;

z_m - minimum distance between surface and antenna beam trajectory of type 2;

$\tau(a,b) = \int_a^b \frac{\alpha(z)dz}{\eta'(\theta_0,z)}$ - optical density of atmosphere;

$$\theta_s = \arcsin\left(\frac{m'(0)\cdot(R_E+H)}{m'(R_E)\cdot R_E}\sin\theta_0\right)$$

$$\eta'(\theta_0,z) = \sqrt{1-\left(\frac{m'(0)\cdot(R_E+H)}{m'(z)(R_E+z)}\sin\theta_0\right)^2}$$

"Polarization Coupling" Effect

The polarization basis of instrument is rotated with respect to the surface basis in scanning sector during aircraft bank. In this case, each radiometer channel receives the sea surface radiation of both vertical and horizontal polarization [6]:

$$\overline{T_b^i} = \begin{pmatrix} T_{bv^i} \\ T_{bh^i} \end{pmatrix} = \begin{pmatrix} \cos^2\Psi & \sin^2\Psi \\ \sin^2\Psi & \cos^2\Psi \end{pmatrix}\begin{pmatrix} T_{bv} \\ T_{bh} \end{pmatrix} = \overline{\overline{U}}(\Psi)\cdot\overline{T_b} \qquad (4)$$

Where

$\overline{T_b}$ - vector of real polarization basis of sea surface;

$\overline{T_b^i}$ - vector of instrument polarization basis;

Ψ - angle of polarization basis rotation.

When antenna beam looks through radiohorizon, Ψ is defined as

$$tg\Psi = \cos\varphi\left(1 + \frac{\sin\varphi + \sin\alpha\cdot A}{\cos\alpha\cdot tg\theta_0\sqrt{\cos^2\varphi + A^2} - \sin\alpha\cdot A}\right)$$

$$A = -\frac{\sin\alpha}{tg\theta_{r.h.}} + \sin\varphi\cdot\cos\alpha\ ;$$

$$\sin\varphi = \frac{1}{tg\theta_{r.h.} \cdot tg\alpha} \cdot \left(\cos 2\theta_0 + \sin 2\theta_0 \sqrt{\frac{1}{4\cos^2\alpha \cdot \cos^2\theta_0 \cdot \sin^2\theta_0} - 1} \right) \alpha -$$

angle of aircraft bank,

θ_0 =75°- angle of scanning cone opening.

Antenna Pattern Smoothing

The brightness temperature received by antenna with aperture d is described as

$$\tilde{T}_b^i = \frac{\int_{\theta_A} P(\theta) \cdot T_b^i \cdot d\theta}{\int_{\theta_A} P(\theta) \cdot d\theta} \qquad (5)$$

Where

$$\frac{P(\theta)}{P(0)} = \left(\frac{J_1(x)}{x} \right)^2, \qquad x = \frac{\pi d}{\lambda} \sin\theta$$

J_1 - one-order Bessel function of the first kind,

λ - wavelength.

DISCUSSION

To determine the significance of this techniques for in flight calibration of radiometer, the calculation of angular brightness temperature distribution at frequencies of 22 GHz and 75 GHz are made (see Fig. 5 and Fig. 6).

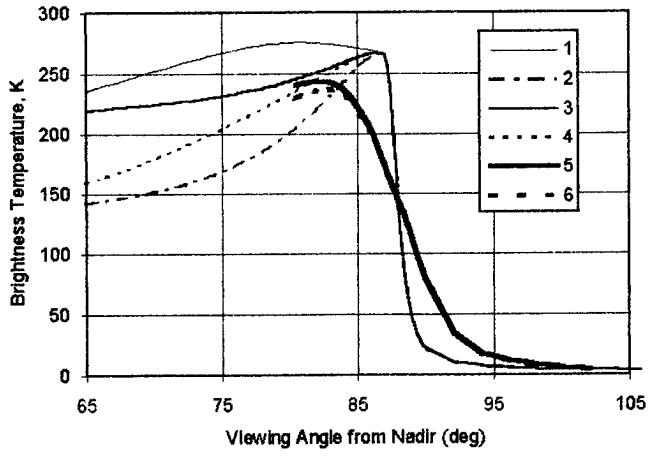


Figure5. Theoretical brightness temperature angular distribution for 22GHz in vertical - 1,3,5 and horizontal - 2,4,6 polarization: 1,2 - T_b ; 3,4 - T_b^i ; 5,6 - $\tilde{T}_b^i$. Calculation for a flat sea surface, d=120 mm, α=25°, other parameters correspond to Fig. 3.

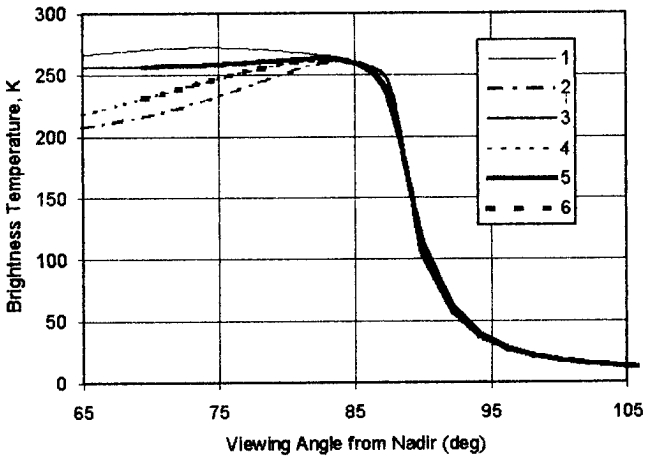


Figure 6. Same as Fig. 5, but for 75GHz.

These figures present the theoretical T_b angular distribution for both polarizations. It is significant that maximum of T_b on vertical polarization, corresponding to Brewster angle (see 1 in Fig.5 and Fig.6), disappears, when "polarization coupling" effect is taken into account (see 3 in Fig.5 and Fig.6). The antenna pattern smoothing results in displacement and decrease of brightness temperature maximum for both vertical and horizontal polarization. This is just the maximum which corresponds to hot scene that can be used for radiometer calibration (Fig. 3). As for cold scene, it is strongly measured at viewing angle more than 10° above horizon.

REFERENCES

[1] I.V.Cherny, A.M.Alesin, N.N.Gorobetz, V.P.Nakonechny, S.Yu.Pantzov, A.I.Zabishny, Advanced Airborne Multi-Spectral mm-Wave Imaging Technique for Ocean and Atmosphere Studies. Proceedings of CO-MEAS'95 Symposium, Atlanta, Georgia, April, 1995.

[2] V.D.Stepanenko, G.G.Schukin, L.P.Bobylev, S.Y.Matrosov, Radiothermosensing in Meteorology, Gidrometeoizdat, Leningrad, 284p., 1987

[3] S.C.McKinley, C.R.Philbrick, Tropospheric Water Wapor Concentration Measured in Penn State/ARL Lidar, Proceedings of CO-MEAS'93 Symposium, Albuquerque, NM, pp.185-188, March, 1993.

[4] H.J.Liebe. MPM - an Atmospheric MM-Wave Propagation model, Intern. Journ. Infrared Millimeter Waves, Vol.10, N4, April, 1989.

[5] P.C.Pandey, R.K.Kakar, An Empirical Microwave Emissivity Model for a Foam Covered Sea, -IEEE J. of Oceanic Engineering, Vol. OE-7, N3, pp.135-140, 1982.

[6] A.J.Gasiewski, D.V.Kunkee, Calibration and Applications of Polarization-Correlating Radiometers, IEEE Transaction on Microwave Theory and Tech., Vol.41,N5, pp.767-772, 1993.

Analysis of MAP Speckle Suppression Algorithms

Valentin V. Zaitsev, Vladimir V. Zaitsev

NPO Mashinostroenia, Gagarina St. 33, Reutov, Moscow Region, 143952, Russia. Tel: (095) 307 91 94. fax: (095) 302 20 01 e-mail: NPO@mashstroy.msk.su

Abstract -- The goal of the paper is to analyze filters based on MAP approach which use for speckle suppression of SAR images. The special attention is paid to such property of MAP estimate as a bias. Effect of bias reduction when number of looks increases is shown. New equations for MAP estimate expected a bias are suggested. The NMMAP filter that is a modification of MAP filter is proposed for point and multiple targets filtering. SIR-C SAR image has been used for the testing of filters.

INTRODUCTION

The MAP algorithm is one of the most perspective, since it more completely takes into account not only SAR images speckle properties but statistics of a signal backscatter from the surface. The main feature of MAP filtration consists in application of adequate describing models presenting SAR data as a pdf (probability density function) set for each particular case (processing intensity or polarimetric images). The most widely known filtering algorithms based on MAP approach were developed in [1-4]. Use of MAP filtration of intensity and polarimetric image processing with consideration of bias is studied in this paper.

In resent years, a combination of filtering and edge detection for SAR image processing are frequently used. Structure Detection Filters (SDF) based on MAP approach and edge detection algorithms are described in [5-7]. The term adaptive for SDF means that it exploits both local statistics and geometrical properties of local areas. The SDF filter procedure is divided into two functional boxes: segmentation box which detects image segments, and filter box. SDF (Refined Gamma MAP and MRGMAP), based on ratio edge detectors is the most universal filters that take in to account geometric position of scatters in the window but this filter complicated in computational respect.

In addition for SDF, the Nagao-Matsuyama MAP Filter (NMMAP) is chosen for its effectiveness in smoothing speckle noise and maintaining the sharpness of point targets. Base application of this NMMAP filter is automatic detection point and multiple targets.

MATHEMATICAL MODEL

1. Intensity image. In this representation, a multiplicative speckle model with an gamma distribution is assumed and can be written as:

$$I(t)=R(t)\, n(t)\,, \qquad (1)$$

where t=(x,y) represents the spatial coordinates of the image, I(t) is the observed image intensity at t=(x,y), R(t) denotes the corresponding terrain reflectivity with E(R) mean and σ_R local standard deviation. Multiplicative speckle noise n(t) is statistically independent of R(t) with unit mean and σ_n local standard deviation. The gamma distribution of backscattering from the surface is used. For these conditions, I(t) has K- distribution.

2.Polarimetric image. For this case each component of the speckled measured scattering matrix is given by [4]:

$$Y_{pq}(t)=S_{pq}\,(t)\; n_{pq}\,(t), \qquad (2)$$

where (pq) - polarization basis (HH,VV,HV), Y_{pq}-complex measured signal , n_{pq} -complex speckle noise. For low look correlation the conditional pdf $P(\Sigma_S/C_S)$ is given by the complex Wishart law [4]. Σ_S is data covariance matrix associated to the Y and C_S is covariance matrix of the denoised vector S.

MAP ESTIMATION PROPERTIES

The estimations which base on the MAP methods are usually rather satisfactory. They have such positive properties , as fortunability and efficiency and, as a rule, are biased, however bias is often eliminated by the simple way [9].

The Gamma-Gamma MAP equation is given by [2]:

$$\hat{R}=\frac{E(I)(\alpha-L-1)+\sqrt{E(I)^2(\alpha-L-1)^2+4\alpha L E(I) I}}{2\alpha} \qquad (3)$$

The mean E(I) and heterogeneity coefficient $\alpha=1/C_R^2$ are determined into the local sliding window of the point I on the intensity's image: $\alpha=(1+C_n^2)/(C_I^2-C_n^2)$, $C_I=\sigma_I/E(I)$, σ_I - local standard deviation, $C_n=1/\sqrt{L}$ (L-number of looks).

Fig.1 shows the MAP estimation versus the input values I normalized by E(R). The estimation (3) is bias due to

$$\lim_{I \to E(I)} \hat{R} \neq E(I)\,.$$

The magnitude of this bias depends on the parameter L and decreases with its growth.

Thus, the equation (3) can be used for the cases of processing the intensity images with the lot of looks. Otherwise, when the large bias of the mean on the processed image is present, and as consequence, the radiometric resolution of the radar image is degradated.

The Non-bias MAP-estimation is given by [10]:

$$\hat{R}^{*}=\frac{E(I)(\alpha-L-1)+\sqrt{E(I)^2(\alpha-L-1)^2+4\alpha L^{*} E(I) I}}{2\alpha} \qquad (4)$$

0-7803-3068-4/96$5.00©1996 IEEE

In the under root expression the parameter $L^*=L+1$ eliminates the bias of the characteristical curves on horizontal axis and the dependence of bias on parameter L, thus the kind and inclination of the curve doesn't vary (Fig. 2). For estimation (3) the next equality:

$$\lim_{I \to E(I)} \hat{R} = E(I),$$

for any L is realized.

Similar expression for MAP estimation with regard to bias for polarimetric images can be written as:

$$\hat{C}_S^* = \frac{(\alpha - L - 1) + \sqrt{(\alpha - L - 1)^2 + 4\alpha L^* \mathrm{Trace}(E(C_S)^{-1}\Sigma_S)}}{2\alpha} \cdot E(C_S),$$

where $E(C_S)$ - is the mean covariance matrix obtained in the adaptive window and α is the heterogeneity parameter [4].

NMMAP FILTER

NMMAP Filter is a modification of the MAP filter that takes into account the geometrical position of the scatters into the filtering window.

In NMMAP filter the local coefficient of variation C_I is compared with the theoretical speckle coefficient of variation C_n. If the value of C_I is smaller than C_n, the average of the pixels within the local window replaces the central pixel value.

In the case when C_I is greater than C_n, the one of nine subwindows (the form of subwindows is similar to filter Nagao-Matsuyama [11]) with the minimum of the standard deviation value and minimum coefficient of variation is determined.

In the case when C_I in selected subwindow is:

a) smaller than C_n, the average of the pixels within the subwindow replaces the central pixel value;

b) between the C_n and $C_{max} = \sqrt{2}C_n$, the replacement central value is determined base of on the MAP estimate.

c) greater than the upper threshold, the central pixel value is preserved .

EXPERIMENT

The SIR-C single look complex (SLC) image of Zhukovskii (Moscow Region, Russia) with corner reflectors of orbit 142.20 was chosen for testing. The pixels of image were presented by the intensity - float format. In Fig.3 the fragments of original and filtered test image in dB scale are shown. In the central part of the images the corner reflectors and hangars are shown. NMMAP filter have been tested, which described above, with the window sizes 11*11 elements. An evaluation of conservation of point and multiple targets using filtered image has been conducted. Measurements of resolution at level -3dB conducted with use corner reflectors have shown a slight degradation of resolution (approximately 0.1 m) with ENL equal to 31. Three-dimensional displays of area with hangars before and after filtering are shown in Fig.4.. The distances between the hangars are comparable to pixel size.

CONCLUSION

MAP approach to the SAR images filtering is one of the most perspective, since they more completely take into account not only the SAR images speckle properties, but the statistics of a signal backscatter from the surface. It is shown, that MAP-estimation is biased and it is necessary to take into account the bias, especially for small number of the looks. The expressions for the non-biased filters are suggested. NMMAP Filter is one of the kind of the MAP filter and more simple for computations than SDF. It may be recommended to detect point and multiple targets.

ACKNOWLEDGMENTS

Authors wish to thank Ellen O'Leary of JPL for providing SIR-C radar data and Andrei Ivanov of NPO Mashinostroenia for useful discussion.

REFERENCES

[1] D.T. Kuan, A.A. Sawchuk, T.C. Strand, P. Chavel "Adaptive Restoration of Images with Speckle", IEEE Trans. on Acous., Speech and Signal Proc., Vol.35, No.3, March 1987, pp. 373-382.

[2] A. Lopes, E. Nezry, R. Touzi, H. Laur "Maximum A Posteriori Speckle Filtering and First Order Texture Models in SAR Images", IGARSS'90, pp. 2409-2412.

[3] A. Lopes, E. Nezry, S. Goze, R. Touzi, G.A. Solaas "Adaptive Processing of Multilook Complex SAR Images", IGARSS'92, pp. 890-892.

[4] A. Lopes, S. Goze, E. Nezry "Polarimetric Speckle Filters for SAR Data", IGARSS'92, pp. 80-82.

[5] E. Nezry, A. Lopes, R. Touzi "Detection of Structural and Textural Features for SAR Images Filtering", IGARSS'91, pp. 2169-2172.

[6] A. Baraldi, F. Parmiggiani "A Modified Version of the SAR Speckle Filter Based on Structure Detection", IGARSS'94, CD-ROM Version, 940052.

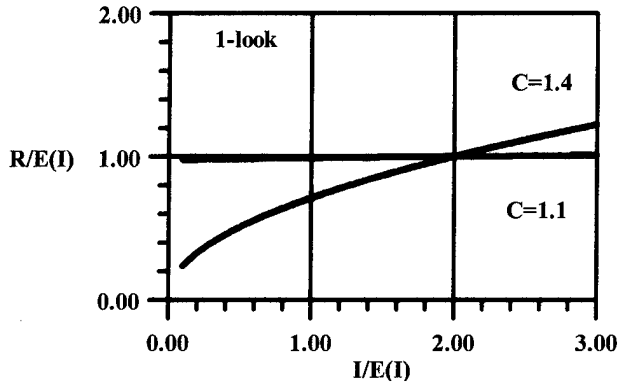
[7] A. Baraldi, F. Parmiggiani "A Refined Gamma MAP SAR Speckle Filter with Improved Geometrical Adaptivity", IEEE Trans., Vol.GE-33, No.5, September 1995, pp.1245-1257.

[8] R. Touzi, Lopes A., Bousquet P. "A Statistical and Geometrical Edge Detector for SAR Images", IEEE Trans., Vol.GE-26, No.6, November 1990, pp.764-773.

[9] K.W. Helstrom "Statistical Theory of Signal Detection", Pergamon Press, 1960, Ch. 7.

[10] V.V. Zaitsev, Vl. V. Zaitsev "Analysis of the Speckle Suppression Algorithms Based on the MAP Approach", Submitted to EUSAR'96.

[11] M.Nagao, T.Matsuyama "Edge preserving smoothing" (in A Structural Analysis of Complex Aerial Photographs), Plenum Press, New York.



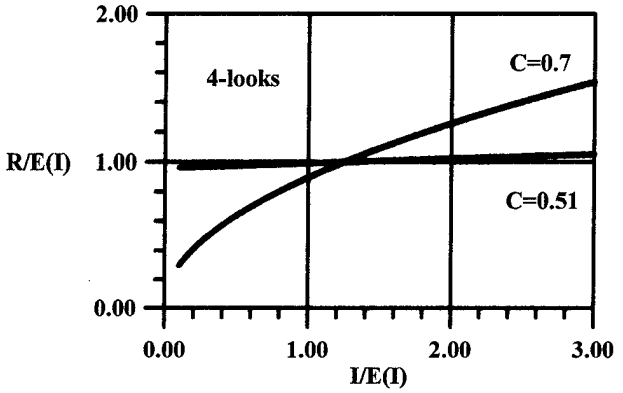
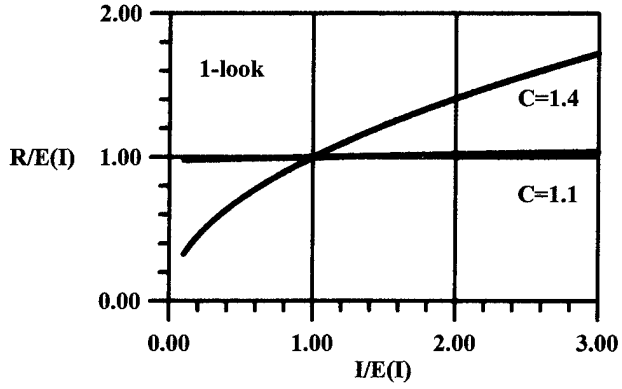


Fig.1 MAP estimation versus the input values



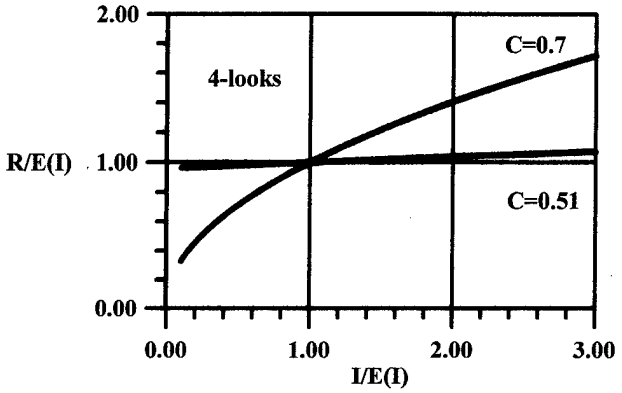


Fig.2 Corrected MAP estimation versus the input values

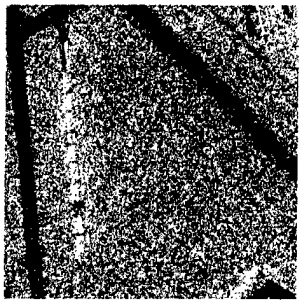


Fig.3a Original image



Fig. 3b Filtered image

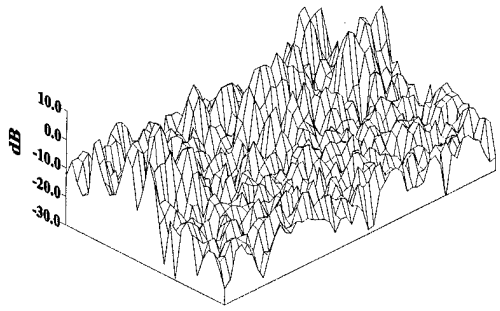


Fig. 4a 3D display of area with hangars in original image

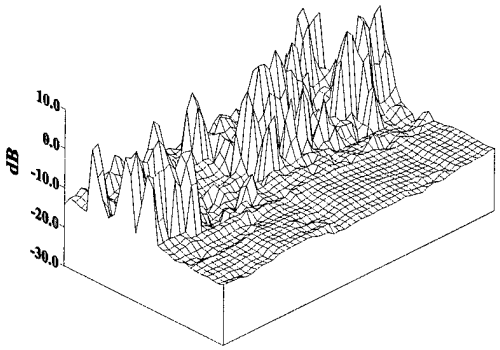


Fig. 4b 3D display of area with hangars in filtered image

Laboratory and In-flight Spectrometer Calibration Technique in Visible and Near Infrared Spectral Ranges

B.I. Belyaev, L.V. Katkovsky, V.P. Nekrasov
Remote Photometry Laboratory, Scientific Research Institute of Applied Physics Problems,
Kurchatova St., 7, Minsk, Republic Belarus, 220064;
Phone: (0172) 780409; Fax: (0172) 780417

The optics remote sensing instruments are used extensively in airspace monitoring of environment and in industry control processes as well. As different researchers and manufacturers attempt to provide a solution to the universal problem of obtaining reliable data, the differences in measured absolute values may arise. Those differences may occur due to the instrument technology, processing procedures, calibration procedures and sources. In-flight absolute calibration is important also because of changes in response of optical sensors with time.

LABORATORY METROLOGICAL COMPLEX

For the laboratory radiometric calibration of various optical sensors in the spectral range of 0.35-2.5 μm the Metrological Complex have been created at our laboratory. The Complex is built up from a number of basic units: monochromatic light source, spectral radiance comparator, reference light source (standardizing lamp), diffuse light source, white light source. The operation of the Complex is based on alternate comparisons of monochromatic, diffuse, and white radiation sources with the sample lamp by using the comparator. On the basis of the ratio of the signals from these sources, spectral radiance is calculated for each source according to the technique of metrological certification, in which measurement of curves of relative spectral distribution of the sources is provided, while the absolute radiance values of the diffused and white light sources are measured then at a single wavelength.

Monochromatic light source is designed for generating parallel flux of radiation in spectral range 0.35-2.5 μm. For this purpose the monochromator is used, that separates monochromatic radiation at the given wavelength. Diffused light source is designed to generate the flux of non-polarized light of continuous spectrum. The device is a photometric integrating sphere (with the diameter 600 mm), the output slit has the diameter 240 mm. The diameter of the photometric sphere is related to the diameter of the output hole by the inequality - $(S_d/S_{sp} \leq 0{,}04)$. The sphere is illuminated from the inside by the set of lamps, with the calibrated field stops. By opening the field stops you can vary the illumination level of the inside surface of the sphere without changing spectral distribution of its radiation. Thus, dynamic range of spectral radiance of continuous spectrum is provided, and it ranges from 0 to 3.62·E-3 Wt/cm^2 μm·sr at the wavelength $\lambda = 0.7$ μm. The white light source includes the lamp, placed in a special holder, that can be moved by the screw system along the axis relatively to the mat glow slate and, thus, according to the law of the square of the distance, we can change the brightness of the mat glow. The white light source allows to obtain the values of brightness of the continuous spectrum much larger than the brightness of the sphere. The standardizing lamp calibrated by spectral radiance is designed for reproduction and transmission of the spectral radiance to the monochromatic, diffuse, and white light sources.

The major sources of errors during absolute radiometric calibration of the spectrometers are: errors, that occur during "transmission" the units of radiance from the standard to standardized means of measurement (no more than 4% in visible and near infrared ranges and 7% at the wavelength $\lambda = 0.35$ μm; errors, caused by the fluctuations of the brightness of the used light source and the fluctuations of the operating electric current value (not more than 1.5%), as well as systematic errors of the radiance of the standardized ribbon filament lamp. So, the resulting mean-square error of the radiance reproduction in visible and NIR ranges does not exceed 6% and in UV range it does not exceed 9%.

THE ALGORITHM FOR THE LABORATORY ABSOLUTE RADIOMETRIC CALIBRATIONS OF THE SPECTRAL DEVICES.

For the energy calibrations we record the calibrated source (sphere) for different brightness and look for dependence in each spectral channel.

$$B_\lambda = f_\lambda(U), \qquad (1)$$

where B_λ - is the brightness corresponding to the given channel, U is the voltage or digital signal of the digitizer for the channel, given by the device. The number of found functions f_λ should equal to the number of the spectral channels.

During the first stage of the procedure of spectral correction the recording of mercury lamp is performed, and

0-7803-3068-4/96$5.00©1996 IEEE

the linking of the numbers of spectral channels with the real wavelengths is done. The numerical values of the functions f_λ in the whole range of U is calculated on the basis of: spectra of the sphere (in U units) registered by the device for the whole range of the brightness for various operational conditions of the spectrometer (exposition times); the curve of the related spectral distribution of the brightness of the sphere; the curve of the absolute values of the brightness of the sphere at the given wavelength (λ_0 = 0.7 μm) depending on the value of the field stops. The found numerical functions are approximated by power series using the least square method.

$$f_\lambda(U) = \sum_{i=1}^{N} k_{i\lambda} P_i(U), \qquad (2)$$

where $P_i(U)$ is the polynomial of degree i from U; $k_{i\lambda}$ - its coefficients. In this particular case we use the polynomials of Chebyshev, defined on the interval (-1;1), and having the following values: P_0=1; P_1= U; $P_n = 2U \cdot P_{n-1} - P_{n-2}$.

The result of the calculation is a set of coefficients in the polynomial of Chebyshev in different degrees from digital counts, brought to the interval (-1;1), as well as the least square errors for each wavelength. In order to recalculate the experimental data to the radiance, it is necessary: to transform the input values U_λ of digital counts to the value from the interval (-1;1); to select the set of the calibrating coefficients, corresponding to the given spectral channel $k_{i\lambda}, i = 0...N$; to calculate the value of radiance for the given spectral channel by using (2).

IN-FLIGHT SPECTROMETER CALIBRATION TECHNIQUE.

The proposed procedure of in-flight calibration of spectrometers with narrow field of view involves the following main steps:

1. Choosing appropriate experimental Earth's surface (with uniform and high enough reflectance's). Carrying out detailed ground based measurements the surface's bidirectional spectral reflectance coefficients.
2. Measuring the spectral radiance of the chosen ground surface by the calibrated spectrometer from the orbit and simultaneously by any similar device from a helicopter or an aircraft.
3. Deriving the analytical formula for upward radiance at the height of the helicopter or the aircraft.
4. Solving the inverse problem for retrieval of the atmospheric parameters, using the ground and the helicopter or the aircraft based measurements.
5. Extrapolating the atmospheric parameters on higher altitudes and using the radiation transfer code for calculation the upward radiance at the top of the atmosphere.

Steps 1 and 2 relate of the field experiments and can be carried out similarly as in [1]. Now we will discuss the steps 3,4, related of the atmospheric correction. There are several methods for determining optical parameters of the atmosphere [2]. If in the region of the field experiment there are two contrasting surfaces present, then we can use the method, which is similar to [2,3].

The spectral brightness of these surfaces, registered from the air, can be put in equations:

$$B_1(\theta_1,\varphi_1) = E_0(\overline{\rho})\pi^{-1}[\ \overline{\rho}T_d(\theta_1) + \rho_1 R_1(\theta_1,\varphi_1) exp(-\tau/\mu_1)\ ] + B_a(\theta_1,\varphi_1), \qquad (3)$$

$$B_2(\theta_2,\varphi_2) = E_0(\overline{\rho})\pi^{-1}[\ \overline{\rho}T_d(\theta_2) + \rho_2 R_2(\theta_2,\varphi_2) exp(-\tau/\mu_2)\ ] + B_a(\theta_2,\varphi_2). \qquad (4)$$

Where $\theta = arccos\,\mu$, φ - the vertical and azimuth angles of view, $E_0(\overline{\rho})$ -- is the irradiance of the surface. $\overline{\rho}$ - is the average of the landscape spectral reflectance coefficient, $T_d(\theta)$ - is the diffuse transmittance function of the atmosphere, ρ_1 and ρ_2 - are the spectral coefficients of the reflection of the two given surfaces. $R(\theta,\varphi)$ is the function, that takes into account the possible anisotropism of the reflection of the surfaces. B_a - is the radiance of the atmospheric haze, τ -total vertical spectral optical thickness between the surface and the airplane. Because the surfaces are located close to each other, from the several kilometers height we can assume that $\theta_1 \cong \theta_2, \varphi_1 \cong \varphi_2$. Then from the (3) and (4) we can obtain (omitting arguments and getting the explicit dependence for λ):

$$\left(B_1^\lambda - B_2^\lambda\right) / \left(\rho_1^\lambda R_1^\lambda - \rho_2^\lambda R_2^\lambda\right) = E_0^\lambda(\overline{\rho}_\lambda)\pi^{-1} exp(-\tau_\lambda/\mu_1) \qquad (5)$$

The every equation of (5) can already be used for determining τ_λ for everyone λ, because all the other values are measured in the experiment: B_i^λ $(i = 1,2)$ - from the airplane, $\rho_i^\lambda, R_i^\lambda, E_0^\lambda$ $(i = 1,2)$ - from the ground experiments. Though we can get more precise results, if we use the following approximation for spectral dependence [3]:

$$\tau_\lambda = \tau_{\lambda_0}^R (\lambda_0/\lambda)^4 + \tau_{\lambda_0}^A (\lambda_0/\lambda)^q, \quad 0 < q \le 2 \qquad (6)$$

where λ_0 - is the fixed given wavelength, $\tau_\lambda^R, \tau_\lambda^A$-spectral optical thickness' for molecular and aerosol scattering, and just $\tau_{\lambda_0}^R, \tau_{\lambda_0}^A, q$ - are considered unknown. The equations (5)

by taking into account (6) (the number of the equations equals to the number of the spectral channels) is used for finding these parameters by using the least square method.

In case if the region of field experiment does not contain the contrast surfaces, the technique can be changed by applying the technique to the uniform background surface. In this case for the radiance, registered from the airplane, using the formulas from [4], we can get

$$B_\lambda(\theta,\varphi) = B_a^\lambda(\theta,\varphi) + \frac{\rho}{1-\rho s} S_0^\lambda \mu_0 T_\lambda(\theta_0) T_\lambda(\theta) \qquad (7)$$

T_λ is a total transmittance; S_0^λ-solar irradiance outside the atmosphere, $\theta_0 = arccos\,\mu_0$ - solar zenith angle, S-spherical albedo of the atmosphere. The following approximations can be used rather accurately [4]:

$$T_\lambda(\theta) \cong \left(1 + b\bar{\tau}_\lambda/\mu_0\right)^{-1} \qquad (8)$$

$$\bar{\tau}_\lambda = 0.50\tau_\lambda^R + 0.16\tau_\lambda^A, \quad b = 0.5(1-g)$$

g - the phase function asymmetry factor. Value of B_a^λ is calculated using the single scattering approximation (which is accurate enough, because the experiments are carried out during sunny weather conditions), but we will not describe it in this article. This expression also includes the phase function parameter g and the parameters of height profile of aerosol. The equations (6)-(8) are used for determining the unknown parameters of the atmosphere $(\tau_{\lambda_0}^A, g, q, \ldots)$ on the basis of the nonlinear regression of the least square method. Note, that $\tau_{\lambda_0}^R$ can be calculated, if we know the ground level barometric pressure. In spectral bands of the gaseous components of the atmosphere the gases' absorption is also included. It is calculated using the standard methods.

Then we extrapolate the parameters up to the top of the atmosphere, using appropriate height profiles of the aerosol and gaseous components, and the radiance is calculated at the orbit height.

We conducted the retrieval of the optical thickness of the atmosphere, using the numerical simulation for the two contrast surfaces (bright circle and dark background) and (5), (6). In order to solve the direct problem of the clear sky atmosphere we used the single scattering approximation and Monte-Carlo method. For the dark surface we took into account the adjacency effect. The whole width of the atmosphere of about 100 km was divided into 30 layers of different width similarly to [3]. The table 1 contains true τ_t and restored τ_{cal} optical thickness for eight wavelengths and two heights h of the surfaces over the see level. Note, that for higher heights of the surfaces the accuracy is better. Thus, the parameters of the atmosphere can be determined with the accuracy 3-4%, and, therefore, the values of radiation for the calibration of spectrometers on the orbit can be determined with the same accuracy.

ACKNOWLEDGMENTS

We wish to thank Vladimir Katkovsky for the translation of the paper.

REFERENCES

[1] P.N. Slater, S.F. Biggar, R.G. Holm, R.D. Jackson, Y. Mao, M.S. Moran, et al, "Reflectance- and radiance-based methods for the in-flight absolute calibration of multispectral sensors", Remote Sens. Environ. , vol. 22, pp. 11-37, 1987.

[2] M.V. Kabanov, D.M. Kabanov, S.M. Sakerin, Aerospace borne methods of optical atmospheric depth and light extinction coefficients determination, Atmospheric Optics, vol. 1, No 1, pp. 107-114, 1988.

[3] L.V. Katkovsky, B.I. Belyaev, V.P. Nekrasov, A.L. Biryukov, "Spectral aureole method of determining parameters of the atmospheric aerosol by using artificial light sources", Atmospheric aerosols, v.1, pp. AT1-5a - AT1-20, 1994. [International aerosol Symposium, March 21-25, 1994, Moscow], Russian Aerosol Society.

[4] P.Y. Deschamps, M. Hermann, D. Tanre, "Definitions of atmospheric radiance and transmittances in remote sensing", Remote Sens. Environ., vol. 13, pp. 89-92, 1983.

Table 1

h, km	λ	0.35 μm	0.41μm	0.47μm	0.53μm	0.59μm	0.65μm	0.69μm	0.75μm
0.1	τ_t	0.381	0.342	0.313	0.289	0.263	0.242	0.229	0.211
	τ_{cal}	0.404	0.353	0.315	0.283	0.259	0.233	0.226	0.211
0.7	τ_t	0.287	0.264	0.247	0.232	0.212	0.196	0.186	0.171
	τ_{cal}	0.310	0.275	0.248	0.225	0.207	0.193	0.183	0.172

Duct detection over the sea by TRANSIT measurements

K.P. Gaikovich
Radiophysical Research Institute,
B.Pecherskaya st., 25, Nizhny Novgorod, Russia, 603600,
Phone: 8312 367294, Fax: 8312 369902,E-mail: gai@nirfi.nnov.su
A.N.Bogaturov, A.S.Gurvich, S.S.Kashkarov
Institute of Atmospheic Physics,
Pyzhevsky per., 3,Moscow, Russia, 109017,
Phone: 095 2316196, Fax: 095 2331652, E-mail: root@iaph.msk.su
S.N.Krivonozhkin, B.M.Shevtcov
Pacific Oceanology Institute,
Radio st., 7, Vladivostok, Russia, 690032,
Phone: 4232 310877, E-mail: poi@stv.iasnet.com
V.K.Ivanov
Institute of Radiophysics and Electronics,
Academician Proskury st.,12 Kharkov, Ukraine, 310085,
Phone: 0572 448515, Fax: 0572 441105, E-mail: ire@ire.kharkov.ua
V.D.Freylikher
Bar-Ilan University,
Ramat-Gan, 52900, Israel,
Phone: 97235318746, Fax: 97235353298, E-mail: frailiv.@alon.cc.biu.ac.il

Abstract--The results of ship-borne measurements (16-th expedition of research vessel "Academician Nesmejanov") of signals from navigation satellites TRANSIT at two frequencies (150 and 400 MHz) are presented. It was discovered that besides the basic modulation related with direct and reflected beams interference there was additional modulation with lesser (2 - 20 times) period. This modulation was evidently related with signal reflection from strong refraction index peculiarities in the atmosphere above the sea. These layers have been observed simultaneously from radiosonde refraction index profiles. The simple four-beam model was found to be in good agreement with measurements data. It appeared possible to estimate the height of reflection layers by measurements parameters.

INTRODUCTION

Ship-borne measurements (16-th expedition of research vessel "Academician Nesmejanov") of power angular dependence of the signal from navigation satellites "Transit" at two frequencies (150 and 400 MHz) and the antenna height level h = 20 m above the sea in various regions of Pacific ocean. The adjusted receiver MAGNA-VOX-702 has been used. The beam width of spiral antenna was 40^{o}. In the measurements regime the frequency band was 200 Hz at both frequencies, and that provided the signal to noise ratio about 40 dB at low elevation angles. The main purpose of measurements was to investigate the possibilities to use the signal parameters for atmosphere remote sensing and for wave propagation prediction.

MEASUREMENTS RESULTS

These measurements showed that in about 20% cases besides the well known (see, for example, [1]) basic modulation related with direct and reflected beams interference there was additional modulation with lesser (2 - 20 times) period. This modulation is superimposed on the basic modulation and it is observed at low elevation angles θ, typically from -1 up to 3 - 5 degrees. The effect have been observed at both frequencies, but it was much more clear at lower frequency 150 MHz. An example of ordinary basic modulation and the case with superimposed additional modulation are shown in the Fig.1,2 respectively.

Such a modulation is obviously related with the signal reflection from atmosphere layers above the sea with the strong refraction index peculiarities. These layers have been observed simultaneously from radiosonde

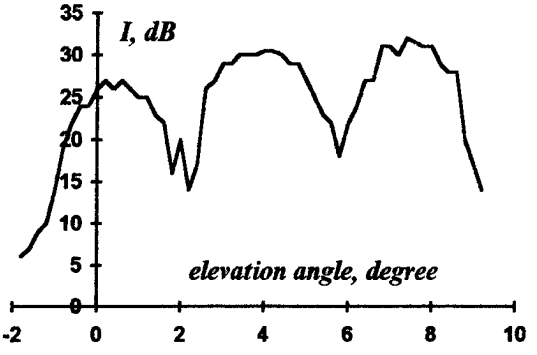


Fig.1. Signal intensity (basic interference) at 150 MHz.

0-7803-3068-4/96$5.00©1996 IEEE

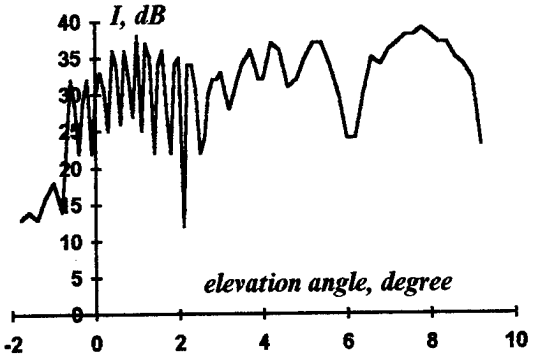


Fig.2. Additional modulation, superimposed on basic modulation.

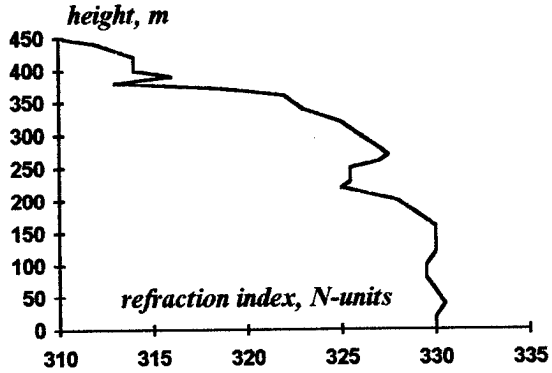


Fig.3. Refraction index height profile measured at the same time as the signal in the Fig.2.

refraction index profiles. The refraction index dependence on height measured at the time of signal measurements shown in Fig.2 is presented in Fig.3.

INTERPRETATION

The simple four-beam model was found to be in good agreement with measurements data. This model takes into account the interference of the direct beam, the beam reflected from sea surface, the beam reflected from the sea and, then, from the atmosphere layer at height level H, and the forth beam reflected from the sea, from atmosphere layer and, for the second time, from the sea. So, only single-reflected from the atmosphere layer beams have been considered. Assuming the reflection coefficient (for field) from sea $R_W = exp(i\pi)$ and that from atmosphere layer $R_a = k\ exp(i\varphi)$ one has the simple expression for angle dependence of the received signal intensity (in the plane Earth surface approach):

$$I = 2[1 - cos(\frac{4\pi h}{\lambda} sin\theta)][1 + k^2 - 2k\ cos(\frac{4\pi H}{\lambda} sin\theta + \varphi)]$$

On the basis of above model it is possible to estimate the reflection height H as antenna height h multiplied by relation of basic and additional modulation periods:

$$H = h\frac{\Delta\theta_{base}}{\Delta\theta_{add}}$$

Applying this formula to the case presented in Fig.2 one obtains H = 200 m, and it easy to see in Fig.3 that the strong inversion of refraction index is located at this height. It is also clear from this that heights of reflection layers are within the interval 50 – 500 m.

It is possible to calculate the signal intensity for spherical-symmetric atmosphere taking also into account standard refraction model. These results (assuming k = 1) are shown in Fig.4. This much more complicated approach gives about the same results as presented above expression for plane case at $\theta > 4^o$. But at lower elevation angles there exist some difference in interference periods and in maxima positions as it is possible to see in Fig.5.

It is clear (see Fig.2), that in reality the reflection coefficient falls drastically with elevation angle. For frequency 400 MHz it falls at lower angles.

Because the additional modulation for ascending satellites differs in about all cases from that for the same descending satellites, it is possible to make the conclusion that the horizontal size of atmosphere reflection layers must be typically some tens kilometers. Also we have observed sharp changes of reflection layers during about one hour time intervals.

In the cases of warm fronts passing above the cold water we have observed very deep additional modulation at simultaneous sharp fading of basic modulation. The most impressive case is shown in Fig.6.

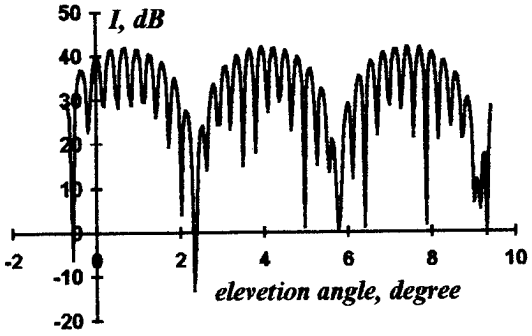


Fig.4. Results of numerical modeling.

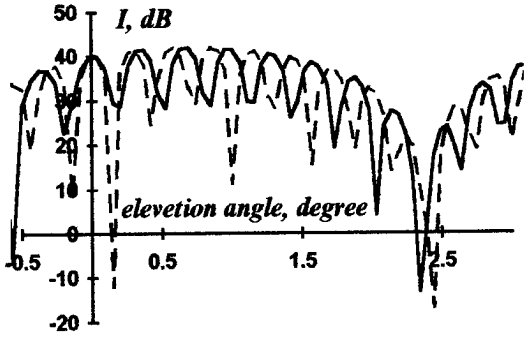


Fig.5. Results of numerical modeling.
solid - spherical geometry; dashed - plane geometry

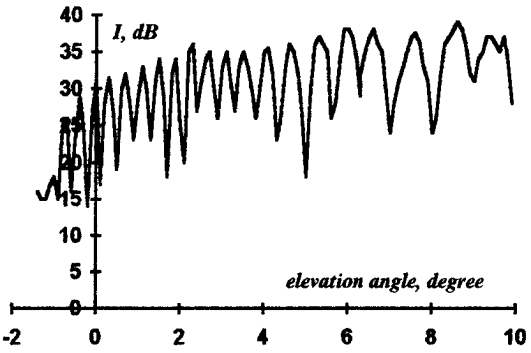


Fig.6. Signal interference during warm front passing

One can see the enhancement of modulation period with elevation angle, which can be explained if to suppose that the height of reflection point from the atmosphere inversion is decreased, i.e. there exist the horizontal inhomogeneity with the scale of some tens kilometers. The fading of basic modulation in this case can be explained taking into account that in the conditions of warm front there exist very strong temperature and humidity overfall nearly the water surface so that the corresponding refraction index inversion leads to full signal reflection not from the water surface but from this inversion at height level nearly the antenna height. In this case the period of basic modulation becomes much larger than in the ordinary case of reflection from water surface.

From the point of view of wave propagation prediction it is very interesting that in the presence of additional modulation it is possible to receive the satellite signals at by 1 - 2° lower elevation angles than in its absence.

CONCLUSION

The results of ship-borne measurements of signals from navigation satellites TRANSIT at two frequencies (150 and 400 MHz) are presented. The main purpose of measurements was to investigate the possibilities to use the signal parameters for atmosphere remote sensing and for wave propagation prediction.

It was discovered that besides the basic modulation related with direct and reflected beams interference there was additional modulation with lesser (2 - 20 times) period. This modulation is explained assuming signal reflection from strong refraction index peculiarities in the atmosphere above the sea. These layers have been observed simultaneously from radiosonde refraction index profiles. The four-beam plane model was found to be in good agreement with measurements data. The method to estimate the height of reflection layers by measurements parameters has been proposed.

REFERENCES

[1] K.D.Anderson. Radio Science, vol.17, No.3, pp.653-663, 1982.

AN INVESTIGATION OF TEXTURAL CHARACTERISTIC FOR GEOLOGICAL PURPOSES

Donitson P P
P3TMGB P.O.Box 1089 CJIA

INTRODUCTION

Spectra features describe the average band to band tonal variance in multiband images whereas textural features describe the spatial distribution of tonal values within a band.

The concept of texture can be investigated through its relationship with tone of the areal changes of boundary of geologic units and topographic features (entrophy and variance) and other parameters (contrast and energy) are useful to discriminate the texture pattern.

Homogenously textured image are not so necessary, but segmentation of areal changes are the important one, and each of which are homogenously textured.

The aim of this study was evaluate statistical parameter and to associate a textural meaning to that parameters in order to perform an image independent feature selection. To reach this objectivity, the statistical analysis will support theoritical consideration based on natural clustering in feature space of segment texture values. Other is to benefit by a better compromise between texture measurement accuracy, computer storage and computation time, a new approximation method of texture image analysis based on spatial distance, range similarity, differences between each element, local average value, probability co-occurence and maximum numbers of pairs. New approximation method of texture image analysis means enhancement of greylevel spatial distribution, contrast, energy, variance and entrophy will be presented.

The statistical analysis supporting theoritical consideration was based on natural clustering in the feature space of segment texture values. The results indicate that statistical parameters can be identified and each set featuring a specific textural meaning. Energy and contrast parameter are considerd become the most efficient for discriminating the differences of textural patterns and for topographic features and boundary of geological units can be observed in the structural features of satellite images in the brightness changes of spectra through variance (standard deviation) and entrophy.

METHOD

Most work in the texture image investigation have been devoted to texture feature analysis within an entire image. Most obvious treatment is to extract the amount of textural information, and if we can assume that the spatial variation of tone as a variation of greylevel , appopriate measure can be done based on variance and entrophy, and discrimination of texture patterns by using contrast and energy. In the statistical method of texture image analysis, we should consider the computational effort in order to neglec the rational independency, texture measurement accuracy, computer storage, computational time and produce a better results of segmentation and can see the heterogeneity /homogeneity area of texture.

To adequate that requirements, the statistical approach is assigned by texture image analysis and statistical parameter based on spatial distance, range similarity, probability co-occurence and maximum number of pairs. The procedures of the approximation method of texture image analysis as follows:

a. calculating the local average
b. substract each element with average value of step a
c. if the result of b≤range similarities (s*average of deviation) , the value of probability co-occurence will add by one (p= p+1), if not no change (p=p)
d. new greylevel value of each element on window operation are equal to multiplication of old greylevel value and square root of ((number of pixel on window operation**2-p**2)/(number of pixel on window operation))/normalization factor

Texture image equation :

$$TI = \sum_i \sum_j X(i,j) * \sqrt{((np^{**}2-p^{**}2)/(win*win))/N}$$

$$Variance=\sum_i \sum_j (sum*sum-sxsq*sxsq) /((win*win)*(win*win-1))$$

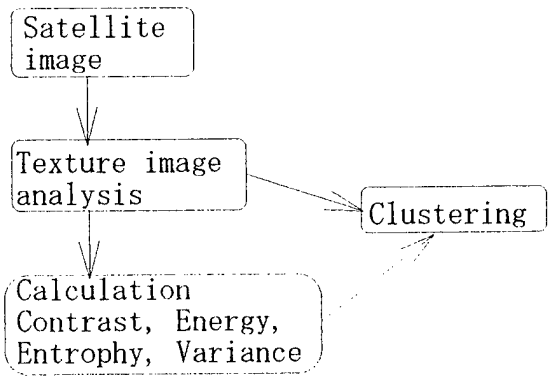
$$Entrophy=(-1)*\sum_i \sum_j (TI(i,j)*sum(TI(i,j)))*\log(\sum_i \sum_j (TI(i,j)* sum(TI)) +0.1)$$

$$Energy=\sum_i \sum_j TI(i,j)*(win*win)/N$$

$$Contrast = (255-\sum_i \sum_j TI(i,j))/(win*win)$$

where :
TI : enhancement of greylevel spatial distribution
sum : local summation on window operation
sxsq : local summation of quadrad of each element
win : size of window operation
N : normalization factor

EXPERIMENT



0-7803-3068-4/96$5.00©1996 IEEE

DISCUSSION

Texture provides the important for image analysis, so textural features can be used to classify images and differences in texture can be used to detect object in an image and one of the problem is segmentation of texture image. By applying the approximation method of texture image analysis ,applied statistical parameter into texture image analysis and do the clustering/isodata process, so we can understand of each set featuring a specific textural meaning. For example, through the theoritical description of energy is to measure textural uniform, contrast is to measure the differences between the highest and the lowest value of a contigunous set of pixel, variance is to measure of heterogeneity/homogeneity and its strongly correlated to first order statistical values (standard deviation) and entrophy is to measure the disorder of an image and the uniformity of texture. We can see the effect of heterogeneity of texture through changes of variation size of cluster. All that information is the important information for geological analysis.

CONCLUSION

Assessment of an investigation of the textural characteristics associated with statistical parameters (variance, entrophy, contrast and energy) was applied into satellite data. This paper has shown a simple investigation of characteristic of image through texture image associated with statistical parameters which will become an important factor for geological analysis. On this study, we found that the necessity of association between characteristic of texture image, and statistical parameters in order to know the heterogeneity/homogeneity and uniformity of texture area, areal changes of boundary of geologic units and topographic features.

REFERENCES

1. A. Rosenfeld and L.S. Davis, " Image segmentation and image models", Proc. of the IEEE, may 1979, pp 764-772
2. R.M. Haralick, "Statistical and structural approaches to texture", Proc. of IEEE, May 1979, pp 768 - 804

Validation of ERS-1/SAR Data to Map the Rio Amazonas Floodplain According to the Cartographic Accuracy Standards

Hermann J. H. Kux
INPE - Instituto Nacional de Pesquisas Espaciais
Caixa Postal 515 - 12.227.010 São José dos Campos, SP, Brazil, Tel. +55-123-256426
{hermann}@ltid.inpe.br

Valério Barbosa da Silva
INCRA - Instituto Nacional de Colonização e Reforma Agrária
Av. André Araújo, 901, 69.060-020 Manaus, AM, Brazil

Abstract - The precise mapping of the border between the *Várzeas* (Floodplain) and the *Terra Firme* (Uplands) along Rio Amazonas, is of fundamental importance for any environmental study of this region. Within this frame, the objective of this study is to analyse if a section of *Várzeas*, close to the city of Santarém (Pará State, Brazil), can be mapped to an accuracy to fit the Cartographic Accuracy Standard (*Padrão de Exatidão Cartográfica - PEC)*. In this study it was verified if the border *Várzea/Terra Firme*, extracted from an ERS-1/SAR scene, texturally analysed, is compatible with PEC. To confirm the results, a TM/LANDSAT scene of this region was analysed separately and registered to the ERS-1/SAR scene. The results indicate that these products present limitations to map the floodplain at the precision required by PEC.

1.0 - INTRODUCTION

In Brazil, the Cartographic Accuracy Standard was established by Federal Government Decree Nr. 89817 on June 20, 1984, establishing the maximum acceptable errors in planimetry and height, as well as the corresponding standard error, according to the map scale. Taking into account that the literature on thematic mapping with remote sensing techniques does not consider the Cartographic Accuracy of the final product, the objective of this paper is to analyse whether a thematic map (*Várzeas*) obtained with ERS-1/SAR and TM-Landsat data, with a detailed field survey, fits the requirements for precision and accuracy of PEC. Due to the lack of plani-altimetric maps that could be used as a reference to extract the border between *Várzea* and *Terra Firme* in the area under study, systematic cartography procedures were applied. Location points of high precision, obtained by GPS and DGPS, were implanted on the extreme points of the area under study.

2.0 - DESCRIPTION OF TEST-SITE

The area under study is localized on the Rio Amazonas Floodplain, at geographical coordinates W 54°30′ - W 54°40′ and S 2°10′ - S 2° 20′. The area of interest is covered by topographic maps SA-21ZB-II (MI-474 and 475) at 1:100,000 scale, elaborated and published by DSG (Mapping Service from the Brazilian Army). This section presents an almost flat relief with several inundation lakes. The border to the *Terra Firme* is made up by a fluvial terrace, with a variable height of 10-20 m.

3.0 - CO-OCCURRENCE MATRICES AND TEXTURAL FEATURES

In the analysis of texture, the gray-level co-occurrence matrix (GLCM) is frequently used to characterize the spatial relationship of the gray level. The GLCM P(i, j, d, θ) denotes the frequency at which two gray levels *i* and *j* occur simultaneously and adjacently, at a given distance d and at a given direction θ. [1] extracted a total of 14 textural characteristics of the co-occurrence matrix. Among these, some characteristics are used extensively to obtain information from digital imagery. Among the textural characteristics defined by [1], 6 were implemented at the software package PCI EASI/PACE Radar Analysis Package, that was used in this study to work with ERS-1/SAR Data: Local Homogeneity, Contrast, Entropy, Average, Standard Deviation, Dissimilarity. A detailed description of these algorithms can be found in [2].

4.0 - MATERIALS AND METHODS

In this study geocoded digital ERS-1/SAR and georeferenced TM-Landsat data (bands 2,3,4 and 7) were used. The ERS-1/SAR data were processed with 6 *looks* to reduce the speckle effects. No specific speckle reduction filter was used, because they would reduce inherent texture of SAR images. On the other hand, according to [3], the smoothing of radar images due to the increase of *looks* is made at the expense of loss of spatial resolution. In this study however the loss of spatial resolution is not an important issue.

5.0 - PROCESSING OF SAR, TM AND FIELD SURVEY DATA

The processing of remote sensing and of field data was made following seven steps, briefly described below: 1. Geocoding of ERS-1/SAR data - The SARPPS (Preliminar Processing System) ERS-1 scene was converted to a geocoded SARGICS (Geocoded Image Correction System) at INPE. The georeferencing of ERS-1 data was made using the EASI-PACE GEOSET software, and the geographical coordinates of points in the field were determined by GPS. 2. ERS-1/SAR and TM-Landsat

0-7803-3068-4/96$5.00©1996 IEEE

registration - Using the GCPWORKS of EASI PACE package, the TM bands 2,4 and 7 were registered to ERS-1/SAR, using 6 control points. During the resampling, the bilinear interpolation was used, because it was the procedure that showed the most natural appearance to the registered image. Due to the low quantity of control points available, a first order polynomial transform was applied. The average quadratic error of registration was ± 0,33 pixel. 3. Textural analysis of ERS-1/SAR data - ERS-1/SAR data were applied to the texture analysis algorithms mentioned above (3.0). None of these algorithms presented satisfactory results. The best result was a contrast enhancement obtained by Standard Deviation features. This scene was used to register the TM-Landsat scene to further extract the borders of interest. Figure 1 shows the SARGICS product without (left) and with (right) the Standard Deviation features. 4. Integration of ERS-1/SAR with TM-Landsat data - The method to transform IHS in RGB space (for references see, [4] and [5]). The color composite TM4(R), TM7(G) and TM2(B) was transformed to IHS space and the component Intensity was replaced by SAR. The scene obtained was converted back to RGB space. Afterwards a visual analysis was made to extract the border *Várzea/Terra Firme.* 5. Maximum likelihood classification - In order to compare results, the TM-Landsat scene was tested separately to verify its' potential for the definition of the area of *Várzeas.* A Maximum Likelihood thematic classification was applied to the composite TM3(R), TM4(G) and TM2(B), and again the border between *Várzea* and *Terra Firme* was extracted. The general precision of the classification was 93%, which is a quite reasonable result for such a complex area like the *Várzea.* 6. Edition of the reference vector - The border between *Várzea* and *Terra Firme,* plotted in the field, was converted into a text file of ARC format, type **.LIN** and afterwards converted in a vectorial layer that can be exhibited on a monitor. This conversion is made by the software GIS LINKS from EASI PACE. 7. Results of visual analysis - After the interpretation of SARGICS/ERS-1 and TM-Landsat scenes together and separately, each class limit was converted to a list of coordinates, in pixels and lines, which were compared to the reference vector by the calculation of the average quadratic error.

6.0 - DISCUSSION AND CONCLUSIONS

1. The quantitative analysis showed that a map at a scale 1:100,000 derived from the hybrid product SARGICS/ERS-1 and TM-Landsat, would have a better result if each one of them is compared separately. The performance of correct classification (78%), in relation to the ground truth points (70), is not sufficient to comply with PEC planimetrically, whose demand is an accuracy of 90%.

2. The map derived from the hybrid product mentioned in 1. above, could be classified as of A type, if the scale is reduced to 1:250,000.

3. The quantitative analysis also showed that the worst performance among the products studied, refers to the one derived from TM-Landsat data when used by itself. This is because the relief, with small ondulations doesn't produce shadows, and without shadows the differentiation among the different environments becomes very difficult. The vegetation cover could be another factor to differentiate among environments, and in fact it became a complicating factor. In several sections there was an "invasion" of vegetation cover from an environment over another one and, in this case, the borders detected by TM-Landsat did not correspond to the effective border among both environments (*Várzea/Terra Firme*).

4. The product SARGICS/ERS-1 analysed separately (raw or processed) didn't allow adequate discrimination of the environments studied, due to several reasons. The small wavelength (5,6 cm) allows only a little penetration into the vegetation canopy, and consequently the details of the *Várzea* morphology could not be perceived. The result of the relative uniformity of the vegetation cover and of the moisture content was a relative homogeneous radar backscatter signal for different areas.

5. The results obtained in this study did not consider the following points: (a) the errors due to georeferencing that, according to theory, are around 3 pixels; (b) the errors due to deformations of relief which was considered as perfectly flat; (c) the assumption that pixels of the features extracted from the image correspond effectively to the points found in the field, which is not the case. Nevertheless, we consider that the pixels interpreted from the features extracted from the images, correspond to the points recorded during the field survey. This approximation is necessary to reconcile this study with the demands of Decree 89.817, considering that pixels obtained with SAR data often do not to agree with ground truth. Being so, while verifying the geometrical quality of the images obtained with SAR data, this approximation cannot be accepted.

REFERENCES

[1] M. Haralick, K. Shanmugam, I. Dinstein "Textural features for image classification", IEEE Trans. on Systems, Man and Cybernetics, SMC-3(6), pp.610-621, Nov. 1973.

[2] Using PCI Software, vol. II, Version 5.2 EASI / PACE, Oct. 1993.

[3] J.P. Ford "Resolution versus speckle relative to geologic interpretability of spaceborne radar images: a survey of user preference", IEEE Trans. on Geoscience and Remote Sensing, GE-20(4), pp.434-444, Oct. 1982.

[4] M.L. Imhoff, C. Vermillion, M.H. Story, A.M. Choudhury, A.M., A. Gafoor, F. Polcyn "Monsoon flood boundary delineation and damage assessment using spaceborne imaging radar and Landsat data"

Photogr. Engin. and Rem. Sensing, 53(4), pp.405-413, Apr. 1987.

[5] R.A. Welch, M. Ehlers "Merging multiresolution SPOT-HRV and Landsat-TM data". Photogr. Engin. and Rem. Sensing, 53(3), pp.301-303, March 1987.

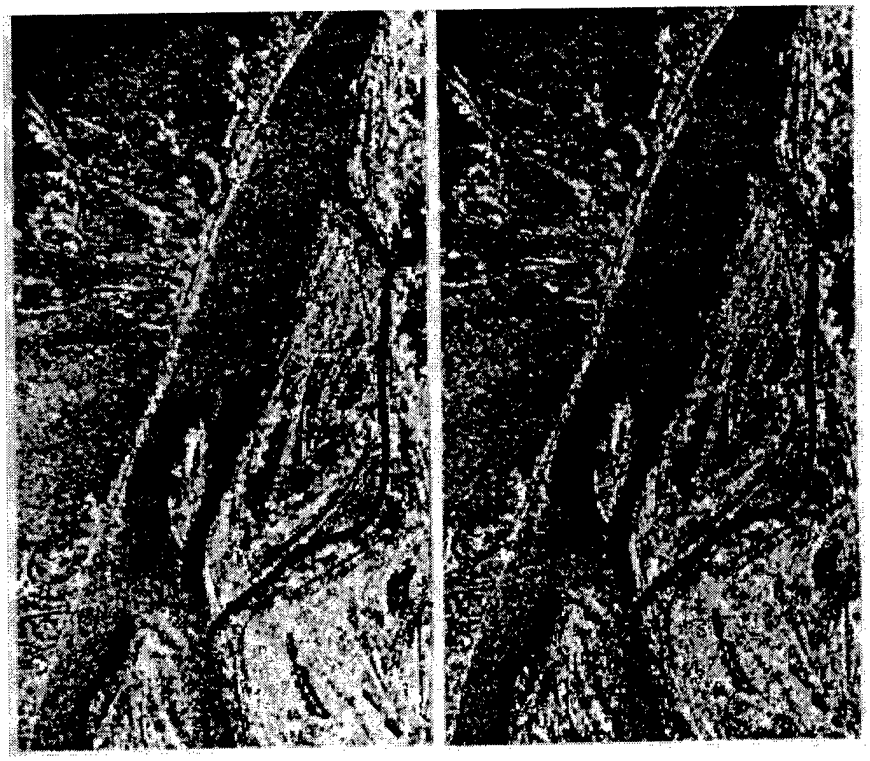


Figure 1 - Comparison between non-processed SARGICS (left) and processed (right) with Standard Deviation feature.

Detail-Preserving Segmentation of Polarimetric SAR Imagery

A. Andreadis, G. Benelli, A. Garzelli
School of Engineering, University of Siena, via Roma, 56, I-53100 Siena, ITALY
Phone: +39-577-263616; Fax: +39-577-263602; E-mail: garzelli@sun1.ing.unisi.it

Abstract -- Polarimetric SAR data help researchers understand and quantify the scattering properties of natural scenes, and their variability under different conditions, better than single polarization SAR data. In this paper, we propose two detail-preserving segmentation algorithms for multiband images and evaluate their performance using real multi-frequency multi-polarization SAR complex data. Adaptive neighborhood structures are selected for modeling the polarimetric complex amplitudes and the region labels, and for achieving detail preservation. Experimental results obtained from multi-band and multi-polarization SIR-C data, selected for archaeological applications studies, show that the novel schemes produce significant visual improvements for detail preservation, and exhibit equivalent or higher classification performance with respect to the classical classification schemes.

INTRODUCTION

Automatic segmentation of polarimetric SAR images is less time-consuming than visual interpretation and can facilitate the inference of geophysical parameters from the surface and the near surface. The information about the scattering properties of real scenarios is essential and it can be uniquely acquired by means of advanced processing techniques working on full polarization data.

When dealing with the unsupervised classification of multi-polarization and multi-frequency images, the main objectives to be reached are the preservation of fine structural details and the smoothing of homogeneous regions, together with an efficient classification at the region boundaries.

A very interesting solution of this problem is given by the unsupervised polarimetric classifier by Rignot, Chellappa and Dubois [1] which provides a maximum *a posteriori* estimate of the region labels, given, for each label, the circular Gaussian model for the conditional distribution of the polarimetric complex measurement vector $X = [HH, HV, VV]$.

This classifier uses contextual information to derive appropriate image models for segmentation purposes, as neighboring surface elements of natural scenes usually have similar polarimetric characteristics that locally define homogeneous regions of similar physical attributes. In that sense, a neighborhood structure N_S and a parameter ß are selected for modeling the polarimetric complex amplitudes and the region labels. These choices produce some undesirable effects:

1. small structural details are lost when data smoothing is obtained; 2. the classification error rate is high at the region boundaries; 3. excessive smoothing and leaking of region labels result when ß is high (ß > 1); 4. a poor Maximum Likelihood estimate is approximately obtained when ß is small (ß < 1).

A higher degree of adaptivity is thus required to solve these problems.

We propose two segmentation schemes, called MICM (Modified Iterative Conditional Modes) and DPICM (Detail-Preserving ICM). The novelty of these schemes resides in the choices of N and ß which allow to define an edge-preserving classifier.

These novel schemes are included into a complete processing system and they are tested on real multi-look multi-polarization SIR-C SAR complex images.

The paper describes the complete system and it is structured as follows.

First, the problem of efficiently filtering the original data is considered as a key point for the correct behavior of the following phase of fuzzy pre-classification. The final classification is then performed by using the two alternative novel approaches. The experimental results, carried out on important archaeological sites, are finally illustrated.

FILTERING

Speckle noise affects the amplitude variance of the signal data which drives many clustering techniques, such as the Fuzzy C-Means (FCM) algorithm used for pre-classification and described in the next Section. Therefore, the reduction of speckle in SAR imagery can significantly improve the global performance of an automatic classification system.

Polarimetric SAR data sets make it possible to reduce the speckle effect by using the correlations among the co-polarized and cross-polarized images.

In [2], an efficient filtering algorithm is proposed, which do not combine HH, HV, and VV images into one image, but produces speckle-reduced HH, HV, and VV images.

Moreover, for multifrequency polarimetric SAR, frequency diversity can be incorporated in addition to polarization diversity by extending the algorithm to n dimensions.

Based on a multiplicative noise model, the algorithm achieves speckle reduction by defining a linear combination of the three polarizations HH, HV and VV, thus providing an

0-7803-3068-4/96$5.00©1996 IEEE

unbiased estimation:

$$\hat{x}_{HH} = (z_{HH} + \alpha_1 z_{HV}/\varepsilon + \alpha_2 z_{VV}/\gamma)(1 + \alpha_1 + \alpha_2)^{-1} \qquad (1)$$
$$\hat{x}_{HV} = \varepsilon \hat{x}_{HH} \qquad \hat{x}_{VV} = \gamma \hat{x}_{HH}$$

where z is the original data, $\hat{x}$ the filtered data,

$$\varepsilon = E[z_{HV}]/E[z_{HH}] \qquad \gamma = E[z_{VV}]/E[z_{HH}] \qquad (2)$$

and α_1, α_2 are chosen such that the mean square error is minimized.

In this way, speckle-reduced HH, HV, and VV images are obtained, which retain the radiometric characteristics of the original signals.

FUZZY PRE-CLASSIFICATION

In this phase, the filtered set of multifrequency, multipolarization images is processed to obtain a preliminary segmentation of the scene.

First a feature vector is defined, whose five components are ten times the logarithm of the parameters composing the polarimetric covariance matrix, i.e. the intensities of the linear polarizations and the amplitude and phase of the complex normalized component HHVV*.

Then the Fuzzy C-Means (FCM) algorithm [3] is applied to the feature vector, choosing $k = 5$ and $m = 2$, where k is the number of classes and m is the parameter which modulates the fuzzy partition function (note that the minimum value $m = 1$ corresponds to a hard partition, that is a binary logic).

Finally, k output images I_1, I_2,..., I_k are obtained, which provide, for each pixel, the fuzzy memberships μ_1, μ_2,..., μ_k to the k classes, respectively. These images are combined into another image F which is the final and only output of the fuzzy pre-classification. The value of a given pixel P of F is the class label i if, for pixel P, is verified $\mu_i \geq \mu_j$ for j=1, 2,..., k.

The pre-segmented image does not provide a very accurate classification, but it represents a good starting point for the iterative polarimetric classifier.

POLARIMETRIC CLASSIFIER

As in the original scheme by Rignot, Chellappa and Dubois [1], we use the Iterative Conditional Modes (ICM) algorithm to obtain a fast and close approximate to the MAP estimate which conversely requires several hundred iterations to converge.

Moreover, contextual information is used to derive appropriate image models for segmentation purposes, as neighboring surface elements of natural scenes usually have similar polarimetric characteristics that locally define homogeneous regions of similar physical attributes. In that sense, a neighborhood structure N_S is selected for modeling the polarimetric complex amplitudes and the region labels.

In [1] N_S is a second order neighborhood window W, i.e. a *3×3 square box*, and ß is a positive value which is kept *constant* for every pixel of the window. The energy function U_2 is defined as:

$$U_2^S(L_S = l/L_r, r \in N_S^0) = -\beta/N \sum_{r \in N_S^0} \delta_k(L_S - L_r) \qquad (3)$$

where δ_k is the Kroneker delta function, N=8, and the other parameters are defined in [1]. The energy term U_2 takes into account the conditional distribution of the region labels. To avoid loss of fine details, high classification error rate at the region boundaries, excessive smoothing and leaking of region labels result when ß > 1, and poor Maximum Likelihood estimate when ß < 1, we propose two segmentation schemes, called MICM (Modified Iterative Conditional Modes) and DPICM (Detail-Preserving ICM). The choices of N and ß are re-defined to achieve edge preservation. In MICM the value of ß is not kept constant over the local window W (*5×5*), but it varies linearly with the maximum number n of pixel in W which have the same label. Therefore, the constant value ß in (3) is substituted by a linear function ß(n).

In DPICM the neighborhood structure N is a *5×1* window whose orientation is determined by the local degree of homogeneity of the original polarimetric data. Let N_i i=1,2,3,4 denote the four windows with different orientations in Fig. 1.

The algorithm uses the modified energy term U_2:

$$U_2 = -\beta/n_m \sum_{r \in N_m^0} \delta_k(L_S - L_r) \qquad (4)$$

where n_m=4 and N_m is the window corresponding to the minimum value

$$m = \min_{i=1,2,3,4} \{var_{N_i}(z_{HH})\}. \qquad (5)$$

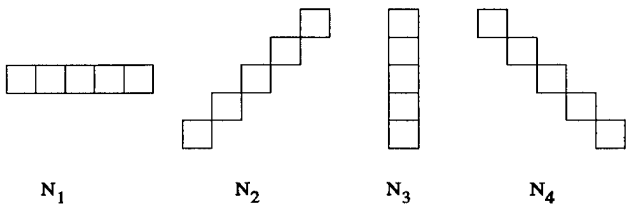


Fig. 1 *Neighborhood structures for the DPICM algorithm*

RESULTS AND COMPARISONS

Experimental results obtained from multi-band and multi-polarization SIR-C data (the test sites have been chosen for archaeological applications studies) show that the two novel schemes produce significant visual improvements for detail preservation, and exhibit equivalent or higher classification performance with respect to the classical scheme. Moreover, both approaches do not need additional topological information based on fuzzy connectivity, as in [4], for preservation of small structures.

Table 1 summarizes some results about the classification accuracy on five classes, detected with unsupervised approach, on polarimetric SAR data of the *Angkor* test site (Cambodia). Data available are SIR-C full complex images acquired during the *Space Shuttle Endeavour* mission in April and October 1994.

Table 1 *Classification accuracy comparisons.*

	class 0	*class 1*	*class 2*	*class 3*	*class 4*	*average*
ML	0.817	0.676	0.555	0.800	0.983	0.766
ICM	0.850	1	0.840	0.910	0.990	0.918
MICM	0,900	0,988	0,840	0,895	0,990	0.923
DPICM	0,972	0,988	1	0,985	0,990	0.987

Fig. 2 illustrates the original L-band HH-polarized amplitude image of the Angkor-Wat site (Cambodia). Fig. 3 shows that both extended regions and linear structures are well preserved by the proposed DPICM algorithm and it confirms the numerical results in Table 1. Also the Maximum Likelihood (ML) solution is reported for comparison.

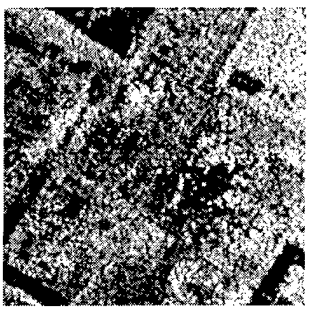


Fig.2 *Original L/HH amplitude image of the Angkor-Wat site (Cambodia)*

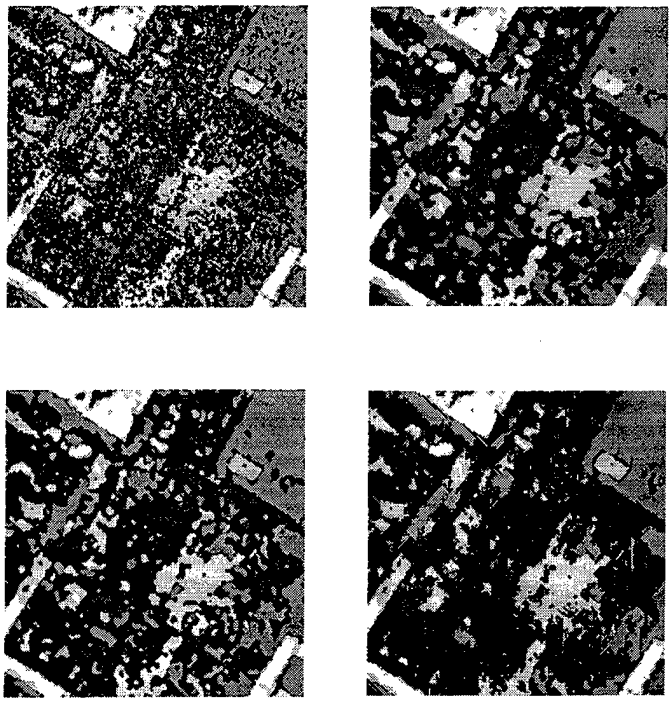


Fig. 3 *Classification maps obtained by ML (top-left), ICM (top-right), MICM (bottom-left), DPICM (bottom-right).*

DPICM outperforms all other techniques because it strongly reduces the problem of over-segmentation without introducing additional loss of details. Regular structures and thin lines are retained by DPICM, thus helping the process of detection of significant classes that, in this case, mainly consist of temples, artificial channels and ancient streets.

References

[1] E. Rignot, R. Chellappa, P. Dubois, "Unsupervised segmentation of polarimetric SAR data using the covariance matrix", IEEE Trans. Geosc., vol.30, pp. 697-705, July 1992.

[2] J.S. Lee, M.R. Grunes, S.A.Mango, "Speckle reduction in multipolarization, multifrequency SAR imagery", IEEE Trans. Geosc., vol. 29, pp. 535-544, July 1991.

[3] J.C. Bezdek, R. Ehrlich, W. Full, "FCM: The fuzzy c-means clustering algorithm", Comp. Geosc., vol. 10, pp. 191-203, 1984.

[4] P.C. Smits, S. Dellepiane, "Processing of SAR data exploiting spatial, polarimetric and topological information", Proc. IEEE IGARSS'95, Firenze, July 10-14 1995, pp.1147-1149.

Detection and Analysis of Ship Waves in ERS-1 SAR Imagery

Chich Y. Peng
Science Systems and Applications, Inc.
Lanham, Maryland 20706-2925
E-mail: peng@neptune.gsfc.nasa.gov

Antony K. Liu
NASA Goddard Space Flight Center, Code 971
Greenbelt, Maryland 20771
E-mail: liu@neptune.gsfc.nasa.gov

Steve Y.-S. Chang
Caelum Research Corporation, Silver Spring, Maryland

Abstract -- From an ERS-1 SAR image over the East China Sea in May 31, 1995, transverse ship waves are detected and analyzed. The original Hough transform is applied to determine the location of the ship its direction of motion and the linear boundary of the V-shaped wake region. Then the one-parameter Hough transform is applied to detect the transverse ship wave pattern in the SAR image. Once detected, the hazy transverse ship wave crests in the SAR image can be best fitted to analytic solutions. From the fitted wave crests, one can estimate the wavelength of the transverse ship wave and hence the speed of the ship.

INTRODUCTION

The wave pattern behind a moving body in water is one of the most consistent phenomena observed in Nature. Whether it is generated by a small duck in a pond or a big aircraft carrier in an ocean, the wave pattern is always confined to a unique V-shaped wake of about 35 degrees. Lord Kelvin [5] has first studied the ship wave pattern by considering an integral solution consisting of the superposition of all the plane waves generated by a ship. The remarkable results derived from his analysis, which are all observable, may be summarized as follows : (1) Significant waves are confined to a V-shaped wake of $35°16'$, (2) at a particular point in the wake exist only two types of waves: diverging and transverse waves with unique propagation direction respectively, and (3) the phase speed of each of these waves relative to the ship is equal to the projection of the speed of the ship along the wavenumber direction. The SAR imagery can be a very useful tool for the observation of such ship wave patterns.. The Kelvin ship wake can be detected automatically from SAR images [3], but observations of the divergent and the transverse Kelvin ship waves have been rarely reported. In this paper, a case study is presented for the detection and analysis of the transverse ship waves from the high-resolution ERS-1 SAR images collected over the East China Sea in May 31, 1995. Based on the Kelvin's model solutions of ship waves, we shall show in the following that the transverse waves can be detected and enhanced in SAR imagery by using the Hough transform techniques.

DETECTION OF TRANSVERSE WAVES

Based on the method of stationary phase, one of the most remarkable conclusions derived from Kelvin's analysis is that at the far field from the ship, only two distinct ship wave components, each with a unique propagation direction, are permissible. In an co-ordinate frame moving with the ship in the positive direction (see Fig.1), the loci of the Kelvin ship wave crest may be expressed parametrically as [4] :

$$x=(A/2)(2\cos\theta - \cos^3\theta) \qquad (1)$$
$$y=(A/2)\sin\theta\cos^2\theta$$

where θ is the angle between the wavenumber vector at location (x, y) and the x-axis . The x-axis is along the ship's motion direction, and the origin is fixed at the ship. A is a parameter , constant for each wave crest. The difference of the values in A between two successive crests may be interpreted as twice the wavelength of the transverse waves at $\theta = 0$. Note that for different values of θ, (1) may represent either divergent waves or transverse waves; for $|\theta| > 35°16'$, it represents the locus of the divergent waves , while for $|\theta|<36°16'$ it represents those of the transverse waves. The locus of a diverging wave crest and a transverse wave crest is plotted in Fig. 1, and the wavenumber vectors at the two extreme locations are also shown.

A SAR image collected over the East China Sea at in May 31, 1995 indicates the presence of a ship wake and a hazy ship wave pattern similar to that of the transverse wave crests. If these features indeed exist, their exact locations and

0-7803-3068-4/96$5.00©1996 IEEE

orientations remian unknown. How can these features be detected automatically ? Can the detected ship waves be quantitatively retrieved from the SAR images and how do they fit to the model solutions in (1)? To give definitive answers to these serious questions, an algorithm based on the application of the Hough transform has been developed. The Hough transform [1], a powerful technique for detecting boundary curves in digital images, basically maps the edge elements in the image into a parameter space. The points on the curves tends to cluster at the relative maxima of the parameter space so that the boundary of the curve can be easily detected. In addition to its advantage of being relatively immune to gaps in the edge elements and to noise, the Hough transform especially fits our purpose of automatic detection and analysis of the transverse ship wave crest shapes, because only one single parameter is involved here so that the Hough transform can be efficiently implemented with an one-dimensional accumulator array .

The procedures for detection and analysis of the ship transverse waves may be summarized as follows:

(1) Apply the two-dimensional wavelet-transform [2] with a Gaussian wavelet to generate an edge map by limiting the wavelet transform results above a threshold.

(2) Apply the Hough transform to detect the boundaries of the ship wake [3] and to determine the location of the ship and its heading.

(3) The co-ordinate of each edge element located in the detected V-shaped wake is transformed into the co-ordinate frame moving with the ship .

(4) With the co-ordinate of each edge element become known, now apply again the Hough transform to detect whether the transverse ship wave crests exits in the wake region. For this purpose, given each location (x, y) of the element in the wake region, solve from (1) for the parameter, A, in terms of (x, y):

$$A=\frac{2x}{\cos\theta(2-\cos^2\theta)} \qquad (2)$$

and

$$\cos\theta=\sqrt{\frac{4(y/x)^2+1+\sqrt{1-8(y/x)^2}}{2(y/x)^2+2}}$$

(5) Accumulate the computed A value into an one-dimensional accumulator array , which is quantized by an increment of one pixel spacing (12.5 m).

(6) When transverse ship waves exist, the accumulator curve will a show a well defined periodicity with period equal to twice the wavelength of the transverse waves. Thus the periodicity of the accumulator curve is used as an indicator of the presence or the absence of the ship transverse waves.

RESULTS

Fig.2a show a subscene of the SAR image centered at (25.911°N, 121.380°E). By visual inspection, we noticed a bright spot with a dark strip and a bright line directly behind it forming a V-shape. More interestingly, hazy curved line features appear to exit, suggesting the presence of the ship transverse waves. The location and orientation of these features still remain unknown. The goal of the this study is to perform automatic detection and quantitative analysis of these features by using computer methods. The results are shown in Fig.2b and Fig.2c respectively. Fig.2c shows the result of the second Hough transform. The horizontal axis represents the parameter, A, in (1), and the vertical axis represents the counts of the edge elements for A particular value of A. We note that the accumulation of the edge elements varies with the parameter, A, periodically with an averaged period of about 212.5m. As noted before, the difference in parameter A between maxima may be considered to be equivalent to twice the wavelength of the transverse wave along the x-axis ($\theta = 0$). Since the wavelength. L, is related to the speed of the ship, U, as $2\pi/L=g/U^2$ at $\theta=0$, we can use this relation and the retrieved wavelength to estimate the speed of the ship. With L = 106.3 m estimated by averaging the highest 9 relative maxima shown in Fig.2b marked by circles, the speed of the ship is estimated to be 25 knots, a reasonable value for perhaps that of a supertanker .

By substituting the relative maximum values of A (those marked by a circle in Fig.2a) into (1) and incrementing θ from -35°16' to 35°16', we can determine the loci of each individual wave crests in the SAR image as shown in Fig.2c. The model curves of the transverse wave crests obtained from the Hough transform agree with the curved line features in the SAR image very well. This again shows that the latter are indeed the signature of the wave crests of the ship transverse waves.

CONCLUSIONS AND SUMMARY

For automatic detection of ship transverse waves in SAR images based on the analytic solutions, there are actually five unknown parameters involved: the x-y coordinate of the ship, the direction of its motion, and the wavelength of the transverse wave. To solve these five parameters simultaneously from the Hough transform, it would requires formidable amount of computer memory and time to implement. Instead, we divide the detection process into two stages. In the first stage, we apply the original Hough

transform to the SAR data to determine the ship's location, its direction of motion and the boundary of V-shaped ship wake region. Then we apply an one-parameter Hough transform to only those pixels confined in the detected ship wake region. The periodicity of the clustering of pixels in the parameter space is then used as an indicator to detect the presence or the absence of transverse ship waves. In the case considered, periodic behavior of the pixel clustering with well defined and equal spacing between the relative maxima are clearly evident , and these results strongly indicate the presence of the transverse ship waves. Once detected, the hazy transverse ship wave crest shapes in the SAR image can be enhanced by fitting the SAR data to the analytic solutions. It would be extremely difficult to obtain such model fit results directly from the SAR image by any other method such as that of non-linear regression. From the spacing of the relative maxima in the parameter space, the wavelength of the ship transverse wave can be estimated and hence the speed of the ship.

ACKNOWLEDGMENTS

This work was supported by the National Aeronautics and Space Administration and the Office of Naval Research.

REFERENCE

[1] D.H.Ballard, "Generalizing the Hough transform to detect arbitrary shapes," Pattern Recognition, Vol. 13, pp. 111-122, 1981.

[2] Liu, A. K., and C. Y. Peng, "Ocean-ice interaction in the marginal ice zone," Proceedings of Second ERS-1 Symposium, 1993.

[3] Liu, A. K., C. Y. Peng, and Y.S.Chang, "Mystery ship detected in SAR image," Trans. American Geophysical Union, vol. 77, pp. 17-18, 1996.

[4] J.N.Newman, "Marine Hydrodynamics," Cambridge: The MIT Press, 1979.

[5] Lord Kelvin, "On ship waves," Proc. Inst. Mech. Eng., vol. 3, 1887.

Fig.2a

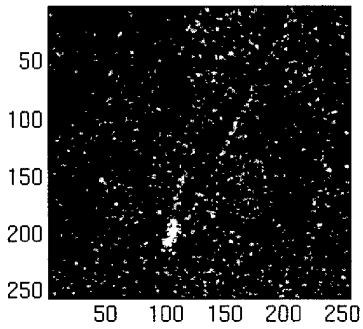


Fig.2b

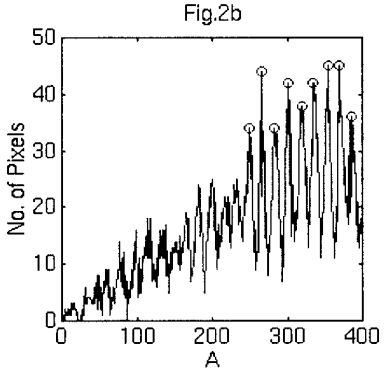
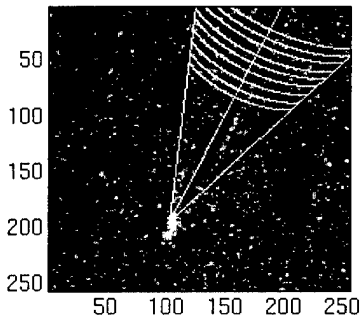


Fig.2c



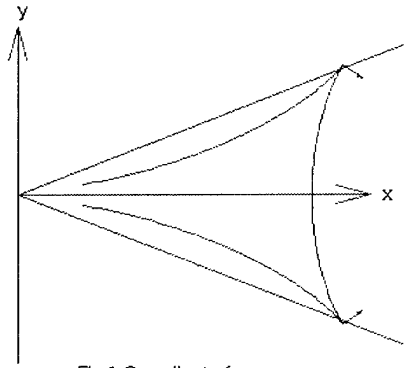


Fig.1 Coordinate frame

ROME: the ROsetta Microwave Experiment for the Investigation of the Cometary Nucleus

Gennaro FEDELE, Giovanni PICARDI and Roberto SEU
INFOCOM Dpt., University of Roma "La Sapienza"
Via Eudossiana, 18 I-00184 Roma, Italy
Tel. +39-6-44585455 - Fax. +39-6-4873300 - e-mail: picar@infocom.ing.uniroma1.it

Abstract -- This paper describes the experiment proposed for the remote sensing of the comet P/Wirtanen. To achieve the experiment objectives a multimode microwave sensor has been designed which accomodates three different modes of operation: radiometer mode, altimetry mode and sounder mode. A discussion of the leading concepts is presented, on which the experiment is based.

INTRODUCTION

The aim of ROME (ROsetta Microwave Experiment) is the remote sensing of the comet nucleus layered surface, basically the first few meters in depth. This task can be achieved by exploiting the capability of microwaves to penetrate to some extent the materials, especially if dry. In this paper we present the multimode microwave sensor designed for the Rosetta mission for the remote sensing of the comet P/Wirtanen. The ROME instrument combines the capability of an active microwave sensor, like a radar altimeter, and a passive microwave instrument, basically a radiometer. Moreover, to locate subsurface discontinuities, also a sounder mode of operation has been designed.

RADIOMETER MODE

Microwave radiometric measurements are capable of providing information about the heat distribution on the surface of comets and they are unique as to give insight also into the subsurface structure of heat flow. For comets and asteroids, it is of utmost importance to get knowledge of thermal distribution and heat flow, because this information is associated to the accretion of comets and differentiation of the solar system. For example, the temperature profile within the comet nucleus allows to understand the history of volatile materials within a comet as well as the composition and structure of the nucleus [3]. The search for the thermal signatures of cometary material, e.g. across the sunlight/shadowed terminator, can be specifically supported by space-borne microwave radiometry delivering a thermal and three-dimensional spatial resolution that can neither be achieved by earth-based observations nor by on-board optical or IR instrumentation. As well known, remote sensing of IR radiation is limited to the very upper layer of surface, then, it is just microwave radiometry that is capable of high penetration depth, being sensitive to thermal radiation emerging from deep subsurface layers at low frequencies. Finally the scientific objectives of the radiometer can be summarized as follows: measure the surface and subsurface brightness temperature, determine the subsurface temperature profile (two layer model) and the associated thermal conductivity and flux, determine the gradient of thermal flux across the terminator deriving the thermal diffusivity and time constant of thermal inertia as well.

The *core temperature* (T_c) and the *temperature profile* across the terminator can be evaluated by means of the following techniques. The temperature T_c will be evaluated well below the skin depth, that is the depth at which a sinusoidal temperature variation with a period equal to the orbital period is reduced by a factor 1/e: in [3] a typical value of the skin depth was evaluated in 6 m. The temperature T_c can be determined from the consideration that in steady state the heat flow q(r) averaged over the orbit is zero at all depths

$$\overline{q(r)} = \frac{1}{U}\int_{U}\int_{4\pi} r^2 K(T)\frac{\partial T(r,\Omega,t)}{\partial r}\,d\Omega\,dt = 0 \qquad (1)$$

where K(T) is the thermal conductivity (function only of temperature T with the assumption of homogeneous nucleus). According to the evaluation reported in [3] and by considering the analytical model suggested in [1] for the K(T), we obtain

- *crystalline ice* $K(T) = \frac{\alpha}{T}$ (α=567 W·m^{-1})

$$T_C = \exp\left(\overline{\ln T_S}\right) \qquad (2)$$

- *amorphous ice* $K(T) = aT + b$
(a=2.34·10^{-3} W·m^{-1}K^{-2}, b=2.8·10^{-2} W·m^{-1}K^{-1})

$$T_c = -\frac{b}{a} + \sqrt{\overline{T_s^2} + \frac{2b}{a}\overline{T_s} + \frac{b^2}{a^2}} \qquad (3)$$

where T_S is the surface temperature and its averages are performed on the spatial and orbital period domains as shown in (1).

To get the temperature profile the one-dimensional solution of the thermal diffusion equation can be considered, neglecting latitudinal effects and assuming an isothermal surface with uniform thermal properties throughout the nucleus. The heat diffusion equation [4] is given by

$$\rho c(T)\frac{\partial T}{\partial t} = \nabla\left[K(T)\cdot\nabla T\right] \qquad (4)$$

This work was partially supported by ASI (Italian Space Agency)

0-7803-3068-4/96$5.00©1996 IEEE

where ρ is the density and c(T) is the specific heat.
By considering a one dimensional model (4) becomes

$$\frac{\partial^2 T}{\partial z^2} = \frac{\rho c(T)}{K}\frac{\partial T}{\partial t} = \gamma \frac{\partial T}{\partial t}. \quad (5)$$

where z is the *depth* spatial coordinate. The solution of (5) based on finite differences, scaling the term $\Delta t = \Delta z^2 \cdot \gamma / 2$, is given by

$$\frac{T_{i+1,j} + T_{i-1,j}}{2} = T_{i,j+1}. \quad (6)$$

In conclusion through the solution by finite differences of the thermal diffusion equation we have a relationship between the temporal (index j) and spatial (index i) temperature variations so that it will be possible to evaluate the temperature profile especially across the terminator where we get the maximum sensitivity.

To accomplish all the above tasks the proposed radiometer makes use of dual frequency capability: X-band has been selected to measure the surface brightness temperature and S-band for the subsurface thermal radiation. In fact, for typical cometary surfaces, microwave emission at X-band is expected to emerge from depths of the order of 500 m (snow), 25 m (ice) and some tens cm (dust), assuming negligible surface and volume scattering. At S-band subsurface microwave emission may effectively be measured as deep as between 2300 m and 5 m, mainly depending on loss tangent and dielectric permittivity.

The radiometric sensitivity provides an accuracy of $\pm$ 0.3 K for the brightness temperature (relative variations) and an absolute accuracy in the order of $\pm$ 1 K. These values are related to results from earth-bound and space-borne observations. For example, the brightness temperature of comet Kohoutek was measured from earth to be 313 $\pm$ 80 K at 8.1 GHz, whereas measurements by S/C Vega 1, 2 and Giotto in the IR and visible range yielded values of brightness temperature for comet Halley larger than 300 °K. So, the dynamic range of cometary brightness temperatures to be expected is estimated to be about 80 K to 400 K. Moreover, the relative accuracy allows the thermal resolution of locally emissive inhomogeneities arranged parallel or perpendicular to the cometary surface.

Finally, it must be noted that the radiometer measures the brightness temperature, but the uncertainity of the physical temperature estimate can be reduced since the ROME radar has the capability to measure the reflection too.

ALTIMETER MODE

The scientific requirements of the altimeter mode are the estimation of first layer composition and elevation profile of the comet nucleus surface; moreover, by on-ground processing surface topographic characteristics like roughness and spatial correlation can be obtained. Note that the multilayered structure of the comet nucleus is supported by theoretical models and experimental measurements [7]. The need to gain information about the surface structure leads to select S-band for the radar sensor. As a matter of fact it has been demonstrated in [6] that the S band represent a good compromise between the achievement of a good penetration depth, needed for sounding purposes, and a negligible volume scattering contribution, which on the contrary could *mask* the surface echo. Moreover the required spatial resolution suggests pulse-limited altimeter and wide bandwidth but, if necessary, the spatial resolution can be enhanced by using synthetic aperture approach via on-ground processing. Finally it must be stressed that the estimate of any parameter of the nucleus surface should be based on the knowledge of a model of the radar received echo, which will be shortly discussed in the following.

When one considers an EM wave illuminating a surface, it is well known that the reflected power depends on the dielectric characteristics of the two media and on the surface roughness σ_h. The radar cross section can be evaluated by calculating the average power of the field scattered by the comet nucleus at distance H

$$\sigma = \left(< E_s E_s^* > / |E_i|^2 \right) 4\pi H^2 = < E_s E_s^* > 4\pi H^4 \quad (7)$$

where it is assumed that the incident field E_i is represented by a spherical wave and that the Kirchoff approximation is valid [5]. The symbol <A> in (7) stands for the average value of A. In the case the radar transmits a Gaussian shaped pulse s(t), whose variance is related to the system bandwidth by $\sigma_t \approx 0.37 / B$, the scattered field can be expressed as:

$$E_s(t) = -j \int_{-\infty}^{\infty} \frac{S(f)}{\lambda} \int_S G(P) R(P) \frac{\hat{n} \cdot \hat{R}_1}{H^2} e^{-2jkR_1} dS e^{j2\pi ft} df, \quad (8)$$

where S(f) is the Fourier spectrum associated to s(t). Solution of (7) leads to [8]:

$$\sigma = \Gamma(0)\pi H^2 P_c + \Gamma(0)\pi H^2 (P_{nc1} - P_{nc2}) = \sigma_c + \sigma_{nc}, \quad (9)$$

which expresses the radar cross section as composed of a coherent plus two noncoherent contributions. Note that in (9) $\Gamma(0)=|R(P)|^2$ is the surface reflectivity which is equal to the square envelope of the Fresnel reflection coefficient.

The coherent contribution in (9) is given by:

$$P_c = \frac{1}{1+F_o} \exp\left[-\frac{F_o}{1+F_o} (4\pi\upsilon)^2 \right] \exp\left[-\frac{(\tau')^2}{2(1+F_o)} \right] \quad (10)$$

where $F_o = 2(\sigma_h / c\sigma_t)^2$ is the normalized surface roughness, $\upsilon = c\sigma_t / \sqrt{2}\lambda$ is the pulse duration normalized to the wavelength and $\tau' = (t - 2H/c)/\sigma_t$ is the normalized time referred to the orbit altitude H. If the surface is very smooth, $F_o << 1$ and, then, from (9) and (10) the maximum value of the coherent contribution ($\tau'=0$) is given by:

$$\sigma_c = \Gamma(0)\pi H^2 \exp\left[-(4\pi\sigma_h / \lambda)^2 \right]. \quad (11)$$

This result agrees with that obtained for a completely flat surface $\sigma_c = \Gamma(0)4\pi(\pi R_{az}^2/\lambda)^2$ since the Fresnel region is given by $R_{az} = \sqrt{\lambda H/2\pi}$ and, then, $\sigma_c = \Gamma(0)\pi H^2$ which coincides with (11) evaluated for $\sigma_h = 0$.

The two noncoherent contributions P_{nc1} and P_{nc2} depend on a surface parameter β [8] given by:

$$\beta = \frac{c\sigma_t}{2Hm^2}\sqrt{1+2F_o}\left(1-\exp\left[-(4\pi\upsilon)^2 F_o\right]\right). \quad (12)$$

where the rms surface slope m is related to the surface correlation lenght l_c by $m = \sqrt{2}\sigma_h / l_c$. With reference to a system bandwidth B=400 Mhz it is possible to show that in all the envisaged conditions, $\beta << 1$ so that P_{nc2} is negligible with respect to P_{nc1} [8] and, then, a satisfactory approximation of the behavior of the noncoherent contribution to the cross section is:

$$P_{nc1} = \frac{\beta}{\sqrt{1+2F_0}}\sqrt{\frac{\pi}{2}}\cdot \mathrm{Erfc}\left[\frac{\tau'}{\sqrt{2}\sqrt{1+2F_0}}\right]. \quad (13)$$

On the other hand, starting from the range resolution $r_x = c/2B$, the ground resolution in a pulse-limited radar altimeter is given by $R_{pl} = \sqrt{2r_x H} = \sqrt{c\sigma_t H/0.37}$ and the max value of (13) becomes:

$$\left(\sigma_{nc}\right)_{max} \approx 0.5\Gamma(0)\pi(R_{pl}/m)^2 = \Gamma(0)\pi H r_x / m^2. \quad (14)$$

Finally, from (11) and (14) we obtain that the coherent-to-noncoherent ratio is a linear function of the height H according to the following relation:

$$\frac{\sigma_c}{\sigma_{nc}} = H\frac{m^2}{r_x}\exp\left[-(4\pi\sigma_h/\lambda)^2\right]. \quad (15)$$

The ratio in (15) is shown in Fig. 1 for an altitude of 1 km. It is worth noting that for altitudes up to 50 km and for relevant values of σ_h/λ the ratio σ_c/σ_{nc} ranges from -15 to 45 dB.

The selection of the pulse repetition frequency (PRF) is dictated by the need to decorrelate consecutive radar echoes. This condition can be achieved if the radar transmit a new pulse after the platform has travelled a distance $d = k(\lambda H/R_{pl})$, where $k \approx 0.3$ [2]. In this way, for a platform velocity v, we obtain:

$$PRF = v/d = (v\sqrt{2r_x H})/(kH\lambda) \approx 4.6(v/\lambda)\sqrt{r_x/H} \quad (16)$$

and, then, the PRF has to be adapted according to the dynamic parameters of the orbit (i.e. v and H). Integration of consecutive pulses allows to enhance the radiometric resolution at constant signal-to-noise ratio (SNR). In fact, for N independent samples, the radiometric resolution is given by:

$$R_r = \left[1+SNR(\sqrt{N}+1)\right]/\left(SNR\sqrt{N}\right) \quad (17)$$

where N can be calculated as $N = R_{pl}/d \approx 6.5 r_x/\lambda$. For the proposed experiment range resolution of some tens of centimeters and radiofrequency in S-band allows to integrate about 20 pulses so that 1 dB of radiometric resolution can be reached with only 6 dB of SNR.

SOUNDER MODE

In the sounding mode the primary tasks are detection and location of subsurface discontinuities and estimation of the first layer composition [9]. Moreover, secondary science objectives can be pursued in sounding mode as, for example, generation of comet nucleus profile and of surface images. The S-band radar system is able to perform these tasks as the wavelength allows a good penetration depth provided that the dielectric constant is not too high. The interfaces between layers can be detected by a pulsed radar provided that its range resolution is lower than the distance between the interfaces.

The strength of the detected echoes is proportional, through the main radar parameters, to the backscattering coefficients of surface and subsurface. In turn the backscattering coefficients can be modeled as the product of the Fresnel reflectivity R(P) by a term that takes into account the geometric contribution to the surface scattering. This last contribution can be evaluated and removed from the received echo so that we are able to estimate the Fresnel reflectivity. For the crust we can write

$$\left|R_{01}(P)\right| = \left|1-\sqrt{\varepsilon_1}\right| / \left|1+\sqrt{\varepsilon_1}\right|, \quad (18)$$

where ε_1 is the crust permittivity which can be estimated by inverting (18):

$$\hat{\varepsilon}_1 = \left(1+\left|R_{01}(P)\right|\right)^2 / \left(1-\left|R_{01}(P)\right|\right)^2. \quad (19)$$

The estimation of the permittivity then allows the identification of the crust.

Similarly, by measuring the strenght of the second echo, it is possible to evaluate the reflectivity of the discontinuity between crust and first layer $|R_{12}(P)|^2$ and, then, to estimate the permittivity ε_2 of the first layer.

Furthermore, by measuring the time delay between the first and the second received echo, it is possible to estimate the depth of the detected subsurface discontinuity, provided that the radar range resolution is good enough.

The sounding could become very critical if the surface roughness scale is greater than the depth of the subsurface discontinuity: in this case a different solution exists based on the analysis of the natural frequencies of the Fresnel reflection coefficient of stratified structures. In fact, it is well known that the reflection coefficient of a two layers structure is a function of the frequency, according to:

$$R(f) = \frac{R_{01} + R_{12}\exp(j2\pi\sqrt{\varepsilon_1}fd/c)}{1+R_{01}R_{12}\exp(j2\pi\sqrt{\varepsilon_1}fd/c)} \quad (20)$$

where d is the depth of the first layer. The frequency displacement Δf between two peaks of the function R(f) is line-

arly related to the discontinuity depth through the relation $d = c/2\Delta f\sqrt{\varepsilon_1}$. Moreover, we can also measure the maximum R_M and the minimum R_m values of $|R(f)|$ with respect to the frequency; then, the solution of the inverse problem allows to estimate the permittivities of the crust (ε_1) and of the first layer (ε_2):

$$\hat{\varepsilon}_2 = (1+R_M)^2/(1-R_M)^2,\ \hat{\varepsilon}_1 = \sqrt{\hat{\varepsilon}_2}(1+R_m)/(1-R_m) \quad (21)$$

For istance, if d=1 m and ε_1=2, the frequency displacement Δf is in the order of 100 MHz, which is well within the bandwidth of the proposed system.

HARDWARE CONSTRAINTS

The design of the ROME instrument has been performed such that a simple and reliable electronics is involved. The main characteristics of the sensor are summarized in the following Table 1.

Table 1

	Active mode	Passive mode
frequency	2.3 GHz	2.3 & 8.4 GHz
T measur. accuracy		1 K
T measur. resolution		0.3 K
spatial resolution	60 m @ 1 km (PL mode)	200 m @ 1 km
bandwidth	400 MHz	100 MHz
dyn. range @ 1 km	-35÷11 dB	
data rate	0.3 kbit/sec	

The hardware has been distributed in 4 boxes with the following figures (see Table 2).

Table 2

PSU	200x100x35 mm	0.8 kg	2.9 w
RAD+TRU+RXU	150x130x40 mm	0.9 kg	3.1 w
APU+DCF+ICU	230x160x48 mm	2.0 kg	6.0 w
FGU+DSG+ UCU+SSPA	230x160x35 mm	1.5 kg	7.5 w
TOTAL		**5.2 kg**	**19.5 w**

The antenna could be a dual frequency array or a stacked array with dedicated dual frequency elements: the mass should be in the order of 2.5 kg, the size 700x700x10 mm.

REFERENCES

[1] J. Klinger, "Some Consequences of a Phase Transition of Water Ice on the Heat Balance of Comet Nuclei", Icarus, 47, pp 320-324, 1981.

[2] E. J. Walsh, "Pulse-to-pulse Correlation in Satellite Radar Altimeters", Radio Science, vol. 17, pp. 786-800, July 1982.

[3] C. P. McKay, S. W. Squyres, and R. T. Reynolds, "Methods for Computing Comet Core Temperature", Icarus, 66, pp. 625-629, 1986.

[4] G. Herman, P. R. Weissman, "Numerical Simulation of Cometary Nuclei", Icarus, 69, pp 314-328, 1987.

[5] F. T. Ulaby, A. K. Fung, and R. K. Moore, Microwave Remote Sensing - Active and Passive, Addison-Wesley: New York, 1988.

[6] CALS: Study and Design of a Comet Approach and Landing System - Comet Microwave Model, ESA Contract No. 7988/88/NL/PB(SC)

[7] D. Prialnik, "Crystallization, Sublimation and Gas Release in Interior of a Porous Comet Nucleus", Astrophysics Journal, 388, pp. 196-202, March 1992.

[8] A. Ciaffone, G. Picardi, and R. Seu, "Application of the PARIS Concept to the GPS Signals", Tech. Rep. n. 1, ESA Contract 142286, 1995.

[9] P. De Marcus, P. T. Melacci, G. Picardi, and R. Seu, "Sounding of Cometary Nucleus via Wideband Radar in the Rosetta Mission", Proc. IGARSS'95, Florence, Italy, 1995.

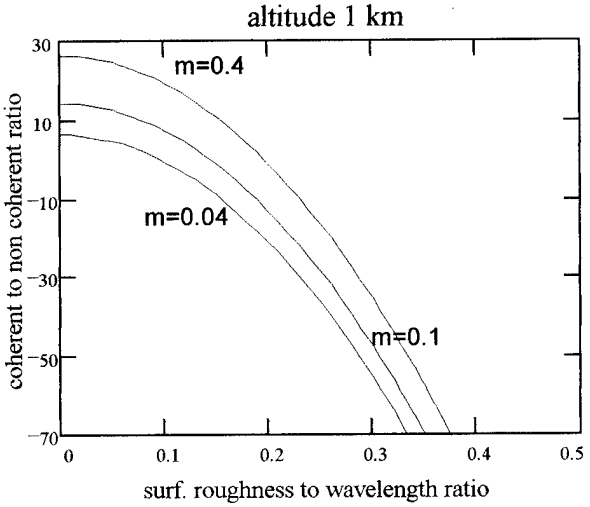


Fig. 1-Coherent to non coherent ratio.

On the Use of the Whitening Filter and Optimal Intensity Summation to Produce Multi-Look SAR images

J. Bruniquel[1,2], A. Lopes[1], J.G. Planès[2], F. Cazaban[2] and M. Deschaux-Beaume[2]

1 : CESBIO (CNES/CNRS/UPS), 18 Av. E. Belin, BPI 2801, 31055 Toulouse Cedex, FRANCE
Phone : (33) 61-55-85-39, Facsimile : (33) 61-55-85-00, E-mail : lopes@cesbio.cnes.fr

2 : ALCATEL ESPACE, 26 Av. J.F. Champollion, BP 1187, 31037 Toulouse Cedex, FRANCE
Phone : (33) 61-19-53-94, Facsimile : (33) 61-19-61-63

ABSTRACT

This paper presents different summations which are used to produce a multi-look intensity image. These summations are more optimal in term of radiometric resolution improvement than the classical incoherent summation. Comparisons and results concerning the radiometric resolution and geometrical quality are presented here.

INTRODUCTION

Because of the speckle noise which is responsible of the granular appearance of Synthetic Aperture Radar (SAR) images, it is necessary to reduce the variance of the signal. One of the various ways to smooth SAR images consists in producing multi-look intensity image. A multi-look intensity image results in the incoherent summation of several looks. The summation is generally done in the spectral image domain but it can be performed in the spatial domain. Hence, the multi-look summation is equivalent to a spatial averaging. Consequently, a spatial degradation occurs by multi-look processing. The speckle noise reduction is proportional to the number of summed samples (i.e. the number of separate looks).

It is possible to use different methods to sum the separate complex looks. Optimal Weighted Intensity Summation (WIS), which has been already presented [1], takes into account the correlation of the separate looks. The Whitening Filter (WF) was initially presented by Novak and Burl [2] for polarimetric data. It has been successfully adapted to multi-channel images [3]. It consists in an optimal complex summation of L channels.

We propose in this paper to use these optimal summations to perform multi-look intensity images. Comparisons with the classical incoherent summation will be presented in terms of compromise between radiometric resolution improvement and spatial degradation.

DESCRIPTION OF THE SUMMATIONS

1 – Intensity Summation (IS)

The classical intensity summation is expressed by

$$z_{is} = \frac{1}{L} \sum_{i=1}^{L} |y_i|^2 \qquad (1)$$

where y is the complex sample of look number i, L is the number of separate looks and i is the look index.

The radiometric improvement involved by the IS depends on the correlation between the looks. If we supposed that the separate looks have the same energy (i.e. the same radiometric level), the Equivalent Number of Look (ENL) is given by

$$ENL = \frac{L}{1 + \frac{2}{L} \sum_{i=1}^{L-1} \sum_{j=i+1}^{L} \rho_{ij}} \qquad (2)$$

where ρ_{ij} is the intensity correlation between look number i and look number j.

2 – Weighted Intensity Summation (WIS)

This summation has been firstly presented by Brooks and Miller [1] for separate looks. It has been adapted and applied to multi-channel data [3][4]. This summation is very similar to the IS except that each channel is weighted by a coefficient. Then we have

$$z_{wis} = \frac{1}{L} \sum_{i=1}^{L} \alpha_i |y_i|^2 \qquad (3)$$

where the weighted coefficients α_i follow the constraint $\sum_{i=1}^{L} \alpha_i = 1$. It has been shown that there are several ways to calculate the α's [3]. In the case of producing a multi-look intensity image, it seems to be optimal to estimate the weighted coefficients by minimizing the variance of the estimator z_{wis}. In that case, they are solution of the following linear system

$$\begin{cases} \sum_{j=1}^{L} \alpha_j = 1 \\ \sum_{j=1}^{L} \alpha_j (\rho_{ij} - \rho_{1j}) = 0 \qquad i = 2,\ldots,L \end{cases} \qquad (4)$$

Hence, the α's depend on look correlation.

0-7803-3068-4/96$5.00©1996 IEEE

Concerning the ENL, we can show that we have

$$ENL = \frac{L}{\sum_{i=1}^{L} \alpha_i^2 + 2 \sum_{\substack{j,k \\ j<k}} \alpha_j \alpha_k \rho_{jk}} \quad (5)$$

3 – Whitening Filter (WF)

Initially presented by Novak and Burl for polarimetric data [2], the WF consists in a transformation of the coordinate system that will make the covariance matrix equal to I (identity matrix). Actually, the Whitening Transformation decorrelates and compensates the radiometric differences of the complex samples [5]. Then, the summation can be optimally performed in term of radiometric resolution. The equation of the WF is given by

$$z_{WF} = {}^t\mathbf{Y}^* \, \mathbf{C}_Y^{-1} \, \mathbf{Y} \quad (6)$$

where $\mathbf{Y} = {}^t[y_1, y_2, \cdots, y_L]$, $\mathbf{C}_Y$ is the covariance matrix expressed by $E[\mathbf{Y}.{}^t\mathbf{Y}^*]$. In that case, the radiometric resolution improvement is optimal and we have

$$ENL = L \quad (7)$$

Moreover, we can prove that the intensity image obtained by the WF is strictly Gamma-distributed, which is not the case, in general, with the IS or WIS.

OBJECTIVES OF THE STUDY

In general, the multi-look processing is done in the azimuthal dimension, i.e. the Doppler spectrum is divided into L parts. There are several ways to extract the separate looks, which can be efficiently weighted before to be summed. This study concerning the choice of the weighting functions has already been done [1][6]. In this paper, we used gate, gaussian and Taylor functions. Examples are given in Fig.1 and Fig.2 in the case of 3 separate looks. In Fig.1, the 3 looks are uncorrelated while in Fig.2, they are strongly correlated.

The various summations previously presented are applied to produce multi-look intensity image. In general, the most largely used summation is the IS. In this paper, we try to estimate if the WIS and the WF summations are able to be better than the IS in term of compromise between the geometrical and the radiometric resolutions.

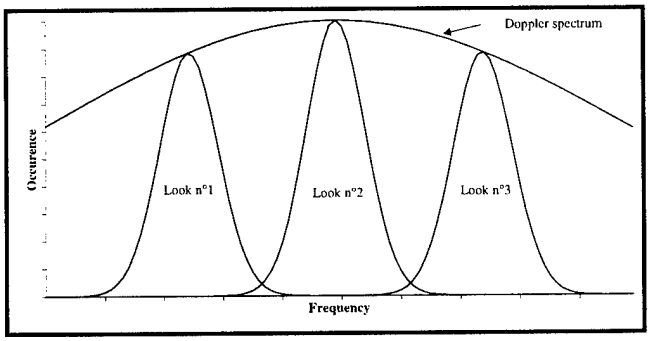


Figure 1 – Uncorrelated separate looks obtained from the Doppler Spectrum

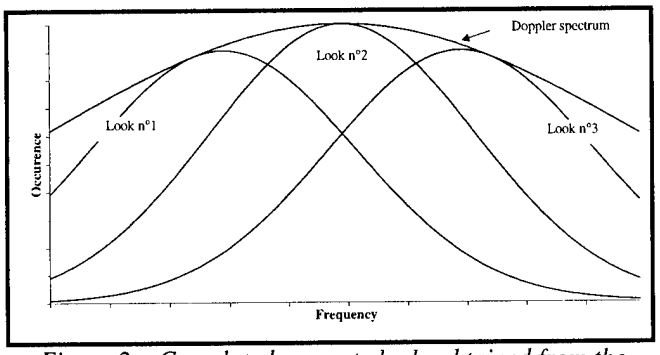


Figure 2 – Correlated separate looks obtained from the Doppler spectrum

RESULTS

The data on which the summations were tested were obtained by the LOCOSAR simulator [7]. LOCOSAR is an end-to-end spaceborne SAR image simulator developed by Alcatel Espace for French DoD (DME/CELAR). It performs the simulation of the SAR raw data and synthetic aperture processing.

1 – Radiometric resolution

The assessment of radiometric resolution is done through the use of the coefficient of variation which is directly related to the ENL

$$C_z^2 = \frac{var(z)}{E^2[z]} = \frac{1}{ENL} \quad (8)$$

The estimation of C_z is done over a 50x50 pixels homogeneous area. The presented results has been obtained with 3 separate looks.

As the correlation between the separate looks grows, the ENL of the IS decreases. The result obtained with the WIS is slightly better than the IS one. Finally, the WF allows us to obtain an optimal ENL, as predicted by theoretical study.

Look correlation	Intensity Summation	Weighted Intensity Summation	Whitening Filter
$\rho_{12} = 0$ $\rho_{13} = 0$ $\rho_{23} = 0$	2.95	2.96	2.97
$\rho_{12} = 0.48$ $\rho_{13} = 0.05$ $\rho_{23} = 0.48$	2.35	2.4	2.95
$\rho_{12} = 0.99$ $\rho_{13} = 0.96$ $\rho_{23} = 0.99$	1.05	1.3	3

Table 1 – ENL obtained by the 3 summations for various look correlation

Weighting functions	Look Correlations	Strong Scatterers		Gaussian clutter
		3 dB beamwidth Width normalised by the initial SLC 3 dB beamwidth	**PSLR (dB)**	Correlation length normalised by the initial SLC correlation length
Gate	$\rho_{12}=0$ $\rho_{13}=0$ $\rho_{23}=0$	**IS** : 2.6 **WIS** : 2.6 **WF** : 2.6	**IS** : -13 **WIS** : -13 **WF** : -13	**IS** : 2.5 **WIS** : 2.5 **WF** : 2.5
Gaussian	$\rho_{12}=0.48$ $\rho_{13}=0.05$ $\rho_{23}=0.48$	**IS** : 2.1 **WIS** : 2.1 **WF** : 3.6	**IS** : -32 **WIS** : -32 **WF** : -27	**IS** : 2.6 **WIS** : 2.6 **WF** : 3.6
Taylor	$\rho_{12}=0.99$ $\rho_{13}=0.96$ $\rho_{23}=0.99$	**IS** : 1.05 **WIS** : 1.05 **WF** : 2.8	**IS** : -27 **WIS** : -32 **WF** : -15	**IS** : 1.0 **WIS** : 1.2 **WF** : 2.6

Table 2 – Estimation of the geometrical degradation involved by the different summations

Hence, the WF permits to sum looks which occupy large spectral band. These large looks are strongly correlated as shown in the last line of Table 1.

2 – Geometrical Quality

The geometrical quality is estimated both on a strong scatterer through 3 dB beamwidth and Peak Side Lobe Ratio (PSLR) and on a gaussian clutter through the autocorrelation coefficient function given by

$$\left|\rho(\Delta x,\Delta d)\right|^2 = \mathrm{ENL}.\left[G_I(\Delta x,\Delta d)-1\right] \qquad (9)$$

where G_I is the intensity autocorrelation function, x and d are respectively the range and azimuth dimensions, Δ represents the spatial variation.

The main results are given in Table 2. It can be seen that the WF is not optimal in term of geometrical quality, since the 3 dB beamwidth grows as the looks correlation increases. The IS and WIS give very similar results.

CONCLUSION

Three different summations have been briefly presented. Two of these are incoherent summations (IS and WIS) while the third one is a coherent summation (WF). These summations are able to sum separate looks to produce intensity multi-look images.

We have shown that the coherent summation (WF) is effectively optimal in term of radiometric resolution enhancement, even if the correlation between the separate looks is very high. That is why we intended to use it to increase the trade-off between the radiometric resolution improvement and the geometrical resolution degradation.

The complete study has shown that the WF degrades the spatial resolution, i.e. it is not able to increase the compromise radiometric/geometrical resolutions.

REFERENCES

[1] S.R. Brooks and P.F. Miller, "The influence of radiometric resolution on synthetic aperture radar design parameters", Proceedings ESA/SEASAT Workshop, ESA SP-154, pp. 79-85, 1979.

[2] L.M. Novak and M.C. Burl, "Optimal Speckle Reduction in Polarimetric SAR imagery", IEEE Trans. On AES, vol. 26, pp. 293-305, 1990.

[3] J. Bruniquel and A. Lopes, "Analysis and enhancement of multi-temporal SAR data", *Proc. of Europto Image Signal Proces. for Rem. Sens. Symp.*, SPIE Vol. 2315, 342-353, Roma Italy, 26-30 Sept. 1994..

[4] J.S. Lee, M.R. Grunes and S.A. Mango, "Speckle Reduction in Multipolarization, Multifrequency SAR imagery", IEEE Trans. On GRS, vol. 29, pp. 535-544, 1991.

[5] K. Fukunaga, "Introduction to statistical pattern recognition", Academic Press Inc. London, 1972.

[6] J.R. Bennett and P.R. McDonnell, "Considerations in the design of optimal multilook processors for image quality", Proceedings of the 3rd SEASAT-SAR Workshop, ESA SPECKLE-172, pp. 5-12, 11-12 December 1980.

[7] F. Cazaban, Y. Le Roy, J.G. Planès and M. Deschaux-Beaume, "SAR Image Simulation with LOCOSAR – Application to Moving Targets and Raw Data Compression Analysis", Proceedings of EUSAR'96, 26-28 March 1996.

Channel Design of The ADEOS-II/GLI (Global Imager)

Takashi Y. Nakajima, Teruyuki Nakajima*, and Masakatsu Nakajima**
NASDA/Earth Observation Research Center
1-9-9, Roppongi, Minato-ku, Tokyo 106, Japan
Tel. +81-3-3224-7089, Fax. +81-3-3224-7052
E-mail nakajima@eorc.nasda.go.jp
* University of Tokyo/CCSR , ** NASDA/EOSD

Abstract -- In order to determine some spectral wavelength specifications of the Global Imager (GLI), the GLI sensor team's Technical Support Group (TCSG) has performed many experimental calculations. An advanced accurate and efficient radiative transfer scheme called GLI Signal Simulator (GSS) was used for these experiments. These calculations were applied to the 3.7 μm band and 6.7 to 7.5 μm band to determine the central wavelength and/or bandwidth of each channel.

The results show that 3.7 μm is better than 3.9 μm to estimate nighttime sea surface temperature and to determine cloud particle size; the combination of 6.7 μm, 7.3 μm and 7.5 μm is the best choice for water vapor profiling.

INTRODUCTION

The National Space Development Agency of Japan (NASDA) is planning to have a new spaceborne multispectral radiometer named Global Imager (GLI). The GLI will be flown aboard the Advanced Earth Observing Satellite II (ADEOS-II) polar orbiter that will be launched by H-II rocket in Feb. 1999. The GLI will be equipped with 36 spectral channels from visible to infrared wavelengths. The spectral wavelength of each channel must be optimized to the mission objectives to obtain desired volume of targets and/or phenomenon The radiation transfer calculation techniques have been gradually developing, predictive simulations calculations of the observed radiance or brightness temperatures have become possible. Thus, it is very important to confirm the possibility of using remotesensing for several targets before launching by using the radiation transfer calculations.

To determine some spectral wavelength specifications of the GLI, the GLI sensor team's Technical Support Group (TCSG) has performed many experimental calculations, using the GLI Signal Simulator (GSS). GSS is based on an accurate and efficient radiative transfer scheme named *"rstar"* [1] [2] with LOWTRAN7's [3] atmospheric models. These calculations were applied to the 3.7 μm band and 6.7 to 7.5 μm band to determine the central wavelength and/or bandwidth of each channel. It must be noticed that scientific requirements, engineering requirements (sometimes they are limitations) and historical requirements (continuation to the previous sensors) must be considered in channel design specifications.

EXPERIMENTAL CALCULATIONS

A. 3.7 μm atmospheric window band issue

Historically, the NOAA/Advanced Very High Resolution Radiometer (AVHRR) and the GOES/VISSR Atmospheric Sounder (VAS) have respectively used 3.75 μm and 3.95 μm channels in the infrared atmospheric window band. To ensure a good Signal to Noise Ratio (SNR), the GLI's 3.7 μm band will have 0.33 μm bandwidth, the same as that of the NASDA's previous ocean color sensor, the ADEOS/Ocean Color and Temperature Scanner (OCTS), which has a 3.715 μm channel and will be launched in the summer of 1996. This atmospheric window band has been utilized to estimate sea surface temperature (SST) during the nighttime [4] and cloud particle size during the daytime [5].

For the former case, the measured radiance at a certain channel should exclude thermal radiation components emitted from atmospheric layers as much as possible. Transmittance at shorter wavelengths is smaller than that at longer wavelengths because of the relatively optically thick water vapor over boundary layer. Figure 1 illustrates the model surface temperature minus simulated brightness temperatures (*Tg-Tbb*) for each model atmosphere and central wavelength of the expected GLI sensor responses with bandwidths of each wavelength set to 0.33 μm. In Fig. 1, wavelengths exceeding 3.8 μm will be unsuitable for the SST estimation with 0.33 μm bandwidth because of the relatively larger *Tg-Tbb*. At the short wavelengths, thermal emission from surface and the optically thick water vapor layer makes measured brightness temperatures large. In contrast, at the long wavelengths, thermal emission from surface is reduced by N2 gaseous absorption located in a relatively higher layer than H2O. Figure 2 illustrates the weighting functions (*WF*) of wavelength from 3.5 μm to 4.1 μm. These weighting functions indicate +10K temperature sensitivities of the measured brightness temperatures. We can find that the upper layer contributions to the brightness temperature are stronger at long wavelengths than at short

0-7803-3068-4/96$5.00©1996 IEEE

wavelengths. This means that radiation in upper layer must be corrected more severely and carefully to estimate SST with long wavelengths. In contrast, at short wavelengths, the magnitude of the weighting functions are smaller and the shapes of the weighting functions are shifted to lower layers. Fig.2 shows that the weighting function around 3.65 μm, at which wavelength the brightness temperature is closest to the corresponding model surface temperatures, is minimum. Almost the same features are obtained by other atmospheric models. This feature makes it easy to estimate SST by using this wavelength.

To utilize of this band for cloud particle size retrieval, the sensitivity of the measured radiance in this band strongly depends on transmittances above the cloud top. Figure 3 illustrates the sensitivity for cloud particle effective radius r_e. We can confirm from Fig. 4 that the maximum values of radaince and the difference between maximum and minimum both occur in 3.6 to 3.7 μm wavelength region. This indicates that this wavelength region is strong sensitive to cloud particles.

C. 6.7 - 7.5 μm water vapor band issue

Two or three wavelengths from the 6.7 to 7.5 μm water vapor band are very common by used to obtain water vapor profile indices. Our main aim is to observe water vapor profiles over as wide a distance area and as low a height as possible. GOES/VAS has used 6.7 μm and 7.3 μm; NIMBUS/Coastal Zone Color Scanner (CZCS), 6.7 μm and 7.5 μm; Sea Wide Field Sensor (SeaWiFS) 6.7 μm and 7.6 μm; and EOS/Moderate Resolution Imaging Spectrometer (MODIS) 6.7 μm and 7.3 μm. Figure 4 illustrates the weighting functions of 6.7 μm, 7.0 μm, 7.3 μm and 7.5 μm obtained by 10% H2O addition for each layer. Since these weighting function should be as evenly spared to obtain water vapor profiles, this combination will be very effective for achieving our purposes. However, restrictions on total satellite weight and electricity supply make it difficult to have four or more channels. Therefore, we have to chose three of the four different channels to obtain the most appropriate combination of channels for our purposes. We find that the peak height gradually decreases with wavelength increasing. In order to determine water vapor profiles over a wide area at low heights, 6.7 μm and 7.5 μm will be chosen. Since the weighting functions of 7.0 μm sometimes are very similar to that of 6.7 μm with another atmospheric models, the 7.3 μm seems the most reasonable choice for the other channel. Therefore, we chose 6.7 μm, 7.3 μm and 7.5 μm for the most appropriate combination.

CONCLUDING REMARKS

It is generally difficult to determine which wavelength is the best choice for the sensors because they have various purposes and sometime the primary purposes are differs. The choice sometimes strongly depends on historical uses and the existence of support channels.

As mentioned in the previous section, the previous sensors have employed 3.7 μm or 3.9 μm wavelengths in this infrared atmospheric window band. We concluded that 3.715 μm is the best choice for the GLI sensor for the reasons below.

(1) The 3.6 to 3.7 μm wavelength region is suitable for estimating SST at nighttime, because of the small differences between model SST and expected measured brightness temperature *Tbb* and because of the small sensitivities of Tbb caused by the change of the atmospheric layer temperatures.

(2) The 3.7 μm wavelength is suitable for estimating cloud particle sizes at daytime, because it has the largest expected measured radiance and sensitivities for the effective radius.

(3) NASDA's ocean color sensor ADEOS/OCTS employs 3.715

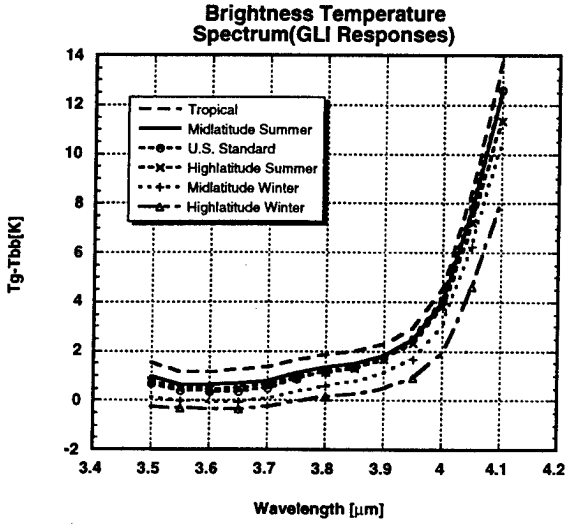


Fig. 1. Brigtness temperature spectrum

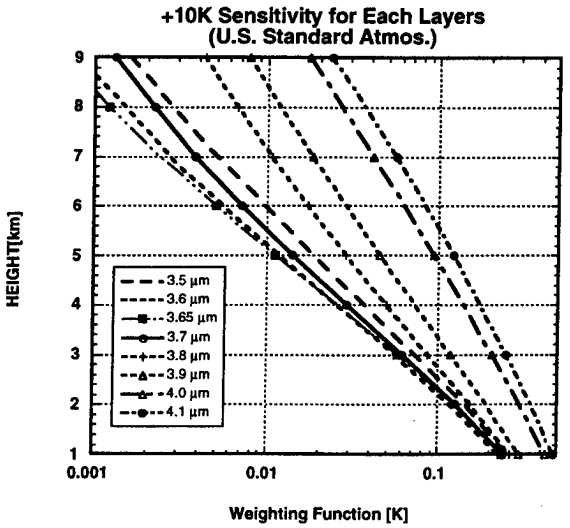


Fig. 2. Weighting function of 3.7μm band

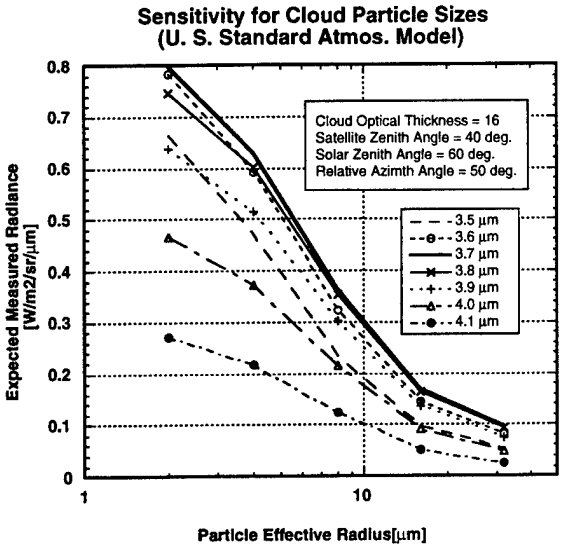


Fig. 3. Sensitiviry for cloud particle sizes

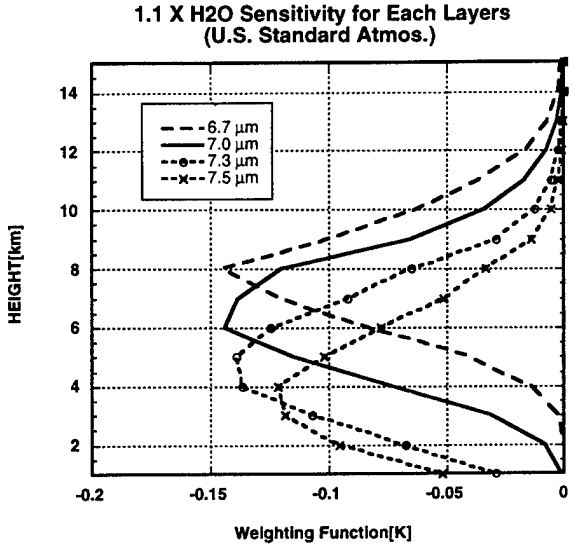


Fig. 2. Weighting function of 6.7 - 7.5 μm water vapor band

μm with a bandwidth of 0.33 μm. The advantage of the 3.6 μm or 3.65 μm wavelength is minimal, and we can't find sufficient reason to choose 3.6 μm or 3.65 μm instead of 3.715 μm.

We chose three of four different channels from the 6.7 μm to 7.5 μm water vapor absorption band to obtain the optimum combination of channels suitable for our purposes. We concluded that the combination of the 6.7 μm, 7.3 μm and 7.5 μm wavelengths is the optimum for our primary purpose for the reasons below.

(1) Main purpose is to observe water vapor profile over as wide as area and as low a height as possible.

(2) The peak height gradually decreases with wavelength increasing. The weighting functions of 7.0 μm sometimes are very similar to that of 6.7 μm for other atmospheric models.

(3) Most previous sensors employed a 6.7 μm channel.

(4) The combination of 6.7 μm, 7.3 μm and 7.5 μm is evenly spared each other.

ACKNOWLEDGMENTS

The authors are grateful to Dr. Steven A. Ackerman of the University of Wisconsin and Dr. Michael D. King of the NASA/ Goddard Space Flight Center for their various suggestions and for providing the HIS data; to Dr. Ryouichi Imasu of the National Institute for Resources and Environment for his helpful calculations. The authors would further like to thank Dr. Bo-Cai Gao of the NASA/Goddard Space Flight Center and Dr. Kohei Arai of the Saga Univeristy for their valuable suggestions and comments for our work.

REFERENCES

[1] T. Nakajima, and M. Tanaka, "Matrix formulation for the transfer of solar radiation in a plane-parallel scattering atmosphere," J. Quant. Spectrosc. Radiat. Transfer, Vol. 35, pp. 13-21, January 1986.

[2] T. Nakajima, and M. Tanaka, "Algorithms for radiative intensity calculations in moderately thick atmospheres using a truncation approximation," J. Quant. Spectrosc. Radiat. Transfer, Vol. 40, pp. 51-69, July 1988.

[3] F. X. Kneizys, E. P. Shettle, L. W. Arbeu, J. H. Chetwynd, G. P. Anderson, W. O. Gallery, J. E. A. Selby, and S. A. Clough, "Users guide to LOWTRAN-7," Air Force Geophysics Laboratory Tech. Rep. AFGL-TR-88-0177, pp. 137, August 1988.

[4] K. Arai, "A method for surface temperature retrieval with ASTER/TIR," Proceedings of the IGARSS'94, MP.CP.01, JPL, 1994.

[5] T. Y. Nakajima and T. Nakajima, "Wide-area determination of cloud microphysical properties from NOAA AVHRR measurements for FIRE and ASTEX regions," J. Atmos. Sci., Vol. 52, pp. 4043-4059, December 1995.

Atmospheric Effects on CO_2 Differential Absorption Lidar Performance

Roger R. Petrin, Doug H. Nelson, John R. Quagliano, Mark J. Schmitt,
Charles R. Quick, Robert K. Sander, Joe J. Tiee, and Michael Whitehead
Los Alamos National Laboratory
MS E543
Los Alamos, NM 87545
Phone: (505) 667-4573 Fax: (505) 665-4267 E-mail: rrp@lanl.gov

Abstract -- CO_2 differential absorption lidar (DIAL) performance can be adversely affected by the ambient atmosphere between the laser transmitter and the target through a number of different processes. This work addresses two sources of atmospheric interference with multi-spectral CO_2 DIAL measurements: effects due to beam propagation through atmospheric turbulence and extinction due to absorption by atmospheric gases. We compare measurements of the effective beam size after propagation to predictions from a beam propagation model that includes turbulence effects such as beam steering and beam spreading. We also compare the experimental measurements of atmospheric extinction to those predicted by both a standard atmospheric transmission model (FASCODE) and a chemometric analysis.

INTRODUCTION

CO_2 differential absorption lidar is an important remote sensing technique and has been used for a variety of applications including chemical effluent detection, geophysical structure identification, and monitoring of meteorological phenomena. Various studies have utilized ground and airborne based systems. Three primary factors contribute to the popularity of CO_2 laser based LIDAR systems: (1) commercial availability, (2) operation in a spectral "atmospheric window", and (3) operation in a "spectral fingerprint" region for many chemicals. The relatively mature laser technology available from commercial CO_2 systems is a major advantage for using CO_2 laser based lidar. A variety of output formats (CW-100kHz, kW average power, 100's kW peak powers) are commercially available, unlike many other laser technologies. A second advantage is the relative transparency of the atmosphere in the CO_2 spectral region allowing long range operation with modest laser energy. This reduces power and size requirements as compared to other laser technologies. The third important factor is the broad tunability (9-11 μm) available in a spectral region where numerous materials exhibit characteristic "fingerprint" spectral signatures. This becomes especially important in applications where identification of numerous components is important.

A number of issues must be considered as part of the design and characterization of a CO_2 LIDAR system for any application. Here we will address issues associated with atmospheric effects that influence both any CO_2 DIAL application and those specific to applications involving multi-spectral DIAL from hard targets. In multi-spectral DIAL, several different wavelengths are used in the measurement rather than just two as in typical DIAL systems. The spectral fingerprint of the material of interest, either the ground in geophysical measurements or the chemicals present in a pollution monitoring system, will be imprinted in the spectral characteristics of the signal return. A large number of wavelengths are necessary for systems required to perform a multiple component chemometric analysis. This need introduces additional system complexity. It is necessary to identify and investigate atmospheric effects that could adversely effect its performance before such a system can be utilized effectively.

MODEL

The CO_2 DIAL model used here is described in detail in [1]. Only a brief overview is given here. The complete model contains the entire DIAL system: transmitter, ambient atmosphere, hard target, and receiver. In the transmitter portion of the model, information about the spatial, spectral, and temporal characteristics of the laser and optical system is used to model the characteristics of the energy output of the system. The receiver portion uses similar information about the detector and receiving optics to predict the signal return strength. A model of the field conditions which includes the effects of atmospheric turbulence, molecular and aerosol absorption and scattering, target spectral response, and speckle on the signal return connect the transmitter and receiver hardware sections of the model. The final output of the model is reported as a signal-to-noise ratio (SNR) for each wavelength used. Detailed descriptions of the sections of the model that predict atmospheric propagation through turbulence can be found in [2,3] while a description of the standard codes (FASCODE and HITRAN) for calculating

This work was supported by the U.S. Department of Energy.
0-7803-3068-4/96$5.00©1996 IEEE

spectral variation in atmospheric transmission can be found in [4-8].

In addition to the standard codes for modeling atmospheric transmission, we have also used a partial least squares chemometric analysis to "fit" the transmission data. This technique is often used to identify and quantify components in a complex mixture. A commercial software package, Grams386/PLSPlus from Galactic Industries, was used. The model was trained with spectra for carbon dioxide, ozone, and water vapor generated using FASCODE. In our analysis, the important result is the spectral residual not the concentrations of the atmospheric constituents. The ability to correct for atmospheric transmission using a partial least squares type chemometric analysis would be extremely useful in situations where background transmission spectra cannot be collected for reference purposes.

RESULTS AND DISCUSSION

A detailed description of the DIAL system used for these measurements can be found in [9]. The measurements were conducted over a 4 week period and performed over terrain consisting of both desert scrub and dry lake bed. The atmospheric temperature varied from 32-40 C and the relative humidity from 3-15%.

Atmospheric Turbulence Effects

The relative increase in beam diameter with turbulence for two initial beam divergences are shown in Fig. 1. As predicted by the model, smaller initial beam divergences are affected much more by atmospheric turbulence than larger initial beam divergences. While the larger divergence beam shows little variation in relative size with turbulence, the smaller initial divergence beam shows a >50% increase at higher levels of turbulence.

Concentrating on the results with the smallest initial beam divergence used, 0.190 mrad, we can examine how well the measurements correspond to model predictions. The best comparison between the model and experiment results when using the Gaussian beam limit for calculating the transverse coherence length. This is not surprising considering the geometry of our system and the general Gaussian shape of our beam. We have calculated the Rayleigh range for our system to be approximately 1.5 km. At 3.39 km to the target, we are at a range of approximately twice the Rayleigh range. This is an intermediate range where neither the plane-wave or spherical-wave approximations are accurate. From the model results, it is apparent that at longer ranges or higher turbulence levels, the results of the Gaussian and spherical wave forms for the transverse coherence length converge, while at shorter ranges or lower turbulence levels, the Gaussian and plane wave forms converge.

An important caveat to these results, however, is the uncertainty in C_n^2 measurements. There are large uncertainties

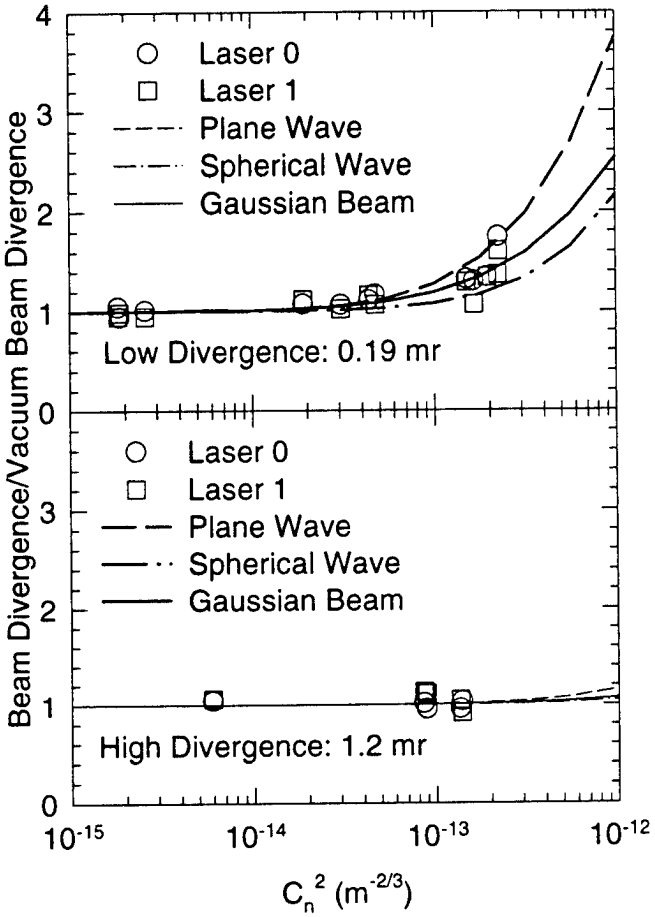


Figure 1. Comparison of propagation measurements and model predictions for different divergences - 3.39 km.

associated with any measurement of C_n^2. Both point probe and optical scintillometer measurements have limitations. The point probes were located near the trailer. They accurately measure C_n^2 (+/- 25%) but give only localized measurements. Any spatial variations of C_n^2 along the beam are not monitored. Even though the Lockheed scintillometer does perform a spatially averaged measurement of the optical turbulence, it only samples a portion of the beam path. When the uncertainty in these measurements and the similarity in the results of the three different methods of calculating the transverse coherence length are considered, it is not possible to specify which method of calculating the transverse coherence length is most accurate.

Atmospheric Transmission

Fig. 2 shows results of one of our measurements of the relative absorption coefficient vs. wavelength to those predicted by FASCODE using HITRAN and by the chemometric analysis. The data has been normalized such that the results are relative to the absorption coefficient of the 10P28 line and do not represent absolute values of the

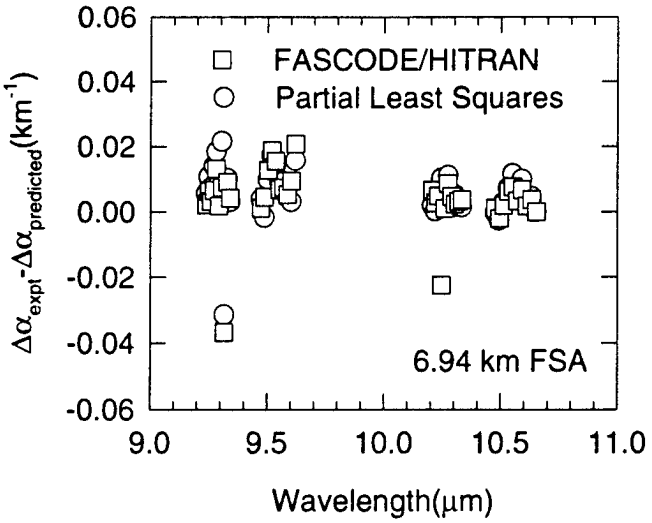


Figure 2. Comparison of FASCODE and chemometric fitting to measured relative atmospheric absorption coefficients.

absorption coefficient. Good agreement is found in the 9-11 μm region with generally less than a 0.02 km^{-1} difference between the predicted and measured values (slightly larger errors, up to 0.04 km^{-1}, appear in some measurements).

Ignoring the 10R20 and the 9R12 lines (lines with strong water vapor absorption and known discrepancies with the HITRAN database [10]) the standard deviation of the difference between measured and predicted values across the spectrum for the FASCODE model is 5.0 x 10^{-3} km^{-1} while for the chemometric analysis it is 5.8 x 10^{-3} km^{-1}. The spectral residual for the chemometric analysis is as small as the that from the FASCODE run. This implies that the three constituents used in the analysis, carbon dioxide, ozone and water vapor, provide adequate information to determine the atmospheric transmission. Additionally, this result indicates that it may be possible to use these three constituents as additional factors in a full chemometric analysis of spectral data with additional information from a target imprinted on it to correct for the atmospheric transmission without using a prior background scan. The spectral residual is a measure of the sensitivity of a multi-wavelength DIAL system. If a separate background scan cannot be obtained, only those variations in absorption coefficient larger than the spectral residual can be attributed to effects other than atmospheric absorption

CONCLUSIONS

We have shown reasonable agreement between our CO_2 DIAL model and our experimental results. The model accurately simulates measurements of beam size after propagating through high levels of atmospheric turbulence. For an initially small beam divergence, the data closely matches the model prediction. Our atmospheric transmission results also agree with the model. The relative absorption coefficients for atmospheric transmission are simulated quite accurately (to better than 0.01 km^{-1}) over a broad spectral range. The results of the chemometric analysis indicate that this method performs as well as the full FASCODE modeling and may lead to a method for correcting for atmospheric transmission without requiring a prior background scan.

ACKNOWLEDGMENTS

The authors would like to acknowledge technical assistance from William M. Porch, John J. Jolin and Charles Fite.

REFERENCES

[1] M. Schmitt, B. Cooke, and G. Busch, "A comprehensive system model for CO_2 DIAL, overview," Los Alamos National Laboratory Unclassified Report 95-2988, 1995.

[2] R.R. Beland, "Propagation through atmospheric turbulence," *The Infrared Electro-optical Systems Handbook*, Vol. 2, SPIE, Bellingham, WA., pp. 157-232, 1993.

[3] R.L. Fante, "Electromagnetic beam propagation in a turbulent media," Proc. IEEE, Vol. 63., pp. 1669-1692, December 1975.

[4] M.E. Thomas and D.D. Duncan, "Atmospheric Transmission," *The Infrared Electro-optical Systems Handbook*, Vol. 2, SPIE, Bellingham, WA., pp. 1-156, 1993.

[5] V.N. Aref'Yev, "Molecular absorption in the 8-13 μm atmospheric window," Izv. Atmos. and Ocean. Phys., Vol. 27, pp. 863-897, 1991.

[6] L.S. Rothman et al, "The HITRAN database: 1986 edition," Appl. Opt., Vol. 26, pp. 4058-4097, 1987.

[7] W.L. Ridgway, R.A. Moose, and A.C. Cogley, "Atmospheric transmittance/radiance computer code FASCOD2," Rep. AFGL-TR-82-0392, U.S. Air Force Geophysics Laboratory, Hanscom Air Force Base, Mass. 1982.

[8] S.A. Clough, F.X. Kneizys, E.P. Shettle, and G.P. Anderson, "Atmospheric radiance and transmittance: FASCOD2," *Proceedings of the Sixth Conference on Atmospheric Radiation*, p. 141, American Meteorological Society, Boston, MA. 1986.

[9] R.R. Petrin, D.H. Nelson, M.J. Schmitt, C.R. Quick, J.J. Tiee, M. Whitehead, "Atmospheric effects on CO_2 differential absortion lidar sensitivity," SPIE Vol. 2702, in press.

[10] W.B. Grant, "Water vapor absorption coefficients in the 8-13-μm spectral region: a critical review," Appl. Opt., Vol. 29, pp. 451-462, February 1990.

Improved Feature Classification by Means of a Polarimetric IR Imaging Sensor

Firooz Sadjadi
Loral Defense Systems-Eagan
3333 Pilot Knob Road
Eagan, Minnesota 55121

Cornell Chun
Physics Innovations
Inver Grove Heights, MN 55076

ABSTRACT

Automatic detection and recognition of targets by means of passive IR sensors suffer from limitations due to lack of sufficient contrast between the targets and their background , and among the facets of a target.

In this paper the results of a suite of polarization-sensitive automatic target detection and recognition algorithms on sets of simulated and real polarimetric IR imagery are presented. A custom designed Polarimetric IR (PIR) imaging sensor is used for collecting real polarimetric target data under a variety of conditions. Then a set of novel algorithms are designed and tested that uses the target and background Stokes parameters for detection, segmentation and classification of targets.

The empirical performance results in terms of the probabilities of detection, false alarm rate, segmentation accuracy, and recognition probabilities as functions of number of pixels on target, aspect and depression angles and several background conditions (clutter densities) of applying this ATR algorithms on the polarimetric data and its comparison with a typical IR only ATR are demonstrated that shows that a noticeable improvement can be achieved.

1. INTRODUCTION

Automatic detection and recognition of targets by means of passive IR sensors suffer from limitations due to lack of sufficient contrast between the targets and their background , and among the facets of a target.

In this paper the results of a suite of polarization-sensitive automatic target detection and recognition algorithms on sets of simulated and real polarimetric IR imagery are presented. A custom designed Polarimetric IR (PIR) imaging sensor [1] is used for collecting real polarimetric target data under a variety of conditions. Then a set of novel algorithms are designed and tested that uses the target andbackground Stokes parameters [2] for detection, segmentation and classification of targets.

0-7803-3068-4/96$5.00©1996 IEEE

Use of polarization in image understanding in the visible band has been attempted. However, in the infrared region of the electromagnetic, to our best knowledge has not been systematically explored.

2. SENSOR DESCRIPTION AND DATA BASES

Polarimetric IR Sensor-The polarimetric IR (PIR) sensor is comprised of four linearly polarized arrays (see the Figure 1) positioned between the infrared detectors and the sensors outside lens.

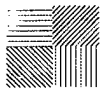


Figure 1. The Four Linear Polarizers Used In The Sensor

Consequently, for every four contiguous pixel set the following functions are computed.

$$\Phi=1/2.\ \mathrm{Arctan}[U/Q] \quad (1)$$

$$P=\sqrt{[Q^2+U^2]}/I \quad (2)$$

Where I, U and Q(the Stokes parameters) are related to the outputs of the four polarizers i_x ; x being the degree of the polarizer's orientation:

$$I=1/2.(i_0+i_{45}+i_{90}+i_{135}) \quad (3)$$

$$Q=i_0-i_{90} \quad (4)$$

$$U=i_{45}-i_{135} \quad (5)$$

Thus three frames corresponding to are input to the target processor I the IR intensity, P the Percent of Polarization, and Φ the Angle of the Polarization. These frames can be represented in a 24 bit RGB or HSI format for simultaneous display.

Data Bases- Two sets of data-bases were used in this project. The main data-base was a set of synthetic imagery of a Russian built Scud Missile and its launcher at

several aspect angles and varying degrees of signal-to-noise ratios (SNR) and background clutter. These images were generated by using a Ray Tracing algorithm and with due considerations for preserving the fidelity of the generated imagery with the polarimetric IR sensor that it is developing.

Towards the end of the study a second data-base consisting of the real polarization-diverse IR imagery of a cube were become available.

The following show a sample of the real data collected by the PIR sensor.



IR P Φ

Figure 2. Image of a real Cube obtained by the PIR sensor

3. TECHNICAL APPROACH

The digitized signal containing three frames of data corresponding to Percent of Polarization, Angle of Polarization and regular IR is inputted to a Target Detection Module. The combined IR and the polarization signatures of the scene is used in this module to segment the scene and extract the regions of interest. This Module extracts both edges and the regions of the targets by using a multi-polarization texture-based technique. The segmentation accuracy of the regions obtained by this module is shown to be twice as good as the regular IR on the data that we used. Similarly, based on the Receiver Characteristic Curves (ROC) for the detected edges obtained for the multi-polarization data and the IR only data it has been shown that the polarization-sensitive regime detects much more correct edges and generates less false edges than the IR only regime does [1].

3.1. Polarization-Sensitive Statistical Segmentation and Labeling Algorithm- The input to this module consists of the input 3-frame imagery, the estimated size of the targets and the first and the second order statistics of the objects of the interest.

The first and the second order statistics of the regions of the original imagery falling under a moving window of the size specified by the estimated size of the objects of interest are computed. Next a measure of the statistical similarity between the extracted statistics and the inputted statistics are made . Fisher Criterion that was used is defined as:

$$F=[n_1(I_1-I_2)^2/(Ivar_1+Ivar_2)+n_2(P_1-P_2)^2 /(Pvar_1+Pvar_2)+n_3(\Phi_1-\Phi_2)^2/(\Phi var_1+\Phi var_2)] \quad (6)$$

Where n_1, n_2, and n_3 are the weighs that can be adjusted to account for the varying degrees of importance for the I, P, and Φ. X refers to the mean value of X and Xvar refers to the the variance of X

The regions that have statistical similarity to the objects statistics will generate low F values. Thus this will produce not only segmentation of the scene but also a classification of them into classes of interest.

3.2. Object Recognition Algorithm- The out put of the Detection Module is fed to the Recognition Module that matches the edge map and the segmented regions with the stored polarization-sensitive models of the objects of interest in a model-based recognition scheme.

The recognition is performed in two ways. In one approach that was described previously an statistical similarity measure (Fisher Criterion) is used to match the extracted target's with a library of stored prototypes. In another approach an image correlator is used to correlate the stored models with the edge map and the segmented target regions. A correlation surface is obtained and then the correlation distances between the best matches corresponding to different object models are compared to decide on the best label for the unknown objects.

4. PERFORMANCE EVALUATION

An experimental design methodology was used to assess the performance of the polarization-sensitive ATR algorithms using the PIR outputs over the algorithms using IR only imagery. The data used in the experiment consisted of the simulated images of a Russian built scud missile described in the Section 2. The following Figure 3 shows a sample of the imagery :



Figure 3. Sample of the PIR Imagery used in the Performance Evaluation

The evaluation was done for each module of the ATR: detection, segementation, and recognition. For each module the performances of the polarimetric IR and regular IR based ATR were obtained. Thus the performance of the textured-based detector, statistical segementor and labelor, and target recognizer were obtained.

4.1. Performance Evaluation of the Polarization-Sensitive Statistical Segmentation and Labeling Algorithm- The performance measure that was used for the this module was Segmentation Accuracy (SA). SA is defined as the ratio of the area of the overlap between the ground truth target (G) area and the actual segmented output (T), and the union of the G and T:

$$SA = \frac{T \cap G}{T \cup G} \qquad (7)$$

The maximum value for SA is 1 and the minimum is zero.

The evaluation results[1] show that over large ranges of elevation and aspect angles, the use of polaimetric data improves segmentation accuracy significantly over the use of intensity data (FLIR). Since in passive ATR segmentation has been a major issue [1], this improvement is indeed significant in passive automatic target recognition. The plots show that there is a dramatic improvement in segmentation accuracy, as much as 55%, when using polarimetric data near the elevation angle of 30 degrees and aspect angle of 30 degrees (Figure 6(b)). For the overhead view, the improvement is as large as 20% (Figure 6(f)). However, for the front and back, and broadside view, there is no improvement over the IR only data

The segmentation accuracy curves for aspect angle of x degrees are similar to those corresponding to the curves corresponding to the aspect angle of 180-x degrees. The improvement using polarimetric data, at aspect angle of 30^{O}, diminishes as the aspect angle is increased. When the aspect angle reaches 50^{O} the improvement reduces to zero.

Thus for aspect angles between 30 and 50 degrees and 130-150 degrees , polarization data contributes a significant improvement over the intensity only data when the elevation angle is increased from 30^{O} to 90^{O} (overhead view).

4.2. Performance Evaluation of Polarization-Sensitive Recognition Algorithm- In the model-based recognition scheme, the sensory derived object was matched against a set of stored target models, and the maximum matching distance was tabulated.

The sensory derived objects corresponded to views of the missile on a mobile launcherseen from an elevation angle of 30 degrees and aspect angles of 0,30, 90, 130, and 180 degrees. The resulting confusion matrix is shown in Table 1.

Table 1 shows that, because of the low contrast in target -to-background intensity, the I -only, or IR sensor data, can not classify correctly among most of the target aspect angles. However, with a combination of percent of polarization P and angle of polarization Φ, all aspect angles were correctly identified exept for 90 degrees (broadside view). This demonstrates that a combination of intensity and polarization data can provide a higher performance than the intensity data alone can provide

Table 1 Confusion Matrix: Matching Results

ϕ only P only I only (FLIR)	Model at 0° Aspect	Model at 30° Aspect	Model at 90° Aspect	Model at 130° Aspect	Model at 180° Aspect
Sensor at 0° Aspect	0.667° 0.836° 0.915	0.488 0.627 0.754	0.204 0.542 0.817	0.546 0.630 0.799	0.511 0.785 0.954°
Sensor at 30° Aspect	0.570 0.788° 0.913	0.642° 0.653 0.741	0.215 0.542 0.815	0.522 0.629 0.792	0.497 0.776 0.954°
Sensor at 90° Aspect	0.559° 0.782° 0.919	0.499 0.623 0.750	0.216 0.583 0.841	0.550 0.616 0.797	0.460 0.774 0.954°
Sensor at 130° Aspect	0.568 0.786° 0.916	0.510 0.619 0.742	0.232 0.544 0.818	0.675° 0.638 0.807	0.477 0.774 0.953°
Sensor at 180° Aspect	0.585° 0.794 0.917	0.499 0.620 0.742	0.207 0.541 0.815	0.547 0.627 0.790	0.524 0.823° 0.964°

5. CONCLUSION AND SUMMARY

In this study we designed and developed and evaluated a suite of novel polarization-sensitive IR target detection, segmentation and recognition algorithms.

These algorithms: Polarization-Diverse Statistical Segmentor and Target Labeler, and Polarization-Diverse Target Recognizer, were tested on sets of synthetic imagery. A set of performance metrics for the evaluation of these algorithms is also defined and are used for evaluating the individual and the end-to-end performance of the algorithm suite. The performance of these algorithms on synthetic imagery has shown that by exploiting the polarization information a significant improvement over the regular IR imagery can be achieved. Evaluating the performance of these algorithms on real PIR data is currently underway.

6. REFERENCES

[1] F. Sadjadi, C. Chun,"Improved Automatic Target Recognition using a Polarimetric IR Imaging Sensor " *Proceedings of Workshop on IR and MMW Radar Polarimetry*, Redstonne Arsenal, AL, Dec. 1995

[2] W. Shurcliff, *Polarized Light*, Harvard University Press, Cambridge, Massachusetts, 1960.

A Comparison of Scintillation Crosswind Methods

Lionel Poggio, Markus Furger, Werner K. Graber

Paul Scherrer Institute
5232 Villigen PSI, Switzerland
tel: +41563104204, fax: +41563102199,
email: Lionel.Poggio@psi.ch

INTRODUCTION

We all are familiar with the shimmering of distant objects on a hot day or the twinkling of stars. These visual effects, known as scintillation, are caused by the drift of refractive-index irregularities in the atmosphere. Scintillation disturbs astronomical observations and optical communication systems. Analysis of scintillation phenomena also provide a method for remotely sensing the atmosphere, since this effect is related to turbulence and wind.

Optical remote sensing is an appealing method to measure wind in complex terrain. A scintillometer was built at our institute, with the aim to measure wind across an Alpine valley. In a first step, we tested this instrument over a flat ground and compared its performance with conventional anemometers.

Different methods of evaluation can be used. We investigated 6 different methods, and the results of these tests are reported here.

CROSSWIND MEASUREMENTS

Optical crosswind techniques are thoroughly described by Wang *et al* [1]. Their theoretical analysis of scintillation lead them to the development of different evaluation techniques.

The wind sensing methods can be grouped into two categories: covariance and frequency techniques.

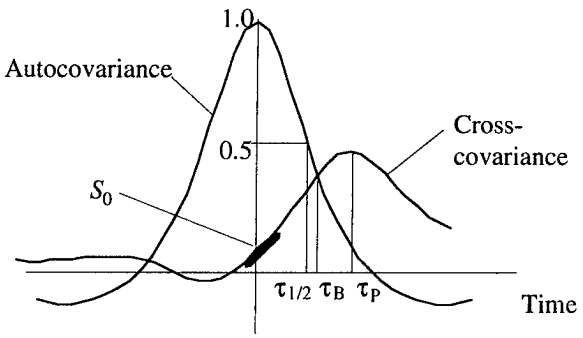


Fig.1 Typical normalized autocovariance and cross-covariance curves. S_0, τ_P, τ_B and $\tau_{1/2}$ are defined in text.

0-7803-3068-4/96$5.00©1996 IEEE

a) Covariance techniques

These techniques use the readings of two spaced detectors. By measuring the normalized time-lagged covariance function, *C(t)*, with the two detectors, the path-averaged wind speed can be found (Fig.1).

Slope technique: The crosswind, V, is proportional to the slope at zero delay of the cross-covariance curve, S_0:

$$V \sim S_0 \quad (1)$$

Peak technique: The crosswind can be obtained from the time delay at the peak of the cross-covariance curve, τ_P:

$$V \sim 1/\tau_P \quad (2)$$

Briggs technique: The crossover time delay of the autocovariance and cross-covariance curves, τ_B, is inversely proportional to V:

$$V \sim 1/\tau_B \quad (3)$$

b) Frequency techniques

These techniques measure the frequency of intensity fluctuations, $\tilde{f}$, of one signal, and cannot discern wind direction. The wind is proportional to the frequency content of the signal.

$$|V| \sim \tilde{f} \quad (4)$$

Autocorrelation technique: The width of the autocovariance curve, $\tau_{1/2}$, is inversely proportional to $\tilde{f}$:

$$\tilde{f} = 1/\tau_{1/2} \quad (5)$$

Fast Fourier Transform (FFT) technique: We determine the Fourier transform, W(f), of the signal. The principal frequency, f_{max}, is the frequency for which W(f) shows its maximum.

$$\tilde{f} = f_{max} \quad (6)$$

Zero-cross technique: This frequency measurement is made by counting the number of zero crossings after substraction of the mean signal:

$$\tilde{f} = count\ . \quad (7)$$

The theory developed by Wang *et al* describes the scintillation phenomenon fairly satisfactory, but makes two assumptions that lead to discrepancies between theoretical prediction and experimental results. First, Wang *et al* assume that the turbulence spectrum follows a universal form and this spectrum does not vary with time. Second, they assume Taylor's 'frozen turbulence' hypothesis. Taylor's hypothesis

implies that the turbulent eddies do not change significantly during the time they drift through the light beam.

EXPERIMENTAL SETUP

A scintillometer based on the model of Wang *et al* [1] was built at PSI. This instrument uses an infrared diode as a light source, operating with a peak wavelength between 0.8 mm and 0.9 mm. Transmitter and receiver apertures have diameters of 15 cm and 5 cm, respectively. The spacing between the two receivers is 6.4 cm. The signal intensity was stored with a sampling rate of 500 Hz on a portable computer, and data processing was subsequently done off-line on a mainframe computer.

During the summer of 1994, the scintillometer was placed on a 1 km path near Würenlingen, Switzerland. Transmitter and receiver were set on platforms, 3.5 m above ground. Nine automatic meteorological stations with conventional cup anemometers were set along the light path. The data from the conventional anemometers was averaged over 5 s, and then used as reference for the comparison with the scintillometer data.

A number of measurement campaigns were carried out. We based the calibration of the scintillometer on campaigns, for which the wind speed range was more than 3 m/s. The duration of these three campaigns was 12h, beginning in early afternoon.

RESULTS AND DISCUSSION

For comparison between the optical measurements and the conventional anemometers, we use different statistical tools. Standard deviations of differences and correlation coefficients are displayed in Table I and II for three averaging times. We see that the agreement improves with longer averaging times. The error due to electronic noise is smoothed out. Table I and II reveal that the best agreement is reached with the autocorrelation and zero-cross techniques, these two techniques showing exactly the same performance.

A closer look at Table I and II show that the peak technique is the least reliable if we consider short averaging times, but for a ten minutes averaging, the peak technique is more reliable than the slope technique. The poor performance for short averaging times is due to problems in direction determination. This effect is flattened by averaging.

Table I: Correlation coefficient between conventional anemometers and scintillometer for six different techniques. Measurements on the 25. July 94.

Averaging time	5 s	1 min	10 min
Slope	0.84	0.89	0.94
Peak	0.79	0.93	0.97
Briggs	0.88	0.94	0.97
Autocorrelation	0.96	0.98	0.99
FFT	0.93	0.97	0.99
Zero-cross	0.96	0.98	0.99

Table II: Standard deviation of the difference between conventional anemometer and scintillometer for the measurement of 25. July 94

Averaging time	5 s	1 min	10 min
Slope	0.36	0.29	0.23
Peak	0.43	0.24	0.17
Briggs	0.31	0.22	0.15
Autocorrelation	0.16	0.14	0.09
FFT	0.22	0.15	0.12
Zero-cross	0.16	0.13	0.09

The factors in the relations (1) to (7) were determined experimentally, and in order to better fit the data we rewrite the relation (4) in

$$|V| \sim \tilde{f}^{\alpha} \tag{8}$$

with α=1.8 for the autocorrelation technique, α=2 for the zero-cross technique, and α=2.3 for the FFT technique. The introduction of the exponent a can be explained by the failure of Taylor's hypothesis. The decay of turbulence eddies during the time they cross the beam has an effect of decorrelation that is proportional to the time delay. This causes the frequency techniques to overestimate the wind. This overestimation becomes greater as the wind decreases. The introduction of (8) counterbalances this effect and coincides better with our experiments.

The effect of eddy decay can be seen if we consider the peak value of the correlation function, $C(\tau_P)$. Taylor's hypothesis implies that for horizontal, crosswind the maximum of the correlation function would be 1. In reality the correlation functions show maxima between 0.3 and 0.8 (Fig.3). For the first four hours of the measurement (afternoon), we observe a good correlation between $C(\tau_P)$ and the wind speed, the value of $C(\tau_P)$ then become large during the nighttime. If we only consider the nighttime period (Fig.4) we see that the correlation is also good during that time. The change of the relation between $C(\tau_P)$ and wind speed is due to the change in the turbulent state of the atmosphere. In the strongly turbulent afternoon atmosphere, the eddy decay is much faster than in the weakly turbulent nighttime atmosphere. This difference in the eddy decay process between weak and strong turbulence leads to changes in the calibration factor for the evaluation techniques. The consequence for our measurements were an overestimation by the covariance techniques of the wind speed during nighttime.

One of our measurements is influenced by a rainy period. Autocorrelation and zero-cross techniques overestimate the wind speed during that period. The additional scintillation due to falling raindrops is interpreted as extra velocity component. We gain a better understanding of the influence of rain on scintillation if we consider the spectra of the intensity fluctuations, W(f). The atmospheric

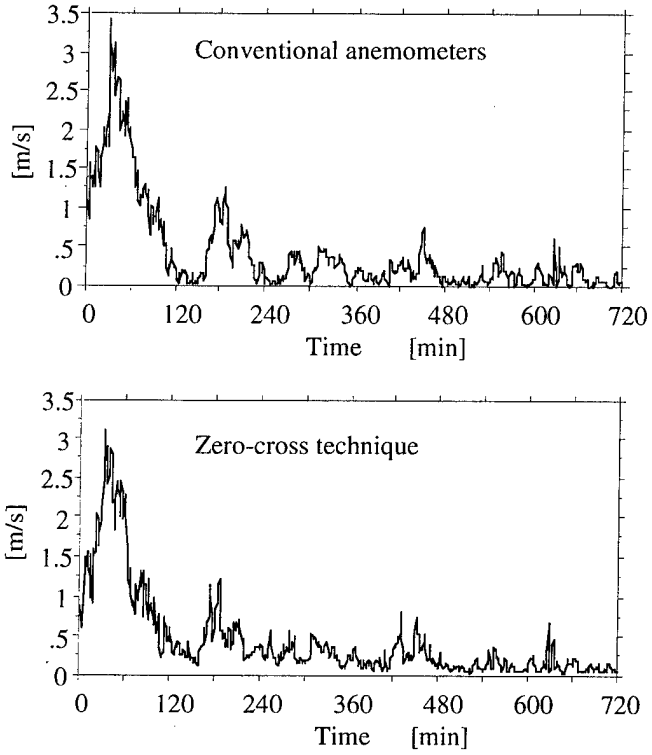


Fig. 2: Measurement over 12h, beginning at 14h10' on the 25. July 94. Both measurements are 1 min averages. The two curves exhibit the same characteristics.

turbulence influences the spectra in the low-frequency region, and precipitation has an effect on the high-frequency region forming a second peak at higher frequencies [2]. The magnitude and frequency of this second peak depends on the precipitation intensity and on the particles fall speed. The FFT technique determines the maximum of W(f) and was not influenced by rain. We tried to change the mode of evaluation and calculated the maximum of the function f·W(f). The high frequency part of the spectrum was consequently magnified, and we then recognize the influence of rain, the wind being overestimated. The covariance techniques are not affected by rain.

SUMMARY AND OUTLOOK

The results of our tests proved that our scintillometer is capable of measuring crosswind. We gained experience in using scintillometer and pointed out possible sources of error.

In a further step, we will use scintillometer with different apertures over longer distances to measure fluxes in an Alpine valley. We will also continue to investigate the effect of precipitation on the scintillation measurements.

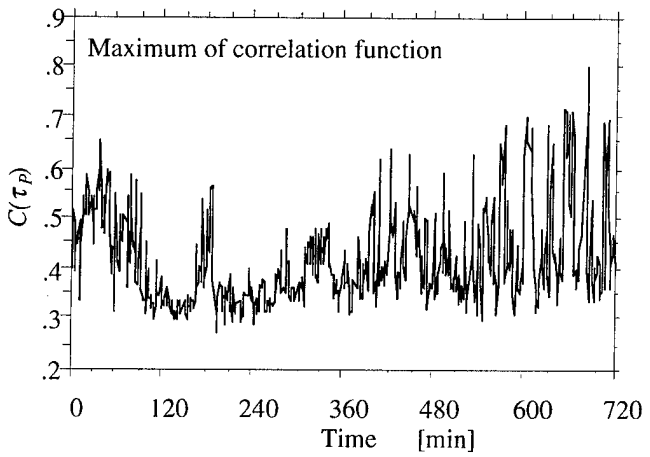


Fig. 3: Peak values of the normalized covariance function, $C(\tau_P)$. Measurement over 12h on the 25.07.94, averaging over 1min.

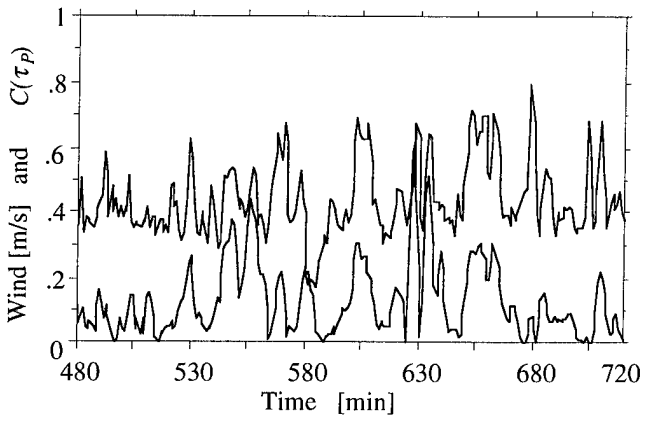


Fig. 4 : Peak value of the normalized covariance function $C(\tau_P)$ (upper curve) and wind measurement (lower curve) for the nighttime period of the 25. July 94 measurement.

ACKNOWLEDGEMENTS

Our thanks go to K. Leutwyler and M. Rohde who built the electronic part of the scintillometer, and to René Richter and Robert Erne for their assistance during the experiments.

REFERENCES

[1] Wang T.I., Ochs G.R., Lawrence R.S., "Wind measurements by the temporal cross-correlation of the optical scintillations", Appl. Opt., vol. 20, pp. 4073-4081, December 1981

[2] A.F. Zhukov, M.V. Kabanov, and R.Sh. Tsvyk, "Temporal fluctuations of laser beam radiation in atmospheric precipitation", Appl. Opt., vol. 27, pp. 578-583, February 1988.

A Multi-Frequency, Dual-Polarization, Microwave Link For Rainfall Estimation

Rafael F. Rincon[1], Steven W. Bidwell[2], Arthur R. Jameson[3] , and Otto W. Thiele[2]
(1) The George Washington University, Washington, D.C. 20052 [rafael@meneg.nasa.gsfsc.gov]
(2) NASA/Goddard Space Flight Center, Greenbelt, MD 20771
(3) RJH Scientific Inc., Alexandria, VA 22303

Abstract-- A ground-based, multi-frequency, dual polarization, microwave link (LINK) is being developed by the NASA/Goddard Space Flight Center for the measurement of precipitation. The LINK is part of a larger ground-based system which will provide a transfer standard permitting a more effective use of conventional sensors for calibrating the various weather radars around the tropics schedule to support the Tropical Rain Measuring Mission (TRMM). The instrument promises a substantial improvement over present techniques in the estimation of important meteorological parameters such as rainwater content and rainfall rate. The LINK, which is currently under testing at the Goddard Space Flight Center, is scheduled for installation at NASA/Wallops Flight Facility, VA in the spring of 1996.

INTRODUCTION

Due to its interaction with atmospheric water, microwave radiation (5 to 40 GHz) provides a unique means of meteorological measurements. Possessing a wavelength on magnitude as the size of raindrops, microwaves are scattered and absorbed by rainfall. The resulting mean electromagnetic field over the rain filled region undergoes amplitude and phase variations that carry information about the meteorological parameters along the propagation path. The measurement of such variations provides a way to estimate important meteorological parameters such as rainwater content (*W*) and rainfall rate (*R*).

The microwave link (LINK) in development by the Microwave Sensors Laboratory at the Goddard Space Flight Center is a coherent, continuous-wave (CW), transmission link capable of measuring path integrated attenuation (A) at several frequencies, and path integrated phase shift (ϕ) at two polarizations. These measurements will render independent simultaneous estimates of W and R for rainfall rates ranging from 1 mm/hr to over 100 mm/hr. Comparisons among LINK estimates, along with measurements from rain gauges and hygrometers should provide a useful transfer standard for rainfall estimation techniques.

0-7803-3068-4/96$5.00©1996 IEEE

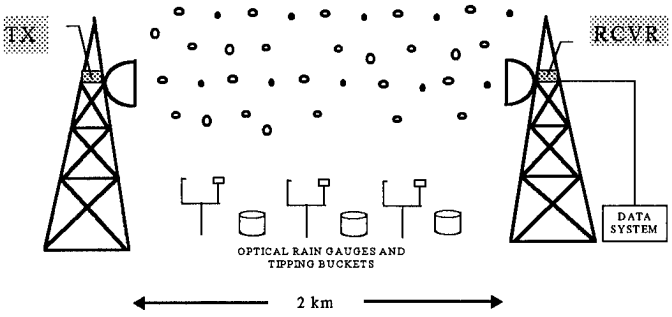


FIG. 1 LINK CONFIGURATION

LINK DESCRIPTION

The multi-frequency, dual polarization, LINK is characterized by a continuous, simultaneous, coherent operation at the frequencies of 8.35 GHz, 8.45 GHz, 25.35 GHz, and 38.025 GHz. The four frequencies were chosen such that independent simultaneous estimates could be made using more than one microwave rainfall estimate. (Measurements above 40 GHz were not included since frequencies in this range are greatly attenuated and rapidly depolarized by precipitation and water vapor). Furthermore, the signals required simple ratios for their synthesis and synchronization.

Consequently, the selection was made of identically polarized signals at 38.025 GHz , 25.35 GHz, 8.45 GHz with ratios 4.5 (38.025 to 8.45), 3.0 (25.35 to 8.45), and 1.5 (38.025 to 25.35). In addition, polarization differential phase shift measurements Φ_{DP} can be achieved by transmitting horizontally (h) and vertically (v) polarized signals at two slightly separated frequencies. The inclusion of a fourth vertically polarized signal at 8.35 GHz would provide, in conjunction with the horizontally polarized signal at 8.45 GHz, Φ_{DP} over a wide range of rain rates.

Fig.1 shows a simplified sketch of the future LINK site on Wallops Island. It consists of two towers, already in place, separated by a distance of approximately 2 km. The transmitter and receiver units will be located on the tower platforms at a height of nearly 20 meters above ground

permitting an on-the-line-of-sight transmission. The four signals will be generated at the transmitter using a common, ultra-stable, 5 MHz local oscillator (LO) in connection with multipliers, amplifiers and phase-locked loops that provide synchronization among the frequencies. The 8.35 GHz (v) and the 8.45 GHz (h) signals will be transmitted through a dual polarization, X-band conical horn antenna, while the 25.35 GHz and 38.025 GHz signals will employ a dual frequency parabolic reflector.

The receiver, with a similar set of antennas co-aligned to the transmitter's set, will phase-lock to the incident 8.45 GHz (v) signal establishing synchronization between the two units. Thereafter, the 8.35 GHz, 8.45 GHz, 25.35 GHz, and 38.025 GHz received signals will be down-converted to 3 KHz, 3 KHz, 9 KHz and 13.5 KHz respectively through the use of a network of ultra-stable LO's, mixers, amplifiers, and phase-locked loops, preserving the same amplitude, phase, and frequency ratio as the microwave signals, and hence, providing the desired meteorological information.

The audio signals will be channeled to the LINK's data system, located at the base of the receiving tower where the four channels will be simultaneously sampled at a rate of 96 KHz. Amplitude and phase information will be recovered with a digital signal co-processing unit capable of performing real-time, 512-point Fast Fourier Transforms (FFT). The results will be contiguously averaged over a period of 3 seconds for noise reduction before being stored in permanent memory.

The LINK will operate in conjunction with a configuration of state-of-the-art optical rain gauges and tipping buckets already on site to improve and cross-check the measurement's accuracy. The addition of a hygrometer, barometer and an anemometer is also scheduled in the near future. All supporting devices will be monitored by the LINK's data system assuring a time concurrence among all the different measurements. The data system will be remotely accessed by modem or through the network allowing data transfers and system monitoring.

ESTIMATION OF RAINFALL PARAMETERS

Attenuation and phase shift of electromagnetic waves due to rainfall over a path can be analytically obtained from the mean electromagnetic field over a given rain-filled region. The results are given by

$$A_{h,v} = 8.686\lambda \int \mathrm{Im}[f_{h,v}]N(D)dD, \quad \text{(dB/km)} \qquad (1)$$

$$\phi_{h,v} = \frac{18.0}{\pi}\lambda \int \mathrm{Re}[f_{h,v}]N(D)dD, \quad \text{(deg/km)} \qquad (2)$$

respectively, where λ is the free space wavelength, $N(D)\,dD$ is the drop-size distribution, and $f_{h,v}$ are the components in the forward direction of the vector scattering amplitudes corresponding to horizontal and vertical polarization (functions of frequency ω, temperature T, polarization, and raindrop diameter D) [1][2].

In the absence of vertical air motion, R and W are given by the following integral relations:

$$R = 0.6 \times 10^4 \pi \rho_w \int v_t(D) D^3 N(D) dD, \quad \text{(mm/hr)} \qquad (3)$$

$$W = 1.667 \times 10^5 \pi \rho_w \int D^3 N(D) dD, \quad \text{(g/m}^3\text{)} \qquad (4)$$

where v_t is the terminal fall speed of the drops in still air, ρ_w is the density of water[3].

The integrands in (1) through (4) can be considered as distributions functions A(D), Φ (D), R(D), and W(D) over the drop sizes. The accuracy of microwave measurement estimators will depend on how strongly A(D) or Φ (D) will relate to R(D) or W(D) since for some drop-size distributions there is a stronger relationship between the distribution functions than for others. In particular, $A_{38\text{-}8}$, $A_{25\text{-}8}$, and $\Phi_{DP\ 8h\text{-}8v}$ are closely related to R , while $A_{38\text{-}25}$, and $\Phi_{DP\ 8h\text{-}8v}$ are closely related to W [4][5].

Many empirical relations have been proposed to make rainfall estimates from microwave measurements. In general, the relations between a microwave measurement X (A or Φ) and a rainfall parameter P (R or W) is of the form $P = k X^{\alpha}$, where k and α depend on drop concentration and frequency. The more α deviates from unity, the greater the explicit dependence of an X-P power law on drop concentration

In particularly, one approach uses the relation $R = k A^{\alpha}$ which is nearly linear ($\alpha \approx 1$) at 25.35 GHz and at 38.025 GHz [5][6] (making A_{38} and A_{25} good estimators of R). However, since LINK differential attenuation measurements are easier and more accurate to make than specific measurements the use of $A_{38\text{-}8}$ and $A_{25\text{-}8}$ promises a direct measure of R.

A similar approach, uses the differential attenuation between the 38.025 GHz and the 25.35 GHz ($A_{38\text{-}25}$) which has been

shown to be well correlated and linearly related to W [3]. The relation is given by

$$W = 0.427 A_{38-25}^{0.9747} . \quad (5)$$

A different approach combines the specific polarization differential phase shift Φ_{DP} and the mass weighted average rain drop diameter Dm to obtain W [3]. Φ_{DP}, defined as one half the difference in the total integrated polarization differential phase, is given by

$$\Phi_{DP} = \frac{\phi_{h,8.45} - (8.45/8.35)\phi_{v,8.35}}{2} . \quad (6)$$

Dm, a useful parameter by itself, can be estimated from the ratio A_{38} / A_{25} through the relation

$$Dm = 0.565 - 0.199(\frac{A_{38}}{A_{25}}) . \quad (7)$$

Rain water content is then estimated from Dm and Φ_{DP} by the relation

$$W = 0.0527(\frac{\Phi_{DP}}{0.03 + 0.62 Dm})^{0.9964} . \quad (8)$$

Based on these three different techniques, the LINK measurements will provide nearly unbiased estimates of R and W. Other techniques have been proposed to estimate additional parameters such as water vapor content and vertical air velocity. These approaches will be explored in the near future on completion and installation of the LINK.

CONCLUSION

The coherent, multi-frequency, dual-polarization microwave link (LINK) will provide a unique facility for increasing our understanding of the potential and limitations of the remote sensing of atmospheric parameters. The LINK measurements of path integrated differential attenuation ($A_{38\text{-}8}$ and $A_{25\text{-}8}$) and path integrated differential phase shift ($\Phi_{DP\ 8h\text{-}8v}$) will permit several simultaneous estimates of rain fall rate R and water vapor W. Since the estimates will be independent and will involve different assumptions, fair confidence could be placed on any one of them for which different approaches would yield the same value. In addition, by comparing the estimates with rain gauge measurements, the most accurate technique could be identified. Finally, the LINK measurements should contribute to improve our understanding of radar rainfall retrieval algorithms for both ground based and space-borne systems.

ACKNOWLEDGMENT

We wish to acknowledge the technical support of Mr. Richard Aldridge and Mr. Michael Triesky at the Goddard Space Flight Center, and Mr. Robert Maddox and Mr. Gene Furness at the Wallops Flight Facility. This work was supported under NASA's Mission to Planet Earth by Dr. Ramesh Kakar at NASA Headquarters.

REFERENCES

[1] H. C. Van de Hulst, Light Scattering by Small Particles, New York: John Wiley, 1957, pp 32-34.

[2] T. Oguci, Attenuation and Phase Rotation of Waves Due to Rain, Radio Science, vol. 8, pp 31-38, January, 1973.

[3] A. R. Jameson, Estimating the Path-Average Rainwater Content and Updraft Speed along a Microwave Link, Journal of Atmospheric and Oceanic Technology, vol. 10, pp 478-485, August 1993.

[4] A. R. Jameson, A Comparison of Microwave Techniques For Measuring Rainfall, Journal of Applied Meteorology, vol. 30, pp 32-54, January, 1991.

[5] D. Atlas and C. W. Ulbrich, The Physical Basis for Attenuation-Rainfall Relations and the Measurement of Rainfall Parameters by Combined Attenuation and Radar Methods, Journal De Recherches Atmospherique, vol. 8, pp 275-298, 1974

[6] A. R. Jameson, A Dual-Frequency Technique for Measuring Rainwater Content, Journal of Atmospheric and Oceanic Technology, vol. 9, pp 28-34, February, 1992.

Cost-Effective Parallel Processing for Remote Sensing Applications

Hyoung Joong Kim and Hyung Soo Kim
Department of Control/Instrumentation Engineering
Kangwon National University
Chunchon 200-701, Korea
FAX: 82 (361) 242-2059 Email: khj@cc.kangwon.ac.kr

Abstract -- Network-based computing with cluster of personal computers or workstations recently has become an important and successful technique. Network-based computing enables fast computation and resolves short of storage with computers on the desks. Cluster of inexpensive computers offers them aggregated computing power and storage to challenge very large-scale problems. Iterative solvers are used for the large sparse linear systems. Preconditioners accelerate the rate of convergence of the iterative solvers. However, parallelization of preconditioners is far from satisfaction so far. Thus, the simplest diagonal scaling is a good alternative for improved convergence and easy parallelization. In order to reduce communication overhead, a data compression technique is considered. Data communication time can be reduced at the cost of convergence rate. MATLAB simulation result is given in this paper. This method is effective to cluster of computers connected through slow networks.

NETWORK-BASED COMPUTING

Finite element approximation of some partial differential equations produces very large linear system. Such linear systems are so large that it is almost impossible to solve with a single computer due to the limited amount of storage. Therefore, network-based computing is considered [1,2,5] in many scientific and engineering applications to cope with the short of storage. Of course, fast computation is another important objective of the network-based parallel computing. Recently, highly cost-effective parallel computing has been possible under clustered computer networks due to the PVM (parallel virtual machine), a public-domain software.

Since PVM from ORNL is freely available by anonymous ftp, it has spread wide over the academic community and has become a standard of message-passing software systems. At last, high-performance computer vendors provide their own version of PVM intended for better exploitation of their hardware architectures. An important motivation for the use of PVM and other cluster computing systems is its cost-effectiveness. The user can perform parallel computing on the workstations and/or personal computers on the desks. Other motivations for the increasing use of PVM include a high degree of portability and a straightforward and robust interface that is well suited for many scientific application development.

0-7803-3068-4/96$5.00©1996 IEEE

ITERATIVE METHOD

Iterative solvers are strongly recommended for large and sparse linear systems. The famous CG (conjugate gradient) method is suitable for Hermitian matrix (and consequently symmetric matrix). Unfortunately, the CG does not work for complex symmetric systems which is not Hermitian and consequently not symmetric. However, the QMR (quasi-minimal residual) method converges to the solution when it is applied to the complex symmetric system of the form

$$A=\begin{bmatrix} 10+j & 3+j & j & 0 & -j \\ 3+j & 10+j & 3+j & j & 0 \\ j & 3+j & 10+j & 3+j & j \\ 0 & j & 3+j & 10+j & 3+j \\ -j & 0 & j & 3+j & 10+j \end{bmatrix}.$$

The convergence rate of those iterative methods depends on spectral properties of the coefficient matrix. To achieve better convergence rate preconditioners has been extensively studied. A preconditioning matrix is an auxiliary matrix that approximates the coefficient matrix or its inverse in some sense. The preconditioning matrix is applied in every step of the iterative method. Unfortunately, preconditioners are often one of the most problematic part of parallelizing an iterative method since certain preconditioners were not developed with parallelism in mind.

Note that parallelization of iterative method is easy. Most of iterative methods are composed of BLAS (Basic Linear Algebra Subroutines) including vector-nector multiplications, matrix-vector multiplications and inner products. The most time-consumingoperation is just matrix-vector multiplication which has been fully studied. Moreover, like PVM, high-performance computer vendors provide their own optimized version of BLAS intended for better exploitation of their hardware architectures.

However, preconditioners are not easy to parallelize. The simplest and the most effective preconditioning is diagonal scaling unless the main diagonal elements of the coefficient matrix are identical [4]. The diagonal scaling is performed once at the beginning of the iteration. Thus, the diagonal scaling is considered as a kind of preprocessing of the iterative method. Its parallelism is rich and easy to implement.

COMMUNICATION OVERHEAD

For each iteration, a direction vector p_n in Figure 1 may be broadcasted through the network over the processors to share the information. During the communication session, all the processors stop processing and wait to receive the vectors broadcasted in a multidrop system. In many slow networks the communication times may be burdensome. Assume that, for example, there are one million unknowns, and they are to be broadcasted through 10 Mbps Ethernet. Then the time for communication lasts at least 26 seconds for each iteration. When the number of iterations is, say, 400,000, the total time for communication only is more than three days.

Reduction of total processing time may be expected either by introducing powerful preconditioners or by applying data compression technique. Good preconditioner may reduce the number iterations. However, applying preconditioners to an iterative method incurs extra computational cost. Hence, there is a trade-off between the gain in computing time and the cost of constructing and applying the preconditioner.

Similarly, the communication time may be reduced at the cost of convergence rate. Data format of the direction vector is usually double-precision. Instead, say, integer format can be used during communication sessions by sacrificing some data precision. There may be various ways to compress data. In this paper, the most simple and easy scheme is used.

QMR Algorithm [3]
without look-ahead and without preconditioner
for complex symmetric systems

0. Choose $x_0 \in C^N$ and set $r_0 = b - Ax_0$.
   Compute $\rho_0 = \|r_0\|$ and set $v_1 = r_0 / \rho_0$.
   Set $p_0 = d_0 = \vartheta_0 = 0$, $c_0 = \varepsilon_0 = 0$, $\eta_0 = -1$.

For $n = 1, 2, \ldots,$ **do**

1. **If** $\varepsilon_{n-1} = 0$, **then** stop.
   Compute $\varepsilon_n = p_n^T A p_n$, **If** $\delta_n = 0$, **then** stop.

2. Compute $p_n = v_n - p_{n-1}(\rho_n \delta_n / \varepsilon_{n-1})$.

3. Compute $\varepsilon_n = p_n^T A p_n$, $\varepsilon_n = p_n^T A p_n$,
   $\tilde{v}_{n+1} = A p_n - v_n \beta_n$, and $\rho_n = \|\tilde{v}_{n+1}\|$.

4. Compute

$$\vartheta_n = \frac{\rho_{n+1}}{c_{n-1}|\beta_n|}, \quad c_n = \frac{1}{\sqrt{1+\vartheta_n^2}}, \quad \eta_n = -\eta_{n-1}\frac{\rho_n c_n^2}{\beta_n c_{n-1}^2},$$

$$d_n = p_n \eta_n + d_{n-1}(\vartheta_n c_n)^2, \quad x_n = x_{n-1} + d_n.$$

5. **If** $\delta_{n+1} = 0$, **then** stop.
   Else $v_{n+1} = \tilde{v}_{n+1} / \rho_{n+1}$.

Figure 1. QMR Algorithm

DATA COMPRESSION TECHNIQUE

At each iteration the direction vector p_n is scaled up by multiplying a constant s_k and rounded to get integers. This simple operation transforms double-precision numbers into integers. The packed integer vector is broadcasted. In this case part of information is lost. Each processor unpacks the integer vector and transforms it into double-precision one by dividing by s_k.

The direction vector in CG or QMR is optimized each time in some sense. The compressed direction vector can not direct the right direction. The compressed direction vector is slightly off the optimized direction. Thus, communication time can be reduced considerably at the cost of total number of iterations. Table 1 shows the number of iterations versus scaling factor s_k.

The simulation is performed on the MATLAB. We place one line of the form

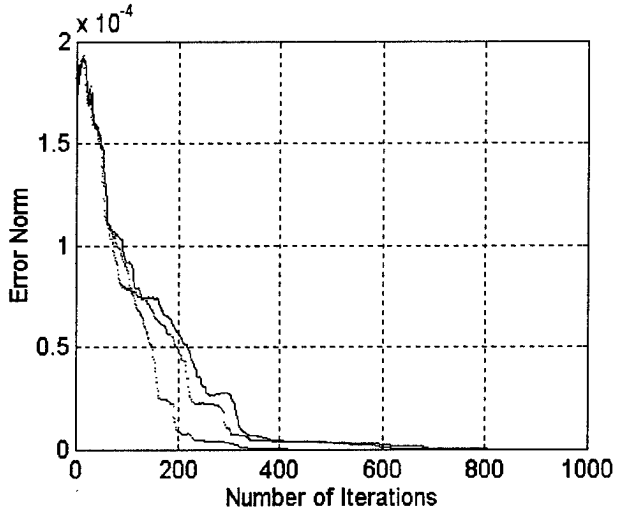
$$p_n = \text{round}(s_n \times p_n) / s_n$$

before Step 2 or Step 3 in Figure 1. Note that the position where the above line places affects the number of iterations. Placing before Step 3 is better than Step 2. When the scaling factor is small, the QMR does not converge. The larger the scaling factor s_k, the better the convergence rate. It complies with our expectation. The scaling factor plays important role in both compression and decompression process. The pseudo-MATLAB line above is so simple that we call it the brute-force compression technique.

The brute-force compression technique works well when the scaling factor is large. The total communication time reduction in IBM-PC is about a eighth since double-precision format requires 8 bytes while integer 2 bytes and the vector is complex such that one complex number requires two double-precision numbers. The communication time reduction in workstations is a quarter since each double-precision requires 8 bytes while integer 4. More sophisticated data compression techniques can be introduced to achieve less communication time.

Table 1. Number of Iterations versus Scaling Factors

Scaling Factor	Number of Iterations	
	Before Step 2	Before Step 3
100	not converge	not converge
1,000	not converge	not converge
10,000	not converge	not converge
100,000	1,619	696
1,000,000	802	371
10,000,000	226	174
100,000,000	217	127
1,000,000,000	134	101



With Scaling factor of 1e+12.
Uppermost line is scaling before Step 2.
Middle line is scaling before Stpe 3.
Lowermost line is without scaling.
Figure 2. Effect of Scaling.

SIMULATION

Simulation tool is MATLAB in this paper. QMR is used as an iterative linear solver. The brute-force data compression technique is applied to a randomly generated matrix which is complex symmetric. Figure 2 shows the convergence behavior. Note that the residual norm with the brute-force technique decreases slower than that without it. As matrix size becomes large, larger scaling factor is required. Thus, implementing the brute-force technique on IBM-PC is not promising. We find that the direction vector is very sensitive to the scaling factor. Figure 2 is obtained with $s_k = 1e+12$.

CONCLUSION

Cost-effective parallel processing technique is studied. To solve a very large and sparse linear equation which is complex symmetric, QMR is used. To cope with short of storage and prohibitively lengthy processing time, network-based cluster of computers is introduced. Parallel computing environments are supported by PVM. The simplest diagonal scaling method is applied as a preconditioning procedure.

Effective and very simple data compression technique is presented. A brute-force compression technique is evaluated using MATLAB. Considerable reduction in communication time is achieved. More sophisticated compression techniques will be studied further. Sensitivity to the scaling factor is also to be studied further.

ACKNOWLEDGMENT

This work was supported in part by the Research Center for Advanced Aggregate Mineral Composite Products (RRC).

REFERENCES

[1] A. Blaszczyk, Z. Andjelic, P. Levin, and A. Ustundag, "Parallel computation of electric fields in a heterogeneous workstation cluster," in High-Performance Computing and Networking, B. Hertzberger and G. Serazzi, Eds. Berlin: Springer-Verlag, 1995, pp. 606-611.

[2] C. Cap, "Massive parallelism with workstation clusters - Challenge or nonsense," in High-Performance Computing and Networking, W. Gentzsch and U. Harms, Eds. Berlin: Springer-Verlag, 1994, pp. 42-52.

[3] R. W. Freund, and N. M. Nachtigal, "An implementation of the QMR method based coupled two-term recurrences," SIAM J. Sci. Comput., vol.15, pp. 313-337, 1994.

[4] G. Golub, and J. M. Ortega, Scientific Computing: An Introduction with Parallel Computing, Academic Press, 1993.

[5] F. Reale, F. Bocchino, and S. Sciortino, "Parallel computing on Unix workstation arrays," Comput. Phys. Comm., vol. 83, pp. 130-140, 1994.

Design of a Geographic Information System Using OPS5

A.K. Menon, *Member, IEEE*, P. Jayaprakash, and P.V. Usha
Department of Computer Science, Cochin University of Science and Technology
Cochin, India 682022
(All Correspondence: Dr. A.K. Menon, XVI/42 Alumparambu, N. Paravur, India 683 513
Telephones: +91 . 484 . 44 2883; +91 . 484 . 62 2903; Email: akm.gis@axcess.net.in)

Abstract -- Geographic Information Systems (GIS) is one technology that is driven more by applications rather than by abstract principles [1]. Existing GISs store spatial data in the form of relations. This leads to ambiguities and inconsistencies in the query processing. A rule-based system (RBS), also known as production system, is a more elegant choice for implementing a GIS, since RBSs address the need to capture, represent, store, and reason about human knowledge on the basis of conditional *if-then* rules. This paper describes the implementation of a GIS using OPS5, a production system language. For the prototype, a medium-sized city, with two rivers, a lake, a railway track, different categories of roads, buildings, and offices, was chosen.

1. INTRODUCTION

The term, Geographic Information System (GIS) refers to the use of computer facilties to handle data referenced in the spatial domain with the capability to interrelate data sets, carry out spatial analysis and display the results. In such a system, the database describes a collection of geographic objects over a two-dimensional map. A GIS stores and manipulates aspatial, spatial, and graphical data. While the graphical data are mainly used for the purpose of displaying answers to the queries, it is the spatial and aspatial data that are manipulated by the query processor of a GIS. Systems for geographic information, like those for remote sensing image analysis and vision analysis, involve processing of spatial data that relate to coordinates or such other properties of geographic objects. Besides the spatial data, the above systems process aspatial data (pertaining to names of places, roads, rivers, population, etc.) and graphical data (for facilitating display of query results in the form of maps or charts). The query/reasoning procedures of a GIS manipulates the spatial and aspatial data and formulates the graphical data by way of partial results.

2. GIS USING RELATIONAL DATABASES

Existing GISs store spatial data in the form of conventional relations in which a spatial object is represented by several tuples. Each relation consists of a set of tuples with the same set of attributes [2], [3]. Relational data models, however, do not lend themselves easily to storage and manipulation of spatial and graphical data. While the table-format data representation in the relational model would be self-explanatory to the user, extraction of semantic information after logically combining several tables becomes tedious and leads to ambiguities [4]. Since graphical data are expensive to capture, there is growing interest in integrating remote sensing systems into a GIS so that the latter can serve as the knowledge source for the former[5]. Remote sensing data, however, are in raster format and hence are incompatible with the vector format representation adopted in the GIS.

This work was supported by a generous equipment grant from the Ministry of Human Resources Development (Dept. of Education), Government of India.

0-7803-3068-4/96$5.00©1996 IEEE

3. PRODUCTION SYSTEMS AND OPS5

An effective GIS has all the characteristics of a knowledge-intensive, problem-solving machine. A rule-based system (RBS), also known as a production system, should therefore be a good choice for implementing GISs, since RBSs constitute the best means available for codifying the problem-solving know-how of a human expert. RBSs address the need to capture, represent, store, and reason about, human knowledge on the basis of conditional *if-then* rules. Because each rule approximates an independent granule of the domain knowledge, an RBS gains in skill and efficiency incrementally as the system acquires new knowledge when new rules are added to the rule base.

OPS5 is a production system language with a forward chaining rule interpreter that has many features to increase its efficiency in handling large rule bases [6]. A production system consists of three modules, *production memory* (PM), *working memory* (WM), and *inference engine* (IE). PM (or the rulebase) consists of an unordered set of conditional statements, with the *if* part (or the condition part) of the rule on the left-hand side and the *then* part (or the action part) on the right-hand side. The productions operate on the elements of WM, a database of temporary data structures. The elements of WM are termed *working memory elements* (WMEs), which are lists of attribute-value pairs. A typical working memory has several hundred objects; each object has between 10 to 100 associated value pairs. An object, together with its attribute-value pairs, constitutes a working memory element.

The general structure of an OPS5 production is

```
(p rule_name
   (condition_element_1)
      .
      .
   (condition_element_n)
--->
   (action_1)
      .
      .
   (action_m))
```

where p is a symbol that identifies a production; "rule_name" is the name of the rule, identified as an atomic symbol; the "condition_elements" are possibly ANDed or ORed antecedents; and the "actions" are the consequents.

4. IMPLEMENTATION

The system that is reported in this work is built around a MicroVax II workstation with a graphics processor and running on VMS operating system. A map of Trivandrum city, the capital of Kerala State, and its environs was used as the primary source of data. The map (Scale 1:125,000) was digitised, paying close attention to natural features like the two rivers that flow through the city, the lake, and the coastal lines; physical features like roads and their intersections, railway tracks, airport, public buildings, schools, etc. Any particular feature such as the road network or the railway track can be displayed alone or overlayed. Any selected subregion of the map can be zoomed for a detailed view. The map was divided into 64 x 64 blocks. Each block was then coded separately so that any one of the several small areas covered by a single block could be displayed, as needed.

OPS5 allows compound data types, referred to as *element classes.* An element class, with a list of attributes and their formats, should be declared before the productions that use it are declared This is accomplished through the *literalize* declaration as in the following:

```
(literalize road

      type        rd_name     start_node
      end_node    junctions   start_xcord
      start_ycord rd_cord)
```

A particular instance of the above declaration can be created in the working memory via the *make* action:

```
(make road
^type state_   highway
^rd_name       |kovalam road|
^start_node    kovalam
^end_node      manacaud
^junctions     jn_list
^start_xcord   2475.0
^start_ycord   985.0
^end_xcord     4254.0
end_ycord      1570.0
^rd_cord       kvlm.dat)
```

The built-in capabilities of OPS5 such as the facilities for creating linked data structures, creating contexts, iteration, recursion, etc., are well-exploited in the implementation to exert high degree of control over the formulation and execution of the production rules. Many type of primitive spatial operations on spatial objects such as ADJACENT, CONTAINS, WITH_IN, INTERSECTS, CLOSEST, FURTHEST, etc., can be constructed very easily.

To find all continental restaurants within 2 km of the State Legislature, we could use the production

```
(p find_restaurant
   (restaurant
      ^name       <name>
      ^location   <location>
      ^meal_type  continental
      ^x_cord     <x_cord>
      ^y_cord     <y_cord>)
   (place
      ^pname      <location>
      ^x_cord     <x_cord1>
      ^y_cord     <y_cord1>)
   (with_in
      ^pname1     |State Legislature|
      ^pname2     <location>
      ^distance   {<distance>  <= 2.0})
--->
   (call plotpoint <name>
         <location>
         <x_cord>
         <y_cord>
```

A sample output of this production is shown as Fig.1 on the next page. The locations of the restaurants, filtered out as per the specifications, are indicated on the map in green numerals (1-4), and their respective names are shown on the side in a list form. Since name placement has not yet been implemented, numeral 1 is overwritten by the locality name, "SPENCER JUNCTION".

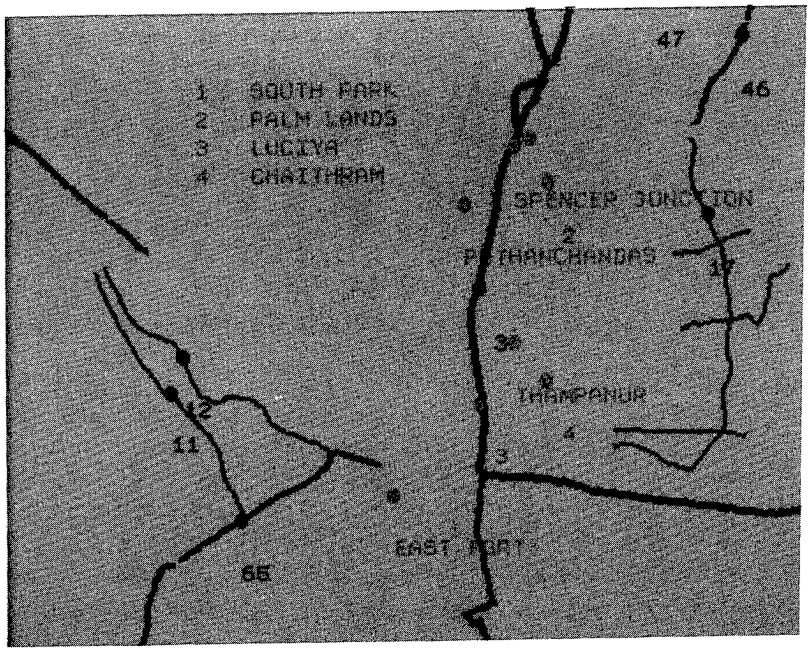


Fig. 1. Output of a production for displaying the locations of continental type restaurants within 2 km of the State Legislature.

5. CONCLUSIONS

A brief description of the problems involved in the representation and analysis of spatial data using relational databases has been given. Adopting the scheme of a production system to represent the known facts for the chosen domain of a geographic information system, in the form of rules, has yielded encouraging results. Production systems are not at all popular for general applications served by relational databases. They are, however, well-suited when the tasks involved is searching through a vast state space. In production systems control and knowledge are separated, allowing for easy modification of the knowledge base without changing the code for control, and vice versa.

ACKNOWLEDGMENTS

The second author (Jayaprakash) is grateful for the Research Fellowship provided to him by the Cochin University of Science & Technology during the work reported here. The third author (Usha) is grateful for the Research Assistantship out of the funds provided by the Ministry of Human Resources Development, Government of India.

REFERENCES

[1] M.F. Goodchild, "A Spatial Analytical Perspective on Geographic Information Systems," Int. J. Geograph. Inform. Syst., vol. 1, no. 4, pp. 327- 334, Oct.-Dec. 1987.

[2] H.M. Raafat, Q. Xiao, and D.A. Gauthier, "An Extended Relational Database for Remotely Sensed Image Data Management Within GIS," IEEE Trans. Geosci. Remote Sensing, vol. 29, no.4, pp. 651-655, July 1991.

[3] A.R. Rao and R. Jain, "Knowledge Representation and Control in Computer Vision Systems," IEEE Expert, vol.3, no.1, pp 64-79, Spring 1988.

[4] L. Mohan and R.L. Kashyap, "An Object-Oriented Knowledge Representation for Spatial Information," IEEE Trans. Software Eng., vol.14, no. 5, pp.675- 681, May 1988.

[5] F. Wang, "Integrating GISs and Remote Sensing Image Analysis Systems by Unifying Knowledge Representation Schemes," IEEE Trans. Geosci. Remote Sensing, vol.29, no. 4, pp. 656-664, July 1991.

[6] L. Brownston, R. Farrell, E. Kant, and N. Martin, Programming Expert Systems in OPS5: An Introduction to Rule-Based Programming. Reading, MA: Addison-Wesley, 1985.

Multiresolution De-Speckle Based on Laplacian Pyramids

B. Aiazzi*, L. Alparone°, S. Baronti*, G. Borri°, C. Susini*

* Istituto di Ricerca sulle Onde Elettromagnetiche "Nello Carrara" - CNR, via Panciatichi, 64, I-50127 Firenze, Italy
Phone: +39-55-4235-275; Facsimile: +39-55-410893; E-mail: baronti@iroe.fi.cnr.it
° Dipartimento di Ingegneria Elettronica, University of Florence, via S. Marta, 3, I-50139 Firenze, Italy
Phone: +39-55-4796-372; Fax: +39-55-494569; E-mail: alparone@cosimo.ing.unifi.it

Abstract -- A multiresolution filtering procedure is derived from the framework of Laplacian pyramids and proposed for edge-preserving MMSE smoothing of images affected by multiplicative noise with speckle statistics. The basic idea of the novel scheme is to apply an MMSE filter (e.g., Kuan's filter) to the different resolution layers in which the noisy image is decomposed. A noise-free image version is achieved by recombining the layers of the pyramid, once they have been filtered. Comparison tests performed on images affected by synthetic speckle, with both one-look and multi-look statistics, show significant SNR improvements over the basic Kuan's scheme, resulting in far lower distortion between noise-free and processed images. Visual comparisons on true and simulated SAR images corroborate the objective results.

INTRODUCTION

Synthetic Aperture Radar (SAR) images are affected by speckle which appears as a granular signal-dependent noise, whose effect is to degrade the performance of image segmentation and classification algorithms. For this reason, a variety techniques are usually employed for speckle reduction [1]. Spatial filtering is used with the objective of smoothing homogeneous areas, in which speckle is fully developed, simultaneously preserving point targets and edges. Moreover, if multi-frequency polarimetric SAR data are available, several images in various polarizations and frequencies can be combined to produce a less noisy version (e.g., polarimetric filtering and principal component analysis).

One of the crucial points of spatial filters is to determine the most suitable neighborhood, for each pixel, in which to estimate the parameters driving the smoothing algorithm. Two approaches are generally possible: the former consists of either adaptively modifying the window shape and/or size at each pixel position based on some local feature within the local window (e.g., mean, variance, edges, point targets), thereby determining the filter response in the presence of such characteristics [2],[3]. The latter parallel approach that has been only recently formalized consists of considering a multiresolution decomposition of the input image, and applying a different filter to each resolution layer. The wavelet decomposition has been employed for multiresolution de-speckle [4],[5], thanks to its capability to capture spatial features within frequency subbands. However, wavelet and subband decompositions are *non-redundant* image descriptions, viz. the image may be exactly synthesized from a number of coefficients as large as the number of pixels. This property implies that connected spatial structures analyzed at increasing resolutions are split into separate subbands, thereby losing their spatial connectivity. On the contrary, Laplacian pyramids (LP) [6],[7], which are *redundant* image descriptions, look attractive because of their full band-pass frequency property [8], which enables connected image structures to be represented onto multiple scales.

In this work, an adaptive filter (Kuan's filter [9]) is applied to the connectivity-preserving different resolution layers in which the noisy image is decomposed by a modified LP-generating procedure, designed for dealing with multiplicative noise. For natural images, each layer of the LP is characterized by an SNR that decreases for increasing spatial resolution. Therefore, each filter may be tuned to the SNR of the related layer, so as to preserve the spatial details of less noisy layers to a larger extent. Once all the resolutions, have been adaptively smoothed, a noise-free image version is achieved by recombining the layers of the LP.

KUAN'S FILTER

Before introducing the multiresolution scheme, let us briefly review the outline of Kuan's *minimum MSE* (MMSE) filter for multiplicative noise model [9].

Denote with $G(m,n) = F(m,n) \times u(m,n)$ the observed pixel value, with $F(m,n)$ the noise-free image, and with $u(m,n)$ the multiplicative noise, independent of $F(m,n)$, stationary and uncorrelated, with unit mean and variance σ_u^2. The MMSE estimate of F at (m,n) may be approximated by

$$\hat{F}(m,n) \approx \overline{G}(m,n) + \left[G(m,n) - \overline{G}(m,n)\right]\left(1 - \frac{\sigma_u^2}{C_v^2(m,n)}\right)\left(\frac{1}{1+\sigma_u^2}\right) \quad (1)$$

where $C_v(m,n) \approx \sigma_G(m,n)/\overline{G}(m,n)$, $\sigma_G(m,n)$ and $\overline{G}(m,n)$ being local standard deviation and average of G, respectively. Such features are evaluated on a suitable neighborhood of (m,n).

0-7803-3068-4/96$5.00©1996 IEEE

LAPLACIAN PYRAMIDS

The Laplacian pyramid is straightforward derived from the Gaussian pyramid (GP) which is a multiresolution image representation obtained through a recursive *reduction*, i.e., low-pass filtering and decimation, of the image data set.

Let $G_0 = \{G(m,n),\ m = 0,...,M-1;\ n = 0,...,N-1\}$, $M = p \times 2^K$, and $N = q \times 2^K$, again denote the observed image, p, q, and K being positive integers. G_0 and the set of *down-sampled* images $\{G_k,\ k = 1,...,K\}$

$$G_k(m,n) = \sum_{i=-I_R}^{I_R} \sum_{j=-I_R}^{I_R} r(i)\, r(j)\, G_{k-1}(2m+i, 2n+j) \qquad (2)$$

for $m = 0,...,M/2^k - 1$, $n = 0,...,N/2^k - 1$ constitute a GP [6],[7]; k denotes the current level of the pyramid and $K > 0$ the $p \times q$ top or *root*. Burt's kernel $\{r(i),\ i = -2,...,2\}$ ($I_R = 2$) has been used for separable reduction:

$$r(0) = a;\ r(\pm 1) = 0.25;\ r(\pm 2) = 0.25 - 0.5a \qquad (3)$$

From the GP, the *Enhanced Laplacian Pyramid* (ELP) [7] is defined for $k = 0,...,K-1$ as:

$$L_k(m,n) = G_k(m,n) - \sum_{\substack{i=-I_E \\ (m+i) \bmod 2,\ (n+j) \bmod 2 = 0}}^{I_E} \sum_{j=-I_E}^{I_E} e(i)e(j)G_{k+1}\left(\frac{m+i}{2}, \frac{n+j}{2}\right) \qquad (4)$$

with $m = 0,...,M/2^k - 1$, $n = 0,...,N/2^k - 1$. The following *7-taps* half-band kernel ($I_E = 3$) has been employed for expansion:

$$e(0) = 1;\ e(\pm 1) = b;\ e(\pm 2) = 0;\ e(\pm 3) = 0.5 - b \qquad (5)$$

b is an adjustable parameter determining the shape of the frequency response, but not the extent of the pass-band, as happens for (3); $b = 0.5$, and $b = 0.5625$ yield *linear* and *cubic* interpolation, respectively. Incidentally, Burt's LP [6] utilizes the same kernel (3), apart from a scale factor to adjust the *DC* gain, for both reduction and expansion.

A *Ratio Laplacian Pyramid* (RLP) may be defined to match the multiplicative nature of speckle noise. The ratio instead of the difference is used to yield a unit-mean pyramid:

$$R_k(m,n) = \frac{G_k(m,n)}{\sum_{\substack{i=-I_E \\ (m+i) \bmod 2,\ (n+j) \bmod 2 = 0}}^{I_E} \sum_{j=-I_E}^{I_E} e(i)e(j)G_{k+1}\left(\frac{m+i}{2}, \frac{n+j}{2}\right)} \qquad (6)$$

The term RLP will be used throughout as a synonymous for *ratio* ELP, with $a = 0.625$ in (3), and $b = 0.5625$ in (5).

MULTIRESOLUTION MMSE FILTERING

For natural (correlated) images, each layer of the RLP is characterized by an SNR that decreases for increasing spatial resolution. Therefore, adaptive filtering (1) may be tuned to the noise variance of the related layer (either R_k, $k < K$, or G_K) to preserve details of less noisy layers to a larger extent.

The noise variance at the kth level of the RLP can be computed from the power gain P_{2r} of the 2D reduction filter and that of the 2D interpolator P_{2e}. Let P_{1r} denote the power gain of the 1D reduction filter (e.g., (3)). Such a gain can be derived from the its frequency response $W_r(\omega)$ as:

$$P_{1r} \triangleq \frac{1}{2\pi}\int_{-\pi}^{\pi} |W_r(\omega)|^2 d\omega = \sum_{i=-I_r}^{I_r} |r(i)|^2 \qquad (7)$$

Since filtering is separable, $P_{2r} = (P_{1r})^2$. Analogously for expansion (e.g., (5)), $P_{2e} = (P_{1e})^2$, where

$$P_{1e} \triangleq \frac{1}{4\pi}\int_{-\pi}^{\pi} |W_e(\omega)|^2 d\omega = \frac{1}{2} \sum_{i=-I_e}^{I_e} |e(i)|^2 \qquad (8)$$

where the *1/2* factor in (8) accounts for up-sampling by *2*.

The variance of speckle at kth level of the GP will be

$$\sigma_u^2(k) \approx (P_{2r})^k \cdot \sigma_u^2 \qquad \left[\sigma_u^2 \triangleq \sigma_u^2(0)\right] \qquad (9)$$

The noise variance at the kth level of the RLP, $\sigma_r^2(k)$, will be

$$\sigma_r^2(k) = \sigma_u^2(k) + P_{2e}\sigma_u^2(k+1) - 2 \cdot cov\left[G_k \cdot G_{k+1}\right] \approx (1 - P_{2r}P_{2e})(P_{2r})^k \sigma_u^2 \qquad (10)$$

in which the covariance of noise between G_k and G_{k+1} was derived in the assumption of constant signal and ideal filters.

The noise-free GP at level $k < K$, namely $\hat{F}_k$ (see (1)), will be recursively given as product of the filtered R_k, i.e., $\hat{R}_k$, and the interpolated up-sampled $\hat{F}_{k+1}$, starting from $k = K - 1$:

$$\hat{F}_k(m,n) = \hat{R}_k(m,n) \times \sum_{\substack{i=-I_E \\ (m+i) \bmod 2,\ (n+j) \bmod 2 = 0}}^{I_E} \sum_{j=-I_E}^{I_E} e(i)e(j)\hat{F}_{k+1}\left(\frac{m+i}{2}, \frac{n+j}{2}\right) \qquad (11)$$

The sizes of windows used for processing at each level k should be progressively reduced for increasing k, e.g., 9×9, 7×7, 5×5, 3×3 for a *4*-layer decomposition ($K = 3$). In any cases, a large K works better. For $K = 0$, the scheme reduces to the plain Kuan's filter (1).

RESULTS AND COMPARISONS

Noisy versions of the *8 bit* test image *Harbor* have been produced from synthetic speckle with unit mean, variance σ_u^2 and amplitude multi-look statistics.

Lee's refined filter [2] has also been used for comparisons. In fact, this scheme exploits multi-scale analysis concepts as a forerunner for more recent researches.

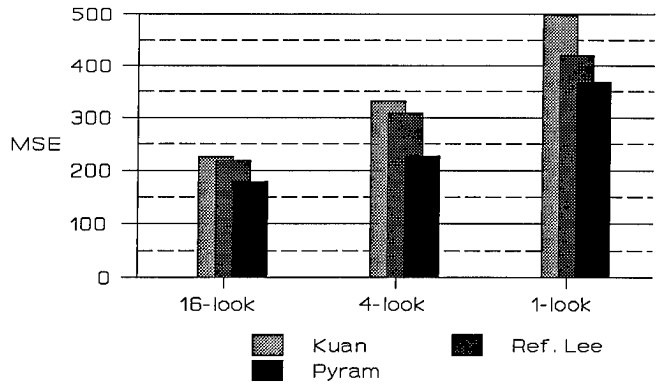


Figure 1. MSE between noise-free and filtered images.

MSE between noise-free and processed noisy versions are reported versus σ_u, expressed as number of equivalent looks, in the plots of Figure 1. The improvement of the multi-resolution filter exhibits a large trend varying with σ_u.

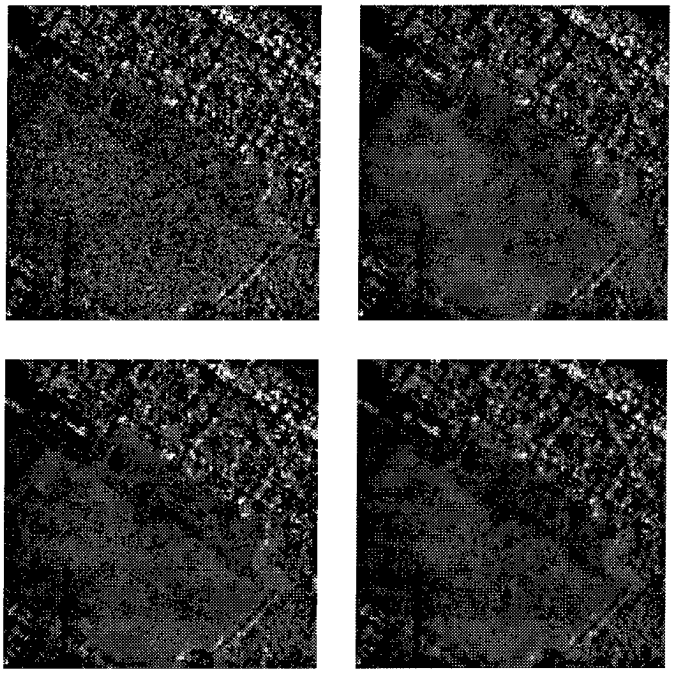


Figure 2. - A 128 × 128 detail from "Airport" image (top left); 7 × 7 Kuan's filter (top right); 7 × 7 Lee's refined filter (bottom left); 4-layer pyramid MMSE filter (bottom right).

Figure 2 shows original and three processed versions of a detail from an ERIM/STAR-1 airborne SAR image (4-looks amplitude) of an airport in Windsor, Ontario. The pyramid MMSE filter is more effective than Kuan's filter in selectively removing noise in proximity of step edges, contours and thin lines, without diminishing image sharpness.

In conclusion, the novel pyramid MMSE scheme is more efficient than Kuan's filter, providing a better estimate of the *noise-free* original, by over *1* dB. Comparisons with Lee's refined filter attest lower *MSE* and comparable visual quality.

ACKNOWLEDGMENTS

The authors are indebted to Dr. J.-S. Lee for kindly providing the code of his refined filter, as well as for useful suggestions throughout.

Work carried out with grants of ASI-Italian Space Agency.

REFERENCES

[1] J.-S. Lee, I. Jurkevich, P. Dewaele, P. Wambacq, and A. Oosterlinck, "Speckle Filtering of Synthetic Aperture Radar Images: A Review", *Remote Sensing Reviews*, Vol. 8, pp. 313-340, 1994.

[2] J.-S. Lee, "Refined filtering of image noise using local statistics", *Comput. Graphics Image Process.*, Vol. 15, No. 2, pp. 380-389, 1981.

[3] P. Meer, R.-H. Park, and K. Cho, "Multiresolution Adaptive Image Smoothing", *CVGIP: Graphic Models Image Process.*, Vol. 56, No. 2, pp. 140-148, Mar. 1994.

[4] M. C. Proença, J. P. Rudant, and G. Flouenzat, "Using wavelets to get SAR images 'free' of speckle", *Proc. IGARSS'92*, pp. 887-889.

[5] D. D. Giusto, L. Böröczky, R. Fioravanti, and S. Fioravanti, "SAR Image Filtering Using Wavelet Transform", *Proc. ICASSP'95*, pp. 2153-2156.

[6] P. J. Burt, and E. H. Adelson, "The Laplacian Pyramid as a Compact Image Code", *IEEE Trans. Commun.*, Vol. 31, pp. 532-540, Apr. 1983.

[7] S. Baronti, A. Casini, F. Lotti, and L. Alparone, "Content-driven differential encoding of an enhanced image pyramid", *Signal Processing: Image Communication*, Vol. 6, No. 5, pp. 463-469, Oct. 1994.

[8] S. Ranganath, "Image Filtering Using Multiresolution Representations", *IEEE Pattern Anal. Machine Intell.*, Vol. 13, No. 5, pp. 426-440, May 1991.

[9] D. T. Kuan, A. A. Sawchuck, T. C. Strand and P. Chavel: "Adaptive Noise Smoothing Filter for Images with Signal-Dependent Noise", *IEEE Trans. Pattern Anal. Machine Intell.*, Vol. 7, No. 2, pp. 165-177, Feb. 1985.

CLASSIFICATION AND FEATURE EXTRACTION WITH ENHANCED STATISTICS[1]

Jon Atli Benediktsson[†], *Kolbeinn Arnason*[†], *Arni Hjartarson*[⋆], *and David A. Landgrebe*[‡]

[†]Engineering Research Institute
University of Iceland
Hjardarhaga 2-6, 107 Reykjavik, Iceland
E-mail: benedikt@verk.hi.is
[⋆]The Icelandic Energy Authority, Grensasveg 9, 108 Reykjavik, Iceland
[‡]School of Electrical and Computer Engineering
Purdue University
W. Lafayette, IN 47907, U.S.A.

ABSTRACT

Classification of AVIRIS data is considered with respect to enhanced statistics. The performance of enhanced statistics is investigated in terms of feature extraction for both pixel and spatial classifiers. The feature extraction methods applied are decision boundary feature extraction and discriminant analysis. The classification results obtained by enhanced statistics are excellent and show the classifiers to be able to distinguish between several geological units with very similar spectral properties.

1. INTRODUCTION

In classification of very-high-dimensional data it is important to design classifiers which can extract the necessary information from the data, and perform classification with sufficient accuracy. The main problem with classification of very-high dimensional data is that in all real cases a limited number of training samples are available. A limited number of training samples usually poses a problem for the estimation of the parameters used in classification. If the parameters are not carefully estimated, the classifiers may not generalize well, i.e., they possibly give low accuracy for test data or may not even work at all. Since for classification of very-high-dimensional data, there are usually never enough training samples available, it is needed to apply methods which are based on estimating the best statistics. In this paper, a recently proposed method of enhanced statistics [1] is investigated in order to see how well the method performs on AVIRIS data in terms of classification accuracy for several different classification methods. The classification methods applied are both pixel based (the Gaussian ML method) [2] and spatial (the ECHO classifier) [3]. The performance of enhanced statistics is also investigated in terms of feature extraction for the different classifiers. The feature extraction methods applied are the recently proposed decision boundary feature extraction (DBFE) [4] and discriminant analysis [5]. All the above-mentioned methods are capabilities of the data analysis software MultiSpec which has been developed at Purdue University. MultiSpec was used for the analysis reported here.

The paper is organized as follows. First, the method of statistical enhancement is discussed. Then, experimental results are given and discussed.

2. STATISTICS ENHANCEMENT IN MULTISPECTRAL ANALYSIS

A well-trained classifier must successfully model the distribution of the entire data set, but the modeling must be done in such a way that the different classes of interest are as distinct from one another as possible. Therefore, it is desired to have the density function of the entire data set modeled as a mixture of class densities [1], i.e.,

$$p(x|\theta) = \sum_{i=1}^{m} \alpha_i p_i(x|\phi_i) \qquad (1)$$

where x is the measured feature vector, p is the probability density function describing the entire data set to be analyzed, p_i is the density function of class i, α_i is the weighting coefficient or probability of class i, and m is the number of classes.

[1]This research is supported in part by the Icelandic Research Council. A copy of MultiSpec can be requested by sending e-mail to landgreb@ecn.purdue.edu

0-7803-3068-4/96$5.00©1996 IEEE

Table 1: Training and Test Samples for Information Classes in the Experiment on the AVIRIS data.

Class #	Information Class	Training Size	Test Size
1	Andesite Lava from 1991	1659	1511
2	Andesite Lava from 1980	1182	1162
3	Andesite Lava from 1970	978	922
4	Old Unvegetated Andesite Lava	2562	2444
5	Andesite Lava with Sparse Moss Cover	1008	1008
6	Andesite Lava with Moss Cover	528	495
7	Andesite Lava with Thick Moss Cover	2863	2733
8	Lichen Covered Basalt Lava	1674	1023
9	Rhyolite	202	202
10	Hyaloclastite	2062	1979
11	Scoria	275	275
12	Lava Covered with Tephra and Scoria	350	350
13	Volcanic Tephra	1654	1608
14	Snow	528	484
15	Firn and Glacier Ice	242	216
	Total	17767	16412

Table 2: Number of Features as a Function of the Cumulative Eigenvalues.

Cumulative Eigenvalues	DBFE	DA
20%	1	
30%	2	
35%	3	
40%	4	
45%	5	
50%	7	
55%	8	1
60%	10	
65%	12	
70%	15	
75%	18	
80%	23	2
85%	28	3
90%	36	4
95%	51	7
99%	86	15

For a well-trained classifier, the probability density function of the entire data set, $p(x|\theta)$, can be modeled by a combination of m Gaussian densities. Therefore, in (1), θ_i contain the mean and covariance matrix for a Gaussian component. However, it is critical that (1) is a good model for the classes in the data. Shahshahani and Landgrebe [1] accomplished the modeling by an iterative calculation based on both the training samples and a systematic sampling of all the pixels in the scene. Their method is called *enhanced statistics*. In the method, the statistics are adjusted or *enhanced* so that, while still being defined by the training samples, the collection of class conditional statistics better fit the entire data set [1]. This amounts to hybrid, supervised/unsupervised training scheme with at least three possible benefits [1]: 1) The process tends to make the training set more robust, providing improved generalization to data other than the training samples. 2) The process tends to mitigate the Hughes phenomenon, thus allowing one to obtain greater accuracy with a limited training set. 3) An estimate is obtained for the prior probabilities of the classes. The estimate is a result of the use of the unlabeled samples, and is something that cannot be computed from training samples alone.

3. EXPERIMENTAL RESULTS

The test area is the region surrounding the volcano Hekla in Iceland. Hekla is one of the most active volcanos in Iceland. It sits on the western margin of the Eastern volcanic zone in South Iceland. Hekla is a ridge, built by repeated eruptions on a volcanic fissure and reaches about 1500 m elevation and about 1000 m above the surroundings. AVIRIS data from the area were collected on June 17th 1991, which was a cloud-free day in the area covered. The AVIRIS sensor operates in the visible to near infrared wavelength range, i.e., from 0.4 μm to 2.4 μm. It has 224 data channels and utilizes 4 spectrometers. During the data collection, spectrometer 4 was not working properly. This particular spectrometer operates in the near-infrared wavelength range, from 1.84 μm to 2.4 μm (64 data channels). These 64 data channels were deleted from the data set along with the first channels for all the other spectrometers, but these channels were blank. When the noisy and blank data channels had been removed, 157 data channels were left. Four full AVIRIS frames were used in the data analysis. Each frame consisted of 614 columns and 512 lines.

Fifteen information classes were defined in the area, and 34179 samples were selected from the classes. Approximately 50% of the reference samples were used for training, and the rest were used to test the data analysis algorithms (see Table 1). The analysis were performed using MultiSpec on a Power PC Macintosh computer.

The data were analyzed in the following manner. First DBFE and DA were performed. For both methods, the cumulative eigenvalues (variance) for different feature sets are shown in Table 2. These feature sets were classified using the Gaussian ML method and the ECHO classifier based on both original statistics and enhanced statistics. The results of the classifications of test data are shown in Figures 1 (DBFE) and 2 (DA). The results are then summarized in Table 3 for the feature sets that had 95% cumulative eigenvalues. From Figures 1 and 2 it can be seen that the ECHO method with enhanced statistics gave the highest accuracies for test data. The test accuracies were in general increasing as a function of the number of features, i.e., up to around 95% variance. When too many features were used, the Hughes phenomenon was observed even for enhanced statistics. The classification results for enhanced statistics are especially interesting for the ECHO classification which gave excellent and improved accuracies for both DA and DBFE feature extraction. The classification maps generated using the DBFE feature set corresponding to 95% cumulative eigenvalues were

Table 3: Summarized Overall Training and Test Accuracies for the Classification Methods Applied to the AVIRIS Data Set (Cumulative Eigenvalues: 95%).

Method	Training Accuracy	Test Accuracy
DA-ML (Original)	95.2%	89.2%
DBFE-ML (Original)	99.9%	94.3%
DA-ML (Enhanced)	91.5%	86.8%
DBFE-ML (Enhanced)	99.4%	94.5%
DA-ECHO (Original)	99.4%	95.5%
DBFE-ECHO (Original)	99.9%	94.5%
DA-ECHO (Enhanced)	98.3%	97.6%
DBFE-ECHO (Enhanced)	99.7%	96.2%
Number of Samples	17767	16412

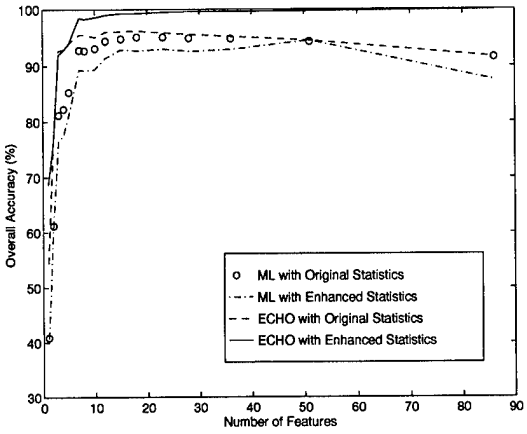


Figure 1: Test Accuracies as a Function of the Number of Features for the Methods that Utilize Decision Boundary Feature Extraction.

in many respects more detailed than existing geological maps. In fact, the classification methods could accurately distinguish between several geological units with very similar spectral properties. Also, the probability maps obtained in classification were much more improved by using enhanced statistics as compared to original statistics.

4. CONCLUSION

The use of enhanced statistics and feature extraction for AVIRIS data has been discussed. The classification results obtained by using enhanced statistics were excellent, especially for the ECHO classifier. The results demonstrate that enhanced statistics, feature extraction, and the choice of classification method are all important when very-high-dimensional data, such as AVIRIS data, are analyzed.

ACKNOWLEDGEMENTS

This work was done in part while J.A. Benediktsson was a visiting scholar in the School of Electrical and Computer Engineering, Purdue University, W. Lafayette, Indiana. The assistance of Larry Biehl of the School of Electrical and Computer Engineering is in particular acknowledged.

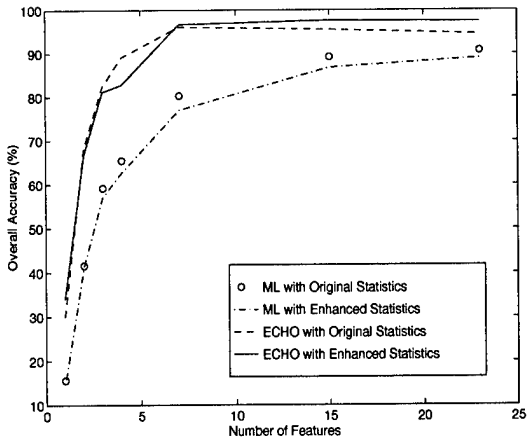


Figure 2: Test Accuracies as a Function of the Number of Features for the Methods that Utilize Discriminant Analysis.

5. REFERENCES

[1] B.M. Shahshahani and D.A. Landgrebe, "The Effect of Unlabeled Samples in Reducing the Small Sample Size Problem and Mitigating the Hughes Phenomenon," *IEEE Transactions on Geoscience and Remote Sensing*, vol. 32, no. 5, pp. 1087-1095, September 1994.

[2] P.H. Swain, "Fundamentals of Pattern Recognition in Remote Sensing," *Remote Sensing - The Quantitative Approach*, edited by P.H. Swain and S. Davis, New York: McGraw-Hill 1978.

[3] R.L. Kettig and D.A. Landgrebe, "Classification of Multispectral Image Data by Extraction and Classification of Homogeneous Objects," *IEEE Transactions on Geoscience Electronics*, GE-14, pp. 19-26, 1976.

[4] K. Fukunaga, *Introduction to Statistical Pattern Recognition*, 2nd Edition, Academic Press, New York, N.Y., 1990.

[5] C. Lee and D.A. Landgrebe, "Feature Extraction Based on Decision Boundaries," *IEEE Transactions on Pattern Analysis and Machine Intelligence*, Vol. 15, No. 4, pp. 388-499, April 1993.

Solar Irradiance Determination by Using ATSR-2 Data

Yong Xue, David T. Llewellyn-Jones and Sean P. Lawrence
University of Leicester

Earth Observation Science Group
Department of Physics and Astronomy
University of Leicester, Leicester, England
Tel: +44-116-2523521, Fax: +44-116-2525262, Email: YX1@LE.AC.UK

Abstract -- In this paper, three physical methods were used to determine solar irradiance by using ERS ATSR-2 data. The schemes were applied to the land and sea areas. The visible and near-infrared reflectance were derived from ERS-2 ATSR-2 spectral bands by using atmospheric radiative transfer model developed by Xue and Cracknell. The narrow-band reflectances are combined into a measure of surface albedo by use of a weighted averaged scheme. The schemes were applied to the land and sea areas. The three schemes are agreement very well each other. All three schemes can also be developed to determine the hourly or daily solar irradiance. However, our current analysis is restricted to a small range of conditions and needs to be extended to a larger dataset.

INTRODUCTION

The retrieval of surface solar flux from satellite radiances is based on the expression of the atmospheric radiative transfer, or on statistical relationships, relating the top of the atmosphere flux to the surface solar flux. Several models have been developed for inferring surface irradiance from satellite-based radiance measurements [1]. After a long period of testing, several of shortwave models matured to a stage where they could be implemented within known limits of accuracy. Two algorithms that have met the required accuracies on a global scale, have been developed at NASA Langley Research Center by W. F. Staylor [2] and at the University of Maryland [3].

With the launch of ERS-2 in April 1995, new possibilities have opened up. ERS-2 carries onboard Along Track Scanning Radiometer (ATSR) which has a unique feature of viewing the Earth's surface from two different angles, i.e., 0° (nadir) and 55° (forward) and in multi-spectral mode. The instantaneous field of view (IFOV) at the nadir on the Earth's surface is a 1 km by 1 km square which is imaged on to the detector element via an off-axis paraboloid mirror. Xue and Cracknell [4] gave the ATSR's technical characteristics.

The paper concentrates on short-wave radiation on sea and land surfaces. In this paper, three physical methods were used to determine solar irradiance by using ERS ATSR-2 data. We referred them as "D scheme", "T scheme" and "O scheme".

EARTH SURFACE ALBEDO

Atmospheric models assuming the ground to be uniform and Lambertian have been studied extensively [5]. The aim of the paper by Xue and Cracknell [6] was to use the computational method to find an operational method which relies on multiple view angle observations or multiple solar zenith angle observations of the surface to accomplish part of this task in a routine manner. In the paper they attempted a solution to the problem of the retrieval of surface reflectance from satellite radiance measurements based on a solution of the radiative transfer equation developed further by Kondratyev [7]. The problem defined for a horizontally-stratified atmosphere is sufficient to cover most applications for light scattering in planetary atmospheres.

Simple calculations lead to the following results of integration of the radiative-transfer equation with the boundary conditions for a downcoming global radiation flux and upgoing global radiation flux. Therefore we find the relation between the surface albedo A and the Earth system albedo, A', as observed from space [6]. The solar zenith angle is calculated from latitude, longitude and time. The atmospheric optical depth (τ_0^{λ}) is determined by the turbidity state of the atmosphere.

For the ERS-2 ATSR sensor with two view angles $\theta'=0$ and $\theta'=\theta_0$, from the model mentioned above, we have simultaneous equation for A' and A'_0, which are the Earth system reflectance observed from space for nadir and zenith angle θ_0, respectively [6]. Numerical solution of above equation, to give the value of the total atmospheric optical thickness, can be carried out by many numerical methods. Having found the value of the total atmospheric optical thickness, we can derive the Earth surface albedo from Earth system albedo.

0-7803-3068-4/96$5.00©1996 IEEE

PARAMETERIZATION OF SHORT-WAVE RADIATION

The usefulness of satellites in climate research is primarily due to the ability to produce global, uniformly distributed, long term records of observations. The three schemes, which were used in the paper are:

D scheme: From Xue and Cracknell's paper [6], we can calculate spectral downcoming radiation flux and upgoing radiation flux.

T scheme: From the boundary conditions used for thermal inertia modelling, Xue and Cracknell [8] used the expression

$$Q_s = (1-A) S_0 C_t \cos Z , \qquad (1)$$

where A is the Earth surface albedo, S_0 is the solar constant, C_t is the atmospheric transmittance in the visible spectrum and cosZ is the function of α (the local latitude), δ (the solar declination) and ω (the angular velocity of rotation of the Earth).

O scheme: Oberhuber [9] calculated the insolation from the daily averaged heat flux at the top of the atmosphere for relative humidity and inclination. the resulting relations required to compute the net short wave radiative flux Q_s are:

$$Q_s = \frac{\alpha\kappa (1-A) S_0 \cos^2\eta (\langle d\rangle/d)^2}{((\cos\eta + 2.7) re(T_a)/p + 1.085\cos\eta + 0.1)} , \qquad (2)$$

where κ is the function of the solar elevation at noon and η the solar elevation. α is a tuning coefficient and is set to 0.9. d denotes the actual distance between the sun and Earth and <d> its annual average. The ratio $(\langle d\rangle/d)^2$ is estimated in terms of the Julian Day β. δ is the solar declination in radians. r is the relative humidity and $e(T_a)$ is the vapour pressure in pascals (1 Pa = 10^{-2} mbar).

TESTS AND RESULTS

The date and time of the ATSR data were 2nd August 1995 and 11:00 GMT. Fig. 1 shows the net spectral solar radiation in 0.87μm channel. Cloudy areas (white plot) were not calculated. D scheme can give spectral reflectance, transmittance and solar radiation for each visible channel. T scheme and O scheme give total net solar radiation. T scheme gives lower values in sea areas. The three schemes are also applied to the ATSR data (4th June 1995) in deforestation area (Rondonia) in Brazil. Figure 2 shows one profile of the area. In T scheme, we can also substitute the extraterritorial solar spectral radiation (ToA radiation) for the solar spectral irradiation on the ground. The absolute error is small because of the linearization relationship between these two parameters.

Comparing T scheme and O scheme, we can see that

$$C_t = \frac{\alpha\kappa\cos\eta (\langle d\rangle/d)^2}{((\cos\eta + 2.7) re(T_a)/p + 1.085\cos\eta + 0.1)} \qquad (3)$$

For most cases, C_t from Eq. (1) is between 0.7 - 0.60. This value is an averaged value of atmospheric transmittance. But, for instantaneous solar radiation calculation, C_t can vary in a big range. From Fig. 2, the results from O scheme and T scheme are agreement with each other for the areas with atmospheric transmittance around 0.7 - 0.60. So T scheme can give instantaneous and daily averaged solar radiation but O scheme can only give daily or monthly averaged solar radiation. O scheme give smaller values than that from T scheme. In this paper, instantaneous radiation fluxes have been calculated. The O scheme was better used to calculate the monthly averaged radiation flux. It smooths the fluxes. The T scheme and D scheme were used to calculate the instantaneous flux. And monthly averaged flux will be obtained from the instantaneous flux.

The net solar radiation from D scheme, which is received by four ATSR visible channels, is only about 20% of total net solar radiation. This agrees with the conclusion in Iqbal [10]. Also, the deforestation areas have great variabilities in solar irradiance, but the O scheme can not give this point. In this paper, instantaneous radiation fluxes have been calculated.

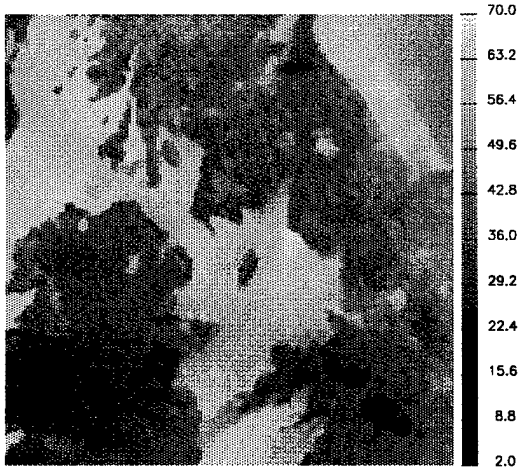


Fig. 1 The instantaneous net solar spectral irradiance in 0.87μm channel (Aug. 2, 1995). The unit is W/m^2.

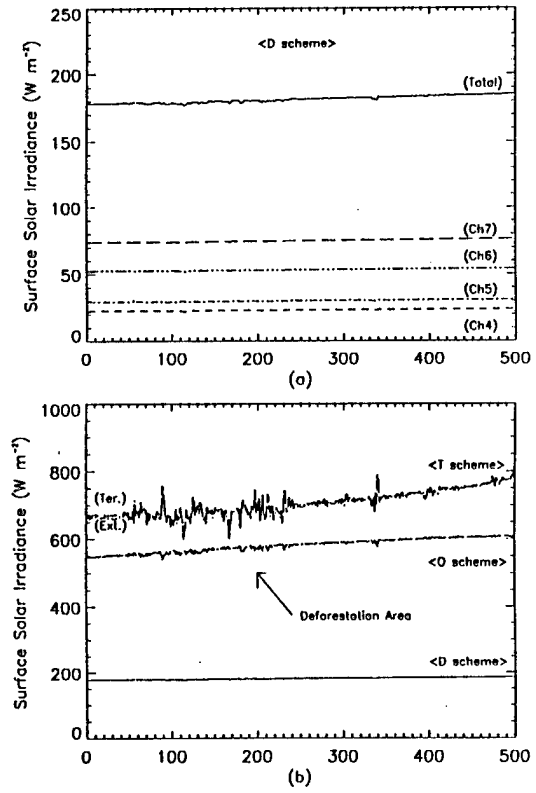


Fig. 2 The comparison of the instantaneous solar irradiance calculated by using three schemes in Rondonia (Jun. 4, 1995).

CONCLUSIONS

The paper demonstrated that ATSR-2 data can be used to determine the solar irradiance which can be used in coupling GCMs to predict and simulate the global climate. The absorbed solar surface irradiance is usually obtained from additional information on the surface albedo [3]. Fortunately, over the ocean the albedo and, therefore, shortwave exitance flux is predictable to good accuracy in contrast to the difficulties that this term causes over land, when attempting to evaluate net shortwave irradiance from space [11]. All three schemes can also be developed to determine the hourly or daily solar irradiance. However, our current analysis is restricted to a small range of conditions and needs to be extended to a larger dataset. With the development of the new generational remote sensor, ATSR, heat fluxes can be calculated by using the ATSR data-set, with its very high radiometric precision, and *in situ* data. We have in hand some research work on this and expect to publish the results in due course.

ACKNOWLEDGEMENT

The authors thank the RAL, Oxford for supplying the ATSR data.

REFERENCES

[1] R. T. Pinker, R. Frouin, and Z. Li, "A review of satellite methods to derive surface shortwave irradiance," Remote Sensing of Environment, Vol 51, pp 108-124, 1995.

[2] W. L. Darnell, W. F. Staylor, S. K. Gupta, N. A. Ritchey, and A. C. Wilber, "Seasonal variation of surface radiation budget derived from international satellite cloud climatology project C1 data. J. Geophy. Res., Vol. 97, pp. 15,741-15,760, 1992.

[3] R. T. Pinker, and I. Laszlo, "Modelling surface solar irradiance for satellite applications on a global scale," J. Appl. Meteo., Vol. 31, pp. 194-211, 1992.

[4] Y. Xue, and A. P. Cracknell, "The earth's surface temperature derivation from satellite data and its prediction by using a second-order approximation thermal inertia model (SoA-TI Model)," In The Determination of Geophysical Parameters from Space, Proceedings of the 43th Scottish Universities Summer School in Physics, N. E. Fancey, ed. 1996, In press.

[5] A. Rosema, and J. L. Fiselier, "Meteosat-based evapotranspiration and thermal inertia mapping for monitoring transgression in the Lake Chad region and Niger Delta." Inter. J. Remote Sensing, Vol. 11, pp. 741-752, 1990.

[6] Y. Xue, and A. P. Cracknell, "Operational bi-angle approach to retrieve the Earth surface albedo from AVHRR data in the visible band," Inter. J. Remote Sensing, Vol. 16, pp. 417-429, 1995.

[7] K. Ya Kondratyev, Radiation in the Atmosphere, New York: Academic Press, 1969.

[8] Y. Xue, and A. P. Cracknell, "Advanced Thermal Inertia Modelling," Inter. J. Remote Sensing, Vol. 16, pp. 431-446, 1995.

[9] J. M. Oberhuber, An atlas based on the COADS data set: the budgets of heat, buoyancy and turbulent kinetic energy at the surface of global ocean. Max-Planck-Institut für Meteorologie, Report No. 15, 1988.

[10] M. Iqbal, An Introduction to Solar Radiation, Toronto, Canada: Academic Press, 1983.

[11] Katsaros, K. B., "Parameterization schemes and models for estimating the surface radiation budget," In Surface Waves and Fluxes, Vol. II, G. L. Geernaert and W. J. Plant, eds. Dordrecht: Kluwer Academic Publishers, 1990, pp.339-368.

Comparison of Linear Least Squares Unmixing Methods and Gaussian Maximum Likelihood Classification

Richard Fernandes[1], John R. Miller[2], Lawrence E. Band[1]
[1]Dept. of Geography, University of Toronto, 100 St. George St., Toronto, Ontario, M5S 1A1, CANADA
Tel: (416)978-5070, fernande@geog.utoronto.ca
[2]Dept. of Physics and Astronomy, York University, 4700 Keele St., North York, Ontario, M3J 1P3, CANADA

ABSTRACT

The study addresses the lack of controlled linear least squares unmixing studies comparing with standard per-pixel classification techniques at the same resolution. A general forward model for scene reflectance is specified and a constrained total least squares solution is described. This solution encompasses previous least squares unmixing methods. The Bayes risk for per-pixel classification is developed to indicate when classification may be inaccurate. Experiments comparing the accuracy of per-pixel classification and least squares unmixing suggest that unmixing is significantly more accurate when complete mixing occurs in the scene.

1.0 INTRODUCTION

Linear least squares (LS) unmixing offers an alternative to standard per pixel Gaussian Maximum Likelihood Classification (MLC) for estimating vegetation cover when pixel size is larger than the size of canopy clumps. Problems unmixing include the tendency of endmembers with low spectral contrast to be completely confused[1];and that estimates of single pixel mixtures of vegetation cover with 20m pixels are "not very accurate" - with an r^2 of less than 0.6 [2].

This study defines the general linear LS inversion model which includes errors in endmember signatures, observation noise, and a priori knowledge. An upper bound on the Bayes risk for MLC of mixed pixels is developed to forecast MLC performance for different targets. Lastly, simulation studies and controlled experiments are conducted to determine if and when spectral unmixing procedures are preferable to MLC for quantitative extraction of scene components

2.0 LINEAR LEAST SQUARES METHODS

One possible linear forward model of pixel reflectance is:

$$[A+E]\underline{x} = [\underline{b}+\underline{r}] \qquad (1)$$

$$\mathrm{E}\{\underline{e}_k\} = 0 \quad and \quad \mathrm{E}\{\underline{e}'_k \underline{e}_k\} = N_k$$
$$\mathrm{E}\{\underline{r}\} = 0 \quad and \quad \mathrm{E}\{r'r\} = M$$
$$\underline{x} \geq 0 \quad and \quad j'\underline{x} = 1$$

where $\underline{b}$ and $\underline{r}$ are m element observed reflectance and additive noise vectors with noise covariance M; $\underline{x}$ is an n element endmember fraction vector; A and E are m by n matrices; with column $\underline{a}_j$ representing the reflectance signature of endmember j; and $\underline{e}_j$ an additive noise vector for this endmember signature with covariance matrix N_k;

The model assume that: the pixel is a 2-D single-scattering surface; the specified endmembers are sufficient; $\underline{a}_j$ is representative of reflectances found in the scene for endmember j;the sensor modulation transfer function is constant over the pixel and zero elsewhere; and that endmember BRDF variations in the scene are modeled or negligible. These assumptions allow the use of radiance instead of reflectance data if endmembers are derived from the image.

The Total Least Squares[3] (TLS) formulation solves (1) by estimating both endmember signatures and fractions. The TLS solution is ill-conditioned and the optimistic model assumptions make it suspect as a robust unmixing method. A more robust method ,Constrained TLS (CTLS), constrains the expected error in the solution to match the errors E and $\underline{e}$:

$$\min \quad \mathrm{E}\left\{\left\|\underline{x}-\bar{\underline{x}}\right\|\right\} \quad \ni \left\|N^{-1}(b-Ax)\right\| = n \qquad (2)$$

$$\text{and } N = \sum_1^n \left[\alpha \underline{x}_k * N_k + (1-\alpha)M\right] \qquad (3)$$

Equation (2) is similar to a LS problem in [4] but here N is a function of both the mixture being estimated and the observation noise. A larger α puts greater weight on endmember signatures errors in

0-7803-3068-4/96$5.00©1996 IEEE

comparison to observation errors. The solution for (2) was estimated by using the normalized MLC probabilities as $\underline{x}$ for each pixel and for computing N for the pixel. The constrained LS problem (SUM2ONE) and non-negative LS problems (NONNEG) are sub-problems of (2) and their solutions are given in [4].

3.0 THEORETICAL ANALYSIS OF MLC RISK

For a two endmember problem with equal a priori probabilities the MLC risk is:

$$r(b) = 0.5 \int_{L2} \{[1 - x_1 + x_2]q_1(\underline{b})p(\underline{b})\}db + 0.5 \int_{L1} \{[1 - x_2 + x_1]q_2(\underline{b})p(\underline{b})\}db \quad (4)$$

$p(\underline{b})$ is the target mixture density function;
$q = 0.5 * p_i(\underline{b}) / p_m(\underline{b})$ is the a posterior probability;
$p_m(\underline{b})$ is the training mixture density function.
L1 and L2 are regions of $\underline{b}$ where MLC decides endmember 1 and 2 respectively.

If p_m is estimated only using pure pixels:

$$p_m = N(\underline{a}_1, N_1) + N(\underline{a}_2, N_2) \quad (5)$$

Where N(m,S) denotes a Gaussian with mean m and covariance S. The Battacharrya bound is:

$$r(b) \leq \int_{\forall b} \left\{ \sqrt{p_1 p_2}\sqrt{x_1 x_2} * \frac{p}{p_m} \right\} db \quad (6)$$

This result does not have the scaling factor sqrt(P1*P2) found with the conventional Battacharya bound. However sqrt(x_1*x_2) is always larger than 0.5; which equals sqrt(P1*P2) for the equal a priori case commonly assumed with MLC. The p/p_m term acts to increase the risk for mixed pixel compared to pure pixel targets. The increase in risk is proportional to the flattening of p which in turn is proportional to the amount of mixing present. Equation. 6 indicates that MLC accuracy reduces gradually until the Mahalanobis distance between target pixels and endmember spectra is large.

Assessing the risk of a LS unmixing algorithm is not straightforward due to the nonlinearities brought about by constraints in (1). Empirical studies were conducted to compare unmixing risk with MLC risk for three cases: pure pixels;boundary mixing; and complete mixing .

4.0 EXPERIMENT 1 - PURE PIXELS

A 15 channel CASI reflectance image of a scale model of an Old Jack Pine site of the BOREAS field campaign was acquired at the York University BRDF facility. A 29.5° illumination angle was used to simulate the low sun angles during snow cover periods where spectral contrast is high. The image resolution permitted on the order of 20 pixels per tree crown. The endmembers used were sunlit crown (SC), shaded crown (ZC), sunlit background (SB) and shaded background (ZB). Identification of pure pixels was performed by visual interpretation.

MLC, and NONNEG and SUMTOONE unmixing were performed on only the pure pixels using a jackknife design for calibration. Table 1 reports classification accuracy and Kappa coefficient where the unmixing label is defined with the class with the largest cover fraction..

Table I - Experiment I Classification Assessment

	SC	ZC	SB	ZB	Kappa
MLC	917	96.9	96.7	98.7	0.947
NONNEG	20.0	27.8	3.5	20.2	-0.05
SUM-ONE	80.2	39.4	57.8	73.2	0.311

MLC was significantly more accurate than NONNEG and SUM-TO-ONE. The lack of covariance information with the unmixing methods resulted in confusions for ZC which lies along a trajectory between ZB and SC in spectral space. The shadowing of ZC also resulted in an apparent NIR reflectance close enough to be confuse it with SB.

5.0 EXPERIMENT II - BOUNDARY MIXING

A 15 Band CASI radiance image of the Northern Fen site of the BOREAS experiment was used. The endmembers identified were: open water, forest canopy, bare ground, and mosses and sedge. These categories were chosen based on the ability to discriminate them visually on a 4m x 4m pixel colour composite. Shadows were minimal due to a 50° solar zenith angle.

Validation and training regions consisting of pure pixels of each category were defined by visual interpretation. Simulated 60m and 116m pixel

scenes were computed using mean filtering and subsampling.. The training areas defined at 4m resolution were registered and subsampled as well.

MLC was performed at each resolution using the training areas at that resolution. SUMTOONE unmixing was applied to the low resolution scenes using endmembers defined by the MLC training areas. All results were re-registered and upsampled to the original 4m resolution validation areas. The unmixing result were classified by labeling each pixel with the class with largest fraction and are given in Table II. The upsampling resulted in duplication of low resolution pixels biases the Kappa statistics. However, even at 116m pixels over 300 independent samples were available before upsampling. The Kappa 1 standard deviation was less than 0.05 for all results.

Table II - Exp. II - Classification Kappa Statistics

	4mx4m	60mx60m	116m
MLC	84.3	84.1	76.8
SUM-ONE	n/a	79.8	79.8

Table II indicates that MLC accuracy dropped gradually with increased mixing. Mixing was not complete since the 116m pixel image still had isolated pure pixels. Unmixing was comparable to MLC at both resolutions tested. This result has not been noted elsewhere since most studies have not performed per pixel classification at the same resolution that unmixing was performed.

6.0 EXPERIMENT III - COMPLETE MIXING

Spectra of red and black paper acquired by the CASI in 10 channels were mixed. Target mixtures of varying proportions and additive noise levels were tested. Unbalanced noise trials used diagonal endmember noise covariance matrices with the mean variance set equal to the mean signal magnitude. Both the magnitude and shape of noise covariance differed for targets and their mixtures. Fig. 1 shows the r.m.s.e red and black fraction errors for classification and constrained TLS unmixing.

MLC has a significantly higher r.m.s.e than CTLS with the exception of either endmembers of an equal mixture. As predicted in Section 3. MLC performs poorly when mixing is very strong. The higher accuracy at the midpoint may be because both endmembers are equidistant from it. This is implicitly considered in the sqrt(q1*q2) term in (3). CTLC had consistently low r.m.s.e

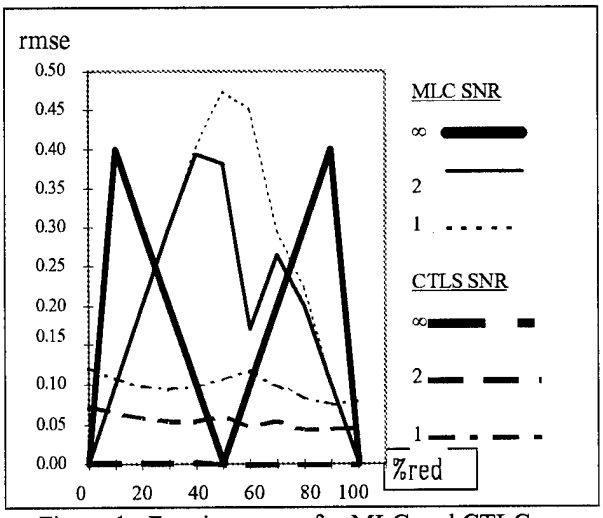


Figure 1. Fraction errors for MLC and CTLC.

7.0 CONCLUSIONS

A general formulation for the linear least squares unmixing problem was presented. The Bayes risk of MLC forecasts poor performance only with complete mixing. Linear LS unmixing was significantly less accurate than MLC when identifying surface cover of scenes with little mixing. Linear LS unmixing was more accurate than MLC as mixing increased. Further research should focus on a controlled scaling experiment to compare MLC and TLS unmixing over a wide range of scales.

8.0 REFERENCES

[1] P. Gong, J. R. Miller and M. Spanner, "Forest Canopy Closure From Classification and Spectral Unmixing of Scene Components - Multisensor evaluation of an Open Canopy. IEEE Trans. Geosci. Rem. Sens., vol. 32, pp. 1067-1081, 1994.

[2] C. Hlavka and M. Spanner, "Unmixing AVHRR Imagery to Assess Clearcuts and Forest Regrowth in Oregon," IEEE. Trans. Geosci. Rem. Sens., vol. 33, pp. 788-795, 1995.

[3] V. Mesarovic, N. Galatsanos, and A. Katsaggelos, "Regularized Constrained Total Least Squares Restoration," IEEE Trans. Image Processing, vol. 4, pp. 1097,1108, 1995.

[4] J.J. Settle and N.A.Drake,"Linear mixing and the estimation of ground cover proportion," Int. J. Rem. Sen., vol 14, pp. 1159-1177, 1993

Development and Test of a Raster Scanning Laser Altimeter for High Resolution Airborne Measurements of Topography

David L. Rabine
Code 924 - NASA
Goddard Space Flight Center, Greenbelt, MD 20771
301-286-4202 voice/301-286-0213 fax/david@eib1.gsfc.nasa.gov

Jack L. Bufton
Code 920 - NASA, Goddard Space Flight Center, Greenbelt, MD 20771

Charles R. Vaughn
Code 972 - NASA, Wallops Flight Facility, Wallops Island, Virginia

INTRODUCTION

The RAster SCanning Airborne Laser (RASCAL) sensor was developed in 1995 at the Goddard Space Flight Center for airborne mapping of surface topography. RASCAL is a second generation laser altimeter with application to both Earth (airborne) and planetary surface (space-based) topography measurement. It differs from earlier nadir-profiling laser altimeters (ref.1) by a two-order of magnitude increase in pulse repetition rate and provision for a near-contiguous scan pattern. It was operated in a NASA airborne remote sensing program in California in September 1995 where it's ability to produce a high-resolution (better than 2 m spatial resolution) three-dimensional image of topography was demonstrated. The design and operational use of the RASCAL sensor are presented below, along with sample data sets that demonstrate its ability to map surface elevation at the sub-meter level of accuracy.

INSTRUMENT AND MISSION DESCRIPTION

The principal of operation of RASCAL is the time-of-flight measurement of 10 nsec wide laser pulses, each of 150 μJ pulse energy, from which the range (i.e. distance) from aircraft to ground can be determined. Optical pulses at 523 nm wavelength are generated by a Nd:YLF Q-switched diode-pumped frequency-doubled laser transmitter and directed at the Earth's surface by a rotating scan mirror. The pulses are then received by a 12.5 cm diam. telescope that is co-located with the laser in the RASCAL sensor, detected by a nsec-response photomultiplier tube, and processed on-board by timing and energy measurement electronics in a microprocessor-controlled data system. The size of each RASCAL laser footprint on the surface is determined by the aircraft height above ground level and laser divergence, and is nominally maintained at 1 m in diameter. To date, the RASCAL instrument has been operated on the NASA Wallops Flight Facility T-39 twin-turbo jet aircraft (N425NA) using a nominal straight-and-level flight pattern with a ground-speed of 100 m/sec at an altitude of 500 m above ground level. Airborne operation of RASCAL at 5,000 laser pulses-per-sec produces a nominal 100 m wide swath of topographic data with 1.67 m along-track and across-track (i.e. spatial) resolution between each measurement footprint. The primary data generated by RASCAL are time-interval-unit (TIU) measurements of the round-trip travel time of each laser pulse between a zero reference surface in the instrument and the Earth's surface. Additionally, the apparent surface reflectivity (i.e. detected pulse energy) of each laser pulse is recorded. Pulse energy data are used to correct the time-interval data for time-walk effects resulting from surface reflectance variability, on the threshold detecting algorithm of the instrument. The RASCAL time-of-flight data must also be corrected for output beam angle, sensor pointing attitude, and the global positioning system (GPS) derived trajectory of the T-39 airborne platform in order to derive accurate values (i.e. geo-referenced values) for the Earth surface elevation and spatial position of each sensor footprint.

Fig. 1 is a block diagram of the RASCAL sensor. Shown are details of the raster scan generator which is based on a 45-sector polygon-shaped aluminum scan mirror. This device was specially fabricated by Lincoln Laser Corp., by means of a diamond-turning process that produced close tolerances for the mirror surface quality of each sector and sub-mrad accuracy in scan pattern generation. The laser transmitter is a diode-pumped Nd:YLF laser (TFR Model from Spectra Physics, Inc.). This frequency doubled laser pulses at 523 nm wavelength producing a visible, mm-size beam with a two-dimensional gaussian intensity cross-section and a 2 mrad divergence. The 15 cm diameter polygon scan mirror, which is mounted with its rotation axis parallel to the aircraft flight direction, directs this high repetition-rate pulsed laser beam across the ground track of

0-7803-3068-4/96$5.00©1996 IEEE

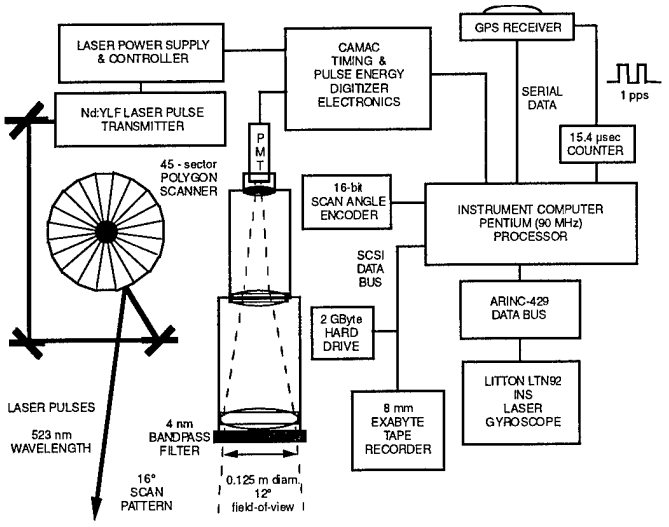


Figure 1 - Block Diagram of the RASCAL altimeter

the aircraft in a raster pattern. Note that the transition between sectors causes an abrupt retrace (i.e. reset) of the scan pattern. The rotation speed of the mirror is servo-controlled and can be fixed to a constant rate. A rotation of 80 rpm creates the contiguous scan pattern for the current platform. At this speed, the mirror produces 60 scans per sec (45 faces multiplied by 80 rpm) to produce the desired across-track pattern. Ground tests showed that laser spots were stable to approximately 1/4 of a spot diameter in pointing angle from the RASCAL sensor and the scan speed was stable to better than 1%. The 45 sectors in the polygon scan mirror each occupy an 8 degree sector of the scan mirror and produce a 16 degree scan pattern by angle-doubling of the reflected laser beam. The RASCAL telescope is a custom-designed refractive optical system based on stock, spherical-surface lenses that focus a 12 degree field-of-view onto a 20 mm diameter blur circle where the photomultiplier tube photocathode is located. A 4 nm bandpass filter covers the entire telescope entrance aperture and provides some degree of rejection of solar background irradiance. The telescope field-of-view was set less than the scan pattern in order to eliminate, by truncation, those laser pulses that reflect from edges of each scan mirror sector. The effective scan pattern is a ± 6 degree swath (i.e., 0.2 radian) that is centered on the aircraft roll axis and consists of 3,600 laser pulses for topography measurements per second. This pattern nominally results in a 60 by 60 grid of measurements that is 100 m square.

The timing and pulse energy digitization electronics of RASCAL are contained in a CAMAC (IEEE 583 Bus) crate along with various supporting electronics consisting of a real-time clock, range-gate, and power supply modules. The time-interval-unit that is the heart of the RASCAL data is a LeCroy, Inc., Model 4204 time-to-digital converter which has 0.15625 nsec timing resolution. These CAMAC electronics are controlled by a custom C-language program running on a 90 MHz Pentium processor. The flight software fires the laser under external trigger control and then reads the TIU and pulse energy data for each laser pulse. Time basis is provided by the 1 Hz signal generated by the GPS receiver. Ancillary data on the polygon scan mirror position are derived from a BEI Motion Systems Co. 16-bit shaft angle encoder and the aircraft roll, pitch, and heading angles from a Litton LTN92 laser gyroscope inertial navigation system (INS) and are read at a rate of 100 measurements per sec by the flight software. Status information and small subsets of data are interleaved to the screen during data collection for quality assurance.

A typical, T-39 airborne science flight of RASCAL spans 2.5 hours of data operations and produces approximately 15 million laser pulse measurements of surface topography. The record from each flight comprises approximately 700 megabytes of range-to-the-surface, pulse energy, GPS, and pointing angle data. Each mission includes deliberate measurements of instrument pointing angle biases. For these measurements the T-39 aircraft is flown in a series of deliberate banking and pitching maneuvers over bodies of water to produce a data record with a wide variety of laser pulse incident angles over a locally-horizontal surface. Pointing angle data collected from a laser gyroscope system mounted on the instrument platform are used in data analysis to compute the pointing biases which reproduce a flat surface from the ranging data. End-to-end length calibration of the ranging data for each flight is accomplished by two passes (in opposite directions) over the ground-based GPS reference station in which the X-Y location of the GPS antenna and its surface elevation appear in the altimetery data. In addition, intersecting passes over the topography of the science flight lines are typically flown to provide self-consistency tests of the data within each flight mission and among all flight missions over the same terrain. Within three hours of landing from each flight mission, all flight and ground data are backed-up on hard drives and data tapes, a GPS trajectory of the aircraft position at 500 msec intervals with ~ 50 cm accuracy is produced, and laser altimeter data quality is assessed. Post flight data analysis takes place over the next few months. In this phase, instrument range and pointing angle biases are combined with a 5 cm-quality GPS trajectory of the aircraft derived from precision orbits for the GPS spacecraft. The end goal of measurements, calibrations, and analysis is sub-10 cm vertical accuracy in geo-referenced topographical data for each RASCAL sensor pulse on the Earth's surface. The final data products are the latitude, longitude, and surface elevation of each laser pulse which constitute digital elevation maps of the scientific study sites.

DATA ANALYSIS METHODOLOGY

The final data product of surface elevation for individual laser pulse measurements requires many steps of data analysis. A suite of Interactive Data Language (IDL) routines were developed for processing laser altimetery data in a UNIX environment on a SUN Sparc 10 workstation. These routines were developed for other laser altimeters and only slight modifications were required for RASCAL's scanning system. Supplemental routines were written to accommodate some of the unique features of the scanning system. There are several steps involved in processing the data.

Determination of biases for pointing angle data and the range data must be done before processing can begin and are the first steps in data analysis. The aircraft, laser gyroscope angle measurements are re-sampled, to match the laser pulse rate, from the smoothed (i.e. filtered) set of 100 samples-per-sec of the INS data record. The INS data are also time shifted to compensate for transport delay from the INS to the data system. The digital encoder's position as a function of time is converted to an output beam angle. These angles are similarly interpolated from the 100 sample-per-sec record of the encoder and inserted into the data structure as a roll bias for each pulse. The aircraft GPS trajectory, which is available only at 2 Hz, is then fit with a cubic-spline to provide a smoothly varying position for the aircraft as a function of time that can be re-sampled for each laser pulse. The next step is application of a range calibration to each laser pulse. Range calibration information is generated in ground testing by operating RASCAL with its scanner stopped over a short (~ 50 m) horizontal path, measuring range as a function of pulse energy, and then measuring the calibration range with a steel tape and a static GPS survey. From these ground-based data a look up table of range vs. pulse energy is created to compensate for time-walk due to variable pulse rise times affecting the threshold detecting range measurement. The range correction is then applied in the data analysis to each laser pulse. A key aspect of this procedure is determining the exact distance between the RASCAL scan mirror surface, which is used as a zero-range reference surface, and the calibration target. Finally, all laser pulse data are passed through a pulse energy filter to eliminate laser pulses with too low or too high pulse energy. The high and low limits are set based on quality of the range calibration. Both high (i.e. saturated) and very low energy laser pulses have excessive (> 20 cm) range errors.

After all data are prepared and filtered, the geo-referencing of each remaining laser pulse proceeds by translation and rotation in a matrix formulation. This procedure is derived from the method of Vaughn et al (ref. 2) and was converted into an IDL procedure. Geo-referencing involves rotation through angular offsets between INS and scanner reference frames, vector displacement of the laser output point to the GPS antenna element, and translation by the RASCAL range measurement to the Earth's surface. All angle biases are taken into consideration when calculating these rotations. The end result is a latitude, longitude and elevation of each valid range measurement in the reference frame that the GPS trajectory was processed. Typically this is the (World Geodedic System) WGS-84 reference ellipsoid.

OPERATIONS COMPLETED AND EXAMPLES

The RASCAL instrument completed its first operational science deployment during October 1995 in eastern and southern California. During a two week period, the RASCAL instrument was shipped to Los Angeles by air cargo, hand carried to Bishop, CA, incorporated into the Wallops Flight Facility T-39 aircraft (N425NA), and employed in two campaigns of science investigations comprising 7 separate flight missions. The first series of flights (5) were conducted from the Bishop Airport over volcanic terrain of Long Valley Caldera and a wide variety of landforms within the Death Valley National Monument. The second series of science flights (2) were conducted from Edwards Air Force Base over terrain along the San Andreas fault and related faults at the southern end of the San Joaquin Valley. These science application data sets will be the subject of future presentations and journal manuscripts. In our current program of data analysis we are verifying the data analysis methodology described herein and investigating data quality. To those ends, we provide examples of data acquired at Bishop, CA and the NASA Dryden Flight Research Center (DFRC) at Edwards Airforce Base, CA.

Fig. 2 is an image of topographic data collected during a RASCAL flight mission on October 13, 1995 over the hangars and support buildings of DFRC. The data show the main hangar complex at DFRC, cars parked around the various buildings, and the concrete ramp area adjacent to the hangars. The RASCAL surface elevation data in this figure were smoothed in IDL by triangulation, gridding and linear surface fitting of all valid measurements. Close examination at the pixel level of these data revealed that part of our ground-based GPS antenna was measured. This permitted us to positively identify the GPS base station antenna at the point indicated by the arrow head in Fig. 2. The RASCAL measurements at this point were a mean surface elevation of 665.30 m (WGS-84 ellipsoidal height), a latitude of North 39.949444140 deg., and a longitude of East 242.11390015 deg. The measured elevation was computed from 10 pixel values of the concrete ramp surrounding the GPS antenna base. These data compare to the following values for the Defense Mapping Agency marker # 1381 GSS, which was embedded in the concrete ramp at the plumb line location of our GPS antenna. It's postion is reported to be North 34.94944147 deg. longitude, East 242.1139071 deg. latitude and an elevation of 665.073

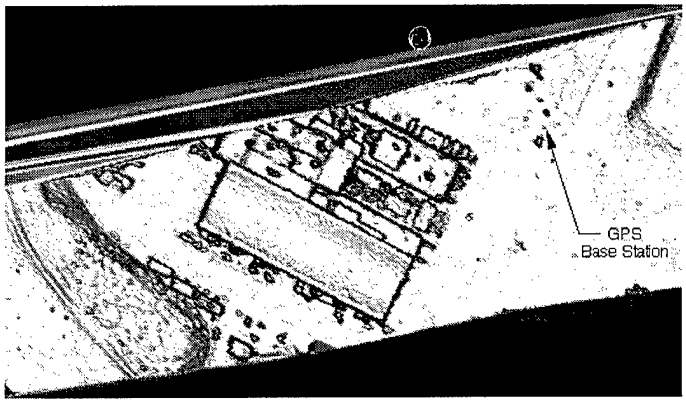


Figure 2 - GPS Ground Station and DFRC Hangars

m. The difference of the measured surface and known location of the area indicate an elevation bias of ~ 25 cm with peak to peak spreading of the elevation values of 10 cm. The spatial measurement determines the location of the antenna to less than 0.5 m. This is an end-to-end verification of RASCAL airborne topography measurement accuracy. A second pass over the same site shortly after this measurement, as well as an additional pass on October 11, 1996 gave similar results.

Fig. 3 presents a gridded digital elevation model (DEM) with 1 m pixels produced from RASCAL data over Lake Crowley Reservoir northwest of Bishop, CA along the Owens River. This image is a composite of six parallel passes flown at an offset of ~ 100 m to create a larger DEM of the area. There are 450,000 topographic measurements in this scene and shading is based on surface elevation. Note the Lake Crowley Dam at the center of the scene. It is a concrete dam with an earthen rampart and service roads on the downstream face. There are some artifacts present in the data (e.g. triangular wedges in the water surface behind the dam) that are produced as the IDL fitting program acts to join data points where there are gaps within a single scan (i.e. pass) or between adjacent scans. This figure serves to demonstrate the high-resolution topography mapping ability of the RASCAL instrument and provides a indication of work to be done to verify the vertical and horizontal positioning of RASCAL data sets over topographic features. We are now in the process of comparing RASCAL data of the water level and Lake Crowley dam structure to independent field measurements with water-level gauges and geodetic surveys.

CONCLUSION

The specific goal of RASCAL airborne laser altimeter operations was the acquisition of geodetic-quality DEM data of sub meter vertical resolution over sets of kilometer length scale, dynamic topography. This development was

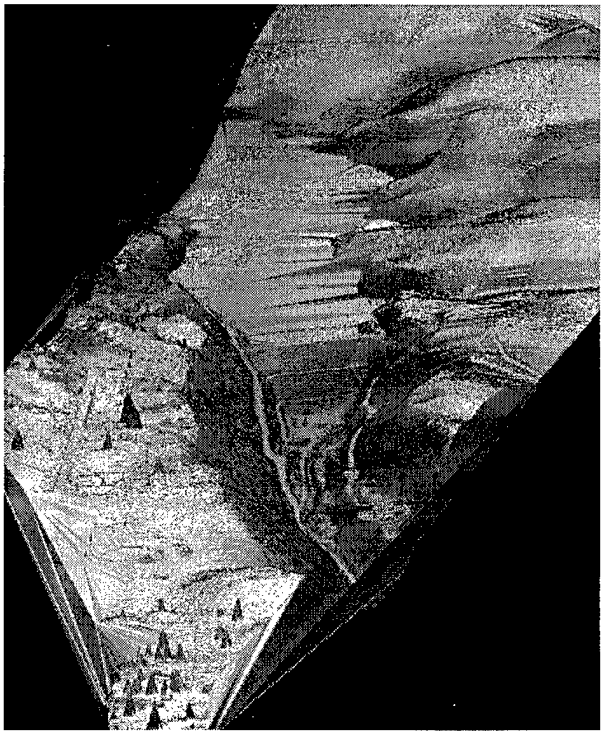


Figure 3 - Lake Crowley Dam and Surroundings

sponsored by the NASA Planetary Program and the Topography and Surface Change Program as a pathfinder investigation for future, NASA space-based topography missions. The initial development of the RASCAL sensor and demonstration of its science measurement potential are complete. The RASCAL instrument worked very well in seven flight missions flown in the fall of 1995 in California and demonstrated a new capability for high-resolution, high-accuracy topography mapping. A data analysis system is also in place to produce georeferenced data products consisting of high accuracy surface elevation from the RASCAL airborne data set. The first steps have been taken to verify the geodetic accuracy of the RASCAL scan observations, and they indicate the sub-meter level-of-performance.

REFERENCES

[1] J. Bufton, J. Garvin, J. Cavanaugh, L. Ramos-Izquierdo, T. Clem, W. Krabill, "Airborne Lidar for Profiling of Surface Topography," in Optical Engineering 30(1), pp. 72-78, Jan. 1991.

[2] C. Vaughn, J. Bufton, W. Krabill, D. Rabine, "Georeferencing of Airborne Laser Altimeter Measurements," November 1995, accepted for publication in the International Journal of Remote Sensing.

Optical Correction of Scene Fractions for Estimating Regional Scale Ocean Coral Abundance in Fiji

Derek R. Peddle, Ellsworth F. LeDrew and Heather M. Holden

Department of Geography, University of Waterloo
Waterloo, Ontario N2L 3G1 Canada
(519) 885-1211 Fax: 888-6768 drp@wateol.uwaterloo.ca

Abstract -- Spectral mixture analysis is used to separate coral and water components at sub-pixel scales for a regional scale transect of SPOT imagery across Savusavu Bay, Fiji. Coral fractions on the ocean floor are estimated using empirical optical corrections from mixture fractions obtained from *in situ* reflectance profile measurements and with reference to a digitised bathymetric chart. Additional corrections are applied to estimate live coral abundance by removing the signal component contributed by coral debris. Issues involved in regional scale applications are discussed in the context of future airborne and satellite image applications.

INTRODUCTION

Coral reefs are highly sensitive to small changes in ocean temperature and light conditions, and are therefore being recognised as potentially one of the most important indicators of global climate change and variability. However, it is difficult to establish a consistent observational technique for monitoring the condition of coral reefs over large areas. Remote sensing imagery offers the necessary information for this purpose, however, previous approaches have been limited to shallow coral shelves and are therefore not well suited to regional scale studies.

To address this problem, we have applied spectral mixture analysis techniques to satellite image data to separate and quantify the water and coral signal components [1]. In this paper, we extend the analysis to now consider the regional scale, for which we present additional methods for analysing and correcting coral fractions at greater depths with respect to the increased heterogeneity of the ocean floor.

STUDY AREA AND DATA

The study area is located in Savusavu Bay on the south coast of Vanua Levu island, Fiji. A mid-winter SPOT image was acquired 30 June 1994 and corrected for atmospheric effects using the 6S model to obtain ocean surface reflectance values. *In situ* optical water properties were measured using a Profiling Reflectance Radiometer (PRR) in August 1994. To obtain estimates of water depth in the Bay, a bathymetric chart was digitised, converted to image format, and co-registered to the SPOT image. A low-pass filter was applied to minimise errors caused by missing data points and irregularities in the original map. For this regional scale analysis, a 33km × 4km transect across the mouth of Savusavu Bay was selected for analysis. The transect encompasses shallow coral shelves in the coastal zone, a series of offshore coral ridges, as well as occurrences of coral heads at a variety of depths.

OPTICAL CORRECTION OF MIXTURE FRACTIONS

Spectral mixture analysis (SMA) involves determining sub-pixel scale fractions of individual scene components (or end-members) which together contribute to the overall signal received by a remote sensing instrument. For oceans, the main components which comprise the pixel level reflectance are the ocean floor and the overlying water which attenuates the bottom signal. The focus of our studies is on the coral environment. Beyond the coral substrate, ocean floor features such as sediments, algae, sand and other materials are also present, however, since these occur primarily at depths which exceed the detection of passive optical remote sensing instruments, these features are not considered in the analysis. Therefore, in the first stage of the SMA, we model sensor level reflectance (ρ_S) in terms of the end-member reflectances of live coral (ρ_C) and water (ρ_W), weighted by their areal fractions (F_C and F_W, respectively) as:

$$\rho_S = \rho_C \cdot F_C + \rho_W \cdot F_W \qquad (1)$$

and solve the resulting system of equations over the set of multispectral channels using a linear least squares approach.

This model formed the basis for the optical correction of scene fractions, as presented in [1]. Here, we apply these corrections to the regional scale transect across the Bay. The major steps in the procedure are summarised as follows:

1. SMA of *in situ* PRR profile spectra to obtain a detailed set of water and coral partial mixture fractions throughout the water column over a known target of high coral abundance.
2. SMA of regional scale SPOT image data. The water end-member was chosen from an area of deep ocean in the middle of the Bay. The coral end-member was selected from a large area of live coral, and represents the maximum spectral response among the varieties of live coral present. The result of this step is coral and water fractions at the ocean surface.
3. Optical correction of ocean surface fractions to provide an estimate of coral abundance on the ocean floor. This involved:

   (a) finding the ocean depth (from digitised bathymetry)
   (b) computing the expected coral fraction at that depth from the set of PRR partial mixture fractions
   (c) estimating the corrected ocean floor coral fraction as the coral surface fraction divided by the PRR fraction from (b).

0-7803-3068-4/96$5.00©1996 IEEE

Detailed descriptions and equations for steps 1-3 were presented in [1] and are not repeated here. Instead, in this paper we illustrate the application of this method to the regional scale transect across Savusavu Bay. Figures 1 and 2 show the western extent of the transect where the dominant feature is a major coral ridge visible in the lower portion of the image. Figure 1 is the uncorrected coral fraction image output from step 2, and represents the fraction of the signal at the ocean surface which can be attributed to coral. Figure 2 shows the corrected coral fractions for the ocean floor (step 3). The main difference between the two images is the larger coral fractions in the corrected image which result from correcting for the optical effects of water as a function of ocean depth. This creates the brighter overall appearance of Figure 2. Although not readily visible in these gray tone renditions, additional patterns of change were noted in the corrected image, particularly along the coral ridge. The coral fractions outside the ridge are also more consistent in the corrected fraction image compared to the uncorrected image.

Regional Scale Spectral Mixture Analyses

In [1], we analysed a sample of image pixels with high fractions of live coral for which the two end-member model was sufficient for estimating coral and water abundance. Over larger areas, however, significant occurrences of coral debris will also be encountered due to the nature of coral evolution and growth. In these areas, debris surfaces often surround occurrences of live coral. Therefore, it is important to account for coral debris so that live coral abundance will not be over-estimated.

The spectral response of coral debris was lower than live coral, however, the location of coral debris in spectral space was aligned along the trajectory defined by the water and live coral end-member reflectance values. Accordingly, at these wavelengths, coral debris could not be considered as an independent end-member. Instead, the relative position of coral debris along the trajectory was determined by a separate SMA with the 2 end-member model, using as input the average spectra from a representative sample of coral debris. Then, in areas of coral debris, the live coral abundance can be corrected by subtracting the SMA coral debris fraction.

This first order correction was tested for a large area of coral debris along the Savusavu Bay transect. The corrected ocean floor coral fractions were adjusted for coral debris to provide an improved estimate of live coral. Coral fraction results before and after the correction were grouped into 10% interval classes as summarised in Figure 3. In areas of high coral abundance (e.g. >30%), the difference between live coral and the original (live coral and debris) fraction is small. These areas are not common, as their frequency in the test site is consistently low (~2% of the total number of pixels per class). Conversely, we observe greater magnitudes of correction throughout the majority of the test sites (coral fractions <30%). In these areas, coral debris comprises a significant portion of the overall coral signal determined from the two end-member SMA model. In particular, for fractions <10%, the difference in occurrence of live coral and the original coral fraction is large, suggesting a dominant coral debris cover in these areas. Although the coral fractions are low in these areas, their large spatial extent makes this correction important as otherwise a significant overestimation of coral fraction would result if the coral debris and live coral signals were not separated.

CONCLUSIONS AND FUTURE WORK

Methods for linking multi-sensor spectral mixture fractions have been presented for determining coral fractions at the ocean surface and for correcting these fractions to provide an estimate of ocean floor coral abundance. At the regional scale, additional corrections are required. In this paper, progress has been made towards correcting the fraction of live coral through the specification and removal of coral debris components. The ability to compute first order estimates of coral and water fractions provides useful information which is also amenable to a variety of different corrections applied to the mixture fractions obtained.

For future work, the increased number of ocean floor features encountered over larger areas highlights the need for increased spectral resolution data. Future use of hyperspectral airborne imaging spectrometers as well as data from the Earth Observing System offer considerable promise. Improved methods for obtaining high quality digital bathymetric information would also be required. Application of the ideas presented in the present study to higher quality data sets linked to field verified sites has the potential to be a valuable component in the monitoring of coral reef ecosystem health within the context of regional and global scale studies of environmental change.

ACKNOWLEDGEMENTS

This work was supported by funding from NSERC. Ocean spectral measurements were acquired using a PRR-600 radiometer from Biospherical Instruments, San Diego. The logistical support of Jean-Michel Cousteau Productions and the Project Ocean Search program is gratefully acknowledged.

REFERENCE

[1] Peddle, D.R., E.F. LeDrew and H.M. Holden, 1995. Spectral mixture analysis of coral reef abundance from satellite imagery and *in situ* ocean spectra, Savusavu Bay, Fiji. *Proc., Third Thematic Conference on Remote Sensing of Marine and Coastal Environments*, Seattle WA. Vol. II, p.563-575.

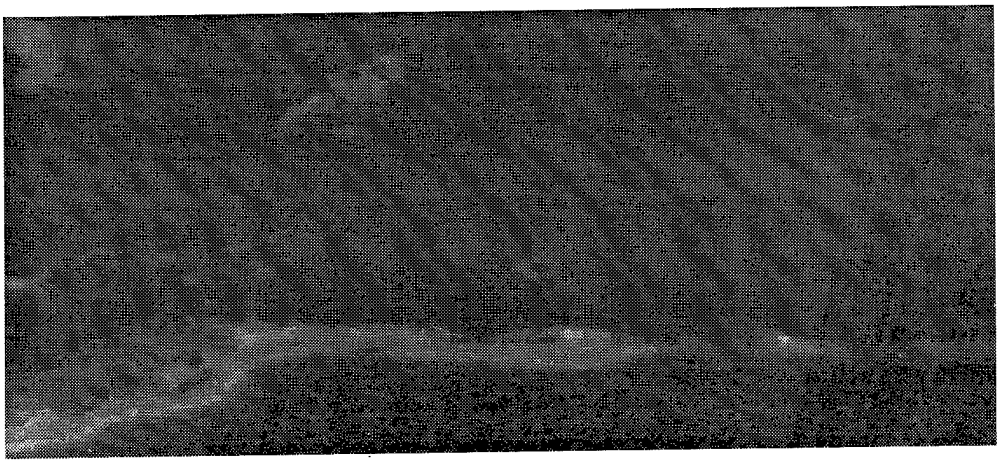


Figure 1: Uncorrected coral fraction image for the ocean surface.

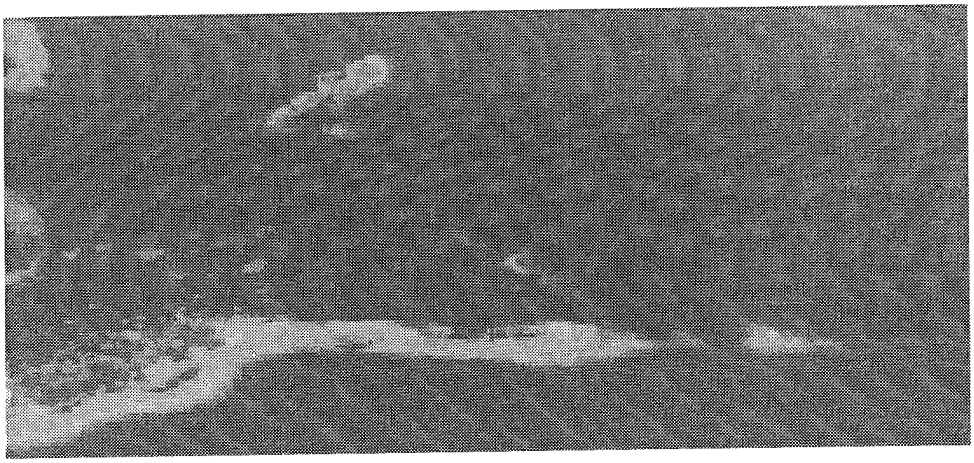


Figure 2: Corrected ocean floor coral fraction image.

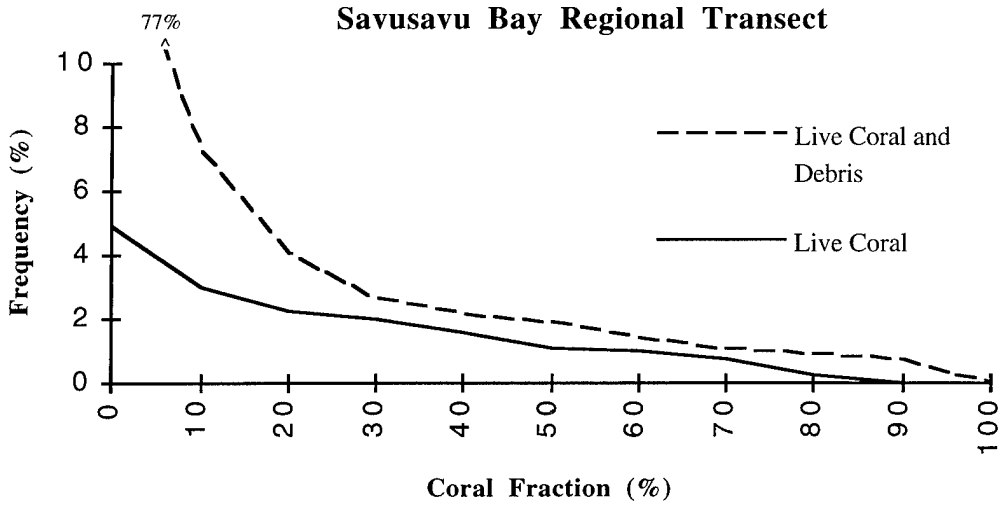


Figure 3: Correction for coral debris for different coral fractions.

Development of SAR Interferometry at IIT Bombay

Jai S. Sukhatme, Vardhan Walavalkar, Y.S.Rao, G.Venkataraman,
M.V.Khire and K.S.Rao
CSRE, Indian Institute of Technology, Bombay - 400 076, India
Fax +91-22-5783480 Email: ksrao@powai.cc.iitb.ernet.in

Abstract -- The emphasis of this paper is on the implementation of SAR Inteferometry at CSRE, Indian Institute of Technology, Bombay. ISAR software by ESA was used for generating the fringes and the phase unwrapping software was developed in-house. A test site around the western ghats was chosen for testing the software.

INTRODUCTION

SAR Interferometry is a promising technique for various applications like producing 3-D relief maps, detecting and monitoring small changes of surface shape caused by crustal movement and land slides, mitigation of volcanic hazard and generally monitoring changes in surface geophysical parameters.

Realising the importance of SAR Interferometry, CSRE at IIT Bombay has taken up the project entitled - "SAR Interferometry for topography and earth surface movement" sponsored by ISRO-IITB Space Technology Cell. Under this project ISAR software, developed by ESA has been implemented on a DEC ALPHA system. The phase unwrapping software was also developed around the same system. The subsequent sections describe the processing the SLC data using the ISAR software, phase unwrapping etc.

TEST SITE AND DATA SETS

The study area is a part of Ratnagiri district on the west coast of Maharashtra lying between 16° 50' to 17° 23' North Latitude and 73° 15' to 73° 46' East Longitude. Physiographically the study area can be divided into three parts as coastal plains, Sahyadri hills and undulating uplands. The height of the terrain varies from 20 m to 400 m above the mean sea level.

Two SAR scenes of ERS-1 acquired on 13th and 19th February 1992 have been obtained from NRSA. The normal baseline for the two scenes is 267m. Several subimages of 512*512 were taken for generating interferometry and one set of images are given as illustration.

IMPLEMENTATION OF THE ISAR SOFTWARE

We have obtained the ISAR (Interferometric SAR) software developed by the Politecnico di Milano, Italy, the details of which are given in [1]. We have used the software for processing the SLC SAR data for the Ratnagiri area and have been successful in generating the interferometric fringes for it. Figures 1-4 illustrate the various steps in the processing of the SLC data.

PHASE UNWRAPPING

The ISAR software leaves us at the stage where we have a "wrapped" phase value corresponding to every pixel in the grid. By wrapped we mean the value (as from any interferometrical experiment) is between $-\pi$ and π. The basic aim of phase unwrapping is to generate the total or $2n\pi$ value of the phase from this wrapped phase.

A variety of techniques have been proposed in the past few years in an attempt to solve this problem. We analyzed most of the techniques such as, integration of differences [2], the incorporation of branch cutting into integration [3], cellular automata [4] and the robust technique [5].

We have implemented the robust technique for which the time taken for

0-7803-3068-4/96$5.00©1996 IEEE

unwrapping is small (of the order of 10 sec. for a 512*512 grid).

Having implemented the Robust technique (till now we have used DCT's to solve the Poisson equn) we have tested it on a variety of synthetically generated images. What we are doing currently is to merge the ideas of the integration technique (the part concerning residue location) and then form a weighted wrapped phase value grid on which we can use the Robust technique.

RESULTS AND DISCUSSION

Figure 1 shows the radar image of a part of the study area in which the ridges on west running North-South and also on the South-East corner are clearly visible. In between there is a valley portion with a drainage line. Figure 2 gives the interference fringes developed for the area corresponding to Figure 1. The fringes corresponding to the ridge lines are clearly visible on both the corners. In the middle of the ridges the shape of the fringes indicates the effects of shadow. Figure 3 and 4 show the slope images in the azimuth and range directions. Due to the viewing geometry of the SAR, only the Eastward slopes are visible. There is an uncertainty in quantifying the slopes which are in the shadow region.

Figures 5 and 6 show the wrapped and unwrapped images for a synthetically generated surface. The unwrapped image agrees well with the simulated surface. We are now working on the fringes generated for the Ratnagiri area.

ACKNOWLEDGMENTS

The authors are thankful to Prof. V.S.Chandrasekharan, Head CSRE, for his encouragement. We are also thankful to Dr. S.N.Coulson, Dr. G.Solaas, ESRIN, Frascati, Italy and Prof. C.Prati, Politecnico di Milano, Italy for having useful discussions and permitting us to use the ISAR software. Finally thanks are due to ISRO-IITB Space Technology Cell for sponsoring the project.

REFERENCES

[1] The *ISAR Interferogram Generator* Manual, ESA-ESRIN, 1995.

[2] R.M.Goldstein, C.L.Zebker, and H.A.Werner, "Satellite Radar Interferometry: two dimensional phase unwrapping", *Radio Science,* 23, pp. 713-720, 1988.

[3] C.Prati, et al, "Seismic Migration for SAR focusing: Interferometrical Applications.", *IEEE Trans. Geosc. & Rem. Sens.,* vol.28, no.4,pp. 627, 1990.

[4] D.Ghiglia, G.Mastin, L.Romero, "Cellular Automata method for phase unwrapping", *J. Opt. Soc. Am. A.,* vol.4, no.1, pp. 267, 1987.

[5] D.Ghiglia, & L.Romero, "Robust 2-d weighted phase unwrapping that uses fast transforms and iterative methods", *J. Opt. Soc. Am. A.,* vol.11, no.1, pp. 107, 1994.

FIGURES

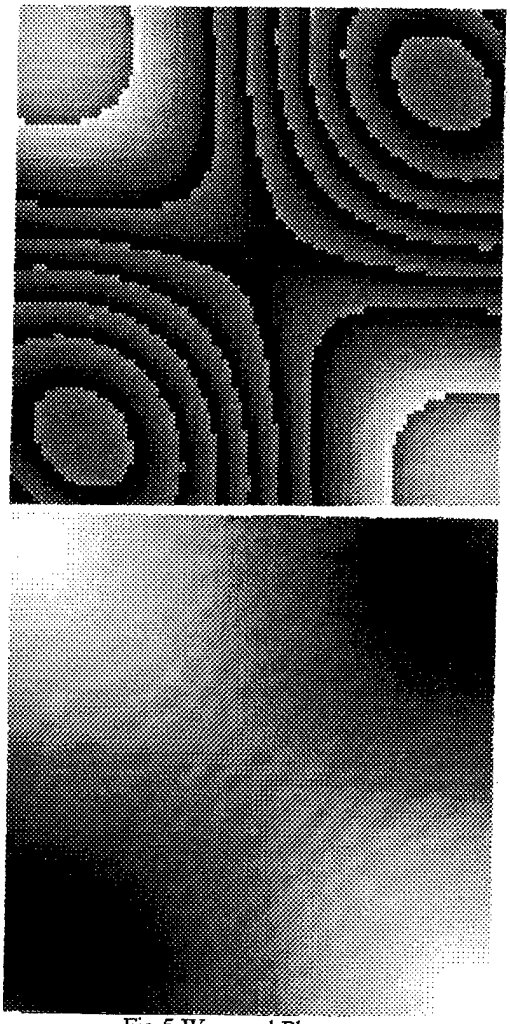


Fig.5 Wrapped Phases.
Fig.6 Unwrapped Phases.

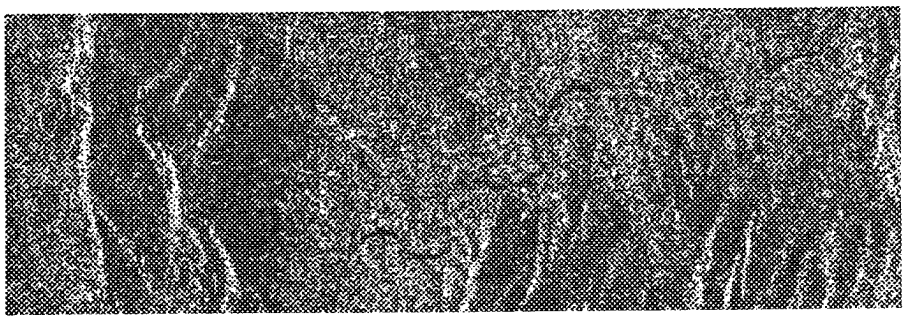


Fig.1 Amplitude Image.

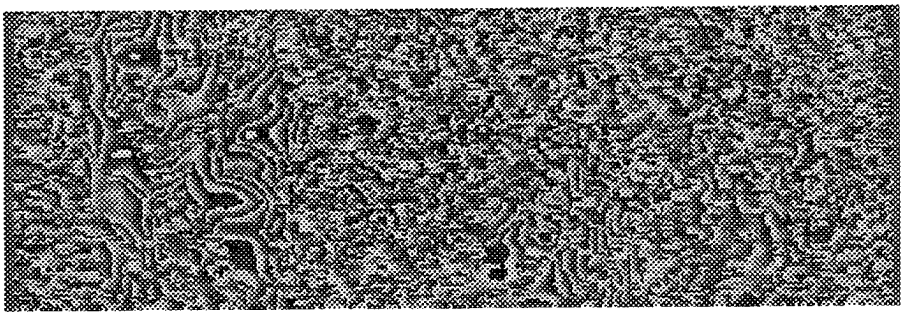


Fig.2 Interferometric Fringes.

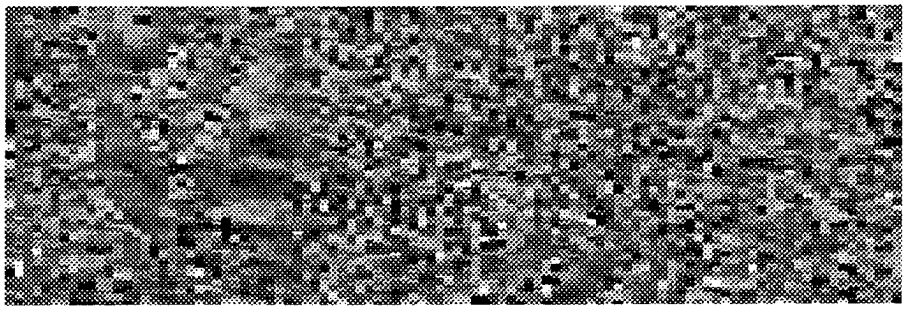


Fig.3 Azimuth Slopes.

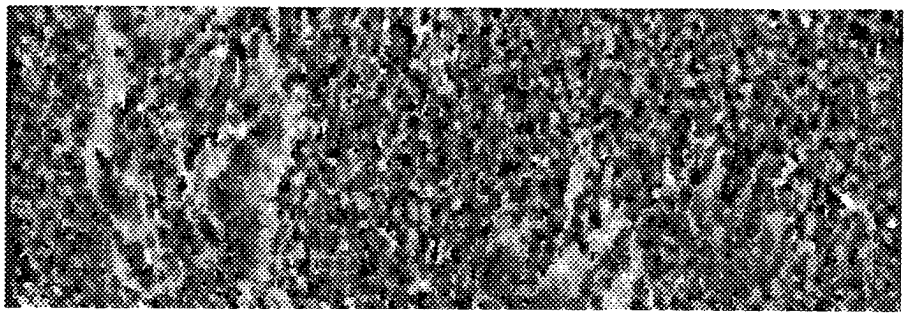


Fig.4 Range Slopes.

Improved Procedures for the Retrieval of Stratospheric Trace Gases from Spectra of a Ground-Based Millimeter Wave Radiometer

Martin Kuntz
Institut für Meteorologie und Klimaforschung
Forschungszentrum Karlsruhe
Postfach 3640, 76021 Karlsruhe, Germany
T: +49 7247 82 4510, F: +49 7247 82 6141, EMail: kuntz@imk.fzk.de

Abstract

Several stratospheric trace gases can be remotely sensed by groundbased millimeterwave radiometry. Altitude profiles of the volume mixing ratios of those gases can be retrieved from measured spectral lineshapes due to the altitude dependent pressure broadening of the line. However, measured spectra are frequently disturbed by device–caused standing waves due to reflections. As a consequence the retrieval of altitude profiles from the spectra requires a more sophisticated analysis. In this paper a new extension of two well known standard inversion algorithms will be given for the inversion of spectra with superimposed standing waves by simultaneously fitting their amplitudes and phases.

INTRODUCTION

A common problem in millimeterwave radiometry is the presence of device–caused standing waves due to manifold reflections. Although these unwanted effects can be reduced by inserting a dielectric periodically or modulating the optical pathlength mechanically a complete elimination of standing waves cannot be achieved in most cases. It is obvious that this complicates the retrieval of altitude profiles considerably, since microwave radiometry as a remote sensing technique obtains it's altitude information solely from the pressure-dependent width of rotational emission lines. To overcome these difficulties one either has to eliminate the remaining standing waves from the measured spectra numerically before inverting them using standard retrieval techniques or has to include the effect of standing waves in the inversion algorithm itself. The first technique turns out to be numerically less attractive, since the standing waves are superimposed on in principle unknown true spectra. As a consequence common optimization techniques cannot be applied and the rigorous elimination of standing waves from the measured spectra becomes numerically extremely expensive (see e. g. [1] for details). The second method seems to be much more promising. As a first approach Nedoluha [2] suggests to incorporate the effect of standing waves in the corresponding error covariance matrix using an optimal estimation technique [3] for inversion. However, a disadvantage of this method is that the influence of the standing waves on the inverted altitude profiles is not completely neutralized and that in addition to the periods of the superimposed standing waves, which can be deduced from the effective length of the resonators in the measurement device, their amplitudes have to be known at least approximately. We therefore suggest a new extension of Twomey's linear constraint inversion (LCI) [4] and Rodgers' optimal estimation technique (OEM) [3] for completely neutralizing the effect of standing waves on the inverted profiles in the inversion procedure itself by simultaneously fitting their amplitudes and phases and assuming their periods to be known.

INVERSION TECHNIQUES

In a first step the nonlinear problem of retrieving atmospheric parameters from a measured spectrum has to be reduced to solving a Fredholm integral equation of the first kind (which has no unique solution in general) by linearizing the radiative transfer equation [5]. The integral equation can then be further simplified by approximating the integral by a sum leading to a linear equation system

$$\boldsymbol{g}_{\mathcal{E}} = \boldsymbol{A}\boldsymbol{f}. \tag{1}$$

In (1) $\boldsymbol{f}$ represents the unknown altitude profile and $\boldsymbol{g}_{\mathcal{E}}$ the observed spectrum along with the measurement noise, which is described by a limited number of sampling frequencies. Given a measured spectrum $\boldsymbol{g}_{\mathcal{E}}$ and the matrix $\boldsymbol{A}$ the fundamental problem in solving (1) lies in the fact that $\boldsymbol{A}$ is always very close to being singular. Thus additional information is needed to make the solution for the profile $\boldsymbol{f}$ unique.

Twomey takes this into account by introducing a priori information (constraints) in form of an additional linear equation system

$$\boldsymbol{r} = \boldsymbol{B}\boldsymbol{f} \tag{2}$$

and combining it with the contribution of the observed spectrum to give the regularized solution

$$\boldsymbol{f}_{\gamma} = \left[\boldsymbol{A}^T\boldsymbol{C}\boldsymbol{A} + \gamma\boldsymbol{B}^T\boldsymbol{B}\right]^{-1}\left[\boldsymbol{A}^T\boldsymbol{C}\boldsymbol{g}_{\mathcal{E}} + \gamma\boldsymbol{B}^T\boldsymbol{r}\right]. \tag{3}$$

In (3) the so-called regularization parameter γ trades the a priori information off against the measurement and has

0-7803-3068-4/96$5.00©1996 IEEE

to be specified by the user; the diagonal matrix $\boldsymbol{C}$ permits weighting the measurements of each channel individually.

Rodgers combines the outcome of the measured spectrum with an a priori profile $\widehat{\boldsymbol{f}}$

$$\boldsymbol{f}_\gamma = \left[\boldsymbol{A}^T\boldsymbol{S}_\varepsilon^{-1}\boldsymbol{A} + \boldsymbol{S}_f^{-1}\right]^{-1}\left[\boldsymbol{A}^T\boldsymbol{S}_\varepsilon^{-1}\boldsymbol{g}_\varepsilon + \boldsymbol{S}_f^{-1}\widehat{\boldsymbol{f}}\right], \quad (4)$$

using the inverse of the measurement noise convariance $\boldsymbol{S}_\varepsilon$ and a priori convariance $\boldsymbol{S}_f$ as weights, respectively.

INCLUDING STANDING WAVES

To incorporate the effect of standing waves in the above linear inversion techniques, the nonlinear problem of fitting the amplitudes A and phases ϕ of sine waves of the type

$$A\sin(k\nu + \phi) \quad (5)$$

must first be linearized. This can be easily achieved by rewriting (5) as

$$a\sin(k\,\nu) + b\cos(k\,\nu) \quad (6)$$

and fitting the parameters a and b, where $A = \sqrt{a^2+b^2}$ and $\tan\phi = b/a$. Thus the superposition of the true spectrum in (1) with a standing wave can be written as[1]

$$\begin{pmatrix} g_{\varepsilon 1} \\ \vdots \\ g_{\varepsilon n} \end{pmatrix} = \begin{pmatrix} a_{11} & \cdots & a_{1m} \\ \vdots & \ddots & \vdots \\ a_{n1} & \cdots & a_{nm} \end{pmatrix}\begin{pmatrix} f_1 \\ \vdots \\ f_m \end{pmatrix} + a\begin{pmatrix} \sin(k\nu_1) \\ \vdots \\ \sin(k\nu_n) \end{pmatrix} + b\begin{pmatrix} \cos(k\nu_1) \\ \vdots \\ \cos(k\nu_n) \end{pmatrix}. \quad (7)$$

Computationally it is more convenient to combine the unknown vector $\boldsymbol{f}$ with the unknown parameters a and b to the new vector $\boldsymbol{f}'$, leading to the new, primed linear equation system

$$\underbrace{\begin{pmatrix} g_{\varepsilon 1} \\ \vdots \\ g_{\varepsilon n} \end{pmatrix}}_{\boldsymbol{g}_\varepsilon} = \underbrace{\begin{pmatrix} a_{11} & \cdots & a_{1m} & \sin(k\nu_1) & \cos(k\nu_1) \\ \vdots & \ddots & \vdots & \vdots & \vdots \\ a_{n1} & \cdots & a_{nm} & \sin(k\nu_n) & \cos(k\nu_n) \end{pmatrix}}_{\boldsymbol{A}'}\underbrace{\begin{pmatrix} f_1 \\ \vdots \\ f_m \\ a \\ b \end{pmatrix}}_{\boldsymbol{f}'}. \quad (8)$$

This new linear equation system can be solved in the same manner as the original equation system (1). However, attention must be paid to the fact that the inverse problem as such is ill conditioned and has to be regularized, while the parameters a and b can be deduced from the above equation unambiguously. The constraint of merely partly regularizing the solution vector $\boldsymbol{f}'$ can be met by setting the corresponding elements of the solutions (3) and (4) to zero, yielding

$$\boldsymbol{f}'_\gamma = \left[\boldsymbol{A}'^T\boldsymbol{C}\boldsymbol{A}' + \gamma^2\begin{pmatrix} \boldsymbol{B}^T\boldsymbol{B} & 0 & 0 \\ 0 & 0 & 0 \\ 0 & 0 & 0 \end{pmatrix}\right]^{-1}\left[\boldsymbol{A}'^T\boldsymbol{C}\boldsymbol{g}_\varepsilon + \gamma^2\begin{pmatrix} \boldsymbol{B}^T\boldsymbol{r} \\ 0 \\ 0 \end{pmatrix}\right] \quad (9)$$

or

$$\boldsymbol{f}'_\gamma = \left[\boldsymbol{A}'^T\boldsymbol{S}_\varepsilon^{-1}\boldsymbol{A}' + \begin{pmatrix} \boldsymbol{S}_f^{-1} & 0 & 0 \\ 0 & 0 & 0 \\ 0 & 0 & 0 \end{pmatrix}\right]^{-1}\left[\boldsymbol{A}'^T\boldsymbol{S}_\varepsilon^{-1}\boldsymbol{g}_\varepsilon + \begin{pmatrix} \boldsymbol{S}_f^{-1}\widehat{\boldsymbol{f}} \\ 0 \\ 0 \end{pmatrix}\right], \quad (10)$$

for the LCI or OEM, respectively. Similar to the way of fitting amplitudes and phases of sine waves, additional linear parameters such as the offset or slope of the measured spectra can be adjusted [6].

RESULTS

In order to demonstrate the utility of the above algorithms, we perform a simple numerical experiment using the 142 GHz line from ozone. Starting from the arbitrarily chosen profile of ozone (dashed line in Fig. 1) we first calculate the synthetic spectrum to be observed from ground at zenith angle, neglecting the effect of the troposphere. We then superimpose three standing waves with amplitudes, periods, and phases according to table 1 (columns 1 to 3) and add a measurement noise of the amplitude 0,1 K for each channel of 1 MHz bandwidth to make the study more realistic. The resulting spectrum is shown in Fig. 2 (broadened dotted line). Finally we apply the extension of Twomey's LCI on this synthetic spectrum and use the smoothness of the profile as a further constraint; for this case the dashed line shown in Fig. 1 serves as a first guess. The retrieved profile is depicted in Fig. 1 (full line) while the corresponding spectrum is shown in Fig. 2 (full line) and is shifted down by 1,5 K for the sake of clarity. It is easily seen in both figures that the retrieval procedure works very satisfactorily, in spite of the presence of standing waves and measurement

Table 1: Fit of standing waves

Nr.	period GHz	ampl. K	phase degrees	ampl.* K	phase* degrees
1.	0,7465	0,8	30	0,804	30,15
2.	0,403	0,6	60	0,596	60,85
3.	0,113	0,4	90	0,401	89,67

[1] For the sake of simplicity we shall assume that only one standing wave is superimposed on the true spectrum. The extension to a superposition with several standing waves of different amplitudes, periods, and phases is obvious.

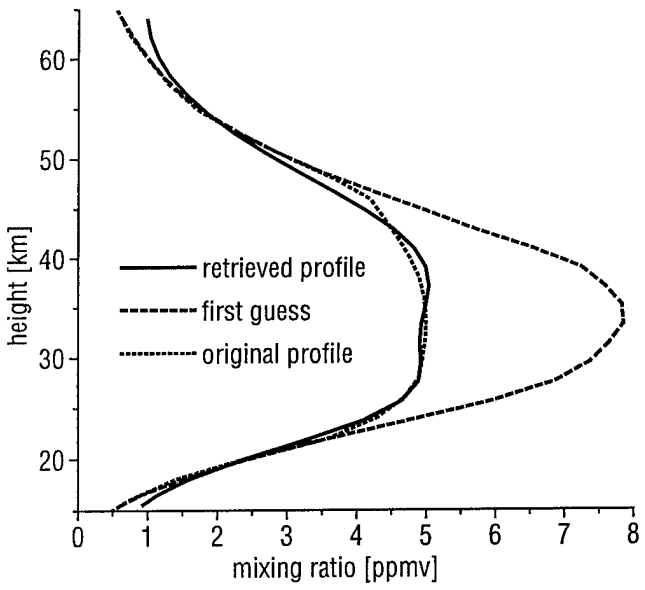


Figure 1: Altitude profiles involved, see also [6].

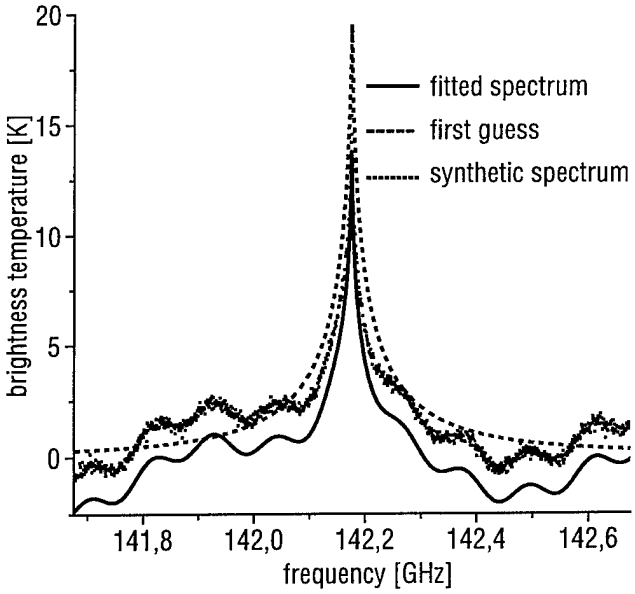


Figure 2: Spectra involved, see also [6]. The fitted spectrum (full line) is shifted down by 1,5 K.

noise in the spectrum. From the parameters a and b, which have been fit for each standing wave, one now can easily deduce the amplitudes and phases of the superimposed standing waves (see columns 4 and 5 in table 1). Since they are in good agreement with the actually superimposed standing waves we deduce that only the true spectrum contributed to the retrieved profile, as desired.

CONCLUSION

A new extension of the LCI and OEM inversion techniques has been suggested and proven to be very successful and reliable in the retrieval of atmospheric profiles from spectra disturbed by device caused standing waves in many cases. In addition it is easy to implement and does not affect the efficiency of the inversion algorithms distinctly.

REFERENCES

[1] U. Klein, "Aufbau und Betrieb eines breitbandigen, bodengestützten Millimeterwellen–Radiometers zur Messung atmosphärscher Spurengase", doctoral thesis, University Bremen, Juli 1993.

[2] G. E. Nedoluha, R. M. Bevilacqua, R. M. Gomez, D. L. Thacker, W. B. Waltman, and T. A. Pauls, "Ground-based measurements of water vapor in the middle atmosphere", J. Geophys. Res, vol. 100, no. D2, pp. 2927-2939, February 1995.

[3] C. D. Rodgers, "Retrieval of atmospheric temperature and composition from remote measurements of thermal radiation", Rev. Geophys., vol. 14, no. 4, pp. 609-624, November 1976.

[4] S. Twomey, Introduction to the Mathematics of Inversion in Remote Sensing and Indirect Measurements. Oxford: Elsevier Scientific Publishing 1977, pp. 115-150.

[5] E. R. Westwater, "Ground-based microwave remote sensing of meteorological variables", in Atmospheric remote sensing by microwave radiometry, M. A. Janssen, Ed. New York: John Wiley, 1993, pp. 145-213.

[6] M. Kuntz, "Bestimmung der Höhenverteilung stratosphärischer Spurengase aus Emissionsspektren eines bodengebundenen Millimeterwellen–Radiometers", doctoral thesis, University Karlsruhe (TH), February 1996.

A New 278 GHz Ground-Based Radiometer for Vertical Profile Sounding of ClO and O_3 in the Upper Atmosphere

G. Hochschild, R. Krupa
Institut für Meteorologie und Klimaforschung
Forschungszentrum Karlsruhe
Postfach 3640, 76021 Karlsruhe, Germany
T: +49 7247 82 2191, F: +49 7247 82 2849, EMail: hochschild@imk.fzk.de, krupa@imk.fzk.de

Abstract – This paper describes the new radiometer system operating in the 278 GHz range, which is intended for long term ground-based monitoring of the vertical profiles of chlorine monoxide and ozone in the stratosphere over the arctic area. To improve the measurement of weak lines, in particular in view of their diurnal variation [3], and to allow operation over a wider range of weather conditions, an advanced balancing technique has been implemented. Results of recent measurements during February and March 1996 at Kiruna, Sweden, are presented.

HARDWARE DESCRIPTION

The frontend consisting of a heterodyne receiver with quasioptical transmission and the calibration system are schematically presented in Fig. 1. To suppress both noise and atmospheric signatures from the unused lower sideband, a Martin-Puplett type interferometer (SSB) with a cooled sideband termination is used, which in particular eliminates the strong ozone line at 274.478 GHz. A second interferometer of the same type acts as diplexer and feeds the local oscillator (LO) to the signal path.

The LO operating at 276.3 GHz uses a Gunn oscillator at 92.1 GHz to drive a tripler. For high frequency stability a phaselock system is included. The downconversion of the millimeterwave signal to the intermediate frequency of 2.1 ± 0.5 GHz is performed by a cryogenic single-ended Schottky mixer operating at a temperature of about 100 K. The dewar for LN_2 bath cooling simultaneously accomodates the low noise IF amplifier and two cold loads. The systems noise temperature including quasioptics and the low-noise cryogenic amplifier is 1200 K in the middle of the observation bandwith. The basic frontend was manufactured in 1993 by Radiometer Physics.

Baseline ripples caused by standing waves in the transmission path are suppressed by a mechanical path length modulator placed in front of the single sideband filter. A rooftop like mirror reciprocating at 65 Hz changes the optical-path length by about 0.4 mm [2].

The high spectral resolution of 1 MHz over an instantaneous IF bandwith of 1 GHz is achieved by the acusto-optical spectrometer, which has been developed and manufactured at the University of Cologne [5].

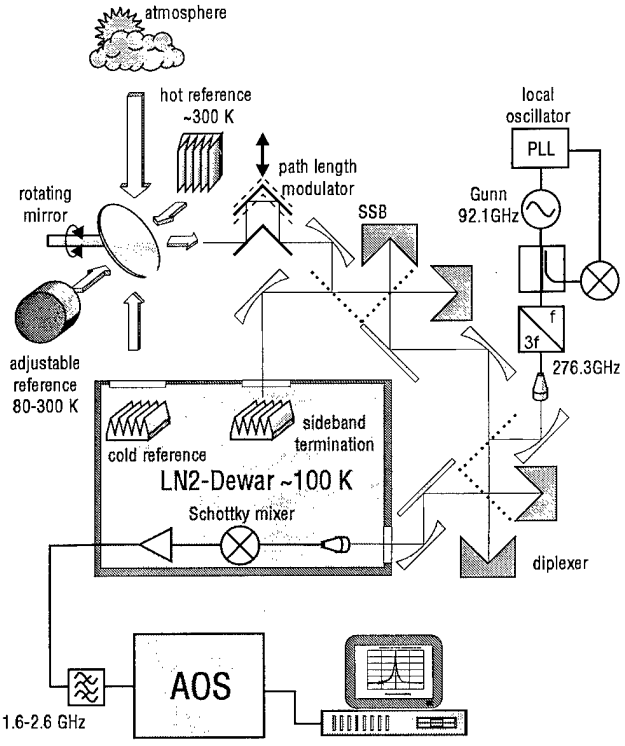


Figure 1: Schematic diagramm of the 278 GHz radiometer

CALIBRATION SCHEME

For the measurement of very weak lines as in the case of ground based ClO profiling, the hot-cold calibration fails to achieve satisfactory results. Baseline distortions due to system nonlinearities are the drawback of this calibration method.

0-7803-3068-4/96$5.00©1996 IEEE

In the radiometer system to be presented, an advanced balancing technique has been implemented. It is based on an innovative calibration load, which provides any necessary brightness temperature within the range from the cryogenic to the ambient temperature with high precision by mechanical adjustment (e.g. using a servo loop). In contrast to the well established external beam switching technique, where a second path from the atmosphere (seen through a lossy dielectric sheet) is used for reference [1], residual spectral lines from the atmosphere are excluded with this adjustable load and thereby a higher signal to noise ratio of the measured spectral line is achieved. This considerably improves the measurement of weak lines and extents the usable range of weather conditions. A separate paper dealing with this new balancing technique in more detail is under preparation.

The spectral line $T_{\theta line}$ measured at the elevation angle θ with this technique is given by

$$T_{\theta line} = \frac{S-R}{R}\,(T_{cont} + T_{rec}) \qquad , \qquad (1)$$

where T_{cont} and T_{rec} are the brightness temperatures of the tropospheric continuum and the receiver noise temperature, respectively. The frequency dependence of all components of (1) is omitted for clarity. To avoid errors caused by fluctuations of the tropospheric continuum or changes of the observation angle (the elevation angle is always chosen for maximum line contrast) one has to correct their influence on the measured line before the data can be integrated. This is done by computing the spectral line T_{zenith} as it would be observed toward zenith and without the presence of the troposphere:

$$T_{zenith} = \frac{S-R}{R}\;\frac{(T_{cont} + T_{rec})}{A_{\theta s}\; e^{\tau_\theta}} \qquad . \qquad (2)$$

The receiver noise temperature T_{rec} as well as the brightness temperature of the troposphere T_{cont} are calculated from supplementary hot-cold calibrated measurements, which are performed periodically every 10 minutes. The stratospheric air mass $A_{\theta s}$ is obtained from spherical geometry, whereas the tropospheric opacity τ_θ results from the continuum temperature T_{cont} and the physical temperature at the site as discribed by [1].

RESULTS

During the recent campaign at Kiruna (67,84°N, 20,41°E), spectra of ClO and other constituents have been measured on a regular schedule, which seem to be suitable for inversion [6]. The new calibration method proved to be suitable at least; a careful evaluation of the merits will follow after a thorough analysis of the measurement results.

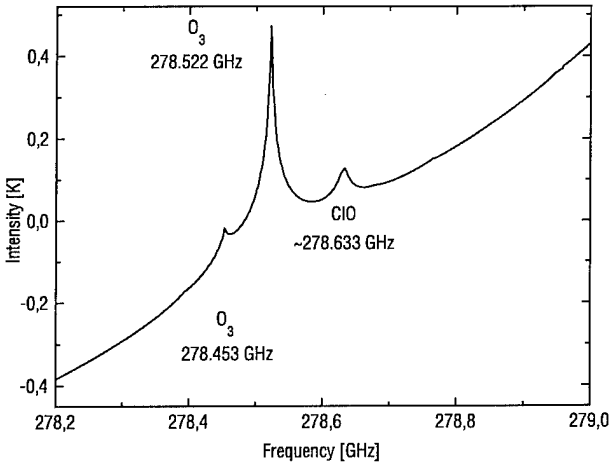


Figure 2: Computed spectrum

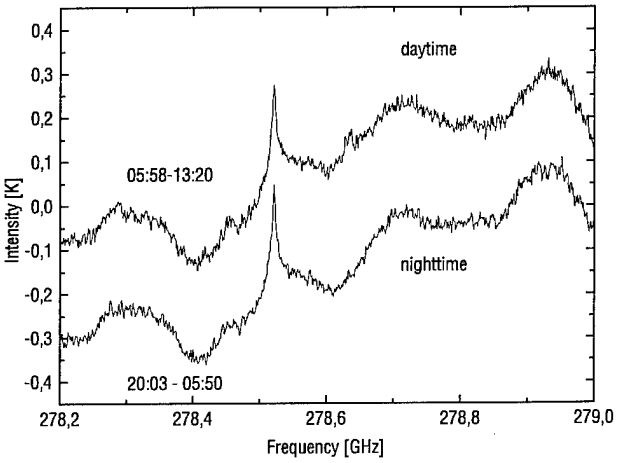


Figure 3: Daytime and nighttime raw spectra measured on March 1-2, 1996. An offset of -0.2 K has been added to the nighttime spectrum for clarity

As an exemple of the recent results, day- and nighttime raw spectra in the vicinity of the 278,633 GHz ClO-line are presented in Fig. 3. For comparison the calculated spectrum is given in Fig. 2. The difference spectrum (Fig. 4) clearly shows the change of the ClO-line, whereas the essentially stronger and overlaping O3-line just 111 MHz below as well as the obvious baseline ripple are almost completely suppressed. The differences of successive measurement periods of typically 2,5 h to a suitable nighttime reference period of similar length (Fig. 5) show the diurnal variation.

CONCLUSION

The weak ClO-line at 278,633 GHz has been measured successfully at the very first attempt in spite of the

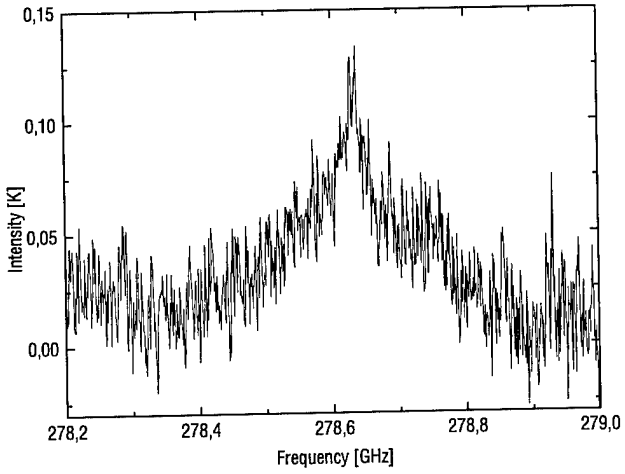


Figure 4: Difference of daytime and nighttime spectra

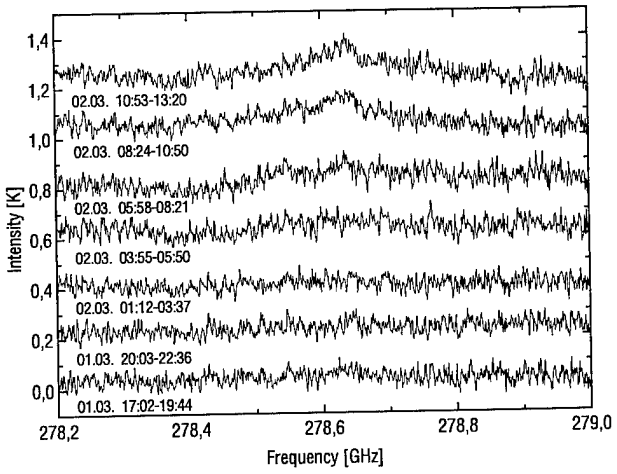


Figure 5: Diurnal variation of the ClO line

residual baseline ripples and instabilities both in the system and in the troposphere. This indicates interesting features of the new calibration method used. Nevertheless continued effort is required to further elaborate the calibration method and to improve the radiometer system.

ACKNOWLEDGMENTS

The authors express their gratitude to Åke Steen and nonnominated institut members at the Swedish Institut for Space Physics at Kiruna for their hospitality and help during the measurement campaign. We also thank Rüdiger Lehm and Hermann Berg for their valuable contributions to the preparation and to the operation of the campaign.

REFERENCES

[1] A. Parrish, R.L. de Zafra, P.M. Solomon and J.W. Barret, "A Ground-based Technique for Millimetre Wave Spectroscopic Observations of Stratospheric Trace Constituents", Radio Science, 23, pp. 106-118 (1988)

[2] J.J. Gustincic, "A Quasi-Optical Receiver Design", IEE MTT-S Int. Microwave Symp. Dig. pp. 99-101. IEEE Catalog No. 77CH1295-5MTT (1977)

[3] D.T. Shindell and R.L. de Zafra, "Chlorine monoxide in the Antarctic spring vortex: 2. A comparision of measured and modeled diurnal cycling over McMurdo Station, 1993", Journal of Geophysical Researach, Vol. 101, NO. D1, pp. 1475-1487, (1996)

[4] L.K. Emmons, D.T. Shindell, J.M. Reevesm and R.L. de Zafra, "Stratospheric ClO profiles from McMurdo Station, Antarctica, Spring 1992" Journal of Geophysical Researach, Vol. 10, NO. D2, pp. 3049-3055, (1996)

[5] R. Schieder, private communication

[6] M.Kuntz, "Improved Procedures for the Retrieval of Stratospheric Trace Gases from Spectra of a Ground-Based Millimeter Wave Radiometer", this conference

Polarimetric SAR image classification based on target decomposition theorem and complex Wishart distribution

L. J. Du and J. S. Lee
Remote Sensing Division, Code 7263, Naval Research Laboratory
Washington, DC 20375, USA
Tel: (202)-767-8249, Fax: (202)-767-5599, e-mail: du@imsy1.nrl.navy.mil

Abstract -- Polarimetric SAR data have been frequently utilized to classify terrain types. This paper compares two terrain classification approaches: 1) classification based on the target decomposition theorem, and 2) classification based on the multivariate complex Wishart distribution.

Target decomposition theorems were developed recently for extracting geophysical information of scattering media. The averaged Mueller matrix or its equivalent was decomposed into components for a thorough study. Parameters were introduced to characterize the physical aspect of the scattering process and they are used for unsupervised classification.

From a different point of view, the statistical property of the polarimetric covariance matrix has been modeled with a complex Wishart distribution. Supervised and unsupervised classification based on this distribution reported good results.

We present results of supervised classifications using both methods. Comparisons are made on the accuracy of these two classification schemes. Possible reasons for the cause of errors are discussed. The NASA/JPL San Francisco data is chosen for illustration.

INTRODUCTION

Polarimetric SAR imaging data have been utilized to analyze the geophysical parameters of the terrain for identification and segmentation. Target decomposition theorems have been developed to decompose the averaged Mueller or equivalent matrices into independent components that characterize the scattering process [1]. The goal is to find a formulation for better predictions on the geophysical compositions of the sensed target area. Cloude approaches it as an eigenvalue problem [1], [2]. He also applied it for unsupervised terrain classification

From a statistical approach, Lee et al. modeled the polarimetric covariance matrix with a complex Wishart distribution [3]. Supervised and unsupervised classification based on this distribution have been applied successfully in terrain classification [4].

In this paper, we adopted the entropy and the angles associated with the maximum eigenvector, that were introduced by Cloude as the feature components for supervised classification. The results are compared with that obtained based on the Wishart distribution. Discussions are made on the merits of these two approaches.

TARGET DECOMPOSITION THEOREM

The Cloude's theorem is based on eigenvector analysis of the multi-look coherency matrix [T]. Coherency matrix and Mueller matrix are uniquely related. The decomposition procedure resolves the coherency matrix into a summation of three independent matrices. Each one corresponds to a statistically independent target component. The associated eigenvalues give the relative strength of each contribution. The data produced from this analysis is then examined for extraction of meaningful information. For a media with reflection symmetry, the general form of an averaged coherency matrix can be expressed as [2]

$$\langle [T] \rangle = \begin{bmatrix} \lambda_1 \cos^2\alpha + \lambda_2 \sin^2\alpha & \cos\alpha \sin\alpha (\lambda_2 - \lambda_1) e^{j(\delta+\phi)} & 0 \\ \cos\alpha \sin\alpha (\lambda_2 - \lambda_1) e^{-j(\delta+\phi)} & \lambda_2 \cos^2\alpha + \lambda_1 \sin^2\alpha & 0 \\ 0 & 0 & \lambda_3 \end{bmatrix} \quad (1)$$

where λ's are the eigenvalues, α and δ are determined from the eigenvector associated with the maximum eigenvalue. To account for the possible deviation from reflection symmetry of the media and the correlations existed between the cross-polarized and co-polarized returns, the maximum eigenvector is modified as

$$\bar{e}_{max} = [\cos\alpha e^{j\phi} \quad \sin\alpha \cos\beta e^{j\delta} \quad \sin\alpha \sin\beta e^{j\rho}]^T \quad (2)$$

where angles β, δ, and ρ are introduced to accommodate the aforementioned physical facts. A quantity describing the relative magnitudes of the three scattering mechanisms in the scene was introduced as the entropy and defined by

$$H = \sum_{i=1}^{3} -P_i \log_3 P_i \qquad P_i = \frac{\lambda_i}{\sum_{j=1}^{3} \lambda_j} . \quad (3)$$

Its value varies between 0 and 1. A smaller value closer to 0 indicates that the radar returns are contributed mainly by a single scattering mechanism. A value closer to 1 signifies a depolarized radar return, and the scattering process is random in nature. It implies that the media is likely to be inhomogeneous in structure and/or in material composition. The value of the parameter α depends on the dominant scattering mechanism, ranging from 0

0-7803-3068-4/96$5.00©1996 IEEE

for surface scattering through $\pi/4$ for dipole scattering to $\pi/2$ for dihedral scattering. Other angles have different physical interpretations. Some of these parameters had been utilized to interpret the scattering from vegetated terrains [5]. They had also been used for unsupervised classifications [6].

Fig. 1 and Fig. 2 display the images of the entropy and α respectively. A linear gray scale is used to show the variations of entropy(0.0 to 1.0) and α(0.0 to $\pi/2$). They were evaluated using 2x2 averaged pixels of the 4-look L-band polarimetric SAR data of San Francisco. Spatial variations of these parameters were revealed in the figures. Similar application to the unaveraged data showed even more fluctuations.

SUPERVISED CLASSIFICATION BASED ON TARGET DECOMPOSITION THEOREM

Fig. 3 shows the classified image using the entropy and α as the feature components. These two parameters have been recognized as the most significant. There are five classes of terrain which are depicted by the ascending level of brightness as ocean, coastal ocean, quasi-natural terrain, parks, and urban area. The same training areas were used as this image was classified previously based on the complex Wishart distribution [4]. A Bayes maximum likelihood classifier produced this image. This classification result is not satisfactory. We proceeded to try the classification using the two large eigenvalues as the features. Better results are obtained and they are shown in Fig. 4.

SUPERVISED CLASSIFICATION BASED ON WISHART DISTRIBUTION

Supervised and unsupervised classification based on the complex Wishart distribution model were applied to the same image. Fig. 5 shows the classified version on the 2x2 averaged image. To compare with the other two algorithms based on the target decomposition theorem, we listed the probabilities of correct classification in Table 1. It was assumed that the training areas are homogeneous and probabilities were calculated as the fraction of the pixels correctly classified in the respective training areas.

DISCUSSIONS AND CONCLUSIONS

For the classification based on the Wishart distribution, the results obtained using the unaveraged data are quite similar to that obtained using the 2x2 averaged data. However, the results based on target decomposition theorem appear to be much noisier if the unaveraged data were used. It implies that averaging is more important in applying target decomposition approach for a clearer segmentation.

Wishart distribution is a very reliable statistical model for the polarimetric SAR data as the good classification confirms this fact. Target decomposition emphasizes the analysis of the physical characteristics of the problem. It enhances our understanding of the scattering nature of the target. The



Fig. 1. Entropy image.

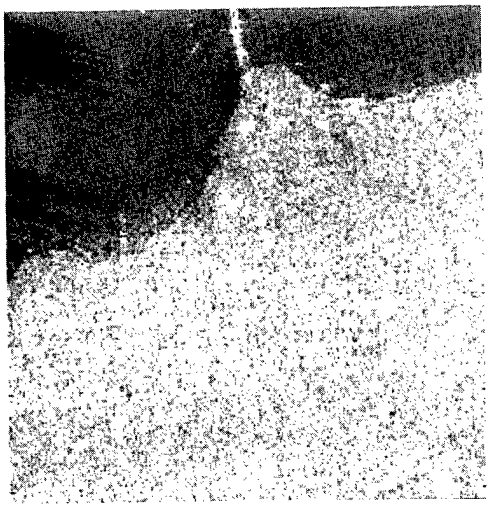


Fig. 2. α image.



Fig. 3. Supervised classification based on entropy and α.



Fig. 4. Supervised classification based on two larger eigenvalues.



Fig. 5. Supervised classification based on Wishart distribution.

Table 1. Comparison of probabilities of correct classification of the results shown in Figures 3, 4, and 5.

class	ocean	coastal ocean	quasi-natural	park	urban area
Wishart dist.	92%	80%	94%	84%	75%
entropy + α	92%	66%	46%	75%	55%
λ's	91%	12%	92%	76%	57%

advantage of the target decomposition approach is in the unsupervised classification that each cluster's physical properties can be used for automated class identification.

Using entropy as a parameter for discrimination, different media may produce similar values as exhibited in Fig. 1 where many spots in the park and urban areas display the same level of strength as that of ocean. The angle α may distinguish clearly dihedral scatterers from surface scatterers. Other angular parameters have different physical meanings, but they are less significant by the fact that natural terrain covers are too complicated to be represented by a simple model. Besides, these angles are evaluated using the eigenvector of the maximum eigenvalue. Their effectiveness in contributing to the discriminating process diminishes when the maximum eigenvalue is not as dominating as compared with the other two eigenvalues. In other words, the judgements made from these angular parameters may not be reliable, if the entropy value is larger than 0.5 [7]. Choosing entropy and these angles as features may produce ambiguities. The classification using two larger eigenvalues as shown in Fig. 4 indicates that the strength of the two larger eigenvalues and their correlations contribute more to the discriminating process than entropy and α angle. Finally, a classifier combining the Wishart distribution approach and the target decomposition theorem may have the potential to yield the best result.

ACKNOWLEDGMENTS

We thank professor Cloude for sending us his classification code. Communications with him have been most helpful.

REFERENCES

[1] S.R. Cloude, and E. Pottier,"A review of target decomoposition theorems in radar polarimetry," PIERS '94, Noordwijk, The Netherlands, July, 1994.

[2] S.R. Cloude,"An entropy based classification scheme for polarimetric SAR data," Proc. IGARSS '95, Firenze, Italy, pp. 2000-2002, 1995.

[3] J.S. Lee, K.W. Hoppel, S.A. Mango, and A.R. Miller,"Intensity and phase statistics of multilook polarimetric and interferometric SAR imagery," IEEE Trans. GRS, vol. 32, pp.1017-1028, Sept. 1994.

[4] J.S. Lee, M.R. Grunes, and R. Kwok,"Classification of multilook polarimetric SAR imagery based on complex Wishart distribution," Int. J. Remote Sensing, vol. 15, pp.2299-2311, 1994.

[5] J.J. van Zyl,"Application of Cloude's target decomposition theorem to polarimetric imaging radar data," SPIE vol. 1748, pp. 184-191, 1992.

[6] E. Pottier,"Radar target decomposition theorems and unsupervised classification of full polarimetric SAR data," Proc. IGARSS '94, Pasadena, U.S.A., pp.1139-1141, 1994.

[7] S.R. Cloude, and E. Pottier,"Concept of polarization entropy in optical scattering," Optical Engineering, vol. 34, pp.1599-1610, June 1995.

Hydrometeors Investigation by Means of 3 Millimeter Coherent Radar

A.S. Kosov, V.D. Gromov, S.N. Maleev, S.S. Kiselev, D.P. Skulachev, I.A.Strukov
All authors are with Space Research Institute, Russian Academy of Sciences
Address: 117810, Profsouznaya, 84/32, Moscow, Russia
Tel: (095)333-2267; Fax: (095)333-1545; E-mail: akosov@esoc1.bitnet

Abstract -- The paper is concerned with the development of the 3 millimeter wave solid state Doppler radar and using the radar for fog and precipitation parameters measurements. The radar is full solid state CW instrument with a sinusoidal frequency modulation. The sounding range is up to 1 km, relative distance resolution is 10%. Backscattering spectra from a weak rain are presented.

1. Background

Millimeter wave Doppler radar may be very useful for investigation of the hydrometeors, consisting of small water drops, primarily because of Rayleigh law of electromagnetic wave scattering. Due to f^4 scattering coefficient frequency dependence fog layers, water clouds and weak rains may be successfully investigated using millimeter waves, which is not so for centimeter waves.

Wavelength selection was based on existing the spectral windows where local minima of atmospheric absorption is occur. We chose the minimum, centred at 94 GHz. At low humidity (less than 1 g/m^3), the one-way absorption is below 0.1 dB/km, but for strong humidity (i.e. 25 g/m^3) it is increased to 2.5 dB/km.

There are few publications, concerning fog and clouds investigations by active remote sensing [1-2]. This is mainly because of low level of radar reflectivity of centimeter waves, which is usually used in meteorology. Using 3 millimeter wave frequency band it is possible to investigate the hydrometeors, consisting of small water drops, such as fog, clouds and weak rain. The first problem, which have been solved using developed radar system was the determination of water drops size distribution in weak rain. The distribution have been obtained from Doppler spectrum in the case of vertical sounding, using the known dependence of speed of falling drops from a drop diameter.

We have used low power transmitter and CW mode of operation. This is related to the problems, which we have solved in current work. We have developed the radar system with the sounding range up to 1 km and distance resolution about 0.1·R, where R - distance of sounding, with the facility of Doppler spectrum measurement and data integration. This is actually needed for fog and weak rain parameters investigation in vicinity of measurement system. In the case of sinusoidal frequency modulation and in the case of second harmonic of modulation frequency component extraction an element of scattering volume at distance R counterparts in signal at detector output as follows [3-4]:

$$s(R) = 0.5 k_R s_V(R) W(R) \cos(\Omega_D t) \qquad (1)$$

where k_R is constant, s_V is scattering coefficient, $\Omega_D = 2\pi f_D$, f_D - Doppler frequency, $W(R)$ is weighting function which can be described as:

$$W(R) = k_W J_2 [m \sin(2\pi f_m R/c)] / R^2 \qquad (2)$$

where: k_W is normalising multiplier, J_2 - Bessel function, modulation index m is defined by frequency excursion $df = m f_m$. In general $W(R)$ is complicated oscillating function. Nevertheless, with optimal choice of modulation index m it is possible to build function $W(R)$ having one dominating peak, which gives maximum altitude resolution, depending on frequency modulation, harmonic number and frequency excursion, Fig.2,3. The altitude displacement of the instrument weighting function peak spatial position can be done by angle scanning (taking into account $H=R\cdot\sin\alpha$) or by tuning the modulation frequency f_m.

2. Experimental System Description

The block diagram of the radar system is shown on Fig. 1. The radar system is CW solid state radar with sinusoidal frequency modulation. The radar antennas A1 and A2 are corrugated horns with the beamwidth about 10 degree at the level of -3 dB. There were two such antennas, one for receiving and the other for transmitting the radiation.

The 3 mm wave oscillator (OSC) was used as LO for mixer M1 and as transmitter source. The RF power of the oscillator was about 20 mW. About 5 mW of this power via directional coupler (DC) was used for LO and about 15 mW for irradiation. This oscillator was InP Gunn-effect device with special high efficiency low consumption power diode [5-7].

Acknowledgments. We are grateful to all collective of Department 61 of the Space Research Institute of Russian Academy of Sciences. We acknowledge the support of the RBSF (Grant 93-02-2930 and 93-02-2931), Cosmion and Soros Foundation (Grant M06-000).

0-7803-3068-4/96$5.00©1996 IEEE

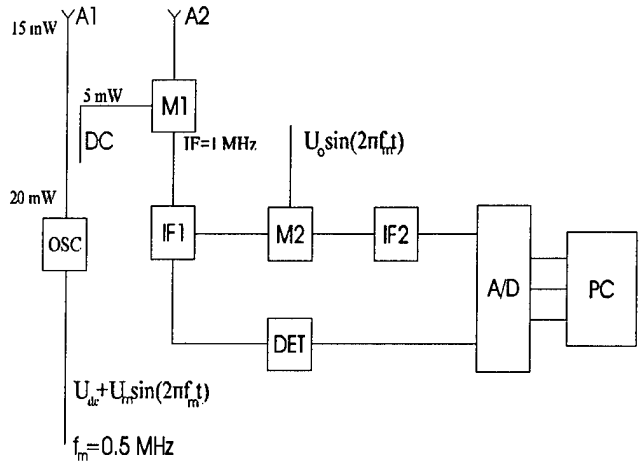


Fig 1. Block diagram of Radar System

The mixer M1 is GaAs Shottky diode balance mixer with conversion loss L ~ 5 dB. Due to low intermediate frequency (we used IF = 1 MHz) the noise temperature of the mixer is high enough T ~ 1000 K. The IF amplifier (IF1) was low noise (T ~ 50 K) FET amplifier. So the equivalent noise temperature of the receiver was T ~ 3000 K. The frequency modulation of the oscillator was produced by changing the bias voltage on the Gunn-effect diode. The modulation sensitivity of the oscillator was about 1 GHz/V. We used the frequency deviation ranged in 1-10 MHz. So the modulation frequency voltage amplitude V was ranged in 1-10 mV. The modulation frequency f_m was about 0.5 MHz and have determined the weighting function spatial position.

Due to the scattering particles motion the Doppler frequencies are ranged in 100 Hz - 10 kHz. To obtain the Doppler spectrum we have used the second conversion by the second mixer M2. The mixer M2 was the subharmonically pump mixer. As a local oscillator power for mixer M2 we used the signal of the reference oscillator OSCR, which was also used for frequency modulation of OSC. So we extracted the second harmonic component of modulation frequency f_m = 0.5 MHz. After second conversion we obtained the Doppler spectrum, which is amplified afterwards by IF2 amplifier. After amplification the signal was converted to digital form by A/D converter. At the same time we have detected the signal of IF1 by detector (DET). The signal after detection was proportional to the total power scattering by investigated targets. All data have been proceeded by Personal Computer PC.

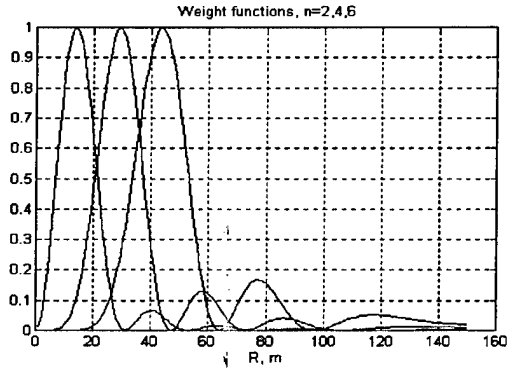


Fig.2. Weighting functions for backscattering sounding of rain or fog using frequency modulation and detection of 2-d, 4-th or 6-th harmonics (peaks from left to right).

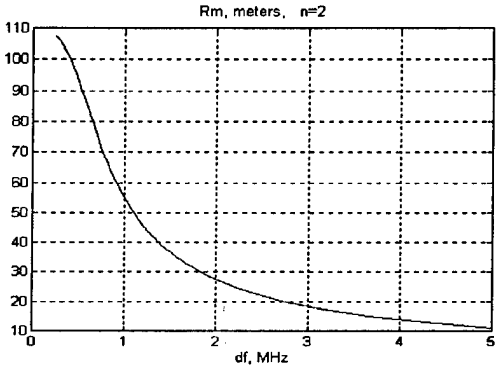


Fig. 3. The position of the maximum of weighting functions depending on frequency excursion *df*.

3. Results of Weak Rain Observation

We have used described above system for hydrometeor (weak rain, fog) parameters measurement. One example is on Fig.4,5, where an evolution of backscattering Doppler spectrum are presented. These spectrum are related to an evolution of rain from very weak to maximum and to the end of the rain. Information, containing in above spectrum can be used for drop size distribution determination and so on. It can be seen from Fig.4 that the mean frequency of the spectra is about 2 kHz at 19.35, then at 19.38 the mean frequency of the spectra have increased to about 3.5 kHz and then at 19.42 the mean frequency is decreased to about 1 kHz. It means that the falling velocity was changed as a result of changing of mean drop diameter. Following to falling velocity vs. drop diameter relation [10]:

$$v(D) = 3.778D^{0.6} \quad [D] = \text{mm}, [v] = \text{m/sec}, \qquad (3)$$

it is possible to determine mean drop diameter. Using (3) and data from Fig.4 we obtained that at 19.35 D_{mean}=1.5 mm; at 19.38 D_{mean}=2.5 mm and at 19.42 D_{mean}=0.5 mm.

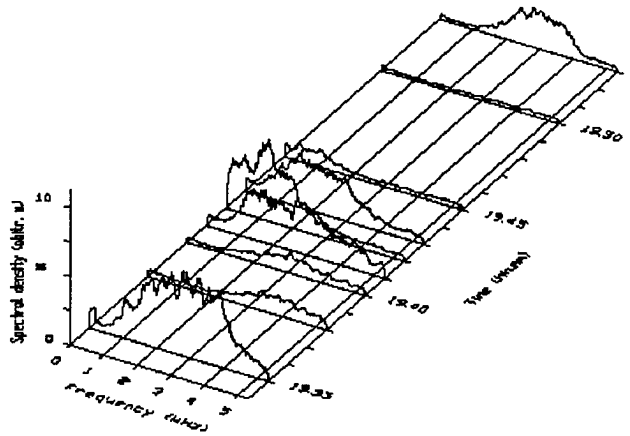


Fig.4. The spectrum of backscatter signal, measured at 60 degree elevation

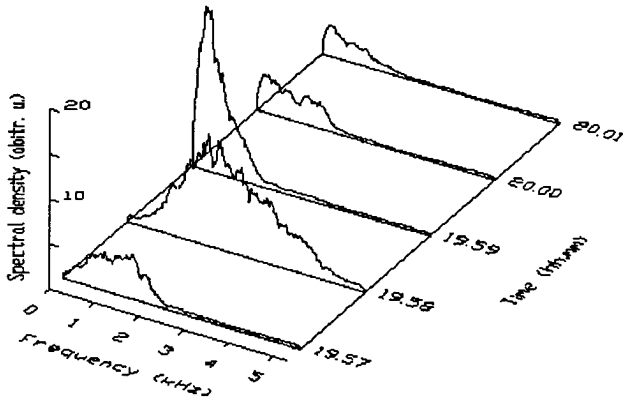


Fig.5. The spectrum of backscatter signal, measured at 30 degree elevation

4. Conclusion

The 3 millimeter wave coherent full solid state CW radar with sinusoidal FM was developed. This instrument allows to conduct measurements of backscattering signal from hydrometeors, consisting from small water drops (fog, weak rain, and possibly clouds) and Doppler spectrum of such hydrometeors. Drops size distribution in precipitation can be obtained from measurement data using calculations of attenuation and scattering (including Mie backscattering by raindrops) of these short wavelengths radiation by hydrometeors. The measurements of Doppler spectrum permit to determine also a wing direction and velocity.

5. References

[1] R.M. Lhermitte, "Cloud and Precipitation Remote Sensing at 94 GHz," IEEE Trans. on Geoscience and Remote Sensing, vol. 26, No 3, pp. 207 - 216, 1988.

[2] J. Nemarich, R.J. Wellman, J. Lacombe, "Backscatter and attenuation by falling snow and rain at 96, 140 and 225 GHz," IEEE Trans. on Geoscience and Remote Sensing, vol. 26, pp. 319 - 329. 1988

[3] M.I. Skolnik, "Introduction to radar systems," Mc.Graw-Hill, 1962.

[4] S.R.J. Axelsson, "Frequency Modulated Doppler Radar for Scatterometry and Surface Profiling," IGARSS'93, 1637-1640, 1993

[5] A.E. Ekzhanov, A.S. Kosov, V.A. Zotov, "Theoretical and experimental investigation of millimeter-wave InP Gunn-effect oscillator," Proceeding of 20-th Int. Europeen Conference, 10-14 Sept., Budapest, P7.15, pp. 1782-1786, 1990

[6] V.D. Gromov, E.N. Kadygrov, A.S. Kosov, "Remote Sensing of the atmospheric boundary layer at 5 mm wavelength," Proc. of URSI Symposium "Wave propagation and remote sensing," Ravenscar North Yorkshire, UK, 8-12 June, 1992

[7] A.V. Troitsky, K.P. Gajkovich, V.D. Gromov, E.N Kadygrov, A.S. Kosov, "Thermal Sounding of Atmosphere Boundary Layer in Oxygen Absorption Band Center at 60 GHz," IEEE Trans. on Geoscience and Remote Sensing, vol. GRS-31, pp. 23-29, 1993

[8] A.S. Kosov, E.N. Kadygrov, A.A. Vlasov, I.A. Strukov, D.P. Skulachev, "Results of balloon measurements of stratosphere radiothermal radiation at 5 mm," In Advance of Space Research, vol. 13, No 2, pp. (2)209-(2)219, 1993

[9] A.S. Kosov, V.D. Gromov, S.N. Maleev, D.P. Skulachev, I.A. Strukov, "Millimeter Wave Radar, Intended for Hydrometeor Parameters Determination," 25-th European Microwave Conference, Bologna, Italy, 3-5 September, 1995

[10] D. Atlas, C. Ulbrich, J. Applied Meteorol., vol. 16, No 10, 1977

Vegetation Obscuration Effects on Mid-Infrared Laser Reflectance of Soil

Brian D. Guenther and Ram M. Narayanan

Department of Electrical Engineering and Center for Electro-Optics
University of Nebraska, Lincoln, NE 68588-0511, USA
T: 402.472.5141 F: 402.472.4732 EMail: eerdrmn@engvms.unl.edu

Abstract— Mid-infrared laser reflectances of soils containing specific minerals show diagnostic features in the 9-11 wavelength range, resulting in their suitability for remote sensing of terrestrial lithology. However, the presence of actively growing vegetation can obscure these diagnostic features, in some cases almost completely, so as to make mineral identification virtually impossible. An experimental study was carried out to determine the effects of growing grass on the mid-infrared laser reflectance of bare soil in order to determine the conditions under which the underlying soil reflectance loses its diagnostic features. Reflectance ratios (indicative of diagnostic features) were investigated as a function of grass-blade height for different grass densities. It was found that, under specific soil conditions, there appeared a grass-blade height value at which the diagnostic ratios level off to a value of 1.0, thereby masking the underlying soil features. These results are expected to be useful for identifying optimal conditions under which soil mineralogy can be identified under overlying vegetation.

INTRODUCTION

Actively growing vegetation usually obscures the diagnostic features in the mid-infrared reflectance of soil brought about by soil mineralogy, in some cases almost completely, so as to make mineral identification virtually impossible [1]. The effects of vegetation are expectedly more pronounced at higher densities and heights. The objective of this study was to identify the conditions under which soil reflectance features were completely masked by overlying vegetation. In this paper, we describe the University of Nebraska's unique laser reflectance sensor operating in the mid-infrared wavelength range for laboratory and field applications. The system was used to collect reflectance data at various wavelengths, incidence angles, and polarization combinations from bare soil and grass-covered soil. Based on the measured data, specific grass-blade heights were determined that resulted in obscuration of the diagnostic features in the soil reflectance.

EXPERIMENTAL SETUP

The laser reflectance sensor used in the experiments is described in detailed in [2], and its block diagram is shown in Fig. 1. It consists of a line-tunable laser that operates in the 9-11 μm wavelength range with an output power of about 5 W. The receiver consists of a lens-detector combination, followed by a matched preamplifier and a lock-in amplifier. Both co-polarized as well as cross-polarized backscattered energy can be measured. The entire optical system is packaged in a box of approximate dimensions 104 cm x 38 cm x 22 cm.

Reflectance measurements were made at four wavelengths in the mid-infrared range, three incidence angles and two polarization combinations, as indicated in Table I. The laser sensor assembly was placed on the optical table, and the beam was directed towards the bare or grass-covered soil target using an adjustable mirror to vary the incidence angle. Soil was placed in a 6-cm deep movable soil container 2.3 m long and 1.1 m wide. The container was divided length-wise into three equally sized areas so that different soil roughnesses could be created. Speckle averaging was performed by physically translating the container during measurements and averaging 50 reflectivity samples for each measurement. Calibration was accomplished using a Labsphere Reflectance Standard of 94% reflectivity.

Initial experiments were made on bare soil under various wetness and surface roughness conditions. The soil was a clayey topsoil containing quartz as the dominant mineral. Varying amounts of soil moisture were induced by completely saturating the soil, mixing it well, and allowing it to dry slowly over a period of a few days. Soil gravimetric wetnesses between 23% and 7% were obtained by this method. Soil surface macroroughness was induced by sieving soil clods formed during wetting through hail screens of different sizes so as to obtain clod sizes less that 0.64 cm, sizes between 0.64 and 1.3 cm, and sizes greater than 1.3 cm.

Grass was then grown on the soil, and three different grass densities were used in different sub-plots of the container. The grass used was Kentucky 31 Tall Fescue, whose planting density was varied using different settings on a standard grass seed spreader. The average grass blade density (number of blades per square meter) obtained thus was determined to be approximately 2500 for the light density, 3800 for the medium density, and 7400 for the high density areas. Reflectance data were gathered from each sub-plot as the grass-blade height increased from 0 (emergent) to about 11 cm.

RESULTS AND DISCUSSION

A complete description of the test results is provided in [3]. This section provides a sample of the data thus obtained. From the bare soil reflectance measurements, it was confirmed that the soil macroroughness at the centimeter scale had no perceptible effect on the reflectance at normal as well as off-normal incidence angles. This

0-7803-3068-4/96$5.00©1996 IEEE

was somewhat expected since under these conditions, the soil could be considered electromagnetically very rough due to the fact that the wavelength is approximately 10 μm. Furthermore, it was confirmed that the soil reflectance dropped with increasing wetness, and its functional dependence was similar to that obtained from a wider variety of soil samples placed in 15-cm diameter Petri dishes [4].

From the bare soil measurements, it was observed that the reflectance ratio obtained by dividing the reflectance at 9.283 μm wavelength to that at 10.633 μm wavelength could be used as the diagnostic ratio. This is expected since quartz (the dominant mineral in our soil sample) has a reststrahlen band close to 9 μm wavelength. In our case, this ratio was approximately 1.25 under all soil roughness and wetness conditions at an incidence angle of 50 degrees. At normal incidence, this ratio was closer to 1 even for the bare soil, and thus it was felt that 50 degree incidence angle would be optimal. This ratio was monitored as the grass grew, and the average grass-blade height was measured. Plots of the reflectance ratio as a function of grass-blade height were generated, and these are shown in Figs. 2-4 for the different grass densities. A definite lowering in a near-linear manner is observed for the reflectance ratio as the grass-blade height increases. From Fig. 2, we note that under light density conditions, the ratio approaches 1.0 at a grass-blade height of about 10 cm. Fig. 3 indicates that under medium density conditions, a grass-blade height of about 8 cm makes the ratio reach 1.0, while Fig. 4 shows that under high grass density, it takes a grass-blade height of 6 cm to mask the soil reflectance features.

CONCLUSIONS

Our study indicates that actively growing vegetation can obscure the spectral characteristics of soil in the mid-infrared. The degree of obscuration increases with vegetation height and vegetation density. Although our study deals with one particular type of grass over one particular type of soil, it is conjectured that similar results would be obtained for other cases. This calls for further experimental study and analysis over a wider variety of vegetation and soil types.

REFERENCES

[1] R.J.Murphy, "The effects of surficial vegetation cover on mineral absorption feature parameters", International Journal of Remote Sensing, vol. 16, pp. 2153-2164, August 1995.

[2] R.M.Narayanan and S.E.Green, "Field measurements of natural and artificial targets using a mid-infrared laser reflectance sensor", IEEE Photonics Technology Letters, vol. 6, pp. 1023-1026, August 1994.

[3] B.D.Guenther, Mid-Infrared Laser Reflectance of Bare and Vegetation-Covered Soil, M.S. Thesis, University of Nebraska- Lincoln, Lincoln, NE, 1994.

[4] R.M.Narayanan, S.E.Green, and D.R.Alexander, "Mid-infrared laser reflectance of moist soils", Applied Optics, vol. 32, pp. 6043-6052, 20 October 1993.

TABLE I
LASER OPERATING CONDITIONS

WAVELENGTHS (μm)	9.283, 9.520, 10.247, 10.633
INCIDENCE ANGLES (deg)	0, 20, 50
POLARIZATIONS	Co-pol, Cross-pol

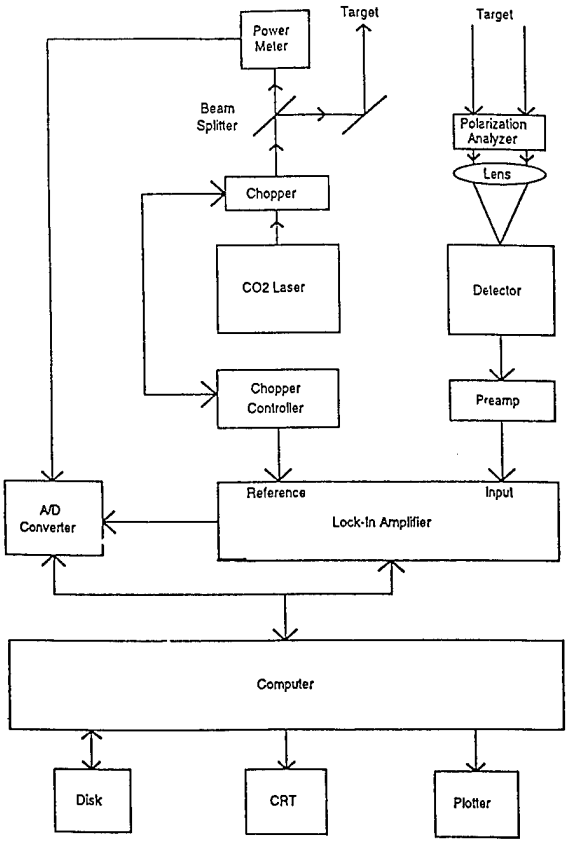


Figure 1: Block diagram of mid-infrared laser reflectance sensor

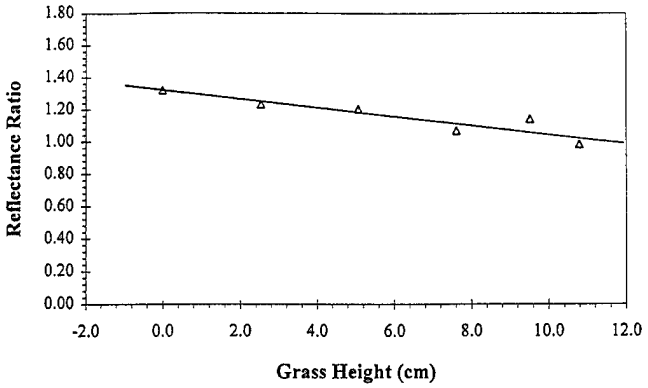


Figure 2: Reflectance ratio as a function of grass-blade height for light density soil

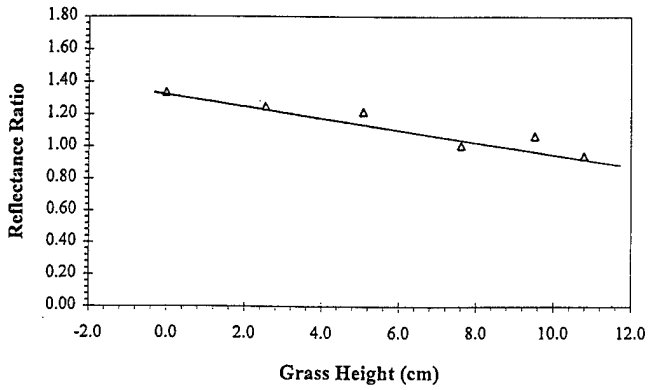


Figure 3: Reflectance ratio as a function of grass-blade height for medium density soil

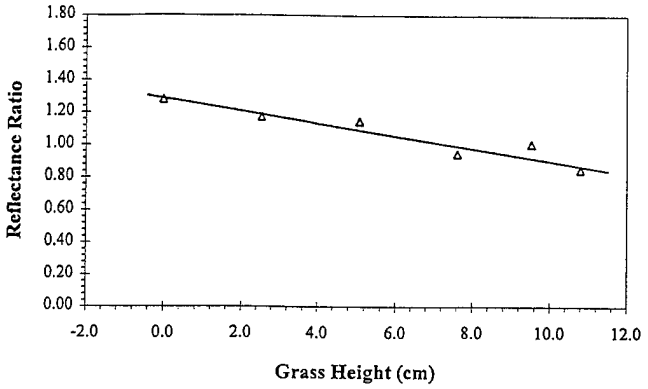


Figure 4: Reflectance ratio as a function of grass-blade height for high density soil

Applying principal components analysis to image time series: effects on scene segmentation and spatial structure

Geoffrey M. Henebry
Kansas State University
Division of Biology/Ackert Hall
Manhattan, KS 66506-4901 USA
T: 913.532.7997 F: 913.532.6653
gmh@unix.konza.ksu.edu

Donna R. Rieck
Kansas State University
Division of Biology/Ackert Hall
Manhattan, KS 66506-4901 USA
T: 913.532.6729 F: 913.532.6653
drieck@unix.konza.ksu.edu

Abstract -- Principal components analysis (PCA) has been applied to multitemporal data for over a decade, frequently in preparation for land cover classification. With the increasing availability of standardized multitemporal datasets, such as Pathfinder AVHRR Land products and the maximum biweekly AVHRR NDVI composites for the conterminous US, we wondered about the efficacy of using PCA to identify the dominant spatio-temporal modes within the data. How many principal components are useful? Does inclusion of higher order components improve scene segmentation or hinder it? What are the effects on the spatial structure of a segmented scene? To address these questions we selected a portion of the North American Great Plains from the Pathfinder AVHRR Land product for 1986. The subset region nominally covers over 2 million km^2 and spans significant temperature and precipitation gradients. The resulting image time series comprised 30 10-day maximum NDVI composites. These data were submitted to a series of PCAs with 3, 6, 9, or 12 principal components output as different images. Each PCA set was then submitted to an unsupervised classification, followed by maximum likelihood decision rule applied to the signature set to yield 4, 6, 8, or 10 classes. Each class was analyzed with lacunarity analysis, which quantifies spatial heterogeneity and anisotropy in binary data. There was a significant effect of the number of PCs used in the classification on the lacunarity of certain classes but not others. Visual inspection revealed that several higher order principal components were compositing artifacts. These results suggest that PCA performed on image time series can effectively filter compositing noise when data are reduced to a small number (<6) of components.

INTRODUCTION

Principal components analysis (PCA) is an important tool for multitemporal analysis [1-3]. PCA of a high temporal resolution image series can attenuate temporal autocorrelation, thereby increasing the suitability of the data for image segmentation and classification procedures [2]. Moreover, principal components (PCs) are of intrinsic interest because they effectively summarize the dominant modes of spatial, spectral, and temporal variation in the data in terms of linear combinations of image frames. As standardized multitemporal datasets are increasingly available, it is relevant to explore the limitations of multitemporal PCA.

How many principal components are useful? Several studies using AVHRR NDVI have found that most of the dataset variance (>90%) lies in the first 3 PCs [1-3]. In particular, [1] suggested that the first PC in their image series related to integrated NDVI and thus to biomass quantity. Further, the sinusoidal trend of the weightings in the first 3 PCs correspond to seasonality [1,2] and the significance of higher order PCs was the subject of speculation [1]. These studies used a limited number of images (<10). Would a significant increase in series length and temporal resolution change these conclusions? A longer data set means more potential PCs. Does inclusion of higher order PCs improve scene segmentation or hinder it? Finally, what are the effects of more PCs on the spatial structure of a segmented scene? Here we present an initial attempt to address these questions.

METHODS

From the 1986 subset of the Pathfinder AVHRR Land (PAL) product, we selected a major portion of the North American Great Plains that exhibits strong abiotic gradients in moisture (E-W) and temperature (S-N) as well as a range of land cover from lightly to intensively managed. Our test region extends from southern Canada into northern Texas, from just east of the Front Range almost to the Mississippi. This area covers more than 2 million km^2 but at 8 km resolution comprises

0-7803-3068-4/96$5.00©1996 IEEE

only a small image: 120 x 278 pixels. The PAL product includes 30 10-day composites of maximum NDVI. While the spatial resolution is coarse, the finer resolution of 10-day versus 14-day composites promises better spatio-temporal tracking for transitory phenomena like the differential onset of spring. Although NASA has cautioned against using the PAL 1986 subset for research, the data are suitable for our purpose.

The image time series was stacked into a 30-band file. The ERDAS Imagine PCA module generated four different images containing 3, 6, 9, or 12 PCs. Each of the four transformed images then underwent an unsupervised classification, followed by maximum likelihood decision rule applied to the signature set to yield 4, 6, 8, or 10 classes. We analyzed each class with lacunarity analysis, which quantifies spatial heterogeneity in binary data [4,5]. The sampling window preserved the aspect ratio of the image and the largest window used was 109x254 or 83% of the image. Lacunarity estimation used the exhaustive sampling of the "gliding-box" algorithm [4].

Lacunarity is sensitive to both the density and the arrangement of "on" pixels in a binary map. At window size of 1, the inverse of the lacunarity index equals the proportion of "on" pixels: larger values of the lacunarity index at the y-intercept indicate sparser coverage. The shape of the decay conveys information about the degree of pixel aggregation. A random arrangement of pixels yields a rapid decay to zero; a linear decay indicates a self-similar spatial distribution of clumps. When clumping occurs at a characteristic scale, the decay is gradual as long as the sampling window is smaller than the clump size. Once the sampling window is greater than the characteristic scale, the decay is rapid. To compare decay curves, it is useful to control for density effects. By combining lacunarity estimates for both "on" and "off" pixels, a normalized lacunarity index can be calculated that is sensitive to aggregation effects alone.

RESULTS

We will focus on the behavior of two adjacent regions in the 8-classification. Class 5 (Fig. 1) is located in the southwestern sector of the image and covers the semi-arid plains and short grass prairies of eastern Colorado, western Kansas and Oklahoma, and northwestern Texas. Located due east, Class 6 (Fig. 2) intermingles extensively with Class 5. This class spans a significant precipitation gradient and a biotic gradient of mixed grass prairie at the western edge to tallgrass prairie at the eastern extremity. Dominant land uses in both classes are dryland and irrigated agriculture and grazing.

As the number of PCs used in segmentation increases, class 6 diminishes and class 5 expands. Importantly, the combined area of these classes remains at about 30% of scene; there appears to be a migration of pixels from class 6 to class 5 as the number of PCs submitted to the classification increases. Moreover, the spatial structure of the classes changes significantly: the inclusion of higher order PCs appears to erode the finer spatial details. The lacunarity plots reveal both the change in class density (Figs. 3&4) and spatial arrangement (Figs. 5&6) as the number of PCs used in classification changes. Note how the spatial configuration of class 5 is perceptibly affected only at 12 PCs; whereas, inclusion of 9 and 12 PCs generate lacunarity curves for class 6 that are significantly different from the nearly identical curves of 3 and 6 PCs. Class 6 at 9 PCs is more diffuse than at 3 or 6 PCs, producing a swifter decay, and class 6 at 12 PCs is more compact, yielding slower decay (Fig. 6).

CONCLUSIONS

Inclusion of higher order PCs in scene segmentation appear to degrade the spatial structure. Why? We think that compositing artifacts and subpixel cloud contamination are the culprits. Distinctive rectilinear features were apparent in most of the PCs > 5 (data not shown). Use of standardized PCA might attentuate this problem [3]. Differential weighting of PCs submitted to the segmentation algorithm is also a possibility. Reducing multitemporal data using PCA can provide a robust preparation for scene segementation, if care is exercised in limiting the compositing error variance captured by higher order PCs.

ACKNOWLEDGMENTS

This research was supported through EPA EMAP grant #R823605-10-0 and NSF LTER grant #BSR-9011662.

REFERENCES

[1] J.R.G. Townshend, T.E. Goff, and C.J. Tucker, "Multitemporal dimensionality of images of normalized difference vegetation index at continental scales," IEEE Trans. Geo. Rem. Sens., vol. GE-23, pp. 888-895, 1985.

[2] R. Benedetti, P. Rossini, and R. Taddei, "Vegetation classification in the middle mediterranean area by satellite data," Int. J. Remote Sens. vol. 15, pp. 583-596, 1994.

[3] L. Eklundh. and A. Singh, "A comparative analysis of standardised and unstandardised principal components analysis in remote sensing," Int. J. Remote Sens. vol.14, pp. 1359-1370, 1993.

[4] R.E.Plotnick, R.H.Gardner, and R.V.O'Neill, "Lacunarity indices as measures of landscape texture," Landscape Ecology, vol. 8, pp. 201-211, 1993.

[5] G.M.Henebry and H.J.H.Kux, "Lacunarity as a texture measure for SAR imagery,". Int. J. Remote Sens., vol. 16, pp.565-571, 1995.

FIGURE 1
Class 5

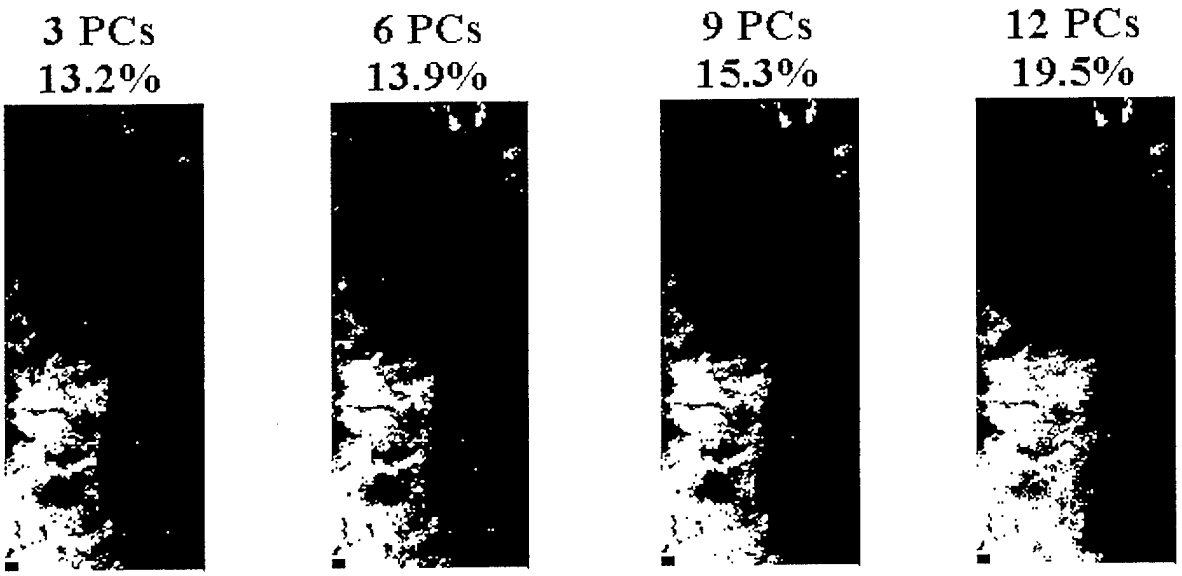
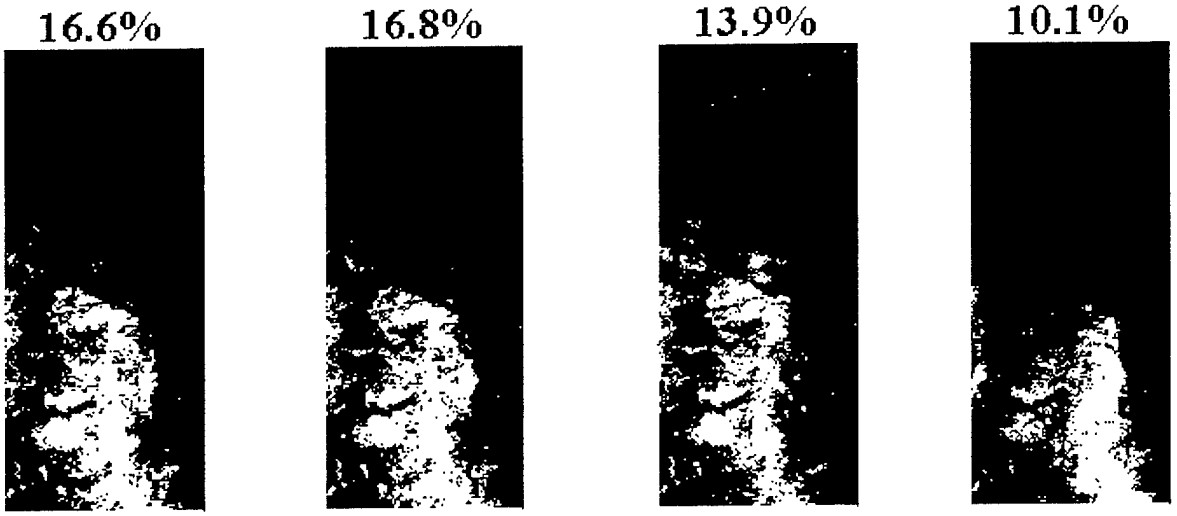
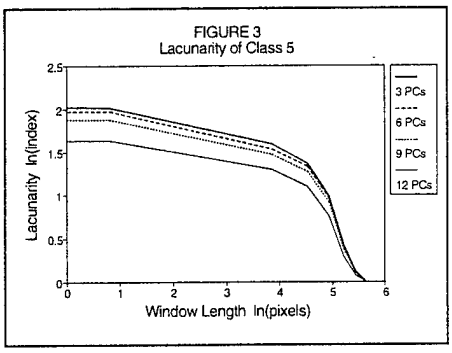
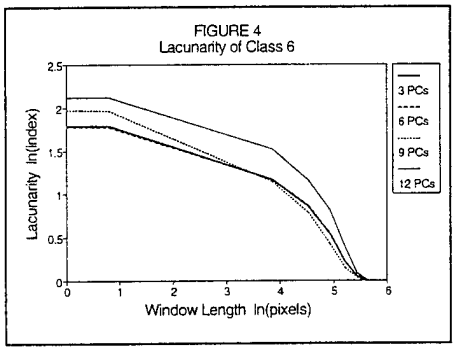
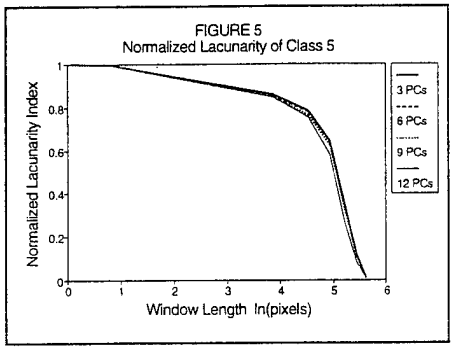


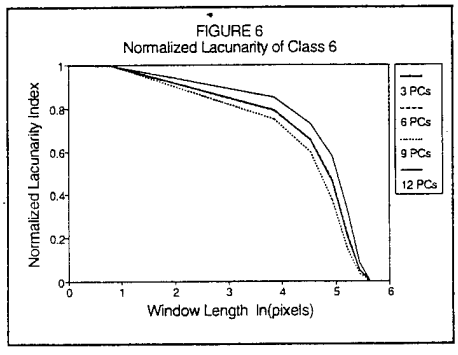
FIGURE 2
Class 6











D.A.T.E. -- Dip Algorithm Testing and Evaluating Workbench

Mark G. Kerzner
Consultant
7522 Apache Plume, Houston, Texas 77071
(713) 728-4210, e-mail 72623.3367@compuserve.com

OVERVIEW

Dipmeter is a well logging tool for measuring formation dip, that is, the angle and the direction of the tilt of the underground formation. It does this by measuring focused microresistivity in a few places (4, 6, or more) on the circumference of the hole. If the formation is dipping, the resulting measurements will be displaced in relation to each other. From these displacements one can compute the dip by applying standard formulas of analytical geometry.

However, finding these displacements is far from a standard problem, and there exists a number of approaches mentioned in [1-3], and more recently in [4], where a similar problem arises for a different tool. The need for effective reservoir description poses ever great challenges and necessitates the development of better, more stable and precise dip computation algorithms.

In this paper we describe a development environment which was designed and programmed specifically to develop and test dip computation algorithms. We describe the geological considerations that went into the design and their implementation. We also briefly discuss the results achieved using this environment, namely, new dip computation algorithms. We will describe the algorithms themselves in greater detail in upcoming publications.

The immediate benefit of the DATE workbench is therefore the development of new dip computation algorithms. In addition, it can serve either as a base or as a model for developing processing algorithms for other tools.

TEST WORKBENCH REQUIREMENTS

An algorithm testing environment has to be able to do the following:

- generate simulated data
- select geological conditions
- modify simulated data according to selection above
- apply algorithms and compare results

For comparison with existing algorithms it also needs to be able to

- import real data from tool recording
- import computation results from other programs

In the following sections we will describe how these steps were implemented in DATE.

DATA GENERATION

Dipmeter tool data contains two distinct sets of curves. The first set is profile curves, which record a given formation property in given point on the circumference of the hole. The second one is orientation data, which measures the position and orientation of the tool and of the well.

The orientation data does not have to be generated, since in computations it will factored out and it is not essential for the correlation algorithm. We will use it, however, when importing real recording.

To create the profile curve data, we first generate a bedding sequence. According to sedimentological studies [5], bed thickness conforms to normal distribution. This means that given the average bed thickness, we can generate a series of beds which will be similar to those found in nature.

This is done using a random number generator. The user can select the seed for generator. This allows to either create a variety of different test by entering different seeds. To repeat the results of the previous test, one enters the seed that was used for this test.

After bed thicknesses have been generated, each bed is assigned a certain resistivity, also using a random number generator. Studies did not indicate a significant dependence between resistivities in adjacent formations, so in DATE this number is generated without regards to the resistivities above and below the given formation.

Finally, we apply a filter to reflect that the tool measure resistivity in a certain volume of formation, rather than at a particular depth point. To truly calculate tool responses, one would have to solve the forward modeling problem of electromagnetic propagation. This is nor needed, however, since for algorithm testing filtering creates curves that look similar to real.

0-7803-3068-4/96$5.00©1996 IEEE

At this stage, we create one curve and duplicate it to create all the others. Curves can be generated in three possible ways: sine wave, random, and random with noise. In the latter case, normally distributed noise is added to each of the pad measurements separately. The intensity of noise is controlled by the user.

SELECTION OF THE DESIRED RESULT

Had the dip been computed at this stage of data generation, it would show that all formations are flat and the dip is equal to 0. Now the user selects the desired dip pattern. Each geological feature, such as an anticline, fault, or thrust, has a dip pattern associated with it. The dip patterns described in [6] were preprogrammed into DATE and can be selected. Other patterns can be used.

The selected dip pattern is imposed on the data. This results in shifting of the profiles curves, stretching and compressing that in certain places. From the distorted curves our algorithms will have to find displacements and then back the selected dip picture. We will measure the success of the algorithm by its ability to restore the given dip pattern.

A set of generated curves and a selected dip pattern are displayed by DATE, as shown in Fig. 1. For this example we used average bed thickness = 0.2 ft, filter length = 0.2 ft, dip pattern = flexures, depth scale = 5 in / 100 ft.

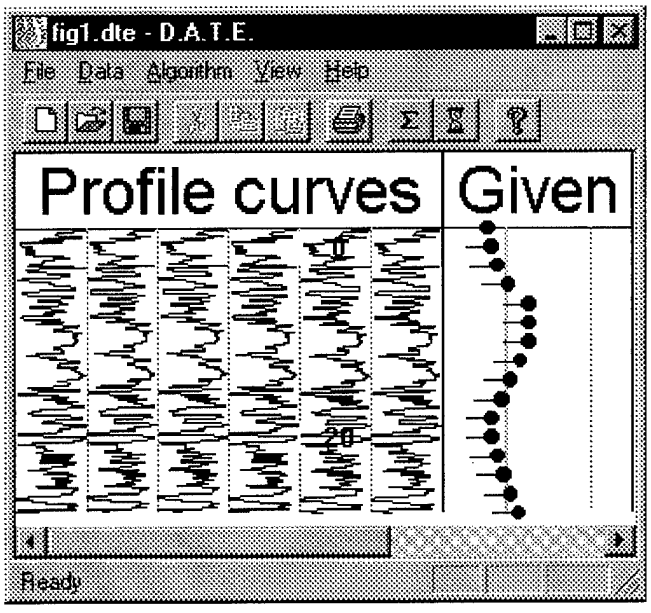


Figure 1. Six-arm dipmeter data generated with DATE.

DATA IMPORT

As an alternative to generating profile curve data and selecting the dip pattern, DATE has an option to import real recording, This is accomplished by dumping any recorded dipmeter format in ASCII, in a predefined way. This approach allows to test with data recorded in any format.

DATE scans an ASCII file, tells the user the file depth interval, and allows to select an interval for processing. Then it reads the profile curve and the tool orientation data. Results of the computation by any dip computing program can likewise be imported from an ASCII dump.

DIP COMPUTATION ALGORITHMS

Algorithms for dip computation can be roughly classified into three groups:

1. Interval correlation (large-scale features).
2. Event correlation (medium resolution).
3. Point-to-point correlation (fine resolution).

Using the DATE workbench we have achieved improvements in all three areas. This is summarized in Table 1. There are therefore six algorithms. All of these algorithms have been programmed and can be used for comparison.

IMPROVEMENTS

There are a number of improvements possible in each of the three groups of the algorithms in Table 1. The DATE workbench provides ample opportunities for this.

It is not feasible to describe them in detail in this paper. Besides, a detail description would necessitates the overview of the old algorithms. This also can not be the subject of the current publication. This is left, therefore, for upcoming publications, one of them being [7].

However, we will in general describe the path which led to these improvement and the advantages to be realized.

The first task which faced the author was to find a technique for processing multipad tool measurements. The algorithms in [1-3] were developed for tools with four pads. They relied on the limited number of pad combinations to form bedding plains. When the number of pads grew, as it happened with modern day tools, the amount of computations grew exponentially or the results became unstable.

The technique found was based on triangle clustering. Virtual reality programs use triangles for rendering scenes as

Table 1. Dip computation algorithms.

Group	Example	Using DATE	New techniques
Interval correlation (large-scale features)	Many	Better interval correlation	Optimization applied for the first time Triangle clustering for multipad correlations
Event correlation (medium resolution)	[3]	Better event correlation	Low-frequency event picking Event-event correlations Triangle clustering for multipad correlations
Point-to-point correlation (fine resolution).	[1]	Microdip®	Profile curve enhancement Better selections of point for matching Changed optimization model Triangle clustering for multipad correlations

a good compromise between efficiency and quality. This happened to be the same in our case.

Now that this was possible, algorithm [1] (group 3) was redesigned in many ways. Profile curve data was enhanced to better analyze the curve character. Algorithm for picking points for matching was improved. Optimization model was changed to arrive at more realistic correlations. Finally, optimization algorithm was reprogrammed in C++ which allowed to use it for various objects in the algorithm, by applying C++ inheritance.

These newly developed techniques were applied to algorithm [3] (group 2). Additionally, two new techniques were added here. One is low frequency event picking (the old algorithm depended upon high frequency of data change). The other one is that event correlation was changed to be true event-event, rather than event-interval correlation.

The interval correlation algorithm (group 1) benefited from the above mentioned new techniques. Since they were never applied to interval correlation, the improvement was immediate. The improvements are summarized in Table 1.

AN EXAMPLE OF BENEFITS

An example of real imported recording comparing the previous method of point-to-point correlations (left) with the improved one, called Microdip® (right), is shown in Figure 2. One can immediately notice the better frequency resolution of the new algorithm. New algorithm's results are also more stable, and the number of computed dips is greater. This stability is even more pronounced in cases of complex recording.

CONCLUSIONS

New requirements for reservoir description lead to work on improved log processing algorithms. This software development effort can benefit from an integrated test facility. An example of such facility is provided by the DATE workbench. This workbench allows to design better dip computation algorithms. It can also be used as a base or model for designing algorithms for other tools.

REFERENCES

[1] Mark G. Kerzner, ""Formation Dip Determination - an Artificial Intelligence Approach"", Log Analyst, vol. 24, no. 5, pp.10-22.

[2] Mark G. Kerzner, Image Processing in Well Log Analysis, IHRDC, Boston, 1986, pp. 21-40.

[3] Mark G. Kerzner, "A Rule-Based Approach to Dipmeter Processing", SPE paper 18128, 1988.

[4] Olivier Faivre, Gerard Catala, "Dip Estimation from Azimuthal Lateralog Tools", SPWLA 36th Annual Logging Symposium, paper CC, June 1995.

[5] Walther Schwarzaher, Sedimentation Models and Quantitative Stratigraphy, Amsterdam, Elsevier, 1975, pp. 20-53.

[6] Fundamentals of Dipmeter Interpretation, Schlumberger, New York, 1970.

[7] Mark G. Kerzner, "Use of Dynamic Programming in Signal Processing", C/C++ User Journal, June 1996.

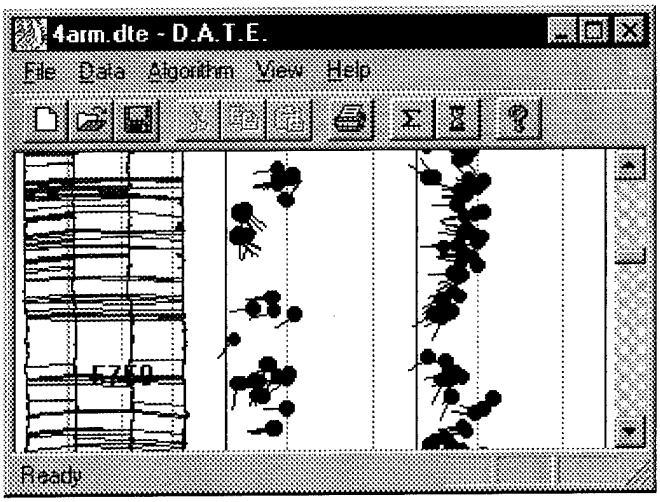


Figure 2. Point-to-point correlation comparison.

High Resolution VHF SAR Processing Using Synthetic Range Profiling

Richard T. Lord and **Michael R. Inggs**
Radar Remote Sensing Group, Dept of Electrical Engineering, University of Cape Town
Private Bag, Rondebosch 7700, South Africa
Tel: +27 21 650 3756 Fax: +27 21 650 3465
Email: rlord@eleceng.uct.ac.za

Abstract—This paper demonstrates the use of stepped-frequency waveforms to obtain high resolution SAR images without imposing severe instantaneous bandwidth requirements on the radar system. Although azimuth compression and motion compensation are essential to obtain high resolution SAR images, this paper only discusses how to obtain high range resolutions. Especially at VHF frequencies it is very difficult to obtain high range resolutions, because the effective pulse bandwidth required would amount to a large percentage of the centre frequency. After briefly introducing the theory of synthetic range profiling as applied to SAR, this paper goes on to discuss the synthetic range profile of an A320 airbus, which serves to demonstrate the feasibility of synthetic range profiling. More attention is then given to simulation results, which introduce the problems encountered when sampling the returning echo waveforms.

INTRODUCTION

Synthetic range profiling (SRP) is a processing technique to obtain high range resolution using stepped-frequency waveforms without imposing severe instantaneous bandwidth requirements on the radar system. A total radar bandwidth of $64 \times 1.5 = 96$ MHz can be synthesized by sequentially transmitting 64 pulses, each pulse stepped in frequency by 1.5 MHz. The final slant-range resolution that can therefore be achieved is about 1.56 m.

This is illustrated in Fig. 1, which shows a surface plot of three point targets that were resolved using SRP. These simulated point targets, which were 6 m apart in ground range, were "illuminated" with 64 monochrome pulses stepped in frequency, each pulse having a bandwidth of 1.5 MHz, which corresponds to a slant-range resolution of only 100 m. However the use of stepped-frequency processing yielded a final slant-range resolution of 1.56 m.

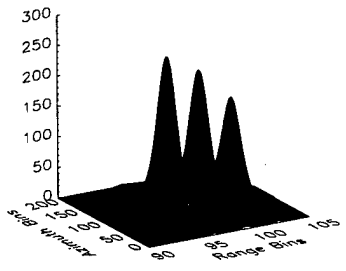


Figure 1: Surface plot of three point targets that were resolved using synthetic range profiling

The CARABAS system is a practical example of an airborne SAR system which operates in the lower part of the VHF-band to produce surface images using stepped-frequency waveforms [2].

SYNTHETIC RANGE PROFILING APPLIED TO SAR

To produce SAR images with stepped-frequency waveforms basically requires the production of one SRP per *coarse* range bin. Obtaining a SRP involves the following steps [5]:

1. Transmit a burst of n pulses, each pulse shifted in frequency by a fixed frequency step size Δf.
2. Collect one I and Q sample of the target's baseband echo response in each coarse range bin for every transmitted pulse. These samples are the frequency-domain measurements of the target's spectral profile.
3. Apply an inverse discrete Fourier transform (DFT^{-1}) on the n complex samples in each coarse range bin to obtain an n-element SRP of the target in the respective coarse range bin.

In contrast with data obtained from pulse-compression radars, the data is already compressed in the range direction at this stage, since the slant-range resolution has been obtained synthetically using the inverse discrete Fourier transform. The azimuth resolution, however, can be obtained as in pulse-compression radars by coherently integrating the range-resolved echo signals that were obtained during the real beam dwell time. This aspect is not addressed in this paper. Furthermore, to obtain high resolution images, motion compensation and range curvature would have to be addressed as well. Another problem not discussed in this paper is the variation of the radar response with frequency and observation angle [1], which varies significantly over the synthetic aperture path.

0-7803-3068-4/96$5.00©1996 IEEE

The synthetic slant-range resolution is given by

$$r_{\text{res}} = \frac{c}{2n\Delta f} \ , \tag{1}$$

and the slant-range ambiguity length is given by

$$w_s = \frac{c}{2\Delta f} \ . \tag{2}$$

Ideally the matched filter integration length, given by $\frac{c\tau_p}{2}$, where τ_p is the pulse length, should equal the slant-range ambiguity length w_s. This leads to a pulse length of

$$\tau_p = \frac{1}{\Delta f} \ . \tag{3}$$

When the integration length is greater than w_s, foldover will occur due to integration of scatterers outside the unambiguous range length. However if the integration length is smaller than w_s, the echo signal will only contain energy integrated from a range depth smaller than the slant-range ambiguity length.

SYNTHETIC RANGE PROFILES OF AEROPLANES

The feasibility of using stepped-frequency waveforms to produce high resolution down-range profiles has already been demonstrated by the production of SRPs of aeroplanes [4]. Fig. 2 shows the SRP of an A320 airbus that has been produced by transmitting linear chirp pulses at 55 different frequencies at L-Band. Two pulses were transmitted at each frequency in order to carry out *moving target indication* (MTI) processing. Each pulse had a bandwidth of 3.6364 MHz, which resulted in a compressed pulse width of $\tau_c = 275$ ns. The pulse resolution was therefore $\frac{c\tau_c}{2} = 41.225$ m, which is about the length of a large aircraft. The frequency spacing was 1.875 MHz, which corresponds to a range-delay extent of 80 m, which is about twice the length of the pulse resolution. The total processed radar bandwidth was 103.125 MHz, which results in a slant-range resolution of 1.45 m.

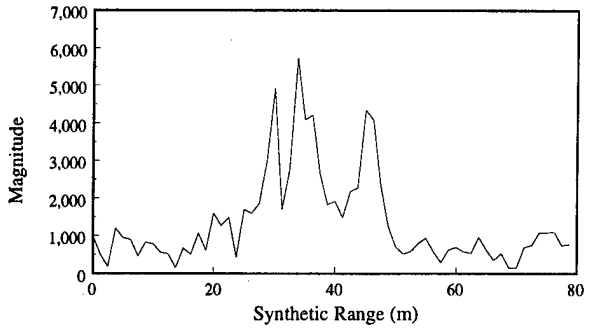


Figure 2: Synthetic Range Profile of an A320 airbus

Table 1: Parameters of radar using SRP

Frequency Step Size	Δf	1.5 MHz
Number of Steps	n	64
Start Frequency	f_0	90.75 MHz
Stop Frequency	f_{63}	185.25 MHz
Total Radar Bandwidth	B	96 MHz
Slant-Range Resolution	r_{res}	1.56 m
A/D sampling frequency	f_{ad}	1.5 MHz
Coarse Range Bin Size	R_{bin}	100 m
Pulse Length	τ_p	666.67 ns
Pulse Repitition Frequency	PRF	11.52 kHz

SIMULATION RESULTS

Table 1 gives the parameters that were used to obtain the simulated SAR data. Fig. 3 shows the magnitude along a range line of a single resolved point target. The dashed line indicates the coarse range bin in which the point target is situated. Samples were collected in four successive coarse range bins, each bin having a slant-range extent of 100 m (corresponding to a 667 ns pulse). Note that the instantaneous bandwidth and the A/D sampling frequency required are only 1.5 MHz, compared with the final processed bandwidth of 96 MHz. The original PRF of 180 Hz was increased by a factor of 64, giving a final PRF of 11.52 kHz. A radar mounted on an aircraft which flies at a height of 10 km, mapping out a 4 km wide swath in slant range, requires a PRF of less than 37.5 kHz to avoid ambiguity problems. However if it is required that one pulse has to be received before the next pulse is transmitted, this increase in PRF will be unacceptable. The technique of *multiple PRF ranging* [3 pg. 116] may be used to solve this problem.

In Fig. 4 a range line displaying three resolved targets is shown. The important thing to note in Fig. 4 is the spill-over of energy into the successive range bin. The next section discusses this problem in more detail.

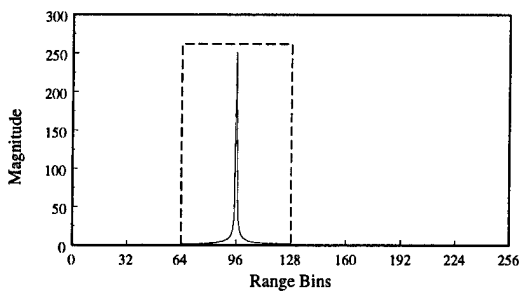


Figure 3: Synthetic range profile of a single point target in one coarse range bin

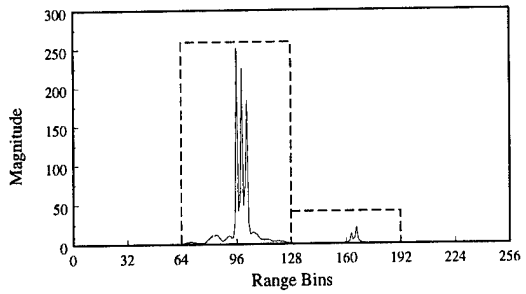


Figure 4: Synthetic range profile of three point targets in one coarse range bin, showing spill-over of energy into successive range bin

SAMPLING CRITERIA

Fig. 5 shows that for a single point target it is possible to avoid spill-over of energy into the successive range bin by sampling the matched filter output exactly at the peak of the triangular waveform. This scenario was followed when the data of Fig. 3 was produced. However as soon as there is more than one point target (which is the case in practice), there will be an inevitable spill-over of energy into the next range bin, as illustrated in Fig. 5. Sampling still takes place at the theoretical peak of the first pulse, but some of the energy of the second pulse and even more energy of the third pulse is also sampled in the next coarse range bin. This explains the decrease in amplitude of the second and third pulse as seen in Fig. 4.

A solution to the problem of spill-over of energy would be to sample every second coarse range bin during one transmitted pulse, and then every other second coarse range bin during the next transmitted pulse. This, however, will increase the PRF by a factor of two. Further investigations are being carried out using windowing functions and overlapping coarse range bins, in order to arrive at a satisfactory solution regarding the sampling of returning waveforms.

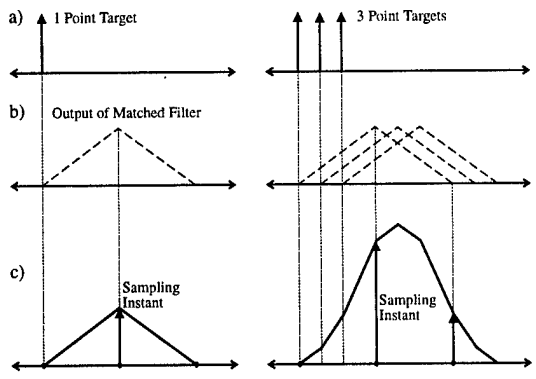


Figure 5: Sampling the output of the matched filter

SKIPPING FREQUENCIES

An important advantage of using stepped-frequency waveforms is the capability of skipping certain frequencies that would otherwise be corrupted by external sources such as broadcast FM and mobile radio. Before transmitting a pulse, the receiver could predict how much interference there will be at a particular frequency, and then decide to skip that frequency. Since the order in which frequencies are transmitted is not important, the radar could try to transmit a skipped frequency at a later stage in the burst. Another way out would be to interpolate the I and Q values of skipped pulses from those I and Q values of surrounding pulses.

CONCLUSIONS

The results that have been obtained from simulated SAR data show that it is feasible to use stepped-frequency waveforms to produce high resolution VHF SAR images. Not only do stepped-frequency waveforms alleviate the instantaneous bandwidth requirements of the radar system, but they also offer the capability of skipping frequency regions that might be polluted by external sources. This is expected to be a major feature of such a system, since the amount of interference at the VHF band is expected to be quite severe.

Further work will have to be carried out to investigate the effects of interpolating missing pulses, to solve the problems of the matched filter effect satisfactorily, to investigate the use of multiple PRF ranging and to implement high resolution SAR azimuth processing.

REFERENCES

[1] S. R. J. Axelsson, "Frequency and Azimuthal Variations of Radar Cross Section and Their Influence Upon Low-Frequency SAR Imaging," IEEE Trans. on Geoscience and Remote Sensing, vol. 33, no. 5, pp. 1258–1265, September 1995.

[2] A. Gustavsson, P. O. Frölind, H. Hellsten, T. Jonsson, B. Larsson, and G. Stenström, "The Airborne VHF SAR System CARABAS," Proc. IEEE Geoscience Remote Sensing Symp., IGARSS'93, Tokyo, Japan, vol. 2, pp. 558–562, August 1993.

[3] S. A. Hovanessian, Radar System Design and Analysis, Norwood, MA 02062: Artech House, 1984.

[4] A. D. Robinson and M. R. Inggs, "Correlation Filters Applied to Synthetic Range Profiles of Aircraft Targets," Proc. of the IEEE South African Communications and Signal Processing Symp., COMSIG'94, October 1994.

[5] D. R. Wehner, High Resolution Radar, Norwood, MA 02062: Artech House, 1987.

A Region-based Approach to the Estimation of Local Statistics in Adaptive Speckle Filters

Roger Fjørtoft Fabien Lebon Franck Sery Armand Lopes Philippe Marthon[1] Eliane Cubero-Castan[2]

CESBIO (CNES/CNRS/UPS), Bpi 2801, 18 avenue Edouard Belin, 31055 Toulouse Cedex, France
Tel: (33) 61-55-85-39 Fax: (33) 61-55-85-00 E-mail: roger.fjortoft@cesbio.cnes.fr

[1]ENSEEIHT (LIMA-IRIT-UMR CNRS 5055), 2 rue Camichel, 31071 Toulouse Cedex, France
Tel: (33) 61-58-83-53 Fax: (33) 61-58-83-53 E-mail: marthon@enseeiht.fr

[2]CNES - French Space Agency, 18 avenue Edouard Belin, 31055 Toulouse Cedex, France
Tel: (33) 61-27-46-12 Fax: (33) 61-27-31-67 E-mail: cubero@qtis.cst.cnes.fr

Abstract — Radar images are inherently degraded by a strong, multiplicative noise known as speckle. The most frequently used speckle filters are adaptive in the sense that the filtering operation depends on estimations of local statistics calculated on a neighbourhood of the considered pixel. The choice of the neighbourhood is consequently an important issue. In this paper we introduce a new method which uses segmentations obtained prior to filtering. This region-based approach is compared to versions using sliding windows. The study is limited to agricultural scenes composed of distinct parcels of relatively homogeneous reflectivity. Without loss of generality, we have restricted ourselves to the LMMSE filter of Kuan *et al.*

INTRODUCTION

Speckle filtering consists in estimating the true reflectivity R as a function of the intensity I of a pixel and some local statistics calculated on a neighbourhood of this pixel. To obtain precise estimations, the neighbourhood must contain a sufficient number of pixels, but it is equally important that the the image is stationary in the neighbourhood. The problem of estimating the underlying reflectivity is consequently closely related to the detection of non-stationarities, such as edges, lines and textural transitions. It is in general necessary to include structural detectors in the filtering process to delimit the neighbourhood on which the local statistics are estimated.

Let us take the scalar LMMSE filter of Kuan *et al* [1] as an example. The linear estimator $\hat{R}$ minimizing the mean square error $E[(R-\hat{R})^2]$ is given by

$$\hat{R} = aI + (1-a)\mu_R, \quad 0 < a < 1. \tag{1}$$

The local mean reflectivity μ_R is estimated by the local mean intensity $\hat{\mu}_I$. The parameter a is a function of the local coefficient of variation σ_I/μ_I: The higher the local heterogeneity, the closer $\hat{R}$ is to I, *ie* the weaker is the smoothing. In a zone of constant reflectivity, the coefficient of variation is related to the equivalent number of looks L by

$$\sigma_I/\mu_I = 1/\sqrt{L}. \tag{2}$$

If $\hat{\sigma}_I/\hat{\mu}_I \leq (1+\epsilon)/\sqrt{L}$, the variations in the neighbourhood may be due entirely to speckle, and the neighbourhood is said to be Gamma-homogeneous. In this case it is reasonable to override (1) and merely set $\hat{R} = \hat{\mu}_I$ [2].

Early versions of the adaptive speckle filters use a fixed size window centered on the pixel to be filtered, as shown in Fig. 1a). On one hand, a large window should be chosen to minimize the variance of the estimations of the local statistics. On the other hand, a large window size is likely to increase the local heterogeneity measure, so that the noise reduction gets weaker. Refined versions include local edge detection, realized by a set of directional masks, to improve the homogeneity of the zone on which the estimations are performed [3]. This method is illustrated in Fig. 1b). The limited number of masks and the sensibility of such local edge detectors to speckle set bounds to the efficacity of this method. A further improvement consists in letting the size of the window increase gradually in order to obtain maximum size Gamma-homogeneous neighbourhoods [4], but for simplicity this method will not be considered here.

REGION-BASED SPECKLE FILTERING

The presence of speckle makes the segmentation of SAR images extremely difficult. A hybrid segmentation technique [5], based on the Ratio Of Exponentially Weighted Averages (ROEWA) operator, the watershed algorithm and region merging, has nevertheless permitted us to obtain satisfactory segmentations of images composed of agricultural parcels without any prior filtering. Our idea is to use the statistics calculated on the entire region when filtering a given pixel, as shown in Fig. 1c). This approach is computationally efficient, as the statistics are not calculated for each pixel, but only once for each region. The segmentation can not be considered as perfect, even though it approaches a thematic partition in regions. It should also be

This study is a result of the cooperation between LIMA/ENSEEIHT and CESBIO on contract 833/CNES/94/1022/00.

0-7803-3068-4/96$5.00©1996 IEEE

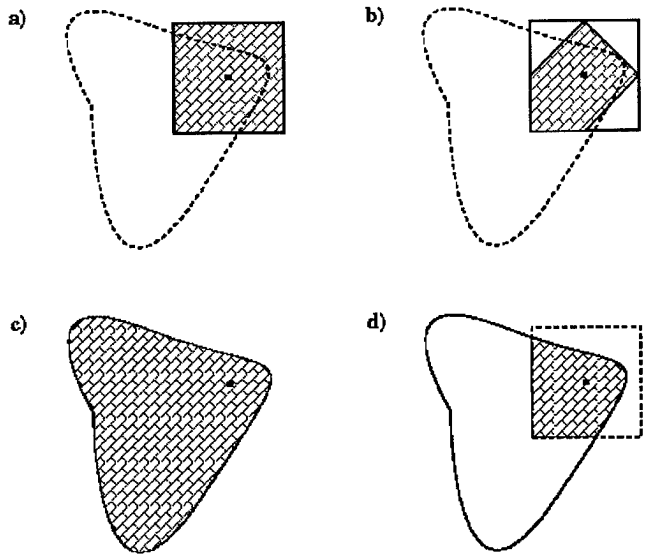


Figure 1: Neighbourhoods for the estimation of local statistics.

noted that thematic regions are not necessarily neither Gamma-homogeneous nor stationary. An intermediate solution, which is more robust to segmentation errors, is to base the estimations on those of the pixels of a fixed size window that belong to the same region as the central pixel, as shown in Fig. 1d).

COMPARISON

The four methods cited above have been tested on ERS1 images of an agricultural scene near Bourges, France. Fig. 2 shows an extract of a raw image and the segmentation obtained by the hybrid segmentation scheme. Fig. 3 shows the speckle reduced images obtained by the different versions of the scalar LMMSE filter. The size of the sliding window was set to 9×9. The version using a set of directional masks to detect edges [2] gives an important improvement compared to the classic version, particularly in preserving edges and other structures, but it introduces artefacts inside the different regions. This effect is greatly reduced when the statistics are calculated on entire regions, defined by a segmentation found prior to filtering. It should be stressed that the performance depends strongly on the segmentation. In our experience, a slight over-segmentation is to prefer, as details that are not represented in the segmentation will be degraded. This problem concerns fine structures as well as slow changes. The majority of the edges, which have been correctly detected, are well preserved. In the filtered image the transitions may actually appear too abrupt, owing to the fact that the edge pixels are attributed to one of the regions, even though they are generally mixed pixels, *ie* the response of elementary scatterers from both regions. The regions defined by the segmentation are in general much larger than a 9×9 window. This seems to increase the local heterogeneity and reduce the strength of the speckle filtering, especially in regions containing a very high number of pixels. The intermediate solution, using only those of the pixels of the region that lie inside a fixed size window, is less sensitive to segmentation errors and offers a better noise reduction at the cost of a higher computation time.

CONCLUSION

This region-based approach to speckle filtering is a computationally efficient way of reducing speckle while retaining significant edges. The segmentation method was developed for agricultural parcels, *ie* scenes composed of distinct regions of approximately constant reflectivity without neither texture nor relief. The edges that have been correctly identified by the segmentation are well preserved, but when we estimate the local statistics by regions, the speckle reduction is not as strong as for the method using directional masks. The intermediate version, using the segmentation in combination with a sliding window, offers a good compromize.

Further progress in SAR image segmentation would undoubtedly improve the results. In order to conserve thin linear structures, such as roads and rivers, appropriate structural detectors must be added. The same applies to transitions in texture. Artificial objects, where the speckle is not fully developed, should be identified and treated separately. The problem of too abrubt radiometric transitions at edges could be reduced by treating edge pixels in a special manner, *eg* using the local statistics estimated on both sides of the edge to compute a weighted average. Inspired by [4], the speckle reduction could be improved by combining the segmentation with a variable size window controlled by a stationarity criterion and guidelines on the minimum and maximum number of pixels.

REFERENCES

[1] D. T. Kuan, A. A. Sawchuk, T. C. Strand, and P. Chavel, "Adaptive restauration of images with speckle", IEEE Trans. ASSP, Vol. 35, No. 3, pp. 373-383, 1987.

[2] A. Lopes, E. Nezry, R. Touzi, and H. Laur, "Structure detection and statistical adaptive speckle filtering in SAR images", Int. Journal on Remote Sensing, Vol. 14, No. 9, pp. 1735-1758, 1993.

[3] J. S. Lee and I. Jurkevich, "Speckle filtering of synthetic aperture radar images: A review", Remote Sensing Reviews, Vol. 8, pp. 313-340, 1994.

[4] Y. Wu and H. Maitre, "A speckle suppression method for SAR images using maximum homogeneous regions", Proc. IGARSS'90, Vol. 3, pp. 2413-2416, Washington DC, May 1990.

[5] R. Fjørtoft, P. Marthon, A. Lopes, and E. Cubero-Castan, "Edge detection in radar images using recursive filters", Proc. ACCV'95, Vol. III, pp. 87-91, Singapore, December 1995.

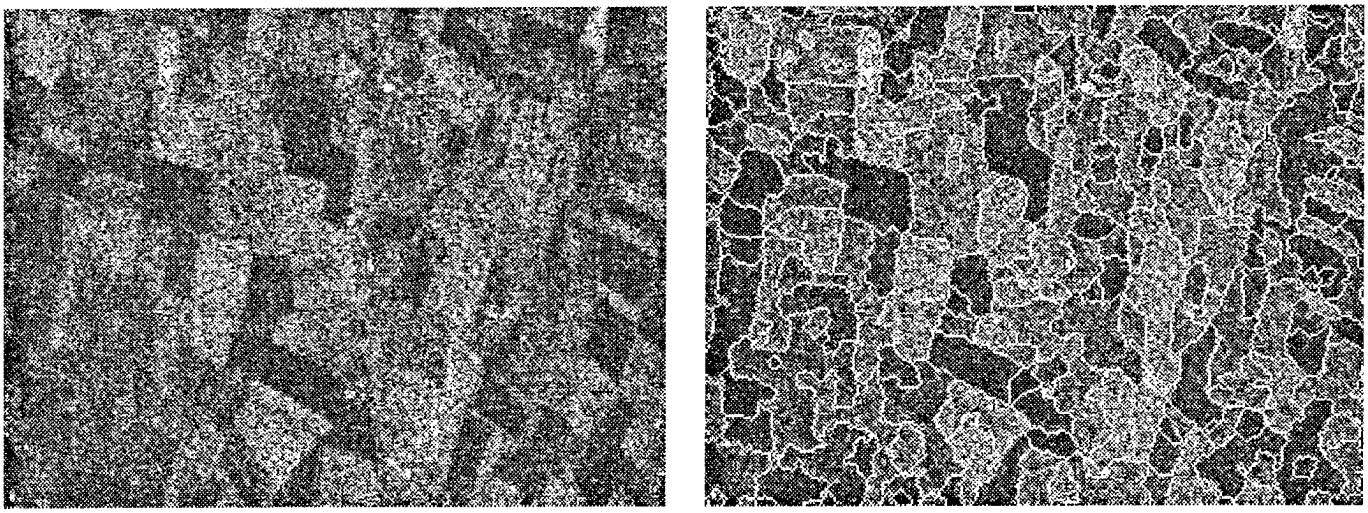


Figure 2: Extract of an amplitude SAR image from Bourges, France ©ESA - ERS1 data - 1993 (left) and its segmentation (right).

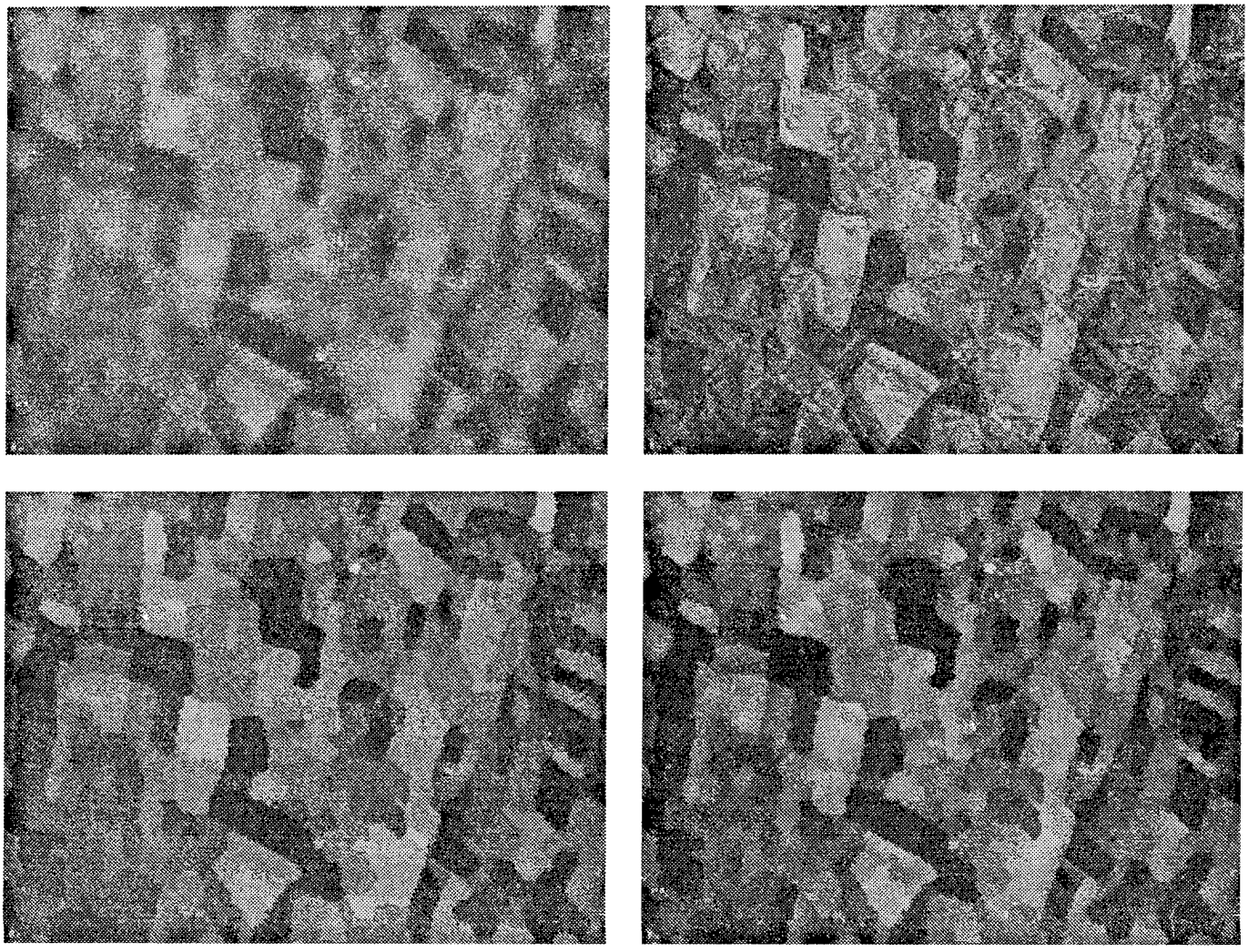


Figure 3: LMMSE filtered images: First row: using a sliding window (left) and a sliding window with edge detection (right). Second row: using the segmentation (left) and the segmentation in combination with a sliding window (right).

Reversible Inter-Frame Compression of Multispectral Images Based on a Previous-Closest-Neighbor Prediction

B. Aiazzi*, P. S. Alba*, L. Alparone°, S. Baronti*, P. Guarnieri°

* Istituto di Ricerca sulle Onde Elettromagnetiche "Nello Carrara" - CNR, via Panciatichi, 64, I-50127 Firenze, Italy
Phone: +39-55-4235-275; Facsimile: +39-55-410893; E-mail: baronti@iroe.fi.cnr.it
° Dipartimento di Ingegneria Elettronica, University of Florence, via S. Marta, 3, I-50139 Firenze, Italy
Phone: +39-55-4796-372; Fax: +39-55-494569; E-mail: alparone@cosimo.ing.unifi.it

Abstract -- *Previous Closest Neighbor* (PCN) prediction has been recently proposed for lossless data compression of multispectral images, in order to take advantage of inter-band data correlation. The basic idea to predict the value of the current pixel in the current band on the basis of the best zero-order predictor on the previously coded band has been applied by extending the set of predictors to those adopted by lossless JPEG. Performances increase of more than 5% when passing from the original set of predictors to the extended set.

INTRODUCTION

Reversible image compression is gaining the attention of an ever increasing audience in the field of remote sensing, in which the availability of high-resolution high-SNR multispectral imaging sensors from aircraft and spacecraft demands robust and efficient coding techniques capable to capture inter-band redundancy without destroying the underlying intra-band correlation [1].

Although *differential pulse code modulation* (DPCM) [2] schemes (e.g., *lossless* JPEG [3]) is employed for error-free compression, their straightforward extension to multispectral image data usually leads to negligible coding gains [4] or even to performance penalties with respect to single-band coding.

Different approaches have been recently investigated based on the largely verified assumption that space details are correlated along neighboring spectral bands. This fact implies that the same spatial edge occurs in two adjacent bands, notwithstanding the two bands may locally differ by a gain factor and an offset due to different sensor responses, which prevents a quantitative prediction from being formulated. A *relative* information of the current band from a neighborhood of pixels in the previously encoded band will be far more useful than an *absolute* prediction (i.e., a predicted value).

This concept has been exploited in [5] by considering a path, scanning all the pixels within an image band, such that the average absolute difference between pairs of adjacent samples is minimized. Such a path, which is indeed a graph connecting all the pixels will not necessarily comprise the minimum-distance branch among the eight-neighbors of each pixel, because of the connectivity constraint (i.e., the scanning path must embrace all pixels once). This fact leads to some locally suboptimal choices to yield a globally optimum graph.

Spectral correlation is exploited by assuming that the optimum prediction graph for a given band will be very similar to the graph of the previously encoded adjacent band. Therefore the graph is computed from the previous band and used to encode the current band without introducing any overhead, since the graph need not be encoded as well.

PCN ALGORITHM

A simplified version of the above scheme is also suggested by Memon *et al.* [5] to dramatically speed up computation (both coding and decoding) at a comparable performance. Each image band, say the kth band, is raster scanned, thereby making prediction to be possible only from four out of the eight-neighbor pixels (causal neighborhood), namely A_k, B_k, C_k, and D_k, as illustrated in Figure 1.

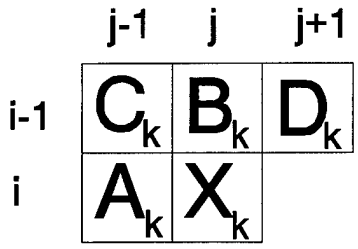


Figure 1. - Causal neighborhood of pixel X in k band, X_k.

The connectivity constraint is granted by the scanning fashion: therefore, all of the four causal neighbors are checked for their minimum absolute difference from the current pixel, thus resulting in an optimum *causal* prediction based on the *Previous Closest Neighbor* (PCN). Again, the underlying assumption that allows inter-band redundancy reduction, is that for each pixel, the PCN on the previously encoded band is likely to be the same as for the current band, and therefore it may be easily computed from the previous band available at the receiving end with a minimum effort.

0-7803-3068-4/96$5.00©1996 IEEE

Let $\hat{X}^l_{k-1}$, $l = 1,...,4$, denote the set of predictors at (i,j) evaluated at k-1th band of a multispectral image with N bands:

$$\begin{aligned} \hat{X}^1_{k-1} &= A_{k-1} \\ \hat{X}^2_{k-1} &= B_{k-1} \\ \hat{X}^3_{k-1} &= C_{k-1} \\ \hat{X}^4_{k-1} &= D_{k-1} \end{aligned} \tag{1}$$

The optimum inter-band PCN prediction at (i,j) in the kth band, $k = 2,...N$, will be given by $\hat{X}^*_k$, where

$$\left|X_{k-1}(i,j) - \hat{X}^*_{k-1}(i,j)\right| = \min_{l=1,...,4}\left\{\left|X_{k-1}(i,j) - \hat{X}^l_{k-1}(i,j)\right|\right\} \tag{2}$$

Hence, the algorithm may be regarded an adaptive *zero-order* predictor driven by the previously encoded band.

INTRA-BAND LOSSLESS JPEG

It is known that zero-order prediction (i.e., a prediction from a single neighbor pixel) can easily be improved by considering a combination of more neighbor pixels simultaneously [2]. In this light, an extension of the set of predictors used by PCN algorithm is introduced. A multispectral *lossless* JPEG, (i.e., DPCM-based [3]) is derived. Again with reference to Fig. 1, prediction is achieved by means of the following set of *8* predictors, which have been standardized by JPEG:

$$\begin{aligned} \hat{X}^0_k &= 0 \qquad (\textit{no prediction}) \\ \hat{X}^1_k &= A_k \\ \hat{X}^2_k &= B_k \\ \hat{X}^3_k &= C_k \\ \hat{X}^4_k &= A_k + B_k - C_k \\ \hat{X}^5_k &= A_k + \frac{B_k - C_k}{2} \\ \hat{X}^6_k &= B_k + \frac{A_k - C_k}{2} \\ \hat{X}^7_k &= \frac{A_k + C_k}{2} \end{aligned} \tag{3}$$

Standard *intra-frame* JPEG works as follows:

for band k, $k = 1,...,N$:
  calculate $E^l_k(i,j) = X_k(i,j) - \hat{X}^l_k(i,j)$, $l = 0,...,7$, over all (i,j);
  calculate H^l_k, zero-order entropy of E^l_k, $l = 0,...7$;
  choose predictor $\hat{X}^*_k$ yielding $min_l\{H^l_k\}$ over whole band;
  encode $E^*_k(i,j)$, $\forall$ (i,j).
stop

Notice that H^l_k, $l = 0$, represents the zeroth order entropy of the kth band, without any decorrelation. Zeroth predictor is never used globally, unless for extremely uncorrelated images.

INTER-BAND LOSSLESS JPEG

An enhanced version of PCN will now be defined from the standard set of eight JPEG predictors (3).

Again, let $\hat{X}^l_{k-1}$, $l = 0,...,7$, denote the set predictors (3) at (i,j) evaluated in the k-1th band. Except for the first band which is intra-coded following the procedure outlined in the previous section, optimum *inter-band* JPEG prediction at (i,j) in the kth band, $k = 2,...N$, will be given by $\hat{X}^*_k$, where again

$$\left|X_{k-1}(i,j) - \hat{X}^*_{k-1}(i,j)\right| = \min_{l=0,...,7}\left\{\left|X_{k-1}(i,j) - \hat{X}^l_{k-1}(i,j)\right|\right\} \tag{4}$$

Hence, the algorithm may be regarded as an adaptive lossless JPEG, in which prediction is driven by the previously encoded band. Notice that if no-prediction ($l = 0$) is locally preferable to any of the $\hat{X}^l_{k-1}$, $l = 1,...,7$, this can be achieved, e.g., for a dark spot surrounded by a brighter background.

For such algorithms as PCN and Inter-Band Lossless JPEG (IB-JPEG), as well as for any multispectral decorrelation method, the order in which the bands are considered is essential for the coding success [6]. In fact, the different bands available should be arranged in a sequence that maximizes the average correlation between two consecutive bands. Such a sequence strongly depends on the multispectral imaging sensor; therefore, once it has been established, it will be the same also for most of the imaged scenes, notwithstanding they exhibit different characteristics. Depending on the correlation coefficient between two successive bands, the second band might better be encoded *intra-band* than *inter-band*. Therefore, a flag bit can be added to each band in order to specify the decorrelation mode, either *intra* or *inter*, along with the label of the optimum global predictor for the intra case.

This strategy is similar to the declarations of *I* (intra-frame), *P* (forward prediction, i.e. causal), and *B* (backward prediction, i.e., non-causal) modes for motion-compensated frames in MPEG-2 video compression standard.

CODING RESULTS AND COMPARISONS

A *2560* × *1536* pels, *8-bit/pel*, *7*-band image of Metaponto, Southern Italy, from Landsat Thematic Mapper (TM) satellite sensor has been used for all coding tests.

Covariance matrix has been calculated over the whole multispectral image and yields the following values of correlation (below diagonal) variance (diagonal) and covariance (above diagonal), as Table 1 reports.

Band	1	2	3	4	5	6	7
1	228	114	121	82	303	193	176
2	0.87	74	107	69	222	78	136
3	0.57	0.88	198	89	394	126	226
4	0.33	0.48	0.38	279	390	119	141
5	0.58	0.74	0.81	0.67	1201	299	916
6	0.73	0.51	0.51	0.40	0.49	310	203
7	0.60	0.81	0.83	0.43	0.92	0.59	376

Table 1. Correlation and covariance from test Landsat image.

The above matrix suggests the best band-ordering to maximize correlation within pair of successive bands. The sequence of bands is: *1 - 2 - 3 - 7 - 5 - 4 - 6*, corresponding to correlation values between neighboring bands of: *0.87, 0.88, 0.83, 0.92, 0.67, 0.40*, as shown in Table 1. It is noteworthy that the optimum sequence found in this work is the same that may be derived from the correlation matrix of different TM images [6], which allows a more general use of results.

Figures 2 and 3 show coding performances compared with PCN, JPEG, and 4-pel auto-regressive DPCM [2],[6].

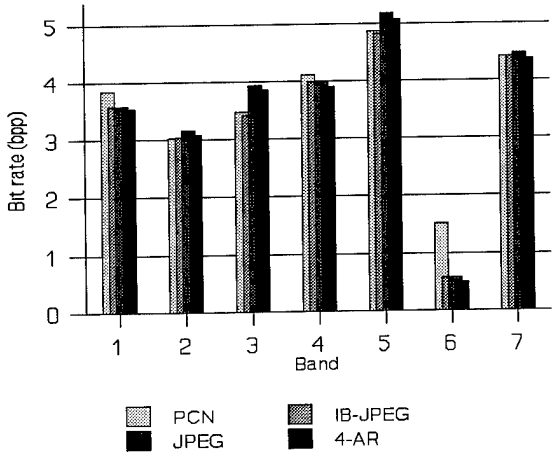


Figure 2. Bit-rates from the 7 TM bands coded with 4 methods: PCN, JPEG, inter-band JPEG, 4-regression DPCM.

CONCLUSIONS

The set of zero-order predictors originally used for PCN has been extended by incorporating the eight spatial predictors used for reversible JPEG, thus resulting in a multispectral lossless JPEG, performing inter-frame decorrelation.

In order to evaluate the capabilities of the method, multi-band correlation has been analyzed in Landsat TM images to yield the sequence of images that maximizes average cross-correlation between any two consecutive bands.

A coding strategy consists of adopting for each band the most advantageous method between intra-frame JPEG and inter-frame JPEG (i.e., the proposed *extended* PCN).

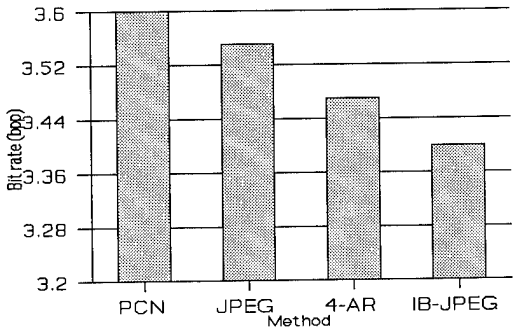


Figure 3. Bit-rate of the four methods averaged over the seven bands: bands 4 and 6 are intra-coded in IB-JPEG; band 6 is intra-coded in PCN (see Fig. 2).

Coding gain has been of the order of 6% with respect to the original PCN, and of about 4% with respect to reversible JPEG. These results are expected to be improved when data with a larger number of bands, like AVIRIS, will be considered, or when spatial predictors more powerful than those used in JPEG will be incorporated in the baseline of the 3-D decorrelation method, first suggested by Memon *et al.*

REFERENCES

[1] R. E. Roger, J. F. Arnold: "Reversible Image Compression Bounded by Noise", *IEEE Trans. Geosci. Remote Sensing*, Vol. 32, No. 1, pp. 19-24, Jan. 94.

[2] A. N. Netravali, and B. G. Haskell: *Digital Picture-Representation and Compression*. Applications of Communications Theory Series. New York, NY: Plenum Press, 1988.

[3] W. B. Pennebaker, and J. L. Mitchell, *JPEG: Still Image Compression Standard*, New York, NY: Van Nostrand Reinhold, 1993.

[4] P. Roos, and M. A. Viergever, "Reversible 3-D Decorrelation of Medical Images", *IEEE Trans. Medical Imaging*, Vol. 12, No. 3, pp. 413-420, Sep. 1993.

[5] N. D. Memon, K. Sayood, and S. S. Magliveras, "Lossless Compression of Multispectral Image Data", *IEEE Trans. Geosci. Remote Sensing*, Vol. 32, No. 2, pp. 282-287, Mar. 1994.

[6] J. Wang, K. Zhang, "Spectral and Spatial Decorrelation of Landsat-TM Data for Lossless Compression", *IEEE Trans. Geosci. Remote Sensing*, Vol. 33, No. 5, pp. 1277-1285, Sep. 1995.

LOSSLESS COMPRESSION OF MULTISPECTRAL IMAGES USING PERMUTATIONS

Ziya Arnavut
Department of Geography and Geology, University of Nebraska, Omaha, NE 68182

Sunil Narumalani
Department of Geography, University of Nebraska, Lincoln, NE 69588

Abstract -- It is well recognized within the remote sensing community that there exists spectral correlation between bands 1, 2, and 3 (which represent reflected blue, green, and red light respectively), and also bands 5 and 7 (which are reflected middle-infrared bands) of the Landsat Thematic Mapper (TM) multispectral image. In this paper, we are presenting the outcome of some experiments which use the spectral correlation as well as spatial correlation of the brightness values (BVs) to compress the TM multispectral data. Our method compresses one of the bands using the standard JPEG compression, and then orders the next band's data with respect to the previous band's *sorting permutation*. Then, a *move to front coding* technique is used to lower the source entropy, before actually encoding the data. It has been observed that our method yields tremendous gain on the visible bands (on the average 0.4 - 0.6 bpp) and can be successfully used for multispectral images where the *spectral distances* are closer.

INTRODUCTION

The goal of data compression is to find shorter representations for any given data. In a data storage application, this is done in order to save storage space on an auxiliary device or in the case of a communication scenario, to increase the channel throughput.

Image compression is divided into two main groups, *lossy* and *lossless*. Most of the literature on image compression deals with lossy techniques, for which the pixel intensities cannot be recovered from an encoded bit stream. Lossless applications, such as digital radiology in the medical sciences and satellite imagery in remote sensing cannot tolerate such irreversible loss of data since the images are subject to further processing, and even minor data losses could render an image useless.

A lossless image compression technique consists of two main components, *modeling* and *encoding* [1]. A model captures the structure inherent in the raw data and extracts it. The *residual*, also called an *error*, is then encoded using an *entropy encoding* technique. Encoding techniques, such as Arithmetic and Huffman encoding, are known to perform optimally in terms of the number of bits used to encode a given data source. Hence, the critical task in data compression is of modeling.

Although much work has been done toward developing algorithms for compressing image data [2], [3], very little is known on the exploitation of spectral relationships to compress the multiband images. A good survey of compression techniques used in remote sensing applications is presented in [4].

Due to the fact that adjacent pixels are correlated in an image, *spatial* correlation is present. Well known image compression techniques, such as JPEG [5] use spatial correlation among the adjacent pixels to decorrelate image data, before actually encoding it. However, unlike single-band images, multispectral images also have *spectral* correlation between adjacent spectral bands. In the case of Landsat Thematic Mapper (TM) data, it is well recognized that bands 1, 2, and 3 are highly correlated with each other, and also bands 5 and 7.

Although spatial correlation is exploited by standard lossless compression techniques, little success has been attained in taking advantage of spectral correlations. In this paper, we present a new compression technique that captures these spectral correlations, as well as the spatial correlation for some bands of the TM images. Our approach indicates that for some TM images an additional 0.4 bits per pixel (bpp) or more may be saved on the average over the standard lossless JPEG technique.

LINEAR PREDICTIVE TECHNIQUES

For a typical image, since the values of adjacent pixels are often highly correlated, a significant amount of information about a pixel value may be obtained by examining the neighboring pixels. Linear Predictive techniques try to exploit these correlations between neighboring pixels. They scan the image in a fixed order and predict the current pixel by taking a linear combination of neighboring pixels that have been previously transmitted. The JPEG still picture compression standard uses linear predictive techniques, and has eight predictive schemes [5].

Linear prediction schemes, such as JPEG, are simple and normally result in a significant reduction in source entropy. However, they do not exploit the spectral correlation among multispectral bands in the case of multi-band images. It is, therefore, important to find good algorithms that can exploit spectral dependencies in order to achieve better compression.

MATHEMATICAL PRELIMINARIES

To set the stage for our later discussions in this paper, we have defined the basic mathematical concepts in this section.

0-7803-3068-4/96$5.00©1996 IEEE

In the study of sorting algorithms, permutations are of special importance since they represent unsorted input data [4].

$$\begin{pmatrix} f_0 + \ \ldots + f_{255} \\ f_0, \ \ldots, f_{255} \end{pmatrix}$$

Knuth [4], explains this relationship with respect to different sorting algorithms. Given a set S, of size $n = |S|$, there are $n!$ unique possible orderings of the set S. Let P be an $n \times n$ digital image, that is, P_{ij} is a pixel representing the i^{th} row and j^{th} column, for $i, j = 1, \ldots, n$, and suppose that P_{ij} is a byte representing any one of 256 gray values. We convert the square array into a linear array P' in the usual way, where $P'_k = P_{ij}$ for $i, j = 1, \ldots, n$, and $k = (i - 1) * n + j$. Thus, k ranges over the $\{1, 2, \ldots, n^2\}$. In this way, each pixel has an *integer index*, and we can regard the image as a sequence of gray values, $[P'_1, P'_2, \ldots, P'_j, \ldots, P'_n 2]$. If π is a permutation of $\{1, 2, \ldots n^2\}$ which sort the sequence $[P'_1, P'_2, \ldots, P'_j, \ldots, P'_n 2]$ in ascending order, then the sorted sequence is:

$$P'_{\pi_1} \leq P'_{\pi_2} \leq \ldots \leq P'_{\pi_{n^2}}.$$

Since n^2 is in fact much larger than the number g of gray values, the sorted sequence gives rise to a partition of $\{1, 2, \ldots, n^2\}$ into blocks, $B_1, B_2, \ldots, B_g$, where $P'_b = i$ for all $b \in B_i$. In other words,

$$P'_{\pi_2} = \ldots = P'_{\pi_{k_1}} < P'_{\pi_{k_1+1}} = \ldots = P'_{\pi_{k_1+k_2}} < \ldots < P'_{\pi_{k_1+k_2+\ldots+k_g}} = \ldots =$$

where: $k_i = |B_i|$ for $1 \leq i \leq g$.

Here, there are g - 1 jumps, where g is the number of gray values attained in the image. This generates a partition of indices into blocks, where the indices in each block can be arranged in any order. Hence, they can be arranged in ascending order. In this work, we call such a sorting permutation based on P' the *canonical sorting permutation* and represent it with π_s.

PERMUTATIONS FOR MULTISPECTRAL IMAGE COMPRESSION

A multispectral image can be compressed using the following protocol. The sender uses the following:

- Obtain the canonical sorting permutation, π_s^1 of b_1 (where b_i represents band i)
- Compress b_1 with JPEG. Encode the data and transmit to the receiver along with 3 bits to indicate which JPEG operator was used.
- Starting from $i = 2$, obtain the canonical sorting permutation, π_s^i, of band b_i. Then, apply π_s^{i-1} to b_i to get b_i'.
- Apply move to front coding to b_i', encode the resulting data and then transmit it to the receiver.

The receiver:

- Decode b_1, undo the effect of JPEG operator and obtain the π_s^1.
- Starting from $i = 2$, for each band received, decode the data, undo the effect of the move to front coding and using π_s^{i-1}, reorder the data and construct band b_i.

From the above algorithms, it is clear that permutations do not require a transmission cost. Hence the important question is "How good are they for compression purposes?"

SIMULATION RESULTS

For our simulations, we used the TM images "Omaha", "Crescent Lake", and "Wyoming" which were obtained from the Center for Advanced Land Management Information Technologies (CALMIT) at the University of Nebraska, Lincoln. Our test images differ in terms of size and are: "Omaha" 1,323 x 1,323; "Crescent Lake" 376 x 331; and "Wyoming" 780 x 664.

In Table 1, under the Band 1 and Band 3 columns, we list the results obtained in terms of first-order entropy when we applied the canonical sorting permutation of band 2 to bands 1 and 3, followed by the move to front coding. Also, in Table 1, for comparison purposes we present the results of the best operator of the standard lossless compression technique JPEG, when applied to bands 1 and 3. By applying the canonical sorting permutation of band 1 to band 2, and band 2 to band 3, improvements over the JPEG technique were observed in most cases. However, our experimentation also shows that the application of the canonical sorting permutation of band 2 to band 1 and 3 yields more gain over the JPEG.

This can be explained by examining the location of TM bands 1, 2, and 3 along the electromagnetic spectrum (EMS). The EMS is a continuum, and the TM bands have been selected as representative components of this continuum based on their utility for a variety of terrestrial applications. TM bands 1, 2, and 3 represent the visible portion of the EMS in almost a continuous manner. Since band 2 is located between bands 1 and 3, it serves as a link or a transition between them. Therefore, it minimizes the *spectral distance* between the bands. For example, the spectral separation between bands 1/2 is 0.00 μm and between 1/3 is 0.11 μm. However, the spectral separation between bands 2/3 is only 0.02 μm. With a minimal *spectral distance* between bands 1/2, and 2/3, band 2 would be the pivotal point where correlations between the 3 bands are maximized.

Table 1. Entropy of applying π_s^2 to TM bands 1 and 3, followed by move to front coding, versus best JPEG.

Image	Band 1	JPEG	Band 3	JPEG
Omaha	3.80	4.23	3.21	3.98
Crescent Lake	3.28	3.58	3.02	3.52
Wyoming	3.29	3.98	2.84	3.94
Average	**3.46**	**3.93**	**3.02**	**3.81**

Tate [7] has presented an algorithm for ordering the multispectral images prior to applying his JPEG like operators to spectrally ordered bands. Wang *et al.* [8] used correlation among the bands for ordering them prior to applying their predictive technique based on regression. For TM data, which consist of 7 bands, we tried different combinations without using Tate's or Wang *et al.* algorithms as there are 7! (i.e., 5,040) possibilities. We observed that the sorting permutation on band 2 is more suitable on bands 1 and 3. In addition, the sorting permutation of band 7 gives better results on band 5.

DISCUSSION

We have demonstrated that for the visible bands of a TM image, permutations can capture the spectral correlation and yield considerable improvement over the standard JPEG compression technique. It is well known that the visible bands are more closer in terms of wavelength distance, hence, its natural to expect that those bands may have higher spectral correlation [9]. Due to this high correlation, the narrower spectral bandwidths, and the continuous spectrum of the visible bands, we may be able to use the canonical sorting permutation of band 2 to increase the locality of reference of data on bands 1 and 3. Hence, the move to front coding can generate a lower source entropy.

In conclusion, this experiment has demonstrated that by using the canonical sorting permutation on the spectral characteristics of remote sensing we can obtain significant gains in compressing these data over the standard JPEG technique. Specifically, these gains were more applicable in the case of the TM visible bands 1, 2, and 3 than the mid-infrared bands 5 and 7, due to the high degree of correlation between the visible bands, their narrower band widths, and their spectral continuity. Additionally, the canonical sorting permutation of band 2 to bands 1 and 3, yielded a higher gain than that of band 1 to band 2, and band 2 to band 3. Therefore, if the bands are more closer in terms of their wavelength distances, and are ordered with respect to their correlationship with each other, then permutations can be used as a method to exploit the spectral correlation and improve the compression gain over the standard JPEG.

REFERENCES

[1] Rissanen, J. J. and G. G. Langdon. "Universal Modeling and Coding," *IEEE Transactions on Information Theory*, 27(1): 12-22, 1981.

[2] Netravili, A. N. and B. G. Haskell. *Digital Pictures - Representation and Compression,* Applications of Communications Theory Series, New York: Plenum Press, 1988.

[3] Rabbani, M. And P. W. Jones. Digital Image Compression Techniques

[4] Sayood, K. "Data Compression in Remote Sensing Applications," *IEEE Geoscience and Remote Sensing Newsletter*, Vol. 84, pp. 7-15, Sept. 1992.

[5] Wallace, G. K. "The JPEG Still Picture Compression Standard," *Communications of the ACM,* 34(4): 31-44, 1991.

[6] Knuth, D. *The Art of Computer Programming*, Vol 3., Reading, MA: Addison-Wesley Publishing Company, 1973.

[7] Tate, S. R. "Band Ordering in Lossless Compression of Multispectral Images," *Proceedings of Data Compression Conference*, Snowbird, UT, Eds. Storer, J. A. & M. Cohn, pp. 311-320, 1994.

[8] Wang, J., Zhang, K., and S. Tang. "Spectral and Spatial Decorrelation of Landsat-TM Data for Lossless Compression, *IEEE Transactions on Geoscience and Remote Sensing*, 33(5): 1277-1285, 1995.

[9] Jensen, J. R., 1996. *Introductory Digital Image Processing: A Remote Sensing Perspective,* Englewood Cliffs, NJ: Prentice Hall, 326 p.

Radar Altimeter Return Noise Signals Identification

Li Maotang, Jiang Jingshan, Wang Jingli, Yu zhiqiang
Center for Space Science and Applied Research
P.O.Box: 8701 Beijing 100080 P.R. China
Tel: +86-10-62559944, Fax: +86-10-62576921, E-mail: mrs3@sun20.cssar.ac.cn

Abstract -- A novel method of radar altimeter return noise signals identification is proposed. The second-order cumulant given by the conventional filtering method can identify the Gaussian signals. The third-order cumulant can distinguish the non-symmetric and non-Gaussian component. The forth-order cumulant that are provided by a special method can discern the symmetric non-Gaussian as well as harmonic components.

I. INTRODUCTION

During recent 20 years, the spaceborne radar altimeter have begun to find wide applicability in studying the oceanology and earth geodesy.

Measured radar altimeter return signals are composed of the real return power signals and the noise signals, and the noise component is rather large. In order to remove the noise signal, we need know the noise distribution. In the past, due to lack of analytical tools, the noise signals is assumed to be a Gaussian distribution. With the new results on higher-order statistics (including higher-order cumulants) in signal processing and system theory it should be possible to reexamine the noise distribution using the higher-order statistics[1].

In this paper, an novel method of radar altimeter return noise signals identification is proposed. The second-order cumulant given by the conventional filtering method can identify the Gaussian noise signals. The third-order cumulant can distinguish the non-symmetric non-Gaussian component. The fourth-order cumulant that are provided by a special method can discern the symmetric non-Gaussian as well as harmonic components.

II. THE DEFINITION OF THE CUMULANTS

For zero-mean real random variables $\{x_i\}$, the second-, third-, and fourth-order cumulants are given by

$$cum(x_1,x_2)=E\{x_1x_2\} \tag{1}$$

$$cum(x_1,x_2,x_3)=E\{x_1x_2x_3\} \tag{2}$$

$$cum(x_1,x_2,x_3,x_4)=E\{x_1x_2x_3x_4\}-E\{x_1x_2\}E\{x_3x_4\} -E\{x_1x_3\}E\{x_2x_4\}-E\{x_1x_4\}E\{x_2x_3\} \tag{3}$$

0-7803-3068-4/96$5.00©1996 IEEE

For a zero-mean stationary random process, the second-, third- and fourth-order cumulants of zero-mean x(t), which follow from (1), (2) and (3), are

$$C_{2,x}(m)=E\{x(t)x(t+m)\} \tag{4}$$

$$C_{3,x}(m_1,m_2)=E\{x(t)x(t+m_1)x(t+m_2)\} \tag{5}$$

$$C_{4,x}(m_1,m_2,m_3)=E\{x(t)x(t+m_1)x(t+m_2)x(t+m_3)\} -C_{2,x}(m_1)C_{2,x}(m_2-m_3)-C_{2,x}(m_2)C_{2,x}(m_3-m_1) -C_{2,x}(m_3)C_{2,x}(m_1-m_2) \tag{6}$$

Of course, the one dimension diagonal slice(1-DDS) can be obtained by setting $m_i=m$, $i=1,2,\cdots,k-1$.

III.NOISE SIGNAL IDENTIFICATION METHOD

Generally speaking, the signals can be classified as Gaussian, non-Gaussian and harmonic signals. Then the non-Gauss signals can be classified as symmetric non-Gaussian and non-symmetric non-Gaussian signals. As in [1], the second-order cumulant of the Gaussian signals is non-zero, but the third-order (or fourth-order) cumulant is zero. For symmetric non-Gaussian and harmonic signals, their odd cumulants is zero, and the even cumulants is non-zero. For non-symmetric non-Gaussian signals their all order cumulants is non-zero. So we can use the second-, third-, and fourth-order cumulants to identify the radar altimeter return noise signals.

There are two kinds of radar return signals. One is consist of radar return power signal and the noise signals. Another is only consist of the noise signals. In this paper the case that only contains the noise signals are discussed. If the measured zero-mean noise signal values y(n) is

$$y(n)=\omega_0(n)+\omega_1(n)+\omega(n) \tag{7}$$

where $\omega_0(n)$, $\omega_1(n)$ and $\omega(n)$ are non-symmetric non-Gaussian, Gaussian and symmetric non-Gaussian (and harmonic) noise signals respectively. According to the cumulant performances. The second-, third- and fourth-order 1-DDS cumulants of the y(n) are respectively

$$C_{2,y}(m)=C_{2,\omega_0}(m)+C_{2,\omega_1}(m)+C_{2,\omega}(m) \tag{8}$$

$$C_{3,y}(m)=C_{3,\omega_0}(m) \tag{9}$$

$$C_{4,y}(m)=C_{4,\omega_0}(m)+C_{4,\omega}(m) \tag{10}$$

where m are lag factor. The $C_{2,\omega_0}(m)$, $C_{2,\omega_1}(m)$ and $C_{2,\omega}(m)$ are the second-order cumulants of $\omega_0(n)$, $\omega_1(n)$, $\omega(n)$ and $C_{2,\omega}(m)$ respectively. The $C_{3,\omega}(m)$ is the third-order cumulants of $\omega_0(n)$. The $C_{4,\omega_0}(m)$ and $C_{4,\omega}(m)$ are the fourth-order cumulants of $\omega_0(n)$ and $\omega(n)$ respectively.

The return noise signal identification method, as Fig. 1, includes three contents:

1) In order to decide whether there is any noise signals the $C_{2,y}(m)$ is calculated and tested. If the $C_{2,y}(m)$ is larger than the threshold 1 there are some noise signals. In order to decide whether there is Gaussian noise signal conventional filter method is used to filter the Gaussian noise signal firstly, then the data filtered are used to calculate second-order cumulant $C'_{2,y}(m)$ and $C''_{2,y}(m) = C_{2,y}(m) - C'_{2,y}(m)$. Finally to judge the $C''_{2,y}(m)$ whether there is any Gaussian signals.

2) Calculate $C_{3,y}(m)$ and judge $C_{3,y}(m)$ whether there is any non-symmetric non-Gaussian signals.

3) To Create the ARMA model outlines these steps: First, the singular-value decomposition(SVD) method for the estimation of autoregressive parameters of the ARMA model of the non-symmetric and non-Gaussian components is discussed. Second , an improved SVD method for estimating the moving average order q_0 of the ARMA model is discussed. Third, the 1-DDS of

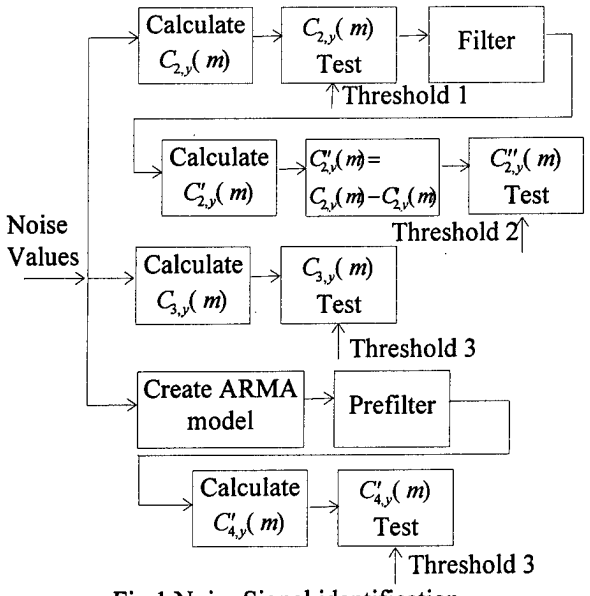


Fig.1 Noise Signal identification

the fourth-order cumulants of the filtered output process are given. This provides the symmetric non-Gaussian and harmonic components[2].

IV.SIMULATION

In order to verify the new method to identify the radar noise signal , some simulations are given.

In (7), $\omega_0(n)$ and $\omega_1(n)$ are produced by GGEXN subroutine in the International Mathematical and Statistical Library(IMSL)[3]. $\omega(n)$ is produced by real harmonic signal.

Because the cumulant performance of the harmonic signals is the same with the cumulant performance of the asymmetric non-Gaussian signals. So the $\omega(n)$ can be represented by the harmonic signals.

During the simulation, we chooses the data number N=2048. The curve and the second-, third-, and fourth-order cumulants of the $\omega_1(n)$ are Fig.A, Fig.B, Fig.C and Fig.D of the Fig.2 respectively. In Fig.A the horizontal ordinate expresses the data number. The vertical ordinate expresses the data magnitude.

Fig.2 suggests that the third- and fourth-order cumulants are zero almost as well as the second-order cumulant is nonzero when m=0. This verifies the conclusion that the second-order cumulant of the $\omega_1(n)$ is nonzero and the third-and fourth-order cumulants of the $\omega_1(n)$ is zero.

The curve and the third-order cumulants of the $\omega(n)$ and $\omega_0(n)$ are Fig.A, Fig.B, Fig.C, and Fig.D of Fig.3 respectively. Fig.3 shows that the third-order cumulants of the $\omega(n)$ is zero. Fig.D verifies the third-order cumulants of the $\omega_0(n)$ are nonzero and the maximum values are given when m=0.

The curve and the second-, third- and fourth-order cumulants of the y(n) are Fig.A, Fig.B, Fig.C, and Fig.D of Fig.4. The second-order cumulant of the y(n) in Fig.4 is the mixed cumulant of $\omega_0(n)$, $\omega_1(n)$ and $\omega(n)$. The third-order cumulant of y(n) is only the cumulant of $\omega_0(n)$.

The fourth-order cumulant of y(n) is the mixed cumulant of $\omega_0(n)$ and $\omega(n)$. The $C'_{4,y}(m)$ after prefiltered only includes the cumulant of $\omega(n)$.

V. EXPERIMENT RESULTS

The airplane radar altimeter data (the data came from the experiment of Qingdao of China at Mar. 1995) are used to calculate the second-, third- and fourth-order cumulants and 50 averages are done.

The third-order cumulant has a large magnitude when m=0. This suggests that there are non-symmetric non-Gaussian noise signals in the return noise signals.

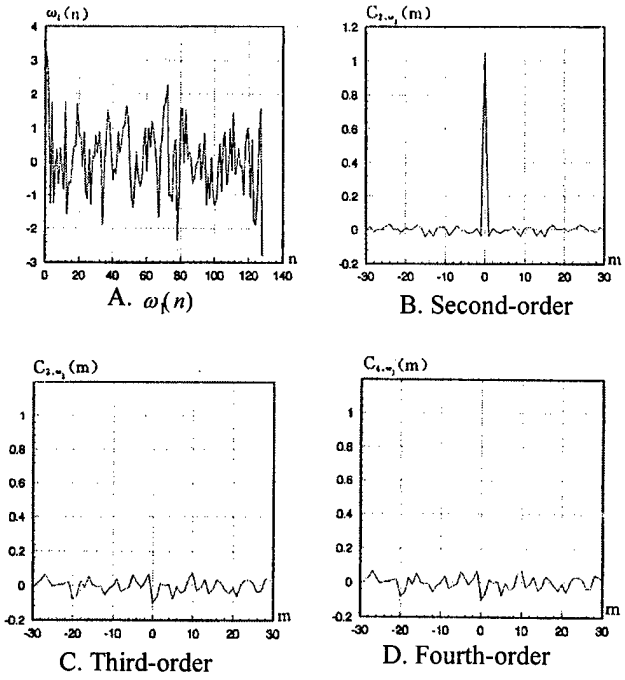


Fig.2 The curve and cumulants of $\omega_1(n)$

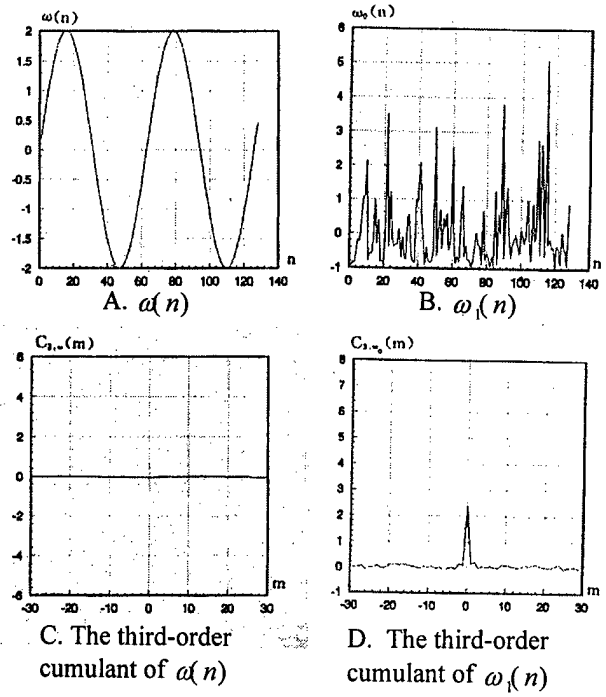


Fig.3 The curve and cumulants of $\alpha(n)$ and $\omega_1(n)$

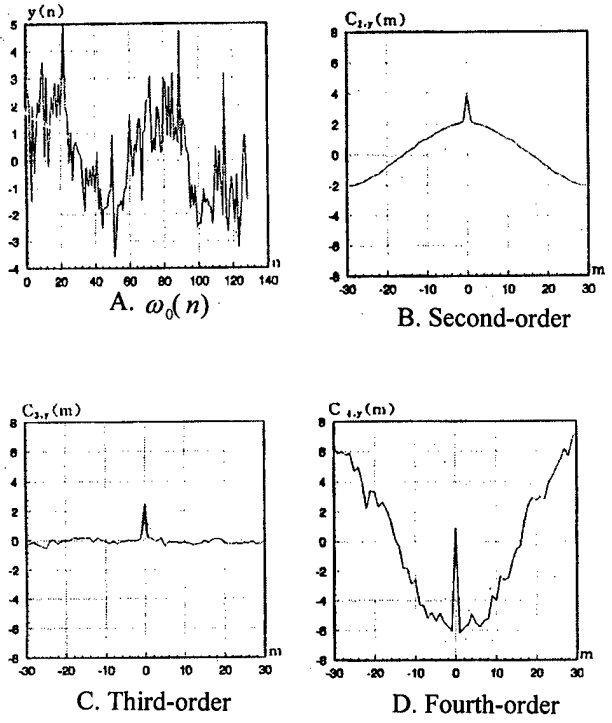


Fig.4 The curve and cumulants of $\omega_0(n)$

VI.CONCLUSION

The radar altimeter return noise signals identification is discussed. A novel method that uses the second-, third- and fourth-order cumulants is proposed. According to the simulation and the experiment results. We can give the conclusion that there are not only Gaussian noise signals but also non-Gaussian noise signals. This will suggest that we should reexamine the correctness and the effectiveness of the some ocean return equations.

REFERENCES

[1] J.M.Mendel, "Tutorial on higher-order statistics (spectra) in signal processing and system theory: theoretical results and some applications," Proceedings of the IEEE, Vol. 79, No. 3, PP. 279-305, March 1991

[2] K.S. Lii, "Non-Gaussian ARMA model identification and estimation," Proc. and Econ. Statistics, PP. 135-141, 1982

[3] C.L. Nikias and R. Pan, "Time delay estimation in unknown Gaussian spatially Correlated Noise," IEEE Trans. On ASSP, Vol. 36, No. 11, PP. 1706-1714, 1988

Range and Angle Error Correction Measure for the Low Elevation Angle in Remote Sensing Data Analysis

Junho Choi
Code 8140.2
Space Systems Development Department
Naval Research Laboratory
4555 Overlook Ave. SW
Washington, DC 20375-5354
Tel. 202-767-9050/9792, Fax. 202-767-1317

Abstract

Effects of tropospheric radiowave propagation were studied based on ray-tracing and parametric approach with empirical data, ECM (European Climatological Medium-range), supplied by the National Climatology Data Center in Asheville, North Carolina. Results indicate that range and angle errors vary dynamically in seasons, months, and regions. The errors in the elevation angles of less than ten degrees are higher than expected, and should not be neglected for higher accuracy requirements.

1. Introduction

A variety of explanations of trpospheric propagational problems have been proposed based on model-based or empirical measurements in terms of frequencies and climatic regions over the years[1 - 6]. However, important details relating to the properties of the received signal are generally less certain; such details might be signal amplitude, delay times between different paths, and individual angles of arrival under multipath conditions. Meteorological uncertainties severely limit the usefulness of models of existing microwave propagation specifically in the presence of precipitation. Many propagational problems on the line-of-sight links arise from the occurrence of anomalous departures in the vertical gradient in the refractive index from the normal value. This value itself will vary slowly with season, time of day, location, and the standard gradient in refractivity often being quoted as -40 N-unit/km corresponding to a 4/3 Earth [7]. The major emphasis here is concentrated on the physical phenomena in the atmosphere using empirical data rather than on building models or analysis based on models developed. Most of the results are directed to quantifying parametric methods, and to investigating correlation among parameters for larger areas than the subgrid levels. Range errors are studied in section 2 for both analytical and experimental aspects with comparison of several alternatives to correct inherent errors. In section 3, angle errors are derived and tested with empirical data for angle error correction in real system. Finally, the conclusion and recommendations are presented in section 4 with references.

2. Range Errors

Many methods have been proposed to take into account refraction effects for the purpose of improving measurements by removing systematic bias. For the case of range error, the error is composed of two parts: the difference between the curved length of the ray path, R, and the true slant range, R_O mainly due to the increase in time necessary to travel over the curved path, R; and the discrepancy caused by the lowered velocity of propagation in a refractive medium as shown in the figure 1. The radio ray path, R, can be expressed [4] by

$$R = \int_O n \csc \theta \, dh \qquad (1)$$

where n represents the refractive index, θ the elevation angle, csc stands for cosecant angle of trigonometry and h the height above the surface. Then the total range error, ΔR, can be computed by

$$\Delta R = R - R_O$$

$$= \int_O n \csc \theta \, dh - R_O \qquad (2)$$

Many of the models are based upon the following assumptions of ray tracing:
1). The refractive index should not change appreciably in a wavelength.
2). The fractional change in the spacing between neighboring rays (initially parallel) must be small in a wavelength.

Note also that equations (1) and (2) are derived with the assumption of a flat Earth. For a flat earth, the attenuation as a function of elevation angle is given by the zenith attenuation multiplied by the cosecant of the elevation angle. The cosecant law does not hold for elevation angles less than 6 to 10^O due to earth curvature and refraction effects. Most satellite communication systems operate at elevation angles

0-7803-3068-4/96$5.00©1996 IEEE

above 6^o or a cosecant of 10. Barton and Ward [9] proposed approximate range and elevation angle errors as follows:

$$\Delta R = 0.007 * N_S \csc \theta_o \quad \text{[meters]} \qquad (3)$$

$$\Delta\theta_o = N_S \cot \theta_o \qquad \text{[mradian]} \qquad (4)$$

where N_S is surface refractivity and θ_o the apparent elevation angle.

Many other models for range and angle error have been proposed over the years [2, 8]. These models are generally developed from either direct integral method or stratified layer method, which can be applied to compute the angular deviation and range inaccuracy introduced when electromagnetic waves traverse a medium other than free space. The latter method, although only approximate in nature, is capable of rendering theoretical estimates of proportional errors to a rather high degree of accuracy, and is presented here by adopting Millman's approach [6] without extensive derivation efforts. Also note that most of the ray-tracing plots drawn here use the stratified layer method. Considering equation (1) by parameters as

$$dh = dr/\sin \theta \qquad (5)$$

$$\sin \theta = [\, 1 - (n_o r_o \cos\theta_o / nr)^2 \,]^{1/2} \qquad (6)$$

where r_o is the radius of the earth; n_o the refractive index at the earth's surface as shown in figure 1. Then the range error can be written as

$$R = (1/n_o r_o \cos \theta_o) \int_h n^2 r \, dr / [\, (nr/n_o r_o \cos \theta_o)^2 - 1]^{1/2} \qquad (7)$$

Considering eq. (7), the denominator inside the integral eq. (7) is going to be zero for the low elevation angles. If the elevation angle, θ_o, is less than 1^o, it is not integrable since n approaches n_o. Thus the integral has a singularity when h goes to zero in the limit, i.e, over the horizon. In other words, eq. (7) is valid if and only if the elevation angle is greater than one degree. Using the trigonometric functions in figure 1, R_o can be derived easily as

$$R_o = [r_o^2 + (r_o + h)^2 - 2r_o(r_o + h) \cos \theta \,]^{1/2} \qquad (8)$$

where θ is the central angle subtended over the Earth's surface. Therefore the range error of equation (2) is derived readily by substituting equations (7) and (8). For the stratified layer approach, equations (7) and (8) can be rewritten in discrete format below by numerical approximation methods such as Gauss's and Simpson's rule approach for numerical approximation of integral equations. The range error, ΔR, of equation (2) may be approximated as

$$\Delta R = \Sigma n_j R_j - R_{om} \qquad (9)$$

Similarly, equations (7) and (8) can be approximated as

$$R_j^2 = r_j^2 + r_{j+1}^2 - 2 r_j r_{j+1} \cos \theta_j \qquad (10)$$

$$R_{om}^2 = r_o^2 + r_{m+1}^2 - 2 r_o r_{m+1} \cos [\, \Sigma \theta_j \,] \qquad (11)$$

where r_o is the Earth's radius at the station and m represents the mth layer.

Figure 2 was plotted for comparison purposes among regional range error behavior by using equations (9) through (11) against elevation angle variations over four seasonal activities in the eastern USA. Figure 2 shows more errors in July.

Figure 3 shows range error versus height plots with elevation angles from 1 to 5.5 degree for July in the eastern USA region. Range errors for 1.0 degree are around low 66 meters. This implies that range errors at 5.5 degree elevation angle are reduced to about 30 % from those at 1.0 degree elevation angle. If we increase the elevation angle to 15 degrees, then the range errors are about 7 meters. This means that range errors at 15 degree elevation angle are reduced to 11 % of the range errors at one degree elevation angle. Finally, it is noticed that range errors vary seasonally as well as monthly from a few meters to about 10 meters range in the low elevation angles.

3. Elevation Angle Errors

Errors in elevation angle are mainly due to the refractive effects. This elevation angle error constitutes a variation in the angle of arrival (or elevation angle errors) of the signal. Corrections can be made for errors in the angle of arrival . These corrections are most useful if they are based on standard or mean models of the radio refractive index such that surface values can be used as a predictor. A successful method of deriving such a model is found in ray tracing through a representative sample of refractive index profiles (or refractivity profiles) and relating refraction variables to surface values using least square techniques. Ordinarily a linear relationship is sufficient with the coefficients being functions of the elevation angle and target height or range. Since the surface value of the refractive index is so central to refraction prediction a detailed examination of its behavior is essential. For a vertical

gradient of refractive index dn/dh, the radius of curvature r is given by [10]

$$1/r = - (1/n) \times (dn/dh) \times \cos \theta_o \qquad (12)$$

where θ_o is the initial elevation angle of the ray at the transmitter with respect to the local horizon as shown in figure 1. The negative sign indicates a decrease in refractive index with height. For terrestrial propagation, where θ_o is generally close to zero, the equation (12) simplifies to

$$1/r = - dn/dh \qquad (13)$$

with n assumed to be unity in equation (12). Since refractive index is relatively insensitive to frequency, ray bending is substantially independent of frequency. It should be noted that the assumption of n = 1 in equation (13) is not true in the troposphere from the ground surface to about 30 kilometers in the space. In general, the value of n is greater than one depending on the value of refractivity at the layers concerned. A relationship between the elevation angle error (or ray bending) and surface refractivity, N_S has been developed [4] for low elevations through a statistical linear regression technique giving

$$\Delta\theta = (bN_S + a) * 10^{-6} \text{ radians} \qquad (14)$$

where the coefficients a and b are provided through graphics or tables [4].
Equation (14) does not apply for regions of climatic extremes, for angles less than 3^o or 4^o. The limiting errors of targets well beyond the atmosphere are given, for $\theta > 5^o$, by

$$\Delta\theta = N_S \cot \theta * 10^{-6} \text{ radians} \qquad (15)$$

Many other ray-tracing models were proposed to improve the accuracy of atmospheric bending or propagation delay [2, 4]. The stratified ray-tracing model has been applied with other integral methods since it gives a better result than other approaches tested. If it is assumed that the refractive index is a function only of height above the surface of a smooth, spherical earth (i.e., it is assumed that the refractive index structure is horizontally homogeneous) and that the refractive index is a monotonically decreasing function of altitude, then the path of a radiowave ray will obey the Snell's law for polar coordinates (Bouger's Rule) as:

$$n_1 r_1 \cos \theta_1 = n_2 r_2 \cos \theta_2 \qquad (16)$$

where n, r, and θ were defined in figure 1. One should keep in mind that equation (16) is subject to the assumptions made in section 2. Snell's law can be expressed in terms of the bending angle τ which is the change of the apparent angle of elevation with altitude.

$$\tau = - \int (dn/n) \cot \theta = - \cot \theta \, dN * 10^{-6} \qquad (17)$$

where the integral limit spans from n1 to n2 for the refractive index of the first integral and from N1 to N2 for the refractivity of the second integral in equation (17) respectively. Applying the law of sines and equation (18) below , it follows that the elevation angle error can be derived for the stratified approach as [6]

$$\alpha_{om} = \cos^{-1} \{(r_{m+1}/R_{om}) \sin [\Sigma_j \theta_j]\} \qquad (18)$$

Then the refraction elevation angle error can be expressed as

$$\Delta\alpha_m = \alpha_o - \alpha_{om} \qquad (19)$$

where α_o is the apparent elevation angle and α_{om} is the true elevation angle

Figure 4 is the ray tracing graph from one to 5.5^o of elevation angle versus the atmospheric height from the ground for the eastern USA region. It is noticed that all angle errors in this low elevation angle range exceed one milliradian (0.0573 degree) and extend to more than 6 milliradian angle errors. Relationship between apparent elevation angle and elevation angle error is presented for seasons in figure 5. The amount of angle error varies by season. It is noticed that some local areas (smaller grid areas) generate larger or smaller angle errors than much larger regional averages (cluster of many grids). This is also true for global average data. It should be noted that elevation angle errors vary dynamically with season and localities; specifically in the low elevation angle. One should be careful in adopting radiowave beam bending and propagation delay models when applying global climatological data to radiowave propagation for radar tracking and antenna pointing applications.

4. Conclusions

Most approaches are here based on empirical data and ray tracing algorithms. Range errors in the lower elevation angles ($\leq 1^o$) are in the range of 70 meters or above and around 7 meters or less for 15^o elevation angles. Notice that range errors vary seasonally from a few meters to 10 meters as well as monthly and locally. Elevation angle errors vary dynamically throughout seasons and regional areas

especially in the low elevation angles ($\leq 6^{o}$). Additional results of correlations between refractivities and meteorological parameters are presented to study direct effects of individual parameters against the refractivity. Results show that a minimum level of range error and elevation angle error can be obtained in the neighborhood of 12^{o} to 15^{o} of apparent elevation angles rather than at the 5^{o} elevation angles which most scientists have presented previously. Error analysis for diurnal and broader regional aspects will be investigated in the future with more relational functions in the sublow elevation angles ($\leq 1^{o}$) and higher elevation angles ($\geq 15^{o}$).

References

1. Derr, V. E., "Remote Sensing of the Troposphere", Wave Propagation Laboratory, Boulder, Colorado, USA, U.S. Government Printing Office, Washington, D.C. 20402 August 1972.

2. Hopfield, H. S., "Two-Quartic Tropospheric Refractivity Profile for Correcting Satellite Data", Journal of Geophysical Research, vol. 74, no. 18, August 1969, pp. 4487 - 4499.

3. Blake, L. V., "Ray Height Computation for a Continuous Nonlinear Atmospheric Refractive-Index Profile", Radio Science, vol. 3, no. 1 January 1968.

4. Bean, B. R. and E. J. Dutton, "Radio Meteorology", National Bureau of Standards Monograph 92, March 1966, U.S. Government Printing Office, Washington, D.C.

5. Campen, C. F. and A. E. Cole, "Tropospheric Variations of Refractive Index at Microwave Frequencies", Air Force Cambridge Research Center, Technical Memorandum #AFCRC TM-55-226, October 1955.

6. Millman, G. H., "Atmospheric Effects on Radio Wave Propagation", Chapter 1 in Modern Radar: Analysis, Evaluation and Design, edited by R. S. Berkowitz in 1965, John Wiley & Sons, Inc., New York, pp. 317 -378.

7. Webster, A. R., "Angles of Arrival and Delay Times on Terrestrial line of sight Microwave Links", IEEE Transactions on Antenna and Propagation, vol. AP-31, no.1, pp. 12 - 17, January 1983.

8. Patterson, W. L. et al., "Engineer's Refractive Effects Prediction System (EREPS) Revision 2.0, Naval Ocean Systems Center, Technical Doc. #1342, Revision 2.0, February 1990.

9. Barton, D. K. and H. R. Ward, "Handbook of Radar Measurement", Artech House, Boston, Mass. 1969.

10. Allnut, J. E., "Satellite-to-Ground Radiowave Propagation: Theory, Practice and System Inpact at Frequencies above 1 GHz", Peter Peregrinus, Ltd, London, England.

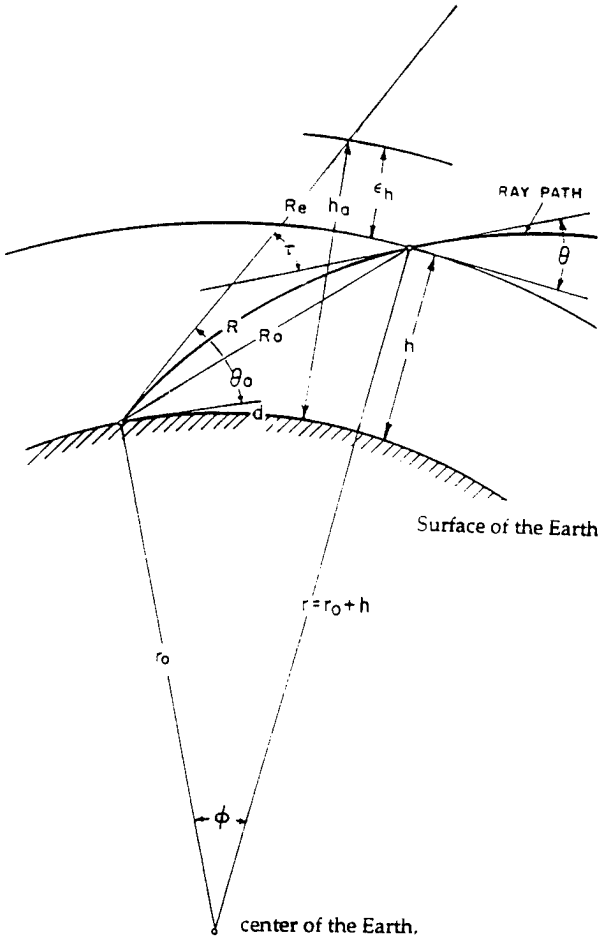
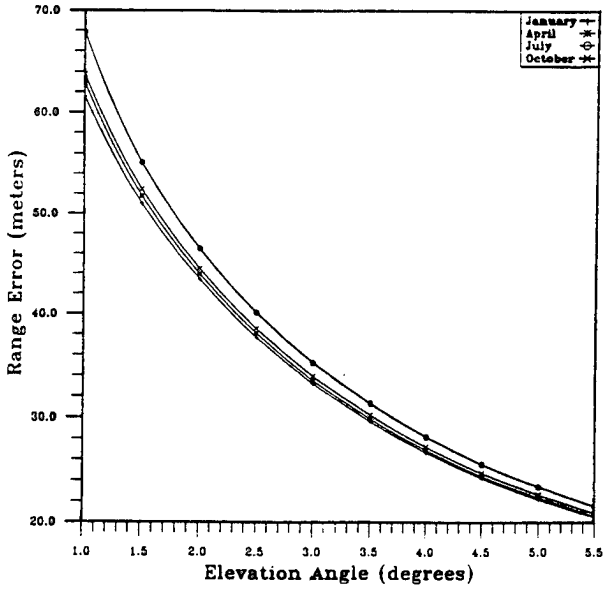
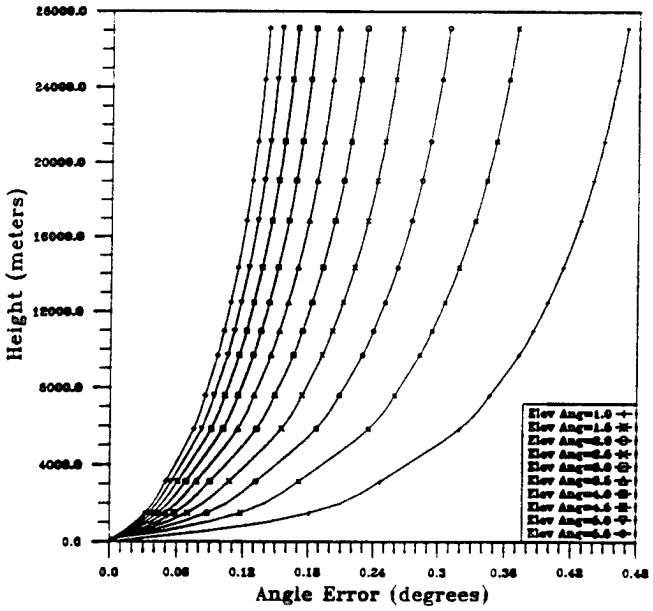


Figure 1. Radiowave propagation geometry of radio ray refraction.



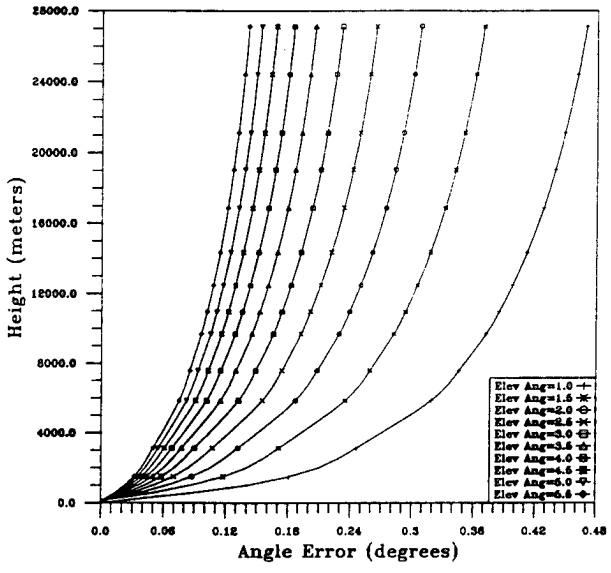
Range Error VS Elevation Angle
EASTERN US - ECM database
10 Year Average

Figure 2. Range error vs. elevation angle.



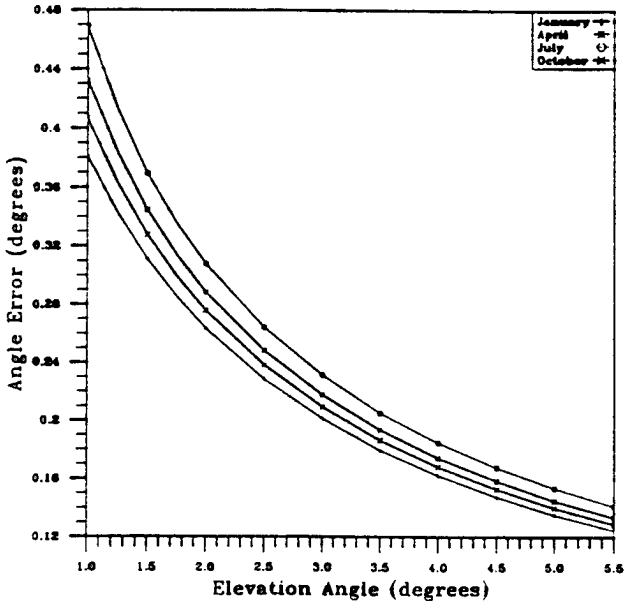
Height VS Angle Error
EAST US - ECM database
NLAT=32.5-47.5 ELON=260-295.0,10 Year Average - July

Figure 4. Angle error vs. height from 1° to 5.5°.



Height VS Angle Error
EAST US - ECM database
NLAT=32.5-47.5 ELON=260-295.0,10 Year Average - July

Figure 3. Range error vs. Height from 1° to 5.5°.



Angle Error VS Elevation Angle
EAST US - ECM database,10 Year Avg
NLAT=32.5-47.5 ELON=260-295.0

Figure 5. Angle error vs. elevation angle from 1° to 5.5°.

Potential And Use of Radar Images for Characterization and Detection of Urban Areas.

Christophe Gouinaud, Florence Tupin, Henri Maître,
Département Images
Ecole Nationale Supérieure des Télécommunications
46 rue Barrault, F - 75013 Paris
e-mail:gouinaud@ima.enst.fr
tel: (33-1) 45 81 76 42 fax: (33-1) 45 81 37 94

Abstract : The resolution of ERS-1 images should let us detect man-made structures like urban areas. After a brief survey of the captor response to urban objects, we propose a method to detect urban aeras. We illustrate the results obtained on two typical landscapes: European agricultural hilly landscapes and tropical zones. Some urban detections are presented both on Aix en Provence and Kourou towns in French Guyana.

1 Introduction

In this paper we present the main lines of our method to detect urban areas (detailed in [1]). The purpose of our work is to provide robust classification criteria permitting automatic segmentation and urban agglomeration density measures.

Our method consists in 2 parts: the first one deals with the detection of bright points characterizing industrial areas, and the second one with more homogeneous regions like large towns, where the concentration of strong reflections becomes very important. We show an example of the use of our detection method in a fusion scheme with classical detection on SPOT image.

2 Backscatter of urban objects.

We propose first an urban object classification in 3 sets, depending on their geometry and roughness, and yielding a model of backscattering law according to [2].

2.1 Smooth surfaces

Following the usual Rayleigh criterion, we consider a surface as smooth when $\Delta h << \frac{\lambda}{8cos(i)}$, where Δh is the mean deviation of height, λ the wavelength, and i its incidence angle. For this type of surface, retrodiffusion laws are close from Snell-Descartes' ones, and thus the object geometry determines the sensor response. Depending on the incidence direction i, objects may have either a strong response or no response at all (taking into account the multiple reflections created by dihedral and trihedral objects).

2.2 Rough surfaces

It is the case of objects with irregularities on the scale of the wavelength, like vegetation for instance. These objects can be well described by Goodman model [3], assuming some properties for the phase and amplitude of elementary reflectors inside a resolution cell. We get an explicit backscattering law (which will be called here "χ"), linking A, the amplitude of the received signal, with L the number of looks (3 for ERS1 Precision Images), and α the parameter of the law [4]:

$$P(A) = \frac{2L^L}{(2\alpha^2)^L \Gamma(L)} A^{2L-1} e^{-\frac{LA^2}{2\alpha^2}} \quad (1)$$

Γ represents the Gamma function. This model also provides a relation linking α with the mean value $\overline{A}$ of the region assumed to be homogeneous.

2.3 Conductor surfaces

This is for instance the case of metallic surfaces, used as rooftops in tropical lands and in industrial areas. They are never plane, and act as periodic lattices. So sometimes a resonnance effect may occur (called Bragg diffraction), involving bright points in the SAR images. For some particular surface shapes (corrugated iron for instance) an approximated model may be proposed, but an explicit law is seldom found.

2.4 Characteristics of the global backscattering law

The global backscattering law of urban areas is the result of the composition of the 3 previous effects, with proportions depending on the areas. This provides some particular characteristics compared to the "χ" law of rough surfaces:

- There are more dark pixels, because of the Snell-Descartes responses in an unfavorable configuration (no response to the sensor).

0-7803-3068-4/96$5.00©1996 IEEE

- There are more bright pixels, because of the Snell-Descartes responses in a favorable configuration, and constructive interferences.
- The intermediate values around the mean caused by speckle are not so much modified.

Using these remarks we aim at estimating the probability that a pixel belongs to a town.

3 Fail of classical approaches

One classical method to detect urban areas consists in calculating first or second order statistics to obtain some discriminant information. We want to emphasize two problems which limit the use of such a method.

First it can be shown that the sizes needed to estimate reliable statistics of speckle samples are very large. For instance the variation coefficient (ratio of standart deviation over mean) estimation with a confidence of 5% around the theoretical value, and with a probability of 99%, needs a 42x42 window size. This corresponds to a 525x525m sample on the ground. So large areas will hardly be homogeneous in many towns. Estimation of skewness will also need similar very large windows. Secondly it can be shown that the statistics of some non-urban areas (forests for instance) are sometimes very close from the statistics of urban areas. It is the case of the radiometric mean.

It is why we propose new detection methods.

4 Detection criteria proposed

In this section we give a description of our method, based on a different approach to estimate pixel nature in SAR image.

4.1 Urban bright point detection

Having a region described by a "χ" law with known parameter, we know the probability of an intensity value A, and the probability for A to exceed a given value. We may compare for any region the measured probability with the theoretical one under hypothesis of fully developed speckle. In order to estimate the parameter of the law in the window, the local histogram is built on a 30x30 window, then it is smoothed, and we deduce α from it, using the last remark of §2.4. A pixel which amplitude value has a probability lower than a fixed threshold is temporary classified as bright. We then calculate the proportion of bright points in a 15 pixel radius disk around any temporary bright pixel. If it is more than 1% (at least 2 temporary bright pixels), the pixel is definitively kept as bright in the final classification.

4.2 Non urban detection.

To initiate a classification scheme non-urban areas have to be characterized. Having no human constructions, these areas have also no specular backsattering points. Therefore the only phenomenon observed is the speckle one. The classification of non-urban areas is based on the comparison of local statistics and χ law based statistics, corresponding to fully developed speckle. In practice, the average value and the first moment (mean) deduced from the χ interpolated histogram on a 30x30 window are compared. In case of equality the region is classified as non urban.

4.3 Urban areas detection

The previous method is well adapted to industrial and suburban areas characterized by isolated bright points. But, when working in in towns, which form very compact regions echoes are combining in a coherent way and cannot be considered as "isolated" at all. To detect these regions, we propose to cut the local histogram (calculated on a 60x60 window) in 2 parts, with a threshold s. In the higher part, $\Sigma = P(A > s)$ is computed and compared to the highest frequency f_{max} of the low part. When $\Sigma > f_{max}$ the central pixel receives s as value, and the threshold is decreased.

The process is iterated until all the pixels are classified. The thresholds have the form $\mu + k\sigma$ (μ is the mean, and σ the standard deviation of an area of totally developed speckle). Then the result is thresholded to obtain urban areas. A blind classification establishes the threshold value k by testing the regions of radii 15 pixels around the detected bright points. We refer to this detection method as ffmax-filter.

5 Classification scheme using our detection method and classical detection in SPOT-images

To do a classification with our detection and classical detection following step are used :

- The bright point detection as seen in (4.1) give training sets for urban classes.
- The speckle zones give training sets for non-urban classes.
- We build a multivariate classical distance based classification based on the ffmax-filter (4.3) and classical detection in SPOT image [5].

This method gives automatic detection of urban areas. not with detecting precise borders, but with a reliable localization. Post treatments could be applied to improve the accuracy of borders. They are not presented here.

6 Results and analysis

The results are illustrated on an image of Kourou (French Guyana) for the bright points detection method,

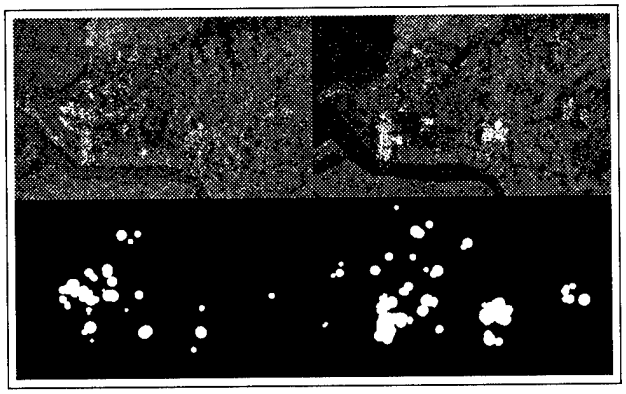


Figure 1: Bright point detection on ERS-1 (left column) and JERS-1 images (right column).

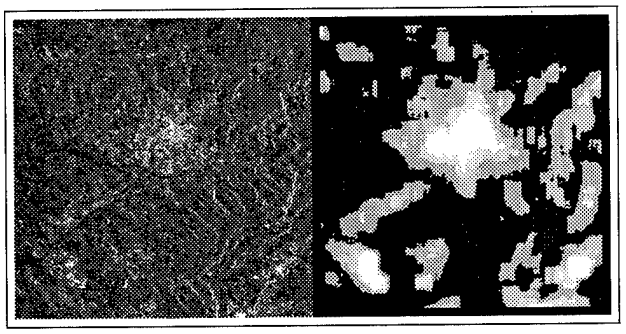


Figure 2: Sar ERS1 image and map of the ffmax-filter values on the region of Aix-en-Provence. This map will be thresholded to select the urban areas.

figure 1, and on an image of Aix en Provence for both methods, figures 2 and 3.

The urban areas detection method is developed to be used with other sensors, like the radar satellite JERS-1 (figure 1b), or SPOT for instance. On SPOT images classical urban detection method is applied [5] [6]. The table below shows the ratio of good detection (urban pixels actually detected by the method), and false detection (detection of pixels which are not in urban areas), in a supervised learning case or an automatic one.

Regions	Captors used	Learning	Detection rates	False alarms rates
Lelystad	ERS-1 JERS-1	supervised	90 %	10 %
Lelystad	ERS-1 JERS-1	automatic	75 %	9 %
Aix en Provence	SPOT ERS-1	supervised	79 %	3 %
Aix en Provence	SPOT ERS-1	automatic	78 %	5 %
Kourou	ERS-1 JERS-1	automatic	70 %	20 %

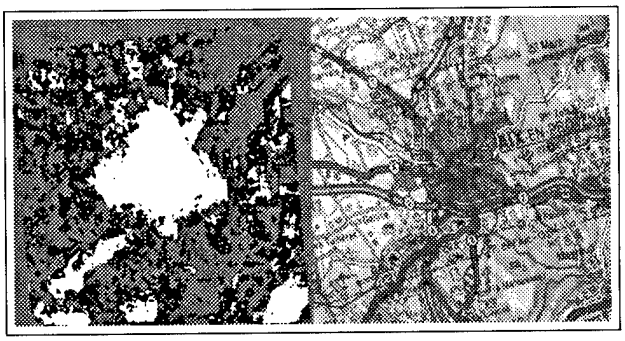


Figure 3: On the left SPOT-SAR automatique urban classification, on the right Map of Aix-en-Provence (Michelin 1/200 000)

To conclude, the proposed method gives good results on any sort of landscapes, and is robust enough to work on hilly regions. The results are improved when used with other captors, radar or optic.

7 Conclusion

Radar images are particularly difficult to interpret. Nethertheless dedicated detectors (adapted to the particular statistics of SAR images) give useful results, allowing a first interpretation of urban zone.

Acknowledgements : We want to thank J.P. Rudant for some of the images illustrating this work.

References

[1] C. Gouinaud and H. Maître. Classification critera for radar images of urban areas. In *Colloque CNES IEEE, Toulouse France*, 1995 à paraitre.

[2] D. J. Weydhal, X. Becquey, and T. Tollefsen. Combining ERS1 SAR with optical satellite data over urban areas. In *IGARSS-95, Firenze*, volume 3, pages 2461–2463, 1995.

[3] J. W. Goodman. Some fundamental properties of speckle. *J. Opt. Soc. Am.*, 66(11):1145–1150, 1976.

[4] H. Laur. *Analyse d'images radar en télédétection.* PhD thesis, Université Paul Sabatier, Toulouse France, 1989.

[5] S. Houzelle. *Extraction automatique d'objets cartographiques par fusion d'informations extraites d'images satellites.* PhD thesis, ENST, Paris France, January 1993.

[6] L. Bousassida, L. Laouni, C.Gouinaud, L.Laurore, and M. Galaup. Etude avec SPOT de la pression urbaine sur les terres agricoles dans le grand Tunis et apport d'ERS1. In CNES, editor, *De l'optique au radar, les applications de SPOT et ERS1*, pages 129–137. CNES-ESA, May 1993.

Phase preservation in SAR processing: The Interferometric Offset Test

B.Rosich Tell, H.Laur
European Space Agency, ESRIN
Via Galileo Galilei, 00044 Frascati, Italy
Tel. +39-6-941801 Fax. +39-6-94180280
betlem@esrin.esa.it, henri@esrin.esa.it

Abstract- SAR Interferometry requires a high accuracy processing of the phase information. The paper describes a practical method to check the phase preservation of a SAR processor. Test results for four different ERS SAR processors are presented.

Keywords:interferometry, phase preserving processing.

INTRODUCTION

Over the years SAR interferometry is becoming more and more attractive, in particular for ERS SAR data users. SAR interferometry is based on the phase information in SAR complex products. However traditional quality requirements for SAR processors are mainly based on measurements of the module of the impulse response function and do not guarantee phase preservation. As a consequence there is a need to establish specific phase quality requirements and corresponding measurements tests on SAR processors [1, 2, 3].

This article presents the current phase preservation tests [7] performed by the European Space Agency following a study described in [1]. Phase preservation tests results are presented for several ERS SAR processors.

PHASE DECORRELATION

The quality of an interferogram is usually represented by the coherence γ between a pair of complex products. Phase aberrations are translated in a coherence degradation and modify the interferogram statistics. Several factors contribute to the interferometric phase decorrelation. For our purposes, they can be divided in two kinds of decorrelation sources:

1. The factors inherent to the SAR system and to the interferometric scenario (as the spatial mis-registration, the temporal decorrelation, the variations in the propagation path or the spectrum mis-alignment): γ_{sys}
2. The factors introduced during the data processing, i.e. the processor phase preservation factors: γ_{proc}

Their contribution to the total coherence can be expressed as:

$$\gamma = \gamma_{sys} \cdot \gamma_{proc} \qquad (1)$$

0-7803-3068-4/96$5.00©1996 IEEE

As our purpose is to analyse the quality of the processor phase preservation, we need to isolate γ_{proc}. This leads to the Interferometric Offset test, which was originally proposed in [1] as a method for checking the phase preservation of SAR processors.

THE INTERFEROMETRIC OFFSET TEST

The test consists basically in:

a. Generate two complex products independently processing the same raw data set twice, but starting at different azimuth and range positions. Usage of the same raw data set will prevent from phase aberration due to inherent SAR effects (γ_{sys}).
b. Evaluate the statistics of the generated interferogram. Since it should ideally have a constant phase of zero, the obtained interferometric phase reveals processor induced aberrations.

Products generation

In generating the products, some points must be carefully observed in order to obtain an appropriated pair for the test:

- Range compression is performed using a nominal chirp or the same chirp replica in both cases.
- The number of offset lines and samples are not integer multiples of the processing blocks dimension (nor in azimuth nor in range). It causes the existence of interferometric areas generated from the same processing data block (which will be referred as *regions a*) and from different data blocks (referred as *regions b*). Their co-existence allows to check the noise level at the processing block boundaries.
- Since usage of different Doppler centroid would produce an spectral envelope misalignment (i.e. it would simulate a system decorrelation source), the same doppler centroid parameters are used to process both products.
- Starting processing positions are chosen, whenever possible, in such a way that the offset between products is an integer value in both directions. If it is not possible, a subpixel misregistration remains with the need of a subpixel coregistration, which increases the phase noise.

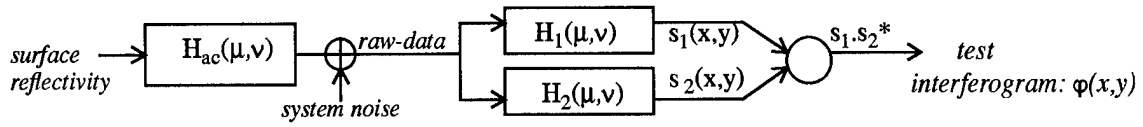


Fig.1 There is a unique acquisition process (H_{ac}) whose output is processed twice (H_1,H_2). Focused signals (s_1,s_2) are combined to form the test interferogram (s_2^* represents the complex conjugate of s_2).

Phase statistics evaluation

A theoretical study on the decorrelation due to the end-to-end SAR system response and on the interferometric phase statistics is carefully presented in [2,3,6]. The analysis is given for the case of an expected interferometric phase equal to zero and therefore it applies for the offset test interferogram if the system considered is the one represented in Fig.1.

The only difference between both transfer functions is the phase term $\phi(.)$, which represents the differential focusing under evaluation:

$$H_2(\mu,\nu) = H_1(\mu,\nu)\cdot e^{-j\phi(\mu,\nu)} \qquad (2)$$

Therefore, the coherence between tested products can be expressed as follows [2,3,4]:

$$\gamma = \frac{E\{s_1\cdot s^*{}_2\}}{\sqrt{E\{|s_1|^2\}\cdot E\{|s_2|^2\}}} = \frac{1}{B_\mu\cdot B_\nu}\cdot\int_{-B_\mu/2}^{B_\mu/2}\int_{-B_\nu/2}^{B_\nu/2} e^{j\phi(\mu,\nu)}\,d\mu\,d\nu \qquad (3)$$

where μ,ν,Bμ and Bν represent the azimuth and range frequency, and the azimuth and range bandwidth respectively.

From this basis, an analytical expression for the phase p.d.f., the phase bias and the phase variance can be derived [2,3]. The interesting result for our analysis is that the interferometric phase decorrelation introduced by the processor can be characterised by:

1. A phase bias value (φ_0) corresponding to the systematic phase errors and equal to the argument of the coherence coefficient. Since it depends on both transfer functions but not on the SNR, it cannot be reduced by averaging.
2. A phase variance ($\sigma^2{}_\varphi$) depending on the module of the coherence coefficient, on both transfer functions and on the SNR. It is very sensitive to data manipulations, but it can be reduced by averaging.

As a consequence, these two statistical parameters are the parameters to be estimated in the offset test interferogram.

The next important point is to identify the contribution of the different processing decorrelation sources on these parameters. The differential focusing phase can be expressed as Taylor series [2,6], where each term represents a different processing decorrelation source:

$$\phi(\mu,\nu) = \phi_{00}+\phi_{10}\cdot\mu+\phi_{01}\cdot\nu+\phi_{11}\cdot\mu\nu+ +\phi_{20}\cdot\mu^2+\phi_{02}\cdot\nu^2+\phi_{21}\cdot\mu^2\nu+\ldots \qquad (4)$$

The meaning of each term together with their evidence in the test results is summarised in Table 1.

Therefore, measured phase bias and standard variation over the generated interferogram correspond to the following phase aberrations:

$$\varphi_0 = \varphi_{00}+\varphi_{20}$$
$$\sigma_\phi^2 = \sigma^2{}_{11}+\sigma^2{}_{21}+\sigma^2_{subpixel-mis}+\sigma^2_{proc-impl} \qquad (5)$$

where $\sigma^2_{poc_impl}$ stands for the phase noise due to the processor implementation. This phase noise is consequence, for instance, of an insufficient amount of data discarded during processing operations which produce only a partial amount of valid data (e.g. when a linear correlation is

Table 1: Measurable processing phase aberrations

	Constant phase offset: ϕ_{00}	Geometric misregistration azimuth:ϕ_{10} & range: ϕ_{01}	Uncompensated range migration linear: ϕ_{11}& quadratic: ϕ_{21}	Defocussing in azimuth: ϕ_{20}	Defocussing in range: ϕ_{02}
φ_0	φ_{00}	*Effect avoided by test conditions*	*No impact*	φ_{20}	*Effect avoided by test conditions*
$\sigma^2{}_\varphi$	*No impact*		$\sigma^2{}_{11}+\sigma^2{}_{21}$	$\sigma^2{}_{20}$	

obtained from a circular one). This noise can be visually detected as a cyclic pattern of regions with high noise (the so-called *regions b*). The presence of $\sigma^2_{subpixel_mis}$ is not due to a processor induced aberration but to the difficulty to generate a testing pair with integer offset values. This noise term represents the noise introduced by the sub-pixel coregistration step needed in such a case.

Test Acceptance Criteria

The test acceptance criteria are based on a maximum systematic error (maximum phase mean) and on a maximum level noise, partially related to the system SNR [1]. The criteria are the following:

- maximum phase mean: 0.1 degrees
- maximum phase standard deviation: 5.0 degrees

TESTS RESULTS

The Interferometric Offset test was applied to four ERS SAR processors: the Verification Mode Processor (VMP) [Range-Doppler], the Italian PAF processor (I-PAF) [Range-Doppler], an experimental Chirp Scaling Algorithm (CSA) and an ωk Processor (ωk).

During the analysis of the statistical parameters, special care has been taken in:

- Avoiding very low backscattering coefficient areas. First part of Table 2 gives the results for the complete generated interferogram, i.e. with 100% of the input data. Second part of Table 2 gives the results obtained when discarding samples corresponding to low backscattering coefficient (equivalent to use about 95% of the input data). This insures a more accurate estimation of the processor induced aberrations.
- Independently measuring the parameters over both kinds of regions previously identified (*regions a* and *b*). No significant difference between these results have been found.

Comments

The results demonstrate that the four SAR processors are phase-preserving. However it is worth mentioning that the first results for the ωk and I-PAF processors were outside the acceptance criteria. This was due to processing inaccuracies and led to slight modifications in the processor design. The last results (Table 2) are obtained after the processor modifications.

The tested processors do not have the same flexibility to follow the test processing recommendations. In some cases, the processor implementation makes difficult the generation of the products required for the test. For example, the VMP processor, which is the main operational ERS processor, indicates the along track position by its associated azimuth time. When the VMP operational mode is used, it is difficult to get an integer azimuth shift between products. Therefore a corregistration step at subpixel level is needed and this is considered to be the main responsible of the measured phase noise. Using the VMP test mode enables the generation of a pair of products shifted by an integer number of lines. In such a case much lower phase noise is obtained.

OTHER TESTS

The Interferometric Offset Test insures that a SAR processor is phase preserving. However the test does not insure that two phase preserving processors are able to provide compatible complex products for interferogram generation. Two possibilities exist and need further investigation:

1. The Point Target Test
   This test is proposed in [1] as a different approach for the offset test and is based on the phase quality analysis of the impulse response function. It is a complement to the classical SAR processing quality analysis.
2. The Cross-Offset Test
   Different processors may implement slightly different transfer functions. The processor differences may not only be related to their phases but also to their modules (e.g. different weighting functions or different weighting coefficients). Therefore, the theoretical statistical analysis for the Offset Test is no more applicable and its independent accomplishment does not guarantee interferometric compatibility. The Cross-Offset overcomes this limitation by performing the Offset Test with a pair of products generated by two different processors (with the same processing requirements as for the Interferometric Offset Test).

CONCLUSIONS

A method to check the phase preservation of a SAR processor has been presented, with special emphasis on its practical aspects. The test was applied to four different ERS SAR processors, demonstrating the test capability to detect processing inaccuracies. Results prove the phase preservation capability of these processors. The test limitations for insuring the quality of an interferogram generated with different phase-preserving processors was pointed out. Additional tests to check this feasibility were proposed.

Table 2: Offset Test results. All phase values are given in degrees.

	VMP	I-PAF	CSA	ωk
Azimuth offset [lines]	332	6718	700	799
Range offset [samples]	99	300	300	300
100 %				
Coherence Module: $\|\gamma\|$	0.996621	0.999861	0.999786	0.999514
Coherence Phase: $\arg\{\gamma\}$	0.056222	0.000010	0.001010	0.004480
Phase mean: φ_0	0.063588	0.001200	0.002127	0.005300
Phase standard deviation: σ_φ	1.908490	1.233000	2.613000	4.583000
95 %				
Coherence Module: $\|\gamma\|$	0.998080	0.999866	0.999799	0.999558
Coherence Phase: $\arg\{\gamma\}$	0.056000	0.000106	0.001003	0.004470
Phase mean: φ_0	0.060897	0.000960	0.000880	0.004370
Phase standard deviation: σ_φ	0.972000	0.599000	1.355000	2.301000

AKNOWLEDGMENTS

The authors thanks B. Schaettler and R. Bamler for useful discussions.

REFERENCES

[1] R.Bamler, B. Schaettler, "Phase-Preservation in SAR Processing: Definition, Requirements and Tests", DLR Tech.Note, Ver.1.0, May 1995.

[2] R.Bamler, D. Just, "Phase Statistics and decorrelation in SAR interferograms", Proc. IGARSS'93, pp. 980-984.

[3] R.Bamler, D. Just, "Phase statistics in interferograms with applications to synthetic aperture radar", Applied Optics, Vol. 33, No. 20, pp. 4361-4368, July 1994.

[4] M. Cattabem, A. Monte-Guarnieri, F. Rocca,"Estimation and improvement of coherence in SAR interferograms", Proc. IGARSS'94, pp. 720-722.

[5] C. Prati, F. Rocca, A. Monte-Guarnieri, P.Pasquali,"Report on ERS-1 SAR interferometric techniques and applications", ESA Study Contract No.3-7439/92/HGE-I, 1994.

[6] L.M.H. Ulanders, J.O. Hagberg, "Radiometric and interferometric calibration of ENVISAT-1 data", ESA Study Contract No. PO/133382, 1995.

[7] "ERS SAR SLC-I Specifications", Issue 1, Dec. 1995.

Robust restoration of microwave brightness contrasts from the DMSP SSM/I data

B.Z.Petrenko

Institute of Radioengineering & Electronics, Russian Academy of Sciences
141120, 1, Vvedenskogo sq., Fryazino, Moscow reg., Russia
Telephone: (095) 526-92-68, Fax: (095) 203-84-14, E-mail: smirnov@mx.iki.rssi.ru

Abstract -- The technique tolerant to an inexactness of the antenna pattern form is developed for resampling microwave radiometer data on the base of robust principles of statistical estimation. Two types of algorithms are considered: a single-channel algorithm and an interchannel algorithm to resample low frequency channel data taking into account higher frequency channel. The performance of the algorithms is demonstrated by results of DMSP SSM/I data processing.

INTRODUCTION

The instrumental spatial resolution of spaceborne microwave scanning radiometers is determined by a field of view size ρ_f, which is typically of 10 to 70 km, and it is critical for many thematic applications. The algorithms for the SSM/I (Special Sensor Microwave/Imager) data interpolation were developed on the base of Backus-Gilbert [1-3] and image restoration [4] techniques to enhance a resolution of microwave images. All these algorithms require the detailed knowledge of the radiometer antenna pattern. However, this requirement is often hard to fulfill. Usually, descriptions of satellite data available for the most of users (e.g., [5]) carry only the information on the 3 Db fields of view diameters. Moreover, elements of a spacecraft design can remarkably change the prelaunch measured antenna pattern. So, there is a demand for an imaging technique which would be tolerant to variations of the antenna pattern form and, at the same time, would provide sufficient resolution of resulting images.

Such technique can be developed basing on robust principles of statistical estimation. This involves separation of abnormal samples from the initial data set so as to make resulting estimates more tolerant to erroneous data. The techniques described below treat as abnormal antenna temperatures sampled at the boundaries of contrast objects which are the most sensitive to the antenna pattern form.

MODEL OF THE SCENE OBSERVED

Generally, the brightness temperature $T_b(\mathbf{p})$ for any pixel $\mathbf{p}$ is estimated by interpolation of a set $\Xi(\mathbf{p})$ of antenna temperatures sampled within a certain aperture surrounding this pixel. The antenna temperature measured at the antenna boresight $\mathbf{r}$ is expressed as

$$T_a(\mathbf{r})=\int G(\mathbf{q},\mathbf{r})T_b(\mathbf{q})ds, \qquad (1)$$

where $G(\mathbf{q},\mathbf{r})$ is the antenna gain function, $\int G(\mathbf{q},\mathbf{r})ds = 1$, and $T_b(\mathbf{q})$ is a brightness temperature of a scene element ds observed in a direction $\mathbf{q}$. Let the scene within the aperture consist of two areas, C_1 and C_2, with $T_b(\mathbf{q})=T_1+\delta T_1(\mathbf{q})$ when $\mathbf{q}\in C_1$ and $T_b(\mathbf{q})=T_2+\delta T_2(\mathbf{q})$ when $\mathbf{q}\in C_2$, where $\delta T_1(\mathbf{q})$ and $\delta T_2(\mathbf{q})$ are spatial fluctuations of brightness temperatures. Then (1) can be written in the following form:

$$T_a(\mathbf{r}) = T_1 + A(\mathbf{r})(T_2 - T_1) + \mathcal{E}(\mathbf{r}), \qquad (2)$$

where

$$\mathcal{E}(\mathbf{r}) = \int_{C_2} G(\mathbf{q},\mathbf{r})\,\delta T_2(\mathbf{q})ds + \int_{C_1} G(\mathbf{q},\mathbf{r})\,\delta T_1(\mathbf{q})ds,$$

$$A(\mathbf{r}) = \int_{C_2} G(\mathbf{q},\mathbf{r})ds. \qquad (3)$$

We shall assume that the areas C_1 and C_2 are contrast, as it takes place for boundaries of many natural surfaces:

$$\mathcal{E}(\mathbf{r}) << \left| T_2 - T_1 \right| \qquad (4)$$

If the field of view is situated at a distance more then ρ_f from the areas boundary then the coefficient $A(\mathbf{r})$ is close to 0 or to 1, and the antenna pattern slightly affects $T_a(\mathbf{r})$ through $\mathcal{E}(\mathbf{r})$ only. On the other hand, the antenna temperatures for fields of view lying closer to the boundary zone, where $A(\mathbf{r})$ varies from 0 to 1, are the most influenced to the antenna pattern variations. So, one can make the estimate of $T_b(\mathbf{p})$ more tolerant to antenna pattern inaccuracy excluding from $\Xi(\mathbf{p})$ antenna temperatures sampled at the boundary zone.

SINGLE CHANNEL DATA IMAGING

While a single channel data interpolation the elements of $\Xi(\mathbf{p})$ most sensitive to the antenna pattern form can be separated by values. If antenna temperatures close to T_1 dominate $\Xi(\mathbf{p})$ then $T_a(\mathbf{r})$ samples for fields of view lying in the boundary zone and in the area C_2 can be treated as anomalies. The estimation of $T_b(\mathbf{p})$ involving abnormal samples separation can be performed by means of median filtering [6]. In order to enhance a capacity of resolving small objects of order ρ_f in diameter a standard range median algorithm was enhanced in a following way. For each data set $\Xi(\mathbf{p})$ both range and weighted medians [6] were taken. The

0-7803-3068-4/96$5.00©1996 IEEE

weighted median was taken by weighting each $T_a(\mathbf{r})$ sample with weights $c(\mathbf{r})$ decreasing with a distance between the pixel $\mathbf{p}$ and antenna boresight vector $\mathbf{r}$. Since 3 Db field of view sizes were assumed to be the only well-known antenna pattern parameters, $c(\mathbf{r})$ were calculated as follows:

$$c(\mathbf{r})= \exp(-|\mathbf{p} - \mathbf{r}|^2/2(k\rho_f /2)^2). \quad (5)$$

The abnormal elements having the smallest weights were iteratively removed from $\Xi(\mathbf{p})$ until the weighted and range medians of the remaining data set became equal.

INTERCHANNEL DATA IMAGING

Due to the diffraction the ρ_f value of multichannel microwave radiometer increases from higher to lower operating frequencies. If the same contrast objects are seen in two channels with a different spatial resolution then brightness contrasts in the low resolution image can be refined with the use of a high resolution image. This idea was expressed in [7]. But the algorithm proposed in [7] hardly relies on the rectangularity of the angular gain function typical for optical sensors. The robust technique solves this problem without detailed suggestions on the antenna patterns.

Let a contrast scene be observed by channels having antenna gain functions G_L and G_H. It follows from (2) and (3) that if $G_L \equiv G_H$ then the relationship between antenna temperatures T_{aL} and T_{aH}, sampled in this channels is well fitted by a linear regression. But if $G_L \neq G_H$ then the pair $\{T_{aL},T_{aH}\}$ sampled at a boundary zone will deviate from a regression line. If the aperture size will be of several ρ_f of a lower frequency channel then strongly deviating points will be a small part of a total amount of samples. Then abnormal samples can be separated from the initial data set by deviations of pairs $\{T_{aL},T_{aH}\}$ from a regression line.

The interchannel algorithm for estimation of a low frequency brightness temperature $T_{bL}^*(\mathbf{p})$ involves following main procedures:

(i) The regression between $T_{aL}(\mathbf{p})$ and $T_{aH}(\mathbf{p})$ is constructed by least squares: $T_{aR}(\mathbf{p})=a+bT_{aH}(\mathbf{p})$, and a standard deviation σ of samples $T_{aL}(\mathbf{p})$ from regressed values $T_{aR}(\mathbf{p})$ is evaluated.

(ii) Single-channel brightness temperature estimates for low and high frequency channels, $T_{bL}(\mathbf{p})$ and $T_{bH}(\mathbf{p})$, are evaluated with the algorithm described above;

(iii) The final brightness temperature estimate $T_{bL}^*(\mathbf{p})$ for a low frequency channel is evaluated as

$$T_{bL}^*(\mathbf{p}) = T_{b\,L}(\mathbf{p}) + (a+bT_{bH}(\mathbf{p})-T_{bL}(\mathbf{p})) \exp\{- \Delta^2/2\sigma^2\} \quad (6)$$

The exponential multiplier in the right part of (6) makes the more stronger correction of a single-channel estimate $T_{b\,L}(\mathbf{p})$ the more relative deviation Δ/σ of a pair $\{T_{bL}(\mathbf{p}), T_{bH}(\mathbf{p})\}$ from a regression line.

The essential feature of this technique is its versatility. It requires no other information on the antenna pattern except ρ_f value. Moreover, since it does not require any suggestions on a nature of data processed, it allows to apply optical or SAR images for enhancing microwave radiometric contrasts. The only requirement is the coincidence of contrast areas boundaries as they are observed by both sensors.

SYNTHESIS OF IMAGES FROM THE SSM/I DATA

Due to the nonlinearity inherent in the the robust algorithms it is hard to analyze their performance theoretically. For this reason it was assessed by the results of processing data of the SSM/I radiometer that is flown on the .DMSP F11 satellite. The ρ_f value was 13 to 15 km at the operating frequency 85.5 GHz and 43 to 69 km at 19.35 GHz with a sampling frequency at 85.5 GHz being twice higher then at 19.35 GHz [5]. Images were made for the channel 19.35 GHz, horizontal polarization (19H), and the channel 85.5 GHz, horizontal polarization (85H) was used for interchannel refinement of 19H images. Cloudless scenes were chosen in order to provide a coincidence of contrast areas boundaries in both channels.

The spatial resolution of resulting images were assessed as a halfwidth of a transition zone between waste (much waster than ρ_f) areas of a land and oceans. For a single-channel algorithm, the resolution of 19H was found to be within 20 to 25 km that is close to limit posed by Nyquist theorem and is consistent with one obtained by the techniques based on an exact knowledge of the antenna pattern. The interchannel algorithm makes the spatial resolution of the 19H images equal to that of that of 85H channel which is approximately of 10 to 12 km.

The more hard problem is to detect contrast object in size of the order of ρ_f or smaller. In this case, a maximum measured antenna temperature contrast is less then the actual brightness contrast. So, the best brightness contrast robust estimate is a maximum antenna contrast.

The images of the Baikal lake area obtained from the DMSP SSM/I F11 measurements made on September, 5, 1994, are shown on Fig. 1. The width of the Baikal lake along the line AB shown on Fig. 1.3 is 70 km that corresponds to 1 to 1.5 ρ_f for the 19H channel. The brightness temperature profiles restored along the line AB are shown on Fig. 2. Due to the procedure of removing abnormal samples the single-channel algorithm allows estimate of brightness temperature contrast close to a maximum antenna contrast. The interchannel algorithm somewhat increases the maximum brightness contrast and narrows the boundary zone between land and water in the 19H channel up to that of 85H. The visual comparison of Fig. 1.1 and 1.2 shows that the interchannel technique resolves contours of contrast objects, such as the Baikal lake and the Angara river in much more details then the single-channel technique. Moreover, a number of actual small objects which are invisible in Fig. 1.1, are well resolved on Fig. 1.2, such as the Olchon island and the St. Nos peninsula on the Baikal lake and the Gusinoe lake to the south of the Baikal lake.

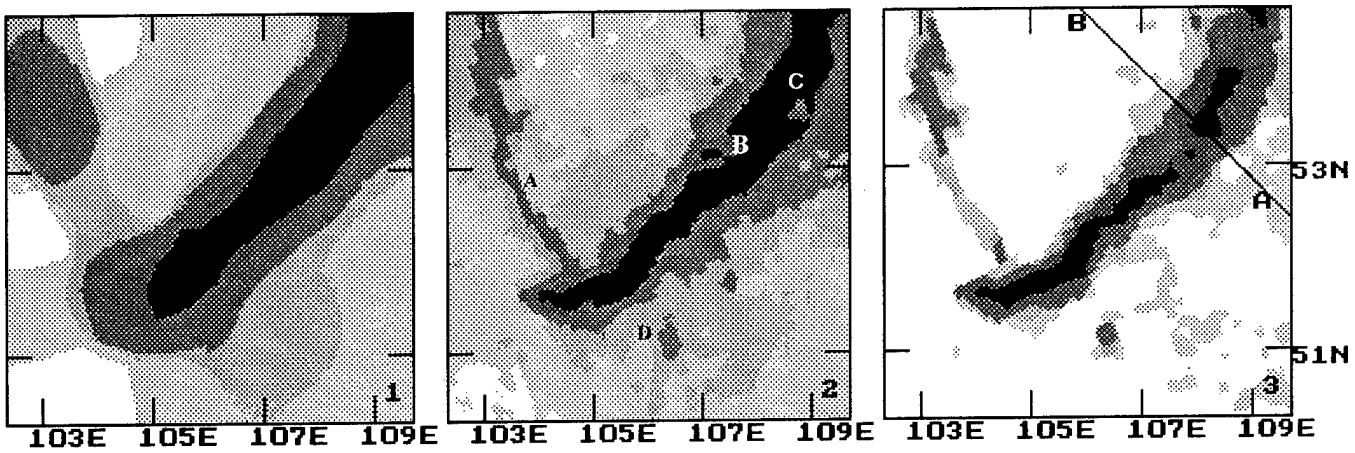


Figure 1. Images of the Baikal lake area obtained from DSMS SSM/I F11 data with a single-channel algorithm of channels 19H (1) and 85H (3) and with interchannel algorithm (2). Objects lettered on Fig. 1.2 are the Angara river (A), the Olchon island (B), the St. Nos peninsula (C), the Gusinoe lake (D)

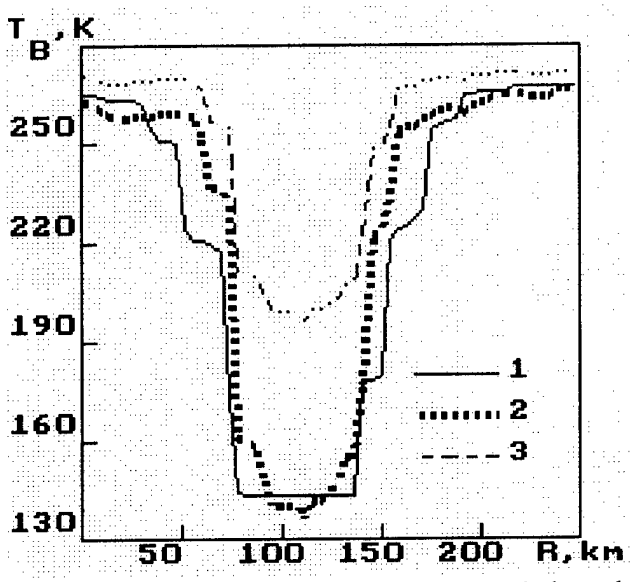


Figure 2. Brightness temperature profiles restored along the line AB on fig. 1.3 by a single-channel interpolation of 19H (1) and 85H (3) and by interchannel interpolation of 19H (2).

CONCLUSIONS

The robust technique for scanning microwave radiometer data imaging is proposed which compensates for the antenna pattern inexact knowledge by the analysys of the structure of the interpolated set of antenna temperatures. While a single channel data processing, this technique provides a spatial resolution of the resulting image comparable with that of the techniques based on the accurate antenna pattern knowledge. Under some natural conditions this technique allows to use the channel with better spatial resolution for the refinement of brightness contrasts on the image obtained in the lower resolution channel. In the last case the spatial resolution of the lower resolution channel image comes close to that of the high resolution channel image.

ACKNOLEDGMENTS

The author thanks Mr. F.J.Wents (Remote Sensing Systems) for delivering SSM/I data. The work was supported by Russian Foundation for Basic Research, project No. 95-05-15275.

REFERENCES

[1] G.A.Poe. Optimum interpolation of imaging microwave radiometer data. IEEE Geosci. Remote Sensing, 1990, v. GE-28, No. 5, pp.800-810.

[2] M.R.Farrar, E.A.Smith E.A. Spatial resolution enhancement of terrestrial features using deconvolved SSM/I microwave brightness temperatures. IEEE Trans. Geosci. Remote Sensing, 1992, V. GE-30, No. 2, pp. 349-355.

[3] Robinson W.D., Kummerow C., W.S.Olson. A technique for enchanting and matching the resolution of microwave measurements from the SSM/I instrument. IEEE Trans. Geosci. Remote Sensing, 1994, V. GE-32, No. 6, pp..419-429.

[4] Sethmann R., Burns B.A., Heygster G.C. Spatial resolution improvement of SSM/I data with image restoration technique. IEEE Trans. Geosci. Remote Sensing, 1994, V. GE-32, No. 6, pp. 1144.

[5] Wentz F.J. User's manual SSM/I antenna temperature tapes. RSS Technical reports 120191 and 120193. Remote Sensing Systems, USA, 1991 and 1993

[6] T.S.Huang, ed. Two-dimensional digital signal processing II. Transforms and median filtering. Springer Verlag, 1981.

[7] B.Zhukov, D. Oertel, F. Lanzl. A multiresolution multisensor technique for satellite remote sensing. Proc. IGARSS'95, 51-53.

Advanced Airplane Version of the HUT 93 GHz Imaging Radiometer

Martti Kemppinen, Tuomo Auer, Ilkka Mononen and Martti Hallikainen
Helsinki University of Technology, Laboratory of Space Technology
Otakaari 5A, 02150 Espoo, Finland
T:+358 0 451 2370 F:+358 0 451 2898 Email:kemppinen@ava.hut.fi

Abstract -- The HUT 93 GHz Airborne Imaging Radiometer (AIR-93) is being modified in an advanced airplane version. The new features include a) the use of an attitude-dGPS instrument to produce gyro data for radiometer beam active stabilization, b) an improved version of the airborne, liquid nitrogen cooled cold calibration target, and c) the digital, computationally stabilized, position oriented optical comparison image system.

INTRODUCTION

The HUT 93 GHz dual channel (horizontal and vertical polarization), conically scanning Airborne Imaging Radiometer, AIR-93 [1, 2], was originally designed and built for Bell JetRanger platform. During the building process, however, our laboratory bought a Shorts Skyvan airplane and modified it into a customized remote sensing platform. To provide multi-sensor capabilities for the EMAC'95 sea ice and snow measurement campaign [3], the instrument was modified to be compatible also with the Skyvan airplane in few weeks after its completion.

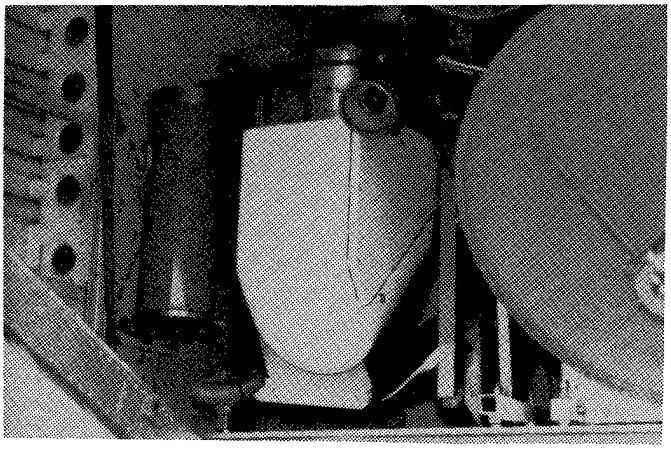


Fig.1 AIR-93 (left) assembly on Skyvan's rear cargo hatch along with profiling radiometers, EMAC'95

The test and measurement campaign flights aboard the two different aircraft types gave valuable, practical information on their applicability for imaging radiometer platform. Compared to the helicopter platform, the airplane was found to have the following advantages (+) and disadvantages (−):

+ The airplane has less angular motion in non-turbulent air (sea ice missions), resulting in less distorted image geometry and radiometric data values.
+ The airplane has a larger range, and there are no restrictions on operating over open sea, while a Finnish JetRanger has not been allowed to exceed the autorotation range from the nearest land since 1993.
+ The airplane has a customized, dGPS-based navigation system that leads to more accurate overflights than the usual helicopter GPS systems.
− The lowest feasible airspeed of the airplane is so high (110 kn) that the flight altitude has to be at least 750 m to compensate for it, providing integration time long enough (τ=10 ms). The higher altitude results in a larger footprint size, 43×68 m (Skyvan, 1000 m nominal) instead of 22×34 m (JetRanger, 500 m nominal).
+ Due to higher airspeed, the cross-wind deficiencies are considerably smaller in airplane use.
− The visibility to the target is poor compared to that of a helicopter.
± Skyvan has double operating costs compared to JetRanger's full-service leasing price. A Skyvan mission also requires more people and effort than a JetRanger flight. However, up to three radiometer systems with a total of ten channels can be operated simultaneously, resulting in 60% less cost/channel.

Excluding the narrower airspeed range and the resulting worse spatial resolution, the Skyvan airplane was considered a better platform for the AIR-93 instrument. Skyvan also provides far better possibilities for the attitude-GPS [4] installation that may also be a permanent one. The attitude-GPS is needed to provide gyro data for the radiometer beam active stabilization system [1], which compensates for the platform's angular motion. In addition, Skyvan has better possibilities to carry a larger airborne cold calibration [1] liquid nitrogen dewar, as the previous one, 2l, was found to be too small.

At present, these possibilities are met by preparing the installation of the attitude-dGPS and the active stabilization system and improving the airborne cold calibration system. Apart from the airplane use customization, the electronics unit is also being modified to improve its reliability and performance, and a new optical comparison image composition technique has been developed. All these modifications are described in more detail in the following sections.

0-7803-3068-4/96$5.00©1996 IEEE

Although not all the new features can be exploited on a helicopter platform, the instrument compatibility with a JetRanger is also restored, as high spatial resolution may be useful in some applications, e.g. precision farming [5].

ELECTRONICS UNIT MODIFICATION

Fig.2 depicts the upgraded control, data acquisition and data processing unit block diagram. The most essential change is replacing the 486 main computer with an 100 MHz Pentium, transferring the temperature control tasks of the third, 8086-computer to the main computer, and discarding the 8086. The motion controlling 286 was replaced by a 586 similar to the main computer to provide the necessary computing capacity for the active stabilization. It boots from a flash disk instead of the previously used diskette drive.

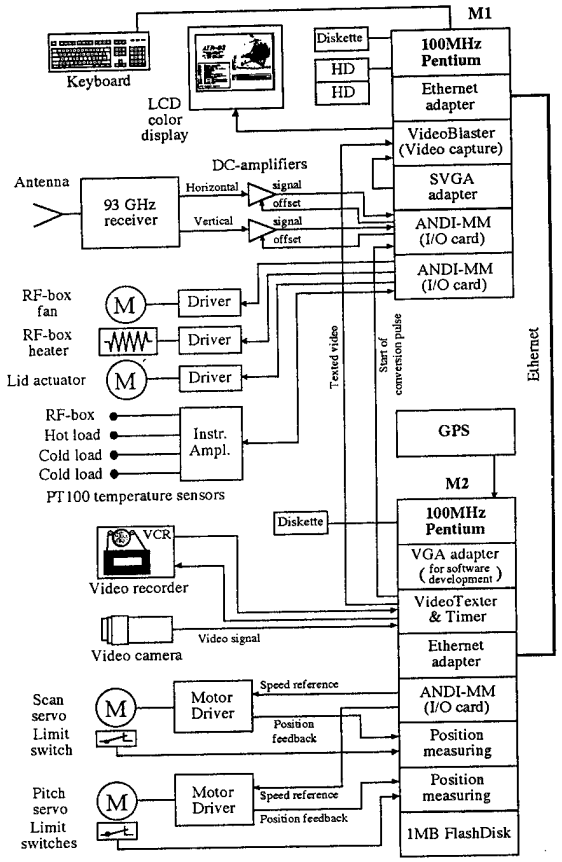


Fig.2 The upgraded AIR-93 system block diagram.

The architecture of the video texter and timer card has been simplified and improved: any graphics can be inserted and the video signal fidelity has been improved from fair to very good. In addition, the graphics grayscale can be stepless varied from white (forest scenes) to black (snow scenes) from the user interface. The electronics unit serviceability has also been improved by replacing the PC-104 card decks by ISA-cards, which are easy to access and can be removed separately for maintenance.

THE ACTIVE STABILIZATION SYSTEM

The purpose of the active stabilization system is to keep the radiometer's beam line-of sight correct despite platform angular motion. The AIR-93 was originally constructed for easy update of the active stabilization: the radiometer is gimballed by two servo drives (the scan and pitch motors), which can be programmed to follow a path that compensates for the platform's angular motion, excluding the residual tilt variation [6].

The necessary real-time gyro data is produced by a commercial attitude-GPS system that is being customized to provide 3-axis attitude and angular velocity data at a rate of 10 Hz at Stanford University [6], while the commercial version outputs 2 Hz attitude data only. The gyro data could also be generated by employing a 3-axis ring-laser gyro, but with 5-10× costs and drift problems. The attitude-GPS has no drift and is assumed to work well, because no banking is required during the straight measurement lines, ensuring full satellite visiblity and integer lock hold on the up-wing Skyvan airplane.

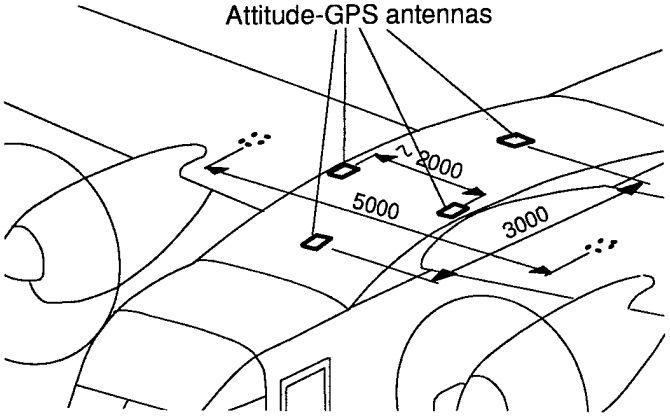


Fig.3 Attitude-GPS antennae accommodation on Skyvan.

The system will be activated as soon as the attitude-GPS is received, assembled and tested on the Skyvan, and AIR-93 servo control programs are supplemented with the compensation path computation formulas presented in [6].

THE AIRBORNE COLD CALIBRATION

The original version of the liquid nitrogen cooled, airborne cold calibration target [1] was tested aboard both helicopter and Skyvan platforms. However, the pressure feed system that was based on controlled evaporization of liquid nitrogen, was not found reliable. In addition, the matched teflon double window had to be warmed so intensively to

prevent moisture condensation that it raised the cold calibration load's apparent brightness temperature by up to 20 K (!). Moreover, the 2l dewar was found to be too small in airplane use, since liquid nitrogen vaporized and flowed all the time, although the heating was off, and could run out during taxi, waiting for takeoff and the transfer flight.

Fig.4 illustrates the new cold calibration target design that has been improved to avoid the previous defects: The liquid nitrogen is stored in a 5l dewar, and transferred by a submersible electrical pump that is put on about one minute before calibration. The pump is controlled according to the feedback of the two PT100 thermal sensors located on the absorber plate. Since the dewar is unpressurized and the fluid is transferred only when needed, it should last for hours. The teflon double-window is replaced by a foam lid that is quickly moved aside for the few seconds a calibration takes. Hence, the radiometer has a direct view of the impregnated absorption plate.

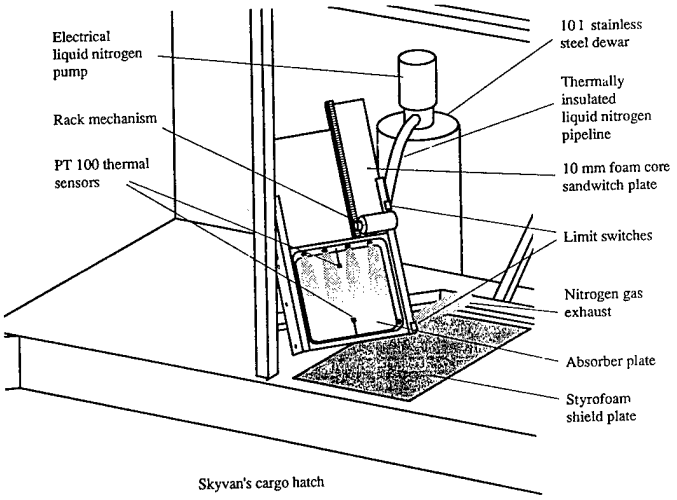


Fig.4 The improved cold calibration target concept.

THE OPTICAL COMPARISON IMAGE

Originally, the AIR-93 had a nadir-looking video camera for optical comparison image production. The video cross-track view angle was set equal to the radiometer swath. The video was recorded on a VHS tape for post processing, and the live video image was grabbed and displayed on the user interface along with the radiometer image for operation convenience. The post processing was performed by digitizing frames from the VHS tape and pasting the frames into a single image manually with the Showcase program. The technique involved a lot of slow manual work, had no position reference data, the frames themselves are slightly distorted, and the composed image may become rather distorted, depending on the platform perturbation.

These problems may be solved by using the video camera as a "line scanner": a cluster of ten middle lines of video image are digitized and stored on a disk each time the airplane has flown forward slightly less than the respective distance. The airplane position and attitude data are also written on the disk along with each cluster. By using these data and the optics across-track correction, it is possible to post-process a totally rectified, almost nondistorted reference image, whose pixel's coordinates are known. Fig.5 presents a test comparison of an original and a 10-line-scanned image that has also been digitized from VHS-tape, without the platform orientation data.

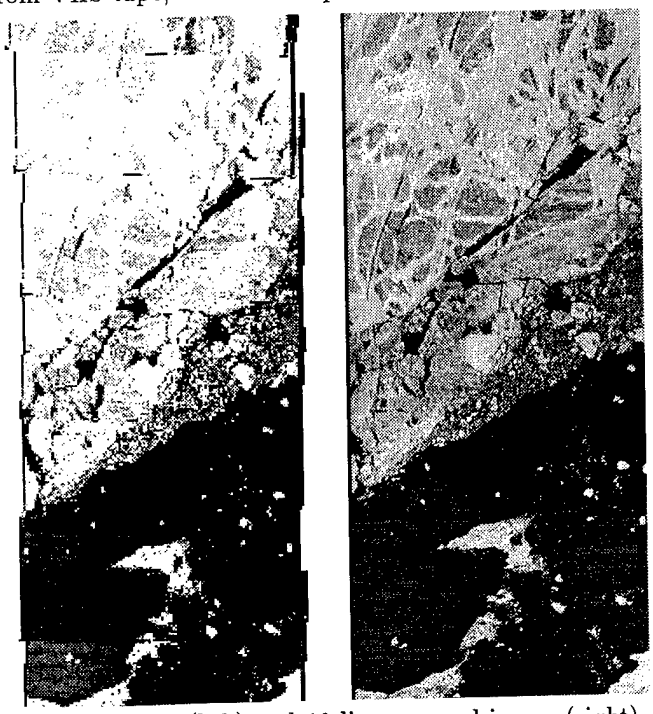


Fig.5 Original (left) and 10-line-scanned image (right).

REFERENCES

[1] M. Kemppinen, J. Pallonen, M. Hallikainen, "93 GHz Airborne Imaging Radiometer," Digest IGARSS'94, pp. 2243-2245, Pasadena, USA, August 1994.

[2] M. Kemppinen, J. Pallonen, E. Lantto, T. Auer, M. Hallikainen, "The first results of a novel 93 GHz airborne imaging radiometer," Digest IGARSS'95, pp. 1814-1816, Firenze, Italy, July 1995.

[3] M. Hallikainen, E. Attema, M. Wooding, "EMAC-95 Snow and Ice Airborne Campaign," Digest IGARSS'95, pp. 1811-1813, Firenze, Italy, July 1995.

[4] P.Y. Montgomery, H. Uematsu, B.W. Parkinson, "Analysis of Angular Velocity Determination Using GPS," Proceedings of ION conference, Salt Lake City, USA, September 1994.

[5] E.S. Haapala, "Position Dependent Control (PDC) of Plant Production," Doctor's thesis, Department of Agricultural Engineering and Household Technology, University of Helsinki, Finland, June 1995.

[6] E. Lantto, M. Kemppinen, "Kuvaavan radiometrin aktiivistabilointi," Teknillinen korkeakoulu, Avaruustekniikan laboratorio, raportti A13, huhtikuu 1993 (in Finnish)

A Low Range-Sidelobe Pulse Compression Technique for Spaceborne Rain Radar

Kenji Sato, Hiroshi Hanado, and Hiroshi Kumagai
Communications Research Laboratory
Hirai 893-1, Kashima-shi, Ibaraki-ken, 314, Japan
Phone : +81-299-7121, Fax : +81-299-7157, E-mail : satoken@crl.go.jp

ABSTRACT

A method using a digital-expansion and analog-compression technique for making a compressed pulse with a very low range-sidelobe level for future application to spaceborne rain radar is studied. In this method, the transmission signal which is modulated both in frequency and in amplitude is generated digitally, and the signal is compressed using a Surface Acoustic Wave Dispersive Delay Line. A range-sidelobe suppression of more than 60 dB is obtained in the calculation, and a 54 dB suppression is attained in test measurement.

INTRODUCTION

The significance of global scale rain measurement as an aid to better understanding of water cycles and climate change has been widely recognized. A spaceborne rain radar is the most attractive instrument for this purpose of the measurement. The TRMM (Tropical Rainfall Measuring Mission) is the first satellite to be equipped with the rain radar (PR : Precipitation Radar) and is scheduled to be launched in 1997. For future rain radar missions, however, further improvement is needed in radar performances. In particular, higher sensitivity and higher resolution are expected to achieve. One way for achieving these improvements is to apply the pulse compression technique to the spaceborne rain radar. There are some difficulties, however, in applying the pulse compression, the most serious one being the presence of the range-sidelobe produced in the compression. For downward looking rain radar, surface echoes are much stronger than light rain signals. Using the pulse compression technique for satelliteborne rain radar may cause the range-sidelobe echo from the surface to mask the rain echo near the surface. When a 14-GHz radar, which has the same frequency as the TRMM-PR is used, a range-sidelobe suppression of more than 60 dB from the mainlobe level is required to measure light rain [1]. The range-sidelobe suppression attained with conventional pulse compression techniques using a pair of SAW DDLs (Surface Acoustic Wave Dispersive Delay Line) is about 40 dB.

One potential method for achieving such a low range-sidelobe level in the pulse compression is to use a digital-expansion and analog-compression technique; the amplitude and/or frequency modulated signal is generated digitally in the transmission and the signal is compressed using a SAW DDL in the receiver as in the conventional method. Because a transmission signal waveform can be generated to correct undesirable defects in the SAW DDL used for the compression, a lower range-sidelobe level can be expected when using this system than when using a pair of SAW DDLs. In this system, data processing is simple and easily completed in real time. This is important especially for spaceborne radar systems.

CALCULATION OF TRANSMISSION SIGNAL

In the digital-expansion and analog-compression system, the most important thing is to determine the transmission signal waveform. When the Fourie transforms of the transmission signal waveform $x(t)$ and the SAW DDL forward transfer response $h(t)$ are denoted as $X(f)$ and $H(f)$ respectively, the spectrum of the compressed pulse $Y(f)$ is expressed as

$$Y(f) = H(f) \cdot X(f). \quad (1)$$

In the digital-expansion and analog-compression case, $H(f)$ is a fixed function representing the response of the SAW DDL used at the receiver. If an output signal waveform $y(t)$ or its spectrum $Y(f)$ is given, $X(f)$ is derived from (1). Therefore the problem is to obtain the optimum $X(f)$ under given $H(f)$ and a target of $Y(f)$.

The test measurement is made using a SAW DDL with a center frequency of 30.5 MHz and bandwidth of 2 MHz. The 3-term Blackman Harris window function [2] is used as a spectrum of the compressed target waveform $Y(f)$ as

0-7803-3068-4/96$5.00©1996 IEEE

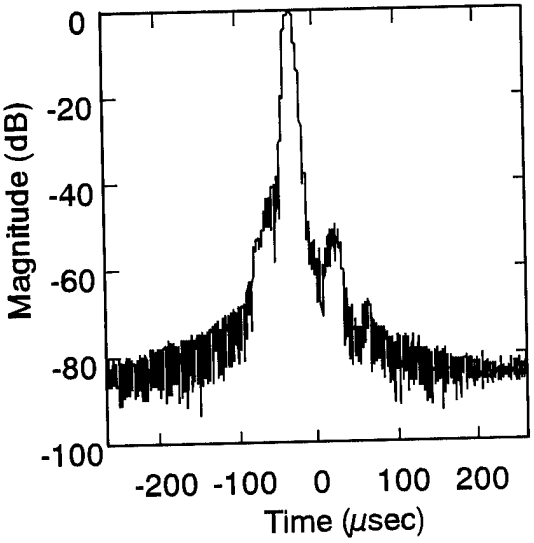


Fig. 1. Transmission signal waveform obtained from calculation using forward transfer function of SAW DDL and a target compressed pulse.

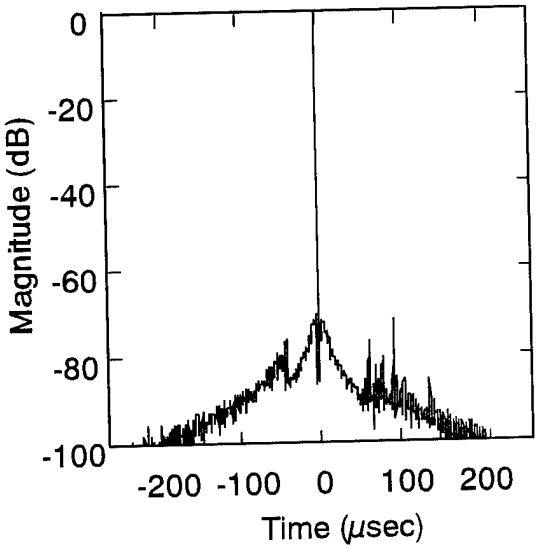


Fig. 2. Compressed pulse obtained from calculation when a time-gate is applied to the signal between -79 μsec and 37 μsec in Fig. 1.

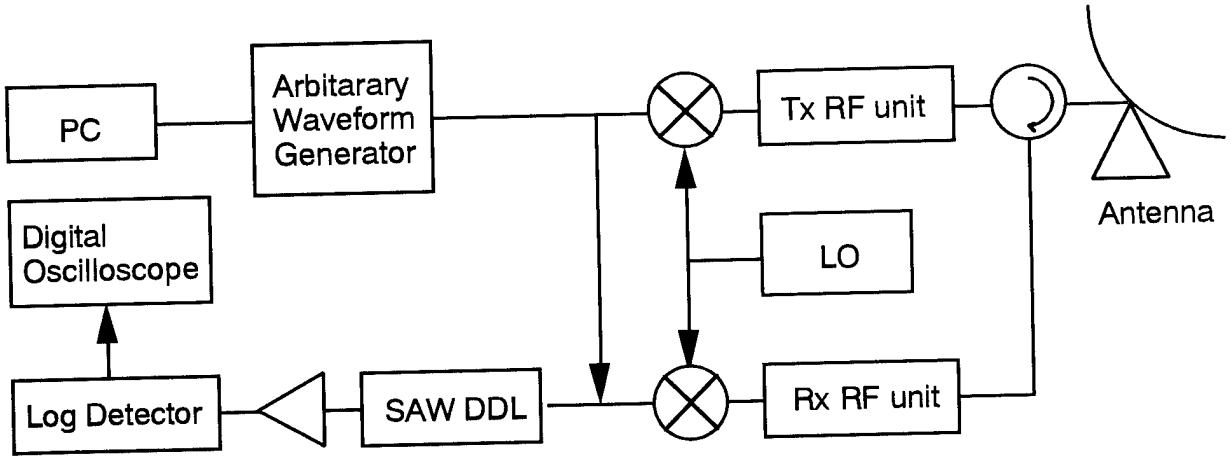


Fig. 3. Block diagram of experimental circuit.

$$Y(f) = a_0 + a_1 \cdot \cos\left[\frac{2\pi(f - f_0)}{B}\right] + a_2 \cdot \cos\left[\frac{4\pi(f - f_0)}{B}\right] \quad (2)$$

when $a_0 = 0.42323$, $a_1 = 0.44755$, $a_2 = 0.07922$.

Though this function has a very simple form, it gives a low enough sidelobe level. In this experiment, the center frequency f_0 is set to 30.5 MHz and the bandwidth B is set to 2.0 MHz.

The calculated transmission signal is shown in Fig. 1. The transmission signal is modulated not only in frequency but also in amplitude, and its pulse width is 9.1 μsec. To send this signal as the radar transmission, a time-gate with a finite length is applied.

Figure 2 shows a calculated compressed signal y(t) under x(t) with a time-gate applied between -79 μsec and 37 μsec in Fig. 1. A compressed pulse with a 70-dB range-sidelobe suppression and a pulse width of 0.8 μsec is obtained (Fig. 2).

RESULTS OF TEST MEASUREMENT

Measurements are taken using a hardware test set to confirm the calculation results. Fig. 3 is a block diagram of the test set. The transmission pulse is generated by an Arbitrary Waveform Generator (AWG) with a 250-MHz clock rate and 12-bits accuracy. The measurement result is shown in Fig. 4 together with the calculated one. In this measurement, the RF unit is not connected but the output of the AWG is hooked directly up the SAW DDL. The figure shows that a range-sidelobe suppression of about 54 dB is attained. There are some discrepancies between the calculated result and the measured one. The range-sidelobe level near mainlobe is higher for the measured pulse than for the calculated one. Insufficient dynamic range and non-linearity in the test circuit are possible causes of this discrepancy. The measured results also show a broad peak at around -30 μsec. This is due to the feed-through effect, which is one of the defects of the SAW DDL. Ideally, this broad peak should be canceled because the input signal contains the component to compensate for the feed-through effect. Although, this cancellation does not work completely. One of possible reasons of this discrepancy is that the transient response of the SAW DDL may cause non-negligible effect in this case. The transient response has not been evaluated enough in our measurement using a network analyzer.

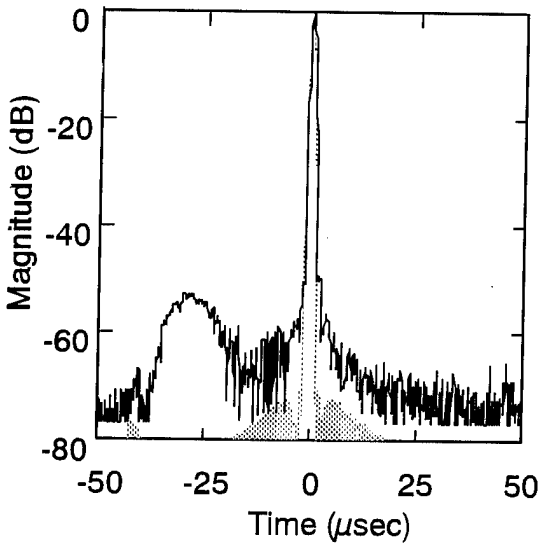


Fig. 4. Compressed pulse (solid line) obtained from measurement using a hardware test set and calculated compressed pulse (dotted line)

CONCLUSION

By calculation, it is shown that enough range-sidelobe suppression can be obtained with the digital-expansion and analog-compression technique. In the test measurement, a 54 -dB sidelobe suppression is attained, although the theoretical calculation marks 70-dB suppression. The possible causes of the discrepancy between the calculation and experiment are transient response effect of the SAW DDL, along with insufficient dynamic range and non-linearity in the test circuit. In this measurement, the transmission signal is optimized to the frequency response of the SAW DDL only. So, better results will be obtained if the transmission signal is optimized to the response of all the receiving system.

Hereafter, the influence of doppler shift to the range-sidelobe level should be studied and the measurement using a radar system including RF unit will be carried out.

REFERENCES

[1] T. Ihara and K. Nakamura, "A Feasibility Study of Rain Radar for the Tropical Rainfall Measuring Mission: 4. A Discussion of Pulse Compression and Adaptive Scanning", J. Commun. Res. Lab., vol. 35, No 145, pp. 149-161, 1988.

[2] F. J. Harris, "On the Use of Windows for the Harmonic Analysis with Discrete Fourie Transform", Proc. IEEE, vol. 66, No. 1, pp. 51-83, 1978.

Pulse compression with -65 dB sidelobe level for a spaceborne meteorological radar

N. Vincent, J. Richard, N. Suinot

ALCATEL ESPACE, 26 av J.F Champollion, 31037 Toulouse Cedex, FRANCE
Phone : (33) 61 19 52 25, Fax : (33) 61 19 61 63, E-Mail : FRDK8N58@IBMMAIL.COM

M. Yarwood, C. Mavrocordatos

ESA-ESTEC, 2200 AG Noordwijk, THE NETHERLANDS
Phone : (31) 71 56 5 40 52, Fax : (31) 71 56 5 45 96

ABSTRACT

With a breadboard activity, funded by ESA, ALCATEL ESPACE associated with four other European companies, demonstrates the feasibility of an all digital generation and compression system, operating in real time and meeting range sidelobes of the compressed pulse lower than -65 dB despite a low pulse bandwidth x pulse duration product.
Chosen pulse compression technique consists in a frequency domain processing taking into account distortions due mainly to IF filters and non linear behavior of the HPA by the implementation of an automatic compensation procedure. After a complete description of the processing technique and the breadboard, this paper presents achieved performances in particular in presence of severe non linear distortions, sinusoidal amplitude and phase ripples.

1. INTRODUCTION

Pulse compression technique is well known for reducing the RF peak power needed by a conventional short pulse radar to meet a given signal to noise ratio which relaxes HPA criticality. In addition, its possible finer range resolution potentially increases the number of independent samples available for a given dwell time which improves the rain rate estimate.

Anyway, in case of spaceborne rain radar, to prevent surface clutter from interfering and obscuring the return from the precipitation field, the range sidelobe level (SLL) of the compressed pulse must be at least lower than -55 to -60 dB which is a big challenge.

The Rain Radar Test Bed demonstrates the feasibility of an all digital generation and compression system, meeting all the requirements as shown in Table 1 and operating at real time. This breadboard has been manufactured by ALCATEL ESPACE associated with four other European companies, and has been funded by ESA.

0-7803-3068-4/96$5.00©1996 IEEE

PARAMETER	REQUIRED	ACHIEVED
Pulse bandwidth	4.5 MHz	4.5 MHz
Pulse duration	< 60 µs	60 µs
PRF	2500 Hz	2500 Hz
Acquisition window	250 µs	256 µs
Doppler spread	+/- 4 kHz	> +/- 4 kHz
Dynamic range	55 dB	~ 60 dB
Compressed pulse response SLL	< - 60 dB	< - 65 dB

***Table 1** : Breadboard requirements and performances*

The implemented compression technique fits with the three different rain radar concepts [1] that are :

- Single Beam Single Frequency (SBSF) at Ku-band,
- Single Beam Dual Frequency (SBDF) at Ku & K-bands,
- Dual Beam Single Frequency (DBSF) at K-band.

2. PULSE WAVEFORM

The determination of the pulse and replica waveforms is preponderant to achieve such a high sidelobe level of the compressed pulse.
Indeed, the weighted linear FM chirp is not adequate because with a 270 (bandwidth . time) product, the Fresnel sidelobes are close to -52 dB [2].
Regarding the full Doppler spread and the HPA saturated operating mode, none phase code gives acceptable performances.
A broken line FM transmit pulse as described in Figure 1 was then selected associated with an optimized replica, computed by the Test Bed in order to take into account distortions due mainly to IF filters and non linear behavior of the HPA. That automatic compensation procedure (ALCATEL ESPACE's patent) enables to relax the radar sensitivity to realistic level of radar hardware distortions.

3. BREADBOARD ARCHITECTURE

The breadboard block diagram is described in Figure 2 as well as main sub-system features. The overall architecture is composed of the five following units :

(i) a Digital Waveform Generation unit (DWG) generates the selected pulse directly at 5 MHz.

(ii) a Digital Waveform Compression unit (DWC) performs the Analog to Digital Conversion, baseband demodulation and pulse compression.

(iii) an Analog Interface unit (ANI) represents the first conversion stage of the radar transmit/receive chains.

(iv) a Distortion unit implemented between 65 MHz ports of the ANI simulates typical distortions and enables to assess the breadboard sensitivity to applied errors.

(v) a Test Bed manages breadboard operation, computes sidelobe ratio and range resolution of the compressed response and displays test results.

The DWG unit is composed of a RAM, a high accuracy Digital to Analog converter and an anti-aliasing filter. An interface module ensures the link with the Test Bed which computes and downloads the waveform in the RAM.

After up-conversion (from 5 to 65 MHz), various types of distortions can be applied on the transmitted pulse : sinusoidal amplitude/phase ripple whose characteristics (amplitude, frequency and start phase) are programmable by external waveform generators, and non linear distortions with AM/AM and AM/PM levels respectively equal to 0.1 dB/dB and 3.5 deg/dB.

The down-converted pulse directly at 5 MHz is fed into compression unit where it is digitized with a high accuracy analog to digital converter, demodulated in I and Q all digitally, filtered for noise reduction and decimated to an appropriate sampling frequency.

At this point samples are either transmitted to the Test Bed for replica computation or compressed in real time by frequency domain multiplication with spectral replica, using 2048-point FFT/inverse FFT functions.

The compressed data are then acquired by the Test Bed for averaging and computation of the range resolution and side-lobe level.

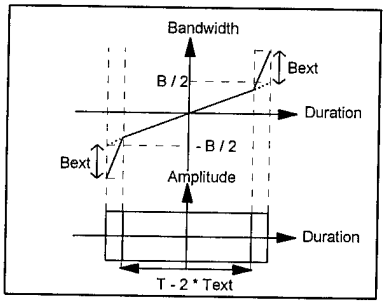


Figure 1 : Pulse waveform

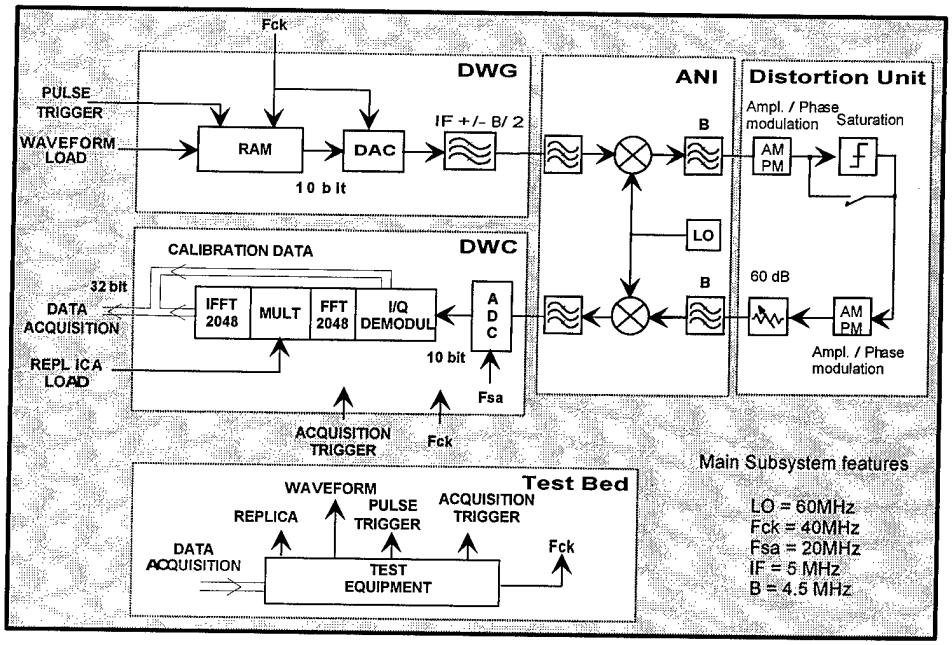


Figure 2 : Breadboard architecture

4. BREADBOARD PERFORMANCES

The following table 2 summarizes a set of typical achieved SLL performances as a result of severe applied distortions. In order to demonstrate the efficiency of the implemented compression procedure, two replicas are considered : a **fixed replica** defined as a Taylor weighted chirp with an opposite slope and an **optimized replica** computed by the Test Bed from the distorted calibration pulse. Given values correspond to a peak value of sidelobe and not to a SLL mean value which is more restricting [3].

APPLIED DISTORTION	SLL with fixed replica	SLL with optimized replica
None	- 58 dBc	- 67 dBc
Amplitude ripple :		
* 0.4 dB pp / 6 periods	- 38 dBc	- 67 dBc
* 2 dB pp / 10 periods	- 24 dBc	- 65 dBc
Phase ripple :		
* 28 deg pp over 7 periods	- 18 dBc	- 63 dBc
* 45 deg pp over 4 periods	- 15 dBc	-66 dBc
Non linear distortion :AM/AM : 0.1 dB/dB & AM/PM : 3.5 deg/dB	- 39 dBc	- 63 dBc

***Table 2** :Measured SLL with different applied errors*

The degradation of the range resolution is very weak, lower than 15 %. In addition, it can be noticed that the optimization of the replica is still effective when the calibration pulse is located at a different position within the acquisition window, than the pulse to be compressed.

As an example, compressed pulse responses in presence of 2 dB peak to peak amplitude ripple over 10 periods are plotted in figure 3 with fixed replica (left) and optimized replica (right).

5. CONCLUSION

This breadboard shows that a -60 dB SLL of the compressed pulse can be met with a large margin despite very pessimistic applied errors. A lower SLL could probably be reached with the proposed procedure but improvements must be performed mainly in terms of ADC number of bits, local oscillator stability and computation noise.

In addition, it would be interesting to determine the impacts of the uncalibrated paths in a realistic spaceborne radar chain as well as the different phenomena which are not taken into account in the existing breadboard.

Such improvement analysis as well as the study of the integration of the generation/compression boards are the objectives of a study, founded by ESA and presently in progress.

6. REFERENCES

[1] J. Testud, P. Amayenc, M. Marzoug, « Rainfall Retrieval from a Spaceborne Radar : comparison between single-frequency, dual-frequency and dual-beam techniques », American Meteorological Society, 1992, Vol.9, p.599.

[2] H. D. Griffiths, L. Vinagre, « Design of low-sidelobe pulse compression waveforms », Electronics letters, June 1994, Vol. 30, n°12.

[3] N. Vincent, J. Richard, N. Suinot, « Very low sidelobe level pulse compression for rain radar », Proc. Europto 1995, Vol. 2584, pp 474-483.

7. ACKNOWLEDGMENTS

This work has been supported by the European Space Agency under contract no. 10002/92/NL/PB. We would like to express our thanks to Mr. P. L. Mancini, M. Yarwood and D. Maccoll of ESTEC.

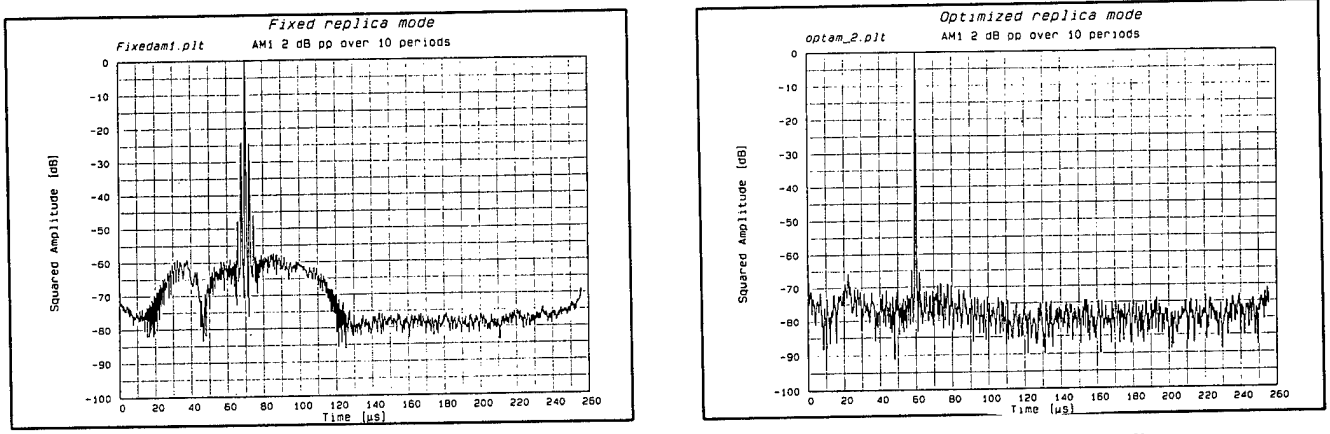


***Figure 3**: Example of breadboard measurement with fixed (left) and optimized (right) replicas*

A SAR antenna calibration method

David Stevens, Peter Bird, Gordon Keyte.
Remote Sensing Section, DRA Farnborough.
Rm 106, R16 Bldg, DRA Farnborough, Farnborough, Hants, GU14 6TD, England.
Tel: +44 (0)1252 394837 Fax:+44 (0)1252 372982 email: dradas@scs.dra.hmg.gb

Abstract -- Corner reflector targets have been used to calibrate ERS-1 and ERS-2's SAR antenna. The analysis method permits resolution of the sources of variation in reflector backscatter into components by considering the different dimensions in the data. This results in the antenna gain pattern; temporal calibration constant series; calibration target differences; and a pure error term. The pure error term may be further reduced into fluctuations from targets, clutter effects, and spatial variations.

The regressional model adopted allows the calculation of a standard deviation in the antenna gain pattern. This was found to be of the order of 0.1dB. t- and χ^2-statistics have been devised to compare the antenna gain pattern with ESA's pattern derived from homogeneous distributed targets.

Analysis during ERS-1's geodetic phase implied that there were significant differences between day time and night time antenna gain patterns. A rms difference of 0.17dB was found. This result has not been confirmed during ERS-2's commissioning phase and a possible explanation has been developed.

INTRODUCTION

SAR systems have found many applications from crop monitoring to digital elevation models. These all require calibrated images and an understanding of the sources of SAR system variation.

ESA's approach to image calibration for its ERS satellites is twofold: distributed homogeneous targets (Amazon rainforest) for the antenna gain calibration; and transponders (Flevoland) for absolute calibration [1]. Here we describe a method using a set of point targets. This allows both antenna gain and absolute calibration, and, with a dataset from a few months, gives values for the system's stability within an image and over time.

METHOD

Eleven 2.57m trihedral corner reflectors [2], spaced evenly across the swath, were used to calibrate the ERS-1 and ERS-2 SARs. Data were taken from 21 passes of ERS-1's geodetic phase and 19 passes of ERS-2's commissioning phase. The commissioning phase dataset was reduced to 12 passes because the amplifier gain was changed on 13 July 1995.

The raw SAR data were processed using DRA Farnborough's Low-Cost SAR Processor. The standard ESA PRI (3-look) specification was used but the images were not calibrated for antenna gain pattern. The integrated target power (ITP) [3] was evaluated for each target using an integration area of 9×9 pixels. A background clutter correction was made from neighbouring pixels. A correction for the effect of ADC saturation [4] was made [5]. Data with ADC saturation corrections greater than 0.5dB were discarded.

The corrected ITP measurements (in dB), y_{ij}, may be written as a function of look angle, x_{ij}, reflector cross section, μ_j, and a pure error term, ε_{ij},

$$y_{ij} = P_n\left(x_{ij}\right) + \mu_j + \varepsilon_{ij}, \qquad (1)$$

where the suffixes i and j denote pass number and reflector number respectively and $P_n(x_{ij})$ is an n^{th} order polynomial (Taylor series expansion). A linear regression for the polynomial coefficients of $P_n(x_{ij})$ is used with the added constraint,

$$\sum_j \frac{\mu_j}{n_j} = \overline{\mu}, \qquad (2)$$

where n_j is the number of measurements of the j^{th} reflector and $\overline{\mu}$ is the known mean reflector signature.

The radar cross sections are included in the regression. This removes 1 degree of freedom for each cross section from the dataset. The total variance is

$$\sigma^2_{total} = \frac{1}{\mathrm{df}} \sum_{ij} \varepsilon^2_{ij}, \qquad (3)$$

where **df** is the number of degrees of freedom.

This may be broken down into components from target variation, clutter, temporal variation and spatial variation. Target variation is estimated from simultaneous measurements of pairs of targets at the same site. The uncertainty in the clutter correction is found from the

0-7803-3068-4/96$5.00©1996 IEEE

background clutter measurements. The rest of the total variance must be from the SAR system. This is divided into temporal and spatial components.

Diagonalising the variance-covariance matrix of the regression [6] transforms the Taylor series into an expansion in orthogonal polynomials. The diagonal elements of the resulting matrix are the variances of the transformed polynomial coefficients. This leads to an error on the polynomial and permits a confidence test of a second polynomial (ESA's calibration curve [1]) using the t- and χ^2-statistics. The following hypotheses may be tested:

H_0: Polynomial A is the same as polynomial B to within experimental error.

H_1: Polynomial A is significantly different from polynomial B.

RESULTS

Table 1 shows the values of the sources of error. Each category was calculated for each dataset. Spatial and temporal categories are dependent on the SAR system; target and clutter categories are not. This assertion is supported since spatial and temporal categories were different for each sensor but target and clutter variations showed little change.

Figure 1 is the antenna gain pattern for ERS-2 (solid line). The points are data values and the dotted line is ESA's calibration curve for ERS-2. The antenna gain pattern's standard error is shown in Figure 2. Over most of the swath, the error is less than 0.07dB.

Table 2 shows the confidence tests. The statistics' values at the 95% confidence level are also shown. Two of the results show significance at the 95% level; the rest all support the null hypothesis.

The two significant results are for the ascending dataset for each sensor. For ERS-1 the result is extremely significant. This implies the antenna gain pattern cycles daily. This is not believed to be true. An explanation is developed in the discussion.

Table 1: Sources of error

	ERS-1	ERS-2
Period	1/5/94 - 13/2/95	19/7/95 - 27/9/95
Data	131	85
Target/dB	0.17	0.17
Clutter/dB	0.05	0.04
Temporal/dB	0.07	0.15
Spatial/dB	0.10	0.24
Total/dB	0.21	0.33

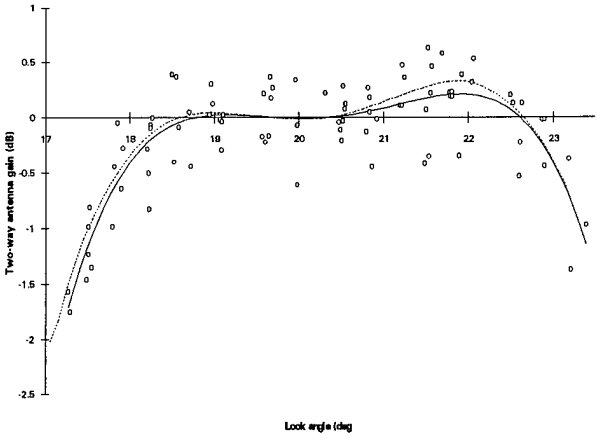


Figure 1: ERS-2's antenna gain pattern

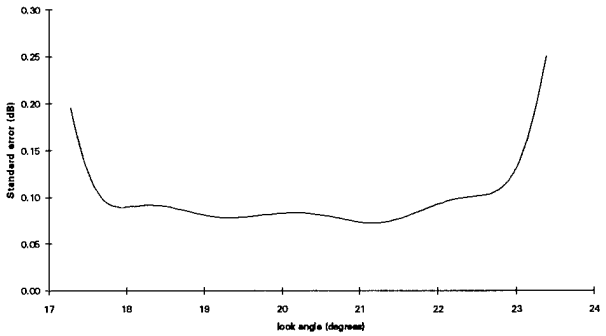


Figure 2: ERS-2's antenna gain pattern standard error

Table 2: Confidence tests applied to ESA's calibration curve

		data	t	chi-squared
ERS-1	95% level	--	2.45	14.07
	all	131	-0.71	7.84
	ascending	62	0.04	23.69
	descending	69	-0.56	7.76
ERS-2	95% level	--	2.78	11.10
	all	85	-1.23	6.54
	ascending	33	-1.79	11.63
	descending	52	0.15	4.90

DISCUSSION

This analysis reveals the sources of error from a SAR image measurement. They are:

- target related variations;
- system related errors.

The system related errors may be divided into spatial and temporal components. These components may be used to decide which errors are present in any set of measurements. For example, a pair of measurements which are *close* in the same image will not be subject to the same errors that a pair *from different images* are. A pair *separated* in the same image will suffer from a different level of error.

How to interpret the word 'close' in the above is not clear. Two measurements from the same field (100m) are 'close' (this was presumed when calculating the target fluctuations) but two measurements from neighbouring calibration sites (10km) are not.

The results of the confidence tests need some attention. Most of the results are not significant. This means that our antenna gain pattern is in agreement with ESA's calibration curve. There are two results which are significant. The ascending pattern for ERS-1 shows extreme significance for the χ^2-test. A possible explanation has been developed. It was discovered that the ascending azimuthal alignment of a few of the reflectors was in error by a few degrees. This leads to a minor attenuation but also to a systematic variation of cross section as a function of azimuth. Since it is known that the azimuthal angle subtended is a monotonic function of look angle this will lead to a slight systematic ramping of the antenna gain pattern. A significance test might detect this. Between the ERS-1 and ERS-2 datasets, the alignment method was modified so that it is to better than 1° in azimuth.

The second significant result is for ERS-2's ascending dataset. Misalignment may be ruled out. It is more likely that the dataset is too small for this kind of analysis. To apply the χ^2-test, the variance of the dataset must be known accurately. There are 33 samples, and 15 degrees of freedom are removed by the analysis (11 reflector cross sections, 5 polynomial coefficients and one constraint). So 18 degrees of freedom remain. Inaccurate knowledge of the variance leads to an uncertainty in the χ^2-statistic.

REFERENCES

[1] J. E. Laycock, H. Laur, "ERS-1 SAR Antenna Pattern Estimation," ESA Report ES-TN-DPE-OM-JL01, Issue 1, Rev. 1, September 1994.

[2] P. J. Bird, G. E. Keyte, D. R. D. Kenward, "An Experiment for the Radiometric Calibration of the ERS-1 SAR", Proceedings of the First ERS-1 Symposium, Vol. 1, pp 195-200, November 1992

[3] A. Laurence Gray, Paris W. Vachon, Charles E. Livingstone, Tom I. Lukowski, "Synthetic Aperture Radar Calibration Using Reference Reflectors," IEE Transactions on Geoscience and Remote Sensing, Vol. 28, No. 3, May 1990.

[4] H. Laur, J. Sanchez, E. Dwyer, P. Meadows, "ERS-1 SAR Radiometric Calibration," CEOS SAR Calibration Workshop, ESA/ESTEC, September 1993.

[5] Phoenix Systems, "LCSP Proposals for Modifications in Support of Improved Data Quality Control", EDS Document ESD/310814/WP0110/3, Issue 1.1, October 1993.

[6] N. Draper, H. Smith, "Applied Regression Analysis, Second Edition," John Wiley & Sons.

© British Crown copyright 1996/DRA
Published with the permission of the Controller of Her Majesty's Stationary Office

Inflight Vertical Antenna Patterns for SIR-C from Amazon Rain-Forest Observations

Yujun Fang and Richard K. Moore
University of Kansas, Radar Systems and Remote Sensing Laboratory
2291 Irving Hill Road, Lawrence, KS 66045-2969, USA
TEL: 913/864-4836 , FAX: 913/864-7789 , E-mail: rmoore@eecs.ukans.edu

Abstract—We measured the vertical pattern of the Shuttle Imaging Radar C (SIR-C) antenna using images of the Amazon rain forest, the largest flat and homogeneous forest in the world. Its scattering coefficient is nearly independent of the incidence angle [1,2]. The images produced by JPL use the standard SIR-C CEOS format. We must use images without radiometric correction to get the antenna pattern, as the radiometric correction depends on preflight patterns. We can only give a small sample of the patterns for the SIR-C antenna in this paper, as the number of Amazon passes was limited, and only a few of the many modes were available. For both L band and C band all possible linear polarizations could be used. In addition, electronic beam steering up to ±20° from the boresight direction [3] could modify the patterns. Also nine "beam spoiling" modes could change the patterns. We previously reported on the SIR-B [4] and X-SAR patterns [5] obtained by the same method.

If all modes had been tested over the Amazon or some other suitable homogenous area, we would have been able to give details of all patterns. Unfortunately the number of passes over suitable areas was very limited, so we can only report on those passes.

IMAGE SELECTION

Regions with homogeneous scattering coefficient can be used to extract the vertical antenna pattern of the antenna. Patterns presented here are from images collected during the first SIR-C/X-SAR mission in April, 1994, from passes 39.60, 55.62, 78.60 and 103.60. We removed segments showing evidence of hills or extensive water areas before processing for the antenna pattern. Table 1 summarizes the image data used.

Table 1. Summary of Image Data Used

Product ID	Data Take ID	Site Name	Latitude	Longitude	Inc. Ang.	Beam Spoiling Mode	Beam Steering Angle
11,389	39.6	Amazon C.	S 0°-32'	W 70°-12'	44.0°	0	2.2°
11,390	39.6	Amazon C.	S 2°-40'	W 68°-24'	44.0°	0	2.1°
11,342	55.62	Amazon Cal.	N 0°-41'	W 69°-19'	26.3°	0	14.7°
12,347	78.6	Amazon Cal.	S 8°-10'	W 62°-26'	29.8°	6	11.3°
12,348	78.6	Amazon Cal.	S 7°-22'	W 61°-58'	29.8°	6	11.3°
12,092	103.6	Sena Madureira	S 21°-20'	W 60°-48'	48.7°	0	6.4°
12,093	103.6	Sena Madureira	S 21°-20'	W 60°-48'	48.7°	0	6.4°

Latitude, longitude and incidence angle are defined at the center of the image.

METHODOLOGY

We first averaged in both along- and across-flight directions by using a suitable window to reduce the effect of fading. Then we applied the preflight correction before making a histogram of the pixel values of the images to determine outliers. The outliers are either very weak (water) or very strong (some man-made objects) and thus should not be used. We define an outlier as a signal level outside a region bounded by the 1% levels on the main peak of the probability density function (27 dB in Fig. 2). Only homogeneous sections are used in the later averaging process. The next step is to undo the radiometric correction. This was easy because the radiometric corrections are provided in a table in the header of the image tape. Finally, we averaged the return powers along the flight lines (excluding outliers). Each line of the output image then becomes a single value corresponding to a particular range.

The radar equation may be simplified to

$$P_r = \frac{KG^2\sigma^0}{R^3\sin\theta} \tag{1}$$

where

G = Antenna Gain
σ^0 = Scattering Coefficient
R = Slant Range
θ = Angle of Incidence
P_r = Return Power from the Target.

K is a constant containing all other factors that do not vary for the system. We may solve this equation for G to obtain the pattern from the measured power.

Shimada and Freeman [6] suggested that additive noise should be included in the radar equation (which tends to narrow the retrieved beamwidth). However, the high SNR of the images we used (over 20 dB in most cases) made this unnecessary. Since the scattering coefficient does not vary significantly with angle over the rain forest, the only variables we need consider are R, θ, and P_r. Using this concept, we obtain an antenna-gain pattern for each image. Finally, we fit a smooth function [i.e., $\cos^b(c_L)$ where b and c are fitting parameters] to the resulting relative vertical antenna pattern $G_{(L)}$. From that function, we are able to calculate the 6-dB elevation beamwidth of the antenna.

RESULTS

Figure 1 shows the histogram of the pixel power return of image 78.60 after averaging to get a square pixel of about 200

0-7803-3068-4/96$5.00©1996 IEEE

x 200 m. The outlier returns caused by the river and possible man-made objects show clearly on the histogram. We discarded these portions of the image in obtaining the pattern. Histograms for other images are similar to the one shown.

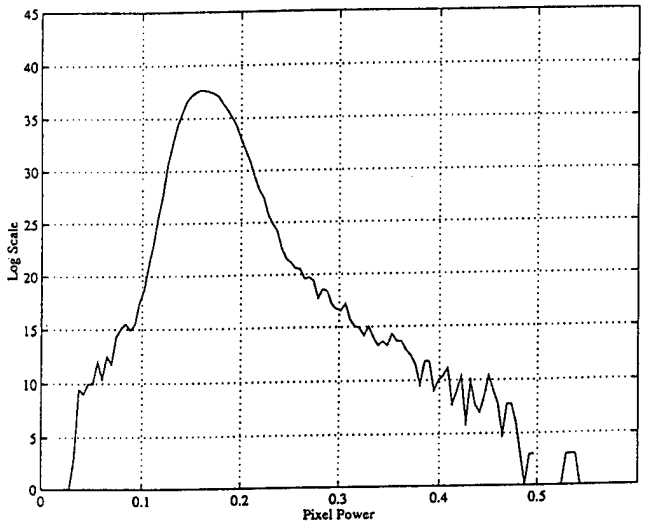


Fig. 1. The histogram of the images after being averaged by using 16 x 16 (200- x 200-m) windows. From the histogram, we can clearly see the outliers and thus are able to determine the upper and lower boundaries for the outlier returns.

We used this technique to obtain the vertical antenna patterns for four scenes from the Amazon forest and then smoothed the patterns by fitting models to them. Three models tested are:

A) $G(\phi) = d \cos^b(c(\phi-a))$

B) $G(\phi) = b + c(\phi-a)^2$ and

C) $G(\phi) = b + c(\phi-a)^2 + d(\phi-a)^4$

Model C was used by [6]. We used a least-squares method to fit these functions to the measured pattern. For pass 103.60, product 12093, the results appear in Fig. 2. Model B (quadratic function) is too inflexible to cover all of the pattern shapes. Model C (quartic without the odd terms) fits reasonably well within the data region, but is unrealistic beyond the data points. Various experiments show that model A can fit most of the antenna patterns we encountered and works well both inside and outside the data region. Table 2 shows the fits and rms deviations for the three models.

Table 2. Fitting Results for Product 12903

Antenna Pattern Model		Beamwidth (degrees)	Error RMS Deviation	
			vertical (dB)	horizontal (deg)
$d\cos^b(c(-a))$	3-dB down	3.42	0.01	0.01
	6-dB down	4.85	0.01	0.02
$b + c(-a)^2$	3-dB down	4.44	0.91	0.46
	6-dB down	5.26	0.84	0.39
$b + c(-a)^2 + d(-a)^4$	3-dB down	3.57	0.06	0.03
	6-dB down	4.79	0.05	0.04

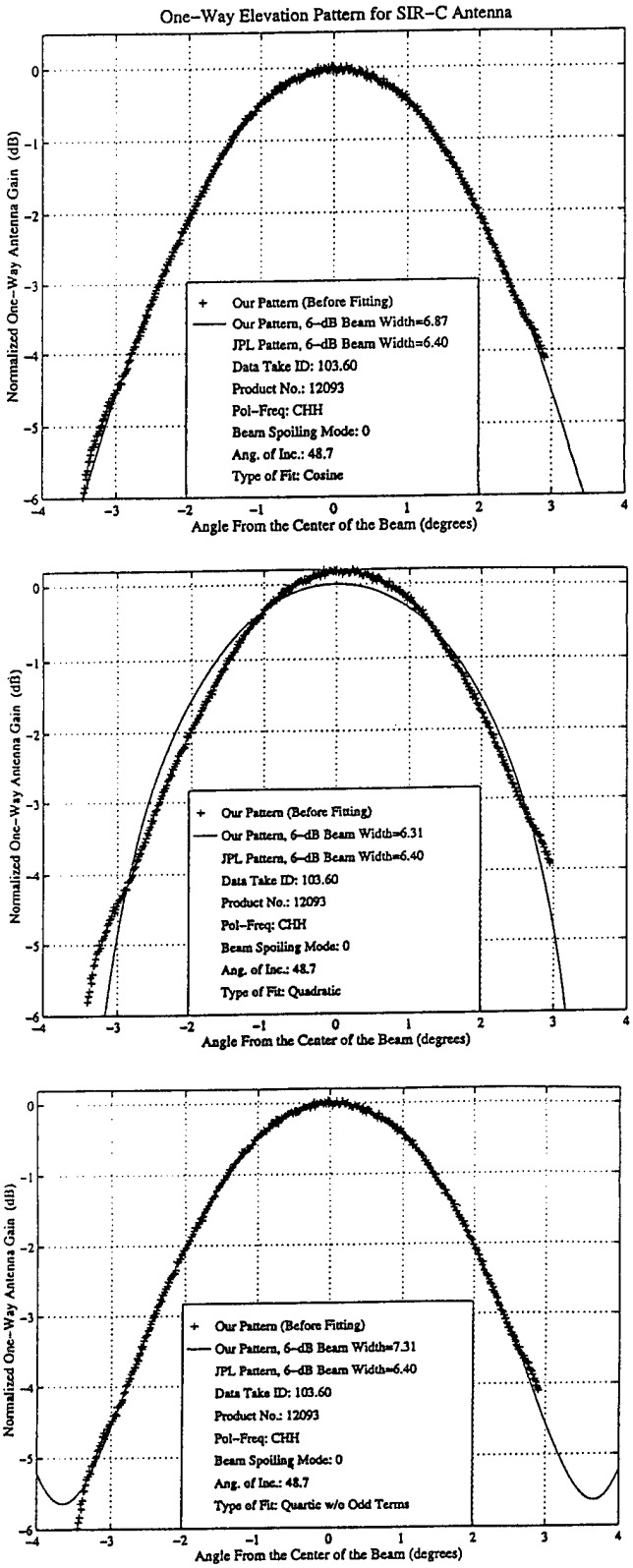


Fig. 2. Resulting patterns for prod. 12093 by using 3 different fitting models. The fitting models used are (a) cosine function, (b) quadratic function and (c) quartic function.

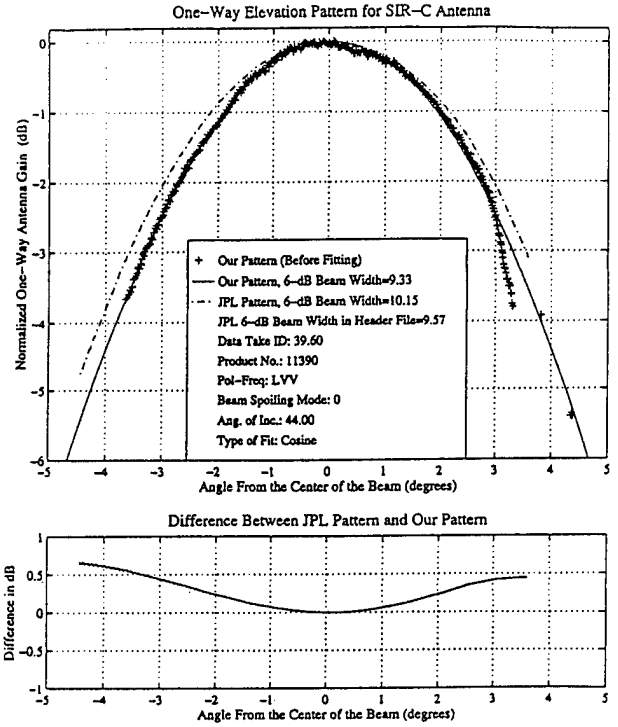


Fig. 3. Example of the composite plots for two-way relative elevation antenna patterns extracted from SIR-C images, no beam spoiling.

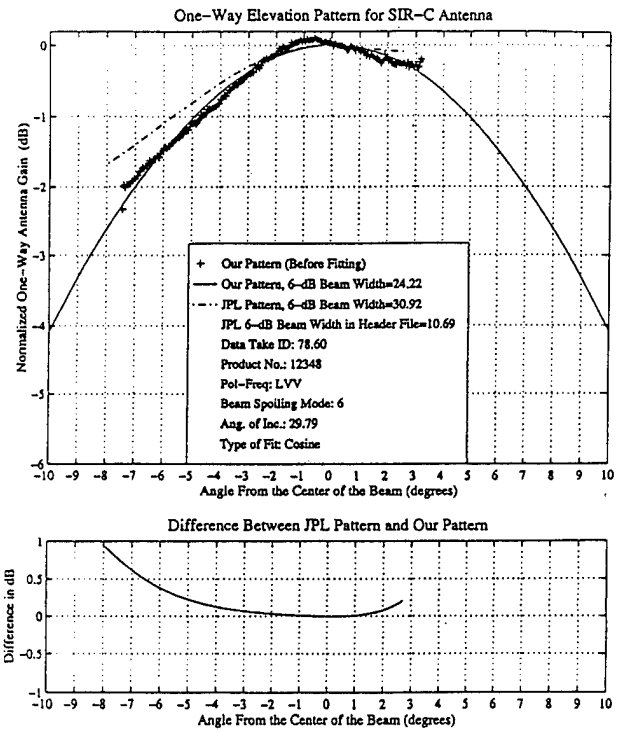


Fig. 4. Example of the composite plots for 2-way relative elevation antenna patterns extracted from SIR-C image, Mode 6 beam spoiling.

The overall results are shown in Fig. 3 for Data Take 39.60, L band, Product 11390. In this case, our pattern and the preflight pattern agree reasonably well. Fig. 4 shows a case where beam spoiling Mode 6 was used (Pass 78.60, Product 12348). In this case the results differ significantly between the measured pattern from the Amazon, the preflight JPL pattern, and the beamwidth shown on the header. Overall results for all passes used are summarized in Table 3. Without beam spoiling our pattern and the JPL preflight pattern (extracted from the radiometric correction table) agree reasonably well. However the difference is large for the beam-spoiling modes, such as mode 6 (in some cases it can be as big as 1 dB beyond 3° from the center of the beam). This result confirms that the radiometric calibration provided with the images can give a relatively large error when the 6-dB beamwidth exceeds 17° [7]. Moreover, the beamwidths given in the tape header are often significantly differently than the beamwidths extracted from the radiometric correction table.

Table 3. Summary of Results[1] [[1] All the results are obtained by using cosine fit; [2] Incident angle are defined at the center of the image; [3] The data in the radiometric correction table was extended by using cosine fit.]

Prod. ID	Data Take ID	Beam Spoil. Mode	Beam Steer. Angle	Inc.[2] Angle	Freq. Pol.	Our 6-dB BeamWidth	JPL 6-dB[3] Beamwidth (Rad. Corr.)
11389	39.60	0	2.2°	44.0°	LVV	6.77°	7.30°
					LHH	6.76°	7.16°
11390	39.60	0	2.1°	44.0°	LVV	6.67°	7.27°
					LHH	6.62°	7.06°
11342	55.62	0	14.7°	26.3°	CVV	8.08°	6.95°
					CHH	7.31°	6.98°
12347	78.60	6	11.3°	29.8°	LVV	16.75°	21.58°
					LHH	17.44°	21.51°
12348	78.60	6	11.3°	29.8°	LVV	15.00°	21.58°
					LHH	16.29°	22.30°
12,092	103.6	0	6.4°	48.7°	LHH	4.85°	N/A
12,093	103.6	0	6.4°	48.7°	CHH	4.67°	N/A

CONCLUSION

The in-flight vertical pattern of the SIR-C antenna agreed well with the preflight pattern used for radiometric correction for most of the cases studied. However, for Pass 78.60 where beam spoiling was used, our best fit is much narrower than that given by the radiometric correction, and much wider than that listed in the tape header. This case contains only a small pattern segment, which may contribute to this discrepancy.

We believe the beam patterns determined by this method should be used in subsequent data analysis. They should represent the true in-flight pattern better than any ground measurements. Unfortunately, the improved patterns are only available for a small fraction of the total complex of SIR-C patterns. Users who need good radiometric data for their applications should consider using only passes without beam spoiling. If radiometric accuracy is not important for an application, beam-spoiled images may be adequate.

ACKNOWLEDGMENTS

This work was supported by NASA/JPL under contract 958434. Many JPL personnel were very helpful for providing the image data and detailed information about the data format.

REFERENCES

[1] A. Sobti and E. C. Davison, "Microwave scattering measurements over Brazil at 13.9 GHz," RSL Technical Report 243-11, Radar Systems & Remote Sensing Laboratory, Lawrence KS, Univ. of Kansas, 1975.

[2] I. Birrer, E. Bracalente, G. Dome, J. Sweet, and G. Berthold, "σ^0 signature of the Amazon rain forest obtained from the Seasat scatterometer," *IEEE Trans.Geosci.Rem.Sens.*, vol. GE-20, pp. 11-17, 1982.

[3] R. L. Jordan, B. L. Huneycutt, and M. Werner, "The SIR-C/X-SAR synthetic aperture radar system," *IEEE Trans. Geosci. Rem. Sens.*, vol. GE-33, pp. 829-839, 1995.

[4] R. K. Moore and M. Hemmat, "Determination of the vertical pattern of the SIR-B antenna," *Int.J.Remote Sensing*, vol.9, pp.839-847, 1988.

[5] Y. Fang and R. K. Moore, "Inflight vertical antenna patterns for X-SAR from Amazon rain-forest observations," *IEEE Trans. Geosci. Rem. Sens.*, vol. GE-33, pp. 1083-1085, 1995.

[6] M. Shimada and A. Freeman, "A technique for measurement of spaceborne SAR antenna patterns using distributed targets," *IEEE Trans. Geosci. Rem. Sensing*, vol. 33, pp. 100-114, 1995.

[7] A. Freeman, M. Alves, B. Chapman, J. Cruz, Y. Kim, S. Shaffer, J. Sun, E. Turner, and K. Sarabandi, "SIR-C data quality and calibration results," *IEEE Trans. Geosci. Rem. Sens.* vol. 33, pp. 848-857, 1995.

A Contribution to Imaging Radiometer Sampling and Integration Period Determination

Martti Kemppinen
Helsinki University of Technology, Laboratory of Space Technology
Otakaari 5A, 02150 Espoo, Finland
T:+358 0 451 2370 F:+358 0 451 2898 Email:kemppinen@ava.hut.fi

Abstract -- Imaging radiometer sampling and integration period determination studies are contributed to by a) performing an empirical study of the sampling rate's effect on the spatial resolution of the resulting image, b) analyzing the effect of supplementing thermal noise on a numerical model expressing the influence of sampling and integration periods on the achievable spatial resolution, and c) discussing the optimal values for the sampling and integration periods on the basis of a scan simulation study.

INTRODUCTION

This paper supplements the scan simulation based study on the optimal sampling and integration period of a conically scanned imaging radiometer [1] by introducing the results of three new investigations:

1. An empirical study of the sampling rate's effect on the spatial resolution of the resulting image.
2. The 1-dimensional numerical model that expresses the influence of sampling and integration periods on the achievable spatial resolution [1], has been supplemented with thermal noise.
3. The general case featuring decoupled integration time and sampling period, has been further studied, raising some new aspects on the optimal relation of the dwell time, integration time and sampling rate.

These items are discussed in Sections 1-3, respectively.

1. THE EMPIRICAL STUDY

The motivation of the study was to verify empirically the results of the scan simulation [1], according to which the optimal sampling period is about 0.5×dwell time, while [3] states the correct period to be around 0.7×dwell time. The performance of the different periods is compared by measuring a target with the AIR-93 instrument [2], varying the sampling period lengths, and comparing the contrasts (separabilities) of the resulting images. As in [3] and the corresponding section of [1], the integration time of AIR-93 is equal to the sampling period. The target was chosen to be an island group, whose shape is as close to that of a test image three-bar group as possible.

The test flights were executed on May 9th 1995 at an altitude of 1000 m over Niittysaaret islands off Helsinki (Fig.1), resulting in a footprint size of 43×68 m. Figs. 2 a-c depict the resulting images employing along- and across-scan sampling periods of 1.0, 0.71 and 0.5 ×dwell time, respectively ($K_{i\beta}$=K_{sy}=1.0, 0.71 and 0.5 [4]).

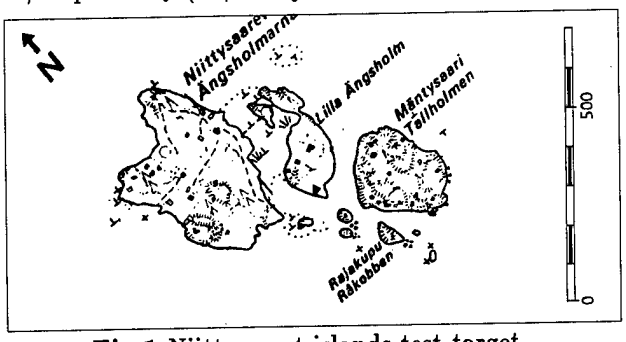


Fig.1 Niittysaaret islands test target.

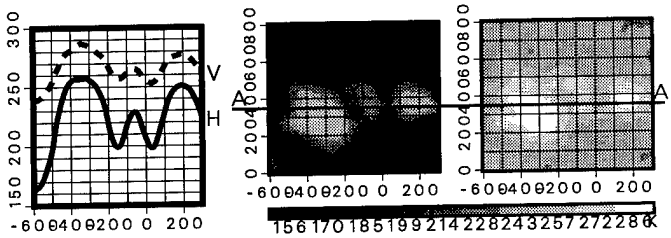


Fig.2a H (middle) and V (right) polarization images and data section A-A (left), $K_{i\beta}$=K_{sy}=1.0.

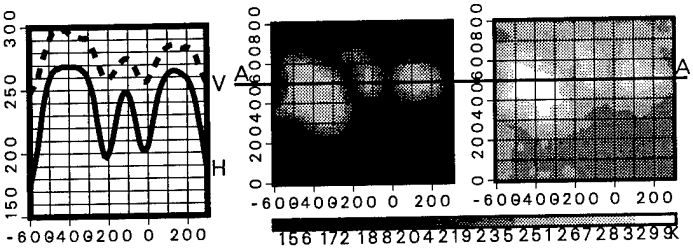


Fig.2b $K_{i\beta}$=K_{sy}=0.71.

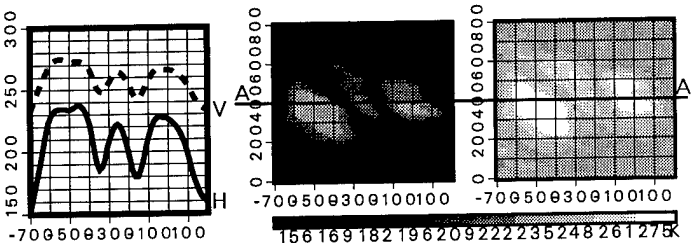


Fig.2c $K_{i\beta}$=K_{sy}=0.5.

Defining the contrast c as the ratio of the mean separation of the middle island and the straits, and the mean

0-7803-3068-4/96$5.00©1996 IEEE

separation of the open sea and outermost islands yields c_H=32% for the H-channel and c_V=21% for the V-channel in the $K_{i\beta}=K_{sy}$=1.0 case. In the $K_{i\beta}=K_{sy}$=0.71 case, the contrasts become c_H=43% and c_V=37%, and in the $K_{i\beta}=K_{sy}$=0.5 case, c_H=66% and c_V=51%. Hence, the separability of $K_{i\beta}=K_{sy}$=0.71 case is on average 34% better than that of $K_{i\beta}=K_{sy}$=1.0 case, but 46 % worse than that of $K_{i\beta}=K_{sy}$=0.5 case. Therefore, the denser sampling is worth employing, whenever technically possible.

As both [1] and [5] assume the same results to apply also in the non-continuously scanned along-track (across scan) direction, this was also empirically verified on May 25th. Fig.3 depicts the "two-bar" island target used for the across-scan verification, and Figs. 4a-c present the results.

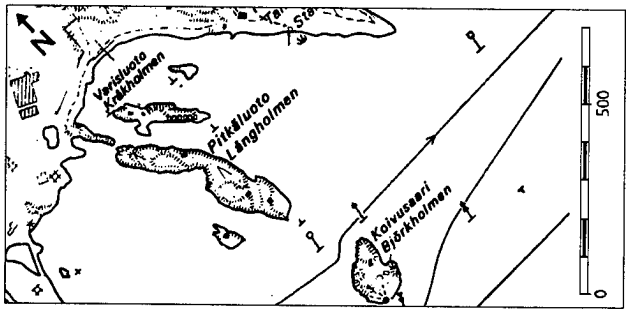


Fig.3 Varisluoto and Pitkäluoto islands test target

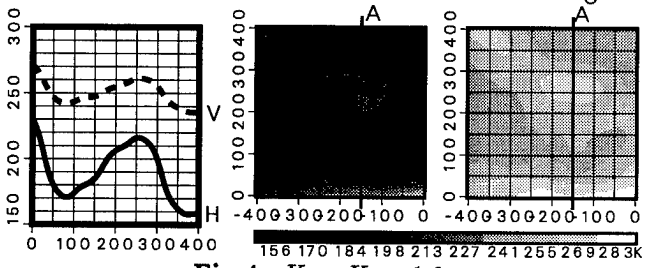


Fig.4a $K_{i\beta}=K_{sy}$=1.0.

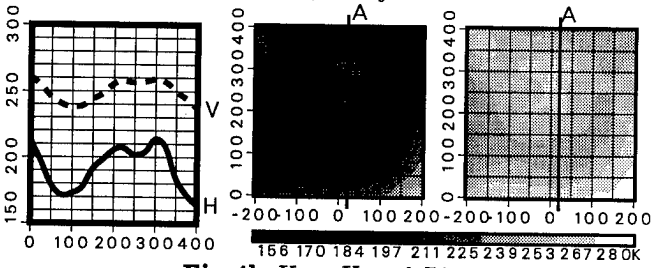


Fig.4b $K_{i\beta}=K_{sy}$=0.71.

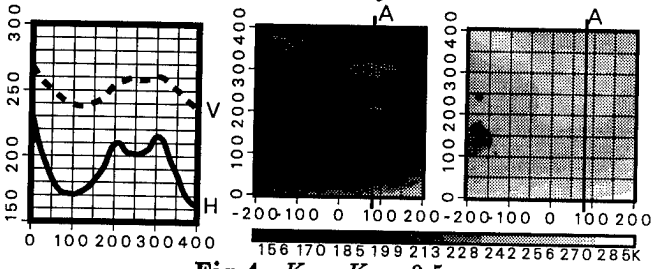


Fig.4c $K_{i\beta}=K_{sy}$=0.5.

Now the contrasts (mean separation of the strait compared to mean separation of open sea and the islands) are c_H=20% and c_V=7% in the $K_{i\beta}=K_{sy}$=0.71 case, and c_H=26% and c_V=10% in the $K_{i\beta}=K_{sy}$=0.5 case, while the $K_{i\beta}=K_{sy}$=1.0 case failed to be resolved. The separability of $K_{i\beta}=K_{sy}$=0.5 case is on average 37% better than that of $K_{i\beta}=K_{sy}$=0.71 case. Hence, the assumption is verified to be a correct one.

2. SUPPLEMENTING THERMAL NOISE

Reference [1] introduced a simulation model that numerically computes the contrast of a two delta-function target convolved with a radiometer antenna power pattern. The result plot presented contrast contour curves as a function of the delta-functions' separation and the sampling (or integration) period. The model did not take into account the radiometer's thermal noise, but now, white noise with a RMS amplitude of 3% of the T_B dynamic range has been incorporated. Comparison of Figs. 5 a and b ensures that the presence of noise does not distort the results in any way, excluding the slight ripple.

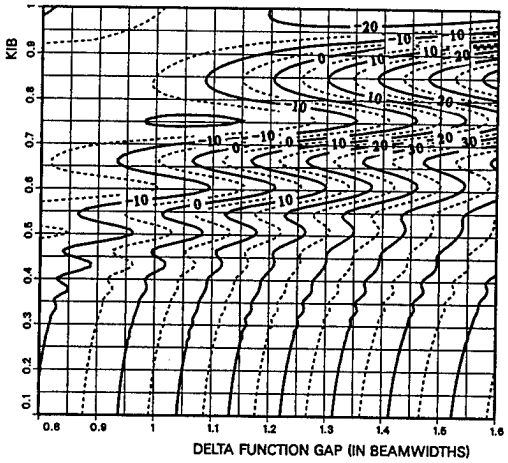


Fig.5a The original contrast contour plot [1].

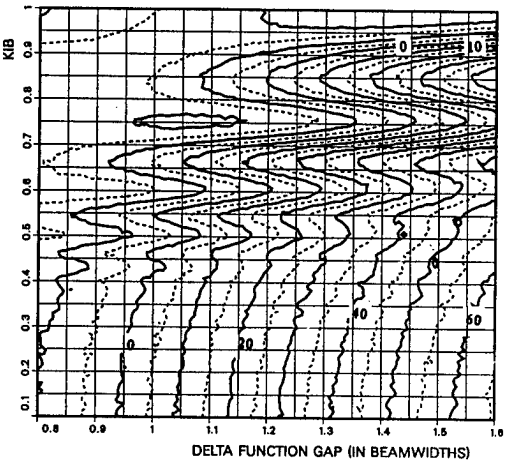


Fig.5b The same in the presence of noise.

3. DECOUPLED CASE STUDIES

A sampling rate frequent enough to prevent aliasing ($K_{i\beta} \leq 0.5$) results either in a relatively short integration time or low scan and platform velocity. Therefore, in some applications it is useful to decouple the integration period from the sampling period to improve sensitivity or scan velocity. As the decoupled contour plot of [1] indicates, the sampling period should not exceed $\approx 0.5 \times$footprint dimensions to prevent aliasing, but the integration period may be somewhat longer at a moderate cost of spatial resolution reduction. Fig. 6 presents quantitave information on the reduction, computed with the model of [1] employing a constant sampling rate of $0.45 \times$footprint dimensions to prevent aliasing.

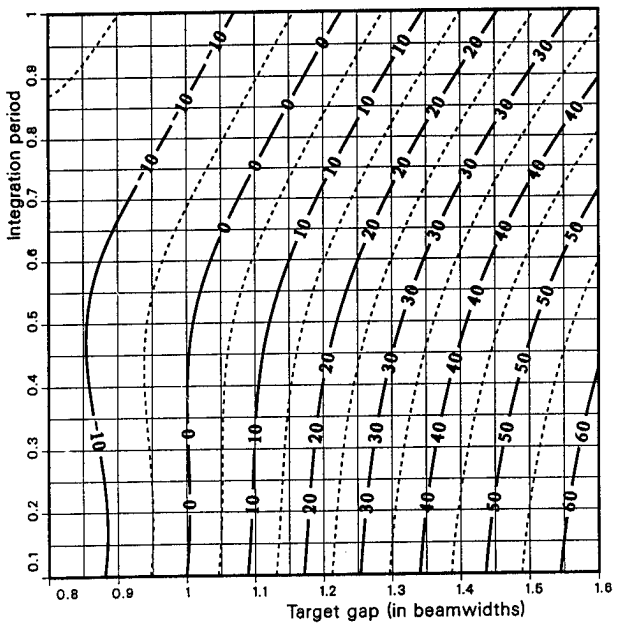


Fig.6 Contrast contours as a function of target separation and integration period.

Due to frequent sampling, there are no signs of aliasing. The contrast curves are very steep at integration periods below $0.5 \times$footprint width, which means that the antenna motion during the integration period may be extended up to $0.5 \times$footprint widths with hardly any reduction in the spatial resolution, as stated in [1]. However, the plot also indicates that the integrator-smearing driven reduction is not dramatic: for example, employing 20 % contrast and an integration period equal to footprint width results in a spatial resolution reduction of $0.3 \times$footprint widths compared to an almost static antenna.

Fig. 7 presents a scan simulation comparison of a case using equal integration and sampling period $K_{i\beta}=K_s=0.5$ and a decoupled case, in which $K_{i\beta}=K_s=0.71$. Both cases employ across-scan (along track) sampling period $K_{sy}=0.5$, which was verified to prevent aliasing in the across-scan direction in Section 1. Both cases have equal 10 ms integration time. The benefit of the decoupled case is that since it has 42 % larger antenna motion during the integration time, the platform velocity becomes 36 % higher than the impractically low velocity (63 km/h) of the coupled case. On the other hand, if the same low velocity were accepted, the decoupled case could have 42 % longer integration time, thus improving the sensitivity.

As Fig. 7 indicates, the x-resolution of the decoupled case is slightly less than on the coupled case. The quantity of the reduction is compatible with the data of Fig. 6. In the y-direction, no visible change can be seen. This was expected, since the antenna motion parameters were changed in the along-scan direction only, and the scan curvature is relatively small, which results in small antenna motion y-component even at the edges of the image.

REFERENCES

[1] Kemppinen M., "Airborne Imaging Radiometer Scan Simulation," IEEE TGARS, Vol. 33, pp. 660-669, May 1995.

[2] Kemppinen M., Pallonen J., Lantto E., Auer T. and Hallikainen M., "The first results of a novel 93 GHz airborne imaging radiometer," Digest IGARSS'95, pp. 1814-1816, July 1995.

[3] Skou N., Microwave Radiometer Systems: Design and Analysis. Artech House Inc., Norwood, MA, USA 1989.

[4] Kemppinen M., Hallikainen M., "The theory and Mechanical Realization of an Ideal Scanning Method for a Single-Channel Imaging Microwave Radiometer," IEEE TGARS, vol 30, pp. 743-749, July 1992.

[5] Feasibility Study for a Multi-frequency Imaging Microwave Radiometer MIMR, Final Report. Marconi Space Systems Limited, Portsmouth, England, 1989.

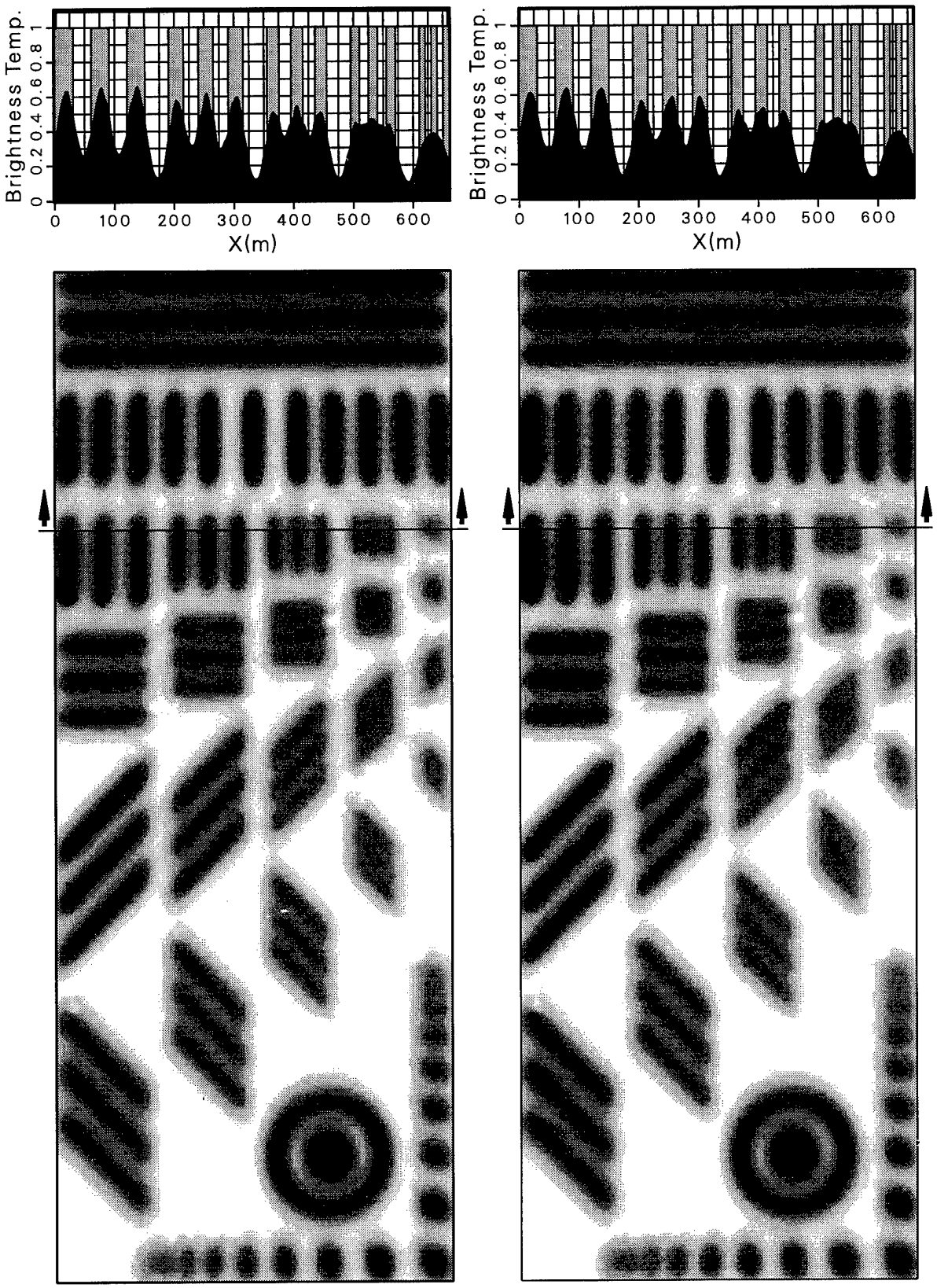


Fig.7 Simulation results employing $K_{i\beta}=K_s=K_{sy}=0.5$ (left) and $K_{i\beta}=0.71$, $K_s=K_{sy}=0.5$ (right).

Radarclinometry for ERS-1 Data Mapping.

Sophie Paquerault, Henri Maître, Jean-Marie Nicolas
ENST Département Images. 46 rue Barrault,
F - 75634 PARIS CEDEX 13 FRANCE
Tel: (33) 1 45 81 81 25 Fax: (33) 1 45 81 37 94
E-mail:paquerau@ima.enst.fr

Abstract: **The availability of SAR images gives us the possibility to map world regions which are not easy to access, or which are generally not visible with optical systems. It is the case of the tropical regions which frequently have an important cloudly cover. Elevation maps, more or less precise, appear more and more important for environment studies and remote sensing applications. Radarclinometry, consisting in exploiting relation between the SAR measures and the geometric orientation of the imaged ground pixel, appears as an efficient and cheap mean to draw elevation maps. We propose and implement an integration method of radarclinometry, taking into account the specificity of ERS-1 images.**

1. Introduction.

The radarclinometry, called *shape from shading* in the robot vision community, consists in estimating the geometric parameters of a ground, from its radiometry and more precisely from the backscattered intensity coming from a piece of imaged ground. This is an interesting technique of relief restoring, because it uses one single image only. Few studies on the radarclinometry have been realized; the leading founder is R.L. Widley who was the first one to apply photometric theories, primilary developped for optics [1], at the radar system [2]. At the first sight, the principle appears oversimple, essentially based on the analysis of the backscattering coefficient, in order to estimate its geometric parameters. This backscattering coefficient has been dealt with in many experimentations [3], so that permits to establish more realist theoretical models of the intensity. The application of this theoretical study has been realized for the topography of the planet Venus [4]; other applications on earth radar images, and on simulated radar images [5] [6] [7] appear more convincing for the robustness point of view; yet, few applications have been accomplished. So, we propose here to describe in detail our analysis of the radarclinometry, and to present some tests made on French Guyana, with radar images acquired by the satellite ERS-1.

2. Theoretical Study.

In order to obtain the elevation map with a radar image, an expression of the backscattered intensity as a function of the geometric parameters of the imaged ground is needed. The inversion of this expression permits us to estimate the geometric parameters, such as the slope, at each pixel, yielding the possibility to obtain the altitude variation δh in each pixel and the altitude by integration. Without taking into account all the details of the SAR system, we consider the SAR image, and we define system parameters and ground ones. With regard to the radar system, we select three parameters (Fig.1): θ, the angle of incidence of the electromagnetic wave emitted by the radar, and calculated from the nadir, R_d and R_a respectively the distance resolution and the azimutal resolution of a flat ground pixel. Also, for simplification, we approximate the electromagnetic waves emitted by the radar, as plane waves. The error of this approximation is very small (with the radar ERS-1, we commit an error of about $0.06mm$ at $10m$ from the tangential point).

With regard to the geometric parameters of the ground, we must define the notion of "parcel". A parcel is the piece of ground which is intercepted by a resolution cell of the radar, and imaged in a pixel. This parcel is considered as a plane surface. So, its area $A(\theta, \alpha, \beta)$ (3) is the one of a parallelogram; from (Fig.2), we have the sides $L(\delta, \alpha)$ (1) and $l(\beta)$ (2), as functions of the two Euler's angles α and β.

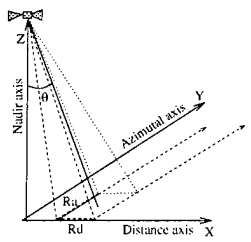


Figure 1: *System parameters.*

0-7803-3068-4/96$5.00©1996 IEEE

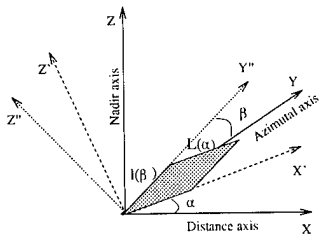


Figure 2: *Geometric parameters of a parcel.*

$$L(\theta,\alpha) = \frac{R_d \sin\theta}{\sin|\theta-\alpha|} \quad (1)$$

$$l(\beta) = \frac{R_a}{\cos\beta} \quad (2)$$

$$A(\theta,\alpha,\beta) = \frac{R_d\, R_a \sin\theta}{\sin|\theta-\alpha|\,\cos\beta} \quad (3)$$

Using the assomption of a Lambertian diffusion, the backscattered intensity may be written:

$$I(\theta,\alpha,\beta) = K\sigma_o A(\theta,\alpha,\beta)\cos^2(\theta-\alpha)\cos^2\beta, \quad (4)$$

where K is the calibration constant of the radar, to be estimated. Then, the radarclinometry treats equation (4), in order to estimate the height map, from the only knowledge of the intensity at each pixel.

3. Reconstruction Method.

After obtaining the backscattered intensity expression, we have to define a strategy for the estimation of the height at each pixel. Two steps are necessary to realize this strategy, the first one for the inversion of expression (4), and the second one for the reconstruction of the elevation map.

3.1. Initial Reconstruction.

In order to solve equation (4), we have to make some assumptions, since there are too many unknowns $(K,\sigma_o,\alpha,\beta)$ for each pixel. At first, we assume the area homogeneous enough so that σ_o is a constant for a large area. This is indeed a realistic assumption on the Amazonian forest which is a quite regular and dense cover. Then, we suppose that the terrain is mostly flat and without noticeable skewness. Again this is a realistic assumption in the area of interest for our application. From these two assumptions, we may obtain the reflectance of flat terrain from the mean value of the intensity.

$$\bar{I} = I_{oo}(\theta) = K\sigma_o A(\theta)\cos^2\theta \quad (5)$$

Knowing the orbital parameters, we can deduce the angle of incidence θ at each position and deduce a $Q(\theta,\alpha,\beta)$ ratio which only depends on two unknowns:

$$Q(\theta,\alpha,\beta) = \frac{I(\theta,\alpha,\beta)}{I_{oo}(\theta)},$$

$$Q(\theta,\alpha,\beta) = \frac{A(\theta,\alpha,\beta)\cos^2(\theta-\alpha)\cos^2\beta}{A(\theta)\cos^2\theta}. \quad (6)$$

(6) is still depending on two unknowns and cannot be solved exactly in α and β for each pixel. We will proceed in two steps. At first, we neglect angle β (this can be justified using a Taylor's expansion of (6) in α and β). We obtain an approximated expression:

$$Q(\theta,\alpha,0) = \frac{A(\theta,\alpha,0)\cos^2(\theta-\alpha)}{A(\theta)\cos^2\theta}, \quad (7)$$

which is inverted in α, and, by using (1), provides the elevation increment δh for each pixel, when scanning the image along a distance line.

$$\delta h(\theta,\alpha) = L(\theta,\alpha)\sin\alpha. \quad (8)$$

The result of this first step is presented on Fig.4. We use radar image acquired by the satellite ERS-1, on the French Guyana (Fig.3). This result is most certainly convincing, because the shape of the relief appears clearly. But, we discover here a drawback in this elevation map, as it exhibits an important linage. Two phenomena can be the cause of this linage. The first one is that we supposed that angle β could be neglected with respect to angle α. The second is that we disregard until now, that the radar image presents speckle. Both effects clearly contribute to the linage.

3.2. Use of the relief context.

It may be easily verified that speckle filtering [8] [9] doesn't contribute efficiently to linage removal. We have chosen to process both deffects (approximation by $\beta = 0$ and speckle noise) by a contextual relaxation technique. It is realized with a Markovian restoration using simulated annealing. Denoting by $I(x)$ the intensity of a pixel x, and by $H^{(k)}(x)$ its elevation at the k^{th} iteration, we express contribution of this pixel to the energy at the k^{th} iteration:

$$U^{(k)}(x) = U_I^{(k)}(x) + \nu\, U_v^{(k)}(x). \quad (9)$$

$U_I^{(k)}$ denotes the data attachment term and equals:

$$U_I^{(k)}(x) = |I(x) - K\sigma_o A(\theta,\alpha^k,\beta^k)\cos^2(\theta-\alpha^k)\cos^2\beta^k|^2$$

where α^k and β^k are the k^{th} estimates of α and β.

And, $U_v^{(k)}$ is the contextual term which will constrain the terrain to be smooth and regular:

$$U_v^{(k)} = \sum_{x_c} \frac{(H^{(k)}(x_c) - H^{(k)}(x))^2}{||x_c - x||},$$

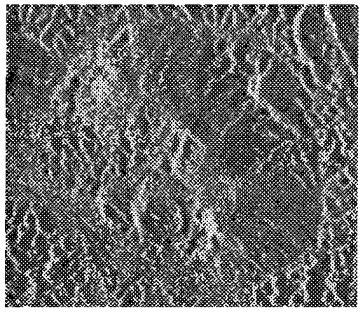


Figure 3: *ERS-1 image of the French Guyana region.*

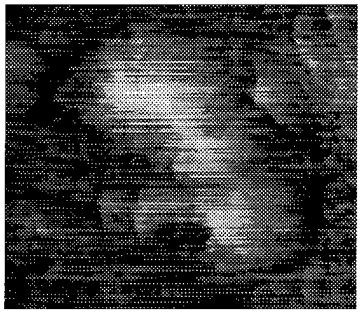


Figure 4: *Elevation map in ground range, estimated with the image (Fig.2).*

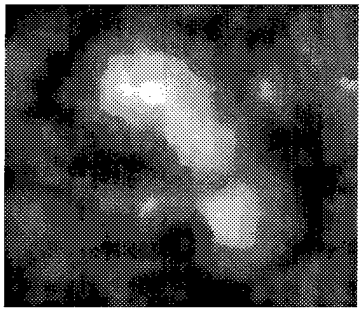


Figure 5: *Elevation map in ground range, after the contextual relaxation technique.*

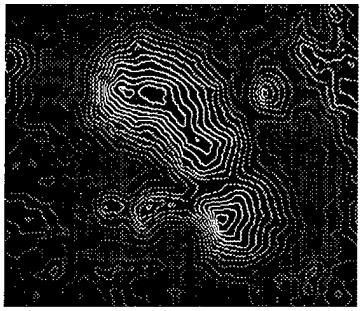


Figure 6: *Contour map extracted.*

x_c being the neighboors of x in 8-connectivity.

Then, we apply this markovian strategy on the radar image (Fig.3), with the initial image of label: the initial elevation map (Fig.4). The obtained result (Fig.5) of this strategy is satisfactory; the linage in the elevation map has disappeared, and the shape of the relief (Fig.6) has been preserved.

4. Conclusion.

The results, which have been obtained with this restitution technique of the relief, are promising. With regard to the contour map extracted from a digital elevation map, the morphological quality of the relief has been correctly restituted. However, the principal problems, like the vegetal occupation of the ground and the local character of the hypotheses have not been resolved. Soon, with the use of RADARSAT images, it will be possible to define the condition on the optimum angle of incidence and, so to apply the radarclinometry with this condition for a better restitution.

References

[1] B. HORN. *Obtaining Shape from Shading Information.* McGraw-Hill Book Company, 1975.

[2] Robert L. WIDLEY. Radarclinometry. *Earth, Moon and Planets*, 36:217–247, 1986.

[3] Fawwaz T. ULABY et M. Craiq DOBSON. *Handbook of Radar Scattering Statistics for Terrain.* Artech House Publishers, 1989.

[4] Robert L. WIDLEY. Radarclinometry for the venus radar mapper. *Photogrammetric Engineering and Remote Sensing*, 51(1):41–50, January 1986.

[5] Robert T. FRANKOT and Rama CHELLAPPA. Application of a shape from shading technique to synthetic aperture radar imagery. *Proceedings of IGARSS'87 Symposium*, pages 1323–1329, May 1987.

[6] R. FRANKOT and R. CHELLAPPA. Estimation of surface topography from sar imagery using shape from shading techniques. *Artificial Intelligence*, (43):271–310, 1990.

[7] Lucien NOCERA. *Reconstruction du Relief à partir d'Images de Satellite Radar à Ouverture de Synthèse : Stéréoscopie et Ombrages.* PhD thesis, Université PARIS VII, 1996.

[8] Y. WU and Henri MAITRE. A speckle suppression method for sar images using maximum homogeneous region filtering. *Proceddings of IGARSS'90*, III:2413–2416, May 1990.

[9] Edmond NEZRY. *Restauration de la réflectivité radar. Application à l'utilisation conjointe des images des radars à synthèse d'ouverture et optiques en télédétection.* PhD thesis, Université Paul SABATIER de Toulouse (Sciences), 1992.

Millimeter-Wave Backscatter Measurements in Support of Surface Navigation Applications

Brett R. J. Snuttjer and Ram M. Narayanan
Department of Electrical Engineering and Center for Electro-Optics
University of Nebraska-Lincoln, Lincoln, NE 68588-0511, USA
T: 402.472.5141, F: 402.472.4732, EMail: eerdrmn@engvms.unl.edu

Abstract—**Millimeter-wave (MMW) radars and radiometers are emerging as reliable and low-cost systems in numerous commercial and military applications. MMW short-range radar systems have a unique advantage are in surface navigation applications, such as military vehicle mobility in inclement conditions, aircraft landing guidance and automobile collison avoidance. MMW short-range systems provide acceptable angular resolutions, but are superior in performance compared to optical systems under conditions of rain, fog, or smoke. Their small size makes them particularly advantageous in space-limited systems. We present 95 GHz MMW grazing angle clutter data obtained from distributed surfaces. Sigma-zero values at grazing angles of 5.0 and 7.5 degrees were obtained from fresh snow and asphalt covered distributed surfaces. The probability distribution of the received clutter power is also discussed. A brief description of the MMW radar system and experimental setup is also included.**

Introduction

The development of millimeter-wave (MMW) radar systems in aircraft landing systems has advanced rapidly in the last 5 years [1]. MMW radar reflectance data and clutter characteristics from common distributed surfaces, such as asphalt and snow, are relatively unknown, especially at low grazing angles. MMW radar grazing angle clutter characteristics are necessary in order to enhance detection and further the development of missile guidance systems and in automated aircraft landing systems.

The University of Nebraska-Lincoln (UNL) has developed a continuous-wave (CW) 95 GHz MMW radar system. The radar is capable of measuring HH, HV, VH and VV polarization combinations. The experimental setup allows radar clutter measurements at grazing angles of 5.0 ° and 7.5 °. Results of sigma-zero vs. grazing angle are presented for asphalt and snow surfaces. The probability distribution characteristics of the received clutter power is also being studied. The received power cumulative distribution function (CDF) is computed from the sample data and compared to the exponential CDF.

Measurement Setup

Figure 1 is a block diagram of the radar system. The transmitter and receiver are housed in separate enclosures. The CW MMW radar is operated in a mono-static configuration. Both the transmit and receive antennas have a beam width of 1.7 °. The 95 GHz transmitted signal is generated by a Gunn Oscillator. The transmitted power is limited to 40 mW. The received signal is down-converted by two IF stages to 60 MHz. The receiver has a SSB noise figure of 13 dB. A 60 MHz log-amp converts the received power to an output voltage. The log-amp has an input power range of -80 to 0 dBm and a 10 MHz bandwidth.

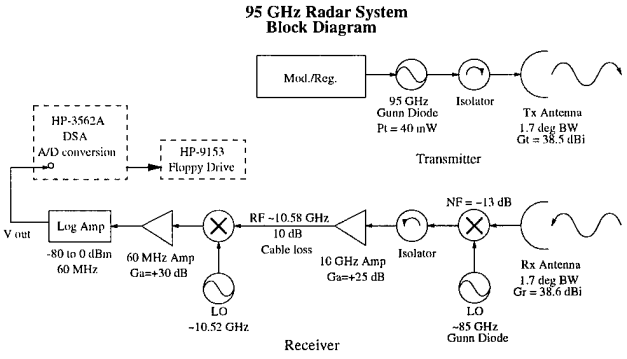


Fig. 1. MMW Radar System Block Diagram

The measurement setup for distributed surface clutter is shown in Figure 2. The Tx and Rx enclosures are both mounted on a 1.2-meter diameter turntable. The turntable is spatially scanned over the distributed surface at a constant depression angle, Θ_d. The received voltage from the log-amp is sampled and stored during the scan.

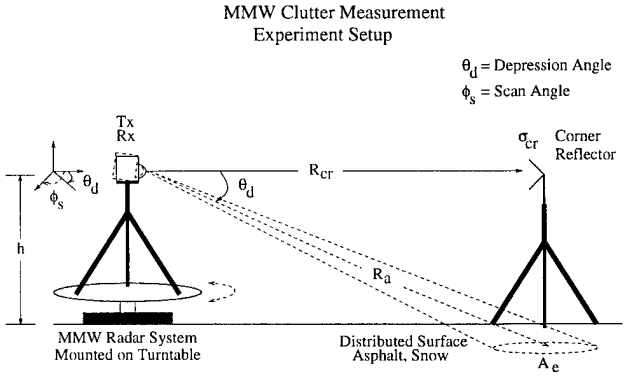


Fig. 2. MMW Clutter Measurement - Experiment Setup

0-7803-3068-4/96$5.00©1996 IEEE

The maximum depression angle, Θ_{dmax}, is limited by the far-field distance, R_{ff} [2].

$$\Theta_{dmax} = 8.56\ ^\circ, R_{ff} = 10.22\ m \quad (1)$$

The minimum depression angle, Θ_{dmin} is limited by the transmitted power, P_T and the noise power, P_n [3].

$$P_t = 40\ mW, P_n = -91.0\ dBm \quad (2)$$

Below Θ_{dmin}, the received clutter power is not above the minimum SNR of the system.

System calibration is performed by measuring the radar reflectance from a corner reflector. The corner reflector is placed at a distance R_c, and the received voltage is recorded. A 14-cm side corner reflector (RCS = 160 m^2) is used for the calibration measurement.

Results

Results of sigma-zero vs. grazing angle, for fresh snow and asphalt, are presented at 7.5 ° and 5.0 ° for HH, VV and VH polarizations. By reciprocity, HV and VH cross-sections are the same. Figure 3 shows the results obtained from new snow and Figure 4 the results for asphalt.

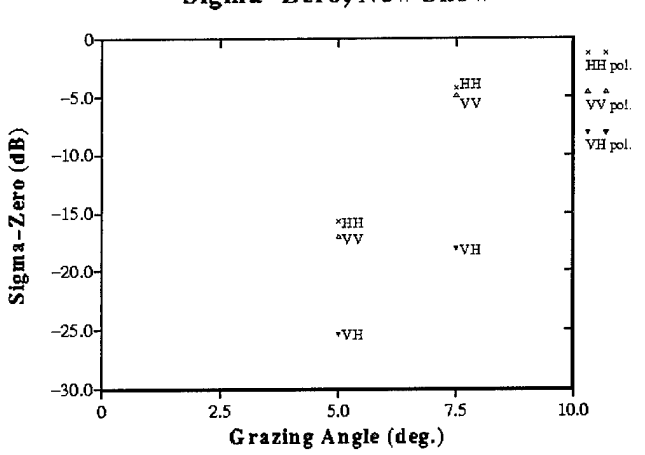


Fig. 3. Sigma-Zero vs. Grazing Angle - New Snow

The received voltage values from the spatial scan are interpolated to yield a resulting power value. The sample mean power value is then computed. The mean value, $P_{Ra(avg)}$, is computed from N samples of P_{Ra}. The received power, P_{Ra}, from a distributed surface, is computed from the mono-static radar range equation [3]. P_{Ra} is given in Equation 3:

$$P_{Ra} = \frac{P_T\ G^2\ \lambda^2\ \sigma^o\ A_e}{64\ \pi^3\ R_a^4}\ A_{sys} \quad (3)$$

The effective antenna aperture, A_e, is given by Equation 4:

$$A_e = \frac{\pi\ R_a^2\ \Theta_{BW}^2}{4\ \sin(\Theta_d)} \quad (4)$$

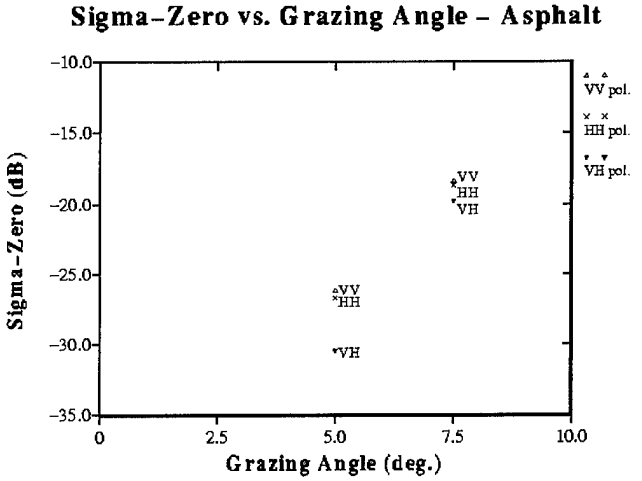


Fig. 4. Sigma-Zero vs. Grazing Angle - Asphalt

It is necessary to compute the co-polarized (HH and VV) sigma-zero values by measuring the received power from the calibration target. All parameters, except the total system gain, A_{sys}, are known in Equation 5:

$$P_{Rcr} = \frac{P_T\ G^2\ \lambda^2\ \sigma_{cr}}{64\ \pi^3\ R_{cr}^4}\ A_{sys} \quad (5)$$

The system loss is eliminated by dividing Equation 5 by Equation 3. Solving for sigma-zero, the result is given by Equation 6:

$$\sigma^o = \frac{\sigma_{cr}\ P_{Ra(avg)}\ R_a^4}{A_e\ P_{Rcr}\ R_{cr}^4} \quad (6)$$

The corner reflector RCS is not known at cross-polarizations, therefore the sigma-zero values at VH pol must be computed in a different method. The VH sigma-zero value is computed from the VH mean power value and the co-polarized sigma-zero value and mean power value at the same grazing angle. σ^o_{VH} is given in Equation 7 as:

$$\sigma^o_{VH} = \frac{\sigma^o_{VV,HH}\ P_{Ra(avg)}|_{VH}}{P_{Ra(avg)}|_{VV,HH}} \quad (7)$$

The probability characteristics of the received power were also considered. The backscatter cumulative distribution function (CDF) was computed from the sample data. The CDF is computed, assuming N samples of received power, by Equation 8 [4]:

$$x_i = \frac{P_i}{P_{avg}},\ with\ P_{avg} = \frac{1}{N}\sum_{i=1}^{N} P_i \quad (8)$$

The resulting normalized power CDF is best approximated by an exponential CDF, F(x), given in Equation 9.

$$F(x) = 1.0 - \exp(-x/b),\ with\ b = 1.0\ (mean\ est.) \quad (9)$$

Figure 5 compares the normalized power CDF from new snow to the exponential CDF. The HH and VV normalized power CDF characteristics are almost identical, hence, only the HH and VH characteristics plotted:

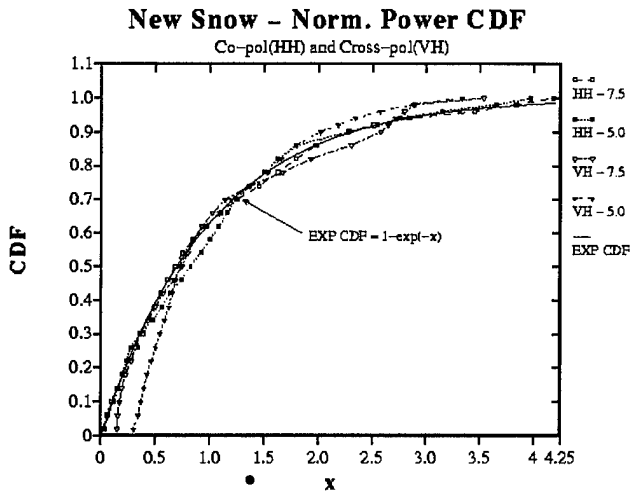


Fig. 5. New Snow - Normalized Power CDF Characteristics

The normalized power CDF from asphalt is compared to the exponential CDF in Figure 6, again only the HH and VH polarization characteristics are considered:

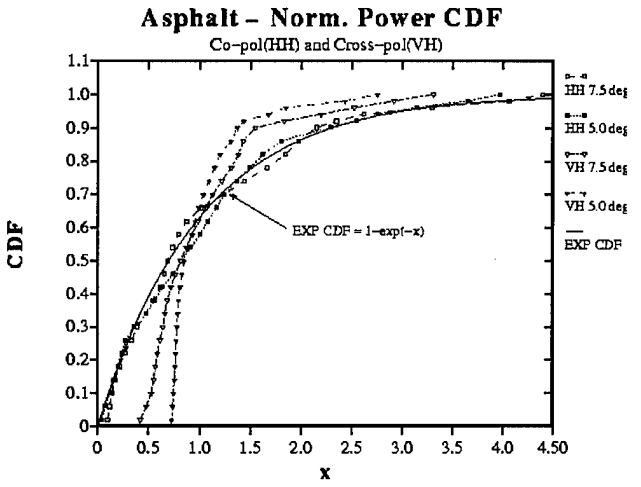


Fig. 6. Asphalt - Normalized Power CDF Characteristics

A Goodness of Fit test compares the normalized power CDF to the exponential CDF. The test parameter χ^2, degree of freedom $\nu = 25$, is listed in Table I for asphalt and new snow surfaces. The new snow and asphalt normalized power data fits the exponential CDF with a significance level $\geq$ 99.5%.

TABLE I
GOODNESS OF FIT TEST - NEW SNOW AND ASPHALT

Pol.	Θ_d	χ^2-New Snow	χ^2-Asphalt
HH	5.0	0.1168	1.7115
HH	7.5	0.0911	0.6007
VV	5.0	0.1185	1.5995
VV	7.5	0.2284	0.5848
HV	5.0	1.1325	3.2342
HV	7.5	0.4079	1.1283

CONCLUSIONS

Grazing angle radar clutter data, at $\Theta_d = 5.0\,^\circ$ and $7.5\,^\circ$ is presented for the asphalt and fresh snow surfaces. The resulting sigma-zero values are substantially lower (by $\approx$ 10 dB) than simulated results using a typical clutter model [5]. Grazing angle data were obtained at only two angles because of the far-field limitations and the low transmitted power level. The received backscatter power, especially for the cross-polarized case, was not measurable at grazing angles less than 5 degrees for both distributed surfaces. No attempt is made to curve fit the sigma-zero vs. grazing angle data because only two angles were measured. Work is continuing at UNL to characterize grazing angle clutter from other distributed surfaces. Other distributed targets of interest include concrete, gravel, and grass covered surfaces.

ACKNOWLEDGMENTS

We gratefully acknowledge the support provided by the U.S. Air Force, AFIT continuing education program, for providing support to 2nd Lt Brett Snuttjer. Thanks are also due to Daniel D. Cox, MSEE-UNL 1993, who originally constructed the radar system.

REFERENCES

[1] B.D. Nordwall, "Millimeter-Wave radar tested as a landing aid," Aviation Week and Space Tech., v142, no.20, pp. 55-56, May 15, 1995.
[2] N.C.Currie and C.E. Brown, "Principles and Applications of Millimeter-Wave Radar," Artech House, 1987, p. 603.
[3] M.I. Skolnik, "Radar Handbook," 2nd ed., Mcgraw-Hill, 1990, pp. 2.4-2.6.
[4] R.M. Narayanan, "Measurement and analy. of electromag. scattering from vegetation and fallen snow at 215 GHz," PhD. Dissertation, Univ. of Massachusetts-Amherst, pp. 41 - 42, Sept. 1988.
[5] N.C. Currie,R.D. Hayes and R.N. Trebits, "Millimeter-Wave Radar Clutter," Artech House, 1992, pp. 138 - 147.

A Novel Design of Return Signal Simulator for Radar Altimeters

Ji Wu, Lin Lin
Center for Space Science and Applied Research
P.O.Box 8701, Beijing 100080, P.R. China
Tel.: +86 10 62 55 99 44 - 3414, Fax: +86 10 6257 6921, e-mail:wuji@sun20.cssar.ac.cn

Abstract -- The design process of return signal simulator (RSS) for radar altimeters is discussed. After analysis of the waveform of ocean return signal and comparison of existing RSS design schemes, a novel design scheme is proposed. The new RSS design has the advantages of not only low cost and compact in dimension, but also the ability of adjusting the slope of the leading edge and the peak value of the waveform.

I. INTRODUCTION

Radar altimeter plays an important role in the ocean observation from space. In order to test and calibrate the sensor before and after the launch, a dedicated instrument called return signal simulator (RSS) is very much needed. A complete RSS should provide the possibilities to simulate different platform altitude, wave height and ocean back scattering coefficients. From the literature, what we found is usually very complicated design such that it could be considered as an independent radar altimeter.

RSS should have the ability to store the transmitting signal (a chirp) for a certain time in order to simulate the propagation time delay from the platform to the ocean surface and return. It should also simulate the distortion of the transmitted chirp after it has been reflected from the ocean surface which will carry the information of the ocean wave height and back scattering characteristics. In order to realize the above two functions, the present paper will discuss and propose a novel design of RSS.

II. DISCRETE OCEAN RETURN SIGNAL

As we known, the principle of the radar altimeter is to transfer the ocean return signal from the time domain to the frequency domain using the so called full deramp technique and analysis the waveform in the frequency domain. A classical ocean return signal excited by a single frequency pulse signal will have the form as shown in Fig.1 (a) in the time domain. However, when excited by a chirp signal as used by an modern radar altimeter, it is a sum of a lot of chirp signals with amplitude and arriving time differences representing back scatterings from difference parts of the illuminated area of the ocean. This return signal, as shown in Fig.1 (b), is very different from (a) and therefore no way to analysis it directly in the time domain.

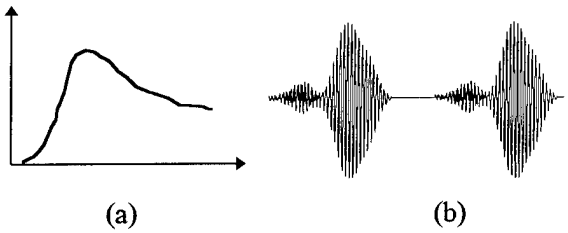


Fig. 1. Ocean return signal.
(a) Pulse excitation, (b) Chirp excitation.

The deramp technique transfers the chirp excited return signal to the frequency domain by mixing the signal with the same chirp as used in the transmit. In the frequency domain, the return chirps with different time delays from the ocean will be separated in the intermediate frequency spectrum and forming the same waveform as shown in Fig.1 (a). To best understand this and simulate the return signals, we could draw a chirp excited return signal in the form of discrete return chirps separately in the time domain as shown in Fig. 2.

In Fig. 2, the first (the earliest) return should be from the ocean wave peak at the nadir region and with a very small magnitude. The return closely followed is reflected from the ocean wave valley at the nadir and the wave peak around the nadir. Since the reflecting area is larger, the signal magnitude is then increased. This is continued until the antenna beam limitation appears resulting a peak point of the waveform is reached. Followed is the trailing edge of the waveform due to the antenna pointing limitations.

Since a continuous return signal must be sampled in the frequency domain during the data processing which

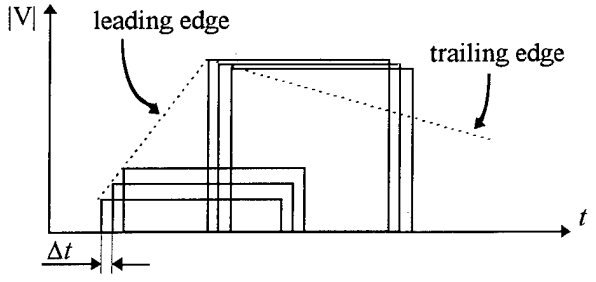


Fig. 2. Discrete ocean return signal.

0-7803-3068-4/96$5.00©1996 IEEE

representing a discrete return signal as shown in Fig.2, we could therefore use the discrete scheme shown in Fig. 2 to simulate the chirp excited ocean return signal.

III. DESIGN SCHEMES OF RSS

It is mentioned in Section I that a RSS should have two functions in simulating an ocean return signal: 1) to provide enough propagation time delay to simulate the distance from ocean surface to the sensor's platform; 2) to simulate the return signal reflected from the ocean surface. In this section we will discuss them in details.

1. Time delay

For an air-based system the platform altitude is from several thousand meters to more than a ten thousand meters corresponding to a few μSec. to 100 μSec. time delay. When it is a few μSec., it is obviously that the best way to obtain the delay is to use a non-dispersed SAW delay line or a bulk acoustic delay line. When the requirement become more than 20 μSec., the acoustic technique will find difficulties to reach such long delay not mention to simulate a space-based system. Therefore we must have an alternative way to realize the long time delay.

Compared with the acoustic technique, optical technique is a very attractive way to fulfil the long time delay requirement. This is because: 1). its small scale and light weight; 2). the low cost of optical fibre after the first investment for the optical transmitter and receiver; 3). for a very long time delay, i,e. the space-based system, we could make an optical fibre loop and let the signal travel through the same length of fibre many times.

For an optical delay system as shown in Fig. 3, the problem may come from the random noise and group delay generated by the optical transmitter and receiver. In order to test the signal distortion of a chirp through the system, a test is made as shown in Fig. 4 on a 31.3 μSec. delay system. It is seen that the group delay for this system is not significant. For a longer delay system, signal distortion may become larger, but as it is in the practical situation, where the orbit position error and antenna pointing error also introduce signal distortions, these random errors and distortions will not be a problem for the simulation of the platform altitude in the RSS.

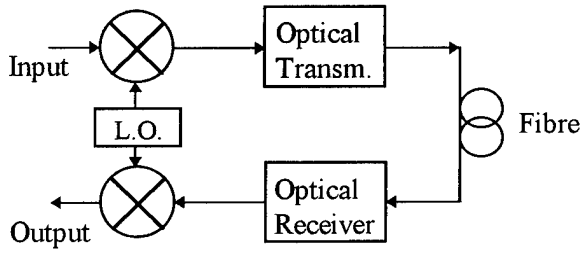


Fig. 3. Optical fibre delay system.

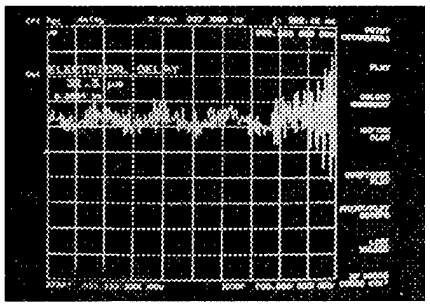


Fig.4. Test result of a 31.3 μSec. optical delay system.

2. Discrete ocean return signal simulator

In Section II, we have expressed the ocean return signal discretely in the time domain in Fig. 2. The time delay Δt (a few nSec. in practice) between each chirp should be equal and corresponds to the sampling interval in the data processing part of the altimeter. The discrete ocean return signal can be expressed as

$$w(t) = \begin{cases} \sum_{i=1}^{n} A_i \cos\left(\omega_o t_i - \frac{\Delta\omega}{2\tau} t_i^2\right) \\ \qquad where \quad i\Delta t \le t_i \le \tau + i\Delta t \\ 0 \qquad otherwise \end{cases} \tag{1}$$

where n is the total number of discrete chirps, A_i is the magnitude of chirp i and τ is the chirp pulse width.

The directly method to convert a single chirp to a multi-chirp as expressed in (1) is to split the input signal into n paths and use delay cables to achieve $i\Delta t$ and use attenuators to achieve A_i as shown in Fig. 5, and finally to combine them together as an output signal. This kind of design could be called the parallel split scheme.

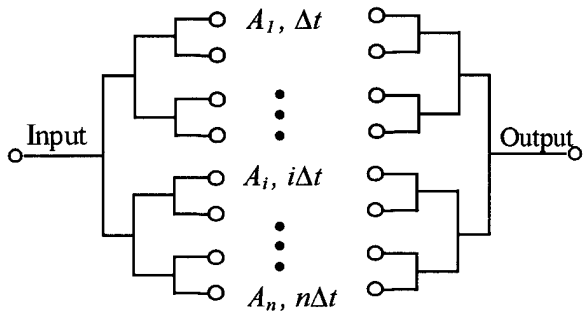


Fig. 5. Parallel split design scheme.

Another direct design is to split the input signal one after the other as shown in Fig. 6, which may be called the series split scheme.

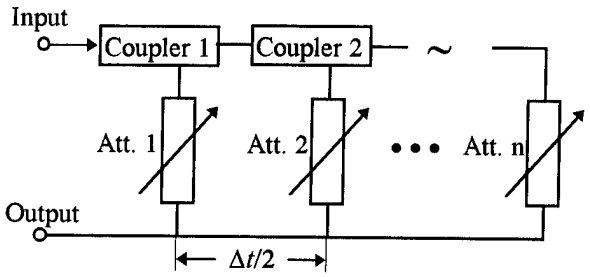


Fig. 6. Series split design scheme

It is feasible to achieve the discrete ocean return signal through the parallel and series split design schemes as shown in Fig.5 and Fig.6. But their weakness is obverse. When n is larger, for example 64, the delay cable needed to obtain $n\Delta t$ will be too long, and the total size of RSS will be too large. In addition, to achieve and adjust A_i in the split branches are also very costly when n is large. Therefore we should consider a better design.

From the above discussion it seems that the most difficult part of the design is to convert the single chirp to the multi-chirp. In differ from splitting the single chirp, we could think about to store the single chirp in a storage component and pick it up a little by little with a Δt time interval. Along this direction, we find that using a closed loop may solve our problem.

As shown in Fig. 7, the input signal (the single chirp) is coupled from the coupling arm of Coupler 1 into the closed loop. Once the signal arrived at Coupler 2, part of the signal will be coupled out as the first output chirp while the rest of the signal is still travelling in the loop. The one cycle time delay for the signal propagate in the loop is adjusted to Δt . Since Δt is much less than the pulse width τ of the chirp, when the head of the chirp in the loop reaches Coupler 2 again the second chirp output will be added on the first one but with the time delay Δt. This will continue for many times until the energy of the signal travelling in the loop has been exhausted.

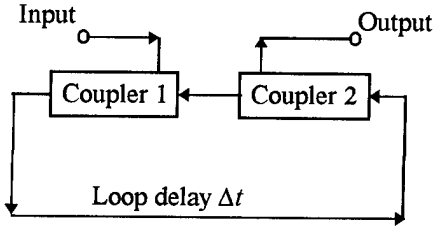


Fig. 7. Principle of closed loop design scheme.

Strictly speaking, this loop is not an energy storage component since there is no energy supplement component in the loop while the signal is attenuating. To compensate this and provide increasing amplitude multi-chirp at the output, we must have a positive loop gain. This could be realized by adding an amplifier in the loop. Once the single chirp is coupled into the loop, it will be amplified after each cycle resulting increasing amplitude on output chirps. It is understood from Fig. 2 that a larger loop gain will produce a steeper slope of the return signal waveform and vice versa. To make the slope of the waveform adjustable, we should use an attenuator together with the amplifier as shown in Fig.8. In practice, since Δt is very small, the required loop gain is also miniature.

After a certain number of cycles, the output chirp will reach a required amplitude which corresponding to a certain peak value of the waveform. At this moment, we must limit the increase of the signal energy. This is down in practice by an amplitude limiter as shown in Fig. 8. If we change the amplitude limiter's effecting point, different return signal's peak values (backscattering coefficients) could be obtained.

IV. CONCLUSIONS

The design schemes of radar altimeter are discussed. To best simulate the ocean return signal, a novel design is proposed. This design uses a closed loop as an energy storage components which has the advantages of 1).compact; 2).low cost; 3).precise Δt for discrete chirps; 4).easy adjustable slopes of waveform leading edge and peak values.

REFERENCES

[1] Alfred R.Ziger, David W.Hancock, George S.Hayne, Craig L.Pardy, "NASA radar altimeter for the TOPEX/ POSEIDON project", proc. IEEE, vol 79, 1991

[2] Ji Wu, Lin Lin "Technical report of optical fibre delay experiment system", Report ITR4-95002, CSSAR, 1995

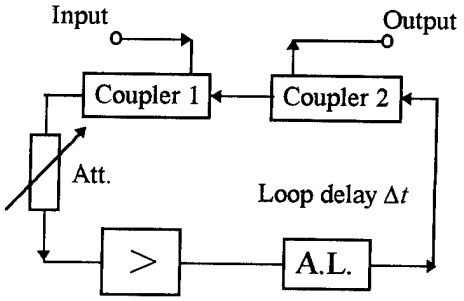


Fig. 8. Complete closed loop design of RSS

Calibration of an Airborne Multiparameter Precipitation Radar with an Active Radar Calibrator

Hiroshi Hanado*, Hiroshi Kumagai, Toshio Iguchi, Toshiaki Kozu,
Kenji Nakamura, and Hiroaki Horie

* Communications Research Laboratory, Japan
893-1, Hirai, Kashima, Ibaraki 314, Japan
Telephone:+81 299 84 7119/Facsimile:+81 299 84 7157
Email:hanado@crl.go.jp

ABSTRACT

A calibration experiment of an airborne precipitation radar was conducted by using an active radar calibrator (ARC). The airborne radar, which is named CAMPR (CRL's Airborne Multiparameter Precipitation Radar), was completed last year. Since a major purpose of CAMPR is to provide validation data for the first space-borne Precipitation Radar (PR) onboard the Tropical Rainfall Measuring Mission (TRMM) satellite, the radar system parameters must be accurately determined. Three flight experiments ware conducted with the ARC, which was developed for calibration of TRMM Precipitation Radar. The ARC was located on a roof of a building. The results are (1) the radar echo thought the ARC was identified clearly with a 30 μs delay both onboard A-scope monitor and at the CAMPR acquired data, (2) the levels of the ARC echoes were consistent with the estimated ones from designed specifications of CAMPR. This experiment result is used to fix the radar system gain of CAMPR.

1. CRL'S AIRBORNE MULTIPARAMETER PRECIPITATION RADAR(CAMPR)

CAMPR [1] was developed to validate the first spaceborne precipitation radar onboard the Tropical Rainfall Measuring Mission (TRMM) satellite. During the TRMM prelaunch period, it takes many flight experiments for collecting various types of rainfall observation data sets to help develop algorithm for the spaceborne precipitation radar (PR). After the TRMM launch, CAMPR will conduct flight experiments to validate the PR onboard TRMM. For these purposes, CAMPR has a capability of wide scanning of the antenna beam, $-57°$ right from nadir and $+75°$ left in cross-track plane. CAMPR is installed on a King-Air B200 which can fly up to 8 km altitude. It can obtain three dimensional distribution of rainfall along the flight track. Along with these functions, CAMPR has both polarimetric and Doppler capabilities. The detail of specification is summarized at Table 1.

Table 1: Specification of CAMPR

Transmit Power(peak)	2 kW
Frequency	13.8 GHz (Ku band)
Antenna	slotted waveguide array antenna
Gain(H), G^H	33.5 dBi
Gain(V), G^V	33.1 dBi
Beam-width(H)	1.95 °(along track)
	4.40 °(cross track)
Beam-width(V)	2.07 °(along track)
	4.35 °(cross track)
Pulse Width	0.5, 1.0, 2.0 μsec
(Range Resolution)	75, 150, 300 m
PRF	2, 4, 8 KHz
Nyquist Velocity	$\pm$10.9, $\pm$21.7, $\pm$43.4 m/sec
Transmit Pattern	H, V, HV, HHVV

2. ACTIVE RADAR CALIBRATOR (ARC)

The active radar calibrator (ARC) is widely recognized as a common and powerful tool for the calibration of spaceborne or airborne SAR [2]. Its compact size and broad antenna beam-width regardless of its radar cross section are major advantages over other passive reflectors. Another important feature implemented in the ARC for the TRMM PR is a signal delay capability [3]. This means that the ARC echo appears at further range bin in the radar A-scope, and is not contaminated from intense surface clutter. Since the signal delay was set at 30μs in

0-7803-3068-4/96$5.00©1996 IEEE

this case, the ARC echo existed at 4.5 km further range bin from the surface range bin. In Fig. 1, an example is shown. In Table 2, the ARC specifications are listed.

Table 2: Specification of ARC

Transmitting antenna gain, G_t	24.1 dBi
Receiving antenna gain, G_r	24.1 dBi
Antenna beam-width (3 dB)	10°
Internal gain, G_{ARC}	56 dB
Radar cross section for 13.8 GHz (0 dBm^2 = 1 m^2)	59.9 dBm^2
Time delay	30 μs

3. CALIBRATION EXPERIMENTS

The ARC was located as its polarization plane was parallel to east-west direction. The airplane equipped with CAMPR flew along the east-west or north-south lines. At first, we planed to fly above the ARC, with the antenna beam fixed to the nadir direction, However, the CAMPR footprint of about 300x600 m oval at 8 km flight level is so small that it was difficult to fly right above the ARC beam center. Hence, CAMPR antenna beam was set to scan fast between -2° and +2°, centered at the nadir direction, with rate of 9°/s. This means that the CAMPR swath size was nearly 2 km, and the ARC echo was obtained easily; moreover, we can judge whether the airplane flew right above the ARC, from the received echo time variation. Two sample records of the ARC echo are shown in Fig. 2. At Fig. 2(a), the airplane flew along the north-south direction. The abscissa is time with unit 32 ms, and the ordinate is a quantity proportional to the received power. Periodic variation of received power, P_{VV}, shows the effect of beam scanning clearly, and this means that the airplane flew right above the ARC in this case. At the east-west direction case (Fig. 2(b)), on the other hand, received power, P_{VV} shows so irregular variation that the airplane did not fly right above the ARC. Other components, P_{VH} and P_{HV} showed the similar variations (not shown in this paper), which contains the information of the airplane attitude; rolling, pitch, and drift angles.

As to one case, Fig. 2(a), observed ARC echo level was compared with estimated one based on the designed specifications of CAMPR. Received power, P_r, is obtained from the radar equation:

$$P_r = \frac{P_t G_t^{(CAMPR)}}{4\pi R^2} \cdot A_{ARC} \cdot G_{ARC} \cdot \frac{G_t^{(ARC)}}{4\pi R^2} \cdot A_{CAMPR}, \quad (1)$$

where P_t: transmit power, G_t: Antenna Gain, A: effective aperture, G_{ARC}: amplifier gain on the ARC. Effective aperture, A, is substituted by $A = \frac{\lambda^2}{4\pi} \cdot G \cdot m_p$, where m_p is polarization effectiveness, and four components of received ARC echo are the following:

$$P_{HH} = \frac{P_t G^H}{4\pi R^2} \frac{\lambda^2}{4\pi} G_r m_{HH} \cdot G_{ARC} \cdot \frac{G_t}{4\pi R^2} \cdot \frac{\lambda^2}{4\pi} G^H m_{HH}, \quad (2)$$

$$P_{HV} = \frac{P_t G^H}{4\pi R^2} \frac{\lambda^2}{4\pi} G_r m_{HH} \cdot G_{ARC} \cdot \frac{G_t}{4\pi R^2} \cdot \frac{\lambda^2}{4\pi} G^V m_{HV}, \quad (3)$$

$$P_{VH} = \frac{P_t G^V}{4\pi R^2} \frac{\lambda^2}{4\pi} G_r m_{VH} \cdot G_{ARC} \cdot \frac{G_t}{4\pi R^2} \cdot \frac{\lambda^2}{4\pi} G^H m_{HH}, \quad (4)$$

$$P_{VV} = \frac{P_t G^V}{4\pi R^2} \frac{\lambda^2}{4\pi} G_r m_{VH} \cdot G_{ARC} \cdot \frac{G_t}{4\pi R^2} \cdot \frac{\lambda^2}{4\pi} G^V m_{HV}. \quad (5)$$

Results from a Fig. 2(a) case are listed in Table 3. The difference between observed ARC echo level and estimated one is 4.0 dB in P_{VV}. Both the antenna directions of CAMPR and the ARC are considered to be uncertainties in this calculation. These uncertainty may be removed by using other cases, which are different in the flight direction.

Table 3: Comparison between observed ARC echo levels and estimated ones

CH	observed	estimated
HH	-79.1 dBm	-82.6 dBm
HV	-78.6 dBm	-77.0 dBm
VH	-80.8 dBm	-77.0 dBm
VV	-75.4 dBm	-71.4 dBm

4. REFERENCES

[1] H. Kumagai, K. Nakamura, H. Hanado, K. Okamoto, N. Hosaka, N. Miyano, T. Kozu, N. Takahashi, T. Iguchi, and H. Miyauchi, "CRL Airborne Multiparameter Precipitation Radar (CAMPR): system description and preliminary results", submitted to IEICE Trans. Commun., 1995.

[2] D.R. Brunfeldt and F.T. Ulaby, "Active reflector for radar calibration", *IEEE Trans. Geosci. Remote Sensing*, vol. GE-22, pp. 165-169, 1984.

[3] H. Kumagai, T. kozu, M. Satake, H. Hanado, and K. Okammoto, "Development of an Active Radar Calibrator for the TRMM Precipitation Radar", *IEEE Trans. Geosci. Remote Sensing*, vol. GE-33, pp. 1316-1318, 1995.

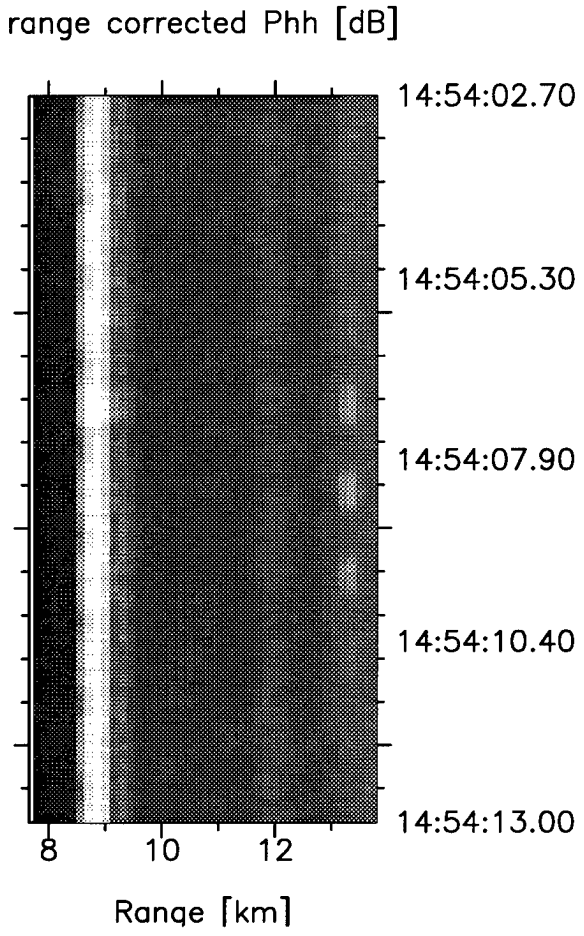


Figure 1: ARC echo appeared at 4.5 km range beyond the surface. At around 9 km range, intense surface clutter appeared stationary. The ARC echo was received at 13.5 km range intermittently. This was explained with the CAMPR antenna beam scanning between -2° and 2°, centered at the nadir direction. Another surface clutter was shown around 12 km.

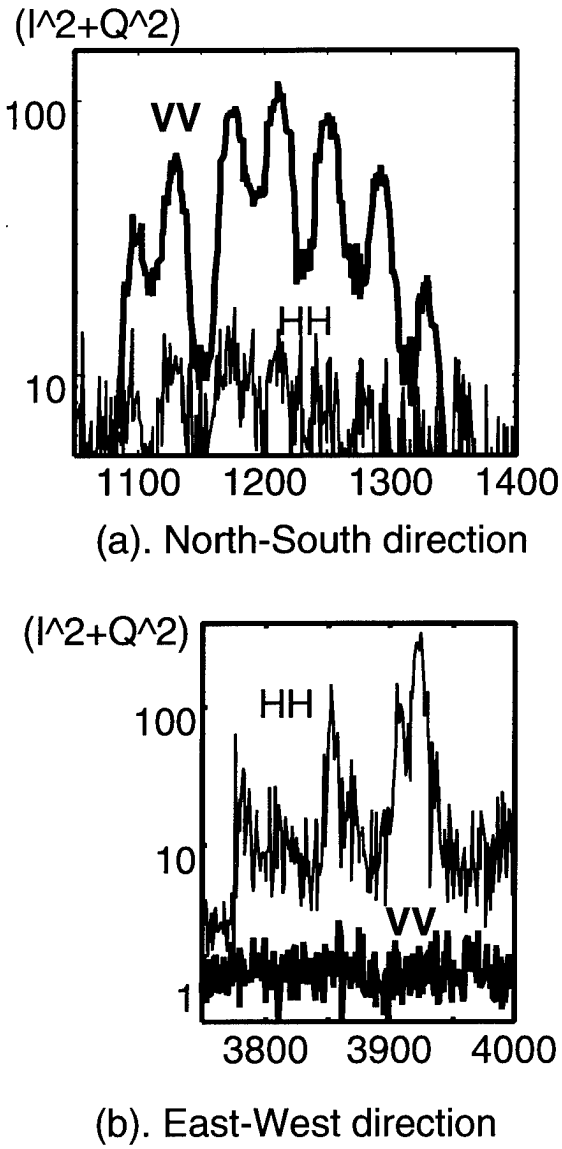


Figure 2: Time variation of Received Powers, P_{HH}, P_{VV}. From its shape, it can be determined whether the airplane flew the right above the ARC or not. (a). was good case example, and (b). was not.

On The Accurate Calibration of The SeaWinds Radar Antenna: A Cylindrical Near-Field Measurement Approach

Ziad A. Hussein[1,2] and Yahya Rahmat-Samii[2,1]

[1]Jet Propulsion Laboratory
California Institute of Technology
Pasadena, California 91109

[2]University of California Los Angeles
Los Angeles, CA 90024-1594

Abstract

A multipolarization, multi-incidence angle conical scanning Ku-band radar antenna is currently being designed and calibrated at the Jet Propulsion Laboratory (JPL) for the SeaWinds Scatterometer instrument. To calibrate the radar's performance, it is essential to accurately determine the antenna gain and radiation pattern characteristics over wide angular range. Such characterizations may be performed on a far-field range or in an indoor near-field measurement facility. Among the advantage of the latter is that the antenna is in a controlled environment. This paper demonstrates the utility of a cylindrical near-field measurement approach for the SeaWinds radar antenna calibration. Both generalized measurement error models and measured tests on a standard gain horn and NASA Scatterometer instrument antenna have been performed to achieve and verify the desired calibration accuracy. A comparison between far-field measured data and those obtained from cylindrical near-field measurements was found in excellent agreement.

1. Introduction

Recent spaceborne scatterometers demand very high quality performance from radar antennas. For example, a recently designed JPL/NASA SeaWinds spaceborne scatterometer for global mapping of dynamic change of ocean circulation requires accurate knowledge of antenna gain, wide-angle antenna patterns, pointing, and beamwidth. The antenna assembled on this instrument is an elliptical parabolic reflector with two independent beams pointing at 40 and 46 degrees from nadir to provide a cross track measurement range of 900 km. The inner beam (40 degrees from nadir) is a horizontal polarization, H-pol, with 1.6 x 1.8 degrees beamwidth in elevation and azimuth plane respectively. The outer beam (46 degrees from nadir) is a vertical polarization,V-pol, with 1.4 x 1.7 degrees beamwidth. The instrument operates at Ku-band, 13.402 GHz.

Near-field measurement has been used for many years to determine the far-field radiation patterns of antennas with high accuracy [1]. In order to accurately characterize the radiation performance of SeaWinds radar antenna at JPL, a cylindrical near-field measurement facility has been developed (Figure 1). It is the objective of this paper to present a cylindrical near-field calibration approach with generalized measurement error models to properly determine the effect of near-field bias errors on antenna gain and far-field radiation patterns, and to critically assess the importance of different error mechanisms in evaluating the achievable accuracy in absolute gain and pattern measurements.

The following is a description of the cylindrical near-field measurement set up at JPL, error analysis technique, a verification of the calibration accuracy with the use of standard gain horn measurement in the cylindrical near-field at 13.402 GHz with those

0-7803-3068-4/96$5.00©1996 IEEE

measured at National Institute of Standard and Technology (NIST) in the far-field range, and the SeaWinds radar antenna comparative performance with those measured in the far-field range.

2. Cylindrical Near-Field Measurement Implementation

The cylindrical near-field measurement facility at JPL, shown in Figure 1, is implemented such that the sampling orthomode probe steps along the vertical direction (3.8 meter long) and the antenna under test rotates in azimuth. The sampling probe measures the amplitude and phase tangential electric field components on a cylindrical surface enclosing the test antenna as illustrated in Figure 2. An RF switch at the input of the sampling probe is used to switch between the electric field components. In order to maintain the relative ratio between the measured field components, the insertion loss difference, amplitude and phase, of the RF switch is determined. This difference is corrected at the front panel of SA 1795 receiver. The antenna under test is then optically aligned to the probe coordinate system. Probe compensation is used to correct for the probe's radiation characteristics [2] including probe antenna gain, patterns and input reflection coefficients. The insertion loss between the antenna under test and the probe, normally taken at the peak of the near-field on the scanning cylindrical surface, is determined. The absolute antenna gain and far-field radiation patterns are then obtained via near-field to far-field transformation [2-4] .

3. Error Analysis

There are two types of bias errors in near-field antenna calibration: electrical and mechanical. The electrical errors are dominated by the probe-antenna under test interaction, scan area truncation, receiver non-linearity and drift, and probe gain and relative patterns. The mechanical errors, which may also induce bias errors in the calculated far-field radiation patterns, are mainly probe position with respect to the center of the rotation of the antenna as it steps along the z-direction, probe orientation, and antenna under test alignment.

Probe tower alignment is critical to the prediction of the antenna pointing accuracy. Misalignment causes a pattern shift that is proportional to the slope of the tower. For example, it has been demonstrated with computer simulation that a 0.02-degree pointing error in elevation necessitates a probe-position alignment to better 1/16 wavelength.

Multiple reflections between the probe and the antenna will greatly affect antenna gain and relative pattern accuracy. Figure 3 depicts the deviations in far-field patterns computed from near-field data measured on successive cylindrical near-field surfaces separated by $\lambda/4$. Near-field truncation along the Z-direction will greatly affect the sidelobe level and angular location in the computed far field radiation patterns in elevation plane [4]. A near-field truncation error in the azimuth direction will deter our ability to predict the backlobe far-field patterns in that direction. It has been observed that the pattern accuracy deteriorates rapidly in azimuth, starting at an angle coinciding with the truncated angular near-field region. Accurate knowledge of the radial separation distance, r_0, between the AUT and the phase center of the probe is important to predict antenna gain and relative patterns. Figure 4 describes the relative change of antenna gain vs. radial error.

4. Standard Gain Horn Antenna Results

A standard gain horn, SGH, model 12-12, has been employed to verify the cylindrical near-field measurement setup and accuracy. The SGH was measured in the cylindrical near-field range at SeaWinds radar antenna operating frequency 13.402 GHz. Far-field patterns and antenna gain were then computed. A comparison between the SGH antenna gain measured at NIST using a generalized three antenna measurement techniques [5] at the same frequency and those measured in the above described approach shows an excellent agreement (within 0.18 dB difference) as shown in Table 1.

Table 1. Comparison between SGH antenna gain measured at NIST and gain measured at JPL

JPL SGH Gain Measurement	NIST SGH Gain Measurement	Difference
23.98 dB	23.80 dB	0.18 dB

Furthermore, a comparison between direct far-field pattern measurement of the SGH at JPL's 3000-foot range and those constructed from cylindrical near-field measurement is shown in Figure 5. As can be seen, the results are in very good agreement down to 40 dB from the peak of the beam. It is worthwhile to note here that the 3000-foot far-field range has a limited dynamic range of 40 dB. This is evident in the far-field patterns shown in Figure 5 at an amplitude level below 40 dB from the peak.

5. SeaWinds Radar Antenna Results

The SeaWinds radar antenna horizontal and vertical polarization were measured in the cylindrical near-field range. The radar antenna performance parameters were then compared to those obtained in the JPL 's 3000-foot range. Figure 6 and 7 depict the radiation patterns of the antenna horizontal polarization in the elevation and azimuth plane respectively. It is seen that the results are in very good agreement. Similarly, the vertical polarization of the SeaWinds radar antenna was measured and compared to the results obtained in the direct far-field measurement in the elevation and azimuth plane as shown in Figure 8 and 9 respectively.

References

[1] Special Issue on Near-Field Scanning Techniques, *IEEE Trans.*, Antennas and Propagat., Vol. Ap-36, June 1988.

[2] Z.A. Hussein and Y. Rahmat-Samii, "Probe Compensation Characterization in Cylindrical Near-Field Scanning" *IEEE AP-S Symp. Digest*, Ann Arbor, Michigan, June 1993.

[3] A.D. Yaghjian, "Near-Field Antenna Measurement On A Cylindrical Surface: A Source Scattering-Matrix Formulation", *NBS Tech. Note 696*, July 1977.

[4] Z.A. Hussein, "Probe Compensation And Error Analysis In Cylindrical Near-Field Scanning" *16th Annual AMTA Symp. Digest*, Long Beach, CA, October 1994.

[5] A.C. Newell, R.C. Baird, and P.F. Wacker, "Accurate Measurement Of Antenna Gain And Polarization At Reduced Distances By An Extrapolation Techniques", *IEEE Trans*, vol. AP-21, No 4, pp. 418-431, July 1973.

Acknowledgment

This work was carried out at the Jet Propulsion Laboratory, California Institute of Technology, under contract with the National Aeronautics and Space Administration. The authors would like to thank Mr. K. Kellogg for his support and Mr. R. Thomas for his assistance in the measurement.

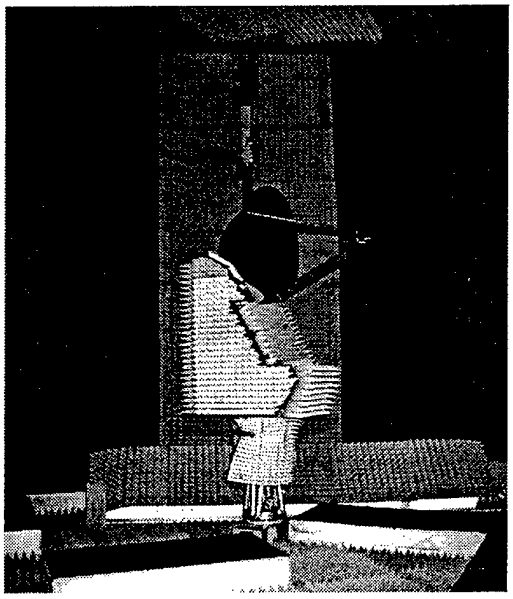


Figure 1. SeaWinds radar Antenna mounted in the cylindrical near-field range facility at the JPL.

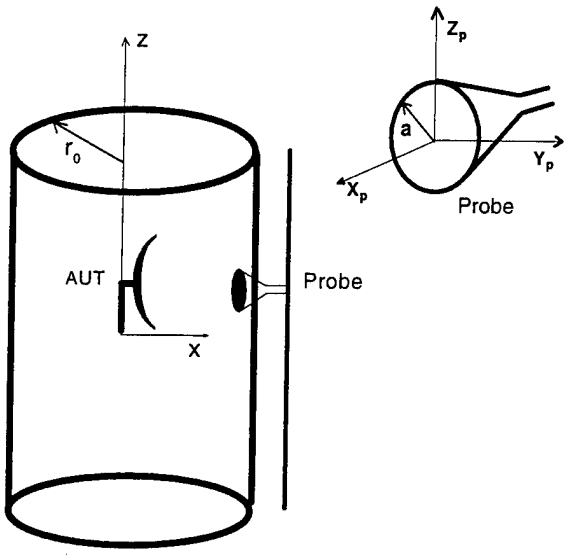


Figure 2. (a) Cylindrical near-field configuration and (b) probe coordinate system.

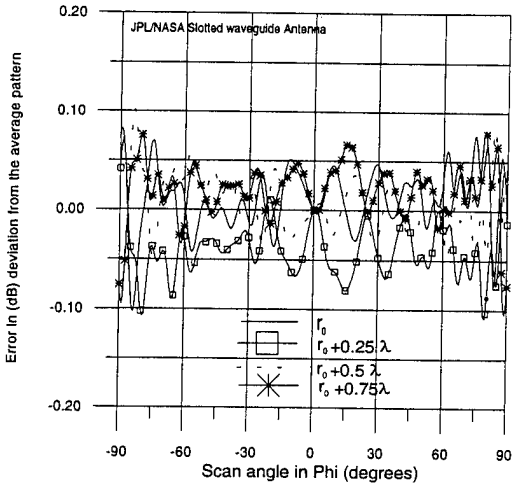


Figure 3. Typical far-field pattern error variation due to near-field multiple reflection between probe and antenna under test.

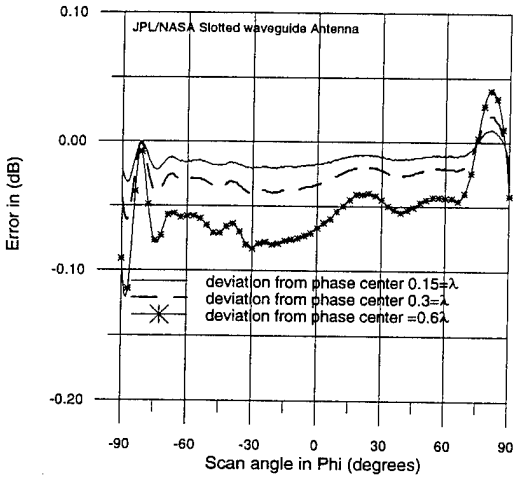


Figure 4. Typical far-field pattern error variation due to lack of accurate knowledge of separation distance between antenna under test and phase center location.

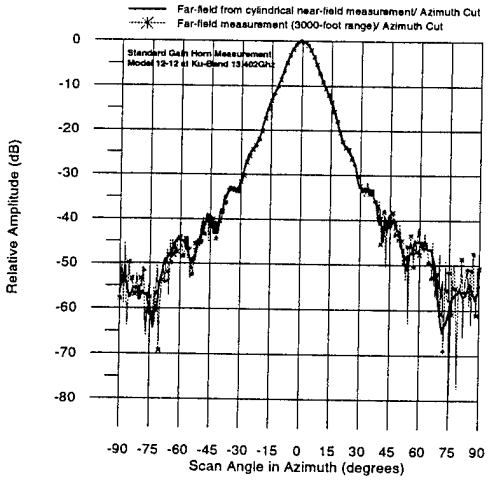


Figure 5. Comparison of standard gain horn far-field pattern obtained from cylindrical near-field measurement and direct far-field measurement.

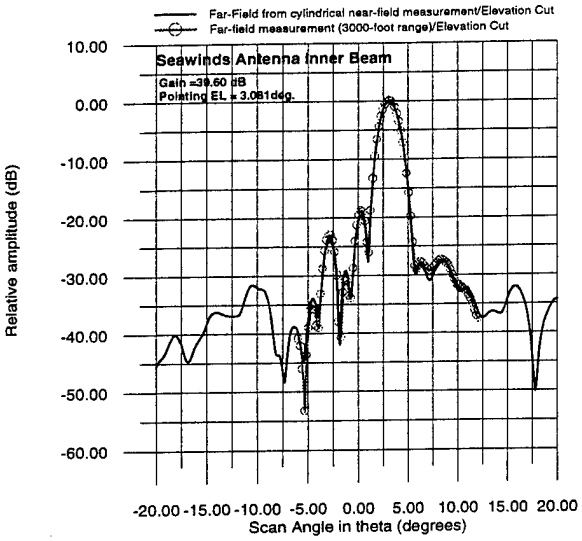


Figure 6. Comparison of H-pol SeaWinds radar antenna elevation plane far-field pattern obtained from cylindrical near-field measurement and direct far-field pattern measurement.

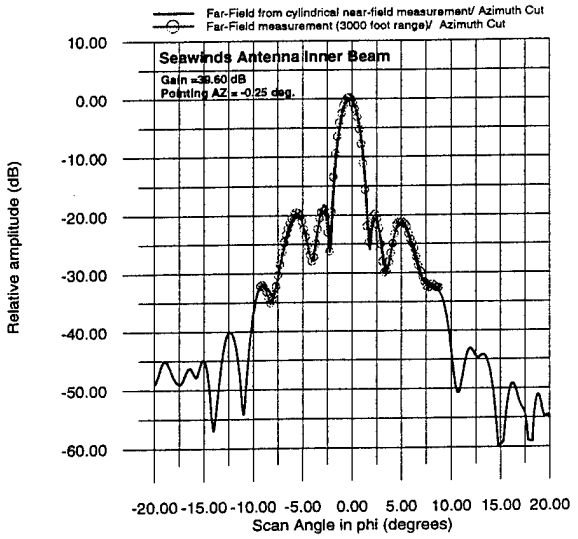


Figure 7. Comparison of H-pol SeaWinds radar antenna azimuth plane far-field pattern obtained from cylindrical near-field measurement and direct far-field pattern measurement.

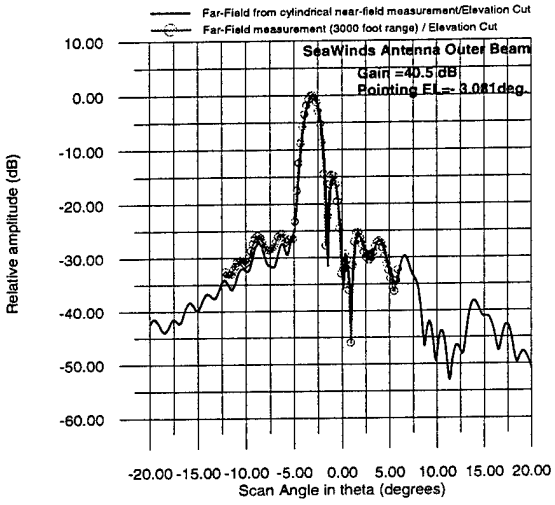


Figure 8. Comparison of V-pol SeaWinds radar antenna elevation plane far-field pattern obtained from cylindrical near-field measurement and direct far-field pattern measurement.

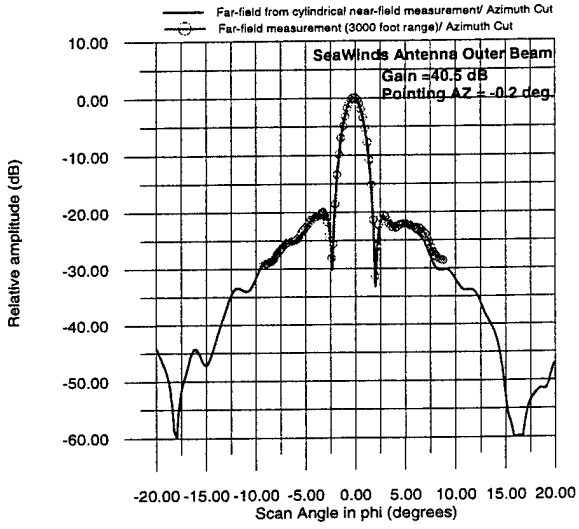


Figure 9. Comparison of V-pol SeaWinds radar antenna azimuth plane far-field pattern obtained from cylindrical near-field measurement and direct far-field pattern measurement.

Detection of Pollutants in Liquids by Laser Induced Breakdown Spectroscopy Technique

G.Arca, A.Ciucci*, V.Palleschi, S.Rastelli and E.Tognoni

IFAM - Istituto di Fisica Atomica e Molecolare del C.N.R.
Via del Giardino, 7 - 56127 PISA
Tel. +39 (50) 888109 - Fax: +39 (50) 888135
e-mail: vince@risc.ifam.pi.cnr.it
WWW: http://www.ifam.pi.cnr.it

* ENEA - Ente per le Nuove tecnologie, l'Energia e l'Ambiente
Centro Ricerche Ambiente Marino
Pozzuolo di Lerici CP 316 - 19100 (SP) I
Tel. +39 (187) 536291

ABSTRACT

LIBS (Laser Induced Breakdown Spectroscopy) is an innovative technique [1-3], which has proven very valuable in the accurate measurement of trace concentration of atomic pollutants in gas [4-6] and solids [7-12].

Given these positive characteristics and the good results obtained on the field by LIBS technique, either in industrial exhausts monitoring and polluted soil analysis, one could ask about the possibility of applying the fundamentals of LIBS method to the study of polluted liquids, in particular water. The group at IFAM-CNR (Pisa) has been conducting extensive researches for verifying the reliability of LIBS analysis of polluted water, with the aim of developing a diagnostic device suitable for *in situ* continuous monitoring operation. Main goal of our research was to keep the experimental setup as simple as possible, but still maintaining a sensitivity for trace pollutants concentrations useful for actual detection of potentially dangerous pollution levels in the sample under analysis.

EXPERIMENTAL SETUP

In order to produce the breakdown on the water surface, a Nd:YAG Laser is used. It delivers about 500 mJ in 8ns FWHM pulses by a 10 Hz repetition rate. The beam is focused by a 30 cm lens on the surface and the discharge light, generated by the emission of the recombination of the excited and ionized atoms, is collected through a suitable optical system and passed on to a 1 m spectrometer. The signal is acquired through an Optical Multi-channel Analyzer. The apparatus is entirely controlled by personal computers, which provide also an automated analysis of the spectrum (Fig. 1).

When setting up a LIBS experiment, one has to deal with the bremsstrahlung radiation which determines a continuum radiation background signal. This signal corresponds to a physical process taking place in the early hundreds of nanoseconds (ionized atom emission) and thus, it can not be reduced using standard averaging procedures. The effect of the continuum background on LIBS analysis can be reduced by starting the spectral acquisition with a given time delay after the breakdown. This delay depends on the characteristics of the LIBS system; in our case we found an optimum configuration using delays of order 1-2 microseconds. However, the drawback of this method is the impossibility to observe discrete emissions lines taking place and decaying within this time.

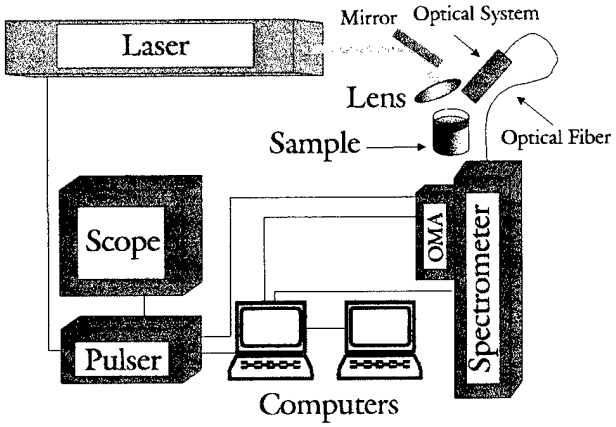


Fig. 1: Experimental LIBS setup at IFAM laboratory.

0-7803-3068-4/96$5.00©1996 IEEE

RESULTS

Inquiries have been focused mostly on atomic species, such as Al, Pb, Cr, Mg, Cu and Ca. The LIBS detection limits, arbitrarily defined as the element concentration which gives a spectral line signal to noise of 2, vary for these elements from a few parts per million (ppm) to a few parts per billion, depending on the solute.

Our first purpose has been testing the feasibility of LIBS technique for trace analysis of water. We started by measuring the concentration of a test drinking water component (Mg) via LIBS and comparing these results with those given by standard chemical analysis [13] on several drinking water samples. Results are given in Fig. 2. The LIBS signal is the integrated intensity of the Mg doublet lines at wavelength 2795.53 Å and 2802.7 Å. As it can be seen, the LIBS intensity is proportional to Mg concentration over a wide range of concentrations. Similar measurements have been conducted on other ionic pollutants and linearity has always been observed. These outcomes enable us to use LIBS intensities to measure trace concentration. With this technique we were able to detect concentration up to 2 ppm.

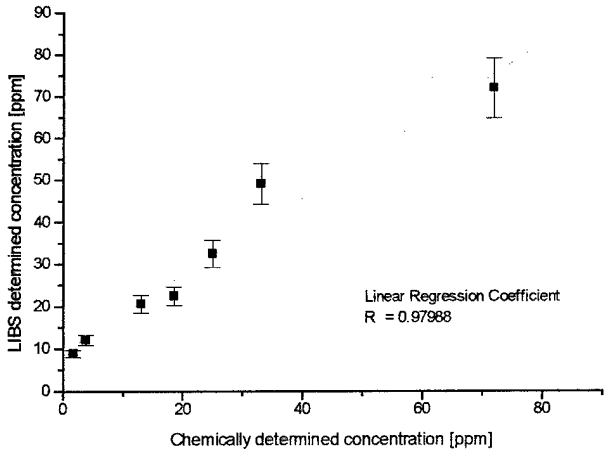


Fig. 2: Comparison between the LIBS results (for Mg concentration) vs. chemically determined concentration. Results corresponding to the two lines of the Mg doublet at 2795.53 Å and 2802.7 Å are shown.

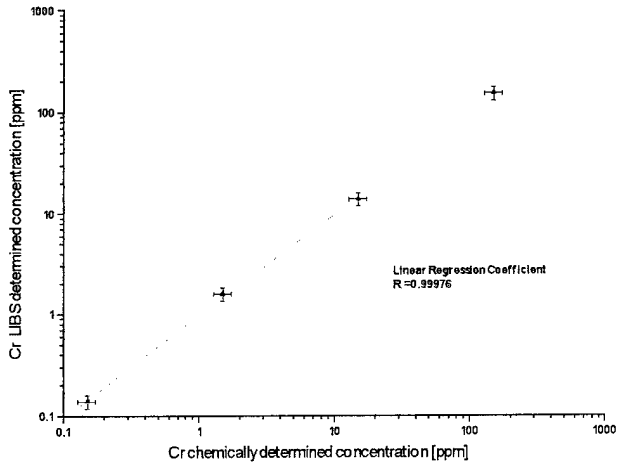


Fig. 3: Comparison between the LIBS results (for Cr concentration) vs. chemically determined concentration on log-log paper. Results corresponding to the Cr line at 2835.63 Å are shown.

The second step of our investigation consisted in polluting a water sample with some metals in very small concentrations. We aimed at determining the LIBS detectability threshold for these elements (for a definition of this limit, we refer the reader to the beginning of this section). Without the pretense of making a systematic classification we limited ourselves to a a few elements, which are relevant to environmental pollution problems: Cu, Cr and Pb. Results are reported in Table 1.

Table 1: Detection limit for several atomic pollutants in water with the reference wavelength indicated.

Element	Wavelength	Detection Limit
Cr	2835.63 Å	100 ppb
Pb	2833.05 Å	100 ppm
Cu	3247.54 Å	50 ppb

Some results relative to several known concentrations of Cr 3 (wavelength 2835.63 Å) can be seen in Fig.3.

The detection limits obtained are an interesting result and suggest possible future applications of the LIBS technique to "in field" continuous monitoring of water, both drinking water and water from industrial plants.

ALTERNATIVE METHOD

The technique just described has a great advantage with respect to laboratory analysis, since it is especially flexible and doesn't require the presence of trained personnel to be employed.

However the sensitivity in the described configuration might not be sufficient for all needs or all pollutants (as it can be seen from Table 1, Pb and Cr have detection thresholds higher than Cu). In order to achieve higher sensitivities we have devised a simple alternative method which has proven capable of increasing the detectability limit of about one order of magnitude, as reported in Table 2.

Table 2: Detection limit for several atomic pollutants on a solid matrix water with the reference wavelength indicated.

Element	Wavelength	Detection Limit
Cr	2835.63 Å	~ 10 ppb
Pb	2833.05 Å	~ 5 ppm
Cu	3247.54 Å	~ 5 ppb

The method consists in preparing a pellet of a solid matrix (KBr) in which we mix a few drops of the liquid to be analyzed. The laser beam is then focused on the KBr solid matrix and the LIBS signal is collected and analyzed in the usual way. The "solid matrix" configuration has several advantages with respect to the "free surface" method: first, a solid doesn't ripple like a liquid surface and therefore the incidence point of the laser light is accurately determined. Second, there is in this case a better laser-material coupling which allows for higher plasma temperatures and electron densities, hence higher signals. Third, whenever the polluted liquid is available in a limited quantity, this "trick" turns out very helpful, since a few ml of water are enough for a complete multielemental analysis.

CONCLUSIONS

The results we have brought in this paper show that it is feasible to apply the LIBS technique for the detection of trace pollutants in water. The "solid matrix" configuration allows for higher sensitivities, while the "free surface" configuration is particularly suited for *in situ* real time monitoring.

REFERENCES

[1] L.J. Radziemsky, T.R. Loree, D.A. Cremers and N.M. Hoffman: Anal. Chem. 55, 1246 (1983).

[2] D.A. Cremers and L.J. Radziemsky: Anal. Chem. 55, 1252 (1983).

[3] J. Belliveau, L. Cadwell, K. Coleman, L. Huwel and H.Griffin: Appl. Spectrosc. 39, 727 (1985).

[4] M. Casini, A. Ciucci, M. De Rosa, F. Famà, V. Palleschi, A. Salvetti, D.P. Singh and M. Vaselli: Optolaser 3, 26 (1990).

[5] M. Casini, M.A. Harith, V. Palleschi, A. Salvetti, D.P.Singh and M. Vaselli: Laser Part. Beams 9, 633 (1991).

[6] C. Lazzari, M. De Rosa, S. Rastelli, A. Ciucci, V.Palleschi and A. Salvetti: Laser Part. Beams 12, 525 (1994).

[7] A.Ciucci, V.Palleschi and S.Rastelli: Trace pollutants analysis in soil by a time-resolved Laser Induced Breakdown Spectroscopy technique, Appl. Physics B (in press 1995)

[8] H. Schroeder, I.Schechter, R.Wisbrun, R.Niessner: "Detection of heavy metals in environmental samples using laser spark analysis" in Excimer lasers and applications (L.D. Laude ed. 1994, The Netherlands) pp. 269-287.

[9] D.K. Ottesen: "The development of laser spark emission spectroscopy for the characterization of ash deposits", in: 24th Int. Symp. on Combustion, The Combustion Institute, pp.1579-1585 (1992).

[10] R. Wisbrun, I. Schechter, R. Niessner, H. Schroeder: Laser-induced Breakdown Spectroscopy for detection of heavy metals in environmental samples, SPIE vol. 1716, 2-14 (1992).

[11] S. Rastelli: Thesis (Physics Department, University of Pisa, 1994).

[12] R. Barbini, R. Fantoni, A. Palucci, F. Colao and S. Ribezzo: ENEA Report RT/INN/94/28 (1994).

[13] Measurements performed at the ENEL-CRT laboratories in Pisa

Contextual dynamic neural networks learning in multispectral images classification

B.Solaiman, M.C.Mouchot and A.Hillion
Ecole Nationale Supérieure des Télécommunications de Bretagne
Dept Image & Traitemet de l'Information
B.P 832, 29285 Brest-Cedex, FRANCE
Tel: 33 98 00 13 08, Fax: 33 98 00 10 98, Email : Basel.Solaiman@enst-bretagne.fr

Abstract :

Various methods for integrating spatial contextual information in multispectral images classification have been developed during the last two decades. These methods have for a large part been of two main types : 1)Pre-classification neighborhood-based using spatial contextual correlation between adjacent pixels in the spectral space, 2)Postprocessing-based smoothing using the contextual correlation between adjacent pixels in the "decision" space. In this paper, an iterative contextual classification algorithm is developed. The aim of this algorithm is to use the spatial contextual correlation between adjacent pixels in order to form the data base to be used in learning a neural network classifier.

I - Introduction :

Multispectral images interpretation using computer-based methods is one of the most important tasks in the analysis of remotely sensed satellite imagery. These methods consider, at the pixel level, the reflected radiation from different spectral bands as a numerical feature vector in the feature space. This permits to consider the multispectral images interpretation problem as a classification (or pattern recognition) one. Therefore, mathematical models already developed in classification theory can be applied in discriminating land covers. Since land use occurs in patches larger than the pixel footprint and since slight misregistration errors may exist between the ground truth and the spectral data, it seems clear that information from neighboring pixels should increase classification accuracy. This information is generally referred to as spatial contextual information. Various methods for integrating spatial contextual information in multispectral images classification have been developed during the last two decades. These methods have, for a large part, been of two types: 1)Pre-classification neighborhood-based using spatial correlation between adjacent pixels in the spectral space, 2)Post processing-based smoothing using the correlation between adjacent pixels in the "decision" space.

In this paper, a new approach permitting the integration of spatial contextual information is proposed. This approach is based on the fact that training pixels extraction (in supervised classification) is time consuming, involves an expensive enterprise of field visits and requires the use of reference data such as topographic maps and air photographs. In addition, the ground truth samples are systematically biased due to constrains induced by the field campaign.

Therefore, the proposed approach starts by learning an initial small size learning base, and then, by using the spatial contextual information in the decision space (obtained thematic map) and in the feature space (spectral images), a new labelled training base is then extracted. This procedure is then repeated in an iterative way and thematic maps are obtained at each iteration. The extraction of new patterns is controlled by :

1) The homogeneity in the decision and the feature spaces using Nagao windows. This control is conducted in order to insure that selected pixels do not belong to edges.

2) The fuzzy classification of selected pixels. Only pixels having been classified (in thematic maps) identical to the most ressemblant class (using the fuzzy classification) will be kept. This control is of extreme importance in order to solve the problem of classes absorption.

II-Contextual iterative base forming :

In this section, we propose to introduce a dynamic contextual classification system. The basic idea of this system is to integrate contextual information issued from both spatial and decision spaces in order to form the data base to be used in the learning process of the neural network. This operation is repeated in an iterative way. It is to be mentioned that this system is completely independent of the neural network to be used in the neural classification process. The general scheme of the proposed system is depicted in figure 1.

As can be noticed, the proposed system starts by learning an initial small size data base containing samples selected manually by an expert. After the end of this learning process, an initial thematic map is obtained. A new learning data base containing the initial one as well as new samples is then formed. The extraction of new samples in the contextual base forming block is governed by :

1) Homogeneity measures in the spatial and in the decision spaces.

2) Information issued from the initial learning data base.

In fact, in order to obtain learning samples that are not issued from edges, homogeneity criteria is needed.

0-7803-3068-4/96$5.00©1996 IEEE

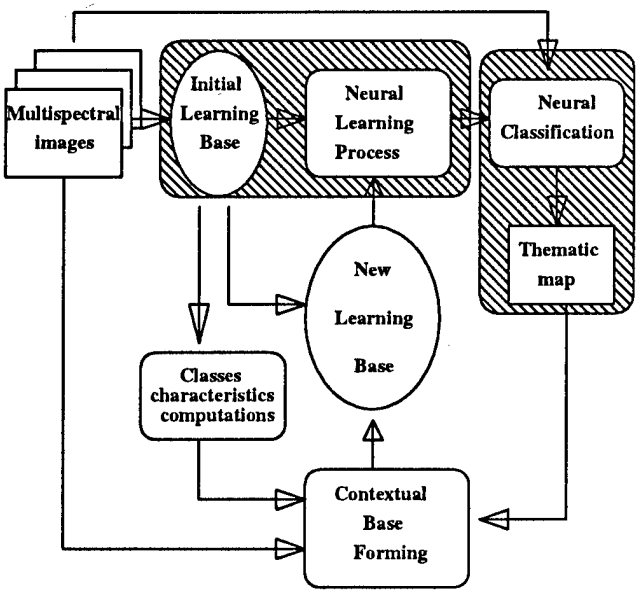


Figure 1. Dynamic contextual system for neural networks multispectral images classification

This criteria is established using both spatial and decisional contextual information. The use of information issued from the initial learning base is of extreme importance in order to prevent the class absorption problem. It is to be noticed that information issued from the initial learning base will be computed only one time and will not be reactualized as a function of new learning basis.

II- a - homogeneity criteria :

In order to give a decision concerning a selected pixel as belonging into a homogeneous region or not, we generally use a rectangular NxN neighboring window. If N is chosen to be equal to 5, then, if considering a Spot image for example, the pixel must be in the centre of a 100m x 100m homogeneous region. This is a severe situation that may be difficult to encounter especially when analysing European images. For this reason, the use of the Nagao cliques is proposed in this study. In fact, Nagao cliques are developed in the context of the Nagao edge preserving filter [1]. In this filter, 8 cliques in a 5x5 window surrounding each pixel are defined (figure 2).

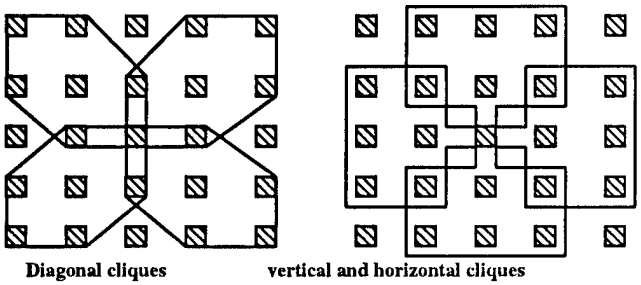


Figure 2: Nagao filter diagonal, vertical and horizontal cliques

Each clique contains 7 pixels. The form of these cliques is determined in such a way that, if the considered pixel is adjacent to an edge pixel, then, at least one of the cliques covers a small size homogeneous region containing this pixel. In the original Nagao filter, each pixel is assigned to the mean value of the clique with the minimal grey level standard deviation. This clique (generally referred to as the winning clique) will have the minimal grey level standard deviation, and thus, the new grey level affected to the pixel will not be significantly different from the old one. Therefore, this filter realizes the smoothing operation while preserving the general appearance of contours in the image.

In this study, each clique is associated with a **clique label** (the label most frequently encountered within the clique in the associated thematic map) as well as a **clique vote** (the number of pixels having this majority vote label).

The decision concerning the membership of a given pixel into a homogeneous region is realized using a selected spectral band as well as the thematic map through the following algorithm :

1. realize the extraction of the 8 Nagao cliques in the considered spectral band : S1(b), S2(b),.. , S8(b) (containing gray levels in the spectral band "b"), as well as the 8 Nagao cliques from the thematic map at the same position T1, T2,... , T8 (containing the decision values),
2. determine the winning clique in the spectral domain : Sw (the clique with the minimal grey level standard deviation),
3. determine the vote, Vote(Tw), and the label, Label(Tw), of the winning clique in the thematic map,
4. if (Vote(Tw) = 7) then the pixel is considered to belong to a homogeneous region.

In fact, the selection of the winning clique, Sw, with the minimal grey level standard deviation, does not necessarily mean that the pixel belongs to a homogeneous region. Therefore, the use of steps 3 and 4 is necessary in order to indicate if all the pixels from the winning clique are classified as belonging to the same thematic class by the classifier.

II- b - Class characteristics computation:

Each individual thematic class, is characterized by two vectors: the mean and the variance vectors. Each component of these vectors corresponds to the mean and the variance values in the corresponding spectral band. These parameters are used in characterising each individual class. They are computed using the initial learning data base containing samples selected manually by the expert. These parameters are not actualized through different iterations in order to preserve the initial knowledge injected by the expert.

This is mainly conducted in order to avoid the class absorption problem.

In fact, some classes are very poorly represented in a studied scene. Therefore, samples issued from other classes may be affected wrongly. This bad classification would generate an important deviation. It is precisely for this reason that :

-the computation of different class parameters are computed using the initial learning base,

- the initial data base is periodically injected to the new learning base at each new iteration.

III - Simulation results :

The simulation of this approach was conducted using a Spot image acquired over the agricultural area of Hillion (Northwest of France). Ten classes are selected and an initial small size learning data base is manually formed by an expert. This base contains 100 pixels from each class.

The classification method used in this study is based on the use of the Hybrid Learning Vector Quantization neural network [2], [3]. This neural network is based on the use of a Self Organizing Feature Map with a hybrid (Supervised/Unsupervised) learning algorithm that has shown to be particularly adapted into the classification of agricultural multispectral data.

During each iteration of the contextual base forming, 100 new pixels issued from each class are added to the learning data base. This small incrementation in the size of the learning base is essential since it is mainly related to the quality of the reconstructed thematic map.

Two simulation studies are then conducted. In the first experimentation, the information characterizing different classes and issued from the initial data base, is not used. Only the homogeneity criteria in the thematic map in establishing the learning basis is used. Obtained results have shown that classes weakly represented in the analysed scene will disappear after few iterations. This is mainly due to the fact in the first obtained thematic maps, where a lot of errors occurs, the pixels injected to the learning base (which are supposed to represent the class) will be issued from other classes. The classification accuracy will loose its significance. Therefore, the integration of the homogeneity criteria in characterizing different classes and issued from the initial learning base is of great importance.

In the second simulation, this criteria in integrated. Obtained results, shown in figure 3, are extremely encouraging in terms of the quality of the obtained thematic maps. The use of homogeneity criterion based on the Nagao windows permits to preserve edges in thematic maps. Obtained results show that this approach has permitted to considerably improve the classification process in terms of generalization.

As can be noticed from figure 3, after 15 iterations (where each class is represented by 1600 pixels), this approach has converged in the sense that further iterations will not improve the quality of the obtained thematic map.

IV - Conclusions :

In this study, we have shown a new approach permitting the integration of contextual information in the phase of the learning data base forming. Several assumptions are made in order to validate the new learning patterns. The only a prior information used through this approach concerns the selection of the initial learning data base as well as the number of thematic land covers (classes).

Recall that this approach is completely independent of the classification method used. Therefore, it may constitute a new methodology in forming learning basis that can be used in any type of classification including the neural network classification approach.

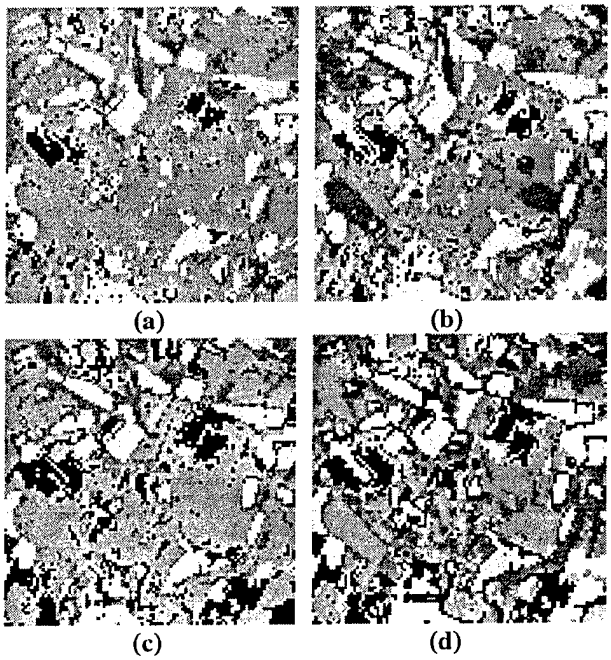


Figure 3 : Obtained thematic maps :
(a) using the initial learning base(100pixels/class),
(b) after one iteration (200 pixels/class),
(c) after 10 iteration (1100 pixels/class), and,
(d) after 15 iteration (1600 pixels/class).

References :

[1]M. Nagao and T. Matsuyama, "Edge preserving smoothing", Computer Graphics and Image Processing, Vol. 9, 1979.

[2]B. Solaiman and M.C. Mouchot, " A comparative study of conventional and Neural Network classification of multispectral data", International Geoscience and Remote Sensing Symposium, IGARSS'94, Pasadena, 8-12 Aug 1994.

[3]B. Solaiman, M.C. Mouchot, R. Brown and B. Brisco, "A comparative study on multispectral agricultural images classification using Bayesian and neural networks approaches", International Symposium on Satellite and remote sensing, 26-30 Sept, Rome, Italy 1994.

From Leaf to Scene: Scaling Problems in Remote Sensing of Vegetation

Narendra S. Goel and Wenhan Qin
Department of Computer Science, Wayne State University
431 State Hall, Detroit, MI 48202
Tel (313) 577-3310 Fax (313) 577-6868
Email: wenhan@epic.cs.wayne.edu

Abstract–Some important spatial scaling issues associated with remote sensing of vegetation are addressed. These include estimation of leaf optical properties and canopy parameters such as LAI, land cover and vegetation type from reflectances of a scene. Based on relationship between canopy architecture and canopy reflectance, we discuss why the above goals are easier to achieve for a homogeneous canopy/scene and very difficult for a heterogeneous one. Some preliminary thoughts on new algorithms which may succeed for the heterogeneous scene are presented.

INTRODUCTION

The reflectance of a leaf depends on the optical properties of its constituents (chrolophyll, water etc.) and how they are structurally arranged within the leaf. The reflectance of a canopy, in turn, depends on the optical properties of its constituents (leaves, branches etc.) and how they are structurally placed within the canopy. The reflectance of a scene, on a km×km level, depends upon the reflectance of its components (canopies) and scene composition.

There are two kinds of spatial scaling problems related to remote sensing: scaling up–calculating canopy/scene reflectance, given information on optical and structural properties of its constituents and scaling down–extracting information on constituents from measured scene reflectance. Remote sensing of the Earth's surface is a scaling down problem.

One approach to assess if one would succeed in a scaling down problem is to investigate the corresponding scaling up problem. For example, if one finds that the scene reflectance is not sufficiently sensitive to changes in the optical properties of the leaves, one should not hope to estimate changes in the chemical properties of the leaves from the scene reflectance data. Even with sufficient sensitivity, there is another issue. In remote sensing, the number of canopy parameters which affect scene reflectance generally exceeds the number of "informationally independent" remote measurements (in a few wavelengths and for a few solar/view directions). Thus, for an accurate estimation for a specific parameter, one needs a procedure and appropriate optimal remote sensing conditions in which the influences of other canopy parameters are least likely. We refer to it as an optimal sampling domain (OSD).

Here, we summarize some scaling results for both homogeneous and heterogeneous vegetation stands, and make inferences about the chances for success in remote sensing of vegetation.

ESTIMATION OF VEGETATION PROPERTIES FROM CANOPY REFLECTANCE

During the last thirty years, especially during the last decade, a number of models have been developed which allow scaling up studies up to a canopy level. These models are most accurate for homogeneous canopies and their accuracy decreases with an increase in the canopy heterogeneity. Likewise, several approaches for estimating leaf or canopy level parameters (scaling down) from canopy/scene reflectance have been investigated including inversion of a scaling up canopy reflectance model, use of vegetation indices (VIs) like NDVI, and training neural networks using measurements about canopy parameters and corresponding canopy reflectances for a variety of canopies. We will now present our views about the feasibility of accurate assessment of various canopy parameters and the corresponding OSD.

Leaf Optical Properties

Leaf optical properties are good indicators for the status of the health of vegetation. By using the derivative $D=dR/d\rho$ (where R is the canopy directional reflectance and ρ is the leaf hemispheric reflectance), one can evaluate the feasibility and OSD for estimating ρ. Obviously, the larger is D, the higher is the possibility to estimate ρ (when the derivative is less than 1.0 in a given spectral region, one should not hope to extract ρ from canopy reflectances in that region). We use the SAIL model, modified to include hotspot effects [1], to calculate D for homogeneous canopies. We find that (1) the higher the LAI or ρ, the larger is the derivative (easier to estimate ρ); (2) D is less than 1.0 for nadir viewing, independent of solar direction (Fig.1) and increases with an increase of view/sun zenith angle. Therefore, it is unlikely to estimate ρ from nadir reflectance; (3) values of D in the hotspot direction at a high solar zenith angle (SZA) is much larger than for other view directions (Fig.2). This suggests that hotspot direction at a high SZA is

This work was partially supported by NASA.
0-7803-3068-4/96$5.00©1996 IEEE

the OSD for leaf optical property estimation; and (4) D increases with ρ, suggesting that leaf optical property estimation is more accurate in the near-infrared (NIR) region than in the visible one.

Canopy Architectural Parameters

We used a model Diana [2], a radiosity based model for calculating radiation regime in architecturally realistic canopies, for scaling up studies for both homogeneous and heterogeneous canopies (like corn and aspen). In these studies, we vary various canopy architectural parameters and calculate how the relationship between canopy reflectance/VI and a parameter of interest changes when other parameters are changed. The details are given in [3-4].

To find the OSD for a specific parameter of interest, a signal-to-noise ratio [3] is applied as an indicator to evaluate the usefulness of all possible view angles in a given view plane (e.g., PP–the principal plane or PC–the principal cone, both being considered as most informative view planes). OSDs for estimating leaf area index (LAI) or percentage ground cover (GC), vegetation type (using leaf size as an index for identification) and Fapar (fraction of the incident photosynthetically active radiation absorbed by the canopy) are summarized below.

LAI: OSD exists only for uniform canopies (e.g., grasslands, crops without distinct row structure) and there is a possibility to estimate LAI for such a canopy. The major "noise" factors to LAI estimation are soil brightness and leaf angle distribution (LAD). Due to the insensitivity of spectral reflectance at high solar/view zenith angles to LAD, the OSD exists in the view directions with high zenith angles in backscattering region at a high SZA. If VI method is used for the estimation, there are two indices which are better than others [3].

GC: Although LAI is unlikely to be estimated for heterogeneous vegetation, GC still can be estimated if reflectance at a low view zenith angle (VZA) in the forward scattering region is used, regardless of SZA.

Leaf Size: The relative leaf size may be useful for identifying vegetation type. It ranges from 0.02 to 0.12 for tree canopies and 0.1 to 0.4 for most crop canopies. It can be estimated by using the normalized reflectance (preferably in NIR wavebands) in the hotspot region (usually in the PC) [4]. Most of the time the OSD is within ±2° off the hotspot direction at a high SZA. For a crop canopy or a tree or leaf canopy with low LAI, this task is easy to achieve. But for a tree canopy with unknown LAI and spacing, it seems unlikely that one can estimate leaf size from canopy reflectance.

Fapar: There exist near-linear relationships between Fapar and most vegetation indices for crops and trees [2]. But these relations vary strongly with soil brightness and sun and/or view geometries. We find that in OSD other VIs, rather than NDVI, are preferred for estimating Fapar because they are least sensitive to the soil brightness and other parameters. In the PP the OSD is almost identical with a high VZA region, depending on vegetation type and sun-view geometry [3].

Plant/tree size/shape: We find that there is no OSD for these parameters even off-nadir reflectance data are used, making their estimation from canopy reflectance highly unlikely.

ISSUES AT SCENE LEVEL

For a scene, there are several levels of heterogeneity in nature–different vegetation/community types (with different optical/morphological properties) or even different kinds of landscape. We are in the process of analyzing the canopy parameter estimation at a scene level. But here we can provide a glimpse of the complications through comparing some results for two types of heterogeneous vegetation–crops and trees.

For these canopies, we chose the spacing distance between trees (or between adjacent rows) as small ($0.5h$, h is the mean canopy height), medium ($1.0h$) and large ($1.5h$). We examined the variation of reflectance in both red and NIR regions and the corresponding NDVI for the same LAI but different spacings. Two SZAs (10 and 60°) and five VZAs (0, ±30, ±60°) in the PP are considered.

The results (Figs.3-4 show two cases) suggest that (1) with the same spacing pattern, reflectance for tree canopies varies much more than for crops (e.g., for high LAI crops at a high SZA, the influence of spacing can be ignored but not for trees); (2) reflectance and NDVI at a low SZA are more sensitive to the heterogeneity of canopy than those at a high SZA; (3) for tree canopies, higher the LAI, the stronger is the influence of spacing; (4) the impact of spacing also varies with the view geometry, being much stronger in the backscattering region than in the forward scattering region. Therefore, among these five VZAs, the reflectance or NDVI at -30° (forward scattering side) is least affected by spacing (Fig.4).

When spacing is small, the red reflectance or NDVI only depends on LAI, almost independent of the vegetation type, SZA, and even VZA except in the hotspot direction. While for NIR in the least sensitive view direction (-30° here), the variation of reflectance is very small (±0.05) if spacing is larger than the canopy's height. This result shows that effect of heterogeneity is also spectral dependent. For the scene concerned here (only consisting of two vegetation types), only when the spacing is small, can the canopy be considered homogeneous for red and NDVI but not for NIR. The strongest influence of spacing occurs for the tree canopies with high LAI at a low SZA, where reflectance in the red (NIR) increases (decreases)

significantly with increasing of spacing. As a result, NDVI decreases dramatically (from 0.85 to 0.45) as spacing increases even when LAI is kept constant. Undoubtedly, the above influences of spacing on reflectance and VIs (here using NDVI as an example) will affect the applicability and extent of results and conclusions of any study limited to crops and grasslands.

To succeed in extraction of scene parameters, one need simple scaling up approaches for scenes. For a tree canopy with quite large spacing, geometric-optical models [5] are available. However, such models are applicable to scenes consisting of single species, dense tree crowns and not to the mixed scene consisting of vegetation, water body and other land types. Due to the strong impact of heterogeneity discussed above, it is desirable to develop more powerful and flexible models to simulate the directional reflectance from such a scene. An approach could be to first divide the whole scene into several uniform subscenes, calculate BRDF of each subscene, and then "couple" BRDF's of neighboring subscenes in an input-output relationship mode. Here, approximating BRDF by a set of spherical harmonics [6] would be computationally advantageous.

REFERENCES

[1] N.S. Goel and A. Kuusk, "Evaluation of one-dimensional analytical models for vegetation canopies," Proc. 12th Int. Geosci. Remote Sens. Symp., pp. 505-1507, 1992.

[2] N.S. Goel, I. Rozehnal and R.L. Thompson, "A computer graphics based model for scattering from objects of arbitrary shapes in the optical region," Remote Sens. Environ., vol. 36, pp. 73-104, 1991.

[3] N.S. Goel and W. Qin, "Influences of canopy architecture on relationships between various vegetation indices and LAI and FPAR: a computer simulation," Remote Sens. Rev., vol. 10, pp. 309-347, 1994.

[4] W. Qin, N.S. Goel, and B. Wang, "Estimation of leaf size from hotspot observations," Proc. 16th Int. Geosci. Remote Sens. Symp., 1996 (in press).

[5] X. Li and A.H. Strahler, "Geometrical-optical modeling of the discrete-crown vegetation canopy: Effect of crown shape and mutual shadowing," IEEE Trans. Geosci Remote Sens., vol. GE-30, pp. 276-292, 1992.

[6] N.S. Goel and N.E. Reynolds, "Bidirectional canopy reflectance and its relationship to vegetation characteristics," Int. J. Remote Sens., vol. 10, pp. 107-132, 1989.

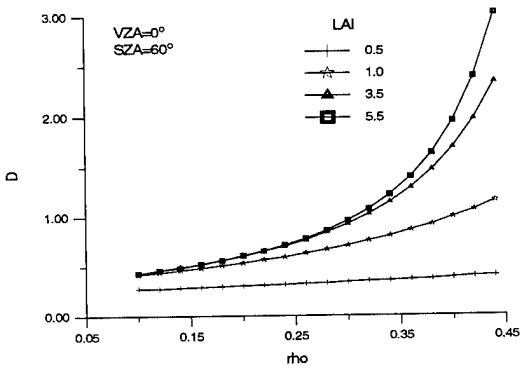


Fig. 1

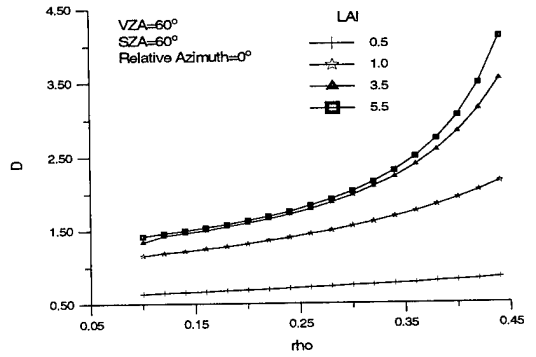


Fig. 2

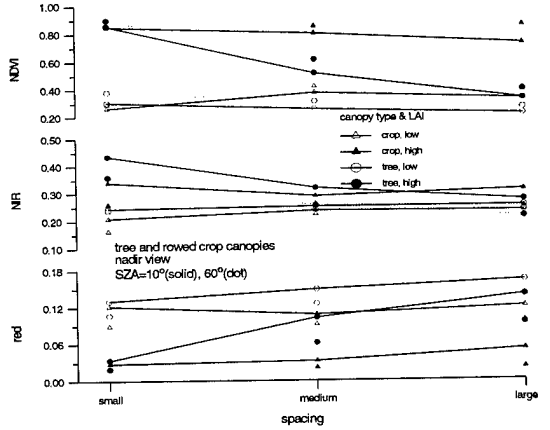


Fig.3

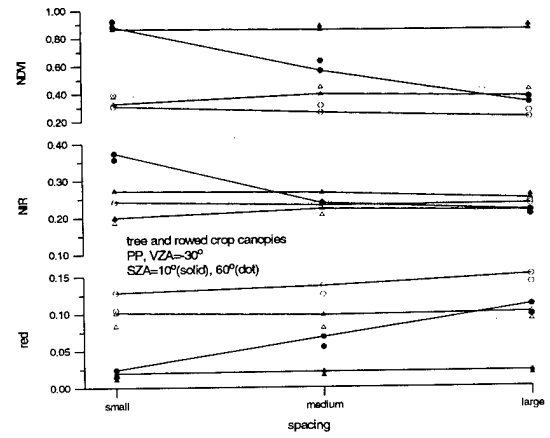


Fig. 4

Fig. 1 Derivative (D) of canopy reflectance vs. leaf reflectance (rho) for homogeneous canopies, spherical LAD, and four LAIs. SZA= 60° and nadir viewing.

Fig. 2 As Fig.1 except for the hotspot direction.

Fig. 3 Canopy reflectances and NDVI for crop and tree canopies for three spacings for VZA=0° (nadir viewing).

Fig. 4 As Fig.3 except for VZA=-30° (PP).

ART Neural Networks for Remote Sensing: Vegetation Classification from Landsat TM and Terrain Data*

Gail A. Carpenter, Marin N. Gjaja, Sucharita Gopal, and Curtis E. Woodcock
Boston University
677 Beacon Street, Boston, Massachusetts 02215 USA

Abstract -- A new methodology for automatic mapping from Landsat Thematic Mapper (TM) and terrain data, based on the fuzzy ARTMAP neural network, is developed. System capabilities are tested on a challenging remote sensing classification problem, using spectral and terrain features for vegetation classification in the Cleveland National Forest. After training at the pixel level, system capabilities are tested at the stand level, using sites not seen during training. Results are compared to those of maximum likelihood classifiers, as well as back propagation neural networks and K Nearest Neighbor algorithms. ARTMAP dynamics are fast, stable, and scalable, overcoming common limitations of back propagation, which did not give satisfactory performance. Best results are obtained using a hybrid system based on a convex combination of fuzzy ARTMAP and maximum likelihood predictions. Fuzzy ARTMAP automatically constructs a minimal number of recognition categories to meet accuracy criteria. A voting strategy improves prediction by training the system several times on different orderings of an input set. Voting assigns confidence estimates to competing predictions.

NEURAL NETWORKS AND REMOTE SENSING

Mapping vegetation from satellite remote sensing data has been an active area of research and development over a twenty year period [1]. Classification of multispectral imagery has proven useful for many mapping purposes [2] but has often been unsuccessful at differentiating species-level vegetation classes. Factors that contribute to these problems include the effects of local topography, background reflectance from soils or understory vegetation, high within-class variance due to the structure and patchiness of vegetation canopies, and the limitations of classification methodologies. To help differentiate vegetation types at the species level, ancillary data have often been used, and it is now common to use topographic variables such as elevation, slope, and aspect in predictive models [3]. Mapping systems that use spectral and ancillary data typically resemble rule-based expert systems [4]. Recently, neural networks have become one of the most exciting developments with respect to improvements in classification. This paper summarizes work that uses the fuzzy ARTMAP neural network [5] as the basis of a systematic methodology for automatic classification of vegetation at the species level from multispectral and ancillary data [6].

* This research was supported in part by the National Science Foundation (NSF SBR 93-00633 and NSF IRI 94-01659) and the Office of Naval Research (ONR N00014-95-1-0409 and ONR N00014-95-0657).

0-7803-3068-4/96$5.00©1996 IEEE

REMOTE SENSING TESTS

Cleveland National Forest test stand data - The data set from the Cleveland National Forest identifies the CALVEG vegetation class for 209 sites, representing 17 vegetation classes. The primary goal of this study is to develop and compare automated classification methods for large-scale remote sensing applications. In order to focus on the methods, the selected prediction problem could not be too easy, but neither could it be dominated by noise or chance. The test data set examined here thus excludes vegetation classes represented by only a few sites, leaving 8 vegetation classes (mixed conifer, canyon live oak, coast live oak, chamise, scrub oak, red shanks, and southern and northern mixed chaparral) and 163 sites. The prediction problem remains challenging and realistic: the pixel-based ($25m \times 25m$) remotely sensed data are typically noisy and unreliable; the number of training set sites (143) is small relative to the number of classes (8); some of the vegetation classes, such as the three different types of oak, are likely to have similar features; and the actual vegetation at each site, where sites range in size from 9 to 610 pixels (5,625 - 381,250 m^2), is, in all likelihood, not a pure sample of just one class.

Input variable combinations - For each pixel, the Cleveland Forest data set provides 6 Landsat Thematic Mapper (TM) band values, 3 linear combinations of the TM band values, and 4 terrain variables. The three linear combinations of TM1-5&7 reflect brightness (B), greenness (G), and wetness (W). Finally, four terrain variables - slope (SL), aspect (A), shade (SH), and elevation (E) - were derived from digital elevation models, warped to fit the Landsat image.

Tests focus primarily on fuzzy ARTMAP and maximum likelihood performance on data sets for which input **a** provides only the 6 TM values (combo 1) and on data sets for which **a** provides all 13 input variables (combo 2) (Table 1). On tests that use each of these input variable combinations, basic fuzzy ARTMAP and maximum likelihood (Table 1.A) have similar predictive accuracies: approximately 45-46% with the 6 TM input variables and 54-57% with all 13 variables. On data sets that provide various subsets of the 13 input variables, performance of the two systems can differ significantly. For example, when pixel inputs provide only the 3 linear combinations B, G, W (combo 3), maximum likelihood performance drops to 40% while fuzzy ARTMAP performance increases to 48%.

The patterns in the results of maximum likelihood classification as a function of inputs are consistent with past experience in remote sensing. Raw spectral bands have frequently produced better results than transforms such as brightness, greenness, and wetness. Similarly, combining the linearly transformed variables brightness,

greenness, and wetness with the original spectral bands yields no improvement.

The results of fuzzy ARTMAP classification are strikingly different, with the brightness, greenness, and wetness transforms resulting in better performance than the original spectral bands (combo 3). Even more divergent from maximum likelihood is the improved performance when fuzzy ARTMAP uses both the six spectral bands and the three linear transforms of the spectral band variables. One of the most interesting results of these tests is the increase in fuzzy ARTMAP performance from 44.7% to 51.9% when linear transforms are combined with the original spectral band inputs (combo 6). This result is in direct contrast with statistically-based classifiers. It also emphasizes the importance of selection of input features and suggests that performance might be further enhanced by other unknown transforms. Ancillary variables affect maximum likelihood and fuzzy ARTMAP performance similarly in the present studies.

K nearest neighbor and back propagation tests - The K nearest neighbor (KNN) algorithm [7] was also tested on the 6-variable and 13-variable input sets (Table 1.B). Predictive accuracy was similar to that of fuzzy ARTMAP and maximum likelihood, varying somewhat with the number of neighbors (K) chosen during testing. However, KNN needs to store all training set pixel vectors (approximately 10,000), while fuzzy ARTMAP compresses memory by a factor of 8 for combo 1, creating about 1200 ART_a categories during learning. Remarkably, using all 13 input variables, the average number of ART_a categories drops to 208, giving a compression ratio of 48:1 compared to KNN.

Although the back propagation neural network has been applied successfully to remote sensing classification problems (e.g., [8]), back propagation performance was not satisfactory on the present remote sensing problem. On combo 1, with TM1-5&7 as inputs, correct prediction rates ranged from 22% to 46% as the number of hidden units ranged from 15 to 60. The best test set prediction rate, obtained using 30 hidden units, was comparable to the average performance rates of maximum likelihood, KNN, and fuzzy ARTMAP. In general, back propagation requires slow learning and many presentations of each input, while fuzzy ARTMAP learning is fast and incremental, or "on-line." In addition, choosing the number of hidden units and optimizing the architecture typically require extensive simulation studies. Fuzzy ARTMAP is thus particularly well suited to ongoing training in situations where new information continues to arrive during use.

Site-level voting - ARTMAP voting, where voters decide on a prediction for each pixel, can boost performance by 3-4%. For mapping problems, however, a site or region fixes a more appropriate measurement scale than individual pixels. On the large-scale remote sensing tests in this section, voting at the site level, rather than the pixel level, proved to be the more successful of the two methods. For site-level voting, a number of fuzzy ARTMAP networks are trained on a given input set, each

Table 1. Test results

A Basic maximum likelihood and fuzzy ARTMAP

Combo #	Input variables	% Correct maximum likelihood	% Correct + (# F_2^a nodes) fuzzy ARTMAP
1	TM1-5&7	46	44.7 (1203 cats)
2	TM1-5&7 B, G, W SL, A, SH, E	54	57.2 (208 cats)
3	B, G, W	40	48.1 (1145 cats)
4	TM1-5&7 SL, A, SH, E	54	47.2 (365 cats)
5	TM1-5&7 SL, A, E	54	48.5 (392 cats)
6	TM1-5&7 B, G, W	46	51.9 (595 cats)
7	B, G, W SL, A, SH, E	52	56.6 (259 cats)

B K Nearest Neighbor (KNN)

Combo #	K=1	K=5	K=10
1	44.3%	47.0%	44.0%
2	56.0%	54.0%	56.0%

C Confidence thresholds and site-level voting

Combo 1 (6 variables)

Maximum likelihood		Fuzzy ARTMAP		
CT=-∞	CT=-21.6	$\overline{\rho}_a$=0	$\overline{\rho}_a$=0.87	$\overline{\rho}_a$=0.87, 5 voters
46.0%	48.8%	44.7%	46.4%	48.6%

Combo 2 (13 variables)

Maximum likelihood		Fuzzy ARTMAP	
CT=-∞	CT=10.0	$\overline{\rho}_a$=0	$\overline{\rho}_a$=0, 5 voters
54.0%	56.5%	57.2%	60.0%

with the inputs presented in a different randomly chosen order. Each voter then predicts the vegetation class of each test set site. Finally, then, the class prediction for each site is taken to be the one made by the largest number of voters.

Rejecting low-confidence predictions - Performance accuracy of fuzzy ARTMAP and maximum likelihood can be boosted by adding a confidence threshold, allowing only high-confidence test set pixels to participate in the site-level vegetation class decision. For fuzzy ARTMAP the matching criterion imposed by a baseline vigilance parameter $\overline{\rho}_a$ provides a natural confidence threshold For maximum likelihood, given a pixel input, the discriminant function value (DFV) for each vegetation class must exceed a confidence threshold (CT) before that pixel may participate in a site-level prediction.

Fuzzy ARTMAP results were found to be fairly constant across wide $\overline{\rho}_a$ intervals. Moderate threshold levels boosted performance somewhat when training produced many categories, as in the 6-variable tests (combo 1) (Table 1.C). As the threshold increases, at some point performance tends to increase for a short interval, then drop steeply, when the threshold is set so high that many useful predictions are discarded. With

both combo 1 and combo 2, maximum likelihood performance shows a similar trend as the confidence threshold increases. In contrast, on the 13-variable input set (combo 2), setting $\overline{\rho}_a$=0 gives optimal performance, and performance begins to drop significantly for $\overline{\rho}_a$>0.5.

Hybrid fuzzy ARTMAP / maximum likelihood classification system - The system variation with the best performance combines the predictions of trained fuzzy ARTMAP and maximum likelihood systems. The success of this method is due to the observation that the two classifiers tend to make predictive errors in somewhat different circumstances. For example, in combo 1 tests (6 variables), fuzzy ARTMAP makes more errors trying to identify red shanks sites than does maximum likelihood. Both classifiers do well on mixed conifer sites, but both do poorly on canyon live oak and northern mixed chaparral. An ideal hybrid system would choose the right decision when the two disagree, but designing such an optimal combination for a given problem would require *a priori* knowledge of the test set. Of a variety of hybrid algorithms tested, all showed some improvement over that of the individual systems. The hybrid that consistently gave best results took a convex combination of the two systems' site-level predictions, as follows.

To select from the 8 vegetation classes, maximum likelihood generates a prediction for each of the pixels in a site. Those pixels for which a definitive prediction is made (i.e., not an "inconclusive" response) can form a vector with components equal to the fraction of definitive pixels in that site assigned to each of the 8 classes. An analogous prediction vector for fuzzy ARTMAP lists the fraction of voters choosing each class. A convex combination of the two vectors, giving weight γ to fuzzy ARTMAP and (1-γ) to maximum likelihood, forms the hybrid prediction vector.

To test performance improvement of a hybrid, fuzzy ARTMAP and maximum likelihood systems were chosen to maximize individual system performance accuracy. For combo 1, fuzzy ARTMAP with 5 voters and $\overline{\rho}_a$ = 0.87 gave 48.6% correct predictions, while maximum likelihood with CT = -21.6 was 48.8% correct (Table 1.C). A convex-combination hybrid with γ = 0.6, which gives 60% weight to fuzzy ARTMAP, improved test set performance to 50.6%. With γ = 0.4, which gives 60% weight to maximum likelihood, performance was almost as high, 50.38% correct. With γ = 0.6, the hybrid system allows maximum likelihood predictions of red shanks and southern mixed chaparral sites to dominate the distributed (and largely incorrect) fuzzy ARTMAP predictions for these classes. For coast live oak sites and northern mixed chaparral, fuzzy ARTMAP compensates for a number of the maximum likelihood errors. At canyon live oak sites, where the two systems make the same errors, hybrid prediction is no better.

For combo 2, with all 13 variables, fuzzy ARTMAP with 5 voters and $\overline{\rho}_a$ = 0.0 gave 60.0% correct predictions, while maximum likelihood with CT = 10.0 was 56.5% correct (Table 1.C). Since optimal performance of the two systems now differs by 3.5%, some hybrids do not give better predictions than fuzzy ARTMAP alone. Nevertheless, a convex combination with γ = 0.6 again gave the best performance, boosting accuracy to 61.1%. However, giving 60% weight to maximum likelihood (γ = 0.4) brought performance back down to the level of maximum likelihood alone.

CONCLUSION

This paper provides an introduction to the fuzzy ARTMAP neural network in the context of remote sensing classification problems. First, the use of a voting strategy improves prediction by training fuzzy ARTMAP several times on different orderings of an input set. This strategy assigns confidence estimates to competing predictions. Second, fuzzy ARTMAP and maximum likelihood perform differently for different combinations of input variables. Fuzzy ARTMAP performance increases using brightness, greenness, and wetness as compared to the original spectral bands, and increases even more when these are combined. Ancillary inputs improve maximum likelihood and fuzzy ARTMAP by similar amounts. Third, a hybrid fuzzy ARTMAP and maximum likelihood classification system can improve overall predictive accuracy since the two classifiers tend to make somewhat different predictive errors. Fourth, results from a group of pixels pooled together form mappings across functional regions or sites, and site-level predictions are more accurate and functionally useful than pixel-level predictions.

REFERENCES

[1] Strahler, A.H., Logan, T.L., and Bryant, N.A. (1978). Improving forest cover classification accuracy from *Proceedings of the 12th International Symposium on Remote Sensing of Environment*, Ann Arbor, MI: Environmental Research Institute of Michigan, 927-942.

[2] Congalton, R.G., Green, K., and Teply, J. (1993). Mapping old growth forests on National Forest and Park Lands in the Pacific Northwest from remotely sensed data. *Photogrammetric Engineering and Remote Sensing*, **59**, 529-535.

[3] Franklin, J., Logan, T.L., Woodcock, C.E., and Strahler, A.H. (1986). Coniferous forest classification and inventory using Landsat and digital terrain data. *IEEE Transactions on Geoscience and Remote Sensing*, **24**, 139-149.

[4] Woodcock, C.E., Collins, J., Gopal, S., Jakabhazy, V., Li, X., Macomber, S., Ryherd, S., Wu, Y., Harward, V.J., Levitan, J., and Warbington, R. (1994). Mapping forest vegetation using Landsat TM imagery and a canopy reflectance model. *Remote Sensing of Environment*, **50**, 240-254.

[5] Carpenter, G.A., Grossberg, S., Markuzon, N., Reynolds, J.H., and Rosen, D.B. (1991). Fuzzy ARTMAP: A neural network architecture for incremental supervised learning of analog multidimensional maps. *IEEE Transactions on Neural Networks*, **3** 698-713.

[6] Carpenter, G.A., Gjaja, M.N., Gopal, S., and Woodcock, C.E. (1995). ART neural networks for remote sensing: Vegetation classification from Landsat TM and terrain data. Submitted to *IEEE Transactions on Geoscience and Remote Sensing*. Technical Report CAS/CNS TR-95-026, Boston, MA: Boston University.

[7] Duda, R.O., and Hart, P.E. (1973). Pattern classification and scene analysis. New York: Wiley.

[8] Benediktsson, J.A. Swain, P.H., and Ersoy, O.K. (1990). Neural network approaches versus statistical methods in classification of multisource remote sensing data. *IEEE Transactions on Geoscience and Remote Sensing*, **28**, 540-552.

New Approaches to Classification in Remote Sensing Using Homogeneous and Hybrid Decision Trees to Map Land Cover

C. E. Brodley
School of Electrical and Computer Engineering
Purdue University
West Lafayette, IN 47906
brodley@ecn.purdue.edu

M. A. Friedl & A.H. Strahler
Department of Geography and Center for Remote Sensing
Boston University
Boston, MA 02215
friedl,alan@crsa.bu.edu

Abstract – Decision tree classification procedures have been largely overlooked in remote sensing applications. In this paper we compare the classification performance of three types of decision trees across three different data sets. The classifiers that are considered include a univariate decision tree, multivariate decision tree, and a hybrid decision tree. Results from an n-fold cross-validation procedure show that for some datasets all the decision trees perform comparably, but for other datasets hybrid decision tree classifiers are superior because of their ability to handle complex relationships among feature attributes and class labels.

INTRODUCTION

Land cover and land cover change represent key controls on Earth system processes including biogeochemical cycles, the annual cycles and spatial distribution of plant biomass and respiration, and coupling between the atmosphere and the biosphere [1]. Remote sensor data collected from satellites possess a variety of desirable attributes for large-scale land cover mapping. These attributes include repetitive coverage of the Earth's land surfaces, multispectral data acquisition, and multiangular sensor viewing geometries. Traditional approaches to automated land cover mapping using remote sensor data have employed pattern recognition techniques including both supervised and unsupervised approaches [2].

Decision tree classification techniques have been used successfully for a wide range of classification problems, but have been largely overlooked by the remote sensing community. In this paper, we assess the utility of decision tree classification algorithms for the task of land cover mapping from remotely sensed data. The techniques described here have substantial advantages for this problem because of their flexibility, intuitive simplicity, and computational efficiency.

DECISION TREE ALGORITHMS

A decision tree is a classification procedure that recursively partitions a data set into smaller sub-divisions based on a set of tests defined at each node in the tree. The tree is composed of a root node (formed from all of the data), a set of intermediate nodes (splits), and a set of terminal nodes (leaves). Each node in a decision tree has only one parent node, and two or more descendant nodes. In this framework, a data set is classified by sequentially sub-dividing it according to the decision framework defined by the tree, and class labels are assigned to each observation according to the leaf node into which the observation falls. To construct an accurate decision tree a set of training samples representative of the population must be available.

Key Issues in Estimating Decision Trees

For any given type of decision tree, a variety of factors related to the implementation of the training algorithm will influence the classification performance of the estimated decision tree. These factors include the different partition merit criteria that can be used to measure the "goodness of a split" [3], and the specific algorithm that is used to perform feature selection at an internal node [4]. Further, a key step in any decision tree estimation problem is to correct the tree for overfitting by pruning the tree back. Conventionally, a tree is grown that classifies all training observations correctly. However, because the tree is "overfit" to the training data, which may contain error, the tree must be pruned back to reduce classification errors when independent data are classified using the tree. Common methods for pruning trees are described in [5, 6].

For this work we consider both homogeneous and hybrid decision tree classifiers. The properties of both of these classes of trees is described below. Here, we examine three types of decision trees: (1) univariate decision trees, (2) multivariate decision trees, and (3) hybrid decision trees; and evaluate their performance using three sets of remotely sensed data with associated land cover class labels.

Univariate decision trees

A univariate decision tree (UDT) is a decision tree where each decision boundary defined by a node of the tree is represented by a single feature of the input data. At each test node

0-7803-3068-4/96$5.00©1996 IEEE

in a UDT the data are split into two more subsets based on a test of a single feature, and where each test is required to have a discrete number of outcomes. In this framework, A UDT classification proceeds by recursively partitioning the input data until a leaf node is reached, and the class value associated with the leaf is then assigned to the observation. The specific values of the decision boundaries in a UDT are estimated empirically from training data. A well known example of this type of approach is the CART model described in [6].

Multivariate Decision Trees

Multivariate decision trees (MDTs) are similar to UDTs, but the test at any node may be based on more than one feature of the input data. For example, we may split the data based on the value of both the NDVI and surface temperature. To do this, a set of linear discriminant functions (LDF) are estimated at each interior node of the tree, where the coefficients for the LDF at any node are estimated from training data. MDTs are often more compact, and may also be more accurate than UDTs [4].

Hybrid decision trees

A hybrid decision tree (HBT) is a decision tree where different classification algorithms may be used in different sub-trees of the larger tree. Here, we use a system named the Model Class Selection system (MCS) [7]. MCS can combine up to three commonly used classification algorithms into a recursive tree-structured hybrid classifier. These algorithms include decision trees, linear discriminant functions and k-means nearest neighbor classifiers. To do this, MCS employs a hill-climbing search guided by a set of heuristic rules to estimate a HBT using the set of training data. As part of this implementation, MCS applies a heuristic pruning procedure to ensure that the resulting classifier does not overfit the training data at the expense of generalization.

To estimate a HBT from a set of training data, a knowledge base has been encoded within MCS. This knowledge base defines a set of heuristic rules to perform automatic algorithm selection depending on the properties of the data (for details, see [7]). These rules are applied recursively to the data set in question to partition it within the framework of a HBT. The resultant decision tree therefore represents a classification structure where the data is successively partitioned into smaller sub-divisions, and where different classification algorithms may be applied to each subset.

ANALYSIS

The general objectives of this work are to present the basic properties of decision tree classification algorithms, and to assess their utility for the purpose of land cover mapping from remotely sensed data. To do this we used three data sets collected at scales ranging from global to regional in scope, and which include both multi-temporal and single date data. Using these data, we assess the classification accuracy produced by each of the candidate classifiers (both across all classes, and between classes), and consider the relative strengths, limitations and potential research areas for decision tree classifiers in remote sensing.

It is important to note that one of the key problems currently confronting the global land cover mapping community is a general lack of high quality training data to use for training, testing, and evaluation of classification algorithms. For the purposes of this work we use data derived from a variety of different sources and that contain significant levels of error in the class labels used to train and test the decision tree algorithms described above. It is important to interpret the results presented below in light of these data limitations. As the availability of better quality ground truth data increases, we expect that the performance of these algorithms will exhibit corresponding improvements. Indeed, we have recently developed an automated method for reducing labeling error in training samples [8].

Data

Three sets of data are used for this work. These data were specifically compiled to assess the performance of decision tree classifiers across a range of spatial resolutions and classification problems within the larger domain of land cover mapping using remote sensing. The attributes of these data-sets are as follows:

1. Global NDVI from AVHRR at 1 degree spatial resolution: This data set is composed of a time series of NDVI measurements collected at monthly time intervals from the NOAA AVHRR during 1987. The training data and associated class labels were compiled by Defries and Townsend [9]. These observations and labels include 3398 1 degree by 1 degree locations where three widely used maps of land cover and vegetation are in agreement.

2. NDVI from AVHRR at 1 Km for North America: This data set was extracted from The 1990 Conterminous US AVHRR Dataset compiled at Eros Data Center (EDC) [10]. The data consists of a time series of NDVI values representing the maximum NDVI during each of eight one month periods spanning the growing season in 1990. Class labels were assigned to these data by reclassifying the fine resolution class labels (159 classes) supplied by [10] to a much coarser classification (17 classes) conforming to the global land cover classification defined by IGBP, and which will also be used as the at-launch land cover product to be used under EOS-MODIS. The data set used here were extracted at 10,000 random locations, and exclude water bodies.

3. TM data at 30 meter resolution for Lake Tahoe: The final data set used for this work is composed of a random sample of roughly 2000 values of raw TM data acquired over a forested area surrounding the Lake Tahoe region of California. These data were extracted from a single image and include all TM

Table 1: Classification Accuracy on the Test Samples

Method	NDVI-1o	NDVI-1Km	TM-30M
UDT	85.61	70.96	75.20
MDT	86.39	71.70	75.88
HBT	87.70	80.09	75.97
LDF	78.66	51.68	70.63

bands except TM6 (thermal). Class labels were assigned using a combination of automated classification procedures which incorporated the use of ancillary data, manual labeling using field data and aerial photography. Details regarding the specifics of the labeling procedure are provided in [11].

CLASSIFICATION PROCEDURES

To evaluate the classification performance of each of the three decision tree algorithms we performed a set of ten-fold cross-validation runs using each classification algorithm to classify each of the data sets. For each of ten runs, we randomly subdivided each dataset into a training set (70%), a pruning set (20%) and a testing set (10%). This subdivision procedure ensures that the trees were estimated, pruned, and evaluated using independent data for each step. By using this procedure the classification results reported should be representative of "average" model performance. The classification accuracies that we report in Table 1 are expressed as averages across the ten runs.

RESULTS AND CONCLUSIONS

The results of our empirical evaluation are shown in Table 1. We include results from a linear classifier (LDF) as a point of reference. For all datasets the decision tree methods outperform the linear classifier.

For the NDVI data at 1 degree of resolution there are small differences among the three decision tree methods with the hybrid tree producing in the highest accuracy. Results for the NDVI data at 1 kilometer, however, show dramatic differences among the different classifiers. Specifically, classification accuracies ranged from 70.96% to 80.09% for the UDT and HDT, respectively. The hybrid decision tree is superior for this data set because different parts of the sample space are best represented using different models. Finally for the TM-30M all methods performed comparably.

Univariate decision trees are restricted to representing boundaries of the sample space that are orthogonal to feature axes, whereas multivariate and hybrid trees can form arbitrary piecewise linear hyperplane boundaries. When each input feature is independently predictive of the class label, then all methods perform comparably. However, dramatic differences can arise when combining the features, either linearly or as in a k-nearest neighbor classifier, which results in a feature combination that is more predictive of the class than each of the individual features. Inspection of the hybrid decision tree for the NDVI data at 1 kilometer of resolution reveal that these data have exactly this property. In conclusion, our empirical evaluation illustrates that decision trees are a viable approach to classification in remote sensing.

REFERENCES

[1] Hall, F.G., Townsend, J.R., & Engman, E.T. (1995) Status of remote sensing algorithms for estimation of land surface state parameters. *Remote Sensing of Environment, 51*, 138-156.

[2] Richards, J.A. (1992). *Remote Sensing Digital Image Analysis*, Springer-Verlag, New York.

[3] Safavian, S.R., & Landgrebe, D. (1991) A survey of decision tree classifier methodology. *IEEE Transactions on Systems, Man, and Cybernetics, 31*, 660-674

[4] Brodley, C.E., & Utgoff, P.E. (1995). Multivariate decision trees, *Machine Learning, 19*, 45-77

[5] Quinlan, J.R. (1987). Simplifying decision trees, *International Journal of Man-Machine Studies, 27* 221-234

[6] Breiman, L., Friedman, J. H., Olshen, R. A., & Stone, C. J. (1984). *Classification and Regression Trees*, Belmont, CA: Wadsworth International Group.

[7] Brodley, C.E. (1995). Recursive automatic bias selection for classifier construction, *Machine Learning, 20*, 63-94

[8] Brodley, C.E. & Friedl, M. A. (1996). Improving automated land cover mapping by identifying and eliminating mislabeled observations from training data, *International Geoscience and Remote Sensing Symposium*, this volume.

[9] Defries, R. S. , & Townsend, J. R. G. (1994). NDVI-derived land cover classifications at a global scale, *International Journal of Remote Sensing, 15*, 3567-3586.

[10] Loveland, T.R., Merchant, J.W., Ohlen, D.O., & Brown, J.F. (1991). Development of a land-cover characteristics database for the conterminous U.S., *Photogrammetric Engineering and Remote Sensing, 57*, 1453-1463.

[11] Macomber, S.A. & Woodcock, C.E. (1994). Mapping and monitoring conifer mortality using remote sensing in the Lake Tahoe basin, *Remote Sensing of Environment, 50*, 255-266.

Proportional Estimation of Land Cover Characteristics from Satellite Data

R. DeFries, M. Hansen, and J. Townshend
Department of Geography, University of Maryland
College Park, MD 20742
tel: 301 405-4884, fax: 301 314-9299, email: rd63@umail.umd.edu

Abstract — The land surface over much of the earth is typically a complex mosaic of different types of vegetation. Traditional approaches that classify vegetation into discrete categories do not allow a description of such mixtures and gradients in vegetation types. Consequently, climate models and other types of global change models that require information on the global distribution of land cover types incorporate these idealized and somewhat unrealistic descriptions of the land surface. Analysis of satellite data potentially can lead to more accurate and realistic descriptions of the land surface as continuous variables of vegetation characteristics. Such variables would describe, for example, proportional mixtures of woody, nonwoody, and no vegetation; deciduous and evergreen vegetation; and broadleaf and needleleaf woody vegetation. This paper explores two approaches to derive such continuous variables. With the first approach, multiresolution data from the NOAA AVHRR and Landsat Multispectral Scanner System (MSS) are used to estimate percentage cover of closed canopy broadleaf evergreen forest in central Africa based on empirical relationships. In the second approach, a linear mixture model is applied using AVHRR Pathfinder Land data to obtain a global map of proportional mixtures of woody vegetation (trees and shrubs), non-woody vegetation (herbaceous vegetation), and bare ground.

INTRODUCTION

Satellite data are used as a basis for characterizing the earth's vegetation at continental and global scales [1, 2, 3, 4]. These analyses describe each grid cell as one of a discrete number of vegetation types. Each grid cell is typically labeled as a single cover type, regardless of the presence of mosaics of different vegetation types present in the cell or vegetation gradients across the landscape. Such descriptions create artificial boundaries between cover types that in many cases are not true representations of the land surface. For example, the vegetation across a north-south transect from the Sahara desert to central Africa is composed of transitions from bare soil in the desert, to shrubs, grasslands, woodlands, and broadleaf evergreen forest in central Africa. Conventional land cover classifications [5] define the region as thin east-west strips of these cover types with discrete boundaries between them. In reality, the vegetation displays gradual transitions between these vegetation types.

Information about the geographic distribution of global vegetation types is a boundary condition for global models that describe exchanges of water, energy, and carbon dioxide between the atmosphere and biosphere. Yet the parameter fields derived from conventional global vegetation data with discrete numbers of cover types depend on the particular vegetation classification scheme and the number of types it includes [6]. Ideally, vegetation characteristics important for controlling these exchanges would be mapped as continuous distributions to capture mixtures and gradients within the cell size of the model. There are a small number of vegetation characteristics important for global models [6, 7], including the spatial extent of woody plant (gradations between bare ground, herbaceous plants, and trees and/or shrubs), seasonality of woody vegetation (deciduous, evergreen), leaf type (broadleaf, coniferous), photosynthetic pathway of nonwoody vegetation (annual, perennial), and disturbance type (e.g., cultivation, fire history). Several of these characteristics, such as woodiness and seasonality, can be detected with satellite data. Other characteristics, such as photosynthetic pathway, would need to be detected with ground-based or other types of information.

The conventional approach toward describing the land surface as discrete cover types arises from a long tradition of vegetation mapping from ground-based observations of physiognomic, floristic, and environmental properties [8] and bioclimatic classification schemes [9, 10]. This approach has been extended to land cover classifications based on satellite data. However, satellite data contain abundant information about the earth's vegetation that could enable richer descriptions of spatial mixtures of some of the important vegetation characteristics [2, 6]. Methodologies for extracting this type of information have not been widely explored and are very much in their infancy.

This paper explores two approaches to mapping one of the important vegetation characteristics, spatial extent of woodiness of the vegetation, as a continuous variable. In such a map, each grid cell is described not as a distinct vegetation type but as a percentage area covered by woody vegetation. One approach uses coregistered multiresolution data in central Africa to derive empirical relationships with percent forest cover in specific locations. These relationships are then extrapolated over larger areas to derive a map of percent woodiness. The other approach, linear mixture modeling, is applied globally to determine percent woodiness from red and near infrared reflectances.

0-7803-3068-4/96$5.00©1996 IEEE

EMPIRICAL ESTIMATION OF PERCENT FOREST USING MULTISENSOR DATA

We derived estimates of percent closed canopy forest in central Africa within grid cells at a spatial resolution of 8 km based on multiresolution, multisensor data [11]. This approach is based on empirical relationships between percent forest cover derived from Landsat Multispectral Scanner System (MSS) data and various metrics, such as mean annual Normalized Difference Vegetation Index (NDVI) and mean annual brightness temperature, derived from AVHRR Pathfinder Land data for 1987 [12]. The relationships, determined from seven MSS scenes, were then extrapolated over the region to obtain estimates of percent closed canopy forest.

The following steps were used to carry out this analysis:

1) reproject MSS scenes into a projection common with the AVHRR Pathfinder Land data (Goode's equal area), using ground control points identified from physical features on 1:250,000 scale maps.

2) coregister MSS scenes with AVHRR data based on the presumption that the optimum coregistration occurs where there is the highest correlation between the NDVI from the AVHRR data and the NDVI calculated from the MSS data. This procedure was necessary because the coarse resolution of the AVHRR Pathfinder data does not permit the location of physical features for determining ground location points and because of the inaccurate navigation of the AVHRR data.

3) classify MSS scenes using a classification tree [13] into closed canopy forest and non-forest classes.

4) calculate percent forest cover for each 8 km grid cell based on the classification of the MSS scenes.

5) analyze relationships between percent forest cover and metrics derived from the AVHRR Pathfinder data. Twenty four metrics were analyzed using two techniques, linear regression and regression trees. These metrics incorporated multitemporal information that indicate seasonality as well as overall "greenness" of the vegetation. The best predictors of percent forest cover included mean annual NDVI and mean annual brightness temperature from AVHRR channel 3. Using half the 8 km grid cells corresponding to the seven MSS scenes for deriving the relationships and the other half for validating the prediction, 90 percent of the grid cells were within 20 percent of the "actual" percent forest cover [11].

The relationships between percent forest cover and metrics derived from AVHRR data were then extrapolated over a larger area to derive estimates of percent closed canopy forest within 8 km grid cells (Fig. 1). The results suggest that multisensor, multiresolution data are useful for estimating subpixel forest cover at coarse spatial resolutions. However, the highly empirical nature of this approach raises questions about the validity of extrapolating the relationships over larger areas.

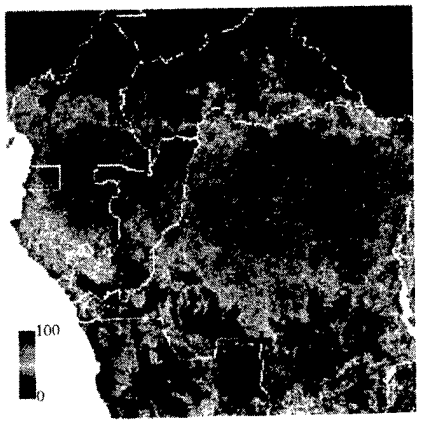


Figure 1. Estimate of percent closed canopy forest in central Africa for 8 km grid cells based on Landsat MSS and Pathfinder AVHRR Land data

LINEAR MIXTURE MODELING TO DERIVE GLOBAL MAP OF PERCENT WOODY COVER

A second approach for estimating continuous distributions of woodiness of the vegetation from satellite data uses a linear unmixing approach [14]. This approach is based on the notion that total reflectances within a coarse resolution grid cell are linear combinations of contributions from each land cover component weighted by the fractional area covered by that component within the cell.

We applied a linear mixture model [15] to derive estimates of woody (trees and shrubs), non-woody (herbaceous), and bare vegetation for the globe using AVHRR Pathfinder data for 1987. The mixture model used locations known to be pure woody, non-woody, or bare vegetation to derive the values for red and near-infrared reflectances corresponding to pure pixels. These locations were determined from overlays of coregistered MSS data. Reflectances were taken from the greenest month, the month with the highest NDVI value in the year, to avoid values influenced by snow. Because the values for red and near infrared reflectances for pure pixels of non-woody vegetation fell between the values for pure pixels of the other two cover types, two mixture models were run, one for mixtures between woody

and non-woody vegetation and one for mixtures between non-woody and bare vegetation. These two results were then combined (Fig. 2).

Linear mixture modeling is an attractive approach to derive continuous distributions of vegetation characteristics over large areas. Validation of the results, however, is a concern due to the difficulties in obtaining field data on mixtures of cover types.

CONCLUSIONS

Satellite data contain information that can lead to richer descriptions of land cover than traditional classifications. Two approaches are described in this paper, an empirical approach applied over a relatively small area based on multisensor data and linear mixture modeling applied globally. Additional approaches for describing continuous distributions of vegetation characteristics from satellite data need to be explored.

ACKNOWLEDGMENTS

This work was supported by NASA under contract NAGW 4206.

REFERENCES

1. J.R.G. Townshend, C.O. Justice, V.T. Kalb, "Characterization and classification of South American land cover types using satellite data", International Journal of Remote Sensing, vol. 8, pp. 1189-1207, 1987.
2. R.S. DeFries, J.R.G. Townshend, "NDVI-derived land cover classification at global scales", International Journal of Remote Sensing, vol. 15, pp. 3567-3586, 1994.
3. N. Laporte, C. Justice, J. Kendall, "Mapping the dense humid forest of Cameroon and Zaire using AVHRR satellite data", International Journal of Remote Sensing, vol. 16, pp. 1127-1145, 1995.
4. T.R. Loveland, J.W. Merchant, D.O. Ohlen, J.F. Brown, "Development of a land-cover characteristics database for the conterminous U.S.", Photogrammetric Engineering and Remote Sensing, vol. 57, pp. 1453-1463, 1991.
5. F. White, "The Vegetation of Africa", Natural Resources Research (UNESCO, Paris, 1983).
6. R.S. DeFries, et al., "Mapping the land surface for global atmosphere-biosphere models: toward continous distributions of vegetation's functional properties", Journal of Geophysical Research, vol. 100, pp. 20,867-20,882, 1995.
7. S.W. Running, T.R. Loveland, L.L. Pierce, "A vegetation classification logic based on remote sensing for use in global biogeochemical models", Ambio, vol. 23, pp. 77-81, 1994.
8. D. Mueller-Dombois, in "Classification and Mapping of Plant Communities: A Review with Emphasis on Tropical Vegetation", G. M. Woodwell, Eds. (John Wiley and Sons, Ltd., U.K., 1984) pp. 21-90.
9. Holdridge, "Determination of world formations from simple climatic data", Science, vol. 105, pp. 367-368, 1947.
10. C. Troll, K. Paffen, "Die Jahreszeitenklimate der erd. (Summary: the seasonal climates of the earth)", Erkunde, vol. 18, pp. 5-28, 1964.
11. R. DeFries, et al., "Subpixel forest cover in Central Africa from multisensor, multitemporal data", Remote Sensing of Environment, submitted, 1995.
12. P.A. Agbu, M.E. James, Goddard Distributed Active Archive Center Publications, GCDG, Greenbelt, MD, The NOAA/NASA Pathfinder AVHRR Land Data Set User's Manual, 1994.
13. M. Hansen, R. Dubayah, R. DeFries, "Classification trees: An alternative to traditional land cover classifiers", International Journal of Remote Sensing letters, submitted.
14. J. Settle, N.A. Drake, "Linear mixing and the estimation of ground cover proportions", International Journal of Remote Sensing, vol. 14, pp. 1159-1177, 1993.
15. Y.E. Shimabukuro, J.A. Smith, "The least-squares mixing models to generate fraction images derived from remote sensing multispectral data", IEEE Transactions on Geoscience and Remote Sensing, vol. 29, pp. 16-20, 1991.



Figure 2. Global estimate of percent woody vegetation (trees and shrubs), non-woody vegetation (herbaceous), and bare ground from linear mixture model based on red and infrared reflectances from AVHRR Pathfinder Land data

Fuzzy ARTMAP Classification of Global Land Cover from AVHRR Data Set

Sucharita Gopal, Curtis E. Woodcock and Alan H. Strahler
Center for Remote Sensing & Department of Geography
Boston University, Boston MA 02215
email: suchi@crsa.bu.edu, curtis@crsa.bu.edu, alan@crsa.bu.edu

ABSTRACT

Phenological differences among broadly defined vegetation types can be a basis for global scale classification at a very coarse spatial scale. Using the annual sequence of composited Normalized Vegetation Index (NDVI) values in an AVHRR data set, DeFries and Townshend (1994) distinguished eleven global cover types and classified global land cover with a maximum likelihood classifier. The present research presents a neural network architecture called fuzzy ARTMAP to classify the same data set. Classification results are analyzed and compared with those obtained from DeFries and Townshend (1994). First, classification accuracy on the training data set is 100% compared with the corresponding accuracy of 86.8% [2]. Second, when fuzzy ARTMAP is trained using 80% of data set and tested on the remaining (unseen) 20% data set, classification accuracy is more than 80%. Third, classification results vary with and without latitude as an input variable similar to those of DeFries and Townshend.

INTRODUCTION

Global monitoring of the earth's land-cover is critical to the study of global change. It is a necessity for understanding land-atmosphere interactions and their effects on global biogeochemical cycles and climate. Changes in land-cover directly affect surface mass and energy budgets through differences in such biophysical parameters as plant transpiration, surface albedo, emissivity and surface roughness. Therefore, mapping, characterizing and monitoring changes in the physical characteristics of land cover has been recognized as a key element in the study of global change [5].

Remote sensing is the only viable means of producing high spatial resolution global land-cover information [12], with data from the NOAA Advanced Very High Resolution Radiometer (AVHRR) being the best source currently available. The primary information source for land-cover studies using AVHRR is the temporal variation in Normalized Difference Vegetation Index (NDVI) [2, 10, 11] which captures the phenological variation between vegetation types. A variety of methods have been used for making these maps, but the best methods for exploiting the temporal variation in NDVI have not yet been determined.

METHODOLOGY

For this study, we have used the same global data set as DeFries and Townshend [2]. The eleven cover types (see Table 1) primarily conform with the requirements of climate models. The training sites for each of the cover types were identified based on agreement between three existing ground-based data sets of land cover [7, 8, 13]. Note that the three data sets agree on cover types for only 26% of the total land surface. Further steps were taken to ensure that cover types in the training set were spectrally distinct from one another. The data set used is a set of monthly Normalized Vegetatation Index (NDVI) values of AVHRR data set at one degree by one degree resolution. The NDVI values were sequenced from the peak value at each pixel in order to standardize seasonal effects. The first NDVI value would represent the maximum value (irrespective of the month in which it occurs), the second value would be the value that occurs in the month following the month in which the maximum value occurs and so on. The data set consists of a total of 3398 pixels.

DeFries and Townshend [2] used a maximum likelihood classifier (MLC) on the entire training data. The main findings of their study are as follows: (i) Incorporating latitude as a variable, (either by stratifying the land surface into latitudinal strips or subdividing the training areas by latitudes), improved training accuracy from 82% to 87%; (ii) NDVI values sequenced from the peak value at each pixel yielded higher accuracy (77% - 84%) compared to using curve characteristics of NDVI profile (69% - 82%); (iii) MLC using monthly values with training areas subdivided by hemisphere yielded slightly better results than MLC run separately on 5-degree latitude strips.

0-7803-3068-4/96$5.00©1996 IEEE

FUZZY ARTMAP NEURAL NETWORKS

Most neural network classification studies in remote sensing have used the backpropagation technique [3, 4]. In this study, we evaluate the performance of a different class of neural networks, called fuzzy ARTMAP [1], for the classification problem. Fuzzy ARTMAP synthesizes fuzzy logic and Adaptive Resonance Theory (ART) models by exploiting the formal similarity between the computations of fuzzy subsethood and the dynamics of ART category choice, search and learning.

The fuzzy ARTMAP network was trained using 80% of the total data (of 3398 pixels) and testing was done on the remaining 20% of unseen data. This method of training offers two advantages. First, there is no definitive data set of global land cover that could be used for assessing classification accuracy. Hence this method of splitting the data set into training and testing provides some independent method of validation of the performance of the neural network classifier. Second, fuzzy ARTMAP is trained until a 100% accuracy is achieved before testing begins. In all simulations, Fuzzy ARTMAP results in 100% training accuracy compared with 87%, the best accuracy obtained using MLC [2]. Results pertaining to the unseen 20% test data will be discussed during the conference.

Three main types of fuzzy ARTMAP neural networks are constructed. Network A consisted of the 12 NDVI values that were sequenced from the peak value at each pixel and included latitude as an input variable. Latitude was entered as distance (in degrees) from the equator. Hence the value of this variable is the same for a location 25-degrees north of the equator and for a location 25-degrees south of the equator. Latitude in Network B was the same as the one in the DeFries and Townshend (1994) study where the North Pole has a value of 0-degrees and South Pole has a value of 180-degrees. The rest of the input vector in B is similar to A. Network C includes only the NDVI values and excludes latitude from the input vector. Each of the three networks had to learn the eleven cover types using the fuzzy ARTMAP supervised learning strategy.

RESULTS AND DISCUSSION

Only global classification results are discussed in this section. Table 1 shows that latitude is an important factor in training fuzzy ARTMAP. Further, different results are obtained using distance from the equator (A) and latitude defined continuously over the earth (B). The classification results are analyzed and summarized as follows: First, the effect of latitude variable is seen looking at differences between predictions made by Networks A and B versus C in Table 1. Network C makes higher estimates for the following classes: *broadleaf evergreen, high latitude deciduous, bare ground, cultivated,* and *broadleaf deciduous forest and woodland.* A comparison of global maps created using the neural networks underscores the effect of latitude. Without latitude, the southern hemisphere seems to be more coarsely classified with large areas attributed to a few classes. Using latitude as the distance from the equator (A) seems to give better results for southern hemisphere.

Second, Network (A), using distance from the equator, can be compared to B and C. It gives smaller estimates for *broadleaf evergreen forest, high latitude deciduous forest, grassland, bare ground,* and *broadleaf deciduous and woodland* compared with other neural networks. In contrast, Network A gives higher estimates for *coniferous evergreen,* and *shrubs and bare ground.* Third, the overall difference between MLC and three neural networks suggest that neural net-

Land Cover Category	Classification Results			
	MLC	Fuzzy ARTMAP		
		A	B	C
Broadlf. evergrn. forest	1240	1692	1770	1954
Conifer. evergrn. forest	2144	2161	1805	1995
High lat. decid. forest	955	574	640	709
Tundra	1947	2559	2723	2332
Mixed deciduous & evergreen	900	409	541	400
Wooded grsslnd.	2110	1328	1675	921
Grassland	2173	2149	2287	2255
Bare ground	1580	1479	1502	1627
Cultivated	1506	3135	2857	3320
Broadleaf decid. forest	499	17	26	28
Shrubs & bare ground	144	698	592	660
No class label	1221	218	1	218
Total	16419	16419	16419	16419

Table 1: Global Classification Results Using Maximum Likelihood and Fuzzy ARTMAP Networks
A - with equatorial distance; B - latitude (DeFries et al. method); C - without latitude.

works estimate larger areas for the following classes: *coniferous evergreen forest woodland, broadleaf evergreen forest, tundra, cultivated* and *shrubs and bare ground*. In contrast, MLC estimates larger areas of *high latitude deciduous forest, mixed deciduous and evergreen, wooded grassland, broadleaf deciduous forest and woodland* compared with the three neural networks. These differences are also seen on the maps produced using the classification results. Maps will be shown during the conference. The differences may be due to a number of factors including the following: fuzzy ARTMAP is sensitive to the size of training classes. It tends to underestimate the class *broadleaf deciduous forest and woodland* that had the least number of training pixels (12). This factor is also demonstrated with network C, which makes broad land cover classes for southern hemisphere since there are no training sites from the southern hemisphere in the data set. DeFries and Townshend used a number of procedures to modify the results obtained from the MLC classifier. None of these modifications were done on the fuzzy ARTMAP results.

In general, the overall results of classification suggest that fuzzy ARTMAP provides a good technique for global land cover classification. It is able to demonstrate the significance of key variables. It also suggests that there is a great deal of uncertainty in global land cover classes. Hence there is an inaccuracy in estimating the exact percentage of land cover under each type. Greater validation results are needed to assess the accuracy of such classification results.

Ongoing analysis involves the use of a voting strategy that improves the prediction results by training the neural network several times on different orderings of the training data set. In addition, attempts to understand the effect of latitude on classification continue. Full results will be available for the conference.

ACKNOWLEDGEMENTS

This research is supported in part by the National Science Foundation (NSF SBR 93-00633) and National Aeronautics and Space Administration (NAS5-31369).

References

[1] Carpenter, G. A., Grossberg, S. and and Rosen, D. B. (1991). Fuzzy ART: Fast stable learning and categorization of analog patterns by an adaptive resonance system, *Neural Networks* 4, 759-771.

[2] DeFries, R. S. and Townshend, J. R. G.(1994). NDVI-derived land-cover classifications at a global scale, *International Journal of Remote Sensing* 15, 3567-3586.

[3] Hara, Y., R. G. Atkins, S. H. Yueh, R. T. Shin, and Kong, J. A. (1994). Application of neural networks to radar image classification, *IEEE Transactions on Geophysics and Remote Sensing* 32, 100-111.

[4] Heermann, P. D. and Khazenie, N. (1992). Classification of multispectral remote sensing data using a back-propagation neural network, *IEEE Transactions on Geophysics and Remote Sensing* 30, 81-88.

[5] Henderson-Sellers, A. and Pitman, A. J. (1992). Land-surface schemes for future climate models: specification, aggregation, and heterogeneity, *Journal of Geophysical Research* 97, D3, 2687-2696.

[6] Matthews, E. (1993). Global vegetation and land use: new high resolution data bases for climate studies. *Journal of Climate and Applied Meteorology* 22, 474-487.

[7] Olson, J.S., Watts, J. A., and Allison, L.J. (1983). Carbon in live vegetation of major world ecosystems, W-7405-ENG-26, U.S. Department of Energy, Oak Ridge National Laboratory.

[8] Sellers, P. J., Tucker, C.J., Collatz, G.J., Los, S.O. Justice, C.O., Dazlich, D.A., and Randall D. A. (1994). A Global 1 by 1 NDVI Data Set for Climate Studies. Part 2: The Generation of Global Fields of Terrestrial Biophysical Parameters From the NDVI, *International Journal of Remote Sensing* 15, 3519-3647.

[9] Sellers, P. J. (1985). Canopy reflectance, photosynthesis, and transpiration, *International Journal of Remote Sensing* 21, 1335-1372.

[10] Townshend, J. R., Justice, C. O. and Kalb, V. (1987). Characterization and classification of South American land-cover types using satellite data, *International Journal of Remote Sensing* 8, 1189-1207.

[11] Wilson, M. F. and Henderson-Sellers, A. (1985). A global archive of land-cover and soils data for use in general circulation models, *Journal of Climatology* 5, 119-143.

Exploring the Interannual Variability of Vegetation Activity using Multitemporal AVHRR NDVI Imagery.

Franz Mora and James W. Merchant.
Center for Advanced Land Management Information Technologies, Conservation and Survey Division, Institute of Agriculture and Natural Resources, University of Nebraska-Lincoln, Lincoln, NE 68588-0517, U.S.A.
Phone: (402) 472-2565, Fax: (402) 472-2410, Email: mora@tan.unl.edu, jm1000@tan.unl.edu

INTRODUCTION

Presently, vegetation activity can be monitored and characterized using remote sensing technology at different scales. At continental or global scales, NOAA/Advanced Very High Resolution Radiometer (AVHRR) data provide unique opportunities to explore the spatial and temporal dynamics of vegetation due to its wide-area and frequent coverage. Vegetation activity is usually processed to Normalized Difference Vegetation Index (NDVI) images, which have been widely used for land cover characterization. Seasonal characteristics of different vegetation types have been used to quantify and correlate vegetation activity with other landscape surface processes, and to describe their patterns of distribution [1][2][3]. With multitemporal AVHRR data, several phenological vegetation metrics have been derived [4][5][6], and empirically correlated with ecological processes such as primary productivity and water balance [7].

While our understanding of annual and seasonal vegetation variability has greatly increased; patterns of interannual variability in natural vegetation are virtually unknown. They are necessary for a consistent description and characterization of land cover, vegetation types, and ecological regions because vegetation is the main landscape feature that controls energy balances, biochemical and hydrological cycles. In addition, analyses of vegetation activity for periods longer than a year are necessary to evaluate vegetation responses to global change. In order to evaluate the magnitude of global change and its effects on ecological processes, it is imperative that human induced changes can be discriminated from natural patterns of vegetation variability.

At present, multitemporal AVHRR/NDVI data acquired for five successive years are available to analyze long-term vegetation dynamics and interannual change for the entire US, and other parts of North America. There are basically two ways to evaluate long-term changes in vegetation activity based on AVHRR-NDVI information: 1] qualitatively, comparing the changes in timing of phenological events that occur year-to-year (e.g., time of the onset and peak of greenness); and 2] quantitatively, based on the intensity of changes in annual NDVI values for annual metrics (such as total integrated measures). Unfortunately, not all the information obtained with multitemporal NDVI images is directly associated to vegetation activity. Their information content can be also associated to solar zenith angle effects, and residual cloud contamination. It is necessary then to develop a strategy for the analysis of NDVI variation that accounts for much of the vegetation activity.

The principal objectives of this research are [1] to identify means to quantify and characterize the interannual variability of vegetation activity as captured by AVHRR/NDVI and [2] to better understand and account for variation in NDVI attributable to variable data quality and cloud contamination.

METHODS

This research has focused on the conterminous U.S. and adjacent areas of North America. AVHRR/NDVI data (1-km resolution) spanning the period 1990-1993 were used in the analysis. Biweekly images were composited to represent maximum NDVI monthly and seasonal values and for every year.

Initially, the metrics for temporal onset and peak of greenness, were derived from the same NDVI dataset. These phenological metrics were obtained using an approach adapted from autoregressive moving average (ARMA) models [6]. Categorical maps representing the timing (in months) of onset and peak of greenness were evaluated by direct comparisons using kappa statistics. Then, several error matrices were obtained to represent year-to-year timing differences in onset and peak of greenness.

Several NDVI-based metrics were obtained for the quantitative comparisons of NDVI variability. Three measures of annual vegetation activity were derived using principal components analysis (PCA) of monthly NDVI maximum value composites. A yearly accumulated (or integrated) greenness (iNDVI) was obtained using the first NDVI principal component. The other two components represented two forms of seasonal variation (s1NDVI and s2NDVI). The interannual comparisons were based on the differences in eigenvalues for every NDVI component. Principal components of NDVI images were used in an

0-7803-3068-4/96$5.00©1996 IEEE

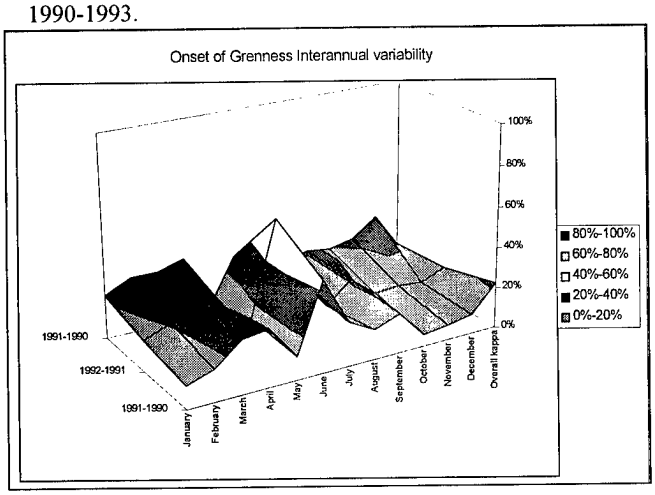
attempt to reduce the effects of data quality and cloud contamination in the interannual change analyses.

Finally, a multitemporal change vector analysis was performed on the differences between seasonal NDVI images on successive years to provide a detailed seasonal comparison. The multitemporal change vector was obtained by applying PCA on the differences between seasonal NDVI values on successive years.

RESULTS AND DISCUSSION

Results of Kappa coefficients indicated that the timing of phenological events exhibited relatively low year-to-year consistency. For the onset of greenness, the overall agreement expressed as kappa statistic was 14%-22%. The year-to-year comparisons evaluated for individual classes (months) indicate that the onset in June is the most consistent phenological attribute. The general interannual pattern agreement observed for the onset of greenness was higher in the spring (peaking in June), decreasing in the following seasons reaching the lowest point in winter (Figure 1).

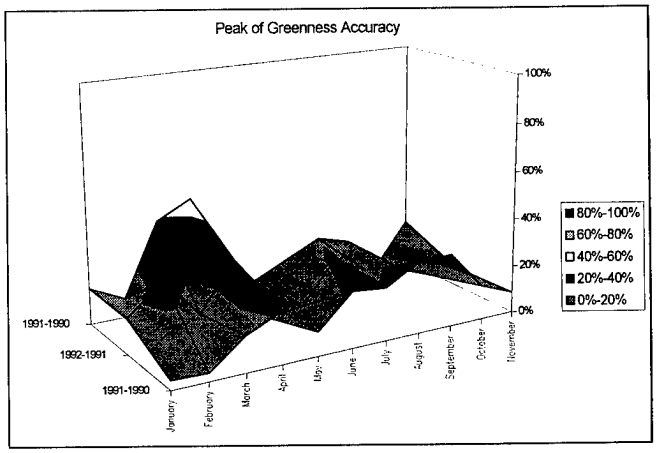
Figure 1. Interannual variability for the Onset of Greenness evaluated as Kappa statistics for successive years between 1990-1993.



Results for the peak of greenness revealed also a low agreement between the peak months on year-to-year comparisons. The overall kappa for the entire images ranged from 14% to 22%. The interannual pattern showed a highest agreement during early spring, with lower values in May (Figure 2).

Principal component analysis of the monthly NDVI variation for every year revealed a consistent pattern of seasonal variation. The first principal component accounted for 60% to 66% of the yearly-multitemporal NDVI variation. The variation explained for second principal component ranged 18%-20%; and the third principal component explained between 4%-6% of the total NDVI variation. Loadings for the first principal component indicate that greenness accumulation over the year is significantly higher during the summer months (June-September), typical of northern latitudes. The second principal component revealed the first source of seasonal variation, highly associated to the summer-winter difference in greenness values. The third principal component identified a seasonal variation associated with low greenness in late spring (May-June) and high in the late summer / early fall (Aug-Sep).

Figure 2. Interannual variability for the Peak of Greenness evaluated as Kappa statistics for successive years between 1990-1993.



The interannual greenness accumulation (iNDVI) showed a consistent temporal pattern over the period analyzed (Figure 3). However, the greater magnitude of negative changes during the winter months (5-8%). This means that NDVI images in the winter tend to be less "green" with each successive year. Additionally, consistent positive differences are observed in the spring, indicating increasing "greenness" with each successive year. A notable difference is observed in the 91-90 period, where NDVI values in 1990 were unusually low (compared to the long term variation). Winter patterns for the 91-92 are an exception to the patterns observed for other years, indicating that year-to-year variations can be dramatic.

Analysis of temporal patterns for the eigenvalues of the second principal showed that seasonal s1NDVI negative differences (greener on previous years) are greater in the winter months, except for the 91-90 period where the seasonal values changed dramatically in May and December giving a positive difference of more than 5% (Figure 4). This trend is also identified in s2NDVI general

pattern, where main seasonal differences occur in the summer (Figure 5).

Figure 3. Interannual variability for iNDVI evaluated with the PC-loading variation for successive years between 1990-1993.

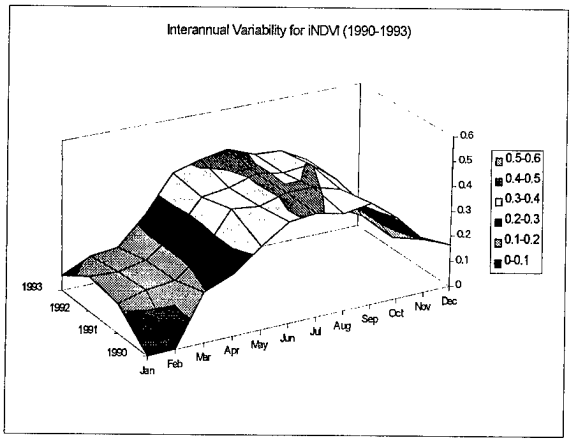


Figure 4. Interannual variability for iNDVI evaluated with the PC-loading variation for successive years between 1990-1993.

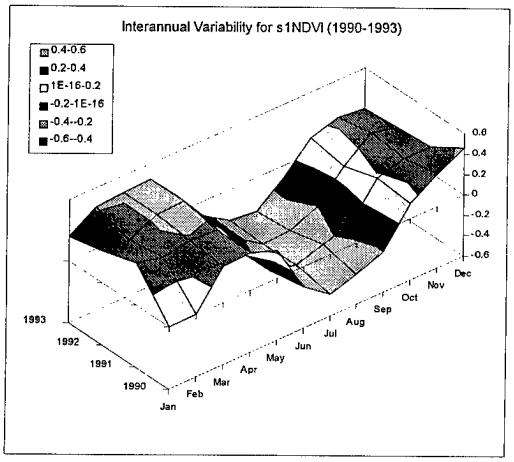
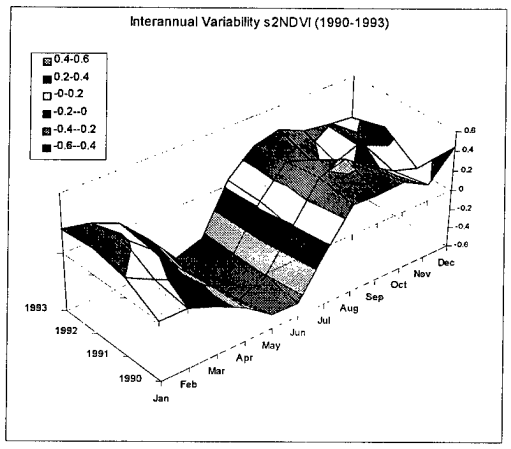


Figure 5. Interannual variability for iNDVI evaluated with the PC-loading variation for successive years between 1990-1993.



CONCLUSIONS

Data analysis resulted in a classification of interannual change. Qualitative changes are determined by the timing of phenological events. However, kappa coefficients indicated that the timing of phenological events exhibited relatively low year-to-year consistency. Results suggest that the methods currently used to compute AVHRR/NDVI seasonal phenological metrics may need to be modified and/or regionally calibrated. Considerable variation is probably associated with noise in the original AVHRR-NDVI dataset. Stratification by similar phenological groups could result in a better characterization of seasonal and phenological events.

The changes were, however, less pronounced when NDVI values were compared among years, especially when the noise in the data was removed by principal component analysis. PCA loadings for each annual vegetation component had almost the same magnitude for every year. The magnitude of interannual variability in iNDVI was not greater than 10%. The maximum variation in s2NDVI was in the order of 20%.

REFERENCES

[1] T.R. Loveland, J.W. Merchant, D.O. Ohlen, and J.F. Brown, "Development of a land cover characteristics database for the conterminous U.S," Photogramm. Eng. Remote Sens., vol. 57, pp.1453-1463, November 1991.

[2] J.R.G.Townshend, T.E. Goff, and C.J. Tucker, "Multitemporal dimensionality of images of normalized difference vegetation index at continental scales," IEE Trans. Geosci. Remote Sens., vol. GE-23, pp. 888-895, November 1985.

[3] R. DeFries, M.Hansen, and J. Townshend, "Global discrimination of land cover types from metrics derived from AVHRR Pathfinder data," Remote Sens. Env., vol.54, pp.209-222.

[4] D. Lloyd, "A phenological classification of terrestrial vegetation cover using shortwave vegetation index imagery," Int. J. of Remote Sens., vol. 15, pp. 2269-2270, 1990.

[5] F. Mora, and L.R. Iverson, "Dynamic stratification of the landscape of Mexico: Analysis of vegetation patterns observed with multitemporal remotely sensed images," in press.

[6] B.C. Reed, J.F. Brown, D. VanderZee, T.R. Loveland, J.W. Merchant, and D.O. Ohlen, "Measuring phenological variability from satellite imagery," J. Veg. Sci., vol. 5, pp. 703-714, 1994.

[7] F. Mora, "Empirical relationships between seasonal vegetation indexes and water balance variables in the landscape of Mexico," Chapter 2, M.S. thesis, University of Illinois at Urbana-Champaign, USA, pp. 26-44, 1994.

Correction of Land-Cover Area Estimates From Low Spatial Resolution Remotely Sensed Data

Aaron Moody

Department of Geography, University of North Carolina at Chapel Hill
205 Saunders Hall, Chapel Hill, NC 27599-3220 (USA).
T: 919.962.5303 EMail: moody@geog.unc.edu

ABSTRACT

A two stage modeling strategy improves area estimates by correcting coarse-resolution measurements of class proportions. *Stage I* models use measurements of landscape spatial properties to estimate the slope and intercept of proportion transition relationships. A *stage II* model uses a regression estimator to predict true class proportions based on measured coarse-scale proportions, and the slope and intercept estimates from the *stage I* models. Model development and testing on a *calibration* site is followed by testing and inversion for a *validation* site. A probabilistic sampling strategy allows statistical assessment of the models and results.

INTRODUCTION

Bias in land-cover area estimates derived from classified remotely sensed data is influenced by image spatial resolution [1]. Models of these resolution effects can therefore help improve area estimates. One might consider two broad types of models in this context. Mixture models, incorporated into the classification process, can estimate the subpixel composition of pixels if pure-class spectra are known [2]. Alternatively, calibrated, post-classification models can improve area estimates from coarse-resolution data if the relationship between "true" and measured proportions can be modeled [1,3].

This paper describes the development and evaluation of linked statistical models that provide post-classification correction of areal bias. The first two models estimate the slope and intercept of a line characterizing the relationship between proportions measured at 30 m and at 1020 m resolutions. The slope and intercept are modeled based on a small set of scale-resistant spatial properties of the landscape. The third model uses the estimated slopes and intercepts to predict 30 m proportions based on proportions measured at 1020 m.

METHODS and RESULTS

Two basic spatial effects contribute to biased area estimates. A *first order* effect is the tendency of large classes to increasingly dominate the landscape when measured at increasingly coarse scales. Accordingly, small classes tend to diminish in size. Figs. 1a and 2a illustrate these patterns for the data used in this study. *Second order* effects refer to modulations of these basic patterns due to specific landscape spatial characteristics [4]. These effects result in the scatter about the smoothed fit notable in Fig. 1a. In either case, scale-dependent changes in the apparent area of classes result from class membership transitions between scales. This effect can be thus characterized in terms of proportion transition lines relating fine and coarse resolution proportions.

Since transition rates depend partly on landscape spatial organization, measures of spatial pattern are used to model the slopes and intercepts of the proportion transition lines for a large set of sampling units in independent calibration and validation sites. These are *stage I* models. Model *inversion*, requires that the landscape pattern measures are relatively scale-resistant.

There are several calibration-based methods for improving coarse resolution area estimates [1,3,5]. The model used here is a form of "classical" model in which known but incorrect values are estimated using unknown correct values [5]. If P_0 represents true proportions and P_r represents measured proportions at some coarse spatial resolution r, then:

$$P_r = \beta_0 + \beta_1 \cdot P_0 + error \qquad (1)$$

where β_0 and β_1 are the intercept and slope of the proportion transition line (supplied by *stage I* models) that relates true proportions to proportions measured at resolution r. Inverting this simple model provides:

$$\hat{P}_0 = P_r - \hat{\beta}_0 / (\hat{\beta}_1) \qquad (2)$$

which is the *stage II* model used in this paper.

A four part strategy is employed as follows: *a*) use a set of scale-resistant spatial measures (calculated at 30 m) to develop *stage I* models for predicting the slope ($\hat{\beta}_1$) and intercept ($\hat{\beta}_0$) of the proportion transition lines for the *calibration* site; *b*) predict 30 m proportions ($\hat{P}_0$) for the calibration site by applying the *stage II* model in (2) using the measured 1020 m proportions (P_r), and the $\hat{\beta}_1$ and $\hat{\beta}_0$ values estimated from the *stage I* models; *c*) using the *stage I* models, repeat *b* using the data from the *validation* site; *d*) for the validation site, invert the model by repeating step *c* using the spatial variables as measured at 1020 m as input to the *stage I* models.

The Plumas and Stanislaus National Forests serve as calibration and validation sites, respectively. Landsat Thematic Mapper data have been classified to produce maps of general land-cover classes for each site. The classes include *barren*, *brush*, *hardwood*, *water*, and *conifer*. The data for each site are aggregated to 1020 m resolution using a plurality-based aggregation procedure. This involves coding each grid cell in a 1020 m sampling grid with the most frequently occurring subgrid-cell class.

Randomly located 238x238 pixel subregions serve as the sampling units for the analyses. Each unit contains 56,644 30 m pixels and 49 1020 m pixels. The Plumas

0-7803-3068-4/96$5.00©1996 IEEE

contains fifty sampling units for model development and initial testing. The Stanislaus contains thirty-five units for model validation and model inversion. The number of units represent 30% of all *possible* such units from each site. Measurements within each sampling unit include: proportions at 30 m for each class, proportions at 1020 m for each class, the $\hat{\beta}_0$ and $\hat{\beta}_1$ values of proportion transition lines between the two scales, a set of spatial measures at 30 m, and the same set of measures at 1020 m. The ultimate goal is to estimate 30 m proportions by supplying 1020 m area measurements and slope and intercept coefficients to the *stage II* model (2). The slopes and intercepts required in (2), are predicted using two multiple regression (*stage I*) models built on the calibration site using the $\hat{\beta}_0$ and $\hat{\beta}_1$ values (respectively) as regressors and a subset of the spatial measures as the predictors.

A number of spatial measures are calculated using the *r.le* software [6]. Five of these demonstrate scale-resistance as determined by the simple correlations between each variable and itself at the two different scales. Of these, three are significant in modeling both $\hat{\beta}_0$ and $\hat{\beta}_1$ values of the proportion transitions as determined within each sampling unit. The four variables used are: **maximum class size** (*mx*), **inverse Simpson's index** (s^{-1}), **contagion** (*c*), and **entropy** (*ent*). Expressions for the latter 3 variables are:

$$s^{-1} = 1 / (\sum_{i=1}^{k} P_i^2) \tag{3}$$

$$c = 2 \cdot \ln(k) - ent \tag{4}$$

$$ent = -\sum_{i=1}^{k}\sum_{j=1}^{k} P_{ij} \cdot \ln(P_{ij}) \tag{5}$$

where k is the number of classes present, P_i is the proportion of class i in the sampling unit, and P_{ij} are elements of a kxk co-occurrence matrix and represent adjacency probabilities between classes i and j. Maximum class size refers to the proportion of the largest class in the sampling unit. Simpson's index indicates the probability of randomly selecting two pixels of the same attribute. Contagion measures the degree of clumping in the landscape. Entropy is maximized when all pixels of a given class are as far away from one another as possible. Table 1 shows the cross-scale correlation matrix for this set of variables.

Table 2 summarizes the two *stage I* models. The predictors are the spatial measures determined at 30 m. The dependent variables are *a)* the intercepts (R^2_{adj}=0.70) and *b)* the slopes (R^2_{adj}=0.63) of a linear least squares fit between 30 and 1020 m proportions in each unit.

Table 1.—Cross-scale correlations

	mx_{1020}	$s^{-1}{}_{1020}$	c_{1020}	ent_{1020}
mx_{30}	0.91	--	--	--
$s^{-1}{}_{30}$	--	0.69	--	--
c_{30}	--	--	-0.07	--
ent_{30}	--	--	--	0.81

Table 2.—Stage I models.

Slope Mod.	Coeff.	St. Err.	t-val.	P > |t|
β_0	-5.77	1.05	-5.49	0.00
mx_{30}	4.95	0.84	5.92	0.00
$s^{-1}{}_{30}$	-0.74	0.22	-3.33	0.002
c_{30}	-0.679	0.17	-4.06	0.0002
ent_{30}	2.83	0.49	5.83	0.00
Intercept Mod.				
β_0	0.0042	0.093	0.045	0.96
mx_{30}	-0.30	0.074	-4.054	0.0002
$s^{-1}{}_{30}$	0.067	0.020	3.3904	0.0015
c_{30}	0.113	0.015	7.68	0.00
ent_{30}	-0.145	0.043	-3.39	0.0015

The *stage I* models estimate the $\hat{\beta}_0$ and $\hat{\beta}_1$ values necessary required for the *stage II* model (2). This sequential modeling process is conducted three times. First, the *stage I* models are developed on the calibration site. The predicted values from these models are then used in (2) to test the overall modeling process for the calibration data. Second, the *stage I* models are applied in a predictive mode using the validation data measured at 30 m. Again predicted $\hat{\beta}_0$ and $\hat{\beta}_1$ values supply the coefficients to run (2) and estimate 30 m proportions for the validation site. Third, *stage I* models are inverted using the variables measured at 1020 m from the Stanislaus and the results are again used to estimate 30 m proportions. The first two cases are *forward* model applications requiring high resolution information to perform the correction. The third is an *inverted* case, because it requires only coarse resolution data. Results from these three tests are presented in Figs. 1, 2, and 3.

DISCUSSION and CONCLUSIONS

Figs. 1a, 2a, and 3a again illustrate the basic scaling effects for class proportions. Note that at 1020 m, the greatest underestimations occur for intermediate-small classes, and the greatest overestimations occur for intermediate-large classes. Very large, very small, and moderate sized classes (at the cross-over point, around 30%) are all reasonably estimated at 1020 m.

The modeling procedure should pull the coarse-resolution area estimates closer to the zero-one line. Figs. 1b and 2b demonstrate that the model improves area estimates for both the calibration and validation sites when operated in the forward mode. The correction performs best for large classes. For small classes a notable dip (albeit reduced) below the zero-one line still occurs. An intercept effect is also evidenced by the vertical alignment of estimates above the zero value of the x-axis. Results from the inverted model (Fig. 3b) also show general improvement, although considerable scatter occurs for very large classes.

Once corrected values are derived, it is possible to tabulate the total absolute error within each sampling unit. For a given sampling unit g, the total error is:

$$TE_g = \sum_{i=1}^{k} |P_{i,1020} - P_{i,30}| \tag{6}$$

where $P_{i,1020}$ and $P_{i,30}$ are the proportions for class i at 1020 and 30 m, respectively. Using these values for both pre- and postcorrection data, the model results can be evaluated. Figs. 1c and 2c show the relationship between pre- and postcorrection error for the calibration and validation sites using the forward model. For any point below the zero-one line, the total error is reduced due to the correction procedure. At both sites, the total error for 90% of the sampling units is either reduced or unchanged after correction. For the inverted model (Fig. 3c) 80% of the regions are either improved or unchanged after correction, with two positive outliers.

Figs. 1d, 2d, and 3d compare the distributions of the pre- and postcorrection TE_g values. In all cases, a significant error reduction is achieved. For the inverted model the t-test was performed after removing the outliers.

Several interesting questions deserve continued attention. Might other scale-resistant measures better predict proportion transitions? Is the general procedure extensible across landscape types? What is the effect of constraining the intercept to zero? What are the sensitivities of the cross-over point seen in Fig. 1? Would a nonlinear model significantly improve results? Resolving these and other issues will help formalize a body of understanding of how class proportions scale. This understanding may lead to improved land-cover area estimates at local, regional and global scales.

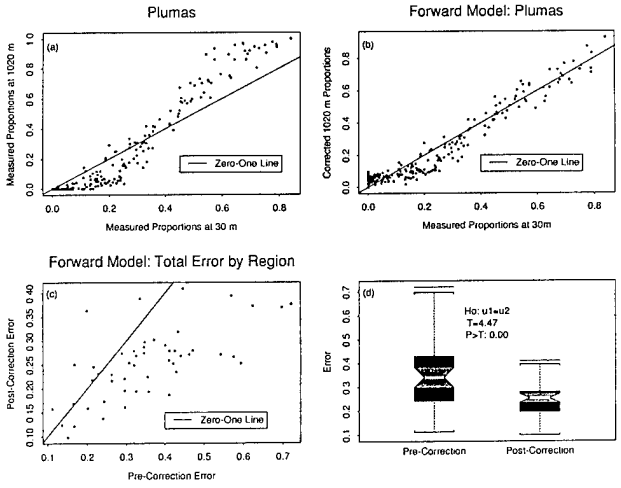


Figure 1

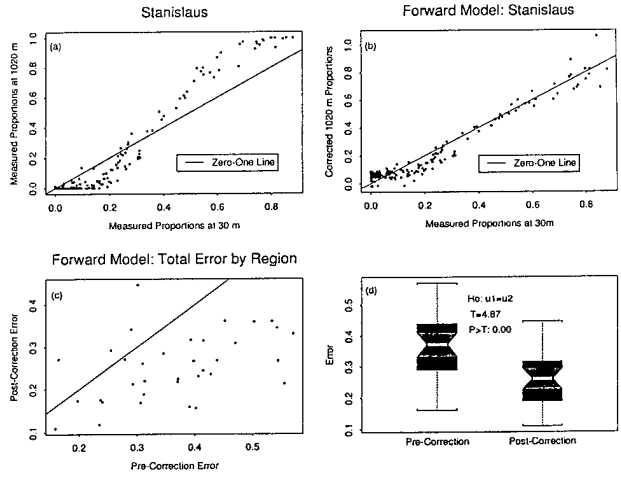


Figure 2

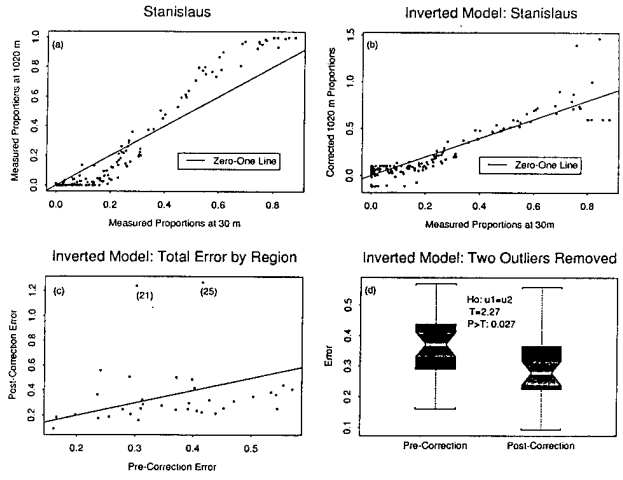


Figure 3

REFERENCES

[1] Mayaux P., and Lambin, E. F. 1995. Estimation of tropical forest area from coarse spatial resolution data: A two step correction function for proportional errors. *Remote Sens. Environ.* 53:1-16.

[2] Adams, J. B., Smith, M. O., and Johnson, P. E. 1986. Spectral mixture modeling: A new analysis of rock and soil types at the Viking Lander 1 site. *J. Geophy. Res.* 91(B8):8098-8112.

[3] Czaplewski, R. L. and Catts, G. P. 1992. Calibration of remotely sensed proportion or area estimates for misclassification error. *Remote Sens. Environ.* 39:29-43.

[4] Moody, A. and Woodcock, C. E. 1995. The influence of scale and the spatial characteristics of landscapes on land-cover mapping using remote sensing. *Landscape Ecology* 10(6):363-379.

[5] Brown, P. J. 1982. Multivariate calibration. *J. Royal Statistical Soc.* 3:287-321.

[6] Baker, W. L. and Cai, Y. 1992. The r.le programs for multiscale analysis of landscape structure using the GRASS geographical information system. *Landscape Ecology* 7(4):291-302.

Landsat Pathfinder Data Sets for Landscape Change Analysis

J.L. Dwyer
Hughes STX Corporation[1/]
EROS Data Center
Sioux Falls, South Dakota 57198
Phone 605-594-6060/Fax 605-594-6529/Email spectra@dg1.cr.usgs.gov

K.L. Sayler
U.S. Geological Survey
EROS Data Center
Sioux Falls, South Dakota 57198
Phone 605-594-6058/Fax 605-594-6529/Email sayler@dg1.cr.usgs.gov

G.J. Zylstra
Hughes STX Corporation[1/]
EROS Data Center
Sioux Falls, South Dakota 57198
Phone 605-594-6153/Fax 605-594-6529/Email zylstra@dg1.cr.usg.gov

Abstract – The North American Landscape Characterization (NALC) project is a component of the National Aeronautics and Space Administration (NASA) Landsat Pathfinder Program which supports scientific research on issues related to global environmental change. The increasing volume of multiresolution satellite data presents researchers with unique opportunities to conduct large-area investigations. More than 20 years of historical Landsat data provide regular observations of consistent measurements at relatively high spatial resolution at increasingly reduced cost to researchers. The NALC project involves the assembly of Landsat multispectral scanner (MSS) data "triplicates" covering the conterminous U.S. and Mexico. The NALC triplicates are comprised of co-registered Landsat MSS data acquired in 1973, 1986, and 1992 (plus or minus one year) and a co-registered digital elevation model (DEM). The 1980's and 1990's data sets also include a normalized difference vegetation index band.

The NALC triplicates are being used to study human-induced land transformations and landscape ecology, to monitor the effects of land management practices on resource condition, to investigate the role of land cover change in biogeochemical cycles, and to study feedbacks between climate and land cover change. Algorithms have been developed for processing Landsat MSS and TM data to identify and characterize landscape change. The change analysis procedure involves: (1) transformation of the imagery to scene-based measures of brightness, greenness, and wetness (TM data only), (2) pairwise differencing of the brightness, greenness, and wetness measures to compute change vectors for each image pixel, (3) encoding the change vectors using hue, saturation, and value for visualization, and (4) formulating a signal-to-noise model by which to isolate areas of "significant" change.

These algorithms have been applied to various NALC data sets, and the results have been provided to collaborators for review and comment. The research topics that have been investigated include regional climatic influence on forest condition and water supplies in the Sierra Nevada from 1985 to 1992, land management practices in natural grasslands in Nebraska, the phenologic response of vegetation to seasonal climatic conditions in semiarid regions, and expansion of urban and suburban land use.

I. INTRODUCTION

The study of landscape (land cover) change encompasses examining human-induced land transformations (deforestation, wetlands loss, agricultural land conversion, and urban sprawl), monitoring the effects of land management practices on resource condition (habitat fragmentation, biodiversity, and land degradation), and analyzing the role of land cover change in biogeochemical cycles. The increasing volume of satellite data having multiple spatial, spectral, and temporal resolutions presents researchers with opportunities to study these problems

[1/] Work performed under U.S. Geological Survey contract 1434-92-C-40004.
0-7803-3068-4/96$5.00©1996 IEEE

over large areas. More than 20 years of historical Landsat data provide regular observations of consistent measurements at relatively high spatial resolution. The North American Landscape Characterization (NALC) project, a component of the NASA Landsat Pathfinder Program, is a collaborative effort between the U.S. Environmental Protection Agency and the U.S. Geological Survey designed to exploit the rich archive of Landsat data for studying land cover changes. The NALC project involves the assembly of Landsat multispectral scanner (MSS) data "triplicates" covering the conterminous United States and Mexico. The NALC triplicates are comprised of co-registered Landsat MSS data acquired in 1973, 1986, and 1992 (plus or minus one year) and a co-registered digital elevation model (DEM). The 1980's and 1990's data sets also include a normalized difference vegetation index band. The NALC triplicates constitute a unique data set that can be used to study large-area land cover change over several decades.

Digital change analysis techniques are predicated on the assumption that pixel brightness values are correlative with the state of the land surface (i.e. land cover type, the phenology of natural vegetation and soil moisture conditions). Monitoring landscape change with remotely-sensed data provides a means for studying ecosystem responses to natural (climatic) and anthropogenic influences at regional scales. Landsat data provide a suitable spatial and temporal context within which to map the extent and characteristics of land cover change. There have been numerous applications of change analysis techniques using Landsat data since the mid-1970's. Several review papers [1], [2] have summarized the various change analysis methods and their applications to natural resource problems. Change analysis procedures have typically been developed for a specific scene or application. The ability to successfully differentiate actual subtle changes in landscape condition from variations in observational conditions and instrument response is particularly problematic.

The goal of our research was to develop methods to identify and characterize land cover change using Landsat data that could be applied to diverse landscapes and geographic areas. Specific objectives included (1) developing a set of radiometric rectification techniques to achieve relative scene-to-scene radiometric calibration, (2) developing an image noise error propagation model to isolate areas of actual landscape change, (3) extracting of proxy measures of physical-based scene characteristics from multispectral image data and implementing of a change vector analysis algorithm, and (4) developing tools for exploratory data analysis and data visualization.

II. RADIOMETRIC RECTIFICATION

A requisite preprocessing step to change analysis, in addition to co-registering the scenes, is to calibrate the images to a common radiometric reference. It is desirable to transform the digital numbers (DN) to physical values (radiance or reflectance) through the use of an empirical instrument calibration model and a radiative transfer model. The types of measurements required to properly constrain these models are not broadly available, particularly for retrospective studies. Alternatively, radiometric rectification [3] can be achieved using a linear transformation in which the additive component corrects for differences in atmospheric path radiance and the multiplicative component corrects for differences in detector calibration, sun angle, Earth-Sun distance, atmospheric attenuation, and phase angle conditions.

Relative calibration techniques assume that atmospheric and surface moisture conditions are uniform across the scenes. Pixels corresponding to temporally invariant features are used as the radiometric control sets with which to derive the gains and offsets for the linear transformation. These features should be topographically flat, be at the same elevation as the land surface of primary interest, and contain minimal vegetation cover to avoid spectral variations caused by phenological differences. Large, flat, homogeneous bright and dark surface areas are the ideal calibration targets, but in many cases a more sophisticated approach is required to gather a sufficient sample of pseudoinvariant features.

The spectral signatures of the radiometric control sets are used to derive coefficients for each band in the image. These sets can be selected by using any of the following methods: extracting identical sets of contiguous pixels corresponding to bright and dark targets in each image; defining similar control sets from brightness-greenness scatter plots that represent bright and dark pixels with low vegetation content [3]; choosing a control set corresponding to the "soil line" pixels, defined in the brightness-greenness scatter plot and having low vegetation content; and using automated scattergram-controlled regression [4]. The first two approaches involve equalizing the means for each band for deriving the linear transformation coefficients, whereas the latter two approaches use a reduced major axis regression model [5]. These methods were used successfully in our research to rectify the pixel brightness values (BV) scale of each subject image to the scale of a reference image, which was selected so that the rectification gains were usually at or greater than one. If sensor calibration data and relevant atmospheric data were available for the reference image, an atmospheric correction algorithm would have been applied to convert the sensor DN values in the rectified images to absolute surface reflectance [3].

III. IMAGE NOISE MODEL

A key step in quantifying landscape change when differencing digital images is to quantify the noise in the image in order to weight the image data for proper analysis and detect spectral changes due to acutal land surface changes. Previous studies have essentially skipped this step, either by adopting a significance threshold based on the statistics of the difference

between the images [1] or by assuming that certain higher order principal components of merged image data represent change [6], [7]. Both methods can highlight extreme change, but neither provides a physically based measure of change. A quantitative estimate and description of the change can only arise by first characterizing the image noise and its effect on the change metrics.

Through systems analysis of the image production process, Maxwell [8] identified dominant sources of image noise. These noise sources include short term variations in surface and atmospheric conditions, sensor noise, and processing noise, part of which arises from misregistration. Ideally, the image noise can be characterized by describing its sources and their contribution to image noise. Unfortunately, though it may be easy to identify sources of image noise, it is extremely difficult, if not impossible, to characterize them and their effects on every image. However, by creating a model of the image noise, researchers can extract some of its characteristics from the image data.

The image noise model adopted in our research assumed that the image noise is white, Gaussian, and not simply additive. Indeed, the noise variance in each band image was modeled as a linear function of pixel brightness value (BV), the parameter values of which are determined from the band image data. Finally, it is further assumed that the scene was not oversampled. On the basis of these assumptions, the image noise variance as a function of BV was extracted from each band image by the following method. First, for each pair of neighboring pixels, the mean BV and the variance about this mean were collected. This collection was then segregated into mean BV bins of equal width, where the width was sufficiently small to correspond accurately to a mean BV, but sufficiently large to include a statistically large number of pixel pairs for most bins. Within each bin with statistically large numbers of pixel pairs, the characteristic variance was defined, corresponding to the pixel pair variance value at the 67 percent level within the cumulative frequency distribution of these variances. A line was then fitted to the resulting set of bin BV's and corresponding characteristic variances, with each point weighted by the number of contributing pixel pairs. This line was extrapolated to the whole BV range, but with the variance limited to its minimum and maximum values found in the set of characteristic variances. The fitted line and its limits were assumed to give the image noise variance as a function of BV for that particular band image. Though the intrinsic structure of the image, particularly the scene texture, contributes to the above estimate of the variance, in the context of differencing co-registered images this contribution must be considered as noise caused by registration errors that can be of the order of one pixel.

Once the image variance as a function of BV was obtained for each band in each image, it was used in weighting the data and in determining a threshold of significant change. For quantities derived from BV, the noise variance in BV was propagated to a noise variance in the derived quantity, assuming that no correlation caused by noise exists between BV's. Consequently, the variance of a derived pixel quantity f(BV) was $\sum_{i=1}^{N_b} (\partial f/\partial BV_i)^2 V(BV_i)$ [9], where N_b is the number of bands, BV_i is the pixel brightness value in band i, and $V(BV_i)$ is the noise variance associated with that pixel brightness value. A significant change corresponded to an absolute difference in pixel brightness or derived quantity between images that exceeded by at least a factor of three the noise variance of this difference. The weight of a given quantity was set to the inverse of its noise variance.

IV. CHANGE VECTOR ANALYSIS

Proxy measures of physical scene characteristics such as brightness and greenness were extracted from each image, and their corresponding noise variances were estimated by error propagation. The Landsat visible and near-infrared bands are chiefly sensitive to vegetation leaf structure, although the addition of the mid-infrared bands in the Landsat thematic mapper add a sensitivity to soil wetness and plant moisture [10], [11]. Because Landsat MSS image data are essentially two-dimensional, brightness and greenness indices were extracted from each MSS image by simple rotation of the scattergram of the image's first two principal components so that the soil line was horizontal and vegetation lay above this line. The resulting horizontal axis corresponded to brightness and the vertical axis to greenness. In practically all of our MSS images, the brightness and greenness indices contained at least 95 percent of the image's information content. The implementation is slightly diffferent in the case of Landsat thematic mapper (TM) data. Brightness, greenness, and wetness indices were extracted from each TM image using the Gram-Schmidt orthogonalization method described in Jackson [12] on samples of dark and bright dry soil, wet soil or water, and dense vegetation selected from the image and falling in appropriate regions in the brightness-greenness plane. Once indices were obtained for each image, the transformation coefficients of the image with the best feature separability were applied to the other images to get indices that could be compared across images. This method of spectral index extraction was validated by ground measurements acquired with a field spectroradiometer.

After consistent measurement scales for the indices were achieved, an image pair was selected and change vectors were computed for each pair of indices at each image pixel. The change vectors were decomposed into magnitude and direction components. Pixels corresponding to actual landscape change were identified by modulating the magnitude component through the image noise and error propagation model. Hue, saturation,

and value (HSV) color space coordinates were used to encode the change vector analysis results for visualization. The direction of change was coded as hue, the magnitude of change as saturation, and an original image band or DEM was rescaled to value (intensity) to provide scene context. The HSV components were then transformed to red, green, and blue color space for displaying the change image. The resultant colors corresponded to the direction of change, and the richness of the color corresponded to the significance of change. Pixels that had not undergone any measureable change were displayed as gray tones corresponding to the characteristics of the intensity component (brightness, elevation).

V. RESULTS

The change detection and analysis techniques described above were applied to Landsat MSS and TM images for numerous areas, achieving consistent results. Landsat MSS images over Senegal were processed to identify areas of changing land use and land degradation from the late 1970's to the early 1990's. Landsat MSS images of the western United States from the middle 1980's to the early 1990's were processed to identify vegetation stress and damage to forested areas as a consequence of drought and infestation. Various stages of vegetation succession were delineated in areas scarred by wildfires. In addition, Landsat MSS images of Las Vegas, Nevada were processed to highlight the expansion of urban and recreational land use from the 1980's to the 1990's. Finally, the impacts of grazing and land management practices on natural grasslands were evident after processing Landsat TM images from the early 1990's.

REFERENCES

[1] A. Singh, "Digital change detection techniques using remotely sensed data," *International Journal of Remote Sensing*, vol. 10, pp. 989-1003, 1989.

[2] D.A. Mouat, G. Mahin, and J. Lancaster, "Remote sensing techniques in the analysis of change detection," *Geocarto International*, vol. 2, pp. 39-50, 1993.

[3] F.G. Hall, D.E. Strebel, J.E. Nickeson, and S.J. Goetz, "Radiometric rectification: toward a common radiometric response among multidate, multisensor images," *Remote Sensing of Environment*, vol. 35, pp.11-27, 1991.

[4] C.D. Elvidge, D. Yuan, R. Weerackoon, R. Lunetta, "Relative radiometric normalization of Landsat multispectral scanner (MSS) data using an automatic scattergram-controlled regression," *Photogramm. Eng. and Rem. Sens.*, vol. 61, pp. 1255-1260, 1995.

[5] J.C. Davis, Statistics and Data Analysis in Geology, 2nd ed., John Wiley and Sons, pp. 200-204, 1986.

[6] T. Fung and E. LeDrew, "Application of principal components analysis to change detection," *Photogramm. Eng. and Rem. Sens.*, vol 53, pp. 1649-1658, 1987.

[7] P.S. Chavez Jr. and D.J. MacKinnon, "Automatic detection of vegetation changes in the southwestern United States using remotely sensed images," *Photogramm. Eng.and Rem. Sens.*, vol. 60, pp. 571-583, 1994.

[8] E.L. Maxwell, "Multivariate system analysis of multispectral imagery," *Photogramm. Eng. and Rem. Sens.*, vol. 42, pp. 1173-1186, 1976.

[9] P.R. Bevington, Data Reduction and Error Analysis for the Physical Sciences, McGraw-Hill Book Company, pp. 56-60, 1969.

[10] E.P. Crist and R.C. Cicone, "Comparisons of the dimensionality and features of simulated Landsat-4 MSS and TM data," *Remote Sensing of Environment*, vol. 14, pp. 235-246, 1984.

[11] E.P. Crist and R.C. Cicone, "A physically-based transformation of Thematic Mapper data -- the TM tasseled cap," *IEEE Transactions on Geoscience and Remote Sensing*, vol. 22, pp. 256-263, 1984.

[12] R.D. Jackson, "Spectral indices in n-space," *Remote Sensing of Environment*, vol. 13, pp. 409-421, 1983.

Factors Affecting NEXRAD-Based Point Rainfall Estimation in the Seattle Area

Thomas A. Seliga and Chi-te Chen
Electromagnetics and Remote Sensing Laboratory
Department of Electrical Engineering, University of Washington
Seattle, Washington 98195-2500
206-685-7092; seliga@ee.washington.edu

Abstract -- Point rainfall rate estimation by radar has many useful purposes, particularly within an urban environment. For example, such monitoring could help define driving conditions related to highway wetness and visibility impairment and predict and assess storm water runoff over spatial scales down to grid sizes of around 1 x 1 km^2. Recent implementation in the U.S. of a national radar system (NEXRAD) with comparable spatial coverage and temporal sampling at approximately five-minute intervals offers great potential for such applications. Thus, an effort to improve point rainfall estimation, using reflectivity factor measurements from the Seattle area NEXRAD WSR-88D radar, is worthwhile investigating. Major factors affecting point rainfall interpretation of radar reflectivity factor include data quantization, rainfall type, spatial filtering, storm motion, melting layer effects and time correspondence of radar and gage measurements. These and other factors are under consideration for development of a robust algorithm to retrieve reliable estimates of point rainfall rates from NEXRAD radar measurements. A sample comparison between radar-derived rainfall rate estimates and gage measurements at a distance of around 60 km from the radar illustrates the methodology in a case where melting layer interference is absent.

INTRODUCTION

The NEXt Generation Weather RADar (NEXRAD) WSR-88D radar system [1-3] offers the public potential access to reliable widespread quantitative estimation of rainfall rates over large spatial domains throughout the U.S. Because of the many highly valuable applications of this capability, continuous improvement of related algorithms is essential. For example, operation of the nation's ground transportation systems may be made safer and more efficient [4-5], flood forecasting will become continuously more reliable [6-7] and better management of water resources for many purposes will emerge [8]. Depending on the application, rainfall estimation takes on different formats. For example, most water resources applications and climatological studies require accurate measurements over relatively long time periods and large spatial domains while most daily personal uses require reliability nearly instantaneously at specific locations. Furthermore, the former may be derived from the latter. Thus, improving point rainfall estimation is not only inherently valuable but also will lead to improvements in estimating rainfall over larger spatial domains and for longer time periods. This paper represents an effort at using the NEXRAD radar system towards this end.

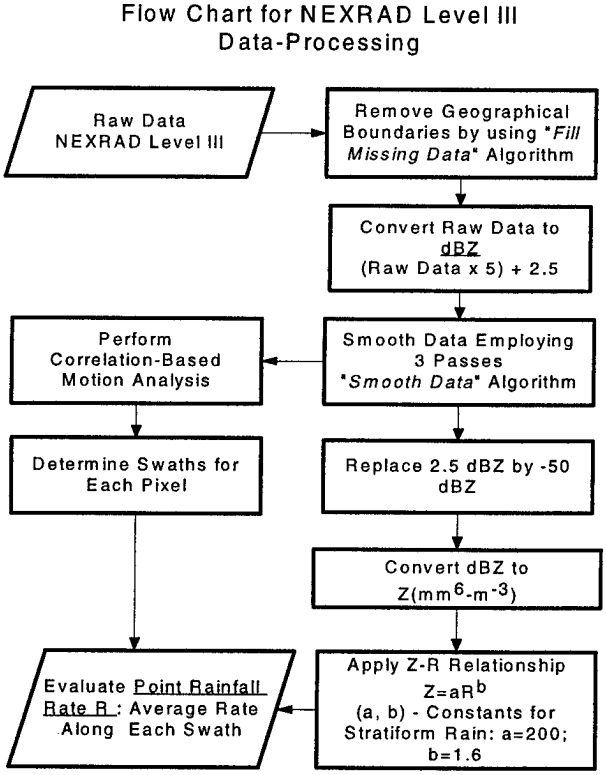


Fig. 1. Radar processing scheme for transforming NEXRAD radar data into point rainfall rate estimates.

METHODOLOGY

Z-R relationships are commonly employed for estimation of rainfall rate R from reflectivity factor Z measurements [9-10]. More recently, multiparameter radar observations have also been introduced. These include dual wavelength methods [11-12] and polarization diversity [13-18]. Sources of possible error in estimating rainfall rates from reflectivity factor and other radar measurements include [10]: horizontal winds that cause ground-level

0-7803-3068-4/96$5.00©1996 IEEE

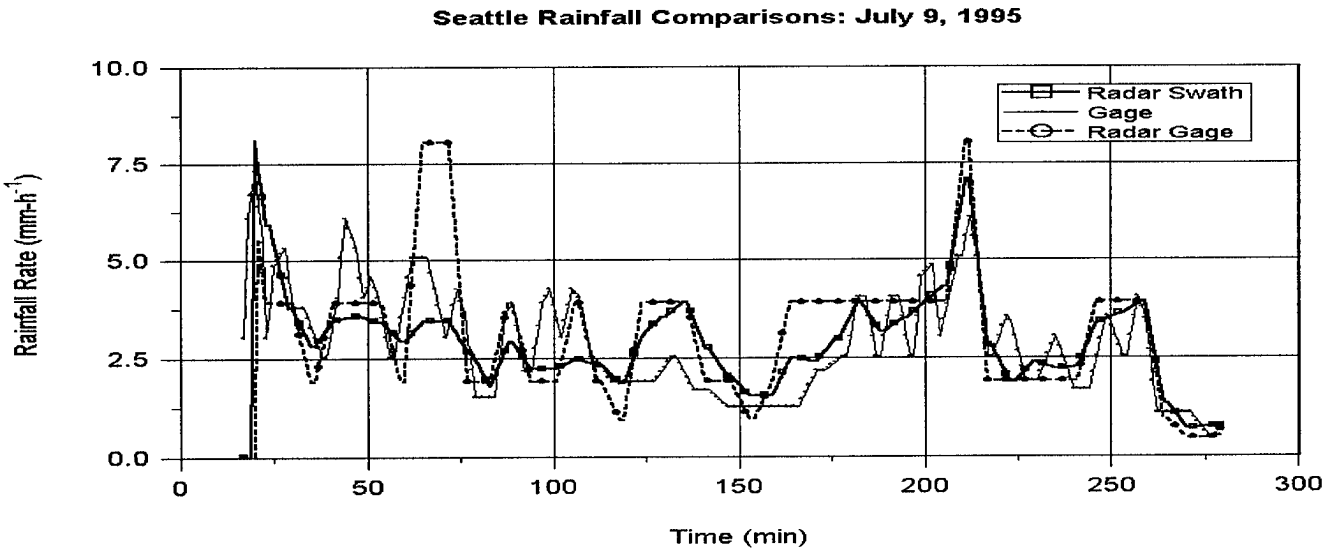


Fig. 2. Radar-based estimates and rain gage measurements of rainfall rates at the University of Washington on July 9, 1995.

raindrops to be displaced from the location of radar measurements; attenuation due to atmospheric gases, rain and wetted radomes; reflectivity enhancements in the melting layer; incomplete beam filling; evaporation; beam blockage; rainrate gradients; polarization effects; and vertical air motions. Other factors that can affect this estimation are: presence of ice phase in the radar scattering volume; radar miscalibration; and inadequacy of the radar measurements to account for intrinsic properties of rainfall such as drop size distribution variability. This paper utilizes Z-R relationships and addresses the first problem, namely, effects of horizontal winds; this is done by estimating storm motion to determine a swath of measurements that approximate corresponding temporal average rainfall rate at a given location on the ground. This approach was previously used successfully in comparisons between ground-based rainfall measurements and inferences from radar polarimetric-based measurements [18].

Fig. 1 illustrates the methodology employed to estimate point rainfall rates from Z In this instance, Level III data which include geographical features are assumed because of their general availability, although Level II data is preferable because of its greater precision (1 dB v. 5 dB) [2-3]. Note that the quantization Q limitations of Level III data are not as restrictive as they appear. Essentially, Q may be interpreted as being from a uniform distribution with each data point representing a sample between Q-levels QL and QL + 5. Spatial filtering, associated with storm motion (to account for horizontal winds), further helps compensate for Q errors. Additional smoothing of the data may also be performed as indicated, but this procedure will ultimately depend on more extensive evaluation. The storm motion is determined through an areal or two-dimensional cross-correlation process that compares the region around a point of interest with similar-sized regions of the just previously sampled measurements. The region with highest correlation is taken as an indication of storm motion over the point of interest. Sample swaths or lengths of volumetric radar measurements, passing over the point of interest, then represent corresponding ground-based observations, recorded over the radar sampling interval (about 5 min for NEXRAD). When using a Z-R relationship, the base radar data is best converted to R at each data point with averaging done in R rather than Z.

JULY 9, 1995 CASE STUDY

Fig. 2 shows results of applying the algorithm, defined in Fig. 1 and without any Z smoothing, for an event that occurred on July 9, 1995 in Seattle at the University of Washington (UW); this location is around 60 km due south of the radar. Estimates from both a swath analysis and radar measurements at the gage are indicated; they utilize the Marshall-Palmer Z-R relationship [19] and include a time shift of around 5 min to account for raindrop fall speeds. The results compare very favorably with five-minute running average tipping bucket (0.01 in) gage results. Corresponding accumulations are shown in Fig. 3. Note that swath smoothing is evident in Fig. 2 which results in a better correspondence to ground truth as seen by the gage.

CONCLUSIONS

This paper presents an approach to NEXRAD estimation of rainfall rates that attempts to account for storm motion or horizontal winds, one of the foremost factors affecting reliable radar estimation of rainfall rate. A summer time case study yielded very good comparisons between radar estimates and ground-based gage measurements. This problem requires further study,

including investigation of errors, differences between estimates from Levels II and III data, other interferences such as effects of vertical air motions, hydrometeor phase uncertainty (especially related to the melting -layer/bright-band) and snowfall. These problems should be resolved or lessened in the future with the addition of polarimetric capabilities on WSR-88D radars, but until this happens efforts must continue to improve algorithms for both areal and point estimation of R from the current set of observations available with the NEXRAD radars. Only in this way will society fully benefit from its major investment in the NEXRAD concept/system.

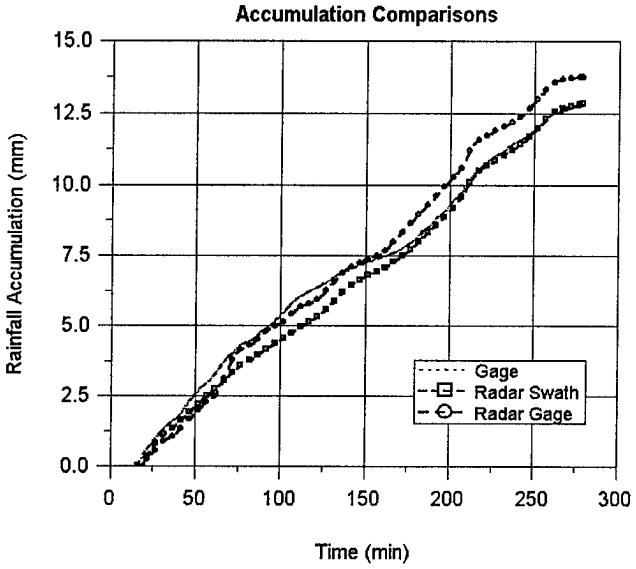


Fig. 3. Rainfall accumulation comparisons between radar estimates and a gage located at the UW on July 9, 1995.

ACKNOWLEDGMENTS

This research was supported by the Washington State Department of Transportation's (WSDOT) Transportation Research Center (TRAC) and the Transportation Northwest Regional Center (*TransNow*) at the UW.

REFERENCES

[1] V. E. Baer, "The transition from the present radar dissemination system to the NEXRAD Information Dissemination System (NIDS)," Bull. Amer. Meteor. Soc., vol. 72, pp. 29-33, 1991.

[2] T. D. Crum, R. L. Alberty and D. W. Burgess, "Recording, archiving, and using WSR-88D data," Bull. Amer. Meteor. Soc., vol. 74, pp. 645-53, 1993.

[3] G. E. Klazura and D. A. Imy, "A description of the initial set of analysis products available from the NEXRAD WSR-88D system," Bull.. Amer. Meteor. Soc., vol. 74, pp. 1293-311, 1993.

[4] T. A. Seliga and L. Wilson, "Applications of the NEXRAD radar system for highway traffic management," Preprints, 27th Int. Conf. on Radar Meteor.,pp. 176-8 , 1995.

[5] T. A. Seliga and K. D. Nguyen, "The NEXRAD radar system: A new tool for highway traffic management and research," Proc. Sixth Annual Mtg. & Exposition, April 15-18,Houston, TX, 1996.

[6] M. D. Hudlow, "Modern era of rainfall estimation,' Int. Symp. Remote Sens and Water Res., 11 pp., 1990

[7] V. Collinge and C. Kirby (eds.), Weather and Flood Forecasting, John Wiley & Sons, NY, 296 pp., 1987.

[8] Council on Environmental Quality & U.S. Department of State, Global 2000. Report to the President, U.S. Govt. Print. Office, Vols. 1,11, III, Washington, DC.

[9] L. J. Battan, Radar Observations of the Atmosphere, Univ. of Chicago Press, Chicago, IL, 323 pp., 1973.

[10] R. J. Doviak and D. S. Zrnic, Doppler Radar and Weather Observations, 2nd ed., Academic Press, NY, 562 pp., 1993.

[11] D. Atlas and C. W. Ulbrich, "The physical basis for attenuation-rainfall relationships and the measurement of rainfall parameters by combined attenuation and radar methods.," J. Rech. Atmos., vol. 8(1-2), pp. 275-98, 1974.

[12] P. J. Eccles, "Comparison of remote measurements by single- and dual-wavelength meteorological radars," IEEE Trans. Geosci. Electron., vol. GE-17, pp. 205-18, 1979.

[13] T. A. Seliga and V. N. Bringi, "Potential use of radar differential reflectivity measurements at orthogonal polarizations for measuring precipitation," J. Appl. Meteorol., vol. 15, pp. 69-76, 1976.

[14] T. A. Seliga and V. N. Bringi, "Differential reflectivity and differential phase shift: Applications in radar meteorology," Radio Sci., vol. 13, pp. 271-5, 1978.

[15] J. W. F. Goddard, S. M. Cherrry and V. N. Bringi, "Comparison of dual-polarization radar measurements of rain with ground-based disdrometer measurements," J. Appl. Meteorol., vol. 21, pp. 252-6, 1982.

[16] M. Saifzadeh, "Microwave differential phase shift in rain-filled media," Electrical Engineering Master's Thesis, The Ohio State University, 111 pp., 1985.

[17] M. Sachidananda and D. S. Zrnic, "Rain rate estimates from differential polarization measurements," J. Atmos. Oceanic Tech., vol. 4, pp. 587-98, 1987.

[18] K. Aydin, Y. M. Lure and T. A. Seliga, "Polarimetric radar measurements of rainfall compared with ground-based rain gauges during MAYPOLE '84," IEEE Trans. Geosci. Rem. Sens., vol. GE-28, pp. 443-9, 1990.

[19] J. S. Marshall and W. M. K. Palmer, "The distribution of raindrops with size," J. Meteor. vol. 5, pp. 165-6, 1948.

Analysis of Dual-Wavelength Dual-Polarization Returns from Frozen Hydrometeors

Robert Meneghini, Code 975, NASA Goddard Space Flight Center, Greenbelt, MD 20771,
Ph: 301-286-9128, FAX: 301-286-1761, email: bob@meneg.gsfc.nasa.gov
Toshio Iguchi, Communications Research Laboratory, Tokyo, 184, Japan
Ph: 81-423-27-7545, FAX: 81-0423-27-6666, email: iguchi@crl.go.jp
Liang Liao, Caelum Research Co., Silver Spring, MD,
Ph: 301-286-5855, FAX: 301-286-1761, email: lliao@meneg.gsfc.nasa.gov

INTRODUCTION AND BACKGROUND

In most situations dual-wavelength radar returns in precipitation are functions of the cumulative path attenuation out to the observation range as well as the backscattering properties of the hydrometeors within the resolution volume. For spaceborne or airborne radars that view the storm from the top, there generally will be a region of frozen hydrometeors that is encountered before regions of partially or fully melted particles. In this region, where attenuation effects are small, the dual-frequency radar returns can be related to two parameters of the size distribution if the scattering at either wavelength is non-Rayleigh [1]. Ambiguities in the estimation procedure remain, however, because of the unknown mass density of the scatterers as well as the effects of particle shape and orientation.

Several approaches are available to resolve at least some of the ambiguities in the microphysical retrievals. One possibility is the addition of radiometric brightness temperature measurements. While the longer wavelengths are sensitive primarily to the total rain water along the radar beam, at wavelengths of about 0.9 cm and shorter, the size distribution and mass density of the frozen hydrometeors become important. Another approach arises from the fact that the measurements from a 3-wavelength radar offer a means by which a 2-parameter size distribution and an averaged mass density can be estimated at each range gate. As of yet, however, no triple wavelength radar data sets have been measured. A third approach is the use of polarimetry. In particular, if the shape and orientation distributions of the particles are known, then the linear depolarization ratio (LDR), the dual-frequency ratio (DFR) and the radar reflectivity factor (Z) can provide, in principle, estimates of the size distribution and average mass density of the particles at each range bin.

In this paper, we illustrate some of the advantages and limitations of the third approach by using data from the dual-wavelength, dual-polarization airborne radar build by the Communications Research Laboratory (CRL) of Japan. For the CaPE (Convective and Precipitation Electrification) experiment, the CRL instrument was installed in the NASA T-39 jet aircraft. In July 1991, 9 data flights were conducted in coordination with ground-based radars and multi-instrumented aircraft.

SAMPLE RADAR RANGE-PROFILES

Shown in Fig. 1 is a set of measured radar reflectivity factors at near-nadir incidence as a function of the distance from the aircraft. The 4 curves correspond to the co- and cross-polarized returns at X-band (10 GHz) and the co- and cross-polarized returns at Ka-band (34.45 GHz). Note that the large spikes in the co- and cross-polarized X-band returns at a range of about 11.5 km correspond to the surface return. The behavior of the DFR (= $dBZ_{co\text{-}pol}$(10 GHz) - $dBZ_{co\text{-}pol}$(34.45 GHz)) with range provides an indication of the region of frozen hydrometeors: in particular, the very sharp increase in the DFR beginning at a radar range of about 6.5 km indicates a region of large melting hail or graupel. By moving upward several kilometers from this point, into a region where the DFR is relatively small and its increase with range gradual, the observation point is assumed to be in a

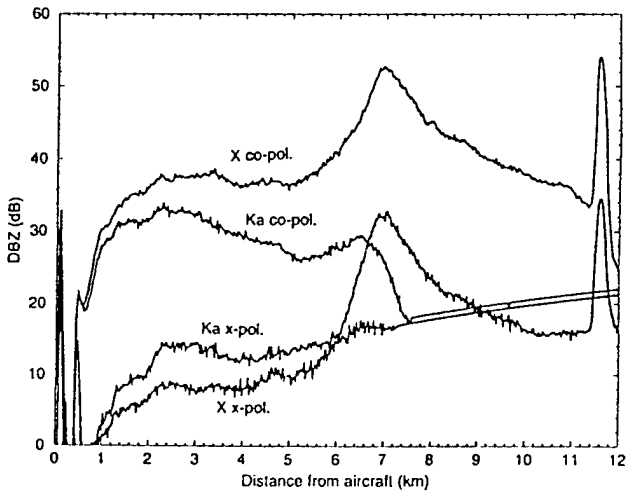


Fig. 1: Co- and Cross-polarized reflectivity factors at 10 and 34.5 GHz versus range; 27 July 1991, 23:16:30 UT.

0-7803-3068-4/96$5.00©1996 IEEE

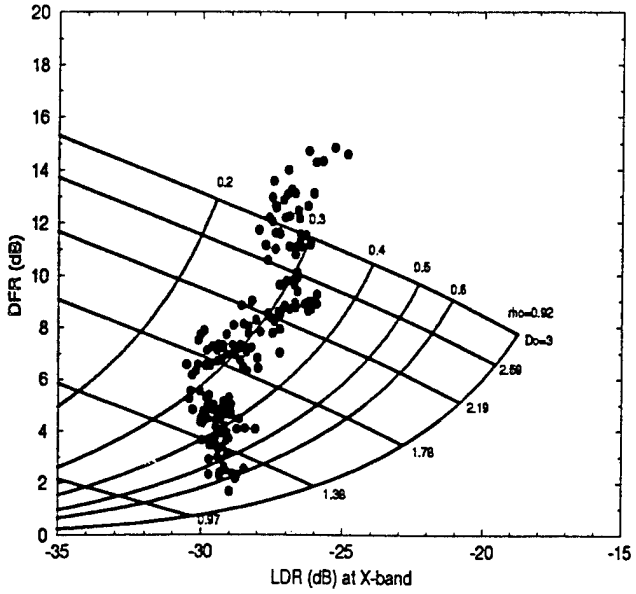


Fig. 2: Lines of constant mass density and median diameter, D_0, superimposed upon a plot of DFR versus LDR; solid circles represent the measurements shown in Fig. 1.

region where the majority of particles are frozen. For the example shown in Fig. 1, the region of frozen hydrometeors is taken to extend from 1 km to 4 km below the aircraft.

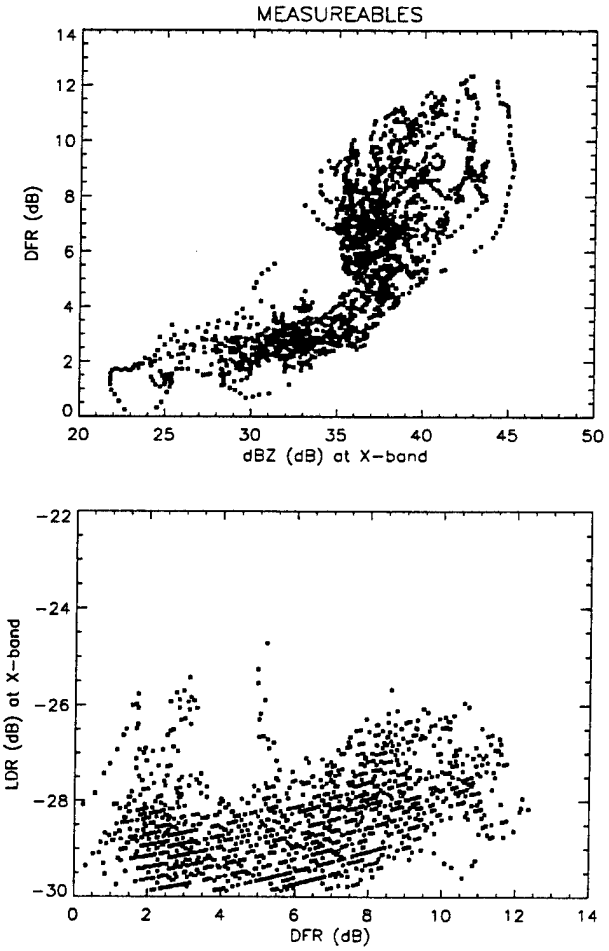
For a particular orientation distribution of particles and a fixed shape-size relationship, lines of constant snow density, ρ, and equivolume, melted median mass diameter, D_0, can be plotted on a graph of DFR (dB) and LDR (dB), where the LDR is given by $dBZ_{x\text{-}pol}$(10 GHz)-$dBZ_{co\text{-}pol}$(10 GHz). In generating the of lines constant (ρ, D_0) shown in Fig. 2 two assumptions are made: the orientation of the particles are random and there is a 1-parameter relationship between shape and size given by:

$$(b/a) = 1.03 - 0.062*p*D_{eq} \qquad (1)$$

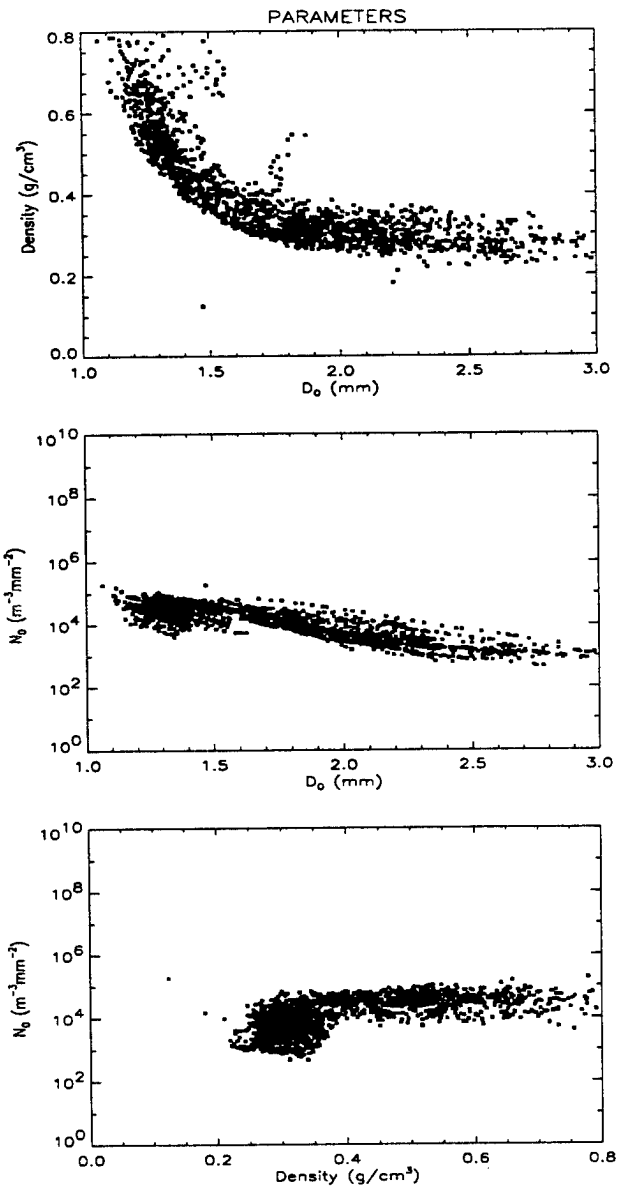
where (b/a) is the ratio of the major to the minor axes of a prolate spheroid, D_{eq} is the equivolume, melted diameter of the particle in millimeters. Note that this relationship is taken from the shape-size relationship for rain drops [2]; in contrast to the case of rain, however, where p = 1, in Fig. 2 we have taken p = 2 so that the average particle shape is taken to be more highly eccentric than a rain drop of the same volume. Obviously, lines of constant (ρ, D_0) change if these assumptions are modified; for example, if the particles are assumed to have a fixed shape, independent of size, the lines of constant mass density shown in Fig. 2 become straighter and more vertically oriented.

Superimposed on the theoretical curves of Fig. 2 are the measurements from Fig. 1 represented by the solid circles. The progression of points as a function of range can be followed by noting that the DFR is approximately a monotonically increasing function of radar range. The results show that the mass density of the particles undergo a slight decrease with distance into the storm along with a significant increase in the median size of the particles.

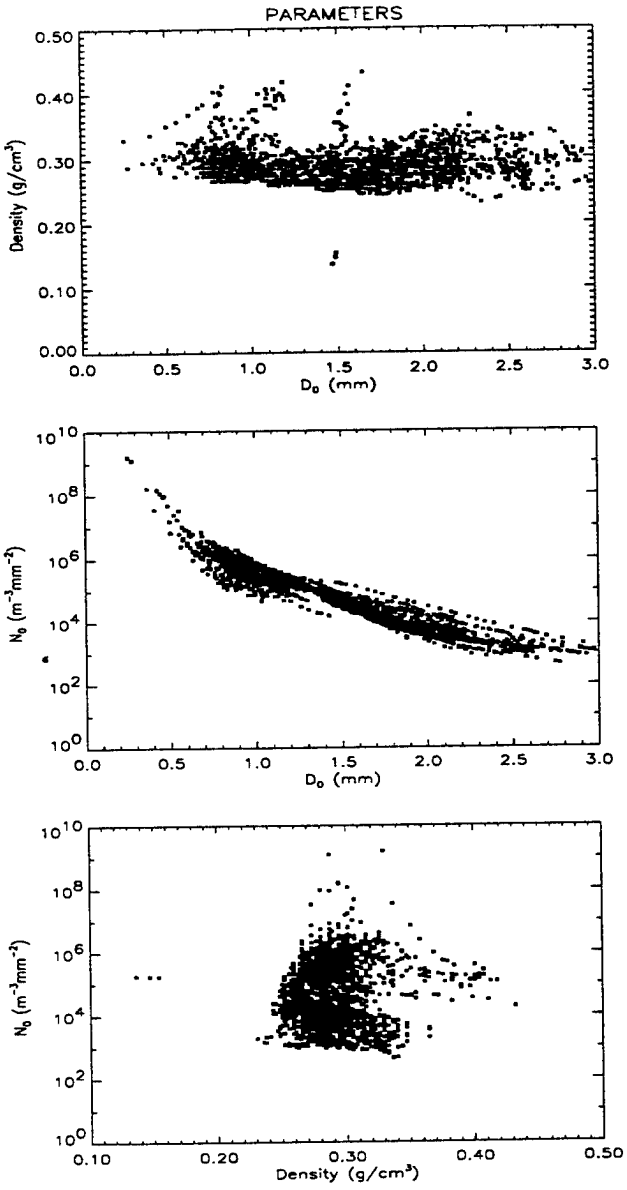
Shown in Figs. 3 are the values of DFR, LDR(10 GHz) and dBZ(10 GHz) measured over a 20 sec. period ($\approx$ 4 km flight line). As in Fig. 1, the radar ranges have been restricted to those regions in which the hydrometeors are frozen. The corresponding estimates of ρ, D_0, and N_0 are shown in Figs. 4 and 5; for the results in Figs. 4, the shape-size relationship is given by Eq. (1) with p = 2 while for Fig. 5 (b/a) = 2.5 so that the prolates are assumed to have a fixed shape, independent of size. Under both assumptions, the N_0 and D_0 are negatively correlated although the D_0 values tend to be smaller and the N_0 larger under the fixed-shape assumption. Both sets of results show the N_0 parameter to be nearly independent of ρ. When the particles are assumed to have a shape-size correlation, the results exhibit a strong negative



Figs. 3: Measurements of DFR, LDR, and dBZ from 23:16:20 - 23:16:40 on 27 July 1991.



Figs. 4: Estimates of ρ, D_0, and N_0 assuming that a shape-size relationship given by Eq. 1 with p = 2.



Figs. 5: Same as Figs. 4 except that the shape of the particles is assumed to be fixed at (b/a) = 2.5.

correlation between density and size; this correlation disappears, however, if shape and size are assumed to be uncorrelated.

SUMMARY

In regions of frozen hydrometeors dual-wavelength, polarimetric radar measurements can eliminate some of the ambiguities in the characterization of size distribution and mass density of the scatterers. In future work, the use of in situ measurements, as well as LDR(34.45 GHz) and ground-based differential reflectivity measurements will be investigated for improving the microphysical retrievals.

REFERENCES

[1] T. Iguchi and R. Meneghini, "Differential Equations for dual-frequency radar returns,", Preprints 27th Conf. Radar Meteor., Oct. 9-13, Vail, CO, p. 190, 1995.

[2] H.R. Pruppacher and K.V. Beard, "A wind tunnel investigation of the internal circulation and shape of water drops falling at terminal velocity in air," Quart. J. Roy. Meteor. Soc., vol. 96, pp. 247-256, 1970

Polarimetric method for ice water content determination

Alexander V. Ryzhkov [1] and Dusan S. Zrnic [2]
[1] Cooperative Institute for Mesoscale Meteorological Studies, University of Oklahoma
[2] National Severe Storms Laboratory
1313 Halley Circle, Norman OK 73069
Ph. (405) 366-05-05, FAX (405) 366-04-72, E-mail: ryzhkov@nssl.gcn.uoknor.edu

1. INTRODUCTION

There have been a number of studies to estimate ice water content (IWC) of snow clouds using radar reflectivity factor Z [1 -4]. All of these studies show extreme variability in the IWC - Z relations, which appear to change from day to day and cloud to cloud. High diversity in the IWC - Z relations is primarily due to the fact that reflectivity factor is proportional to the product of IWC and average mass of ice hydrometeors; therefore at least one more independent measurement is needed to resolve this ambiguity.

Since ice and snow hydrometeors are nonspherical the use of polarimetry is a natural way for estimation of bulk properties of snow clouds and precipitaion [5].

In this paper we develop a radar polarimetric model of a cloud of ice hydrometeors and obtain a polarimetric relation for computing IWC . We account for the diversity of crystal shape and the dependence of shape and density of scatterers on their size. Finally, we use polarimetric data from four Oklahoma snowstorms to check the consistency of the IWC estimates (obtained from the proposed polarimetric algorithm) with those derived using conventional IWC - Z relations.

2. ASSUMPTIONS

We model ice particles as oblate and prolate spheroids with axes a and b, where axis a is always the axis of rotation.The oblates are assumed oriented so that the axis of rotation is vertical whereas prolates are considered to be randomly oriented in the horizontal plane.

We attempt to model the transition from elementary pristine crystals to aggregates taking into account the dependence of dry snow density on the size of snow particles as specified by Brown and Francis [6]:

$$\rho = 0.07\, D^{-1.1} \qquad (1)$$

In (1) and throughout the paper ρ is in g cm^{-3} and D in mm.

The shape of ice hydrometeor is highly variable. It depends on the type of crystal and its size. Following Matrosov et al. [7] we examine 11 categories of ice particles with distinctly different dependencies of their aspect ratios on size. These categories are listed in Table 1. The relation between the crystal's smaller and larger dimensions (h and L respectively) can be expressed by the power law [7]

Table 1. The coefficients α and β for different classes of crystals [7]

Crystal class	α	β
1. Dendrites	0.038	0.377
2. Solid thick plates	0.230	0.778
3. Hexagonal plates	0.047	0.474
4. Solid columns (L/h ≤ 2)	0.637	0.958
5. Solid columns (L/h > 2)	0.308	0.927
6. Hollow columns (L/h ≤ 2)	0.541	0.892
7. Hollow columns (L/h > 2)	0.309	0.930
8. Long solid columns	0.128	0.437
9. Solid bullets (L ≤ 0.3 mm)	0.250	0.786
10. Hollow bullets (L > 0.3 mm)	0.185	0.532
11. Elementary needles	0.073	0.611

$$h = \alpha\, L^{\beta} \qquad (2)$$

where the coefficients α and β in (2) are listed in the second and third columns of Table 1, for h and L expressed in mm.

3. BASIC RELATIONS

In the model we use the Rayleigh approximation. Therefore, the final results are valid at least for the centimeter wavelengths. In the Rayleigh region the scattering amplitudes of spheroidal particles in forward and backward directions are equal and can be expressed as [8]:

$$f_{a,b} = f_{a,b}(0) = f_{a,b}(\pi) = \frac{\pi^2 D^3}{6\lambda^2}\, \xi_{a,b} \qquad (3)$$

where

$$\xi_{a,b} = \frac{1}{L_{a,b} + \dfrac{1}{\epsilon - 1}} \qquad (4)$$

In (3) λ is the wavelength in mm, f_a is the scattering amplitude if the electric field vector is parralel to the axis of rotation of the hydrometeor, and f_b stands for the scattering amplitude if the electric vector is perpendicular to the axis of

0-7803-3068-4/96$5.00©1996 IEEE

rotation. The parameter $L_{a,b}$ determines the shape of the hydrometeor [8]. The radar cross-section of a snow particle is given by

$$\sigma_{a,b} = 4\pi\ |f_{a,b}|^2 = \frac{\pi^5 D^6}{9\lambda^4}\ \xi^2_{a,b} \qquad (5)$$

We consider the case of hydrometeor illumination at low elevation angles. Thus, the expressions for radar reflectivity factors at orthogonal linear polarizations and specific differential phase are as follows:

$$Z_{h,v} = \frac{\lambda^4}{\pi^5 K^2} \int \sigma_{h,v} N(D)\, dD \qquad (6)$$

and

$$K_{DP} = \frac{180\lambda}{\pi} \int Re\ (f_h - f_v)\ N(D)\, dD \qquad (7)$$

where $f_h = f_b$, $f_v = f_a$, $\sigma_h = \sigma_b$, $\sigma_v = \sigma_a$ for oblate hydrometeors. In (6) $K = \left| (\varepsilon_w - 1)/(\varepsilon_w + 2) \right|$, ε_w is the dielectric constant of water. $Z_{h,v}$ is expressed in $mm^6 m^{-3}$, K_{DP} - is in deg km^{-1}.

Our objective is to obtain the relation between ice water content IWC and radar variables Z_h, K_{DP} and either $Z_{DP} = Z_h - Z_v$ or $Z_{DR} = Z_h/Z_v$. These variables are readily available if measurements are performed in linear vertical - horizontal polarization basis.

It follows from (1) that the density ρ of ice hydrometeor is usually quite low if its size is larger than 0.5 mm. At low densities $\varepsilon - 1$ is roughly proportional to ρ, $\varepsilon - 1 = \mu\rho$. Furthermore, $L_{a,b} << 1/(\varepsilon - 1)$ in (4) and the expression for $\xi_{a,b}$ can be expanded as follows

$$\xi_{a,b} \approx \mu\rho\ (1 - L_{a,b}\mu\rho) \qquad (8)$$

At the first approximation for oblate particles $\sigma_h = \sigma_b \sim \rho^2 D^6 \sim M^2$ where M is mass of the particle. Therefore for a narrow intreval of particle size (or mass) the reflectivity factor is proportional to the product of partcle concentration N and square of their mass $Z_h \sim N M^2$. At the same time ice water content is proportional to the product of concentration and mass: IWC ~ N M. Both IWC and Z_h do not depend on the shape of ice hydrometeor. To estimate IWC we need to determine N and M independently. In order to accomplish this it is necessary to find an independent polarimetric parameter from which either N or M can be derived. Such a parameter could be the ratio Z_{DP}/K_{DP} which can be written as

$$\frac{Z_{DP}}{K_{DP}} \sim \frac{D^6(\xi_b^2 - \xi_a^2)}{D^3(\xi_b - \xi_a)} \sim D^3(\xi_b + \xi_a) \sim \rho D^3 \sim M \qquad (9)$$

Note that both K_{DP} and Z_{DP} are highly dependent on the particle shape because $\xi_b - \xi_a \approx \mu^2\rho^2 (L_a - L_b)$ according to (4) whereas their ratio does not depend on the shape and is determined only by the particle mass. Combining Z_h and Z_{DP}/K_{DP} we obtain

$$IWC = C\ Z_h K_{DP}/Z_{DP} = C\ K_{DP}/(1 - Z_{DR}^{-1}) \qquad (10)$$

Thus, IWC can be estimated using K_{DP} and Z_{DR}.

Using (3 - 5) we can derive power low relations between the mass of the particle M and parameters σ_h and $Re(f_h - f_v)$ for all eleven classes of hydrometeors

$$\sigma_h = \frac{\pi^5}{9\lambda^4}\ a_1\ M^2 \qquad (11)$$

$$Re\ (f_h - f_v) = \frac{\pi^2}{6\lambda^2}\ a_2\ M^{b_2} \qquad (12)$$

The coefficients $a_{1,2}$ and b_2 are different for different categories of crystals.

Remarkably, the ratio $(\sigma_h - \sigma_v)/Re\ (f_h - f_v)$ is almost linearly proportional to the mass of the ice particle:

$$\frac{\sigma_h - \sigma_v}{Re\ (f_h - f_v)} = \frac{2\pi^2}{3\lambda^3}\ a_3 M \qquad (13)$$

In (13) the coefficient a_3 is about 5.2 and practically doesn't depend on the type of ice crystals and their density.

It is easy to obtain the expressions for the integral parameters Z_h, K_{DP}, and Z_{DP} using (6 - 7) and (11 - 13) and assuming exponential type of particle size distribution. Combining IWC, Z_h, K_{DP}, and Z_{DP} in (10) yields the coeffcient $C = \lambda C_1$, where $C_1 \approx 4.4\ 10^{-3}$ if λ is expressed in mm and IWC - in g m^{-3}. The coefficient C_1 is quite stable for all types of crystals examined. The RMS deviation of C_1 about ther mean is 5%. This means that the relation (10) practically is not sensitive to the shape of snow particles. We have examined the susceptibility of (10) to the variations in the density dependence on particle size. Several possible dependencies were simulated matching experimental data from [6]. The corresponding changes in C_1 do not exceed 20 %. The coeffcient increases slowly as average ρ increases.

The advantage of the method is that it is immune to radar calibration errors because the absolute value of the radar reflectivity factor is not involved. However, the suggested technique has two limitations: first, it doesn't work well for very low values of K_{DP} and Z_{DR} and, second, it overestimates the actual ice water content if heavy aggregation of crystals takes place. The second limitation is a reflection of the fact that large low-density aggregates contribute much to IWC

and Z_h but practically do not affect K_{DP} and Z_{DP}.

4. EXPERIMENTAL EVALUATION

We have examined four Oklahoma snowfall events for which data from the S-band Cimarron polarimetric radar were available (Z_h, K_{DP} and Z_{DR}). There were no aircraft penetrations in these storms, so direct (in-situ) measurements of ice water content have not been made. The only possibility left was to estimate IWC using the suggested method and compare the results with IWC estimates obtained from traditional IWC - Z relations.

For the two snowfalls selected (03.01.95 and 03.02.95) the observations were performed far behind a cold front in regions of surface temperature below -5°C. In these two cases crystals were dominant type of ice particles. The other two snowstorms (01.05.95 and 03.08.94) were observed near the frontal boundary with warm air, so the presence of aggregates together with pristine crystals was more likely for the latter storms.

Ice water content estimates computed from K_{DP} and Z_{DR} are plotted against measured Z_h in Fig. 1 for all four snowfalls. Different symbols stand for four different days. Plotted on the same graph are the lines representing three IWC - Z dependencies reported in the literature. One of them IWC = $0.064\ Z^{0.58}$ was presented by Atlas et al [4] and represents the best fit for cirrus clouds in the range of reflectivities between -50 and 10 dBZ. The second one , IWC = $0.035\ Z^{0.51}$ suggested by Heymsfield [2] summarizes the results obtained for stratiform ice clouds in the Z interval between -15 and 25 dBZ. And, finally, the third one: IWC = $0.013\ Z^{0.39}$ is supposed to be valid for snowfalls with reflectivities larger than 20 dBZ [1].

The estimated values of IWC are in best agreement with the dependence reported by Atlas et al. [4] and its extrapolation to larger reflectivity factors (line 1 in Fig.1). The majority of data points lie slightly above the Heymsfield line (curve 2) and no data fit Sekhon - Srivastava dependence (curve 3). The data for two colder days of 03.01.95 and 03.02.95 when crystals were a dominant scatterers agree better with the Atlas et al. and Heymsfield dependencies. As expected, the worst correspondence (large overestimation) is evident for the case of 03.08.94 (triangles in Fig. 1) when heavy aggregation was more likely than for other cases.

These preliminary tests of the proposed polarimetric technique for ice water content determination indicate that the polarimetric method shows good consistency with the traditional one based on IWC - Z relations if ice crystals are dominant scatterers in a cloud. In the presence of heavy aggregation the suggested method is likely to overestimate the actual ice water content.

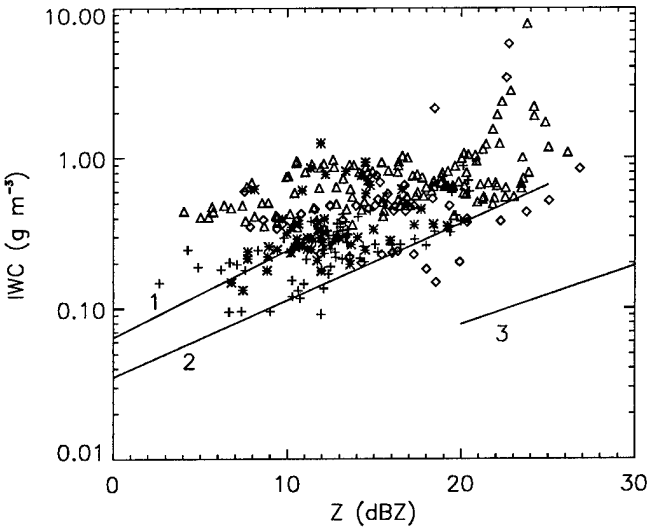


Fig. 1. IWC estimates obtained from polarimetric variables versus measured values of radar reflectivity factor for four Oklahoma snowstorms: 03.01.95 (+), 03.02.95 (*), 01.05.95 (◇), 03.08.94 (Δ). 1 - Atlas et al [4]; 2 - Heymsfield [2]; 3 - Sekhon and Srivastava [1].

REFERENCES

[1] R. S. Sekhon and R. C. Srivastava, "Snow size spectra and radar reflectivity", *J. Atmos.Sci.*, vol. 27, pp. 299 - 307, 1970.

[2] A. J. Heymsfield, "Precipitation development in stratiform ice clouds: a microphysical and dynamical study," *J. Atmos. Sci.*, vol. 34, pp. 367 - 381, 1977.

[3] K. D. Sassen, "Ice cloud content from radar reflectivity", *J. Appl. Meteor.*, vol. 26, pp. 1293 - 1299, 1987

[4] D. Atlas, S. Y. Matrosov, A.J. Heymsfield, M.-D. Chou, D. B. Wolff, "Radar and radiation properties of ice clouds", *J. Appl. Meteor.*, vol. 34, pp. 2329 - 2345, 1995.

[5] J. Vivekanandan, V. N. Bringi, M. Hagen, P. Meischner, "Polarimetric radar studies of atmospheric ice particles", *IEEE Trans. Geosci. Rem. Sens.*, vol. 32, pp. 1 - 10, 1994.

[6] P. R. A. Brown and P. N. Francis, "Improved measurements of the ice water content in cirrus using a total-water probe", *J. Atmos. Ocean. Tech.*, vol. 12, pp. 410 - 414, 1995.

[7] S. Y. Matrosov, R. F. Reinking, R. A. Kropfli, B. W. Bartram, "Estimation of ice hydrometeor types and shapes from radar polarization measurements", *J. Ocean. Atm. Tech.*, vol. 13, pp. 85 - 96, 1996.

[8] H. C. Van de Hulst, *Light Scattering by Small Particles*, Dover Publications, Inc., New York, 470 pp., 1981.

Simulation of Dual-Polarization Bistatic Scattering from Rain and Hail

K. Aydin and S-H. Park
The Pennsylvania State University
Department of Electrical Engineering
University Park, PA 16802
Phone: (814) 865-2355
FAX: (814) 863-8457
e-mail: aydin@cloud1.ee.psu.edu

ABSTRACT -- S-band bistatic radar parameters are simulated to evaluate their potential for discriminating rain and hail and estimating their median size. In this paper, results for vertically polarized transmission with co- and cross-polarized reception are considered for several bistatic directions. The linear depolarization ratio, the effective reflectivity factor, the bistatic to backscatter reflectivity ratio (BBR_v), and the correlation coefficient between the co- and cross-polarized returns are evaluated. It is observed that each one of these parameters can differentiate rain from hail under certain conditions. However, when all of them are used in combination they can be effective over a broader range of possibilities. It is also noted that BBR_v may be a good estimator of median size.

INTRODUCTION

A bistatic radar system for measuring dual-Doppler vector wind fields has recently been demonstrated [1]. It is of interest to evaluate the utility of polarization with such a system for differentiating hail from rain and estimating hailstone size (e.g., median size). This paper presents simulations of S-band dual-polarization bistatic radar parameters in rain and hail. A three dimensional canting distribution is used with oblate spheroidal model raindrops and hailstones. Exponential size distributions reported in the literature are incorporated in these simulations. The scattering computations are performed with the extended boundary condition method [2].

RAIN AND HAIL MODELS

Raindrops and hailstones are modeled as oblate spheroids. The axial ratios of hailstones are assumed to be independent of size and chosen equal to 0.8 [3]. Raindrop axial ratios are calculated from Green's formula [4].

The S-band scattering computations are performed at 2.75 *GHz*. The dielectric constant of a raindrop at 5 *°C* is 80.89 - j19.92 [5]. The dielectric constant of water at 0 *°C* is 80.92-j23.51 and of solid ice is 3.17-j0.004. Hailstones made of solid ice and a mixture of 10% water and 90% ice are considered here. The latter mixture leads to a dielectric constant of 8.63-j1.63 [6].

The orientation of an oblate spheroidal particle can be described by the polar (θ) and azimuthal (ϕ) angles of its symmetry axis in a coordinate system where the z-axis is along the vertical direction, Fig.1. Both angles are assumed to be size independent. The azimuth angle ϕ is assumed to be uniformly distributed between 0 and 2π. The polar angle θ is assumed to have a truncated Gaussian distribution. The mean and standard deviation of θ are chosen as 0° and 5° for raindrops, and 0° and 30° for hailstones, respectively. The results presented here do not change appreciably if the mean angle for hailstones is set to 90°.

The exponential size distribution

$$N(D) = N_0 \exp(-\Lambda D) \tag{1}$$

is used for both rain and hail. Here D is the equivolume spherical diameter of the particle. Two different exponential distributions are considered for rain: the Marshall-Palmer (MP) [7] and Joss thunderstorm (J-T), [8]. For the MP distribution $N_0 = 8000\ mm^{-1}m^{-3}$, the maximum drop diameter is 6 *mm*, and Λ is varied between 1.5 to 4 mm^{-1}, which corresponds to rainfall rate in the range 1 to 120 $mm\ h^{-1}$. For the J-T distribution $N_0 = 1400\ mm^{-1}m^{-3}$, the maximum drop diameter is 8 *mm*, and Λ is varied between 1 to 3 mm^{-1}, corresponding to rainfall rate in the range 1 to 187 $mm\ h^{-1}$. The hailstone size distribution follows the model given in [9], which relates N_0 and Λ as $N_0 = 4000\ \Lambda^{5.3}\ mm^{-1}m^{-3}$ with Λ in mm^{-1} units. Here we have truncated the distribution at a maximum size of 50 *mm* and varied Λ from 0.1 to 0.8 mm^{-1}, which corresponds to a median size range of 4.6 to 30.5 *mm*.

RESULTS AND DISCUSSIONS

The results presented in this paper focus on transmission of v polarization only and reception of both the co-

This research was supported by the National Science Foundation under the grant ATM-9225116.

0-7803-3068-4/96$5.00©1996 IEEE

polarized and the cross-polarized (h) components. The v and h polarization directions are chosen as the $\hat{\theta}$ and $\hat{\phi}$ unit vector directions, respectively, in a spherical coordinate system with the z-axis pointing vertically up. The radar parameters of interest are the effective reflectivity factor at v polarization Z_v, the linear depolarization ratio $LDR_v = Z_{hv} / Z_v$, where Z_{hv} is the cross-polarized reflectivity factor, the bistatic to backscattering reflectivity ratio $BBR_v = Z_v$(bistatic) / Z_v(backscatter), and the correlation between the co- and cross-polarized signals, ρ_{xv}.

Figure 2 shows plots of LDR_v vs. Z_v, BBR_v vs. ρ_{xv} and BBR_v vs. Λ for several bistatic scattering angles with θ_s = 100° and ϕ_s = 30°, 60°, 90°, 120° and 150° (the subscript s indicates scattering direction). The transmitted wave is incident on the scattering volume from the θ_i = 90° and ϕ_i = 0° direction (the subscript i indicates the incidence direction). Hence, for back and forward scattering we have (θ_s = 90°, ϕ_s = 0°) and (θ_s = 90°, ϕ_s = 180°), respectively.

It is clear that slightly wet hail has significantly higher LDR_v values than rain, whereas dry hail (solid ice) has values comparable to rain. Also, it appears that the differences in LDR_v for rain and hail are larger in the ϕ_s = 30°, 60° and 90° directions (backward quadrant).

For the models used in these simulations Z_v > 60 *dBZ* clearly indicates hail. However, as in the monostatic radar case, using Z_v alone may not be reliable for detecting hail.

BBR_v appears to be most useful for differentiating rain and hail (both dry and wet) in the ϕ_s = 90°, 120° and 150° directions (forward quadrant). Furthermore, BBR_v is not sensitive to particle orientation (not shown here). Finally, the nearly one-to-one dependence of BBR_v on Λ in these directions indicates that it may be used for estimating the median diameter D_0, since D_0 relates to Λ.

The lower values of BBR_v corresponding to small hail coincide with those of rain. However, when combined with ρ_{xv}, even small hail may be distinguished from rain since small hail exhibits ρ_{xv} values below that of rain. As a result, by combining all of these radar parameters one can discriminate rain from hail with more confidence and possibly estimate hailstone median size. If a dual polarization transmitter is used, then the number of available radar parameters that must be interpreted self consistently will be more than doubled. This can enhance the level of confidence in the interpretation of polarimetric radar parameters. It is also worth noting that these parameters may prove useful in identifying the melting layer.

REFERENCES

[1] J. Wurman, "Vector winds from a single-transmitter bistatic dual Doppler radar network," Bull. Amer. Meteor. Soc., vol. 75, pp. 983-994, 1994.

[2] P.C. Waterman, "Scattering by dielectric obstacles," Alta Freq., vol. 38, pp. 348-352, 1969.

[3] N.C. Knight, "Hailstone shape factor and its relation to radar interpretation of hail," J. Climate Appl. Meteorol., vol. 25, pp. 1956-1958, 1986.

[4] A.W. Green, "An approximation for the shapes of large raindrops," J. Appl. Meteor., vol. 14, pp. 1578-1583, 1975.

[5] P.S. Ray, "Broadband complex refractive indices of ice and water," Appl. Opt., vol. 11, pp. 1836-1844, 1972.

[6] C.F. Bohren, and L.J. Battan, "Radar backscattering of microwaves by spongy ice spheres," J. Atmos. Sci., vol. 39, pp. 2623-2628, 1982.

[7] J.S. Marshall, and W.M.K. Palmer, "The distribution of raindrops with size," J. Meteor., vol. 5, pp. 165-166, 1948.

[8] J. Joss, J.C. Thams, and A. Waldvogel, "The variation of raindrop size distributions at Locarno," Proc. Int. Conf. Cloud Physics, pp. 369-373, 1968.

[9] L. Cheng and M. English, "Hailstones concentration and size at the ground and the melting level," Preprints, Conf. Cloud Physics, Boston, MA: Amer. Meteorol., Soc., pp. 423-426, 1982.

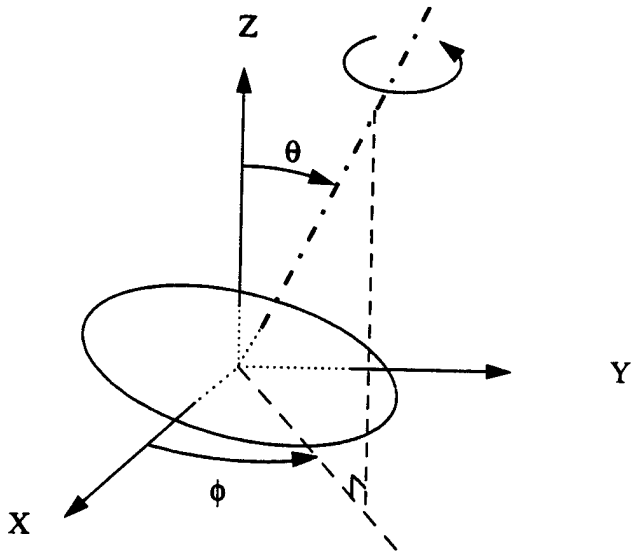


Fig.1 Canting angles for an oblate spheroidal particle.

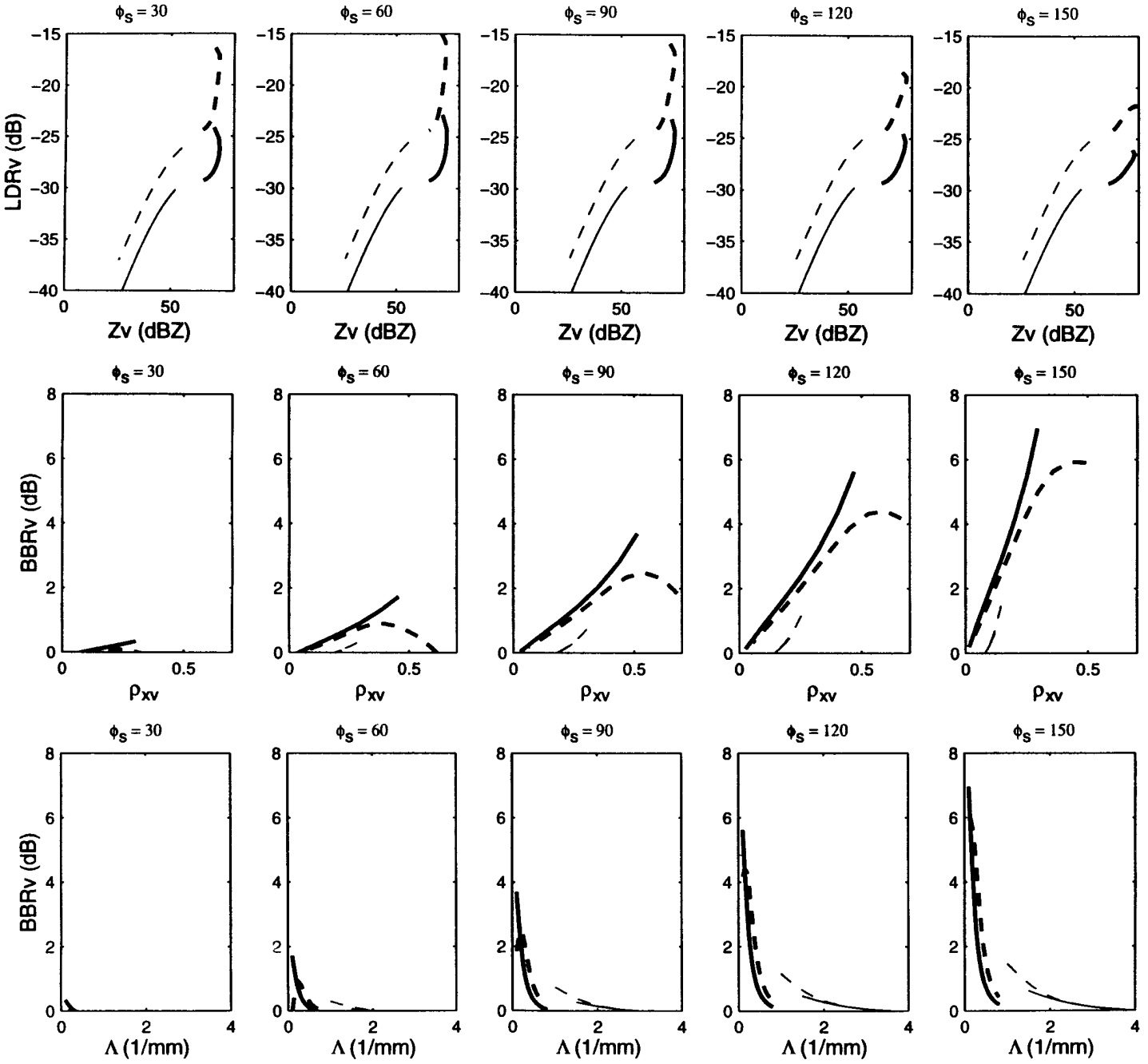


Fig. 2 Bistatic radar parameters corresponding to $\theta_s = 100°$ and the given ϕ_s values on each plot. The backscattering direction (not shown here) corresponds to $\theta_s = 90°$, $\phi_s = 0°$. The thin lines are for rain, solid line for MP and dashed line for J-T size distributions. The thick lines are for hail, solid line for dry hail (all ice) and the dashed line for wet hail (10% water and 90% ice mixture).

Computational Study of Millimeter Wave Scattering from Bullet Rosette Type Ice Crystals

K. Aydin and T. M. Walsh
The Pennsylvania State University
Department of Electrical Engineering
University Park, PA 16802
Phone: (814) 865-2355
FAX: (814) 863-8457
e-mail: aydin@cloud1.ee.psu.edu

ABSTRACT -- Some interesting aspects of millimeter-wave (35, 94, 220 *GHz*) scattering properties of various types of ice crystals are presented. These ice crystals include three types of bullet rosettes which are compared with hexagonal columns and hexagonal plates. The elevation angle dependence of differential reflectivity and linear depolarization ratio for certain bullet rosettes show distinct signatures that are different than columns and plates.

INTRODUCTION

Millimeter-wave (*mm*-wave) radars at 35 and 94 *GHz* are now being used for probing clouds both from ground-based and airborne platforms [1]-[5]. A major challenge in practice is the interpretation of these measurements for differentiating ice crystal types. For this purpose it is necessary to evaluate the scattering characteristics of different ice crystals through model computations. Hexagonal columns, hexagonal plates and stellar crystals have already been studied at 35, 94 and 220 *GHz* [5]-[10]. This paper focuses on some interesting aspects of the scattering properties of bullet rosettes and their differences with columns and plates. The finite-difference time-domain method is used for the scattering computations [11].

MODEL ICE CRYSTALS

The model bullet rosettes and hexagonal columns and plates are shown in Fig.1. The elemental bullets, which look like columns that narrow down at the connection point in the rosette structure [12], are modeled as columns here. This is not expected to have any significant effect on their scattering characteristics at millimeter wave frequencies. Note that all four branches of the 4-4 rosette lie on the same plane. Four branches of the 6-3 rosette also lie on the same plane with two branches orthogonal to that plane. In the case of the 8-1 rosette, each of the two sets of four branches lie on a plane. These planes make an angle of 70° with each other. The ice crystals are assumed to have a density of 0.9 $g\ cm^{-3}$, resulting in dielectric constants 3.1307-j0.0298, 3.1307-j0.0111, and 3.1307-j0047 at 35, 94 and 220 *GHz* frequencies, respectively.

The relationship between the maximum (d) and minimum dimensions of hexagonal columns and plates are given in [13] and [7]. For the rosettes each branch has a length L and a width w. These are related as [14]:

$$w = 0.25\,L^{0.7856} \quad for\ L \le 0.3\,mm, \qquad w = 0.185\,L^{0.5320} \quad for\ L > 0.3\,mm, \tag{1}$$

where both w and L are in *mm* units. Hence, the maximum dimension of any rosette considered here is $d = 2L$.

For the purpose of describing the orientation model of the ice crystals let us define a symmetry axis for each one. The symmetry axis of a plate is perpendicular to its broad surface. The axis of a column is its symmetry axis. For a 4-4 rosette it is perpendicular to the plane formed by the four branches. For a 6-3 rosette it is the same as the axes of two branches that are perpendicular to the remaining four. In the case of the 8-1 rosette, the symmetry axis is perpendicular to the line formed by the intersection of the two planes, each containing four branches, and bisects the larger angle (110° angle) between the two planes. The orientation of an ice crystal is determined by the polar and azimuthal angles θ and ϕ of its symmetry axis and the rotation angle ψ of the crystal around its symmetry axis. Here we assume that all three angles are independent and ϕ and ψ are uniformly distributed between 0 and 2π. The polar angle θ is assumed to have a Gaussian distribution with mean $\bar{\theta} = 0°$ (except for columns for which $\bar{\theta} = 90°$) and 10° standard deviation, [8].

RESULTS AND DISCUSSIONS

Due to limited space we present only two scattering parameters of interest for radar applications, differential reflectivity (Z_{DR}) and linear depolarization ratio (LDR). For a single scatterer these can be expressed as:

$$Z_{DR} = \sigma_{hh}/\sigma_{vv} \tag{2.a}$$

$$LDR_h = \sigma_{vh}/\sigma_{hh} \tag{2.b}$$

where the σ's are the orientation averaged radar cross sections; σ_{hh} and σ_{vv} are the co-polarized cross sections and σ_{vh} is the cross-polarized cross section (transmit h and

This research was supported by the National Science Foundation under the grant ATM-9225116.

0-7803-3068-4/96$5.00©1996 IEEE

receive v polarization). The results for the five ice crystal models with $d = 2$ *mm* are shown in Fig.2. LDR is less than -40 *dB* at 35 *GHz* for the 6-3 and 8-1 rosettes, hence they do not appear on these graphs which show only those values above -40 *dB*. Also note that $Z_{DR} \cong 0$ *dB* at 35 *GHz* for these two rosette types at all radar elevation angles. Hence, based on Z_{DR} and LDR measurements at 35 *GHz*, these two crystal types would appear like spherical particles.

The general trends in both LDR and Z_{DR} that are discussed below are valid for smaller sizes down to several tenths of a *mm*. It should be noted that LDR decreases (becomes more negative) with decreasing size for all crystal types, however, this decrease is most dramatic for the 6-3 and 8-1 rosettes. Z_{DR} tends towards 0 *dB* with decreasing size, again most rapidly for the 6-3 and 8-1 rosettes.

It is interesting to note that the variations of Z_{DR} and LDR as a function of radar elevation angle (α) are different for the bullet rosettes and the hexagonal columns and plates. It has been noted before that with increasing α the depolarization ratio steadily increases for columns and decreases for plates [4],[8]. For the 6-3 and 8-1 rosettes the 94 *GHz* LDR_h has a peak at about $\alpha = 45°$ and the 220 *GHz* LDR_h oscillates. The 4-4 rosette and the plate have a similar LDR_h trend at 35 and 94 *GHz*, but at 220 *GHz* LDR_h has a peak near $\alpha = 60°$.

Z_{DR} shows a similar trend for the column, plate and 4-4 rosette, it decreases from positive values down to 0 *dB* with increasing elevation angle. For the 6-3 rosette the 94 and 220 *GHz* Z_{DR} is negative at $\alpha = 0°$ and has a maximum (positive peak) at $\alpha = 45°$. For the 8-1 rosette Z_{DR} is positive at $\alpha = 0°$ and has a minimum (negative peak) near $\alpha = 60°$.

Hence, using the elevation angle dependence of Z_{DR} and LDR one can discriminate between columns, plates and bullet rosettes. The 94 and 220 *GHz* millimeter-wave frequencies appear to be more sensitive than 35 *GHz* for identifying bullet rosettes with these linear polarization parameters.

REFERENCES

[1] R. Lhermitte, "A 94-GHz Doppler radar for cloud observations," J. Atmos. Oceanic Technol., vol. 4, pp. 36-48, March 1987.

[2] K. Aydin, C. Tang, A. Pazmany, J. Mead, R. McIntosh, M. Hervig, R. Kelly, and G. Vali, "95 GHz polarimetric radar measurements in a cloud compared with model computations," Atmos. Res., vol. 34, pp. 135-144, 1994.

[3] A. Pazmany, J. Mead, R. McIntosh, M. Hervig, R. Kelly, and G. Vali, "95 GHz polarimetric measurements of orographic cap clouds," J. Atmos. Oceanic Technol., vol. 11, pp. 140-153, February 1994.

[4] E.E. Clothiaux, M.A. Miller, B.A. Albrecht, T.P. Ackerman, J. Verlinde, D.M. Babb, R.M. Peters, and W.J. Syrett, "An evaluation of a 94-GHz radar for remote sensing of cloud properties," J. Atmos. Oceanic Technol., vol. 12, pp. 201-229, April 1995.

[5] S.Y. Matrosov, R.F. Reinking, R.A. Kropfli, and B.W. Bartram, "Estimation of ice hydrometeor types and shapes from radar polarization measurements," J. Atmos. Oceanic Technol., vol. 13, pp. 85-96, February 1996.

[6] C.E. Dungey, C.F. Bohren, "Backscattering by nonspherical hydrometers as calculated by the coupled-dipole method: An application in radar meteorology," J. Atmos. Oceanic Technol., vol. 10, pp. 526-532, August 1993.

[7] C. Tang, "Millimeter wave polarimetric radar remote sensing of ice crystals," PhD Thesis, The Penn. State Univ., May 1994.

[8] C. Tang, and K. Aydin, "Scattering from ice crystals at 94 and 220 GHz millimeter wave frequencies," IEEE Trans. Geosci. Remote Sensing, vol. 33, pp. 93-99, January 1995.

[9] K. Aydin, and C. Tang, "Millimeter wave polarimetric scattering from ice crystals," Preprints, 26th Int. Conf. on Radar Meteorology, Amer. Meteorol. Soc., 24-28 May, 1993, Norman, OK, pp. 123-125.

[10] T.L. Schneider, and G.L. Stephens, "Theoretical aspects of modeling backscattering by cirrus ice particles at millimeter wavelengths," J. Atmos. Sci., vol. 52, pp. 4367-4385, December 1995.

[11] K.S. Kunz, and R.J. Luebbers, "The finite difference time domain method for electromagnetics," CRC Press, Boca Raton, Florida, 1993.

[12] J. Iaquinta, H. Isaka, and P. Personne, "Scattering phase function of bullet rosette ice crystals," J. Atmos. Sci., vol. 52, pp. 1401-1413, May 1995.

[13] A.H. Auer, and D.L. Veal, "The dimensions of ice crystals in natural clouds," J. Atmos. Sci., vol. 27, pp. 919-926, September 1970.

[14] A.J. Heymsfield, and R.G. Knollenberg, "Properties of cirrus generating cells," J. Atmos. Sci., vol. 29, pp. 1358-1366, October 1972.

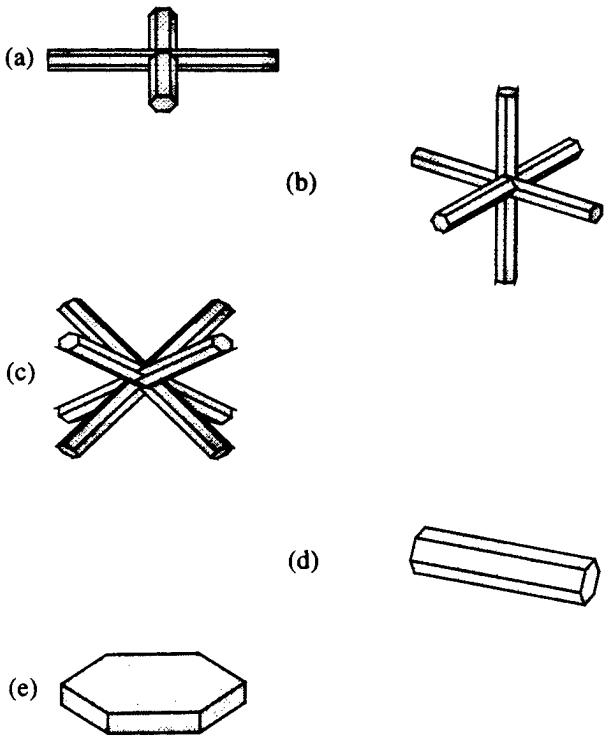


Fig. 1 Ice crystal models, a) 4-4 bullet rosette, b) 6-3 bullet rosette, c) 8-1 bullet rosette, d) hexagonal column, and e) hexagonal plate. (The branches of a rosette are identical in size.)

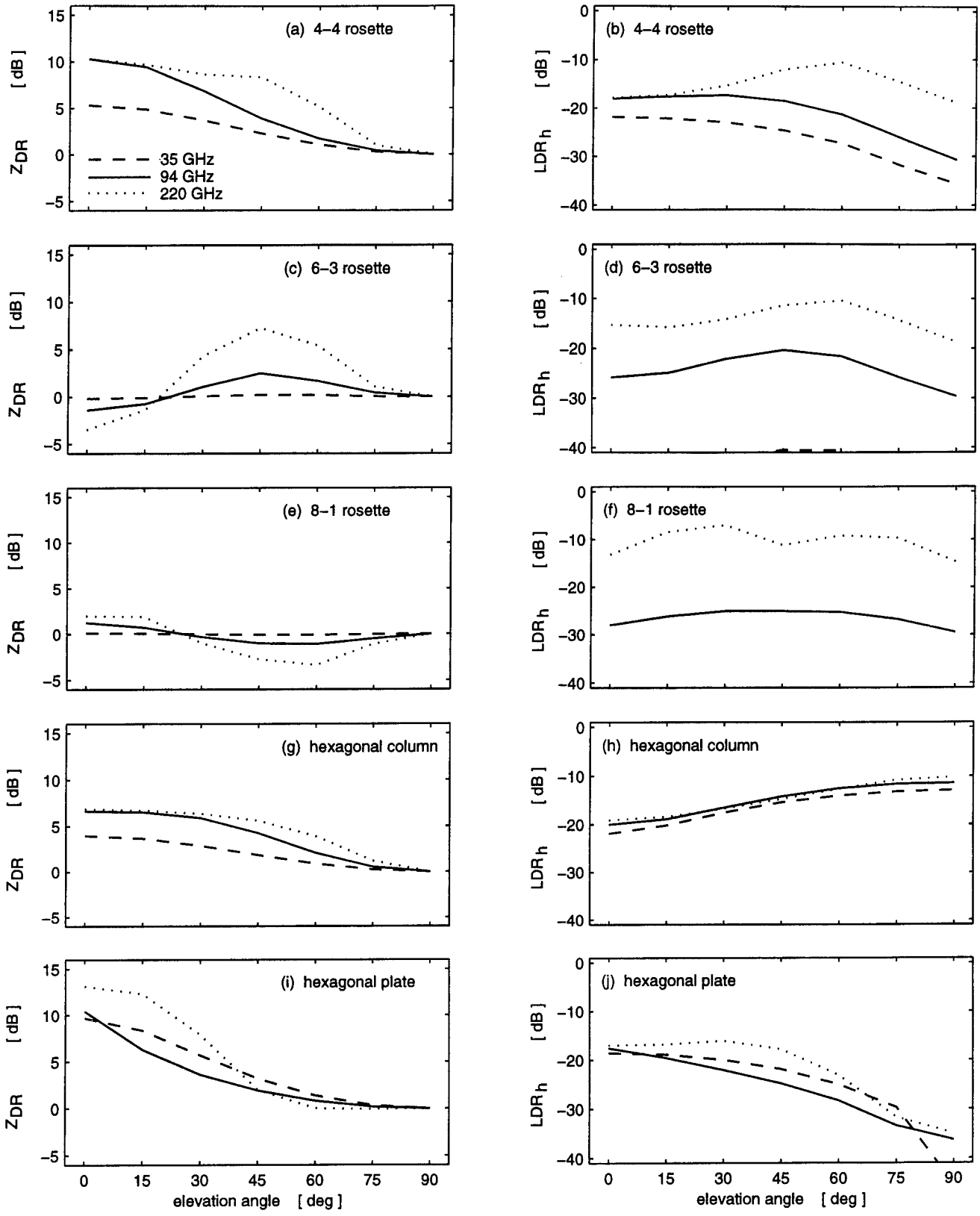


Fig. 2 Z_{DR} and LDR_h as a function of radar elevation angle for five different ice crystals each with a maximum dimension of 2 mm.

Multiparameter Radar Snowfall Estimation Using Neural Network Techniques

Rongrui Xiao and V. Chandrasekar
Dept. of Electrical Engineering
Colorado State University
Fort Collins, Colorado 80523
T: (970) 491-6758, F: (970) 491-2249, E-Mail: rx515948@lance.colostate.edu

ABSTRACT

WISP94 CSU-CHILL radar data and ground snowgage measurements at Stapleton International Airport (SIA) and Denver International Airport (DIA), Denver, Colorado, are analyzed in this paper. Traditionally, the radar estimation of ground snowfall is estimated by Z-S relations. The performance of such parametric relations are not satisfactory due to the complexities of the snow process. In this paper a radial-basis function neural network based algorithm is applied to map the relationship between the radar observations and ground snowfall measurements. The development of the neural network based technique, and the snowfall estimation results are presented.

INTRODUCTION

Using radar to measure snowfall has been the research topic for radar meteorologists for decades. Traditionally, a parametric reflectivity-snowfall (Z-S) relation is used to estimate ground snowfall based on radar observations. However, the accuracy and reliability of Z-S relations are limited by two important factors. First, the nature of snowfall varies greatly from storm to storm and location to location due to the difference in ice crystal types, degree of rimming, snow intensity and fall speeds, etc. Second, most weather radar systems are conventionly calibrated to measure the reflectivity factor of water drops instead of snowflakes and ice crystals. Thus many factors need to be considered to substantiate the Z-S relations.

Due to the universal function approximation capability of the multilayer feedforward neural networks (MFNN), multilayer perceptron (MLP) networks have been proposed for the rainfall estimation problems [1]. In this paper, another structure of MFNN, the radial-basis function (RBF) network [2], is developed for snowfall estimation. The whole radar observed vertical reflectivity profile over the cloud are applied to the RBF network as the input. The network is first trained to approximate the functional relationship between the vertical profiles and ground snow depths by using the snowgage measurements as the target outputs. Then, separate data which are not part of the training data are used to test the generalization performance of the RBF network.

Radar reflectivity data collected by CSU-CHILL multiparameter radar and ground snowfall measurements recorded by snowgages located at the Stapleton International Airport (SIA) and the Denver International Airport (DIA), Denver, Colorado during the Winter and Icing and Storms Projects (WISP94) were used for this study.

RADAR AND SNOWGAGE DATA

WISP94 was conducted from 25 January to 25 March 1994 along the Colorado Front Range area [3]. Data collected during two snow storm events (26 and 29 January 1994) were analyzed in this paper. The three snowgages considered were the "diaasos" located at the DIA and the "sianws" and "siaual", both located at the SIA. Table I lists the relative locations of the CSU-CHILL radar and the three snowgages in Cartesian coordinate.

Table I. Relative locations of the radar and snowgages

Instrument	X (km)	Y (km)
CSU-CHILL	0.0	0.0
diaasos	-1.7836	-68.1277
sianws	-20.0543	-75.6591
siaual	-22.5181	-75.3258

For each PPI volume scan, radar reflectivity measurements were averaged over a 3 × 3 km area to get a mean value at each level starting from height of 0.5 km to 5 km with vertical spacing of 0.5 km. Thus 10 such averaged reflectivity values were obtained representing the vertical profile. Fig. 1 shows examples of the mean vertical reflectivity profiles obtained above the three snowgage sites at around 1335 UTC, January 26, 1994.

Snowgage measurements were given as equivalent liquid depth in inches. 15-minute snowfall accumulations were computed based on snowgage measurements to obtain meaningful

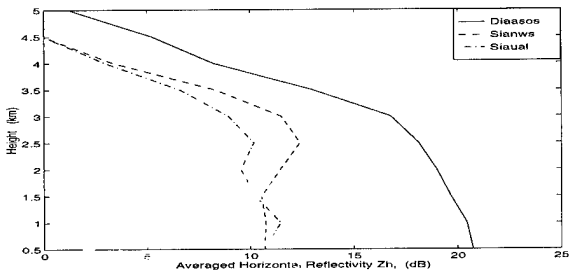


Fig. 1. Vertical reflectivity profiles above three snowgage site, at 1335 UTC, Jan. 26, 1994.

0-7803-3068-4/96$5.00©1996 IEEE

snow depth data. For each radar volume scan, the corresponding ground snowfall was defined as the 15-minute snowfall accumulation with the same starting time as the radar volume scan. Finally, the vertical reflectivity profiles were combined with the corresponding 15-minute snowfall accumulations to form a data set for the whole storm. The total number of samples is 67 for 26 January (15 from "diaasos", 26 from "sianws" and 26 from "siaual"), and is 11 for 29 January (6 from "sianws" and 5 from "siaual"). This data set was further divided into two parts, one contains the training data to be used to train the RBF network, the other is the testing data set to be used to test the performance of the network.

THE RBF NEURAL NETWORK

The radial-basis function (RBF) network belongs to the multilayer feedforward neural network (MFNN). Fig. 2 shows the structure of a RBF network. It contains three layers which are the input layer, the hidden layer and the output layer, respectively. The input layer accepts input vectors from outside and pass them to the hidden layer. The hidden layer units (neuron) contain many nonlinear radial-basis functions with different centers and widths, and the output of the hidden layer are obtained by computing the radial-basis function value of the Euclidean norm between the input vector and the center vector. The output layer contains a layer of linear units, i.e., these units just compute the weighted summation for outputs coming from the hidden layer.

In this study, the input vector is the vertical reflectivity profile and the output is the corresponding 15-minute snowfall accumulation. The connection weights $w_{i,j}$ and the centers are to be decided during the training process. An orthogonal least squares (OLS) learning algorithm [4] is implemented to train the RBF network in this paper.

SNOWFALL ESTIMATION RESULTS

Mixed Data for Training/Testing

For the first case study, about half of the data from all three snowgages on 26 January (8 from "diaasos", 18 from "sianws" and 8 from "siaual", total 34) were used to form a training data set, and the rest data on 26 January were used to form the testing data set (7 from "diaasos", 8 from "sianws" and 18 from "siaual", total 33). This is to test the learning and generalization capability of the RBF network for the functional relationship between the vertical profiles and ground snowfall

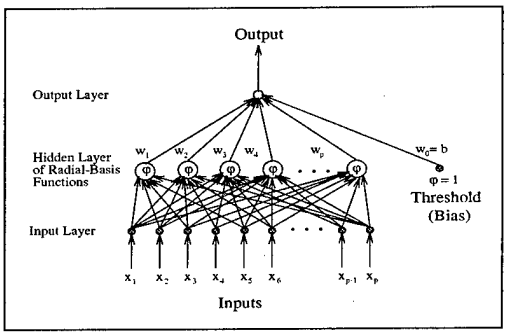


Fig. 2. The structure of radial-basis function network.

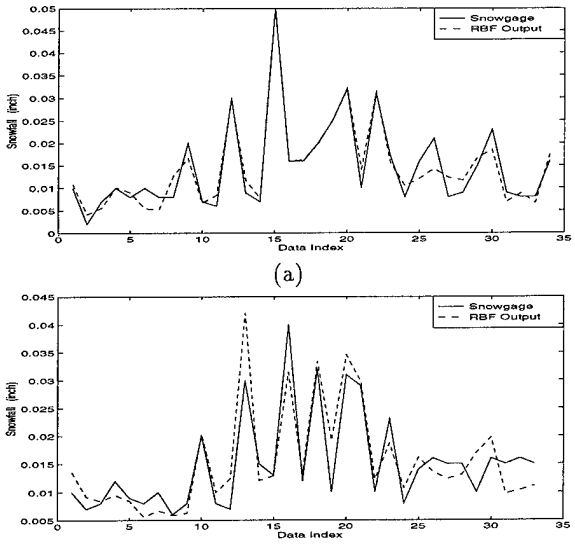


Fig. 3. Comparison of snowgage measurements and RBF network estimated snowfall. (a) Training data (34 samples, 01/26/94). (b) Testing data (33 samples, 01/26/94)

depth based on a well representative training data set. After applying the OLS learning algorithm, the number of hidden layer neuron was decided to be 19 with an error goal of 0.001. Fig. 3a shows the comparison of RBF network estimated ground snowfall depth and the corresponding snowgage measurements for the training data set. Fig. 3b is similar to Fig. 3a except for the testing data set.

Data from Different Locations for Training/Testing

For the second case study, all data from one snowgage ("sianws") on 26 January was used to form the training data set (26 samples) whereas data from the other two snowgages, "diaasos" and "siaual", were used to form the testing data set (41 samples). This is to test the generalization capability of the RBF network for the vertical reflectivity profile versus ground snowfall relationship from one location to others inside a snow storm. After training the RBF network using the OLS learning algorithm, the number of hidden layer neuron was decided to be 7, with an error goal of 0.001. Fig. 4a and 4b show the comparison of snowgage measurements and RBF network estimated ground snowfall depth for the training and testing data, respectively.

Data from Different Days for Training/Testing

For the third case study, data from two snowgages, "sianws" and "siaual", on 26 January were used to form the training set (total 52 samples) whereas data from the same two snowgages on 29 January were used to test the RBF network (total 11 samples). This is to test how well a RBF network can generalize the vertical profile versus ground snowfall relationship to different snow storms. Again, after training with the OLS learning algorithm, the number of hidden layer neuron was decided to be 7 with an error goal of 0.004. Fig. 5a and 5b show the comparison of snowgage measurements and RBF network

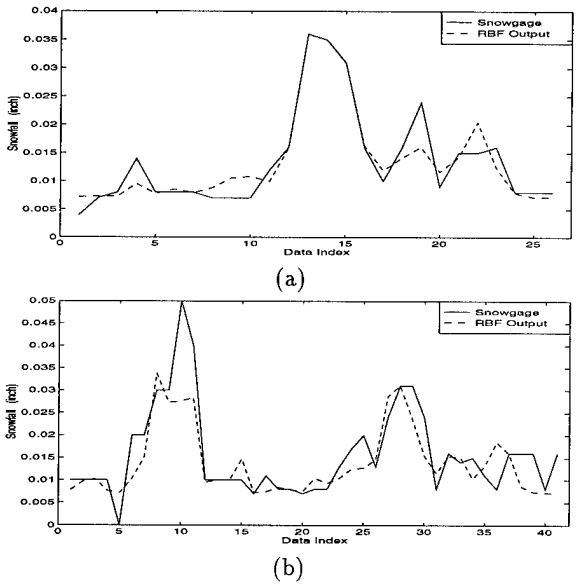


Fig. 4. Comparison of snowgage measurements and RBF network estimated snowfall. (a) Training data (sianws, 26 samples, 01/26/94). (b) Testing data (diaasos and siaual, 41 samples, 01/26/94).

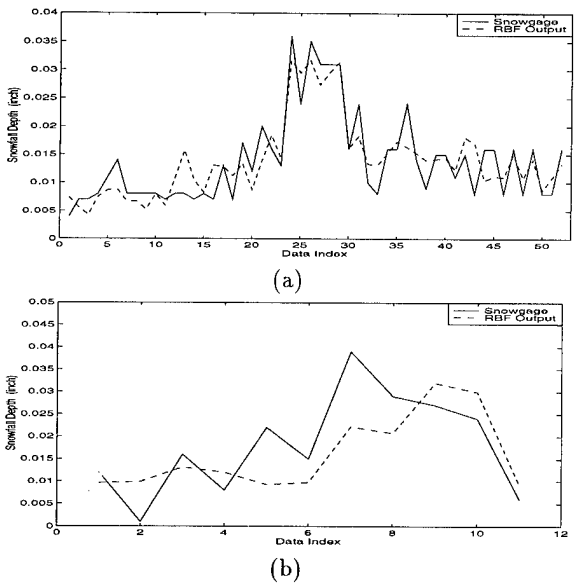


Fig. 5. Comparison of snowgage measurements and RBF network estimated snowfall. (a) Training data (52 samples, 01/26/94). (b) Testing data (11 samples, 01/29/94).

estimated ground snowfall depth for the training and testing data, respectively.

Comparison with Z-S Relation

A Z-S relation proposed by Smart and McGinley was also applied to obtain snowfall estimates for above three cases [5]. This Z-S relation is given as $Z_h = 200S^{1.60}$, where S is in cm. Smart and McGinley found that snow accumulation estimates based on this Z-S relation closely represent the observed snow depth over the northeastern Colorado area in their study. Statistical evaluation parameters such as bias, root mean squared error (rmse), correlation coefficient (corr) and fractional standard error (FSE) between snowgage measurements and snowfall estimates obtained by the RBF network and the Z-S relation were computed. Table II summarizes these parameters for the RBF network estimates and Z-S relation estimates based on the three testing data sets.

Table II. Statistics of RBF network and Z-S relation

Case # (Data #)		Statistical Parameter			
		bias (in)	rmse (in)	corr	FSE
1	RBF	-0.0004	0.0043	0.86	0.22
(33)	Z-S	-0.0138	0.0121	0.79	0.98
2	RBF	0.0019	0.0058	0.80	0.26
(41)	Z-S	-0.0176	0.0186	0.55	1.19
3	RBF	0.0019	0.0082	0.63	0.38
(11)	Z-S	-0.0104	0.0267	0.60	1.00

CONCLUSION

A RBF neural network based technique using the radar observed vertical reflectivity profiles to estimate ground snowfall depth is studied. Results from three different training and testing data sets show that the RBF network is able to approximate and then generalize the functional relationship between the vertical profiles and ground snowfall depth. Comparison with a Z-S relation also shows that the RBF network can give more accurate and reliable snowfall estimates. RBF neural network may provide a promising tool for the snowfall estimation problem pending further investigation.

ACKNOWLEDGMENTS

This work was supported by the National Science Foundation (ATM-9413453) and NCAR. The authors acknowledge helpful discussions with Professor V. N. Bringi.

REFERENCES

[1] R. Xiao and V. Chandrasekar, "Multiparameter radar rainfall estimation using neural network techniques," *Preprint of 27th Conference on Radar Meteorology,*, pp. 199-201, Vail, CO, Oct. 9-13, 1995, Amer. Meteor. Soc.

[2] S. Haykin, Neural Networks, Macmillan College Publishing Company, 1994.

[3] R. Rasmussen and W. A. Cooper, Winter Icing and Storm Project 1994: Scientific Overview, Technical report, Boulder, CO, 1993.

[4] S. Chen, C. F. N. Cowan, and P. M. Grant, "Orthogonal least squares learning algorithm for radial-basis function networks," *IEEE Trans. Neural Networks,* vol. 2, No. 2, March 1991, pp. 302-309.

[5] J. R. Smart and J. A. McGinley, "The use of radar reflectivity to determine snowfall over northeast Colorado", *Preprint of 12th Conference on Weather Analysis and Forecasting,* pp. 390-395, Boston, MA, 1989, Amer. Meteor. Soc.

Probing Electric Fields Near Sprites and Jets Using Multiparameter Radar and Chaff

Thomas A. Seliga, John D. Sahr and Robert H. Holzworth*
Electromagnetics and Remote Sensing Laboratory
Department of Electrical Engineering and *Department of Geophysics
University of Washington: Seattle, Washington 98195-2500
206-685-7092; seliga@ee.washington.edu

Abstract -- The discovery of electric discharges above thunderstorms has generated intense scientific interest. Studies of these 'sprites' and 'jets' have focused on their characterization by optical and radio techniques, with radar measurements of the causative storms providing insight into related weather. We describe a method for investigating the electric field structure above thunderstorms using ground-based radar to observe chaff dispersed by rockets. Slender conducting or dielectric chaff will generally align itself with the ambient electric field. This alignment is readily detected by appropriate configurations of polarimetric radar(s) such as are now used in meteorology to observe the nature and motion of hydrometeors. This is especially convenient as it permits the thunderstorms associated with sprites and jets to be characterized with the same experimental facility. This paper renders a preliminary examination of factors such experiments would entail and features that a multiparameter radar might utilize to probe chaff dispersed by small rockets. Monostatic and bistatic radar measurements of scatter from chaff provide a powerful tool to study electric fields associated with sprites and jets as well as other atmospheric electric fields.

SCIENTIFIC BACKGROUND

Until the 1980's the middle atmosphere (10-100 km) was thought to be a relatively passive medium which held limited interest for study. However, recent discoveries indicate that the middle atmosphere is electrically active with important implications for both atmospheric/space physics. It is well known that ionospheric and magnetospheric electric fields penetrate into the stratosphere [1], and thunderstorm related electric fields and currents strongly affect the middle atmosphere [2]. This knowledge has been advanced by the discovery that unique electrical phenomena occur in the middle atmosphere.

A new source of electric currents in the stratosphere associated with internal gravity waves or inertial waves (26 km) was found [2]; strong vertical electric fields at mesospheric altitudes (60-80 km) were also discovered [3]. In addition to large scale, slowly varying fields, thunderstorms have dramatic influence on the middle atmosphere. For example, coordinated balloon and rocket experiments over a thunderstorm indicated that lightning transient effects track upward into the lower ionosphere [4]. Atmospheric conductivity is also strongly affected by thunderstorms [5]. Most interestingly, rocket flights in 1987-88 detected optical phenomena tentatively associated with high altitude electric discharges over thunderstorms [6]. Then, a high altitude optical discharge was captured in an optical image [7].

By the late 1980's, observations accumulated that extended scientific interest in middle atmospheric electrodynamics. This newly invigorated area of atmospheric physics gained public attention via NASA experiments on these upward optical discharges [8]; these led to the designation of the observations as Red Sprites and Blue Jets in accordance with the colors of the emissions. Sprites are red luminous, very transient structures which stretch from near 40 to 90 km altitude with a horizontally striated structure which points backward to a spot in the large anvil structure of a mesoscale convective complex (MCC) [9]. Blue Jets appear to arise out of the tops of MCC's as a luminous fountain that reaches upwards to 35 or 40 km. Sprites and Jets, as well as the recently discovered Elves [10], are distinct middle atmosphere phenomena, none of which have ever been detected in-situ. Their electrical nature has been investigated theoretically [11], but the actual in-situ experimental parameters, such as the time-dependence of the charge density and electric field, needed to validate these theories, remain an educated guess.

While quasistatic middle atmosphere electrical structure can be studied with successive rocket flights, it is nearly impossible to obtain in-situ electrodynamic measurements during transient Red Sprite or Blue Jet events. It appears that Sprites are associated with large, positive cloud to ground lightning strokes [10,12]. Unusually large numbers of positive lightning strokes can often be found in the trailing regions of large thunderstorm complexes such as MCC's. These active Sprite producing regions may be hundreds of km^2 in area; prediction with higher spatial resolution is not possible yet. Therefore, a traditional rocket-borne payload, with a lifetime of a few minutes, seems highly unlikely to be in the right place at the right time to capture one of these transient events.

The technique described here promises to detect both transient and ambient electric fields in the middle atmosphere over a wide altitude range. If a meteorological

0-7803-3068-4/96$5.00©1996 IEEE

rocket or high altitude airplane is used to dispense chaff over a thunderstorm complex, the electrical structure of the middle atmosphere, which connects the thunderstorm complex into the global electrical circuit [13], can then be studied with dual polarimetric-based radars. Such chaff clouds will have lifetimes of a half hour or more and are more likely to be aloft during the rare Sprite or Jet events, capturing essential features of related electric fields.

CHAFF-RADAR INTERRELATIONSHIPS

Chaff consist of scatterers that are introduced into the atmosphere or propagation medium of interest for the purpose of producing known radar targets for a specified objective or set of objectives. They have been especially useful in military operations for radar decoying [14], but also in atmospheric research. The latter includes the study of middle atmosphere dynamics [15-16], atmospheric boundary layer investigations [17] and tracking of air within clouds [18]. The advent of polarimetric-based radar observations in meteorology [19-22] has not only revolutionized traditional radar meteorology but has also been found useful in conjunction with chaff releases to follow air flow and its mixing within clouds containing hydrometeor targets [18]. This capability offers an effective means of investigating the influence of mixing on such cloud systems and the possibility of improving targeting of weather modification agents to specific regions of clouds [18].

Chaff, dispersed in the atmosphere during military exercises, also interferes with radar meteorological operations [23]. In this instance, chaff produces echoes that may be wrongly interpreted as weather, alter the operational mode of weather radars and/or contaminate archival records. Future polarimetric-based capabilities in operational radars should prove useful for identifying chaff, thereby removing this interference in the future.

This paper envisions another use of chaff, namely, to map the direction of atmospheric electric fields associated with thunderstorms and other atmospheric phenomena. In this case, the natural well-known tendency of dielectric and conducting bodies to orient themselves with their longest dimensions parallel to the ambient electric field intensity [24] can be used in conjunction with polarimetric-based radars to discern essential information on the direction of the ambient electric field. Relevant observations in monostatic, bistatic and dual mode configurations deserve attention. Discussion is limited to the case of short dipoles and a few observables, although it is clear that other features may prove equally or more useful for similar applications.

CHARACTERISTICS OF NEEDLE CHAFF

Chaff response is characterized by the short electric dipole [25-26]. The essential features are the length and radius of the cylinder; the chaff cylinder is excited by the projection of the applied field in the direction of the cylinder which re-radiates as a short electric dipole. A spatial ensemble of equally-sized, aligned chaff particles will return an average power related to the propagation direction and polarization of the incident field, the orientation of the chaff and the scatter direction and polarization of the receiving system. In addition to covariance or power-based observables, Doppler velocity measurements should also be useful for deducing important behavior of the chaff embedded in a medium which combines influences of electric field, gravitational and fluidic forces. Although the latter two influences can be important or even dominate chaff behavior, they are not examined here, since techniques are available for minimizing such effects.

The following set of primary observations are presumed: a) reflectivity factors at horizontal H and vertical V polarizations Z_H , Z_V; b) differential reflectivity Z_{DR}; c) linear depolarization ratio LDR; d) phase difference between co-polar returns $\Delta\Phi_{HV} = \Phi_{HH} - \Phi_{VV}$; e) phase difference between co- and cross-polar returns $\Phi_{LDR} = \Phi_{HH} - \Phi_{VH}$; and f) zero-lag cross-correlation coefficient $\rho_{HV}(0)$ between Z_H and Z_V [20-22]. These parameters entail measurements in monostatic, bistatic and/or dual radar modes. They relate to a combination of H and apparent V orientations where the H polarization is aligned with the local horizontal and V is orthogonal to H and in the plane of incidence, defined by the propagation vector and the local zenith. In certain instances, it is useful to rotate these respective linear polarizations (e.g., $\pm$ 45 °) or to use circular polarization states. These possibilities are excluded from discussion here.

COORDINATE FRAME AND CHAFF MODEL

The concept may be examined with reference to a fixed (x,y,z) Cartesian coordinate frame where the directions of incidence and scatter are arbitrary so as to include all monostatic and bistatic configurations. Cylindrical chaff are presumed to reside in this system at directions defined by the spherical coordinate angles θ from the zenith and ϕ from the x-axis. All radar observable are presented with reference to this fixed frame and direction angles.

A simple model was selected to determine polarimetric radar's response to chaff,. It consists of a cylindrical conductor of length 5.0 mm and radius 0.25 mm. Such a particle will approximate a short dipole at 10 cm, the preferred wavelength for both operations and research. The apparent maximum Z_H that such a radar would record at a density of one particle m^{-3} is 29.2 dBZ; the Z_H for an ensemble of similar chaff particles that are uniformly distributed in all spatial directions is 22.2 dBZ; and LDR of this same ensemble is -4.77 dB. The model results presented below relate to dual-radar observations at incident directions $(\theta_I, \phi_I) = (135°, 0°)$ and $(135°, 90°)$.

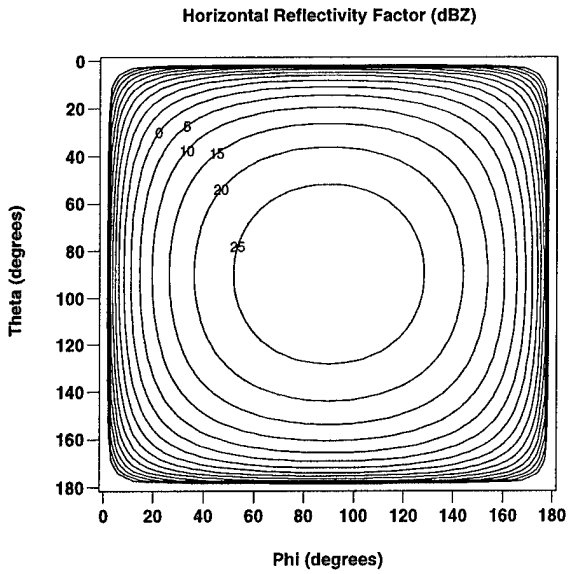


Fig. 1. Z_H dependence on spatial orientation of chaff at a density of one particle per m^3.

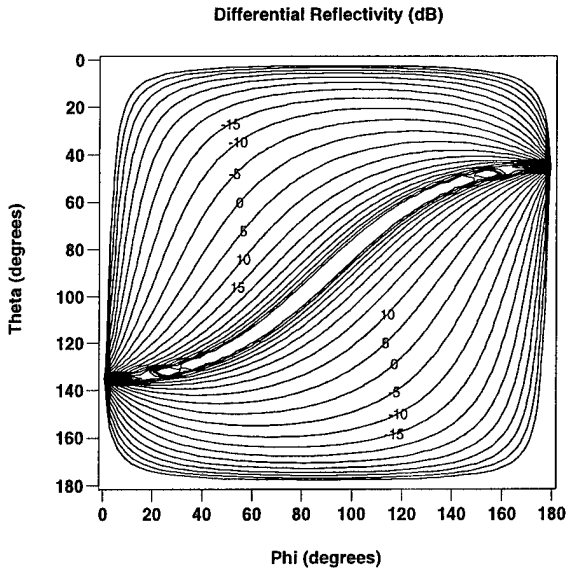


Fig. 2. Z_{DR} dependence on spatial orientation of chaff at a density of one particle per m^3.

Z_H - Z_{DR} MEASUREMENTS

Figs. 1 and 2. illustrate the Z_H and Z_{DR} response of a monostatic radar when a short chaff cylindrical particle is aligned in the (θ, ϕ) direction and the incident wave direction is [-0.707 0 0.707]. As expected, maximum Z_H occurs when the chaff is horizontal (θ = 90°) and broadside to the propagation direction; the minimum response occurs when the chaff is aligned in the plane of incidence (ϕ = 0°, 180°). Z_{DR} defines the relative response of the co-polar returns Z_H and Z_V [20]. If the chaff is constrained in some fashion, e.g., a vertical plane, this information may be used to find its orientation, provided the particle is not in or near (due to radar sensitivity) the plane of incidence. Since Z_H depends on both the orientation of the particle relative to the polarization of the wave plus the number density of particles, its use is limited unless additional information such as the exact direction of the particle is known. Another view of the scatterers is required, and this results from either a second radar or bistatic measurements. Before this configuration is examined, the relationship of the direction of the chaff to the relative phases of the respective co-polar and cross-polar radar signals deserves attention.

Essentially, cylindrical chaff, aligned in the upper right-half quadrant (or lower left-half quadrant) to the plane of incidence as seen from the radar will return in-phase signals between co-polar and cross-polar returns (relative to the incident polarization directions) while chaff directed in the lower right-half (or upper left-half) quadrant will yield out-of-phase signals. Thus, either of these simple measurements resolves whether the particle is directed upwards or downwards when considered relative to the right-half plane to the plane of incidence. Combining this observation with Z_{DR} then determines a sector orientation as well as the surface in which this orientation resides. This is clearly indicated in Fig. 2 which defines the spatial location of Z_{DR} contours.

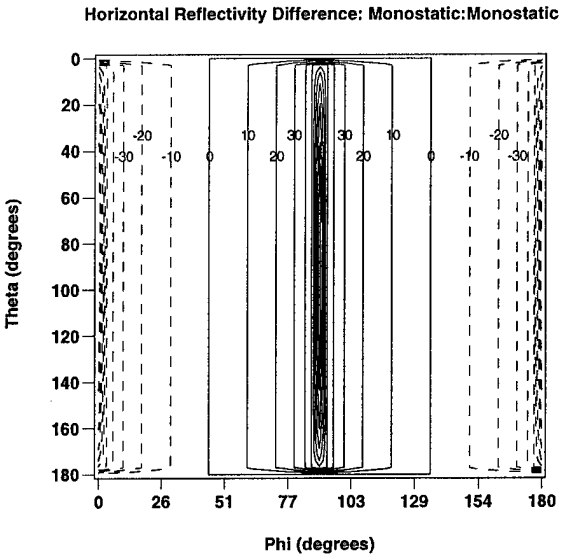


Fig. 3. Difference in Z_H as measured by two radars observing the same scattering volume at orthogonal viewing directions.

Absent *a priori* information on the direction of the chaff, it is not possible to completely determine its direction. Observations at another aspect are required, using either bistatic- or dual-radar measurements at an orientation substantially different from that of the single monostatic radar (ideally 90°). These measurements need not include

the same number of observations. For example, measurement of Z_H would reduce the possible directions to two which are then resolved by Φ_{LDR}. Conceptually, dual-radars, each with (Z_H, Z_{DR}, LDR, Φ_{LDR}) capabilities, would suffice to resolve all possibilities. Fig. 3 shows the difference in Z_H between two such radars with the second incident at [0 -.707 0.707]. A similar result derives from a bistatic configuration. Examination of Fig. 3 in relation to those in Figs. 1 and 2 shows that the combination is capable of resolving the orientation of the chaff; in the case where the particle resides in the plane of incidence of either radar, that radar would produce an infinite value of Z_{DR} while the other radar's Z_{DR} would uniquely determine its orientation in that plane.

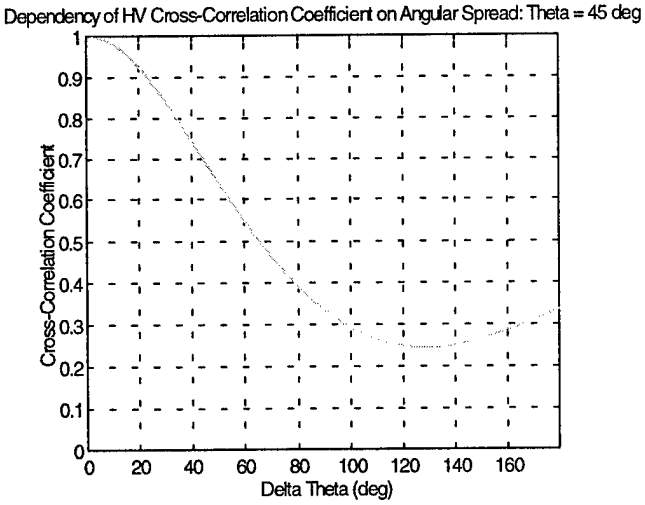


Fig. 4. Illustration of the dependence of $\rho_{HV}(0)$ on angular spread ($\Delta\theta$) of a uniformly distributed ensemble of chaff centered at 45° from the vertical in the plane perpendicular to the radar propagation direction.

DISTRIBUTED ORIENTATIONS AND $\rho_{HV}(0)$

Chaff is expected to exhibit fluctuating directions about a preferred orientation, presumed to represent the ambient electric field direction. The polarimetric observables will then depend on both the mean orientation and the spread of directions about this mean. This circumstance is not treated here. However, $\rho_{HV}(0)$ is significantly dependent on the distribution of chaff directions (34,43). Thus, $\rho_{HV}(0)$, along with the other parameters, may be used to determine the orientation spread present in a given measurement set. Consistency among parameters can then be used to derive the mean field direction. The behavior of $\rho_{HV}(0)$ is illustrated in Fig. 4 which is the case where chaff resides in a plane transverse to the propagation direction, points in the mean direction $\theta_o = 45°$ from the vertical and is uniformly distributed over $(\theta_o - \Delta\theta/2) \le \theta \le (\theta_o + \Delta\theta/2)$. Note that $\rho_{HV}(0) = 1$ for equally aligned chaff and decreases with $\Delta\theta$; its value at $\Delta\theta = 180°$ is 0.33, corresponding to total randomness in orientation within the transverse plane. Note also that a broad minimum occurs at $\Delta\theta = 135°$. $\rho_{HV}(0)$ depends on both θ_o and $\Delta\theta$, but this dependence differs little over reasonable ranges of θ_o. Thus, $\rho_{HV}(0)$ should also be measured, since it provides a means of estimating the angular spread, thereby guiding the interpretation of the other radar observables in terms of the ambient electric field.

CONCLUSIONS

This paper has demonstrated that multiparameter radar measurements of chaff have potential significance for scientific investigations of atmospheric electric fields. The concept has, to a degree, been already proven from technologies employed by a number of investigators. Chaff of various forms and shapes are available, chaff has been deployed successfully by rockets in the middle atmosphere at the altitudes of interest for many years, and a number of previous radar observations strongly support electric field induced alignment of ice phase hydrometeors within thunderstorms [28-29].

Much future research and study are required on this topic. Ferreting out the details of experimental scenarios should include selection of locations (Kennedy Space Flight Center, Wallops Island, Alaska, Kwajalein, Trömso, etc.), radar facilities (NCAR S-POLE, CSU CHILL, NASA SPANDAR, etc.), chaff design and vehicle (rocket /aircraft) selection for chaff disbursement. Additional theoretical work and simulation modeling are also needed, focusing on both the physical phenomena and its relation to the experimental approach. The behavior of chaff under the influence of gravitational, electrical and fluidic forces also deserves additional attention. For example, basic physics suggests that chaff may oscillate about a mean direction determined by whether gravitational-fluidic forces dominate or electrical forces dominate. This is a rich field for investigation, particularly since polarimetric radar now offers an effective means of remotely sensing such behavior. Furthermore, preliminary investigations by the authors suggest that light weight, low dielectric constant spherical particles or shells, impregnated with a conducting needle would present uniform resistance to the atmosphere while retaining electrical alignment properties that are detectable with radar. Theory also predicts relatively long relaxation times for chaff needles to become aligned with the oscillation frequency and relaxation time both dependent on electric field intensity. It is likely that such motions would be detectable with coherent Doppler techniques. Thus, it appears that polarimetric-Doppler radar measurements of chaff constitute a powerful means for studying the entire vector electric field of the middle atmosphere - a truly wondrous capability worthy of intense scientific investigation.

REFERENCES

[1] F. S. Mozer and R. Serlin, " Magnetospheric electric field measurements with balloons," J. Geophys. Res., vol. 74, pp. 4739- , 1969.

[2] R. H. Holzworth, "High latitude stratospheric electrical measurements in fair and foul weather under various solar conditions," J. Atmos. Terres. Phys., vol. 43, pp. 1115-25, 1981.

[3] L. C. Hale, C. L. Croskey and J. D. Mitchell, "Measurements of middle-atmospheric electric fields and associated electrical conductivities," Geophys. Res. Lett., vol. 8, p. 927, 1981.

[4] M. C. Kelley et al., "Electrical measurements in the atmosphere and ionosphere over an active thunderstorm: 1.," J. Geophys. Res., vol. 90, pp. 9815-23, 1985.

[5] R. H. Holzworth, K. W. Norville, P. M. Kintner and S. P. Powell, "Stratospheric conductivity variations over thunderstorms," J. Geophys. Res., vol. 91, pp. 13257-63, 1986.

[6] Y. Q. Li et al., " Anomalous optical events detected by rocket-borne sensors in the WIPP campaign," J. Geophys. Res., vol. 96, pp. 1315-26., 1991.

[7] R. C. Franz, R. J. Nemzek and J. R. Winckler, "Television image of a huge cloud-to-space discharge above a thunderstorm," Science, vol. 249, p. 48, 1990.

[8] D. D. Sentman and E. M. Wescott, "Observations of upper atmosphere optical flashes recorded from an aircraft," Geophys. Res. Lett., vol. 20, pp. 2857-60, 1993.

[9] J. R. Winckler, W. A. Lyons, T. E. Nelson and R. J. Nemzek, " Further observations of cloud-ionosphere electrical discharges above thunderstorms," J. Geophys. Res., vol. 100, pp. 14335-45, 1995.

[10] W. A. Lyons and T. E. Nelson, "Processing, integrating and displaying disparate data sources from the Sprites'95 field program," Preprints, 12th IIPS for Meteor., Oceanog. and Hydrology, AMS, 1996.

[11] V. P. Pasko et al., "Heating, ionization and upward discharges in the mesosphere due to intense quasi-electrostatic thundercloud fields," Geophys. Res. Lett., vol. 22, pp. 365-8, 1995.

[12] W. A. Lyons, "The Sprites '95 field campaign: Initial results - Characteristics of sprites and the mesoscale convective systems that produce them," 18th Conf. on Severe Local Storms, Amer. Meteor. Soc., 1996.

[13] R. G. Roble and I. Tzur, "The global atmospheric-electrical circuit," in The Earth's Electrical Environment, ed. Geophys. Study Comm., pp. 206-31, National Academy Press, Washington, DC, 1986.

[14] R. J. James, "A history of radar," IEE Review, vol. 35, pp. 343-9, 1989.

[15] L. B. Smith, "The measurement of winds between 100,000 and 300,000 ft by use of chaff rockets," J. Meteorol. vol. 17, pp. 296-310, 1960.

[16] H. U. Widdel, "Foil clouds as a tool for measuring wind structure and irregularities in the lower thermosphere (92-50 km)," Radio Science, vol. 20, pp. 803-812, 1985.

[17] W. L. Eberhard, W. R. Moninger and G. A. Briggs, "Plume dispersion in the convective boundary layer. I.," J. Appl. Meteor., vol. 27, pp. 599-616, 1988.

[18] B. E. Martner and R. A. Kropfli, "TRACIR: A radar technique for observing the exchange of air between clouds and their environment," Atmos. Env., vol. 23, pp. 2715-21, 1989.

[19] G. C. McCormick and A. Hendry, "Principles for the radar determination of the polarization properties of precipitation," Radio Sci., vol. 10, pp. 421-34, 1975.

[20] T. A. Seliga and V. N. Bringi, "Potential use of radar differential reflectivity measurements at orthogonal polarizations for measuring precipitation," J. Appl. Meteor., vol. 15, pp. 69-76, 1976.

[21] V. N. Bringi, T. A. Seliga and S. M. Cherry, "Statistical characteristics of the differential reflectivity radar signal," IEEE Trans. Geosci. Remote Sens., vol. GE-21, pp. 215-20, 1983.

[22] R. J. Doviak and D. S. Zrnic, Doppler Radar and Weather Observations, 2nd ed., Acad. Press, Inc., New York, 562 pp., 1993.

[23] D. Hazen, W. Roeder, B. Boyd, J. Lorens and T. Wilde, "Weather impact on launch operations at the Eastern Range and Kennedy Space Center," 6th Conf. on Aviation Weather Systems, Amer. Meteorol. Soc., pp. 270-5, 1995.

[24] J. D. Stratton, Electromagnetic Theory, McGraw-Hill Book Co., Inc., New York, 615 pp., 1941.

[25] J. H. Van Vleck, F. Bloch and M. Hamermesh, "Theory of radar reflection from wires or thin metallic strips," J. Appl. Phys., vol. 18:274, 1947.

[26] G. T. Ruck, D. E. Barrick, W. D. Stuart and C. K. Krichbaum, Radar Cross Section Handbook, Vol. 1, Plenum Press, NY, 472 pp., 1970.

[27] M. Sachidananda and D. S. Zrnic, "ZDR measurement considerations for a fast scan capability radar," Radio Sci., vol. 20, pp. 907-22, 1985.

[28] A. Hendry and G. C. McCormick, "Radar observations of the alignment of precipitation particles by electrostatic fields in thunderstorms," J. Geophys. Res., vol. 81, pp. 5353-57, 1976.

[29] T. A. Seliga, K. Aydin, H. Direskeneli and V. N. Bringi, "Possible evidence for strong vertical electric fields in thunderstorms from differential reflectivity measurements," Preprints, 21st Int. Conf. Radar Meteorology, Amer. Meteor. Soc., pp. 500-2, 1983.

Weather Radars with Pulse Compression using Complementary Codes: Simulation and Evaluation

A. Mudukutore V. Chandrasekar
Department of Electrical Engineering, Colorado State University, Fort Collins, CO 80523.
R.J. Keeler
National Center for Atmospheric Research, P.O. Box 3000, Boulder, CO 80307.

ABSTRACT

Using complementary codes in conjunction with wideband pulse compression waveforms can yield high resolution spatial and temporal weather measurements with low range sidelobe contamination. For extended targets such as precipitation systems, range sidelobes mask and corrupt observations of weak phenomena occurring near areas of strong echoes. Therefore, having low range sidelobes is extremely important in precisely determining the echo scattering region. In this paper, we evaluate the performance of complementary phase codes in the context of time-varying, distributed weather targets. A simulation procedure has been developed to describe the signal returns from distributed targets using phase-coded pulse compression transmit waveforms with complementary coding for both single and dual polarization operations. The evaluation is based on the integrated sidelobe level and Doppler sensitivity after matched filter processing.

INTRODUCTION

Pulse compression techniques involve transmission of a long coded pulse and compression of the received echo using a matched filter to obtain a narrow pulse. This results in an increased detection performance associated with a long-pulse radar system while still maintaining the fine range resolution of a short-pulse system. The matched filter maximizes the output signal-to-noise ratio (SNR). A measure of the degree to which the pulse is compressed is given by the *compression ratio* defined as

$$CR = \frac{T}{\tau} = TB \tag{1}$$

where T = transmitted pulse length, $\tau = 1/B$ = compressed pulse length, and B is the bandwidth of the transmitted waveform. A major drawback to the application of pulse compression for meteorological purposes is the presence of range sidelobes which tend to smear the returns in range. The following measures are often used to quantify the level of range sidelobes:

- Peak Sidelobe Level (PSL), defined as

$$PSL = 10 \log \frac{\text{maximum sidelobe power}}{\text{peak response}}. \tag{2}$$

- Integrated Sidelobe Level (ISL), defined as

$$ISL = 10 \log \frac{\text{total power in sidelobes}}{\text{peak response}}. \tag{3}$$

Complementary codes consist of two sequences of equal length N having the special property that the sum of their autocorrelation functions has a peak of $2N$ at lag 0 and a value of zero at all other lags. Biphase complementary codes are available in lengths of $N(2^k)$, where k is any integer 0, 1, 2, 3, $\cdots$, and N is the kernel length given by 2, 10, and 26. In addition to the code lengths listed above, quadriphase complementary codes can also be constructed for kernel length $N = 3$ [1]. While implementing complementary codes, the two sequences are separated in time, frequency or polarization. This results in decorrelation of the returns so that complete sidelobe cancellation does not occur. This poses a serious limitation, especially when the reflecting medium consists of random fluctuating weather targets.

SIMULATION DESCRIPTION

Nearly all analyses of sidelobe suppression schemes, thus far, have been done on hard targets. The simulation procedure used here differs from previous schemes in that we are modelling a fluctuating weather target. This method improves on earlier work which assume that the scatterers are *frozen* in space during the pulse propagation time. Therefore, this simulation procedure models weather systems more accurately, especially for longer pulses at higher transmit frequencies. The details of the simulation are skipped for brevity. However, to summarize, the simulation procedure yields time records of signals that satisfy the joint distribution properties in range-time and sample-time and is an extension of the procedure described in [2].

0-7803-3068-4/96$5.00©1996 IEEE

RESULTS

The results shown in this paper are based on using the following:
(i) Input reflectivity profile to simulation: 100 dB spike at center range bin compared to all other ranges.
(ii) Modulation waveform: 12-bit quadriphase complementary code pair

$$C_1 = \{+1,+1,-1,+1,+j,+1,+1, +1,-1,-1,-j,-1\} \quad (4)$$

$$C_2 = \{+1,+1,-1,+1,+j,+1,-1, -1,+1,+1,+j,+1\}. \quad (5)$$

If the transmission of the two codes were staggered in time, then the sidelobe suppression performance degrades by an amount proportional to the Doppler phase shift that occurs during the time interval between the two codes. Fig. 1 plots the ISL as a function of Doppler velocity for various time separations (TS) between the two codes. Simultaneous transmission ($TS = 0$) performs the best with $ISL < -40$ dB over Doppler velocities in the range [0,50] m/s. However, with increasing time separations, the ISL's get progressively higher. Therefore, in these cases, the Doppler phase shift that occurs over the duration of the time separation needs to be accounted for to achieve reasonably low sidelobe levels.

The following two implementation schemes for complementary codes are evaluated here:

1. C_1 and C_2 transmitted every alternate pulse at same polarization.
2. Simultaneous transmission of the two codes where C_1 is transmitted at **H** polarization and C_2 at **V** polarization [3].

From Fig. 1, we see that the performance of scheme (1) is affected by the decorrelation in the returns for the two codes due to target Doppler phase shift. Therefore, we need simultaneous measurements of C_1 and C_2 complex samples to account for the Doppler shift that occurs during the time separation T_{PRT} between the two codes. This is accomplished by a rotating-phasor interpolation (magnitude and phase averaged separately). The resulting time series has measurements for each code separated by T_{PRT}. There is an inherent ambiguity in the interpolation scheme which occurs when the phase-shift between two consecutive samples of the original series is greater than $\pm\pi$ radians. Fig. 2 shows the ISL vs. velocity for the 100 dB fluctuating spike target. Low ISL of about -40 dB are observed for velocities less than half the Nyquist velocity, i.e., [0,12.5] m/s, and in the interval [37.5,50] m/s where the signal is doubly aliased. However in the velocity interval [12.5,37.5], due to the ambiguity in the interpolation scheme, the interpolated samples are off by π radians and result in poor sidelobe suppression.

The performance of scheme (2) is affected by two factors. (i) Cross-coupling between the **H** and **V** polarization signals due to the radar system components and those due to the reflecting medium itself (i.e., the linear depolarization ratio LDR) limits the ISL that can be achieved. This is due to the fact that the cross-polar component of the signal is incoherent with respect to the co-polar matched filter coefficients and this appears as an increase in the noise level at the filter output. (ii) Decorrelation in the H and V returns due to the differential phase shift ϕ_{DP} and the differential reflectivity Z_{DR} prevent complete cancellation of the range sidelobes. The limiting effects of Z_{DR} and ϕ_{DP}, individually, on ISL can be seen in Fig. 3(a) and (b) respectively. The curves for $Z_{DR} = 0$ dB and $\phi_{DP} = 0^o$ are equivalent to the curve for $TS = 0$ in Fig. 1. We account for Z_{DR} and ϕ_{DP} by scaling and shifting either the **H** or **V** phasor with respect to the other before summing up the signals at the output of the matched filters. However, estimates of Z_{DR} and ϕ_{DP} are extremely noisy because they are computed from subtraction of independent random variables having large variance with little averaging performed. An FIR filter is used to reduce these fluctuations in Z_{DR} and ϕ_{DP} before using them to rotate and scale the **V** phasor with respect to the **H**. The ISL vs. Doppler velocity plots are shown in Fig. 4. The different curves represent different (Z_{DR} (dB), ϕ_{DP} (degrees)) combinations. On an average, the ISL values are about -25 dB (higher compared to -40 dB for single polarization case). This can be attributed to poor Z_{DR} and ϕ_{DP} estimates. However, due to the availability of simultaneous samples of C_1 and C_2, there is no sensitivity of the ISL on Doppler velocity, which makes the scheme usable over a wide range of velocities. It should be pointed out here that both schemes yield poor estimates of radar variables, especially in high reflectivity gradients, and do not perform as well as Barker phase coded waveforms of similar length in conjunction with least squares inverse sidelobe suppression filters which yield ISLs in the range -35 to -50 dB over [0,50] m/s[4].

References

[1] Sivaswamy, R. Multiphase complementary codes. *IEEE Trans. Information Theory*, IT-24:546–552, Sept. 1978.

[2] Chandrasekar, V., et. al. Statistical properties of dual-polarized radar signals. *Proc., 23rd Conf. Radar Meteor.*, pp 193–196, Snowmass, CO, 1986.

[3] Keeler, R.J., et. al. Pulse compression polarization waveforms for rapid scan doppler radar. *Prepr., 26th Conf. Radar Meteor.*, pp 255–257, Norman, OK, 1993.

[4] Mudukutore, A., et. al. Range sidelobe suppression for weather radars with pulse compression: Simulation and evaluation. *Prepr., 27th Conf. Radar Meteor.*, pp 763–766, Vail, CO, 1995.

ACKNOWLEDGEMENTS

This research is supported by the US Air Force Office of Scientific Research (F49620-95-1-0133), NSF (ATM-9413453) and the FAA/TASS Program Office.

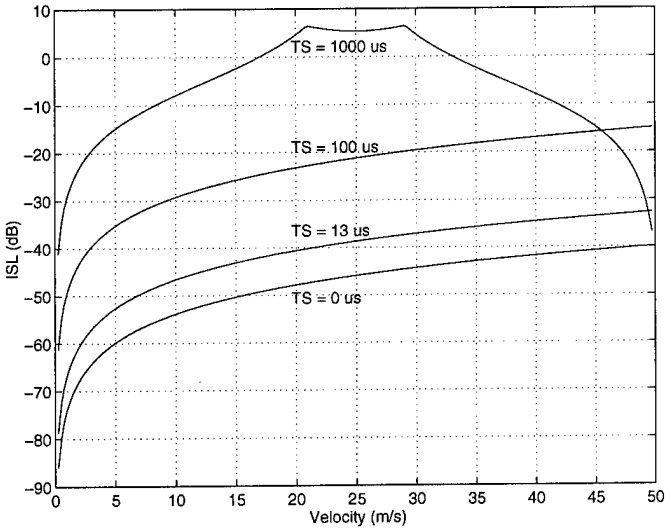


Figure 1: ISL vs. Doppler velocity for different time separations between the two codes.

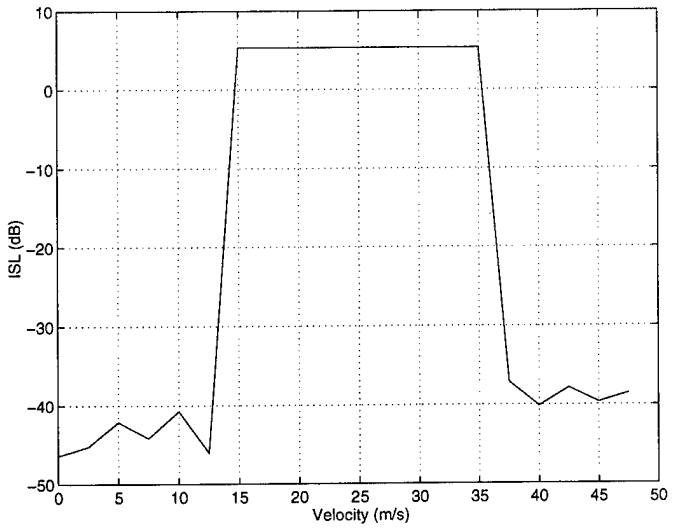


Figure 2: ISL vs. Doppler velocity for time-varying spike target using single polarization where C_1 and C_2 are transmitted every alternate pulse.

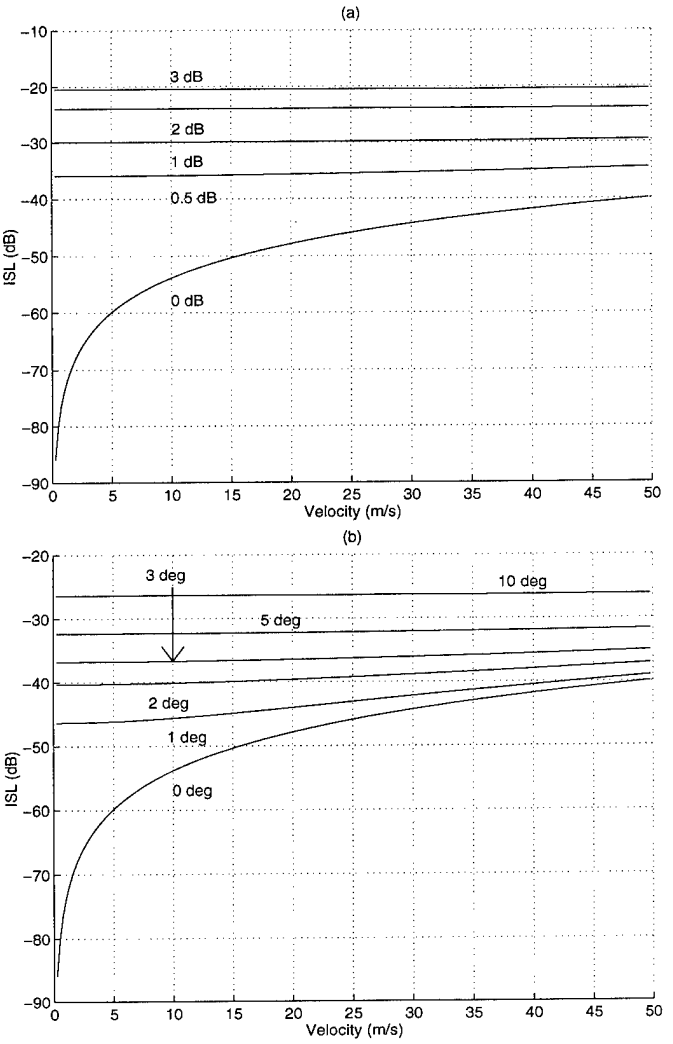


Figure 3: ISL vs. Doppler velocity when varying (a) Z_{DR} values; (b) ϕ_{DP} values.

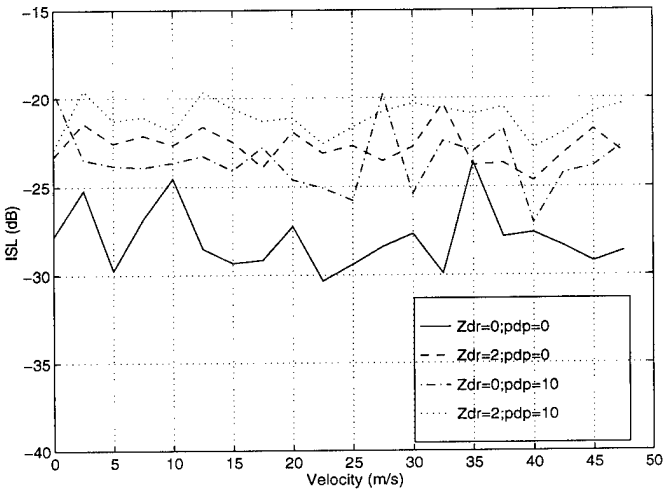


Figure 4: ISL vs. Doppler velocity for time-varying spike target using simultaneously transmitted, dual polarization with complementary coding.

Mapping Of Boreal Forest Biomass Using SAR

K. Jon Ranson[1], Guoqing Sun[2], Brian Montgomery[3] and Roger H. Lang[4]

[1]Biospheric Sciences Branch, Code 923, Goddard Space Flight Center, Greenbelt, MD 20771, USA.
Phone: (301)286-4041, Fax: (301)286-1757, E-mail: jon@taiga.gsfc.nasa.gov
[2]Science Systems and Applications, Inc. 5900 Princess Garden Parkway, Suite 300, Lanham, MD, 20706 USA
[3]Hughes STX, Lanham, MD 20706
[4]Electrical Engineering and Computer Science Dept., The George Washington University, Washington, DC USA

Abstract -- Knowledge of the distribution and structure of forests can lead to improved estimates of the carbon balance in terms of above ground storage and exchange with the atmosphere from maintenance respiration. As part of the Boreal Ecosystem Atmosphere Study (BOREAS) a study is being made of the use of remote sensing data for estimating land cover and biophysical characteristics of boreal forest study sites in Canada. Earlier work by the authors and others have developed maps of forest cover and above ground biomass. The biomass maps are produced using a regression equation developed from forest measurements and radar backscatter data. Other researchers have made a case for stratifying forest cover and constructing separate biomass relationships for each strata.

In this paper we examine the use of forest classification maps derived from SIR-C/XSAR images to improve estimates of total biomass. The classification procedure used a supervised Bayesian Classifier to map the forest area into several forest and non-forest classes. Forest classes were combined into Dry Conifer, Wet Conifer and Deciduous. Regression equations of dry biomass and radar backscatter were developed for each forest type and applied to the radar data. A stepwise technique was used to determine the best set or combinations of radar channels for mapping biomass.

The best channels for biomass estimation was determined to be LHV and CHV for conifers and a combination of LHH, LHV and CHV worked best for the limited deciduous data available. Analysis of the results indicates that forest type should be considered when mapping biomass in this type of forest. However, the results from a more general equation were adequate.

INTRODUCTION

Estimating biomass of forests with synthetic aperture radar (SAR) has received much attention over the past 5 years. Several studies have reported good results using one or more SAR channels to map biomass below 25 kg/m^2. Kasischke et al [1] and LeToan et al [2] used different techniques to estimate biomass in pine plantation forests in the US and France, respectively. Dobson et al. [3] used forest structure for a biomass estimation approach for northern US forest. Ranson et al. [4] and Ranson and Sun [5] used a general relationship to estimate biomass in the northern US and Canada. In this paper we examine the effect of forest canopy structure on SAR biomass estimation in a portion of the Boreal Ecosystems Atmosphere Study (BOREAS) study area in Canada using multichannel SIR-C/XSAR image data.

SIR-C/XSAR

The SIR-C/X-SAR spaceborne imaging radar missions were successfully conducted during April 9-19, 1994 and September 30-October 10, 1994. The instrument was a multichannel system with L-band (λ=23 cm), C-band (λ=5.7 cm) with quad-polarization (HH,HV,VV,VH) and X-band (λ=3 cm) with VV polarization. These channels cover the current configurations of orbiting radars such as L-band HH polarized JERS-1, C-band VV-polarized ERS-1, and C-band HH-polarized RADARSAT systems. The mission was a cooperative experiment between NASA, the German Space Agency, and the Italian Space Agency. SIR-C/X-SAR was launched on space shuttle Endeavour and acquired multiple data takes covering over 6% of the Earth's surface including a variety of land, ocean and polar ice targets. The SIR-C/X-SAR design includes bandwidths of 10, 20, and 40 MHz. The SIR-C/XSAR images used in this study were acquired with a bandwidth of 20MHz and processed with twelve looks. The images were acquired on April 13 and October 6, 1994 with incidence angles of 33° and 53°, respectively.

BOREAS

The BOREAS project [6] is designed to acquire necessary data to understand the interactions of land and the atmosphere and the relationships to global climate change. Scientists are working to interface models of climate and land processes to provide tools for understanding the mechanisms and consequences of this change.

The BOREAS Southern Study Area (SSA) covers an area about 130 km in the east-west direction and 90 km from north to south (see Figure 1). The southern boundary is located approximately 40 km north of the town of Prince Albert, Saskatchewan, Canada. The SSA topography is gentle, with local elevations ranging from 550m to 730m. The western part of SSA is in the Prince Albert National Park (PANP) and the eastern region falls within and around the Narrow Hills Provincial Forest. The SSA is near the southern limit of the boreal forest and the transition to natural prairie grassland and agricultural lands occurs 15 km to the southeast.

The image data discussed in this paper is located in the eastern portion of the SSA (53° 53' N, 104 45'° W) and covers portions of an intensive BOREAS modeling study area

*Trade names are used for information only and do not imply endorsement by the US Government.

This work was supported in part by NASA MTPE SIR-C/XSAR project (POP No. 665-31) and the BOREAS project (RTOP No. 462-33).

0-7803-3068-4/96$5.00©1996 IEEE

(Figure 1). The vegetation in this area is classified as mixed boreal forest. On well drained and or sandy soil the predominant species is jack pine (*Pinus banksiana*). Poorly drained sites support black spruce (*Picea mariana*). Mixed stands of aspen (*Populus tremuloides*,) balsam poplar (*Populus balsamifera)* and white spruce (*Picea glauca)* are found on well drained glacial deposits. Localized logging for paper pulp and fence posts is common within the area. The fen areas are composed mostly of sedge (*Carex spp.*) vegetation with discontinuous cover of tamarack (*Larix spp.*)or swamp birch (*Betula pumila)*. The north-east portion of the study area experienced a wild fire in the late 1970's.

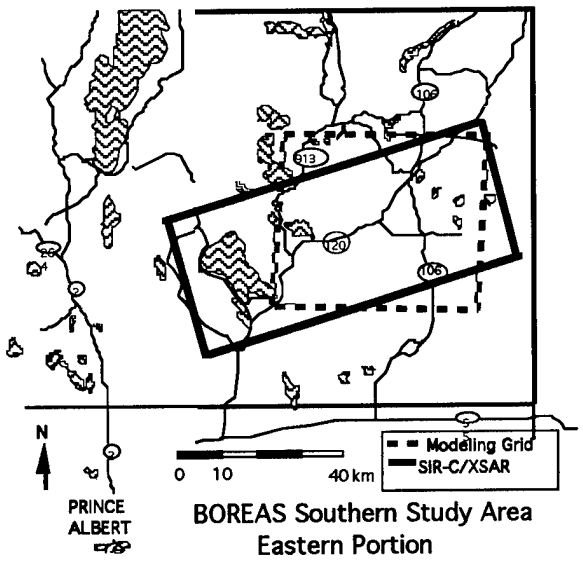


Figure 1. BOREAS SSA study location

METHODS

Forest Classification

Commercially available, PCI* imaging processing software was used for image classification. A supervised maximum likelihood classifier data was used. Training set locations were identified on the images for eleven classes shown in Table 1. GPS derived site coordinates were used to aid in site location. All channels from combining the April and October SIR-C/XSAR images were used. Radar backscatter signatures were determined from the images for each training set. For all classes except black spruce single large training sets were used. For black spruce multiple training sets were combined to get representative signatures. The signatures were then used as inputs for the Maximum Likelihood Classifier (MLC) to produce a classified map. Classification performance was determined by analyzing classified training sets and also comparing classification results to 56 test sites located throughout the study area.

For the purpose of this study a more general classification map was needed. The detailed classes on the left side of Table 1 were combined to produce a four class map which was used to stratify forest type for biomass estimation (Table 1, right side).

Table 1. Forest classification set. Detailed list was combined to form new four class set as shown at right.

Original Class	Combined Class
Regeneration	Dry Conifer
Young Jack Pine	
Jack Pine	
White Spruce	
Black Spruce	Wet Conifer
Treed Muskeg	
Young Aspen	Deciduous
Aspen	
Clearing	Other
Fen	
Water	

Biomass Estimation

Forest measurements including species and diameter breast height were made for over 60 forest stands throughout the study area. Stands selected were, as much as possible, uniform in stand structure (species, age, density) and large enough to locate accurately and extract at least a 3X3 window of image pixels. The forest stands were stratified into the three classes Dry Conifer, Wet Conifer and Deciduous on the basis of dominant recorded species. Above ground total dry biomass was calculated using the species and DBH data with published weight tables for Canadian Prairie Provinces [7]. No attempt was made to examine, bole, branch or foliage biomass separately here.

A stepwise regression routine available in Splus* [8] was used to determine a best set of SAR channels from LHH, LHV, LVV, CHH, CHV, CVV and XVV backscatter (σ°). This was done for data for each of the three forest types separately. In addition, similar analysis was performed using all of the data. The best fit equations were:

Dry conifer:

$$B^{1/3} = 2.472 + 0.247\,\sigma^\circ\text{LHV} - 0.210\,\sigma^\circ\text{CHV}, r^2 = 0.71 \quad (1)$$

Wet Conifer:

$$B^{1/3} = 2.650 + 0.160\,\sigma^\circ\text{LHV} - 0.1192\,\sigma^\circ\text{CHV}, r^2 = 0.63 \quad (2)$$

Deciduous:

$$B^{1/3} = 2.087 - 0.231\,\sigma^\circ\text{LHH} + 0.280\,\sigma^\circ\text{LHV} - 0.383\,\sigma^\circ\text{CHV}, r^2 = 0.66 \quad (3)$$

All Data Combined:

$$B^{1/3} = 2.678 + 0.227\,\sigma^\circ\text{LHV} - 0.2343\,\sigma^\circ\text{CHV} - 0.0836\,\sigma^\circ\text{CVV}, r^2 = 0.70 \quad (4)$$

Each of the equations for forest type are different from each other and Eq. 4, either in the bands selected or in the magnitude of the coefficients. This indicates that biomass estimation is dependent on forest type as discussed by

Dobson et al [3]. Note that each of these equations contains L- and C-band cross-polarized channels. In fact Eqs. 1 and 2 for Dry and Wet conifer show similar coefficients for LHV and CHV suggesting a relationship similar to that reported by Ranson et al. [4].

RESULTS

Classification results are shown for this four-class map as pooled training set results(Table 2a) and test plot results (Table 2b). Training set classification accuracy was very good for all forest classes. For the field plot data Dry Conifer and Deciduous showed excellent classification accuracy. Wet conifer was confused with Deciduous 40% of the time.. The percent of the area classified as Deciduous was 21%, Dry Conifer (24%) and Wet Conifer(21%). The non-forested classes accounted for 35% of the imaged area.

Table 2a. Training set classification accuracy(%).

	Deciduous	Dry Conifer	Wet Conifer	Other
Deciduous	86.2	12.3	1.4	0.1
Dry Conifer	4.7	88.5	0.7	6.1
Wet Conifer	0.3	0.7	99.0	0.0
Other	0.1	0.3	0.1	99.5

Table 2b. Sample plot classification accuracy(%).

	Deciduous	Dry Conifer	Wet Conifer	Other
Deciduous	91.7	0.0	0.0	8.3
Dry Conifer	0.0	78.3	8.7	13.0
Wet Conifer	40.0	6.7	40.0	13.3
Other	40.0	0.0	0.0	60.0

Comparing SAR biomass with field biomass for the three forest types produced the relationships shown as Eqs. 5-7. The comparison is also provided for pooling all the data in Eq. (7).

Dry conifer:
SAR biomass = 2.077 + 0.700 Field biomass, (5)
r^2 = 0.64 RMSE=2.9 kg/m^2

Wet Conifer:
SAR biomass = 0.911 + 0.731 Field biomass, (6)
r^2 = 0.65 RMSE=3.2 kg/m^2

Deciduous:
SAR biomass = 3.15 + 0.696 Field biomass, (8)
r^2 = 0.56, RMSE=5.06 kg/m^2.

All data:
SAR biomass = 2.691 + 0.643 Field biomass, (7)
r^2 = 0.65, RMSE=2.2 kg/m^2

The root mean square error (RMSE) results show that biomass may be estimated to within about $\pm$2-3 kg/m^2 using forest type specific relationships for Dry and Wet Conifer.. The RMSE for the Deciduous estimator equation was over 5 kg/m^2 which may be due to the small number of deciduous stands in our sample. The slopes of all the Equations 5-8 are less than unity indicating that biomass estimates may be underestimated. Restricting the analysis to biomass levels less than 15 kg/m^2 tended to reduce the observed bias. Using the general relationship (Eq. 4) resulted in only slightly more error than using individual forest type relationships.

SUMMARY

A portion of the BOREAS SSA was mapped into forest classes and biomass estimation equations derived for each forest class. SIR-C/XSAR data was able to produce a reasonable forest type map. The good classification results are among growing evidence that the mutlichannel SAR data is very useful for forest classification. The confusion of Wet conifer with Deciduous and Dry Conifer (Table 2b) based on the field plot data needs further study and will be addressed during field work in 1996. The results show there is species effect for biomass estimates, but the more general equation performed only slightly worse. The next step in the process is to generate a combined biomass image to use for initializing and testing ecosystem models for BOREAS.

REFERENCES

[1] Kasischke, E.S., N.L. Christensen,Jr., and L.L. Bourgeau-Chavez,"Correlating radar backscatter with components of biomass in loblolly pine forests,"Trans. Geosci. Remote Sens.,vol. 33, pp. 643-659,1995

[2] Le Toan, T., A. Beaudoin, J. Riom, and D. Guyon, "Relating forest biomass to SAR data,",IEEE Trans. Geosci. Remote Sens. vol 30,pp. 403-411, 1992.

[3] Dobson, M.C. et al., "Estimation of forest biophysical characteristics in northern Michigan with SIR-C/XSAR," IEEE Trans. Geosci. Remote Sens., vol. 33, pp. 877-895, 1995.

[4] Ranson, K. J., S. Saatchi and G. Sun, "Boreal forest ecosystem characterization with SIR-C/XSAR" IEEE Trans. Geosci. Remote Sens., vol. 33, pp. 867-876, 1995.

[5] Ranson, K.J. and G. Sun "Mapping biomass for a northern forest using multifrequency SAR data," IEEE Trans. Geosci. Remote Sens., vol. 32, pp. 388-396.

[6] BOREAS, "Boreal Ecosystem Atmosphere Study (BOREAS) Experiment Plan Ver. 3.1", NASA GSFC Code 923, Greenbelt, MD July 1995.

[7] Singh, T., "Biomass equations for ten major tree species of the Prairie Provinces," Northern Forest Research Centre, Canadian Forestry Service, Environment Canada, Info. Rep. NOR-X-242, 1982.

[8] MathSoft, S-PLUS guide to statistical and mathematical analysis, Version 3.2, 1993.

Carbon Dynamics in Northern Forests using SIR-C/X-SAR Imagery

Kathleen M. Bergen, M. Craig Dobson, Leland E. Pierce

The University of Michigan, Radiation Laboratory, EECS Dept.
Ann Arbor, MI 48109-2122 USA
Tel: +1-313-764-0501, FAX: +1-313-747-2106, email: kbergen@eecs.umich.edu

ABSTRACT

A key large-scale question in ecology is the amount of carbon stored in terrestrial vegetation. The need to determine this over large regions is most efficiently met by remote sensing programs and is currently being tested using SIR-C/X-SAR imagery at the NASA Michigan Forests supersite. There are three goals in the present study. The first is to estimate carbon stored in living vegetation at the site. The second is to measure changes in carbon balance related to forest disturbance (clearcutting and thinning). The third is to determine carbon gain from annual growth (NPP).

Biomass has been mapped in the image domain, and by applying an allometric relationship, results show that 12.82×10^9 kg of carbon are stored in the portion of the test site represented in the imagery. Clearcuts which were made between SRL-1 and SRL-2 have been extracted from the classified imagery and this analysis shows an estimated 300 ha of forest or 6.02×10^6 kg of carbon were removed. Ground data have been analyzed for annual growth; SIR-C/X-SAR images are currently being processed to demonstrate the sensor's sensitivity to this parameter.

1. INTRODUCTION

The terrestrial component of the carbon cycle has been and continues to be extensively studied at the level of internal organism and local ecosystem processes. Of more recent emphasis is the regional to global scale modeling of these processes due to the centrality of CO^2 to the issues of global warming. The current best estimate is that 1×10^{15} to 2×10^{15} g of carbon per year entering the atmosphere is from terrestrial ecosystems equalling approximately 20% to 40% of fossil fuel input [1]. Harvesting of tropical forest biomass (especially burning) is the largest component of the carbon flux into the atmosphere from terrestrial ecosystems. Boreal and north-temperate forest ecosystems, such as those found at the Michigan Forests site, are also potential carbon sources, as they contain a smaller, but significant amount of the worlds vegetative biomass.

With this interest in measuring and modeling carbon flux comes the need to acquire information over large areas and this is being met by remote sensing programs such as that of the SIR-C/X-SAR instrument recently carried aboard the shuttle Endeavor. This microwave sensor is expected to perform well in the estimation of biophysical parameters related to carbon dynamics, and this objective is currently being tested using imagery for the NASA Michigan Forests Supersite in northern Michigan. Recently, success in deriving biophysical parameters, including biomass, from SIR-C/X-SAR imagery has been demonstrated through analysis of image data from the site [4]. The present project builds on on this to study carbon dynamics.

2. GOALS

We explore the use of SIR-C/X-SAR imagery to directly estimate carbon flux associated with living woody vegetation. Previous publications have discussed SAR's particular capabilities and advantages as a remote sensor in such efforts [4][7]. There are three goals in the present project. The first is to estimate carbon stored in living vegetation at the test site. The second is to demonstrate applicability of the SIR-C/X-SAR dual mission to measuring changes in carbon balance having to do with forest disturbance, in particular, complete (clearcutting) and partial (thinning) harvesting, practices common in most private and public managed forests in North America. The third is to determine above-ground net primary production [ANPP] from annual growth as the dual mission incorporated one annual growing season.

3. METHODOLOGY

3.1. Site and Ground Data

The Michigan Forests test site, centered on 46.390° N. Latitude and 84.880° W. Longitude, is located in the Hiawatha National Forest in the eastern part of Michigan's Upper Peninsula. The greater study area encompassing the entire ascending and descending SIR-C/X-SAR swaths is approximately 60 km E-W and 50 km N-S.

The site is situated on the ecotone between the north-temperate and boreal forest biomes and thus contains communities common to both. A complexity of physiographic regions and a moisture/productivity gradient ranging from xeric,

0-7803-3068-4/96$5.00©1996 IEEE

low productivity, to mesic, relatively high productivity, plus wetlands, also contributes to the diversity of forest communities and to stands of varying ages and densities. This combination of significant community diversity and numerous stands of large geographical extent has made it possible to select a large number of long term test stands of sufficient size. Seventy four-hectare (200m x 200m) plots were established and measured at the supersite beginning in 1991. Communities present are listed in Table 1 as classification categories. Stand selection proceeded by further stratifying by age group where applicable to meet a distribution of seedling, sapling, pole, and mature stands.

Detailed measurements were made in each stand to quantify composition, structure, and biomass. Biomass for the stands was estimated using field measurements combined with allometric biomass equations developed on trees in the lake states [6]. This data has been analyzed to have error rates of 15% or better. Total above-ground biomass for the 70 stands ranges from $< 2.5 kg/m^2$ for clear-cut seedling stands to $27.3 kg/m^2$ for a mature northern hardwoods stand. The 70 stands were measured over the course of 1-3 years prior to the 1994 SIR-C overflights.

In addition to these base measurements, a number of the stands were remeasured after the 1994 growing season had terminated. These re-measurements form a database of stands biomass/carbon accrual over either one, two, or three growing seasons. In young ecosystems the rate of primary production (PP) or total gross photosynthesis (P) exceeds the rate of community respiration (R) so that P/R is > 1.0. P/R approaches 1 as succession occurs where the energy fixed tends to be balanced by the energy cost of maintenance. This means that net community production in an annual cycle is large in young, smaller in maturing, and tending toward a zero carbon balance at maturity. For these reasons, younger aged stands will be emphasized in investigating SAR sensitivity to annual growth.

Table 2 lists the stands for which average annual biomass accrual has been determined. It can be seen that these young stands are generally rapidly adding biomass. Some variation is present; low values are attributable to known, very low site quality. In addition to measures of annual growth, the test region has undergone events of disturbance. Clearcutting activity has been documented from personal observation and Forest Service records.

3.2. Image Processing

In order to meet each of the three goals, SIR-C/X-SAR imagery must be classified. To date three scenes have been classified: SRL-1 22.2 (April 10), SRL-2 22-2 (October 1), SRL-1 102.41 (April 15). These three scenes have been classified to levels I, II, and III (see Table 1) [2]. A Level I multi-temporal classification achieved a mean accuracy of 99%, and level II 94%. At level III, or species/species group level, accuracy is 70%'s-90%'s; this is an area of ongoing work.

Table 1: Classification Categories

Level I	Level II	Level III
surface		
short veg		
tall veg	upland conifer	red pine
		jack pine
	lowland conifer	northern white-cedar
		black spruce
	deciduous	northern hardwoods
		aspen

To meet the first goal of determining carbon storage at the site, biomass must first be estimated. To date, the SRL-1 102.41 April 15, 1994 data has been used to derive empirical estimations of biomass. Height, basal area (BA), trunk biomass, crown biomass, and total above-ground biomass has been empirically determined for each structural class in the classified image. The rms error for total above-ground biomass (0-25) kg/m^2 was 1.4 kg/m^2. Application of the same procedure for estimation of biomass for the remaining three images is currently being carried out.

4. RESULTS

Given the biomass images, it is possible to estimate the amount of carbon held in the imaged portion of the test site in above-ground living vegetation. This is done to a first approximation by applying a widely used allometric rule that biomass is approximately 47% carbon. Application of this shows that the imaged region contains 5.98×10^9 kg biomass or 2.82×10^9 kg carbon. Further work will be done to determine the amount in each community and to refine the estimate based on herbaceous, foliar, and woody component. Below-ground biomass and carbon storage will be estimated based on community and age group.

Because level I classified results are accurate to 99% in terms of the presence of trees vs. short vegetation or surfaces, clearcutting activity can be located and measured. To do this several steps were taken. First, April level I classified imagery was further post-processed to sieve out any small clusters of pixels erroneously classified as trees. The same was done for short vegetation errors in the October imagery. This was done to assure location of only major clearcuts which would have been tall vegetation (trees) in April and short vegetation (clear-cut) in October. After this was done, the two images were differenced. The results showed a number of obvious and known clearcuts. Results also produced a number of much smaller isolated groups of pixels which were known to be slight errors (generally edge

Table 2: Growth of Young Forest Test Stands

Stand	Community	Time 1 Biomass (kg/ha)	Time 2 Biomass (kg/ha)	Msmnt Lag (yrs)	Total Accrual (kg/ha)	Avg Annual Accrual (kg/ha/yr)	Annual Percent Accrual
78	red pine	158	217	1	60	60	37.3
66	jack pine	1319	1702	1	383	383	29.0
40	red pine	3155	7090	2	3935	1968	49.9
37	jack pine	3381	4044	2	663	332	9.4
45	aspen	7925	13751	2	5826	2913	31.7
38	jack pine	8473	13177	2	4704	2352	24.7
58	jack pine	8712	13828	1	5116	5116	58.7
36	jack pine	10071	14732	3	4661	1554	13.5
49	aspen	12291	18652	2	6361	3180	23.2
41	red pine	16138	20962	2	4824	2412	14.0
82	red pine	19581	20292	1	711	711	3.6
81	jack pine	28961	35889	1	6928	6928	23.9
51	red pine	37097	59349	2	22252	11126	26.5
33	aspen	41532	63635	3	22103	7368	15.3
22	red pine	46168	57950	3	11782	3927	7.9

Table 3: Biomass and Carbon Storage & Removal

	Storage (April 1994)	Removed (April - Oct. 1994)
Biomass (kg)	5.98×10^9	12.82×10^6
Carbon (kg)	2.82×10^9	6.022×10^6
Area (ha)	53,057	300

pixels) in the original classification. These were sieved from the imagery.

The output clearcut areas are then co-located with the biomass images to determine the amount of biomass removed. This process has shown that approximately 300 ha of forest was removed during the period between April 10, and October 1, 1994. Most of this occurred in the Raco Plains area, an area of highly xeric sandy outwash supporting primarily jack pine, but also red pine, plantations. Due to jack pine budworm infestation, there is an active salvage clear-cutting program. From the biomass imagery it was determined that this amounts to 12.82×10^6 kg of biomass removed. Applying the allometric relationship, approximately 6.022×10^6 kg of carbon was removed. These results are collected in Table 3.

When the second scene is analyzed for biomass, the amount of annual growth in the test stands listed in Table 2 will be determined. It is expected that an outcome image of carbon flux will show a large negative carbon flux in clear-cut (as demonstrated above) and heavily thinned areas, slight increase in younger test stands and other younger communities in the area, and little to no flux in maturing or mature communities.

5. REFERENCES

[1] Aber, J.D., and J.M. Melillo, *Terrestrial Ecosystems.* Holt, Rinehart and Winston Inc., Orlando, FL, 1991.

[2] Anderson, J.R, E.H. Hardy, J.T. Roach, and R.E. Witmer, *A land use and land cover classification system for use with remote sensor data.* U.S. Geological Survey, GPO, Washington, 1976.

[3] Bergen, K.M., M.C. Dobson, T.L. Sharik, I.J. Brodie, *Structure, composition, and above-ground biomass of SIR-C/X-SAR and ERS-1 Forest Test Stands 1991-1994, Raco, Michigan site.* Radiation Lab Tech. Rep. 026511-7-T, Radiation Lab, EECS Dept., The University of Michigan, Ann Arbor, MI, Oct. 1995.

[4] Dobson, M.C., F.T. Ulaby, L.E. Pierce,T.L. Sharik, K.M. Bergen, et al., "Estimation of forest biophysical characteristics in northern Michigan with SIR-C/X-SAR," *IEEE Trans. Geosci. and Remote Sensing,* Vol. 33, No. 4, July 1995.

[5] Dobson, M.C., F.T. Ulaby, L.E. Pierce, "Land-cover classification and estimation of terrain attributes using synthetic aperture radar," *Remote Sensing of Env.* , Vol. 51, No. 1, Jan. 1995.

[6] Perala, D.A., and D.H. Alban. *Allometric biomass estimators for aspen-dominated ecosystems in the upper great lakes.* USDA North Central Forest Experiment Station, Research Paper NC-314, 1994.

[7] Way, J.B., E.J.M. Rignot, K.C. McDonald, R. Oren, R. Kwok et al., "Evaluating the type and state of Alaska taiga forests with imaging radar for use in ecosystem models," *IEEE Trans. Geosci. and Remote Sensing,* Vol. 32, March 1994

Land Applications of ERS-1 Wind Scatterometer in Boreal Forest Zone

Jouni Pulliainen, Nicholas Walker(*), Terhikki Manninen(**), Martti Hallikainen and Jochen Grandell
Helsinki University of Technology, Laboratory of Space Technology
Otakaari 5A, 02150 Espoo, Finland, Fax: +358 0 460224, email: pulliainen@ava.hut.fi
(*) GEC-Marconi Research Centre, Chelmsford, UK, (**) Technical Research Centre of Finland

Abstract -- The feasibility of the ERS-1 Wind Scatterometer (WS) for land applications in boreal forest zone was analyzed using data (1) from test areas located in Finland and (2) covering the European boreal forest zone. The results show that the ERS-1 Wind Scatterometer has potential for some applications: the monitoring of soil frost and the retrieval of soil moisture/vegetation water content. The major problem in the employment of the ERS-1 scatterometer for land applications is its poor spatial resolution (47 km). This paper will also address the problem of improving the spatial resolution of the ERS-1 scatterometer data. It is shown that a realistic figure for the improved resolution is 25 km.

INTRODUCTION

The C-band backscattering properties of boreal forests have been found to change drastically depending on weather and season. During summer, the backscattering properties are dependent on the vegetation and soil moisture. During winter, soil freezing and snow cover cause changes in σ^o. The estimation and monitoring of environmental characteristics is possible if the backscattering properties can be described by an appropriate model.

The ERS-1 Wind Scatterometer measures the target with a spatial resolution of 47 km employing three separate antenna beams. Each resolution cell is measured at two angles of incidence (two of the beams have the same angle of incidence). In this paper, the multi-angular WS data is used for the estimation of the soil moisture and for detecting the soil frost. This is carried out by employing a previously developed semi-empirical forest backscattering model in the inversion [1].

STUDY SITES AND MATERIAL

The study material includes ERS-1 Wind Scatterometer data and reference information interpolated into a fixed 25 km by 25 km grid for two test areas in Finland (both sized 500 km by 500 km). The reference data include (1) land use characteristics, (2) daily air temperature and precipitation information, (3) daily hydrological model-based soil moisture values for some sub-areas and (4) soil frost/snow cover information. The additional reference information for the European boreal forest zone includes NOAA AVHRR-based forest biomass estimates.

The average relative forest cover in land areas of the Finnish test areas is 77 %. However, mixed pixels with inland lakes and agricultural areas are usual. The grid cell-wise reference data includes the distributions of different land use categories, forest biomass and soil types. The forests are relatively sparse and the dominant tree species are Scots pine and Norway spruce.

The main reference data employed are the hydrological model-based soil moisture estimates, precipitation information and *in situ* soil frost measurements. The soil frost information includes the depth of frost measured separately for open areas and forests. These data were available for 19 ground stations (three values per month).

RETRIEVAL OF SOIL FROST/MOISTURE

Inversion method

The inversion method is based on the idea of searching the maximum likelihood inverse solution for the semi-empirical forest backscattering model [1]. The inversion algorithm employs the three-beam WS data, and it requires the land-use and forest cover information as *a priori* data. The inverse problem is to find the solution which maximises the following conditional probability:

$$p\left(\overline{\sigma^o} \mid (V, \bar{\theta}, m_{v,v}, m_{v,s}, c)\right) = \quad (1)$$

$$B_1 \cdot \exp\Big(-\sum_{i=1}^{3} \frac{1}{2\sigma_i^2}\{c \cdot [(1-f_w)\cdot[\sigma_V^o(V,\theta_i,m_{v,v}) + t^2(V,\theta_i,m_{v,v})\cdot\sigma_g^o(\theta_i,m_{v,s})] + f_w\sigma_w^o(\theta_i)] - \sigma_i^o\}^2\Big)$$

where

- $\overline{\sigma^o}$ = $((\sigma^o)_1, (\sigma^o)_2, (\sigma^o)_3)$, vector containing grid cell-wise interpolated backscattering coefficients
- V = average forest stem volume of the grid cell
- θ = angle of incidence
- $m_{v,v}$ = average volumetric canopy moisture
- $m_{v,s}$ = average volumetric soil moisture
- B_1 = norming constant
- f_w = fraction of water areas (lakes and sea)
- σ_i = standard deviation of σ^o for the ith antenna beam
- c = calibration constant due to the systematic difference between the model and ERS-1 WS data
- σ_V^o = modelled forest canopy backscattering contribution
- t = modelled forest canopy transmissivity
- σ_g^o = modelled soil backscattering contribution
- σ_w^o = modelled backscattering coefficient of water areas.

In order to estimate the soil moisture, $m_{v,s}$, for a single pixel, (1) yields the following iteration problem:

0-7803-3068-4/96$5.00©1996 IEEE

$$Minimize \quad \sum_{i=1}^{3} \frac{1}{2\sigma_i^2}\{c\cdot(1-f_w)\cdot[\sigma_v^o(V,\theta_i,m_{v,v})+t^2(V,\theta_i,m_{v,v})\cdot\sigma_g^o(\theta_i,m_{v,s})]$$

$$+ \quad c\cdot f_w\cdot\sigma_w^o(\theta_i) \quad - \quad \sigma_i^o\}^2 \quad + \quad \frac{1}{2\lambda_c^2}(c-\hat{c})^2 \quad + \quad \frac{1}{2\lambda_{m_{v,v}}^2}(m_{v,v}-\hat{m}_{v,v})^2, \qquad (2)$$

where

$\lambda_{m_{v,v}}$ = standard deviation of volumetric canopy moisture

$\hat{m}_{v,v}$ = average value of volumetric canopy moisture

λ_c = standard deviation of ERS-1 WS calibration accuracy (assumed to be 0.1 dB)

$\hat{c}$ = systematic difference between the backscattering model and ERS-1 WS-derived σ^o (assumed to be 1.3 dB).

Soil moisture retrieval results

Fig.1 presents the comparison between the ERS-1 WS-based soil moisture estimates and hydrological model-based reference values. The results include values obtained for 323 cases from a total of 32 grid cells (18 dates). The results show that on dry conditions the soil moisture estimate is nearer the reference value than on wet conditions. Since the radar response to variations in the soil moisture saturates at volumetric moistures higher than about 30%, the estimates disperse towards high values.

Fig.2 shows the relation between the two-day cumulative precipitation and the daily soil moisture estimate (mean value for 32 grid cells), and additionally, the combined effect of soil moisture and precipitation. These results clearly show that:

* It is possible to obtain good estimates for soil moisture in forested areas using ERS-1 Wind Scatterometer data when considerable precipitation has not occurred directly prior to image acquisition.
* The soil estimate obtained is actually related to the soil moisture and incident precipitation, probably due to the fact that precipitation increases the amount of loose water on surface vegetation or on ground which amplifies the backscatter from forest floor. Since the forest floor backscattering contribution is assumed to be only related to the soil moisture in the estimation procedure, the possible loose water causes an overestimated soil moisture. Hence, the soil moisture estimate really estimates the total effective amount of water in top soil layer and on ground vegetation.

Monitoring of soil frost

The detection of soil freezing was tested using the ERS-1 WS data from the autumn 1993. The inversion algorithm (2) estimates the soil moisture using a modelled relation between the dielectric constant and the volumetric soil moisture [2]. When soil freezes its dielectric constant decreases significantly and, as a consequence, the model predicts a low soil moisture (from the model point of view, a frozen soil behaves as a very dry soil). Therefore, when (2) suggests an unrealistic low soil moisture value, it really detects a frozen area. Since the microwave backscatter is related to both vegetation and soil, the scatterometer-based soil moisture estimate is also affected by the freezing of vegetation.

Fig.3 depicts the average behavior of soil frost depth and WS-based soil moisture estimate. The comparison is carried out for six occasions. The conclusion from the results is that under non-frost conditions the soil moisture estimates typically show values well above 10% (which can be also noticed in Figure 1), but in the case of frozen soil the estimates obtained are usually below 10%. The soil moisture estimate appears to correlate with the depth of soil frost.

Fig.4 shows the grid cell-wise behavior of the depth of soil frost as a function of the average WS-based soil moisture estimate. The results show that when the soil moisture estimate obtained is below 9.5%, the soil is either frozen or at least the mean air temperature is below freezing point (which may indicate that the forest/ground vegetation is partially frozen).

RESOLUTION ENHANCEMENT

Due to the low spatial resolution (47 km) of ERS-1 scatterometer images, there is an interest in techniques which can improve the resolution of the scatterometer data. One method which was originally developed for use with Seasat scatterometer (SASS) data [3] involves combining the data from different antenna passes. When this technique was applied to ERS-1 data, improved nominal resolution levels of 14 km were reported [4]. However, the ERS-1 scatterometer processing chain ensures that its resultant images are adequately sampled and therefore combining different images will not help to improve the spatial resolution. In addition, the process of combining data from different antenna passes would not, in itself, increase the resolution of the image beyond that determined by the instrument impulse response function.

The ERS-1 scatterometer processing chain involves the spatial integration of returned pulses which are weighted using a 85x85 km^2 Hamming window. The pixel sampling rate for ERS-1 scatterometer data is 25 km. The Hamming function is widely used in signal processing [5] and takes the form of a cosine squared function which sits on a pedestal above the zero level. The vast majority of the energy in the power spectrum is contained within the sampling limit and (in comparison to noise and possible mis-registration effects) there is virtually no information which can be obtained by combining data sets taken at different times or with different antennas. Therefore, in the absence of any *a priori* information about the scene under consideration a realistic limit that can be placed on the possible resolution enhancement of ERS-1 scatterometer data is 25 km, which might be achieved using linear deconvolution methods.

CONCLUSIONS

Our results indicate that in the case of boreal forest zone, the ERS-1 Wind Scatterometer has considerable potential in mapping of soil/vegetation freezing and some potential in soil moisture monitoring. The potential for forest biomass retrieval is poor. Moreover, the results show that extensive image resolution enhancement is not possible.

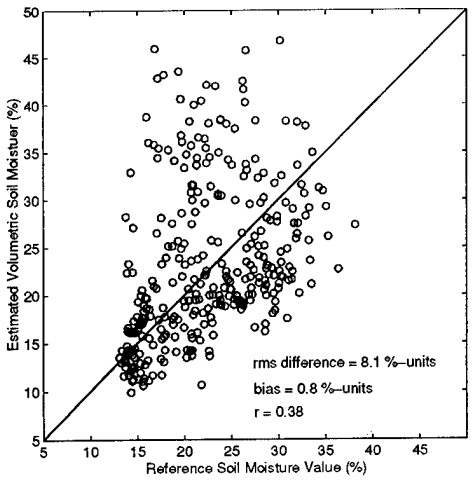


Figure 1. Soil moisture retrieval results for the time period from June to September 1993. The results are determined for 323 pixel-wise measurements on 18 occasions for 32 grid cells.

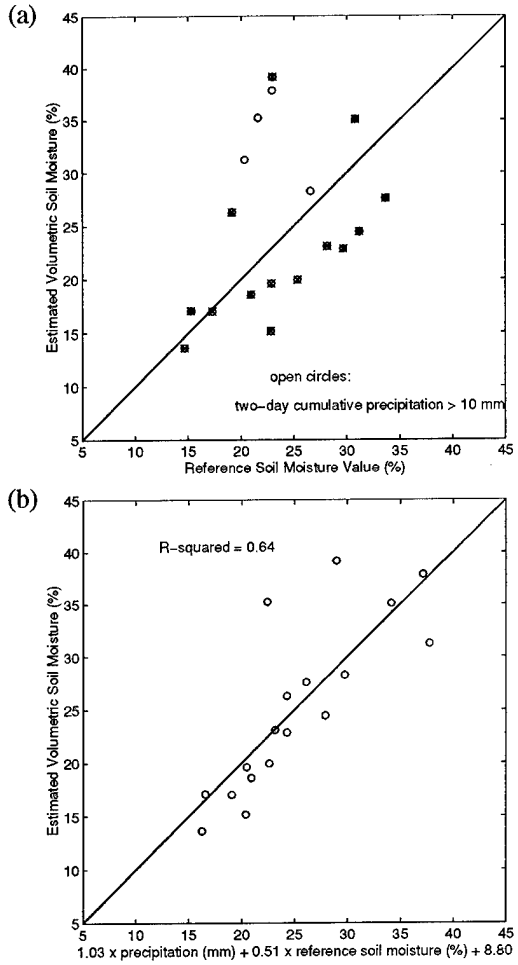


Figure 2. (a) Comparison of the daily WS-based average soil moisture estimate with the reference soil moisture. (b) Regression relation between the soil moisture estimate and the sum of reference soil moisture and two-day cumulative precipitation.

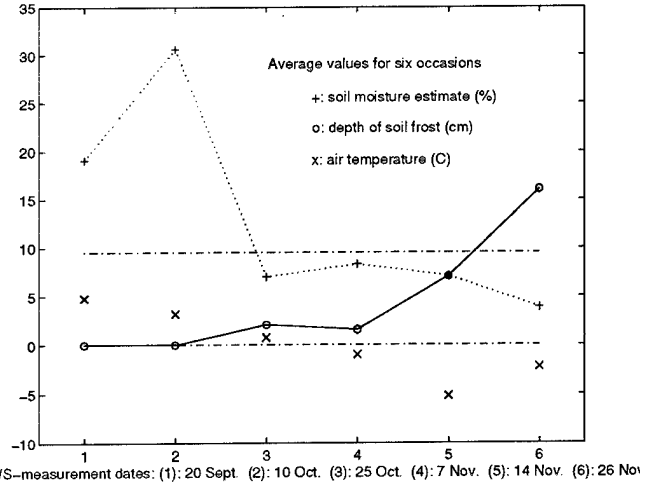


Figure 3. Behavior of WS-based soil moisture estimate (soil frost detector), depth of soil frost and daily mean air temperature for the autumn 1993. The daily average values calculated from 19 grid cells are presented.

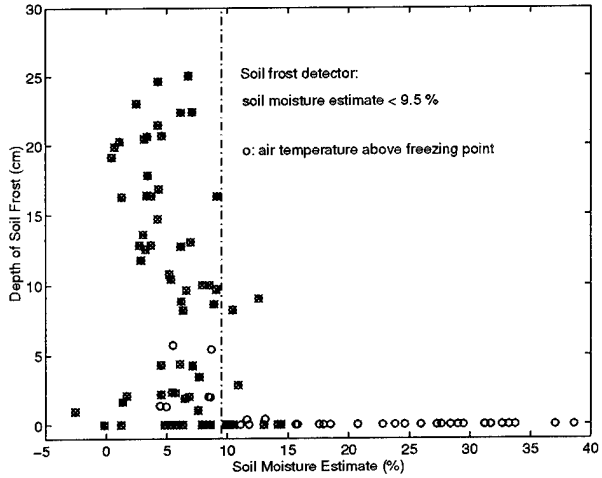


Figure 4. Relation between WS-based soil moisture estimate and the depth of soil frost. The cross-marked circles present the cases where mean air temperature has been below (or equal to) the freezing point.

REFERENCES

[1] Pulliainen, J., Heiska, K., Hyyppä, J., Hallikainen, M, "Backscattering properties of boreal forests at the C- and X-bands", *IEEE Trans. Geosci. Remote Sensing*, vol. 32, no. 5, pp. 1041-1050, 1994.

[2] Hallikainen, M.,T., Ulaby, F.T, Dobson, M.C., El-Rayes, M.A., Wu, L.K., "Microwave dielectric behavior of wet soil Part I: empirical equations and experimental observations", *IEEE Trans. Geosci. Remote Sensing*, vol. 23, pp. 25-34, 1985.

[3] Long, D.G., Hardin, P.J., Whiting, P.T., "Resolution enhancement of spaceborne scatterometer data," *IEEE Trans. Geosci. Remote Sensing*, vol. 31, pp. 700-715, 1993.

[4] Early, D.S., Long, D.G., Drinkwater, M.R., "Comparison of enhanced resolution images of Greenland from ERS-1 and Seasat scatterometers," *Proceedings of IGARSS'94, Pasadena, 8-12 Aug. 1994*, pp. 2382-2384, 1994.

[5] Harris, F., "On the use of windows for harmonic analysis with the discrete Fourier transform," *Proceedings of the IEEE*, vol. 66, pp. 51-83, 1978.

Spatial and Temporal Variability of Surface Cover at BOREAS Using Reflectance from a Helicopter Platform

Sara E. Loechel +
Phone: 301/504-6823 ; Email: sloechel@geog.umd.edu
Charles L. Walthall *
Phone: 301/504-6074 ; Email: cwalthal@asrr.arsusda.gov
Eric Brown de Colstoun +
Phone: 301/405-3043 ; Email: ebrownde@geog.umd.edu
Jing M. Chen ☆
Phone: 613/947-1266 ; Email: Chen@ccrs.emr.ca
Brian L. Markham °
Phone: 301/286-5240; Email: markham@highwire.gsfc.nasa.gov

+ Laboratory for Global Remote Sensing Studies, University of Maryland, College Park, Maryland 20742
* Remote Sensing and Modeling Laboratory, Beltsville Agricultural Research Center, Beltsville, Maryland 20705
☆ Canadian Centre for Remote Sensing, Ottawa, Ontario K1A 1Y7
° Laboratory for Terrestrial Physics, Goddard Space Flight Center, Greenbelt, MD 20771

Abstract -- Helicopter-based radiometric measurements of forested sites acquired during the Boreal Ecosystem-Atmosphere Study (BOREAS) were used to examine the spatial, temporal, and spectral variability in surface reflectance and vegetation indices (VI), including the normalized difference vegetation index (NDVI) and the simple ratio (SR), and for comparison with surface cover and fluxes. In this analysis, the sensors, which were employed during all three intensive field campaigns (IFC) of 1994, consisted of an eight-channel modular multiband radiometer (MMR), ground-based sun photometer used for atmospheric correction, and LICOR LAI-2000, hemispherical photographs, and a ceptometer for retrieval of surface biophysical variables. Means and coefficients of variation were calculated and linear regression analysis performed on reflectances, VIs, and surface variables over the entire data set and as a function of season and cover type. Surface biophysical variables included leaf area index (LAI), effective LAI, and the fraction of absorbed photosynthetically-active radiation (green fAPAR). While each dominant species displayed recognizable reflectance spectra, variability in reflectance, which was high in every channel, was most likely strongly influenced by understory and ground reflectances, and by atmospheric effects. Of the eight MMR bands, those most responsive to surface variations were the third and second middle infrared (IR) (2.08-2.37 and 1.57-1.80 μm, respectively), the red (0.63-0.68 μm), and the blue (0.45-0.52 μm). Of the two VIs examined, our results showed that the NDVI offered more predictive information than the SR regarding temporal and spatial variations in surface characteristics. Linear regression analyses between the surface biophysical measurements and the helicopter reflectances and VIs resulted in low r^2 values (consistently < 0.5), which may be explained by the effects of incomplete canopy cover and background effects. Only among sites that were mainly vegetated by Aspen (*Populus tremuloides*) and observed during the summer IFC was a stronger relationship observed. Atmospheric contamination of the radiometric signal by clouds and smoke from forest fires may also have contributed to the unsatisfactory results. Improved estimates of aerosol optical depth, taken from a sun photometer mounted on the helicopter, will be available in the future.

0-7803-3068-4/96$5.00©1996 IEEE

INTRODUCTION

A central objective of the Boreal Ecosystem-Atmosphere Study (BOREAS) was to achieve an improved understanding of the behavior of the boreal biome for use in more accurately predicting the effects of global change [6]. Remote sensing techniques which estimate relevant biophysical and climatic variables are frequently used in models which predict global change. Therefore, the objective for remote sensing studies at BOREAS was to improve those techniques used for parameter retrieval. In particular, one objective of this research was to assess the utility of vegetation indices (VI), derived from helicopter-based modular multiband radiometer (MMR) reflectances, in estimating surface biophysical variables during all three intensive field campaigns (IFC) of 1994 at BOREAS [11]. This assessment should also assist in clarifying the methods used to estimate those same variables at global scales from satellite observations. A secondary objective of this preliminary analysis was to assess the quality of the helicopter and surface measurements at BOREAS to eliminate sources of error in evaluations of the predictive capabilities of VIs.

The current understanding of the use of satellite reflectance factors to categorize forest canopy characteristics is changing.

The relationships and models which are applied to forest canopies were developed over homogeneous agricultural crops or grassland canopies. Those relationships have not consistently applied to the forest environment with its natural variability, unique geometry, and layering characteristics. In agricultural crops and forests with full canopy cover, the relationship between LAI and reflectance factors in the red, near infra-red, and mid-infrared have been found to be negative, positive, and negative, respectively [2]. In incomplete canopies, however, a negative relationship was found between red reflectance and LAI, but no relationship between near infra-red reflectance and LAI [8]. In addition, analysis over Oregon forests (where LAI was correlated to canopy closure) showed a positive near IR-to-LAI relationship in deciduous and coniferous stands [7]. Thus, over the boreal forests where the relationship of canopy closure to LAI is unknown, this may be a factor when utilizing reflectance and VIs in modeling forest canopy processes.

METHODOLOGY

The analysis was performed in three stages. First, the helicopter MMR observations were converted to at surface reflectance factors through the processes of radiometric calibration and atmospheric correction. Second, an initial assessment in the form of measures of central tendency and variability in the MMR reflectance factors, MMR-derived VI products, and surface biophysical variables was made. This provided a broad understanding of the behavior of the variables and a glimpse at possible trends and patterns, as well as an assessment of data quality. Third, linear regression was used to assess the predictive capability of reflectances and VIs relative to the surface biophysical variables, which are commonly applied with satellite data, and as a function of dominant species and season. The dominant vegetation types which we focused on are Aspen (*Populus tremuloides*), Black Spruce (*Picea mariana*), and Jack Pine (*Pinus banksiana*) [6].

The helicopter and surface data used in this analysis were collected during all 3 IFCs of 1994 at numerous tower and auxiliary sites in both the northern and southern study areas at BOREAS. The dates of the IFCs were as follows: 24 May-16 June, 19 July-10 August, and 30 August-19 September, in sequence. The NASA Goddard Space Flight Center/Wallops Flight Facility (GSFC/WFF) helicopter was deployed and the data was acquired with a Barnes Modular Multispectral Radiometer (MMR) while the helicopter was hovering at an altitude of approximately 300 meters above ground level yielding an instantaneous field of view (IFOV) of ~ 23 m. The spectral bands of the MMR are as follows: 0.45-0.52 μm for MMR1 (blue), 0.51-0.52 μm for MMR2 (green), 0.63-0.68 μm for MMR3 (red), 0.75-0.88 μm for MMR4 (near infra-red (IR)), 1.17-1.33 μm for MMR5 (first middle IR), 1.57-1.80 μm for MMR6 (second middle IR), and 2.08-2.37 μm for MMR7 (farthest middle IR). The MMR voltages were processed to at-sensor radiances ($Wm^{-2}\mu m^{-1}sr^{-1}$) following procedures described in [4] and using calibration coefficients obtained during post-season calibrations performed at NASA/GSFC. The individual scans were examined and those with spurious values were removed. The mean helicopter MMR radiances and sun photometer data collected near-simultaneously on the ground were then input into Version 3.2 of the Second Simulation of the Satellite Signal in the Solar Spectrum (6S) atmospheric correction program [9] to obtain surface reflectance factors. The sun photometer data set provided estimates of aerosol optical depths, which varied spatially and temporally especially during the summer due to the prevalence of forest fires. Descriptions of the methods used in deriving LAI and green fAPAR estimates are available in the literature [1,3,5]. The surface measurements used in the analysis were collected by BOREAS science teams (Chen, Cihlar and Penner; Gower; Plummer and Curran; Rich) and are defined as follows: (1) LAI -- one half the total leaf area per unit ground surface area (m^2m^{-2}); (2) effective LAI -- the product of LAI and a species-specific foliage clumping index; and (3) green fAPAR -- the fraction of photosynthetically active radiation absorbed by green plant matter (fAPAR). Time elasped between surface and helicopter observations was confined to less than three weeks for the conifer sites where seasonal variability was low, and to appoximately two weeks for the temporally-variable Aspen stands.

RESULTS AND DISCUSSION

Analysis of Central Tendency and Variability

BOREAS-Wide Analysis. The mean and coefficient of variation of surface reflectance, VIs, and surface biophysical variables in the data set are given inTable 1. Mean reflectance

Table 1: Mean and %CV for Collected MMR Spectral Reflectances, VIs, and Surface Biophysical Data Sets

	MMR1	MMR2	MMR3	MMR4	MMR5	MMR6	MMR7	SR	NDVI	LAI	EffLAI	fAPAR
N	214	214	214	214	214	214	214	214	214	96	80	85
Mean	0.019	0.032	0.03	0.191	0.203	0.125	0.054	7.475	0.717	2.929	2.088	0.694
%CV	39.3	31.2	40.6	35.7	32.2	35.7	44.1	55.2	15.5	41.3	40.8	20.8

clearly followed the spectral pattern expected for green vegetation. Low reflectance (and high absorption) was associated with the visible part of the spectrum, while high reflectance was found in the near infra-red (IR). In addition, the mean VIs (SR=MMR4/MMR3=7.5 and NDVI=(MMR4-MMR3)/ (MMR4+MMR3)=0.72) and surface parameters (LAI=2.93 and fAPAR=0.69) fell within expected values.

The variability of the SR (CV=55%) and of reflectance factors in the blue (MMR1 CV=39%), red (MMR3 CV=41%) and middle IR (MMR7 CV=44%) bands -- associated with leaf senescence, chlorophyll absorption, and tissue water content, respectively -- demonstrated markedly higher variability over the NDVI (CV=15%) and slightly higher variability relative to the other bands. The surface measurements showed similar ranges in variability (LAI CV=41%, Effective LAI CV=40%, and fAPAR CV=21%). At the First International Satellite Land Surface Climatology (ISLSCP) Field Experiment (FIFE), a similar experiment was carried out over the predominantly grass canopies of the Konza Prairie in Kansas [10]. A strong pattern of increased variability in those same variables was shown (with markedly lower variance in the other wavelengths) and was associated with a greater predictive capability. The weakness of this pattern at BOREAS suggests that the complexity and variability of forest ecosystems, variability in understory composition, and/or atmospheric effects may have introduced bias into the data set.

Figure 1 is a correlation matrix of MMR surface reflectances. High correlations (> approximately 0.8) were displayed between bands 1 through 3 and 7, while similarly high associations were seen in bands 4 and 5. This finding was consistent with the results found in Kansas [10]. However, a seasonal trend in correlations in our results indicated that the reflectances may have also been responding to other processes not associated with overstory vegetation. For example, the blue and the farthest IR (MMR1 and MMR7) showed decreasing correlations of 0.859, 0.756, and 0.689 for IFCs 1, 2, and 3, respectively. These two bands (which respond to leaf senescence and water content, respectively) should have exhibited consistently high associations, especially in the drier conditions that prevailed during the third IFC and that should have influenced both causal factors strongly. This absence of strong cross-seasonal correlations again implied the presence of complicating factors in the BOREAS data set.

Analysis of Variability Within Each Species and IFC. Mean vegetation indices and measured biophysical properties for the data set are presented in Table 2. Overall agreement in broad seasonal/cover type patterns were shown between VIs and surface biophysical variables in the helicopter data. For example, seasonal trends in SR and NDVI were observed in each species, and their relationship to cover type was observed at predominantly Aspen sites, which showed higher SR and NDVI than the Jack Pine or Black Spruce sites. Trends were less evident in the surface data, which was sampled with

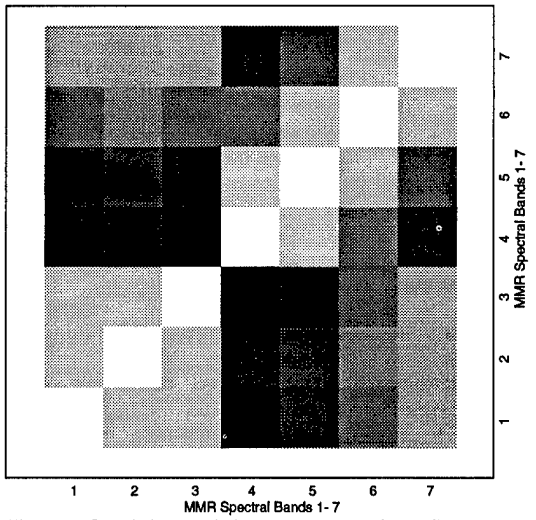


Figure 1: Correlation matrix between MMR surface reflectances. Grey scale indicates strengh of correlation ranging from 0 (black) to 1 (white); 20 greyscale steps.

less frequency and regularity. For example, the same Aspen sites were not consistently sampled in every IFC. The density of the Aspen stands (relative to the conifer sites) was especially evident in the fAPAR estimates. Mild seasonal patterns were observed in the Pine and Spruce stands in both the surface and helicopter data. The sampling of LAI and effective LAI varied, especially in the second and third IFCs. Therefore, some trends were indistinguishable, as shown in Table 2 where N gives both the number of MMR and LAI samples in each dominant species type. The other surface parameters were sampled with slightly lower frequency than LAI. The inconsistent sampling regime of the surface measurements justified the further stratification of the data set.

Regression Analysis

BOREAS-Wide Analysis. The results of regression analyses (Table 3) showed poor relationships between surface variables and vegetation indices. Our results showed, however, implied the higher information content and predictive capability of the NDVI ($0.106 \leq r^2 \leq 0.276$) compared to the SR ($0.029 \leq r^2 \leq 0.162$). In each case, the addition of a quadratic term of LAI improved the results only slightly. The poor performance of the relationship between effective LAI and the VIs was clearly evident. Histograms of the data (which showed normal distributions in the surface variables and in the NDVI, while the SR did not) confirmed bias in the data set, though they offered little insight into causes or interactions.

Some improved relationships were found between reflectance factors in individual channels and the surface variables (Table 4). MMR bands 1-3 and 6-7 showed the strongest relationships to the surface vegetation. This confirmed the results of the analysis of mean and variability with suggested higher information content at those wavelengths. However,

Table 2: Mean Surface Variables and VIs by Species and IFC						
IFC	N_{MMR} /N_{LAI}	SR	NDVI	LAI	EffLAI	fAPAR
			Aspen			
1	11/1	10.70	0.81	3.65	2.91	NA
2	28/7	14.42	0.85	2.90	1.82	0.80
3	6/1	6.63	0.70	2.66	2.21	0.84
			Pine			
1	21/12	4.16	0.59	2.17	1.62	0.60
2	37/25	5.96	0.68	2.46	1.92	0.64
3	12/6	5.62	0.68	2.84	1.64	0.79
			Spruce			
1	25/14	6.23	0.71	3.30	2.29	0.69
2	41/26	6.45	0.72	3.38	2.36	0.72
3	6/3	7.14	0.75	4.29	1.92	0.85

the slope of the regression lines were all negative, including that of near IR to LAI. The lack of a strong positive relationship between near IR reflectance and forest canopy LAI suggested, based on previous work [2,7,8], that canopy closure and LAI are not strongly correlated. Therefore, the reflectance factors were possibly influenced or biased by canopy closure, understory, and background cover.

Regression Analysis Within Species. To address the questions of the information content and predictive capability of the VIs for each species, the data set was confined to tower sites (those with intensive data collection from surface-based towers). Table 5 gives the results (r^2) of the species-by-species linear regression of the VIs and red and near IR reflectance against the three surface vegetation measurements at the tower sites. Although the quantity of sites was reduced by this restriction, as was shown in the number of observations in each analysis (N), some temporal consistency in sampling was attained. The most striking result, however, was the strong relationship (r^2>0.97) shown in the regressions of Aspen VI and individual band reflectances against surface variables. This confirms previous research [8,12], which implied that canopy closure and background effects are issues confined to coniferous tree species. The r^2 value of a regression of MMR4 and LAI in the full data set of Aspen sites was 0.61 with a positive slope, superior to the relationship for all Aspen stands in the full data set (r^2<0.03 in Table 4). This demonstrated the strength of the MMR4-LAI relationship over Aspen sites, and its weakness with coniferous species. However, SR- and NDVI-to-LAI regressions in the same data set resulted in r^2 values of only 0.32 and 0.27, respectively. Although this represented an increase relative to the significance for the entire data set (Table 3), the implication of this decrease in the significance of the relationship relative to the more restricted tower site data set was that atmospheric and aerosol contributions to the signal may have affected the visible bands. The Pine and Spruce tower site analysis showed much weaker relationships to each surface variable, which again suggested the interaction of canopy structure and background reflectance in the reflectance factors of these species. Again, effective LAI showed weak relationships in both conifer species.

Table 3: Regression Analyses for VIs (r^2)			
	Predictor Variables		
Surface Variables	N	SR	NDVI
LAI	96	0.056	0.174
Eff LAI	80	0.029	0.106
fAPAR	85	0.162	0.276

The quality of performance of the NDVI in predicting surface biophysical quantities was demonstrated numerically in the slope and strength of their relationships with red and near IR reflectances. In the Aspen stands, high r^2 values and slopes conformed to expected values (red: negative; near IR: positive) which maximize the information content of the SR and NDVI [2]. The two conifer stands, however, had weak relationships, and the absence of the expected slope contributed to the weakness of the SR and NDVI relationships. A graphical depiction of this relationship is given in Figure 2. This plot of reflectance in the near IR (MMR4) as a function of LAI demonstrated the distinct behavior of the three tree species. In addition to distinct relationships as defined by the slope of the relationship (given in Table 5), the area occupied by each species in Cartesian space was mutually exclusive.

SUMMARY

The BOREAS field experiment allowed a critical assessment of the performance of vegetation indices in predicting surface conditions, a common satellite application, while use of the helicopter reflectances eliminated the issues of georegistration and scale which affect satellite observations. This preliminary analysis confirmed the utility of VIs in predicting surface conditions, and focused on an issue of concern in

Table 4: Regression Analyses for MMR Reflectance Factors and Surface Biophysical Variables (r^2)								
	Predictor Variables							
Surface Variables	N	MMR1	MMR2	MMR3	MMR4	MMR5	MMR6	MMR7
LAI	96	0.268	0.271	0.332	0.027	0.183	0.403	0.450
Eff LAI	80	0.222	0.190	0.242	0.006	0.066	0.233	0.325
fAPAR	85	0.304	0.301	0.370	0.003	0.162	0.385	0.486

Table 5: Regression Analyses of VIs and Reflectances vs. Surface Variables for Each Species: Tower Sites Only							
Predictor Variables							
Surface Variables	NLAI	SR (r^2)	NDVI (r^2)	MMR3 (r^2, slope)		MMR4 (r^2, slope)	
			Aspen				
LAI	3	0.998	0.999	0.99	neg	0.97	pos
Eff LAI	3	0.998	0.999				
fAPAR	3	0.998	0.999				
			Pine				
LAI	21	0.381	0.363	0.43	neg	0.00	no
Eff LAI	21	0.041	0.047				
fAPAR	21	0.086	0.198				
			Spruce				
LAI	10	0.274	0.265	0.24	no	0.02	no
Eff LAI	10	0.363	0.342				
fAPAR	10	0.362	0.309				

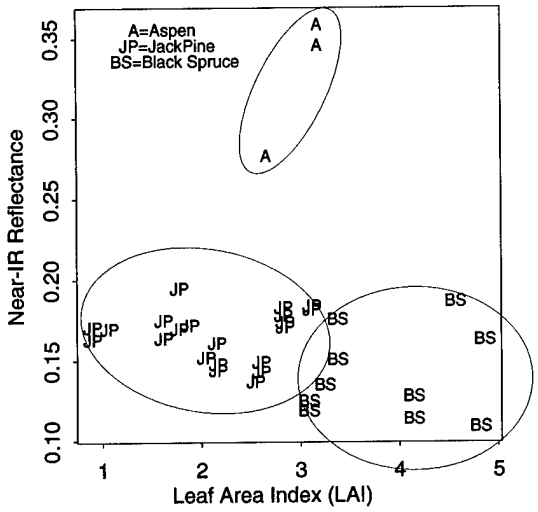


Figure 2: Near IR Reflectance as a function of LAI for the three tree species.

recent research: the behavior of the reflectance factor over coniferous forests and the interaction of leaf area index, canopy cover, understory and background composition in that behavior. However, the utility of VIs was reinforced over the Aspen sites. We observed a marked decrease in the predictive ability of the VIs over coniferous stands. In addition to an initial assessment of the application of remote sensing methods in the boreal forest, weaknesses or bias in the helicopter and surface variables were identified. Atmospheric correction using aerosol depths derived from a sun photometer mounted on the helicopter will strengthen the MMR observations. Options to improve the surface measurements include further restricting observations based on sampling consistency and methods and to account for understory and background reflectance factors when explaining the behavior of the VI-LAI relationships for conifers.

REFERENCES

[1] J.M. Chen and J. Cihlar, "Quantifying the effect of canopy architecture on optical measurements of leaf area index of plant canopies using two gap size analysis methods." IEEE Trans. Geosci. Remote Sens., vol. 33, pp. 777-787, 1995.

[2] F.M. Danson, "Developments in the Remote Sensing of Forest Canopy Structure," in Advances in Environmental Remote Sensing, F.M. Danson and S.E. Plummer, Eds. Chichester, England: John Wiley & Sons, 1995, pp. 53-69.

[3] S.T. Gower and J.M. Norman, 1991, "Rapid estimation of leaf area index in forests using the LI-COR LAI-2000," Ecology, vol. 72, pp. 1896-1900.

[4] B.L. Markham, F. M. Wood Jr., and S.P. Ahmad, Radiometric calibration of the reflective bands of NS001-thematic mapper simulator (TMS) and modular multispectral radiometers (MMR) in Recent Advances in Sensors, Radiometry, and Data Processing for Remote Sensing, Proc. SPIE, 24, pp. 96-108, 1988.

[5] P.M. Rich, "Characterizing plant canopies with hemispherical photographs," in Instrumentation for studying vegetation canopies for remote sensing in optical and thermal infrared regions, N.S. Goel and J.M. Norman, Eds., Remote Sensing Reviews, vol. 5, pp. 13-29, 1990.

[6] P.J. Sellers, F.G. Hall, M. Apps, D. Baldocchi, J. Cihlar, J. Den Hartog et al., BOREAS Experiment Plan (Version 3.0), NASA/GSFC, Greenbelt, Md. 20771, May 1994, pp 358 plus Appendices.

[7] M. Spanner, L. Johnson, J. Miller, R. McCreight, J. Freemantle, J. Runyon, and P. Gong, "Remote sensing of seasonal leaf area index across the Oregon transect," Ecological Applications, vol. 4, no. 2, pp. 258-271, 1994.

[8] M. Spanner, L. Pierce, D. Peterson, and S. Running, "Remote sensing of temperate coniferous forest leaf area index: The influence of canopy closure, understory vegetation, and background reflectance," Intl. J. Rem. Sen., vol. 11, pp. 95-111, January 1990.

[9] E. Vermote, D. Tanre, J. Deuz, M. Herman, and J. Morcrette, "Second simulation of the satellite signal in the solar spectrum: an overview," IEEE Trans. Geosci. Remote Sens., in press.

[10] C. Walthall and E. Middleton, "Assessing spatial and seasonal variations in grasslands with spectral reflectances from a helicopter platform," J. Geophys. Res., vol. 97, no. D17, pp. 18905-18912, November 1992.

[11] C. Walthall, D.L. Williams, B. Markham, J. Kalshoven, R. Nelson, "Development and present configuration of the NASA GSFC/WFF helicopter-based remote sensing system," this issue.

[12] D. Williams, "A comparison of spectral reflectance properties at the needle, branch, and canopy level for selected conifer species," Remote Sens. Environ., vol. 35, no. 2, pp. 79-93, February 1991.

Modeling Solar Radiation Transmission In Boreal Conifer Forests

W. Ni[1], X. Li[1], C.E. Woodcock[1], J.L. Roujean[2], R. Davis[3] and A. Strahler[1]
[1] Center for Remote Sensing and Department of Geography, Boston University, 725 Commonwealth Ave., Boston MA, 02215, USA Tel. +1-617-353-2088, Fax +1-617-353-3200, e-mail: wenge/lix/curtis/alan@crsa.bu.edu
[2] Meteo France Centre National de Recherches Meteorologiques,42 avenue Gustave Coriolis, 31057 Toulouse Cedex, France, Tel. +33-61079343, Fax +33-61079626 e-mail: roujean@meteo.fr
[3] Cold Regions Engineering Research Laboratory, U. S. Army Corps of Engineers Hanover, New Hampshire, USA, e-mail: u2rg9red@crrel41.crrel.usace.army.mil

Abstract – A hybrid geometric-optical and radiative transfer (GORT) model [1], developed for the radiation regime in discontinuous vegetation canopies, is modified to include branch orientation properties. This new version of the model was used to estimate solar radiation transmission in old Jack Pine (OJP) and old black spruce (OBS) forests in Canada.

Radiation measurements collected in OJP and OBS forests in Canada show that radiation transmission as a function of solar zenith angle and height in the canopy deviates from what is predicted by Beer's law. By considering gap probabilities between crowns in addition to within individual crowns, GORT estimates more accurately transmission distribution in the canopy.

Modification of the GORT model to include branch orientation improves the ability to model the observed patterns of solar radiation transmission as a function of solar zenith angle and height in the canopy in the SOJP site. Branch orientation distributions are derived from PARABOLA measurements by the Geometric-Optical Mutual Shadowing (GOMS) model [2].

INTRODUCTION

The Boreal Ecosystem-Atmosphere Study (BOREAS) experiment has been undertaken for better understanding of the interactions between the boreal forest biome and the atmosphere. The radiation environment below, within and above conifer stands plays a crucial role. Both airborne canopy reflectance and snowmelting patterns [3] collected over BOREAS test sites showed strong heterogeneity which reveals that the effect of the conifer forests on the solar radiation regime differs significantly from the one of a more homogeneous turbid medium, like deciduous forests and grass canopies. Large uncertainties of the surface radiation inputs used in the climate models, as well in hydrology and ecology schemes, come from this insufficient knowledge of the partitioning of radiative energy within the snow-covered boreal landscape.

The architecture of conifer forests is quite complex due to the clumping of branches into crowns, of shoots into branches, and of needles into shoots. This yields a strong landscape heterogeneity at all spatial scales since a light ray may be trapped in or transfered through any element of the canopy layer. Incorporating the conifer stand structure into a classical radiative transfer approach proved to be rather difficult as a result of the specific heterogeneity [4]. The geometric-optical (GO) model [2] was developed for describing the light transfer in discontinuous vegetation canopies, which incorporated directly the three-dimensional tree geometry structure effect on the radiation regime. With the basic GO approach, the newly developed geometric-optical and radiative-transfer (GORT) model [1] incorporates the effect of not only the three-dimensional tree geometry structure, but also the foliage spectral properties on the radiation regime. This model is tested hereafter against measurements of solar radiation transmission collected during BOREAS field campaigns over Old Jack Pine (OJP) and Old Black Spruce (OBS) forests.

0-7803-3068-4/96$5.00©1996 IEEE

RESULTS OF MODELING

Distribution of total radiation within the forest canopy includes three components: direct incoming solar radiation, diffuse skylight filling into gaps, and the field of solar radiation scattered by elements of the canopy and understory background. In the visible range, the only spectrum treated here, large absorption by needles allows for ignoring multiple scattering and so only the first two contributions are considered.

In GORT, the discontinuous vegetation canopy was modeled as an assemblage of many individual tree crowns of ellipsoidal shape randomly centered between height h_1 and h_2, where h_1 and h_2 are the lower and upper bounds of crown center height. Within each single crown the foliage and branches are assumed to be uniformly distributed. The incoming direct and diffuse shortwave irradiance can pass through the gaps between crowns, stems, branches, or leaves, and enters canopies at different heights, with some of the photons scattered and some unscattered. The proportion of the scattered and unscattered direct beam at any height and at any solar zenith angle was simulated by the total gap probabilities, including the between-crown and within-crown gap probabilities.

In this study, the gap probability calculated in the GORT model is used to model the shortwave radiation transmission of conifer stands. Fig. 1 and Fig. 2 show the vertical profiles of the beam and diffuse skylight transmittance over OJP forest for various sun angles using the GORT model and Beer's law. Measurements of tree geometry and foliage density served as inputs. These figures show that vertical distribution of the radiation predicted from GORT resembles a logistic curve in sigmoid shape as a function of height. Most of the radiation is intercepted between h_1 and h_2. Deviation from an exponential function like Beer's law is essentially caused by the between-crown gap probability, taken into account in the GORT model. At smaller solar zenith angles, the radiation beam reaching the

forest floor has two components, which are the between-crown and within-crown gap probabilities. The former is dominant for large solar zenith angles where the radiation interception by the forests is much closer to the prediction by Beer's law.

Field measurements [5] and tree parameters retrieved by bidirectional reflectance inversion of the geometric optical mutual shadowing (GOMS) model [6] in BOREAS test sites showed that the horizontal whorls of branches within a single crown act somewhat like a pile of horizontally oriented disks within an ellipsoid envelope [7]. This makes more light pass through the crowns at large solar zenith angles. With the assumption of randomly oriented branches within a single crown, the GORT model will underestimate the gap probability. In this study, the original GORT model was modified to account for the effect of the horizontal whorl branch structure on the gap probability. Here an empirical formula, $G_b(\theta) = 0.7cos^2(\theta)+0.3$, describing the orientation of branches for the SOJP site was used in the calculation of between-crown gap probability. It was obtained from the inverted tree coverage results [6]. Fig. 3 depicts the modeled radiation transmission distribution with height and solar zenith angle in SOJP sites by the original and modified GORT model for a clear day. Fig. 3 shows that the radiation transmittance first decreases and then increases with increasing solar zenith angle. The reason is that at smaller solar zenith angles, radiation transmission arises mainly from beam radiation, whereas at larger solar zenith angles, more contribution is from diffuse skylight though openness.

COMPARISON WITH FIELD MEASUREMENTS

During 1994 and 1995 field campaigns in BOREAS, radiation measurements were implemented in SOJP, SOBS, and NOBS sites. Fig. 4 and Fig. 5 show the measured (averaged over days 157, 158, 201, 202, 208, 216 in SOJP and days 157, 158, 164, 201, 202, 205, 206, 207, 208, 211, and 216 in SOBS) and modeled vertical distribution of daily radiation transmittance in SOJP and SOBS sites. Fig. 6 and Fig. 7 show the radiation transmission at the snow covered forest floor in SOJP and NOBS sites.

Comparison of field measurements in SOJP and SOBS with the modeled results shows that GORT can model the vertical radiation transmission distribution in SOJP better than in SOBS site. The explanation is due to the difference of the tree distribution between SOJP and SOBS sites. The tree heights are more uniform for SOJP than SOBS: the range of the tree height is 12-15 m in SOJP whereas it is 0-11 m in SOBS site according to [5]; 60% of the trees were recorded as 6 meters high, 30% were 8 meters and 10 % of 10.5 meters. This tree distribution in SOBS deviates from what is assumed by the GORT model. Fig. 4 and Fig. 6 show that the modified GORT model can simulate better radiation transmittance than the original GORT in the SOJP site. Because of too many uncertainties for the distribution of vertical crown centers in the canopy, we did not explore the ability of the modified GORT to model nonuniform tree-distributed SOBS sites.

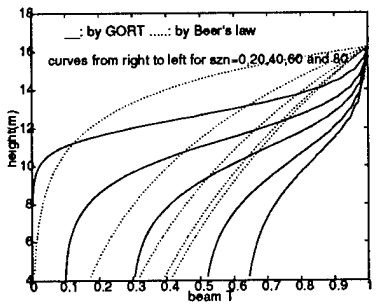


Figure 1: Modeled beam transmittance in SOJP

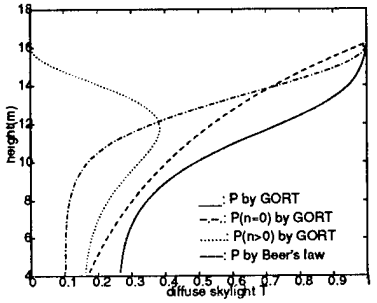


Figure 2: Modeled diffuse skylight transmittance in SOJP, contributed by between-crown, P(n=0) and within-crown, (P(n>0)) gap probabilities

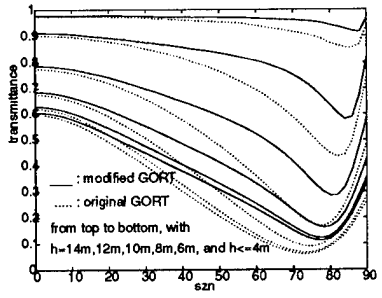


Figure 3: Modeled shortwave radiation transmittance in SOJP by original and modified GORT

Notice that the values of the input parameters h_1 and h_2 are not sensitive to the radiation transmission at the forest floor, although they are sensitive to its vertical distribution. This may be important for the future work on the application of GORT in snowmelting models at landscape scale, since we have to use remotely sensed measurements for the inputs of GORT at landscape scale, by which the input values of h_1 and h_2 are usually hard to obtain.

CONCLUSION

The comparison of solar radiation transmission between the field measurements and simulated results by GORT shows its ability to model the effect of the three dimensional conifer

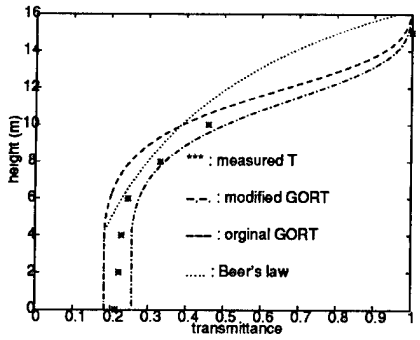


Figure 4: Comparison of modeled and measured daily averaged transmittance in SOJP

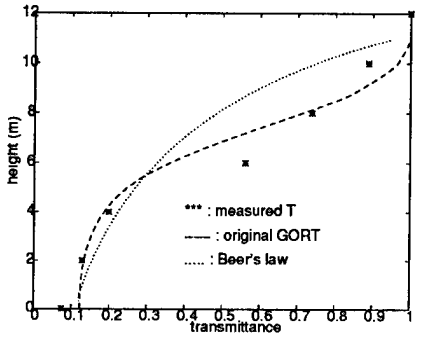


Figure 5: Comparison of modeled and measured daily averaged transmittance in SOBS

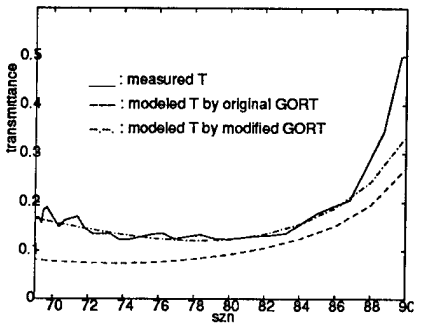


Figure 6: Comparison of modeled and measured transmittance in SOJP on day 38, 39,40

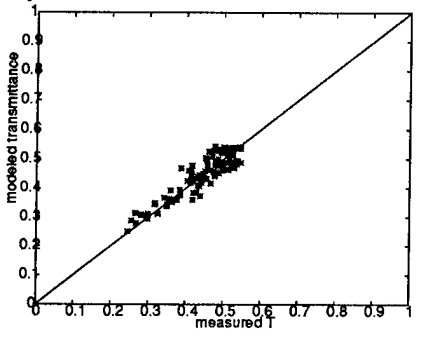


Figure 7: Comparison of modeled and measured radiation transmittance in NOBS on day 81, 82, 83, 84, 85 in 1995

stand structure on the solar radiation environments within and below the canopy. The combination of both GO and RT approaches has more advantages than either pure RT or pure GO approaches. GO accounts for the influence of crown structure and RT accounts for the influence of the optical properties of the foliage structure. Moreover, the combination of these two approaches allows one to incorporate more easily the complicated conifer tree structure in the model (e.g. accounting the effect of the horizontal whorl branch structure). GORT has high potential for application at landscape scale in BOREAS.

ACKNOWLEDGMENT

This work is supported in part by U.S. Army Corps of Engineerings under contract DACA89-93-k-00012, by NASA under contract NAS5-31369 and by China's NSF under grant 49331020. The authors also thank Meteo France and Programme National de Teledetection Spatiale (PNTS) for the support.

References

[1] Li, Xiaowen, Strahler A. H. and Woodcock C.E., "A hybrid geometric optical-radiative transfer approach for modeling albedo and directional reflectance of discontinuous canopies", IEEE Transactions on Geoscience and Remote Sensing, 1995, vol.33, pp.466-480.

[2] Li, Xiaowen and Strahler A. H., "Geometric-optical bidirectional reflectance modeling of mutual shadowing effects of crowns in a forest canopy", IEEE Transactions on Geoscience and Remote Sensing, 1992, vol.30, pp.276-292.

[3] Hardy, J. and R. E. Davis "Snow distribution around trees: incorporation of snow interception patterns into spatially distributed snow models", 1995, EOS, Transactions, American Geophysical Union, Vol.76, No.46, pp202.

[4] Oker-Blom, J. Lappi and H. Smolander, "Radiation Regime and Photosynthesis of Coniferous Stands", in Photon-Vegetation Interactions – Application in Optical Remote Sensing and Plant Ecology, R.B. Myneni and J. Ross,Eds, Springer-Verlag, 1991.

[5] Chen, J. M., "Optically-based methods for measuring seasonable variation of leaf area index in Boreal conifer stands", Agri. For. Meteorol., 1996, in press.

[6] Li, Xiaowen, Strahler A. H., "A knowledge-based inversion of physical BRDF models and three case studies", 1996 International Geoscience and Remote Sensing Symposium.

[7] Ross, J. K. and A. Marshak," Monte Carlo Methods", Photon-Vegetation Interactions – Application in Optical Remote Sensing and Plant Ecology, R.B. Myneni and J. Ross, Eds, Springer-Verlag, 1991.

The Impacts Of Environmental Conditions On Microwave Radiometry Of Vegetation : A Physical Approach

Mostafa A. Karam
GenCorp Aerojet
1100 W. Hollyvale Street, Azusa, CA 91702 USA
Phone : (818) 812-1154, Fax :(818) 969-5772, e-mail : karamm@post.aes.com

ABSTRACT

The physical microwave vegetation radiometry model developed at Aerojet is employed to investigate the impacts of environmental conditions on microwave radiometry of vegetation / forest. The model is based on solution of the radiative transfer equations and it operates over a wide frequency band in the microwave and millimeter wave regions for both coniferous and deciduous forest as well as grass and agriculture crops. Numerical simulations based on the model showed that the horizontally polarized temperature is more sensitive to the seasonal variations than the vertically polarized temperature.

INTRODUCTION

Environmental conditions such as freezing, thawing, dryness, and wind storms, affect vegetation and forest canopies in three different aspects. They change the canopy structures through defoliating or foliating (seasonal variation) or through changing orientation (wind storm). They change dielectric properties through changing water content or changing physical temperature. They also change the canopy physical temperature profiles through wind storms. In this study the vegetation microwave radiometry model developed at Aerojet [1-3] is employed to investigate the impacts of some of those conditions on the radiometer response.

In this study, the effect of the variation in canopy physical temperature profile associated with wind storm is investigated. Also the effect of seasonal variation in canopy structure is investigated through foliating or defoliating the canopy trees.

MODEL DESCRIPTION

The model is constructed through developing and integrating a hierarchy of models : (i) upper-level model relating the radiometer brightness temperature to the scattering amplitude tensors of the canopy constituents [2], (ii) intermediate-level models relating the scattering amplitude tensors of the canopy constituents to the geometric and dielectric properties of such constituents, and (iii) lower-level models relating the dielectric properties of vegetation constituents to the canopy biophysical parameters. The upper-level model is developed through an iterative solution for the radiative transfer equations inside a multi-layered random medium containing discrete scatterers representing the canopy constituents [1-2]. The deciduous leaves are represented by randomly oriented elliptic discs. The branches, trunks, stems, and coniferous leaves are represented by randomly oriented finite length cylinders. The intermediate-level models are represented by (a) disc scattering amplitude tensors bridging those derived via the physical optics approximation and those derived via the generalized Rayleigh-Gans approximation [3], and (b) finite cylinder scattering amplitude tensors working over a wide frequency bands[3]. The scattering amplitude tensors are derived from electromagnetic theory. The lower-level models are based on semi - empirical formulae reported in the open literature for soil and vegetation dielectric constants [4-5].

NUMERICAL SIMULATIONS

The numerical simulations performed in the present section are aimed at investigating some effects of wind storms and season variations on the radiometer response. The numerical simulations are performed through using walnut canopy parameters as an input for the model. The canopy is treated as a two layered medium above a rough surface. The upper layer stands for the crown and it contains tree leaves, secondary branches and primary branches. The lower layer contains the tree trunks. The rough surface represents the soil-canopy interface. The geometric properties of the leaves, branches, trunk, and soil roughness are given in [3].

0-7803-3068-4/96$5.00©1996 IEEE

Figure 1 is presented to illustrate the effect of wind storms on the vertically polarized temperature at 6.6 GHz. The effect of wind storm is represented by an exponential physical temperature profile along the canopy height. The physical temperature value is equal to T_c at the canopy-air interface, and is equal to T_s at the canopy-soil interface.

Figures 2 - 4 are presented to investigate the impacts of season variations on both canopy brightness temperature and attenuation. Two different seasons of the year are considered in Figs. 2 - 4 : spring and winter. In spring, the canopy trees are foliated and in winter the trees are defoliated. Figure 2 depicts the vertically polarized brightness temperature calculated as a function of frequency at 53° angle of incidence for both winter and spring seasons. Figure 3 gives the horizontally polarized brightness temperature under the same conditions used in Fig. 2. The attenuation values are depicted at Fig. 4 for both vertically and horizontally polarized radiations. Two sets of attenuation values are calculated for each polarization : values at spring time, and values at winter time. In the legend of Fig. 4, the first letter stands for polarization, and the second letter stands for the season. of the year. For instance V(s) means the vertically polarized attenuation calculated at spring time.

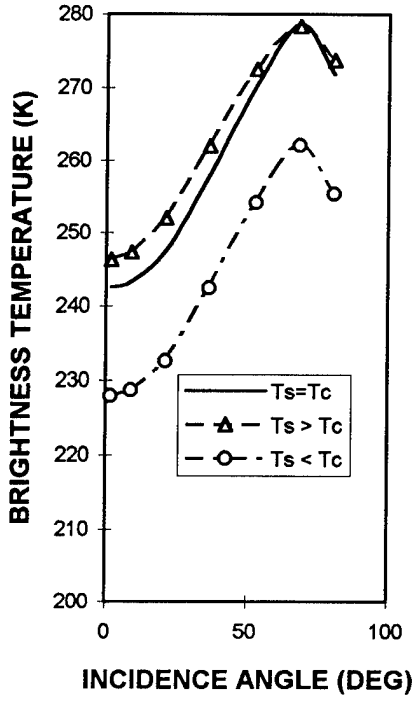


Fig. 1 The vertically polarized temperature for different physical temperature profile (Frequency = 6.6 GHz, soil moisture = 29.5%)

DISCUSSIONS

With regard to the effect of wind storm which is represented by the variations in canopy physical temperature profile, from Fig. 1 we see that such an effect has a pronounced impact on the canopy brightness temperature. The brightness temperature follows the variations in canopy-soil temperature. Higher values for the canopy-soil temperature are associated with higher values for the canopy brightness temperature and vise versa. The results reported in Fig. 1 are true for the walnut canopy under consideration and for the radiometer configurations (frequency, angle, polarization) considered in the figure. They may vary for other canopies and other radiometer configurations.

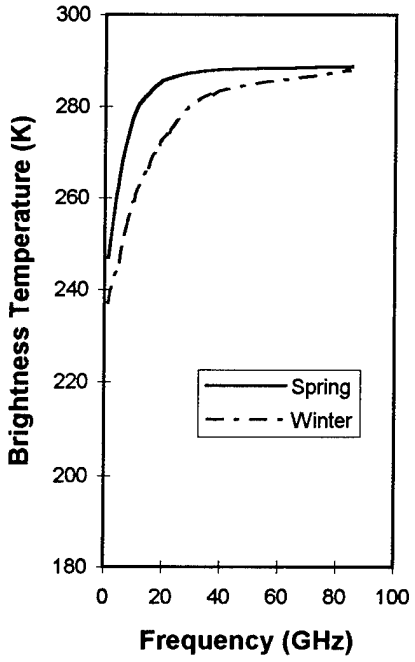


Fig. 2 The seasonal variations in the vertically polarized temperature (Angle = 53°)

As for the variations in the canopy structure associated with the season variations, their impacts can be inferred from Figs. 2 - 4. Form Figs. 2 and 3 we see that defoliating the canopy trees which

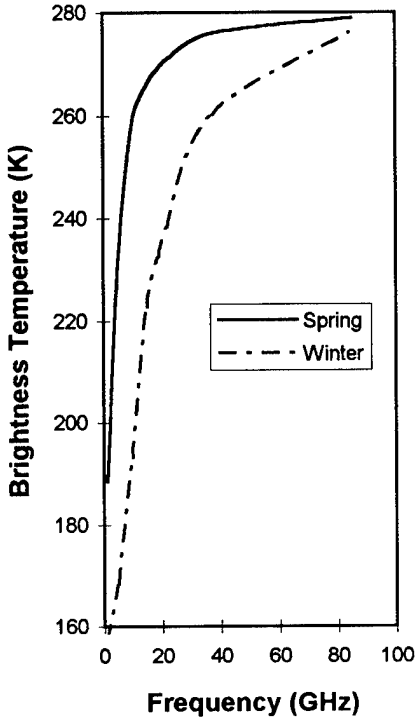


Fig. 3 The seasonal variations in the horizontally polarized temperature (Angle = 53°).

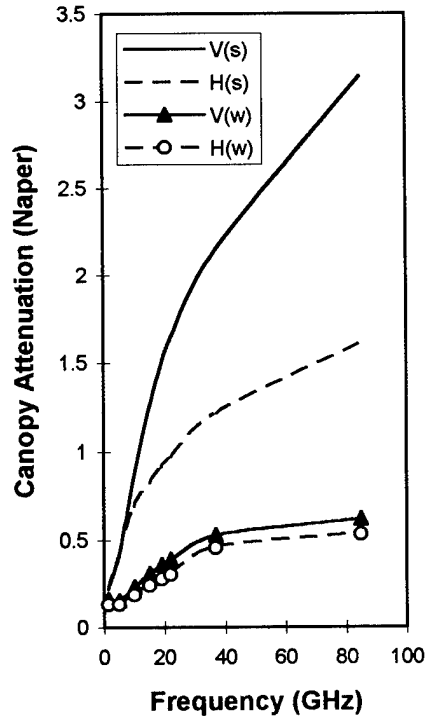


Fig. 4 The seasonal variations in the canopy attenuation (Angle =53°).

takes place during winter times is associated with a decrease in both radiometer brightness temperature and attentions. The decrease in canopy brightness temperature during winter season is more at lower frequencies than at higher frequencies, and it is more for horizontally polarized radiations than vertically polarized radiations. On the other hand the decrease in attenuation is more at higher frequencies than at lower frequencies. This is expected because tree leaves have lower attenuation values at lower frequencies than at higher frequencies. From Figs. 2 and 3 we also see some interesting feature. We see that the horizontally polarized brightness temperature is sensitive to the variation in canopy structure over a wide frequency band. This indicates its potential in monitoring the seasonal variations in canopy structures over a frequency values ranging from L-band (1.4 GHz) frequencies to Ka - band (37 GHz) frequencies.

REFERENCES

[1] M. A. Karam, " The potential of microwave radiometers in monitoring forest biomass," Digest of IGARSS'94, pp. 1860 - 1862, 1994.

[2] M. A. Karam, " A physical model for microwave radiometry of vegetation, I . Brightness temperature formulation " Unpublished.

[3] M. A. Karam, " A physical model for microwave radiometry of vegetation, II . Scattering amplitude tensors and preliminary results, " Unpublished.

[4] F. T. Ulaby, and M. A. El-Rayes, " Microwave dielectric spectrum of vegetation- Part II : Dual-dispersion model, " IEEE Trans. Geoscience and Remote Sensing, vol. GE-25, pp. 550-557, 1987.

[5] M. C. Dobson, F. T. Ulaby, M. T. Hallikainen, and M. A. El-Rayes, " Microwave dielectric behavior of wet soil-Part II : Dielectric mixing models, " IEEE Trans. Geoscience and Remote Sensing, vol. GE-23, pp. 35-46, 1985.

Optimization of a Composite Surface Model for the Radar Backscattering Cross Section of the Ocean Surface as Measured by Wind Scatterometers

Roland Romeiser

University of Hamburg, Institute of Oceanography, Troplowitzstr. 7, 22529 Hamburg, Germany
Phone: +49 40 4123 5430 Fax: +49 40 4123 5713 E-Mail: romeiser@ifm.uni-hamburg.de

Abstract -- A calibrated composite surface model for the calculation of absolute normalized radar backscattering cross sections (NRCS) of the ocean surface is presented. The model is based on a Taylor expansion of the NRCS, as given by Bragg scattering theory, up to second order in the surface slope. Measured NRCS values for a variety of radar frequencies, polarizations, incidence angles, azimuthal radar look directions, and wind speeds can be well reproduced after some reasonable tuning of the input ocean wave spectrum. The model can thus be considered as an advanced wind scatterometer model based on physical principles. Due to this fact it is also well suited for general applications like the calculation of NRCS variations associated with distortions of the wave spectrum in the presence of surface current gradients.

INTRODUCTION

Remote sensing of the ocean by microwave radar requires imaging models for the relationship between features at the sea surface and their radar signatures. Major applications are the derivation of surface winds from absolute normalized radar backscattering cross section (NRCS) measurements (wind scatterometry) and the interpretation of relative spatial NRCS variations due to the presence of long ocean waves, current gradients, or surface films. Suitable models for these applications have been obtained by different approaches.

Wind scatterometry requires a simple but well calibrated algorithm for the conversion of NRCS values into wind speed vectors. The coarse spatial resolution and the constant radar parameters of spaceborne wind scatterometers allow the utilization of completely empirical models. In contrast to this, the interpretation of radar signatures associated with surface current gradients and related features requires detailed knowledge of the physics of the imaging mechanism. Sophisticated models have been developed which account for the impact of the complete ocean wave spectrum and its spatial variations on the backscattered radar signal. Observed NRCS variations could normally be explained quite well this way.

A shortcoming of most "physical" imaging models is that they have not been optimized for the reproduction of absolute NRCS values and their dependence on parameters like the radar frequency and polarization and the wind speed. Their quantitative performance is thus somewhat questionable. On the other hand, existing calibrated physical models are quite complex and require time-consuming integrations or very detailed input parameter sets. Such models are not ideally suited for general applications.

In this paper we present an optimized composite surface model which combines some advantages in a unique way. The proposed model is based on physical principles, but it does not require complex fundamental integrations. It is well calibrated, but it requires as input only the radar frequency, polarization, incidence angle, wind speed, and the azimuthal radar look direction with respect to the wind direction. After some reasonable tuning of the equilibrium waveheight spectrum, measured mean NRCS values for a variety of parameter values can be reproduced quite well. The proposed model can thus be considered as a "physical" wind scatterometer model which can consistently be used for many applications that require NRCS calculations.

THEORY OF THE MODEL

The proposed model is a composite surface model based on a Taylor expansion of the NRCS up to second order in the surface slope. According to resonant Bragg scattering theory [1], the normalized radar backscattering cross section σ_0 of a horizontal facet at the ocean surface is given as

$$\sigma_0 = 8\pi k_e^4 \cos^4\theta_0 \left|b(\theta_0)\right|^2 \left(\Psi(\underline{k}_B) + \Psi(-\underline{k}_B)\right). \quad (1)$$

Here k_e is the electromagnetic wavenumber, and θ_0 is the nominal incidence angle of the radar. The magnitude of the Bragg wavenumber vector $\underline{k}_B$ is given as

$$k_B = 2k_e \sin\theta_0, \quad (2)$$

while its direction ϕ_B is equal to the nominal azimuthal look direction of the radar, ϕ_0. The complex scattering coefficient b in (1) depends on the polarization of the radar and on the relative dielectric constant of seawater, which varies with the electromagnetic wavelength. The waveheight spectrum Ψ is defined such that its integral yields the mean square surface elevation.

In the general case of a slightly tilted Bragg-scattering facet with slopes s_p parallel and s_n normal to the radar look direction, the relatively simple expressions (1), (2) become more complicated. Furthermore, a correction factor may be intro-

This work has been supported by the Deutsche Forschungsgemeinschaft, Grant No. Al 88/2, by the European Community, Grant Nos. MAST-0040-C and MAS2-CT94-0104, and by the Deutsche Agentur für Raumfahrtangelegenheiten, Grant Nos. 50 QS 9014 and 50 QS 9016.

0-7803-3068-4/96$5.00©1996 IEEE

duced which accounts for geometric weighting effects associated with backscattering facets which are tilted with respect to the horizontal plane or elevated from nominal sea level. The expectation value $\langle\sigma\rangle$ of the NRCS of a realistic sea surface can then be computed by taking a Taylor expansion of the local NRCS up to second order in the surface slopes and averaging over the illuminated area in space and time. In addition to the zeroth-order term of the NRCS as given by (1), some terms of second order in the surface slopes survive the averaging procedure.

Details of the Taylor expansion have already been described elsewhere [2]. In view of the limited space of this publication we want to mention only that, in contrast to most other approaches, our model includes not only geometric terms but also an explicit hydrodynamic modulation transfer function (MTF) which accounts for the asymmetric distribution of the Bragg waves along longer ocean waves [3]. Furthermore, we resolve the dependence of the hydrodynamic MTF and of some geometric terms on the wavenumber of the modulating waves by keeping some integrals over the waveheight spectrum in the resulting terms of $\langle\sigma\rangle$.

Finally, $\langle\sigma\rangle$ can be written as

$$\langle\sigma\rangle = \sigma^{(0)} + \langle\sigma^{(2)}\rangle , \tag{3}$$

where $\sigma^{(0)}$ is the undisturbed zeroth-order term, and $\langle\sigma^{(2)}\rangle$ is composed of second-order contributions which depend on the mean square surface slopes parallel (p) and normal (n) to the azimuthal radar look direction and on the mean product of the two slope components, respectively:

$$\langle\sigma^{(2)}\rangle = \langle\sigma^{pp}\rangle + \langle\sigma^{nn}\rangle + \langle\sigma^{pn}\rangle . \tag{4}$$

Inserting all components of the Taylor expansion, each of the three terms of (4) can be further decomposed into six terms which account for different modulation mechanisms:

$$\langle\sigma^{j}\rangle = \langle\sigma^{j}_{gg}\rangle + \langle\sigma^{j}_{tt}\rangle + \langle\sigma^{j}_{hh}\rangle + \langle\sigma^{j}_{gt}\rangle + \langle\sigma^{j}_{gh}\rangle + \langle\sigma^{j}_{th}\rangle , \tag{5}$$

where $j = pp$, nn, pn. Here the subscript gg denotes pure second-order "geometric" modulation, tt denotes second-order "tilt" modulation, that is, modulation of σ_0 due to variations of the surface slope and to the corresponding variations of the Bragg wave vector, and hh denotes second-order hydrodynamic modulation of the waveheight spectral density of the Bragg waves. The other three terms are cross terms resulting from the correlation of first-order geometric, tilt, and hydrodynamic modulation. All second-order terms can be written in terms of integrals of the waveheight spectrum which cover all two-dimensional wavenumbers up to a maximum wavenumber which is determined by the size of the Bragg scattering facets. We choose $1/6\ k_B$ for this limit.

Finally, we obtain one set of zeroth-order and second-order terms for each of the two Bragg wave components traveling towards and away from the radar antenna, which yields totally 38 terms.

MODEL OPTIMIZATION AND EVALUATION

Aside from electrodynamic effects, the variation of the theoretical NRCS with radar frequency, wind speed, and azimuthal radar look direction depends mainly on the form of the waveheight spectrum. The variety of parameterizations proposed by different authors suggests that the waveheight spectrum may be tuned to some extent in order to fit model results to measured NRCS values.

A reference data set for the model optimization was composed of data from four different airborne scatterometers and experimental campaigns as described in [4], [5], [6], [7], covering radar frequencies between 1.2 and 34.4 GHz, horizontal (HH) and vertical (VV) polarization, incidence angles between 30° and 52°, and wind speeds between 2 and 20 m/s. The total number of reference data points is 507.

For basic test calculations, the so-called Donelan-Banner-Jähne waveheight spectrum proposed by J. Apel [8] was used. Promising advantages of this spectrum are its well defined dependence on wavenumber and wind speed and the fact that it is continuous and differentiable for all wavenumbers. It turned out, however, that neither the wavenumber dependence nor its wind speed dependence is completely satisfactory for the model calculations: For low wind speeds like 2 m/s, all measured NRCS values were reproduced relatively well. For 14 m/s winds, the NRCS values for Bragg wavenumbers up to about 200 rad/m were clearly underestimated, while the NRCS values for higher Bragg wavenumbers were overestimated by up to one order of magnitude. Further analysis has shown that also the directional behavior of the waveheight spectrum according to [8] does not lead to the desired cross-wind / downwind differences of the NRCS.

An improved parameterization for the waveheight spectrum has been developed in an iterative procedure, trying to keep the spectral shape as close as possible to the original shape by focusing modifications on the Bragg wave region at wavenumbers between approx. 25 and 1100 rad/m.

Fig.1 shows a graph of the proposed spectrum for a wind speed of 10 m/s. Also shown is the corresponding spectrum according to [8] and the spectrum proposed by Bjerkaas and Riedel [9] which has been used often in the literature. The figure shows that the proposed optimized spectrum agrees better with the Bjerkaas-Riedel spectrum than with Apel's spectrum on which it is based. Furthermore, the differences between the latter two spectra appear to be bigger than the differences between the proposed spectrum and the Bjerkaas-Riedel spectrum. Our optimization procedure appears to have not resulted in a completely unrealistic wave spectrum.

For the wind speed dependence of the waveheight spectrum we propose a power law as known from most wind scatterometer models, with a wavenumber-dependent wind speed exponent that has a maximum value of approx. 1.6 at a wavenumber of approx. 250 rad/m. It vanishes for low wavenumbers below 1 rad/m, where the spectral shape changes with the

peak wavenumber as function of wind speed in a conventional way. For the directional spreading function we adopt the Gaussian expression from [8], but we reduce its width at high wavenumbers by approx. 1/2 in order to reproduce the measured crosswind / downwind differences of the NRCS.

It is no surprise that the dependence of the simulated NRCS on radar frequency and wind speed must be in good agreement with measurements after the optimization procedure described above. It is encouraging to see that also other properties of the experimental results are reproduced quite well without dedicated tuning activities.

As examples, Figs. 2 and 3 show simulated upwind / downwind ratios and HH / VV ratios of the NRCS, respectively, vs. the corresponding reference values. Without any tuning, the hydrodynamic MTF according to [3] leads to reasonable upwind / downwind differences of the NRCS. Also the measured HH / VV differences are well reproduced, which is not the case if only the zeroth-order term $\sigma^{(0)}$ of the NRCS is taken into account.

The proposed model in combination with the optimized wave spectrum appears to be a powerful tool, which should be well suited for wind scatterometry applications as well as for general applications like the conversion of arbitrary measured or calculated wave spectra into realistic NRCS values.

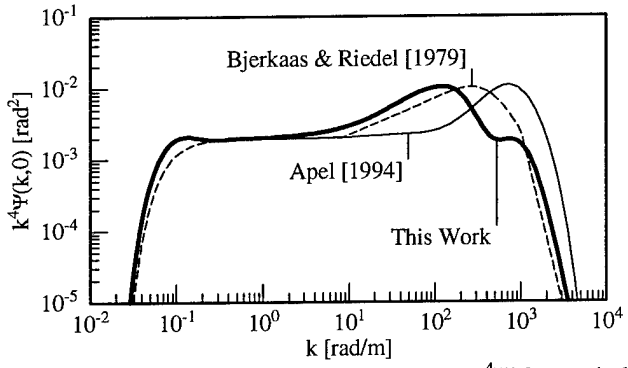


Figure 1: Cross section of curvature spectra $k^4\Psi$ for a wind speed of 10 m/s, as proposed in this work and in [8] and [9].

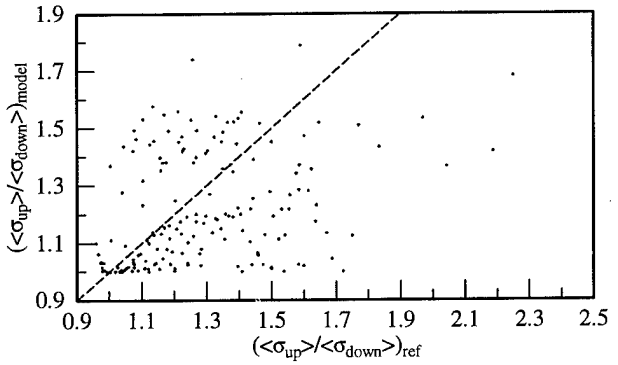


Figure 2: Simulated vs. measured upwind / downwind ratios of the NRCS (no dedicated optimization has been applied).

REFERENCES

[1] G.R. Valenzuela, "Theories for the interaction of electromagnetic and ocean waves – a review," Boundary Layer Meteorol., vol. 13, 1978, pp. 61-85.

[2] R. Romeiser, A. Schmidt, and W. Alpers, "A three-scale composite surface model for the ocean wave–radar modulation transfer function," J. Geophys. Res., vol. 99, 1994, pp. 9,785-9,801.

[3] W. Alpers and K. Hasselmann, "The two-frequency microwave technique for measuring ocean wave spectra from an airplane or satellite," Boundary Layer Meteorol., vol. 13, 1978, pp. 215-230.

[4] M.A. Donelan and W.J. Pierson, "Radar scattering and equilibrium ranges in wind-generated waves with application to scatterometry," J. Geophys. Res., vol. 92, 1987, pp. 4,971-5,029.

[5] H. Masuko, K. Okamoto, M. Shimada, and S. Niwa, "Measurement of microwave backscattering signatures of the ocean surface using X band and K_a band airborne scatterometers," J. Geophys. Res., vol. 91, 1986, pp. 13,065-13,083.

[6] P.E. Snoeij, P.J.F. Swart, and C.M.H. Unal, "Study of the response of the radar echo from the ocean surface to the surface wind vector at frequencies between 1 and 18 GHz," Final Rep., ESA Contr. 8722/89/F/FL(SC), Delft Univ. of Technology, Delft, Netherlands, 1992, 146 pp.

[7] V. Wismann, "Ocean wind vector measurements by the rotating antenna C-band scatterometer during the ERS-1 Calibration and Validation Campaign," Proc. IGARSS '92, Houston, TX, 1992, pp. 699-702.

[8] J.R. Apel, "An improved model of the ocean surface wave vector spectrum and its effects on radar backscatter," J. Geophys. Res., vol. 99, 1994, pp. 16,269-16,291.

[9] A.W. Bjerkaas and F.W. Riedel, "Proposed model for the elevation spectrum of a wind-roughened sea surface," Technical Memorandum, TG 13528, Johns Hopkins Univ., APL, Laurel, Md., 1979, 32 pp.

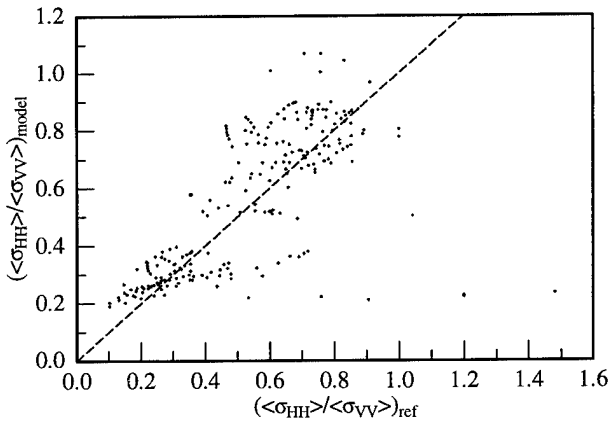


Figure 3: Simulated vs. measured HH / VV ratios of the NRCS (no dedicated optimization has been applied).

A Physically-Based Two-scale Electromagnetic Model For Backscatter From Ocean-Like Surfaces.

T. Elfouhaily and B. Chapron
IFREMER centre de Brest
DRO/OS, BP 70
29270 Plouzané France
(33).98.22.43.12 (V) or .45.33 (FAX)
Tanos.El.Fouhaily@ifremer.fr (email)

Abstract -- In this communication, we discuss the development of a two-scale radar sea scatter model including use of a directional spectrum and bispectrum of the water surface. Such a development seeks to quantify the involvement of complex surface hydrodynamic processes. Upwind-crosswind difference is retrieved from the spreading function of the short and long waves while upwind-downwind asymmetry is reproduced from the skewness function of the small features on the water surface. Hydrodynamic contribution is included to model longer wave system influences (amplitude and direction of swell systems). Thus, this two-scale model compares well against CMOD4, CMOD_IFREMER and SASS-II models for C-band VV pol., and Ku-band VV- and HH-pol., respectively.

INTRODUCTION

The Normalized Radar Cross Section (NRCS) is known to be strongly correlated with the wind field at the water surface [2][4]. To estimate wind vector from space, model functions that relate NRCS measurements to geophysical reality of the ocean surface have been empirically developed [1][4]. Nowadays, operational models for several frequency bands and polarizations exist [9][13]. Those empirical models are based upon statistical analysis and physical knowledge of the a-priori behavior of the backscatter signal. Although estimation for moderate wind speed is accurate enough from these algorithms, wind direction retrieval is still a weak point. This inconvenience occurs even for fully developed wind seas. Acknowledging the diversity of meteorological situations, global inversion schemes are even tougher. Consequently, theoretically-based developments are needed to help modelers to elaborate more accurate models that can infer wind vector for all kind of situations.

An ocean surface varies in time and space under the action of several perturbative agents. By describing the moving surface as a random process limited to a certain number of statistical moments, one simplifies, to some extent, the e.m. analysis of the interaction. In fact, one needs to make assumptions regarding the random rough surface in order to be able to find a simple closed-form solution of the e.m problem. The major assumptions always needed in e.m. modeling when one deals with random process of rough surfaces are:

- Stationarity; statistical properties of the water surface are unchanged with an arbitrary horizontal translation of the observation point.
- Ergodicity; ensemble average of several independent surface realizations is equivalent to time-average of the evolution of one random realization.
- Correlation length; foot-print dimensions are larger than surface correlation lengths of water waves. Homogeneity of the foot-print is necessary for numerical computations.
- Radius of curvature; all features on the surface are interpreted as waves with finite radius of curvature. Tangent plan can always be determined at each point of the surface in order to derive the standard Fresnel reflection and transmission coefficients.
- Far zone; the distance between the observer and the surface scattering point is large compared to surface and e.m. wave wavelengths. This allows modelers to simplify Green's function of free space.
- Rayleigh criterion; if $k_z\sigma \ll 1$ then the surface is 'smooth', otherwise it is 'rough', where k_z is the vertical component of the e.m wavenumber and σ is the surface rms height.

For a review of theories for e.m. models, the reader is invited to refer to Valenzuela [11] and Brown [3]. In this paper, we use the so-called IEM model for randomly rough dielectric surface because of its tractable ability to approximate both Kirchhoff and Bragg mechanism. The expressions of IEM field coefficients are simplified and given by means of a concise Fresnel reflection coefficients notation for both vertical and horizontal polarizations.

We demonstrate that in order to reproduce the polarization sensibility, the entire wave spectrum cannot enter the IEM solutions. IEM separately deals with long and short waves. An extension of this model is thus needed to account for short wave tilting by long waves. Traditionally, hydrodynamics enters e.m. equations via; the height or slope PDF, the wave vector spectrum or its Fourier transform the 2D wave height autocovariance. The hydrodynamic modulation of short waves that ride on top of long waves is shown to be responsible for the departure from the standard Gaussian statistics. This departure is recognized in the third order surface statistics or the skewness function. Therefore, suggested expressions for the skewness and its Fourier transform the Bispectrum of ocean-like surfaces presented to fully understand upwind-downwind asymmetry as measured by microwave instruments.

0-7803-3068-4/96$5.00©1996 IEEE

IEM SOLUTIONS

Assuming small slope approximation for perfectly conducting random surfaces, Fung and Pan [7] proposed e.m. solutions in terms of scalar tangential surface fields and found that the far-zone *backscatter* field contains two components: one is the Kirchhoff scattered field and the other is a complementary field:

$$E_p^s = E_p^k + E_p^c \tag{1}$$

where subscript (p) denotes polarization ($p=H$ for horizontal- transmit/horizontal receive and $p=V$ for vertical-transmit/vertical-receive).

Consequently, the coherent scattered power is:

$$P_p = \langle |E_p^s|^2 \rangle = \langle |E_p^k|^2 \rangle + 2\Re \langle E_p^k E_p^{c*} \rangle + \langle |E_p^c|^2 \rangle \tag{2}$$

and by using the definition of the Normalized Radar Cross Section (NRCS or sigma naught):

$$\sigma_p^0 = \lim_{R \to \infty} 4\pi R^2 (\langle |E_p^s|^2 \rangle / \langle |E_p^i|^2 \rangle) \tag{3}$$

Equation 2 and eq. 3 yield the IEM model for backscatter from dielectric random surface that one can write under integral form as follows:

$$\sigma_p^0 = \frac{k_0^2}{2} \int \left\{ |f_p|^2 \Gamma_2 + \Re(f_p F_p^*) a\Gamma_1 + \frac{|F_p|^2}{4} a\Gamma_0 \right\} \tag{4}$$

where k_0 is the e.m. wavenumber, k_z is the vertical component of k_0. The coefficient (a) is dependent on Rayleigh criterion,

$$a = \exp\left\{ -(k_z \sigma)^2 \right\} \tag{5}$$

Γ_n is the Fourier transform at $(-2\vec{k}_H)$ of the IEM generalized characteristic function C_n, i.e.;

$$\Gamma_n = \frac{1}{2\pi} \int C_n \exp\{-j2(\vec{k}_H \cdot \vec{r})\} d\vec{r} \tag{6}$$

where $\vec{k}_H$ is the horizontal component of the e.m. wavenumber vector and $\vec{r}$ is the horizontal spatial lag between two scatter points at the surface and the expression of the generalized characteristic function of vertical displacements for a Gaussian rough surface is,

$$C_n(\vec{r}) = \exp\left\{ -2^n (k_z \sigma)^2 (1 - \rho(\vec{r})) \right\} \tag{7}$$

where $\rho(\vec{r})$ is the two dimensional correlation function which is related to the vector spectrum of wind-driven waves through a 2D Fourier transform.

SIMPLIFIED FIELD COEFFICIENTS

f_p and F_p in eq. 4 are the field coefficients for Kirchhoff and complementary e.m. field, respectively. They depend on surface properties and e.m. incidence angle (θ). Expressions for these field coefficients are explicitly given in [8] for backscattering under single scattering condition and for dielectric rough surfaces. We simplify the rather complicated original field coefficient by means of the Q_coefficient based upon the Fresnel reflection coefficient for vertical polarization:

$$Q_V = \frac{1}{2}\left(1 - \frac{1}{\varepsilon_r}\right)(1 + R_V)^2 \tag{8}$$

where ε_r is the relative complex permittivity of sea water. The IEM field coefficients simplify to:

$$f_V = 2\cos(\theta)\sec^2(\theta) \cdot R_V \tag{9}$$

$$f_H = -2\cos(\theta)\sec^2(\theta) \cdot R_H \tag{10}$$

$$F_V = -8\cos(\theta)\tan^2(\theta) \cdot (R_V - Q_V) \tag{11}$$

$$F_H = 8\cos(\theta)\tan^2(\theta) \cdot R_H \tag{12}$$

where R stands for the Fresnel reflection coefficients and V, H subscripts means vertical and horizontal polarizations, respectively.

HYDRODYNAMIC MODULATION

The second and third terms in eq. 4 are the complementary solutions to the Kirchhoff approximation that takes care of the polarization sensitivity. One can easily notice that those complementary terms are weighted by the negative exponential of the squared Rayleigh criterion (eq. 5) which vanishes for large values of the rms height. Thus, in order to preserve polarization sensitivity, only small scale waves (ripples) could enter the IEM formulation. Therefore, IEM is not a two-scale model but a hybrid model which has limits (1) in the Kirchhoff solution for high frequency and low incidence angles and (2) in the small perturbation approximation for high incidence angles and small rms heights. Therefore, short and long waves exclusively enter the IEM model. When long waves are introduced short waves are not and vice versa.

Wright [14] was the first investigator to formulate a composite-surface scattering model for the ocean. The sea is assumed to be formed by an infinite number of slightly rough patches and the backscatter power is an average of backscatter from single rough patches over the distribution of slopes of longer waves. More precisely, this average is a convolution of the NRCS of small rough patches by slope probability distribution of longer waves. One can use this idea to extend IEM model over both long and short waves without neglecting the hydrodynamic modulation of short waves by the longer ones.

To account for hydrodynamic modulation, the IEM generalized characteristic function of vertical displacements (eq. 4) should be split into two characteristic functions. The first one is the long wave characteristic functions as one could

easily get by a simple Fourier transform of the Gaussian slope PDF. While the second is the short wave generalized characteristic function same as in (eq. 4). An additional term that accounts for third order statistics namely the surface skewness functions is then introduced when this latter contribution is averaged over the longer waves. The skewness can be interpreted as advection effects of the short waves riding on top the longer ones. A typical normalized skewness function in polar coordinate should read

$$S = \cos(\varphi) \cdot \left(\frac{r}{s_0}\right)^3 \cdot \exp\left\{-\alpha\left(\frac{r}{s_0}\right)^\gamma\right\} \quad (13)$$

where α, γ are arbitrary constants and s_0 is the skewness parameter defined as a "correlation length" of the short wave advection by long waves. We defined it as the ratio of the small wave rms height over the long wave mean-square slopes.

$$s_0 = \frac{1}{2} \cdot \frac{rms(Short)}{mss(Long)} \quad (14)$$

Typical value of those constants for sea surface waves under moderate surface wind speeds are $\gamma \sim 1$, $\alpha \sim 1$ and $s_0 = 1cm$. The 2D Fourier transform of the skewness function or the well-known Bispectrum ($B(k, \phi)$) has a simple closed-form for any α when γ only equals 2.

$$B = -js_0^2 \frac{ks_0}{(2\alpha)^4}\left\{8\alpha - (ks_0)^2\right\}\exp\left\{-\frac{(ks_0)^2}{4\alpha}\right\}\cos(\phi) \quad (15)$$

This development slightly differs from the one initiated by Chen and its collaborators [5][6]. Moreover, introduction of skewness as proposed above is comparable with the so-called 3-scale e.m. model [10].

DISCUSSION AND CONCLUSIONS

In order to compare this two-scale model and its hydrodynamic properties with empirical models; CMOD_IFREMER C-band VV pol. [9], CMOD4 C-band VV pol. [11], and Ku-band VV- and HH-pol. [13], one can perform a Fourier expansion of eq. 4 as follows,

$$\sigma_p^0 = a_0 + a_1\cos(\varphi) + a_2\cos(2\varphi) + \ldots \quad (16)$$

This decomposition permits a simpler physical interpretation of the involvement of each Fourier harmonic; a_0 is the omni-direction response of the surface which is dominated by the omni-directional spectral; a_1 reproduce the upwind/downwind asymmetry by means of the surface skewness function; a_2 is responsible for most of the upwind/crosswind anisotropy in which the spreading of short waves is highly involved. The variability of the Fourier harmonics from our model with incidence angle θ for both frequency bands and polarizations can be summarized as follows:

- a_0 is a monotonic decreasing positive function.
- a_1 is a bimodal function that has a positive maximum at $\theta > 30^o$. And a negative minimum at a certain angle $\theta < 20^o$. Therefore, a_1 crosses zero at angles between 20 and 30 degrees. So, every radar instrument that observes ocean surface at incidence angle close to 25^o cannot differentiate the upwind from the downwind direction. In contrast, the upwind/downwind is always captured for $\theta < 20^o$ and $\theta > 30^o$.
- a_2 is a unimodal positive function that has a single maximum at a low incidence angle ($\theta < 20^o$). This coefficient is responsible for most of the anisotropy between upwind and crosswind directions.

So, the development presented above includes hydrodynamic contribution through third order statistical description coming from short wave modulation over the slope of longer waves. According to eq. 13 such a contribution will directly affect a_1 but also a_0 and a_2 at second order. More attention should then be focused on properly model tilt-hydrodynamic modulation to better retrieve wind direction from empirical algorithms.

REFERENCES

[1] Bentamy A., Y. Quilfen, P. Queffeulou and A. Cavanié. Calibration of the ERS-1 Scatterometer C-band model. IFREMER Technical Report, BP. 70, 29280 Plouzané. DRO/OS 94.0.1., January 1994.

[2] Brown, G. S., H.R. Stanley, and N.A. Roy, The wind speed measurement capability of spaceborne radar altimeters, IEEE J. of Oceanic Engrg., OE-6, No. 2, pp. 59-63, 1981.

[3] Brown, G. S., A comparison of approximate theories for scattering from rough surfaces, Wave Motion, 7, pp. 195-205, 1985.

[4] Brown, R.A., On satellite sctterometer capabilities in air-sea interaction, JGR, 91, C2, pp. 2221-2232, Feb 15, 1986.

[5] Chen, K. S., A. K. Fung, and D.E. Weissman, A backscattering model for ocean surface, IEEE Trans. Geosci. and Remothe Sendsing, Vol. 30, No. 4, pp 838-850, 1992,

[6] Chen, K. S., A. K. Fung and A. Faouzi, An empirical bispectrum model for sea surface scattering, IEEE Geo. Remote Sens., Vol. 31, No. 4, 820-835, 1993.

[7] Fung A.K., and G.W. Pan, A scattering model for perfectly conducting random surfaces, I. Model development, Int. J. Remote Sensing, Vol. 8, No. 11, 1579-1593, 1987.

[8] Fung A. K., Microwave scattering and emission models and their applications, ARTECH House, Norwood MA, 1994.

[9] Quilfen Y. ERS-1 off-line wind scatterometer products. ERS-SCAT/IOA/DOS-01 IFREMER.

[10] Romeiser, R., A. Schmidt, and W. Alpers, A three-scale composite surface model for the ocean wave-radar modulation tranfer function, J. Geophys. Res., 99, 9785-9803, 1994.

[11] Stoffenlen A. and A. Anderson, The ECMWF contribution to the characterisation, interpretation, calibration and validation of ERS-1 scatterometer backscatter xeasurements and winds, and their use in numerical weather prediction models, ESA contract report, 9097/90/NL/BI, Feb. 1995.

[12] Valenzuela, G.R., Theories for the interaction of electromagnetic and oceanic waves- A review, Boundary Layer Met., 13, pp. 61-85, 1978.

[13] Wentz F.J., S. Peterheruch and L.A. Thomas, A model for ocean radar cross section at 14.6 GHz, J. of Geophys. Res., 89, C3, 3689-3704, May 20, 1984.

[14] Wright, J.W., A new model for sea clutter. IEEE Transactions on Antennas and Propagation, AP-16, 217-223, 1968.

An Application of the Two-Scale Model from the Point of View of the Small-Slope Approximation to Radar Observations from the Ocean

***E.A. Skirta, A.N. Keane**
***NOAA/ERL/Environmental Technology Laboratory**
325 Broadway, Boulder, CO 80303-3328
Tel./Fax: 303-497-7732/303-497-3577, E-mail: eskirta@etl.noaa.gov
University of Colorado/CIRES & NOAA/ERL/Environmental Technology Laboratory
325 Broadway, Boulder, CO 80303-3328
Tel./Fax: 303-497-7424/303-497-6978; E-mail: akeane@etl.noaa.gov

Abstract --The angular and polarization dependencies of the radar backscatter from the ocean at low grazing angles at X-band are discussed. Analysis of recent backscattering data, obtained as a result of small grazing-angle radar observations, indicates that the Bragg mechanism alone cannot explain all the peculiarities of the experimental results in the presence of surface stratification and hydrodynamical modulation. The two-scale model, from the point of view of the small-slope approximation (SSA), takes into account the effects of modulation of the scattering cross section due to small-scale roughness, caused by the local slopes of a large-scale undulating surface. The two-dimensional JONSWAP spectrum has been used to calculate the cross sections derived. The results obtained are compared with San Clemente Ocean Probing Experiment (SCOPE) measurements and some Coastal Ocean Probing Experiment (COPE) results.

INTRODUCTION

At moderate incidence angles the scattering characteristics of the ocean surface can be largely explained by a composite or a two-scale model. The difference between the results of theoretical calculations and measurements increases as grazing incidence is approached. Recent field measurements were conducted to identify the fundamental scattering mechanisms from the ocean at low incidence angles [1-3]. On the other hand, low grazing angles are of significant practical and theoretical interest, and the corresponding problem has been addressed many times (e.g., [3, 4]). The results observed are in disagreement with composite surface theory, which cannot explain horizontally polarized radar cross sections at low grazing angles from wind-roughened water surfaces.

X-BAND RADAR BACKSCATTER FROM THE OCEAN AT LOW GRAZING ANGLES

In addition to the features of low grazing-angle dependence of normalized radar cross sections (NRCS) and Doppler velocities presented in [1] from SCOPE radar observation, several other results concerning grazing angle dependence on wind speed, wind direction, and stability of air-sea surface conditions, were reported recently [5].

SCOPE data selected for analysis allow the closest time comparison of horizontal (HH) and vertical (VV) polarizations for the broadest range of environmental conditions. Both HH and VV cross sections were computed from the linear channel to increase the sensitivity of the measurements. The analysis demonstrates several peculiarities of radar signals collected at light winds of 3-5 m/s, unstable stratification, and other contributing environmental conditions.

Two examples of radar images, obtained as a result of COPE observations made in 1995 by NOAA/ERL/ETL are presented in Fig. 1 (a, b) at the angles of depression $\alpha=2^0$ and $\alpha=2.9^0$, respectively, with NRCS (VV) on the left, and NRCS (HH) on the right of each figure. The data was collected on September 30, 1995 at 19:58 hrs. EST; wind direction is 310^0; wind speed is 4.5 m/s under stable surface conditions. Surface manifestation of hydrodynamic modulation in the presence of internal waves and swell is seen both at VV and HH polarizations. NRCS at HH (dashed line) and VV (solid line) along the range of propagation R are shown in Fig. 2 at $\alpha=3.7^0$. These figures indicate that hydrodynamic-electromagnetic interactions should be included in a theoretical scattering model to study the impact of these effects on sea surface response.

THE SCATTERING MODEL

Most of the previous studies of microwave backscattering from the ocean surface have been made to obtain relationships between the microwave backscattered cross sections and the parameter of the wind-wave field. Though those models have been successful in accounting for microwave backscattering from the ocean surface at middle incidence, the physical mechanism of backscattering from wind-wave surfaces still is not well understood. One of the reasons for it is that the two-scale model, widely used for radar data interpretations, assumes the large- and small-scale roughnesses to be statistically independent. However, the fact that real surfaces have a continuous spectrum of roughness scales, with the consequence that the partition between short scales and large scales has to be

This document has been generated as part of a joint NOAA/DOD - Advanced Sensors Applications Program.
0-7803-3068-4/96$5.00©1996 IEEE

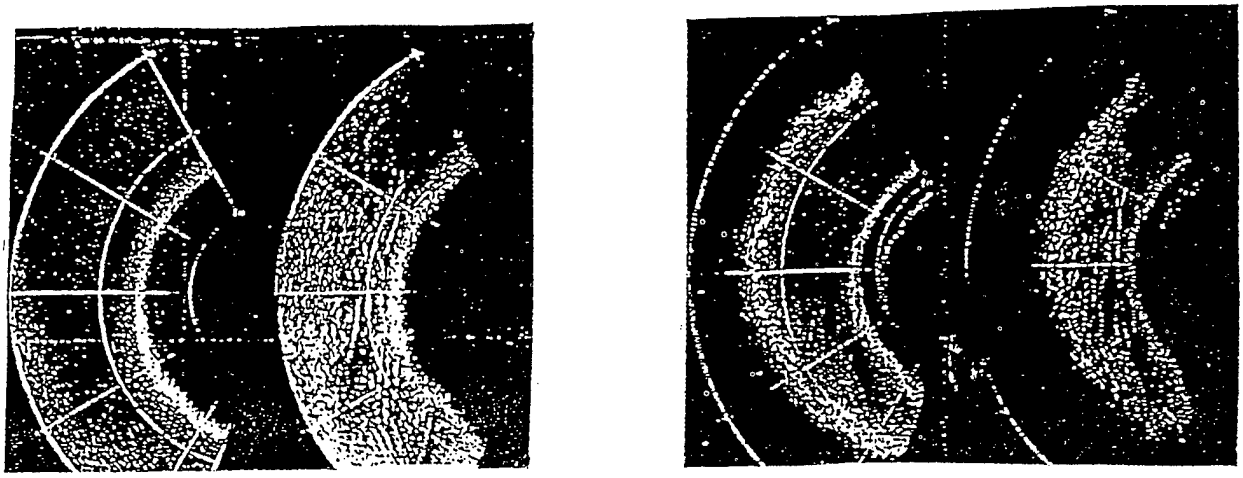


Fig. 1. Radar images of NRCS at the angles of depression 2^0 (on the left) and 2.9^0 (on the right) of the figure.

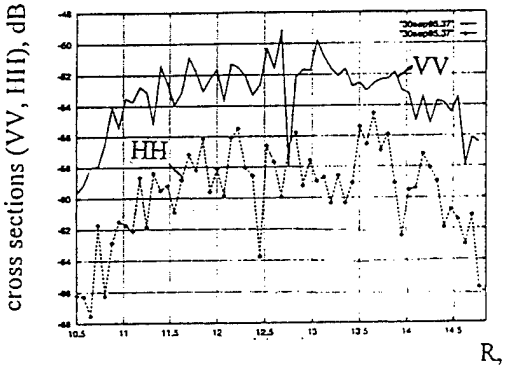


Fig. 2. NRCS along the range of observation at $\alpha=3.7^0$.

introduced, cannot be neglected.

The general expressions for a scattering cross section following from the small-slope approximation (SSA) [6] have been simplified recently for the case of two-scale roughness [7]. The results demonstrate that SSA takes into account the effect of modulation of the scattering cross section due to small-scale roughness by the local slopes of a large-scale undulating surface.

SEA SURFACE DESCRIPTION

The main problem in numerical modeling of electromagnetic wave scattering from a wind roughened surface is the choice of the wave spectrum and the definition of the splitting frequency on the basis of which the roughness parameters are calculated. Numerical calculations were carried out for the JONSWAP model of the surface spectrum [8], represented in the form of the product of a wave number spectrum and a frequency-dependent spreading function $Q(k,\varphi)$:

$$W(k,\varphi) = (\alpha/2)k^{-4}\exp\left\{-1.25(k/k_m)^{-2} + \ln\gamma \times \exp\left[-\left(\sqrt{k/k_m}-1\right)^2/2a^2\right]\right\} Q(k,\varphi), \qquad (1)$$

$$Q(k,\varphi) = \left[\Gamma(1+p/2)/\pi^{1/2}\Gamma((1+p)/2)\right]\cos^{2p}(\varphi-\varphi_w),$$

where $\alpha=0.0081$; $a=0.07$, $k<k_m$ and $a=0.09$, $k>k_m$; $k_m=\omega_m^2/g$ is the wave number corresponding to the peak frequency ω_m of the spectrum; g is the acceleration due to gravity; γ is the peak enhancement factor; φ_w is the angle determining wave propagation direction, with $|\varphi-\varphi_w| \le \pi/2$;

$$p = \begin{cases} 0.46(k/k_m)^{-1.25} p_m, & k \ge k_m \\ 0.46(k/k_m)^{2.5} p_m, & k \le k_m, \end{cases}$$

$p_m = 11.5\,(U/C_m)^{-2.5}$; U denotes the wind speed at a height of 19.5 m; $C_m=(g/k_m)^{1/2}$. The friction velocity U_* is introduced [9].

The variances in slope as a function of U_* as well as a function of wind speed U_{10} were calculated. The theoretical slope variances from the present scattering model versus wind speed for along-wind and cross-wind directions are integrated over the wave numbers corresponding to a transition from gravity short waves to capillary waves ($0.5 \le \Lambda \le 2.5$ cm, $2.5 \le k \le 12.5$ cm^{-1}). The calculated slope variances are about twice as large as those inferred from the model of Cox and Munk. One of the examples of the two-dimensional curvature spectrum (Fig. 3) demonstrates the azimuth dependence in the gravity-capillary and capillary regimes at $u=4$ m/s in the presence of the swell ($\Lambda_1=150$ m). The short gravity waves are the main source of capillary waves via the process of cresting and breaking.

In Fig. 4 the cross sections emphasizing the grazing-angle dependence were calculated with the following parameters: $\gamma=1$, the dielectric permittivity of sea water $\varepsilon_2 = 52.44+i39.47$ at $f=10$ GHz, $T=20^0$, S=35 ppt; $U_*=12$ cm/s, HH - solid line, VV - dashed line; azimuth direction is downwind. These results

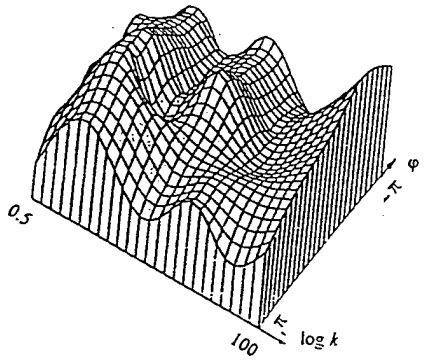


Fig. 3. Curvature spectrum in the presence of the swell (Λ_1=150 m).

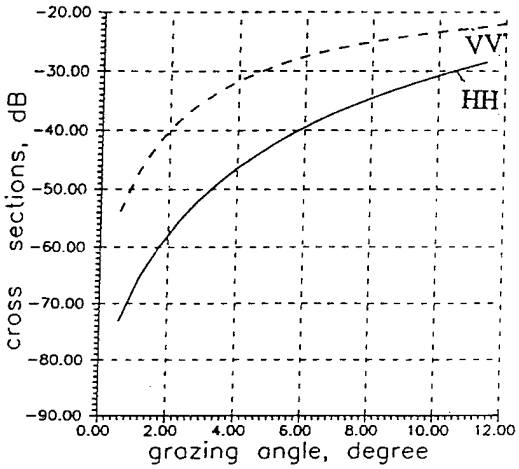


Fig. 4. Cross sections (VV, HH) as a function of grazing angle.

and others, calculated at higher U_* of 17-23 cm/s (U_0 = 5-6.5m/s) produce quantitative coincidences with SCOPE and COPE measurements collected under light winds due to spatial anisotropy of small-scale waves taken into account, and the mean square slopes obtained. Within the limits of applicability of the two-scale model the division of the spectrum into large- and small-scale parts is controlled by the limits of the relations for the roughness parameters, and the characteristic radius of the curvature of undulating surface (if taken into account). The Rayleigh parameter $(kh)^2$ is chosen to be less or equal 0.1, where h^2 is the variance of the elevations of the small-scale waves (ripples).

At the low winds of 2-3 m/s, NRCS calculated and observed from SCOPE, decrease sharply and are sensitive to sea-surface temperature as well as to the air-sea temperature difference, that was varied from -1° C to -(5-6)° C for some sets of data.

CONCLUSIONS

Some improvement in the agreement between theoretical cross sections and X-band radar observations is achieved by using the two-scale model from the point of view of the SSA. The expression of the modified small-scale spectrum demonstrates a correlation between small- and large-scale roughness. The results of the calculations allow us to determine that the influence of the partitioning of the spectrum turns out to be less significant, than the contribution of the high-frequency part of the spectrum for stable surface conditions. In radar probing a wind sea surface with one general direction of wave propagation (single-mode wind waves) the azimuth variations of NRCS are explained primarily by the spatial anisotropy of the ripples for along-wind and cross-wind directions, which can be related to the conditions of their formation on large-scale surfaces. At small grazing angles under the wind speed of 3-4.5 m/s, the Bragg scattering mechanism in the presence of unstable stratification and a two-mode wind-wave system (wind and swell) is being carried out more in detail to test a portion of the spectrum probed by radar.

ACKNOWLEDGMENTS

The authors are grateful to Alexander G. Voronovich for valuable discussions and helpful comments.

REFERENCES

[1] R.A. Kropfli and S.F. Clifford, "The San Clemente Ocean Probing Experiment: A study of air-sea interaction with remote and In Situ sensors," Proc. IGARSS Symp., Pasadena, Calif., pp. 2407-2409, 1994.

[2] P.H.Y. Lee et al, "X band microwave backscattering from the ocean waves," J. Geophys. Res., vol. 100, pp. 2591-2611, 1995.

[3] D.B. Trizna, "Statistics of low grazing angle radar sea scatter for moderate and fully developed ocean waves," IEEE Trans. Antenna Propagat., vol. 39, pp. 1681-1690, 1991.

[4] L.B. Wetzel, "Electromagnetic scattering from the sea at low grazing angles," in Surface Waves and Fluxes, vol. II. G.L. Geernaert and J .Plant, Eds., The Netherlands: Kluwer Academic Publishers, pp. 109-171, 1990.

[5] A.N. Keane, E.A. Skirta, "X-band polarization dependency of radar backscatter from the ocean at low grazing angles," The National Radio Science Meeting, Boulder, CO, p. 124, 1996.

[6] A.G. Voronovich, "Small slope approximation for electromagnetic wave scattering at a rough interface of two dielectric half-spaces," Waves in Random Media, 4, pp. 337-367, 1994.

[7] A.G. Voronovich, "A two scale model from the point of view of the small slope approximation," in press.

[8] D.E. Hasselmann, M. Dunkel, and J.A. Ewing, "Directional wave spectra observed during JONSWAP, 1973," J. Phys. Oceanogr., 10, pp. 1264-1280, 1980.

[9] J. Wu, "Effects of atmospheric stability on ocean ripples: a comparison between optical and microwave measurements," J. Geophys. Res., 96, pp. 7265-7269, 1991.

A Comparison of Wind Wave Spectra Used in Ocean Remote Sensing Modeling.

T. Elfouhaily and B. Chapron
IFREMER centre de Brest
DRO/OS, BP 70
29270 Plouzané France
(33).98.22.43.12 (V) or .45.33 (FAX)
Tanos.El.Fouhaily@ifremer.fr (e-mail)

Abstract -- Nowadays, remote sensing techniques from space become routine application to get valuable information on ocean surface processes. Nevertheless, knowledge about electromagnetic mechanisms depending upon water surface representation are needed to properly interpret those information. Consequently, a reliable ocean surface description in terms of wind wave vector spectrum is necessary to correctly model hydrodynamic properties near the water surface. This two-dimensional spectrum should account for long waves as well as short waves. As well known, capillary-gravity waves play a major role in microwave scattering. Thus, a reliable interpretation of microwave measurements is constrained to accurate modeling of the capillary-gravity portion of the wind wave directional spectrum. Although gravity waves have been accurately measured and properly modeled in the past, a great effort is still needed in both measurements and modeling of short waves. In spite of the rarity of direct short wave measurements, one still can find in the literature some proposed ocean wave spectra. Comparison of those spectra is reported, along with remarks that may guide investigators who are concerned with models elaboration of geophysical processes at the air-water interface.

INTRODUCTION

A reliable statistical description of wind-generated surface waves is of crucial interest to fully understand perpetual motions and exchanges at the air-sea interface. Satellite surveillance, engineering design of marine vessels, wave forecasting, atmosphere-ocean interactions, are basic field applications of directional wind wave spectra. Among statistical description, spectral formulation is generally privileged.

Spectral representation of the wind driven surface waves separates nowadays scientists into two major schools of thoughts: the first school challenges the (-4) spectral slope and its wind independent saturation range pioneered by Phillips, in 1958; e.g., Toba [20], Kitaigorodskii et al. [12], and finally Phillips [15]. The second school is formed by ones who still use Phillips' spectral form (k-4); e.g., Banner [3], and Apel [1]. However, for most of these authors the spectral equilibrium range may also be wind speed dependent.

Spectral shape of long waves has been correctly measured and modeled in the past. While, in contrast, behavior of small waves (~centimeter wavelength) is still under refinement. Sparsity of short-wave measurements is mainly caused by the difficulty to measure slope and curvature of the water surface while measuring elevation of waves still relatively much easier. To measure the displacement spatial spectrum, Barber [4] developed a technique using array of vertical probes. To date, slope measurements have been made either by observing sun glitter over the water surface Cox and Munk [8] (C&M hereinafter) or by new techniques based upon advanced technologies such as scanning laser probes and stereophotography ([19][11]).

We will select, from the myriad of wind-wave spectra offered by the literature, spectra that describe both short and long waves in a large range of wind speeds. In general, spectra are divided into two categories. The physically based spectra and the empirically based spectra. In the first category, we will present the composite Bjerkaas and Riedel [5] model, and the well known spectrum of Donelan and Pierson [10]. In the second category, we will present the empirical Rodriguez et al. [18] spectrum and the one derived by Apel [1]. Those names will be abbreviated hereinafter by, B&R, D&P, R+, and A. respectively. A brief description of all those spectra is given.

REVIEW OF WAVE SPECTRA

1- Bjerkaas and Riedel spectrum

The Bjerkaas and Riedel spectrum [5] (B&R) is widely used in the literature especially for its ability to satisfy most of available surface displacement measurements based on open ocean data for low frequencies and wind-wave tank data for high frequencies. This spectrum and its subsequent versions are defined in four wavenumber ranges. The first spectral range near the spectral peak of gravity waves corresponds to the Pierson-Moskowitz spectrum. Gravity and short gravity waves are from Pierson [16] while small gravity to gravity-capillary waves are from Kitaigorodskii [13] and Leykin-Rosenberg [14]. Finally, the capillary wave range is modeled by means of the slope spectra measured by Cox [7]. B&R have gathered all these chunks of spectra to form their "mosaic" spectrum by adjusting different arbitrary constants to match curves at the disconnection limits. The major drawback of this

0-7803-3068-4/96$5.00©1996 IEEE

spectrum is the great number of tuning parameters needed to connect together spectra which are themselves already fitted to uncertain data. In addition, only close to fully-developed sea conditions can be reproduced with these spectra. Fig.1 shows the omni-directional curvature spectrum of B&R for 10 m/s wind speed. The gravity-capillary secondary peak is located at 1.7 cm. Fig.2 compares inferred and measured mean square slopes (mss) for clean and slick surfaces from B&R and C&M, respectively.

2- Donelan and Pierson Spectrum.

In this advanced model [10] (D&P), the equilibrium range spectrum is divided into two parts. A gravity wave part which is derived from the JONSWAP formulation [9], and a short wave part where wind input is balanced by local dissipation: viscous damping and breaking losses. In this latter part, wave-wave interactions are thus assumed to be negligible. Fig.1 shows the omni-directional curvature spectrum of D&P for 10 m/s wind speed. Fig.2 compares inferred and measured mean square slopes for clean and slick surfaces from D&P and C&M, respectively.

3- Rodriguez et al. spectrum

To assess the effect of hydrodynamic modulation of small waves by large waves Rodriguez et al. [18] (R+) developed an idealized omni-directional full wavenumber spectrum that respects, on one hand, the k-2.5 spectral decay with a linear increase of the spectral strength with wind speed, and on the other hand, the total mean square slope. This kind of approach aims to retain key features of the ocean surface observed at nadir incidence, since altimeter returns are dominated by the slopes of the surface filtered up to certain wavelength dependent on electromagnetic frequency. Fig.1 shows the omni-directional curvature spectrum of R+ for 10 m/s wind speed. The gravity-capillary secondary peak is located at 4 cm. Fig.2 compares inferred and measured mean square slopes for clean and slick surfaces from R+ and C&M, respectively.

4- Apel spectrum

Apel [1] (A.) built up a full spectral model to be the bare for electromagnetic computations. This analytical 'improved' spectrum is supposed to be valid across the entire range of ocean waves. It gathers together spectral branches already modeled by many investigators and integrates new laboratory data especially in the gravity-capillary wave region. The author called his spectrum the "Donelan-Banner-Jähne" spectrum because of the spreading function made up to match the one from Donelan, the omni-directional spectral slope to be (-4) from Banner, and finally the saturation spectral level of the secondary gravity-capillary peak at 750 rd/m from laboratory measurement of Jähne and colleagues (e.g. [11]). Fig.1 shows the omni-directional curvature spectrum of A. for 10 m/s wind speed. The gravity-capillary secondary peak is located at 0.8 cm. Fig.2 compares inferred and measured mean square slopes for clean and slick surfaces from A. and

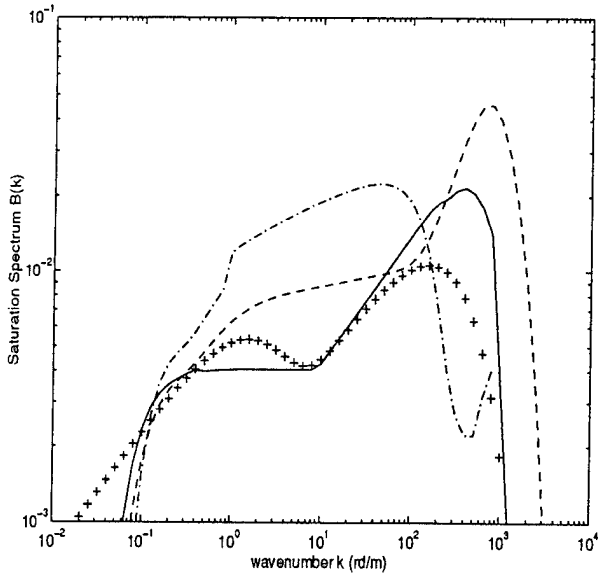


Figure 1: shows comparison between four widely used curvature spectra. The wind speed is 10 m/s. B&R (solid), D&P (dashed-dotted), R+ (crosses), and A. (dashed) have gravity-capillary waves at 1.7 cm, 11 cm, 4 cm, 0.8 cm, respectively.

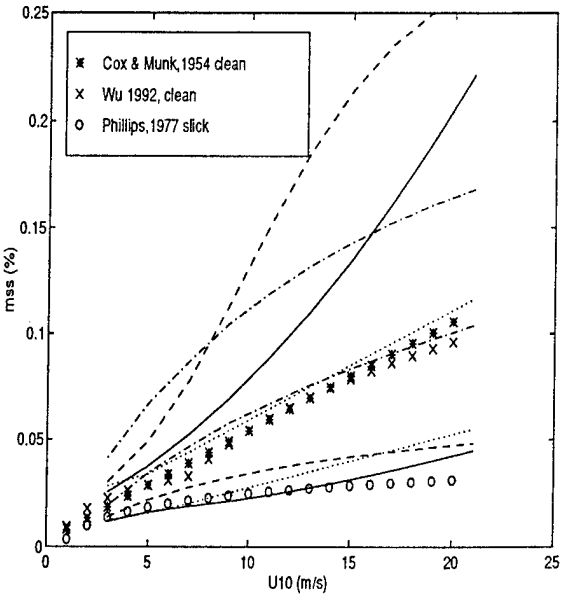


Figure 2: depicts measured mean square slopes from C&M for both clean and slick surfaces versus inferred mss from the four spectra. B&R (solid), D&P (dashed-doted), R+ (dotted), and A. (Dashed).

C&M, respectively.

DISCUSSION

The shape of surface wave spectra is still under investigations due to the absence of a unified universal form. Fig.1 illustrates how much the spectra presented above differ. Huge differences exist between these spectra and unfortunately, there are still some other ones in the literature that exhibit similar divergence.

Weaknesses of each spectrum presented above can be stated as follows: (1) B&R is dependent on too many arbitrary constants of segment matching and level adjustments which make its use very limited. (2) Although D&P seems to be well constructed for the long waves, short wave branch is questionable. As a matter of fact, D&P overestimates mean square slopes by a factor of 1.7 compared to C&M optical measurements (Fig.2). The total mean-square slope is highly sensitive to the shape of the spectral tail. Shemdin and Hwang [19] showed discrepancies with the D&P spectral tail by measuring slope frequency spectra up to 300 Hz with a laser-optical sensor. They found that D&P has an early sharp spectral cutoff at frequencies higher than 8Hz which was not substantiated by their TOWARD and MARSEN observations. (3) R+ spectrum is the most simplified one. His author built it up to simplify altimetry EM bias calculations. A slope variance criteria is of crucial importance to ensure that scattering models reproduce altimeter returns. Although, R+ satisfies the total slope variance, it doesn't for partial integration of the slope spectrum. In fact, altimeter returns have been shown to be inversely proportional to the filtered and not the total variance [6]. Moreover, this spectrum is not adequate to fetch effect analyses on the water surface since it roughly describes the spectrum around the spectral peak. (4) Finally, A. is a relatively simple algebraic form that uses the long wave spectrum of Donelan, data and spectral shape of Banner and measurements for gravity-capillary waves of Jähne and colleagues. Gravity-capillary secondary peak was misplaced by A. to lie around 0.8 cm rather than 1.7 cm as Apel should have concluded from Jähne and colleagues optical data. These gravity-capillary waves have a minimum phase speed and correspond to rapid growth.

CONCLUSION

The presented above spectra are widely used in the literature. As discussed, most of the integrated variables criteria are not satisfied by those spectra. Among others, the total mean-square slope exceed the Plant's limit $2 \times (0.04 \pm 0.02)$. Based on this review, we developed a "unified directional spectrum for long and short wind-driven waves" (Tech. Rep. DROS/OS/96-2, pp 1-30) which takes advantage of all reliable information from the former spectra and new measurements in the high frequency part of the wavenumber domain. In particular, wave-induced stress computation is shown to be more reliable from such a spectrum, which tend to prove that mss parameter is of crucial importance.

REFERENCES

[1] Apel J.R., An improved model of the ocean surface wave vector spectrum and its effects on radar backscatter, J. Of Geophysical Research/Oceans, Vol. 99, 16.269-16.291, 1994.

[2] Banner, M. L., I. S. F. Jones, and J. C. Trinder, Wavenumber spectra of short gravity waves, J. Fluid Mech., 198, 321-344, 1989.

[3] Banner, M.L., Equilibrium spectra of wind waves, J. Phys. Oceanog., 20, 966-984, 1990.

[4] Barber, N. F., The directional resolving power of an array of wave recorders. Ocean wave spectra, Englewood Cliffs, N. J.: prentice-Hall Inc., pp. 137-150, 1963.

[5] Bjerkaas, A. W., and F. W. Riedel, Proposed model for the elevation spectrum of a wind-roughened sea surface, Rep. APL-TG-1328-I-31, 31 pp., Appl. Phys. Lab., Johns Hopkins Univ., Laurel, Md., 1979.

[6] Brown, G. S., Quasi-specular scattering from the air-sea interface, Surface Waves and Fluxes, Edt. Gernaert and Plant editors, Vol. II, 1-40, 1990.

[7] Cox, C., Measurements of slopes of high frequency waves, J. Mar. Res., 16, 199-225, 1958.

[8] Cox C.S. and W.H. Munk. Statistics of the sea surface derived from sun glitter. J. Mar. Res., 13, 198-227, 1954.

[9] Donelan M.A., J. Hamilton and W.H. Hui. Directional spectra of wind generated waves. Philos. Trans. R. Soc. London, Ser. A, 315, 509-562, 1985.

[10] Donelan, M. A., and W. J. P. Pierson, Radar scattering and equilibrium ranges in wind-generated waves with application to scatterometry, J. Geophys. Res., 92, 4971-5029, 1987.

[11] Jähne B. and K. S. Riemer,1990, Two-dimensional wave number spectra of small-scale water surface waves, J. of Geophys. Res., Vol. 95, No. C7, pages 11,531-11,546, July 15, 1990.

[12] Kitaigorodskii, S. A., V. P. Krasitskii, and M.M. Zaslavskii, On Phillips' theory of equilibrium range in the spectra of wind-generated gravity waves, J. Phys. Ocean., 5, 410-420, 1975.

[13] Kitaigorodskii, S. A., On the theory of the equilibrium range in the spectrum of wind-generated gravity waves, J. Phys. Ocean., 13, 816-827,1983.

[14] Leykin I.A. and A.D. Rosenberg, Sea-tower measurements of wind-wave spectra in the Caspian Sea, J. Phys. Ocean., 14(1), 168-176, 1984.

[15] Phillips O.M. , Spectral and Statistical properties of the equilibrium range in the wind-generated gravity waves. J. of Fluid Mech., 156, 505-531, 1985.

[16] Pierson, W.J., The theory and applications of ocean wave measuring systems at and below the sea surface, on the land, from aircraft and from spacecraft, NASA Contract Rep., CR-2646, N76-17775, 1976.

[17] Pierson W.J., and R.A. Stacy, The elevation slope, and curvature spectra of a wind roughened sea surface, NASA Contract Rep., CR-2646, 126 pp., 1973.

[18] Rodriguez E., Y. Kim and J.M. Martin, The effect of small-wave modulation on the electromagnetic bias. J. of Geophysical Research, Vol. 97, No. C2,2379-2389, February 15,1992.

[19] Shemdin, H., and P. A. Hwang, Comparison of measured and predicted sea surface spectra of short waves, J. of Geophys. Res., 93, C11, 13.883-13.890, Nov 15, 1988.

[20] Toba Y., Local balance in the air-sea boundary processes, III, on the spectrum of wind waves, J. Ocean. Soc. Japan, 29, 209-225, 1973.

Evolution of Surface Waves of Finite Amplitude in Field of Inhomogeneous Current[1]

Bakhanov,V.V., O.N.Kemarskaya
Institution of Applied Physics, Russian Academy of Science
46 Uljanov Str. Nizhny Novgorod 603600
RUSSIA
T: 7.8312.384356 F: 7.8312.365976 EMail: bakh@hydro.nnov.su
V.P.Pozdnyakova, I.A.Okomel'kova, I.A.Shereshevsky
Institution for Physics of Microstructure
Nizhny Novgorod GSP-105, 603600
RUSSIA
T: 7.8312.675732 F: 7.8312.675553 EMail: ilya@ipm.sci-nnov.ru

ABSTRACT

The evolution of gravity surface waves of finite amplitude on a localized two-dimensional inhomogeneous current is investigated. A model equation describing the variation of surface wave amplitude has been derived and solved numerically. The time evolution of a two-dimensional pattern of surface waves amplitude, when the inhomogeneous current arises at a certain moment of time is investigated. It is shown, that even a relatively weak inhomogeneous current modifies appreciably the regime of surface waves long-wave instability develop. With increasing time the maximum amplitudes of surface waves at first increase, and then run into constant values, but the surface anomaly structure still continues to grow in complexity. The dependence of surface wave field evolution on the amplitude, wave-length and propagation direction of surface waves is investigated.

INTRODUCTION

Much attention is given recently to research of nonlinear gravitat surface waves evolution [1]. At the same time the transformation of surface wave in a field of non-uniform currents is usually considered in linear approximation for surface waves [2]. This work deals with transformation of nonlinear surface waves in a field of various inhomogeneous currents on the basis of a model equation.

FORMULATION OF A PROBLEM. BASIC EQUATIONS.

The evolution of nonlinear surface waves propagating against a current $-V\vec{x}_0$ on weak perturbation of the current $\vec{u}$ is considered. It is assumed, that characteristic scales of $\vec{u}$ non-uniformity (vertical and horizontal near a surface) are much larger, than the scattered surface wave length. Then $\vec{u}$ is considered as function only of horizontal coordinates and it is possible to write dispersion relation [1,3]:

$$\left[n-\vec{k}\left(-V\vec{x}_0+\vec{u}(x,y,t)\right)\right]^2 = gk\left(1+k^2a^2\right) \qquad (1),$$

where n, $\vec{k}$ and a -frequency, wave vector and amplitude of surface wave. We shall consider evolution of the most effective scattering by inhomogeneous flow surface waves, whose group speed is close to V, and wave vector, accordingly, to $\vec{k} = g/\left(4V^2\right)\vec{x}_0 = k_*\vec{x}_0$. Assuming $|\vec{u}| << V$, we expand (1) in a power series of small perturbation of the wave vector $\tilde{\vec{k}}$ in the inhomogeneous flow $\vec{k} = k_*\vec{x}_0 + \tilde{\vec{k}}$:

$$\tilde{n} = 1 + v_x(x,y,t) - p_x^{\,2}/4 + p_y^{\,2}/2 + \tilde{a}^2/4 \qquad (2),$$

where $\tilde{n} = n/(k_*V)$, $v_x = u_x/V$, $p_x = \tilde{k}_x/k_*$, $p_y = \tilde{k}_y/k_*$, $\tilde{a} = 2ak_*$. It was assumed when obtaining (2), that $k_*^{\,2}a^2 \sim p_x^{\,2}, p_y^{\,2}$. Using (2) one can write down the model equation for complex amplitude of surface waves field A :

$$4i\frac{\partial A}{\partial \tilde{t}} + \frac{\partial^2 A}{\partial \tilde{x}^2} - 2\frac{\partial^2 A}{\partial \tilde{y}^2} + |A|^2 A + 4v_x\left(\tilde{x},\tilde{y},\tilde{t}\right)A = 0 \qquad (3),$$

where $\tilde{t} = k_*Vt$, $\tilde{x} = k_*x$, $\tilde{y} = k_*y$. The behaviour of nonlinear surface waves envelope on the basis of a equation (3) without last term related to perturbation of current, is in detail considered in work [1]. In it, in particular, diagram of the homogeneous solution stability in two dimensions is indicated, which in many respects determines character of surface waves transformation on non-uniform current.

RESULTS OF NUMERICAL CALCULATIONS.

[1] The work was suppoted by Russian Fund of Fundamental Investigation (code No 96-05-65128)

0-7803-3068-4/96$5.00©1996 IEEE

The time evolution of the initially homogeneous wave field when the current perturbation v_x arises at a moment of time $t = 0$ is investigated in given work in framework (3). First we shall consider one-dimensional inhomogeneous flow $v_x = v_x(\tilde{x})$, and then - two-dimensonal inhomogeneous localized flow $v_x = v_x(\tilde{x}, \tilde{y})$.

One-dimensional perturbation of current.

The first case corresponds to transformation of surface waves in a field of an internal wave, speed of propagation of which equals V and dimensionless amplitude - $\max(|v_x|)$. We shall write v_x in the following form $v_x = v_0 \cos(q\tilde{x})$, where q - dimensionless wave number of an internal wave. A large difference of scales is typycal for internal waves and surface waves being in synchronism with them. Dimensionless length of internal wave in calculations was equal to 4096. Weak internal waves with dimensionless amplitude equal to 0.01 were selected. At the initial stage of surface anomaly development transformation of linear and nonlinear surface waves is similar (so at $A_0 = |A|(\tilde{t} = 0) = 0.1$ up to $\tilde{t} \approx 4000$). At large $\tilde{t}$ for nonlinear surface waves in the dependence $|A|$ on $\tilde{x}$ at the background of large-scale variability (with characteristic scale of internal wavelength) there is reasonably small-scale variability (Fig.1), which at $\tilde{t} > 6000$ (for $A_0 = 0.1$) determines the kind $|A|(\tilde{x})$. In this case value $K = (\max(|A|) - \min(|A|)) / A_0$ quickly grows. The instability of surface waves envelope, causing the small-scale variability $|A|(\tilde{x})$ in the absence of a internal wave is not developed at such values of $\tilde{t}$. As growth of instability of surface waves envelope on scales of internal waves is small, the action of nonlinearity of surface waves does not result in significant amplification of modulation $|A|$ with scale of internal waves. However the transformation of surface waves in a field of an internal one results in development of smaller-scale instability. The time of output $|A|(\tilde{x})$ on a stage of small-scale variability is sharply reduced at the increase A_0. So at $A_0 = 0.2$ it yields 1200.

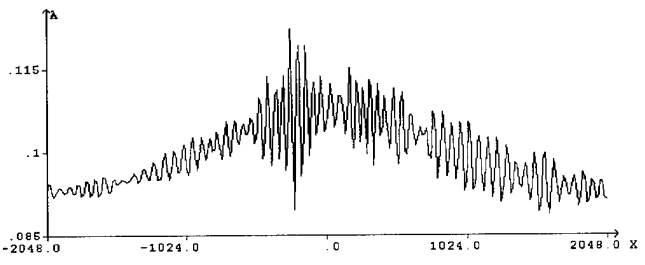


Fig.1. The dependence of $|A|$ from $\tilde{x}$ in field of internal wave at $A_0 = 0.1, q = 2\pi / 4096$, $v_0 = 0.01$, $\tilde{t} = 5000$.

We shall note, that occurrence of small-scale dependence $|A|(\tilde{x})$ for linear surface waves at $\tilde{t} > 16000$ is also observed, which is due to non-isochronious movement of surface wave packets captured by internal wave [4]. Here K reaches values essentially large than for nonlinear surface waves at all values of $\tilde{t}$. That will lead first of all to occurrence of scales $|A|(\tilde{x})$ smaller than lengths of an internal wave: non-isochronious movement of captured surface wave packets or the development of instability of surface waves envelope in a field of an internal wave, depends on a ratio of parameters v_0 and A_0.

Two-dimensional perturbation of current.

In the two-dimensional non-uniform case flow on a surface from dipole, oriented along the axis x and located at a depth h was chosen as current perturbation:

$$v_x = c \frac{2\tilde{x}^2 - \tilde{y}^2 - \tilde{h}^2}{\left(\tilde{x}^2 + \tilde{y}^2 + \tilde{h}^2\right)^{5/2}}$$

where c is the dipole power, $\tilde{h} = k_* h$. The following values are taken in calculations: $c = 10$, $h = 10$, the calculations were executed in a square with the sizes 1024 x1024 of dimensionless units $\tilde{x}$ and $\tilde{y}$. The behaviour of linear surface waves in a field of similar perturbation of current is considered in [5]. At a the initial stage a spatial structure of fields $|A|(\tilde{x}, \tilde{y})$ for nonlinear surface waves is the same as in the linear case. For $p_x(\tilde{t} = 0) = p_x^0 = p_y(\tilde{t} = 0) = p_y^0 = 0$ there are prefferatle directions, making an angle the axis x $\pm 55^0$. The speed of increase K for linear surface waves at $\tilde{t} > 120$ decreases and at $\tilde{t} > 600$ K is established at a level 0.9. The speed of increase K for the nonlinear surface waves is conserved up to the large values $\tilde{t}$. So at $A_0 = 1.7$ the speed of increase K is saved up to $\tilde{t} = 350$ and K by this becomes value 1.7. In the latter case at $\tilde{t} > 600$ a picture of space distribution becomes complicated $|A|$ (Fig.2) and fast increase of value K is observed, which at $\tilde{t} > 800$ is established at a level 2.5 Speed of expansion of the region, where there is surface anomaly, also grows. Up to this moment of time it was practically constant and close to speed of expansion of the surface anomaly region for linear surface waves. Probably, modulation $|A|$ which occurc as a result of transformation on non-uniform current results in fast development of Benjamin-Feir instability of surface wave

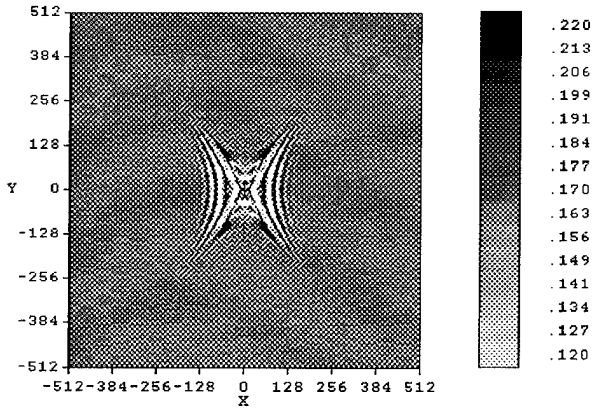


Fig.2. Spatial distibution of $|A|$ at $c=10$, $h=10$, $A_0=1.7$, $\tilde{t}=900$.

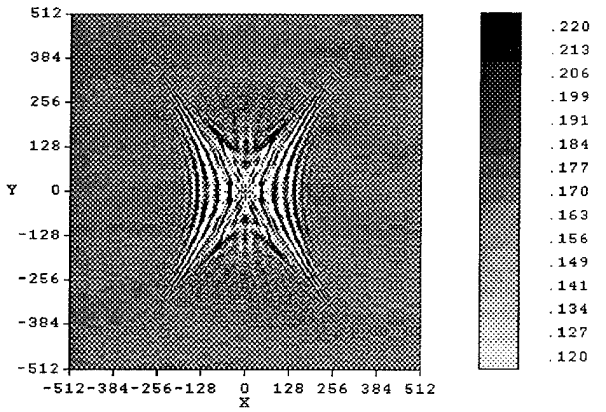


Fig.3. Spatial distibution of $|A|$ at $c=10$, $h=10$, $A_0=1.7$, $\tilde{t}=1500$.

envelope. In this case the increase of variability $|A|$ scales with time of scales ofon a non-uniform flow provides their reaching the area of maximum growth. The field $|A|$ for case of nonlinear surface waves becomes more complicated with time (fig. 3). The non-uniformity scales of the fields A decrease, and higher derivative on $\tilde{x}$ and $\tilde{y}$ should be taken into account in (3) for correct calculations.

The time of development of instability of surface wave envelope and occurrence of significant contrasts in surface anomaly decreases for increased A_0 ,so at $A_0=0.2$ it is less than 400.

Essential reduction of $\max(K)$ at the deviation of p_x^0 and p_y^0 from zero is characteristic for transformation of linear surface waves. Calculations show for nonlinear surface waves at the reasonably large values A_0 that difference p_x^0 and p_y^0 from zero within the applicability limits of (3) ($p_x, p_y << 1$) results in some change of a structure of fields $|A|(\tilde{x},\tilde{y})$, but the value of $\max(K)$ and sizes of the surface anomaly area are weakly dependet on it.

REFERENCES

[1] H.C.Yuen, and B.M.Lake, "Nonlinear dynamics of deep-water gravity waves," Advances in Appl. Mech., vol.22, pp.67-229, 1982.

[2] D.H.Peregrine, and I.G.Jonsson, "Interaction of Waves and Currents," Report No83-6, Coastal Engineering Research Center, USA, 1983, 88p.

[3] A.Ya.Basovich, and V.I.Talanov, "On the transformation of short surfsce waves on non-uniform currents," Izv. AN SSSR, FAO, vol.13, No.7, pp.766-773, 1977.

[4] A.Ya.Basovich, "Transformation of the surface waves spectrum due to the action of an internal wave," Izv. AN SSSR, FAO, vol.15, No.6, pp.448-452, 1979.

[5] V.V.Bakhanov, V.I.Kazakov, O.N.Kemarskaya, I.A.Shereshevsky, and A.Ya. Basovich, "Effect of two-dimensional inhomogeneous flow on surface waves," 1995 International Geoscience and Remote Sensing Simposium Proceedings, vol.1, pp.340-342.

Study of the Second Order Approximation of the Velocity Bunching in the SAR Imaging Process Using the Bispectrum.

J.M. Le Caillec, R. Garello
Télécom Bretagne, Dpt ITI, BP 832
29285 Brest Cedex, France

B. Chapron
IFREMER, BP 70, Plouzané, France

ABSTRACT

In this paper, we comment some simulations of the SAR imaging process obtained by using, firstly the complete nonlinear transform (i.e. the velocity bunching), and secondly its second order approximation (i.e. a second order Volterra model), in order to study the quadratic nonlinear interaction strength and localization and to compare with results obtained on ERS-1 images.

1. INTRODUCTION

The first part of this paper is devoted to a brief background on nonlinearity detection with the bispectrum. The second part develops the Second Order Volterra Model (SOVM) for the Velocity Bunching. Some results about the quadratic nonlinearity detection over the exact Velocity Bunching and over its closed version are related in the third part and general conclusions are drawn in the last section.

2. BACKGROUND ON NONLINEARITIES DETECTION USING THE BISPECTRUM

The third order spectrum or bispectrum, which can be defined as the mathematical DFT coefficients expectation,

$$B(k_1,k_2) = E\{\tilde{X}(k_1).\tilde{X}(k_2).\tilde{X}^*(k_1+k_2)\} \quad (1)$$

allows the quadratic nonlinearities detection. For instance, if we consider the following signal

$$\begin{aligned} X(i) &= A_1.\cos(k_1.i+\varphi_1) + A_2.\cos(k_2.i+\varphi_2) \\ &+ A_3.\cos((k_1+k_2).i+\varphi_1+\varphi_2) \\ &+ B.\cos((k_1+k_2).i+\varphi_3) + N(i) \end{aligned} \quad (2)$$

where $\varphi_i|_{i=1,2,3}$ are random phases and $N(i)$ a gaussian noise, only the bispectrum of the part in phase coupling (i.e. the first three sinusoids) is non null, whereas the bispectrum of the non phase coupled signal (the first two sinusoids and the last one) is null. The phase coupling detection is relevant for the SOVM model which is divided into two parallel paths, a linear one and a quadratic one as described on Fig 1. The SOVM output signal is composed of waves in phase coupling provided by each path (see [1] and [4]). The energy part in phase coupling can be quantified by using the bicoherence defined by (see [1])

$$P(k_1,k_2) = \frac{B(k_1,k_2)}{\sqrt{S(k_1).S(k_2).S(k_1+k_2)}} \quad (3)$$

For instance, the bicoherence $P(k_1,k_2)$ is equal, for the signal of (2), to $\frac{A_3}{\sqrt{(A_3)^2+B^2}}$. However the information extraction from the bicoherence (which is a 4D structure for 2D signals) is rather difficult. The cross variable bicoherence table introduced in [5] and defined by

$$T_{RA}(k_x^1,k_y^1) = \sum_{k_x^2}\sum_{k_y^2} P^2(k_x^1,k_y^1,k_x^2,k_y^2) \quad (4)$$

can be seen, for a given wavelength $k = (k_x,k_y)$, as the ratio between the nonlinear "interaction" energy part (provided by all original spectrum interactions). This statistical tool has been demonstrated to be very useful for SOVM quadratic nonlinearity detection [4]. In order to understand results already obtained on ERS-1 images we have firtsly derived the VB second order approximation.

3. SECOND ORDER VOLTERRA MODELING.

The DFT coefficients of an ocean SAR image can be expressed as a function of the RAR modulation [2][3]:

$$\tilde{X}^{sar}(k) = \sum_A (1+X^{rar}(i)).e^{-j.\beta.v(i).k_x}.e^{-j.k.i} \quad (5)$$

i describing a predefined sampled area of the sea surface A, $\beta = R/V$, and $v(i)$ the wave orbital velocity. The RAR modulation and the displacement are linearly derived from the sea surface DFT coefficients. The Volterra

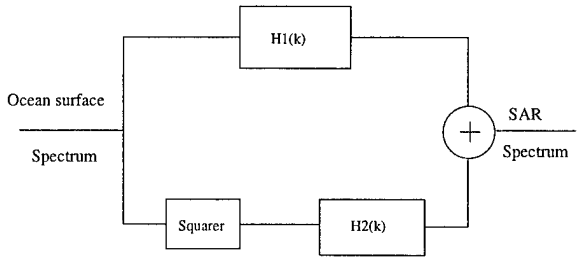


Figure 1: Second Order Volterra Model

0-7803-3068-4/96$5.00©1996 IEEE

series decomposition assumes to expend the exponential of (5) over the Taylor series.

$$e^{-jk_x\beta v(i)} = \sum_{n=0}^{+\infty} \frac{(-j.\beta v(i).k_x)^n}{n!} \quad (6)$$

The second term of the expansion is equal to :

$$i_2^{dd}(i,k_x) = \frac{(jk_x\beta)^2}{2!}.d^2(i) = \frac{(j.k_x\beta)^2}{2!}.\sum_{k_1}\sum_{k_2}\tilde{v}_{k_1}.\tilde{v}_{k_2}.e^{j.(k_1+k_2).i} \quad (7)$$

Where $\tilde{v}_{k_i}$ denotes the DFT coefficients of the orbital velocity, and $\sum_{k_1}$ is 2D summation over the spectrum support. For a finite bandwidth spectrum (as we can approximate the sea surface spectrum, and consequently the displacement spectrum), i.e. $\epsilon(k_1) \simeq 0$ if $k_1 \notin S$, it is well-known that "constructive" interactions are centered around twice the central peak frequency of the original spectrum and "destructive" interactions are located around the continuous component (see [4]). In this case, when the quadratic part and the linear one are separated in frequency, we use the term quadratic spectrum and linear spectrum. Moreover the second order term is not the only one to strongly contribute to the quadratic interactions. As a matter of fact, by considering the fourth order interactions.

$$i_4^{dd}(i,k_x) = \frac{(jk_x\beta)^4}{4!}.v^4(i) = \frac{(jk_x\beta)^4}{4!}.\sum_{k_1}\sum_{k_2}\sum_{k_3}\sum_{k_4} \tilde{v}_{k_1}.\tilde{v}_{k_2}.\tilde{v}_{k_3}.\tilde{v}_{k_4}.e^{j.(k_1+k_2+k_3+k_4).i} \quad (8)$$

and if we assume $k_3 = -k_4$ then the interations are:

$$i_4^{dd}(i,k_x) = \frac{1}{2}\frac{(jk_x\beta)^4}{4!}.\binom{4}{3}|Vs|^2\sum_{k_1}\sum_{k_2}.\tilde{v}_{k_1}.\tilde{v}_{k_2}.e^{j.(k_1+k_2).i} \quad (9)$$

with $\sum_{k_3}|d(k_3)|^2 = V_s^2$. Let note that $\beta^2 E\{V_s^2\} = \rho_{dd}^2(0)$ where $\rho_{dd}(x)$ is the autocorrelation function of the displacement. $\binom{4}{3}$ takes into account the number of possible combinations. The fourth order interactions are, in this case, "degenerated" into quadratic interactions. All even order interactions contribute to the quadratic interactions and it is easy to verify that:

$$i_{2p}^{dd}(i,k_x) = \frac{1}{2^{p-1}}\frac{(jk_x\beta)^{2.p}}{2p!}.\binom{2p}{p-1}.(Vs)^{2p} \sum_{k_1}\sum_{k_2}\tilde{v}_{k_1}.\tilde{v}_{k_2}.e^{j.(k_1+k_2).i} \quad (10)$$

The quadratic interaction DFT coefficient part, for a given wavelength k, due only to the velocity interactions is equal to:

$$\tilde{X}_{dd}^{sar}(k) = g(k_x,V_s)\sum_{k_1}D(k_1).D(k-k_1).\tilde{\epsilon}_{k_1}.\tilde{\epsilon}_{k-k_1} \quad (11)$$

Where $\tilde{\epsilon}_k$ is the DFT coefficients of the ocean surface, $D(k)$ the linear transfer function between the sea surface and the orbital velocity, with:

$$g(k_x,V_s) = \sum_{p=1}^{+\infty}\frac{(jk_x\beta)^{2p}}{(p+1)!(p-1)!}\frac{V_s^{2p-2}}{2^{p-1}} \quad (12)$$

The velocity interactions are not the only ones because as it can be seen in (5), quadratic interactions can occur between the RAR modulation and the velocity. For instance the quadratic term is:

$$i_2^{rd}(i,k_x) = -jk_x\beta v(i).X^{rar}(i) = -jk_x\beta\sum_{k_1}\sum_{k_2}\tilde{d}_{k_1}.\tilde{X}_{k_2}^{rar} \quad (13)$$

As for the velocity-velocity interactions, higher order nonlinearities interfere in the quadratic nonlinearity

$$i_4^{rd}(i,k_x) = \frac{(-jk_x\beta)^3}{3!}.v^3(i) = \frac{(-jk_x\beta)^3}{3!}.\sum_{k_1}\sum_{k_2}\sum_{k_3}\sum_{k_4} \tilde{v}_{k_1}.\tilde{v}_{k_2}.\tilde{v}_{k_3}.\tilde{X}_{k_4}^{rar}.e^{j.(k_1+k_2+k_3+k_4).i} \quad (14)$$

Two cases must be distinguished. Either $-k_4 = k_i$ or $k_j = k_i$ with $i,j = (1,2,3)$, i.e either there is a RAR modulation-velocity interaction or a velocity-velocity interaction. So by summation over all the nonlinearities we obtain that the Fourier coefficient part due to this interaction is :

$$\tilde{X}_{Rd}^{sar}(k) = h_1(k_x,V_s,RV_s)\sum_{k_1}D(k_1).D(k-k_1).\tilde{\epsilon}_{k_1}.\tilde{\epsilon}_{k-k_1} + h_2(k_x,V_s)\sum_{k_1}D(k_1).M^{rar}(k-k_1).\tilde{\epsilon}_{k_1}.\tilde{\epsilon}_{k-k_1} \quad (15)$$

with

$$h_1(k_x,V_s,RV_s) = \sum_{p=1}^{+\infty}\frac{(jk_x\beta)^{2p-1}}{2^{p-2}}\frac{V_s^{2p-4}}{(p+1)!(p-2)!}Re\{RV_s\} \quad (16)$$

$$h_2(k_x,V_s) = \sum_{p=1}^{+\infty}\frac{(jk_x\beta)^{2p-1}}{2^{p-2}}\frac{V_s^{2p-2}}{(p+1)!(p-1)!} \quad (17)$$

With $\sum_{k_3}\tilde{v}(k_3).\tilde{M}^{rar}(k_3) = RV_s^2$ and $\beta E\{RV_s^2\} = \rho_{Rd}^2(0)$ where $\rho_{Rd}(x)$ is the cross correlation between the RAR modulation and the SAR displacenent.

An important remark is that these "modulations" are high pass filters and consequently, nonlinearities are strongly attenuated near the range axis. Moreover as all spectrum components, they are also attenuated, for components far from this range axis, due to the azimuth smearing. The SOVM "linear" part is in fact the more difficult to simulate, because two competitive phenomena are involved for the linear spectrum components. Higher order nonlinearities infer in the transfer function between the sea spectrum and the SAR spectrum linear part, but also, aliasing due to "constructive" interactions, the frequency of which being greater than twice the frequency sampling can be located over the "linear" spectrum components. We found that a good approximation is to identify the SOVM linear part to the classical modulations (RAR and Velocity Bunching). In order to study such a model we have made some SAR simulations and SOVM simulations to compare them.

4. SECOND ORDER VOLTERRA MODEL VALIDATION.

We have first simulated a sea surface using the JONSWAP spectrum and therefore a SAR image as described in [6].

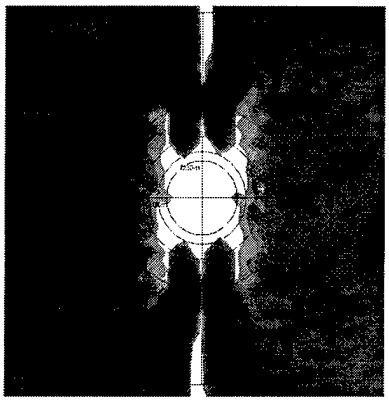


Figure 2: Velocity Bunghing Bicoherence Table



Figure 3: SOVM Bicoherence Table

In our simulations, the significant wave height H_s, the wind speed and the wave propagation angle have been varied whereas the peak spectrum wavelength has been fixed to 200m. The spectrum and bispectrum have been estimated by averaging over sixty four independent signal realizations. The fitting of the SOVM spectrum and the SAR one is rather good for low H_s, but the SOVM linear part spectrum is also well fitted (we found also that in every case the velocity-velocity interactions are stronger than the RAR modulation-displacement interactions). For intermediate H_s the SOVM provides better results than the linear part, and both are unfitted for high H_s (due to the higher order nonlinearities). The SOVM and VB bicoherence tables are very similar (an example of these tables is given for the complete VB, the SOVM and the SOVM linear part in Fig 2-4), proving that the quadratic nonlinearities can be detected in the process of the ocean surface and are not completely blurred by higher order nonlinearities, for realistic H_s. As already said, the quadratic nonlinearities are pass-band filtered and an unexpected result is that "destructive" interactions are located in the band when the waves travel in the range direction, providing higher nonlinearity rate in this case than when the waves travel in other directions. For instance the high nonlinearity rates in Fig 2-4 (i.e. the darker parts) are located in the range direction (these

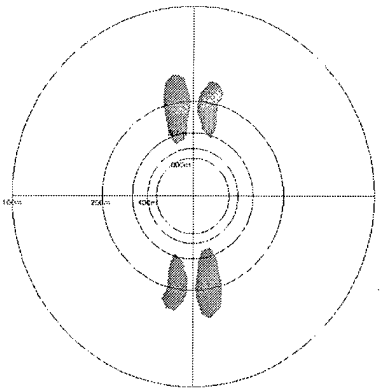


Figure 4: Linear Part Bicoherence Table

wave having quadratically interacted) and in the azimuth direction where the waves have been generated by interactions (as expected, even if the linear part can provide a rather good spectrum approximation, it can not give so good results for the bispectrum).

5. CONCLUSIONS

As seen in the previous section, the highest nonlinearity rates occur for waves propagating in the range direction. For other wave propagation directions, "constructive" interactions have been removed by the azimuth smearing and the "destructive" interactions have been widely attenuated by the high pass filtering inherent to the quadratic interactions. However if the H_s becomes too high, the destructive interactions become sufficiently strong to remain, meanwhile the original spectrum is filtered by the azimuth smearing. Some other phenomena must be also taken into account for a complete study such as aliasing and speckel noise effects which will be included in the next set of simulations. Moreover, and it is for us the prime point, the results of these simulations agree with the ones obtained on ERS-1 images [4] where we have verified that the highest nonlinearity rates were for waves traveling in the range direction.

References:

[1] Nikias C.L., A.P. Petropulu, Higher-Order Spectra Analysis, A nonlinear signal processing framework, Prentice Hall.

[2] Hasselmann K.,S. Hasselmann, "On the non linear Mapping of an Ocean Wave Spectrum Into a Synthetic Aperture Radar Image Spectrum and its Inversion", Journal of Geophysical Research Vol 96, No C6, pp 10 713-10 729 June 1991.

[3] Alpers W.R.,D.B. Ross, C.L. Rufenach "On the Detectability of Ocean Surface Wave by Real and Synthetic Aperture Radar" Journal of Geophysical Research Vol 86, No C7, pp 6481-6468 July 1981

[4] Le Caillec J.M., R. Garello, B. Chapron, "2D Bispectral Estimates from Ocean SAR Images", unpublished

[5] Le Caillec J.M., R. Garello, B. Chapron, "Detection of Nonlinearity in Sea Surface SAR Imaging Process Using Bispectrum Method Estimation", ICASSP 95, Detroit May 95

[6] Bruning C.,W.R. Alpers,K. Hasselmann,"Monte-Carlo simulation of the nonlinear imaging of a two dimensional surface wave field by a synthetic aperture radar", International Journal of Remote Sensing Vol 11 No 10 pp 1695-1727 1990

BISTATIC SEA CLUTTER : SIMULATIONS AND MEASUREMENTS

A.KHENCHAF, F.DAOUT, Y.HURTAUD* and J.SAILLARD
Lab. SEI/EP 63 CNRS - IRESTE, University of Nantes, La Chantrerie, CP 3003,
44087, Nantes Cedex 03, FRANCE,Tel (33)40 68 30 43 ,Fax (33)40 68 32 33, Email akenchaf@ireste.fr
* Centre d'Electronique de L'ARmement, Division GEOS/SOP -35170 Bruz France

Abstract

The problem of electromagnetic scattering from a randomly rough surface is analyzed using the Kirchhoff approximation *(stationnary phase, scalar approximation)*, the small perturbation model and the two-scale model. We show that physical and geometrical optics approximation can be used for rough sea surface. A small perturbation model gives a satisfactory solution. Unfortunately, it only applies to smooth sea surface. Therefore, these methods have been shown to be limited in their regions of validity [1][2].

Comparisons between the numerical calculations and the models are made for various surface rms height and correlation length both normalized to the incident wave number (*denoted by kσ and kL, respectively*). The two-scale model proposed in this paper is the method trying to conciliate the two previous aspects. One application is made in the ocean surface case. A set of experimental data, describing simultaneous bistatic radar cross section and forward radar cross section measurements of sea clutter taken with a moderately high resolution X-band scatterometer system operating near grazing incidence for both horizontal and vertical polarizations over a range of low grazing bistatic angles, is used but not presented in this paper to examine the applicability of bistatic scattering models.

INTRODUCTION

Accurate prediction of the performance of a radar system depends upon accurate models of not only the target and radar, but also the background signals. For a surface search radar operating over the ocean, the predominant background signal interfering with the target return is often sea clutter. Although descriptions of both amplitude distribution shapes and temporal behaviour of sea return are required for a complete model, the most generally useful statistic in a sea clutter model is the average cross section per unit area.

For a bistatic link over the sea surface, it is necessary to combat multipath fading caused by sea reflection that can disrupt an electromagnetic system near the sea surface, understanding the effect of the scattering by this natural surface is an absolute necessity. The rough surface leads to an unpolarized wave. The crosspolarized coefficients are produced by the diffuse scatter of the sea surface when illuminated.

0-7803-3068-4/96$5.00©1996 IEEE

These coefficients are calculated from the incoherent summation of echoes projected by each surface element. In order to describe the scattering of an electromagnetic wave, an appropriate theory has to be chosen. Existing theories may be classified in three main groups : * Kirchhoff model [4], * Small perturbation model [5], [6], [7], * Two-scale model.

Using Kirchhoff and small perturbation model the effect of the salinity and temperature on the electromagnetic field scattered by sea surface is studied in [3].

The geometry of the reflection process is shown in Fig 1.

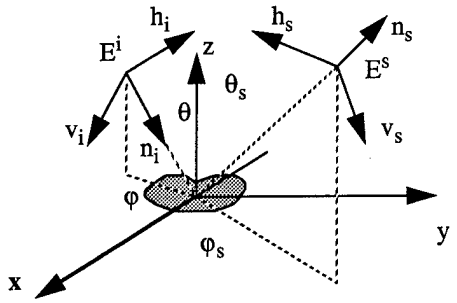


Fig 1. Geometry of the surface scattering problem

II- KIRCHHOFF METHOD

The vector formulation of the Kirchhoff method [4] is based upon the vector second Green's theorem, which states that the scattered field at any point within a source-free region bounded by a closed surface can be expressed in terms of the tangential fields on the surface. A mathematical statement of this fact is formulated by Stratton and Chu and modified for the far zone by Silver [5]. For process with Gaussian correlation coefficient, the validity conditions using the wavelength λ, the surface correlation length L and the rms surface height can be written as [1] [2]:

$$\frac{L}{\lambda} > \frac{3}{\pi} \cong 0{,}955 \qquad \text{and} \qquad \frac{L}{\lambda} > \sqrt{\frac{\sigma}{\lambda}\sqrt{\frac{8}{\pi}}} \cong 1{,}26\sqrt{\frac{\sigma}{\lambda}} \qquad (1)$$

Under this assumption it is still difficult to evaluate the scattered field analytically. Two additional simplifying approximations have appeared in the literature : The stationary phase approximation and the scalar approximation.

II-1 Stationary phase (Geometrical Optics)

After using the stationary phase approximation [6] to simplify the scattered field expression, the scattering coefficient can be written as

$$\sigma_{pq}^{s} = \frac{\pi (kq|U_{pq}|)^2}{q_z^4} Prob\{Z_x, Z_y\} \qquad (2)$$

$Prob\{Z_x, Z_y\}$ is the probability density function of the surface slopes, $q_x=k(\sin(\theta_s)\cos(\phi_s)-\sin(\theta)\cos(\phi))$, $Z_x=-q_x/q_z$, $q_y=k(\sin(\theta_s)\sin(\phi_s)-\sin(\theta)\sin(\phi))$, $Zy=-q_y/q_z$, $q_z=k(\cos(\theta_s)+\cos(\theta))$, $q^2=q_x^2+q_y^2+q_z^2$

U_{pq} are polarization-dependent coefficients.

When the surface height is a Gaussian distributed with zero mean, the validity conditions can be written as [1] [2] :

$$\frac{L}{\lambda} > \frac{\sqrt{\sqrt{6\pi}}}{\pi}\sqrt{k\sigma}, \quad \left(\frac{L}{\lambda} > \frac{3}{\pi}\right) \text{ and } \left(\frac{\sigma}{\lambda} > \frac{\sqrt{10}}{2\pi}\frac{1}{|\cos\theta_s + \cos\theta|}\right) \qquad (3)$$

II-2 Scalar approximation (*Physical Optics*)

For the GO model, we assumed that the variance of the surface height was large compared to the incident wave length. This restriction is not required with the PO model. Instead, we assume that the rms surface slope is small. Under this approximation the scattering coefficient can be written as [5], [4] : $\sigma^s_{pq}=\sigma^s_{pqc}+\sigma^s_{pqn}+\sigma^s_{pqs}$

When the surface height is Gaussian distribution, the conditions of validity are [1] [2]

$$\frac{L}{\lambda} > \frac{3}{\pi} \cong 0{,}95 \qquad \text{and} \qquad \frac{L}{\lambda} > \frac{\sqrt{2}}{0{,}25}\frac{\sigma}{\lambda} \cong 5{,}66\frac{\sigma}{\lambda} \qquad (4)$$

III - SMALL PERTURBATION MODEL

In the previous section the Kirchhoff method was applied to surface with horizontal roughness scale and average radius of curvature larger than the electromagnetic wavelength. When both the surface standard deviation and correlation length are smaller than the surface standard deviation and correlation length are smaller than the wavelength, one standard approach that we considered is the small perturbation method. The bistatic scattering coefficient for either a horizontally or vertically polarized incident wave from slightly irregular surface within the incident medium is

$$\sigma_{pq}^{s} = 8\left|k^2\sigma\cos\theta\cos\theta_s\right|^2 |\alpha_{pq}|^2 W(k_x - k\sin\theta, k_y) \qquad (5)$$

Where W is the two-dimensional wave-number spectral density of the surface roughness *(ocean)*, α_{pq}: polarization-dependent coefficients. For the Gaussian case the validity conditions are given [1] [2] :

$$\frac{\sigma}{\lambda} < \frac{0{,}3}{2\pi} \cong 0{,}048 \qquad \text{and} \qquad \frac{L}{\lambda} > \frac{\sqrt{2}}{0{,}3}\frac{\sigma}{\lambda} \cong 4{,}71\frac{c}{\lambda} \qquad (6)$$

IV- TWO-SCALE MODEL

In sections II and III two special types of rough surfaces were considered. The surface roughness had to be either large or small compared with the incident wave length.

Naturally occuring surfaces, however, may include both types of roughness in various proportions. Some surfaces may have one continuous distribution of roughness instead of two significantly different average sizes. In this case the surfaces can be modeled as having only two average sizes of roughness with one large and the other small compared with the incident wavelength. Fig 2 shows the geometry of the surface scattering problem. The transmitter and the receiver are positioned in a reference (x, y, z) by the angles θ, φ, θ_s and φ_s.

Assume the incident wave $\vec{E}^i$ to be :

$$\vec{E}^i = \hat{a}E_o \qquad \text{with} \qquad E_0 = |E_o| exp\{-jk(\hat{n}_i \cdot \vec{r})\} \qquad (7)$$

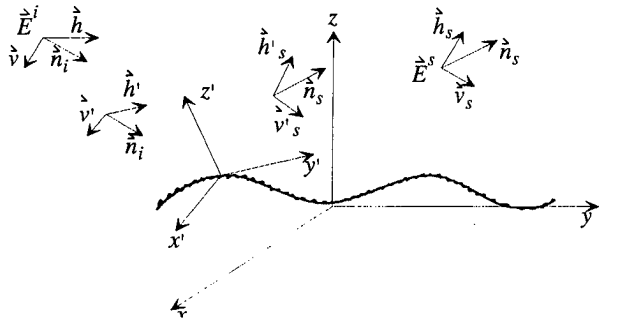


Fig 2.Geometry of surface scattering problem

In the local reference :

$$\vec{E}^i = E^i_{v'}\hat{v}' + E^i_{h'}\hat{h}' = [(\hat{a}\cdot\hat{v}')\hat{v}' + (\hat{a}\cdot\hat{h}')\hat{h}']E_o \qquad (8)$$

The locally scattered fields due to incident waves are :

$$\begin{bmatrix} E^s_{v'} \\ E^s_{h'} \end{bmatrix} = \begin{bmatrix} S_{v'v'} & S_{v'h'} \\ S_{h'v'} & S_{h'h'} \end{bmatrix} \begin{bmatrix} E^i_{v'} \\ E^i_{h'} \end{bmatrix} \qquad (9)$$

Then the scattering coefficients are given by :

$$\begin{bmatrix} E^s_{vh} \\ E^s_{hh} \end{bmatrix} = \begin{bmatrix} \hat{v}_s\cdot\hat{v}'_s & \hat{v}_s\cdot\hat{h}'_s \\ \hat{h}_s\cdot\hat{v}'_s & \hat{h}_s\cdot\hat{h}'_s \end{bmatrix} \begin{bmatrix} E^s_{v'} \\ E^s_{h'} \end{bmatrix} \qquad (10)$$

So the average $\langle E^s_{hh}E^{s\,*}_{hh}\rangle$ of $E^s_{hh}E^{s\,*}_{hh}$ can be calculated.

$\langle E^s_{hv}E^{s\,*}_{hv}\rangle$ can be calculated if we use $\langle E^s_{hh}E^{s\,*}_{hh}\rangle$ and the transformation given by (11) :

$$\hat{h}_s \leftrightarrow \hat{v}_s \qquad \hat{h}'_s \leftrightarrow \hat{v}'_s \qquad \hat{h}' \leftrightarrow \hat{v}' \qquad (11)$$

To calculate $\langle E^s_{vv}E^{s\,*}_{vv}\rangle$ and $\langle E^s_{vh}E^{s\,*}_{vh}\rangle$ the following transformation can be used :

$$\hat{h}_s \leftrightarrow \hat{v}_s \qquad \hat{h} \leftrightarrow \hat{v} \qquad (12)$$

Then the first bistatic coefficient scattering is given by :

$$\sigma^s_{hh} = \langle (\hat{h}_s \cdot \hat{h}'_s)^2 (\hat{h}' \cdot \hat{h})^2 \sigma^s_{h'h'} \rangle + \langle (\hat{h}_s \cdot \hat{h}'_s)^2 (\hat{v}' \cdot \hat{h})^2 \sigma^s_{h'v'} \rangle +$$
$$\langle (\hat{h}_s \cdot \hat{v}'_s)^2 (\hat{h}' \cdot \hat{h})^2 \sigma^s_{v'h'} \rangle + \langle (\hat{h}_s \cdot \hat{v}'_s)^2 (\hat{v}' \cdot \hat{h})^2 \sigma^s_{v'v'} \rangle +$$
$$\langle (\hat{h}_s \cdot \hat{v}'_s)^2 (\hat{v}' \cdot \hat{h}) (\hat{h}' \cdot \hat{h}) \sigma^s_{v'v'v'h'} \rangle +$$
$$\langle (\hat{h}_s \cdot \hat{v}'_s) (\hat{v}' \cdot \hat{h})^2 (\hat{h}'_s \cdot \hat{h}_s) \sigma^s_{v'v'h'v'} \rangle +$$
$$\langle (\hat{h}_s \cdot \hat{v}'_s) (\hat{v}' \cdot \hat{h}) (\hat{h}'_s \cdot \hat{h}_s) (\hat{h}' \cdot \hat{h}) \sigma^s_{v'v'h'h'} \rangle +$$
$$\langle (\hat{h}_s \cdot \hat{v}'_s) (\hat{v}' \cdot \hat{h}) (\hat{h}'_s \cdot \hat{h}_s) (\hat{h}' \cdot \hat{h}) \sigma^s_{v'h'h'v'} \rangle +$$
$$\langle (\hat{h}_s \cdot \hat{v}'_s) (\hat{h}' \cdot \hat{h})^2 (\hat{h}'_s \cdot \hat{h}_s) \sigma^s_{v'h'h'h'} \rangle +$$
$$\langle (\hat{h}_s \cdot \hat{h}'_s)^2 (\hat{v}' \cdot \hat{h}) (\hat{h}' \cdot \hat{h}) \sigma^s_{h'h'h'v'} \rangle \qquad (13)$$

$$\sigma^s_{pqp'q'} =$$

$$16 \left| k^2 \sigma \cos\theta' \cos\theta'_s \right|^2 Re\,(\alpha_{pq} \alpha_{p'q'}{}^*)\, W(k_x + k\sin\theta', k_y) \qquad (14)$$

$$\sigma^s_{pq} = 8 \left| k^2 \sigma \cos\theta' \cos\theta'_s \right|^2 |\alpha_{pq}|^2 W(k_x + k\sin\theta', k_y) \qquad (15)$$

The other coefficients are obtained by using transformations (11) and (12).

V- NUMERICAL RESULTS

The validity conditions of stationary phase, scalar approximation and for the small perturbation model are studied [1][2]. It can be observed that the scalar approximation and the small perturbation model can be simultaneously applied for ($kL > 6$ and $k\sigma < 0,3$). Stationary phase and scalar approximation can be applied concurrently for ($kL > 17$ and $k\sigma > 3$). For the simulation two surface types are chosen ($kL = 1$, $k\sigma = 0,1$ and $kL = 6,5$, $k\sigma = 1$), for the slope standard deviation m ($m = \sqrt{2}\frac{\sigma}{L}$), two frequenties (*10 and 15 GHz*), salinity $S = 35 ppm$ and with a temperature $T = 20°C$.

The monostatic coefficients σ^s_{vv} for the three models stated before are plotted in Fig 3 for $kL = 1$ and $k\sigma = 0,1$, F=10 or 15 GHz. The validity conditions for scalar approximation are not satisfied so this model is divergent for $\theta > 10°$. The stationary phase approximation is not represented for the same reason. In Fig 4 the monostatic coefficients σ^s_{vv} are plotted for the four scattering models, $kL = 6,5$ and $k\sigma = 1$, F=10 and 15 GHz. Another example for the simulation is processed for the sea surface using the Pierson-Moscowitz's spectrum [8] and the slope distribution given by Cox and Munk [9]. The results will be presented during the symposium.

VII- CONCLUSION

The numerical results are computed for the bistatic radar cross-section from a rough sea surface using Gaussian model for the correlation and wave height.

The major new consideration is the development of the composite model in the bistatic case. Good agreements are obtained between this model and measurements.

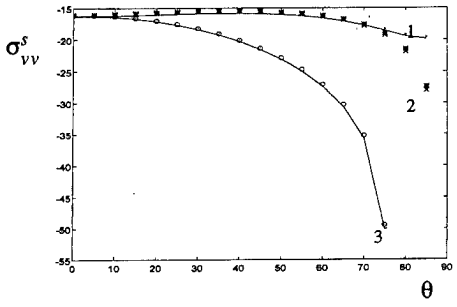


Fig.3 F=10 GHz-15 GHz for kL=1, kσ=0.1
small perturbation model (1), two-scale model (2),
scalar approximation (3)

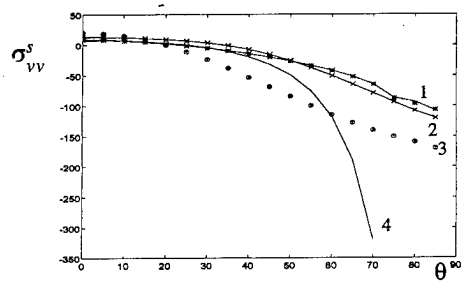


Fig.4 F=10GHz-15GHz for kL=6.5, kσ=1:
scalar approximation (1),stationary phase approximation (4)
small perturbation model (3), two-scale model (2)

ACKNOWLEDGMENT

This work was supported by the " Centre d'Electronique de L'ARmement", convention No 0064192.

REFERENCES

[1] A.Khenchaf, F.Daout, J.Saillard, *"Bistatic polarized scattering by rough surface"*, JIPR, Third International workshop on Radar Polarimetry, Nantes, France, March 21-23 1995.

[2] A.Khenchaf, F.Daout, J.Saillard, *"Polarization degradation in the sea surface environment"*, OCEANS'95, San Diego, USA, October 9-12, 1995.

[3] F.Daout, A. Khenchaf, J. Saillard, *"Effect of the salinity and tremperature on the electromagnetic field scattered by the sea surface"*, OCEANS' 94, Brest, France, September 13-16, 1994.

[4] J.A. Ogilvy, *"Theory of wave scattering from random rough surfaces"*, Adam Higler, 1991.

[5] F.T.Ulaby, R.K.Moore,,A.K.Fung, "*Microwave remote sensing - Active and passive*", vol. II, Adison-Wesley publishing company, 1982.

[6] F.T. Ulaby and C. Elachi, *"Radar polarimetry for geoscience applications"*, norwood, MA: Artech house, 1990.

[7] S.O. Rice, *"Reflection of electromagnetic waves from slightly rough surfaces"*, commun. Pure. appli. Math., vol.4, pp 351-378- 1951.

[8] A.K. Fung, K.K. Lee, *"A semi-empirical sea-spectrum model for scattering coefficient estimation"*, IEEE Journal of oceanic Engeering, vol. OE.7, No 4, pp 166-176, October 1982.

[9] C.Cox and W.Munk, *"Measurement of the roughness of the sea surface from photographs of sun glitter"*, J. Opt. Soc. Amer., vol. 44, No 11, pp 838-850, 1954.

Verification of Microwave Scattering Mechanisms Using Optical Polarimetric Imagery

J.D. Barter and P.H.Y. Lee

TRW, R1-1008, 1 Space Park, Redondo Beach, CA 90278, USA
Tel: 310.812.0450; Fax: 310.814.2359; e-mail: James_Barter@atdmac.sp.trw.com

Abstract - Observations of microwave backscattering from the sea surface have indicated the presence of scattering mechanisms other than Bragg resonant mechanisms[1]. These conclusions are supported by the study of the line shapes of Doppler spectra[2] and of the dependence of the backscatter on grazing angle[1], polarization[1], wind-direction[1] and wind speed[3]. Conjectured non-Bragg scattering mechanisms include specular reflection from facet-like portions of a wave surface as well as double bounce reflections including reflections at the Brewster angle. Using a novel polarimetric optical specular event detector (OSED)[4], temporal correlations have been made with microwave scattering returns allowing spatially resolved identification of wave structures which give rise to the microwave returns and provide direct verification of the presence of the conjectured scattering mechanisms.

INTRODUCTION

The OSED diagnostic has been used in conjunction with a fully polarimetric X-band radar to provide temporally correlated and spatially resolved polarimetrically coded visual images of mechanically breaking waves at the Ocean Engineering Laboratory (OEL) of the University of California at Santa Barbara (UCSB) wind-wave tank facility. The spatially resolved images allow the direct identification of wave structures responsible for backscatter returns while the polarimetric capabilities of the OSED provide strong evidence of the equivalence of the polarization activity of the wave structures across a large range of wavelength (~3 cm - ~580 nm).

INSTRUMENT DESCRIPTION

The OSED detector consists of two standard black-and-white (RS-170) video cameras whose fields of view are precisely overlaid by means of a beamsplitter - mirror system. Dichroic polarizers introduced separately into each camera view provide simultaneous images of the system field of view in s-polarized (horizontal) and p-polarized (vertical) light. If the illumination is unpolarized, the two images record intensities equivalent to microwave returns of $(HH+VH)$ and $(VV+HV)$. Similarly, s- or p-polarized illumination would yield information equivalent to (HH and HV) or (VV and VH) respectively. Thus, while the OSED does not at present measure the full polarization state, within the statistical equivalence of an ensemble of wave breaking events, the OSED can provide information at visible wavelengths equivalent to the four polarization matrix elements available from the X-band radar by recording successive equivalent wave ensembles under appropriate illumination.

In addition to the polarization information, the image intensity contains information on the equivalent backscatter cross-section at visible wavelengths. In the presence of an absolute calibration of the illumination intensity, an estimate of the surface curvatures of the scattering objects may also be obtained.

Simple frame subtraction of image intensities can be calculated and displayed in near real time. The OSED s- and p-polarization images are stored as the red and green images of a standard color (NTSC) TV frame on a Magneto-Optic Disk (MOD) recorder which allows offline analysis and display of synchronized images.

The OSED and its Illuminator are mounted symmetrically with respect to the radar as shown in Figure 1 to obtain the same specular reflection condition as applies to the Radar in a quasi-monostatic backscatter mode. IRIG time codes are impressed on the OSED images and associated with the Radar data records to enable synchronization of the two data streams.

ALIGNMENT AND IMAGE ANALYSIS

Alignment of the two camera images involves translational and rotational alignment by means of the beam splitter, turning mirror and camera attitude adjustments, and balancing of the image sizes and exposure levels by means of the matched zoom lens focal length and f-stop adjustments.

Assessment of the alignment is achieved by the use of a non-polarizing, high-contrast checkerboard target at a nominal 10 m range illuminated with unpolarized light. The basic 2-dimensionally resolved image processing functions available for cross-section and polarimetric analysis of the target are the pixel-by-pixel sum and difference images where each resultant pixel intensity is described by

$$I_{SUM} = \left(I_s + I_p\right)/2 \ , \tag{1}$$

$$I_{DIF} = \left(I_s - I_p + 255\right)/2 \ , \tag{2}$$

for an 8-bit image digitization system. Optimum alignment of the system is found by minimizing the variance of the difference image (Eqn 2) about the median gray level $I_{DIF} = 127.5$. A statistical treatment of the misalignment and exposure level imbalance over the region of interest in the field of view shows that this system is able to achieve an equivalent misalignment of ± 0.2 pixels over a range of illumination levels.

By the symmetry of the breaking wave with respect to the vertical, it is reasonable to assume that an ensemble of scatterers comprising a breaking event will not favor rotations of

0-7803-3068-4/96$5.00©1996 IEEE

the polarization in either direction. It is therefore convenient to take as a measure of the degree of polarization the ratio

$$P = \left(I_s - I_p\right) / \left(I_s + I_p\right) = \left(I_{DIF} - 255/2\right) / I_{SUM} \quad . \tag{3}$$

Calculation of this ratio is performed pixel-by-pixel and displayed in false color, where the target cross-section (image intensity) is suppressed. For comparison with the radar Polarization Ratio (defined as HH/VV), appropriate sums can be performed over the image to yield

$$Pol.\ Rat. = \sum_{pixel} I_s \Big/ \sum_{pixel} I_p \quad . \tag{4}$$

Relative cross-section in the visible is obtained directly from the sum-image as

$$\sigma = \sum_{pixel} \left(2 * I_{SUM}\right) \quad . \tag{5}$$

IMPLEMENTATION AND RESULTS

The combined, synchronized system of OSED and Radar have been used to study 4 *m* mechanically generated breaking waves at low grazing angles (4.5° - 11°) at the OEL / UCSB facility. A representative example will be shown to demonstrated some of the capabilities of the system. Examples of further use of the system will also be presented at this meeting[5,6]. A 51 second record of Radar Cross Section (RCS) of backscatter from 4 *m* breaking waves at 4.5° grazing angle and 10 *m* nominal range is shown in Figure 2. Breaking wave events which occur within the elliptical radar footprint (~1 x 3 *m* at the -3 *dB* contour) give rise to greatly enhanced radar cross-sections visible as four groups of cross-section peaks. For clarity, only the *HH* and *VV* returns of the radar are shown. Variation of peak cross-section depends amongst other things on the position of the breaking event within the radar footprint. Similarity of the breaking events can be seen in the consistent increase of *HH* returns over *VV* returns (*i.e.*, Super Events[1]) during each event. The breaking event near t = 29 *s* is chosen for a more detailed look in Figures 3 - 6.

In Figure 3, all four polarization matrix elements of the radar return are shown for times 27 - 30 *s*. Again, the dominance of the *HH* over the *VV* during such a breaking event is representative of these mechanically generated waves. Since unpolarized illumination was used for the OSED, the OSED channels correspond to radar cross-sections of $(HH + VH)$ and $(VV + HV)$. Figure 4 compares the radar $HH + VH$ cross-section to the OSED s-polarization return, similarly Figure 5 compares the radar $VV + HV$ cross-section to the OSED p-polarization return. It will be seen that the radar cross-section rises approximately 0.5 *s* before the OSED return. The first specular facet is visible in the OSED image at t = 28.17 *s* near the rise of the radar cross-section, but the rise of the OSED cross-section does not occur until the wave crest strikes the front face of the wave and dissolves into a disordered surface. Therefore, the early rise of the radar cross-section is thought to be due to diffractive processes from the tip of the gravity wave at the earliest stage of breaking. The increased range of the radar cross-section compared to the OSED may arise from a combination of two effects. First, the characteristic structure size of facets on a breaking wave are in the Rayleigh regime, being considerably smaller than the radar wavelength (~3 *cm*). Second, the noise floor of the OSED is presently limited by upwelling light reflected from the wave tank floor.

Figure 6 compares the polarization ratio of the OSED and radar. Again, since the OSED illumination is unpolarized, the OSED polarization ratio (Eqn 4) is compared to the radar power ratio $(HH + VH)/(VV + HV)$. Due to the large fluctuations of the ratio at small cross-section, the ratio is only plotted from 28 to 30 *s*. Note, however, that the polarization ratio in the visible closely follows the shape of the ratio at X-band. The difference in magnitude is thought to be related to the disparity in Brewster incidence angles at visible (~54°) and X-band (~83°) wavelengths. Double bounce reflections from the breaking wave greatly favor *HH* radar returns near 4.5° - 7° grazing angle where the Brewster effect in the visible is only partial.

Temporal sequences of 2-dimensionally resolved images of the OSED degree of polarization are available but are not shown in this paper due to the space limitation. However, these images allow the visible identification of scatterers which give rise to the OSED polarized returns. At early times (28 - 28.5 *s*) the polarized OSED returns come from portions of the large curvature, leading edge of the unbroken wave crest that satisfy the specular condition. Near 28.5 *s* the wave crest strikes the front face of the wave and dissolves into a large disordered surface which scatters largely depolarized light isotropically. At this time a large area of the front face of the wave, having an approximately parabolic profile[7], supports a backscatter reflection of the bright crest at incidence angles very near the Brewster angle in the radar regime which dominates over the unpolarized returns from the crest. At later times (~29.5 *s*) the Brewster reflection in the front face disappears, leaving only the bright, unpolarized crest which, however, may also support polarized structures.

ACKNOWLEDGMENTS

This work was supported by ASAP/ISSO, Department of Defense, Contract No. DMA 800-94-C-6008. The authors are grateful to Professor Marshall Tulin and his staff at USCB/OEL for the use of the OEL wavetank facility.

REFERENCES

[1] P.H.Y. Lee et al., *J. Geophys. Res.* **100**, 2591-2611 (1995)

[2] P.H.Y. Lee et al., *IEE Proc.-Radar, Sonar Navig.* **142**, 252-258 (1995).

[3] P.H.Y. Lee et al., *IEEE Trans. Antennas & Propagation* **AP-44**, 333-340 (1996)

[4] J.D. Barter and P.H.Y. Lee, Submitted to *Appl. Opt.*
[5] P.H.Y. Lee et al., *IGARSS '96*, Paper No. 96.0088.
[6] P.H.Y. Lee et al., *IGARSS '96*, Paper No. 96.0089.
[7] M.P. Tulin, Private Communication.

FIGURE CAPTIONS

Fig. 1. Schematic of the OSED mounting with respect to the Radar, such that the OSED views the same foot print with the same specular reflection condition.

Fig. 2. Time record of the Radar HH and VV backscatter cross-sections for a 4 m mechanically generated breaking wave.

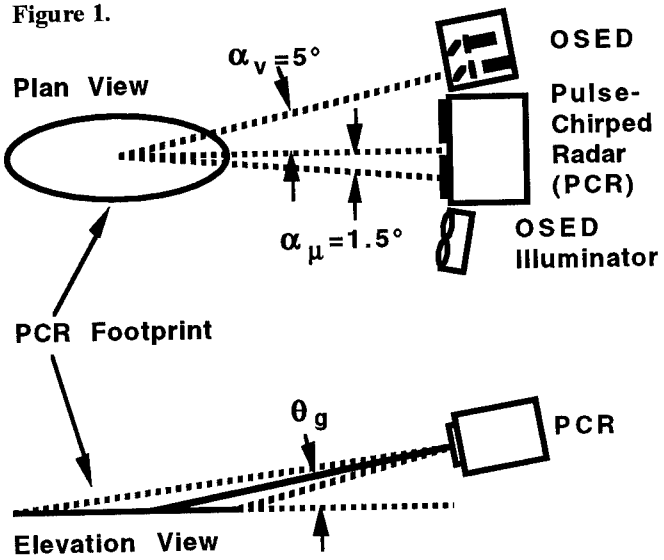
Fig. 3. Time record of the four Radar return polarization matrix elements HH, VV, VH, and HV for the expanded time scale from 27 to 30 s.

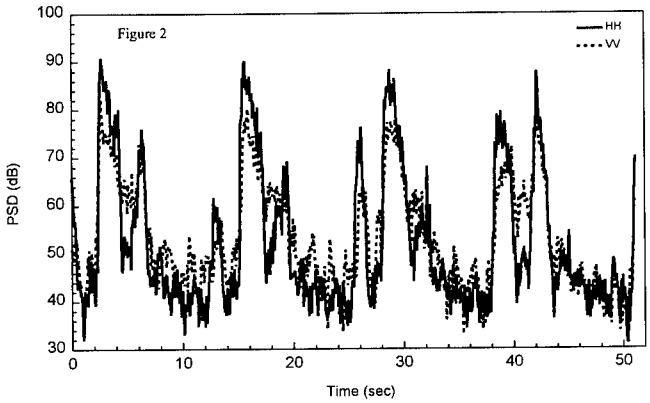
Fig. 4. Comparison of the OSED s-polarization cross-section to the equivalent Radar cross-section $(HH + VH)$.

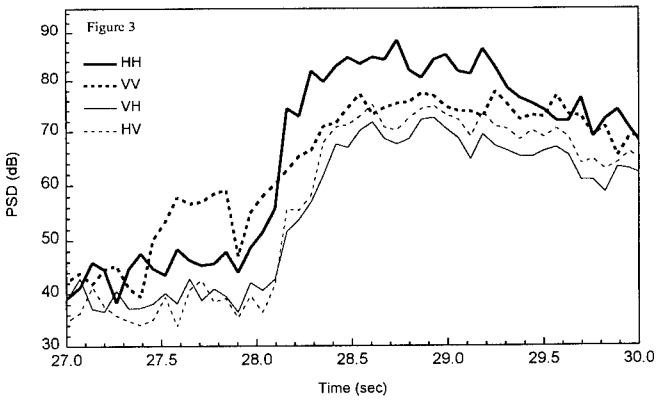
Fig. 5. Comparison of the OSED p-polarization cross-section to the equivalent Radar cross-section $(VV + HV)$.

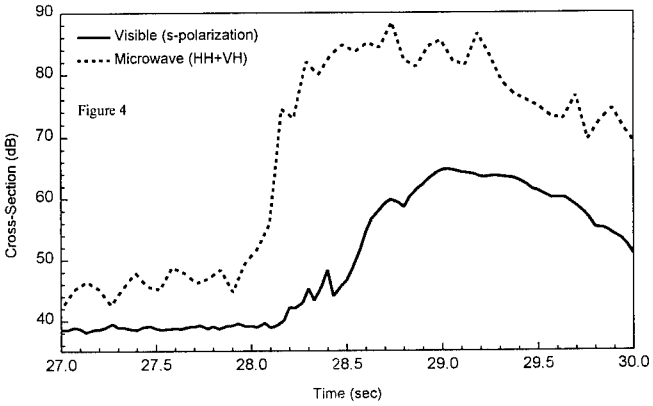
Fig. 6. Comparison of the OSED polarization ratio $\sum_{pixel} I_s \Big/ \sum_{pixel} I_p$ to the equivalent Radar power ratio $(HH + VH)/(VV + HV)$.

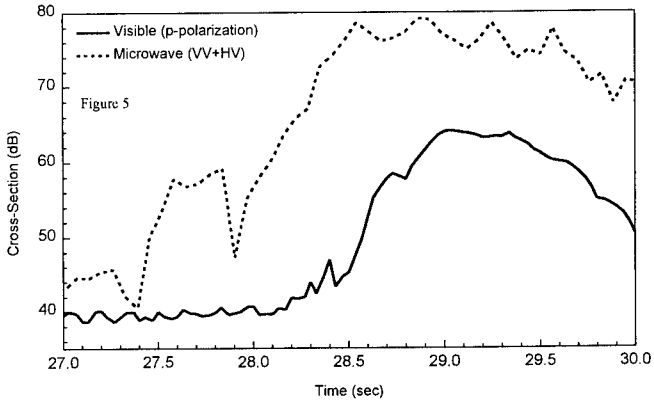
Figure 1.

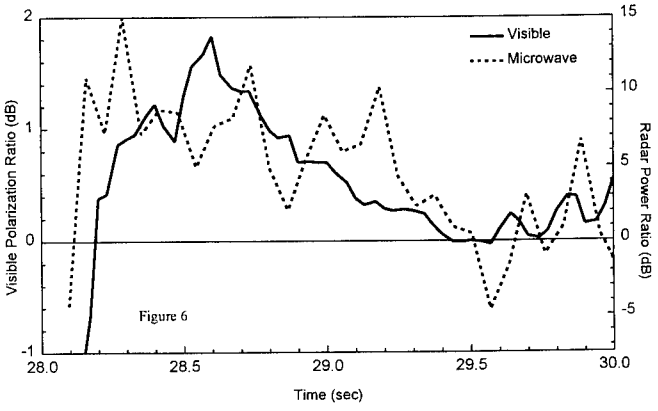












Fetch and Wind Dependence of SAR Azimuth Cutoff and Higher Order Statistics in a Mistral Wind Case.

Vincent KERBAOL[1], *Bertrand CHAPRON*[1], *Tanos EL FOUHAILY*[1], *René GARELLO*[2]

[1] IFREMER, centre de Brest, Département d'Océanographie Spatiale,
BP 70, 29280 Plouzané, France
[2] Télécom Bretagne, Département ITI, BP 832, 29285 Brest Cedex, France

Abstract – Fetch dependence of SAR azimuth cutoff and image statistics on ERS-1 SAR images is discussed. Azimuth cutoff accounts for motions on sea surface and is a kinematic parameter. Wind estimation through cutoff analysis is presented as well as limitations of this method for fetch limited sea states. In addition, SAR higher order statistics have proved to be well correlated with estimated SAR azimuth cutoffs. Their behaviour are presented together with breaking events density probability. A first attempt is proposed to better localize the short lifetime scatterers that are expected to arise and fade within the integration time by bandpass filtering the Doppler spectrum derivated from a SLC image.

1. PRESENTATION

In this paper, a case study of an ERS-1 SAR scene acquired on March 23 1992 at 10:28 A.M. near the french southern mediterranean shore over the Gulf of Lion is discussed. Two successive ERS-1 Precision Images (PRI) on a descending path (195°) were at our disposal as well as Single Look Complex Images (SLC) and Raw data. According to weather chart, a steady wind of $13\,ms^{-1}$ was blowing 300° relative to North (e.g. 15° to range) over most of the part of the second PRI image, except at both early and late azimuth where the wind speed was expected to be lower. Earlier in the night, the wind speed was measured as high as $25\,ms^{-1}$.

2. SAR WIND SPEED ESTIMATION

Many attemps have been conducted to retrieve wind and waves characteristics from SAR images. A successful inversion method based on a closed non-linear integral transformation has been proposed by Hasselmann and Hasselmann [1]. Moreover, the issue of estimating the wind speed by opposing the measured SAR backscattered intensity to scattering model (such as CMOD) has revealed to be of few interest because of the lack of calibration of ERS-1 PRI images [2]. Improvements have been carried out in this domain for data processed after November 1992, the reliability still remains limited, in particular due to the non negligeable effect of the ADC saturation at near range.

Hereafter, wind speed retrieval is discussed through azimuthal cutoff analysis. Imaging of ocean surfaces by SAR is known to be strongly affected by the orbital motions of the surface waves. Doppler shifts induced by these motions distort the phase history of the backscattered signal which is used to synthetise the azimuthal resolution. Consequently, the image is azimuthally low-pass filtered by the characteristic function of azimuthal displacements as shown using the quasi-linear approximation [1]:

$$P_S(k) = \exp\{-k_{az}^2 \rho_{\xi\xi}(0)\}\, P_R(k) \tag{1}$$

where P_S and P_R are the SAR and the RAR power spectrum respectively, and $\rho_{\xi\xi}(0)$ is well approached by the vertical component of orbital velocities (incidence angle $\approx 23.5°$):

$$\rho_{\xi\xi}(0) = (\frac{R}{V})^2 \int \omega^2 S(k) dk \tag{2}$$

Cutoff parameter estimation has already been discussed elsewhere [3, 4]. Here we propose to use the intercorrelation function between different looks generated from SLC image in order to eliminate the non-coherent scattering correlation term (Fig.1). The intercorrelation function is fitted as follows:

$$C(x) \sim e^{-\pi^2 \frac{x^2}{\lambda^2}} \tag{3}$$

where:

$$\lambda = \pi \sqrt{\rho_{\xi\xi}(0)} \tag{4}$$

SAR azimuth cutoff λ is then directly bound to the standard deviation of the total azimuthal displacements field. Furthermore, this kinematic parameter has proved to be a robust wind speed indicator [4]. Indeed, cutoff

0-7803-3068-4/96$5.00©1996 IEEE

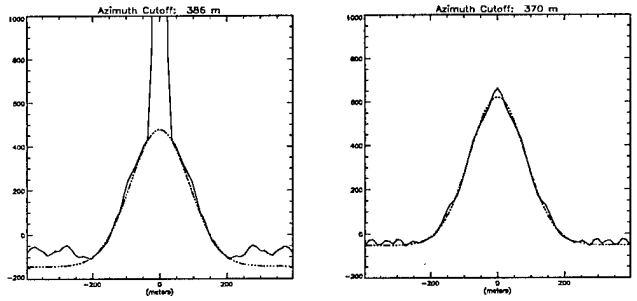


Figure 1: Estimation of the azimuth cutoff through the azimuthal correlation function (left). The narrow central peak of the non-coherent scattering has been removed by using intercorrelation between two independent looks (right).

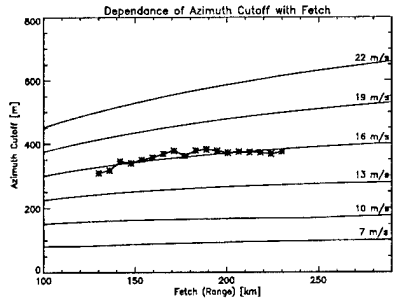


Figure 2: Estimation of the azimuth cutoff along the range axis (thick) and fetch dependent theoretical values for different wind speeds (thin).

values, estimated on a global data set of more than 1200 ERS-1 SAR Wave mode images, have been opposed to wind speeds derived from ERS-1 Scatterometer U_{10}. They have shown to be linearly related (with a coefficient of 23.2) for the whole range of wind speeds. This empirical relationship can be compared using a JONSWAP-like sea spectral model. From (2) and (4), we have:

$$\lambda = \pi \frac{R}{V} \sqrt{\int \omega^2 S(k) dk} \simeq 25\, U_{10} \qquad (5)$$

This relationship has been obtained under the assumption that all wavelengths were equally fully developed which is not always true under high winds conditions. Introduction of an age factor would give a coefficient even closer to the empirical one.

3. SAR OBSERVATIONS

3.1. Azimuth cutoff analysis

Though the wind was nearly steady in speed and direction, the estimated cutoff appeared to vary across the track and to underestimate the wind speed. Assuming the wind was almost blowing in range direction, it seemed then reasonable to consider that the sea was fetch limited along the range axis. Estimated cutoff values have then been compared with theoretical values inferred from a fetch dependent sea spectral model (Fig.2). Eq. (5) becomes:

$$\lambda(x) = \pi \frac{R}{V} \sqrt{\int \omega^2 S(k, \Omega(x)) dk} \qquad (6)$$

where x is the fetch distance, extending from 130 to $230km$ between far and near range and $\Omega(x)$ represents the corresponding inverse wave age. The estimated wind speed is $16\, ms^{-1}$ which is higher than the expected value ($13\, ms^{-1}$).

3.2. Peak wavelength analysis

In addition to azimuth cutoff, peak wavelength and associated phase analysis have also been carried out from the cross spectrum between the first and the third of the three processed looks. This wavelength is compared with the theoretical value of fetch limited wavelength, using the same sea spectral model (Fig.3(left)). The estimated wind speed of $16\, ms^{-1}$ is still greater than the real wind speed. Possible interpretation is that the rough sea state raised under stronger wind conditions during the previous night has not totally relaxed, leading to both SAR peak wavelength and cutoff greater than expected for a $13\, ms^{-1}$ wind.

The phase of cross spectrum represents the propagation of wavelength between the first and third look acquisition time ($\Delta T = \frac{2}{3}\, 0.577 = 0.38s$ for ERS1):

$$\phi_{predicted} = \omega\, \Delta T = \sqrt{g \frac{2\pi}{l}}\, \Delta T \qquad (7)$$

where g is the acceleration of gravity and l the peak wavelength. Both phases, measured at SAR peak cross spectrum and predicted from the measured wavelength, are plotted Fig.3(right). As expected predicted phase decreases with increasing fetch.

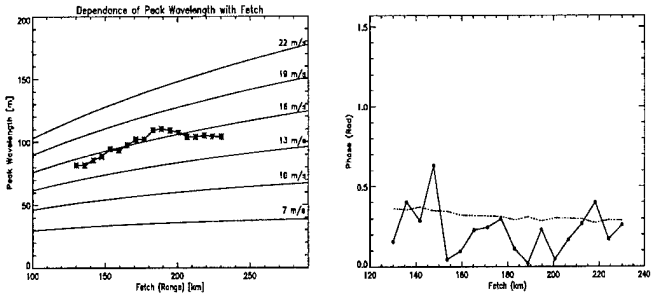


Figure 3: **Left:** Estimation of the SAR cross spectrum peak wavelength along range axis (thick) and fetch dependent peak values for different wind speeds (thin). **Right:** Predicted phase (dash) and measured phase (solid).

4. STATISTICS

Interpretation of SAR image higher order statistics still remains a topical problem. It has often been observed that both skewness ($\sqrt{\beta_1}$) and kurtosis (β_2) tend to increase with wind speed but the reason of this is unclear.

The non-linearity of SAR mapping transformation is often invoked to explain the deviation of SAR statistitics from Rayleigh distribution (or χ^2 for multi-look images). Yet, considering that azimuthal displacements occuring during the integration time turn into a facet superposition effect [5], SAR distribution should tend to Gaussian law following central limit theorem. This is in contradiction whith the fact that β_1 and β_2 keep increasing with wind speed. Our opinion is that non-coherent specular scattering, like breaking events, will play a major role as wind speed increases. Tilley [6] suggested that when the cross section is dominated by sea spikes density clipped in amplitude, the cross section measurement can be approximated by the number of point scattering processes occuring during the integration time. Mean rate of this number must also be weighted by a non-detection probability accounting for SAR Doppler bandpass limitation [7] or shadowing effect for instance. SAR image amplitude should then be associated with Poisson law to lead to K-statistics [8].

Referring to Barrick [9], the mean number of backscattered specular glints per unit area varies as follows:

$$N \sim exp\{-\frac{tan^2(\theta)}{mss}\} \qquad (8)$$

where θ is the incidence angle and mss the mean square slope. Fetch dependence of N should be weak. Indeed the mss parameter is known to be mostly dominated by gravity-capillary waves for moderate to high winds. Such a range of waves is not expected to vary for fetch as long as $100\,km$. Thus, N will not change with fetch but rather from its incidence angle dependence ($tan\theta$) along range axis.

4.1. Wind dependence

As shown above, higher order statistics will not be fetch dependent in our case study. However, they are strongly related to wind speed variation along the track. Skewness and azimuth cutoff have been estimated from PRI 3-looks amplitude image in this direction for a fixed fetch of $180\,km$ (Fig.4). As one can see, the wind speed increases from the shore and decreases at late azimuth. A remarkable feature is the excellent correlation between cutoff and skewness parameter.

An empirical relationship between azimuth cutoff and β_1 was derived from the analysis of the ERS-1 imagette global data set. Cutoff parameter was found to vary with

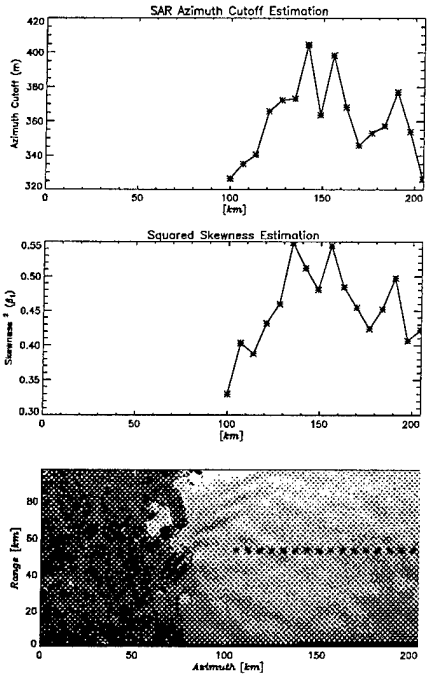


Figure 4: Azimuth cutoff and Skewness plotted in the along track direction.

$\beta_1^{2/3}$. Using wind speed estimated through azimuth cutoff analysis and the probability B of crest breaking given by Srokosz [10], squared skewness have then been related to B (Fig.5):

$$B = exp\{-\frac{\alpha^2 g^2}{2\int \omega^4 S(k) dk}\} \qquad (9)$$

where α is 0.5. It can be seen that results obtained in our case study are in good agreement with our empirical relationship.

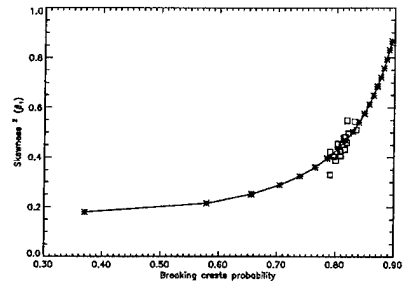


Figure 5: Squared skewness versus Breaking crest probability for imagette data set (asterisk) and Mistral case (squares).

4.2. Time-frequency analysis

It has been shown that knowledge of the number of short lifetime detected events is important. Indeed it is possi-

ble to localize in time, within integration period, short-lifetime backscattered echoes by bandpass filtering Doppler spectrum. This process is similar to multi-looking process. The time resolution is obtained by moving the bandpass filter along Doppler frequencies. As an example, we present an azimuth line extracted from SLC image on which two strong echoes have been detected (Fig.6 (bottom)). After bandpass filtering process, one oberve that they have occured at different times during the integration (top). The peak located at early azimuth has been detected at the beginning of integration time. It would then appear on the forward look and vanish on the successive ones. The other peak would rather be detected on the central look.

Such a process should help in counting peaks of strong intensity. Moreover, this should give information concerning time-breaking duration.

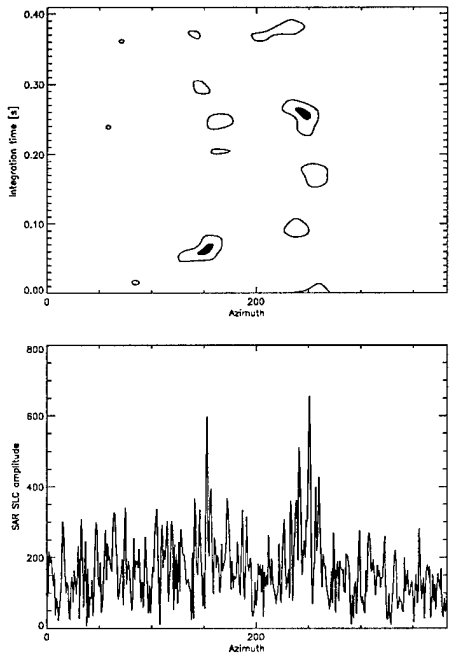


Figure 6: **Bottom:** Azimuth line extracted from SLC image. **Top:** Distribution of SAR intensity during integration time.

5. CONCLUSION

In this paper, the issue of retrieving wind speed through azimuth cutoff analysis is adressed. This method has been shown to be a robust wind indicator. Such an estimation would give underestimated wind speeds in case of fetch limited sea. A solution based on the use of sea spectral model including wave age parameter is proposed to recover true wind speed. In addition, increase of higher order statistics with wind speed has clearly been pointed out. An interpretation is proposed in relation with the wave breaking probability. It has raised the necessity to better know the detected scatterers density. A time-frequency approach has then been proposed to localize these events during the integration time.

6. REFERENCES

[1] K. Hasselmann and S. Hasselmann. On the nonlinear mapping of an ocean wave spectrum into a synthetic aperture radar image spectrum and its inversion. *J. of Geophys. Res.*, 96(C6):10,713–10,729, June 1991.

[2] I.S. Robinson A. Scoon and P.J. Meadows. Demonstration of an improved calibration scheme for ers-1 sar imagery using a scatterometer wind model. *Int. J. Remote Sens.*, 17(2):413–418, 1996.

[3] P.W. Vachon and H.E. Krogstad. Airborne and spaceborne synthetic aperture radar observations of ocean waves. *Atmosphere-Ocean*, 32(1):83–112, March 1994.

[4] B. Chapron, T. El Fouhaily, and V. Kerbaol. A sar speckle wind algorithm. *Proceedings of Second ERS-1 Workshop, DRO/OS, IFREMER Brest*, 15-17 March 1994.

[5] B. Chapron, R. Garello, V. Kerbaol, and J.M. Lefevre. Nonlinear theory of ocean-sar transformation and statistical analysis of ers-1 sar-wave mode imagettes. *Proceedings Second ERS-1 Symposium*, Jan. 1994.

[6] D.G. Tilley and Y.V. Sarma. A comparison of synthetic aperture radars applied for satellite remote sensing of the ocean surface. *Trends in Geophys. Res.*, 2, 1993.

[7] D. P. Winebrenner and K. Hasselmann. Specular point scattering contribution to the mean synthetic aperture radar image of the ocean surface. *J. Geophys. Res.*, 93(C8):9281–9294, Aug. 1988.

[8] E. Jakeman and R.J.A. Tough. Non-gaussian models for the statistics of scattered waves. *Advances in Physics*, 37(5):471–529, 1988.

[9] D.E. Barrick. Rough surface scattering based on the specular point theory. *IEEE Trans. Ant. Prop.*, AP-16:449, 1968.

[10] M.A. Srokosz. On the probability of wave breaking in deep water. *J. Phys. Oceanography*, 16:382–385, Feb. 1986.

COMBINED RADAR AND CROSS POLARIZATIONAL RADIOMETER SYSTEM FOR DETECTION AND IDENTIFICATION OF SOME ANOMALOUS FORMATIONS ORIGINATED ON SEA SURFACE DUE TO CHANGES OF LONG AND SHORT WAVES SPECTRUM COMPONENTS

Artashes K.ARAKELIAN and * Astgik K.HAMBARYAN

Institute of Radiophysics & Electronics
of Armenian National Academy of Sciences
Ashtarak-2, Armenia, 378410, C.I.S.
Tel:(+7-8852) 28-78-50, E-mail:irphe@arminco.com
* Holding "Shinzargatsoum" Ministry of Construction of Armenia
35 Komitas St., Yerevan, 375051, Armenia.
Tel. (+7-8852) 22-58-60

ABSTRACT

The results of theoretical estimation of relationship between the absolute values of radar cross section and brightness temperature, as well as between the variances of these absolute values, due to changes of wind speed and sea surface wave principal characteristics are presented. Cross polarization microwave active-passive method of detection and identification, as well as combined in space and in time X-band radar - radiometer detector-identifier of some anomalous formations, originated on sea surface due to changes of wind wave spectrum different components, are developed.

INTRODUCTION

The sea state ecological control by radiophysical methods of remote sensing suggest detection and identification of sea surface lots, differing from surrounding background by their physical-chemical and biological parameters. Analysis of the results of numerous researches has shown, that various inhomogeneities may exert the same influence on the changes of natural background microwave radiation and reflection characteristics. Therefore, preliminary filtration of any types of anomalous formations may increase detection and classification efficiency. Since, the anomalous formations coming out of which are connected with changes of sea wave spectrum components due to wind field characteristics fluctuation, internal waves going out, streams, etc, are very spread on sea surface and are the main interference at the process of detection and identification of any types of sea surface natural and artificial anomalies. Therefore, the development of the methods of sea surface anomalous formations detection and identification, originating on sea surface due to changes of sea surface wave spectrum short and long components characteristics, is actual problem and may find wide application in the sphere of sea state diagnostics and wind speed and sea water physical and chemical characteristics estimations.

SOME THEORETICAL ESTIMATIONS

The using of the sea surface two scale model allows to investigate relationships of sea surface radar cross section σ_{ii} and brightness temperature T_{Bi} at fully developed wind wave, when sea surface state may be perfectly characterized by wind speed and direction only. But mostly, on the sea surface there are situations, when the sea surface wave is differed by its parameters from fully developed wind-generated waves. And in these cases, ripples height $\sigma_h^2=\{\sigma_{hx}^2;\sigma_{hy}^2\}$ and long waves slope variances $m^2=\{m_x^2;m_y^2\}$, with the wind speed and direction, may be considered as the main parameters describing sea surface wave.

In Fig.1 the curves of angular

0-7803-3068-4/96$5.00©1996 IEEE

dependencies of sea surface radar cross section increments $\Delta\sigma_{ii}(\Delta\sigma^2_h)$ due to change of sea surface short waves parameters at wind gust from 6.3m/s to 9.8m/s and 15.4m/s, that is $\Delta v=(9.8-6.3)$m/s and $\Delta v=(15.4-6.3)$m/s, during of which, the parameters of sea surface long scale waves is not changed, are shown. These curves correspond to estimations carried out at radio wave length λ = 2,16cm, salinity $S_s \sim$ 20%., air t_a and water t_v temperatures 11°C, practically the same for all centimeter range of radio waves. In Fig.1 the curves of angular dependencies of sea surface radar cross section increments $\Delta\sigma_{ii}(\Delta m^2)$, due to changes of sea surface long waves slope variances, are shown too. These changes correspond to breach of condition of fully developed wind-generated waves at wind speed ~6.3m/s due to coming out supplementary ripples (long waves), carrying out to increasing of long waves slope variance from $m^2_{6.3}$ to $m^2_{9.8}$ and $m^2_{15.4}$, corresponding to the long waves slope variances at $v \sim$ 9.8m/s and 15.4m/s respectively. The results of Fig.1 are correct for both vertical and horizontal polarizations of radiation.

In Fig.2 the curves of angular dependencies of sea surface brightness temperature cross polarized components increments $\Delta T_{Bv}(\Delta\sigma^2_h)$ and $\Delta T_{Bh}(\Delta\sigma^2_h)$at the gust of the wind from 6.3m/s to 9.8m/s and 15.4m/s are shown. In the same place the curves of angular dependencies of $\Delta T_{Bv}(\Delta m^2)$ and $\Delta T_{Bh}(\Delta m^2)$ due to changes of long waves parameters only at increasing of long waves slope variance from $m^2_{6.3}$ to $m^2_{9.8}$ and $m^2_{15.4}$ are presented.

DETECTION-IDENTIFICATION METHOD

Analysis of the results of Fig.1 and 2 have shown, that at the stage of solution of problems connected with anomalous formations detection and identification, originated on sea surface due to changes of short and long waves characteristics, as the parameter for identification it is worth while to use the values of the ratios $D_v=\Delta T_{Bv}/\Delta\sigma_{vv}$ and $D_h=\Delta T_{Bh}/\Delta\sigma_{hh}$.

In Fig.3 the curves of angular dependencies of $D_{v,h}$ at different changes of sea surface wave short and long components parameters are presented. These curves correspond to the gust of wind speed from 6.3m/s to 15.4m/s and change $m^2_{6.3}$ to $m^2_{15.4}$ at $t_a = t_v$ =11°C. In Fig.3 the limits of any changes of these dependencies due to the changes of all conditions for Δv, Δm, t_a t_v and λ, are presented. According to the results of Fig.3, there are sufficient differences between the curves of $D_v(\Delta v,\Delta m)$ and $D_h(\Delta v,\Delta m)$, which may be used as a basis for detection and identification of such anomalous formation, originated on sea surface due to only the changes of sea surface wave short or long components characteristics. For detection and identification it is necessary to determine the values of D_v and D_h at incidence angle from 45° - 75° and compare these values with certain thresholds.

COMBINED RADAR-RADIOMETER DETECTOR-IDENTIFIER

In Fig.4 a block diagram of detector-identifier are presented. This detector - identifier consist of antenna 1, combined radar - radiometer module 2, in the outputs of that the signals σ_{vv}, T_{Bh} and T_{Bv} are formed, handlers 3, in the outputs of the each signals $\Delta\sigma_{vv}$ and $\Delta T_{Bv,h}$ are formed, dividers 4, thresholders 5, module for detection and identification 6, register 7.

CONCLUSION

Thus, on the basis of results of carried out theoretical investigations, cross polarization radar - radiometer principle for sea surface anomalous formations detection and identification are suggested. This method allows to identify sea surface anomalous formations originated due to chan-

ges of sea surface wave various components characteristics.

Combined radar and cross polarization radiometer detector-identifier developed at the Institute of Radiophysics and Electronics of Armenian National Academy of Sciences is described.

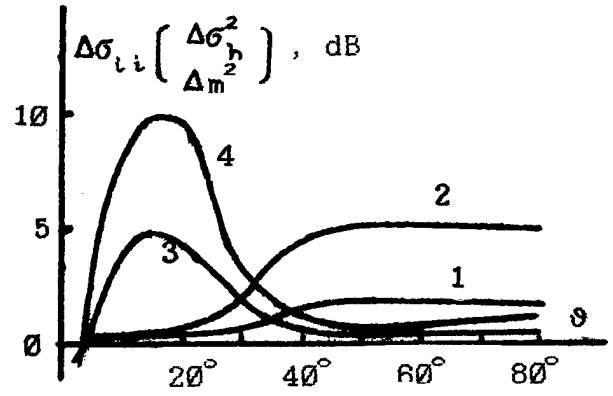


Fig. 1

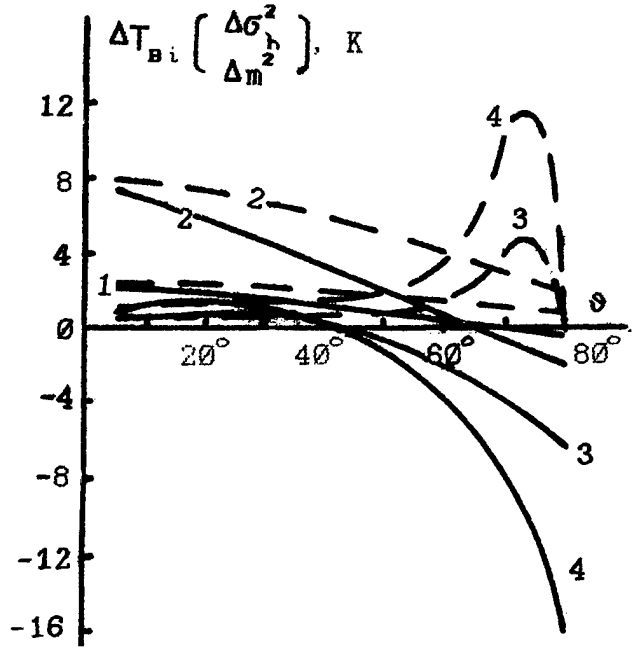


Fig. 2

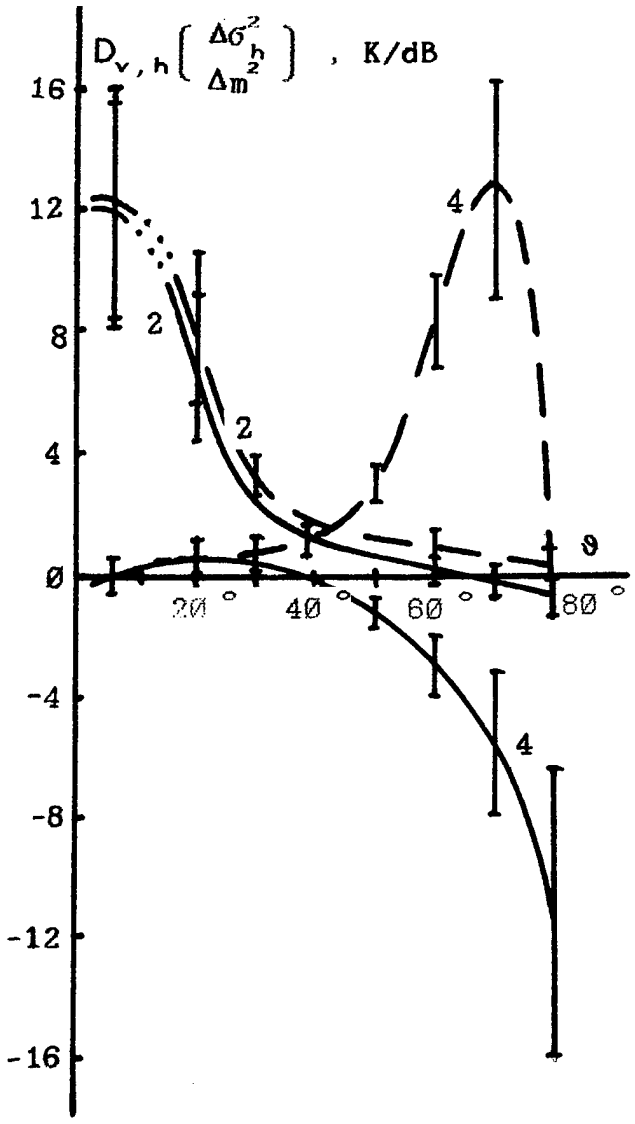


Fig. 3

——————— - Vert.polarization; -- -- -- - horiz.polarization
1.- Gust of Wind from 6.3m/s to 9.8m/s; 3.- Change $m^2_{6.3}$ to $m^2_{9.8}$
2.- Gust of Wind from 6.3m/s to 15.4m/s; 4.- Change $m^2_{6.3}$ to $m^2_{15.4}$

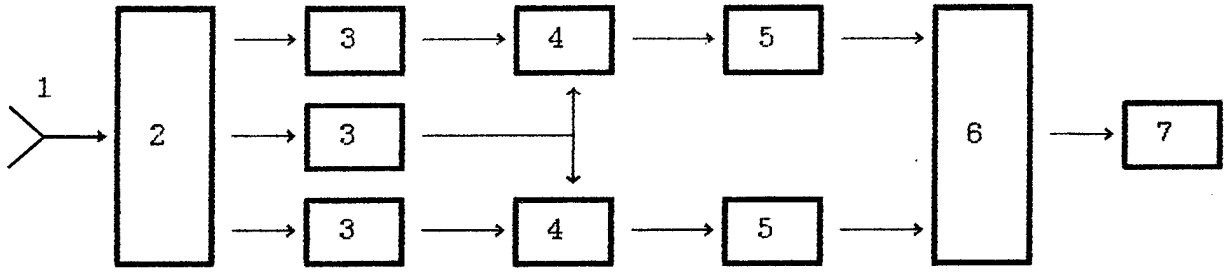


Fig.4 A Block Diagram of Detector-Identifier

1996 International Geoscience and Remote Sensing Society

KidSat: Youth Enhancing Space

Moon-Young Choi, Go Nagatani
La Canada High School, Pasadena, CA

JoBea Way
Jet Propulsion Laboratory, California Institute of Technology
Mail Stop 300-233, 4800 Oak Grove Dr., Pasadena, CA 91109
818-354-8225, Fax: 818-354-9476, Email: way@lor.jpl.nasa.gov

Elizabeth Jones Stork
Institute for Academic Advancement of Youth, The Johns Hopkins University

Abstract -- The mission of KidSat is to identify how middle school students can utilize images of Earth to promote inquiry and foster knowledge by using mounted cameras onboard the Space Shuttle. Students engage in scientific inquiry by using content rich middle school curricula based on images of Earth taken during Shuttle flights. The students use the tools of modern technology to distribute the images and results widely. A research and discovery model promotes individual student growth, inquiry and achievement while helping students solve real-world problems. Teamwork, mentoring and the active participation of precollegiate and collegiate students, educators, engineers and scientists further enhances this educational process.

INTRODUCTION

Imagine how beautiful Earth is from space [1]. And imagine how much we could learn about the world we call home from a vantage point high above Earth's clouds, tallest peaks and deepest canyons.

The KidSat Project is designed and operated by students who want to explore Earth from space and learn more about its past and its fragile, ever-changing environment [2]. KidSat provides students with the necessary tools to study Earth, just as astronauts and scientists do during Space Shuttle missions [3].

0-7803-3068-4/96$5.00©1996 IEEE

KidSat includes a payload of digital still and video cameras that fly on the Space Shuttle. Students command these cameras from their classrooms, sending instructions to a KidSat Mission Control Center via the Internet to photograph specific regions of Earth they wish to study. Image data are sent to the KidSat Data System during the mission and these images are accessible in the classroom in real time, again using the Internet. Students are then responsible for analyzing the images; these enhanced images are sent back to the KidSat Data System and are available on-line so that students can see each other's discoveries

Students and teachers are working to develop this program in collaboration with scientists, engineers and educators from NASA and academic institutions. Eventually KidSat may fly aboard the new International Space Station, giving students and educators a permanent platform for studying the Earth from space.

THE KIDSAT CONCEPT

One of the most compelling facts about the KidSat Project is that the instruments and the mission operations and data system infrastructures are configured by students with the help of scientists and engineers. The instruments are operated not by the astronauts on a Space Shuttle flight, or by scientists at NASA's Mission Control Center, but by students in their own classrooms [4].

Students are determining the exact specifications for each KidSat mission. This means they decide what instruments they want to fly, what lenses are needed, and which areas of the world they want to image. For the first Shuttle flight, the payload includes a Kodak digital still camera, mounted in the Shuttle's overhead window, that provides high resolution color images of the Earth; and a NASA video camera mounted in the Shuttle's payload bay that monitors the Earth along the Shuttle's flight path. The commands, telemetry and images are transmitted back and forth from space to students' classrooms using orbiting communications satellites and the Internet. The video is available live in the classrooms via NASA TV.

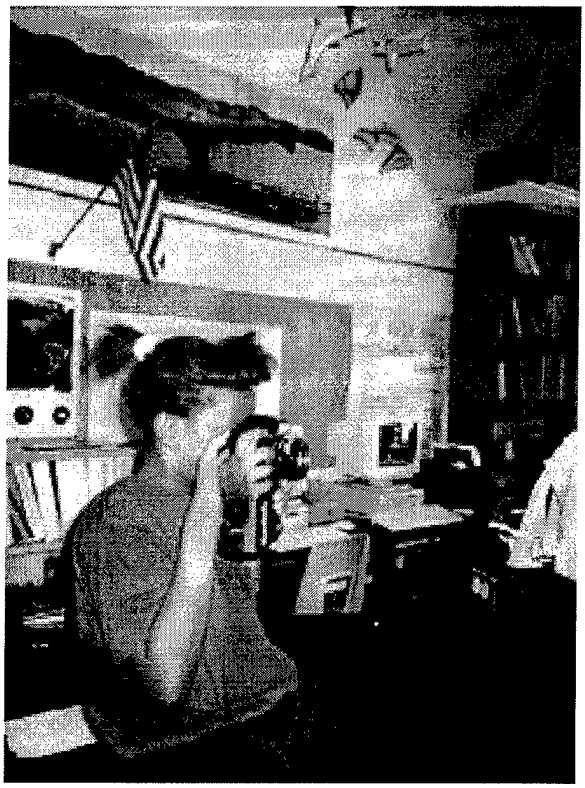


Figure 1: A student at the Charleston Pilot School examines the KidSat digital still camera.

WHO IS INVOLVED

KidSat was inspired by high school students from a Johns Hopkins University challenge Awards Program working on a Space Shuttle project with scientists at NASA's Jet Propulsion Laboratory (JPL) [3]. Since then the concept has been developed by JPL, The Johns Hopkins University Institute for Academic Advancement of Youth, and the University of California, San Diego. The project is sponsored by NASA's Education Division with support from NASA's Offices of Space Flight, Space Science, and Mission to Planet Earth.

The KidSat philosophy is that students are actively involved in every aspect of the project. At the heart of the program is the effort to actively engage large numbers of K-12 students in the process of planning observations and incorporating images into their classroom studies. It is also central to the program that students (in necessarily smaller numbers) are involved in the selection and configuration of the instruments, and the design and operation of the mission control and data systems.

Each partner institution has responsibility for developing specific aspects of the KidSat Project. JPL has the lead role in project management, in implementing the flight instruments, and, initially, in developing the data system. At JPL, students from La Canada High School and the California Institute of Technology are working on these KidSat project elements. UCSD has the lead in mission operations. Undergraduate students at the university are developing a KidSat Mission Operations Gateway that links classrooms to Space Shuttle operations and uplinks student commands to their cameras. High school students from San Diego join the undergraduate students to operate the Gateway during the mission. The Johns Hopkins University Institute for Academic Advancement of Youth is leading a team of educators from across the country to develop the KidSat curriculum, design teacher training workshops, and evaluate the pilot classrooms at Buist Academy in Charleston, South Carolina, Gompers Secondary School in San Diego, California, and the Washington Accelerated Learning Center in Pasadena, California. In the next two years, KidSat will add classrooms in Omaha, Nebraska, Houston, Texas and

Baltimore, Maryland. NASA's Johnson Space Center is also playing a major role in providing access to existing Space Shuttle flight cameras, assisting in the development of the mission operations infrastructure, and integrating the student payload onboard the Space Shuttle.

PILOT PROJECT

KidSat is currently a pilot project designed to develop the infrastructure and curriculum such that, in the future, many classrooms across the country may participate via the Internet. In the pilot program, a small number of schools are involved in the development process. Any school may find out about KidSat and follow its development using the Internet.

AN INVESTMENT IN OUR FUTURE

The theme for KidSat is Youth Enhancing Space. This theme was developed by a group of high school students working with the pilot classrooms. KidSat gives America's youth an opportunity to actively participate in the country's space program. It acknowledges students' value as young explorers and citizens of the future. In the long run, that knowledge gained may bring about a whole new perspective about humanity's role in helping to preserve life on Earth.

PUBLIC INTERNET SITES

You may access the KidSat Home Pages through the following public Internet site:

http://www.jpl.nasa.gov/kidsat

ACKNOWLEDGMENTS

The KidSat Youth Enhancing Space project has developed with support from many students, teachers, engineers and scientists. We acknowledge this support as well as that of the National Aeronautics and Space Administration. This work was carried out under contract to the National Aeronautics and Space Administration.

REFERENCES

[1] Ride, S. and T. O'Shaughnessy, The Third Planet, Exploring the Earth from Space. Crown Publishing Company, New York, NY, 1994.

[2] Way, J. B., E. J. Stork and S. Ride, 1995. KidSat. IGARSS '95, Florence, Italy.

[3] Way, J. B., B. Holt, M. Schier, V. Connors, L. Godwin, T. Jones, A. Campbell, F. Dean, T. Garrett, H. Hartley, A. Moshiashwili, J. Woodring, E. Cooper, E. Mortenson, D. Ouellette, R. Parrott, M. Rivas, Earth Observations for the SRL Mission. Geocarto Int., 9, 61-80, 1994.

[4] Nicholson, J., Students with a Mission, NASA Puts "Can Do" Project in Orbit. National Geographic, 186, 54-69, 1994.

The Education Element of the KidSat/Youth Enhancing Space Project

John McGuire
Pacific Union School, Arcata, CA
Institute for the Academic Advancement of Youth, Johns Hopkins University
Western Regional Office, 206 North Jackson Avenue, Suite 304, Glendale, CA 912 06
818-500-9034, Fax. 818-500-9058, Email: mjones@lor.jpl.nasa.gov

Bruce Fisher
Fortuna Elementary, Fortuna, CA

Roger Kassebaum, NE
Millard North High School, Omaha

Dan Barstow
Teacher Education Resource Center, Cambridge, MA

Kathy Rackley
Buist Academy, Charleston, SC

Paul Bixler
Gompers Secondary School, San Diego, CA

Dr. Mark Jones
Institute for the Academic Advancement of Youth, Johns Hopkins University

Jackie Hunt
Institute for the Academic Advancement of Youth, Johns Hopkins University

ABSTRACT

Affording a greater accessibility to technology is recognized as imperative to the education of tomorrow's students. KidSat/Youth Enhancing Space Project uses a progressive approach to entice students' curiosity. Utilizing an interdisciplinary approach to the implementation of KidSat/Youth Enhancing Space Project curriculum, students are involved in transferring their new knowledge to other disciplines, which facilitates their learning process.

Defining features of KidSat/Youth Enhancing Space are its innovative method of promoting teacher and student ownership and collaborative relationships in development of a curriculum that is salient to the child; one that is diligently monitored by teachers for content and high standards. Students' understanding of science, mathematics and technology concepts is enhanced by student involvement in project design and implementation and with teachers, scientists, and engineers serving as content advisors. This process not only enriches student learning, but also fosters teacher involvement in their own professional growth and development.

The educational objectives for KidSat/Youth Enhancing Space are (1) to advance the learning of middle school students through the use of science, math, space technology, geography and other subject areas, (2) to develop an infrastructure that will foster student intellectual exploration and discovery, and (3) to develop and implement teacher training institutes geared to achieving mastery of technology, subject knowledge, and the reasoning skills imparted to students.

INTRODUCTION

KidSat/Youth Enhancing Space gives young people a piece of space program. It acknowledges their value as young explorers and citizens of the future. KidSat/Youth Enhancing Space is designed to capture the imagination of students and motivate them to learn by engaging them in an exciting, hands-on project that significantly contributes to their education. It addresses new challenges in educational technology including how to bring high quality affordable learning tools into the classroom, effective use of the Internet, and how to involve students in scientific investigations as part of human exploration.

The education element of KidSat/Youth Enhancing Space advances the learning of students through the use of science, mathematics, geography, and earth viewing technology. The KidSat/Youth Enhancing Space educational philosophy places student ownership at the heart of the program. Students are actively involved in all aspects of the program which includes planning observations and incorporating KidSat/Youth Enhancing Space images into their studies. Core educational student activities include: (a) designing and select the KidSat/Youth Enhancing Space instruments, (b) discovering and

0-7803-3068-4/96$5.00©1996 IEEE

constructing meaning from KidSat/Youth Enhancing Space images of the earth, (c) designing and operating the KidSat/Youth Enhancing Space mission control system, (d) applying new visual perspectives of the earth and (e) identifying and resolving issues with regard to downlinking information and distribution of data. Innovative curricular activities and the development of new data sets enhance students current knowledge base and serves to develop the basis and motivation for further learning.

The educational goals for KidSat/Youth Enhancing Space encompass curriculum development, student learning, and professional development for classroom teachers. Curriculum goals include activities that stress inquiry and discovery with rich content that embellish current national educational standards. Students learning is advanced through the use of science, mathematics, geography, and space technology, developed through an infrastructure which fosters student intellectual growth. Though-out this process the program undergoes continuous evaluation, revision, and development. Additional goals focus on developing and implementing teacher training institutes geared to achieving subject knowledge, mastery of technology, and pedagogical skills.

CORE CURRICULUM DESIGN TEAM

A Core Curriculum Design Team consisting of educators, scientists, and engineers creates the supplementary curriculum modules to be integrated into targeted schools. The unique partnership which exists between scientists and educators in KidSat/Youth Enhancing Space Project provides the opportunity to create inquiry based science curricula that is rich in content. Scientists, engineers, and educators work together sharing individual expertise through ongoing collaboration. As lessons in modules are developed each element of the educational team works together to review, revise, and refine the lessons.

EDUCATION MODULES

Educational modules feature "learning by doing" allowing students to attain skill mastery and determine a the direction of investigation leading to discoveries. Students may be differentiating the biomes in a particular image as a specific objective of a lesson, yet generate interest concerning how the image is captured and produced. Such exploration may generate discussion on light, lenses, and cameras which leads to further investigation. This inquiry is a foundation of the modules. Students individuality of learning is address through this method.- optimal match

Viewing Earth From Space

This module teaches students how to view the Earth from space and introduces them to the basic elements of the KidSat/Youth Enhancing Space Project. In Unit 1, students develop an understanding of how a shuttle or piloted platform reaches and maintains an orbit around the Earth, what role communication plays, as well as a historical perspective of piloted space exploration. The remote sensing supplementary curriculum developed as part of the SIR-C educational CD at JPL(Freeman, et al. 1994) and Can Do educational material form a base for this module. Basic principles of physics, mathematical concepts of scale, as well as the importance of communication are emphasized. Unit 2 revolves around the interpretation of images of the Earth. Viewing Image of Weather from Space and Familiar Places and Patterns provide students the opportunity to explore and hypothesize about conditions on the Earth. Optical images are the source of data for this unit. The introduction to the Internet and KidSat/Youth Enhancing Space Data System are the main components of Unit 3. Students access optical images via the Internet based and use authoring software to enhance the images.

Mission Operations

Acquiring images and videos of sites with the KidSat/Youth Enhancing Space instruments is the primary objective of the *Mission Operations* module. Students study concepts involved in the acquisition of images from an instrument in space and basic mission operation techniques. These include targeting, flight operations, weather observation, current events, and communications. Communications between Student Mission Operations Centers and Mission Control Gateway is emphasized as well as communication within the SMOC. Students will predict the orbital paths of the Shuttle or Space Station. With this mapping students decide optimal image opportunities based on attitude, weather, previous investigation of sites, and other conditions. Motions and forces, Earth rotation, seasonal patterns, meteorology, day/night relationships, as well as geometry and coordinate graphing are also emphasized in the module.

The Impact Of Water On Earth

This module introduces students to the "blue planet": its population, resources, and environments that are intricately related to and dependent upon water. Students using images from space will investigate weather, ice/glaciers, oceans, ecosystems, and landforms. Students model scientific procedures through the use of image driven curriculum. In all cases curricular processes emphasize content acquisitions from in depth student investigations. Each of the components of this modules stresses the interdependency of the elements of our planet as a system with complex interactions. Students examine, identify planet features and analyze the impact of human interaction

on our planet. The lessons provide a scaffold for individual student research with open ended entry and departure points.

Future Modules

The IAAY and Core Curriculum Design Team will create additional modules each year. Currently under development are the Student Investigations and the Instrument Design Module.

ASSESSMENT AND EVALUATION

Lessons contained in each module have built in assessment checkpoints. Activities incorporated into the lessons and units have prescribed skill expectations to determine each student's understanding and progress. The assessments are unique to each lesson or unit and are based on each unit's key elements and goals. Both content and process objectives are measured through a variety of methods including student journals, products, portfolios, and standardized assessment. The embedded assessments provide another diagnostic opportunity to aid in individualizing curriculum within the lesson/module. All modular units include an end of unit assessment point. Evaluation of student's understanding of the content and processes within a module can be determined through a student project.

Standardized assessment will be administered before the implementation of the curriculum and at the end of the program instruction. Four sub-tests of the Comprehensive Testing Program (CTP III) will be administered to all participating students at the Pilot School Sites as well a non-participating comparison group. Testing will focus upon: Mathematics Achievement; Writing Process Achievement; Verbal Aptitude; and Quantitative Aptitude.

Future Opportunities and Issues in Radar Remote Sensing of Earth's High Latitudes

Frank Carsey
California Institute of Technology Jet Propulsion Laboratory
JPL ms 300-323
Pasadena, CA 91109

Carl Wales
Alaska SAR Facility
Geophysical Institute of the University of Alaska Fairbanks
Fairbanks AK 997750

Abstract. The Alaska SAR Facility (ASF) is now downlinking data for science and operational users from 4 satellites, ERS-1 and -2, JERS-1, and RADARSAT; ASF thus processes data generated by three non-US space agencies, ESA, NASDA, and CSA. All of these satellites may well be still functioning at the turn of the millennium. Scientific plans are now in place for these data sets, and more opportunities for their use are planned. The future is also promising: In 1998 ESA plans an exciting new radar, the ASAR, as part of the ENVISAT payload; in 2000 CSA plans to launch and operate RADARSAT 2; and in 2001 or 2002 NASDA plans to launch ALOS. These future satellite programs promise increased observational capability. ASF, plans to provide users with steadily increasing quantity and quality of data as well as increased access to higher-level data products and specialized data sets such as interferometric SAR. Among the higher-level products envisioned are weekly, Arctic-wide ice motion, age, and thickness, a complete RADARSAT SAR map of Antarctica, JERS-1 mosaics of the Amazon and African rain forests, ERS Tandem Mission fringe maps of Antarctica and parts of Alaska, and other user-generated products. With the increased coverage and frequency selection, the value of fused data sets consisting of SAR and other data sets will be far greater. We feel that the next 5-10 years will see the maturation of routine SAR observations in a number of exciting scientific and operational applications. Thus, over the next decade the satellite radar data sets available to researchers in the high latitudes will evolve significantly, especially if the user community can exert some influence over flight agencies in the area of data availability.

CURRENT SITUATION

The high latitudes traditionally have excellent coverage from satellites. This situation is partly the natural consequence of the convergence of orbits of polar orbiters at the poles, but that coincidence would not be sufficient as active ground stations and archiving facilities are also required. In the case of satellite radar data sets, the ground station support required is demanding due to the high data rates and sophisticated data processing involved. Motivation is required, and it is provided by the utility that satellite SAR data sets have demonstrated in polar applications.

There are 3 radar ground stations in each polar region and additional stations in the high sub-polar regions; thus, at this time, it is possible to obtain radar data from any point poleward of about 55° N or S in the form of either L-band or C-band images (from JERS-1 or ERS-1). This is, by comparison to much of the world, exceptionally good data availability, and it is augmented by good collection schemes for visible-light and IR images and passive microwave observations in addition to various sounding data. In the case of the radar data, there are some obstacles to the free availability and exchange of data, and this is an issue that should receive continued examination and vigorous lobbying to correct so that scientific use of data is enhanced.

ASF is responsible for data acquired at Fairbanks, Alaska and McMurdo Station, Antarctica. The ASF mask includes an area stretching from Siberia to Oregon, Alberta, and a substantial amount of the Arctic Ocean, and the McMurdo mask covers 2/3 of Antarctica and a great expanse of the Ross-Amundsen Seas. All data acquired at these sites is available to approved scientific users.

The current data holding situation for ASF includes ERS-1 and 2 and JERS-1 and a collection of ice motion information for the Beaufort Sea derived from ERS-1 winter data. Current acquisitions include ERS-1 and 2 and JERS-1 including taped JERS-1 data from a variety of locations. The ERS-1 data collection started in 1991; JERS-1 in 1992. Data acquisition at McMurdo is from ERS and RADARSAT and officially began in January, 1996, but there are some data acquisitions prior to that.

Support provided by NASA through contracts to Caltech and the University of Alaska Fairbanks

0-7803-3068-4/96$5.00©1996 IEEE

ERS-1+2 TANDEM MISSION

By far the most exciting development to date in high-latitude SAR opportunities is the ERS Tandem Mission (ETM) in which ERS 1 and 2 fly in identical orbits with a time interval of 1 day between their coverage. This data set is ideal for interferometric analysis and will be useful for DEM generation and for observing environmental changes such as ice stream motion and volcanic and seismic deformation.

The objective of ETM was to map the Earth's land-surfaces 5-6 times in descending passes augmented with ascending passes where terrain would call for the additional acquisitions. ASF requested that extra ascending data be acquired for Antarctica and some of the Alaska mask so that ice vector motion could be better determined. (Interferometry is sensitive only to the motion along the transmit vector; two measurements are required to resolve horizontal motion.) In Antarctica the ETM data will allow terrain correction of the SAR images themselves with the consequence that this data can be analyzed for geologic and tectonic information. Also, the ETM data over the ice sheets will resolve their topography in the steeply-sloping regions where satellite altimetry is not applicable.

ASF now holds the Alaska mask ETM data and some of the McMurdo mask data, and the remainder of the McMurdo data will be in hand by year's end. The data set will be so large that the processing and analysis of it will require several years, but the results will be exciting and useful.

RADARSAT

RADARSAT was launched in November, 1995 and has been in commissioning phases until early this month (May, 1996). There are approximately 50 Applications Development and Research Opportunity (ADRO) investigators associated with the US component of the program, which is supported with data by ASF. These programs stress the polar regions, but they are global in distribution. Data acquired for the research program by ASF will be available to investigators whose research proposals are accepted; these can be submitted to ASF at any time. RADARSAT represents an advance in the SAR data available to users in that there are some 26 beams including ScanSAR which has quite wide swath, up to 500 km. The beam selection also includes the capability to observe a site at a variety of incidence angles. As discussed below, RADARSAT data acquisitions already planned will extend new type of radar data product, repeat large-scale mappings.

RAMP.

A key aspect of the RADARSAT program is the RADARSAT Antarctic Mapping Project (RAMP) which is described further in other papers in these *Proceedings*. RAMP will result in two complete mappings of Antarctica, and they will be merged into maps of the entire continent. The first mapping is planned to occur in October, 1996. ASF will also make available the original SAR frames from which the maps will be derived.

RGPS and the Arctic Snapshot.

Another key RADARSAT data set will be the "Arctic Snapshot," a sequence of ScanSAR swaths acquired over 2 days which will cover the entire Arctic Ocean on a weekly basis. This data set is for use in the RADARSAT Geophysical Processing System (RGPS) which has the long-term goal of estimating surface heat and brine fluxes for the northern ice-covered seas. Generating a complex, long-term, basin-scale geophysical data set from routine SAR observations has never been attempted previously; it is a significant challenge. The RGPS is now in development phase for operation in the 1997-98 timeframe. When operational the RGPS may be implemented at ASF so that data can flow immediately from the SAR processor to be processed into geophysical products and go to the user community. The Arctic Snapshot will also be utilized in the ice monitoring activity of the National Ice Center, and, of course these data sets will also be available to approved scientific users.

ENVISAT and ALOS

From a strong current position in SAR observations, ASF is planning for enhanced capability in future. Crucial to this future is access to the next generation of satellite SAR data, in particular to ASAR on ENVISAT, planned for flight by ESA in 1998 or 1999, and ALOS, planned for flight by NASDA in 2001 or 2002. ASAR will continue the ESA use of C-band and will include incidence angle, polarization and swath selection including a ScanSAR mode. ALOS is planned to be a fully polarimetric L-band system. At present the requisite international agreements have not been signed to make ASF an approved ground station for these systems, but it is anticipated and hoped that this will occur.

CONCLUSION

ASF is a key resource supporting polar research and operations with SAR data and products. Ongoing activities are vital and interesting, and the future holds enormous promise. These SAR data sets should receive ever increasing attention in the generation of high-level data products for use in studies of climate, air-sea-ice interactions, seismic and volcanic deformation, northern ecosystems, and operations.

Expected Errors in Satellite–derived Estimates of the High Latitude Surface Radiation Budget

Jeffrey R. Key
Dept. Of Geography, Boston University
675 Commonwealth Ave., Boston, MA 02215
Phone: (617) 353-2841, Fax: (617) 353-8399, jkey@bu.edu

Robert S. Stone
Cooperative Institute for Research in Environmental Sciences, University of Colorado, Boulder, Colorado

Axel J. Schweiger
Polar Science Center, University of Washington, Seattle, Washington

INTRODUCTION

An analysis of the spatial and temporal variations of the polar radiation budget will undoubtedly require the use of multi-spectral satellite data. How well we can estimate the radiation balance depends on how well we can estimate the physical and microphysical properties of the surface and atmosphere that directly affect it; e.g., surface temperature and albedo, cloud particle effective radius, cloud optical depth, cloud thickness and cloud height. However, the retrieval of cloud and surface parameters is particularly problematic at high-latitudes. Here we examine our current ability to retrieve these geophysical parameters using visible and thermal satellite data, in particular the Advanced Very High Resolution Radiometer (AVHRR) on-board the NOAA polar-orbiting satellites. Both empirical and theoretical methods used in their retrieval are briefly described and the expected accuracy for each of these parameters is quantified. On the basis of our uncertainty analysis we speculate on the utility of estimating radiative fluxes derived from satellite data for the study of climate change in polar regions.

PARAMETER RETRIEVAL

In this section we ascribe uncertainties to each of the surface and cloud parameters that are used in the computation of radiative fluxes. The parameter retrieval algorithms are described elsewhere [1] [2].

Skin temperature T_S and surface albedo α_S summarize the physical aspects of the surface such as snow and ice thickness, grain size, and water content. They occur explicitly in the energy balance equation, and therefore their retrieval from satellite data is desirable. From what little validation data are available (e.g., [3] [4] [1]), errors in clear sky IST are on the order of 0.5 K for summer and 0.5-2 K for winter conditions.

This work was supported by NASA grant NAGW-2407 and NSF grants OPP-9320938 and OPP-9220938.

These errors are largely a result of inaccuracies in cloud detection, which is particularly problematic when lower tropospheric ice crystals are present. Equating the clear sky temperatures to cloudy sky conditions, necessary because the temperature under cloud cover cannot be obtained from thermal data, introduces additional error.

Narrow-band surface albedo or reflectance is retrieved by correcting the satellite radiance or albedo for atmospheric attenuation, and further correcting it for anisotropic reflectance of the surface. These steps were followed by [5] where satellite-derived albedos were compared to in situ data. Calibration is the largest source of uncertainty, with unknown aerosol amounts and questionable anisotropic reflectance factors being important contributors. Uncertainty is on the order of 0.05, absolute.

Because the retrieval of surface temperature and albedo as described above are done for clear sky only, accurate cloud detection is critical. Our error assessment for cloud detection here assumes a spectral thresholding method, but one that incorporates time; i.e., the temporal variability of each location is examined under the assumption that clear sky spectral characteristics will change little over short periods of time [1]. With this procedure we estimate the error in cloud fraction A_c to be 0.1 absolute during the polar day and 0.15 during the polar night.

Cloud particle effective radius *Re* and optical depth τ_c can be estimated using multi-band reflectances during the day and brightness temperature differences at night. Due to uncertainties in the shortwave channel calibration, the small signal to noise ratio in channel 3 (3.7 μm) at low temperatures, and cloud phase uncertainties, we place a potential error of 50% on optical depth and errors of 2 μm and 10 μm for water and ice cloud effective radii, respectively.

Cloud top height Z_c and temperature are determined from the channel 4 brightness temperature, the temperature profile, and the cloud optical depth. The uncertainty in cloud top height is approximately 400 m in summer water clouds and 1500 m in winter ice clouds.

0-7803-3068-4/96$5.00©1996 IEEE

Other

In this study it is assumed that TOVS data are only being used to provide temperature and humidity profiles, although it can also be used in the retrieval of cloud parameters [6]. It has been found that, while low-level inversions can be retrieved, they are generally less intense. Also, summer retrievals are better than winter retrievals. We use errors in the temperature profile, *T(z)*, determined for typical winter conditions, of a few degrees in the lower troposphere to less than one degree in the mid- and upper troposphere (S.J.S. Khalsa, personal communication, 1994). No quantitative assessment of the uncertainty in the humidity profile has been done, so precipitable water, *W*, is varied by plus and minus 20%.

Total column ozone amount, O_3, can also be obtained from TOVS, although its accuracy is unknown to the authors. Climatological means plus and minus one standard deviation are used for summer and winter sensitivity tests. Aerosol optical depth τ_{aer} is in general not retrievable from the AVHRR over highly reflective surfaces such as snow and ice. Two cases are examined, one with a high aerosol loading in the troposphere, τ_h, and one with a high volcanic loading in the stratosphere, τ_v.

FLUX SENSITIVITIES

The estimated uncertainties in the retrieved values of surface and cloud properties are now used to assess the accuracy with which surface radiative fluxes can be estimated using satellite data. We present surface net radiative fluxes computed using typical values of these parameters plus and minus the stated uncertainties. Net radiation, rather than upwelling or downwelling fluxes, is examined since this is what ultimately affects the surface energy balance. Results are summarized by season for clear and cloudy conditions. In the clear sky analyses, snow and open water surfaces are considered separately. The radiative transfer model used is described in [7].

Clear Sky

Tables 1 and 2 list the parameters used in the net flux sensitivity studies for typical Arctic summer and winter clear sky conditions. Snow and open water surfaces are considered separately. Also given are the estimated uncertainties in the retrieved values using the AVHRR as the primary instrument. The effects of the uncertainties on the surface net flux are listed as the percent difference from the baseline case.

It is clear from the tables that expected errors in the retrieval of surface temperature and albedo yield the largest uncertainty in the surface net flux under clear sky conditions. This is particularly true for snow surfaces. Aerosols, on the other hand, play an important role in the radiation balance over open water since they increase the planetary albedo and decrease the downwelling shortwave flux. Note also that increased aerosol amounts have opposite effects on the net flux in summer and winter over open water. In summer an increase in aerosol amount decreases the net flux at the surface, whereas in winter the net flux would increase due to the increase in the downwelling longwave flux. In winter estimated errors in the temperature profile retrievals have a significant effect on the surface radiation balance. In the range of ozone considered (plus and minus one standard deviation), this parameter is relatively unimportant for net flux calculations.

Table 1. Net flux sensitivities for clear summer over snow and over open water.

Parameter	Baseline Value	Error (±)	Difference (%)
SNOW:			
T_s (K)	272	1	16
α_s (0.6 m)	0.90	0.05	49
O_3 (g m-2)	7.15	0.1	<0.1
W (mm)	11	20%	0.6
τ_h	0.660	10%	1
τ_v	0.30	10%	1
WATER:			
T_s (K)	271.4	1	2
α_s	0.07	0.05	5
O_3 (g m-2)	7.15	0.1	<0.1
W (mm)	11	20%	0.3
τ_h	0.660	10%	3
τ_v	0.30	10%	2

Table 2. Net flux sensitivities for clear winter over snow and over open water.

Parameter	Baseline Value	Error (±)	Difference (%)
SNOW:			
T_s (K)	242	3	17
O_3 (g m-2)	7.22	0.36	<0.1
W (mm)	2	20%	4
τ_h	0.660	10%	3
τ_v	0.30	10%	2
T(z) (K)	245	+	10
WATER:			
T_s (K)	272	1	3
O_3 (g m-2)	7.22	0.36	<0.1
W (mm)	2	20%	1
τ_h	0.660	10%	1
τ_v	0.30	10%	0.5

Cloudy Sky

Results for the cloudy sky tests are given in Tables 3 and 4. As in the clear sky cases, probable errors in the retrieval of

surface temperature and albedo have a large effect on the net surface flux. Errors in cloud effective radius and cloud thickness are acceptable for summer conditions, but need to be reduced for wintertime studies. Cloud amount and optical depth also exert a significant influence on the net flux and their retrievals from satellite data need to be improved.

Table 3. Net flux sensitivities for cloudy summer (stratus).

Parameter	Baseline Value	Error (±)	Difference (%)
T_s (K)	268	4	25
α_s (0.6 m)	0.87	0.05	15
O3 (g m-2)	7.15	0.1	<0.1
W (mm)	11	20%	<0.1
Re (m)	8	2	2
Z_c (m)	1200	400	2
A_c	0.7	0.1	4
τ_c	2.5	1.25	8

Table 4. Net flux sensitivities for cloudy winter (cirrus).

Parameter	Baseline Value	Error (±)	Difference (%)
T_s (K)	247	4	23
O_3 (g m-2)	7.22	0.36	<0.1
W (mm)	2	20%	3
Re (m)	40	10	2
Z_c (m)	7500	1500	3
A_c	0.5	0.15	6
τ_c	1.5	0.75	8

CONCLUSIONS

The sensitivity of the net surface radiation flux to estimated errors in satellite retrievals of surface temperature and albedo imply that improvement in these algorithms is needed. Results indicate that errors in the retrievals are largely a result of uncertainties in cloud masking and the calibration of the AVHRR shortwave channels, affecting primarily the estimates of surface temperature, surface albedo, and cloud optical depth. Validation studies using hourly surface radiation measurements at Barrow, Alaska indicate that on a point-by-point basis the net surface radiative flux can be estimated to within about 10%. We can expect some improvement on this when data are averaged over time and space but, since many of the uncertainties are not Gaussian (e.g., calibration errors will introduce a bias), errors will not average out.

Future work should include the validation of retrieval algorithms, particularly for cloud properties, using in situ data from experiments such as BASE (Beaufort and Arctic Storms Experiment) and SHEBA (Surface HEat Budget of the Arctic Ocean). These field campaigns will allow us to better quantify retrieval accuracies for individual parameters as well as the combined accuracy of radiative flux estimates.

REFERENCES

[1] Key, J., 1966, An integrated approach to estimating surface radiative fluxes from satellite data, *Remote Sensing Environ.*, submitted.

[2] Key, J., 1966, The Cloud and Surface Parameter Retrieval (CASPR) User's Guide, Department of Geography, Boston University, 90 pp., unpublished.

[3] Key, J., R. Stone, and M. Rehder, 1994: Estimating high latitude radiative fluxes from satellite data: problems and successes. **IGARSS'94 Proceedings**, Vol. 2, 8-12 August, Pasadena, 1018-1020.

[4] Key, J., J.A. Maslanik, T. Papakyriakou, M.C. Serreze, and A.J. Schweiger, 1994: On the validation of satellite-derived sea ice surface temperature, *Arctic*, in press.

[5] DeAbreu, R.A., J. Key, J.A. Maslanik, M.C. Serreze, and E.F. LeDrew, 1994: Comparison of *in situ* and AVHRR-derived surface broadband albedo over Arctic sea ice. *Arctic*, in press.

[6] Francis, J., 1994: Improvements to TOVS retrievals over sea ice and applications to estimating Arctic energy fluxes, *J. Geophys. Res.*, 99(D5), 10395-10408.

[7] Key, J., 1966, Streamer User's Guide, Department of Geography, Boston University, 72 pp., unpublished.

Multitemporal Analysis Of Fast Sea Ice Albedo Using AVHRR Data

Roger A. De Abreu and E.F. LeDrew

Waterloo Laboratory for Earth Observations
Dept. of Geography, University of Waterloo
Waterloo, Ontario. N2L 3G1 CANADA

Ph.: (519)885-1211 ext, 2689 Fax: (519) 888-6768
Internet: roger@wateol.uwaterloo.ca

Abstract - Using AVHRR 1 and 2 data, the spatial and seasonal variability of sea ice visible and infrared albedo is examined through non-standardized principal component analysis (PCA). PCA reveals the importance of the time of ice consolidation in controlling the spatial and temporal variability of sea ice albedo during the spring melt season.

INTRODUCTION

In this paper, we utilize Advanced Very High Resolution Radiometer (AVHRR) visible channel 1 (0.58-0.68 μm) and near-infrared channel 2 (0.72-1.1 μm) to characterize the regional variability of broadband visible (0.28-0.69 μm) and infrared (0.7-4.0 μm) sea ice albedo over the entire spring melt season. Our objective is to describe the spatial and temporal variability of sea ice albedo in a fast ice regime. To this end, we use principal component analysis (PCA) to identify the major and minor scale variance structures in a multitemporal satellite albedo dataset collected during the 1993 Sea Ice Monitoring and Modelling Site (SIMMS) experiment.

SITE DESCRIPTION AND SURFACE MEASUREMENTS

SIMMS '93 was located in Resolute Passage (74°41.1'N, 95°35.22'W), N.W.T. in the Canadian Arctic Archipelago. The experiment is located in the middle of an early consolidation regime, the Barrow Strait regime, and a late consolidation area known as the Lancaster Sound regime (see fig. 1). The Barrow Strait regime consolidates in January and the Lancaster Sound regime can consolidate as late as April. As a result, the area contains fast sea ice that varies widely in terms of age and morphological characteristics. Intensive surface observations were made primarily at intensive sampling sites located in the middle of these two zones from April 22 to June 22. A further description of the surface measurements can be found in [1].

AVHRR SATELLITE DATA

Canada's Atmospheric Environment Service (AES) provided us with geocorrected NOAA 12 AVHRR data registered to a common map projection. The following clear sky data are used for multitemporal analysis: April 30, May 3, June 4, June 9, June 16, June 20, July 7 and July 29. The data span the entire melt season. Visible and infrared surface albedos were extracted from raw satellite data using the method described in [2] with the following two exceptions. Coincidental Landsat Thematic Mapper data were used to update the NOAA 12 AVHRR 1 and 2 pre-launch calibration and the narrow to broadband conversion was performed after the atmospheric correction to produce broadband visible and infrared albedos. The satellite-derived albedos resemble closely the *in situ*-measurements and are considered accurate to ±0.05 albedo units.

PRINCIPAL COMPONENT ANALYSIS

Principal component analysis, or eigenvector analysis, has been used extensively in the remote sensing community as a means of image enhancement, image compression and change detection in multitemporal image data. More specifically, in the polar remote sensing community, this technique has been utilized to examine the variability and interrelationships of sea ice and various atmospheric variables [3] and towards the classification of sea ice [4].

In this investigation, PCA is used to identify the underlying multitemporal dimensionality of the satellite-derived albedo dataset. Since we are concerned with the changes that are attributed to time, we perform the analysis on the visible and infrared data separately to eliminate the spectral component. Since the albedo data are commensurable, principal components of the data are extracted from the covariance matrix of the respective broadband data. In table 1, the calculated eigenvalues for each component are given as a percentage of the total variance. The first three components explain over ninety percent of the albedo variation over the sampled period. In order to aid in interpreting these components, we calculate the component loadings for each image dataset, i.e. the correlation of each image with each component. These loadings are presented graphically in fig. 2 for the first three components of each band. The first two components of the visible and infrared albedo are contoured in figs. 3 and 4 respectively. Our first interpretation of these data is presented below. In this limited space, we restrict our analysis to only the first two components of each band.

0-7803-3068-4/96$5.00©1996 IEEE

INTERPRETATION OF PRINCIPAL COMPONENTS

Visible Albedo

The visible albedo of sea ice is sensitive to the scattering characteristics of the sea ice volume. Surface observations indicate that, when covered by snow, sea ice visible albedo was typically high ranging from 0.7-0.95 [1] However, the seasonal ablation of the snow volume and the decay of the ice cover rapidly decreased this albedo with time.

The first component represents sixty percent of the variance in the dataset and suggests that, in 1993, visible albedo was most variable from April to the end of June when the snow-covered sea ice (α_{vis}=0.92) transformed into low-albedo melt ponds (α_{vis}=0.40). The component image essentially describes visible albedo integrated over the season. The mapped scores highlight those ice areas responsible for most of the seasonal variation in visible albedo. Generally, rough ice areas and near shore areas score high in this component. All of these areas are within the early consolidation zone and all have appreciable snow volumes (>20 cm). Significantly, melt ponds formed first and were extensive in these areas. Conversely, in the late consolidation area, melt ponds did not begin to form until after June 20.

The second component loads positively on June 20 and negatively on July 7. This component captures an interesting late season albedo pattern. The loadings suggest an inverse in albedo patterns for these two dates which is defined spatially by the time of ice consolidation. In the early consolidation area, surface albedo slightly increased in melt areas as melt water drained leaving behind a higher albedo ice surface. However, in the late consolidation area, the visible albedo of the white ice surface decreased from 0.61 to 0.32 as the ice surface melted and surface ponding finally began to form in this area. New areas of open water (shore leads) also scored similarly to these areas.

Infrared Albedo

Due to the absorptive properties of ice and water, the infrared albedo of sea ice is controlled by the conditions of the very near surface layers of sea ice. Infrared sea ice albedo decreases steadily throughout the melt season as snowpack grain size and the amount of surface water increases.

The first infrared principal component loads positively on all dates and most heavily on the dates June 9, 16 and 20. Essentially, like the first visible component, this component image represents infrared albedo integrated over the melt season and describes the general pattern of infrared albedo over this period. The dominant June period covers the onset and extent of surface ponding in the early consolidation area. This component suggests that the infrared albedo is consistently lower in the early consolidation zone and this pattern is somewhat dependent on the extensive ponding in this ice regime.

The second component accounts for 24 % of the seasonal variation and appears to load heavily on those dates (April 30, May 3 and June 4) when the ice in the region was predominantly covered by snow. This suggests that the component describes the variability in infrared albedo when melt ponds were absent. Since infrared snow albedo is sensitive to snow grain size, the component image is most representative of snow conditions. Significant is the fact that the component image shows a spatial structure similar to that of component 1, i.e. the sharp distinction between the consolidation zones. This suggests that these consolidation zones also drive the spatial pattern of infrared albedo early in the year through their distinctive snow conditions.

CONCLUDING REMARKS

This investigation has highlighted the importance of ice consolidation in controlling the spring patterns of sea ice albedo. In 1993, early consolidation areas had significantly deeper snow volumes due to their propensity for snow catchment. As a result, surface ponds appeared first and were more extensive in these zones. This appears to be the most important environmental factor behind the pattern of sea ice albedo in the SIMMS '93 experiment region.

ACKNOWLEDGMENTS

The authors would like to acknowledge the assistance of the following agencies: Natural Science and Engineering Research Council (Scholarship-R. De Abreu, Operating Grant-E.LeDrew), the Institute of Space and Terrestrial Sciences (Contract E. LeDrew), Northern Studies Scientific Training Grant, the Polar Continental Shelf Project. and the Atmospheric Environment Service. A special thanks to the members of SIMMS '93.

REFERENCES

[1] De Abreu, R.A., D.G. Barber, K. Misurak and E.F. LeDrew, "Spectral albedo of snow-covered first-year and multi-year sea ice during spring melt," Annals of Glaciology, vol. 21, pp. 337-342, 1995.

[2] De Abreu, R.A., J. Key, J.A. Maslanik, M.C. Serreze and E.F. LeDrew, "Comparison of in situ and AVHRR-derived broadband albedo over Arctic sea ice. Arctic," vol. 47(3), p. 288-297, 1994.

[3] Crane, R.G., "Spring melt patterns in the Kara/Barents Sea," GeoJournal, vol. 18(1), p. 25-33, 1984.

[4] Rothrock, D.A. and D.R. Thomas, "Principal component analysis of satellite passive microwave data over sea ice", vol. 93(C3), p. 2321-2332, 1988.

Table 1. Eigenvalues (λ) of Covariance Matrix for Visible and Infrared Albedo. Note: % refers to percentage of total variance explained by component

Principal	Visible Albedo		Infrared Albedo	
Component	λ	%	λ	%
1	0.024	59.9	0.016	65.0
2	0.010	23.6	0.006	23.9
3	0.004	10.5	0.001	4.2
4	0.001	2.8	0.001	3.7
5	0.001	1.4	0.001	2.1
6	0.001	1.1	0.000	0.6
7	0.000	0.5	0.000	0.4
8	0.000	0.2	0.000	0.2

Fig. 1. SIMMS Experiment Region

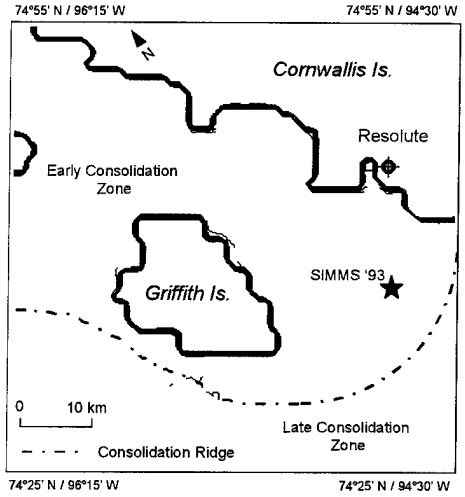
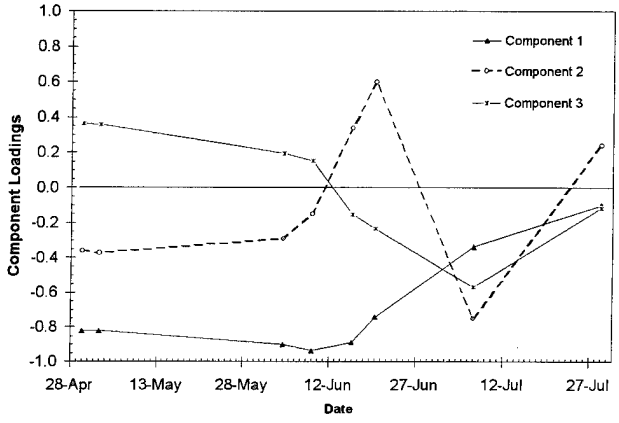


Fig. 2 Component loadings for (a) visible albedo and (b) infrared albedo

(a)



(b)

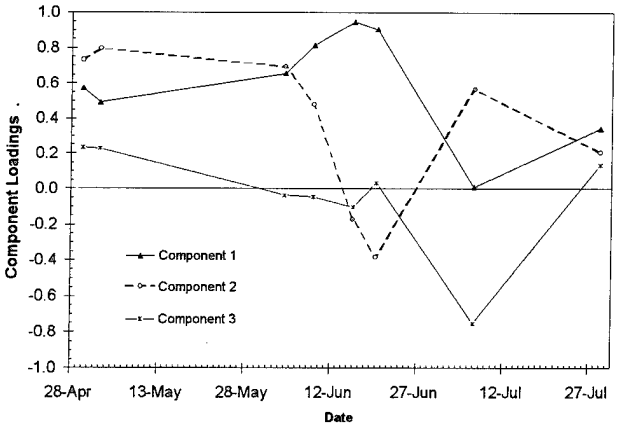


Fig. 3. Mapped visible albedo components (a) 1 and (b) 2.

(a) (b)

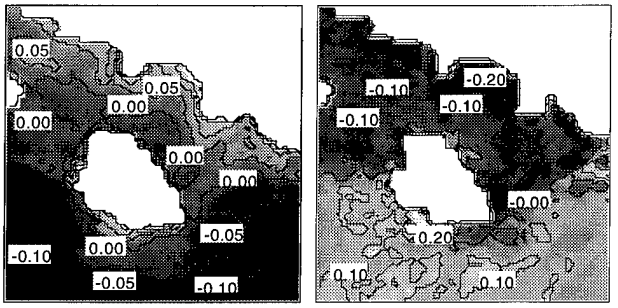
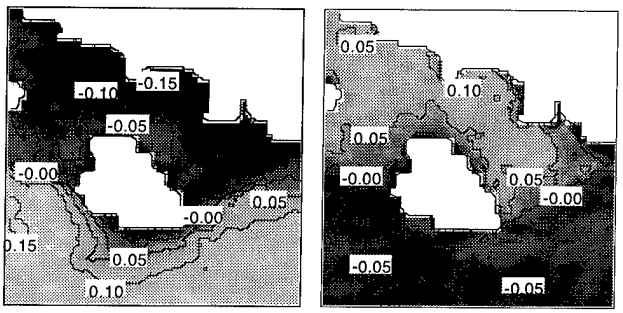


Fig. 4 Mapped infrared components (a) 1 and (b) 2.

(a) (b)



Assessing Variability and Trends in Arctic Sea Ice Distribution Using Satellite Data

Gennady I. Belchansky, Ilia N.Mordvintsev
Institute of Ecology and Evolution,Russian Academy of Sciences
Leninsky prospect 33, Moscow, 117071, Russia
Tel:(095)135-9725/Fax:(095)954-5534/E-mail:animals@sovamsu.sovusa.com
&
David C. Douglas
Alaska Science Center, National Biological Service 1011 East Tudor Road, Anchorage, Alaska, USA
Tel:(907) 786-3473/Fax:(907)876-3676/E-mail:David_Douglas@nbs.gov

ABSTRACT

Trends in the annual minimum, minimum monthly-mean, and the sea ice extent at the end of August were investigated for the Barents and western Kara Seas and adjacent parts of the Arctic Ocean during 1966 to 1994 using data from Russian ice maps (1974-1994), Kosmos-Okean and ALMAZ SAR satellite series (1984-1994), and published literature. Four definitions of sea ice extent were examined based on thresholds of ice concentration: > 90%, > 70%, > 40% and > 10% (E1, E2, E3, and E4, respectively). Root-mean-square differences between sea ice maps and satellite-image sea ice classifications for coincident areas were subjected to Monte-Carlo analyses to construct confidence intervals for the 20-year ice-map trends. With probability p=0.8, the average 20-year change in the minimum monthly-mean sea ice extent (followed in brackets by the average change in the absolute annual minimum ice extent) was between 30-60% [19-71%], 29-61% [15-67%], 31-63% [18-69%] and 18-48% [7-55%] in the Barents sea; (-24)-(-4)% [(-25)-(12)%], (-27)-(-9)% [(-34)-(-4)%], (-32)-(-15)% [(-39)-(-9)%] and (-33)-(-15)% [(-38)-(-8)%] in the western Kara sea; and (-3)-19% [(-8)-29%], (-4)-18% [(-11)-26%], (-6)-16% [(-11)-24)%] and (-7)-15% [(-12)-24%] in the combined Barents and Kara Seas, for sea ice concentration E1-E4, respectively. Including published data from 1966-1983, the trend in minimum monthly-mean sea ice extent for the combined 30-year period showed an average increasing of 11.8% in the Barents Sea and of 47.4% reduction in the western Kara Sea ;sea ice extent at the end of August showed an average reduction of 4.7% in the Barents Sea.

INTRODUCTION

A number of studies have suggested that changes in the global average air temperature might be detectable by observing changes in the extents of the polar sea ice covers [1]-[3]. Minimum ice extent and ice concentration during the summer provide indirect information required the evaluate heat and humidity fluxes between the ocean, the atmosphere and the perennial ice pack. One sensitive region in the context of global change is the Barents-Kara Seas and adjacent parts of the Arctic Ocean. Documenting variations in the annual minimum ice extent and concentration is important for establishing baseline data, for understanding historical periodicity, and for investigating long-term trends. However, long-term trends derived from ice maps are fixed estimates without variance. In our previous work [2] satellite data were used to estimate confidence intervals for the 1984-1993 map-derived ice trends in the Barents-Kara Seas. The reported work describes the results of using object-oriented satellite data processing techniques to estimate the efficiency of Kosmos-Okean satellite data for investigating variability in Arctic Sea Ice distribution and documenting variations in annual minimum Sea Ice extent, concentration, confidence intervals for the 1974-1994 map-derived ice trends in the Barents-Kara seas, to examine long-term trend during a 30-year period (1966-1995) based on [3].

METHODOLOGY

The study area included the Barents and Kara Seas, and adjacent parts of the Arctic Ocean (70N, 20E; 84N, 86E). Two subregions encompassing the Barents and western Kara Seas were analyzed separately for comparability with results reported in [3]. Remote sensing data were collected by the satellites Kosmos-1500, 1766, 1869, Okean-01-06, and ALMAZ SAR (32 digital images, 1984-1994). The Kosmos-Okean polar-orbiting satellite series data include simultaneously recording passive microwave (RM-08, 0.8 cm wavelength, 500 km swath width, 15 km resolution), side-looking radar (SLR, 3.0 cm wavelenght, 450 km swath width, 1.2 km resolution) and optical (MSU-M, four visible and near-infrared bands, 900 km swath width, 1.0 km resolution) imagery. Almaz SAR (9.6 cm wavelength, 11 m resolution) data included four images (19.07.91) [2]. Ice maps (1:5,000,000 scale) for 10-day intervals (July through October, 1974-1995) were manually derived from (depending on availability) shipboard and aircraft observations, Scandinavian and American ice maps, and Russian and American satellite

0-7803-3068-4/96$5.00©1996 IEEE

data. Minimum ice-extent data in the Barents and western Kara Seas for the period 1966-1983 were extracted from [3].

The sea-ice extent, surface characteristics, and trends were studied with using geographical and remote sensing data bases. For this goal problem-oriented Data Processing System has been developed. It included: Okean-Almaz Imagery, Control points and Sea Ice databases; Image Restoration, Data Interpretation and Statistical Analysis Subsystems. The databases include, respectively, a set of satellite images for the period 1984-1994 (July-October) and a set of ice maps for the period 1974-1994 (July-October) digitized into ARC/INFO database. For each year, 1974-1994, the total area covered by sea ice was quantified for the absolute annual minimum, the minimum monthly-mean, and the sea ice extent at the end of August. Four definitions of ice extent, based on ice concentration, were considered: E1=>90%, E2=>70 %, E3=>40% and E4=>10%. Imagery analysis included radiometric calibration and georegistration. Derivative bands were calculated for Okean data that included SLR/RM-08 ratio and the first principal component (PC1) of RM-08, SLR and MSU-M. Supervised ice classification procedures were developed using randomly selected training polygons extracted from corresponding ice maps. An algorithm was developed with minimum loss function criteria [2] to ascertain the most efficient classification procedure for discriminating five ice concentration classes: <10%, 10-40%, 40-70%, 70-90% and >90%. Differences between the satellite-derived classifications and the ice maps were calculated and the results were used in a Monte-Carlo analyses to statistically estimate confidence limits for the ice map trends. Ice extent trends during the 1966-1995 period were calculated with data from [3].

RESULTS

Optimal ice classification was achieved with RM-08 and PC1 for Okean-01,03,06 data; SLR and MSU-M were optimal for Okean-02 and Kosmos-1500 data; and SLR was used for the Kosmos-1766 data. The satellite-derived ice concentration classes had, on average, 75% agreement with the ice-map training polygons. Root-mean-square differences between ice maps and the satellite-derived classes were 15.3%, 19.4%, 18.6% and 11.8% for ice extensions E1-E4, respectively. Minimum monthly-mean sea ice extent in the Barents Sea showed an average increasing trend during the 1974-1994 (Table). Results of Monte-Carlo analyses established upper and lower confidence limits (P=0.8) that corroborated the increasing trend (Table). Over the 30-year period this region showed an average 11.8% increasing trend. Minimum monthly-mean sea ice extent in the western Kara Sea showed an average decreasing trend during the 1974-1994 (Table). Results of Monte-Carlo analyses established upper and lower confidence limits (P=0.8) that corroborated the decreasing trend. Over the 30-year period this region showed an average 47.4% decreasing trend in minimum monthly-mean sea ice extent (Fig.). The recent 20-year changes in minimum monthly-mean sea ice extent appeared consistent with annual variations and periodic cycles characteristic of the extended 30-year database. In general, within year comparisons between the Barents and western Kara Seas showed little consistency with respect to the magnitude of ice extension (e.g., relatively high and low ice years in the Barents Sea were not closely associated with similar conditions in the western Kara Sea.

During 1974-1994, the absolute annual minimum sea ice extension in the Barents and western Kara Seas also showed increasing and decreasing trends (Table). The pattern of annual variations was very similar to that observed for the minimum monthly-mean, however, the rates of increase and decrease for the derived 20-year trends were higher for the minimum monthly mean ice extent. The greatest 20-year increase was observed in the Barents Sea for ice extension E2 (>70% concentration). The increasing trend in sea ice extension, 1974-1994, persisted when data were combined for the Barents-Kara Seas and neighbouring areas of the Arctic Ocean. For the combined study area, 20-year trends had less variability among the four ice extensions compared to the trends detected for the Barents and western Kara Seas individually. Also for the combined study area, the rate of increasing ice extent was more pronounced for the absolute annual minimum ice extent compared to the minimum monthly-mean (Table). The sea-ice extent at the end of August (1974-1994) also showed an increasing trend in the Barents Sea and decreasing trend in the western Kara Sea. However, when combined with data [3], the 30-year trend showed an average 4.7% reduction in the Barents Sea (Fig.).

DISCUSSION

During the 1974-1994 period analyses of the Russian ice maps indicated an increasing and decreasing trends in the extent of minimum sea ice cover for the Barents and Kara Seas. An important constraint to such interpretations lies in the presumed accuracy of the ice maps. Although the magnitude of error inherent to ice maps could not be directly assessed, using satellite remote sensing to generate an alternative measure of ice conditions provided data for estimating one plausible degree of map error. After including all possible combinations of the observed disparities between the ice maps and the satellite ice classifications in a Monte-Carlo analyses, the trends of minimum ice cover extent in the Barents and Kara Seas remained evident (P=0.8; Table). The decreasing trend of minimum sea ice extent during the extended 30-year period demonstrates the importance of long-term

databases for interpreting short-term results (e.g., 10-year periods). The increasing 10-year trend in minimum ice extent, 1984-1994, appears consistent with respect to the mid-term variability and possible cyclic conditions in the Barents and Kara Seas during the past 30 years. Analyses of recalibrated Nimbus-7 scanning multichannel microwave radiometer (SMMR) images and historical U.S.NAVY-NOAA ice maps revealed substantial quantitative differences, and demonstrated the need for consistently calibrated remote sensing data. Furthermore, consistent criteria for defining the limits of ice extent are required for long-term trend analysis [1]. This study detected notable differences between the four definitions of ice extension (E1-E4) with respect to the magnitude of derived trends (Table). Preliminary comparisons between Okean and ALMAZ (SAR) images in the Kara Sea showed good consistency for detecting ice concentration classes. ALMAZ SAR data are valuable for discriminating sea ice flows, grey ice, first-year ice, and multi-year ice; and for future refinement of Okean data interpretation. However, all microwave remote sensing, such as SLR, RM-08 and SAR, have identical problems with an inability to effectively distinguish ice cover during the presence of meltponding, wet snow, or flooding, as often associated with seasonal temperature changes or diurnal freeze-thaw cycles. An analysis of the multichannel passive microwave radiometers data onboard the Nimbus (ESMR, SMMR) and DMSP (SSMI) satellite series with higher-resolution data, such as Okean or ALMAZ SAR, could enhance current methodologies for characterizing the Arctic summer sea ice cover and trends. An integrated multisensor remote sensing approach could take advantage of differing sensitivities to different surface types, enhanced temporal resolution, and multiscale spatial resolution that could be used to assess the precision of broad-scale or long-term interpretations.

Table. 20-Year Average Change Trends in the Extent of the Minimum Monthly-Mean, the Absolute Annual Minimum Sea Ice Cover and Ice Cover in the End of August in the Barents, Western Kara, and Combined Barents-Kara Seas During the 1974-1993 Period.

Sea Ice Extent Definition (% Ice Concentration)							
>90% (E1)		>70% (E2)		>40% (E3)		>10% (E4)	
Trend (%)	P=0.8 (%)	Trend (%)	P=0.8 (%)	Trend (%)	P=0.8 (%)	Trend (%)	P=0.8 (%)
MINIMUM-MOUTHLY-MEAN:							
BARENTS SEA							
40.0	30-60	43.4	29-61	45.5	31-63	28.3	18-48
KARA SEA							
-14.7	(-24)-(-4)	-19	(-27)-(-9)	-26.9	(-32)-(-15)	-24.7	(-33)-15
BARENTS and KARA SEAS							
6.9	(-30)-19	6.5	(-4)-18	1.9	(-6)-16	3.0	(-7)-15
ANNUAL MINIMUM:							
BARENTS SEA							
36	19-71	38.6	15-67	37.1	18-69	28.2	7-55
KARA SEA							
-4.1	(-25)-12	-23.7	(-34)-(-4)	-31.1	(-39)-(-9)	-26.2	(-38)-(-8)
BARENTS and KARA SEAS							
11.6	(-8)-29	5.6	(-11)-26	2.5	(-11)-24	5.2	(-12)-24
THE END OF AUGUST							
BARENTS SEA							
58.5	31-92	52.6	25-85	55.3	27-88	28.1	4-56
KARA SEA							
-29.2	(-43)-(10)	-30.1	(-43)-(-13)	-19	(-34)-(-4)	-18.7	(-33)-(-3)
BARENTS and KARA SEAS							
1.5	(-16)-24	-0.6	(-18)-21	6.7	(-12)-30	4.8	(-14)-28

REFERENCES

[1] C.L.Parkinson, "Strengths and weaknesses of sea ice as a potential early indicator of climate change". In: Weller, G., C.L.Wilson and B.B.Severin (editors). International conference on the role of polar regions in global change. Geophysical Institute, University of Alaska, Fairbanks, pp. 17-21, 1991.

[2] G.I.Belchansky, D.C.Douglas, I.N.Mordvintsev, and G.K.Ovchinnikov, "Assessing trends in Arctic Sea Ice distribution in the Barents and Kara seas using the Kosmos-Okean sattellite series", Polar Record, Cambrige University press, vol.31, n.177, pp.129-134, 1995.

[3] T.Vinje, "Sea ice variability in the Nordic Seas". In: Weller,G., C.L.Wilson and B.B.Severin (editors), International conference on the role of polar regions in global change, Geophysical Institute, University of Alaska, Fairbanks, pp. 23-27, 1991.

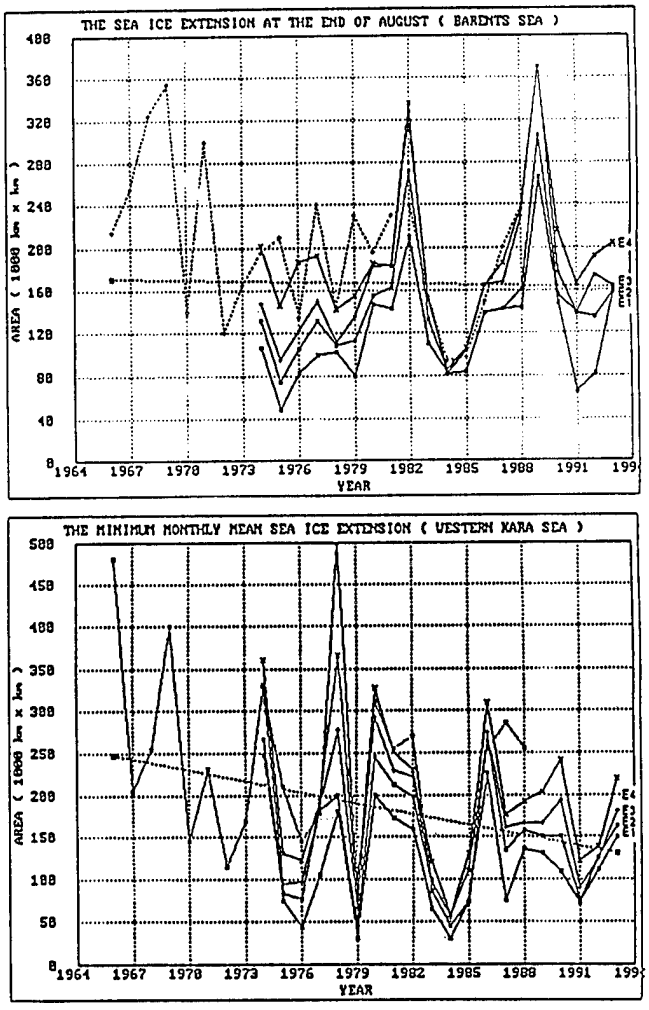


Figure. Sea ice extention trends.

Image Time Series Analysis of Arctic Sea Ice

Joseph M. Piwowar[1], Gudrun R.I. Wessel[2], and Ellsworth F. LeDrew[1]
[1]Waterloo Laboratory for Earth Observations
Department of Geography
[2]Department of Statistics
and Actuarial Science
University of Waterloo
Waterloo, ON, Canada N2L 3G1
e-mail: piwowar@wateol.uwaterloo.ca

Abstract -- We describe the application of per-pixel time series modelling to a sequence of 108 monthly images of Arctic sea ice concentrations. We outline a semi-automated model fitting procedure which we used to fit AutoRegressive - Moving Average (ARMA) models to the time series at each pixel in a hypertemporal image stack. After deseasonalizing each series, we found that most of the variability in sea ice concentrations in the Arctic follow a first-order autoregressive (i.e., AR(1)) process. The strongest autoregressive autocorrelations are found in the central Arctic Basin and generally become weaker closer to the southern limit of the seasonal ice extent. In the marginal sea ice zone the mean ice concentration for a given month is shown to become less dependent on past month's values.

INTRODUCTION

Routine, repetitive, and continuous observations of the Earth's surface from operational remote sensing systems began in the early 1970s with the launch of the Landsat 1 and Nimbus 5 satellites. The Landsat series of platforms, and other more recent systems (e.g., NOAA, SPOT, IRS-1), carry optical sensors which continue to supply us with valuable Earth resource information, primarily over sub-polar land surfaces. Similarly, the primary sensors aboard the Nimbus 5, Nimbus 7, and DMSP satellite sequence have allowed polar scientists to amass a continuous record (except for a 2-year gap between Nimbus 5 and Nimbus 7) of the Earth's cryosphere. We are fast approaching the time at which data from these systems can be used to define 30-year climatic normals. There is a critical need for the development of new hypertemporal image analysis techniques to extract temporal signals from long sequences of satellite imagery.

Time series analysis (TSA) is the procedure of fitting stochastic models to observations available at discrete points in time. In particular, they attempt to explain and characterize the occurrence of observed temporal phenomena, and when properly constructed, can be used to identify other temporal sequences of the same process [1]. In this analysis of temporal variations in Arctic sea ice concentration, the class of time series models known as ARMA (AutoRegressive - Moving Average) models is considered. Although there are other types of time series models which are typically used in a variety of other applications, [2] justify the use of ARMA class models for describing hydrologic and other kinds of environmental data sets. They show that, in addition to having a sound physical basis, ARMA models have the ability to forecast environmental time series at least as well as, and usually better than, their competitors.

ARMA models can contain just autoregressive (AR) components, just moving average (MA) components, or combinations of the two. Following the accepted nomenclature for these processes, a purely autoregressive model of order p could be specified as ARMA(p,0), or simply AR(p). Similarly, the notation ARMA(0,q) or MA(q) denotes a pure moving average process of order q, and ARMA(p,q) references a mixed autoregressive - moving average process of the specified orders. In an AR process, an observation is modelled as a function of previous observations' values; MA models are based on how much a previous observation's value differs from its average value according to the model (i.e., the previous period's error term).

SCANNING MULTICHANNEL MICROWAVE RADIOMETER DATA

The Scanning Multichannel Microwave Radiometer (SMMR) was a 10-channel instrument which operated on the Nimbus-7 spacecraft between November 1978 and August 1987. It measured emitted Earth radiation at five dual-polarized frequencies between 6.63 and 37 GHz in the microwave portion of the electromagnetic spectrum. The SMMR data used in this study are derived from those published on the *Nimbus-7 SMMR Radiances and Sea Ice Concentrations* CD-ROM (Volume 7) produced by the NASA Oceans and Ice Branch at the Goddard Space Flight Center. We extracted the processed sea ice concentration data from the CD-ROM for our analyses. Ice concentration is the percentage of a given area of ocean (a pixel, in this analysis) which is covered by ice and is a measure of the amount of open water within the ice margins. Even in the middle of winter, concentrations of less than 90% can be found in the middle of the Arctic pack ice largely as a result of open leads and polynyas. The SMMR data on the CD-ROM are composited into polar stereographic images with a nominal pixel size of 25 km near the poles and are ideal for hemispheric-scale global change analyses [3].

All of the ice concentration files within each month were averaged to create 108 monthly images. The image sequence was then *deseasonalized* for time series analysis by subtracting each monthly image from the 9-year average for that month and divided by the 9-year monthly standard deviation average (i.e., normalized monthly anomaly images were created). A hypertemporal data set was created by "stacking" all of the monthly anomaly images and per-pixel time series were extracted from the image stack by reading the ice concentration anomaly value from the same pixel in each monthly image.

0-7803-3068-4/96$5.00©1996 IEEE

TIME SERIES MODELLING OF THE SMMR DATA SET

Time series modelling is necessarily a manual process, based on heuristic evaluation of graphical displays and summary statistics at each step of the modelling procedure. Clearly, a manual analysis of the 136,192 pixels (i.e., potential time series) in the SMMR data set was impractical so initial model identification was based on 12 sample time series selected from "critical" regions previously identified during linear regression analysis [4] and from additional locations which were thought to be representative of more general conditions. Following accepted ARMA modelling procedures [5] a variety of models were evaluated for these series and we concluded that the temporal dynamics of Arctic sea ice likely follow an AR(1) process.

Consequently, AR(1) models were fit to the entire SMMR anomalies data stack. Of 136,192 potential time series, only 61,513 AR(1) models were actually calculated due to low variance in many of the series over the open ocean and land. Just because an ARMA model can be calculated for a given time series, however, does not necessarily mean it is an adequate representation of the data. The residual series (modelled - observed values) must be analyzed to determine if there is any remaining autocorrelation or trends which could indicate that the tested model does not adequately describe the data. Diagnostic checks made on the residual autocorrelation functions of the fitted models revealed that 68% of the Arctic sea ice zone is appropriately modelled by an AR(1) process (Fig.1). This suggests that for these locations, mean monthly sea ice concentrations can be accurately estimated by knowing the long-term average concentration for that month and the previous month's value at that location. This statistical analysis matches the geophysical reality of the Earth's sea ice cover by noting that an annual cycle is induced on the cryosphere by planetary factors and that the thermal properties of ice make it relatively persistent with respect to adjacent atmospheric and oceanic influences.

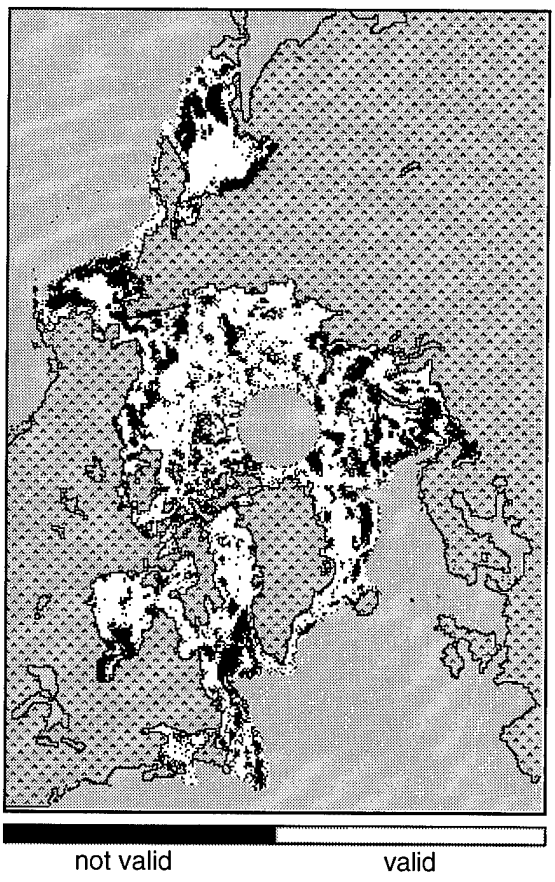


Fig.1: AR(1) Model Validation Summary

What about the 32% of the Arctic sea ice zone where an AR(1) model does not appear to fit the data? Data obtained during the modelling exercise gives us some clues which might help explain the poor fit. For example, a review of the diagnostic residual checks reveals some locations in the central Arctic Basin, north of the Canadian Archipelago, where there are significant residual autocorrelations at lag 2 (which would invalidate an AR(1) model). This indicates a longer temporal persistence of the ice features and a need for more AR parameters. This is substantiated by modelling at a nearby location in the Beaufort Sea where an AR(6) model (with the AR(3-5) parameters constrained to zero) was found to be appropriate. Thus the ice concentrations in this area depend not only on that of the previous month, but also on values from the second and fifth previous months. These observations fit the geophysical reality that this region is the domain of the least amount of ice motion in the Arctic leading to very little change in ice concentrations from month to month, or even from season to season.

Another area of problematic AR(1) modelling is in the East Siberian Sea where there are significant autocorrelations at lags 2 and 24 in the residual series. When a new time series model was fit to some of these data, the resulting AR(12) model (with the AR(3-11) parameters constrained to zero) does much better in explaining the strong monthly and seasonal autocorrelations in these data. The seasonal AR(12) parameter of the fit model is difficult to explain given that the time series had been deseasonalized prior to modelling. There is some evidence of residual seasonality in the time series plot of the ice concentration anomalies which may support the call for additional seasonal differencing. This analysis leads to the conclusion that ice concentration anomalies in this region can be expected to be repeated on an annual cycle.

An interesting dichotomy is revealed in the Davis Strait - Labrador Sea region, where the sea ice features in the western half strongly follow an AR(1) process, but the temporal characteristics of the ice in the eastern portion strongly contradict the AR(1) models fit there. To examine this phenomenon in greater detail, 3 time series were extracted at locations in the western region, eastern region, and at a point in the middle and fit with AR(1), ARMA(12,2), and ARMA(1,1) models, respectively. The eastern location is at the margin of the seasonal sea ice zone, experiencing very

little winter iciness over the SMMR data record, except during the first six months of 1983 and 1984 when ice concentrations in this region exceeded 80%, likely the result of a particularly strong El Niño event during 1982-83. This regional phenomenon might be explained by reviewing the ocean currents in this region. The western half of the Davis Strait - Labrador Sea region is be dominated by the southerly Labrador Current which is responsible for carrying much of the sea ice which is exported from the Canadian Archipelago southward. In the eastern half, warmer water is carried northward along the West Greenland Current. Evidently in years of very heavy ice conditions across the Canadian Arctic, such as in 1983 and 1984, the volume of southerly ice export along the Labrador Current increases and is forced to spill over into the waters typically occupied by the West Greenland Current producing the heavy ice anomalies observed here.

Another interesting observation which can be made from the three Labrador Sea time series shown above is the change from a pure AR process for the (western) series in the seasonal sea ice zone, through a mixed ARMA model along the sea ice margin, and to an almost pure MA process at a point (in the eastern Labrador Sea) which can be considered to be outside of the seasonal sea ice zone. This would suggest that as the seasonal cycle of ice concentrations becomes more irregular, its autoregressive nature is gradually replaced by a stronger relationship with past month's residuals than their observations. This observation is substantiated by paired time series extracted from the Sea of Okhotsk, the Barents Sea, and in the East Greenland Sea. In each region, pure AR processes were appropriate for the series farther into the ice pack while MA parameters were more dominant at locations closer to the ice edge.

SUMMARY

The principal objective of applying the methods of time series analysis to the SMMR data was to derive a spatial summary of the temporal characteristics of monthly sea ice concentrations in the Arctic. ARMA modelling of the anomaly data stack revealed that 68% of the 27,500 time series in the Arctic sea ice zone is shown to be adequately represented by AR(1) models. From a geophysical perspective, this is not surprising since an inter-month coherence is expected due to the persistent nature of sea ice arising from its thermal inertia. The results of the temporal modelling show that this is not consistent across the Arctic sea ice zone, however. As might be expected, the strongest autoregressive autocorrelations are found in the central Arctic Basin and generally become weaker closer to the southern limit of the seasonal ice extent. As the autoregressive nature of the temporal processes decreases in a southward progression, the mean ice concentration for a given month is shown to become less dependent on past month's values and more related to previous observation's residuals, i.e., the processes are increasingly more closely fit by moving average models. Again, from a geophysical perspective this makes sense since the presence of sea ice becomes much more irregular along the lower bounds of the seasonal sea ice zone.

Time Series Analysis provides a unique view of the temporal variability and repetitiveness of an image time series by forcing a critical examination of the temporal structure of the phenomenon being modelled. Since the procedure treats a time series as an entity, TSA may fail to reveal short-term temporal anomalies present in the data.

Time series modelling is a powerful tool for simulation and forecasting. Statistically based forecasts are necessary for continued resource development in the Arctic. Sea ice simulations could provide valuable input to climate and engineering models by defining the spatial distribution of sea ice concentration as a probability surface. Further, when it becomes possible to create ARMA models based on climatically significant time series (i.e., 30 years), they may be useful for identifying statistically significant climatic anomalies.

The sometimes extreme variability of sea ice, especially during the melt period, is well documented. In spite of this, the spatial coherence in the derived images from the time series modelling is remarkable. Distinct time-based regions are revealed, which are different from spatial groups defined elsewhere in this report and in other published studies. This new regionalism adds another dimension to the study of cryospheric, atmospheric, and oceanic processes in the Arctic.

ACKNOWLEDGMENTS

Financial Support from the Natural Science and Engineering Research Council and the Institute for Space and Terrestrial Science is gratefully acknowledged.

REFERENCES

[1] L.R. Rabiner and B.H. Juang, "An Introduction to Hidden Markov Models", *IEEE ASSP Magazine*, Vol. 3, No. 1, pp. 4-16, 1986.

[2] Keith W. Hipel and A. Ian McLeod, *Time Series Modelling of Water Resources and Environmental Systems*. Amsterdam: Elsevier, 1994.

[3] Per Gloersen, William J. Campbell, Donald J. Cavalieri, Josefino C. Comiso, Claire L. Parkinson and H. Jay Zwally, *Arctic and Antarctic Sea Ice, 1978-1987: Satellite Passive-Microwave Observations and Analysis*, Washington: NASA SP-511, 1993.

[4] Joseph M. Piwowar and Ellsworth F. LeDrew, "Climate Change and Arctic Sea Ice: Some Observations from Hypertemporal Image Analysis", *Proceedings, Third Thematic Conference on Remote Sensing for Marine and Coastal Environments*, Vol. I, pp. 625-636, September 1995.

[5] G.E.P. Box and G.M. Jenkins, *Time Series Analysis: Forecasting and Control, revised ed.* Oakland, CA: Holden-Day, 1976.

An Analysis of Odden Event Intra- and Inter-Annual Variability

Kenneth W. Fischer, Catherine A. Russel, Robert A. Shuchman
Center for Earth Sciences, Environmental Research Institute of Michigan
P.O. Box 134001, Ann Arbor, MI 48113-4001
313-994-1200, ext. 2239 (Ph.); 313-994-5824 (Fax)
email: fischer@erim.org, russel@erim.org, shuchman@erim.org

Edward G. Josberger
Ice and Climate Project, US Geological Survey
University of Puget Sound, Tacoma, WA 98416
206-593-6516 (Ph.); 206-383-7967 (Fax), ice@ups.edu

Abstract -- The "Odden" is a large sea ice feature that forms in the East Greenland Sea. During the winter, the ice edge of the Odden may advance and retreat by several hundred kilometers on relatively short time scales. An analysis of the satellite passive microwave derived ice area and extent time series along with meteorological data from the Arctic Drifting Buoy Network determined the meteorological forcing required for Odden growth, maintenance and decay.

INTRODUCTION

The "Odden" is a large sea ice feature that forms in the East Greenland Sea, it may protrude eastward to 5° E from the main sea ice pack between 73° and 76° N. It generally forms at the beginning of the winter season and can cover 300,000 km^2. Throughout the winter, the outer edge of the Odden may advance and retreat by several hundred kilometers on time scales of a few days to weeks.

The Odden ice is believed to play a key role in controlling deep water formation in the Greenland Sea through the process of deep water convection. The brine rejection by the rapid freezing during the Odden growth period may be instrumental in controlling the deep convection. In particular, recent theory suggests that the primary Greenland Sea deep water formation site is located in the "Nordbukta" open water region which frequently forms on the north side of the Odden [1].

An analysis of the satellite passive microwave derived ice area and extent time series along with meteorological data from the Arctic Drifting Buoy Network determined the meteorological forcing required for Odden growth, maintenance and decay. The key meteorological parameters which cause the rapid ice formation and decay associated with the Odden are, in order of importance, air temperature, wind speed, and wind direction. Atmospheric pressure was found not to play a significant role in the Odden events. Air temperature and wind direction are the dominant variables with temperatures below -9.5°C and winds from the west required to trigger significant Odden events.

SATELLITE AND *IN SITU* DATA SETS

The Scanning Multichannel Microwave Radiometer (SMMR) and the Special Sensor Microwave / Imager (SSM/I) have provided all-weather, all-season imagery of global sea ice from 1978 - present [2]. While both of these sensors provide low resolution imagery (25 km), the Odden event can clearly be seen in the imagery due to its large size.

While the SMMR and SSM/I data sets provided good estimates of the Odden occurrence and its areal coverage, drifting buoys deployed in the Arctic provided the necessary coincident meteorological data for this analysis. A network of drifting buoys is currently maintained by the International Arctic Buoy Program (IABP). Processed data sets provide atmospheric pressure and temperature at the ocean surface [3]. Estimates of the temperature and pressure in the general location of the Odden were derived by averaging all data points in the grid from 71°N to 77°N and 15°W to 5°E--six data points in all. Geostrophic wind speed and direction were also calculated from the buoy data by calculating the pressure gradient from the gridded pressure data fields.

INTRA-ANNUAL ODDEN VARIABILITY

Many questions have been raised regarding the occurrence of the Odden such as why does it occur at certain times but not others, and during some years but not others. To address these questions, an analysis was performed using both the remotely-sensed ice cover data and the interpolated *in situ* buoy meteorological data to determine the atmospheric conditions which cause the Odden to form, decay, remain stagnant or not appear at all.

The methodology first identified specific formation and decay events in the ice area coverage time series and then correlated these events with the meteorology time series to determine which meteorological variables most strongly influence Odden formation and what, if any, thresholds could be identified for triggering an Odden event. The

0-7803-3068-4/96$5.00©1996 IEEE

analysis was later broadened to include conditions under which the Odden ice pack maintained itself above certain minimum area levels and when no Odden occurred at all.

Identification of Odden Formation and Decay Events

Annual time series of sea ice extent and total ice covered area for the Odden region (70°N-79°N and 20°W-6°E) were calculated from the daily maps and the October average conditions. The Odden ice extent was derived by summing the areas of the pixels with at least 30% ice concentration beyond the derived winter ice edge in the defined Odden region. The Odden ice area was derived by summing the total ice concentration for a pixel times the pixel area.

Figure 1 shows a particularly active winter season (November 1981 - April 1982) in which numerous growth and decay events occurred. The Odden is easily distinguished from the rest of the ice pack in part because of its location and shape and also, in sequential images, because of its rapid formation and dissipation.

Meteorological Conditions Associated with Odden Growth and Decay

Once growth, decay, and stagnant periods were identified, a statistical analysis was done to determine the meteorological conditions associated with each of the Odden ice cases. For each case, meteorological data from all of the days fitting the ice criteria were averaged and standard deviations calculated. The results of this analysis are summarized in Fig. 2.

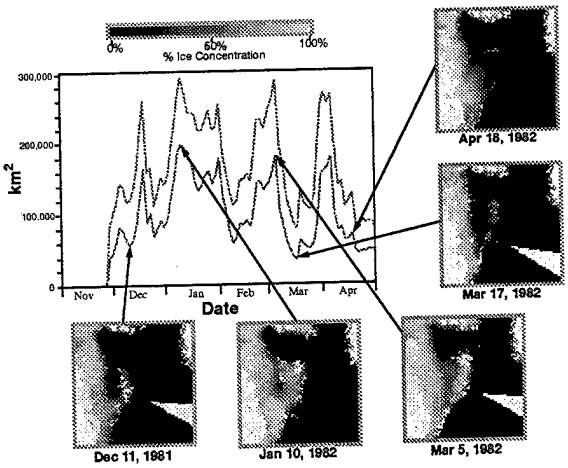


Figure 1. Time series of Odden area (bottom curve) and extent (top curve) for the 1981-82 Winter season. Extreme variability in the Odden is illustrated by the pullouts of SMMR derived ice concentration maps at specific points in the time series.

As can be seen from Fig. 2, temperature and wind both play key roles in the Odden ice formation. Atmospheric pressure was not found to correlate significantly with any of the cases and will not be considered here. Based on the analysis, atmospheric temperature appears to play the most significant role in causing the Odden to form. All of the temperature results make intuitive sense with the coldest conditions being associated with Odden growth and the warmest with no Odden forming at all.

Wind speed and direction also play a role in the Odden ice pack formation and decay; influencing the surface heat flux, the ice drift and upper ocean currents. As shown in Fig. 2, Odden formation occurs when winds are moderate and out of the west, bringing very cold air from the Greenland Ice Sheet.

At the other extreme, Odden decay is associated with very high winds, 12.4 m/s on average, from the north, and air temperatures of -6.0 C. This appears to be contradictory: strong winds and moderately cold temperatures should yield ice growth and not ice decay. The explanation lies in the Ekman transport in the ocean that is generated by the surface winds. The surface winds will be, on average, to the south and east, generating an Ekman transport of relatively warm water to the west and south. The net effect is a strong on ice flow of the relatively warm surface waters in the Greenland Sea that results in rapid melting and compacting of the ice edge.

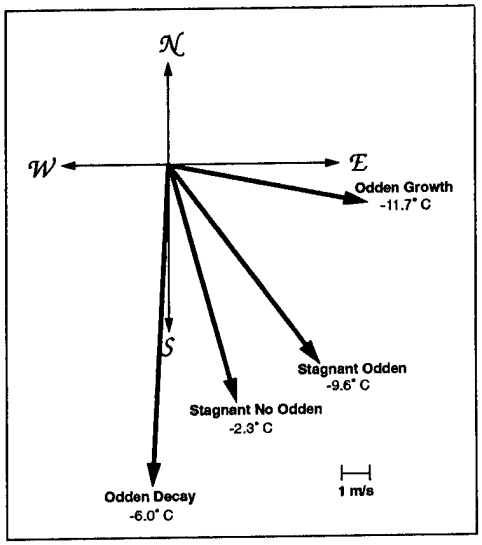


Figure 2. Results of meteorological analysis showing mean wind speed, direction, and temperature for Odden growth, Odden decay, stagnant Odden, and stagnant no Odden cases.

In addition to the statistics calculated for each of the four Odden cases, correlations between various pairs of time series were carried out to determine if there was any delay

between the meteorological forcing and the ice formation. The strongest correlations were found between the temperature and growth rate time series.

Fig. 3 shows the Odden Growth Rate along with the meteorological data for the 60 day time period from Jan 21 through March 20, 1979. The Growth Rate was calculated by first upsampling the SMMR derived Odden area to twice daily (to correspond to the temperature sampling rate), then taking the difference between every two successive points and finally running a 7 point running boxcar filter. The temperature time series has been averaged with a 5 point running boxcar filter. As can be seen from the figure, growth rate is anti-correlated with air temperature and in phase.

The correlation coefficient for this particularly time series was -0.68. The conclusion from this analysis was that while ocean surface mixed layer preconditioning plays a role in the long-term winter average Odden ice area, the ice growth responds almost immediately to low temperature forcing and ice decay to warm temperature forcing. Wind speed and direction were also found to correlate well in time with low to moderate winds out of the west correlating with ice growth and high winds out of the north/northeast with decay. Wind speed and direction are not independent of temperature, so this correlation is expected to some extent.

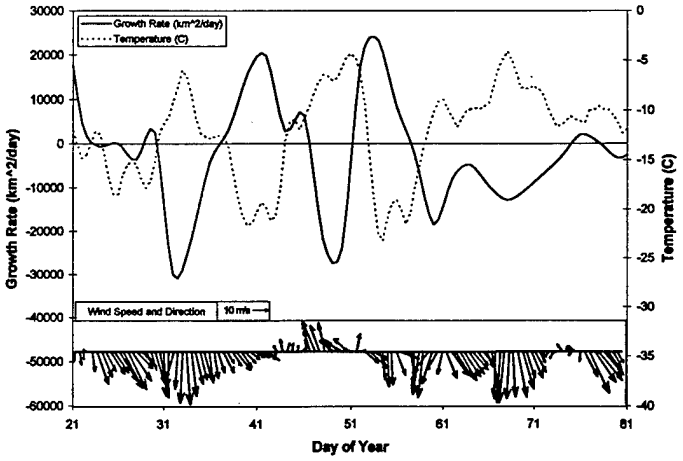


Figure 3. Sixty day time series showing SMMR derived Odden ice growth rate with corresponding buoy derived meteorological parameters during the period January 21 - March 20, 1979.

INTER-ANNUAL ODDEN VARIABILITY

Meteorological conditions also play a key role in Odden inter-annual variability. Temperature in particular was observed to be well-correlated with Odden ice area statistics. Years when there were larger numbers of occurrences of temperatures below -9.5°C showed larger Odden ice area mean, maximum, and integrated growth. Additionally, the years when no Odden formed whatsoever had average temperatures 1.5-3°C higher than the average of the other years. As with intra-annual variability, wind speed played a less dominant role than temperature and wind direction occurrences appeared not to play a role in inter-annual Odden variability.

Overall, we have shown meteorological forcing to play an important if not dominant role in the formation and variability of the Odden ice and this must be taken into account when considering both ice growth and deep water formation in the Greenland Sea.

ACKNOWLEDGMENTS

The ERIM portion of this analysis was supported by Office of Naval Research (ONR) Contract N00014-81-C-0295, Mr. Charles A. Luther, Technical Monitor. The USGS involvement was supported by the Global Change Program, Dr. Harry Lins, Water Resources Division Global Change Research Coordinator. The authors would also like to acknowledge the contributions of Jeff Rash to the meteorological analysis.

REFERENCES

[1] Visbeck, M., J. Fischer, and F. Schott, "Preconditioning the Greenland Sea for Deep Convection: Ice Formation and Ice Drift," *Journal of Geophysical Research*, Vol. 100, pp. 18489-18502, 1995.

[2] Gloersen, P., W.J. Campbell, D.J. Cavalieri, J.C. Comiso, C.L. Parkinson, H.J. Zwally, Arctic and Antarctic Sea Ice, 1978-1987: Satellite Passive-Microwave Observations and Analysis, NASA SP-511, National Aeronautics and Space Administration, Washington, D.C., 290 pp., 1992.

[3] Colony, R.I. and I. Rigor, "International Arctic Buoy Program Data Report, 1 January 1993 - 31 December 1993", Applied Physics Laboratory Technical Memorandum TM 04-95, APL, University of Washington, Seattle, WA, 1995.

Remote Sensing Data Availability from the Earth Observation System (EOS) Via the Distributed Active Archive Center (DAAC) at NSIDC

R. L. Weaver and V. J. Troisi
National Snow and Ice Data Center/CIRES
University of Colorado-Boulder
Campus Box 449
Boulder, Colorado 80309-0449 USA
(303) 492-7624 (voice); (303) 492-2468 (fax); weaver@kryos.colorado.edu
(303) 492-1827 (voice); (303) 492-2468 (fax); troisi@kryos.colorado.edu

Abstract – – In 1989 NSIDC was invited to become one of eight Distributed Active Archive Centers (DAACs) in the Earth Observing System Data and Information System (EOSDIS). The Earth Observing System (EOS) is a long-term interdisciplinary and multi-disciplinary research effort to study global-scale processes that shape and influence the Earth as a system. Recent deliberations within the EOS community is fostering change in the originally planned EOSDIS structure towards a federated system.

This paper will report on the current status of the federated approach to EOSDIS, and offer an assessment as to the impact this will have on provision of remote sensing data from EOS sensor systems to the polar research community.

INTRODUCTION

In 1990, NASA's Mission to Planet Earth undertook the development of the Earth Observation System. The Earth Observation System (EOS) is comprised of three major elements; satellite platforms and instrumentation, a data and information system, and science teams developing and implementing algorithms to generate products in 24 general measurement groups which encompass atmosphere (9), solar radiation (2), land (6), ocean (4), and cryosphere (3). The cryosphere elements of the measurement plan are presented in Table 1.

Table 1: Cryosphere Measurements in EOS

Category/Variable	Sensor System
Land Ice (ice sheet topography, ice sheet volume change, glacier change	GLAS, ASTER, ETM+/LATI
Sea Ice (extent, concentration, motion, temperature)	AMSR, DFA/MR, MODIS ETM+/LATI, ASTER
Snow Cover (extent, water equivalent)	MODIS, AMSR, ASTER, ETM+/LATI

NSIDC ROLE IN EOSDIS

The National Snow and Ice Data Center (NSIDC) operates a Distributed Active Archive Center in association with its other programs. The NSIDC DAAC serves the snow and ice (cryospheric) community with products derived from EOS and other sensor systems. To date efforts have focused on the passive microwave data provided by the Special Sensor Microwave Imager (SSM/I) and visible and infrared data provided by the Advanced Very High Resolution Radiometer (AVHRR). NSIDC has also provided access to numerous in-situ data sets useful to sea ice and snowcover researchers. NSIDC DAAC data are available on-line via the Version 0 Information Management System (V0 IMS; WWW URL http://www-nsidc.colorado.edu) The NSIDC DAAC is scheduled to produce and deliver snow and sea ice products from the MODIS sensor on AM-1 in 1998.

PROVISION OF DATA RELEVANT TO SNOW AND ICE RESEARCH BY EOSDIS

What Can Remote Sensing Data Measure of the Cryosphere?

The ability of remote sensing data to measure components of the cryosphere depends on the sensor system used and the nature of the problem being addressed. Many cryospheric parameters (ice mass changes, snow depth, sea ice type) can only be measured using indirect techniques. That is, what the satellite sensor sees in terms of spectral radiance/emittances must be empirically interpreted to obtain geophysically meaningful quantities.

Data requirements for snow and ice parameters have been compiled by several groups. The Global Climate Observing System [1] provided a list of terrestrial observational needs, including cryospheric parameters and Tables 2-4 offer high level assessments of how remote sensing data can be applied to measure relevant cryosphere variables. These tables were prepared by the

0-7803-3068-4/96$5.00©1996 IEEE

Polar DAAC User Working Group (PoDAG) and NSIDC staff for use by NSIDC DAAC to prioritize data sets.

Mapping of Science Priorities to NSIDC DAAC and EOS Data Sets

Based upon the priorities presented in Tables 2-4, NSIDC has focused its activities in a few key areas to provide data and information about the cryosphere. In addition, the measurement suite of the EOS sensors will add new parameters in the needed observations and/or offer better calibrated, more precise measurements of existing parameters.

An important new role for remote sensing data in the EOS era will be data assimilation into global and regional computer climate models. Model simulations of the climatic impact of greenhouse gases typically show enhanced warming at high latitudes, largely a result of positive feedbacks involving sea ice. Sea ice has been treated rather simply in computer models, and emerging new products could help alleviate this situation. Ice motion fields derived from AVHRR Polar Pathfinder (and later MODIS) data, sea ice albedo from MODIS, and possibly MISR, and inferred ice thickness from SAR are but a few examples of data sets which directly support climate models [2].

NSIDC continually updates and re-prioritizes its data holdings and proposed new products to reflect the perceived needs of the cryospheric user community. Listings of currently active data sets and products may be found on the NSIDC WWW site (URL http://www-nsidc.colorado.edu) and in the EOSDIS Science Data Plan [3].

REVISIONS TO THE EOSDIS

EOS has undergone more or less continual review since it's inception in 1990. It has been "reshaped", "rescoped", "re-engineered", and "regiggered" over the past several years. The driving force behind all of these changes has been primarily budgetary, but also the revised science goals of the EOS program. In July 1995 the Board on Sustainable Development (BSD) of the National Research Council reviewed EOSDIS as part of an all-encompassing review of the USGCRP and NASA MTPE [4]. The BSD concluded that components of EOSDIS which provide "flight control, data downlink, and initial processing should be retained but streamlined" and that "product generation, publication, and user services should be transferred to a federation of partners selected through a competitive process open to all". NASA MTPE decided in August 1995 to develop and implement plans to accomplish the above two BSD conclusions.

NASA MTPE hopes that the "recompetion" and movement towards a "Environmental Information Federation" (EIF) will expand the sense of ownership among the user community, introduce greater innovation, flexibility and responsiveness in the provision of information services from EOS instruments. It is also hoped that the system will also be more cost effective [5].

What Changes are Planned?

The key to the EIF is the distribution of services among "Environmental Sciences Information Partners (ESIP) and the establishment of an "Integrating Organization". The ESIPs will compute, and distribute products derived from the EOS and other instruments which meet the stated scientific goals of the EOS measurement program, (See Figure 1). The "Integrating Organization" will provide guidance to the ESIPs on how they must interact. Such guidance should include definition of the inter-connecting network and computer system standards and protocols, and the data management services roles and responsibilities.

The schedule for implementation of these changes is not yet fully known. Our best guess at this time is that some of the products and services currently operating or under development at the current DAACs will be recompeted prior to May 1997. A significant portion of the first EOS satellite (AM-1) product set may be recompeted, as well as some of the current Version 0 functions of selected DAACs.

What Will these Changes Mean to Cryospheric Data Management and Research?

EOS cryospheric data, products and services currently scheduled to be provided by the NSIDC DAAC will be recompeted in the 1996-1997 timeframe. This will probably include sea ice products from the MODIS instrument on AM-1. The NSIDC DAAC Version 0 efforts will also undergo an in-depth review, but may be recompeted before AM-1 launch in mid-1998. Other near-term products (such as AM-1 cloud products or surface temperatures from MODIS) of interest to the cryosphere community may be affected by recompetition. Certainly products from the PM-1 and GLAS satellite systems will be recompeted in the 1999 timeframe.

CONCLUDING REMARKS

What are the Risks and the Benefits?

NASA MTPE suggests that the benefits from the current recompetition exercise includes placing EOSDIS data management elements on a firmer basis through the competitive selection process which is open to all; improving ownership of EOSDIS by the community; and increasing information system evolution by introducing new players to the effort. In addition, it is hoped that the EIF will provide opportunity for expansion of the system beyond NASA sponsored data systems, possibly into commercial sectors.

The potential risks include the real possibility that production schedules of the present EOSDIS cannot be met; the current high level of user services support at the DAACs will not continue; the "Integrating Organization" will fail in its critical tasks to tie the system together. There is concern that the user support role of the current DAACs will be lost in the transition to the federation. This very important function, especially to the new, uninitiated user of remote sensing information, must play a central role in whatever system evolves to distribute EOS data and products.

There are also pressures to re-align product generation facilities by instrument types rather than by scientific discipline linkages. For example, snow cover products from MODIS may be bundled with other land-based products (net primary productivity etc.). Remote sensing of snow and ice regions is not instrument specific. Data have been and will be merged from visible, infrared, passive microwave, and active microwave sensor systems.

The cryosphere interdisciplinary, in its nature because it encompasses oceans, land, and atmosphere may lose much of the synergy that now exists at the data and research centers within EOS.

REFERENCES

[1] Townshend, J. *et. al.* 1995. GCOS/GTOS Plan for Terrestrial Climate-related Observations, Version 1.0. GCOS 21, WMO/TD-No. 721, Global Climate Observing System. WMO/UNESCO/WNEP/ICSU. WMO Geneva, 113 pp.

[2] The Polar Pathfinder Group, 1996. The Polar Pathfinders: Data Products and Science Plans. EOS (in preparation)

[3] Schwaller, Mathew, Brian Krupp, and William North (editors), 1995. Science Data Plan for the EOS Data and Information System, Document Version 4, July 1995. NASA EOSDIS ESDIS Project Office.

[4] Board on Sustainable Development, 1995. A Review of the U. S. Global Change Research Program and NASA's Mission to Planet Earth/Earth Observing System. National Research Council. (URL http://www.gcrio.org/USGCRP/LaJolla/cover.html)

[5] Butler, Dixon, 1996. NASA's Response to the NRC Board on Sustainable Development, Recommendations Regarding EOSDIS. Presentation Viewgraphs and Narrative. (URL: http://mercury.hq.nasa.hq.gov/eosdis/sustainable.html)

ACKNOWLEDGMENTS

Funding for the NSIDC DAAC is provided by the National Aeronautics and Space Administration under Contract NAS5-32392.

Table 2: Data Requirements from Satellites; Sea Ice

Variable	*Present Sensor*	*Spatial Resolution*	*Time Resolution*	*EOS Sensor*	*Other Data Sources*	*Status of Data*	*Spatial Resolution*	*Temporal Resolution*	*Accuracy Needed*	*Accuracy Available*
Ice mass balance										
Ice extent	SSM/I	55 km	daily	MIMR	RADARSAT	good	25 km	daily	20 km	20 km
Ice concentration	SSM/I	55 km	daily	MIMR	RADARSAT	good	25 km	daily	1%	7%
Multiyear ice concentration	SSM/I	55 km	daily	MIMR	RADARSAT	good	25 km	daily	3%	30%
Ice displacement	RADARSAT	5 km	twice weekly	MODIS	buoys	needs dev.	25 km	daily	1 km	300 m
Ice deformation (%)	RADARSAT	5 km	twice weekly	MODIS		needs dev.	25 km	daily	0.5%	0.1%
Ice thickness distribution					sonar, models, RADARSAT	sparse	200 km	weekly	10% of thickness, 3% of area	50% of thickness, 30% of area
Ice growth / melt rate										
Snow thickness					climatology	sparse	100 km	weekly	5 cm	20 cm
Ocean heat flux to ice					climatology, models	almost no data	100 km	weekly	5 W/m^2	- -
Sea surf. temp. near ice edge	AVHRR	20 km	daily	MODIS		poor	25 km	daily	0.5 K	
Surface SW flux										
Surface albedo	AVHRR	1 km	daily	MODIS	climatology	needs dev.	100 km	twice daily	0.05	0.1
Cloud fraction	AVHRR	1 km	daily	MODIS	climatology, stations	needs dev.	100 km	twice daily	4%	30%
Ice extinction coefficient					field observations	sufficient	- - -	- - -	- - -	- - -
Surface LW flux										
Ice surface temperature	AVHRR, TOVS	1, 100 km	twice daily	MODIS	buoys, stations	needs dev.	100 km	twice daily	1 K	2 K
Atmos. temp. profile	TOVS	100 km	twice daily	AIRS, AMSU	stations	needs dev.	100 km	twice daily	1 K	10 K
Atmos. humidity profile	TOVS	100 km	twice daily	AIRS, AMSU, MHS	stations	needs dev.	100 km	twice daily	0.2	
Cloud bottom height	TOVS	100 km	twice daily	AIRS, AMSU		needs dev.	100 km	twice daily	5%	Atmos. ice crystal precip.
Atmospheric ice crystal precipitation				GLAS	aircraft	needs climatology	- - -	- - -	- - -	- - -
Atmospheric aerosols				GLAS	aircraft	needs climatology	- - -	- - -	- - -	- - -
Surface sensible heat flux										
Wind speed, 10 m			twice daily		buoys, NWP models	good	100 km	twice daily	1 m/s	
Ice surface temp. distribution	AVHRR	1 km	twice daily	MODIS		needs dev.	100 km	twice daily	0.3 K	
Air temp., 10 m					NWP models	poor	100 km	twice daily	1 K	
Air temp., lowest level	TOVS	100 km	twice daily	AIRS, AMSU	NWP models	needs dev.	100 km	twice daily	1 K	3 K
Surface/air temp. difference	TOVS	100 km	twice daily	AIRS, AMSU	NWP models		100 km	twice daily	0.2 K	1 K
Surface roughness						no technique				
Floe size statistics	SAR (AVHRR)	100 km	weekly	MODIS	RADARSAT	needs dev.	100 km	weekly	10%	- - -
Ridge statistics	SAR (L-band)	100 km	weekly	- - -	RADARSAT	needs dev.	100 km	weekly	10%	- - -
Ice momentum balance										
Wind velocity, 10 m					buoys, NWP models		25 km	daily	1 m/s	
Ocean mixed layer stability					models		25 km	daily		
Also requires atmospheric planetary boundary layer stability (from sensible heat flux), surface roughness, ice mass, and internal ice stress gradient.										
Salt Flux										
Water, salt flux through straits					ship observations, models	rough climatology				

TM Landsat Thematic Mapper
MSS Landsat Multispectral Scanner
AVHRR NOAA Advanced Very High Resolution Radiometer
OLS DMSP Optical Line Scanner

SAR Synthetic Aperture Radar
ALT Radar Altimeter
SPOT Système Probatoire pour l'Oservation de al Terre
SCAT Scatterometer
SSM/I DMSP Special Sensor Microwave Imager
ATSR Along Track Scanning Radiometer

Prioriy: 1 = critical, 2 = essential, 3 = useful

MIMR EOS Multifrequency Imaging Microwave Radiometer
MISR EOS Multi-Angle Imaging Spectroradiometer
GLAS EOS Geoscience Laser Altimeter System
ASTER EOS Advanced Spaceborne Thermal Emission and Refl. Radiometer
MODIS EOS Moderate Resolution Imaging Spectrometer
AIRS EOS Atmospheric Infrared Sounder
AMSU EOS Advanced Microwave Sounding Unit
SAGE III EOS Stratosphere Aerosol and Gas Experiment III
ALT EOS Radar Altimeter

Table 3: Data Requirements from Satellites: Ice Sheets

Variable	*Satellite Sensor (present)*	*EOS Sensors*	*Status*	*Temporal Resolution*	*Spatial Resolution*	*Single Point Accuracy*	***Priority***
Snow & Ice Mass Balance							
Accumulation Rate	SSM/I, TOVS	MIMR, GLAS	research mode	annual	20 km	2 cm w.e./y	1
Snow Facies Boundaries	TM, AVHRR, SSM/I SAR, SCAT	MISR, MODIS MIMR, ASTER	research mode	weekly no winter	5 km	1 km	2
Ice Thickening/Thinning	ALT	ALT GLAS	proven technique not until early C21	seasonal annual	20 km (ALT) 5 km (GLAS)	50 cm/y 10 cm/y	1
Morphology & Dynamics							
Precise Mapping	TM, SPOT, SAR	ASTER, MISR	proven technique	monthly	100 m	100 m	1
Coarse Scale Morphology	AVHRR, OLS	MODIS	proven technique	annual	1-4 km	1 km	2
Ice Topography	ALT, SAR interferometry	GLAS	proven technique not until early C21	once	500 m along track 1-5 km across track	2 m	1
Mapping Ice Margin	TM, SPOT, AVHRR,SAR	ASTER, GLAS	proven technique	seasonal	instr. depend.	100 m	1
Ice-Stream and Glacier Motion	TM, SPOT, SAR	ASTER	proven technique needs adequate data	annual	1 km	25 m/y	1
Climatology							
Surface Temperature	TM, AVHRR ATSR	MISR, ASTER MODIS	research mode	daily	4 km	1 K	2
Atm. Humidity Profile	TOVS	AIRS, AMSU	needs data	daily	1 km vertical	20 %	2
Atm. Temperature Profile	TOVS	AIRS, AMSU	needs data	daily	1 km vertical	1 K	2
Aerosol Concentration		SAGE III	research mode	daily	1 km vertical	TBD	2
Albedo ($S\uparrow$, $S\downarrow$)	AVHRR, TOVS,OLS	MODIS	research mode	daily	4 km	2 %	1
Radiation Balance	AVHRR, ATSR	MODIS, ASTER	research mode	daily	4 km	20 Wm^{-2}	1
Cloud Fraction	AVHRR	ASTER, MODIS	research mode	daily	4 km	5 %	1
Cloud Bottom Height	TOVS	AIRS, AMSU	research mode	daily	4 km	100 m	1
Surface Wind Speed & Direction			no technique	daily	4 km	1 m/s	2
Surface Air Temperature			no technique	daily	4 km	1 K	1
Precipitation			no technique	daily	4 km	5 cm w.e./y	3

Table 4: Data Requirements from Satellites; Snow Cover (after Crane, 1993)

Variable	*Satellite Sensor (present)*	*EOS Sensors*	*Status*	*Temporal Resolution*	*Spatial Resolution*	*Single Point Accuracy*	*Priority*
Snow Cover Extent, Visible/IR	AVHRR	MODIS	research mode	daily, weekly, monthly	1-2 km	1 km	1
Snow Cover Extent, Passive Microwave	SSM/I	AMSR	operational	daily, weekly	25 km	25 km	1
Snow Water Equivalent	SSM/I	AMSR	research mode	daily, weekly	25 km	+/- 50mm WE	1
Wet Snow/Dry Snow Boundary	SSM/I	AMSR	research mode	daily, weekly	25 km	25 km	3
Albedo (Broadband Surface)	AVHRR	MODIS	proven technique	daily, weekly	1-2 km	0.1	2

Algorithms for Calculation of Digital Surface Models from the Unwrapped Interferometric Phase

Wolfgang Goblirsch, Paolo Pasquali
Remote Sensing Laboratories, Department of Geography, University of Zürich
Winterthurerstrasse 190, CH-8057 Zürich - Switzerland
fax: +41 1 362 52 27, email: gobi@rsl.geogr.unizh.ch

ABSTRACT

The focus of this paper is on interferometric DEM generation algorithms from imaging geometry analysis. The proper description of the interferometric imaging geometry is presented. As a result of solving the two sets of range-Doppler equations one also obtains the interferometric alongtrack baseline component. This fixes the imaging positions of each pixel in the case of known antenna tracks. Conversely, if the relative positions of the antenna tracks are not precisely known, one may adjust the interferometric baseline by comparing the azimuth-offsets from image correlation to the calculated alongtrack baseline. As an example, the angle of convergence is estimated using single-pass interferometric DOSAR data motion compensated to individual reference tracks. A new method of estimating the absolute phase difference is suggested which exploits the range-offsets obtained from correlating the complex image pair. Finally, it is shown that layover produces a residual tilt in interferometric DEM's if the crosstrack-coordinate is left unfiltered.

1. INTRODUCTION

Airborne interferometric SAR allows the generation of potentially high resolution Digital Surface Models (DSM) since the interferometric phase is a function of the mapped terrain surface. In order to map the interferometric phase to the surface of the terrain model, two different operations have to be executed.

The first step is the phase unwrapping operation which aims to guarantee the correct multiplicity to the phase difference between 0 and 2π. Due to the inherently noisy interferometric phase this operation is already subject to intense scrutiny by the remote sensing scientific community in order to develop better noise compensating algorithms. The second step transforms the unwrapped phase difference to the surface of the terrain model. Methods are presented for improving this second step.

This transformation follows both from two sets of range-Doppler equations representing the imaging geometry, one for each antenna, and from the phase difference relation involving the slantrange difference of the antennas. We will term this set of five equations the Interferometric Range-Doppler Equations (IRDE).

In this paper we first focus on the description of the IRDE. Then we suggest a new phase calibration method. From the exact solution of the IRDE follows a baseline adjustment approach. Finally, we demonstrate how separate filtering of the vertical- and crosstrack-DSM-coordinates improve the precision of the DSM.

2. THE INTERFEROMETRIC RANGE-DOPPLER EQUATIONS

The IRDE describe the imaging geometry of a processed interferometric image pair based on the two antenna flight tracks denoted by $\vec{p}(t) = (p_1(t), p_2(t), p_3(t))$ and $\vec{q}(t)$ where t is the along-track, or azimuth time, referenced to one track (master track). This time is found with the pixel number j_p in azimuth as well as the azimuth pixel spacing δ_{az} as follows: $t_p = (j_p - 1)\,\delta_{az}/v_p$, where v_p is the averaged velocity on track p. The imaging time t_q of the corresponding pixel on the slave track is found with an analogous relation. In a similar fashion the range r_p from the master track is found from the slantrange pixel spacing δr_p, the range pixel number i_p, and the range r_{po} to the first image pixel with: $r = r_p = r_{po} + i_p \delta r_p$.

The range r_q to the corresponding slave pixel is obtained from the interferometric phase difference relation:

$$\Delta r = r_q - r_p = \frac{\Delta\phi\lambda}{4\pi} \qquad (1)$$

where $\Delta\phi$ denotes the calibrated unwrapped phase difference and λ denotes the wavelength. The range-Doppler equations are:

$$\left|\vec{p}(t_p) - \vec{x}(t_p)\right| = r_p \qquad (2)$$

$$\left(\dot{\vec{x}}(t_p) - \dot{\vec{p}}(t_p)\right) \cdot \left(\vec{p}(t_p) - \vec{x}(t_p)\right) = r_p \left|\dot{\vec{x}}(t_p) - \dot{\vec{p}}(t_p)\right| \sin\alpha \qquad (3)$$

$$\left|\vec{q}(t_q) - \vec{x}(t_q)\right| = r_q \qquad (4)$$

$$\left(\dot{\vec{x}}(t_q) - \dot{\vec{q}}(t_q)\right) \cdot \left(\vec{q}(t_q) - \vec{x}(t_q)\right) = r_q \left|\dot{\vec{x}}(t_q) - \dot{\vec{q}}(t_q)\right| \sin\beta \qquad (5)$$

where: $\vec{x}$ = *(x, y, z), position of the imaged groundpoint*
$\dot{\vec{p}}(t_p)$ = *velocity of antenna p*
$\dot{\vec{q}}(t_q)$ = *velocity of antenna q*
$\dot{\vec{x}}$ = *velocity of the groundpoint*
α = *processed squint angle track p*
β = *processed squint angle track q*

Geometrically, the two range equations represent two spheres centered at the imaging positions on the two tracks. The Doppler equations represent cones with their tips located at the imaging positions, and their axes pointing in the direction of the velocity vectors. For zero squint the Doppler cones degenerate into zero-Doppler planes.

3. A NEW PHASE CALIBRATION APPROACH

Now the final step in interferometric DSM generation is the calculation of the groundpoint coordinates for each matched image pixel on the basis of the antenna tracks and the unwrapped phase difference. In order to do this we first have to find the correct phase difference offset $\Delta\phi_k$ to be added to the original unwrapped phase difference $\Delta\phi_o$ so that equation (1) will result in the true range difference. This operation is termed phase calibration and if no special calibration setup is implemented in the interferometric SAR system usually requires a ground control point (gcp). In certain cases, however, the use of ground control might be avoided using the range-offsets Δr_c obtained from image correlation.

In the case when the range-offsets Δr_c from the correlation of the complex image pair represent the absolute range difference Δr in equation (1) we are able to calculate $\Delta\phi_k$ with the help of equation (6):

$$\Delta\phi_k = \frac{4\pi\Delta r_c}{\lambda} - \Delta\phi_o \qquad (6)$$

where $\Delta\phi_k$ is averaged over all matched pixels with a sufficiently high correlation coefficient. We use the same window-size for filtering $\Delta\phi_o$ used in correlating the complex image pair.

As an example, given a range pixel size of 0.624 m and an offset precision of 1/100 of a pixel we would get an acceptable error in the phase-offset of about 8^0 by averaging over 100 pixels.

Unfortunately, in airborne interferometric SAR-systems both antennas usually have different internal delay times so there is an unkown constant range-offset which has to be found by careful range-calibration. With data from two identical antennas in one-pass interferometry or from one antenna in two-pass interferomertry, the new phase calibration approach should work since the offsets from complex image correlation should offer sufficient precision and the number of pixels used can be quite large.

0-7803-3068-4/96$5.00©1996 IEEE

4. SOLUTION OF THE INTERFEROMETRIC RANGE-DOPPLER EQUATIONS

Once the absolute range-offset has been established with the help of the calibrated phase difference, we are able to solve the 4 range-Doppler equations for the groundpoint coordinates $\vec{x}$ and the nominal azimuth-offset $t_q - t_p$. The nominal azimuth-offset disappears for parallel tracks and zero-Doppler imaging geometry in which case we only have to solve the two range equations and one zero-Doppler plane equation. In all other cases we have to solve 4 different equations, two of which are quadratic and the other two linear for the groundpoint coordinates. In the general case of nonlinear tracks, an analytic expression of the solution cannot be given. However, we can always solve two range equations and one Doppler equation in an analytic fashion, starting with an initial azimuth-offset, and then testing the solution with the remaining Doppler equation. This establishes an iterative approach for solving the IRDE with arbitrary precision [3].

For the case of linear tracks a noniterative solution can be given which results from the real roots of a fourth order polynomial in the vertical DSM-coordinate z or the crosstrack DSM-coordinate y. The DSM x-coordinate is conveniently selected in the groundtrack-direction of the master track and is thus given by:

$$x = (p_1 + r\sin\alpha)\cos\theta_p \qquad (7)$$

where θ_p denotes the pitch angle of the master track velocity vector. The variable $p_1 = j_q\delta_{az}$ denotes the alongtrack coordinate of the scene, where j_p denotes the alongtrack pixel number and δ_{az} is the alongtrack pixel spacing. The transformation between the vertical- and the crosstrack-coordinate is found with:

$$y = \sqrt{r^2(\cos\alpha)^2 - (p_3 - z)^2} \qquad (8)$$

Typically in airborne SAR, one motion compensates with respect to a fixed sensor altitude for which the azimuth-offset or alongtrack interferometric baseline component B_x can be expressed in simpler terms:

$$B_x = \frac{e(\tan\gamma)^2 - y\tan\gamma + r\sin\alpha - (r+\Delta r)\sin\beta\sqrt{1+(\tan\gamma)^2}}{1+(\tan\gamma)^2} \qquad (9)$$

where:

γ = angle of convergence

d_o = groundtrack separation at the first image pixel

$e = -(d_o/\tan\gamma + p_1)$ = distance to groundtrack intersection

$B_y = (B_x - e)\tan\gamma$ = crosstrack baseline

The projection of the imaging geometry to the tangent plane is pictured in Figure 2 for right pointing antennae.

In the case of horizontal tracks we require γ and d_o for the calculation of the vertical, or the crosstrack, DSM-coordinate. The variable d_o can be given as a function of the absolute platform attitude angles at the start of the scene for an airborne single-pass interferometric SAR-system. One has to use a gcp for adjusting d_o if these angles are not precise. If the platform roll angle variation is available we might find the angle of convergence with the following equation:

$$\gamma = \operatorname{atan}\left(\frac{B\sin\Delta\rho}{L_{az}}\right) \qquad (10)$$

where B is the physical baseline length, L_{az} denotes the alongtrack length of the processed scene, and $\Delta\rho$ is the difference of the platform roll angles at the beginning and at the end of the processed scene segment. This works especially well when the roll variation is nearly linear as demonstrated with IMU data pertaining to the interferometric data set gathered by DOSAR during the 1994 campaign in Switzerland [1], [2]. Figure 1 shows the roll angle variation for a particular scene segment which was used to generate a DSM with the help of the IRDE for crossed tracks. The crossed-tracks geometry was caused by motion compensating with respect to individual reference track-directions.

In the given example we obtained 0.0008° for γ by inserting the values of B = 1.06 m, $\Delta\rho = 0.75°$ and $L_{az} = 960$ m into equation (10). The value of γ was confirmed by using gcp's for adjustment of the imaging geometry during DSM generation.

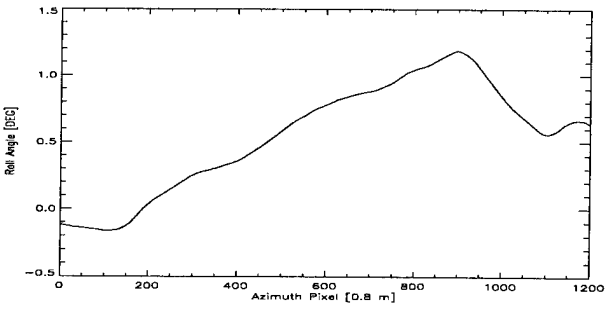


Figure 1: Roll angle variation

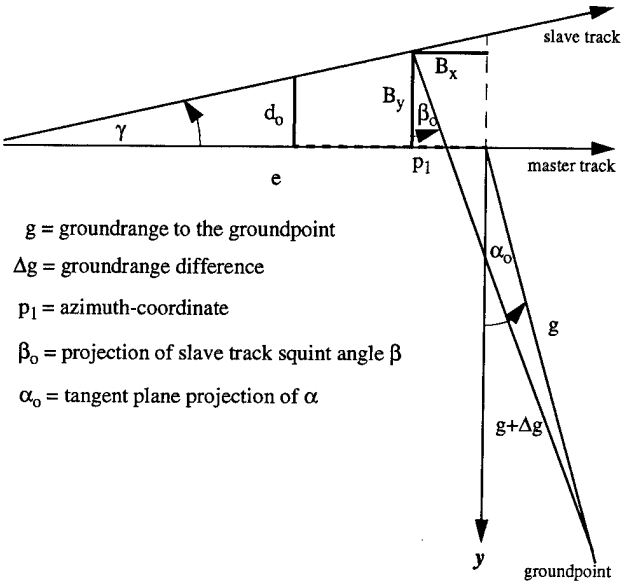


Figure 2: Imaging geometry in the tangent plane for horizontal linear tracks

5. ESTIMATING THE ANGLE OF CONVERGENCE FROM THE CORRELATION AZIMUTH-OFFSETS

We exploit equation (9) for an alternative method in estimating γ. For airborne two-antennae interferometric SAR systems we usually have $|\gamma| < 0.01°$ and $\alpha = \beta$. In this case equation (9) simplifies to:

$$B_x \cong -(y\tan\gamma + \Delta r\sin\alpha) \qquad (11)$$

which shows that the absolute value of the azimuth-offset increases with range in the crossed-tracks case and is also terrain dependent.

The azimuth-offset Δx from correlating the complex image pair usually is the along-track baseline component B_x plus a constant Δ_x. Thus in order to calculate γ we must use the difference of the correlation azimuth-offset obtained at different ranges where $y(r_2) \neq y(r_1)$:

$$\tan\gamma = \frac{(\Delta x(r_1) - \Delta x(r_2)) + \sin\alpha(\Delta r(r_1) - \Delta r(r_2))}{y(r_2) - y(r_1)} \qquad (12)$$

Of course y is still a function of γ so we would have to use an iterative approach to find the angle of convergence. But if we are only interested in the order of magnitude of γ we can use an approximated crosstrack-coordinate obtained, for example, from a low resolution reference DEM.

We correlated the complex image pair processed from 200 MHz DOSAR data [1] with a 16×16 window. The pixel-size of the used data set was 0.58×0.62 m^2 (azimuth×range). The offset precision was set to pixel-size/20. The offsets were updated at 9.3 m intervals in azimuth, and at 10 m intervals in range. When we inserted the corresponding offsets into equation (12) for all $r_2 - r_1 = 10$ m no trend could be detected. Averaging γ over all samples resulted in $\gamma = 0.001°$. We have yet to confirm this method with additional data sets.

6. LAYOVER AND NOISE INFLUENCE IN THE DSM CROSSTRACK-COORDINATE

It is not adviseable to filter the phase difference heavily before DSM calculation because this will reduce singular DSM-elevation values unnecessarily. On the other hand, leaving the phase difference essentially unfiltered will cause DSM deformation in the vertical and crosstrack DSM-coordinates. If we want to measure the elevations of individual objects more precisely we might want to accept a certain degree of noise in the vertical DSM-coordinate z. However, the same degree of noise is unacceptable in the crosstrack-coordinate y since it will turn the slantrange into a less monotonic function of y [1]. But even if we have strongly reduced the noise influence by filtering the interferometric phase will we measure some crosstrack displacements of steep surface features. This can be attributed to the layover effect resulting from the SAR slantrange geometry:

When the slope facing the radar is greater than the off-nadir angle we have more than one ground location corresponding to the same slantrange; a situation which is equivalent to a nonmonotonic slantrange as a function of groundrange. As a result, signatures from locations whose ranges correspond to the same range sample mix and we obtain only one elevation value per slantrange pixel, thereby changing the form of the imaged features upon slantrange-to-crosstrack transformation with equation (8).

These layover areas are not masked with DOSAR data for two reasons:

- Their correlation coefficient reaches values in excess of 0.87 where correct elevations are obtained in non-overlaid regions.
- Due to the high range resolution of the 200 MHz range-chirp data, very small surface objects are resolved which tend to have radar facing slopes greater than the off-nadir angle. Therefore, we also want to preserve as well as possible the form of these objects in the surface model.

Without signal mixing, a symmetric peak in groundrange pictured in Figure 3 would be tilted towards the radar in slantrange-coordinates as in Figure 4. The tilt is such that it would be exactly offset when going from slantrange to groundrange, thereby restoring the original form again. But in reality the peak in slantrange will be more symmetric because one can obtain only one elevation for each range pixel. Transforming the more symmetric peak back to groundrange, however, results in a net tilt away from nadir.

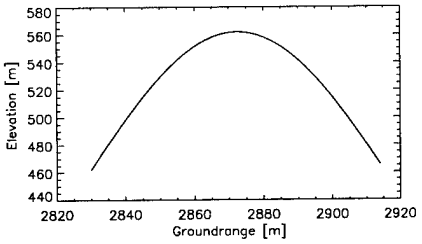


Figure 3: Peak in groundrange-coordinates

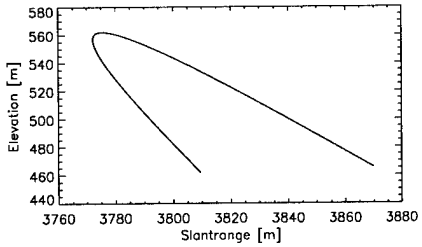


Figure 4: Peak in slantrange-coordinates

This happens with all surface features having sufficiently steep radar facing slopes which is the case for mostly small-scale objects. Thus when we straighten out the crosstrack-coordinate relative to slantrange so much that local ambiguities disappear we will obtain a monotonic slantrange which removes the tilt in the DSM. This has been done with 27×27 moving average filter of y in Figure 6. Smaller window sizes resulted in more or less residual tilt which a crosstrack filtering window size of of 3×3 demonstrates in Figure 5. The filtering window size has to be adjusted to the expected overlaid slantrange intervals. On the other hand, one should not filter too strongly in order to preserve crosstrack topographic information as much as possible. As a rule of thumb the maximum window size n for crosstrack smoothing may be calculated with the following equation:

$$n = [(r_2 - r_1)/\delta r] \qquad (13)$$

where: $r_1 = \sqrt{(y_0 + \Delta y)^2 + (p_3 - (z_{ref} + \Delta z))^2}$

$r_2 = \sqrt{y_0^2 + (p_3 - z_{ref})^2}$

Δz and Δy are the vertical and illuminated crosstrack dimensions of the overlaid object, y_0 is the minimum groundrange, and z_{ref} is medium elevation of the scene.

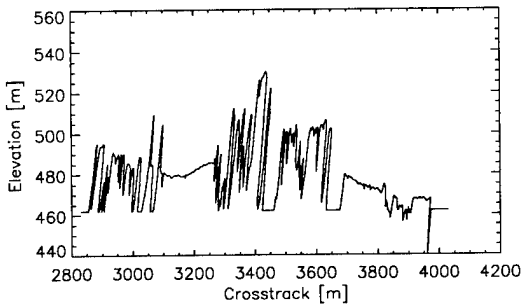


Figure 5: Crosstrack elevation profile filtered with 3×3 window size

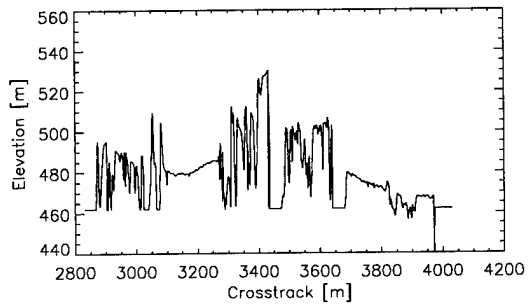


Figure 6: Crosstrack elevation profile filtered with 27×27 window size

7. CONCLUSION

It was found that one has to solve the Interferometric Range-Doppler Equations for a correct description of the interferometric imaging geometry. Doing so one also obtains a model of the alongtrack interferometric baseline which may be adjusted with offsets from complex image correlation in the case of crossed-tracks geometry. Using the range-offsets in combination with the suggested phase calibration approach one would be less dependent on ground control points; a situation especially convenient in spaceborne interferometry for large area investigations.

High resolution interferometric DSM generation requires separate filtering of the DSM crosstrack-coordinate. The window size has to be adjusted to the local ambiguities which occur as a result of layover.

REFERENCES

[1] W. Goblirsch et al: Accuracy of Interferometric Elevation Models Generated from DOSAR Airborne Data, IGARSS'95 vol. 1, pp. 770 - 774

[2] N. Faller, E. Meier: First Results with the Airborne Single-Pass DO-SAR Interferometer, IEEE Transactions on Geoscience and Remote Sensing, vol. 33, no. 5, 1995, pp. 1230-1237

[3] W. Goblirsch: Error Sources in Optimization of Parameters of Airborne Interferometric Synthetic Aperture Radar. Thesis, Department of Geography, University of Zürich 1996, in press

Elevation Correction and Building Extraction from Interferometric SAR Imagery

G.R. Burkhart, Z. Bergen and R. Carande
Vexcel Corporation,
2477 55th Streat, Boulder, CO 80301
(303) 444-0094, fax:(303)444-0470, burkhart@vexcel.com
W. Hensley, D. Bickel and J. R. Fellerhoff
Sandia National Laboratory,
P.O. Box 5800 M/S 0531, Albuquerque, NM97185-0531
(505) 845-8112, fax:(505) 845-8609, whhensl@sandia.gov

Abstract -- The development of high (2m) resolution interferometric SAR (IFSAR) instrumentation makes extraction of man made and natural urban structures feasible. In particular, we consider building extraction from imagery of an urban/industrial area. IFSAR imagery are particularly well suited for this task because these data include the measured elevation as well as the coherence and intensity of the back scattered radiation. Gradients in the IFSAR elevation correspond directly to elevation edges. Coherence and intensity data can be combined to give specific information about the scattering properties of the viewed surface. The disadvantage of IFSAR imagery is that these data are typically of lower resolution and contain greater noise than other data such as optical photography, also the data contain specific artifacts that must be removed. Indeed, the motivation for building and tree extraction behind this work is the need to remove noise and artifacts from the IFSAR data. Techniques for removing artifacts that are peculiar to IFSAR data are particularly discussed.

OVERVIEW

The goal of this project was to develop tools that can be used to improve digital elevation models (DEMs) that were produced from interferometric synthetic aperture radar (IFSAR). We obtained data for two different sites at Sandia National Laboratory. The data that we could use for the two sites included (1) the *backscattered power*, (2) the *IFSAR elevation* in meters from sea level (3) the *binning number* and (4) the *maximum correlation.* The binning number and maximum correlation arise from the rectification of the power and elevation. The data are originally processed into range and azimuth, but for rectification the range and azimuth data are transformed into the horizontal coordinate system This transformation is accomplished with the use of the IFSAR elevation. Since the range and azimuth data do not transform uniformly to the horizontal coordinate system (because of differing elevations), the data are collected into uniformly spaced bins. The binning number is the number of range and azimuth measurements to fall into a bin normalized to the average. The binning number gives additional information: regions of rising elevation have a smaller binning number and regions of decreasing elevation have larger binning number. As we shall see, the binning number can be very helpful, particularly for the removal of front-porch anomalies.

Although many measurements fall into a given bin, the final elevation assigned to that bin is taken from only one measurement, the measurement with the greatest correlation. If s_1 and s_2 are the complex signals received by each of the antennas, the correlation is $s_1 s_2^* / |s_1||s_2|$. The maximum correlation is the greatest correlation of the measurements to fall in a bin.

Our work with DEM reconstruction follows four approaches. The first approach is image filtering; the second, tree recognition and extraction; the third, building recognition and extraction, and the fourth is building model construction and DEM reconstruction using the building models and the "bare-earth" DEM.

IMAGE FILTERNG

The first step in the DEM improvement is noise reduction through digital filtering. Noise in the DEM is due to phase noise in the interferogram. Essentially, the idea with digital filtering is that noise scale lengths are typically smaller than scale lengths of real features. Application of the filter alters the signal at small scales leaving the large scales intact. Any features on the noise scale are always destroyed by the filter.

Context-Sensitive Diffusion

For noise filtering, we use a true multi-length scale method based upon the diffusion equation. The diffusion length scale, which is the scale length that is diffused in a single iteration, is large in regions with no feature edges, but small near feature edges. Thus, noise is removed to the greatest extent possible, but at the same time the position and abruptness of feature edges are preserved.

0-7803-3068-4/96$5.00©1996 IEEE

Consider the vector gradient $\mathbf{g}_l$, where $g_{x,l} = h_{i+l,j} - h_{i-l,j}$ and $g_{y,l} = h_{i,j+l} - h_{i,j+l}$. The length-scale-average gradient is

$$\langle \mathbf{g} \rangle = \left(\frac{1}{l_{\max}} \right) \sum_{l=1}^{l=l_{\max}} \mathbf{g}_l .$$

This gives the gradient that is consistently present across different length scales. The anisotropic diffusion coefficient is now a tensor:

$$\mathbf{D} = c \frac{\langle \mathbf{gg} \rangle - \langle \mathbf{g} \rangle \langle \mathbf{g} \rangle}{\langle \mathbf{g} \rangle \langle \mathbf{g} \rangle}$$

and the diffusion equation is

$$\frac{\partial h}{\partial t} = \nabla \bullet \mathbf{D} \bullet \nabla h .$$

Consider, for example

$$D_{xx} = c \frac{\langle g_x^2 \rangle - \langle g_x \rangle^2}{\langle g_x \rangle^2}$$

If the length-scale-average gradient $\langle g_x \rangle$ is large, that is, if the gradient persists across length scales, then it is probably a feature edge and the diffusion is small. On the other hand, if the deviation, $\langle g_x^2 \rangle - \langle g_x \rangle^2$ is large, then the gradients do not persist across length scales, and the diffusion is large. The diffusion tensor will be nearly diagonal in a coordinate system that has one coordinate aligned with the local feature edge and one coordinate that is normal to the local feature edge, and so the anisotropic formulation has the virtue that it is capable of smoothing along edges while, at the same time, preserving the edge's position and steepness.

Front Porch Removal

In Fig. 1, we show an example of a building with a prominent "front porch" anomaly. This effect appears as an extended region on the near-range side of the building that is characterized by elevations in between the elevation at the ground and the elevation at the building top.

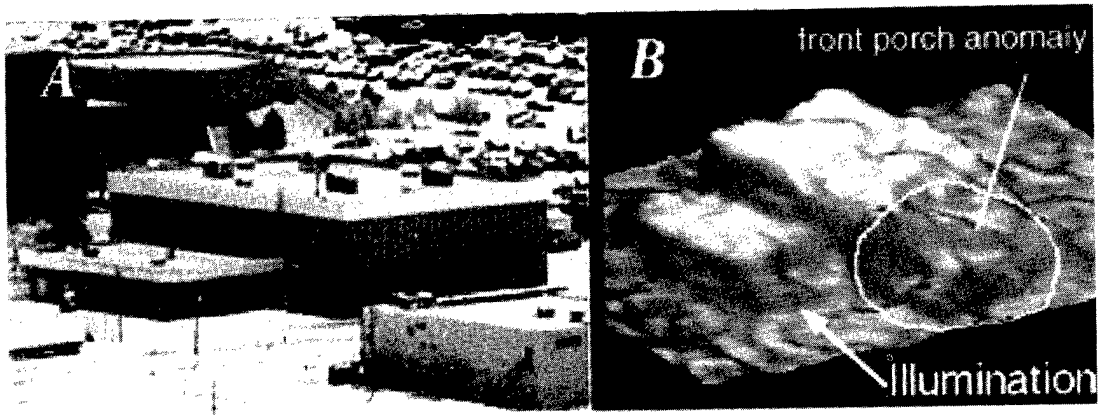


Fig. 1: Perspective optical view of a building in the B-894 scene (A), and a perspective view of the IFSAR elevation for the same building (B). The sloped region in front of the building in the IFSAR elevation is due to the front porch effect.

Cuts of elevation, intensity and normalized binning number, for the same building as was seen in Fig. 1, are shown in Fig. 2 We see that the front porch region is characterized by intermediate elevation and enhanced intensity, and it begins and is terminated by anomalously low binning numbers. Based on geometric considerations, we expect the overall length of the front porch region to be $2\Delta h \sin(\theta_i)$, where Δh is the height of the building above the surrounding terrain and θ_i is the incidence angle to the terrain in front of the building. Since the nominal incidence angle is about 45°, we expect that the length of the front porch will be approximately $2\Delta h$.

In the case of Fig. 2, $\Delta h \approx 13$ m and the length of the front porch is about 26 m.

We use these signatures to identify and correct for front porch regions, however, it should be noted that in the process, any actual features in the front porch region (such as real front porches!) are lost.

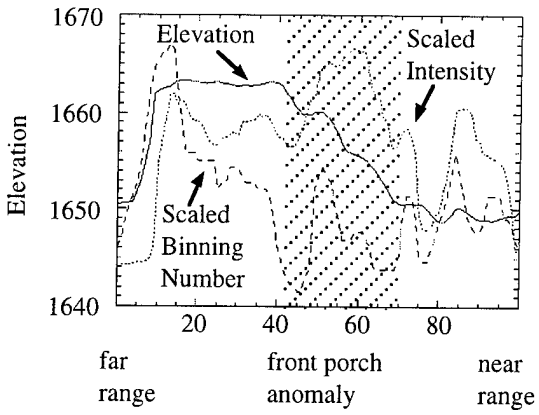


Fig. 2: The elevation, intensity and binning number for cuts through the building shown in Fig. 1. The cross hatched region is the front porch anomaly.

The comparison between the IFSAR elevation and the manually derived elevation is given in a more quantitative manner in Figure 3. Figure 3a shows the comparison between the IFSAR elevation (3x3 median filtered) and the manually derived elevation, and 3b shows a comparison between the IFSAR elevation that has been processed with context sensitive diffusion and front porch removal and the manually derived elevation. First, considering the back and side edges of buildings, we see that the context-sensitive diffusion has completely maintained the gradients on these edges, but in the flat regions, the context-sensitive diffusion has substantially reduced the error that is due to thermal noise. The front edges of buildings in Figure 3a are characterized by first white, indicating that the IFSAR elevation is greater than the manually derived elevation, followed by black, indicating the opposite. We see that the black regions are almost completely removed by front porch removal andwhite regions are reduced substantially.

CONCLUSIONS

We have achieved remarkable progress toward automatic DEM reconstruction. The combination of context-sensitive diffusion and front porch removal yields dramatic improvement in the DEMs, and DEMs that compare very well to the manually derived DEM. Due to space limitations, we cannot further discuss building extraction except to note that an approach such as given in [1] seems to work well for this problem.

ACKNOWLEDGMENTS

This work was supported by the United States Department of Energy under Contract DE-AC04-94AL85000.

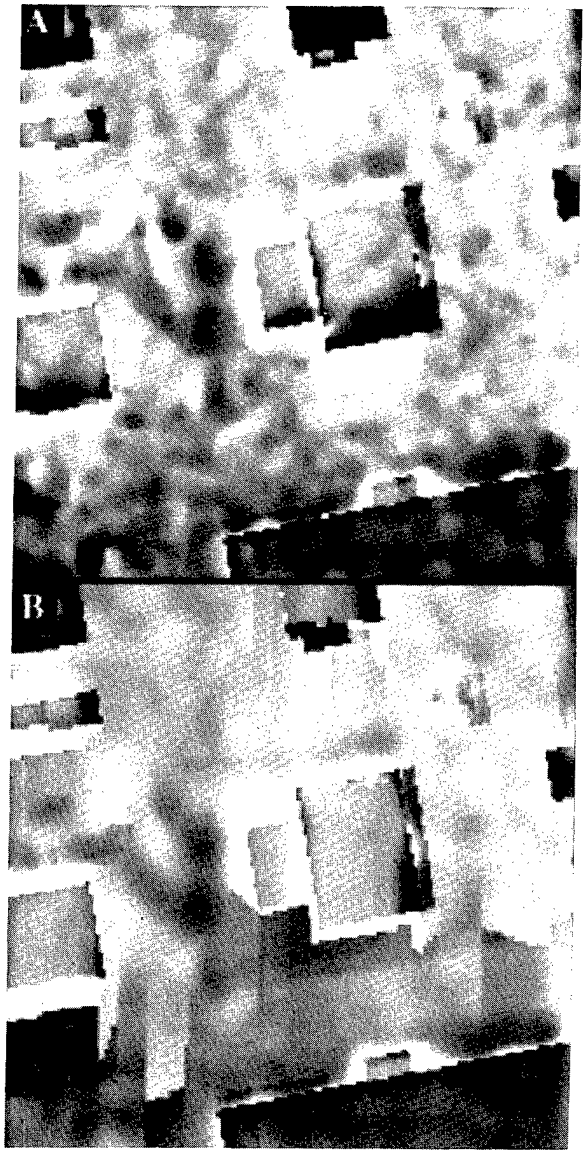


Fig. 3: Quantitative result of DEM improvement. (a) The difference between the manually derived elevation and IFSAR elevation (3x3 median filtered). (b) The difference between the manually derived elevation and the IFSAR elevation after diffusion and front porch removal.

REFERENCES

[1] W. Weidner and W. Förstner, "Towards automatic building extraction from high-resolution digital elevation models," ISPRS Journal of Photogrammetry and Remote Sensing, vol. 50, p. 38, 1995.

Unbiased estimation of the coherence from multi-look SAR data

R. Touzi, A. Lopes*, J. Bruniquel**, P. Vachon

Canada Centre for Remote Sensing, 588 Booth Street, Ottawa Ontario, Canada K1A OY7

* CESBIO (CNES/CNRS/UPS), 18 Av. Ed. Belin 31055 Toulouse, France

**Alcatel Espace, 26 Av.J.F. Champollion, 31073 Toulouse, France

Abstract – The statistics of the classical coherence estimator are derived for Gaussian scenes. It is shown that the coherence estimator is generally biased towards higher values for partially coherent areas. The multi-look coherence estimator is then analyzed, and the statistics of the classical coherence estimator are used to remove the bias from the coherence estimate. A new method for coherence estimation from the multi-look complex coherence, is introduced. It is shown that the multi-look complex coherence estimate is less biased than the multi-look magnitude coherence. The statistics of the complex coherence estimator are derived and used to remove the coherence bias.

INTRODUCTION

In different modes of Synthetic Aperture Radar (SAR) imaging such as interferometry, multi-temporal acquisition, and polarimetry, the radar signal is measured in mutiple channels and the information provided by the channel correlation may be used as a source of information. The degree of coherence, called the coherence, is defined in [1] as the magnitude of the correlation coefficient of the complex signal data. The coherence is calculated to provide a coherence map [2], which is currently used for target classification [3, 4]. Quantitative coherence information is very important in many applications and as such the coherence should be estimated accurately.

In interferometry, the two original complex channels z_1 and z_2 are generally combined to output different multi-look products such as the interferogram and a coherence map. Each pixel value of the multi-look coherence map corresponds to the coherence value calculated with L independent samples contained in each pixel. Generally, the original complex files are not stored, and only the multi-look information is available. The multi-look coherence map pixel values of the selected area are averaged to provide an estimate of the coherence.

In this paper, the statistics of the classical coherence estimator are derived for Gaussian scenes. The multi-look coherence estimator is analysed and a method is proposed to remove the estimate bias using the statistics of the classical coherence estimator. A new method is then introduced for coherence estimation from multi-look complex coherence. The statistics of the complex coherence estimator are derived and used to remove the coherence bias.

CLASSICAL COHERENCE ESTIMATOR: DEFINITION AND STATSISTICS

Definition:

The complex coherence of two complex signals z_1 and z_2 is defined in [1] by:

$$\gamma = \frac{E(z_1 z_2*)}{\sqrt{E(|z_1|^2}\sqrt{E(|z_2|^2)}} \tag{1}$$

where $E(x)$ is the expectation of x . The coherence is the magnitude D of the complex coherence. Given N signal measurements, the classical estimator of the complex coherence is:

$$\hat{\gamma} = \frac{< z_1 z_2* >}{\sqrt{< |z_1|^2 >}\sqrt{< (|z_2|^2 >}} \tag{2}$$

where $< z_1 >= \frac{1}{N}\sum_{i=1}^{N} z_{1i}$, and i is the sample number.

The coherence estimator $d = \hat{D}$ is defined as the magnitude of the complex coherence estimate: $\hat{D} = |\hat{\gamma}|$. It is shown in [5] that d is the maximum likelihood estimator of the coherence.

STATISTICS OF THE CLASSICAL ESTIMATOR WITH GAUSSIAN AREAS

The probability density function (pdf) of the classical coherence estimator $d = \hat{D}$ is derived in [6] for two circular Gaussian processes. The pdf expression is used to derive the moments of k order:

$$m_k = \frac{\Gamma(L)\Gamma(1+k/2)}{\Gamma(L+k/2)}(1-D^2)^L \cdot {}_3F_2(1+k/2, L, L; L+k/2; 1; D^2) \tag{3}$$

0-7803-3068-4/96$5.00©1996 IEEE

This equation can be used to deduce the mean and the variance of d. Figure 1 presents the mean of the estimated coherence $E(d) = E(\hat{D})$ as a function of the real coherence value D. As can be seen, the coherence estimator d is unbiased for highly coherent areas, i.e. with high D values. The estimator becomes biased towards higher values for partially coherent areas, i.e. low D values, with a resulting reduction of contrast between areas of different coherence. The bias decreases with increasing number of independent samples L. It becomes insignificant within areas of lower D values if an infinite number of independent samples are integrated during the estimation process.

UNBIASED ESTIMATION OF THE COHERENCE FROM MULTI-LOOK COHERENCE DATA

Multi-look coherence estimator:

Given N independent L-look coherence samples, the multi-look coherence estimator $\bar{d}_L = \hat{D}$ is defined as the average of the N sample values: $\bar{d}_L = \frac{1}{N}\sum_{i=1}^{N} d_{Li}$, where d_L is the multi-look coherence, i is the sample number, and N is the number of integrated multi-look coherence samples. It can be shown that $E(\bar{d}_L) = E(d_L)$, and $var(\bar{d}_L) = var(d_L)/N$.

Hence, the dispersion of the estimate around the mean coherence $E(d_L)$ becomes narrower after the sample averaging process. The probability distribution becomes tightly concentrated around $E(d_L)$ and the bias can be removed using equation (3) with the known number of independent looks L contained in each sample. The error bar is derived in [5] as a function of the number N of independent multi-look (L) samples integrated, and the standard deviation of the coherence estimate d_L.

This method called the "multi-look magnitude coherence estimate method" is validated in [5] using actual SAR data. The results obtained for Gaussian areas can be extended to K-distributed areas as it was done in [7]. This allows the user to extend the application of such results to a wide range of natural extended targets (forest, rock, and ocean). The method is used in [8] to remove the bias from coherence estimated Gaussian and K-distributed scenes on ERS-1 data.

UNBIASED ESTIMATION OF THE COHERENCE FROM MULTI-LOOK COMPLEX COHERENCE DATA

Multi-look complex coherence estimator:

In interferometry, the multi-look channel phase difference is stored in addition to the multi-look (magnitude) coherence. This phase difference is the argument of the muti-look complex coherence. The classical estimator γ of the complex coherence Υ over L independent samples is defined by:

$$\gamma = \frac{\sum_{i=1}^{L} z_{1i} z_{2i}*}{\sqrt{\sum_{i=1}^{L} |z_1|^2}\sqrt{\sum_{i=1}^{L} |z_2|^2}} \quad (4)$$

An estimate of the complex coherence Υ can be obtained by averaging the N multi-look complex coherence estimates γ_{Li} (the L-look complex coherence calculated over the sample i) over the area under study: $\Upsilon = \bar{\gamma}_L = \frac{1}{N}\sum_{i=1}^{N} \gamma_{Li}$.

The multi-look complex coherence estimator is defined as the magnitude of the integrated complex coherence: $d = |\hat{\Upsilon}| = |\bar{\gamma}_L|$. Compared to the multi-look magnitude coherence estimator discussed previously, the multi-look complex coherence estimator uses the phase during the averaging process. This should lead to more accurate coherence estimation, as shown below. Since $\hat{\Upsilon}$ is taken here as the estimate of $E(\gamma)$, the first order statistics of the complex coherence estimator γ have to be derived in order to remove an eventual bias, and to calculate the precision of the estimate.

Statistics of the complex coherence estimator for Gaussian areas:

The bias expression for the complex coherence estimate γ is derived in [5] for Gaussian scene. Figure 2 presents the bias on the estimate $|E(\gamma)|$ as a function of the real value D, for different values of L. The two following points are noted:

- The bias on the magnitude of the integrated complex coherence is lower than the bias on the classical coherence estimator d presented in Figure 2.
- The bias of the multi-look complex coherence estimate decreases very rapidly with the increasing L. It becomes practically insignificant for relatively large L ($L \geq 20$). For the same L value (i.e. $L = 20$), the classical estimator is largely biased for low coherence areas, as can be seen in Figure 1.

This method called "the multi-look complex coherence estimate method" is validated in [5] using actual SAR data. The error bar is derived in [5] as a function of the number N of independent multi-look samples integrated, and the standard deviation of the complex coherence estimate γ_L. Since, the complex coherence statistics derived for Gaussian scene are still available for K-distributed scenes, the method can be applied to both Gaussian and K-distributed scenes.

CONCLUSION

The classical coherence estimator is biased towards higher values for partially coherent areas. Even if a large number of samples are integrated during the estimation process, the coherence estimated from one-look complex data might still be biased for very low coherence values. The estimator statistics have to be used for the accuracy assessement of the coherence estimation from one-look complex data.

For coherence estimation using multi-look coherence data, the statistics of the classical estimator can be used to remove the bias of the coherence estimated over Gaussian or K-distributed scenes. The precision of the coherence estimate can also be assessed using the values of the number of looks L contained in each sample, and of the number N of averaged multi-look samples.

The multi-look complex coherence method is less biased than the multi-look magnitude coherence method. For Gaussian or K-distributed scenes, the coherence might be estimated from multi-look complex coherence data with a relatively large number of looks. This yields a coherence estimate which does not need any bias removal in a practical sense, as is the case for a multi-look magnitude coherence estimator. For low L values, the statistics of the complex coherence estimator can be used to remove the bias on the coherence estimate.

REFERENCES

[1] Born, M. and Wolf, E., *Principles of Optics: Electromagnetic Theory of Propagation, Interference and Diffraction of Light*, Fifth. ed., Elmsford NY: Pergamon Press, 1985.

[2] Prati, C. and Rocca, F., Range resolution enhancement with multiple SAR surveys combination, *Proc. of, IGARSS'92 Symp.*, pp. 1576-1578, Houston, Texas, 1992.

[3] Hagberg, J.O., Ulander, L.M.H., and Askne, J., Repeat-pass interferometry over forested terrain, *IEEE Trans. Geosci. Rem. Sens.*, Vol. 33, No. 2, pp. 331-340, Mar. 1995.

[4] Rignot, E.J.M., and Van Zyl, J.V., Change detection techniques for ERS-1 SAR data, *IEEE Trans. Geosci. Rem. Sens.*, Vol. 31, No. 4, pp. 896-906, July 1993.

[5] Touzi, R., Lopes, A., Bruniquel, J. and Vachon, P.W., Unbiased estimation of the coherence function: Implications in SAR interferometry, *IEEE Trans. Geosci. Rem. Sens.*, in review, 1996.

[6] Touzi, R., and Lopes, A., Statistics of the Stokes parameters and of the complex coherence parameters in one-look and multi-look speckle field, *IEEE Trans. Geosci. Rem. Sens.*, in press, March, 1996.

[7] Joughin, I.R., Winebrenner, D.P., and Percival, D.B., Probability density functions for multi-look polarimetric signatures, *IEEE Trans. Geosci. Rem. Sens.*, Vol. 32, No. 3, pp. 562-574, May 1994.

[8] Vachon, P.W., Geudtner, D., Gray, A.L., and Touzi R., ERS-1 Synthetic Aperture Radar Repeat-Pass Interferometry Studies: Implications for Radarsat, *Can. J. Rem. Sens.*, Vol. 21, No. 4, pp. 441-454, 1995.

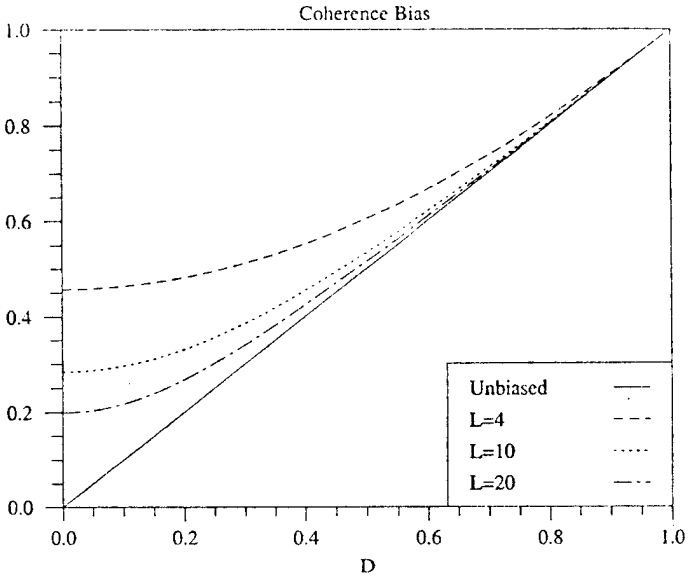


Figure 1: Coherence bias for various looks.

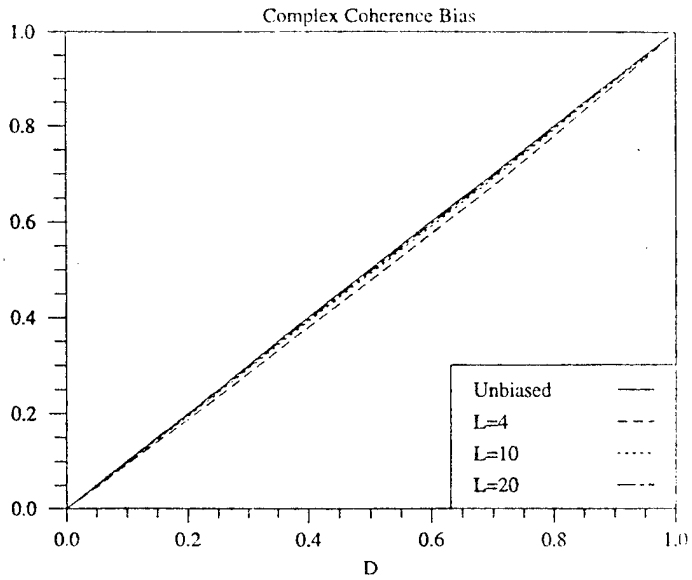


Figure 2: Complex coherence bias for various looks

Automated Rapid Mapping with Interferometric Synthetic Aperture Radar Data

Francis M. Ngai
ngai@vexcel.com
(303) 444-0094 x212

Richard E. Carande
carande@vexcel.com
(303) 444-0094 x220

Vexcel Corporation, 2477 55th Street, Boulder, Colorado 80301, U.S.A.

Abstract

This paper describes automated algorithms that generate map products in a rapid fashion with interferometric synthetic aperture radar (IFSAR) data set. The input IFSAR data set consists of backscatter, elevation and correlation images and the automatically extracted map elements include land-use polygons, transportation networks, buildings/man-made structures, bald-earth elevation contours and hydrology networks. A calculator computes five feature images from the IFSAR data set and the five feature images serve as inputs to a hybrid unsupervised classification algorithm which segments the scene into five classes. The five classes include fields, trees, urban area/man-made structure, water and unknown. The classification results allows a bald-earth terrain model to be extracted from the IFSAR terrain model using a novel algorithm. The difference between the bald-earth elevation and the original IFSAR elevation can be used in conjunction with the classification map to identify and estimate the heights of buildings, man-made structures and trees. Elevation contours and hydrology networks derived from the bald-earth model can be shown to be more accurate than that derived from the IFSAR model. Transportation networks are identified using a road extraction technique based on rotational energy summation. Sample map products are shown to demonstrate the efficiency and accuracy of the automated algorithms.

1 INTRODUCTION

This report summarizes work in the area of feature-based classification of interferometric synthetic aperture radar (IFSAR) imagery for rapid mapping. Conventional mapping science relies upon passive optical instruments to provide data for map construction. Topography is extracted by viewing stereo images and plotting contour lines. The derived topography is used to correct (orthorectify) geometric distortions in the imagery. Features of interest are identified and traced from the orthorectified imagery and stored in a data base. The operations described above are typically performed manually which translates into high production costs. Furthermore, optical sensors require daylight and favorable weather conditions for successful operations.

Interferometic synthetic aperture radar can address these optical limitations. Radar systems are active sensors which can operate during day or night, as well as adverse weather conditions. The use of two antennas simultaneously provides the capability of deriving elevation measurement for each pixel using interferometric techniques [1]. Not only does this proivde a registered elevation map, but also allows the imagery to be geometrically corrected for terrain effects as it is processed. In addition, topographic contours can be immediately extracted.

The three-imagery IFSAR data set, which consists of backscatter, elevation and correlation measurements, is well matched for land-use classification. The three measurements can be considered as features and a feature vector for a particular pixel in the scene is the collection of feature values at that location. Pixels of a particular land-type, or class, can possess a particular signature in the data set, where a signature is the global feature vector of the corresponding class. Land-use classification can be accomplished by partitioning the classes of pixels according to the signatures.

2 DATA SET

The three-imagery IFSAR data set was collected by the Army Topographic Engineering Center's IFSAR airborne system, which is operated by the Evironmental Research Institute of Michigan. The ERIM/TEC sensor is known as *IFSARE*. The output IFSARE data set consists of 2.5m square pixels of backscatter, elevation and correlation measurements. The data set used here was of a test site near Ann Arbor, Michigan, known as the *Dexter/Chelsea* site. The site is approximately 15 km by 12 km and is a mix of mostly farms, fields and small stands of trees. The area is quite flat, with dominant topographic features being the tree stands and man-made structures. The acquisition date for this data was in February 1995.

The backscatter file corresponds to the multilooked-orthorectified imagery of the scene. Elevation is calculated from the phase difference in processed complex imagery of the two interferometric antennas. The measurements in the correlation file indicates the coherence between the measurements made by the two antennas on the airborne platform. Correlation can be represented as the product of decorrelating effects. For the IFSARE system, there are three main decorrelating effects which must be considered: spatial baseline decorrelation, thermal noise decorrelation

0-7803-3068-4/96$5.00©1996 IEEE

and volume scattering decorrelation. Since the spatial baseline decorrelation effect can be modeled [2], and the signal-to-noise ratio of the data is known, one can estimate the relative volume scattering by correcting the correlation values for these two effects. The volume scattering parameter is particularly useful for finding tree canopies and other vegetation [3, 4].

3 FEATURE CALCULATOR

The feature calculator extracts feature information from the IFSARE data set for land-use classification. The inputs to the feature calculator are the backscatter file, the elevation file and the correlation file. All input files are in floating point format, as provided directly by the IFSARE processor. The outputs consists of five byte-format files: backscatter file, correlation file, volume scattering file, RMS backscatter file and RMS slope file. The five features are used by the classifier to determine land use.

4 LAND-USE CLASSIFICATION

The purpose of the land-use classifier is to segment the scene into five classes: 1) fields, 2) trees, 3) urban area/man-made structure, 4) water and 5) unknown. A hybrid unsupervised classification technique was used to perform land-use classification on the Dexter/Chelsea data.

In this hybrid approach, the scene is first segmented with the ISODATA K-means algorithm. This algorithm is an unsupervised classification algorithm which partitions the feature space into N number of classes. N is user-defined and is greater than the desired number of classes. Next the user would examine each of the N classes and utilizes his/her knowledge of SAR imagery to classify each class as fields, trees, urban area/man-made structure, water or unknown. We are currently investigating automating ths process by performing restrictive relative analysis on the class signature vectors in the feature space.

5 FEATURE EXTRACTION

In conjunction with IFSARE data set, the results of land-use classification allow features such as land-use polygons, bald-earth digital elevation model, trees, buildings, power poles, as well as transportation networks to be identified and located.

The dominant topographic features in the Dexter/Chelsea data set are trees and man-made structures. Hence, drainage networks derived from the IFSARE digital elevation model (DEM) are inaccurate. To alleviate this problem, pixels which have been classified as trees or urban area/man-made structure are masked out from the IFSARE DEM. The bald-earth DEM is obtained by resampling the elevation measurements which have not been masked out.

A difference DEM can be created from the IFSARE DEM and the bald-earth DEM. With the difference DEM, the location and height of man-made structures such as buildings and power poles can be estimated. Figure 1 shows an example of power line extraction. Tree height can be derived from the difference DEM as well.

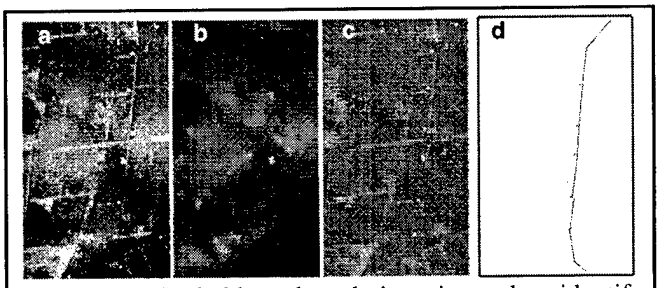


Figure 1. The bald earth technique is used to identify power poles above 17.5 meters in height. The original DEM in a shows the poles clearly. These are not in the bald earth elevation shown in b, and therefore are obvious in the difference image shown in c. In d the vectors connecting the power poles, which should correspond to the power lines, are shown.

Transportation networks are identified using a road extraction technique based on rotational energy summation which assumes that roads are dark piece-wise linear structures [5].

Figure 2. presents the end-to-end data flow for converting the raw IFSAR data to map elements using the approach outlined above. Figure 3 shows a symbolic map generated using this algorithm directly from the Dexter/Chelsea IFSARE data.

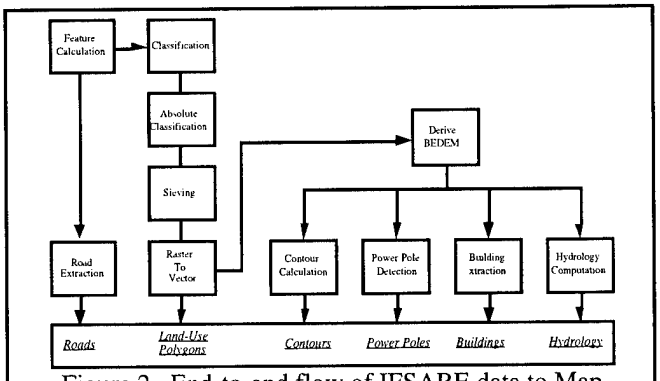


Figure 2. End-to-end flow of IFSARE data to Map Elements

6 CONCLUSIONS

The ability to produce rapid maps from IFSAR data has been shown to be feasible and the algorithm for automatic extraction of map features have been demonstrated. The land-use polygons generated by the land-use classifier

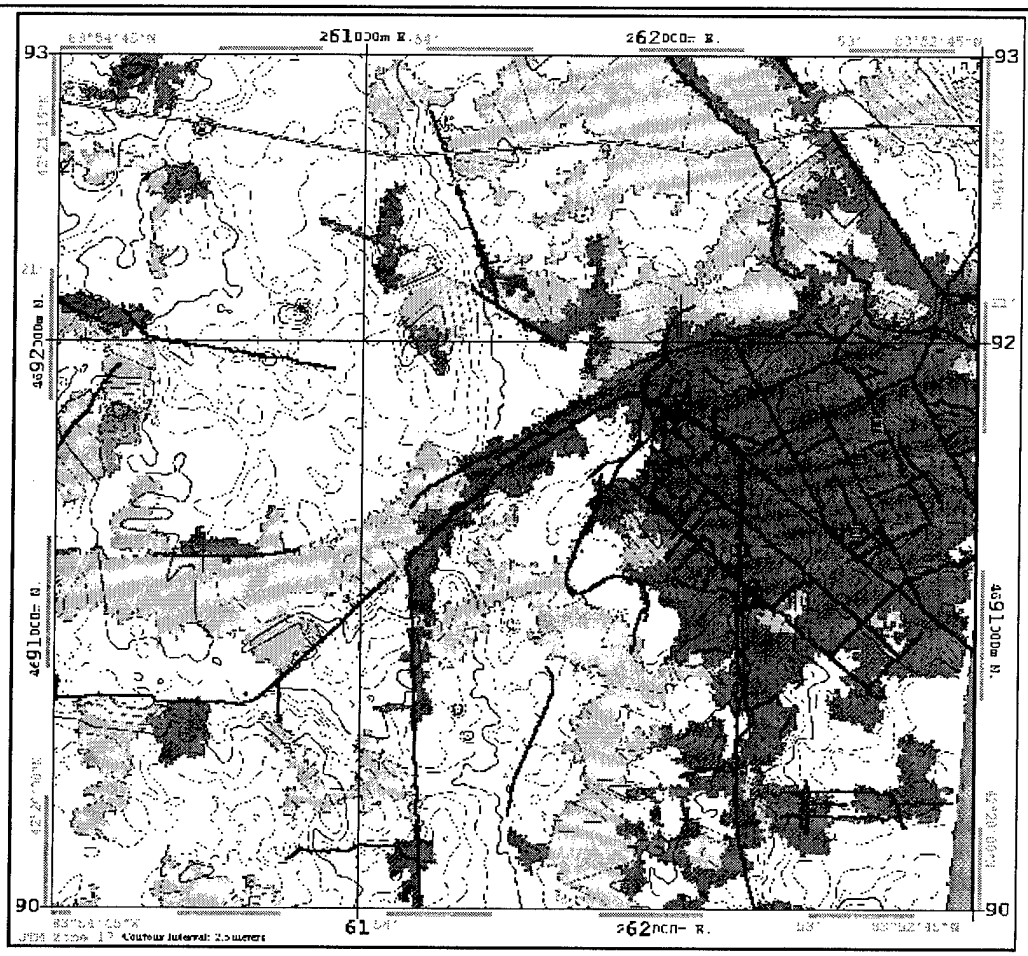


Figure 3. Example map product of the IFSARE data produced from the Dexter-Chelsea data set. This product is a purely symbolic representation of the surface feature. Land use shown: dark grey = urban, light grey = tree, white = field and black = unkown.

allows a bald-earth digital elevation model to extracted from its counter-part in IFSAR data set. The bald-earth DEM proves to be a power tool in finding structures such as buildings and power lines.

7 ACKNOWLEDGEMENTS

The work described here was performed under contract DACA76-95-C-0007 from U.S. Army Topographic Engineering Center, Fort Belvoir, VA.

8 REFERENCES

[1] H. A. Zebker and R. M. Goldstein, "Topographic mapping from interferometric synthetic aperture radar observations," *J. Geophys. Res.*, vol. 91, no. B5, pp. 4993-4999, 1986.

[2] H. A. Zebker and J. Villasenor, "Decorrelation in Interferometric Radar Echoes," *IEEE Trans. Geosci. Remote Sensing,* vol. 30, pp. 924-932, 1992.

[3] J. O. Hagberg, *et al.*, "Repeat-Pass SAR Ineterferometry Over Forested Terrain," *IEEE Trans. Geosci. Remote Sensing,* vol. 33, pp. 331-340, 1995.

[4] U. Wegmuller, *et al.*, "Interferometric Signatures of Temperate Forest From ERS-1 SAR Data," Proceedings of IGARSS'94, Pasadena, CA, Aug 8-12.

[5] Z. Bergen, D. Kaiser and R. Carande, "REX: An Automated Road Extraction Algorithm for SAR Imagery," IGARSS '96, Lincoln, Nebraska.

Ultra-Wideband and Low-Frequency SAR Interferometry

L.M.H. Ulander and P.O. Frölind
National Defence Research Establishment (FOA)
P.O. Box 1165, S-581 11 Linköping, Sweden
Phone: (+46)-13-318044, Fax: (+46)-13-318100, email: ulander@lin.foa.se

Abstract -- We analyse different techniques for 3D SAR-mapping. Interferometry using narrow-band SAR enables retrieval of topography but gives an ambiguous height. Stereoscopy can also be used but has degraded resolution due to speckle. For ultra-wide band SAR, i.e. wavelength-order resolution, these techniques converge and give similar vertical resolution. A significant advantage, however, is that the interferometric height becomes unambiguous since the depth of focus is only one fringe.

INTRODUCTION

A SAR produces high-resolution images of a ground area projected into the slant range and azimuth plane. Most SAR systems are narrow-band and narrow-beam, i.e. the spatial resolution is much larger than the wavelength. This implies speckle noise over distributed targets, i.e. random amplitude and phase fluctuations generated when several scatterers contribute to the image within the resolution cell. Ultra-wideband SAR drives the spatial resolution to the wavelength limit. A consequence of the latter is that surface speckle disappears although volume speckle remains.

Three-dimensional (3D) mapping of the ground is desirable in many applications. Unambiguous volumetric mapping can be achieved by creating a synthetic 2D aperture from many tracks. A much simpler technique to estimate topography is (speckle) interferometry using two parallel but offset antennas or flight tracks. The main drawbacks with this technique are that the measured height is ambiguous and that the speckle introduces a maximum baseline-to-distance ratio.

In this paper, we investigate the possibility to perform three-dimensional mapping with ultra-wideband and wide-beam SAR systems. The techniques will be applied to data from the CARABAS VHF-band SAR [1]. It is an ultra-wideband SAR system operating in the 20-90 MHz band.

SPECKLE INTERFEROMETRY

Speckle interferometry is based on cross-correlating two SAR images of the same scene with slightly different incidence angles as illustrated in Fig. 1. The 3D position is estimated by measuring the slant range r and the phase difference $2kd$ where k is the radar wavenumber. The speckle in the two images is the same if the imaging geometry and scene properties are constant, and thus cancels when determining the phase difference. The small change of incidence angle in Fig. 1, however, gives a random change in the speckle pattern which introduces noise in the phase difference. The speckle patterns are correlated up to a maximum angle difference given by [2]

$$\Delta\theta_{\max} = \frac{\lambda \tan\theta}{2\rho_r} \tag{1}$$

where λ is the wavelength, θ is the incidence angle, and ρ_r is the slant range resolution. Note that the maximum angular change in (1) is small when the resolution is much larger than the wavelength. The RMS height error σ_h is directly related to the RMS phase noise σ_φ according to

$$\sigma_h = \frac{\lambda}{2}\frac{\sin\theta}{\Delta\theta}\frac{\sigma_\varphi}{2\pi} \tag{2}$$

We note that the height error in (2) is controlled by two competing processes: 1) The phase error which increases with $\Delta\theta$ since the speckle correlation decreases, and 2) the geometrical error which decreases with $\Delta\theta$ since the height sensitivity increases. We also note that the minimum height error is independent of wavelength since (1) sets an upper limit to $\Delta\theta$. This also implies that the minimum height error is of the same order as the slant range resolution.

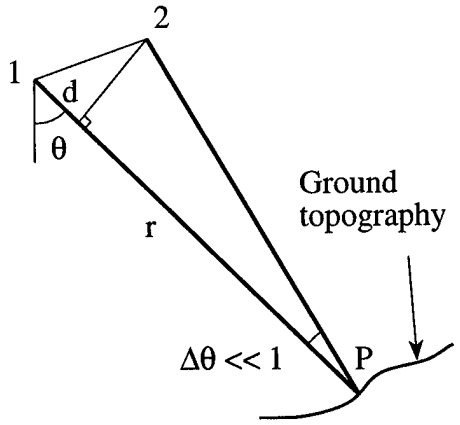


Fig. 1. Basic interferometry geometry. Two antennas image the point P from slightly difference incidence angles.

0-7803-3068-4/96$5.00©1996 IEEE

STEREOSCOPIC SAR

The 3D position of a point object is straightforward to retrieve from two SAR images acquired from different flight tracks. For simplicity, we consider only parallel but displaced flight tracks as in Fig. 2. Knowledge of the two ranges r_1 and r_2 together with the baseline components b_y and b_z enables the height h_1 to be determined from the following equations

$$\begin{cases} r_1^2 = h_1^2 + y_1^2 \\ r_2^2 = (h_1 + b_z)^2 + (y_1 - b_y)^2 \end{cases} \tag{3}$$

Elimination of y_1 in (1) and (2) results in a second-order equation, from which h_1 may be determined. An error analysis gives the height error Δz and the across-track error Δy according to

$$\begin{cases} \Delta z = \Delta r_1 \dfrac{\sin\theta_2}{\sin(\theta_1 - \theta_2)} + \Delta r_2 \dfrac{\sin\theta_1}{\sin(\theta_2 - \theta_1)} \\ \Delta y = \Delta r_1 \dfrac{\cos\theta_2}{\sin(\theta_1 - \theta_2)} + \Delta r_2 \dfrac{\cos\theta_1}{\sin(\theta_2 - \theta_1)} \end{cases} \tag{4}$$

where Δr_1 and Δr_2 are the line-of-sight errors for the corresponding flight tracks. From (4) we conclude that the errors are controlled by the common denominator. The required range accuracy for a given precision Δz or Δy is thus proportional to $\sin(\theta_1 - \theta_2)$. This means that a smaller incidence angle difference must be compensated by a higher precision of the range.

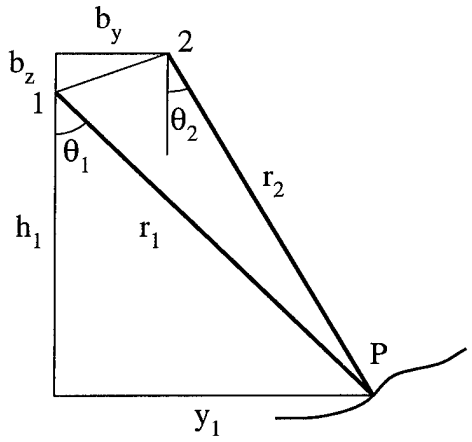


Fig. 2. SAR stereoscopy enables the 3D position of P to be determined from measurements of r_1, r_2, b_x, and b_y.

From (4), we again conclude that the position can be determined with an accuracy of the same order as the slant range resolution. This requires that the incidence angles and the incidence angle difference are of the same order of magnitude. Finer resolution may be determined by interpolation of the point target response, but interfering clutter and noise will set a lower resolution limit.

ULTRA-WIDEBAND INTERFEROMETRY

Both stereoscopy and speckle interferometry can provide the 3D position with a precision of the same order of magnitude as the slant range resolution. However, both techniques suffer from some major short-comings. For stereoscopy, one problem is that of identifying the same objects in the two images. For interferometry, the phase is only measured modulo-2π which means that only relative height variations can be retrieved. Sophisticated phase unwrapping techniques have been developed to take care of this problem, but a number of reference points are nevertheless needed to calibrate the height measurements.

Both of these short-comings can be circumvented by using a resolution of wavelength order. A fully deterministic approach can now be applied. The basic idea is that the speckle becomes correlated for large changes in incidence angle as the resolution becomes finer, and fully disappears when the wavelength limit is reached. This means that we may use larger incidence angle changes to increase height sensitivity. As a consequence, the 3D position of an object may be determined with wavelength accuracy. At least two problems are obvious with this approach. Firstly, a large incidence angle change means that single-pass interferometry is not possible and repeat passes must be used instead. This suggests using lower frequencies to ease the requirement on navigational accuracy and scattering stability. Secondly, it becomes a problem to identify the same object in the two images solely based on their appearance. We suggest two methods for solving this problem, one for distributed targets and one for isolated point targets. The distributed targets may be treated in an automatic manner, assuming a gently undulating topography which will be coherent over an extended area. The single point target, on the other hand, probably needs to be (coarsely) identified in both images before its position can be evaluated using the stereoscopic technique.

The first step in ultra-wideband interferometry is to project the two SAR images onto a common horizontal ground reference plane. This is convenient since we expect the topography to be least variable relative this plane. All objects which are situated on the reference plane will thus match perfectly after the transformation. Any deviation from the reference plane, on the other hand, will give a mis-match.

The two images will thus be correlated as long as the mismatch is less than the resolution,. We call this the depth-of-focus (DOF), and it can be determined using the geometry in Fig. 3 according to

$$DOF = \rho_r \frac{\frac{1}{\sin\theta_2} + \frac{1}{\sin\theta_1}}{\frac{1}{\tan\theta_2} - \frac{1}{\tan\theta_1}} \qquad (5)$$

We note that the depth-of-focus is large for speckle interferometry but small for ultra-wideband interferometry.

Fringes will appear within the depth-of-focus from the reference plane. The resulting phase variation can be separated into one term due to the reference plane and a second term due to the height variations from the same plane. After subtraction of the former, the residual phase variations can be directly converted to topographic height. The height change corresponding to 2π radians is called the ambiguity height which is given by

$$\Delta z = \frac{\lambda_c}{4} \frac{\sin[(\theta_1 + \theta_2)/2]}{\sin[(\theta_1 - \theta_2)/2]} \qquad (6)$$

where λ_c is the wavelength corresponding to the centre frequency. Equation (6) shows that the ambiguity height varies across the swath so that the scaling between differential phase and height changes accordingly.

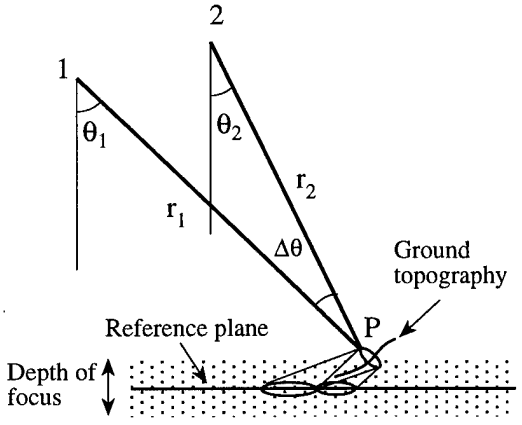


Fig. 3. Illustration of depth-of-focus relative a reference plane. P is out of focus since the responses are disjoint.

It can be shown that the trigonometric factor in (5) and (6) are in fact identical despite their different appearance. We may thus express the depth of focus in the following fundamental equation

$$DOF = \frac{4\rho_r}{\lambda_c} \Delta z \qquad (7)$$

Equation (7) says that the depth of focus is proportional to the ambiguity height and the resolution expressed in quarter wavelengths. For the ultimate resolution $\rho_r = \lambda_c/4$ we thus obtain one fringe within the depth of focus, i.e. the height measurement becomes unambiguous. The limited depth of focus implies that only a small height interval can be analysed at a time. Repeating the process by varying the reference plane completes the measurement.

3D VOLUME PROCESSING

An alternative to interferometry is to process the SAR data set directly as a function of an assumed 3D position. The result is a 3D image, with an extra vertical component compared to a ground range image. The simplest is by cross-correlation of the two images after SAR processing, which gives an identical result as interferometric processing. Another possibility is to first cross correlate the range-compressed raw data and then perform a 3D inversion processing. It is anticipated that the latter method will give lower sidelobes but at the expense of increased noise. Other techniques for processing are also possible using multi-baseline data to partly fill out a synthetic 2D aperture.

CONCLUSIONS

We have analysed a number of techniques for 3D mapping using SAR. Interferometry using narrow-band SAR is limited by speckle and scene decorrelation, and also gives an ambiguous height which must be unwrapped. Stereoscopy is another technique which can be applied to a pair of SAR images but it has degraded performance due to speckle. We have shown that interferometry and stereoscopy converge and give similar vertical resolution for ultra-wide band SAR systems. The interferometric height becomes unambiguous in this limit since the depth of focus is only one fringe. These techniques will be applied to CARABAS VHF-band SAR data. The lower operating frequency will increase scene correlation and enable multi-baseline repeat-track data.

REFERENCES

[1] Gustavsson, A., P.O. Frölind, H. Hellsten, T. Jonsson, B. Larsson and G. Stenström, 1993, The Airborne VHF SAR System CARABAS, Proceedings of IGARSS'93 held in Tokyo, Japan, 18-21 August 1993, pp. 558-562.

[2] Hagberg, J.O., L.M.H. Ulander and J. Askne, 1995, Repeat-Pass SAR Interferometry over Forested Terrain, IEEE Transactions on Geoscience and Remote Sensing, Vol. 33, No. 2, 331-340.

Medium Resolution Efficient Phase Preserving Focusing for Interferometry.

F. Gatelli, A. Monti Guarnieri, C. Prati, F. Rocca.
Dipartimento di Elettronica - Politecnico di Milano
Piazza L. da Vinci, 32 - 20133 Milano - Italy
Fax: +39-2-23993585, e-mail: monti@elet.polimi.it

Abstract – A real time technique to get strip-map SAR interferograms and coherence maps with common Unix Workstations is presented. For the ERS mission, the "real time" throughput corresponds to approximately 1/8 of PRF: e.g. $\sim$ 4 min for processing a 100 $\times$ 100 km image pair. The proposed algorithm achieves that goal on a medium cost 160 Mflops/s Unix Workstation. The output is a 5 looks averaged interferogram, with a geometric resolution of 50 $\times$ 50 m.

INTRODUCTION

With the huge amount of satellite SAR data available from ERS-1 and ERS-2 [1] the generation of fast, low resolution interferometric products for data browsing and large scale analysis is a relevant problem. Algorithms for the generation of interferograms and coherence maps are known and established [2], however, some of the processing steps should be revisited when computational efficiency becomes the main request.

PRESUMMING AND FOCUSING

The first processing step of the proposed algorithm consists of a range and azimuth presumming of the SAR raw data. The cost of these operations is minimized by means of an integer implementation (e.g. by storing one complex sample in one 16 bit word) and by using polyphase filter banks [3]. The main goal of presumming is to reduce the amount of data to be processed with the minimum loss of quality. It can be done by canceling the contributions coming form the incorrelated parts of SAR images spectra [3,4]. The range spectral decorrelation is basically due to the baseline, whereas the azimuth spectral decorrelation is due to sidelobes and to variations of the Doppler centroid. A good compromise between quality and efficiency could be achieved by dropping half of the range band, and 3/8 of the azimuth band, e.g. by choosing subsampling ratios 2×8 (range, azimuth) and by processing 1 look in range and 5 looks in azimuth. As an example, for acquisitions with a baseline of 300 m the range spectral shift is ~5 MHz (for flat earth). A range presumming of 2 allows to recover 81% of the useful bandwidth (e.g. 9 MHz with respect of 11 MHz), if the center frequencies of the presumming filters are tuned according to the spectral shift [2,4]: $f_0 = \pm 2.5$ MHz. Yet, the data rate is halved with evident computational advantages.

For azimuth presumming the two raw data set should be filtered with the same central frequencies, that are equal to the average of Doppler Centroid (for the fist look). An advantage of azimuth presumming is to reduce the length of the Doppler history so that smaller processing blocks can be exploited by azimuth focusing.

The five sub-looks created by raw data presumming are then range and azimuth focused. For ERS, an efficient 1-D range-Doppler processor has provided enough quality for the goal. That processor has passed the CEOS phase-preserving test (e.g. phase errors are one order of magnitude lower than the requirements).

COHERENCE ESTIMATE

A new technique has been developed for a quick estimate of the image coherence "unpublished"[5]. The technique exploits the images absolute values, according to the expression:

$$\rho = \frac{E\left(|v_1|^2 - E\left[|v_1|^2\right]\right)\left(|v_2|^2 - E\left[|v_2|^2\right]\right)}{\sqrt{\left(E\left[|v_1|^4\right] - \overline{|v_1|^2}^2\right)\left(E\left[|v_2|^4\right] - \overline{|v_2|^2}^2\right)}} = \gamma^2$$

being v_1, v_2 the two images, ρ the correlation coefficient of their modulus and γ the absolute values of the coherence. The following coherence estimator is thus derived:

$$\hat{\gamma}_M = \begin{cases} \sqrt{2\hat{\rho} - 1} & \hat{\rho} > \frac{1}{2} \\ 0 & \hat{\rho} \leq \frac{1}{2} \end{cases} \qquad (1)$$

$$\text{where} \quad \hat{\rho} = \frac{\sum_{n,m} |v_1(n,m)|^2 \cdot |v_2(n,m)|^2}{\sqrt{\sum_{n,m} |v_1(n,m)|^4 \cdot \sum_{n,m} |v_2(n,m)|^4}}$$

It can be shown that this estimator has a larger variance than the usual coherence estimator, yet it is much faster (e.g. it does not require the estimate of local frequency), robust and simpler:

i- no stationarity of the local interferometric phase is required

0-7803-3068-4/96$5.00©1996 IEEE

ii- it is independent of any focusing phase error that do not affect speckle

iii- it can be directly applied to detected images

iv- it is independent of any fringes' frequency estimation error.

The main drawback of the estimator $\hat{\gamma}_M$ could be its sensitivity to image non-stationarities, however this problem can be solved by equalizing the images' mean amplitude (at a modest computational cost) [5].

IMAGES COREGISTRATION

An efficient image coregistration requires both a fast estimate of alignment parameters, and a low-cost image resampling. In the ERS case, the following deformation model can be assumed between the two images:

$$\begin{bmatrix} x'' \\ r'' \end{bmatrix} = \begin{bmatrix} \cos\beta & -\sin\beta \\ \sin\beta & \cos\beta \end{bmatrix} \begin{bmatrix} x_1 & 0 \\ 0 & r_1 \end{bmatrix} \begin{bmatrix} x \\ r \end{bmatrix} + \begin{bmatrix} x_0 \\ r_0 \end{bmatrix} \underset{\beta \ll 1}{\simeq} \begin{bmatrix} x_1 & -r_1\beta \\ x\beta & r_2 \end{bmatrix} \begin{bmatrix} x \\ r \end{bmatrix} + \begin{bmatrix} x_0 \\ r_0 \end{bmatrix} \quad (2)$$

being x'', r'' the reference coordinate of one image and x, r those of the other. The images shift (x_0, r_0), stretch (x_1,r_1) and skew (β) parameters can be estimated by exploring the relative shift of at least three small-windows, possibly close the corners of the images. The shifts between corresponding windows can be found by maximizing coherence, e.g. the figure of merit use expressed by (1). The accuracy can be $\ll 1/10$ of a resolution cell, that is enough for a medium resolution product, however the measured coherence should exceed a proper threshold to avoid larger errors. As an example, Fig.1 shows the probability that the estimated cross-correlation has a maximum for a random position, different from the right one.

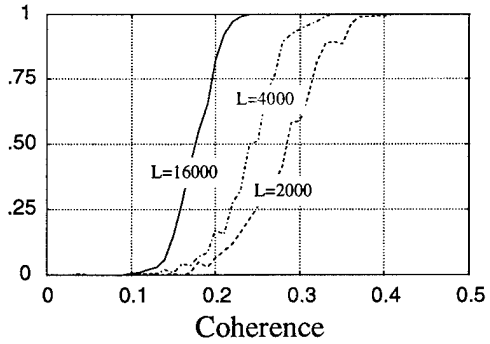


Figure 1: *Probability of "correct detection" (e.g. the estimated shift is within ±1 sample from the correct value) for different numbers of independent pixels, L.*

Once that the parameters for images coregistration are known, the necessary images resampling can be implemented, together with 1:2 range oversampling, according to (3), e.g. by means of 1-D resampling along azimuth and then along range. These resampling can be given in the space domain by exploiting the FIR kernels:

$$h_\Delta(n) = h_{lp}(n) \cdot \frac{\sin(\pi(n-\Delta))}{\pi(n-\Delta)} \cdot \exp(-j2\pi f_{dc}(n-\Delta)) \exp\left(-j2\pi \frac{f_s}{N_l}\Delta d\right) \quad (3)$$

being Δ the local shift, f_{dc} the Doppler centroid, d the look number (N_l the number of looks), and $h_{lp}(n)$ a proper smoothing window. The two exponentials in (4) are requested to shift the kernel spectrum around the Doppler centroid (for azimuth resampling) and to compensate the phase offset due to looks' subsampling.

The size of the kernel, e.g. the extent of the window $h_{lp}(n)$, depends on the level of phase noise that can be tolerated. For example, it can be shown that a 6 samples window, gives a decorrelation of 0.1% (SNR=27 dB) for $\Delta = 0.5$ (that is the case of image range oversampling ×2). In general, the optimum window size is a function of the azimuth power spectrum density and of the displacement Δ, therefore a Look-Up-Table of N kernels can be built by optimizing the kernels for the shifts: $\Delta = 0 \ldots 1/N$. The noise due to the quantization of Δ can be made negligible (SNR<32 dB) by assuming $N \geq 64$. Notice that the use of small kernels of 6-7 samples makes space domain resampling (and oversampling) more efficient than the frequency domain approach [6].

STRIP-MAP INTERFEROGRAM GENERATION

The generation of an interferogram is accomplished, as usual, by complex multiplication of two surveys after coregistration and range oversampling. At this step, it is possible to add in-phase the contribution of different looks. Then, the interferogram is flattened, low-pass filtered and subsampled. A strip-map interferogram is obtained by mosaicking small azimuth strips, say 32 km wide. In the ERS case, the variation of Doppler parameters in strips of that extent causes negligible defocusing (and phase distortion) at the edges of the blocks. There is no need of space registration if the images were registered at zero Doppler while focusing. The only phase registration necessary could be performed to compensate the variation of flattening functions in two adjacent blocks. However, that is quite easy since both functions are known.

An example of a 5 looks averaged ERS-1/ERS-2 tandem interferogram got by mosaicking two strips of 32 km (azimuth) × 100 km (range) is given in Fig.2,3. The total computing time was 14 minutes with a 30 Mflops/s Workstation (DEC alpha), the time for each processing step is specified in Tab.1.

ACKNOWLEDGMENTS

The authors would like to thank *ACS* for partial sponsoring this work.

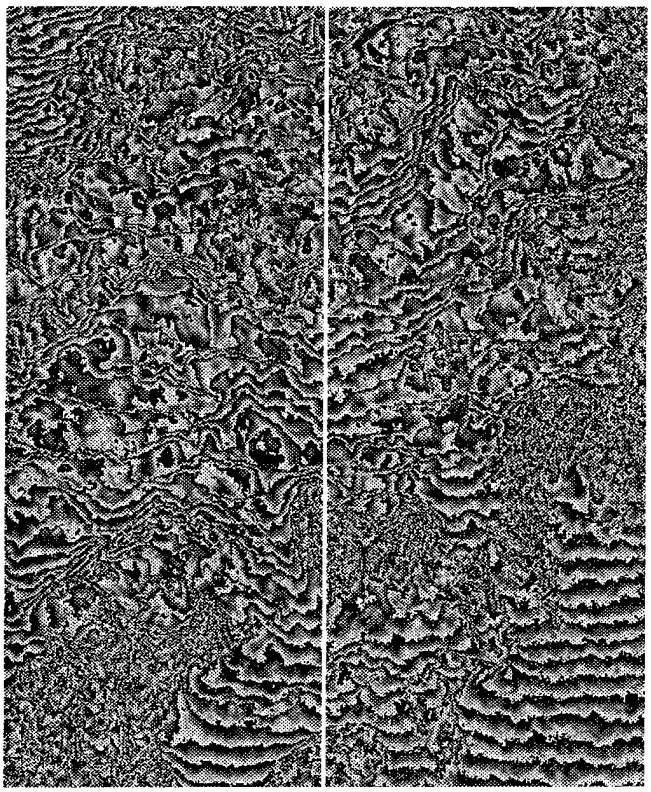


Figure 2: *ERS-1/ERS-2 tandem interferogram (area of Benevento, Italy), 66 km azimuth (horizontal) × 100 km range (vertical), 5 looks.*

Table 1: *Computational complexity and computing time for the proposed quick-look interferogram.*

Processing	**Complexity** [Mflops]	**CPU time** [min:sec] *DEC 3000/500*
Raw data Presumming	2800	1:45
Focusing	4830	3:00
Registration params. estimate		0:03
Image #1 Resampling	2665	1:40
Image #2 Oversampling	760	0:25
Interferogram Generation	227	0:07
Coherence Estimate	450	0:25
TOTAL	~11700	6:55

CONCLUSIONS

A "real-time" algorithm to get ERS SAR interferograms and coherence maps has been proposed. The algorithm efficiency comes from the following items:

i. raw data presumming is performed to reduce redundancy with the minimum loss of quality. Polyphase filters banks and integer implementation are exploited.

ii. a novel coherence estimator, that exploits a the images modulus, is introduced. It is used both for estimating the images shifts and stretches, and for computing coherence maps.

iii. image resampling and oversampling is performed in the space domain by means of very short, tabulated kernels optimized for low phase noise.

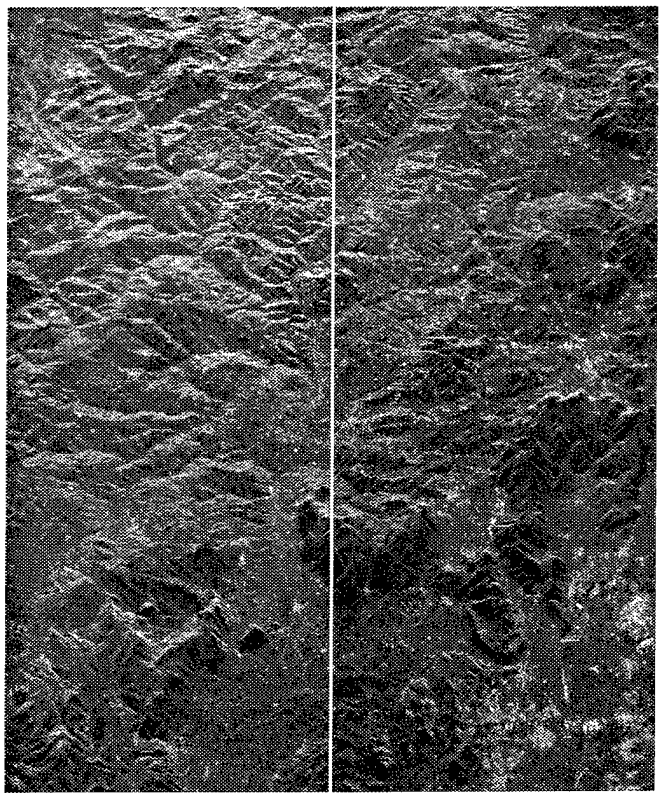


Figure 3: *Tandem interferogram: Absolute values.*

REFERENCES

[1] Solaas G. A., *An Assessment of ERS SAR Low REsolution Imagery*, ESA rep. n. ES-TN-DPE-OM-GS01, Jul. 1993.

[2] Rocca F., Prati C., Pasquali P., Monti Guarnieri A., *ERS-1 SAR Interferometry techniques and applications*, ESA report n.3-7439/92/HGE-I, 1994.

[3] Monti-Guarnieri A., Prati C., F. Rocca F., *SAR interferometric quick-look* in *Proc. IGARSS' 93* (Tokyo, Japan), Aug. 93, Vol. 3, pp. 988-990.

[4] Gatelli F., Monti Guarnieri A., Parizzi F., Pasquali P., Prati C., Rocca F., *The wavenumber shift in SAR interferometry IEEE Trans. on Geosci. and Remote Sens.*, Vol. 32, No. 4, pp. 855-865, Jul 1994.

[5] Monti Guarnieri A., Prati C., *SAR Interferometry: a "Quick and Dirty" Coherence Estimator for Data Browsing*, submitted to IEEE Trans. Geosc. and Remote Sensing, Jan. 1995.

[6] G. Fornaro, G. Franceschetti, E. S. Marzouk, "A new approach for image registration in interferometric processing" , in *Proc. IGARSS' 94* (Pasadena, CA), Aug. 94, Vol. 4, pp. 1983–1985.

EMISAR Single pass Topographic SAR interferometer modes

S. N. Madsen, N. Skou, K. Woelders, and J. Granholm

Danish Center for Remote Sensing, Dept. of Electromagnetic Systems
Technical University of Denmark, B-348, DK-2800 Lyngby, Denmark
Phone: +45 4525 3800, Fax: +45 4593 1634, E-mail: snm@emi.dtu.dk

Abstract — The Danish Center for Remote Sensing (DCRS[1]) has augmented its dual-frequency polarimetric synthetic aperture radar system (EMISAR[2]) with single pass across-track interferometric (XTI) modes. This paper will describe the system configuration, specifications and the operating modes. Analysis of data acquired in 1995 indicates that height resolutions better than one meter should be attainable at least in areas with benign topography where overlay, shadows and phase unwrapping errors are minimal. Calibration procedures applied to correct for multipath and limited channel isolation are discussed.

INTRODUCTION

A single pass across-track interferometer uses two antennas displaced across-track to acquire two images observing all image points from two slightly different angles of incidence. By overlaying the two complex SAR images during processing and determining the phase differences (interference generation), slant range differences can be determined with fractional wavelength accuracy. From slant range, differential slant range measurements, and knowledge of the baseline (= displacement from one antenna to the other) the 3-D target location can be determined. A single pass system acquires the two complex images forming the interferogram simultaneously thus there is no temporal decorrelation due to target displacement. As the antennas forming the baseline are rigidly connected, and the orientation can be measured by an inertial navigation system, the baseline is well defined and generally known to great accuracy which is seldom the case in repeat pass systems. The single pass concept does, however, limit the baseline to a length which can practically be implemented on the aircraft platform available.

Defining the interferogram as the product of channel 1 and the complex conjugate of channel 2, the interferometric phase is,

$$\phi = \phi_1 - \phi_2 = p\frac{2\pi}{\lambda}(\rho_2 - \rho_1) \tag{1}$$

$p = 1$ if the transmit antenna is common for the two channels, $p = 2$ if each channel uses only one antenna to both transmit and receive. λ is wavelength and ρ_i is slant range. The phase measured in the interferogram, ϕ_M, is the absolute phase of (1) modulus 2π. Getting from ϕ_M to ϕ, involves two steps called phase-unwrapping and absolute phase determination, see for instance [1] and [2]. Assuming the geometry of Fig. 1, the look angle θ and the interferometric phase are related by (assuming $B << \rho$):

$$\sin(\theta - \alpha) = \cos(\theta - \theta_{21}) \approx \frac{\rho_1 - \rho_2}{B} = \frac{-\lambda\phi}{2\pi p B} \tag{2}$$

α is the baseline orientation relative to horizontal. It is trivial to solve for the target height and across-track position:

$$\theta = \alpha - \arcsin\left(\frac{\lambda\phi}{2\pi p B}\right) \tag{3}$$

$$h = H - \rho_1 \cos\theta \tag{4}$$

$$y = \rho_1 \sin\theta \tag{5}$$

A more general geometry allowing for non zero Doppler geometry is discussed in [3] and analyses of accuracies and error sources are presented in [4] and [5]. As it is intuitively clear, the signal-to-noise ratio will limit performance as thermal noise induces phase errors which via (3) couple to the look angle leading to wrong height and cross track positions. Similarly, baseline orientation errors (here presented by α) will cause position errors although these errors will be slowly varying over the image.

A less intuitive error source is baseline decorrelation which occurs because not all targets within the resolution cell contribute the same interferometric phase. For the very short baselines applied in the system discussed here, baseline

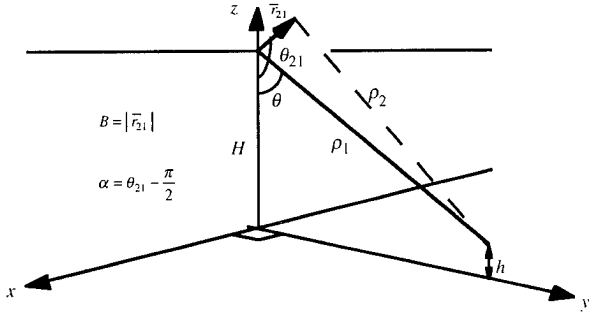


Fig. 1. Across-track interferometric geometry.

[1] The Danish Center for Remote Sensing is finansed by the Danish National Research Foundation.

[2] Development of EMISAR has been supported by the Thomas B. Thriges Foundation, the Danish Technical Research Counsil (STVF), the Royal Danish Air Force (RDAF), the Technical University of Denmark, the Joint Research Centre (JRC) and by the Danish National Research Foundation.

0-7803-3068-4/96$5.00©1996 IEEE

Table 1. EMISAR system parameters for polarimetric and interferometric modes.

Parameter	*C-band*	*L-band*
Polarimetry:		
wavelength	5.67 cm	24.0 cm
transmit power	2 kW	6 kW
antenna gain	27 dB	18 dB
max. bandwidth	100 MHz	
digitization	8192 I/Q samples	
	I+Q = 8 + 8 bits	
polarization	quad-pol, hh/vv/hv/vh	
look direction	left	
nominal altitude	41,000 ft.	
Interferometry:		
wavelength	5.67 cm	
polarization	dual-pol: HH/VV	
baseline length	1137 mm	
baseline angle, α	34.0°	(from horizontal)
nominal altitude	25,000 or 41,000 ft.	

decorrelation is a minor importance.

SAR SYSTEM

The radar used, EMISAR, is an L– and C–band polarimetric SAR developed at the Electromagnetics Institute since 1986. The system is flown on a Danish Air Force Gulfstream G–3. The transmitted bandwidth is up to 100 MHz, and the system is usually operated at 41.000 ft altitude. Some system parameters are listed in Table 1. Two flush mounted C-band antennas have been added to the system to support the single pass interferometric mode, Fig. 2.

The system presently use a combination of an inertial navigation system and a P-code GPS system to provide the required navigational information.

The XTI antennas are (like the existing pod antenna) fully polarimetric, and they are connected to a switch matrix mounted in the pod. Both antennas can be operated in a polarimetric mode, and interferometric data can be collected on both like polarizations, HH and/or VV. The radar front-end and data rate limitations does not presently support polarimetric interferometric data to be collected at high resolution. Several interferometric modes of operation are possible, including: 1) single baseline (transmit on one antenna, receive on both); 2) double baseline (sequentially transmit and receive on one antenna then transmit and receive on the other); and 3) dual baseline (sequentially transmit on one antenna and receive on both, then transmit on the other and receive on both).

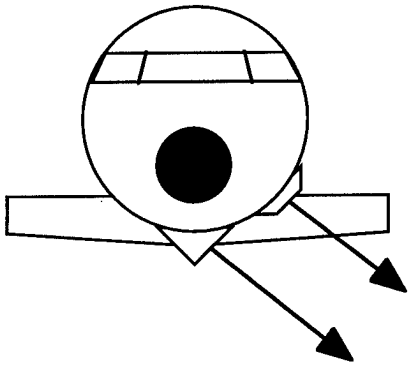


Fig. 2. Single pass interferometry use two polarimetric antennas flush mounted on G-3 fuselage in front of wing.

MULTIPATH CORRECTION

The initial test of the EMISAR single pass mode showed that the limiting performance factor was multipath on the radar platform. It is import to note that the interferometric derivations (1–5) assumes a single signal path with the signal propagating from the transmit antenna, to the target, and back to the receive antenna. In any practical system there will, however, be reflections of parts of the aircraft platform which will also be received, and limited isolation between the two interferometric antennas also leads to multi-path. A leakage to/from the other antenna can be seen to be equivalent to a multipath reflection of the other antenna.

If the ideal signal for channel i is $c_i = a_i \exp\{j\phi_i\}$ then the injection of a leakage signal from channel 2 to channel 1 will modify the interferometric phase as

$$(c_1 + \varepsilon c_2)c_2^* = (a_1 \exp\{j\phi_1\} + \varepsilon a_2 \exp\{j\phi_2\})a_2 \exp\{-j\phi_2\}$$

$$= a_1 a_2 \exp\{j\phi\}(1 + \varepsilon \frac{a_2}{a_1} \exp\{j\phi\})$$

and even for more complex situations it is easily seem that the measured phase is a function of the ideal phase,

$$\phi_m = \phi + \Delta\phi(\phi) \tag{6}$$

As a full discussion of parameter calibration in an interferometric system is very complex we assume in the following that parameters such as baseline (length and orientation), aircraft orientation, channels delays and phases are already calibrated. Differentiating (4) with respect to the absolute phase provides

$$\partial h = \rho \sin\left(\alpha - \arcsin\left(\frac{\lambda\phi}{2\pi pB}\right)\right) \frac{-1}{\sqrt{1-\left(\frac{\lambda\phi}{2\pi pB}\right)^2}} \frac{\lambda}{2\pi pB} \partial\phi$$

$$= \frac{-y}{\sqrt{1-\left(\frac{\lambda\phi}{2\pi pB}\right)^2}} \frac{\lambda}{2\pi pB} \partial\phi \tag{7}$$

This shows that for small errors in the absolute phase (a requirement meet for any reasonable system), the error can be determined if the height error is known as a function of the across-track ground range and the absolute phase. The EMISAR system has been calibrated on several occasions by mapping ocean that provides a well defined height reference. It has been found that there seem to be two dominating multipath sources, one is a channel cross coupling at an

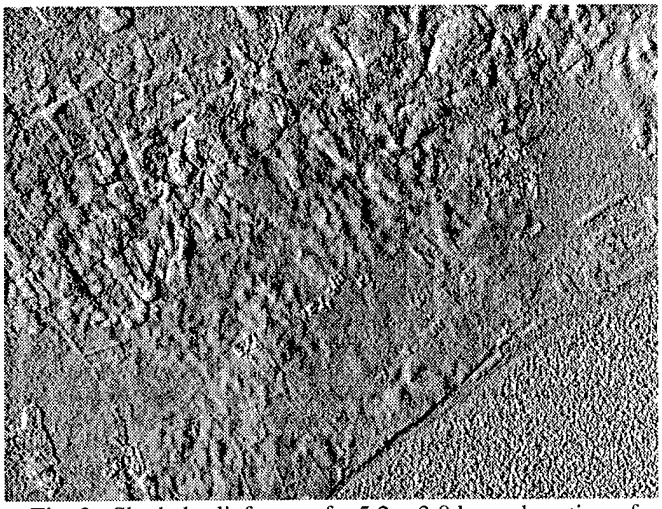


Fig. 3. Shaded relief map of a 5.2 × 3.8 km subsection of a radar generated height map. Data were acquired from an altitude of 25,000 ft. Note the clear signature of the buildings near the center of the image. The area in the lower right hand corner is water.

approximately –40 dB level, the other is an unknown reflection of the fuselage or antenna fairings with an equivalent baseline of approximately 20 cm. The calibration phase screen has been found to be basically identical from mission to mission.

PROCESSING

The EMISAR azimuth presummers are presently not able to process Doppler off-sets varying with range, thus interferometric acquisitions are data rate limited to 6144 complex range samples. In the high resolution mode this gives a slant range swath of 6500 m after range pulse compression. Depending on the actual data acquisition geometry this translates into between 8 and 10 km ground range swath. The processing scheme applied is based on processing techniques developed at JPL, [3], [6]. The processor simultaneously processes the two interferometric channels which are then motion compensated to a common reference line, [7]. The processor also includes automatic determination of the absolute phase, [2]. The output products include co-registered amplitude data, height map, correlation map, and for calibration runs also absolute phase maps. The output data sets are orthorectified to a spherical (s, c, h) coordinate system, [8]. Usually output products are generated at 5 or 10 m ground range pixel spacing.

RESULTS

Significant amounts of data were acquired during 1995 in both Denmark and Greenland indicating height accuracies before multipath calibration on the order of 5 to 10 meter. By applying the above described phase screen calibration technique, systematic errors have been drastically reduced. Analyses of data acquired in Denmark where the topographic relief is moderate (heights vary from 0 to 137 m in the data analyzed) indicates that the height error after removing a tilted plane is from 1 m in the near range to 3 m in the far range (at 10 m horizontal pixel spacing) when operating from 41,000 ft. Data acquired in the double baseline mode on a 25,000 ft. pass over the same area indicates stochastic height errors of 0.6 m rms. in the far range. Studies are presently on-going to evaluate the height error performance in more detail, however, sufficiently accurate reference data are not readily available. A shaded relief image of a subsection of a 25,000 ft. pass is shown in Fig. 2.

CONCLUSION

The upgrade of the EMISAR system has provided the DCRS with a high resolution topographic mapping instrument. Initial test have shown that the system has the potential to generate height images with vertical accuracies of less than one meter. To obtain high quality data consistently an airborne interferometer needs to be very accurately calibrated with respect to all parameters involved in the process. This work is in progress. The automatic generation of height maps without ground reference points also requires a very accurate navigation and attitude measurement system, which is presently under procurement. Careful evaluation experiments are on-going, but are most difficult as reference maps or data with sufficient height accuracy are not readily available.

REFERENCES

[1] R.M. Goldstein, H.A. Zebker, and C. Werner, "Satellite radar interferometry: two-dimensional phase unwrapping," Radioscience, vol.23, pp.713–720, Jul.-Aug. 1988

[2] S.N. Madsen, "On absolute phase determination techniques in SAR interferometry", SPIE conference proceedings, Orlando, Florida, April 1995

[3] S.N. Madsen, H.A. Zebker, and J. Martin, "Topographic mapping using radar interferometry", IEEE trans. Geoscience and Remote Sensing, vol. 31, no. 1, pp. 246–256, Jan. 1993.

[4] E. Rodriguez and J. Martin, "Theory and design of interferometric synthetic aperture radars", IEE proc.–F, vol. 139, no. 2, pp. 147–159, Apr. 1992.

[5] E. Rodriguez, D.A. Imel, and S.N. Madsen, "The accuracy of airborne interferometric SAR", IEEE trans. Aerospace and Electronic Syst., accepted for publication.

[6] S.N. Madsen, P.A Rosen, D.A. Imel, J. Martin, and S. Hensley "A third generation interferometric processor for interferometric processing", in preparation.

[7] David R. Stevens, Ian G. Cumming, and A. Lawrence Gray, "Options for Airborne Interferometric SAR Motion Compensation", IEEE Trans. GRS, vol. 33, pp. 409-420, March 1995

[8] Søren N. Madsen and Howard Zebker, "Imaging Radar Interferometry", chapter 17 in Manual of Remote Sensing, Vol. III, 1996, in press.

Parametric Estimation of Time Varying Baselines in Airborne Interferometric SAR

Johan Jacob Mohr, Søren Nørvang Madsen

Danish Center for Remote Sensing, Dept. of Electromagnetic Systems
Technical University of Denmark, B-348, DK-2800 Lyngby, Denmark
Phone: +45 4525 3800, Fax: +45 4593 1634, Email: jm@emi.dtu.dk

ABSTRACT

In this paper a method for estimation of time varying spatial baselines in airborne interferometric Synthetic Aperture Radar (SAR) is described. The range and azimuth distortions between two images acquired with a non-linear baseline are derived. A parametric model of the baseline is then, in a least square sense, estimated from image shifts obtained by cross correlation of numerous small patches throughout the image. The method has been applied to airborne EMISAR† imagery from the 1995 campaign over the Storstrømmen Glacier in North East Greenland conducted by the Danish Center for Remote Sensing††. This has reduced the baseline uncertainties from several meters to the centimeter level in a 36 km scene. Though developed for airborne SAR the method can easily be adopted to satellite data.

INTRODUCTION

The application of repeat pass interferometric techniques to airborne SAR imagery, though very similar to satellite interferometry, comprises quite different problems with respect to baseline estimation. During data acquisition an airplane, as opposed to a satellite, continuously has to be controlled to ensure a proper spatial baseline. The airborne EMISAR is in the repeat pass mode controlled via the Instrument Landing System (ILS) by the radar control computer which again receives navigational information from a P-code GPS receiver.

The actual trajectory is typically oscillating around the desired track and the deviations must be compensated in the processing and taken into account in the interpretation of the interferograms. The high frequency motion components can be accurately measured by an Inertial Navigation Unit (INU), but this measurement has to be augmented for baseline estimations due to drift. The meter level absolute accuracy provided by P-code GPS utilized by EMISAR is far from the requirement, but even the decimeter accuracy potential with differential GPS is not sufficiently accurate.

†Development of the EMISAR was sponsored by the Thomas B. Thriges Foundation, the Danish Technical Research Counsil (STVF), the Royal Danish Air Force (RDAF), the Technical University of Denmark and the Joint Research Centre (JRC).
††The Danish Center for Remote Sensing is established and funded by the Danish National Research Foundation.

The required accuracy for the baseline knowledge is dependent on the application on the order of sub millimeter to centimeters.

A method for estimation of the linear terms (azimuth offset, skew and stretch) on the basis of radar data is described in [1]. This method is generalized here and a third order polynomial error model, corresponding to an INU with a linearly varying drift in the acceleration biases, is investigated. Experiments with EMISAR data from Storstrømmen, though, tends to suggest that second order polynomials is sufficient.

The INU measurements also requires synchronization with radar data. In the EMISAR system an internal 9 ms delay in the INU has also been estimated on the basis of a co-registration of the images.

MODEL

For simplicity the problem is here described in a rectangular coordinate system, (s,c,h), where s is the along track coordinate, c across track (positive to the left) and h is up.

Track 1 is assumed to be a straight line at an altitude, H, with a constant sample spacing, see Fig. 1a. The baseline to be estimated is the displacement of track 2 relative to track 1. Thus, track 2 is given by $(\mathrm{s}(t),\mathrm{c}(s),H+\mathrm{h}(s))$, where $\mathrm{c}(s)$ and $\mathrm{h}(s)$ constitutes the spatial baseline. What can be measured by a correlation of small patches of the amplitude images is range off-set from track 1 to track 2, n_{ra}, and the corresponding azimuth off-sets, n_{az}, in bins. Any pixel coordinate in either of the two images can be converted to slant range distance, ρ_i, and azimuth position, s_i, by

$$\rho_1 = \rho_{01} + n_{ra,1}dr,$$
$$\rho_2 = \rho_{02} + n_{ra,2}dr,$$
$$s_1 = s_{01} + n_{az,1}da,$$
$$s_2 = s_{02} + n_{az,2}da,$$

where ρ_0 is slant range to first bin, s_0 is azimuth of first bin, dr and da are range and azimuth pixel spacing respectively and the index denotes image number. Since it is assumed that the first image is acquired from a ideal track, $\rho_1 \equiv k$ and $s_1 \equiv s$, see Fig. 1. For track 2 we have

$$s = s_2 + \Delta\mathrm{s}(s_2) = s_2 + \sum_{i=0,ns} \sigma_i \mathrm{T}_i(s_2), \quad (1)$$

$$\mathrm{c}(s) = \sum_{i=0,nc} \chi_i \mathrm{T}_i(s), \quad (2)$$

$$\mathrm{h}(s) = \sum_{i=0,nh} \eta_i \mathrm{T}_i(s), \quad (3)$$

0-7803-3068-4/96$5.00©1996 IEEE

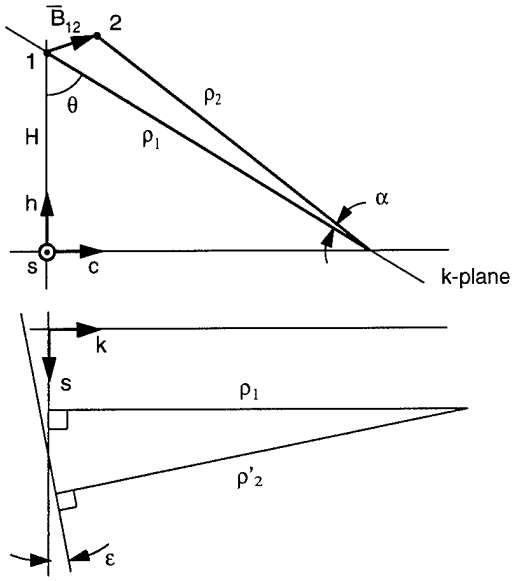


Fig. 1. The geometry a) projected on a plane perpendicular to $\hat{s}$, b) projected on the slant range plane.

where σ_i, χ_i and η_i are the unknown coefficients in an decomposition of track 2 in some error functions $T_i(s)$, e.g. a polynomial of degree i.

The next step is to express the range and azimuth image off-sets in terms of the unknown baseline parameters. The geometry is projected on a plane perpendicular to the s-direction and a projection onto the slant range plane, Fig. 1. The auxiliary angles α and ε can be determined from

$$\sin\alpha = \frac{1}{\rho_2}(c\cos\theta + h\sin\theta)$$

and

$$\tan\varepsilon = \frac{\partial c}{\partial s}\sin\theta - \frac{\partial h}{\partial s}\cos\theta.$$

The azimuth shift between the images, readily calculated as

$$[s_2 + \Delta s(s_2)] - s_1 = \rho_2' \sin\varepsilon$$

are not used directly, but with small α and ε the equation set for each image point become

$$s_2 - s_1 = -\Delta s(s_2) + \rho_2 \cos\alpha\left(\frac{\partial c}{\partial s}(s)\sin\theta - \frac{\partial h}{\partial s}(s)\cos\theta\right), \quad (4)$$

$$\rho_2 \cos\alpha\cos\varepsilon - \rho_1 = -c(s)\sin\theta + h(s)\cos\theta. \quad (5)$$

Finally (1)-(3) and their derivatives are substituted into (4)-(5) forming two independent (virtual) linear equations in the baseline parameters σ_i, χ_i and η_i. With several well spread estimated image shifts, sets of (4)-(5) will form a equation system with sufficient rank to determine the baseline.

The outlined method gives a well determined baseline estimate, since the azimuth shift is very sensitive to the derivative of $c(s)$ and $h(s)$. Also note that the method in principle requires knowledge of the topography (through θ), but to first order a flat earth assumption is sufficient.

MOTION COMPENSATION

In airborne SAR imperfect motion compensation also gives rise to a misregistration of the images. In this section the importance of (unknown) topography and accelerations in c and h is addressed. Imperfections due to unknown topography is considered first. From Fig. 2, the shift, $\Delta\rho$, to be compensated is seen to be

$$\Delta\rho = -\hat{n}(\theta)\cdot\bar{b}(s) = -c\sin\theta + h\cos\theta.$$

A height "error", δ_z, will give an uncompensated shift of

$$\delta_{ra} = \frac{\partial\Delta\rho}{\partial z}\delta_z = -(c\cos\theta + h\sin\theta)\frac{1}{\rho\sin\theta}\delta_z \quad (6)$$

in the range direction as compared to an image with perfect compensated motion. Note that the deviation from an actual track to a reference track is compensated by a procedure which is basically similar to how one data set of an interferometric pair is overlaid the other data set. Reversely this relationship between height offsets and slant range offsets is the very reason that interferometry works, [2]. An unknown scene height also give rise to a shift in the azimuth direction,

$$\delta_{az} = \frac{\partial}{\partial z}\left(\rho\frac{\partial\Delta\rho}{\partial s}\right)\delta_z = -\left(\frac{\partial c}{\partial s}\cos\theta + \frac{\partial h}{\partial s}\sin\theta\right)\frac{1}{\sin\theta}\delta_z, \quad (7)$$

in generale much larger, but not as severe in the sense that it does not affect the phase. On the other hand it is most undesirable since it causes misalignment of the images. The cross track velocities must therefore be minimized, during the control of the airplane. Note that it is the absolute heights which are of importance - not the variations within the scene.

Another important issue is delay of navigation data relative to the radar data. Such a delay results in an error in the measurement of the antenna phase center. This delay will mainly cause a shift in the azimuth direction and thus cause misalignment of the data sets. If the delay, δ_s, is measured in meter ($= vt_{delay}$) the shift is

$$\delta_{az} = \frac{\partial}{\partial s}\left(\rho\frac{\partial\Delta\rho}{\partial s}\right)\delta_s = \left(-\frac{\partial^2 c}{\partial s^2}\sin\theta + \frac{\partial^2 h}{\partial s^2}\cos\theta\right)\rho\,\delta_s. \quad (8)$$

It is therefore of importance that the accelerations in the control of the airplane is minimized. On the other hand (8) enables the estimation of the delay as two independent aircraft tracks generally will have a baseline acceleration.

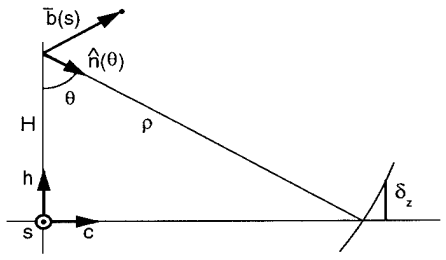


Fig. 2. Motion compensation of a target at height δ_z. $\hat{n}(\theta)$ is the LOS unit vector; $b(s)$ deviation from the reference track.

RESULTS

DCRS has on two consecutive days in august 1995 acquired L-band (HH+VV) repeat track interferometry data over Storstrømmen glacier in Northeast Greenland. The nominally 36 km long imagery were acquired from an altitude of H = 12500 m with incidence angles ranging from 26° to 58°.

Two typical tracks with a perpendicular baseline of about 10 m were selected to illustrate the three step baseline estimation procedure. The navigation data and the radar data are synchronized via an accurate time tagging. Local image misregistrations are found by a cross correlation of 25 range patches by 79 azimuth patches with a size of 128x128 pixels.

1. Initial processing of the two data sets with motion compensation to a common reference line. Cross correlation. Estimation of the linear baseline residuals by solving equations (4) and (5) in a least squares sense, see Table 1. Correction of the navigation data.
2. Reprocessing and cross correlation. The misregistrations are shown on Fig. 3. Now a third order model is fitted, and a navigation data delay of 3 ms estimated by an application of (8).
3. Reprocessing and cross correlation. A third order model is again fitted, see Table 1, The navigation data are corrected and the baselines can now be extracted.

For verification a final processing and cross correlation has been performed and the results plotted on Fig. 3, and it is seen that the higher order baseline terms significantly reduce the registration errors. The third order terms are significant in a F-test on all reasonable levels. If the apparent remaining systematic errors are taken into account, e.g, by a factor 10 reduction in number of independent observations in the F-test, the third order terms are significant only on the 90% level, thus being obvious subjects for elimination.

The accuracy of the estimated baseline is addressed via an analysis of the dispersion matrix of the estimated 'baseline residual coefficients.' The standard deviations on the sum off the cross track coefficients, $\chi_0 - \chi_3$ and $\eta_0 - \eta_3$, are 1.4 cm and 1.7 cm respectively, (with an assumption of complete uncorrelated misregistrations).

Table 1. Estimated baseline residual after first and third processing. Residuals is expressed as in (1)-(3), where $T_i(s)$ is an i-order Chebychev polynomial with s scaled to [-1;1].

i	σ_i [m]	χ_i [m]	η_i [m]
0	-1.246	-6.363	-11.978
1	0.989	-0.802	1.168
Std. dev. ra–residual:			0.221 [m]
Std. dev. az–residual:			0.781 [m]
0	-0.374	-0.154	-0.004
1	-1.858	-0.006	-0.003
2	-1.151	-0.488	-0.017
3	0.031	0.016	0.021
Std. dev. ra-residual:			0.044 [m]
Std. dev. az-residual:			0.133 [m]

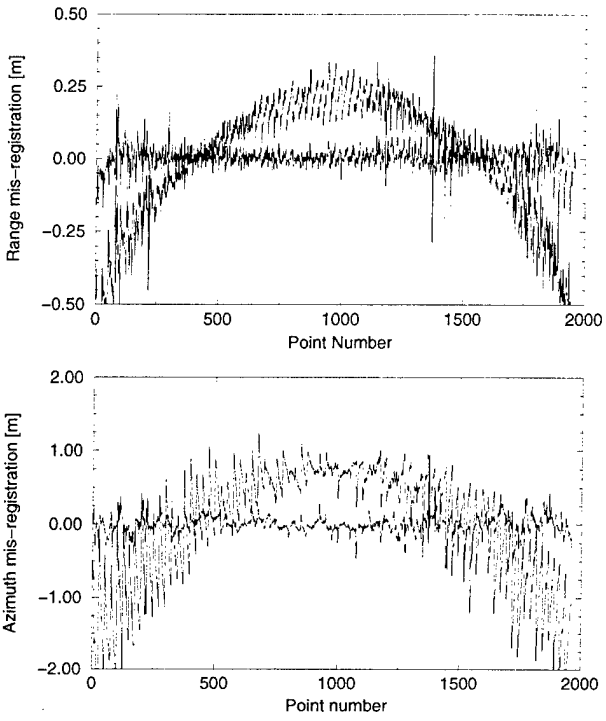


Fig. 3. The range and azimuth misregistrations after removal of the linear (parabolic curves) and the 3'rd order (flat curves) baselines errors. The patches are numbered consecutively.

CONCLUSION

Track estimation as well as navigation data synchronization have been shown to reduce uncertainties on the baseline from several meters to centimeter level in the typically 36 km long EMISAR imagery of Storstrømmen. Though accurate enough for some applications, for others it might be necessary to take motion compensation errors into account in the estimation scheme, via a coarse DEM. Alternatively, Kiruma has proposed a multi track technique for stationary scenes, which are easily modifed to take higher order motion components into account, [3]. However, this does not utilize the azimuth distortions which contains useful information and must be taken into account in the airborne case.

REFERENCES

[1] Søren N. Madsen and Howard Zebker, "Imaging Radar Interferometry", chapter 17 in Manual of Remote Sensing, Vol. III, chapter 17, 1996, in press.

[2] David R. Stevens, Ian G. Cumming, and A. Lawrence Gray, "Options for Airborne Interferometric SAR Motion Compensation", IEEE Trans. GRS, vol. 33, pp. 409-420, March 1995.

[3] Kimura, Hiroshi, "A Method to Estimate Baseline and Platform Altitude for SAR Interferometry", Proceedings of IGARSS'95, pp. 199-201, Firenze, Italy, July 1995.

On the Baseline Decorrelation

Giorgio Franceschetti[1,2], *IEEE Fellow,* Antonio Iodice[2], Maurizio Migliaccio[3], *IEEE Member,* Daniele Riccio[1], *IEEE Member*

[1]Università di Napoli Federico II, *Dipartimento di Ingegneria Elettronica,* Via Claudio 21, 80125 Napoli, Italy.
☎ +(39)-81-7681111 fax+(39)-81-5934438 email: francesc@irece1.irece. na.cnr.it
[2]Consiglio Nazionale delle Ricerche, *Istituto di Ricerca per l'Elettromagnetismo e i Componenti Elettronici (I.R.E.C.E.),* Via Diocleziano 328, 80124 Napoli, Italy. ☎+(39)-81-5704945 fax +(39)-81-5705734 email: iodicea@irece1.irece.na.cnr.it
[3]Istituto Universitario Navale, *Istituto Teoria e Tecnica delle Onde Elettromagnetiche,* Via A.Acton 38, 80133 Napoli, Italy.
☎ +(39)-81-5513976 fax +(39)-81-5521485 email: migliaccio@nava1.uninav.it

Abstract -- SAR Interferometry is a relevant tool for Earth monitoring. Across-track mode is capable to generate high-resolution terrain elevation maps. Their quality is governed by the correlation of the SAR image pair which are used to generate the interferogram. The baseline decorrelation is here considered emphasizing the importance of the surface scattering.

INTRODUCTION

SAR interferometry (IFSAR) is a widespreading technique which is able to open a new perspective into geo and marine science, see, for instance [1-4]. In particular, across-track interferometry is able to generate from a SAR image pair an interferogram which is related to the terrain elevation of the scene under survey. The ability to estimate the terrain elevation from the interferogram is dictated by the correlation of the SAR image pair [5]. This is a fundamental and very important problem: on one side it sets a limit on the height accuracy of the terrain elevation map [2,5] and on the other it permits to extract some information over the temporal changes of the scene [5,6].

The main sources of decorrelation are [5]: the system thermal noise, the temporal changes of the scene, the IFSAR processing errors and the spatial diversity. The decorrelation due to thermal noise can be easily modelled by an additive noise model, the decorrelation due to temporal changes is present only in the repeat-pass interferometry mode and the IFSAR processing sources of decorrelation can be minimized by accurate processing. Conversely, the baseline decorrelation, which is related to spatial diversity, is unavoidable [5] and intrinsic in any IFSAR system even if it can be reduced at the expenses of image resolution [7]. Any information about the decorrelation process is of great relevance when designing an IFSAR system.

In this paper we investigate the influence of the scattering surface properties on the baseline decorrelation, also in view of a future realization of an IFSAR simulator.

We represent the illuminated patch by means of a two-scale model: the low frequency part of the surface profile's spectrum is described by planar facets, while its high frequency part is modelled by a superimposed microscopic roughness whose heigth profile is a second-order stationary isotropic process with zero mean. We analytically evaluate the correlation between the electromagnetic fields backscattered to the two synthetic SAR antennas. We show that generally the correlation is not only affected by the sensor geometry but also by the surface roughness. By using system parameters typical of a real IFSAR sensor and considering the case study of a Gaussian surface, we show that the predicted dependence on the roughness standard deviation σ becomes appreciable for high values of σ/λ and/or for large baselines. Note finally that the importance of surface scattering has been addressed also in [8]; in this paper we use a more general approach which does not require the backscattered field to be delta-correlated. In addition, a general and compact formulation is here provided.

The paper is organized as follows. First, a complete formulation of the problem is given. The scattering model is depicted under the hypothesis of surface scattering and Physical Optics (PO) solution of the scattering integral. Then, the relevant case of Gaussian surface is specialized. Finally, a set of meaningful numerical examples is provided.

THE MODEL

In this Section we depict the very general model we employ in order to evaluate the baseline decorrelation as function of the surface scattering characteristics of the scene under survey.

The decorrelation coefficient γ is defined as follows:

$$\gamma = 1 - \frac{\left|E[e_1 e_2^*]\right|}{\sqrt{E[|e_1|^2]E[|e_2|^2]}} \quad , \tag{1}$$

wherein * stands for complex conjugate, $E[\cdot]$ for statistical mean and e_1 and e_2 are the two electromagnetic fields received at the two synthetic antennas forming the IFSAR system, see Fig.1.

In order to obtain γ we need to evaluate the mean square value of the two backscattered electric fields and their mutual coherence. In the PO approximation we have [9]:

$$e_{1,2} = KF_{1,2} e^{-jkR_{1,2}} \iint dxdy\, e^{-j2k_{1,2}\xi} W(x - x_0, y - y_0) \quad , \tag{2}$$

wherein (Fig.1) the pedixes 1 and 2 apply to the first and second antenna, respectively, $R_{1,2}$ are the antennas - facet

0-7803-3068-4/96$5.00©1996 IEEE

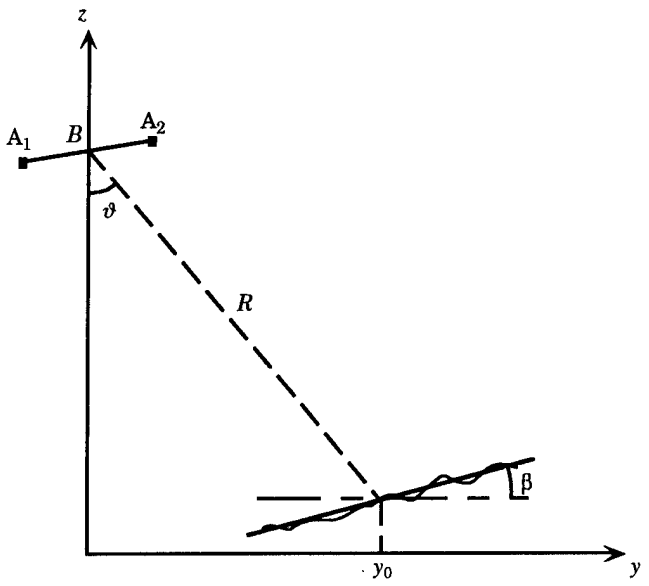


Fig.1: Relevant to the geometry of the problem

center ranges, $\boldsymbol{k}_{1,2}$ are the wavenumber vectors and $\boldsymbol{\ell}$ is the vector describing the facet roughness with reference to its center. The factor K accounts for the free-space attenuation, F is a complex function depending on the Fresnel coefficients at the mean plane [9] and $W(x,y)$ is the SAR ground illumination function (after processing).

If $W(x,y)$ is a factorizable function, we can write:

$$W(x,y) = \Xi(x/\Delta x)\Theta(y/\Delta y) \quad , \tag{3}$$

wherein Δx and Δy are the azimuth and ground range resolution, and $\Xi(\cdot)$, $\Theta(\cdot)$ can have, for instance the usual sinc(·) expression. This quoted assumption (eq. (3)) can be relaxed, but it is used here for the sake of simplicity.

In the hypothesis that the microscopic roughness $\epsilon(x,y)$ is a second-order stationary isotropic statistical process, we have that the mean square values of the two e.m. field are [10]:

$$E[|e_1|^2] = 2\pi K^2 |F_1|^2 \Delta x \Delta y \Re_{11}(s') \quad , \tag{4}$$

$$E[|e_2|^2] = 2\pi K^2 |F_2|^2 \Delta x \Delta y \Re_{22}(s'') \quad , \tag{5}$$

whereas their mutual coherence is given by [10]:

$$\begin{aligned} E[e_1 e_2^*] = {} & 2\pi K^2 F_1 F_2^* e^{-j\boldsymbol{k}(R_1 - R_2)} \Re_{12}(s''') \cdot \\ & \Im[\Xi^2](2\Delta x B_\perp \tan\alpha \sin\vartheta / \lambda R) \\ & \Im[\Theta^2](2\Delta r B_\perp / \tan(\vartheta - \beta)\lambda R) \, . \end{aligned} \tag{6}$$

In eq.(4-6) $\Re(\cdot)$ are the Hankel Transforms of a combination of the self and joint characteristic functions of ϵ [10] and $\Im$ means Fourier Transform. Others parameters are the average antenna - facet center range R, the average look angle ϑ, the baseline component perpendicular to the look direction $B_\perp$, the slant range resolution Δr, and the tilt angles α,β of the mean plane along x and y directions, respectively. More details can be found in [10].

Inserting eqs. (4-6) into eq. (1) we get:

$$\begin{aligned} \gamma = 1 - {} & \Im[\Xi^2](2\Delta x B_\perp \tan\alpha \sin\vartheta / \lambda R) \cdot \\ & \Im[\Theta^2](2\Delta r B_\perp / \tan(\vartheta - \beta)\lambda R) \frac{\Re_{12}(s''')}{\sqrt{\Re_{11}(s')\Re_{22}(s'')}} \quad , \end{aligned} \tag{7}$$

where the dependence on the roughness statistics is expressed by the last factor.

It is here instructive to specialize γ in the relevant case of a Gaussian surface, that is whenever $\epsilon(x,y)$ is characterized by Gaussian self and joint probability density functions (pdf).. In particular, the self pdf has a zero-mean and σ-standard deviation and the normalized correlation function is given by:

$$C(\tau) = \exp(-\tau^2 / T^2) \quad , \tag{8}$$

wherein T is the usual correlation distance.

In such a case, if we assume the sinc(·) SAR ground illumination function and consider large values of σ/λ, we have:

$$\begin{aligned} \gamma = 1 - {} & \Lambda\left[\frac{2\Delta x B_\perp \tan\alpha \sin\vartheta}{\lambda R}\right] \Lambda\left[\frac{2\Delta r B_\perp}{\tan(\vartheta - \beta)\lambda R}\right] \cdot \\ & \exp\left[-\frac{1}{2}\left(\frac{4\pi\sigma \sin\vartheta \, B_\perp}{\lambda R}\right)^2\right] \quad , \end{aligned} \tag{9}$$

wherein $\Lambda(\cdot)$ is the triangle function.

The last factor of eq. (9) can be approximated to unity if:

$$B_\perp \sigma << \frac{\lambda R}{4\pi \sin\vartheta} \quad . \tag{10}$$

In this case, letting $\alpha=\beta=0$, we obtain the well known result that the decorrelation linearly increases with the baseline [2,5,7]. The validity of this approximation for a real IFSAR sensor is discussed in the next Section.

RESULTS

In this Section, we analyze the baseline decorrelation behavior in the case of the X-SAR interferometer, whose main system parameters are listed in Table I.

We consider an untilted surface ($\alpha=\beta=0$) and an average look angle ϑ equal to 45°. In this case, the baseline decorrelation γ, evaluated by means of eq.(9) as a function of $B_\perp$ and for different values of σ can be determined.

Results for $B_\perp$ ranging from 0 to the critical baseline [5] and σ ranging from 0 m to 2 m with a step of 0.5 m, are depicted in Fig.2.

TABLE I: Relevant to some X-SAR system parameters

Spacecraft altitude	220 km
Look angle	15° to 65°
Wavelength	0.031 m
Nominal slant range resolution	7.89 m

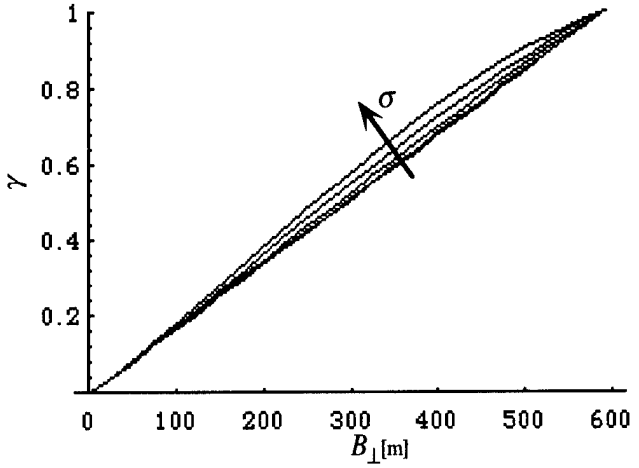


Fig.2: γ vs. $B_\perp$. Curves are parametrized to σ ranging from 0 m to 2 m with a 0.5 m step.

We note that except for low values of σ the linear model [2,5] is not appropriate. This is emphasized in Fig. 3 where the difference $\Delta\gamma$ between γ evaluated by eq.(9) and $\gamma=\gamma_0$ evaluated via the linear model is plotted. For example, for $B_\perp$ equal to 100 m we have that $\Delta\gamma$ is 0.001, 0.004, 0.008, 0.015 for σ equal to 0.5 m, 1.0 m, 1.5 m, and 2.0 m, respectively. Accordingly for $B_\perp$ equal to 300 m we have that $\Delta\gamma$ is 0.005, 0.020, 0.043, 0.074. In general, it can be demonstrated by eq.(9) that:

$$\left.\frac{\Delta\gamma}{\gamma_o}\right|_{\max} = \frac{1}{2}\left(\frac{\pi\sigma\sin\vartheta\tan\vartheta}{\Delta r}\right)^2 , \qquad (11)$$

and is achieved at half of the critical baseline.

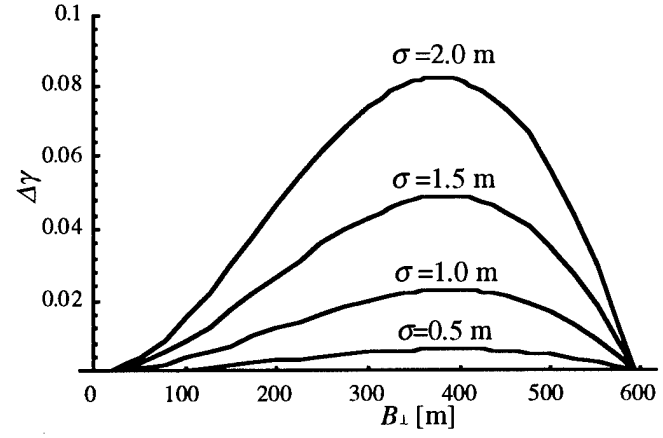


Fig.3: $\Delta\gamma$ vs. $B_\perp$ for different values of σ.

As a consequence, we can state that as soon the baseline is much shorter than the critical one, the linear model is practically coincident with the one depicted by eq.(9), at least in the examined Gaussian case.

Differently, if the baseline is around half of the critical baseline, the effect of the surface roughness becomes appreciable.

CONCLUSIONS

In this paper a new general and compact formulation of the baseline decorrelation coefficient, which takes into account the surface roughness statistics, has been provided. It has been shown that the dependence on the roughness statistics is appreciable for very rough surfaces and for long baselines.

REFERENCES

[1] T.H.Dixon et al., *SAR Interferometry and Surface Change Detection,* RSMAS Technical Report TR 95-003, University of Miami - Rosenstiel School of Marine and Atmospheric Science, 1995.

[2] F.K.Li and R.M.Goldstein, "Studies of Multibaseline Spaceborne Interferometric Synthetic Aperture Radars", *IEEE Trans. Geosci. Remote Sensing, GE-28,* 88-97, 1990.

[3] R.M.Goldstein and H.A.Zebker, "Interferometric Radar Map of Ocean Currents", *Nature,*328, 707-709, 1987.

[4] D.R.Lyzenga and J.R.Bennet, "Estimation of Ocean Wave Spectra Using Two-Antenna SAR Systems", *IEEE Trans. Geosc. Remote Sensing, GE-29,* 463-465, 1991.

[5] H.A.Zebker and J.Villasenor, "Decorrelation in Interferometric Radar Echoes", *IEEE Trans. Geosci. Remote Sensing, GE-30,* 950-959, 1992.

[6] U.Wegmüller and C.L.Werner, "SAR Interferometric Signatures of Forests", *IEEE Trans. Geosci; Remote Sensing, GE-33,* 1153-1161, 1995.

[7] F.Gatelli, A.Monti Guarneri, F.Parizzi, P.Pasquali, C.Prati, and F.Rocca, "The Wavenumber Shift in SAR Interferometry", *IEEE Trans. Geosci. Remote Sensing, GE-32,* 855-865, 1994.

[8] E.Rodriguez and J.M.Martin, "Theory and Design of Interferometric Synthetic Aperture Radars" *IEE Proc.-F, 139,* 147-159, 1992.

[9] L.Tsang, J.A.Kong and R.T.Shin, *Theory of Microwave Remote Sensing,* New York: John Wiley, 1985.

[10] G.Franceschetti, A.Iodice, M.Migliaccio, D.Riccio, "The Effect of Surface Scattering on the IFSAR Baseline Decorrelation", submitted.

This work has been partly supported by the project of the Italian Ministry of the University and Scientific Research, M.U.R.S.T. 40% "Telerilevamento dell'ambiente: modelli e sperimentazione".

Micro Pulse Lidar Daytime Performance: Simulations and Observations

J.A. Reagan*, A.E. Galbraith*, and J.D. Spinhirne†
*University of Arizona, ECE Dept., Tucson, AZ 85721-0104
Tel (520) 621-6203, Fax (520) 621-8076, reagan@ece.arizona.edu
NASA Goddard Spaceflight Center, Code 912, Greenbelt, MD 20771†
Tel (301) 286-9099, Fax (301) 286-1762, jspin@virl.gsfc.nasa.gov

Abstract -- Relatively low-cost, eye-safe lidars are now possible with recent technological advances in lasers and detectors. Both diode pumped Nd:YAG/YLF and AlGaAs diode lasers are viable candidates for the low energy, high rep-rate lidar transmitter sources required for eye safety. High quantum efficiency photon counting avalanche photodiodes (APD's) permit efficient detection of the weak lidar returns plus an effective means for averaging over the large number of pulses needed to achieve acceptable signal to noise ratios (SNR's). A critical question as to the feasibility of this micro pulse lidar (MPL) approach is whether acceptable SNR's can be obtained for daytime operation. This paper presents simulations of expected performance for an MPL similar to a system now under field test at the DOE ARM CART site, the results of which are compared with sample observations obtained with this field system.

INTRODUCTION

Lidar offers an effective approach for profiling aerosol and cloud structural features as has been demonstrated numerous times (e.g., [1]). However, even more than thirty years since its inception, lidar has yet to achieve truly widespread appreciation. While there are many reasons for this, including the need for research demonstrations before committing to operational use, two of the most significant reasons are that lidars have generally not been eye-safe and lidars have been quite expensive.

Relatively low-cost, eye-safe lidars are now possible with recent technological advances in lasers and detectors. Candidate lasers for eye-safe visible and near-IR lidars include diode pumped, frequency-doubled Nd:YAG/YLF lasers and GaAlAs laser diodes, both of which are capable of producing microjoule (μJ) or higher pulse energies at pulse repetition frequencies (PRF's) of a few kHz or higher. Eye-safety for such low energy pulses can be readily achieved by expanding the laser beam through a collimator to a diameter not greater than ~25 cm. The weak photon returns from such low energy transmitted pulses can be efficiently sensed with photon counting silicon avalanche photodiode (APD) detectors now available with quantum efficiencies greater than ~30 % and count rates of ~10 MHz. Micro pulse lidars (MPL's) based on these technological innovations are being investigated for both aerosol/cloud [2] and water vapor [3] profiling applications, and a first version MPL cloud lidar, employing a frequency-doubled ND:YLF laser, has successfully completed over a year of testing as an autonomous field instrument at the DOE Atmospheric Radiation Measurements (ARM) Oklahoma Cloud and Radiation Testbed (CART) site.

A critical question as to the feasibility of the MPL approach for operational applications is whether acceptable signal to noise ratios (SNR's) can be achieved in reasonably short time intervals (within several minutes) even for daytime operation. This paper presents simulations of expected night and daytime performance for an MPL system with parameters equal to those of the recently upgraded DOE ARM instrument, MPL-2. The simulations are compared with sample observations to demonstrate that the upgraded system indeed operates effectively and as predicted.

THEORETICAL CONSIDERATIONS

The received lidar signal for one transmitted laser pulse of energy E_0 at wavelength λ, expressed in received primary (unmultiplied) photoelectrons, $n(r)$, for backscattering received from a range bin Δr centered at a distance r from the lidar may be expressed by

$$n(r) = \frac{\lambda \delta_\lambda}{hc} \times \frac{E_0 A_R \Delta r \beta(r) T^2(r)}{r^2} \qquad (1)$$

Here, δ_λ is the detector quantum efficiency, h is Planck's constant, c is the speed of light, A_R is the effective receiver aperture, $\beta(r)$ is the atmospheric unit volume backscattering coefficient and $T^2(r)$ is the atmospheric round-trip transmittance which is related to the unit volume atmospheric extinction coefficient $\sigma(r')$ along the path by

This work supported in part by NASA Goddard Space Flight Center under contract NCC-05-77.

0-7803-3068-4/96$5.00©1996 IEEE

$$T^2(r) = e^{-2\int_0^r \sigma(r')dr'} \quad (2)$$

If noise n_{BD} is also present due to background radiation and detector noise, the ideal quantum limited rms SNR is given by

$$SNR = n/\sqrt{n + n_{BD}} \quad (3)$$

for one pulse and is increased by $\sqrt{M}$ for M pulses. If n_{BD} is negligible as should be the case for a dark night and a very low dark count detector, then SNR $\approx \sqrt{n}$.

Background radiation, n_B, is a significant concern for daytime operation, for which case $n_{BD} \approx n_B$ for a low dark count detector. The background counts per range bin Δr may be expressed in the form

$$n_B = \frac{\lambda \delta_\lambda}{hc} \times A_R \Omega_R \Delta\lambda_R L_{\lambda B} \Delta r \times \frac{2}{c} \quad (4)$$

where, in addition to the terms defined earlier, Ω_R is the receiver solid angle, $\Delta\lambda_R$ is the receiver spectral bandpass and $L_{\lambda B}$ is the sky spectral radiance (wm^{-2} sr^{-1} nm^{-1}) along the direction r, which is along the zenith for a vertical pointing lidar.

For λ selected to avoid molecular absorption $\beta(r)$ and $\sigma(r)$ are due to the combined effects of air molecules (Rayleigh scattering) and aerosol particles;

$$\beta(r) = \beta_R(r) + \beta_a(r) \quad (5)$$

$$\sigma(r) = \sigma_R(r) + \beta_a(r) \quad (6)$$

where the R and a subscripts identify the Rayleigh and aerosol coefficients, respectively.

The Rayleigh terms $\beta_R(r)$ and $\sigma_R(r)$ may be computed from the Rayleigh scattering law and a knowledge of atmospheric temperature and pressure versus r. This leaves $\beta_a(r)$ and $\sigma_a(r)$ as unknowns, but there is only one known, $n(r)$, at any r. Hence, $\beta_a(r)$ and $\sigma_a(r)$, as well as the aerosol extinction-to-backscatter ratio $S_a = \sigma_a/\beta_a$, cannot be retrieved without invoking certain assumptions or special circumstances. For example, knowing or assuming a modeled value for S_a permits retrieval of the aerosol extinction profile, $\sigma_a(r)$.

Aerosol concentrations are typically high enough near the surface so that $\beta(r) \approx \beta_a(r)$ and $\sigma(r) \approx \sigma_a(r)$ for the first several hundreds of meters at an operating wavelength of λ = 523 nm. However, high aerosol concentrations are generally limited to a well mixed region that extends no more than a few km above the earth's surface. Thus, under clean, cloud free conditions for λ = 523 nm, it is reasonable to approximate $\beta(r) \approx \beta_R(r)$ and $\sigma(r) \approx \sigma_R(r)$ in the upper troposphere for heights greater than about 5 km above ground. This provides a good test region to compare theoretically predicted lidar performance against actual observations.

SIMULATIONS AND OBSERVATIONS

To generate simulations representative of reasonably clean conditions, an aerosol profile model for λ = 523 nm was chosen with a mixed layer height of about 3 km, an optical depth (integrated extinction) of about 0.1, an aerosol extinction to backscatter ratio, σ_a/β_a, of 25 and $\beta_R/\beta_a > 10$ between 5 and 10 km above ground. One minute average (150,000 laser pulses) SNR values were computed for this aerosol model using the signal and noise relations given in (1) through (6) and the following parameters representative of the upgraded MPL-2 system:

E_0 = 1→8 μJ @ 2.5 kHz PRF
A_R = $\pi \times 10^{-2} m^2$ (20 cm diameter)
δ_λ = 55% @ 523 nm
$\Delta\lambda_R$ = 0.14 nm
Ω_R = 9.5×10^{-9} sr (110 μrad full-angle FOV)
system optical transmission efficiency of ~7%

The system optical transmission efficiency is multiplied times A_R to account for internal optical losses. The transmitted laser pulse energy is about 8 μJ if the system exit window is clean, but several weeks have often passed between cleanings. The signal has been observed to increase as much as 7 or 8 fold after the window was cleaned; hence, the reason for listing E_0=1→8 μJ. A value of 4 μJ was assumed for E_0 in the simulations. The background and detector noise count, n_{BD}, was assumed negligible for nighttime, while the daytime value of n_{BD} was assumed to be dominated by background radiation (i.e., $n_{BD} \approx n_B$). Estimates of the background radiance, $L_{\lambda B}$, needed to compute n_B were obtained by running a radiative transfer code for λ = 523 nm using nominal values for surface albedo (~ 0.2), aerosol optical depth (0.1 to 0.2), aerosol size distribution (Junge model with ν = 2.5), aerosol refractive index (1.44 - i 0.005) and sun angles (zenith angles ≤ 30°). For zenith viewing, $L_{\lambda B}$ was estimated to be bounded between 0.05 to 0.1 wm^{-2} sr^{-1} nm^{-1}. A range bin size of Δr = 300 m was used in the simulations as this corresponds to the bin size used in the collection of data currently available for comparison with the simulations.

Results of the SNR simulations are listed in Table 1 for heights in 1 km steps from 5 km to 10 km. The nighttime values are quite good throughout the height range and even the daytime values are all greater than ~10. An SNR > 5 is adequate for distinguishing mixing layer/cloud boundaries, while an SNR > 20 is sufficient for implementing aerosol retrieval algorithms. Hence, the

simulation results indicate that MPL data should be quite useful day or night even for a relatively short averaging period of one minute. Considerably larger SNR's would be expected for lower heights both due to the inverse squared range effect and the typically much larger aerosol concentrations. Averaging for periods of 10 to 30 minutes would further increase the SNR's and still provide adequate temporal resolution for many applications.

To select MPL data to compare against the simulations, time-height images of MPL returns were scanned for a period of several weeks to identify cloud free, apparently fairly clean periods of 24 hours or more. The range dependent decreases in these clear period returns were then checked in the 5 to 10 km range to confirm whether their range-squared compensated signals decreased with height close to what would be expected for a Rayleigh scattering profile. This resulted in the selection of a 24 hour data period beginning on 10/1/95.

To extract SNR estimates from the data required several processing steps. The one minute summed range bin counts recorded by the MPL data acquisition system are totals of both signal and noise, $n_t(r) = n(r) + n_{BD}$. A detector count-rate correction factor must first be applied to $n_t(r)$ to correct counts summed at rates close to the detector maximum count rate. To extract the signal from the corrected $n_t(r)$ count requires subtraction of n_{BD}, taken as the corrected average count for bins near the maximum unambiguous range (~60 km) where n(r) is negligible. The extracted signals for selected heights were then time averaged to determine means, $\bar{n}$, and standard deviations, σ_n, of n for 15 minute running averages. Finally, the ratio $\bar{n}/\sigma_n$ was taken as the estimated SNR of n. Results obtained by averaging for an hour period at night and for an hour during the day around solar noon, at heights in 1 km steps between 5 km and 10 km, are shown in Table 2.

Comparing the values in Table 2 to the simulations (Table 1), it can be seen that the observations are somewhat lower but exhibit a range dependent trend similar to the simulations. The nighttime results are about a factor 1.5 lower than the simulations, indicating E_0 was more likely about 2 μJ (nighttime SNR $\propto \sqrt{E_0}$), which is within the 'dirty window' derated energy range noted earlier. Thus, the observations fall within the performance range as predicted from system parameters. Moreover, results show that this lidar can achieve sufficiently high SNR's in short averaging periods of one to several minutes to be quite useful in aerosol and cloud sensing applications even during the daytime.

REFERENCES

[1] J.A. Reagan, M.P. McCormick, and J.D. Spinhirne, "Lidar sensing of aerosols and clouds in the troposphere and stratosphere," *Proc. IEEE,* vol. 77, pp. 433-448, March 1989.

[2] J.D. Spinhirne, "Micro pulse lidar," *IEEE Trans. Geosci. Remote Sensing,* vol. 31, pp. 48-55, Jan. 1993.

[3] J.A. Reagan, T.W. Cooley and J.A. Shaw, "Prospects for an Economical, Eye-Safe Water Vapor Lidar," *Proc. IGARSS'93 Symposium*, Tokyo, Japan, pp. 872-874, August, 1993, IEEE Publication 93CH3294-6.

[4] J.D. Spinhirne, V.S. Scott, J.A. Reagan, and A. Galbraith, "Cirrus and Aerosol Lidar Profilometer - Analysis and Results," *Proc. ARM Science Team Meeting*, San Diego, CA, March 1995.

Table 1 MPL-2 SNR Simulations

Height (km)	SNR		
	Night	Day $L_{\lambda B}$(wm^{-2} sr^{-1} nm^{-1}) 0.05	0.1
5	155	82	63
6	123	54	41
7	98	37	27
8	81	25	18
9	67	17	12
10	57	12	9

Table 2 MPL-2 SNR Performance (observations: 10/1/95 - ARM Oklahoma CART Site)

Height (km)	SNR	
	Night	Day
5	97	27
6	79	21
7	65	17
8	53	13
9	44	11
10	37	7

Rayleigh Lidar Observations During Arctic Summer Conditions

J. P. Thayer
SRI International
333 Ravenswood Avenue, G-275, Menlo Park, CA 94025
(415) 859-3557/Fax (415) 322-2318/Email jeff_thayer@qm.sri.com

N. B. Nielsen
SRI International
333 Ravenswood Avenue, 30617, Menlo Park, CA 94025
(415) 859-2841/Fax (415) 859-5036

R. B. Kerr
Boston University, Center for Space Physics
Department of Astronomy, 725 Commonwealth Avenue, Boston, MA 02215
(617) 353-6139/Fax (617) 353-6463/Email kerr@moe.bu.edu

J. Noto
Boston University, Center for Space Physics
Department of Astronomy, 725 Commonwealth Avenue, Boston, MA 02215
(617) 353-6363/Fax (617) 353-6463/Email noto@moe.bu.edu

ABSTRACT

Summer observations by a Rayleigh lidar in Greenland are often hindered by the prolonged presence of high solar background. To reduce the contribution of solar background to the lidar signal we have employed polarization and narrowband filtering techniques. These techniques combine to extend lidar operations to about 5° solar elevation angle. Further background rejection can be gained by employing multiple etalons of relatively high resolution. This capability is becoming more feasible for lidar applications with the development of liquid crystal etalons. Here, we demonstrate the lidar system performance separately using polarization and narrowband filtering techniques and introduce the development of a unique liquid crystal etalon system for lidar applications.

INTRODUCTION

In the winter of 1992/1993, a Rayleigh lidar system was installed at the NSF Sondrestrom atmospheric research facility located on the west coast of Greenland near the town of Kangerlussuaq (67.0°N, 50.9°W). The vertically directed lidar system samples the elastically backscattered laser energy from molecules (Rayleigh) and aerosols (Mie) over the altitude range from 15 to 90 km at high spatial resolution with the present resolution set at 192 m. The lidar system consists of an injection-seeded, frequency-doubled, 42W Nd:YAG laser, a 92 cm Newtonian telescope, and a two-channel photon counting receiver. A broadband 10 Å filter centered on 532.0 nm with about 60% peak transmission is used in the receiver during nighttime observations. The principal objective of the lidar project is to contribute to studies concerned with the climatology and phenomenology of the arctic middle atmosphere.

Because of the site's location above the arctic circle, frequent observations are made during sustained periods of twilight. To reduce the solar background during these times, we use a combination of optical elements including a narrowband filter, half-wave plate, and a polarizer in the receiver optics. This combination of optical elements presently extends lidar operations from solar elevation angles of about –2° to solar elevation angles of about 5°. For the arctic, this improved range in solar elevation angle can result in many hours of extended lidar operations in the summer. To evaluate the individual performance of the narrowband filter and the polarizer in rejecting solar background, we describe in the following section lidar measurements using each technique. Following this section, we discuss issues related to employing high-resolution etalons within a lidar receiver system and present information concerning the development of a unique liquid crystal etalon system to improve daytime operations of the Rayleigh lidar. This novel device exploits the variable index of refraction effect inherent in liquid crystals to allow for a stable, rugged, flexible, compact device that is ideal for lidar applications.

BACKGROUND REJECTION TECHNIQUES

Polarization

It is well known that unpolarized light from the twilight sun is almost completely polarized when viewed at a 90° scattering angle. The degree of polarization at the 90° scattering angle is wavelength-dependent and, for the receiver wavelength of 532 nm, is nearly 90% vertically polarized [1].

0-7803-3068-4/96$5.00©1996 IEEE

Therefore, during these times the background light observed from a vertically viewing lidar receiver will be highly polarized (multiple scattering and ground reflections will cause some depolarization). By incorporating a half-wave plate and polarizer into the receiver optics, we can, theoretically, reject 99% of the vertically polarized light and transmit 95% of the horizontally polarized light. Once the background rejection is optimized, the linearly polarized laser pulses at 532 nm can be transmitted in the horizontal plane of polarization and scattered back to the receiver with little modification to its original polarization.

Polarization measurements of the background signal alone during twilight conditions resulted in a 75% reduction when the polarizer was placed in the optical path with the broadband filter. The impact of the polarizer on the laser signal was tested during low background conditions (i.e., night). This test resulted in a laser transmission through the polarizer of better than 90% after fine tuning the polarization plane of the transmitted beam. Thus, the use of the polarizer improves lidar performance during twilight conditions by a factor of three to four. The polarization technique alone becomes ineffective for solar zenith angles less than 85°, partly due to the linear decrease in the degree of polarization with decreasing solar zenith angle, but mostly due to the exponential increase in the background intensity with decreasing solar zenith angle. It should be noted, however, that it is necessary to rotate the polarization plane of the receiver and the transmitter to compensate for the sun's azimuthal position changing with time. As the sun changes its azimuthal position, the plane of highly polarized backscattered light will rotate with that change. As a result, the effectiveness of a polarizer with a fixed half-wave plate will range from maximum to minimum as the sun azimuth changes from 0 to 90°. As the summertime sun rises at our latitude the azimuthal angle has changed by nearly 90° from sunset and, therefore, the plane of highly polarized scattered background light has rotated 90°. This causes an increase in the background by a factor of three to four compared to the measurements made during sunset at the same solar zenith angle, basically illustrating the polarizer's ineffectiveness at dawn. To remedy this situation we have implemented computer-controlled, half-wave plate rotators in the transmitter and receiver to rotate the plane of polarization of the transmitted beam and the receiver with the sun's position to optimize the background rejection at all solar azimuth angles.

Narrowband Filtering

It has been shown by [2] that for a continuous spectrum the output flux from a dispersive element, such as a prism, grating spectrometer, or Fabry-Perot spectrometer, is inversely proportional to the square of the resolving power (R). Thus, for lidar operations during high solar background conditions, it is of great advantage to reduce the spectral passband of the system by employing narrowband filters. Reference [2] also demonstrated that for the same resolving power the Fabry-Perot (FP) provides the greatest luminosity (L). These properties favor the use of FP etalons in daytime Rayleigh lidar work. This leads to the concept of the luminosity–resolution (LR) product

$$LR = 2\pi A_{FP}\tau = \tau U_{FP} R,$$

illustrating the constancy of this relationship with the working area of the FP etalon A_{FP} and the total transmittance factor of the optical system. Maximizing this product results in a trade-off between the étendue (U) of the FP and its resolving power. In general, étendue is equal to the product of $A\Omega$, which for any optical system should be conserved to ensure maximum throughput. For an FP etalon, the solid angle subtended by the etalon plates is expressed as $\Omega = 2\pi R^{-1}$ which limits the resolving power of the etalon. The telescope étendue is determined by the area of the primary mirror and its field of view. Thus, for lidar applications the étendue of the etalon with the greatest resolving power should be equal or greater than the étendue of the collecting telescope. By definition, low-resolution filters have small resolving powers and, therefore, interference filters of one-inch diameter or more and greater than about 10 Å bandwidth may be used in lidar receivers without much concern about limiting the étendue or throughput of the system.

Currently, we employ in our receiver during high background conditions a Daystar filter, consisting of a solid mica etalon and an interference filter, centered on 5320.5 Å with a 0.8 Å bandwidth and approximately 25% peak transmission. By etalon standards, this is a low-resolution filter with an étendue that exceeds the étendue of our collecting telescope. Fig. 1a compares the performance of this Daystar filter with the polarizer configuration discussed previously in terms of signal percent error versus solar zenith angle. The comparison is based on dusk observations made on August 26, 1995 using only the Daystar filter in the receiver and dusk observations made on August 27 using the half-wave plate, polarizer, and 10 Å interference filter in the receiver. Five altitudes of 30.42 km, 40.02 km, 50.58 km, 60.18 km, and 70.74 km were used in computing the percent error from the data sets with lower percent error meaning better system performance.

We calculated the percent error after integrating the data for 3 min and 5 range gates (or about 1 km). Due to the increasing background variance, the noise-subtracted signal estimates worsened with decreasing solar zenith angle, particularly for data above 50 km altitude. As a result, we decided to determine the percent error using signal estimates from the dark period of observations using the Daystar filter and another set of signal estimates from the dark period of observations using the polarizer setup. This allowed the percent error to be reliably determined during the high

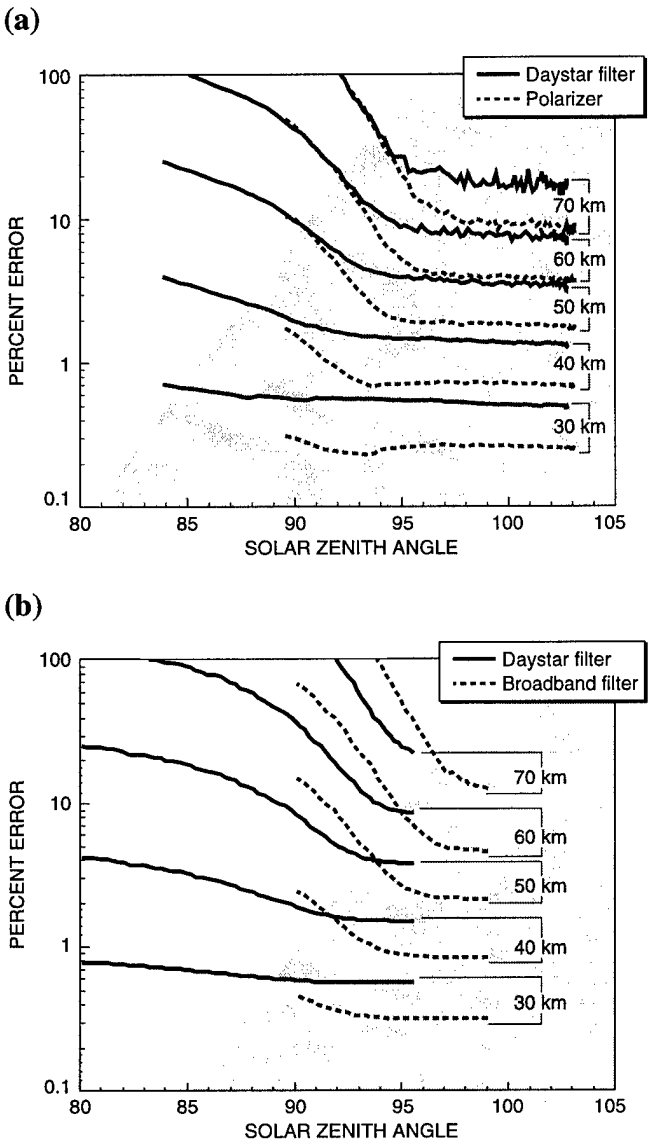


Fig 1. System performance at 5 different altitudes expressed in terms of percent error for observations of a) August 26 and 27, 1995 and b) April 25, 1995. The August data is a comparison between observations made using the polarizer configuration, dotted line, and the Daystar Filter, solid line. The April data is a comparison between observations made using a broadband 10Å filter, dotted line, and the Daystar Filter, solid line. The shaded region highlights the performance of the polarizer in a) and the broadband filter in b).

background conditions for all altitudes. The percent error associated with the Daystar filter is shown by the solid line in Fig. 1a while the percent error associated with the polarizer is shown by the dashed line. The shaded region in Fig. 1a highlights the system performance using the polarizer. The polarizer observations were limited to solar zenith angles greater than about 90° due to the high background saturating the counters.

As shown by the boundary of the shaded region in Fig. 1a, the time or solar zenith angle where the percent error of the two techniques cross is altitude-dependent. This is because of the different influences the two optical elements have on the laser signal and on the time-varying background signal. This results in a tradeoff between the temporally increasing solar background and the spatially decreasing backscattered laser signal with altitude. This effect can be explained by expressing the percent error in a signal-dominated regime as $1/\sqrt{\langle s(k)\rangle}$, where <s(k)> is the mean signal count, and the percent error in a noise-dominated regime as $\sqrt{\langle b\rangle}/\langle s(k)\rangle$, where <b> is the mean background count. For solar zenith angles greater than about 95°, the lidar return signal is signal-dominated. Due to the greater transmission of the laser light by the combination of polarizer and broadband filter over the Daystar filter, the percent error is smaller than that associated with the Daystar filter during these times at all altitudes. As the solar background increases with decreasing solar zenith angle, the polarizer allows more background signal than the Daystar and, thus, shows a much steeper slope with decreasing solar zenith angle. At 30 km altitude, the observations with the Daystar filter will show better system performance than the observations with the polarizer for solar zenith angles less than about 85°. At higher altitudes we see this cross-over occurs at even greater solar zenith angles (87.5° for 40 km, 90.5° for 50 km, and 92° for 60 km) as the backscattered laser signal is weaker and, thus, influenced by the increasing background at greater solar zenith angles. Thus, for signal-dominated regimes the polarizer provides optimal system performance while for background-dominated regimes the Daystar filter is best. In practice, we use the Daystar filter and the polarizer together to reap the benefits of both techniques with the signal requirements for the specific experiment determining when to implement the Daystar filter.

A similar experiment was carried out on April 25, 1995 but with the polarizer out of the receiver optical path, thus, comparing the Daystar filter performance with the broadband 10 Å filter. This comparison is presented in Fig. 1b in the same format as Fig. 1a but with the dotted line representing the percent error of the 10 Å filter. This plot reflects the improvements made when using polarization, as the performance cross-over between the Daystar and broadband filter occur at much greater solar zenith angles than those illustrated in Fig. 1a. The Daystar performance has basically not changed between the two experiments as can be seen by comparing the solid curves in Fig. 1a,b. Note that the slope of the shaded region boundary in both plots is the same but shifted to greater zenith angles for the Fig. 1b observations. Thus, for the same system performance, the use of the

polarizer roughly extends the observations by reducing the solar zenith angle by an additional 4°.

For middle atmosphere studies this analysis helps determine the proper time to position the Daystar filter to improve system performance. For example, noctilucent clouds are unique to the earth's polar regions and occur only in the summer months near an altitude of about 83 km. To detect noctilucent clouds in the backscattered lidar signal it is desirable to optimize system performance at the 50 to 60 km altitude range as the backscattered signal from these clouds is equivalent to Rayleigh backscatter in this altitude range [3]. Therefore, Fig. 1a shows it to be best to insert the Daystar filter near 90° solar zenith angle or less to provide better than 10% error in the signal at 50 km, while becoming less accurate at lower altitudes where the loss can be afforded.

MULTIPLE ETALON APPROACH

Etalons of higher resolving power than currently employed in our receiver can be used to reject further the continuum solar background as the Doppler-broadened backscattered signal, transmitted by the injection-seeded laser (105 MHz or 0.099 pm linewidth), has a linewidth of about 2970 MHz or 2.8 pm. Multiple etalons are necessary to extend the free spectral range to the point where interference filters can be used to reject the overlapping orders of the Fabry-Perot. It is critical, however, to consider the LR product of the system and, thus, match the étendue of the etalon of highest resolving power with that of the collecting telescope. This condition then determines the resolving power limits for the etalon as will be shown by the following.

The étendue of the telescope is given by

$$U_T = A_T \Omega_T \cong A_T \pi \theta_T^2 = \pi^2 r_T^2 \theta_T^2$$

and the étendue of the FP is given by

$$U_{FP} = A_{FP} \Omega_{FP} = \frac{2\pi A_{FP}}{R} = 2\pi A_{FP} \frac{\Delta\lambda}{\lambda} = 2\pi^2 r_{FP}^2 \frac{\Delta\lambda}{\lambda},$$

where θ_T is the telescope field of view, and $\Delta\lambda$ is the limiting spectral resolution of the etalon. Thus, the spectral resolution for the etalon is defined as

$$\Delta\lambda = \frac{\lambda A_T \theta_T^2}{2A_{FP}} = \frac{\lambda r_T^2 \theta_T^2}{2r_{FP}^2}.$$

The telescope field of view is related to the beam divergence of the laser which should be minimized during high background operations.

Presently, the laser beam divergence of the Greenland system is about 0.1 mrad and our telescope field of view is set at 0.5 mrad. Further background rejection can be made if the laser beam divergence, and therefore the telescope field of view, was reduced even more. From the above equation it is also clear that a reduction in the telescope field of view would allow for an increase in resolution of the etalon without a loss in system étendue. For our present lidar setup of $r_T = 0.457$ m, $\theta_T = 0.5$ mrad, $r_{FP} = 29 \times 10^{-3}$ m, $\lambda = 532 \times 10^{-9}$ m, our limiting resolution is $\Delta\lambda = 0.165$ Å. To approach the linewidth of the backscattered signal we need to either increase the working area of the etalon plates by a factor of 2 (which can get rather expensive) or decrease the laser beam divergence by a factor of 2. The second option being more economically feasible results in $\theta_T = 0.25$ mrad and the limiting resolution becomes $\Delta\lambda = 0.041$ Å. For an etalon finesse of near 20, the free spectral range for a single etalon of this resolution becomes 0.826 Å with a gap spacing of about d = 1.14 mm. Employing two etalons with a spacer ratio of near one (a vernier ratio) will effectively extend the free spectral range by approximately a factor of 10 to 8.26 Å allowing for a broadband interference filter to suppress the overlapping orders.

LIQUID CRYSTAL ETALON

In constructing the double etalon system described above, great care must be taken to ensure the two etalons are properly configured. Fine tuning of the etalons is desirable during installation to peak the overall performance of the system. Fine adjustments of the etalon system has been done by a number of techniques including pressure tuning of the fixed air gap within the etalon, mechanically changing the distance between the etalon plates, or tilting of the entire etalon. These techniques (aside from simply tilting the plates) often add significant complexity to a multiple etalon system. A liquid crystal etalon that exploits the variable index of refraction effect inherent in liquid crystals simplifies the process of fine tuning significantly and provides a stable, rugged, flexible, and compact device for implementation into lidar receivers. Birefringent liquid crystals exhibit an index of refraction that depends on the polarization parameters of the incident light. Liquid crystals will transmit either left- or right-handed polarization, depending on the helical ordering of the crystals, and will reflect the opposite polarization. Applying an electric field parallel to the optical axis causes the crystals to rotate in the plane perpendicular to the electric field. This rotation changes the index of refraction of the crystal by changing the position of the crystal relative to the optical axis [4]. Employing this process within the fixed gap of the etalon allows for the FP to be tuned easily, quickly, and repeatably during lidar applications. Recent advances in

polymer technology have allowed the construction of multi-stage, polarization-based, broadband tunable filters. The technology used to construct these filters is identical to the technology needed to produce a liquid crystal etalon. A double etalon system based on liquid crystal technology is under development and should be available for 1997 summer operations in Greenland.

CONCLUSION

We have demonstrated the use of polarization and narrow-band filtering techniques for improving Rayleigh lidar observations during summertime conditions in the arctic. We have also discussed issues related to employing high-resolution etalons within a lidar receiver system and present information concerning the development of a unique liquid crystal etalon system to improve further the daytime operations of the Rayleigh lidar. These improvements will significantly benefit middle atmosphere research in the arctic, in particular, the study of noctilucent clouds.

ACKNOWLEDGMENTS

This work was supported by the NSF Coupling of Energetics and Dynamics of Atmospheric Regions (CEDAR) program under the cooperative agreement, ATM-9317167.

REFERENCES

[1] K. L. Coulson, Polarization and Intensity of Light in the Atmosphere, A. Deepak Publishing, 596 pp. (1988).

[2] P. Jacquinot, "The Luminosity of Spectrometers With Prisms, Gratings, or Fabry-Perot Etalons," Journal of the Optical Society of America, Vol. 44, No. 10, p. 761, 1954.

[3] J. P. Thayer, N. B. Nielsen, and J. Jacobsen, "Noctilucent Cloud Observations Over Greenland by a Rayleigh Lidar," Geophys. Res. Letters, Vol. 22, No. 21, 2961-2964, 1995.

[4] D. W. Craig, J. Staromlynska, "Comparison of Variable Birefringence Devices and Fabry-Perot Etalons for use as Tunable Filters," IEEE J. of Quant. Elect., 24, p. 1440, 1990.

Daytime Tropospheric Water Vapor Profile Measurements by Raman Lidar

Scott E. Bisson and J. E. M. Goldsmith
Sandia National Laboratories
Livermore, CA 94551-0969
Mail Stop 9057
Ph. (510) 294-2467, E-Mail: sebisso@sandia.gov

Abstract -- We describe a high performance Raman lidar system capable of both nighttime and daytime operation. The key elements of this system are a narrow-band, dual field-of-view detection system, fast photon counters and a high average power excimer laser. This system has been used to measure daytime water vapor profiles up to 5 km with high spatial (75-150 m) and high temporal (10 min) resolution. In this paper, we discuss this system and a novel method for calibration.

INTRODUCTION

One of the most important atmospheric constituents needed for climate and meteorological studies is water vapor. Water vapor plays an important role in driving atmospheric circulations through latent heat release and in determining the earth's radiation budget, both through its radiative effects (water vapor is the major greenhouse gas) and cloud formation. The vertical distribution of water vapor is particularly important because it not only determines convective stability but radiative effects are also strongly altitude dependent. It is highly variable, both spatially and temporally and is one of the most uncertain parameters in GCM's (General Circulation Models). Therefore, knowledge of the vertical and temporal variations of water vapor are essential for understanding atmospheric processes.

A powerful, proven technique for the measurement of water vapor in clear skies or up the lowest cloud level is Raman lidar [1,2]. Raman lidar operates by sending out a pulse of laser light and recording both the elastically (Rayleigh and aerosol) and inelastically (Raman) backscattered radiation due to water vapor and nitrogen. The water vapor profile is obtained by ratioing the water vapor signal with the nitrogen signal. This eliminates effects due to laser pulse energy fluctuations and overlap between the laser beam and telescope field-of-view (fov). This ratio is then normalized to a radiosonde. Unlike DIAL (Differential Absorption Lidar) which requires a laser precisely tuned to a water vapor absorption feature, Raman lidar is a non-resonant technique which relaxes constraints on the laser and reduces complexity. Raman lidar is a high performance, robust technique for the measurement of nighttime water vapor profiles.

This research was supported by the Environmental Sciences Division of the U. S. Department of Energy as part of the Atmospheric Radiation Measurement (ARM) Program.

Whiteman et al [2] have developed a Raman lidar system to measure sustained nighttime water vapor profiles with high accuracy (>90%) at altitudes up to 9 km, which encompasses most of the earth's water vapor. Integration times were 1 minute with 75 m vertical resolution. While the nighttime capabilities of Raman lidar are well established the daytime capabilities are not. The need for a continuous data record and the influence of solar radiative forcing provide strong motivation for similar daytime capabilities. Daytime measurements however, are limited by the difficulty of detecting the weak backscattered Raman signal against the large solar background. At Sandia, we have developed a high performance, narrow-band, narrow fov Raman lidar system capable of both day/night operation. The key features of this system are its dual fov capability and narrow-band, high transmission UV interference filter system. Recent measurements with this system indicate that daytime measurements up to 5 km with 75 m range resolution and a few minutes integration time are possible.

DAYTIME ISSUES

The central problem in the development of a daytime capable Raman lidar is the detection of the weak backscattered Raman signal against the large solar background. This problem has been partially overcome by operating in the solar blind region of the spectrum (wavelengths less than about 290 nm) [3,4]. In this region the sky is effectively black due to absorption of sun light by tropospheric and stratospheric ozone. Unfortunately tropospheric ozone also significantly attenuates the laser beam. In an alternate approach, the background skylight reaching the detector is reduced by using a narrow fov receiver and narrow-band detection. Ansmann et al [5] have used this approach and have obtained daytime water vapor profiles up to 2.5 km. Integration times were approximately 15 min with 180 m range resolution. By reducing the receiver fov the number of detected background sky photons can be reduced. Unfortunately, this increases the altitude at which the receiver fov and laser beam overlap. A solution to this problem is to use a dual fov detection system. In a dual fov system, the weak high altitude signals are directed through a narrow field stop (which reduces background light) whereas the low altitude signals pass through a separate wide field stop. Since the low altitude signals are much stronger, the increased background light associated with the wider fov is

0-7803-3068-4/96$5.00©1996 IEEE

not a problem. The receiver fov must not be narrower than the laser beam divergence otherwise signal will be lost at high altitudes. The number of detected background sky photons can be reduced further by using narrow bandwidth detection. For optimum efficiency, this requires a laser with a bandwidth substantially narrower than the water vapor Raman linewidth. The narrow-band, narrow fov approach is particularly attractive as it is easy to switch from nighttime to daytime operation simply by reducing the receiver fov and changing the receiver filters from wide-band (1-3 nm) to narrow-band (.3-1 nm). Furthermore, it is possible in principle to use the background skylight to calibrate the lidar. By ratioing the background signals in the nitrogen and water vapor channels an absolute calibration may be obtained. In the solar-blind approach, it is desirable to change the wavelength of the laser to achieve optimum nighttime performance. In practice this may be difficult.

Another issue which needs to be considered is the repetition rate of the laser. For nighttime operation the performance is roughly independent of the repetition rate. In the daytime however, with a constant average power, the performance is strongly dependent on the laser repetition rate. For maximum daytime performance it is desirable to have a high pulse energy, low rep-rate laser. The reason for this is simple: as the laser energy is increased and the rep-rate lowered, more laser photons are detected in a shorter time thus reducing the observation time and hence the integrated background signal.

INSTRUMENT

Fig. 1 shows a schematic of the Sandia lidar system. The transmitter is based around a Lambda Physik LPX 150T injection-locked, tunable XeCl laser operating at 308 nm. Injection locking was beneficial for reducing the beam divergence and the linewidth of the laser beam. The output from this laser was further amplified by a single-pass Lambda Physik LPX-220 XeCl amplifier producing outputs up to 250 mJ @ 200 Hz. Much higher outputs were possible but with reduced gas lifetime and the possibility of optical damage. The receiver is a .76m f 4.5 Dall-Kirkham telescope with an fov that can be reduced to .2 mr, which is comparable to the laser beam divergence. The detection system consists of wide and narrow fov portions with 3 channels each. Three species (N_2 @ 331 nm, H_2O @ 347 nm, and aerosols @ 308 nm) are detected. A beamsplitter, mounted at 45° with respect to the optical axis of the telescope, splits off about 5% of the received signal into the wide fov channels with the transmitted portion (95%) into the narrow fov. This configuration provides maximum range coverage and increased dynamic range. At high altitudes, where the signals are weak, the field stop reduces the number of detected background sky photons but does not reduce the strength of the high altitude backscattered Raman signal.

Photon counting is used for all of the high altitude channels whereas analog detection is used for all of the low altitude channels. Unfortunately the photon counters could not respond to the high background count rates (~ 80 MHz) so neutral density filters were used to reduce the background sky light to more manageable count rates (~ 8 MHz).

High transmission (35%), high background rejection, narrow-band (.35 nm) UV interference filters are used to separate the different Raman components. Traditionally, polychromators have been used for this purpose since the

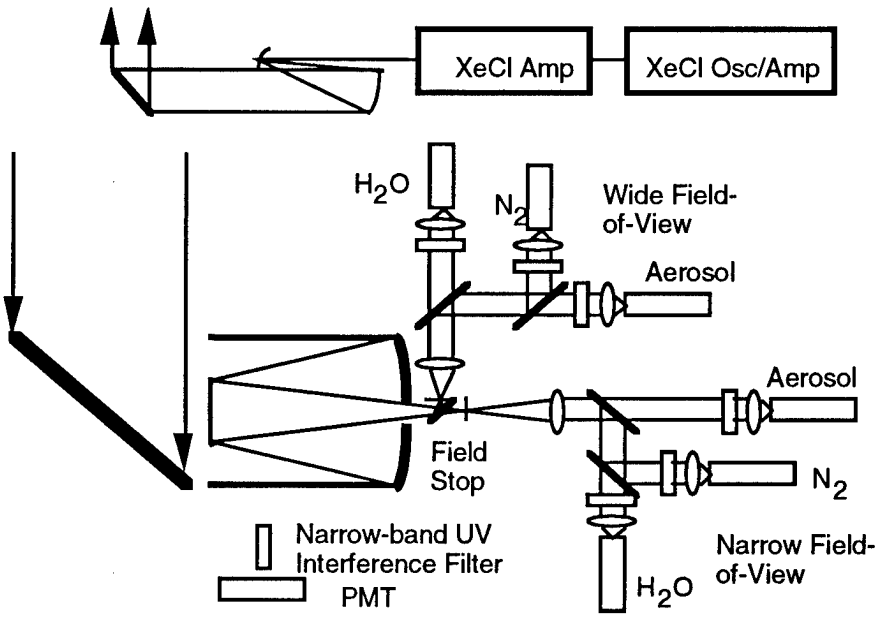


Figure 1. Schematic of the narrow band, narrow field-of-view Raman lidar system.

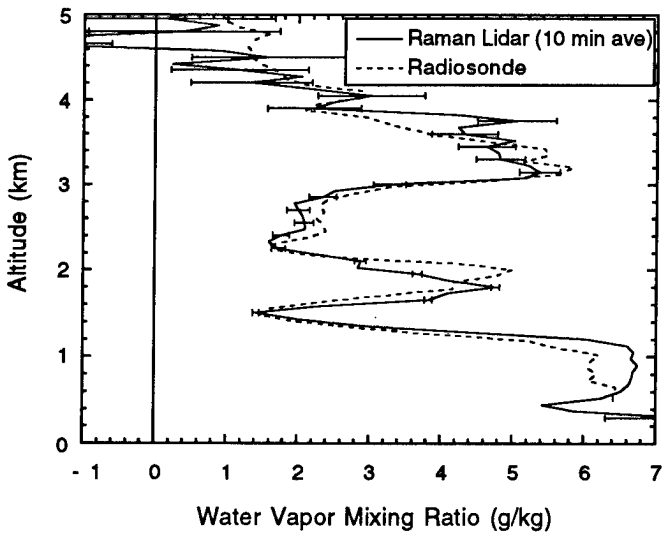


Fig. 2. Comparison of a daytime Raman lidar measurement with a coincident radiosonde. The error bars on the lidar data indicate statistical error only. This data was acquired with the Sandia Raman lidar at the US Department of Energy's Cloud and Radiation Testbed (CART) site in north central Oklahoma.

bandwidth can be made quite narrow. Unfortunately, the throughput is typically low (5%) and the complexity is high. Narrow-band, UV interference filters of the type described here have not been commercially available until recently.

RESULTS

Fig. 2 shows a daytime water vapor profile obtained with an integration time of 10 minutes and 75 m range resolution. This profile was constructed from the high altitude photon counting data only. A coincident radiosonde profile is overlaid for comparison. From this comparison, it was evident that the maximum daytime range was around 4-5 km, but higher ranges may be possible depending on sun light levels and water vapor concentrations. There was some disagreement at low altitudes due to the fact that only the high altitude data was used for the daytime measurements. This data was acquired with the signals attenuated by a factor of 10 to avoid high background sky photon count rates. We have recently installed faster photon counters (150 MHz) which should significantly improve the daytime performance. The performance above 5 km has yet to be determined due to the lack of sufficient moisture conditions.

ACKNOWLEDGMENTS

We thank Mark Mitchell for his technical assistance with the experiments.

REFERENCES

[1] S. H. Melfi and D. Whiteman, "Observation of Lower-Atmospheric Moisture Structure and its Evolution using a Raman Lidar," Bull. Am. Meteor. Soc., vol. 66, 1288-1292 (1985).

[2] D. N. Whiteman, S. H. Melfi, and R. A. Ferrare, "Raman Lidar System for the Measurement of Water Vapor and Aerosols in the Earth's Atmosphere," Appl. Opt., vol. 31, 3068-3082 (1992)

[3] D. Renaut and R. Capitini, "Boundary-Layer Water Vapor Probing with a Solar Blind Raman Lidar: Validations, Meteorological Observations and Prospects," J. Atm. and Oceanic Technol., vol. 5, 585-601 (1988)

[4] D. Renaut, J. C. Pourny, and R. Capitini, "Daytime Raman-Lidar Measurements of Water Vapor," Opt. Lett., vol. 5, 233-235 (1980).

[5] A. Ansmann, M. Riebesell, U. Wandinger, C. Weitkamp, E. Voss, W. Lahmann, and W. Michaelis, "Combined Raman Elastic-Backscatter Lidar for Vertical Profiling of Moisture, Aerosol Extinction, Backscatter, and Lidar Ratio," Appl. Phys. B, vol. 42, 1-11 (1992)

High Spectral Resolution, Low-Coherence Technique for Daytime Doppler Wind Measurements with Lidar

Ken W. Fischer
Center for Earth Sciences, Environmental Research Institute of Michigan
P.O. Box 134001, Ann Arbor, MI 48113-4001
313-994-1200, ext. 2239 (Ph.); 313-994-5824 (Fax); email: fischer@erim.org

Abstract -- This paper describes a high spectral resolution lidar technique which can be used to make Doppler wind field measurements using low-coherence lidar during the day. In particular the use of multiple Fabry-Perot étalons and narrowband interference filters in series are considered and measurements made using the technique are presented.

INTRODUCTION

Atmospheric lidar systems offer the power to make a wide variety of unique profiling measurements but suffer from limitations in the areas of clouds, daytime operation, and long-term unattended operation. This paper describes a high spectral resolution lidar technique which can be used to make Doppler wind field measurements using low-coherence lidar during the day and night.

In particular the use of multiple Fabry-Perot étalons and narrowband interference filters in series to attenuate background daylight signal is considered. This combination provides the high spectral resolution needed to determine Doppler shift and also attenuate the background daylight signal. Measurements can be made with this technique using either aerosol or molecular scattered signal allowing measurements to be made from the surface to the maximum altitude allowed by available signal without breaks due to presence or lack of aerosols. The technique has been demonstrated in the visible and can also be used in the near-ultraviolet portion of the spectrum.

The use of a low-coherence (non-heterodyne) measurement allows signal to be integrated over any desired period before a Doppler determination is made and allows the use of multiple detection apertures, both distinct advantages in considering space-based lidar measurements. This offers distinct advantages over a coherent heterodyne measurement in terms of the effect of laser speckle which fundamentally limits the lower end of measurement sensitivity for heterodyne detection lidars. Daytime wind data collected using the University of Michigan Doppler lidar will be presented and discussed.

LOW-COHERENCE DAYTIME DOPPLER LIDAR TECHNIQUE

Ground based low coherence lidar systems working in the yellow-green wavelength (0.5 μm) region have demonstrated the capability to measure vector wind with an accuracy of approximately 1 m/s [1-4]. This technique of determining wind velocity relies on detecting the Doppler shift experienced by a pulse of narrow band laser light as it is scattered by the atmosphere. The detection is done using an incoherent interferometric determination of the laser wavelength before and after scattering.

The incoherent lidar technique described here makes use of a Fabry-Perot interferometer as a high resolution element, capable of detecting Doppler shifts of the backscattered signal of the order of 5×10^{-6} nm. Laser light scattered by the atmosphere is gathered by a telescope and collimated before passing through an étalon. The Fabry-Perot interference pattern (set of concentric rings) appears at the infinity focus of the interferometer objective lens, where a detector system is placed. A spatial scan of one order of the interferometer in the image plane provides the line shape of the backscattered laser signal. It is from this line shape that Doppler shift information is obtained.

To attenuate the high background daylight signal in this portion of the spectrum, a second Fabry-Perot étalon and a narrowband interference filter have been added. To illustrate the effect of adding the second (low) resolution étalon and the narrowband filter, Fig. 1 shows a wavelength scan of fringes produced by the high resolution étalon with and without the low-resolution étalon and narrowband filter. Fig. 1 a) plots transmission versus wavelength of the high resolution étalon for +/- 0.05 nm centered at the laser frequency (~75 orders). Fig. 1 b) shows the response over the same spectral range for the low resolution étalon and the narrowband filter. Fig. 1 c) shows the effect of combining all three elements in series. Note that most of the extra orders from the high resolution étalon are strongly attenuated. This trend continues to orders outside of those displayed in Fig. 1.

DOPPLER LIDAR SYSTEM DESCRIPTION

The University of Michigan has constructed a lidar system which uses the technique described above to measure horizontal winds. The lidar system uses a Nd:YAG laser source frequency-doubled to operate at 532 nm. The core of the receiving system is a Fabry-Perot interferometer and matching detector as described above. An overview schematic of the system is shown in Fig. 2.

0-7803-3068-4/96$5.00©1996 IEEE

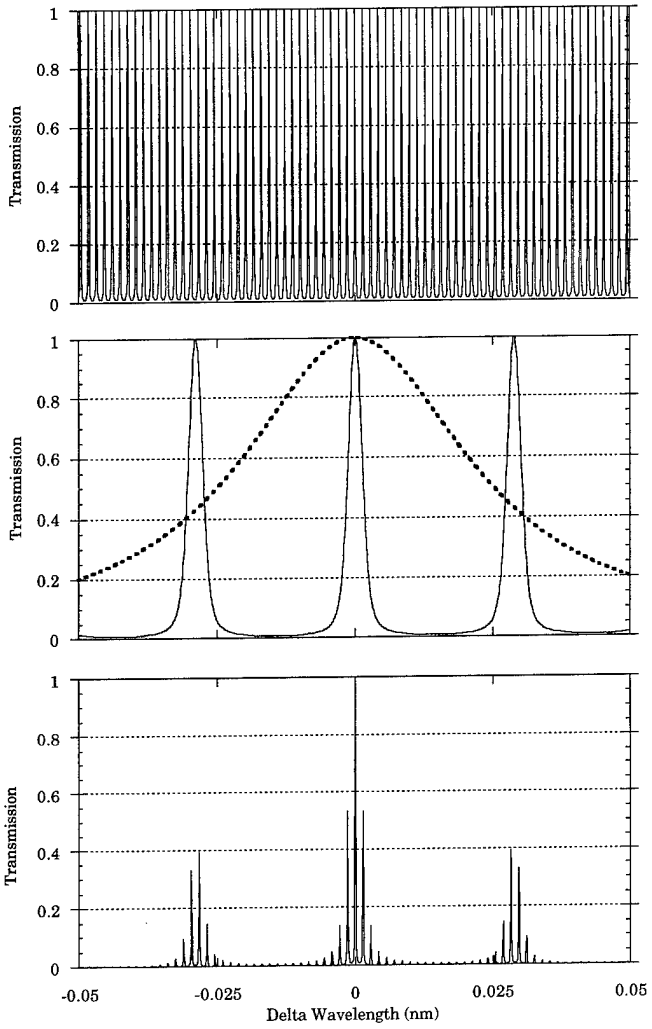


Figure 1 **a)** Normalized transmission vs. wavelength plot of the high resolution étalon for +/- 0.1 nm centered at the laser frequency (150 orders). **b)** Response over the same spectral range for the low resolution étalon (solid étalon) and the narrowband filter (dashed line) individually. **c)** Spectral response of system with all three elements combined in series.

A special detector is necessary in order to spatially scan the interferometer's image plane due to the circular nature of the pattern. The ring pattern from the high resolution Fabry-Perot étalon is projected by a telephoto lens pair onto a thirty-two channel image plane detector (IPD). The IPD is a micro-channel plate photo-multiplier tube and provides a gain of $\sim 10^6$. It is similar to the type used on the Fabry-Perot Interferometer instrument flown on the Dynamics Explorer satellite [5] and the High Resolution Doppler Imager instrument on the Upper Atmosphere Research Satellite.

The IPD has thirty-two concentric annular anodes, each anode having equal surface area. This is done to spatially match the interference pattern of the Fabry-Perot interferometer which allows the IPD to effect a spatial scan which is linear in wavelength. During the initial measurement demonstrations, only the inner twelve anodes were used. A more thorough description of the detector and its capabilities can be found in [6]. This type of detector was used to demonstrate the low-coherence Doppler lidar technique and for early field measurements. The detector is currently in the process of being upgraded to a CCD array.

The return-signal spectra are scanned linearly in wavelength by the detector. The resulting output are the spectra sampled in wavelength at twelve equally spaced points. This is the form of the raw instrument data before any type of processing is done. To illustrate how the system measures $\Delta\lambda$, two modeled spectra are shown in Fig. 3 a) a laser reference spectra centered exactly in channel (anode) 6 and another shifted by +3.5 m/s towards channel 7 (wind going away from observer). As a spectrum shifts in wavelength, the number of counts in each channel changes relative to the unshifted reference spectrum. Fig. 3 b) shows the change in counts for each channel relative to the reference for the +3.5 m/s shift. Measuring the change in photon counts in each channel relative to the unshifted reference allows measurement of shifts of much less than one channel width.

DEMONSTRATION DATA

Fig. 4 shows a time-series map of the horizontal wind field during the night and day of August 19, 1992 over Atlanta, Georgia. Each arrow corresponds to the horizontal wind speed and direction at a given altitude and time. The length of each arrow is proportional to the horizontal wind speed and its direction indicates the compass direction in which the wind was blowing with north along the positive

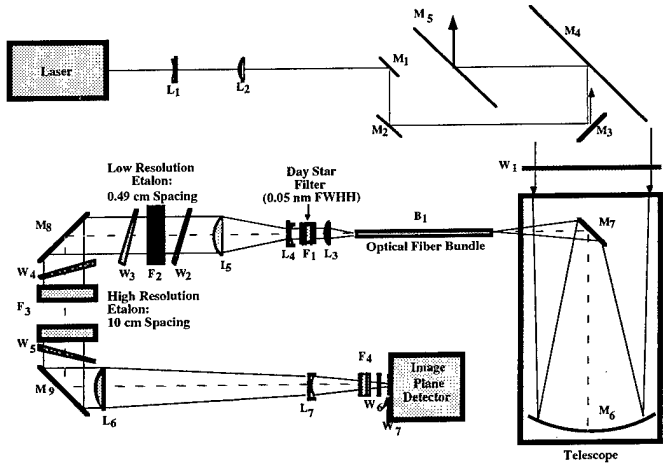


Figure 2. Schematic of daytime Doppler lidar optical components, including laser.

y-axis and east along the positive x-axis. A 5 m/s (~11 miles/hour) indicator arrow is shown at the lower left for scale. Winds have been smoothed using a running average of three consecutive data points to remove high frequency variability in the data.

Wind flow aloft overnight was generally from the west-southwest. During the night, the flow above and below the nocturnal inversion at ~300 m is largely de-coupled with stronger steady winds above and lighter more variable winds below. Between 0200 and 0930 EDT, a possible example of a Ekman spiral can be seen by noting the change in wind direction from southeast (near the surface) to southwest (at approximately 500 m). This rotation of the wind vector is a well known meteorological phenomenon caused by ground friction slowing the near surface flow and reducing the turning effect of the Coriolis force. Winds aloft are not exposed to surface drag and flow is in the expected geostrophic direction. Winds after 0800 EDT were observed to be lighter and more variable, typical of days in the Atlanta area.

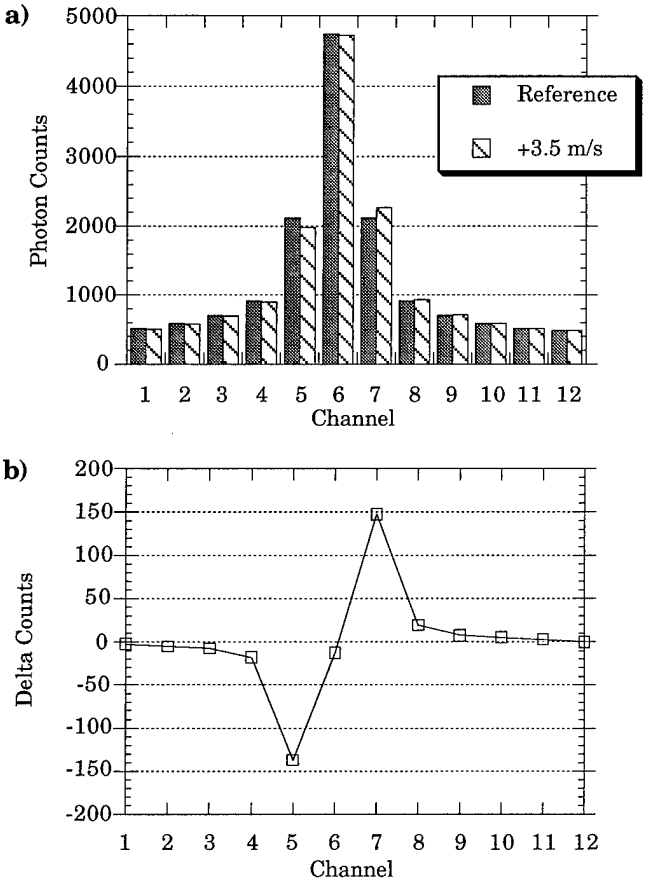


Figure 3 **a)** Modeled reference spectra centered in channel 6 with modeled signal spectra shifted +3.5 m/s (i.e. - wind going away from observer). **b)** Change in counts on each channel for a +3.5 m/s Doppler shift.

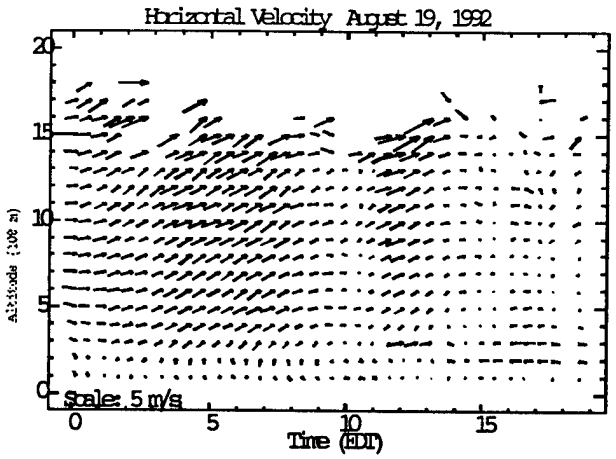


Figure 4 Horizontal wind field map over Atlanta, Georgia for August 19, 1992

ACKNOWLEDGMENTS

The author wishes to gratefully acknowledge the following individuals who have made significant contributions to the development and implementation of this lidar technique: Vincent Abreu, John Barnes, Paul Hays, Todd Irgang, Matt McGill, and Wilbert Skinner.

REFERENCES

[1] G. Benedetti-Michelangeli, F. Congeduti, and G. Fiocco, "Measurement of aerosol motion and wind velocity in the lower troposphere by Doppler optical radar," *J. Atmos. Sci.*, Vol. 29, pp. 906-910, 1972.

[2] M. L. Chanin, A. Garnier, A. Hauchecorne, and J. Porteneuve, "A Doppler lidar for measuring winds in the middle atmosphere," *Geophys. Res. Lett.*, Vol. 16, pp. 1273-1276, 1989.

[3] C. A. Tepley, S. I. Sargoytchev, and C. O. Hines, "Initial Doppler Rayleigh lidar results from Arecibo," *Geophys. Res. Lett.*, Vol. 18, pp. 167-170, 1991.

[4] K. Fischer, V. Abreu, W. Skinner, J. Barnes, M. McGill, T. Irgang, "Visible Wavelength Doppler Lidar for Measurement of Wind and Aerosol Profiles During Day and Night), *Opt. Engr.*, Vol. 34, pp. 499-511, 1995.

[5] P. B. Hays, T. L. Killeen, and B. C. Kennedy, "The Fabry-Perot interferometer on Dynamics Explorer," *Space Sci. Instrum*, Vol. 5, pp. 395-416, 1981.

[6] P. B. Hays and J Wang, "Image plane detector for Fabry-Perot interferometers: physical model and improvement with anticoincidence detection," *Appl. Optics* , Vol. 30, pp. 3100-3107, 1991.

Field Calibration and Sensitivity Analysis of Coherent Infrared Differential Absorption Lidars

P.I. Richter, I Peczeli, Sz. Borocz and L. Gazdag
Department of Atomic Physics, Technical University of Budapest
Budafoki ut 8. IIII.Budapest, Hungary

J. Leonelli and T. Dolash
Battelle Memorial Institute
505 King Avenue, Columbus, OH 43201-2693
(614)424-3985, Fax (614)424-7759

Abstract - Field tests were conducted with two identical infrared differential absorption lidars for the remote measurement of low concentrations of gases in the atmosphere. An FTIR spectrometer was also used to provide quantitative calibration of the systems with each other and with the FTIR. Statistical analyses of the lidar signals were used to determine the sensitivity limits for range and minimum detectable path-integrated concentration.

1. INTRODUCTION

Infrared differential absorption lidar (IR DIAL) techniques allow remote sensing of low concentrations of gases in the atmosphere from distances up to several kilometers. The nature of the measurement technique, namely the propagation of the laser beams through uncontrolled time-varying atmospheric paths and topographic backscatterers, makes calibration of these optical remote sensing devices difficult. Field tests were carried out with two nearly identical coherent CO_2-laser based DIAL systems with nearly coincident beam paths to prove data validation for rapidly fluctuating gas concentrations. A commercially available fourier transform infrared (FTIR) spectrometer, manufacturered by ETG Inc, measuring along the lidar beams was used for quantitative calibration of the systems. Statistical analysis of the time fluctuating lidar signals was used to determine the demonstrated sensitivity limits (range and minimum detectable path-integrated concentrations) for the DIAL systems.

2. THE LIDAR SYSTEMS

The differential absorption lidar techniques allows laser remote sensing systems to be designed for the remote sensing of atmospheric trace gases[1] Due to the spectral coincidence and tunability of the CO_2 laser[2] and the characteristic absorption spectrum of numerous volatile organic compounds (VOCs), chlorinated hydrocarbons, and hazardous air pollutant (HAP) molecules[3], a tunable CO_2 laser is a superior light source for infrared differential absorption lidar measurements. When the volume of space undergoing measurement is trans-illuminated with two co-linear laser beams with wavelengths λ_1 and λ_2 corresponding to different absorption cross sections $\sigma(\lambda_1)$ and $\sigma(\lambda_2)$ of the molecule of interest, and when the ratio of the intensities $I(\lambda_1)$ and $I(\lambda_2)$ of the beams that have traveled across the space of concern is measured, then according to the Lambert-Beer law, the path-integrated concentration (CL) of the contaminant for a coherent DIAL system is given by :

$$CL = \frac{1}{\sigma(\lambda_1)-\sigma(\lambda_2)} \ln\frac{I(\lambda_2)}{I(\lambda_1)}$$

The main goal of this project was to design a relatively small system with low power consumption and simple layout as well as rugged construction and reliable field operation. These goals were achieved by using an enhanced optical heterodyne detection scheme based on an autodyne arrangement that makes the sensing of extremely low level backscattered light intensities ($<10^{-18}$ W) possible. Optical heterodyne detection is based on interferometric mixing of the weak signal beam to the detected with a frequency-offset local oscillator beam on the surface of the detector. It can be shown that, in principle, ideal (quantum limited) detection can be achieved; however, it generally requires complex optoelectronic system with rigorous mechanical tolerances.

Extreme simplicity, self-alignment and the same sensitivity can be achieved when the signal beam is reinjected into the operating laser (with frequency shift), sometimes called autodyne detection. The systems used this autodyne arrangement[5]. See Figure 1. However it was observed that performance of the system was greatly influenced by the properties of the CO_2 laser sources used, as discussed in a previous paper[6]. In the LRS-3 system, a saw-tooth voltage signal drives a piezoelectric transducer (PZT) located at the end of each CO_2 laser, to physically change the cavity length of the laser. The linear modulation of the laser cavity by the PZT provides a frequency modulation (FM) of 100 kHz or greater of the output wavelength of the laser and thereby produces the frequency shift needed for heterodyne detection. The backscattered signal returns to the laser cavity with a frequency that is dependent on the time of flight to the topographic or

0-7803-3068-4/96$5.00©1996 IEEE

backscattered signals are amplified in the laser cavity and mixed with the local oscillator to produce a high frequency beat signal which is the signal of interest. In the VTB-2 system a moving target provides the frequency shift needed for heterodyne detection. The output beams are chopped with a common chopper wheel, but transmit at different time intervals. Fractions of both beams are directed by a beamsplitter through filters and onto the only detector in the system. These fractions are the local oscillator beams of the two channels. The remaining portion of the beams is transmitted through a common transmitter/receiver telescope.

This common beam path between the local oscillator signal and the returning backscatter signal maintains a self-adjusted coherent relationship between the beams. This self-adjusting relationship is important because it minimizes misalignment and vibration effects, making the system more robust. The photocurrent produced by the detector contains both low and high frequency components. The low frequency signals are at the chopping frequency, while the high frequency signals are at the heterodyne frequency. The local oscillator signals and the heterodyne signals are processed by four voltage-to-frequency converters which are in turn counted by a laptop personal computer. The extreme sensitivity of the system[5] allows for the use of low power (few Watts CW) lasers. These lasers are tuned to the absorption maximum and minimum of the molecular component to be detected. The lasers are grating tuned (line selection) and the cavity length is trimmed to give maximum output power by a piezoelectric actuator. Absorption peaks of pollutant compounds in the air are typically 0.01 - 0.05 μm wide (full width half maximum (FWHM))[3] so an appropriate laser line pair must be selected for each compound to be detected. The telescope shines the beams on remote topographic surfaces and collects the backscattered light for reinjection into the lasers. The modulated light reaches the detector, providing four electronically separable signals: the high frequency heterodyne signals S_1 and S_2, and L_1 and L_2 used for normalization. Minimum integration time is one second. The path-integrated concentration is calculated according to the following equation:

$$CL = \frac{1}{\sigma(\lambda_1)-\sigma(\lambda_2)} \ln \frac{S_2/L_2}{S_1/L_1}$$

3. Data Validation and Calibration

Propagation of the laser beams in the lidar backscatter mode is influenced by several uncontrollable[1] factors like absorption along the beam path, scattering along the beam path, nature of topographic backscatter, and fluctuation of the refractive index of the air which can influence the results of the measurements. In addition, these properties of the propagation path can vary in space and time that may cause uncontrollable variation of the measured signal.

To study the uncontrollable variations influencing long path lidar measurements two similar lidar systems were used along optical paths very close to one another (maximum distance 4 m at the source) using the same target. Lidar-target distances were about 400 m, a styrofoam target simulated the topographic backscatter. Ethanol was released by a spray compressor at a distance of about 300 m from the lidars for two minutes. A cross-wind of about 1 m/s transported the cloud across the beams between the lidars and the target. Measurement laser lines were λ_{on} = 9.6767 μm ≡ 9P34 and λ_{off} = 9.6392 μm ≡ 9P30, where the differential absorption cross section[3] is 10^3 $atm^{-1}m^{-1}$. Temporal variation of the two signals were observed while an absorbing gas was introduced into the beam paths. Figure 2 shows the path-integrated concentration as a function of time measured by LRS-3 and VTB-2, with integration times of 10 seconds. The extremely good correlation between the temporal variation of the two lidar signals show that the concentration fluctuations were real. This allows application of these types of lidar systems for the study of transport of gases in the atmosphere with high temporal resolution. It is very difficult to calibrate lidar systems with field conditions. Point measurements with sampling and further laboratory analysis are inaccurate and cumbersome. Field instruments based on gas chromatography or spectrophotometry are available for in situ measurements. However none of these measurements compares to the instantaneous response of lidar systems not to mention that it is impossible to gain information along extended paths or volumes. Optical remote sensors based on Fourier transform infrared (FTIR) spectroscopy[7] are the best alternatives that can achieve 1-200 meter range with retroreflector. However these cannot cover the full operating range of the lidars that can reach several kilometers, and require long integration and processing times. Figure 3 shows data on simultaneous measurement of C_2H_4 release with the lidar and an MDA FTIR spectrometer. The spectrometer was approximately 150 m from the retroreflector. Eight scans were averaged for each data point. Peak concentrations measured were similar, however it is apparent that the information of the temporal variation of the concentration measured by the lidar is much more detailed.

Table I presents some of the results from the field measurement program.

4. Experimental Sensitivity Analysis

Sensitivity was analyzed in terms of measurement conditions (range, reflection coefficient, integration time) and minimum detectable concentration. Sensitivity of the measurements is

(range, reflection coefficient, integration time) and minimum detectable concentration. Sensitivity of the measurements is demonstrated on the basis of a 30 minute time window of the heterodyne signal on one of the measurement channels. During this time period the output of the lidar was covered for several intervals to measure the noise level of the heterodyne signal (system noise). This test was carried out from range of 800 m using an artificial (styrofoam) backscattering target and one second integration time. $P_{het}/N \approx 50$ was measured. This allows evaluation of the limits over which the system can operate. Namely, the range is limited directly by the signal/system noise ratio. The advantage of the heterodyne detection is that the heterodyne signal is proportional to the square root of the received light intensity, therefore the external parameters only modestly influence the performance of the system. For example, using topographic backscattering one can assume for the backscattering coefficient of typical topographic targets $\rho_{topographic} \geq 0.04\rho_{styrofoam}$, i.e .$(P_{het}/N) \geq 10$ for range of 800 m with one second integration time.

5. CONCLUSIONS

It was shown by field experiments that coherent infrared differential absorption lidars can be used as remote sensors for broad range of atmospheric gases. Due to their fast response they are ideal to detect rapid changes over large ranges. Measurement parameters can be optimized for various gases and measurement conditions to achieve maximum performance.

REFERENCES

(1) Measures, R.M.,1984, Laser Remote Sensing (New York: Wiley)

(2) Witteman, W.J., 1987, The CO_2 Laser (Berling: Springer)

(3) Hanst, P.L. and Hanst, S.T., 1990, Gas Analysis Manual for Analytical Chemists (Anaheim: Infrared Analysis, Inc.)

(4) Smith, F.G. (ed) 1993, Atmospheric Propagation of Radiation, The Infrared and Electro-Optical Systems Handbook (Bellingham).

(5) Richter, P., 1991, Proceedings of the Second International Symposium on Field Screening Methods for Hazardous Wastes and Toxic Chemicals, Las Vegas, P. 167.

(6) Richter, P., Péczel, I., and Böröcz, SZ. Journ. Mod. Opt. 41, 2079 (1994)

(7) MDA FTIR Remote Sensor, Environmental Technologies Group 4708 S. Old Peachtree Rd. Norcross Ga. 30071

Gas	$\Delta\sigma$ (10^{-4} ppm^{-1}m^{-1})	λ_1/λ_2	VTB-2 ppm.m	LRS-3
Ethanol	460	9P16/10R18	532	780
Methanol	1860	9P34/9P30	144	104
Ethylene	1890	9P16/10R18	89	70
TCE	1440	10P20/9R24	147	178
SF_6	52200	10P20/9R24	3.5	1

Table 1. Results from Field Measurement Test

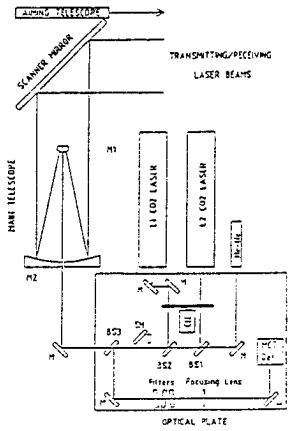


Figure 1. Coherent DIAL System Layout

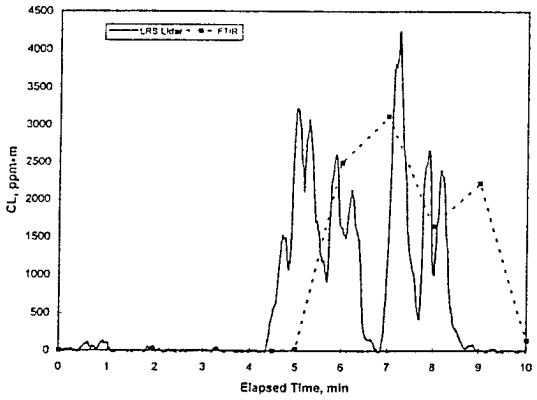


Figure 2. Comparison of Temporal Variation in CL of Ethanol as measured by LRS-3 and VTB-2 Lidars

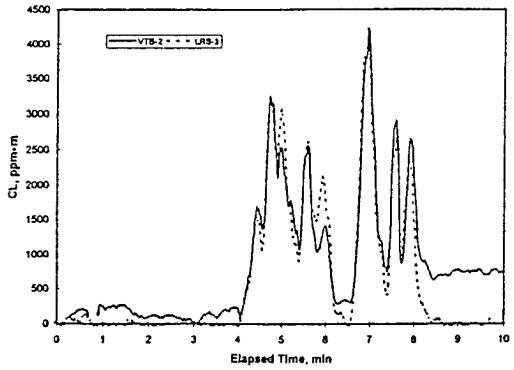


Figure 3. Comparison of CL VS time for Lidar and FTIR

Task-Specific Segmentation of Remote Sensing Images

Jianhua Xuan and Tülay Adalı

Department of Computer Science and Electrical Engineering,
University of Maryland Baltimore County, Baltimore, MD 21228
Phone: (410) 455-3500, Fax: (410) 455-1048, E-mail: {xuanj,adali}@engr.umbc.edu

ABSTRACT

In this paper, we present a task-specific segmentation method that incorporates semantic knowledge into data-driven segmentation process through different region merge scores. Starting from a simple region growing algorithm which results in over-segmented regions, we apply region merging method designed specifically for each task such as road extraction or vegetation area identification. Further, edge information is integrated to verify and correct region boundaries. The experimental results show that this method can reliably extract areas of interest such as roads and vegetation areas in Landsat images.

I. INTRODUCTION

Automatic segmentation of aerial photographs is a key step in remote sensing image interpretation. Many methods have been developed for segmenting remotely sensed imagery, which fall into two categories of segmentation techniques: bottom-up approach and top-down approach. The bottom-up approach segments an image into homogeneous regions without any *a priori* knowledge about the image content, while the top-down approach employs available semantic knowledge in the segmentation process. A combination of top-down and bottom-up strategies is an often-used segmentation approach that yields far better results than those of using either method alone. However, such a combination approach can exhibit some problems, e.g., existence of a loose relationship between the data-driven segmentation and knowledge rules, and lack of spatial guidance rules. Reference [1] proposes a knowledge-based segmentation scheme where classification is achieved in a category-oriented fashion achieving good segmentation at the cost of increased complexity.

In this paper, to overcome the problems mentioned above, we propose a task-specific segmentation method which incorporates the knowledge into data-driven segmentation process through different region merge-scores. The region growing algorithm performs an initial segmentation on edge-preserving smoothed Landsat images, which usually produces a large amount of small regions. A region merging algorithm is needed to resolve those over-segmented regions. A task-specific region merging algorithm is designed and performed to incorporate various kinds of the domain knowledge. After identifying that the basic task in Landsat image segmentation is to segment roads, rivers, vegetation/non-vegetation areas, etc., we can apply this domain knowledge to design a specific merge-score for each particular task. For example, roads are spectrally bright objects in Landsat images and they are well-connected, and this knowledge is used to define a merge-score for those bright regions in terms of gray-level similarity, size, and connectivity. Vegetation areas correspond to dark regions and their texture property implies that they have large variances. Thus we can define a merge-score for dark regions in terms of gray-level similarity, variance similarity, and the size constraint and connectivity. Similarly, we can apply the available knowledge on rivers and non-vegetation areas to define suitable merge-scores, respectively. Furthermore, the edge information can be integrated with the region information, which yields reliable and meaningful segmentation results as demonstrated in [7].

The remainder of the paper is organized as follows: In section II, we present the proposed task-specific segmentation technique and define suitable merge-scores for different tasks such as segmentation of roads and vegetation areas. Section III gives experimental results for Landsat images. Section IV concludes with suggestions for future research.

II. TASK-SPECIFIC SEGMENTATION METHOD

A block diagram for the task-specific segmentation method is shown in Fig. 1. The segmentation scheme consists of three main components: preprocessing, task-specific region merging, and integrating edge information, which are described as follows:

Preprocessing: Edge detection is achieved by using Canny's edge detector since it provides good detection,

0-7803-3068-4/96$5.00©1996 IEEE

good localization and a single edge response [2]. These characteristics are of particular importance for combination of region and edge information in the subsequent boundary elimination and contour modification stages. An adaptive smoothing filter developed by Chen and Medioni [3] is used to remove noises while all the edges can be well preserved. Then, the region growing algorithm performs an initial segmentation on edge-preserving smoothed images. The choice of a conservative threshold guarantees that erroneous merging does not take place. However, one drawback is that a large amount of small regions are produced, which can be resolved by a region merging algorithm which is described next.

Task-specific region merging: The region merging algorithm we have employed has been successfully applied to the segmentation of images of natural scenes [4], hand-wrist radiography [5], and magnetic resonance brain images [7]. A merge-score usually combines scores based on certain region features: grey-level similarity, region size and region connectivity, etc. All the scores can be mathematically formulated. For instance, the similarity score between regions a and b can be defined as:

$$S_{sim}(a,b) = \frac{|\mu_a - \mu_b|}{\max(1.0, \sigma_a + \sigma_b)}, \quad (1)$$

where μ is the mean gray level and σ is the standard deviation. The connectivity measure between regions a and b is defined as:

$$S_{conn} = \begin{cases} c(a,b) & \text{if } 0.5 \le c(a,b) \le 2.0 \\ 0.5 & \text{if } c(a,b) < 0.5 \\ 2.0 & \text{otherwise} \end{cases}, \quad (2)$$

where $c(a,b) = \min(l(a), l(b))/(4*l_s(a,b))$ with $l_s(a,b)$ the length, in pixels, of the shared boundary between regions a and b, and $l(x)$ the circumference of region x. Now we can define some task-specific merging scores as follows:

Region merging for roads: Roads are commonly occurring objects in Landsat images. Observing that roads are spectrally bright objects and well-connected, we can construct a merging score for roads in terms of gray-level similarity and connectivity measure as follows:

$$S_{road}(a,b) = S_{sim} \times (S_{conn}(a,b)/2.0)^2. \quad (3)$$

where the connectivity measure is especially emphasized to capture the characteristic of roads being strongly connected, i.e., connected regions with similar high gray-level are encouraged to be merged.

Region merging for vegetation areas: Vegetation areas usually correspond to dark regions and exhibit large variances in Landsat images. Therefore, we first extract dark areas as candidates for vegetation areas. Then we can define a merge score for vegetation areas in terms of variance similarity and connectivity measure. The variance similarity score between regions a and b is simply defined as:

$$S_{var}(a,b) = |\sigma_a - \sigma_b|. \quad (4)$$

The merge score for vegetation areas is defined as:

$$S_{veg}(a,b) = \sqrt{S_{var}(a,b)} \times S_{conn}(a,b). \quad (5)$$

Integrating edge information: The edge information can be integrated to verify and, where necessary, to correct region boundaries, which yields more reliable and meaningful segmentation results as demonstrated in [6] [7]. In particular, we use edge information to serve two purposes: 1) eliminating false boundaries and 2) modifying the contours. For the implementation details, see [7].

III. EXPERIMENTAL RESULTS

We apply the segmentation method described in the previous section to Lansat images. Sample set of results are shown in figures 2 and 3. In Fig. 2, the original image and the contours of region growing are shown to illustrate the complexity of Landsat images and over-segmented results obtained from region growing. Fig. 3 illustrates the initial road contours and the contours after region merging. As we can see, the connectivity score for roads dominates the road merging score, which results in a fairly good segmentation of the roads. Fig. 3 also shows the results for segmenting vegetation areas. At each stage, since there are some parameters that need to be specified, we have developed an interface for interactive manipulation of segmentation results and study of the sensitivity of these parameters. Notice that the task-specific knowledge can be used to design the merging scores such as similarity scores and connectivity measures in many ways, this approach provides us a general framework for incorporating the domain knowledge.

IV. CONCLUSION

The task-specific segmentation method has been applied to Landsat images. The experimental results show that this method can be successful in segmenting complicated Landsat images. For future work, a complete segmentation system may consist of two parts: 1) the proposed task-specific segmentation method and 2) a knowledge based segmentation technique as in [1], to further exploit the knowledge on various tasks.

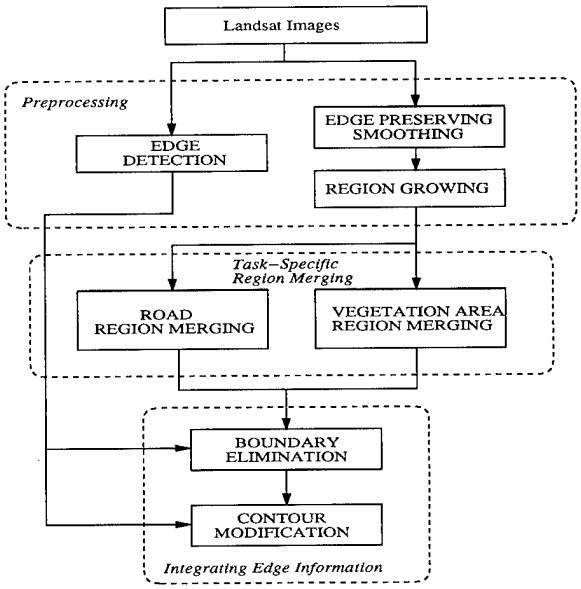


Figure 1: Block diagram of the task-specific segmentation system

V. REFERENCES

[1] J. Ton, J. Sticklen, and A. K. Jain, "Knowledge-based segmentation of Landsat images", *IEEE Trans. Geosci. Rem. Sens.*, Vol. 29, No. 2, pp. 222-231, Mar. 1991.

[2] J. Canny, "Computational approach to edge detection," *IEEE Trans. Pattern Anal. Machine Intell.*, Vol. 8, No. 6, pp. 679-698, Nov. 1986.

[3] J. S. Chen and G. Medioni, "Adaptive smoothing: principles and applications," *Advances in Image Analysis*, (Y. Mahdavieh and R. C. Gonzalez (ed.)), SPIE Optical Engineering Press, 1992.

[4] J. Beveridge, J. Grifith, R. Kohler, A. Hanson and E. Riseman, "Segmentation of images using localized histograms and region merging," *Int. Comput. Vision*, Vol. 2, pp. 311-347, 1989.

[5] G. Manos, A. Y. Cairns, I. W. Ricketts and D. Sinclair, "Automatic segmentation of hand-wrist radiographs," *Image and Vision Computing*, Vol. 11, No. 2, pp. 100-111, Mar. 1993

[6] T. Pavlidis and Y. Liow, "Integrating region growing and edge detection," *IEEE Trans. Pattern Anal. Machine Intell.*, Vol. 12, No. 3, pp. 225-233, Mar. 1990.

[7] J. Xuan, T. Adalı, and Y. Wang, "Segmentation of magnetic resonance brain image: integrating region growing and edge detection", *Proc. IEEE Intl. Conf. on Image Processing*, Vol. III, pp. 544-547, Washington, D.C., Oct. 23-26, 1995.

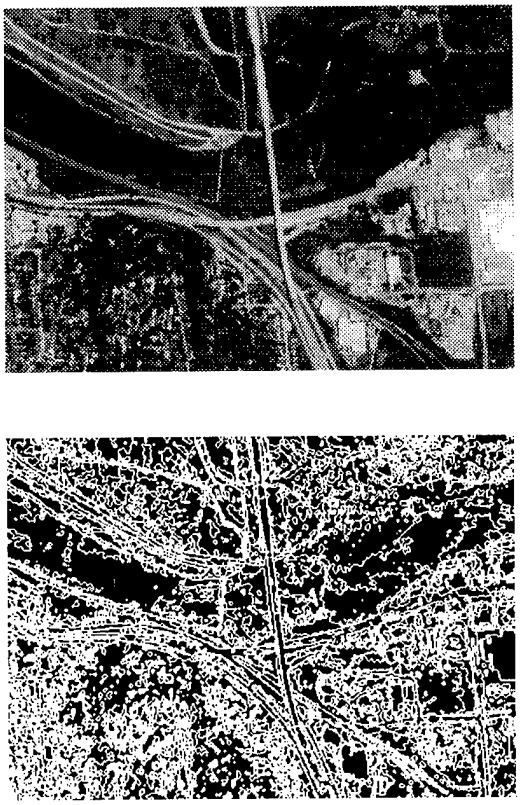


Figure 2: Landsat images: (top) original image, (bottom) region growing.

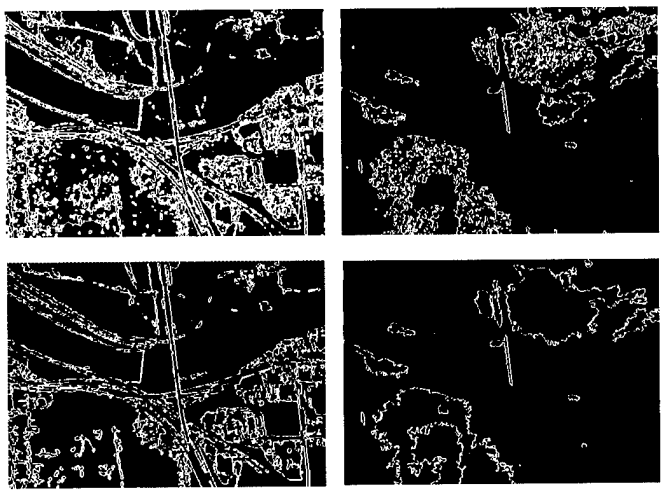


Figure 3: Roads and Vegetation Areas: (top left) initial roads, (bottom left) road region merging, (top right) initial vegetation areas, (bottom right) vegetation area region merging.

Hybrid Image Segmentation for Earth Remote Sensing Data Analysis

James C. Tilton
Information Sciences and Technology Branch
NASA Goddard Space Flight Center
Mail Code 935
Greenbelt, MD 20771, USA
Tel: (301) 286-9510
FAX: (301) 286-1776
E-Mail: tilton@chrpisis.gsfc.nasa.gov

Abstract -- Image segmentation is a partitioning of an image into constituent parts using image attributes such as pixel intensity, spectral values, and/or textural properties. Image segmentation produces an image representation in terms of edges and regions of various shapes and interrelationships. It is a key step in several approaches to image compression and image analysis.

We have devised a hybrid image segmentation approach that combines region growing and boundary detection. The core of this image segmentation approach is an iterative parallel region growing algorithm that we developed over the past several years [1,2,3]. The question of where to stop the region growing process is solved by not allowing the region growing process to grow regions past boundaries defined by a boundary detection algorithm. We have found an edge detector based on an optimal difference recursive filter [4,5] to be most suitable for this boundary detection. This edge detector provides highly localized edge boundaries and is relatively insensitive to noise. It also provides a convenient threshold parameter through which an application appropriate edge density can be selected.

INTRODUCTION

Image segmentation is a partitioning of an image into constituent parts using image attributes such as pixel intensity, spectral values, and/or textural properties. Image segmentation produces an image representation in terms of edges and regions of various shapes and interrelationships. It is a key step in several approaches to image compression and image analysis.

Most image segmentation approaches can be placed in one of three categories:

i. characteristic feature thresholding or clustering,
ii. boundary detection, and
iii. region growing.

Characteristic feature thresholding or clustering is often ineffective because it does not exploit spatial information. Boundary detection does exploit spatial information through examining local edges found throughout the image. For simple noise-free images, detection of edges results in straightforward boundary delineation. However, edge detection on noisy, complex images often produces missing edges and extra edges which cause the detected boundaries to not necessarily form a set of closed connected curves that surround connected regions. Region growing exploits spatial information and guarantees the formation of closed connected regions, but it is often unclear at what point to stop the region growing process.

We have devised a hybrid image segmentation approach that combines region growing and boundary detection. The core of this image segmentation approach is an iterative parallel region growing algorithm that we developed over the past several years [1,2,3]. The question of where to stop the region growing process is solved by not allowing the region growing process to grow regions past boundaries defined by a boundary detection algorithm. We have found an edge detector based on an optimal difference recursive filter [4,5] to be most suitable for this boundary detection. This edge detector provides highly localized edge boundaries and is relatively insensitive to noise. It also provides a convenient threshold parameter through which an application appropriate edge density can be selected.

OPTIMAL DIFFERENCE RECURSIVE FILTER FOR EDGE DETECTION

The Khoros software system [6] contains a wide range of image processing tools, including several edge detection algorithms. The Khoros edge detection algorithm that we have found to be most useful with remotely sensed imagery data is the "optimal difference recursive filter for edge detection," which is the "vdrf" routine under Khoros V2.0.2.

This edge detection algorithm was first described by Shen and Castan in [4]. A more detailed description in [5]. In these papers, Shen and Castan note that since the differential operators most commonly for edge detection are very sensitive to the noise present in most natural images, a preprocessing such as smoothing is usually required to reduce the noise. However, the most common approaches employed for image smoothing have the undesirable side effect of reducing the accuracy to which the edge detector can localize the detected edges. Through an analysis of the "traditional" mono-step edge model, Shen and Castan conclude that an optimal low-pass filter for smoothing images prior to edge detection is a symmetric exponential filter of infinite size (ISEF, Infinite Symmetric Exponential Filter). They show that this filter has a better signal to noise ratio and a better precision of localization than Gaussian-based filters. In [5], Shen and Castan propose a multiedge model, and show that the ISEF is also optimal in this case.

A symmetric exponential filter can be written as:

$$f(x) = a*b^{|x|} \qquad (1)$$

where, for the discrete case, $b = (1-a)/(1+a)$ and $0<a<1$ (implying $0<b<1$).

The Khoros "vdrf" routine has several parameters. Parameters a_1 and a_2 are parameters for the exponential filter parameters for the difference recursive implementation of the

0-7803-3068-4/96$5.00©1996 IEEE

ISEF for the first and second pass of the filter. A second pass is required in the recursive implementation for use in the calculation of the first and second derivative of the smoothed image required for the edge detection step. In (1), $a=a_{\#}/2$, where #=(1,2).

After the ISEF is performed, an adaptive gradient is calculated at the zero crossings of the 2nd derivative of the ISEF smoothed image, and the edges are detected through thresholding [5]. Here a segment is output as a valid edge segment if the gradient threshold value along its length is above a low threshold, t_1, for its entire length, and if the value is above a high threshold, t_2, for at least part of its length. The segment must also have at least a minimum number, l, of pixels in it. These parameters, t_1, t_2, and l - along with the parameter w (the window size for calculating the adaptive gradient) - are additional parameters for the Khoros "vdrf" routine.

ITERATIVE PARALLEL REGION GROWING

Over the past several years we have investigated a powerful image segmentation approach we call Iterative Parallel Region Growing (IPRG) [1,2]. The basic outline of IPRG has changed very little from our earliest work [3]:

i. Initialize the segmentation process.
ii. Calculate a (dis)similarity criterion between each pair of spatially adjacent regions.
iii. Merge pairs of regions that meet the merge constraints.
iv. Check for convergence. If converged, stop. Otherwise return to step ii.

However, in order to bring in information from an additional source such as edge detection, we have (optionally) changed details mainly in the initialization and convergence steps, with some minor changes in merge constraints. We will note these changes as we discuss the key elements of the IPRG algorithm in turn below: the initialization process, the (dis)similarity criterion, the merge constraints, and convergence criterion.

Initialization

Until recently, the segmentation process was initialized by simply labeling each pixel as a separate region, and then merging all spatially adjacent pixels with identical feature values. Our current hybrid version of IPRG has options to initialize the segmentation process in two additional ways.

IPRG can be initialized by simply providing a region label map. This region label map could be obtained by any means, but it makes most sense to create it through a high quality clustering algorithm that allows thresholding out (non-classification) of pixels that are not near the center of the clusters. In our future work, we plan to experimented with using such a clustering algorithms.

The hybrid IPRG can also be initialized from an input edge map. In this case a "distance from edge map" (*dem*) is generated by initializing *dem* to one for each pixel on an edge and zero otherwise. *dem* is then iteratively grown out from each edge pixel as follows: If a pixel with *dem*=0 has a neighbor with *dem*=*i*, set *dem*=*i*+1 for that pixel. This continues iteratively until *i* reaches a preset maximum value (*idem*). Then set *dem*=*idem* for all pixels with *dem*=0. Finally, the initial segmentation is set by performing connected component labeling on all pixels with *dem*=*idem*.

Similarity Criterion

In general, the best similarity criterion depends on the application the resulting segmentations will be used for, and on the characteristics of the image data. Nevertheless, we have developed and studied a few general purpose similarity criterion for use with the IPRG algorithm, including criterion based on minimizing mean-square error and minimizing change in image entropy [7]. (These are actually *dis*similarity criteria rather than similarity criteria because their values decrease with increasing similarity.)

In the past couple years we have implemented two additional dissimilarity criteria. One is a Normalized Vector Distance (NVD) from Baraldi and Parmiggiani [8]. They define the factors σ_1 and σ_2 based on the match, respectively, between the modulus and the angle of the feature vectors being compared. These factors are constructed such that $\sigma_1 = 1$ and $\sigma_2 = 1$ signify vector equivalence, and σ_1 and σ_2 both range from 0 to 1. σ is defined as the product of σ_1 and σ_2. Finally, NVD is defined as $1-\sigma$.

The second new dissimilarity criteria is a Euclidean spectral distance from Schoenmakers [9]. For two regions i and j, characterized by the vectors $X_i = (x_{1i}, x_{2i}, \ldots, x_{ci})^T$ and $X_j = (x_{1j}, x_{2j}, \ldots, x_{cj})^T$, this criteria is defined as:

$$EUC_{ij} = [(x_{1i}-x_{1j})^2+\ldots+(x_{1i}-m_{cj})^2]^{-1/2}$$

where c is the number of spectral channels.

Both Baraldi and Parmiggiani and Schoenmakers note that their dissimilarity criterion are not influenced by the size of the regions being compared. In contrast, the mean-square error and entropy based criterion explicitly contain the number of pixels in each region in their formulation. This results in a bias against small regions for both of these criterion.

Merge Constraints

At each iteration, the IPRG algorithm selects a set of region pairs to be merged. In doing this, the image is first divided into a set of subimages. The size of these subimages depend on the "constraint level" employed (see below). The most similar pair of spatially adjacent regions is noted within each subimage (ties are broken arbitrarily), and is selected for merging at that iteration. After each iteration, the set of subimages is redefined appropriately.

A subimage with respect to a particular region is defined recursively as follows: A level 0 subimage for any region is the empty set. A level 1 subimage, with respect to a region, is the region itself. A level 2 subimage, with respect to a region, is the level 1 subimage, with respect to that region, plus all regions that are spatially adjacent to the level 1 subimage. Finally, a level n subimage, with respect to a region, is the level $n-1$ subimage, with respect to that region, plus all regions that are spatially adjacent to the $(n-1)^{st}$ level subimage.

For merge constraint level n, merges are limited to be the best merges within the union of the level n subimages with respect to each of the potentially merging region pairs. Constraint level $n-0.5$ signifies merges are constrained to be the best merge within the level n subimage with respect to

only one of the potentially merging region pairs. For a merge constraint level of 1.0 or higher, the subimages overlap each other.

Employing merge constraint level 0.5 is equivalent to performing the best merge for each region, without regard to what the best merge is for any neighboring region. This generally gives poor results. The merge constraint level 1.0 is equivalent to performing the pairwise mutually best merges for all pairs of spatially adjacent regions (with ties broken arbitrarily). This generally sufficient to give good results. The higher the merge control level, however, the closer this scheme comes to matching the scheme of one best merge per iteration over the whole image.

Convergence Criterion

In the hybrid version of IPRG, an edge map from a previously run edge detection as the convergence criterion for the region growing process. At each iteration of the region growing process, the result is checked against the edge map. If any edge pixel comes to be more than a preset maximum distance, *maxdem*, from a region boundary, the merge causing this effect is suppressed. If this is the first time this edge pixel triggered this merge suppression, the pixels up to a certain distance, *spltdem*, are also reinitialized to one pixel per region. This region splitting is only performed the first time an edge pixel triggers a merge suppression. Finally, when the cumulative merge suppressions throughout the image make it such that no more merges can occur, convergence is achieved.

TEST RESULTS

Due to space constraints, we'll just give here a synopsis of the parameter settings and method of combination of the edge maps and region growing process that appears to give the best results. The full presentation (complete with pictures of edge maps and segmentation label maps, along with the original data) will have to wait for the oral presentation.

The recommended value for both a_1 and a_2 is 0.3. While, we have found that this value does a good job for Landsat TM data, setting a_1 to 0.1 and leaving a_2 at 0.3 seems to do a better job of extracting edge detail. Generally higher values of these parameters (especially a_1) tend to wash out edge detail, while lower value of a_1 (but not a_2 lower than 0.3) tends to extract more edge detail. Noisier data than Landsat TM data would require higher settings for these parameters.

A window size, w, of 5 seems to perform best. A size of 3 gives spurious results, and a size of 5 seems to do better than 7 in extracting appropriate edge detail. Again, a higher setting may work better for noisier data.

Shen and Castan recommend values of 12 for t_1 and 15 for t_2. We found that a lower value for t_1 (=6) brought out more edge detail in Landsat TM data. The recommended value would be more appropriate for noisier data, as the additional detail would probably be due to noise in that case.

Again, due to the relatively noise-free condition of the Landsat TM data we tested on, we found a smaller value for l (minimum number of pixels in a segment) than recommended by Shen and Castan was more satisfactory. We found that, for Landsat TM data, a value of 5 worked better than the recommended value of 10.

Since the initial iterations go so fast in our massively parallel implementation of IPRG, we find it unnecessary to initialize IPRG with the edge detection results. However, convergence based on the edge detection results does give excellent results.

We did find, however, that since the edge detection results are so detailed (with overlapping edges at some locations), it is best to run IPRG in two stages. In the first stage, we mask out the data where the edges are very dense (where an edge pixel is surrounded by 5 other edge pixels) and run IPRG to convergence based on the edge map with *maxdem*=1 and *spltdem*=1. In the second stage we turn off the mask and continue IPRG with the addition of a global threshold on the dissimilarity criterion. A value of 1.0e-03 seems to perform well for the average mean squared error criterion on the Landsat TM data. We also used merge constraint level 1.0 in our tests.

In the oral presentation, we will also present results from AVHRR and GOES data.

ACKNOWLEDGMENTS

This research effort is supported by RTOP funding from the Office of Mission to Planet Earth, NASA Headquarters, Washington, DC.

REFERENCES

[1] J. C. Tilton, "Image segmentation by iterative parallel region growing with applications to data compression and image analysis," Proceedings of the Second Symposium on the Frontiers of Massively Parallel Computation, Fairfax, VA, pp. 357-360, 1988.

[2] J. C. Tilton, "Image segmentation by iterative parallel region growing and splitting," Proc. of the 1989 International Geoscience and Remote Sensing Symposium, Vancouver, BC, Canada, pp. 2420-2423, 1989.

[3] J. C. Tilton and S. C. Cox, "Segmentation of remotely sensed data using parallel region growing," Digest of the 1983 International Geoscience and Remote Sensing Symposium, San Francisco, CA, pp. 9.1-9.6, 1983.

[4] J. Shen and S. Castan, "An optimal linear operator for edge detection," Proceedings of CVPR '86, Miami Beach, FL, pp. 109-114, 1986.

[5] J. Shen and S. Castan, "An optimal linear operator for step edge detection," Graphical Models and Image Processing, Vol. 54, No. 2, pp. 112-133, 1992.

[6] K. Konstantinides and J. R. Rasure, "The Khoros software development environment for image and signal processing," IEEE Trans. on Image Processing, Vol. 3, No. 3, pp. 243-252, 1994.

[7] J. C. Tilton, "Experiences using TAE-Plus command language for am image segmentation program interface," Proceedings of the TAE Ninth Users' Conference, New Carrollton, MD, pp. 297-312, 1991.

[8] A. Baraldi and F. Parmiggiani, "A neural network for unsupervised categorization of multivalued input patterns: an application to satellite image clustering," IEEE Transactions on Geoscience and Remote Sensing, vol. 33, no. 2, pp. 305-316, 1995.

[9] R. P. H. M. Schoenmakers, Integrated Methodology for Segmentation of Large Optical Satellite Images in Land Applications of Remote Sensing, Agriculture series, Catalogue number: CL-NA-16292-EN-C, Luxembourg: Office for Official Publications of the European Communities, 1995.

UNSUPERVISED STATISTICAL SEGMENTATION OF MULTISPECTRAL SAR IMAGES USING GENERALIZED MIXTURE ESTIMATION

Abdelwaheb Marzouki * Yves Delignon * Wojciech Pieczynski **

*Département Electronique, École Nouvelle d'Ingénieurs en Communication,
Rue Guglielmo Marconi, 59650 Villeneuve d'Ascq, France
**Département Signal et Image, Institut National des Télécommunications,
9, rue Charles Fourier, 91011 Evry Cédex, France
phone 33 1 60 76 44 25, fax 33 1 60 76 44 33, E-mail Wojciech.Pieczynski@int-evry.fr

Abstract
This work deals with the estimation of generalized mixtures with applications to unsupervised statistical multisensor image segmentation. A mixture is said to be "generalized" when the exact nature of the noise components is not known; one assumes, however, that each belongs to a finite known set of families of distributions. We propose some methods of estimation of such mixtures based on Expectation-Maximization (EM), and Iterative Conditional Estimation (ICE, [6]) algorithms. The set of families of distributions is assumed to lie in Pearson's system.

1. INTRODUCTION

It is well established that statistical methods of segmentation can show exceptional efficiency. One can distinguish global methods, which use Markovian models [1], [3], [4], [6], and local ones [5], [8]. When unsupervised segmentation is concerned, one has to estimate the required model parameters in a previous step. The corresponding statistical problem is that of mixture estimation, and techniques like EM or SEM [5] can generally be used. In "classical" mixtures the nature of the noise distributions is known: for instance, they are all Gaussian, or Gamma, or Beta, etc. In real situations it can happen that this nature differs with the class. Furthermore, in the multisensor case, it can differ with the sensor for a given class. Moreover, for a given class and a given sensor this nature can vary in time. Thus it would be very useful to be able to automatically find the right nature of the distribution for each class and each sensor. Pioneer results of such works are presented in [7].

Our work addresses the problem of a generalized multispectral mixture estimation with application to unsupervised segmentation of SAR images. A mixture is said to be "generalized" when the exact nature of the noise components is not known; we assume, however, that each belongs to a finite known set of families of distributions. For instance, in the case of three classes and two sensors, if each component can be exponential or Gaussian, there are thirty-six possibilities of "classical" mixture. Thus the observed process is a distribution mixture and the problem of estimating such a "generalized" mixture contains a supplementary difficulty: one has to label, for each class and each sensor, the exact nature of the corresponding distribution.

When considering both global and local methods, classical mixture estimation algorithms such as EM, ICE, and SEM, can be adapted to such situations. Among different possibilities, we describe one of the generalized mixture estimation methods, valid in the context of Hidden Multisensor Markov Fields, using the Pearson system and ICE.

Different algorithms are then applied to the problem of unsupervised Bayesian multispectral SAR image segmentation. We propose an adaptive version of SEM in the case of "blind", i.e., "pixel by pixel", segmentation and compare its efficiency to the global ICE based method.

2. PEARSON'S SYSTEM

In this section we specify the set of families $\Phi = \{F_1, \ldots, F_8\}$ we will use in the unsupervised radar image segmentation. Our description of Pearson's system is brief as further details can be found in [2].

A probability density function f on R belongs to Pearson's system if it satisfies :

$$\frac{1}{f(y)}\frac{df(y)}{dy} = -\frac{y+a}{c_0 + c_1 y + c_2 y^2} \qquad (1)$$

The variation of the parameters a, c_0, c_1, c_2 provides distributions of different shape and, for each shape, defines the parameters fixing a given distribution. Let Y be a real random variable whose distribution belongs to Pearson's system. For $q = 1,2,3,4$ let us consider the moments of Y defined by :

$$\mu_1 = E[Y] \qquad \mu_q = E[(Y - E(Y))^q] \quad \text{for } q \geq 2 \qquad (2)$$

0-7803-3068-4/96$5.00©1996 IEEE

and two parameters γ_1, γ_2 defined by :

$$\gamma_1 = \frac{(\mu_3)^2}{(\mu_2)^3} \qquad \gamma_2 = \frac{\mu_4}{(\mu_2)^2} \tag{3}$$

$\sqrt{\gamma_1}$ is called "skewness" and γ_2 "kurtosis".

On the one hand, the coefficients a, c_0, c_1, c_2 are then linked with $\mu_1, \mu_2, \gamma_1, \gamma_2$ by the following formula :

$$a = \frac{(\gamma_1 - \gamma_2 + 1)\mu_1 + (\gamma_2 + 3)\sqrt{\gamma_1 \mu_2}}{10\gamma_2 - 12\gamma_1 - 18}$$

$$c_0 = \frac{\mu_2(4\gamma_2 - 3\gamma_1)}{10\gamma_2 - 12\gamma_1 - 18} \quad c_1 = \frac{\sqrt{\gamma_1 \mu_2}(\gamma_2 + 3)}{10\gamma_2 - 12\gamma_1 - 18} \tag{4}$$

$$c_2 = \frac{(2\gamma_2 - 3\gamma_1 - 6)}{10\gamma_2 - 12\gamma_1 - 18}$$

On the other hand, putting

$$\lambda = \frac{\gamma_1(\gamma_2 + 3)^2}{4(4\gamma_2 - 3\gamma_1)(2\gamma_2 - 3\gamma_1 - 6)} \tag{5}$$

the eight families of the set $\Phi = \{F_1, \ldots, F_8\}$ are defined by :

$$\begin{aligned}
&[P_Y \in F_1] \Leftrightarrow [\lambda < 0] \quad [P_Y \in F_2] \Leftrightarrow [\gamma_1 = 0 \, and \, \gamma_2 < 3] \\
&[P_Y \in F_3] \Leftrightarrow [2\gamma_2 - 3\gamma_1 - 6 = 0] \\
&[P_Y \in F_4] \Leftrightarrow [0 < \lambda < 1] \quad [P_Y \in F_5] \Leftrightarrow [\lambda = 1] \\
&[P_Y \in F_6] \Leftrightarrow [\lambda > 1] \\
&[P_Y \in F_7] \Leftrightarrow [\gamma_1 = 0 \, and \, \gamma_2 > 3] \\
&[P_Y \in F_8] \Leftrightarrow [\gamma_1 = 0 \, and \, \gamma_2 = 3]
\end{aligned} \tag{6}$$

The exact form of different densities can be seen in [2]. In particular we have, F_1: beta distributions of the first kind; F_3: gamma distributions; F_5: Inverse gamma distributions; F_6 : beta distributions of the second kind; and F_8 : Gaussian distributions.

Note that the moments $\mu_1, \ldots, \mu_4$ can be easily estimated by empirical moments, from which we deduce the estimated values of γ_1, γ_2 by (3) and, finally, we estimate the family using (6).

3. GENERALIZED ICE

Let us briefly describe how generalized ICE runs in the context of Multisensor Hidden Markov Fields. For a set of pixels S, we consider two sets of random variables $X = (X_s)_{s \in S}$, $Y = (Y_s)_{s \in S}$ called "random fields". Each X_s takes its values in a finite set of classes $\Omega = \{\omega_1, \ldots, \omega_m\}$ and each Y_s takes its values in R^m. The field X is Markovian and we will denote by α all parameters defining its distribution P_X. The random variables $(Y_s)_{s \in S}$ will be assumed independent conditionally to X, and furthermore, the distribution of each Y_s conditional to X will be assumed equal to its distribution conditional on X_s. Under these hypotheses all distributions of Y conditional to X are defined by the k distributions of Y_s conditional to $X_s = \omega_1, \ldots, \omega_k$ respectively, whose densities will be denoted by $f_1, \ldots, f_k$. The sensors will be assumed independent, which implies

$$f_i(y_s) = f_i(y_s^1, \ldots, y_s^m) = f_{i1}(y_s^1) \times \ldots \times f_{im}(y_s^m) \tag{7}$$

Note that realizations of X according to its posterior distribution are possible (Gibbs sampler).

Thus each f_{ij} lies in one of the eight families of Pearson's system and the problem is to find each of them. We assume that we dispose of an estimator $\hat{\alpha} = \hat{\alpha}(X)$ of the parameters α.

The ICE-PEAR is an iterative procedure which runs as follows:

(i) Initialize the procedure in some way. For instance, take all f_{ij} Gaussian with parameters estimated by some classical algorithm.

(ii) Calculate $(\alpha^{q+1}, f_{ij}^{q+1})$ from $Y = y$ and (α^q, f_{ij}^q) in the following way:

(a) Simulate x^q, a realization of X according to its α^q and $f_1^q, \ldots, f_k^q$ based distribution conditional to $Y = y$.

(b) Calculate $\alpha^{q+1} = \hat{\alpha}(x^q)$.

(c) For $i = 1, \ldots, k$, consider $S_i = \{s \in S \,/\, x_s^q = \omega_i\}$. For each sensor j calculate the four first moments from $y_i^j = (y_s^j)_{s \in S_i}$ and decide, using (3), (5), and (6), in which family among $F_1, \ldots, F_8$ the distribution f_{ij} lies. Use (4) in order to calculate the parameters.

(d) Consider the densities f_{ij} found in (c) as (f_{ij}^{q+1})

It is possible to propose an analogous "blind", i.e. "pixel by pixel" SEM based algorithm and its adaptive version, in which priors depend on pixels [7].

4. EXPERIMENTS

4.1 Synthetic image

Let us consider a synthetic image "Ring" below and its noisy versions in three sensors. ICE-PEAR is the result of the Maximum Posterior Mode (MPM [4]) segmentation based on ICE-PEAR estimates and Adaptive Generalized SEM designates the result of the classical local Bayesian segmentation based on estimates with Adaptive Generalized SEM .

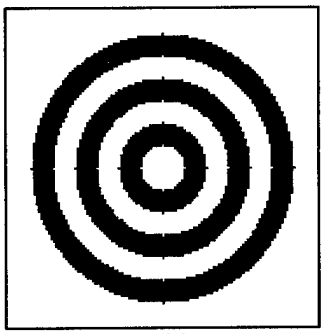
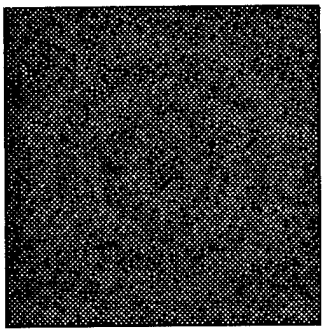
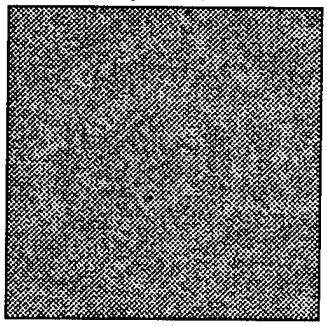


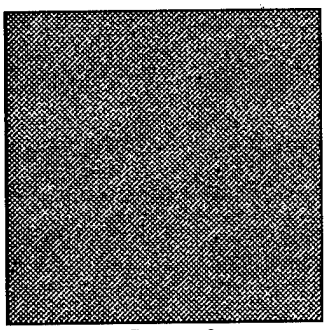
Image Ring



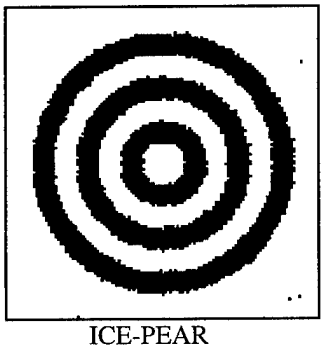
Sensor 1



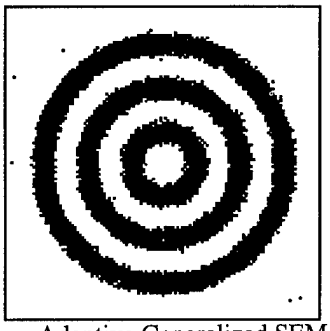
Sensor 2



Sensor 3

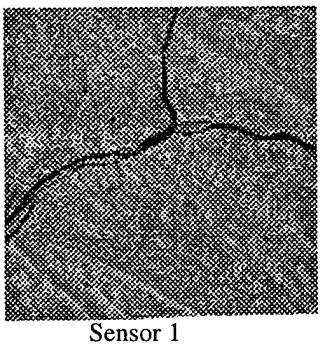


ICE-PEAR

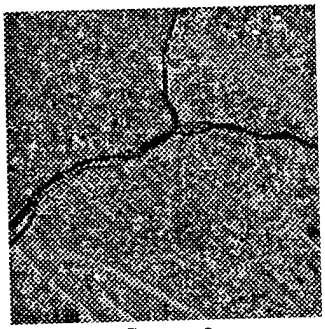


Adaptive Generalized SEM

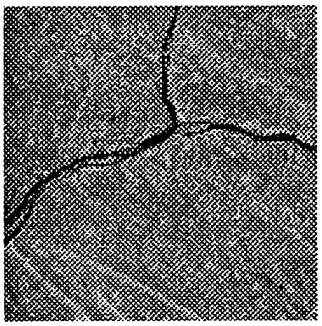
4.2 Real image



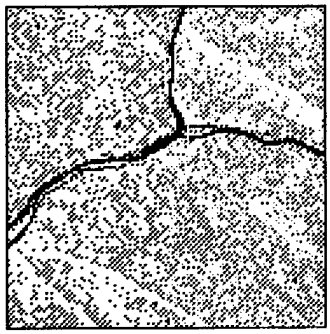
Sensor 1



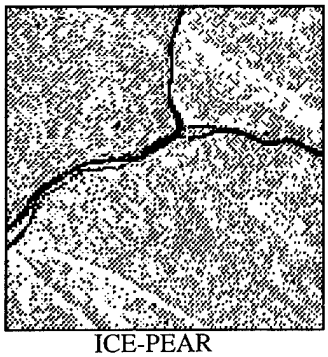
Sensor 2



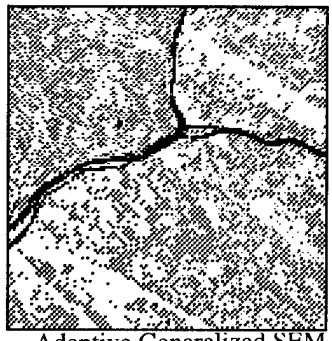
Sensor 3



Generalized SEM



ICE-PEAR



Adaptive Generalized SEM

5.CONCLUSION

Different generalized mixture estimation algorithms allow one to find automatically the correct form of the noise for each class and each sensor, which allow one to generalize the classical unsupervised image segmentation methods.

REFERENCES

[1] S. Geman, and G. Geman, Stochastic relaxation, Gibbs distributions and the Bayesian restoration of images, *IEEE Transactions on PAMI*, Vol. 6, pp. 721-741, 1984.

[2] N.L. Johnson, and S. Kotz, Distributions in Statistics: Continuous Univariate Distributions, Vol. 1, Wiley J., 1970.

[3] S. Lakshmanan, and H. Derin, Simultaneous parameter estimation and segmentation of Gibbs random fields, *IEEE Transactions on PAMI*, Vol. 11, pp. 799-813, 1989.

[4] J. Marroquin, S. Mitter, and T. Poggio, Probabilistic solution of ill-posed problems in computational vision, *Journal of the American Statistical Association*, 82, pp. 76-89, 1987.

[5] P. Masson, and W. Pieczynski, SEM algorithm and unsupervised segmentation of satellite images, *IEEE Transactions on GRS*, Vol. 31, No 3, pp. 618-633, 1993.

[6] W. Pieczynski, Statistical image segmentation, *Machine Graphics and Vision*, Vol. 1, No. 1/2, pp. 261-268, 1992.

[7] H.C. Quelle, Y. Delignon, and A. Marzouki, Unsupervised Bayesian segmentation of SAR images using the Pearson system, Proceedings of IGARSS'93, Tokyo, pp. 1538-1540, 1993.

[8] J. Tilton, S. Vardeman, and P. Swain, Estimation of context for statistical classification of multispectral image data, *IEEE Transactions on GRS*, GE-20, pp. 445-452, 1982.

Segmentation of SAR images by means of Gabor filters working at different spatial resolution

A.Baraldi and F.Parmiggiani
IMGA-CNR
Mailing address: via Emilia Est 770, 41100 Modena (Italy)
Tel.: +39-59-362388; Fax: +39-59-374506; E-mail: andrea@katabatic.bo.cnr.it

Abstract

The traditional approaches to contour detection in SAR images employ *a priori* models of the speckle. In this paper, we propose to apply to SAR images a new contour detection algorithm which is intended to be data-independent, i.e., it does not exploit any domain specific knowledge about the contents of the scene. This new contour detector must feature some degree of biological plausibility in order to simulate the behavior of a human photo-interpreter who is able to segment at one glance images acquired by optical as well as by SAR sensors. This means that, in order to improve the performance of the contour detector, we are not exclusively restricted to the exploitation of SAR images, but we can apply the algorithm to a wide variety of test images which refer to well known physiological and psychophysical experiences.

After the contour detection stage, we employ a second stage which extracts (closed) regions from non-connected binary contours, and a third stage which performs (conservative) region-merging. The third stage employs a neural network clustering algorithm whose input sequence consists of segment-based textural parameters. The statistical regularities detected by the network in the random input sequence are equivalent to categories of segments which can be successively used by a knowledge-based, domain dependent, hierarchical classification scheme.

The proposed segmentation procedure is applied to SAR images depicting sea ice. The performance of the contour detection stage seems to encourage the development of a new category of biologically plausible algorithms to perform low-level visual tasks.

Introduction

The scientific community has identified ice classification as a priority item because of its importance for global climate and weather, and for ship navigation. In recent years, the objective of ice classification has become more feasible due to the availability of suitable data. In particular, SAR images have demonstrated a great potential in monitoring sea ice in every day/night and weather condition. Thus, an efficient sea ice classification scheme, either supervised or unsupervised, should employ SAR imagery to extract ice classes.

The development of SAR image processing algorithms featuring robustness is a difficult task because of the complex features which characterize the interactions between the SAR signal and the surface of the earth. For example, in order to remove the presence of speckle noise, a great variety of SAR speckle filters has been developed (e.g., see [1],[2]). In SAR imagery: i) pixel-based classification approaches, whose local statistics are extracted from individual pixels and their close neighbors, heavily rely upon a speckle filtering stage; and ii) region-based classification approaches are thought to provide better overall performance than pixel-based approaches, although they may feature poor detection of linear features and narrow areas (e.g., ice ridges) [3],[4]. In this paper, we aim to develop a SAR segmentation procedure to be employed within a region-based SAR classification scheme.

A SAR segmentation procedure typically exploits a contour detection stage. Contour detection methods are generally less computationally expensive than region growing methods, and although they are sensitive to thresholds, this drawback may be partially compensated for by the exploitation of a later region-merging stage. When a contour detector especially suited for SAR images (such as [5]) employs an *a priori* model of the speckle noise, no speckle filter pre-processing is required in the SAR region-based approach (e.g., see [3]). This reduces the overall computation time of the SAR region-based approach with respect to that required by the pixel-based approach which is intrinsically simpler but also needs speckle pre-processing.

The traditional approach to SAR filtering and contour detection employs *a priori* knowledge about the data domain (e.g., a multiplicative speckle model is adopted in [1], [2] and [5]). In [2], an attempt to combine the properties of a biologically plausible contour detector, whose peculiar features are robustness and data-independence, with a domain-specific *a priori* speckle model was discussed. In the present paper, we propose a completely different strategy to approach the problem of SAR contour detection. This approach ignores any *a priori* domain-

0-7803-3068-4/96$5.00©1996 IEEE

specific model of the SAR signal, and tries to focus its attention on the biological aspects of a general-purpose contour detection algorithm (which must be able to process SAR images as well as images from other sensors). This approach to SAR contour detection is justified by the behavior of a human photo-interpreter who is able to segment optical imagery as well as SAR images at one glance (i.e., in a pre-attentive manner), regardless of the different physical and pictorial properties of these two types of images. This means that, whereas the human interpretation (classification) system uses domain specific knowledge about the contents of the scene, the human low-level visual system exclusively employs general purpose models that contain knowledge about images and grouping criteria which are independent of the scene under analysis [6]-[8]. An advantage of the proposed alternative approach to contour detection is that we can improve our general-purpose model by assessing its performance on several well-known test images (in particular, those that refer to physiological and psychophysical effects such as the Mach band illusion [9]).

After the contour detection stage, a SAR image segmentation procedure must employ a second stage where (closed) segments are extracted starting from non-connected binary contours. This module can be implemented by means of traditional image processing algorithms which exploit geometric information extracted from the non-connected binary contours, i.e., the raw SAR image is not employed at this stage [2]. As a consequence, this second module must apply a conservative segmentation strategy to deal with the non-connected contour pixels, i.e., every contour pixel is selected to form one segment on its own (conservative choice). This aspect stresses the need of a third SAR segmentation stage which employs pixel similarity measures to perform region-merging, in order to reduce local oversegmentation phenomena.

1 Planning

Let us introduce the three stages of the proposed SAR segmentation procedure: 1) contour detection; 2) segment extraction from non-connected contours; and 3) region-merging.

1. Contour detection. We propose to detect contours in SAR images by means of a new low-level vision module, termed Chromatic and Achromatic Contour Detector (CACD), which features some degree of biological plausibility [9]. CACD is intended as a data-independent algorithm which is not specifically developed to deal with SAR images. For example, when CACD is applied to (achromatic) SAR images, its chromatic contrast detection channel is actually inhibited. An interesting aspect of CACD, which performs multi-scale analysis, is that it features simultaneous ability in detecting contours and textures. This means that when CACD is applied to SAR images, it does not require any pre-processing stage to remove speckle.

CACD tries to address some of the major problems investigated by neurophysiological and neuropsychological studies of the mammalian visual sistem. In particular, CACD: i) defines a neuron transfer function which accounts for both chromatic and achromatic contrast; ii) defines odd- and even-symmetric neurons, whose specific receptive fields and sensibility profiles are computed by means of "normalized" Gabor functions (such that both their excitatory and inhibitory subsets feature connection weights whose sum is equal to 1): the activity of these neurons should be related to that of the simple cells in the Primary Visual Cortex (PVC) [8]; iii) combines odd- and even-symmetric filter responses (these responses should be related to the activity of the complex cells of PVC [8]); iv) combines responses of filters working at different spatial scales.

The exploitation of a bank of multi-scale filters allows CACD to detect, simultaneously, contours (e.g., texels) at high spatial resolution and textures at low spatial resolution. CACD employs filters featuring four different dimensions because at least four spatial scales are required to model human vision [10]. We introduce the terms: i) CACDH as the implementation of CACD which combines high resolution oriented filters of 3×3 and 5×5 pixels in size; ii) CACDL as the implementation of CACD which combines low resolution oriented filters of 13×13 and 25×25 pixels in size. These four square Gabor filters feature their σ parameter equal to 0.5, 1, 2 and 4, respectively, and center frequencies which mutually differ by one octave in the spatial frequency domain.

2. Segment extraction from non-connected contours. The second stage of the SAR segmentation procedure is an automatic region-extraction module to be applied to the binary contour image generated by CACD. In line with [2], this module employs the non-connected binary contour pixels to extract (closed) segments by means of geometrical rules, i.e., no backscatter information from the input raw image is exploited at this stage. The procedure which extracts segments from non-connected contour pixels consists of the following steps [2]: i) computing the distance image made of chamfer 3-4 distance values from contour pixels; ii) computing gradients in the distance image; iii) detecting distance local maxima; iv) clustering distance local maxima to detect segment seed pixels; v) applying region growing strategies around seed pixels to detect segments; vi) assigning every contour pixel to a new segment (which is a conservative choice).

3. Region-merging. In order to reduce local oversegmentation phenomena which may affect the segmented image

generated by the second stage of the SAR segmentation procedure, a Neural Network (NN) clustering algorithm is employed [11],[12]. A NN of this type detects statistical regularities in a random sequence of multi-valued (i.e., not necessarily binary) input patterns. Segment-based statistics provide the NN with a sequence of input patterns.

According to the textural feature selection proposed in [13], some of the most uncorrelated texture statistics which also feature a clear physical meaning are: mean, standard deviation, recursivity and contrast. The latter two parameters are extracted from the Upper-triangular Gray-Level Cooccurrence Matrix (UGLCM). With regard to the textural properties of images, let us refer to the most recent version of the Julesz conjecture which states: two pictures (e.g., textures) with identical third-order statistics must be physically identical, i.e., they cannot be discriminated between because identical third-order statistics imply identical second- and first-order statistics [14]. Thus, discrimination between textures becomes increasingly difficult as their third-order statistics become more similar [14]. We conclude that the exploitation of third-order statistics, e.g., extracted from a third-order UGLCM (see also [15]), would increase the reliability of the segment-based feature extraction stage at the cost of an increase in memory requirement and processing time. At the current time, our feature extraction stage can extract from the detected segments the following two within-segment data sets: i) mean, standard deviation, second order UGLCM recursivity, second order UGLCM contrast; or ii) third order UGLCM recursivity, third order UGLCM contrast.

While in the first stage of the SAR segmentation procedure, Gabor filters exploit a joint space/spatial frequency domain to detect local discontinuities in the image intensity [9], the NN clustering procedure is applied to a measurement space where topological attributes of segments are lost, i.e., NN exploits no spatial information. This implies that NN is not affected by discontinuities of local information in the spatial domain (e.g., according to spatial analysis, the presence of a step edge reveals that two adjacent segments cannot be merged even though their within-segment average statistics are equal). This behavior is consistent with the goals of the NN clustering stage which are: i) the extraction of global statistics (image regularities or categories) from local (segment-based) properties; and ii) the reduction of oversegmentation phenomena.

In order to avoid undersegmentation phenomena, NN must be run in a conservative framework, i.e., the NN input parameters must be severe.

NN clustering algorithms are based on a parallel and distributed system, i.e., a system composed of several processing units whose competitive/cooperative activities are defined by simple local rules. In [11], we proposed a NN model, termed Simplified Adaptive Resonance Theory (SART), which is an evolution of that presented in [12]. SART features self-organizing properties inherited from both ART-based models [16] and Kohonen's Self-Organizing Map (SOM) [17]. The interesting functional characteristics of SART are that: i) it requires only two user-defined parameters to run (these parameters have a clear physical meaning: one normalized parameter represents the expected degree of difficulty of the pattern recognition process, the second parameter represents the time available to the net to acquire knowledge from the input data set); ii) it self-adjusts the size of the net, i.e., it generates neurons dynamically, therefore neither an *a priori* decision regarding the size of net is required to the user nor dead units will affect the net; iii) it initializes neurons automatically, therefore no neuron randomization pre-processing is required; and iv) it performs on-line learning, i.e., it processes new data immediately without having to retrain or to refer to any of the previous training data. We wish to stress that point iv) listed above also implies that SART is affected by the order of presentation of the input sequence. This aspect of SART, which is also typical of every biological cognitive system, is reduced: a) when the neurons' plasticity, which is a monotone decreasing function of time, decreases slowly, i.e., when the input parameter which defines the time available for learning increases (this behavior of SART is in line with those of biological cognitive systems); and b) because the cooperative mechanisms employed in SART (in line with those of SOM) allow several neurons to gain the same input pattern, i.e., the impact of one input pattern "diffuses" (and "fades away") through the net.

4 Implementation

In the first stage of the proposed SAR image segmentation procedure, we apply CACD according to the following strategy: a) CACDH is run and a user-defined treshold is chosen interactively in order to extract contours of interest; b) CACDL is run while no user-defined threshold is required; c) a logic AND operation is applied to the two binary contour images in order to generate one final contour image. Therefore, the user must choose one threshold interactively. Since CACD is a rather robust and data-independent procedure, this threshold may vary slightly with the SAR image to be processed.

The second stage automatically extracts segments from non-closed contour polylines. The feature extraction stage automatically extracts segment-based textural features to be processed by SART.

When SART is employed to process data sets which combine information of different sources, i.e., information characterized by different semantics and dynamic ranges, SART enforces the development of a structured network systems. In particular, each SART subnet must employ

one user-defined severity threshold to deal with one data source at a time. For example, in order to process the first segment-based data set described above (made of four statistics), four SART subnets must be developed. The output categories resulting from these independent subnets are further combined into macro-categories, which are 4-tuple of subnet categories.

5 Experimental results

A 3-look ERS-1 Precision Image (PRI) of the Bellingshausen Sea located in Antarctica, 512×512 pixels in size, with a pixel size of 12.5 × 12.5 m, acquired November 14, 1992 (© ESA 1992), is shown in Fig. 1. Fig. 2 shows the output of CACDH, and Fig. 3 is the output binary image generated by CACDL (see Section 4). Fig. 4 shows the superposition (average) of Figs. 2 and 3. Only the pixels which appear white (local maxima) in Fig. 4 are processed by the segment extraction stage, whose output is shown in Fig. 5. The segment extraction stage features some typical behaviors: e.g., where two contour lines which ran parallel form a bottle neck, the procedure starts detecting a new segment. Fig. 5 features 6170 regions. Fig. 6 is the output of SART whose inputs are the segment-based statistics extracted from Fig. 1 according to the segments described in Fig. 5. Fig. 6 features 5760 segments: most of the segments which have been merged with adjacent ones actually belong to contour pixels. Since SART is employed in a conservative way, in order to avoid undersegmentation, some bright areas of Fig. 1 appear to be oversegmented in Fig. 6. The oversegmentation of bright areas actually stems from the fact that CACD features higher sensitivity at the upper values of the gray-value scale, as shown in Figs. 2 and 3.

From this observation, we conclude that further developments of the segmentation procedure should improve the neuron transfer function employed in the current version of CACD. Further CACD versions are expected to lose sensitivity at the upper values of the gray-level scale.

References

[1] E. Nezry, M. Leysen and G. De Grandi, "Speckle and scene spatial statistical estimators for SAR image filtering and texture analysis: some applications to agriculture, forestry and point target detection," in SAR Data Processing for Remote Sensing, Proc. SPIE, Paris (France), Sept. 1995, vol. 2584, pp. 25-28.

[2] A. Baraldi and F. Parmiggiani, "A refined Gamma MAP SAR speckle filter with improved geometrical adaptivity," *IEEE Trans. Geosci. Remote Sensing*, vol. 33, no. 5, pp. 1245-1257, Sept. 1995.

[3] Y. Sun, A. Carlström and J.Askne, "SAR image classification of ice in the gulf of Bothnia," *Int. J. Remote Sensing*, vol. 13, no. 13, pp. 2489-2514, 1992.

[4] A. Sephton, L. Brown, J. Macklin, K. Partington and N. Veck, "Segmentation of synthetic-aperture radar imagery of sea ice," *Int. J. Remote Sensing*, vol. 15, no. 4, pp. 803-825, 1994.

[5] R. Touzi, A. Lopes and P. Bousquet, "A Statistical and geometrical edge detector for SAR images," *IEEE Trans. Geosci. Remote Sensing*, vol. 26, no. 6, pp. 764-773, Nov. 1988.

[6] J. M. Beaulieu and M. Goldberg, "Hierarchy in picture segmentation: a stepwise optimization approach," *IEEE Trans. Pattern Anal. Machine Intell.*, vol. 11, no. 2, pp. 150-163, Feb. 1989.

[7] D. Marr, Vision, New York: W. H. Freeman and Company, 1982.

[8] C. Mason and E. R. Kandel, "Central visual pathways," in Principles of Neural Science, E. Kandel and J. Schwartz, Eds., Norwalk, Connecticut: Appleton and Lange, 1991, pp. 420-439.

[9] A. Baraldi and F. Parmiggiani, "Combined detection of intensity and chromatic contours in computer vision," *Optical Engineering*, vol. 35, no. 5, May 1996, in press.

[10] H. R. Wilson and J. R. Bergen, "A four mechanism model for threshold spatial vision," *Vision Res.*, vol. 19, pp. 19-32, 1979.

[11] A. Baraldi and F. Parmiggiani, "A self-organizing neural network merging Kohonen's and ART models," *Proc. International Conference on Neural Networks '95*, Perth, Australia, Dec. 1995, vol. 5, pp. 2444-2449.

[12] A. Baraldi and F. Parmiggiani, "A neural network for unsupervised categorization of multivalued input patterns: an application to satellite image clustering," *IEEE Trans. Geosci. Remote Sensing*, vol. 33, no. 2, pp. 305-316, 1995.

[13] A. Baraldi and F. Parmiggiani, "An investigation of textural characteristics associated with gray level cooccurence matrix statistical parameters," *IEEE Trans. Geosci. Remote Sensing*, vol. 33, no. 2, pp. 293-304, March 1995.

[14] J. I. Yellott, "Implications of triple correlation uniqueness for texture statistics and the Julesz conjecture," *J. Opt. Soc. Am. A*, vol. 10, no. 5, pp. 777-793, 1993.

[15] H. Anys and D. He, "Evaluation of textural and multipolarization radar features for crop classification," *IEEE Trans. Geosci. Remote Sensing*, vol. 33, no. 5, pp. 1170-1181, Sept. 1995.

[16] G. A. Carpenter, S. Grossberg, and D. B. Rosen, "Fuzzy ART: fast stable learning and categorization of analog patterns by an adaptive resonance system," *Neural Networks*, vol. 4, pp. 759-771, 1991.

[17] T. Kohonen, "The self-organizing map," *Proceedings of the IEEE*, vol. 78, no. 9, pp. 1464-1480, Sept. 1990.

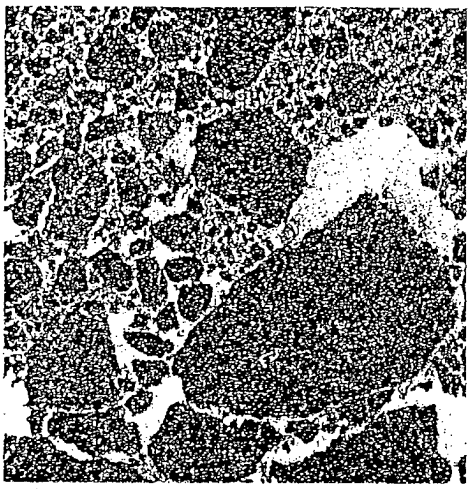


Fig. 1

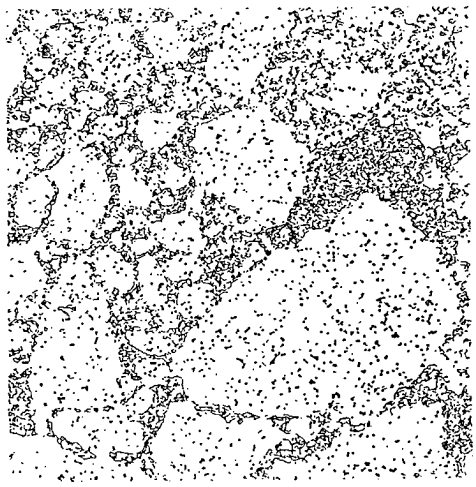


Fig. 2



Fig. 3

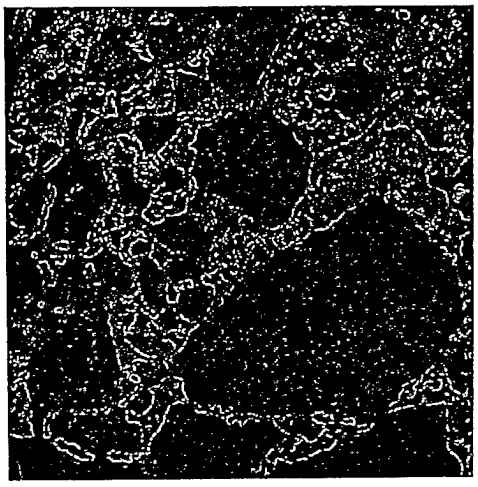


Fig. 4

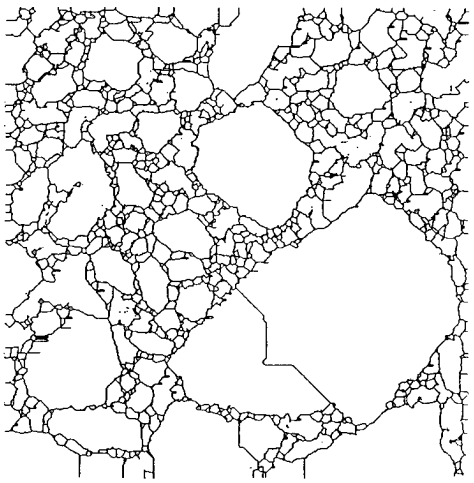


Fig. 5

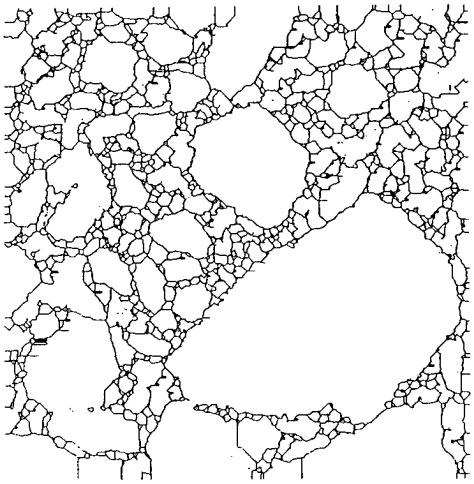


Fig. 6

Markov Random Field based Image Segmentation with Adaptive Neighborhoods to the detection of Fine Structures in SAR Data

P.C. Smits, S. Dellepiane, and S.B. Serpico
University of Genoa - Department of Biophysical and Electronic Engineering
Via all'Opera Pia 11a, I-16145 Genova ITALY
Phone +39 10 3532662 / Fax +39 10 3532134
E-mail: [smits,silvana,vulcano]@dibe.unige.it

Abstract - In the Markov Random Field (MRF) region label approach for Synthetic Aperture Radar (SAR) image segmentation small structures may be lost. This is due to the filtering effect of the MRF region label model, which is desirable in homogeneously labelled areas like agricultural regions. End-users also interested in resource management, may wish to preserve the small structures such as small roads and rivers. To this end, the neighborhood set used in the MRF region label model has been made adaptive, based on a simple Bayesian network (BN). Results using Synthetic Aperture Radar (SAR) data show that an important improvement of the representation of small structures is possible if they can be detected to some extend using the Maximum Likelihood approach.

INTRODUCTION

The main drawbacks of SAR image segmentation based on the MRF region label model are that fine structures, like, for instance, 1-3 pixel wide line segments, usually disappear and region borders are not exactly detected. This is the cost one has to pay for the hypothesis that the image under test consists of homogeneously textured areas. Preserving fine structures would increase the effectiveness of the MRF approach, for instance, for end-users who are thrown on the use of SAR data for the cartography, urban planning and the analysis of agricultural sites [1,2].

The mentioned drawbacks may be due to two reasons. The first reason is that the statistical image model is not accurate enough; this may cause confusion at region borders as well as close to fine structures. The second reason is that the Markovian property is usually simplified through a configuration of adjacent pixels, whose shape is fixed and predefined for a whole image [3].

The peculiarity of the present paper is to propose the use of adaptive neighborhoods within the MRF region label approach, as they contribute to a better preservation of fine structures and to a more correct detection of region borders. In the literature, neighborhood sets are sometimes chosen according to some prior knowledge of the application domain, but they cannot be changed or automatically adapted during processing.

This work has been carried out as part of the European Community Training and Mobility for Researchers (TMR) program and has been financed by the European Commission, contract number ERBFMBICT950257.

0-7803-3068-4/96$5.00©1996 IEEE

SEGMENTATION BASED ON AN MRF REGION LABEL APPROACH

The Maximum a-posteriori probability (MAP) classifier adapted from [3] includes two energy terms. One term describes the imaging process (the statistics of the SAR data), the other describes the imaged objects (the MRF region label process).

Statistics of the SAR data Considering the measurement vector X_S = [HH, HV, VV]$_S$ at the pixel site s, i.e., the vector of the polarimetric complex amplitudes measured at the site s of the polarimetric radar, we can express the conditional distribution of the polarimetric measurement vector X_S, as its region label L_S is assumed to be circular Gaussian, as follows:

$$U_1^s(X_s / L_s = l) = X_s^{*T} C_{l_s}^{-1} X_s + \ln\left|C_{l_s}\right| \qquad (1)$$

where $C_l = \left\langle X^* X^T \right\rangle_l$ is the 3 x 3 polarimetric covariance matrix of the training data of the class l.

MRF region label model The imaged objects are considered to be mainly homogeneous classes. The application of the MRF region label model is justified only if the true region label of each pixel depends mainly on the neighbouring labels. In this case, the conditional distribution of the region label L_S, given the region labels elsewhere, is expressed as the Gibbs energy function

$$U_2^s(L_s = l / L_r, r \in N_s^o) = -\frac{\beta}{\left|N_s^0\right|} \sum_{r \in N_s^0} \delta_k(L_s - L_r).$$

This is called the region label process, where δ_k is the Kronecker delta function which returns the value 1 if L_S is equal to L_r and the value 0 otherwise; $\left|N_s^0\right|$ is the dimension of the neighbourhood N_s^0. The region label process expresses the Gibbs energy function of the probability that the pixel site s has a label L_S, given the labels of its neighbourhood N_s^0. In the experiments that follow, the value of the attraction parameter β was set to 1.4. The MAP estimate of L, expressed in terms of energy, minimizes $E_{MAP} = \sum_s \left\{U_1^s + U_2^s\right\}$.

THE MRF REGION LABEL PROCESS WITH ADAPTIVE NEIGHBOURHOOD SYSTEMS

In an MRF region label process defined on a lattice S, a set of pixels $N_s^\alpha \subseteq N_s^* \subseteq S$ is called a strictly Markovian

neighbourhood or a minimum neighborhood if all the elements in the neighborhood system are meaningful. In the following, N_s^α will be called the adaptive neighbourhood. To test whether a proposed neighborhood system is efficient or not, the *hypothesize-and-test* paradigm is used. The hypothesis can be formulated as follows. Let the proposition $A_s = N_s^\alpha$ mean "N_s^α *is the minimum neighborhood in the Markovian sense*". As more evidence is gathered, the belief value $BEL\left(N_s^\alpha\right)$ of each proposition $A = N_s^\alpha$ changes. Suppose that there exists an extra source of knowledge $\boldsymbol{K}$ containing information about the image content. Let $\boldsymbol{K}_s^*$ represent the knowledge about a subimage N_s^*, including the site s. Let $\boldsymbol{X}_s^*$ and $\boldsymbol{L}_s^*$ be the observations and the labels assigned to the subimage N_s^*, respectively. In this case, the belief function can derive information from three resources: the observations $\boldsymbol{X}_s^*$, the label image $\boldsymbol{L}_s^*$, and the knowledge $\boldsymbol{K}_s^*$, as shown in Fig 1.

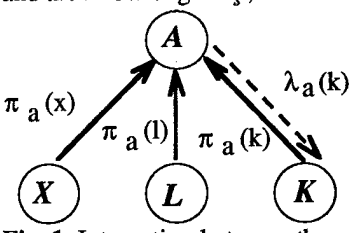


Fig. 1. Interaction between the prop. A and different information sources.

Let $\pi_A(..)$, be the current strengths of the causal supports contributed by incoming links to A. A causal support represents evidence propagated forward from the parent nodes to their sons. The belief updating concerning the proposition $A_s = N_s^\alpha$ ("N_s^α *is the minimum neighbourhood in the Markovian sense*") is given by the formula

$$\mathrm{BEL}\left(N_s^\alpha\right) = \gamma P\left(N_s^\alpha \,/\, \boldsymbol{x}_s^*, \boldsymbol{l}_s^*, \boldsymbol{k}_s^*\right)\pi\left(\boldsymbol{l}_s^*\right)\pi\left(\boldsymbol{x}_s^*\right)\pi\left(\boldsymbol{k}_s^*\right),$$

where γ is a normalizing constant that makes $\sum_\alpha BEL\left(N_s^\alpha\right) = 1$. Due to the simplicity of this Bayesian belief network (the nodes K, X, and L do not have successors) the diagnostic supports $\lambda_A(..)$ are set to 1. $P\left(N_s^\alpha \,/\, \boldsymbol{x}_s^*, \boldsymbol{l}_s^*, \boldsymbol{k}_s^*\right)$ is the fixed conditional probability matrix that relates the proposition $A_s = N_s^\alpha$ to its immediate parents $\boldsymbol{x}_s^*$, $\boldsymbol{l}_s^*$, and $\boldsymbol{k}_s^*$. To the causal supports $\pi_a(..)$ a function is to be assigned that properly takes into account the support from every node, i.e., from every source of information. Then, a connected neighbourhood system $N_s^\alpha \subseteq N_s^*$ is believed to be Markovian if $\forall \varepsilon \neq \alpha$: $BEL\left(a_s^\alpha\right) > BEL\left(a_s^\varepsilon\right)$.

Focusing attention on the MRF region label model again, we are looking for a set of pixels that are Markovian neighbours. To reduce the computational burden, we reduce heuristically the number of possible neighbour sets. Consider the case where we have additional knowledge $\boldsymbol{K}_s^*$, which, for instance, may be a digitized and registrated map. In the experiments that follow, the neighbourhood systems are allowed to assume five different shapes: the default 3x3 system, and the four, 5 pixel long, straight lines (\,|,/,-) crossing the site s. $P\left(N_s^\alpha \,/\, \boldsymbol{x}_s^*, \boldsymbol{l}_s^*, \boldsymbol{k}_s^*\right) = 0.2$ for all five propositions N_s^α, α=0, 1, .., 4. Since $s \in N_s^\alpha$, the causal supports have positive minima. For the results that follow, the causal supports $\pi_a(..)$ are modelled as the similarities of the information (e.g., in the next examples the label image, and eventually other knowledge) at the site s (the pixel under test) to the neighbouring pixels: $\pi_A\left(\boldsymbol{l}_s^*\right) =$,

$$\frac{1}{\left|N_s^\alpha\right|}\sum_{r\in N_s^\alpha}\delta\left(l_s - l_r\right), \quad \pi_A\left(\boldsymbol{k}_s^*\right) = \frac{1}{\left|N_s^\alpha\right|}\sum_{r\in N_s^\alpha}\delta\left(k_s - k_r\right),$$

and $\pi_A\left(\boldsymbol{x}_s^*\right) = 1$.. The best N_s^α replaces N_s^α in the MRF region label model.

RESULTS

In order to have more insight in the success and failure of the BN to select the right most appropriate Markovian neighborhood, its operating characteristics were determined, using two corrupted synthetic images: one with a certain neighborhood shapes to detect, and one without [5]. Feeding the BN with 400 shape estimation problems for every signal to noise ratio (SNR) with different (Gaussian, additive) noise realizations, we obtained the operating characteristics depicted in Fig. 2. P(M) indicates the misdetection probability (i.e., the right neighborhood shape has not been selected), and P(F) the probability of false alarm (i.e., the neighbourhood shape has been selected when in reality it was not there). The evidence strength used to produce the data was the difference between the belief value of the expected shape and the belief value of the best shape found, excluding the expected shape:

$$d_\alpha = BEL\left(A = N_s^\alpha\right) - \max_{\beta\neq\alpha} BEL\left(A = N_s^\beta\right)$$

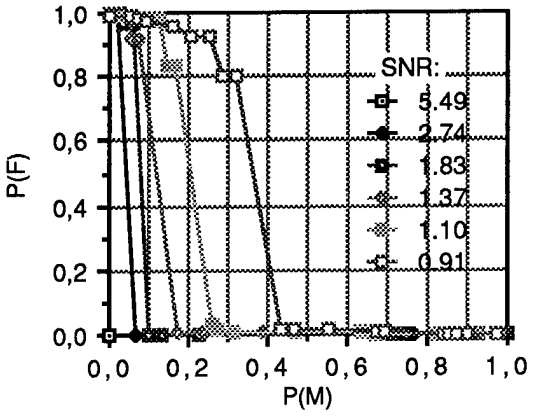


Fig. 2. Operating characteristics for the BN neighborhood shape detection algorithm.

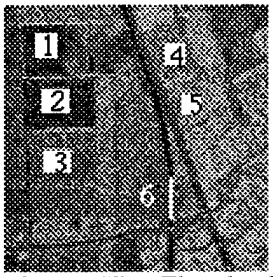


Fig. 3. The Flevoland scene with training areas.

From the operating characteristics one can derive the best evidence criterion (i.e., the best threshold for the belief difference) for various SNRs. The evidence criterion for the performed experiments was set to 0.012, corresponding to a SNR of approximately 1.83.

The SAR data to illustrate the MRF-AN approach consist of portions of the L-band image of the Flevoland (NL) scene, HH and VV polarization. Fig. 3 shows the training areas that are applied to calculate the statistics in the image model (1). Simulated Annealing used 300 iterations to minimize the MAP criterion, both for the MRF and for the MRF-AN approach [4]. Fig. 4 and 5 are two sections of the scene, with a) and b) the HH and VV polarizations, respectively, and c) to e) the ML result, the result of the MRF approach by [3], and the MRF-AN approach, respectively.

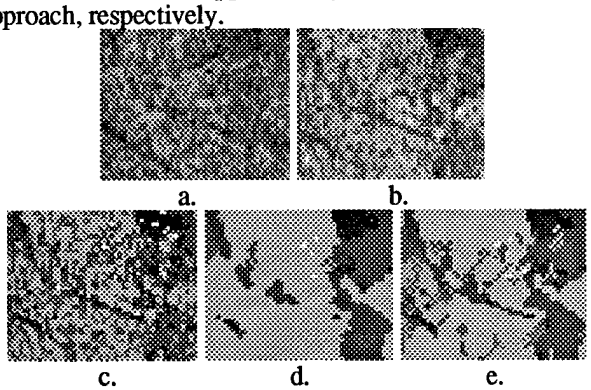


Fig. 4. Detail of the Flevoland scene, L-band. a) HH and b) VV polarization. Results: c) ML; d) MRF; e) MRF-AN.

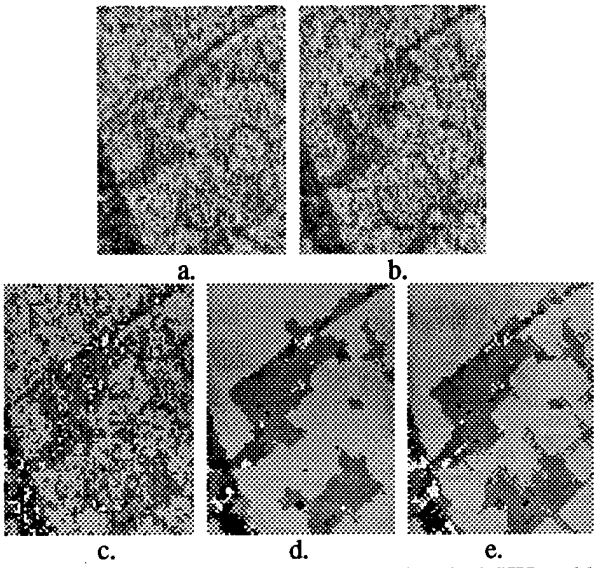


Fig. 5. Detail of the Flevoland scene, L-band. a) HH and b) VV polarization. Results: c) ML; d) MRF; e) MRF-AN.

Visual inspection of the results show that an improvement of the preservation of small structures is achieved, only if the ML approach is able to detect these structures to some extend. Moreover, using conventional error measures, the overall accuracy of MRF-AN is slightly better in comparison with results of the MRF without adaptive cliques.

SUMMARY AND DISCUSSION

The presented modification to the MRF region label approach for segmentation, called MRF region label model with adaptive neighbourhoods (MRF-AN) approach, concerns the integration of various sources of information to choose the shape of a neighbourhood that is the most appropriate for the local image around the pixel site under test. The choice is based on a belief value of the proposition that the proposed neighborhood is a minimum Markovian neighbourhood. From among the different alternatives of shapes, the one with the highest belief value is chosen to compute the MRF region label process. The MRF-AN approach is enable to recover 1 and 2 pixel-wide structures, and allows one to merge different sources of information. Although P(F) errors in the neighborhood detection may introduce disturbing effects, it is concluded that, for the images and objects of interest and for the a-priori assumptions made, the proposed method is valid and practically feasible.

REFERENCES

[1] D. Geman and B. Jedynak, "An active testing model for tracking roads in satellite images," IEEE Trans. PAMI, Vol. 18, No. 1, Jan. 1996, pp. 1-14.

[2] P. Kelly and F. Chen, "Iterative segmentation algorithms using morphological operations," Proc. IEEE Int. Conf. ASSP, pp. v49-v52, April 1993.

[3] E. Rignot and R. Chellappa, "Segmentation of polarimetric synthetic aperture radar data," IEEE Transactions on Image Processing, Vol. 1, No. 3, pp. 281-300, July 1992.

[4] B.S. Manjunath, T. Simchony, and R. Chellappa, "Stochastic and deterministic networks for texture segmentation," IEEE Trans. Acoustics, Speech and Signal Proc., Vol. 38, No. 6, June 1990, pp. 1039-1049.

[5] T. Kanungo, M.Y. Jaisimha, J. Palmer, and R.M. Haralick, "A methodology for quantitative performance evaluation of detection algorithms," IEEE Trans. Image Processing, Vol. 4, No. 12, Dec. 1995, pp. 1667-1674.

SAR image segmentation by mathematical morphology and texture analysis

Benoit Ogor, Véronique Haese-coat and Joseph Ronsin

INSA, laboratoire ARTIST
20 avenue des Buttes de Coesmes 35043 RENNES Cedex, France
Tel : (33) 99 28 65 05, Fax : (33) 99 28 64 95
Email : ogor@insa-rennes.fr

Abstract - This paper presents a promising segmentation method for synthetic aperture radar (SAR) imagery designed in the context of agricultural remote sensing using a morphological region based image analysis. The region based approach is really appropriate for land use applications given that land cover is naturally built-up from regions. The method is divided into two principal steps : a morphological image partitioning resulting in a severe oversegmentation and a further region growing process exploiting information from a textural edge detector.

INTRODUCTION

Due to its all-time disposition and its frequency range, SAR active sensor is a complementary system of optical sensors. Prior to exploit this complementarity, it is necessary to perform the registration of both multisensor images. One interesting solution to this problem is to establish correspondence between images by matching invariant primitives. Significant contours representing salient region boundaries can be useful stable descriptors in the image given that they are preserved in most cases. It's with the precise objective to delineate these features that we are interested in the segmentation of SAR images.

We propose a morphological approach, to the segmentation of SAR image, consisting of an initial image subdivision algorithm refined by a hierarchical region growing process. The merit of this method is that the segmentation process is essentially based on new advanced tools derived from mathematical morphology, a theory which represents a challenging alternative to the traditionnal techniques of SAR image analysis. Indeed, mathematical morphology is very attractive for segmentation in so far as it can efficiently deal with geometrical features such as size, shape, contrast or connectivity that can be considered as region oriented features. Mathematical morphology provides powerful tools for segmentation, namely the watershed transformation [1] and the waterfall algorithm [2]. But due to the specific peculiarities of SAR imagery (speckle noise, strong scene texture) and the grey level based nature of the original morphological segmentation, the proposed method can involve sequentially running a chain of adaptive tools to prevent the severe gradient watershed oversegmentation.

DESCRIPTION OF THE SEGMENTATION

The segmentation method decomposes into four distinct phases that are briefly described below. It uses, at the most, techniques of morphological origin. The three first steps, made of a morphological filtering operator, a constant false alarm rate (CFAR) texture edge detector combined with the watershed transformation, constitute the preliminary part of the algorithm resulting in a systematic over-fine segmentation. The last phase consists in the oversegmentation removal by a hierarchical region merging process exploiting the output of the previous texture edge detector. It will allow the extraction of the most probable real boundaries in the image separating textured fields.

(1) *image smoothing* : the purpose here is to smooth the original image in order to reduce as much as possible oversegmentation effects due to speckle and texture while retaining the salient image edges. Morphological filters by reconstruction are proved to be attractive for this task, having the property of simplifying an image by producing flat zones (i.e. regions of constant grey level) while preserving efficiently sharp edges due to a fundamental pyramidal property related to the flat zones connectivity [3]. Morphological filters by reconstruction are composed of morphological opening and closing by reconstruction. A promising filter called connected alternating sequential filter, cascading alternatively morphological openings and closings by reconstruction of increasing structuring element size, was applied to average out speckle. Directional structuring elements (from (3×1) to (5×1)) defined in the four usual orientations were considered to preserve as much as possible strong scatterers or structural features (e.g. edges or lines) in the original image.

(2) *edge detection* : instead of applying usual gradient edge detectors based on the difference between pixel values that used to fail in the presence of speckle noise, a more suitable edge detector for SAR images, is chosen. It is based on the

0-7803-3068-4/96$5.00©1996 IEEE

famous coefficient of variation (CV) (i.e. ratio of standard deviation to mean). It is well known that this first order statistical parameter is a good indicator of texture heterogeneity within the image [4]. Indeed, it has a precise numerical value in homogeneous areas where only texture speckle exists (e.g. agricultural fields). Moreover, it is sensitive to the presence of a contour irrespective of its direction. The larger CV is, the more likely there exists an edge in the neighborhood. Computed in a (3×3) window, CV is then a good textural edge detector on which the watershed algorithm can be directly applied.

(3) *waterfall algorithm* : the watershed transformation, at the basis of the morphological approach to segmentation [1], is a very fast image segmentation method, looking like a topographic region growing process by its construction mode. Its principle is as follows : the contours of an image are the highest crest lines of its gradient module. Therefore, it is most often performed on the gradient image computed from the original image (i.e. on the CV edge detector output image in our case). As the watershed algorithm is very sensitive to local gradient variations (indeed, it precisely locates the contours at the local maxima of the gradient edge image), it generally tends to produce a severe oversegmentation. This phenomenon is obviously more pronounced for SAR imagery given the strongly textured nature of a SAR image and even its morphologically filtered gradient version. It's the reason why the watershed transformation is not operational in that way and is replaced by a constrained watershed (i.e. the waterfall algorithm) regularizing more the SAR texture edge image and detecting much less contours than with the original unconstrained watershed version. A postprocessing operator is nevertheless essential for a SAR image given the actual segmentation quality level (see Fig.2). At this stage, the image is divided up into a large amount of size-variable connected regions. One interesting solution to the removal of the remaining oversegmentation is to extend the algorithm by a region growing-type segmentation method with the regions, coming from the watershed algorithm, chosen as starting germs of the region merging process.

(4) *region growing* : it consists of refining the previous segmentation by performing a hierarchical iterative region merging process. The principle is as follows : at each iteration of the process, a distance (measuring the similarity between adjacent regions) is computed for all regions pairs and we decide to merge exclusively the most similar pair of regions. As the watershed transformation produces a map of closed contours that most of them are unsignificant and spurious, a solution is to consider the textural edge information taken on the contour arcs separating waterfall regions as similarity parameter. The textural parameter used to measure the watershed contours strength is the mean CV of the pixels along the common boundary of watershed regions. If this mean CV is low, it means that the contour is irrelevant and located in a homogeneous region. Otherwise, it's a significant and informative edge. By merging exclusively the regions pairs with the lowest mean CV at their border, that allows us to merge at first the most similar regions without modifying the sharpest edges in the oversegmented image. The process is iterated until a prefixed number of regions is reached.

RESULTS AND DISCUSSION

The segmentation method is tested on the SAR 7-look airborne image of an intensive agricultural scene (Fig.1). The result of the initial morphological segmentation (until step (3)) is showed in Fig.2. Despite the high level of oversegmentation due to the strong textured nature of the SAR image, we can already perceive the road network and the separation between some large units of land cover. The Fig.3 and Fig.4 show the results of the hierarchical region growing process (step 4) with the explicite decreasing number of regions. The final resulting segmentation (Fig.4) is quite faithful with respect to the original SAR image by delineating the boundaries of the most significant texturally homogeneous fields. Finally, these works underlined the considerable potentialities offered by mathematical morphology in the context of SAR image analysis. Unlike the usual region growing methods, this algorithm does not suffer from the blocky region boundaries effect due to the initial morphological segmentation method used.

REFERENCES

[1] S.Beucher and F.Meyer, "The morphological approach to segmentation : the watershed transformation", Mathematical Morphology in Image Processing, edited by Dougherty (E.R.), pp 433-482, Marcel Dekker Inc, New York, 1993.

[2] S.Beucher, "Watershed, hierarchical segmentation and waterfall algorithm", International. Symposium on Mathematical Morphology and Its Applications to Image Processing, J.Serra and P.Soille (editors), Kluwer Academic Publishers, pp 69-76, Paris, 1994.

[3] P.Salembier and J.Serra, "Flat zones filtering, connected operators and filters by reconstruction", IEEE transactions on Image Processing, vol.4, n°8, pp 1153-1160, 1995.

[4] H.Laur, T.Le Toan and A.Lopes, "Textural segmentation of SAR images using first order parameters", proceedings of IGARSS'87, Ann Arbor, USA, pp 1463-1468, 1987.

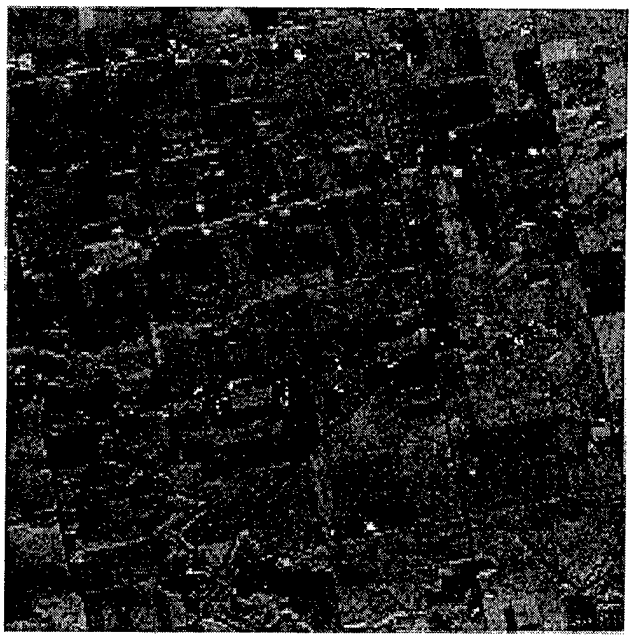


Fig.1 : SAR original image (480×480)

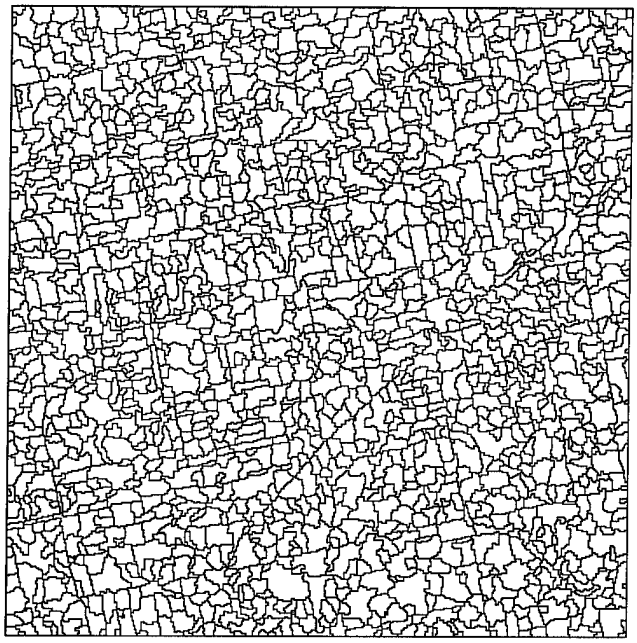


Fig.2 : waterfall segmented image (2230 regions)

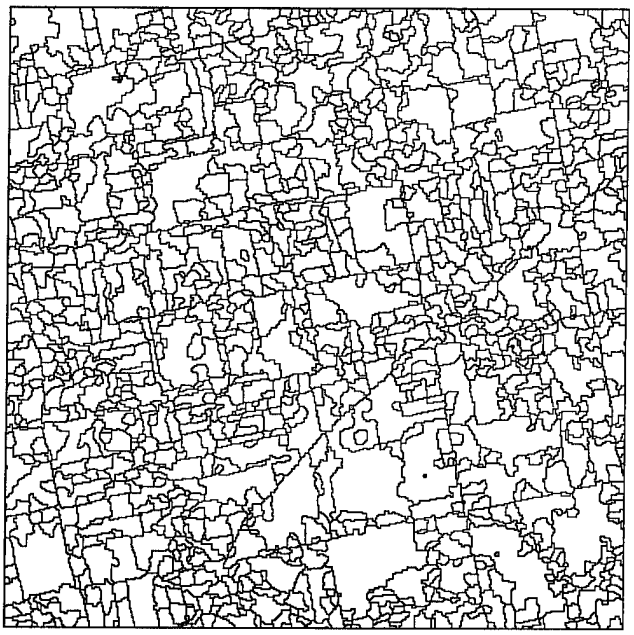


Fig.3 : draft segmented image (1500 regions)

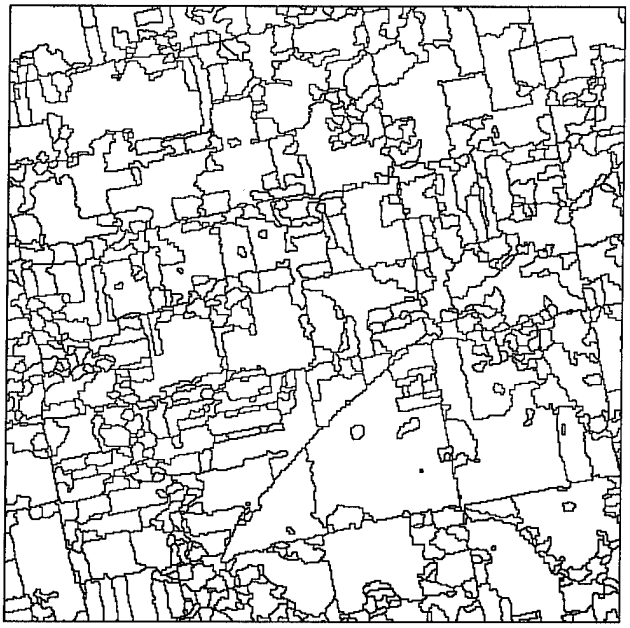


Fig.4 : final segmented image (900 regions)

ACKNOWLEDGEMENTS

The authors wish to thank Dr D.C.He from the CARTEL, university of Sherbrooke, Quebec, Canada for supplying the image used in this study.

SCATTERING FROM CULTURAL GRASS CANOPIES: A PHASE COHERENT MODEL

James M.Stiles
Radar Systems and Remote Sensing Lab
The University of Kansas, Lawrence KS
Tel:(913) 864-7744, Fax:(913) 864-7789
e-mail: jstiles@rsl.ukans.edu

Kamal Sarabandi
The Radiation Laboratory
The University of Michigan, Ann Arbor MI
Tel:(313) 936-1575, Fax:(313) 747-2106

Abstract – A microwave scattering formulation is presented for grassland and other short vegetation canopies. The fact that the constituent elements of these targets can be as large as the vegetation layer make this formulation problematic. For example, a grass element may extend from the soil surface to the top of the canopy, an thus the upper portion of the element can be illuminated with far greater energy than the bottom. By modeling the long, thin elements of this type of vegetation as line dipole elements, this non-uniform illumination can be accounted for.

Additionally, the stature and structure of grass plants can result in situations where the average inner-product or coherent terms are significant at lower frequencies. As a result, the backscattering coefficient cannot be modeled simply as the incoherent addition of the power from each element and scattering mechanism. To determine these coherent terms, a coherent model which considers scattered fields, and not power, is provided.

Finally, a major component of the grass family are cultural grasses, such as wheat and barley. This vegetation is often planted in row structures, a periodic organization which can likewise result in significant coherent scattering effects, depending on the frequency and illumination pattern. Therefore, a formulation is also provided which accounts for the unique scattering of these structures.

INTRODUCTION

When applying random media scattering techniques to grassland canopies, several unique problems arise which must be overcome. Grassland constituents are often neither straight, nor circular in cross-section. Thus, it becomes difficult to approximate the structure of grass plants as a collection of simple canonical elements where the scattering is well known. In addition, the relative position of the elements often cannot be described as uniformly distributed throughout the canopy layer. Instead, the elements begin at the bottom of the scattering layer and traverse vertically to the top. The position of these structures are only slightly random in the vertical dimension, with a variance far smaller than the canopy height. An additional result is that the coherent wave illuminating the element is non-uniform, that is the intensity of the wave varies from the top to the bottom of a long scattering element.

Finally, perhaps the most significant problem when dealing with grass canopies is due to potential for the scattered fields from dissimilar elements to be correlated. As a result, the total scattering power cannot be reduced to a summation of the scattering power from each separate plant element, the plant structure as a whole must be considered [4].

ELEMENT SCATTERING

The scattering from the long, thin dielectric elements found in grassland canopies can be attributed to electric line-dipoles lying along the cylinder axis [2,5]. The total scattering from the cylinder can be thought of as a coherent addition of the scattering from elemental or incremental dipoles, each with a dipole moment described as $\mathbf{p}_{2d}d\ell$. The dipole moment is a function of the incident electric field along the element axis, as well as a function of the 2-dimensional polarizability tensor $\mathcal{P}_{2d}$. We seek to find a scattering solution for a line-dipole element embedded in an extinction layer (vegetation) over a dielectric half-space (soil).

This formulation will consider only the first order scattering mechanisms, of which there are four [1]. The total scattered field is therefore the *coherent* summation of these four terms. To correctly determine this value, each of the four scattering mechanisms must be referenced to a single equi-phase plane ($\bar{r} \cdot \bar{k}_0 = C$). The propagation by each of the four scattering mechanisms can be modeled as a sum of two complex propagation paths, the direct path and the reflected or image path. Using ray optics, the propagation from the equi-phase plane (arbitrarily taken to pass through the origin, $C = 0$) directly to the particle is:

$$\begin{aligned}\Phi_1(\bar{r}') =& (\bar{r}_1 - \bar{r}_p) \cdot \bar{k}_0 + (\bar{r}' - \bar{r}_1) \cdot \bar{k}_1 \\ =& \bar{r}_1 \cdot \bar{k}_0 + (\bar{r}' - \bar{r}_1) \cdot \bar{k}_1 \end{aligned} \quad (1)$$

where $\bar{r}_1$ defines the location where the ray intersects the top of the vegetation layer, and $\bar{r}_p$ defines the location where the ray intersects the equi-phase plane. Note the boundary is assumed to be diffuse, and refraction is not considered.

The propagation along path 1 is therefore described as $\exp\left[\imath\Phi_1(\bar{r}')\right]$ where $\Phi_1(\bar{r}')$ is a complex function given as:

$$\Phi_1(\bar{r}') = k_0^x x' + k_0^y y' - \frac{k_\rho^2 z'}{k_0 \cos\theta} + \frac{k_1 z'}{\cos\theta} \quad (2)$$

0-7803-3068-4/96$5.00©1996 IEEE

Using the same sequence of steps as shown for Φ_1, the image, or ground bounce term is found to be:

$$\Phi_2(\bar{r}') = k_0^x x' + k_0^y y' + \frac{k_\rho^2(z'+2d)}{k_0\cos\theta} - \frac{k_1(z'+2d)}{\cos\theta} \tag{3}$$

with the propagation defined as $R\exp\left[\imath\Phi_2(\bar{r}')\right]$. The value R is the appropriate complex reflection coefficient for the soil, an artifact of the specular ground reflection encountered by this image path.

These two propagation expressions can be used in combination to determine the relative propagation of the coherent electric field to and from a location in the vegetation canopy, for any of the four first-order scattering mechanisms. This location, for example, could define a position on a line-dipole element, defining therefore an incremental dipole element.

A scattering matrix element for an incremental dipole with polarizability $\mathcal{P}_{2d}$ is given as:

$$S_{\chi\psi} = \frac{k_0^2}{4\pi}\hat{\chi}_s \cdot \mathcal{P}_{2d} d\ell \cdot \hat{\psi}_i \tag{4}$$

where S is an element of the scattering matrix for receive/transmit polarizations χ, ψ, and P is the complex 3×3 polarizability tensor which completely defines the scattering of a dipole element.

This incremental dipole lies along a contour defined by the long element upon which dipole lies. The scattering from a complete line-dipole element can be determined by integrating the scattering from the incremental dipoles along the length of the thin element, while accounting for the complex propagation to/from each point ($\bar{r}_\ell$) on the element:

$$S_{\chi\psi}^n = \frac{k_0^2}{4\pi}\int_L \hat{\chi}_n(\hat{k}^i)\cdot\mathcal{P}_{2d}(\bar{r}_\ell)\cdot\hat{\psi}_n(\hat{k}^i)\,\exp\left[\imath\Phi_{\chi\psi}^n(\hat{k}^i;\bar{r}_\ell)\right]d\ell \tag{5}$$

where n refers to the parameters associated with the nth scattering mechanism.

Note this solution provides for the coherent addition of the scattered *fields* for each of the four first-order scattering mechanisms($\sum_{n=1}^4 S_{\chi\psi}^n$), rather than the scattered *power*, the parameter most often evaluated. The importance of this can be seen when multiplying this sum of four values by its complex conjugate. Sixteen terms will result, four of which represent the scattered power associated with each mechanism. The remaining twelve terms are the "inner product" values which can significantly increase or decrease the total scattering power.

Additionally, note this is not a solution for the scattering of a thin dielectric element, but instead of a dielectric element in an extinction layer over a dielectric half space. The effect of the extinction layer and the reflection from the half space are comprehended in the solution. Finally, perhaps the most significant aspect of this model is that it accurately represents the illumination of the element by the coherent wave. Since the propagation both to and from an each arbitrary point on the scatterer is determined, the effect of the extinction layer on the scattering element is accurately represented.

WAVE PROPAGATION

The complex propagation constant describing the coherent wave in a medium consisting of sparsely populated elements can be expressed as $k_1 = k_0 - \imath M_{\chi\psi}$, where $M_{\chi\psi}$ is a function resulting from Foldy's approximation and determined by computing the average forward scattering of the constituent elements [3,pp.458-461]. However, since a Rayleigh solution was used to determine the polarizability of the line dipoles, the forward scattering solution does not reflect the losses due to scattering. Additionally, the line dipole elements may be of similar size to the extinction layer, thus they cannot be considered "point" targets in a scattering volume.

The first problem is solved by explicitly determining the scattering loss from a line-dipole element. As the electrical length of the element becomes large, this loss becomes proportional to the physical length, and the scattering loss can be expressed in terms of (unit length)$^{-1}$. The 2-dimensional polarizability tensors can be modified to reflect this loss:

$$P_{xx}'^{2d} = P_{xx}^{2d} + \frac{\imath k_0^2}{8}|P_{xx}^{2d}|^2(1+\cos^2\theta_i') \tag{6}$$

$$P_{yy}'^{2d} = P_{yy}^{2d} + \frac{\imath k_0^2}{8}|P_{yy}^{2d}|^2(1+\cos^2\theta_i') \tag{7}$$

$$P_{zz}'^{2d} = P_{zz}^{2d} + \frac{\imath k_0^2}{8}|P_{zz}^{2d}|^2 2\sin^2\theta_i' \tag{8}$$

where $\cos\theta_i' = \hat{k}_i\cdot\hat{z}'$ and $\hat{z}'$ defines the axial direction of the incremental dipole element. Utilizing these modified values in Foldy's approximation will provide a solution which accounts for both absorption and scattering losses.

Again using the concept of an incremental dipole element, the effective propagation constant resulting from a collection of line dipole elements can be computed. We first consider a layer of thickness Δz with a collection of line dipole elements passing completely through the layer. The section of each line dipole element passing through this layer can be considered an elemental dipole with polarizability tensor $\mathcal{P}^{2d}\Delta\ell$. The particle density of these elements, defined as n_0 particles per unit volume, is therefore $n_0 = N_{epa}/\Delta z$, where N_{epa} is the average number of elements intersecting a unit area of the layer. Taking the limit as Δz approaches zero leads to this form of Foldy's approximation:

$$M_{\psi\psi}(z) = \frac{\imath N_{epa}(z)k_0^3}{2}\langle\hat{\psi}\cdot\mathcal{P}^{2d}\cdot\hat{\psi}\rangle\sqrt{1+\left(\frac{d\rho}{dz}\right)^2} \tag{9}$$

PLANT SCATTERING

We assume that a grass plant consists of a stalk which extends from the soil, with a grain head and its apex and thin leaves originating from random positions along the stalk. The scattered field from a grass plant can thus be expressed as the coherent sum of the scattering from its constituent elements:

$$S_{\chi\psi}^{plant} = S_{\chi\psi}^{grain} + S_{\chi\psi}^{stalk} + \sum_{n=1}^{N} S_{\chi\psi}^{leaf\ n} \tag{10}$$

A general element of the covariance matrix can thus be written as:

$$\begin{aligned}\langle S_{\chi\psi}^{plant} S_{\lambda\mu}^{*plant}\rangle &= \langle S_{\chi\psi}^{grain} S_{\lambda\mu}^{*grain}\rangle + \langle S_{\chi\psi}^{stalk} S_{\lambda\mu}^{*stalk}\rangle + \\ &\sum_{n=1}^{N}\langle S_{\chi\psi}^{leaf\ n} S_{\lambda\mu}^{*leaf\ n}\rangle + \langle S_{\chi\psi}^{grain} S_{\lambda\mu}^{*stalk}\rangle + \langle S_{\chi\psi}^{stalk} S_{\lambda\mu}^{*grain}\rangle \\ &+ \sum_{n=1}^{N}\langle S_{\chi\psi}^{grain} S_{\lambda\mu}^{*leaf\ n}\rangle + \sum_{n=1}^{N}\langle S_{\chi\psi}^{stalk} S_{\lambda\mu}^{*leaf\ n}\rangle + \\ &\sum_{n=1}^{N}\langle S_{\chi\psi}^{leaf\ n} S_{\lambda\mu}^{*grain}\rangle + \sum_{n=1}^{N}\langle S_{\chi\psi}^{leaf\ n} S_{\lambda\mu}^{*stalk}\rangle + \\ &\sum_{n=1}^{N}\sum_{m\neq n}^{N}\langle S_{\chi\psi}^{leaf\ n} S_{\lambda\mu}^{*leafm}\rangle \end{aligned} \tag{11}$$

where $\chi\psi$ and $\lambda\mu$ represent an arbitrary element of set $\{vv, vh, hv, hh\}$. If $\chi\psi = \lambda\mu$, then the covariance matrix element represents real scattered power $\langle|S^{plant}|^2\rangle$, with the first three terms of (11) providing the incoherent scattering power, and the remaining terms providing the inner product or coherent scattering power. Recall each term, such as $\langle S_{\chi\psi}^{grain} S_{\lambda\mu}^{*stalk}\rangle$ likewise represents 16 terms, representing the correlation between the 4 first order scattering mechanisms.

If the plant contains four leaves, then the number of terms in (11) totals 576. This is contrasted to an incoherent formulation, such as radiative transfer, where just 24 terms are considered. Whereas these incoherent terms are certainly the most significant, the question remains whether the remaining 552 coherent terms are *insignificant* when taken in total. Both the small stature and the simple structure of a grass plant may lead to conditions where the coherent terms are important.

CANOPY SCATTERING

Many of the plants comprising the grass family, such as wheat and barley, are agricultural crops which grow not in a random fashion, but instead are planted in straight, periodic rows. The coherent scattering term can be greatly influenced by this structure, and thus the coherent solution for this distribution will be presented here. The scattering covariance from a row section can be expressed as:

$$\begin{aligned}&\langle S_{\chi\psi}^{row} S_{\lambda\mu}^{*row}\rangle = N_p\langle S_{\chi\psi}^{plant} S_{\lambda\mu}^{*plant}\rangle + \\ &N_p(N_p-1)\langle S_{\chi\psi}^{plant}\rangle\langle S_{\lambda\mu}^{*plant}\rangle\langle\exp[\imath 2k_0\bar{k}_p\cdot(\bar{\rho}_n-\bar{\rho}_m)]\rangle_{n\neq m}\end{aligned} \tag{12}$$

where N_p is the number of plants and the two terms can again be interpreted as the incoherent and coherent scattering terms.

The scattering from an area A encompassing a section of row-structured plants can likewise be modeled as the scattering from a collection of row sections located at $\bar{\rho}_{row}^{r} = rX_{row}\hat{x}$, where X_{row} is the spacing between adjacent rows and r is an integer value:

$$\begin{aligned}\langle S_{\chi\psi}^{canopy} S_{\lambda\mu}^{*canopy}\rangle &= \sum_{r=-N_{row}/2}^{N_{row}/2}\langle S_{\chi\psi}^{row} S_{\lambda\mu}^{*row}\rangle_r + \\ &\sum_{r=-N_{row}/2}^{N_{row}/2}\sum_{s=-N_{row}/2, r\neq s}^{N_{row}/2}\langle S_{\chi\psi}^{row}\rangle_r\langle S_{\lambda\mu}^{*row}\rangle_s e^{\imath 2k_x^i X_{row}(r-s)}\end{aligned} \tag{13}$$

and $\langle S_{\chi\psi}^{row}\rangle_r$ is the average scattered field of row r. The phase term in equation (13) is not written as an expected value, as the rows are modeled as a periodic array with spacing X_{row}. Because of this periodicity, the rows generate a Bragg scattering phenomenon, with the average scattered field from each row constructively adding in phase at a set of specific incidence angles.

REFERENCES

[1] Y. Kuga, M.W. Whitt, K.C. McDonald, and F.T. Ulaby, "Scattering models for distributed targets", in *Radar Polarimetry for Geoscience Applications* (ed. F.T. Ulaby and C. Elachi), Artech House, Norwood, MA, 1990.

[2] K. Sarabandi, T.B.A Senior, "Low-frequency scattering from cylindrical structures at oblique incidence," *IEEE Trans. on Geoscience and Remote Sensing*, Vol. 28, No. 5, pp. 879-885,1990.

[3] Tsang, L., J.A. Kong, and R.T. Shin, *Theory of Microwave Remote Sensing*, John Wiley and Sons, New York, 1985, chapter 3.

[4] S.H. Yueh, et al., "Branching Model for Vegetation", *IEEE Trans. on Geoscience and Remote Sensing*, Vol. 30, No. 2, pp. 390-401, 1992.

[5] J.M. Stiles and K. Sarabandi, "A Scattering Model for Thin Dielectric Cylinders of Arbitrary Cross-Section and Electrical Length", *IEEE Trans. Antennas Propagat*, vol. 44, pp.260-266, Feb. 1996.

SCATTERING FROM CULTURAL GRASS CANOPIES: MEASURED AND MODELED DATA

James M.Stiles
Radar Systems and Remote Sensing Lab
The University of Kansas, Lawrence KS
Tel:(913) 864-7744, Fax:(913) 864-7789
e-mail: jstiles@rsl.ukans.edu

Kamal Sarabandi and Fawwaz Ulaby
The Radiation Laboratory
The University of Michigan, Ann Arbor MI
Tel:(313) 936-1575, Fax:(313) 747-2106

Abstract – The validity of a coherent grassland scattering model is determined by comparing the model predictions with direct measurements of a representative grass canopy. A wheat field was selected as this test target, and polarimetric, multi-frequency backscattering data was collected over an entire growing season, along with a complete set of ground-truth data. The L-band measured data demonstrated a strong dependence on azimuthal look direction, in relation to the row direction of the wheat. The C-band measurements likewise resulted in interesting backscattering data, with σ^0_{vv} actually increasing with incidence angle for many cases.

The coherent scattering model provides backscattering data which match and predict these measured data, and most of the other measured data quite well. The model shows that at L-band, the incoherent scattering power alone is insufficient for predicting the measured results, as the coherent terms can dominate the total scattered energy. Additionally, the model, which accounts for this non-uniform illumination of the wheat elements, likewise demonstrates the peculiar data observed for C-band.

INTRODUCTION

During the summer of 1993, an experiment was conducted to measure and quantify the microwave scattering from a grassland canopy. Wheat vegetation was selected as a representative grassland target, as a wheat plant dramatically and continuously changes form during its brief growing period. Thus, each measurement opportunity consisted of observing a canopy which was significantly different than the previous measurement. Additionally, polarization, frequency, incidence angle, and azimuth look angle were all variables at which multiple data points were collected.

Along with the scattering data, a thorough set of ancillary data, precisely describing the grass canopy was likewise measured. All parameters which effect the microwave scattering were evaluated and quantified, regardless of there ultimate significance to remote sensing users. This complete ground-truth data set was used to determine the model results presented in this paper, no free-parameters were involved and the data was not "tweeked" to better match the measured data.

GRASS MODEL

The constituent elements of a grassland canopy are primarily long, thin dielectric elements, thus they can be modeled in an electromagnetic sense as line-dipole elements. Furthermore, these elements reside in a vegetation layer which attenuates and modifies the coherent incident wave as it propagates through the layer, a vegetation layer located on a soil surface. Thus, a formulation which provides the first-order scattering solution for a line-dipole element in an extinction layer over dielectric half-space was implemented to solve the scattering from grassland vegetation [2].

The structure of the grass plant modeled consists of, completely or partially, leaf, stalk and grain elements. In many cases, grassland constituents are modeled as straight elements with circular cross-sections. However, grass structures are often curved elements with decidedly non-circular cross-sections. Using the line dipole element model, the scattering effect of element cross-section can be accounted for completely by a two-dimensional polarizability tensor P_{2d}. For blade-shaped cross-sections, the tensor elements have been determined as a function of three shape parameters [1]. To account for the axial curvature displayed by leaf elements, a curve was defined based on a second order polynomial.

Added to these parameters were values required to statistically describe the orientation, shape, and position of the leaf elements. As a result, twenty parameters were required to specify the leaf element alone. Similar descriptions were developed for the other elements, providing physical analogs which match the wheat structures with high fidelity. Additionally, the model computes the coherent scattering terms not normally accounted for. Therefore, additional statistically parameters were required to specify physical correlations between dissimilar elements and plants. The result was a model of significantly increase fidelity, albeit with a corresponding increase in complexity.

L-BAND RESULTS

The measured scattering data exhibited a strong dependence on azimuth look angle, with significant changes from at least -40 to 40 degrees. The variation is similar to a $\sin x/x$ pattern, and suggests a coherent effect in the data. Another interesting behavior is the fact that this variation is quite dependent on incidence angle with the maximum

0-7803-3068-4/96$5.00©1996 IEEE

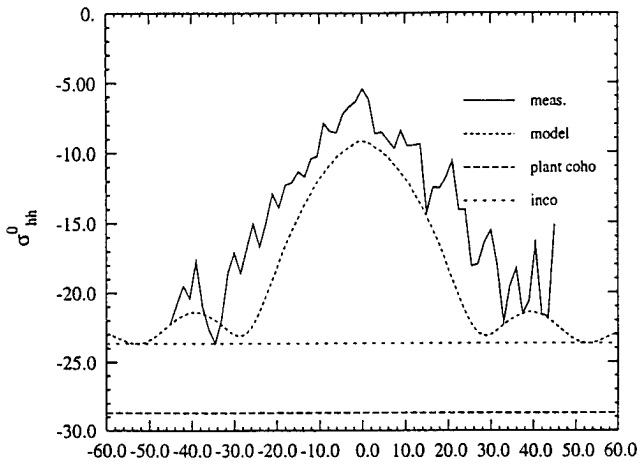


Fig. 1: The measured and modeled backscattering coefficient σ^0_{hh} as a function of azimuth angle for May 25.

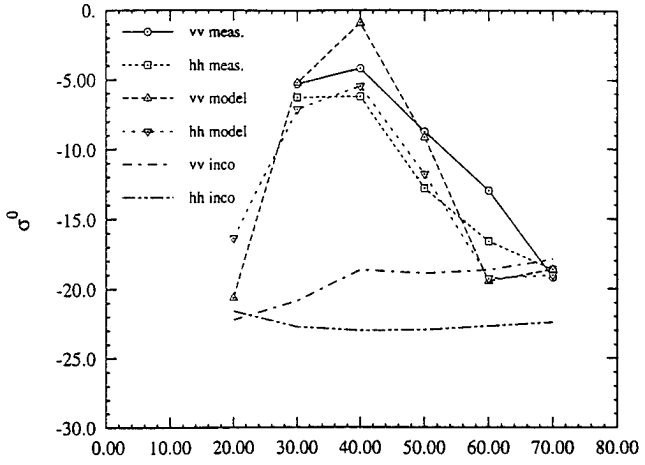


Fig. 2: The measured and modeled backscattering coefficient at zero degrees azimuth, plotted as a function of incidence angle for June 10.

value occurring at 40 degrees incidence. This provides more evidence as to a coherent effect, as the first Bragg mode for a periodic scatterer with the wheat row spacing (20 cm) is approximately 40 degrees at L-band.

For example, Figure 1 shows σ^0_{hh}, at an incidence angle of 40 degrees, as a function of azimuth angle. The model provides a good match to the measured data, but the true significance of the results are seen when observing the lower two traces of the plots. The lowest trace is that of the incoherent scattered power, the summation of the scattered power from each of the individual elements of the vegetation canopy. This quantity, which is generally used to model the scattering from grass vegetation, is as much as 25 dB in error from the measured data. Also plotted on the graphs is the total plant power, that is, the incoherent power plus coherent terms resulting from the correlation between dissimilar mechanisms or elements (row coherence is neglected). Thus, the coherent scattering terms not only are significant, they can in aggregate be much greater than incoherent power.

Note the coherent effects of the row structure are dependent on the illumination of the wheat canopy. This leads to a major difficulty which arises from the coherent effects of the row structure. For the coherent effect from the row structure, the scattering is not proportional to the illumination area, and thus different sensors will measure different σ^0 values.

Figure 2 displays the scattering as a function of incidence angle when the radar is looking perpendicular to the row structure ($\phi_i = 0$). The Bragg scattering effect is evident, peaking at 40 degrees and then falling off rapidly as incidence angle increases. The figures likewise display the incoherent scattering, and the large discrepancy between the incoherent power and the total power at this azimuth angle is quite apparent.

C-BAND RESULTS

The C-band radar frequency of 5.3 GHz is more than four times the center frequency of the L-band data. As a result, the expected value of the coherent terms are small and insignificant when compared to incoherent scattering data. The measured C-band scattering data, however, revealed an interesting phenomenon when plotted as a function of incidence angle. This general behavior shows σ^0_{vv} initially decreasing with incidence angle, but then sharply increasing from 40 to 70 degrees. For several test days, the largest value of σ^0_{vv} actually occurs at 70 degrees incidence. This is in marked contrast to the scattering behavior of most random media, where σ^0 decreases monotonically as a function of incidence angle, as σ^0_{hh} does in this data.

Additionally, the scattering data reveals something about the dependence on soil moisture. By contrasting backscattering data taken both before and after a significant rain event, we note that the horizontal co-polarized backscattering coefficient has increased on the second day for every incidence angle. The vertical coefficient has likewise increased for small incidence angles, but at large angles σ^0_{vv} is nearly identical for both sets of test data. The inference derived from this data is that σ^0_{hh} is significantly effected by scattering mechanisms which involve scattering from the soil surface. The same is true for σ^0_{vv} at small incidence angles, however at incidence angles of 40 degrees and above, the lack of sensitivity indicates that the direct scattering from the vegetation dominates in this region.

The scattering response σ^0_{hh} as a function of incidence

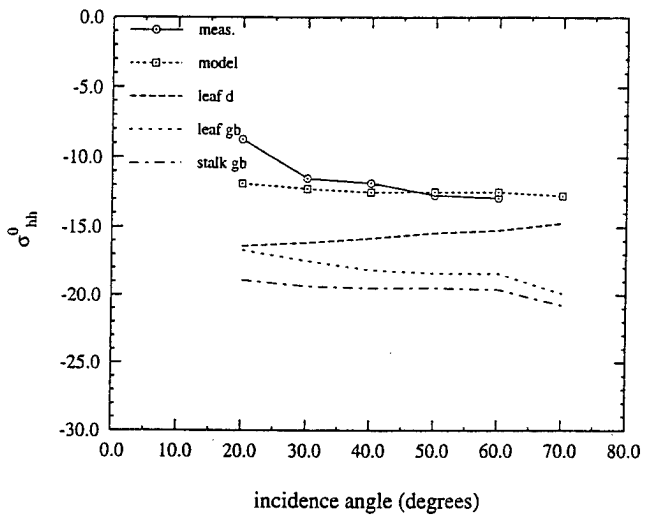


Fig. 3: The measured and modeled backscattering coefficient σ^0_{hh} at C-band, plotted as a function of incidence angle for May 17 (gb= ground bounce, d=direct).

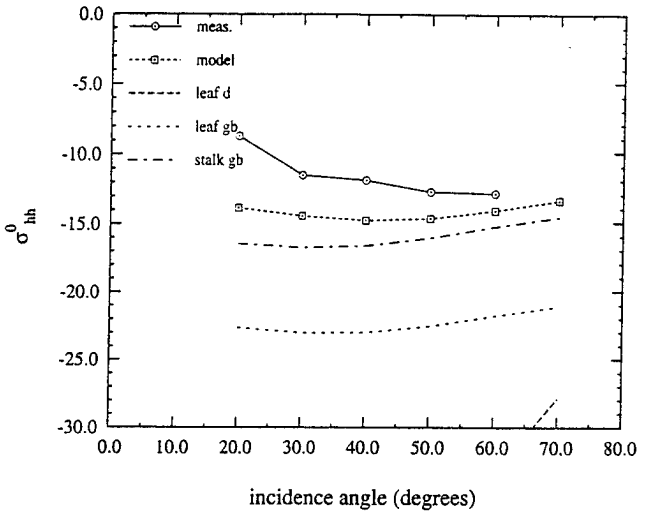


Fig. 4: The measured and modeled backscattering coefficient σ^0_{hh} at C-band, evaluated with straight leaves of circular cross-section.

angle is given by Figure 3 for a test day early in the growing season. No single scattering term dominates, but instead the total is mainly a function of three scattering terms.

The measurements suggested that σ^0_{hh} is sensitive to soil moisture for all incidence angles. The dominance of the ground-bounce term for this polarization confirms this, as the ground-bounce scattering is directly proportional to the reflection coefficient of the soil surface. However, this value is likewise dependent on the size of the wheat vegetation, so that the scattering is essentially a reflection of both biomass and soil moisture.

Finally, recall that both the cross-section shape, as well as leaf curvature, are considered in the leaf scattering model. The model data of May 17 provides an excellent opportunity to test the importance of this added fidelity. The model data not only matches the measured data well for this date, but also shows that the leaf scattering is the major contributor to the response. Therefore, the data was again computed with leaves of the same cross-sectional area, average length, and angular distribution as before, however this time the cross-section was assumed to be circular, and the leaves to be straight. The results are provided in Figure 4, and graphically demonstrate the tremendous difference between the two cases.

The accuracy of the model predictions for *vv* polarization, although adequate, did not match that of the *hh* case. However, the general response of the scattering is matched well, giving insight into the reasons for the peculiar concave response exhibited by this polarization.

As the incidence angle increases, the attenuation through the vegetation causes the ground-bounce terms to diminish, and the scattering decreases to a minimum at approximately 40 degrees. At incidence angles at 40 and above the direct scattering from the grain (with a little from the stalk) increases, again forming the general concave shape of the scattering response. It should be noted that the model confirms the inference from the measured data, that σ^0_{vv} at C-band is sensitive to soil moisture at all incidence angles 20 and 30 degrees only

X-BAND RESULTS

When examining this data at X-band, the data needs to be divided into vegetation with and without a grain head element. When no grain head exists, the model displays a good match to the measured data with generally less than 2 dB error for all data points. Conversely, the model data for the days where the grain head is prevalent exhibits very poor accuracy, with the error often exceeding 5 dB. This error, particularly when compared to the good performance when the grain is not present, again suggests that the grain model is a poor estimator of grain head scattering for at high frequencies. Additionally, the cross-pol data at all frequencies exhibited significant errors, suggesting that second-order scattering terms are significant for these polarizations.

REFERENCES

[1] J.M. Stiles, et al.,"Microwave Scattering Model for Grass Blade Structures', *IEEE Trans. on Geoscience and Remote Sensing*, Vol. 31, No. 5, pp. 1051-1059, Sept. 1993.

[2] J.M. Stiles and K. Sarabandi,"Scattering from Cultural Grass Canopies: A Phase Coherent Model", submitted to *Proc. Int. Geosci. Remote Sensing Symp.*, Lincoln, Nebraska, 1996.

Forest Backscatter Modeling: Simulation Versus Discrete Random Media Approach

Roger H. Lang* and Robert Landry**

*Dept of Electrical Engineering & Computer Science
The George Washington University
Washington, DC 0052 USA
lang@seas.gwu.edu

** Canada Centre for Remote Sensing
Ottawa, Ontario K1a 0Y7 Canada
landry@ccrs.emr.ca

Abstract --The radar backscatter is computed from a forest by using two different techniques and the results are compared. The basis for the comparison is tree architecture information obtained by Landry. Using his technique the coordinates of all branch nodes of the tree are reconstructed. With this information, the backscatter is computed by coherently adding up the backscatter from individual branch links. The results are compared to the standard statistical approach where branches are treated independently with prescribed orientation statistics. The procedure is applied to red pine and jack pine trees at L band frequencies. The results show that when trunks are the dominant scatterers, the backscatter is approximately the same while when volume scatter is dominant, differences of as much as 6 db can be observed.

INTRODUCTION

The backscatter modeling of forests at microwave frequencies has been of interest for many years. By treating forests as a two layer random media, statistically based backscatter formulas have been derived by the distorted Born approximation [1] or by a transport approach [2]. Using these approaches trunks, branches, leaves and needles are replaced by lossy dielectric cylinders and discs with prescribed orientation statistics.

Investigators have tried to improve upon these models in two directions. First, they have examined coherence effects between scatterers. They have considered the coherent interaction between cylinders and spheres [3] and the enhancement effect of parallel trunks [4]. The effects of scatter shape have been considered by Lang et al [5]. They modeled a tapered trunk by coherently adding cylindrical sections of varying size.

Recently, the two efforts have been combined in a tree simulation. Using data obtained by Landry et al [6], Lang et al [7] computed the backscatter from a reconstructed red pine tree by coherently adding the scatter from each cylindrical segment. This procedure not only accounted for all first order coherent effects between scatterers but also accounted for the tapering of trunks and the tapering and the bending of branches.

In this paper we will compare the results of this simulation method to the results one obtains by using the statistical distorted Born model. In the next section, a brief review of the architectural tree modeling is given. This is followed by short discussions of the simulation procedure and the statistical approach. Finally, a comparison of the backscatter coefficients for a red pine forest and BOREAS jack pine trees is given for each of the two methods.

TREE ARCHITECTURE MEASUREMENTS

Landry has developed a procedure for obtaining the complete architectural description of a tree. The procedure is known as the "Tree Vectorization" technique [5]. A selected tree is fallen, cut into manageable sections. These sections are erected in a vertical position and several representative branches are chosen for vectorization. A surveying instrument is used to obtain the three dimensional coordinates of the branching nodes of the selected branches. In addition, other data is taken on trunk and branch dimensions.

This information is used in a reconstruction process whereby the coordinates of all branching nodes are generated. The reconstructed nodes are not exactly

0-7803-3068-4/96$5.00©1996 IEEE

those of the original tree but closely resemble it. The simulated tree not only looks like the real tree but, on close inspection, has the detailed characteristics the mother tree.

The methodology has been used to measure several tree types. Two of these will be examined in this paper. The first is a sixty year old red pine (pinus resinosa) measured in the Petawawa National Forest located in Chalk River, Ontario Canada (July, 1992). The second is a young jack pine tree (pinus banksiana) measured in the BOREAS Southern Study Area [8] in Saskatchewan, Canada (August, 1995).

SIMULATION METHOD

The simulation method is used to compute the backscatter from a stand of trees over a rough surface. The stand is constructed by dividing the forested area into a grid and by placing a simulated tree at each intersection. Trees are given a random azimuthal rotation to make the collection appear random. Since the positions of all branch nodes are known, each tree can be considered to be a collection of lossy dielectric cylinders whose coordinates are known.

The scattered fields are computed by coherently adding the scattered field from each cylinder. Attenuation in the forest medium is accounted for by immersing the stand in an equivalent medium whose properties are calculated using a form of the Foldy approximation. Direct scattering from the cylinders and scattering between the cylinders and the ground are considered but second order scattering between cylinders is not taken into account. More details of the methodology can be found in Lang et al [7].

STATISTICAL TECHNIQUE

In the treatment of scattering from a forest stand by the statistical method, the forest is considered to be a two layered random medium. The upper layer is composed of randomly oriented dielectric cylinders representing branches of different sizes and needles. The lower layer consists of tapered cylinders representing trunks. These cylinders may extend into the upper layer but for the purposes of scattering are considered to be members of the trunk layer. The distorted Born theory is used to calculate the scattered fields. The method only considers single scattering and all scatterers are assumed independent of each other.

One difficulty, in appling the technique, is to derive the classes of cylinders needed to represented the branches. There are many ways of doing this and it is not clear which is the best. One methodology is detailed in [1]. In this paper the procedure will be as follows: first, break the tree up into branches, second, replace each branch by a cylinder; third, form a histogram of cylinder diameters, fourth, partition the histogram into classes and choose an average cylinder from each class.

When breaking the tree into branches, start at the bole and follow each primary branch to its terminus. This is not always a unique process since branches fork or make sharp turns. Select the next link by choosing the branch whose diameter and direction change the least. It is hoped that the number of truly ambiguous cases will be small compared to the whole. For each primary branch follow all secondary branches to their termini and so on.

For each branch an equivalent cylinder must be chosen. The following rules will be used. The cylinder length will be the sum of the branch segment lengths. The branch diameter will be an average over the segment diameter which is weighted by their length. The inclination and azimuth angles are again averages over the segment angles weighted by the segment's length.

Using this methodology branch classes have been chosen for the red pine and jack pine trees. For example, the red pine branch classes are shown in Table I.

Table 1

Branch Type	Diameter(cm)	Length(cm)
Secondary 1	.32	4.20
Secondary 2	.33	19.3
Secondary 3	.47	6.5
Primary 1	.75	105.
Primary 2	1.05	234

Densities have been computed, as well as, angular distributions.

NUMERICAL RESULTS

The comparison of the two methods was done at P and L band frequencies for the red pine tree. The vectorized tree had a dbh of 23.5 cm and a trunk height of 20.8 m. The needles were chosen to have a radius of .06 cm and a length of 10.3 cm. For the statistical model

the crown layer thickness was 7.1 m and the trunk layer was 15.1 m. The underlying ground had a surface roughness of 2 cm and a large correlation length so that incoherent surface scatter contributed in a measurable way only at angles below 5 degrees.

The results of the comparison are shown in Fig. 1 for like polarization. The plots HHSIM and VVSIM are for the horizontal and vertical simulation while HHSTAT and VVSTAT are for the horizontal and vertical statistical method respectively. In the case of horizontal polarization the simulation results follow the statistical calculations quite closely for angles less than 65 degrees. In this range of angle, the double bounce (direct-reflected) is the main contributor. Since both models have identical trunks, the results are expected to be the same.

In the VV case the attenuation is stronger and the direct -reflected term is only important for angles less than 35 degrees. From Fig. 1 it is seen that the simulation results are somewhat higher than the results of the statistical method in this angular region.

For angles greater than 65 degrees for HH and greater than 35 degrees for VV, the statistical values are higher than the simulation results. In this region direct backscatter from the trees is the main contributor. It is observed that differences between the two results can be larger than 5 db. The differences are due to the different treatment of branches in each case and possible coherence effects.

The results of scattering from red pine at P band are trunk dominated over a broader range of angles. The calculations from the young jack pine tree show that the results are trunk dominated for both P and L band. However, in a real situation surface scatter becomes important and must be treated more carefully to obtain realistic results. This implies that the assumed large correlation length used in the red pine case must be lowered.

REFERENCES

[1] N.S. Chauhan, R.H. Lang and K.J. Ranson,"Radar modeling of boreal forest," IEEE TGRS, 29, pp.627-638,1991.

[2] M.A. Karam, A.K. Fung, R.H. Lang and N.S. Chauhan, "A microwave scattering model for layered vegetation," IEEE TGRS, 30, pp.767-784, 1992.

[3] P.F. Polatin, K. Sarabandi and F.T. Ulaby, " Monte carlo simulation of electromagnetic scattering from a heterogeneous two-component medium," IEEE TAP, 43, pp.1048-1057, 1995.

[4] L. Tsang, K. Ding, G. Zhang, C.C. Hsu and J. A. Kong, " Backscattering enhancement and clustering effects of randomly distributed dielectric cylinders overlying a dielectric half space based on monte-carlo simulations," IEEE TAP, 43, 488-499, 1995.

[5] R. Landry, R.H.Lang and R.Cacciola, Fine tree architecture reconstruction in support of microwave models," in Inter. Symposium on Retrieval of Bio- and Geophysical Parameters from SAR Data fpr Land Applications, Toulouse, France, 1995 in press.

[6] R.H. Lang, N.S. Chauhan and O. Kilic, "Modeling P-band SAR returns from a red pine stand," Remote Sens. Environ, 47, pp.132-141. 1994.

[7] R. H. Lang, R. Landry, O. Kavakhioglu and J.C. Deguise, " Simulation of microwave backscatter from a red pine stand," in Multispectral and Microwave Sensing of Forestry, Hydrology and Natural Resources, editors, E. Mougin, J. Ranson and J. Smith, SPIE, Rome Italy, vol 2314, pp.538-548, 1994

[8] F.G. Hall, P.J. Sellers, M. Apps, D. Baldocci, J. Cihlar, B. Goodison, H. Margolis and A. Nelson, " BOREAS: Boreal Ecosystem-Atmosphere Study," IEEE TGRS Newsletter, pp.9-17, 1993.

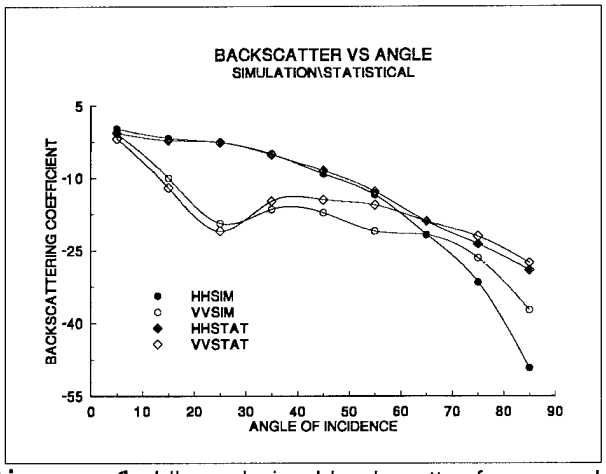


Figure 1 Like polarized backscatter from a red pine stand a L band.

Wave Scattering and Scene Image of Trees Generated by Lindenmayer Systems

Guifu Zhang and Leung Tsang
Electromagnetics and Remote Sensing Laboratory
Department of Electrical Engineering
Box 352500
University of Washington, Seattle, WA 98195-2500
Telephone: (206)685-7537 Fax: (206)543-3842

Abstract

When the distances between branches and leaves are not far away or a wavelength scale, branches and leaves scatter collectively. Collective scattering effects depend on the relative locations of branches and leaves in a tree. We used Stochastic Lindenmayer Systems to generate trees. The tree generated by Lindenmayer systems has the realistic appearance so that the relative locations of branches and leaves are reasonably represented. The wave scattering by branches and leaves is calculated by using coherent addition approximation (CCA). The scattering of rough surface and that of grass are included. The scene images of the Lindenmayer tree are provided for vv, hh, hv polarizations at L-band.

1. Introduction

Wave scattering by vegetation has been studied by using independent scattering approximation (Ind), coherent addition approximation (CAA), and coherent mutual interaction model (CIM) in previous papers[1-3]. It was shown that coherent addition approximation is valid for most problems of wave scattering by vegetation, In CAA, the relative phase information of wave scattering from branches and leaves is retained, and the structure of plants is important. Instead of using the pair-distribution function which is difficult to obtain for vegetation, we use Lindenmayer systems to generate plants and trees which are quite realistic in appearance to natural trees. In this paper, we present results of scene images of vegetation at microwave frequencies based on simulations. Rough surface scattering effects are also included. The scene image of the tree is provided for vv, hh, hv polarizations.

0-7803-3068-4/96$5.00©1996 IEEE

2. Formulation and Method

Consider a tree above a random rough surface with grass around it. The tree scattering coefficient $\sigma_{\beta\alpha}^{(T)}$ is calculated by using coherent addition approximation, given as

$$\begin{aligned}\sigma_{\beta\alpha}^{(T)}(\hat{k}_s,\hat{k}_i) = \frac{4\pi}{A}|\sum_{i_{bl}=1}^{N_{bl}}[&f_{\beta\alpha}^{(i_{bl})}(\hat{k}_s,\hat{k}_i) \\ &+f_{\beta\alpha}^{(i_{bl})}(\hat{k}_s,\hat{k}_{iu})\cdot R_\alpha \\ &+R_\beta\cdot f_{\beta\alpha}^{(i_{bl})}(\hat{k}_{sd},\hat{k}_i) \\ &+R_\beta\cdot f_{\beta\alpha}^{(i_{bl})}(\hat{k}_{sd},\hat{k}_{iu})\cdot R_\alpha]|^2 \end{aligned} \quad (1)$$

where $f_{\beta\alpha}^{(i_{bl})}(\hat{k}_s,\hat{k}_i)$ is the scattering amplitude of a branch or a leaf. R is the modified Fresnel reflection coefficient, in which the roughness effect on the reflection is included. N_{bl} is the number of branches and leaves which contribute to the scattering in the pixel. It is noted that for the SAR image with fine resolution, the 4 terms in Eq. (2) do not always contribute a pixel simultaneouly due to the limited time range. So, the position of a pixel, the azimuth resolution and range resolution together determine whether a branch or a leaf has contribution, and which term contributes to the pixel.

The wave scattering from the tree, grass and rough surface are assumed to be independent. We have

$$\sigma_{\beta\alpha} = \sigma_{\beta\alpha}^{(S)} + \sigma_{\beta\alpha}^{(G)} + \sigma_{\beta\alpha}^{(T)} \quad (2)$$

$\sigma_{\beta\alpha}^{(S)}$ is the scattering coefficient of rough surfaces, which is calculated by using Kirchhoff approximation or small perturbation method [1]. Grass scattering coefficient $\sigma_{\beta\alpha}^{(G)}$ is evaluated by using grass independent scattering approximation.

3. Results

We first use Lindenmayer systems to generate an evergreen tree as shown in figure 1. It is 15.5 meters high with 7162 branches in which there are 3577 end branches. A leaf is attached to each of the end branch.

Figure 2 shows the scene images of vv, hh, and hv polarization for the resolution of $1m$X$1m$. The backgrounds are the scattering by rough surface and grass, which is the sum of the first two terms in Eq. (2). They are obtained by generating random numbers based on Rayleigh distribution. We can see main features of the tree in both co- and cross- polarization. However, it is much clearer in hv polarization because the background scattering due to rough surface and grass has minimal cross polarization.

4. Reference

[1] L. Tsang, J. A. Kong, and R. T. Shin, *Theory of Microwave Remote Sensing*, Wiley Interscience, New York, 1985.

[2] Z. Chen, L. Tsang, and G. Zhang, " Microwave Scattering by Vegetation Based on Wave Approach and Stochastic Lindenmayer System," *Microwave and Optical Technology Letters,* vol. 8, no. 1, pp. 30-33, 1995.

[3] G. Zhang, L. Tsang, and Z. Chen, "Collective scattering effects of trees generated by stochastic Lindenmayer systems," *Microwave and Optical Technology Letters,* vol. 11, no. 2, pp. 107-111, 1995.

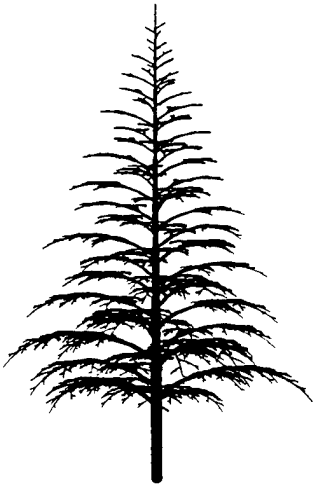
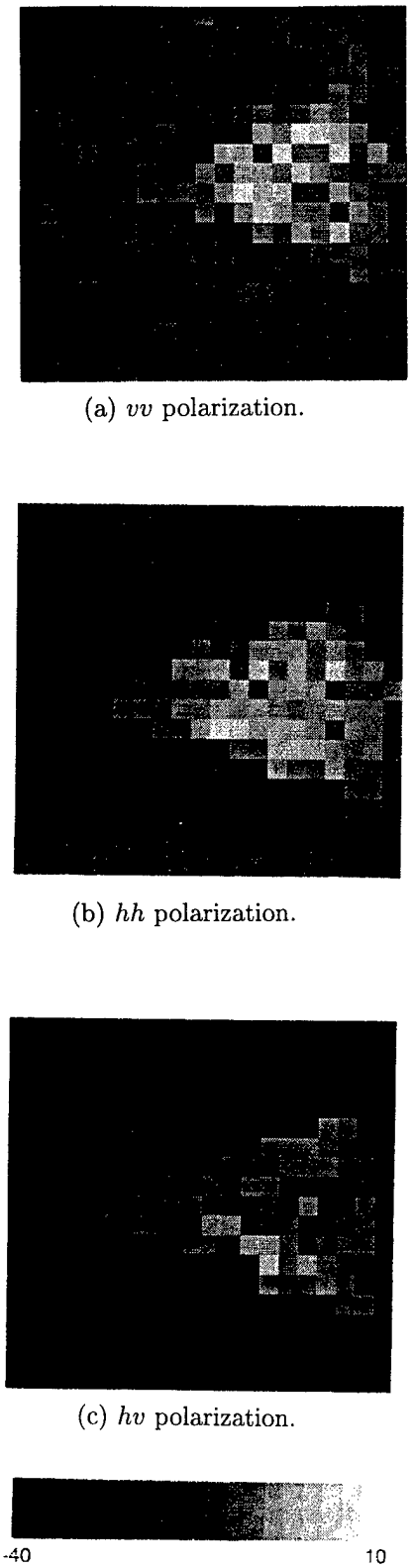


Figure 1: *A tree generated by Lindenmayer systems. It is 15.5 meters high with 7162 branches.*



(a) *vv* polarization.

(b) *hh* polarization.

(c) *hv* polarization.

Figure 2: *Simulated scene images for vv, hh, and hv polarizations. Incident angle is* 45^o. *Resolution is* $1mX1m$. *Frequency is* $1.25GHz$.

Estimation of Moisture Content of Forest Canopy from SAR Data

Mahta Moghaddam and Sasan Saatchi
Jet Propulsion Laboratory, California Institute of Technology
4800 Oak Grove Drive
Pasadena, CA 91109
Phone: 818-354-1591, Fax: 818-393-5285, email: Mahta.Moghaddam@jpl.nasa.gov

Abstract - During several field campaigns in spring and summer of '94, the NASA/JPL airborne synthetic aperture radar (AIRSAR) collected data over the southern and northern study sites of BOREAS. Among the areas over which radar data were collected was the young jack pine (YJP) tower site, which is generally characterized as having short (2-4 m) but closely spaced trees with a dense crown layer. In this work, we use the AIRSAR data over this YJP stand from several different dates, and estimate the dielectric constant and hence the moisture content of its branch layer components. This is accomplished by applying a nonlinear estimation algorithm to the data assuming a parametric model of scattering derived from a discrete-component forest model. The results thus obtained show how the environmental conditions affected the moisture state of this forest stand over a period of six months. The results are compared to the available ground-truth measurements of moisture content and dielectric constant.

1. INTRODUCTION

The area used for this work is part of a larger region used in the boreal ecosystem atmosphere study (BOREAS) project [1]. During several focused and intensive field campaigns in 1994, SAR images were acquired over BOREAS study sites with the intention of mapping forest types and estimating parameters important in ecosystem modeling. The images we have chosen in this study were acquired over an area containing primarily jack pine stands: young jack pine (YJP) at a regeneration stage with average age of 10-15 years, and old jack pine (OJP) with average age of 65 years. These are located in the BOREAS Southern study area (SSA), near the Prince Albert National Park in Saskatchewan.

The images were obtained with the NASA/JPL airborne synthetic aperture radar (AIRSAR), which measures polarimetric C-, L-, and P-band backscattering data. In this work, we have chosen data from six different dates: 17, 20, and 26 April, 11 June, 28 July, and 20 September. The three April data sets are chosen since they present the changes taking place during the thaw season. The remaining three data sets represent the state of the forest during the spring and summer growing seasons.

0-7803-3068-4/96$5.00©1996 IEEE

The young jack pine (YJP) stand was well characterized by performing comprehensive ground truth measurements. The parameters measured are related to the structure and architecture of the forest canopy, which are slowly varying functions of time, and on small time scales (days, weeks, or even months), not dependent on environmental conditions such as temperature and precipitation. To study the interaction of the forest stand with atmosphere, energy exchanges, and growth rate, it is necessary to measure parameters which are more dynamically related to changes in the environmental conditions. One such parameter is the moisture content of the canopy, which is directly related to the dielectric constant of the forest canopy components, and hence can, in principle, be studied with scattering measurements using SAR.

In this work, our goal is to determine the moisture state (water content) of the branch layer in the YJP forest by inverting dielectric constant values from SAR data. The methodology can be summarized as follows:

1. Assuming the backscattered field is mainly due to branch layer volume scattering, derive parametric models that relate the radar backscattered cross section for multiple frequencies and polarizations to the complex dielectric constant of branch layer components. Since the YJP forest has a rather dense crown layer, at C- and L-bands the backscattering cross section is almost entirely due to branch layer volume scattering.
2. Given the parametric models, use a nonlinear optimization scheme to derive the real and imaginary parts of the dielectric constant using SAR data from each of the six data takes.

2. PARAMETRIC MODELS

The backscattered field from a forest contains contributions from four major sources: forest floor, trunk-ground and branch-ground double-bounce, and branch layer volume scattering. Since only a limited number of measurements are available for each pixel, we consider cases where the scattered fields are mainly due to one mechanism, so that the number of unknowns is reduced. Here, we will focus on branch layer volume scattering, which can be shown [2] to be dominant in the YJP site for L- and C-bands.

To derive a parametric model for volume scattering from branches, we used a discrete component forest scattering model [3], defined a forest as characterized by our ground truth measurements of YJP, and calculated the radar backscatter for L- and C-bands for all polarizations as the real and imaginary parts of the dielectric constant of branch layer constituents were varied. A sample of synthetic data such generated is shown in Figure 1. Parametric curves in the form of polynomials were used to fit the data. Once the coefficients of these two-dimensional polynomials are found, they can be used in an estimation algorithm to retrieve the unknowns from SAR data.

3. ESTIMATION ALGORITHM

The estimation technique (also loosely referred to as inversion technique) is a nonlinear one, since the data and unknowns are related via nonlinear functions, in this case polynomials of order up to 4. The parameter estimates are obtained by defining a least squares criterion based on minimizing the distance between data and model calculations, and is carried out in an iterative fashion, each time updating the solution for the unknowns until an acceptably small error is reached. Issues of concern are the method of calculating direction and step length in the direction of solution update at each iteration, and incorporating the statistics of data and unknowns in the estimation procedure. Here, we have used a preconditioned conjugate gradient algorithm to carry out each iteration of the solution. The statistics of the problem are taken into account through appropriate covariance operators.

This algorithm was tested using synthetic data, and it was found that the estimation error for "typical" values of unknowns is small (about 5%), and no more than 25% overall.

4. RESULTS

Figure 2 shows a sample (C-VV) of the variation in radar backscatter over the six data take dates. The above inversion algorithm was applied to the BOREAS YJP data. The results are summarized in Figures 3(a) and 3(b). These figures show the generally increasing trend of both the real and imaginary parts of the dielctric, although each in a different fashion. The real part decreases at the last data take. These will be discussed at the presentation.

To our knowledge, specific measurements or models relating the moisture content of the branch layer to the dielectric constant of its components do not exist for the YJP forest. However, similar data exist for other types of conifers relating the trunk dielectric constant, as a function of radial distance into the trunk, to its moisture content [4]. Based on these measurements and moisture content data obtained for the YJP forest in the summer of 1994, the values shown in Figure 4 were obtained.

5. CONCLUDING REMARKS

An inversion algorithm based on a nonlinear least-squares estimation was used to invert a subset of forest parameters from a parametric model. This model was derived from a discrete component forest scattering model, and was constructed for the volume scattering case. The free parameters were the real and imaginary part of the dielectric constant of branch layer components. The algorithm was first tested and validated with synthetic data and later applied to six data sets from the BOREAS YJP site. The results clearly indicate the distinct moisture states of the forest canopy at the dates of the data takes.

This inversion algorithm will later be extended to cases where a larger set of forest parameters will be treated as unknowns, using the same methodology as described here. In its current form, this could be a valuable tool for monitoring the change in canopy moisture states for various forest stands over short- or long-term temporal scales.

ACKNOWLEDGEMENT

The work described here was performed by the Jet Propulsion Laboratory, C lifornia Institute of Technology, under a contract from the National Aeronautics and Space Administration.

REFERENCES

[1] BOREAS Experiment Plan, Chapter 1, Version 3.0, May 1994.

[2] M. Moghaddam and S. Saatchi, "Analysis of scattering mechanisms in SAR imagery over boreal forest: Results from BOREAS'93," *IEEE Trans. Geosci. Remote Sensing*, vol. 33, no. 5, pp. 1290-1296, September 1995.

[3] S. L. Durden, J. J. van Zyl, and H. A. Zebker, "Modeling and Observation of the Radar Polarization Signature of Forested Areas," *IEEE Trans. Geosci. Remote Sensing*, vol. 27, pp. 290-301, 1989.

[4] W. A. Salas, K. J. Ranson, B. N. Rock, and K. T. Smith, "Temporal and spatial variations in dielectric constant and water status of dominant forest species from New England," *Remote Sensing Environ.*, vol. 47, pp. 109-119, Feb. 1994.

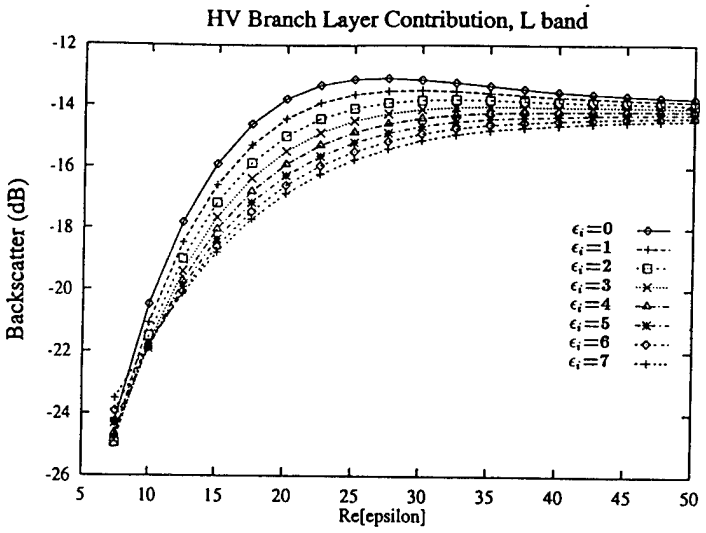


Figure 1

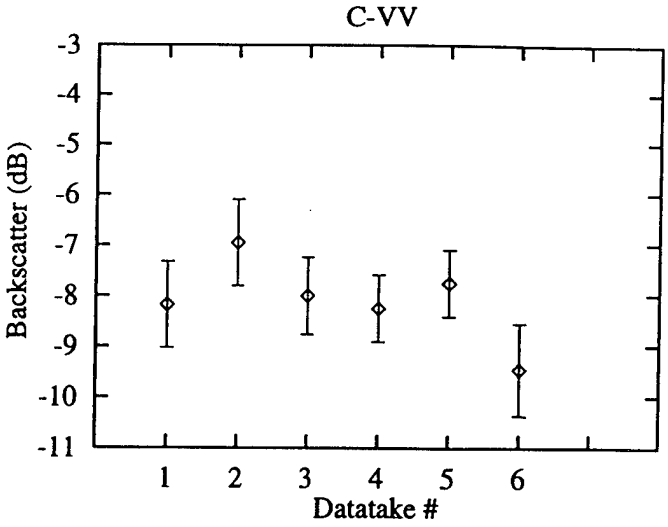


Figure 2

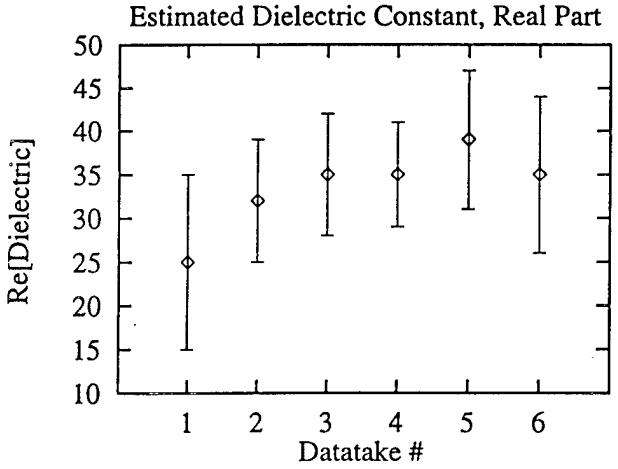


Figure 3(a)

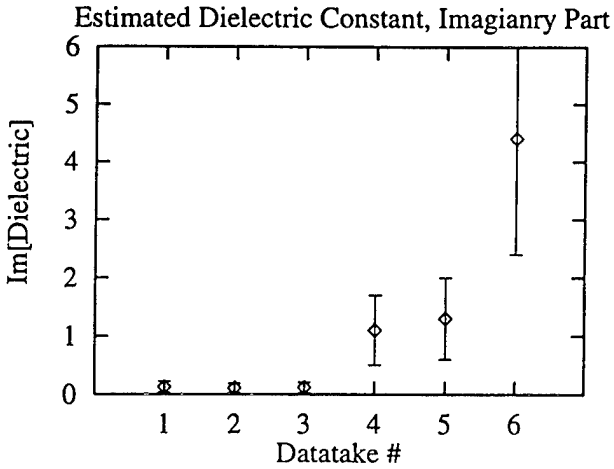


Figure 3(b)

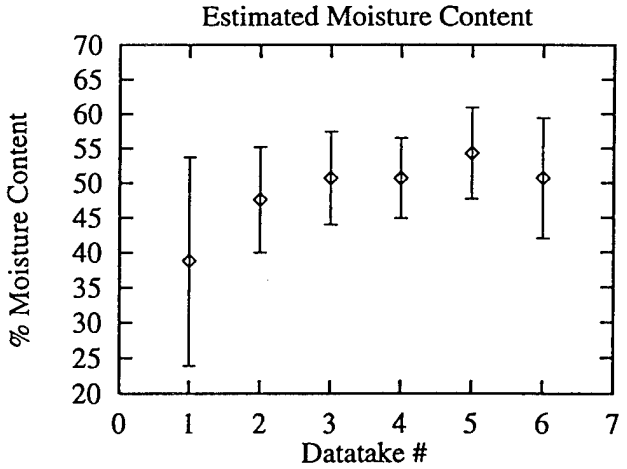


Figure 4

Datatake	Date
1	17 Apr 94
2	20 Apr 94
3	26 Apr 94
4	11 Jun 94
5	28 Jul 94
6	20 Sep 94

Investigating correlations between radar data and mangrove forests characteristics

C. Proisy[1], E. Mougin[1], F. Fromard[2]

1 - Centre d'Etudes Spatiales de la Biosphère
CNES/CNRS/Université Paul Sabatier
bpi 2801, 18 avenue Edouard. Belin, 31055 Toulouse Cedex, France
Phone Number : (33) 61.55.85.19 Fax Number : (33) 61.55.85.00 Email : proisy@cesbio.cnes.fr
2 - Laboratoire d'Ecologie Terrestre, 13 avenue du Colonel Roche, BPI 4403 31405 Toulouse Cedex, France

Abstract -- In this paper, we present a statistical analysis of multifrequency and multipolarisation SAR data acquired over mangrove forests of French Guyana. A large SAR data set, acquired by both spaceborne (ERS-1, JERS-1, SIR-C) and airborne (NASA/JPL AIRSAR) systems has been collected. Different test sites were selected in French Guyana, in order to picture the successionnal stages of mangrove dynamics, characterized by their specific floristic, structural and functionning parameters. Intensive field measurements were performed over these sites. Standing biomass values are then derived. This data set is used to assess the capability of SAR systems to retrieve structural parameters of mangrove forests. Here, statistical relationships between AIRSAR multipolarisation data and mangrove parameters are shown.

INTRODUCTION

Mangrove forests grow exclusively in the intertidal zone, with an extent of about 10 millions hectares throughout the intertropical regions. In spite of being considered economically and scientifically of prime importance, mangrove forests are the less well known terrestrial ecosystems, and particularly, their functionning and associated dynamics have rarely been studied. This lack of fundamental information can be explained by the difficulties encountered during field studies in such media. The monitoring of the mangrove dynamics can be advantageously undertaken by using remote sensing systems. However, a quasi-permanent cloud cover over the regions considered does not allow repetitive observations to be performed with the sensors operating in the visible and near infrared domain. In this context, information delivered by imaging radars deserve our attention since SAR systems have already been successfully used for mapping and discriminating between different flooded forests and low vegetation canopies [1]. In this paper, we present a statistical analysis of multipolarisation AIRSAR data versus French Guyanese mangrove parameters.

0-7803-3068-4/96$5.00©1996 IEEE

TEST SITE

Description

The French Guyanese coast can be seen as a uniform mangrove forest stretching over 350 km long and only 1 to 2 km wide, with a total extent of about 70 000 hectares. In French Guyana, only three mangrove species can be found : the grey mangrove (*Laguncularia racemosa*), the white mangrove (*Avicennia Germinans*) and the red mangrove (*Rhizophora Mangle*) [2]. The colonization of coastal mudbanks by the mangrove forest starts with the grey mangrove. Along a transect from the sea onto the land, the canopy height and the standing biomass of the grey mangrove increases progressively whereas tree density decreases. As we move farther, the white mangrove is encountered; this latter progressively eliminating the first species. The farther we move away from the sea, the older is the population of *Avicennia Germinans*. The canopy height and standing biomass thus continue to increase as tree density decreases. At this development stage, which can be considered as the mature stage, the mangrove canopy is a monospecific forest characterized by a height of about 25-30m. Then as trees increase in height and decrease in density, other species are observed like the red mangrove. Farther on, the mangrove forest disappears and is replaced by a flooded forest. The disappearence of the mangrove forest can also occur in a different way leading to swamps or lowland forest. Along the Guyanese coast, in several locations, decaying mangrove zones covered by dead trunks of the white mangrove can be observed. In short, the dynamics of mangrove forests of French Guyana can be characterized by 4 development stages as follows : 1) mangrove establishment and early growth stage, 2) mature stage, 3) senescent stage and transformation into flooded forests and swamps, 4) decaying and dead mangrove. These different stages are situated almost parallel to the coast. Mapping Guyanese mangrove forests has previously been presented elsewhere [3]; Here, emphasis is put on the retrieval of structural parameters, including aboveground biomass.

SAR Data Acquisition

The test site was imaged on June 11, 1993 by the NASA/JPL AIRSAR instrument at P- (0.44 GHz), L- (1.25 Ghz) and C-bands (5.3 Ghz), in four combinations of polarization (HH, VV, HV, VH). Data was collected at a mean incidence angle of 35°. The compressed delivered data was calibrated using the POLCAL method developped by JPL [4]. Intensities at P-, L-, C-bands, phase differences, coherence degrees were then derived.

Ground Data Collection

Ground data have been collected on an extensive basis for the general characteristics of the test sites including delineation of mangrove forest, inventory of species, vegetation and soil characteristics. Allometric relationships between tree d.b.h (diameter at breast height) and tree height and biomass by part (leaves, branches and trunks) were derived from in situ measurements [5]. Furthermore along a selected transect, density of trees, tree heights and distribution of tree diameters were measured. Then, aboveground biomasses were estimated using the allometric equations. The transect was divided into 11 large plots representative of different development stages of mangrove forests.

DATA ANALYSIS AND RESULTS

Only intensities at P-, L- C-bands are analysed as a function of structural parameters (tree diameters, tree heights, density of trees and basal area) and above ground biomass by part (foliar, branches, trunk, total biomass).

Correlations with Mangrove Characteristics

Table I shows linear correlation coefficients between radar parameters and mangrove structural parameters , *i.e.* tree diameter (d.b.h), tree height, tree density and basal area. Overall, the bests results are obtained for the cross polarizations, P-HV, L-HV, C-HV. Particularly, for the three frequencies, a correlation coefficient r^2 of about 0.89 is found with tree density The best estimator for tree height is given by P-VV (r^2 = -0.65). The minus sign show a negative correlation expressing the attenuation of signal due to increasing tree height.

As an illustration, Figure 1 shows the relationships between P-band backscattering coefficients and tree basal area.

Correlation with Biomass Quantities

P-HV configuration shows the highest correlations with the dry biomass quantities, from 0.65 for foliar biomass to 0.82 for branch biomass (Table II). L-HV and C-VV have the second highest correlations (higher than 0.73 and 0.68 respectively) at the exception of foliar biomass (0.56 and 0.63). The weakest correlations are found for L-HH and L-VV configurations.

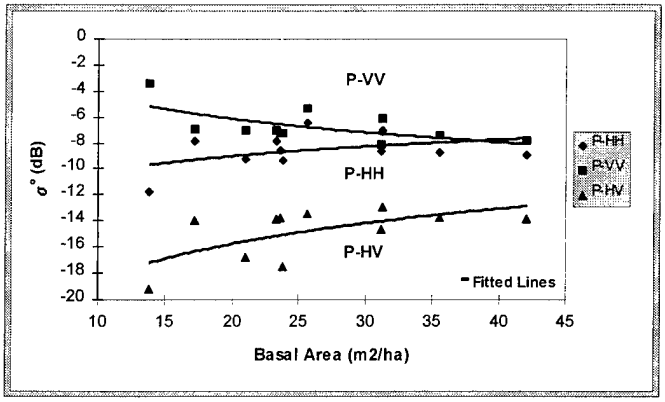


Figure 1 : P-band response versus basal area

	Diameter	Height	Density	Basal Area
C-HH	0,67	0,47	-0,47	0,44
C-VV	0,72	0,58	-0,69	0,54
C-HV	0,53	0,54	-0,89	0,45
L-HH	0,31	0,03	0,03	0,02
L-VV	0,27	0,02	0,32	-0,07
L-HV	0,77	0,60	-0,89	0,58
P-HH	0,41	0,29	-0,83	0,31
P-VV	-0,50	-0,65	0,78	-0,57
P-HV	0,69	0,52	-0,89	0,56

Table I : *Correlation Coefficients between radar data (for C-, L-, P-bands respectively,) and structural parameters of mangrove forests.*

	Bfoliar	Bbranch	Btrunk	Btotal
C-HH	0,49	0,73	0,69	0,70
C-VV	0,56	0,78	0,73	0,74
C-HV	0,41	0,45	0,41	0,43
L-HH	0,11	0,23	0,22	0,23
L-VV	0,00	0,23	0,20	0,20
L-HV	0,63	0,79	0,68	0,73
P-HH	0,42	0,53	0,46	0,49
P-VV	-0,45	-0,43	-0,31	-0,36
P-HV	0,65	0,82	0,74	0,78

Table II : *Correlation Coefficients between radar data (for C-, L-, P-bands respectively) and aboveground dry biomass.*

Figures 2, 3 and 4 shows σ variations for all the frequencies and polarizations versus total aboveground biomass. Overall, σ° increases with biophysical quantities, except for low

biomass levels, where VV- polarized P-Band response decreases. This might be explained by the attenuation of ground component with increasing standing biomass. The saturation levels are about 50 tDM/ha, 130 tDM/ha, 160 tDM/ha at C-, L-, P-bands, respectively.

The largest dynamics in σ° are observed for all the HV-polarized bands (about 6 dB at P-band).

A stepwise multiple linear analysis reveals that the best estimation of total dry biomass is obtained with P-HV configuration as described as follows :

$$\mathbf{Log(\ Bt\ ) = 4.63 + 0.161\ \sigma°P\text{-}HV} \qquad (r^2=0.84)$$

CONCLUSION

In this study, we have presented a preliminary analysis of SAR data versus biophysical properties of mangrove forests. HV-polarized bands show the highest correlations with structural parameters and aboveground biomass.

ACKNOWLEGDMENTS

AIRSAR data were kindly provided by JPL.

REFERENCES

[1] L.L. Hess, J. M. Melack and D. S. Simonett, "Radar detection of flooding benath the canopy : a review" Int. J. Remote Sensing, vol. 14, n°11, pp. 1313-1325, 1990.

[2] J.P. Lescure and O. Tostain, "Les mangroves guyanaises" Bois et Forêts des Tropiques, n° spécial Guyane 220, pp. 35-42.

[3] F. Sery, D. Ducrot-Gambart, E. Mougin, F. Fromard, J. P. Rudant, "Mapping on mangrove forest using multisource data ", Proc. IGARSS'95, vol II, pp.1222-1224, 1995.

[4] J. J. van Zyl, C. F. Burnette, H. Zebker, A. Freeman, and A. J. Holt "POLCAL user's manual " JPL D-7715. JPL. Pasadena. CA. 1990

[5] Fromard F., Puig H., Peltier A., Betoulle J. L., Mougin E., Marty G. "Structural Properties and above-ground biomass of the French Guiana mangrove forest", IIIe Workshop Ecolab. Belem, Brazil, Mar. 6-13, 1995 - in press

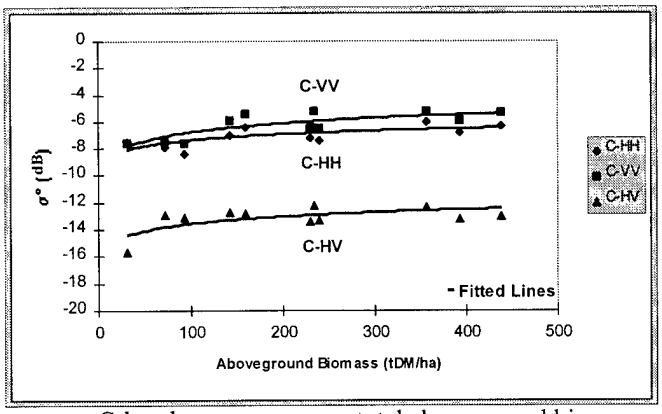


Figure 2 : C-band response versus total aboveground biomass

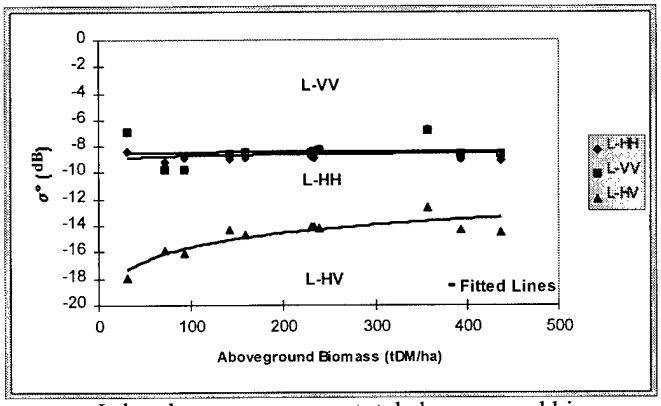


Figure 3 : L-band response versus total aboveground biomass

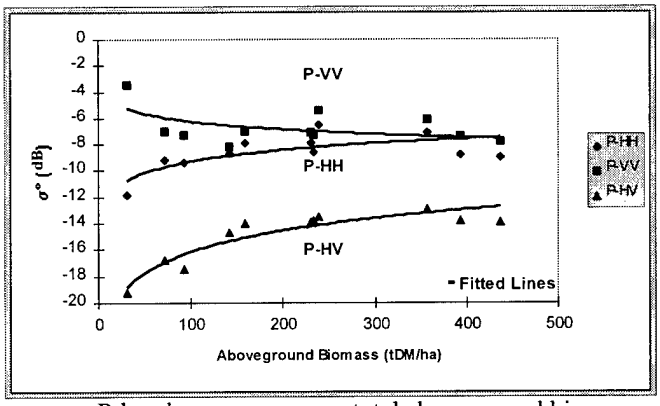


Figure 4 : P-band response versus total aboveground biomass

Monitoring vegetation features with multi-temporal SAR data

G. Amodeo[1],P. de Matthaeis[2], P.Ferrazzoli[2], S. Paloscia[1], P. Pampaloni[1]
G. Schiavon[2], S. Sigismondi[3] and D. Solimini[2]

[1] IROE- CNR - via Panciatichi 64, Firenze, Italy
FAX: 39 55 4235290 - E-Mail Microrad@IROE.FI.CNR.IT

[2] Dipartimento di Informatica, Sistemi e Produzione, Università Tor Vergata
via della Ricerca Scientifica, 00133 Roma, FAX: 39 6 2020519

[3] Dept. of Earth Sciences - Univ. of Florence, Via La Pira 4 - 50122 Firenze FAX: 39 55 218628

Abstract - Polarimetric data collected by AIRSAR and SIR-C / X-SAR over the Italian Montespertoli site are analyzed with the purpose of evaluating the potential of multifrequency SAR in discriminating crops and estimating vegetation biomass.

INTRODUCTION

Discriminating among the various vegetation species and retrieving biomass are two major application objectives of radar remote sensing. Results from previous investigations indicated that a combined use of P-, L - and C- bands allows one to separate several classes of crop covers and to monitor vegetation biomass [1]. In this paper the experiments carried out at Montespertoli are briefly described: information is given about site characteristics, ground measurements and radar parameters; the backscattering coefficients measured during MAC-Europe and SIR-C/X-SAR experiments on the same terrain types are critically compared.A simple classification algorithm is proposed, and its performance is tested with the data collected during the 3 flights of the MAC-Europe Campaign. Finally the sensitivity of the backscattering coeffcient $\sigma^{\circ}$to biomass is investigated, after subdividing vegetation into homogeneous groups, according to plant geometrical properties.

THE EXPERIMENTS

In the framework of the MAC-Europe 91 Campaign [2] and the SIR-C/X-SAR experiment [3], the Italian Montespertoli site was imaged by polarimetric SAR systems several times in summer 1991 and in April and October 1994. In order to cover the most significant areas of the site with different incidence angles between 20° and 50°, three parallel passes were performed on each flight date (June 22, 29 and July 14) of MAC-91, whilst daily data takes at different angles with SIR-C/X-SAR were carried out in April (between 12 and 18) and in October (between 3 and 9). Nominal pixel sizes obtained with AIRSAR on the 16 look images were 6.66 m in range and 12 m in azimuth; the corresponding values for the 4 look SIR-C/X-SAR images were 25 m both in azimuth and range. Most of data were delivered already calibrated; however calibration was improved by means of trihedral corner reflectors deployed parallel to the flight lines.

More than half of the Montespertoli site is hilly, with forests, vineyards, olive groves, pastures and some urbanization. The remaining part is flat with agricultural fields of sunflower, corn, sorghum, colza, wheat and alfalfa. This paper presents results obtained over agricultural fields, some small forests and some olive groves.

The ground data, which were collected on selected fields at the same time as the remote sensing measurements, regarded some general information (tree height, forest density, crop type, crop height, soil moisture) and, for a significant set of agricultural fields, all the significant soil and vegetation parameters, such as Leaf Area Index (LAI), Plant Water Content (PWC), dimensions of leaves and stalks, soil moisture content and roughness. Forests are dense, with basal areas (i.e. normalized trunk base areas) in the range 70-150 m^2/ha, trunk densities in the range 2000-8000 ha^{-1}, while tree heights are in the range 10-20 m. Olive groves basal areas are about 10 m^2/ha for all selected fields, densities are about 300 ha^{-1}, while tree heights are about 3 m. A significant number and variety of agricultural fields was present during the three MAC-Europe flights (between 22 June 91 and 14 July 91), while only few early stage wheat fields were present in April 94. The range of variations of the Plant Water Content (in kg/m^2) was about 0.5-5.0 for sunflower, about 0.2-1.5 for corn, about 0.2-1.0 for sorghum and about 0.2--3.0 for alfalfa. Wheat and colza fields were in the ripening stage during the first two 1991 flights, while most of them were harvested before the 3rd flight. For sunflower and corn the plant density is < 10 m^{-2}; these crops are characterized by large vertical

0-7803-3068-4/96$5.00©1996 IEEE

stalks (stalk diameter=1-3 cm), and wide leaves (average leaf area = 10-40 cm^2). For colza, wheat and alfalfa the plant density is in the range 80-500 m^{-2}; these crops are characterizedby small vertical stalks (stalk diameter = 0.2-1.2 cm), while leaves are small (< 1 cm^2) or absent.

The polarimetric radars measure both the amplitude and the phase of the backscattered signal for each of the 4 linearly polarized components (HH, VV, HV, VH).The calibration accuracy of AIRSAR (at P, L, and C band), SIR-C (at L and C band) and X-SAR data was checked and improved by means of the corner reflectors deployed on the site. In this paper we will use backscattering data measured at linear and circular (copolar and crosspolar) polarizations and at 35° and 50°incidence angles.

A comparison between AIRSAR and SIR-C data, carried out at L and C band and at HH, HV and VV polarizations, has shown a good correspondence between the data of the two experiments. For two forests, which are located over hilly terrains and have a fairly high slope with the same orientation almost perpendicular to the flight line, the SIR-C backscatter is higher than the AIRSAR response at all frequencies and polarizations. This discrepancy is probably due to the lower local incidence angle of the SIR-C observation. Indeed the two radars flew over the site approximately along the same track but looking at opposite azimuthal directions.

THE RESULTS

Classification

The analysis of collected data demonstrated that radar systems are effective in separating agricultural fields from other types of surface and in discriminating among classes of agricultural species [4,5]. The scattering properties of the various types of surfaces provided the essential guidelines to devise and develop a classification algorithm which uses HH,HV,VV,RR and RL polarizations at P, L, and C bands and exploits some a-priori knowledge. In particular, such a technique requires that the number of classes be specified in advance and that certain features (backscattering coefficients, in our case), including the extreme values of each class, are known. The algorithm was tuned by using the MAC-Europe'91 data averaged over homogeneous zones of nine types of surface, i.e. urban areas, water bodies, forests, vineyards, olive groves, bare soils, wide leaf (mainly well developed sunflower), colza, mixed 'small'' vegetation (which included wheat, alfalfa and pastures), which are characterized by different scattering properties. The developed algorithm was then tested on a pixel-by-pixel basis for the data taken by the three AIRSAR passes over the Montespertoli area.

The algorithm starts from P band data discriminating between two broad classes: urban areas and forests. A high difference between HH and VV polarizations at P band isolates vineyards with rows in the direction of the flight line, while a more complex condition must be applied in other cases. Olive groves can be identified since, in general, on these areas σ° is higher at P- band than at L- band, even at HV polarization. Water bodies can be separated from the other classes since, in our site, σ°_{HV} at C- band is lower than -22 dB. As far as agricultural crops are concerned, the difference σ°_{RL}- σ°_{RR} at C- band allows the separation between two broad classes: bare soils and wide leaf crops on one hand and other herbaceous crops (wheat, alfalfa and colza) on the other. Bare soil can be separated from vegetated soils since even short vegetation at C- band produces an appreciable increase of the crosspolarized backscatter, whereas colza is easily identified by the very high value of σ°_{HV} at C band. Finally, L-band crosspolarized σ°may be used to separate well- developed wide leaf crops from the early growth stages of the same crops. The confusion matrix, obtained on a "pixel-by-pixel'' classification, for some land cover categories in the whole area show that the results are generally good for all classes, the lowest percentage of right classification being that of mixed vegetation (65%) and olive groves (76%) and the highest that of bare soils (96%) and forests (92%).

Sensitivity to biomass

On the basis of the main scattering sources identified within the area the vegetation species of Montespertoli have been subdivided into the following 3 groups:

- Forests, Olive Groves (characterized by large cylinders),
- Corn, Sunflower, Sorghum (characterizedby intermediate cylinders),
- Colza, Wheat, Alfalfa (characterizedby small cylinders).

A regression analysis has been carried out, by adopting the following linear relationships:

$\sigma^\circ = a + b \times B$ (for forests and olive groves)
$\sigma^\circ = a + b \times PWC$ (for agricultural fields)

where B and PWC are respectively the forest fresh biomass per square meter and the plant water content (Kg/m^2) of crops.

The analysis of data collected at $\theta = 35°$ showed that, in general, there is a better correlations at HV polarization than at HH polarization. For forests and olive groves the correlation between σ°_{HV} and biomass slightly decreases when frequency increases: for our data, the correlation coefficient R^2 is 0.93 at P band, 0.84 at L band, 0.77 at C band. Both

MAC and SIR-C data confirm that, for values higher than about 40 kg/m^2, no significant σ°_{HV} increase with biomass may be observed, even at P- band.

In many other experiments [e.g. 6,7], where forests less dense than those of Montespertoli were present, a saturation effect was observed even at much lower biomass values, especially at L- and C- band. It must be stressed that the good linear correlations observed between σ°_{HV} and wood biomass are partially due to the peculiarity of Montespertoli site, where only species with very low (i.e. olive groves) or very high biomass (i.e. dense forests) were present.

For corn, sunflower and sorghum the correlation is low at P band (R^2=0.14) where crop elements are transparent, increases at L band (R^2 = 0.73) and decreases again at C band (R^2 = 0.31), where the early saturation effect is well evident. For colza, wheat and alfalfa there is almost no correlation at P band (R^2=0.18), a moderate increase is noted at L band (R^2 = 0.66) with a further improvement at C band (R^2=0.75).In both the latter cases, the correlation is mostly due to two ripening colza fields, characterized by high σ°_{HV} values and a PWC higher than 6 kg/m ^{2}.

It should be noted that, at θ= 35°, the correlations obtained at HV, RR, 45X polarizations (where soil backscatter is low) are generally higher than those obtained at HH, VV, RL, 45 C polarizations (where soil backscatter is relatively high). At θ = 50°, soil backscatter is low even in the copolar case and correlation coefficients are close to those obtained at 35° for HV, RR, 45X polarizations, whereas for HH, VV, RL, 45C polarizations they show, in general, an appreciable increase.

CONCLUSIONS

The results of this investigation indicate that a radar system operating at P- and L- band is able to separate agricultural fields from other targets, while a system operating at L- and C- band is able to discriminate within agricultural areas. The availability of polarimetric data allows a significant improvement in land classification. An algorithm trained on the average polarimetric features of vegetation types cultivated in the area has been implemented and successfully tested to separate at a pixel scale nine classes of land cover. To monitor biomass, P-band shows the best sensitivity for forests and olive groves, L-band is valid for crops with low plant density while both L- and C-band give useful information for high plant density crops. It should also be noted that biomass retrieval too benefits from the availability of polarimetric data (or, at least, HV polarization data).

ACKNOWLEDGMENTS

This work has been partially supported by ASI, Agenzia Spaziale Italiana and by the EC under contract EV5V CT94 0502.

REFERENCES

[1] P. Ferrazzoli, S. Paloscia, P. Pampaloni, G. Schiavon, S. Sigismondi and D. Solimini, , "The potential of multifrequency polarimetric SAR in assessing agricultural and arboreous biomass," submitted to IEEE Trans. Geosci. Remote Sensing, 1996.

[2] D.E. Wickland, R.E. Murphy, and A.C. Janetos, "Overview of MAC Europe '91 Campaign and NASA Airborne Imaging Spectrometry and Radar Programs", Proceedings of 25th ERIM International Symposium on Remote Sensing and Global Environmental Change, Graz (Austria), 1993, I66-I75.

[3] E.R. Stofan, D.L. Evans, C. Schmullius, B. Holt, J.J. Plaut, J. van Zyl, S.D. Wall, and J. Way,"Overview of results of spaceborne imaging Radar-C, X-band Synthetic Aperture Radar (SIR-C/X-SAR)", IEEE Trans. Geosci. Rem. Sens., Vol. GE-33, 817-828, 1995.

[4] A. Freeman, J. Villasenor, J. D. Klein, P. Hoogeboom, and J. Groot, "On the use of multifrequency and polarimetric radar backscatter features for classification of agricultural crops", Int. J. Remote Sensing, Vol.15, 1799-1812, 1994.

[5] S. Baronti, F. Del Frate, P. Ferrazzoli, S. Paloscia, P. Pampaloni, and G. Schiavon, "SAR polarimetric features of agricultural areas", Int. J. Remote Sensing, Vol.16, 2639-2656, 1995.

[6] M.C. Dobson, F.T. Ulaby, T. Le Toan, A. Beaudoin, E. S. Kasischke,and N. Christensen, "Dependence of radar backscatter on coniferous forest biomass", IEEE Trans. Geosci. Rem. Sens.,Vol. GE-30, 412-415, 1992.

[7] P. Ferrazzoli and L. Guerriero, "Radar sensitivity to tree geometry and woody volume: a model analysis", IEEE Trans. Geosci. Rem. Sens., Vol. GE-33, 360-371, 1995

Near-Field Effect of Extended Targets on Absolute Calibration of Microwave Sensors

Ji Wu, Jingshan Jiang
Center for Space Science and Applied Research
P.O.Box 8701, Beijing 100080, P.R. China
Tel.:+86 10 6255 9944-3414, Fax:+86 10 6257 6921, e-mail:wuji@sun20.cssar.ac.cn

Abstract -- The near-field effect of extended target, i.e. the illuminated ground area of an active microwave sensor, is discussed. It is shown by both analysis and numerical examples that all measurements are taken in the near-field and the value of normalized backscattering coefficients are varying periodically even for a uniformly distributed scattering characteristics target while the platform altitude is increasing. In order to compensate this variation, a practical platform relocation technique is proposed.

I. INTRODUCTION

Uncertainties of normalized backscattering coefficients obtained by active microwave sensors at different platform altitudes are often observed in practice while the target is an extended area (illuminated ground area) [1][2]. This phenomenon happens even if the area has uniformly distributed backscattering characteristics and the sensor has been through accurate external calibration. In the literature, explanations of the above uncertainty are often given in three reasons: the extended target effect, the volume scattering effect and the scale problem (related to platform altitude). There is, however, no further quantitative analysis and people often use the Amazon rain forest as the absolute calibration site [3], which has been proven to have a uniform response during the past years.

The difference between an extended (or illuminated) area and a point target used during the external calibration is that the dimension of the illuminated area is changing together with the platform altitude. Historically, this has not been considered when calculating the far-field condition of the measurement distance due to the reason that the phases of the return wave from the area are random. In this paper, however, it is shown that the illuminated area has a near-field effect to the sensor's receiving signal even when the phases are completely random.

II. THE FAR-FIELD CONDITION

The geometrical relation of a normal incident receiving antenna with the illuminated area is shown in Fig. 1. The dimension of the illuminated ground area is

$$D = 2h\, tg(\theta_{0.5}/2) \tag{1}$$

where $\theta_{0.5}$ is the half power beam width of the receiving antenna. From the far field condition $r \geq 2D^2/\lambda$, and substitute (1) into the far-field condition, we obtain

$$r \geq 8\left(h^2/\lambda\right) tg^2\left(\theta_{0.5}/2\right) . \tag{2}$$

This means that when h is increasing linearly, r is increasing quadratically, therefore the far field condition will never be fulfilled. This formula also tells us that for different h, the location of the receiving antenna in the near-field region, i.e. the ratio of h/r, is also different. In other words, the higher platform altitude is, the closer it is to the near-field electrically.

The impact of the above is important. For example, in most of the modelling works for ground scattering, only the plane wave incident is considered which produce a theoretical backscattering coefficient under the far-field condition. However, as Equ. (2) tells us, the receiving antenna of the sensor is always located in the near-field of the illuminated ground area. The measured backscattering coefficient will also be the near-field result which must not have the same value as it is predicted in the theory.

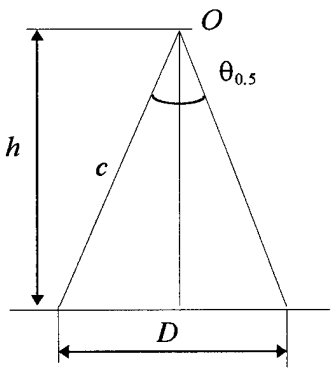


Fig. 1. Normal incident antenna beam coverage.

0-7803-3068-4/96$5.00©1996 IEEE

III. THE NEAR-FIELD EFFECT

The near-field effect is produced by phase delay from the edge of the illuminated area. From Fig. 1 the difference between c and h is expressed as

$$c-h=\frac{h}{\cos(\theta_{0.5}/2)}-h\ . \tag{3}$$

When $c-h$ is an integer number of λ, the composed field from all scattering points on the ground at the receiving antenna will be minimum, that is at

$$h_n=\frac{n\lambda\cos(\theta_{0.5}/2)}{1-\cos(\theta_{0.5}/2)}\ . \tag{4}$$

While h is changing, the minimum composed field will then appear periodically with a period T, which is obtained from (4) as

$$T=h_{n+1}-h_n\ =\ \frac{\cos(\theta_{0.5}/2)}{1-\cos(\theta_{0.5}/2)}\lambda\ . \tag{5}$$

The corresponding frequency $f=1/T$.

Although the above is derived under the assumption that the ground scattering has uniform phase response under the illumination of the transmitting antenna, it is also true for random phase response over the entire area. The reason is that for a uniformly distributed random phase response between 0~2π and when h is large, the contributions from discrete scattering points on the equal distance contours (which are circles centered at the nadir) are statistically symmetrical therefore will still follow the rule given in (5).

For situations which are not normal incident, since the equal distance contours are not circles any more, as shown in Fig. 2, the edge contributions will not be in phase and the predicted variations of σ° due to the near-field effect will be determined by many frequencies. Omit the derivation, we here give only the results. The periods of the low frequency variations are given by

$$T_n=\frac{\cos\theta_i\cos(\theta_n/2)}{1-\cos(\theta_n/2)}\lambda \tag{6}$$

where θ_i is the incident angle, θ_n is the look angle from platfmrm to each contour edges, as shown in Fig. 2, on the illuminated area with the largest angle equals to $\theta_{0.5}$. On top of the low frequency variations, a fast variation exists and the frequency is determined by the nearest and farthest points on the illuminated area to the receiving antenna and given by period

$$T=\frac{\cos(\theta_i-\theta_{0.5}/2)\cos(\theta_i+\theta_{0.5}/2)}{\cos(\theta_i-\theta_{0.5}/2)-\cos(\theta_i+\theta_{0.5}/2)}\lambda\ . \tag{7}$$

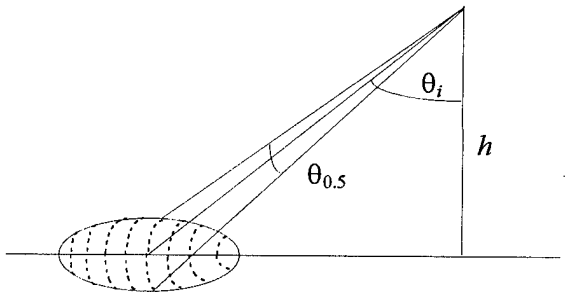


Fig. 2. Side looking incident geometry, dashed lines in the coverage area are equal distance contours.

IV. DISCRETE GROUND SCATTERING MODEL

To prove the above analysis we developed a simple discrete ground scattering model. The model uses small discs as scattering elements and change the element amplitude and phase excitations to simulate random ground scattering characteristics. From the far-field expression of a small disc with radius α, we have

$$E_n=E_i\frac{2\pi\alpha}{k\sin\theta_n}J_1\left(k\alpha\sin\theta_n\right)jk\frac{e^{-jkr_n}}{2\pi r_n}\cos\theta_n \tag{8}$$

where E_i is the element excitations of the small disc, J_1 is the first order Bessel function, r_n and θ_n are the distance and incident angle from the n'th small disc to the receiving antenna respectively, and k is the wave number. To simulate a general ground scattering, it is important to set E_i correctly. Considering the transmitting antenna beam taper on the illuminated area, the variations of the small disc orientation and the polarization coupling, the ground backscattering characteristics, etc., let

$$E_i=\gamma_n\left[0.707+0.293\left(1-\frac{r_n'}{r_o}\right)^2\right]\frac{e^{-jkr_n}}{kr_n} \tag{9}$$

where r_n' is the distance from the n'th small disc to the center of the illuminated area and r_o is the radius of the area, γ_n is a complex random number with amplitude variation from t to 1 and phase variation from 0 to 2π. t

could be set from 0.2 to 0.8 representing the roughness of the ground surface.

Substitute (9) into (8) and add the fields from all small discs on the illuminated area at O, we obtain

$$E_s = \sum_{n=1}^{N} j\gamma_n k\alpha\left[0.707+0293\left(1-r_n'/r_o\right)^2\right] \cos\theta_n \frac{J_1\left(k\alpha\sin\theta_n\right)}{\left(k\alpha\sin\theta_n\right)} \frac{e^{-j2kr_n}}{\left(kr_n\right)^2} \quad (10)$$

where N is the total number of small discs in the area. Finally, we place the small discs randomly with 0 to 1.414λ in spacing inside the illuminated area as shown in an example in Fig. 3.

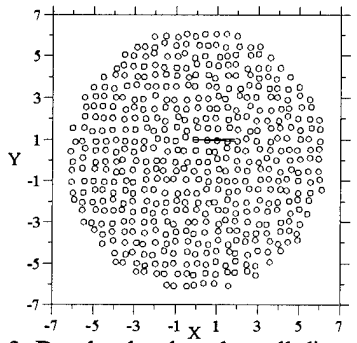


Fig. 3. Randomly placed small discs inside an illuminated area on the ground.

V. EXAMPLES

The above small disc model has been used to calculate the ground back scattering for various platform altitude. According to the definition of the radar cross section [4],

$$\sigma = \lim_{R\to\infty} 4\pi R^2 \left|E_s\right|^2 / \left|E_{in}\right|^2 \quad (11)$$

where R is the platform altitude h in case of normal incident and E_{in} is the incident field at the center of the illuminated area. As we have discussed in the Section II that no mater what platform altitude is, the far-field condition will never be satisfied. In fact, what we use in practice when calculating the backscattering coefficients is the approximation of (11),

$$\sigma \approx 4\pi h^2 \left|E_s\right|^2 / \left|E_{in}\right|^2 \quad (12)$$

and for the normalized backscattering coefficient,

$$\sigma^o \approx \frac{4\pi h^2}{\pi r_o^{\,2}} \left|E_s\right|^2 / \left|E_{in}\right|^2 . \quad (13)$$

Fig. 4 shows two examples, where σ^o are calculated using the small disc model for different platform altitudes. The high frequency variation is fading due to the random phase excitations. The low frequency variation is however due to the near-field effect discussed in Section III.

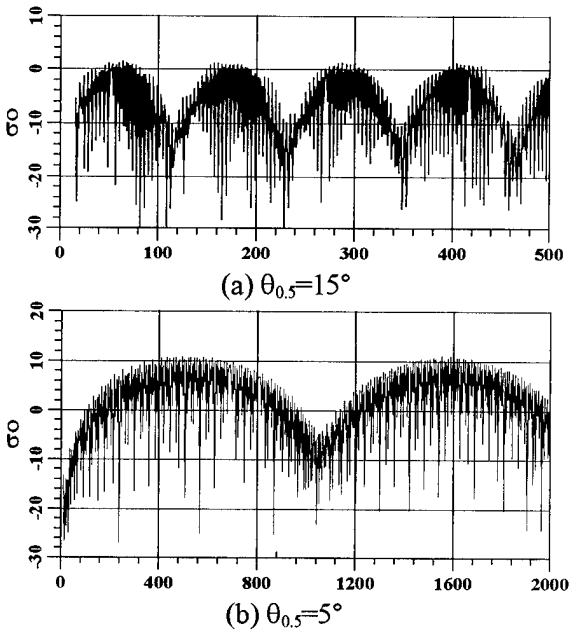


Fig. 4. Calculated σ^o in dB for different h/λ.

VI. ABSOLUTE CALIBRATION

In practice, absolute calibration of an active microwave sensor is made by measuring a point target with known radar cross section [5]. As we have discussed in Section I, this calibration is valid only for point targets which can be measured in the far-field. For the extended targets, i.e. the illuminated ground area, there are two problems now remaining unsolved for absolute calibration. Problem one, how to get the same backscattering coefficient from the same illuminated area (the scattering characteristics of this area must be quite uniform, such as an agriculture field) in different platform altitudes; problem two, how to transform this near-field measurement result to the far-field, which can be easily used in applications.

For the first problem, let us consider the periodical near-field effect again for normal incident cases. From the analysis and the examples, we know that the back-scattering coefficients measured in different platform altitudes are varying periodically. It is to say that if two

measurements are taken at different altitudes but in the same position in the period given by (5), for example both at the peak of the variation pattern, they will produce the same result. In practice, if the difference between two platform altitudes is happened to be just an integer number of times of the period T, the measurement results will be the same, where the two receiving antenna beam widths should be the same if the two measurement systems are different.

The above may be called the platform relocation property of the periodical phenomena caused by the near field effect. However, since T may become quite large when $\theta_{0.5}$ is small (for instance when $\theta_{0.5}$=2.5° and λ=3cm, T=126m), it is difficult to relocate an air-based measurement to a ground-based measurement for comparison. Therefore, we need a technique to move the platform within one period distance but still keep the measurement result unchanged.

It is well known in the near-field antenna measurement theory that the antenna main beam is formed gradually while the observation point is moving from the near-field to the far-field. In other words, the antenna radiation pattern has different properties in different near-field regions. For the extended target problem, the location of the platform in the near-field, i.e. h/r, also carries the information of the near-field effect. From (2) we obtain,

$$\theta_{0.5} = 2tg^{-1}\sqrt{\frac{1}{8e}\cdot\frac{1}{h/\lambda}} \qquad (14)$$

where $e=h/r$ is from 0 to 1 covering all platform altitudes. For a fixed value of e, (14) is actually the relation between the receiving antenna beam width and the platform altitude. For a fixed platform altitude, (14) shows also the relation between the antenna beam and the near-field location e. That is to say, at a certain platform altitude, we can zoom the antenna beam in order to reach a certain e, or backscattering measurement result.

Let us now take an example to demonstrate how could we obtain the same measurement value at two very different platform altitude. We now consider one measurement is taken in an 3cm band air-based system at 10000m platform with a receiving antenna $\theta_{0.5}$=2.5° and θ_i=0°, using the platform relocation property, we could relocate the platform to 43.25m (10000-int [10000/T] T). Next we use this altitude to calculate the near-field location e. Substitute 43.25, the wavelength and $\theta_{0.5}$ into (2) we obtain r=237.5m and e=0.1821. Now let us consider a ground-based system making a simultaneous measurement at 20m platform altitude. In order to obtain the same measurement result, from (14) the ground-based system should use a receiving antenna with $\theta_{0.5}$=3.68°.

For the second problem addressed above, we are now considering a near-field to far-field transformation method. As the content of this paper is limited, we will not discussed it further in this paper.

VII. CONCLUSIONS

The near-field effect of the backscattering coefficient measurement of extended targets is discussed. Conclusion may draw in the following points: 1). Receiving antenna of an active microwave sensor is always located in the near-field of the ground scattering area; 2). Different platform altitudes of the same receiving antenna may produce different measurement results due to near-field effect; 3). The measured σ° will vary periodically while the platform altitude is changing and the period of the variation could be easily predicted for normal incident case but not very easy to predict for other cases; 4). Absolute calibration by point targets is not valid for extended target measurement unless the near-field result is transformed to the far-field after the measurement; 5). Period relocation property and beam zooming technique are proposed to solve the uncertainty problem caused by different platform altitude measurements.

ACKNOWLEDGEMENT

The work has been partially sponsored by the President foundation of the Chinese Academy of Sceinces. J.W. thanks Professor Binqiang Zheng, Bo Sun at CSSAR and Mr. Jiankang Ji at EMI, Technical University of Denmark for stimulating discussions.

REFERENCES

[1] James R. Wang, et al., "The SIR-B Observations of Microwave Backscatter Dependence on Soil Moisture, Surface Roughness, and Vegetation Covers", IEEE Trans. on GRS, Vol. GE-24. No. 4, July 1986

[2] Loepold J. Cantafio, Space-Based Radar Handbook, Artech House, Inc. 1989

[3] I.J. Birrer et al. "Signature of the Amazon Rain Forest Obtained with the Seasat Scatterometer", IEEE Trans. on GRS, Vol. GE-20, 1982

[4] M.I. Skolnik, Radar Handbook, McGraw-Hill, New York, 1990

[5] F.T.Ulaby, R.K.Moore and A.K.Fung, Microwave Remote Sensing, Addison-Wesley Publishing Comp., London 1982

Calibration of an Airborne W-Band Polarimeter Using Drizzle and a Trihedral Corner Reflector

John Galloway, Andy Pazmany, Robert McIntosh
Microwave Remote Sensing Lab
Knowles Engineering Building, University of Massachusetts at Amherst, Amherst, MA 01003
T: (413) 545-0723, F: (413) 545-4652, galloway@alex.ecs.umass.edu
Robert Kelly and Gabor Vali
University of Wyoming, Department of Atmospheric Science
Laramie, WY 82071
T: (307) 766-4955, F: (307) 766-2635, rkelly@grizzly.uwyo.edu

Abstract — Calibration of an airborne 95 GHz polarimetric radar was accomplished using measurements of a corner reflector and freezing drizzle. The calibrated data products included: Z_{eHH}, Z_{DR}, and LDR. This paper presents the measurements made to calibrate the 95 GHz polarimeter's cloud measurements and an analysis of measurement sensitivity to calibration errors.

INTRODUCTION

Recent work making use of an airborne 95 GHz polarimetric radar to study cloud microphysics from the University of Wyoming King Air facility required calibration of the radar measurements to relate the radar data to aircraft probe data. The W-Band radar is a monostatic, dual receiver system with programmable switched linear (horizontal or vertical) transmit pulse polarization [1]. The products desired from the radar system include Z_{eHH}, ZDR, LDR, and ρ_{HV}. Calibration of Z_{eHH} requires an absolute measurement of the system gain and transmitter power. Calibration of ZDR, and LDR requires characterization of the relative response between the H and V receivers. Calibration of W-Band polarimeters has been performed frequently over the last few years at the University of Massachusetts using a procedure documented in [2]. This requires use of a polarization grid and corner reflector. The position and mounting of the polarimeter in the King Air make it difficult to steer the radar beam to a corner reflector in the field with a grid mounted over the antenna. Without a polarization grid, no separate characterization of the receiver and transmitter distortion of the polarizations is available, therefore, an alternative method for characterizing the system gain imbalance and crosspolar isolation was required.

SYSTEM CALIBRATION MODEL

At the time this calibration method was adopted, the data products available from the radar system included averaged auto- and crosscorrelation estimates from both vertical (V) and horizontal (H) receiver channels. The products available to calibrate the system included: P_{HH}, P_{HV}, P_{VH}, P_{VV}, R_{HV}, and R_{HH}, where P_{ij} represents the sample average of the power received in the i polarization receiver from transmission of a j polarization pulse, and R_{HV} is the single pulse repetition period (PRT) lag crosscorrelation estimate. The single PRT lag autocorrelation estimate from the H channel, R_{HH}, is the pulse pair estimator used to measure the Doppler velocity mean and spectral width.

Both a corner reflector and volume distributed target were used to calibrate. The system model used for the corner reflector response was the following form of the radar range equation for a point reflector:

$$\begin{bmatrix} P_{Hr} \\ P_{Vr} \end{bmatrix} = [R]\frac{K_{cr}}{r_{cr}^4}\begin{bmatrix} \sigma_{cr} & 0 \\ 0 & \sigma_{cr} \end{bmatrix}[T]\begin{bmatrix} P_{Hs} \\ P_{Vs} \end{bmatrix}, \quad (1)$$

where, $P_{Hr,Vr}$ are the return power measurements, $P_{Hs,Vs}$ are the peak power in the transmit pulse, σ_{cr} is the corner reflector cross-section, r_{cr} is the corner reflector range, K_{cr} is the point target radar constant and $[R]$ and $[T]$ are 2x2 real matrices expressing polarization crosstalk and channel gain imbalance from the receive and transmit processes respectively. The same kind of relation may be used when considering a measurement of a volume distributed target [3]:

$$\begin{bmatrix} P_{Hr} \\ P_{Vr} \end{bmatrix} = [R]\frac{K_{vol}}{r^2}\begin{bmatrix} \sigma_{HH} & \sigma_{HV} \\ \sigma_{VH} & \sigma_{VV} \end{bmatrix}[T]\begin{bmatrix} P_{Hs} \\ P_{Vs} \end{bmatrix}, \quad (2)$$

where σ_{ij} is the volume backscatter cross-section, r is the range to center of a given volume resolution cell, and K_{vol} is the radar constant for a volume distributed target.

The ratio of K_{cr} to K_{vol} is the volume of a radar resolution cell. Therefore, K_{cr} may be estimated from power measurements on a corner reflector, and K_{vol} may then be calculated from known radar system parameters. Estimation of K_{cr} involves inversion of (1). Since the cross section matrix for a corner reflector is known (see [4]), the corner reflector calibration data may be used to find the product of $K_{cr}[R][T]$ and the transmit power. This means (1) may be rewritten as:

$$\frac{r_{cr}^4}{\sigma_{cr}}\begin{bmatrix} 1 & m_{HV} \\ m_{VH} & m_{VV} \end{bmatrix}\begin{bmatrix} P_{Hr} \\ P_{Vr} \end{bmatrix} = K_{cr}\begin{bmatrix} P_{Hs} \\ P_{Vs} \end{bmatrix}, \quad (3)$$

where the elements of $[M]$ are formed as the inverse of $[R][T]$. The product of K_{cr} and transmit power was found using P_{HH} measurements of the corner reflector, and assuming that $m_{HV}P_{VH} << P_{HH}$, which holds true for the case of a corner reflector.

This work was supported by NSF Grant No. ATM-9320672.
0-7803-3068-4/96$5.00©1996 IEEE

Given that independent measures of $[R]$ and $[T]$ are not available, any inversion in the case of a volume scatterer to find $[M]$ requires an assumption about one of the two distortion matrices. For these measurements, it was assumed that the matrix of cross-sections commuted with $[T]$, and that the principal distortion was due to the receiver. The values of m_{VH}, m_{HV} (polarization isolation) and m_{VV} (gain mismatch) may be found, in principle, by making power measurements in both receivers for H and V transmit cases. In the case of a volume scatterer with negligible LDR and 0 dB ZDR, the cross section matrix is similar to that of a corner reflector and a similar inversion may be used to obtain the values of m_{VH}, m_{HV} and m_{VV}, but not K_{vol} as there is no a priori knowledge about the cross section of a given volume filled with hydrometeors.

Measurement Sensitivity to Calibration

Radar measurements of clouds used in comparisons with the in situ probes available on the UWyo King Air include the reflectivity, Z_{eHH}, differential reflectivity, Z_{DR}, linear depolarization ratio, LDR, and copolar correlation coefficient, ρ_{HV}. The radar reflectivity measurement is defined by [5]:

$$Z_{eHH} = \lambda^4 \pi^{-5} |K_w|^{-2} \sigma_{HH}, \tag{4}$$

where λ is the wavelength, and K_w is a factor depending on the dielectric constant of water at 95 GHz. The relation used to calculate σ_{HH} may be derived from (2):

$$\sigma_{HH} = r^2 K_{vol}^{-1} P_{HH}. \tag{5}$$

Estimation error in K_{vol} is simply inversely proportional to error in the final estimate of Z_{eHH}. Differential reflectivity is defined by:

$$\begin{aligned} Z_{DR} &= 10 \log_{10} \left(\sigma_{HH} \sigma_{VV}^{-1} \right) \\ &= 10 \log_{10}(P_{HH}) - 10 \log_{10}(m_{VV} P_{VV}). \end{aligned} \tag{6}$$

In the case of Z_{DR}, the measurement bias varies inversely as m_{VV}. The linear depolarization ratio is defined by:

$$\begin{aligned} LDR &= 10 \log_{10} \left(\sigma_{HV} \sigma_{VV}^{-1} \right) \\ &= 10 \log_{10}(P_{HV} + m_{HV} P_{VV}) \\ &\quad -10 \log_{10}(m_{VV} P_{VV}) \end{aligned} \tag{7}$$

where estimation of σ_{HV} was accomplished using the procedure outlined in [1]. Errors in m_{VV} produce an inversely proportional error in LDR estimates. The impact of error in estimation of the polarization isolation, m_{HV}, however, depends on the relative values of the P_{HV} and P_{VV} measurements.

The normalization required to make ρ_{HV} a zero-lag correlation coefficient using a single PRT lag correlation estimate is detailed in [6]. The definition and implementation of ρ_{HV} are:

$$\begin{aligned} \rho_{HV} &= < S_{HH} S_{VV}^* > (< |S_{HH}|^2 >< |S_{VV}|^2 >)^{-0.5} \\ &= \frac{R_{HV}}{\sqrt{P_{HH} P_{VV}}} \frac{P_{HH}}{R_{HH}} \end{aligned} \tag{8}$$

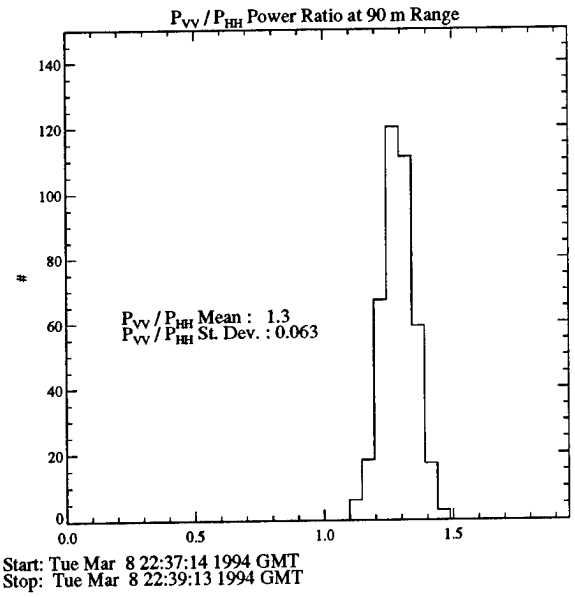


Fig. 1. Histogram of ratio of P_{VV} to P_{HH} for case of overhead drizzle.

Since the calibration factor, K_{vol}, cancels in this ratio, error in that value does not influence the result. Neither do any of m_{HV}, m_{VH}, and m_{VV} appear, making ρ_{HV} entirely insensitive to the calibration errors.

Drizzle Data

A measurement on freezing drizzle was made at vertical incidence during a missed approach to the Norman airport in Oklahoma on March 8, 1994. The data available from this observation are presented as histograms of the power ratios used to find m_{VV}, m_{VH}, and m_{HV} in figures 1 and 2. Each of the sample averages in power indicated in the histogram count involved 100 independent samples of the radar return available from the drizzle. The values of m_{VV}, m_{VH}, and m_{HV} determined from the drizzle were 0.74, -0.022 and -0.020 respectively. The expected ZDR value from drizzle is clearly 0 dB, and the offset from that value measured from the drizzle represents the system channel gain imbalance, in this case 1.1 dB. The ratio of P_{HV} to P_{HH} for drizzle provided an estimate of the system crosspolar isolation (17 dB or about 0.02) which was assumed to be substantially greater than the LDR possible from drizzle (less than -34 dB [3, p. 271]).

Figure (3) displays the Z_{DR} data taken at vertical incidence from all observations made on March 6 and 8, 1994. The values are expected to fall near 0 dB, since the hydrometeors should not present a preferred orientation in the H, V basis looking upward. The histogram shows that the distribution of Z_{DR} values is centered on about 0.2 dB and has a spread of around 0.5 dB or so. This may be taken to mean that the channel gain imbalance calculated from the data on freezing drizzle applies reasonably well to the data taken on both days. Since the expected standard error in Z_{DR} given sampling and

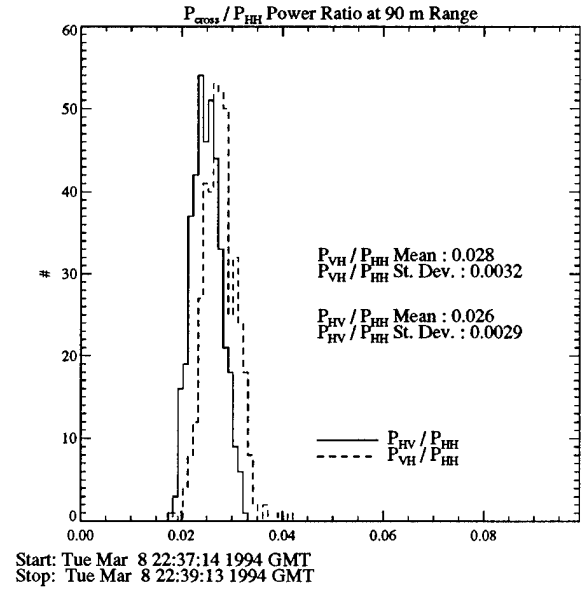


Fig. 2. Histograms of P_{HV}/P_{HH} and P_{VH}/P_{HH} for case of overhead drizzle.

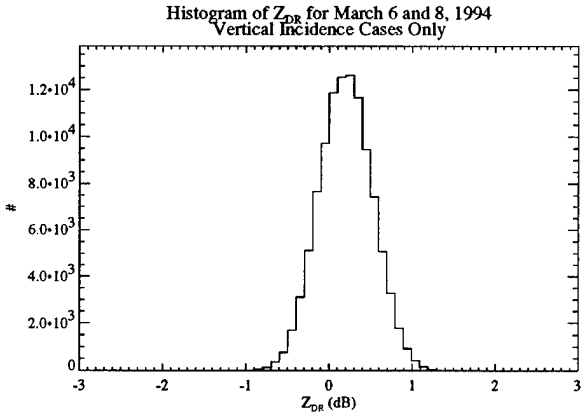


Fig. 3. Histogram of Z_{DR} values for all vertical incidence observations from March 6 and 8, 1994. Each point in the count represents the Z_{DR} calculated from P_{HH} and P_{VV} sample averages over 100 independent samples of the radar return.

SNR considerations is around 0.5 dB, the offset of 0.2 dB is acceptably close to 0 dB.

Corner Reflector Data

A trihedral corner reflector mounted on a 20 ft. mast located at the University of Wyoming Flight Facility about 370 m away from the aircraft was used to measure the product of K_{cr} and transmitter power. An adjustable reflector plate mounted above the antenna was used to steer the radar beam in the field to the corner reflector. The values obtained for m_{VV}, m_{VH}, and m_{HV} were 0.53, -0.019 and -0.010 respectively, indicating about a 2.8 dB channel gain imbalance, and 20 dB crosspolar isolation. The values for channel gain imbalance from the measurements of overhead drizzle provide a test for the validity of the corner reflector calibration estimates aside from the total cross section. Neither the system channel gain imbalance nor the crosspolar isolation values could be characterized with these corner reflector measurements. It is probable that the mast behind the corner reflector biased the values of channel gain imbalance through its contribution to the V channel return power. The crosspolar response measured with the corner reflector cannot accurately represent the system crosspolar isolation for a volume target because it does not include crosspolar return power from angles away from the antenna pattern boresight.

Conclusions

Known reference targets, both man-made (corner reflector) and naturally occurring (drizzle), provided the data necessary to calibrate parameters of interest (Z_{eHH}, Z_{DR}, LDR, and ρ_{HV}) for use in studying clouds using a W-Band polarimeter from an airborne platform. The system model adopted provides straightforward relations between the measured calibration constants and error in the final data products.

References

[1] A. L. Pazmany, R. E. McIntosh, R. Kelly, and G. Vali, "An Airborne 95 GHz Dual Polarization Radar for Cloud Studies", *IEEE Transactions on Geoscience and Remote Sensing*, vol. 1, 1994.

[2] Wood M. A., "A Theoretical Study of Calibration Procedures for Coherent and Non-coherent Polarimetric Radars.", Tech. Rep. 86011, Royal Signals and Radar Establishment, Malverne, 1986.

[3] R.J. Doviak and D.S. Zrnić, *Doppler Radar and Weather Observations*, Academic Press, Inc., 1993.

[4] F. Ulaby and ed. Elachi, C., *Radar Polarimetry for Geoscience Applications*, Artech House, 1990.

[5] J.B. Mead, A.L. Pazmany, S.M. Sekelsky, and R.E. McIntosh, "Millimeter-Wavelength Radars for Remotely Sensing Clouds and Precipitation", *Proceedings of the IEEE*, vol. 82, no. 12, pp. 1891–1906, December 1994.

[6] N. Balakrishnan and D.S. Zrnić, "Use of Polarization to Characterize Precipitation and Discriminate Large Hail", *Journal of the Atmospheric Sciences*, vol. 47, pp. 1525–1540, July 1990.

CALIBRATION OF BISTATIC POLARIMETRIC SCATTEROMETERS

F. Daout, A. Khenchaf, and J. Saillard
Lab. SEI/EP 63 CNRS - IRESTE, University of Nantes, La Chantrerie, CP 3003,
44087, Nantes Cedex 03, FRANCE
Tel. 40 68 30 20, Telefax 40 68 32 33 email: fdaout@ireste.fr

Abstract:
The recent interest in bistatic and multistatic radar has led to a need for information concerning the bistatic reflectivity of clutter viewed by such systems. Unfortunately, little information is available describing calibration for a bistatic radar system.

This paper presents a new calibration technique for bistatic scatterometers. This technique assumes perfect isolation between antenna ports. It is shown that all magnitudes and phases (*relative to one of the similary polarized linear polarization configurations*) of the radar transfer function can be calibrated without knowledge of the scattering matrix of a reference target. Only the use of the direct path between the transmitter and receiver is required.

The technique is particularly useful for calibrating a radar under field conditions, because it does not require a set of calibration targets.

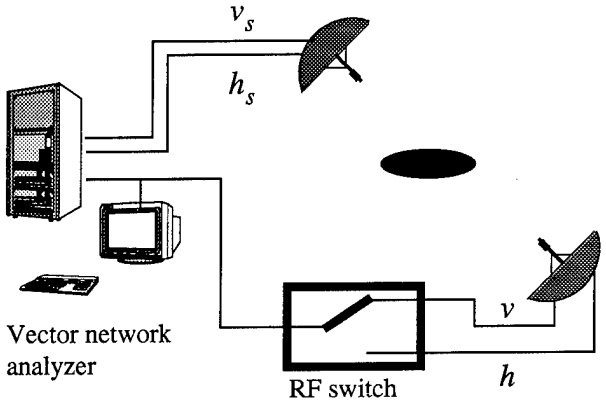


Fig. 1 General bistatic polarimetric instrumentation based on a vector network analyser

INTRODUCTION

Scatterometers have been used to determine the radar response of surfaces at different frequencies, polarizations and incidence angles in a monostatic case. These studies show that more detailed information regarding the geometric and electric structure of surface would be inferred when employing a bistatic configuration. To systematically advance to quantitative analysis of bistatic radar scatter from such data, will require stable, well-calibrated systems.

The calibration of monostatic radar systems has been considerably improved in the past [1], [2]. In the last few years the interest in bistatic scatterometers has increased rapidly. The calibration of such a system is performed by using two external reference targets. This technique is similar to the monostatic case [3].

This paper is concerned with a new approach for polarimetric bistatic radar systems, primarily for ground based application. The proposed technique uses the direct path between the receiver and transmitter, plus the rotation of one antenna into an orthogonal base of polarization.

0-7803-3068-4/96$5.00©1996 IEEE

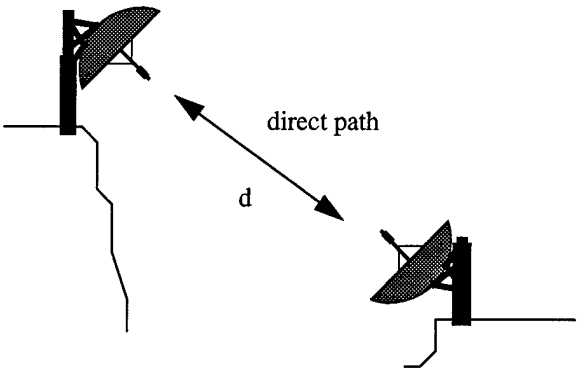
SYSTEM DISTORSION MATRIX

When using an ideal polarimetric radar, the measured scattering matrix $[S^m]$ is equal to its theoretical scattering matrix $[S]$. Usually however, these two matrices are different and it is necessary to characterise the errors introduced by the radar system. Then the process must be inverted to obtain an estimate of the actual scattering matrix.

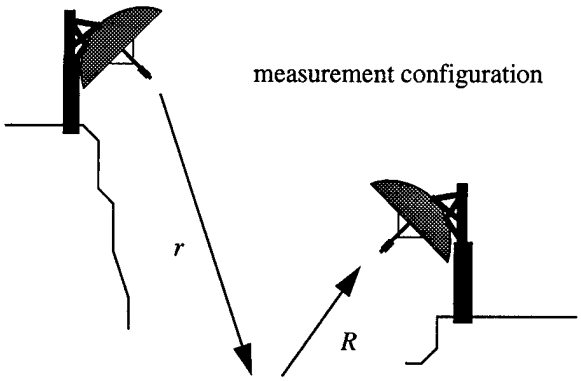
As in monostatic radar systems, the measurement made by the radar is related to the target scattering matrix $[S]$ by:

$$\begin{bmatrix} S^m_{hsh} & S^m_{hsv} \\ S^m_{vsh} & S^m_{vsv} \end{bmatrix} = Ae^{i\phi} \begin{bmatrix} R_{hshs} & R_{hsvs} \\ R_{vshs} & R_{vsvs} \end{bmatrix} \begin{bmatrix} S_{hsh} & S_{hsv} \\ S_{vsh} & S_{vsv} \end{bmatrix} \begin{bmatrix} T_{hh} & T_{hv} \\ T_{vh} & T_{vv} \end{bmatrix} \quad (1)$$

where A represents the radar system gain and losses, ϕ is the phase due to the delay between the transmitting antenna, the target and the receiving antenna and any losses in the system. The receive and transmit matrices $[R]$ and $[T]$ describe the polarization characteristics of the receiving and the transmitting system. The terms T_{hh} or T_{vv} represent the amplitude



(a) calibration configuration



(b) measurement configuration

Fig. 2 Schematic representation of the transmitting and receiving antennas -(a) calibration configuration - (b) measurement configuration

and phase errors in the transmitted signal and T_{hv} or T_{vh} represent the cross-polarization coupling. In the same way, R_{hshs} or R_{vsvs} represent the amplitude and phase errors introduced by the receiver and R_{hsvs} or R_{vshs} represent the cross-polarization coupling terms of the receiver.

CALIBRATION APPROACH

When you use a bistatic polarimetric instrumentation based on a network analyser (Fig. 1) outdoors, it can be assumed that the transmit and receive antennas of the measurement system each have excellent isolation between their h and v ports [2], thus the distortion matrices are approximately diagonal, i. e

$$\begin{bmatrix} S^m_{hsh} & S^m_{hsv} \\ S^m_{vsh} & S^m_{vsv} \end{bmatrix} = Ae^{i\phi} \begin{bmatrix} R_{hshs} & 0 \\ 0 & R_{vsvs} \end{bmatrix} \begin{bmatrix} S_{hsh} & S_{hsv} \\ S_{vsh} & S_{vsv} \end{bmatrix} \begin{bmatrix} T_{hh} & 0 \\ 0 & T_{vv} \end{bmatrix} \quad (2)$$

In order to obtain the 4 unknown coefficients, a measurement of the direct path between the two positions is made (Fig. 2.a)

Next, the system is moved to a measurement configuration.

CALIBRATION PROCEDURE

In the following a bistatic calibration procedure for the determination of the scattering coefficient will be shown, which requires only the use of the direct path (Fig. 2.a).

A- First step: Calibration of the co-polarized terms

First, the system is on a calibration configuration (Fig. 2.a) where the two antennas are in the same line. The matrix of the received voltage $[E^{ro}]$ is given by

$$\begin{bmatrix} E^{ro}_{hsh} & E^{ro}_{hsv} \\ E^{ro}_{vsh} & E^{ro}_{vsv} \end{bmatrix} = \left(\frac{2\eta_o G_T P_T}{4\pi}\right)^{\frac{1}{2}} \left(\frac{G_r \lambda^2}{4\pi}\right)^{\frac{1}{2}} \frac{e^{ikd}}{d} \begin{bmatrix} R_{hshs} & 0 \\ 0 & R_{vsvs} \end{bmatrix} \begin{bmatrix} T_{hh} & 0 \\ 0 & T_{vv} \end{bmatrix} \begin{bmatrix} 1 & 0 \\ 0 & 1 \end{bmatrix} \quad (3)$$

where $P_T = E_o^2/2\eta_o$ is the transmitted power, G_T is the nominal gain of the transmitting antenna, G_r is the nominal gain for the receiving antenna, kd is a phase factor that accounts for the propagation between the target and the radar, d is the range between the two antennas.The subscript o denotes quantities associated with the direct path.

For a target with unknown scattering matrix $[S]$ located at a distance r from the transmitting antenna and R from the receiving antenna, the received voltages for the different polarizations are:

$$\begin{aligned} E^r_{hsh} &= \left(\frac{2\eta_o G_T P_T}{4\pi}\right)^{\frac{1}{2}} \left(\frac{G_r \lambda^2}{4\pi}\right)^{\frac{1}{2}} \frac{e^{ik(R+r)}}{Rr} R_{hshs} S_{hsh} T_{hh} \\ E^r_{hsv} &= \left(\frac{2\eta_o G_T P_T}{4\pi}\right)^{\frac{1}{2}} \left(\frac{G_r \lambda^2}{4\pi}\right)^{\frac{1}{2}} \frac{e^{ik(R+r)}}{Rr} R_{hshs} S_{hsv} T_{vv} \\ E^r_{vsh} &= \left(\frac{2\eta_o G_T P_T}{4\pi}\right)^{\frac{1}{2}} \left(\frac{G_r \lambda^2}{4\pi}\right)^{\frac{1}{2}} \frac{e^{ik(R+r)}}{Rr} R_{vsvs} S_{vsh} T_{hh} \\ E^r_{vsv} &= \left(\frac{2\eta_o G_T P_T}{4\pi}\right)^{\frac{1}{2}} \left(\frac{G_r \lambda^2}{4\pi}\right)^{\frac{1}{2}} \frac{e^{ik(R+r)}}{Rr} R_{vsvs} S_{vsv} T_{vv} \end{aligned} \quad (4)$$

With (3) and (4) it is possible to calibrate the co-polarized terms and to obtain the following expression for the co-polar-

ized scattering amplitude:

$$S_{hsh} = \frac{Rr}{d} e^{ik(d-R-r)} \frac{E^r_{hsh}}{E^{ro}_{hsh}}$$
$$S_{vsv} = \frac{Rr}{d} e^{ik(d-R-r)} \frac{E^r_{vsv}}{E^{ro}_{vsv}} \quad (5)$$

A small error in the term d, r or R will have a minor effect on the magnitude of S_{hsh} or S_{vsv} but may cause a large error in the phase angle of S_{hsh} or S_{vsv}. However the phase of S_{hsh} relative to that of S_{vsv} is independent of $(d-r-R)$.

With only this measure, it is not possible to calibrate the cross-polarized component of the bistatic scattering matrix.

B- Second step: calibration of the cross-polarized terms

The direct path is very useful for the calibration of the co-polarized terms but unfortunately, it cannot be used for the cross-polarized components. To do this, it is necessary to use any target with a strong cross-polarized RCS. To simulate this target, the receiving or transmitting antennas (*or both of them*) are rotated by an angle α . By means of this rotation a second target is simulated with a scattering matrix which can be calculated as a function of the rotation angle α.

The received voltage matrix for the direct path $[E^{r\alpha}]$ is:

$$[E^{r\alpha}] = \left(\frac{2\eta_o G_T P_T}{4\pi}\right)^{\frac{1}{2}} \left(\frac{G_r \lambda^2}{4\pi}\right)^{\frac{1}{2}} \frac{e^{ikd}}{d} \begin{bmatrix} R_{hshs} & 0 \\ 0 & R_{vsvs} \end{bmatrix} \begin{bmatrix} \cos\alpha & \sin\alpha \\ -\sin\alpha & \cos\alpha \end{bmatrix} \begin{bmatrix} T_{hh} & 0 \\ 0 & T_{vv} \end{bmatrix} \begin{bmatrix} 1 & 0 \\ 0 & 1 \end{bmatrix} \quad (6)$$

The subscript α refers to the rotation angle.

If we define additional quantity K_1 and K_2 as in [4] as:

$$K_1 = \frac{E^{r\alpha}_{vsh}}{E^{r\alpha}_{hsv}} = -\frac{R_{vsvs} T_{hh}}{R_{hshs} T_{vv}} \quad (7)$$

and

$$K_2 = E^{ro}_{hsh} E^{ro}_{vsv} = \left(\frac{2\eta_o G_T P_T}{4\pi}\right)\left(\frac{G_r \lambda^2}{4\pi}\right)\frac{e^{i2kd}}{d^2} R_{hshs} T_{hh} R_{vsvs} T_{vv} \quad (8)$$

Then using these in combination with (4), we can obtain the following expression for the cross-polarized scattering components of the target:

$$S_{hsv} = \frac{Rr}{d} e^{ik(d-R-r)+i\frac{\pi}{2}} \left(\frac{K_1}{K_2}\right)^{\frac{1}{2}} E^r_{hsv}$$
$$S_{vsh} = \frac{\frac{Rr}{d} e^{ik(d-R-r)-i\frac{\pi}{2}} E^r_{vsh}}{(K_1 K_2)^{\frac{1}{2}}} \quad (9)$$

We notice that the value of angle α has no effect in the method.

CONCLUSION

The bistatic calibration procedure described in the previous sections allows the calibration of a bistatic scatterometers based on a vector network analyser. Only the direct path between the transmitting and receiving antennas is necessary, no calibrate target such as a metallic sphere or a trihedral corner reflector is required. The main advantage of this method is the absence of a calibration target, so no target error alignments are introduced. In the same way, the angle of the rotation of the antennas is arbitrary. The receiver or the transmitter can be rotated by any angle α which can permit the simulation of a target with strong cross-polarized terms.

The technique is very useful for field operation because it does not require a calibration target.

Currently the procedure is used for the measurement of the bistatic scattering matrix of the sea surface using two different positions for the transmitter and receiver and by the use of a vector network analyser.

ACKNOWLEDGMENTS

This research was supported by the C.E.L.A.R. (Centre d'Electronique de L'ARmement, division GEOS/SOP, Bruz, France) convention No 01/93/SA.AR.

REFERENCES

[1]H.A. Yueh, J.A. Kong, R.M. Barnes and R.T.Shin "Calibration of polarimetric radars using in-scene reflectors" J. electromagnetic waves, Jan 1990

[2]K.Sarabandi, F.T. Ulaby and M.A. Tassoudji, 'Calibration of polarimetric radar with good polarization isolation", IEEE Trans. Geosci. Remote Sensing,vol. 28, pp 70-75, Jan. 90.

[3]D. Kaehny, k. Schmitt and W.Wiesbeck, "Calibration of bistatic polarimetric radars systems", IEEE Trans. Geossci. Remote Sensing, vol.30, pp 847-852, Sept 92.

[4]F.T. Ulaby and C.Elachi, "Radar polarimetry for geoscience application", Artech house, 1990

Accurate Antenna Reflector Loss Measurements for Radiometer Calibration Budget

Niels Skou
Danish Center for Remote Sensing, Electromagnetics Institute
Technical University of Denmark (TUD), B-348, DK-2800 Lyngby, Denmark.
Phone: (45) 45 88 14 44, Fax: (45) 45 93 16 34, E-mail: ns@emi.dtu.dk

ABSTRACT

Antenna reflector losses may play an important role in the calibration budget for a microwave radiometer. If the losses are small they are difficult to measure by traditional means. However, they can be assessed directly by radiometric means using the sky brightness temperature as incident radiation. The paper describes how such measurements are carried out as well as a suitable experimental set-up. The main reflector of the European Space Agency's MIMR system is used to demonstrate the principle.

INTRODUCTION

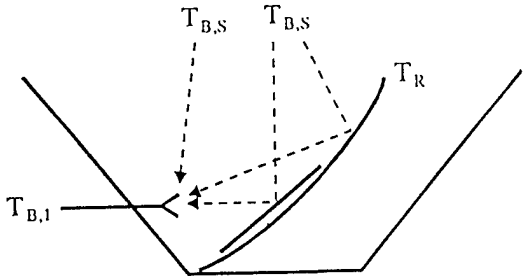
The fundamental pre-launch calibration of spaceborne radiometer systems is normally carried out with the instrument inside a thermal vacuum chamber which also includes a calibration target viewed by the radiometers antenna system. The calibration target is very accurately temperature controlled and is able to provide brightness temperatures over a wide range, typically some 77 K to some 300 K. Such a target is difficult and expensive to develop - especially if it has to be large in order to serve a large aperture system. A thermal vacuum chamber is also not a cheap and trivial installation - especially if it has to be large. For these reasons it may be necessary to dismount the antenna reflector and carry out the calibration with the feed horns viewing the calibration target. Thus reflector losses must be accurately assessed so that they can be compensated for in the data analysis.

The reflection coefficient for a specimen of the reflector material can be measured on a network analyzer. However, if the reflection coefficient is close to 1, which it will be for a decent reflector, it turns out to be difficult if not impossible to achieve the necessary measurement accuracy. On the other hand it is really the emissivity of the reflector material we need for the radiometric calibration correction, and this can be measured directly and accurately down to very small values by radiometric means.

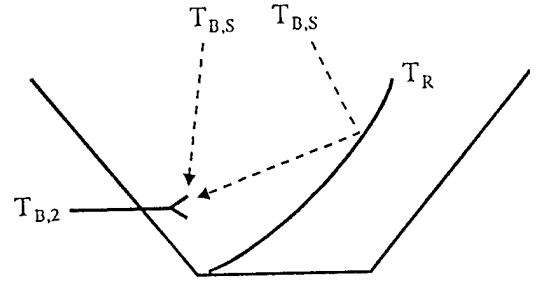
MEASUREMENT SETUP

The reflector to be measured, or a specimen of its material, is placed in a large metal bucket together with a radiometer and a suitable horn antenna. The device under test reflects the clear sky brightness temperature into the radiometer horn. The bucket diverts antenna sidelobes and spillover towards clear sky.

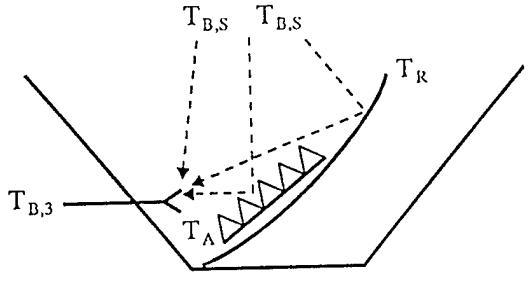
Figure 1 shows how the reflector emissivity is measured in a 3-step process using the sky temperature as radiation



(a) Reflector and lossless plate



(b) Reflector



(c) Reflector and absorber

Figure 1: Measurement schedule

source. First the sky temperature $T_{B,S}$ is measured using a lossless plate (in this case a silver plated aluminium plate):

$$T_{B,1} = n \cdot T_{B,S} + (1 - n\ ) T_{B,S} = T_{B,S}$$

0-7803-3068-4/96$5.00©1996 IEEE

where n is the beam filling factor of the plate. n is assumed large and the emissivities of the reflector and the bucket are assumed small. This step can be regarded as an inter-calibration of the radiometer and the sky temperature. Secondly, the reflector alone is measured:

$$T_{B,2} = n\left(T_R \cdot \varepsilon + T_{B,S}(1-\varepsilon)\right) + (1-n)T_{B,S}$$

where T_R is the temperature of the reflector and ε is its emissivity. If the reflector is very good (low loss) the difference between $T_{B,1}$ and $T_{B,2}$ is small. Finally, in the 3rd step an absorber having the same physical size as the lossless plate is measured:

$$T_{B,3} = n \cdot T_{B,A} + (1-n) \cdot T_{B,S}$$

where $T_{B,A}$ is the physical (hence also the brightness) temperature of the absorber.

Solving the above 3 equations we find:

$$n = \frac{T_{B,3} - T_{B,1}}{T_{B,A} - T_{B,1}} \quad (1)$$

$$\varepsilon = \frac{T_{B,2} - T_{B,1}}{n(T_R - T_{B,1})} \quad (2)$$

It is seen that $T_{B,S}$ has to be constant throughout the experiment. So, only clear days without clouds can be used. Also the radiometer must be stable throughout an experiment. If the reflector is very good the difference $T_{B,2}$ - $T_{B,1}$ (which is the dominating factor in determining the emissivity) become small and the requirement to stability become stringent. The crucial steps (a) and (b) are measured several times alternating between them. The time between successive measurements is kept to 2 minutes. Thus the time difference (important versus stability) is short and measurements of the same situation is repeated enabling drifts to be checked.

The aluminium lined bucket has an opening of 3 x 3 m and a height of 1.2 m. The lossless plate is 0.5 x 0.5 m. 3 noise-injection radiometers (5, 17 and 34 GHz) with associated 25 dB standard gain horns are used for the measurements. The brightness temperatures are measured with a standard deviation of 0.1 K.

The 5 GHz standard gain horn is very large compared with the lossless plate and it has been found useful to also employ a smaller horn (see later).

THEORETICAL EMISSIVITY

With the notation R_S = surface resistivity, and η = impedance of intrinsic medium, the power reflectivity for a good conductor is:

$$\rho = 1 - \frac{4R_s}{\eta}$$

η = 377 when the intrinsic medium is air as in our case. ρ = 1-ε in case of no transmission which we can assume with good confidence, considering our relatively thick metal plates.

For the surface resistivity we find: $R_S = \sqrt{\frac{\pi f \mu}{\sigma}}$ or for non-magnetic material:

$$R_S = \sqrt{\frac{\pi \cdot f \cdot \mu_0}{\sigma}} = 2\pi \cdot \sqrt{\frac{f}{\sigma \cdot 10^7}}$$

where σ is the conductivity, and f the frequency. Hence we find

$$\varepsilon = \frac{1}{15}\sqrt{\frac{f}{\sigma \cdot 10^7}}$$

Inserting the conductivity for typical metals we find the values shown in Table 1.

	Conductivity s (s/m)	Emissivity 17 GHz	Emissivity 34 GHz
Silver	6.17×10^7	0.00035	0.00049
Copper	5.80×10^7	0.00036	0.00051
Aluminium	3.72×10^7	0.00045	0.00064
Brass	1.57×10^7	0.00069	0.00098
Iron	1.12×10^7	0.00082 *	0.0012 *

* neglecting magnetic properties at frequency in question

Table 1: Emissivity of some conductors

It is seen that the difference between silver and copper is minute but also aluminium is very close.

If we want to measure emissivities in the 0.01 range then the silver plate can be considered lossless. However, if emissivity measurements in the range around 0.001 is wanted then corrections are needed.

MEASUREMENTS ON METAL PLATES

From preliminary network analyzer measurements it is expected that the emissivity of the MIMR reflector is quite small. Hence, it is of interest to assess "emissivity resolution" i.e. the lower limit of what can be measured with the present setup. To this end different metal plates have been measured against the "lossless" plate in the bucket. Like for the normal measurement procedure the test plate and the lossless plate are measured several times alternating between them and with 2 minutes between measurements. Also the absorber is measured to determine the beam filling factor the usual way.

The test plates are of course exactly the same size as the "lossless" plate.

Figure 2 presents results from a preparatory exercise measuring the difference between an iron plate and the lossless plate. The magnetic properties of the iron plate is not known so the actual value of the emissivity is not known. It is evident from looking at the bar diagram in Figure 2 that the iron plate has an emissivity large enough to be measurable by the method employed. The reflected brightness temperatures are in the iron case systematically larger than in the lossless case. By averaging we find for iron: $T_{B,2}$ = 17.94 K, for the lossless case: $T_{B,1}$ = 17.50 K. Inserting in formulas (1) and (2), we find: n = 0.9814 and ε = 0.0017. The beam filling factor is good. The emissivity value and the systematic behaviour of the bar diagram lead us to state that the method can measure emissivity values somewhat smaller than 0.0017.

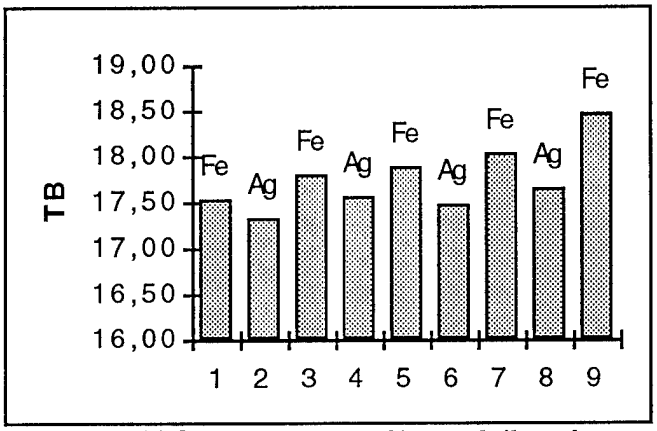


Figure 2: 34 Ghz measurement of iron and silver plates

In an attempt to find the limiting value of emissivity that we can measure, a brass plate is used in the following experiments. Figure 3 reports a 17 GHz measurement and it is noted that good stability prevails but there is no systematic pattern in the bar chart. The calculated emissivity is as low as ε = -0.0002 also indicating that we cannot see the difference between brass and silver. Hence, we cannot measure the emissivity of brass at 17 GHz (0.00069 theoretically).

The next experiment, see Figure 4, concerns the measurement of brass at 34 GHz. At this frequency the theoretical emissivity is ε = 0.001. A careful inspection of the bar chart shows that in all cases, but measurement "4", going from brass to silver results in lower brightness temperature while going from silver to brass results in higher brightness temperature. Hence, there is a systematic and reasonable pattern in the bars and we can feel confident that we can perform an emissivity assessment. By proper averaging and using the usual formula we find ε = 0.0008 which is in fair agreement with the theoretical value bearing in mind that it is not corrected for losses in the so-called "lossless" plate.

Hence, it is seen that we can measure an emissivity of 0.001. However, the results from similar other experiments not reported here show that in some cases we can see the difference between the lossless plate and the brass plate, in others not. In no case can a difference be detected at 17 GHz.

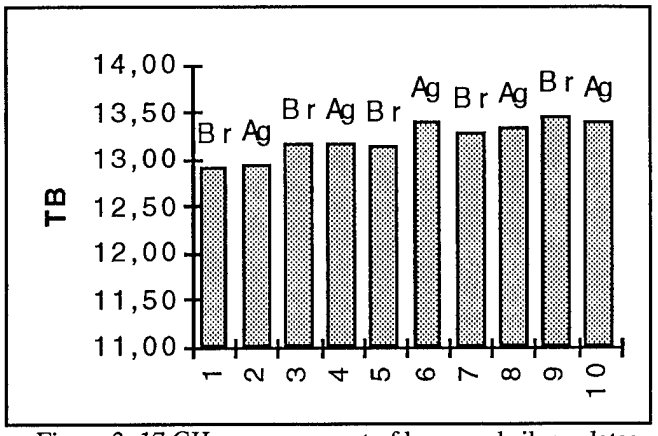


Figure 3: 17 GHz measurement of brass and silver plates

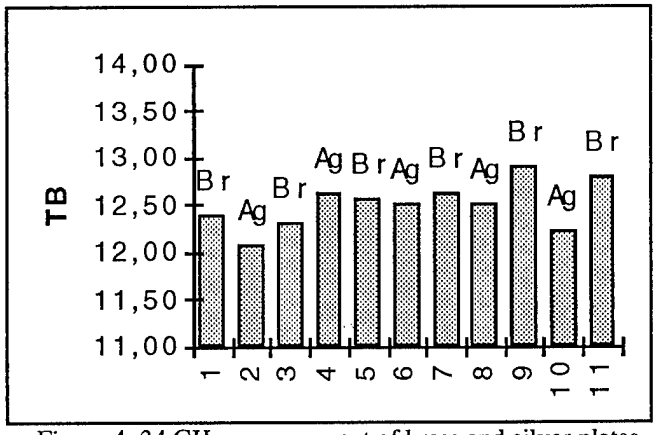


Figure 4: 34 GHz measurement of brass and silver plates

This indicates that even this figure is marginal and we can certainly not measure smaller values. We conclude that the lower limit for emissivity measurable by the present setup is 0.001.

MIMR REFLECTOR MEASUREMENTS

In the following a few examples of measurements on the MIMR reflector itself shall be presented. Figure 5 shows 34 GHz results. (a) and (b) refer to the measurement steps, see Figure 1. Stability is good and by proper averaging we find:

$T_{B,1}$ = 13.02 K, $T_{B,2}$ = 13.07 K, $T_{B,A} = T_R$ = 273 K, $T_{B,3}$ = 252.11 K, and using the usual formulas (1) and (2): n = 0.9196, ε = 0.0002

The beam filling factor is good, but we cannot measure any difference between the reflector and the lossless plate. This is indicated by the low emissivity value, and also evident from the bar diagram in Figure 5.

Several experiments were carried out spread out over the period from August to December covering physical temperatures from 27°C to -4°C. In no case could any statistically significant difference be observed. This was also the case at 17 GHz.

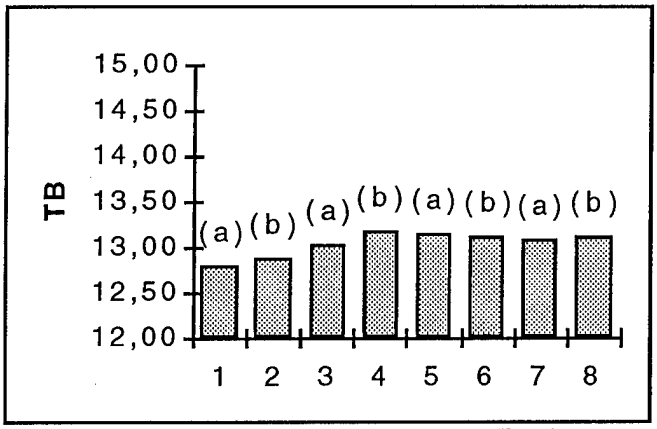


Figure 5: 34 GHz measurement of the MIMR reflector

The 5 GHz measurements are of special interest. The MIMR reflecter is manufactured in carbon fibre with a very thin metallization as reflecting surface. One could be nervous about the performance at the low frequency with its larger skin depth.

The 5 GHz measurements start out with an example where the large standard gain horn is used, see Figure 6. We find n = 0.7589, and ε = -0.0043. This measurement indicates that the MIMR reflector is better than the lossless plate which is of course nonsense. The beam filling factor is poor due to the large horn. In Figure 7 the situation is rectified by using the small horn. Here we find n = 0.8824 and ε = -0.0003. Now we find the well known situation: provided satisfactory beam filling factor we cannot measure the difference between the MIMR reflector and the lossless plate.

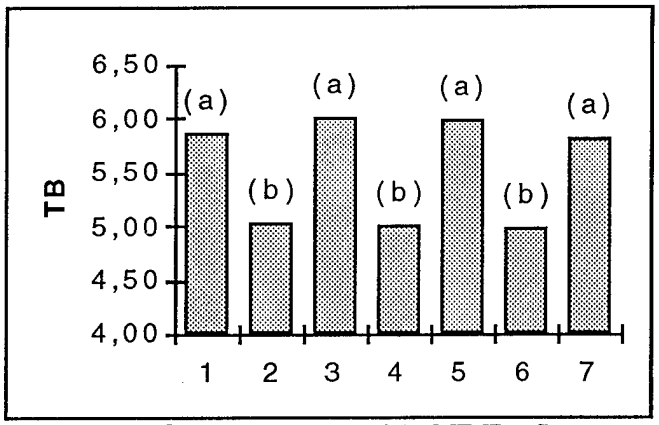


Figure 6: 5 GHz measurement of the MIMR reflector, large horn.

The question of beam filling factor was examined by further experiments also at the higher frequencies by varying the distance between the horn and the reflector / lossless plate. As soon as the beam filling factor reaches close to 90% we get reasonable measurements, and things do not change even if the factor is further enlarged The explanation to this behaviour is sought in edge illumination problems: When the beam filling factor is inadequate for whatever reason (distance too large, horn too big) reflections / diffraction in the edges of the lossless plate contributes significantly to the received radiation. The bias by these contributions can only go in one direction since the nadir brightness temperature is the lowest possible and could thus explain our problems.

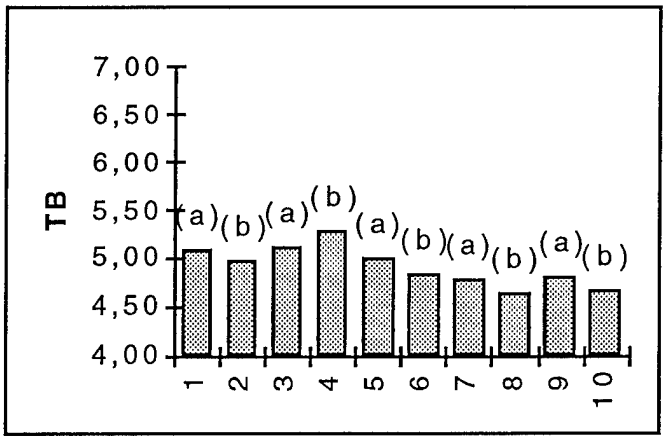


Figure 7: 5 GHz measurements of the MIMT reflector, small horn

DISCUSSIONS AND CONCLUSIONS

- The experiments with different metal plates indicate that the present measurement setup cannot measure emissivities below 0.001. It is for example obvious that we cannot measure the difference between aluminium and silver (the "lossless" plate), and the bucket can be regarded as lossless.
- The experiments with the MIMR reflector show that in the frequency range 5-34 GHz we cannot see any difference between the reflector and the lossless plate. It is believed that the reflector (which is manufactured in carbon fibre and coated with a thin layer of aluminium) concerning emissivity approaches that of an aluminium plate (emissivity in the range of 0.00024 - 0.00064). This cannot, however, be proven by the present measurements due to the ε = 0.001 limit stated above. But we can conclude that in the frequency range 5 - 34 GHz the emissivity of the MIMR reflector is below 0.001.
- Measurements have been carried out in the temperature range +27° C to -4° C. No dependence on temperature is found.
- The sky brightness temperature reflected in a reflector having an emissivity of 0.001 and a physical temperature of 300 K is only modified by 0.3 K. The somewhat higher brightness temperatures from Earth targets are modified correspondingly less (some 0.2 K worst case). This means that correction for MIMR main reflector losses are hardly warranted. 0.2 K must be included in the calibration budget.
- If better values for the emissivity of the MIMR reflector are needed the way forward is to adopt a slightly different measurement concept: a specimen of the reflector material having the shape and size of the lossless plate must be manufactured. The specimen and

the lossless plate are again measured alternatively in the metal bucket. It is possible to make a mechanism so the specimen and the lossless plate can be interchanged in seconds - speed is a major factor considering instrument and atmosphere instabilities. At the same time geometry is consistent and edge effects will cancel. This way very accurate measurements are possible.

ACKNOWLEDGMENTS

The work described in the present paper was carried out under contract with the European Space Agency through Alenia Spazio. Mr. R. Bordi and Mr. P. Spera of Alenia have contributed to the work through fruitful discussions.

REFERENCES

Although not directly referred to during the work and in this paper the following references contain valuable information about the subject in question:

K. R. Carver; "Antenna and Radome Loss Measurements for MFMR and PIMS," Report, Physical Science Laboratory, New Mexico State University, 1975.

R. F. Harrison and H-J. C. Blume, "Determination of Electromagnetic Properties of Mesh Material Using Advanced Radiometer Techniques," NASA Langley Research Center. In NASA Conference Publication 2368: Large Space Antenna Systems Technology, 1984.

Electromagnetic Scattering Based on Pair Distribution Functions Retrieved from Planar Snow Sections

L. M. Zurk[1]
M.I.T. Lincoln Laboratory
244 Wood St., Lexington, MA 02173 USA
phone: 617-981-3431 fax : 617-981-3905 email : zurk@ll.mit.edu

L. Tsang
Electrical Engineering Department , University of Washington
Seattle, WA 98195 USA

Jiancheng Shi
Center for Remote Sensing and Environmental Optics, University of California
Santa Barbara, CA 93106 USA

Robert E. Davis
U.S. Army Cold Regions Research and Engineering Laboratory
Hanover, NH 03755-1290 USA

1. Work was completed when author was with the Applied Physics Laboratory, Seattle WA

ABSTRACT

Electromagnetic wave propagation and scattering in dense media depends on the 3-D pair distribution function of particle positions [1]. In the past researchers have assumed a form, such as Percus-Yevick (PY), for the pair function in snow. Recent efforts in the snow community have concentrated on analyzing planar snow sections to obtain 2-D stereological data. In this paper we calculate the volume 3-D pair distribution function from the 2-D stereological data by solving Hanisch's integral equation [2]. We first use Monte Carlo simulations for single and multi-size particles to verify the inversion procedure with good results. Next we apply the procedure to available planar snow sections. A log-normal distribution of particle sizes is assumed for the ice grains in snow with the distribution parameters derived from stereological measurements. The 3-D pair function can be expressed as a weighted sum of size specific pair functions which are necessary for scattering calculations. We choose a small number of representative particle sizes and use a least squares non-linear fit to decompose the 3-D pair function into pair functions for those particles. The fit procedure is constrained by a set of physically meaningful rules and can only be applied to those sizes with sufficient number densities. Analysis of scattering from log-normally distributed spheres indicates the larger particles contribute strongly to the independent scattering but have relatively small interaction terms. Since the large, sparsely distributed particles are not retrievable from the fit and have relatively small iteraction terms we include their scattering contribution by using the hole correction approximation. The family of recovered pair distribution functions gives scattering rates comparable to those calculated under the PY approximation.

PAIR DISTRIBUTION FUNCTION

The pair districution function $g_v(r)$ represents the probability that two particles in 3-D space are separated by a distance r. An expression for gv(r) is given by Hanisch [2] :

$$g_v(r) = \frac{1}{4\pi r}\frac{dK_v(r)}{dr} \qquad (1)$$

where $N_vK_v(r)$ can be interpreted as the mean number of particles in a sphere of radius r and N_v is the mean number of particles per unit volume. For a single particle size, $g_v(r)$ is the same as the pair distribution function used in dense media theory to calculate scattering. A similar form exists for $g_A(r)$ which is the area pair distribution function and is measurable from section data.

There has been much effort in quantitative stereolgy to relate 3-D quantities to those that can be measured from 1-D and 2-D cross section data. When the particles are spherical in size and their size distribution is known, an integral equation due to Hansich [2] can be developed for a section of thickness t:

$$g_A(r) = \frac{1}{4(E[\xi]+t)^2}\int_0^\infty f(u,t)g_v\left(\sqrt{r^2+u^2}\right)du \qquad (2)$$

where $E[\xi] = r_0$ is the mean radius of the ice grains and f(u,t) is related to the cumulative distribution function for the sphere size.

0-7803-3068-4/96$5.00©1996 IEEE

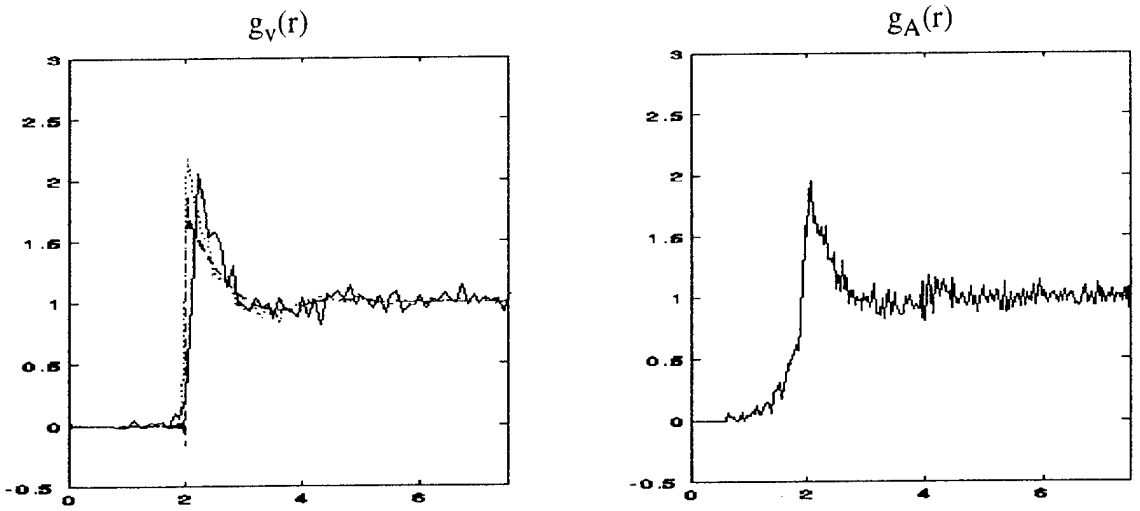


Figure 1: Left-hand plot is gv(r) from computer simulation (solid line) , calculated from Percus Yevick (dotted line). Right-hand plot is $g_A(r)$ from computer simulation. The x axis for both plots are normalized to r_0.

RESULTS FROM MONTE CARLO DATA

The Metropolis technique was used to deposit N=3500 spheres with radius r_0 into a test cube so they occupied 30% by volume. The cube was cut into 17 section planes which were used to calculate $g_A(r)$ shown in the right-hand plot of Fig.1. Hanisch's integral equation was then inverted to yield the volume pair distribution function that is shown in the left of Fig. 1 (solid line) along with $g_V(r)$ calculated from the Percus-Yevick approximation (dotted line). Note that for this single size case, there is zero probability that the particles are separated by a distance less than 2 r_0.

SCATTERING FROM MULTI-SIZED SPHERES

For a system of particles with L different sizes i = 1,2,.. .L and number density n_i , $g_v(r)$ can be represented in terms of the pair distribution function between species s_i and s_j, $g_{ij}(r)$, as

$$g_v(r) = \sum_{i,j}^{L} \frac{n_i n_j}{n_0} g_{ij}(r) \qquad (3)$$

where n_0 is the total number density of the particles.

The effective wavenumber for a system of particles can be calculated from the Fourier transform of the correlation function, $h_{ij}(r) = g_{ij}(r) - 1$, under the quasi-crystalline approximation (QCA) and the quasi-crystalline approximation with coherent potential (QCA-CP) [3]. In these calculations, h_{ij} is weighted by the cube of the particle radius and number density of the particle.

SNOW SUBSECTIONS

The 2-D subsections of snow were prepared by saturating the pore void with filler, then cutting, polishing and enhancing the contrast so the snow grain profiles can be automatically classified against the pore filler [4]. One snow section prepared in this fashion at the Cold Regions Research and Engineering Laboratory (CRREL) is shown in Fig. 2. It has been observed that the diameters of the snow grains follow a log-normal distribution [5] and furthermore that the parameters of the distribution can be obtained from stereological data. We use five representative sizes for the log-normal distribution.

To determine $g_A(r)$ from snow subsections the grain profiles were fitted with area equivalent circles and the separation distances between the circles were recorded.

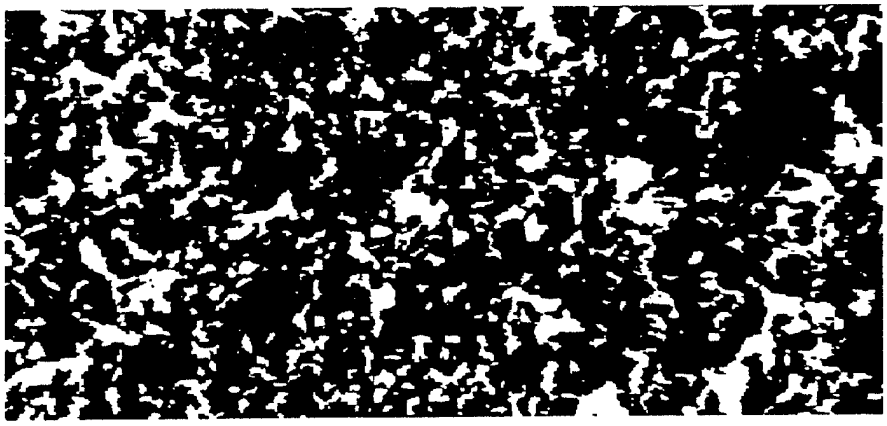


Figure 2 :
Snow section from
March 3, 1993
site in Fairbanks, Alaska
ice grain volume 22%

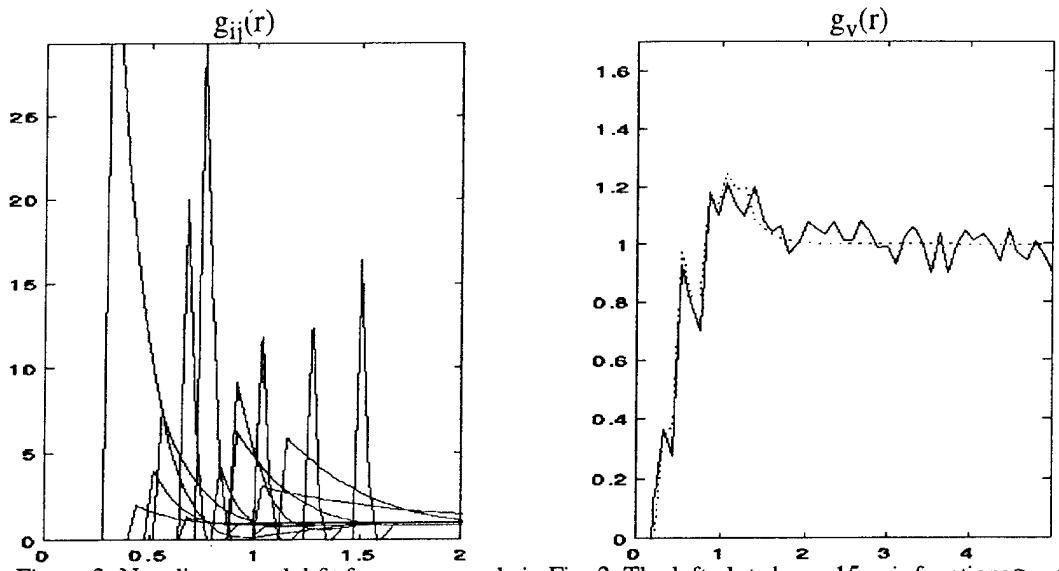


Figure 3: Non-linear model fit for snow sample in Fig. 2. The left plot shows 15 pair functions g_{ij} and the right shows the total pair function g_v from fit (dotted line) and from snow section (solid line).

G_{IJ} FROM PLANAR SNOW SECTIONS

The volume pair distribution function $g_V(r)$ can be obtained from inversion of (2) once the area pair distribution function $g_A(r)$ and the size distribution have been determined from section data. The recovered volume pair distribution function for the snow section in Fig. 2 is shown in the right-hand plot of Fig. 3 as a function of r in mm.

To calculate the scattering from the ice grains, $g_V(r)$ needs to be decomposed into size specific $g_{ij}(r)$ as in (3). We represent $g_v(r)$ as a sum of basis functions with the functional form

$$X_k(r) = h(r-r_k)\frac{A_k}{r}(\exp(-\mu_k(r-r_k))\cos(\mu_k(r-r_k))+1) \qquad (4)$$

where the double index i,j has been collapsed into a single index k with $r_k=r_i + r_j$ and h(r) is the step function. Equation (4) contains two adjustable parameters A_k and μ_k which represent the amplitude of the pair function and the strength of the oscillation and decay. These parameters are determined by an iterative minimization of the least squares error between the $g_v(r)$ recovered from the snow section and that given by the sum of the basis functions in (4). The right-hand plot of Fig. 3 shows a comparison of this sum (dotted line) and the retrieved $g_v(r)$.

The size specific pair distributions functions resulting from this procedure are shown in the left plot of Fig. 3. Scattering calculated with these pair functions compares well with that calculated under the Percus-Yevick approximation for the same size distribution under the QCA-CP approximation.

CONCLUSIONS

Scattering characteristics of dense media depends on 3-D particle statistics. We have demonstrated the recovery of the volume pair distribution function from 2-D sections of both computer generated data and actual snow samples. The process requires 1) measurement of $g_A(r)$, 2) inversion of Hansich's integral equation with a specific size distribution, and 3) decomposition into size specific pair functions. Further details of the process can be found in [6].

REFERENCES

[1] L.M. Zurk, L. Tsang, K.H. Ding, and D.P. Winebrenner, "Monte Carlo Simulations of the Extinction Rate of Densely Packed Spheres with Clustered and Non-Clustered Geometries", J. of the Opt. Soc. of Am, Vol. 12, No. 8, Aug. 1995

[2] K.H. Hanisch, "On Stereological Estimation of Second order Characteristics and of the Hard-core Distance of Systems of Sphere Centres", Biometrical Journal, Vol. 25, No. 8, 731-743, 1983

[3] K.H. Ding and L. Tsang, "Effective Propagation Constants of Dense Nontenuous Media with Multi-Species of Particles", Journal of Electromagnetic Waes and Applications, Vol. 2, No. 8, 757-777, 1988

[4] R. Perla, J. Dozier and R.E. Davis, "Preparation of serial subsections in dry snow specimens", Journal of Microscopy, Vol. 141, 111-114, April 1986

[5] Jiancheng Shi, Robert E. Davis, Jeff Dozier, ``Stereological determination of dry-snow parameters for discrete-scatterer microwave modeling", Annals of Glac., 17, 1993

[6] L.M. Zurk, "Electromagnetic Wave Propagation and Scattering in Dense, Discrete Random Media with Application to Remote Sensing of Snow", PhD Thesis, University of Washington, Dec. 1995

Modeling of Electromagnetic Wave Scattering from Time-Varying Snowcover *

K.H. Ding, Y.E. Yang, S.E. Shih, and J.A. Kong
Department of Electrical Engineering and Computer Science and
Research Laboratory of Electronics, Massachusetts Institute of Technology
Cambridge, MA 02139

R.E. Davis
U.S. Army Cold Regions Research and Engineering Laboratory
Hanover, NH 03755-1290

Abstract - - In this paper, a study of the effects of time-varying snowcovers on the radar backscatter signatures is presented. To this objective, a snow physics model, known as SNTHERM, is applied to enable the simulation of the dynamical behavior of snowpacks. The SNTHERM model can provide thermal and physical properties such as the temperature profile, liquid water content, and the layering structure which affect the electromagnetic properties of snowpacks. To calculate the backscattering coefficients from snowcovers, we employ the dense medium radiative transfer (DMRT) theory with a clustered snow grain microstructure. This coupled model is then used to predict the influence of environmental variation on the millimeter wave radar response, and compare simulation results with snow backscatter measurements. Good agreement is obtained between model and measured data in both timing and magnitude.

INTRODUCTION

The seasonal snowcover is a major environmental factor over the earth surface. On the ground, snow is a highly inhomogeneous medium consisting of mixture of ice, air, and liquid water. The unbonded spherical particle has been widely used in the modeling of snow grains. However, natural snow grains are in a clustered form. In order to account for the clustering behavior of ice particles, we apply the sticky hard sphere model [1], assuming the presence of surface adhesion between particles, to simulate a system of spherical particles that are not only randomly organized but also have a tendency to form bonds with each other. It is also possible to describe adhesive particles statistically with Percus-Yevick sticky particle pair distribution function [1], which can be utilized in the dense medium radiative transfer (DMRT) theory to study the electromagnetic interactions with snowpacks [2-4].

Seasonal snowpacks are also highly variable in their temporal and spatial behavior. Knowledge of the snowcover physics which govern the heat and mass transfer is essential for predicting the dynamically changing snow texture under varying environmental conditions. The SNTHERM model developed at the U.S. Army Cold Regions Research and Engineering Laboratory (CRREL) [5] can provide insight into the snow densification and metamorphosis process, as well as the thermal and physical properties, such as the temperature profile, liquid water content, and the layering structure. In this study, we coupled the DMRT three-dimensional scattering model with the SNTHERM one-dimensional snow physics model to interpret the diurnal variations of the millimeter wave radar returns from a series of experiments conducted by the University of Massachusetts at Amherst during March 1993 [6].

DMRT: SNOW SCATTERING MODEL

In a snowpack, the ice particles occupy an appreciable volume fraction such that the classical assumption of independent scattering is no longer valid. This deficiency is corrected by the dense medium radiative transfer (DMRT) theory [2]. The DMRT theory has been applied to study the active and passive remote sensing of snow terrain [3,4]. The layered geometry of a snowcover is depicted in Figure 1: the upper half space is air; the lower half space is soil with complex permittivity ϵ_g; and the middle layers represent snow. Within the l-th snow layer, the constituent ice particles are random clusters of small primary spherical particles of radius a_l with complex permittivity ϵ_s. The stickiness τ is applied to parameterized the clustering nature of snow grains [1]. The aggregated ice particles are randomly distributed in a background medium of complex permittivity ϵ_{bl}.

All four Stokes parameters can be included in the vector DMRT equation (1) which describes the propagation of specific intensities inside the l-th layer,

$$\cos\theta \frac{d}{dz}\bar{I}_l(\theta,\phi,z) = -\kappa_{el}\bar{I}_l(\theta,\phi,z) + \int_0^{2\pi} d\phi' \int_0^{\pi} d\theta' \sin\theta' \bar{\bar{P}}_l(\theta,\phi;\theta',\phi') \cdot \bar{I}_l(\theta',\phi',z) \quad (1)$$

with elevation angles $0 \le \theta \le \pi$. $\bar{I}_l(\theta,\phi,z)$ is the Stokes vector in the direction (θ,ϕ), κ_{el} is the effective extinction

*This work was supported by the U.S. Army Cold Regions Research and Engineering Laboratory.
0-7803-3068-4/96$5.00©1996 IEEE

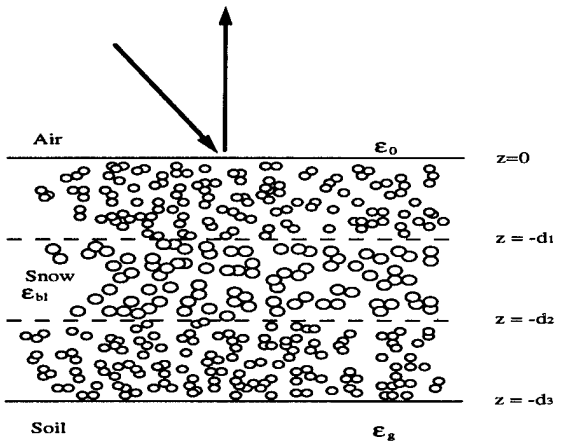


Figure 1: A schematic diagram of multilayer snow medium. The upper and lower half spaces are homogeneous with permittivities ϵ_o and ϵ_g, respectively.

rate, and $\overline{\overline{P}}_l(\theta,\phi;\theta',\phi')$ is the phase matrix which has been modified to be dependent upon the extinction rate and albedo [2-4]. The boundary conditions for the specific intensities at $z=d_l$ are, for $0<\theta_l<\pi/2$,

$$\begin{aligned} & \overline{I}^-_{l+1}(\pi-\theta_{l+1},\phi_{l+1},z=-d_l) \\ = \; & \overline{\overline{T}}_{l(l+1)}(\theta_l)\cdot\overline{I}^-_l(\pi-\theta_l,\phi_l,z=-d_l) \\ + \; & \overline{\overline{R}}_{(l+1)l}(\theta_{l+1})\cdot\overline{I}^+_{l+1}(\theta_{l+1},\phi_{l+1},z=-d_l) \qquad (2) \\ & \overline{I}^+_l(\theta_l,\phi_l,z=-d_l) \\ = \; & \overline{\overline{T}}_{(l+1)l}(\theta_{l+1})\cdot\overline{I}^+_{l+1}(\theta_{l+1},\phi_{l+1},z=-d_l) \\ + \; & \overline{\overline{R}}_{l(l+1)}(\theta_l)\cdot\overline{I}^-_l(\pi-\theta_l,\phi_l,z=-d_l) \qquad (3) \end{aligned}$$

where the intensities in the scattering layer have been broken into upward going intensities $\overline{I}^+_l(\theta,\phi,z)$ and downward going intensities $\overline{I}^-_l(\pi-\theta,\phi,z)$. In the above equations $\overline{\overline{T}}_{l(l+1)}(\theta_l)$ is the transmission matrix which represents the coupling from region l to region $l+1$, and $\overline{\overline{R}}_{l(l+1)}(\theta_l)$ is the reflection matrix which represents the coupling from upward going intensities into downward going intensities at the boundary of region l and region $l+1$. The angles θ_l and θ_{l+1} in layers l and $l+1$, respectively, are related to each other by Snell's law. The discrete-ordinate eigenanalysis technique is used in solving (1) and the quadrature rule used here is the method that adopted by Tanaka and Nakajima [7].

SNTHERM: SNOW PHYSICS MODEL

SNTHERM is a one-dimensional snowpack physics model that was developed at the U.S. Army Cold Regions Research and Engineering Laboratory (CRREL) [5]. The model considers a snowcover over soil ground and can predict temperature profile within the strata of snow and frozen soil. SNTHERM also simulates various physical and hydrological processes within a snowcover, including water flow, compaction, grain growth, and snow ablation and accumulation. In the model, the snowcover and soil ground are subdivided into stacked layers with horizontally infinite control volumes, each of which is then subject to the governing equations for heat and mass balance. The mass of ice and water is assumed to be conserved under the contraction of control volume, whereas the displaced portion of air and water vapor are expelled. At each time step, the mass balance equations are solved first and water flux and snow density from this computation are used in the subsequent solution of the energy equation. The detailed description of theoretical models and numerical methods of SNTHERM are referred to Jordan [5].

Table 1: Sample SNTHERM Output File

layer thickness (cm)	snow density (kg/m^3)	liquid density (kg/m^3)	grain diameter (m)	temperature ($^\circ K$)
2	289.2959	40.83261	0.001054	273.1251
6	281.7177	38.72473	0.001652	273.1249
8	279.3642	25.37651	0.002019	273.1112

Giving the initial temperature profile, water content, grain sizes, and layer densities of snow layers, plus the subsequent meteorological conditions such as air temperature, wind speed, precipitation, and solar radiation, SNTHERM can provide various snow parameters at hourly intervals. Among them, the stratified structure of snow layers, grain size, bulk snow density and liquid density are important inputs to the DMRT scattering model. Table 1 presents a partial listing of a SNTHERM output file for a 3-layer structure of a wet snow case. It indicates that the density, size, and wetness varies with the layer structure and the temperature profile.

COMPARISON OF MODEL AND MEASUREMENTS

The experimental data sets are from a series of snow measurements conducted by the University of Massachusetts at Amherst, 1 March (day 60) to 8 March (day 67) 1993 [6]. In these experiments, three radar systems operating at 35, 95, and 225 GHz were used. The 95 and 225 GHz radars are fully polarimetric. The 35 GHz radar was only capable of VV-polarized radar cross-section measurements. Besides the radar signatures, the meteorological and ground information were also recorded, including air temperature, wind speed, and relative humidity, snow liquid water content per volume, average ice grain diameter and volume fraction, and snow depth. Meteorological data were used to drive SNTHERM, whose predictions compared very closely with the field measurements. Theoretical calculations based on the DMRT and the SNTHERM models are compared with the backscattering coefficients σ_{vv} at 35 GHz in Figure 2, and with the σ_{vv} and σ_{hh} at 95 GHz in Figures 3 and 4, respectively. The radar response shows a strong diurnal fluctuation which is due to the effects of liquid water within the snowpack. The backscatter drops during daytime periods

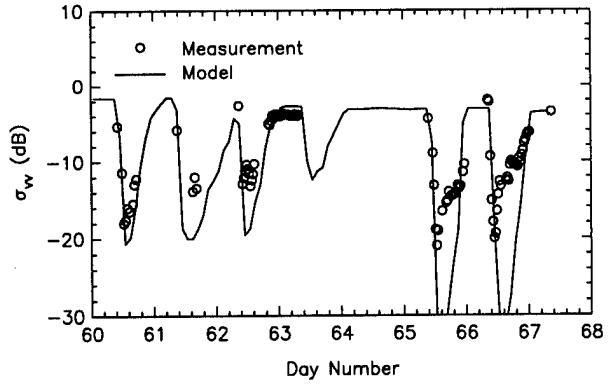


Figure 2: Comparison of models with snow measurements at 35 GHz and 60° incident angle [6].

when the temperature rises and liquid water content increases. While in cold nights, the backscatter tends to rise again because of the refreezing of the snow. It can be seen that there is good agreement between the model and the measured data in both timing and magnitude.

CONCLUSION

In this paper, we have investigated the relationship between the electromagnetic sensor response and the snowcover changes under time-varying environmental conditions. The DMRT and SNTHERM models are applied to study the influence of surface energy exchange over snow on the backscatter, and compare with experimental data. We demonstrated that SNTHERM can provide the linkage between the snow metamorphsis and the electromagnetic properties of snowcovers. It predicts important snow model parameters which are difficult to obtain from ground truth measurements. Also, the coupled DMRT and SNTHERM model can be useful in predicting the multi-temporal radar response of snowcovers, and in retrieving snow parameters for remote sensing applications.

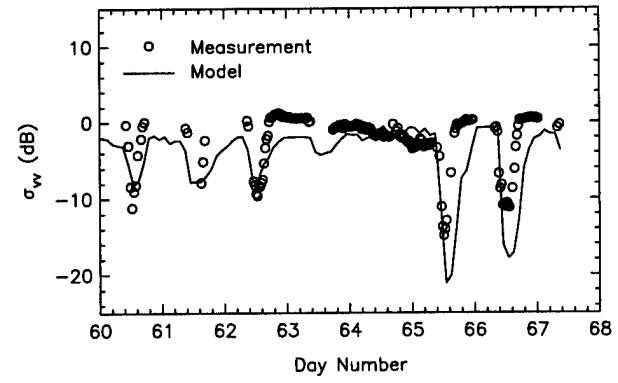


Figure 3: Comparison of models with snow measurements at 95 GHz and 60° incident angle [6].

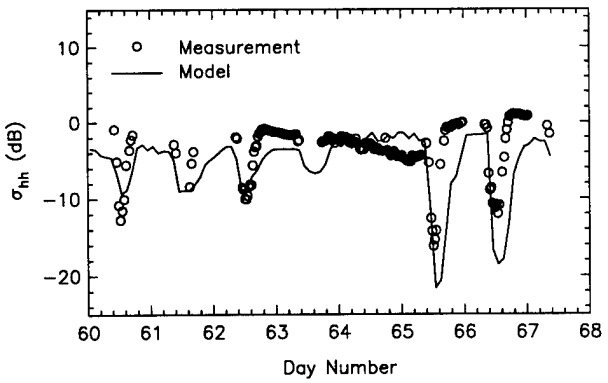


Figure 4: Comparison of models with snow measurements at 95 GHz and 60° incident angle [6].

ACKNOWLEDGMENTS

The authors would like to acknowledge Janet Hardy for her help in providing updated SNTHERM output files.

REFERENCES

[1] K.H. Ding, L. Zurk, and L. Tsang, "Pair distribution functions and attenuation rates for sticky particles in dense media," *J. Electro. Waves Applic.*, Vol. 8, pp. 1585–1604, 1994.

[2] L. Tsang, and A. Ishimaru, "Radiative wave equations for vector electromagnetic propagation in dense nontenuous media," *J. Electro. Waves Applic.*, Vol. 1, pp. 59–72, 1987.

[3] L. Tsang, "Dense medium radiative transfer theory for dense discrete random media with particles of multiple sizes and permittivities," in *Progress in Electromagnetic Research,* Volume 6, A. Priou, ed., Elsevier, New York, 1991.

[4] R. West, L. Tsang, and D.P. Winebrenner, "Dense medium radiative transfer theory for two scattering layers with a Rayleigh distribution of particle sizes," *IEEE Trans. Geosci. Remote Sensing,* Vol. GE-31, pp. 426–437, 1993.

[5] R. Jordan, "A one-dimensional temperature model for a snow cover: Technical documentation for SNTHERM.89," Spec. Rep. 91-16, U.S. Army Cold Reg. Res. and Eng. Lab., Hanover, NH, 1991.

[6] P. Chang, J. Mead, R. McIntosh, R. Davis, and H. Boyne, "A detailed study of the backscatter characteristics of snowcover measured at 35, 95 and 225 GHz," in *Proc. IGARSS '94 Symp.*, Pasadena, CA, August, 1994, pp. 1932–1934.

[7] M. Tanaka, and T. Nakajima, "Effects of oceanic turbidity and index of refraction of hydrosols on the flux of solar radiation in the atmosphere-ocean system," *J. Quant. Spectrosc. Radiat. Transfer,* Vol. 18, pp. 93–111, 1977.

Pulsed Beam Scattering from a Layer of Discrete Random Medium: With Applications to Spaceborne Weather Radars

Ö. Kılıç, R. H. Lang
The George Washington University
Dept. of Electrical Engineering and Computer Science
Washington, D.C. 20052
tel: (202) 994-5921 fax: (202) 994-0227
e-mail: kilic@seas.gwu.edu

Abstract -- Transient response of a Gaussian beam scattering from a layer of discrete random medium is examined for the case of a narrowband pulse. The scattered fields from the medium are calculated by using the analytical wave theory in conjunction with the distorted Born approximation. The model is used to generate results using the configuration for the TRMM satellite overlooking rain. The response of the medium is examined in terms of the different components of the received power for different look angles varying from nadir to 18^o.

INTRODUCTION

Electromagnetic backscattering from a layer of discrete random medium illuminated by a short pulse is studied. The layer has a thickness, d and lies over a flat ground, modeled as an homogenous half space with a dielectric constant, ϵ_g. The particles, which have a dielectric constant, ϵ_r are identical and distributed randomly inside the layer with free space in the background. The coordinate system of the medium is described by (x, y, z). A two dimensional Gaussian beam, which is obtained in the far field of an aperture antenna with excitation fields given by $\boldsymbol{E}_{ap} = \hat{\boldsymbol{y}}\, g(x_a)$, is incident on the particles. The coordinate system of the antenna is denoted by (x_a, y, z_a) where z_a corresponds to the normal to the antenna plane. The incident pulse, $p(t)$ is a short pulse which can be assumed to be a narrowband signal for practical purposes. The analysis is confined to the scalar treatment for the hh polarization. The configuration of the problem is shown in Fig. (1).

FORMULATION

The problem can be reduced to a time harmonic problem by decomposing the incident pulse, $p(t)$ into its frequency components by a Fourier transform:

$$p(t) = \int P(w)\, e^{-iwt}\, dw \qquad (1)$$

The transient response from the medium can then be determined by superposing the time harmonic response for all frequencies in (1), [3]. Due to the random nature of the medium, each time harmonic component of the received field consists of a mean and a fluctuating component, such as:

$$\Psi(\boldsymbol{r}; w) = <\Psi(\boldsymbol{r}; w)> + \widetilde{\Psi}(\boldsymbol{r}; w), \quad <\widetilde{\Psi}(\boldsymbol{r}; w)> = 0 \quad (2)$$

Consequently, the stochastic average for the correlation of the received field can be broken into two parts:

$$<\Psi(\boldsymbol{r}, w)\Psi(\boldsymbol{r}', w)> = <\Psi(\boldsymbol{r}, w)><\Psi^*(\boldsymbol{r}, w)> + <\widetilde{\Psi}(\boldsymbol{r}, w)\,\widetilde{\Psi}^*(\boldsymbol{r}, w)> \qquad (3)$$

The first term on the right in (3) is associated with the mean wave and is refered to as the *coherent* term. It depends on the specular reflection of the mean field from the ground. It has the shape of a Gaussian beam, traveling in the direction of the specular reflection. For the backscatter case, only the normal looking component of the mean field contributes to the received power, Fig. (2). The reflected beam is determined by multiplying the Gaussian beam traveling in the specular direction with the reflection coefficient of the surface. In Fig. (2), the shaded region shows an equivalent medium which has the same attenuation characteristics as the layer of particles in Fig. (1). As implied in Fig. (2), the coherent response involves no particle effects other than the attenuation as it travels inside

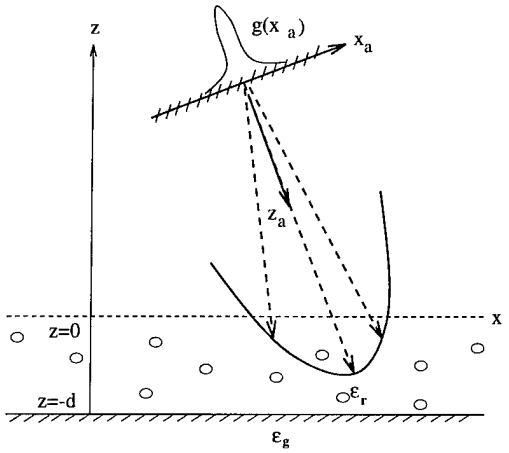


Figure 1. Problem Configuration

0-7803-3068-4/96$5.00©1996 IEEE

the equivalent layer. Assuming that the illuminated medium is in the far field of the antenna, the coherent term can be calculated asymptotically, from the superposition of the time harmonic components, [5] as:

$$P_{coh}(t) = a_{coh}|\Gamma_o|^2\, \widehat{g}^4(\hat{z})\, p^2(t - \tfrac{2z_o}{c})) \qquad (4)$$

where, $\Gamma_o(\hat{z})$ denotes the equivalent reflection coefficient from the surface at $z = 0$ and $\widehat{g}$ is the Fourier transform of the Gaussian excitation, $g(x_a)$ at the aperture plane. In the derivations for the expression above, a narrowband approximation is invoked so that expressions like the reflection coefficient, Γ_o or the Gaussian function, $\widehat{g}$ are assumed to stay constant over the frequency range.

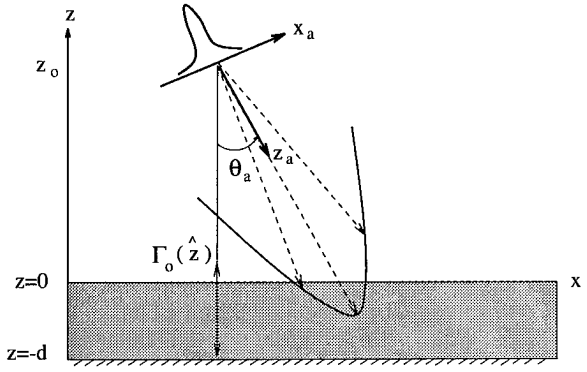


Figure 2. Coherent Response

Particle scattering effects are included in the *incoherent* term which is the second term on the right in (3). This term will be calculated using a single scattering mechanism, known as the distorted Born approximation. The advantages over the usual Born approximation are: (i) mean wave is incident on the particles; (ii) attenuation of the mean wave as it propagates inside the layer is accounted for. Using the distorted Born approximation, the incoherent term in (3) is calculated as an average over the particle position and orientation inside the medium as follows:

$$<\widetilde{\Psi}(\boldsymbol{r},w)\,\widetilde{\Psi}^*(\boldsymbol{r},w)> = \int d\boldsymbol{s}\,\rho(\boldsymbol{s})\,\overline{\phi_s(\boldsymbol{r},\boldsymbol{s})\,\phi_s^*(\boldsymbol{r},\boldsymbol{s})} \qquad (5)$$

In the equation above, $\phi_s(\boldsymbol{r},\boldsymbol{s})$ denotes the scattered field from a particle located at $\boldsymbol{s}$ inside the layer. The overbar refers to the average over the orientation, and the integration over $\boldsymbol{s}$ corresponds to the average over position, with $\rho(\boldsymbol{s})$ defined as the particle density. Using the distorted Born approximation, $\phi_s(\boldsymbol{r},\boldsymbol{s})$ is calculated in terms of the mean field as:

$$\phi_s(\boldsymbol{r},\boldsymbol{s}) = \int d\boldsymbol{r}'d\boldsymbol{r}''\, G(\boldsymbol{r},\boldsymbol{r}')\, t(\boldsymbol{r}'-\boldsymbol{s},\boldsymbol{r}''-\boldsymbol{s})\, <\Psi(\boldsymbol{r}'')> \qquad (6)$$

where, $t(\boldsymbol{r},\boldsymbol{r}')$ is the transition operator which relates the incident field on a particle to an equivalent source within the boundaries of that particle and $G(\boldsymbol{r},\boldsymbol{r}')$ is the Green's function for the medium. The mean wave, $<\Psi(\boldsymbol{r})>$ is determined using the Foldy-Lax approximation. The Green's function is obtained by first considering a half space of particles and applying the boundary conditions at the ground, [2]. The remaining unknown in (6) is the transition operator, $t(\boldsymbol{r},\boldsymbol{r}')$. It is related to the scattering amplitudes, $f(\boldsymbol{a},\boldsymbol{b})$ through a Fourier transform, when the slowly varying part of the mean wave is constant over the size of the particle, [1].

Using the expressions for these terms in (6), and employing (6) in (5), the incoherent power can be represented by three dominant returns: (1) direct term, which involves scattering of the incident wave directly back to the antenna; (2) direct-reflected term, which is due to the scattering of the incident wave through a single interaction between a particle and the ground; (3) reflected term, which occurs when the incident wave arrives at the antenna after a diuble bounce from the ground. The behavior of these components are shown in Fig. (3). As we observe in the figure, the direct-reflected component

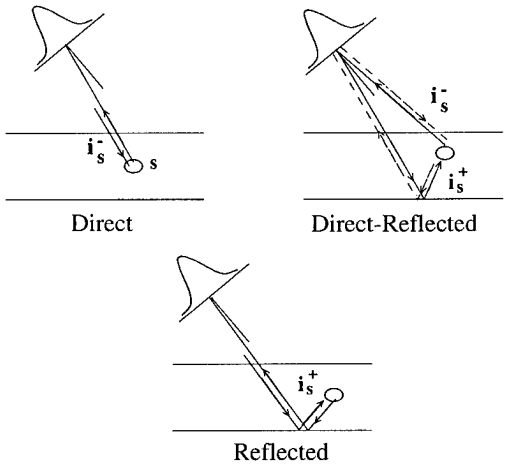


Figure 3. Components of Incoherent Response

is composed of two terms, where the field is incident on a particle either directly, along $\hat{\boldsymbol{i}}_s^-$; or through a reflection from the ground, along $\hat{\boldsymbol{i}}_s^+$. Both terms have the same phase when they arrive at the antenna. In the power calculations, these two terms couple in four different ways. It is the coupling of these two terms with each other that can cause a diferrence of upto 3 dB with the radiative transfer theory. Denoting the three cases of the incoherent power by dd for the direct term, dr for the direct-reflected terms, and rr for the reflected term, the incoherent power is written as:

$$P_{inc}(t) = P_{inc}^{dd}(t) + P_{inc}^{dr}(t) + P_{inc}^{rr}(t) \qquad (7)$$

Invoking the narrowband approximation as before, and assuming that all particles are in the far field of the antenna, the three components of the incoherent power is calculated asymptotically [6], as follows:

$$P_{inc}^{dd}(t) = \int ds\bar{\sigma}_{dd}\left[\widehat{g}(\hat{\boldsymbol{i}}_s^-)\right]^4 \frac{e^{\alpha_{dd}s_z}}{r_s^2}\, p^2(t - t_{dd}(s)) \qquad (8)$$

$$P_{inc}^{dr}(t) = \int ds \overline{\sigma}_{dr} \left[\widehat{g}(\hat{i}_s^-)\, \widehat{g}(\hat{i}_s^+) \right]^2 \frac{e^{\alpha_{dr} s_z}}{r_s\, r_{s_I}}\, p^2(t - t_{dr}(s)) \quad (9)$$

$$P_{inc}^{rr}(t) = \int ds \overline{\sigma}_{rr} \left[\widehat{g}(\hat{i}_s^+) \right]^4 \frac{e^{\alpha_{rr} s_z}}{r_{s_I}^2}\, p^2(t - t_{rr}(s)) \quad (10)$$

where $\overline{\sigma}_\beta$, $\beta \in \{dd, dr, rr\}$ is a function of the scattering cross section of the particle under the associated condition. It also involves the particle density and the reflection coefficient for the terms that experience reflection from the ground. The time delays, $t_\beta(s)$ correspond to the pathlengths traveled for each case;

$$t_{dd}(s) = \frac{2r_s}{c},\ t_{dr}(s) = \frac{r_s + r_{s_I}}{c},\ t_{rr}(s) = \frac{2r_{s_I}}{c} \quad (11)$$

where r_s and r_{s_I} correspond to the direct and reflected paths for a particle at s and c is the speed of light. Finally, $\alpha_\beta$corresponds to the attenuation associated with the path traveled by each component to the particle.

NUMERICAL DISCUSSIONS

In this section, the configuration for the TRMM satellite will be adapted to observe the received power from a layer of rain. Parameters to describe the medium are chosen so that moderate rain conditions are simulated. Spherical particles with a diameter of 1 mm are used to represent an average rain drop. The density of the particles are determined for a single layer, by assuming a rain rate of 1 mm/hr and integrating the Marshall-Palmer distribution over all possible sizes. The layer depth is chosen as 5.7 km using the CaPe (Convective and Precipitation-Electrification Experiment) data, [4]. The radiation pattern for TRMM satellite, which overlooks the medium at a height of 350 km, is approximated to the first order by a Gaussian beam with a width of 1.0^o. The operating frequency is 13.8 GHz, and the look angle varies from nadir to 18^o. Figure (4) shows the total received power for various look angles as a function of distance from the satellite. As we see, the three terms in (8)-(10) are observed in consecutive order. The direct term, which arrives first and the reflected term which arrives last form a symmetric geometry with respect to the sharp direct reflected term, which is observed at the center. The distance between the starting positions of the direct and the direct reflected term corresponds to the layer depth, d. The difference in the levels of the direct and the reflected components is due to the attenuation of the reflected signal as it travels a longer path inside the medium. This can be utilized in the estimation of the total attenuation inside the layer.

ACKNOWLEDGMENTS

O.K. would like to thank R. Meneghini for his valuable insights.

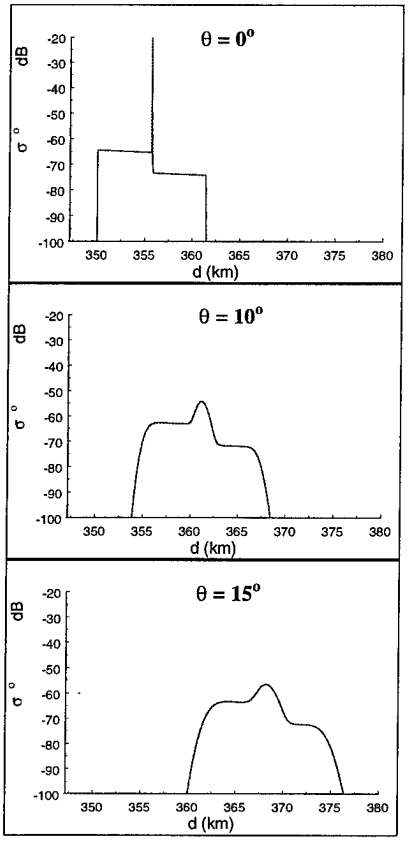


Figure 4. Transient Response of Rain for TRMM Configuration

REFERENCES

[1] Lang, R. H. *Electromagnetic backscattering from a sparse distribution of lossy dielectric scatterers*, Radio Sci. V.16, No:1, pp.15-30, 1981.

[2] Seker, S. *Resonant scattering from sparsely distributed lossy dielectric scatterers*, Ph.D. thesis, the George Washington University, Washington, DC, 1982.

[3] Le Vine D. M., Lang R. H. and Lin, Y. *Transient response of a layer of discrete random media over a dielectric half space* IEEE Trans. Geosci. Remote Sensing, vol. 30, pp.1034-1045, 1992

[4] Liao, L., Meneghini, R. and Iguchi, T. *Simulations of mirror image returns in rain from spaceborne and airborne radars over ocean*, Proc. 27th Int. Conf. on Radar Meteorology, pp.800-802, Vail, CO, 1995.

[5] Kilic, O. *Multibeam approach to pulse scattering from discrete random media*, Ph.D. thesis, the George Washington University, Washington DC, 1996

[6] Kilic, O. and Lang, R. H. *Transient response of a discrete random medium illuminated by a pulsed aperture*, unpublished.

TM Wave Scattering by Multiple Two-Dimensional Scatterers Buried under One-Dimensional Multi-Layered Media *

T. J. Cui† and W. Wiesbeck, Fellow, IEEE

Institut für Höchstfrequenztechnik und Elektronik, University of Karlsruhe,

Kaiserstr.12, 76128 Karlsruhe, Germany

(Telephon: +49 721/6086136, Telefax: +49 721/691865, E-mail: cui@iheaal.etec.uni-karlsruhe.de)

Abstract—**An exact and general theory is developed for the TM wave scattering by two-dimensional dielectric cylinders and perfect conducting cylinders buried under one-dimensional multi-layered media. From the Green's function under the layered media, electric field integral equations are obtained. Compared with the published methods, the theory has clearer physical significance, but can be used for treating the coupling of multiple scatterers.**

I. INTRODUCTION

Electromagnetic scattering is a very important research topics, because it has been found wide applications in the electromagnetic theory and engineering. For this topics a lot of research methods have been presented for different emphasis. However they were originally developed for scatterers residing in a homogeneous space. Although this restriction is suitable for some aerospace applications where the effect of the environment can be neglected, it does exclude many problems of practical interest where the existence of the earth must be taken into account. For example, in many cases the influence of the ground or the ocean, which often can be adequately represented by a model consisting of one or more planar dielectric layers, is the dominant effect in the problem. Therefore, the research for the scattering by buried scatterers is of great importance. Recently numerous papers have been published on the subject of scatterers in layered media, for example [1]-[2]. These works give excellent solutions for different problems. However there is a restriction for these methods. That is, they are not suitable simultaneously for buried dielectric and conducting scatterers.

In this paper we present a general method to investigate the TM wave scattering problem for multiple two-dimensional (2-D) dielectric cylinders and (or) perfect conducting cylinders buried under one-dimensional (1-D) multi-layered media.

*This work is supported by the Alexander von Humboldt Foundation, Germany.

†T. J. Cui was with the Department of Electromagnetic Field Engineering, Xidian University, Xi'an 710071, P. R. China.

0-7803-3068-4/96$5.00©1996 IEEE

II. 2-D GREEN'S FUNCTION UNDER THE 1-D MULTI-LAYERED MEDIA

To set up the general theory, we first investigate the two-dimensional Green's function under the layered media.

Consider a medium consisting of $n+1$ dielectric layers separated by n planar interfaces parallel to the xoy plane of a Cartesian coordinate system and located at $z = z_i, i = 1, 2, \ldots, n$, as illustrated in Fig.1. The relative permittivity of the ith layer is characterized by ϵ_i. The half spaces $z < 0$ and $z > z_n$ are homogeneous dielectric regions, whose relative permittivities are characterized by ϵ_b and ϵ_a. All the relative permittivities may be complex if the medium is lossy. An infinite-long line electric current I is perpendicular to the xoy plane, which is located at $z = -h$, as shown in Fig.1.

According to the electromagnetic field theory, the electric field excited by the electric current I is of only y-direction component, and can be written as [3]

$$E_b^i(x,z) = -\frac{k_b^2 I}{4\omega\epsilon_0\epsilon_b} H_0^{(2)}[k_b\sqrt{x^2+(z+h)^2}] \qquad (1)$$

where $k_b = \omega\sqrt{\mu_0\epsilon_0\epsilon_b} = k_0\sqrt{\epsilon_b}$ is the wave number in the half space $z < 0$, and $H_0^{(2)}(\cdot)$ is the second-kind zero-order Hankel's function. From the results of Harrington [3] and Wait [4], the incident electric field $E_b^i(x,z)$ can be expanded as the summation of infinite plane waves

$$E_b^i(x,z) = \frac{\omega\mu_0 I}{4\pi}\int_{-\infty}^{+\infty} \beta_b^{-1} e^{-j\beta_b|z+h|} e^{j\xi x} d\xi, \qquad (2)$$

where $\beta_b = \sqrt{k_b^2 - \xi^2} = \sqrt{k_0^2\epsilon_b - \xi^2}$ is the phase factor.

Because of the one-dimensional boundary of the multi-layered media, the total electric field in the region $z < 0$ will then be written as

$$E_b(x,z) = \frac{\omega\mu_0 I}{4\pi}\int_{-\infty}^{+\infty} \beta_b^{-1}\left[e^{-j\beta_b|z+h|} + r^+(k_0,\xi) \cdot e^{j\beta_b(z-h)}\right] e^{j\xi x} d\xi, \qquad (3)$$

the transmitted electric field in the region of $z > z_n$ is

$$E_a^s(x,z) = \frac{\omega\mu_0 I}{4\pi}\int_{-\infty}^{+\infty} \beta_b^{-1} t^+(k_0,\xi) e^{-j(\beta_a z + \beta_b h)} e^{j\xi x} d\xi, \qquad (4)$$

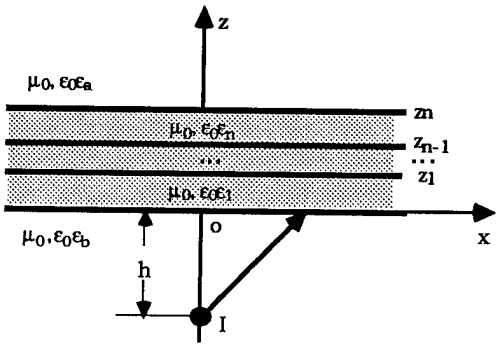


Figure 1: An infinite-long electric current under multi-layered media

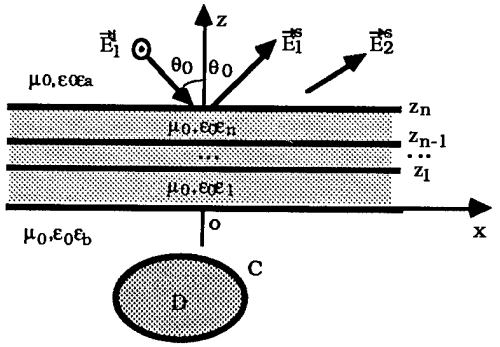


Figure 2: A scatterer buried under the multi-layered media

where $\beta_a = \sqrt{k_a^2 - \xi^2} = \sqrt{k_0^2\epsilon_a - \xi^2}$; and $r^+(k_0,\xi)$ and $t^+(k_0,\xi)$ are the reflection and transmission coefficients when a plane wave is incident from ϵ_b to ϵ_a by passing $\epsilon_1, \epsilon_2, \ldots,$ and ϵ_n, which can be calculated by using the electromagnetic wave theory [5].

If the electric current source I is located at any point (x', z') in the region $z < 0$, the electric fields in the regions of $z < 0$ and $z > z_n$ can be easily obtained from a coordinate transform

$$E_b(x,z,x',z') = \frac{\omega\mu_0 I}{4\pi}\int_{-\infty}^{+\infty}\beta_b^{-1}\left[e^{-j\beta_b|z-z'|} + r^+(k_0,\xi)e^{j\beta_b(z+z')}\right]e^{j\xi(x-x')}d\xi, \quad (5)$$

$$E_a^s(x,z,x',z') = \frac{\omega\mu_0 I}{4\pi}\int_{-\infty}^{+\infty}\beta_b^{-1}t^+(k_0,\xi)\cdot e^{-j(\beta_a z - \beta_b z')}e^{j\xi(x-x')}d\xi \quad (6)$$

which we call the two-dimensional Green's functions under one-dimensional layers for scattering use.

III. ELECTRIC FIELD INTEGRAL EQUATION FOR BURIED DIELECTRIC CYLINDERS

Now we consider the TM wave scattering problem for buried dielectric cylinders. See Fig.2, an arbitrarily shaped two-dimensional dielectric cylinder **D** with relative permittivity $\epsilon_r(x,z)$ is buried under the one-dimensional multi-layered media. A plane-polarized electromagnetic wave with electric field perpendicular to the xoz plane is incident from the region $z > z_n$ to the interface $z = z_n$ at an oblique angle θ_0, as shown in Fig.2. According to the electromagnetic wave theory [5], the reflected electric field by the one-dimensional medium can be written as

$$E_1^s(x,z) = r^-(k_0,\theta)e^{-jk_0(\sqrt{\epsilon_a - \sin^2\theta}z + x\sin\theta)}; \quad (7)$$

and the transmitted electric field through the one dimensional medium is

$$E^i(x,z) = t^-(k_0,\theta)e^{jk_0(\sqrt{\epsilon_b - \sin^2\theta}z - x\sin\theta)}, \quad (8)$$

where $r^-(k_0,\theta)$ and $t^-(k_0,\theta)$ are the reflection and transmission coefficients when the plane wave is incident from ϵ_a to ϵ_b by passing $\epsilon_n, \epsilon_{n-1}, \ldots, \epsilon_1$; θ can be determined by the Snell's law: $\sin\theta = \sqrt{\epsilon_a}\sin\theta_0$.

From Fig.2, the transmitted electric field through the multi-layered media is just the incident electric field of the dielectric cylinder. Under the illumination of the incident field $E^i(x,z)$, the internal electric field $E(x,z)$ and scattered electric field $E^s(x,z)$ inside the cylinder have the following relation

$$E(x,z) = E^s(x,z) + E^i(x,z). \quad (9)$$

From the results obtained in Section II, the scattered electric field generated by the dielectric cylinder can be obtained. It is an integral. Substituting the integral into (9), we have

$$-E(x,z) + j\frac{k_0^2}{4\pi}\int_{\mathbf{D}}[\epsilon_r(x',z') - \epsilon_b]E(x',z')\int_{-\infty}^{+\infty}\beta_b^{-1}\cdot\left[e^{-j\beta_b|z-z'|} + r^+(k_0,\xi)e^{j\beta_b(z+z')}\right]e^{j\xi(x-x')}d\xi dx'dz' = -E^i(x,z), \quad (x,z)\in\mathbf{D} \quad (10)$$

which is the electric field integral equation for the internal electric field $E(x,z)$ inside the buried dielectric cylinder.

Solving (10), $E(x,z)$ can be determined. So the total scattered electric field in the region $z > z_n$ is obtained

$$E_{\text{total}}^s(x,z) = E_1^s(x,z) + j\frac{k_0^2}{4\pi}\int_{\mathbf{D}}[\epsilon_r(x',z') - \epsilon_b]E(x',z')\cdot\int_{-\infty}^{+\infty}\beta_b^{-1}t^+(k_0,\xi)e^{-j(\beta_a z - \beta_b z')}e^{j\xi(x-x')}d\xi dx'dz'. \quad (11)$$

IV. ELECTRIC FIELD INTEGRAL EQUATION FOR BURIED CONDUCTING CYLINDERS

See Fig.2, an arbitrarily shaped conducting cylinder with boundary **C** lies under the multi-layered media. When the plane wave described in Section III is incident to the interface $z = z_n$, a surface electric current density $J(x,z)$ is induced around the conducting cylinder. Accordance with

the discussion in Section II, the scattered electric field generated by $J(x,z)$ can be formulated. When $(x,z) \in \mathbf{C}$, using the boundary condition

$$E(x,z)|_{(x,z)\in\mathbf{C}} = 0, \tag{12}$$

we will obtain an electric field integral equation for the induced current $J(x,z)$

$$\frac{\omega\mu_0}{4\pi}\int_{\mathbf{C}} J(x',z')\int_{-\infty}^{+\infty}\beta_b^{-1}\left[e^{-j\beta_b|z-z'|}+r^+(k_0,\xi)\right.$$

$$\left.\cdot\, e^{j\beta_b(z+z')}\right]e^{j\xi(x-x')}d\xi ds' = -E^i(x,z), \tag{13}$$

from which $J(x,z)$ can be determined. Thus the total scattered electric field in the region $z > z_n$ is

$$E^s_{\text{total}}(x,z) = E^s_1(x,z) + \frac{\omega\mu_0}{4\pi}\int_{\mathbf{C}} J(x',z')\int_{-\infty}^{+\infty}\beta_b^{-1}$$

$$\cdot t^+(k_0,\xi)e^{-j(\beta_a z-\beta_b z')}e^{j\xi(x-x')}d\xi ds'. \tag{14}$$

V. ELECTRIC FIELD INTEGRAL EQUATIONS FOR MULTIPLE BURIED SCATTERERS

Now we consider the general case. There supposed to be M dielectric cylinders $\mathbf{D}_1, \mathbf{D}_2, \ldots, \mathbf{D}_M$ and N conducting cylinders $\mathbf{C}_1, \mathbf{C}_2, \ldots, \mathbf{C}_N$ buried under the multi-layered media. When the plane wave is incident from the upper space, there will be internal electric field $E_m(x,z)$ inside the mth buried dielectric cylinder $\mathbf{D}_m, m = 1,2,\ldots,M$, and surface electric current $J_n(x,z)$ around the nth buried conducting cylinder $\mathbf{C}_n, n = 1,2,\ldots,N$, induced. Then the scattered electric field excited by $E_m(x,z)$ and $J_n(x,z)$ in the region $z < 0$ can be expressed as

$$E^s(x,z) = j\frac{k_0^2}{4\pi}\sum_{m=1}^{M}\int_{\mathbf{D}_m}[\epsilon_{rm}(x',z')-\epsilon_b]E_m(x',z')\cdot$$

$$\int_{-\infty}^{+\infty}\beta_b^{-1}\left[e^{-j\beta_b|z-z'|}+r^+(k_0,\xi)e^{j\beta_b(z+z')}\right]\cdot$$

$$e^{j\xi(x-x')}d\xi dx'dz' + \frac{k_0\eta_0}{4\pi}\sum_{n=1}^{N}\int_{\mathbf{C}_n}J_n(x',z')\cdot$$

$$\int_{-\infty}^{+\infty}\beta_b^{-1}\left[e^{-j\beta_b|z-z'|}+r^+(k_0,\xi)e^{j\beta_b(z+z')}\right]e^{j\xi(x-x')}d\xi ds' \tag{15}$$

where $\epsilon_{rm}(x,z)$ is the relative permittivity of the mth dielectric cylinder ($m = 1,2,\ldots,M$). When the observing point $(x,z) \in \mathbf{D}_m$, we obtain from the boundary condition

$$\left[E_m(x,z) - E^s(x,z) - E^i(x,z)\right]|_{(x,z)\in\mathbf{D}_m} = 0; \tag{16}$$

when the observing point $(x,z) \in \mathbf{C}_n$, we have

$$\left[E^s(x,z) + E^i(x,z)\right]|_{(x,z)\in\mathbf{C}_n} = 0. \tag{17}$$

Substituting (15) into (16) and (17), there will be $M+N$ coupled integral equations for $E_m(x,z)$ and $J_n(x,z)$.

The total scattered electric field in the upper region $z > z_n$ is then obtained

$$E^s_{\text{total}}(x,z) = E^s_1(x,z) + j\frac{k_0^2}{4\pi}\sum_{m=1}^{M}\int_{\mathbf{D}_m}[\epsilon_{rm}(x',z')-\epsilon_b]\cdot$$

$$E_m(x',z')\int_{-\infty}^{+\infty}\beta_b^{-1}t^+(k_0,\xi)e^{-j(\beta_a z-\beta_b z')}e^{j\xi(x-x')}d\xi dx'dz'$$

$$+\frac{k_0\eta_0}{4\pi}\sum_{n=1}^{N}\int_{\mathbf{C}_n}J_n(x',z')\int_{-\infty}^{+\infty}\beta_b^{-1}t^+(k_0,\xi)\cdot$$

$$e^{-j(\beta_a z-\beta_b z')}e^{j\xi(x-x')}d\xi ds'. \tag{18}$$

The above theory is exact. But it is difficult to solve the concerned integral equations by analytical methods. The numerical implementation of the theory will be investigated in other paper.

VI. CONCLUSIONS

This paper presents a general theory for the TM wave scattering by dielectric cylinders and conducting cylinders buried under one-dimensional multi-layered media. This theory has a clear physical significance. For example, in the scattered electric field in the upper space there are two parts: one is contributed by the multi-layered media; one is contributed by the buried scatterers in which the influence of the layers has been involved. Similar conclusion is true for the electric field integral equations. This theory is also suitable for the lossy case and **continuous one-dimensional medium**.

References

[1] X.B. Xu and C.M. Butler, "Scattering of TM excitation by coupled and partially buried cylinders at the interface between two media," IEEE Trans. Antennas Propagat., vol.AP-35, pp.529-538, 1987.

[2] K.A. Michalski and D. Zheng, "Electromagnetic scattering and radiation by surfaces of arbitrary shape in layered media, Part I: Theory; Part II: Implementation and results for contiguous half-spaces," IEEE Trans. Antennas Propagat., vol.AP-38, pp.335-352, 1990.

[3] R.F. Harrington, Time-harmonic Electromagnetic fields. New York: McGRAW-HILL, 1961.

[4] J.R. Wait, Electromagnetic Waves in Stratified media. London: Pergamon Press, 1962.

[5] J.A. Kong, Electromagnetic Wave Theory. New York: Wiley,1986.

TE Wave Scattering by Multiple Two-Dimensional Scatterers Buried under One-Dimensional Multi-Layered Media *

T. J. Cui† and W. Wiesbeck, Fellow, IEEE
Institut für Höchstfrequenztechnik und Elektronik, University of Karlsruhe,
Kaiserstr.12, 76128 Karlsruhe, Germany
(Telephon: +49 721/6086136, Telefax: +49 721/691865, E-mail: cui@iheaal.etec.uni-karlsruhe.de)

Abstract—**A general theory is presented for the TE wave scattering by multiple two-dimensional scatterers buried under one-dimensional multi-layered media. Closed-form formulations for the electric and magnetic fields excited by an arbitrarily oriented electric current strip under the layered media are derived at first, from which an electric field integral equation for the buried dielectric cylinder, a magnetic field integral equation for the buried conducting cylinder, and coupled mixed electromagnetic field integral equations for multiple buried scatterers are then obtained.**

I. INTRODUCTION

The electromagnetic scattering and radiation by objects buried in one-dimensional medium have been considered by many authors [1]-[3]. However there is a restriction in these considerations, that is, the methods involved are not suitable simultaneously for treating buried dielectric and conducting scatterers, which is important in many applications. For this reason, we have investigated the electromagnetic scattering by multiple dielectric and conducting cylinders buried under multi-layered media [4]. But we considered only the simplest case — TM wave excitation.

In this paper, we will present a general theory for the TE wave scattering by multiple scatterers buried under the multi-layered media.

II. THE FIELDS EXCITED BY A CURRENT STRIP UNDER MULTI-LAYERED MEDIA

In this section, we give the formulations for electric and magnetic fields excited by an arbitrarily oriented electric current strip buried under one-dimensional multi-layered media. See Fig.1, we consider a medium consisting of $n+1$ dielectric layers separated by n planar interfaces parallel to the xoy plane and located at $z = z_i, i = 1, 2, \ldots, n$. The relative permittivity of the ith layer is characterized by ϵ_i. The half spaces $z < 0$ and $z > z_n$ are homogeneous dielectric regions, whose relative permittivities are characterized by ϵ_b and ϵ_a. When the medium is lossy, all the permittivities may be complex.

From the electromagnetic theory and Fourier transform, when an arbitrarily oriented electric current strip $\vec{J}dl = (\hat{x}J_x + \hat{z}J_z)dl$ is located at any point (x', z') under the layered media, its radiation fields can be formulated by a complicated deduction. In the region of $z < 0$,

$$H_{by}(x,z) = -\frac{k_b}{4j}[(z-z')J_x - (x-x')J_z]dl\frac{H_1^{(2)}(k_bR)}{R} + \frac{dl}{4\pi}\int_{-\infty}^{+\infty}(J_x + \beta_b^{-1}\xi J_z)r^+(k,\xi)e^{j\beta_b(z+z')}e^{j\xi(x-x')}d\xi, \quad (1)$$

$$E_{bx}(x,z) = -\frac{k_b dl}{4\omega\epsilon_0\epsilon_b R^3}\{R^2H_1^{(2)}(k_bR)J_x - (z-z')[(z-z')\cdot J_x - (x-x')J_z][2H_1^{(2)}(k_bR) - k_bRH_0^{(2)}(k_bR)]\} - \frac{dl}{4\pi\omega\epsilon_0\epsilon_b}\int_{-\infty}^{+\infty}(\beta_bJ_x + \xi J_z)r^+(k,\xi)e^{j\beta_b(z+z')}e^{j\xi(x-x')}d\xi, \quad (2)$$

$$E_{bz}(x,z) = -\frac{k_b dl}{4\omega\epsilon_0\epsilon_b R^3}\{R^2H_1^{(2)}(k_bR)J_z - (x-x')[(x-x')\cdot J_z - (z-z')J_x][2H_1^{(2)}(k_bR) - k_bRH_0^{(2)}(k_bR)]\} + \frac{dl}{4\pi\omega\epsilon_0\epsilon_b}\int_{-\infty}^{+\infty}\xi(J_x + \beta_b^{-1}\xi J_z)r^+(k,\xi)e^{j\beta_b(z+z')}e^{j\xi(x-x')}d\xi; \quad (3)$$

in the upper region $z > z_n$, only the magnetic field is interested

$$H_{ay}(x,z) = \frac{dl}{4\pi}\int_{-\infty}^{+\infty}(J_x + \beta_b^{-1}\xi J_z)t^+(k,\xi)\cdot e^{-j(\beta_a z - \beta_b z')}e^{j\xi(x-x')}d\xi, \quad (4)$$

where $R = \sqrt{(x-x')^2 + (z-z')^2}$ is the distance between field point and source point; $\beta_b = \sqrt{k_0^2\epsilon_b - \xi^2}$ and $\beta_a = \sqrt{k_0^2\epsilon_a - \xi^2}$ are the phase factors in Region b and a; and $r^+(k,\xi)$ and $t^+(k,\xi)$ are the reflection and transmission coefficients when a plane wave with its magnetic field perpendicular to the incident plane is incident from $\epsilon_b \to \epsilon_1 \to \cdots \to \epsilon_n \to \epsilon_a$.

*This work is supported by the Alexander von Humboldt Foundation, Germany.

†T. J. Cui was with the Department of Electromagnetic Field Engineering, Xidian University, Xi'an 710071, P. R. China.

0-7803-3068-4/96$5.00©1996 IEEE

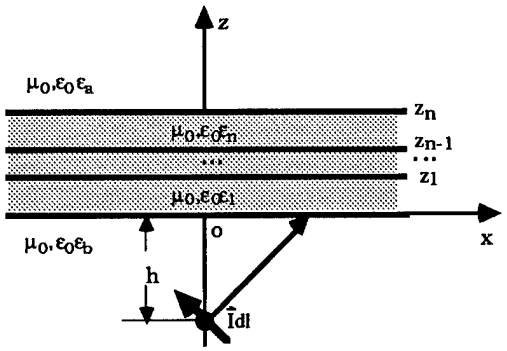


Figure 1: An arbitrarily-oriented electric current strip under multi-layered media

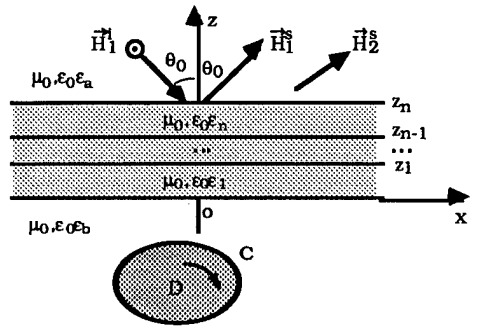


Figure 2: A scatterer buried under the multi-layered media

III. MAGNETIC FIELD INTEGRAL EQUATION FOR BURIED CONDUCTING CYLINDERS

In this section we consider the TE wave scattering by buried conducting cylinders. See Fig.2, an arbitrarily shaped conducting cylinder **C** is buried under the multi-layered media. A plane-polarized electromagnetic wave with magnetic field perpendicular to the xoz plane, a TE wave, is incident from the upper space to the interface $z = z_n$ at an oblique angle θ_0. From the electromagnetic wave theory [5], the reflected magnetic field by the multi-layered media can be written as

$$\vec{H}_1^s(x,z) = \hat{y} r^-(k,\theta) e^{-jk(\sqrt{\epsilon_a - \sin^2\theta} z + x\sin\theta)}; \quad (5)$$

the transmitted magnetic field through the layers, that is the incident magnetic field to the buried conducting cylinder, is

$$\vec{H}_b^i(x,z) = \hat{y} t^-(k,\theta) e^{jk(\sqrt{\epsilon_b - \sin^2\theta} z - x\sin\theta)} \quad (6)$$

where $r^-(k,\theta)$ and $t^-(k,\theta)$ are the reflection and transmission coefficients when the plane wave (TE wave) is incident from ϵ_a to ϵ_b by passing $\epsilon_n, \epsilon_{n-1}, \ldots, \epsilon_1$, respectively; θ is an equivalent angle in the free space, which can be determined by the Snell's law: $\sin\theta = \sqrt{\epsilon_a}\sin\theta_0$.

Under the illumination of the incident field $\vec{H}_b^i(x,z)$, there will be surface electric current $\vec{J}(x,z) = (\hat{x}\cos\phi + \hat{z}\sin\phi)J(x,z)$ induced around the contours of the conducting cylinder **C**. Here, ϕ is the angle between the tangent line at point (x,z) and the x-axis when **C** rotates clockwise. From (1), the scattered magnetic field excited by $\vec{J}(x,z)$ in the region $z < 0$ can be expressed as an integral. When the point $(x,z) \in \mathbf{C}$, from the electromagnetic boundary condition $\hat{n} \times \vec{H}_b(x,z) = \vec{J}(x,z)$, we will obtain

$$\frac{k_b}{4j}\int_{\mathbf{C}} J(x',z')[(z-z')\cos\phi' - (x-x')\sin\phi']\frac{H_1^{(2)}(k_bR)}{R}ds'$$

$$-\frac{1}{4\pi}\int_{\mathbf{C}} J(x',z')\int_{-\infty}^{+\infty}(\cos\phi' + \beta_b^{-1}\xi\sin\phi')\cdot$$

$$r^+(k,\xi)e^{j\beta_b(z+z')}e^{j\xi(x-x')}d\xi ds' - J(x,z) = H_{by}^i(x,z). \quad (7)$$

This is the magnetic field integral equation for the induced electric current around the buried conducting cylinder, from which $J(x,z)$ can be determined. Thus the total scattered magnetic field in the region $z > z_n$ can be calculated

$$\vec{H}_a^s(x,z) = \vec{H}_1^s(x,z) + \hat{y}\frac{1}{4\pi}\int_{\mathbf{C}} J(x',z')\int_{-\infty}^{+\infty}(\cos\phi'$$

$$+\beta_b^{-1}\xi\sin\phi')t^+(k,\xi)e^{-j(\beta_a z - \beta_b z')}e^{j\xi(x-x')}d\xi ds'. \quad (8)$$

IV. ELECTRIC FIELD INTEGRAL EQUATION FOR BURIED DIELECTRIC CYLINDERS

Now we consider an arbitrarily shaped dielectric cylinder **D** with relative permittivity $\epsilon_r(x,z)$ buried under the multi-layered media, as shown in Fig.2. When a TE wave is incident to the interface $z = z_n$, the transmitted electric field, i.e., the incident electric field to the buried dielectric cylinder, can be expressed as

$$\vec{E}_b^i(x,z) = -\frac{\eta_0}{\epsilon_b}t^-(k,\theta)(\hat{x}\sqrt{\epsilon_b - \sin^2\theta} + \hat{z}\sin\theta)\cdot$$

$$e^{jk(\sqrt{\epsilon_b - \sin^2\theta} z - x\sin\theta)}. \quad (9)$$

Under the illumination of the incident wave, the internal electric field $\vec{E}_b(x,z)$ will be induced inside the buried dielectric cylinder, which is the summation of scattered and incident electric fields

$$\vec{E}_b(x,z) = \vec{E}_b^s(x,z) + \vec{E}_b^i(x,z). \quad (10)$$

From (2) and (3), $\vec{E}_b^s(x,z)$ can be formulated

$$E_{bx}^s(x,z) = -\frac{jk_b}{4\epsilon_b}\int_{\mathbf{D}}\frac{\epsilon_r(x',z') - \epsilon_b}{R^3}\{[R^2H_1^{(2)}(k_bR) -$$

$$(z-z')^2 f(k_bR)]E_{bx}(x',z') +$$

$$(x-x')(z-z')f(k_bR)]E_{bz}(x',z')\}dx'dz' -$$

$$\frac{j}{4\pi\epsilon_b}\int_{\mathbf{D}}[\epsilon_r(x',z')-\epsilon_b]\int_{-\infty}^{+\infty}[\beta_b E_{bx}(x',z')+$$

$$\xi E_{bz}(x',z')]r^+(k,\xi)e^{j\beta_b(z+z')}e^{j\xi(x-x')}d\xi dx'dz', \quad (11)$$

$$E^s_{bz}(x,z)=-\frac{jk_b}{4\epsilon_b}\int_{\mathbf{D}}\frac{\epsilon_r(x',z')-\epsilon_b}{R^3}\{[R^2H_1^{(2)}(k_bR)-$$

$$(x-x')^2 f(k_bR)]E_{bz}(x',z')+$$

$$(x-x')(z-z')f(k_bR)]E_{bx}(x',z')\}dx'dz'+$$

$$\frac{j}{4\pi\epsilon_b}\int_{\mathbf{D}}[\epsilon_r(x',z')-\epsilon_b]\int_{-\infty}^{+\infty}\xi[E_{bx}(x',z')+$$

$$\beta_b^{-1}\xi E_{bz}(x',z')]r^+(k,\xi)e^{j\beta_b(z+z')}e^{j\xi(x-x')}d\xi dx'dz' \quad (12)$$

where $f(u)$ is the following function

$$f(u)=2H_1^{(2)}(u)-uH_0^{(2)}(u). \quad (13)$$

Substituting (11) and (12) into (10), we will obtain electric field integral equations for the internal electric fields $E_{bx}(x,z)$ and $E_{bz}(x,z)$ inside the dielectric cylinder. Then the total scattered magnetic field in the upper space can be written as

$$\vec{H}^s_a(x,z)=\vec{H}^s_1(x,z)+\hat{y}\frac{j\omega\epsilon_0}{4\pi}\int_{\mathbf{D}}[\epsilon_r(x',z')-\epsilon_b]$$

$$\int_{-\infty}^{+\infty}[E_{bx}(x',z')+\beta_b^{-1}\xi E_{bz}(x',z')]t^+(k,\xi)\cdot$$

$$e^{-j(\beta_a z-\beta_b z')}e^{j\xi(x-x')}d\xi dx'dz'. \quad (14)$$

V. MIXED FIELD INTEGRAL EQUATIONS FOR MULTIPLE BURIED SCATTERERS

There supposed to be M dielectric cylinders $\mathbf{D}_1,\ldots,\mathbf{D}_M$ and N conducting cylinders $\mathbf{C}_1,\ldots,\mathbf{C}_N$ buried under the multi-layered media. The relative permittivity of the mth dielectric cylinder is $\epsilon_{rm}(x,z)$.

Similar to the above sections, when a TE wave strikes the interface $z=z_n$, there will be internal electric field $\vec{E}_{bm}(x,z)$ inside the buried dielectric cylinder $\mathbf{D}_m, m=1,2,\ldots,M$, and surface electric current $\vec{J}_n(x,z)$ around the buried conducting cylinder $\mathbf{C}_n, n=1,2,\ldots,N$, induced. In the region $z<0$, the scattered magnetic field excited by $\vec{E}_m(x,z)$ and $\vec{J}_n(x,z)$ can be formulated

$$H^s_{by}(x,z)=-\frac{k_b\omega\epsilon_0}{4}\sum_{m=1}^{M}\left\{\int_{\mathbf{D}_m}[\epsilon_{rm}(x',z')-\epsilon_b][(z-z')\cdot\right.$$

$$E_{bmx}(x',z')-(x-x')E_{bmz}(x',z')]\frac{H_1^{(2)}(k_bR)}{R}dx'dz'-$$

$$-\frac{j}{\pi k_b}\int_{\mathbf{D}_m}[\epsilon_{rm}(x',z')-\epsilon_b]\int_{-\infty}^{+\infty}[E_{bmx}(x',z')+\beta_b^{-1}\xi\cdot$$

$$\left.E_{bmz}(x',z')]r^+(k,\xi)e^{j\beta_b(z+z')}e^{j\xi(x-x')}d\xi dx'dz'\right\}-$$

$$\frac{k_b}{4j}\sum_{n=1}^{N}\left\{\int_{\mathbf{C}_n}J_n(x',z')[(z-z')\cos\phi'-(x-x')\sin\phi']\cdot\right.$$

$$\frac{H_1^{(2)}(k_bR)}{R}ds'-\frac{j}{\pi k_b}\int_{\mathbf{C}_n}J_n(x',z')\int_{-\infty}^{+\infty}$$

$$\left.(\cos\phi'+\beta_b^{-1}\xi\sin\phi')r^+(k,\xi)e^{j\beta_b(z+z')}e^{j\xi(x-x')}d\xi ds'\right\}. \quad (15)$$

Similarly, the formulations for scattered electric fields are also availabe, which are not written here for pages reason.

From the boundary condition, when the observation point $(x,z)\in\mathbf{D}_m$ $(m=1,2,\ldots,M)$, we have

$$\left[E_{bmu}(x,z)-E^s_{bu}(x,z)-E^i_{bu}(x,z)\right]|_{(x,z)\in\mathbf{D}_m}=0, \quad (16)$$

where $u=x,z$; when $(x,z)\in\mathbf{C}_n(n=1,2,\ldots,N)$,

$$\left[J_n(x,z)+H^s_{by}(x,z)+H^i_{by}(x,z)\right]|_{(x,z)\in\mathbf{C}_n}=0. \quad (17)$$

Equations (16)-(17) constitute the mixed electric and magnetic field integral equations for the internal electric fields $\vec{E}_{bm}(x,z)$ and the induced electric current $J_n(x,z)$.

VI. CONCLUSIONS

Like the TM case [4], the theory presented in this paper is suitable for lossy case and one-dimensional inhomogeneous medium.

References

[1] X.B. Xu and C.M. Butler, "Scattering of TM excitation by coupled and partially buried cylinders at the interface between two media," IEEE Trans. Antennas Propagat., vol.AP-35, pp.529-538, 1987.

[2] X.B. Xu and C.M. Butler, "Current induced by TE excitation on coupled and partially buried cylinders at the interface between two media," IEEE Trans. Antennas Propagat., vol.AP-38, pp.1823-1828, 1990.

[3] K.A. Michalski and D. Zheng, "Electromagnetic scattering and radiation by surfaces of arbitrary shape in layered media, Part I: Theory; Part II: Implementation and results for contiguous half-spaces," IEEE Trans. Antennas Propagat., vol.AP-38, pp.335-352, 1990.

[4] T.J. Cui and W. Wiesbeck, "TM wave scattering by multiple two-dimensional scatterers buried under one-dimensional multi-layered media," Proc. IEEE International Geoscience and Remote Sensing Symposium, Lincoln, 27-31 May, 1996.

[5] J.A. Kong, Electromagnetic Wave Theory. New York: Wiley,1986.

High Resolution Imaging Techniques in Step-Frequency Subsurface Radars

Juan J. Martínez-Madrid*, José R. Casar Corredera, Gonzalo de Miguel-Vela****
*** Universidad Alfonso X el Sabio, Avda. de la Universidad 1, Villanueva de la Cañada, 28691 Madrid. Phone: +(34)-1-8109248; Fax:+(34)-1-8109101; e-mail: jjmadrid@uax.es**
**** GPSS-ETSIT, Universidad Politécnica de Madrid, Ciudad Universitaria s/n, 28040 Madrid. Phone: +(34)-1-3367225; Fax: 1-34-3367350; e-mail: jramon@gtts.ssr.upm.es**

Abstract -- Imaging of buried objects with subsurface radars is affected by the resolution limits imposed by the constraints in bandwitwh and antenna beamwidth. In this contribution, the step-frequency radar capabilities are exploited through the application of various signal processing methods that alleviate the resolution problem. Depth resolution is improved with a high-resolution technique based on signal extrapolation. Horizontal resolution is achieved via migration techniques similar to those used in seismic sounding, that exploit the peculiar characteristics of a step-frequency system. Selected examples are included to illustrate the improvements.

INTRODUCTION

Subsurface radars have shown their validity as a remote sensing tool, specially for those problems related to non-destructive probing of material media such as earth, ice, concrete... Applications range from civil engineering, geophysical studies and resource prospecting, archaeology, security,... [1].

Unfortunately, there are a number of limitations to their practical operation. The strongest one is set by the heavy losses associated with the transmission of electromagnetic waves in material media which limit the maximun usable bandwidth and, accordingly, depth resolution.

A number of radar system concepts have been proposed to cope with these problems: narrow-pulse, FM-CW and Step-Frequency [2]; this last one has been our choice for a number of reasons which include reduced peak power, noise reduction, better bandwidth control and suitability to subsequent digital signal processing techniques.

This contribution deals with those applications whose main purpose is that of providing an image of the region beneath the surface. This image can either be directly handled to the final user or be further processed by traditional image analysis procedures. In producing such an image, we must be concerned with achieving good contrast between buried objects and the background as well as maximum resolution, both in the vertical (depth) and horizontal coordinates.

Vertical resolution depends on the transmitted bandwidth and is usually achieved via matched filtering in pulsed systems or via FFT in a step-frequency system. In this latter approach a twofold improvement in vertical resolution can be achieved in practical operation through the use of parametric spectral analysis [3]. Horizontal resolution depends on the antenna footprint. Due to the short operating ranges, unprocessed traces retrieval result in the typical parabolic smearing which can only be corrected through the use of migration techniques similar to those previously developed for geophysical acoustic sounding.

Our contribution is centered on the implementation of those methods using the original frequency domain samples supplied by a step-frequency radar, thus performing vertical and horizontal compression simultaneously. We also discuss how parametric spectral analysis techniques (which usually preclude further application of migration processing due to the loss of phase information) can be included in the process through the use of extrapolation techniques.

STEP-FREQUENCY RADAR

The principle of operation of a step-frequency radar is based on the duality betwwen the time and frequency domains and can be related to the design and implementation of matched filters in the frequency domain. A step frequency radar operates by transmitting a waveform composed of a number of increasing stepped frequencies. A coherent I-Q detector measures both the in-phase and in-quadrature components of the received signal at each of the frequency steps. If this detected samples are Fourier transfomed, a new sequence is obtained, that corresponds to the range (depth) distribution of the energy scattered from the scanned volume.

From spectral analysis theory, it is known that the resolution attainable in this way is bounded by the reciprocal of the sampling period in the original domain (the frequency step Δf). In distance units we have:

$$\Delta z = c / (2N\Delta f) \qquad (1)$$

where c is the speed of light in the medium, and N is the number of transmitted frequencies ($N\Delta f$ is the total bandwidth).

There are several features of the step-frequency technique which make it attractive in comparison to pulse-based systems: it requires much lower peak power; the receiver is instantaneously narrowband (thus allowing for significant

0-7803-3068-4/96$5.00©1996 IEEE

noise reduction), accurate antenna and system calibration can be performed at each discrete frequency... Finally, substantial cancellation of the surface return can be achieved by measuring a reference signal in a target-free area and substracting it from the received waveform.

Improving the Vertical Resolution.

A Fourier transform is not the only way of obtaining the range profile; in fact, the problem can be stated as the dual case of the well studied spectral analysis problem. Thus, all the techniques there developed can be considered. Among them, parametric spectral analysis based on autoregressive models [4] was successfully tested [3], yielding a twofold improvement in operating conditions. Its main drawback is the loss in phase information, which is critical when migration is to be carried on.

An alternative is to use the estimated model coefficients to extrapolate the received sequence. The range profile can now be computed by Fourier analysis on the 'extended bandwidth' data, preserving all phase information. The resolution improvement is comparable to the formerly obtained; besides, resolution can be exchanged for sidelobe control through the use of suitable windows.

MIGRATION

Horizontal resolution is directly related to the antenna beamwidth, but, as a result of the tight constraints on the frequency of operation, wideband operation and size (portability) of the antennas, narrow beamwidths are very difficult to achieve. This very fact, which could be considered as a drawback, enables the adoption of the same approach as the migration techniques developed in acoustical geophysical sounding [5]; adapted for operation in a step-frequency setup. We have considered two different approaches: the so-called Kirchhoff method and the wave-equation migration method.

Kirchhoff Method.

It is based on the Kirchhoff integral theorem and results, basicly, in a depth-dependent bidimensional filtering. The interesting point is that we can re-formulate the solution in the azimut-frequency domain, where the received signal appears naturally sampled. The filtering kernel must compensate two effects: first, a phase shift that depends both on the transmitted frequency and distance from the measuring point x_m, and second, an amplitude factor which is not considered (it is hard to estimate, as it depends on the antenna pattern, but will just result in an implicit windowing of the data).

For each of the transmitted frequencies, the signal coming from a specific depth under the surface point x_m can be computed 'focusing' the samples received in a neighborhood of x_m. Finally, the contributions at each frequency (Δf) must be coherently summed to obtain the final image. The resulting expression is

$$s(x_m, z) = \sum_{n=0}^{N-1} \sum_{k=-L}^{L} v(m-k, n) \cdot \cdot \exp(-j(4\pi / c) f_n z \sqrt{1 + \left| x_m - k\Delta x \right|^2 / z^2} \quad (2)$$

It is worth to point out that the FFT processing deemed necessary to achieve range compression is implicit in the process, reducing the number of operations with respect to the case where range compression is performed in advance to migration.

Wave Equation Migration.

This method comes from another formulation of the same wave-equation ruled problem. Here, the wave equation is directly solved for, using the received samples as boundary conditions. This method is specially well-suited for step-frequency data, as the first step in the calssical solution involves a transformation of the data to the frequency-wavenumber domain, where the desired solution is:

$$s(x,z) = \sum_{f} \sum_{k_x} E(k, f, z=0) \cdot \exp(jk_z z) . \exp(jk_x x) \quad (3)$$

which can be obtained in successive steps for every depth of interest, or by means of mapping and interpolation into the k_z-k_x domain, followed by an inverse Fourier transform. In this case, the solution is found for the whole scanned area.

EXPERIMENTS AND RESULTS

Our main aim was to test the feasibility of the proposed methods and their capabilities to improve the resolution of the images in a step-frequency subsurface radar system.

The incoming samples were generated by means of simulation, based on the finite difference time domain method [5]. Although this is a time-domain approach, the generated signals can be converted to the frequency domain where only the proper complex amplitudes at selected frequencies are extracted. In this way, it is possible to change different parameters at will (dielectric constants, frequencies, size and shape of targets,...).

In the results here discussed, a horn antenna was scanned at 10 cm. over a homogeneous material half-space, whose surface showed a certain degree of roughness (2-4 cm. rms). The measurements were taken at 32 equally spaced frequencies. The frequency step was 12.5 Mhz. and the total bandwidth 400 Mhz., which yields a free-space resolution cell of 38 cm. (or 24 cm. in the considered material).

There is some amount of preprocessing before the data are fed to the migration algorithms. In first place, some calibration and equalization is applied; then, an independently measured reference signal is subtracted to the received data in order to cancel the interface return. In this way, cancellation ratios up to 27-29 dB were achieved.

Fig. 1, shows the result obtained for a point-like target

buried at a depth of 30 cm. The Kirchhoff and the wave-equation methods do not show significant differences. Depth resolution was improved from 24 cm. to 10-12 cm. Horizontal resolution was improved from 26 cm. To 12 cm. (Measured at 3dB from the peak value).

Fig. 2, shows the case of two targets (6x6 cm) whose centers are placed 16 cm. apart at the same depth. The results in the dept coordinate are similar to those in the previous example. As for the horizontal coordinate, the targets cannot be resolved when no migration is applied: both returns are mixed producing a sharp peak. When the migration processing is included, the targets are resolved. In this situation, it was observed that the Kirchhoff method performs better. This might be a consequence of the limited beamwidth of the antenna; in an acoustical system, propagation is nearly onmidirectional and the wave-equation method is able to integrate more contributions. In a radar system, extending the integration area only results in adding clutter returns to the final estimate.

CONCLUSIONS

Migration processing and high resolution techniques have been successfully applied to improve resolution in subsurface radar images. Bandwidth extrapolation techniques double depth resolution without affecting the migration process. The migration techniques are formulated in the frequency domain, which reduces the computational load. The Kirchoff method appears to perform better in terms of closely-spaced target discrimination; besides it can be applied (with a small delay) as the scanning proceeds. Other experiments show that the algorithm also performs well when imaging extended targets.

REFERENCES

[1] D. J. Daniels, D. J. Gunton, H. F. Scott, "Introduction to subsurface radar", IEE Proc. , vol. 135 Pt. F, No 4, August 1988, pp 278-320.

[2] K. Iizuka, A. P. Freundorfer et al. "Step-frequency radar". J. Appl. Phys., 56(9), 1, November 1984, pp 2572-2583.

[3] J. J. Martínez, J.R. Casar, G. de Miguel, F.J. Jiménez "Detection of Shallowly Buried Objects with Subsurface Radars". Proc. of IGARSS'93 Symposium, Tokyo, Japan, August 1993, pp 1897-1899.

[4] S. M. Kay, Modern Spectral Estimation. Prentice-Hall, 1988.

[5] J. Gazdag, P. Sguazzero, "Migration of Seismic Data". IEEE Proc., Vol. 72, No. 10, October 1984, pp. 1302-1315.

[6] K. S. Kunz, R. J. Luebbers, The Finite Difference Time Domain Method for Electromagnetics. CRC Press, 1993.

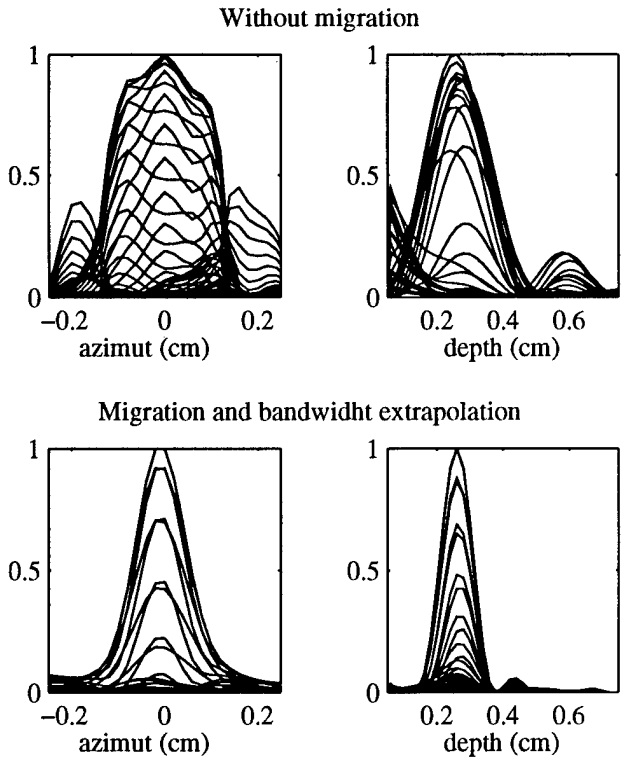


Fig1. Point target buried at 30 cm

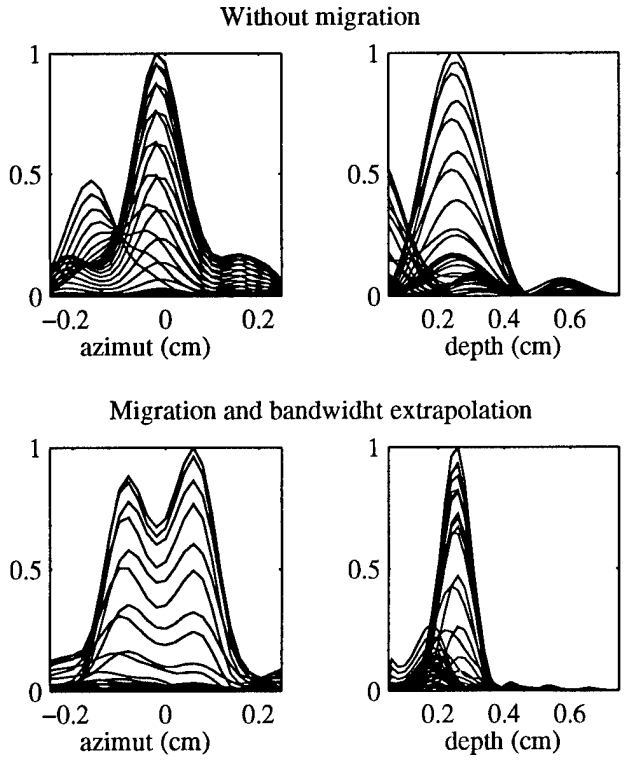


Fig. 2, Two targets at +/- 8 cm. and buried at 30 cm.

Numerical Simulation of Scattering From Object Embedded in A Medium with Randomly Rough Boundary

Saibun Tjuatja, Zhi-Jian Li, Adrian K. Fung, and Carlos Terre

Wave Scattering Research Center, Department of Electrical Engineering
University of Texas at Arlington
Box 19016, Arlington, TX 76019, U.S.A.

Phone: (817) 273-3974 Fax: (817) 273-3443 Email: eetjuatj@utacnvx.uta.edu

Abstract – An FD-TD algorithm is used to compute the scattering from objects embedded in a homogeneous medium with a rough top boundary. The rough top boundary is modeled as a randomly rough surface with Gaussian correlation function and height distribution. A three dimensional randomly rough surface with specified correlation length and height standard deviation is generated on the computer. To reduce computation, the volume of grids above the rough boundary (observation region) is chosen to be small. A near-to-far field transformation is utilized to determine the far-zone scattered field due to the rough boundary and the object underneath. Possible errors near the edge of the surface are suppressed by the absorbing boundary condition and by introducing a windowing function. The far-field scattering patterns of a cylindrical-shaped object embedded in a medium with rough top boundary are generated and presented in this paper.

INTRODUCTION

For a medium with buried object there are discontinuities at the object-medium boundary and the air-medium boundary. An impinging wave will experience multiple scattering between the object and the medium boundary as well as within the object. We expect complex wave, object and medium boundary interactions to occur. Except for special, idealized cases, analytical methods are ineffective for such problems. Numerical methods designed to solve frequency domain problems such as moment methods are also not suitable because of the wide band nature of the problem. On the other hand, the finite difference time domain method (FD-TD) offers many advantages as an electromagnetic modeling, simulation, and analysis tool with capabilities including [1]: broadband response predictions; arbitrary 3-D model geometries; interaction with an object of any conductivity; frequency-dependent constitutive parameters for modeling most materials such as lossy dielectrics; and any type of response, including far fields to near fields.

The finite difference time domain (FD-TD) approach has many formulations: scattered field, total field, potential, implicit etc. [1]. For scattering calculations where the amplitude of the scattered field is significantly smaller than the incident, it is particularly advantageous to use the scattered field formulation. This is the case for many scattering problems because in the real world many objects or land surfaces have small or moderate dielectric values. Another advantage of this approach is that the incident field is evaluated analytically and hence is not subject to numerical error inherent in the FD-TD algorithm. For the scattering problem under consideration, the scattered field formulation does produce lower noise level. This is because in this formulation only the scattered field experiences dielectric discontinuity and is required to satisfy truncation boundary conditions. An earlier study on three dimensional rough surface scattering was based on the total field formulation [2] and it has a higher signal to noise compared with the scattered field approach.

The formulation of the FD-TD method is summarized in the following section along with the criteria for selecting time, space, target resolution requirements. The truncation condition is discussed in the subsection. The implementation of a window function to obtain the scattering coefficient of a randomly rough surface with buried object are given in the subsequent section. Numerical results and summary are presented in the last two sections.

FD-TD: A SCATTERED FIELD APPROACH

This section discusses the FD-TD formulation starting with the Maxwell's equations and then a conversion of them to finite difference forms. The conditions for acceptable time and spatial increments are also given.

The Maxwell's time dependent curl equations for the total field, $\vec{E} = \vec{E}^s + \vec{E}^i$, are given by

$$\nabla \times \vec{E} = -\mu \frac{\partial}{\partial t}\vec{H} \quad \text{and} \quad \nabla \times \vec{H} = \sigma \vec{E} + \varepsilon \frac{\partial}{\partial t}\vec{E} \tag{1}$$

The incident field satisfies the following equations everywhere, i.e.

$$\nabla \times \vec{E}^i = -\mu_0 \frac{\partial}{\partial t}\vec{H}^i \quad \text{and} \quad \nabla \times \vec{H}^i = \varepsilon_0 \frac{\partial}{\partial t}\vec{E}^i \tag{2}$$

A set of governing equations for the scattered fields in the medium defined by μ and ε is obtained by taking the difference between the above two sets of equations. The governing equations are

$$\nabla \times \vec{E}^s = -\mu \frac{\partial}{\partial t}\vec{H}^s - \sigma_m \vec{H}^s - \sigma_m \vec{H}^i - (\mu - \mu_0)\frac{\partial}{\partial t}\vec{H}^i \tag{3}$$

$$\nabla \times \vec{H}^s = \varepsilon \frac{\partial}{\partial t}\vec{E}^s + \sigma \vec{E}^s + \sigma \vec{E}^i + (\varepsilon - \varepsilon_0)\frac{\partial}{\partial t}\vec{E}^i \tag{4}$$

0-7803-3068-4/96$5.00©1996 IEEE

Applying the central difference approximation to the differential operations in Eq. (3), we obtain three scalar difference equations for $\vec{H}^s$, and one of them is given by

$$H_{sx}^{n+1/2}\{i,j,k\} = \left(\frac{2\mu - \sigma_m \delta t}{2\mu + \sigma_m \delta t}\right) H_{sx}^{n-1/2}\{i,j,k\}$$
$$+ \left(\frac{-2\delta t/\delta y}{2\mu + \sigma_m \delta t}\right)[E_{sz}^n\{i,j+1,k\} - E_{sz}^n\{i,j,k\}]$$
$$+ \left(\frac{-2\delta t/\delta z}{2\mu + \sigma_m \delta t}\right)[-E_{sy}^n\{i,j,k+1\} + E_{sy}^n\{i,j,k\}]$$
$$+ \left(\frac{-2\sigma_m \delta t}{2\mu + \sigma_m \delta t}\right) H_{ix}^n\{i,j+1/2,k+1/2\}$$
$$+ \left(\frac{-2(\mu - \dot{\mu}_0)\delta t}{2\mu + \sigma_m \delta t}\right) H_{ix}^n\{i,j+1/2,k+1/2\} \qquad (5)$$

where a sampled scalar function of time and space is denoted as $F^n\{i,j,k\} = F\{i\delta x, j\delta y, k\delta z, n\delta t\}$, and δt, δx, δy, and δz are the time and spatial sampling periods respectively. The three scalar difference equations for $\vec{E}^s$ are also obtained using a similar procedure. Note that in this formulation, the transmitted field below the rough interface is the sum of the incident and scattered fields.

To ensure an algorithm which is stable and accurate, the conditions on the spatial increment and the time increment δt have been derived in [3]. The spatial sampling periods, δx, δy, and δz are chosen to be less than $\lambda/10$ so that the uncertainty of the FD-TD solution is less than ± 0.6 dB. To ensure stability of the time stepping algorithm, δt is chosen to satisfy the inequality

$$\delta t \le \frac{1}{c}\left[\frac{1}{(\delta x)^2} + \frac{1}{(\delta y)^2} + \frac{1}{(\delta z)^2}\right]^{-1/2} \qquad (6)$$

The resolution needed to represent the randomly rough surface variations may be defined in terms of σ, surface *rms* height, and L, surface correlation length. The resolution requirement for L may be the same as for λ, i.e. the spatial sampling period should be less than $L/10$. Let n_0 be the number of sampling points per unit length for the horizontal dimension. Then, to represent σ with as many points as for L requires a resolution which is a factor of L/σ times finer, i.e., $n_0(L/\sigma)$ points per unit length.

Truncation Condition

A radiation boundary condition or truncation boundary condition is needed at the boundary of the FD-TD computation domain (grid). The first order Mur's radiation boundary conditions [4] is used in this study. It has the form

$$E_x^{n+1}\{i,0,k\} = E_x^n\{i,1,k\}$$
$$+ \left(\frac{c\delta t - \delta y}{c\delta t + \delta y}\right)[E_x^{n+1}\{i,1,k\} - E_x^n\{i,0,k\}]. \qquad (7)$$

This condition is preferred because it provides good results for all angles of incidence.

THE RADAR CROSS SECTION AND SCATTERING COEFFICIENT

The Radar Cross Section (RCS)

Near to far field transformations are well known for frequency domain (time harmonic) fields [7]. To utilize the existing near to far field transformation method, a discrete Fourier transform is first applied to the time domain near fields, i.e., the FD-TD solutions, giving the frequency domain near fields. The equivalent surface currents are determined using the frequency domain near fields by applying the equivalence theorem. The use of equivalence theorem, however, requires a virtual surface surrounding the scatterer. For an area extensive target, i.e. the rough boundary of the medium, the virtual surface is a horizontal plane. The equivalent currents on the virtual surface are given by

$$\vec{J}_{Seq} = \hat{n} \times \vec{H}^s(\omega) \quad \text{and} \quad \vec{M}_{Seq} = -\hat{n} \times \vec{E}^s(\omega) \qquad (8)$$

where $\hat{n}$ is the outward unit normal vector of the surface. The scattered far fields (in frequency domain) are obtained by transforming the equivalent currents over free space Green's function [7]. The radar cross section is computed using

$$\text{RCS} = \lim_{r \to \infty} 4\pi r^2 \left[\frac{E_{\phi\,\text{far}}^2 + E_{\theta\,\text{far}}^2}{E_{\phi\,\text{inc}}^2 + E_{\theta\,\text{inc}}^2}\right] \qquad (9)$$

where $E_{\phi\,\text{inc}}$ and $E_{\theta\,\text{inc}}$ are the components of the incident (excitation) plane wave.

Window Function And Scattering Coefficient

To reduce the error due to boundary reflection and finite surface size, a window (or weighting) function is applied to the truncated surface such that fields near the surface edges are weighted down in the scattering coefficient calculation. A Gaussian window function is used in this study, and it is given by

$$G(x,y) = \exp\left(\frac{-[(x - x_{\text{cen}})^2 + (y - y_{\text{cen}})^2]}{T^2}\right) \qquad (10)$$

where T is a constant which determine the width of the window, it is chosen such that fields at the truncated surface edges are attenuated by 60 dB. Formulation of the window function has been discussed by Chen and Bai [5].

The window is applied to the fields (in frequency domain) prior to the near-to-far field transformation. Following the transformation, the radar cross section (RCS) is calculated using the scattered far fields. The scattering coefficient is obtained by normalizing the RCS to the effective area of the truncated surface.

NUMERICAL RESULTS

The top rough boundary of a homogeneous medium with $\varepsilon = 5.1$ and $\sigma = 10^{-6}$ [S/m] is generated using the method reported in Fung and Chen [6]. The rough boundary has Gaussian correlation function and height distribution with $k\sigma = 0.35$ and $kL = 5.5$, where k is the free space wave number. An incident wave with an incident angle of 30° and wavelength, λ, of 100 cm are used in the calculations.

Fig. 2 shows the bistatic scattering coefficients of the medium with the generated rough boundary for VV polarization. Note that the scattering pattern shown in Fig. 2 is due entirely to the surface roughness of the medium.

A perfect conducting object (a rod with rectangular cross-section) with dimensions $l_x = 10$ cm, $l_y = 80$ cm, and $l_z = 7$ cm is introduced into the lower medium. The vertical position of the object is 14 cm below the mean height of the boundary. Fig. 3 shows the bistatic scattering coefficients of the medium with buried object for VV polarization. Note that the difference between Fig. 2 and Fig. 3 is caused by the presence of the buried object only.

SUMMARY

FD-TD simulation of scattering from object embedded in a medium with rough boundary has been carried out in this study. The FD-TD formulation is developed based on the scattered field approach. Simulation results which show the effects of buried object on the scattering pattern of medium with rough boundary are presented in this paper.

REFERENCES

[1] Kunz, K.S., and Luebbers, J., *The finite difference time-domain method for electromagnetics*, CRC Press, Boca Raton, FL, 1993.

[2] Fung, A.K., Shah, M., and Tjuatja, S., "Numerical simulation of scattering from three-dimensional randomly rough surfaces," *IEEE Trans. Geosci. Remote Sensing*, Vol. 32, No. 5, pp.986–994, September 1994.

[3] Taflove, A., and Umashankar, K., "Review of FD-TD numerical Modeling of Electromagnetic Wave Scattering and Radar Cross Section," Invited paper, *Proc. of the IEEE*, Vol. 77, No. 5, May 1989.

[4] Mur, G., "Absorbing boundary conditions for the Finite-difference approximation of the time-domain electromagnetic field equations," *IEEE Trans. Electromagnetic Compatibility*, EMC-23, pp. 377-382, 1981.

[5] Chen, M.F., and Bai, S.Y., "Computer simulation of wave scattering from a dielectric random surface in two dimensions - Cylindrical case," *J. Elec. Waves Appl.*, vol. 4, no. 10, pp. 963-982, 1990.

[6] Fung, A.K. and Chen, M.F., "Numerical Simulation of Scattering from Simple and Composite Random Surfaces," *J. Optical Society of America*, Vol. 2, No. 12, pp. 2274 - 2284, December 1985.

[7] Ramo, S., Whinnery, J., and Van Duzer, T., Fields and Waves in Communication Electronics, 3rd ed., John Wiley & Sons, 1994.

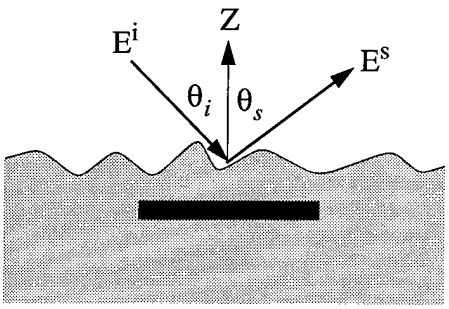


Figure 1. Geometry of the scattering from rough surface with buried object.

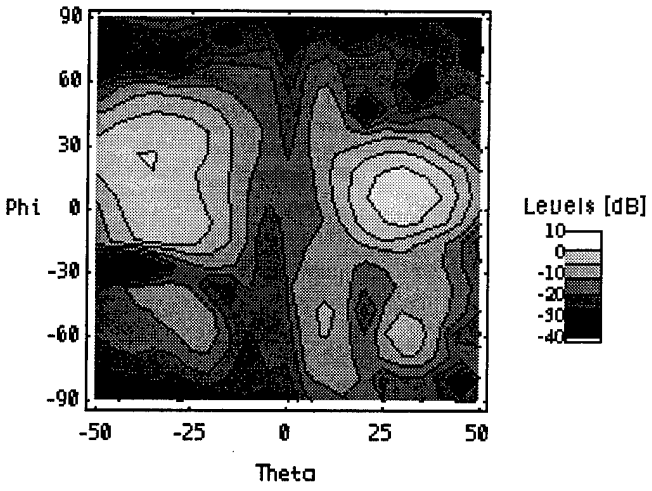


Figure 2. Bistatic scattering coefficients from the randomly rough surface (VV).

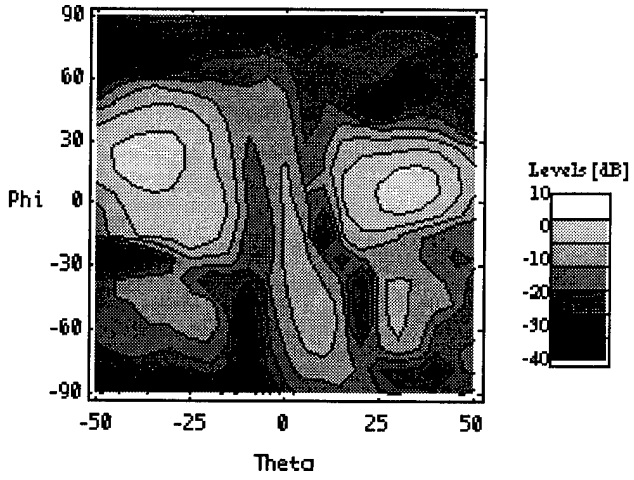


Figure 3. Bistatic scattering coefficients from the randomly rough surface with buried object (VV).

A High-Resolution Imaging of Small Objects for Subsurface Radar Data Processing

Toru Sato, Toshio Wakayama*, Kazuhisa Takemura, and Iwane Kimura
Department of Electronics and Communication, Kyoto University
Kyoto 606-01, Japan
***: now with Mitsubishi Electric Corporation.**
Corresponding Author: T. Sato
Phone: +81-75-753-5960, Fax: +81-75-751-8201
E-mail: tsato@kuee.kyoto-u.ac.jp

INTRODUCTION

In subsurface radar applications, it is often experienced that the requirements for the resolution and the penetration depth contradict each other. For example, pre-excavation survey of archaeological sites may require to detect buried objects of the order of 10cm at a depth of 1m. In such a case, the compromise will be the use of around 500MHz, for which the target is on the order of a radar wavelength. We refer to the target in such a situation as a 'small object'. It is thus hard to identify the shape of the object with conventional signal processing technique as the synthetic aperture method.

Our objective is to develop a robust high-resolution imaging algorithm applicable to targets whose dimension is close to the radar wavelength. In order to avoid instabilities in super-resolution techniques, we limit the number of freedom in the estimation by properly modeling the target as well as the parameters of the medium.

DISCRETE MODEL FITTING ALGORITHM

Our algorithm, which is called discrete model fitting (DMF) method[1], solves the inverse problem of imaging the subsurface object by iteratively compare the estimated received signal waveforms computed from the model of the target with those of the received signal, and by adjusting the parameters which describes the model so that the variance between the waveforms are minimized. Currently it deals with two-dimensional imaging based on a one-dimensional scan of the radar sensor, although both monostatic and multistatic cases can be treated.

At the first step, outstanding targets are estimated as a group of point targets. Position of each target is estimated from the peaks in the received signal waveform, which gives the distance of the points from each antenna. All possible combinations of these points determined from two received signals at different antenna locations are plotted on a plane. A consensus analysis distinguishes the true points from spurious ones. Discontinuity in the medium are also estimated based on the consensus analysis of the received time series at each point during the scan. Non-linear least squares fitting is used to improve the model in an iterative manner in estimating the layer boundaries and the point targets[2].

For each prominent target found in the first step, the shape estimation procedure is applied. The shape of the target is expressed in terms of the points which represents its outer boundary. These points are selected so that the distance between adjacent points are on the order of 1/10 of the radar wavelength, and they are connected smoothly. Fig. 1 schematically shows the arrangements of these points. Location of large circles are varied only in the radial direction from its virtual center, which is determined in each iteration, and the location of small circles are computed by Lagrangian interpolation. In this manner, the set of parameters which describes the model shape is minimized to (x_c, y_c), and r_i $(i = 1, \ldots, N)$, where N is the number of variable points, which is 4 in the case of Fig. 2.

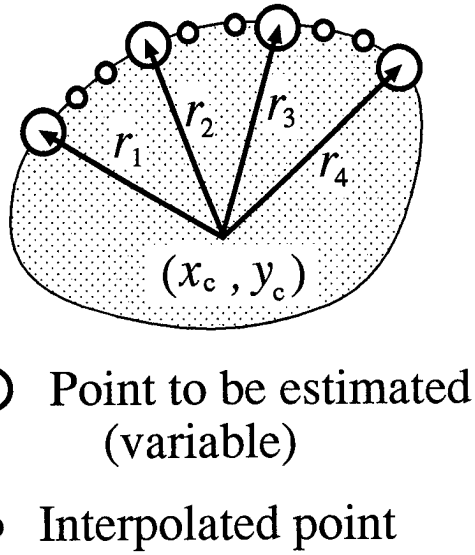


Figure 1: Arrangements of variable and interpolated points in the modeling.

The reflections from these connected points are computed by the ray tracing method, and the edge refraction component is appended to the reflection component with the aid of physical optics so that the two components connect smoothly. Fig. 2 shows an example of the rays thus generated. In the ray tracing, only the location of wavefront and the energy associated

0-7803-3068-4/96$5.00©1996 IEEE

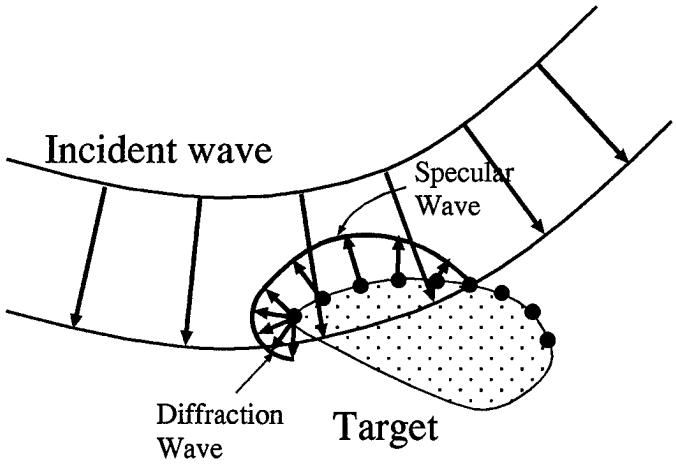


Figure 2: Scattering of rays from a finite object.

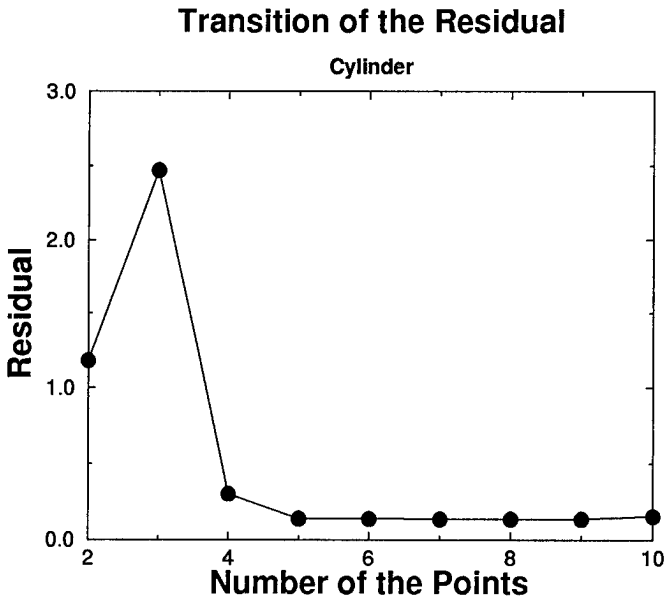


Figure 4: Transition of the residual of fitting in each iteration of the imaging as the number of variable point is increased.

it is computed at each time step. In order to generate the estimated signal waveform at the location of receiving antennas, the waveform for the reflected waves are computed using the FDTD method, and convolved with the impulses which represent individual rays corresponding to various scattering paths. For the edge reflection component, the reference waveform is prepared in a form of a table for possible combination of the incident and reflected directions, and synthesized each time for the desired directions.

IMAGING OF SIMPLE TARGET SHAPES

The major restriction of this imaging technique is that proper initial guesses are required for the model parameters in each non-linear fitting process. Automated procedures for finding such initial parameters have been devised for various cases, including the one for an arbitrary shaped perfectly conducting object. It starts with the prominent point target, and gradually expands its surface by modifying the points which represent the boundary. The expansion terminates when the surface is extended one wavelength beyond the reflection boundary on both sides. Extension of the surface more than this limit usually results in an expansion into the direction from which no echo returns to the direction of antennas.

We have examined the performance of this imaging technique with numerical simulations. We assume a case where the radar sensor scans linearly along the ground surface, and transmit a mono-cycle pulse at a fixed interval. We neglect the effect of the ground since it can be removed from the data fairly easily by subtracting the DC component in the direction of the scan. Fig. 3 shows the process of reconfiguring the shape of a perfectly conducting cylinder. Squares indicate the location of antennas, each of which is used for both transmission and reception, and is used alternately in a monostatic operation. The abscissa and the ordinate is expressed in the unit of the radar wavelength at the center frequency of the transmitted pulse. The shaded circle represents the cross section of the given cylinder, and the small circles along its border indicate the reconstructed image. The simulated data is generated by using FDTD method with the second order absorbing boundary[3], and compared with the estimated received signal computed from the reconstructed image using the ray tracing algorithm. Fig. 4 shows the residual of the fitting in each iteration.

Similar results are obtained for other simple shapes such as a conducting plate. We also made a test site experiments, which confirmed the performance of the proposed algorithm examined by this simulation.

SUMMARY

A model fitting algorithm was developed for imaging an object whose size is on the order of the radar wavelength, which is often the case for subsurface radar applications. The performance of the algorithm is examined for simple shapes with numerical simulations and test site experiments. Although the cases examined in this paper assumed that the medium is uniform, the DMF algorithm has been extended to the case of layered media. The ultimate limitation of this algorithm is the total number of parameters and the appropriateness of the model, which need to be constructed for individual situations.

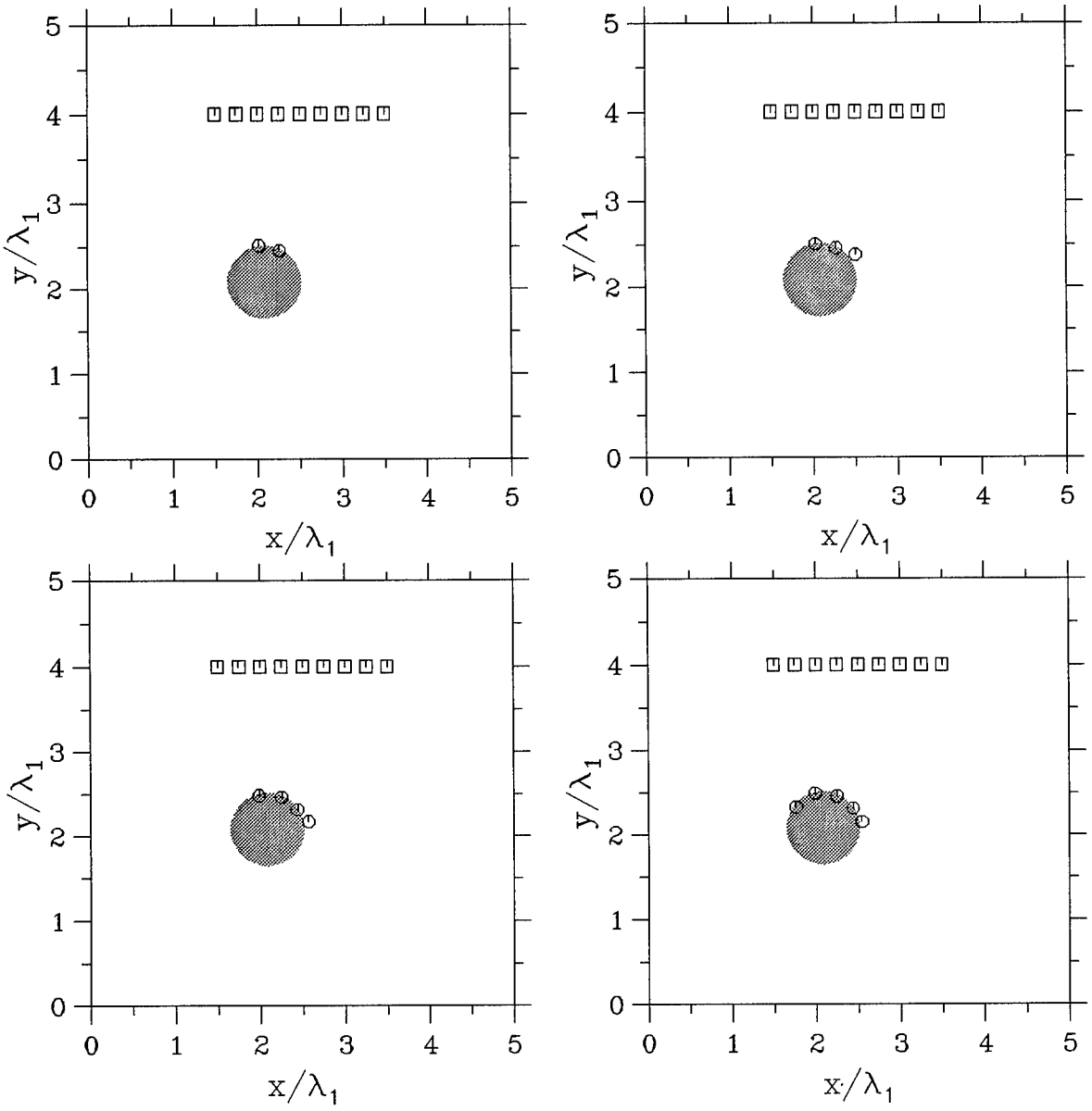


Figure 3: Evolution of the model shape in the estimation process of a conducting cylinder.

REFERENCES

[1] T. Wakayama, T. Sato and I. Kimura, "High-Resolution Radar Image Reconstruction Using an Arbitrary Array", *IEICE Trans. Commun.*, Vol. E76-B, No. 10, pp. 1305–1312, 1993.

[2] T. Wakayama, T. Sato and I. Kimura, "Radar Image Reconstruction by Discrete Model Fitting in a Layered Inhomogeneous Medium", *Proc. Fifth Int. Conf. Ground Penetrating Radar*, pp. 223–237, 1994.

[3] G. Mur, "Absorbing boundary conditions for the finite-difference approximation of the time-domain electromagnetic-field equations", *IEEE Trans. Electromagn. Compat.*, Vol. EMC-23, No. 4, pp. 377–384, 1981.

Ground-Penetrating Radar Antenna Modeling

Zhubo Huang, Kenneth Demarest, and Richard Plumb
University of Kansas, Radar Systems and Remote Sensing Laboratory
2291 Irving Hill Road, Lawrence, Kansas 66045, USA
Tel: 913/864-7395 , FAX: 913/864-7789 , E-mail: demarest@eecs.ukans.edu

Abstract--Detecting subsurface objects by using Ground-Penetrating Radar (GPR) has received considerable interest in recent years. In order to interpret radar signals from buried objects, one must have the ability to model a large range of objects, grounds and radar antennas, theoretically or numerically, so that a real GPR system can be simulated. Many investigations have been done for modeling objects (scatterers) and grounds, but few have involved realistic antennas. This paper presents a technique to model real GPR antennas located above a ground in which an object is buried. Numerical results are presented to verify this technique.

INTRODUCTION

The increasing use of ground-penetrating radar systems has brought about the need for sophisticated GPR modeling tools that are capable of interpreting the radar returns from objects buried in a variety of grounds. The interpretation of radar returns involves several research subjects, such as the modeling of radar antennas, grounds and buried objects. The interpretation of radar returns can be helpful for understanding how to detect and identify buried objects with GPR systems.

A computer code that is used to simulate the performance of GPR systems is called a GPR simulator. In general, a good GPR simulator is capable of correctly modeling the characteristics of the antennas, the ground, and the scatterers. Unfortunately, techniques that are good at modeling one aspect of the problem are usually not well suited for others. For example, the finite-difference time-domain technique (FDTD) [1] is well suited for modeling dielectric spaces, such as grounds and scatterers, but is not well suited for modeling complex antennas. Conversely, the method of moments (MOM) [2] is well suited for modeling complex antennas, but not penetrable objects and real grounds. Since accurate ground modeling is usually essential, most GPR simulators concentrate on accurate ground-scatterer modeling at the expense of modeling complex antennas.

This paper presents a technique that is able to model complex antennas in the presence of real grounds and scatterers. This technique makes use of the well-known equivalence principle from electromagnetics, which allows the overall GPR geometry to be divided into two sub-geometries. Different numerical techniques can then be used to model different aspects of the overall problem. An iterative procedure is used to link two sub-geometries to the actual geometry being modeled. This technique is described in the following section, along with numerical results.

0-7803-3068-4/96$5.00©1996 IEEE

FORMULATION OF THE PROBLEM

Consider the typical GPR geometry which is shown in Fig. 1. Here, an antenna is located above a ground in which an object (scatterer) is buried. The antenna transmits an incident field toward the ground. This field is partially transmitted into the ground and then scattered by the buried object.

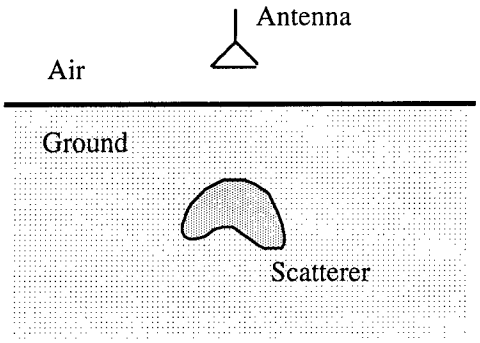


Figure 1. A typical ground-penetrating radar geometry.

Unfortunately, no one technique is well suited for modeling this typical GPR geometry. This is because there is an interaction between the antenna and the ground-scatterer, which requires the technique to model both antenna and ground-scatterer, as well as their interaction.

We can analyze this GPR geometry by using the Schelkunoff equivalence principle [3] to split the original geometry into two sub-geometries. This is accomplished by surrounding the antenna in Fig. 1 with a mathematical surface S and removing either the interior elements or the exterior elements. The fields generated by these removed objects are supported by a set of equivalent electric and magnetic surface currents that are impressed on S. In this way, the complicated geometry can be divided into two sub-geometries: an antenna geometry and a ground-scatterer geometry.

Fig. 2 shows these sub-geometries. The antenna geometry consists only of the antenna and the equivalent currents. In this geometry, the fields inside S are identical to the fields inside S in the original geometry, and zero outside S. The ground-scatterer geometry consists only of the ground, the

scatterer, and the equivalent currents on S. The fields outside S in this sub-geometry are identical to those in the original geometry, and zero inside S. The equivalent surface currents that must be placed on S in both sub-geometries are given by

$$\mathbf{J}_s = \mathbf{n} \times \mathbf{H} \tag{1}$$

$$\mathbf{M}_s = \mathbf{E} \times \mathbf{n} \tag{2}$$

where $\mathbf{n}$ is the outwardly pointing unit vector of S, $\mathbf{J}_s$ and $\mathbf{M}_s$ are the electric and magnetic surface currents respectively, and $\mathbf{E}$ and $\mathbf{H}$ are the electric and magnetic fields on S in the original geometry, respectively. The values of these surface currents can be determined by modeling the two sub-separately and passing field information between them using an iterative procedure. This procedure models the interaction between the antenna and the ground-scatterer.

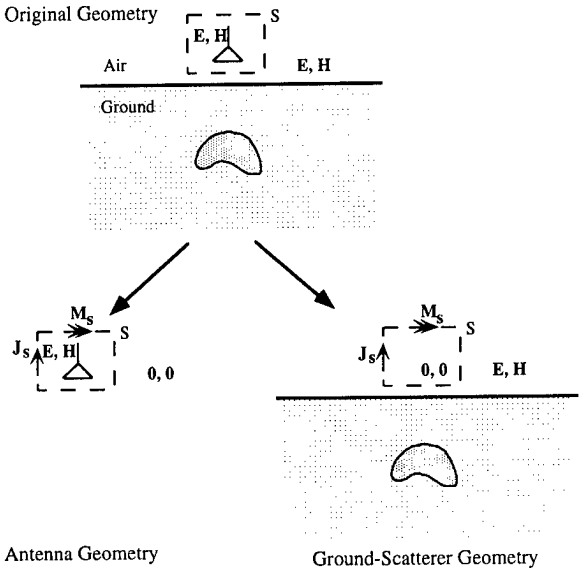


Figure 2. The geometry of the equivalent problem.

The iterative procedure starts by modeling the antenna geometry to get an initial estimate of surface currents on S. Then, one can impress these surface currents on S to model the ground-scatterer geometry. By sampling the fields on S, one can then obtain an improved estimate of the surface currents that includes the initial currents and the currents due to the effect of the ground-scatterer. The next step is to model the antenna geometry again, while impressing the new surface currents on S. By sampling the fields on S, the initial surface currents on S can be updated. These updated currents are impressed on S to repeat modeling the ground-scatterer geometry. A more accurate solution (surface current or field) can be obtained by performing more iterations.

Many numerical methods can be used for modeling each sub-geometry depending on the complexity of the problem. For example, if the antenna is simple, such as a thin wire dipole, the FDTD method can be used for both sub-geometries. In many GPR applications, the antenna usually is too complicated for the FDTD method to model. Therefore, in order to handle more complicated antennas, one can use the MOM to model the antenna and the FDTD to model the ground-scatterer geometry.

SIMULATION

In this section, a numerical experiment is presented to verify this iterative technique. The geometry of the experiment is shown in Fig. 3. Here, the radar antenna is selected as a thin wire dipole, driven by a voltage source. This antenna is simple enough so that the whole problem can be solved by either the FDTD method directly or by the iterative method. The result obtained by solving the whole problem by using the FDTD directly can be considered as an *exact* solution. Therefore, the iterative results can be compared with the exact result to verify the iterative technique.

In this experiment, the thin wire dipole (0.6-meter long) is located 0.4 meters above a ground. The ground is a stratified medium [4] with a relative dielectric constant that changes linearly from the surface (6.0) to 1.6 meters below the surface (8.0), with a uniform conductivity of 0.01 s/m. A perfectly conducting cube, 0.2 meter^3, is buried in the ground 0.6 meters below the ground surface. The exact solution is obtained in a 50 x 50 x 70-cell FDTD space, in which the ground contains 40 cells in the vertical direction and the equivalence surface encloses 20 x 10 x 10 cells. The FDTD cell size is 0.04 meters. The voltage source is a 6-ns-double-peak Gaussian pulse.

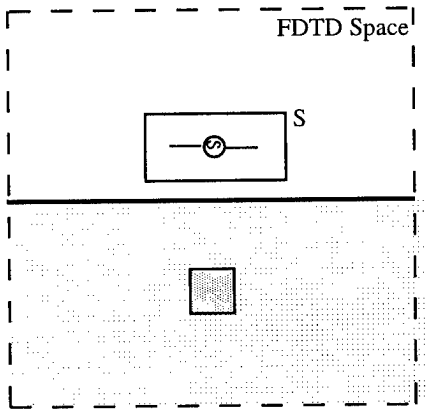


Figure 3. The geometry of the numerical experiment.

Fig. 4 shows the comparisons between the exact result (solid line) and iterative result (dashed line) when the antenna is excited with a voltage pulse. Here, the electric field 0.8 meters above the ground is shown. As can be seen, the difference between the exact result and the iterative result becomes smaller as more iterations are performed. The result of the fourth iteration is very close to the exact result.

Fig. 5 shows the relative mean of absolute value of the scattered-field error. Here, the error field is the difference between the exact field and the iterative field. As can be seen in this figure, the relative mean error becomes smaller as more iterations are performed, indicating that the iterative procedure is capable of correctly modeling the antenna, the ground, and the scatterer.

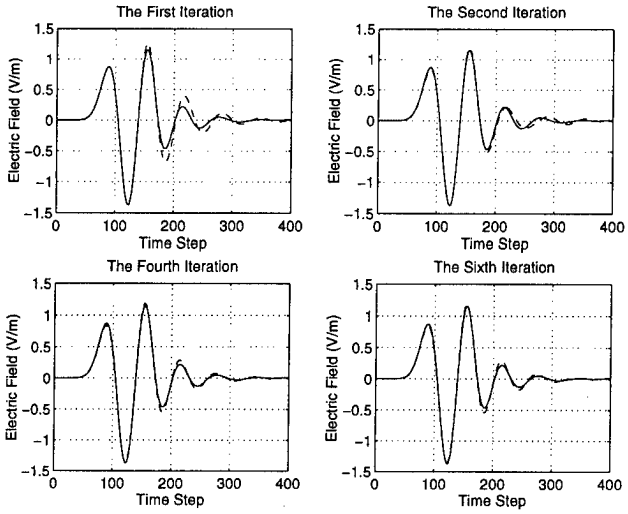


Figure 4: Electric field at one point above the ground.

CONCLUSION

In this paper we have presented an iterative technique that is capable of modeling complex antennas, grounds, and scatterers. This technique allows the antenna to be modeled separately from the ground-scatterer geometry, thus allowing different numerical techniques to model both parts of the overall geometry.

Although the numerical results presented here used the same numerical technique (FDTD) to model both parts of the overall problem, this is not a restriction of the overall technique itself.

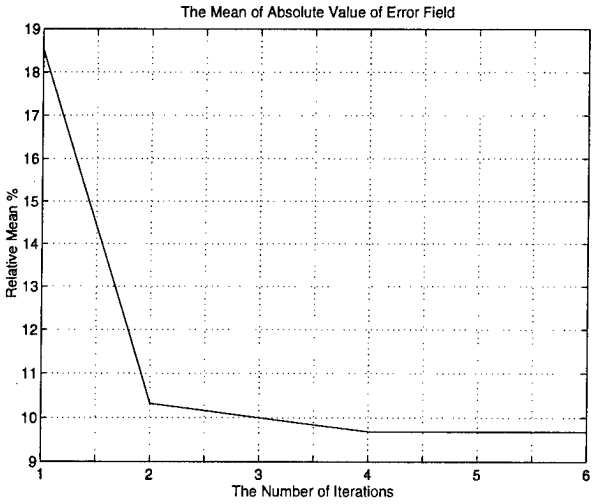


Figure 5: Relative mean of the error field.

REFERENCES

[1] K. S. Yee, "Numerical Solution of Initial Boundary Value Problems Involving Maxwell's Equations in Isotropic Media," *IEEE Transaction on Antenna and Propagation,* vol. AP-14, no. 3, pp. 302-307, May 1966.

[2] Roger F. Harrington, *Field Computation by Moment Methods,* New York, IEEE Press, 1993.

[3] Roger F. Harrington, *Time-Harmonic Electromagnetic Fields,* New York, McGraw-Hill Book Company, 1961.

[4] K. R. Demarest, R. G. Plumb, and Z. Huang, " FDTD Modeling of Scatterers in Stratified Media," *IEEE Transaction on Antenna and Propagation,* vol. AP-43, no. 10, pp. 1164-1168, October 1995.

A Hierarchical Fuzzy Clustering Algorithm using Pyramid Linking Data and Land-cover Classification Experiments

Masao NAKA[1], Tadakuni Miyazaki[2], Yoshitaka IWATA[3]

1) Remote Sensing Technology Center of Japan
1-9-9 Roppongi, Minato-ku, Tokyo, 106, Japan
Phone; +81-3-5561-9775, Fax; +81-3-5561-9542,
Email; naka@restec.or.jp

2) National Institute for Environment Studies
16-2 Onogawa ,Tsukuba,Ibaragi, 305, JAPAN
Phone; +81-298-51-6111, Fax; +81-298-51-4732

3) Fujits F.I.P. Inc.
4-14 Kamiya-cho Sibuya,Tokyo150,JAPAN
Phone; +81-3-3481-4186, Fax; +81-3-3481-9554

Abstract – This paper proposes a hierarchical fuzzy clustering algorithm using pyramid linking data. The authors implemented computational code of the hierarchical fuzzy clustering scheme on Sun workstation. The code incorporates flexible computational modes.
The authors evaluated the code experimentally using hypothetical data and image data of Earth observation satellites. Three levels of pyramid linking data system from these data are generated using 1 to 16 neighbor pixel averaging according to the pyramid linking information. The hypothetical data has been efficiently segmented. Some test sites of satellite image are experimentally classified by this code.

INTRODUCTIONS

To effectively utilize of remotely sensed data from Earth observation satellites for global resource monitoring and vegetation mapping, it is necessary to develop automatic, high-speed land cover classification methods applicable to huge volumes of image data with multispectral bands and various spatial resolutions.

The fuzzy c-means(FCM) clustering algorithm can provide a non-parametric and unsupervised approach to the cluster analysis of remote sensing data. Several efforts of fuzzy clustering have been undertaken by J.C. Bezdek and others[1),2)]. Some earlier studies suffer from problems due to the setting of optimum initial conditions, low classification accuracy and high computational load.

In the next section, this paper presents a new hierarchical fuzzy clustering method (HFCM) using pyramid link data based on the fuzzy c-means algorithm and the computational characteristics of implemented code. It next discusses experimental results of applying this clustering method to hypothetical data and satellite images then presents conclusions of the study.

A HIERARCHICAL FUZZY CLUSTERING USING PYRAMID LINK DATA

Our hierarchical fuzzy clustering algorithm is a modified version of the hierarchical approach based on a fuzzy c-means (FCM) algorithm proposed by M. M. Trivedi et al[1)]. We first implemented an elemental FCM code, then this code was integrated into a hierarchical scheme so we could use pyramid link data structures(PDS) that were generated from single and/or multiple imaging sensor data . Figure 1 shows the concept of the hierarchical fuzzy clustering using pyramid link data. We used the FCM clustering algorithm to partition the measurement spectral space for each iteration then tested each

0-7803-3068-4/96$5.00©1996 IEEE

partitioned region for a homogeneity.

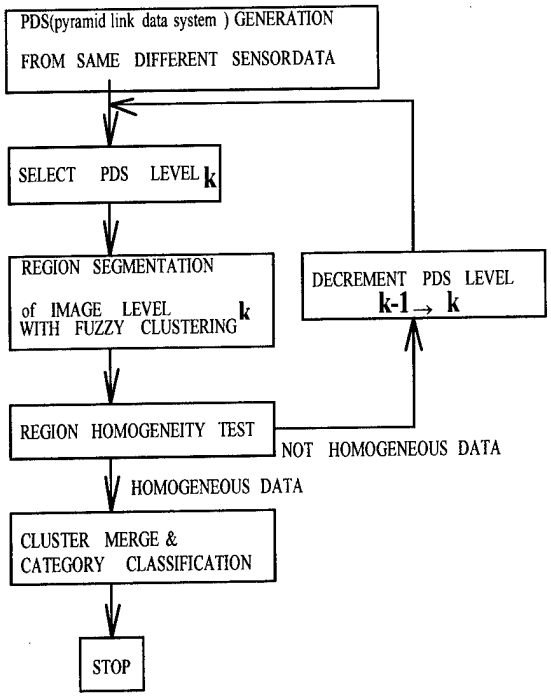


Fig. 1 Concept of Hierarchical Fuzzy Clustering

If the region is non homogeneous (the fuzzy membership value of a pixel is less than the threshold value, U_{th}), we split it into smaller regions using FCM clustering at next PDS level(finer resolution level). Coarse-to-fine processing is performed; The processing results from coarse resolution are propagated to finer resolution. This PDS enable us allows to represent the original image of a single sensor or multiple sensors data at various levels that differ in resolution. The resolution of data decreases as the pyramid level increases. The data size decreases by a factor of four due to sub-sampling horizontally and vertically. In a typical PDS, upper level image versions are generated using four neighbors pixel averaging from a lower level image. In our PDS, however, we generate pyramid link information on the Euclid distance between consecutive PDS levels. We will compute the level k+1 version of the images froma single sensor using 1 to 16 pixel averaging of the level k version of an image with the link information between image level k+1 and k. For multiple sensors, the PDS will be composed of different resolution data from different sensor. For example, TM data (IFOV ;30m) of LANDSAT and the Advanced Visible and Near Infrared Radiometer (AVNIR ; IFOV 16m) data of the Advanced Earth Observing Satellite(ADEOS) of Japan, which will be launched in 1996, will be combined to generate the PDS.

This code version has the following features: 1) Initial clustering centers for iteration are assigned from random sampling of each level of PDS generated from original image data. 2) The degrees to which each pixel belongings to the initial clusters is assigned from the Euclidean distances between gray level of the pixel to the cluster center or arbitrary constants. 3) The fuzzy cluster centers in the previous PDS level may become a part of the initial cluster centers of the next PDS level. 4) The fuzzy membership values of a pixel for each cluster are represented by 4 bytes of real data in stead of 0 to 255 (8 bit integer). 5) Category correspondence processing between cluster and category is performed by similarity measure. 6) Flexible computational modes of hierarchical fuzzy clustering are implemented into the code: single stage, two stages, three stages etc.

EVALUATION EXPERIMENTS

We conducted experiments using hypothetical data of 3 spectral bands and real image data from SPOT on a Sun 4/2 work station to evaluate the implemented code.

The hypothetical data composed of 12 homogeneous sub-regions of data from 3 bands with random noise is shown in Fig.2. The standard deviation of added noise is 3 for band 1, 5 for band 2 , 5 for band 3. The mean value of added noise is zero for each band. We

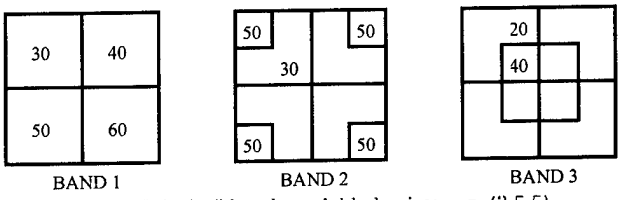


Fig. 2 Hypothetical Data (3 Band, 12 Classes)

generated three levels of PDS from this hypothetical data and sequentially processed each PDS

level data I_3, I_2, and I_1 using the hierarchical fuzzyclustering (HFCM) code. We were then able to successfully segment the hypothetical data into 12 homogeneous regions. In this experiment, we applied HFCM (three stages (1st , 2nd, and 3rd) to hypothetical data. Table 1 compares the average classification accuracy for various classification methods using hypothetical 3-band data. This table shows that a hierarchical fuzzy clustering (HFCM, three stages) using pyramid link data has the highest classification accuracy in these methods. In this table, the average segmentation accuracy of hierarchical fuzzy clustering (HFCM, 3 stages) is 91.27% in contrast with 62.62 % for conventional fuzzy clustering (HFCM, single stage). Computation time for hierarchical fuzzy clustering (HFCM,three stages) was less than that of conventional fuzzy clustering (HFCM,single stage).

We experimentally applied the hierarchical fuzzy clustering code to three levels of PDS generated from a SPOT satellite HRV image. The test site is a sub-area of the HRV image (512 x 400 pixels, 3 bands) of the Sagami River basin near Yokohama, Japan that taken on January 14, 1989 by SPOT 2. We applied hierarchical fuzzy clustering (HFCM, three stages) procedure using pyramid linka data to this test site using the following processing parameters; m=2.0; *l*max=50; U_{th};0.9 (1st), 0.8 (2nd), 0.1 (3rd), 36 clusters (first, second, and third).

We then classified all 108 clusters into five categories using similarity measures between clusters and ground categories. The classification accuracy is currently being investigated. Results from these preliminary experiments show that the hierarchical fuzzy clustering code implemented for a Sun4/2 workstation enables efficient segmentation of coverage types of Earth surfaces

Table 1 Comparison of Averaged Classification Accuracy for Hypothetical Data

Classification Method	Averaged Classification Accuracy (%)	Comments
HFCM three stages	91.27	# of itr; ;22, 45, 50 # of cls; 12, 12, 12 (1st→2nd→3rd) Uth; 0.8, 0.5, 0,2 ε ;0.032, rej; 255
HFCM single stage	62.42	# of itr; 50 # of cls ;36(3rd only) Uth; 0.2 , ε ; 0.120, rej; 5293
Maximum Likelihood	88.97	threshold; 3.0

CONCLUDING REMARKS

From the experiments on a hierarchical fuzzy clustering code using pyramid link data, we can concluded the following. (1) this code is superior to conventional FCM or the maximum likelihood method in clustering capability and ability to detect more reliable clusters. (2) The computation time for hierarchical fuzzy cluster analysis of image data using this code is less than that ofconventional FCM. (3) The smoothing effect of coarse stage PDS of this code is less sensitive to noise than conventional FCM. We will perform further detailed experiments using various sensor data.

ACKNOWLEDGMENTS

The authors wish to thanks Prof. H. Simoda and associate Prof. K. FUKUE of Research and Information Center of Tokai University for useful comments and providing us the satellites observation data and truth data on the test site.

REFERENCES

[1] M.M. Trivedi, J.C. Bezdek, et al, "Low-level Segmentation of Aerial Images with Fuzzy Clustering",IEEE Trans.SMC,vol.16,pp589-597,1986

[2] K.Hirota, "Fuzzy Clustering: An Application to Remote Sensing Images", Tech. Rep. SICE of Japan, Remote Sensing Symp. vol.13 pp67-70,1987

Fractal Concept to the Classification of Crop and Forest Type in IRS Data

K.JEYARANI K.JAYARAM HEBBAR

Computer Processing group
National Remote Sensing Agency
Balanagar,Hyderabad,India
Tel:278866 Fax:040-277190

ABSTRACT

The objective of the paper is to assess the use of fractal dimension as discriminators in Indian Remote Sensing Satellite (IRS) image for different forest and crop pattern. In this study, a kernal of a pre-defined size has been moved on a single band image and corresponding fractal dimension is found using Triangular Prism Surface Area method. The measured dimension is used as a classification factor and applied over the kernal. A preliminary study is performed using IRS LISS II Band-4 data. The results are motivating and significant improvement has been obtained in this procedure in case of a homogeneous pattern occurred in this data.

INTRODUCTION

In recent years, fractals have been shown to be very useful for the characterization of natural objects such as mountains, clouds, trees, coastlines etc. Further more, the fractal theory has been used with efficiency for the analysis of chaotic signals[1]. The central concept of fractal is the notation of self-similarity[2]. The fractal differs from the cartesian dimension. The later is an integer with value one for a linear and two for a surface. The fractal dimension differs from one for a straight line to two for a surface to three for an infinity controlled surface as real value depends upon the amount of complexity or roughness of the surface[3]. In general, the classifications are using the reflectance value of training pixels to characterize the spectral behavior of several land cover types. The mean and variance of these spectral data are used to classify the entire image. In this paper, the fractal's roughness theory is applied to classify the IRS images without using training sites.

An attempt has been made on IRS-1B, LISS II, BAND-4 data acquired on January 93 covering a part of Surguja district, M.P of size 500X500 pixels. The study area is covered with different land cover classes viz. Forest, Agriculture and Water body. Procedure of obtaining fractal dimension from data and tests of classification performance are presented.

CLASSIFICATION PROCEDURE

To obtain the fractal dimension, we apply the Triangular Prism Surface Area method[4]. The method is briefly described as follows. To determine the fractal dimension of an area around a given pixel, we choose a set of pixels surrounding that pixel. This set of pixels form a window. At each position of the window, the surface area is calculated at several spatial resolution. The digital values at the corners of the window are read from the image and the average value at the center of the window is calculated. Four triangles can be calculated by Heron's formula. The sum of the surface area of all triangles gives the surface area of part of the image. This calculation is repeated at each window position for spatial resolution from 1x1 pixel up to the number of pixels of the window size. Finally, for each window the surface

0-7803-3068-4/96$5.00©1996 IEEE

area and the spatial resolution are both log transformed and a linear function is fit through the calculated data points. The fractal dimension for a surface is defined as

$$D = 2 - r$$

where 'r' is the slope of the line through the log transformed surface area and log transformed resolution, '2' is added to reflect the higher geometric dimension of "Topographic Surface" compared to a line.

After obtaining the fractal dimension, the amount of roughness of the surface is computed from the fractal dimension. The computed value has been applied to the corresponding window to reduce the irregularity. At certain stage, there is no fractal dimension due to the smoothness of the surface. This is the indication that the image has been classified. The final output shows a range of classes from '0' to the number of classes presented in the image, depending upon the window size chosen. The size of the window can affect the value of the fractal dimension. We found more number of classes with 5X5 size window than with 8X8 size window.

RESULTS

The IRS BAND-4 raw image of the study area is presented in Fig.1. Since the data used was January month, where the total agriculture is generally harvested (rice crop), the separability of different forest cover type canopy density classes can be very well observed in this image. The classified image of the same area is exhibited in fig-2. The harvested agriculture class has been further classified as Agriculture_A and Agriculture_B depending upon the irrigability condition.The discriminating factor obtained from the fractal dimension for each class with the number of pixels presented in each class are shown in Table-1. From this we can easily identify that Agriculture_A and Agriculture_B classes are dominating area compared to other classes[5]. The Sal forest area is predominantly covered by Shorea Robusta.

These observations are reinforced by the fractal results of Table-1 of 8X8 window size, which provides insights about the classes and their labels. The roughness factor of the water body is less when compared to Sal forest. There is not much difference between the roughness factor for Agriculture_A and Agriculture_B.

DISCUSSION AND CONCLUSION

The classification procedure as described in this study provides significant improvement in differentiating the classes. The fractal dimension of classes have shown to have distinctive distributions, especially in case of Agriculture type. The discontinuity of water body has been found in this classified image (Fig.2). This may be due to the insufficient testing window size of the class. The continuty has occurred well with testing window of 5X5 size kernal whereas the number of classes has been doubled than 8x8 size kernal. The results obtained in this preliminary study are motivating and suggest further works to investigate the correlation between the ground truth and more classes obtained from the small size of testing window.

Table-1:

No.	Class	Window Size	No. of Pixels Presented	Fractal Dimension
1	Water body	8X8	9408	2.0591
2	Agriculture A	8X8	71298	2.1784
3	Agriculture B	8X8	93269	2.1772
4	Sal Forest	8X8	76025	2.8189



Fig.1: IRS LISS-II BAND_4 Raw Image of Study Area.

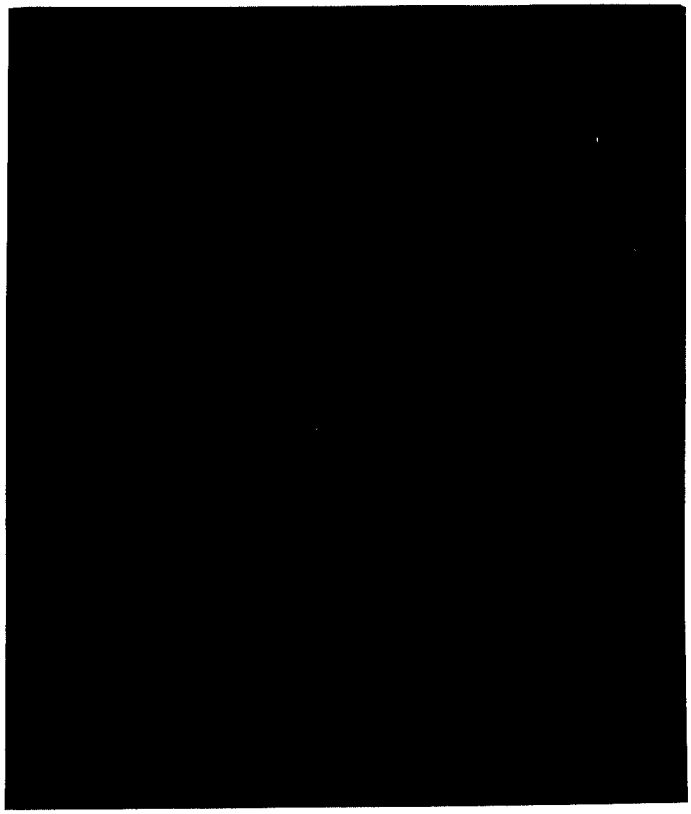


Fig.2: Fractal Classified Image Depicting the Forest and Agriculture Type.

ACKNOWLEDGEMENT

The authors wish to thank Prof.B.L.Deekshatulu, Director, NRSA, for his constant encouragement. The authors are grateful to Dr.Dutt, Dr.Murthy and Mr.Bishwadeep,Forestry Division, NRSA for providing the data and their valuable suggestions to complete this paper.

REFERENCES:

[1] K.J.Falconer,"Fractal Geometry"-Mathamatical Foundation and Applications, John Whiley & sons Ed.,1990

[2] Mandelbrot B.B, 1982, "The Fractal Geometry of Nature", Freeman,Sanfracisco,460pp

[3] Sergrey V Buldyrev et al., "Fractal in Natural Science", World Scientific Publication, Singapore, 1994, pp453-465

[4] Keith C Clarke, 1986, "Computation of the fractal dimension of topgraphic surfaces using the Triangular Prism Surface Area Method", Computers & Geoscience,Vol-2,No5,pp713-722

[5] Dr.C.B.S. Dutt et al.," Forest Cover Mapping and Vegetation Analysis Using Remote Sensing as part of Environmental Imapact Analysis of Mining in Surguja District", Forestry and Ecology Division Report, NRSA,1994, pp11-40

A Comparison of Three Neural Network Classifiers for Remote Sensing Classification

Sucharita Gopal
Dept. of Geography
Boston University
Boston MA 02215
suchi@crsa.bu.edu

Manfred Fischer
Dept. of Economic Geography
Wirtschafsuniversität, Wien
Wien, Austria
mmf@isis.wu-wien.ac.at

Abstract

This paper evaluates the use of neural network classifiers for the pattern classification problem in remote sensing. The performance of Multi-Layer Perceptron (MLP), Radial Basis Function, and Fuzzy ARTMAP networks is evaluated using a Landsat-5 TM scene of the northern section of the city of Vienna, Austria. Classification accuracies obtained from the neural network classifiers are compared with a benchmark, the maximum likelihood classifier. In addition to the evaluation of classification accuracy, the neural networks are analyzed for their generalization capability and stability of results. Best overall results (in terms of accuracy and convergence time) are obtained using fuzzy ARTMAP followed by MLP (with weight elimination). Their classification error on training data set are zero and 7.87% respectively; classification error on testing data set are 10.24% and less than 2 percent. Simulation results serve to illustrate the properties of various classifiers in general, as well as the stability of the result with respect to various critical control parameters, initial parameter conditions, training time, and different training and testing data sets.

Neural Networks

Satellite remote sensing has become a valuable tool for gathering information about planet earth. Images received by satellites are useful not only for observing but monitoring changes in the natural environment. High-spatial resolution images acquired by earth-orbiting sensors may also be used to monitor both the extent of urban areas and their composition in terms of land use. Unfortunately, many of the commonly used image processing techniques, such as parametric pixel-by-pixel classification algorithms, tend to perform poorly in this context. This is because urban areas comprise a complex spatial assemblage of disparate land cover types - including built structures, numerous vegetation types, bare soil and water bodies - each of which has different spectral reflectance characteristics. As a result, pattern recognition in urban areas is one of the most demanding issues in classifying satellite remote sensing data. The present research uses artificial neural networks for classification of urban areas.

0-7803-3068-4/96$5.00©1996 IEEE

Neural Networks

The neural networks used in this paper include two types of the Multi-Layer Perceptron (MLP) network, radial basis function network [2], and fuzzy ARTMAP. MLP are feed-forward networks with one or more layers of nodes between input and output nodes. These additional layers contain the hidden units or nodes. In the present study, the input layer consists of six units representing the six spectral channels (TM1, TM2, TM3, TM4, TM5, and TM7) and the output layer represents the eight a priori land use categories (see Table 1). The specification of the activation function is a critical issue in successful application of a MLP classifier. We have used two types of activation functions in the present study. The first MLP network, called MLP-1, uses a logistic function; the second MLP network, called MLP-2, uses a hyperbolical tangent activation function. Both MLP-1 and MLP-2 are trained using the backpropagation algorithm [3]. In a Radial Basis Function (RBF) network the hidden units compute radial basis functions of the inputs. The net input to the hidden layer is the distance from the input to the weight vector. The RBF classifier in the present study uses softmax ouput units and Gaussian functions in the hidden layer. For complete details on the three classifiers, see [2]. Fuzzy ARTMAP [1] synthesizes fuzzy logic and Adaptive Resonance Theory (ART) models by exploiting the formal similarity between the computations of fuzzy subsethood and the dynamics of ART category choice, search and learning. The advantages of fuzzy ARTMAP are that it constructs the minimum number of recognition categories to meet accuracy criteria. In contrast, the number of hidden units in MLP has to be determined by

trial-and-error. In addition, ARTMAP dynamics are fast, stable and scalable, overcoming common limitations of backpropagation algorithm, including lengthy training time and convergence to a local minima. A normal (conventional) classifier, maximum likelihood, is used as a benchmark to evaluate the performance of the three neural network classifiers. All classifiers are given the same feature sets in training and testing.

Data and Data Representation

The data used for training and testing the classification accuracy of the classifiers is a section (270 X 360 pixels) of a Landsat-5 Thematic Mapper (TM) scene. The image covers the northern section of the city of Vienna (Austria) and has an area of 8.1X10.8 km^2. Six TM bands are used (TM1, TM2, TM3, TM4, Tm5, TM7); each has a spectral value between 0-255. Each TM pixel represents a ground area of 30x30 m^2. The purpose of the multispectral classification was to identify the eight land cover categories listed in Table 1.

Category Number	Land Use Category	Pixels	
		Train.	Test.
C1	Mixed grass & arable farmland	167	83
C2	Vineyards & areas with sparse veg.	285	142
C3	Asphalt & concrete surfaces	128	64
C4	Woodland & public gardens with trees	402	200
C5	Low density residen. & industrial areas	102	52
C6	Densely built-up residential areas	296	148
C7	Water courses	153	77
C8	Stagnant water bodies	107	54
	Total pixels	1640	820

Table 1: Categories Used for Classification and Number of Training/Testing Pixels

Suitable training sites were selected for each of the eight classes using ancillary information and orthophotos. This approach resulted in a database of 2,460 pixels (about 2.5% of all pixels in the scene) that are divided into a training set (two thirds of the database) and a testing set by stratified random sampling. Thus each training/testing run consists of 1,640 training and 820 testing vectors (see Table 1). This moderately large size for each training run makes the classification problem non-trivial on one hand, but still allows for extensive tests on in-sample and out-of-sample performance of classifiers. Data preprocessing (i.e. transforming the raw input data) is an important step in classification. This step reduces the effect of poor quality (noisy) data and generally leads to better predictions. In the present study, data are scaled to the interval [0,1].

Effect of Various Control Parameters on Performance

Neural networks are known to be sensitive to changes in network design, control parameters (including learning and initial parameter conditions), the size and number of training patterns, etc. This issue is the major focus of our simulation experiments. The central objective in real world applications using neural networks is to identify intervals of the control parameters that give robust results, and to demonstrate that these results persist across different training and testing sets.

In-sample performance of a classifier is important since it determines the convergence ability and sets a target of feasible out-of-sample performance which might be achieved by fine-tuning the control parameters [2]. Out-of-sample performance measures the ability of a classifier to recognize patterns outside the training set, i.e. data never seen by the classifier during training. All simulations were carried out on a Sun SPARCserver 10-GS with 128 MB RAM.

We summarize the effect of training time, initial parameter conditions, the gradient descent control term, and training and testing sets, on the performance of MLP and RBF classifiers. First, simulation results show the effect of training time (in terms of epochs) on the in-sample performance of networks. The performance tends to oscillate initially and stabilizes given sufficient training. MLP-1 (with weight elimination, [2]) and MLP-2 networks tends to converge asympotically at a minimum that is found at about 17,000 epochs, while the RBF converged at about 36,000 epochs. (In all cases, learning parameter is 0.8, network is trained for 50,000 epochs with equal random initializations). Second, simulation results demonstrate that different initial conditions can lead to more or less major differences in the starting stage of the training process. The in-sample and out-of-sample performance varies widely with different initial starting conditions. After about 15,000 epochs, such performance differences more or less vanish. However, it should be emphasized that the issue of stability with initial conditions deserves attention when training a classifier. Third, the choice of the control parame-

ter for the gradient descent is a crucial parameter in backpropagation training. A stability analysis with respect to this parameter shows that both in-sample and out-of-sample performance of the classifier remain very stable in the range of 0.4 and 0.8, while a small change from 0.4 to 0.2 yields a dramatic loss in classification accuracy. The optimal learning rate in this experiment was found to be 0.8. Fourth, different training and testing samples affect in-sample and out-of-sample performance. In one simulation, the performance was significantly different with a different order of training/testing data.

Critical parameters affecting performance of fuzzy ARTMAP are: vigilance (ρ), choice (θ), different order of presentation of the training set, and size of the training set. Increasing vigilance creates more ART_a categories and improves classification performance. When $\rho = 0$, the average in-sample and out-of-sample classification accuracy is 92% and 91% respectively. When $\rho = 0.95$, the average in-sample and out-of-sample classification accuracy is 96.36% and 95.82% respectively. The average number of ART_a categories increases from 37 to 284 (across 5 simulations). The number of ART_a categories and training epochs increases with α. Different orders of presentation of the training set leads to differences in performance. This was evaluated using five different orders of the training set. Simulation results indicate that the the size of training set improves performance.

Classification Results and Analysis of Performance

The major objective of this paper is to evaluate the classification accuracy of the neural classifiers, MLP-1, MLP-2, RBF [2] and fuzzy ARTMAP (FA) against the benchmark, maximum likelihood (ML). Table 2 shows the comparison between classifiers in terms of: (i) epochs required (column 2) (ii) number of hidden units in the case of the first three neural classifiers and the number of ART_a categories (column 3) for the fuzzy ARTMAP, (the figure in the bracket of this column refers to the number of connections), (iii) in-sample (column 4) and out-of-sample (column 5) classification accuracy and (iv) CPU time (column 6; given in seconds). Note that while attempts were made to choose the best MLP's, no similar attempts were made in choosing parameters critical to RBFs. The RBF classifier did not train and generalize as well as the MLP-networks. MLP-1 and MLP-2 generally train and generalize at the same rate, but MLP-1's training is faster, by about 30%. The best MLP results are provided by MLP-1 classifier with 14 hidden units and 196 free parameters, followed by MLP-2, and RBF. The overall results show that fuzzy ARTMAP performs the best. In terms of classification accuracy, both in-sample as well as out-of-sample, it is superior to the other neural classifiers and the conventional model. More significantly, it trained much faster than the other neural classifiers.

Type	Ep.	# Hid./ Cats.	Class. Accuracy		CPU
			I-S.%	O-S.%	(sec.)
MLP1	92	14(196)	92.13	89.76	15.1
MLP2	92	22(338)	90.91	90.00	21.0
RBF	92	22(338)	90.91	90.00	21.0
FA	8	116(812)	100.00	99.26	2.1
ML			90.85	85.24	1.4

Table 2: A Comparison Between Classifiers

In addition, the error matrices for in-sample and out-of-sample performance of the various classifiers highlight that neural classifiers, in general, outperform the conventional classifier and fuzzy ARTMAP gives the best performance amongst the neural classifiers.

Acknowledgements

This research is supported in part by the National Science Foundation (NSF SBR 93-00633) and the Austrian zur Förderung der Wissenschaftlichen Forschung (P-09972-TEC). The authors thank Prof. Karl Kraus, Department of Photogrammetric Engineering and Remote Sensing, Vienna Technical University and Petra Staufer, Wirtschafsuniversität, Vienna, Austria for their help and assitance.

References

[1] Carpenter, G. A., Grossberg, S., Markuzon, N., Reynolds, J.H., and Rosen, D. B. (1992). Fuzzy ART: A neural network architecture for incremental supervised learning of analog multidimensional maps, *IEEE Transactions on Neural Networks* 3, 698-713.

[2] Fischer, M.M., Gopal, S., Staufer, P. and Steinocher, K. (1995). 'Evaluation of neural pattern classifiers for a remote sensing application', Manuscript in Review, *Geographical Systems*, WSG-Discussion Papers, 46, Department of Economic & Social Geography, Wirtschafsuniversität, Wien, Austria.

[3] Rummelhart, D.E., Hinton, G.E. and Williams, R.J. (1986): Learning representations by back-propagating errors, *Nature 323*, pp. 533-536.

A Decision Tree Classifier Design for High-dimensional Data with Limited Training Samples

Saldju Tadjudin
School of Electrical and Computer Engineering
Purdue University
West Lafayette, IN 47907-1285
Phone (317) 494-1743
Fax (317) 494-3358
tadjudin@ecn.purdue.edu

David A. Landgrebe
School of Electrical and Computer Engineering
Purdue University
West Lafayette, IN 47907-1285
Phone (317) 494-3486
Fax (317) 494-3358
landgreb@ecn.purdue.edu

Abstract -- Recent advances in sensor technology have increased the spectral resolution of remote sensing data significantly. Higher spectral resolution for each pixel should make possible the discrimination of a larger number of classes in more detail. However, due to the scarcity of training samples in remote sensing applications, the increase in spectral dimensionality only complicates the design of classifiers which, if not properly done, may cause the deterioration of classification accuracy. In this work, we propose a new design procedure for a hybrid decision tree classifier which improves the classification efficiency and accuracy for classifying high-dimensional data with a small training sample size. We further propose to use a feature extraction technique based on maximizing the statistical distance between two subgroups. Experimental results show that the proposed tree classifier is more effective in classifying high-dimensional data with limited training samples than a single-layer classifier and a previously proposed hybrid tree classifier.

INTRODUCTION

Remote sensing technology has provided a relatively cheap and effective means to measure the radiation reflected from the earth's surface. In recent years, sensors have been developed to gather data in hundreds of spectral bands. For example, the Airborne Visible/Infrared Imaging Spectrometer (AVIRIS) collects data in 224 spectral bands covering 0.4-2.5 μm wavelength region with 20 m spatial resolution. By representing the spectrum of a pixel in an image as a random process, statistical pattern recognition methods have been successfully applied to process multispectral data. Supervised classification methods typically assume that the parameters of the underlying data distribution can be approximated by the training samples. The availability of a large number of spectral bands should allow more detailed classes to be identified with higher accuracy. However, a large number of features produces large variances in the parameter estimates. Typically, the performance of the classifier improves up to a certain point as additional features are added, and then deteriorates. This is referred to as the Hughes phenomenon[1]. Another immediate complication of high dimensionality is that the computation time may become large. Therefore, high dimensionality can become a liability rather than an asset for a conventional one-stage classifier. In this work, we propose a new procedure for designing a parametric, hybrid decision tree that would circumvent these dimensionality problems The organization of this paper is as follows: the following section describes the decision tree classifier (DTC) and our proposed classifier, followed by a discussion on feature reduction, experimental results and conclusions.

DESIGN OF DECISION TREE CLASSIFIERS

The decision tree classifier (DTC) has been used for classification and other purposes since the 1960's [2]. In principle, it divides a complex decision into several simpler ones in a hierarchical fashion. The hierarchical structure of decision tree classifiers has several desirable properties: 1) The classification process can be done in O(log(N)) instead of O(N) where N is the number of classes; 2) A tree classifier is more flexible than a single-stage one in that the nodes can have different decision rules and different features. In single-stage classifiers, a subset of features and the decision rule are selected by optimizing a global criterion and are used to discriminate among all classes. In contrast, a tree classifier offers the flexibility to select different features and a unique decision rule for each node; 3) A tree classifier may circumvent the effects due to small training sample size by focusing on fewer classes and using fewer features at each node. In particular, there are fewer nodes near the root of the tree and consequently more training samples are available per node. The tradeoff for these benefits is a more complex design process.

We propose to use the hybrid approach to construct the DTC. The hybrid method combines both top-down and bottom-up approaches. The bottom-up approach[3] typically computes the statistical distance between each pair of classes. At each node the two classes with the smallest distance are merged to form a new group. The mean vector and covariance matrix for the new group are computed from the training samples in that group, and the merging process is repeated until two groups are left to form two cluster centers. We propose a new bottom-up method with fewer computations and better classification performance. We first compute the pairwise distance between pre-defined classes. At each node, instead of repeatedly merging classes and subgroups with the smaller distance until two groups emerge, we select two classes with the largest separation as two cluster centers and merge the rest of classes into the clusters based on their statistical "closeness" to the cluster centers. This approach has the benefit of computing the pairwise distances only once and hence reducing computational time.

0-7803-3068-4/96$5.00©1996 IEEE

The top-down design consists of the following tasks: 1) selection of a node decision rule; 2) termination rule; 3) decision tree structure; and 4) feature reduction. These different aspects of a tree classifier should be considered simultaneously for an optimal design. Unfortunately, this problem of optimization is non-trivial. To simplify the design problem, we adopt a binary structure. The termination rule is simply the majority rule, i.e. the class label in the terminal node is assigned to the class with the most training samples at that node. Furthermore, the classes and subclasses are assumed to be normally distributed. Therefore, the decision rule for node splitting is a maximum-likelihood classification of Gaussian classes and subclasses. The proposed DTC design algorithm is summarized as follows:

Bottom-up approach:

(1) Compute the statistical separability between each class pair. When the number of training samples is less than a threshold, the Euclidean distance is computed. Otherwise, the Bhattacharyya distance is computed instead. The threshold is chosen as (2n+1) where n is the number of training samples.
(2) Select two classes with the largest separation as two cluster centers.
(3) Merge the remaining classes with the one of two clusters whichever has the smaller distance.

Hybrid design:

(1) Use the bottom-up approach to divide the data set into two subgroups.
(2) Compute the mean vectors and covariance matrices of the two subgroups and redivide the samples into two nodes using the decision rule. In a two class Gaussian maximum likelihood classification, the decision rule is given by the following:

$$J_i = \left(x-\hat{M}_i\right)^T \hat{\Sigma}_i^{-1}\left(x-\hat{M}_i\right) + ln\left|\hat{\Sigma}_i\right| \qquad i = n_L \text{ or } n_R$$

$$x \in n_L \text{ if } J_{n_L} < J_{n_R} \; x \in n_L \text{ if } J_{n_L} < J_{n_R} \qquad (1)$$

where x is the data sample of N dimensions

$\hat{M}_i$ is the sample mean of node i

$\hat{\Sigma}_i$ is the sample covariance of node i

n_L and n_R represent left and right node, respectively.

(3) When the majority of the samples in the separated group consist of one class, the design is complete. Otherwise, return to step 1 for each subgroup.

FEATURE REDUCTION

The benefits of performing feature reduction for remote sensing applications are twofold: 1) to circumvent the Hughes phenomenon and 2) to reduce the amount of computation required for classification. Feature reduction methods can be roughly divided into two categories: feature selection and feature extraction. In feature selection, features that do not contribute to the discrimination of classes can be eliminated by evaluating some criteria before and after the removal. Feature extraction involves the transformation of data into a new set of coordinates where the least effective features are more obvious. The transformation is usually linear and based on the optimization of some criteria. In this work, we only consider feature extraction techniques. This section describes two feature extraction algorithms and discusses their relative strengths and weaknesses when applied to a binary tree classifier. The following discussion uses the decision rule as in (1).

Canonical or discriminant analysis [4] extracts features that maximize the ratio of the between-class scatter matrix to the within-class scatter matrix. Although this method performs well for most cases, there are several drawbacks. First, the approach delivers features only up to the number of classes L minus one. For a binary tree classifier, it means there is only one feature extracted at each node. One feature may not be optimal to discriminate between classes with a complex decision boundary. Second, if the mean values are similar or the same, the extracted feature vectors are not reliable. Furthermore, for multiple classes, if a class has a mean vector very different from the other classes, the between-class scatter matrix is biased towards that class, resulting in ineffective features.

The Bhattacharyya distance is a convenient measure of class separability for two classes. Furthermore, it gives an upper bound of Bayes error for normal distributions [4]. The Bhattacharyya distance is given as

$$\mu(1/2) = \frac{1}{8}\left(M_2 - M_1\right)^T \left[\frac{\Sigma_1+\Sigma_2}{2}\right]^{-1}\left(M_2 - M_1\right) + \frac{1}{2} ln \frac{\left|\frac{\Sigma_1+\Sigma_2}{2}\right|}{\sqrt{|\Sigma_1||\Sigma_2|}} \qquad (2)$$

We can extract features that maximize the Bhattacharyya distance between two classes. However, the optimization of $\mu(1/2)$ is non-trivial. so we perform a suboptimal procedure to find the effective features[4]. The method proceeds as follows:

(1) Compute the eigenvalues λ_i and orthonormal eigenvectors ϕ_i of $\overline{\Sigma}^{-1}(M_2 - M_1)(M_2 - M_1)^T$ where $\overline{\Sigma} = (\Sigma_1 + \Sigma_2)/2$. Since the rank of the matrix is one, only the first eigenvalue λ_1 is non-zero. The class separability due to the mean difference is then preserved by the transformation $\phi_1^T x$.

(2) Perform the transformation $y = [\phi_2 \cdots \phi_N]^T x$ by which x is mapped to the (N-1) dimensional subspace where there is no information due to mean difference. Let $\Phi_{N-1} = [\phi_2 \cdots \phi_N]$.

(3) Extract (M-1) features, $\Psi=[\psi_1 \cdots \psi_{M-1}]$, by optimizing the second term of $\mu(1/2)$ on y. These features preserve the information due to covariance difference. The overall transformation is then given by

$$z=[\phi_1 \vdots \Phi_{N-1}\Psi]^T x. \quad (3)$$

Step 1 is equivalent to discriminant analysis when the prior probabilities are assumed equal. In Step 2 and 3, features that contribute to the covariance difference are further extracted. Therefore, this method has an advantage of generating more than one feature at each node of a binary tree compared to the discriminant analysis approach. In addition, the Bhattacharyya distance is an optimal criterion for two normal classes and the node splitting of a binary tree is assumed to involve two normal classes. In contrast, when the Bhattacharrya distance is used for feature reduction for more than two classes in one-stage classifiers, the minimum or average pairwise distance between all class combinations is usually used as the sub-optimal criterion for optimization. For a binary tree classifier, this suboptimal choice of criterion can be avoided.

EXPERIMENTAL RESULTS

In the following experiment we compare the performances of the proposed algorithm (New), decision tree algorithm in [3] (Prev), and the single-stage maximum likelihood classifier (ML). The data set consists of a portion of an AVIRIS data taken in June, 1992, which covers a mixture of agricultural/forestry land in the Indian Pine Test Site in Indiana. The water absorption bands were removed to leave a total of 196 bands for the experiment. The test samples are composed of 6 classes. The classes and the number of labeled samples are shown in Table 1.

Table 1 Class description of the data set

Class No.	Class Name	No. of Samples
1	Corn-notill	628
2	Corn-min	692
3	Grass/trees	609
4	Soybeans-notill	724
5	Soybeans-min	688
6	Woods	605

In the experiment, the training samples are randomly selected from the sample pool, and the rest of samples are used for testing. We perform 10 trials for each experiment and obtain the mean and standard deviation of the classification accuracy. For the single stage classifier, we use discriminant analysis feature extraction to extract 5 features for the 6 classes. For the binary trees, we use Bhattacharyya distance feature extraction to select 50 features at each node. The results are shown in Table 2. Fig. 1 illustrates the average accuracy of the classifiers.

Table 2 Classification results

No. of training samples	ML % (std dev)	Prev % (std dev)	New % (std dev)
200	85.2 (0.03)	85.4 (0.03)	88.2 (0.03)
300	87.4 (0.02)	86.3 (0.02)	88.6 (0.02)
400	89.2 (0.02)	88.6 (0.02)	89.9 (0.02)

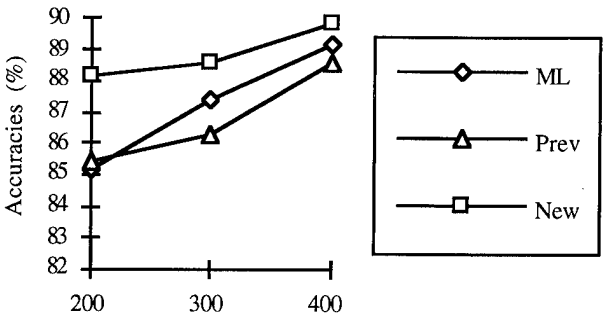


Figure 1 Classification results

CONCLUSION

Our goal in this research is to circumvent the classification problems incurred by an increase in the number of features while the training samples remain limited. The problems are namely the increase in computation time and decline in performance. We have proposed a new decision tree algorithm and incorporated a feature extraction algorithm suitable for a binary tree. The experimental results have shown that the proposed algorithm performs best under the small training sample size situation using the feature extraction method based on maximizing the Bhattacharyya distance at each node.

REFERENCES

[1] G.F. Hughes, "On the mean accuracy of statistical pattern recognizers," IEEE Trans. Inform. Theory., Vol IT-14, pp. 55-63, 1968.

[2] S.R. Safavian and D.A. Landgrebe, "A survey of decision tree classifier methodology", IEEE Trans. on Systems, Man and Cybernetics, vol. 21, No. 3, pp. 660-674, May/June 1991.

[3] B. Kim and D.A. Landgrebe, "Hierarchical decision tree classifiers in high-dimensional, numerous class cases," IEEE Trans. Geoscience and Remote Sensing, vol. 29, No 4, pp. 518-528, July 1991.

[4] K. Fukunaga, Introduction to Statistical Pattern Recognition, 2nd ed., Academic Press, New York, 1990.

Classification Accuracy Improvement and Delineation of Mixed Pixels Using Hierarchical Image Classification

Jayantha Ediriwickrema, Computer Graphics Center, P. O. Box 7106, NCSU, Raleigh, NC 27695

Siamak Khorram, Professor and Director, Computer Graphics Center, P. O. Box 7106, NCSU, Raleigh, NC 27695, and Dean of International Space University, Parc d'Innovation, Communaute Urbaine de Strasbourg, Blvd. Gonthier d' Andernach, 67400 Ilkirch, France

Abstract -- Among the supervised parametric classification methods, the maximum likelihood (MLH) classifier has become popular in remote sensing. Reliable prior probabilities (PPs) are not always freely available, and it is a common practice to perform the MLH classification with equal PPs. When equal PPs are used, the advantages of the MLH classification may not be attained. This study explores a hierarchical image classification (HIC) method to estimate PPs for the spectral classes using Landsat Thematic Mapper (TM) data and spectral class signatures. The TM pixels are visualized in spectral space relative to the spectral class probability surfaces. Prior probabilities are estimated from the pixels which fall within spectral class probability regions. The pixels likely to be misclassified are classified with the MLH classification with the estimated PPs. Besides the classified image, the HIC delineates mixed pixels and their land use/land cover class components at the specified significance level. The classified image resulting from the HIC shows increased accuracy over three classification methods. Delineated mixed pixels and their class components show visual agreement to the false color composites and aerial photographs.

INTRODUCTION

The maximum likelihood (MLH) classification has become the most widely used method in digital image processing of remotely sensed data. The algorithm was developed in terms of prior probabilities (PPs), and its potential was not optimum when PPs are assumed equal [1]. Because PPs often unavailable, equal PPs are approximated. It is desirable to obtain reliable PPs for each spectral class and use them at least to classify the pixels likely to be misclassified. Robust approaches are necessary to determine PPs within the same time frame and to the spectral classes selected. In this study, the hierarchical image classification (HIC) visualized the Thematic Mapper (TM) pixels in spectral space relative to the spectral class probability regions at a specified significance level. When the distribution of a spectral class was assumed to be multivariate normal, a quadratic equation with a constant equal to χ^2 value was commonly used to delineate the constant probability contours [2]. The pixels which fell within spectral class probability regions were used to estimate PPs, and were grouped as the pixels most likely to be correctly classified and allocated directly to the respective spectral class. The pixels which fell within more than one probability region and outside all probability regions were categorized as the pixels likely to be misclassified. The pixels likely to be misclassified were classified by the MLH classification with the PPs estimated from the pixels most likely to be correctly classified. Visualization of pixels relative to all spectral class probability surfaces suggest spectral classes that have a chance of being assigned for each pixel. Along with the improved classified image, this study identified mixed pixels and their mixed class components.

0-7803-3068-4/96$5.00©1996 IEEE

METHODOLOGY

Study Area

The north-west of the Greater Nashville, Tennessee metropolitan area was selected as the study area. This area encompasses a wide variety of land use/land cover (LU/LC) patterns with different levels of frequency of land cover variations. Mixed pixels can be anticipated due to heterogeneous and frequent changes in LU/LC patterns. High frequency LU/LC patterns provide a fairly good background to evaluate pixels likely to be misclassified.

Data

Sub image of 256 columns and 256 rows was selected from the rectified six-bands TM data set which was used in [3]. Aerial photographs and the false color composite of the TM data were used to select homogeneous training sites and assess accuracies.

Hierarchical Image Classification

The classification scheme included five LU/LC classes (i) Hardwood Forests (ii) Conifer-Mixed Conifer/Hardwood Forests (iii) Non-Forested Vegetation (iv) Developed, and (v) Water. A detailed description of the classification scheme can be found in [3]. Initially 113 training sites were selected from fairly homogeneous areas representing the five LU/LC classes. It is important to select training sites to minimize spectral overlap while covering the entire spectral gradient of the TM data [4]. Training sites which showed spectral confusion were gradually removed from the signature file and the final signature file was developed with 59 training sites.

These 59 signatures were used to classify the TM data by HIC based on spectral class probability regions at a five percent significance level of χ^2 with six degrees of freedom.

Estimation of Prior Probabilities: In the HIC, the spectral class probability regions were defined to meet the five percent significance level of χ^2 with six degrees of freedom. When the measurement vector "y" (the pixel coordinates in p-dimensional spectral space) is distributed as $N_p(\mathbf{m}, \Sigma)$ with $|\Sigma| > 0$, then the probability of "y" being in the solid ellipsoid is 1- α (1).

$$(y-m)^T \Sigma^{-1}(y-m) \le \chi_p^2(\alpha), \quad (1)$$

where $\chi_p^2(\alpha) = \chi^2$ distribution with "p" degrees of freedom at α significance level. All probability regions were specified at one probability density level. At the specified significance level, it was possible to overlap probability regions. Since the training sites represented different spectral classes with narrow spectral variances, the Gaussian assumption for the spectral class distributions may be considered as valid. Therefore, relative to the pixels which fell within all probability regions, the fraction of pixels which fell within each probability region was considered as a good estimate for the PP for each spectral class.

Classification of the Pixels Likely to be Misclassified: The HIC categorized the TM pixels into two groups. The pixels which fell within only one probability region were grouped as the pixels most likely to be correctly classified. These pixels were directly classified into the corresponding spectral classes. The pixels which fell within more than one probability region or outside all probability regions were grouped as the pixels likely to be misclassified. The MLH algorithm (2) with the estimated PPs was used to classify the pixels likely to be misclassified. The negative log likelihood function was defined to derive positive weighted distances.

$$L = -\ln(\omega_c) + 0.5\{\ln(|\Sigma_c|) + (y-m_c)^T \Sigma_c^{-1}(y-m_c)\}, \quad (2)$$

where L = weighted distance, ω_C = PP of spectral class "c," $\mathbf{m}_c$ = the mean vector of spectral class "c," and Σ_C = the variance-covariance matrix of spectral class "c." In this equation class "c" was chosen for the pixel where the "L" was lowest. Weighted distance "L" was computed for each pixel taking each spectral class separately.

Output Image Files: Three image files, (i) the classified image, (ii) the summary image, and (iii) the distance image [4] were produced by the HIC, and all input and output data files were in Hierarchical File Architecture (HFA) [5].

Cross Validation

To evaluate the performance of the classified image produced by the HIC, three classified images were developed: (i) MLH with equal PPs, (ii) MLH classification with PPs estimated from the classified image in the previous one, and (iii) MLH classification with PPs estimated from the threshold image.

MLH with Equal PPs: The primary object of this study was to evaluate the performance of the HIC over the MLH classification with equal PPs. The MLH procedure was used along with 59 training signatures to classify the TM data. A distance file was also developed with the classified image to create a threshold image.

MLH with Estimated PPs from the Classified Image: The original TM image was classified again with PPs which were estimated from the image that was classified with equal PPs. The frequency of the assigned pixels in each spectral class was used as the PP of the respective spectral class.

MLH with Estimated PPs from Threshold Image: The threshold image was developed from the distance image. A five percent significant level of χ^2 with six degrees of freedom was used in developing the threshold image. The fraction of pixels classified into each spectral class in the threshold image was used as the estimated PP. These estimated PPs were used to reclassify the original TM image using the MLH classifier.

Delineation of Mixed Pixels and their Components

The summary image file was used to delineate mixed pixels and their components for the pixels which fell within more than one spectral class probability region. For the pixels which fell outside all probability regions, both the summary and the distance image files were used. A threshold value was derived from the sum of the lowest weighted distance and the maximum weighted distance of the corresponding probability region. The spectral classes, whose weighted distances were less than the threshold values, were used as those spectral classes likely to be assigned for each pixel. Quantitative analysis of the mixed LU/LC class components requires large scale highly detailed maps. Therefore, the patterns and the distributions of the mixed pixels and their components were visually compared instead of performing quantitative analysis.

Accuracy Assessment

The HIC was designed to improve classification accuracies for the pixels likely to be misclassified, and it was appropriate to analyze such pixels in the validation. If there was any improvement of the HIC over the MLH with equal PPs, the improvement should have been from the pixels classified differently in both images. Therefore, the pixels classified differently in both images (the HIC and the MLH with equal PPs) were extracted, and from them 423 (an arbitrary number) pixels were randomly selected for accuracy assessment. The selected pixels were located on both false color composite and the aerial photographs, and a separate

raster file was developed as the reference class image. The 423 selected pixels were assigned the corresponding LU/LC numbers, and the remaining pixels were assigned zero. Using the "summary" procedure in the ERDAS/IMAGINE, omission and commission error matrices were developed [4]. Kappa coefficients (KCs) were calculated to evaluate the HIC over the three classification methods. The accuracies calculated in this study were based totally on the pixels likely to be misclassified. Therefore, the accuracies describe the standards of the classified images relative to the pixels likely to be misclassified and not relative to the entire image. The KC statistic is generally used in comparing different error matrices and was used in this study to compare the classification methods.

RESULTS

Overall, four different classified images were produced in this study: (Method-a) Standard MLH classification with equal PPs, (Method-b) MLH with PPs estimated from the classified image with equal PPs, (Method-c) MLH with PPs estimated from the threshold map, and (Method-d) HIC. Even though different approaches were used, all images looked similar at a glance [4]. When the images were carefully examined, differently classified pixels were mostly found around the LU/LC class boundaries as expected.

Assessment of the HIC

The KCs and the overall accuracies (OAs) are shown in Table 1. Both OA and the KC were found to be lowest in the MLH classification with equal PPs. The KC and the OA were generally high in all methods when PPs were used. Out of the classifications with unequal PPs, the lowest KC and OA were shown by the method which estimated PPs from the classified image with equal PPs. The KC and the OA were increased when PPs were estimated from the threshold image. The HIC showed the highest KC and the OA. The increase of the KC and the OA in HIC was 30% relative to the standard MLH classification with equal PPs. The accuracy increase was around four percent in the HIC relative to the method which used the threshold image in three passes.

Mixed Pixels and their Components

The image of the distribution of mixed pixels at the specified significance level is shown in [4]. This image was developed from the summary and the distance image files which resulted in the HIC and summarizes the number of pixels in each mixed pixel category. More than half of the pixels (52.72%) were found to be pure pixels. Pixels with two and three LU/LC components were found to be 34.09% and 6.76%. Mixed pixels with more than two components were 8.18%. Hardwood Forests in valleys often resulted in two component

Table 1. Kappa coefficients and overall accuracies.

	Method-a	Method-b	Method-c	Method-d
KC	0.24	0.39	0.50	0.54
OA	43.74	60.76	68.32	72.10

mixed pixels. Mixed pixels with more than three components were often found in sparsely distributed Conifer-Mixed Conifer/Hardwood Forests and on the shaded lower slopes of mountains.

CONCLUSION

The proposed HIC method is effective and easy to implement. The estimated PPs in the HIC method are closer to the classification model than the estimated PPs in the classified image with equal PPs or the threshold image. The estimated PPs in the HIC possess a significant amount of information capable of improving the classification accuracy over the MLH classification with equal PPs. Furthermore, the method enhances the value of the classified image by indicating the most likely LU/LC class components for each pixel while providing a favorable base to analyze mixed pixels.

REFERENCES

[1] P. M. Mather, "A Computationally-Efficient Maximum-Likelihood Classifier Employing Prior Probabilities for Remotely Sensed Data," *International Journal of Remote Sensing*, vol. 6, pp. 369-376., 1985.

[2] G. M. Foody, N. A. Campbell, N. M. Trodd, and T. F. Wood, "Derivation and Applications of Probabilistic Measures of Class Membership form the Maximum-Likelihood Classification," *Photogrammetric Engineering and Remote Sensing*, vol. 58, pp. 1335-1341, 1992.

[3] S. Khorram, D. J. Ediriwickrema, and J. T. Morisette, "Characterization of Forest Canopy Species Composition for the Nashville, Metropolitan Area," Computer Graphics Center, North Carolina State University, Raleigh, North Carolina, Final Report Submitted to Southern Oxidant Study 204, May 1995.

[4] D. J. Ediriwickrema, "Modeling and Analysis of AVHRR Data for Biogenic Emission Inventory System (BEIS)," in *Computer Graphics Center, College of Forest Resources*. Raleigh: North Carolina State University, Raleigh, NC 27695, 1995, pp. 165.

[5] ERDAS/IMAGINE, *ERDAS IMAGINE Version 8.2 Production Tour Guides*, First ed. Atlanta, Georgia: ERDAS, Inc., 1995.

High resolution 3-D SAR via multi-baseline interferometry

J. Homer I.D. Longstaff G. Callaghan
Department of Electrical and Computer Engineering,
The University of Queensland, Brisbane, Qld 4072, Australia and
Cooperative Research Centre for Sensor Signal and Information Processing
Ph: +61 7 3365 3697, Fax: +61 7 3365 3684, Email: homerj@elec.uq.edu.au

Abstract – The ability of interferometric SAR (InSAR) to provide terrain height estimation can be interpreted as being due to the baseline (of the two SAR imaging flight paths) acting as an aperture in the normal-to-slant-range ($\vec{n}$) direction. However, the aperture, because it consists of only two nodes, has effectively no resolving power. In this paper we introduce and examine a technique which synthesises an $N > 2$ node aperture in the $\vec{n}$ direction from $N-1$ connected baselines. This, together with the slant-range and azimuth resolving capability of SAR imaging systems, enables the generation of high resolution 3-D imagery. A theoretical analysis and procedural outline of the proposed technique are presented.

INTRODUCTION

Synthetic aperture radar (SAR) systems provide high resolution terrain imagery in the slant range $\vec{s}$ and azimuth $\vec{a}$ directions. The resolution in the $\vec{a}$ direction is achieved through the synthesis of an extended aperture in that direction. Interferometric SAR (InSAR) is a technique which uses two SAR imaging flight paths to provide terrain measurements in the third — normal-to-slant range $\vec{n}$ — dimension. This ability can be interpreted as being due to the flight path pair synthesizing an aperture in the $\vec{n}$ direction. The synthesised aperture, however, contains only two nodes or sample points. This results in the beam-pattern, produced by the synthesised $\vec{n}$ aperture, being sinusoidal. As a result, InSAR provides only a measurement capability, rather than a resolving capability, in the $\vec{n}$ direction.

In this paper we propose and examine an extension of standard single-baseline InSAR which provides resolution in the $\vec{n}$ direction. The technique involves filling the 2-node aperture with additional flight paths — Figure 1. The $N > 2$ node synthesised aperture leads to a focussed beam-pattern and, consequently, resolution in the $\vec{n}$ direction — Figure 2. The use of $N > 2$ flight paths also leads to the ability of increasing the length B_n of the $\vec{n}$ aperture beyond B_{crit} — the critical value in single-baseline InSAR above which the two SAR images become decorrelated. The ability to generate high resolution 3-dimensional images is the result.

The paper is set out as follows. Section 2 provides a brief theoretical treatment of the multi-baseline InSAR technique — including achievable $\vec{n}$ resolution, improvements in ground range resolution and conditions to avoid aperture sampling imaging ambiguities. Section 3 presents a procedure for synthesising the $\vec{n}$ aperture and, subsequently, to generate 3-D imagery.

THEORY — MULTI-BASELINE INSAR

We begin by considering standard single-baseline InSAR. Consider two single look complex (SLC) SAR image data sets of the same terrain acquired from separate satellite passes. Assume the data sets are co-registered so that a point on the terrain corresponds to the same pixel coordinates (k,l) in both data sets. Let $\phi(k,l) = \phi_1(k,l) - \phi_2(k,l)$ be the corresponding phase difference image. Consider two nearby pixels (k,l), $(k+\delta k, l+\delta l)$ of the SLC-SAR data sets. For sufficiently small δ_k, δ_l, the change in phase difference between these two pixels: $\Delta\phi(k,l) = \phi(k,l) - \phi(k+\delta_k, l+\delta_l)$ is related to the change in terrain normal-to-slant-range $\Delta n(k,l) = n(k,l) - n(k+\delta k, l+\delta l)$ by [1]: $\Delta\phi(k,l) = 4\pi B_n \Delta n(k,l)/(s\lambda)$ where $s =$ slant range, $\lambda =$ radar wavelength and $B_n =$ component of baseline in direction $\vec{n}$.

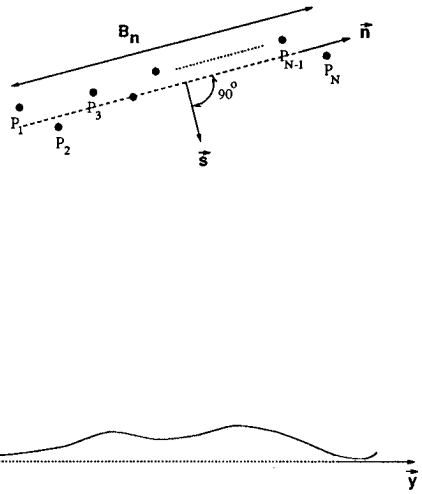


Figure 1: The proposed configuration for multi-baseline InSAR - $N > 2$ flight paths imaging the same terrain.

This capability of single-baseline InSAR to measure differences in the normal-to-slant range direction $\vec{n}$ can be extended to a resolving capability in $\vec{n}$ by using additional flight paths to synthesise an $N > 2$ node $\vec{n}$ aperture. The approximate $\vec{n}$ resolution element size is given by: $\rho_n = \frac{s\lambda}{2B_{n,N}}$, where $B_{n,N}$ is the length of the $\vec{n}$ synthesised aperture formed from the $N-1$ connected baselines.

In single-baseline InSAR the value of B_n must not exceed the following critical value:

$$B_n < B_{crit} \triangleq min_{k,l} \left| \frac{\lambda s(k,l) tan(\theta(k,l) - \vartheta(k,l))}{2\rho_s} \right| \quad (1)$$

where ρ_s = slant range resolution, θ = radar incident angle, ϑ = angular slope of the terrain above the horizontal. This condition is due to the two SAR images becoming essentially decorrelated [2], [3] and hence unsuitable for InSAR, when B_n exceeds B_{crit}. By using

0-7803-3068-4/96$5.00©1996 IEEE

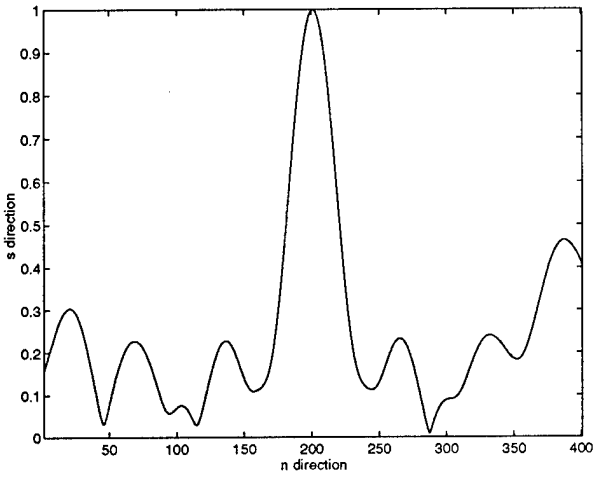


Figure 2: The beam-pattern in $s-n$ plane synthesised by the set of N flight paths.

$N-2$ additional flight paths, as illustrated in Figure 1, this condition is replaced by: $B_n^{(i)} < B_{crit}, i = 1,2,...,N-1$ where $B_n^{(i)}$ is the normal-baseline between adjacent paths P_i, P_{i+1}. Since $B_{n,N} = \sum_{i=1}^{N} B_n^{(i)}$ the aperture length $B_{n,N}$ in the proposed multi-baseline technique may significantly exceed B_{crit}. The result is fine resolution in the $\vec{n}$ direction and, consequently, high resolution 3-D imagery.

Ground-range resolution enhancement

The size of the ground-range resolution element $\rho_g = \rho_{g,s}$ in an individual (single-pass) SAR image is determined by the slant-range resolution $\rho_s = c/2W$, where W is the bandwidth of the chirp: $\rho_g = \rho_s cos\vartheta / sin(\theta - \vartheta)$. In a similar way, a finite normal-to-slant-range resolution element ρ_n leads to a finite ground-range resolution element $\rho_{g,n} = \rho_n cos\vartheta / cos(\theta - \vartheta)$. From the definition of B_{crit} it follows that synthesis of an $\vec{n}$ aperture of length $B_{n,N} > B_{crit}$ leads to $\rho_{g,n} < \rho_{g,s}$, and an improved ground-range resolution. In general, however, even better improvements in ground-range resolution are attainable. This is because the point spread function (psf) in the $\vec{s}-\vec{n}$ plane is sinc-like rather than box-like. The cross section of the former is an ellipse, the principle diameters of which are ρ_n, ρ_s. Accordingly, the ground-range resolution is given approximately by:

$$\frac{1}{\rho_g} = \sqrt{\left(\frac{1}{\rho_{g,s}}\right)^2 + \left(\frac{1}{\rho_{g,n}}\right)^2}. \qquad (2)$$

Thus the ground-range resolution element ρ_g is smaller than both $\rho_{g,n}$ and $\rho_{g,s}$.

Imaging ambiguities due to aperture sampling

The aperture synthesised in the $\vec{n}$ direction by the multi-baseline InSAR method is sampled, rather than continuous. As a result, the synthesised beam-pattern shows large grating-lobes, as indicated in the far right of Figure 2. Such grating lobes can lead to spatial aliasing or imaging ambiguities. The occurrence of these ambiguities depends on (i) the angular separation of the grating-lobes from the main-lobe and (ii) the slope of the terrain. The former depends on the sampling interval of the synthesised aperture. In the case of an aperture with a uniform sampling interval of δB, it can be shown that a sufficient condition for no grating lobe related ambiguities is:

$$2\delta B < (s\lambda) / \left[\frac{\rho_s}{tan(\theta - \vartheta)} + \rho_n\right] \qquad (3)$$

For the more general case of a nonuniformly sampled aperture, the associated beam pattern has a less regular shape, as indicated in Figure 2, and is more difficult to characterise. A rule of thumb for minimising imaging ambiguities is:

$$2\delta B_{max} < (s\lambda) / \left[\frac{\rho_s}{tan(\theta - \vartheta)} + \rho_n\right] \qquad (4)$$

where δB_{max} is the maximum sampling interval.

APERTURE SYNTHESIS FOR 3-D IMAGING

For simplicity we make the following assumption.

Assumption 1 (i) All N flight paths are described by straight lines, are parallel to the ground plane $z = 0$ and parallel with each other. (ii) All N SLC-SAR images are acquired with a zero squint angle $\varphi_i = 0$, $i = 1,2,...,N$.

We foreshadow here a more detailed treatment which allows for the invalidity of Assumption 1.

The $\vec{n}$ aperture synthesis approach we propose here is basically the same as that used in standard single-pass SAR to synthesise an aperture in the azimuth $\vec{a}$ direction. In short, a highly focussed beam in the $\vec{n}-\vec{s}$ plane aimed at a particular terrain target T_m, is generated by applying a particular set of phase rotations $\{\phi_{i,m}\}$, $i = 1,2,...,N$ to the set of SLC-SAR images $\{D_i\}$, $i = 1,2,...,N$. The required phase rotation for SAR image D_i is given by:

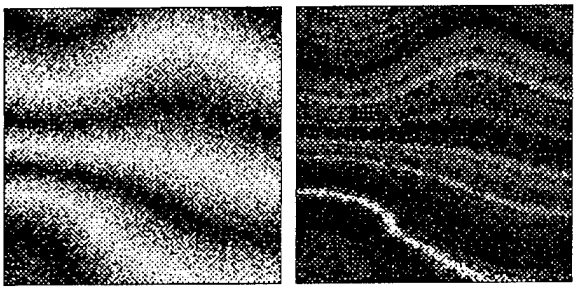
$$\phi_{i,m} = \frac{4\pi d_{i,m}}{\lambda} \qquad (5)$$

where $d_{i,m}$ is the distance in the $\vec{n}-\vec{s}$ plane (*i.e.* in the direction perpendicular to the flight path) between the corresponding flight path P_i and the terrain target T_m being imaged. In effect, the application of $\{\phi_{i,m}\}$ to $\{D_i\}$ leads to the reflected signals from T_m being in-phase while reflected signals from other terrain points being out-of-phase. Addition of the phase rotated images:

$$\bar{D}_m(k,l) = |\sum_{i=1}^{N} D_i(k,l) exp(j\phi_{i,m})|$$

leads to focussing of T_m and provides an estimation of the backscattering strength of T_m. The generation of a 3-D image involves constructing a grid of points m, which covers the terrain region being imaged. Appropriate phase rotations are then applied to focus and obtain the backscattering strength of each grid point. Since, in general, a band of terrain points have the same normal-to-slant-range n indice, the summed image, in general, shows a focussed band or fringe - see Figure 3(b).

In this light, the summed image $\bar{D}_m(k,l)$ can also be interpreted as a multi-baseline interferogram which has been generated by phase aligning and summing the $N-1$ interferograms obtained from the $N-1$ connected baselines $B_n^{(i)}$. In particular, $\bar{D}_m(k,l)$ shows a focussed fringe along the terrain band corresponding to the particular n indice being focussed. This is illustrated in Figure 3. Figure 3(a) is a simulated single-baseline interferogram and Figure 3(b) a simulated multi-baseline interferogram corresponding to the same 'hilly' terrain topography. The values of the imaging parameters such as radar wavelength, satellite height etc used in the simulations are based on those of ERS-1. The signal(phase) to noise ratio $SNR = 7dB$. The single-baseline of Figure 3(a) is $B_n = 400m$ while the multi-baseline had an overall length of $B_n = 4080m$ and consisted of 10 connected baselines each chosen from a random distribution with a mean of $400m$. Note that the narrow focussed fringe of the multi-baseline interferogram clearly shows the presence of a 'dip' running up the side of a 'hill' of the terrain, while this 'dip' is essentially lost in the noise and broad fringe pattern of the single-baseline interferogram.



(a) (b)

Figure 3: (a) Single-baseline interferogram $B_n = 400m$, (b) multi-baseline interferogram $B_n = 4080$ corresponding to the same terrain topography.

Flight Path Parameter Determination

As indicated by (5), aperture synthesis in the $\vec{n}$ direction requires accurate knowledge of each of the flight path vectors $\vec{P}_i$. Under the validity of Assumption 1, two parameters are required for each flight path: the elevation or z co-ordinate $P_{i,z}$ and cross track or y co-ordinate $P_{i,y}$. We briefly discuss here two approaches for determining these $2N$ path parameters.

Change in Phase Difference Method: Under the ideal conditions of zero noise, the change in phase difference:

$$\Delta_{m,n}\phi_{1,2} = \phi_2(T_n) - \phi_1(T_n) - (\phi_2(T_m) - \phi_1(T_m))$$

within a single-baseline interferogram between two targets T_m, T_n is related to the four parameters $P_{i,z}, P_{i,y}$, $i = 1,2$ of the two flight paths as well as the two target positions. In particular, M targets lead to $M-1$ equations, each relating the four flight path parameters to a measured change in phase difference. It follows that $M \geq 5$ targets of known position are required to determine the parameters of two flight paths. For the more general case of N flight paths, parameter determination requires $M \geq 3 + 2/(N-1)$ targets of known position. If the target positions are not known, flight path parameter determination requires the following condition to be met: $(M-1)(N-1) \geq 2(M+N)$. A meaningful solution to this inequality exists only four $N \geq 4$ flight paths.

In the presence of noise the set of phase difference equations, in general, can not be solved uniquely. Instead an estimate of the flight path parameters can be obtained through minimization of a non-negative cost function, such as the squared error function V_M:

$$V_M = \sum_{i=1}^{N-1}\sum_{m=1}^{M-1}[\Delta_{m,m+1}\phi_{i,i+1} - \hat{\Delta}_{m,m+1}\phi_{i,i+1}]^2 \geq 0$$

where $\Delta_{m,m+1}\phi_{i,i+1}$ is the measured change in phase difference and $\hat{\Delta}_{m,m+1}\phi_{i,i+1}$ is the change in phase difference which corresponds to a particular set of values for the unknown parameters. In practice, minimisation of the cost function is achieved through an iterative process.

Sharpness Method: This method is based on determining the flight paths' parameters which maximise the 'sharpness' of the focussed fringe. In more detail, focussing of the multi-baseline aperture beampattern on a particular terrain target T_m requires application of appropriate phase rotations to the set of N SAR images. Any errors in the applied phase rotations, resulting from errors in the flight path parameters, lead to a reduction in the focussing quality of the beampattern or sharpness of the associated fringe. It follows that an estimate of the set of flight path parameters may be obtained through maximisation of the fringe sharpness S_m. Sharpness may be measured by a number of functions [4]. Results to date indicate that for our purposes — estimation of flight path parameters — the following two measures perform well:

$$S^{(1)}_{nj,al} = \sum_{sk}[\Delta A_{nj}(sk,al)]^2$$

$$S^{(2)}_{nj,al} = \sum_{sk}[\Delta A_{nj}(sk,al) - \Delta A_{nj}(sk-1,al)]^2$$

where $\Delta A_{nj}(sk,al) = A_{nj}(sk+1,al) - A_{nj}(sk,al)$ and $A_{nj}(sk,al)$ = amplitude at $(s,a) = (sk,al)$ of the multi-baseline interferogram generated for the normal-to-slant-range indice $n = nj$. To reduce the effect of noise we average the values for a given function $S_{nj,al}$ over azimuth indices al and/or normal-to-slant-range indices nj.

REFERENCES

[1] C. Prati, F. Rocca, "Limits to the resolution of elevation maps from stereo SAR images", *Int. J. Remote Sensing*, Vol. 11, No. 12, 1990, pp 2215-2235.

[2] H.A. Zebker, J. Villasenor, "Decorrelation in Interferometric Radar Echoes", *IEEE Trans. Geosci. Remote Sensing*, Vol. 30, No. 5, Sept. 1992, pp 950-959.

[3] A. Gabriel, R.M. Goldstein, "Crossed orbit interferometry: theory and experimental results from SIR-B", *Int. J. Remote Sensing*, Vol. 9, No. 5, 1988, pp 857-872.

[4] M. Goris, *Towed-Array Calibration*, PhD dissertation, The Australian National University, Canberra, Dec. 1995.

Registration of SAR images using the chirp scaling algorithm

David Fernandes[1,2], Günter Waller[1], João Roberto Moreira[1]

[1]German Aerospace Research Establishment (DLR)
Institute for Radio Frequency Technology (HF)
D-82230 Wessling Germany, tel. +49 8103 282320, FAX: +49 8103 281449
fernandes@ohf015.hf.op.dlr.de joao.moreira@dlr.de

[2]Centro Técnico Aeroespacial (CTA)
Instituto Tecnológico de Aeronáutica (ITA)
12228-900 São José dos Campos SP Brasil

Abstract – This paper provides a procedure to process and register simultaneously SAR data from spaceborne sensors. The procedure is based on the Extended Chirp Scaling Algorithm described in correlated papers. The performance of the developed processor has been tested with simulated and real SAR data.

INTRODUCTION

Registration of SAR images is an important part of activities which require correlation of temporal, frequencial, polarimetric, or spatial information.

It has been shown that registration simultaneous with image processing will result in processing time reduction and increased image quality, [1].

This paper describes a procedure which allows simultaneous processing and registration of SAR data from spaceborne sensors. The basic algorithm used is the Extended Chirp Scaling Algorithm, [2], [3], [4].

The functional and interferometric performance of the developed processor has been approved with simulated data and real ERS-1 SAR data.

AZIMUTH REGISTRATION

We assumed two SAR sensors S_i, $i = 1, 2$, circling the Earth in parallel orbits with the equal flight velocity V. The genereted scenes I_i are formated by the signals $x_i(.,.)$ backscattered from the targets on ground. The pulse repetition periods of the signals transmited by S_1 and S_2 are, respectively, T_{r1} and T_{r2}.

The pulse echoes backscattered from a certain point target on ground at slant range r_i and azimuth time $t = t_o$ are $x_i(\tau, t; r_i, t_o)$. Herein τ is the range time, t the azimuth time, and $t = 0$ the scene center time in azimuth.

By that, the time-varing slant range equals, [2]:

$R(t; r_i, t_o) = \sqrt{r_i^2 + V^2(t - t_o)^2}$, or approximately

$\rho(t; r_i, t_o) = r_i + V^2\,(t - t_o)^2\,/\,(2\,r_i)$.

Now, we suppose that sensor S_1 is the reference sensor and that the scenes center pixels with $x_1(\tau, t = 0; r_1, t_o)$ and $x_2(\tau, t = 0; r_2, t_o)$ are registrated. With

$$K_a = 2\,V^2\,/\,(\lambda\,r_2) \tag{1}$$

$$F_a = T_{r1}/T_{r2}, \tag{2}$$

and the wavelength λ, we define the linearly frequency modulated (LFM) azimuthal signal

$x_a(\tau, t; r_2) = \exp\{-j\,\pi\,(F_a - 1)\,K_a\,t^2\}$.

Subsequently, $x_a(\tau, t; r_2)$ is applied to scale the signal $x_2(\tau, t; r_2, t_o)$ given by [2]:

$$\begin{aligned} y_2(\tau, t; r_2, t_o) &= x_2(\tau, t; r_2, t_o)\; x_a(\tau, t; r_2) \qquad (3)\\ &= a(t)\, s_o\,(\tau - 2\,R(t; r_2, t_o)\,/\,c_o) \\ &\quad \times \exp\left\{-j\,\pi\,K_r\,(\tau - 2\,R(t; r_2, t_o)\,/\,c_o)^2\right\} \\ &\quad \times \exp\left\{-j\,\pi\,K_a\,(F_a - 1)\,t_o^2/\,F_a\right\} \\ &\quad \times \exp\left\{-j\,4\,\pi\,R_c(t; r_2, t_o)\,/\,\lambda\right\} \qquad (4) \end{aligned}$$

with,

$$R_c(t; r_2, t_o) = \sqrt{r_2^2 + F_a\,V^2(t - t_o/F_a)^2} \tag{5}$$

In (4) $s_o(.)$ describes the LFM transmit pulse with FM rate K_r and $a(.)$ the azimuthal antenna function.

Equation (4) has some notable features:

(i) Though the terms $\rho(t; r_2, t_o)$ and the aproximation

$\rho_c(t; r_2, t_o) = r_2 + F_a\,V^2\,(t - t_o/F_a)^2\,/\,(2\,r_2)$

of $R_c(t; r_2, t_o)$ were used for derivation of $y_2(\tau, t; r_2, t_o)$ they don't appear in (4).

(ii) For $T_{r1} = T_{r2}$ the equation (4) reduces to

$y_2(\tau, t; r_2, t_o) = x_2(\tau, t; r_2, t_o)$.

(iii) The phase term

$\pi\,K_a\,(F_a - 1)\,t_o^2/F_a$

describes the scaling deviation to be corrected.

(iv) The azimuth resolution to pixel spacing ratio of the reference signal $x_1(\tau, t; r_1, t_o)$ is given by

$l_1 = 1\,/\,(T_a\,K_a\,T_{r1})$,

where T_a is the illumination time. The corresponding ratio for the scaled signal $y_2(\tau, t; r_2, t_o)$ equals

$l_2 = 1\,/\,(T_a\,K_a\,F_a\,T_{r2})$.

With F_a given by (2) we get the desired result $l_2 = l_1$. Consequently, additional to the registration of the central pixels defined by $x_1(\tau, t = 0; r_1, t_o)$ and $x_2(\tau, t =$

0-7803-3068-4/96$5.00©1996 IEEE

$0; r_2, t_o)$, the other pixels described by, $y_2(\tau, t; r_2, t_o)$ and $x_1(\tau, t; r_1, t_o)$ are registrated.

RANGE REGISTRATION

For sensors S_i $i = 1, 2$ shown in Fig. 1, we assume inicial range delay T_i, sample time period T_{si}, and echo signal:

$\{x_i(\tau_{i,m})\}$ with: $\tau_{i,m} = mT_{si} + T_i$, $m = 0, 1, .. M-1$.

The sample $x_i(\tau_{i,m})$ represents the backscatter from the resolution cell $RC_i(m)$ with center P_i locate at a slant range:

$$r_i(\tau_{i,m}) = c_o\,(mT_{si} + T_i)\,/\,2 \quad c_o : \text{light speed} \qquad (6)$$

The horizontal separation between $RC_1(m)$ and $RC_2(n)$ with m and $n = 0, 1, .. M-1$ is given by

$HS(\tau_{1,m}, \tau_{2,n}) = d_{1,m} - B\cos\alpha - d_{2,n}$, where

B is the baseline, α is the baseline slope angle, and

$$d_{1,m} = r_1(\tau_{1,m})\cos\theta_{1,m} \qquad (7)$$

$$d_{2,n} = r_2(\tau_{2,n})\cos\theta_{2,n} \qquad (8)$$

$\theta_{1,m}$ and $\theta_{2,n}$ are the grazing angles and $d_{1,m}$ and $d_{2,n}$ are the horizontal projections of $r_1(\tau_{1,m})$ and $r_2(\tau_{2,n})$, respectively.

Note that, for $HS(\tau_{1,m}, \tau_{2,n}) = 0$ the samples $x_1(\tau_{1,m})$ and $x_2(\tau_{2,n})$ are registrated.

We supposed that $\tau_{1,m}$ is the reference time for the registration and that the scenes center pixels $x_1(\tau_{1,M/2})$ and $x_2(\tau_{2,M/2})$ are registrated, $HS(\tau_{1,M/2}, \tau_{2,M/2}) = 0$.

We consider the samples set $\{x_2(\nu_{2,m})\}$ of S_2, with $\nu_{2,m} \in \Re$, where $\Re$ is the set of real number and $m = 0, 1, .. M-1$, so that:

$HS(t_{1,m}, \nu_{2,m}) = 0.$

Therefore, $\nu_{2,M/2} = \tau_{2,M/2}$ and, taking into account (6), (7) and (8):

$$\nu_{2,m} = 2\,\delta_{2,m}\,/\,(c_o\cos\phi_{2,m}) \qquad (9)$$

$$\delta_{2,m} = -B\cos\alpha + c_o\,(mT_{s1} + T_1)\cos\theta_{1,m}\,/\,2 \qquad (10)$$

where $\phi_{2,m}$ is the grazing angle of the slant range $r_2(\nu_{2,m})$ related to $x_2(\nu_{2,m})$, and $\delta_{2,m}$ is the horizontal projection of $r_2(\nu_{2,m})$.

Equation (9) gives the required radial delay to be performed the registration of the samples $x_1(\tau_{1,m})$ and $x_2(\nu_{2,m})$ by the Chirp Scaling Algorithm.

The time between samples $x_2(\nu_{m+n})$ and $x_2(\nu_m)$ is:

$\Delta_{\nu 2}(n; m) = 2\,(\delta_{2,m+n}/\cos\phi_{2,m+n} - \delta_{2,m}/\cos\phi_{2,m})/c_o$

Note that:

(i) $\Delta_{\nu 2}(n = 1; m)$ is the new sample rate of the registrated samples $x_2(\nu_{2,m})$.

(ii) $\cos\phi_{2,m}$ and $\cos\theta_{1,m}$ in (9) and (10) may be estimated by the baseline B, the slope angle α, the altitude h_1, the altitude h_2, and the slant range $r_1(\tau_{1,m})$ given by (6).

(iii) For $\theta_{1,m}$ and $\phi_{2,m}$ constantes and equal to the grazing angles in the scene center $\theta_{1,M/2}$ and $\phi_{2,M/2}$, respectively, $\Delta_{\nu 2}(n = 1; m)$ is independent of m and has the form

$$\Delta_{\nu 2} = T_{s1}\cos\theta_{1,M/2}\,/\,\cos\phi_{2,M/2} \qquad (11)$$

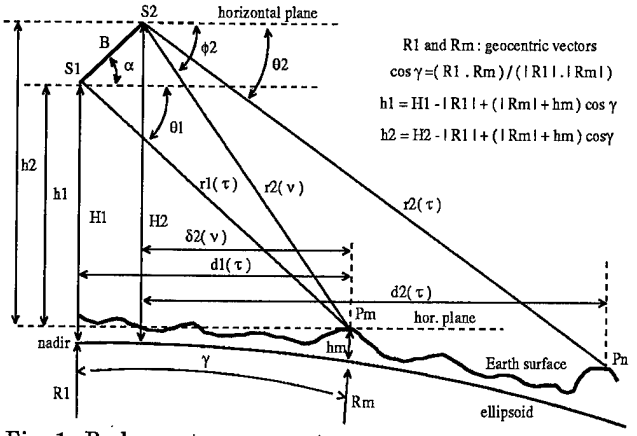


Fig. 1. Radar systems geometry

CHIRP SCALING PROCESSOR

The Chirp Scaling Processor, [2], with the extended approach, [3], [4], is shown in the Fig. 2.

For simplicity we suppose $T_{s1} \le T_{s2}$ and $T_{r2} \le T_{r1}$.

In Fig. 2, for $F_a = 1$, C_s is the curvature factor, A_s is the range distortion factor, K_{sm} is the effective FM rate in range and τ_{ref} is the time locus of the reference range in the range signal/Doppler domain given by [2]. For $K = T_{s2}/\Delta_{\nu 2} = 1$ we have $C_{sm} = C_s$.

For the raw data $x_1(\tau, t)$ of the radar system S_1, F_a and K must be set equal to 1.

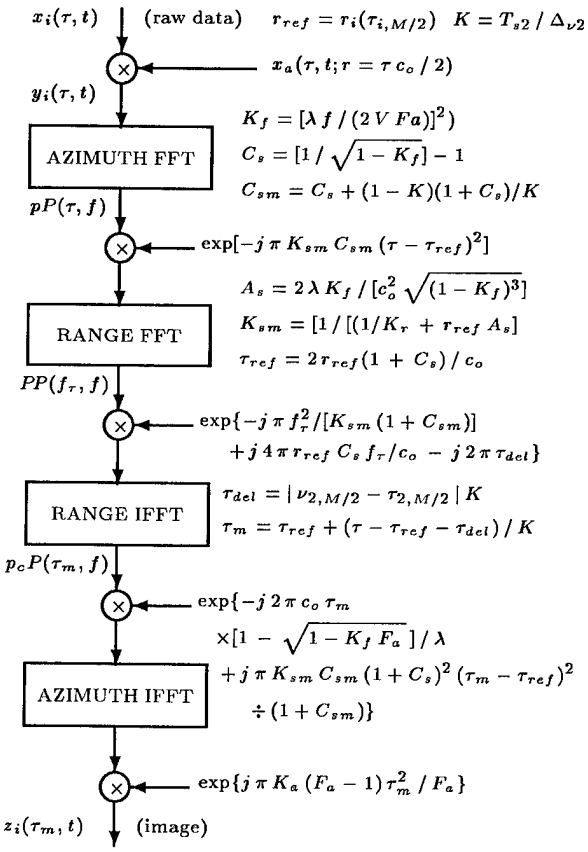


Fig. 2. Chirp Scaling Processor

RESULTS

The raw data of four point targets were simulated with the parameters:
(i) $T_{s1} = 52.72ns$ (pixel spacing in range: 7.91m), $1/T_{r1} = 1634.55Hz$ (pixel spacing in azimuth: 4.34m), $h_1 = 800.0km$,
(ii) $T_{s2} = 66.07ns$ (pixel spacing in range: 9.91m), $1/T_{r2} = 1934.55Hz$ (pixel spacing in azimuth: 3.67m), $h_2 = 800.2km$,
(iii) $B = 538.52m$, $\alpha = 21.80^o$ and
(iv) radial and azimuthal resolution: 15.0m .

The Fig. 3 shows the point target responses of four point targets before and Fig. 4 after registration.

Fig. 5 emphasizes the capability of the processor for interferometric SAR processing. The scene shows the phase interferogram after Flat Earth removal of an area (35Km in range, 32km in azimuth) near Cairo imaged by ERS-1.

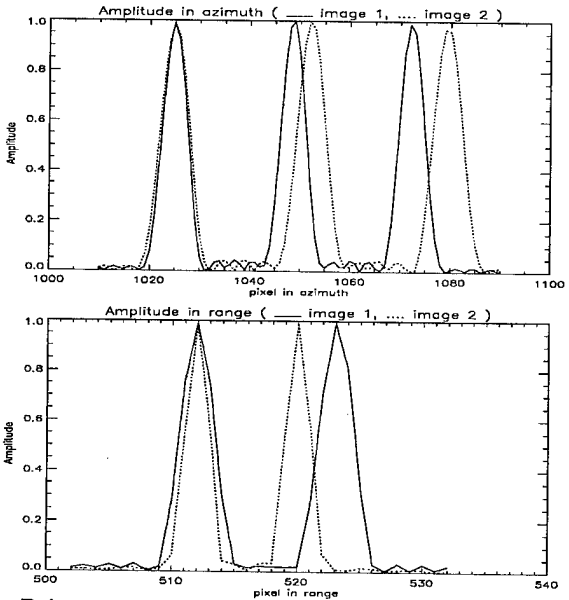


Fig. 3. Point targets without registration

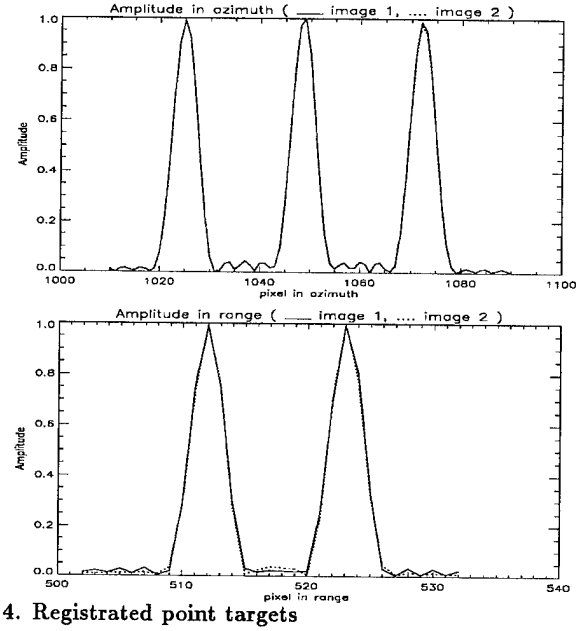
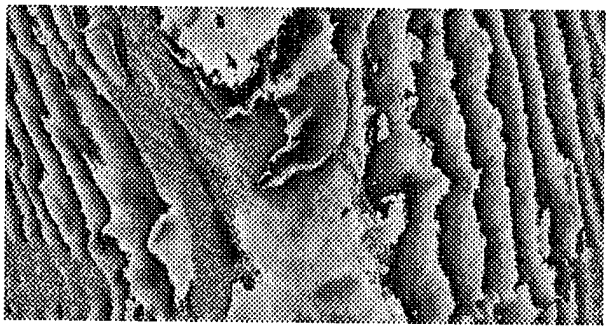


Fig. 4. Registrated point targets



↑ *azimuth* → *range*

Fig. 5. Phase interferogram after Flat Earth removal

CONCLUSIONS

A processor has been developed which tightly combine both, SAR processing and image registration. Compared to conventional methods this integrated processing reduces computer time and preserves image quality. Besides that, all the advantages of the Extendet Chirp Scaling Algorithm are kept.

The performance of the processor has been approved by the registration of simulated point targets and the interferometric processing of real ERS-1 raw data.

ACKNOWLEDGMENTS

DLR International Cooperation Office, Fundacão de Amparo à Pesquisa do Estado de São Paulo (FAPESP Proj. Eng. Elet. 95/1484-1), and DARA-ESA (Proj. RAPID : A02.D114).

REFERENCES

[1] G. Fornaro, G. Franceschetti and E. S. Marzouk, "A new approach for image registration in interferometric processing", Proc. IGARSS'94, pp. 1983-1985, 1994

[2] R. K. Raney, H. Runge, R. Bamler, I. G. Cumming and F. H. Wong, "Precision SAR processing using chirp scaling", IEEE Trans. Geosci. Remote Sensing, vol.32, pp.786-799, July 1994.

[3] A. Moreira, J. Mittermayer and R. Scheiber, "Extended chirp scaling algorithm for air- and spaceborne SAR data processing in stripmap and scansar imaging modes", paper submitted to IEEE Trans. Geosci. Remote Sensing.

[4] A. Moreira, J. Mittermayer and R. Scheiber, "Azimuth and range scaling for SAR and ScanSAR processing", Proc. IGARSS'96, 1996.

Quality Assessment of InSAR–derived DEMs generated with ERS Tandem Data

M. Schwäbisch, M. Matschke, W. Knöpfle, A. Roth

German Aerospace Research Establishment (DLR)
German Remote Sensing Data Center (DFD)
D–82230 Oberpfaffenhofen, Germany
Tel.: ++49–8153–28–1379
Fax: ++49–8153–281445
email: schwaeb@dfd.dlr.de

Abstract — This paper provides a quality assessment of digital elevation models generated by means of SAR interferometry and the use of ERS tandem data. A total of 8 scene pairs have been investigated, acquired at different dates but covering the same site to allow a study of the different parameters such as temporal decorrelation, baseline, and varying incidence angles. The ERS tandem configuration implies some characteristics that are examined, concerning in particular the system parameters. Moreover, peculiarities detected during the interferometric processing are reported. The achieved results are compared to an existing reference DEM. Additionally, the InSAR–derived DEMs are compared to each other to study SAR–specific effects.

Keywords: SAR, interferometry, digital elevation models

INTRODUCTION

With the launch of ERS–2 a new interferometric sensor configuration was established which was expected to improve the quality of InSAR–derived DEMs generated with spaceborne SAR data. In particular, the reduction of the orbit repeat period to only one day in combination with the well–known ERS features like orbit stability or quality of SAR instrumentation and processing should lead to a substantial decrease of the coherence problem, which up to now has considerably marked the limitations of DEM generation.

In this paper we present results obtained with ERS Tandem data sets acquired at three different dates in October 1995 and covering a part of the upper Rhine valley and its surrounding hills of the 'Black Forest'. Emphasis was laid on a quality assessment of the DEMs, including a study of the tandem characteristics. First, some features of the interferometric processing are analyzed, followed by a presentation of the achieved results. At the end a summary and conclusions are given.

INTERFEROMETRIC PROCESSING

The interferometric data processing revealed some noteworthy characteristics which are outlined in the following.

ERS system parameters

In several tandem data pairs the PRF value differs slightly between ERS–1 and ERS–2. The difference is about 1 pixel along the azimuth extension of a quater scene. It has to be compensated in the resampling step of the image fine registration.

In addition to that the azimuth and range time parameters are occasionally found to contain a certain offset, leading to a shift of the image with respect to ground. Using the common geolocation procedure [1], this shift was measured to reach up to 20 pixel in range and 15 pixel in azimuth. In order to guarantee a precise geopositioning of the interferometric products the time parameters must be corrected by the use of tie points.

Phase Unwrapping

The phase unwrapping was performed using the least squares methods described in [2]. The static (unweighted) method led to disappointing results due to its strange behaviour at the residues locations. In addition to the local $-\pi \rightarrow \pi$ leaps global phase ramps have been detected that are not present in the wrapped phase image. Fig. 2 depicts the phase difference between the original interferogram (Fig. 1) and the (rewrapped) absolute phase pattern in the static case. About 3 fringe lines are introduced between the lower left and upper right part of the image, corresponding to a height difference of 240 m. Due to its non–linear behaviour it is practically impossible to compensate the residual phase pattern after phase unwrapping, using e.g. tie points.

Application of the weighted least squares method led to much better results (Fig. 3). A 4×4 box around each residue was weighted by 0 to eliminate their disturbing impact. After each iteration step the residues had to be recalculated since new residues can occur at locations where the residue condition was slightly missed in the preceding step. However, even the weighted method cannot reconstruct the absolute phase pattern precisely due to its slope–underestimating nature in the presence of phase noise [3]. Furthermore, terrain information corrupted by severe phase disturbances naturally cannot be recovered if entire fringe lines had got lost, as can be seen in Fig. 3 in the right part of the image.

0-7803-3068-4/96$5.00©1996 IEEE

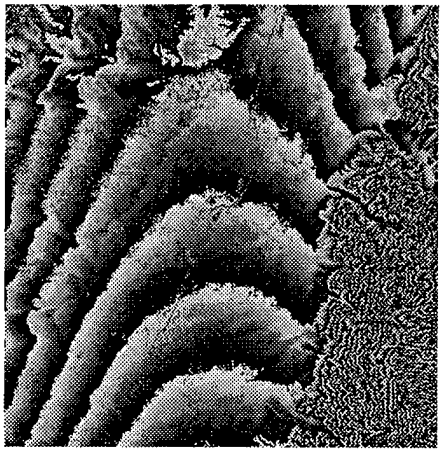


Fig. 1: Interferogram of the upper Rhine valley near the city of Strasbourg, including a part of the Black Forest

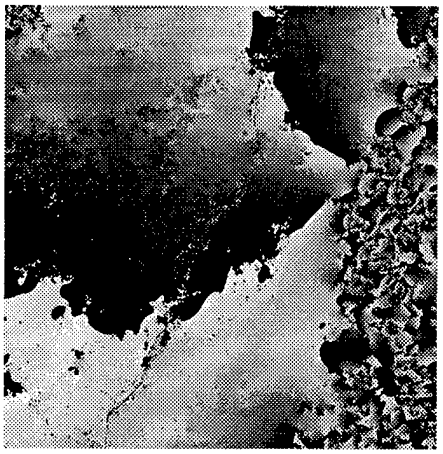


Fig. 2: Phase difference between original interferogram and rewrapped absolute phase image (unweighted least squares method)



Fig. 3: Phase difference between original interferogram and rewrapped absolute phase image (weighted least squares method)

Orbit optimization

Although ERS orbit data reach accuracies in the order of 30 cm the highly sensitive interferometer configuration needs much more precise baseline information in the mm order to allow an accurate phase–to–height conversion. An orbit optimization procedure was applied to compensate for baseline errors as well as for errors introduced in the interferometric processing steps. It is based on a minimization algorithm which is fed with tie points and calculates the residual height differences. The constant and linear terms of the orbit polynomials are iteratively corrected until a minimum of the residual heights is detected. It has to be noted that the tie points must be selected in areas which are not affected by phase unwrapping errors, as depicted in Fig. 3.

Geocoding

The terrain height map was transformed into map coordinates to allow an easy comparison with an existing reference DEM which was originally generated by digitizing the height contour lines of a topographic map. The geocoding algorithm is described in [4][5]. A new inverse method which is expected to reduce the computing time efficiently is currently under investigation.

RESULTS

A total of 8 tandem quater scenes were processed in the aforementioned area, acquired at three different dates in October 1995. Although the acquisition time and weather conditions were quite promising concerning the expected temporal decorrelation, all of the data sets show extended areas of low coherence especially in the forested regions. Fig. 4 gives an impression of one of the favorable coherence results, where the values are close to 1 in the agricultural and urban areas and go down to 0.2 in the forested regions. In Fig. 5 the corresponding DEM is displayed.

As an example, Table I reports the measured results for two almost completely overlapping quater scene pairs. Besides the differences in baseline and average coherence the data pairs are characterized by an incidence angle difference of about 3°. The height differences with respect to the reference DEM are in the order of 10 m (std. dev.) for flat terrain. Unfortunately, the most part of the hilly areas is covered by coniferous forests and is therefore characterized by low coherence, causing the height differences to increase significantly (Fig. 6).

Table I: Results of the comparison of two tandem data pairs with a reference DEM

InSAR–DEM			difference to reference DEM		difference to InSAR–DEM of 22./23. Oct. 95
date	baseline	average coherence	flat terrain	hilly terrain	highly coherent hilly area
3./4. Oct. 95	340 m	0.53	2.3 m mean	–105 m mean	–4.1 m mean
			6.6 m std. dev.	85 m std. dev.	4.2 m std. dev.
22./23. Oct. 95	104 m	0.63	–7.1 m mean	30 m mean	–
			10.8 m std. dev.	66 m std. dev.	–

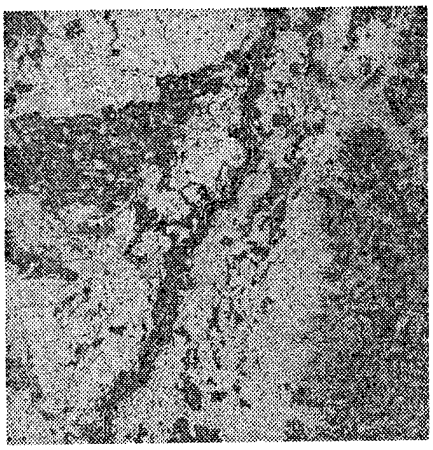


Fig. 4: Coherence map of the upper Rhine valley (see Fig. 1); The low coherent areas mark the forested regions

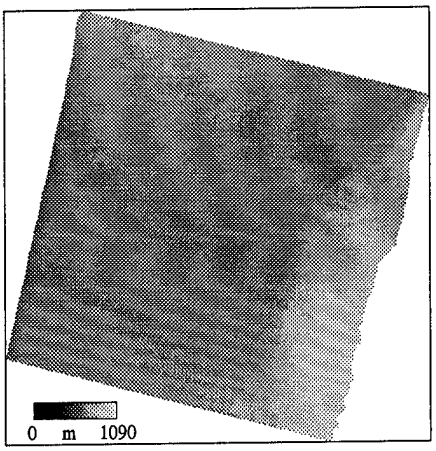


Fig. 5: InSAR–derived DEM of the data pair 22./23. Oct. 95 (see Figs. 1 and 4)

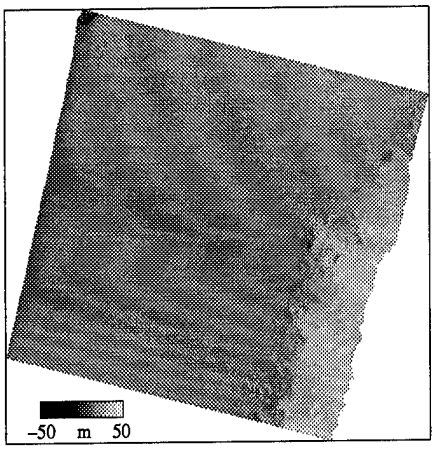


Fig. 6: Height differences between InSAR–DEM (Fig. 5) and reference DEM; The values increase significantly in the hilly areas (lower right part)

A comparison of the two overlapping InSAR–DEMs in a highly coherent hilly part shows a good coincidence. No significant deviations that might be caused by the incidence angle difference can be observed (see also Table I).

SUMMARY AND CONCLUSIONS

We have investigated several data pairs of the ERS tandem mission to assess the potential of this interferometer configuration regarding the derivation of digital elevation models. The data were acquired at three different dates, two of them characterized by dry and stable weather conditions. They cover an area with different types of vegetation and terrain slopes, partly overlapping to ensure an observation of the same ground element under slightly varying incidence angles.

Despite the considerably good preconditions the quality of the derived DEMs proves to be quite disappointing. The achieved height accuracy suffers from the extensive temporal decorrelation that occurs in the vegetated areas, namely the forested regions, a fact that is well–known from ERS–1 interferometric investigations. The decrease of the orbit repeat period to one day turns up to be no significant advantage compared to the 3–day cycle of ERS–1.

We conclude that the ERS tandem interferometer is not the awaited instrument to overcome the problem of temporal decorrelation in order to allow DEM generation on a large scale basis. Nevertheless, its great advantage lies in the global data coverage that was not yet achieved by ERS–1 (3–day cycle) or SIR–C/X–SAR. Up to now no spaceborne SAR sensor can exhaust the entire potential of the interferometric principle.

REFERENCES

[1] A. Roth, A. Craubner, T. Hügel, "Standard Geocoded Ellipsoid Corrected Images," in: G. Schreier (Ed.), SAR Geocoding: Data and Systems, Wichmann, Karlsruhe, pp. 159–185, 1993

[2] D. C. Ghiglia and L. A. Romero, "Robust Two–Dimensional Weighted and Unweighted Phase Unwrapping that Uses Fast Transforms and Iterative Methods," J. Opt. Soc. Am., Vol. A 11, pp. 107–117, 1994

[3] R. Bamler, N. Adam, G. W. Davidson, D. Just, "Noise–induced Slope Distortion in 2–D Phase Unwrapping by Linear Estimators with Application to SAR Interferometry," submitted to IEEE Trans. Geosc. Rem. Sens., 1996

[4] M. Schwäbisch, "Die SAR–Interferometrie zur Erzeugung digitaler Geländemodelle," DLR Technical Report 95–25, 1995 (in german)

[5] R. Lanari, G. Fornaro, D. Riccio, M. Migliaccio, K. Papathanassiou, J. Moreira, M. Schwäbisch, L. Dutra, G. Puglisi, G. Franceschetti, M. Coltelli, "Generation of Digital Elevation Models using SIR–C/X–SAR Multifrequency Two–Pass Interferometry: the Etna Case Study," to be published in IEEE Trans. Geosc. Rem. Sens.

SURFACE WINDS IN A MIDLATITUDE STORM SEEN BY SATELLITES AND NUMERICAL MODELS

Kristina B. Katsaros[1,2], Suzanne Dickinson[1,2], Abderrahim Bentamy[1], Yves Quilfen[1], Serhad S. Atakturk[2], Robert A. Brown[2]

1) Département d'Océanographie Spatiale, Intitut Francais de Recherche pour l'Exploitatation de la Mer, 29280 Plouzané, France

2) Department of Atmospheric Sciences, 351640
University of Washington, Seattle, Washington 98198-1640, USA

1. INTRODUCTION

Sea surface winds are observed from polar orbiting satellites by active and passive microwave instruments. The scatterometer on the European Remote Sensing Satellite-1 (ERS-1) has been operating since 1991 providing vector winds at 50 km resolution over a 500 km wide swath, and ERS-2, a twin, was launched in 1995. The Special Sensor Microwave Imager, SSM/I, (on several Defense Meteorological Program satellites since 1987) provides wind speed in non-raining areas over a 1400 km swath. Several altimeters such as those on the ERS satellites and TOPEX-Poseidon (since 1992) sample a 10 km wide path at nadir providing wind speed over the footprint. All these data can be used singly, in conjunction or after assimilation into numerical models to form gridded wind fields that may represent the surface wind over periods ranging from the instantaneous swath view to hours, days, weeks or months. These wind fields are used to drive surface wave models, ocean circulation models or to calculate climatological means of turbulent fluxes of momentum, the wind divergence or curl. In this paper we examine how the sampling and the method to form the wind field influences the resulting means of certain wind parameters during the passage of a midlatitude cyclone in the North Pacific Ocean. The main objective is to understand the possible adverse effects of limited sampling of the storm systems moving across the sea.

2. METHODS AND PROCEDURES

We examine the following wind parameters that enter into different oceanographic or meteorological studies:

the average wind speed (modulus), $U_{AVE,\,MOD}$:

$$U_{AVE,MOD} = \frac{1}{N}\sum\sqrt{u^2+v^2} \qquad (1)$$

the modulus of the averaged zonal and meridional wind components, $U_{MOD,AVE}$:

$$U_{MOD,\,AVE} = \sqrt{(\frac{1}{N}\sum u)^2 + (\frac{1}{N}\sum v)^2}$$

the wind stress vector, τ_{AVE} :

$$\tau_{AVE} = \frac{1}{N}\Sigma\,(\rho C_D U_{MOD}\,\vec{U}) \qquad (3)$$

the kinetic energy transferred to the sea, K.E. :

$$K.E. = \frac{1}{N}\Sigma\,(u^2+v^2) \qquad (4)$$

where u and v are horizontal and vertical wind components, respectively, ρ is the air density, C_D the drag coefficient (a function of U_{MOD}). $\vec{U}$ and U_{MOD} are the instantaneous wind vector and modulus respectively, Σ implies a sum over N individual points.

To examine the effects of sampling and averaging procedures we need to have a wind field that we can consider the truth, so that it can be used as a control in evaluating the other procedures. Such a gridded wind field has been constructed from all available information and evaluated at 20 minute intervals. There are no continuous measurements at enough points on the ocean to ever have such a wind field from direct *in situ* observations. The constructed wind field we take as *representative* of the true surface wind employs data from the ERS-1 scatterometer and SSM/I radiometers assimilated into either :

a) the global numerical weather prediction model of the European Centre for Medium Range Weather Forecasts (ECMWF) at the hour nearest to overpass time, or

b) a surface wind field produced with the University of Washington (UW) planetary boundary layer model, which

0-7803-3068-4/96$5.00©1996 IEEE

first calculates the geostrophic surface wind employing the ECMWF surface pressure data (Dickinson and Brown, 1996). An interpolation scheme to obtain the model field at the overpass time takes into account both the translation and evolution of the weather system. 19 satellite swaths passed over the domain during the three and a half day period of study (83 hours). The data were assimilated into the model fields whenever and wherever there was satellite data obtained in the domain. The data was given twice the weight of the model wind values and they were simply averaged together with some smoothing. The fields were then interpolated to 20 min intervals using information on the translation and evolution of the storm. Intersections between isobars and isotherms on the surface chart were used as tracers of the storm, and a fit over the domain of the translation and rotation of these points was obtained to use in the interpolations (Dickinson and Brown, 1996). Average wind fields based only on ECMWF surface wind, the University of Washington model winds, or on the 19 swaths of satellite wind estimates for the domain of the cyclone are also obtained to compare with the control field. For the satellite winds alone the kriging method for merging data has been used (Bentamy et al, 1995).

The Storm : The midlatitude cyclone studied here is a rather typical winter storm with a minimum central pressure of 985 hPa on day one of our study period and 977 hPa as it crosses the American coastline 3 ½ days later. It translates across the ocean at an average speed of 38 km/hr along the track illustrated by circles on the figures in the results section. (See further Dickinson and Brown, 1996.).

Sampling and averaging : We examine the wind field on a 0.5 latitude degree resolution in the domain influenced by the storm. Averages over the life of the storm, are calculated from different sampling schemes including the most complete possible, that is every 20 min, which we call the control, 6 hourly, 12 hourly and 24 hourly. The control represents an average of 250 wind estimates, while the 24 hour samples represent 4 estimates. The 24 hour samples can be started at 21, 00 or 03 UTC.
In truth the 20 min samples are, of course not completely independent, since the ECMWF data that forms the background is available at 6 hourly intervals, and the satellite samples are obtained on the average every 5.8 hours, but not falling at the synoptic map times and not at the same place in the domain. The fact that the interpolation scheme allows for translation, rotation and evolution should render the interpolated fields somewhat more independent than for the case of linear interpolation.

3. RESULTS

The effect of the structure of the wind field with respect to the cyclone circulation center is seen in all the fields. Figure 1a formed from the field *representative of the surface truth* shows the modulus with the UW model background. The storm track is clearly seen as a region of low mean wind speed surrounded by high mean wind speeds . When the sign of the vectors enters into the averages as in the modulus of the averages of wind components. Fig. 1b, or the stress vector, the region affected by alternatingly southerly and northerly winds also shows low mean values. The kinetic energy pattern is that of a double dipole with two regions of high and two regions of low mean kinetic energy transfer (not shown). Means obtained in storm-following coordinates show identical fields for $U_{AVE,MOD}$ and $U_{MOD,AVE}$.

We found that sampling every 6 hrs did not substantially change the resulting fields, but for increasing time separation between samples the maximum percent differences in the means from the control (the average based on the 20 min fields) increased from about 5% for 6 hourly samples to 14 % for 24 hour samples. The timing of these four samples per average also influenced the resulting average wind fields noticably. Errors in the kinetic energy were as high at ± 20 % for the 24 hour samples. The satellite data alone look quite similar in shape to the control and retains the higher values. The ECMWF model alone shows generally good agreement with the control and the satellite data.

4. DISCUSSION

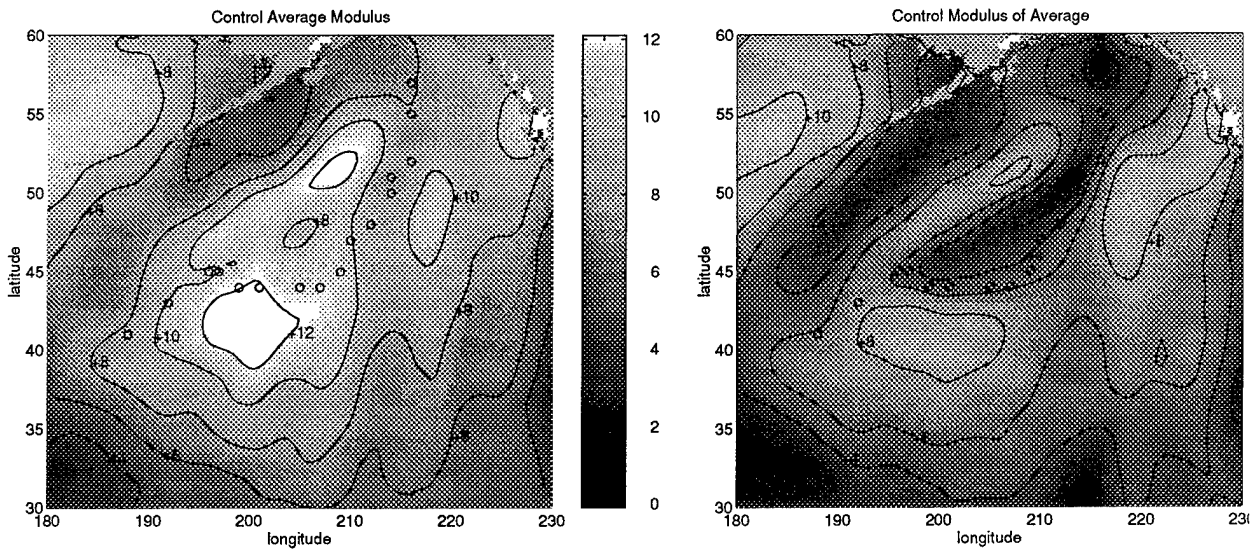
For variable wind fields it is clear that the position in the domain may strongly influence the mean wind experienced by the underlying ocean. The sampling by a point observing system (buoy or ship) can severly under- or overestimate the mean value in the domain. 12 and 24 hour samples are biased.

This case study, taking advantage of the available 20 min wind fields *representing the truth* allowed us to examine the effect of limited sampling in a translating and evolving weather system and has allowed studies of variability within the storm domain.

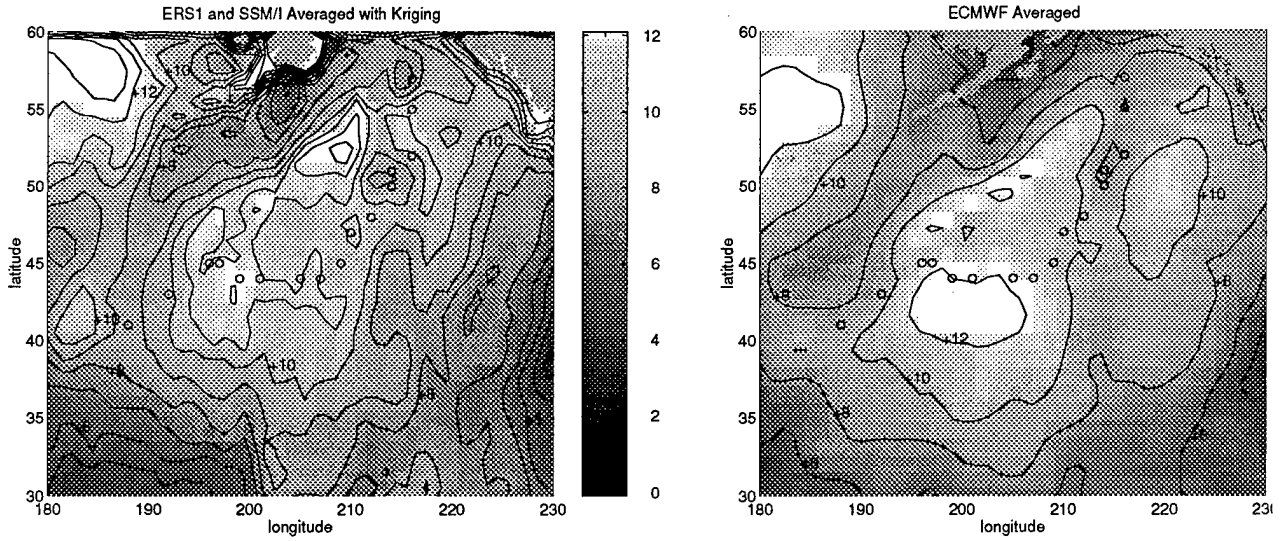
Acknowledgments :
This work has been supported by a NASA-Jet Propulsion Laboratory grant to the University of Washington and Institut Francais de Recherche pour l'Exploitation de la Mer.

References

Bentamy A., Y. Quilfen, F. Gohin, N. Grima, M. Lenaour and J. Servain, 1995 : Determination and validation of average wind fields from ERS-1 scatterometer measurements. *Global Atmosphere and Ocean. Syst.* (in press)
Dickinson, S. and R.A. Brown, 1996 : A study of near-surface winds in marine cyclones using multiple sensors, *J. Applied Meteorology*, (in press).



a) b)



d) c)

Figure 1: Averages of wind parameters (m/s) for a three and a half day period (Nov. 10 - Nov. 14 1992) over a North Pacific Cyclone. Disregard the outside 5 degrees of latitude and longitude of the figure. This region does not have the same satellite coverage as the storm itself. Circles identify storm centers every 6 hours.

a) Average of the modulus for the 20 minutes fields using satellite data with UW model background.

b) Modulus of the averages for the 20 minutes fields using satellite data with UW model background.

c) The 19 satellite swaths averaged together with kriging.

d) Average of the 6 hourly ECMWF wind fields.

Microwave Backscatter from the Sea Surface at Grazing Incidence

Joseph R. Buckley and Ryan S. Johnson[1]
Physics Department, Royal Military College of Canada, Kingston, Ont., K7K 5L0, CANADA
Phone: (613)541-6000 ext 6275 Fax: (613) 541-6040 E-mail: buckley-jrmc.ca

[1]14 Software Engineering Squadron, CFB Greenwood, NS, B0P 1N0 CANADA

Abstract— As part of the Sea Truth and Radar Systems '94 experiment on the Grand Banks of Newfoundland in December, 1994, we collected high resolution digital images of radar backscatter from the sea surface at low grazing angle incidence. Analysis of these images and other data collected concurrently allowed validation of certain theories of formation of the two chief components of low grazing angle sea clutter. The modulation of the low amplitude distributed scatter is strongest near the crests of the waves. The association of "sea spikes" with the crests of breaking waves was confirmed, and the amplitude and distribution of these spikes was related to both wind speed and to maximum breaking crest length. These observations favour the cylindrical plume model[1] for the formation of spikes.

1. INTRODUCTION

The focus of The Sea Truth and Radar Systems experiment of December, 1994 (STARS'94) on the Grand Banks of Newfoundland was the simultaneous collection of ocean surface wave information from satellite, aircraft and ship-borne microwave instruments, from traditional surface-following buoys and from numerical models, along with measurements of the meteorology of the air-sea interface. In this experiment, the Marine Microwave Research Group of Royal Roads Military College collected high-resolution digital radar backscatter imagery in a 2 km radius circle around the ship *CSS Parizeau* at the centre of the data collection region. The principal purpose of these measurements was to provide precise information through spectral techniques on the wavelength and direction of all components of the sea surface wave field with wavelengths longer than 15m. This objective was achieved, but the data also provided insights into the mechanisms of radar backscatter from the sea surface.

In this paper, we describe the results of our experimental exploration of these mechanisms.

This work was supported by the Academic Research Program of the Department of National Defence, Canada under project 3705-908
0-7803-3068-4/96$5.00©1996 IEEE

2. BACKSCATTER MODELS FOR LOW GRAZING ANGLES

Low grazing angle microwave backscatter from the sea surface is of two distinct types: distributed scatter, which is spread out over the surface, and sea spikes, which are more powerful, discrete echoes. The distributed scatter is attributed to Bragg scattering off capillary waves which are generated by the wind[2]. What is most important in the imaging of ocean surface waves is the modulation of this scatter, due to tilting of the surface, to change in amplitude of the capillary waves by the orbital velocity of the longer surface waves[3], to wind drag at the wave crests[4], to spontaneous generation of capillary waves in the high curvature region near wave crests[5], or to shadowing of the wave troughs by intervening wave crests [6].

Sea spikes seem to be associated with breaking waves. Their strong reflections have been modeled as specular reflections from capillary waves near the crests of larger waves [7], as reflections from the face of the bubble plume formed as a wave breaks [1], or as constructive multi-path interference [8]. Analysis of the data we collected during this experiment allows us to assess the validity of these models under the specific conditions we encountered.

3. DATA COLLECTION AND ANALYSIS

Microwave backscatter data were collected using a standard marine radar and a 20MHz, 8 bit digitizer and recorder connected to the logarithmic output of the radar's IF stage. Resultant images of the sea surface, collected in synchronization with the rotation of the radar antenna, covered a region 2km in radius about the ship, with a pixel size of 7.5m. Bursts of 16 or 32 images were collected at least every 15 minutes throughout the experiment. In all, over 10,000 images were collected. Photogrammetrically calibrated video and still photographs of the sea surface were taken simultaneously with the radar imagery when conditions permitted.

We performed a laboratory calibration of the radar receiver response to measured inputs through the entire dynamic range, and therefore, with application of the nominal antenna gain,

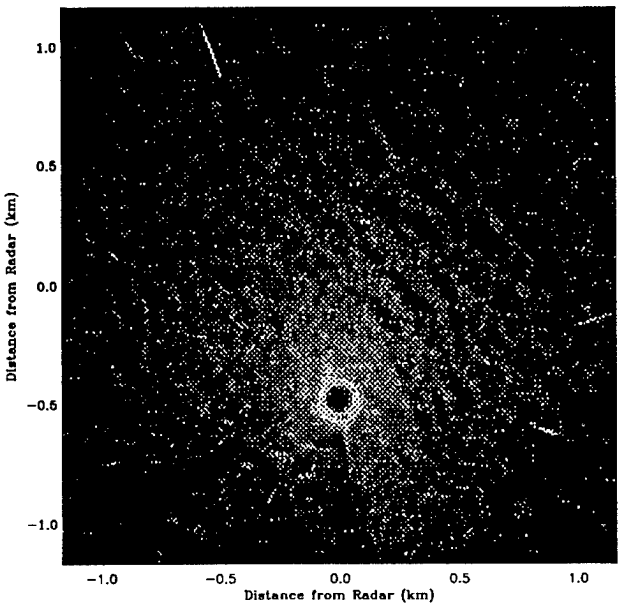


Figure 1: Radar image of the sea surface, 0140Z, 04 Dec 94.

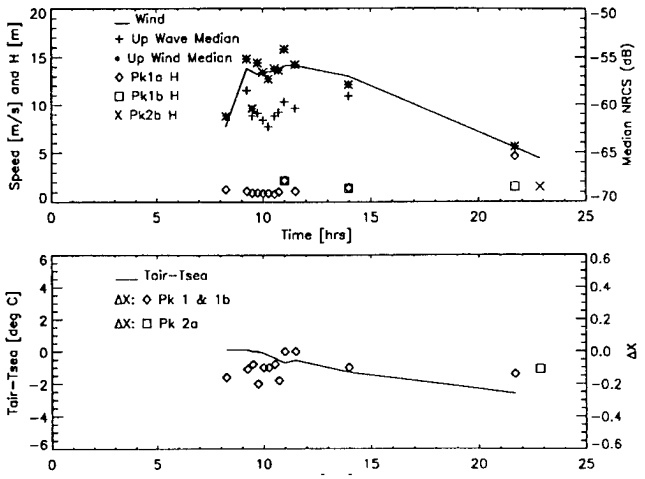


Figure 2: Derived image parameters, 04 Dec 94. (top) Median up-wind and up-wave NRCS, wind speed and estimated wave height. (bottom) Wave shape asymmetry (ΔX) and air–sea temperature difference.

were able to convert digitized voltages from the radar's IF to corresponding true normalized radar cross section (NRCS) values.

In fig. 1, a typical radar image, the distributed backscatter appears to have a very "wavelike" pattern, and, indeed, the spectrum of this pattern has been shown to resemble closely the spectrum of sea surface elevation[9].

Close examination of figures like this one show that the region of maximum backscatter on each wave usually occurred just before the onset of the shadow zone between waves, *i. e.* at or near the crest of the wave. The advancing faces of the waves generally appeared brighter than the retreating faces. The azimuthal maximum value for the NRCS was aligned with the wind direction, even when the wind and wave directions differed, except in the case of rapidly shifting wind direction. The median NRCS in each image was correlated with the wind speed. This behaviour is shown in the top panel of fig.2.

The distance from the radar to the first shadow zone in the up-wave or down-wave direction was correlated with the wave height as measured independently by a surface following wave buoy. The distance to the nearest shadow zone was usually shorter in the up-wave direction, consistent with the observation that forward faces of wind waves are steeper than back faces. In the bottom panel of fig.2, measurements of closest shadows give an approximate wave height of 2m, and an asymmetry of -0.1 (forward face steeper). Visual observations at the time estimated the wave height at 2–3m, and noted that the seas were decaying, and assuming a more sinusoidal nature.

"Sea spikes", visible as points of high intensity in fig.1, were found to be almost exclusively associated with the brightest parts of the distributed backscatter, *i. e.* near the crests of the waves. Their intensity was seen to vary with wind speed, increasing when the wind became stronger, and decreasing when the wind weakened. The only deviation from this behaviour came during a gale, when the sea was covered with large areas of foam, which presumably damped the spike-causing breaking events.

Plotting the cumulative distribution of NRCS values on a Rayleigh probability scale, showed that, invariably, two separate populations were present and could be described with individual Weibull models. These populations are evidently the distributed scatter at the smaller NRCS values, and the sea spikes at the larger. The intersection of these models indicated the percentage of sea spikes in the image, typically between 5 and 10%. These plots also gave directly the median NRCS, and the 1%NRCS values. The 1% NRCS value has been shown [1] to be a stable estimate of the strength of the largest spikes. Fig. 3 shows how this quantity varies with the wind speed.

Analysis of the photographic record allowed determination of the median and maximum lengths of the breaking crests of the waves present in the corresponding radar images. Results of this analysis (fig. 3, bottom), show that the maximum crest length is much more highly correlated with the 1% NRCS and the wind speed than is the median crest length.

4. CONCLUSIONS

Intensity variations in the distributed backscatter along the faces of the waves are consistent with the model in which the principal modulation mechanism for distributed scatterers is a capillary wave concentration at the crests of the larger gravity waves caused either by the surface wind field, or hydrodynamic insta-

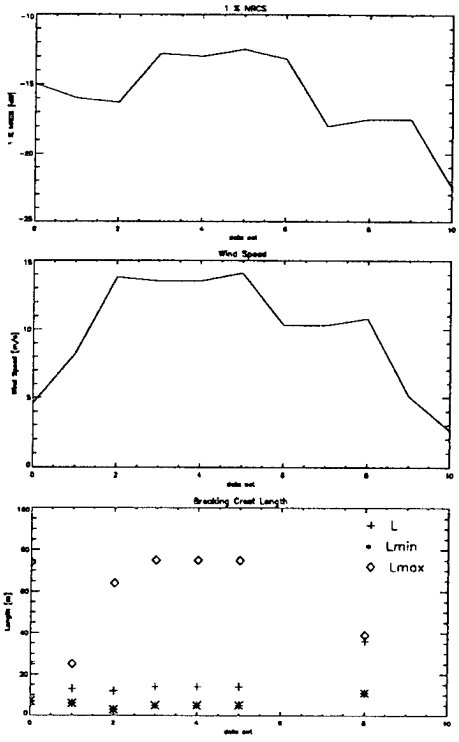


Figure 3: Observations of 1% NRCS (top), wind speed (middle) and observed breaking crest length, L (bottom) at 10 times during the experiment.

bility.

The agreement between variations in sea spike intensity, wind speed and maximum crest length offers better support to the cylindrical plume model of sea spike formation than the others mentioned earlier, however, there are some discrepancies in the detailed application of this model which will require further work to resolve.

Other aspects of these measurements show that shallow grazing incidence microwave backscatter has potential for the estimation of wind speed, wind direction, wave height and the state of wave development.

5. ACKNOWLEDGMENTS

This work was carried out while the authors were associated with Royal Roads Military College, in Victoria, B. C., Canada, and is described in much greater detail in [10]. The College has since been closed, and we lament its passing. The work continues with the transfer of the group to the Royal Military College of Canada.

We wish to thank the other participants in STARS'94 for their support and cooperation, and in particular, the officers and crew of the *CSS Parizeau* for their unfailing perseverance in enabling the collection of data under very trying circumstances and foul weather, and Fred Dobson of the Bedford Institute of Oceanography for his leadership and persistence in making the experiment come together and happen.

6. REFERENCES

[1] D.B. Trizna. Statistics of low grazing angle radar sea scatter for moderate and fully developed ocean waves. *IEEE Trans. on Antennas and Propagation*, 39:1681–1690, 1991.

[2] F.T Ulaby, R.K. Moore, and A. K. Fung. *Microwave remote sensing, active and passive. Vol II: Radar remote sensing and surface scattering and emission theory.* Addison-Wesley, London, 1982. 1064p.

[3] I. S. Robinson. *Satellite oceanography: an introduction for oceanographers and remote sensing scientists.* Ellis Horwood, Chichester, 1985. 455p.

[4] T. Hara and W. J. Plant. Hydrodynamic modulation of short wind-wave spectra by long waves and its measurement using microwave backscatter. *J. Geophys. Res*, 99 C(5):9767–9784, 1994.

[5] D.B. Trizna, J. P. Hansen, P. Hwang, and J. Wu. Ultra-wideband radar studies of steep crested waves with scanning laser measurements of wave slope profiles. *Dynamics of Atmospheres and Oceans*, 20:33–53, 1993.

[6] L. B. Wetzel. Models for electromagnetic scattering from the sea at extermely low grazing angles. Technical Report NRL-MR-6098, Naval Research Laboratory, Washington, DC, 1987. 78pp.

[7] L. B. Wetzel. Electromagnetic scattering from the sea at low grazing angles. In G. L. Geenaert and W. L. Plant, editors, *Surface Waves and Fluxes*, volume 11, No 2, pages 109–172. Kluwer Academic Publishers, Boston, 1990.

[8] M. Katzin. On the mechanisms of radar sea clutter. *Proceedings of the Institute of Radio Engineers*, 45:44–54, 1957.

[9] J. R. Buckley, M. Allingham, and R. Michaud. On the determination of directional spectra from marine radar imagery of the sea surface. *Atmosphere-Ocean*, 32:195–213, 1994.

[10] R. S. Johnson. Low grazing angle microwave backscatter from the sea surface. Master's thesis, Royal Roads Military College, FMO Victoria, BC, Canada, 1995. 151p.

DOPPLER-RADAR-RADIOMETER METHOD OF NEAR SEA SURFACE WIND SPEED, LONG WAVES ROUGHNESS DEGREE, WATER AND AIR TEMPERATURES DETERMINATION

Artashes K.ARAKELIAN and *Astgik K.HAMBARYAN

Institute of Radiophysics and Electronics
Armenian National Academy of Sciences
Ashtarak-2, 378410, Armenia
Tel: (7-8852) 287-850; E-mail:irphe@arminco.com

* Holding "Shinzargatsum" Ministry of Construction
35 Komitas St., # 209, Yerevan, 375051, Armenia
Tel. (7-8852) 255-860

ABSTRACT

The spectral, angular, polarizing, air and water temperatures, sea surface waves and wind features of reflected from the sea surface radar signal frequency Doppler shift distribution variance, sea surface radar cross section and brightness temperature are considered. The method and device of simultaneous Doppler-radar and cross-polarized radiometer sensing for sea surface roughness degree, wind speed, water and air temperatures determination are described.

INTRODUCTION

Radiothermal radiation of the objects of nature in radio frequency range is characterized by brightness temperature $T_{Bi}(\vartheta)$. Reflective properties of observed surfaces, determining the intensity of reflected radiation, are characterized by radar cross section $\sigma_{ii}(\vartheta)$ of these surfaces. Therefore, to solve the microwave remote sensing inverse-problem it means to determine the values of wanted parameter by measured values of $\sigma_{ii}(\vartheta)$ and $T_{Bi}(\vartheta)$ or their some combinations. Since, $\sigma_{ii}(\vartheta)$ and $T_{Bi}(\vartheta)$ are the rather complex function of many variables, it is necessary to form a set of independent measurements and to exclude the influence of other factors by their giving as a priori information or by choosing of corresponding conditions for $\sigma_{ii}(\vartheta)$ and $T_{Bi}(\vartheta)$ measurements with taking into account the polarizing, angular or frequency features of them. Difficulties of microwave remote sensing inverse - problem solution are consisted in necessity of $\sigma_{ii}(\vartheta)$ and $T_{Bi}(\vartheta)$ absolute measurements, so as any relative measurements carry out to increasing of numbers of independent measurements, and to requirements of using of supplementary priori information about observed objects. Therefore, the solution of microwave remote sensing inverse problem supposes the necessity of carrying out of multi-frequency, multi-channel, multi-position, polarizing, circle and panoramic observations.Today's methods of near surface wind speed and water temperature determination are subdivided in the following way: generally, parameters of wind field are determined by radars (side looking radars, scatterometers, Doppler-radars, etc.), and sea surface temperature is determined by systems of infrared or microwave radiometers. Thereat, the following characteristics of measurements accuracy are supposed: ±2m/s and 1-1.5K for wind speed and water temperature respectively. In fact, these accuracies are the limits of the possible for using devices and existing algorithms of information handling, and farther

0-7803-3068-4/96$5.00©1996 IEEE

improvement of these accuracies does not connect with the improvement of today's using devices characteristics, which are sufficiently high. Difficulties of wind speed and water temperature remote determination accuracies are connected with difficulties of physical problem, included ambiguous solution simultaneously by several independent parameters.

In this paper, on the basis of the results of sea surface microwave reflection, proper radiothermal radiation and backscattered radar signal Doppler characteristics spectral, angular, polarizing, temperature and wind changes theoretical and experimental investigations, the method and device of near sea surface wind speed, sea surface roughness degree, water and air temperatures simultaneous determination is developed.

METHOD OF WIND SPEED AND WATER TEMPERATURE DETERMINATION

The absence of priori information about air temperature and difference of sea wave real spectrum from fully developed wind wave condition may lead to sufficient mistakes at wind speed and water temperature determination by radar, radiometer or combined radar-radiometer sensing. Really, since, all of these methods are connected with sea surface radar and radiometer observations at nadir (0° - 25°) or (25°-85°) angles, when sufficient contribution in absolute values of $\sigma_{ii}(\vartheta)$ and $T_{Bi}(\vartheta)$ are carried by difference of air t_a and water t_v temperatures and by sea waves long structures, which are inert to the fast changes of wind speed, then to increase the accuracies of wind speed and water temperatures determination it is necessary to estimate by other methods t_a and the variance $m^2\{m_x^2; m_y^2\}$ of long waves slope distribution, which characterizes the sea surface roughness degree.

As, in view of the fact that the sea surface radar cross section and brightness temperature are the rather complex functions of such parameters as: radio wavelength λ, incidence angle ϑ, wind speed v or its equivalent, ripples height variance σ_h^2, wind direction φ, water and air temperatures, long waves slope variance m^2, salinity S_s and polarization, then to solve the problem of wind speed and water temperature determination it is necessary to solve this set of equations at least:

$$\sigma_{ii}(\vartheta_1) = f\{\lambda,\vartheta,\varphi,v,t_v,t_a,m^2,S_s\}$$

$$\sigma_{ii}(\vartheta_2) = f\{\lambda,\vartheta,\varphi,v,t_v,t_a,m^2,S_s\}$$

$$T_{Bv}(\vartheta_{1,2}) = f\{\lambda,\vartheta,\varphi,v,t_v,t_a,m^2,S_s\}$$

$$T_{Bh}(\vartheta_{1,2}) = f\{\lambda,\vartheta,\varphi,v,t_v,t_a,m^2,S_s\}$$

$$0^\circ < \vartheta_1 < 25^\circ \quad ; \quad 25^\circ < \vartheta_2 < 85^\circ$$

at fixed or priori known values of $\lambda=\lambda_o$; $\vartheta_{1,2}=\vartheta_{1,2,o}$; $\varphi=\varphi_o$ and $S_s=S_{so}$. However, even this set of equations, that suppose bi-polarizing and bi-position radar and radiometer sensing of sea surface, does not allow to carry out the necessary estimation, since, it has not unambiguous solution on parameters σ_h^2, m^2, t_a and t_v. Therefore, it is necessary to exclude one of the equations for $\sigma_{ii}(\vartheta)$ and to supplement the set with another independent equation.

The results of [1] have shown, that as a forth independent equation may be used the expression for variance σ_ϑ^2 of averaged on resolution cell backscattered radar signal frequency Doppler shift distribution.

$$\sigma_\vartheta^2 = 8\pi(3\lambda)^{-1}[1+\cos^2\vartheta + (1-R)\sin^2\vartheta/(1+R)]\sum_{i=1}^{5}(D_i+B_i)$$

$$D_i = \int_{K_{i-1}}^{K_i} K(g+\alpha_n K^2/\rho)S(K_i)\exp(-r_o K^2)dK$$

$$B_i = \int_{K_{i-1}}^{K_i} K(g+\alpha_n K^2/\rho)S(K_i)dK$$

$S(K_i)$ is the wave number sea spectrum, r_o -the mean geometric radius of resolution cell, α_n-surface ten-

sion coefficient, ρ-water density.

Analysis of the results of some theoretical estimations has shown, that unambiguity of the set of equations

$$\sigma_{ii}(\vartheta)=f\{\lambda,\vartheta,\varphi,v,t_v,t_a,m^2,S_s\}$$

$$\sigma^2_{\vartheta}(\vartheta)=f\{\lambda,\vartheta,\varphi,v,t_v,t_a,m^2,S_s\}$$

$$T_{Bv}(\vartheta)=f\{\lambda,\vartheta,\varphi,v,t_v,t_a,m^2,S_s\} \quad (1)$$

$$T_{Bh}(\vartheta)=f\{\lambda,\vartheta,\varphi,v,t_v,t_a,m^2,S_s\} \quad (2)$$

on parameters v, t_v, t_a and m^2 may be provided at ϑ from 60°- 70°. This is conditioned by unambiguity of solution of equations (1), (2) on parameters (σ^2_h;m^2) and t_v at a priori known values of $t_a=t^{ao}_a$, that is provided only at ϑ from 57°-75°. However, the choice of ϑ for measurements of $\sigma_{ii}(\vartheta_o)$ and $\sigma^2_{\vartheta}(\vartheta_o)$ may be carried out from interval 30°-85°. It means, that at radiometer measurements data comparison ϑ must be chosen from the interval 60°-70°, but at scatterometer and Doppler radar measurements data comparison, ϑ may be chosen from 30°-85°.

In Fig.1 a block diagram of Doppler-radar- radiometer system for wind speed and water temperature remote determination is shown. This system realizes a solution of the set of equations.

where T_{ASO} and T_{AAO} are the brightness temperatures of Atmosphere on the sea surface and antenna levels, τ_{AO} is the value of Atmosphere optical width.

This set allows at $v>v_{min}$ (where v_{min} = 2-3m/s is the threshold values of wind speed necessary for sea wave generation) simultaneously to estimate the values of v, m^2, t_v and t_a. At $v < v_{min}$, when the ripples are absent, this system allows simultaneously to estimate the values of m^2, t_v and the condition $v < v_{min}$.

CONCLUSION

Thus, we have developed microwave Doppler-radar and bi- polarizing radiometer method and system for near sea surface wind speed, sea wave degree, air and water temperatures determination.

REFERENCE

1.A.K.Arakelian " Some features of the backscattered from sea surface radar signal frequency Doppler shift distribution statistical characteristics" the Digest of IGARSS'94, Pasadena, California, USA, 1994, vol.2, p.p.785-787.

$$\sigma^2_{\vartheta}=f\{\lambda,\vartheta,\varphi,v,t_v,t_a,m^2,S_s\} \;;\; T^r_{Bv}=f\{\lambda,\vartheta,\varphi,v,t_v,t_a,m^2,S_s,T_{ASO},T_{AAO},\tau_{AO}\}$$

$$\sigma_{ii}=f\{\lambda,\vartheta,\varphi,v,t_v,t_a,m^2,S_s\} \;;\; T^r_{Bh}=f\{\lambda,\vartheta,\varphi,v,t_v,t_a,m^2,S_s,T_{ASO},T_{AAO},\tau_{AO}\}$$

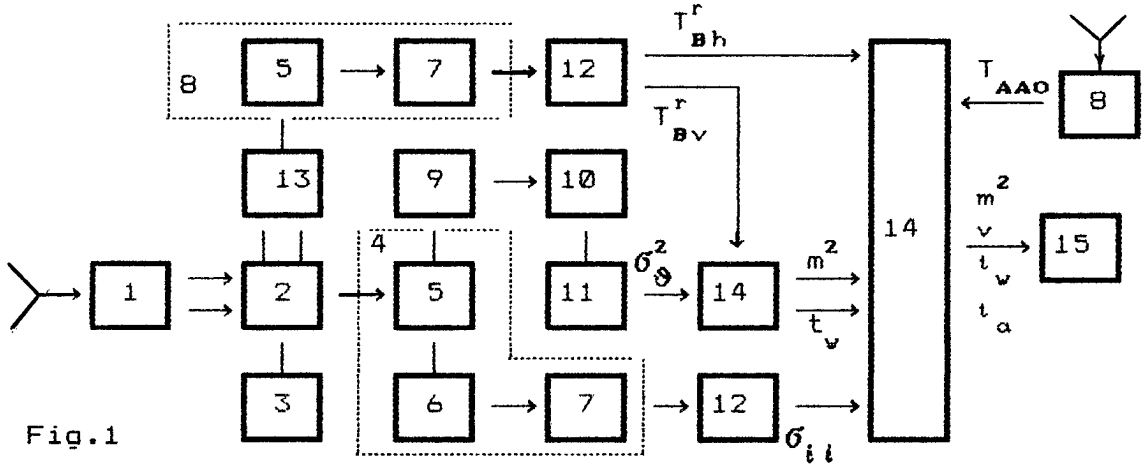


Fig.1

1- Polarizing Splitter, 2- Antenna (Transmittion/Reception) and Polarizing Switch, 3- Transmitter, 4- Radar Receiver, 5- Microwave Module, 6- Intermediate Freq. Module, 7- Low Freq. Module, 8- Radiometer Receiver, 9- Square-Low Detector, 10- Module of σ^2_{ϑ}, 11- Module of $\vartheta(t_n)$, 12- Modul of Normalization, 13- Module of Defense, 14- Solver, 15- Register, $T^r_{Bv,h}$ are real values of brightness temperature.

AN OFFSET BETWEEN SCATTEROMETER DIRECTIONAL ANISOTROPY AND WIND DIRECTION ACROSS THE EQUATORIAL PACIFIC OCEAN

Clifford L. Rufenach
University of Colorado/CIRES, Boulder CO 80309-0449 USA
email:clr@cdc.noaa.gov, Tel. (303)492-4988, FAX: (303)497-7013

ABSTRACT

The functional form usually employed for retrieving global winds constrains the cross-sectional maxima into lines parallel to the wind. We propose a generalized form allowing cross-section maxima offset from these streamlines. We fit parameters from these two models using collocated ERS-1 spacecraft scatterometer and equatorial buoy measurements. These models exhibit similar residuals but different directional dependencies for each of three years. Consequently, neither of these two models can convincing be identified as more accurate than the other when fit to extensive measurements unless other factors are considered. For example, the generalized model exhibits an average offset, near 10°, for each of these years lending confidence to the significance of this modeled offset. Equatorial swell systematically oriented at an angle to the local prevailing wind could cause this offset.

INTRODUCTION

Cross-sections calculated from scatterometer measurements have been related to radar incidence angle θ, radar polarization, and mean wind speed U and mean wind-direction φ.
This microwave backscatter increases with wind speed and varies sinusoidally with wind-direction due to Bragg scattering from centimeter-scale waves. The short wind-driven waves modified by the longer waves, are not necessarily aligned with the local wind. Consequently, the cross-section directional anisotropy due to these short waves is not necessarily aligned with the wind-direction. We investigate two models with and without a cross-sectional angular offset.

The cross-section measurements exhibit maxima near the upwind and downwind directions and minima near the crosswind directions. In the past some workers have suggested the maxima occur along the wind streamlines. We believe these maxima are nearly aligned with the streamlines on some occasions but not on others. Li et al. [1] analyzed the alignment of the minima but not the maxima. We suspect the maxima have similar scatter relative to the streamlines as the minima.

The cross-section also depends on a number of secondary ocean parameters including: boundary layer stability, surface tension and water viscosity. Several workers have examined the modification of Bragg waves by long waves; although, only the wind speed dependence have been reported; see, e. g., [2-3]. We believe the orientation of the long surface waves can cause an offset in the cross-section directional anisotropy relative to the streamlines.

GEOPHYSICAL MODEL

A general model relationship between the cross-section σ_o (in dB) and the near-surface wind vector (U, φ) is of the form,

$$\sigma_o = \langle\sigma_o(\theta, U)\rangle + \sum_{n=1}^{N} [A_n \cos n\varphi + B_n \sin n\varphi] \quad (1)$$

where N is usually taken as 2, $\langle\sigma_o(\theta,U)\rangle$ denotes the wind speed portion of the model (angular brackets denote averaging over all directions) and the remaining terms denote the wind-direction dependence. φ denotes the wind-direction relative to the antenna look-direction (i. e., $\varphi = 0°$ corresponds to a wind-direction blowing toward the antenna when $B_n = 0$). Two simplifications of (1) have been employed for fitting directional models to the scatterometer measurements. These two models are denoted: (a) the aligned model and (b) the offset model given respectively by,

$$\sigma_o(\varphi) = \sum_{n=1}^{2} [a_n \cos n\varphi] \quad (2)$$

where $\sigma_o(\phi) = \sigma_o - \langle\sigma_o(\theta, U)\rangle$ is an even function of ϕ in (2) and,

$$\sigma_o(\phi) = \sum_{n=1}^{2} C_n \cos n(\varphi - \varphi_o) \quad (3)$$

where $C_n = (A_n^2 + B_n^2)$, $\tan(n\phi_o) = B_n/A_n$ and ϕ_o denotes the angular offset when n = 2 provided the ϕ_o contribution due to n = 1 is small compared to n = 2. The n = 1 terms are usually small for vertical polarization at both C-band and Ku-band. Modifications of (2) are investigated by: (a) adding a third-order cosinusoidal terms in (2) denoted modified model and, (b) adding sinusoidal terms in (2) resulting in a cross-section maxima and minima offset from both the streamlines and crosswind lines; respectively, see (3).

The addition of a third order term in (2) is given by,

0-7803-3068-4/96$5.00©1996 IEEE

$$\sigma_o(\phi) = \sum_{n=1}^{3} a_n \cos n\varphi \qquad (4)$$

The expressions (2), (3), and (4) give the functional form of models previously employed by others.

MODEL AND MEASUREMENT COMPARISON

The ERS-1 scatterometer measurements were collocated within ± 25 km of the equatorial Pacific TAO (Tropical Atmosphere Ocean) buoys for the calendar years 1992, 1993 and 1994. A description of this collocation technique and the measurement accuracy is given in [4]. The hourly buoy wind speed and direction at a height of 4 m above the ocean surface are employed in conjunction with the scatterometer measurements in all model fits.

The aligned and offset models are based on either two or four adjustable parameters for the wind-direction. The wind speed portion of the model is based on six adjustable parameters valid for U > 3 m/s employing an exponential form developed in[4]. The smallest residuals for the three data sets was obtained during 1994 using 10,236 collocated measurements. We select this data set for detailed analysis.

The adjustable parameters for the wind-direction portion of the model are given in Table 1. The aligned, modified and offset models are fit using (2), (3) and (5) denoted by 2 parameters, 3 parameters and offset model, see Table 1. The additional coefficient a_3 is numerically small. Therefore, we compare the aligned model given by (2) and the offset model given by (3). The individual measurements and these two models are displayed in Figure 1. The angle in the offset model ϕ_o is near 11° and the minima angle in the aligned model is near $\Delta\phi_o = \pm 0.2°$. The adjustable parameters are all statistically significant . That is, both models are fit to this data with similar residuals. However, the offset model exhibiting slightly smaller residuals; i. e., the RMS deviations are 1.00 dB and 1.06 dB based on the offset and aligned models, respectively. We note these models exhibit similar fits but show substantially different directional characteristics.

The other two data sets, 1992 and 1993, also exhibit similar characteristics; the yearly average offsets varying from 9° to 11°. More precisely, the offset model exhibits slightly smaller residuals (scatter) than the aligned model but different directional characteristics.

This offset could be caused by the swell orientation relative to the prevailing wind [6] itself or the swell modification of the wind-driven waves in a preferential way, such that the wind-wave crests tend to be offset toward the swell crests. That is, limited measurements show that these waves can be offset from the wind by 10° to 20° with the sense (clockwise or counter-cloclwise dependent on the swell orientation [5]. This mechanism could be more realistic since the inferred cross-section offset is the same order. The wind-driven waves in the equatorial Pacific are characterized by dominant wavelengths of say 20 m to 40 m because the average and maximum wind are only about 5 m/s and 10 m/s. These intermediate dominant waves must modify the short Bragg waves. Further discussion of these mechanisms is beyond the scope of the present work.

Spacecraft scatterometer algorithms have mostly used a geophysical model based on the aligned model. Therefore, the inferred offset based on equatorial buoy measurments is a new tenative result employed in one oceanic region which means this functional form may not be needed in other oceanic regions.

We examine possible biases in cross-section due to the directional form based on the offset and aligned models. These two forms are applied to the model fits across the equatorial Pacific during 1994. An average offset of about 11° has been inferred from this data set. Therefore, the aligned model could underestimate the magnitude of the directional modulation. These modulations are C_2 = 1.36 dB and a_2 = 1.31 dB for the offset and aligned models, respectively. We note a small decrease in the modulation (bias) as expected in the aligned form result compared tothe offset result. Similar biases were inferred for the 1992 and 1993 data sets.

REFERENCES

[1] Li, F., G. Neumann, S. Schaffer and S. L. Durden, Studiesof the location of azimuth modulation minima for Ku-band ocean radar backscatter, J. Goephys. Res., 93(C7), 8229-8238, 1988.

[2] Durden, S. L., and J. F. Vesecky, A physical radar cross-section model for wind driven sea with swell. IEEE J. Oceanic Eng., OE-10, 445-451, 1985.

[3] Nghiem, S. V., F. K, Li, S. Lou, G. Neumann, R. McIntosh, S. C. Carson, J. R. Carswell, E. J. Walsh, M. A. Donelan and W. M. Drennan, Observations of radar backscatter at Ku and C bands in the presence of large waves during the surface wave dynamics experiment, IEEE Trans. Geosci. Remote Sens., 33(3), 1995

[4] Rufenach, C., A new relationship between radar cross-section and ocean surface wind using ERS-1 scatterometer and buoy measurements, Int. J. Remote Sensing, 16(18), 3629-2647, 1995.

[5] Long, S. R., N. E. Huang, E. Mollo-Christensen, F. C. Jackson and G. L. Geernaert, Directional Wind Wave Development, Geophys. Res. Letters, 21(23), 2503-2506, 1994.

[6] Hasselmann, K., S. Hasselmann, E. Bauer, C. Brüning, S. Lehner, H. Graber, P. Lionello, Development of a satellite SAR image spectra and altimeter wave height data assimilation system for ERS-1, Max Planck Institut für Meteteorolgie Report No. 19, Hamburg, Germany, 1988.

TABLE 1 EQUATORIAL MODEL DIRECTIONAL PARAMETERS FIT BASED ON COLLOCATED ERS-1 AND BUOYS MEASUREMENTS DURING 1994[a]

(a) ALIGNED MODEL PARAMETERS

NUMBER OF PARAMETERS	a_1	a_2	a_3	RMS dev.	ϕ_{min}
	(dB)	(dB)	(dB)	(dB)	(°)
2	-0.219	1.31		1.07	0.2
3	-0.209	1.31	-0.117	1.06	

(b) OFFSET MODEL PARAMETERS

A_1	B_1	A_2	B_2	C_2^*	RMS dev.	ϕ_o
(dB)	(dB)	(dB)	(dB)	(dB)	(dB)	(°)
-0.268	-0.118	1.27	0.487	1.36	1.00	11.5

[a] 10,236 measurements.
* $C_2^2 = A_2^2 + B_2^2$.

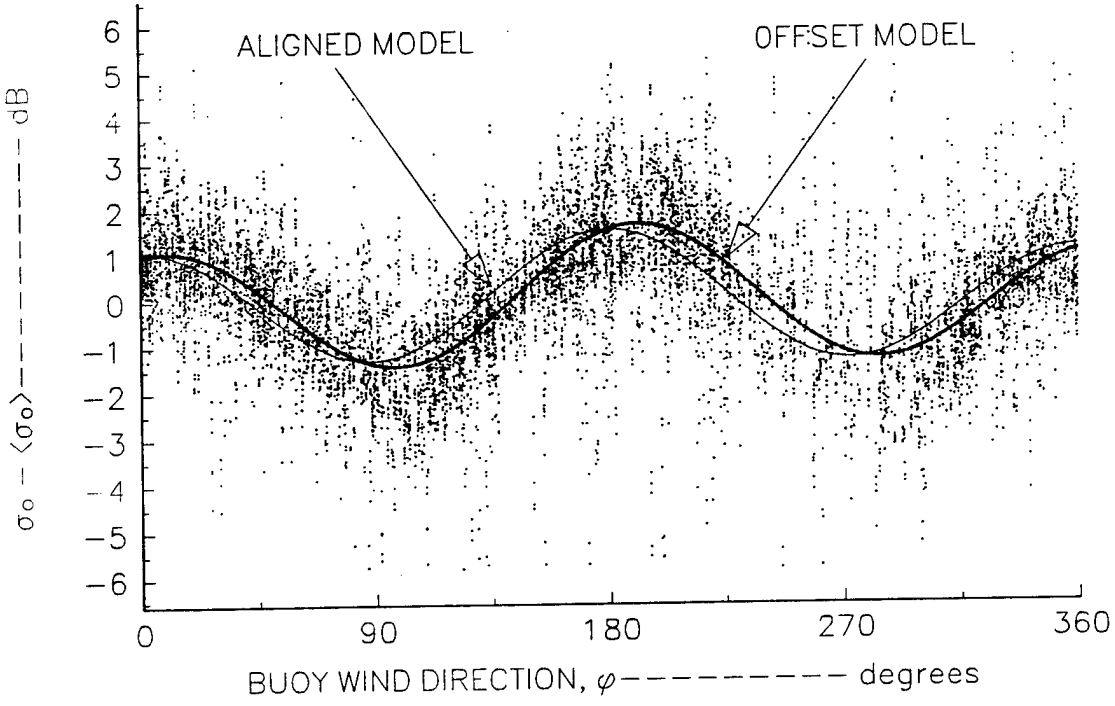


Figure 1. Rectangular plot of equatorial Pacific measurements during 1994 and the aligned and offset model fits to these measurements. The relatively large scatter in the data points implies that either model can be fit to the measurements. The two models show significant different cross-sections variation with wind-direction ϕ: up to about 0.5 dB difference

The role of Remote Sensing in training activity of Tuscany Region

S. Cuomo[+], D.Giuli[°], G.Federici[°]

[+]PIN - Centro Studi Ingegneria, P.zza Ciardi 25, 50047 - Prato (ITALY), e-mail: cuomo@pinet.ing.unifi.it
[°] Facolta' di Ingegneria - Universita' di Firenze, via di S. Marta 3, 50139 - Firenze (ITALY)

Abstract -- The European Community has focused on the development of human resources one of the main goal to be achieved for the improvement of our society. This idea, as stated by J. DeLors, considers educational and training activities, as a whole, among the main tasks of the European Community. In this scenario the Tuscany Region wants to play a leading role and has issued a regulation to discipline the activities in the field of vocational training activities by defining a global frame concerning both objectives and organization.

At the same time, the social growing cannot be split up from the safeguard of our environment: in this sense one of the most important aspects is the developing of curricula and educational methodologies for the Monitoring and Control of the Environment (MCE), that can be able to put remote sensing and geoscience products and knowledge together with advanced learning technologies.

In the MCE field a non-profit organization, PIN - Centro Studi Ingegneria, acts as a C.I.R. in Tuscany region having been charged, for its specific knowledge in the field of geoscience and remote sensing, to operate as a reference center for the development of training activities in the field of environmental monitoring and Remote Sensing.

One of the main goals of the C.I.R. of Prato is the achievement and sharing of these methodologies in Italy and in the European Union. For this purpose educational tools are going to be realized, as multimedia software, educational supports for self learning and remote educational techniques based upon the telematics network existent for the interconnections of Universities and other educational centers in Tuscany region.

In this paper the main activities and the first results of educational projects are presented

THE ROLE OF RS IN THE ACTIVITIES OF TUSCANY REGION

As assessed by several statements of the EU [1], in the field of the Vocational Training, one of the main aspects we have to consider for a correct development of human resources, is to find a kind of vocational training which could be able to solve the trade-off between two opposite needs. The first is to give people a high specialization, the second is to give them a high capability to convert quickly their own know-how in order to follow the ever changing rhythms of the labour market.

0-7803-3068-4/96$5.00©1996 IEEE

These needs are often in contrast with a school background, at a basic but also at University level, that generally does not follows rapidly with difficulty technological changes but even less the employment's requirements.

In this scenario is therefore necessary to propose vocational training activities which can offer to unemployed people a real chance of finding a job in the particular (even in geographic sense) occupational context, but nevertheless the educational content quality should a high one, in order to ensure to the employed people their knowledge to be always up to date.

The Tuscany Region has decided to invest a considerable part of its budget in vocational training activities, in the different fields of economic interest present in Tuscany, such as tourism, handicrafts and industry.

Furthermore, in its development guidelines, the Tuscany Region has decided to try itself in some non traditional sectors of economy, in particular the Environment. The environment should be regarded as an economic resource to be safeguarded and developed. In this context we can focus two main fields of interest: the first is devoted to the management of environmental heritage (of particular interest in Tuscany) i.e. by the institution of new Parks, and a more efficient management of the existing ones. The second is more linked to specific problems in the field of the RS, for the MCE. In order to exploit in a correct way this resource, it is necessary to adopt specific professional figures, able to easily pass from decisional aspects to hard technological problems.

In order to develop this kind of professional figure, the Tuscany Region, following the EU suggestions in the field of vocational training activities, has set up some Centers of Regional Interest (C.I.R.) for the professional activities: one of them, in particular, the PIN - Centro Studi Ingegneria (Prato) is specifically devoted to the activities in the environmental field.

THE ACTIVITIES OF C.I.R. FOR THE ENVIRONMENT

In order to ensure a reference frame for training activities, the Tuscany Region has approved a specific law (n° 70, Sep. 94 [2]) setting up some Centers (C.I.R.) whose task is to feed and support the qualifying processes for training activities, by operating with reference to definite economic sectors or homogeneous professional groups. In addition to training activities is furthermore it has been established that these

Centers, should develop experimental activities and applied researches.

In the Environmental field a C.I.R. is operated by the PIN - Centro Studi Ingegneria which is located in Prato. This new institution, operating in agreement with the Universities of Florence, Pisa and Siena, has among its institutional purposes the development of an integration between vocational training activities and University educational system: in this sense an outstanding example is represented by the setting up of a unitary system for regional tele learning based upon three high speed Metropolitan Area Networks (MAN) linked over the regional territory(Fig. 1).

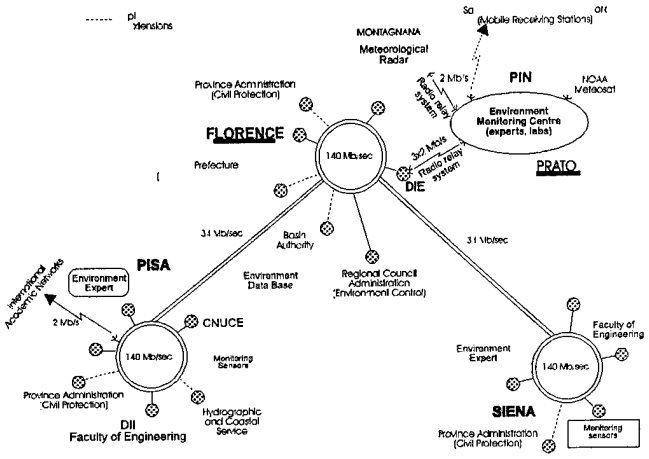


Fig.1 - The Tuscany MAN

The PIN - Centro Studi Ingegneria has high technology available for its tasks, such as real time multisensor data for Environmental Control purposes, particularly for evaluation and managing of hydrogeological hazard.

For RS activities at PIN's, a RS station is present for direct receiving and analysis of data coming from Meteosat and NOAA series satellites, and furthermore a direct radio link with a meteorological radar station which is located in the middle of Tuscany.

The direct connection to the Tuscany MAN makes possible high speed link with technological resources available in the other research Laboratories in Tuscany.

As to vocational training, the PIN has planned a series of activities to be carried out from 1995 to 1998, with specific tasks in technical and professional sectors (vertical competencies) and in the basics for the development and support of educational activities (horizontal competencies) as well.

Among the main aspects of these activities we can mention:

- the systematic development of advanced research in the MCE and RS
- the use of innovative educational methodologies such as tele learning and multimedia technologies
- the institution of innovative professional profiles in the environmental field
- services and consultancies for the Public Administration

In Fig. 2 a schema regarding project activities of C.I.R. is reported focusing the different areas of application.

It is important to stress how, for any sector of interest, one of more project is in progress or just terminated.

For the project activities we can individuate these main topics:

- development of multimedia methodologies and educational support
- systematic development of educational paths
- leading projects in the environmental fields, both for MCE and RS
- leading projects for tele education and tele training

As this work is presented about 30 projects the in environmental field - at different levels, from regional to European - are in progress having PIN in a leading role both for applied research and education.

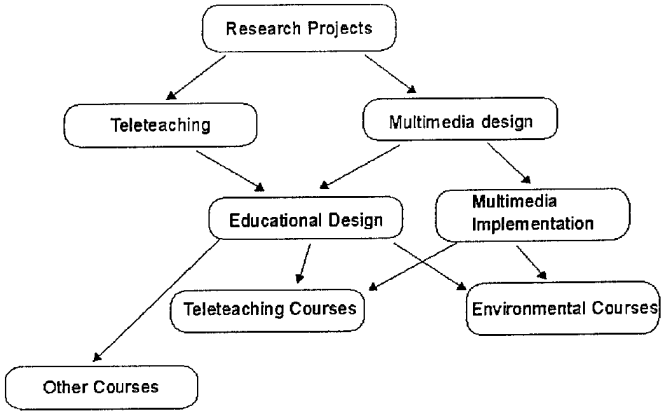


Fig.2 - A scheme of C.I.R.'s activities

RESULTS FROM THE MONICA PROJECT.

As a result we can refer to one project, just terminated for its first phase, that has carried out interesting results, the so called *MONICA* that has led to the development of experimental educational methodologies in the field of RS and MCE in which who is writing has been deeply involved.

For the design of this project two guidelines have been focused:

- the need of defining, in an organic way, the educational activities in the different areas of environmental interest and, in particular, those regarding water, air and soil
- the design and implementation of innovative educational methodologies (such as CD-ROM,

multimedia, auto learning...) to give an effective support to the activities for training and professional qualification for subject employed in the environmental field

The educational program has been designed for subjects - employed and unemployed as well - to whom a high specialization is addressed in the MCE and RS field, such as operators in the Public Administration.

Four courses have therefore been designed in cooperation with the Universities of Florence, Pisa and Siena (with the contribution of Elea F.P.), about this subjects:

- Management of water cycle
- Management of hydrogeological resources
- Monitoring of air pollution
- Monitoring of pollutant transfer on large scale

The educational contents for this courses have been transferred on a CD-ROM (Fig. 3) exploiting multimedia capabilities such as sound and animation.

These courses have then been held from December 1995 to February 1996, with classes At about 12 students, alternating traditional teaching methodologies (with a teacher present in the classroom) and innovative methodologies of learning, i.e. based upon CD-ROM supported or not by a tutor.

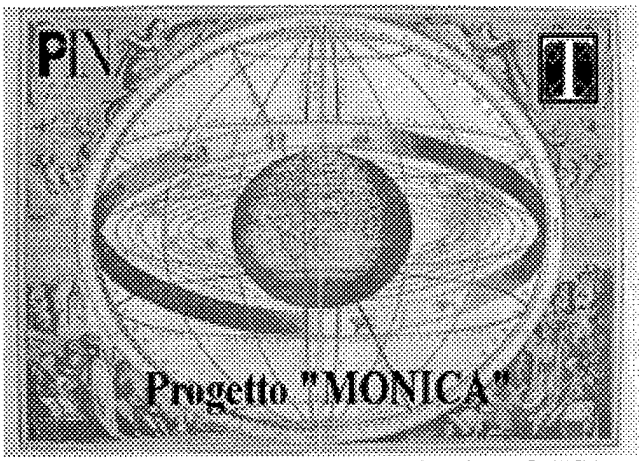


Fig. 3 - A sample from CD-ROM for MONICA

In order to estimate the degree of effective learning and the appreciation of students with regard to these methodologies, evaluating tests have been carried out.

A crossed estimation of the results has pointed out that, in spite of the peculiarity of the courses, learning and appreciation have been so satisfactory that this project will flow into new courses in collaboration with the Tuscany Region.

CONCLUSIONS AND PERSPECTIVES

The Tuscany Region has considered environmental monitoring and remote sensing as the pillars of the vocational training. In this context the PIN has been set up in 1995 as a Center of Regional Interest in solving all those problems in relationship to the environmental field.

In this first year the educational training activity from 1995 to 1998 has been planned: it takes into account 30 projects at a regional and a European level.

As to certain projects, the first phase has already been achieved, at the end of which we have observed a high degree of appreciation towards the contents of these training courses.

As to the future, the other training projects are in progress. One of the most relevant, in the field of RS is the so called METEOSSE, whose tasks are the design and the implementation of courses in the field of meteorological observations, based upon the use and the integration of multisensor data coming from advanced sensors for RS (radar, satellite, and so on). One of the main goals of this project is to define professional profiles to be employed in the field of the advances of MCE and RS.

ACKNOWLEDGMENTS

A lot of people have dealt with the institution of the C.I.R. at PIN's, and it is important to thank them as a whole.

In particular, as to MONICA project, it is dutiful to mention, among people of our team, Ing. Elena Palmisano - Coordinator and Ing. Maurizio Masseti - Editor of Multimedia Support.

REFERENCES

[1] Commission of the European Communities "Growth, Competitiveness, Employment. The challenges and ways forward into the 21st century- White Paper"

[2] Regione Toscana "Nuova Disciplina in Materia di Formazione Professionale". L.R. n° 70, 31-08-1994

[2] D. Giuli "Piano di Sviluppo Triennale " Internal Report, July 1995

[3] S. Cuomo "Progetto MONICA, Valutazioni didattiche" to be published

[4] D. Giuli. *et alii* "Progetto MONICA. Final report" to be published

Development of a Remote Sensing Core Curriculum
submitted for the sessions on educational initiatives in Geoscience and Remote Sensing

Dr. John E. Estes (corresponding author)
Professor, Department of Geography
University of California
Santa Barbara, California 93106
phone: 805 893 3649/fax: 805 893 3703/email: estes@geog.ucsb.edu
and
Dr. Timothy Foresman
Assistant Professor, Department of Geography
University of Maryland
Baltimore County, 21228-5398
phone: 410 455 3149/fax: 410 455 1056/email: foresman@umbc.edu

A Remote Sensing Core Curriculum (RSCC) development project is currently underway. This project is being conducted under the auspices of the National Center for Geographic Information and Analysis (NCGIA). RSCC is an outgrowth of the NCGIA GIS Core Curriculum project. It grew out of discussions begun at NCGIA, Initiative 12 (I-12): "Integration of Remote Sensing and Geographic Information Systems". I-12 participants stressed the need for up-to-date classroom materials to stimulate remote sensing education in our colleges and universities. This curriculum development project focuses on providing professors, teachers and instructors in undergraduate and graduate institutions with course materials from experts in specific subject matter for areas use in the class room.

Currently, curriculum materials are being developed for four courses: 1. Aerial Photographic Interpretation; 2. Remote Sensing of the Environment; 3. Introductory Digital Image Processing; and 4. Remote Sensing Applications. Each course in the curriculum will be composed of approximately 25 separate lecture modules. The modules for the applications of remote sensing can also be employed in support of the other three courses. Experts from around the United States are contributing materials. Classroom testing of these materials will occur in the 1996/97 academic year and the curricula will be ready for dissemination, at the cost of reproduction by NCGIA in the summer or 1997.

The RSCC project is coordinated by Dr. Timothy Foresman of the University of Maryland, Baltimore County. Funding for the project is being provided by a number of organizations including among others: The National Aeronautics and Space Administration and EOSAT Corporation. Project steering committee members come from academic institutions across the United States and EOSAT. These academic institutions include: The University of California, Santa Barbara; the University of Maryland, Baltimore County; Clark University; Georgia Tech; The University of South Carolina; and the Desert Research Institute of the University of Nevada, Reno.

0-7803-3068-4/96$5.00©1996 IEEE

Creation of a "Remote Sensing Core Curriculum" represents a logical extension of the National Center for Geographic Information and Analysis's activities towards establishing curriculum materials. Creation of this curriculum an outgrowth of ASPRS Education Committee activities; but more directly NCGIA research initiative #12 titled "Remote Sensing and Geographic Information Systems." This initiative, identified the "urgent need for educational materials stressing the integration of remote sensing and GIS" [1]. At this time Dr. Arturo Silvestrini, president of EOSAT, approached Dr. John Estes with an offer of support to initiate a remote sensing core curriculum. With EOSAT's sponsorship, a meeting was held in September, 1992, and a steering committee of university and industry specialists established to develop the Remote Sensing Core Curriculum program. This steering committee generated a conceptual framework for a national and international remote sensing education curriculum that was presented to the ASPRS membership [1]. A set of eleven core courses was suggested to represent the fundamental topics for comprehensive education in the discipline and technologies of remote sensing. These include: Introduction to Electromagnetic Energy Theory; Airphoto/Photogrammetry; Overview of Remote Sensing for the Environment; Remote Sensing Field Techniques; Thermal Infrared Remote Sensing; Microwave (Active and Passive) Remote Sensing; Introductory Digital Image Processing; Advanced Digital Image Processing; Interface of Remote Sensing and GIS; Remote Sensing Applications; and Database Development.

As a practical matter the steering committee selected a set of four high priority topics with principal volume authors for initial emphasis. It was envisioned that each volume would have approximately 15 lecture modules developed in cooperation with contributing author/experts.

- Vol. 1. Airphoto/Photogrammetry - Star (deceased 1994), Estes, and Jensen.
- Vol. 2. Overview of Remote Sensing for the Environment - Cary, Estes, and Faust.

- Vol. 3. Introductory Digital Image Processing - Jensen, Faust, and Eastman.
- Vol. 4. Remote Sensing Applications - Foresman, Eastman, Cary, and Shupin.

A proposal was submitted in 1994 to the National Aeronautic and Space Administration's (NASA) Office of Mission to Planet Earth (MTPE) seeking development funding for the initial four volumes listed above [2]. A two-year award was granted by NASA MTPE in May of 1995 to create the "NCGIA Remote Sensing Core Curriculum." Currently the program is focused on development of the draft volumes with an expected beta-testing release date of early summer 1996. An operational release date for all four volumes is summer 1997.

The academic community targeted by the Remote Sensing Core Curriculum encompasses the variety of engineering, Earth science, life science, and social science departments that represent the multidisciplinary community interested in remote sensing technology and applications [3, 4, 5, 6, 7]. Instructors from agronomy, biology, ecology, geography, geology, soils and Earth science, marine biology, and oceanography can expect to incorporate the RSCC materials into their own lectures. This approach provides a robust set of resources to any specific or hybrid discipline dealing with Earth's surface and human interaction phenomena.

The development of any curriculum materials at the collegiate level must anticipated some level of academic background on the part of the student. RSCC materials are being developed so that students with a basic, general science background can begin the sequence of courses. This general science background would include basic biology, chemistry and physics along with math to the level of beginning calculus. Due to the varying nature of exposure of today's students to differential and integral calculus, however, where ever possible materials and exercises will present mathematical concepts in algebraic form. While many of the courses in the RSCC will build upon one another, they need not be taken in strict sequence. It is generally recommended that the students enter through the air photo interpretation/ photogrammetry or Introduction to Remote Sensing courses.

The educational setting for which this sequence is designed is somewhat of a shifting target. The assumptions for distribution of RSCC materials have been in a constant state of change since the first meetings of the steering committee in 1992. We have shifted from pseudo static printed media, to a discussion of CD ROMS, to a dynamically updated Internet medium with printed text support. Today, University faculty access to the Internet is almost universal. This ability, to acquire data over the Internet, marks a significant change in the manner in which we as educators can access remote sensing data and information for use in the classroom. While computing resources many vary significantly from campus to campus, both nationally and internationally [8], the Internet medium has, for the purposes of this effort, dampened this disparity in educational resources. Basically, the Internet has helped to make the data/information access playing field a little more level. There is, however, still a significant range in performance capabilities and Internet interface software at the university workstation level (UNIX, PC, and Macintosh). This variation in performance capabilities may impact the ease with which faculty may access and use RSCC resources.

The development of the four courses which make up the initial RSCC offering can be monitored by accessing the RSCC Homepage at: http//www.umbc.edu.rscc. Each volume under development will eventually contain some 20-25 lecture outlines (referred to as modules). These modules maybe in either outline or text form. It should be noted here that RSCC materials are not a text for a course in any of the subjects covered. they are to be used by instructors to enrich their lectures with materials and presentation flows employed by recognized experts in the field covered by that particular module. The modules cover the topic in each course in the sequence that would normally be followed by an instructor. Many of the modules are being developed by recognized experts who have responded to advertised solicitations for the input of materials. Again, topic module may be in outline or text form and they contain selected references and graphics along with excercises where appropriate; hopefully, providing additional resources to instructors trying to cover a wide range of topics interdisciplinary subject matter in these courses.

A critical requirement to understanding the the principles and methodologies of remote sensing is access to excercises and applications that build upon and reinforce the knowledge base of student which they have gained through lectures. RSCC Excercise are being formatted through the the resources of the Idrisi project at Clark University. Each excercise and application module containing remotely sensed data and ancillary field data sets will be tested for performance at downloading via the Internet and operated on computing platforms typically found in university departments (i.e., operating system: DOS, Windows, Macintosh and UNIX). Our goal is to provide RSCC u with the tools, techniques and methods necessary to convert the volume excercises, and accompanying remote sensing data into their university's existing software environment.

Principals with NASA MTPE'S Educational Programs Office have outlined a policy oriented towards interconnections and coordination among its sponsored grant activities. RSCC has initiated communication with a variety of Earth science and remote sensing education programs. Most of these programs are for a general audience, targeting the K-12 education community. A few of these programs target high school and junior college levels. Industry and commercial vendor information will become an integral part of the RSCC Homepage to facilitate access to remote sensing information and software support resources. This information

can assist faculty in making informed decisions on the performance characteristics of software, hardware and peripherals, as well as digital data products appropriate to university settings. The remote sensing business community has been very supportive in the past of continued education and training. Major industry leaders, such as EOSAT (Lanham, MD), ESRI (Redlands, CA), and Intergraph (Huntsville, AL), have fully endorsed the RSCC since is inception [2]. Recently, many other software vendors such as ERDAS Corp (Atlanta, GA), PCI Inc. (Toronto, Canada) and ER Mapper (San Diego, CA) have pledged their support to help the RSCC a successful international, collegiate educational program.

In the era of Mission to Planet Earth's Earth Observing System and the tremendous growth in commercial remote sensing systems, the need for highly-trained professionals becomes paramount for the health and viability of the remote sensing community. The Remote Sensing Core Curriculum is attempting to provide state-of-the-practice resource materials and curriculum guidance to reach the nation's, as well as international, universities and colleges that might not otherwise have the resources necessary to meet this increasing educational demand. The remote sensing demand has been well documented [9, 10, 11] and can only be expected to rise as new discoveries and results from the orbiting satellite platforms reach the scientific community. Access to advanced computing technology, and the paradigm shift in communications afforded through the Internet, offer impressive opportunities to reach the broad national and international collegiate audiences. Under the capable management of ASPRS, the RSCC can be expected to provide a major foundation for tomorrow's technology leaders.

ACKNOWLEDGMENT

EOSAT and under NASA Grant #NAGW4419 have provided support for this work. Appreciation is extended to our colleagues on the Steering Committee, Tina Cary, Ron Eastman, Nick Faust, Karen Kemp, John Jensen, Ken McGwire, and Tony Shupin.

REFERENCES

[1] Jensen, J., 1993. The NCGIA Core Curriculum in Remote Sensing., Photogrammetric Engineering & Remote Sensing, 59 (6):945-948.

[2] Foresman, T. W., 1994. NASA Headquarters Research Grant No. NAGW 4419, "Research and Development for Remote Sensing Applications Supporting a National Remote Sensing Core Curriculum: A Necessary Precursor to Earth Systems Science Education.

[3] Dalhlberg, R., and J. Jensen, 1986. Education for Cartography and Remote Sensing in the Service of an Information Society: the U.S. Case, The American Cartography, 13; 51-71.

[4] Kiefer, R. W., 1988. Survey of Photogrammetry and Remote Sensing Programs and Courses in the United States and Canada, America Society for Photogrammetry and Remote Sensing, Bethesda, Maryland.

[5] Morain, S., 1992. Status of Photogrammetry, Remote Sensing, and GIS in the U.S., Photogrammetric Engineering & Remote Sensing, 58(8):1073-1076.

[6] Nellis, M. D., R. Lougeay, and K. Lulla, 1989. Interfacing remote sensing research and instruction. Proceedings of Current Trends in Remote Sensing Education, Geocarto International Center, Hong Kong, pp. 1-3-3.

[7] Sader, S. A., R. M. Hoffer, and E. W. Johnson, 1989. The status of remote sensing education. Journal of Forestry (10): 25-30.

[8] Foresman, T. W., 1995. Academic Research and Education in GIS, GIS World Source Book 1996.

[9] Civco, D. L., R. W. Kiefer, and A. Maclean, 1992. Perspectives on Earth Resources Mapping Education in the United States., Photogrammetric Engineering & Remote Sensing, 58 (8): 1087 1091.

[10] Estes, J. E., J. Star, and M. Goodchild, 1990. Educational activities in remote sensing and GIS at the national Center for Geographic Information and Analysis. Proceedings for the ISPRS Working Group VI/VII on "Education, Training, and Educational Standards for Remote Sensing and GIS," Rhodes, Greece.

[11] Jensen, J., 1989. Remote sensing education: Present realities and future potential. Proceedings of Current Trends in Remote Sensing Education, Geocarto International Center, Hong Kong, pp. 81-86.

What kind of images do I need ? What is the delay to obtain them ?

S. Houzelle, P. Bellemain, J. Amalric, P. Herry
Aerospatiale, B.P. 99, 06322 Cannes la Bocca Cedex, FRANCE
Tel : (+33) 92 92 74 76, Fax : (+33) 92 92 71 60, email : setot@cannes.aerospatiale.fr

Abstract -- This paper presents a software architecture that first suggests concurrent sets of images that can be used to answer a thematic issue, second, sorts the sets of solutions to match user preferences, and third, gives a mission planning scheme for image acquisition in order to have an estimation of the overall delay required to solve the thematic problem. The main characteristics of this architecture are that problem analysis and decision making are separated in order to satisfy a large number of users and that mission planning uses a scheduling algorithm that globally plans all ground based and on orbit activities from problem statement to problem resolution.

INTRODUCTION

Nowadays, several kinds of satellite images are available, and selecting an image, or a set of images, to solve a particular problem (a cartographic problem, an agriculture related problem...) can be a real headache for someone who doesn't have a serious background in remote sensing and image processing. There is a risk to order non adapted images, and to loose time in processing these images or in ordering other ones.
Another important point is to be able to know how long it is going to take to solve the problem. To answer this question the time required to acquire images must be known. This mission planning problem requires also serious orbitographic knowledge to be solved.
Different approaches of mission planning can be found in literature [1,2], but no one proposes the suggestion of appropriate images associated to it.
Thus, this paper presents a software which, to answer a thematic issue (in cartography, geology, telecommunication...), aims at :

- suggesting concurrent sets of images, possible solutions to the problem,
- sorting the solutions to match user preferences,
- giving a mission planning scheme for image acquisition in order to estimate the delay required to solve the problem.

This software architecture is dedicated to non experts in image processing who realize all the potentialities of satellite images but don't know which ones they need for their application.
First the general architecture of the software is presented. Then the main functions of the architecture are presented : Problem Formulation, suggestion of a concurrent set of images (Problem Analysis), Solution Sorting and Mission Planning.

ARCHITECTURE

As depicted on Figure 1, the system is divided into four main functions :

Problem Formulation : This function is a user interface. The user selects a *product* and its characteristics.
The notion of product has been chosen to be quite general in the way of formalizing a domain specific problem.

Problem Analysis : This function analyses the product and translates it into images to acquire.
Analysis is performed using a modeling of defined sensors, definition of the product, and expert rules.

Solution Sorting : This function sorts solutions using user defined criteria.

Mission Planning : For each solution, this function gives an estimate of the overall time required to answer the thematic query with this solution.

Each function is activated once. Thus, Problem Analysis function has to generate enough solutions, all as different as possible, to ensure an effective sort of these solutions, and to give maximum chances to mission planning to succeed on at least one solution.

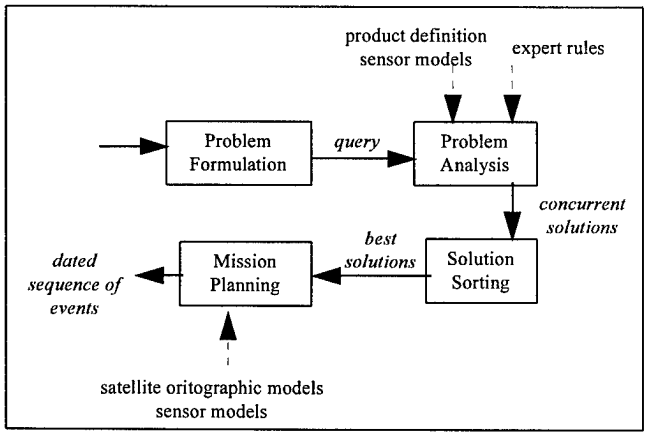


Figure 1 : general scheme

0-7803-3068-4/96$5.00©1996 IEEE

Solution generation (Problem Analysis) and solution selection (Solution Sorting) are independent. This ensures that a solution won't be declared non adapted before being compared with other solutions.

Mission Planning can be performed on a selection of solutions because this function is time consuming.

We do think this architecture is quite general and can be applied to a wide range of application domains. If the domain changes, the user interface, the products and the expert rules have to be modified, but the generic architecture can remain unchanged.

PROBLEM FORMULATION

A user queries the system by choosing a product among pre-defined ones. A product can be image related (DTM, image classification...) or domain specific (soil humidity, ice classification, urban area detection...). Its definition generally contains objects that have to be observed in images in order to make the product.
Temporal acquisition constraints can also be specified if, for example, more than one acquisition is desired. The user can also specify the maximum number of images he wants and their maximum cost. Finally, restrictions on desired images can be directly specified, for advanced users who have notions of images they need. For example, a user can specify he only wants radar images, or images with better resolution than 10m...

PROBLEM ANALYSIS

This function analyses the user defined product and translates it into images to acquire or to retrieve from an archive. Each image included in a solution is specified with the following characteristics :

- satellite family (ex : SPOT-1-2-3). The name of a particular satellite within a family (ex : SPOT-1) is not fixed. Mission planning will choose which satellite is better to minimize acquisition time.
- sensor (ex: HRV)
- sensor mode (ex : XS)
- incidence angle range
- geographic coordinates of area of interest
- observation date ranges
- polarization and number of look for radar images

Analysis is performed in two steps (cf. Figure 2). The first one is an initialization step and consists in creating an initial set of solutions. This set contains one solution per defined sensors and mode of sensors. The second step is an expertise step and consists in evaluating the solutions already created, fixing their characteristics, and creating new solutions by adding images to a solution to improve it, if necessary. Hence, solutions are multisensor and are based on redundancy or complementary of sensors depending on the user product.

To be adaptable to various kind of application domains, expertise is performed using *specialist modules*. Each specialist is in charge of evaluating a particular characteristic of a solution. Some specialists are domain specific, and their functionality depends on the products defined in the system. It is the case of the sensor specialist which evaluates the adequacy between sensors indicated in a solution and the user product. The resolution specialist is also specific and evaluates the sensor resolution adequacy with the product...
Other specialists are more general, like the cost specialist that evaluates the cost of a solution (sum of image prices) and check its compatibility with user financial constraints.
Specialists use expert knowledge and user product specification for their evaluations.
Output of this function is a set of concurrent solutions. Each solution is evaluated from different points of view. Basically there is one point of view per specialist. For example, each solution may contain a sensor adequacy evaluation, a resolution adequacy evaluation,...

SOLUTION SORTING

This function allows sorting solutions to find out what are the best ones for each user. Therefore, the user chooses a *sorting strategy* (during Problem Formulation). This strategy is composed of a list or sorting criteria. The first criterion is the most important for the user, and the last, the less important. Sorting criteria are those defined in specialist modules during the preceding Problem Analysis.

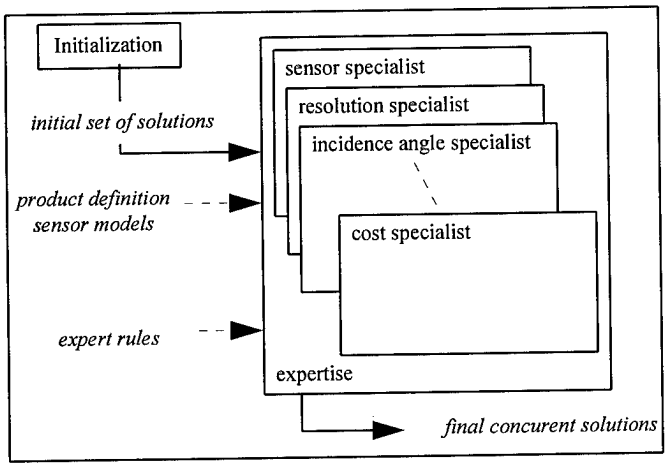


Figure 2 : Initialization and Expertise by specialist modules

Sort is being processed on the first criterion. Equivalent solutions from this point of view are then sorted with the second criterion, etc.
Using this method, each user can sort solutions taking into account his own needs.

MISSION PLANNING

This function takes as input a solution and schedules all its activities from problem statement to problem resolution. It answers the following questions : When my problem can be solved, and is it compatible with the time I have ?
For each image acquisition included in the solution, following ground based and on orbit activities are modeled (cf. Figure 3) :

- Problem formulation (system query) at the query analysis center,
- Processing of image ordering at mission planning center,
- Satellite programming at a command ground station,
- Satellite observation,
- Data acquisition at a reception ground station,
- Data processing at satellite data processing center to create images,
- Image processing to answer the problem.

First, activity duration and precedence delays between these activities are evaluated. Then, all activities are scheduled and resources are allocated.
Scheduling of activities of all images is performed in a single process. Thus, conflicts between concurrent resources (ground stations for example) are managed correctly.
Principal constraints taken into account are :

- Geometrical accessibility to an area of interest from an orbit,
- Ground station/satellite visibility,
- Operational availability of ground centers,
- Sun lightning of the area of interest(day, night).

Satellite orbitographic model used by the system is generic for all satellites. Hence it is simplified and cannot be compared to any ground station satellite programming models. More over, external conflicts of scheduling, and system failures cannot be modeled. Thus output of this function is only a rough estimation of satellite system planning that can be reconsidered due to model precision or external problems.

CONCLUSION

We have presented a software architecture that suggests a set of images that can be used to answer an image based problem, and gives a mission planning scheme for image acquisition in order to estimate the delay required to solve the problem.
The architecture design verifies the following main characteristics : formalizing of query is made in terms of product, problem analysis is divided into points of view that are general or domain specific, solution creation and solution selection (sorting) are independent, and mission planning is performed globally on all activities.
This design ensures reliability, performance and reusability in various domains of application.

REFERENCES

[1] A. Charalambides, « SIMIS : A Mission Operation Simulator », Third Workshop on Simulators for European Space Programs, ESTEC Noordwijk, The Netherlands, 1994.

[2] V. Gabrel, « Methologie pour la planification de production de systèmes d'observation de la terre par satellites », These de l'université Paris-Dauphine, 1994. In French.

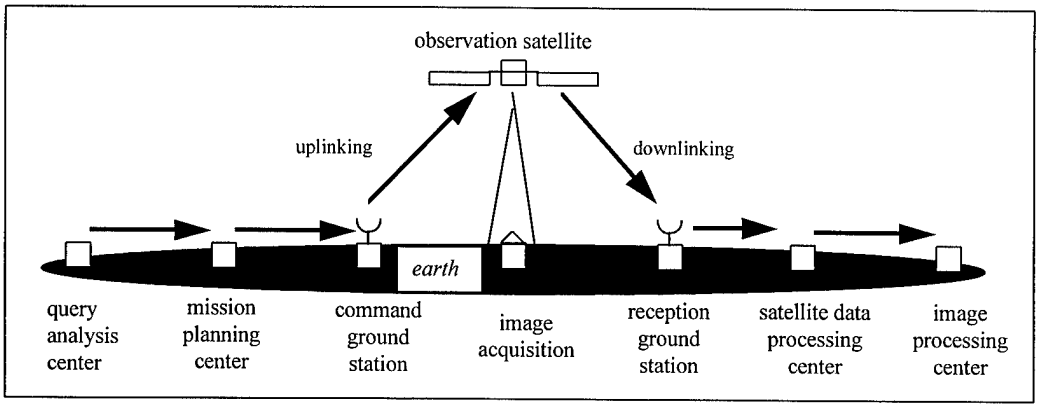


Figure 3 : Details of modeled activities and communications

Conference Author Index

A

Aarholt, E. 1736
Aas, K. 2307
Abel, P. 1816
Abshire, J. B. 1538
Abuelgasim, A. A. 1426
Adah, T. 700
Advokatov, V. R. 1947
Ahamad, A. 1266
Ahmed, R. H. 2369
Ahola, P. 1998
Ahuja, L. R. 1058
Aiazzi, B. 411, 460, 1042
Akpa, S. *
Alba, P. S. 460, 1042
Alberta, T. A. 1911
Alexander, D. R. 857
Alfoldi, T. T. 324
Alfultis, M. A. 1165, 1504
Alhumaidi, S. M. 1526
Allan, N. 905, 1745
Allen, C. 1932, 2033, 2036
Alparone, L. 411, 460, 1042
Alpers, W. 860, 1370, 1478, 1487
Alumbaugh, D. L. 1941
Alves, M. 830
Amalric, J. *
Amar, F. *
Amodeo, G. 736
Amsbury, D. L. 929
Andary, J. 2160
Anderson, L. E. 1877
Anderson, M. C. 2104, 2358
Anderson, M. R. 959
Anderson, R. *
Andreadis, A. 377
Andres, P. *
Angarkhaeva, L. H. 1945, 1947
Anterrieu, E. 869
Antoniou, A. 990
Arakelian, A. K. 625, 811, 885
Arakelian, K. A. 885
Arbelo, M. *
Arca, G. 520, 854
Armour, B. 339
Arnason, K. 414
Arnaud, A. *
Arnavut, Z. 463
Arnold, D. V. 1475, 1892
Arnon, I. *
Arst, H. 76
Arvidson, T. 2160
Asae, M. 1666
Askari, F. 1141
Asner, G. P. 1663
Atakturk, S. S. 805
Attema, E. 1995
Auer, T. 484
Austin, A. *
Awaya, Y. *
Axelsson, S. R. J. *
Aydin, K. 560, 563
Azimi-Sadjadi, M. R. 1105, 1108

B

Bachem, A. 282
Bachmann, C. M. 356
Baggeroer, P. A. 145
Bahar, E. 1794, 2170, 2177, 2180
Baikalova, T. V. *
Baker, J. *
Bakhanov, V. P. *
Bakhanov, V. V. 609
Baldini, L. 7, 1367
Ballard, J. 2146
Balsiger, F. 1826
Balzer, W. 2291
Bambha, R. 1553
Bamler, R. 1217, 2050
Band, L. E. 212, 420
Banik, R. 1290
Bao, M. 860, 1370
Bara, J. 315, 869
Baraldi, A. 709
Barber, D. G. 953, 1187, 1552, 1992
Barbier, C. 251
Barbosa da Silva, V. 374
Barclay, H. 1873
Barker, J. L. *, 1270, 1276, 1600
Barkerm, J. L. 1273
Barnett, J. 2149
Baronti, S. 411, 460, 1042
Barstow, D. 631, 925
Bartel, L. C. 1935
Barter, J. D. 618, 2201, 2213
Bartoloni, A. *
Barwell, B. R. 1438
Bashkuev, Yu. B. 1945, 1947
Bates, J. J. 1710
Bateson, C. A. 1663
Batista, G. *
Batz, O. 872
Bauer, A. *
Bayma, R. W. 1615
Beach, K. L. 2201, 2213
Beal, R. C. *, 896, 1143
Bearman, G. H. *
Beaven, S. G. *, 115
Becchi, I. 1312
Beh, B. 996, 1266
Belchansky, G. I. 642
Belisle, W. R. 1315
Bellemain, P. *
Belliss, S. 1839
Belongie, M. 1035
Belova, N. I. *
Belward, A. *
Belyaev, B. I. 19, 366
Belyaeva, T. A. 1323
Bencherif, H. 10
Benediktsson, J. A. 63, 414, 1848
Benelli, G. 377
Bennardo, A. *
Bennett, J. C. 2344
Benson, C. S. 2246
Bentamy, A. 805
Bergen, K. M. 580, 1092, 1568
Bergen, Z. D. *
Bergen, Z. 659
Berizzi, F. 1230
Bersano-Begey, T. F. 1520, 2077
Berthod, M. *, 25, 345
Bertram, R. R. 2219
Bertrand, J. 2080
Bertrand, P. 2080
Bessafi, M. 10
Betty, C. L. 2183
Betty, C. 2186
Beus, S. E. 1263
Bhogal, A. S. 1873, 2303
Bianchi, R. *
Bicheron, P. 1901
Bickel, D. L. 2063
Bickel, D. 659
Bidwell, S. W. 402, 1550
Bird, P. 493
Bisson, S. E. 691
Bixler, P. *, 631
Bjerkelund, C. 1155
Bjorgo, E. 932
Blair, J. M. 2361
Blanchard, A. J. *
Blanco, A. 76
Blankenship, C. B. *
Blari, J. B. 1806
Blonda, P. *
Blurton, C. 917
Boback, J. P. 1692
Bobrov, P. P. 2192
Bock, E. J. *
Boehnke, K. *, 839, 2014, 2264
Bogaturov, A. N. 369
Boller, B. D. 269
Bolus, R. L. 1073, 2375
Boncyk, W. C. 1270, 1273
Boncyk, W. 1276
Borak, J. S. 243
Borak, J. 233
Borderies, P. 2167
Borel, C. C. *
Borocz, S. 697
Bosdogianni, P. 1379
Bostater, C. *
Botman, A. M. 324
Bottger, H. 2341
Botti, J. A. 1506
Boucher, D. J. 1704
Bourbigot, K. *
Bourdeau, M. 833
Boutry, J. M. *
Boyarskii, D. A. *
Brakke, T. W. 1657
Brammer, C. *
Brandt, P. 1487

*Author's paper not available at the time of printing.

Braswell, B. H. *
Breaker, L. C. 1712
Bredow, J. W. 863, 947, 2288
Brennan, T. J. 2222
Bresci, E. 1312
Briggs, J. M. 2361
Brisco, B. G. *
Brisco, B. *
Brodley, C. E. 532, 1382
Brown de Colstoun, E. C. 1904
Brown de Coulston, E. 586
Brown, G. S. 2119
Brown, R. A. 805
Brown, R. J. *
Brownsword, C. 1141
Bruegge, C. 1279
Brugman, M. 2255
Bruniquel, J. 387, 662
Bruzzone, L. *
Buckley, J. R. 808
Buckley, J. 1155
Budge, A. *
Bufton, J. L. 423
Bugden, P. *
Bulatov, M. G. 1490
Bulgarelli, B. 1584
Bullock, P. R. 1992
Bundschuh, B. O. 999
Bur, M. C. *
Burgess, M. P. 1618
Burkhart, G. R. 659
Burns, B. E. 2020
Burns, B. 1881
Byrd, M. *

C

Caffey, T. W. H. 2023
Callaghan, G. 796
Cames, A. 869
Campbell, J. W. M. 1146
Campbell, J. W. 1621
Campbell, J. 1155
Capms, A. 315
Capolino, F. 13
Carande, R. E. *, 665, 1211
Carande, R. 659
Carayon, G. 273
Carello, R. 1953
Carlotto, M. J. 34, 2089, 2164
Carpenter, G. A. 529
Carsey, F. 634, 1181, 1775
Carswell, A. I. *
Carswell, J. 1385, 1466
Casar Corredera, J. R. *
Caselles, V. *
Cavalier, D. J. 2246
Cavalieri, D. J. *, 956, 1523, 1529
Cavalli, R. M. *
Cavallo, A. *
Cavayas, F. 236
Caylor, I. J. 1550
Cazaban, F. 387
Cazzaniga, G. 1845
Celani, C. *
Cespedes, E. R. *, 857
Chabert, M. 1842
Chadwick, D. J. 2134
Chadwick, R. B. *
Chagnon, R. *
Chakrabarti, S. 1867
Chan, S. S. 1005
Chan, T. K. 2137, 2140
Chandrasekar, V. 566, 574
Chang, A. T. C. 2011, 2246
Chang, P. *, 1123, 1707
Chang, S. Y. S. 85
Chapman, B. 823, 830
Chapman, R. D. 1736
Chappelle, E. W. 1812
Chapron, B. 600, 606, 612, 621, 1385, 1389
Charlebois, D. 1873, 2303
Chauhan, N. 2146
Che, C. Y. *
Che, X. *
Chen, C. 551
Chen, G. 2240
Chen, H. *
Chen, J. M. 586, 1651
Chen, J. *
Chen, K. S. *, 1297
Chen, L. 1908
Chen, M. *, 43
Chenebault, J. 279
Chenerie, I. 2167
Cheng, H. D. 133
Cheng, S. Y. S. 380
Cherny, I. V. 360, 1968
Cheshire, H. 1609
Cheung, K. 1035
Chiaradia, M. T. 2060
Chinchilla, N. 891
Chiu, T. C. 1070
Chiu, T. 2122
Cho, J. Y. N. 1926
Cho, S. 1977
Choi, J. 469
Choi, M. Y, 628
Choi, S. K. *
Chong, C. C. 180
Choudhury, B. J. 106
Chrien, T. G. *
Chu, A. *, 43
Chubb, S . R. 902, 911
Chugurin, V. V. *
Chun, C. 396
Churilov, V. P. *
Churnside, J. H. 1328
Cialella, A. T. 1904
Cihlar, J. *
Cipollini, P. 91, 1398
Ciucci, A. 520, 854
Clabau, P. 70
Clark, J. H. 1146
Clark, S. 881
Claude, J. 869
Clifford, S. F. 1739
Clift, S. 1293
Clothiaux, E. E. 356
Cloutier, C. *, 1290
Coan, S. M. *
Cohn, S. A. 1914
Coleman, T. L. 1315
Collins, J. D. *
Collins, M. J. 2068
Collins, M. 1141, 2027
Colpitts, B. G. 2189
Coltelli, M. 350
Comiso, J. C. 2008
Compton, M. 1211
Console, E. 1376
Cooper, A. L. 902, 911
Cooper, D. I. *
Cooper, D. *
Coppo, P. 2131
Corbella, I. 315, 869
Corner, B. R. 1920
Cornwall, J. M. 2347
Corp, L. A. 1812
Corsini, G. 290, 1230, 1398
Cowen, R. *
Coyle, D. B. 1806
Crawford, J. P. 1775
Crawford, M. M. *, 263, 1870
Cremers, D. A. *
Cress, D. H. 1935
Crevier, Y. *
Croft, S. K. *
Cromwell, D. 91
Crowley, R. D. 269
Cruz Pol, S. L. 1435
Csillag, F. 2377
Csiszar, I. 1114
Cubero-Castan, E. 457
Cuddy, D. 1358
Cui, T. J. 763, 766, 1340
Cumming, I. 336, 2044, 2255
Cuomo, S. 817
Curlander, J. 1775
Curtis, J. O. 2030, 2282

D

Dabney, P. W. *
Dahl, P. 2270
Dai, X. 1609
Daida, J. M. 891, 1520, 2077, 2219
Dall, J. 276, 1629
D'Amelio, C. *
Damen, M. C. J. 2240
Damiao, D. P. *
Dano, E. B. 2195, 2198
Dano, E. 1158
Daout, F. 615, 746
Das, J. *
Datcu, M. *, 310, 2054
Daughtry, C. S. T. 224, 1803, 1812
Daum, D. R. 1606
Davidson, A. 2377
Davidson, G. W. 2050
Davidson, G. 1217
Davidson, K. L. 1260
Davidson, K. 1158
Davidson, M. W. J. 1980
Davis, C. H. 1783
Davis, F. W. 1077, 1083
Davis, R. E. 254, 754, 757
Davis, R. 591
Davis, S. *
Dawn, D. R. 848
Dawson, M. S. *, 1297
Day, J. L. 1083
De Abreu, R. A. 639
Debinski, D. 2300
De Carolis, G. 1306

Dechambre, M. 833
Dedieu, G. 2366
Deering, D. W. 1654, 1897
DeFries, R. 535
De Grandi, G. 1574, 2086
Dekker, A. G. *
Delaney, P. A. 987
Delignon, Y. 70, 706
Dellepiane, S. 714
Demarest, K. 778
Demarez, V. 1002, 1660
de Matthaeis, P. 736
de Miguel-Vela, G. *
Derksen, C. P. 127
Desachy, J. 2074
Deschaux-Beaume, M. 387
Desjardins, R. 236
Desnos, Y. L. 1217, 1355
De Troch, F. P. 1303
Diak, G. R. 2104, 2358
Diani, M. 1230
Diaz, J. P. *
Di Bisceglie, M. 1580
Dickinson, S. 805
Dietrich, S. *
Diffendal, R. F., Jr. 1017
Dimaio, S. P. 2020
Diner, D. 1279
Ding, K. H. 757, 1208
Dionisio, C. 28
Dmitriev, W. V. 1950
Dobson, F. W. 1155
Dobson, M. C. 580, 1092, 1093, 1568, 2335
Dolash, T. 697
Domanov, M. M. *
Donato, T. 1141
Donelan, M. A. 2210
Donelan, M. *
Dong, Y. 1556
Donnelly, W. 1385, 1466
Douglas, D. C. 642
Doviak, R. J. 1914
Dozier, J. 2002, 2249
Driese, K. L. 186
Drobot, S. D. 1187
Drucker, R. 1190
Du, L. J. 439
Dubayah, R. O. 2149
Dubbert, D. 1881
Dubina, I. N. *
Dufrene, E. 1002
Dugan, J. *
Dunagan, S. E. 2276
Dupont, S. 25, 345
Dutra, L. *
Dwyer, J. L. 547

E

Early, D. S. 124
Eastwood, M. L. *
Ebel, R. *
Echavarria, F. R. *
Eck, T. F. 1897
Edelsohn, C. R. *
Ediriwickrema, D. J. 793
Edson, J. B. *
Ehrismann, J. 339
Eichinger, W. *
Eis, K. E. 1105, 1108
El-Khattib, H. M. 1756
El-Mowilhi, N. M. 1756
El-Shenawee, M. 2170
Elachi, C. *
Elfouhaily, T. 600, 606, 621, 1389
Eloranta, E. *
Emblanch, C. 1067
Emery, W. J. 186, 1138
Emery, W. 192
Ender, J. H. C. *
England, A. W. 2155, 2267, 2270
Engman, E. T. 1058, 1064, 1297, 2237
Entekhabi, D. 1076
Erasmi, S. *
Erbie, E. 2011
Eriksson, M. *
Ersoy, O. K. *
Erxleben, W. H. 1014
Espedal, H. A. 1158
Estes, J. E. 198, 820, 2242, 2321
Etling, D. 1478
Evans, K. *
Exposito, F. J. *

F

Facheris, L. 7, 13
Falls, M. J. 1681
Fang, Y. 496, 1266
Fedele, G. 383
Federici, G. 817
Fedor, L. S. 1450, 1681
Fedoseev, Y. G. *
Fellerhoff, J. R. 659
Fellerhoff, R. 1881
Ferguson, S. 1526
Fernandes, D. 1227
Fernandes, R. 212, 420
Fernandez, D. M. *, 1749
Fernandez, D. *
Ferrare, R. A. 1685
Ferrare, R. *
Ferrazzoli, P. 736
Ferris, M. J. *
Field, C. T. 1800
Filho, O. R. 1986
Firda, J. M. 1
Fischer, A. 2366
Fischer, K. W. 648, 694
Fischer, M. 787
Fiset, R. 236
Fisher, B. 631
Fitzgerald, R. W. *
Fjortoft, R. 457
Flamant, P. H. 4
Floury, N. 836, 842, 975, 1306, 2167
Flynn, T. J. 2057
Fochesatto, G. J. 4
Ford, R. E. 1501
Foresman, T. W. 2242
Foresman, T. 820
Fornaro, G. *, 350, 2047
Forster, B. 1080, 1556
Fortner, R. W. *, 1166
Fortuny, J. *
Foster, J. L. 2011, 2246
Fotedar, L. K. 239
Fowler, C. 73
Franceschetti, G. 51, 350, 680, 2047
Frasier, S. 984, 1730
Frattura, F. 7
Freeman, A. 823, 830
Freemantle, J. *
Frei, M. 1833
Freilikher, V. *
French, N. B. *
Freylikher, V. D. 369
Friedl, M. A. 532, 1382, 2152
Frison, P. L. *
Fritsch, B. *
Frohn, R. C. 2321
Frolind, P. O. 668, 1877
Fromard, F. 733
Frost, E. 925
Frulla, L. A. *
Frulla, L. *
Fuglistaler, S. 342
Fukao, S. 1929
Fung, A. K. *, 772, 947, 1202, 1297, 2008, 2116, 2183, 2186
Furger, M. 399

G

Gade, M. 860
Gagliardini, D. A. *
Gaikovich, K. P. 369
Gaiserl, P. W. *, 1123
Galantowicz, J. F. 1076, 2270
Galbraith, A. E. 683, 1244
Galdi, C. 1580
Galloway, J. 743
Gamba, P. 266, 2071
Garegnani, J. J. 2242
Garello, M. 1584
Garello, R. 612, 621, 1956
Garzelli, A. 377
Gasiewski, A. J. 1120, 1129, 1688
Gasparini, O. 315
Gastellu-Etchegorry, J. P. 1002, 1660
Gatelli, F. 671
Gault, K. A. *, 1221
Gautier, C. 2149
Gazdag, L. 697
Gelautz, M. 31
Gemmill, W. H. 1712
German, M. L. 1441
Gerstl, S. A. W. *, 1642
Geudtner, D. 966, 2255
Giarrusso, J. M. *
Gibas-Tracy, D. R. 2234
Gibbs, D. P. 1541
Gibeaut, J. C. *, 263
Gimond, M. *
Ginzburg, A. I. *
Gird, R. *
Girou, D. *
Gitelson, A. A. *, 2355
Gitelson, A. 209
Giuli, D. 7, 13, 817, 1367
Givri, J. R. *
Gjaja, M. N. 529
Glushko, E. V. 2324
Goblirsch, W. 656

Goel, N. S. 526, 1645
Gogineni, P. 1867
Gogineni, S. P. 115, 1196
Gogineni, S. 1932
Golden, K. M. *
Goldsmith, J. E. M. 691
Golovachev, S. 175
Gomarasca, M. A. *
Gong, P. 2068
Gonzalez, K. D. 1506
Goodberlet, M. A. *
Goodenough, D. G. 1873, 2303
Goodin, D. G. 215
Goodman, N. 2033, 2036
Gopal, S. 529, 538, 787, 1426
Goto, A. 920
Gottfried, J. 1178
Gotwols, B. L. *, 1736
Gouinaud, C. 257, 474
Gourrion, J. 1389
Goutoule, J. M. 869
Gow, A. J. 1184, 1190
Goward, S. N. 1803
Gowda, K. C. 1858
Gower, J. 1146
Graber, W. K. 399
Graf, G. 1355
Grandell, J. *, 583, 1998, 2110
Granhohm, J. 674, 1629
Grankov, A. 175
Grassin, S. 1956
Gray, A. L. 1146, 1155, 1621
Gray, L. 2255
Gray, R. B. 1290
Gray, R. 1352
Green, R. O. *
Greidanus, H. 1633
Grenfell, T. C. 1199
Grindel, M. 999
Grits, Y. 2355
Grodsky, S. A. 1971
Gromov, V. D. 442
Gross, G. 1478
Grunes, M. R. 1574
Guarnieri, A. M. *
Guarnieri, P. 460
Guenther, B. D. 445
Guerra, J. C. *
Guerriero, L. 2060
Guijarro, J. 1355
Guindon, B. *
Guneriussen, T. *
Gurvich, A. S. 369
Gustafson-Bold, C. L. 1283
Gustavsson, A. 1877
Gutierrez, R. O. *, 263
Gutman, S. I. *
Gwilliam, B. L. 1073, 2375

H

Haake, K. 1597
Haas, A. 1080
Haese-Coat, V. 717
Hahn, T. 842
Hall, D. K. 139, 956, 2011, 2246
Hall, F. G. 230, 1657
Hall, K. 254
Hall, S. E. 1498
Hallidin, S. *
Hallikainen, M. *, 484, 583, 1089, 1759, 1998, 2110, 2285
Halthore, R. N. 1904
Haltrin, V. I. 285, 305
Hambaryan, A. K. 625, 811
Hammer, P. D. 2276
Han, L. 1395
Han, Y. 1685
Hanado, H. 487, 512
Hansen, M. 535
Happ, L. 2027
Haptanov, V. B. 1945
Hara, T. *
Hardin, P. J. 827, 848, 1606
Harding, D. J. 1806
Harris, R. 1826
Hart, D. G. 145
Hartnett, J. 1111
Hashimoto, S. 1695
Hassol, S. 1169
Haugen, H. *
Haung, Z. 778
Hautecoeur, O. 204, 1901
Haverkamp, D. 109, 1532
Hawela, F. 1756
Hawkins, R. K. *, 1290, 1621
Hayes, K. *, 1733
Hazen, D. A. 1432
Heer, C. 2341
Hehr, L. H. *
Hein, A. *
Heinrichs, J. 950
Helder, D. L. 1270, 1273
Helder, D. 1276
Hellsten, H. 1877
Hellwich, O. 330, 1836
Henebry, G. M. 166, 195, 215, 448
Henry, J. C. *
Henschel, M. *
Hensley, S. 31
Hensley, W. H. 2063
Hensley, W. 659
Henson, J. M. 254
Herland, E. A. *
Hernandez, P. A. *
Herrera, F. *
Herry, P. *
Hesany, V. *, 888, 1733, 2210
Hesany, *
Hess, L. L. *
Hevizi, L. G. *
Heygster, G. C. 1788
Heymsfield, G. M. 1550
Hicks, M. R. 1504
Hillion, A. 523
Hines, D. 1257, 1385
Hipple, J. 1501
Hirsave, P. P. 1073
Hjartarson, A. 414
Ho, L. L. *
Hochheim, K. P. 1992
Hochschild, G. 436
Hoekman, D. H. 260, 845
Hoffmeyer, P. D. 2030, 2282
Holden, H. M. 427
Holden, H. 88
Holecz, F. 248
Holloway, C. L. 1914
Holt, B. *
Holzworth, R. H. 569
Homer, J. 796
Hood, R. E. 1460
Hoogeboom, P. 1633
Hoogenboom, H. J. *
Hopcraft, G. 1923
Horie, H. 512, 1364
Horn, R. 1624
Hosomura, T. *
Hou, S. 1032
Houzelle, S. *
Howard, S. 246
Howarth, P. J. 1986
Howell, P. B. 1926
Hoyt, P. *
Hsieh, C. Y. 2116
Hsieh, P. 1855
Hsu, A. Y. 1061, 1297
Hsu, A. 1064
Hsu, C. C. 836, 1208
Hu, B. 1587, 1669
Huan, S. 60
Huang, S. *, 1571
Huddleston, J. N. 1718
Huehnerfuss, H. 860
Huemmrich, K. F. 2372
Huete, A. R. *, 157, 1423
Hug, J. F. *
Hughes, W. *, 1221
Huguenin, G. R. 1544
Hummelbrunner, W. *
Hunt, J. 631
Hurlemann, P. *
Hurtaud, Y. 615
Hussein, Z. A. 515
Hwang, J. N. 130
Hyyppa, J. 1089

I

Iacozza, J. 1187
Ignatov, A. *
Iguchi, T. *, 512, 554, 1364
Iisaka, J. *
Inggs, M. R. 454, 2020
Inggs, M. 1889
Iodice, A. 680
Irisov, V. G. 1126, 1450, 1457, 1672
Irons, J. R. *, 1657, 1904, 2161
Irons, J. 2183, 2186
Isernia, T. 1241, 2083
Ishimaru, A. 2128, 2137, 2140
Itten, K. I. 2326
Ivanov, A. Y. 1971
Ivanov, A. Yu. *
Ivanov, V. K. 369
Ivlev, O. V. *
Iwata, Y. 781

J

Jaaskelainen, V. *
Jackson, S. R. 2258
Jackson, T. J. 1058, 1061, 1064
Jacobson, M. D. 1138, 1678

Jain, A. K. 1851
Jakob, G. 31
Jakubauskas, M. E. 2300
Jameson, A. R. 402
Jamsa, S. 2092
Jansen, R. W. 902
Jayaprakash, P. 408
Jayaram Hebbr, K. 784
Jeffries, W. 1352
Jelinski, D. E. *
Jen, L. *
Jenkins, A. D. 1158
Jensen, J. R. 2279
Jenserud, T. 1141
Jessup, A. T. *
Jeyarani, K. 784
Jezek, K. C. 142, 145, 148, 1775
Jezek, K. 118, 1196, 1772
Ji, J. 1300
Ji, W. 2225
Jia, J. C. 180
Jia, S. *, 1423
Jiang, J. 739
Jiang, W. W. *
Jiao, J. *
Jin, M. *
Jin, Y. Q. 2380
Jingli, W. 466
Jingshan, J. 466
Johannessen, J. A. 1158
Johannessen, O. M. 932, 1158
Johansen, B. *
John, H. 2338
Johnsen, H. 1155
Johnson, D. R. *, 1175
Johnson, J. T. *, 1401
Johnson, L. F. 2276
Johnson, P. E. 1721
Johnson, R. S. 808
Jones, M. A. *, 631
Jones, W. L. 1526
Jonsson, T. 1877
Jordan, A. K. 1208
Jordan, L. E., III 2228
Jordan, M. S. 1260
Josberger, E. G. 648
Judge, J. 2270
Jung, M. 1870
Jurczyk, S. 2160
Juying, J. 947

K

Kabashnikov, V. P. 19
Kadygrov, E. N. *
Kaiser, D. *
Kaiser, J. A. C. *, 911
Kaita, E. 1273
Kalb, M. 1175
Kalshoven, J. E. 1797, 1809
Kambhammettu, N. 1392
Kanagaratnam, P. 115, 1196, 1867
Kandus, P. *
Kane, T. J. 993
Kanevsky, M. B. 1493
Kanzieper, E. *
Karaev, V. Y. 1493
Karam, M. A. 154, 594
Karlinsey, T. 1892
Karszenbaum, H. *
Kashkarov, S. S. 369
Kasilingam, D. *
Kassebaum, R. *, 631
Katehi, L. P. B. 1346
Katkovsky, L. V. 19, 366
Kato, Y. 875
Katou, K. *
Katsaros, K. B. 805
Katsaros, K. 1389
Katsev, I. L. *
Katzenberger, J. 1509
Kaupp, V. H. *
Kawata, Y. *, 1250, 1666
Kazandjiev, V. *
Kazmin, A. S. *
Keane, A. N. 603
Keck, C. L. *
Keeler, M. *
Keeler, R. J. 574
Keihm, S. J. 1435
Keithley, C. *, 227
Kellenberger, T. W. 2326
Keller, M. R. *
Keller, M. *, 248
Keller, W. C. *, 888, 1733, 2210
Kellndorfer, J. M. 1093, 2335
Kellndorfer, J. 2329
Kelly, R. E. 1938
Kemarskaya, O. N. 609
Kemppinen, M. 484, 499, 1998, 2285
Kenyi, L. W. 353
Kerbaol, V. 621, 1389
Kerenyi, J. 1114
Kerr, R. B. 686
Kertesz, M. 2377
Kerzner, M. G. 451
Kess, B. L. 1048
Key, J. R. 636
Key, J. 73
Keyte, G. 493
Kheeroug, S. S. 189
Khenchaf, A. 615, 746
Khire, M. V. 430
Khlif, M. S. 857
Khorram, S. 793, 1609
Kiang, R. K. 1864
Kietzmann, H. 1086
Kilic, O. 760
Kim, C. 1977
Kim, E. J. 2267
Kim, H. J. 405
Kim, H. S. 405
Kim, M. S. 1812
Kim, Y. *, 1612
Kimbreau, G. 891
Kimura, I. 775, 1361
Kindscher, K. 2300
Kirchner, C. *
Kirscht, M. 333
Kiselev, S. S. 442
Kishi, A. M. 1704
Kittler, J. 1379
Knapp, A. K. 166, 2361
Knight, A. 869
Knoepfle, W. 2332
Knopfle, W. 802
Knowles, D. S. *
Knudson, C. 296
Knulst, J. 1158
Kobjakova, N. *
Kogan, F. 209
Koh, G. *
Kokhanovsky, A. A. *
Komarov, S. A. *
Komiyama, K. 875
Kong, J. A. *, 757, 836, 1190, 1208, 1401
Kontar, E. A. *
Kooi, P. S. *
Koomen, P. 1633
Koren, H. 2307
Kosmann, D. 2338
Kosov, A. S. 442
Kostina, V. L. 172, 178
Kovalick, W. M. *
Kowk, R. 935
Kozlov, A. I. 299
Kozu, T. *, 512
Kraemer, R. *
Kraft, U. R. 866
Kraft, U. 872
Krasnopolsky, V. M. 1712
Kravtsov, Y. A. 103
Kravtsov, Yu. A. 1454
Krenek, B. *, 1541
Krishen, K. 239
Krishna, A. P. 221
Krivonozhkin, S. N. 369
Kropfli, R. A. 1739
Krueger, D. A. *
Krummell, J. R. 2361
Krupa, R. 436
Kudryavtsev, V. N. 1971
Kuga, Y. 2128, 2137, 2140
Kuhbauch, W. 1980
Kumagai, H. 487, 512
Kumar, S. R. 1858
Kummerow, C. 1429
Kunkee, D. B. 1129
Kuntz, M. 433
Kurtz, J. 2027
Kurvonen, L. 1759
Kusaka, T. *, 1250
Kusneirkeiwicz, D. Y. 1143
Kustas, W. P. 2104
Kutser, T. 76
Kux, H. J. H. *, 195, 374
Kuzmenko, Yu. A. *
Kuzmin, A. V. *, 1454
Kwok, R. *, 1190

L

Labrousse, D. *, 345
la Forgia, V. *
Lahtinen, J. 1998
Lai, S. J. *
Lake, B. M. 2201, 2213
Lalbeharry, R. 1155
Lalonde, M. 1621
Lamont-Smith, T. 1742
Lanari, R. *, 350, 2047
Landgrebe, D. A. 790, 1855
Landgrebe, D. 414
Landry, R. 726

Landsfeld, M. 2149
Lane, J. *
Lang, R. H. 577, 726, 760
Langford, A. O. *
Langford, G. 2276
Langham, C. W. 324
Langlois, P. M. 1917
Langman, A. 2020
Lannes, A. 869
Laroussinie, O. *
Larsen, M. F. 1926
Larsson, B. 1877
Lataitis, R. J. 1914
Lauknes, I. *
Laur, H. 477
Laursen, V. 869
Lavorato, M. B. 4
Lavrenov, I. 1495
Lawrence, S. P. 417, 2158
Lawson, J. *
Lay, W. L. 57
Le, C. T. C. 2128, 2137
Leach, A. *
Leavitt, B. C. 2273
Lebed, L. 209
Leberl, F. 31
Le Ber, J. *
Leblanc, E. 224
Leblanc, S. G. 1651
Lebon, F. 457
Le Caillec, J. M. 612
Le Dantec, V. 1002
LeDrew, E. F. 127, 230, 639, 645, 938
LeDrew, E. P. 427
LeDrew, E. 88
Lee, B. S. 1794, 2180
Lee, J. S. 439, 1162, 1574, 2086
Lee, L. *
Lee, M. E. *
Lee, P. H. Y. 618, 2201, 2213
Lee, R. 118
Le Hegarat-Mascle, S. 1067
Lehmann, F. 2107
Lemaire, P. 251
Leone, A. 1584
Leonelli, J. 697
Leong, M. S. *
Leroy, M. 204, 1654, 1901
Lesht, B. M. 1675
Le Toan, T. 836, 842, 975, 1306, 1983, 2167
Leu, C. H. 160
Leung, K. *, 43, 1358
Leuschen, C. 2033, 2036
Leuskiy, V. Ye. 1672
Leveau, J. 10
Le Vine, D. M. *, 878, 1547
Lewis, J. E. *
Lewis, M. R. *
Lewis, P. 1405, 1408
Lewis, T. B. *
Li, F. K. 1132, 1469, 1959
Li, J. *
Li, L. W. *
Li, L. 1123, 1707
Li, T. L. 1064
Li, X. 293, 591, 1587, 1669, 2173
Li, Z. J. 772
Li, Z. *, 136, 2186
Liang, S. 1648
Liao, L. 16, 554
Liberman, B. 175, 1320
Lieberman, S. H. *
Lightstone, L. *
Liljegren, J. C. 1675
Lim, I. 57, 67
Lin, I. I. 2261
Lin, L. 509
Lin, Y. C. 1334
Lindemer, W. 872
Lindgren, P. D. 1172
Lintz Christensen, E. 1629
Liou, Y. A. 2155
Litovechenko, K. 251
Liu, A. K. 85, 380
Liu, G. *, 1571
Liu, H. 1535
Liu, W. 1515
Livingstone, C. E. 1515, 1621
Llewellyn-Jones, D. T. 417, 2158
Loechel, S. E. 586
Loechel, S. 2149
Loffeld, O. *
Logvin, A. I. 299
Lohi, A. *
Loizzo, R. *
Lombardo, P. 347
Long, D. G. 124, 218, 827, 848, 1463, 1475, 1606, 1715, 1721, 1724, 1892
Longstaff, D. 796
Lopes, A. 387, 457, 662
Lord, R. T. 454
Lou, S. H. 935, 1959
Lou, Y. *, 1612
Loumagne, C. 1067
Loutin, E. A. 299
Loveberg, J. 881
Loveland, T. R. *, 2318
Lu, Y. H. 57, 67
Ludwig, F. L. 891
Lukin, V. P. 1830
Lukin, V. 22
Lukowski, T. I. *, 1290, 1621
Lund, D. E. 2195, 2219
Luong, D. Q. 356
Luscombe, A. P. 1290, 1352
Luvall, J. 1286
Lyzenga, D. R. *, 899, 908, 1158, 2195, 2198, 2219
Lyzenga, D. 1141

M

Ma, W. *
MacArthur, J. L. 1143
Macauley, M. K. 2222
MacDonald, H. C. *
MacDonald, M. C. *, 183
Macelloni, G. 2131
MacGregor, D. *
Mack, J. M. 1938
Madisetti, V. K. 1592
Madsen, S. N. 276, 674, 677, 972, 1629
Magotra, N. 1029
Mahlke, J. 1769
Mahootian, F. *
Maitre, H. 474, 503
Makisara, K. 1010
Makkonen, P. 1998
Makynen, M. 1998
Malaret, E. 1141
Maldonado, L. 1612
Maleev, S. N. 442
Malinovski, V. *
Malliot, H. A. 2349
Manara, G. 290
Mancini, P. L. 279
Mancini, P. 1355
Mandyam, G. 1029
Manninen, T. 583
Manning, W. *
Manohar, M. 1023
Manry, M. T. *
Maotang, L. 466
Marazzi, A. 266, 2071
Marchand, R. 2119
Marechal, N. *, 1233
Marenco, A. L. 1592
Mariani, A. *
Markham, B. L. 586, 1270, 1273, 1276, 1797, 2121
Markina, N. N. 1698
Markus, T. 1247, 1529, 1791
Marmorino, G. O. *
Marra, J. 100, 296
Marthon, P. 457
Martin, S. *, 1190
Martin-Neira, M. 315, 869
Martinez, P. 37
Martinez-Madrid, J. J. *
Marty, G. 1002
Martynov, O. V. *
Marzano, F. S. *
Marzouki, A. 706
Maslanik, J. A. 186
Maslanik, J. 73, 192, 950
Matschke, M. 802, 2332, 2338
Mattar, K. E. 1146
Mattar, K. 1621, 2255
Mattia, F. 1306
Mattikalli, N. M. 1058, 2237
Matwin, S. 1873, 2303
Maupin, P. 1373
Mauser, W. 1974
Mavrocordatos, C. 490
May, G. C. 947, 2288
Mayer, T. S. 993
Mayer, V. J. 1166
Mayor, S. 1911
Mazetti, P. 1367
McBride, W. E., III 285
McCalmont, J. F. 1535
McCleese, D. *
McColl, K. C. 1710
McCoy, W. 1029
McDonald, K. *
McDonnell, J. J. 133
McGee, S. 917
McGuire, J. 631
McIntosh R. E. 1, 984, 1553, 1917, 1923
McIntosh, R. 743, 1466, 1730
McKim, H. A. 1073
McKim, H. L. 2375
McLaughlin, C. D. 929
McLaughlin, D. J. 905, 1745
McLauglin, D. J. *
McMurtrey, J. E. 1812

McNally, T. *
McNeill, S. 1839
Mead, J. B. 1553, 1917, 1923
Meadows, G. A. 2219
Meadows, G. 2195, 2198
Mecocci, A. 2071
Meier, D. 1352
Meier, W. 73
Melack, J. M. *
Melfi, S. H. *, 1257
Melnikov, V. M. *
Melsheimer, C. 1370
Melville, W. K. 2204
Memon, N. D. 1039
Menegasssi Menchik, M. T. *
Meneghini, R. *, 16, 554, 1364
Menon, A. K. 408
Merchant, J. W. 541, 2315
Merzlyak, M. N. 2355
Mesarch, M. A. 1005, 1908
Mesnager, G. 1842
Meyers, R. J. 1506
Michel, T. R. 248
Middleton, E. E. 1005
Miewald, T. 929
Migliaccio, M. *, 680
Migliacio, M. 350
Mikami, T. 1695
Mikheev, P. V. 189
Mikkela, P. 1759
Mikulin, L. *
Miles, M. W. 932
Milillo, G. *
Millar, P. S. 1800
Miller, J. R. *, 212, 1411
Miller, J. 420
Miller, T. 1612
Miller, W. H. 1032
Milovich, J. *
Milshin, A. 175, 1320
Miner, G. F. 1892
Minino, M. *
Minnis, P. 1911
Mironov, V. L. *
Mitchell, S. 2377
Mittermayer, J. 1214, 1217
Mityagina, M. I. *, 103
Miyawaki, M. 1639
Miyazaki, T. 781
Mochi, M. *
Moens, J. B. *
Moghaddam, M. *, 730, 978
Mogili, A. 1266
Mohling, W. *
Mohr, J. J. 677, 972
Moldenhauer, O. 94
Molinaro, F. 10
Moller, D. 984
Monaldo, F. M. 1143, 1149
Mononen, I. 484
Monorchio, A. 290
Montgomery, B. 577
Monti Guarnieri, A. 671, 1845
Moody, A. 544
Moon, C. J. *
Moon, W. M. *
Moore, J. D. 922
Moore, R. K. 496, 996, 1266, 1392
Moore, S. L. *
Mora, F. 541
Morain, S. *
Moran, M. S. 157, 1420
Mordvintsev, I. N. 642
Moreau, L. *, 70
Moreira, A. 1214, 1217
Moreira, J. R. *, 350, 799, 1227
Moreira, J. *
Moreno, J. F. 1823, 1861
Morrison, K. 2344
Moses, R. W. 1938
Mouchot, M. C. 236, 523, 1376, 1753
Mougin, E. *, 733, 1002
Moulin, S. 2366
Mourad, P. D. *
Mozley, E. C. *
Muchoney, D. 233
Mudukutore, A. 574
Mueller, H. J *
Mueshen, B. 2338
Mugnai, A. *
Mukherjee, D. P. *
Mulchi, C. L. 224
Muller, J. 1775
Muller, M. R. 1618
Murata, M. 1639
Murni, A. 1851
Murphy, T. J. *
Myers, R. J. *
Myneni, R. *

N

Nadimi, S. A. 863, 947, 2288
Naeije, M. C. 97
Nagabhushan, P. 1045, 1858
Nagata, H. 1639
Nagatani, G. 628
Nagler, P. L. 1803
Naka, M. 781
Nakajima, M. 390
Nakajima, T. Y. 390
Nakajima, T. 390
Nakamura, K. 512
Nakamura, S. *
Nakamura, T. 1929
Nakonechny, V. P. 1968
Narayanan, R. M. 445, 506, 1017, 1073, 1920, 1926, 2030, 2258, 2282, 2375
Narumalani, S. *, 463
Nash, G. G. *
Nassar, E. 118
Nativi, S. 1367
Naumov, A. P. 1698
Neale, C. M. U. 133, 2369
Nekrasov, V. P. 19, 366, 1441
Nelson, B. *
Nelson, D. H. 393
Nelson, R. F. 1797
Nemani, R. *
Nervi, A. 1603
Neuenschwander, A. 1512
Neumann, G. 1469, 1959
Newman, G. A. 1941
Nezry, E. 1574
Ng, W. E. 57, 67
Ngai, F. M. 665
Nghiem, S. V. 1190, 1208, 1469, 1959
Nguyen, L. 1911
Ni, W. 293, 591
Nichol, J. 2113
Nicolas, J. M. 503
Nielsen, F. 1766
Nielsen, N. B. 686
Niemann, O. 1873
Nikulainen, M. 1998
Nirchio, F. *
Nithack, J. *
Njoku, E. G. 1054
Nocera, L. 25
Nogotov, E. F. 1441
Nohmi, H. 1639
Noll, J. *, 1995
Noltimier, K. F. 142
Norikane, L. 1772, 1775, 2329
Norman, J. M. 2104, 2358
Normand, M. 1067
North, P. R. 1654
Noto, J. 686
Nuesch, D. *
Nunez, M. 1417
Nunnelee, W. M. 1678

O

Oaku, H. 1636
Oden, S. F. 1143
Oertel, D. 2107
Ogor, B. 717
Ohura, Y. 1639
Ojima, D. *
Okamoto, K. *
Okomel'kova, J. A. 609
O'Leary, E. 823
Oleson, K. W. 186
Oleson, K. 192
Oliphant, T. E. 1715, 1721, 1724
Olsen, R. B. *
Olson, W. 1429
O'Neill, P. E. 1061, 1064
O'Neill, P. O. 1297
Onstott, R. G. 944, 1193, 1202, 1520
Onstott, R. 2195
Osharin, A. M. *
Otterman, J. 1657
Oudart, P. 273

P

Paar, G. 31
Paduan, J. D. 1749
Pahl, U. 1478
Painter, T. H. 2249
Pairman, D. 1839
Pak, K. *, 1401, 2125, 2137, 2143
Pal, P. *
Palleschi, V. 520, 854
Palm, S. P. 1257
Palmer, R. D. 1920, 1926, 1929
Paloscia, S. 736, 2131
Pampaloni, P. 736, 2131
Panah, A. A. *
Panegrossi, G. *
Pangburn, T. 1073, 2375
Pankin, A. A. 360

Pantzov, S. Y. 360
Papathanassiou, K. P. *, 350, 799
Paquerault, S. 503
Parishikov, S. V. *
Park, J. D. 1526
Park, S. H. 560
Parkin, S. H. 1102
Parmiggiani, F. 709
Parra, G. A. 1753
Pasaribu, D. P. 372, 1590
Pascazio, V. 1241, 1577, 2083
Pasquali, P. *, 342, 656
Pasquariello, G. *, 1306, 1562, 2060
Payne, B. 321
Payton, S. L. 2273
Pazmany, A. L. 1553
Pazmany, A. 743
Peat, H. 2377
Peczeli, I. 697
Peddle, D. R. 212, 230, 427, 938
Peddle, D. 88
Pellegrini, P. F. 1603
Peltoniemi, J. I. *
Peng, C. Y. 380
Pepin, M. P. 54
Pereira, J. *
Perfiliev, Y. P. 1701
Perona, G. 1584
Perov, A. O. *
Perovich, D. K. 1184, 1190
Peterson, D. L. 2276
Peterson, J. R. *
Petrenko, B. Z. 481
Petrin, R. R. 393
Petrou, M. 1379
Pham, K. 37
Philbrick, C. R. 1253, 1826
Piazza, E. 1603
Picardi, G. 383
Pieczynski, W. 706
Piepmeier, J. R. 1120
Pierce, L. E. 580, 1092, 1568
Pierce, L. 40, 2329
Pierri, R. 1241, 2083
Pignatti, S. *
Pihlflyckt, J. 1998, 2285
Piironen, A. *
Pilant, D. *, 121
Pillai, S. R. 990
Pinel, V. 1660
Piwowar, J. M. 127, 645, 938
Planes, J. G. 387
Plant, W. J. *, 888, 1733, 2210
Plotnizky, S. *
Plumb, R. 778, 2033, 2036
Plummer, S. E. 1654
Plutchak, J. 1498
Poggio, L. 399
Pollard, B. 1923
Pons, I. 257
Porter, D. L. 1152, 2242
Posa, F. 1306
Pospelov, M. N. 1135, 1454
Poulain, D. E. 857
Poulton, M. M. *
Pouwels, H. 1633
Pozdnyakova, V. P. 609
Prakash, H. N. S. 1858
Prati, C. *, 671
Prevosto, M. 1956
Prietzsch, C. 282
Prikhach, A. S. *
Princz, J. *, 1221
Privette, J. L. *, 1663
Proffitt, M. H. *
Proisy, C. 733
Ptichnokov, A. V. 2324
Puglisi, G. 350
Pulliainen, J. 1759
Pullianinen, J. 583, 2110
Pultz, T. J. *
Pungin, V. G. 103
Pyhalahti, T. *

Q

Qi, J. 1420
Qin, P. 1989
Qin, W. 526, 1645
Qiu, Z. 2318
Quagliano, J. R. 393
Quartly, G. D. 91
Quel, E. J. 4
Quick, C. R. 393
Quilfen, Y. 805
Quintanilha, J. A. *

R

Rabine, D. L. 423
Racette, P. 1429
Rackley, K. *, 631
Raev, M. D. 1490
Raggam, H. *, 353
Rague, B. W. 1054
Rahmat-Samii, Y. 515
Rais, J. 1851
Raizer, V. Yu. *
Rall, J. A. R. 1538
Ramamurthy, M. K. 1498
Ramirez, A. *
Rampa, V. 2038
Raney, R. K. 2279
Rango, A. 2011
Ranson, K. J. 577, 1096
Ranzi, R. 266
Rao, C. R. N. *
Rao, K. S. 163, 201, 430
Rao, P. V. N. 163, 201
Rao, Y. S. 163, 201, 430
Rapoport, V. O. *
Rastelli, S. 520, 854
Rautiainen, K. 1998, 2285
Reagan, J. A. 683, 987, 1014, 1244, 1535
Reagan, J. T. 1020
Reed, B. *
Reed, R. 1475
Rees, W. G. 2261
Refice, A. 2060
Refling, J. P. 1102
Reichel, H. 872
Reichenbach, S. E. 1048, 1597
Reiners, W. A. 186
Reinke, D. 1105
Reistad, M. 1158
Remund, Q. P. 827, 848
Ren, Y. 1929
Ressler, M. A. 1886
Rey, L. 273
Reynaud, J. *
Ribbes, F. 842, 1983
Ricci, D. N. 1704
Riccio, D. *, 350, 680
Richard, J. 490
Richter, P. I. 697
Ride, S. *
Rieck, D. R. 448
Riggs, G. 139
Rignot, E. *
Rijkeboer, M. *
Rincon, R. F. 402
Ritter, M. 2204
Roberts, D. A. *
Roberts, M. 227
Rocca, F. *, 671
Rodenas, J. A. 1953
Roeder, R. S. 269
Roenko, A. N. 172, 178
Roli, F. *
Romeiser, R. 597, 981, 1962
Romig P. R., III 1048
Ronsin, J. 717
Roschier, M. 1998
Rosello, J. 1224
Rosenkranz, P. W. *
Rosenthal, W. 2252
Rosich Tell, B. 477
Ross, S. J. 1520, 2077
Rossi, M. *
Rostan, F. 2294
Rosten, D. P. 1809
Roth, A. 802, 2332, 2338
Roth, L. *
Rothrock, D. A. *
Rothrock, D. *
Rott, H. 2125
Rougean, J. L. 1408
Roujean, R. J. 591
Rouvier, S. 2167
Roux, C. 1753
Rozenberg, A. 2204
Rubertone, F. 1571
Rubino, A. 1487
Ruddick, K. G. *
Ruf, C. S. *, 1263, 1435, 1692
Rufenach, C. L. 814
Rungaldier, H. 2201, 2213
Running, S. *
Russell, C. A. *, 648
Russell, M. 1417
Ruzek, M. 1175
Ruzhentsev, N. V. *
Ryzhkov, A. V. *, 557

S

Saatchi, S. S. *, 1861
Saatchi, S. *, 730
Sabet, K. F. 1346
Sabinin, K. D. 103
Sacchini, J. J. 54
Sadjadi, F. 396
Sado, S. *
Saghri, J. A. 1020

Sahr, J. D. 569
Saillard, J. 615, 746
Saint-Joan, D. 2074
Sakurai-Amano, T. *
Salomonson, V. V. 139
Samal, A. 1048
Samuel, P. 1158
Sand, K. *
Sandberg, D. 1181
Sander, G. 1881
Sander, R. K. 393
Sano, E. E. 157
Sansosti, E. 2047
Sarabandi, K. 720, 723, 969, 978, 1070, 1334, 1337, 1346, 2122
Sarita, S. 1045
Sarture, C. M. *
Satalino, G. 1562
Sato, K. 487
Sato, S. 339
Sato, T. 775, 1361, 1612
Sausa, R. C. 851
Savazzi, P. 2071
Savtchenko, A. 2216
Sayler, K. L. 547
Sayood, K. 1026
Sazonov, Y. A. *
Scepan, J. 198
Scharroo, R. 97
Scheiber, R. 1214
Schertzer, D. 37
Schetkin, I. M. 2192
Schiavon, G. 736
Schiller, S. 1286
Schimel, D. S. *
Schirinzi, G. 1241, 1577
Schistad Solberg, A. H. 1484, 2307
Schloss, A. L. 106
Schlueter, N. 1247
Schmidt, G. M. 2101
Schmitt, M. J. 393
Schmugge, T. J. 2101
Schmugge, T. 1051
Schmullius, C. *
Schneider, D. 999
Schoening, V. L. 987
Schuler, D. L. 1162, 2086
Schulze, E. D. *
Schuster, G. L. 1911
Schwabisch, M. *, 350, 802
Schweiger, A. J. 636
Schwemmer, G. *, 1257
Schwichow, H. 339
Seifert, F. M. 1086
Seiferth, J. C. 1600
Sekelsky, S. M. 1, 1553
Seliga, T. A. 551, 569
Sergi, R. *, 1562
Serpico, S. B. *, 714
Servomaa, H. 1998
Sery, F. 457
Sessenrath, G. *
Seu, R. 383
Shaikh, M. A. 1105, 1108
Sharma, A. 1315
Shaw, J. A. 1328
Sheen, D. R. *
Shelton, J. C. 2201, 2213
Shen, C. Y 902
Sheng, Y. 48, 1559
Shepherd, N. W. 1290
Shepherd, N. 1352
Shepherd, P. R. *
Shereshevsky, I. A. 609
Shevtcov, B. M. 369
Shi, J. C. 2125
Shi, J. 136, 754, 2022, 2249
Shih, S. E. 757, 1208
Shimada, J. 43
Shimada, M. 1636
Shin, R. T. *, 1401
Shinme, H. 1639
Shinohara, H. 1639
Shippert, M. M. 169
Shire, H. N. 896
Shirer, H. N. *
Showman, G. A. 1688
Shuchman, R. A. 648
Shuchman, R. 1158
Siddiqui, K. J. 1099
Sieber, A. J. *
Sigismondi, S. 736, 2131
Sikora, T. D. *, 893, 896
Singh, R. *
Siqueira, P. 1337
Skirta, E. A. 603
Skoelv, A. 1141
Skofronick, G. M. 1688
Skotnicki, W. 1612
Skou, N. 674, 749, 869, 1629
Skriver, H. 1300, 1766
Skulachev, D. P. 442
Skvortsov, E. I. 1490
Slatton, K. C. *, 263
Sletten, M. A. 2017, 2207
Small, D. 342
Smirnov, A. I. 1454
Smirnov, A. V. 1481
Smith, G. L. 1414
Smith, J. A. 2146
Smith, M. C. 269
Smith, N. 1414
Smith, R. 1618
Smith, W. H. 2276
Smith, W. L., Jr. 1911
Smits, P. C. 714
Smokty, O. *
Snider, J. B. 1432
Snoeij, P. 1633
Snuttjer, B. R. J. 506
Snyder, W. 2095
So, C. S. *
Soffer, R. 1411
Soh, L. K. 112, 1532, 1565
Sohl, T. 246
Sohn, H. G. 148
Sohus, A. 321
Solaiman, B. 236, 523, 1373, 1562
Solberg, R. *, 1484, 2307
Solimini, D. 736
Solov'ev, D. M. *, 1971
Song, S. 996, 1392
Sosnovsky, Yu. M. 1323
Sottili, F. 13
Souffez, S. H. *
Souffez, S. S. *
Soulis, E. D. 1986
Souyris, J. C. 975, 1306, 2167
Soyris, J. C. 836
Spagnolini, U. 2038
Spencer, M. W. 82, 1463
Spencer, R. W. 1460
Spidaliere, P. 2160
Spinhirne, J. D. 683, 1244
Spring, F. 1515
Sridhar, M. 1498
Srivastava, S. K. 1290
Srivastava, S. 1352
St. Germain, K. M. 1026, 1523
Stacey, N. J. S. 1618
Stacy, N. J. S. *
Stalino, G. *
Stanhope, S. A. 2219
Stanichny, S. V. *
Staples, G. C. *
Starmer, W. J. 198
Steffen, K. 950
Steinauer, R. *
Steingieer, R. 1980
Stenstrom, G. 1877
Stern, H. *
Sternberg, B. K. *
Sterner R. E., II 1736
Stevens, D. 493
Stevens, T. D. 1253
Steyn-Ross, D. A. 94, 1293, 2098
Steyn-Ross, M. L. 94, 1293, 2098
Stiles, J. M. 720, 723
Stogryn, A. 154
Stolz, R. 1974
Stone, R. S. 636
Stork, E. J. 628
Stowe, L. *
Strahler, A. H. 243, 532, 538, 1405, 1426, 1587, 1669
Strahler, A. 233, 293, 591, 2173
Strawa, A. W. 2276
Streck, C. 330, 1836
Stretch, L. *
Strobl, P. 2107
Strukov, I. A. 442
Stuopis, P. A. 254
Sturgess, K. 2027
Sturm, J. M. 2207
Su, H. 2361
Su, Z. *, 1303
Subra, W. 2231
Subramanya, B. 1816
Suchall, J. L. 1355
Sud'bin, A. I. 100
Suga, Y. 1763
Sugawara, M. 1639
Sugimura, T. 79
Suinot, N. 273, 279, 490
Sukhatme, J. S. 430
Sun, C. 133
Sun, G. 577, 1096
Susini, C. 411
Sveinsson, J. R. 63, 1848
Swain, P. H. 1848
Swift, C. T. *, 1547
Sylvester, J. 1205
Syvertson, M. *

T

Taconet, O. 1067
Tadjudin, S. 790
Tait, A. 2005
Takasaki, K. 79
Takemata, K. 1666
Takemura, K. 775
Takeuchi, S. 1763
Talitsky, V. G. *
Tamlourrino, A. 2083
Tamoikin, V. V. *
Tan, S. Y. 67
Tanaka, S. 79
Tang, S. 2216
Tano, F. 1980
Tarchi, D. *
Taskinen, H. 1998
Tauriainen, S. 1998
Teany, L. D. *, 1290
Teraoka, T. 1361
Terre, C. 772
Tesauro, M. 51
Tescher, A. G. 1020
Thames, P. 192
Thayer, J. P. 686
Thiele, O. W. 402
Thomas, A. 953
Thomas, B. H. 1704
Thomas, C. H. 1788
Thomasson, L. 836
Thome, K. J. 1283
Thompson, D. G. 1892
Thompson, D. R. *, 893, 896, 981, 1152
Thompson, H. R., Jr. 2201, 2213
Thompson, L. L. *
Thompson, M. 1881
Thomsen, A. 1300, 1766
Thursby, M. H. 1526
Tian, B. 1105, 1108
Ticehurst, C. 1556
Tiee, J. J. 393
Tierney, M. R. *
Tighe, L. *
Tikhonov, V. V. *
Tikunov, V. S. 2324
Tilton, J. C. 703, 1023
Timchenko, A. I. *
Ting, C. M. *
Tirri, T. 1998
Titov, V. I. 1331
Tjuatja, S. 772, 2008, 2186
Todhunter, J. S. 189
Tognoni, E. 520, 854
Tommervik, H. *
Tomppo, E. 1010
Tong, K. 1035
Torre, A. *, 60, 1571
Torres, F. 315, 869
Torres, R. 1355
Totuka, H. 1639
Tournadre, J. 1389
Tourneret, J. Y. 1842
Touzi, R. 662
Townshend, J. 535
Tracy, B. T. 1073, 2375
Treitz, P. M. 1986
Treuhaft, R. 978
Trimble, J. 823
Trizna, D. B. 905, 2017
Troch, P. A. *, 1303
Trofimov, V. T. *
Troisi, V. J. 651
Troitsky, A. V. *
Trokhimovski, Yu. G. 1126, 1450, 1457, 1672
Troufleau, D. 157
Trump, C. L. *
Tsai, W. Y. 935, 1718
Tsang, L. *, 130, 728, 754, 1401, 2125, 2143
Tsatsoulis, C. 109, 112, 1532, 1565
Tseng, W. Y. 85
Tsu, H. 1763
Tucker, C. J. 1169
Tupin, F. 474
Twarog, E. M. 1745

U

Ueda, K. 1250
Ulaby, F. T. 723, 1070, 1092, 1093, 1568, 2335
Ulaby, F. 2329
Ulander, L. M. H. 668, 1877
Ungar, S. G. *
Usha, P. V. 408

V

Vachon, P. W. 966, 1155, 1621, 2255
Vachon, P. W. 966
Vachon, P. 662
Vadkovsky, V. N. *
Vadon, H. *
Valero, J. L. 336, 2255
Vandemark, D. 1257, 1385, 1389
van den Berg, J. H. 2240
van der Keur, P. 1300
van der Kooij, M. W. A. 339, 963
Vandersteene, F. *
van Gelder, A. 2240
van Halsema, D. 963
van Leeuwen, W. J. D. *, 1423
VanSumeren, H. 2195
Van Woert, M. L. 1117
van Zuidam, R. 2240
van Zyl, J. J. 2294
van Zyl, J. 978, 1612
Vasilevsky, A. F. *
Vasilyev, Yu. F. 172, 178
Vaugh, C. R. 423
Vedel, S. *
Velipasaoglu, E. O. *
Veltroni, M. 1230
Veneziani, N. 2060
Venkataraman, G. 430
Venkataratnam, L. 163, 201
Vermotel, E. R. 1904
Vescoui, F. 1980
Vesecky, J. F. 891, 1520, 2077, 2219, 2347
Vidal, A. 157, 1224
Vidal-Madjar, D. 1067
Vierling, L. A. 1897
Viggian, R. *
Vincent, N. 279, 490
Vishniakov, V. 175
Vogelmann, J. E. 246
Vogelzang, J. *
Volynsky, V. A. *, 100, 296
Von Ahn, J. *
Vorosmarty, C. L. 106

W

Waite, W. P. *
Wakayama, T. 775
Walavalkar, V. 430
Wales, C. 634, 1775, 1777
Walker, B. 1881
Walker, D. T. 2219
Walker, N. 583
Wall, S. *, 51
Wallace, B. 881
Waller, G. 1227
Walsh, T. M. 563
Walter-Shea, E. A. 1005, 1908
Walthall, C. L. 586, 1423, 1797, 1904
Wan, Z. 2095
Wang, B. 1645
Wang, J. R. 956, 1429, 2134, 2246
Wang, J. 1297
Wang, M. X. *
Wang, N. 1989
Wang, Y. *, 1077, 1083
Wanner, W. 1405, 1408, 1411, 1669
Ward, E. 914
Warner, K. K. 1017
Wash, C. H. 1260
Wasrin, U. R. 842
Waters, J. 2231
Way, J. B. *, 628
Weaver, R. L. 651
Wedin, D. 2377
Weeks, R. 2125
Weidemann, A. D. 285, 305
Weinman, J. A. *
Weissman, D. E. 878, 888, 1472
Wergin, W. 2011
Wersinger, J. M. 914
Wessel, G. R. I. 645
Wessman, C. A. 1663
West, J. C. 2207
West, R. D. 1718, 1727
Westwater, E. R. 1138, 1450, 1672, 1681, 1685
Wever, T. 1833
Weydahl, D. J. 151
Weydal, D. *
White, H. P. 212, 1411
White, M. A. *
Whitehead, M. 393
Whiteman, D. *
Whitlock, C. H. 1911
Wick, G. A. *
Wiesbeck, W. 763, 766, 1340, 2294
Wilheit, T. T. *
Wilhelmson, R. B. 1498
Wilkner, D. 881
Williams, D. L. 1797, 2161
Williams, J. 1780
Williams, R. N. 1111
Willis, K. J. 929
Willmott, C. J. 106
Wilson, B. 1772
Wilson, C. J., III 218

Wilson, J. J. 2341
Wilson, L. L. 130
Wilson, W. J. *, 1132
Winebrenner, D. P. 941, 1205
Winokur, R. S. *
Winstead, N. S. *, 893
Winter, R. 966
Wismann, V. R. 839, 2014, 2264
Wismann, V. *
Woelders, K. 276, 674, 1629
Wojtowicz, D. 1498
Wolf, C. 2219
Wolfe, D. E. *
Wolhletz, B. P. 1932
Wood, E. F. 1061, 1064
Woodcock, C. E. 529, 538, 591
Woodcock, C. 293
Woodhouse, I. H. 260, 845
Woodhouse, R. 1279
Wooding, M. 1995
Wu, J. 509, 739, 1965, 2216
Wu, S. T. S. 1309
Wylie, B. 2377

X

Xia, Z. G. 48, 1559, 2310
Xiao, R. 566
Xiong, H. *
Xu, W. 2044
Xu, Y. 2030, 2282
Xuan, J. 700
Xue, Y. 417, 2158

Y

Yacobi, Y. Z. *
Yakin, G. Y. 189
Yakovlev, V. V. *, 103
Yamaguchi, Y. *
Yamanashi, M. 1636, 1929
Yamashita, N. 1695
Yamazaki, A. 1250
Yang, G. 2068
Yang, J. *
Yang, L. 2318
Yang, W. 2315
Yang, X. 1989, 2240
Yang, Y. E. 757
Yankielun, N. E. *
Yanovsky, F. J. 2297
Yanow, G. 321
Yarwood, M. 490
Yea, J. H. 2137
Yee, R. 2201, 2213
Yeh, P. S. 1032
Yeo, T. S. *, 57, 67
Yevtyushkin, A. V. *
Yildirim, O. 1343, 1444
Yonekura, T. 1666
Yook, J. G. 1346
Young, G. S. *, 893, 896
Young, J. 118
Yu, Y. 60
Yueh, S. H. *, 935, 1132, 1190, 1718, 1727
Yueh, S. Y. *
Yushakov, V. N. *
Yutsis, V. V. *

Z

Zagolski, F. 1002
Zaitsev, V. A. 1971
Zaitsev, V. V. *, 363
Zakarin, E. 209
Zakharov, A. I. *
Zamaraev, B. D. 172, 178
Zege, E. P. *
Zeng, Q. *
Zhan, J. 1429
Zhang, B. 1405
Zhang, C. B. 57, 67
Zhang, G. 728, 2143
Zhang, J. 2375
Zhang, N. *
Zhang, Y. 2095, 2177
Zheng, X. *
Zhiqiang, Y. 466
Zhu, K. 2041
Zhukov, B. 2107
Zimmermann, R. *
Zinichev, V. A. *
Zink, M. 1086
Zion, M. 1061
Zlystra, G. J. 547
Zott, J. 2276
Zribi, M. 1067
Zrnic, D. S. 557
Zurk, L. M. 754
Zuykova, E. M. 1331